ECCM

20

26-30 JUNE

2022

LAUSANNE

SWITZERLAND

Proceedings of the 20th European Conference on Composite Materials

COMPOSITES MEET SUSTAINABILITY

Vol 3 – Characterization

Editors : Anastasios P. Vassilopoulos, Véronique Michaud

Organized by :

EPFL

Under the patronage of :

CCLAB Composite Construction Laboratory

LPAC Laboratory for Processing of Advanced Composites

ESCM EUROPEAN SOCIETY FOR COMPOSITE MATERIALS

ECCM 20
26-30 JUNE 2022
LAUSANNE SWITZERLAND

EPFL CCLAB Composite Construction Laboratory LPAC Laboratory for Processing of Advanced Composites

Proceedings of the 20th European Conference on Composite Materials ECCM20 26-30 June 2022, EPFL Lausanne Switzerland

Edited By :

Prof. Anastasios P. Vassilopoulos, CCLab/EPFL
Prof. Véronique Michaud, LPAC/EPFL

Oragnized by:

Composite Construction Laboratory (CCLab)
Laboratory for Processing of Advanced Composites (LPAC)
Ecole Polytechnique Fédérale de Lausanne (EPFL)

ISBN: 978-2-9701614-0-0
DOI: http://dx.doi.org/10.5075/epfl-298799_978-2-9701614-0-0

Published by :

Composite Construction Laboratory (CCLab)
Ecole Polytechnique Fédérale de Lausanne (EPFL)
BP 2225 (Bâtiment BP), Station 16
1015, Lausanne, Switzerland

https://cclab.epfl.ch

Laboratory for Processing of Advanced Composites (LPAC)
Ecole Polytechnique Fédérale de Lausanne (EPFL)
MXG 139 (Bâtiment MXG), Station 12
1015, Lausanne, Switzerland

https://lpac.epfl.ch

Cover:

Swiss Tech Convention Center
© Edouard Venceslau - CompuWeb SA

Cover Design:

Composite Construction Laboratory (CCLab)
Ecole Polytechnique Fédérale de Lausanne (EPFL)
Lausanne, Switzerland

©2022 ECCM20/The publishers

Disclaimer:

The ECCM20 organizing committee and the Editors of these proceedings assume no responsibility or liability for the content, statements and opinions expressed by the authors in their corresponding publication.

Editorial

This collection gathers all the articles that were submitted and presented at the 20th European Conference on Composite Materials (ECCM20) which took place in Lausanne, Switzerland, June 26-30, 2022.

ECCM20 is the 20th edition of a conference series having its roots back in time, organized each two years by members of the European Society of Composite Materials (ESCM).

The ECCM20 event was organized by the Composite Construction laboratory (CCLab) and the Laboratory for Processing of Advanced Composites (LPAC) of the Ecole Polytechnique Fédérale de Lausanne (EPFL).

The Conference Theme this year was “Composites meet Sustainability”. As a result, even if all topics related to composite processing, properties and applications have been covered, sustainability aspects were highlighted with specific lectures, roundtables and sessions on a range of topics, from bio-based composites to energy efficiency in materials production and use phases, as well as end-of-life scenarios and recycling.

More than 1000 participants shared their recent research results and participated to fruitful discussions during the five conference days, while they contributed more than 850 papers which form the six volumes of the conference proceedings. Each volume gathers contributions on specific topics:

Vol 1 – Materials

Vol 2 – Manufacturing

Vol 3 – Characterization

Vol 4 – Modeling and Prediction

Vol 5 – Applications and Structures

Vol 6 – Life Cycle Assessment

We enjoyed the event; we had the chance to meet each other in person again, shake hands, hold friendly talks and maintain our long-lasting collaborations. We appreciated the high level of the research presented at the conference and the quality of the submissions that are now collected in these six volumes. We hope that everyone interested in the status of the European Composites’ research in 2022 will be fascinated by this publication.

The Conference Chairs

Anastasios P. Vassilopoulos, Véronique Michaud

ECCM 20
26-30 JUNE 2022
LAUSANNE SWITZERLAND

Hosting Organizations

Composite Construction Laboratory (CCLab)
Laboratory for Processing of Advanced Composites (LPAC)
Ecole Polytechnique Fédérale de Lausanne (EPFL)

Venue

Swiss Tech Convention Center (https://www.stcc.ch)

Conference Chairs

Chair : Prof. Anastasios P. Vassilopoulos, EPFL, Switzerland
Co-Chair: Prof Véronique Michaud, EPFL, Switzerland

International Scientific Committee

Prof. Malin Åkermo SE
Dr. Emmanuel Baranger FR
Prof. Christophe Binetruy FR
Prof. Pedro Camanho PT
Prof. Konstantinos Dassios GR
Prof. Brian Falzon UK
Prof. Kristofer Gamstedt SE
Prof. Sotiris Grammatikos NO
Prof. Christian Hochard FR
Prof. Marcin Kozlowski PL
Prof. Stepan Lomov BE
Dr. David May DE
Prof. Stephen Ogin UK
Prof. Gerald Pinter AT
Prof. Silvestre Pinho UK
Prof. Yentl Swolfs BE
Dr. Julie Teuwen NL
Dr. Panayota Tsotra CH
Prof. Wim van Paepegem BE
Prof. Dimitrios Zarouchas NL
Dr. Andrey Aniskevich LV
Prof. Christian Berggreen DK
Dr. Nicolas Boyard FR
Prof. Valter Carvelli IT
Prof. Klaus Drechsler DE
Prof. Bodo Fiedler DE
Dr. Nathalie Godin FR
Prof. Roland Hinterholzl AT
Prof. Ian Kinloch UK
Dr. Thomas Kruse DE
Prof. Theodoros Loutas GR
Prof. Veronique Michaud CH
Prof. Alessandro Pegoretti IT
Prof. Joao Ramoa Correia PT
Prof. Jose Sena-Cruz PT
Prof. Antonio T. Marques PT
Prof. Thanasis Triantafillou GR
Prof. Albert Turon ES
Prof. Anastasios P. Vassilopoulos CH
Prof. Martin Fagerström SE
Dr. Alexandros Antoniou DE
Prof. Lars Berglund SE
Prof. Michal Budzik DK
Prof. Lucas Da Silva PT
Dr. Andreas Endruweit UK
Prof. Mariaenrica Frigione IT
Dr. Larissa Gorbatikh BE
Dr. Martin Hirsekorn FR
Prof. Vassilis Kostopoulos GR
Prof. Jacques Lamon FR
Prof. Staffan Lundstrom SE
Prof. Peter Mitschang DE
Dr. Soraia Pimenta UK
Prof. Paul Robinson UK
Dr. Olesja Starkova LT
Prof. Sofia Teixeira de Freitas NL
Dr. Stavros Tsantzalis GR
Prof. Danny van Hemelrijck BE
Prof. Michele Zappalorto IT
Dr. Miroslav Cerny CZ

Local Organizing Committee

Prof. Anastasios P. Vassilopoulos, EPFL
Prof. Véronique Michaud, EPFL
Angélique Crettenand and Mirjam Kiener, Lausanne Tourisme
And all those who helped, colleagues who reviewed abstracts and chaired sessions, and CCLab and LPAC students and collaborators who worked hard to make this conference a success.

ECCM 20
26-30 JUNE 2022
LAUSANNE SWITZERLAND

Sponsors

SHIMADZU
Excellence in Science

Bristol Composites Institute

JEC GROUP

suprem

Surface Measurement Systems
World Leader in Sorption Science

INSTRON

9T LABS

Anton Paar

DIA-STRON
DELIVERING MEASUREMENT SOLUTIONS

AELER

HRC

ICCM 23
BELFAST 2023
30 JULY – 4 AUGUST

TEIJIN

Functional Composite Materials

materials
an Open Access Journal by MDPI

ELSEVIER

Supporting partners

JEC

CertBond
COST Action CA18120

EsSENce

Switzerland Tourism.

SWISS

SBB CFF FFS

sampe
Switzerland

COMPOSITES UNITED | SWITZERLAND

canton de vaud

Lausanne

Contents

IMPLEMENTING STRUCTURAL FUSES IN CFRP COMPONENTS VIA MICROSTRUCTURALLY-ENGINEERED CRACK PATHS

M.Erfan Kazemi[a], Victor Medeau[a], Emile Greenhalgh[a], Soraia Pimenta[a], James Finlayson[b] and Silvestre T Pinho[a]

a: Faculty of Engineering, Imperial College London
Exhibition Rd, South Kensington, London SW7 2BU, UK – m.kazemi@imperial.ac.uk

b: Composites - Structural Systems Design, Rolls-Royce
PO Box 31, Derby, DE24 8BJ, UK

Abstract: *This study aims to develop and implement actual carbon fibre-reinforced polymer (CFRP) solutions for realising structural fuses in real components. To this end, we have developed various concepts for structural fuses, applied to generic idealised components and aimed at engaging different in-plane and through-the-thickness damage propagation mechanisms. Micro-cut patterns (MCPs) / crack path combinations have been engraved on thin-ply CFRP prepregs (by using a laser cut machine) for manufacturing CFRP specimens. Afterwards, we have carried out a series of experimental studies to evaluate the fracture properties of various MCPs under three-point bending (3PB). Then, 3PB results were used to refine and down-select our concepts, for use in our generic idealised component design to test them under indentation test using a cantilever beam rig. The test results demonstrated that MCPs can provide significant control over the fracture locus and path, additionally allowing the failure initiation load and energy dissipation to be tailored.*

Keywords: Microstructure design; Carbon fibre-reinforced polymer (CFRP); Structural fuse; damage-control; crack path

1. Introduction

Carbon fibre-reinforced polymer (CFRP) composites are being increasingly used in various industries such as aeronautics due to their high performance to weight ratio. Nonetheless, because of their inherently brittle nature, CFRPs are susceptible to sudden uncontrolled failure, which can endanger the integrity of entire CFRP components [1]. When a CFRP component separates into two parts due to fracture, typically, the actual fracture path is a consequence of the geometry of the component and of the loading, rather than a characteristic designed into the component. However, in many applications (e.g. fan blade-off events) there are significant advantages in controlling the fracture path via a form of structural fuse (e.g. to reduce the portion of the blade ejected) to reduce the energy transmitted into the casing.

Thin-ply CFRPs provide greater design possibilities, improved homogenization and more possible stacking sequences than conventional thick plies-based counterparts [2]. As extensively studied in the literature, the ply thickness affects the initiation and propagation of micro-cracks as well as delamination [3]. It is known that translaminar fracture depends on the microstructure (in particular on the crack path shape) [4] and that applying micro-cut patterns (MCPs) on thin-ply CFRP prepregs is a powerful tool for developing engineered CFRP micro-structures with

  doi:10.5075/epfl-298799_978-2-9701614-0-0

enhanced fracture performance [5]. In a previous study, we demonstrated that applying MCPs can increase the fracture toughness of the laminates up to 180% compared to that of QI laminates in a compact tension (CT) test [5]. However, new tests and concepts are needed to examine the behaviour of engineered micro-structures when applied as structural fuses for real CFRP components. Hence, the main goal of this study is to propose innovative designs of engineered crack paths with tailored properties for practical applications. To this end, we have proposed an innovative microstructure design through various studies and down-selected potential MCP concepts to create a predictive controlled failure along a chosen (crack) path, while retaining the strength and toughness of the structure (compared to that of the baseline (quasi-isotropic (QI)) material. These engineered crack paths can be used to promote or prevent selected failure mechanisms.

2. Experimental Procedure

Unidirectional thin-ply SkyFlex USN20A prepregs (a 20gsm UD fabric of TR30S, high strength carbon fibres from Mitsubishi with K51 epoxy resin from SK Chemicals) with an uncured thickness of 0.05 mm are used in this study. To manufacture panels, we have cut each thin-ply prepreg at the desired angle (using an automated cutting table) and placed on top of each other ply with the help of alignment holes to guide the layup (Figure 1, a). While laying up, micro-cut patterns (MCP) (see Figure 1, e-f) were engraved using the Oxford Lasers Diode Pumped Solid State micro-machining system with specific patterns in each ply (Figure 1, b) to manufacture CFRP specimens with the stacking sequence of $\left[(0,45,90,-45)_{16}, 0_{1/2}\right]_{s}$. Then, we cured the panels at 125 ℃ under 5 bar pressure in an autoclave machine. After curing, we cut the specimens via the abrasive waterjet cutting method and tested them under three-point bending (3PB) as well as indentation tests (Figure 1, c-d).

To assess the optimum geometrical properties of MCP, we investigated a large range of MCPs to evaluate the variation of fracture parameters in a compact tension (CT) test [6]. An example of ST MCP is illustrated in Figure 1, e-f. The rationale behind selecting various MCPs / crack path combinations is mainly based on: (1) studying the ability of the MCP to deflect the crack away from the inherent (critical) stress path; (2) promoting desirable failure mechanisms, mainly delamination; (3) protecting uncut plies so that they act as crack stopping barriers; and (4) designing MCP properties so that the specimen does not fail under other unwanted failure modes (namely compressive failure). With these in mind, we have carried out multiple studies in terms of various MCP parameters / crack path combinations (as shown in Figure 2 and Table 1) and presented some of which here to address the aforementioned objectives.

  doi:10.5075/epfl-298799_978-2-9701614-0-0

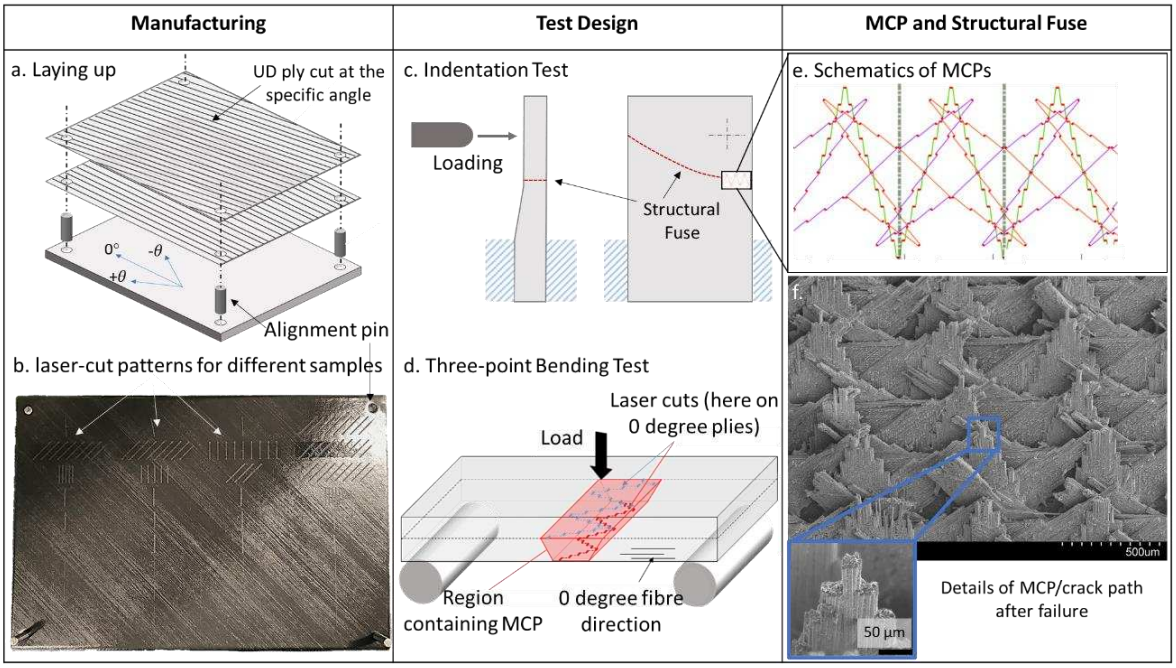

Figure 1: Design, manufacture, and test of engineered structural fuses made of CFRP composites

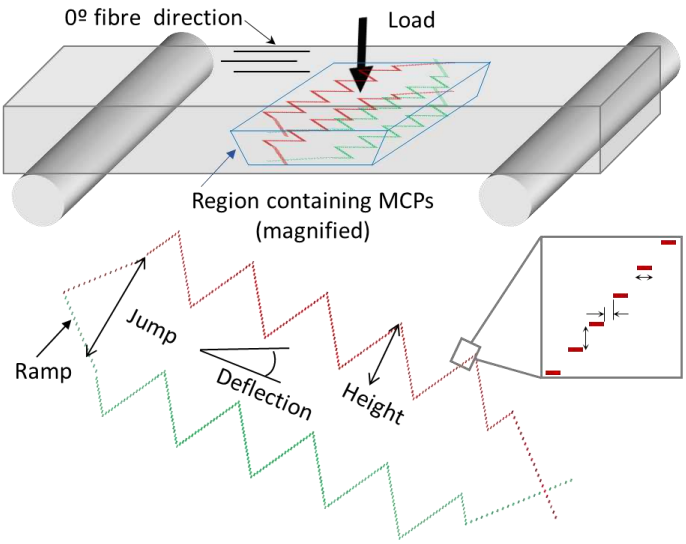

Figure 2: Schematic of a shark teeth (ST) MCP and associated parameters

  doi:10.5075/epfl-298799_978-2-9701614-0-0

Table 1. Various parameters of micro-cut patterns (MCPs) investigated in this study

Study	Parameter	Specimen number
1	Jump size	Sp1-Sp4
2	Ramp up and Jump Size	Sp5-Sp8
3	Deflection and amount of fibres cut	Sp9-Sp12
4	MCP height and type	Sp13-Sp16
5	Using 45°/-45° plies	Sp17-Sp20

3. Results and discussion

Study 1 investigates the effect of jump size from 1.0 mm to 2.0 mm on the fracture path as well as delamination size/jump. For study 1, we observed that increasing the jump size from 1.0 mm to 2.0 mm results in more significant delamination, see Figure 3-b. By comparing the fracture paths of Sp2-Sp4 (see Figure 3-a, b) with those of the baseline material (Sp1) without micro-cut patterns (MCPs), we have noticed that MCPs give microstructures the ability to guide the crack along its engineered path, while the baseline material without MCPs lacks such characteristic and shows an uncontrolled brittle path after failure, Figure 3-a,b. In addition, measured strength and energy dissipation are still close to those of the non-engineered material, although Sp4 still shows a 15% and 13% decrease in work of fracture and peak stress compared to those of the baseline material, respectively, Figure 4, a-b.

Study 2 (through Sp5-Sp8) investigates the effect of ramp-up and jump value on the fracture properties. By comparing the results to those of study 1, we conclude that ramping up is a successful tool that promotes failure in 90° plies and shows a potential for improvement of delamination jump. It is also concluded that the baseline ramp is a good balance of a few cuts and also can guide the crack. Test results demonstrate that adding targeted partial cuts in the 45°/-45° can help guide the crack. However, applying Teflon or silicon spray to weaken the interface to promote delamination does not seem to affect the behaviour. Moreover, the challenge with this particular MCP is that the crack does not alternate sign and create delamination in every block (similar to non-engineered material). Hence, the MCP could be modified so that it would alternate every two or three blocks to make sure the crack always follows the pattern and increases delamination, Figure 3-c. Nonetheless, by comparing to Study 1, we can observe that normalised work of fracture and peak stress values improve slightly, see Figure 4. a-b.

  doi:10.5075/epfl-298799_978-2-9701614-0-0

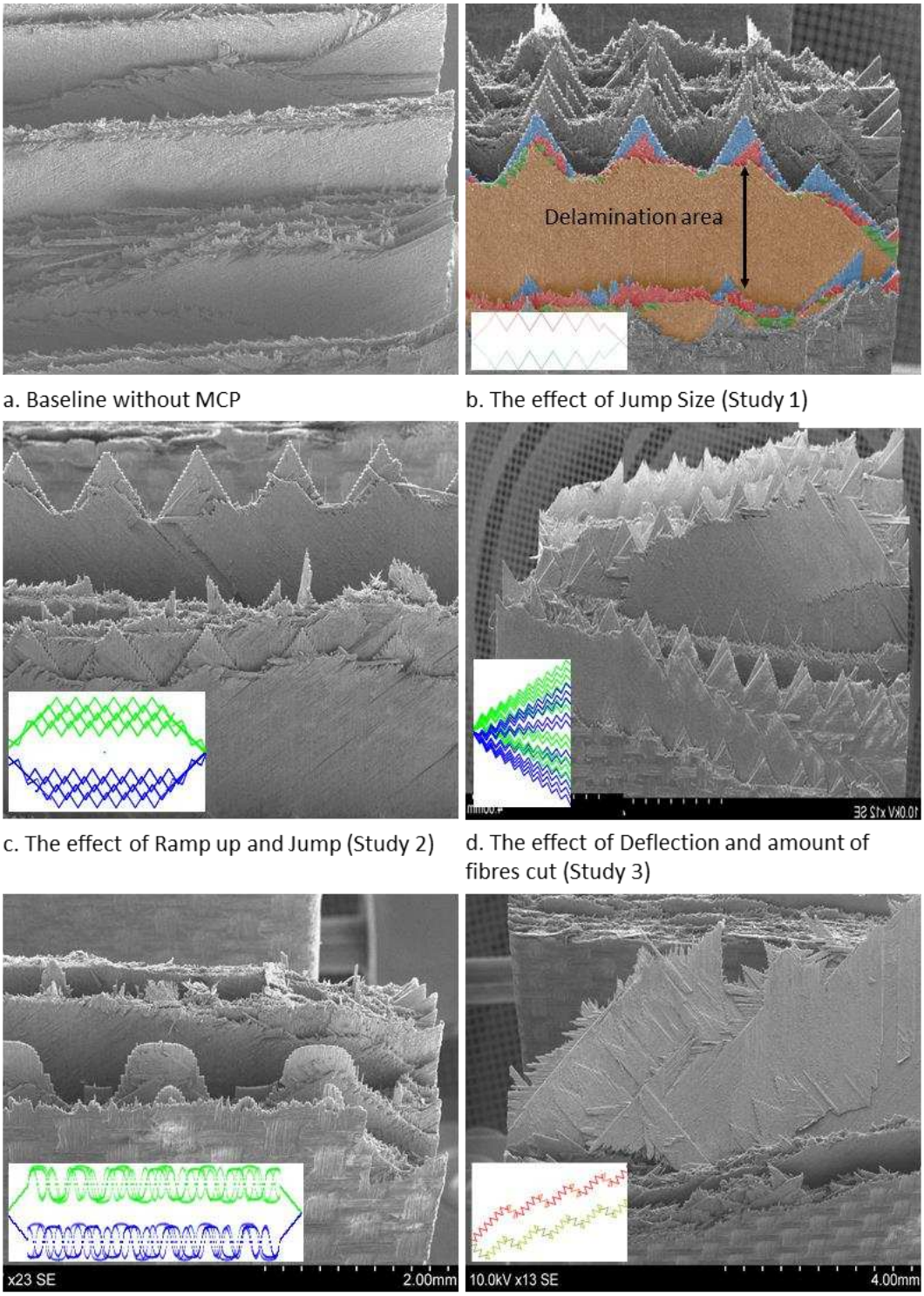

a. Baseline without MCP

b. The effect of Jump Size (Study 1)

c. The effect of Ramp up and Jump (Study 2)

d. The effect of Deflection and amount of fibres cut (Study 3)

e. The effect of MCP height and type (Mogul field) (Study 4)

f. The effect of Using 45°/-45° plies (Study 5)

Figure 3: Fracture surfaces of the failed specimens in different studies

  doi:10.5075/epfl-298799_978-2-9701614-0-0

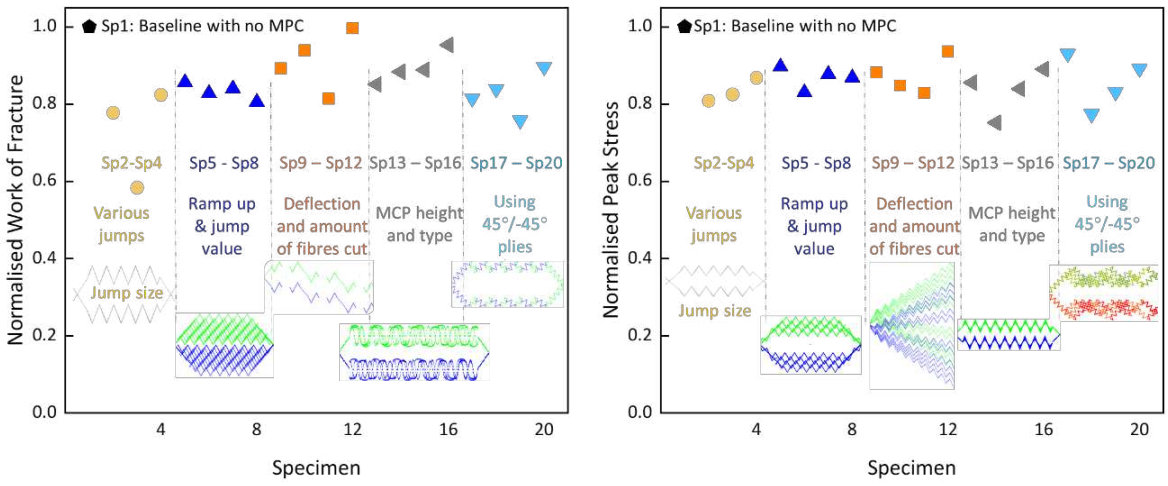

a. Normalised work of fracture

b. Normalised peak stress

Figure 4: Normalised (a) work of fracture and (b) peak stress values of engineered crack path specimens under three-point bending (3PB)

To demonstrate one of the promising design concepts, the force-displacement curves for study 3 specimens (Sp9-Sp12) are depicted in Figure 5-a. We have examined the variations of deflection and amount of fibres cut, showing that this particular design is successful to deflect the in-plane crack, see Figure 3-c and Figure 5,c-d. Moreover, partially cut MCPs can still guide the crack and increase strength and energy dissipation (see Sp 12 values in Figure 5, b). The test results suggest that there is a potential for a partial cut of MCPs in 0° plies. In the fourth study, we investigate the roles of MCP height and type on fracture performance. Regarding the type of MCPs, in addition to ST MCPs, we also apply mogul field (MF) MCP to examine its feasibility and performance. By analysing Figure 3-d and Figure 4 a-b, we can observe that changing a MCP type can have a positive effect in deflecting the crack, while retaining fracture properties. By comparing the results in Figure 4-a,b, we can confirm that slightly higher shark-teeth (ST+) patterns can be used, though it does not significantly increase the fracture properties. As a result, we can conclude that there is still some room for using longer features in the MCPs if needed; however, the limited effect of the MCP used should be examined to that of ramp/crack jump height.

  doi:10.5075/epfl-298799_978-2-9701614-0-0

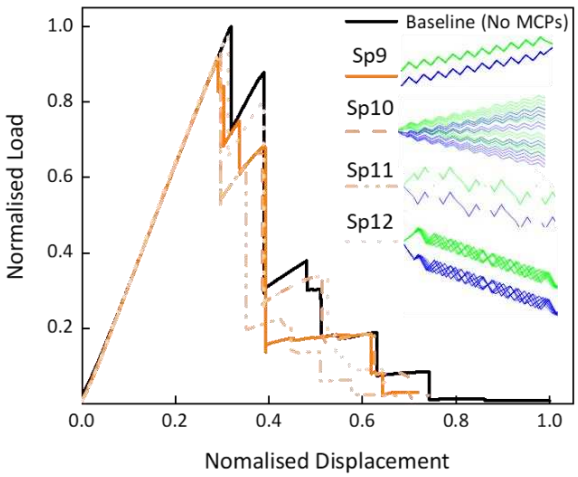

a. Force-displacement results under 3PB (Study 3)

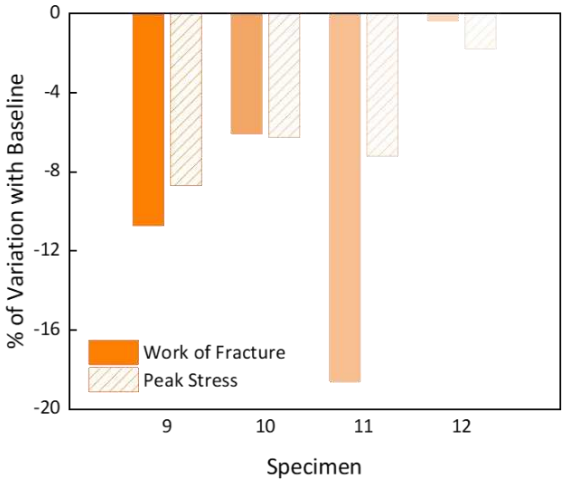

b. Variation of normalised work of fracture and peak stress (Study 3)

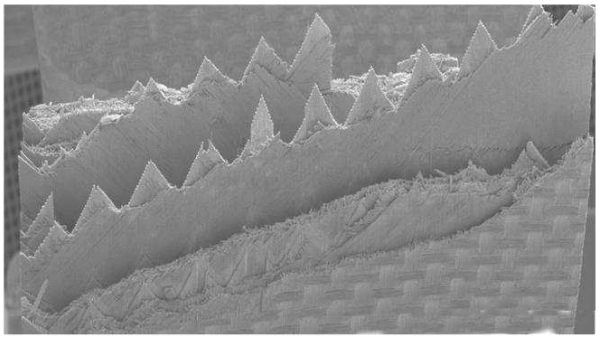

c. Constant deflection through the thickness (TTT) in Sp9 (Study 3) - front view

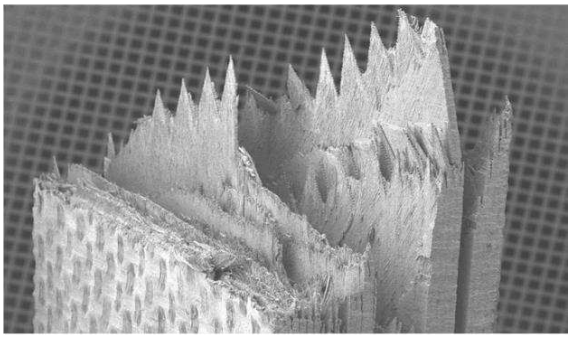

d. Constant deflection TTT in Sp9 (Study 3) - side view

Figure 5: (a) Force-displacement curves of study 3 specimens and corresponding MCP schematics, (b) their percentage of variation (in terms of work of fracture and peak stress) with the baseline, and (c-d) fracture surface of one of the samples in study 3 (Sp9)

In the last study, we examined using MCPs on 45°/-45° plies on the fracture performance. The fractographic analyses of failed specimens (Figure 3-e) show that using MPCs on the 45°/-45° may be somewhat less effective at controlling the crack position in those plies. Comparing the work of fracture and peak stress values reveals that using MCD on 45°/-45° plies does not improve the performance significantly compared to previous studies. In addition, we did not observe any strong knock-off of the strength/work of fracture despite micro-cuts being present in every two plies (versus every four plies in Sp4). This concept is perhaps less promising than MCPs in 0° plies to control the crack; however, targeted MCP in 45° still can be used to help deflect the crack.

To further evaluate the feasibility of applying these engineered crack paths to real applications, such as blade-off events in engines, engineered crack paths are applied to more realistic specimens and will be investigated under indentation test using a cantilever beam test, which its results will be provided at the conference.

  doi:10.5075/epfl-298799_978-2-9701614-0-0

4. Conclusion

In this paper, we carried out multiple studies to design concepts of structural fuses made of thin-ply carbon fibre-reinforced polymer (CFRP) for generic idealised components. A series of micro-cut patterns (MCPs) and crack path combinations were engraved on multiple CFRP specimens and we tested them under three-point bending (3PB). It was concluded that:

1- carefully-designed micro-cuts can be applied to create engineered crack paths in thin-ply composite structures, which can deflect the crack away from the inherent (critical) path and steer it along chosen planes;
2- MCPs can be used to promote desired failure mechanisms, namely delamination, to retain energy dissipation, not necessarily present in the baseline material;
3- engineered crack paths can be applied so that the specimen does not fail under unwanted failure modes (namely compressive failure); and
4- by applying engineered crack paths, uncut plies are protected so that they can act as crack stopping barriers.

These results motivate ongoing work where we are investigating this structural fuse concept in more complex structures.

Acknowledgements

The funding from Innovate UK under the UKRI FANDANGO project No. 113232 (https://gtr.ukri.org/projects?ref=113232) is gratefully acknowledged.

References

1. Kazemi, M.E., et al., *Investigating the roles of fiber, resin, and stacking sequence on the low-velocity impact response of novel hybrid thermoplastic composites.* Composites Part B: Engineering, 2021. **207**: p. 108554.
2. Yokozeki, T., et al., *Damage characterization in thin-ply composite laminates under out-of-plane transverse loadings.* Composite Structures, 2010. **93**(1): p. 49-57.
3. Wisnom, M.R., S.R. Hallett, and C. Soutis, *Scaling Effects in Notched Composites.* Journal of Composite Materials, 2010. **44**(2): p. 195-210.
4. Teixeira, R., S. Pinho, and P. Robinson, *Thickness-dependence of the translaminar fracture toughness: experimental study using thin-ply composites.* Composites Part A: Applied Science and Manufacturing, 2016. **90**: p. 33-44.
5. Bullegas, G., S.T. Pinho, and S. Pimenta, *Engineering the translaminar fracture behaviour of thin-ply composites.* Composites Science and Technology, 2016. **131**: p. 110-122.
6. V Medeau, E.G., S Pimenta, J Finlayson, S T Pinho, *Optimizing engineered micro-structures fracture properties for CFRP crack path design*, in *10th International Conference on Composites Testing and Model Identification*. 2021: Lille, France.

  doi:10.5075/epfl-298799_978-2-9701614-0-0

FRACTOGRAPHY OF POLYMER COMPOSITES: FUTURE ADVANCES

Tomas J. Katafiasz[a], Emile S. Greenhalgh[a]*

a: The Composites Centre, Department of Aeronautics, Imperial College London, UK
*tomas.katafiasz11@imperial.ac.uk

Abstract: *Fractography is a useful research tool which enables engineers to bridge the gap between numerical modelling and experimental testing, support material design development, and aid in the failure investigation of in-service (and laboratory-based) failures. This paper presents the current issues and direction of research for the fractography of polymer composites and highlights the future challenges. These include: fretting failures between delaminated neighbouring plies, gleaning environmental effects (i.e. the influence of moisture and/or temperature on fracture morphology), and the sequencing of physically isolated failures. The latter is addressed by the proposed new methodology in which fractography and numerical modelling are synergistically coupled. This methodology is becoming increasingly important across a range of industries as the uptake of composites becomes wider.*

Keywords: fractography, failure investigation, fretting, hygrothermal, FEM (finite element modelling)

1. Introduction

Fractographic analysis of polymer composites gives a deep insight into composite failure mechanisms and has supported the development of test methods and predictive tools in composite engineering. It is also an invaluable tool for post-failure investigation of components and in-service failures [1]. However, fractographic techniques need to keep abreast of the advances in new composite material architectures, constituents, processing routes, and applications. In this paper, the current state-of-the-art in polymer composite fractography is presented alongside the challenges which lie ahead. Some of these are highlighted by the need to link semi-qualitative analysis, relating to the specific conditions of failure and loading history, to the fracture morphologies. Other challenges concern the influence of environmental factors (hygrothermal effects: temperature and moisture uptake) and cyclic loading (where fretting damage is induced), both of which are particularly pertinent in primary aerospace structures. Furthermore, as new composite interleave and interlaminar reinforcement technologies are developed, the requirement to fully characterise their failure modes becomes critical in the validation and certification of full structural components.

Another important issue arising from the investigation of in-service failures is the global sequencing of physically isolated failures. For example, the failure of composite forks and a seat tube during a bicycle accident, or multiple stiffeners debonding and fracturing from the skin in a stiffened wing section, where both failures often occur during a single event but are not physically connected. Such physically isolated failures are often impossible to sequence through purely fractographic analysis since they are not physically connected by a common local failure initiation site. Thus, a new methodology has been proposed to incorporate Finite Element Modelling alongside traditional fractographic methods. This paper will outline this methodology

  doi:10.5075/epfl-298799_978-2-9701614-0-0

which can be applied to both laboratory experiments (where instrumentation is unable to capture events) and in-service failures.

2. Fretting and environmental conditions

2.1 Fretting

It should be noted that fretting is differentiated from fatigue, which has been discussed in detail fractographically in polymer composites by Greenhalgh [1]. Fatigue failure results from cyclic loading whereas fretting failure is a morphological process of wear where previously failed (or un-failed) surfaces are damaged through frictional loads in an oscillating mode II fashion. Fretting can occur between two undamaged surfaces, or as more often observed in composite structures and pertinent to failure investigations, between two previously delaminated neighbouring plies. Such preexisting damage can occur through means unassociated with the fretting load, such as impact or buckling, but the driving force for fretting to extend these delaminations often originates from a resonance or other cyclic load. The fractography of fretting in composites is particularly applicable to failure investigations, where the extent of fretting (i.e. number of cycles) can be matched to the resulting fracture morphologies. This morphological correlation, although noticed in failed composite parts (Figure 1), has not yet been covered by research, particularly within polymer composites. Early work by Daoud [2] and Schulte et al. [3] have outlined mechanical test rigs to induce fretting damage on glass fibre and carbon fibre composites, respectively (Figure 2). Both rigs utilised normal clamping loads to produce varying levels of frictional force. Unfortunately the fractography of fretting damage on composite-composite interfaces was not presented.

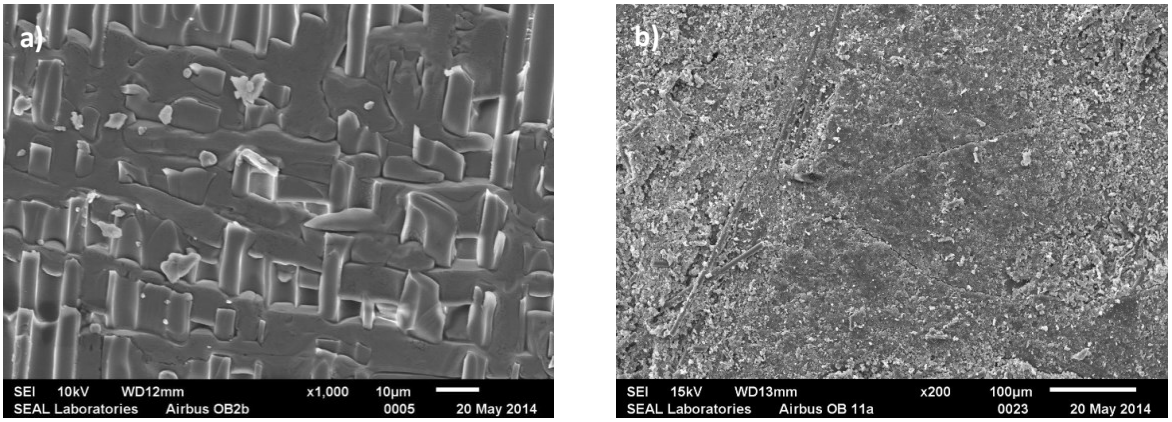

Figure 1. Scanning Electron Microscope images of fretted polymer composites, post-failure [4]

Although previous fretting research has been conducted on metal-metal and metal-composite interfaces, very little, if any, fractography has been conducted on fretted composite-composite interfaces. Composite on composite fretting becomes crucial as they become more widely utilised in primary structures.

  doi:10.5075/epfl-298799_978-2-9701614-0-0

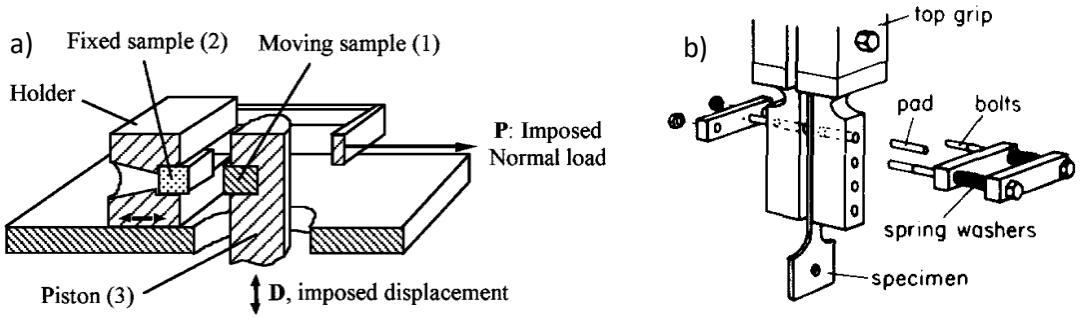

Figure 2. Fretting rigs developed by a) Daoud [2], and b) Schulte et al. [3]

Recent work by at Imperial College London investigated cycling a 3-point bending specimen (previously partially delaminated mid-thickness in both mode I or mode II) to study the effects of mode II fretting on a T700/M21 composite laminate [5]. It was noted that the fretting damage after an initial mode I type delamination resulted in no morphological changes due to fibre bridging caused by the mode I crack which held the surfaces apart and disallowed any friction between them. It was also noted that fretting after a mode II delamination caused rounding on the pre-existing cusps and produced some debris, Figure 3. Due to the nature of the test set-up (i.e. 3-point bending), it was deemed that a variable compressive through-thickness force was imperative in producing the required friction associated with in-service fretting load cases. Thus, a new test rig has been designed to account for this. An electric motor is used in conjunction with a fixed base plate and uniaxial top plate, where previously delaminated specimens are placed. Weights can be applied to the top plate to adjust the frictional forces during the fretting process.

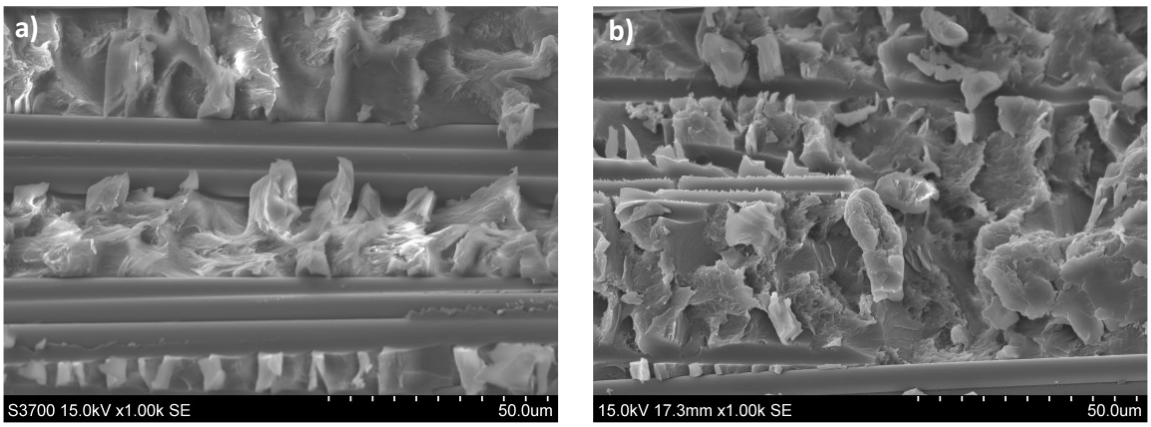

Figure 3. T700/M21 self-fretting after a mode II delamination after a) 0 cycles, and b) $5x10^5$ cycles [5]

2.2 Environmental conditions

It is well known that the hygrothermal (moisture and temperature) conditions can affect the mechanical performance of composites under various loading modes [6], and especially those dominated by the integrity of the fibre/matrix interface [7]. As new composite matrix toughening systems are developed, the effect of the environmental conditions on the

mechanical performance of composite systems is critical in composite design for high performance applications, particularly in demanding environments.

Recent work by Katafiasz et al. [8] has shown that the mode I interlaminar facture toughness of a moisture saturated highly toughened CF/epoxy system is severely degraded at -55°C. Moisture saturation within a primary aerospace structure would typically arise whilst remaining stationary on a runway at a hot and humid country whereby moisture ingresses into the epoxy system. Then, as the flight reaches cruising altitude (typically at -55°C), and since the toughening particle/epoxy interface is degraded due to the moisture and the matrix system embrittles due to the cold temperature, the particles are seen to be plucked from the surrounding resin, hence reducing the overall mode I interlaminar fracture toughness, Figure 4.

Other processes noticed in the same work showed that at 90°C both the epoxy and toughening particles become highly ductile, and moisture degrades the fibre/matrix interface, both increasing the mode I fracture toughness compared to those tested at room temperature and at -55°C, Figure 5. Although the level of moisture and the failure temperature cannot be quantifiably deduced from the fracture morphologies, a first step has been taken towards this goal. Realistically, the in-service moisture content of composites varies through the thickness (unless fully saturated and in a state of equilibrium), therefore care must be taken when relating laboratory-based morphologies to in-service failures. More research is needed for temperatures closer to the T_g of the matrix, or where the in-service temperatures are particularly extreme. Further fractographic work on the effect of temperature and moisture on other polymeric composite systems will also provide understanding to which environmental degradation processes are material specific and which are general to polymeric composites.

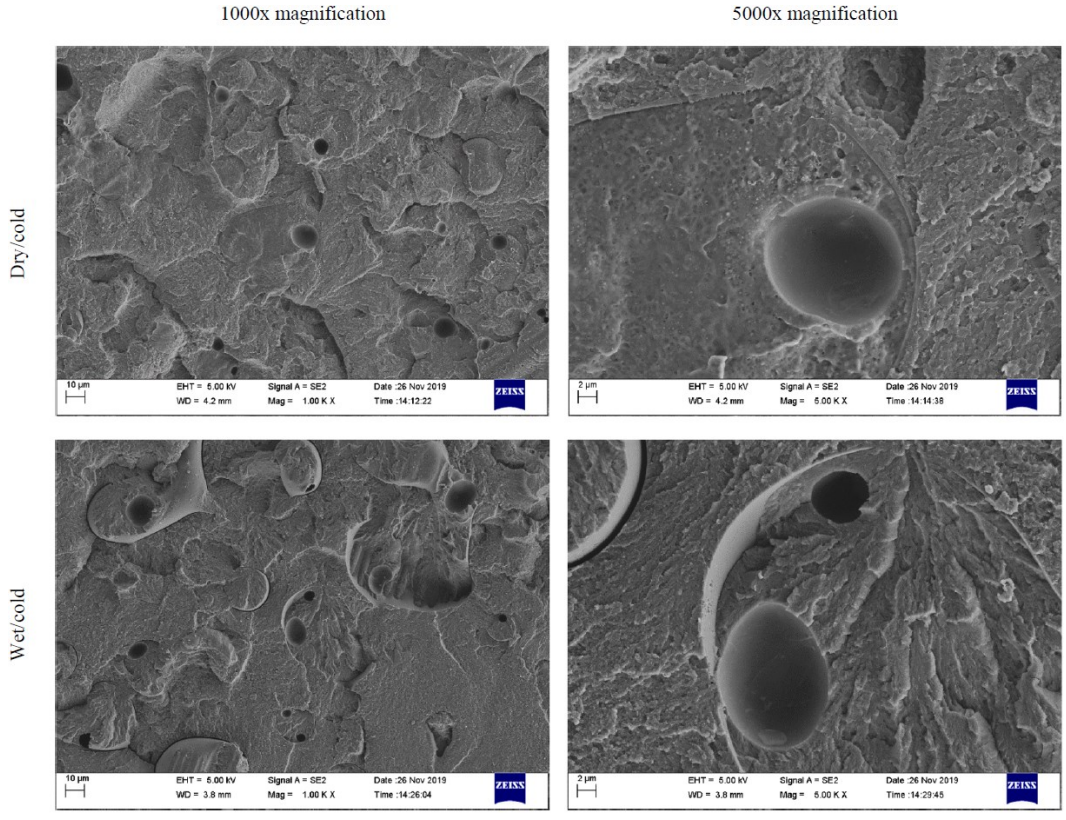

Figure 4. Micrographs showing toughening particle/epoxy debonding under mode I interlaminar fracture in the wet/cold condition [8] (Courtesy of Rolls Royce)

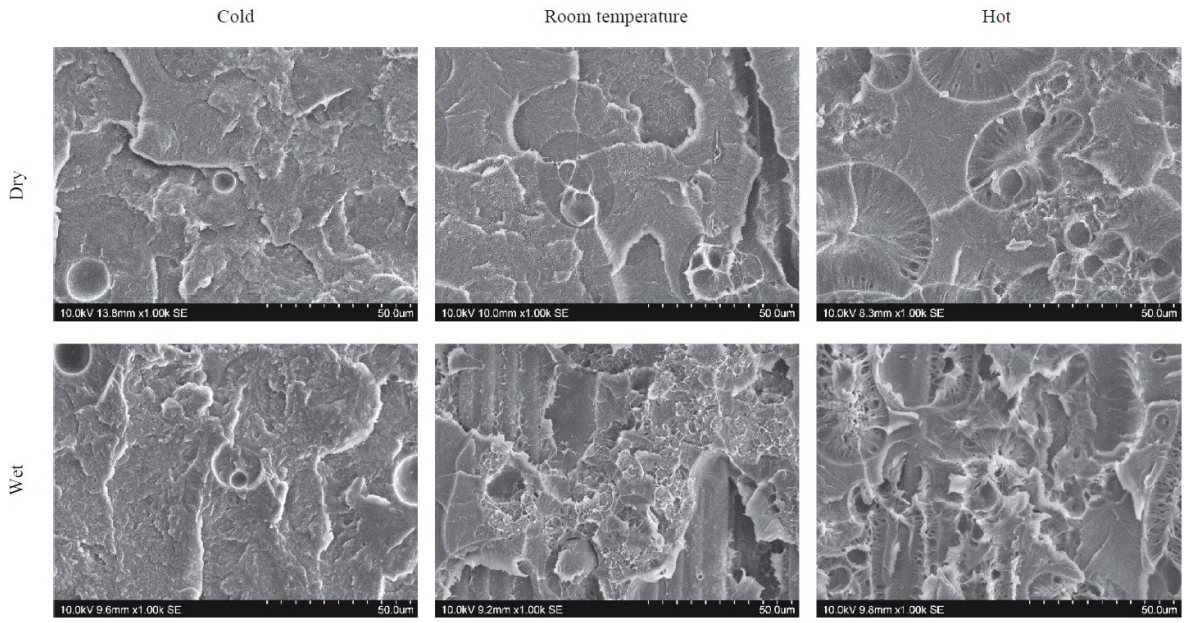

Figure 5. Micrographs showing the effect of both moisture and temperature on the mode I interlaminar fracture toughness of a highly toughened CF/epoxy system [8] (Courtesy of Rolls Royce)

3. Sequencing physically isolated failures

3.1 Challenges

Fractography can be used to sequence failures within failed composite components by, amongst other morphological features, mapping the: interlaminar crack directions from the mode II shear cusps (Figure 6a), tensile translaminar fracture directions from DAFFs (Directly Attributable Fibre Failures) (Figure 6b), and compressive translaminar fracture directions from kink banding (Figure 7a) and arrow heads (Figure 7b) [9]. This has led to the fractography post-failed components being a vital tool in supporting future design to mitigate failure, and in some cases, providing evidence for failure investigation.

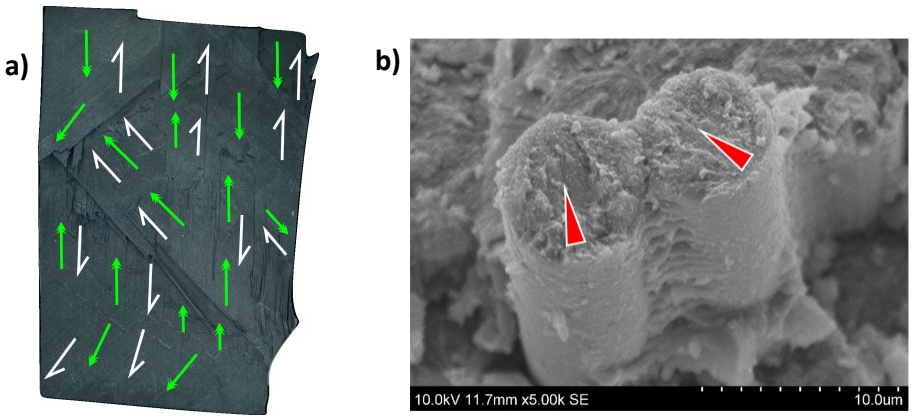

Figure 6. a) Mode II shear and crack growth directions in a failed aerospace component, b) Directly Attributable Fibre Failures showing the tensile translaminar growth direction [9]

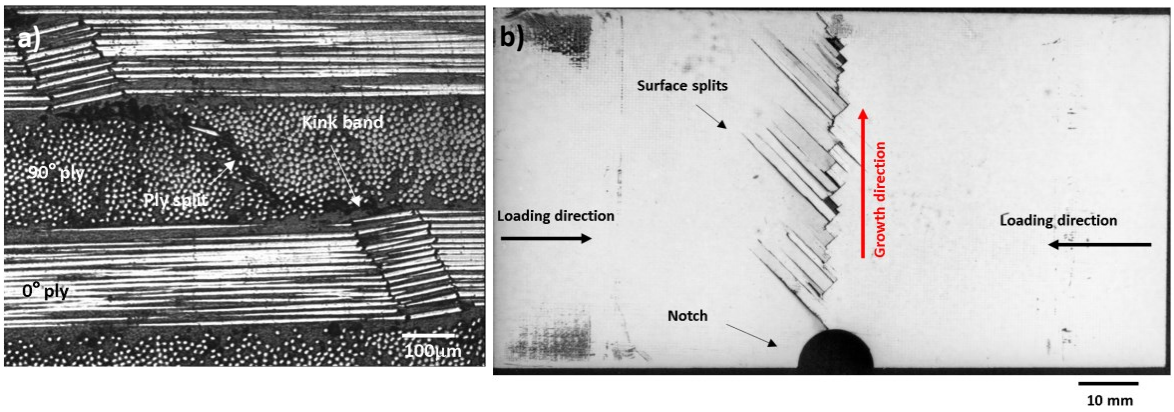

Figure 7. a) Optical microscopy showing kink banding, b) Compressive arrow heads indicating compressive translaminar growth direction [9]

Challenges arise when multiple failures within one structure or component are physically isolated, such that pristine material exists between two or more areas of failure. Examples of these include seat tube and fork failures in a bicycle accident, or multiple stiffener debonding in a stiffened wing section (Figure 8).

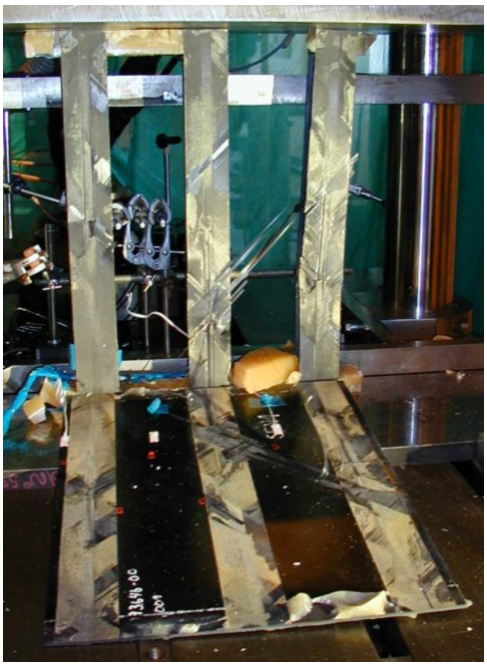

Figure 8. Multiple stiffeners debonding from a panel under compression [1] (courtesy of Ministry of Defence)

To sequence these failures high speed video footage is needed but often unavailable or unfeasible. Thus, a new methodology is required.

3.2 Methodology

The methodology outlined here considers Finite Element Modelling coupled with fractographic observations. First, the physically isolated failures are identified and characterised experimentally using traditional fractographic methods. Then, a wholly elastic FE model is

constructed for the entire structure or component. The damage associated with the isolated failures are then implanted into the elastic model to make up separate models, each with one local failure informed by the fractographic evidence. The separate models are then run independently and the resulting stress distributions are compared to the experimental fractography. Whichever FE model produces stress concentrations in the applicable mode at one (or more) of the other sites of failure can be assumed to have occurred first. This process, shown diagrammatically in Figure 9 below, can then be iterated for the further failures (if there are more than two). This methodology must be developed further and verified before being used reliably.

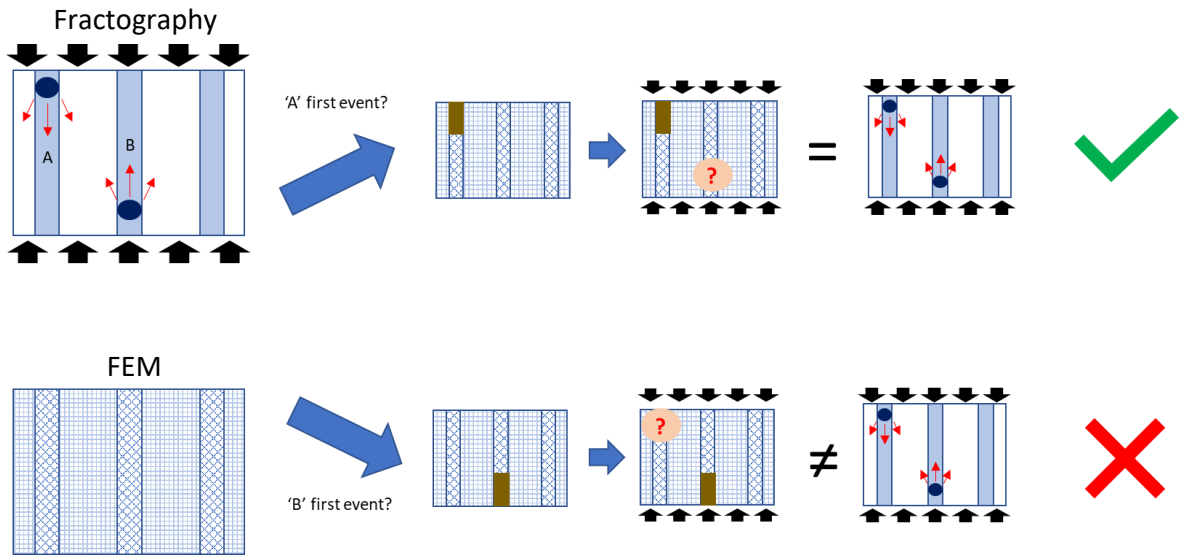

Figure 9. Outline of the FE/fractography methodology for a stiffened panel

4. Summary

This paper has outlined some of the challenges associated with the future of polymer composite fractography. These have been categorised into three general topics: composite-to-composite fretting, hygrothermal effects, and the sequencing of physically isolated failures. As polymer composites become more widespread throughout multiple industries, and increasingly diverse composite systems are developed, fractography provides a useful tool in determining how new material systems fail, post-failure analysis, and in aiding composite design to mitigate in-service failures.

Acknowledgements

The authors acknowledge funding from ATI and Rolls-Royce plc via the collaborative research projects 'CTI Composite Fan Technology' [grant number 113085] and 'FANTASTICAL' [grant number 113190]. The authors would also like to thank Mr Ryan Clarke for his work on the fretting work presented, Mr Gary Senior and Mr Jon Cole for their assistance with material manufacture, and Mr Keith Wolstenholme and Mr Joseph Meggyesi for their assistance with mechanical testing.

5. References

1. Greenhalgh ES. Failure analysis and fractography of polymer composites. Woodhead Publishing; 2009.
2. Daoud M, Chateauminois A, Vincent L. Fretting of glass fibre reinforced composites. Journal of Materials Science. 1999;34(1):191–194.
3. Schulte K, Friedrich K, Kutter S. Fretting fatigue studies on carbon fibre/epoxy resin laminates: I—Design of a fretting fatigue test apparatus. Composites Science and Technology. 1987;30(1):19–34.
4. Greenhalgh ES, Ritchens L, Routledge D, Lewis P, Watkinson K, Ingle M, Hiley M. Methodologies for Handling of Non-Metallic Failures (Polymers and Polymer Composites). Presentation at TWI, Cambridge, UK, 2017.
5. Clarke, R. Characterisation of Fretting Damage in Support of Composite In-Service Failures. MEng Final Year Project Report, Department of Aeronautics, Imperial College London, 2019.
6. Friedrich K, Application of Fracture Mechanics to Composite Materials, Elsevier, 1987.
7. Kishore Maiti A. Compressive behavior and fracture features of rubber bearing glass-epoxy composites exposed to aqueous media. J Reinf Plast Compos 2001;20:1546–54. https://doi.org/10.1106/92BG-4C2Q-DBN7-LL4G.
8. Katafiasz TJ, Greenhalgh ES, Allegri, G Pinho ST, Robinson P. The influence of temperature and moisture on the mode I fracture toughness and associated fracture morphology of a highly toughened aerospace CFRP. Composites: Part A 2021;142 https://doi.org/10.1016/j.compositesa.2020.106241.
9. Greenhalgh ES, Katafiasz TJ. Fractography of Polymer Composites, ASM Handbook, Volume 12, *Fractography*, 2023, *pre-publication.*

  doi:10.5075/epfl-298799_978-2-9701614-0-0

STUDY ON THE MECHANICAL BEHAVIORS OF 3D PRINTED HYBRID COMPOSITES WITH VARIOUS COMBINATION PATTERNS BETWEEN CARBON FIBER AND GLASS FIBER

Na-Hyun Jeon[a], Hui-Jin Um[a], Hak-Sung Kim[a,b]*

a: Department of Mechanical Convergence Engineering, Hanyang University, 222 Wangsimni-ro, Seongdog-gu, Seoul, Republic of Korea
b: Institute of Nano Science and Technology, Hanyang University, 222, Wangsimni-ro, Seoungdong-gu, Seoul, Republic of Korea
*Email: nahyun.j11@gmail.com

Abstract: *Carbon fiber reinforced polymer (CFRP) composites have been applied into many applications due to high specific strength and modulus. However, CFRP composites have very low failure strain, along with unexpected fracture, which is a disadvantage in engineering design. In this study, mechanical behavior of hybrid composites with various carbon fiber/glass fiber patterns were investigated to implement the composites that compensates for disadvantages of each material. Traditionally, while it is difficult to manufacture hybrid composite in intralayer level, 3D printing technology could make various complicated hybrid patterns by micro scale. Hybrid composites specimens were fabricated by intrayarn level using 3D printing. Tensile test and three-point-bending test were performed to investigate the mechanical behavior of HFRP composites. Consequently, hybrid composites with higher dispersion showed improved tensile strength and modulus. Flexural strength and modulus could be increased by 71.3, 84.8, and 56% in hybrid composite than glass fiber reinforced polymer (GFRP) composites.*

Keywords: Hybrid composite; intrayarn; Carbon fiber reinforced polymer (CFRP); Glass fiber reinforced polymer (GFRP); 3D printing

1. Introduction

Recently, as the regulations of carbon emission have been strengthened due to growing attraction of environment protection, the weight reduction is one of the critical issues in automotive industry field [1]. To meet these criteria, the carbon fiber reinforced polymer (CFRP) composites have been widely applied to the automotive components [2-4]. Since the CFRP composites have high specific strength and modulus, it can be achieved up to 40~60% of weight reduction in automotive field along with excellent mechanical properties [5]. However, CFRP composites have very low failure strain characteristic, abrupt and premature failure often occurs which is the disadvantages in engineering design [6]. To improve the weakness, the studies of hybrid composites have been increasing due to their complementary advantages of each material such as CF with high strength and GF with high failure strain. Hybrid composites could be classified by 3 types: Interlayer, Intralayer, and Intrayarn hybrid composites as shown in Fig.1 [7]. The interlayer hybrid composites have been most widely studied since it was relatively easy to handle by varying the stacking sequence and angle with different ply materials [8-10]. Although hybrid composites on the intralayer level is more difficult to fabricate than previous case, it shows more improved mechanical properties such as out-of-plane strength and fatigue behavior due to high dispersion [6,11]. Mixing fiber level called “intrayarn” would be expected

  doi:10.5075/epfl-298799_978-2-9701614-0-0

to show further enhanced mechanical behavior due to mutual influence between different materials. However, conventional fabrication process faces problem with manufacturing intrayarn hybrid composite because of its time consuming and difficulties with delicate arrangement of fiber. Nowadays, due to the development of three-dimensional (3D) printing technology, the hybrid composites with various and complicated patterns could be implemented on fiber level [12].

In this study, mechanical behavior of hybrid composites with various carbon fiber/glass fiber patterns in intrayarn level were investigated to implement the composites that compensates for the disadvantages of each material. The hybrid composites with various combination patterns were fabricated through 3D printing method. Tensile and three-point-test were performed to investigate the mechanical behavior with respect to the hybrid patterns. The fracture surfaces were taken by digital microscope to observe failure mode after flexural test.

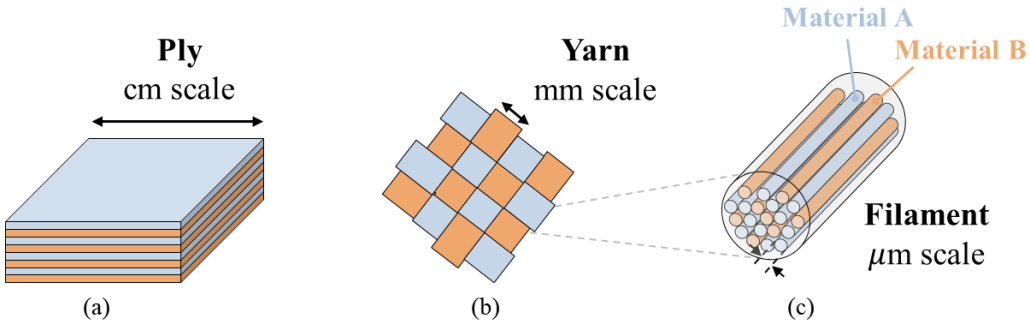

Figure 1. The constituent unit of hybrid composites: (a) interlayer, (b) intralayer, and (c) intrayarn.

2. Experiments

2.1 Materials

As indicated in Fig. 2 (a-b), the two types of filaments were used to fabricate the hybrid composites: continuous carbon fiber (CCF) filaments and high strength high temperature (HSHT) glass fiber filaments (Markforged®, USA). Table 1 shows the mechanical properties of each filament provided by manufacturer [13]. The continuous fibers of each filament are pre-impregnated in nylon 6 with a melting point of about 220°C. The diameter of carbon fiber filament is 0.34 - 0.38 mm, and HSHT glass fiber's either.

Figure 2. Continuous fiber filament of Markforged: (a) carbon fiber filament, and (b) HSHT glass fiber filament (c) Desktop 3D printer (composer A3, Anisoprint)

  doi:10.5075/epfl-298799_978-2-9701614-0-0

2.2 Specimen fabrications

The mechanical test specimens were 3D printed using composer A3 (Anisoprint LLC) as shown Fig. 2 (c). All continuous fiber filaments were 3D printed with the nozzle temperature of 235℃. There were types of fiber reinforced composites: carbon fiber reinforced polymer (CFRP) composites, glass fiber reinforced polymer (GFRP) composites, and hybrid fiber reinforced polymer (HFRP) composites. Since the 3D printing generally proceeds with one material per layer, intrayarn hybrid composites with various combination patterns in a layer were implemented by editing G-code of 3D printer. Fig. 3 shows hybrid composite patterns in the cross-sectional direction, where blue color denotes CF and orange color means GF. The volume fraction between CF(C) and GF(G) was the same for all specimens as CF 50 : GF 50 (see Table 2).

Table 1: The mechanical properties of constituent materials [13]

Material	Tensile strength (MPa)	Tensile modulus (GPa)	Flexural strength (MPa)	Flexural modulus (GPa)
Carbon fiber	800	60	540	51
HSHT glass fiber	600	21	420	21

Table 2: The volume fraction of hybrid composite according to the patterns.

Pattern case	Volume fraction ratio (C : G)
Carbon fiber	100 : 0
HSHT glass fiber	0 : 100
C-G-C	50 : 50
C-G-C-G-C	50 : 50
CG-CG-CG-CG	50 : 50

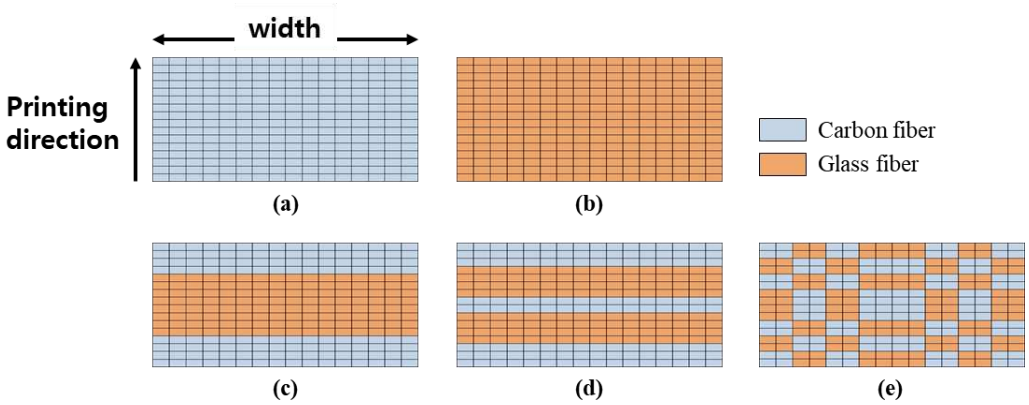

Figure 3. Combination patterns: (a) CFRP; blue (B) GFRP; orange, (c) HFRP case 1, (d) HFRP case2, and (e) HFRP case 3

  doi:10.5075/epfl-298799_978-2-9701614-0-0

The specimens were 3D printed in the thickness direction by 8 layers in a $[0]_{4s}$ for tensile test. The dimensions of tensile specimen are 1 mm in thickness, 10 mm in width, and 200 mm in length (see Fig. 4 (b)). For flexural test, specimens were printed by 16 layers in a $[0]_{8s}$ with thickness of 2 mm, and width of 20mm. The length is same as 200mm with tensile test specimen (see Fig. 5 (b)).

2.3 Mechanical tests

Tensile test was performed according to ASTM D 3039 with the displacement loading rate of 2mm/min using a universal tensile machine (RB 301 UNITECH-M, R&B, South Korea) (see Fig. 4 (a)).

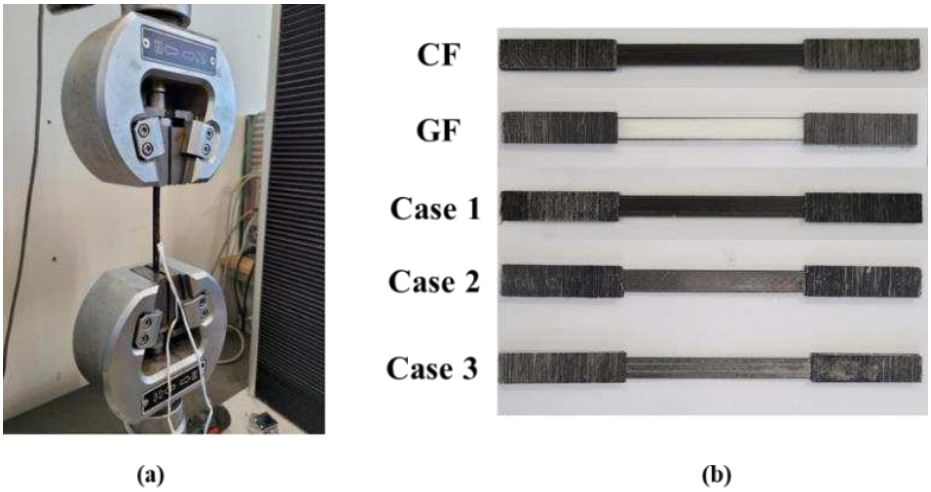

Figure 4. (a) Tensile test equipment and (b) test specimen according to the printing pattern

To investigate the flexural properties, three-point-bending (3PB) test was conducted based on the ASTM D790 using a universal tensile machine either (see Fig. 5 (a)). Displacement loading was applied with the speed of 2mm/min and radius of supports and loading jig are 20mm. Fracture surfaces of specimens were analyzed after mechanical properties test using digital microscope (AM4113ZT, Dino-Lite, Taiwan).

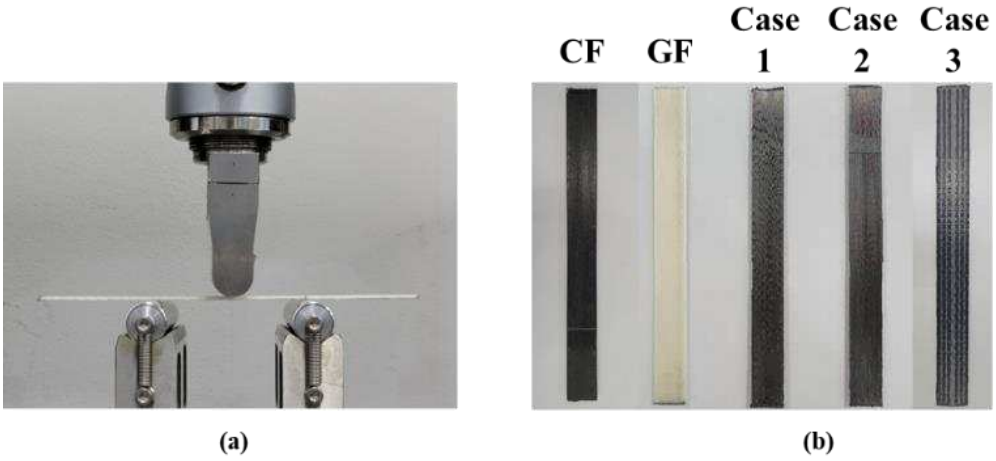

Figure 5. (a) Three-point-bending test equipment (b) flexural test specimens according to the printing pattern

  doi:10.5075/epfl-298799_978-2-9701614-0-0

3. Results and discussion

3.1 Tensile properties

The hybrid effect was defined from the rule of mixtures (ROM). It presents that enhancement or decline of hybrid composite's mechanical properties comparing by ROM and it could be calculated as follows [14]:

$$\lambda = \frac{\sigma_T}{\sigma_H} - 1 \quad (1)$$

where, λ is the hybrid effect for tensile properties, σ_T is the tensile strength or modulus of the hybrid composite, and σ_H means tensile strength or modulus of the hybrid composites calculated from the ROM. The Hybrid effects is presented as a positive or negative deviation, calculated hybrid effects for tensile properties are given in Table 3. As shown, the hybrid effects for both tensile strength and tensile modulus are negative. The degree of dispersion increases in the order case 1, 2, and 3, and the hybrid effect for strength and modulus is near at 0 as the dispersion increases. It is noteworthy that in hybrid composites, higher dispersion leads higher tensile properties.

Table 3: Tensile properties of HFRP composites according to the combination patterns.

Specimen	Tensile Strength (GPa)	Hybrid effects for Strength	Tensile Modulus (MPa)	Hybrid effect for Modulus
Case 1	399.0	-0.198	37.4	-0.160
Case 2	375.1	-0.246	41.2	-0.074
Case 3	401.3	-0.193	42.5	-0.045

3.2 Flexural properties

Fig. 6 shows load-displacement curve as results of flexural test, and the significantly different flexural behavior was observed according to the HFRP type. The catastrophic failure was observed in CFRP (see Fig.6(a)), whereas no sudden load drop was found in (see Fig.6(b)). Rather, the load was maintained even under large deformations. In case of HFRP composites, both CF and GF properties were exhibited as shown in Fig. 6(c-e). The more load drops appeared in HFRP case2 than that of HFRP case1. Since the HFRP case 2 has more interfaces between CF and GF layer, they prevent crack propagation with no rapid load drop. However, the maximum load of case2 was lower than that of case1 because the ratio of CF fibers on the compressed surface, that is, the outer layer, was less in case2 than in case1 [10]. The case3 shows completely different LD curve behavior compared to the case1 and 2 as shown in Fig. 6(e). There was no sudden load drop which was similar to the GFRP behavior, and the maximum load was similar to case1. In case3, CF and GF were 3D printed alternately with highest dispersion. As a result, it was found that the higher dispersion of the hybrid composite, the higher strength characteristics and the smooth LD curve behavior such as GFRP. As shown in Fig. 7, the highest flexural strength was found in case1 compared to other HFRP due to the more CF layer on outer surface. Although there was less carbon fiber layer at the compressive side in case3 compared to the case2, the higher flexural strength appeared than that of case2 even with same volume fraction due to the

  doi:10.5075/epfl-298799_978-2-9701614-0-0

higher dispersion. Consequently, HFRP case2 showed 84.8% higher flexural modulus than that of GFRP composites.

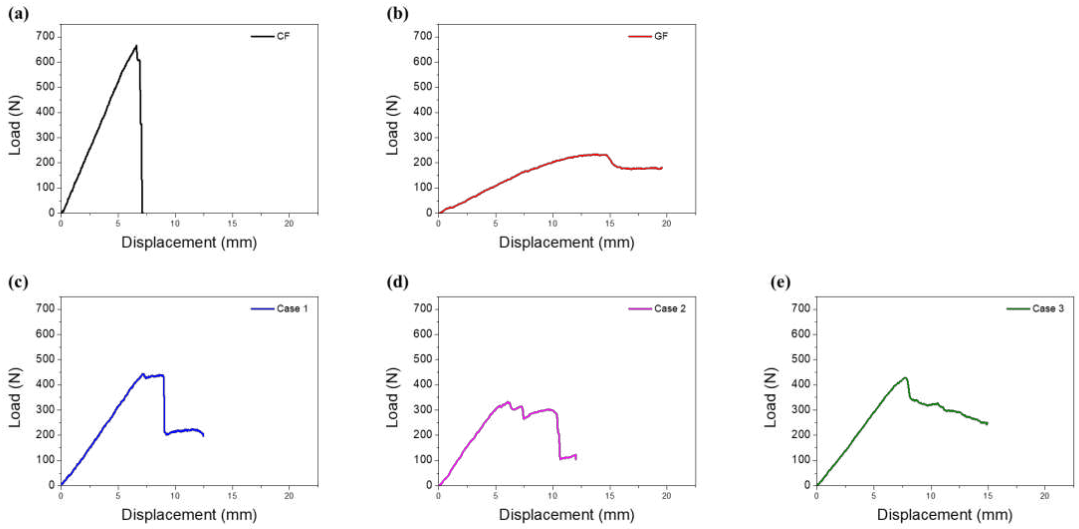

Figure 6. LD curve (a) CFRP (b) GFRP (c) HFRP case1 (d) HFRP case2, and (e) HFRP case3

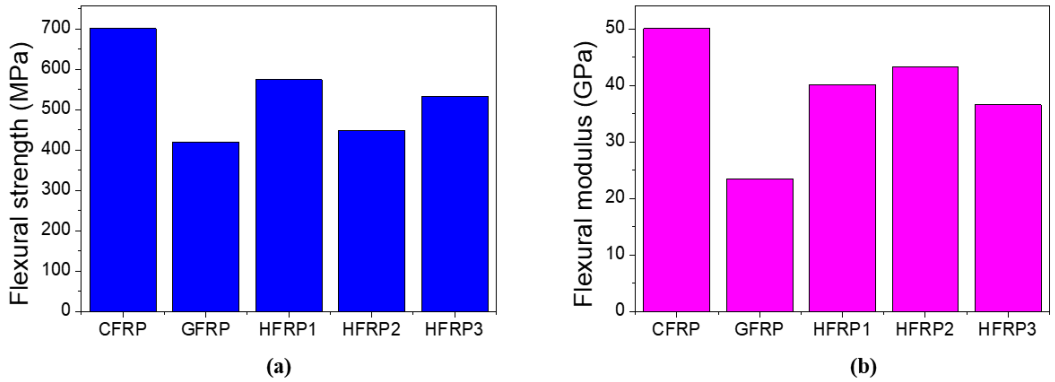

Figure 7. Flexural test result according to the composites type; (a) Flexural strength and (b) Flexural modulus-

3.3 Fracture surface

In CFRP composites, the crack was initiated in tensile side and cracks has grown as strain incresed. As shown Fig. 8 (a), that fractures occured slowly in tensile side, and broken single fiber was observed in fiber fracture area. After the cracks have grown to some extent, complete failure occurred abruptly. After compressive failure in an instant, fracture surfaes were formed relatively smoothly. The GFRP composite showed completely different fracture mode with CFRP composite. In GFRP composite, a few fiber fractures were shown, while cracks at compresive side did not lead to complete fracture until 20 mm in displacement (see Fig. 8 (b)). For HFRP case 1 and 2, the compressive fiber failure were found at surface layer similar with CFRP, but the delamination occured dominatly along with the interface between CF and GF as indicated in Fig. 8 (c) and (d). Microbuckling, a kind of compressive fracture, lead to delaminaton. In Case3, carbon fibers have broked, whereas no fracture could be seen in glass fiber. This is related to the LD curve behavior of it which was similar with the GFRP composites (see Fig.6 (e)).

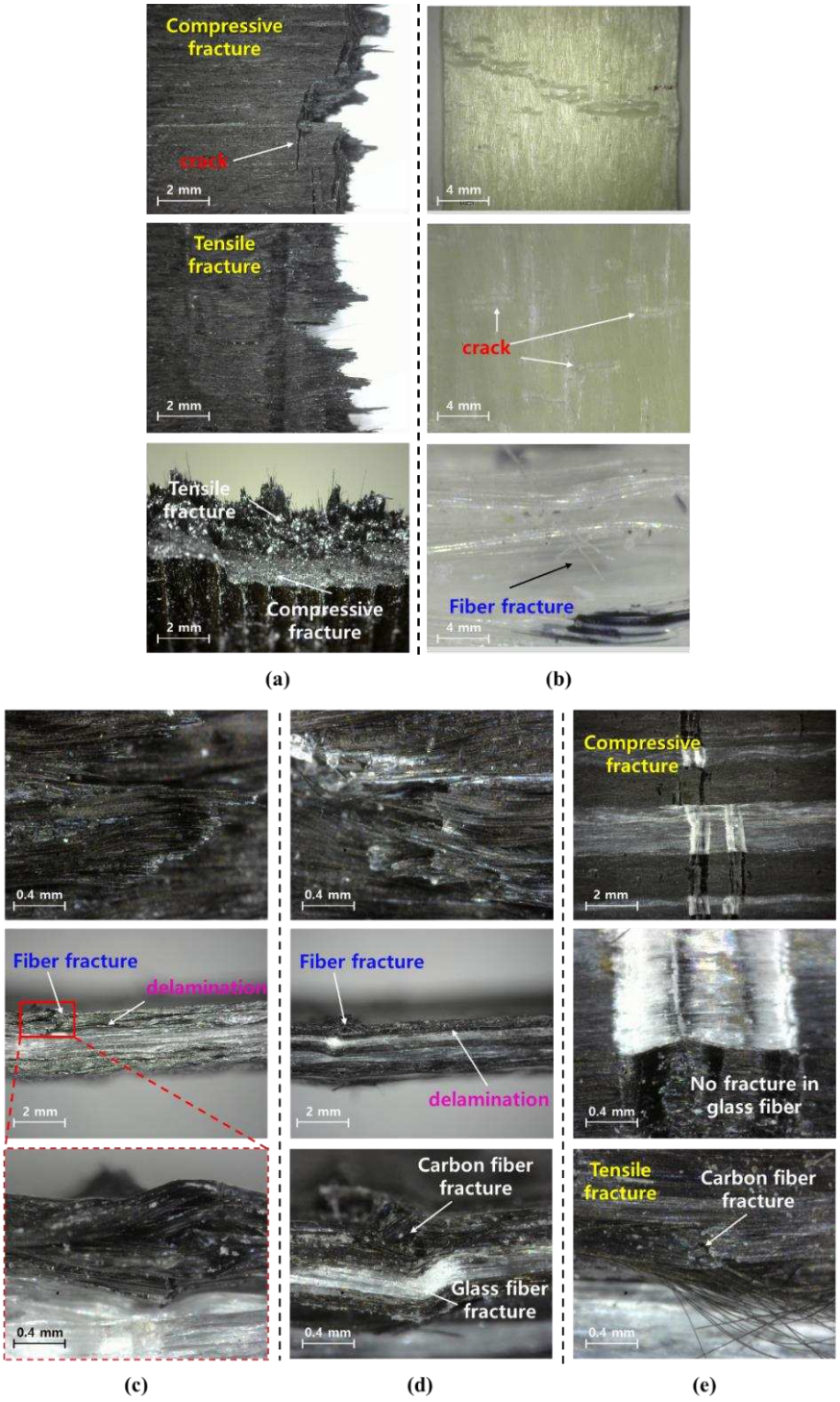

Figure 8. Optical images of fracture surface as a result of flexural test: (a) CFRP, (b) GFRP, (c) HFRP case1, (d) HFRP case2, and (e) HFRP case3.

4. Conclusion

In this study, mechanical behavior of intrayarn hybrid composite were investigated to complement disadvantages of composite that use one kind of fiber. To fabricate intrayarn hybrid composite, carbon fiber filaments and glass fiber filaments were used, and HFRP composites specimens were fabricated by 3D printing. Tensile test and flexural test were conducted. Then, fracture surfaces were observed by digital microscope to analyze flexural behaviours. As a result,

  doi:10.5075/epfl-298799_978-2-9701614-0-0

hybrid caes3 showed highest tensile hybrid effect due to the high dispersion. Moreover, the higher the hybrid dispersion, the better the disadvantages of each material were compensated, and the complementary properties of each material were realized much better.

Acknowledgements

This work was supported by Korea Institute of Energy Technology Evaluation and Planning (KETEP) grand funded by the Korea government (MOTIE)(20212020800090, Development and Demonstration of Energy-Efficiency Enhanced Technology for Temperature-Controlled Transportation and Logistics Center).

References

1. W.S. Miller, L. Zhunag, J. Bottema, A.J. Wittebrood, P.D. Smet, A. Haszler, Recent development in aluminium alloys for the automotive industry. Material Science and Engineering. 2000; 37-49
2. Erica R.H., Frank R., Randolph E. K., Strategic materials selection in the automobile body: Economic opportunities for polymer composite design. Composite Science and Technology. 2008; 68
3. Kim K.S., Bae K.M., Oh S.Y., Seo M.K., Kang C.G., Park S.J., Trend of Carbon Fiber-reinforced Composites for Lightweight Vehicles. Elastomers and Composites 2012; Vol. 47 No.1 65-74
4. Lee J.M., Lee K.H., Kim B.M., Ko D.C., Design of roof panel with required bending stiffness using CRFP laminates. International Journal of Precision Engineering and Manufacturing 2016; 17(4), 479-485
5. Das S., The cost of automotive polymer composites: A review and assessment of DOE's lightweight materials composites research 2001; 1-49
6. Filip S., Daniel J., James D., Lucas I., Gaspard M., Luke C., Improved out-of-plane strength and weight reduction using hybrid interface composites. Composites Science and Technology 2019; 107730
7. Yentl S., Liesbet C., Eline V.B., Larissa G., Peter H., Ian W., Ignaas V., Tensile behaviour of intralayer hybrid composites of carbon fibre and self-reinforced polypropylene. Composites: Part A. 2014; 78-84
8. Yongli Z., Yan L., Hao M., Tao Y., Tensile and interfacial properties of unidirectional flax/glass fiber reinforced hybrid composites. Composites Science and Technology. 2013; 172-177
9. Zhongyo L., Junyuan Z., Alexander J., Luise K., Low-velocity impact behavior of hybrid CFRP-elastomer-metal laminates in comparison with conventional fiber-metal laminates. Composite structures. 2022; 115340
10. I.D.G. Ary S., Younjig K., Leonard D.T., Kim C.S., Ho Kong S. Effect of stacking sequence on the flexural properties of hybrid composites reinforced with carbon and basalt fibers. Composites: Part B. 2014;251-258
11. Peijs A.A.J.M., J.M.M. Dekok, Hybrid composites based on polyethylene and carbon fibres part 6: tensile and fatigue carbon fibres. Journal of Materials Science Letters. 1992; 520-522
12. Seyed Hamid Reza Sanei, Diana P., 3D-Printed Carbon Fiber Reinforced Polymer Composites: A Systematic Review. Journal of Composites Science 2020; 98
13. Markforged. Composites material datasheet. 2019, p.1, https://static.markforged.com/markforged composites datasheet.pdf.
14. Hasan I., Qingtao W., Ahmend A., Wei L., GF/CF Hybrid Laminates Made Through Intra-tow Hybridization for Automobile Applications. Fibers and Polymers 2016; Vol.17 No.9, 1505-1521
15. F. Chen, S. Bazhenov, A. Hiltner, E. Baer, Flexural failure mechanisms in unidirectional glass fibre-reinforced thermoplastics. Composites 1993; 25(1): 11–20
16. Chensong D. Heshan A. Ian J., Flexural properties of hybrid composites reinforced by S-2 glass and T700S carbon fibres. Composites: Part B 2012; 573-581

  doi:10.5075/epfl-298799_978-2-9701614-0-0

EFFECT OF WEAVING PATTERNS ON THE WETTABILITY AND MECHANICAL PROPERTIES OF 3D WOVEN I-BEAM COMPOSITES

Emir, Karci[a], Muhammed Ali,Vural[a], Melisa, Dincer[a-b], Mert, Celikturk[a-c], İbrahim Halil, Sahin[a-c], Burak, Yatkin[a-c], Cagin, Emre[a-c], Basak, Ozkendirci[d], Elif Ozden, Yenigun[e], Hulya, Cebeci[a-b-c]

a: Aerospace Research Center, Istanbul Technical University, Istanbul, 34469, Turkey- karci15@itu.edu.tr
b: Aviation Institute, Istanbul Technical University, Istanbul, 34469, Turkey
c: Department of Aeronautical and Astronautical Engineering, Istanbul Technical University, Istanbul, 34469, Turkey
d: Faculty of Fine Arts and Design, Dogus University, Istanbul, 34437, Turkey
e: School of Design Textiles, Royal College of Art, SW7 2EU, London, United Kingdom

Abstract: *3D woven composites can be of great benefit in increasing delamination resistance. With fiber reinforcement through-the-thickness, 3D composites prevent delamination cracks from impact fracture, thereby reducing the occurrence of matrix separation damages of laminate structures. When a novel design as 3D weaving is implemented for special geometries composites in I, T, and C forms, optimization studies need to be performed. This study aims to investigate how the load-carrying capacity of I-beams changes when the vertical load carrying wall has different weaving patterns. A comparison was performed between regular weaving pattern has a cross-link point of load bearing wall (LB-X) and a novel design without cross-link point of load bearing wall (LB-II). I-beam composites were manufactured with 3D-weaved I-beam LB-X and LB-II fabrics by vacuum infusion process (VIP). Void content analysis was studied to examine the composite quality after VIP. The mechanical properties of LB-X and LB-II were studied with 3-point bending tests. The results presented a significant change in bending loads of LB-X and LB-II with 793 N and 1421 N presenting the increased load carrying capability when a novel weaving pattern has been implemented. Void contents were presented for LB-X and LB-II with 2.64% and 1.70%, respectively.*

Keywords: 3D weaving; structural composite; woven preform; flexural strength; composite quality.

1. Introduction

Laminated structures commonly used in the aerospace industry consist of 2D woven ply reinforcements and thermoset resins. 2D laminated structures completely provide excellent mechanical properties, light-weight properties, and easy production (1). However, the poor interlaminar and intralaminar properties in 2D lamina structures, the presence of matrix and fiber cracks under transverse load, poor damage tolerance, and low delamination resistance limit the load-bearing properties of lamina structures through the thickness. This limitation has a particularly profound effect on composite structures having I shapes, such as ribs, stringers, and spar. The exposure of these structures to radial and shear forces throughout the thickness leads to delamination and early undesired failures (2). Delamination damage is one of the most common types of damage in composite materials. The formation and growth of delamination cracks in composite laminates can lead to serious structural problems, such as reduced

  doi:10.5075/epfl-298799_978-2-9701614-0-0

structural stiffness, subjecting the structure to internal stresses, and resulting fracture of the material, which can lead to eventual failure (3). Many researchers reported that these failures can be solved by using the 3D weaving method, which increases damage tolerance and delamination resistance (4–6).

Unlike traditional in-plane 2D laminated composites, 3D woven composites improve the interlaminar properties of composites by preventing delamination since the presence of yarns is oriented along the thickness direction. Another advantage of 3D weaving is to enable the production of preforms with complex architecture, near to net shape (7). Furthermore, 3D fabrics exhibit much higher wettability capability than stacked 2D laminated structures, resulting in increased matrix infusion rates and reduced infusion time during the fabrication of structures. The higher wetting ability of 3D woven preforms provides ease of production in complex structures (8,9). Several engineering components such as I, T, C beams are widely used in aerospace structures(10). Hence, weaving studies of spacer (hollow) fabric are essential to create such preforms will avoid the possibility of forming composites without any joining. Behera et.al. have studied the weaving of 3D spacer fabrics and their composites on various shapes including I beams (4–6,11). These investigations indicated how the mechanical property and failure behavior of 3D woven composites are influenced by the different geometries and vertical wall patterns. In their weaving patterns, at the vertical walls of I beams cross-linking point forming the X profile is present similar to several studies from literature (11). The aim of this study is to examine the effect of a novel weave design on the load-bearing capacity of a 3D woven I-beam with and without this cross-linking point. Vertical load bearing walls with cross-linking point (LB-X) and without cross-linking point (LB-II), are presented in Figure 1.

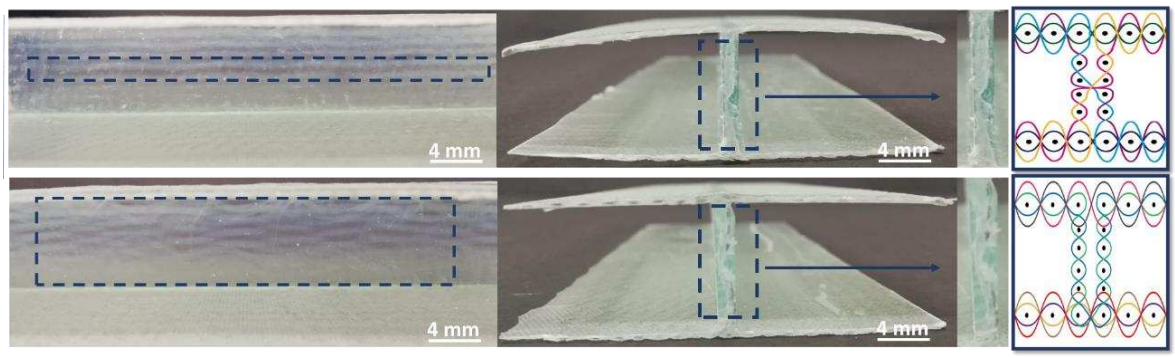

Figure 1. 3D I-beam composites a) LB-X design with crosslink point b) LB-II design without crosslink point.

3D I beam composites were manufactured by vacuum infusion process (VIP). The quality assurance of all composites is performed by void content analysis through image processing. The mechanical properties were examined with 3-point bending tests to study the behavior of vertical wall when LB-X and LB-II designs are present.

2. Experimental

2.1. Weaving of I-beam preforms

3D woven rectangular spacer fabric is produced by weaving with a custom-built 2D weaving machine. The 3D woven rectangular spacer fabrics have a flange width of 7 cm, a vertical wall height of 2 cm, and a width in the weft direction is 20 cm. To obtain I-shaped fabric structures,

  doi:10.5075/epfl-298799_978-2-9701614-0-0

fabrics are cut from half of the flange to obtain LB-X and LB-II I-beam fabrics with a width of 7 cm, a wall height of 2 cm, and width of weft direction of 14 cm.

The production of LB-X and LB-II I-beam fabrics varies according to the weaving plan by changing the fiber orientation on vertical walls. The weaving process of LB-X I-beams is provided by using 2 beams as mentioned in the literature and by pulling one of the beams to form the vertical walls (6,11,12). In LB-II I-beam weaving, four warp beams are employed differently from the weaving process and LB-II beams are obtained through pulling three different beams of floating fabrics sequentially. In LB-X and LB-II I-beam preforms, the fabrics forming the upper and lower surfaces have a warp density of 20/inches and a weft density of 4/inch, and the vertical walls consist of layers with a weft and warp density of 4/inch.

2.2. Fabricating of I-beam composites

The 3D LB-X and LB-II I-beam composites were fabricated via a vacuum infusion process (VIP). A two-component thermoset epoxy resin (HEXION MGS L160/H160) was mixed at a mixing ratio of 4:1 and cured for 24 hours at room temperature. To manufacture 3D I beam composites, a molding was performed from wooden blocks wrapped with non-porous PTFE-coated fiberglass fabrics. The molds were inserted to the hollow preforms and then the resin was infused followed by a vacuum process to avoid the formation of excess of void content. The vacuum infusion process was applied on the glass plate and infusion mesh was placed for the I-shaped fabric to ease impregnation of the resin and peel plies were placed on the top and bottom of the preform for easy demolding.

In addition, to obtain a homogeneous vertical wall thickness, aluminum plate pieces of 2 mm thickness and 1 cm^2 area were placed between the molds in the production of LB-X and LB-II I-beam composites. After the production of LB-X and LB-II I-beam composites, the fiber volume fraction was appointed by weighing composites before and after infusion, and calculated as %34 and %40, respectively.

2.3. Characterization

The LB-X and LB-II I-beam composites were tested with 3-point bending to investigate their flexural performance by SHIMADZU AGS-X 50 kN Universal Testing Machine with three rollers of supports diameter of 60 mm. Also, the testing speed of the crosshead was 1 mm/min. The span length of 80 mm was kept constant for all I-beam composites, while the dimensions of the specimen were at 20x60x140 mm for each structure. The force to stroke values obtained resulting from the test were converted into flexural stress to flexural strain values solving equations (1) and (2).

$$\sigma_f = 3PL/2bd^2 \quad (1)$$

$$\varepsilon_f = 6Dd/L^2 \quad (2)$$

Another parameter that has a crucial effect on the difference in mechanical properties of LB-X and LB-II I-beam composites and the quality of I-beam composites was void content. Since, it is critical to produce reliable and high-quality 3D I beam composites, the void content of the 3D structures was studied by an image processing through ImageJ software. The results were correlated with the mechanical properties to also discuss the quality of composite manufacturing process with the custom-built molding tools as presented in here. The pictures

  doi:10.5075/epfl-298799_978-2-9701614-0-0

of the vertical walls of both LB-X and LB-II were taken by optical microscopy and processed through ImageJ software. The amount of voids were calculated as follows:

$$V_v = \frac{The\ area\ of\ void\ in\ the\ optic\ microscope\ image}{The\ total\ area\ of\ the\ optic\ microscope\ image} \times 100$$

3. Results and Discussion

3.1. Void Content analysis

Void content of composite structures is very critical to achieve the required mechanical characteristics. The increase in void content causes the composite to fail at lower strength than it supposed to be. Hence, such in 3D I beam composites the wetting of resin and curing stages should be well controlled to have lower void contents. With such a complex geometry than a 2D laminated structure, higher void content will cause stress concentrations around the void which will facilitate the formation of matrix-fiber cracks. Optical microscope images of I-beam composites with 600 TEX LB-X and LB-II vertical walls were fabricated at ambient conditions and with similar parameters in Figure 4. The results presented an average of 2.20% void for LB-X I beam composites, and 1.65% void for LB-II I beam composites. All imaging was performed at the vertical walls of the 3D I beam composites. The results were further studied for the mechanical property investigation with 3-point bending tests.

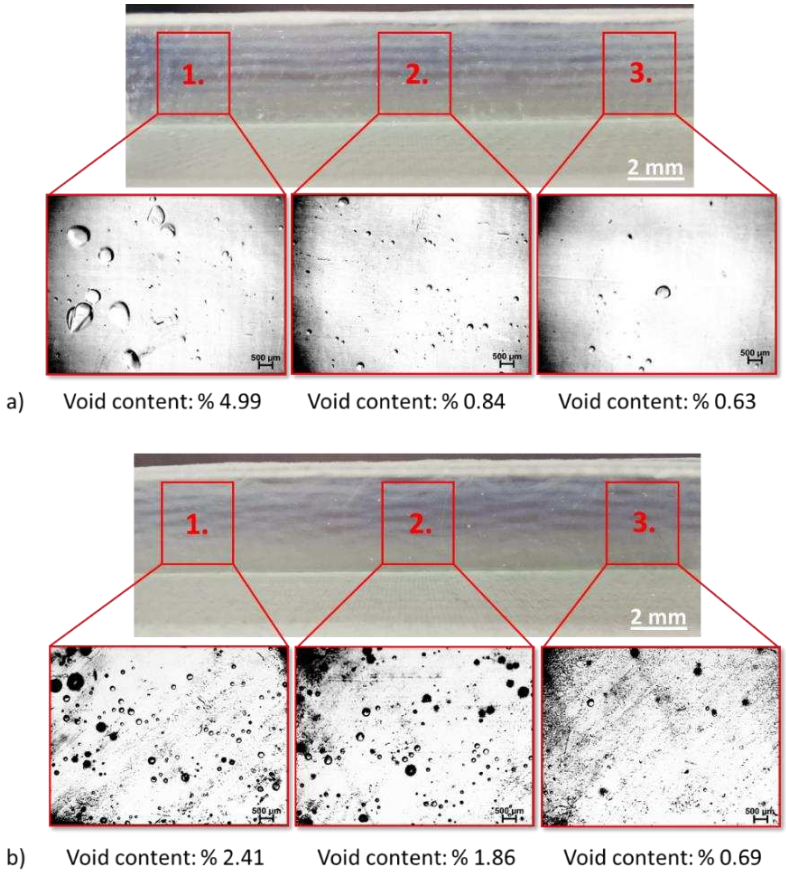

Figure 4. The optical microscope image of a) LB-X and b) LB-II 3D I-beam composites with void content analysis

3.2. Three-point-bending test results

The load-bearing capabilities and flexural stress values varying according to the vertical wall weaving pattern were studied. The flexural stress and load-bearing forces are given in Figure 2. Higher flexural stress has been observed with the advantage of the LB-II geometry arising from the design of the vertical wall. All 3D I beams composites were manufactured from 600 TEX yarns hence a minimal fiber weight fraction changes have been observed during the composite manufacturing. The LB-X weave pattern with a cross-linking point is susceptible of creating stress accumulation at the intersection point. Hence, the changes in the vertical wall design resulted an approximately 20% more efficient and durable mechanical property when LB-II was considered.

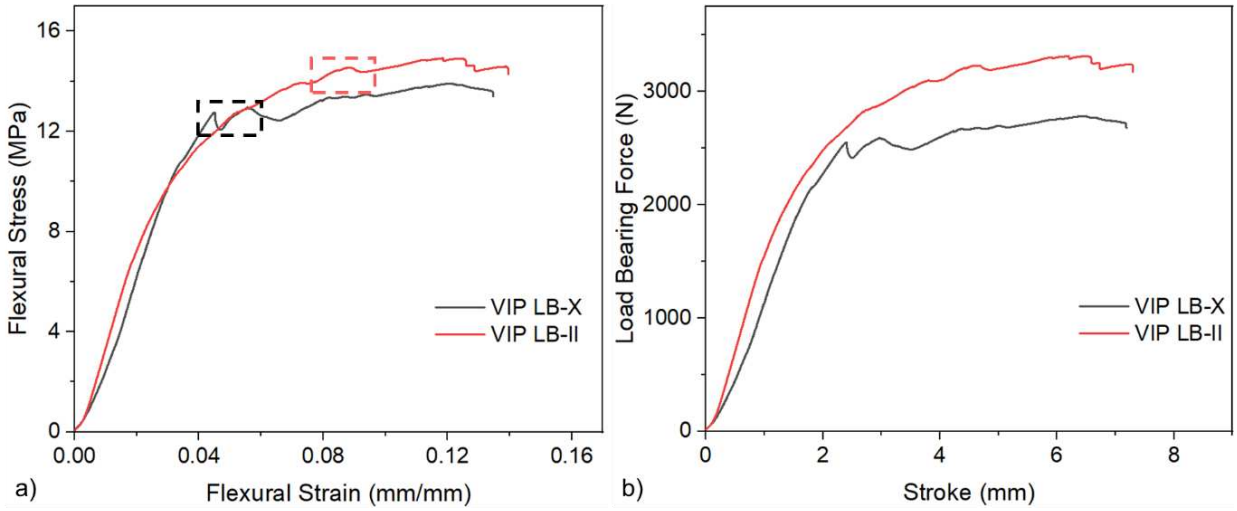

Figure 2. The 3-point bending test results of 600 TEX LB-II and LB-X I-beam composites produced by vacuum infusion process a) Flexural stress-flexural strain graph b) Load Bearing Force-Stroke graph

The flexural stress to strain results presented in the figure 2., the stress value at which the first fracture occurs in the LB-X design is 12.71 MPa whereas this was 14.91 MPa in the LB-II I-beam composites. The maximum stress and load bearing force values obtained resulting from the 3-point bending tests performed on LB-X and LB-II I-beam composites are given in Table 1.

Table 1: Maximum load bearing force and flexural stress

Production Method	Weaving Pattern	Load Bearing Force [N]	Flexural Stress [MPa]
VIP	LB-X	2773	12.71
VIP	LB-II	3310	14.91

Failure mode situations that occur according to the difference in weaving patterns are clearly shown in the Figure 3. The local failure of LB-X and LB-II I beam composites the vertical wall was apparently given in Figure 6a and 6b. Under the loading condition, it has been observed that fractures occur at lower forces due to the fact that the I-beam composite with LB-X weaving pattern has a stress accumulation region with the increase in stress and strain values. Fractures

  doi:10.5075/epfl-298799_978-2-9701614-0-0

reaching the cross-point region continue to increase and thusly cause buckling and distortion of the structure.

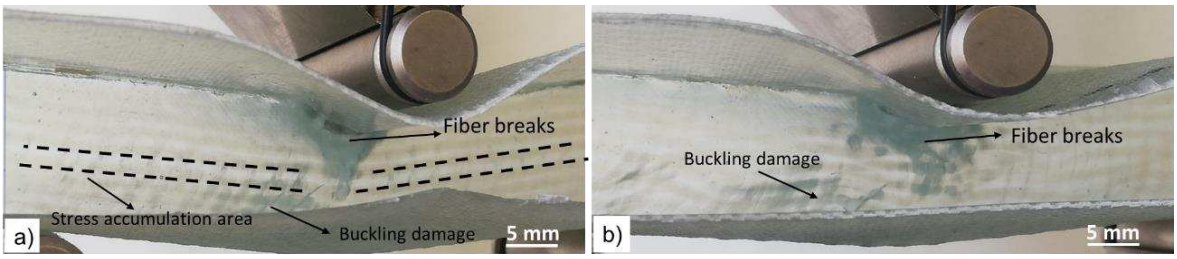

Figure 3. Failure modes of LB-X and LB-II I-beam composites under flexural loading conditions

4. Conclusion

3D I-beam composites with a novel weaving pattern of LB-II presented a higher load carrying capability compared to more widely studied weaving designs of the vertical wall as LB-X in an I beam structure. To examine the mechanical properties and resin permeability of LB-II 3D I-beam composites, void content and 3-point bending test analysis were applied to the composites. It was also presented that LB-II woven patterned composites provide lower void content. The results clearly demonstrated that such a novel weaving design of LB-II 3D I-beam composites were more durable than LB-X I-beam composites. Since the flexural stress of the LB-X I beam composites was increased after eliminated of crosslink point on the vertical wall, the failure mode of I-beam composites under bending load changed and the mechanical performance increased by 20%.

Acknowledgments

This study was funded by the Scientific and Technological Research Council of Turkey (TUBITAK: project number 218M703 (218M704)) 1003 Primary Subjects R&D Funding Program. The authors would also like to thank to the conference funding for Mr. Emir Karcı provided by the TUBITAK 2224-A Support Program for Participation in Abroad Scientific Events.

We would like to thank Şişecam Elyaf, Turkey's glass fiber producer, for the material support of glass fibers provided for this study.

5. References

1. Turgut F, Neje G, Behera B, Ozden-yenigun E, Cebeci H. Growth of High-yield Aligned CNTs onto 3D Woven Preforms for Multifunctional Structural Composites. 2018;(March):28–9.

2. Hu Q, Zhang Y, Mao Y, Memon H, Qiu Y, Wei Y, et al. A Comparative Study on Interlaminar Properties of L-shaped Two-Dimensional (2D) and Three-Dimensional (3D) Woven Composites. Appl Compos Mater. 2019;26(3):723–44.

3. Wisnom MR. The role of delamination in failure of fibre-reinforced composites. Philos Trans R Soc A Math Phys Eng Sci. 2012;370(1965):1850–70.

4. Neje G, Behera BK. Comparative analysis of mechanical behavior of 3D woven spacer sandwich composites with single and double level structures. Polym Compos. 2020;41(11):4885–98.

  doi:10.5075/epfl-298799_978-2-9701614-0-0

5. Neje G, Behera BK. Influence of cell geometrical parameters on the mechanical properties of 3D integrally woven spacer sandwich composites. Compos Part B Eng [Internet]. 2020;182(August):107659. Available from: https://doi.org/10.1016/j.compositesb.2019.107659

6. Neje G. Lateral Compressive Properties of Spacer Fabric Composites with Different Cell Shapes Content courtesy of Springer Nature , terms of use apply . Rights reserved . Content courtesy of Springer Nature , terms of use apply . Rights reserved . 2018;725–34.

7. Gandhi K. Woven Textiles : Principles, Technologies and Applications. Woodhead Publishing. 2019.

8. Gerlach R, Siviour CR, Wiegand J, Petrinic N. In-plane and through-thickness properties, failure modes, damage and delamination in 3D woven carbon fibre composites subjected to impact loading. Compos Sci Technol. 2012;72(3):397–411.

9. Bogdanovich AE. Multi-scale modeling, stress and failure analyses of 3-D woven composites. Vol. 41, Journal of Materials Science. 2006. 6547–6590 p.

10. Tong L, Mouritz AP, Bannister MK. 3D Fibre Reinforced Polymer Composites. 2002.

11. Manjunath RN, Khatkar V, Behera BK. Influence of augmented tuning of core architecture in 3D woven sandwich structures on flexural and compression properties of their composites. Adv Compos Mater [Internet]. 2020;29(4):317–33. Available from: https://doi.org/10.1080/09243046.2019.1680925

12. Turgut F, Koycu A, Cebeci H, Neje G, Behera BK, Ozden-Yenigun E. Hierarchical cnts grown multifunctional 3d woven composite beams for aerospace applications. Vol. 1 PartF, AIAA Scitech 2020 Forum. 2020.

DAMAGE CHARACTERIZATION IN MULTIDIRECTIONAL GLASS FIBRE REINFORCED POLYPROPYLENE LAMINATES UNDER QUASI-STATIC LOADING: EXPERIMENT & SIMULATION

J. Sommer[a,b], M. Hajikazemi[a,b], I. De Baere[a], W. Van Paepegem[a]*

a: Department of Materials, Textiles and Chemical Engineering, Faculty of Engineering and Architecture, Ghent University, Technologiepark Zwijnaarde 46, Ghent, Belgium
b: Dutch Polymer Institute (DPI), P.O. Box 902, 5600 AX, Eindhoven, Netherlands
*Corresponding author: josef.sommer@ugent.be

Abstract: *The quantification of matrix cracking during in-plane tensile experiments is challenging, particularly when opaque composites with complex lay-ups are concerned. In this study, experimental damage characterizations are performed for multidirectional laminates made of Glass/Polypropylene tapes under uniaxial tension loadings. Stereo Digital Image Correlation is implemented to measure strain fields and crack evolutions on the front and the edge surfaces of flat coupons. A damage detection methodology is developed to detect matrix cracking in the off-axis plies based on displacement discontinuities. Four multidirectional laminates with $[0_2/90]_{2s}$, $[90_2/0_2]_s$, $[0/45/0/-45]_s$, and $[0/45/90/-45]_s$ lay-ups are characterized to investigate the effects on crack initiation and growth. To validate the experimental measurements, post-mortem in-situ microscopy and a recent physics-based modelling technique are considered that can predict ply cracking, delamination and fibre breakage evolution and estimate the effects of damage modes on laminate properties. Good agreements are observed between the experimental and modelling results.*

Keywords: Thermoplastic composite; multidirectional laminates; damage characterization; in-situ instrumentation; physics-based modelling

1. Introduction

The observation of damage modes in multidirectional composite laminates without stopping the test is a cumbersome task. Visual inspection methods, such as photographs or advanced illumination techniques can provide useful insights into crack characteristics for transparent composites (e.g. glass/epoxy). Unfortunately, a broad range of composites is rather opaque, as is the case for Glass/Polypropylene (glass/PP). Recently, Digital Image Correlation, an optical-based instrumentation technique, has been used to assess matrix cracks in multidirectional carbon/epoxy laminates under bending loads [1] and in glass/epoxy laminates under in-plane loadings [2] with good agreement to post-mortem microscopy.

In the current research, we aim to perform a comprehensive damage characterization under uniaxial quasi-static tensile loading for multidirectional glass/PP laminates as this composite is an interesting alternative in large batch applications. To do so, a consistent manufacturing process based on hot-press moulding is implemented to produce glass/PP plates with reliable material properties, e.g. same fibre volume fraction for different stacking sequences. Four lay-ups, $[0_2/90_2]_s$, $[90_2/0_2]_s$, $[0/45/0/-45]_s$ and $[0/45/90/-45]_s$ are investigated to study the effects of laminate stacking sequence and ply thickness on the mechanical performance, crack initiation

  doi:10.5075/epfl-298799_978-2-9701614-0-0

and progression. The effective mechanical performance and damage quantification are measured by two Stereo Digital Image Correlation (3D-DIC) systems. One 3D-DIC system is devoted to measuring full-field strains with validation by an extensometer in the axial direction. The other 3D-DIC system is designed for in-situ damage measurements on the specimen's edge surface with validation by post-mortem microscopy. For each laminate, the axial and transverse strains together with crack density in different off-axis plies are determined. The experimental results are further validated using a recently developed physics-based modelling technique [3, 4] based on the variational approach [5] and energy-based [6] failure criteria. To provide the required elastic properties for modelling inputs, basic laminates, $[0]_8$, $[90]_8$ and $[\pm45]_{2s}$ are manufactured and tested.

2. Material and experimental methods

2.1 The manufacturing process and sample preparation

Unidirectional glass fibre reinforced polypropylene (glass/PP) tapes, namely UDMAX™ GPP 45-70 (SABIC FRT Tapes) are used for the production of uni- and multidirectional laminates by hot-pressing. The initial tape fibre volume fraction is 45 % with a nominal ply thickness of 0.25 mm. A maleic-anhydride modified isotactic polypropylene is used in the glass/PP tapes to improve the fibre-polymer adhesion and mechanical performance. All laminates are produced in a closed mould with (i) a heating phase to 210 °C with 4.5 K/min under 0.5 bar pressure, (ii) a holding phase of 10 minutes to ensure homogeneous temperature distribution, and (iii) a cooling phase to 50 °C with -8.5 K/min while applying 37 bar pressure for unidirectional and 45 bar for multidirectional laminates, respectively during consolidation. The pressure profiles are adjusted to achieve comparable plate properties and fibre volume fraction (see Table 1) without having voids in multidirectional laminates (see Figure 1) caused by the shrinkage behaviour of PP.

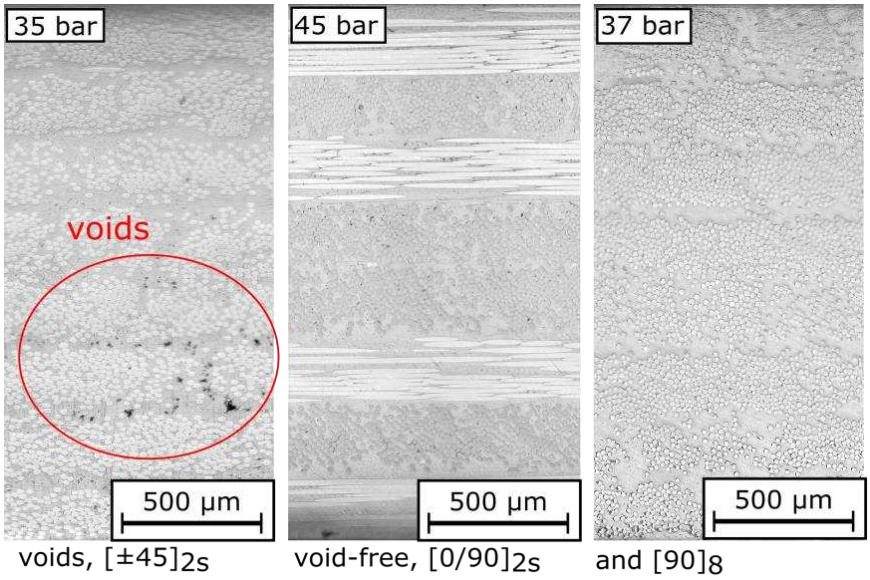

Figure 1. Microstructures for some lay-ups by applying different maximum pressure profiles.

Rectangular samples, 200 mm x 20 mm, were cut from the produced plates by a water-cooled diamond disc and 50 mm long tabs were prepared of $[\pm45]_{2s}$ glass/PP laminates. Poor adhesion was obtained when using adhesives to bond the tab material onto the PP surfaces. Therefore, tabs are welded onto the glass/PP specimen by ultrasonic vibration welding.

  doi:10.5075/epfl-298799_978-2-9701614-0-0

Table 1: Plate properties for used maximum pressure and stacking sequences (five repetitions), selected consolidation pressure and properties are in bold

Stacking sequence	multidirectional		Unidirectional		
Applied pressure [bar]	35	**45**	40	35	**37**
density [g/cm^3]	1.69	**1.71**	1.74	1.69	**1.71**
(acc. ASTM B962)	± 0.02	± 0.03	± 0.01	± 0.01	± 0.01
fibre vol. [vol%]	-	**49.56**	51.01	49.01	**49.68**
(acc. ASTM D3171)		±0.48	± 0.56	±0.19	±0.24
microscopy	voids	void-free			

2.1 Testing methodology and details of crack detection by using 3D-DIC

All tensile tests are performed on a servo-hydraulic INSTRON 8801 with a load cell of ±100 kN using a testing speed of 2mm/min. All multidirectional laminates for the study of damage behaviour are tested up to 2.4 % axial strain, controlled by an extensometer. The final failure was avoided to allow matrix crack inspection after the experiment for validation purposes. In all experiments, strains are measured on the front surface by 3D-DIC that were later post-processed to obtain the axial stiffness reduction by using the secant modulus and Poisson's ratio evolution. The damage detection is performed on the polished edge surface by the second 3D-DIC system. An automated damage algorithm is developed to quantify matrix cracking based on the measured axial displacement field. Therefore, the post-processed axial displacement field by ViC-3D software is exported to the Matlab software for the crack detection approach. The criterion to define a crack in the off-axis ply is based on displacement discontinuities caused by the separation of crack surfaces [2]. Several crack detection paths are considered and equally spaced over the off-axis ply thickness to include also crack growth over the thickness. Post-mortem microscopic observations were performed after every single experiment by a Keyence microscope to identify cracks and to validate the crack detection algorithm to provide finally the crack progression during the performed tensile experiment.

3. Results and Discussions

3.1 Cross-ply $[0_2/90_2]_s$ laminate with embedded off-axis ply

The measured mechanical performance and average crack density evolution together with modelling results of $[0_2/90_2]_s$ glass/PP laminates are illustrated in Figure 2. In figure 2a) are the measured axial and transverse strains illustrated, in b) the evolution of Poisson's ratio and in c) the axial stiffness reduction versus the applied load for three samples, respectively. These results are measured by 3D-DIC on the front surface of every sample and validated by an attached extensometer. Excellent agreement is observed between both axial strain measurements. Very small scatter between the tensile performance of three samples can be seen, although in-plane fibre waviness cannot be denied for glass/PP. The detected cracks in the embedded 90 ply were obtained by performing 3D-DIC on the edge surface. An average crack density (Figure 2d) is used to consider the observed crack pattern (Figure 2e) by reporting the average of the crack numbers detected in every single path over the maximum crack distance. The majority of cracks are not fully propagated through the ply thickness caused by crack arresting phenomena due to localized matrix yielding in polymer-rich areas.

  doi:10.5075/epfl-298799_978-2-9701614-0-0

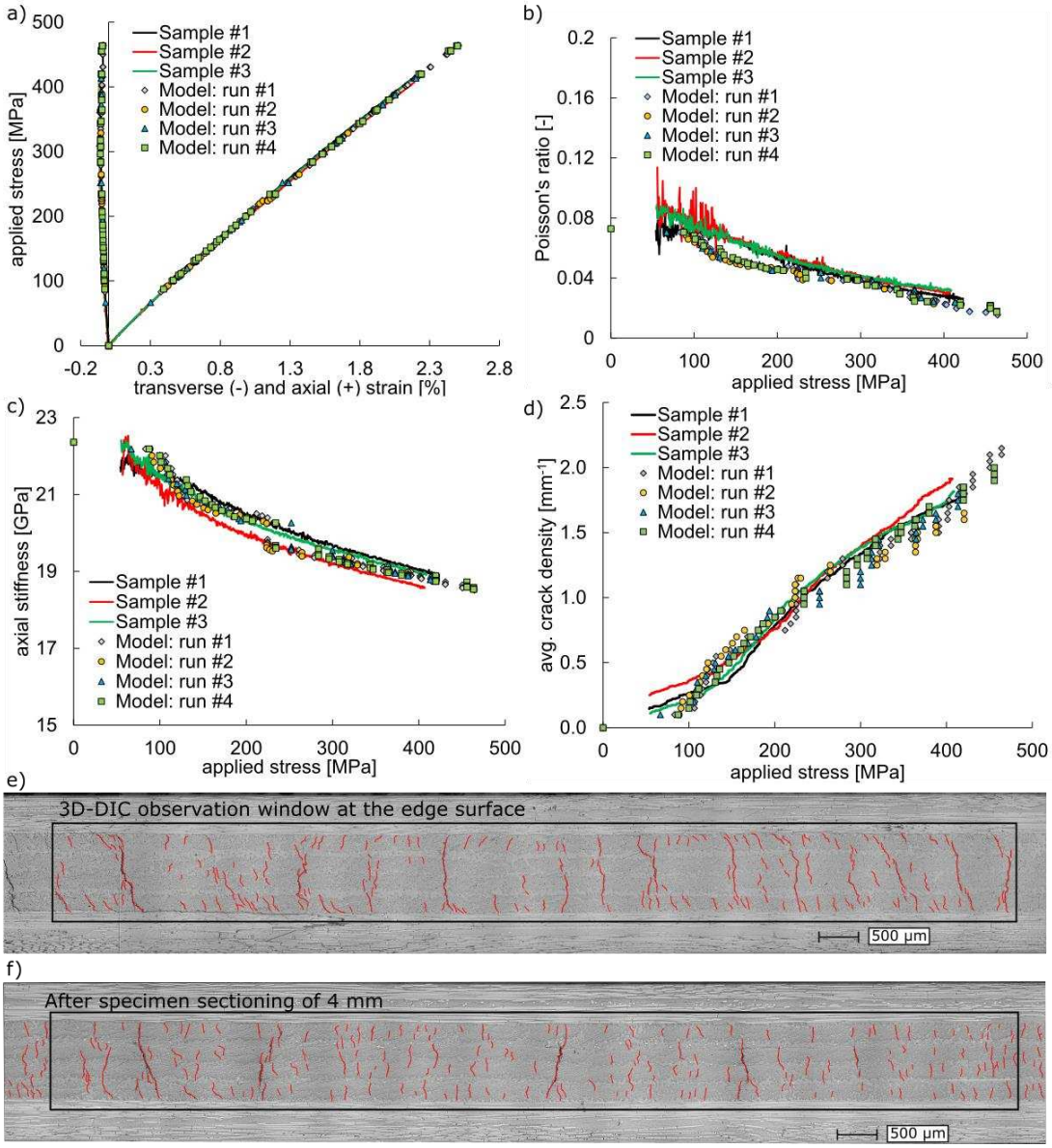

Figure 2. Quasi-static tensile behaviour of glass/PP $[0_2/90_2]_s$ laminate, measurements and modelling results. a) stress-strain performance, b) Poisson's ratio evolution, c) axial stiffness reduction, d) crack density evolution, microstructure after e) testing and f) sectioning

The first observation is that the model can be calibrated to predict a similar crack density growth as measured in the experiments for an average ply cracking fracture energy of 120 J/m^2 without consideration of residual stresses. This value is taken as a statistical value using a normal distribution with a standard deviation of 25% when performing four simulations using the variational approach [5]. Secondly, the model can accurately predict the axial and transverse strain evolutions while delivering very good predictions for the Poisson's ratio and axial stiffness reduction using the measured elastic material properties of E_{11} = 38.97 GPa, E_{22} = 5.39 GPa, G_{12} = 2.04 GPa and ν_{12} = 0.3 from testing basic laminates. Thus, when testing $[0]_8$ laminates, minor stiffness reduction of approx. 5% starting from 1 to 2 % axial strain was measured and included in the model. The latter observation confirms consistency between the observed damage modes, the reported average crack densities and a small amount of fibre breakage, and the measured laminate properties verifying the accuracy of both experiment and modelling. Finally,

it is noteworthy that the observation of ply cracks is performed on the laminate edge surface and one might ask whether the same damage pattern exists inside the laminate. Sample sectioning by grinding and polishing over a depth of 4 mm from the edges was therefore performed (Figure 2f). The same number of cracks is observed as it was measured by 3D-DIC and manually counted in post-mortem microscopy before. However, due to the fibre waviness and matrix yielding effects, cracks are not exactly at the same location as before on the edge surface.

3.2 Cross-ply $[90_2/0_2]_s$ laminate with external off-axis ply

To observe crack propagation through the sample width, the $[90_2/0_2]_s$ cross-ply laminate is investigated with external 90 off-axis plies. The study of the results showed that an individual crack initiated at the edge and does not completely propagate through the sample width. However, there is almost always the same crack density measured at each considered detection path placed along the axial direction. This effect is mainly due to the presence of fibre waviness and polymer-rich areas inside the individual off-axis ply causing crack arresting by local matrix yielding, while there is another crack at a site very close by (Figure 3).

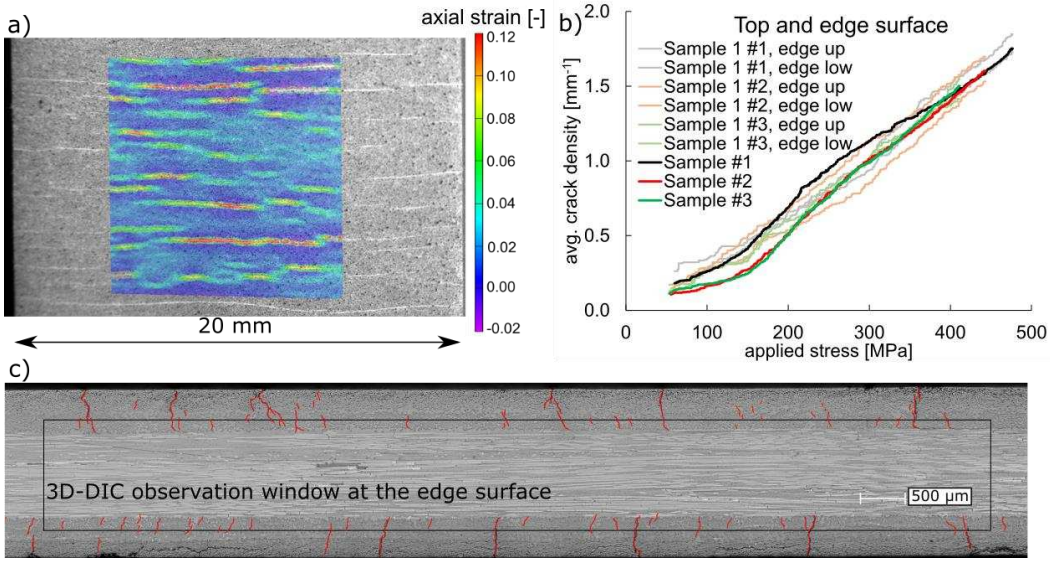

Figure 3. Crack detection on an externally attached 90 ply in a $[90_2/0_2]_s$ glass/PP laminate, a) axial strain map at 2.2 % global axial strain, b) comparison of average crack densities measured on the front and edge surface, c) damaged microstructure.

The mechanical performance and the detected average crack densities are in very good agreement between experiments and modelling using the same modelling inputs. The measured crack evolution on the top and the edge surface for the upper and lower 90 plies are very similar (Figure 3b). Although the 3D-DIC observation window (Fig. 3c) on the edge surface could only partially capture both 90 plies, no differences were observed by counting cracks manually.

3.3 $[0/45/0/-45]_s$ laminate with embedded 45 and -45 off-axis plies

The orientation of the off-axis plies can induce internal shear stresses which might affect the crack propagation. Figure 4 shows the mechanical performance (a-c), the measured average crack density evolution for the thick -45 ply (d) and the damaged microstructure after the test (e) and after sectioning (f). Cracks are present in both off-axis plies, but the thin 45 plies could not be fully captured by 3D-DIC and have been excluded from the measurements. The modelling

has been performed using the same input material parameters as before. In summary, there is good agreement between the modelling and experimental results for both the effective mechanical properties and the microscopic matrix crack evolution. This states that although in the modelling, ply cracks are assumed to be fully propagated through the ply thickness, it has small effects on the effective laminate properties. Furthermore, the measured average crack density is a suitable parameter to characterize the damage extent.

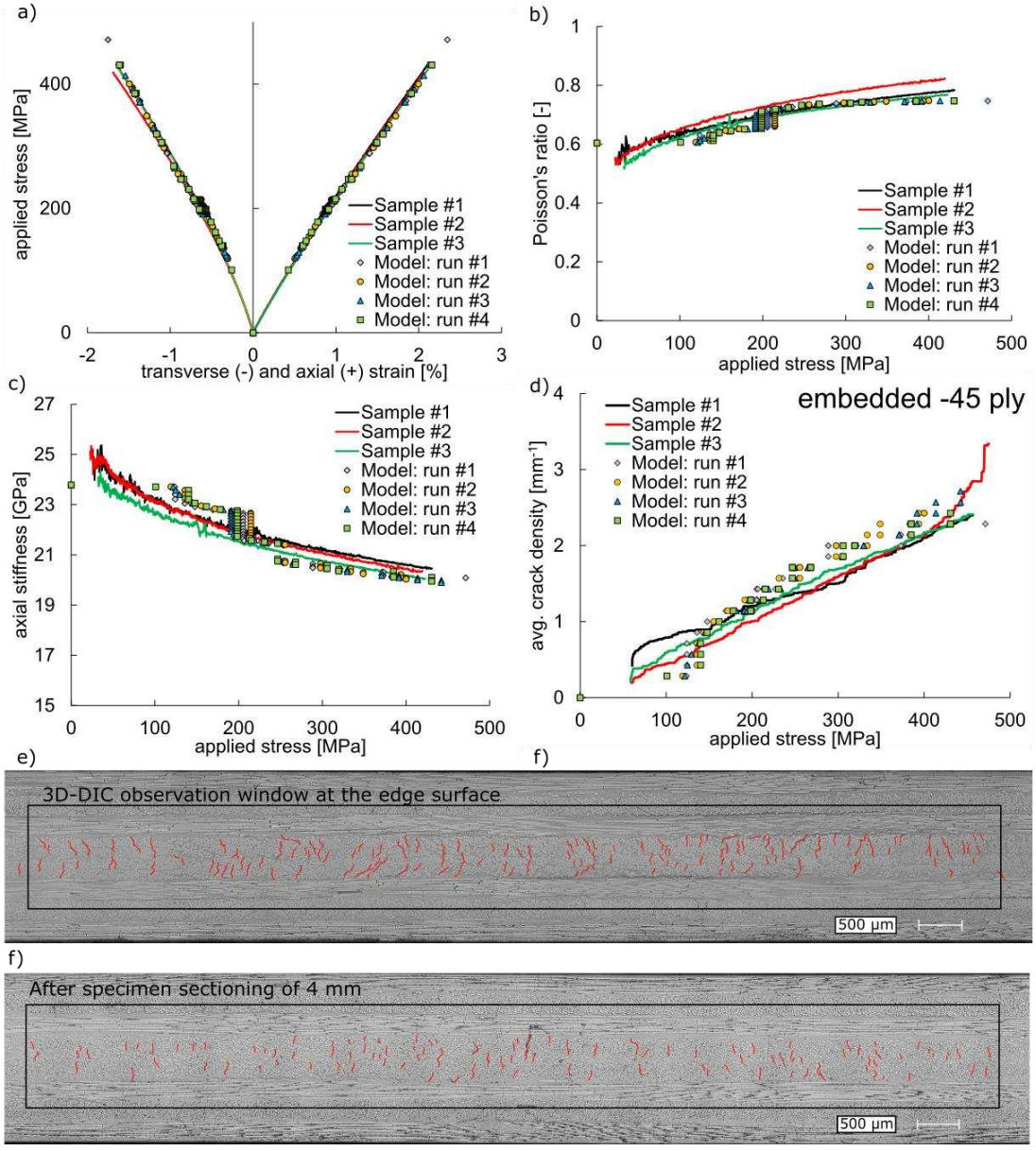

Figure 4. Quasi-static tensile behaviour of glass/PP $[0/45/0/-45]_s$ laminate, measurements and modelling results. a) stress-strain performance, b) Poisson's ratio evolution, c) axial stiffness reduction, d) crack density of -45 ply, microstructure after f) testing and g) sectioning.

3.4 Quasi-isotropic [0/45/90/-45]s laminate

It is useful now to characterize the mechanical behaviour of a more complex quasi-isotropic [0/45/90/-45]s laminate. Figure 5 shows the mechanical performance (a-c), the measured average crack density evolutions for -45 ply (d) and both 90 plies (e), the damaged microstructure after the test (g) and after sectioning (h).

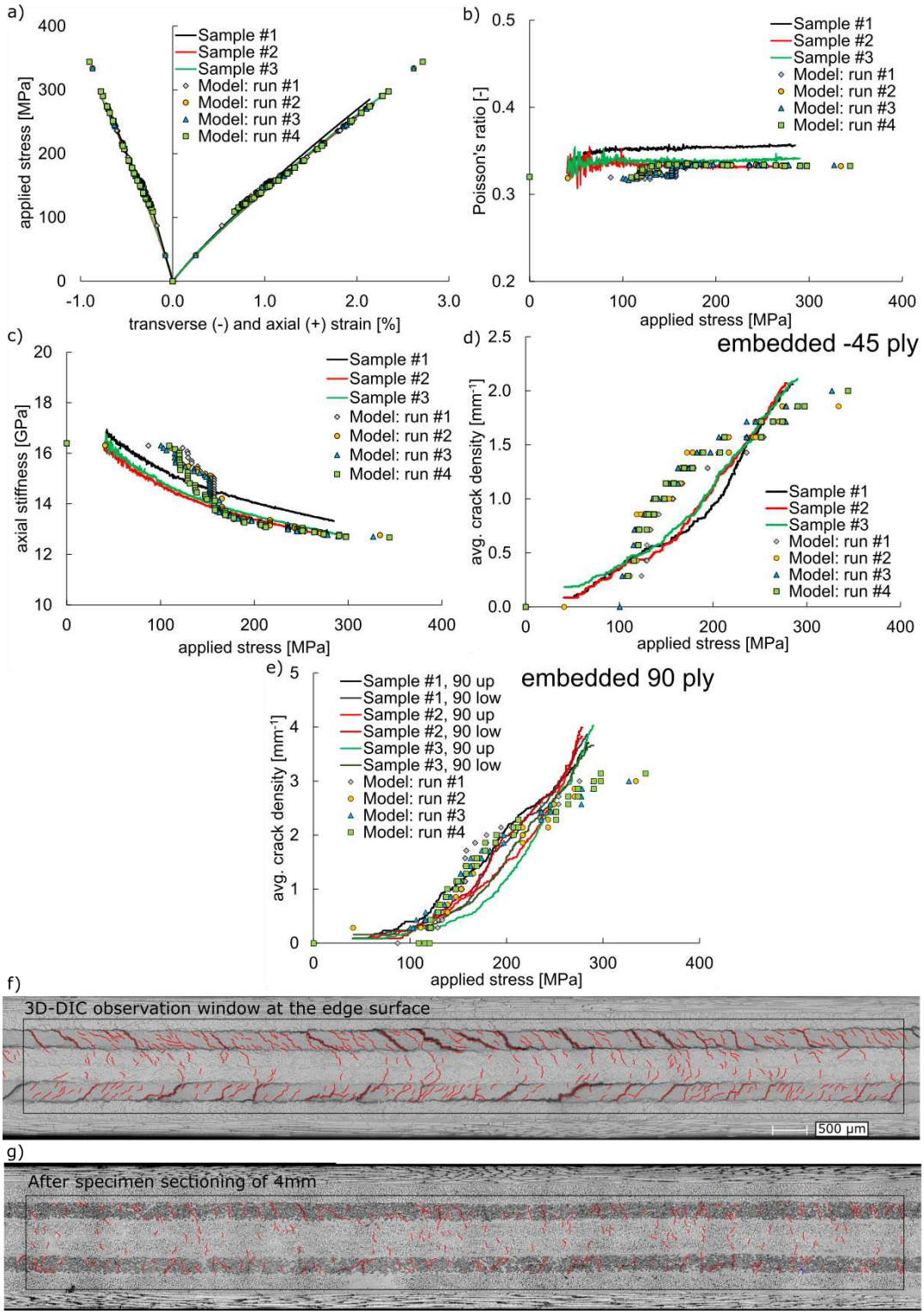

Figure 5. Quasi-static tensile behaviour of glass/PP [0/45/90/-45]s laminate, measurements and modelling results. a) stress-strain performance, b) Poisson's ratio evolution, c) axial stiffness reduction, crack density of d) -45 ply, e) both 90 plies, microstructure after f) test and g) sectioning

There is a rather good agreement between modelling and experimental results for the effective laminate properties but the crack densities are slightly over predicted. This can be explained by the assumption of fully propagated ply cracks through the thickness, while in reality more load

is needed to propagate those cracks through the thickness. Another issue is that cracks in -45 ply are propagating under a mixed-mode condition and different oriented neighbouring plies as was the case previously. However, the same average fracture energy of 120 J/m^2 is assumed. The microscopic observations show that the entire interfaces of the 90 plies are delaminated and even some transverse cracks merged with delaminations (Fig. 5e) and caused large crack openings. Considering this aspect in the model requires measurements of the initiation and propagation of delaminations and the displacement opening of single cracks. The assumed average fracture energy of 120 J/m^2 can reasonably well predict the initiation and propagation of ply cracks in glass/PP off-axis plies and more importantly their effects on effective laminate properties for different lay-ups. Therefore, a physics-based damage modelling approach based on energy failure criteria can potentially predict the mechanical performance in the presence of different interactive damage mechanisms.

4. Conclusion

A novel instrumentation technique consisting of optical measurements by 3D-DIC is developed to measure quantitatively average crack densities in embedded and external off-axis plies including validations by microscopy for opaque multidirectional glass/PP laminate. The measured average number of cracks on the edge surface is validated by post mortem microscopy and sample sectioning confirmed the same number of cracks inside. The observed damage modes in multidirectional glass/PP laminates are in agreement with commonly reported damage modes, although localized matrix yielding and fabrication-induced fibre waviness influence the damage progression. Overall, a very good agreement between the experiments and modelling was obtained for all investigated multidirectional laminates by using the same modelling input parameters.

Acknowledgments

This work forms part of the research programme of the Dutch Polymer Institute (DPI), project 812T17. M. Hajikazemi acknowledges the financial support of Fonds voor Wetenschappelijk Onderzoek FWO–Vlaanderen (Grant No. 1202522N).

5. References

1. Mehdikhani, M., et al., *Multi-scale digital image correlation for detection and quantification of matrix cracks in carbon fiber composite laminates in the absence and presence of voids controlled by the cure cycle.* Composites Part B: Engineering, (2018).138-147.
2. Miskdjian, I., M. Hajikazemi, and W. Van Paepegem, *Automatic edge detection of ply cracks in glass fiber composite laminates under quasi-static and fatigue loading using multi-scale Digital Image Correlation.* Composites Science and Technology, (2020).108401.
3. Hajikazemi, M., *Physics-based methodology for predicting ply cracking and laminate failure in symmetric composite laminates under multiaxial loading condition*, in, *Multi-Scale Continuum Mechanics Modelling of Fibre-Reinforced Polymer Composites*, Woodhead Publishing, 2021. p. 509-553.
4. Hajikazemi, M., L. McCartney, and W. Van Paepegem, *Matrix cracking initiation, propagation and laminate failure in multiple plies of general symmetric composite laminates.* Composites Part A: Applied Science and Manufacturing, (2020).105963.
5. Hajikazemi, M., et al., *Variational analysis of cracking in general composite laminates subject to triaxial and bending loads.* Composite Structures, (2020).111993.
6. McCartney, L., *Energy methods for modelling damage in laminates.* Journal of Composite Materials, (2013).2613-2640.

  doi:10.5075/epfl-298799_978-2-9701614-0-0

INVESTIGATING THE EFFECT OF SILANE COUPLING AGENT ON GLASS FIBRE/THERMOPLASTIC INTERFACIAL ADHESION

Roya Akrami[a], Liu Yang[a], James L. Thomason[a]

a: Department of Mechanical and Aerospace Engineering, University of Strathclyde, Glasgow, UK.

Abstract: *Fibre coating (sizing) is a key component for controlling interface integrity and functionality, as well as governing long-term performance characteristics of glass fibre composites. Silane coupling agent is the crucial component in glass fibre sizing contributing to interfacial adhesion, and its role needs to be fully understood in order to develop efficient sizing formulations. This study investigates the effect of a number of different silanes, typically used in glass fibre sizings, on the interfacial shear strength (IFSS) when combined with different thermoplastic polymers. IFSS was measured using the microbond test for both bare and silane sized glass fibres. The results showed that IFSS increased by sizing the fibres with silane. This improvement was observed for Polypropylene (PP) in all the applied silanes, whereas* maleic anhydride grafted polypropylene *(MaPP),* polyamide 6 (*PA6) and* polybutylene terephthalate (*PBT) did not show significant improvement in some of the applied silanes.*

Keywords: Microbond, Interface, Silane, Glass Fibre, Thermoplastics

1. Introduction

Glass fibre reinforced polymers are the most widely used polymeric composites due to the specific mechanical characteristics and low cost of glass fibre. In recent years, the development and applications of fibre-reinforced thermoplastic polymer composites have increased in different industries such as automotive and aerospace. Glass fibre thermoplastic composites are emerging technology that is being researched significantly these days as they usually exhibit a higher range of toughness and recyclability and have less complex processing requirements in comparison with thermosets [1].

Fibre, matrix, and the fibre–matrix interface properties are important parameters affecting the thermoplastic composites properties. To have desirable composite properties, the fibre-matrix interface should have the ability to effectively transfer stresses across the interface. During manufacturing of glass fibre, a thin surface coating (called Sizing) of mainly polymeric materials is applied on the surface of fibre. Sizing is a key component for controlling the interface integrity and functionality of glass fibre thermoplastic composites.

Organofunctional silanes are key components of sizing, which are usually referred as coupling agents. These silanes are reported to improve the interfacial strength and hydrothermal resistance of the interface [2]. The general structure for a silane coupling agent is [X-Si$(OR)_3$], where R is a methyl or ethyl group and X is a chemically reactive group that can interact with the composite matrix and/or the film former [2]. The interaction is usually known to be a chemical one, where the matrix is a thermoset polymer and the X group on the silane reacts with the matrix elements. It is not well understood whether a high molecular weight thermoplastic polymer matrix would have the same chemical interaction [3]. There are only a few studies on interfacial properties on glass fibre thermoplastics compared to glass fibre thermosets [3].

  doi:10.5075/epfl-298799_978-2-9701614-0-0

This study investigates the effect of a number of different silanes typically used in glass fibre sizings, namely γ-aminopropyltriethoxysilane (APS), γ-glycidoxypropyltrimethoxysilane (GPS) and γ-methacryloxypropyltrimethoxysilane (MPS), on the interfacial shear strength (IFSS) when combined with different thermoplastic polymers. Microbond testing, which is a wildly accepted method in polymer composites research has been used to evaluate the IFSS [4]. Microdroplets have been created from different thermoplastics i.e., PP, MaPP, PA6, PBT on unsized and silane sized glass fibres. The significance of differences in the averaged IFSS for the investigated systems is evaluated by two-tailed Student's T-Test [5]. An example of SEM observations of debonded fibre matrix is illustrated. Furthermore, compatibility of the thermoplastics with different silane sized fibres is reported and discussed.

2 Materials and method

2.1 Materials

The experiments were conducted using bare (water-sized) E-glass fibres taken from a large roving supplied by Sisecam. The thermoplastic polymers used were, PP (PETOPLEN EH102), MaPP (Polybond® 3200), PA6 (Tecomid® NB40 NL) and PBT (Tecodur® PB30 NL) supplied by Petkim, Addivant and Eurotec respectively. APS, GPS and MPS were purchased from Sigma Aldrich. The bare fibres were coated with 1% solutions of APS, GPS and MPS. The silane sized fibres used for the investigation are summarized in Table 1.

Table 1: Glass fibre summary.

Designation	Sizing	Mean fibre diameter (μm)
BF	Bare (water size)	17.5
APS	γ-aminopropyltriethoxysilane	17.7
MPS	γ-methacryloxypropyltrimethoxysilane	18.6
GPS	γ-glycidoxypropyltrimethoxysilane	17.9

2.2 Silane treatment

The process of applying the silane coatings started with calibrating a pH meter using buffer solutions of pH 4, 7 and 10. For adjusting the pH of deionised water to 5-5.5, a dilute acetic acid solution was used. This is to promote hydrolysis of the GPS and MPS in water. 1 mL of silane was mixed with 100mL of acidified deionised water then left to hydrolyse for 24 h in a sealed plastic container (Figure 1). APS solution was made at pH 7, as that's the optimised pH level for APS [2]. 30 cm BF bundles were completely immersed in the silane solutions, as shown in Figure 1 for 15 minutes, then removed and dried in an oven for 30 minutes at 110°C.

  doi:10.5075/epfl-298799_978-2-9701614-0-0

Figure 1. Silane solution (left), immersed fibre bundles in the silane solution (right)

1.2 Microbond test

Sample preparation was done similar to a previous publication by Nagel et al. [6]. Steel washers were employed as the sample holders for the microbond test. Individual fibres were removed from bundles and applied on a steel washer, attached first with double-sided tape then secured with superglue. Long fibres were extruded from thermoplastics pellets and then they were used to make a knot around the fixed glass fibre on the washer. The samples were then proceed at 220°C for PP, 200°C for MaPP and 260°C for PA6 and PBT in a vacuum oven under nitrogen flow and left to reach the ambient temperature under nitrogen. The droplets were examined under an optical microscope (200x). Only axisymmetric droplets were chosen for the test. Figure 2 shows an example of a fine PP droplet that is prepared for the test. The fibre diameter, length of the droplet (embedded length) and droplet diameter were measured using the image processing software package ImageJ. A total of 30 samples were prepared for each batch and were subjected to microbond test using an Instron 3342 universal tensile testing machine as shown in Figure 4. The droplet was brought to just below the blades and the blades were closed until touching the fibre. The details of the sample were then inputted into the Instron software and the test began at a rate of 0.1mm/min using a 10N load cell. Eq. (1) formulates the calculation method for the IFSS.

$$\tau = \frac{F_{max}}{\pi D_f L_e} \quad (1)$$

Where τ is the interfacial shear strength, F_{max} is the maximum load, D_f is the diameter of the fibre and L_e is the embedded length.

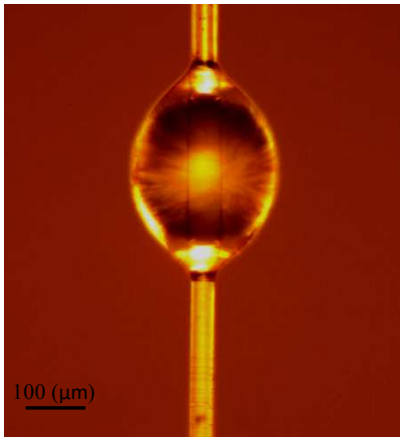

Figure 2. An example of a PP droplet

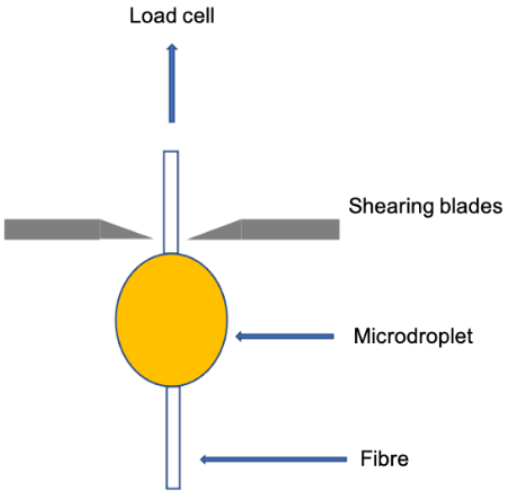

Figure 3. Microbond set up

3. Results and discussions

Although it is not fully accepted whether micromechanical testing methods provide realistic approximations of the true interfacial properties, the microbond test is widely used by many researchers as an effective method for screening and comparing various sizings and it allows testing almost any combination of fibre and matrix [7, 8].

The microbond testing results were based around bare and three different silane coated fibres (APS, GPS, MPS) with four different thermoplastics. The plot of maximum load against embedded area provides information on the spread of the data to be easily assessed. Figure 4 shows a typical plot, exhibiting the scatter in data characteristic in the microbond test.

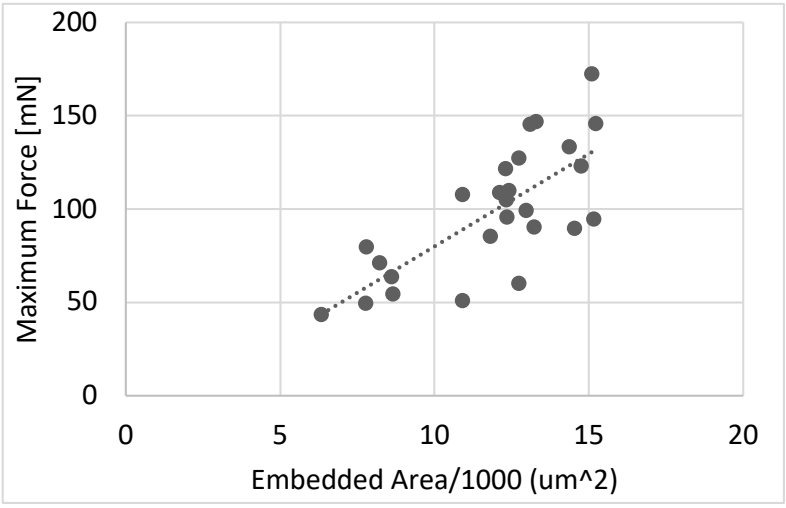

Figure 4. Maximum load vs embedded area for APS with PP matrix.

Figure 5 shows the IFSS results obtained by the microbond tests on PP, MaPP, PA6 and PBT systems. All the IFSS and Student T.test results are also summarized in Tables 2 and 3. Overall, the PBT system has the highest IFSS values of all the investigated fibre/matrix systems. MaPP has the second highest IFSS value, followed by PA6 and PP.

For PP systems, the application of any form of sizing contributed to an improved IFSS compared to a bare fibre. The silane sized fibres generally exhibited IFSS in the region of around 8 MPa, which shows the improvement in IFSS compared to BF. The p values obtained from the two-tailed Student's T-Test, see Table 3, between Bare and Silane sized fibres show that the difference in average apparent IFSS values for these systems are significant at the 95% confidence level, while there is a small difference when comparing the silane sized fibres with each other.

It can be seen that IFSS for MaPP systems are much higher than PP systems for BF and silane sized fibre, this is in agreement with previous observation by Nygård et al. [9]. The results show that APS had the highest IFSS value of 21.9 MPa among all the samples in the MaPP system, and there is a little difference between the MPS and GPS. The T.test results in Table 3 also certifies these results.

The IFSS results for PA6 systems show that APS has the highest IFSS value of 19.8 MPa, whereas Bare and GPS has the lowest value 16.7 MPa and 17.1 MPa respectively. However, the T.test results indicate that the differences in average apparent IFSS values for these batches are not significant.

Microbond results for PBT systems stand as the highest value (approximately 30 MPa for BF and MPS, and 32 MPa for APS and GPS) among all the systems. However, there is only a small improvement in silane sized fibres compared to BF.

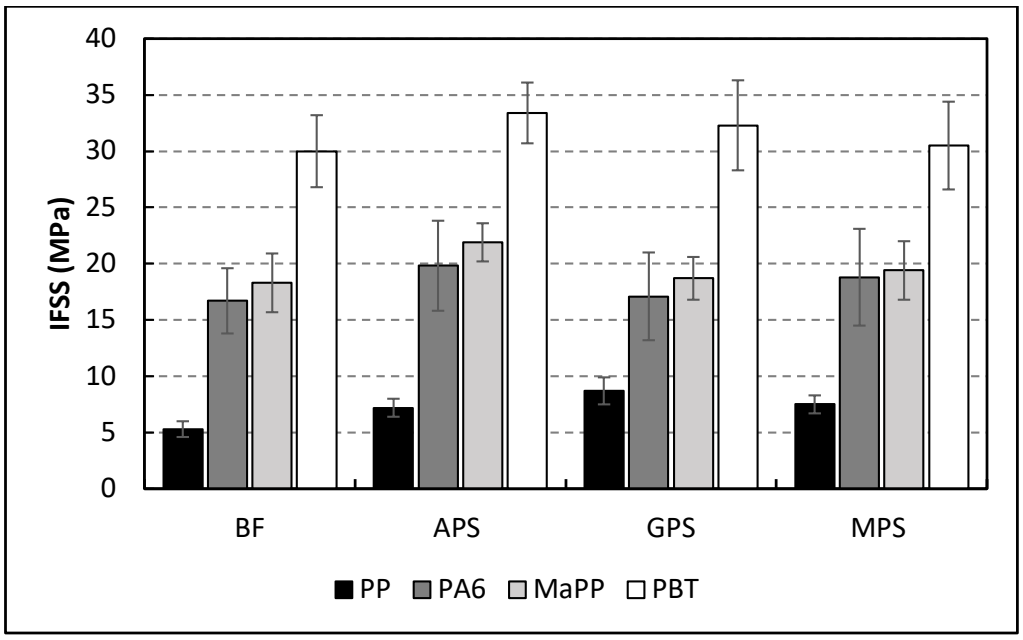

Figure 5. IFSS results for the investigated systems.

Table 2. Summary of Microbond Testing Results

Designation	IFSS (MPa) PP	IFSS (MPa) MaPP	IFSS (MPa) PA6	IFSS (MPa) PBT
BF	5.1±0.6	18.3±2.6	16.7±2.9	30.0±3.5
APS	7.2±0.8	21.9±1.7	19.8±4.2	31.9±3.9
GPS	8.7±1.2	18.7±1.9	17.1±4.3	32.3±4.5
MPS	7.5±0.8	19.4±2.6	18.8±4.9	30.5±3.7

Table 3. Two-tailed Student's t-Test between Bare and Silane sized fibres

Paired samples	p value in different Thermoplastic systems			
	PP	MaPP	PA6	PBT
BF/APS	0.003*	0.02*	0.30	0.29
BF/GPS	0.0002*	0.82	0.82	0.28
BF/MPS	0.0006*	0.29	0.43	0.60
APS/GPS	0.07	0.005*	0.27	0.89
APS/MPS	0.62	0.14	0.74	0.59
GPS/MPS	0.12	0.16	0.51	0.53

* Significant at 0.05 level, 95% confidence limit

From the results, the application of silane has some improvement in the IFSS of the thermoplastic composites. Given that there is not a significant difference between the IFSS results using different silane sizing, it is reasonable to suggest that the improvement might be due to both physical and chemical bonds in the interface.

Figure 8 shows SEM images of a debonded PP micro-droplet sample. The SEM observations confirm the validity of the test, as the debonding can be seen clearly without any damage to the matrix or fibre.

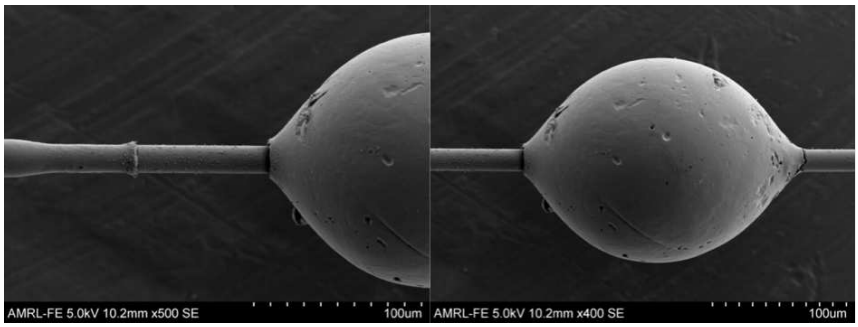

Figure 8. SEM image of debonded PP droplet.

4. Conclusion

This study investigated the effect of different silane coatings and the adhesion of glass fibres with different thermoplastic matrices including PP, MAPP, PA6 and PBT. The microbond test was used to evaluate the effectiveness of silane coupling agents for coating glass fibres to improve the interfacial properties. In addition, SEM observation was used to study the morphology of the debonded droplets. SEM observations revealed the successful nature of debond, confirming the test accuracy. In most of the studied polymers, silane only increased average IFSS by small amounts which were generally not significant at 95%CL. There were some exceptions as IFSS improved for PP in all the silane sized fibres and MaPP in APS sized fibres. Previous studies suggest that this increase might be associated with the improvement of a chemical bond because of silane reacting with the matrix components. However, the IFSS increase observed in this study may instead be of a physical nature as the increase in the IFSS does not significantly vary by changing the matrix-reactive group on the silane. This conclusion needs to be supported with more technical analysis to better understand the bond nature to pave the way towards improved glass fibre reinforced thermoplastic materials. As a result, it is suggested that further analysis such as surface morphology measurement using atomic force microscopy and surface energy evaluation using contact angle measurements are required to carefully differentiate the contribution of physical and chemical nature of interfacial bonds.

Acknowledgements

The authors would like to extend thanks to Şişecam company and the University of Strathclyde as the sponsors of this project.

5. References

1. Biron M. Thermoplastics and thermoplastic composites: William Andrew; 2012.
2. Plueddemann EP. General Concepts. In: Plueddemann EP, editor. Silane Coupling Agents. Boston, MA: Springer US; 1982. p. 1-28.
3. Thomason JL. Glass fibre sizing: A review. Composites Part A: Applied Science and Manufacturing. 2019;127.
4. Sockalingam S, Nilakantan G. Fiber-matrix interface characterization through the microbond test. International Journal of Aeronautical and Space Sciences. 2012;13(3):282-95.
5. DeVries H, Fritsma GA. 2 - Quality assurance in hematology and hemostasis testing. In: Keohane EM, Otto CN, Walenga JM, editors. Rodak's Hematology (Sixth Edition). St. Louis (MO): Elsevier; 2020. p. 8-30.
6. Nagel U, Yang L, Kao C, Thomason J. Effects of thermal recycling temperatures on the reinforcement potential of glass fibers. Polymer Composites. 2018;39(4):1032-40.
7. Zinck P, Wagner H, Salmon L, Gerard J. Are microcomposites realistic models of the fibre/matrix interface? I. Micromechanical modelling. Polymer. 2001;42(12):5401-13.
8. Zinck P, Wagner H, Salmon L, Gerard J. Are microcomposites realistic models of the fibre/matrix interface? II. Physico-chemical approach. Polymer. 2001;42(15):6641-50.

9. Nygård P, Redford K, Gustafson C-G. Interfacial strength in glass fibre-polypropylene composites: influence of chemical bonding and physical entanglement. Composite Interfaces. 2002;9(4):365-88.

HYBRIDIZATION AND CHEMICAL TREATMENTS APPLIED ON CARBON AND FLAX FIBER REINFORCED COMPOSITES

Jean-Charles, Agopian[a], Olivier, Téraube[b], Karine, Charlet[a], Marc, Dubois[b]

a: Université Clermont Auvergne, Clermont Auvergne INP, CNRS, Institut Pascal, F-63000 Clermont–Ferrand, France – Mail: jean-charles.agopian@sigma-clermont.fr
b: Université Clermont Auvergne, Clermont Auvergne INP, CNRS, ICCF, F-63000 Clermont–Ferrand, France

Abstract: *Knowing that carbon-flax hybrid composites combine both the properties of carbon (C) and flax (F) fibers, several stacking sequences of unidirectional (0°, 45°, 90°) epoxy-based non-hybrid and hybrid carbon-flax composites were produced using vacuum infusion: $[C_6]$, $[CF_2]_s$, $[F_2C]_s$, $[F_6]$. Ageing treatments in hot (60°C) or room-temperature water were achieved to study water absorption depending on both stacking sequence and water temperature. Tensile, bending, drop-weight and creep tests were processed on both unaged and aged samples. With standard deviations, an effect of the stacking sequence on the composite properties was highlighted. Carbon fibers were also fluorinated in order to increase their hydrophobic properties and potentially improve the adhesion between carbon fibers and matrix.*

Keywords: Carbon fiber; Flax fiber; Hybrid composite; Ageing

1. Introduction

Natural fibers are increasingly used as composite material reinforcement for several reasons, *e.g.* their good specific properties, their low price, their damping properties, and their ecological aspect. Among others, flax fibers are particularly interesting, as their specific properties compete with the ones of E-glass fibers, and that France is their biggest producer. However, natural fibers have drawbacks, *e.g.* hydrophilicity, poor adhesion with most of polymer matrices, or hardly-predictable mechanical properties, which may disqualify them to reinforce composite materials for structural applications [1].

Hybridization of natural fibers with synthetic ones, *e.g.* carbon or glass, is a way to obtain the advantages of both fibers while reducing their intrinsic drawbacks. Carbon-flax fiber reinforced composites were already studied, and are well-known for their good balance between damping and mechanical properties, with a lower water absorption than flax fiber reinforced composites.

In this study, flax and carbon fiber fabrics were mixed in order to keep the lightness, damping properties and ecological aspect of flax fibers, while carbon fibers were used to increase both the mechanical and water-ageing properties of the composite materials. The study of tensile mechanical properties highlighted an evolution of elasticity and shear moduli and of Poisson's ratios with the stacking sequence, modifying the whole compliance matrix.

As fluorination of carbon fibers is known as a way to increase their hydrophobicity under judicious conditions [2], carbon fibers were fluorinated at various temperatures in this study. A future objective is to use them as composite reinforcement, in order to increase the resistance to water of these composite materials.

  doi:10.5075/epfl-298799_978-2-9701614-0-0

2. Materials and methods

2.1 Fabrication of composite samples

Composite materials were epoxy-based and reinforced with carbon and flax fibers. Carbon fiber fabric is a 12K HiMaxTM FCIM 313 from Hexcel. Flax fiber fabric is a unidirectional FlaxPlyTM fabric from Eco-Technilin. The resin used is the 1050 epoxy resin from Resoltech, combined with their 1056S hardener in 100:35 proportions.

Composite materials were fabricated using vacuum resin infusion. 40 cm x 4 cm bands of fibers were first introduced in a waxed PMMA mold closed with clamps. Felt was stuffed into the mold entry and output holes to slow the resin flow. The mold was then connected to the vacuum system. The mix {resin + hardener} was also vacuumed for 5 minutes to avoid future porosities. The mix was then put to ambient air and aspirated by depression into the mold. The vacuum system was stopped once the fibers in the mold were completely impregnated with resin.

The following 6-ply stacking sequences were made, where F and C stand for Flax and Carbon: $[C_6]$, $[CF_2]_s$, $[F_2C]_s$, $[F_6]$. For each stacking sequence, three fiber orientation were investigated: 0°, 45°, and 90°, leading to 12 unidirectional sequences. Pure resin samples were also fabricated.

Glass-epoxy composites were fabricated to be used as tabs for tensile tests. The same protocol was used, with a 30 cm x 30 cm x 3 mm mold and Resoltech 1055S hardener. 4 plies of double-ply +45°/-45° glass fabric were used, leading to the stacking sequence $[+45/-45/+45/-45]_s$.

After demolding, composite plates were left 14 days at room temperature (RT) to achieve post-reticulation. Specimens were cut using a diamond saw with a water jet, and dried shortly after.

2.2 Fiber fluorination

Carbon fiber samples (consisting in 8 10 cm-long bundles) were treated with static fluorination. Fluorination apparatus consists of a reactor linked to a pure fluorine gas and a nitrogen gas bottles. A soda lime trap is set up at the reactor output, in order to trap residual F_2 molecules.

Fibers were put in a passivated-nickel basket in the reactor, which was then closed, and vacuumed (10^{-3} bar). The pump valve was then switched off, meaning the reactor was a closed system. Different fluorination temperatures were applied: RT, 230°C, 280°C, 330°C, and 380°C.

N_2 was first introduced up to a pressure of 0.03 MPa and then molecular fluorine up to 0.06 MPa. Atmospheric pressure (0.1 MPa) was reached with N_2. 20 minutes were then timed. The reactor was then flushed for at least 2 hours with N_2 (flux of 600 mL/min) to eliminate both the remaining fluorine and side products through the trap. Fibers were then removed from the reactor, and their contact angle with water was measured using the method described in [2].

2.3 Water ageing and mechanical tests

Water ageing was performed to study the influence of the stacking sequence on water absorption. The fiber orientation of aged composite materials was 0°. Two water ageing were implemented: for the first one, specimens were immerged for 3 months in 60°C demineralized water in a WeissTechnik climatic chamber. For the other one, specimens were immerged for 1 year in RT demineralized water. For both ageing methods, tensile, bending and creep specimens were aged. In order to maximize water uptake, edges were not protected during ageing. Specimens were regularly weighted. To do so, specimens were got out of water, quickly dried

  doi:10.5075/epfl-298799_978-2-9701614-0-0

with absorbent paper, weighted and immediately replaced into water. Once steady state was reached, samples were dried at 60°C in 0% relative humidity until their weight was constant. For each stacking sequence, ageing method, and nature of specimen, 4 specimens were tested.

Fick's law, given in Equation (1), was used to study the water uptake of composites [3]:

$$\log\left(\frac{M_t}{M_s}\right) = \log(k) + n\log(t) \quad (1)$$

In this equation, M_t is the water weight in the sample at a given time, M_s the water weight at steady state, k a constant describing the relationship between the sample and water molecules, and n a constant describing the water absorption mode. In a Fickian or pseudo-Fickian diffusion model (n ≤ 0.5), the diffusion coefficient can be expressed as in Equation 2, where D is the diffusion coefficient, m the initial slope of M_t/M_s vs. time $t^{1/2}$, and h the sample thickness:

$$D = \pi\left(\frac{mh}{4}\right)^2 \quad (2)$$

Tensile tests were performed as much as possible in compliance with ASTM D3039 standard. Specimen dimensions were 170 mm x 15 mm x 3 mm. Tabs, whose dimensions were 50 mm x 15 mm x 3 mm, were stuck with two-component glue to the specimens.

The elastic region was investigated through tensile tests using a ZwickRoell UTS20K equipped with a 20 kN load cell, manual-clamping jaws, and a gauge acquisition station. Tests were performed at a 1 mm/min speed at RT. For unaged composites, FCAB-2-11 0°-90° strain gauges from TML were used to acquire both longitudinal and transversal deformations. Displacements of aged composites were measured using an extensometer with a stroke of 2.5 mm. To allow comparison, the 0° orientation of unaged composites was also tested with the extensometer. For each sequence, ageing method and fiber orientation, 4 specimens were tested.

Compliance matrices of unaged samples were determined assuming that non-hybrid stacking sequences ($[C_6]$, $[F_6]$) were transversely isotropic, hybrid sequences ($[CF_2]_s$, $[F_2C]_s$) were orthotropic, and pure resin samples were isotropic. Based on Kirchhoff-Love plate theory, the elements of the compliance matrix linked to the normal direction (Poisson's ratios ν_{x3}, shear moduli G_{x3}, and E_{33} modulus) were neglected. To ease interpretation, only moduli and Poisson's ratios were given, matrices being obtainable with these values. It should be noted that the matrices may not be symmetric, which could be due to standard deviation. Moreover, the obtained moduli may differ depending on the measurement system (gauges or extensometer).

Once elastic properties were acquired, specimens were tested on a Schenck Hydropuls PSB250 machine, equipped with a 100 kN load cell and hydraulic jaws. Jaw pressure was set at 100 MPa, and specimens were tensile tested until rupture at a speed of 1 mm/min, displacements being measured with a 1 mm extensometer. For each stacking sequence and composite ageing, 4 specimens were tested.

Three-point bending tests were realized as much as possible in compliance with ASTM D790 standard. Specimen dimensions were 120 mm x 18 mm x 3 mm. Tests were performed on a ZwickRoell UTS20K equipped with a 20 kN load cell. The speed was set at 1 mm/min speed and tests were made at RT. Displacements were acquired through the traverse displacement. For each stacking sequence and composite ageing method, 4 specimens were tested.

  doi:10.5075/epfl-298799_978-2-9701614-0-0

Creep tests were performed on a VA2000 MetraVib viscoanalyzer as much as possible in compliance with ASTM D7337 standard. Specimen dimensions were 50 mm x 15 mm x 3 mm. A constant load of 30 N was applied for 4500 s at RT. For each stacking sequence and composite ageing method, 4 specimens were tested.

Creep parameters J_0, J_1 and η_1 were determined using Inokuchi's method [4], while the equivalence between generalized Maxwell and Kelvin-Voigt models, Maxwell relaxation function and Laplace-Carson transform were used to determine the damping factor *tan(δ)*, using the same method than [5].

Drop-weight impact tests were performed on specimens whose dimensions were 80 mm x 80 mm x 4 mm, with the following stacking sequences: $[C_8]$, $[C_2F_2]_s$, $[F_2C_2]_s$, $[F_8]$. A CEAST 9310 droptower impact system from Instron was used. Two energy levels (11 J and 22 J) were investigated to compare the behavior of each material depending on the chosen energy. If the specimen is not broken, a damage degree μ can be defined as the ratio of the absorbed energy by the impact energy. As absorbed energy is the area under the strength-displacement curve, it can be obtained by integrating this curve. Both energies can also be read on the energy-time curve. For each stacking sequence and energy level, 2 specimens were tested.

3. Results and discussion

3.1 Carbon fiber fluorination

Contact angles of water drops with fluorinated fibers are given in Table 1, with polytetrafluoroethylene (PTFE) as reference value. As already shown in literature, fluorination appears as a mean to increase the hydrophobicity of carbon fibers. Here, it appears that sufficiently high fluorination temperatures do not impact the treatment quality. In the case where mechanical properties of the fibers were maintained, such fibers could be integrated in composite materials to increase their resistance to water sorption.

Table 1: Contact angles with water depending on the fluorination temperature

Fluorination temperature (°C)	Non-fluorinated	20	230	280	380	PTFE
Contact angle with water (°)	50 ± 9	114 ± 4	131 ± 10	131 ± 8	127 ± 1	108-114 [6]

3.2 Water ageing

Water absorption curves are given in Figure 1. For both ageing temperatures, the influence of the stacking sequence is similar. The more there are flax fibers outside, the higher the water absorption is, highlighting the hydrophilicity of flax fibers. Higher water temperature leads to faster and higher water absorption, independently of the stacking sequence. It should be noted that RT-aged samples did not reach steady state due to time constraint.

Fick's law parameters were calculated and are given in Table 2. For both ageing temperatures, values of D for $[CF_2]_s$ and $[F_2C]_s$ were expected to be between the ones of $[C_6]$ and $[F_6]$. However, the following order has been reached: $[CF_2]_s < [C_6] < [F_6] < [F_2C]_s$. This highlights the high positive ($[CF_2]_s$) or negative ($[F_2C]_s$) effect that hybridization has on the diffusion coefficient. Moreover, the higher the ageing temperature, the higher the diffusion coefficient and the closer n is to 0.5, showing that diffusion kinetics strongly depends on the chosen temperature. Concerning n,

  doi:10.5075/epfl-298799_978-2-9701614-0-0

increasing the flax fiber proportion on the outside of the material leads to a transition from a pseudo-Fickian ($n < 0.5$) to a Fickian diffusion behavior ($n = 0.5$).

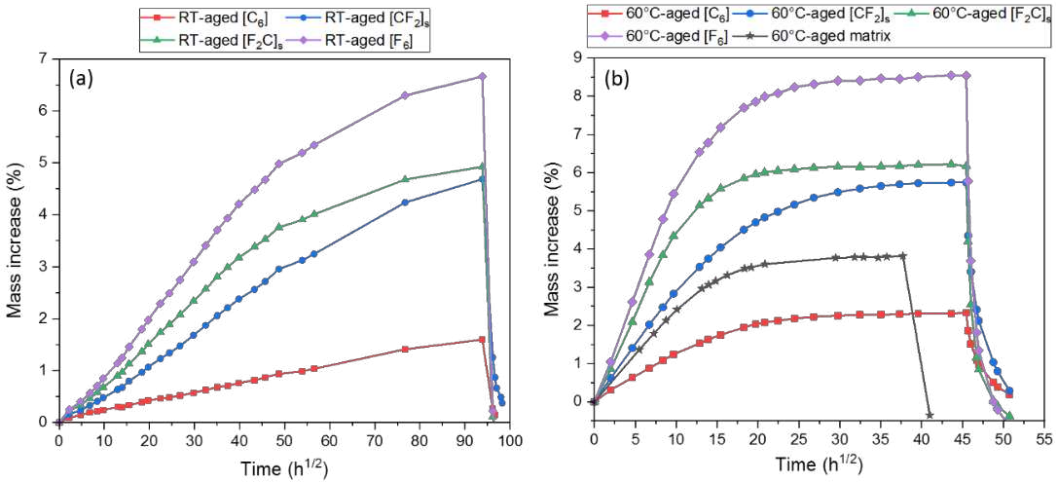

Figure 1. Water absorption curves depending on the stacking sequence and ageing temperature: (a) RT, (b) 60°C

Table 2: Fick's law parameters depending on the stacking sequence

	D [m²/s] (10^{-14})		n	
Sequence	RT ageing	60°C ageing	RT ageing	60°C ageing
$[C_6]$	7.5 ± 0.4	150 ± 30	0.34 ± 0.03	0.43 ± 0.02
$[CF_2]_s$	6.7 ± 0.1	130 ± 10	0.42 ± 0.02	0.46 ± 0.01
$[F_2C]_s$	11.0 ± 0.2	290 ± 20	0.43 ± 0.01	0.52 ± 0.02
$[F_6]$	9.8 ± 0.7	220 ± 10	0.46 ± 0.03	0.53 ± 0.02
Matrix	-	210 ± 20	-	0.445 ± 0.005

3.3 Tensile and bending properties

Tensile and bending properties of unaged and aged materials are given in Figure 2. Tensile properties of hybrid materials are between those of non-hybrid ones, with equivalent properties for $[CF_2]_s$ and $[F_2C]_s$. Thus, the effect of stacking sequence is not primordial for tensile properties, which might be explained by the fact that all fibers are similarly stressed, independently of their localization in the composite section.

It can also be noted that hybridization of carbon fibers with flax ones reduces the strengthening and stiffening of tensile $[C_6]$ samples after ageing. Except for the $[C_6]$ sequence, ageing barely affects the composite tensile properties, which acts in favor of hybridization with flax fibers.

Parameters to obtain the compliance matrix of each stacking sequence are given in Table 3. The scattering of the values with the sequence is noticeable: $[C_6] > [CF_2]_s \approx [F_2C]_s > [L_6]$ for moduli, and the opposite for Poisson's ratios, highlighting both the reinforcement provided by carbon fiber addition through the shear and elasticity moduli, and the higher transversal contraction of pure flax-reinforced material in both directions (0° and 90°) under tensile stress.

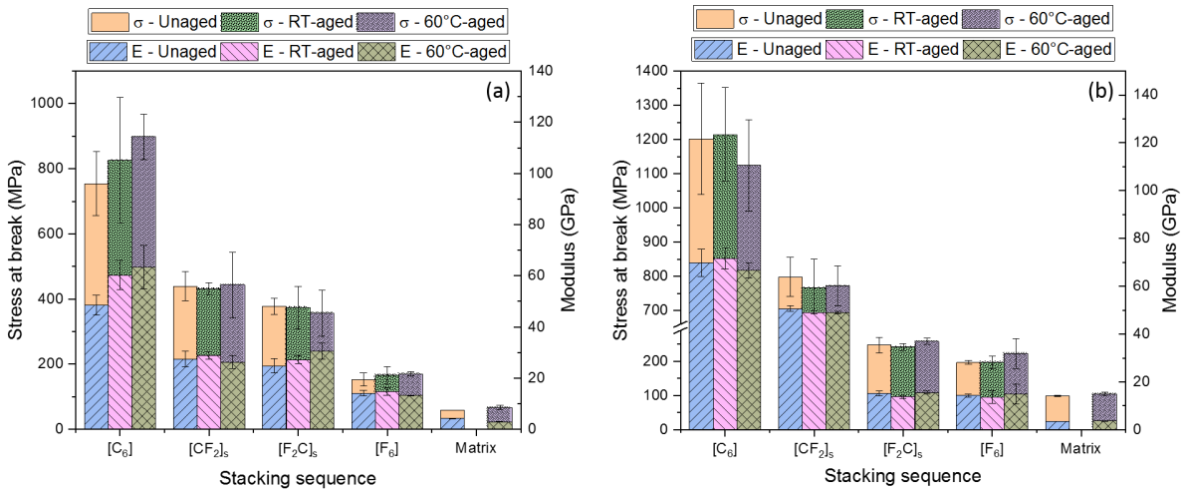

Figure 2. Mechanical properties depending on the stacking sequence and ageing conditions, (a) tensile, (b) bending

Table 3: Moduli and Poisson's ratios depending on the stacking sequence

Sequence	E_{11} (GPa)	E_{22} (GPa)	E_{45} (GPa)	ν_{12}	ν_{21}	G_{12} (GPa)
$[C_6]$	99	8.5	14.1	0.24	0.03	6.2
$[CF_2]_s$	46	6.5	8.1	0.32	0.04	3
$[F_2C]_s$	45	5.8	7.6	0.38	0.06	2.8
$[F_6]$	22	5.4	6.1	0.34	0.11	2.2

As for tensile properties, ageing only has few effect on the bending properties of all materials. However, the stacking sequence is much more important here, as $[F_2C]_s$ has properties close to $[F_6]$, while the ones of $[CF_2]_s$ are much better, which could be due to the creation of tensile and compressive stresses in the material outer layers by bending test. As seen in Figure 2, as the tensile properties of $[C_6]$ are higher than the $[F_6]$ ones, it can explain that bending properties are higher for $[CF_2]_s$ than $[F_2C]_s$.

3.4 Creep properties

Creep compliances of unaged and aged materials are given in Figure 3. If compliance J_0 is roughly scattered with the stacking sequence (with $[F_2C]_s > [F_6]$, which was not expected as $[F_6]$ tensile modulus was higher than $[F_2C]_s$ one), the values of J_1 are much less dependent on the stacking sequence. Concerning the ageing, if J_1 is rather decreased for aged materials, J_0 highly increases with both ageing temperatures, which is surprising as it highlights a stiffness decrease not evidenced by tensile tests.

Damping properties η_1 and *tan(δ)* were calculated and are given in Table 4. Standard deviations are high, meaning that all results should be carefully considered. For both values, an opposite evolution with the stacking sequence is found: $[CF_2]_s < [F_2C]_s < [F_6] < [C_6]$ for η_1, and the opposite for *tan(δ)*, highlighting the benefits of hybridization on these values. Ageing also has opposite effects, as it tends to increase η_1, while it decreases *tan(δ)*. However, in both cases, RT ageing has a stronger effect than 60°C ageing.

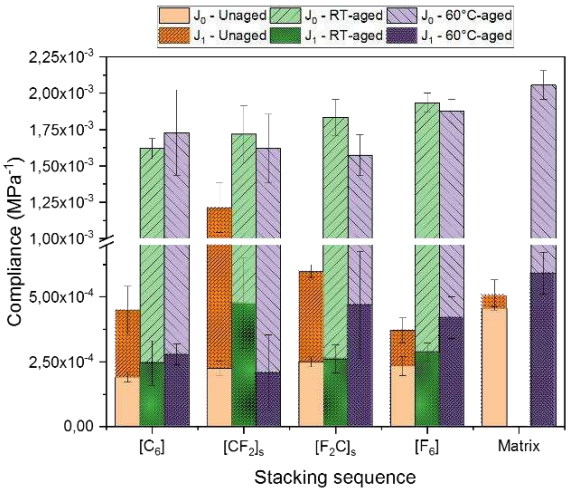

Figure 3. Creep compliances depending on the stacking sequence and ageing conditions

Table 4: Creep properties depending on the stacking sequence and ageing conditions

	η_1 (10^6 [MPa.s])			*tan(δ)* at 20 Hz (10^{-6})		
Stacking sequence	Unaged	RT-aged	60°C-aged	Unaged	RT-aged	60°C-aged
$[C_6]$	2.3 ± 1.8	2.8 ± 3.1	1.6 ± 1.6	8.1 ± 2.9	1.4 ± 0.4	2.2 ± 0.9
$[CF_2]_s$	1.3 ± 0.2	3.3 ± 2.3	1.0 ± 1.4	32.5 ± 8.0	6.7 ± 4.4	24.8 ± 7.1
$[F_2C]_s$	1.50 ± 0.01	3.9 ± 0.9	1.3 ± 1.2	21.8 ± 1.8	1.2 ± 0.1	16.2 ± 8.5
$[F_6]$	1.8 ± 0.5	6.3 ± 1.2	3.5 ± 0.5	17.0 ± 2.6	0.8 ± 0.2	2.5 ± 0.1
Matrix	4.4 ± 1.3	-	5.6 ± 0.7	4.1 ± 1.2	-	0.9 ± 0.3

To conclude this section about creep properties, hybridization appears to confer better damping properties than non-hybrid materials. A possible assumption may be that some energy-dissipative phenomena take place at the interface region between different natures of fibers.

3.5 Drop-weight impact properties

Drop-weight impact properties of unaged materials are given in Figure 4. Only the $[F_8]$ composite has a different behavior than the other ones, with a lower peak force but high displacements. It can be noted than hybrid sequences have lower post-test displacements than non-hybrid ones.

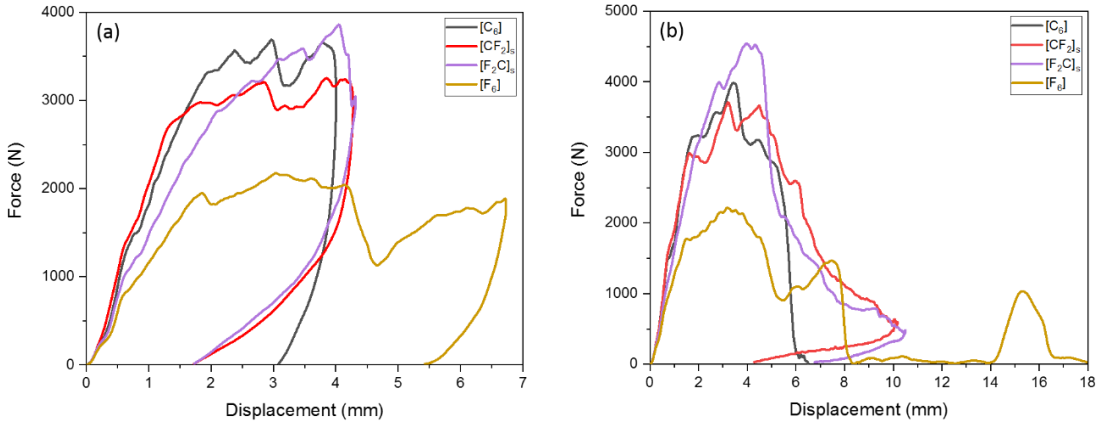

Figure 4. Drop-weight impact properties depending on stacking sequence and impact energy, (a) 11 J, (b) 22 J

Damage degrees for each sequence are given in Table 5. Hybrid sequences are stronger than non-hybrid ones, as they were less damaged by the 11 J test. Moreover, the $[C_2F_2]_s$ sequence was the only one that was not halved by the 22 J test, highlighting its better impact absorption. Bold values underline the perforation of the sequences, as the damage degree cannot decrease with increasing impact energy. Hybridization is thus an asset for impact properties.

Table 5: Damage degree depending on the stacking sequence

Impact energy	μ $[C_8]$ (%)	μ $[C_2F_2]_s$ (%)	μ $[F_2C_2]_s$ (%)	μ $[F_8]$ (%)
11 J	94 ± 1	83 ± 1	77 ± 3	98 ± 3
22 J	**74 ± 1**	96 ± 1	**94 ± 6**	**66 ± 2**

4. Conclusion

Carbon fibers were fluorinated under various temperatures, and an increase of their contact angle with water was found. Flax and carbon fiber based non-hybrid and hybrid composite materials were fabricated and characterized. Their water sorption behavior was investigated and linked to the stacking sequence. Tensile, bending and creep properties were also studied, and the moduli and Poisson's ratios of each stacking sequence were determined and discussed as a function of the stacking sequence. Finally, drop-weight impact tests outlined the interest of hybridization of composite materials. The next step of the study is the use of fluorinated carbon fibers as composite reinforcement. A potential enhancement of resistance to water is expected.

Acknowledgements

The authors wish to thank SIGMA Clermont, which has funded this work. They also thank A. Béakou and A. Gravier for their help during the experimental phase and its scheduling.

5. References

[1] V. Fiore, A. Valenza, G. Di Bella, Mechanical behavior of carbon/flax hybrid composites for structural applications, Journal of Composite Materials. 46 (2012) 2089–2096. https://doi.org/10.1177/0021998311429884.

[2] J.-C. Agopian, O. Teraube, M. Dubois, K. Charlet, Fluorination of carbon fibre sizing without mechanical or chemical loss of the fibre, Appl. Surf. Sci. 534 (2020) 147647. https://doi.org/10.1016/j.apsusc.2020.147647.

[3] Z. Al-Hajaj, R. Zdero, H. Bougherara, Mechanical, morphological, and water absorption properties of a new hybrid composite material made from 4 harness satin woven carbon fibres and flax fibres in an epoxy matrix, Composites Part A: Applied Science and Manufacturing. 115 (2018) 46–56. https://doi.org/10.1016/j.compositesa.2018.09.015.

[4] M.D. Alvarez, W. Canet, F. Cuesta, M. Lamua, Viscoelastic characterization of solid foods from creep compliance data: application to potato tissues, Z Lebensm-Unters Forsch A. 207 (1998) 356–362. https://doi.org/10.1007/s002170050345.

[5] V.-D. Do, A. Beakou, T.-P. Le, Caractérisation du comportement viscoélastique d'un composite hybride carbone-lin, in: Brest, France, 2019.

[6] M.K. Bernett, W.A. Zisman, Relation of Wettability by Aqueous Solutions to the Surface Constitution of Low-energy Solids, J. Phys. Chem. 63 (1959) 1241–1246. https://doi.org/10.1021/j150578a006.

MANUFACTURING AND MECHANICAL CHARACTERISATION OF ADVANCED RE-FORMABLE FIBRE-REINFORCED VITRIMER COMPOSITES

Virginia Amfilochiou[a], Tapas Debsharma[b], Ives De Baere[a], Filip Du Prez[b], Wim Van Paepegem[a]

a: Department of Materials, Textiles and Chemical Engineering, Mechanics of Materials and Structures Group, Ghent University, Technologiepark 46, 9052 Zwijnaarde, Belgium – virginia.amfilochiou@UGent.be

b: Department of Organic and Macromolecular Chemistry, Polymer Chemistry Research Group, Ghent University, Krijgslaan 281 S4-bis, B-9000 Gent, Belgium

Abstract: *Vitrimers are a new category of polymers with a dynamic covalently cross-linked network. This gives to vitrimers the chemical resistance and high mechanical properties of thermosets as they have a cross-linked structure, and the re-processability of thermoplastics thanks to the dynamic character of their network bonds. Such a unique combination of features makes vitrimers interesting for composite applications. However, the research on manufacturing and reprocessing of vitrimer composites is limited. In this work, a new epoxy-based vitrimer was used for the production of fibre-reinforced composites. Glass-Fibre-Reinforced Vitrimers (GFRVs) were produced by Vacuum Assisted Resin Infusion (VARI) and their quality was visually evaluated. The re-processability of the composite was assessed by means of thermoforming after curing and the quality of the thermoformed specimens was evaluated by digital microscopy.*

Keywords: Glass-fibre; vitrimer composites; manufacturing; covalent adaptable networks; thermoforming;

1. Introduction

Fibre reinforced composites are essential for applications in industry such as aerospace, wind energy, automotive, sporting goods. For fibre-reinforced materials two polymer categories are most commonly used as matrices; thermosets and thermoplastics. The use of thermoset composites is predominant at the moment due to their high mechanical properties and chemical resistance. However, their end-of-life scheme is not ideal as thermosets are most commonly landfilled or incinerated [1]. On the other hand, thermoplastics can be recycled but most of them exhibit low chemical and creep resistance while others that are chemically resistant and have superior mechanical performance, have also restricting prices for high volume production industries [2]. Thus, as the demand for sustainability and circular economy is increasing, there is a need for a new recyclable composite material [3].

In 2011, Leibler et al. discovered a new generation of polymeric materials comprising of a crosslinked network structure with dynamic covalent bonds [4]. This unique network provides structural properties similar to thermosets in combination with the malleability of thermoplastics, bridging the two types of polymers. The dynamic covalent bonds of the network can undergo an associative exchange when heat is introduced to the system without compromising the cross-links' density. As a result of this heat triggered associative exchange, the viscosity of this material is gradually decreasing with increasing of temperature following the Arrhenius Law; a characteristic that until then was distinctive only for vitreous silica. Thus, the new material was named Vitrimer [5]. Since the work of Leibler and his co-workers, many

  doi:10.5075/epfl-298799_978-2-9701614-0-0

different chemistries have been used to produce a wide range of vitrimer materials, including but not limited to transesterification, transamination, transalkylation, siloxane exchange, disulfide exchange and imine-amine exchange reactions. All are exhibiting three common features that are also the criteria for a material to be characterised as vitrimer [4-9]:

- After curing the polymer's viscosity drops due to an increase of temperature following the Arrhenius Law;
- When immersed in solvents below its degradation temperature, the material cannot be dissolved;
- The material exhibits two transition temperatures: a glass transition temperature T_g characteristic to all polymer networks, and a second transition temperature T_v that indicates the material's transition from a viscoelastic solid to a viscoelastic liquid. The latter is related to the speed of the covalent bonds exchange reactions. The T_v is set when the material viscosity is equal to or higher than 10^{12} Pa.s.

In theory, these unique and interesting vitrimer characteristics should also be transferrable to fibre-reinforced composites made with vitrimers as their matrix. Some of the dynamic chemistries in literature have been used to produce composites in smaller scales and show some re-processing capabilities [9, 10, 11]. However, these published researches, while being good examples of proof-of-concept, they usually lack in-depth technical information regarding manufacturing of fibre-reinforced vitrimers by industrial composite-manufacturing methods at an acceptable scale. Furthermore, to the best of our knowledge and until now, there are no publications that characterise vitrimer composites in terms of their quality and mechanical performance, either before or after reprocessing.

In this work, a novel low viscosity (< 500 mPa.s at room temperature) vitrimer based on epoxy with a relative high T_g of 85 °C and a high characteristic stress relaxation time ($\tau^* \approx 6$ sec), was used to manufacture continuous-glass-fibre reinforced composite plates [12]. The low viscosity of less than 500 mPa.s at room temperature, and long pot-life that this vitrimer resin exhibits, are essential for continuous fibre infusion processes such as VARI, which was also chosen in order to produce the composites. In addition, a T_g higher than 80°C is also targeted for composite applications in automotive, wind energy and sports equipment, which was a contributing factor for selecting the vitrimer chemistry [13].

In the following paragraphs, the materials and experimental procedures followed are described. Then, the thermoforming of the cured vitrimer composite is described and the microscopy images of the thermoformed samples are analysed. In the last part, some conclusions are drawn regarding the demonstrated properties and the related future work is described.

2. Experimental Procedures

2.1. Materials

Bisphenol A diglycidyl ether (DGEBA, D.E.R.™ 332) was purchased from Sigma Aldrich and used as epoxy resin for the vitrimer polymer system in combination with a dynamic hardener and a catalyst that provided the polymer with its re-processing characteristics. Regarding the fibre reinforcement, Interglas 92626 Glass-Fibre Fabric of 8H Satin Weave was purchased from MCTechnics and used for the composite manufacturing.

  doi:10.5075/epfl-298799_978-2-9701614-0-0

2.2. Synthesis of Epoxy-based Vitrimer system

The synthesis of the vitrimer material was performed at the Polymer Chemistry Research Group of Ghent University, in Belgium. After mixing, the vitrimer system showed viscosity of 300 mPa.s and a long pot-life at 25 °C of at least 90 min. The system was cured 14h at 120 °C to ensure the completion of the cure as well as achieve a higher T_g above 80 °C. Furthermore, this vitrimer system exhibited a fast stress relaxation time ($\tau^* \approx 6s$, determined by stress relaxation experiments using the Maxwell model of single exponential decay), in comparison with other vitrimer chemistries presented in literature [5 - 12]. The above characteristics make this system suitable to be considered for composite applications in wind energy, maritime, sports equipment, as well as some applications in the automotive industry.

2.3. Manufacturing of GFRVs

Composite plates of both $[0°]_8$ and $[\pm 45°]_{2s}$ were manufactured by using the vitrimer system. The warp (0°) direction of the fabric was set along the length of the composite laminate plate. The process is illustrated in Figure 1. The composites were cured under vacuum for 14h at 120°C. The blue perpendicular and parallel lines on the plate are the guiding lines for the warp and weft direction of the glass fabric that was infused.

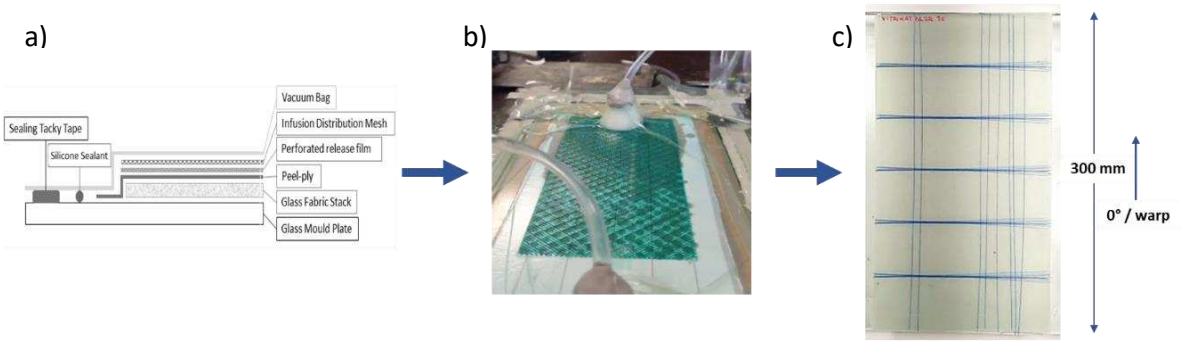

Figure 1 Manufacturing by VARI of the vitrimer composite plates; a) VARI schematic set-up and lay-up of consumables b) Image of infusion process by VARI c) Final cured GFRV plate

2.4. Thermoforming of GFRVs

A thermoforming process was used to examine if the reprocessing behaviour of the vitrimer polymer is transferred to the final composite. The process was considered as a first assessment of the thermoforming characteristics of the glass-fibre vitrimer composite. Specimens of 50 mm x 50 mm were cut from the pristine vitrimer composite plates. To reshape these specimens a steel-zigzag mould was used that was attached on an Instron tensile machine with 100 kN load-cell fitted with a heating chamber (shown in Figure 2a). The specimens were hot-pressed by applying different sets of thermoforming parameters to evaluate their effect on the quality of the vitrimer composite (shown in Table 1). A second cycle of thermoforming was performed on the reshaped specimens in order to return them to their original flat shape. In this second thermoforming two flat-compression plates attached to the same Instron tensile machine were used and the same sets of thermoforming parameters were applied (Figure 2b).

  doi:10.5075/epfl-298799_978-2-9701614-0-0

a) b)

Figure 2. Thermoforming set-up mounted on a tensile machine; a) 1st Thermoforming set-up of zigzag mould. b) 2nd Thermoforming set-up of flat compression plates

Table 1. Thermoforming parameters of specimens VC1 and VC2

Specimen ID	Pressure (bar)	Temperature (°C)	Pre-heating Time (min)	Closing Speed [mm/min]	Thermoforming Time (min)
VC1	15	180	10	0.5	10
VC2	30	190	10	0.5	10

3. Results and Discussion

3.1. Quality of Manufactured Composite plates

As the composite is reinforced with glass fibres and the vitrimer resin has a clear colour the quality of the plates was visually evaluated. In Figure 3 we can see the produced high quality GFRV plate with lack of air bubbles or defects that was later on verified by microscopy.

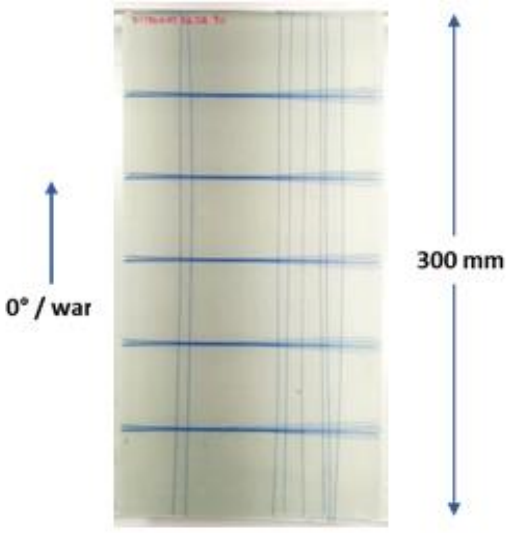

Figure 3. Image of one of the high-quality final $[0°]_8$ lay-up composite plate

3.2. Thermoforming

The pristine vitrimer composite specimens VC1 and VC2 were successfully thermoformed into an omega-profile shape of a stiffener after curing, as shown in Figure 4, illustrating the reshaping capabilities of these epoxy-based vitrimer composites. After thermoforming, a change of colour

  doi:10.5075/epfl-298799_978-2-9701614-0-0

of the material is evident. It is hypothesised that this is due to a partial oxidation of the system. Further tests are needed to evaluate if this discoloration also indicates an effect of the thermoforming process on the material properties.

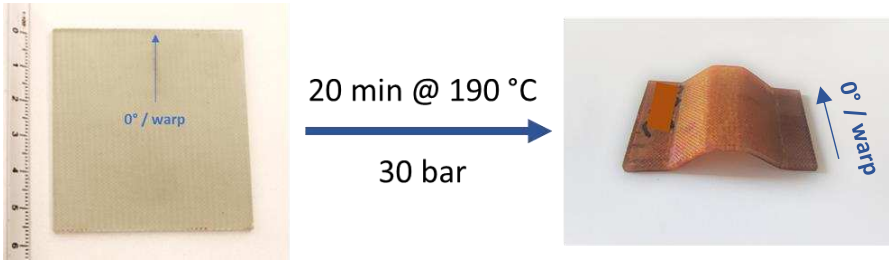

Figure 4. First cycle of thermoforming of specimen VC1 20 min at 190 °C, 30 bar of pressure

The thermoformed specimens were later on cut into two specimens each, perpendicular to the 0°/warp direction. Specimens VC1-2 and VC2-2 were reshaped back to their original flat shape through a 2nd thermoforming cycle following the parameters from Table 1, respectively . The specimens are depicted in Figure 5. Finally, the edges perpendicular to the 0°/warp direction of all specimens were examined by microscopy to evaluate the quality of the thermoforming (Figure 6 and Figure 7).

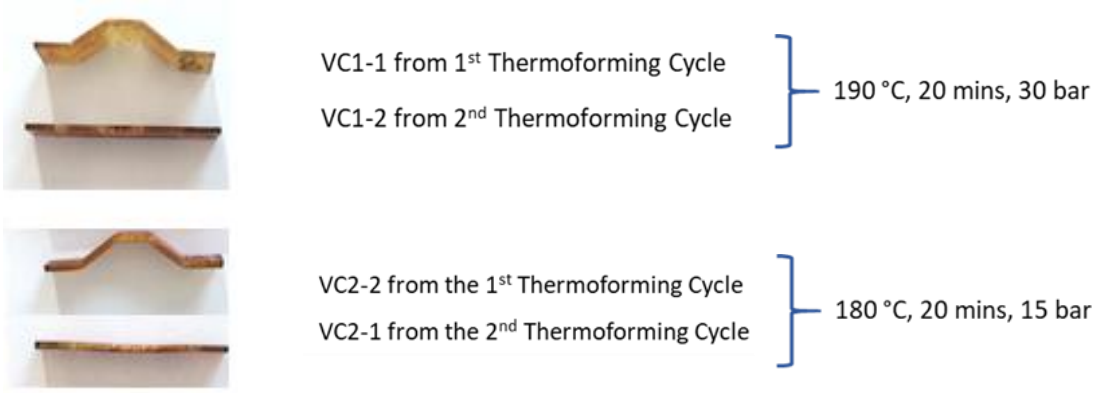

Figure 5. Specimens VC1-1 AND VC2-1 after the first thermoforming cycle and specimens VC1-2 and VC2-2 after the second thermoforming

From the microscopy images we can see that higher temperature and pressure values improve the reshaping process of the GFRVs as the final thermoformed specimen shows less fibre buckling compared to the ones produced by lower temperature and pressure. After the second thermoforming matrix cracking was visible for both specimens. However, these cracks were less and smaller for the specimen thermoformed at 190 °C with 30 bar. Fibre buckling and microcracking during thermoforming is an issue arising often during thermoplastic composites' thermoforming and it is not limited to our case. It has been shown to be affected by fabric weave patterns, composite lay-up and thermoforming parameters [14,15]. These trials demonstrate that the thermoforming of vitrimer composites is possible and can be improved by tuning the thermoforming parameters of temperature and pressure. Hence, the results of this study agree with literature on thermoplastic composite thermoforming and demonstrate that regarding re-processability vitrimer composites behave in a way similar to thermoplastic ones.

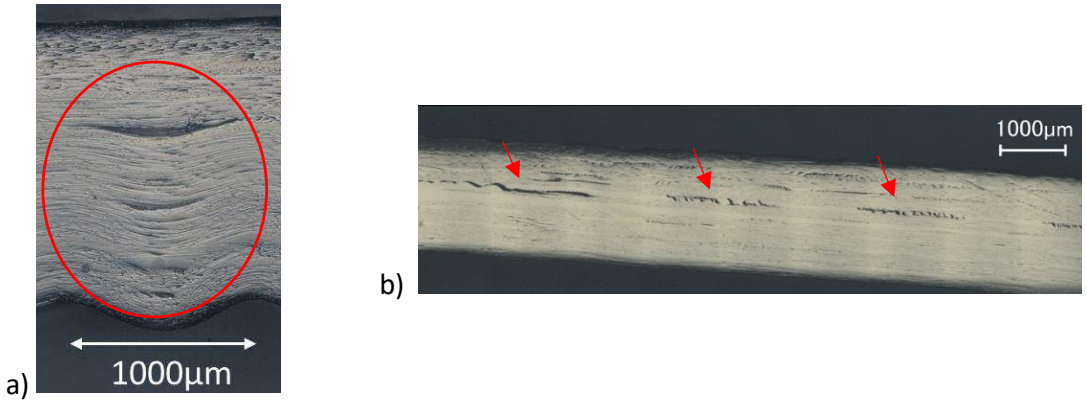

Figure 6. Thermoforming of vitrimer composite at 180 °C and 15 bar of pressure for 20 min; a) Depiction of extensive fibre buckling after the 1st thermoforming b) Depiction of extensive matrix cracking after the 2nd thermoforming

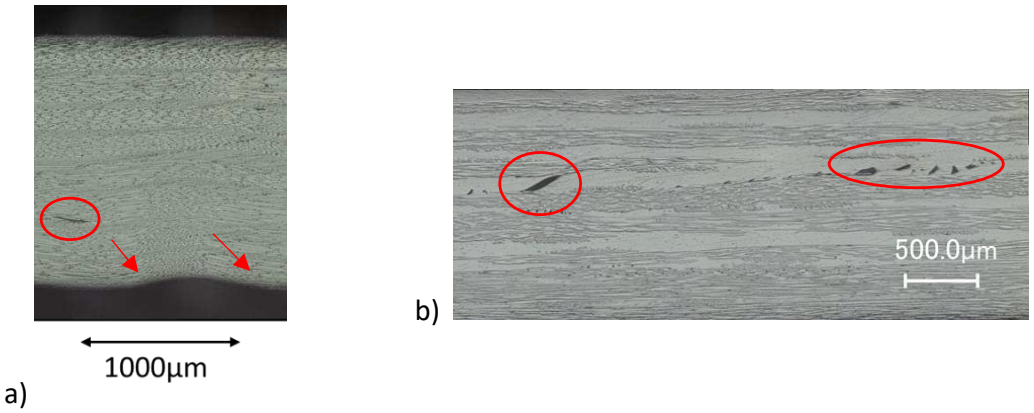

Figure 7. Thermoforming of vitrimer composite at 190 °C and 30 bar of pressure for 20 min; a) Depiction of minor fibre buckling after the 1st thermoforming b) Depiction of minor matrix cracking after the 2nd thermoforming

4. Conclusions

An innovative epoxy-based vitrimer material was evaluated for its applicability as a matrix for glass-fibre reinforced composites. The selected vitrimer chemistry resulted in promising thermomechanical properties, as it exhibited a relatively high T_g and low viscosity coupled with fast stress relaxation time.

In a following step, the vitrimer polymer synthesis was used to impregnate continuous-glass-fibre fabric of different lay-ups by means of industrially available processes (VARI). The resulted composite plates were of high-quality with no visible defects.

Finally, it was verified by means of thermoforming that the reprocessing capabilities of the matrix are transferred to the pristine composites when sufficient temperature and pressure are applied. The thermoformed samples were analysed by digital microscopy after their first and second thermoforming cycle. The microscopy results showcased that a fine tuning of the reprocessing parameters, especially for the first thermoforming cycle, can provide high quality

  doi:10.5075/epfl-298799_978-2-9701614-0-0

GFRVs that are re-processable. This indicates future possibilities regarding repairability and mechanical recycling.

Taking the above into consideration, it can be concluded that this particular vitrimer chemistry is promising and could be considered for repairable, recyclable and thermoformable epoxy-based composites with glass-fibre reinforcement. However, further investigation and optimisation is needed to evaluate the mechanical performance of such composites.

Acknowledgements

This project has received funding from the European Union's Horizon 2020 research and innovation programme under the Marie Skłodowska-Curie grant agreement No 860911.

5. References

1. Anna, H.-Å., Model for End of Life Treatment of Polymer Composite Materials. 2005, KTH: Stockholm: KTH. p. 104, 24, 29.
2. 2012, Composite Materials Handbook vol 3, Poymer Matrix Composites Materials Usage, Design, and Analysis: SAE International on behalf of CMH-17 devision Whichita State University
3. Juaidi A, Abdallah R, Ayadi O, Salameh T, Hasan A A and Ibrik I. 2021, Recent Advances in Renewable Energy Technologies: Elsevier Inc. pp 177-210
4. Montarnal D, Capelot M, Tournilhac F and Leibler L. 2011, Silica-Like Malleable Materials from Permanent Organic Networks: Science 334 965-8
5. Denissen, W., J.M. Winne, and F.E. Du Prez. 2016, Vitrimers: permanent organic networks with glass-like fluidity: Chemical Science, 7(1): p. 30-38.
6. Krishnakumar B, Sanka R V S P, Binder W H, Parthasarthy V, Rana S and Karak N. 2020, Vitrimers: Associative dynamic covalent adaptive networks in thermoset polymers: Chemical Engineering Journal 385 123820
7. Yang Y, Xu Y, Ji Y and Wei Y. 2020, Functional epoxy vitrimers and composites: Progress in Materials Science 100710
8. Alabiso W and Schlögl S. 2020, The Impact of Vitrimers on the Industry of the Future: Chemistry, Properties and Sustainable Forward-Looking Applications: Polymers 12 1660
9. Aranberri I, Landa M, Elorza E, Salaberria A M and Rekondo A. 2021, Thermoformable and recyclable CFRP pultruded profile manufactured from an epoxy vitrimer: Polymer Testing 93 106931
10. Denissen W, De Baere I, Van Paepegem W, Leibler L, Winne J and Du Prez F E. 2018, Vinylogous Urea Vitrimers and Their Application in Fiber Reinforced Composites: Macromolecules 51 2054-64
11. Spiesschaert Y, Guerre M, De Baere I, Van Paepegem W, Winne J M and Du Prez F E. 2020, Dynamic Curing Agents for Amine-Hardened Epoxy Vitrimers with Short (Re)processing Times: Macromolecules 53 2485-95
12. Debsharma T, Amfilochiou V, Wróblewska A A, De Baere I, Van Paepegem W, Du Prez F E. 2022, Fast dynamic siloxane exchange mechanism for reshapable vitrimer composites: Submitted in Journal of the American Chemistry Society
13. Mallick P K. 2007, FIBER-REINFORCED COMPOSITES Materials, Manufacturing, and Design: LLC: CRC Press Taylor & Francis Group
14. Friedrich K, Hou M and Krebs J. 1997, Composite Sheet Forming, pp 91-162
15. Suresh S and Kumar V S S. 2018, Investigation on influence of stamp forming parameters on formability of thermoplastic composite: Polímeros 28 422-32

  doi:10.5075/epfl-298799_978-2-9701614-0-0

EXPERIMENTAL STUDY ON THE MECHANICAL BEHAVIOUR OF CARBON-FIBRE Z-PIN REINFORCED CURVED COMPOSITE LAMINATES UNDER FOUR-POINT BENDING

Mudan Chen [a], Bing Zhang [a], Xiaodong Xu [a, b], Giuliano Allegri [a], Stephen R. Hallett [a]*

a: Bristol Composites Institute, University of Bristol, Queen's Building, Bristol, BS8 1TR, UK
b: University of the West of England, Coldharbour Lane, Bristol, BS16 1QY, UK

Abstract: *This study investigates the influence of the most commonly used Z-pin type, i.e., carbon-fibre composite Z-pin on the four-point bending strength of curved laminates through experiments. The layup has been carefully designed through performing finite element analysis (FEA) to reduce the probability of edge delamination. Three types of samples have been manufactured: unpinned, and Z-pinned with 0.27% and 0.54% areal densities. HexPly® IM7/8552 carbon/epoxy unidirectional prepreg and 0.28 mm diameter T300/BMI pins were employed to manufacture the specimens. It was found that the through-thickness tensile strength decreased by 26% and 37% for 0.27% and 0.54% Z-pinned samples respectively. The surface bonding-frictional force between the pin and laminate interface is not enough to resist the damage initiation, and the pins cause additional disturbance to the laminate, leading to the strength reduction.*

Keywords: Z-pin; curved laminates; delamination; four-point bending.

1. Introduction

Fibre-reinforced polymer composite laminates have an inherent weakness in their out-of-plane direction relative to in-plane strength. As a typical example, when a curved laminate structure is subjected to a bending moment, delamination is observed to be the dominant failure mode due to the prevalent through-thickness tensile stress [1,2]. Thus, several through-thickness reinforcement technologies have been proposed to upgrade the delamination resistance of composite laminates.

Z-pinning has been developed as an effective and discrete through-thickness reinforcement technology. Almost all the mechanical applications of Z-pins [3–5] were demonstrated on resisting delamination propagation in flat laminates, and there is much less research on the application of Z-pins for suppressing or delaying delamination in irregular geometries [6].

Ju et al. [2] studied the delamination strength of curved laminates with grooved stainless-steel Z-pins. The pin surface was treated by physical and chemical methods to increase the friction force between the pins and their embedded laminate intentionally. It was found the curved beam strength was increased by 21, 27 and 42% for 0.3 mm diameter pins and 8.7, 12 and 32% for 0.5 mm ones, at the areal densities of 0.5, 1 and 2% respectively.

Different from the work in Ref. [2], this study investigates the most commonly used Z-pin type, i.e. carbon-fibre composite Z-pin at two different aerial densities. There is no treatment applied to the pin surface, thus the surface is relatively smooth and the pin/laminate interface bonding-frictional force is expected to be lower than the aforementioned grooved metal pins [3].

  doi:10.5075/epfl-298799_978-2-9701614-0-0

2. Sample design and preparation

In the previous research of Xu et al. [1], two pristine cases without deliberately introduced wrinkles have been studied in terms of the layup effect on the failure mode, experimentally and numerically. By dispersing the differently oriented plies at the surface, the delamination location has changed from the inner radius to the middle. Similarly, to avoid the undesirable delamination caused by free-edge effect at the inner radius, finite element analysis (FEA) was carried out for the layup design at the beginning of this study. The newly designed layup is $[0, (+45/0/-45/0)_2\ (+45_2/-45_2/0_2)_3]_s$. There are 54 plies for each laminate, and the thickness is 6.75 mm.

The sample geometry is shown in Fig. 1 (a). HexPly® IM7/8552 carbon/epoxy unidirectional prepreg and T300/BMI pins were used. The pin diameter is 0.28 mm. Three types of samples have been manufactured, i.e., unpinned, 0.27% and 0.54% Z-pinned. The aerial density is calculated based on the mid-plane of the curved area. As the laminates have an unconventional curved shape, a zigzag configuration has been designed to minimise the pin touching at the inner radius as shown in Fig. 1 (b, c). The manufacturing process mainly includes the following steps:

- Layup the prepreg onto a steel mould by aligning centrelines of the prepreg and mould.
- Debulk inside a sealed bag for 15 mins after every four plies.
- Heat the laminate in an oven to soften the resin, then insert the pins manually through the thickness of the curved section.
- Cure the laminate in an autoclave, following the material cure cycle [7].
- Cut individual specimens from the cured laminate.

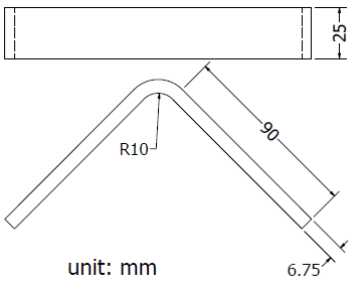

(a) Sample geometry

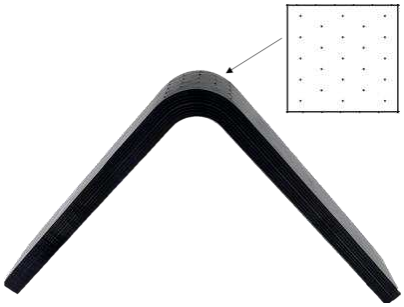

(b) 0.27% Z-pinned sample

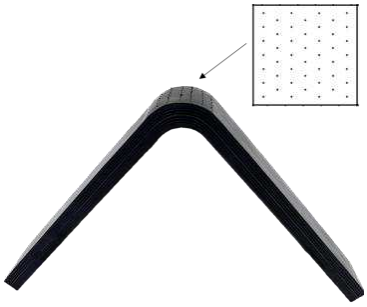

(c) 0.54% Z-pinned sample

Figure 1. Specimen geometry and photos

3. Test setup and result discussion

The test method follows the ASTM D6415/D6415M – 06a standard [8]. The four-point bending test set-up is shown in Fig. 2 (a). A hydraulic-driven Instron 8872 with a load capacity of 25 kN was used for the loading. The specimen was loaded under a displacement control with a rate of 1 mm/min. A video gauge and a high-speed camera were set in front of the specimen to capture the crack events. The tests were stopped manually when the load drop was over 50%.

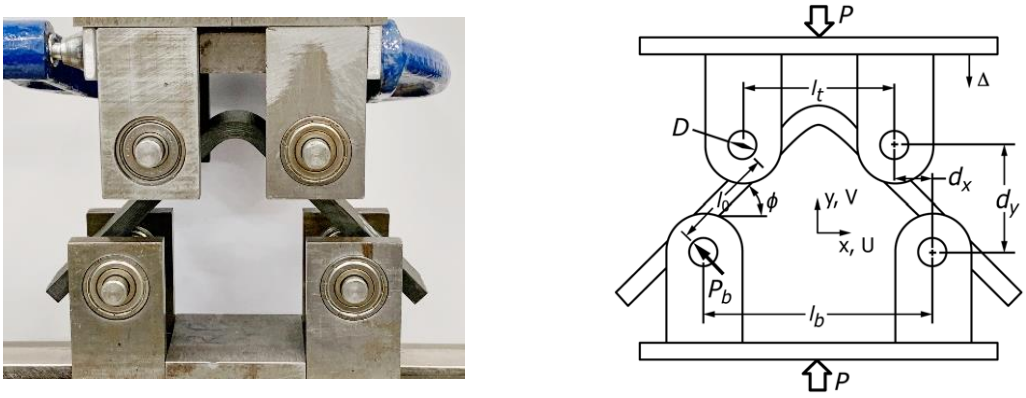

(a) Test set-up (b) Set-up details [8]

Figure 2. Four-point bending test of curved beam

Fig. 3 shows that the load-displacement curves increase linearly until critical delamination happens. The final load drops of the three different types of samples are all due to the catastrophic delamination in the middle. Five specimens were tested for each group, and three of them that showed similar failure modes are presented here. For the unpinned samples, small cracks appeared in the upper radius at the beginning, which were caused by manufacturing defects and didn't cause a load drop (Fig. 3 (a)). There was no inner radius failure observed, and the final failure was in the middle. In terms of the 0.27% Z-pinned ones, the first drop mainly appeared near the inner radius, but the drop amount was more than 10% but less than 50%, the structure could still carry some loads until the mid-part failed (Fig. 3 (b)). Most 0.54% Z-pinned samples only had one failure at the end, and no cracks were observed before that (Fig. 3 (c)).

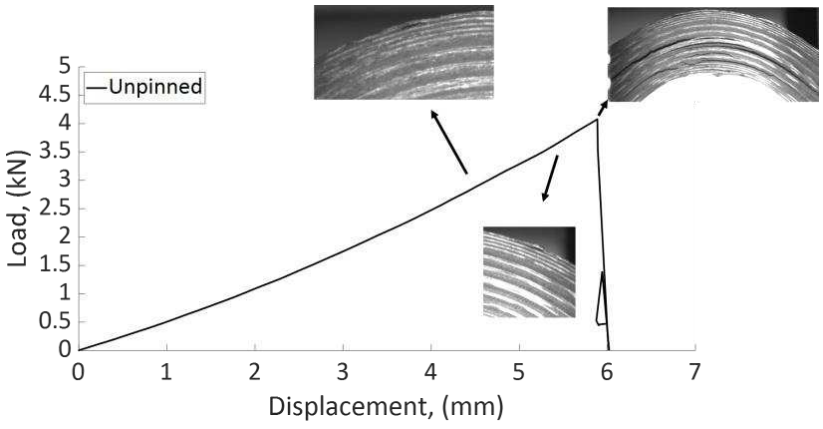

(a)

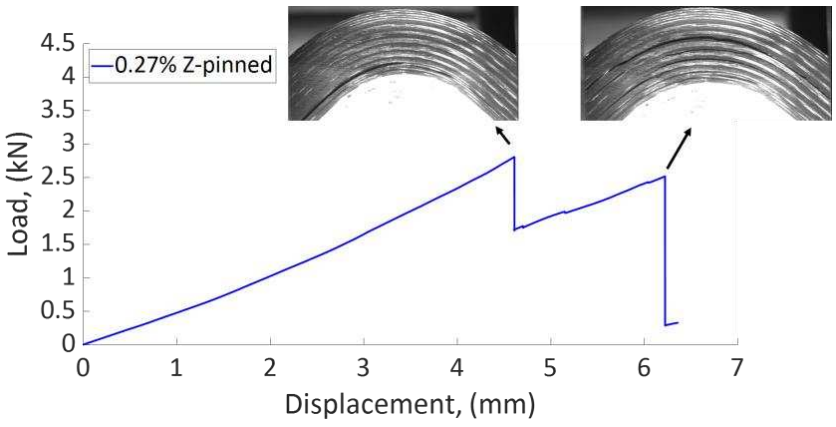

(b)

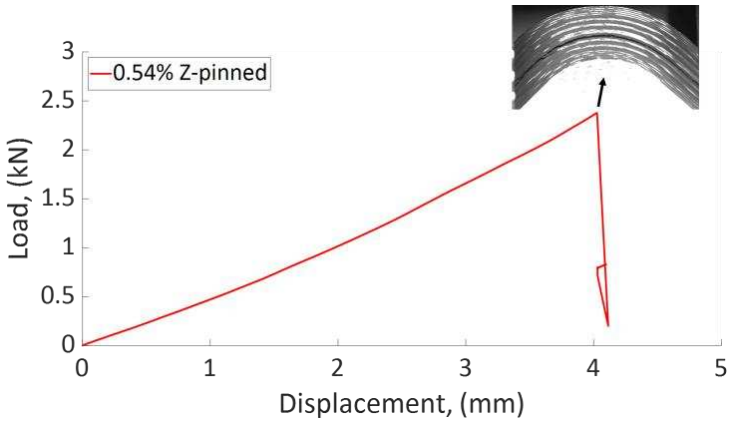

(c)

Figure 3. Load-displacement curves and observed failures during the test

The Curved Beam Strength (CBS) and through-thickness tensile strength σ_I^{max} can be calculated with the following equations according to the ASTM D6415/D6415M – 06a standard:

$$CBS = \left(\frac{P}{2w\cos(\varphi)}\right)\left(\frac{d_x}{\cos(\varphi)} + (D+t)\tan(\varphi)\right) \quad (1)$$

$$d_y = d_x\tan(\varphi_i) + \frac{D+t}{\cos(\varphi_i)} - \Delta \quad (2)$$

$$\varphi = \sin^{-1}\left(\frac{-d_x(D+t)+d_y\sqrt{d_x^2+d_y^2-D^2-2Dt-t^2}}{d_x^2+d_y^2}\right) \quad (3)$$

$$\sigma_I^{max} = \frac{3\cdot CBS}{2t\sqrt{r_i r_o}} \quad (4)$$

The detailed set-up and some parameters are shown in Fig. 2 (b). P is the failure load, defined as the ultimate load before 10% load drop. w and t are specimen width and thickness, which equal 25 mm and 6.75 mm respectively. $D = 20\ mm$ is the roller diameter. φ is the angle from horizontal to the specimen legs in degrees, and $\varphi_i = 45°$ is the initial value of φ, representing the beginning of the test. d_x and d_y are the horizontal and vertical distances between two rollers. d_x equals to 16 mm. Δ is the vertical relative displacement. r_i and r_0 are the inner and

outer radii of the specimen, which are 10 mm and 16.75 mm. The calculated result is summarised in Table. 1.

Table 1: Summary of experimental results

ID	Unpinned			0.27% Z-pinned			0.54% Z-pinned		
	P [kN]	CBS [kN]	σ_I^{max} [MPa]	P [kN]	CBS [kN]	σ_I^{max} [MPa]	P [kN]	CBS [kN]	σ_I^{max} [MPa]
1	3.90	4.35	74.70	2.95	3.43	58.96	2.06	2.52	43.34
2	4.08	4.54	77.96	2.81	3.29	56.54	2.61	3.09	53.08
3	4.12	4.55	78.11	2.70	3.20	54.96	2.38	2.85	49.00
Mean	**4.03**	**4.48**	**76.92**	**2.82**	**3.31**	**56.82**	**2.35**	**2.82**	**48.47**

The comparison of CBS and σ_I^{max} for Z-pinned and unpinned specimens are plotted in the bar chart with error bars in Fig. 4. By inserting pins, the through-thickness tensile strength has decreased by 26% and 37% for 0.27% and 0.54% Z-pinned samples respectively. The pins have shown resistance on crack propagation in the previous research [3–5], due to the bonding and friction forces between pins and laminate, while the curved beam under four-point bending test is in principle a crack initiation case. The bonding-frictional forces between traditional carbon fibre pins and the laminates are not large enough to delay the crack initiation. The additional in-plane damage and stress concentration around the pins might be the reasons that caused the delamination initiation at a lower load than in unpinned laminates.

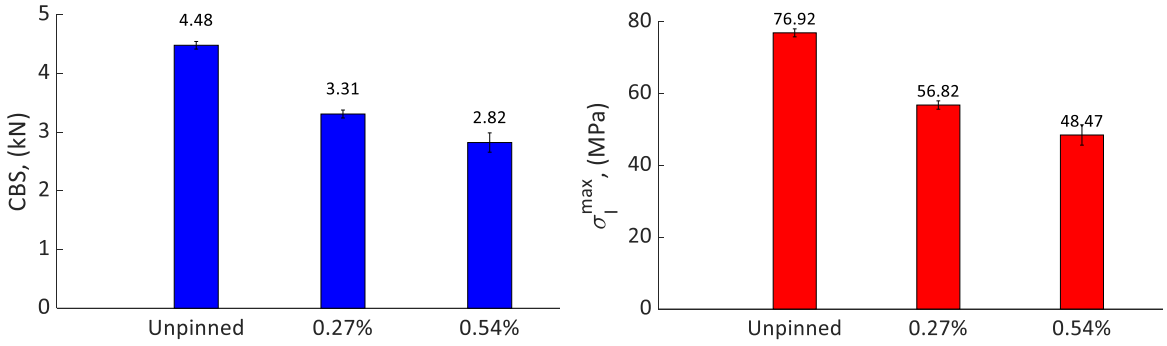

Figure 4. Comparison of test results for three different types of samples

4. Conclusions

The effect of Z-pins on the four-point bending test of curved beams has been studied experimentally. The traditional carbon fibre pins have been inserted in the curved area with a zigzag configuration at two aerial densities. Compared with the grooved metal pins in previous research [2], the carbon fibre pin has a relatively smooth surface. The through-thickness tensile strength was found to decrease by adding the composites pins, which implies that the bonding and friction force between the pin and laminate interface is not enough to delay the crack initiation. On the contrary, additional disturbance has been added to the laminate. In the future

work, a different type of pin with greater surface roughness will be employed to increase the interface friction force.

Acknowledgements

This work was supported by the Engineering and Physical Sciences Research Council through the Centre for Doctoral Training in Advanced Composites for Innovation and Science (grant number EP/L016028/1).

5. References

1. Xu X, Jones MI, Ali H, Wisnom MR, Hallett SR. Effect of out-of-plane wrinkles in curved multi-directional carbon/epoxy laminates. Composites Science and Technology 2020; 197:108282.
2. Ju H, Nguyen KH, Chae SS, Kweon JH. Delamination strength of composite curved beams reinforced by grooved stainless-steel Z-pins. Composite Structures 2017; 180:497–506.
3. Zhang B, Allegri G, Yasaee M, Hallett SR. Micro-mechanical finite element analysis of Z-pins under mixed-mode loading. Composites Part A: Applied Science and Manufacturing 2015; 78:424–35.
4. Liu HY, Yan W, Yu XY, Mai YW. Experimental study on effect of loading rate on mode I delamination of z-pin reinforced laminates. Composites Science and Technology 2007; 67(7):1294–301.
5. Pegorin F, Pingkarawat K, Daynes S, Mouritz AP. Influence of z-pin length on the delamination fracture toughness and fatigue resistance of pinned composites. Composites Part B: Engineering 2015; 78:298–307.
6. Mouritz AP. Review of z-pinned laminates and sandwich composites. Composites Part A: Applied Science and Manufacturing 2020; 139:106128.
7. Prepreg Data Sheet | Hexcel [Internet]. 2020. Available from: https://www.hexcel.com.
8. D30 Committee. Test Method for Measuring the Curved Beam Strength of a Fiber-Reinforced Polymer-Matrix Composite. ASTM International.

  doi:10.5075/epfl-298799_978-2-9701614-0-0

Effects of stacking sequences on the Interlaminar Shear Strength of CF/PEKK composites

Enrico Chemello[a], Marco Apostolo[b], Giuseppe Sala[a], Antonio Mattia Grande[a]

a: Department of Aerospace Science and Technology, Politecnico di Milano, via La Masa 34, 20156 Milano, Italy – enrico.chemello@polimi.it, antoniomattia.grande@polimi.it
b: Solvay, Thermoplastic Composite Platform, 4500 McGinnis Ferry Rd, Alpharetta, GA 30005 USA

Abstract: *High performance thermoplastic composites for aerospace primary structures are increasingly studied in the last years. However few articles report the properties of the PEKK/CF composite material for structural applications. In this paper the Interlaminar Shear Strength of laminates obtained with different stacking sequencies of unidirectional layer obtained from a PEKK/CF prepreg tape was evaluated. A modification of the ASTM D2344 standard is proposed for obtaining a valid failure mode, considering the less brittle behaviour of the thermoplastic matrix compared to thermosets. Furthermore, this testing campaign was carried out performing a 2D Digital Image Correlation. Results show how, the modified testing parameter are crucial to obtain shear failure mode for the considered carbon fibre reinforced thermoplastic composite.*

Keywords: TPC; PEKK; ILSS; Composites; DIC

1. Introduction

Polymer matrix composites (PCM) are more and more used for the development of primary structures in the aerospace industry due to their high strength-to-density and stiffness-to-density ratios and superior physical performances that enables a weight reduction of the aircrafts' overall weight, without the reduction in the structure's performance [1]. In the last decade, the usage of thermoplastic polymers for the matrix composition has drawn the attention of researchers and industries due to some advantages given by the nature of these materials. The main advantages of these polymers are related to their production process that is faster and cheaper. Indeed, since nowadays most of the used matrix are thermoset resins, where a long cure process is needed with associated high production costs. The thermoplastic composites do not need a curing step making the production process faster and simpler. For this reason, it is considered of great importance to study the performances of these materials obtained through out-of-autoclave production processes as thermoforming or automated tape layering [2].
Even if thermoplastic matrices are usually tougher than their thermoset counterparts [7], thermoplastic based composites (TPC) are subjected to the phenomenon of delamination too. Delamination can be also caused by a poor adhesion between the fibres and the matrix, a potential source of lower overall mechanical properties in TPC [3]. Due to this fact, in literature there are many experimental data regarding the performances of TPC about the inter-lamina fracture toughness with exception to the ones composed by poly-ether-ketone-ketone (PEKK) matrix where few data are available.
PEKK is an aerospace grade semicrystalline polymer with a wide operational temperature range and capable to withstand high mechanical loads. It is therefore an aim of this work to provide

  doi:10.5075/epfl-298799_978-2-9701614-0-0

information regarding the interlaminar properties of the carbon fibre reinforced PEKK composites, in particular on the Interlaminar Shear Strength (ILSS) of the component produced by thermoforming.

2. Material

For the testing campaign, it has been used APC PEKK-CF from Solvay, a prepreg tape whose typical applications include aircraft structures, space components and other structural engineering parts. The prepreg is characterized by a 60% of fibre content in volume. The laminates were processed through hot-press moulding. The lay-up of the different prepreg sheets was wrapped up using Kapton foils to avoid the flow of the matrix and to maintain the desired geometry of the laminate. The package was then heated up to 370 °C without pressure applied, once reached the final temperature it has been applied a pressure of 10 bar for 20 minutes. Finally, the lamina was left to cool down in air with and the pressure was released once the temperature was lower than the expected glass transition (about 159 °C).
Three laminates were produced varying the stacking sequences to study the interlaminar properties changes with the variation of the fibre orientation along the thickness. Three representative sequencies were selected: Unidirectional 0°, $[90°/0°]_{8S}$ and $[0°/90°/45°/-45°]_{4S}$. All the three laminates are symmetric. Subsequently, the three laminates of dimensions 120x120x4 mm have been cut through waterjet to obtain the Short Beam Test specimens.

3. Method

For the evaluation of the Interlaminar Shear Strength (ILSS), it has been followed the ASTM standard D2344/D2344M, initially using cylinders of diameters of 6 mm and 3 mm for the loading nose and supports, respectively, as specified in the normative. As described in ASTM D2344, the tests were conducted on specimens nominally 4 mm thick, 8 mm wide and 24 mm long and the span between the support rollers was set to 16 mm. The rate of the loading nose's movement was set to 1 mm/min as specified in the standard.
To obtain a valid failure mode caused by interlaminar shear, in the case of $[90°/0°]_{8S}$ specimens, the dimension of the cylinders has been increased to avoid localised crushing on the specimen given by the stress concentration that arise in the interfaces between specimen and support/loading rollers. This aspect may underestimate the ILSS value caused by a compressive damage that may occurs before shear failure [4-6]. The diameter of the support rollers was then set to 4.5 mm while the diameter of the loading nose was incremented until a correct failure mode was obtained. Tests were conducted with a diameter of 8 mm, 10 mm, 12 mm, 16 mm and 20mm. This test method, in the case of unidirectional specimens, is useful also to determine the shear behaviour of the material through the creation of stress stain curves [6].
The strain field on the lateral surface was reconstructed using the 2D digital image correlation (DIC). For this aim, the surface of the specimen was preliminary coated with an opaque white water-based spray paint and subsequently a random pattern of black dots on the white background was created with a black paint as it is shown in Figure 1.
The tests were recorded using a Canon EOS 70D camera with a resolution of 1920×1080 pixels and 24 photograms per second. The images were calibrated manually obtaining a scale of 0.033 mm/pixel. For the analysis, the commercial software GOM Correlate version 2020 was used.
The shear strain values, obtained through the DIC analysis, were validated performing a SBS test with a strain gauge of grid dimension of 0.6x1 mm, placed at 45° in the midway between the loading nose and the support roller. The strain gauge was applied in the thickness midplane, on the opposite face with respect the one recorded by the camera.

  doi:10.5075/epfl-298799_978-2-9701614-0-0

After the test, the failure modes on the specimens were analysed with the optical microscope, Nikon model Eclipse LV105N.

Figure 1. Picture of the test validated through strain gauge

4. Results and discussion

As specified in the ASTM D2344 standard, the short beam strength is evaluated using the classical beam theory which states that the shear stress varies parabolically through the thickness of the specimen reaching, in the midway plane, the maximum value given by Eq. (1) in the case of a beam with rectangular cross section:

$$\sigma_{xy} = \frac{3}{4}\frac{P_M}{b \cdot h} \tag{1}$$

where P_M is the maximum value of the reaction force experienced by the test machine during the test, b is the width of the specimen and h is its thickness. Despite the simplicity of the theory used it has been shown that provides a good approximation of the real state of stress experienced by the specimen [6].

Values obtained with the different stacking sequencies can be seen in Figure 2. As it was expected, the unidirectional specimens have a higher value of ILSS. Indeed, in the case of layers with the same direction, during the production process of the laminate the fibres from adjacent plies tend to interlace between them making the laminate more homogeneous. The distinction between plies is faded and fibre bridging phenomenon can occur [3].

The specimen with a stacking sequence of $[0°/90°/45°/-45°]_{4S}$ are the ones with the lowest value of ILSS. It has been also noted a higher standard deviation on the values of the short beam strength. The reason of the higher variability on the ILSS values could be the fact that usually the non-zero ply interfaces are characterised by a higher level of variability regarding the thickness of the matrix region between plies, causing a high variability on the interlaminar fracture toughness [7]. As it can be seen in Figure 3, multiple delamination occurs along the thickness of the specimen, in some cases the interlaminar fracture branches and some smaller intralaminar fractures of the matrix are observed in the non-zero direction plies.

  doi:10.5075/epfl-298799_978-2-9701614-0-0

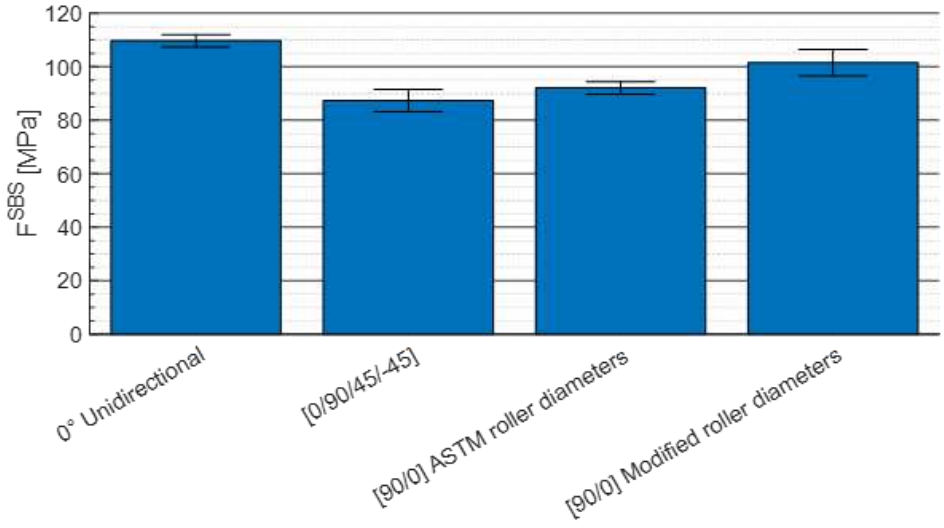

Figure 2. ILSS values of the different lay-up sequencies

Regarding the $[90°/0°]_{8S}$ specimens, it has been observed a failure mechanism not valid for the determination of the ILSS. As can be observed in Figure 3, the failure is triggered by a compression buckling failure next to the loading nose position. The cause of this behaviour could be the ductile nature of the thermoplastic matrix that experience an extensive compression yielding below the loading nose position [8]. Stress concentration in this region leads to intensive deformation of the matrix. the result of the elevated deformation gradient with respect the region on the side of the loading nose position leads to the matrix cracking in the plies with a 90° direction and to a tensile failure of the carbon fibres in the 0° plies.

The presence of this failure behaviour prior to the delamination can give an underestimation of the ILSS. Since this problem is caused by the stress concentration due to the contact of the loading nose on the specimen's surface, the dimensions of the loading nose and the support rollers were increased to assure a larger contact area and reducing the local stress values. The same technique was adopted in other research works on different materials [5-6]. The compressive failure was avoided using a loading nose diameter of 20 mm and a diameter for the support rollers of 4.5 mm.

The test was repeated with this configuration and as expected, higher values of short beam strength were obtained (see Figure 2). It is worth noting how the variability of the results with the new configuration has increased significantly, indeed as in the case of the $[0/90/45°/-45°]_{4S}$ specimens, the ILSS for non-zero ply interface is characterised with a high variability, and this is not true for the compressive failure mode experienced by the specimen tested with the standard ASTM dimension of the rollers.

As it is possible to see in Figure 3, the fracture is interlaminar but there is also present delamination migration inside the 90° plies. This happens because of the shearing directions that tends to drive the fracture upward or downward, inside the laminate until it reaches the interface with the ply with the fibers directed in the delamination growth [8]. The presence of the fibers along the length of the specimen avoids the propagation of the fracture along the direction of the thickness, while in the 90° plies the fracture is free to grow in the matrix.

  doi:10.5075/epfl-298799_978-2-9701614-0-0

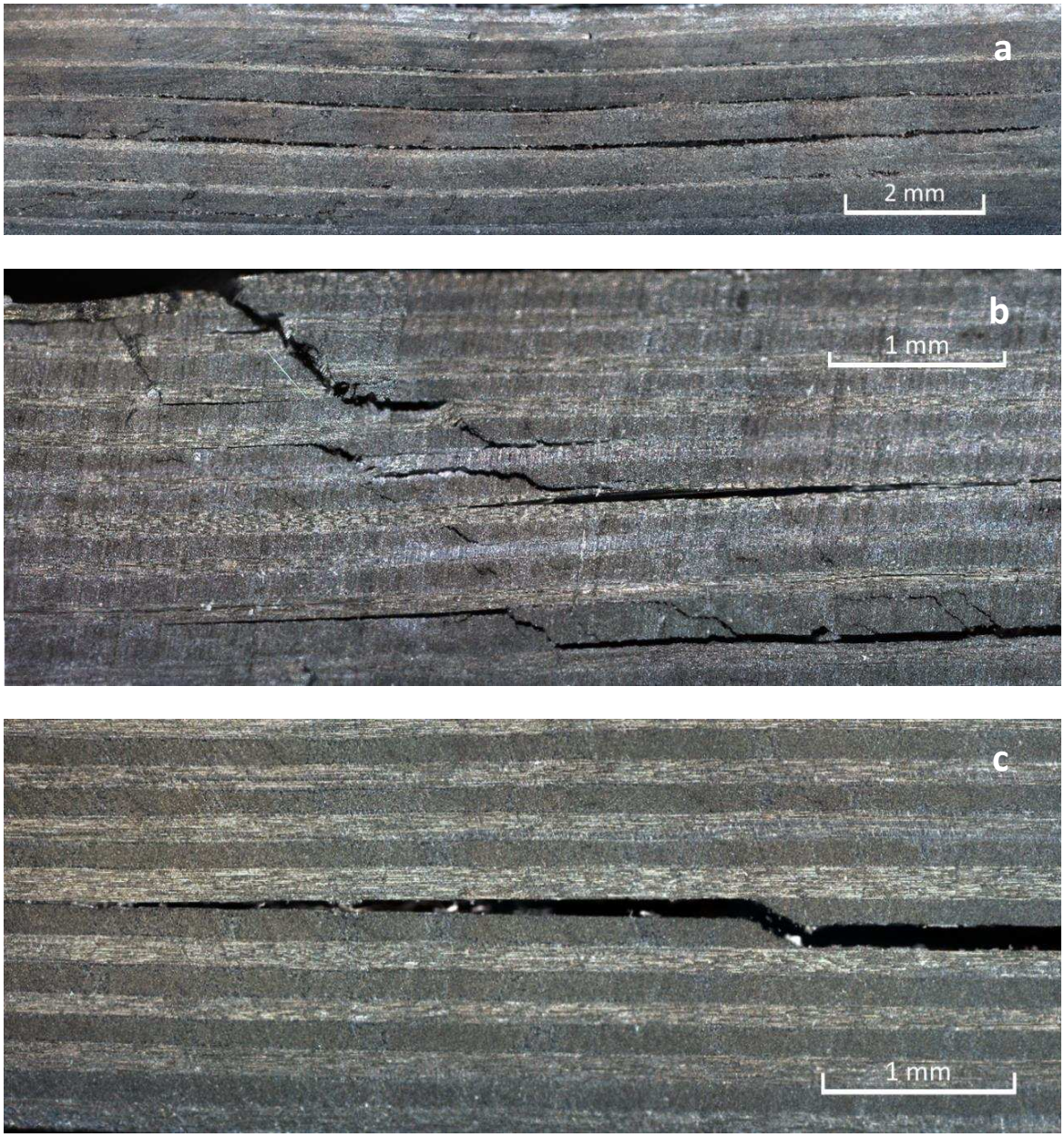

Figure 3. Fracture morphology in a $[0°/90°/45°/-45°]_{4S}$ specimen (a), $[90°/0°]_{8S}$ specimen tested with standard roller dimensions (b) and $[90°/0°]_{8S}$ specimen tested with modified roller dimensions (c).

In Figure 4 is reported the result of the DIC regarding the shear distribution exhibited by a unidirectional specimen during the test. The strains refer to a frame taken during the linear part of the loading curve. The distribution of the shear strain along the thickness is in accordance with the theory and the maximum values are in the midplane thickness, in the region between the loading nose and the support rollers. In this region, where most of delamination occurs (indicated in the figures with the red boxes), the shearing contributions are predominant, and the low gradient allows to evaluate the maximum shear strain by spatial averaging the strain values obtained through DIC.

  doi:10.5075/epfl-298799_978-2-9701614-0-0

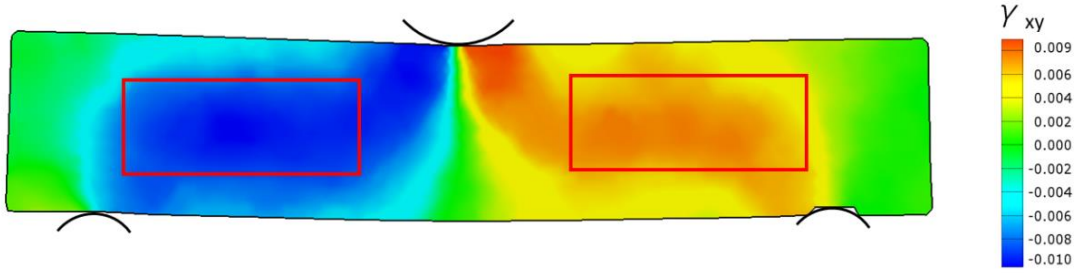

Figure 4. Shera stain field evaluated through DIC on a unidirectional specimen

5. Conclusions

From the results obtained with the short beam strength test campaign it is clear how a modification on the ASTM standard regarding the loading roller dimensions should evaluated considering the nature of the polymeric matrix. For matrices that tends to experience a higher plastic response, as most of the thermoplastic polymers, the dimensions of the rollers need to be increased.

The results of the DIC can also be used for the assessment of the shear stress-strain strain constitutive law of the material and to model the interlaminar and intralaminar fracture behaviour. Due to the nature of the thermoplastic matrix, the composites can exhibit plastic behaviour in the directions perpendicular to the fibres' direction. A correction on the Eq. (1) may be necessary for the evaluation of the maximum shearing stress experienced by the specimen at higher loads where non-linearities cannot be neglected.

6. References

1. Quilter A. Composites in aerospace applications. IHS White Paper. 2001;444(1):264.
2. Barile M, Lecce L, Iannone M, Pappadà S, Roberti P. Thermoplastic composites for aerospace applications. Revolutionizing aircraft materials and processes 2020 (pp. 87-114). Springer, Cham.
3. Bascom WD, Yon KJ, Jensen RM, Cordner L. The adhesion of carbon fibers to thermoset and thermoplastic polymers. The Journal of Adhesion. 1991 Jun 1;34(1-4):79-98.
4. Cui W, Wisnom MR, Jones M. Effect of specimen size on interlaminar shear strength of unidirectional carbon fibre-epoxy. Composites engineering. 1994 Jan 1;4(3):299-307.
5. Allott NR, Czabaj MW. Characterization of the interlaminar shear strength of IM7/8552 using small-scale short beam shear tests. Composites Part A: Applied Science and Manufacturing. 2021 Mar 1;142:106200.
6. Makeev A, He Y, Schreier H. Short-beam Shear Method for Assessment of Stress–Strain Curves for Fibre-reinforced Polymer Matrix Composite Materials. Strain. 2013 Oct;49(5):440-50.
7. Greenhalgh ES. Delamination-dominated failures in polymer composites. Failure analysis and fractography of polymer composites. 2009:164-237.
8. Whitney JM, Browning CE. On short-beam shear tests for composite materials. Experimental Mechanics. 1985 Sep;25(3):294-300.

  doi:10.5075/epfl-298799_978-2-9701614-0-0

TEST METHODS FOR DYNAMIC CHARACTERIZATION OF POLYMER-BASED COMPOSITE MATERIALS

Emilio V. González[a], José A. Artero-Guerrero[b], José González[c], Elisabeth De Blanpre[d], Vincent Jacques[d]

a: AMADE - Escola Politècnica Superior, Universitat de Girona, Girona, Spain;
emilio.gonzalez@udg.edu
b: Department of Continuum Mechanics and Structural Analysis, Universidad Carlos III de Madrid, Leganés, Madrid, Spain
c: COMPOXI, Girona, Spain
d: Dassault Aviation, Paris, France

Abstract: *The methodology of designing aeronautical structural components made with advanced polymer-based composite materials is quite mature and well stablished for static loads, and even, for fatigue loads. However, for intermediate and high dynamic loading conditions, the methodology is not clear and the test methods are often limited to academic research levels without any type of standardization. The Clean Sky project "Development of a methodology to characterize the behaviour of composite structures under dynamic loading" is focused, in part, on the definition of well-suited experimental tests at the coupon level for a whole characterization of polymer-based composite materials under dynamic loading. A definition is purposed at each of the large number of material properties that must be characterized to later simulate a composite structure. In the present communication, an overview of the test methods considered for the dynamic characterization and additional analysis of composite materials will be described within the framework of the project.*

Keywords: high-strain rates; dynamic loading; polymer-based composite

1. Introduction

When advanced polymer-based composite materials are to be used in aeronautical structural components, a design development program is generally initiated during which the performance of the structure is assessed prior to its use. Typically, the process of design starts with the analysis of a large set of simple small specimens and, when sufficient knowledge is acquired at this level, it is changed over to a more complex structure but carrying out fewer tests. This methodology is quite mature and well stablished for static and even for fatigue loads. However, for intermediate and high dynamic loading conditions, the methods are still under development and often limited to academic research levels, without any type of standardization.

During their service life, aerospace structures can be subjected to a variety of dynamic loading cases. Crash/impact is one of the most concerning cases due to its possible disastrous consequences. Impacts on aerospace structures can be produced by the accidental or deliberate hit of an object into aircraft. Hailstones, bird strikes, runaway debris, tyre fragments or even other fragments from the aircraft structure that could be ejected in case of an accident (i.e. uncontained rotor engine failure) are examples that occur in the aerospace sector. Therefore, it

is crucial to understand how the materials used in the aerospace sector behaves under dynamic loadings.

Composite materials may exhibit strain rate effects, therefore robust and industrial dedicated dynamic coupon and element level tests, analysis and modelling methods are then necessary to design and certify composite airframe structures. The analysis tools based on static formulations could be far away from the actual material and structural response, and hence a dedicated methodology is needed for dynamic loading states. This is what the European project entitled *Development of a methodology to characterize the BEhaviour of composite structures under DYNamic loading*, with the acronym BEDYN, will deal with.

1.1 Project details

BEDYN is a granted Clean Sky 2 Joint Undertaking (JU) project for call H2020-CS2-CFP10-2019-01 (Grant Agreement No. 886519), with Dassault Aviation as Topic Manager (TM). The project will be carried out by a consortium with different and complementary background and capabilities. The consortium is formed by: two universities, AMADE-UdG and UC3M; and a company, COMPOXI.

The topic of the project is collected to Airframe Integrated Technology Demonstrator (ITD), Part A WP A-1.4 oriented to "Virtual Modelling for Certification", and specifically to WP A-1.4-2 on "Advanced criteria for rapid dynamic / crash modelling for safety" (see Fig. 1). Globally, WP A-1.4 focuses on the enhancement of virtual modelling in the design process for certification purposes. For the particular case of "Advanced criteria for rapid dynamic / crash modelling for safety", the expected outcome is to increase the PRL (Process Readiness Level) of rapid dynamic analyses by developing adapted calculation methodologies and sizing criteria. This will contribute to support future certification processes for discrete damage and emergency situations (crash, bird strike, etc.) providing validated methods and tools against elementary tests.

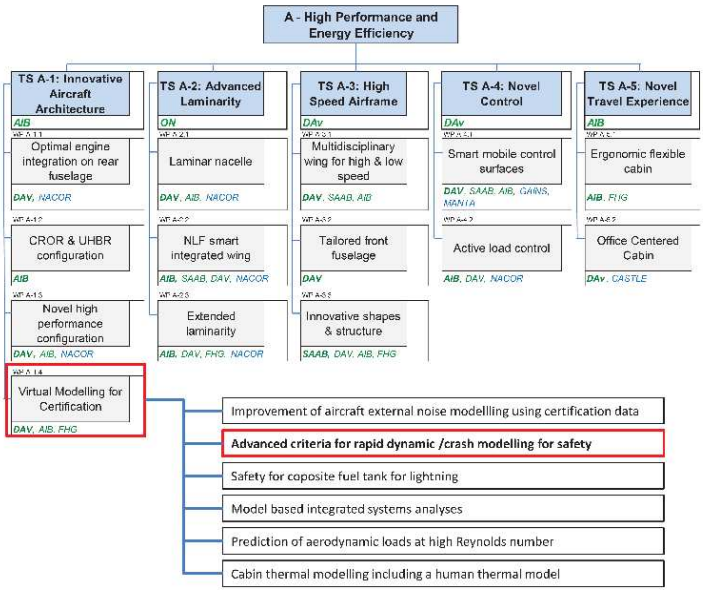

Figure 1. Airframe Integrated Technology Demonstrator (ITD), Part A WP A-1.4.

76/1211 ©2022 Gonzalez et al. doi:10.5075/epfl-298799_978-2-9701614-0-0 published under CC BY-NC 4.0 license

2. Project Work Packages

Basically, BEDYN project can be split into two differentiable sets of works: numerical and experimental. In accordance with the objectives of the project, the experimental part corresponds to defining the appropriate test methods to fully characterize thermoset-based composite materials under dynamic conditions, and to analyse different topics such as flexure response, notch effect and bearing response. The numerical part is focused on defining constitutive models and a simulation strategy accounting for dynamic effects, aligned with industrial purposes and thus a good balance of accuracy and computational analysis times.

These works are organized into 7 Work Packages (WP), the first 5 dedicated to technical tasks and the last 2 focused on management and communication activities. The relationship among the different WPs is schematically shown in Fig. 2. The specifications and inputs from TM are key-points at each of the WPs.

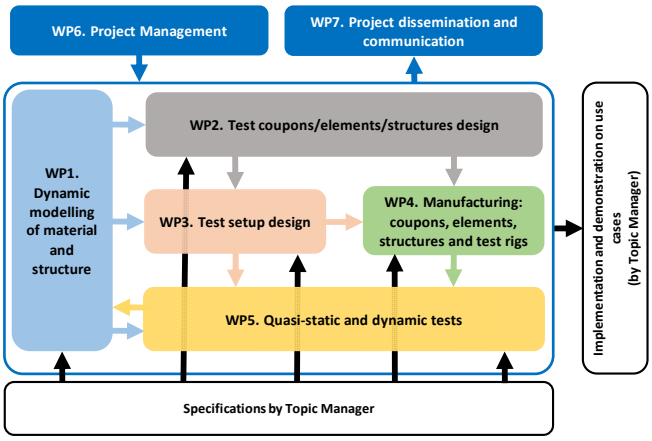

Figure 2. BEDYN's Work Packages.

The project starts and finishes in WP1, which contains the numerical activities to be performed (including the review, formulation and implementation of constitutive models and modelling strategy), but also, it includes the analysis of experimental results carried in the other WPs, as well as the validation of the whole methodology proposed for dynamic analysis.

All other technical WPs, are focused on experimental activities. On one side, these experimental activities deal with the complete characterization of a thermoset composite material under dynamic loading, including elastic properties (E_{11}, E_{22}, ν_{12}, G_{12}), strength properties (fibre: X_T, X_C; matrix: Y_T, Y_C; shear: S_L) and fracture toughness (interlaminar: G_{IC}, G_{IIC}, $G_{\%C}$; translaminar for a given laminate). The characterization also includes an adhesive bonded joint, thus in addition to the dynamic characterization of the associated fracture toughness, the strengths must be also described. On the other hand, other topics will be analysed experimentally: flexure response, notch effect and bearing. For all tests, specimens, test setups and well-suited data reduction methods must be defined based on literature reviews or novel test methods. Since in the literature there is no agreement on the effect of dynamic loads on some material properties (for both material characterizations: ply and delamination), and in some cases, it has never been studied, this topic is a challenge. Finally, simple flat-shaped structures will be manufactured for testing under out-of-plane gelatine-impact, as experimental data for the validation of the whole methodology. Accordingly, three different specimen types can be identified: "coupon", for

77/1211 ©2022 Gonzalez et al. doi:10.5075/epfl-298799_978-2-9701614-0-0 published under CC BY-NC 4.0 license

characterizing basic properties of the composite material (ply), interlaminar (delamination) and adhesive interfaces; “element”, they include what can be understood as small size demonstrator; “structure”, they are devoted for characterizing the behaviour at a subcomponent level under out-of-plane dynamic loads. These experimental tasks will be carried out in four different WPs: WP2, definition of specimens; WP3, design of test setups and data reduction methods; WP4, manufacturing of specimens and new test rigs; and finally, WP5 the execution of the experimental test campaign.

3. Methodology

For the development of the project, there are several Key Steps (KS) on which the BEDYN methodology will rely. The KSs associated with the dynamic testing, which is the topic of the present communication, are described below.

3.1 Dynamic material characterization

In the Building Block Approach method, different structure levels must be tested to increase test complexity while maintaining confidence levels on the experimental and numerical results. In BEDYN project, it is proposed to perform a basic material characterization in both, intralaminar and interlaminar levels (the last includes co-bonded interface and delamination interface). The tests considered are summarized in Table 1 and Table 2. The use of the Split Hopkinson Pressure Bar (SHPB) bar will be required for both compressive and tensile configurations. Different coupon geometries will be used to obtain the different properties at desired strain rates. However, there are still particular properties at which there is no available tests, such as for the dynamic interlaminar fracture toughness characterization. AMADE-UdG and UC3M were working in the development of this experimental characterization and it will be used for the project (limited to pure mode I crack propagation; see sketches of the test rig in Fig. 3). The selection of the specimen and test setups will be mainly done by Finite Element simulations. An important result to be satisfied is the load equilibrium during the dynamic SHPB tests to properly obtain the corresponding characterization without any inertial effect.

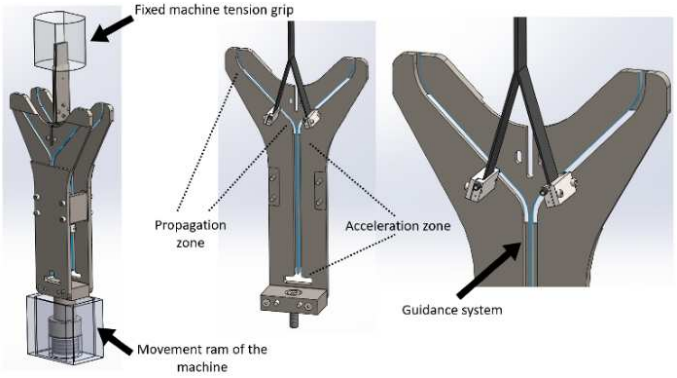

Figure 3. Test rig to characterize fracture toughness in pure mode I using a high-speed servo-hydraulic machine (patented with international application number PCT/ES2021/070415 and publication number WO/2022/003219).

For SHPB test, the use of high speed camera will allow to apply Digital Image Correlation (DIC) method to obtain displacement and strain rate fields. To obtain the stress state and static equilibrium, the SHPB theory will be used.

78/1211 ©2022 Gonzalez et al. doi:10.5075/epfl-298799_978-2-9701614-0-0 published under CC BY-NC 4.0 license ToC

A unidirectional tape of epoxy/carbon fibre prepreg material and an epoxy adhesive film will be used (see Table 3). Two different strain rates, plus static tests will be performed. It is worth mentioning that the static tests will be based, whenever possible, on standardized test methods. The specimen sample considered for each test configuration will be of 3+1 specimens (three for testing plus one for reserve). All specimens will be stored and tested at laboratory conditions, 23ºC and 50%RH.

Table 1: Coupon specimens I/II.

Type	Tester	Reference	Results
Longitudinal compression	SHPB-C	Ploeckl et al. (2017) [1] BEDYN research	E_{11C}, ν_{12}, X_C
Transverse and off-axis tensile	SHPB-T	Kuhn et al. (2015) [2] Quino et al. (2020) [3] BEDYN research	E_{22T}, ν_{12}, Y_T Failure envelope: σ_{22T} - σ_{12}
Transverse and off-axis compression	SHPB-C	Koerber et al. (2010) [4] Ploeckl et al. (2017) [1] BEDYN research	E_{22C}, Y_C Failure envelope: σ_{22C} - σ_{12}

Table 2: Coupon specimens II/II: interlaminar and adhesive bonded joint specimens.

Type	Tester	Reference	Results
Double Cantilever Beam - Pure mode I (DCB)	Instron servo hydraulic dynamic	AMADE-UdG procedure (see Fig. 3)	G_{IC}: onset and propagation, interlaminar and adhesive bonded joint
End Notched Flexure - Pure mode II (ENF)	SHPB-C	Lißner et al. (2020) [5] Shamchi et al. (2022) [6] BEDYN research	G_{IIC}: onset and propagation, interlaminar and adhesive bonded joint
Single Leg Bending Test - Mixed-mode 41% (SLB)	SHPB-C	Lißner et al. (2020) [5] BEDYN research	$G_{\%C}$: onset and propagation, interlaminar and adhesive bonded joint
Butt Joint (BJ)	SHPB-T	Neumayer et al. (2016) [7] BEDYN research	τ_I: pure mode I strength adhesive bonded joint
Single Lap Shear - SLS	SHPB-C	BEDYN research	τ_{II}: pure mode II strength adhesive bonded joint

Table 3: Material specifications and loading rates.

Item	Definition
Composite Material	Hexply® M21EV/34%/UD200/IMA/150ATL
Adhesive	FM® 300M

Loading rates	Quasi-static + 2 dynamic (focus: 20 s^{-1} and 100 s^{-1})

3.2 Dynamic structure characterization

In order to analyse the effect of different properties as the notch effect (size effect), flexural behaviour and the bearing effect, element (i.e. small size demonstrator) and structure (i.e. subcomponent level) specimens will be considered in the test matrix. The element and structure tests considered are collected in Table 4 and Table 5.

The scope of these tests are: two stacking sequences, two notch sizes and two fastener diameters for bearing tests (see Table 6). The use of the SHPB bar will be required for both compressive and tensile configurations. It has to be noted that if specimen sizes are not adequate, it may be difficult to detect any clear dynamic effect. The specimen sample considered for each test configuration will be of 3+1 specimens (three for testing plus one for reserve). Also, two different high strain rates plus the quasi-static tests will be performed. To avoid any possible size effect, the specimens used for quasi-static testing will be with the same features as the ones used dynamically.

Table 4: Element type specimens.

Type	Tester	Reference	Results
Three point bending (3PB)	SHPB-C	Zhang et al. (2012) [8] BEDYN research	Flexural strength
Filled Hole Tension (FHT)	SHPB-T	BEDYN research	Notch effect: Remote strength
Filled Hole Compression (FHC)	SHPB-C	BEDYN research	Notch effect: Remote strength
Compact Tension (CT)	SHPB-T	Hoffman et al. (2018) [9] BEDYN research	Notch effect: G_C translaminar fracture toughness. A cross-ply laminate is considered for G_{X_TC}
Composite-aluminium bolted joint (Bearing)	SHPB-T	BEDYN research	Bearing: Remote strength

Table 5: Structure specimens.

Type	Tester	Reference	Results
Out-of-plane gelatine impact on flat-shaped laminates (500 mm x 500 mm)	Gas gun	BEDYN research	DIC - high speed cameras Non-destructive Inspections

Regarding the testing at the subcomponent level, it will be used the pneumatic launcher from UC3M lab in which a bird substitute projectile will impact against a flat panel. The results of these tests will be used for the validation and verification of the BEDYN methodology by the TM.

A total of 4 specimens will be manufactured, 2 for each stacking sequence to be tested at 2 different gelatine impact velocities, with 1 repetition for each configuration. All impact tests will be recorded with at least 3 high speed video-cameras, allowing also to obtain the strain rate and the strain field of the structure. Testing at a component level and beyond will not be considered in this proposal.

Table 6: Summary of specifications for Element type specimens.

Item	Definition
Fasteners: FHT, FHC and Bearing	Titanium
Aluminium plate: Bearing	2024-T3
Lay-ups for *Element* and *Structure* type specimens	Layup #1: $[-45/0_2/45/90/45/0_2/-45/0]_S$ Layup #2: $[45/0/-45/90/-45/0/45/90/-45/0/45/90]_S$
FHT and Bearing (FHC, just Size #1 is tested)	Size #1: hole 4 mm; width 24 mm (Torque: 2 mN) Size #2: hole 8 mm; width 48 mm (Torque: 16 mN)

The total number of tests to be performed including material characterization, elements and structures is of 476, 184 quasi-static plus 292 dynamic.

4. Conclusions

The BEDYN project will address a methodology to properly characterize the dynamic behaviour up to rupture of thermoset polymer-based composite structures submitted to dynamic loading. The methodology includes the definition of test methods for the complete characterization of composite materials under dynamic loading. The project is challenging since dynamic test methods are scarce in the literature, without no standardization and often without consensus in the associated works for a given property. Therefore, the project implies the selection of specimens, test setups (tester and instrumentation) and well-suited data reduction methods. The methodology is completed with the selection of a modelling strategy for industrial purposes which will be fed by the dynamic material data cards defined.

Acknowledgements

This project has received funding from the Clean Sky 2 Joint Undertaking (JU) under grant agreement No. 886519. The JU receives support from the European Union's Horizon 2020 research and innovation programme and the Clean Sky 2 JU members other than the Union.

5. References

1. M. Ploeckl, P. Kuhn, J. Grosser, M. Wolfahrt, and H. Koerber, 'A dynamic test methodology for analyzing the strain-rate effect on the longitudinal compressive behavior of fiber-reinforced composites', Composite Structures, vol. 180, pp. 429–438, 2017.

2. P. Kuhn, M. Ploeckl, and H. Koerber, 'Experimental investigation of the failure envelope of unidirectional carbon-epoxy composite under high strain rate transverse and off-axis tensile loading', in EPJ Web of Conferences, 2015, vol. 94, p. 01040.

3. G. Quino, V. L. Tagarielli, and N. Petrinic, 'Effects of water absorption on the mechanical properties of GFRPs', Composites Science and Technology, vol. 199, p. 108316, Oct. 2020, doi: 10.1016/j.compscitech.2020.108316.

4. H. Koerber, J. Xavier, and P. P. Camanho, 'High strain rate characterisation of unidirectional carbon-epoxy IM7-8552 in transverse compression and in-plane shear using digital image correlation', Mechanics of Materials, vol. 42, no. 11, Art. no. 11, 2010.

5. M. Lißner, E. Alabort, B. Erice, H. Cui, B. R. Blackman, and N. Petrinic, 'On the dynamic response of adhesively bonded structures', International Journal of Impact Engineering, vol. 138, p. 103479, 2020.

6. S. P. Shamchi, M. F. S. F. de Moura, Z. Zhao, X. Yi, and P. M. G. P. Moreira, 'Dynamic mode II interlaminar fracture toughness of electrically modified carbon/epoxy composites', International Journal of Impact Engineering, vol. 159, p. 104030, 2022, doi: https://doi.org/10.1016/j.ijimpeng.2021.104030.

7. J. Neumayer, P. Kuhn, H. Koerber, and R. Hinterhölzl, 'Experimental determination of the tensile and shear behaviour of adhesives under impact loading', The Journal of Adhesion, vol. 92, no. 7–9, Art. no. 7–9, 2016.

8. Y. Zhang, B. Sun, and B. Gu, 'Experimental characterization of transverse impact behaviors of four-step 3-D rectangular braided composites', Journal of composite materials, vol. 46, no. 24, Art. no. 24, 2012.

9. J. Hoffmann, H. Cui, and N. Petrinic, 'Determination of the strain-energy release rate of a composite laminate under high-rate tensile deformation in fibre direction', Composites Science and Technology, vol. 164, pp. 110–119, 2018.

CHARACTERISATION OF ORTHOTROPIC ELECTRICAL CONDUCTIVITY OF UNIDIRECTIONAL C/PAEK THERMOPLASTIC COMPOSITES

Yannick Buser[ab], Gerben Bieleman[ab], Wouter Grouve[a], Sebastiaan Wijskamp[b] and Remko Akkerman[ab]

a: University of Twente, Faculty of Engineering Technology, Chair of Production Technology, Drienerlolaan 5, 7522NB Enschede, the Netherlands – y.m.buser@utwente.nl
b: ThermoPlastic composites Research Center, Palatijn 15, 7521PN Enschede, the Netherlands

Abstract: *Induction welding is a promising fusion bonding technology for carbon fibre reinforced thermoplastic composites. In this process, an alternating electromagnetic field induces eddy currents in a composite susceptor. The amount of resultant heat generated is governed by the electrical conductivity of the carbon fibre network, making accurate determination of this orthotropic property important for physics-based process simulations. This work focusses on characterisation of the conductivity in unidirectionally reinforced PAEK using the six-probe method. Special attention has been given to the distribution of the current density in the specimens during each characterisation experiment. Acquired resistance data was subsequently interpreted either analytically or numerically, depending on the current distribution detected. The longitudinal component of the conductivity tensor was found in agreement with the rule of mixtures and the transverse and through-thickness conductivities matched earlier characterisation attempts where a conventional two-probe analysis was employed.*

Keywords: Characterisation; Electrical conductivity; Six-probe method; Induction welding

1. Introduction

Thermoplastic composite (TPC) parts are increasingly used as structural components in modern aircraft. Initially, their application was limited to clips and brackets to connect the metal or thermoset composite aircraft skin to its stiffening frame. These successful early adaptations have paved the way for application on a larger scale. Nowadays, both skin and stiffeners are considered candidate for manufacturing out of unidirectional (UD) TPC tapes, mainly due to the automation opportunities it represents [1]. The assembly of substructures built entirely from UD ply-based TPCs is therefore an increasingly relevant subject.

A key advantage of TPC substructures when compared to their thermoset equivalents, is the potential for assembly via fusion bonding, which can negate the need for adhesives. In essence, fusion bonding involves the local application of time, heat and pressure to melt and consolidate the joint, establishing a weld. The various welding technologies that exist as of today mainly differ in how sufficient heat is localised at the joint. Induction welding (IW), one of these technologies, is an attractive method because heat is generated directly inside the material, instead of being transferred via tooling or directed to the interface by introducing foreign materials at the joint. Additionally, the process is very suited for automation.

The internal heat generation during IW is attained through the electrically conductive network of carbon fibres. This network features coil-like characteristics and is therefore receptive to electromagnetic flux. Application of an external electromagnetic field emitted by a welding coil

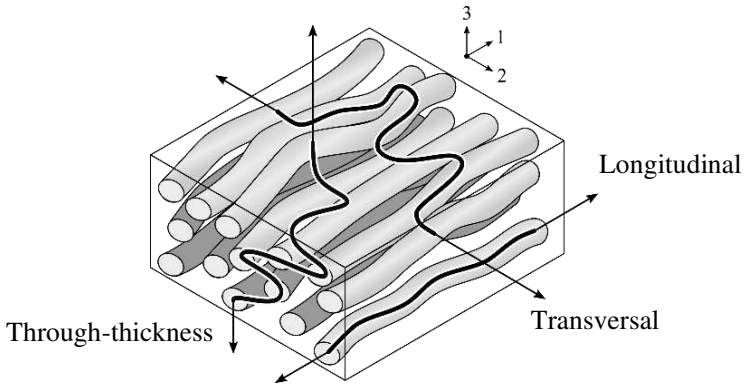

Figure 1: Schematic of longitudinal, transverse and through-thickness current flow in an UD ply

will therefore induce opposing current loops in the composite. These so called eddy currents generate heat due to the inherent resistance of the carbon fibres (Joule heating) and the resistive junctions present between them. It is challenging to inductively generate heat in UD reinforced plies. In the transverse direction (and equally true for the through-thickness direction) current flow is governed by the coincidence of fibre-fibre contacts caused by morphological phenomenon such as fibre waviness and clustering (illustrated by Figure 1) [2-3]. The limited number of contacts and small contact areas result in a poor transverse conductivity and thus acts as a barrier to the formation of significant intra-ply current loops. In actual UD ply-based laminates, formation of eddy currents therefore relies on the ply interfaces where changes in stacking orientation allow the current to utilise the conductive nature of the different fibre directions to form an eddy [4]. Nevertheless, the contact incidence mechanisms remain of importance for the distribution of current to and from the ply interfaces. The magnitude and distribution of the resultant heat during IW thus remains, among others, a function of the electrical conductivity in all three principal directions.

Despite successful applications of IW technology in industrial settings, such as the woven fabric reinforced rudder and elevator of the Gulfstream G650 by GKN Fokker [5], large scale application, let alone of UD ply-based reinforcements, has yet to take flight. In current practice, a quality weld is preceded by an extensive experimental investigation of the process window, matching the power input of the welding rig to achieved weld-line temperatures. And for UD ply-based components specifically, the temperature response is very sensitive to variations in material behaviour, as the electrical conductivity is partly governed by the amount and quality of fibre-contacts and, closely related, the volume fraction in which the constituents are present. Consequently, improved process control will require quantification of and insight in the orthotropic electrical conductivity of UD-ply based TPCs, aiding process modelling capabilities.

In preceding work by Grouve et al. [4] the orthotropic electrical conductivity of UD reinforced PEKK was determined (see Table 1) using a conventional two- and four-probe approach, methods typically associated with isotropic material systems. The found conductivities were used as input for numerical validation of induction heating experiments performed. Discrepancies between numerical and experimental data remained, which might be attributed to an underprediction of the conductivities found. The present study will therefore re-evaluate the characterisation procedure to gather further insight.

Table 1: Orthotropic electrical conductivity as obtained from the work of Grouve et al. [4]

Material	**Orthotropic electrical conductivity**		
	Longitudinal, σ_1	Transverse, σ_2	Through-thickness, σ_3
Solvay AS4D/PEKK, 59% FVF	22.9 ± 0.05 kS/m	3.37 ± 0.06 S/m	0.40 ± 0.22 S/m

This work addresses the characterisation of orthotropic electrical conductivity in UD ply-based TPCs using a direct current (DC) six-probe method. In particular, careful attention is paid to the boundary conditions involved in characterisation, that is considering the validity of assumptions made about the uniformity of the current distribution during the experiment. For this purpose, two morphologically distinct and commercially available UD reinforced PAEK prepregs are characterised. There will be reflected on the properties found by comparing the results to theoretical values and the results presented in Table 1.

2. Materials and methodology

2.1 Six-probe method

This work will employ the six-probe method as the basis for characterisation. A schematic of the method is shown in Figure 2 in which a DC current I is one-sidedly applied over the width w of a specimen via the outer probes. This creates an electric field that is uniform across the width, but non-uniform across the thickness t. Four inner probes are used for sampling the voltage response on both sides of the specimen, V_t and V_b. Besides the in-plane conductivity σ_x, this allows determination of the through-plane conductivity σ_z in the same run, which can be deduced from the difference measured between V_t and V_b. Additionally, the parallel configuration of the voltage terminals to the current flow eliminates lead and contact resistance from the measurement data.

It should be noted that, depending on the distance between the probes, the specimen geometry and the degree of anisotropy in the xz-plane, a fully uniform current can develop between the voltage terminals, such that $V = V_t = V_b$. In such a case, a simplistic relation can be used to determine the conductivity in x-direction:

$$\sigma_x = \frac{\delta}{wt}\frac{I}{V} = \frac{\delta}{wt}\frac{1}{R} \tag{1}$$

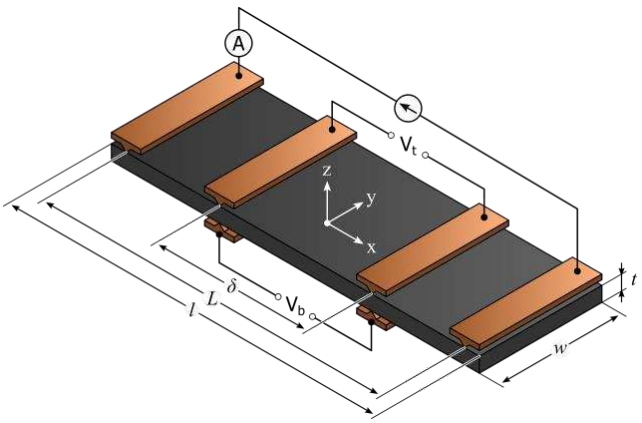

Figure 2: Schematic of the six-probe method and parameters involved

In any other case, the six-probe method relies on assumptions regarding the current density throughout the coupon for determination of the anisotropic conductivity from test data. However, as a consequence of the heterogeneous architecture of the UD reinforcement, both the inherent anisotropy and distribution of the insulating polymer lead to complexities in satisfying the assumed current distribution. The conductivity in longitudinal direction is shown four to five orders of magnitude higher compared to its perpendicular components (Table 1). This implies that local variations in the fibrous architecture and/or poor contact between probe and test coupon can amount to clusters of preference paths in the fibre network, acting as a short-circuit. In such circumstances, the electrical conductivity will be underpredicted by the data analysis since most of the current density is passed through an effective cross-sectional area smaller than the coupon cross-section wt. It is thus important to determine transversal and through-thickness conductivity, to the extent possible, uncoupled from current flow in fibre direction. This consideration is reflected in the work presented by measuring longitudinal conductivity in a separate set of experiments.

2.2 The rule of mixtures for electrical conductivity

The rule of mixtures (RoM) provides a theoretical estimate for the principal conductivity in fibre direction, given as

$$\sigma_1 = f\sigma_f + (1-f)\sigma_m \approx f\sigma_f \tag{2}$$

in which f is the fibre volume fraction and σ_f and σ_m the electrical conductivity of the constituents, respectively fibre and matrix, with the latter being negligible compared to the fibre conductivity. The RoM will serve as a comparison for the results presented later.

2.3 As-received prepregs

Unidirectionally carbon fibre reinforced PEEK (Toray TC1200) and PEKK (Solvay APC) with an average consolidated ply thickness (CPT) of 0.14 mm were used for this study. The pre-impregnated (prepreg) tapes contain carbon fibre from Hexcel (resp. 12K AS4 and 12K AS4D) in a volume fraction of 59%, a fibre areal weight of 145 g/m^2 and a fibre conductivity of 59 kS/m [6]. The prepregs have been selected for their prominent contrast in morphology, depicted in Figure 3, where it can be observed the prepregs differ in terms of uniformity of the fibre-matrix distribution.

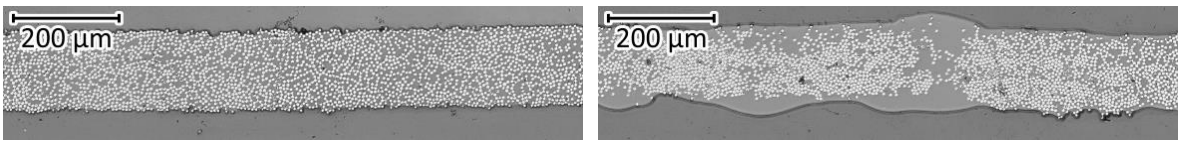

Figure 3: Micrographs of Toray PEEK (left) and Solvay PEKK (right) as-received prepregs

2.4 Specimen preparation

Two sets of specimens are used in this study. For measurements of longitudinal conductivity, 10 slender strips of both prepregs were cut from the roll, dimensioning approx. 250 × 50 mm^2, with fibres oriented in length direction. The exact width of the strip was measured using a digital calliper. The high aspect ratio (length-over-thickness) was chosen for current to develop as uniformly as possible over the thickness of the ply. The strips were subsequently pre-treated to

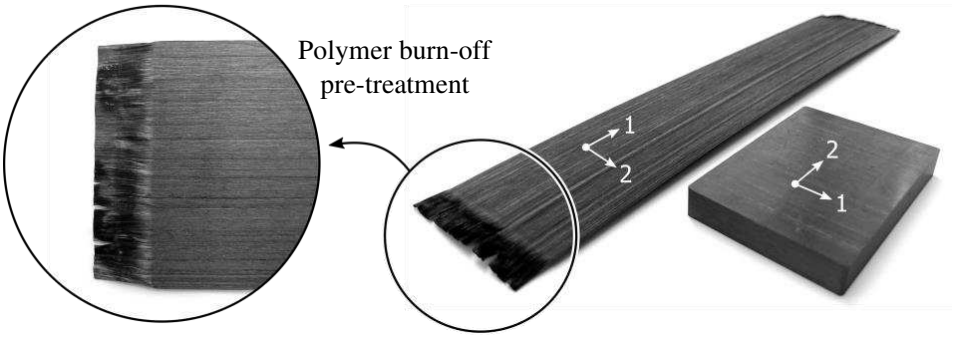

Figure 4: Photograph of a slender prepreg (left) and 64-ply consolidated (right) specimen

enhance the electrical contact with the current supply terminals. To this purpose, a length of approx. 10 mm at both tape ends was subjected to polymer burn-off using a gas torch, exposing the fibrous constituent, while the remaining tape was shielded using a metal heatsink (Figure 4).

For the second category of specimens, a hot press was used to consolidate thick 12 × 12 in^2 laminates with a $[0]_{32s}$ and $[0]_{16s}$ fully UD lay-up using a picture frame mould. An overview of the consolidation cycles is given in Table 2. From each laminate, 15 specimens with in-plane dimensions of 65 × 45 mm^2 were precision milled with the fibres oriented in width direction (Figure 4 and 5). The thickness of each specimen was measured with a micrometer in a 6-point grid. This set of specimens is used for characterisation of transverse and through-thickness electrical conductivity.

Table 2: Consolidation parameters and average thickness of the parent laminates

Material	**Consolidation cycle**				**Thickness [mm]**	
	Temperature	Pressure	Dwell	Cooling rate	$[0]_{32s}$	$[0]_{16s}$
AS4/PEEK	385 °C	20 bar	20 min	5 °C/min	8.99 ± 0.04	4.51 ± 0.04
AS4D/PEKK	380 °C	20 bar	30 min	5 °C/min	9.15 ± 0.05	4.55 ± 0.05

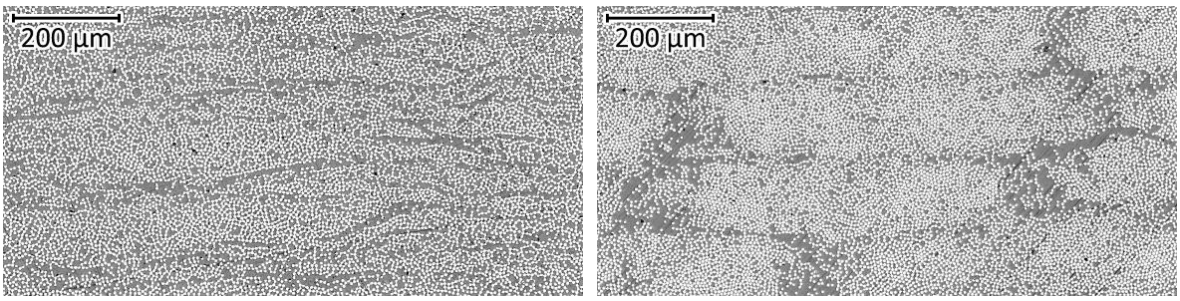

Figure 5: Micrographs of Toray PEEK (left) and Solvay PEKK (right) $[0]_{16s}$ consolidated specimens

2.5 Electrical conductivity measurements

A six-probe test fixture was manufactured following the schematic depicted in Figure 2. The spacing of the inner probes δ and outer probes L were set to resp. 100 mm and 240 mm for the longitudinal conductivity specimens (the slender tapes) and resp. 25 mm and 55 mm for the transversely oriented consolidated specimens.

A Tenma 72-13360 DC power supply was used to perform a pre-programmed current sweep from 0.1 to 1 A with increments of 0.1 A. A few specimens required modification of this range due to power output limitations of the supply. At each increment, current was maintained for 1 second. Under these conditions, Joule heating in the specimens was kept at a minimum, hence measurements are regarded isothermal. A TiePie HS6D differential oscilloscope was used for continuous acquisition (at a 1 kHz sample rate) of the actual supplied current via a connected current clamp and the potential difference over the voltage terminals. In further analysis current and voltage data was taken as the average over each 1 second interval. Measurements were performed twice for the transversely oriented specimens, with the specimen mounted upside-down in the second run.

Conductivity measurements on the prepreg tapes were preceded by an analysis of the current distribution over the width of the specimens. The contact resistance between the current terminal and tape has a significant contribution to the total resistance of the circuit, thus it should be verified whether variations in contact resistance cause uneven insertion of current in the tape. To this end, tapes were subjected to a 10 A supply current first, such that the increase of surface temperature through resistive losses could be monitored using a FLIR A65 infrared camera. Such verification is regarded trivial for the transversely oriented coupons, because the electrical anisotropy actually promotes the sideways flow of current in this configuration.

Determination of the electrical conductivity has been approached numerically in cases where V_t exceeded V_b. A 2D model of the xz-plane was constructed in COMSOL Multiphysics, iteratively solving for the anisotropic electrical conductivities σ_x and σ_z. The data measured with both voltage terminals was defined as the objective for the solver for a given supply current as boundary condition. With an educated first guess, this approach can be remarkably fast.

3. Results and discussion

3.1 Lateral current homogeneity

Figure 6 shows the thermogram of the typical initial heating response of a PEEK prepreg specimen not subjected to the pre-treatment, loaded with a 10 A DC current. As anticipated, lateral uniformity of the current density is not satisfied in absence of a pre-treatment, resulting in the resistive heating of selective fibre clusters only. The apparent underlying variations in probe-ply contact resistance can be attributed to a combination of prepreg roughness and uneven distribution of insulating polymer at the wetted surface. The poor transverse electrical conductivity of the UD reinforcement is also clearly illustrated by this experiment, as the heating pattern does not homogenise further away from the probes. Prepreg specimens treated with the local burn-off procedure feature a contrastingly uniform heating behaviour upon current application (Figure 6). The polymer removal likely both lowers and homogenises the contact resistance at the line contact with the probes, such that lateral uniformity is satisfied.

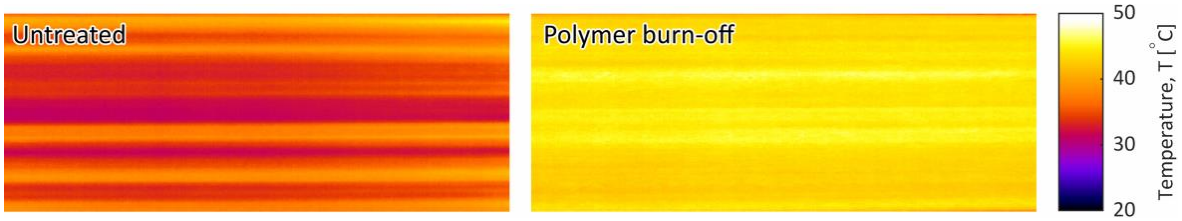

Figure 6: Surface heatmaps of a PEEK specimen before (left) and after (right) pre-treatment

3.2 I-V linearity analysis and data reduction

The current sweep performed during each characterisation experiment can be used to verify the isothermal Ohmic behaviour of the specimens, required for application of the constitutive relations involved in data analysis. Figure 7 and 8 show the typical plots of such analysis for a prepreg specimen and a consolidated stack respectively. Both figures show a constant resistance, the slope of the regression.

For most prepreg specimens, the resistance over the top and bottom voltage terminals was regarded equal (see Figure 7), hence $R = R_t \approx R_b$, such that Eq. (1) for a fully uniform current density distribution could be applied to determine the longitudinal electrical conductivity σ_1. The threshold for equality was set as $|R_t/R_b| \leq 2\%$, which is based on cases where a negative resistance difference was measured, that is when R_b exceeded R_t in magnitude. For a select few measurements the numerical model had to be employed.

Figure 8 shows the exemplary I-V curves for a current sweep on a 64-ply transversely oriented specimen. It can be observed that the chosen probe configuration and specimen thickness(es) do accommodate the non-uniformity required in through-thickness current distribution for a lower voltage reading at the bottom terminals, while still being sufficiently detectable. More interestingly, reversing (flipping) the orientation of the specimen has a large influence on the voltage readings. This observation highlights the statistical nature of the fibre contact incidence dictating the transverse current flow. Consequently, each specimen response has been further homogenised by taking R_t and R_b as the closest fit through both measurements, represented by the solid lines in Figure 8. For all specimens, the numerical method was subsequently used to fit σ_2 and σ_3 to these averaged trends.

3.3 Orthotropic electrical conductivity

Figure 9 shows the characterised longitudinal electrical conductivities of both the PEEK and PEKK prepreg specimens. A close agreement is found with the theoretical longitudinal conductivity predicted by the Eq. (2) as 35 kS/m, validating its applicability. The error bars in Figure 9 represent the standard deviation of the dataset. Especially for the PEEK specimens evident

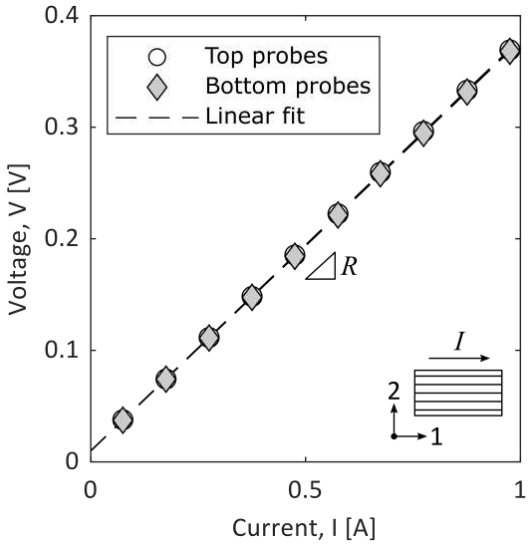

Figure 7: Current and voltage data of a PEEK prepreg specimen

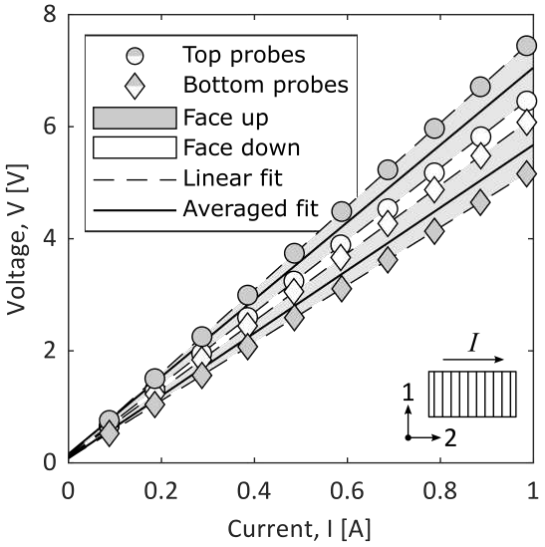

Figure 8: Current and voltage data of a 64-ply PEEK consolidated specimen

variance is present in the data. This could well be the result of assumptions made about the prepreg thickness, which was taken as the average CPT specified by the manufacturer. This lead to variations in prepreg thickness not being accounted for in the data processing.

The characterised conductivities in transverse and through-thickness direction are shown in Figure 10. No significant effect of the ply-count is found in the dataset. Between suppliers however, the PEEK sample features a greater transverse conductivity compared to the PEKK sample. A possible explanation for this behaviour can be found in the morphological differences between the two prepregs. The less homogeneous distribution of the constituents in the as-received PEKK prepreg amounts to polymer pockets that clearly remain present in the consolidated specimens, as can be observed in Figure 5. These pockets obstruct transverse current flow and, since they are typically continuous in fibre direction, might require a bypass via the adjacent plies. Ply-scale transverse conductivity measurements could confirm this hypothesis, as in absence of adjacent plies a bypass cannot be facilitated, further increasing the resistance.

Two key observations are notable when comparing the six-probe test results for PEKK with the two-probe results (Table 1) on the same material. Regarding the longitudinal conductivity, the present study validated the applicability of the RoM, in contrast to the earlier work. In retrospect, it seems therefore unlikely that the four-probe characterisation procedure lead to the same quality of current uniformity as achieved by the novel pre-treatment presented, thus underpredicting the RoM. The transverse and through-thickness conductivities found, however, are in agreement with the earlier work. This result hides a remarkable observation. The two-probe specimens tested in [4] dimensioned 16 mm in width, about three times narrower than the six-probe specimens. The fact that, despite this difference, the narrower two-probe specimens did not exhibit a significantly lower conductivity, suggests that at the scale tested the statistical nature of contact incidence and resulting preference paths has reached it saturation.

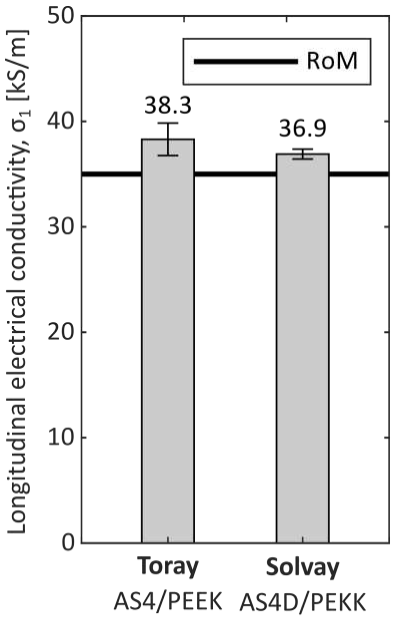

Figure 9: Bar plot of the characterised longitudinal conductivities

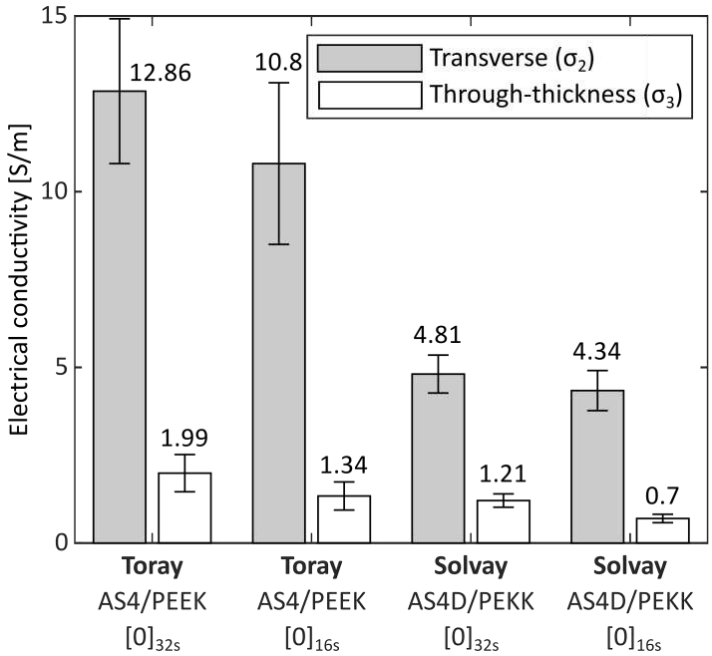

Figure 10: Bar plot of the characterised transverse and through-thickness conductivities

Further research should be performed on a range of six-probe specimen widths to verify this hypothesis under similar test conditions.

4. Conclusion

Electrical conductivity experiments were performed on UD carbon fibre reinforced PEEK and PEKK specimens using a six-probe method. As expected, attention to the distribution of current density in the specimen during the experiment is crucial for reliable characterisation of the intrinsic properties. The electrical conductivity in longitudinal direction is found in agreement with the rule of mixtures. For the transverse and through-thickness directions, a methodology is showcased that grants characterisation of both remaining properties in a single experiment which are in agreement with measurements from earlier work using a two-probe method. For further research, it is recommended to apply the six-probe approach presented to a broader range of widths for the transversely oriented specimens to intentionally adjust the degree of contact incidence in the fibre network.

Acknowledgements

This work is part of the "Connecting Industries" framework which is funded by the Topsector HTSM, the University of Twente, and the ThermoPlastic composites Research Center. The authors gratefully acknowledge the financial support as well as the technical support from the industrial and academic partners of the ThermoPlastic composites Research Center.

5. References

1. Gardner Business Media. Thermoplastic Composites Collection. Retrieved from https://www.compositesworld.com/kc/cw-collections on January 28, 2021.
2. Yu H, Heider D, Advani S. A 3D microstructure based resistor network model for the electrical resistivity of unidirectional carbon composites. Composite Structures. 2015; 134:740-749.
3. Zhang JN, Wang CY, Guo Z, Zhou YG, Wu HH. Prediction on electrical resistivity of thin-ply unidirectional composites considering electric tunnel effect. Polymer Composites 2020; 41(10): 4318-4328.
4. Grouve WJB, Vruggink E, Sacchetti F, Akkerman R. Induction heating of UD C/PEKK cross-ply laminates. Procedia Manufacturing 2020; 47:29-35.
5. Van Ingen J, Buitenhuis A, Van Wijngaarden M, Simmons F. Development of the Gulfstream G650 induction welded thermoplastic elevators and rudder. In: International SAMPE Symposium and Exhibition, Seattle, WA, USA, 2010.
6. Data Sheet Hexcel. HexTow® AS4 Carbon Fiber.

MECHANICAL CHARACTERIZATION OF HOT COMPACTED SELF-REINFORCED POLYPROPYLENE LAMINATES IN COMPARISON WITH CURV

Anna Kandinskaia[a], Pauline Koslowski[b], Laurens van Audenaerde[b], Larissa Gorbatikh[a], Ignaas Verpoest[a] and Yentl Swolfs[a]
a: Composite Materials Group, Materials Engineering Department, KU Leuven,
Kasteelpark Arenberg 44 bus 2450, Belgium – anna.kandinskaia@kuleuven.be
b: Samsonite Europe NV Westerring 17, B-9700 Oudenaarde, Belgium

Abstract: *In this study, anisotropic biaxially stretched polypropylene film laminates were investigated. Different combinations of process parameters such as temperature and dwell time were used to understand the influence on penetration impact resistance and tensile behavior in machine and transverse directions. It was shown that the process parameters used during the hot compaction do not have a significant impact on properties unless the processing temperature exceeds the melting temperature. The observed correlations reveal the optimal processing conditions for the specific film type and deepens the knowledge towards an alternative to self-reinforced composites.*

Keywords: oriented polymers; polypropylene laminates; self-reinforced composites

1. Introduction

Self-reinforced composite materials are gradually gaining popularity in a wide range of applications due to improved mechanical performance compared to regular polymers. They also ensure good compatibility between the matrix and reinforcement. Up to now, oriented polymer films are mainly used in the packaging industry, while making laminates out of it was shown by Samsonite to have an enormous potential in suitcase applications [1].

When semicrystalline polymers undergo a stretching process, the molecules align along the stretching direction. Orientation is used to improve the stiffness, strength and toughness of polymers allowing the aligned molecules to contribute to bearing the load. The amount of enhancement reached, depends on the drawing ratio and hence orientation degree. The anisotropy introduced by unidirectional stretching is partially eliminated by drawing a polymer in the second perpendicular direction allowing to have good properties and thickness stability in the plane of the film [2].

The mechanical performance of semicrystalline oriented polymers depends mainly on its crystallinity and on molecular orientation. In a film stretching process, crystallization and orientation processes happen simultaneously and cause more complexity. Still, semicrystalline polymers are known to be less sensitive to temperature variations compared to amorphous polymers [3]. However, analysis of how process parameters affect the mechanical properties of the final product gets more complicated when polymer is subjected to yet another thermal process. Many studies have been conducted on biaxially oriented polymer films itself. Nevertheless, no reports exist on the processing of multilayer laminates made of such thin films nor on the characterization of these laminates.

  doi:10.5075/epfl-298799_978-2-9701614-0-0

2. Materials and methods

2.1 Materials

Commercially available biaxially oriented polypropylene film was used with an average thickness of 40 µm. The film has a multilayered structure and consists of a core and two heat sealable layers on the top and on the bottom (see fig. 1). One of the heat sealable layers is corona treated to improve adhesion.

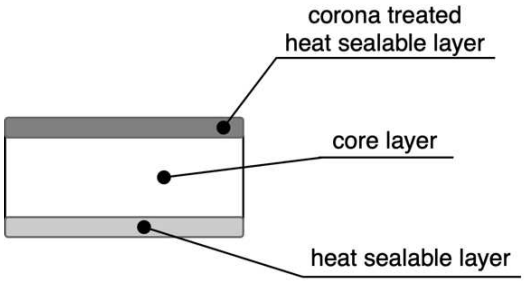

Figure 1. Polypropylene film structure

The film is stretched more along the main orientation direction called transverse direction (TD) and less in the other, named machine direction (MD).

2.2 Production

Every laminate was produced by hot compaction method and has a size of 320x320 mm^2. All 28 precut layers were stacked on top of each other in the same orientation, forming a sheet with an average thickness of 1,1 mm.

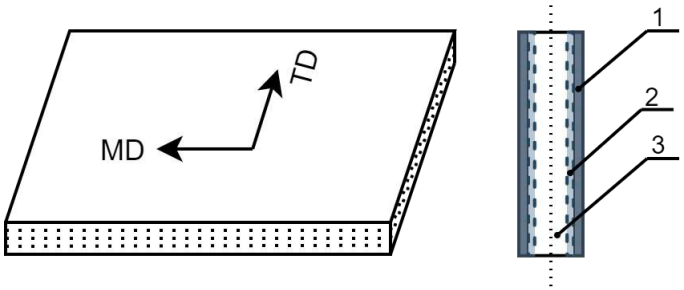

Figure 2. The lay-up consisting of 1 – aluminum plates, 2- Teflon sheets, 3- stack of polypropylene films.

The press platens were pre-heated and kept at the desired temperature for 10 minutes to ensure temperature homogeneity. Then, the stack consisting of 1mm thick aluminum plates with the PP films in between separated with Teflon sheets (see fig. 2) was compacted at different temperatures and dwell time. A pressure of 39 bar was used in all configurations. After the hot compaction, the laminate is cooled down to 40℃ while pressure is maintained.

SRPP laminates were investigated by Swolfs [4] and optimized its production parameters for the hot compaction method. Woven layers of SRPP were stacked onto each other accounting in total of 8 layers. The lay-up was also undergoing the same procedure as BOPP with the only difference

in temperature of 188℃ and dwell time of 5 minutes. Throughout the current paper, values for comparison with SRPP were taken from his research.

Table 1 provides an overview of different combination of process parameters which were investigated in this study. Overall, 11 configurations were analyzed.

Table 1: An overview of the process parameters.

ID number	Temperature [℃]	Dwell time [sec]
1	125	30
2	125	60
3	130	60
4	135	60
5	150	60
6	165	60
7	180	60
8	120	120
9	125	120
10	120	300
11	125	300
SRPP	188	300

2.3 Tensile test

Tensile tests were performed according to ASTM D3039 "Standard Test Method for Tensile Properties of Polymer Matrix Composite Materials." At least four samples were cut using a guillotine and tested on Instron 5567 with a load cell of 30kN for all BOPP panels. Mechanical grips were used to grip the samples. The nominal strain rate was 6%/min. At least five samples were water jet cut and tested on Instron 4505 with a load cell of 100kN for the hot-compacted SRPP panels [4]. Hydraulic grips were used to grip the samples. The strain rate was 5%/min. All specimens were rectangular and measured 25×250 mm^2. They were tested at a 150mm gauge length. End tabs were not used but sandpaper was used to avoid slippage in grips.

The average surface strain was calculated using digital image correlation. All samples were covered by a speckle pattern along the length and half-width of the specimen. The tensile modulus was calculated as the slope of the stress-strain diagram between 0.1 and 0.3% strain.

2.4 Impact test

Penetration impact tests were performed according to standard ISO 6603-2. A hemispherical striker of 20mm in diameter was dropped from a height of 1 m with a weight of 26.41 kg 259J Square samples of 100x100mm^2 were cut and tested. Penetration impact resistance was

  doi:10.5075/epfl-298799_978-2-9701614-0-0

calculated as an energy underneath the whole force-displacement curve normalized by the thickness of the specimen.

2.5 T-peel test

T-peel test was performed according to standard ASTM D1876-08. 10 rectangular samples of 250x20mm^2 were cut from a 0,6 mm thick panel with an unbonded side of 76mm in length. During the manufacturing a released film was inserted in the middle of the stack leaving on side of the panel unbonded. The total number of layers was decreased from 28 to 14 to ensure peel stresses dominate over bending stresses during the test. These samples were cut and tested on an Instron 5943 gripping and pulling the ends apart at a rate of 254mm/min. The peel strength was calculated as the averaged peel load normalized by the width after the first initial peak.

2.6 DSC

Differential scanning calorimetry was only performed for the pure film. Four samples have been tested according to the standard ASTM D3417-99 on TA instruments Q2000. A 50/50 helium/nitrogen flow of 50ml/min was used. A heating and cooling rate at 10K/min was maintained.

3. Results and discussion

The polypropylene film is not significantly influenced by process temperature nor dwell time (fig.4). With respect to the temperature, tensile stiffness varies between 3,9-4,6 GPa with the slight decline towards higher temperatures. A similar trend is observed in the penetration impact resistance. This resistance does not vary significantly (29-45 J/mm) until the temperature rises above 170°C, where it drops down to 23 J/mm. Note that all BOPP configurations consistently exhibit higher values for both stiffness and penetration impact resistance than SRPP.

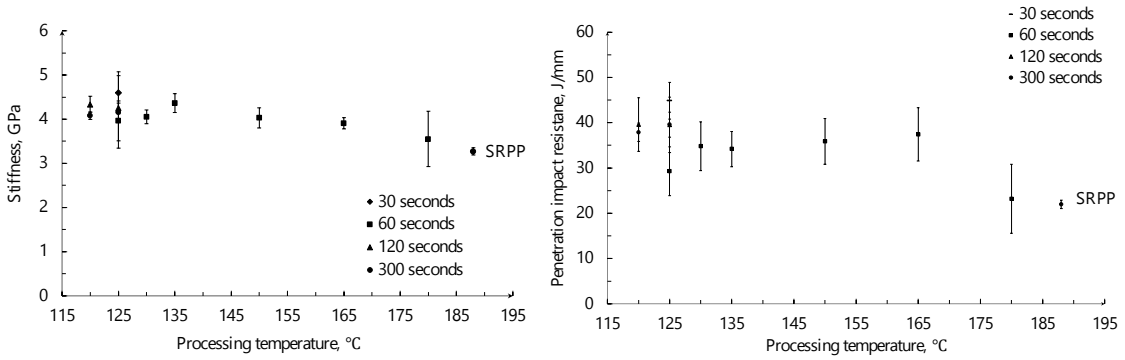

Figure 4. Mechanical properties of the laminates as a function of temperature: (a) tensile stiffness and (b) penetration impact resistance.

If the processing temperature does not exceed the melting temperature, which is determined using DSC to be 169°C (see fig. 5), then both stiffness and penetration impact resistance reveal a slight decrease. Closer to the melting point, molecular relaxation occurs, and the material starts flowing out, thus reducing panel thickness.

  doi:10.5075/epfl-298799_978-2-9701614-0-0

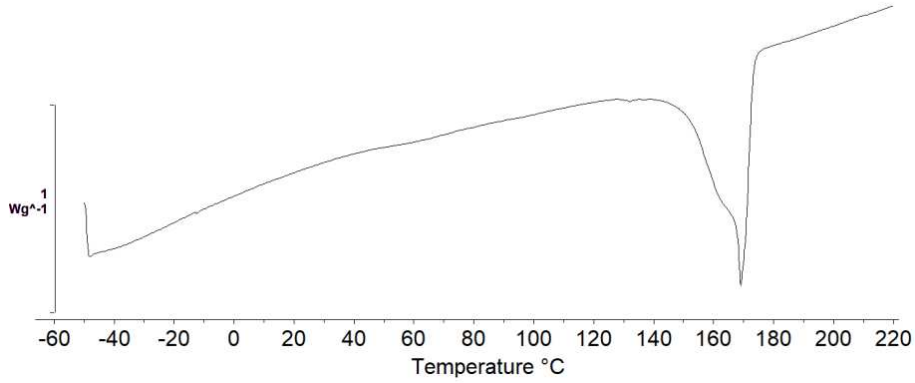

Figure 5. DSC thermogram for the oriented polypropylene film

The interlayer bonding was quantified using a T-peel test. The test was performed for the configuration #2 which has an average value of stiffness and penetration impact resistance, and is considered to be representative for determining the peel strength. The peel strength (see fig. 6) for the BOPP laminate is in line with the data for SRPP (Swolfs et al. 2014).

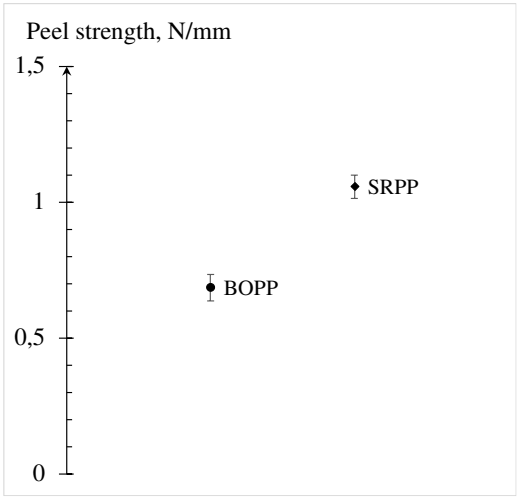

Figure 6. Peel strength for one BOPP configuration in comparison with SRPP

4. Conclusions

The study discussed 11 configurations of BOPP laminates produced at different process parameters and compared with the well-studied SRPP material. It was demonstrated that the BOPP laminate was not significantly influenced by the processing parameters; hence providing a wide processing window. Analysis of the tensile and impact behavior demonstrates that BOPP laminates are stiffer and more impact resistant than standard SRPP material. Moreover, it still offers a decent peel strength.

Acknowledgements

We would like to acknowledge funding from VLAIO in the framework of the NextGenBOB project (HBC.2020.2530).

  doi:10.5075/epfl-298799_978-2-9701614-0-0

5. References

1. Koslowski P, Hillaert R. (2018) Biaxially oriented thermoplastic polymer laminate films for luggage articles and methods of making the same (Belgium Patent.no. WO2018167233A1)
2. Ward IM. Structure and properties of oriented polymers. Applied Science Publishers LTD. 1975
3. Ward IM, Sweeney J. The mechanical properties of solid polymers. John Wiley & Sons Ltd. 2004
4. Swolfs Y. Hybridisation of self-reinforced composites: modelling and verifying a novel hybrid concept. Katholieke Universiteit Leuven, PhD thesis.2015
5. Swolfs Y., Van den fonteyne W, Baets J., Verpoest I., Failure behaviour of self-reinforced polypropylene at and below room temperature, Composites Part A: Applied Science and Manufacturing 65 (2014) p. 100-107.

  doi:10.5075/epfl-298799_978-2-9701614-0-0

EFFECT OF HYBRIDIZATION ON THE FAILURE MECHANISMS OF THIN/THICK HYBRID CARBON/GLASS FIBER-REINFORCED COMPOSITES UNDER FLEXURAL LOADING

Saher Gul[a,b,c], Isa Emami Tabrizi[d], Burcu Saner Okan[a,b,c], Mehmet Yildiz[a,b,c], Adnan Kefal[a,b,c,]*

a: Integrated Manufacturing Technologies Research and Application Center, Sabanci University, Tuzla, Istanbul, Turkey
b: Faculty of Engineering and Natural Sciences, Sabanci University, Tuzla, Istanbul, Turkey
c: Composite Technologies Center of Excellence, Istanbul Technology Development Zone, Sabanci University-Kordsa Global, Pendik, Istanbul, Turkey
d: School of Engineering, University of Liverpool, Liverpool, UK
*adnankefal@sabanciuniv.edu

Abstract: *In this study, the effect of inter-ply hybridization on flexural properties and the hybrid effect exhibited by thin and thick carbon/glass fiber reinforced hybrid composites is investigated. Under flexural loading, the multi-scale damage mechanisms demonstrated by thick laminates are compared with their thin counterparts using optical fractography and acoustic emission techniques. Moreover, digital image correlation is used to monitor the through-thickness strains in thick composites. Results showed that upon the addition of glass fibers, the failure strain of thick all-carbon (AC) laminate is improved by 89% with a hybrid effect of 65%, and hybrid samples show higher flexural strength than AC specimens. Substituting top/bottom carbon fibers with glass fibers in thick AC laminates resulted in dissipation of bending stress through the thickness of laminates, thus actively delaying the instantaneous global failure. Compared to non-hybrid specimens, failure paths of thick hybrid composites were predictable and repeatable.*

Keywords: Fiber hybridization; hybrid composites; thick composites; CFRP; failure mechanism

1. Introduction

Carbon fiber reinforced polymer composites (CFRPs) are one of the widely employed structural materials in the aerospace industry, e.g., the airframe of Boeing 787 is nearly 50% CFRP by mass (1). Although CFRPs exhibit excellent mechanical properties and a high strength-to-weight ratio, they often have low toughness, low failure strain, and a high manufacturing cost. Furthermore, the characteristic brittle nature of carbon fibers can cause stress concentration, and the gradual buildup of minor cracks usually results in an abrupt catastrophic failure (2). To mitigate these problems, fiber hybridization is used; in this method, another fiber is incorporated in the same matrix along with the low-elongation carbon fiber. Glass fiber is an appropriate hybrid material candidate for CFRPs due to its relatively low cost and higher strain-to-failure ratio. The flexural strength of hybridized composite (with an optimized layer sequence) can reach 96% of an all-carbon laminate at only a 0.51 hybrid ratio (3). Hybrid glass/carbon fiber composites also increase the "apparent failure strain" of carbon fibers, which is called the "*hybrid effect*". For instance, up to a 95% increase in apparent failure strain of carbon fibers can be obtained by sandwiching carbon fiber layers between glass fibers in hybrid composites (4). Thus, rationally placing carbon or glass fiber plies at critically stressed locations in hybrid composites can improve their cost-weight-performance effectiveness.

  doi:10.5075/epfl-298799_978-2-9701614-0-0

Determination of potential weight saving associated with composite materials requires that the damage behavior of carbon/glass fiber hybrid composites be a major design consideration. In this context, the flexural performance of composite structures becomes important since the laminate is simultaneously subjected to a dynamic combination of tensile, compressive, and shear forces. Although the mechanical response of thin laminates has been extensively studied (5)(6), the flexural behavior of thick laminates is relatively poorly understood in the literature. Thus, a thorough understanding of damage characterization in hybridized thick laminates would be crucial in the robust design of future composite materials for use in aerospace and marine structures.

In this work, a hybrid composite design is generated by choosing two levels of laminate thickness, and an experimental investigation of the flexural behavior and hybrid effect of thin and thick carbon/glass fiber reinforced hybrid composites is performed. By changing the number of fiber plies and their stacking sequence, various damage modes exhibited by laminates are identified and compared through optical fractography and acoustic emission techniques. Furthermore, the evolution of surface strains in the thickness direction during the pure bending condition in thick laminates is tracked by the digital image correlation method.

2. Materials & methods

2.1 Composite design and manufacturing

Unidirectional carbon fiber-epoxy resin prepreg (300 g/m^2 areal weight) with fiber volume fraction of 37% and glass fiber-epoxy prepreg (300 g/m^2 areal weight) with fiber volume fraction of 35% was purchased from Kordsa A.S. (Turkey). According to the chosen stacking sequence (*Figure 1*a), a total of 6 or 48 prepreg plies were stacked upon each other to design 'thin' or 'thick' laminates, respectively. For hybrid specimens, four symmetric layup configurations i.e.,

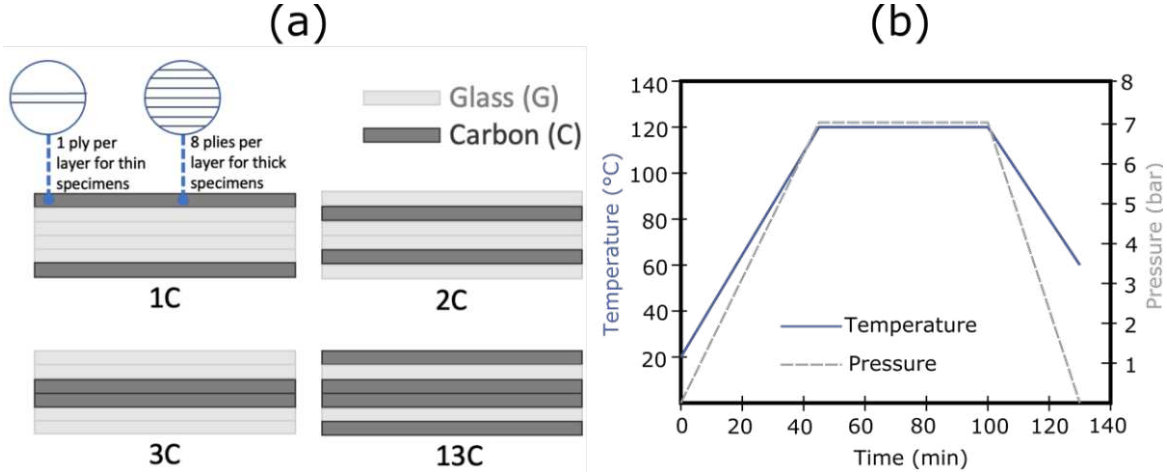

Figure 1. (a) Stacking sequence used for hybrid laminates. (b) Cure cycle used for manufacturing of composite specimens

[C_x/G_x/G_x], [G_x/C_x/G_x], [G_x/G_x/C_x], [C_x/G_x/C_x] named as 1C, 2C, 3C, and 13C were utilized, where x=1 for thin specimens, and x=8 for thick specimens. Non-hybrid all-carbon (AC) or all-glass (AG) were also prepared to be used as reference samples. A manual hot press (MSE Teknoloji Ltd.) was utilized to cure the prepregs into the final form by following the curing parameters provided by the prepreg manufacturer (*Figure 1*b). The manufactured laminates were cut to suitable

dimensions according to the ASTM D790-A standard, and flexural tests were performed on Instron 5982 universal testing machine. Optical micrographs of specimens at the global failure sites were obtained using a Nikon-LV100ND optical microscope.

2.2 Acoustic emission (AE) technique and digital image correlation (DIC) method

Mistras PCI 2 apparatus with the AEwin PCI2-4 software was used to monitor the generation and propagation of various damage types in the bending specimens. Two piezoelectric sensors (PICO-2-750 kHz Lightweight Miniature AE sensors, Mistras) attached to the top side of samples were utilized to detect the elastic acoustic waves generated during mechanical deformation. Based on the K-means algorithm and Davies-Boulding dissimilarity function, the optimum number of clusters was calculated for the post-processed AE data (4), and clusters were subsequently linked to various damage types as provided later in Section 3.2. Through-thickness local strain maps along the span length of the bending specimens were obtained using a digital image correlation (DIC) technique with a GOM (Braunschweig, Germany) 12M sensor system. The experimental set-up for the DIC testing during flexural loading of thick composite laminates is shown in *Figure 2*.

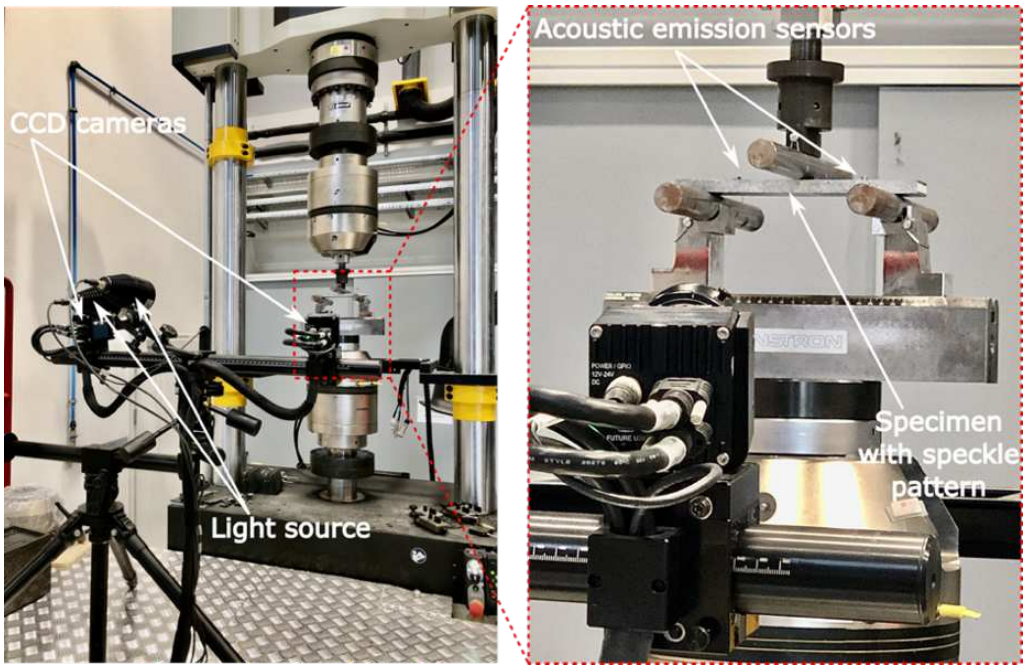

Figure 2. Set up for DIC testing of the thick composite during flexural tests

3. Results

3.1 Effect of interply hybridization on the flexural performance

Figure 3 shows the stress *versus* strain plots of thin and thick laminates during flexural loading. Among thin hybrid specimens, 3C laminate exhibited the highest flexural strength i.e., 1072 MPa, while for the thick hybrid specimens, 2C laminate had the highest strength i.e., 976 MPa. Upon replacing top/bottom carbon plies with glass fibers, and the placement of carbon plies along the horizontal midplane of the thin or thick samples, the flexural modulus changes compared to non-hybrid samples. As per the structural requirements, the ply stacking sequence can be utilized to tune the toughness of a thin or thick hybrid laminate. Although the first stress

  doi:10.5075/epfl-298799_978-2-9701614-0-0

drop value for thick AC laminate is 23.82% less than the thin specimen, its strain to failure is improved, and the higher number of carbon plies delay the global failure. Furthermore, upon hybridization of thick AC laminate in a 3C sequence, the flexural strain to failure significantly increased by 89%. The stepwise profile of the stress-strain curves of thin or thick hybrid specimens implies that the sudden failure exhibited by an all-carbon specimen can be prevented upon its interply hybridization with glass fibers.

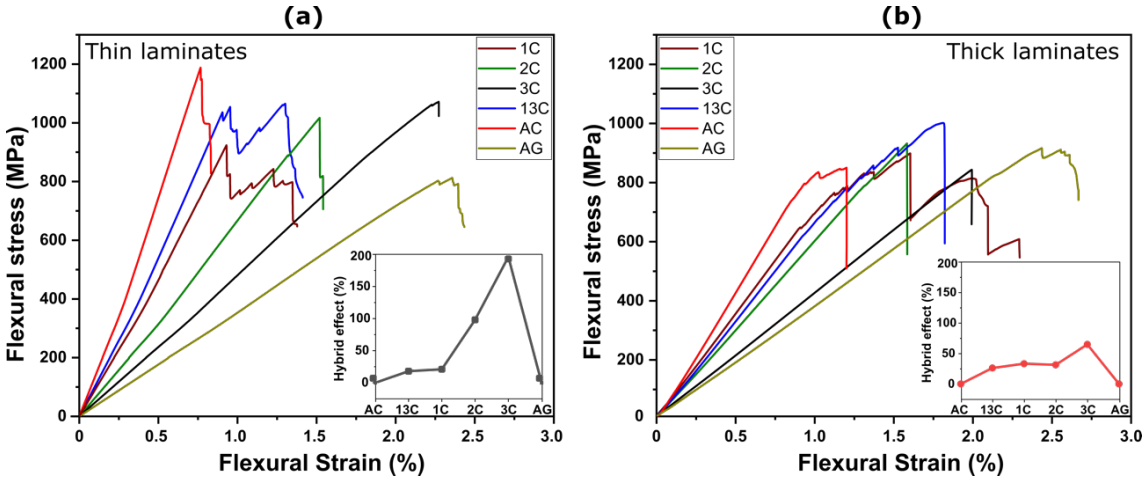

Figure 3. Flexural stress vs. strain curves of (a) thin composite laminates(4) *and (b) thick composite laminates* (7)*. Inset shows the hybrid effect as a function of specimen type*

The existence of plies with varying toughness in hybrid specimens of a particular stacking sequence triggers a more complex failure path. The result of interply hybridization in the form of the "*hybrid effect*" (8) is presented as an inset in *Figure 3*. The highest hybrid effect of 196.15% and 65% is exhibited by the thin 3C and thick 3C specimens, respectively. For the thick 1C, 2C, and 13C laminates, the hybridization effect does not differ much under flexural loading conditions, at 33.05%, 31.22%, and 26.10%, respectively.

3.2 Characterization of damage mechanisms in thin/thick laminates through optical fractography and acoustic emission technique

In this section, thin laminates' failure initiation and damage behavior are compared with their thick counterparts to look for any similarities or patterns. For the non-hybrid thin AC laminate, damage initiates due to compressive failure of top carbon plies, and global failure is due to kinking and buckling (*Figure 4*a). While for thick AC laminate, two damage modes are activated, (i) compressive failure on the top carbon plies and (ii) tensile failure of bottom carbon plies. Like thick AC, the thick 1C specimen showed a tensile failure of bottom carbon plies (*Figure 4*b). Compressive failure at the top layers (Figure 4c) and tensile failure at the bottom layers characterized global failure for the thin AG specimen. In contrast, extensive buckling at the compressive side caused the failure of the thick AG sample. In thin 1C and 13C specimens, similar damage behavior was observed, whereby a kink band formation in carbon plies on the top initiated the damage (*Figure 4*d). The presence of less-stiff fibers on the top surface in thin 2C laminate caused the complete failure of glass fibers, but the damage did not propagate through the thickness. However, for the thick 2C specimen, in addition to the breakage of top glass fibers, a transverse crack formation was also observed in the carbon plies beneath them, causing interfacial delamination (*Figure 4*e). For the 3C stacking sequence, the thin laminate underwent

  doi:10.5075/epfl-298799_978-2-9701614-0-0

buckling and fiber rupture of top and bottom glass plies, unlike the thick 3C specimen, where the top and bottom plies did not exhibit any visible damage but rather an extensive premature delamination failure at the neutral axis occurred. Moreover, the thin and thick 13C laminates exhibited identical failure paths, i.e., shear-driven delamination global failure (*Figure 4*f). Global failure in thick laminates was always in the form of interlaminar delamination. Thus, the stress vs. strain evolution of hybrid laminates and their damage initiation and manifestation depends upon the stacking sequence and thickness of the specimen.

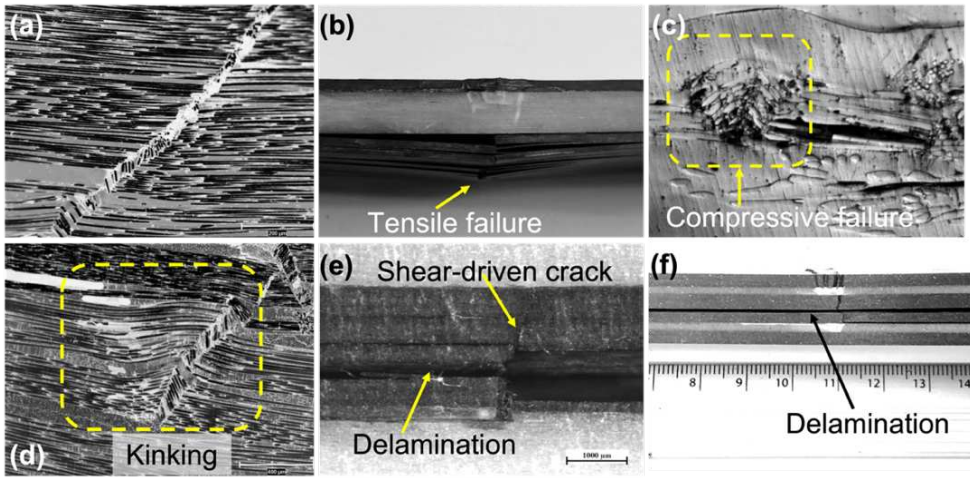

Figure 4. Composite specimens exhibit various damage mechanisms. (a) Kink band formation in thin AC specimen, (b) Tensile failure in bottom carbon layers in thick 1C specimen, (c) Compressive failure on top layers in thin AG specimen, (d) Kinking failure in thin 1C specimen, (e) shear-driven crack formation and interlaminar delamination in thick 2C specimen, (f) extensive shear-driven delamination failure in carbon plies along the horizontal midplane of thick 13C specimen.

Hybridization of thick AC laminate with glass fibers dissipates the bending stress through the laminate thickness, thus actively delaying the instant of global failure observed. Furthermore, compared to non-hybrid specimens, the failure paths of thick hybrid composites were predictable. For instance, upon repeating the bending tests several times, the failure path preferred by a laminate with a 3C stacking sequence was shear-driven mode II delamination at the horizontal midplane. The global failure predictability provided by thick section laminates can be useful during structural health monitoring of load-bearing elements as it can help choose an efficient placement of embedded sensors.

Although the stress-strain curves obtained during flexural loading can be a good indicator of the instant where the loss of material's structural integrity starts, it cannot distinguish between the various failure paths taken by the material up to the final fracture. To overcome this limitation, acoustic emission (AE) testing is performed on the composite laminates to scrutinize and distinguish the initiation of failure and damage modes within the samples. Different failure types generate sound waves of the distinct frequency range (4)(7). Correlating the AE data with the stress-strain curves provides the details of flexural strain values related to the first registry and the type of initial damage for thin and thick laminates. As seen in *Figure 5*(a) for the thin AC laminate, micro-damage originates in the form of matrix cracking at 59.25% of failure strain, followed by fiber breakage, fiber pull-out, and fiber breakage at 79.59%, 95.29%, and 97.45% of failure strain, respectively.

  doi:10.5075/epfl-298799_978-2-9701614-0-0

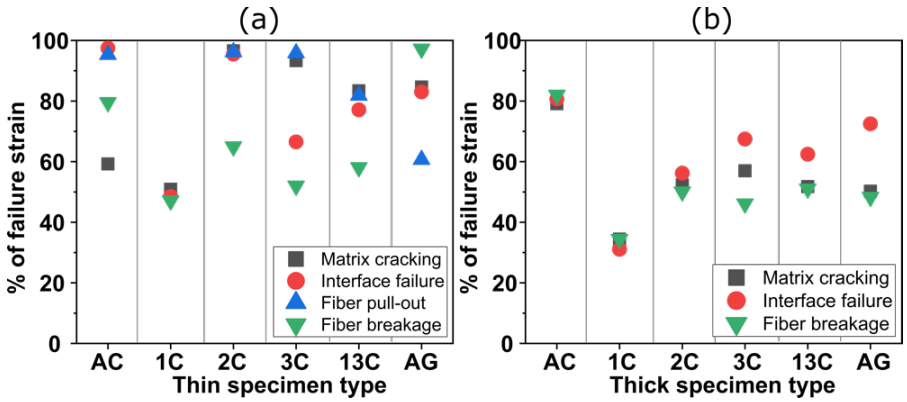

Figure 5. Initiation of acoustic emission data acquisition for various failure types as a function of percentage of final failure strain and specimen type (a) for thin laminates, (b) for thick laminates.

For thin and thick hybrid laminates, the AE data suggests that the damage initiation is in the form of fiber breakage. In thick AC laminate (*Figure 5*b), the registration of acoustic data happens at ~80% of failure strain, suggesting an abrupt failure with no prior indication. However, upon hybridization with glass fibers (e.g., in thick 3C laminate), acoustic data is registered at 51% of failure strain, even though its stress-strain profile is similar to the thick AC specimen. A detailed description of the AE profiles of thin and thick laminates can be found in (4) and (7), respectively.

3.3. Evolution of through-thickness strain in thick composite laminates

To monitor the surface strains at the top, middle, and bottom of specimens, three virtual strain gages were generated during DIC analysis (*Figure 6*). The distribution of transverse strain (ε_{xx}) and shear strain (ε_{xy}) at 90% of the ultimate flexural strength (σ_{ult}) for the non-hybrid and hybrid samples is shown in *Figure 7* and *Figure 8*, respectively. It can be observed in *Figure 7*(a) that a transverse strain localization of compressive nature is present below the loading tip for the thick AC sample, reaching -1.8%. A similar trend is observed for the v-SG data obtained for the thick AC specimen (*Figure 7*b), showing that ε_{xx} along the horizontal midplane of AC specimen is negligible. *Figure 7*(c), shows the shear strain (ε_{xy}) distribution of the thick AC specimen, and generation of narrow band shaped profile parallel to the loading axis can be readily seen, which resulted in crack initiation, and ultimately a delamination failure in lower plies of the specimen. In comparison, the ε_{xx} profile of the thick AG specimen is symmetric in nature, and the specimen reaches a compressive strain of -2.5%, and tensile strain of nearly +2.6%, respectively, as shown in *Figure 7*(d). High compressive strength and high ductility of glass fibers prevent fiber breakage, allowing the AG specimen to reach higher strain values than the thick AC specimen under bending. Localization of transverse strain in the all-glass specimen at the chosen loading level is not observed, as evident from the v-SG profiles (*Figure 7*e). Furthermore, the shear strain profile of the thick AG sample also

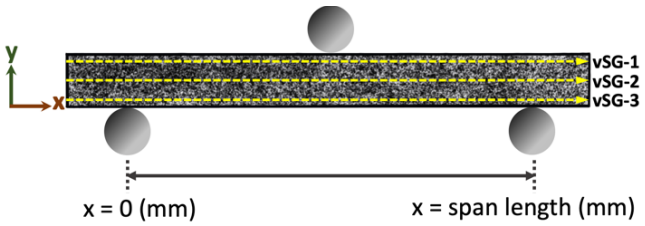

Figure 6. Location of virtual strain gages generated on the surface of thick laminate specimens for DIC analysis

exhibits similar behavior, and strain is symmetric about the vertical midplane of the laminate (*Figure 7*f), leading up to shear-driven delamination.

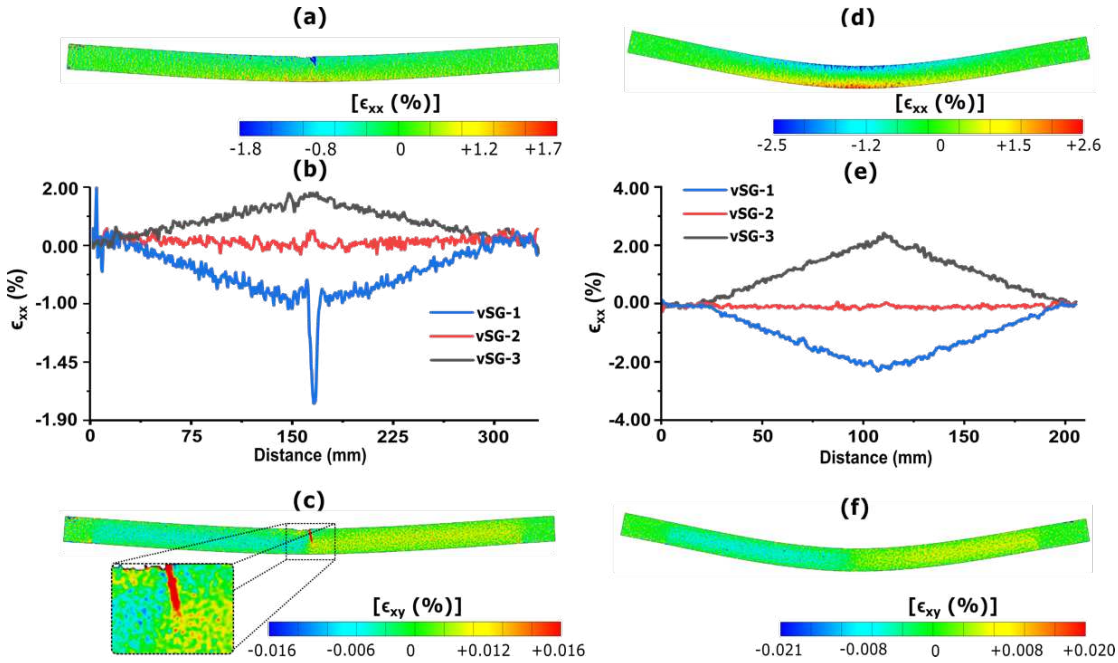

Figure 7. DIC results at 90% of σ_{ult}. For thick AC laminate: (a) transverse strain (ε_{xx}) field (c) shear strain (ε_{xy}) field. For thick AG laminate (d) transverse strain (ε_{xx}) field, (f) shear strain (ε_{xy}) field. Evolution of transverse strain along the span length of (b) thick AC laminate and (e) thick AG laminate

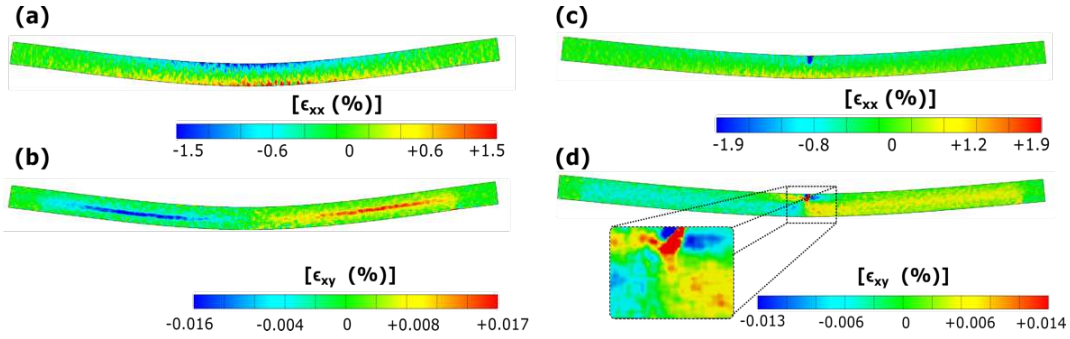

Figure 8. DIC results at 90% of σ_{ult}. For thick 3C specimen: (a) transverse strain (ε_{xx}) field, (b) shear strain (ε_{xy}) field. For thick 13C specimen: (c) transverse strain (ε_{xx}) field, (d) shear strain (ε_{xy}) field

Among the thick hybrid specimens, 3C and 13C configurations are chosen as an example to demonstrate the usefulness of DIC technique to monitor surface strains. It can be seen in *Figure 8*(a) that the ε_{xx} profile of 3C specimen is similar to AG laminate and is mainly concentrated around the glass plies of 3C while being symmetric about the horizontal midplane. On the other hand, a very prominent shear strain concentration is observed for the 3C laminate in *Figure 8*(b), predicting a shear-driven delamination failure, being in excellent agreement with the observed global failure mode in the 3C specimen. For the 13C specimen, in addition to the presence of a symmetric transverse strain profile (similar to 3C), a concertation of compressive strain (ε_{xx} = -

  doi:10.5075/epfl-298799_978-2-9701614-0-0

1.9%) can also be observed (*Figure 8*c), since 13C laminate contains carbon plies on the top bounding surface. Moreover, the shear strain observed on the 13C specimen surface is not only highly concentrated below the loading tip but also present along the middle carbon fiber plies (*Figure 8*d). As a result, 13C laminate exhibited a crack formation in top carbon plies and an extensive shear-driven delamination failure along the horizontal midplane.

4. Conclusion

The effect of interply hybridization on flexural properties, failure initiation, and damage propagation in thin (6-ply) and thick (48-ply) carbon/glass fiber hybrid composites have been investigated. Flexural modulus in hybrid laminates (of both thicknesses) is strongly correlated with the position of carbon-fiber plies, undergoing an increment on placement of carbon fibers away from the horizontal midplane. Furthermore, the apparent failure strain of thin and thick AC laminates is significantly improved by replacing the top and bottom carbon plies with glass fibers. Characteristic stress drops observed during flexural loading of hybrid specimens indicate the arrest of initial damage by plies of variable stiffness through the thickness, and global failure is no longer abrupt as in all-carbon specimens. Among the various failure modes active within specimens during deformation, damage predominately initiates in the form of fiber breakage in thin and thick laminates. Macro-damage sites are predictable through surface-strain monitoring using DIC technique, and global failure modes of thick composites are repeatable.

References

1. Boeing: 787 By Design: By Design: Advanced Composite Use [Internet]. [cited 2021 Jan 15]. Available from: https://www.boeing.com/commercial/787/by-design/#/advanced-composite-use

2. Yamamoto G, Koizumi K, Nakamura T, Hirano N, Okabe T. Tensile-strength-controlling factors in unidirectional carbon fiber reinforced plastic composites. Compos Part A Appl Sci Manuf. 2021 Jan 1;140:106140.

3. Prusty RK, Rathore DK, Singh BP, Mohanty SC, Mahato KK, Ray BC. Experimental optimization of flexural behaviour through inter-ply fibre hybridization in FRP composite. Constr Build Mater. 2016 Aug 15;118:327–36.

4. Tabrizi IE, Kefal A, Zanjani JSM, Akalin C, Yildiz M. Experimental and numerical investigation on fracture behavior of glass/carbon fiber hybrid composites using acoustic emission method and refined zigzag theory. Compos Struct [Internet]. 2019;223:110971. Available from: http://www.sciencedirect.com/science/article/pii/S0263822319304313

5. Zhang J, Chaisombat K, He S, Wang CH. Hybrid composite laminates reinforced with glass/carbon woven fabrics for lightweight load bearing structures. Mater Des [Internet]. 2012;36:75–80. Available from: http://www.sciencedirect.com/science/article/pii/S0261306911007667

6. Dong C, Davies IJ. Flexural and tensile strengths of unidirectional hybrid epoxy composites reinforced by S-2 glass and T700S carbon fibres. Mater Des. 2014;54:955–66.

7. Gul S, Tabrizi IE, Okan BS, Kefal A, Yildiz M. An experimental investigation on damage mechanisms of thick hybrid composite structures under flexural loading using multi-instrument measurements. Aerosp Sci Technol. 2021 Oct 1;117:106921.

8. Swolfs Y, Gorbatikh L, Verpoest I. Fibre hybridisation in polymer composites: A review. Vol. 67, Composites Part A: Applied Science and Manufacturing. Elsevier Ltd; 2014. p. 181–200.

  doi:10.5075/epfl-298799_978-2-9701614-0-0

HOW DO WE DEFINE AND MEASURE STRENGTH OF A COMPOSITE?

Michael R. Wisnom[a], Federico París[b], Yentl Swolfs[c]
a: Bristol Composites Institute, University of Bristol, UK, M.Wisnom@bristol.ac.uk
b: Escuela Superior de Ingeniería, Universidad de Sevilla, Spain
c : Department of Materials Engineering, KU Leuven, Belgium

Abstract: *The outputs from a series of online workshops on defining and measuring strength of composites and the factors affecting it are presented. The meaning of the strength of a composite is discussed and a definition is proposed. Issues in measuring fibre direction tensile and compressive strength are discussed, with potential ways to overcome them. Recommendations are made on how to use the term strength, and how to address the remaining challenges.*

Keywords: strength; failure; testing; tension; compression

1. Introduction

Strength of composites has been a key area of research for many years, and yet there are still huge variations in reported values of strengths. For example, a recent study on compressive strength of UD IM7/8552 showed a variation of more than a factor of two between different test methods [1]. This is a major reason "why progress on the failure of fiber composite materials has been so retarded" [2] as identified by Christensen, who highlighted the difficulties of performing accurate testing, suggesting that "the data of these observed behaviors must be completely uncorrupted by the inadvertent and uncontrolled influences that almost inevitably creep in" [2]. This paper addresses the question: "how do we define and measure strength of a composite?" and summarises some of the key points arising from a workshop on this topic [3] and two further workshops on measuring fibre direction tensile and compressive strength [4,5]. A fourth workshop was also recently held on shear strength [6].

2. Definition of strength

An online workshop was organized in October 2020 to address the definition and measurement of strength. A panel of invited speakers debated the topic, with over 100 people attending the session [3]. There are many ways to define the strength of a composite, and different reasons for wanting to specify it – as a measure of the intrinsic strength to compare materials, as input into models for predicting the strength of components or as a conservative value to establish safe design allowables. Regarding the ultimate strength of a unidirectional composite, we contend that the only unambiguous definition is the maximum stress that the material can sustain under uniform uniaxial loading and in the absence of other stress components. Other definitions such as damage initiation stress are difficult to establish and more subjective. Tests with in-situ SEM and X-ray CT have shown that there is often damage before any load is applied due to intrinsic defects or residual stresses. The point at which macroscopic damage is noted in a test depends on how closely it is monitored and so is arbitrary.

Concepts such as in-situ strength are even more problematic as fundamental definitions because they depend on other factors, as discussed later. Such measures may be useful in establishing

  doi:10.5075/epfl-298799_978-2-9701614-0-0

fitness for purpose for a particular design, but they are not appropriate as basic material parameters. The maximum stress may be achieved after considerable damage, which may cause premature failure if the direction or type of loading is changed, but it is still valid as a simple measure of ultimate material performance.

There are significant differences between metals and composites in the relation between stress state and failure. The local triaxial stress state is not directly related to the macroscopically applied stress. There is not a single failure mechanism or a smooth variation of strength under different stress states. It is therefore necessary to consider the different potential failure mechanisms of fibre direction tension and compression; in-plane transverse tension, compression and shear; interlaminar tension, compression and shear; and also their interaction. The definition above can be applied to all these principal failure modes.

Even with this simple definition it must be recognised that the value obtained may depend on a number of factors, such as the volume of material tested, strain rate, temperature and moisture condition, and so these must be specified alongside the strength. Measurements should be made under uniaxial loading with a uniform stress state as stress gradients can increase the maximum stress at failure, and the presence of stress concentrations and other stress components can also affect it. With these caveats, the maximum stress is useful as a material property, representing what may be attained under ideal conditions and a basis for comparison of different materials.

There is inherent variability in composites and hence a distribution of strengths rather than a single value. However, it is undesirable to have strengths that are linked to theories which may not be fully validated or accepted. For example, the variation of strength with specimen size may be accounted for by means of a Weibull characteristic strength and modulus, but it is preferable to quote the strength at a specified volume to avoid the dependence on any underlying theory.

There are many challenges in carrying out practical tests to measure strength, to avoid stress concentrations and other parasitic stress components. These are discussed in the next sections for fibre direction tensile and compressive strength. In principle it is possible to measure stresses at failure under combinations of different stress components, but in practice this is even more challenging and requires more research both on the tests and the use of the obtained values in criteria to predict failure.

This measure of strength can strictly only be applied to unidirectional composites under simple stress states. Even simple flat laminates have multiple potential failure modes that depend on different factors and can interact in different ways depending on many parameters. Transverse cracking and delamination can interact with fibre direction response, especially at free edges, and so the failure stress may depend on the stacking sequence and ply thickness. Also, in a laminate subject to uniform applied stress there are other stress components present in the different plies, as well as residual thermal stresses and constraint from other plies. Theoretically it might be possible to define and measure an ideal ultimate laminate strength, for example by selecting stacking sequences and ply thicknesses to avoid premature damage, or using tubular specimens to eliminate free edges, but even if this was successful, it is not clear if it would be useful since such values would not necessarily apply to practical situations.

Measures such as notched strength depend on further factors in addition to those above, including the notch size, laminate thickness, and width to notch ratio. They are nevertheless

  doi:10.5075/epfl-298799_978-2-9701614-0-0

useful for design and comparative purposes but should not be regarded as material properties. Compression after impact testing is even more problematic, and should be treated as a pragmatic way to gauge impact response rather than measuring a material property. Strength of components is a structural rather than material phenomenon due to complex stress distributions and interactions between through thickness and in-plane failure mechanisms as a result of three dimensional-geometry.

The term “failure strength” is commonly used, but is really a contradiction in terms and should be avoided. Strength and failure stress are often used interchangeably, but should really be distinguished, with strength reserved for basic unidirectional materials and failure stress used elsewhere. Terms such as compression-after-impact (CAI) strength or open hole tensile (OHT) strength should be replaced by CAI or OHT failure stress. In all cases there should be full specification of the conditions under which the measurements have been made. Failure strain is also very useful as it can be more directly measured and is widely used in industry.

3. Fibre direction tensile strength

A second online workshop was organised in March 2021 to discuss measuring tensile strength [4]. This is not easy because of the difficulty of introducing the high loads necessary without inducing stress concentrations. Even with careful tabbing arrangements, test specimens usually fail at the ends, e.g. Fig. 1.

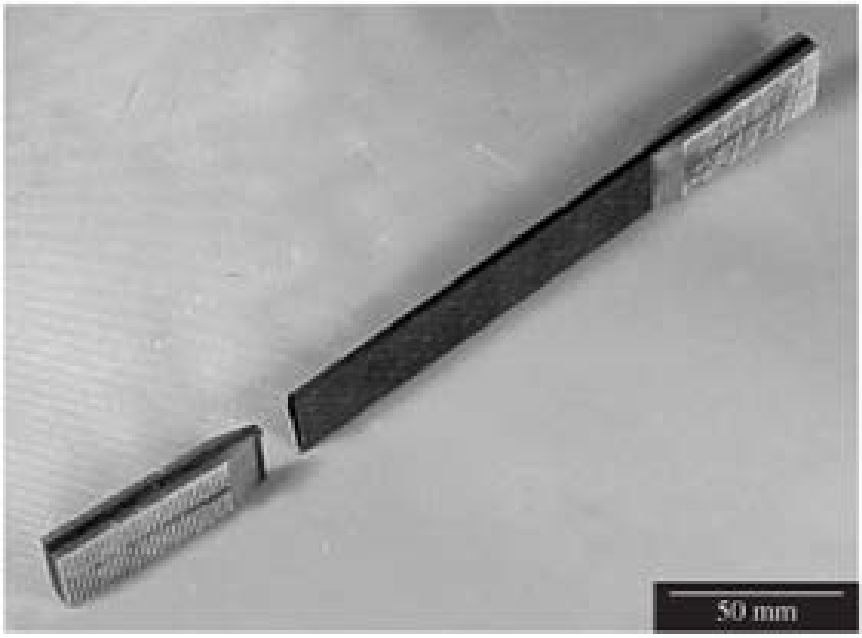

Figure 1. Typical failure of tensile specimen at the end of the tab

One approach to this is to machine the specimens to produce a waisted section with reduced cross-sectional area. Waisting can be carried out through the thickness, across the width, or both, and needs to be very gentle in order to avoid the specimens splitting, Fig. 2 [7]. With care it may be possible to produce consistent gauge section failures, but the specimen dimensions are typically large, and the machining or manufacturing can be expensive and time consuming.

  doi:10.5075/epfl-298799_978-2-9701614-0-0

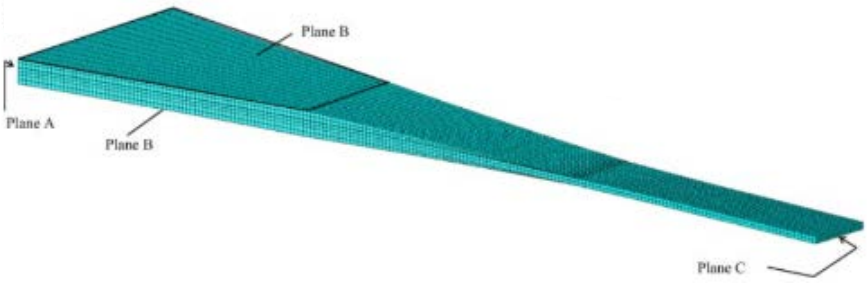

Figure 2. Very gradually waisted tensile specimen [7]

Recent work has shown that with the right equipment this can be done quite easily with prepreg, Fig. 3 [8]. Hybrid specimens can also be used to measure tensile strength, for example with carbon fibre plies sandwiched between glass fibre plies with a lower modulus and higher strain to failure. This has been shown to completely eliminate the stress concentration at the grips, producing consistent gauge section failures, Fig. 4 [9]. It is a very easy technique to use, and also eliminates the need for tabs, however it only measures strain at failure directly, rather than stress, and also needs a small correction for thermal residual strains. Bending tests can also eliminate failure at the points of load introduction, but only have a small volume of material at the maximum stress, and there is also a question as to whether the stress gradient may result in a different strength than in pure tension [10].

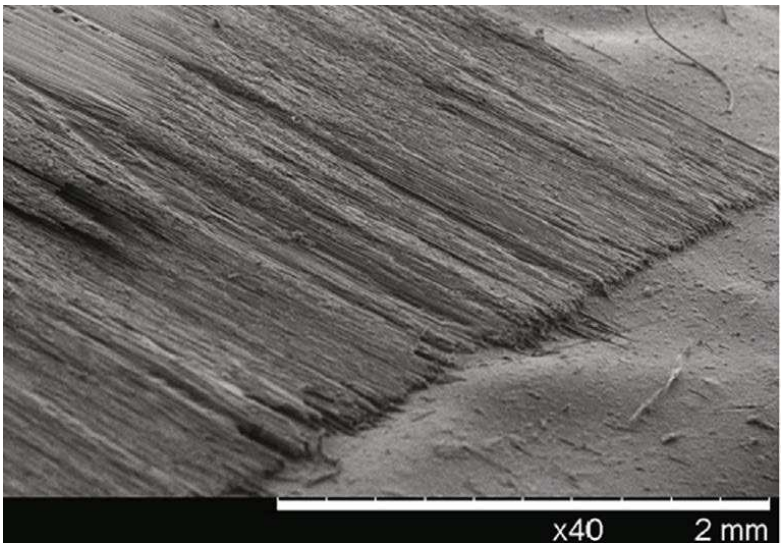

Figure 3. Gradually chamfered ply [8]

The size effect due to the volume of stressed material is well established [e.g. 11,12] but there are still questions as to the relative effect of changes in length and cross-section. Strain rate, temperature and humidity are generally considered to have less influence since the fibres themselves are not sensitive to these effects, at least for carbon. Some studies have shown that these factors can cause differences in strength, but are the test methods sufficiently robust?

  doi:10.5075/epfl-298799_978-2-9701614-0-0

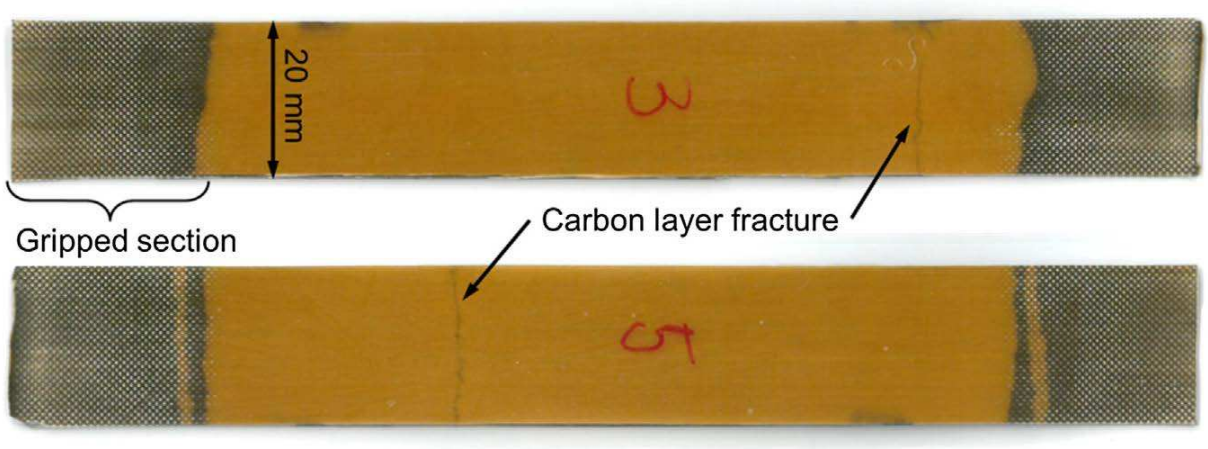

Figure 4. Clear gauge section failure in carbon fibre / glass sandwich specimens [9]

Many failure criteria such as Tsai-Hill or Tsai-Wu imply strong interaction between other stress components, but recent work using hybrid specimens has indicated very little effect of in-plane shear and transverse compression on fibre direction tensile failure strain [13,14].

A good test method should give consistent high values, with low variability. Several methods appear promising and it is important to compare them for the same material, also taking account of the stressed volume. Different tests methods should give similar results if they are valid and all measuring the same quantity. This is being put to the test in a round-robin exercise that was started as a consequence of the tensile strength workshop. The round-robin exercise is comparing tensile strengths obtained by waisted specimens, flexural specimens, and ones with continuous, rectangular, tapered and arrow-shaped end tabs. Once the best methods have been established, they can be used to further investigate the factors affecting tensile strength. The final goal is to develop an ISO standard specifically for unidirectional composites.

4. Fibre direction compressive strength

A third workshop was held in October 2021 on measuring compressive strength [5]. It is clear that special care must be taken to avoid buckling. Consistent gauge section failures may in fact be initiated by overall buckling, which occurs at a much lower stress than the simple Euler equation would suggest due to the effect of shear deformation, and the substantial reduction in modulus with applied compressive strain in carbon fibre composites [15]. The obvious solution is to reduce the gauge length, which typically is of the order of 10 mm, but this causes the stress state to be non-uniform along the length, creating uncertainty about whether the obtained strength is representative of the behaviour of the same material under uniform stress. It is important to eliminate bending which may be caused by transverse displacements between the grips of the test machine or non-uniformities in the tabbing.

There is also the question of whether to introduce the load by compression at the ends of the specimen or by shear. The latter is more straight-forward, but causes stress concentrations at the ends of the tabs. Also unlike in tension, shear stresses greatly reduce compressive strength, as has been shown in combined compression and torsion tests on tubes [16].

  doi:10.5075/epfl-298799_978-2-9701614-0-0

In conventional specimens loaded through tabs, interlaminar shear stresses inevitably occur [17], as shown in Fig. 5a. Hence failure typically initiates at the grips unless there is some form of defect or stress concentration in the gauge section. There are also indications that transverse tensile and compressive stresses can be important [e.g. 18,19].

At the corner points, where geometry and material properties change abruptly, nominal stress singularities appear [20] contributing to premature failures in standard tests of composite materials that have been reported [21]. In the particular case of the compression test of unidirectional laminates, these stress intensifications can be reduced, as proposed in [22] where a chamfer, filled with adhesive, is included at the end tab (see Fig.5c) and the 45° chamfer was demonstrated to be a less severe configuration [21].

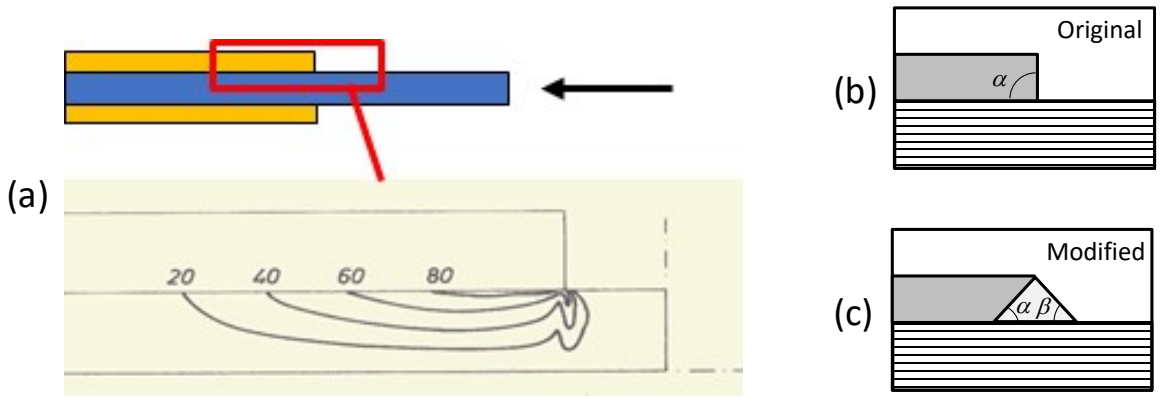

Figure 5. (a) Shear stress concentrations at end of tabs [17], (b) original geometry, (c) modified geometry to reduce the order of the stress singularity.

If specimens are end-loaded, they need to be ground very flat and perpendicular and even with extremely careful preparation tend to fail by splitting or brooming. Combined end and shear loading therefore tends to give the best results [23]. Tabs should carry just enough load to avoid end failure, but be as thin as possible to minimise the stress concentration at the start of the gauge section. This can be further reduced by encouraging the tabs to debond at the tips [23]. Accurate alignment of the specimen and fibres is crucial, and local misalignment induced at the exit from the test fixture by gripping pressure may have an effect.

Bending tests can also be used to measure compressive failure strain, provided tensile and interlaminar shear failures are avoided. Care has to be taken to avoid roller failure due to stress concentrations. This can be done by using very large rollers or by pin-ended buckling tests where a long specimen is allowed to buckle and then fail in compression in the middle. Scaled pin-ended buckling tests have shown a strong size effect, Fig. 6, which is mainly due to the strain gradient [24] although there could be a contribution from the difference in stressed volume. Recent tests with wood sandwich beams have separated these factors and demonstrated the effect of strain gradient on specimens with the same stressed volume [25].

  doi:10.5075/epfl-298799_978-2-9701614-0-0

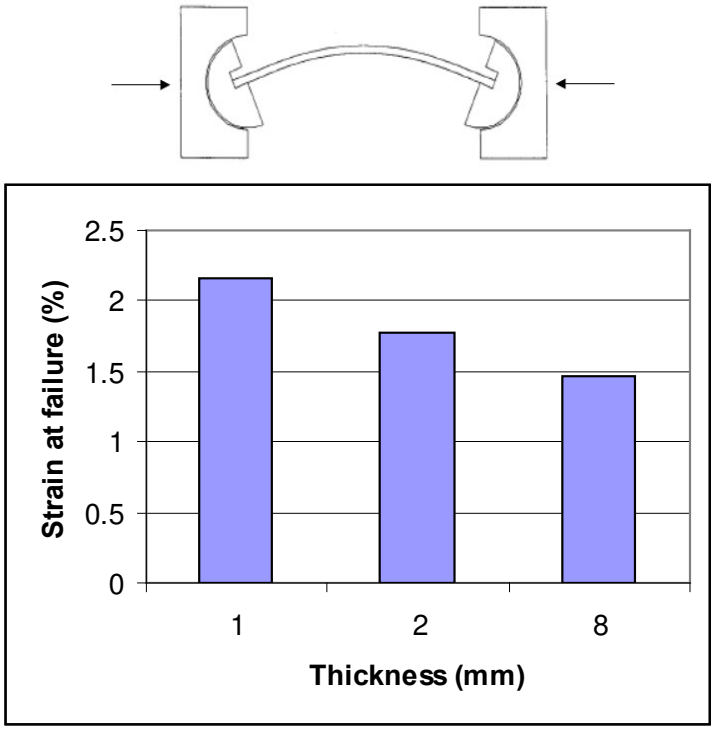

Figure 6. Strain gradient effect in scaled buckling tests [24]

A different approach is to use a specially designed laminate that when subjected to tensile loading, fails in compression in its central 90°-ply due to the Poisson effect. It has been shown that gauge section failures can be obtained, although transverse tension is also present [26].

Strain rate, temperature and humidity have all been demonstrated to have significant effects on compressive strength since these conditions can greatly affect the matrix behaviour [e.g. 27,28]. However due to the difficulties in testing, there is limited evidence on other factors. Sandwich tests on thin ply specimens have shown that failure strains increase with decreasing ply thickness [29], believed to be due to greater homogeneity and better fibre alignment. This highlights the importance of the manufacturing process, and the possibility of much lower compressive strength in full scale structures than small test coupons of the same material due to misalignment defects such as wrinkles.

Hybridisation can also affect compressive failure. For example, compressive failure strains of 2.5% have been reported for high strength carbon/epoxy embedded in glass/epoxy four-point bending specimens [30]. Higher failure strains have been reported for 0° plies embedded in laminates with many 45° plies [31] although the layup may also reduce the stress concentrations. Theoretical modelling has suggested that the stacking sequence affects compressive strength [18] but it is challenging to verify this experimentally.

Further work is needed to compare the different methods and reach a consensus on the best way to measure compressive strength.

  doi:10.5075/epfl-298799_978-2-9701614-0-0

5. Summary and Recommendations

Strength as a material property should only be used for unidirectional composites under simple uniaxial stress states measured under uniform loading.

Strength should be defined as the maximum stress that can be attained prior to total rupture and should be stated together with the volume of material and conditions under which it was measured.

Results of laminate and structural tests should be referred to as failure stresses rather than strengths.

Round-robin exercises should be undertaken to compare the different test methods and reach conclusions on the best ones. A round-robin is underway on tensile strength measurement and others are needed for compression and other failure modes.

Once the best test methods have been established, further work should be undertaken on the factors that affect failure. A consensus should be sought on what research is needed to build a modelling framework on a firm foundation to be able to predict laminate and structural failure from basic material strengths.

The presentations and videos of the workshops are available online [3-6].

6. References

1. Thomson D, Cui H, Erice B, Petrinic N. A study on the longitudinal compression strength of fibre reinforced composites under uniaxial and off-axis loads using cross-ply laminate specimens. Composites Part A 2019; 121:213–222. https://doi.org/10.1016/j.compositesa.2019.03.034
2. Christensen RM. Why progress on the failure of fiber composite materials has been so retarded. Journal of Reinforced Plastics and Composites 2017; 36:1615-17. https://doi.org/10.1177/0731684417733550
3. Workshop: How do we define and measure strength of a composite? https://www.bristol.ac.uk/engineering/news/2020/composite-strength-workshop.html
4. Workshop: Measuring UD tensile strength and the factors affecting it https://www.bristol.ac.uk/engineering/news/2021/tensile-strength-workshop.html
5. Workshop: Measuring UD compression strength and the factors affecting it https://www.bristol.ac.uk/engineering/news/2021/ud-compression-strength-workshop.html
6. Workshop: Measuring shear strength of composites and the factors affecting it https://www.bristol.ac.uk/engineering/news/2022/fourth-international-workshop-in-the-measuring-strength-series.html
7. Korkiakoski S, Bronsted P, Sarlin E, Saarela O. Influence of specimen type and reinforcement on measured tension–tension fatigue life of unidirectional GFRP laminates. International Journal of Fatigue 2016; 85:114-129. https://doi.org/10.1016/j.ijfatigue.2015.12.008
8. Gordon T, Xu X, Wisnom MR, Kim BC. Novel tape termination method for automated fibre placement: Cutting characteristics and delamination suppression. Composites Part A 2020; 137:106023. https://doi.org/10.1016/j.compositesa.2020.106023

  doi:10.5075/epfl-298799_978-2-9701614-0-0

9. Czél G, Jalalvand M, Wisnom MR. Hybrid specimens eliminating stress concentrations in tensile and compressive testing of unidirectional composites. Composites Part A 2016; 91: 436–447. https://doi.org/10.1016/j.compositesa.2016.07.021
10. Wisnom MR. The relationship between flexural and tensile strength of unidirectional carbon fibre-epoxy. Journal of Composite Materials 1992; 26(8):1173-1180. https://doi.org/10.1177/002199839202600805
11. Okabe T, Takeda N. Size effect on tensile strength of unidirectional CFRP composites - experiment and simulation. Composites Science and Technology 2002; 62:2053-2064. https://doi.org/10.1016/S0266-3538(02)00146-X
12. Wisnom MR, Khan B, Hallett SR. Size effects in unnotched tensile strength of unidirectional and quasi-isotropic carbon/epoxy composites. Composite Structures 2008; 84:21-28. https://doi.org/10.1016/j.compstruct.2007.06.002
13. Jalalvand M, Fotouhi M, Leong MC, Wisnom MR. A novel technique to accurately measure the fibre failure strain in composite laminates under a combined in-plane tension and shear stress state. Proc. ICCM21, Xian, China, 20-25 August 2017. https://www.iccm-central.org/Proceedings/ICCM21proceedings/papers/4014.pdf
14. Rev T, Czél G, Wisnom MR. The effect of transverse compressive stresses on tensile failure of carbon fibre/epoxy composites. Composites Part A 2022; 156:106894. https://doi.org/10.1016/j.compositesa.2022.106894
15. Wisnom MR, Haberle JG. Prediction of buckling and failure of unidirectional carbon fibre-epoxy struts. Composite Structures 1994; 28:229-239. https://doi.org/10.1016/0263-8223(94)90011-6
16. Jelf, PM, Fleck NA. The failure of composite tubes due to combined compression and torsion. Journal of Materials Science 1994; 29:3080-3084. https://doi.org/10.1007/BF01117623
17. Wisnom MR. Effect of shear stresses in indirect compression tests on unidirectional carbon fibre-epoxy. AIAA Journal 1991; 29:1692-7. https://doi.org/10.2514/3.10792
18. Davidson P, Waas AM. Compressive failure due to kink band formation in the presence of transverse loading, and accounting for mesoscale and microscale misalignment. Composite Structures 2021; 265:113760. https://doi.org/10.1016/j.compstruct.2021.113760
19. Wang L, Kawaguchi K, Xu J, Han Q. Effects of transverse constraints on the longitudinal compressive strength of unidirectional CFRP pultruded plates and rods. Composite Structures 2019; 207:740–751. https://doi.org/10.1016/j.compstruct.2018.09.071
20. Barroso A, Mantič V, París F. Singularity analysis of anisotropic multimaterial corners. International Journal of Fracture 2013; 119:1-23. https://doi.org/10.1023/A:1023937819943
21. Barroso A, Marín JC, Mantič V, París F. Premature failures in standard test specimens with composite materials induced by stress singularities in adhesive joints, Int. J. Adhes. Adhes. 2020; 97:102478, https://doi.org/10.1016/j.ijadhadh.2019.102478
22. Dogra J, Hodgkinson JM, Robinson P, Pinho ST. Development of a compression test for thick composite laminates: finite element analysis. 16th International Conference on composite materials, Kyoto, Japan, (2007). https://www.iccm-central.org/Proceedings/ICCM16proceedings/papers/WeBM1-02sp_dograj223496p.pdf
23. Häberle JG, Matthews FL. An improved technique for compression testing of unidirectional fibre-reinforced plastics; development and results. Composites 1994; 25:358-371. https://doi.org/10.1016/S0010-4361(94)80006-5

24. Wisnom MR, Atkinson JA, Jones MI. Reduction in compressive strain to failure with increasing specimen size in pin-ended buckling tests. Composites Science and Technology 1997; 57:1303-1308. https://doi.org/10.1016/S0266-3538(97)00057-2
25. Wu X, Wisnom MR. Compressive failure strain of unidirectional carbon fibre composites from bending tests. submitted, 2022.
26. Laurin F, Paulmier P, Irisarri FX. Determination of the longitudinal compressive strength of a CFRP ply through a tensile test on a laminate. Composites Part A 2018; 113:209–219. https://doi.org/10.1016/j.compositesa.2018.07.026
27. Soutis C, Turkmen D. Moisture and temperature effects of the compressive failure of CFRP unidirectional laminates. Journal of Composite Materials 1997; 31:832-849. https://doi.org/10.1177/002199839703100805
28. Koerber H, Camanho PP. High strain rate characterisation of unidirectional carbon-epoxy IM7-8552 in longitudinal compression. Composites Part A 2011; 42:462-470. https://doi.org/10.1016/j.compositesa.2011.01.002
29. Amacher R, Cugnoni J, Botsis J, Sorensen L, Smith W, Dransfeld C. Thin ply composites: Experimental characterization and modelling of size-effects. Composites Science and Technology 2014; 101:121–132. https://doi.org/10.1016/j.compscitech.2014.06.027
30. Czél G, Jalalvand M, Wisnom MR. Hybrid specimens eliminating stress concentrations in tensile and compressive testing of unidirectional composites. Composites Part A 2016; 91:436–447. https://doi.org/10.1016/j.compositesa.2016.07.021
31. Berbinau P, Soutis C, Goutas P, Curtis PT. Effect of off-axis ply orientation on 0°-fibre microbuckling. Composites Part A 1999; 30:1197–1207. https://doi.org/10.1016/S1359-835X(99)00026-3

  doi:10.5075/epfl-298799_978-2-9701614-0-0

DEVELOPMENT OF ADVANCED COMPOSITES THROUGH SURFACE CHARACTERIZATION OF FIBERS AND FILLERS BY INVERSE GAS CHROMATOGRAPHY

Anett Kondor[a], Daniel J. Burnett[b]

a: Surface Measurement Systems Ltd. London, UK –
AKondor@surfacemeasurementsystems.com
b: Surface Measurement Systems NA, Allentown, USA

Graphical Abstract:

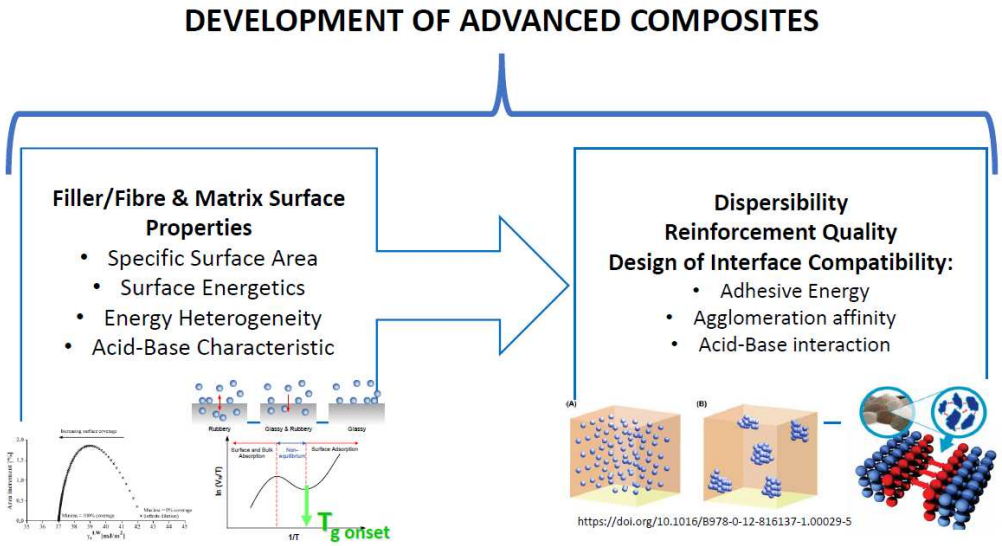

Abstract: *The ultimate quality and performance of fiber/nano-fiber composites depends strongly on the interfacial interaction of the components. In particular, the surface energy and surface area of fibers and fillers are directly related to the compatibility, dispersibility and reinforcement quality. To enhance the adhesion properties at the interface, fibers/fillers are often exposed to various surface treatments. In this studies, surface areas and energies of fillers and natural fibers from different origins and surface treatments have been investigated by Inverse Gas Chromatography (IGC).*

Keywords: surface energy; compatibility; reinforcement; IGC, adhesion

1. Introduction

Development of new advanced composites requires more understanding of the component properties and the interfacial interactions between the reinforcement and the matrix material. Surface properties, such as surface energy, specific surface area, acid-base properties, of the reinforcement material helps to select the most compatible matrix for it. Ability to measure the surface energy of these materials is essential for ensuring compatibility between them. Adhesion between the matrix and filler/fiber is crucial for reinforcement composites. During the manufacture of filler or fiber, surface treatment and modification are performed to enhance this

adhesion. Additionally, it helps to understand its behavior during the processes and predict the performance. Inverse Gas Chromatography (IGC) is a powerful analytical tool to determine the surface energy, specific surface area, acid-base properties and solubility parameters which can be used to help predict the reinforcement quality, interface compatibility and composite performance.

One of the most commonly used parameters for the description of the energetic situation on the surface of a solid is the surface energy. The surface energy is analogous to the surface tension of a liquid. Surface energy describes the interaction between cohesive and adhesive forces which, in turn, dictate if wetting occurs. In practical terms, the higher the surface energy, the more reactive the surface. The surface energy parameter can be divided into a dispersive and a specific component. The dispersive surface energy can be directly calculated from the retention times of a series of injected n-alkanes [1]. The specific contribution of the surface energy is obtained indirectly via the specific free energy, obtained by injecting a range of polar probe molecules. By applying an appropriate concept, the acid-base numbers can be calculated from the specific free energies. The study of acid-base properties by IGC has the additional benefit that changes in the orientation of surface groups can be studied. Those changes are not necessarily related to variations in composition. For this reason spectroscopic methods are less appropriate for the study of these effects [2].

A common approach for acid-base calculations used in IGC is the van Oss concept [3], which provides acid and base numbers in the same units as the dispersive surface energy.

$$\Delta G_i^{sp} = N_A \cdot a_i \cdot 2 \cdot \left[(\gamma_l^+ \cdot \gamma_s^-)^{1/2} + (\gamma_l^- \cdot \gamma_s^+)^{1/2}\right] \quad (1)$$

In Eq. 1 γ_s^+ and γ_s^- are the electron acceptor (acid) and electron donor (base) parameters of the surface and γ_l^+ and γ_l^- are the electron acceptor and donor parameters of the probe molecule. Unfortunately, in its original form, this equation can only be used for relative comparison due to inaccurate starting parameters leading to an overestimation of the basicity [4]. To correct this and decrease probe sensitivity, the input parameters have been rescaled for a more reliable determination of acid/base values according to Della Volpe [4]. With this rescaling, the van Oss concept is useful for the determination of the specific surface energy. The specific surface energy can be obtained from the γ_s^+ and γ_s^- numbers according to Equation 2:

$$\gamma_s^{sp} = 2 \cdot \sqrt{\gamma_s^+ \cdot \gamma_s^-} \quad (2)$$

The thermodynamic work of adhesion (particle-matrix interactions) compared to the work of cohesion (particle-particle interactions) for all particle/fiber-matrix pairs can be calculated from the surface energy values of the individual composite components as shown in Eq.3 and Eq 4. With a higher surface energy, there are greater cohesive forces (particle-particle interactions), which could lead to increased agglomeration (or poor dispersion) and decreased load transfer.

$$W_{Ad} = 2 \cdot \left[\left(\gamma^d_{particle/fiber} \cdot \gamma^d_{matrix}\right)^{1/2} + \left(\gamma^{sp}_{lparticle/fiber} \cdot \gamma^{sp}_{matrix}\right)^{1/2}\right] \quad (3)$$

$$W_{Coh} = 2 \cdot \left[\left(\gamma^d_{particle} \cdot \gamma^d_{particle}\right)^{1/2} + \left(\gamma^{sp}_{lparticle} \cdot \gamma^{sp}_{particle}\right)^{1/2}\right] \quad (4)$$

2. Surface Characterization of fibers and fillers

2.1 Untreated and treated carbon fibers

The carbon fibers used in this study were PAN based high tensile strength materials. Two AS4 carbon fibers were investigated: AS4-12K and AS4-GP-3K. They were kindly supplied by Hexcel, Salt Lake City, USA. Both types of fibers were oxidized and AS4-GP was also sized with an epoxy-based agent. A third fiber C320.00A, Sigri SGL Carbon, Germany, unoxidized and unsized was studied for comparison. The three samples will be referred to as AS4 unsized, AS4 sized and CA. All experiments were conducted with an IGC2000 from SMS Ltd and the samples were packed into silanised glass columns (30 cm long, 4 mm ID). Prior to measurement the sample was pre-treated at 303 K for 2 hours in situ. The samples were measured at 303 K with a carrier gas flow rate of 10 ml/min. Probe molecules were undecane, decane, nonane, octane, dichloromethane, acetone, ethyl acetate, ethanol and acetonitrile. All solvents were supplied by Aldrich and were HPLC grade. The probe molecules were injected from the head-space via a loop with 250 µl volume. The injection concentration was 0.03 p/p0 to obtain infinite dilution conditions. The deadtime was determined by a methane injection. The specific interactions, expressed by the specific free energy (Eq 1), are listed in Table 1. Most probes interact strongest with the AS4 unsized sample. However, the AS4 sized sample interacts stronger than the untreated CA fiber. This suggests that polar probes interact significantly with the epoxy layer. From the specific free energies acid-base numbers have been calculated using the Gutmann concept. These numbers are displayed in Figure 1 for the carbon fibers.

Table 1: Specific Free Energy values of the polar probes on the fiber surfaces at 303K in [kJ/Mol]

Fiber name	$\Delta G^{sp}_{Acetone}$	$\Delta G^{sp}_{EthylAcetate}$	ΔG^{sp}_{DCM}	ΔG^{sp}_{EtOH}	$\Delta G^{sp}_{Acetonitrile}$
CA fiber	6.16	7.43	6.75	8.13	11.07
AS4-12K	10.48	14.29	8.43	16.89	15.17
AS4-GP-3K	9.39	10.21	10.05	9.01	13.53

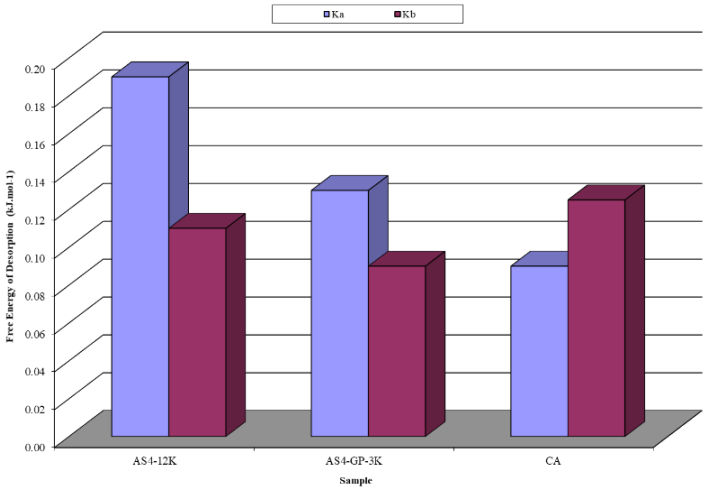

Figure 1. Acid (Ka) and base (Kb) numbers for different carbon fibers calculated from specific free energies

All samples appear amphoteric. The untreated CA fibre seems to be predominately basic while oxidation causes a shift towards a dominating acidity. When the Ka numbers are compared

directly the trend AS4-12K (unsized) > AS4-GP-3K (sized) > CA can be observed. This can be explained by the fact that oxidation increases the amount of oxygen functionalities, so AS4-12K unsized shows the highest acidity. A comparison of the Kb numbers shows the following trend: CA > AS4-12K (unsized) > AS4-GP-3K (sized). The change in basicity from the untreated CA to the AS4 unsized sample can be explained by the decrease in the graphitic nature of the fibre due to the oxidation. Sizing seems to decrease the basicity even further.

2.2 Cellulose fibers

Three fibre samples were used in this work [6]. Two types of bast fibres were chosen, a Canadian linseed flax (variety unknown), supplied by the Composites Innovation Centre (CIC), Winnipeg, Manitoba, and a Kenaf fibre (variety KK60), provided by Engage Eco Products Co. Ltd., Thailand. The third fibre sample tested was BioMid® cellulose fibers, supplied by ENC International. All experiments were conducted with an Inverse Gas Chromatograph Surface Energy Analyser (IGC-SEA) from Surface Measurement Systems (London, UK). About 0.7–1 g of chopped fibers (~10 cm long) with a sample bed length of ~ 30 mm were packed into individual 4 mm internal diameter iGC silanised glass column. Carrier gas was helium, and methane was the reference gas to determine the dead time, which represents the time necessary for a molecule to travel across the column without any interaction. Series of normal alkanes (C7-C10) were injected to build the alkane line, while dichloromethane and ethyl-acetate were injected as the mono polar acid probe and basic probe respectively [6]. The individual surface energy components, γ_S^D and γ_S^{SP}, and the total surface, γ_S^{TOT} of the BioMid® cellulose, flax and kenaf fibers are listed in Table 2 and the distribution profiles are given in Figure 2.

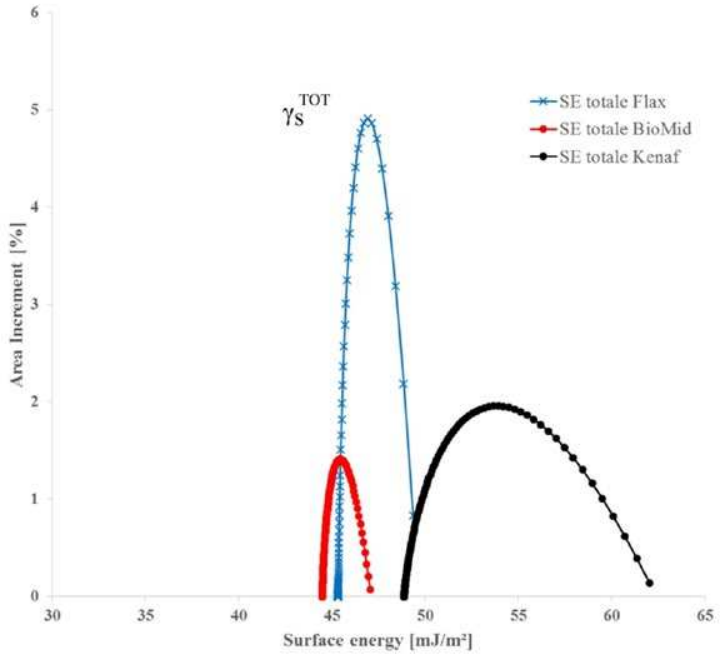

Figure 2. Distribution of the total surface energy for the cellulose BioMid®, kenaf and linseed flax fibers [6]

Table 2: Surface energy components [mJ/m^2] at 30° C, 0 % RH, Min value corresponds to maximal coverage, Max value corresponds to minimal coverage and Mean value is the median where half of the population lies below this value [6].

  doi:10.5075/epfl-298799_978-2-9701614-0-0

	γ_S^D			γ_S^{SP}			γ_S^{TOT}		
Fiber name	Min	Max	Mean	Min	Max	Mean	Min	Max	Mean
BioMid®	40.7	42.8	41.1	3.8	4.3	3.9	44.5	47.1	45.0
Flax	38.6	41.0	39.1	6.6	8.3	6.9	45.3	49.4	46.1
Kenaf	37.7	43.6	38.8	11.1	18.4	12.5	48.9	62.0	51.3

BioMid® fibres are produced by a spinning process from cellulose and other biomass components in solution and would thus be expected to have a regular smooth surface. Since the individual components have some degree of mobility during this processing method, it could be expected that if different chemical moieties are present, they would rearrange to give a relatively homogeneous low energy surface. This was reflected in the lowest γ_S^{TOT} for the BioMid® fibres and the narrowest distribution of the fibres tested. Flax fibres' surface contained polar groups of lower energy than that of kenaf fibres' surface, which is consistent with the assumption that the former surface was rich in waxes and the kenaf fibres contained a variety polar component. Kenaf fibres' surface likely comprised more Lewis acid-base functional groups than that of flax, for instance lignins, pectins and extractives [6].

2.3Ultrafine silk particles

In one of our study in collaboration with Deakin University, the surface energy and the acid-base properties of ultrafine silk powders as new lightweight composite fillers were measured by IGC-SEA system and the surface energy values were correlated with the cohesiveness and flow ability of the silk powders [7]. The measured surface energetics and compressibility of the silk powder are shown on Figure 3. Linear correlation was observed between the surface energy and compressibility of silk powders due to the trend between samples was the same at both properties.

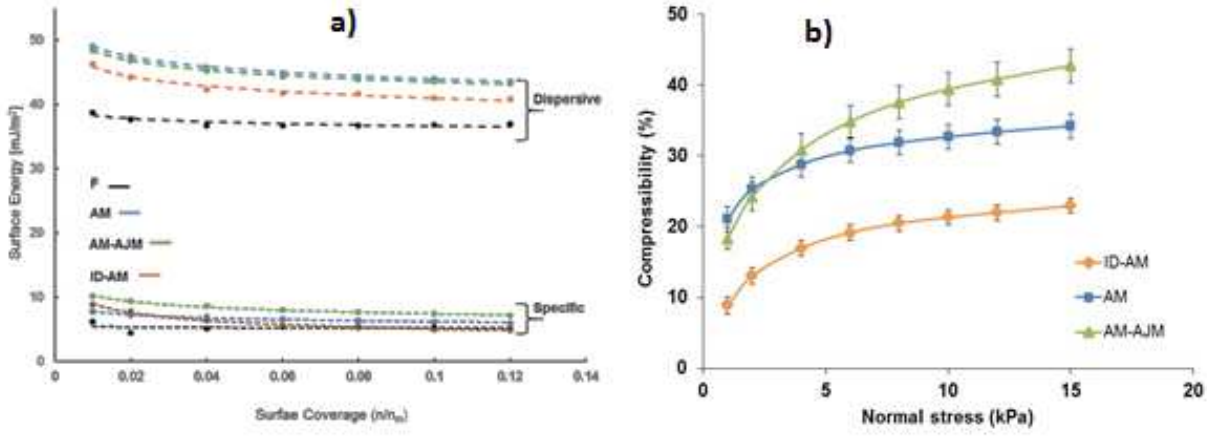

Figure 3. a) Profiles of surface energies and b) compressibility of silk powders [7]

  doi:10.5075/epfl-298799_978-2-9701614-0-0

3. Conclusion

Inverse Gas Chromatography technique is a powerful tool to determine the essential surface properties of reinforcement materials and the matrix, which make important role in the interactions between them, and thermodynamic work of adhesion in reinforcement composites. IGC is useful tool also to investigate and to understand the process-induced effects on the surface properties. The surface energy distribution profiles instructive for natural fiber / polymer matrix composite design. Not only is it important to match the average surface energy of the fibers and matrix polymer, but also to evaluate the potential for polar interactions between the fiber and matrix to give good fiber adhesion. In addition, a broad distribution of surface energy of the fiber may result in sections of the fiber showing adequate adhesion while other sections are poorly wetted. These poorly adhered sections in the interface can act as flaws which are known to lower the interfacial adhesion. In summary, information what IGC can provide about the composite components helps to develop and design more advanced composites with exterior performance and properties.

Acknowledgements

Surface Measurement Systems thank Frank Thielman, Alexander Bismarck, Angelica Legras and Rangam Rajkhowa for their contributions to the studies.

4. References

1. Schultz J, et al. The Role of the Interface in Carbon Fiber-Epoxy Composites, J. Adhesion 1987, Vol 23, 1:45-60.
2. Buckton G, Beezer A.E. The applications of microcalorimetry in the field of physical pharmacy, Intern. J. Pharm.1991, Vol 72, 3:181-191.
3. Van Oss CJ, Good RJ, Chaudhury MK, Additive and nonadditive surface tension components and the interpretation of contact angles, Langmuir 1988, 4, 4:884–891
4. Della Volpe C, Sigioni S. Some Reflections on Acid–Base Solid Surface Free Energy Theories, J. of Coll. and Int Science 1997, Vol 195, 1:121-136
5. Thielmann F, Burnett D, Bismarck A. Determination of Carbon Fibre-Polymer Interactions by Inverse Gas Chromatography, SMS Ltd. 2006, Case Study 604
6. Legras A, et al. Inverse gas chromatography for natural fibre characterisation: dispersive and acid-base distribution profiles of the surface energy, Cellulose 2017, 24:4691–470
7. Rajkhowa R, et al. Relationship between processing, surface energy and bulk properties of ultrafine silk particles, Powder Technology 2015, 270:112-120

  doi:10.5075/epfl-298799_978-2-9701614-0-0

EXPERIMENTAL AND NUMERICAL ANALYSIS OF HEAT DISSIPATION IN HYBRID CARBON/GLASS THIN-PLY COMPOSITES FOR MULTIFUNCTIONAL APPLICATIONS

Viesturs, Lācis[a], Alens, Šņepsts[a], Andrejs, Pupurs[a], Zainab, Al-Maqdasi[b]

a: Riga Technical university, andrejs.pupurs@rtu.lv
b: Lulea University of Technology

Abstract: *Thermal behavior of hybrid carbon/glass thin-ply laminates with different layer thickness ratios were investigated experimentally. Two different approaches were used for applying thermal loads: in one experiment small-scale external heater was attached on the surface of laminate specimen; in the second approach cyclic mechanical loading with high frequency was applied to generate internal heating within materials. In both experiments transient temperature distribution along the thickness of specimens was measured and recorded using high performance thermal imaging camera. Obtained results demonstrate temperature distribution in reference and hybrid laminate layers during the transient and steady state thermal conditions. Relatively large differences between carbon/epoxy and glass/epoxy layers were found in terms of internal heat generation and heat transfer. Parametric analysis results on reference and various hybrid lay-ups from this study could aid the lay-up design for composites in multifunctional applications with various thermal processes.*

Keywords: thin-ply laminates; heat dissipation; thermal imaging

1. Introduction

Developments in spread-tow fabric technology during the last decade have opened up new possibilities to design new carbon/glass hybrid thin-ply laminates obtaining lightweight and flexible structural components with increased damage resistance and ductility compared to conventional composites [1-3]. Along excellent mechanical damage resistance properties such hybrid laminates could also simultaneously utilize beneficial physical properties of materials, such as electrical insulation properties of glass fibers and thermal conductivity properties of carbon fibers ultimately designing a multifunctional material. Such materials have great potential in structural electronics [4], structural batteries [5], aerospace and automotive applications among others.

Such hybrid laminates with thin carbon and glass layers could be of particular interest in developing structural electronic components, where a significant weight reduction could be additionally achieved on the system level by, for example, integrating thermal conductivity function in the hybrid structural laminate for conducting away the excess heat from electronic components and thus eliminating the need for heavy liquid cooling and ventilation components. In the context of glass/carbon laminates, the carbon fiber layers would be very suitable for performing the heat conduction. Initial attempts in applications of such multifunctional glass/carbon hybrid laminates in printable circuit boards have been reported in [4].

  doi:10.5075/epfl-298799_978-2-9701614-0-0

The present paper aims to contribute to understanding of thermal behavior of hybrid thin-ply laminates. Hybrid carbon/epoxy and glass/epoxy thin-ply laminates with different carbon and glass fiber layer thickness ratios were investigated experimentally. Two different approaches were used for applying thermal loads: in one experiment small-scale external heaters were attached on the surface of laminate specimens; in the second approach cyclic mechanical loading was applied to generate internal heating within materials. 2D transient temperature distribution along the thickness and length of the specimens was measured. The main objective of the study was to evaluate the heat transfer from the externally heated surface layer to the internal layers (in case of external heating) and to analyze heat flow and temperature distribution in hybrid laminate layers during self-heating.

2. Materials and manufacturing

Thin-ply laminates were manufactured using Textreme carbon fiber thin-ply plain weave fabrics from Oxeon (Sweden) with areal weight of 100g/m^2 and glass fiber plain weave fabrics from Interglas (Germany) with an areal weight of 80g/m^2. Epoxy resin LY1564 from Huntsman (USA) with XB 3404-1 hardener was used as the matrix. Composite plates were hand stacked into desired lay-ups and vacuum infusion technique was used for epoxy infusion into the stacked fabrics. To enhance the flow of resin through the densely packed fabrics, small size metal pins were used to provide better flow conditions prior to the vacuum infusion process. The hybrid composite plates were cured in an oven at 80°C temperature for 8 hours. Hybrid carbon/glass laminates with various combinations of single, double and quadruple carbon and glass fiber layers were manufactured. All plates including the reference plates consisted of 16 layers. The lay-ups and their notations are schematically shown in Fig.1.

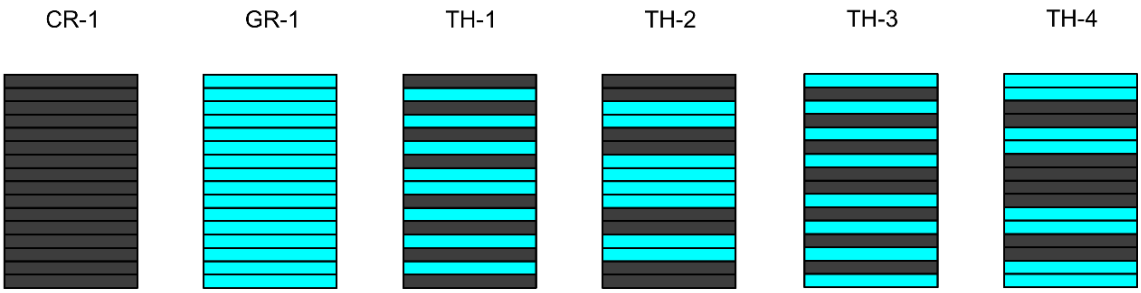

Figure 1. Schematic illustration of hybrid thin-ply laminate lay-ups

In Fig.1. CR-1 and GR-1 denote carbon/epoxy and glass/epoxy reference materials respectively. TH-1 to TH-4 are the used notations for hybrid carbon/epoxy and glass/epoxy laminate plates with different layer configurations and thickness ratios. Notably the hybrid composite plates TH-1 to TH-4 all consist of 8 layers of carbon/epoxy and 8 layers of glass/epoxy layers.

3. Experimental tests

Experimental part of the present study consisted of two different thermal tests. In the first experiment a small-scale (21 x 60 x 5 mm) self-regulating electrical heater with 15W capacity was attached on external surface layer of laminate specimen and the heat transfer to the internal layers was measured. In typical room temperature conditions, the external heater reaches 60°C temperature on the contact surface within approximately 60 seconds. The heater was attached to the test specimen with a thin double-sided scotch tape ensuring a uniform

  doi:10.5075/epfl-298799_978-2-9701614-0-0

contact between the heater and the test specimen surface. The heating tests were conducted starting from room temperature both on the heater and the specimen. Recording of temperature distribution along the thickness of the specimens was performed using high performance thermography and thermal imaging camera model A6752sc from FLIR. The camera was equipped with FLIR 1X microscope lens (field of view 9,6 mm x 7,7 mm) allowing to accurately capture temperature distribution within the layers of laminate specimens with total thickness in the range between 1.6 to 2.0 mm. During the heating the specimens were mounted vertically in a holder and the camera was placed perpendicularly to the specimen edge.

The second type of thermal experiment was self-heating test by subjecting the test specimens to cyclic mechanical loading. Cyclic mechanical loading was performed on Instron E10000 dynamic testing machine, equipped with a 10 kN load cell. The tests were carried out in tension-tension cyclic loading regime with fixed maximum and minimum strain levels. The load ratio was R=0.1 and the loading frequency of 20Hz was used unless stated otherwise. For sake of parametric analysis, loading cases with frequencies of 25Hz and 30Hz were also conducted on selected specimens. Maximum tensile strain levels in the range of 0.5% up to 0.9% were applied. Heat generation and temperature distribution within laminate layers were measured using the same set-up as for external heating tests, namely the FLIR A6752sc camera equipped with FLIR 1X microscope lens (Fig.2). Tests were started at room temperature and the cyclic loading of specimens was conducted until reaching steady state thermal conditions. After reaching the steady state (typically within 7-8 minutes) the cyclic loading was stopped but the specimen left in the tensile machine grips, and the cooling of specimen down to room temperature was also recorded with the thermal imaging camera.

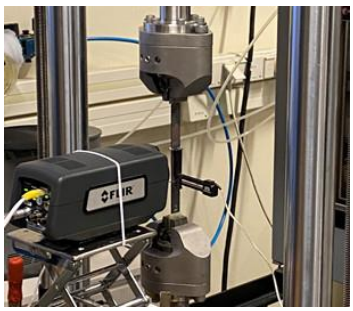

Figure 2. FLIR A6752sc thermal imaging camera positioned to measure self-heating during cyclic mechanical loading

2D transient temperature distribution along the thickness and length of the specimens was recorded in both of the described experiments and the data were processed with FLIR Research IR Max software.

Typical images of temperature distribution in specimens during external heating experiment and self-heating experiment are shown in Fig.3a and 3b respectively.

  doi:10.5075/epfl-298799_978-2-9701614-0-0

a) b)

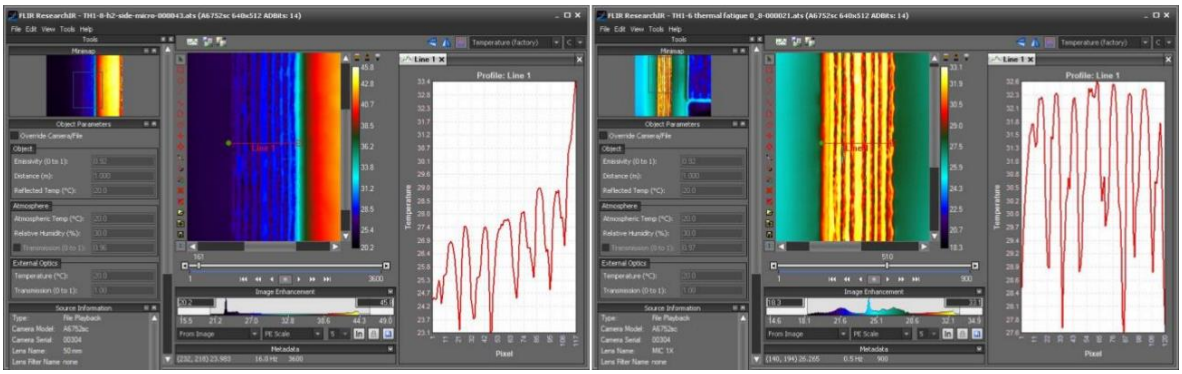

Figure 3. Examples of recorded temperature distributions in laminate layers during: a) external heating test; b) self-heating test

4. Results

4.1 External heating tests

Comparison of transient temperature distribution in reference materials, CR-1 and GR-1 is shown in Fig.4. The graphs show temperature distribution along the width of the specimen with the external heat source (60°C) being on the right hand side of the specimen. Results in Fig.4 clearly indicate differences between carbon (CR-1) and glass (GR-1) fiber composites in terms of thermal conductivity with relatively small gradient for carbon and relatively larger gradient for glass fiber composites as a result of lower thermal conductivity.

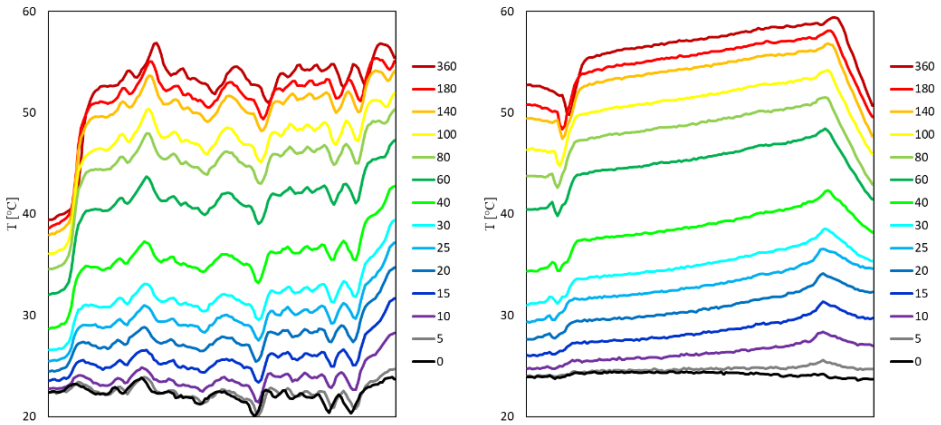

Figure 4. Transient temperature distribution in CR-1 (left) and GR-1(right) laminates

Fig.5 shows a comparison of transient temperature distributions in TH-1 and TH-2 laminates which both have carbon/epoxy external layers, however different layer thickness ratios.

Finally, Fig.6 shows a comparison of transient temperature distributions in TH-3 and TH-4 laminates which both have glass/epoxy external layers. From Fig.5 and 6 it appears that the hybrid laminates exhibit larger gradients as carbon/epoxy reference materials, however, much smaller gradients compared to reference glass/epoxy materials. The thickness ratio in different hybrid laminates seems to have a significant influence on local temperature distribution.

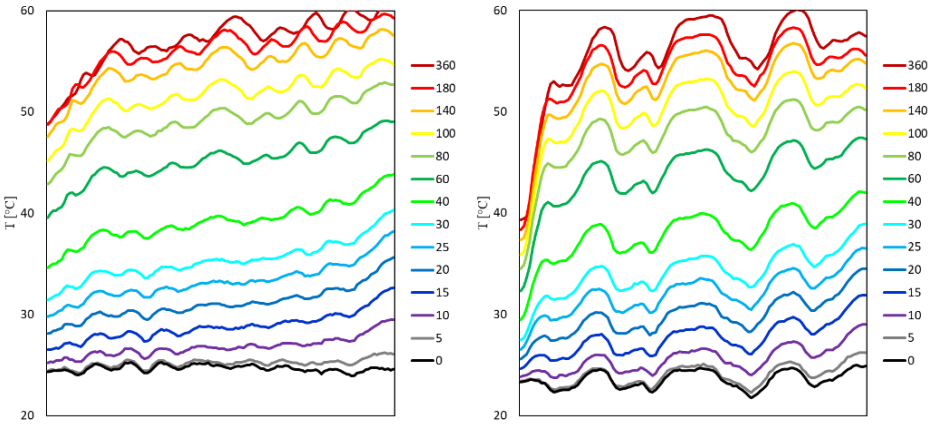

Figure 5. Transient temperature distribution in TH-1 (left) and TH-2 (right) laminates during external heating

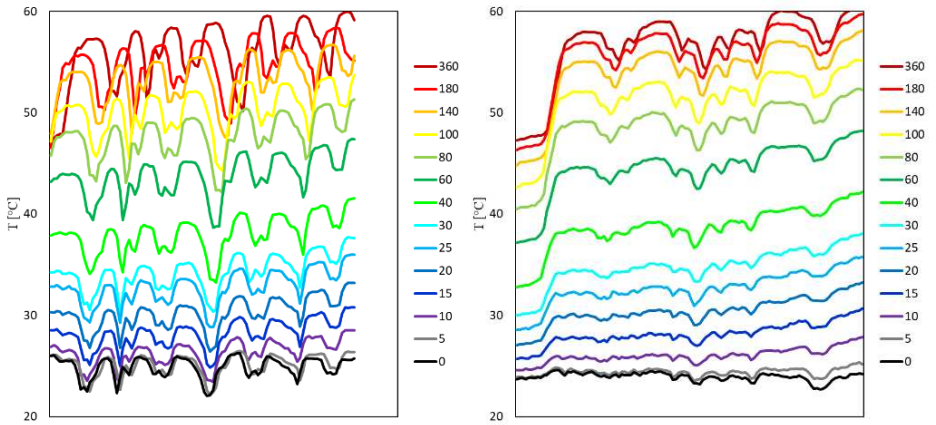

Figure 6. Transient temperature distribution in TH-3 (left) and TH-4 (right) laminates during external heating

4.2 Self-heating tests

Regarding self-heating test results, Fig.7 demonstrates the results for reference carbon/epoxy laminates (CR-1). Fig. 7a shows the effect of applied maximum strain level on self-heating under 20 Hz loading frequency. A relative increase of temperature (ΔT) from room temperature in the laminate mid/plane is depicted on vertical axis in Fig.7 and in the further text. Expectedly, higher maximum strain level leads to larger self-heating/higher temperature. Fig.7b shows the effect of loading frequency showing relatively small effect of loading frequency on self-heating in the range between 20 Hz up to 30 Hz.

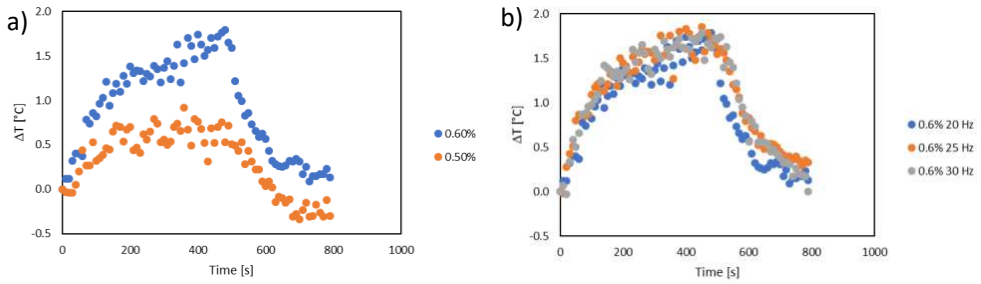

Figure 7. Average temperature in laminate mid-plane during self-heating of CR-1 laminates

Fig.8 shows the self heating and how it is affected by maximum strain level for reference glass/epoxy material (GR-1). Results indicate slightly higher self-heating of GR-1 laminates compared to CR-1 laminates. Fig.8 also shows self-heating behavior under maximum strain levels up to 0.9% at which mechanical failure was observed.

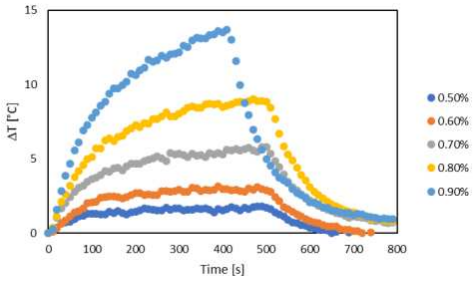

Figure 8. Average temperature in laminate mid-plane during self-heating of GR-1 laminates

Finally, Fig.9 and Fig.10 demonstrates self-heating behavior of TH-1 – TH-4 hybrid thin-ply laminates. A clear dependency of self-heating on maximum strain level can be observed. Notably, the hybrid laminate lay-up TH-1 with thinnest possible layer configuration and with carbon/epoxy external layers demonstrates the highest self-heating compared to other hybrid laminate lay-ups.

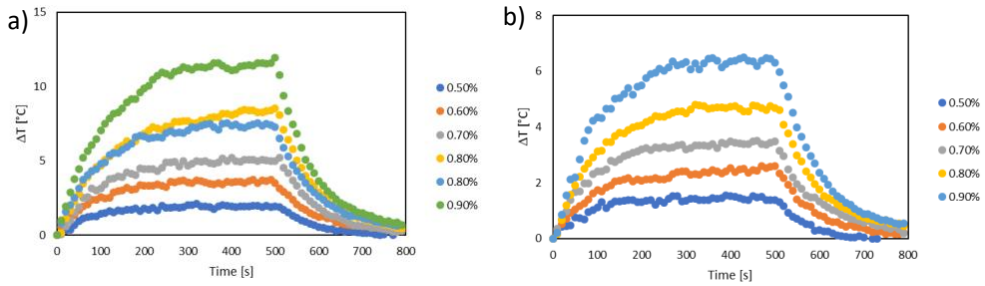

Figure 9. Average temperature in laminate mid-plane during self-heating of a) TH-1 laminates; b) TH-3 laminates

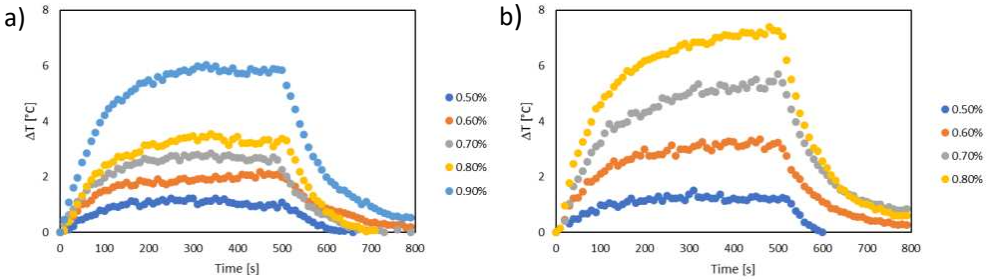

Figure 10. Average temperature in laminate mid-plane during self-heating of of a) TH-2 laminates; b) TH-4 laminates

5. Conclusions

It can be concluded from the present work that external heating can lead to notable temperature gradients in glass/epoxy laminates, while carbon/epoxy laminates demonstrate rather uniform temperature distribution. Temperature gradients in hybrid thin-ply laminates consisting of carbon/epoxy and glass/epoxy laminate layers significantly depends on the actual layer thickness. It was also shown that laminate lay-up significantly influences the self-heating behavior of hybrid thin-ply laminates.

Acknowledgements

This work has been supported by the European Regional Development Fund within the Activity 1.1.1.2 “Post-doctoral Research Aid” of the Specific Aid Objective 1.1.1 “To increase the research and innovative capacity of scientific institutions of Latvia and the ability to attract external financing, investing in human resources and infrastructure” of the Operational Programme “Growth and Employment”, project No.1.1.1.2/VIAA/3/19/408.

6. References

1. Manders PW, Bader MG. The strength of hybrid glass/carbon fibre composites - Part 1 Failure strain enhancement and failure mode. Journal of Materials Science 1981; 16(8):2233-2245.
2. Swolfs Y, Gorbatikh L, Verpoest I. Fibre hybridisation in polymer composites: A review, Composites Part A: Applied Science and Manufacturing 2014; 67:181-200. DOI: 10.1016/j.compositesa.2014.08.027
3. Wisnom MR, Czél G, Swolfs Y, Jalalvand M, Gorbatikh L, Verpoest I. Hybrid effects in thin ply carbon/glass unidirectional laminates: Accurate experimental determination and prediction, Composites Part A: Applied Science and Manufacturing 2016; 88:131-139.
4. Schatzel D. Reliability of Carbon Core Laminate Construction in Printed Circuit Boards Utilizing Stablcor™, National Aeronautics and Space Administration (NASA), NASA WBS: NAS7-03001 report 2009.
5. Carlstedt D, Runesson K, Larsson F, Asp LE. On the coupled thermo–electro–chemo–mechanical performance of structural batteries with emphasis on thermal effects. European Journal of Mechanics, A/Solids 2022; 94, art. no. 104586.
6. Tong X, Chen X, Xu JS, Zheng Y, Zhi SJ. The heat build-up of a polymer matrix composite under cyclic loading: Experimental assessment and numerical simulation. International Journal of Fatigue 2018; 116: 323-333.
7. Katunin A, Wronkowicz A. Characterization of failure mechanisms of composite structures subjected to fatigue dominated by the self-heating effect. Composite Structures 2017; 180: 1-8.

DEVELOPMENT OF GLASS FIBER/TALC-FILLED POLYPROPYLENE COMPOSITES FOR USE IN MULTILAYER SEWAGE PIPES APPLICATION

Helena, Khoury Moussa[a,b], Georges, Challita[b], Wadih, Yared[c], Marwan, Abi rizk[c], Houssem, Badreddine[a], Akram Alhussein[d]

a: UR LASMIS, Université de Technologie de Troyes, 12 Rue Marie Curie, CS 42060, 10004, Troyes, France – Helena.khoury_moussa@utt.fr

b: Équipe MMC, CRSI, Lebanese University, Faculty of Engineering, Roumieh, El-Metn, Lebanon.

c: Advanced Plastic Industries – API Company, Dbayeh highway, Seaside road, Dbayeh, El-Metn, Lebanon.

d: UR LASMIS, Université de Technologie de Troyes, Pôle Technologique Sud Champagne, 26 rue Lavoisier, 52800 Nogent, France.

Abstract: *In this study, two different composite materials; 30 wt.% talc-filled polypropylene and 30 wt.% glass fiber filled polypropylene, were elaborated and characterized in order to be used as a middle layer in a three-layer sewage pipe. Various tensile tests were performed on specimens produced by injection molding. The obtained results show an increase of approximately 124 % and 289 % in Young's moduli after adding talc and glass fiber, respectively. This significant increase in the rigidity of the material could allow manufacturing pipes with reduced weight and consequently induce an important cost saving. In addition, the use of differential scanning calorimetry analysis revealed that the addition of fillers enhances the crystallization temperature of the polypropylene matrix; this is related to the improvement in tensile properties. Also, the morphology of the materials was studied using a scanning electron microscope.*

Keywords: Multilayer pipe; Polypropylene – Talc; Polypropylene - Glass Fiber; Ring Stiffness; Mechanical Properties.

1. Introduction

The majority of old sewer pipes were constructed from brittle rigid materials like concrete or clay, which failed due to stone impingement or ground movement. Internal concrete corrosion is caused by sulfuric acid produced by domestic/municipal wastewater, which weakens the structure and is a key problem in hot, dry climates [1–3]. The majority of the requirements of modern sewage pipe systems can now be met by flexible plastic pipe systems. When compared to rigid materials, they also have enhanced properties [4–9]. In sewage applications, polyvinyl chloride (PVC), high density polyethylene (HDPE), and glass fiber reinforced plastic (GFRP) were commonly used. Polypropylene (PP) has gradually gained a greater place as a pipe material for non-pressure sewerage applications over the last few decades, owing to its superior stiffness to weight ratio, high temperature resistance, chemical resistance across a wide pH range, good abrasion resistance, and excellent long-term properties [10–12].

Incorporating inorganic particle fillers into a PP matrix has been found to be an effective way to improve mechanical properties. Reinforcements that are much stiffer and stronger than the

  doi:10.5075/epfl-298799_978-2-9701614-0-0

polymer improve its modulus and strength [13]. As a result, the modification of mechanical properties can be considered their primary function. Leong et al. [14] investigated the effects of filler loading on the mechanical, flow, and thermal properties of PP composites filled with talc, kaolin, and $CaCO_3$. Talc and kaolin were discovered to reinforce PP by increasing tensile and flexural moduli with filler load. However, at higher filler loadings, talc tends to agglomerate, resulting in a significant loss of talc-filled PP composite strength and toughness. Impact resistance is extremely high in $CaCO_3$-filled PP composites. However, the increased impact toughness of PP – $CaCO_3$ composites comes at the expense of tensile and flexural strength. Wang et al. [15] found that adding talc fillers to the PP matrix increased thermal stability, melting temperature, crystallization temperature, crystallinity percentage, and Young's modulus contrary to the reduction of glass transition temperature and elongation behavior. Furthermore, they observed that yield strength increase at low tensile speed and decrease at high tensile speed. In addition, Panthapulakkal and Sain [16] investigated the mechanical, water absorption, and thermal properties of Injection-Molded Short Hemp Fiber/Glass Fiber-filled Polypropylene Hybrid Composites. They found that incorporating glass fiber improves the tensile, flexural, and impact properties of short hemp fiber composites. In another study [17], 30 wt.% glass fibers, talc, or $CaCO_3$ were added to a recycled PP (RPP) matrix to achieve properties similar to or greater than those of the original PP. The elasticity modulus of the RPP polymer was increased by the three types of fillers. However, the addition of talc and $CaCO_3$ reduced tensile, yield, and impact strengths, whereas the use of glass fiber resulted in a significant increase. In addition, for glass fiber filled RPP, a better filler matrix interface was observed.

After the development of multilayer pipe systems, another chapter in the success story of polyolefin pipes in drinking water, sewage, gas, and industrial applications was added. All of the distinct requirements imposed on sewage pipes can be met through the combination of individual layers. Hutar et al. [18] assessed the failure of a three-layer composite plastic pipe made up of two protective layers and a main HDPE pipe layer using a fracture mechanics approach. They reported that, under certain conditions, a crack can be stopped at the interface, significantly increases the pipe lifetime. Estrada et al. [19], on the other hand, investigated the effect of the boundary condition on the first ply failure and stress distribution of a multilayer composite pipe using the finite element method. Indeed, the main property that distinguishes a non-pressure pipe is ring stiffness. It is the ability of a pipe to withstand ring deflection caused by radial forces. A pipe ring stiffness is determined by the stiffness of its material and the structural design of its wall. Park et al. [20] used the parallel plate loading test, finite element modeling, and theoretical analysis to investigate the pipe stiffness of GFRP flexible pipes. Furthermore, numerous researchers have published a wealth of information on the stiffness of flexible plain pipes [7,21–23]. In this study, two different composite materials were elaborated and characterized in order to be used as a middle layer in a three-layer sewage pipe. This can be useful to manufacture pipes with thin walls and lightweight that significantly leads to cost savings as a result. Advanced Plastic Industries – API (Lebanon, Zouk Mosbeh, www.api.com.lb), a manufacturer of plastic pipes and fittings, is collaborating on this study. The company is investing in this research in order to produce a new sewer pipe with improved mechanical properties, lower cost and retaining the ideal chemical resistance of PP pipes.

2. Experimental procedure

2.1 Materials

  doi:10.5075/epfl-298799_978-2-9701614-0-0

The matrix of the composite materials was elaborated for combining a high modulus PP block copolymer (BorECO BA212E – Borouge, Borealis Group, Singapore 049145) and a PP homopolymer (TASNEE PPH2250 – TASNEE, 11496 Kingdom of Saudi Arabia) with an equal density of 900 kg/m^3 and melt flow indexes of 0.3 g/10min and 25 g/10min, respectively. As reinforcements for the composite materials, fiber glass (DS 1125-10N – BRAJ BINANI Group, B-1560 Hoeilaart, Belgium) with a 10 µm diameter and a 4 mm length, and talc grade (Mikron's talk premier – Mircon'S, 34674 Üsküdar, Turkey) with a mean particle size of 5.3 µm were used.

Two different composite materials were produced, which are designed by PP-MT30 and PP-GF30. PP-MT30 and PP-GF30 each consist of a matrix of 50 wt.% BA212E and 20 wt.% PPH2250 filled with 30 wt.% talc or 30 wt.% glass fiber, respectively.

2.2 Tensile test

Tensile tests were performed on the various materials in accordance with ASTM D638 [24]. ASTM D638 specifies a test method for determining the tensile properties of unreinforced and reinforced plastics in the form of standard dumbbell-shaped test specimens. Specimens were mounted and loaded on a tensile machine (INSTRON-4411 H4155-5 KN, England) and loaded up to failure with a loading speed of 5 mm/min, at room temperature. A video extensometer based on the digital image correlation technique was used to measure deformation and strain. The averages of five measurements for each material are presented in all reported results.

2.3 Differential scanning calorimetry

Differential scanning calorimetry (DSC) was used to investigate the crystallization behavior and melting characteristics of the materials in accordance with ISO 11357-3 [25]. The measurements were performed with a simultaneous TGA/DSC SETARAM instrument (Caluire, France) under 200 ml/min argon flow and a heating and cooling rate of 10°C/min. The samples were heated from 25°C to 220°C and held at that temperature for 5 minutes to eliminate thermal history; then, the nonisothermal crystallization process was recorded from 220 to 25°C, and a standard crystallization status was created; the crystallization temperature (T_c) of the PP phase was measured from this cooling stage. The melting temperature of PP (T_m) was measured during a second heating stage under the same conditions as the first.

2.4 Materials morphology

The fracture surfaces of tensile samples were observed to examine the morphologies of talc and glass fiber reinforced polymer composites. This was done using a scanning electron microscope (SU8030, Hitachi); the fracture surfaces of the tensile specimens were sputter-coated with a thin gold–palladium layer to prevent electrical charge accumulation during the examination, and the specimens were analyzed at a 10 kV accelerating voltage.

3. Results and discussion

3.1 Tensile properties

Young's modulus of two polymers blend is calculated according Eq. (1) [26,27].

$$E^{1/5} = E_1^{1/5}\phi_1 + E_2^{1/5}\phi_2 \quad (1)$$

Where,

E: modulus of the blend.

  doi:10.5075/epfl-298799_978-2-9701614-0-0

E_i: modulus of phase i.
ϕ_i : volume fraction of phase i.
Therefore, it could be deduced from Eq. (1) that the Young's modulus of the matrix is equal to 1422.76 MPa. However, material properties such as Young's modulus and tensile strength listed in Table 1, are determined from the experimental tests. The obtained results show an increase of 124 % and 289 % in Young's moduli by the use of talc-filled PP and glass fiber-filled PP, respectively. This finding is consistent with previous research [17,28,29]. However, Tensile strength of talc-filled composite is steady while that of the glass fiber filled composite increased by approximately 118%. Because glass fiber is stronger and stiffer than talc, this increase in strength is expected.

Table 1: Young's modulus and tensile strength of the different materials.

Material	Young's modulus [MPa]	Tensile strength [MPa]
BA212E	1448 ± 31	27 ± 1
PPH2250	1361 ± 42	29 ± 1
PP-GF30	5535 ± 339	61 ± 2
PP-MT30	3189 ± 106	27 ± 1

3.2 Differential scanning calorimetry results

The results of melting and crystallization temperatures determined from DSC thermograms are summarized in Table 2. Difference in melting temperatures of the pure PP grades that constitute the matrix is negligible, and the melting temperature does not change when talc or glass fiber is added. However, in terms of crystallinity, BA212E has a high crystallinity, whereas PPH2250 has a low crystallization temperature; thus, blending these two grades must result in a matrix with a lower crystallization temperature than BA212E. The crystallization temperatures obtained for the two composites are very close to that of BA212E. Indeed, talc is an effective nucleating agent that enhances the crystallinity of a PP matrix, as the crystallinity of the polymer matrix increases, the composite is expected to have a greater modulus and improved strength [14,15,30–33]. As a consequence, it could be concluded that the developed composites maintain the good crystallinity of BA212E.

Table 2: Meting and crystallization temperatures.

Material	T_c [˚C]	T_m [˚C]
BA212E	126.2	165.4
PPH2250	112	163.3
PP-GF30	124.7	162.2
PP-MT30	127.1	161.6

3.3 Scanning electron microscopy results

SEM images of PP-MT30 and PP-GF30 obtained from the fracture surfaces of tensile specimens are shown in Figure 1. Figure 1 (a) depicts talc filler particles deeply embedded indicating good filler-matrix interactions, and no large voids are visible between the particles and the matrix. On the other hand, Figure 1 (b) shows that small amount of glass fibers is pulled out and broken; there is a strong bond interface between the glass fiber and the PP matrix. Therefore, Because of the high number of glass fibers and the improved interface bonding between the fillers and the PP matrix, PP-GF30 has good mechanical properties.

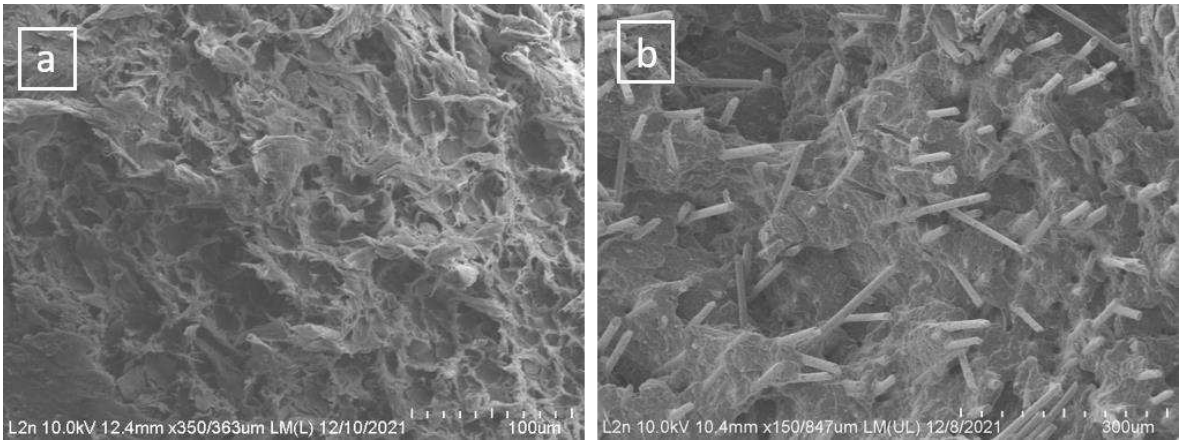

Figure 1. SEM micrographs for (a) PP-MT30 and (b) PP-GF30.

4. Conclusion

Two different composite materials, PP-MT30 and PP-GF30, were elaborated and characterized in this study in order to be used as a middle layer in a three-layer sewage pipe. Several tensile tests were performed on injection molded specimens. The results showed that using talc-filled PP and glass fiber-filled PP increased Young's moduli by 124 % and 289 %, respectively. This significant increase in material rigidity may allow for the production of pipes with reduced thickness, resulting in significant cost savings. Furthermore, differential scanning calorimetry (DSC) analysis revealed that the addition of fillers increased the polypropylene matrix crystallization temperature. This increase in crystallinity of filled polypropylene composites is related to improved tensile properties. Also, SEM micrographs showed a good filler-matrix interaction in addition to a good filler distribution and dispersion.

5. References

1. Mori T, Nonaka T, Tazaki K, Koga M, Hikosaka Y, Noda S. Interactions of nutrients, moisture and pH on microbial corrosion of concrete sewer pipes. Water Research 1992; 26:29–37.
2. Yuan L, Kyriakides S. Liner wrinkling and collapse of bi-material pipe under axial compression. International Journal of Solids and Structures 2015; 60–61:48–59.
3. Mu S, Zhou H, Shi L, Liu J, Cai J, Wang F. Research on performance and microstructure of sewage pipe mortar strengthened with different anti-corrosion technologies. IOP Conf. Series: Materials Science and Engineering 2017; 250:012036.
4. Farshad M, Necola A. Strain corrosion of glass fibre-reinforced plastics pipes. Polymer Testing 2004; 23:517–21.

  doi:10.5075/epfl-298799_978-2-9701614-0-0

5. Klaiber FW, Lohnes RA, and Wipf TJ, Investigation of High-Density Polyethylene pipe for highway applications, final report: Phase I. Iowa DOT Project HR-373, Iowa State University, College of Engineering, Department of Transportation. 1996.
6. Frank T. PE-HD spiral pipes for sewage pipelines - Electrofusion socket welding up to DN 1800. Proceedings of Plastics Pipes 2001.
7. Chaallal O, Arockiasamy M, Godat A. Laboratory tests to evaluate mechanical properties and performance of various flexible pipes. Journal of Performance of Constructed Facilities 2015; 29:04014130.
8. Martins JDN, Freire E, Hemadipour H. Applications and market of PVC for piping industry. Polímeros 2009; 19:58–62.
9. Yuan Y, Liu C, Huang M. The structure and performance of short glass fiber/High-Density Polyethylene/Polypropylene composite pipes extruded using a shearing–drawing compound stress field. Materials 2019; 12:1323.
10. Jansen N, Polypropylene: a tried and proven pipe material. 3R international 2/3 1998; 113-116.
11. Brochure, Borouge. Polypropylene materials for non-pressure sewage and drainage systems
URL:http://www.borouge.com/IndustrySolution/PDF%20Files/BorEco/2011%2012_Polypropylene%20materials%20for%20Non-Pressure%20Sewage%20Drainage%20Systems.pdf (accessed 28 august, 2019).
12. Wassenaar J. Polypropylene materials for sewerage & drainage pipes with reduced energy and carbon footprints. Journal of Materials Science and Engineering B 2016; 11-12:283-290
13. Xanthos M, Polymers and polymer composites. Functional Fillers for Plastics: Second, updated and enlarged edition. 2010.
14. Leong YW, Bakar MBA, Ishak ZAM, Ariffin A, Pukanszky B. Comparison of the mechanical properties and interfacial interactions between talc, kaolin, and calcium carbonate filled polypropylene composites. Journal of Applied Polymer Science 2004; 91:3315–3326.
15. Wang K, Bahlouli N, Addiego F, Ahzi S, Rémond Y, Ruch D, Muller R. Effect of talc content on the degradation of re-extruded polypropylene/talc composites. Polymer Degradation and Stability 2013; 98:1275–1286.
16. Panthapulakkal S, Sain M. Injection-molded short hemp fiber/glass fiber-reinforced polypropylene hybrid composites—Mechanical, water absorption and thermal properties. Journal of Applied Polymer Science 2007; 103:2432–2441.
17. Soy U, Findik F, Yetgin SH, Gokkurt T, Yıldırım F. Fabrication and mechanical properties of Glass Fiber/Talc/$CaCO_3$ filled recycled PP composites. American Journal of Applied Sciences 2017; 14:878–885.
18. Hutař P, Zouhar M, Náhlík L, Ševčík M, Máša B. Multilayer polymer pipes failure assessment based on a fracture mechanics approach. Engineering Failure Analysis 2013; 33:151–162.
19. González-Estrada OA, León JS, Pertuz A. Influence of the boundary condition on the first ply failure and stress distribution on a multilayer composite pipe by the finite element method. Journal of Physics: Conference Series 2019; 1159:012013.
20. Park J-S, Hong W-H, Lee W, Park J-H, Yoon S-J. Pipe stiffness prediction of buried GFRP flexible pipe. Polymers and Polymer Composites 2014; 22:17–24.
21. Farshad M, Necola A. Effect of aqueous environment on the long-term behavior of glass fiber-reinforced plastic pipes. Polymer Testing 2004; 23:163–167.
22. Lee JH, Kim SH, Choi WC, Yoon SJ. Pipe stiffness prediction of buried glass fiber reinforced polymer plastic (GFRP) and polymer mortar pipe. Key Engineering Materials 2017; 753:3–7.

23. Thomas NK, George SP, John SM, George SP. Stress analysis of underground GRP pipe subjected to internal and external loading conditions. International Journal of Advanced Mechanical Engineering 2014; 4:435-440
24. D20 Committee. Test Method for Tensile Properties of Plastics [Internet]. ASTM International; 2020 [cited 2020 Jun 24]. Available from: http://www.astm.org/cgi-bin/resolver.cgi?D638-14
25. ISO 11357-3: 2018. Plastics - Differential scanning calorimetry (DSC), Switzerland 2018.
26. Davies WEA. The theory of elastic composite materials. Journal of Physics D: Applied Physics 1971; 4:1325–1339.
27. Willemse RC, Speijer A, Langeraar AE, Posthuma de Boer A. Tensile moduli of co-continuous polymer blends. Polymer 1999; 40:6645–6650.
28. AlMaadeed MA, Kahraman R, Noorunnisa Khanam P, Madi N. Date palm wood flour/glass fibre reinforced hybrid composites of recycled polypropylene: Mechanical and thermal properties. Materials & Design 2012; 42:289–294.
29. Serrano A, Espinach FX, Tresserras J, Pellicer N, Alcala M, Mutje P. Study on the technical feasibility of replacing glass fibers by old newspaper recycled fibers as polypropylene reinforcement. Journal of Cleaner Production 2014; 65:489–496.
30. Leong YW, Ishak ZA, Ariffin A. Mechanical and thermal properties of talc and calcium carbonate filled polypropylene hybrid composites. Journal of Applied Polymer Science 2004; 91:3327–3336.
31. Ammar O, Bouaziz Y, Haddar N, Mnif N, Talc as reinforcing filler in polypropylene compounds: Effect on morphology and mechanical properties. Polymer Sciences 2017; 3.
32. Wang SH. The mechanical properties and thermodynamic study on polypropylene/talc composites. Advanced Materials Research 2014; 915–916:751–754.
33. Makhlouf A, Satha H, Frihi D, Gherib S, Seguela R. Optimization of the crystallinity of polypropylene/submicronic-talc composites: The role of filler ratio and cooling rate. eXPRESS Polymer Letters 2016; 10:237–247.

  doi:10.5075/epfl-298799_978-2-9701614-0-0

THE EFFECT OF POLYMERIC MATRIX TYPE ON THE THERMOMECHANICAL PERFORMANCE AND SYNERGY OF CARBONACEOUS HYBRID NANOCOMPOSITES

Evagelia Kontou[a], Ilias Charitos[a]

a: *Mechanics Department, School of Applied Mathematical and Physical Sciences, National Technical University of Athens, Iroon Polytechniou 9, Zografou 15780, Athens, Greece*

Abstract: *The scope of the present work is the preparation and the experimental study of carbonaceous hybrid nanocomposites based on two different polymeric types, namely Polylactic acid (PLA) and linear low-density polyethylene (mLLDPE), produced by metallocene catalyst. Blends of carbon nanofibers (CNFs) or carbon nanotubes (CNTs) and graphene oxide (GO) at equal ratio, and various total contents were prepared at equivalent processing conditions by a melt mixing procedure. Experimental methods, as scanning electron microscopy (SEM), broadband dielectric spectroscopy (BDS), differential scanning calorimetry (DSC), dynamic mechanical analysis (DMA), tensile testing have been carried out. A better thermomechanical performance of the hybrid nanocomposites was found, while further, a collaboration between GO and CNTs, has been detected by BDS, which results to the establishment of conductive paths into the bulk matrix, at a lower nanofiller content, compared to the monofiller nanocomposites. This cooperation is assigned to an effective coupling of gaps between GO and CNTs.*

Keywords: Polylactic Acid; Hybrid nanocomposites; Mechanical properties; Electrical properties.

1. Introduction

Over the last years, various types of carbon/based nanofillers, including carbon nanotubes (CNTs), carbon nanofibers (CNFs) and graphene nanoparticles, have been utilized as additives into a bulk polymeric matrix, to adapt their mechanical, thermal, and electrical properties for a number of targeted applications. The obtained optimization of the prepared nanocomposites' macroscopic properties is due to the nanofillers' special structures and properties, such as low density, high aspect ratio, high modulus, tensile strength, and remarkable electrical and thermal conductivities [1]. Concerning CNFs, they are characterized by diameters ranging between 50-200 nm, being different from the conventional carbon fibers having diameters of the order of micrometers. Pristine PLA exhibits poor thermal and mechanical properties, while it's mechanical performance, and electrical/ thermal properties can be improved by the incorporation of nanosized fillers, expanding this way the PLA's application fields [2]. Typical applications to this trend are antistatic, electromagnetic interference materials, sensors, and heaters. On the other hand, linear low density polyethylene (LLDPE) [3] polymerized by metallocene catalysts (mLLDPE) have several advantages over LLDPE produced by Ziegler–Natta catalysts, such as strength, optical properties, narrow molecular weight distribution, and low extractables. A limited number of works is referring to the reinforcing of LLDPE with carbonaceous nanofillers [4]. The incorporation of carbonaceous nanofillers into mLLDPE leads to a substantial improvement of its thermomechanical performance. In this way, the mLLDPE/nanocomposites meet the requirements for a number of applications such as in medical and packaging fields. PLA/GO/CNT, PLA/GO/CNF, mLLDPE/GO/CNT and

  doi:10.5075/epfl-298799_978-2-9701614-0-0

mLLDPE/GO/CNF hybrid nanocomposites, at various weight fractions, at equal ratio GO/CNT and GO/CNF, were prepared with a melt-mixing procedure, and experimentally studied.

2. Experimental

2.1 Materials

Two series of polymer hybrid nanocomposites, based on PLA and mLLDPE, designated as PLA/GO/CNT , PLA/GO/CNF, mLLDPE/GO/CNT and mLLDPE/GO/CNF hybrid nanocomposites, at various weight fractions, at equal ratio GO/CNT and GO/CNF, were prepared with a melt-mixing procedure, and experimentally studied [5]. The PLA matrix utilized is under the commercial name Ingeo™ Biopolymer 2003D, produced by NatureWorks LLC, while the LLDPE type employed, is based on octene comonomer, and prepared by metallocene catalyst, and designated as mLLDPE. The carbonaceous nanofillers used in the present work, are: Graphene oxide (GO), provided by United Nanotech Innovations PVT.LTD., functionalized with OH groups As provided by the manufacturer, the number of layers was 3–6 in average, the thickness average in Z dimension was 2–3 nm and the length average in X and Y dimensions was approximately 5 μm. Multiwalled carbon nanotubes (MWCNTs) were provided by Aldrich with in average, the outer diameter of 10 ± 1 nm, the inner diameter of 4,5 ± 0,5 nm, and 3–6 μm in length. Carbon nanofibers (CNFs) provided by Aldrich, were of a length ranging between 20-200 μm while the average diameter was 100 nm.

2.2 Experiments

The prepared nanocomposites were experimentally studied, by SEM, DSC, BDS, DMA, RAMAN spectroscopy, and tensile testing. The relative experimental results are presented and analyzed in the following.

3. Results and Discussion

The dispersion quality of the nanocomposites is representatively illustrated in Figs 1 and 2, for PLA and mLLDPE/based hybrid nanocomposites correspondingly.

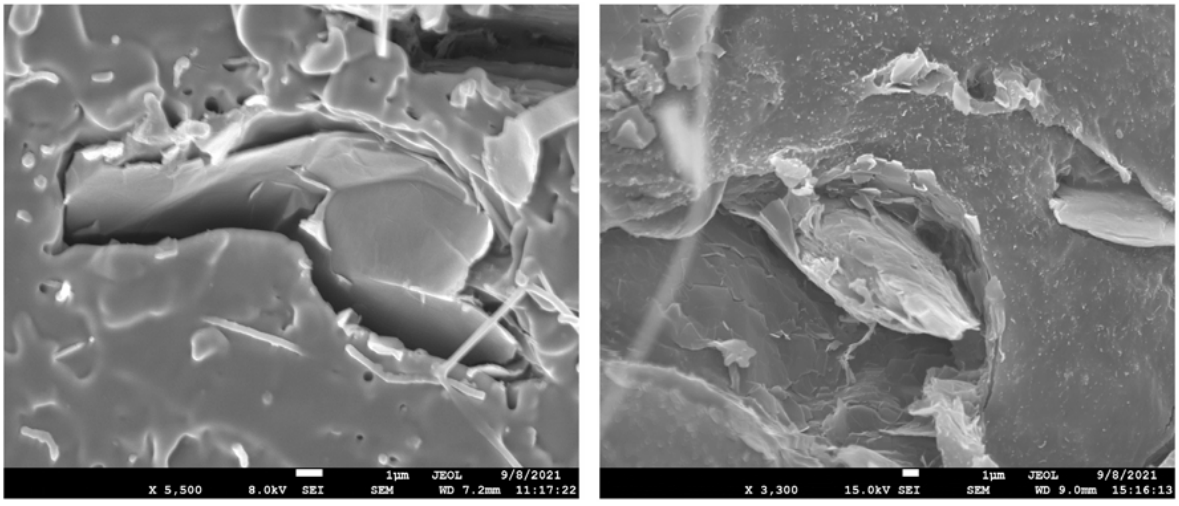

Figure 1. Scanning Electron Microscopy image for PLA/GO/CNF/3.84%, and PLA/GO/CNT/8%

In both Figures, a generally good dispersion quality of nanofillers has been achieved, as far as CNTs and CNFs is concerned, while the GO sheets exhibit a partial exfoliation.

  doi:10.5075/epfl-298799_978-2-9701614-0-0

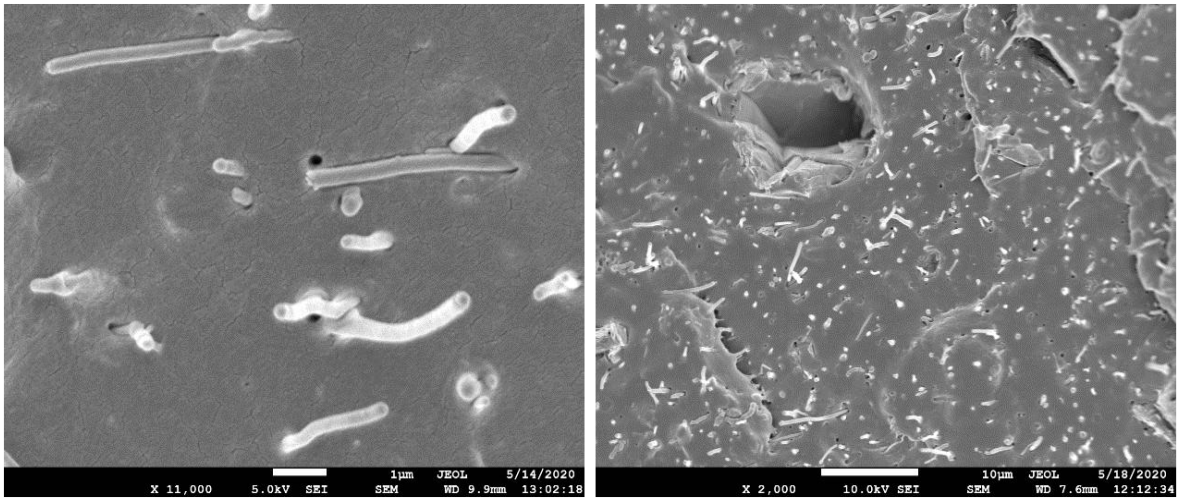

Figure 2. Scanning Electron Microscopy image for mLLDPE/GO/CNF/3.84%, and mLLDPE/GO/CNT/3.84%

The DSC results of all hybrid nanocomposites examined are summarized in Table 1. The glass transition temperature Tg and the melting temperature Tm are unaffected by the nanofillers' presence. The PLA/hybrids exhibit a cold crystallization temperature, which is higher for the nanocomposites. The T_{cc} increment of the nanocomposites indicates that the presence of the nanofillers hinders the kinetics of crystallization on heating. In addition, a substantial crystallinity increment is obtained, mainly for the PLA/GO/CNT materials. This is not the same for the mLLDPE/hybrids, where a low crystallinity increment is observed.

Table 1: DSC results of all polymer hybrid nanocomposites examined.

Material	T_g (°C)	T_m (°C)	T_{cc} (°C)	ΔH^*_{cc} J/g	ΔH^*_m J/g	ΔH^* J/g	X_c %	Crystal. Increment %
PLA	60	154	105	-24	28.1	4.1	4.4	-
PLA/GO/CNT/3.84%	59	152	110	-13	29.8	16.8	18	310
PLA/GO/CNT/6.25%	61	152	123	-10.7	22.4	11.7	12.6	186
PLA/GO/CNT/8%	60	152	124	-11.6	20.8	9.2	10	127
PLA/GO/CNF/3.84%	60	153	109	-21	23.8	2.8	3	-
PLA/GO/CNF/6.25%	60	150	110	-25.5	29.4	3.9	4.2	-
PLA/GO/CNF/8%	60	150	110	-22	31.1	9.1	9.8	122
mLLDPE		103			68.0		24.6	-
mLLDPE/GO/CNF/1.31%		103			74.2		26.9	9.3
mLLDPE/GO/CNF/3.84%		103			75.5		27.3	11.0
mLLDPE/GO/CNF/6.25%		102			82.0		29.7	20.7
mLLDPE/GO/CNT/1.31%		102			68.0		24.6	-
mLLDPE/GO/CNT/3.84%		101			71.8		26.0	5.7
mLLDPE/GO/CNT/6.25%		101			70.7		25.6	4.1

The tensile experiments were performed at room temperature, and the corresponding results are presented in Table 2.

  doi:10.5075/epfl-298799_978-2-9701614-0-0

Table 2: Tensile results of PLA and mLLDPE hybrid nanocomposites.

Material	Young's modulus E (MPa)	Modulus increment (%)	Yield stress σ_y (MPa)	Yield strain ε_y (%)	Tensile strength σ_b (MPa)	Failure strain ε_b (%)
PLA	3064 ± 150	-	34.4 ± 6.5	1.52	27.0 ± 5.5	7.39
PLA/GO/CNT/3.84	3218 ± 160	5.0	40.2 ± 8.0	1.48	29.5 ± 7.1	4.21
PLA/GO/CNT/6.25	4265 ± 230	39.2	40.4 ± 8.0	1.43	25.9 ± 6.3	7.18
PLA/GO/CNT/8	5652 ± 300	84.5	47.4 ± 9.8	1.43	32.3 ± 7.9	6.19
PLA/GO/CNF/3.84	3460 ± 190	12.9	38.5 ± 7.6	1.28	28.9 ± 7.2	6.01
PLA/GO/CNF/6.25	3796 ± 208	23.9	-	-	43.9 ± 10.9	1.51
PLA/GO/CNF/8	4000 ± 212	30.5	-	-	41.4 ± 10.2	0.01
mLLDPE	92± 4.0	-	4.0 / 5.4	23.1	29.5± 6.5	1939
mLLDPE/GO/CNF/1.31	142± 7.0	54.3	4.6 / 6.0	30.1	32.0± 8.0	1924
mLLDPE/GO/CNF/3.84	184± 8.5	100.0	5.6 / 6.5	32.0	28.7± 7.4	1809
mLLDPE/GO/CNF/6.25	204± 8.0	121.7	6.9 / 7.2	49.5	30.5± 8.7	1610
mLLDPE/GO/CNT/1.31	118± 5.0	28.3	4.8 / 6.2	30.2	30.9± 6.8	1900
mLLDPE/GO/CNT/3.84	154± 7.3	60.8	5.4 / 6.7	30.3	31.8± 7.7	1707
mLLDPE/GO/CNT/6.25	180± 8.4	95.6	7.2 / 8.4	32.1	33.3± 7.4	1576

The reinforcing effect of nanofillers is obvious in all nanocomposites examined. In the PLA/hybrids the higher Young's modulus enhancement is obtained for PLA/GO/CNT, whereas in the mLLDPE/hybrids, the higher Young's modulus increment is obtained for mLLDPE/GO/CNF nanocomposites. The yield stress is increased in almost all nanocomposites, while it is to be noted that the ductility for the mLLDPE /hybrids is retained for all nanofiller weight fractions. Comparing the two series with different polymeric matrix, it can be seen that the higher Young's modulus enhancement is obtained for mLLDPE/GO/CNF hybrid nanocomposites. It is therefore extracted that the polymeric matrix type plays a decisive role on the nanocomposite' properties.

The BDS results for all polymer nanocomposites examined are shown in Fig.3, in terms of the real part of the complex electrical conductivity plotted versus frequency.

  doi:10.5075/epfl-298799_978-2-9701614-0-0

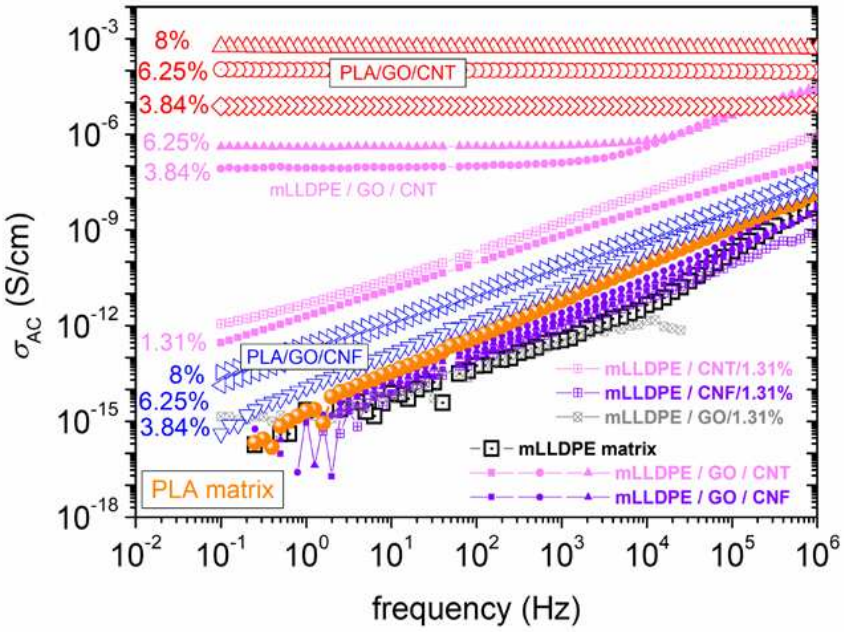

Figure 3: Comparison of BDS results for the real part of the complex electrical conductivity $\sigma_{AC}(f)$ with varying frequency, between the PLA-and mLLDPE, -based nanocomposites.

The PLA/GO/CNF, and the mLLDPE/GO/CNF nanocomposites demonstrate an almost linear increment of the σ_{AC} with increasing frequency, which is typical response for insulating material. The same trend is obtained for monofillers mLLDPE, which are shown comparatively. On the other hand, the PLA/GO/CNT nanocomposites, as well as the mLLDPE/GO/CNT ones at 3.84 and 6.25 wt.%, exhibit the so-called 'DC plateau', where the σ_{AC} is independent of the frequency in Figure 3. These results are indicative of electrical percolation of the GO/CNTs throughout the nanocomposites volume [6]. Therefore, it can be assumed that a synergistic effect may arise from the presence of the flexible MWCNTs, which favor the bridging of planar graphene oxide nanoplatelets and thus helping the development of a 3D network. The σ_{AC} values, are about ten orders of magnitude lower for mLLDPE/hybrid nanocomposites compared with the PLA/hybrid nanocomposites at the same hybrid nanofiller loadings. It can thus be further extracted that the PLA matrix favors additionally this type of synergy, compared to the mLLDPE. From the RAMAN results (not presented here) the shifting of the peak centers D, G and G', was attributed to the polymer-nanofiller and nanofiller-nanofiller interactions. It has been postulated that the CNTs have a higher degree of disorder. In addition, the important role of CNTs with the highest surface area, to the quality dispersion into the polymeric material, has been detected and associated with the formation of nucleation sites for crystal growth. Therefore, the RAMAN results are compatible with the BDS results regarding a synergistic effect for this type of hybrid nanocomposites.

In Figures 4, 5 the master curves of the storage modulus E' of all types of nanocomposites examined are shown.

  doi:10.5075/epfl-298799_978-2-9701614-0-0

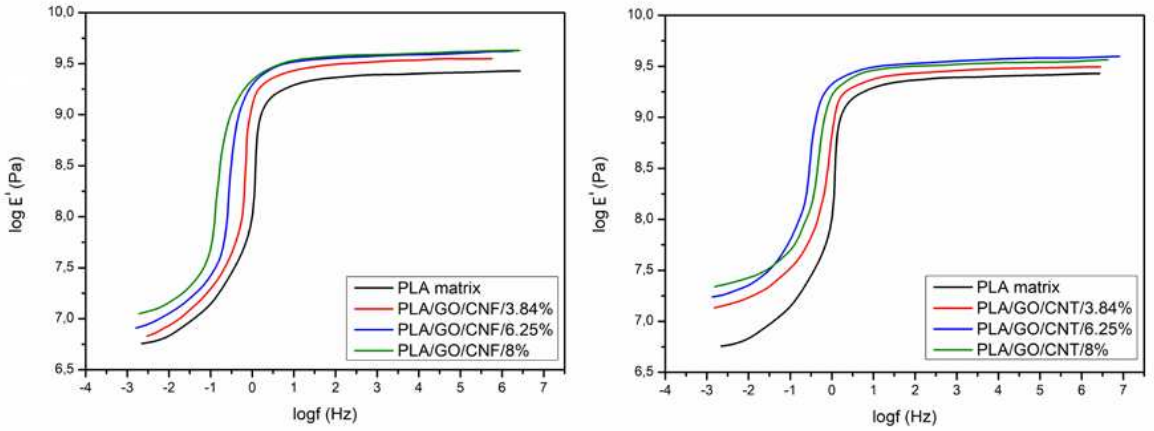

Figure 4: Master curves of the storage modulus for the PLA/hybrid nanocomposites

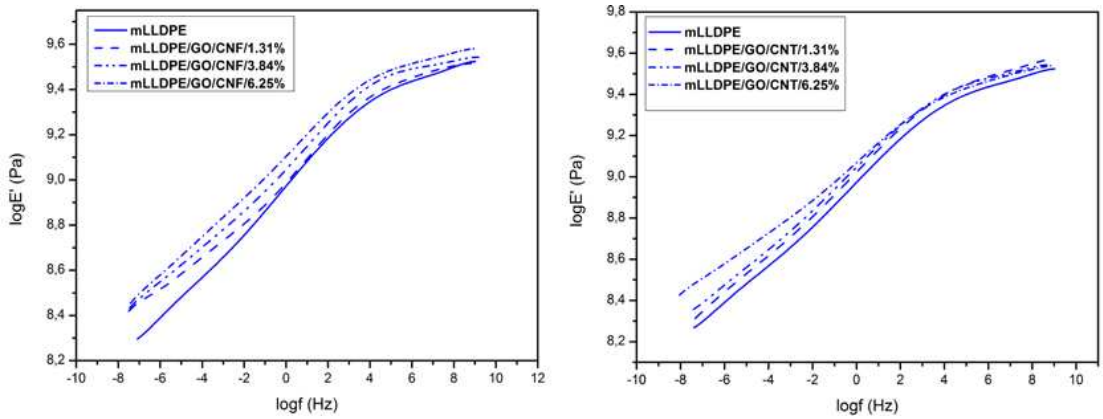

Figure 5: Master curves of the storage modulus for the mLLDPE/hybrid nanocomposites

In all cases, the storage modulus of the nanocomposites is higher than that of the polymeric matrix. For the PLA/based hybrids, it is observed that the nanocomposites attain higher values of E′ while the PLA/GO/CNF/6.25% and PLA/GO/CNF/8% exhibit almost the same value, whereas PLA/GO/CNT/6.25% appear to have the highest storage modulus at high frequency range, followed by a slightly lower value for the PLA/GO/CNT/8%. In the transition region, the storage modulus curves are distinct and it is an indication of an effective nanoparticle dispersion, while in the opposite case the master curves usually overlap each other. In the low frequency range (rubbery region), a monotonic dependence of the storage modulus values on the nanofiller loading is obtained. In addition, the decrement of the softening dispersion, which is the height difference between the glassy and rubbery state, can be observed. This effect is related with the fact that the elastic nanofillers result to a more solid – like response. In the mLLDPE/based nanocomposites, a monotonic reinforcing effect with increasing nanofillers weight fraction, along the whole frequency range is observed. In the low frequency range, a slope reduction can be observed, in both material series, which is more obvious in the PLA/GO/CNT nanocomposites. This slope reduction is an additional indication of the establishment of a network correlating the matrix and the dispersed GO/CNT nanofillers, arising from the optimized interaction between them. The loss modulus master curves (not presented here), appear to have no essential differences, regarding the frequency of the peak value and the relative position between them.

  doi:10.5075/epfl-298799_978-2-9701614-0-0

4. Modeling of the Young's modulus

The Young's modulus was modeled by the analytical model of Mori-Tanaka [7], extended by Benveniste [8] and Odegard et al. [9], in two steps and shown in Figure 6. In the first step, the Young's modulus of the fictitious matrix (polymer matrix + effective fiber-type filler) was calculated. In the second step the Young's modulus of the hybrid nanocomposites was calculated by adding the phase of GOs into the fictitious matrix. Polymer matrix (E_{mLLDPE}=92MPa, v_{mLLDPE}=0.4 & E_{PLA}=3064MPa, v_{PLA} =0.3) and GOs (E=250GPa, v=0.17) were treated as isotropic materials and the fiber-type fillers were treated as transversely isotropic materials (E_{Lcnt}=910GPa, E_{Tcnt}=304GPa, G_{12cnt}=194GPa, v_{Lcnt}=0.2 , v_{Tcnt} =0.3 & E_{Lcnf}=230GPa, E_{Tcnf}=8GPa, G_{12cnf}=27.3GPa, v_{Lcnf}=0.256 , v_{Tcnf} =0.3). The Mori Tanaka model is very successful in predicting the effective properties of two-phase composites. In theory, it is restricted to moderate volume fractions of inclusions, but in practice it can give good predictions well beyond this range.

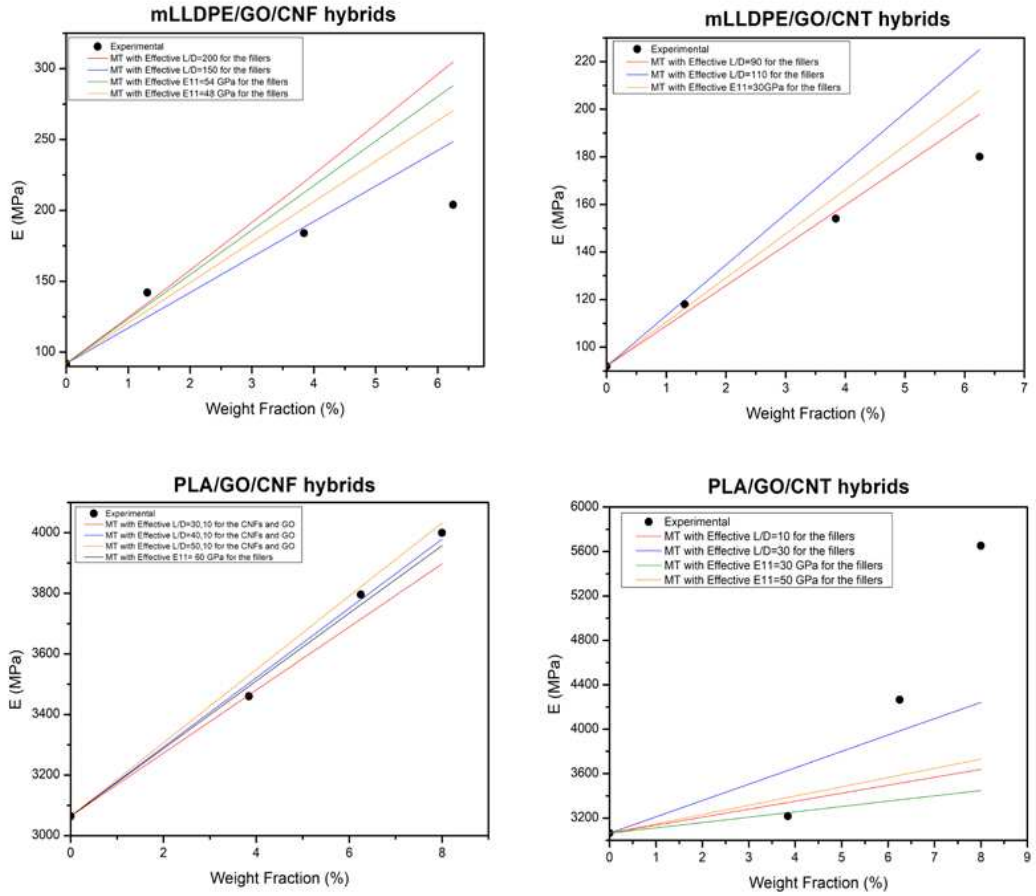

Figure 6: Young's modulus by Mori-Tanaka model, in comparison with the experimental results for all hybrid nanocomposites examined.

The parameters in the captions are used to obtain a good approximation of the experimental data. The approximation of the experimental Young's modulus is very good for the hybrid materials, whose Young's Modulus increases linearly with the weight fraction. For PLA/GO/CNT hybrids, the model is unable to approach the experimental data for fillers' contents greater than 4%wt, because of the rapid and non-linear increase of the Young's modulus at these contents.

  doi:10.5075/epfl-298799_978-2-9701614-0-0

5. References

1. Xiuyi Lin, Xu Liu, Jingjing Jia, Xi Shen, Jang-Kyo Kim. Electrical and mechanical properties of carbon nanofiber/graphene oxide hybrid paper. Composites Science and Technology 2014; 100 : 166–73.
2. Fredi G, Rigotti D, Bikiaris DN, Dorigato A. Tuning thermo-mechanical properties of poly(lactic acid) films through blending with bioderived poly(alkylene furanoate)s with different alkyl chain length for sustainable packaging. Polymer 202; 218: 123527. https://doi.org/10.1016/j.polymer.2021.123527.
3. Kuila T, Bose S, Hong CE, Uddin ME, Khanra P, Kim NH, et al. Preparation of functionalized graphene/linear low density polyethylene composites by a solution mixing method. Carbon 2011; 49: 1033-37.
4. Aalaie J, Rahmatpour A, Maghami S. Preparation and characterization of linear low density polyethylene/carbon nanotube nanocomposite. J. Macromol. Sci. Phys. B 2007; 46: 877- 89.
5. Charitos I, Georgousis G, Klonos PA, Kyritsis A, Mouzakis D, Raptis Y, Kontos A, Kontou E. The synergistic effect on the thermomechanical and electrical properties of carbonaceous hybrid polymer nanocomposites. *Polymer Testing* 2021; 95:107102. https://doi.org/10.1016/j.polymertesting.2021.107102.
6. Charitos I, Georgousis G, Kontou E. Preparation and Thermomechanical Characterization of Metallocene Linear Low-Density Polyethylene/ Carbon Nanotube Nanocomposites. Polymer Composites 2019;40:1263-73. DOI 10.1002/pc.24961.
7. Mori T, Tanaka K. Average stress in matrix and average elastic energy of materials with misfitting inclusions, *Acta Metall*. 1973; 21: 571–74.
8. Benveniste Y. A new approach to the application of Mori-Tanaka's theory in composite materials, Mechanics of Materials 1987;6(2):147-157.
9. Odegard GM, Gates TS, Wise KE, Park C, Siochi EJ. Constitutive Modeling of nanotube-reinforced polymer composites, Composites Science and Technology, 2003;63:1671-87.

  doi:10.5075/epfl-298799_978-2-9701614-0-0

GLASS-FIBER REINFORCED POLYURETHANE FOAM COMPOSITE MANUFACTURED BY LONG FIBER INJECTION PROCESS LFI: LIGHTWEIGHT POTENTIAL INVESTIGATIONS THROUGH MECHANICAL PROPERTIES AND MICRO- STRUCTURE CHARACTERIZATION

FREDERIC LEONARDI[a], QUENTIN HOQUI[a], THOMAS CAPELLE[b], JOCELIN LABORDE[b]

a: IPREM, Université de Pau et Pays de l'Adour, Av de l'Université 64000 PAU (France)
frederic.leonardi@univ-pau.fr
b: AXYAL, Rue du Bruscos, 64230 SAUVAGNON (France)

Abstract: *The Long Fiber Injection (LFI) is an innovative economic competitive manufacture process which combines injection and fiber spray-up technology to produce Glass Fiber Reinforced PU Foam composite (GFRPUF). Projected into open molds, LFI process allows complex shape, integrations of functionals components, a large weight reduction. We explored the lightweight potential of GFRPUF composites by using a highly foamed PU matrix about 175 kg.m^3 and incorporating fiber mass content up to 50%. Mechanical properties tests were performed in compression and 3 points bending, while the real sprayed up fiber content and the fiber orientations were checked with a burn-off procedure and image processing. Influence of fibers incorporated contents on foam microstructure were also evaluated with Scanning Electron Microscopy and micro-computed tomography. Correlation on mechanical properties / microstructure was clearly demonstrated and wide alteration of the foam structure was observed starting from 30-35% mass content for the prepared GFRPUF composites.*

Keywords: PUR foams; GFRPUF; Long Fiber Injection (LFI); mechanical properties; lightweight composites

1. Introduction

The Long Fiber Injection (LFI) is a recent innovative economic competitive PUR process developed at the end of 20th/beginning 21st century [1,2]. It is a hybrid process which combine injection and fiber spray-up technology. Fiber glass rovings are simultaneously cut and mix with the reactive two-components polyurethane and finally spray on the mold by a blowing air flow into the mixing head. This spray up system enable composite with massive fiber amount because there is no real apparent viscosity for the reactive PUR mixture. The moving robotized head allow the process a tailored spray on the mold with automatized adjustable robot passes program. LFI manufacture methods is fully automatized and also characterized by moderate pressure processing which enable functional component integration [3]. Chen *et al.* evaluated the quality the content and the length of fiber were the most significant factors, and mold temperature and ratio of raw materials were the least significant factors on bending properties [4]. Mechanical properties can thus be locally fitted to stress specifications requirements, fiber mass content as main key adjusting level. F. Hufenbach *et al.* exhibited on little foamed

  doi:10.5075/epfl-298799_978-2-9701614-0-0

composite quite linear tensile properties according to fiber mass content [5]. Serban *et al*. examined mechanical and morphological properties of LFI GFRPUF composites. They observed on the structure that fiber mass content increased mechanical properties and size of the cells but no significative influence of fiber length was noticed [6]. The present study investigates the lightweighting potential of GFRPUF composite at a higher level using a highly foamed PU matrix and larger fiber mass content enable up to 50% as innovative LFI process permit. Three point bending and compression properties were evaluated, micro-structure of composite observed with tomography and SEM analysis.

2. Composite manufacturing

In the present study LFI airflow parameters was chosen in a way to have orthotropic panels material, the randomness of fibers orientation distribution was evaluated to check this point by pyrolisys. AXYFOAM foam polyurethane system was used as matrix composite for the study, in this configuration the reactive PU resulted unreinforced foams with density of 175 kg/m^3. Glass fiber rovings used as mechanical fiber reinforcement composite were E6-CR-180 from JUSHI Compagny and LFI manufacture process. Roving are characterized by a linear density of 2400 tex, fiber by a 82 GPa elastic modulus and a 17 µm fiber unit diameter according to technical data sheet. The ratio isocyanate/polyol was keeping constant to ensure same kinetic PU reaction. Composites were manufactured in panel rectangular mold with 10 mm thickness by one-shot spray-up of the robotized head. After the spray-up step in the open mold, the locking was conducted by spring clips and clamps for 50 minutes at temperature mold of 65°C.

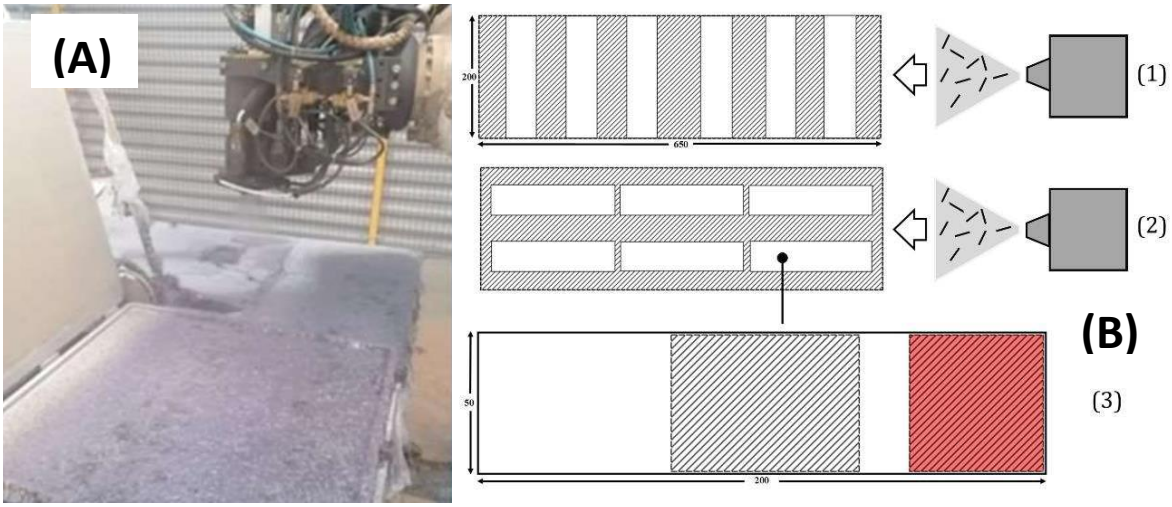

Figure 1 : (A) GFRPUF composites from LFI process, (B) selected samples areas: (1) 90° direction and (2) 0° spray-up direction, 3 points bending samples (3): in red compression sample, hatched areas representing pyrolyzed for each sample parts

3. Experiments

Experimental procedures were carried out to evaluate the mechanical characterization of GFRPUF composite created by LFI technology manufacture. Tests were performed in bending and compression on a Alliance RT/50 testing machine using 10kN loadcell. All the tests were realized at room temperature. The sampling protocol were the same for each configuration composite panels, the selected sampling areas (figure 1 B) were taken by large margin of mold edges to disregard the associated complex phenomenon.

  doi:10.5075/epfl-298799_978-2-9701614-0-0

3.1 Three-point bending tests

Three points bending tests were performed according to the ISO 178 standard Plastics – Determination of flexural properties on rectangular 50 x 200 mm and 10 mm thickness samples. Six samples were taking off the panels and tested, length in the robotized spray up direction. The tests were executed at the speed of 2 mm/min. Anisotropy behavior were also evaluated with bending properties for the GFRPUF 20%/25mm and the 40%/25mm with 90° cut samples (figure 1 B). Bending test allows better reliability and repeatability over tensile ones appreciated for the investigated composites here.

3. 2. Compression tests

Compression tests were realized according to the ISO 844 standard Rigid cellular plastics – Determination of compression properties on a 50 mm square-base and 10 mm thickness samples. The tests were executed at the test speed of 1 mm/min. The compression tests focused on Young modulus properties, only the elastic material behavior was investigated.

3. 3. Pyrolysis analyzes

Several parameters like ratio fiber lengths / sample dimensions, low foam matrix density and sprayed-up fibers' technology manufacture make the GFRPUF composites of the study quite affected by local inhomogeneity gradients. To evaluate and reduce results scatters, post pyrolysis degradation was realized on mechanical-tested samples. The degradation procedure has been defined after TGA analysis (60°C/min ; air atmosphere), it consisted to an extreme heat treatment at 1000°C for three hours to ensure foam matrix sample part were totally degraded. By registration the weight and the dimensions of the composite before/after the pyrolyze, the aim of this treatment was to obtain the effective mass and volume fibers rates into the GFRPUF composite but also local densities of the foam. Determined effective rates have been then directly related with the measured mechanical properties. In a way to be more representative the entire compression samples were pyrolyzed while only the center of bending tested ones were. Post cut into smaller 65*50 pieces, this area is the most stressed during the bending test and is the one which lead the mechanical properties of the entire sample. The figure 1 illustrates these different sampling cuts and selected areas for the pyrolyze procedure (hatched zone).

4. Results and discussion

4.1 Bending properties

Mechanical values in three points bending are consistently increasing with fiber mass content as expected for classical composites mechanical behavior. This classical evolution of composite behavior is obtained as the fiber content increasing the stiffer the material response is. This known behavior is materialized on the testing curves by a higher slope but also a reduced yield range for the elastic linear composite behavior. Unlike the unreinforced foam which completely break in one single rupture, the reinforced PUF composite still has strength after the first break. The first break appeared at the center sample, leading a by first crack into the fiberglass. In addition, foam cohesive fractures along the bundle fibers also randomly appeared, locating next to the central sample areas. The effective volume glass fiber of composite extracted from pyrolysis degradation replace thus each configuration to its real contribution and make a clear view on the bending properties influence of the fiber content presented in figure 2.

  doi:10.5075/epfl-298799_978-2-9701614-0-0

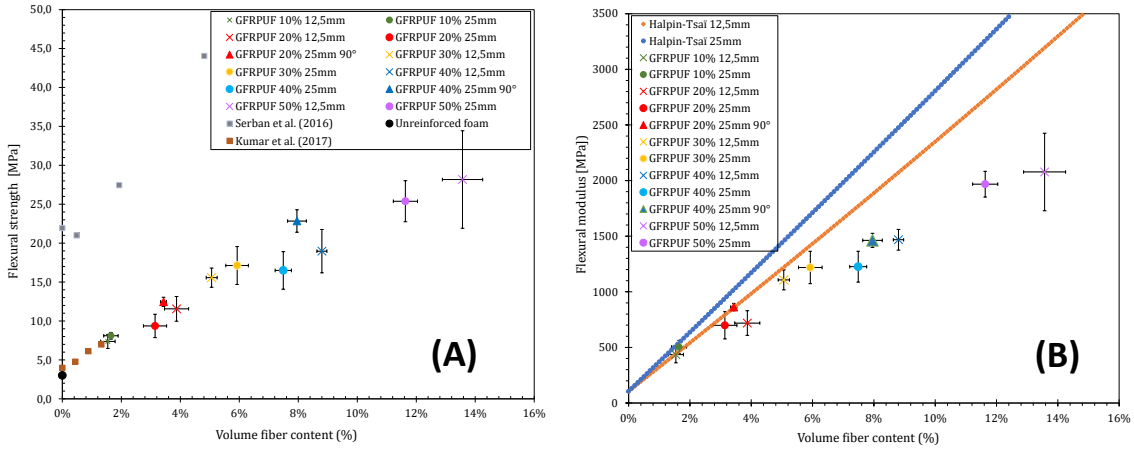

Figure 2 : Maximum flexural strength (A) and flexural modulus (B) versus volume fiber content for two fiber length in the GFRPUF composites. Comparison with Halpin-Tsai model.

For both stiffness and max strength values, two domains can be identified. Until 5-6% fiber volume content representing 30-40% fiber mass composite, properties are increasing proportionally with the fiber content [6, 7}. After this point a slow decrease of the previous proportionally trend is noticed, this reduced slope seems to reveal a lower reinforcing influence of fiber content on the bending properties composite. This difference of the mechanical stress response interrogates to a potential change on the structure composite. On the other hand, the results don't show a significantly fiber length influence on flexural properties. The composite configuration with 20% and 40% of mass content were cut on 90° to evaluate a potential anisotropy on the panel properties. Experimental results show a little more value on modulus about (15%) and higher on max strength (35%). This minor anisotropy of properties is not related with different fiber orientation evaluated further. It is resulting from locally little more densified areas in the center part of length mold just over where the robot trajectory during composite manufacture is more efficiently spraying. The entire experimental results show an important part of scatter although reduced by pyrolysis. For low mass fiber contents this trend is intensified because of very low fiber volume content create by density ratio of foam/glass and the fact that fibers were aggregated in large bundle which enhance the probability of uncertain mechanical solicitation. Furthermore, 90°experimentals results present a much lower degree of scatter. This observation reveals an better uniform fibers disposition between each sample took off the panel in the width direction of the manufacture mold. All real effective fiber mass contents are above the theorical content due to a over pressure feeding fiber manufacture parameter

4.2 Compression properties

Composites were tested on the thickness direction, the weakest one considering the fact the fiber spraying is disposed in a plan perpendicular to the thickness / foaming rise direction. Compression test curves are presented in figure 3A . As reported for bending mechanical properties, two domains of mechanical behavior composite can be identified. On the first part, at low fiber volume content, there is an irregular increasing trend ending with a maximum of compressive response for the 5-6% volume fiber content composite. Until this content, the filling fiber is thus reinforcing the foam. After this point, the compression modulus is totally dropping and reach values below the unreinforced foam compressive performances.

  doi:10.5075/epfl-298799_978-2-9701614-0-0

Like on bending properties, for a given content, the fiber length doesn't have any major influence on the properties. Both studied fiber lengths are following the same trend. In this configuration test, the z orientation of fibers is a key factor which can lead to enhanced properties. The fiber length chosen in this study may be too long to get a significant orientation in the rise foaming (z direction). On the figure 3B, the compression curves of representative configuration composites are presented, this figure make an overview of the different observed compression behaviors in relation to the compressive modulus data. On the unreinforced and 30% GFRPUF curves, the classical compression foam behavior is shown but for the 50% GFRPUF, the curve is totally different: the elastic part is not clearly identifiable.

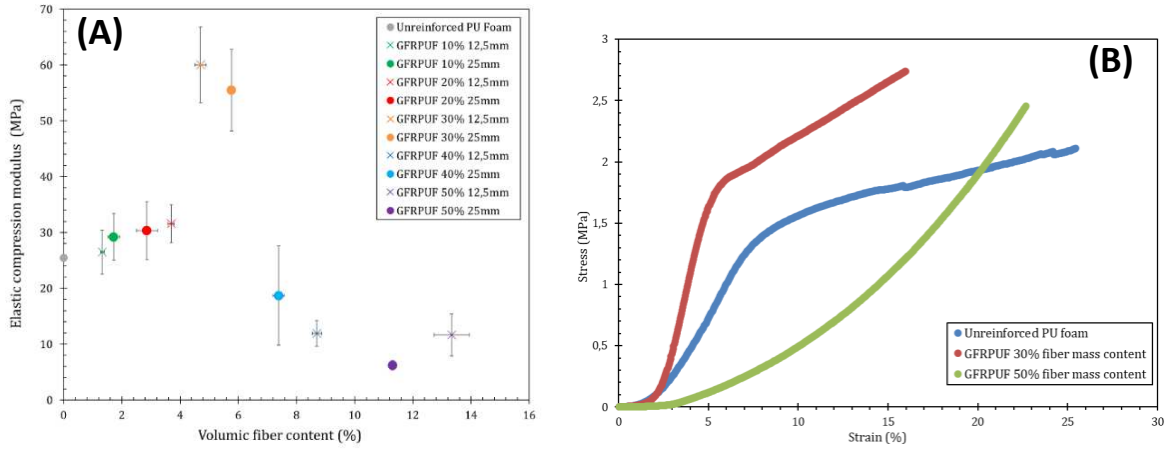

Figure 3 : Elastic compression modulus versus fiber content in volume for two fiber length (A) and compression tests for unfilled, 30 w% and 50 w% in fiberglass of 12.5 mm (B)

4.3. Halpin Tsaï model

A modeling confrontation attempt was performed to characterize the trend of mechanical properties regarding the fiber content. The Halpin-Tsaï (H-T) model is one of the commonly used methods to predict the effective stiffness moduli of composites reinforced. Investigations on bending stiffness properties were carried out and confronted to experimental results. Hypothesis of constant foam matrix modulus was considered in the Halpin-Tsaï model and evaluate from the unreinforced PU foam modulus. Following equation (1) are presenting the H-T model of fiber-reinforced composites [8], with the determination of E_L and E_T modulus components (respectively Longitudinal and Transverse):

$$E_c = aE_L + (1-a)E_T \quad (1)$$

The a parameter is an orientation efficiency factor which is chosen according to the leading fiber orientation trend into the composite structure. It is generally considered at 1 for completely aligned fibers composites, 1/5 for randomly 3D oriented fibers composites and 3/8 for randomly 2D oriented fibers composites (which is the case of this study, confirm by pyrolysis analysis). Longitudinal and transverse parts are determined with the following equations (2) where E_m/E_f representing the elastic modulus of the fiber / matrix respectively. The ζ parameter is characterizing the form factor of fibers.

$$E_L = E_m \frac{1+\zeta\eta_L\Phi_{Vf}}{1-\eta_L\Phi_{Vf}} \; ; \; E_T = E_m \frac{1+2\eta_T\Phi_{Vf}}{1-\eta_T\Phi_{Vf}} \; with \; \zeta = {}^{2l}/_{d}, \eta_L = \frac{{}^{E_f}/_{E_m} - 1}{{}^{E_f}/_{E_m} - \zeta}, \eta_T = \frac{{}^{E_f}/_{E_m} - 1}{{}^{E_f}/_{E_m} + 2} \quad (2)$$

4.4 Microstructure and morphology of the composite

GFRPUF of the study, were analyzed by several characterization imaging. Image processing of pyrolyzed samples, SEM scan and computer micro tomography were realized to report cell structure and fiber composite layout. Firstly, investigations on the laid fiber orientation of the composite were performed to check the reality of manufacture fiber spray and potential effect on the mechanical properties involving. ImageJ free image processing software and its Directionality plugin were run on pyrolyzed composite samples. After an optimization on taken picture with a image processing steps, Directionality plugin were run. Based on Fourier spectrum analysis, the plugin determines the preferred orientation of picture structures here the fibers and display a distribution histogram of these orientations. The figure 4 describes the process steps, (A) part presents a picture of 20% GFRPUF pyrolyzed sample and shows that fibers are present in form of bundles but more scattered than raw fiber roving. (B) part present the fiber detection with a color for each orientation, finally a distribution of detected angles is displayed (C). Both face of each sample was evaluated and no preferential fiber orientation into all configurations of composites was noticed, these observations validate the randomness of spray up LFI manufacture process.

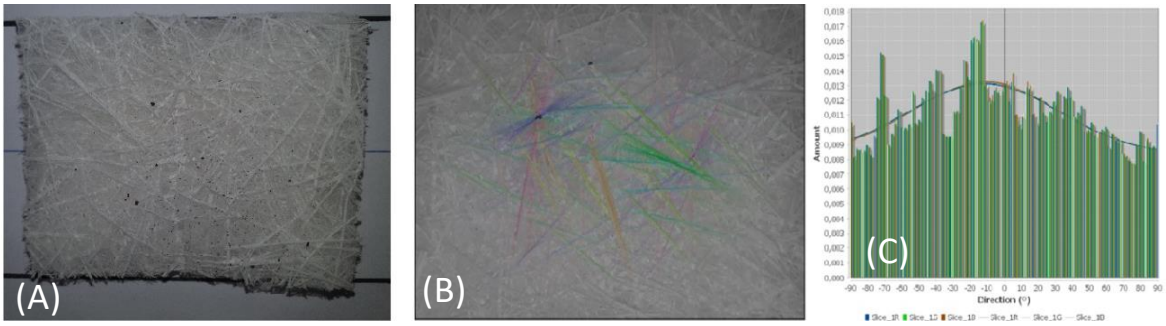

Figure 4 : 20% GFRPUF pyrolyzed sample (A), Directionality plugin Image J analysis (B), histogram of detected angles (C).

Fractured areas of bending tested composite samples were viewed with Scanning Electron Microscopy device. The figure 5 shows one of them, bundles of fibers are clearly observed on the right. In the center of the figure an area of fiber peeled off can be perceived, here crack propagation is located at the interface of the fiber bundle/PU. In the figure 5A foam cells are trapped into the bundle where they grew along them. The following phenomena is observed: if there is enough space between fibers PU matrix expands and still regularly arrange.

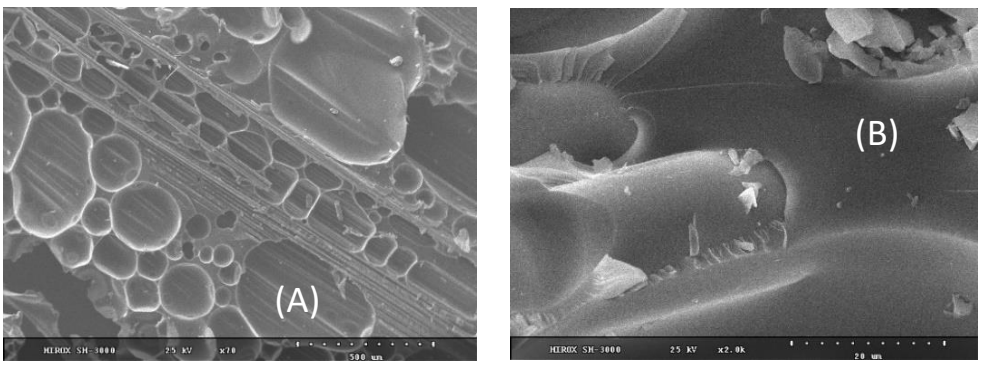

Figure 5: SEM images of fractured GFRPUF composites (A), zoom on the interface of PU matrix/fiberglass (B)

The figure 5B presents a zoom on crack interface which highlighted that fibers bundle were actually totally PU embedded and a non-expansion of PU matrix in tightly bundle areas. This observation shows firstly the manufacture process is giving a good wettability enough to ensure there isn't dry fiber and secondly that the more the sprayed fibers bundles are scattered the more foamed composite microstructure is uniformly arranged. Untested specimens of all GFRPUF composite configurations of the study were scanned with a Easytom 150 micro-computed tomography device of RX Solutions. Scanned composite samples were a 1 cm^3 cube shape, image resolution of approximatively 10 µm was reach according to recorded voxel unit. The aim of these scans was to characterize the influence of the fiber content on the microstructure composite. Global structure was observed on thickness side.

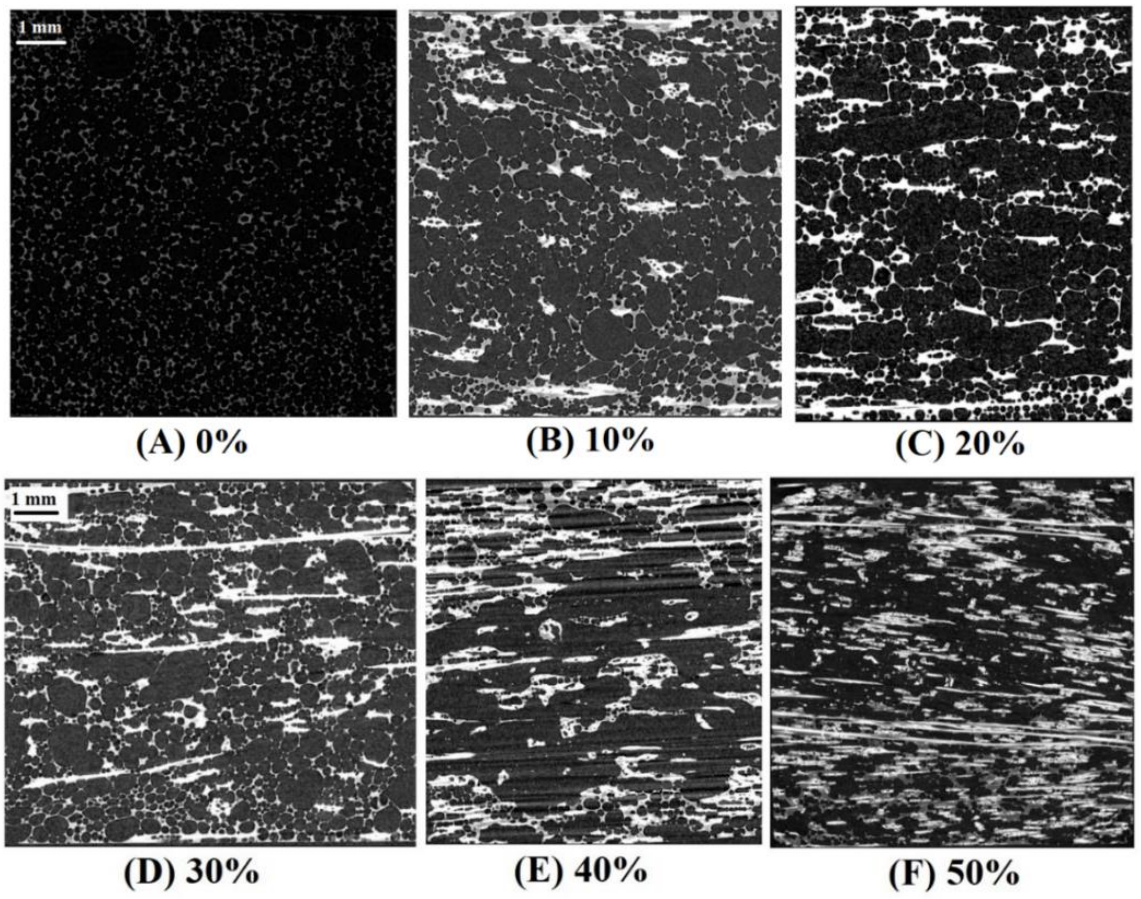

Figure 6 : Micro-computed tomography of unfilled and GFRPUF *composites*

Unreinforced foam is presented on part of figure 6(A). Quite regular size distribution and spherical shape are observed. When fibers are is incorporated, foam structure is starting to change and becomes less homogeneous with a more extended cell size distribution, part (B) displays the 10% GFRPUF composite and associated observations. Same trend is found on 20% GFPRUF part (C) but larger cells are visible, this fact could be in direct correlation with its compressive results where modulus value is slightly lowered compared as it could be expected in respect to a classical linearity between 10% and 30% fiber mass content composites. Until 30% of mass fiber content presented in figure 6 part (A), a continuity of the overall microstructure is clearly demonstrated. After this content, a breaking point is reached as illustrated by the figure 6 part (B) 40% and part (C) 50% composites. Large localized void parts are highlighted in the structure, meaning that PU matrix didn't expend.

  doi:10.5075/epfl-298799_978-2-9701614-0-0

5. Conclusions

Correlation between mechanical and micro-structure of GFRPUF composites, obtained from automatized LFI process, were clearly shown. An optimum was reached for the 30-35% of mass fiber content while a decreasing properties trend for higher content was observed. Compression test demonstrate that foaming process is deeply perturbated when filler content reached 40% in weight. We have also shown also that fiber length (12.5 or 25 mm) have no significantly influence on mechanical properties of the composite as already found in literature.

Acknowledgements

The work was carried out within the framework of the FUI 25 MATIMELEC project (2018-2021). The authors thank BPI France for financial support.

6. References

1. Frehsdorf W, Söchtig W. High requirements – Low investment costs: LFI-PU process: Ripe flexible technology. Kunststoffe Plast Europe. 2001; 91(3):23–25.
2. Mason K. Long-Fiber Injection Advances Polyurethane Composites. Composites World. 2006 [cited 2022 apr. 19]. Available on : https://www.compositesworld.com/articles/long-fiber-injection-advances-polyurethane-composites.
3. Hufenbach W, Fischer WJ, Gude M, Geller S, Tyczynski T. Processing Studies for the Development of a Manufacture Process for Intelligent Lightweight Structures with Integrated Sensor Systems and Adapted Electronics. Procedia Materials Science. 2013; 2:74–82.
4. Chen F, Cao CP, Zhang W, Sun Y. Optimization of Parameters in Long Fiber Reinforced Reaction Injection Molding on Bending Properties. AMR. 2010; 154–155:981–6.
5. Hufenbach W, Gude M, Geller S. Cellular Fiber-Reinforced Polyurethane Composites with Sensory Properties. Adv Eng Mater. 2014; 16(3):272–5.
6. Şerban DA, Weissenborn O, Geller S, Marşavina L, Gude M. Evaluation of the mechanical and morphological properties of long fibre reinforced polyurethane rigid foams. Polymer Testing. 2016; 49:121–7.
7. Kumar M, Kaur R. Glass fiber reinforced rigid polyurethane foam: Synthesis and characterization. E-Polymers. 2017; 17(6):517-521.
8. Affdl JCH, Kardos JL. The Halpin-Tsai equations: A review. Polym Eng Sci. 1976; 16(5):344–52.

  doi:10.5075/epfl-298799_978-2-9701614-0-0

THE EFFECT OF GRAPHENE-BASED MATERIALS IN POLYAMIDE 6 OBTAINED BY *IN SITU* THERMOPLASTIC RESIN TRANSFER MOULDING (T-RTM) POLYMERIZATION

J. N., Lagarinhos[a,b], J.M., Oliveira[a,b]

a: EMaRT Group – Emerging: Materials, Research, Technology, School of Design, Management and Production Technologies, University of Aveiro, Estrada do Cercal 449, 3720-509 Oliveira de Azeméis, Portugal
b: CICECO - Aveiro Institute of Materials, University of Aveiro, Campus Universitário de Santiago, 3810-193 Aveiro, Portugal
email – joanalagarinhos@ua.pt

Abstract: *Polyamide 6 (PA6) and PA6 reinforced with graphene (APGBM) were developed by an in situ anionic ring opening polymerization of ε-caprolactam through thermoplastic resin transfer moulding (T-RTM) technology. In low viscosity raw materials, the dispersion of nanoparticles namely graphene, is a demanding challenge. The effect of different loadings of GBM was studied along with the thermal and mechanical properties of nanocomposites. It was found that the introduction of GBM had a nucleating effect on PA6 crystallization and increased crystallinity degree. Mechanical analyses of nanocomposites, including tensile and flexural tests, showed an improvement in mechanical performance with the addition of GBM. The APGBM prepared with 0.75 wt.% revealed better mechanical performance among.*

Keywords: polyamide 6; *in situ* polymerization; graphene; thermoplastics; T-RTM technology

1. Introduction

The use of plastic materials in automotive parts have arouse great interest in the industry. Some automotive structures are based on thermoset matrices, but nowadays, global market is slowly replacing the thermosets with thermoplastic matrices looking for better environment performance (1).

Thermoplastic resin transfer moulding (T-RTM) is an efficient processing technology for large-scale production of thermoplastics via *in situ* polymerization (2,3). This technology is based in the injection of a reactive mixture (low viscosity monomer with suitable catalyst and activator) to a preheated mould, in which a *in situ* polymerization occurs (4,5) Anionic polymerization of ε-caprolactam monomer combined with a catalyst and activator system can be used to produce PA6 *via* T-RTM. This is possible since anionic polymerization occurs at relatively low temperatures with short mould cycle times (6).

Polyamide 6 (PA6) obtained from T-RTM shows relatively high molecular weight, high crystallinity and superior mechanical performance which enable to replace metallic materials of structural components in automotive industry (7). However, its mechanical performance, such as strength and elasticity modulus, can limits its applications (8). To expand the use of PA6 in

  doi:10.5075/epfl-298799_978-2-9701614-0-0

areas with increasing performance demands, many attempts have been made to improve its mechanical properties.

The incorporation of nanofillers, such graphene-based materials have been studied, with special focus on the improvement of mechanical properties (9–11). Graphene, a two dimensional honeycomb layer of sp^2 bonded carbon, has a high potential to be an effective filler to prepare high performance nanocomposites. Its electrical, thermal, and mechanical properties can substantial increase the performance of composites (12–14). It has been reported as the strongest material tested with a ultimate strength of 130 GPa and Young modulus of 1 TPa (15).

Several studies have focused on the effect of graphene-based materials on PA6 performance (16–18). However, the dispersion of graphene within low viscosity raw materials and its interfacial adhesion are a key factor to determine the properties of the final nanocomposites (19). Several approaches to achieve of uniformly nano dispersed graphene has been reported (20,21). Although, *in situ* polymerization has been proven to be a more efficient method due to the reduced processing time (22). Furthermore, the low monomer viscosity, turn it a better medium for dispersing graphene allowing a more efficient retention of its properties (23–25).

Herein, a simple and effective method to prepare PA6 and PA6 reinforced with GBM (APGBM) via *in situ* polymerization by using T-RTM technology is reported. The influence of GBM loadings on thermal and mechanical properties of samples were analysed.

2. Materials and methods

2.1 Materials

The monomer AP-Nylon® caprolactam (CL), mixed with a catalyst Bruggolen® C10 (C10) and activator Bruggolen® C20P (C20P) were used for anionic polymerization of PA6. These components were purchased from L. Brüggemann GmbH and Co. KG, Germany. In this study, a formulation of 95% CL, 3% C10 and 2% C20P, was developed and denominated AP. Powder graphene (GBM) was purchased from NanoXplore (Canada). APGBM samples were prepared adding different amounts of GBM to raw materials. The compositions of the different formulations developed are described in Table 1:

Table 1: Compositions of the developed APGBM nanocomposites.

Samples	GBM (wt.%)	PA6
AP	0	100
APGBM1	0.1	99.9
APGBM2	0.25	99.75
APGBM3	0.5	99.5
APGBM4	0.75	99.25
APGBM5	1.0	99.0

  doi:10.5075/epfl-298799_978-2-9701614-0-0

2.2 AP and APGBM preparation

AP and APGBM samples were prepared by *in situ* ring-opening polymerization of CL monomer using a semiautomatic T-RTM laboratory equipment.

The laboratory T-RTM setup consists of a dosing unit with two tanks, a mixing head, and a mould system equipped with a heating, a pressure, and a vacuum control units. For AP preparation, the CL was divided into two equal parts and placed into the two tanks. C10 was added to one of the tanks and C20P was added to the other. The temperature in each tank was set to 90 ^{o}C under stirring, at a speed of 350 rpm for a period of 7 min. After melting the components, the CL/C10 and CL/C20P flow in separated channels into the mixing head (110 ^{o}C) under controlled pressure. Through impingement, the reactive mixture was injected into a preheated mould (160 ^{o}C), under vacuum. The polymerization reaction occurs inside the mould. Following polymerization time (≈6 min), a plate (280mm x 150mm x 2mm) was demoulded at room temperature, and samples prepared for further characterization.

For APGBM nanocomposites preparation, GBM loadings were pre-dispersed in the molten CL-catalyst tank under stirring at a speed of 550 rpm for a period of 15 min. Subsequently, the catalyst and activator were added, and the process proceed as described previously.

2.3 Thermal analyses

A differential scanning calorimeter (DSC) equipment (Shimadzu DSC-60) was used to study thermal behaviour of AP and APGBM. Samples were heated from room temperature to 250 ^{o}C at a heating rate of 20 ^{o}C/min and held for 2 min to eliminate the thermal history, and then cooled to -25 ^{o}C, and reheated to 250 ^{o}C at 10 ^{o}C/min. The crystallinity degree, X_c, was determined by the following equation:

$$Xc\ (\%) = \frac{\Delta H_m}{\Delta H_m^0\ (1-\varphi)} \times 100 \quad (1)$$

where ΔH_m is the melting enthalpy of sample, φ is the weight fraction of GBM, and ΔH_m^0 corresponds to the melting enthalpy of PA6 in 100% crystalline state (PA6 = 190 J/g) (26).

Thermogravimetric analysis (TGA) (not shown) was performed on a Hitachi STA300 equipment. A heating rate of 10 °C/min was used from room temperature to 600 ^{o}C, under N_2 atmosphere (flow rate of 100 mL/min). Conversion degree (DC) of CL, through loss of mass, was calculated using equation:

$$DC\ (\%) = \frac{W_a}{W_b} \times 100\% \quad (2)$$

where W_a is the weight measured at 240 ^{o}C (inflexion point between monomer evaporation and polymer degradation), and W_b is the initial weight of the sample.

2.4 Mechanical analyses

Tensile and flexural properties were evaluated through an Autograph AG-IS (Shimadzu) universal testing machine with a 10kN load cell. Tensile tests were measured according to ISO 527-2 standard (Type 1BA) with a constant crosshead speed of 1mm/min. A video extensometer (Shimadzu DVE-101/201) was used to determine the elongation of each specimen.

  doi:10.5075/epfl-298799_978-2-9701614-0-0

The flexural properties were assessed following ISO 178, with a crosshead speed of 1mm/min. Each group of specimens contained, at least, five specimens. The average and standard deviation values of the measured properties were used in the reported data.

3. Results and discussion

3.1 Thermal behavior

The influence of GBM on melting (T_m) and crystallization (T_c) behaviour of APGBM nanocomposites was analysed by DSC. The cooling and second heating thermograms of AP and APGBM are shown in Figure 1 and data are summarized in Table 2.

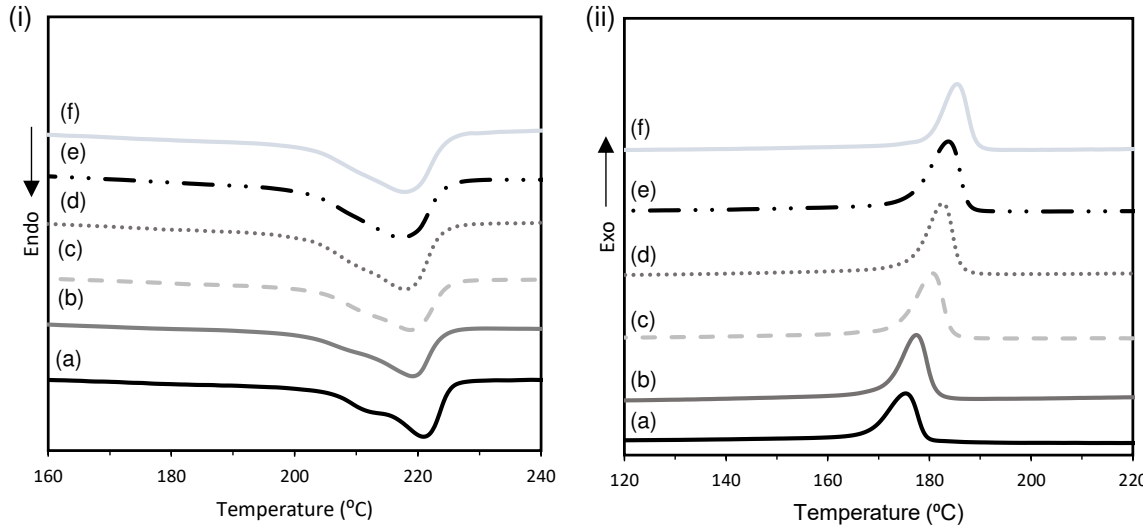

Figure 1. DSC heating scans (i) and cooling scans (ii) of AP and APGBM nanocomposites (from bottom to top): (a) AP; (b) APGBM1; (c) PGBM2; (d) APGBM3; (e) APGBM4; (f) APGBM5. The curves are vertically offset for clarity.

Table 2: Thermal parameters of AP matrix and APGBM nanocomposites.

Samples	T_m [°C]	T_c [°C]	ΔH_m [J/g]	Xc [%]	DC (%)
AP	220.9 ± 0.4	175.4 ± 0.3	59.9 ± 0.3	31.5 ± 0.3	98
APGBM1	219.1 ± 0.1	177.3 ± 0.2	62.1 ± 0.2	33.7 ± 0.5	98
APGBM2	219.3 ± 0.5	180.7 ± 0.1	63.6 ± 0.3	35.3 ± 1.2	97
APGBM3	218.0 ± 0.2	182.8 ± 0.2	64.4 ± 0.7	35.9 ± 0.9	97
APGBM4	217.4 ± 0.2	184.2± 0.1	61.8 ± 0.8	34.5 ± 0.1	97
APGBM5	217.2 ± 0.4	185.3 ± 0.2	58.4 ± 0.5	33.2 ± 0.1	97

DSC heating curves showed that the addition of GBM had a slightly effect on melting temperature of AP. From melting endotherms, it can be seen that there are two melting peaks

in AP, one main peak at about 221 ^{o}C (T_{m1}) and a small shoulder peak at about 212 ^{o}C (T_{m2}), indicating the co-existence of α and γ crystal structures of PA6, respectively (27). From APGBM heating curves it was possible to observe that with increasing GBM loading, T_{m2} peak was attenuated. As seen from Figure 1-ii, T_c of nanocomposites was higher than that of AP. The T_c increased from 175.4 ^{o}C for AP to 185.4 ^{o}C for APGBM5. This significant increase of T_c is attributed to strong nucleation effect of graphene during the crystallization of the AP (8).

X_c also increases compared to AP matrix. As mentioned above, GBM can promote crystallization by acting as nucleating agent, thus crystallization can be facilitated. A slightly decreases in X_c if observed in AGBM5. It is probably due to the excess of nanoparticles that hinders the mobility of PA6 chains (10).

DC values, calculated using equation 2, revealed a high conversion rate (between 97-98 wt.%), for both samples, which means that the polymerization was almost complete, and a low residual monomer content was achieved.

3.2 Mechanical behavior

Tensile tests were performed to evaluate the influence of graphene on the mechanical properties (Figure 2).

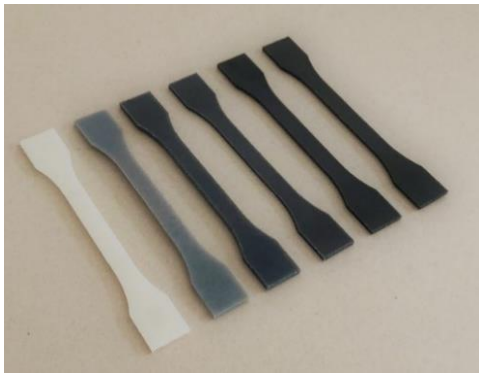

*Figure 2. Specimens for tensile tests. From right to left: AP, A*PGBM1*, A*PGBM *2, A*PGBM3*, A*PGBM*4 and A*PGBM5.

The tensile properties of these materials, and its standards deviations are given in Table 3.

Table 3: Tensile properties of AP and APGBM nanocomposites.

Samples	σ_{max} [MPa]	ε_{max} [%]	E [GPa]
AP	63.5 ± 2.1	14.3 ± 3.5	2.6 ± 0.3
APGBM1	52.7 ± 4.0	8.9 ± 2.2	3.4 ± 0.6
APGBM2	55.8 ± 6.1	13.4 ± 8.8	3.5 ± 0.3
APGBM3	65.9 ± 7.6	28.3 ± 16.9	3.8 ± 0.5
APGBM4	66.0 ± 4.9	35.3 ± 14.8	4.1 ± 0.7
APGBM5	60.2 ± 1.4	10.5 ± 4.4	3.4 ± 0.7

  doi:10.5075/epfl-298799_978-2-9701614-0-0

For lower additions of GBM (0.1 wt.% and 0.25 wt.%), a slightly reduction of tensile strength was observed. For higher contents no significant changes were noted. The Young modulus increased with increasing GBM loadings. When the content is 0.75 wt.% GBM, the Young modulus of APGBM4 is enhanced by ~58% and the elongation at break by ~174%. When the GBM loading reaches 1.0 wt.%, the mechanical properties showed a decrease. Commonly, the mechanical properties of the nanocomposites improve significantly with the addition of different loadings, however, an excess of GBM may form small agglomerates, thus the molecular interaction decreased, lead to a reduction in tensile strength (28). Another possible explanation for this decreasing, is due to agglomerates that can act as stress concentration sites.

Table 4 presented the flexural properties of AP and APGBM. Unlike the tensile strength, the flexural strength of APGBM samples showed an initial increase followed by a decrease. When incorporated with 0.1 wt.% of GBM, the flexural strength of APGBM1 was about 193% higher than that of AP. With a further increase of GBM content, the flexural strength falls, however the values remain higher than that exhibited by AP. The flexural modulus of AP is increased by 92%, from 2.6 to 5.0 GPa for APGBM3.

Table 4: Flexural properties of AP and APGBM nanocomposites.

Samples	σ_{max} [MPa]	ε_{max} [%]	E [GPa]
AP	91.6 ± 3.4	7.9 ± 0.6	2.6 ± 0.1
APGBM1	193.4 ± 16.4	7.3 ± 0.2	4.2 ± 0.6
APGBM2	190.5 ± 9.8	7.7 ± 0.8	4.8 ± 0.9
APGBM3	182.2 ± 13.0	7.4 ± 0.2	5.0 ± 0.2
APGBM4	154.0 ± 4.7	7.3 ± 0.2	4.3 ± 0.2
APGBM5	138.6 ± 2.1	7.2 ± 0.3	3.4 ± 0.2

It is interesting to note that unlike tensile strength, flexural strength of APGBM samples do not show an initial decreasing tendency. This might be due to the GBM loading do not reach the critical level at lower amounts, once the loading mode of a tensile test is different from that of a flexural tests (29).

4. Conclusions

The present work demonstrated an effective approach to AP and APGBM production by *in situ* polymerization through T-RTM technology. The polymer/GBM loadings influence on thermal and mechanical behaviour was investigated.

Different GBM loadings affected the melting temperature of AP towards lower values. The crystallization temperature shifted to higher temperatures, as well as crystallinity degree that increases with increasing GBM loadings. Even very low loadings of GBM promote a relevant increasing in tensile and flexural moduli.

  doi:10.5075/epfl-298799_978-2-9701614-0-0

Based on the results, GBM were successfully incorporated in low viscosity raw materials using T-RTM technology. The improvement on mechanical properties at low loadings of GBM, offer great promises of this technology applications to produce APGBM nanocomposites for automotive industry applications.

Acknowledgements

This work was partially supported by Simoldes Group. This work was also developed within the scope of the project CICECO-Aveiro Institute of Materials, UIDB/50011/2020 & UIDP/50011/2020, financed by national funds through the Portuguese Foundation for Science and Technology/MCTES.

5. References

1. Elmarakbi A, El-Safty S, Martorana B, Azoti W. Nanocomposites for Automotive: Enhanced Graphene-based Polyer Materials and Multi-Scale Approach. Int J Automot Compos. 2017;2:155–66.
2. Miranda Campos B, Bourbigot S, Fontaine G, Bonnet F. Thermoplastic matrix-based composites produced by resin transfer molding: A review. Polym Compos.
3. Louisy E, Samyn F, Bourbigot S, Fontaine G, Bonnet F. Preparation of glass fabric/poly (L-lactide) composites by Thermoplastic Resin Transfer Molding. Polymers (Basel). 2019;11(2):339.
4. Sibikin I, Karger-Kocsis J. Toward industrial use of anionically activated lactam polymers: Past, present and future. Adv Ind Eng Polym Res. 2018;1(1):48–60.
5. Ageyeva T, Sibikin I, Karger-Kocsis J. Polymers and related composites via anionic ring-opening polymerization of lactams: Recent developments and future trends. Polymers (Basel). 2018;10(4):357.
6. Zaldua N, Maiz J, de la Calle A, García-Arrieta S, Elizetxea C, Harismendy I, et al. Nucleation and crystallization of PA6 composites prepared by T-RTM: Effects of carbon and glass fiber loading. Polymers (Basel). 2019;11(10):1680.
7. Xu S, Zhao X, Ye L. Effect of heat treatment on the structure and properties of MC nylon 6. Polym Plast Technol Eng. 2012;51(7):689–95.
8. Liu H, Hou L, Peng W, Zhang Q, Zhang X. Fabrication and characterization of polyamide 6-functionalized graphene nanocomposite fiber. J Mater Sci. 2012;47(23):8052–60.
9. Li J, Tian L, Pan N, Pan Z. Mechanical and electrical properties of the PA6/SWNTs nanofiber yarn by electrospinning. Polym Eng Sci. 2014;54(7):1618–24.
10. Wang Y, Liu S, Zhang Q, Meng Q. In situ polymerization to prepare graphene-toughened monomer cast nylon composites. J Mater Sci. 2015;50(19):6291–301.
11. Fu X, Liu Y, Zhao X, Zhao D, Yang G. A commercial production route to prepare polymer-based nanocomposites by unmodified multilayer graphene. J Appl Polym Sci. 2015;132(44).
12. Huang X, Qi X, Boey F, Zhang H. Graphene-based composites. Chem Soc Rev. 2012;41:666–86.
13. Sham AYW, Notley SM. A review of fundamental properties and applications of polymer–graphene hybrid materials. Soft Matter. 2013;9(29):6645–53.
14. Lee S-K, Rana K, Ahn J-H. Graphene films for flexible organic and energy storage devices. J Phys Chem Lett. 2013;4(5):831–41.

  doi:10.5075/epfl-298799_978-2-9701614-0-0

15. Lee C, Wei X, Kysar JW, Hone J. Measurement of the elastic properties and intrinsic strength of monolayer graphene. Science (80-). 2008;321(5887):385–8.
16. Jin J, Rafiq R, Gill YQ, Song M. Preparation and characterization of high performance of graphene/nylon nanocomposites. Eur Polym J. 2013;49:2617–26.
17. Li C, Xiang M, Ye L. Intercalation structure and highly enhancing tribological performance of monomer casting nylon-6/graphene nano-composites. Compos Part A Appl Sci Manuf. 2017;95:274–85.
18. Zhuang YF, Cao XY, Zhang JN, Ma YY, Shang XX, Lu JX, et al. Monomer casting nylon/graphene nanocomposite with both improved thermal conductivity and mechanical performance. Compos Part A Appl Sci Manuf. 2019;120:49–55.
19. Perumal S, Atchudan R, Cheong IW. Recent Studies on Dispersion of Graphene–Polymer Composites. Polymers (Basel). 2021;13(14):2375.
20. Sanes J, Sánchez C, Pamies R, Avilés M-D, Bermúdez M-D. Extrusion of polymer nanocomposites with graphene and graphene derivative nanofillers: An overview of recent developments. Materials (Basel). 2020;13(3):549.
21. Yu X, Dong X, Song Z, Gui J. Fabrication of polyamide 6 nanocomposites reinforced by the exfoliated graphene. Plast Rubber Compos. 2020;49(7):281–8.
22. Vasiljević J, Demšar A, Leskovšek M, Simončič B, Čelan Korošin N, Jerman I, et al. Characterization of polyamide 6/multilayer graphene nanoplatelet composite textile filaments obtained via in situ polymerization and melt spinning. Polymers (Basel). 2020;12(8):1787.
23. Kashani Rahimi S, Otaigbe JU. Polyamide 6 nanocomposites incorporating cellulose nanocrystals prepared by In situ ring-opening polymerization: Viscoelasticity, creep behavior, and melt rheological properties. Polym Eng Sci. 2016;56:1045–60.
24. Meng F, Huang F, Guo Y, Chen J, Chen X, Hui D, et al. In situ intercalation polymerization approach to polyamide-6/graphite nanoflakes for enhanced thermal conductivity. Compos Part B Eng. 2017;117:165–73.
25. Xiang M, Li C, Ye L. In situ synthesis of monomer casting nylon-6 / reduced graphene oxide nanocomposites : Intercalation structure and electrically conductive properties. J Ind Eng Chem [Internet]. 2017;50:123–32. Available from: http://dx.doi.org/10.1016/j.jiec.2017.02.005
26. Cartledge HCY, Baillie CA. Studies of microstructural and mechanical properties of nylon/glass composite Part I The effect of thermal processing on crystallinity, transcrystallinity and crystal phases. J Mater Sci. 1999;34(20):5099–111.
27. Zhang X, Fan X, Li H, Yan C. Facile preparation route for graphene oxide reinforced polyamide 6 composites via in situ anionic ring-opening polymerization. J Mater Chem. 2012;22:24081–91.
28. Wang J, Song F, Ding Y, Shao M. The incorporation of graphene to enhance mechanical properties of polypropylene self-reinforced polymer composites. Mater Des. 2020;195:109073.
29. Stankovich S, Dikin DA, Dommett GHB, Kohlhaas KM, Zimney EJ, Stach EA, et al. Graphene-based composite materials. Nature. 2006;442(7100):282–6.

  doi:10.5075/epfl-298799_978-2-9701614-0-0

AN INVESTIGATION INTO THE PERFORMANCE OF ALIGNED, DISCONTINUOUS CARBON FIBRE COMPOSITES PRODUCED WITH HIPERDIF 3G

Chantal, Lewis[a], Rhys, Tapper[b], Mark, Harriman[c], Marco L., Longana[a], Carwyn, Ward[a], and Ian, Hamerton[a]

a: Bristol Composites Institute, University of Bristol, Queen's Building, University Walk, Bristol, BS8 1TR, UK – chantal.lewis@bristol.ac.uk
b: Solvay Materials, Sinclair Close, Heanor, Wrexham, Derbyshire, DE75 7SP, UK
c: Solvay Materials, Abenbury Way, Wrexham Industrial Estate, Wrexham, Clywd, LL13 9UX, UK

Abstract: *Aligned discontinuous fibre reinforced composites (ADFRCs) have the capability to exhibit mechanical properties close to that of continuous fibres when they are highly aligned with fibres longer than critical length. ADFRCs also offer better handling and forming capabilities, a feature that has the potential to reduce manufacturing defects. The HiPerDiF technology, invented at the University of Bristol has been upscaled to a new third-generation machine capable of producing larger quantities of ADFRC feedstock with more consistency. This research aims to investigate the quality and performance of the new material in comparison with unidirectional continuous fibre composites of similar constituent material.*

Keywords: Aligned discontinuous fibre-reinforced composites (ADFRC); Mechanical characterization

1. Introduction

Fibre reinforced polymer composites provide the opportunity to produce lighter, cheaper, and more durable products thanks to their superior specific strength and modulus when compared with metals. However, owing to the complexities of the designs, manufacturing processes, and material variability, they are susceptible to manufacturing defects like fibre kinking and wrinkling, fibre bridging, and resin rich pockets. Aligned discontinuous fibre reinforced composites (ADFRCs) have the potential to reduce these manufacturing defects because the use of discontinuous fibres leads to better handling and forming capabilities, especially when manufacturing complex parts [1]. However, their main drawback is the reduction in mechanical performance, due the discontinuity and the misalignment of the fibres. Therefore, to create a valuable product with high performance, it is necessary to use fibres that are highly aligned and longer than their critical length [2].

The HiPerDiF technology, invented and patented at the University of Bristol, can produce tailorable and highly aligned discontinuous fibre preforms which can achieve mechanical properties comparable to those of their continuous counterparts [2]. This technology can process a variety of types of fibre feedstock including reclaimed and natural fibres [3] which can be combined with different types of resin systems [4]. The mechanical and functional properties of the feedstock can be tailored by either using different fibre types or the same fibres with different mechanical properties [5]. This makes the HiPerDiF technology more flexible and

  doi:10.5075/epfl-298799_978-2-9701614-0-0

sustainable with the capability to become part of a closed loop recycling process [7, 8, 9]. When prepared from hybridized fibres, ADFRCs have also been shown to present a pseudo-ductile response under tensile loading instead of failing catastrophically like continuous fibre composites [6]. Until recently, the HiPerDiF technology, has been mainly laboratory-based with a low throughput, and consequently only a limited characterisation of the produced material has been possible. A new, third-generation machine, HiPerDiF 3G illustrated in Figure 1, capable of producing m/hr quantities of aligned discontinuous fibre feedstock has recently been produced within an EPSRC-funded research project (EP/P027393/1) and is located within the National Composites Centre (NCC). With the increased production rate, sufficient volumes of material can now be produced to allow an increased range of characterisation activities. The advantages of upscaling this technology will mean more opportunity to incorporate this new material into a variety of manufacturing processes. This will provide a better understanding of the material, its behaviour, and the opportunity to improve this technology. As a result, this will increase its applicability and give more industries access to higher performing aerospace-grade materials in a discontinuous form.

The aim of this research is to investigate the quality and performance of the material and identify any new risks associated with a large-scale production. To achieve this, ADFRC panels were manufactured using 3 mm long virgin discontinuous fibres and a high-performance resin system (CYCOM® 977-2) provided by the Solvay Group. The panels were manually placed in a 0° unidirectional fibre orientation and tested in tension. The results of the tensile test were compared against tensile results of continuous fibre panels with similar constituent materials.

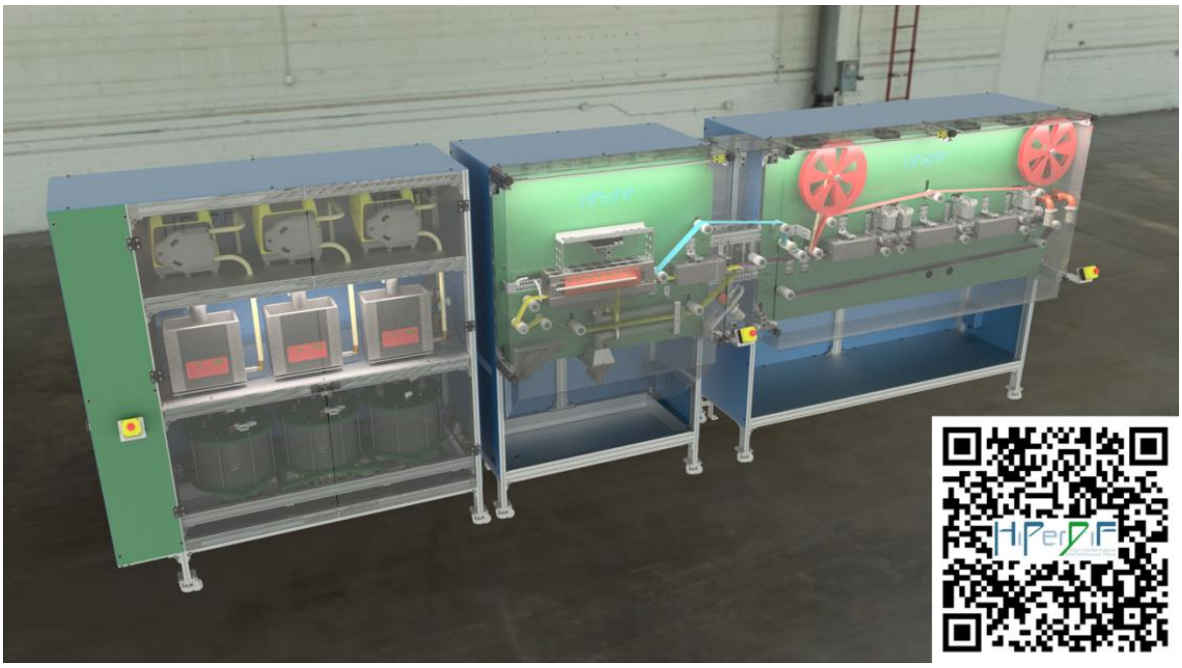

Figure 1. 3D rendered image of the HiPerDiF 3G machine

  doi:10.5075/epfl-298799_978-2-9701614-0-0

2. Methodology

2.1 The HiPerDiF Method

The upscaled HiPerDiF 3G machine shown in Figure 1 is capable of highly aligning discontinuous fibres between 1 and 10 mm. The fibres are dispersed in water and sprayed using a series of nozzles between a series of thinly spaced parallel plates that compose the alignment head. The fibre suspension falls on to a moving mesh belt and the change in direction coupled with the momentum of the suspension causes the fibres to align in the direction of the belt. A series of vacuum pumps and heaters are used to remove the water and dry the fibres as they move along the belt without affecting their alignment. By applying heat and pressure, the HiPerDiF 3G machine can impregnate the dry preform with the chosen resin system to produce rolls of prepreg in a tape form. To achieve the desired areal weight of preform, the process variables such as the fibre length, fibre to water ratio, and the belt speed can be varied.

2.2 Materials

Using HiPerDiF 3G, the preform was produced with virgin carbon fibres (Tenax HT C124, Teijin, USA) to achieve an estimated fibre areal weight of 35.9 gsm calculated using the machine parameters. The properties of the reinforcement fibres used are listed in Table 1

Table 1: Fibre Properties

Fibre property	Unit	Teijin Tenax HT C124
Fibre length	mm	3
Density	g/cm^3	1.79
Filament diameter	μm	7
Tensile strength	MPa	4350
Tensile modulus	GPa	225

The dry preform was impregnated with CYCOM® 977-2 toughened epoxy resin provided by Solvay with an areal weight of 36 gsm.

2.3 Specimen manufacturing

HiPerDiF prepreg tapes, 30 mm wide, were manually placed side by side to form a ply layer of length 270 mm and width 150 mm. Each tape was laid unidirectionally in the 0° direction. 8 plies were stacked up to form a laminate and care was taken to minimize gaps and overlaps between the prepreg strips and between each ply layer. The laminate was cured in an autoclave for 180 mins at 180°C and 6 bar pressure. After curing, the laminate was debagged, and deburred and glass fibre/epoxy end tabs were bonded on to the panel using a two-component epoxy paste adhesive (Araldite 2014-2, Huntsman Advanced Materials GmbH). The prepared panel was then cut into 8 samples with an end tab length of 56 mm in accordance with Figure 2. To provide baseline data to compare material properties, CYCOM® 977-2-HTS unidirectional continuous prepreg material provided by Solvay was used to manufacture composite test samples. The

  doi:10.5075/epfl-298799_978-2-9701614-0-0

same manufacturing techniques were used and the layup configuration and sample dimensions were the same as the HiPerDiF 3G test samples.

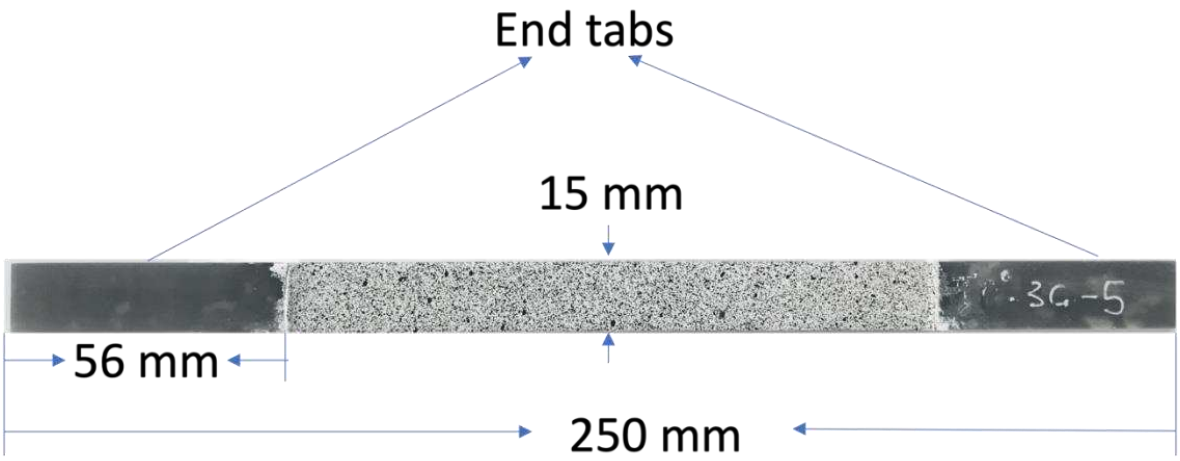

Figure 2. Representative image of tensile test specimen

2.4 Tensile testing

Tensile tests were performed with a servo hydraulic testing machine equipped with a 100 kN load cell at a testing rate of 0.5 mm/min. The strain was measured using digital image correlation (DIC) and analysed using DaVis 10 software. DIC is an optical method that provides a full field three-dimensional analysis of the deformation and strain behaviour across the entire sample. To allow the strain to be measured using DIC, the surface of the specimens in the gauge length, was prepared with black spray paint in a speckled pattern over a white painted background as shown in Figure 2. The gauge length used for strain measurement was approximately 138 mm for all specimens. The tensile tests were performed in accordance with ASTM guidelines [10].

2.5 Fibre volume fraction measurement

A thermogravimetric analyser (TGA Q500) was used to determine the fibre volume fraction of samples. Samples (*ca.* 10 mg) were heated in air up to 500°C for 90 mins. The samples were weighed before and after heating to a resolution of 0.1 μg. The fibre volume fraction was determined using the measured weights of the samples and the known densities of fibre and resin.

3. Results/Discussion

The fibre volume fraction of the composite determined using TGA was approximately 38%. Figure 3 shows that under SEM, the surface of the fibres remain undamaged with some ash present. This indicates that most of the resin has degraded, and the fibre volume content determined using TGA is acceptable. The composite fibre volume fraction was also theoretically predicted using the resin density which is 1.79 g/cm^3 and the fibre properties listed in Table 1.

  doi:10.5075/epfl-298799_978-2-9701614-0-0

Compared against the theoretical prediction of 42%, the value determined by TGA is slightly lower than expected. This could be as a result of the quantity of misaligned fibres in the produced preform. The results of the tensile test of the HiPerDiF 3G samples are shown in Figure 4. The stress strain curve shows a linear elastic and brittle failure, similar to what might be expect for sample of a continuous fibres. To compare the mechanical properties of the HiPerDiF 3G samples with CYCOM® 977-2 HTS prepreg samples, all data were normalized to 65% fibre volume fraction. Figure 5 shows a comparison of the mechanical properties with CYCOM® 977-2 HTS tensile test data. HiPerDiF 3G samples achieved a tensile modulus of 77 GPa and tensile strength of 751 MPa at a failure strain of 0.97%. In comparison, CYCOM® 977-2 HTS samples achieved a tensile modulus of 151 GPa and tensile strength of 2274 MPa at a failure strain of 1.5%.

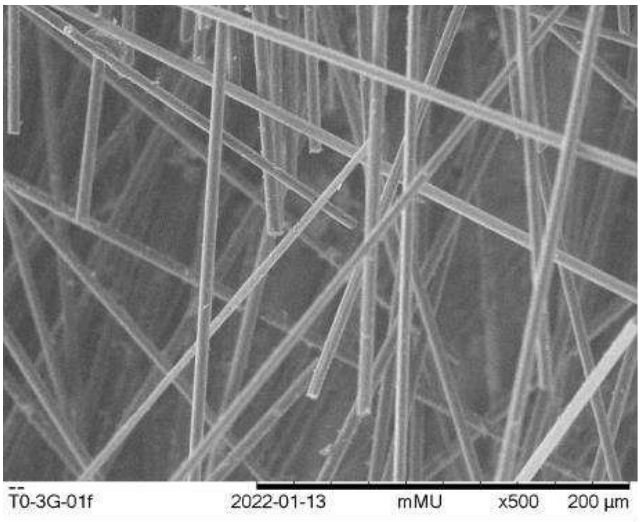

Figure 3. SEM image of HiPerDiF 3g samples after TGA

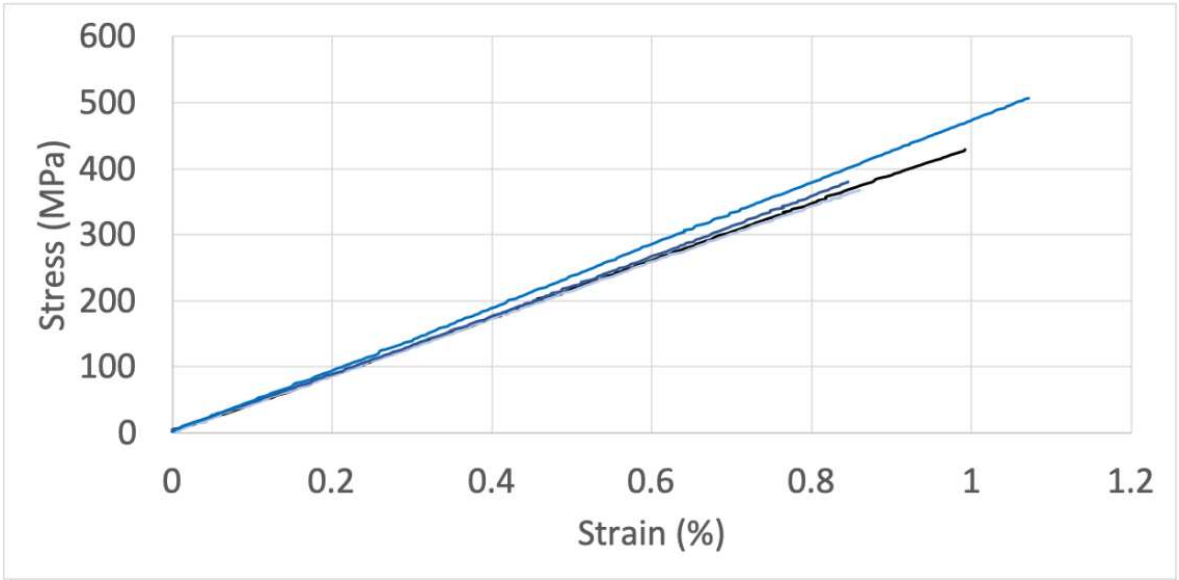

Figure 4. Stress strain curve of HiPerDiF 3G samples with 38% fibre volume fraction

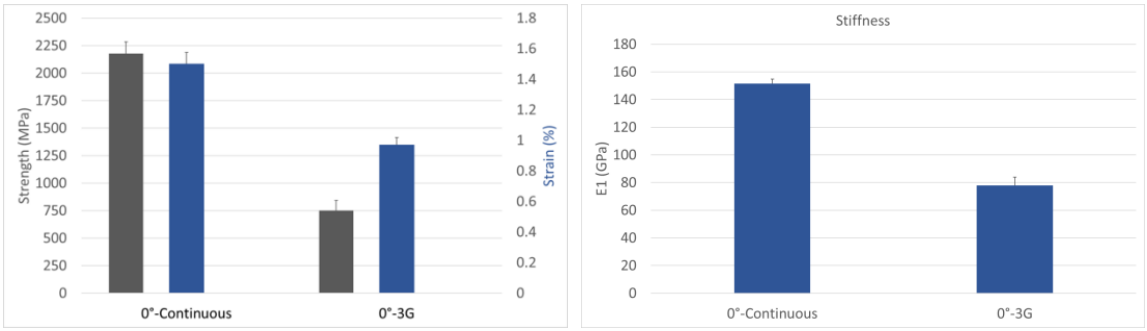

Figure 5. Mechanical properties of HIPerDiF-3G compared with UD Continuous CYCOM® 977-2 HTS prepreg samples normalised at a fibre volume fraction of 65%.

4. Conclusion and Future work

In this paper the manufacturing process and tensile results of composite samples made using the HiPerDiF 3G machine has been summarized. The possibility of applying the same techniques used for continuous fibre prepregs to ADFRC prepregs to manufacture high performance composite parts has been demonstrated. From the experimental results obtained, it can be concluded that the overall behaviour of HiPerDiF 3G composites are similar that of UD continuous composites. However, the mechanical properties achieved are significantly lower, which indicates that the present level of alignment achieved is not as high as expected. Therefore, the next step would be to understand the alignment of the samples which were tested and determine how it be optimised. To achieve this, it will be necessary to investigate the microstructure using image analysis techniques. In addition, a variety of machine settings of the HiPerDiF 3G machine will be used in order to improve the quality of the tape.

Acknowledgements

This work was funded under the UK Engineering and Physical Sciences Research Council (EPSRC) Project [grant EP/P027393/1] “High Performance Discontinuous Fibre Composites—a sustainable route to the next generation of composites” and the EPSRC Centre for Doctoral Training in Composites Science, Engineering and Manufacturing (ACCIS, Grant number EP/S021728/1) and the contribution of Solvay Group.

5. References

1. Okine, R. K., Edison, D. H., & Little, N. K. Properties and formability of an aligned discontinuous fiber thermoplastic composite sheet. Journal of Reinforced Plastics and Composites 1990; 9(1): 70–90.
2. Yu, H., Potter, K. D., & Wisnom, M. R. A novel manufacturing method for aligned discontinuous fibre composites (High Performance-Discontinuous Fibre method). Composites Part A - Applied Science and Manufacturing 2014; 65: 175-185.
3. Longana, M., Ondra, V., Yu, H., Potter, K., & Hamerton, I. Reclaimed carbon and flax fibre composites: manufacturing and mechanical properties. Recycling 2018, 3, 52.
4. Tapper, R., Longana, M., Yu, H., Hamerton, I., and Potter, K. A closed-loop recycling process for discontinuous carbon fibre polyamide 6 composites. Composites Part B 2019 179 107418

  doi:10.5075/epfl-298799_978-2-9701614-0-0 published under CC BY-NC 4.0 license

5. Longana, M., Yu, H., Jalavand, M., Wisnom, R., Potter, K. Aligned discontinuous intermingled reclaimed/virgin carbon fibre composites for high performance and pseudo-ductile behaviour in interlaminated carbon-glass hybrids. Composites Science and Technology 2017, 143, 13-21.
6. Longana, M., Yu, H., Lee, J., Pozegic, T., Huntley, S., Rendall, T., Potter, K., & Hamerton, I. Quasi-isotropic and pseudo-ductile highly aligned discontinuous fibre composites manufactured with the HiPerDiF (High Performance Discontinuous Fibre) technology. Materials 2019, 12, 1794.
7. Tapper, R., Longana, M., Yu, H., Hamerton, I., and Potter, K. Development of a closed-loop recycling process for discontinuous carbon fibre polypropylene composites. Composites Part B 2018, 146, 222-231.
8. Tapper, R., Longana, M., Norton, A., Potter, K., and Hamerton, I. An evaluation of life cycle assessment and its application to the closed-loop recycling of carbon fibre reinforced polymers. Composites Part B 2020, 184, 107665.
9. Fitzgerald, A., Proud, W., Kandemir, A., Murphy, R., Jesson, D., Trask, R., Hamerton, I., and Longana, M. A life cycle engineering perspective on biocomposites as a solution for sustainable recovery. Sustainability 2021, 13(3), 1160.
10. ASTM D3039/D3039M-17 Standard Test Method for tensile Properties of Polymer matrix Composite Materials; ASTM International: West Conshohocken, PA, USA, 2017.

  doi:10.5075/epfl-298799_978-2-9701614-0-0

DESIGN OF A BENDING EXPERIMENT FOR MECHANICAL CHARACTERISATION OF PULTRUDED RODS UNDER COMPRESSION

Gustavo, Quino[a], Paul, Robinson[b], Richard S., Trask[a]

a: Bristol Composites Institute, Faculty of Engineering, University of Bristol, BS8 1TL, UK
b: Department of Aeronautics, Imperial College London, SW7 2AZ, UK

Abstract: *Carbon fibre pultruded rods are used in structural applications across a wide range of industries due to their lightweight, corrosion/fatigue resistance and outstanding properties in the axial direction. While there is available literature on the mechanical characterisation of pultruded rods under tension and bending, very little has been reported about their compression response. The characterisation of the mechanical performance of pultruded rods under uniaxial direct compression is challenging due to the high sensitivity to alignment, stress concentrations in the gripping zone, and the complexity of specimen manufacturing, especially when the rods can be of small diameter (~1mm).*

Existing literature reports the use of the compression side of a beam under bending to test materials with high axial stiffness and strength such as carbon fibre laminates. In this work, we show the applicability of such idea on pultruded rods. We report on the design of a novel bending experiment to characterise the compression behaviour of pultruded rods, ensuring low strain gradient and consistent failure within the gauge section.

Keywords: compression; pultruded rod; CFRP; mechanical test

1. Introduction

Continuous fibre non-crimped composite materials usually display their maximum strength and modulus in the direction of the fibre, in particular, under tensile loads. However, in compression, due to various factors such as fibre waviness and pre-existing defects, instabilities such as micro buckling, lead to premature failure, and a poorer compression performance [1-4]. Literature reports compressive strengths in the fibre direction below 60% the tensile strength [1].

Composite pultruded rods tend to exhibit a better fibre alignment than laminates; therefore, they stand as an alternative to improve the compression performance of fibre composites [2]. However, measuring the improved compression performance poses a challenge from the experimental point of view. Materials with high axial stiffness like composites tend to fail in the gripping areas due to stress concentrations caused by system applying the load.

Direct compression experiments have been previously reported in literature. For example, Soutis [2] and Clarke [3] made use of direct compression to measure the strength and strain to failure of carbon fibre pultruded rods. Both studies reported that failure would sometimes take place in the vicinity of the loading endcaps, due to stress concentrations. In addition, sample preparation was costly and time consuming, and the system would be highly sensitive to the final alignment of the assembly.

  doi:10.5075/epfl-298799_978-2-9701614-0-0

An alternative method to introduce compression in a specimen is via bending. In a beam subjected to bending, one side would be in tension while the opposite side would be loaded in compression. This approach has been used in composite laminates and sandwich beams [5]. In this work, we extend that approach to design a novel four-point bending test to conduct compression tests in pultruded rods that can provide with consistent failure within the gauge section.

2. Experiment design

2.1 Material and specimen concept

The concept is shown in Figure 1a. It consists of a pultruded rod glued on top a channelled beam under bending. The beam is loaded symmetrically in four-point bending mode with a total force P. The span length is L and distance between loading pins of D (Figure 1b). The rod will be loaded in compression due to bending of the assembly, while the bottom side of the beam will be in tension. The beam also has a through thickness cut to allow direct view of the composite pultruded rod.

The material considered for this design exercise was a 0.8mm diameter carbon fibre pultruded rod, commercially available from Easy Composites (Easy Composites Ltd, UK). The beam was made of Poly (methyl methacrylate) (PMMA).

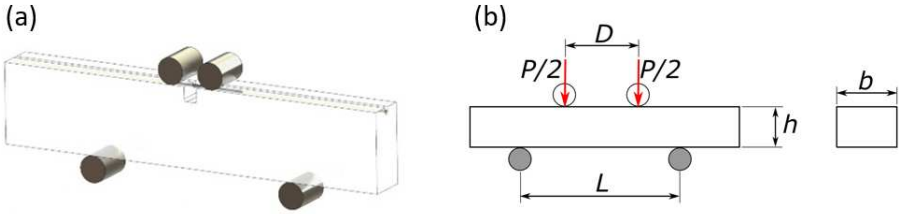

Figure 1. Beam: a) Concept; b) Geometric parameters.

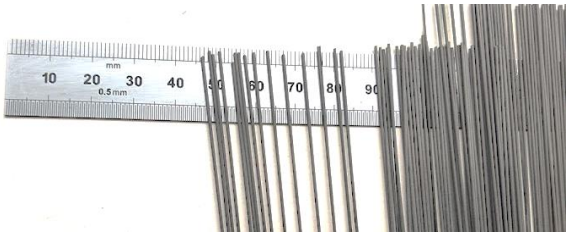

Figure 2. CFRP Pultruded rods used in the study.

2.2 Design criteria

The following 6 design criteria/guidelines were followed for the design of the experiment.

a. Beam theory

From beam theory, a beam under symmetric four-point bending will have a maximum flexural stress σ_f of:

$$\sigma_f = \frac{PL}{2bh^2}\left(1 - \frac{D}{L}\right) \quad (1)$$

Keeping the total load P constant, a smaller ratio $\frac{D}{L}$ will be required to obtain a higher maximum flexural stress. A ratio D/L=1/4 was chosen for this design exercise.

b. Buckling of rod free length

The exposed free length of the pultruded rod is at risk of buckling as it can be considered a slender structure. Analytically, the critical length for Eulerian buckling was calculated to be 7.4 mm, for the extreme case of pinned ends. A free length of 5mm was selected.

c. Total load

The total load *P* required to introduce a compressive stress in the pultruded rod high enough to trigger compressive failure, should be within the limits of available testing equipment.

d. Beam structural integrity

The beam material should not fail in tension or compression before the pultruded rod has reached a stress equal to its compressive strength.

e. Bending percent in the rod

Under direct compression of a rectangular laminate specimen, the standard ASTM D6641 recommends the use of 2 strain gauges. Even though the specimens do not buckle, opposite sides of the coupons will exhibit different strains due to a certain degree of bending. The strain measured with the two strain gauges ε_1 and ε_2 define the bending percent B_y as in Eq. (2). According to the standard, the bending percent is acceptable when it is under 10%.

$$B_y = \frac{\varepsilon_1 - \varepsilon_2}{\varepsilon_1 + \varepsilon_2} \times 100\% \quad (2)$$

Similarly, in our proposed experiment, the strains in opposite ends of the specimen will not be the same. Fig. 3 shows the detail of the exposed free length of the pultruded rod. Following the definition of bending percent, the strain ε_1 was measured in the "orange" dot, while ε_2 was measured in the "green" point, in the axial direction in both cases.

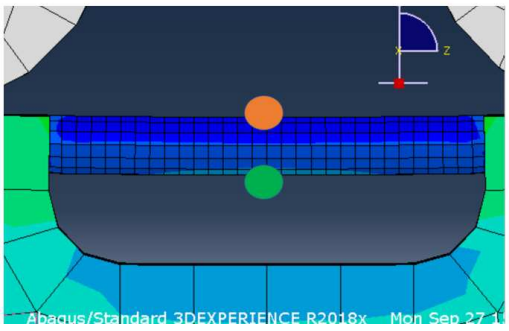

Figure 3. Detail of the exposed free length of the pultruded rod. The "orange" side will be at a higher compressive strain than the "green side"

f. Maximum stresses in rod

The final design should yield a maximum stress within the gauge length of the pultruded rod.

Criteria *c, d, e,* and *f* were verified via the virtual experiment described in the next section.

2.4 Geometry optimisation and virtual experiment

A virtual experiment (see Fig. 4) was setup using Abaqus 2017 (Dassault Systèmes Simulia Corp, USA). The rods and beam were meshed with linear brick solid elements C3D8R. The behaviour of the composite pultruded rod and the beam were assumed linear elastic. The loading pins and roller supports were modelled as rigid parts. The material properties assigned to all parts in the FE model are summarised in Table 1.

Table 1: Material properties used for the PMMA beam and the CFRP rod within the FE model.

	$E, E_{11}(GPa)$	$E_{22}(GPa)$	$\nu\ (\nu_{12})$	$G_{12}(GPa)$	$G_{23}(GPa)$
PMMA	3.2		0.33		
CFRP	174	8.34	0.31	4.55	2.6
Loading pins/ Roller supports	Rigid				

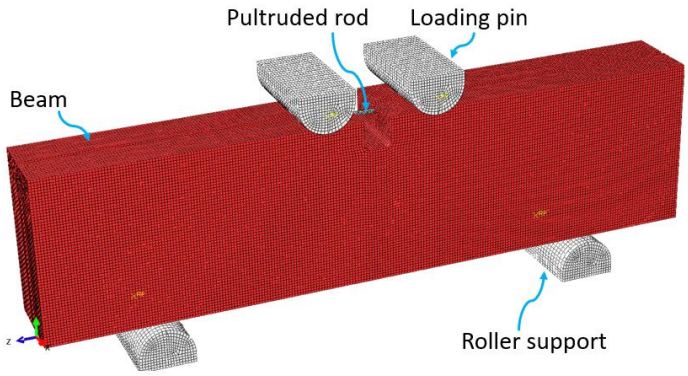

Figure 4. Meshed model of the experiment.

The geometry of the beam was optimised to minimise the bend percent on the pultruded rod specimen defined in Eq. 2. A manual iteration of the various geometric parameters h, D, L was conducted to ensure that the resulting B_y is within the acceptable range. The results of the various values of bending percent for 3 different combinations of geometric parameters, with the rod loaded at the same compressive stress of 1.2 GPa are shown in Table 2.

Table 2: Iteration of geometric parameters.

Iteration	$h\ (mm)$	$D\ (mm)$	$L\ (mm)$	$B_y(\%)$
1	20	20	60	10.8
2	20	20	80	11.1
3	30	20	80	3.0

The values of $h = 30mm, D = 20mm, L = 80mm$ was chosen for the final design. For that case, the axial stresses along 40 mm of the central section of the pultruded rod (Fig. 5a) is displayed in Fig. 5b. It is observed that the higher stresses are within the gauge section. The simulation results also showed strains under 2% in the PMMA beam, ensuring that it will not fail during the test.

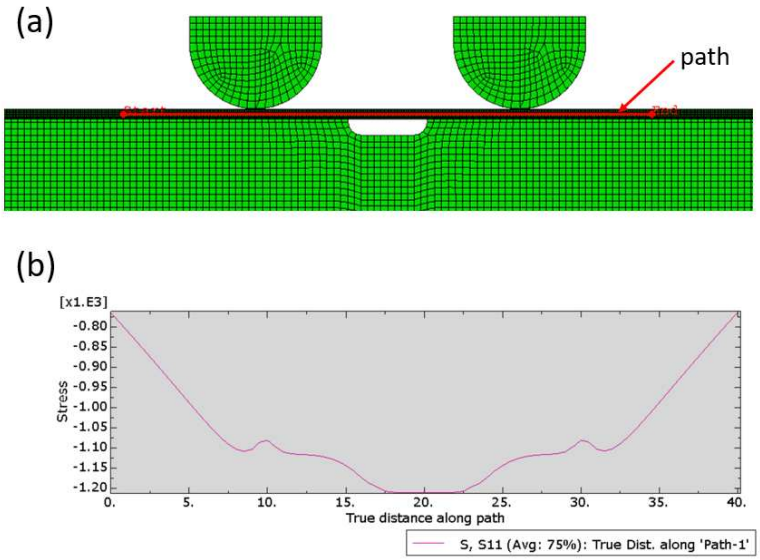

Figure 5. Axial stress along the centreline of the rod: a) Centreline path, b) Axial stress along path.

3. Experimental

The experiment was conducted in quasi-static regime in the servo-hydraulic machine Instron 8872. The load was acquired with a 25 kN load cell. The pultruded rod was prepared with black speckle over a white background to obtain the history of strains via digital image correlation.

Fig. 6 shows a snapshot of the free length of the pultruded rod specimen, right after fracture. The fracture took place within the gauge length suggesting that the design process successfully minimised stress concentration at the ends.

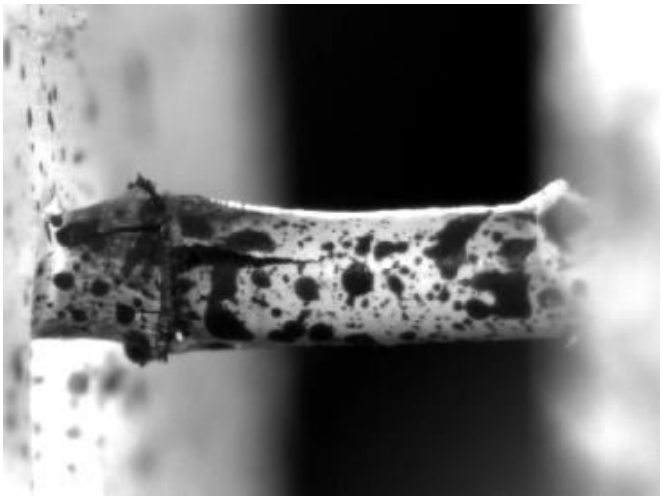

Figure 6. Compressive failure of the pultruded rod.

  doi:10.5075/epfl-298799_978-2-9701614-0-0

4. Conclusions and future work

The proposed methodology provides with compression fracture within the gauge length and stands as an advantageous alternative to direct compression due to the simpler specimen preparation, and the reduction of stress concentrations. The method will be used for a complete series of specimens of various composite rod systems obtained by pultrusion.

Acknowledgements

The authors would like to acknowledge the funding provided by UK Engineering and Physical Sciences Research Council (EPSRC) programme Grant EP/T011653/1 NextCOMP, Next Generation Fibre-Reinforced Composites: a Full Scale Redesign for Compression.

5. References

1. Fleck, N.A. 1997. “Compressive Failure of Fiber Composites.” In Advances in Applied Mechanics, 33:43–117.
2. Soutis, C. 2000. “Compression Testing of Pultruded Carbon Fibre-Epoxy Cylindrical Rods.” Journal of Materials Science 34: 3441–46.
3. Clarke, A. B. 1998. “Mechanical Properties and Process Conversion of a Novel Form of Unidirectional Carbon Fibre/Epoxy Rod.” University of Bristol.
4. Thomson, D., Quino G., Cui H., Pellegrino A., Erice B., and Petrinic N.. 2020. “Strain-Rate and off-Axis Loading Effects on the Fibre Compression Strength of CFRP Laminates: Experiments and Constitutive Modelling.” Composites Science and Technology 195 (July): 108210.
5. ASTM. 2002. “Standard Test Method for Compressive Properties of Unidirectional Polymer Matrix Composite Materials Using a Sandwich Beam.” Annual Book of ASTM Standards 08 (Reapproved): 1–9.

  doi:10.5075/epfl-298799_978-2-9701614-0-0

MECHANICAL TESTING OF 3D COMPOSITES – A ROUTE TO BEST PRACTICE

Matt Poole[a], Michael Gower[a], Stefanos Giannis[a]

a: National Physical Laboratory – matt.poole@npl.co.uk

Abstract: *Currently 3D composites are unrepresented within the majority of composite test standards. As such, NPL undertook a programme of work to determine the applicability of current test standards for use with 3D composites. Good practice guidance has been proposed after a thorough assessment of the applicability of existing mechanical test standards covering tension, compression, flexure, shear, fracture toughness and impact/post-impact loading. For the test method assessments undertaken, two 3D woven composite architectures, a glass fibre-reinforced epoxy orthogonal and a carbon fibre-reinforced epoxy layer-to-layer, have been studied. Due to the relatively large unit cell sizes found in 3D composite formats, testing was conducted using both standard and non-standard test specimen dimensions. The aim was to provide an understanding of the mechanical performance of 3D composite materials, as well as good practice recommendations not included in existing standards.*

Keywords: 3D woven; Mechanical testing

1. Introduction

Three-dimensionally reinforced (3D) composites are beginning to gain application in a variety of components, especially within the aerospace and automotive sectors. This is due in part to the desirability of features such as enhanced out-of-plane properties and the ability to be woven into structural elements. However, effective design of components requires accurate characterisation and/or prediction of the mechanical behaviour of these materials under a range of loading conditions. Typically, mechanical characterisation of a composite material is achieved through the performance of numerous experimental methods, many of which are covered within both national and international standards. These standards are often accompanied with precision data to evidence the repeatability and reproducibility of the methods. Unfortunately, representation of 3D composites within the majority of these mechanical test standards is non-existent, with the assessment of test method applicability equally not well covered in the available literature.

Although there are no explicit statements within mechanical test standards restricting use on 3D composites, their suitability for characterising the mechanical properties of these materials is unclear. Generally, material properties should be measured across volumetric elements considered representative of the bulk material, which for 3D composites, due to the inclusion of a through-thickness reinforcement, can become large. As such, for 3D composites, the recommended test specimen geometries in current methods can result in an underrepresentation of the bulk material. However, it should be realised that bulk material representation alone does not determine if the correct mode of failure occurs. From studies in the literature, standard test methods are often treated as applicable to all composite material formats. While the observed modes of failure are often discussed, assessment of their representation relevant to the mode of loading and material properties measured are rarely

  doi:10.5075/epfl-298799_978-2-9701614-0-0

challenged. By having both in-plane and out-of-plane fibres, the stress state becomes more complex and cannot always be assumed representative of the "pure" loading mode expected by the test method chosen.

To address the underrepresentation of 3D composites in current composite mechanical test standards, NPL undertook a programme of work to examine many test standards, covering a range of different test methods and loading types. Within this programme, two 3D woven material formats (glass fibre-reinforced epoxy orthogonal and carbon fibre-reinforced epoxy layer-to-layer) were tested using a range of composite mechanical test standards. While the work was limited to 3D woven materials, many of the observations will be relevant to other 3D reinforcement formats e.g., stitched, tufted etc. A good practice guide was produced from the outcome of this work, with the aim to provide guidance on the suitability of current international material test standards for determining the mechanical properties of 3D composites. Work presented here aims to highlight some of key observations made during this programme.

2. Experimental

When testing to obtain fundamental material properties, such as strength and stiffness, it is preferred that measurements are considered representative of the bulk material response. This can typically be achieved by making sure that there is at least one representative unit volume contained within the test area of the specimen. Unfortunately, many test standards limit the dimensions of test specimens, which for materials with large unit cell volumes may be quite restrictive. In these cases, modification to non-standard test specimen dimensions is required. However, it must be noted that this is not possible for all tests due to the limitations inbuilt to the specific test method and fixtures used. In the work conducted and reported here, both standard and non-standard test dimensions were used where possible. Testing was also undertaken along both the warp- and weft-directions unless otherwise noted.

2.1 Materials

To assess current international test standards for suitability in determining the mechanical properties of 3D composites, two 3D woven FRP composite materials were tested: a glass fibre-reinforced epoxy (GFRE) orthogonal (ORT) material, and a carbon fibre-reinforced epoxy (CFRE) layer-to-layer (LTL) woven material.

The GFRE ORT material consists of five warp tow layers and six weft tow layers, with a through-thickness z-binder running along the same direction as the warp tows, Figure 1a. The thickness of the GFRE ORT material is approximately 3 mm and has unit lengths along the warp and weft directions of approximately 8 and 10 mm, respectively. The CFRE LTL material has seven warp tow layers and eight weft tow layers. Unlike the GFRE ORT material, multiple z-binders are stacked through-the-thickness of the CFRE LTL material, see Figure 1b. Each z-binder traverses two weft tow layers through-the-thickness and across five weft tow columns, interlacing between each. There are an equal number of z-binders to warp tow layers. This material has an approximate thickness of 5 mm and unit lengths along the warp and weft directions of approximately 10 and 17 mm, respectively.

  doi:10.5075/epfl-298799_978-2-9701614-0-0

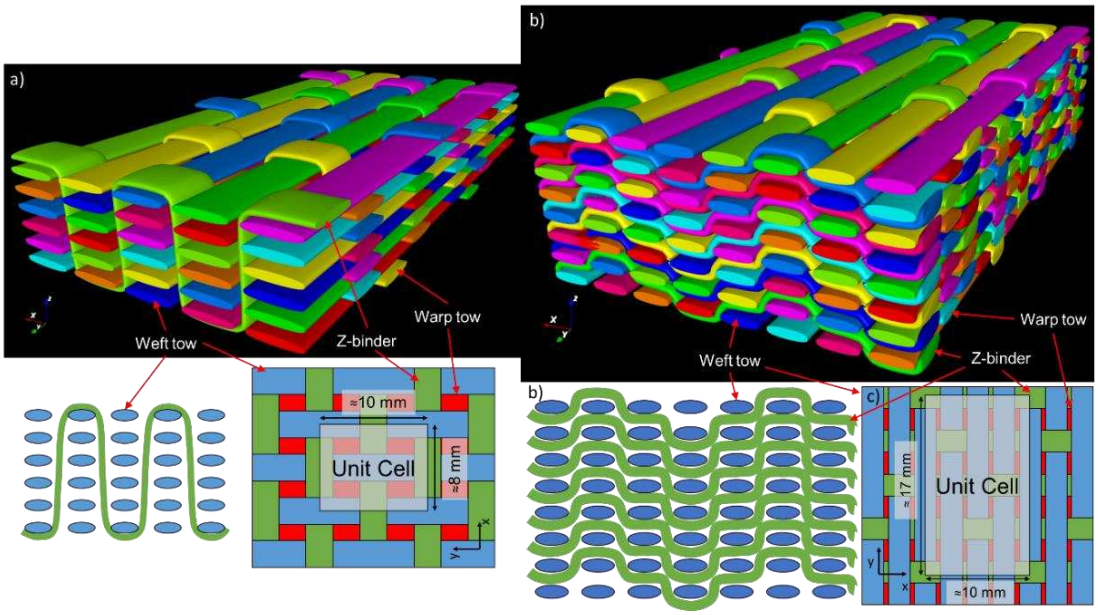

Figure 1: Structures of the 3D woven composite materials used in this work. a) 3D orthogonal woven glass fibre-reinforced epoxy (GFRE ORT); b) 3D layer-to-layer woven carbon fibre-reinforced epoxy (CFRE LTL)

2.2 Tension

Unnotched Tension: Tension testing was undertaken using ISO 527-4 [1] type 3 test specimens, i.e. straight-sided and end-tabbed. Tests were conducted using both standard and non-standard specimen widths of 25 mm and 35 mm, respectively. Strain was measured over a gauge length of 50 mm using back-to-back longitudinal extensometers.

Open-hole (notched) Tension (OHT): OHT testing was conducted in accordance with ASTM D5766 [2]. As for unnotched tension, both standard and non-standard test specimen dimensions were used. The ratio of width-to-hole diameter was maintained at 6 for all test specimens. As such, specimen widths of 24, 36, and 48 mm were tested with 4-, 6- and 8-mm diameter holes, respectively.

2.3 Compression

Unnotched Compression: Compression testing was conducted in accordance with method 2 (combined loading) of ISO 14126 [3]. Compared to other compression testing methods, ISO 14126 was chosen due to its flexibility with regards to both the method of load introduction and test fixture. Both standard and non-standard specimen dimensions were used. For the GFRE ORT material, both the width and gauge length were changed, while for the CFRE LTL only the width was adjusted. Strain was measured over the gauge area using 3D DIC on both sides of the test specimen.

Open-hole (notched) Compression (OHC): OHC testing was undertaken following method 2 of ISO 12817 [4] as it allows the use of combined loading test fixtures. As for notched tension, standard and non-standard specimen dimensions were used, while maintaining a width-to-hole diameter ratio of 6. Specimen dimensions of 24 and 36 mm wide were tested with a hole diameter of 4 and 6 mm, respectively.

  doi:10.5075/epfl-298799_978-2-9701614-0-0

2.4 Flexure

ISO 14125 [5] was used for four-point flexural testing. Unlike other flexural test standards, ISO 14125 helps the user to determine the most suitable specimen dimensions by splitting materials into four classes. Each class is based on the ratio of the longitudinal flexural stiffness to the through-thickness shear stiffness, though the standard does provide suggestions of typical materials in each class should the material properties not be known. Dimensions relating to class III and IV, as well as variations between were used in this study to determine suitability of flexural testing of 3D composites.

2.5 Shear

Compared to other means of loading, shear loading methods tend to have the greatest variety, with test standards associated with many. In this work, a number of these shear test standards were tested to determine if any were applicable to the testing of 3D composites.

±45° tension: ±45° tension testing was undertaken following guidance in ISO 14129 [6]. This standard is used to determine in-plane shear strength and modulus of composite materials. Like tensile testing, specimens were straight-sided and end-tabbed, with the same standard and non-standard dimensions being used. Strain was measured using 3D DIC on either side of the test specimen.

V-notch beam: The V-notch beam test, also known as the Iosipescu test, was conducted according to ASTM D5379 [7] using rectangular specimens with V-notches located centrally along the length. These test specimens produce a thin band of pure shear between the V-notches. Shear load is introduced into the test specimen via end-loading through an asymmetric four-point bend fixture. In this work, shear loading was conducted along the 1-2 and 2-1 shear planes, where 1 and 2 represent the warp- and weft-directions, respectively, allowing for the determination of in-plane shear strength and modulus. Unlike other test methods reported here, only standard specimen dimensions were used. Due to the limit view of the test specimen in the fixture, strain was measured using front and back 2D DIC.

V-notch rail shear: The V-notch rail shear test is like the V-notch beam test in that a thin band of shear develops between the notches during loading, but the specimen dimensions are larger. Guidance for testing is provided in ASTM D7078 [8]. Load is introduced into the test specimen by shear loading through grip faces. Shear properties were measured across the 1-2 and 2-1 shear planes. Shear strain was measured using 2D DIC on the front and back of the test specimen due to limitations of specimen viewing in the test fixture. V-notch rail shear is suggested to be used with textile-based composites where the structure is relatively coarse.

Short beam shear: There are currently two test standards for determining the interlaminar shear strength (ILSS) of materials using the short beam shear test method, ASTM D2344 [9] and ISO 14130 [10]. The main difference between these two standards is recommended specimen dimensions and specimen span length. As such, in this work a comparative study was undertaken using both standards.

Plate twist: Plate twist is a method for determining the in-plane shear modulus. Testing was conducted according to the test standard ISO 15310 [11]. Test specimens are plates that are loaded at opposing corners using flexural rigs orientated at 90° to each other. Both standard and non-standard dimensions were tested.

  doi:10.5075/epfl-298799_978-2-9701614-0-0

2.6 Fracture Toughness

For all fracture toughness testing, specimens had standard dimensions with CFRP tabs bonded to each arm to increase their stiffness to aid with crack propagation. No film insert could be put into the material and therefore a starter crack was machined into the material using a diamond wire saw. The diameter of the wire was 0.13 mm.

Mode I: Mode I testing was conducted according to ISO 15024 [12]. It uses double cantilever beam (DCB) specimens to produce the correct loading mode.

Mode II: Mode II testing was done following ISO 15114 [13] which uses the calibrated end-load split (C-ELS) test method. Due to the design of the test method, stable crack growth should be possible during loading.

2.7 Compression-After-Impact (CAI)

CAI testing was conducted according to ISO 18352 [14] using standard test dimensions. Specimens were initially impacted with an energy per unit thickness of material of 6.7 J/mm. These were then scanned using flash thermography and ultrasonic c-scanning to determine the extent of damage. Finally, the specimens were then loaded in compression until failure. DIC was used to observe some of the strain profile of the test specimens during compression loading.

3. Key Findings and Recommendations

The following subsections contain key findings and recommendations from the programme of work carried out. Further detail and general good practice can be found in the NPL Good Practice Guide No. 151 [15].

3.1 Tension

Unnotched tension testing using the recommended test dimensions in ISO 527-4 (and ASTM D3039 [16]) are suitable for use with 3D composites. However, the unit cell size of the material must be considered and ideally the specimen width should encompass several unit cells, though it is recommended that there is at least one unit cell length. Non-standard test dimensions should be used where necessary to ensure sufficient representation of the bulk material, but 25 mm widths should be treated as a minimum.

For OHT it is recommended that a better evaluation of the material performance, and degree of notch sensitivity, can be achieved by testing with multiple specimen dimensions and maintaining a width-to-hole diameter ratio of 6. Optional further analysis would be to vary the width-to-hole diameter ratio. Additionally, the number of test specimens per dimension should be increased to better assess the scatter in results due to the influence of hole position relative to the material structure. Depending on the material format it may be necessary to conduct a Weibull statistical distribution to evaluate the material performance better.

3.2 Compression

For unnotched compression testing, the unsupported gauge length should be short to avoid buckling failures during loading. Unfortunately, for materials with coarse structures or large unit cell areas, this can mean that the bulk material is not well represented. As such, it is recommended that the unsupported gauge area of a test specimen should contain at least one

  doi:10.5075/epfl-298799_978-2-9701614-0-0

unit cell across both the length and width. However, to avoid buckling failures, the size of the gauge area needs to be balanced according to the buckling limit for the material as determined by the Euler buckling criteria.

Measurement of strain using small strain gauges only produces a local, rather than global, measure of the strain on materials with coarse structures or large unit cell areas. As such, the measurement of strain should be taken across an area of at least a unit cell, though the larger the area the better the representation of the bulk material. To ensure adequate coverage, non-contact measurement techniques such as DIC are high recommended for this.

For OHC testing, the materials tested show a strong notch sensitivity and clear strength dependence on the size and position of the hole relative to the material structure. Like OHT, it is recommended that for 3D composites, and coarse material structures generally, multiple test specimen dimensions and an increase in the number of repeats tests is needed to better evaluate the performance of the material.

3.3 Flexure

For flexural testing, interlaminar failures are considered unacceptable as they indicate the presence of shear stresses. This can generally be remedied by increasing the span length but can then also result in large bending deflections occurring. In the materials tested, the balance between interlaminar failures and large bending deflections makes it difficult to determine suitable test spans. As such, flexural testing would be better for quality assurance testing. Regardless, the following are general recommendations for flexural testing.

- Choose a test span that a) minimises shear contribution, and b) ensures deflection can be measured fully – a support span ratio greater than 30:1 but less than 40:1 would likely be suitable for 3D composites. A long travel LVDT or another suitable device should be used.
- Determine what level of interlaminar shear failure can be considered acceptable (the smaller the better) before a peak load is reached. While it is ideal to avoid shear failures completely, the qualitative comparison between specimens is important and small amounts of shear may not be avoidable. Allowing a small proportion of shear failure to develop may enable easier and faster testing.
- [***Optional***] Select a suitable strain limit to stop the test at if large bending deflections occur – this can be very much dependent on the material being tested but stopping the test at 5% flexural strain, as suggested within ASTM D790 and D6272, seems reasonable.

3.4 Shear

Measurements of the in-plane shear modulus were undertaken using the test methods ±45° tension (ISO 14129), V-notch beam (ASTM D5379), V-notch rail shear (ASTM D7078) and Plate Twist (ISO 15310). All four test methods produced average shear modulus measurements of very similar values, but with varying degrees of repeatability and therefore appear suitable for determining the shear modulus of 3D composites. However, material uniformity and unit cell size should be considered when choosing which method to use. As such it is recommended that any of these test methods could be used to measure shear modulus depending on the user's preference.

  doi:10.5075/epfl-298799_978-2-9701614-0-0

In all cases, the materials were able to be loaded well beyond 5% shear strain, which is an arbitrary test termination point suggested within each standard to minimise the influence of other loading modes on the measurement of shear strength. The 5% shear strain termination point means that the true shear strength cannot be obtained using these methods. In addition, despite good repeatability, invalid failures, especially in V-notch beam and V-notch rail specimens, suggest none of these tests are suitable for measuring shear strength of these materials. Therefore, it is recommended that none of these methods be used for the determination of shear strength. However, each of these methods could be used for quality assurance purposes. Further work would be needed to determine an acceptable method for measuring shear strength effectively.

ILSS was measured using both SBS methods outlined in ASTM D2344 and ISO 14130. Although good repeatability was achieved for all tests, tensile cracking occurred regardless of test dimensions. This is considered an unacceptable failure mode and therefore not representative of ILSS. As such, neither test method is recommended for measurement of ILSS.

3.5 Fracture Toughness

Due to the through-thickness reinforcement in 3D composites, the initiation and propagation of a crack front for mode I and mode II loading can be difficult. Flexural failure in the specimen with little propagation of the crack front is not uncommon but can be eliminated by increasing the stiffness of the arms. Bonding tabs of CFRP to the material is recommended. However, it should be noted that beam arm stiffening is not guaranteed to enable crack propagation as it is highly dependent on the 3D composite structure being tested. For instance, in this work the crack front of the GFRE ORT would not propagate in either mode I or mode II, while the CFRE LTL crack front did.

It is not always possible to place a thin film insert to act a start defect. One recommended alternative is to use a thin diamond wire saw to produce a start defect. Currently the thinnest diamond wire available is 0.13 mm in diameter, which is about 10 times thicker than a standard film insert.

In the case of crack propagation, 3D composites tend to display both crack branching and fibre bridging. The data reduction techniques suggested within ISO 15024 and ISO 15114, which are based on linear elastic fracture mechanics, do not consider the influence of large-scale fibre bridging or crack branching and are therefore not recommended for use with materials such as 3D composites. As such, further work would be required to develop suitable reduction techniques for these materials.

3.6 Compression-After-Impact

The 3D composites tested in this work both showed localised damage around the impact site due to the z-binders providing extra surface area for energy absorption. When compressively loaded the GFRE ORT material failed by buckling, while the CFRE LTL failed acceptably through the image region. Here, the GFRE ORT is couple of millimetres thinner than the dimensions recommended in ISO 18352, while the CFRE LTL has the recommended material thickness, and likely influences the difference modes of failure observed. There are no alternative dimensions suggested by ISO 18352, especially for thinner materials, and therefore further work would be required determine sufficient scaling.

  doi:10.5075/epfl-298799_978-2-9701614-0-0

Acknowledgements

The work reported in this paper was carried out by NPL as part of the National Measurement System (NMS) programme funded by the United Kingdom Department of Business, Energy and Industrial Strategy (BEIS).

4. References

1. British Standards Institution, "BS EN ISO 527-4: 1997 Plastics - Determination of tensile properties - Part 4: Test conditions for isotropic and orthotropic fibre-reinforced plastic composites," BSI, 1997
2. ASTM International, "ASTM D5766/D5766M - 11 Standard Test Method for Open-Hole Tensile Strength of Polymer Matrix Laminates," Wst Conshohocken, PA, 2011
3. British Standards Institution, "BS EN ISO 14126:1999 Fibre-reinforced plastic composites - Determination of compressive properties in the in-plane direction," BSI, 1999.
4. British Standards Institution, "BS ISO 12817:2013 Fibre-reinforced plastic composites - Determination of open-hole compression strength," BSI, 2013.
5. British Standards Institution, "BS EN ISO 14125:1998+A1:2011 Fibre-reinforced plastic composites - Determination of flexural properties," BSI, 1998
6. British Standards Institution, "BS EN ISO 14129:1998 Fibre-reinforced plastic composites - Determination of the in-plane shear stress-shear strain response, including the in-plane shear modulus and strength by the ±45° tension test method," BSI, 1998.
7. ASTM International, "ASTM D5379/D5379M - 12 Standard Test Method for Shear Properties of Composite Materials by the V-notched Beam Method," West Conshohocken, PA, 2012.
8. ASTM International, "ASTM D7078/D7078M - 12 Standard Test Method for Shear Properties of Composite Materials by V-Notched Rail Shear Method," West Conshohocken, PA, 2012
9. ASTM International, "ASTM D2344/D2344M - 16 Standard Test Method for Short-Beam Strength of Polymer Matrix Composite Materials and Their Laminates," West Conshohocken, PA, 2016
10. British Standards Institution, "BS EN ISO 14130:1998 Fibre-reinforced plastic composites - Determination of apparent interlaminar shear strength by short-beam method," BSI, 1998
11. British Standards Institute, "BS EN ISO 15310:2005 - Reinforced plastics - Determination of the in-plane shear modulus by the plate twist method," BSI, 2005
12. Bristish Stanards Institution, "BS ISO 15024:2001 Fibre-reinforced plastic composites - Determination of mode I interlaminar fracture toughness, Gic, for unidirectionally reinforced materials," BSI, 2001.
13. British Standards Institution, "BS ISO 15114:2014 Fibre-reinforced plastic composites - Determination of the mode II fracture resistance for unidirectionally reinforced materials using the calibrated end-loaded split (C-ELS) test and an effective crack length approach," BSI, 2014
14. British Standards Institution, "BS ISO 18352:2009 Carbon-fibre-reinforced plastics - Determination of compression-after-impact properties at a specified impact-energy level," BSI, 2009
15. M. Poole and M. Gower, "NPL Good Practice Guide No. 151: Mechanical Characterisation of 3D Fibre-Reinforced Plastic (FRP) Composites," NPL, London, 2021.
16. ASTM International, "ASTM D3039/D3039M - 14 Standard Test Method for Tensile Properties of Polymer Matrix Composite Materials," West Conshohocken, PA, 2014

  doi:10.5075/epfl-298799_978-2-9701614-0-0

TAPERED GEOMETRY FOR TESTING CONTINUOUS FIBER REINFORCED THERMOPLASTICS UNDER TENSION

Sebastian Schmeer[a], Florian Mischo[b], David Scheliga[b]

a: Leibniz-Institut für Verbundwerkstoffe, Kaiserslautern (IVW) – sebastian.schmeer@ivw.uni-kl.de
b: Leibniz-Institut für Verbundwerkstoffe (IVW), Kaiserslautern

Abstract: *Continuous fiber reinforced thermoplastics (cFRTP) are attractive materials for many applications especially for structural parts. It is very important that not only proven experts with years of testing experience but also large parts of the industry are able to characterize those materials in an accurate, robust and effective way. Actual standards recommend rectangular specimens with tabs for such materials, which often leads to problems based on the thermoplastic matrices. A novel geometry is presented here for testing multi-axial cFRTP (organo sheets and tape-based multi-axial laminates). The main goal was to achieve advantages in efficiency and robustness while reaching the same level of accuracy without using tabs. The presented geometry results from an FEM optimization and is slightly tapered within the testing section. A round-robin test with five international participants was performed to compare the tabbed rectangular specimen (ISO 527-4, type 3 [1]) with the new tapered tensile specimen (TTS) without tabs.*

Keywords: Continuous fiber reinforced plastics; thermoplastic composites; material characterization; tensile strength

1. Introduction

Continuous fiber reinforced thermoplastics (cFRTP) are prominent lightweight materials based on their excellent specific stiffness and especially specific strength properties. Due to their attractive further advantages, e.g. fast manufacturing in large series, recyclability and weldability, these materials are used in a rising number of applications. [2–4] The material behavior (stress-strain relation) and important performance values like stiffness and strength are evaluated experimentally in e.g. tensile tests. Continuous fiber reinforced plastics usually have high stiffness and strength values in fiber direction and significantly lower properties in transversal fiber direction. Therefore, when clamping such materials, high transverse pressure is required in the grips to prevent the specimen from slipping out. This often leads to specimen failure in its clamping area instead of in its testing section. Here, critical stress peaks occur due to the high transversal clamping pressure and the stiff clamping jaws. This can lead to lower strength values being calculated in the tests than the real tensile strength of the material. [5]

Typically, bonded tabs are used to strengthen the clamping area and to prevent a clamping failure in the specimens (see Figure 1). Procedures using this method can be found in several standards (e.g. [1,6]). It was developed for thermoset-based composites and provides reliable results when performed properly implying that there mustn't be any asymmetries in the bond or tab positioning and the bond must be defect-free. Unfortunately, bonding is a very

  doi:10.5075/epfl-298799_978-2-9701614-0-0

challenging procedure for thermoplastic composites (in terms of time, quality and knowledge). The various thermoplastics require tailor-made adhesives, sometimes combined with coupling agents. [7,8] The necessary know-how, care and effort are often not available to a sufficient extent for material characterization. Insufficient bonding causes the specimen to break away from the tab and slip out of the clamping. The countermeasure is to increase the clamping force, which above a certain level leads to the specimen's clamping failure. However, this leads to calculated lowered strength values and/or to large deviations if a material is characterized by different laboratories. [5]

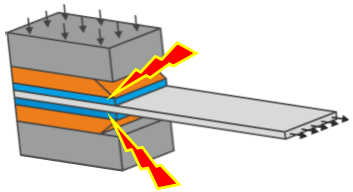

Figure 1: Critical clamping condition for specimens according to ISO 527-4

2. Geometries

Tensile tests are usually used to determine the stress-strain behavior and the characteristic values of tensile Young's modulus, tensile strength and Poisson's ratio. In order to prevent the strength-reducing influence of the stress peaks in the clamps and at the same time to avoid glued-on tabs, the approach taken here is to design the testing area with a smaller width than the clamping area. As the specimen width changes, shear stresses inevitably result from force flow redirection. However, the determination of the above-mentioned characteristic values should not be negatively influenced. Therefore, a shape optimization was carried out based on basic considerations and FE analyses. The material selected for the FE optimization was a purely unidirectional (UD) fiber reinforced thermoplastic as it reacts most sensitively to deviations from the pure tensile stress state. The exemplary failure body for the plane stress state of unidirectional reinforced composites according to Puck [9,10] is shown in Figure *2*. The tensile test is intended to produce fiber failure (FF) in the test specimen and takes place in the marked plane. In addition to the targeted tensile stresses (green), unwanted shear stresses (red) also occur due to the width variation. It should be avoided that the shear stress becomes dominant as this induces interfiber failure (IFF). The stress exposure is the ratio of the actual stress to the failure stress and can be distinguished for FF stress exposure and IFF stress exposure. [11]

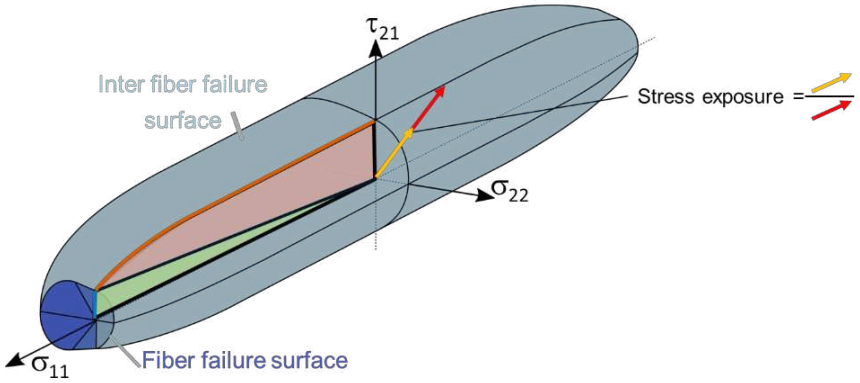

Figure 2: Fracture surfaces for the plane stress state of unidirectional reinforced composites according to Puck

Figure 3a depicts several considerations: To avoid high notch stress peaks, angular geometries for width minimization are ruled out. Non-circular inner cutouts are more complex in machining than outer applied tapers and therefore are not followed up either.

Local width variations are expected to produce larger stress peaks than global ones. In an FE analysis, the magnitude of these stress peaks was investigated. Figure 3b presents the stress exposure ratio in the UD material as an example of a local width reduction when the tensile test specimen for unreinforced thermoplastics from ISO 527-2 [12] is used. Here, the ratio of maximum IFF stress exposure to FF stress exposure in the specimen exceeds 1. Therefore, the test geometry is unsuitable, since IFF occurs first before the targeted FF can be achieved in the material.

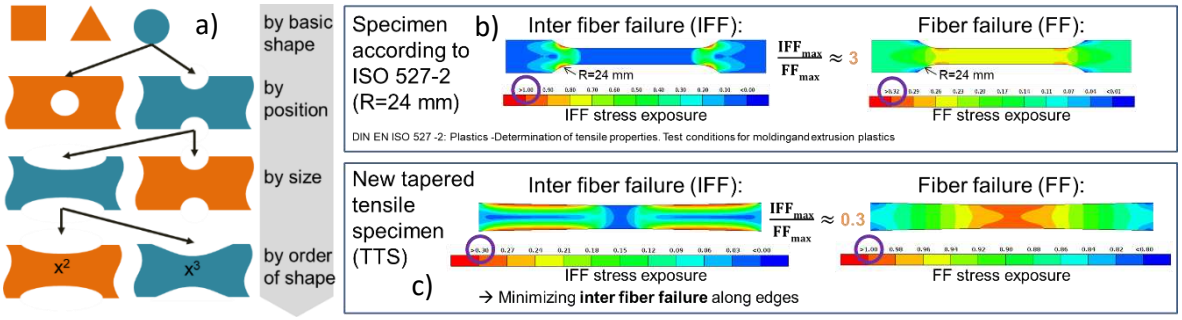

Figure 3 : a) Geometry optimization path, b) stress exposure analysis of a local width reduction based on a square shape c) stress exposure analysis of a global width reduction based on a cubic shape

Many other FE analyses were performed obtaining best results for a global width reduction using a cubic approach. In this case, the shear stresses can be uniformly distributed over the entire length of the width reduction without generating stress peaks. This leads to a low IFF stress exposure and thus to FF in the material (Figure 3c). In this theoretical study, the same (realistic) material properties were used in all cases. Since the specific properties for different cFRTP variate, the statement here is not absolute but relative.

Figure 4 shows the position of the investigated specimen geometry types in the section plane of the Puck failure body from Figure *2*. Here, the effect of excessive shear stress fractions in the specimen becomes graphically evident. The normal stress fraction Sigma 11, which is reached at specimen fracture and gives the strength from the test, is significantly lower than the value that can be achieved in fact. In the case of the cubic-tapered specimen, the maximum shear stresses in this example remain sufficiently low so that FF is reached.

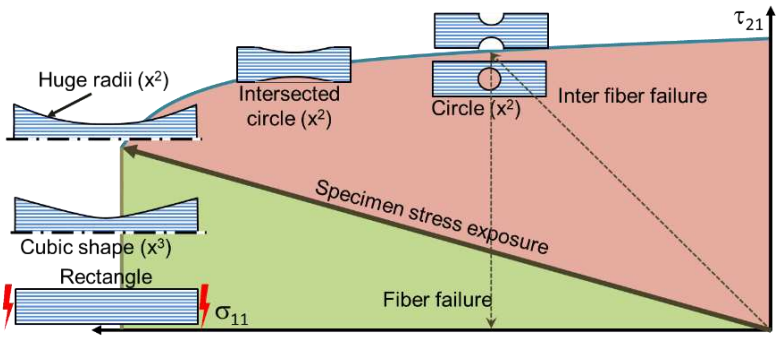

Figure 4: Position of the investigated geometry types in the section plane of the Puck failure body

Figure *5* shows the resulting geometry with the test area having the same width as the established reference geometry from ISO 527-4: 1992 [1]. The overall length is 50 mm longer to keep the shear stress low. From the test section to the clamping section, the specimen is increased in width by a total of 3 mm following a cubic function. In the center of the specimen is a parallel test area (25 x 25 mm²) to determine the Young's modulus and the Poisson's ratio.

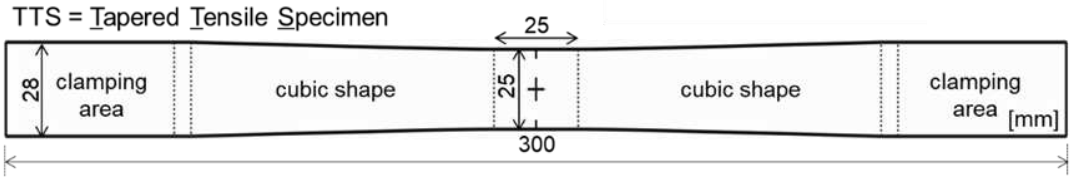

Figure 5: New optimized Tapered Tensile Specimen (TTS) geometry without tabs

3. Round robin testing procedure

To prove the accuracy, robustness and efficiency of the TTS in comparison to the standardized rectangular specimen geometry with tabs (according to ISO 527-4 [1]), an international round robin test was performed. For this reason, apart from IVW, international operating material suppliers participated as test laboratories and two cFRTP materials for usage in large series productions were selected out of the group of multidirectional reinforced thermoplastics as round robin test materials. A glass-fiber fabric reinforced polypropylene with a balanced orientation of fibers (47 % fiber volume content [FVC]; 2 mm plate thickness) and a glass-fiber fabric reinforced polyamide with an unbalanced fiber orientation (80% fibers oriented in 0°, 20 % in 90°; 47 % FVC; 2 mm plate thickness) were investigated.

To consider manufacturing influences on the specimens, one batch was centrally cut and distributed to the test participants by a laboratory using water jet cutting. Each round robin participant individually cut all other specimens themselves by milling. The cutting out of the plate material as well as the specimen testing is performed in agreement with the ISO 527-4 standard. [1] Hence, different testing fixtures and strain measurement devices (e.g. extensometer, digital image correlation [DIC]) were used by the laboratories. After testing and documentation of the results, the data was centrally summarized and anonymously evaluated.

4. Results

In the round robin test the Young's modulus and tensile strength of each testing material and specimen geometry was evaluated. Figure 6 summarizes the overall testing results. It is obvious that for both geometries (type 3 specimen of ISO 527-4 and TTS) and both materials (GF-PP and GF-PA66), the modulus and tensile strength values show comparable mean values and standard deviations (see also Table 1). The different measuring techniques used and machining methods performed (milling/water jet cutting) also had no measurable influence on the characteristic determined values.

  doi:10.5075/epfl-298799_978-2-9701614-0-0

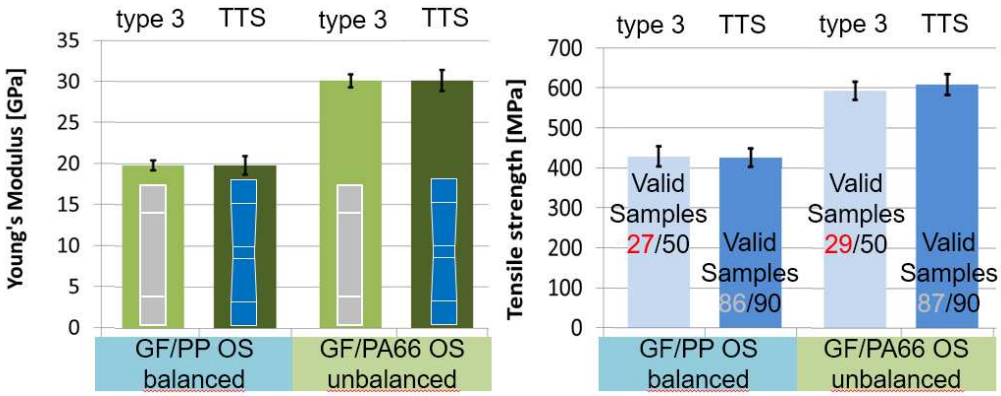

Figure 6: Results of international round robin testing campaign, ISO 527-4 type 3 vs. TTS geometry

Table 1 : Mechanical material values of the round robin testing campaign

Material	Tensile Properties	Mean value	Standard deviation
Specimen type 3			
GF-PP	σ_{11}	428.33 MPa	25.01
	E_{11}	19.90 GPa	0.63
GF-PA66	σ_{11}	593.50 MPa	21.78
	E_{11}	30.21 GPa	0.62
TTS			
GF-PP	σ_{11}	430.36 MPa	23.22
	E_{11}	20.10 GPa	0.98
GF-PA66	σ_{11}	603.30 MPa	27.01
	E_{11}	30.42 GPa	0.73

When evaluating tensile strength, the validity of the tensile test as described above is of particular importance. ISO 527-4 defines invalid testing by slipping of the specimen or failure in the clamping or the edge region of the clamping area. Due to the adhesive tab application and the required transversal pressure, the specimen type 3 of ISO 527-4 [1] often triggers failure in the clamping area and therefore invalid failure. The TTS specimen, due to its tapered shape, shows a significantly higher robustness indicated by the high valid sample count in Figure 6.

  doi:10.5075/epfl-298799_978-2-9701614-0-0

Figure 7 : Exemplary results (failure modes) of GF-PA66 specimens (green tick: valid failure; orange question mark: uncertain failure mode; red cross: invalid failure mode)

Figure 7 shows an exemplary GF-PA66 specimens test batch of a testing campaign participant. It indicates the clearly valid tested specimens with a green tick and the clearly invalid failed ones with a red cross. In this exemplary test batch, only the rectangular specimens show invalid failure at the edge of the clamping area or adhesive failure. The question marks visualize an “uncertain” failure mode because the crack is located in both valid and invalid areas. Such cracks lead to an uncertain failure mode because it is not possible to determine whether the crack originated in the invalid or valid area. The tapered shape of the TTS also prevents these unknown failures due to a triggered and clear failure beginning in the specimen’s middle section.

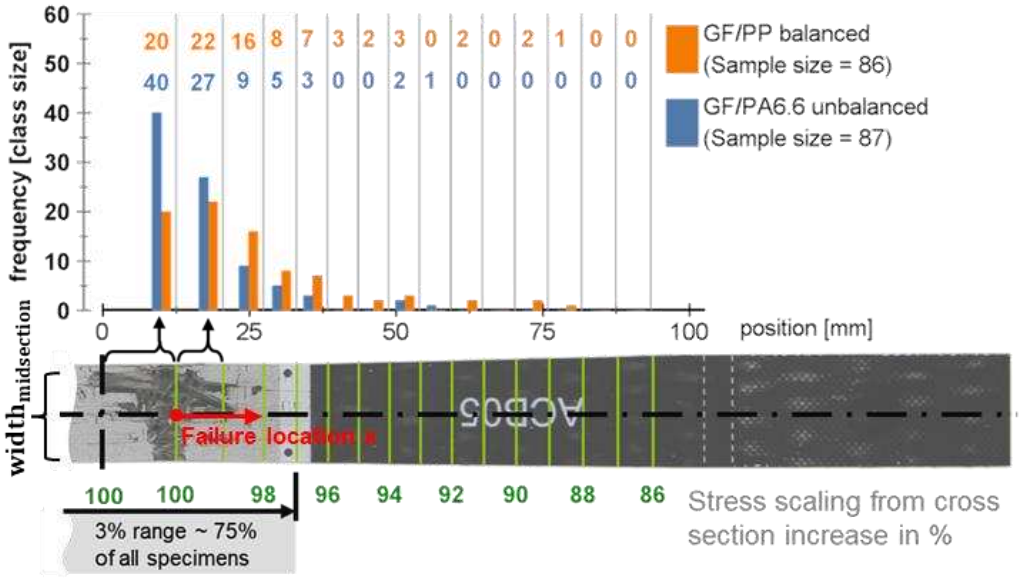

Figure 8: Analysis of failure position and calculation of stress depending on failure position of TTS

In the majority of tests, the failure occurred in the parallel specimen region (see Figure 8). Due to slight inhomogeneities in the test material, specimen failures are sometimes initiated outside of the parallel, non-tapered measurement area of the TTS specimen. In this case, a recalculation of the specimen’s failure area/failure stress is necessary and thus was performed. By knowing

the cubic spline of the edge curve, the calculation of the specimen area A at failure position x (A(x)) is possible using Equation 1 with the measured specimen width in the parallel mid-section ($\mathrm{width}_{\mathrm{midsection}}$, see Figure 8).

$$A(x) = \mathrm{thickness} * (\tan^{-1}(x a_1) * x * a_2 + \mathrm{width}_{\mathrm{midsection}}) \quad (1)$$
$$\text{with } a_1 = 0.06047 \text{ and } a_2 = 0.0246$$

5. Conclusion

The newly developed TTS has been successfully applied to multiaxial materials. It is analyzed by its accuracy, efficiency and robustness in an international round robin test compared to the standard ISO 527-4 type 3 specimen geometry in Figure 9. Due to equivalent testing results for Young's modulus and tensile strength, the TTS geometry shows the same testing accuracy as the type 3 specimen. However, in terms of robustness and efficiency the TTS indicates better results. Almost all tested TTS samples failed validly and only less than 5% invalidly but then clearly identifiable. In comparison, the type 3 specimens only achieved a validity of almost 60% in both materials and also showed an uncertain failure mode in 10% of the cases. In this round robin test TTS geometry performed 10 times more robust.

Due to the high success rate and the significantly lower preparation effort in terms of time and knowledge, the TTS samples lead to an approximately 10 times higher effectiveness. All this advantages based on the specific tapered specimen edge and the absence of tabs that have to be bonded, prepared and cured for the ISO 527-4 type 3 specimen [1].

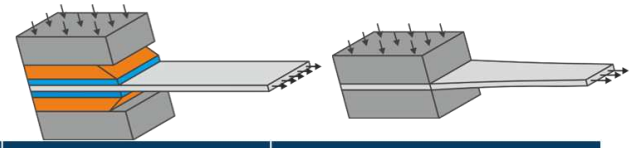

		ISO 527-4 Type 3	New (TTS)	
Accuracy	Young's modulus	Same results		
	Strength	Same results		
Robustness	GF/PP organic sheet balanced	~54% valid (27/50) ~10% uncertain fail	~96% valid (86/90) 0% uncertain fail	TTS 10 x more robust
	GF/PA organic sheet unbalanced	~58% valid (29/50) ~10% uncertain fail	~97% valid (87/90) 0% uncertain fail	
Efficiency	Testing effort	High effort	Low effort	TTS 10 x more efficient
	Recommended knowledge	High	Low	
	Specimen preparation	Cutting, Bonding, Curing	Cutting → ~6 times faster → No costs for glue	

Figure 9: Summary and conclusion of round robin test results

The advantages and positive results of the TTS lead to the standardization of the geometry and the addition of this new specimen geometry into ISO 527-4 as new type 4. Revised ISO 527-4 is stated to be published very soon. Until this standard newly published, the TTS geometry (as CAD-file) can be requested from the author of this paper.

In upcoming investigations a transfer of the test method to unidirectional reinforced specimens will be focused on, where the success of the geometry depend on the ratio of the material's shear to tensile strength.

Acknowledgements

These investigations were conducted for the working group "Continuous fiber reinforced thermoplastics" under the umbrella of the AVK (Federation of reinforced plastics e.V.) and led by IVW. The work has been funded by the participating companies Arkema, Mitsui Chemicals Europe GmbH, Lanxess/Bond-Laminates GmbH, Covestro AG, Evonik Industries AG, DSM Engineering plastics, Sabic, Solvay S.A., DuPont.

6. References

[1] International Organization for Standardization. ISO 527-Part 4: Test conditions for isotropic and orthotropic fibre-reinforced plastic composites(ISO 527-4:1997); 1997.
[2] Alshammari BA, Alsuhybani MS, Almushaikeh AM, Alotaibi BM, Alenad AM, Alqahtani NB et al. Comprehensive Review of the Properties and Modifications of Carbon Fiber-Reinforced Thermoplastic Composites. Polymers (Basel) 2021;13(15).
[3] Premium AEROTEC. Press release: Premium AEROTEC zeigt Zukunftspotenzial von CFK mit thermoplastischer Matrix: Weltweit erster Demonstrator für A320-Druckkalotte steht im Mittelpunkt des ILA-Auftritts.
[4] ElringKlinger AG. Press release: ElringKlinger erhält Großserienauftrag für ein globales Leichtbau-Projekt; 2016.
[5] Belingardi G, Paolino DS, Koricho EG. Investigation of influence of tab types on tensile strength of E-glass/epoxy fiber reinforced composite materials. Procedia Engineering 2011;10:3279–84.
[6] ASTM International. ASTM D 3039/D 3039M – 00: Standard Test Method for Tensile Properties of Polymer Matrix Composite Materials: ASTM International; 2002.
[7] Blackman B, Kinloch AJ, Watts JF. The plasma treatment of thermoplastic fibre composites for adhesive bonding. Composites 1994;25(5):332–41.
[8] Scarselli G, Quan D, Murphy N, Deegan B, Dowling D, Ivankovic A. Adhesion Improvement of Thermoplastics-Based Composites by Atmospheric Plasma and UV Treatments. Appl Compos Mater 2021;28(1):71–89.
[9] Schürmann H. Konstruieren mit Faser-Kunststoff-Verbunden: Mit 39 Tabellen. 2nd ed. Berlin, Heidelberg: Springer; 2007.
[10] Puck A. Festigkeitsanalyse von Faser-Matrix-Laminaten: Modelle für die Praxis. München, Wien: Hanser; 1996.
[11] Knops M. Analysis of Failure in Fiber Polymer Laminates: The Theory of Alfred Puck. Berlin, Heidelberg: Springer Berlin Heidelberg; 2008.
[12] International Organization for Standardization. ISO 527-Part 2: Test conditions for moulding and extrusion plastics(ISO 527-2:2012); 2012.

  doi:10.5075/epfl-298799_978-2-9701614-0-0

NUMERICAL AND DIGITAL IMAGE CORRELATION BASED EXPERIMENTAL ANALYSIS OF THE DEFORMATION BEHAVIOUR OF STITCHED UNIDIRECTIONAL CONTINUOUS CARBON FIBRE/EPOXY COMPOSITES WITH DIFFERENT STITCH PATTERNS UNDER TENSILE LOADING

Kai Uhlig[a], Lars Bittrich[a], Axel Spickenheuer[a], Markus Stommel[a,b]

[a]: Leibniz-Institut für Polymerforschung Dresden e.V., Germany
[b]: Faculty of Mechanical Science and Engineering, Institute of Materials Science, TU Dresden, Dresden, Germany

Abstract:

Continuous carbon fibre / epoxy composites (CF/EP) based on Tailored Fibre Placement (TFP) are increasingly used in the industry to produce lightweight parts due to the resource efficient and reliable fibre placement process. Due to the required stitching yarn the morphology of TFP based CF/EP composites is inhomogeneous. The displacement volume of the necessary stitching yarn in combination with the stitch pattern causes a slight waviness of the CF in-plane and out-of-plane which results in a reduction of the tensile modulus and strength. The resulting waviness depends on user defined TFP manufacturing parameters. The aim of the study is the numerical and experimental investigation of the effect of different TFP stitch patterns on the deformation behaviour and the mechanical properties of TFP based unidirectional CF/EP laminates. Therefore, six TFP based CF/EP laminates with different but typical stitch patterns are analysed under tensile loading using a 3D digital image correlation (DIC) system with high spatial resolution. The DIC data are compared with numerical results of a 3D representative volume element (RVE) finite element model developed for TFP based composites. Both qualitatively and quantitatively, the numerical and experimental determined strain data showed a good agreement.

Keywords: Tailored Fibre Placement; Continuous Fibre Reinforced Plastics; Variable Angle Tow; Digital Image Correlation; Representative Volume Element

1. Introduction

Due to their high specific strength and stiffness, CF/EP are used in structural lightweight components. Several manufacturing techniques exist to produce advanced CF/EP composite laminates and structures. Usually, CF/EP structures are manufactured by stacking unidirectional plies with several fibre angles to attain a quasi-isotropic behaviour. In certain applications with few dominant load cases, such conventional laminates do not fully exploit the potential of highly orthotropic CF/EP materials and the cut off waste is relatively high. To overcome these issues the TFP Technology was developed [1]. TFP is an embroidery-based preform manufacturing technique that allows a flexible orientation of any fibre roving (e.g. carbon, glass, aramid). As shown in Figure 1, a continuous roving is placed along programmable paths within the plane (2D) and fixated by a stitching yarn onto a flat textile base material using a double locked stitch in a zig-zag stitch pattern. The roving is deposited following a pre-defined path by rotating the roving pipe and moving the base material in two perpendicular directions [2]. Mattheij et al. [1], Crothers et al. [3], Gliesche et al. [4] and Aschenbrenner et al. [5] have studied the application of the TFP technology for composite materials.

  doi:10.5075/epfl-298799_978-2-9701614-0-0

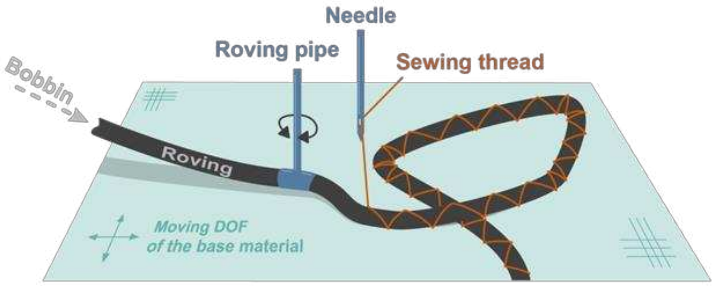

Figure 1 TFP Principle [2]

To access the potential of the TFP technology in real composite parts Spickenheuer et al. [6] developed a design tool to numerically derive fibre paths along principal stress directions. Based on that work Bittrich et al. [7] developed the direct fibre path optimization concept to derive optimized variable-axial fibre-reinforced composites. Due to the presence of the stitching yarn, the morphology of TFP-based composites differ from either UD prepregs or woven fabrics. Both displacement volume of the stitching yarn and zig-zag stitch pattern cause fibre waviness (*Figure 2*). Furthermore, due to the added stitching yarn, the fibre volume content is not homogeneous and typically lower when compared to perfectly aligned unidirectional prepregs [2]. Considering the material behaviour of a UD layer, in which both strength and stiffness are highly dependent on the fibre orientation, the induced waviness leads to a reduction on both stiffness and strength [2]. In contrast to AFP-based laminates, where fibre patches exhibit rectangular cross sections, at TFP rovings smoothly overlap during their placement. This even occurs for parallel placement in laminates with constant thickness. Thus, for TFP laminates, one does not observe the typical disadvantages that follow discontinuous overlapping of rectangular patches, and gaps provide more of exactly such discontinuities. Furthermore, the stitching yarn of one roving regularly penetrates the neighbouring roving [2]. Hence, a TFP-based layer consists of a resin infiltrated roving, a stitching yarn and resin-rich zones around the stitching yarn. The resulting morphology of a TFP-based laminate depends on roving type, stitching yarn type, roving path, and subsequently the stitching yarn path, which is a function of the adjustable machine parameter stitch distance d_S and stitch width w_S (see *Figure 3*). The roving distance d_R and stitch sequence between two adjacent rovings constitute further variables affecting the resulting morphology [2].

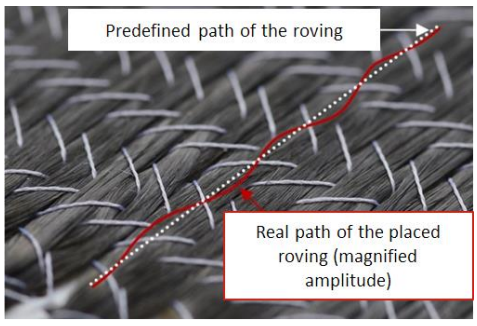

Figure 2 Waviness formation of a roving during fibre placement via TFP

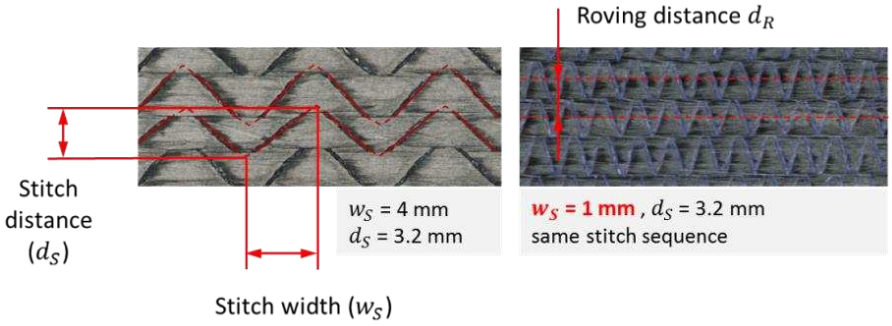

Figure 3 Description of the TFP parameter stitch distance d_S, stitch width w_S, roving distance d_S between two adjacent rovings

Experimental methods to estimate the waviness in prepreg-based laminates are described in [8]. In this work Leipprand et al. investigated the influence of three different w_S (3, 4 and 5 mm) on the waviness of TFP-based UD laminates. Based on the waviness data of the laminates determined in [8] and additional morphology data based on micro sections Uhlig et al. [2] developed a representative volume element (RVE) for TFP-based laminates to evaluate the geometrical influence of the local fibre volume content on the stress and strain distribution under uniaxial tensile loading in the elastic regime. The RVE consist of separate zones for the resin infiltrated roving, the base material and resin rich areas around the upper and lower stitching yarn. The in-plane waviness and the out-of-plane waviness of the roving reinforcement fibres are included in the RVE. Due to an almost equivalent tensile modulus of resin material and stitching yarn, they are combined and modelled as one volume in the RVE [2]. In Figure 4 three RVEs positioned adjacent with different visible layers are shown. While [2] and [8] giving fundamental information about the resulting morphology of TFP-based laminates, the experimentally investigated parameters of [8] did not exploit all manufacturing parameter possibilities of typical TFP devices.

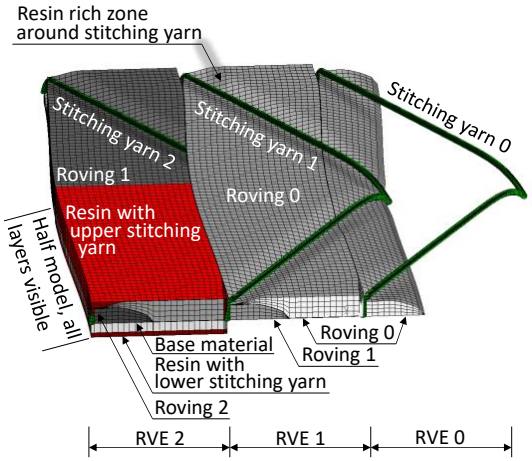

Figure 4 TFP-RVE - The illustration shows three RVEs positioned adjacent to each other with different visibility of the individual RVE layers. The stitching yarn is shown only in this illustration but is considered as resin material in the RVE [2].

In the present work, the influence of technically relevant TFP parameters on the deformation behaviour under uniaxial tensile loading and thus on the mechanical properties is investigated experimentally and numerically using the RVE developed by Uhlig et al [2]. Compared to the

  doi:10.5075/epfl-298799_978-2-9701614-0-0 published under CC BY-NC 4.0 license

experimental work of Leipprand et al. [8] the TFP parameter space is extended to include technical relevant short and long stitch widths. Furthermore, an improved test setup with significantly increased spatial resolution is used for the experimental analysis of the deformation behaviour.

2. Methodology

2.1 TFP laminate configuration

Six different TFP-based laminates were produced by using an 800 tex Toho Tenax® HTS carbon fibre rovings; 10 tex Amann® Serafil polyester stitching yarn; paper (base material); and epoxy resin Hexion EPR L20 with curing agent Hexion EPH 161. The roving distance in each laminate configuration was 2.2 mm. After preform manufacturing via TFP, the laminates were produced using Resin Transfer Molding (RTM) in a cavity with a constant thickness of 1 mm. The manufacturing conditions were identical to the laminates produced by Leipprand et al. [8]. All manufactured laminate configurations and their specifications are shown in

Table 1. Setup C1 is herein considered as the baseline configuration and all further setups vary in relation to Setup C1, whereby the variation is highlighted in bold letters in

Table 1.

Table 1 TFP Laminate configurations in this study, FVC stands for fibre volume content

Setup	Top view	Cross section	Stitch distance d_s [mm]	Stitch width w_s [mm]	FVC Lami-nate [%]	FVC TFP CF/EP Layer [%]
C1			3.2	4	35.6	54.0
C2		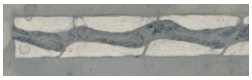	3.2	**1**	33.7	57.0
C3		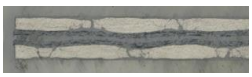	3.2	**2**	34.4	56.0
C4			3.2	**10**	35.4	53.1
C5	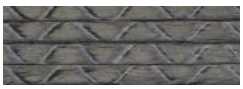	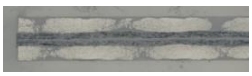	**2.8**	4	34.4	48.1
C6		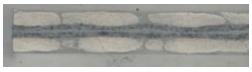	**4.6**	4	33.7	53.1

As it can be seen in the cross sections in

Table 1, an additional waviness perpendicular to the placement plane surface occurs at short stitch widths due to the high amount of stitching yarn (especially at C1). As shown in Table 1, the fibre volume content in the laminate is low due to the included embroidery base material (paper). Within the CF rovings deposited by TFP, the fibre volume content is between 48.1 % and 57.0 %. They differ due to the variation of sewing thread lengths, which are specified by the

  doi:10.5075/epfl-298799_978-2-9701614-0-0

TFP parameters. With increasing stitch width and/or decreasing stitch distance, the sewing thread length decreases and, in a cavity with constant volume, the volume available for the roving increases. After the laminate production, six specimens of each configuration were cut using a water-cooled diamond saw with dimensions according to DIN EN ISO 527-5 standard (length 250 mm, width 10 mm, thickness 1 mm). Afterwards all specimens received GF/EP end tabs in the clamping zone for a homogenous load transfer. Two specimens of each configuration were prepared with a speckle pattern for DIC analysis.

2.2 Experimental setup

Tensile properties in fibre direction were determined according DIN EN ISO 527-5 standard in standard climate conditions using a ZwickRoell tensile test rig with a 100 kN load cell and wedge jaws. Six specimens of each configuration were tested. A laser extensometer was used for global strain measurement. On two specimens of each configuration, the local deformation behaviour on the specimen surface was additionally investigated during the tensile tests with a 5 Megapixel GOM ARAMIS DIC system (sensor resolution 2448 x 2050 pixel, measurement field 20 x 15 mm). Prior to the tests the DIC system was calibrated. The calibration deviation was 0.03 Pixel. For the evaluation of the DIC results, a facet size of 40 pixels with a facet spacing of 25 pixels was set for all samples. Considering the image acquisition field, the strain reference length is 0.38 mm, which is equivalent to 50 Pixel. Based on the calibration, the average absolute error of the calculated strain data at the investigated load level is $\pm$ 0.06 %. Figure 5 exemplarily shows the area investigated by DIC with strain distribution results (strain in load direction) on a specimen from configuration C3. In parallel, the strain distribution results determined by means of the RVE with the same TFP parameter under identical loading conditions is shown. The RVE considers only one row of rovings within the sample.

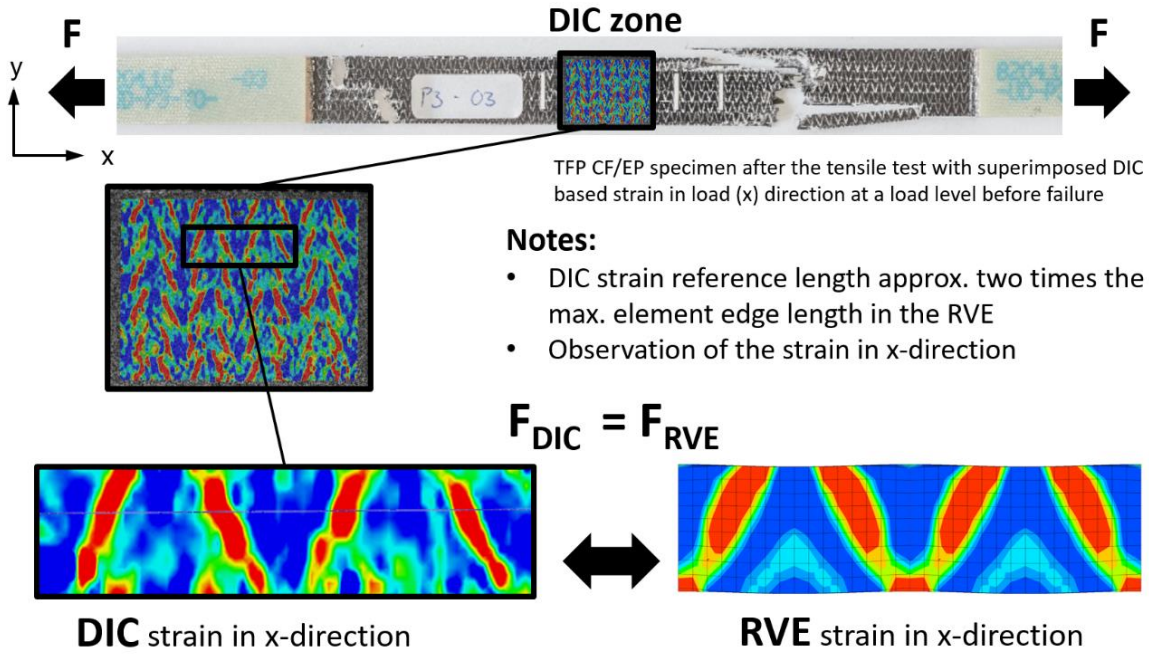

Figure 5 Superimposed DIC zone on an already tested specimen (C3) with displayed strain in load direction, additionally the RVE based result at identical load level and with identical scaling is shown

  doi:10.5075/epfl-298799_978-2-9701614-0-0

2.3 FE – Analysis setup

In this study, the RVE approach developed by Uhlig et al [2] is used. The RVE was developed using the ANSYS Parametric Design Language (APDL) of the commercially available Finite element software ANSYS. The RVE was set with the relevant material data (CF roving and EP matrix) and TFP parameter for each configuration. For modelling, an 8-node structural solid element with the option of orthotropic material properties (SOLID185) was chosen. Due to a detailed volume description, a regular mesh is ensured and the further alignment of each element coordinate system is possible. These element coordinate systems form the basis for the orthotropic material orientations. Here, the element edges of each element are used to form average vectors. The generated vectors are used to orientate the element coordinate system, whereas the x-axis is orientated in fibre direction. The element edge length is a maximum of 0.2 mm, which is approximately twice the value of the strain reference length of the DIC measurement. The element size was set to approximately 0.2 mm, which is half of the strain reference length. With the RVE the displacement volume of the stitching yarn induced waviness and the inhomogeneous fibre volume content in the resin infiltrated CF roving can be calculated (Figure 6).

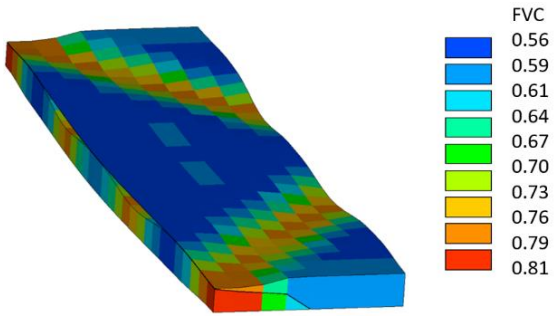

Figure 6 RVE - Local fibre volume content within the resin infiltrated CF roving at laminate C1, the waviness in the CF roving due to the displacement volume of the stitching yarn is visible

To compare the DIC results with the numerical derived RVE results an identical load was set in the simulation (see Figure 5). The chosen load was approximately at 80 % of the fracture load to reach sufficient strain values, which are above the noise level of the DIC system. The RVE also makes it possible to calculate the local stress in the fibres under tensile loading and thus to draw a conclusion about the achievable strength of the laminate in fibre-parallel direction.

3. Results

Table 2 summarizes the results of the study. In addition to fracture patterns, the numerically and experimentally determined characteristic values for tensile strength and tensile modulus are listed. The theoretically possible characteristic values with perfect unidirectional orientation (i.e. without any fibre waviness and fibre damage) are also listed. Furthermore, the deformation images determined by means of the RVE and the deformation images determined by means of the DIC with representation of the strain in the load direction and identical scaling are compared. The DIC results for configurations C1 to C3 show very good quantitative agreement with the deformation data determined by RVE. Strain concentrations occur in the stitching yarn environment and the stitching yarn course is perfectly recognizable in the DIC and RVE data. In configuration C4, due to the lower amount of stitching yarn and the reduced waviness, the strain

  doi:10.5075/epfl-298799_978-2-9701614-0-0

concentrations in the RVE are lower and the sewing thread course cannot be clearly found in the DIC images.

Table 2 Summary of the results

Configuration / Property	Unit/scaling	C1	C2	C3	C4	C5	C6
Fracture image							
Tensile strength Experiment	[N/mm²]	1223 ± 54	1184 ± 26	1260 ± 40	1267 ± 58	1204 ± 42	1144 ± 26
Tensile strength RVE	[N/mm²]	1206	1141	1200	1212	1186	1148
Tensile modulus Experiment	[N/mm²]	82325 ± 1279	77749 ± 1030	81500 ± 1170	82832 ± 698	80875 ± 2580	76660 ± 1836
Tensile modulus RVE	[N/mm²]	86802	77600	81854	90138	84083	80935
DIC strain in load direction	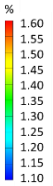	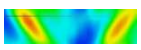		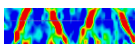	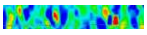	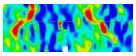	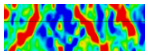
RVE strain in load direction		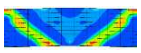		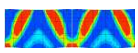		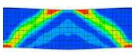	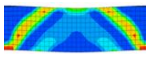

However, the differences are within the range of measurement uncertainty of the DIC system. In configurations 5 and 6, the sewing thread course can be recognized in the DIC images to some extent. The maximum and minimum strain values correspond to the RVE results, but the DIC data are of inferior quality here. The experimentally determined values for the tensile modulus for configuration C2 and C3 show very good agreement with the values determined by RVE. The difference between simulation and experiment for the other configurations amounts to a maximum of 8.2 % (configuration C3). The differences in tensile strength between simulation and experiment are smaller and do not exceed 4.4 %. Considering the fact that the waviness in the RVE was determined from micro sections and thus small deviations are possible in reality, and that effects such as broken filaments occurring during the TFP process are not considered here, the results obtained are very good. By using the RVE, the principal effects of different TFP parameters on the morphology and thus the mechanical properties can be reliably calculated. Concomitantly this work shows that DIC is a method to resolve strain inhomogeneities on the surface of TFP-based composites under deformation, if the spatial resolution is appropriate.

  doi:10.5075/epfl-298799_978-2-9701614-0-0

Acknowledgements

The authors wish to thank the Institute for lightweight engineering and polymer technology (TU Dresden) for the support while testing the samples. In parallel, the authors wish to thank Frank Engelmann from the IMA Dresden for production of the CF-EP laminates and our IPF colleague Nicole Schmidt for preparing the samples for testing.

4. References

1. Mattheij, P.; Gliesche, K. & Feltin, D., Tailored Fibre Placement - Mechanical Properties and Applications, Journal of Reinforced Plastics and Composites, 1998, 17-9, 774-786
2. K. Uhlig, M. Tosch, L. Bittrich, A. Leipprand, S. Dey, A. Spickenheuer and G. Heinrich, "Meso-scaled finite element analysis of fibre reinforced plastics made by tailored fibre placement.," Composite Structures, pp. 53-62, 2016.Mays GC, Hutchinson AR. Adhesives in civil engineering. Cambridge University Press. 1992.
3. P. Crothers, K. Dreschler, D. Feltin, I. Herzberg and M. Bannister, "The design and application of tailored fibre placement," in *Proceedings 11th International Conference on Composite Materials*, Gold Coast, Australia, 5 (1997), pp. 1-10.
4. K. Gliesche, T. Hübner and H. Orawetz, "Application of the tailored fibre placement (tfp) process for a local reinforcement on an open-hole tension plate from carbon/epoxy laminates," in *Composites Science and Technology 63*, 2003, pp. 81-88
5. L. Aschenbrenner, T. H. and R. Degenhardt, "Tailored fibre placement technology - optimisation and computation of cfrp structures," in *Proceedings Advances in Design and Analysis of Composite Structures - ESAComp Users' Meeting*, Braunschweig
6. A. Spickenheuer, M. Schulz, K. Gliesche and H. Heinrich, "Using tailored fibre placement technology for stress adapted design of composite structures," in *Plastics, Rubber and Composites 37-5/6*, 2007, pp. 227-232.
7. L. Bittrich, A. Spickenheuer, J. H. S. Almeida Jr, S. Müller, L. Kroll and G. Heinrich, "Optimizing variable-axial fibre-reinforced composites: the direct fibre path optimization concept," *Mathematical Problems in Engineering,* pp. 1-11, 2019.
8. Leipprand, A.; Spickenheuer, A.; Bittrich L.; Heinrich G.: „Experimental and numerical analysis of material properties of unidirectional composites manufactured by tailored fibre placement.” ANTEC - The plastics conference – Las Vegas, USA, 28.04.2014-30.04.2014, - S. 2591-2954, 2014

  doi:10.5075/epfl-298799_978-2-9701614-0-0

COMPARISON OF INTERLAMINAR AND INTERFACIAL SHEAR STRENGTH WITH RECYCLED CARBON FIBER

Jesse Savolainen[a], Sarianna Palola[a], Essi Sarlin[a]

a: Tampere University, Materials Science and Environmental Engineering, P. O. Box 589, 33101, Tampere, Finland – jesse.savolainen@tuni.fi

Abstract: *Testing the interlaminar shear strength (ILSS) of composites using a short beam shear (SBS) test takes time. Micro-scale interfacial shear strength values (IFSS) need to be scaled back to the macro-level if a more reliable picture of the composite behavior on the right scale is desired. Here, the objective is to find out what kind of relation the ILSS and the IFSS values have for recycled carbon fibers (rCF) and epoxy matrix. Factors affecting the reliability of both tests are considered.*

A slope-based method was used to obtain the IFSS values from the micro-scale results. The microbond test gave a 43.6 MPa IFSS value and the SBS test a 36.4 MPa ILSS value. There were a lot of variables associated with the SBS for rCF, due to which there is uncertainty in the results. The data from the microbond tests were more reliable due to the high sampling volume.

Keywords: ILSS; IFSS; recycled carbon fiber; short beam shear test; microbond test

1. Introduction

The importance of composite recycling has increased, which can be noticed in the legislation of the European union considering recycling and circularity. Pyrolytic recycling has been developed to recover carbon fiber, but it is known to have a detrimental effect on the mechanical properties of the fibers [1]. For recycled carbon fiber (rCF) to meet the mechanical requirements of the reuse application, the properties of different recycling batches should be tested reliably and quickly. The established method to test interlaminar shear strength (ILSS) of composites is the short beam shear (SBS) test, but there are problems [2] considering the test, such as identifying the failure mode of the sample and thus validating the result for ILSS. In addition, making the laminate samples takes time. The different manufacturing steps increase the possibility of distortion of the fabric and therefore deviation of the results. Testing the micro-scale properties and reliable scaling of results to the macro level will be able to save hours and avoid possible errors [7].

In this study, macro and micro-scale shear strength is compared for a rCF and reinforced epoxy matrix. Macro-scale data was obtained by SBS and ILSS values were calculated. Micro-scale data and the interfacial shear strength (IFSS) were analyzed by the slope-based approach of microbond test. Questions, how the traditional ILSS values relate to IFSS values, and what magnitude the results, are answered. The reliability of the results is also considered.

2. Materials and methods

2.1 Recycled carbon fiber and matrix

  doi:10.5075/epfl-298799_978-2-9701614-0-0

The original carbon fiber roll [4] (Toho Tenax, Japan) was pre-impregnated with epoxy, where the weight percentage of carbon fiber was 70%. Recycling was done using pyrolysis as part of the previous study conducted by Palola et al. [4]. The yield was 67% and the virgin carbon fiber fabric's weave was Twill. Other characteristics of the carbon fiber are noted in Palola's et al. publication [4].

The matrix was epoxy Araldite® LY 5052 and hardener Aradur® 5052 CH (Huntsmann, USA) and they were mixed by weight in a ratio of 100 to 38, respectively, as recommended by the manufacturer [5].

2.2 Short beam shear test

SBS samples were manufactured using vacuum assisted resin transfer infusion (VARI). Eight plies of rCF were dried in oven for 30 min at 100 °C and stacked in sequence of $[0°_8]$. Vacuum pressure of 0.6 bar was used. The laminate was cured at room temperature for 20 h and post-cured for 12 h at 60 °C. The ILSS was tested using a universal testing machine (Instron 5967, UK) according to standard ASTM D 2344 [7]. Nine samples were cut to approximate dimension of 12.5 mm x 4.2 mm with circular saw (Proxxon, Germany), which had a diamond coated blade. Average thickness for the samples was 2.14 mm. Three-point bending configuration was used with span length of 5.67 and displacement rate of 1.0 mm/min. The samples were pre-tensioned to 3 N to get the same initial set-up. ILSS is calculated using the Eq. (1):

$$ILSS = \frac{3}{4}\frac{F_{max}}{b*h}, \quad (1)$$

where F_{max} is the maximum force in the three-point bending, b and h are the sample thickness and width, respectively. The fiber weight percentage was calculated to be 59.4 % for the laminate.

2.3 Microbond test

The FIBRObond micro testing device (Fibrobotics, Finland) was used for microlevel adhesion testing [7] [8] to get IFSS. The operator disconnects individual epoxy droplets from the fiber by controlling the blades with piezoelectric locators. Figure 1. shows an illustrative picture of fiber, droplet, the sample holder, as well as the blades with which the droplet is removed.

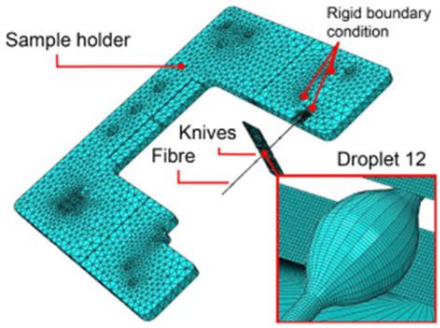

Figure 1. FIBRObond testing configuration [9].

The fibers were selected from a carbon fiber fabric area that represented the entire fabric. The droplets were prepared for six fibers after which they were cured at ambient laboratory temperature for 60 h. The same epoxy was used for laminates. The force-displacement curve of

  doi:10.5075/epfl-298799_978-2-9701614-0-0

each droplet was recorded with a 1 N force cell (Futek jr. S-beam, USA) and droplet length was measured using machine vision. The displacement rate was 0.008 mm/s. The six individual rCF filaments were tested and each filament contained 8 - 40 tested droplets. To calculate IFSS, a slope-based approach was used, where the maximum force to detach each droplet is drawn on the graph as a function of the droplet's surface area. Linear regression fit is then used to get IFSS. The microbond data is further discussed in [4].

2.4 Scanning electron microscopy

To ensure the fracture mode of the SBS samples were interlaminar, a scanning electron microscopy (SEM, Zeiss ULTRAplus, Germany) was used. Pictures of the fracture surfaces were taken from the samples L6, L7 and L8 (see Table 1.). In addition, one cross-sectional sample was prepared from the laminate to ensure the matrix's adhesion to fibers is sufficient. The cross-section sample was cut from the laminate using a diamond coated blade and was cast in transparent resin EpoFix (Struers, Denmark) in vacuum impregnation unit CitoVac (Struers, Denmark). A vacuum pressure of 0.2 bar was used. After curing at room temperature for 4 days the cross-section sample was sanded with water using #500, #1000, #2000, and # 4000 grit paper and polished with polishing cloth and 3 µm and 1 µm diamond suspension in succession. The SEM samples were coated with a ~3 nm layer of palladium and platinum mixture (ratio: Pt/Pd 80/20 wt%).

3. Results and discussion

3.1 Interlaminar shear strength

The SEM images confirmed the matrix had wet the fiber and the laminates were of high quality (see Figure 3. a) and 3.b)). The dominant fracture mode for the tested samples was noted to be an interlaminar fracture in the three samples imaged.

In Figure 2. are the SBS samples' flexural stress and strain behavior. The samples L4 and L9 had 30 % force drop during the test, which caused the test to stop. This limit was user-defined according to standard ASTM D 2344 [7]. Samples L5 and L8 have a different flexural behavior after 1 mm of flexural elongation compared to other samples as seen in Figure 2. This can be explained by the difference in the thicknesses. L5 is thicker (2.31 mm) and L8 is thinnest (2.05 mm).

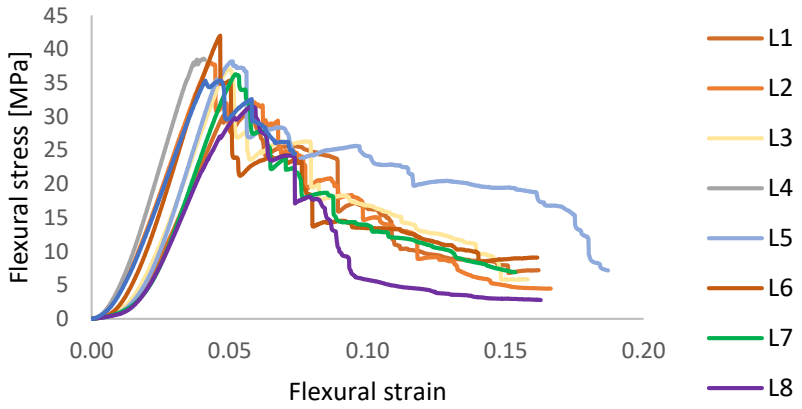

Figure 2. ILSS samples' flexural stress as a function of flexural strain.

Table 1: SBS samples' dimensions, ILSS values, mean (x), standard deviation (s) and coefficient of variation (CV).

Sample	Lenght [mm]	Thickness [mm]	Width [mm]	ILSS [MPa]	x [MPa]	s	CV [%]
L1	12.59	2.15	4.37	30.28			
L2	12.67	2.13	4.35	38.07			
L3	12.57	2.13	4.35	37.03			
L4	12.45	2.08	4.10	38.59			
L5	12.50	2.31	4.07	38.18	36.36	3.62	9.96
L6	12.46	2.14	4.20	42.00			
L7	12.35	2.03	4.00	36.28			
L8	12.48	2.05	4.09	31.53			
L9	12.81	2.24	4.24	35.32			

The laminate had abnormal epoxy-free area that is depicted in Figure 3. c). The lowest carbon fiber layer was distorted during layup or infusion. Whether there are distortions in other layers of the laminate was unknown. However, this is one good example of the challenging sample preparation of the SBS test with rCF. The uneven quality and the surface of the fiber can cause uneven distribution of the load in the sample and increase the likelihood of stress concentrations [10]. In this case, the laminate is also more likely to break under the load when compared to virgin carbon fiber. Palola et al. observed surface unevenness on individual rCF [4].

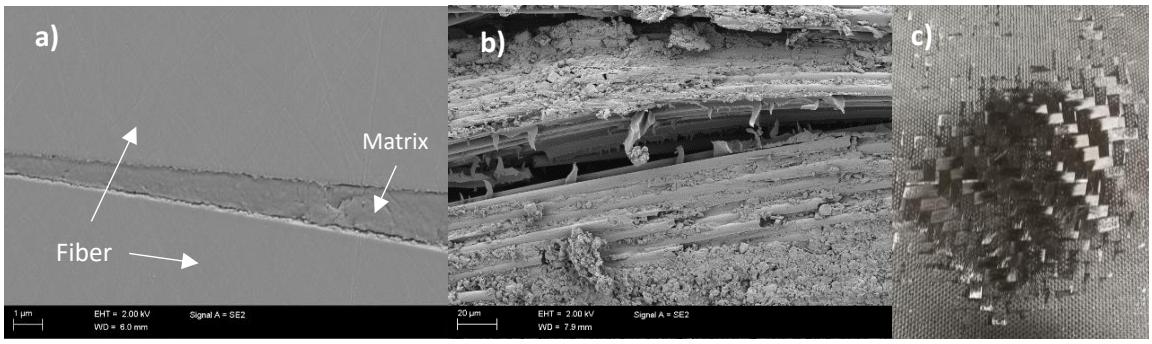

Figure 3. a) SEM image from the cross section of the laminate, b) fracture surface with interlaminar debonding, and c) distorted ply where there is little to no resin.

Factors affecting ILSS are, among other things, carbon fiber fabric weaving, reinforcement layup, and thickness [2]. Carbon fibers have low surface activity and adhesion to resins, which decreases ILSS [10] and IFSS. Also, the recycled carbon fiber fabric was not of the best quality. Instead, there were obvious gaps, which are due to the method of recycling the carbon fiber. Since carbon fiber fabric weaving was not the best possible the poor quality might have had some effect on ILSS, although good areas of fabric were selected visually for the laminate plies.

3.2 Interfacial shear strength

  doi:10.5075/epfl-298799_978-2-9701614-0-0

The IFSS was 43.6 MPa and had a standard deviation of 2.5 MPa [4] (see Table 2.). Palola et al. conducted the microbond tests on rCF and analyzed the results and considered the factors that contributed to them in their study. The strength of recycled carbon fiber had been eroded in recycling because the embedded length of the largest droplets the fiber withstood during the test was 42 µm. Palola et al. noticed a 60 % drop in tensile strength of the rCF compared to virgin carbon fiber [4]. The FIBRObond measuring device was able to achieve good linear regression, which the disturbance term (R^2) indicates, although the rCF had significantly lower tensile strength.

Laurikainen et al. [8] address the high scatter and error sources of microbond testing in their study, as well as the factors contributing to these. The high scatter of the microbond test was largely due to variation in the quality of fibers and the quality of the fiber surfaces, rather than the FIBRObond measurement apparatus itself. The total number of droplets they tested was 1527.

Table 2: The results of the microbond test for rCF with number of tested droplets, IFSS values, disturbance terms (R^2), mean (x) and standard deviation (s) [4].

Sample	Number of tested droplets	IFSS [MPa]	R^2	x [MPa]	s
M1	8	41.5	0.89	43.6	2.5
M2	11	40.6	0.93		
M3	44	37.6	0.95		
M4	31	50.9	0.97		
M5	43	41.2	0.95		
M6	40	49.7	0.98		

3.3 Comparison between micro and macro-scale

Measured ILSS was 16.6 % lower compared to IFSS gotten from the microbond test. A bar chart with the shear strengths and standard deviations is presented in Figure 4. The coefficient of variation (CV) for the microbond results was 5.7 % and for the SBS 9.96 %. The higher CV for SBS can be explained by other fracture modes that might have be present but were not noticed on SEM. rCF is more vulnerable to uneven stress distribution in the SBS since fibers might break in a longitudinal direction during loading. The microbond test ensures comparability between results with identical loading scenarios.

The effect of carbon fiber fabric quality makes comparing different recycled batches challenging with the SBS, as the laminate can have bad areas, where weaving has gaps and distortion. Producing the SBS samples could be impossible if there is not enough good fabric to make the samples. The effect of weaving must also be considered in the SBS, as it is known to affect the distribution of stresses between the matrix and the reinforcement [2]. The microbond test eliminates the effects of weaving quality and stacking sequence of the laminate.

  doi:10.5075/epfl-298799_978-2-9701614-0-0

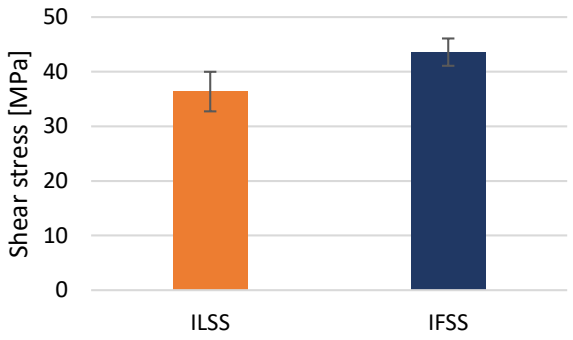

Figure 4. ILSS and IFSS values with standard deviation.

The uneven surface of rCF has a different effect in both tests. In the microbond test, the effect of the uneven surface is emphasized compared to other contributing factors. The uneven surface allows resin droplets to attach to the fiber better through mechanical interlocking, which increases the force required to remove the droplet. The results show to have a good linear fit. The average R^2 value is 0.94. A conclusion about the similar attachment of droplets to the fiber between different samples can be drawn. In the SBS, an uneven surface might increase the likelihood of uneven distribution of the load in the fibers, and thus increases the probability of stress concentrations. The contact stress from the loading points of the SBS will also negatively affect the stress distribution lowering the ILSS and inducing unwanted fracture modes [2].

Stojcevski et al. [11] compared the shear stresses and test methods in the micro-, meso- and macro-scales for carbon fiber and epoxy matrix. The sizing concentrations and the surface treatment of carbon fibers were varied. There were also unsized and carbon fibers. As a micro-scale test, they used a single fiber fragmentation test (SFFS). In their article, they found the shear strength for the unsized fibers to be higher at the macro-scale, than the shear strength of the micro-scale with each surface treatment. Their results differ from the results of this research, where macro-scale results were lower compared to the micro-scale. This is explained by significantly different micro-scale testing methods. The microbond test gives higher results when compared to SFFS. The matrix used was not the same as in this study, but epoxy, nonetheless. The adhesion mechanism can be assumed to be the same for the functional groups on the interface, so a careful comparison can be made between the results.

4. Conclusions

In this study, ILSS and IFSS values were compared, ILSS being 16.6 % lower than IFSS. The microbond test does not consider the volume fraction of fibers, which significantly affects the shear strength on the macro-scale. The fibers carry the load and the more reinforcement there is, the stronger the composite will be. However, SBS sampling is challenging on rCF if there are unevenness and distortion in the fabric. Because of this, the microbond test is a more reliable way to obtain shear strength for a given system when there are no resources in use to verify the quality of the laminate and tested samples and the fabric used is of poor quality. This allows the fiber recycler to compare reliably different manufacturing parameters' effects on shear strength.

Reliability is also increased by many measuring points in the microbond test. The FIBRObond testing device removes the possibility of uneven stress distribution, which produces unwanted fracture modes. In addition, a significant number of droplets from different sizes are tested in

  doi:10.5075/epfl-298799_978-2-9701614-0-0

the microbond test, allowing the use of reliable linear regression. The results are statistically averaged by the many data points and gives a sufficient view of the fiber's interfacial strength when several fibers are tested from different places of fabric, as was done in this study.

Acknowledgements

This research was partly funded by EU H2020-IND-CE project "FiberEUse" (grant agreement number 730323). This work made use of the Tampere Microscopy Center facilities at Tampere University (33014 Tampere, Finland).

5. References

1. Pimenta S, Pinho ST. The effect of recycling on the mechanical response of carbon fibres and their composites. Composite Structures 2012; 12: 3669-3684.
2. Kadlec M, Nováková L, Růžek R. An experimental investigation of factors considered for the short beam shear strength evaluation of carbon fiber-reinforced thermoplastic laminates. Journal of testing and evaluation 2014; 3:580-592.
3. Jawaid M, Thariq M, Saba N. Mechanical and physical testing of biocomposites, fibre-reinforced composites and hybrid composites. Woodhead Publishing. 2019: 377, 380.
4. Palola S, Matrenichev V, Laurikainen P, García-Arrieta S, Elizetxea C, Sarlin E. Properties of pyrolytically recycled carbon fiber and their re-use in composites. SAMPE Europe Conference 2019.
5. Advanced materials Araldite ® LY 5052 / Aradur ® 5052* Cold curing epoxy systems, Huntsman. 2012.
6. ASTM D 2344/D 2344 M. Standard test method for short-beam strength of polymer matrix composite materials and their laminates. American Society for Testing and Materials. 2000.
7. von Essen M, Sarlin E, Tanhuanpää O, Kakkonen M, Laurikainen P, Hoikkanen M, et al. Automated high-throughput microbond tester for interfacial shear strength studies. SAMPE Europe Conference 2017.
8. Laurikainen P, Kakkonen M, von Essen M, Tanhuanpää O, Kallio P, Sarlin E. Identification and compensation of error sources in the microbond test utilising a reliable high-throughput device. Composites Part A: Applied science and manufacturing 2020; 137 :105988
9. Kanerva M, Korkiakoski S, Lahtonen K, Jokinen J, Sarlin E, Palola S, et al. DLC-treated aramid-fibre composites: tailoring nanoscale-coating for macroscale performance. Composites science and technology 2019; 171: 62-69.
10. Wang R, Zheng S, Zheng Y. Polymer matrix composites and technology. Wood-head Publishing 2011; 65, 176.
11. Stojcevski F, Hilditch T, Henderson L. A comparison of interfacial testing methods and sensitivities to carbon fiber surface treatment conditions. Composites Part A: Applied Science and Manufacturing 2019; 118: 293-301.

  doi:10.5075/epfl-298799_978-2-9701614-0-0

EXPERIMENTAL INVESTIGATION OF SHIELDING EFFECTIVENESS OF CARBON/EPOXY COMPOSITE MATERIALS

Gang Zhou[a], Ewa Mikinka[a], Xujin Bao[b], Weiwei Sun[c]

a: Department of Aeronautical and Automotive Engineering, Loughborough University, Loughborough LE11 3TU, UK – E.E.Mikinka@Lboro.ac.uk
b: Department of Materials, Loughborough University, Loughborough LE11 3TU, UK
c: C-Power Ltd, No 5 Huake Si Road, Tianjing, China

Abstract: *Limited research in the shielding effectiveness (SE) of carbon/epoxy composite laminates is available but an in-depth understanding of complex nature of shielding mechanisms relating to laminate details is not. This paper investigated the SE of carbon/epoxy laminates against electromagnetic waves using the 2 port coaxial transmission line method for the range of frequencies between 30 MHz and 1.5 GHz. Laminate panels of two different thicknesses were used, each in both cross-ply and quasi-isotropic lay-ups. The anisotropic nature of electrical conductivity of these panels was also characterised. The obtained scattering parameters were analysed to differentiate the contributions of reflection and absorption modes. It was found that SE was dominated by the absorption losses with the reflection losses making only the small contribution. Both lay-up and laminate thickness had only modest effects, due to that the significant part of incident electromagnetic power was consumed by the reflection losses.*

Keywords: carbon/epoxy; composites; shielding effectiveness; electrical conductivity; electromagnetic interference.

1. Introduction

The shielding of operationally vital electronic devices against the interference of electromagnetic waves (EMI) has been tremendously important in various industrial sectors for decades [1-14]. Examples include navigation, radar, telecommunication systems, wireless electronic devices and mobile phones. The requirements of their shielding performances vary, dependent on the size, frequency and shielding protection level, among others. While shielding enclosures for less demanding applications are often made of conductive metal-coated thermoplastics, for relatively large operationally vital electronic systems, conductive metals have been used for enclosure structures. With the increasing development of high-speed and greater-power electronic systems with ever greater number of functionality, lightweight carbon fibre reinforced composite structures have attracted the significant attention for replacing heavy and corrosion-sensitive metallic enclosures. However, due to their electrically anisotropic nature, an analytical assessment of their shielding effectiveness (SE) is very challenging. This study aimed investigating the SE characteristics of anisotropic carbon/epoxy laminate plates with two different thicknesses, each of two lay-ups. Focus was on the contributions of different shielding modes to SE. Both data and knowledge of this investigation would be essential to eventual design and manufacture of composite enclosure structures.

2. Composite materials and specimen preparations

  doi:10.5075/epfl-298799_978-2-9701614-0-0

Carbon/epoxy laminates were made of unidirectional tape-based LTM45/34–700 prepreg with a nominal ply thickness of 0.128mm. Individual plies with the dimensions of 300 × 300 mm were laid up in a lay-up of either cross ply (CP) or quasi-isotropic (QI) and the laminate stacks were cured in an autoclave at 60°C under the pressure of 0.62 MPa for 16 hour to have a nominal thickness of 2.0 mm for the 16 ply and 1.0 mm for the 8 ply laminate, respectively. The load (aka test) and reference plates shown in Figure 1 were cut from the 300 x 300mm laminates using a CNC machine. For electrical conductivity measurement, rectangular coupon samples in various sizes were cut with a water-cooled diamond bench saw and the four larger surfaces of each specimen were milled to improve their flatness and parallel. Silver paint (RS PRO silver conductive paint) was applied on the contact surfaces for the half of all samples to reduce contact resistance.

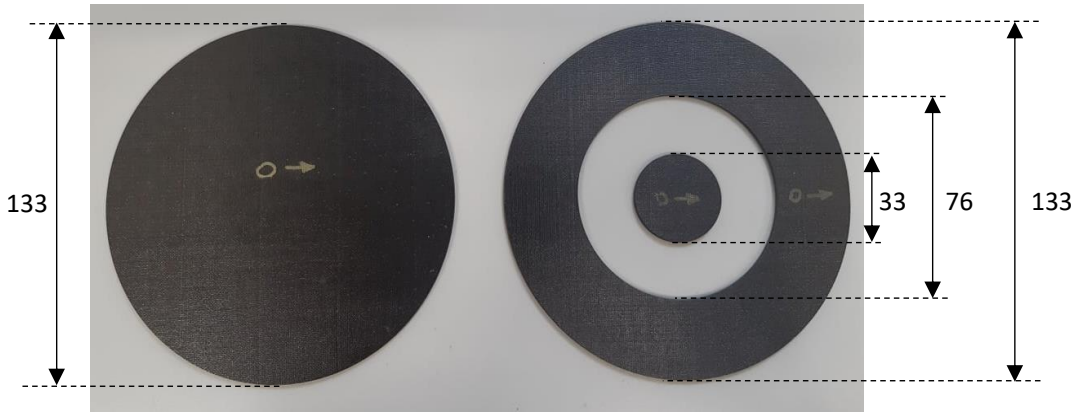

Figure 1. Load and reference plates used for SE measuremenint (all dimensions in mm)

3. Shielding effectiveness measurement and experimental set-up

3.1 Method of shielding effectiveness assessment

It is well known that when EM waves impinges the surface of a structure made of isotropic and homogeneous conductive material, part of the waves are reflected (R) at the surface, whereas the remaining penetrate into the thickness of the structure and that if either the intensity or power of the EM waves is high or the thickness of the structure is thin, part of the penetrated waves would transmit through the distal surface of the structure (T), as shown in Figure 2. The difference of the two is regarded as absorbed (A), with the overall power balance of R + A + T = 1. For current layered composite laminates, these physical mechanisms ought to be similar. Moreover, the fibre-matrix interfaces symbolised by the interior black vertical lines could increase interior reflections or diffractions. For a shielding of a layered composite laminate, none of EM waves is supposed to transmit through its thickness and thus this perception is represented by the summary of three contributing energy or power losses via surface reflections, penetrative absorptions and multiple interior reflections or diffractions in Eq. (1). This equation has been used to exhibit the SE.

$$SE = SE_R + SE_A + SE_{MR} \quad (1)$$

  doi:10.5075/epfl-298799_978-2-9701614-0-0

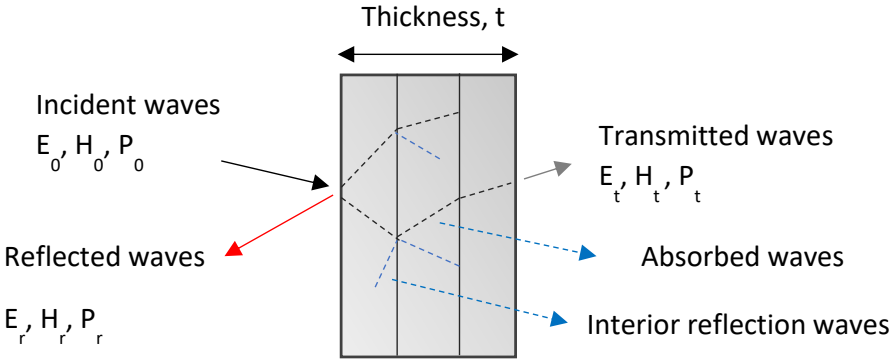

Figure 2. Electromagnetic shielding process

As the surface reflection loss SE_R is dependent on the mismatch of impedance between wave propagation medium of air η_0 and shielding material η_s, it could be defined by

$$SE_R = 20\log\left[\frac{(\eta_o+\eta_s)^2}{4\eta_o\eta_s}\right],\ \eta_s = \sqrt{\frac{j\omega\mu}{\sigma+j\omega\varepsilon}} \quad (2)$$

Where σ is the electrical conductivity of the shielding material, ε dielectric permittivity, μ magnetic permeability and ω the angular frequency of the incident EM waves. For a highly conductive material, we have $\eta_o \gg \eta_s$ and $\sigma >> j\omega\varepsilon$. Thus, Eq. (2) becomes

$$SE_R = 20\log\left(\frac{\eta_o}{4\eta_s}\right) = 20\log\left(\frac{\eta_o}{4\times\sqrt{\frac{j\omega\mu}{\sigma}}}\right),\ \eta_o = \sqrt{\frac{\mu_o}{\varepsilon_o}} = 377\Omega \text{ with } \sigma << j\omega\varepsilon \text{ for air} \quad (3)$$

As carbon/epoxy laminates is largely non-magnetic, the reflection loss takes the form of

$$SE_R = 50 + 10\ log_{10}\left(\frac{\sigma}{f}\right) \quad (4)$$

in which f denotes frequency. The absorption loss SE_A is attributed to the Joule heating loss generated in the shield and to the interaction between the EM field and electric and/or magnetic dipoles (polarisation loss). Since such absorption loss decreases exponentially with the increase in the shield thickness t, it is given by

$$SE_A = 20\log\left(e^{-\frac{t}{\delta}}\right) = 20\frac{t}{\delta}\log(e),\ \delta = \sqrt{\frac{1}{\pi\mu f\sigma}} \quad (5)$$

where the penetration depth δ is dependent on magnetic permeability μ. If the intensity of incident EM waves could be reduced to 37% of its original strength in non-magnetic shielding material [5,13-14], Eq. (5) becomes

$$SE_A = 15.4\ \times t \times \sqrt{\mu f\sigma} = 1.7 \times t \times \sqrt{f\sigma} \quad (6)$$

The energy loss associated with multiple interior reflections or diffractions SE_{MR} is related to the impedance mismatch at the fibre-matrix interfaces and is given by

$$SE_{MR} = 20log\left|1 - \frac{(\eta_s-\eta_o)^2}{(\eta_s+\eta_o)^2}e^{-\frac{2t}{\delta}}\right| \quad (7)$$

As a result, Eq. (1) becomes

$$SE = 50 + 10\ log_{10}(\frac{\sigma}{f}) + 1.7 \times t \times \sqrt{f\sigma}\ + 20log\left|1 - \frac{(\eta_s - \eta_o)^2}{(\eta_s + \eta_o)^2} e^{-\frac{2t}{\delta}}\right| \quad (8)$$

Since, realistically, it is extremely difficult to differentiate the mechanism of interior penetrative absorptions from the mechanism of multiple interior reflections or diffractions, they are not distinguished here. In this way, a simpler form of the SE can be obtained

$$SE = 50 + 10\ log_{10}(\frac{\sigma}{f}) + 1.7 \times t \times \sqrt{f\sigma} \quad (9)$$

3.2 Experimental set-up of shielding effectiveness measurements

The SE measurements were carried out using a coaxial transmission line apparatus, which was designed and manufactured according to the ASTM D4935 standard for planar materials [15]. The 2 port set-up, which is illustrated in Figure 3, consisted of ZNLE3 vector network analyser (VNA) coupled with a flanged coaxial specimen holder made of brass. Before measurement, VNA was calibrated using a dedicated calibration kit. All measurements were performed with 1 kHz bandwidth and input power of 0 dBm in the frequency range from 30 MHz to 1.5 GHz. The quantities of the total shielding (SE), absorption (SE_A) and reflection (SE_R) loss were obtained from scattering parameters using the following expressions [12]:

$$SE = 10log\left(\frac{P_\mathrm{I}}{P_\mathrm{T}}\right) = 10\log\left(\frac{1}{\mathrm{T}}\right) = 10\log\left(\frac{1}{|S_{21}|^2_{load}}\right) - 10log\left(\frac{1}{|S_{21}|^2_{ref}}\right) \quad (10)$$

$$SE_R = 10log\left(\frac{P_\mathrm{I}}{P_R}\right) = 10\log\left(\frac{1}{1-\mathrm{R}}\right) = 10log\left(\frac{1}{1-|S_{11}|^2_{load}}\right) - 10log\left(\frac{1}{1-|S_{11}|^2_{ref}}\right) \quad (11)$$

$$SE_A = 10log\left(\frac{P_\mathrm{I}}{P_\mathrm{A}}\right) = 10\log\left(\frac{1}{\mathrm{A}}\right) = 10\log\left(\frac{1-\mathrm{R}}{\mathrm{T}}\right)$$

$$= 10\log\left(\frac{1-|S_{11}|^2_{load}}{|S_{21}|^2_{load}}\right) - 10\log\left(\frac{1-|S_{11}|^2_{ref}}{|S_{21}|^2_{ref}}\right) \quad (12)$$

in which S_{11} is the reflection coefficient (i.e. the ratio of the reflected to the input power), S_{21} is the transmitted coefficient, P denotes EM power with subscripts I, R, A and T indicating incident, reflected, absorbed and transmitted values, respectively.

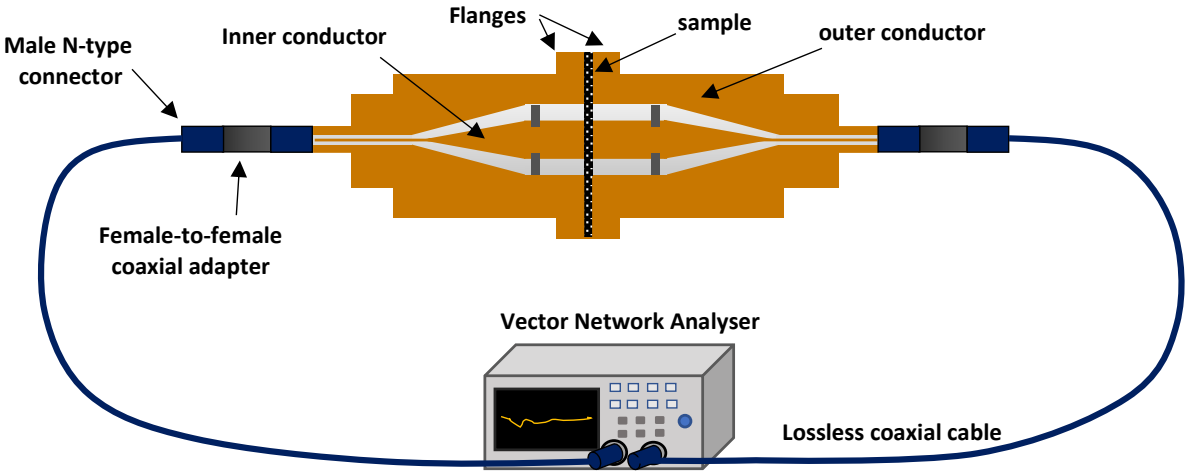

Figure 3. Coaxial transmission line method for measuring shielding effectiveness

4. Results and discussion

4.1 General characteristics of SE responses

Figure 4 shows the reflection and absorption attenuation spectra in the frequency range of 30-1500 MHz for a 8 ply laminate in a lay-up of QI. In the figure, it can clearly be seen that the spectra are oscillatory initially in the region between 30 and 150 MHz and then settled to remain steady for the rest of the frequency range. In particular, the reflection part was small, whereas the absorption part was very dominant, with the SE of about 60 dB. Similar results were reported in [10] for similar carbon/epoxy plates. For the laminates of twice the thickness, the overall attenuation characteristics shown in Figure 5 are very similar, except that the SE had gone up by about 10 dB, as expected. Further observations of the surface reflection losses of the CP laminate plates confirmed that the reflection loss was not altered when lay-up was switched. Moreover, the surface reflection losses consumed the overwhelming majority of the incident EM intensity or power, as shown in Figure 6. As a result, these findings appeared to suggest that in this frequency range, even the 16 ply thick carbon/epoxy laminates could be excellent in the performance of SE. In addition, it appeared that the increase in frequency could lead to the reduction in electrical conductivity values [16]. These opposite trends, when taken into account into Eq. (6), might have a cancelling effect so that they showed little net effect.

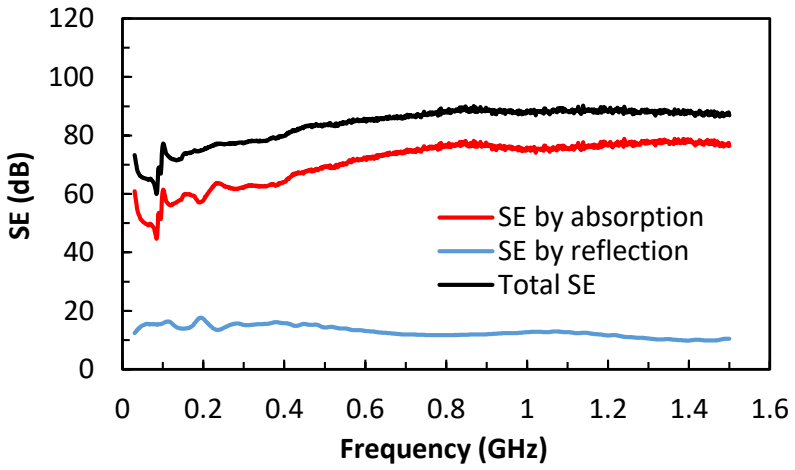

Figure 4. Attenuation spectra with two different shielding modes in a 8 ply QI laminate

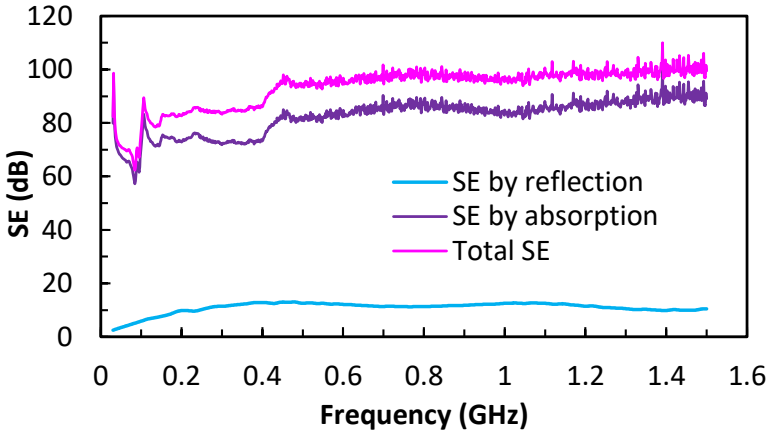

Figure 5. Attenuation spectra with two different shielding modes in a 16-ply QI laminate

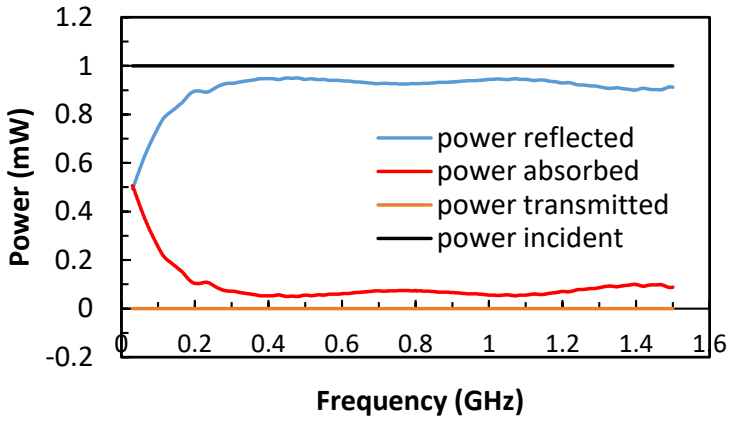

Figure 6. Incident, reflected, absorbed and transmitted power for a 16-ply QI laminate

4.2 Effects of lay-up and thickness on SE

The present carbon/epoxy laminates had the in-plane fibres oriented either in the two orthogonal directions (CP) or in four directions with a 45^0 ply-to-ply increment (QI) but had no fibres in the TTT direction. As a result, the forward transmission direction of the EM waves was nearly insulative, though the fibre surface-to-fibre surface distances in the TTT direction could be as small as less than one hundred micron so that dielectric breakdown of epoxy and fibre-to-fibre contact provided some limited electric current path network. This is why the average in-plane electrical conductivity value of 16 ply QI carbon/epoxy laminates was 11064 S/m, whereas the average TTT electrical conductivity value was only 37 S/m, which was nevertheless still many orders of magnitude greater than a nominal value of 1.4×10^{-12} S/m for current epoxy [17]. These characteristics coincided with the present SE measurements in such a way that not only the surface reflection loss consumed the majority of incident EM power but also the lay-up effect shown in Figure 8 appeared to be marginal, as expected.

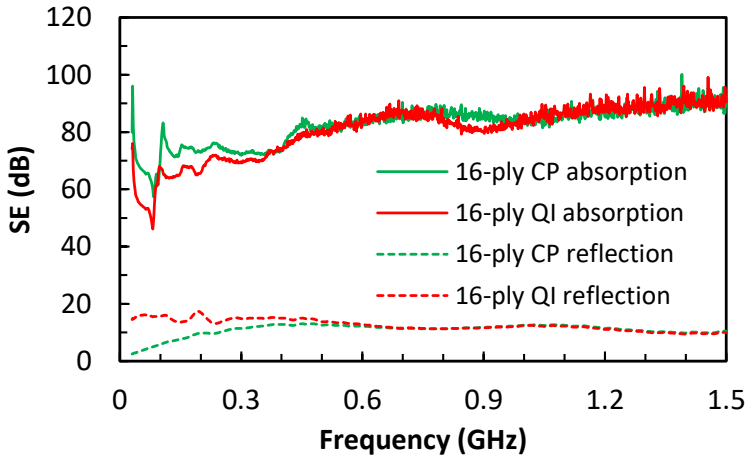

Figure 7. Lay-up effect of SE in 16 ply CP and QI laminates

For the same reasoning relating to the anisotropic electrical conductivity values, doubling the laminate thickness was found to generate only a very modest SE enhancement by about 10 dB, as shown in Figure 8. Predictions of Eq. (6) for conductive shields were such that doubling the thickness could double SE_A at the same frequency. However, for the present anisotropic laminates with very modest electrical conductivities, doubling the thickness led only modest

enhancement on the absorption losses. In addition, not much difference in absorption loss was observed between CP and QI lay-ups, as expected.

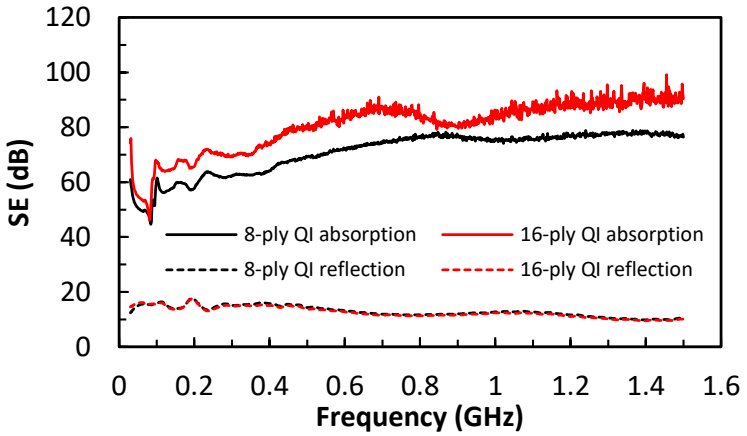

Figure 8. Reflection and absorption for 8 and 16 ply QI composites

5. Closing remarks

Carbon/epoxy laminates of two different thicknesses, each in both CP and QI lay-ups, have been evaluated for SE using the 2 port coaxial transmission line method for the range of frequencies between 30MHz and 1.5GHz. The obtained scattering parameters were analysed and the contributions of reflection and absorption mechanisms to SE were differentiated. It was found that the shielding performance of these laminates was completely dominated by the absorption losses, whereas the reflection losses made only the small contributions. Both lay-up and laminate thickness had only modest effects, due to that the significant part of incident electromagnetic power was consumed by the reflection losses. These findings offered a comprehensive insight into the shielding properties of carbon/epoxy laminates, which will be vital to design and manufacture of composite enclosures.

Acknowledgements

The first author would like to acknowledge the financial support from the C-Power Ltd and Loughborough University for this project.

5. References

1. Schelkunoff S. The electromagnetic theory of coaxial transmission lines and cylindrical shields. Bell System Technical Journal 1934; 13:532-579.
2. Schulz R, Plantz V, Brush D. Shielding theory and practice. IEEE Transactions on Electromagnetic Compatibility 1988; 30:187-201.
3. Celozzi S, Araneo R, Lovat G. Electromagnetic shielding, Encyclopedia of RF and Microwave Engineering. IEEE Press. 2005.
4. Tong X. Advanced materials and design for electromagnetic interference shielding. CRC Press. 2016.
5. Guan H, Chung D. Effect of the planar coil and linear arrangements of continuous carbon fiber tow on the electromagnetic interference shielding effectiveness, with comparison of carbon fibres with and without nickel coating. Carbon 2019; 152:898-908.

  doi:10.5075/epfl-298799_978-2-9701614-0-0 published under CC BY-NC 4.0 license

6. Luo X, Chung D. Electromagnetic interference shielding using continuous carbon-fibre carbon-matrix and polymer-matrix composites. Composites Part B 1999; 30:227-231.
7. Kim H, Shin H, Kim G, Park H, Moon H, Kwac L. Electromagnetic interference shielding characteristics for orientation angle and number of plies of carbon fiber reinforced plastics. Carbon Letters 2014; 15:268-276.
8. Chung D, Eddib A. Effect of fiber lay-up configuration on the electromagnetic interference shielding effectiveness of continuous carbon fiber polymer-matrix composites. Carbon 2019; 141:685-691.
9. Angulo L, Francisco P, Gallardo B, Martinez D, Cabello M, Bocanegra D, Garcia S. Modelling and measuring the shielding effectiveness of carbon fiber composites. IEEE Journal on Multiscale and Multiphysics Computational Techniques 2019; 4:207-213.
10. Gallardo B, Francisco P, Romero S, Rebate I, Somolinos D, Martinez D. Limitations in the shielding effectiveness measurement methods for carbon fiber composites. IEEE Electromagnetic Compatibility Magazine 2021; 10:52-61.
11. Tserpes K, Tzatzadakis V, Bachmann J. Electrical conductivity and electromagnetic shielding effectiveness of bio-composites. Journal of Composites Sciences 2020; 4:28-36.
12. Ni Q, Inoue M, Zhang L. Electromagnetic shielding property of CFRP composite laminates, 18th International Conference on Composite Materials, South Korea, August 2011.
13. Munalli D, Dimitrakis G, Chronopolous D, Greedy S, Long A. Electromagnetic shielding effectiveness of carbon fibre reinforced composites. Composites Part B 2019; 173:106906.
14. Li Z, Haigh A, Soutis C, Gibson A. X-band microwave characterization and analysis of carbon fibre-reinforced polymer composites. Composite Structures 2019; 208:224-232.
15. -. American Society for Testing and Materials. ASTM D4935-18 Standard test method for measuring the electromagnetic shielding effectiveness of planar materials. American Society for Testing and Materials 2018.
16. Headifen GR, Fahrenthold EP. Mechanical and electrical properties of glass and carbon fiber-reinforced composites. ASME Transaction, Journal of Energy Resources Technology 1991;113:176-181.
17. Todoroki A, Yoshida J. Electrical resistance change of unidirectional CFRP due to applied load. JSME International Journal 2004; 47:357–364.

  doi:10.5075/epfl-298799_978-2-9701614-0-0

INTERFACIAL SHEAR STRENGTH OF FLAX FIBRE WITH SUSTAINABLE MATRICES

Ali Kandemir[a], Marco L. Longana[a], Ian Hamerton[a], Stephen J. Eichhorn[a]

[a] Bristol Composites Institute, Department of Aerospace Engineering, School of Civil, Aerospace, and Mechanical Engineering, University of Bristol, Queen's Building, University Walk, Bristol BS8 1TR, UK – presenter email: ali.kandemir@bristol.ac.uk

Abstract: *In this study, the interfacial properties of a sustainable natural fibre, based on flax, with three potentially sustainable advanced matrices are examined. These commercial advanced matrices are (i) a vitrimer that combines the beneficial properties of both thermosets and thermoplastics, (ii) an entirely bio-based thermoset, and (iii) an advanced thermoplastic resin, are investigated for sustainable high-performance fibre reinforced polymer composites. Each of the selected matrices offers either recyclability, repairability, reusability, or the use of renewable sources and a reduction in the emissions of volatile organic compounds. Microbond tests are used to evaluate the interface performance of flax fibres coupled with each of the three matrices: interfacial shear strength and critical fibre length are reported. In conclusion, it is found that the vitrimer and the bio-based thermoset matrices have better adhesion with flax fibre compared to a traditional epoxy matrix, and the advanced thermoplastic resin shows the poorest adhesion with flax fibre.*

Keywords: bio-based; flax; interfacial properties; sustainability; vitrimer

1. Introduction

Sustainability in fibre reinforced polymer composites (FRPs) has become vital for reaching the global sustainable development goals such as climate action, and affordable and clean energy [1]. Natural fibres based on or derived from virgin, renewable, and/or biodegradable biomass have attracted huge interest as a possible sustainable solution in FRPs [2]. Amongst those, flax is a promising reinforcement for sustainable composites since the plant is widely cultivated and competitive with synthetic counterparts such as glass fibre in terms of specific mechanical properties [3]. Traditional thermoset matrices offer attractive mechanical properties (*e.g.* typical unreinforced Young's moduli are *ca.* 3 GPa; ultimate tensile strength in the range 80-90 MPa) but cannot be recycled or reused due to the existence of covalent crosslinks between the chains [2]. Conversely, thermoplastics have the potential to be recycled, but their mechanical properties are often weaker than thermosets, as the polymer chains are held by non-covalent associations. In this study, the interfacial properties of flax fibres are examined for sustainable high-performance FRPs, when combined with three potentially sustainable advanced matrices:

i. an advanced thermoplastic resin, which offers recyclability and reformability,
ii. an entirely bio-based thermoset, which offers the use of renewable sources and a reduction in volatile organic compounds (VOC) emissions,
iii. a vitrimer that combines the beneficial properties of both thermosets and thermoplastics; offering recyclability, repairability and reusability.

  doi:10.5075/epfl-298799_978-2-9701614-0-0

The interfacial performance of the flax fibres when coupled with each of the three matrices was investigated using the microbond test method [4].

2. Materials and Methods

2.1 Fibre and Matrices

The flax fibres, sourced from Eco-Technilin-Flaxtape™ (Normandy, Northern France), were produced *via* the use of a proprietary process and were used as received. The tensile strength and diameter of the flax fibres were reported in a previous study [5], namely 580 MPa and 64 µm, respectively.

Arkema Elium®150 was selected as an example of an advanced thermoplastic resin due to its properties such as post-thermoformability, recyclability, and mechanical properties similar to epoxy composites [6]. The following steps were applied to prepare the resin; a blend of resin to hardener (100:2 ratio), was well mixed, heated in an oven at 40°C for 20 minutes and then held at room temperature overnight.

Furacure, a poly(furfural alcohol)(PFA)-based developmental resin, provided from Bitrez Ltd., was chosen as an example of a bio-based resin, being a REACH compliant polymer[7], of high bio-based grade with fire resistance, which is advantageous in natural fibre composites [8]. The resin is prepared using a 24:1 resin to hardener ratio and cured at 160°C for 120 minutes in an oven according to recommendations by the manufacturer.

Vitrimax T100™, imine-linked vitrimer procured from Mallinda Inc., was selected as an example from a dynamically exchangeable covalent polymer network, offering both thermoplastic and thermoset features. Commercial vitrimers are comparative newcomers to the field of matrix chemistry, although the concept was first observed in a laboratory scale over a decade ago [9]. Vitrimers offer remouldability, reshaping, covalent welding, recyclability, reusability, and high mechanical performance [10,11]. The following procedures, recommended by the manufacturers, were applied to prepare the resin blend: the hardener and resin were blended in the ratio (2.5:1), well mixed, and cured in an air circulating oven at 135°C for 60 minutes.

2.2 Microbond Test

The microbond method [4] was carried out to determine the interfacial shear strength (IFSS) of flax fibres with each of the advanced matrices, and a schematic test setup is illustrated in Fig. 1.

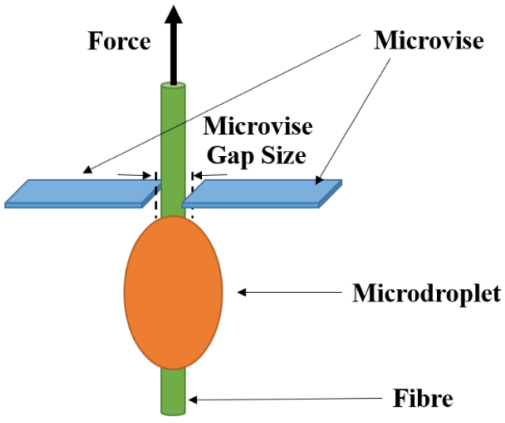

Figure 1. A schematic setup of the microbond test [5].

  doi:10.5075/epfl-298799_978-2-9701614-0-0

The fibres were attached to plastic tabs arranged in a silicone holder to maintain a gauge length of 40 mm. Dynamax 3139 adhesive was used to attach the fibres to plastic tabs, subsequently cured at ambient temperature (*ca.* 20°C) under UV light (λ = 368 nm) for at least 2 hours. After this point, the resin droplets were applied to the fibres and cured by following the procedures outlined in Section 2.1. An optical microscope, Zeiss Axio Imager M2 (Carl Zeiss AG, Oberkochen, Germany), was used to measure the droplet position on the fibre, its size, and embedded area for each microbond test. A Dia-stron LEX820 Extensometer (Dia-Stron Ltd., Andover, UK) was used with the microbond apparatus, which comprises a thin metallic plate (microvice) with a narrow cut in the middle to accommodate the fibre but to prevent the microdroplet from passing through. An appropriate microvice gap separation (gap sizes; 50, 80, 150, 180, 225, 275, and 330 µm) was used depending on the size of the droplet to achieve an ideal shear stress distribution. After the tests, each fibre was observed using an optical microscope to determine the correct failure type. The data for the specimens that showed acceptable debonding failure mechanism were deemed admissible for IFSS calculation and critical fibre length. IFSS was calculated using Eq. (1):

$$IFSS\ (MPa) = \frac{F_d(N)}{A_e(mm^2)} = \frac{F_d(N)}{\pi \times d \times l_e\ (mm^2)} \quad (1)$$

where F_d and A_e (d and l_e) denote debonding force and embedded area (fibre diameter and embedded length), respectively.

3. Result and Discussion

Figures 2, 3, and 4 show admissible experiment examples from the performed microbond tests for Elium, Furacure, and Vitrimax – flax fibre systems.

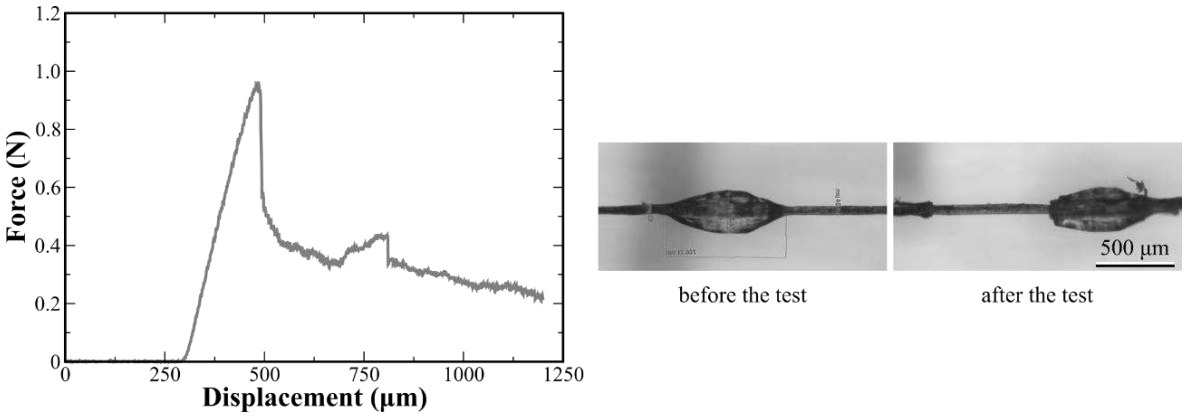

Figure 2. An example of the microbond test: test data, droplet positions before and after the test, respectively, for Arkema Elium®150 - flax fibre systems.

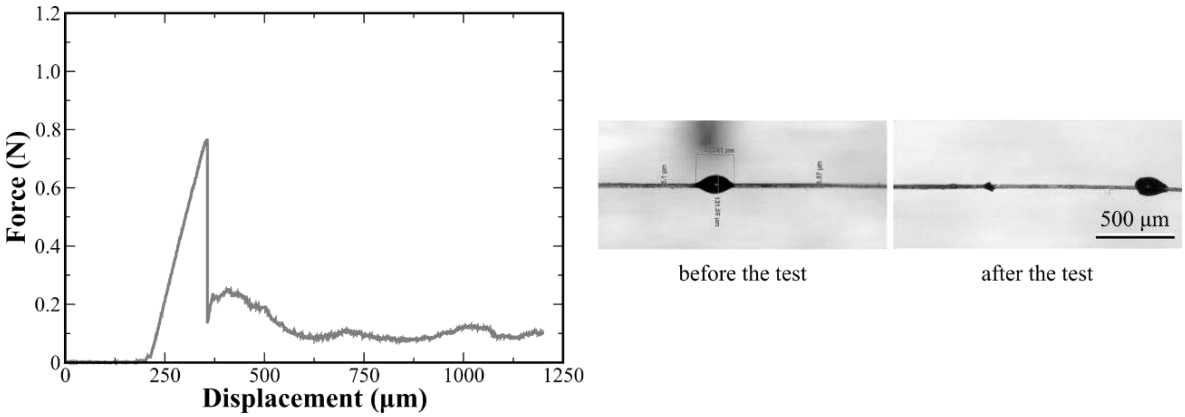

Figure 3. An example of the microbond test: test data, droplet positions before and after the test, respectively, for Furacure (PFA) flax fibre system

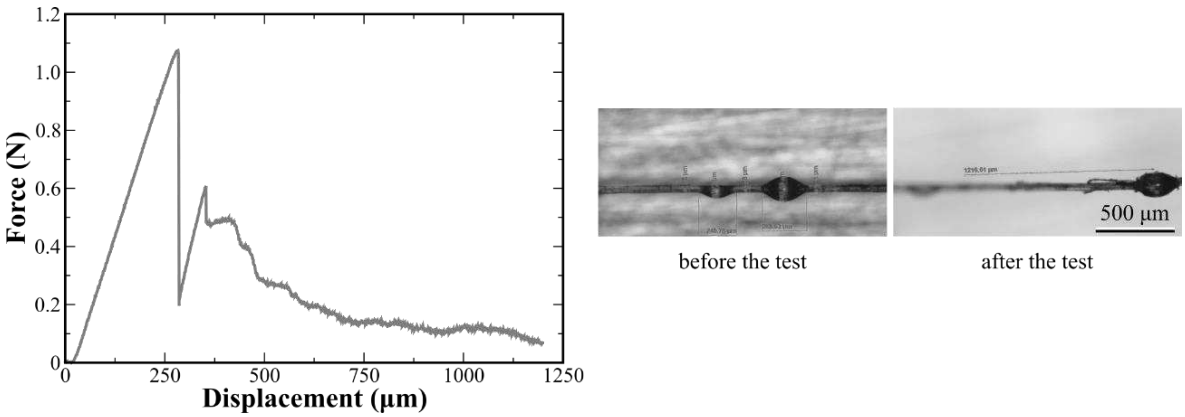

Figure 4. An example of the microbond test: test data, droplet positions before and after the test, respectively, for Vitrimax T100™ - flax fibre system.

The test data in the figures are represented as force *versus* crosshead displacement. Moreover, the figures also show the droplet positions before and after the test, respectively. During the experiments, the targeted droplet experiences shear force debonding from the fibre at the peak force point, which is determined as the 'debonding force', and slides into the endpoint of the fibre. Figure 5 shows IFSS values of the all matrix – flax fibre systems, in addition to an epoxy–flax fibre system for comparison. As seen in the figure, the mean and standard error of IFSS values were calculated for each of the resins systems with flax for Elium (5.91 ± 0.18 MPa), epoxy (11.83 ± 0.79 MPa), Furacure (23.68 ± 1.53 MPa), and Vitrimax (19.96 ± 1.45 MPa).

  doi:10.5075/epfl-298799_978-2-9701614-0-0

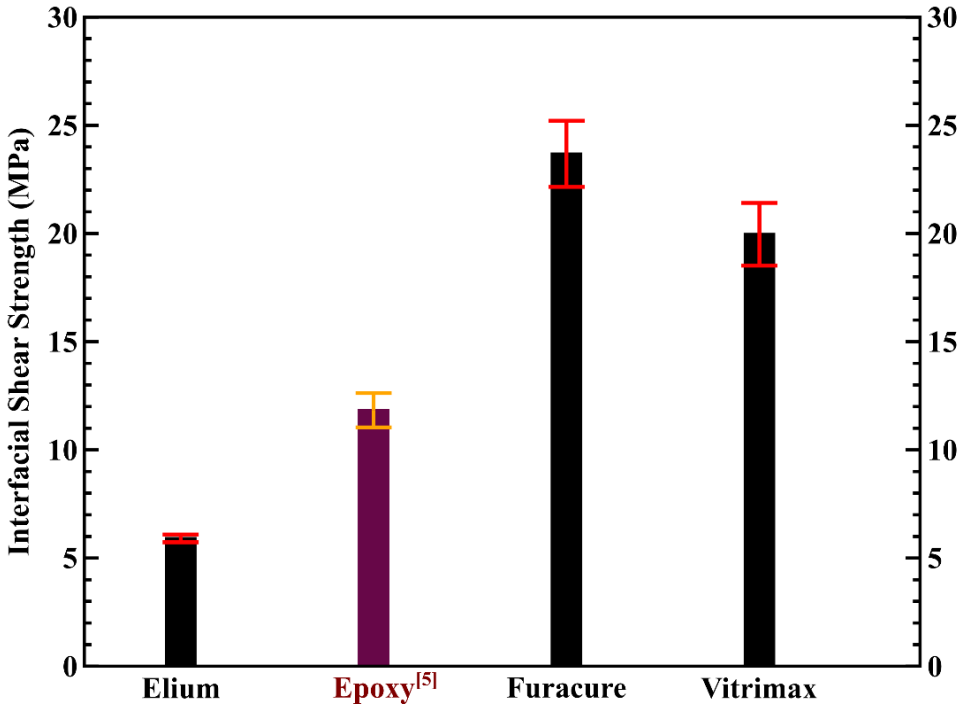

Figure 5. Interfacial shear strength of Arkema Elium®150, Furacure (PFA) and Vitrimax T100™ with flax fibres. Error bars represent the standard error of the mean (SEM). For comparison, the Prime20LV epoxy–flax fibre system was also used from previous work [5].

It can be seen that Elium showed the lowest adhesion performance with flax fibre. On the other hand, the Furacure and Vitrimax resins showed the highest level of adhesion, and they have better adhesion with flax fibre than the standard Prime20LV epoxy system. Moreover, the IFSS values for flax with different epoxy systems have been reported variously as 33 MPa (24 MPa with maleic anhydride sizing) [12] by using single fibre fragmentation tests, 23 MPa [13], and 13–17 MPa [14] by pull-out tests. It is noted here that the 'round-robin' test programme has also shown that pull-out tests give a higher IFSS value than the microbond tests [15]. Therefore, Furacure and Vitrimax resin are expected to have higher IFSS values where different pull-out or fibre fragmentations tests are carried out.

For efficient reinforcement in short or discontinuous fibre reinforced composites, the fibres must have a longer length than the critical fibre length because this allows maximum stress transfer amongst fibres, and the failure of the composite material is likely to be initiated by the fibres rather than fibre-matrix debonding. The critical fibre length is calculated from the following Eq. (2):

$$l_c(mm) = \frac{\sigma_f(MPa) \times d\ (mm)}{2 \times IFSS\ (MPa)} \quad (2)$$

where l_c, d, and σ_f represent the critical fibre length, diameter (at the droplet), and fibre tensile strength, respectively. Figure 6 shows the critical fibre length values of the all matrix – flax fibre systems, in addition to an epoxy–flax fibre system for comparison. In this study, l_c values of the matrix–flax fibre systems were found to be 3.12 ± 0.67 mm (Elium), 1.56 ± 0.39 mm (epoxy), 0.78 ± 0.19 mm (Furacure), and 0.92 ± 0.24 mm (Vitrimer). Therefore, better reinforcement in discontinuous flax FRP can be obtained when fibres with longer lengths than reported l_c are used in manufacturing stages.

  doi:10.5075/epfl-298799_978-2-9701614-0-0

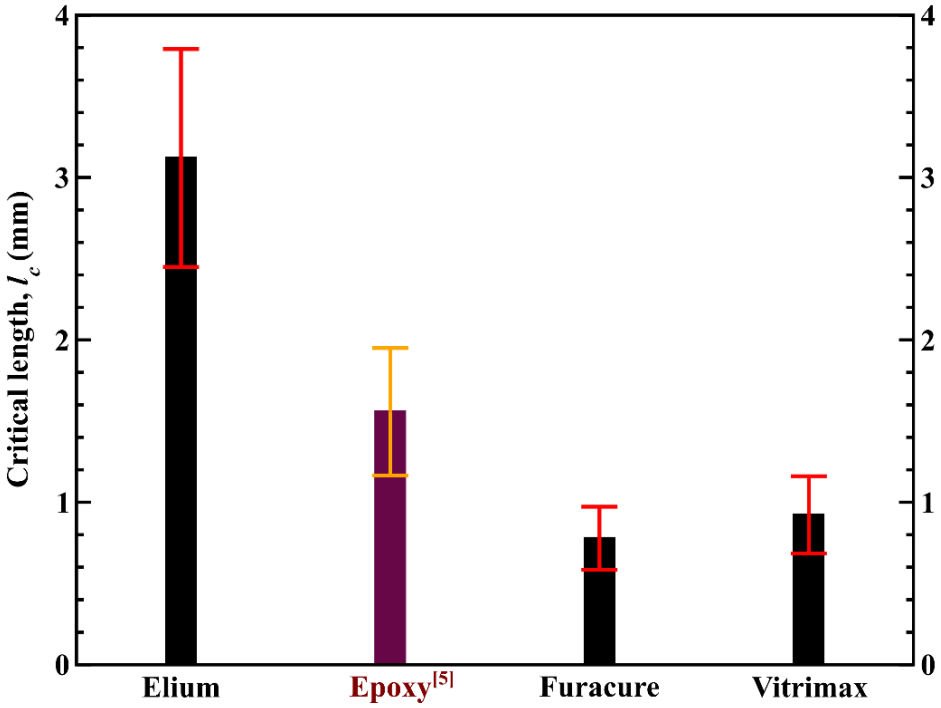

Figure 6. The critical fibre length of Arkema Elium®150, Furacure (PFA) and Vitrimax T100™ with flax fibres. Error bars represent the standard error of the mean (SEM). For comparison, the Prime20LV epoxy–flax fibre system was also used from previous work [5].

4. Conclusions

This study investigated the interfacial properties of flax fibres with three potentially sustainable advanced matrices and compared them with a commonly used commercial epoxy matrix that is recommended for infusion. The bio-based (PFA) and vitrimer (imine-linked) resins were observed to be good candidates with making composites with flax fibres due to high interfacial bonding. Both resins offer sustainability features due to their use of renewable sources, decreasing VOC emission, or allowing reuse, recycling, and repair options, and the latter is the subject of a future manuscript.

Acknowledgements

This work was funded under the UK Engineering and Physical Sciences Research Council (EPSRC) Project [grant EP/P027393/1] “High Performance Discontinuous Fibre Composites—a sustainable route to the next generation of composites” and the EPSRC Centre for Doctoral Training at the Advanced Composites Centre for Innovation and Science (ACCIS, Grant number EP/L016028/1). A.K. acknowledges support from the Turkish Ministry of National Education YLSY grant. The authors thank Ecotechnilin, Fabrizio Scarpa, and Charles de Kergariou for supplying flax-ft fibres. The authors also thank Mallinda Inc. (especially Heather Rubin) and Bitrez Ltd. (especially Dominic Hopwood) for providing polymer matrix materials.

  doi:10.5075/epfl-298799_978-2-9701614-0-0

5. References

1. Globalgoals.org. The global goals for sustainable development [Internet] 2022 [cited 2022 March 08] Available from: https://www.globalgoals.org/
2. Fitzgerald A, Proud W, Kandemir A, Murphy RJ, Jesson DA, Trask RS, Hamerton I, Longana ML. A Life Cycle Engineering Perspective on Biocomposites as a Solution for a Sustainable Recovery. Sustainability 2021;13:1160.
3. Kandemir A, Longana ML, Panzera TH, del Pino GG, Hamerton I, Eichhorn SJ. Natural Fibres as a Sustainable Reinforcement Constituent in Aligned Discontinuous Polymer Composites Produced by the HiPerDiF Method. Materials 2021;14:1885.
4. Miller B, Muri P, Rebenfeld L. A microbond method for determination of the shear strength of a fiber/resin interface. Composites Science and Technology 1987;28:17-32.
5. Kandemir A, Pozegic TR, Hamerton I, Eichhorn SJ, Longana ML. Characterisation of Natural Fibres for Sustainable Discontinuous Fibre Composite Materials. Materials 2020;13:2129.
6. Arkema.com. Elium Resins [Internet] 2022 [cited 2022 March 08] Available from: https://www.arkema.com/global/en/products/product-finder/product-range/incubator/elium_resins
7. Europa.eu. Understanding REACH [Internet] 2022 [cited 2022 March 14] Available from: https://echa.europa.eu/regulations/reach/understanding-reach#:~:text=REACH%20is%20a%20regulation%20of,of%20the%20EU%20chemicals%20industry.
8. Bitrez.com. Furacure (PFA) [Internet] 2022 [cited 2022 March 08] Available from: https://www.bitrez.com/products/furacure-pfa/
9. Montarnal D, Capelot M, Tournilhac F, Leibler L. Silica-like malleable materials from permanent organic networks. Science. 2011;334:965-8.
10. Mallinda.com. VITRIMAX™ product: the technology [Internet] 2022 [cited 2022 March 08] Available from: https://mallinda.com/product/
11. Taynton P, Yu K, Shoemaker RK, Jin Y, Qi HJ, Zhang W. Heat-or water-driven malleability in a highly recyclable covalent network polymer. Advanced materials 2014;26:3938-42.
12. Joffe R, Andersons J, Wallström L. Interfacial shear strength of flax fiber/thermoset polymers estimated by fiber fragmentation tests. Journal of materials Science. 2005;40:2721-2.
13. Eichhorn SJ, Baillie CA, Zafeiropoulos N, Mwaikambo LY, Ansell MP, Dufresne A, Entwistle KM, Herrera-Franco PJ, Escamilla GC, Groom L, Hughes M. Current international research into cellulosic fibres and composites. Journal of materials Science 2001;36:2107-31.
14. Spārniņš E, Nyström B, Andersons J. Interfacial shear strength of flax fibers in thermoset resins evaluated via tensile tests of UD composites. International Journal of Adhesion and Adhesives 2012;36:39-43.
15. Pitkethly MJ, Favre JP, Gaur U, Jakubowski J, Mudrich SF, Caldwell DL, Drzal LT, Nardin M, Wagner HD, Di Landro L, Hampe A. A round-robin programme on interfacial test methods. Composites Science and Technology 1993;48:205-14.

  doi:10.5075/epfl-298799_978-2-9701614-0-0

NOVEL Z-PIN TECHNOLOGIES FOR THROUGH THICKNESS REINFORCEMENT

Irene Jiménez-Fortunato[a], Mario A. Valverde[a], Giuliano Allegri[a], Stephen R. Hallett[a]

a: Bristol Composite Institute (BCI), University of Bristol – irene.jimenez-fortunato@bristol.ac.uk

Abstract: *Z-pins provide effective Through-Thickness Reinforcement (TTR) for prepreg-based laminated composite structures. Carbon fibre z-pins yield much higher fracture toughness enhancement in pure Mode I than in Mode II. On the contrary, metal (e.g. steel) z-pins provide significantly higher apparent fracture toughness in Mode II dominated regimes than their carbon-based counterparts. The work presented here combines the properties of carbon fibre and metallic z-pins across the mode mixity range by developing hybrid z-pins. An experimental parametric study involving single z-pin coupons with different TTR constituents is presented here. An Arcan-like rig is used to explore a range of mixed-mode angles, spanning from Mode I to Mode II. Commonly used 0.28 mm diameter carbon-fibre z-pin are considered as baseline in this study.*

Keywords: Fracture Toughness; Z-pins; Through Thickness Reinforcement

1. Introduction

Prepreg Fibre Reinforced Polymers (FRPs) present excellent in-plane mechanical properties along the fibre directions due to the load-carrying fibres and moulding matrix [1]. However, their properties out-of-plane are poor and Through-Thickness Reinforcement (TTR) techniques are required [2-4]. There are two common methodologies for TTR: stitching and pinning. Stitching process uses an industrial sewing machine or loom to introduce TTR prior to curing the prepreg or before resin infusion. However, stitching prepregs can create damage such as in-plane fibre rupture and stitch needle breakage [5]. Pinning consists on inserting z-pins that secure the laminate plies together by friction and adhesion [6]. The first use of this technique was done manually in the 1970s, and in the 1980s the process was automated. Z-pins are made of high stiffness and strength materials such as titanium alloy, steel or pultruded carbon fibres [6]. Z-pinning has been demonstrated as the preferred technique for large scale production of TTR in laminates as it only needs an additional step in manufacturing and the usual prepreg manufacturing steps are performed [4, 6].

The most common z-pins for aerospace structures are made of carbon fibre. Carbon-fibre z-pins provide a higher apparent fracture toughness in pure Mode I than in Mode II. This is because, at relatively low mode-mixities, z-pins experience pull-out and friction develops at the interface between the laminate and the z-pin, enhancing the dissipation of mechanical energy and, hence, the apparent fracture toughness. However, at high mixed-mode angles, carbon fibre z-pins experience brittle failure with very small or negligible pull-out. Conversely, metal (e.g. steel) z-pins provide significantly higher apparent fracture toughness in Mode II dominated regimes than carbon fibre z-pins due to the ductility of the metal that causes energy dissipation via plastic deformation [7]. However, the fracture toughness enhancement achieved by metal z-pins in Mode I dominated regimes is usually far lower than for carbon TTR, because of the properties

  doi:10.5075/epfl-298799_978-2-9701614-0-0

(friction in particular) of the metal TTR with the laminate interface [6-9]. Hence, a new z-pin concept has been put forward here with a carbon fibre skin (hollow carbon rodstock) with a metal core, so-called hybrid z-pins, which combine the benefits of both carbon fibre and metal z-pins in Mode I and Mode II respectively, providing a balanced toughening action across the full mode-mixity range, i.e. Mode I and Mode II and mixed Mode I/II.

2. Experimental set-up

Single z-pin samples were manufactured in a quasi-isotropic (QI) IM7/8552 [10] laminate. The top sub-laminate stacking sequence is $[0/-45/90/45]_{4s}$ while the bottom sub-laminate is $[90/-45/0/45]_{4s}$ to create a fibre mismatch of 90° at the mid-plane to prevent fibre nesting. An insert of PTFE release film was placed between the top and bottom sub-laminates to avoid bonding of the through-thickness mid-plane during the curing process. Single z-pins were manually inserted into the laminate after heating up the uncured laminate on a hot plate. The single z-pin sample dimensions were 18 mm x 18 mm x 8 mm. Different z-pins are considered in this paper: (1) commonly used 0.28 mm T300 carbon/BMI pin (baseline in this study), (2) 0.5 mm T300 carbon/BMI, (3) hollow CFRP rodstock with 0.5 mm external diameter and 0.3 ± 0.05 mm internal diameter, and (4) hybrid z-pins formed by hollow carbon rodstock and a metallic core as shown in Figure 1. The hollow CFRP rodstock has a larger internal diameter to allow for the insertion of a core. It has also been tested on its own to quantify the benefits of inserting a core. In the absence of core, the hollow CFRP rodstock is filled with resin from the laminate during the curing process. Additionally, solid 0.5 mm CFRP z-pins were considered to evaluate the apparent fracture toughness of laminates reinforced with larger diameter z-pins and to directly compare with hybrid z-pins.

Figure 1. Hybrid z-pin illustration

An Arcan-like rig (Figure 2) was used to explore a range of mixed-mode angles, spanning from pull-out in Mode I (0°) to pure shear in Mode II (90°). The disc rotates in 15° intervals allowing the testing of 7 configurations. The tests were carried out using a calibrated 1 kN load cell and bespoke fixture in an electromechanical test machine i.e. AGS-X Shimadzu [11].

  doi:10.5075/epfl-298799_978-2-9701614-0-0

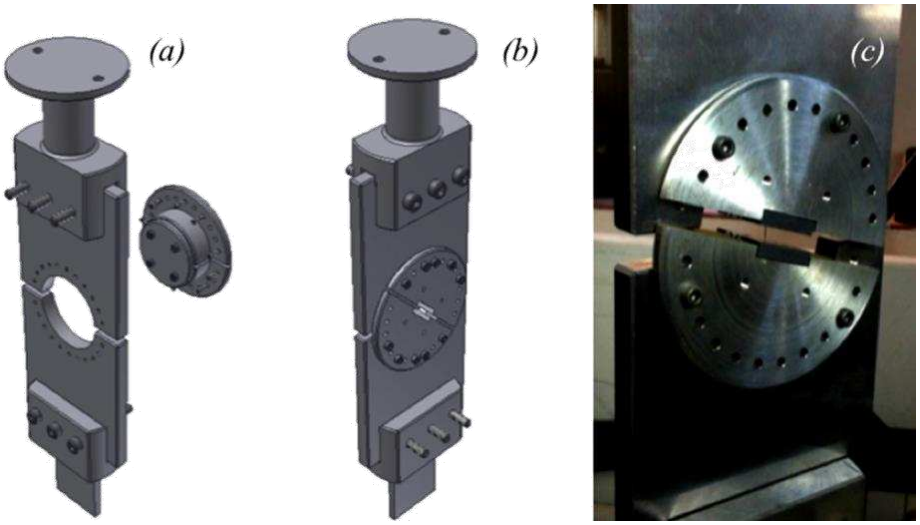

Figure 2. Arcan rig for single Z-pin testing; (a) back view; (b) front view; (c) assembled jig during a z-pin pull out test [12]

3. Experimental results

A minimum of three samples per Arcan rig configuration were tested, with up to 5 samples at the transition region, where some z-pins experienced total pull-out and others breakage at the same position during the experiments. The apparent fracture toughness, G^*, has been calculated following the procedure in [12, 13] considering the z-pin misalignment angle inside the laminate. To compare the different diameter z-pins, G^* has been normalised considering 2% areal density. Hence, Figure 3 shows the apparent fracture toughness with respect the corrected mixed mode angle for the different z-pins tested. The experimental results for the standard 0.28 mm CFRP z-pins are taken from [12, 13]. It can be seen that all the z-pins provide a similar apparent fracture toughness at low mode-mixity angles. However, the 0.5 mm CFRP z-pins present a significant lower value of G^* than expected as larger diameter z-pins, i.e. lower frictional energy than 0.28 mm diameter z-pins. This fact is currently under investigation as the CFRP z-pins should have the same outer surface. Regarding Mode II dominated regimes, it can be seen that the hybrid CFRP/nitinol z-pin produces almost double the apparent fracture toughness of the hollow CFRP rodstock and the solid CFRP z-pins. That is due to the core dissipating energy through plastic deformation at shear dominated angles whereas the solid CFRP z-pins and the hollow CFRP rodstock experience brittle fracture. The transition region for all z-pins is between 20° and 40° corrected mixed mode angle.

  doi:10.5075/epfl-298799_978-2-9701614-0-0

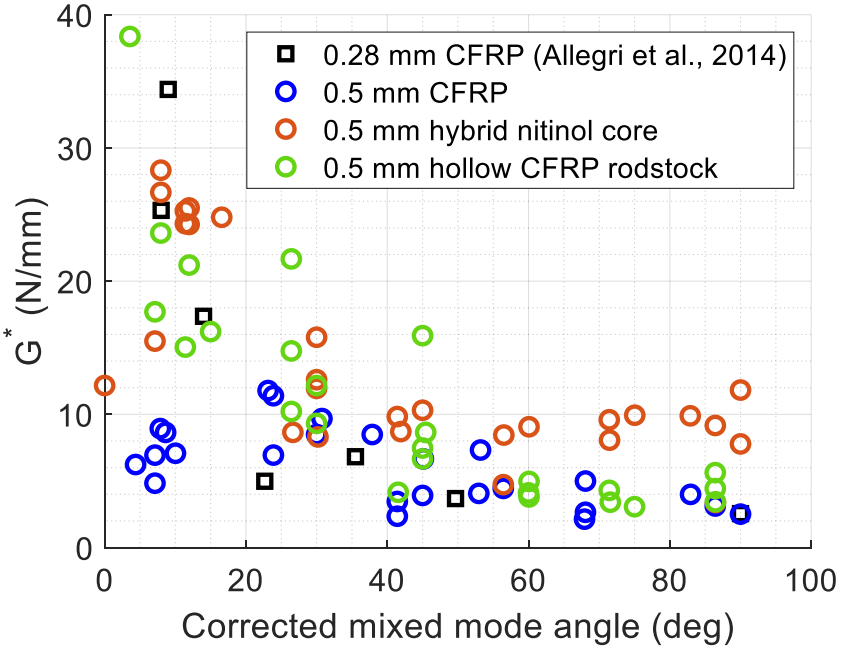

Figure 3. Comparison of different z-pins

4. Conclusions and future work

The performance of different single z-pins have been studied across a range of mode mixities. It has been demonstrated that hybrid z-pins increase the apparent fracture toughness in Mode II dominated regimes in comparison to CFRP z-pins by a factor of two due to the dissipation of energy via plastic deformation of the metallic core. Additional core materials will be considered in future experiments to potentially enhanced even more the apparent fracture toughness in Mode II. In addition, there is need to understand the difference between 0.5 mm CFRP z-pins in Mode I dominated regimes in comparison to the 0.28 mm and hollow CFRP z-pins. The insertion and failure mechanism will be investigated by using Scanning Electron Microscopy (SEM).

Acknowledgements

The authors wish to acknowledge the support of Rolls-Royce plc through Composites University Technology Centre (UTC) at the University of Bristol.

5. References

[1] J. Hoffmann, A. Brast, and G. Scharr, "Z-pin insertion process for through-thickness reinforced thermoplastic composites," *Journal of Composite Materials,* vol. 53, no. 2, 2019, doi: https://doi.org/10.1177%2F0021998318781233.

[2] I. Gnaba, X. Legrand, P. Wang, and D. Soulat, "Through-the-thickness reinforcement for composite structures: A review," *Journal of Industrial Textiles,* vol. 49, no. 1, 2019, doi: https://doi.org/10.1177%2F1528083718772299.

[3] A. P. Mouritz, P. Chang, and M. D. Isa, "Z-Pin Composites: Aerospace Structural Design Considerations," *Journal of Aerospace Engineering,* vol. 24, no. 4, 2011, doi: https://doi.org/10.1061/%28ASCE%29AS.1943-5525.0000078.

  doi:10.5075/epfl-298799_978-2-9701614-0-0 published under CC BY-NC 4.0 license

[4] *Composite Laminates: Properties, Performance and Applications* (Materials Science and Technologies Series). New York, USA: Nova Science Publishers, Inc., 2009.

[5] D. A. Drake, R. W. Sullivan, A. E. Lovejoy, S. B. Clay, and D. C. Jegley, "Influence of stitching on the out-of-plane behavior of composite materials – A mechanistic review," *Journal of Composite Materials,* vol. 55, no. 23, 2021, doi: https://doi.org/10.1177%2F00219983211009290.

[6] A. P. Mouritz, "Review of z-pinned composite laminates," *Composites: Part A,* vol. 38, 2007, doi: https://doi.org/10.1016/j.compositesa.2007.08.016.

[7] B. M'membe, "Novel Through Thickness Reinforcement Development for Composite Materials," PhD, Department of Aerosspace Engineering, University of Bristol, 2016.

[8] K. Pingkarawat and A. P. Mouritz, "Comparative study of metal and composite z-pins for delamination fracture and fatigue strengthening of composites," *Engineering Fracture Mechanics,* vol. 154, pp. 180 - 190, 2016, doi: http://dx.doi.org/10.1016/j.engfracmech.2016.01.003.

[9] B. M'membe, M. Yasaee, S. R. Hallett, and I. K. Partridge, "Effective use of metallic z-pins for composites' through thickness reinforcement," *Composites Science and Technology,* vol. 175, 2019, doi: https://doi.org/10.1016/j.compscitech.2019.02.024.

[10] Hexcel, "HexPly 8552," in *Product Data Sheet*, ed, 2020.

[11] Shimadzu Scientific Instruments. "AGS-X Series Universal Electromechanical Test Frames." https://www.ssi.shimadzu.com/products/universal-tensile-testing/ags-x.html (accessed.

[12] G. Allegri, M. Yasaee, I. K. Partridge, and S. R. Hallett, "A novel model of delamination bridging via Z-pins in composite laminates," *International Journal of Solids and Structures,* vol. 51, pp. 3314-3332, 2014, doi: http://dx.doi.org/10.1016/j.ijsolstr.2014.05.017.

[13] M. Yasaee, J. K. Lander, G. Allegri, and S. R. Hallett, "Experimental characterisation of mixed mode traction–displacement relationships for a single carbon composite Z-pin," *Composites Science and Technology,* vol. 94, pp. 123 -131, 2014, doi: https://doi.org/10.1016/j.compscitech.2014.02.001.

Temperature Dependence of Thermophysical Properties of Carbon/Polyamide Composite

*Kasahun Niguse Asfew [a, c, *], Jan Ivens [a], David Moens [b]*

a: Department of Materials Engineering, KU Leuven Campus De Nayer, J. De Nayerlaan 5, BE-2860 Sint-Katelijne-Waver, Belgium – kasahunniguse.asfew@kuleuven.be
b: Department of Mechanical Engineering, KU Leuven Campus De Nayer, J. De Nayerlaan 5, BE-2860 Sint-Katelijne-Waver, Belgium
c: Department of Mechanical Engineering, Adama Science and Technology University, P.O. Box: 1888, Adama, Ethiopia

Abstract: *In this study, the temperature dependence of heat capacity, thermal expansion, density, and thermal conductivity of carbon/polyamide composites has been studied. Results showed that the specific heat capacity of the C/PA composite increases with temperature, and major transitions have been observed at glass transition (Tg) and melting (Tm) temperatures. Due to the presence of fibers, the CTE values in the fiber direction of C/PA samples were smaller by an order of magnitude than in the transverse direction. The density measurement results showed that with an increase in temperature, volume increases, so density decreases. The laser flash technique has been used to measure the heat diffusivity of the C/PA composite, which is then used to calculate thermal conductivity. Results showed that the average thermal conductivity increases with temperature along the fiber direction and increases with a small rate in the beginning and is almost uniformly distributed later, in the transverse direction.*

Keywords: Temperature Dependence; Carbon/Polyamide Composites; Specific Heat Capacity; Coefficient of Thermal Expansion; Thermal Conductivity

1. Introduction

In thermoplastic composite production, the material must be processed at high temperatures, which impacts the thermophysical properties of the material and accurate thermal simulations require the knowledge of temperature dependent thermo physical properties. As a result, it's becoming increasingly vital to study the behavior of thermoplastic composites at high temperatures. Several researchers studied different methods to study the effect of temperature on thermal diffusivity, thermal conductivity, heat capacity, coefficient of thermal expansion (CTE), and density of isotropic or anisotropic materials. (1–4) used the laser flash method to measure the thermal diffusivity and the derived heat capacity and thermal conductivity of isotropic metals and fiber-reinforced polymer composites (FRPC).

The effects of the finite width of the laser flash pulse, heat loss, and sample thickness in thermal diffusivity measurement (5) and the influence of stacking sequence of composite samples and frequency of the source on thermal wave distribution (6) in the laser flash method have been studied. The temperature dependence of specific heat capacity, thermal diffusivity, and thermal conductivity of different composite materials has been studied by several researchers (3). The thermal conductivity of semi-crystalline and four amorphous polymers was determined starting at room temperature and going up to temperatures above the polymer melting point (Tm) for semi-crystalline polymers or above the glass transition temperature (Tg) for amorphous

  doi:10.5075/epfl-298799_978-2-9701614-0-0

polymers, and the peak thermal conductivity values are observed around Tg for amorphous and around Tm for semi-crystalline polymers (7). The coefficient of thermal expansion (CTE) of different FRPCs was measured over a range of temperatures, and CTE was greatly affected by temperature and fiber direction (8,9). The temperature dependance of carbon/epoxy was determined and both the in-plane and through-thickness thermal conductivities increase with temperature linearly, although the in-plane one increases at a slightly greater rate (10). In this study, the temperature dependence of heat capacity, thermal expansion, density, and thermal conductivity of carbon/polyamide410 composites has been studied.

2. Temperature dependance of Heat Capacity of C/PA410 composites

2.1 Equipment and Methods

In this experiment, DSC thermograms were recorded with a DSC Q2000 V24.11 Build 124 (TA Instruments). Standard samples of UD C/PA410 composite tapes with approximately 8-10 mg of mass were used. Liquid nitrogen was used as a purge gas at a flow rate of 50 mL/min. The samples were equilibrated at -50 °C and the data were collected at a heating and cooling rate of 3.00 °C/min over a temperature range of -50 to 300 °C. There was an isothermal dwell of five minutes between each step.

2.2 Results and Discussions

The specific heat capacity results of the measurements are presented in three transition temperature ranges (Table 1).

Table 1: Average Specific heat capacity of C/PA410 composite with temperature variation

	Average Specific Heat Capacity (J/g °C)		
	Up to Tg	Tg to Tm	Above Tm
Sample 1	0.645	1.703	2.086
Sample 2	0.686	1.848	2.322
Sample 3	0.63	1.775	2.157
Sample 4	0.94	2.334	2.918
Sample 5	0.627	2.016	2.732
Sample 6	0.882	1.94	2.424
Mean	0.74	1.94	2.44

As we see from the heat capacity Vs temperature plot of all samples (Figure 1), the heat capacity of the samples increases slightly up to Tg, and the mean specific heat capacity was 0.74 J/g°C. Above Tg, the polymer structure is floppy and has sufficient free volume for various molecular motions to be able to absorb the added heat. The mean specific heat capacity between Tg and Tm is then becomes 1.96 J/g°C. Then at Tm, crystalline regions of the polymer melt. At this stage, first, the polymer absorbs a certain amount of heat (the latent heat of melting), and second, the polymer undergoes a change in heat capacity. Due to this, the mean specific heat capacity above Tm further increases to 2.44 J/g°C.

  doi:10.5075/epfl-298799_978-2-9701614-0-0

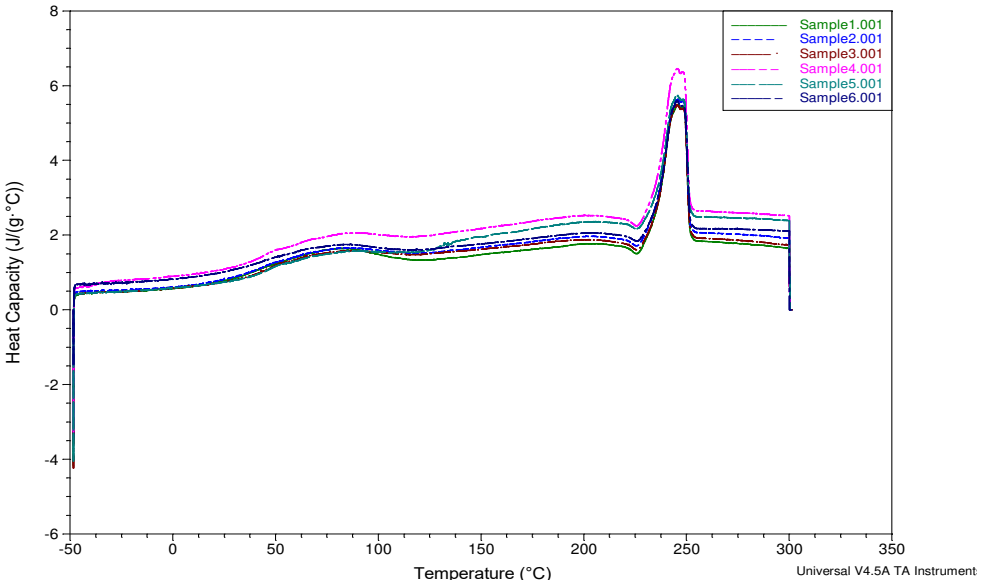

Figure 1: overlay of heat capacity Vs temperature curves of all samples

3. Temperature dependance of coefficient of thermal expansion (CTE) of C/PA410 composites

3.1 Equipment and Methods

Thermal energy is responsible for atomic or molecular vibrations about a mean position in any material. As the temperature of the materials is increased, the amplitude of thermal energy-induced vibrations increases, and interatomic or intermolecular spacing increases, i.e., an expansion of the body occurs. In this work, thermo-mechanical measurements are performed on a C/PA410 composite material using a TA Instruments Q400 thermomechanical analyzer in expansion mode. The procedure used in this study is presented in table 2.

Table 2: TMA measurement procedure

	CTE (Longitudinal)	CTE(Transverse)
1	Ramped heating (10 °C/min) to 200 °C	Cooling to -30°C
2	Cooling (10°C/min) up to -30°C	Ramped heating (3 °C/min) to 200 °C
3	Ramped heating (3 °C/min) to 200 °C	Cooling (3°C/min) up to 20°C
4	Cooling (5°C/min) up to 20°C	

3.2 Results and Discussions

An idealized TMA curve has a linear section below the transition (expansion below Tg) and a linear section above the transition (expansion above Tg). The results of the TMA measurement of all the samples are summarized in Tables 3 and 4 for fiber and transverse directions, respectively. The results of this study showed a significant difference in CTE according to fiber orientation.

  doi:10.5075/epfl-298799_978-2-9701614-0-0

Table 3: Summary of the CTE values along longitudinal direction

Samples	CTE below Tg $\mu m/(m°C)$	CTE above Tg $\mu m/(m°C)$
Sample 1	2.916	8.014
Sample 3	2.731	6.8
Sample 6	1.843	5.99
Sample 7	2.814	6.241
CTE $= \mu \pm$ SD	**2.5 +/- 0.4**	**6.75 +/- 0.77**

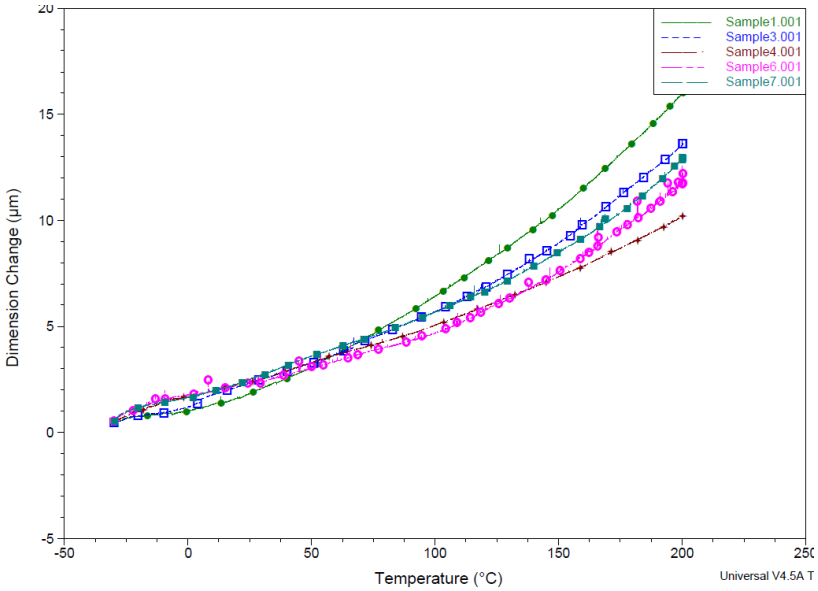

Figure 2: Overlay of Dimension change vs Temperature curves in longitudinal direction

In the direction of fibers, the CTE is small because of the mechanical restraints imposed by the fibers. On the other hand, compared to the CTE in the fiber direction, more than an order of magnitude increase in CTE values is observed in the transverse direction. This effect is even more pronounced with increasing temperatures.

Table 4: Summary of the CTE values along transverse direction

Samples	CTE below Tg $\mu m/(m°C)$	CTE above Tg $\mu m/(m°C)$
Sample 2	69.72	166
Sample 3	56.55	147.5
Sample 4	65.46	160.6
Sample 5	58.05	163.4
Sample 7	78.95	157.2
CTE $= \mu \pm$ SD	**65.75 +/- 8.1**	**158.9 +/- 6.4**

The higher CTE value of the polymer matrix mainly contributed to the higher expansion of the composite in the transverse direction. In addition, the rigid fibers mostly prevent the expansion of the matrix in the fiber direction, so the matrix is forced to expand even more in the transversal direction.

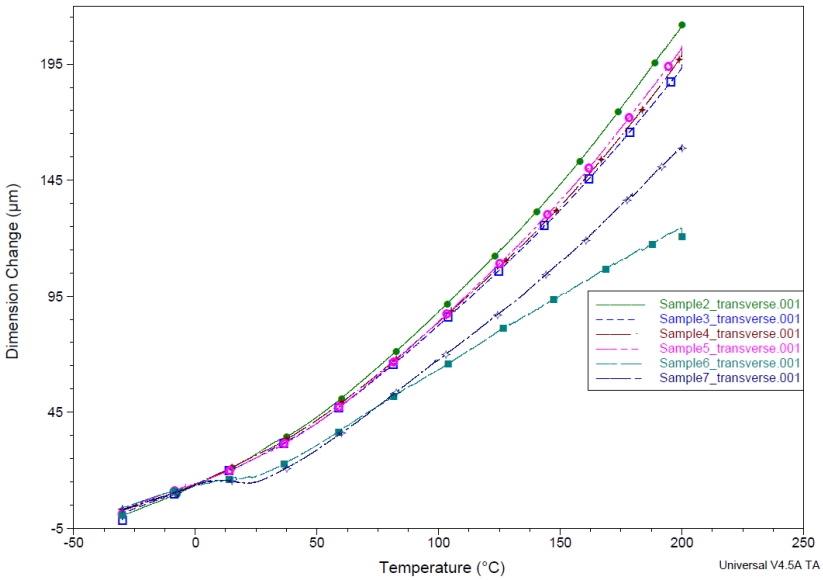

Figure 3: Overlay of Dimension change vs Temperature curves in transverse direction

When Tg is reached, a significant increase in the rate of expansion and a change in the slope of the curves are observed both in the fiber and transverse direction of the composite. Figure 2 and 3 showed that the slopes of all curves in the overlay plots showed good agreement, except that of sample 4 in the fiber direction and sample 6 in the transverse direction.

4. Temperature dependance of the density of C/PA410 composites

Evolution of density with temperature can be calculated from the volumetric expansion values at varying temperatures and density at room temperature. The Quantachrome Instruments' Multipycnometer density measuring device was used to measure the density of the C/PA410 composite and was found to be 1.22g/cm3. The calculated evolution of the density of the C/PA410 composite over the temperature range of 20–200 C (Figure 4) showed that the density drops as temperature increases.

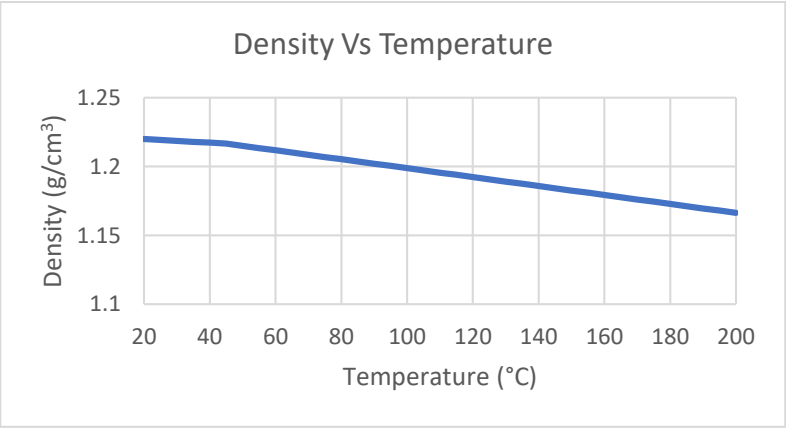

Figure 4: Temperature dependance of density of C/PA410 composite.

  doi:10.5075/epfl-298799_978-2-9701614-0-0

5. Temperature dependance of thermal diffusivity and thermal conductivity of C/PA410 composites

5.1 Equipment and Methods

A diode laser source (MDL-N-808/7~10W) with an 808 nm wavelength was used to produce a thermal contrast on the specimens' surface to assess the thermal diffusivity of the C/PA410 sample. A cylindrical lens expanded the laser beam to a vertical line (2mm*6mm), reflected it in the mirror, and focused on the sample surface using a convex lens (f200), as shown in the figure 5. The laser was directed to the surface of the sample for two seconds during each run of the experiment, whereby the illuminated strip heated up and the heat began to disperse out of the lit zone. The laser source will then be blocked, allowing the heat to shrink back. With a sampling frequency of 50 Hz, an IR camera (CEDIP JADE UC J330R, 8-12 micron, 80mK@F/0.8@30C typical, 14 bits, 320x240 pixels) set perpendicular to the sample surface at 10cm records. For each run of the experiment, the camera detected the IR radiation emitted by the sample for 15 seconds (2 seconds before the heating started, 2 seconds while heating, and 11 seconds during cooling). The amount of IR radiation observed is related to the change in temperature.

The test was performed on four identical samples (30mm*30mm*1.5mm) at four distinct temperatures: room temperature, 50 °C, 85 °C, and 100 °C. At each temperature, two sets of experiments were carried out, with the fibers aligned horizontally and vertically to quantify heat diffusion along with the fiber and perpendicular to it. The temperature of the sample was measured using a thermometer (thin-film standard PT1000 element, 2*10mm) affixed to the center part of the sample as indicated in the figure 5. A digital multimeter (34401A) from Keysight Technologies was used for data acquisition, and the LabVIEW (National Instruments Corporation, USA) environment was used for the temperature readings.

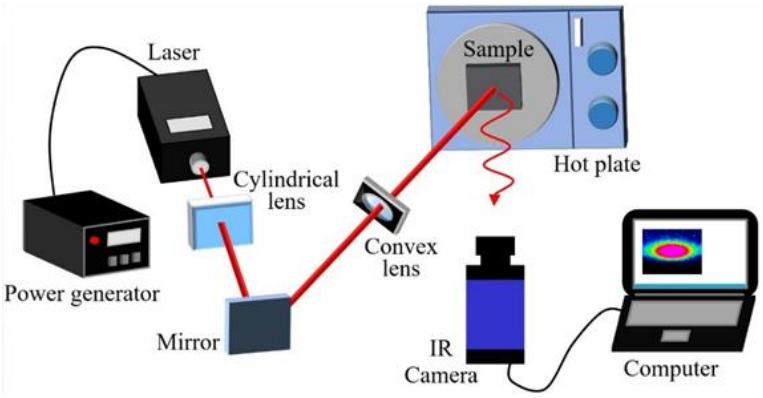

Figure 5: Experimental setup for the thermal diffusivity measurement

5.2 Result and Discussion

The recoded IR pictures of each sample at different temperatures are analyzed using MATLAB software. The temperature profiles over the width of the laser line were extracted and fitted using the Gaussian equation for each collected frame. From this, the FWHM progress with time is plotted. The slope of a linearly fitted cooling section of the FWHM with sqrt (t) graph is used to compute the thermal diffusivity. Since the FWHM=2.35*√2α*√t, the slope of a linearly fitted cooling section of the FWHM with sqrt(t) graph is used to calculate the thermal diffusivity (α) using Eq. (1):

  doi:10.5075/epfl-298799_978-2-9701614-0-0

$$\alpha = \frac{Slope}{2.35 * \sqrt{2}} \quad (1)$$

As shown in the figure 6, the average thermal diffusivity increased with temperature along the fiber direction and was distributed almost uniformly in the transverse direction.

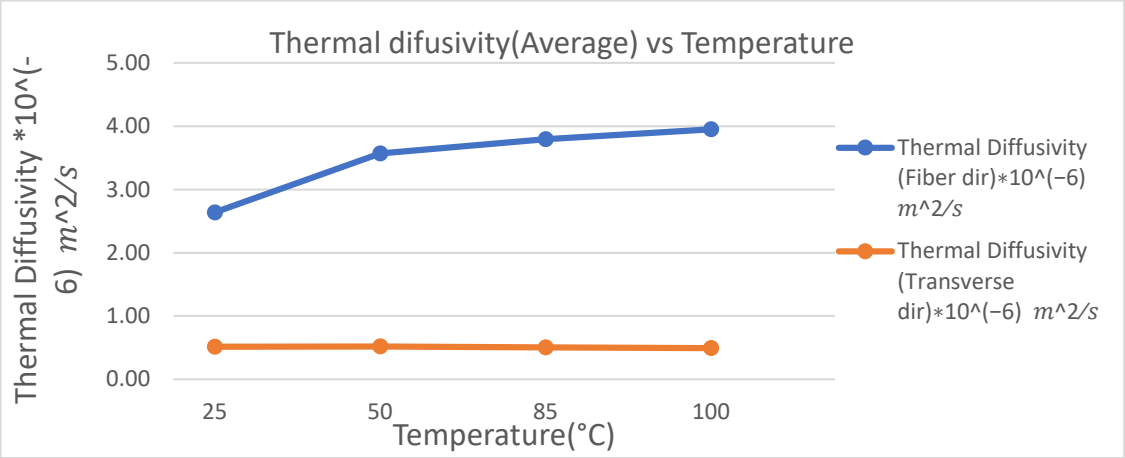

Figure 6: Average temperature dependency of average thermal diffusivity(m2/s) of C/PA410 samples

Thermal conductivity at each temperature is calculated from the average thermal diffusivity, specific heat capacity, and density values at each temperature. Figure 7 shows that the thermal conductivity of C/PA410 composites increases progressively with temperature along the fiber direction and with a small increase in the beginning and distributed almost uniformly later in the transverse direction for the temperature range between room temperature and 100 °C.

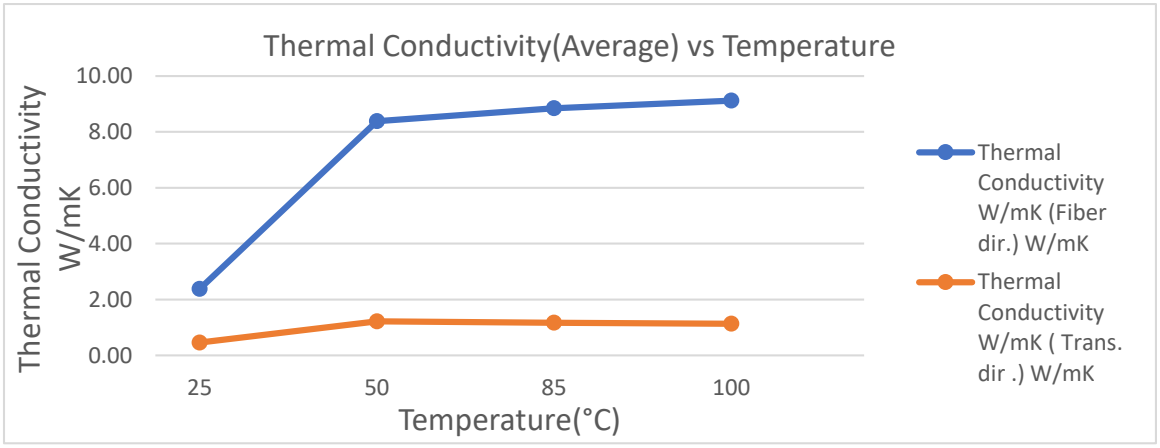

Figure 7: Temperature dependency of average thermal conductivity (W/mK) of C/PA410 samples

In nonmetals, increasing temperature increases the lattice vibration, giving higher phonon propagation. On the other hand, the density of the composite drops, and the heat capacity increases at higher temperatures. Therefore, the thermal conductivity along the fiber direction increases with temperature because of the presence of highly conductive continuous carbon fibers, and the heat conduction is dominated by lattice vibrations, while this effect is less potent along the transverse direction.

  doi:10.5075/epfl-298799_978-2-9701614-0-0

6. Conclusion

The thermophysical properties of the C/PA410 composite have been examined in relation to temperature. The heat capacity of the samples increased as the temperature rises, but the density decreases. CTE of the samples increased with temperature increment and at Tg, a significant increase in the rate of expansion is observed both in the fiber and transverse direction of the composite. Experimental results of the laser flash method showed that the thermal diffusivity and thermal conductivity of the samples increase progressively with temperature along the fiber direction and distributed almost uniformly in the transverse direction.

Acknowledgements

This research work was carried out in the frame of the HGPP project (International University Partnership Services for the Establishment of Postgraduate Programmes in Ethiopia) funded through GIZ GmbH and the International University Partnership for the Establishment of PhD Programmes in Ethiopia funded by the Ethiopian Ministry of Science and Higher Education

7. References

1. Boué C, Fournier D. Infrared thermography measurement of the thermal parameters (Effusivity, diffusivity and conductivity) of materials. Quant Infrared Thermogr J. 2009;6(2):175–88.
2. Krapez JC, Spagnolo L, Frieß M, Maier HP, Neuer G ünter. Measurement of in-plane diffusivity in non-homogeneous slabs by applying flash thermography. Int J Therm Sci. 2004;43(10):967–77.
3. Spinelli G, Guarini R, Kotsilkova R, Batakliev T, Ivanov E, Romano V. Experimental and Simulation Studies of Temperature Effect on Thermophysical Properties of Graphene-Based Polylactic Acid. Materials (Basel). 2022;15(3).
4. Lee S, Kim D. The evaluation of cross-plane/in-plane thermal diffusivity using laser flash apparatus. Thermochim Acta. 2017;653(June 2016):126–32.
5. Lim KH, Kim SK, Chung MK. Improvement of the thermal diffusivity measurement of thin samples by the flash method. Thermochim Acta. 2009;494(1–2):71–9.
6. Kalogiannakis G, Van Hemelrijck D, Longuemart S, Ravi J, Okasha A, Glorieux C. Thermal characterization of anisotropic media in photothermal point, line, and grating configuration. J Appl Phys. 2006;100(6):1–12.
7. Dos Santos WN, De Sousa JA, Gregorio R. Thermal conductivity behaviour of polymers around glass transition and crystalline melting temperatures. Polym Test [Internet]. 2013;32(5):987–94. Available from: http://dx.doi.org/10.1016/j.polymertesting.2013.05.007
8. Ran Z, Yan Y, Li J, Qi Z, Yang L. Determination of thermal expansion coefficients for unidirectional fiber-reinforced composites. Chinese J Aeronaut [Internet]. 2014;27(5):1180–7. Available from: http://dx.doi.org/10.1016/j.cja.2014.03.010
9. Dong C, Li K, Jiang Y, Arola D, Zhang D. Evaluation of thermal expansion coefficient of carbon fiber reinforced composites using electronic speckle interferometry. Opt Express. 2018;26(1):531.
10. Sweeting RD, Liu XL. Measurement of thermal conductivity for fibre-reinforced composites. Compos Part A Appl Sci Manuf. 2004;35(7–8):933–8.

INTEGRATIVE MATERIAL CHARACTERIZATION OF CRYSTALLINE NANOCELLULOSE REINFORCED FILAMENTS FOR FUSED-FILAMENT FABRICATION

Helena, Weingrill[a], Stefan, Wurzer[a], Joamin, Gonzalez-Gutierrez[b]

a: Anton Paar GmbH, Graz – stefan.wurzer@anton-paar.com
b: Luxembourg Institute of Science and Technology, Luxembourg

Recently crystalline nanocellulose (CNC) has received increased attention in the scientific community following a universal push for more environmentally conscious engineering and increased sustainability. Due to the combination of high stiffness and low density of CNC, a high specific modulus of approximately 90 MPa/(kg·m³) [1] is achieved. However, during processing via fused filament fabrication (FFF), the material is exposed to a series of thermal and mechanical loads. Therefore, the load history must be considered when characterizing and predicting the composite's properties in the final 3D-printed construction part. A recycled 3D-printable polypropylene modified with CNC up to 15 vol% content was examined in this study. Since the CNC's reinforcement effect is mainly determined by the interactions between the cellulose and the matrix [2], a maleic-acid-anhydride-based compatibilizer was used. To characterize the novel composite shear rheological investigations, dynamic-mechanical analysis (DMA) and measurements regarding shrinkage were performed. An unexpected decrease in viscosity with increasing filler content was observed. This decrease was attributed to (I) the increased use of low viscosity compatibilizer with increased filler content and (II) the thermal degradation of the compatibilizer manifested in a color change of the tested material. This hypothesis was verified by differential scanning calorimetry (DSC) measurements. These measurements enabled a reliable material characterization, which can help to predict the properties of the final printed part.

Keywords: Fused Filament Fabrication (FFF); CNC; Material characterization; Sustainability; Recycled PP

1. Introduction

Following extensive efforts to develop lightweight and stiff materials from renewable sources cellulose and its nanoscale derivates have only recently received increased interest. Nanocellulose can be defined as a cellulose material with at least one dimension in the nanometer scale exhibiting high tensile strength and stiffness, high flexibility and large surface to volume ratio while also being lightweight. Due to these properties, crystalline nanocellulose (CNC) has generated high interest as a filler in various composite materials [3]. Using CNC with recycled polypropylene (PP) yields a sustainable high-strength nanocomposite material with a high potential for processing via fused filament fabrication (FFF), a well-known processing method in the realm of additive manufacturing. The reinforcement effect of the CNC can be increased by the use of a compatibilizer, since the interactions between matrix and filler are crucial for such [2]. However, the interactions between fillers and the polymer chains do typically not only impact the material's mechanical behavior in the final part but may also affect two crucial properties for 3D printing: the viscosity and the shrinkage behavior [4] [5]. Whereas the

  doi:10.5075/epfl-298799_978-2-9701614-0-0

viscosity needs to stay below a certain level to guarantee the material's overall printability, the shrinkage behavior is crucial for successfully predicting the dimensions of the printed part. Furthermore, to efficiently design parts out of the novel composite accurate information about the material's stiffness is required. The fact that the material behavior of the printed part is significantly influenced by the thermal and mechanical loads to which the polymer is subjected during the printing process, must be considered in the characterization. Understanding the changes that occur in the material due to processing can help to decrease the amount of testing necessary on the final part to ensure proper functionality. In this study a series of test methods (shear rheological tests, DMA, DSC, shrinkage tests) were performed on recycled PP with different volume contents of CNC and a maleic-acid-anhydride-based compatibilizer to accurately determine material behavior during and after printing considering the thermal and mechanical loads occurring during FFF.

2. Materials and Specimen Preparations

In this study the recycled PP Kruplene-C PP multicolor MFR 0.4-1 supplied by Kruschitz GmbH (Völkermarkt, Austria) was used as the matrix material. The composite material was produced by melt mixing of the PP together with the CNC CelluForve NCCTM (CelluForce Inc., Montreal, Canada) and the maleic-acid-anhydride-based compatibilizer SCONA TSPP 10213 GB (BYK-Chemie, Wesel, Germany) at 175 °C with a kneader (Brabender Technologie GmbH, Duisburg, Germany). As a first step, the PP was melted for 2 min and kneaded for 1 min. The compatibilizer was added afterwards, and kneading proceeded for another minute. Lastly, the CNC was added to the compound and kneaded again for 17 min. The filaments with diameters ranging from 1.5 mm to 1.8 mm used for the FFF were produced from the compounds with different vol% of CNC using a capillary rheometer (Göttfert, Werkstoff-Prüfmaschinen GmbH, Buchen, Germany). In Figure 1, the compounds, and the produced filaments with the different volume contents of CNC are shown. The compatibilizer amount in the formulation depends on the amount of CNC in the compound, with the volume content of the compatibilizer being 1/10th of the volume content of the CNC.

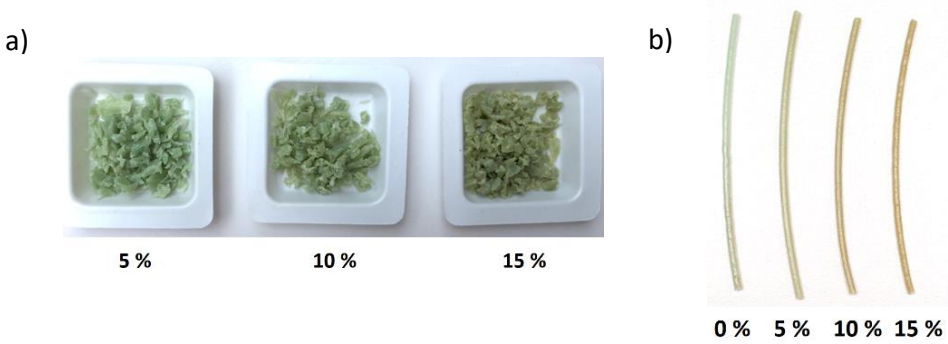

Figure 1. a) Kneaded compounds with 5 vol%, 10 vol% and 15 vol% (from left to right) CNC in a recycled polypropylene matrix b) Filaments with filler contents of CNC produced via a capillary rheometer

3. Material characterization

3.1 Shear rheological tests

The MCR 702 MultiDrive (Anton Paar GmbH, Austria) with a plate-plate geometry was used for shear rheological characterizations. Disks with a diameter of 25 mm and a height of 2 mm were

molded in a vacuum press (Dr. Collin GmbH, Maitenbeth, Germany). After determining the limit of the viscoelastic range (LVE) in an amplitude sweep, a frequency sweep with logarithmically decreasing angular frequency in the range from ω = 628 rad/s to 1 rad/s was performed using a shear strain of γ = 0.1 %. The tests were performed at 185 °C, which equals the representative printing temperature for PP. Additionally, an oscillatory test at a constant angular frequency of ω = 100 rad/s (approximate shear rates occurring during 3D printing) was performed at 185 °C with γ = 0.1 % to investigate the degradation behavior under combined thermal and mechanical load of selected materials for 60 min.

3.2 Dynamic calorimetric scanning (DSC)

To further analyze the thermal stability of the compound, DSC measurements were carried out. The DSC measurements of the nanocomposite with different filler contents, the recycled PP, the CNC, and the compatibilizer were performed in a temperature range from 25 °C to 375 °C under an air atmosphere using a heating rate of 10 K/min. Furthermore, a DSC measurement at a fixed temperature of 185 °C for 60 min was performed to investigate potential degradation over time at the printing temperature.

3.3 Shrinkage tests

Shrinkage tests were performed using the MCR 702 MultiDrive to analyze the shrinkage behavior of the filaments during cooling after the FFF printing process. For the measurements a free sample length of 33 mm was used. The samples were heated from ambient temperature to 150 °C with a heating rate of 10 K/min while being subjected to a small load of 0.05 N. Once 150 °C was reached, the temperature chamber (CTD 600 MDR) was opened to imitate the exposure of the filaments to ambient conditions when exiting the printing nozzle. The extensional strain of the sample was detected as a function of time and used to characterize the sample's shrinkage.

3.4 Dynamic mechanical analysis

Dynamic mechanical analysis of the filaments was performed using the MCR 702 MultiDrive in tension and torsion. The test parameters for the measurements are summed up in Table 1. To ensure the used amplitudes are within the LVE range of the material, amplitude sweeps at -60 °C were performed. For the measurements a free sample length of 33 mm was used.

Table 1: Parameters for the DMA measurements in torsion and tension.

Set parameter	DMA in torsion	DMA in tension
Heating rate	2 K/min	2 K/min
Temperature range	-60 °C – 150 °C	-60 °C – 150 °C
Frequency	1 Hz	1 Hz
Deformation	0.1 %	0.03 %
Constant tensile force	-0.5 N	Proportional to dynamic load (120 %)

  doi:10.5075/epfl-298799_978-2-9701614-0-0

4. Results

4.1 Shear rheological measurements

In Figure 2, the results from the frequency sweeps are displayed. Interestingly, with increasing filler content, the complex viscosity η* decreased. This effect was attributed to the lower viscosity of the compatibilizer (purple curve at the bottom in Figure 2) and its increased content at higher volume contents of the CNC in the composite. However, the test procedure resulted in a distinct color change in the samples as well. Thus, to investigate a possible degradation behavior, selected samples were additionally subjected to oscillatory shear for 60 minutes at a constant frequency. In Figure 3, the result from the oscillatory shear test at constant frequency is given for the pure PP, the PP with a filler content of 15 vol% CNC and the compatibilizer. Whereas η* remained constant over the test time of 60 minutes for the pure PP, it decreased for the nanocomposite and the compatibilizer.

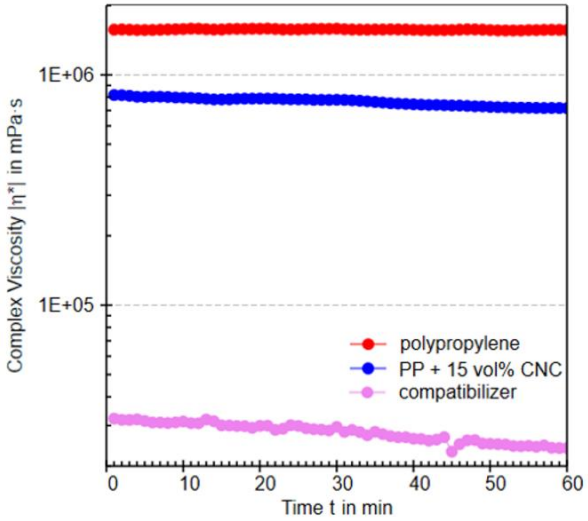

Figure 2. Complex viscosity curves of PP, composites with different volume contents of CNC and the compatibilizer as a function of the frequency at 185 °C

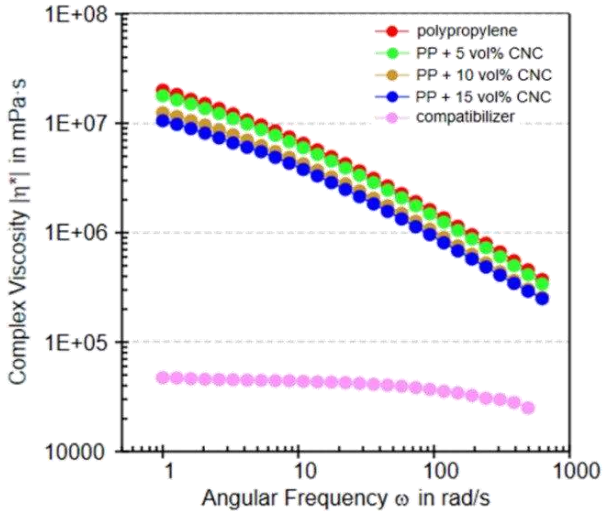

Figure 3. Complex viscosity of PP, the composite with 15 vol% CNC and the compatibilizer over time at a constant angular frequency of 100 rad/s at 185 °C

The changes in the complex viscosity |η*| are displayed in Table 2. A decrease of 12 % and 25 % could be observed for the nanocomposite containing 15 vol% CNC and the compatibilizer, respectively. Thus, the unexpected decrease in viscosity with increasing filler content, as seen in the frequency sweeps (Figure 2), was also attributed to the degradation of the compatibilizer. This decrease highlights the sensitivity of the compatibilizer towards combined shear and thermal loads. Special attention must be given to the kneading and the printing parameters to prevent degradation of the material during processing.

Table 2: Changes in η over 60 minutes of PP, PP with 15 vol% CNC and compatibilizer*

Material	Initial η* in mPa·s	η* after 60 min in mPa·s	Change in η* in %
polypropylene	$1.57 * 10^6$	$1.56 * 10^6$	< -0.1
PP + 15 vol% CNC	$8.18 * 10^5$	$7.17 * 10^5$	-12
compatibilizer	$3.22 * 10^4$	$2.0 * 10^4$	-25

4.2 Dynamic calorimetric scanning (DSC)

In Figure 4, the DSC measurements of the PP, compounds with different filler contents and the compatibilizer are shown. PP (red line) exhibits a melting peak at 162 °C, which subsequently is also observable for the nanocomposites. While the pure PP, CNC, and nanocomposites with different volume contents of CNC exhibit thermal stability well beyond the printing temperature of 185 °C, the onset oxidation temperature for maleic-acid-anhydride-based compatibilizer can be found at approximately 198 °C.

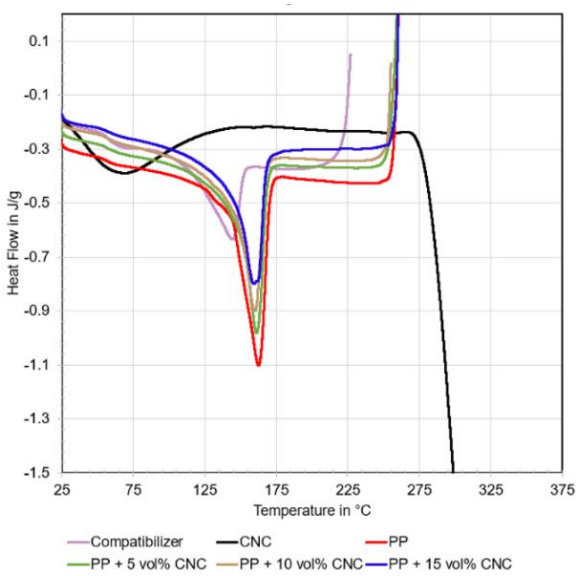

Figure 4. DSC measurements of PP, CNC, composites with different volume contents of CNC and the compatibilizer under air atmosphere with a heating rate of 10 K/min

To further analyze the degradation behavior, DSC measurements over time at a constant temperature of 185 °C under an air atmosphere were performed. The results of the DSC measurements are shown in Figure 5. While no degradation over time could be determined for

the pure PP and the nanocomposites, the compatibilizer displayed significant degradation beyond 40 min. It can be concluded that the compatibilizer is stable over a relevant period of time at printing temperature while no additional loads are applied.

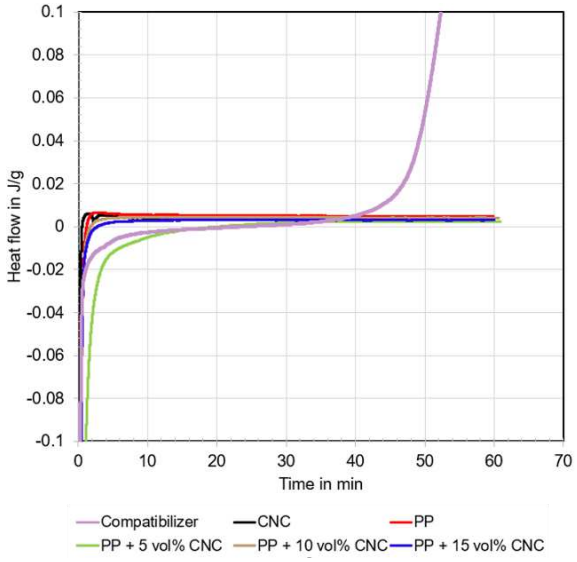

Figure 5. DSC measurements of PP, composites with different volume contents of CNC and the compatibilizer under air atmosphere at a constant temperature of 185 °C

4.3 Shrinkage tests

The results of the shrinkage tests are presented in Figure 6. With increasing filler content, smaller shrinkage was detected. After 30 minutes of cooling at ambient temperature, the filament sample of the pure PP shrunk by 5.00 %, whereas the filament sample of the PP-based nanocomposite containing 15 vol% CNC shrunk by 3.52 %. The percentage of shrinkage is applied for designing the printed parts so that the dimensions match the constructional requirements. Furthermore, using this data, an estimation of the warpage of the final printed part can be performed.

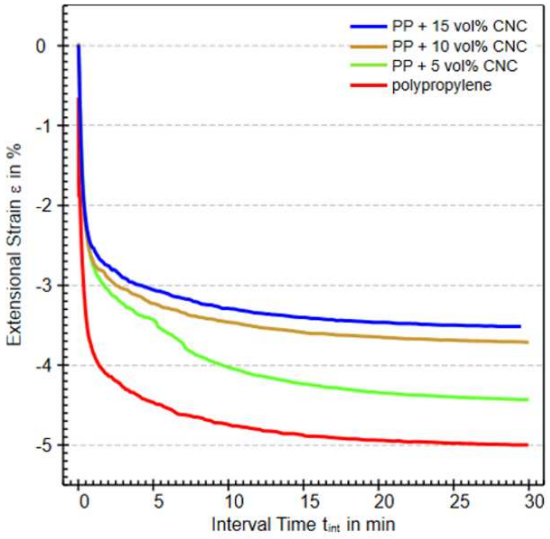

Figure 6. Shrinkage measurements of PP and composites with different volume contents of CNC at ambient temperature after heated up to 150 °C

4.4 Dynamic response characterization

In Figure 7, the thermograms of the torsional and tensile DMA are displayed. As expected, with increasing filler content of CNC, the material's stiffness increased as demonstrated by the increase of the storage moduli G' and E'. However, a significant increase in E' was only detected for the nanocomposite with of 10 vol% and 15 vol% CNC filler content. These results led credibility to the assumption that agglomeration of the filler occurred, and thus mechanical reinforcement was only achieved at the highest filler contents.

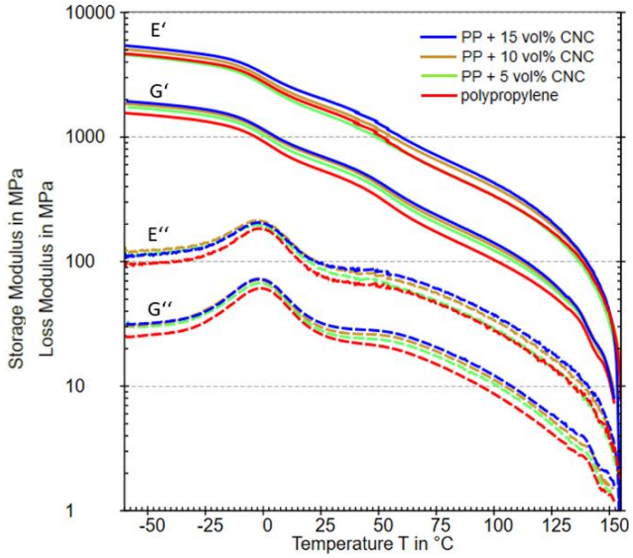

Figure 7. Temperature dependent storage and loss moduli of PP and composites with different volume contents in torsion and tension

5. Conclusions

Extensive rheological, thermal, and mechanical characterization of PP CNC nanocomposites was performed in this study. It can be concluded that the addition of CNC and a maleic-acid-anhydride-based compatibilizer to recycled PP has a significant impact on the rheological properties as well as on the mechanical and shrinkage behavior of the nanocomposite compared to pure PP. However, special attention must be given to the thermal and mechanical loads occurring during the nanocomposite preparation and further processing. The maleic-acid-anhydride-based compatibilizer used in this study is especially susceptible to degradation. While the compatibilizer exhibited thermal stability for a relevant time frame when no mechanical load was applied, the combination of thermal and mechanical load lead to degradation and a subsequent decrease in viscosity of the nanocomposite. This behavior must be considered when processing the nanocomposite via FFF by avoiding excessively high temperatures. Additionally, a decrease in the compound shrinkage compared to the pure PP material under cooling conditions present after extrusion of the FFF nozzle could be observed. A lower shrinkage is generally advantageous for the processing via FFF since lower warpage of the final part can be expected. Furthermore, an increase in stiffness can be observed with increased filler volume content. For the lowest filler content, the increase of stiffness is only minimal. It is suspected that this is caused by the agglomeration of the CNC inside the composite. This knowledge gives an insight into the behavior of PP CNC nanocomposites processable via FFF and can help reduce the test effort on the 3D-printed part to ensure the proper functionality of the final product.

  doi:10.5075/epfl-298799_978-2-9701614-0-0

Acknowledgements

The research was partially carried out within the FFG-funded project "Natural3D" under Project No. 860384

References

1. Chen J, Lin N, Huang J, Dufresne A. Highly alkynyl-functionalization of cellulose nanocrystals and advanced nanocomposites thereof via click chemistry. Polymer Chemistry 6: 4385-4395. 2015
2. Peterson A, Mehandzhiyski AY, Svenningsson L, Ziolkowska A, Kádár R., et al. A Combined Theoretical and Experimental Study of the Polymer Matrix-Mediated Stress Transfer in a Cellulose Nanocomposite. Macromolecules 54: 3507–3516
3. Poletto M, Ornaghi H, Cellulose - Fundamental Aspects and Current Trends. Intech, 2015
4. Hristov V, Vlachopoulos J. Effects of Polymer Molecular Weight and Filler Particle Size on Flow Behavior of Wood Polymer Composites. Polymer Composites 29: 831-839. 2008
5. Ryu Y, Sohn J S, Kweon BC, Cha SW. Shrinkage Optimization in Talc- and Glass-Fiber-Reinforced Polypropylene Composites. Materials. 2019

  doi:10.5075/epfl-298799_978-2-9701614-0-0

EXPERIMENTAL ANALYSIS OF GLASS FIBRE REINFORCED NYLON-66 UNDER COMBINED LOADING AT LOW AND HIGH RATES OF STRAIN

Yuan Xu[a], Junyi Zhou[a], Gustavo Quino[b], Antonio Pellegrino[a]

a: Department of Engineering Science, University of Oxford, Oxford, OX1 3PJ, UK
b: Bristol Composites Institute, Faculty of Engineering, University of Bristol, BS8 1TL, UK
(yuan.xu@eng.ox.ac.uk)

Abstract: *Reinforced polymer composites are increasingly used in various industrial applications because of their lightweight and superior stiffness-strength combination. In these engineering practices, composites are commonly subjected to multiaxial loads and behave at strain rates ranging from low to high. However, most existing studies that focus on the mechanical characterisation of composites are limited to single loading modes involving tensile, flexural, compressive, and fatigue. The multiaxial behaviour of 30% glass fibre reinforced nylon-66 (PA66-GF30) is investigated in this study through combined tension-torsion experiments. A thin-walled tube geometry of specimens and gripping fixtures are designed to enable appropriate failure of the material under tensile and torsional loading. The quasi-static experimental data depict the multiaxial failure of PA66-GF30 subjected to different stress states including pure shear, combined shear-tension, and plain strain tension. High-rate combined loading experiments are implemented using a novel split Hopkinson tension-torsion bar system to unravel the rate dependence.*

Keywords: Glass fibre reinforced nylon-66; Combined tension-torsion; Thin-walled tube specimen; Rate dependence; Hopkinson bar

1. Introduction

Among reinforced polymer composites, glass fibre reinforced polyamide 66 is widely used in aerospace and automotive industries because of their excellent mechanical, thermal and chemical properties [1]. The broad application in various environments calls for the development of constitutive models that are representative of the material behaviours in complex loading regimes experienced within realistic scenarios. The material data at different stress states and strain rates will be of significance to the improvement of structural design and integrity assessment practices [2-3].

A number of studies have been carried out focusing on the mechanical properties of reinforced polymer composites. Eriksson et al. [4] investigated the effect of thermal-oxidative aging on tensile strength, modulus, and elongation at break of unreinforced and glass-fibre-reinforced recycled polyamide 66. Sattar et al. [5] studied the variability of the meso-structure on the flexural and tensile behaviours of glass fibre nylon composite. Kuram et al. [6] conducted tensile and impact tests and investigated the effects of recycling number and injection parameters on the mechanical properties of glass-fibre reinforced nylon 6. However, existing experimental approaches are limited to single loading modes involving tensile, flexural, compressive, and fatigue. The realisation of complex mechanical environment, especially featuring multiaxial

  doi:10.5075/epfl-298799_978-2-9701614-0-0

loading and high deformation rate, remains challenging in a controlled laboratory environment, thus resulting in the behaviours of glass fibre reinforced polyamide 66 under such extreme mechanical conditions unanswered.

This study describes combined tension-torsion experiments conducted to reveal the multiaxial deformation and failure responses of 30% glass fibre reinforced nylon-66 (PA66-GF30). A specimen geometry of hollow cylinder is designed to allow for appropriate failure of the material under tensile and torsional loading. Quasi-static stress-strain responses are obtained at a range of stress states including pure shear, combined shear-tension, and plain strain tension. A novel split Hopkinson tension-torsion bar system is employed to measure the high-rate combined loading behaviours.

2. Material and Specimen

The material under investigation is 30 wt% glass fibre reinforced nylon 66 (TECAMID® 6/6 GF30 black) with a density of 1350 kg m^{-3}. The plastic was obtained from commercial sources supplied by Ensinger Inc. and was received in the form of thick plates of dimensions 305 x 250 x 40 mm^3. 30% glass fibre reinforced nylon 66 was coded as PA66-GF30 through this study.

The specimens employed in both tension and torsion experiments are designed as hollow thin-walled cylinders (Fig. 1) with large and flat ends. The gauge section has wall thickness of 0.5 mm, internal diameter of 15.8 mm, and gauge length of 2 mm. PA66-GF30 is easy to machine, and the test samples were extracted from the as-received plates via subtractive manufacturing methods. The axis of the tubular specimen corresponds to thickness direction of the plates. The ends of the specimen are bonded to a pair of aluminium holders via epoxy-based adhesive. The holder has a hollow stud with external thread and an octagon hole internally to transmit both the axial and torsional loads.

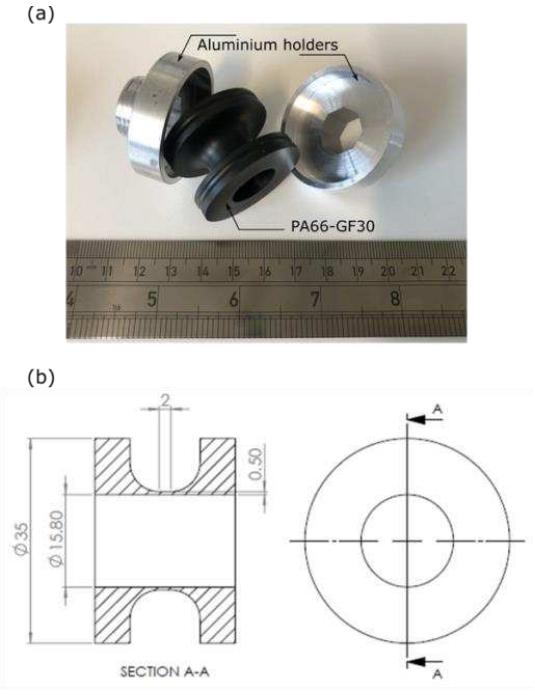

Figure 1. (a) Photo of a PA66-GF30 specimen and aluminium holders; (b) geometry and dimensions of the specimen

  doi:10.5075/epfl-298799_978-2-9701614-0-0

3. Experimental Method

Quasi-static tension, torsion, and combined tension-torsion experiments were conducted in a Zwick/Roell Z250 screw-driven universal testing machine (Fig. 2). The tensile load was applied under displacement control at a speed of 0.002 mm/s, while the torsional load 0.03 degree/s. In combined tension-torsion tests, the loading velocity of each component was varied to alter the contribution of tension and torsion loads. Two combinations (0.002 mm/s and 0.01 degree/s, 0.001 mm/s and 0.03 degree/s) were selected to obtain tension-dominated and torsion-dominated stress states, respectively. The applied force and torque were recorded via the respective resistive load cells, Zwick Force 100 kN and Zwick Torque Transducer 1000 Nm.

Two iDs UEye USB 3.0 Cameras were synchronised to video-record the macroscopic deformation and failure mechanism of the tubular specimens. The surface of the specimen was painted with a fine speckle pattern. High-resolution (2456 x 2054 pixels) pictures were recorded at a frame rate of 1 fps via a CMOS sensor. The full-field tensile and shear displacement was calculated from the footage through digital image correlation (DIC) analysis. The history of the average axial and shear strain within the gauge section of the specimen were then measured from DIC using commercial software LaVision Davis.

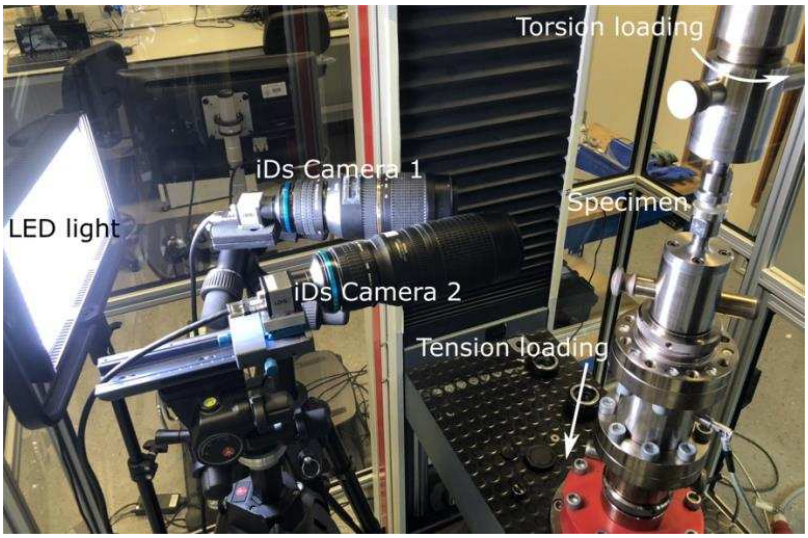

Figure 2. Quasi-static testing setup

High-rate combined loading experiments were implemented using a novel split Hopkinson tension-torsion bar system that was designed at the Impact and Shock Mechanics Laboratory, University of Oxford [4-5]. Deformation and failure of were observed using two Photron SA5 high-speed cameras positioned perpendicularly to the axis of the tubular sample. The two high speed cameras were triggered simultaneously, and the recorded images synchronised with the strain gauges signals from the Hopkinson incident bar. The average strain histories on the surface of the specimen were obtained by means of DIC analysis of the high-speed images and the synchronised stress histories measured by strain gauges located on the transmitted bar.

4. Results and Discussion

Experiments presented in this study are summarised in Table 1, categorised according to the type of tests by tension, torsion, and combined tension-torsion.

  doi:10.5075/epfl-298799_978-2-9701614-0-0

A parameter named biaxial loading angle β(Eq. 1), proportional to the ratio of the direct stress σ over the shear stress τ, is introduced to describe the relative contribution of tension and torsion during combined loading:

$$\tan\beta = \frac{\sigma}{\sqrt{3}\tau} \quad (1)$$

In this study, the biaxial loading angle was limited to $0° \leq \beta \leq 90°$, where $\beta = 0°$ corresponds to torsion loading, whist $\beta = 90°$ tension loading. Any β in the interval $0° < \beta < 90°$ represents an arbitrary combination of tension and torsion, in which torsion-dominated combined loading can be identified by $\beta < 45°$ while tension-dominated loading by $\beta > 45°$. The larger the biaxial loading angle, the more tension dominated was the combined loading.

Table 1

Summary of quasi-static experiments

Type of test	Specimen label	Biaxial loading angle °	Ultimate stress MPa		Elongation at break %	
			Tension	Shear	Tension	Shear
Tension	Tension1	90	61.9		25.3	
	Tension2	90	59.4		26.0	
Combined tension-torsion	TT1	65	50.5	13.4	20.9	21.0
	TT2	15	20.9	45.8	14.7	73.1
Torsion	Torsion1	0		55.8		84.3
	Torsion2	0		55.4		90.0

Tensile and shear stress versus strain responses are presented in Fig. 3, including the tension-only experiment with one repetition (Fig. 3a), the tension-only experiment with one repetition (Fig. 3b), and two representative combined tension-torsion experiments with tension-dominated loading (Fig. 3c) and torsion-dominated loading (Fig. 3d). A classical viscoplastic deformation behaviour can be observed from the engineering tensile and shear stress-strain curves. The ultimate tensile strength was measured averagely 60.7 MPa with the deviation not more than 2%. The onset of macroscopic fracture was identified from the video footage at strain about 25%. It is worth noting a small 'tooth' appears way after the yielding point at strain around 10%. The engineering shear stress-strain curves are highly consistent. The ultimate shear strength was measured about 55.6 MPa. Large deformation was observed until failure at strain varying from 84% to 90%.

Due to the concurrent effects of the longitudinal and torsional loading, the combined-loading cases present a compromise in terms of the ultimate stress and the strain to failure compared with the tension-only or torsion-only cases. Furthermore, the extent of this compromise varies with different stress states. The tensile elongation at break in tension-dominated combined loading ($\beta = 65°$) and torsion-dominated combined loading ($\beta = 15°$) decreased by 18% and 80%, respectively, compared to the case of simple tension. While compared to the case of simple torsion, the shear elongation at break in these two combined loading cases ($\beta = 65°$ and $\beta = 15°$) decreased by 43% and 20%, respectively.

  doi:10.5075/epfl-298799_978-2-9701614-0-0

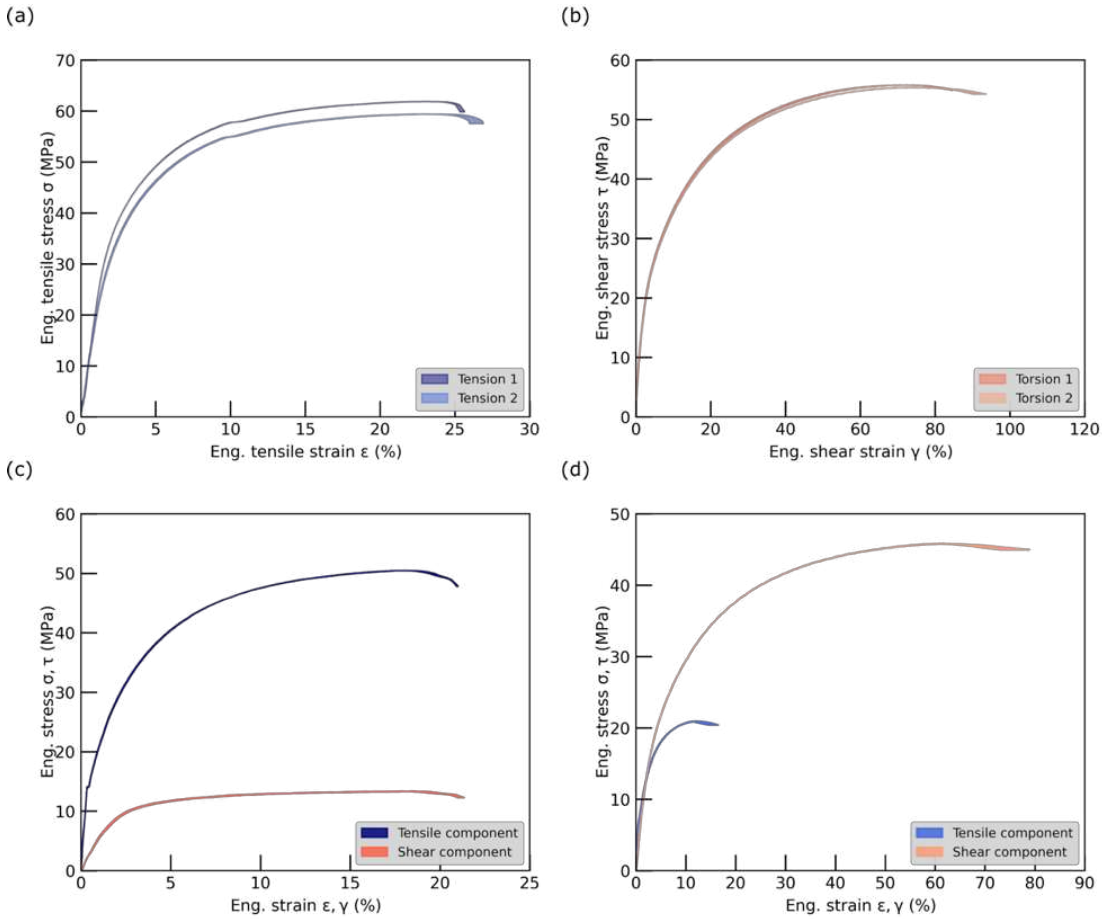

Figure 3. Engineering stress-strain curves measured from (a) tension-only tests #Tension1 and #Tension2, (b) torsion-only tests #Torsion1 and #Torsion2, (c) tension-dominated combined loading test #TT1, and (d) torsion-dominated combined loading test #TT2

The trajectories of the measured engineering normal and shear strain are presented in Fig. 4a. The ratio between the normal strain and the shear strain is nearly constant as demonstrated by the linear trend of the strain path. This indicates a constant strain rate loading in tension and torsion during the combined loading experiment. Figure 4b illustrates the paths of the engineering normal stress and shear stress, which appear bilinear during combined loading ($\beta = 65°$ and $\beta = 15°$). The turning point approximately corresponds to the yielding point, after which the development of the shear stress is lower than its component. This is attributed to different viscoplastic behaviours of PA66-GF30 in tension and shear as the material undergoes strain hardening in tension whilst it quickly saturates and maintains a flow stress plateau in shear until failure, as addressed in Fig. 3c and 3d.

The field of engineering axial strain Eyy and shear strain Exy of the tubular specimen in representative tension loading, torsion loading, and combined loading experiments is presented in Fig. 5. Two typical moments are selected to reflect the deformation process, followed by a post-failure stage showing the fracture pattern. The homogenous distribution of the axial strain and shear strain within the gauge section indicates uniform deformation of the material prior to failure. Fracture under tension loading consisted of a series of discrete short cracks oriented along the circumference of the gauge section while slightly tilted. The video footage indicates the crack propagated with

  doi:10.5075/epfl-298799_978-2-9701614-0-0

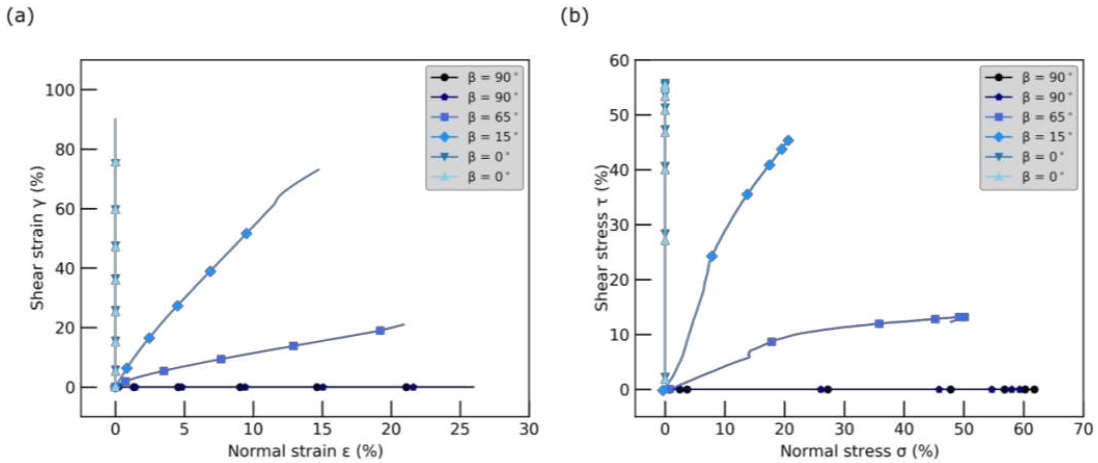

Figure 4. Loading path in (a) strain and (b) stress

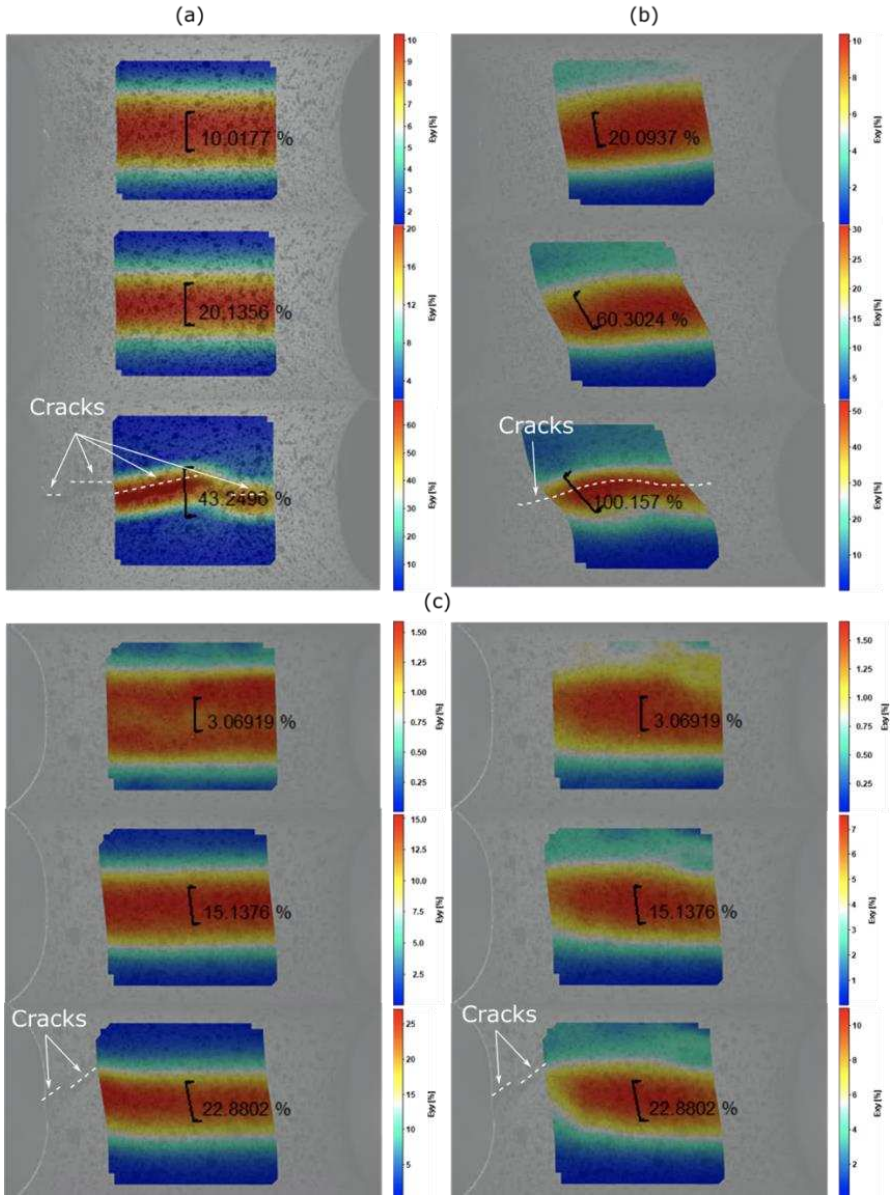

Figure 5. Deformation process in (a) tension-only tests #Tension1, (b) torsion-only tests #Torsion1, and (c) tension-dominated combined loading test #TT1

  doi:10.5075/epfl-298799_978-2-9701614-0-0

a speed at the order of millimetre per second. Fracture under torsion loading appeared more wavy but continuous within the gauge section. As a result of the collective effects of the axial and rotary loads, fracture under combined loading was composed of intermittent cracks along the circumference but significantly tilted.

5. Conclusions

The present study details the deformation and failure of PA66-GF30 subjected to tension, torsion, and combined tension-torsion loading conditions. A classical viscoplastic deformation behaviour was obtained from the engineering tensile and shear stress-strain responses. The ultimate strength and elongation at break measured from multiaxial loading decreased when compared with the single loading behaviour. The loading trajectories demonstrated a constant ratio between the normal strain and shear strain, while bilinear development of the normal stress and shear stress was observed. High-rate combined loading experiments were implemented using a novel split Hopkinson tension-torsion bar system. The experimental results will be discussed in future study to unravel the rate dependence of the multiaxial behaviour.

Acknowledgements

The authors would like to thank Rolls-Royce plc and the EPSRC for the support under the Prosperity Partnership Grant\Cornerstone: Mechanical Engineering Science to Enable Aero Propulsion Futures, Grant Ref: EP/R004951/1.

6. References

1. Surampadi NL, Ramisetti NK, Misra RDK. On scratch deformation of glass fiber reinforced nylon 66. Material Science and Engineering A 2007; 456(1–2): 230–235.
2. Ghorbel E. A viscoplastic constitutive model for polymeric materials. International Journal of Plasticity 2008; 24(11):2032–2058. doi: 10.1016/j.ijplas.2008.01.003.
3. Donato GHB, Bianchi M. Pressure dependent yield criteria applied for improving design practices and integrity assessments against yielding of engineering polymers. Journal of Material Research and Technology 2012 1(1): 2–7. doi: 10.1016/S2238-7854(12)70002-9.
4. Eriksson P-A, Boydell P, Eriksson K, Månson J-AE, Albertsson A-C. Effect of thermal-oxidative aging on mechanical, chemical, and thermal properties of recycled polyamide 66. Journal of Applied Polymer Science 1997;65:1619–30.
5. Sattar S, Beltran B, Laredo, Pedrazzoli D, Zhang M, Kravchenko SG, Kravchenko OG. Mechanical behavior of long discontinuous glass fiber nylon composite produced by in-situ polymerization. Composites Part A: Applied Science and Manufacturing 2022;154:106779. doi: 10.1016/J.COMPOSITESA.2021.106779.
6. Kuram E, Tasci E, Altan AI, Medar MM, Yilmaz F, Ozcelik B. Investigating the effects of recycling number and injection parameters on the mechanical properties of glass-fibre reinforced nylon 6 using Taguchi method. Materials and Design 2013;49:139–150. doi: 10.1016/J.MATDES.2013.02.027.
7. Xu Y, Farbaniec L, Siviour C, Eakins D, Pellegrino A. the development of split Hopkinson tension-torsion bar for the understanding of complex stress states at high rate. In L. Lamberson, S. Mates, & V. Eliasson (Eds.), Dynamic Behavior of Materials (2021;1:89-93).

Conference Proceedings of the Society for Experimental Mechanics Series. Springer, Cham.
8. Farbaniec L, Xu Y, Zhou J, Patsias S, Macdougall D, Reed J, Petrinic N, Siviour CPellegrino A, Eakins D. Application of the photon doppler velocimetry (pdv) technique in tension-torsion hopkinson bar experiments. EPJ Web of Conferences 250, 01025, DYMAT 2021.

  doi:10.5075/epfl-298799_978-2-9701614-0-0

TENSILE CHARACTERISATION OF HIPERDIF PLA/CARBON FIBRE TAPE UNDER PROCESSING CONDITIONS

Burak Ogun Yavuz[a], Ian Hamerton[b], Marco L. Longana[b], and Jonathan P.-H. Belnoue[b]

a: Bristol Composites Institute, University of Bristol – lj20825@bristol.ac.uk
b: Bristol Composites Institute, University of Bristol

Abstract: *Although composite materials can, through lightweighting, play a role part in the decarbonisation of transport, they are inherently challenging in terms of sustainability. This is because high-performance composites used in the aerospace and automotive sector are often made of carbon fibres and thermosets resins that are difficult to recycle. The HiPerDiF (High-Performance Discontinuous Fibre) method invented at the University of Bristol offers a way to remanufacture composites from reclaimed fibres. The method allows the production of composites comprising high volume fractions of highly aligned discontinuous fibres, with high processability and performance. Still, greater sustainability credentials can be gained by using thermoplastic matrices which have a greater potential for recycling. In this study, the tensile properties along the fibre direction of a HiPerDiF PLA/carbon fibre tape under process conditions (high temperature below the melting point of the matrix) are investigated. This allows to create a formability database that can be used as a basis for the development of process models that can help in the development of a robust manufacturing process for the highly formable HiPerDiF thermoplastic matrix tapes.*

Keywords: PLA; aligned short carbon fibre, forming, high temperature, fibre volume fraction

1. Introduction

Despite the potential that composites offer to save fuel or increase efficiency during a lightweight structure's functional life, their production and end of life management impact heavily on environmental pollution [1]. More specifically, thermoset composites have been contributing to both pollution with a 0% recycle ratio and a logarithmic increase in the production volume of composites [2]. Pyrolysis is a commercial option to reclaim fibres by burning the thermoset resin. The comminution of the reinforcement into short fibres (3-100 mm) is a necessary second step to reprocess them into a recycled composite [2]. Using a thermoplastic as a matrix will make the end-of-life recycling possible without the need for pyrolysis, and therefore reclaiming both matrix and fibres. Moreover, using recycled thermoplastic can save about 50% of production embodied energy [3] and would decrease the carbon emission by 50%, thus greatly reducing the concerns associated with waste management. An easy existing option is through the use of randomly distributed short fibres, which are mostly used to reinforce structures with low requirements for structural properties as they are characterised by a low fibre volume fraction (V_f). The HiPerDiF (High-Performance Discontinuous Fibre) method allows to produce composite tapes with high mechanical properties by increasing fibre alignment and volume fraction [4]. There are two main advantages of aligned discontinuous fibre composites: high mechanical properties compared to randomly oriented ones and the potential for high formability [5, 6]. The forming process should help to solve some of the handleability issues (that come with increased material formability) but

  doi:10.5075/epfl-298799_978-2-9701614-0-0

setting up the right process conditions is typically a very empirical process guided by experience and numerous physical trials. A different approach is suggested here whereby a forming simulation tool for the HiPerDiF material will be built and used to optimise the forming conditions (i.e., temperature, boundary condition, *etc.*). The present study is a starting point toward the manufacturing of defect-free sustainable composite parts with complex geometries by forming aligned discontinuous fibre thermoplastic (HiPerDiF) prepreg. The manuscript, more specifically, presents new results on the tensile behaviour (of PLA/carbon fibre tapes) under processing conditions. This behaviour is assumed to be one of the key mechanisms at play in the forming of the HiPerDiF material.

2. Specimen preparation

In order to successfully simulate a forming process, the in-plane material properties of the prepreg tape are needed. To this effect, tensile test specimens were produced to characterise the longitudinal (along with the fibre direction) properties of the tape. The specimen production consists of three main steps: reshaping the matrix material, aligning the fibres, and finally, the impregnation process. Poly(lactic acid) (PLA) filaments (3D4MAKERS) were used as the matrix material [7]. Tenax-J HT C124 of 3 mm length carbon fibres were chosen [8, 9]. The material properties of these two-component are given in Table 1.

Table 1. General properties of matrix and reinforcement [7, 8, 9]

Properties	3D4MAKERS PLA
Tensile Strength [MPa]	110
Tensile Modulus [GPa]	3309
Elongation [%]	160
Density [g/cm^3]	1.24
Melting Point [°C]	145-160
Process Temperature [°C]	170-220

Properties	Tenax-J Carbon fibre
Tensile Strength [MPa]	4400
Tensile Modulus [GPa]	240
Elongation [%]	1.8
Density [g/cm^3]	1.77
Type	HT C124
Sizing	Water-soluble
Cut Length [mm]	3
Diameter [μm]	7.0

Short carbon fibres, coated with a water-soluble sizing, are dispersed into water. The water mixture is pressurised to push out through a nozzle targeting the alignment plates. The space between the plates is the leading parameter controlling fibre alignment because the maximum horizontal distance between the top and bottom of a single 3 mm fibre cannot pass the distance between plates. Fibres drop on a drain belt where the water is removed by suction. After that, aligned fibres are fully dried with infrared heaters. The detailed HiPerDiF manufacturing process can be found in [4]. After the alignment process with the HiPerDiF machine, the 5 mm wide dry fibre tapes (aligned fibres) are ready for impregnation: a dry fibre tape was sandwiched between layers of PLA tapes during the impregnation process inside the mould (Figure 1). The PLA tapes were printed from a filament. A fibre volume fraction of 35% was achieved by sandwiching 9

  doi:10.5075/epfl-298799_978-2-9701614-0-0

layers of fibre tapes between 10 PLA tapes. These sets of layers were placed in the 5 mm slot of the female mould. The male mould was placed on top of the tapes and then placed into a vacuum bag where impregnation was undertaken under vacuum pressure at 195°C for 4 hours. One batch of specimens is shown in Figure 2. To perform digital image correlation (DIC), random white dots were sprayed on the specimen, as shown in Figure 3. As also illustrated in the figure, the specimen in-plane dimensions were 5 mm x 75 mm. The fibres were oriented along the length of the specimen. One of the samples' cross-sections, with a V_f of about 35% was confirmed via thermogravimetric analysis (TGA), is shown in Figure 4.

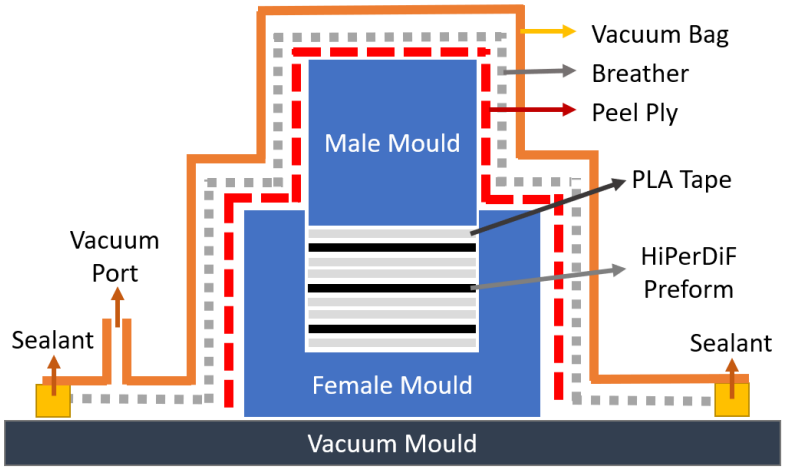

Figure 1: Representative illustration of the impregnation process

Figure 2: One batch of production

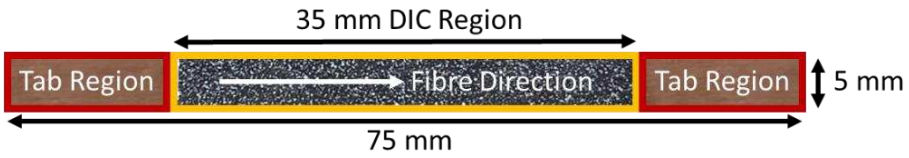

Figure 3: Specimen dimension

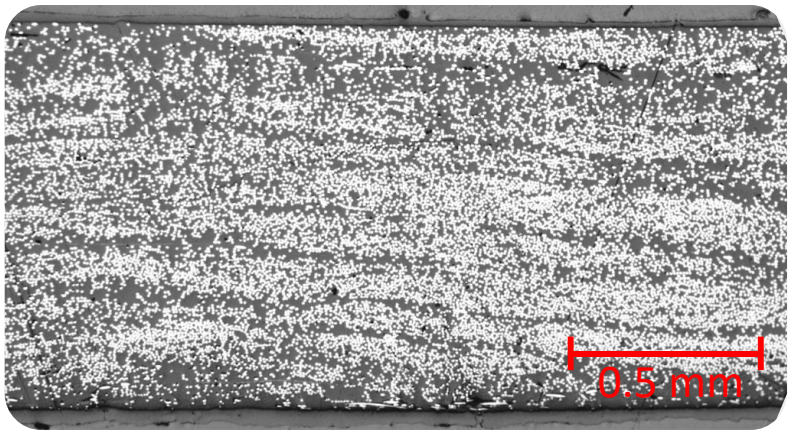

Figure 4: Microscope image of the specimen's cross-section

3. Test setup

Tensile tests with the fibres parallel to the loading direction were performed at different temperatures. The test setup is illustrated in Figure 5. A 10 kN Shimadzu electromechanical tensile test machine with a thermal chamber was used. Specimens were loaded quasi-statically (1 mm/min) at 20°C, 80°C, 120°C, and 140°C. Four tests were performed for each temperature. DIC cameras were placed vertically along with the specimen. To allow the specimen to be observed through the narrow gate whilst avoiding light reflection from the glass (in the thermal-chamber door), the thermal chamber was opened from below and a high-powered light source was used to illuminate the specimen. It was assumed that there was not much hot air loss from the lower gate, as the hot hair rises with decreasing density. Two thermocouples were used: one for measuring the temperature variation inside the chamber (which is about ±5°C due to the on-off controller) and another for monitoring the temperature of the specimen until it had reached equilibrium (with an error of about ±1°C). While the load data were recorded by the Shimadzu test machine, the elongation and strain were measured *via* DIC.

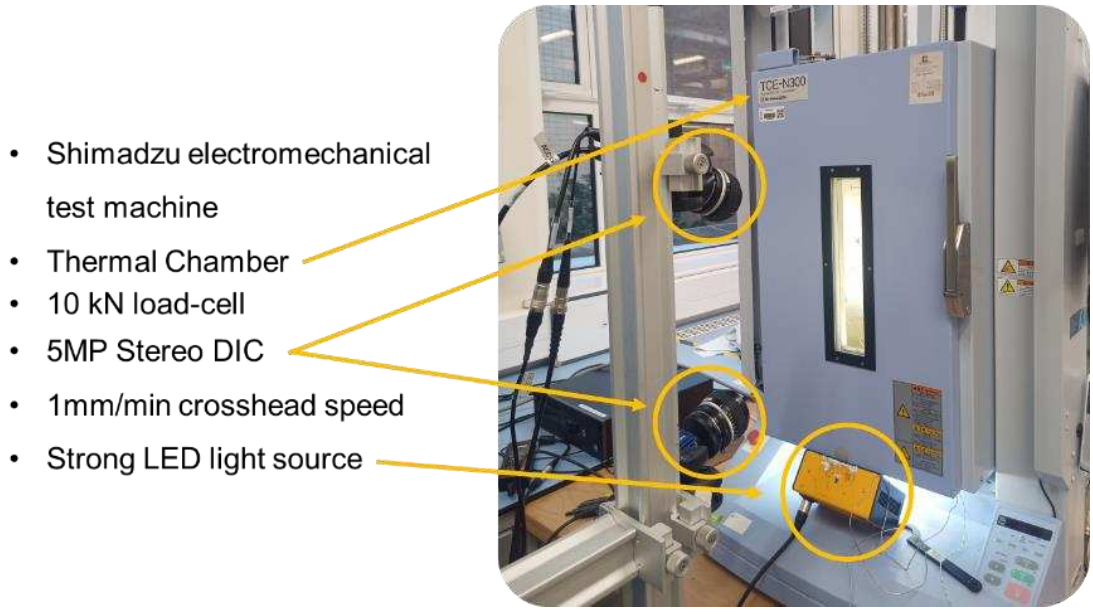

Figure 5: Test set-up

  doi:10.5075/epfl-298799_978-2-9701614-0-0

4. Data post-processing

The stress was calculated as the tensile force applied by the machine divided by the specimen's cross-sectional area. The strain data were computed from the average of 8 digital extensometers around the necking region which is shown in Figure 6. This is essential to measure the strain within the necking region correctly since the average value around the necking region includes low strain regions and causes errors in the calculated strain.

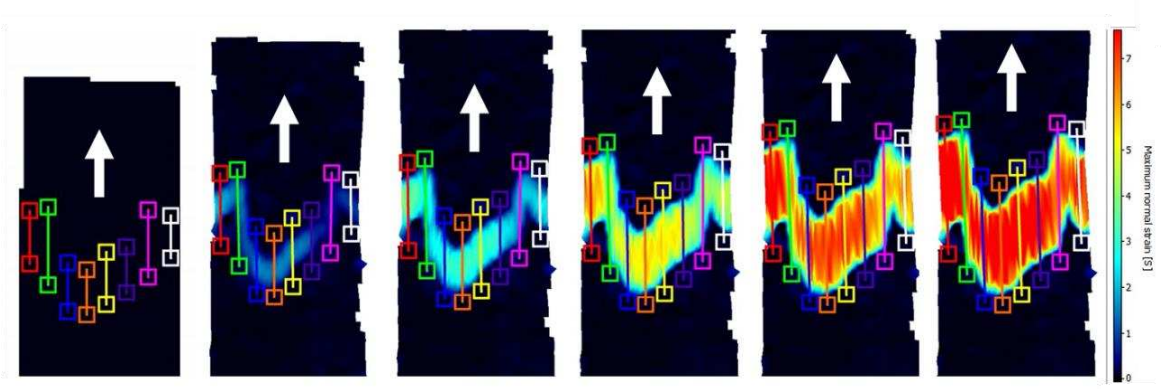

Figure 6: Strain measurement with digital extensometer within necking region

5. Results and discussions

The results from the experiments described in section 3 are presented in Figure 7 where the stress *vs.* strain curves are plotted. The 20°C results are represented with black dots while 80°C, 100°C, 120°C, and 140°C tests are plotted in blue, green, yellow and red dots respectively.

At room temperature, the average strength and average specific strength were measured to be 645 MPa as the average strength and 463 MPa*cm^3/g. This is respectively 13% and 118% higher than the aluminium 7075-T6[10]. Good stiffness properties were also obtained with an elastic modulus of 63.1 GPa (only 8% lower than aluminium [10]) and a specific modulus of 44.3 GPa*cm^3/g (75% higher than aluminium [10]). It is also worth noting that, a fibre volume fraction as high as 55% could be reached with better fibre alignment [11]. The failure strain was measured to be about 1.19%.

To illustrate the effect of temperature better, a zoomed-in version of the curves is provided on the right-hand side of Figure 7. Since the load-carrying capacity of the specimen depends on load transfer between short fibres, decreasing viscosity with increasing temperature decreases the load carried by the specimens. After an initial linear region (at low strains), the fibres start sliding on each other and transfer less load (as the overlap distance between them decreases). When the strain reaches around 50% there is not much fibre overlap remaining and the measured stresses are nearing 0. Load transfer decreases with the resin viscosity and becomes very low near the melting point of PLA (*i.e.*, 150°C).

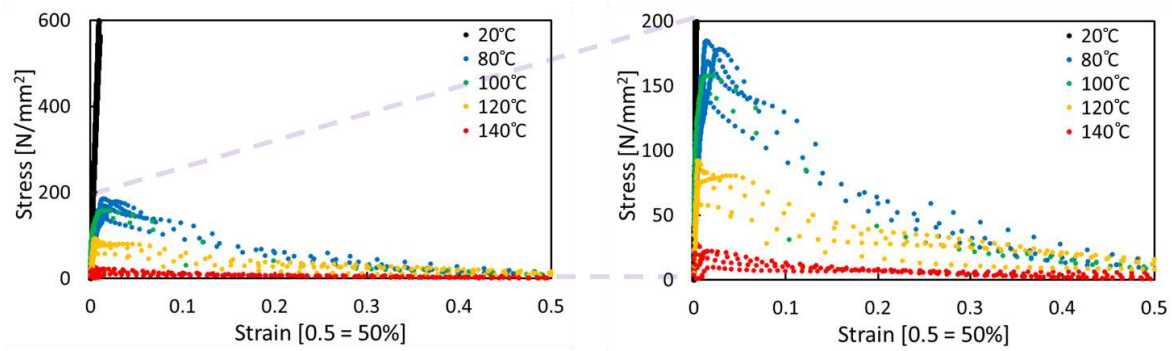

Figure 7: Stress vs. strain results at all temperatures

6. Conclusion

The effect of temperature on the tensile properties of HiPerDiF PLA/carbon fibre tape was experimentally characterised. At room temperature, the tape showed good specific properties that overmatch aluminium, suggesting a possible use in secondary structures not exposed to high temperatures (above 60°C). To reach a better quality and higher volume fraction, better alignment is needed and impregnation at higher temperatures can be tried in order to let excessive PLA out of the mould and increase V_f. As for high-temperature results for forming, the dataset was produced and will be used to guide the derivation of constitutive models that could be used for the forming simulations. The data revealed the matrix viscosity importance on the measured properties and it is anticipated that the fibre length will also play a key role.

To be able to perform comprehensive forming simulations and produce defect-free structures with reduced physical trails, shear and transverse mechanical properties are also needed, besides the tensile longitudinal ones. These will be characterised in the near future.

Acknowledgements

This study was supported by the Engineering and Physical Sciences Research Council (EPSRC) (grant no. EP/S021728/1) through the Centre for Doctoral Training in Composites Science, Engineering and Manufacturing (CoSEM CDT), Simulation of New Manufacturing Processes for Composite Structures (SIMPROCS) (grant no. EP/P027350/1) and a scholarship (started by Atatürk) from the Republic of Türkiye Ministry of National Education. The authors also would like to thank Yusuf Mahadik and Narongkorn Krajangsawasdi for their help in the experimental study and manufacturing process.

7. References

1. Singh RL, Singh PK. Global Environmental Problems. Principles and Applications of Environmental Biotechnology for a Sustainable Future 2016, 13–41. doi:10.1007/978-981-10-1866-4_2.
2. Bledzki AK, Seidlitz H, Goracy K, Urbaniak M, Rösch JJ. Recycling of carbon fiber reinforced composite polymers—review—part 1: Volume of Production, Recycling TECHNOLOGIES, Legislative Aspects. Polymers, 2021 13(2), 300. doi:10.3390/polym130203000.

3. Ashby MF, Shercliff H, Cebon D. Materials: Engineering, science, processing and design. Kidlington, Oxford, United Kingdom: Butterworth-Heinemann is an imprint of Elsevier 2019.
4. Yu H, Potter KD. Method and apparatus for aligning discontinuous fibre. UK patent, Patent application number 1306762.4, April, 2013.
5. Such M, Ward C, Potter K. Aligned discontinuous fibre composites: a short history, Journal of Multifunctional Composites 2014, Vol. 2 (3) - Pag 155-168.
6. Armiger TE, Edison DH, Lauterbach HG, Layton JR, Okine RK. Composites of stretch broken aligned fibres of carbon and glass reinforced resin. European Patent 0,272,088 1994.
7. Product data. (n.d.). Retrieved August 11, 2021, from https://www.3d4makers.com/pages/product-data
8. Tenax™ short fibers. (n.d.). Retrieved August 11, 2021, from https://www.teijincarbon.com/products/tenaxr-carbon-fiber/tenaxr-short-fibers
9. Tenax™ filament Yarn. (n.d.). Retrieved August 11, 2021, from https://www.teijincarbon.com/products/tenaxr-carbon-fiber/tenaxr-filament-yarn
10. Ferrous and Non-Ferrous Metals Stockist May 17, 2005. (2020, October 16). Aluminium: Specifications, properties, classifications and classes. Retrieved September 07, 2021, from https://www.azom.com/article.aspx?ArticleID=2863.
11. Yu H, Potter KD, Wisnom MR. A novel manufacturing method for aligned discontinuous fibre composites (high performance-discontinuous fibre method). Composites Part A: Applied Science and Manufacturing, 2014, 65, 175-185. doi:10.1016/j.compositesa.2014.06.005

  doi:10.5075/epfl-298799_978-2-9701614-0-0

DAMAGE ARREST MECHANISMS IN NANOPARTICLE INTERLEAVED COMPOSITE INTERFACES

Nithya Subramanian [a], Chiara Bisagni [b]

a: Marie Sklodowska-Curie Postdoctoral Fellow, Aerospace Structures & Computational Mechanics, Faculty of Aerospace Engineering, Delft University of Technology, The Netherlands; n.subramanian-1@tudelft.nl

b: Professor, Aerospace Structures and Computational Mechanics, Faculty of Aerospace Engineering, Delft University of Technology, The Netherlands

Abstract: *The effectiveness of carbonaceous nanoparticles in arresting and delaying damage in nanocomposites has been attributed to multiscale toughening mechanisms. To explore their application in joined interfaces of composites, this study investigates the use of carbon nanotube (CNT) interleaved films for co-cured joining of composite parts and their consequent effects on the interfacial fracture toughness. Carbon nanotubes dispersed in a thermoset resin into thin films of two discrete thicknesses (200 µ and 500 µ) and three concentrations of CNT dispersion were chosen for this study (0.5% wt., 1% wt., and 2% wt.). The films were semi-cured in the oven before being incorporated as interleaves in the composite laminate interface. Fracture toughness of the interface in mode I loading conditions was determined through double cantilever beam (DCB). Micrographs of the fracture surfaces reveal a slip-and-stick based crack jump and arrest phenomena in mode I when nanoparticles are added to the interleaved interface. The thickness of the interleaves has a more significant effect on mode I toughening mechanisms than the concentration of the nanoparticles.*

Keywords: Co-cured composite interface; Interleaf; Carbon nanotubes; Fracture toughness

1. Introduction

Composite structures for aeronautical applications can be traditionally joined via adhesive co-bonding, co-curing, and/or mechanical fastening, which induce interfacial defects and stress concentrations under operational loads and increases structural weight. Co-cured joints, unlike co-bonded joints have no discernible interface due to diffusion of the adhesive into the laminate during cure [1,2]. However, controlling the flow of epoxy in the co-cure region as well as mitigating misalignment of the sub-components during co-cure are challenging and lead to irregularities. The incorporation of a partially cured epoxy film in the co-cured region ensures uniform thickness and restrains the relative sliding of the sub-components during co-cure, thus preventing misalignments. This technique also allows for an easier method to integrate the adhesive epoxy layer in the composite lay-up process.

Interleaved composite laminates with a discrete layer of epoxy films between joining surfaces have been studied as a strategy to improve damage tolerance during co-cured joining [3–5] and limit the need for accompanying mechanical fasteners. Owing to the presence of an interleaf film at the interface, larger damage zones arising from microcrack diffusion and crack path tortuosity are observed leading to higher interfacial fracture toughness [6]. Research over the past two decades has probed the effectiveness of dispersed and aligned carbonaceous

  doi:10.5075/epfl-298799_978-2-9701614-0-0

nanoparticles (graphene platelets, carbon nanotubes, etc.) in enhancing the mechanical and multifunctional properties of polymers [7,8]. Various studies of CNT reinforced polymers have shown improved toughness over the neat matrix [9–11] inducing toughening mechanisms, such as crack deflection [12], crack pinning [11], CNT pull-out [13,14], microscale and nanoscale crack bridging [15]. However, these mechanisms require some degree of interaction between the crack front and the CNTs. Recent studies postulate the benefits of adding nanoparticles in a targeted fashion with controlled nanoparticle network morphology to trigger/activate multiscale damage suppression events as opposed to the less effective technique of homogenously dispersing the nanoparticles in a host polymer [12,16].

In this study, the authors explore the role of interleaf films containing CNT only in co-cured interfaces to delay and diffuse damage propagation [17,18] by allowing the CNT to directly interact with the crack front. This targeted reinforcement approach is preferred over the option to disperse the CNT in the entire matrix phase of the composite. A related previous study involving molecular simulations of CNT-dispersed matrix showed that elastic mechanical properties of the nanocomposite can be improved by adding CNT up to 2% wt. Loading levels beyond 2% wt. were shown to interfere with the epoxy crosslinking process and lead to deterioration of mechanical properties [19]. Therefore, we investigate CNT loading levels up to 2% wt. in the epoxy used for interleaving and consider two different interleaf thicknesses and their combined effects on damage propagation mechanisms.

Motivated by the effectiveness of nano-interleaves on toughening composite interfaces and their potential for expanded applications in co-cured composite joints, this study investigates the damage mechanisms in the interleaved interface from experiments performed under mode I load with double cantilever beam (DCB) specimens. The main parameters studied are the nanoparticle concentration and interleaf thickness. Following the mechanical tests, in order to investigate the type of interfacial failure (adhesive/cohesive), microcracking in the interleaf, and migration of the crack path, the fracture surfaces were examined with optical and confocal microscopes.

2. Experimental Work

2.1 Materials

The prepreg used for this study was unidirectional carbon IM7 fiber with HexPly® 8552 epoxy resin system of ply thickness 0.13 *mm*. Neat epoxy interleaves (containing no nanoparticles) in the study were manufactured with the API-60 epoxy system – an aerospace grade resin – purchased from Kaneka Aerospace Inc. with a compatible thermal cure cycle and properties with the HexPly® 8552 proprietary resin system. Filmed interleaves containing multi-walled CNT were procured from NanoSperse with the same host epoxy matrix at three nanoparticle concentrations (0.5% wt., 1% wt., 2% wt.) and two interleaf thicknesses (200 μ and 500 μ).

2.2 Laminate manufacturing with interleaves

All laminate specimens in the study consist of a [$0°_{12}$/interleaf/$0°_{12}$] lay-up and a unidirectional fracture interface. Both the neat epoxy interleaf as well as the CNT interleaves are staged (semi-cured) in the oven, subsequent to their complete cure kinetics characterization [3], to attain a resulting degree of cure between 0.3 – 0.35. An initial delamination is embedded in the laminate

  doi:10.5075/epfl-298799_978-2-9701614-0-0

spanning 35 *mm* using a Teflon release film of 25 *μ* thickness. During the laminate consolidation process, the interleaf film was introduced at the edge where the Teflon delamination insert ended. Figure 1 shows the staged interleaves and their consolidation into the laminate, which was cured in the autoclave according to the recommended prepreg cure cycle. The cured plates were trimmed and cut into samples of approximately 150 - 160 *mm* in length and 25 *mm* in width with a diamond-tipped circular saw for the fracture toughness tests. It must be noted that the total length of the actual specimen does not affect the test results as long as it is over 100 *mm*. The thickness of the specimens varied between 3.3 and 3.8 *mm* depending on the embedded interleaf thickness.

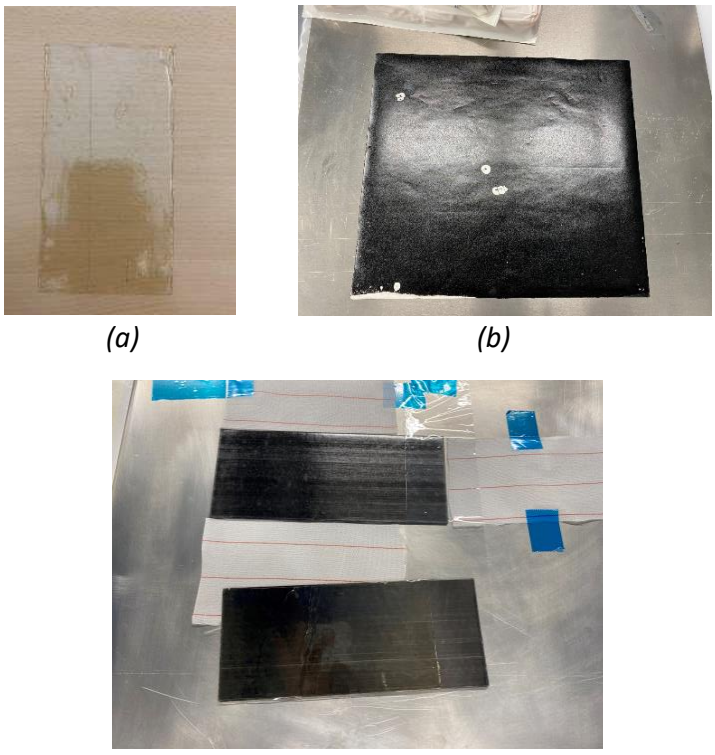

(a) *(b)*

(c)

Figure 1. Manufacturing and consolidation of the laminate with interleaved interface (a) Neat epoxy interleaf (200 *μ thickness); (b) CNT interleaf (0.5% wt., 200 μ thickness); (c) integration of interleaf in the laminate midplane*

2.3 Test setup and analysis scheme

Double cantilever beam samples were tested in mode I loading conditions conforming to ASTM standards [20] to calculate fracture toughness values and resistance effects to damage propagation. The samples tested and their corresponding nomenclature in the rest of this paper are reported in Table 1. All fracture tests were performed on a Zwick tension/compression test frame with 10 *kN* maximum capacity. The load frame was attached to a 1 *kN* load cell for the DCB tests. The samples were painted white, and 1 *mm* markings were made in black ink to track crack length propagation. Images from two monochromatic cameras perpendicular of the longitudinal axis of the samples were acquired every second to monitor crack length. Images from the two cameras were also helpful to determine if the crack front is asymmetric resulting in different crack lengths on either side.

  doi:10.5075/epfl-298799_978-2-9701614-0-0

Table 1. Number of samples and nomenclature based on interleaf type and thickness

Plate no.	Interleaf thickness [μ]	CNT conc. [% wt.]	Nomenclature	No. of samples
1	200	0 (Neat)	Neat200μDCB	2
2	200	0.5	0.5%CNT200μDCB	3
3	500	0.5	0.5%CNT500 μDCB	3
4	200	1	1%CNT200μDCB	3
5	500	1	1%CNT500μDCB	3
6	200	2	2%CNT200μDCB	3
7	500	2	2%CNT500μDCB	3

Figure 2 illustrates the mode I test with a piano hinge bonded to the sample. The samples in mode I were loaded at a constant crosshead displacement of 0.3 *mm/min.* It was expected as well as confirmed with subsequent microscopy that the limited flow of the interleaf epoxy during the cure cycle would allow for the crack front to be in contact with the interleaf layer. But a sharp and straight crack front with every point fully embedded in the interleaf layer could not be verified. Therefore, all samples were pre-cracked using the prescribed pre-cracking technique in ASTM D5528 to achieve an initial crack length between 28 and 32 *mm*.

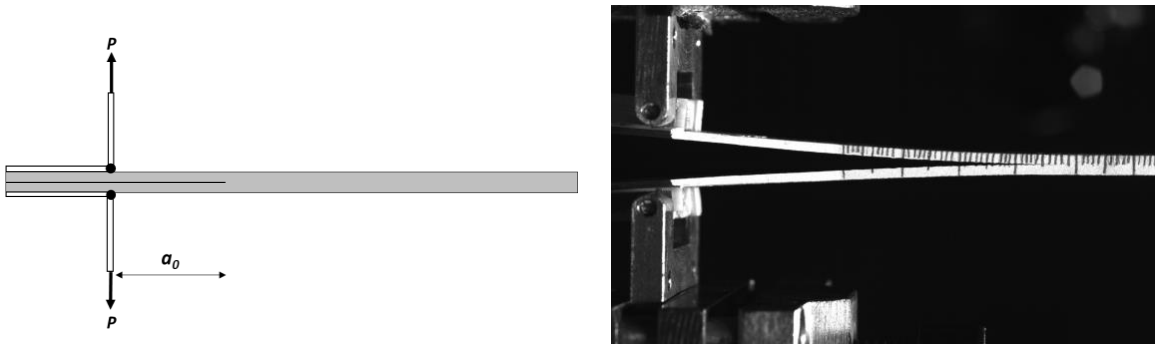

(a) *(b)*

Figure 2. Test setup for mode I fracture toughness testing (a) schematic of the DCB sample test with piano hinges; (b) image captured from monochromatic camera of DCB sample

Data reduction to compute mode I fracture toughness is performed on the load-displacement *(P-δ)* data from the test machine as well as the crack lengths from the captured images using the modified compliance calibration (MCC) approach [21]. This approach is chosen because it allows to account for the thickness differences among the samples while calculating mode I fracture toughness (G_I). A least squared plot of the crack length normalized by sample thickness *(a/h)* as a function of the cube root of compliance $(C^{1/3})$ is generated and the slope of this fit corresponds to A_1; *P is the load and b* is the sample width. The critical initiation fracture toughness (G_{Ic}) is computed by using the critical load (P_{crit}) instead of *P* in Eq. (1).

$$G_I = \frac{3P^2\, C^{2/3}}{2A_1 bh} \tag{1}$$

  doi:10.5075/epfl-298799_978-2-9701614-0-0

3. Results and Discussion

The load-displacement data obtained from the Zwick test frame for a representative sample from each set (described in Table 1) are plotted in Figure 3. The data is categorized based on the nanoparticle content and compared to the neat epoxy interleaved laminate in each case. While the *P-δ* profile of the neat epoxy interleaved interface indicates a stable, typical crack propagation, the inclusion of nanoparticles to the interface remarkably alters the damage mechanisms. In each case, the addition of nanoparticles leads to a significant improvement in the flexural stiffness of the sample. The slope of the linear *P-δ* section remains fairly constant for a specific CNT wt. content but appears to increase with increasing CNT content. The saw-tooth profiles in Figure 3 imply unstable crack growth followed by a strong arrest mechanism. The peak of each saw-tooth corresponds to the initiation load to propagate the crack at that specific crack length; however, the troughs of the saw-tooth indicate an arrest mechanism, subsequent to which the sample continues to behave 'elastically' with a reduced stiffness but no change to the crack length, until the next initiation load. The overall strain energy (area under the curve) is higher than the baseline laminate (with neat epoxy interleaf) even at low wt. contents of CNT.

The damage propagation in mode I for CNT interleaved interfaces can be described by a 'slip-stick' mechanism [22] as illustrated in Figure 4, where each sudden load drop in Figure 3 results in a crack slip/jump (sudden increase in crack length) but this slip is then arrested by a 'stick' phenomenon and held intact until the next slip event. The higher the load drop, the larger the crack slip tends to be. Although the mechanism of damage propagation is altered, the forces for crack arrest (troughs of the saw-tooth) are consistent with the forces in the baseline laminate containing the same interleaf thickness, i.e., each CNT interleaved laminate containing a 200 μ interleaf possesses a *P-δ* profile that falls to the baseline laminate *P-δ* profile at the end of a crack slip event.

Interleaf thickness exhibits a significant effect on the peak initiation loads, arrest loads, as well as the overall strain energy of the samples. As mentioned earlier, the thickness of the interleaf with no nanoparticles (neat epoxy) determines the lower bound for the *P-δ* profile when nanoparticles are added to the interface. Comparing the laminates with the same CNT wt. content but different interleaf thicknesses (Figures 4 (a)-(c)), it can be noted that the slip events are 'delayed' in the interfaces containing a thicker interleaf. This is demonstrated by the fact that each load drop in the *P-δ* curve occurs at a higher displacement for the 500 μ interleaved samples when compared to their thinner interleaved equivalent.

Micrographs obtained via a Zeiss Keyence Wide-angle laser microscope, as shown in Figure 5, also display higher tortuosity to the crack path and undulations in the interface for thicker interleaves. The undulations in the micrographs confirm cohesive-dominated failure in the thicker interleaf while suggesting a mix of adhesive and cohesive failure regions in Figure 5(a) as illustrated by regions of adhesive peeling [23]. Furthermore, Figure 5(b) reveals that the waviness of the undulations are clustered close to the mid-line (shorter wave-lengths) and they become sparser (with longer wave-lengths) towards the edge of the specimen. This indicates that the delamination front is not a straight line but curved and quasi-parabolic. The striations as well as the post-processed images from both cameras confirm that the crack length is nearly equal on both edges during the test thus implying that the quasi-parabolic crack front is symmetric [24].

  doi:10.5075/epfl-298799_978-2-9701614-0-0

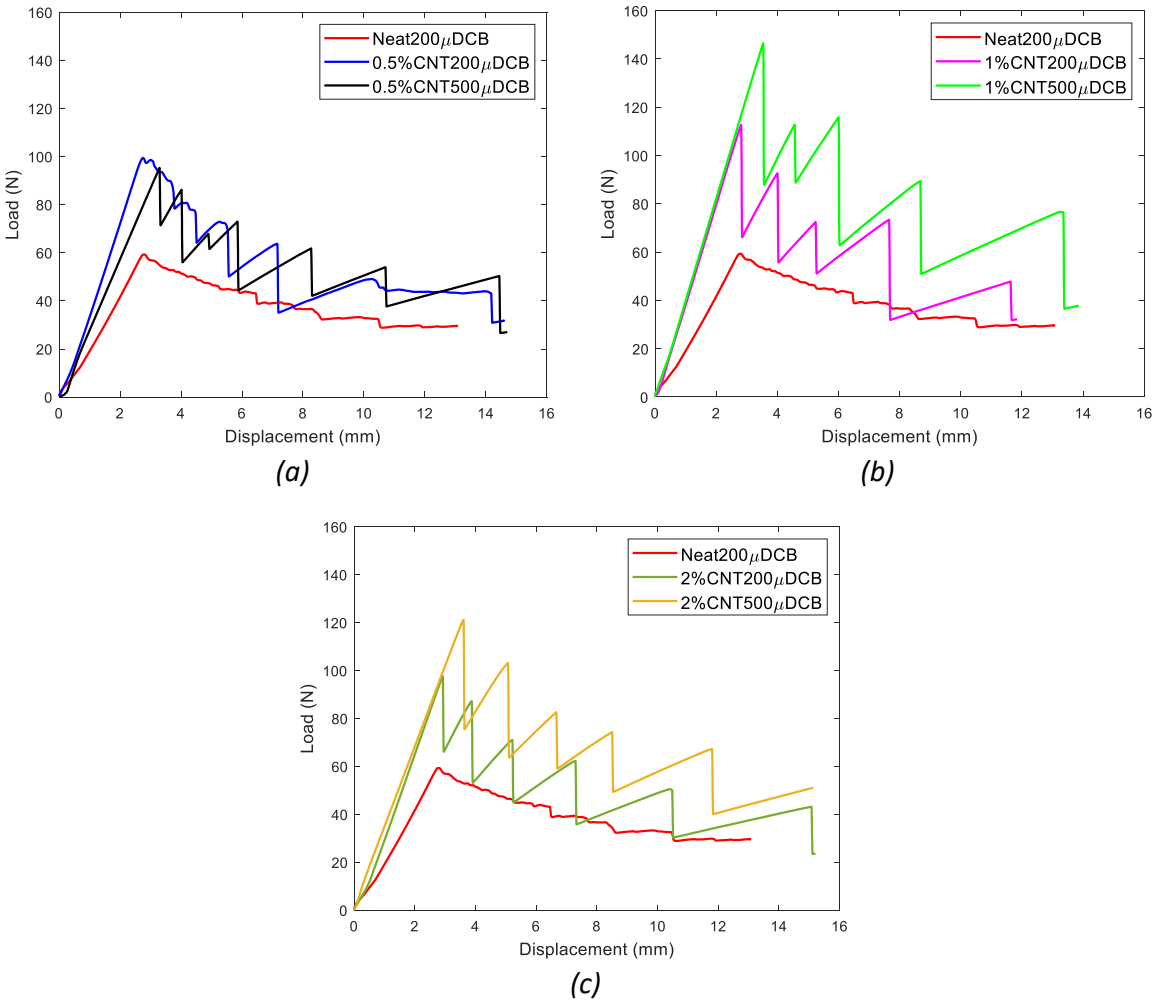

Figure 3. Comparison of load-displacement curves from DCB tests with neat epoxy interleaved interface (a) 0.5% CNT interleaves; (b) 1% CNT interleaves; (c) 2% CNT interleaves

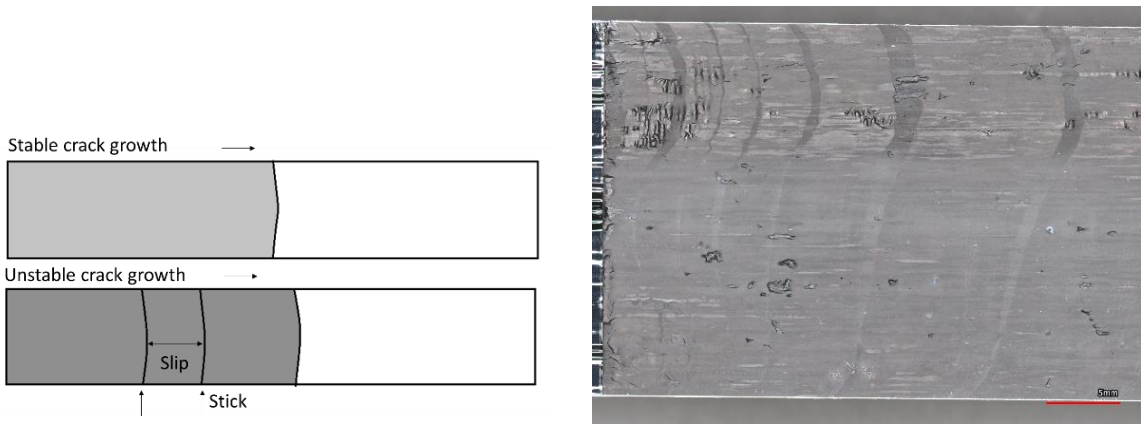

Figure 4. Slip-stick damage propagation (a) schematic of the fracture surface; (b) micrograph of failure surface from 1%CNT200μDCB with slip-stick striations

  doi:10.5075/epfl-298799_978-2-9701614-0-0

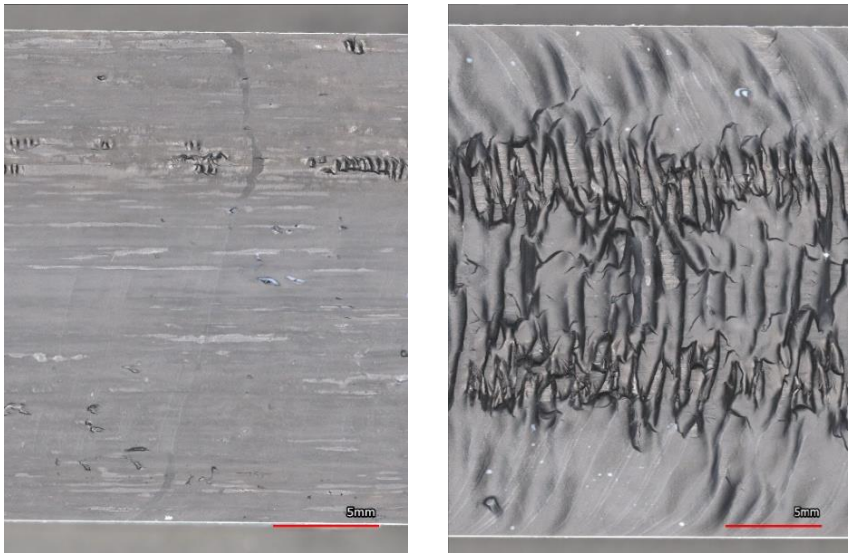

(a) *(b)*

Figure 5. Fracture striations and undulations on failed surface (a) in 1%CNT200µDCB; (b) in 1%CNT500µDCB

Data in literature places the critical mode I fracture toughness for IM7/8552 composites in the 0.2 – 0.23 kJ/m^2 range [25]. A larger spread is observed (between 0.2 – 0.27 kJ/m^2) [26] when using different approaches to determine the critical load (P_{crit}) in Eq. (1) such as visually observed deviation from linearity, or the 5% offset method described in ASTM D5528. Composite interfaces also exhibit a toughening effect to crack propagation owing to fiber bridging ahead of the crack front, represented generally with R-curves. As the crack length increases, more energy is required to further propagate the crack due to pinning and bridging effects between the fibers. The R-curves in Figure 6 contain mean fracture toughness values from multiple samples (as described in Table 1) in a sample set. In this study, the presence of an interleaf region does not allow for microscale fiber bridging across the fracture interface thus resulting in no R-curve effect.

A neat epoxy interleaf interacting with the crack front improves the mode I initiation resistance to the range: 0.25 – 0.3 kJ/m^2 [3] according to a previous study by the authors. In this batch of samples, however, no statistical difference between the neat epoxy interleaved interface and a laminate with no interleaf is observed here. Another remarkable characteristic of interleaved interfaces is the absence of any additional resistance as the crack length increases. The R-curves remain fairly flat in all cases although significant gains in toughness are observed as a result of the addition of CNT to the interleaves. We observe no statistically significant difference between laminates containing varying concentrations of CNT within a 200 μ interleaf. This indicates that toughening mechanisms in mode I are more sensitive/responsive to the thickness of the interleaf than the concentration of nanoparticles. Toughness of the interleaved laminate improves up to nearly 4 times with CNT concentrations ≥1% and an interleaf thickness of 500 μ.

The test data and micrograph striations demonstrate a crack arrest mechanism in CNT-interleaved laminates. This arrest seems to occur at a load nearly equal to that of a neat epoxy interleaved laminate of the same interleaf thickness. Therefore, a neat epoxy interleaf appears to set the lower bound for the force-displacement profile of a CNT-interleaved laminate. At

  doi:10.5075/epfl-298799_978-2-9701614-0-0

higher CNT wt. %, we observe higher initiation loads but larger load drops (corresponding to larger crack jumps), whereas increasing interleaf thickness shifts the load drop events (slip) to higher displacements indicating a damage delay mechanism. The *P-δ* data and the micrographs affirm that crack growth processes are altered at two scales due to nanoparticle interleaving: at the macroscale via slip-stick based jump and via microscale tortuosity behind the quasi-parabolic crack front.

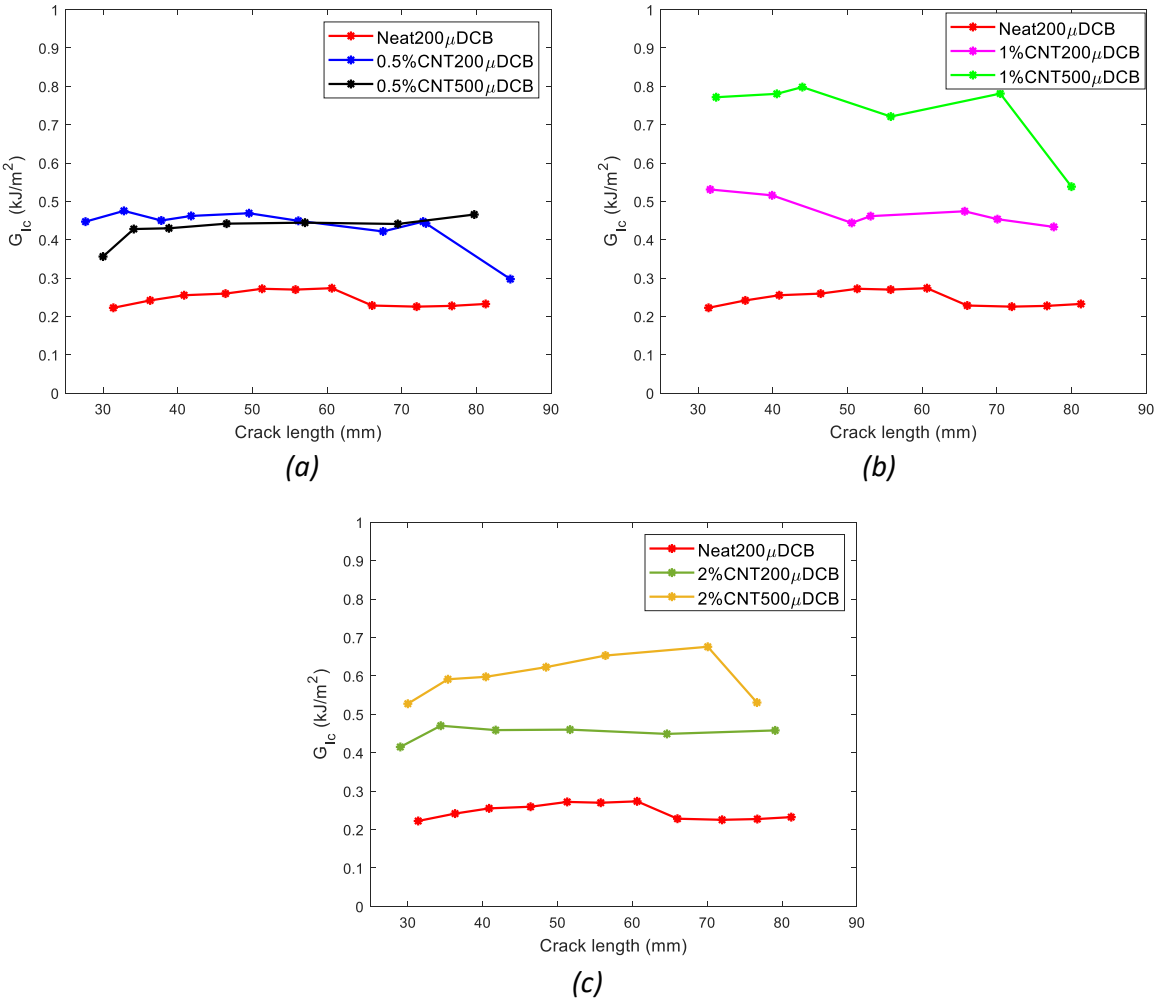

Figure 6. R-curves from DCB tests compared with neat epoxy interleaved interface (a) 0.5% CNT interleaves; (b) 1% CNT interleaves; (c) 2% CNT interleaves

4. Conclusions

This study was focused on the incorporation of semi-cured interleaves containing nanoparticles in the composite consolidation process and its effectiveness in mode I fracture resistance. Interleaves with neat epoxy as well as different concentrations of CNT were staged to a predefined degree of cure to maintain their integrity and thickness during consolidation into the laminate. Interleaves of two different thicknesses were considered in this study. The double cantilever beam samples prepared using this approach were tested under mode I loading.

The load-displacement data as well as micrographs of failed surfaces revealed a remarkable change in the underlying damage mechanisms governing crack propagation in mode I. The

  doi:10.5075/epfl-298799_978-2-9701614-0-0

addition of nanoparticles to the interleaf resulted in a higher flexural stiffness of the sample whereas the critical fracture initiation loads were more sensitive to interleaf thickness. A slip-stick phenomenon was observed with damage progression where the crack arrest load for a CNT interleaf could be predicted by the load-displacement profile of a neat epoxy interleaf of same thickness. Improvements in mode I fracture toughness of up to 4 times were observed with the inclusion of CNT within a thicker 500 μ interleaf when compared to a baseline interleaf without nanoparticles. There is no significant resistance behaviour (R-curve effects) to crack propagation as a function of crack length as no bridging effects were observed. Data from the fracture toughness tests were augmented with wide-angle microscopy of the fractured surfaces to shed light on crack front progression and the microscale mechanisms that lead to damage delay.

Acknowledgements

This project has received funding from the European Union's Horizon 2020 research and innovation programme under the Marie Skłodowska-Curie grant agreement No. 835672. The authors acknowledge the support from the Delft Aerospace Materials and Structures Lab (DASML), particularly Alexander Uithol, to conduct experiments and post-process image data.

5. References

[1] Mohan, J., Ivanković, A., and Murphy, N. "Mode I Fracture Toughness of Co-Cured and Secondary Bonded Composite Joints." *International Journal of Adhesion and Adhesives*, Vol. 51, 2014, pp. 13–22.

[2] Brito, C. B. G., Contini, R. de C. M. S., Gouvêa, R. F., Oliveira, A. S. de, Arbelo, M. A., and Donadon, M. V. "Mode I Interlaminar Fracture Toughness Analysis of Co-Bonded and Secondary Bonded Carbon Fiber Reinforced Composites Joints." *Materials Research*, Vol. 20, No. suppl 2, 2018, pp. 873–882.

[3] Subramanian, N., and Bisagni, C. Multiscale damage in co-cured composites—perspectives from experiments and modelling. Presented at the Thirty-sixth Technical Conference, 2021.

[4] Chen, S. F., and Jang, B. Z. "Fracture Behaviour of Interleaved Fiber-Resin Composites." *Composites Science and Technology*, Vol. 41, No. 1, 1991, pp. 77–97.

[5] Marino, S. G., and Czél, G. "Improving the Performance of Pseudo-Ductile Hybrid Composites by Film-Interleaving." *Composites Part A: Applied Science and Manufacturing*, Vol. 142, 2021, p. 106233.

[6] Singh, S., and Partridge, I. K. "Mixed-Mode Fracture in an Interleaved Carbon-Fibre/Epoxy Composite." *Composites Science and Technology*, Vol. 55, No. 4, 1995, pp. 319–327.

[7] Avilés, F., Oliva-Avilés, A. I., and Cen-Puc, M. "Piezoresistivity, Strain, and Damage Self-Sensing of Polymer Composites Filled with Carbon Nanostructures." *Advanced Engineering Materials*, Vol. 20, No. 7, 2018, p. 1701159.

[8] Rai, A., Subramanian, N., and Chattopadhyay, A. Investigation of Piezo-Resistivity in CNT Nano-Composites under Damage. Presented at the SPIE Smart Structures and Materials + Nondestructive Evaluation and Health Monitoring, Las Vegas, Nevada, United States, 2016.

[9] Zainol Abidin, M. S., Herceg, T., Greenhalgh, E. S., Shaffer, M., and Bismarck, A. "Enhanced Fracture Toughness of Hierarchical Carbon Nanotube Reinforced Carbon Fibre Epoxy Composites with Engineered Matrix Microstructure." *Composites Science and Technology*, Vol. 170, 2019, pp. 85–92.

[10] Wichmann, M. H. G., Schulte, K., and Wagner, H. D. "On Nanocomposite Toughness." *Composites Science and Technology*, Vol. 68, No. 1, 2008, pp. 329–331.

  doi:10.5075/epfl-298799_978-2-9701614-0-0

[11] Wetzel, B., Rosso, P., Haupert, F., and Friedrich, K. “Epoxy Nanocomposites – Fracture and Toughening Mechanisms.” *Engineering Fracture Mechanics*, Vol. 73, No. 16, 2006, pp. 2375–2398.

[12] Liu, Q., Lomov, S. V., and Gorbatikh, L. “The Interplay between Multiple Toughening Mechanisms in Nanocomposites with Spatially Distributed and Oriented Carbon Nanotubes as Revealed by Dual-Scale Simulations.” *Carbon*, Vol. 142, 2019, pp. 141–149.

[13] Rai, A., Subramanian, N., Koo, B., and Chattopadhyay, A. “Multiscale Damage Analysis of Carbon Nanotube Nanocomposite Using a Continuum Damage Mechanics Approach.” *Journal of Composite Materials*, Vol. 51, No. 6, 2017, pp. 847–858.

[14] Subramanian, N. *Physics-Based Modeling of Material Behavior and Damage Initiation in Nanoengineered Composites*. Doctoral Dissertation Aerospace Engineering 2018. Arizona State University, Tempe, Arizona, USA, 2018.

[15] Garcia, E. J., Wardle, B. L., and John Hart, A. “Joining Prepreg Composite Interfaces with Aligned Carbon Nanotubes.” *Composites Part A: Applied Science and Manufacturing*, Vol. 39, No. 6, 2008, pp. 1065–1070.

[16] Liu, Q., Lomov, S. V., and Gorbatikh, L. “Enhancing Strength and Toughness of Hierarchical Composites through Optimization of Position and Orientation of Nanotubes: A Computational Study.” *Journal of Composites Science*, Vol. 4, No. 2, 2020, p. 34.

[17] Warren, Graham Leicester. *EPOXY/SINGLE WALLED CARBON NANOTUBE NANOCOMPOSITE THIN FILMS FOR COMPOSITES REINFORCEMENT*. Texas A&M University, 2009.

[18] Shin, Y. C., Lee, W. I., and Kim, H. S. “Mode II Interlaminar Fracture Toughness of Carbon Nanotubes/Epoxy Film-Interleaved Carbon Fiber Composites.” *Composite Structures*, Vol. 236, 2020, p. 111808.

[19] Subramanian, N., Rai, A., and Chattopadhyay, A. “Atomistically Informed Stochastic Multiscale Model to Predict the Behavior of Carbon Nanotube-Enhanced Nanocomposites.” *Carbon*, Vol. 94, 2015, pp. 661–672.

[20] D30 Committee. *Test Method for Mode I Interlaminar Fracture Toughness of Unidirectional Fiber-Reinforced Polymer Matrix Composites*. ASTM International.

[21] Kageyama, K., and Hojo, M. Proposed Methods for Interlaminar Fracture Toughness Tests of Composite Laminates. Presented at the Achievement in composites in Japan and the United States, 1990.

[22] Zhou, Y., Xiao, Y., Wu, Q., and Xue, Y. “A Multi-State Progressive Cohesive Law for the Prediction of Unstable Propagation and Arrest of Mode-I Delamination Cracks in Composite Laminates.” *Engineering Fracture Mechanics*, Vol. 248, 2021, p. 107684.

[23] Silveira, N. N. A., Sales, R. C. M., Brito, C. B. G., Cândido, G. M., and Donadon, M. V. “Comparative Fractographic Analysis of Composites Adhesive Joints Subjected to Mode I Delamination.” *Polymer Composites*, Vol. 40, No. 8, 2019, pp. 2973–2983.

[24] Guo, S., Xia, Y., Wei, X., and Zhou, Q. “Investigation on the Stable and Stick-Slip Crack Propagation Behaviors in Double Cantilever Beam Test.” *The Journal of Adhesion*, Vol. 96, No. 13, 2020, pp. 1198–1218.

[25] Krueger, R. “A Summary of Benchmark Examples to Assess the Performance of Quasi-Static Delamination Propagation Prediction Capabilities in Finite Element Codes.” *Journal of Composite Materials*, Vol. 49, No. 26, 2015, pp. 3297–3316.

[26] Raimondo, A., Urcelay Oca, I., and Bisagni, C. “Influence of Interface Ply Orientation on Delamination Growth in Composite Laminates.” *Journal of Composite Materials*, No. in press, 2021.

  doi:10.5075/epfl-298799_978-2-9701614-0-0

EXPERIMENTAL CHARACTERISATION OF ELECTRICAL CONDUCTIVITIES OF CARBON/EPOXY LAMINATES

Gang Zhou[a], Ewa Mikinka[a], Xujin Bao[b], Weiwei Sun[c]

a: Aeronautical and Automotive Engineering, Loughborough University, Loughborough LE11 3TU, UK – G.Zhou@Lboro.ac.uk
b: Department of Materials, Loughborough University, Loughborough LE11 3TU, UK
c: C-Power Ltd, No 5 Huake Si Road, Tianjing, China

Abstract: *This work investigated some key issues of anisotropic electrical conduction in carbon/epoxy laminates, made of the same carbon fibres and epoxy resin, with three different lengths and areas, fibre waviness and various electrode-specimen contact conditions. The objectives were to ensure that the contributions of extrinsic factors to the electrical conductivities not be erroneously attributed to intrinsic ones and to develop an understanding for the variation of the electrical conductivities under elevated temperatures. It was found that the electrical conductivities were independent of dimensions. It was shown that the increase in clamping force increased electrical conductivities. It was found that the paint enhancement was modest in the in-plane direction but significant in the through-the-thickness direction. These findings suggest that the paint effect was an artefact. It was found that when the level of electrical current was increased up to 3 A, the raised temperatures could reach as much as 50^{0}C.*

Keywords: carbon/epoxy laminate; electrical conductivity; electrical current; clamping force; temperature.

1. Introduction

The electrical conduction and current-induced thermal behaviour of carbon fibre-reinforced laminates have attracted lots of attention in the fields of lighting strike protection [1-2], electromagnetic interference (EMI) shielding [3-4], electro-thermal de-icing systems [5], high-speed rotors [6-7] and electrification of composite aircraft [8-9]. Research investigations proved extremely challenging, as (a) composite laminates are anisotropic, (b) there is the lack of test standard of electrical conductivities for composite laminates even at the coupon level, (c) the effects of extrinsic factors on electrical conductivities could erroneously be attributed to those of intrinsic parameters and (d) the direct adaptations of standard electrical measurement methods for isotropic and homogeneous materials were used for anisotropic composite laminates. As a result, not only are the values of electrical conductivities widely varying but also there is little accurate and reliable data. Moreover, the relationships between the values of electrical conductivities and key intrinsic and extrinsic parameters were not established with confidence. This has led to significant difficulties to explore multi-functionalities of lightweight composite structures in design, analysis, and numerical modelling.

Although several findings on the electrical conductivities of carbon/epoxy laminates were reported [1-2,4], there is a dearth of knowledge of how laminate specimen dimensions,

  doi:10.5075/epfl-298799_978-2-9701614-0-0

current level, silver paint and clamping pressures, fibre waviness and raised temperature affect electrical conduction characteristics. A systematic experimental investigation on the electrical conduction and electro-thermal behaviour of carbon/epoxy laminates was conducted at Loughborough University. Two different carbon/epoxy material systems were employed, namely, unidirectional (UD) tape-based and plain weave fabric-based with the same type of carbon fibre and epoxy resin. Specimens consisted of rectangular shapes of three different lengths for in-plane measurements, square and circular shapes of three different areas for through-the-thickness (TTT) measurements. The objectives were to develop an in-depth understanding of electrical conduction mechanisms and to examine the effects of both intrinsic and extrinsic factors on the anisotropic nature of electrical conduction and electro-thermal behaviour using two-probe method via solid electrodes. While intrinsic factors were lay-up and fibre waviness, extrinsic factors included specimen size, clamping force, conductive paint, current level and raised temperature. In this work, the results primarily from the tape-based laminates were presented.

2. Carbon/epoxy laminates and measurement methods

2.1 Carbon/epoxy specimens and preparations

Two types of carbon/epoxy laminates were made of UD tape and plain weave fabric prepregs, respectively, in which both used the same 12k PAN-based Grafil 34-700 carbon fibres and LTM45 epoxy resin. The UD tape-based laminate panel of 300×300 mm was laid up symmetrically with 16 plies in a QI lay-up of $(45^0/0^0/–45^0/90^0)_{2s}$, with a cured ply thickness of 0.128 mm. The fabric-based laminate panel of the same size was also laid up with 8 plies in a QI lay-up in $(\pm45^0/0^0/90^0)_{2s}$, with a cured ply thickness of 0.428 mm. Both types of the laminate panels were cured in an autoclave at 60^0C under a pressure of 0.62 MPa for 16 hours to have a nominal thickness of 2 and 3.4 mm, respectively. A nominal value of electrical conductivity is 55556 S/m for Grafil 34-700 carbon fibres [10] and is 1.4x10-12 S/m for LTM45 epoxy resin [11]. The respective fibre volume fractions were 61% and 58%.

To achieve best contact between solid electrodes and specimen faces for both rectangular and square shapes, the entire surfaces of each of the two panels were milled symmetrically to parallel on a milling machine first. The respective thicknesses of the two panels became 1.86 and 3.18 mm. For the tape-based laminates, about half of a cured ply thickness was machined off from each surface, whereas for the fabric-based laminates, about a third of a cured ply thickness was machined off. This operation achieved a geometric flatness and parallel of the two surfaces and exposed sufficient carbon fibre filaments. Strips of specifically selected widths were then cut using a bench saw with the two cut cross sections of each strip being milled to parallel. Individual test specimens of both rectangular and square shapes were finally cut off the milled strips. The nominal dimensions of the square specimens were 10x10 mm, 20x20 mm and 30x30 mm, respectively. The rectangular specimens with the same width of 10 mm had the respective lengths of 10 mm, 20 mm and 30 mm. The half of all specimens had silver paint applied uniformly on their contact faces. The tape-based 16 ply cylindrical specimens were extracted with core drills of three different sizes.

2.2 Measurement method and experimental set-up for volume electrical conductivities

Since there is no established method for measuring the electrical conductivity of anisotropic fibre-reinforced composite laminates, the present method was adapted from a 2-probe

  doi:10.5075/epfl-298799_978-2-9701614-0-0

method (2PM) in ASTM D4496 [12] recommended for moderately conductive materials. Primary considerations for its validity were given to ensure that the composite materials at both current and voltage probe contact locations were the same not only in in-plane but also in TTT measurements. A composite specimen with a length of *L*, a width (or diameter) of *b* (or *d*) and a thickness of *t* was clamped between two solid electrode boards, as shown in Figure 1. When electric current with a selected value flowed in its length direction, the volume electrical resistance *R* was calculated from the measured voltage drops. Then, with the known specimen dimensions, the volume electrical conductivity *k* in S/m was calculated by Ohm's law as

$$k = \frac{L}{Rbt} = \frac{1}{Rt}\left(\frac{L}{b}\right) = \frac{JL}{\Delta V} \quad (1)$$

in which *J* denotes the current density over the given area of *bt* and Δ*V* is the voltage drop. A digital torque screwdriver Norbar 13850 with a range of 0.3 to 1.5 Nm and an accuracy of ±6% was used to apply precise clamping pressures. An IR dual laser noncontact thermometer RS820 with a digital display was used for rapid precise temperature measurements in a range of -50 to 380°C with an accuracy of ±1%.

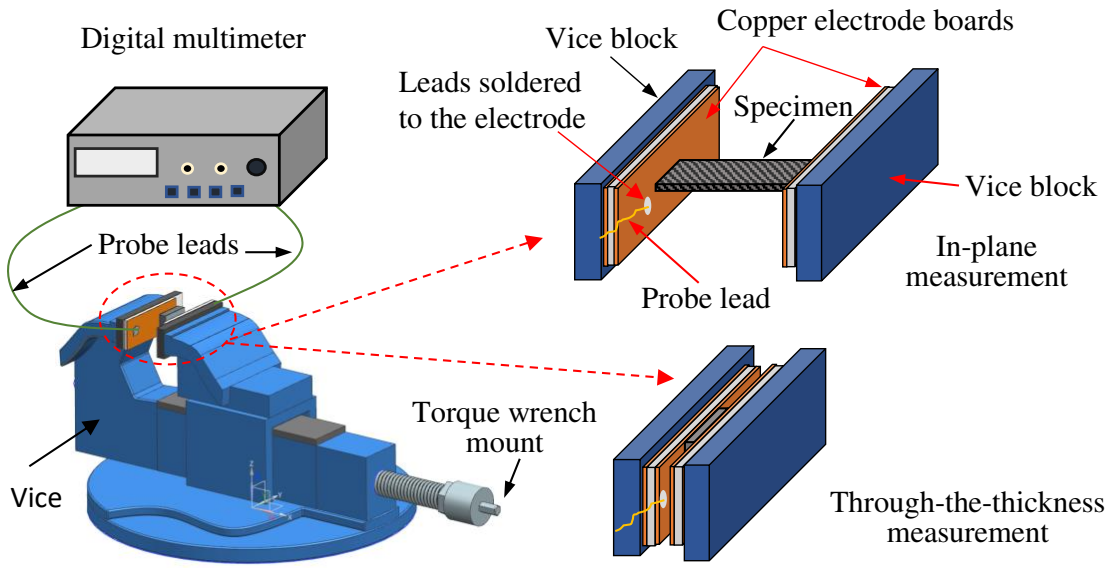

Figure 1. Two-probe method for measurement of volume electrical conductivity

3. Results and Discussion

3.1 Anisotropic electrical conduction path networks

It is well known that carbon/epoxy laminates are significantly anisotropic electrically, as carbon fibre tows in the lamination plane are conductive, whereas epoxy that keeps carbon fibres separated in both the in-plane transverse and TTT directions is insulative. Thus, an in-plane conduction path network was dominated by the axial electrical conduction of carbon fibre tows. The overall in-plane average values from the two in-plane directions shown in Figure 2 were 11064 S/m for the tape-based laminates.

For the TTT direction, an electrical conduction path network was commonly attributed to the existence of interior randomly distributed fibre-to-fibre contact points. If that were the case, the average TTT values would be much greater than the present values of about 37.3 S/m for

  doi:10.5075/epfl-298799_978-2-9701614-0-0

tape-based laminates shown in Figure 3, as a nominal value of electrical conductivity of 333 S/m for PAN-based carbon fibres in the diametric direction [13] is about an order of magnitude greater. Moreover, the present laminates were well made of commercial prepregs using autoclave so that majority of individual fibre filaments were surrounded by epoxy, though distances among some of filaments may well be tiny. It can thus be speculated that a TTT conduction path could also have short resin tracks among the filaments of both in the same ply and at the ply crossing interfaces, in addition to the 'fibre-to-fibre physical contact', and that those tiny resin tracks may have broken down dielectrically under local raised breakdown voltages at the interfaces of the resin tracks. In addition, the voluminous distributions of these contact points could be affected by other intrinsic factors such as fibre volume fraction [14], lay-up [8], fibre waviness [15] and manufacturing-related consolidation pressures [16].

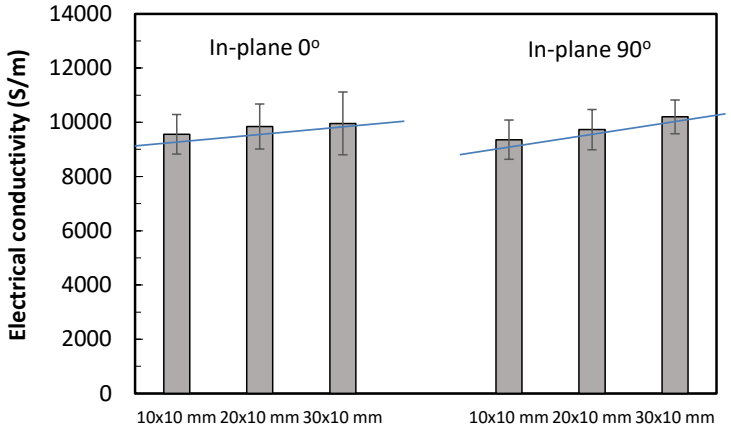

Figure 2. In-plane electrical conductivities of tape-based laminates without silver paint

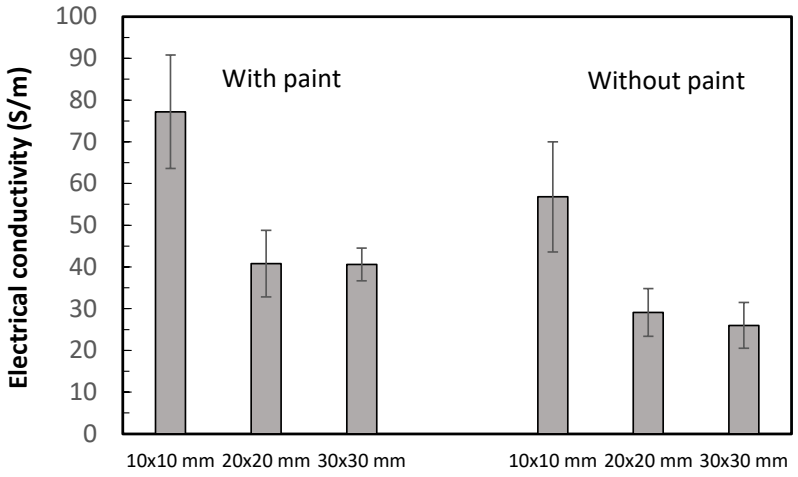

Figure 3. Through-the-thickness electrical conductivities of tape-based laminates

3.2 Effects of specimen sizes

Figure 4 shows that a specimen length had a linear relationship with the corresponding electrical resistance. This linear trend agreed with prediction of Eq. (1) and confirmed that the in-plane electrical conductivities remained independent of specimen length. Figure 5 shows that a cross-sectional area had an exponential relationship with the TTT values of electrical conductivities, which also agreed with prediction of Eq. (1). This also confirmed that the TTT electrical conductivities were independent of the cross-sectional areas of specimens.

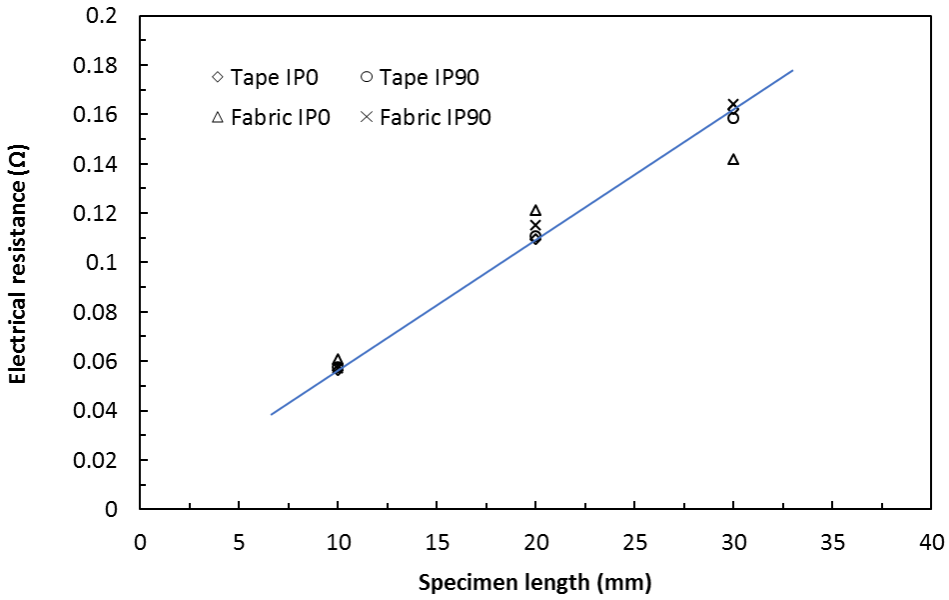

Figure 4. In-plane resistance variation with specimen length for tape- and fabric-based laminates without silver paint

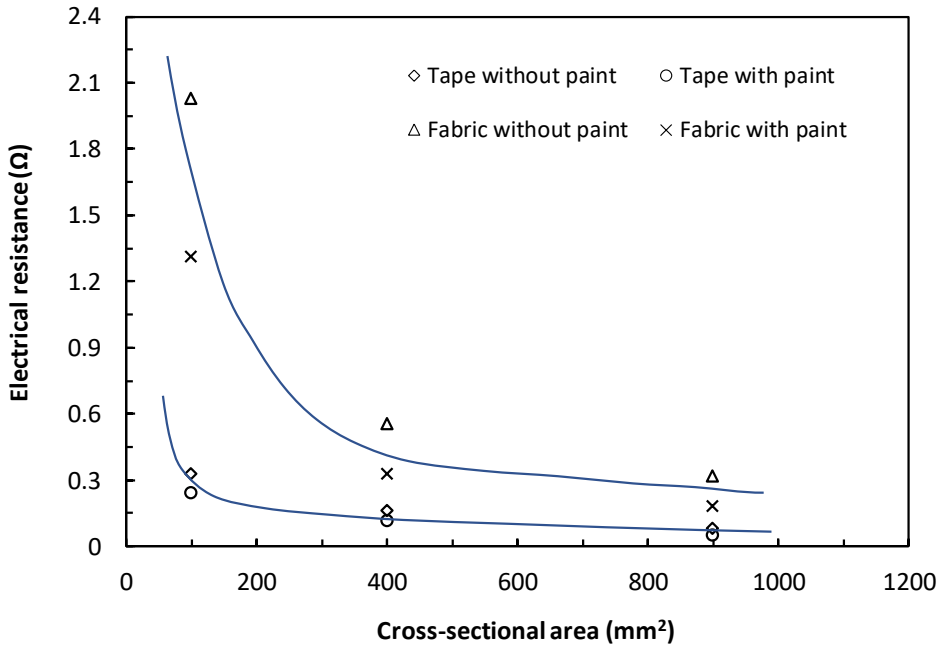

Figure 5. Through-the-thickness resistance variation with cross-sectional area for tape- and fabric-based laminates without and with silver paint

3.3 Effects of clamping force

Figure 6 shows the variations of the in-plane electrical conductivities with the level of clamping torques in a range of 0.5 to 1.3 Nm for the tape-based carbon/epoxy samples without silver paint. The established trends appear to be linear and consistent. The tape-based carbon/epoxy samples with silver paint exhibited the similar linear trends but with the slightly lesser slopes. Although the contact faces of all present samples were carefully controlled to be flat and parallel, when using solid electrodes, the values of the electrical conductivities could vary as much as 50% in the present torque range.

  doi:10.5075/epfl-298799_978-2-9701614-0-0

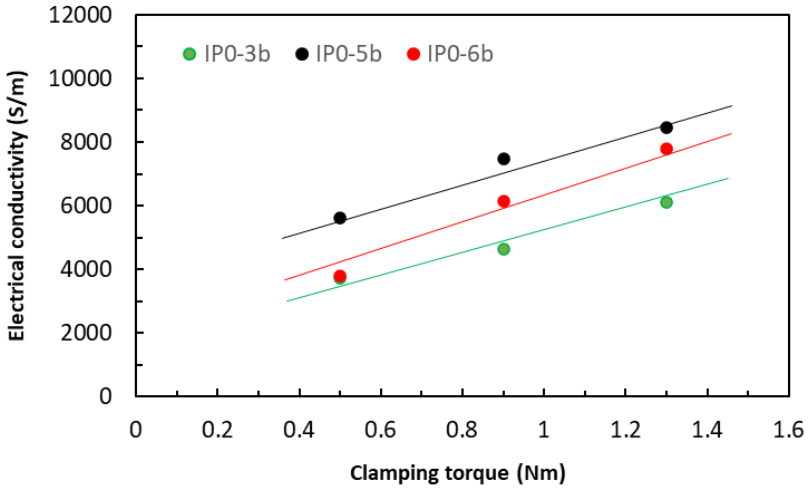

Figure 6. Variations of in-plane electrical conductivity with clamping torque for tape-based carbon/epoxy samples without silver paint

3.4 Effects of conductive silver paint

Appyling conductive paint (or paste) to the contact faces of composite specimens in electrical conductivity measurements has been a common practice. The present data in Figures 3 and 5 demonstrated that when used with solid electrodes, the paint enhancement on the values of the electrical conductivities were significant, especially in the TTT direction. They were 42% for the tape-based carbon/epoxy laminates and 67% for the fabric-based laminates. Since the use of silver paint on specimen contact faces could not alter the interior conduction path network, these significant enhancements thus reflected the lack of achieving the designated current densities at the contact faces on the unpainted specimens, rather than the genuine indication of the physical properties of the painted specimens. This was again in agreement with prediction of Eq. (1) that the value of electrical conductivity was linearly proportional to the value of current density. The paint enhancement effets on the in-plane electrical conductivities were very modest (less than 20%) due primarily to that the much greater contact with carbon fibres existed. All these appear to suggest that the paint enhancing effects on the values of electrical conductivities should be viewed either as an artefact or, at the best, as the idealised upper limits of the measured values. Therefore, the electrical conductivities values obtained from the specimens without conductive paint should be closer to true values of the materials.

3.5 Effects of electrical current level and raised temperature

In Figure 7, the variations of raised surface temperatures with the increase in electrical current were shown for the in-plane electrical conductivities of the tape-based laminates. Under various given levels of clamping torques, a parabolic trend of surface temperatures was consistently established from mA to 3 A. There were a couple of attempts of taking the current level to 5 A, which led to the destruction of the samples with the temperatures reaching 90^0C and beyond. The temperatures in interior carbon fibres were expected to increase with the increased current levels due to Joule heating and thus epoxy separating them was also heated rapidly. As epoxy is electrically insulative, its rate of the temperature raises was significantly slower than that of carbon fibres, leading to the nonlinear parabolic trend. It was clear from Figure 8 that such moderate increase of temperatures led to very little change in electrical conductivities.

  doi:10.5075/epfl-298799_978-2-9701614-0-0

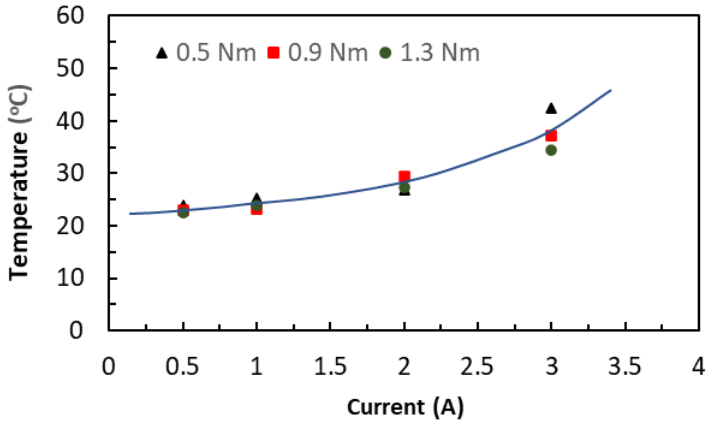

Figure 7. Variations of raised temperature with increase current on in-plane laminate surfaces

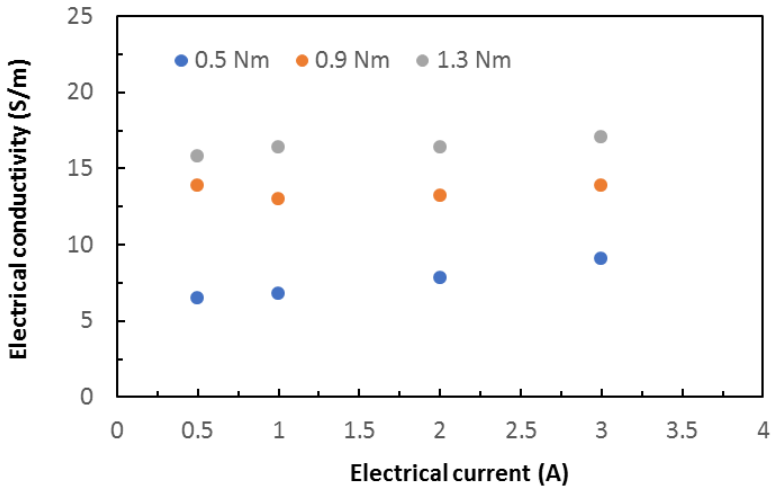

Figure 8. Variations of raised temperature with increase current on in-plane laminate surfaces

4. Conclusions

The electrical conduction and current-induced thermal behaviour of both tape- and fabric-based carbon/epoxy laminates were investigated using 2-port method via solid electrodes to ascertain the anisotropic nature of conduction path network and the extent of both intrinsic and extrinsic factors on the electrical conductivities. The findings suggested that while the in-plane conduction path network was dictated by continuous carbon fibres, an interior TTT conduction path network was formed not only by fibre-to-fibre contact but also by dielectric breakdowns of minute resin tracks between filament/fibre tow and filament/fibre tow. It was shown that the electrical conductivities were independent of dimensions for both laminates. The increase of clamping forces was shown to increase the electrical conductivities linearly. It was found that the application of conductive paint enhanced the in-plane electrical conductivities only by the modest amount but in the TTT direction the enhancement was significant. The increase of current level, albeit increased surface temperatures, did not affect the values of electrical conductivities. Since the extrinsic factors such as clamping forces and application of conductive paint did not change the conduction path networks, the measured volume electrical conductivities were apparent values and therefore the values of electrical conductivities obtained without paint ought to be used.

  doi:10.5075/epfl-298799_978-2-9701614-0-0

Acknowledgements

The first author would like to acknowledge the financial support from the C-Power Ltd and Loughborough University for the project.

5. References

1. Cinquin J, Heinrich C, Balland E, Pons F, Gaztelumendi I, Vavouliotis A, Kostopoulos V, Kostagiannakopoulou C. Volume electrical conductivity measurement on organic composite material. In: Proc of SETEC13 Conf, Wuppertal, Germany, Sept 2013; pp192-204.
2. Yokozeki T, Goto T, Takahashi T, Qian D, Itou S, Hirano Y, Ishida Y, Ishibashi M, Ogasawara T. Development and characterization of CFRP using a polyaniline-based conductive thermoset matrix. Composites Science and Technology 2015; 117:277-81.
3. Luo X, Chung D. Electromagnetic interference shielding using continuous carbon-fibre carbon-matrix and polymer-matrix composites. Composites Part B 1999; 30:227-31.
4. Munalli D, Dimitrakis G, Chronopoulos D, Greedy S, Long A. Electromagnetic shielding effectiveness of carbon fibre reinforced composites. Composites Part B 2019; 173:106906.
5. Yao X, Falzon B, Hawkins S, Tsantzalis S, Aligned carbon nanotube webs embedded in a composite laminate: A route towards a highly tunable electro-thermal system. Carbon 2018; 129:486-94.
6. Headifen GR, Fahrenthold EP. Mechanical and electrical properties of glass and carbon fiber-reinforced composites. ASME Transaction Journal of Energy Resources Technology 1991; 113:176-81.
7. Li W, Qiu H, Zhang X, Cao J, Yi R. Analyses on electromagnetic and temperature fields of super high-speed permanent-magnet generator with different sleeve materials. IEEE Transactions on Industrial Electronics 2014; 61:3056-63.
8. Zantout, A., Zhupanska, O., On the electrical resistance of carbon fiber polymer matrix composites. Composites Part A 2010; 41:1719-27.
9. Jones C, Norman P, Galloway S, Burt G, Kawashita L, Jones M, Hallett S. Electrical model of carbon fibre reinforced polymers for the development of electrical protection systems for more-electric aircraft. 18th European Conference on Power Electronics and Applications 2016; 1-10.
10. Chung D, Eddib A. Effect of fiber lay-up configuration on the electromagnetic interference shielding effectiveness of continuous carbon fiber polymer-matrix composite. Carbon 2019; 141:685-91.
11. Todoroki A, Yoshida J. Electrical resistance change of unidirectional CFRP due to applied load. JSME International Journal 2004; 47:357–64.
12. -. ASTM D4496-13, Standard test method for D-C resistance or conductance of moderately conductive materials, American Society for Testing and Materials, USA.
13. Pierson HO. Handbook of carbon, graphite, diamond, and fullerenes: properties, processing, and applications. Noyes Publications. 1993.
14. Park J, Hwang T, Kim H, Doh Y. Experimental and numerical study of the electrical anisotropy in unidirectional carbon fibre reinforced polymer composites. Smart Materials and Structures 2007; 16:57-66.
15. Yu H, Heider D, Advani S. A 3D microstructure based resistor network model for the electrical resistivity of unidirectional carbon composites. Composite Structures 2015; 134: 740–49.
16. Khan JB, Smith AC, Tuohy PM, Gresil M, Soutis C, Lambourne A. Experimental electrical characterisation of carbon fibre composites for use in future aircraft applications. IET-Science, Measurement and Technology 2019; 13:1131-38.

  doi:10.5075/epfl-298799_978-2-9701614-0-0

INVESTIGATION AND SIMULATION OF THE INTRA-PLY SHEAR PROPERTY FOR THE UNIDIRECTIONAL PREPREG FORMING

Hao Yuan[a], Muhammad Khan[a], Connie Qian[a], Neil Reynolds[a], Kenneth Kendall[a]

a: Automotive Composites Research Centre, Warwick Manufacturing Group, University of Warwick, Coventry, United Kingdom, CV4 7AL – hao.yuan@warwick.ac.uk

Abstract: *Intra-ply shear behaviour of uncured composite plies plays a key role to influence the component quality in high-volume manufacturing processes for high performance composites. This study proposes a simple way to characterise and analyse the intra-ply shear behaviour of a carbon fibre/epoxy UD prepreg using picture-frame test with small modifications where the pure shear behaviour can be characterised without involving inter-ply friction as observed in cross-plied UD prepregs. 3D digital image correlation (DIC) are adopted to monitor the out-of-plane deformation during the test and identify the valid data range corresponding to pure shear deformation. The major advantage of this test is that only load-extension data are required to generate correct shear stress-strain relationship and to identify the valid data range if sufficient repeats are conducted for each test configuration. Further, a hypo-elastic material model is implemented through user subroutines in ABAQUS/Explicit and the simulation model is compared against the experimental results.*

Keywords: Prepreg processing; intra-ply shear; picture-frame test; digital image correlation.

1. Introduction

The recent advance in rapid cure resin systems makes the high volume manufacturing of structural composites possible through prepreg compression moulding (PCM) and double diaphragm die-match forming (3DF) processes. In these processes, the stacked prepreg sheets will be formed into the desired 3D shapes at high temperature in a preforming or forming stage. To correctly predict the material behaviour during the manufacturing process, the most important challenge is the proper characterisation of relevant deformation behaviours of prepreg laminates. The intra-ply shear is the most predominant deformation modes when forming complex structures with double-curvatures. Although this deformation mode for woven prepregs has been studied extensively, the intra-ply shear for UD prepregs occurs in form of the relative slippage between individual fibres along the fibre direction, which is different to that for woven materials. In addition, UD prepregs are far more compliant in the transverse, posing some difficulties on the correct characterisation where the pure shear deformation and material integrity should be guaranteed.

Many efforts have been made to tackle the challenges involved in the intra-ply shear characterisation for UD prepregs. Groves developed a testing method in which UD prepregs are placed between two parallel platens on a rheometer and the shear is induced by the rotation of one of the platens in oscillation or steady motion [1]. It is challenging to covert the results for modelling due to the fact that shear deformation is not uniformly distributed along the radial coordinates. The parallel-shear-plate test developed by Scobbo and Nakajima induces the shear deformation via translational motion [2]. Two laminated and consolidated UD prepreg stacks

  doi:10.5075/epfl-298799_978-2-9701614-0-0

are placed in the gap of three parallel platens. Two platens on both sides are fixed while the central platen could oscillate translationally [2] or be pulled out at a constant velocity for steady-shear characterisation [3]. However, the parallel-shear-plate test suffers the major challenge of susceptible inter-ply shear/friction occurring locally at resin rich regions in ply-ply interfaces. More recently, Haanappel and Akkerman designed a torsion bar test that involves twisting a prismatic specimen made from 80 plies of UD prepregs via the standard torsion fixture on a rheometer [4]. Due to the limitation of the rheometer, large strains and high strain rates cannot be achieved at the same time in this test. Potter made an initial attempt to address the in-plane deformation of UD prepregs via the off-axis tensile test with different fibre angles between 15° and 90° [5].

The standardised methods for in-plane shear characterisation for biaxial fabrics (i.e. picture-frame and bias-extension tests) have also been adopted for intra-ply shear tests for UD prepregs [6-8]. However, to the best of the author's knowledge, all existing studies based on these two methods only used UD prepregs laminated in the cross-ply lay-up, therefore, the issue of ambiguity in intra-ply shear and inter-ply friction is induced again at the cross-over region of the specimen for these tests.

This study proposes the use of standardised picture-frame test for intra-ply shear characterisation of UD prepregs due to its simplicity and convenience in terms of both experiment and data analysis. A specially designed picture-frame was used for testing UD prepregs without involving inter-ply friction that is normally experienced for cross-plied UD specimens. DIC analysis was adopted to help identify the out-of-plane deformation during the test and extract the correct data for shear deformation. A comparison of shear stress-strain data was made among different test conditions to investigate the different factors influencing the intra-ply shear response. A simulation model based on hypo-elastic constitutive law was created and the results are compared with the experimental observations.

2. Materials and test setup

2.1 Material investigated

The material investigated in this work is PYROFIL™ TR366250S unidirectional carbon fibre/epoxy thermoset prepreg from Mitsubishi Rayon Co., Ltd. As one of candidates for high volume automotive applications, this prepreg is specially designed for compression moulding and has a 5 minute curing cycle at 140°C and 8 MPa pressure. The preforming or forming process for this material is usually conducted at around 80°C. It has a nominal thickness of 0.226 mm.

2.2 Test setup and specimen preparation

So far the picture-frame test has only been used for shear characterisation for cross-plied UD prepregs which involves possible inter-ply shear at the centre of the specimen. In this study, a specially designed picture-frame testing rig (Fig. 1) allows specimens in two fibre directions to be placed with a gap in between, hence, the influence of inter-ply shear deformation can be eliminated. The test was performed in an environmental chamber on a INSTRON 5985 universal testing machine at three different temperatures and two crosshead speeds. To investigate the influence of the specimen size, specimens with different widths and ply numbers are used for some of these test conditions. The full test conditions used in this study are summarised in Table 1 and five repeats were done for each condition. Specimens with 3 plies were made by

  doi:10.5075/epfl-298799_978-2-9701614-0-0

consolidation under the vacuum for 90 minutes to minimise the influence of resin rich regions at ply-ply interface and the nominal thickness is 0.66 mm.

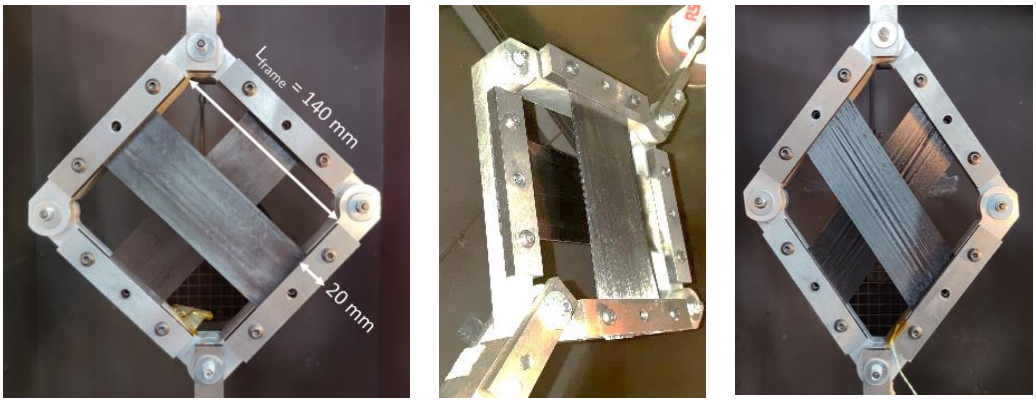

Figure 1. Picture-frame testing rig designed for UD prepreg intra-ply shear characterisation

Table 1: Test matrix for investigation on temperature, deformation rate and size effects.

		Temperature		
		21°C	50°C	80°C
Crosshead speed	0.25 mm/s	1 ply – 50 mm 1 ply – 25 mm 1 ply – 15 mm 3 plies – 50 mm	1 ply – 50 mm 3 plies – 50 mm	1 ply – 50 mm 3 plies – 50 mm
	1 mm/s	1 ply – 50 mm	1 ply – 50 mm	1 ply – 50 mm

Note: Each entry denotes the specimen configuration tested (i.e. number of plies – width)

2.3 Specimen behaviour

As shown in Fig. 1, the deformed specimen can undergo buckling or wrinkling at increased shear angles. This is due to the reduction in specimen width during the test (Fig. 2 (a)) causing some level of compaction in transverse direction. As the wrinkling may lead to non-uniform strain distribution and induce other deformation modes, the onset of wrinkling needs to be defined to ensure the data accuracy and minimum interruption from out-of-plane deformation.

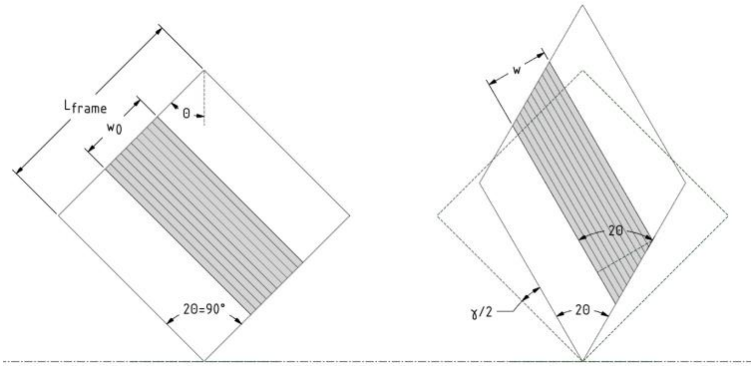

Figure 2. Reduction of specimen width in the test

A DIC system (GOM 12M), synchronised with testing machine via analogue-digital convertor, was used to visualise the deformation and identify the range of valid testing data. A matt-finish white acrylic paint was sprayed directly on the specimen surface to create a high contrast

  doi:10.5075/epfl-298799_978-2-9701614-0-0 published under CC BY-NC 4.0 license

speckle pattern for DIC. The strain results in DIC post-processing software GOM Aramis v6 is expressed in terms of a global coordinate system which is fixed to the DIC system. Due to the rigid body rotation of fibres occurring throughout the test, x-axis of the coordinate system should be aligned with fibre direction to generate correct strain maps. The transformation of coordinate system is performed directly in GOM Aramis for each stage based on the rotation angle of testing rig measured using ImageJ image processing software.

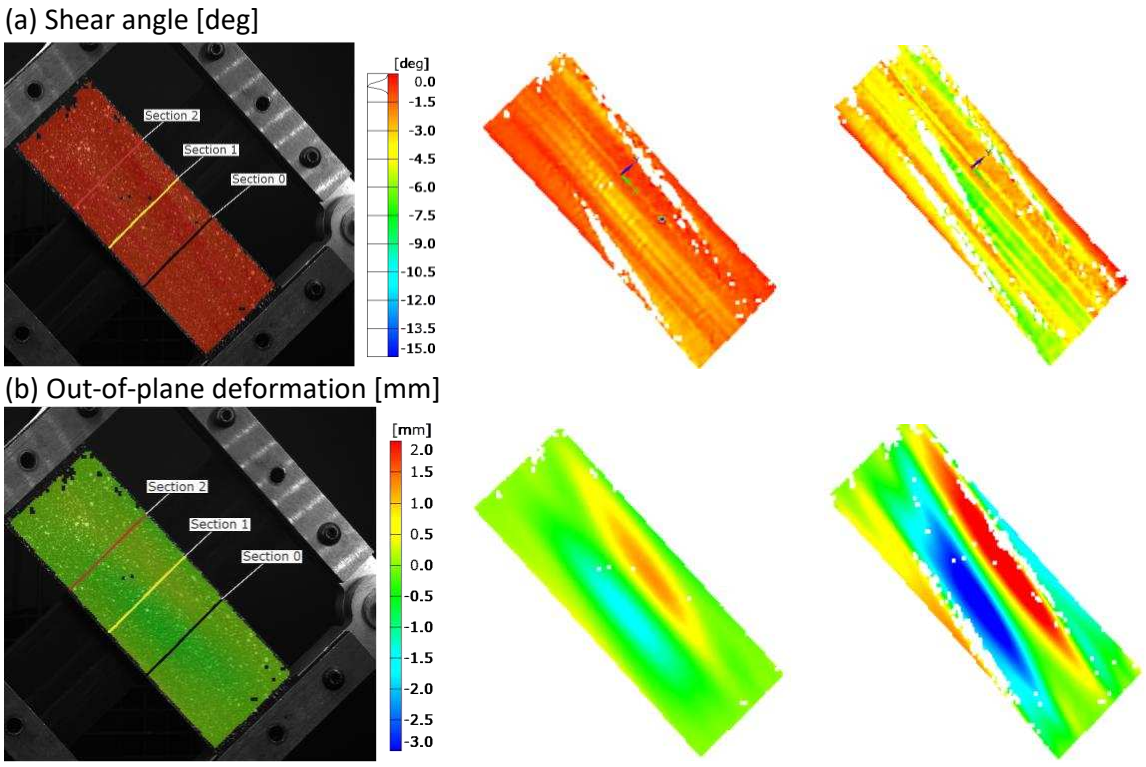

Figure 3. DIC analysis results at three stages: (a) shear angle and (b) out-of-plane deformation for a specimen with 1 ply and 50 mm width tested at 21°C and 0.25 mm/s

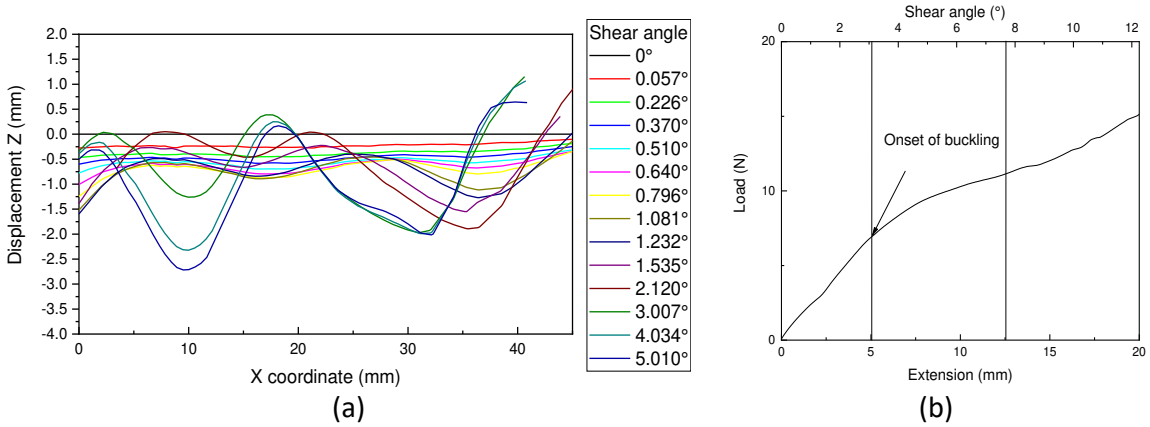

Figure 4. (a) DIC out-of-plane deformation history along centre section line and (b) load-extension curve of a specimen with 1ply and 50mm width tested at 21°C and 0.25 mm/s

DIC results in Fig. 3 shows a relative uniform shear angle distribution in initial stages of the test as indicated by the shear angle histogram in the legend. The uniform shear deformation will no longer exist as the specimen deforms further when large out-of-plane deformation occurs. Fig. 8 (a) shows the history of out-of-plane deformation along the centre line of specimen (Section 1 in Fig. 3) extracted from the DIC data at different nominal shear angles. As UD prepregs are

extremely compliant, it is almost impossible to mount the specimen onto the rig while keeping it completely flat, leading to small out-of-plane deformations at the beginning stage (< 1° nominal shear angle). At the shear angle of around 3°, there is a sudden change of the deformation shape and decrease in specimen width, suggesting the onset of transverse buckling. Further evidence can be found from the load-extension curve (Fig. 4 (b)), where the increase of load starts slowing down after the initial linear increase. After this stage the representative curve may show a further quick increase in load which is mainly caused by the tensile force from possible fibre misalignment. In this study the onset of buckling is yet to be determined for each test configuration and only the testing data below the nominal shear angle of 3° are considered as pure shear with minimum disturbance from other deformation modes.

2.4 Data reduction

The shear stress-strain curves can be extracted from the load-extension data following the established procedure for picture-frame test as Eq. (1) – (5) below:

$$\gamma = 90° - 2 \cdot \cos^{-1}\left(\frac{\sqrt{2}L_{frame}+d}{2 \cdot L_{frame}}\right) \quad (1)$$

$$F_s = \frac{F}{2 \cdot \cos\theta} \quad (2)$$

$$F_{norm} = F_s \cdot \frac{L_{frame}}{{L_{eff}}^2} \quad (3)$$

$$L_{eff} = \sqrt{2 \cdot w_0 \cdot L_{frame}} \quad (4)$$

$$\tau = \frac{F_{norm}}{t} \quad (5)$$

where L_{frame}, w_0, γ and θ are the frame length, specimen initial width, shear angle and frame angle, respectively, as indicated in Fig. 2. d denotes the crosshead extension, F denotes the measured force subtracted by the force from dry run without specimen, F_s denotes the shear force, F_{norm} denotes the normalised shear force, τ denotes the shear stress and t denotes the specimen thickness. For UD prepregs, the effective specimen length (L_{eff}) is calculated based on the equivalent shearing area (Eq. (4)) and a uniform shear deformation is assumed.

3. Results and discussions

In Fig. 5, result curves are presented in error bands where the coloured area indicates the standard deviation calculated from all test repeats performed at the same test condition and the dash line in the centre represents the averaged results. As shown in Fig. 5 (a), the normalised shear force has relative small variations for specimens with different widths. However, results for narrower specimens shows larger scatter in the material response due to the high sensitivity to the disturbance from undesired forces, such as forces required to deform the rig and tension in fibres caused by misalignment. Higher normalised shear forces for smaller specimens towards later stage also suggests the possible large contribution from the fibre tension. From stress-strain results (Fig. 5 (b) – (d)), it can be found that the turning point of curve for specimens with 3 plies occurs at a later stage, especially at 21°C, as larger thickness provides more resistance to the transverse buckling. Although a late onset of wrinkling for 3 plies cannot be identified from results at 80°C, specimens with 3 plies can still provide a more consistent material response due to lower sensitivity to unwanted forces. Moreover, a sudden change in the scatter can always

be found at the similar strain level of the buckling onset (turning point) as the material behaviour gets unstable.

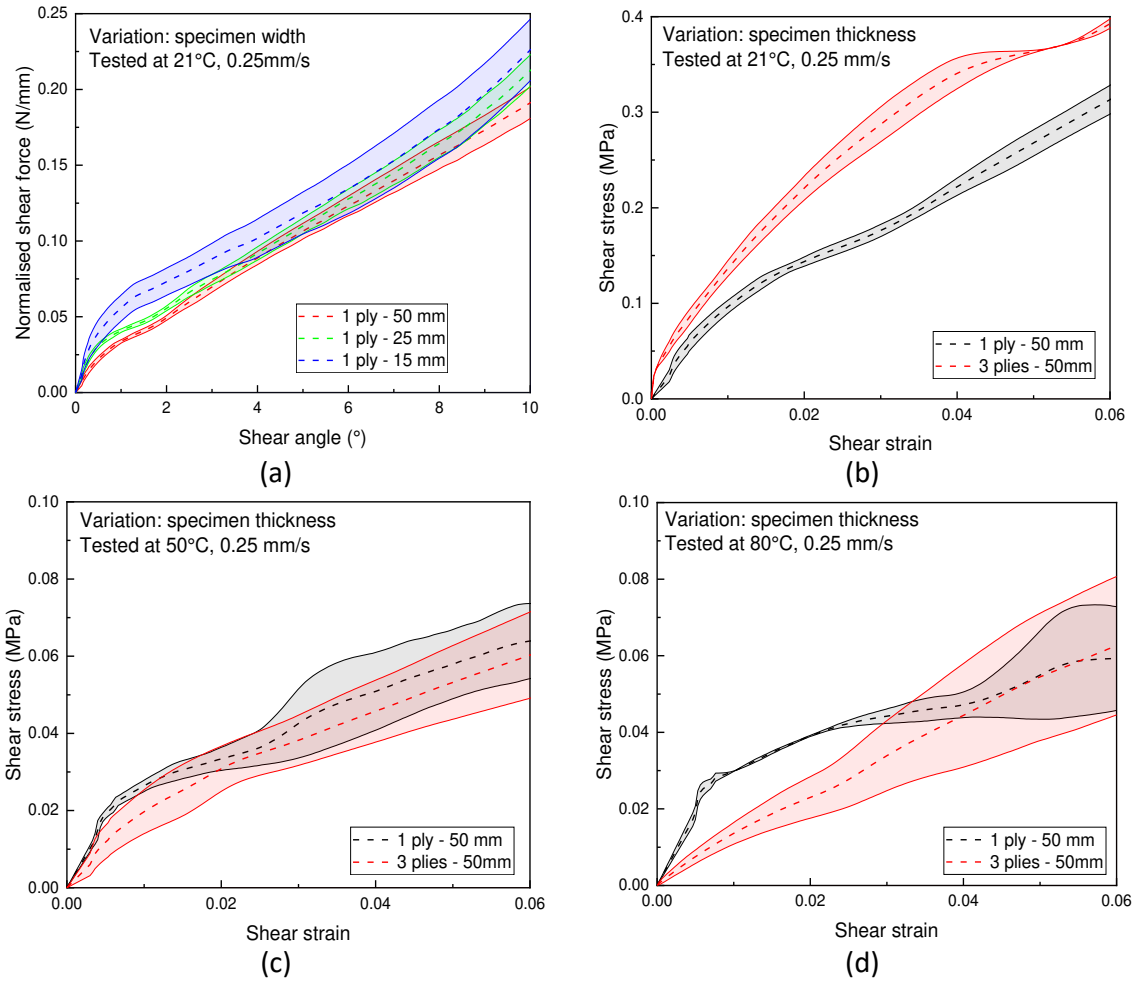

Figure 5. Size effects study: (a) Normalised shear force-shear angle curves for specimens with different widths tested at 0.25 mm/s and 21°C; shear stress-strain curves for specimens with different thickness tested at 0.25 mm/s and (b) 21°C, (c) 50°C and (d) 80°C

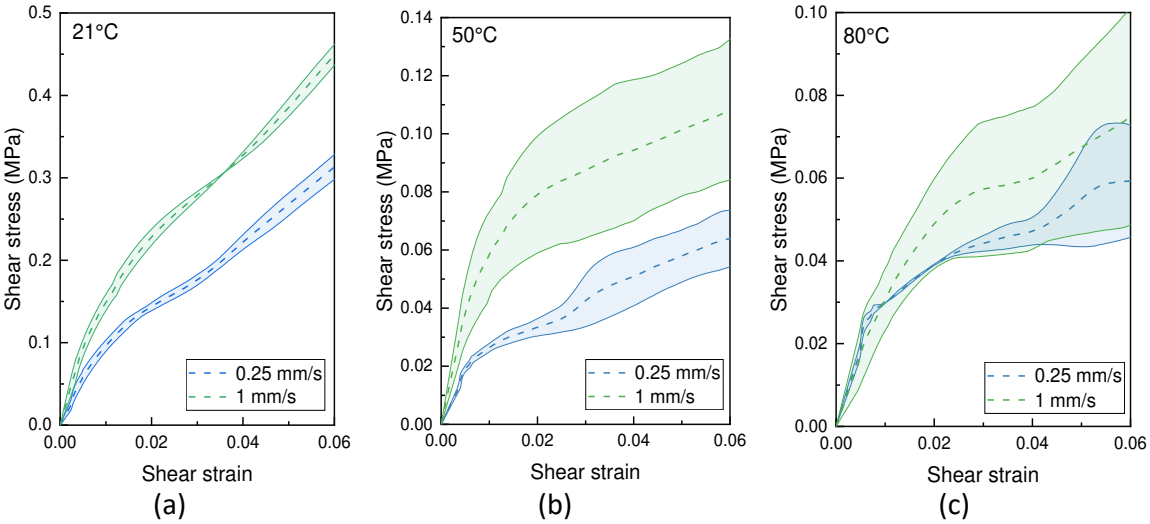

Figure 6. Shear stress-strain curves for specimens with 1 ply and 50 mm width tested at (a) 21°C, (b) 50°C and (c) 80°C

  doi:10.5075/epfl-298799_978-2-9701614-0-0

Stress-strain results in Fig. 6 shows both temperature- and rate-dependent intra-ply shear behaviour of the material. Shear stresses are significantly lower for the test at higher temperatures and higher for the test at higher deformation rate. The buckling onset is also found to show the temperature and rate dependence. The buckling onset for the test at 21°C occurs at around 0.03 and 0.04 shear strain for crosshead speed 0.25 mm/s and 1 mm/s, respectively. The buckling onset for high temperature tests all occurs at around 0.02 and just below 0.01 shear strain for test speeds of 0.25 mm/s and 1mm/s respectively. Specimens made of more plies would be a potential improvement to differentiate the buckling criteria for the test at different high temperatures while increasing the range of valid data.

4. Simulation of UD prepreg in picture-frame test

In an initial simulation attempt, the hypo-elastic constitutive model developed for describing the large deformation behaviour of 2D fibrous materials [9] is implemented through the user subroutine VUMAT in ABAQUS/Explicit for the UD prepreg in this study. Only one corotational fibre frame was used due to the absence of second fibre direction in UD prepregs. Superimposed membrane (M3D4R) and shell elements (S4R) with a seed size of 2 mm sharing the same nodes are created to decouple the high in-plane tensile stiffness and weak out-of-plane stiffness in the fibre direction. The representative material properties used are E_1 = 100 GPa, E_2 = 0.1 GPa for membrane elements and E_1 = 50 MPa, E_2 = 5 MPa, G_{12} = 0 for shell elements. The non-linear in-plane shear stiffness derived from testing results above is applied to membrane elements only.

The results of simulation (Fig. 7) shows a uniform shear distribution at the beginning stage of test and the out-of-plane deformation is in a similar pattern with that has been observed during the experiment (Fig. 3). However, the magnitude of the out-of-plane deformation is significantly lower and the buckling occurs at a later stage in simulation results. A further parametric study on the factors influencing this behaviour, including transverse out-of-plane rigidity, non-linearity of intra-ply shear stiffness, properties in transverse direction, is required to capture the correct wrinkling onset in the simulation.

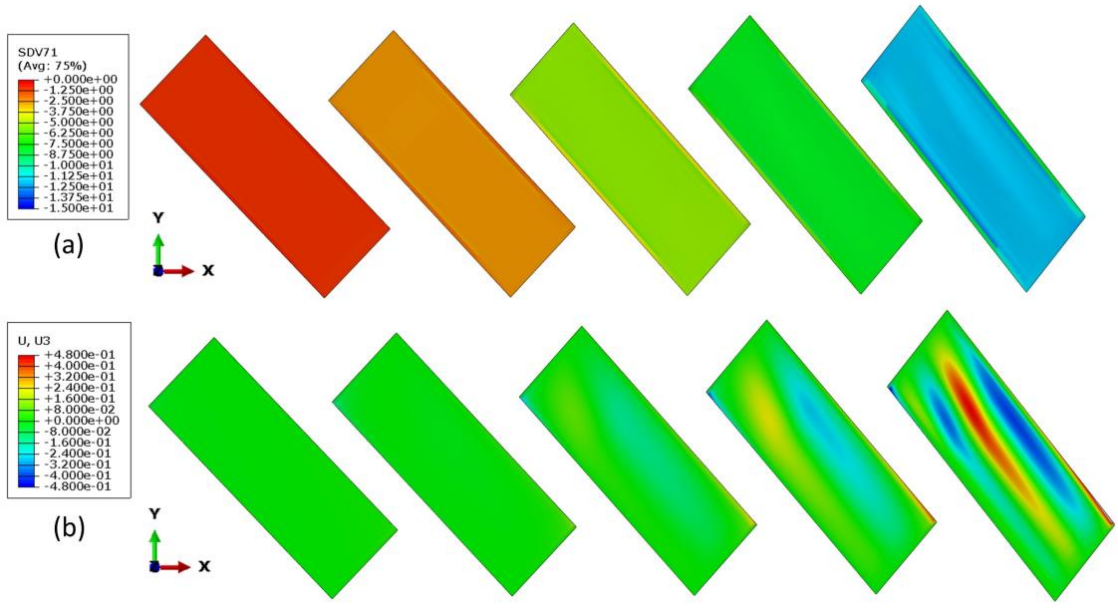

Figure 7. Representative FE results: (a) Shear angle [°] and (b) out-of-plane deformation [mm] at nominal shear angle of 0.8°, 2.4°, 5.2°, 8° and 12°

  doi:10.5075/epfl-298799_978-2-9701614-0-0

5. Conclusions

The feasibility of using the standard picture-frame test for intra-ply shear characterisation of UD prepregs was investigated with a specially designed testing rig. A relatively uniform shear deformation can be observed at the beginning stage of the test until large out-of-plane wrinkling caused by transverse compaction disrupts the pure shear deformation. DIC analysis was used to help identify the onset of transverse buckling and the range of valid testing data. Experimental results shows the high dependence of intra-ply shear properties and buckling onset on the temperature- and deformation rate. The results from an initial simulation of the test using hypo-elastic model suggests that a parametric study is required to provide an insight into the contributions from additional material properties to the buckling.

Overall, the simplicity in specimen preparation, experiment and data analysis is the major advantage of the test. With sufficient repeats, the buckling onset can be identified as a sudden change of scatter in testing results without the need for DIC, hence, only load-extension data would be required for the analysis. Specimens with multiple plies of prepregs are recommended for tests at higher temperature in order to acquire the valid data over a wider range of strain.

Acknowledgement

The authors acknowledge the support from China Scholarship Council (CSC).

6. References

1. Groves DJ. A characterization of shear flow in continuous fibre thermoplastic laminates. Composites 1989; 20:28-32.
2. Scobbo JJ, Nakajima N. Modification of the mechanical energy resolver for high temperature and rigid material applications. Polymer Testing 1990; 9:245–255.
3. Goshawk JA, Jones RS. Structure reorganization during the rheological characterization of continuous fibre-reinforced composites in plane shear. Composites Part A: Applied Science and Manufacturing 1996; 27:279–286.
4. Haanappel SP, Akkerman R. Shear characterisation of uni-directional fibre reinforced thermoplastic melts by means of torsion. Composites Part A: Applied Science and Manufacturing 2014; 56:8–26.
5. Potter K. In-plane and out-of-plane deformation properties of unidirectional preimpregnated reinforcement. Composites Part A: Applied Science and Manufacturing 2002; 33:1469–1477.
6. Dangora LM, Hansen CJ, Mitchell CJ, et al. Challenges associated with shear characterization of a cross-ply thermoplastic lamina using picture frame tests. Composites Part A: Applied Science and Manufacturing 2012; 78:181–190.
7. Larberg YR, Åkermo M, Norrby M. On the in-plane deformability of cross-plied unidirectional prepreg. Journal of Composite Materials 2012; 46:929–939.
8. Khan MA, Pasco C, Reynolds N, Kendall KN. On the validity of bias-extension test method for the characterisation of in-plane shear properties of rapid-cure prepregs. Composite Structures 2020; 246:112399.
9. Khan MA, Mabrouki T, Vidal-Sallé E, Boisse P. Numerical and experimental analyses of woven composite reinforcement forming using a hypoelastic behaviour. Application to the double dome benchmark. Journal of Materials Processing Technology 2010; 210:378–388.

  doi:10.5075/epfl-298799_978-2-9701614-0-0

INTERLEAF THICKNESS, INTERLEAF PARTICLES, AND INTERLAMINAR CRACK PATH MIGRATION

Robin Hartley[a], Ivana K. Partridge[a], James Kratz[a]

a: Bristol Composites Institute, University of Bristol, Bristol, BS3 4TT, United Kingdom

Abstract: *Interlaminar fracture is one of the most critical failure modes for laminated composites. A common method to mitigate this is adding preformed micro-particle filled interleaves between the fibre layers. Mode I static fracture tests were carried out on laminates containing either glass or polyamide 12 particle reinforced interleaves, to determine the effects particle material and interleaf thickness had on the location of crack propagation within the laminate. It was found that increasing interleaf thickness delayed interlaminar to intralaminar crack migration and promoted cohesive failure through the tough interleaf while delaying fibre bridging. Failure of the fibre-matrix interface in the fibre layers either side of the interleaf was identified as the primary catalyst for crack migration whilst some limited percolation of fibres into the interleaf allowed fibre bridging and cohesive failure to occur simultaneously. These findings are pertinent to understanding interlaminar failure and developing new damage tolerant interleaf toughened materials.*

Keywords: interleaf; particle toughening; thermoset; composite; model system

1. Introduction

The high specific strength and stiffness of carbon fibre reinforced polymer (CFRP) composites make them ideal for high performance engineering applications. However, their lack of through thickness reinforcement results in matrix dominated out of plane properties leaving laminates especially vulnerable to impact damage [1]. This type of damage propagates through the thickness of laminates by intraply cracks, which are diverted and become delaminations when they meet plys with a transverse fibre orientation [2]. Resistance to delamination is a matrix driven property. However composite interlaminar critical strain energy release rates (G_{IC}) are often significantly lower than the those of the base resin and increasing the base resin toughness does not result in an equivalent increase in composite G_{IC} [3]. This been demonstrated to be due to crack tip constraint from adjacent plies which prevents the formation of a full crack tip process zone prior to fracture [4]. Research into separating fibre layers and reducing this constraint using preformed micro-particles to form tough interleaves has led to the development of commercially successful material systems [5]. However, the incorporation of tough interleaves [6] and choice of interleaf particle material [7] has been shown to affect the crack path, causing migration from interlaminar to intralaminar failure. In this work a method of manufacturing micro-particle (glass and polyamide 12) toughened interleaves that allows for control the interleaf thickness in the cured laminate is described. Static mode I fracture tests were performed to determine how interleaf thickness and particle material affect crack path migration to the intralayer. Interlaminar vs intralaminar cracks have different energy release rates [8] and hence this work aids in understanding the effect of interleaf architecture on the damage tolerance of interleaved CFRP laminates.

  doi:10.5075/epfl-298799_978-2-9701614-0-0

2. Materials and Methods

2.1. Materials

A model resin system was created consisting of diglycidyl ether of bisphenol F (DGEBF), Triglycidyl p aminophenol (TGPAP) and 4,4'-diaminodiphenylsulfone (4,4'-DDS). A commonly used phase separating thermoplastic modifier that forms sub-micron morphology, polyether suphone (PES), was also added to the blend. The constituent masses used in the blend to create this stoichiometry are detailed in Table 1. This model resin system was used to manufacture unidirectional prepreg with AS4A carbon fibres. Interleaf film materials were made using a filming machine with the self-same resin described above with the addition of one of two types of pre-formed micro particles at 14 wt%; i) polyamide 12 (Orgasol® 2009, diameter: 15±3 µm), and ii) silane coupling agent coated silica glass (Microperl® 050 20, diameter 11±6 µm). Henceforth, the naming convention will be PA and GL the polyamide and glass particles, respectively.

Table 1: Formulation constituent masses

		Constituent masses / g	
Constituent	Equivalent weight / g mol^{-1}	Epoxy	Epoxy + particle
DGEBF	165.00	29.79	25.62
TGPAP	96.00	28.89	24.84
4,4'-DDS	62.00	21.32	18.34
PES	-	20.00	17.20
Particle	-	-	14.00
Total	-	100.00	100.00

Table 2. Laminates and their interleaf film contents

Laminate name	Particle type	Interleaf film areal weight / g m^{-2}	No. of films	Total interleaf areal weight / g m^{-2}
Baseline	-	-	0	0
10gsm14wt%PA	Polyamide 12	10 gsm	1	10
30gsm14wt%PA	Polyamide 12	30 gsm	1	30
150gsm14wt%PA	Polyamide 12	30 gsm	5	150
10gsm14wt%GL	Glass	10 gsm	1	10
30gsm14wt%GL	Glass	30 gsm	1	30
150gsm14wt%GL	Glass	30 gsm	5	150

2.3. Interleaved Laminate Manufacture

A manufacturing method was developed to produce unidirectional laminates containing particle filled interleaves of tailorable thickness at their midplanes. Two six ply sub-laminates were laid up with particle-filled interleaf films stacked between them. These laminates were used to make fracture specimens, and therefore a PTFE film initial delamination was also inserted, carefully butted up to the interleaf in the midplane (Figure 2.1a). Table 2 shows how by controlling the areal weight of the individual films and their stacking sequence, the total interleaf areal weight and thereby the thickness of the interleaf can be controlled. To mitigate in-cure resin bleeding

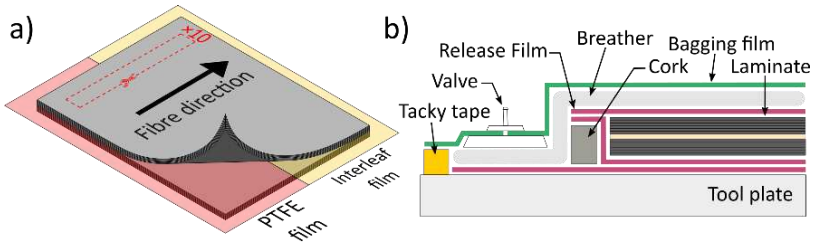

Figure 2.1. a) Interleaved laminate layup scheme. b) Interleaved laminate bagging scheme.

from the laminates caused by high total interleaf areal weights, cork picture frames lined with release film were placed around the laminates as shown in the bagging scheme in Figure 2.1b. To reduce the occurrence of fibres from either side of the midplane nesting into one another and thereby producing indistinct interleaves, the two plies adjacent to the midplane were oriented at ± 5°. The laminates were cured in an autoclave, ramping at 2 °C min^{-1} up to a 170 °C isothermal hold for 4 hours. This temperature was chosen as it is below the PA particle melting point and therefore conserves the particle crystallinity and dimensions.

2.4. DCB Testing

Figure 2.2 shows the double cantilever beam (DCB) specimen dimensions and mode I testing configuration used for fracture testing. The ASTM D5528-13 [9] standard was followed to perform three tests per laminate using a Shimadzu AGS-X universal testing machine set up with a 1 kN load cell and a crosshead speed of 2 mm min^{-1}. Tests were recorded using an iMetrum Video Guage to measure load point displacement and allow crack extension (the distance from the load point to the crack tip (a)) to be tracked with the aid of rulers added to the edges of the specimens with a thin coat of paint. The modified compliance calibration method was used for data reduction as it provided the most conservative G_I values calculated using Equation 1:

$$G_I = \frac{3P^2C^{\frac{1}{3}}}{2Abh} \tag{1}$$

where P is the load, C is the specimen compliance, b is the specimen width, h is the specimen half thickness, and A is a constant calculated from the slope of a least squares plot of $C^{1/3}$ vs a/h. Critical values (G_{IC}) were calculated from the loads at the first point of visual crack extension and propagation values were calculated from the loads at each mm of additional extension for the first 10 mm of propagation, followed by every 5 mm until the crack had propagated 50 mm.

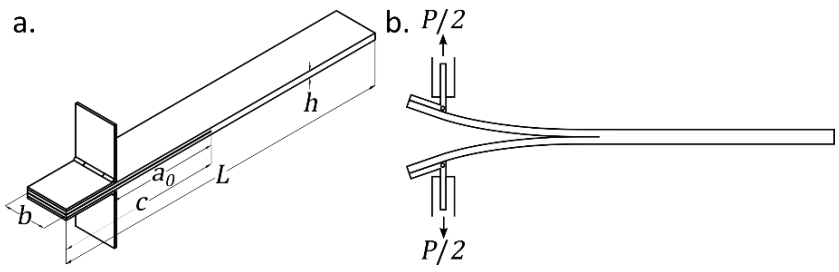

Figure 2.2. a) DCB specimen dimensions: PTFE film length (c = 75 mm), delamination length ahead of the load point (a_0 = 50 mm), specimen thickness (h ≈ 3.2 mm), specimen width (b = 20 mm), and specimen length (L = 160 mm). b) DCB test configuration.

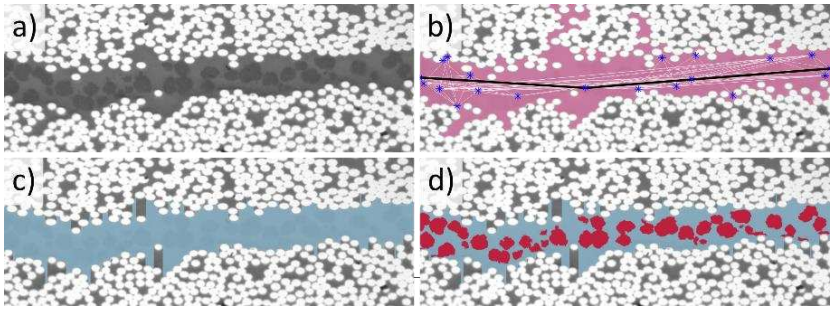

Figure 2.3. Image analysis steps for a 300 µm subsection of an interleaf micrograph cross-section. a) Original greyscale image. b) Area detected with a region growing algorithm (pink) overlaid with a path calculated through the interleaf using Dijkstra's algorithm [10]. c) Final segmented interleaf region (blue) calculated by dividing (b) into 1-pixel wide columns and selecting only the pink regions contiguous with the black path. d) Interleaf particles thresholded (red) using an adaptive, automatic algorithm developed by Landini et.al. [11].

2.5. Analysis of Interleaf Cross-section

The particle volume fraction (V_f) and thickness of the different interleaves were measured from optical micrographs of polished 20 mm wide cross-sections cut from the cured laminates using a robust and repeatable image processing methodology. This methodology is depicted and described in Figure 2.3 using an example 300 µm wide subsection of a micrograph. The average height in pixels of the blue segmented region in Figure 2.3c was calculated and converted into micrometers to give the interleaf thickness. Particle V_f was calculated by dividing the total number of particle pixels (red, Figure 2.3d) by the total number of interleaf pixels (blue, Figure 2.4c).

3. Results and Discussion

3.1. Measured Interleaf Thicknesses and Particle Volume Fractions

Figure 3.1 shows 300 × 200 µm micrograph subsections of the interleaves from each of the laminates in Table 3, which details their interleaf film contents and theoretical/experimental thicknesses and particle V_f. For the 10 and 30 gsm interleaves, the experimental thicknesses exceed those predicted by theory (calculated from the resin density and interleaf areal weight). This is a result of the largest particles exceeding the theoretical interleaf thickness and the stiff fibres being unable to bend around them. The 150 gsm interleafs are thick enough for the particles to densify during consolidation, a process that is accompanied by resin infiltrating the fibre layers at the same time as fibres percolating into the interleaf. This percolation of stray fibres blurs the boundary between interlayer and intralayer and occurs to a greater degree in the interleaves containing GL particles. This is because both particles are added at 14 wt% resulting in a lower V_f of GL particles in the interleaf due to their density being roughly double that of the PA particles.

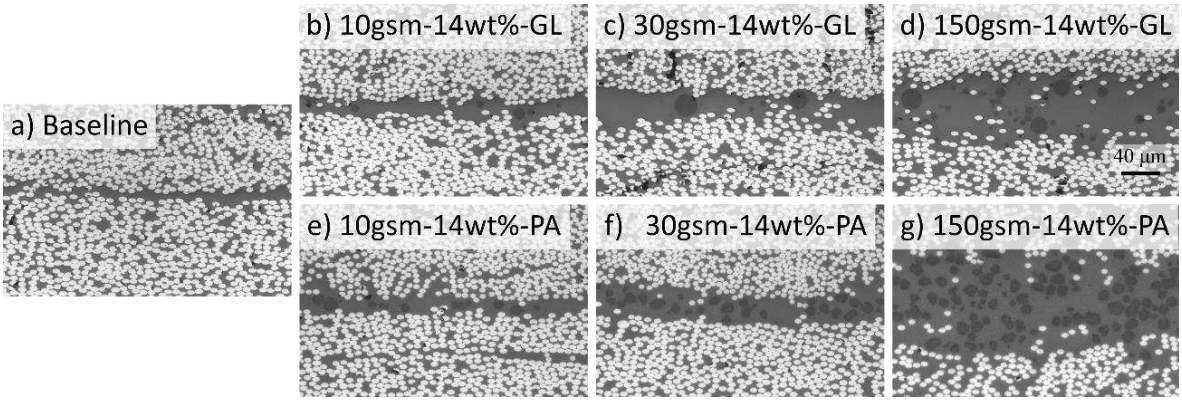

Figure 3.1. Optical micrographs of interleaf cross-sections.

Table 3. Laminates and their interleaf film contents

Name	Areal density / g m^{-2}	Theoretical thickness / µm	Experimental thickness / µm	Theoretical particle V_f	Experimental particle V_f
Baseline	N/A	-	15 ± 10	0	0
10gsm-14wt%-GL	10	7	26 ± 11	0.08	0.02
30gsm-14wt%-GL	30	21	33 ± 16	0.08	0.05
150gsm-14wt%-GL	150	106	82 ± 31	0.08	0.09
10gsm-14wt%-PA	10	8	24 ± 10	0.18	0.08
30gsm-14wt%-PA	30	24	31 ± 15	0.18	0.12
150gsm-14wt%-PA	150	120	107 ± 44	0.18	0.22

3.2. Propagation Strain Energy Release Rates and Crack Path Migration

The effect that particle material, particle V_f, and interleaf thickness have on the path the crack takes through the laminate is evident from the shapes of the R-curves for GL and PA containing laminates in Figures 3.2a and 3.2b, respectively. R-curves (resistance curves) show the how the resistance to propagation changes with crack extension and are hence sensitive to the location of the crack within the laminate.

At the start of the tests (extension = 0), the tips of the cracks are at the centre of the interleaves and hence the initiation strain energy release rates are referred to as critical strain energy release rates (G_{IC}). These values capture the full energy absorbing potential of the particle filled resin rich interleaves. For both the PA and GL filled interleaves, interleaf thickness is directly correlated to G_{IC}. Crack tips centred in a thick interleaf are less constrained by the adjacent fibre layers, and hence a larger plastic zone can develop prior to fracture. Shear deformation within the plastic zone is the key toughening mechanism contributing towards interlaminar toughness, with particles maintaining interlaminar separation. The PA particles contribute additional energy absorbing mechanisms through their plasticity relative to the surrounding matrix, which enables them to bridge and provide traction across the crack faces as they stretch and deform in the wake of crack tip. In contrast the GL particles are relatively inert, acting primarily as spacers with limited additional contribution to energy absorption. This explains the significantly higher initial energy release rates in laminates containing PA particles.

  doi:10.5075/epfl-298799_978-2-9701614-0-0

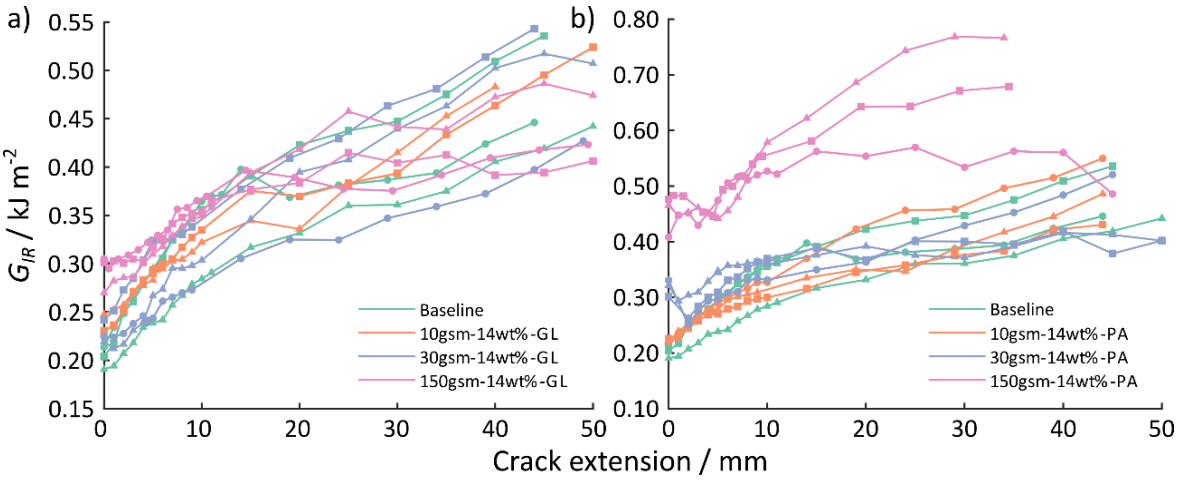

Figure 3.2. Mode I resistance curves for a) GL particle reinforced interleaves and b) PA particle reinforced interleaves.

Analysing the fracture surface optical micrographs in Figure 3.3, reveals how the interleaf characteristics influence the crack path, and using this information in conjunction with the R-curves reveals the how the location of the crack within the laminate impacts the G_{IR}. The presence of the ±5° plies either side of the interleaf make it clear from the fracture surfaces where the crack propagated during the test. The orientation of the fibres in Figure 3.3 indicates that for all laminates, the failure process rapidly directs the crack out of the interleaf and into the intralayer either above or below the interleaf at different points across the width. This crack migration and resulting intralayer propagation results in both individual and bundles of fibres building up as ligaments that provide traction across the crack face. Energy is required to either pull out or fracture bridging fibres, which contributes to the G_{IR}. The length of the bridging region in the wake of the crack increases with crack extension until it reaches a steady state, reflected in the asymptotic R-curves in Figure 3.2. The most significant differences between the shapes of the GL and PA R-curves occur in the initial stages of the test where the thicker 30 and 150 gsm PA interleaved laminates show a clear transitory drop in G_{IR}. The drop in G_{IR} can be clearly correlated to the proportion of the crack front propagating cohesively. Cohesive failure within the interleaves shows up as dark areas absent from fibre markings close to the initial delaminations in Figure 3.3. These regions are much more extensive in the PA interleaves and their extent is directly proportional to the thickness of the interleaf.

The propensity for cracks to migrate to the intralayer demonstrates that failure of the fibre-matrix interface is more energetically favourable than cohesive failure within the tough interleaf. However, for migration to occur, the elevated stress field at the crack tip must both overlap with fibres in the adjacent plies and, at the point of overlap, exceed the interfacial strength of the fibre-matrix interface. The thicker the interleaf, the greater the distance between the crack tip and the adjacent fibre layer. As crack tip stresses are proportional to r^{-2} from the crack tip, it is less likely in a thick interleaf for this critical stress overlap to occur prior to cohesive interleaf failure. The random nature of local crack growth means that as the crack extends the likelihood that this overlap occurs increases and as a result, even the cracks in the 150 gsm interleaves end up almost entirely in the intralayer.

In the GL particle interleaves, there is no drop in G_{IR} despite visible regions of cohesive failure on the 30 and 150 gsm fracture surfaces. This is because in the GL particle interleaves, fibre

bridging is prevalent even whilst the crack is failing cohesively. The cross-section of the 150gsm-14wt%-GL shows that the to the lower V_f of GL particles allows stray fibres to percolate into the interleaf, as described in Section 3.1. This results in crack bridging from the onset of the test as evidence from the presence of fibre marks right up to the initial delamination in the SEM image in Figure 3.4a. Contrasting this to the complete lack of fibre marks in the cohesive failure region of the 150gsm-14wt%-PA laminate in Figure 3.4b tells the story of how particle volume fraction can dictate local crack migration and initiate intralaminar failure.

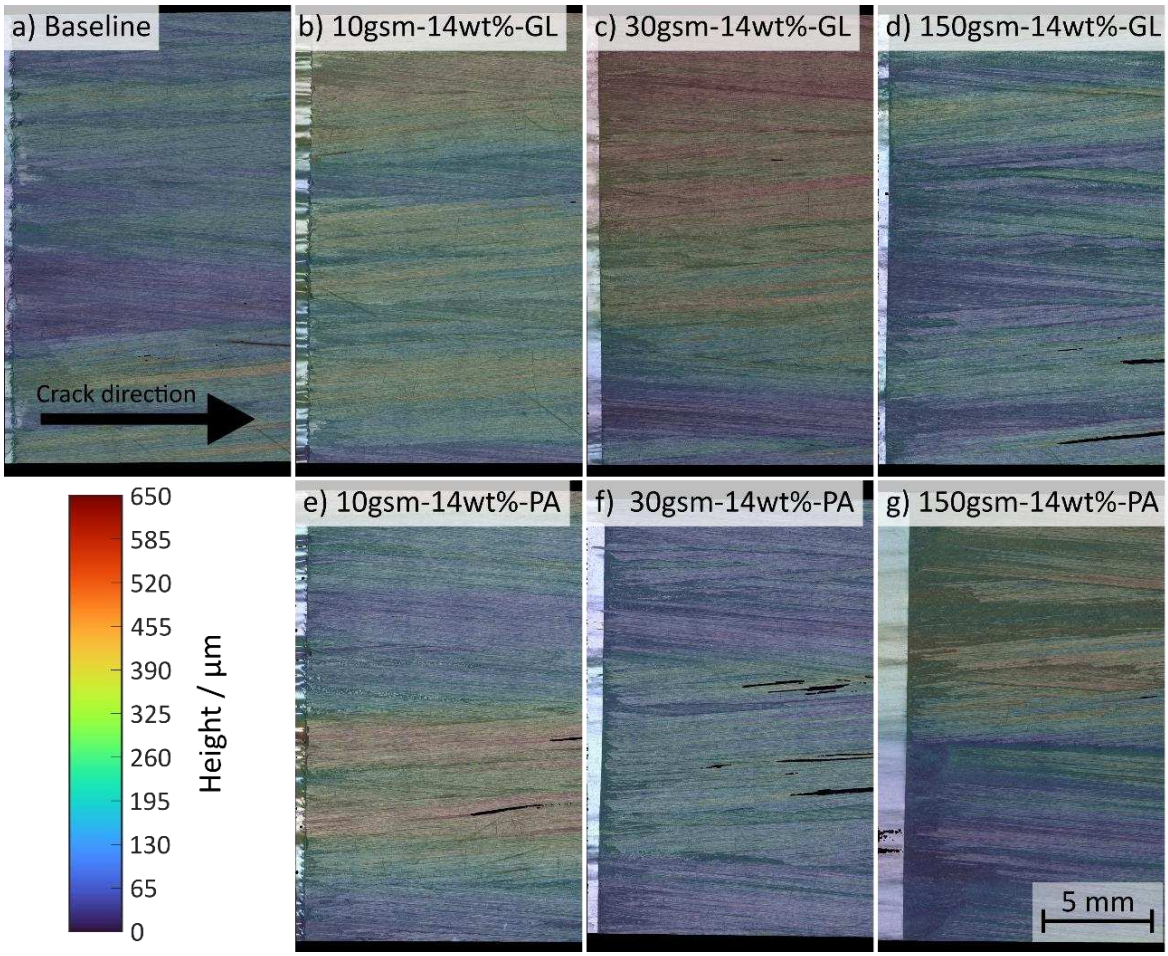

Figure 3.3. DCB fracture surfaces with the height of the surface overlaid. The bright regions on the left of each micrograph show the location of the initial delamination and the global crack propagation direction is indicated by the arrow.

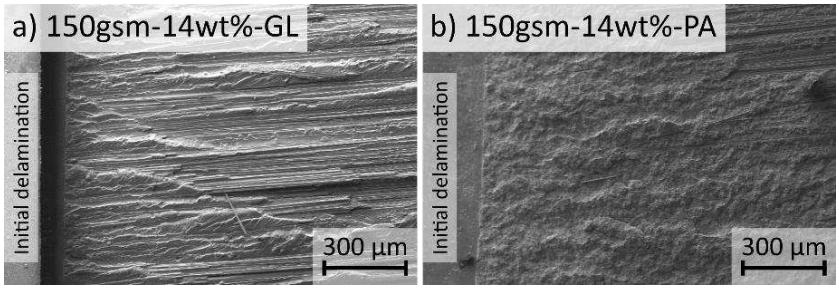

Figure 3.4. SEM images of DCB fracture surfaces showing the differences in fibre penetration into the interleaf.

4. Conclusion

In this work, static mode I fracture tests were performed in order the study the nature of crack propagation within micro-particle interleaved laminates. The results show that creating thicker interleaves is critical to maximising the G_{IC} of laminates, as less constraint from adjacent fibre layers can allow a more fully developed plastic zone to form at the crack tip. Pre-formed interleaf micro particles play a crucial spacing role in maintaining that thickness, but their material can further maximise G_{IC}. Of the two materials studied, glass particles provide little in the way of additional toughening whereas polyamide 12 particles absorb energy by bridging the crack faces plastically and deforming to the point of fracture.

Interleaf to intralayer crack migration occurred in laminates containing interleaves of all thicknesses regardless of interleaf particle material. Increasing the thickness of the interleaves served to delay crack migration, which was attributed to the increased distance between the crack tip and adjacent fibre layer. As a result, the elevated stress field at the crack tip is less likely to exceed the fibre matrix interfacial stress if it overlaps with the fibre layer. Thus, fibre-matrix interfacial failure in the vicinity of an interlaminar crack is the likely catalyst for crack migration as these regions of failure then draw the crack towards them as intralaminar propagation serves as the path of least resistance.

Acknowledgements

This research was supported by the EPSRC Centre for Doctoral Training in Advanced Composites for Innovation and Science (EP/L016028/1).

References

[1] Cantwell WJ, Curtis PT, Morton J. Impact and subsequent fatigue damage growth in carbon fibre laminates. Int. J. Fatigue. 1984;6(2):113–8.

[2] Hull D, Shi YB. Damage mechanism characterization in composite damage tolerance investigations. Compos. Struct. 1993;23:99–120.

[3] Hunston DL, Moulton RJ, Johnston NJ, Bascom WD. Matrix Resin Effects in Composite Delamination: Mode I Fracture Aspects. Toughened Compos. 1987;74–94.

[4] Singh S, Partridge IK. Mixed-mode fracture in an interleaved carbon-fibre/epoxy composite. Compos. Sci. Technol. 1995;55(4):319–27.

[5] Odagiri N, Kishi H, Yamashita M. Development of TORAYCA prepreg P2302 carbon fiber reinforced plastic for aircraft primary structural materials. Adv. Compos. Mater. 1996;5(2):249-52.

[6] Ni X, Furtado C, Fritz NK, Kopp R, Camanho PP, Wardle BL. Interlaminar to intralaminar mode I and II crack bifurcation due to aligned carbon nanotube reinforcement of aerospace-grade advanced composites. Compos. Sci. Technol. 2020;190

[7] Borstnar G, Mavrogordato MN, Helfen L, Sinclair I, Spearing SM. Interlaminar fracture micro-mechanisms in toughened carbon fibre reinforced plastics investigated via synchrotron

radiation computed tomography and laminography. Compos. - Part A Appl. Sci. Manuf. 2015;71:176-83.

[8] Chen C, Nesbitt S, Reiner J, Vaziri R, Poursartip A. Cure path dependency of static and dynamic mode II interlaminar fracture toughness of interlayer toughened composite laminates. Compos. Sci. Technol. 2020;200(March).

[9] ASTM D5528-13. Standard test method for mode I interlaminar fracture toughness of unidirectional fiber-reinforced polymer matrix composites. Am. Stand. Test Methods 2014;1-12.

[10] Dijkstra EW. A note on two problems in connexion with graphs. Numer. Math. 1959;1(1):269-71.

[11] Landini G, Randell DA, Foad S, Galton A. Automatic thresholding from the gradients of region boundaries. J. Microsc. 2017;265:185-95.

  doi:10.5075/epfl-298799_978-2-9701614-0-0

PROCESS SIMULATION OF CARBON FIBER REINFORCED POLYAMIDE 6/METAL-HYBRID LAMINATES

Christoph, Zanghellini[a], Franz, Maier[a], Michael, Paulitsch[a], Roland, Hinterhölzl[a]

a: Research Group of Lightweight Design and Composite Materials, University of Applied Sciences Upper Austria, Wels, Austria – christoph.zanghellini@fh-wels.at

Abstract: Process simulation of composites became a powerful tool to predict process-induced deformations over the last decades and increases the cost-effectiveness of the development of composite parts. In this paper, the thermo-mechanical properties of a CF-PA6 tape were characterized by performing DSC and DMA experiments. Modelling parameters were determined from experimental data and added to the material database of the commercially available process simulation software COMPRO (Convergent). Consequently, the compression molding process of CF-PA6 plates and CF-PA6/metal-hybrid laminate plates was simulated using finite element analysis. The resulting process induced deformations were compared with 3D scans of manufactured plates. The predicted shapes and deformations matched the manufactured CF-PA6 plates reasonably well, supporting the functionality of the characterized CF-PA6 material data. However, for the hybrid laminates further investigations will be necessary to gain a better understanding of the process and the materials, especially the adhesion promoter involved, to further improve the accuracy of the PID prediction.

Keywords: Process simulation; CF-PA6; metal-hybrid laminates; process-induced deformation

1. Introduction

Thermoplastic composites gained a lot of attention in many industrial applications over the last decades. Industries like automotive and aerospace are main drivers for the development and widespread utilization of thermoplastic composite parts. Thermoplastic composites allow for short cycle times of typically only a few minutes. When heated above melting temperature, they can be formed in the desired shape in a molding tool. During subsequent cooling, the thermoplastic matrix solidifies quickly and the mechanical properties are reestablished. This is a major benefit compared to thermoset composites, where many undergo time consuming curing cycles, lasting up to multiple hours. Process induced deformations occur in thermoplastic and thermoset composites during manufacturing, i.e. shrinkage arises during cooling/curing due to various mechanisms. Semi-crystalline thermoplastics, e.g. Polyamide 6 (PA6), crystallize partially during cooling, which leads to physical shrinkage of the matrix. Additionally, thermal shrinkage occurs due to the temperature change. The resulting shrinkage strains contribute to the development of residual stresses in a composite part during manufacturing, beside various other mechanisms, e.g. tool-part interactions. Residual stresses lead to process-induced deformations (PID) in the part and are typically unwanted. Process simulation became a powerful tool to predict PID, considering multiphysical phenomena that occur during composite processing [1–3].

Composite/metal-hybrid laminates, or hybrid structures, are composed of at least two different layers consisting of either metals or composites. The development and utilization of hybrid

  doi:10.5075/epfl-298799_978-2-9701614-0-0

laminates is mainly driven by the aerospace and automotive industry. This material combination offers new possibilities for the engineering of structural components. In general, hybrid laminates are a good choice for all components that must withstand impacts while being lightweight at the same time [4,5]. However, it is still challenging to understand the processing of composites and especially of hybrid structures. This study focuses on the characterization of the thermo-mechanical behavior of a carbon fiber reinforced polyamide 6 (CF-PA6) tape to obtain modelling parameters to further generate a material input file for the commercially available process simulation tools COMPRO and RAVEN (Convergent Manufacturing Technologies, Canada). Furthermore, the CF-PA6 material file is used in finite element (FE) process simulations of composite and metal-hybrid laminate plates to predict arising residual stresses during the process and the resulting PID using ABAQUS/CAE and the COMPRO plug-in.

2. Experiments and Methodology

The characterized material is the SIGRAPREG®TP C U157-0/NF-T340/46% from SGL Carbon. Table 1 provides a brief overview on the tape's properties, according to the data sheet. All evaluations, calculations and modelling approaches which follow were realized with custom Python scripts.

Table 1: Material properties of the CF-PA6 tape.

Property	**CF-PA6**
Fiber	SIGRAFIL®C T50-4.4/255-T140
Matrix	PA6
Fiber mass fraction (%)	54
Fiber volume fraction (%)	42
Melt temperature (°C)	220
Glass transition temperature (°C)	58
Tape thickness (mm)	0.2

2.1 Crystallization Kinetics

Crystallization shrinkage is a major contributor in the development of residual stresses. Models have been developed to predict the crystallization shrinkage by calculating the volume change depending on the actual state of crystallinity [2]. The material model that is implemented in COMPRO was developed by Gordnian (2017) as part of his doctoral thesis [6]. This model was initially developed to describe the crystallization kinetics of CF-PEEK. Due to the similar nature of PEEK and PA6 as semi-crystalline thermoplastics, it was assumed that the approach from [6] will also work to describe the crystallization behavior of CF-PA6. Differential scanning calorimetry (DSC) was used to perform dynamic and isothermal experiments on samples taken from the CF-PA6 tape. Samples (n=5) of 5–6 mg were prepared and placed in 40 µL aluminum crucibles. All experiments initiated with a heating ramp at 10°C/min to a temperature of 260°C followed by an isothermal hold at this temperature for 10 min, to remove any potential thermal history from tape manufacturing. Subsequently, in case of the isothermal experiments the samples were rapidly (100°C/min) cooled down to the desired isothermal hold temperature

below melting temperature (200°C, 202°C, 205°C, 207°C, 209°C, 210°C) and in case of the dynamic experiments the samples were cooled down with the desired cooling rate (1°C/min, 3°C/min, 5°C/min, 7°C/min, 10°C/min, 20°C/min) to room temperature. The experiments were performed with a Mettler-Toledo DSC3.

The recorded heat flow during these experiments was used to calculate the degree of crystallinity of the PA6 matrix using the following equation:

$$X_{mc}(t) = \frac{\Delta H(t)}{(1-X_{mr})H_f^0} \quad (1)$$

where $X_{mc}(t)$ is the mass fraction crystallinity, $\Delta H(t)$ is the crystallization enthalpy, X_{mr} is the mass fraction of the reinforcing carbon fibers and H_f^0 is the heat of fusion for 100 % crystallinity. The value of the heat of fusion for PA6 is assumed as 188 J/g [7]. Figure 1 shows the measured heat flow, the established baseline for integration, as well as the calculated crystallinity versus time for a dynamic and isothermal experiment, respectively.

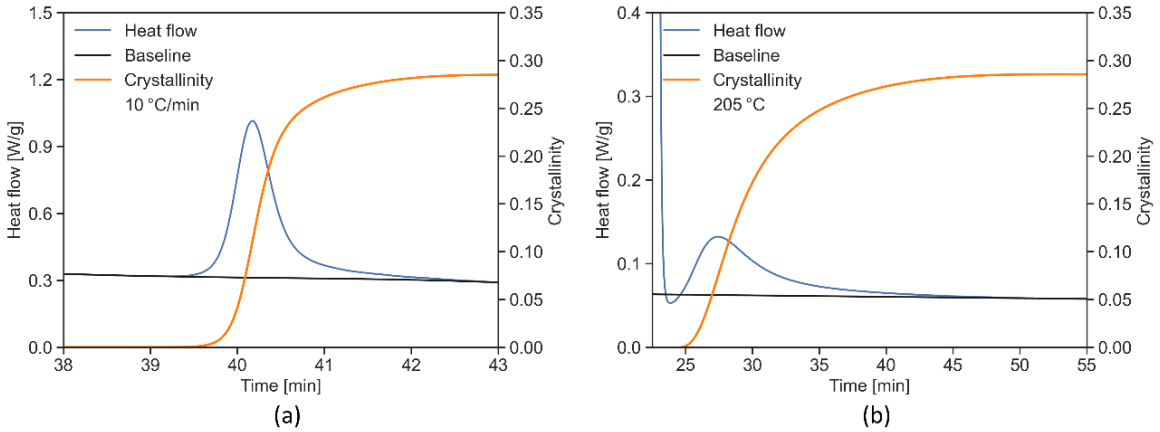

Figure 1. Heat flow curve (blue) and crystallinity (orange) with the established baseline (black) for a dynamic experiment (a) and an isothermal experiment (b).

The differential form model (rate-type kinetics model) for the description of the crystallization kinetics [6] is given in its base form as:

$$\frac{dX}{dt} = k(T)f(X) \quad (2)$$

where dX/dt is the crystallization rate, $k(T)$ is the temperature dependency of the crystallization rate and the dependency of the crystallization rate on the current crystallinity is described by $f(X)$. Following the modelling approach in [6], the modelling parameters for the prediction of the degree of crystallinity as well as the crystallization onset time (induction time) were derived from the experimental crystallization data obtained from DSC experiments and included in COMPRO. For a more detailed description of the entire modelling approach, one is referred to [6].

2.2 Modulus Development

A 'cure hardening instantaneously linear elastic' (CHILE) material model is employed by COMPRO in the stress analysis. Hence, the mechanical behavior of the matrix is assumed to behave linear elastic at each instance of the process. Experiments with a dynamic mechanical thermal analysis (DMTA) with unidirectional (UD) CF-PA6 specimen in a 90° 3-point bending test

setup (Figure 2) were conducted. Measurements with the DMTA were conducted with samples at room temperature, which were then heated up. Starting from the molten state would not be feasible because after the onset of melting and the reduction of crystallinity, no reliable force response can be detected. Thus, for the considered temperature range, the degree of crystallinity can be assumed to be constant (i.e. maximum value determined with DSC) and thus, only the temperature dependent modulus *E(T)* is measured. The CHILE model for thermoplastic matrices included in the COMPRO model library was initially developed for PEEK and is presented in detail in [8].

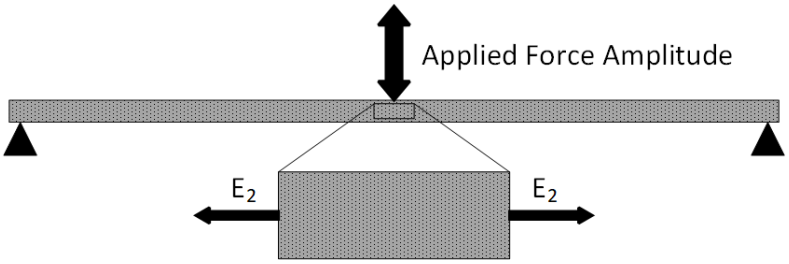

Figure 2. 90° 3-point bending test for the measurement of the composite's transversal modulus E_2.

The setup parameters for the DMTA measurements (*n*=5), which were performed with a Mettler-Toledo DMA/SDTA861e, are summarized in Table 2. As UD composite samples were used for the characterization, the resin modulus was not directly measured. Consequently, the transversal elastic modulus E_2 of the composite is measured with DMTA over a wide temperature range and in the following the isotropic resin modulus E_r of the PA6 matrix was calculated with the Chamis micromechanical model [9]:

$$E_2 = \frac{E_r}{1-\sqrt{\varphi_f}\left(1-\frac{E_r}{E_{f,2}}\right)} \tag{3}$$

where φ_f is the fiber volume fraction and $E_{f,2}$ is the modulus of the reinforcing fiber in its transversal direction. The obtained averaged result for E_r over temperature was then used to determine the modelling parameters for COMPRO.

Table 2: DMTA experimental setup.

Property	**Value**
Sample dimension (mm^3)	70 x 10 x 2
Bending length (mm)	60
Displacement amplitude (µm)	120
Pre-load force (N)	5
Frequency (Hz)	1
Temperature range (°C)	25–210
Heat rate (°C/min)	2

2.3 Simulations

We simulated the processing of flat CF-PA6 plates and flat CF-PA6/metal-hybrid laminate plates. The three-dimensional FE process simulation model, using 2400 quadratic solid elements (C3D20), was built in ABAQUS/CAE with the COMPRO plug-in including the CF-PA6 material input file. The plates had a length and width of 200 x 100 mm^2 and a total thickness of 4 mm. Hybrid plates were composed of a 2 mm composite layup, a metal layer and a layer of adhesion promoter in between (VESTAMELT® Hylink, Evonik), with neglectable thickness. The investigated laminate configurations were as follows: [0_{12}, 90_8] for the CF-PA6 plate and [0_{10}]/Aluminum, [0_2, 90_2, 0_2, 90_2, 0_2]/Aluminum, [0_{10}]/Steel and [0_2, 90_2, 0_2, 90_2, 0_2]/Steel for the hybrid laminates. The compression molding tool was represented by two flat plates on the lower and upper side of the composite or hybrid plate. The tool segments had a dimension of 200 x 100 x 10 mm^3. All necessary material parameters for CF-PA6 were included in the material file, i.e. CTE from thermomechanical analysis (TMA) data and typical values for heat capacity (1700 J/kg K), heat conductivity (0.25 W/m K) and densities (1.23 g/cm^3 and 1.09 g/cm^3 for the crystalline and amorphous phase, respectively). The material properties of the used tooling steel and metal layers (aluminum and steel) were also included as non-curing materials in the COMRPO material library.

In the thermal analysis, the entire model (tool segments and laminate) was set to processing temperature (260°C) with a predefined field. Cooling was realized in two steps, from 260°C to 110°C and from 110°C to 80°C via heat conduction. This split was required to implement a modification at the interface, i.e. a change in the contact definition, in the following stress analysis. The cooling temperature profile, based on thermocouple data measured during the compression molding process, was applied as temperature boundary condition to surfaces of the tool segment in contact with the laminate. In a third step, the tool segments were removed (deactivated) and cooling of the laminate was modelled as convective heat transfer (cooling by ambient air) from 80°C to 25°C. The heat convection was realized with a surface film condition that was defined on the exterior surfaces of the laminate with an assumed heat transfer coefficient of 5 W/m^2K for static ambient air.

In the subsequent stress analysis, the resulting temperature distribution from the previously performed heat transfer analysis were used for each corresponding step. A flow compaction analysis was skipped because micrographs from processed CF-PA6 specimen showed that the resin flow is neglectable and therefore the layer thickness and fiber distribution were assumed to be constant. The process pressure of 50 bar was applied on the upper tool segment. The bonding, enforced by the adhesion promoter, at the composite/metal interface is thermally activated (curable copolyamide bonding agent according to Evonik data sheet). Bonding was assumed to occur below melting temperature (approx. 135°C) of the adhesion promoter during the cooling process, and this temperature served as starting value for iteratively adjusting the simulation. To account for the temperature dependent bonding in the cooling simulation the contact interaction properties between the composite and metal layer were modified after the first step. In the first step of the stress analysis the contact behavior between the composite and metal layer was defined with a frictional penalty behavior and normal hard contact without separation. This allowed for some relative movement of the metal and the CF-PA6 laminate. In the second step the tangential behavior was changed to rough friction, completely preventing tangential sliding. In combination with the normal contact condition this changed contact

definition simulates perfect bonding between the composite and metal layer, i.e. a fully cured adhesion promoter. In the third step, the tool segments were removed (deactivated) and the laminate was able to freely warp. Figure 3 shows an exemplary FE mesh of a process model as well as the simulated PID. To simulate CF-PA6 plates only two simulation steps were needed, i.e. cooling and tool-removal.

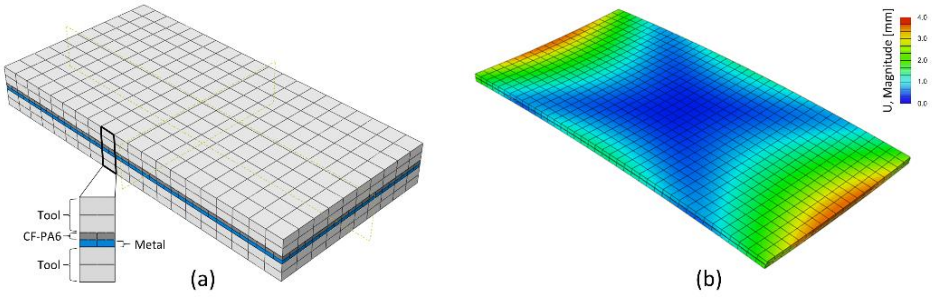

Figure 3. Meshed FE process model (a) and simulated process-induced distortions (b) of a CF-PA6/metal-hybrid plate.

The simulation results were then compared to experimentally manufactured plates by calculating the out-of-plane deviations of simulation and 3D scans (RS6, Hexagon) of the experiments. The geometry comparisons were carried out with Geomagic® Control X™.

3. Results

3.1 Crystallization Kinetics and Modulus Development

The modelled degree of crystallinity during cooling compared with the experiments is shown in Figure 4 (a). The comparisons show that the crystallinity growth can be predicted in all considered cases. Excellent agreement is shown for cooling rates between 3°C/min–10°C/min and still an acceptable agreement for the lower and upper bound of the cooling rate range, i.e. 1°C/min and 20°C/min, is observed. Thus, the adopted model from [6] is suited for the crystallization prediction of CF-PA6. The extracted resin modulus curve obtained from the DMTA experiments compared to the predicted PA6 modulus development curve by the CHILE model for thermoplastics [8] is shown in Figure 4 (b). Good agreement between the experimental data and the model was achieved.

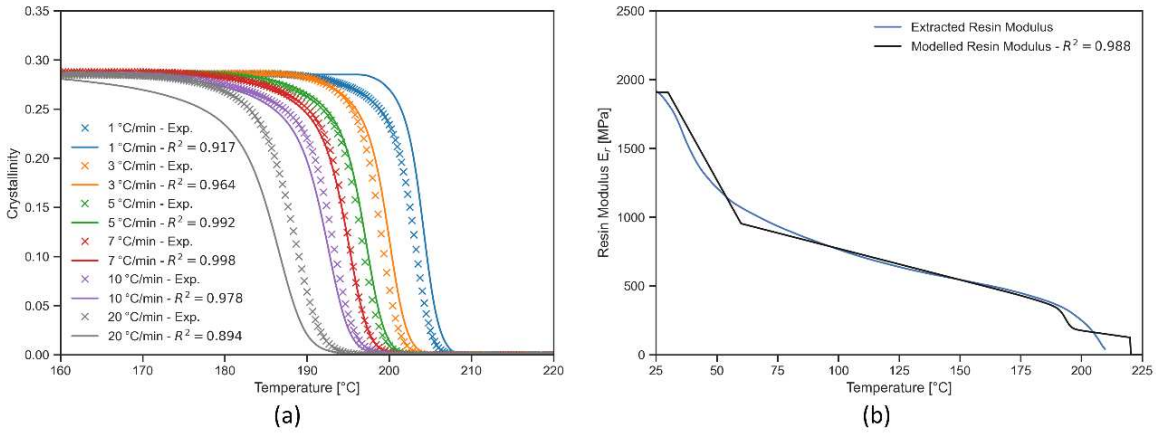

Figure 4. Predicted crystallinity vs. measured crystallinity by DSC at different cooling rates (a) and modelled resin modulus vs. extracted resin modulus obtained from DMTA experiments (b).

3.2 Simulations

Figure 5 shows the comparison of predicted PID and 3D surface scans of the experimental plates. Generally, in terms of shape prediction, all simulation results were in good agreement with the experiments. All plates show the same shape as the corresponding experiment, either a saddle shape or a convex shape, depending on the laminate configuration. The deviations of PID between simulation and experiment were within an acceptable range of ± 0.3 mm (approx. 7.0 mm absolute deformation) for the considered CF-PA6 plate, validating the functionality of the CF-PA6 material input file. For the hybrid laminates the PID deviations between simulation and experiment were within a range of ± 0.25 mm in case of the steel configurations (approx. 3.0 mm absolute deformation) and within a range of ± 0.75 mm in case of the aluminum configurations (approx. 3.5 mm absolute deformation). All simulations overestimated the occurring deformations. The chosen bonding temperature (application of full adhesion by switching the contact interaction properties) in the simulation of 110°C was iteratively determined. Simulations with different adherence temperatures were conducted and compared. A bonding temperature of 110°C resulted in acceptable deviation to the experiments. However, a more specific clarification (through suited thermo-mechanical experiments) for the assumed bonding temperature will be needed.

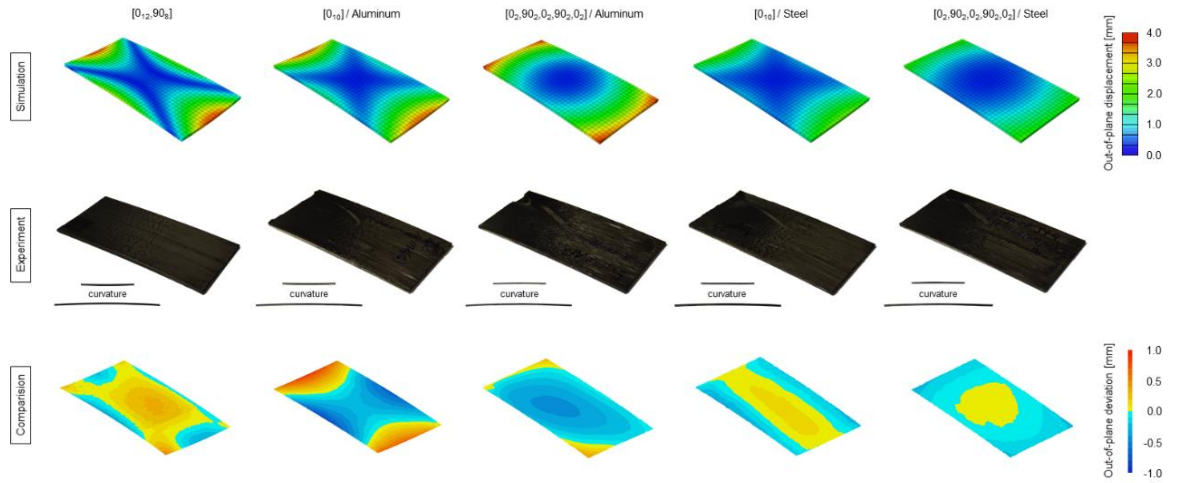

Figure 5. Top row: simulated out-of-plane deformations for all laminate configurations, middle row: corresponding experiments and bottom row: comparison between the simulation results and the surface scans of the experiments (PID deviation).

4. Conclusions

Crystallization kinetics experiments with DSC as well as modulus development experiments with DMTA were executed to determine and model the thermo-mechanical behavior of CF-PA6 and included in COMPRO. Good agreement between the experiments and models was achieved. Crystallization as well as the development of the orthotropic properties based on the actual state of temperature and crystallinity for CF-PA6 can be predicted in simulations. Consequently, the crystallization shrinkage can be calculated and considered together with other effects (thermal anisotropy, tool-part interactions etc.) in the prediction of residual stresses and PID in CF-PA6 composites and hybrid laminates. Comparisons of the predicted PID between the simulations and experiments were conducted. The simulation of the CF-PA6 plate was in good

  doi:10.5075/epfl-298799_978-2-9701614-0-0

agreement with the experiment and predicted the shape of the manufactured part accurately. In case of the CF-PA6/metal-hybrid plates a process simulation with separated steps was introduced to account for temperature dependent bonding enforced by the thermally activated adhesion promoter at the composite/metal interface. The onset (bonding temperature) of full adherence between the composite and metal layer during the cooling simulation was identified as a crucial factor to influence the magnitude of the predicted PID. However, the onset of interface bonding was only based on an assumption derived from an iterative comparison procedure. These iterations were carried out within a temperature range where bonding could potentially occur during cooling (the temperature range was assumed due to the properties of the adhesion promoter and the PA6 matrix). Hence, further investigations of the thermo-mechanical behavior or more precisely, the bonding activation of the adhesion promoter might provide better understanding and further improve the accuracy of the simulation of the CF-PA6/metal-hybrid laminates.

Acknowledgements

We gratefully acknowledge the financial support of the Upper Austrian Government under the FTI-structural-funding program in the scope of the project ‘Erforschung von Methoden für die Mobilität der Zukunft’, project number “Wi-2018-466449/18-WieM”.

5. References

1. Parlevliet P, Bersee H, Beukers A. Residual stresses in thermoplastic composites-A study of the literature-Part I: Formation of residual stresses. Composites Part A: Applied Science and Manufacturing. 2006; 37(11): 1847–1857.
2. Baran I, Cinar K, Ersoy N, Akkerman R, Hattel J. A review on the mechanical modeling of composite manufacturing processes. Archives of Computational Methods in Engineering. 2016; 24(2): 365–395.
3. Wisnom M, Gigliotti M, Ersoy N, Campbell M, Potter K. Mechanisms generating residual stresses and distortion during manufacture of polymer-matrix composite structures. Composites Part A: Applied Science and Manufacturing. 2006; 37(4): 522–529.
4. Lin Y, Min J, Teng H, Lin J, Hu J, Xu N. Flexural performance of steel–FRP composites for automotive applications. Automotive Innovation. 2020; 3(3): 280–295.
5. Wang Z, Jin X, Li Q, Sun G. On crashworthiness design of hybrid metal-composite structures. International Journal of Mechanical Sciences. 2020; 171.
6. Gordnian K. Crystallization and thermo-viscoelastic modelling of polymer composites [dissertation]. Vancouver: University of British Columbia; 2017.
7. Da Paz R, Leite A, Araújo E, Da Nóbrega Medeiros V, De Melo T, Pessan L. Mechanical and thermomechanical properties of polyamide 6/Brazilian organoclay nanocomposites. Polimeros. 2016; 26(1): 52–60.
8. Chapman T, Gillespie J, Pipes R, Manson J, Seferis J. Prediction of process-induced residual stresses in thermoplastic composites. Journal of Composite Materials. 1990; 24(6): 616–643.
9. Vignoli L, Savi M, Pacheco P, Kalamkarov A. Comparative analysis of micromechanical models for the elastic composite laminae. Composites Part B: Engineering. 2019; 174.

  doi:10.5075/epfl-298799_978-2-9701614-0-0

INVESTIGATION AND CHARACTERIZATION OF THERMAL PROPERTIES OF A METAL MATRIX COMPOSITE REINFORCED WITH A METALLIC GLASS FOAM (NI60NB20TA20)

Kerstin Dittmann[a], Anna Trauth[a], Kay Weidenmann[a]

a: Institute of Materials Resource Management (MRM), Augsburg University,
Am Technologiezentrum 8, 86159 Augsburg, Germany
kerstin.dittmann@mrm.uni-augsburg.de

Abstract: *The metallic glass presented in this work with alloy composition $Ni_{60}Nb_{20}Ta_{20}$ (at.-%) obtained its amorphous structure through a powder atomization process and was processed into an open-porous foam using laser powder bed fusion. Subsequently, the open-porous structure was infiltrated with an AlSi12 eutectic aluminum alloy by gas pressure infiltration. For manufacturing processes and applications, knowledge of thermal properties of the metallic glass foam as well as metal matrix composite is essential. Therefore, characteristics of thermal expansion were determined experimentally by dilatometry, specific heat capacity by differential scanning calorimetry and thermal conductivity by laser flash analysis. Thermal expansion as well as specific heat capacity are measured for the metallic glass foam as well as infiltrated composite. Laser flash analysis method was applied to the infiltrated composite only, as this method is not suitable for an open-porous structure. Thermal investigations revealed a relaxation in the metallic glass, which was investigated in detail.*

Keywords: metallic glass; metal matrix composite; thermal expansion; specific heat capacity; thermal conductivity

1. Introduction

Compared to crystalline metals, metallic glasses exhibit remarkable properties such as high strength, hardness, elastic strain limit due to their amorphous structure [1–3]. Conversely, they also exhibit low toughness and high susceptibility to brittle fracture, making them less qualified for the use as monolithic structural components [4]. To compensate for brittleness, metallic glasses are increasingly used as a reinforcing phase in a hybrid material, such as metal matrix composites (MMC) with interpenetrating structures. This requires that the metallic glass has an open-porous foam structure so that it can be infiltrated with a metal that has more ductile properties [5, 6]. The metallic glass used in this work with alloy composition $Ni_{60}Nb_{20}Ta_{20}$ (at.-%) obtained its amorphous structure through a powder atomization process and was processed into an open-porous foam using laser powder bed fusion (LPBF). Subsequently, the open-porous structure was infiltrated with an AlSi12 eutectic aluminum alloy by gas pressure infiltration. Due to the high crystallization temperature of the metallic glass $Ni_{60}Nb_{20}Ta_{20}$ alloy (721 °C [7]) and the low melting temperature of the AlSi12 alloy (577 °C [8]), it was possible to select a corresponding process temperature of 660 °C to maintain the amorphous structure of the metallic glass. For manufacturing processes and applications, the knowledge of thermal properties of the metallic glass foam as well as the MMC is essential. Therefore, the characteristics of thermal expansion were determined experimentally and characterized by dilatometer measurements, specific heat capacity by differential scanning calorimetry (DSC) and

  doi:10.5075/epfl-298799_978-2-9701614-0-0

thermal conductivity by laser flash analysis (LFA). The thermal expansion as well as specific heat capacity are measured and investigated on the metallic glass foam as well as on the infiltrated composite. The LFA method was applied to the infiltrated composite only, as this method is not suitable for an open-porous structure. In addition, the thermal investigations revealed a relaxation in the metallic glass, which was also investigated in detail. Metallic glasses are formed by supercooling a liquid melt at very high cooling rates (10^2-10^8 K/s) [9, 10]. During this process, free volume is frozen, and the metallic glass is in a thermodynamic metastable state. Upon reheating (below crystallization temperature), a relaxation process begins. Thermally activated diffusion closes the free volume and a thermodynamic equilibrium is reached [11–13].

2. Material and experimental methods

2.1 Material

The metallic glass presented in this work with an alloy composition $Ni_{60}Nb_{20}Ta_{20}$ (TaNi39.1Nb20.7 wt.-%) obtained its amorphous structure through a gas atomization process by the company Nanoval GmbH & Co.KG (Berlin, Germany). The Nanoval process is crucible-free [14] and was carried out in an inert argon atmosphere. Rapid cooling causes the material to solidify into an amorphous powder with particle size d_{50} = 44 µm. The powder was further processed into an open-porous foam with a measured reinforcement volume fraction of 37.7 % using LPBF. This Process was conducted by the research group “Production and Component Behavior” at the Institute for Applied Materials – Materials Science and Engineering, Karlsruhe Institute of Technology. Subsequently, the open-porous structure was infiltrated with an AlSi12 eutectic aluminum alloy by gas pressure infiltration. Due to the high crystallization temperature of the metallic glass $Ni_{60}Nb_{20}Ta_{20}$ alloy (721 °C [7]) and the low melting temperature of the AlSi12 alloy (577 °C [8]), a corresponding process temperature of 660 °C was selected to maintain the amorphous structure of the metallic glass. This results in an interpenetrating MMC with metallic glass as reinforcement phase.

2.2 Experimental methods

Investigations on thermal expansion of the $Ni_{60}Nb_{20}Ta_{20}$ open-porous foam, the infiltrated MMC as well as the AlSi12 for comparison were carried out in a dilatometer type DIL 402 Expedis from Netzsch (Selb, Germany). The examined samples were cuboid-shaped with dimensions of 5 x 5 x 10 mm³ and plane-parallel surfaces. Due to the different structure of the $Ni_{60}Nb_{20}Ta_{20}$ open-porous foam along and across the building direction caused by the LPBF process, the material is investigated in both directions regarding thermal expansion. Figure 1 shows on the

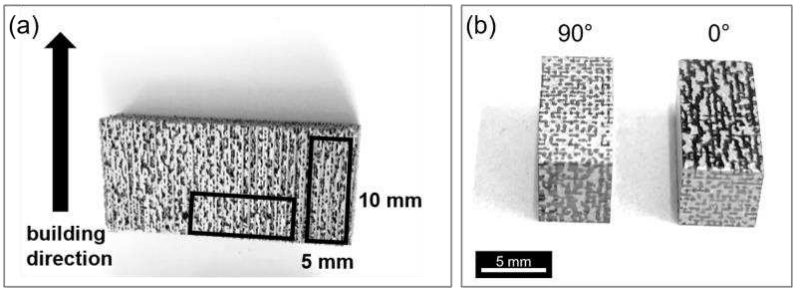

Figure 1. Samples for dilatometer measurements parallel (0°) and perpendicular (90°) to building direction. (a) Samples of $Ni_{60}Nb_{20}Ta_{20}$ open-porous foam. (b) Samples of infiltrated MMC with AlSi12.

  doi:10.5075/epfl-298799_978-2-9701614-0-0

left side the $Ni_{60}Nb_{20}Ta_{20}$ open-porous foam and on the right side the MMC infiltrated with AlSi12.Measurements parallel to building direction are identified with 0° and perpendicular to building direction with 90°. Three thermal cycles of 20 °C to 500 °C with a constant heating and cooling rate of 5.5 K/min were carried out for each sample. The upper temperature limit was chosen to remain below crystallization temperature of the metallic glass and melting temperature of the AlSi12 (577 °C [8]). The contact force was set to 0.2 mN. To avoid oxidation all measurements were performed in an inert argon atmosphere. Therefore, the dilatometer was evacuated to a vacuum of 10^{-4} mbar and purged three times with argon to minimize the residual oxygen content. A reference measurement was performed with a Al_2O_3 sample to eliminate any effects of the testing device. All measurements were carried out and evaluated according to DIN 51045-1. The coefficients of thermal expansion (CTE) were evaluated in a range of 60 °C to 480 °C.

The specific heat capacity was determined by means of dynamic differential calorimetry in a DSC 214 Polyma from Netzsch (Selb, Germany) according to DIN 51007. For comparison and validation of the results, an Al_2O_3 sample was again used as reference. Accordingly, a sample size of approximately 1 x 2 x 3 mm³ of the $Ni_{60}Nb_{20}Ta_{20}$ foam and the MMC was chosen. The temperature program for the heat capacity measurements is composed of an isothermal start phase at 0 °C, a dynamic phase with constant heating rate of 20 K/min up to 200 °C and a final isothermal end phase at 200 °C. Since relaxation in metallic glasses has an influence on the specific heat capacity, the relaxation temperature T_r was first determined. For this purpose, four DSC measurements from ambient temperature to 500 °C (20 K/min) were carried out on one sample. All measurements were performed in an inert argon atmosphere.

Thermal conductivity was determined using laser flash analysis. The measurements were carried out with a LFA 1000 of the company Linseis (Selb, Germany) according to ASTM E 1461. In this method, the thermal diffusivity (a) of the material is measured, and the thermal conductivity (λ) is calculated with the density (ρ) and specific heat capacity (c_p) using equation 1.

$$\lambda = a\rho c_p \tag{1}$$

The specimens must have plane-parallel top and bottom surfaces and a defined thickness. This resulted in a specimen size of 10 x 10 x 1.6 mm³ as shown in Figure 2.

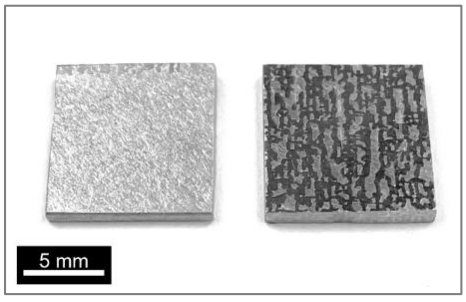

Figure 2. Samples for LFA. Left: Sample of AlSi12. Right: Sample of the infiltrated MMC.

Furthermore, the measurements require a continuous sample body, which is why the $Ni_{60}Nb_{20}Ta_{20}$ open-porous foam could not be investigated with this method. Therefore, the measurement was additionally performed on an AlSi12 sample for comparison.

  doi:10.5075/epfl-298799_978-2-9701614-0-0

3. Results

3.1 Thermal expansion

Figure 3 shows the temperature-dependent evolution of the thermal strain during the three thermal cycles of the $Ni_{60}Nb_{20}Ta_{20}$ open-porous foam (Fig.3 (a)), the infiltrated MMC $Ni_{60}Nb_{20}Ta_{20}$-AlSi12 (Fig.3 (b)), and for comparison of the AlSi12 matrix itself (Fig. 3 (c)).

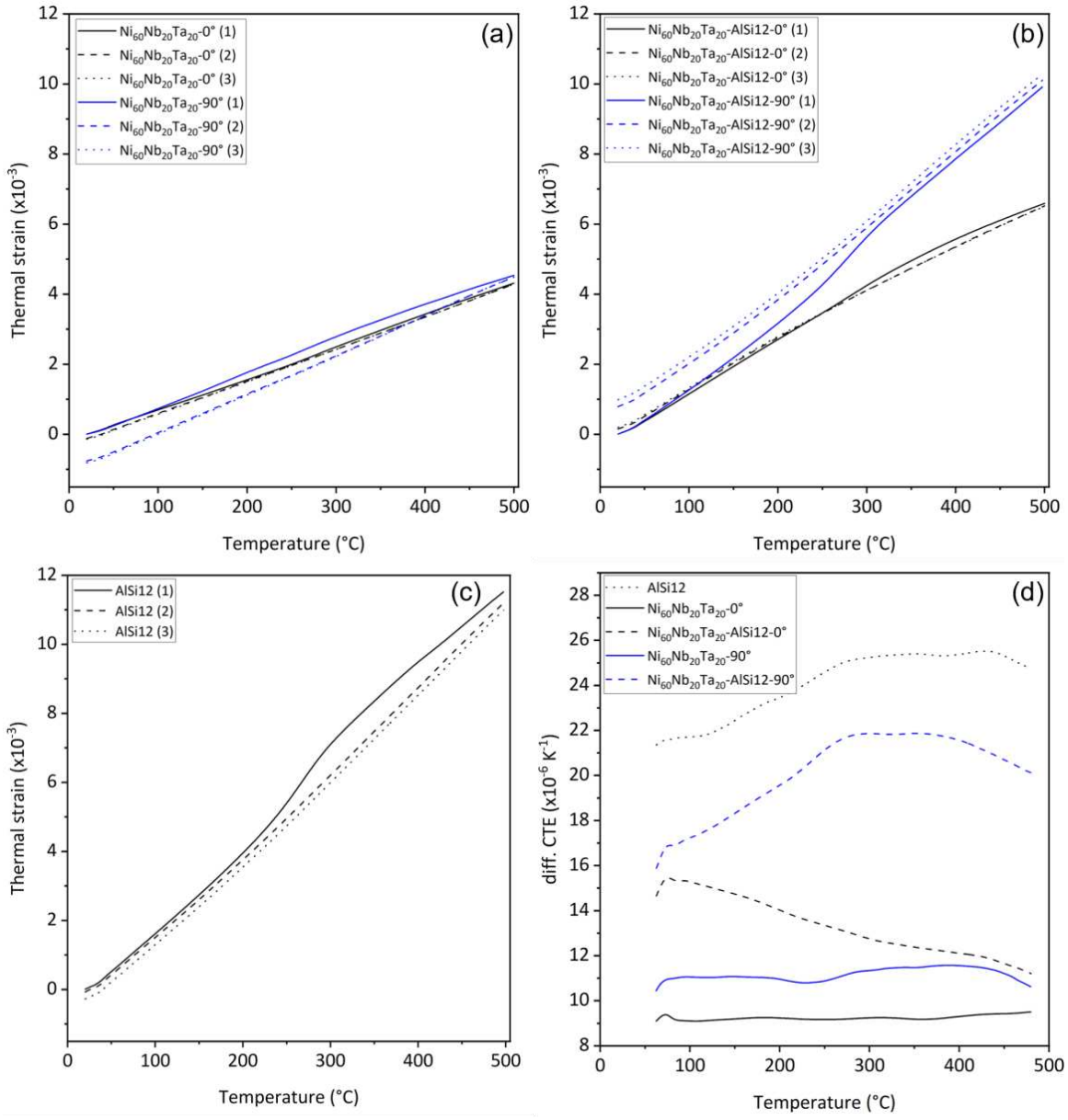

Figure 3. Results of dilatometer measurements. (a) Thermal strain of $Ni_{60}Nb_{20}Ta_{20}$ open-porous foam in 0° and 90° direction. (b) Thermal strain of infiltrated MMC $Ni_{60}Nb_{20}Ta_{20}$-AlSi12 in 0° and 90° direction. (c) Thermal strain of AlSi12. (d) Differential CTE results for all samples.

The first heating cycle of all samples exhibit a distinct increase starting at 200 °C, whereas the following second and third cycle are on the same track. The $Ni_{60}Nb_{20}Ta_{20}$ open-porous foam exhibits with 0.43 % in 0°- and 0.45 % in 90°-direction nearly the same expansion in both directions. However, the sample in 90°-direction shows some remaining negative thermal strain after the cycles, as do the sample of AlSi12. AlSi12 exhibits a max. thermal strain of 1.11 %. The

  doi:10.5075/epfl-298799_978-2-9701614-0-0

infiltrated MMC combines metallic glass $Ni_{60}Nb_{20}Ta_{20}$ and AlSi12 and results in a max. thermal strain of 0.66 % in 0°-direction and 1.0 % in 90°-direction. Additionally, the samples in 90°-direction exhibit a positive remaining negative thermal strain after the second and third heating cycle. The increase in the first cycle can be attributed to relaxation in the metallic glass [11] and to an internal stress generated in MMCs during solidification at manufacturing process [15]. In order to exclude these influences, only the average value from the second and third heating process is considered in the analysis of CTEs shown in Figure 3 (d). The determined CTE of the metallic glass $Ni_{60}Nb_{20}Ta_{20}$-0° is constant value of $(9.24 \pm 0.10) \times 10^{-6} K^{-1}$ with increasing temperature. The CTE of $Ni_{60}Nb_{20}Ta_{20}$-90° remains nearly the same at $(11.17 \pm 0.26) \times 10^{-6} K^{-1}$ with a small increase starting at 250 °C. In contrast, the CTEs of the MMC as well as the matrix material AlSi12 are not linear with increasing temperature. The CTE of the $Ni_{60}Nb_{20}Ta_{20}$-AlSi12 in 0°-direction decreases with increasing temperature from $(14.65 \pm 0.19) \times 10^{-6} K^{-1}$ at 60 °C to $(11.21 \pm 0.96) \times 10^{-6} K^{-1}$ at 480 °C. Whereas, the CTE of the $Ni_{60}Nb_{20}Ta_{20}$-AlSi12-90° is $(15.88 \pm 0.32) \times 10^{-6} K^{-1}$ at 60 °C and increases to a maximum of approx. $21 \times 10^{-6} K^{-1}$ at 300 °C. Subsequently, the value decreases again to $(20.12 \pm 0.94) \times 10^{-6} K^{-1}$ at 480 °C. Similar behavior is observed for the AlSi12-matrix. The CTE starts with $(21.35 \pm 0.25) \times 10^{-6} K^{-1}$, increases to a maximum of approx. $25 \times 10^{-6} K^{-1}$ between 300 - 400 °C and decreases to $(24.72 \pm 2.88) \times 10^{-6} K^{-1}$.

3.2 Specific heat capacity and relaxation

In order to obtain a specific heat capacity independent of the thermal history of the material, an upper temperature limit was first determined experimentally using DSC measurements (Fig. 4 (b)). The DSC signals of the first heating cycle differs from the three following ones.

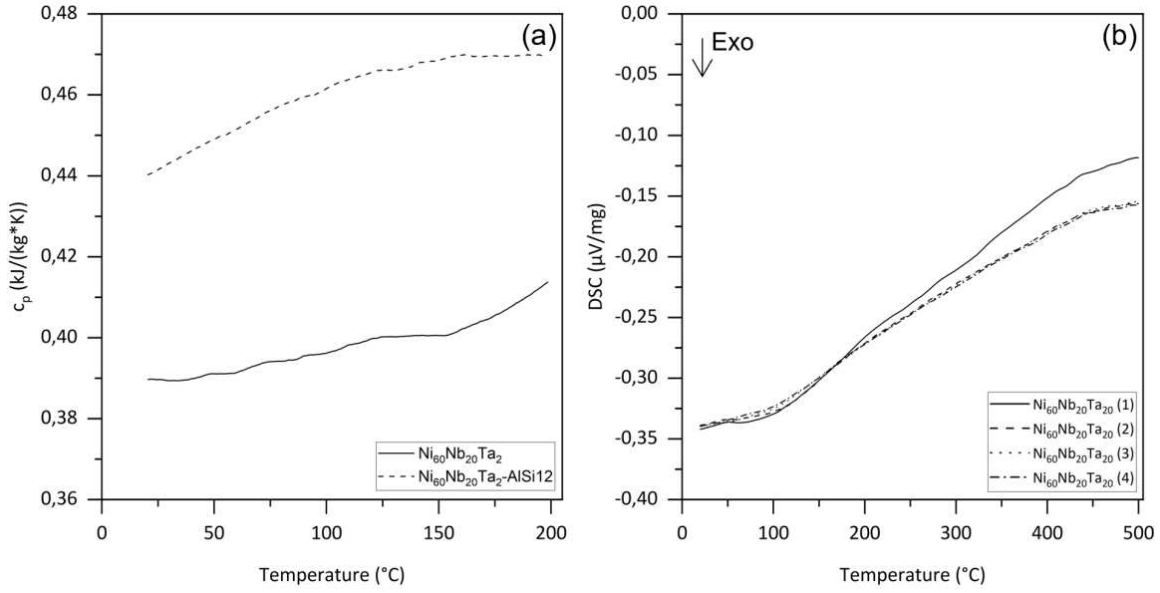

Figure 4. Results of DSC measurements. (a) Specific heat capacity of $Ni_{60}Nb_{20}Ta_{20}$ open-porous foam MMC $Ni_{60}Nb_{20}Ta_{20}$-AlSi12. (b) DSC signal of $Ni_{60}Nb_{20}Ta_{20}$ open-porous foam.

The relaxation temperature T_r therefore corresponds to the temperature at which the DSC signals start to diverge at approximately 200 °C. Consequently, this value was chosen as upper temperature limit for the determination of the specific heat capacity of the metallic glass $Ni_{60}Nb_{20}Ta_{20}$ and the MMC $Ni_{60}Nb_{20}Ta_{20}$-AlSi12 (Fig. 4 (a)). Both c_p values increase with increasing temperature. $Ni_{60}Nb_{20}Ta_{20}$ starts at 0.39 ± 0.01 kJ/kgK at ambient temperature (20 °C) and

increases until 0.42 ± 0.01 kJ/kgK at 200 °C. Whereas, the MMC $Ni_{60}Nb_{20}Ta_{20}$-AlSi12 starts with a much higher value at 0.44 ± 0.01 kJ/kgK at 20 °C and increases until 0.47 ± 0.01 kJ/kgK at 200 °C.

3.3 Thermal conductivity

For the evaluation of the AlSi12 sample a density of 2640 kg/m³ and a heat capacity of 0.90 kJ/kgK was used according to literature [16], with a measured thermal diffusivity of $(0.65 \pm 0.02) \times 10^{-4}$ m²/s resulting in a thermal conductivity of 154.43 ± 4.21 W/mK. The thermal conductivity of the infiltrated MMC $Ni_{60}Nb_{20}Ta_{20}$-AlSi12 is 59.44 ± 1.01 W/mK and was calculated with a measured density of 5690 kg/m³, the result of the investigated heat capacity of 0.44 kJ/kgK at ambient temperature and a measured thermal diffusivity of $(0.24 \pm 0.01) \times 10^{-4}$ m²/s. All results are summarized in Table 1.

Table 1. Results of thermal conductivity measured by LFA.

Material	ρ (kg/m³)	$c_{p,20°C}$ (kJ/kgK)	a ($\times 10^{-4}$ m²/s)	λ (W/mK)
AlSi12	2640 [8]	0.90 [16]	0.65 ± 0.02	154.43 ± 4.21
$Ni_{60}Nb_{20}Ta_{20}$	10790	0.39 ± 0.01	-	-
$Ni_{60}Nb_{20}Ta_{20}$-AlSi12	5690	0.44 ± 0.01	0.24 ± 0.01	59.44 ± 1.01

4. Discussion

The results show that the thermal expansion of the two components of the MMC differ strongly. Whereas the AlSi12 has a high max. thermal strain of 1.11 % and CTE of 21 to 25×10^{-6} K^{-1}, which corresponds with literature [17, 18], the metallic glass $Ni_{60}Nb_{20}Ta_{20}$ exhibits a significantly lower max. thermal strain of 0.43 % and 0.45 % and CTE of 9 to 11×10^{-6} K^{-1}. There is no data published for the metallic glass $Ni_{60}Nb_{20}Ta_{20}$ yet, but an estimation according to [19] leads to an approx. CTE of 8.97×10^{-6} K^{-1} by using the glass transition temperature $T_g = 936$ K of the same composition in [20], which confirms the results. The metallic glass shows an increase in thermal expansion during the first heating cycle starting at 200 °C, due to thermal relaxation as confirmed by the DSC measurements. In addition, a slight anisotropy between the sample parallel (0°) and perpendicular (90°) to building direction is apparent. AlSi12 also shows an increase during the first heating cycle, starting at 300 °C, which suggests that internal residual stresses already exist in the material. MMC with components whose CTE differ greatly exhibit thermal residual stresses after manufacturing. These are generally expected to be compressive stresses in the reinforcement phase and tensile stresses in the matrix when the CTE of the matrix material is higher than the CTE of the reinforcement phase [15, 21]. All these effects combined lead to the resulting thermal expansion of the MMC $Ni_{60}Nb_{20}Ta_{20}$-AlSi12. Due to the structure of the $Ni_{60}Nb_{20}Ta_{20}$ open-porous foam, the samples exhibit anisotropy in 0°- and 90°-direction. This is further enhanced by the different component proportions in the respective directions. The properties of the metallic glass dominate in 0°- and of the AlSi12 in 90°-direction. Therefore, the MMC in 90°-direction has a significantly higher thermal expansion of 1.0 % than the MMC in 0°-direction with 0.66 %. The anisotropy in the CTE is equally evident. The AlSi12 dominated MMC (90°) behaves similarly to the CTE of AlSi12 and increases from 15 to 21×10^{-6} K^{-1}, with increasing temperature. Whereas the metallic glass dominated MMC (0°) decreases linearly from 14 to 11×10^{-6} K^{-1}, and thus a linear behavior more typical for metallic glasses [19]. All thermal

  doi:10.5075/epfl-298799_978-2-9701614-0-0

expansion results are consistent with results of a MMC with $Ni_{60}Nb_{20}Ta_{20}$ as particle reinforcement phase in literature [18].
The resulted specific heat capacity show that AlSI12 with 0.90 kJ/kgK (20 °C) combined with $Ni_{60}Nb_{20}Ta_{20}$ with 0.39 kJ/kgK (20 °C) increases the c_p of the MMC to 0.44 kJ/kgK. The c_p of the metallic glass has not yet been determined, which is why there are no comparative values. However, if the value is compared with the c_p of the individual components ($c_{p,Ni}$ = 0.45 kJ/kgK, $c_{p,Nb}$ = 0.26 kJ/kgK, $c_{p,Ta}$ = 0.14 kJ/kgK [16]), it can be seen that the values correspond well and lead to the conclusion that the results of the MMC also appear realistic.
Same applies to the heat capacity of the MMC, no comparable literature values are yet available. However, the result of the AlSi12 shows that the method provides realistic results, since 154 W/mK corresponds to literature [8, 16]. Considering that nickel (67 W/mK), niobium (54 W/mK) and tantalum (54 W/mK) [16] have a significantly lower thermal conductivity than AlSi12, it can be concluded that the results of the MMC with 59 W/mK appear realistic.

5. Conclusion

A metallic glassy $Ni_{60}Nb_{20}Ta_{20}$ open-porous foam and infiltrated MMC were successfully investigated in terms of thermal expansion, specific heat capacity and thermal conductivity. Thermal expansion was investigated parallel (0°) and perpendicular (90°) to building direction and a pronounced anisotropy was determined. Samples in 90°-direction exhibit a significantly higher thermal expansion with increasing temperature than samples in 0°-direction. The determined heat capacity and thermal conductivity also provide new values for the metallic glass $Ni_{60}Nb_{20}Ta_{20}$ as well as the MMC.

Acknowledgements

The authors are especially thankful to Steffen Czink from the research group "Production and Component Behavior" at the Institute of Applied Materials - Materials Science and Engineering, Karlsruhe Institute of Technology for carrying out the LPBF procedure. Also, special thanks to R. Horny and M. Belli for their technical and experimental support. The financial support of the German Research Foundation (DFG) within the project WE 4273/19-1 is gratefully acknowledged.

6. References

[1] Inoue A, Shen B, Koshiba H, Kato H, Yavari AR. Cobalt-based bulk glassy alloy with ultrahigh strength and soft magnetic properties. Nat. Mater. 2003; 2(10): 661–3 [https://doi.org/10.1038/nmat982]
[2] Inoue A, Shen BL, Chang CT. Fe- and Co-based bulk glassy alloys with ultrahigh strength of over 4000MPa. Intermetallics 2006; 14(8-9): 936–44 [https://doi.org/10.1016/j.intermet.2006.01.038]
[3] Schroers J. Processing of bulk metallic glass. Adv. Mater. 2010; 22(14): 1566–97 [https://doi.org/10.1002/adma.200902776]
[4] Ashby M, Greer A. Metallic glasses as structural materials. Scr. Mater. 2006; 54(3): 321–6 [https://doi.org/10.1016/j.scriptamat.2005.09.051]
[5] Zhang H, Wang A, Li H*, et al.* Quasi-static compressive property of metallic glass/porous tungsten bi-continuous phase composite. J. Mater. Res. 2006; 21(6): 1351–4 [https://doi.org/10.1557/jmr.2006.0166]

[6] Sun Y, Zhang HF, Wang AM*, et al.* Mg-based metallic glass/titanium interpenetrating phase composite with high mechanical performance. Appl. Phys. Lett. 2009; 95(17): 171910 [https://doi.org/10.1063/1.3257699]
[7] Lee M, Bae D, Kim W, Kim D. Ni-based refractory bulk amorphous alloys with high thermal stability. Mater. Trans. 2003; 44(10): 2084–7 [https://doi.org/10.2320/matertrans.44.2084]
[8] Mondolfo LF. Aluminum alloys: Structure and properties. London and Boston: Butterworths 1976.
[9] Johnson WL. Bulk glass-forming metallic alloys: Science and technology. MRS Bull. 1999; 24(10): 42–56 [https://doi.org/10.1557/S0883769400053252]
[10] Inoue A, Takeuchi A. Recent development and application products of bulk glassy alloys. Acta Mater. 2011; 59(6): 2243–67 [https://doi.org/10.1016/j.actamat.2010.11.027]
[11] Egami T. Structural relaxation in metallic glasses. Ann. N. Y. Acad. Sci. 1981; 371: 238–51 [https://doi.org/10.1111/j.1749-6632.1981.tb55664.x]
[12] van den Beukel A, Radelaar S. On the kinetics of structural relaxation in metallic glasses. Acta Mater. 1983; 31(3): 419–27 [https://doi.org/10.1016/0001-6160(83)90219-5]
[13] Tiwari G, Ramanujan R, Gonal M*, et al.* Structural relaxation in metallic glasses. Mater. Sci. Eng. A 2001; 304-306: 499–504 [https://doi.org/10.1016/S0921-5093(00)01503-3]
[14] DDMC2018 Fraunhofer Direct Digital Manufacturing Conference: Proceedings. Stuttgart: Fraunhofer Verlag; 2018.
[15] Huber T, Degischer HP, Lefranc G, Schmitt T. Thermal expansion studies on aluminium-matrix composites with different reinforcement architecture of SiC particles. Compos. Sci. Technol. 2006; 66(13): 2206–17 [https://doi.org/10.1016/j.compscitech.2005.12.012]
[16] GRANTA EduPack; 2020.
[17] Roy S, Nagel A, Weidenmann KA. Anisotropic thermal expansion behavior of an interpenetrating metal/ceramic composite. Thermochim. Acta 2020; 684: 178488 [https://doi.org/10.1016/j.tca.2019.178488]
[18] Lichtenberg K, Weidenmann KA. Effect of reinforcement size and orientation on the thermal expansion behavior of metallic glass reinforced metal matrix composites produced by gas pressure infiltration. Thermochim. Acta 2017; 654: 85–92 [https://doi.org/10.1016/j.tca.2017.05.010]
[19] Kato H, Chen H-S, Inoue A. Relationship between thermal expansion coefficient and glass transition temperature in metallic glasses. Scr. Mater. 2008; 58(12): 1106–9 [https://doi.org/10.1016/j.scriptamat.2008.02.006]
[20] Lichtenberg K. Metallmatrixverbunde mit Verstärkungselementen aus metallischem Glas Ni60Nb20Ta20: Herstellung und Charakterisierung. Dissertation Karlsruhe Institute of Technology 2017.
[21] Bourke M, Goldstone JA, Stour MG, Needleman A. Characterization of Residual Stresses in Composites. In: Fundamentals of Metal-Matrix Composites. Elsevier 1993; 61–80.

TENSILE STRENGTH OF CARBON FIBER TOW/EPOXY COMPOSITES WITH RESPECT TO THE MICROSTRUCTURE OF CARBON FIBER TOW

Su Hyun Lim[a], Wonvin Kim[a], Seong Su Kim[a]

a: Department of Mechanical Engineering, Korea Advanced Institute of Science and Technology (KAIST), Daejeon, Republic of Korea – limsu@kaist.ac.kr

Abstract: *Mechanical properties of continuous fiber reinforced composites are affected by the microstructure within carbon fiber (CF) tows. Herein, the effect of fiber distribution and fiber interlacing within CF tows on the tensile strength of CF tow/epoxy composites was studied. Three types of T700 grade CF tows with different microstructure and sizing treatment were prepared. Fiber distribution was evaluated by scanning electron microscope (SEM). Fiber volume fraction and minimum distance between CFs were calculated using numerical simulations. Quantitative evaluation of fiber interlacing was proposed, and it was applied to the three CF tows. Tensile strength of CF tow and CF tow/epoxy composites were measured, and compared with interfacial shear strength. Finally, two fiber interlacing models were proposed: core-shell structure model and uniform distribution model. Uniform distribution model with high fraction of 0° aligned CFs was advantageous to enhance the tensile strength of CF tow and the composites.*

Keywords: Carbon fiber reinforced polymers; Microstructure; Fiber distribution; Fiber interlacing; Tensile strength

1. Introduction

Fiber distribution and fiber interlacing, which is related to the relative distance and angle between CFs, become non-uniform during the CF tow manufacturing process. It is clear that material properties of CF tows with arbitrary microstructure have different values from those predicted theoretically.

Previous studies have focused on fiber distribution in the cross-section of composite materials and its effect on material properties at microscale using scanning electron microscopy (SEM) and micro-computed tomography [1]. Further, attempts have been made to reflect the orientation of reinforcements in the case of short fiber or particle reinforced plastics [2]. To the best of our knowledge, there has been no study challenging the quantitative evaluation of fiber interlacing to find the correlation with the mechanical properties of carbon fiber reinforced polymers (CFRPs).

In this paper, we investigate the effect of microstructure of CF tows on the tensile strength of the CF tow/epoxy composites. Three types of T700 grade CF tows with different microstructures were compared each other. Tensile strength of CF and interfacial shear strength were measured. Fiber volume fraction and the nearest distance between the CFs were evaluated by using SEM images. New method to quantitatively measure the degree of fiber interlacing was proposed, and applied to three CF tows. Tensile strength of CF tow and CF tow/epoxy composites were measured according to the ASTM standard. Comparing the experimental results, we proposed the core-shell structure model and uniform distribution model to characterize the microstructures within CF tows.

  doi:10.5075/epfl-298799_978-2-9701614-0-0

2. Experiments

2.1 Materials

Three kinds of 12K tows consisted of T700 grade CFs with different sizing agents were prepared. The CF tows have same fiber diameter of 7 μm, elongation at breakage of 2.1 %, and sizing level of 1 %. However, they have differences in tensile strength of CF and the interfacial shear strength (IFSS) as shown in Table 1, which were measured by ASTM D3379-75 and micro-droplet test, respectively [3,4].

Epoxy resin (YD114, Kukdo Chemicals, Republic of Korea) and curing agent (Jeffamine D230, Huntsman, USA) were mixed in a volume ratio of 3:1 and used as a matrix of the CF tow/epoxy composites.

Table 1: Sample designations and mechanical properties with respect to the sizing agents

Sizing agents	A	B	C
Sample designation	A_CF	B_CF	C_CF
Tensile strength of CF (MPa)	4673	5165	5083
IFSS (MPa)*	26	10.4	22.9

* : IFSS between each CF and YD114/Jeffamine D230 mixture

2.2 Evaluation of fiber distribution parameters

CF tow/epoxy composites were made by impregnating the three kinds of CF tows with an epoxy resin/curing agent mixture and curing at 80°C for 2 hrs. Cross-section of fabricated specimen was polished and immersed in aqueous sulfuric acid solution to expose CFs by dissolving the matrix. Fiber distribution was evaluated by observing the pre-treated cross-section of the CF tow/epoxy composites using scanning electron microscope (SEM; AIS1800C, Seron Technologies Inc, Republic of Korea). Using in-house MALAB code, fiber volume fraction and minimum distance between CFs were calculated from SEM images and compared each other [1,5].

2.3 Evaluation of the degree of fiber interlacing

Figure 1 shows the experimental setup to generate the fragmented fiber debris by passing the CF tows through a roll mill with thinner gap than the thickness of CF tows. We assumed that the fiber interlaced points are most vulnerable to stress concentration when subjected to shear force, so all the debris was generated by cutting the fiber interlaced regions. Test was conducted with respect to the observation length from 16 m to 128 m, and mass of CF tow specimen was measured before and after the test to get the mass of fiber debris. Breakage/tow weight ratio, which is the mass of broken fibers per initial mass of CF tow, was calculated for quantitative evaluation of the degree of fiber interlacing.

2.4 Tensile test of CF tow and CF tow/epoxy composites

Tensile test of CF tow and CF tow/epoxy composites was conducted in accordance with ASTM D4018-99 [6]. For CF tow/epoxy composite specimen, impregnated and consolidated CF tows with an epoxy resin/curing agent mixture content of about 35 % were prepared. End tab of CF tow and CF tow/epoxy composite specimens were fabricated using 2-mm-thick glass fiber

  doi:10.5075/epfl-298799_978-2-9701614-0-0

reinforced plastic and leaflet paper, respectively, and film type epoxy adhesive was used for attachment. Specimens with gauge length from 50 mm to 150 mm were tested at a loading speed of 10 mm/min. Maximum load for failure was measured using universal testing machine (INSTRON 4469, Instron Corp, USA), and converted into tensile strength.

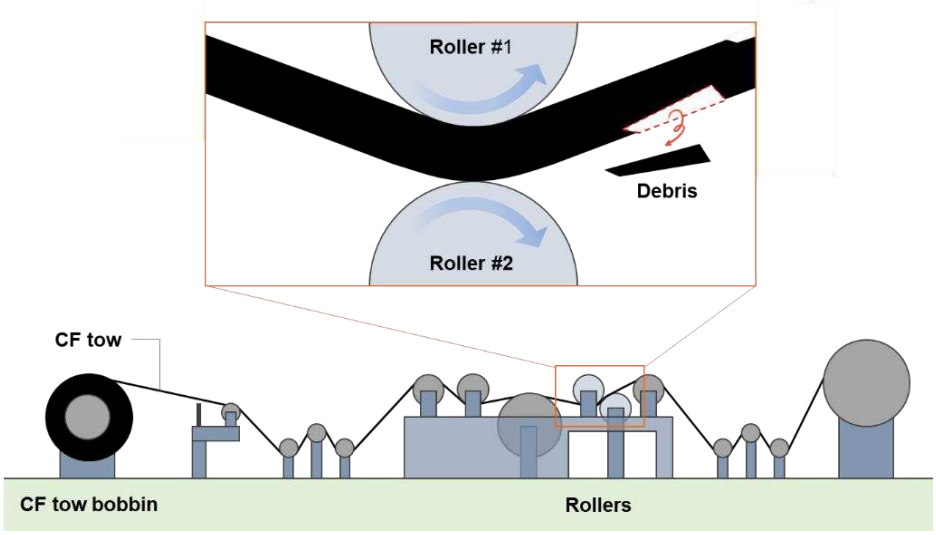

Figure 1. Experimental setup to evaluate the degree of fiber interlacing within CF tow

3. Results and discussion

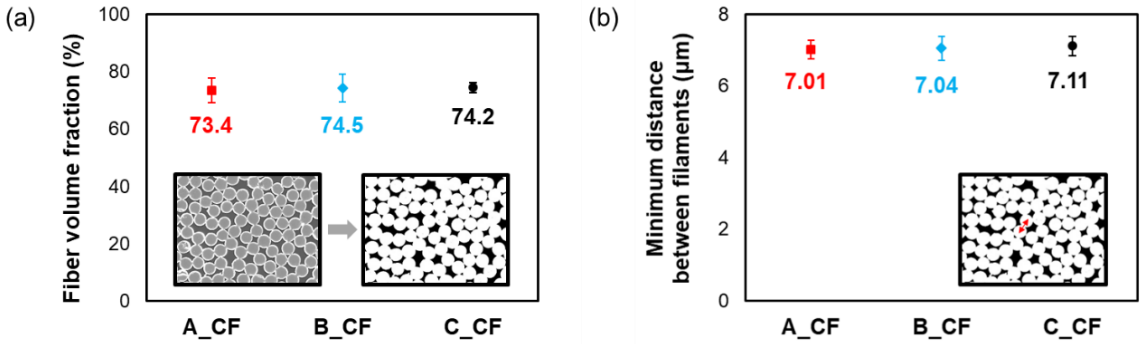

Figure 2. Fiber distribution parameters: (a) fiber volume fraction, (b) minimum distance between CFs

Figure 2 represents the two parameters of fiber distribution within CF tows. Three CF tows had almost the same fiber volume fraction and the distance between nearest CFs when the deviation is considered. Therefore, CF tows can be assumed to have no difference on fiber distribution.

Figure 3 shows the breakage/tow weight ratio of CF tows with respect to the observation length. The breakage/tow weight ratio tended to converge as the observation length increased in all three kinds of CF tow. This is because fiber interlacing in the spinning process is not only caused by artificial factors, but also occurs unintentionally, so that it becomes probabilistically stable as the observation length increases. Comparing the three CF tows based on the observation length of 128 m, breakage occurred the most frequently in A_CF, followed by B_CF and C_CF. Therefore, the degree of fiber interlacing of A_CF is the largest among the three CF tows, which means the highest frequency of fiber contact.

  doi:10.5075/epfl-298799_978-2-9701614-0-0

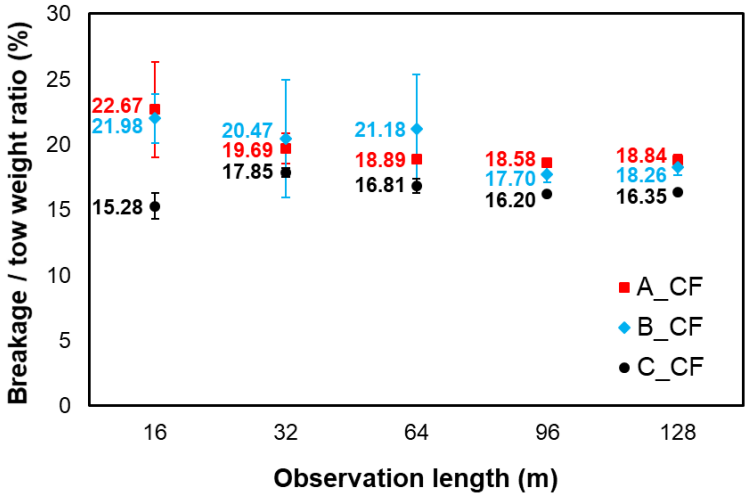

Figure 3. Degree of breakage generation with respect to CF tow observation length

Figure 4 represents the tensile strength of CF tows with respect to gauge length. Tensile strength of CF tow was higher in the order of B_CF, C_CF, and A_CF. Because three CF tows are composed of CFs with different tensile strength, compensation was done by calculate and compare the tensile strength ratio of CF tow and CF as shown in Table 2. A_CF has the highest tensile strength ratio and decreases in the order of B_CF and C_CF. It can be predicted that the fraction of 0° aligned CFs in A_CF will be higher than that of B_CF and C_CF, so well-aligned microstructure is effective to maintain the tensile strength during up-scale from CF to CF tow.

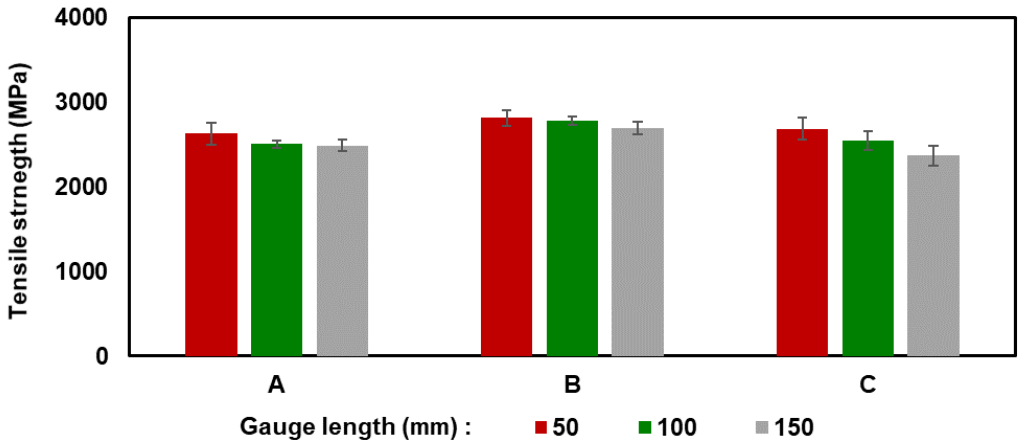

Figure 4. Tensile strength of CF tows with respect to gauge length

Table 2: Maintenance of tensile strength of CF tows compared to CFs

Gauge length (mm)	CF tow tensile strength / single CF tensile strength (%)		
	A_CF	B_CF	C_CF
50	56.26	54.48	52.88
100	53.61	53.86	50.01
150	53.26	52.18	46.65

  doi:10.5075/epfl-298799_978-2-9701614-0-0

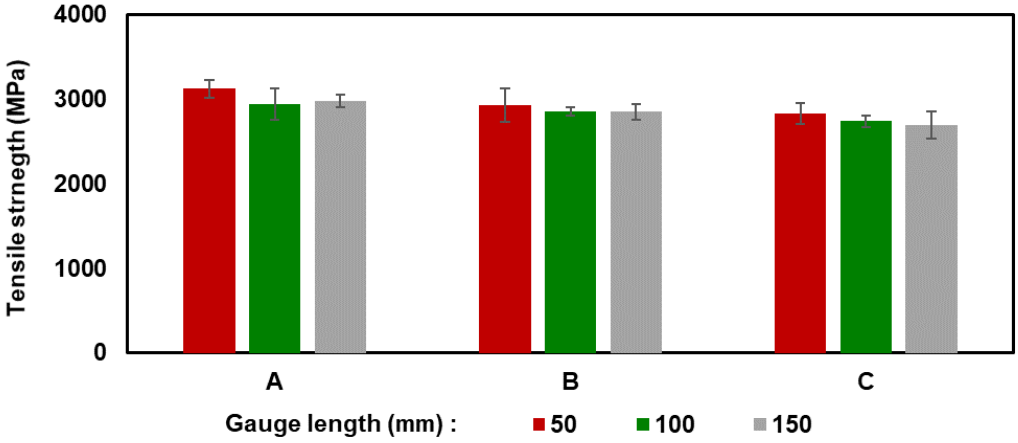

Figure 5. Tensile strength of CF tow/epoxy composites with respect to gauge length

Figure 5 shows the tensile strength of CF tow/epoxy composites. Tensile strength of A_CF was the highest for all gauge length and decreased in the order of B_CF and C_CF. It should be noted that the tensile strength of CF tow/epoxy composites has the same tendency with the tensile strength ratio of CF tow and CF. Moreover, A_CF with the highest IFSS showed definitely high tensile strength of CF tow/epoxy composites despite the absolute low tensile strength of CF and CF tow.

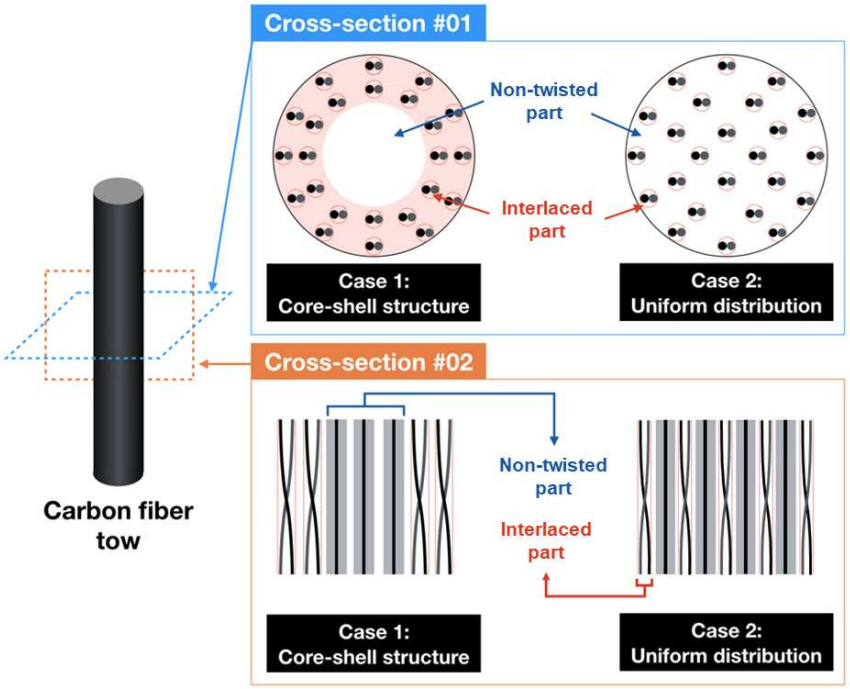

Figure 6. Fiber interlacing models within CF tows

Based on the experimental results, two types of fiber interlacing model were proposed as shown in Figure 6. Core-shell structure model is for fiber interlacing morphology of B_CF and C_CF. On the other hand, microstructure of A_CF was modeled as uniform distribution model. The uniform distribution model was more advantageous than the core-shell model in enhancing the tensile properties of the CF tow due to a higher degree of CF alignment and more uniformly interlaced geometry. The uniform distribution model was also favorable in increasing the tensile

strength of CF tow/epoxy composites. Since the stress generated at the fiber/matrix interface by tensile loading decreases as the degree of fiber alignment increases, uniform distribution model delays the CF/matrix interface failure up to higher tensile load than core-shell model, resulting in better tensile strength. In conclusion, fiber interlacing has a dominant effect on the tensile strength of CFRPs, and the uniform distribution model is advantageous on tensile loading by lowering the stress on fiber/matrix interface.

4. Conclusion

In this study, effect of fiber interlacing on the tensile strength of CF tow and CF tow/epoxy composites was investigated. Based on the newly proposed method to evaluate the fiber interlacing, two fiber interlacing models were suggested for each kinds of CF tows. According to the experimental results, following conclusions were derived:

(1) Three kinds of CF tows were assumed to have the same fiber distribution.

(2) Degree of fiber interlacing within CF tow was evaluated by applying shear force on CF tow and measuring the mass of fiber debris.

(3) Tensile strength of CF tow and CF tow/epoxy composites were measured. Tensile strength ratio of CF tow and CF was calculated to predict the fraction of well-aligned fibers.

(4) Two fiber interlacing models were proposed: core-shell structure model and uniform distribution model. Uniform distribution model was efficient to enhance the tensile strength of both the CF tow and CF tow/epoxy composites.

Acknowledgements

This work was supported by the Korea Evaluation Institute of Industrial Technology, granted financial resource from the Ministry of Trade, Industry & Energy, Republic of Korea (No.20010509). This paper was partly supported by Korea Institute for Advancement of Technology (KIAT) grant funded by the Korea Government (MOTIE) (P0017006. The Competency Development Program for Industry Specialist in 2022).

References

1. Wang W, et al. Micromechanical modeling of fiber-reinforced composites with statistically equivalent random fiber distribution. Materials. 2016;9(8):624.
2. Breuer K, Stommel M. RVE modelling of short fiber reinforced thermoplastics with discrete fiber orientation and fiber length distribution. SN Applied Sciences. 2020;2(1):1-13.
3. ASTM A. Standard test method for tensile strength and Young's Modulus for high-modulus single-filament materials. ASTM International West Conshohocken, PA, USA; 1989. p. 128-31.
4. Lim, SH, et al. Resin impregnation and interfacial adhesion behaviors in carbon fiber/epoxy composites: Effects of polymer slip and normalized surface free energy with respect to the sizing agents. Composites Part A: Applied Science and Manufacturing. 2021;146:106424.
5. Jeong, GS. A study on behavior of tow-prepreg and resin flow characteristics according to temperature and pressure. Master thesis. 2020.
6. ASTM D. Standard test methods for properties of continuous filament carbon and graphite fiber tows. 2011.

  doi:10.5075/epfl-298799_978-2-9701614-0-0

UNDERSTANDING THE INFLUENCE OF MANUFACTURING DEFECTS ON THE TENSILE BEHAVIOR OF SIC/SIC FILAMENT WOUND TUBES FROM A UNIDIRECTIONAL COMPOSITE MODEL

Claire, Morel[a,b], Christophe, Lorrette[a], James, Braun[a], Jacques, Lamon[b], Emmanuel, Baranger[b]

[a]: Université Paris-Saclay, CEA, Service de Recherches Métallurgiques Appliquées, 91191, Gif-sur-Yvette, France – claire.morel@cea.fr ;
[b]: Université Paris-Saclay, Centrale Supélec, ENS Paris-Saclay, CNRS, LMPS - Laboratoire de Mécanique Paris-Saclay, 91190, Gif-sur-Yvette, France.

Abstract: *SiC/SiC ceramic matrix composites are promising cladding candidates to improve the accident tolerance of the fuel in pressurized water reactors. Indeed, their excellent mechanical properties at high temperatures (above 1200°C) would give them additional margins to face a loss of coolant. In this work, the mechanical behavior of a filament wound tube under cyclic tensile stress is performed in order to investigate the impact of two types of manufacturing defects on the mechanical behavior. The defects studied correspond to local modifications of the composite microstructure. For both classes of defects, the same methodology is used, consisting in performing mechanical cyclic tensile tests in the tube axis direction with post-analysis to assess fine parameters. The results allow characterizing the elastic behavior, as well as, the behavior during matrix microcracking through the consideration of unload-reload cycles. Microstructiral analyses are performed to establish the mechanical properties/microstructures relationship.*

Keywords: mechanical behavior; manufacturing defects; SiC/SiC; tubes

1. Introduction

Ceramic matrix composites (CMC) are attractive materials for high-temperature applications, due to their stability up to 1600°C [1]. Therefore, they are studied with a view to application in many high value-added fields. For example, these materials, and more specially the SiC/SiC composites are prime candidates for fuel cladding in pressurized water reactors, because of their high temperature resistance and their stability under irradiation when materials are pure and well-crystallized [2]. Using SiC/SiC composites could increase reactor safety, especially for E-ATF (Enhanced Accident Tolerant Fuels) applications, aiming to improve fuel cladding properties in the event of a loss-of-coolant accident (LOCA) [3]. In fact, unlike zirconium-based fuel cladding, SiC/SiC composites can maintain their geometry and integrity in extreme situations (beyond 1200°C in oxidizing steam environment). They show a strongly reduced oxidation compared to zirconium-based fuel cladding under such accident conditions.

The mechanical behavior of SiC/SiC CMC has been studied widely in the literature either experimentally or by modeling. Unidirectional composite have been investigated with the shear lag model [4, 5] and 2D plate architectures have already been characterized [6]. Attention will then be focused on tubular architecture in this work. Less data are found in the literature in this field because few applications use this geometry, outside nuclear and some aeronautical ones [7].

In this paper, two batches of tubular test specimens representative with dimensions of fuel cladding tubes were studied [8]. Each batch presented a local modification of the morphology,

  doi:10.5075/epfl-298799_978-2-9701614-0-0

the first one consisting in variation of core chemical composition while the second one in surface defects. The objective of this paper is to describe the damage phenomena of various SiC/SiC tubes with various microstructure characteristics by relying on a damage models for unidirectional composites. In a first part, the material is described, as well as the experimental protocol of the tensile tests. In a second part, the analysis of the mechanical behavior is carried out.

2. Description of material and tensile tests

2.1 Manufacturing process of SiC/SiC tubes

The tubes were made of three components: silicon carbide (SiC) fibers, SiC matrix and pyrocarbon (PyC) fiber/matrix interphase. The fibrous preform was made of 3rd generation Hi-Nicalon type S fibers. Two reinforcement layers were produced by filament winding with an angle of +/-45° along the tube axis, using cylindrical tooling to ensure tubular geometry and good surface finish. The PyC and SiC were deposited by Chemical Vapor Infiltration (CVI). In a first step, pyrocarbon interphase with a thickness between 50 and 100 nm was deposited on fibers, in order to optimize fiber/matrix coupling and to promote deflection of the matrix cracks. Then, a first layer of matrix was deposited to consolidate the structure and allow the mandrel removal by chemical attack [9]. Two successive infiltration cycles finalized the tubes densification. Finally, external and internal finishing surface treatment steps were possible. In this study, only the influence on grinding will be conducted for this step. The dimensions of the tubes were given in Table 1 and 2; the average cross section area of tubes was 17mm².

2.2 Manufacturing defects

The two types of local morphology changes investigated are referred to as defects in the following. The first defect type refers to a change in core composition, while the second results from grinding step. The tubes were assumed to be composed of two parts: the plies, consisting of matrix, fibers and porosity and the outer surfaces of the tube, called seal coat, composed of matrix only.

Table 1 details the composition of the two grades of tubes of batch 1. Within the plies, porosity was lower in grade 1-B than in grade 1-A. Indeed, in grade 1-B, the matrix within the plies, deposited during the first CVI step, was not pure and contained silicon, unlike grade 1-A which contained only SiC. This can been explained by the conditions during the CVI cycles that differed from the nominal conditions.

Batch 2 was dedicated to the investigation of the influence of surface defects. For this purpose, different amounts of seal coat were removed by grinding from the inner and the outer surfaces. 2-RR grade denotes reference as-manufactured tubes. The following grades (2-OI, 2-O+I and 2-O+I+) refer to all outer and inner grinded tubes, respectively noted O and I. Thickness of remaining seal coat and tube dimensions for the different grades are given in Table 2.. The seal coat had been completely removed during the grinding operation for those tubes labelled with a "+". On those surfaces, plies are directly uncovered and some fibers have been damaged by the grinding operation. On the other tubes, the seal coat was still present on the surface of fiber preform and it was expected to smooth the external surfaces.

Table 1: Characteristics of the microstructures of the two grades of the batch 1.

Batch 1		1-A	1-B
Tube	Outer diameter	9.59 mm	9.50 mm
	Inner diameter	8.31 mm	8.22 mm
External layers	Outer thickness	65 µm	30 µm
	Inner thickness	53 µm	100 µm
Plies	Fiber fraction	40 %	34 %
	Porosity	7.7 %	5.3 %
	Matrix fraction	52.3 %	60.7 %

Table 2: Characteristics of the microstructures of the two grades of the batch 2.

Batch n°2		2-RR	2-OI	2-O+I	2-O+I+
Tube	Outer diameter	9.68 mm	9.53 mm	9.28 mm	9.31 mm
	Inner diameter	8.31 mm	8.32 mm	8.28 mm	8.43 mm
External layers	Outer thickness	84 µm	75 µm	0 µm	0 µm
	Inner thickness	58 µm	61 µm	58 µm	0 µm
Plies	Fiber fraction	37 %			
	Porosity	8.5 %			
	Matrix fraction	54.5 %			

2.3 Cyclic tensile test protocol

Figure 1. Set-up of cyclic tensile tests.

Tensile tests were performed on tubes from both batches. Load was applied parallel to tube axis leading to a local multi-axial loading of each ply. The test procedure is described in ISO 20323 standard [10]. The specimens were 65 mm and 70 mm long for batch 1 and 2, respectively. The tubes were glued in a mandrel with epoxy adhesive. The tube and gripping clamp assembly was

installed on the testing device. The upper part was screwed on it, while the lower part was directly glued to a grip itself screwed to the lower part of the tensile machine (see Fig. 1). This method guarantees tube alignment with respect to the loading direction [10]. The force was measured with a 25 kN load cell (HBM U10M). The strain was measured thanks to longitudinal extensometers with 25 mm (INSTRON 2620-603) and 30 mm (MFA1) gauges length for the batch 1 and 2, respectively. Loading rate was 0.05 mm/min.

Cyclic as well as monotonic loading mode was applied on batch 1. A maximum of 4 cycles were performed, with a single one is in the elastic domain, with a minimum stress of - 50 MPa at each cycle. The number of cycles and the level of damage were sufficiently low to avoid fatigue phenomena [8]. An example of the stress-strain curve for a cyclic test is shown in Figure 2.

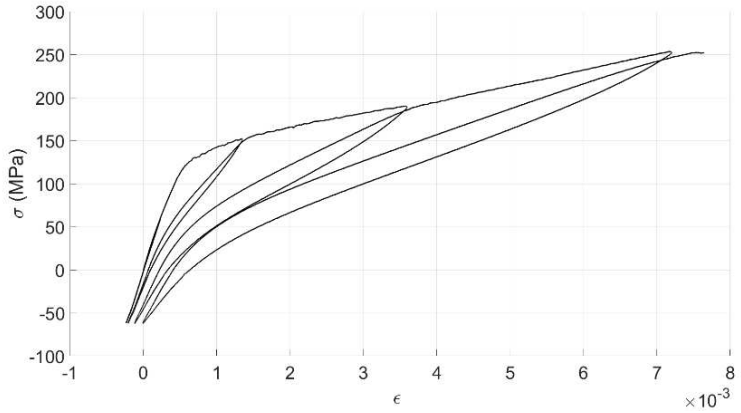

Figure 2. Mechanical behavior curve for grade 1-A.

3. Mechanical behavior

3.1 Elastic behavior

The Young's moduli are given in Figure 3. It can be noticed that the 1-B grade presents a softer behavior than 1-A (resp. 213 GPa on average against 271 GPa). This was attributed to the presence of silicon in the matrix core. Indeed, the elastic modulus of silicon is around 150 GPa against 416 GPa for the CVI-SiC (β-SiC) matrix [11]. For the 2nd batch, when the seal coat is removed, the elastic modulus of tube decreases. The seal coat matrix is stiffer than the core composed of fiber, matrix and porosity.

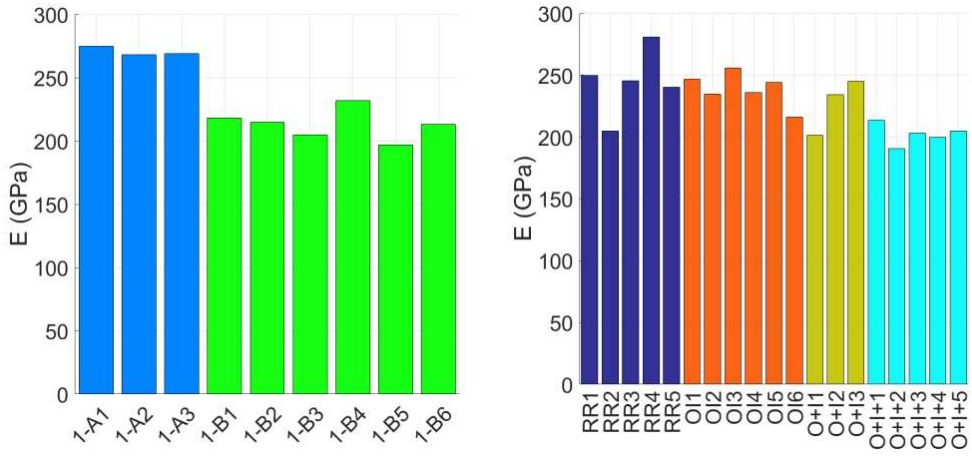

Figure 3. Elastic modulus for batch 1 (left) and batch 2 (right).

In parallel, an analytical model was developed to simulate tube elastic behavior as a function of the composition. This model is based on the equations of the continuous media mechanics (hypothesis of small perturbations and equilibrium). For each layer of tube, a behavior law was determined. For the seal coat, an isotropic behavior was assumed [11]. For the core layers, the behavior was determined in three steps. At first, only the isotropic matrix was considered then pores were added by assimilating them to blunt cracks [12] and finally, the behavior of the fibers fiber was added only in the fiber axis.

The experimental and analytical analysis of elastic behavior enabled to assess the role of the external layers of matrix. The latter stiffen the composite owing to their composition (i.e. layers with only matrix, without porosity) and increase the isotropy of tube structure. When the thickness of tubes is reduced, the external layer tend to play the same role as the internal layer of matrix, for the same thickness. On the other hand, the study of the onset of matrix cracking, not detailed in this paper, shows that the external seal coat layers crack first, especially the outer matrix layer. The outer SiC grains present a more fragile behavior because of their specific microstructure consisting in large columnar arrangement.

3.2 Damage behavior

The tube damage behavior was then studied. In the case of unidirectional CMC, the first cracks appear in the matrix. These cracks are then deflected at the fiber/matrix interface (Figure 4). Therefore, a load transfer occurred from the matrix onto the fibers. In addition, around the cracked areas, debonding between the fiber and the matrix appeared. Slip between the fiber and the matrix took place, characterized by the shear stressτ. Different quantities characterize the damage in the composite, particularly in cyclic tests [4]. In this paper, a focus on two quantities highlighting the impact of the two defects was studied.

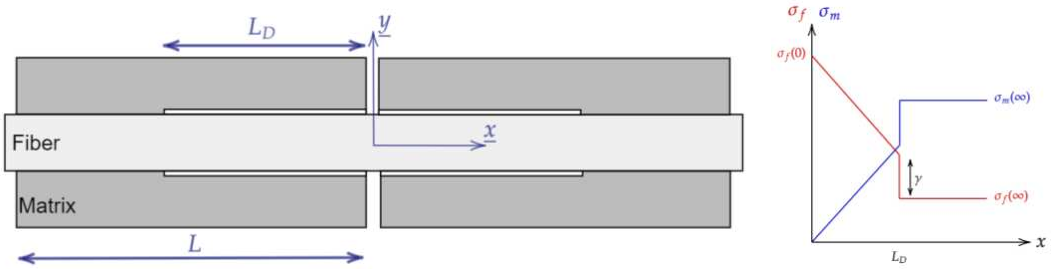

Figure 4. Shear lag model.

The cycle width at half-maximum characterizes the slippage in the composite [4] (see Fig. 2). Indeed, during a cycle, no new crack occurs; the hysteresis induced by the energy loss was only due to slippage. In unidirectional composites, slippage is located at the fiber/matrix interface. However, slippage in the tubes can occur between fiber and matrix in the core preform or between the plies. Figure 4 shows the evolution of the slippage during the cycles for the two batches as a function of the strain at the beginning of the cycle.

On the 2nd batch, no difference between the grades was observed. The external layers of the matrix had no impact. Slippage was essentially located in the fibrous preform, at the fiber/matrix interface or between the plies. Therefore, the shear lag model can be applied.

On the 1st batch, a difference was observed. The slippage is more important on grade 1-A. In a first approximation, it was assumed that the preform behaves like a unidirectional composite. Thus, the effect of the fiber orientation and the shear stress associated with this orientation were neglected. According to the shear lag model [5,6], the stresses in the matrix at a given level of a crack were defined by equation Eq. (1).

$$\frac{2\tau L_D}{R_f} = \sigma_m(\infty) - \gamma + \sigma_m^T \quad (1)$$

withR_f the fiber radius, γ the equivalent stress of the energy jump at the level of matrix break, σ_m^T the thermal residual stress and $\sigma_m(\infty)$ the stress in the matrix away from the crack. Debonding length was defined by Eq. (2). Thus, as the elastic matrix modulus E_m in the matrix decreased, debonding length decreased. The fiber/matrix slippage occurred over a shorter area, leading to thinner cycles width, which confirmed the experimental observations (Figure 5).

$$L_D = \frac{R_f}{2\tau}(E_m\epsilon(\infty) - \gamma + \sigma_m^T) \quad (2)$$

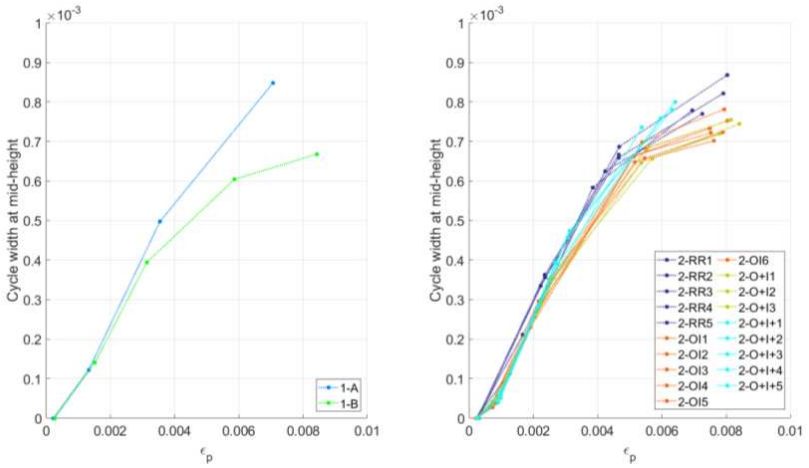

Figure 5. Cyclic width at mid-height in function of the strain for batch n°1 (left) and batch n°2 (right).

The second characteristic quantity considered is the evolution of the tangent modulus at the beginning of discharge$1/E^*$. Figure 5 shows its evolution for the two batches as a function of the strain at the beginning of the cycle. This quantity characterizes the damage evolution within the composite.

First, the impact of matrix seal coat on the damage was studied on the 2nd batch. By analyzing the micrographs in the final state and studying the properties at breakage of the different components, it was evidenced that the external layers of the tube were cracked. However, the presence of matrix seal coat seemed to have no impact on the tube damage. In order to justify this experimental observation, a simplified model was considered. It was composed of two layers: the first one ($\cdot_c$), in the core, and two external layers ($\cdot_e$). In the following, the cross-sectional area, the damage and the elastic modulus of each layer will be noted as $S_.$, $d_.$ and $E_.^0$ respectively. The damage behavior of this two-layer material as given in Eq. (3), allowed the strength N and the strainϵ to be related. The equivalent damage of the two layers $\overline{d}$, was deduced as Eq. (4).

$$N = [S_e E_e^0(1 - d_e) + S_c E_c^0(1 - d_c)]\epsilon \quad (3)$$

$$\overline{d} = 1 - \frac{S_e E_e^0 (1-d_e) + S_c E_c^0 (1-d_c)}{S_e E_e^0 + S_c E_c^0} \quad (4)$$

$$\alpha = S_e E_e^0 / S_c E_c^0 \quad (5)$$

Moreover, by considering the section ratios and by performing a Taylor expansion of α defined by Eq. (5), Eq. (6) is obtained. Therefore, the core layer was well predominant in the damageable behavior of the composite.

$$\overline{d} \approx d_c + \alpha(d_e - d_c) \quad (6)$$

On the 1st batch, a slight difference was noticed between the two grades, which is due to the differences measured in the elastic domain (≈ 20%). The core composition change modified in a similar way the tangent modulus E^* but did not influence the damage evolution. The measurement of the tangent modulus $E^*$was difficult and subject to error. The measurement error is in the order of magnitude of the differences in elastic behavior, so it is difficult to analyze further.

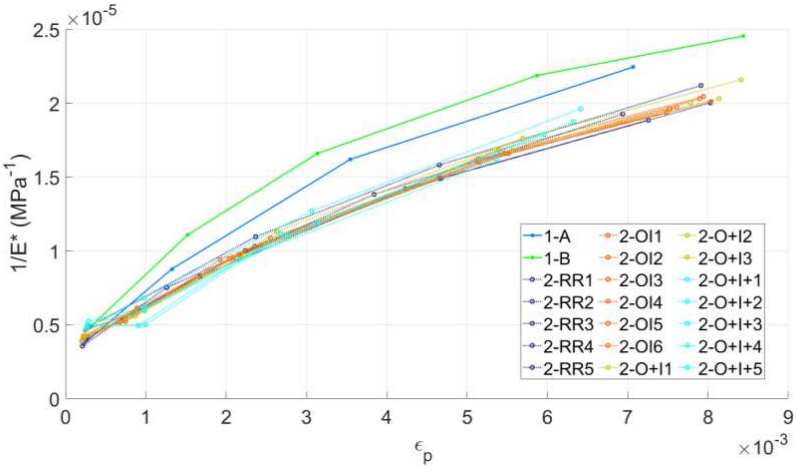

Figure 6. Evolution of at the tangent modulus $1/E^*$ in function of the strain at the beginning of the discharge for the both batches.

In summary, the seal coat layers had limited impact on the slippage and the evolution of the E^* modulus. Indeed, even if they cracked, the thickness of the matrix remained small compared to the core of the material. Their damage was therefore negligible. On the other hand, the changes in the plies composition had an influence on the mechanical behavior. A softer matrix decreased the interfaces slippage but softened the damageable behavior.

4. Conclusion

First, the characteristics of two different batches of tubes were described to investigate the impact of a morphological modification within the plies and the impact of the seal coat layers, respectively. In a second step, the mechanical behavior was analyzed by focusing on the elastic modulus and two characteristic quantities for the matrix cracking part, describing the sliding and the damage progression. Simplified modelling considering the plies as unidirectional composites, allowed relationship with microstructure to be established. Thus, it was highlighted that the seal coat layers allow stiffening and making the composite more isotropic in the elastic part while they have no impact on the behavior in the matrix cracking part. The presence of Si

in the plies makes the matrix in the core more flexible, which results in a decrease of the $E$and E^* moduli, in comparison with reference tubes. A softer matrix also leads to a decrease of the cycle width, which corresponds to the description of the shear-lag model.

For further study, it would be now interesting to describe the cycled behavior in compression. As the cracks perpendicular to the loading direction are closed under compressive loading, it will be possible to obtain additional information on the cracks in shear. These different descriptions would make it possible to evidence the different mechanisms that appear during the matrix-cracking phase of the tubes to describe the damage mechanisms of the composite in more details. This will allow building a damage model representative of the mechanisms based on the shear lag model.

5. References

1. Saucedo-Mora L, Lowe T, Zhao S, Lee PD, Mummery PM, Marrow TJ. In situ observation of mechanical damage within a SiC-SiC ceramic matrix composite. Journal of Nuclear Materials 2016; 481:13-23.
2. Bansal NP, Lamon J. Ceramic matrix composites: materials, modeling and technology. John Wiley & Sons 2014, chapter 13.
3. Terrani KA. Accident tolerant fuel cladding development: Promise, status, and challenges. Journal of Nuclear Materials 2018; 501:13-30.
4. Vagaggini E, Domergue JM, Evans AG. Relationship between hysteresis measurements and the constituent properties of ceramic matric composites: I, theory. Journal of American Ceramic Society 1995; 78:2709-2720.
5. Lissart N, Lamon J. Damage and failure in ceramic matrix minicomposites: experimental study and model. Acta Materialia 1997; 45.3:1025-1044.
6. Lamon J. A micromechanics-based approach to the mechanical behavior of brittle-matrix composites. Composites science and technology 2001; 61.15: 2259-2272.
7. Yun HM, DiCarlo JA, Fox DS. Issues on fabrication and evaluation of SiC/SiC tubes with various fiber architectures. HTCMC-5 2004; NASA/TM-2004-213335.
8. Braun J, Sauder C, Lamon J, Balbaud-Célérier F. Influence of an original manufacturing process on the properties and microstructure of SiC/SiC tubular composites. Composites Part A: Applied Science and Manufacturing 2019; 123:170-179.
9. Sauder C, Lorrette C. Method for producing a composite including a ceramic matrix. U.S. Patent No. 9,145,338. 2015.
10. ISO 20323, Fine ceramics (advanced ceramics, advanced technical ceramics) – Mechanical properties of ceramic composites at ambient temperature in air atmospheric pressure - Determination of tensile properties of tubes, 2018.
11. Michaux A, et al. Young's modulus, thermal expansion coefficient and fracture behavior of selected Si–B–C based carbides in the 20–1200°C temperature range as derived from the behavior of carbon fiber reinforced microcomposites. Journal of the European Ceramic Society 2007; 27.12:3551-3560.
12. Pensée V, Kondo D, Dormieux L. Micromechanical analysis of anisotropic damage in brittle materials. Journal of Engineering Mechanics 2002; 128.8: 889-897.

  doi:10.5075/epfl-298799_978-2-9701614-0-0

Characterization of damage of a laminated composite with a barrier layer under thermomechanical loading

Yann Accettura[a,b], Christophe Bois[b], Jean-Christophe Wahl[b], Tanguy Briand[a]

a: CMP Composites, 37 impasse du Taillan, 33320 Eysines, France. Email : Yann.accettura@cmpcomposites.fr

b: Univ.Bordeaux, I2M : UMR 5295,33400-Talence, France.

Abstract: *The search for technological solutions decoupling the sealing function from the mechanical strength of composite tanks would allow a significant reduction in the cost/performance ratio of launchers. Moreover, the use of particular propellants can lead to chemical incompatibilities between the container and the content, causing the failure of the storage systems. The deposition of a polymer coating on the internal surface of the tank can thus act as a protective layer against chemical incompatibilities and at the same time guarantee the tightness of the tank in spite of composite damage. However, coating process may induce temperature aging that affects cracks development in the composite laminate. The coating has therefore an ambivalent effect regarding permeability issue.*

Keywords: coating; damage; barrier layer; thermomechanical load; micro-crack

1. Introduction

The lightening of space structures remains a crucial issue, but today it cannot be dissociated from those related to the reduction of production costs and sustainable development. With the emergence of numerous players, the space sector has become extremely competitive, thus encouraging the development of new technologies. Thus, the concept of a reusable launcher, still considered utopian ten years ago, is today a reality. By combining this technology with more easily recyclable materials and robust industrialization methods that limit waste and energy resources, the space sector can aim for the same high environmental standards as other sectors such as the automotive and aeronautics industries. Industrial players are looking for innovative solutions to improve performance, and the potential for performance gains on tanks remains high. A coefficient is used to compare the mechanical performance between the different type of tank: (Pressure x Volume)/ Mass (in bar. L. kg^{-1}). At present, Type IV tanks allow to gain +278% of performance compared to Type I aluminum tanks, but the development of Type V tanks could further improve this potential [1] provided that other functions are fulfilled. Therefore, the use of an internal coating allows to decouple the structural function and the sealing function of the composite tanks but also to free itself from the problems of incompatibility of composite materials with cryogenic propellant such as liquid oxygen [2,3].

This study proposes to characterize the mechanical properties at room temperature as well as in a cryogenic environment more likely to correspond to a liquid oxygen environment of a laminated composite after the deposition of a polymer coating. The deposition process of the latter and its impact are studied. Firstly, the manufacturing of samples used in this study will be presented. Secondly, the experimental methods dedicated to the study of transverse cracking process is detailed. Then the results will be exposed, to finish on a conclusion of the study and the perspectives of work. The purpose of this study is to ensure the sealing of our tank, and can only be achieved by controlling these cracks. Indeed, only this measure seems

  doi:10.5075/epfl-298799_978-2-9701614-0-0

2. Experimental methods

2.1 Materials

The composite samples are manufactured with a specific tooling for filament winding that can be visualized on figure 1, allowing to realize two composite plates of dimension 330 mm x 330 mm.

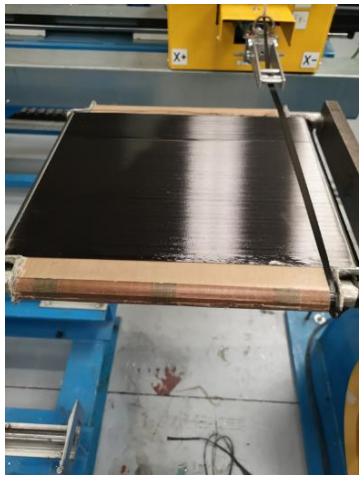

Figure 1 Dry filament winding

The specimens are made by dry filament winding of T700SC 24K fibres from Toray® (see figure 1) and then infused to make a composite plate with an epoxy resin coupled with two different hardeners, and following their complete polymerization cycles. The lay-up used in this study is [0/90/0] in order to observe transverse cracking in 90° ply. At the end of the composite manufacturing process, a coating with a controlled thickness based on thermosetting resin with embedded polytetrafluoroethylene (PTFE) particles is applied to half of one plate. This coating cycle consists of a linear temperature rise, then a plateau at 140°C for 20 minutes during which the glass transition temperature of the composite material is exceeded, and finally a decrease up to the room temperature. The thermal cycle of the coating process, is shown in figure 2. It is worth noting that applying the coating on half the plates allows producing a composite laminate without coating but having the same temperature history than the coated composite.

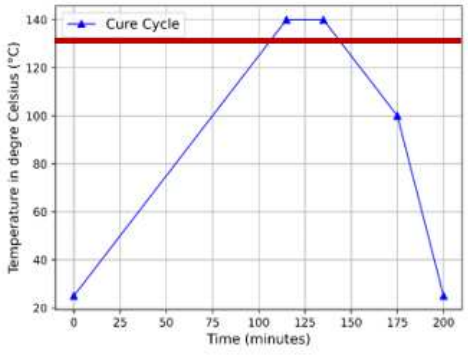

Figure 2 Thermal cycle of the deposit process

Two batches of 6 tensile specimens are then cut to the dimensions 240 mm x 25 mm within the 2 plates (see Figure 3). The specimens are then tested using a previously used setup detailed in Section 2.2 [4,5].

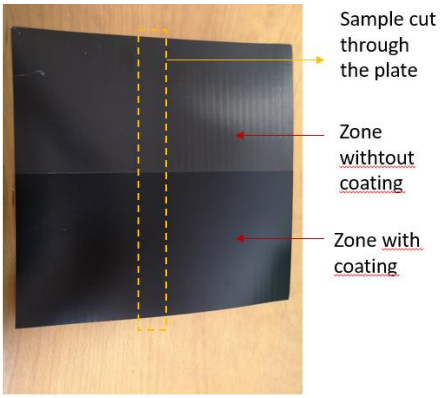

Figure 3 Laminate plate with coating on half a face

2.2 Cracking test

The tests aim to evaluate the impact of the coating process on the mechanism and creation of through cracks in the composite. The cracking test (see figure 4) allows to visualize the appearance of damage, mainly through cracks, within the specimens.

3 specimens of each batch are then tested:

- Blank specimens, at room temperature
- Half-coated specimens, at room temperature
- Blank specimens, at cryogenic temperature
- Half-coated specimens, at cryogenic temperature

The Table below shows all the specimen used for this study:

Specimen (Range)	Coated (PTFE)/Uncoated	Temperature (Kelvin)	Lay-up	Ply thickness
1 to 3	Uncoated*	Room (293 K)	[0/90/0]	200 µm
4 to 6	Half-coated	Room (293 K)	[0/90/0]	200 µm
7 to 9	Uncoated*	143 K	[0/90/0]	200 µm
10 to 12	Half-coated	143 K	[0/90/0]	200 µm

Tableau 1 List of specimens

*No temperature cycle

The specimens tested at room temperature make it possible to discriminate the influence of cryogenic conditions from the tests in case of influence of the latter on the laminated

  doi:10.5075/epfl-298799_978-2-9701614-0-0

composite. The so-called "cold" or "cryogenic" conditions represent a controlled temperature environment at -130 degrees Celsius (143 K).

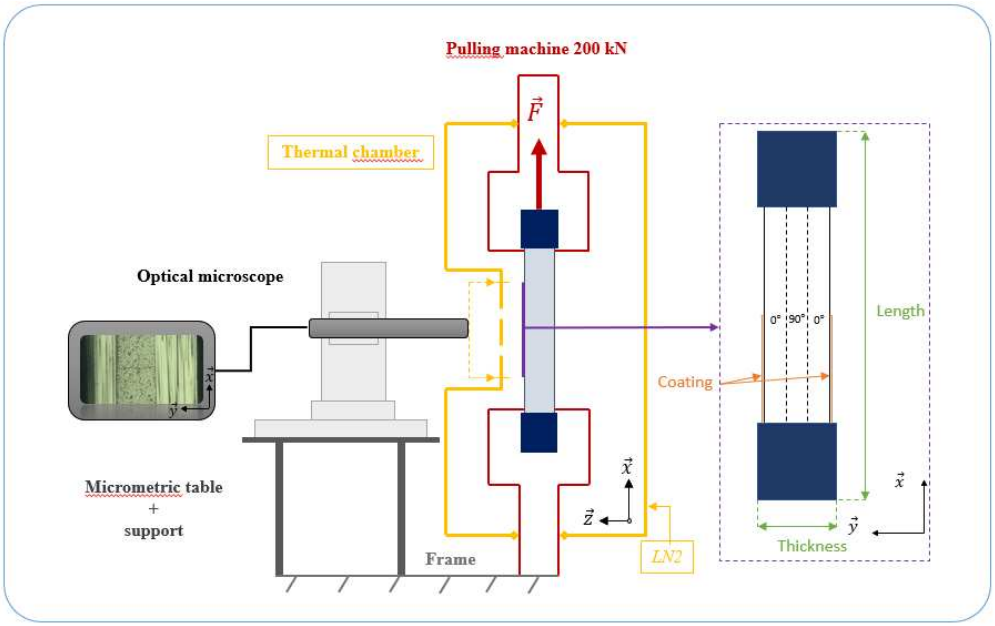

Figure 4 Test bench for observations under thermomechanical load

In order to identify the damage and to evaluate it, we will use, as in the literature, a damage variable noted ρ and called cracking rate [6,7]. This variable is generally scaled to allow comparison between different ply thicknesses. The reduced cracking rate $\bar{\rho}$ is defined as follows (Equation 1):

$$\bar{\rho} = \frac{N^{crack}}{Observation\ length}.Thickness^{90°\ ply} \quad (1)$$

where N^{crack} is the number of transverse cracking and $Thickness^{90°\ ply}$ is the thickness of 90° ply.

The results will be presented thanks to the evolution of this variable as a function of the deformation applied to the laminate. Note that the observation length is 80 mm as defined in [5,6].

3. Results

The 80 mm long specimens are cut into 4 observation sections (areas) of 20 mm each. The observation face is previously polished to allow the observation of the reduced cracking rate. In a first step, the analysis of the semi-coated specimens was performed. This value is large enough to manage material dispersion [5]. Firstly, the study of the damage within a half-coated specimen at room temperature was carried out. This first analysis allows to differentiate the impact of the coating and the impact of the coating process on the laminate composite. The results are presented in figure 5.

  doi:10.5075/epfl-298799_978-2-9701614-0-0

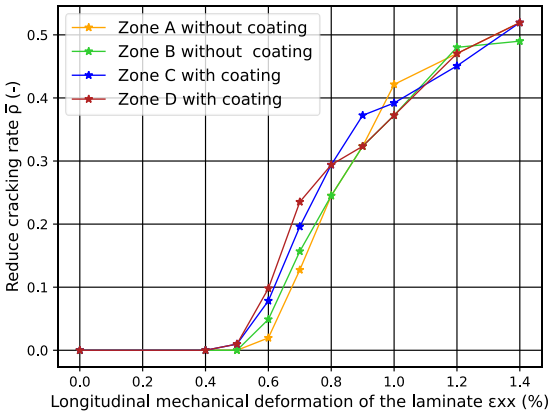

Figure 5 Evolution of the reduced cracking rate of the central ply of [0/90/0] laminate in specimen 4 as a function of the mechanical strain applied to the laminate

The analysis was repeated on the 3 half-coated specimens to verify the trend of the results and confirm them. No significant difference could be detected between the different areas of each specimen. Clearly, the coating does not influence the physicochemical properties that contribute to the onset and development of transverse cracks in the laminate.

The 2 following figures (figure 6 & 7) present the results of all the test specimens:

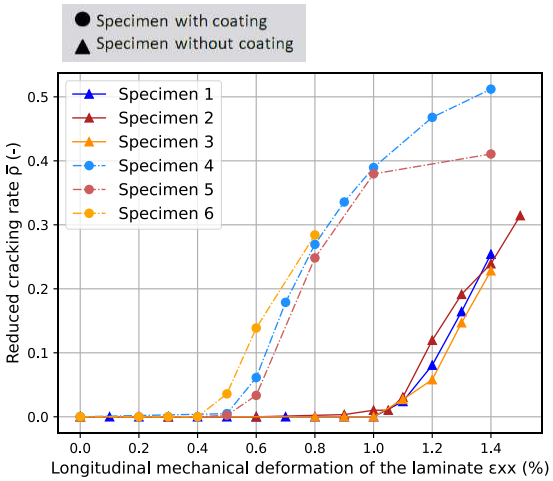

Figure 6 Evolution of the reduced cracking rate,at room T° of the central ply of a [0/90/0] laminate as a function of the mechanical strain applied to the laminate

  doi:10.5075/epfl-298799_978-2-9701614-0-0

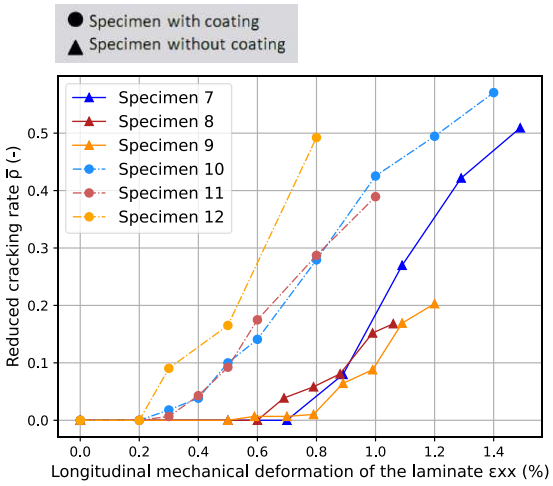

Figure 7 Evolution of the reduced cracking rate, at -130°C of the central ply of a [0/90/0] as a function of the mechanical strain applied to the laminate

The figure 6 highlights the good reproducibility of the results on all the specimens tested. A truly clear tendency emerges: the onset of cracking occurs much earlier on all the specimens treated (the onset occurs respectively 52% earlier at room temperature and 64% earlier at cryogenic temperature). The cracking kinetics remains similar for the specimens at room temperature, but a slight dispersion appeared for the specimens tested at cryogenic temperature.

Potentials sources of these early primers will be discussed in the following section.

4. Conclusion & future work

In this study, laminated specimens were tested following a heat treatment, allowing to evaluate the impact of a coating process on the mechanical properties of a composite, and more particularly on the appearance of transverse cracks. Specimens were also tested under cryogenic temperature conditions to simulate a real cryogenic tank environment. The study showed that the coating process reduces the cracking threshold for both tested temperatures. The phenomenon triggering this early initiation probably comes from the heat cycle applied for the deposition of the PTFE coating. Indeed, tests on the half-coated specimens showed that there is no influence of the coating on the initiation threshold and kinetics of the cracking process of the laminated composite. Phenomena induced by heat cycle are complex as it involves various potential physicochemical mechanisms. Several authors deal with similar issues [8,9]. However, in this study, it seems that physicochemical degradations are related to the overtaking of glass transition. A non-exhaustive list of potential mechanisms is presented below:

- The overshoot of the glass transition can lead to a reorganization of the polymer chains inducing a narrowing of the bonds [9]. In addition, the heat treatment may induce a post-cure on the uncross linked molecular chains after the curing of the laminated composite. This phenomenon can be defined as an increase in the rate of matrix crosslinking.
- The thermo-oxidation is an aging effect of polymer matrix undergoing thermal loading under oxygen environment [10]. It occurs mainly at temperatures above 120°C [8]. Thermo-oxydation modifies the structure of materials linked to their instabilities and their interactions with atmospheric oxygen. This phenomenon cuts the chains of the

  doi:10.5075/epfl-298799_978-2-9701614-0-0

macromolecular network. Thermo-oxidation is able to influence the initiation of cracking of composite laminates under mechanical loading [8,11].

- The complexity of polymer industry can induce other chemical changes due to polymer history (curing process of composite, coating process). However, it is the least preferred cause in our case, because of the absence of the appearance of this phenomenon in the literature.

These working hypotheses will influence a part of our future work. Further studies are necessary to confirm the results. Indeed, by using analyses in particular of differential scanning calorimetry one could detect if the matrix has a complete rate of cross-linking and thus affirmed or invalidated the hypothesis of the complete cross-linking.

Concerning thermo-oxidation, one element confirms this hypothesis, namely the change in color of the matrix after exposure to the oxygen environment [12]. However, the exposure times are generally much longer than those used in our study and exceed several hundred hours. Microscopic analysis were used to evaluate the degradation of the surface of the matrix, but they have been unsuccessful. IR spectroscopy on virgin and treated sample will be analyzed thereafter to detect a difference in molecular composition and thus verify the presence or not of oxidation [13]. Another evaluation of oxidation using Vickers micro/nano-indentation could be performed.

The change of chemical composition inducing a mechanical change will remain more difficult to foresee. Additional chemical analysis could be implemented if neither of the two hypotheses above is validated. However, this study shows a clear trend, a coating process with a heat cycle above the glass transition temperature is not adequate to maintain the initial transverse cracking threshold of the laminated composite.

After the work on composite cracking, a study on the transfer of cracking from the laminate composite to the coating will be performed. It will allow to define if a potential cracking of the composite leads to a transverse cracking of the coating and thus of potential leakage path.

5. References

1. Krawczak P. Réservoirs haute pression en composites. 2002;17.

2. L'Intermy J. Développement d'un matériau de liner pour réservoir cryogénique de lanceur. 2013;282.

3. Malenfant J-C. Influence de l'endommagement sur la perméabilité des matériaux composites application à la conception d'une capacité cryogénique sans liner. Bordeaux; 2011.

4. Briand T. Caractérisation et modélisation de la relation entre l'endommagement et la perméabilité d'un composite stratifié en condition cryogénique : Université Bordeaux ; 2021. Available at : https://tel.archives-ouvertes.fr/tel-03322713

5. Laeuffer H. Caractérisation et modélisation des réseaux de fissures pour la prédiction de la perméabilité des réservoirs composites stratifiés sans liner, Arts et Métiers ParisTech; 2017.Available at: https://hal.archives-ouvertes.fr/tel-01812568

6. Huchette C. Sur la complémentarité des approches expérimentales et numériques pour la modélisation des mécanismes d'endommagement des composites stratifiés, Université Paris 6; 2005. Available at: https://nuxeo.u-bordeaux1.fr/nuxeo/site/esupversions/84fc0382-e34c-4c96-a5e8-09502c9597f3

  doi:10.5075/epfl-298799_978-2-9701614-0-0

7. Huchette C, Lévêque D, Carrère N. A mutiscale damage model for composite laminate based on numerical and experimental complementary tests. In: Sadowski T, éditeur. IUTAM Symposium on Multiscale Modelling of Damage and Fracture Processes in Composite Materials. Dordrecht: Springer Netherlands; 2006. p. 241-8. (SOLID MECHANICS AND ITS APPLICATIONS).

8. Vu AT. Endommagement de stratifiés aéronautiques à fibres de carbone et matrice polymère soumis à des chargements monotones ou cycliques à plusieurs températures. Expériences et modélisation. ISAE-ENSMA Poitiers ; 2010. Available at: https://tel.archives-ouvertes.fr/tel-00523580/document

9. Ogi K. Influence of thermal history on transverse cracking in a carbon ber reinforced epoxy composite. :13.

10. Decelle J, Huet N, Bellenger V. Oxidation induced shrinkage for thermally aged epoxy networks. Polymer Degradation and Stability. 1 janv 2003;81(2):239-48.

11. Mercadé C. Modélisation de la dégradation d'un matériau composite carbone-époxy soumis à une sollicitation thermo-mécanique couplée. Application aux réservoirs d'hydrogène de type IV. 2017;200.

12. Buch X, Shanahan MER. Thermal and thermo-oxidative ageing of an epoxy adhesive. Polymer Degradation and Stability. 11 mai 2000;68(3):403-11.

13. Zahra Y, Djouani F, Fayolle B, Kuntz M, Verdu J. Thermo-oxidative aging of epoxy coating systems. Progress in Organic Coatings. 1 févr 2014;77(2):380-7.

  doi:10.5075/epfl-298799_978-2-9701614-0-0

MULTI-SACLE INVESTIGATION OF THE EFFECT OF SIZING CHEMISTRY ON ADHESION AND INTERFACIAL PROPERTIES OF GLASS FIBRES-REINFORCED EPOXY COMPOSITES

Armand Fahs[a], Sigrid Assengone Otogo Be[a], Lénaïk Belec[a], Saadia Belkessam[a], Guy Louarn[b], Jean-François Chailan[a]

[a] Laboratoire MAPIEM, Université de Toulon, CS 60584, 83041 Toulon Cedex 9, France.
[b] Université de Nantes, CNRS, Institut des Matériaux Jean Rouxel, IMN, 2 Rue de la Houssinière, 44000 Nantes, France.

Abstract: In this research, two model interphases between E-glass fibres and epoxy resin were designed and studied in terms of adhesion and mechanical strength from nano to macroscale. The first one is made from a reactive sizing of APTMS silane coupling agent and DGEBA pre-polymer film-former. The other one contains a non-reactive MTES silane and neutralized DGEBA film-former. The sizings were evidenced by SEM/AFM observations and XPS spectroscopy. The characterization of the elaborated composites by AFM nano-mechanic mode, micromechanical tests revealed the effect of the sizing chemistry on the interfacial properties between glass fibres and matrix. The interfacial strength is more important for the composites reinforced with APTMS-DGEBA sized fibres than those elaborated with MTES-BGEA sized fibres. In each case, an interphase area of around 200 nm width is detected at fibres vicinity. In this area, the elastic modulus is more than 25% lower than the bulk matrix modulus.

Keywords: Sizing chemistry; interface/interphase; glass fibres; epoxy composites; nano and micro-mechanics.

1. Introduction

Glass fibre-reinforced composites merge excellent mechanical properties with light weight, which justifies their increasing use in areas such as automobile, aircraft, sports equipment, or construction. The properties of a composite depend on the intrinsic properties of the fibres and the matrix. It is admitted that fibre-matrix interface region plays an important role in defining the composite properties and especially, the strength of the bonds across this interface. Considerable efforts have been devoted over the last 25 years to understand and monitor this interfacial area between the fibre and the matrix. Indeed, this area propagates in the matrix to form an interphase [1].

Several studies [2-5] have been published to predict and improve the properties of the composite by controlling the interphase, but the investigation of this complex region remains difficult. The properties of the interphase are substantially influenced by the surface treatment of the fibres [6-8]. Increasing research efforts on interphase study indicated that the microstructure and mechanical property gradients within the interphase are ranging from nanometres to micrometres [9-13].

The objective of this work is to study composite materials with simplified sizing systems, from nano to macroscopic scale. This study aims to understand how the main constituents of sizing modify the interfacial strength, the mechanical properties of composites as well as their

  doi:10.5075/epfl-298799_978-2-9701614-0-0

durability. To achieve this goal, two model interphases between glass fibres and epoxy resin with opposite behaviours were designed. The first one contains a reactive sizing made of a coupling agent and a film-former to create chemical bonds between the glass fibres and the epoxy matrix. The other one contains a non-reactive silane and a neutralized film former, which cannot form chemical bonds between the epoxy matrix and the glass fibres. Model composites are then elaborated with the different sized fibres and characterized at different scales.

2. Experimental section

E-glass fibres are cleaned to remove the organic impurities from their surface. The silanes used for reactive sizing is 3-Aminopropyltrimethoxysilane γ-APTMS, and that of non-reactive sizing is methyltriethoxysilane MTES. A Bisphenol A diglycidyl ether-based epoxy DGEBA, Diethylenetriamine DETA and Diethylamine DEA were used in this study. A DGEBA pre-polymer was used as reactive film former in the sizing. A neutralized film former Bisphenol A glycerolate diethylamine BGEA (or neutralized DGEBA) was synthesized in the laboratory and used as non-reactive film former.

2.1. Silane-grafting and film former deposition on glass fibres

The glass fibres were immersed either in APTMS or in MTES solutions (1% wt.) in ethanol for 1h at room temperature. Afterwards, the fibres were rinsed and treated for 30 min at 110°C in the oven, followed by a condensation overnight at room temperature. Regarding the film-forming agents, the APTMS and MTES silane-grafted fibres were immersed 20 min in respectively the DGEBA and the BGEA film former solutions at a concentration of 0.005 mol L^{-1} in acetone. The glass fibres were then removed and cured overnight in the oven at 60°C. The sized fibres have been characterized by SEM/AFM microscopy and XPS spectroscopy to confirm the sizing deposition (results not shown).

2.2. Elaboration of resin and of glass fibre-reinforced epoxy composites

DGEBA pre-polymer was mixed with DETA hardener in an amine/epoxy stoichiometric ratio r of 1. The mixture was well stirred until it becomes homogeneous. To elaborate the resin and the composite plates, the DGEBA-DETA mixture was deposited respectively in empty molds and molds containing 25%-30% sized fibres. All samples were cured in the oven during 2h at 60°C followed by 2h at 120°C and finally 4h at 140°C.

2.3. Characterization methods

The microfractography of the composite materials were observed using scanning electron microscopy (Zeiss-Supra 40 VP/ Gemini column) in secondary electron mode SE2. The samples were previously coated with thin layer of carbon. AFM experiments were performed on a Multimode 8 microscope (Bruker) using the PeakForce Quantitative Nano-Mechanics mode (PF-QNM). The reduced modulus can be fitted according to the DMT model [14]. AFM measurements were done with an RTESPA-300 probe and the spring constant of the cantilever was determined by the SADER method [15]. The typical spring constant k was 40 N/m and the cantilever tip radius was calibrated using a polystyrene sample.

The thermo-mechanical properties of composite materials were investigated using DMA Q800 (TA Instruments). Experiments were performed by using the single cantilever mode at a heating rate of 3°C min^{-1}. DMA was operated with an amplitude of 20 µm at a frequency of 1 Hz. The mechanical test was carried out on resin and composite plates using an INSTRON machine

equipped with a force cell of 100 kN according to standard NF EN 2746. The specimen was stressed at a constant test speed of 1 mm min^{-1}. Each result is an average of five test specimens.

Two micro-mechanical tests based on fragmentation and pull-out methods were carried out to show the influence of sizing chemistry on the mechanical properties and the interfacial strength between fibres and matrix. These tests were performed with a DMA machine on unidirectional micro-composites under longitudinal tension, which enables the detection of low forces [16,17]. The samples were carefully handled and at least 10 specimens were analysed for each test. The pulling speed used for fragmentation and pull-out experiments was 0.5 % min^{-1}.

3. Results and discussion

3.1. Mechanical and thermomechanical properties of the composite plates

The storage modulus and the loss factor (Tan δ) curves of the composite plates elaborated with the reactive sizing (EP-APTMS-DGEBA) and the non-reactive sizing (EP-MTES-BGEA) are presented in fig. 1. The storage modulus curves exhibit a similar behaviour. At glassy state, the storage modulus remains constant and then sharply drops in the temperature range between 140 and 160°C, followed by a plateau at higher temperature. The glassy storage modulus of EP-APTMS-DGEBA is around 20 % higher than EP-MTES-BGEA, which could be attributed to stronger interfacial properties between the fibre and the matrix. The Tα of the EP-APTMS-DGEBA is around 150°C, similar to that of the EP-MTES-BGEA.

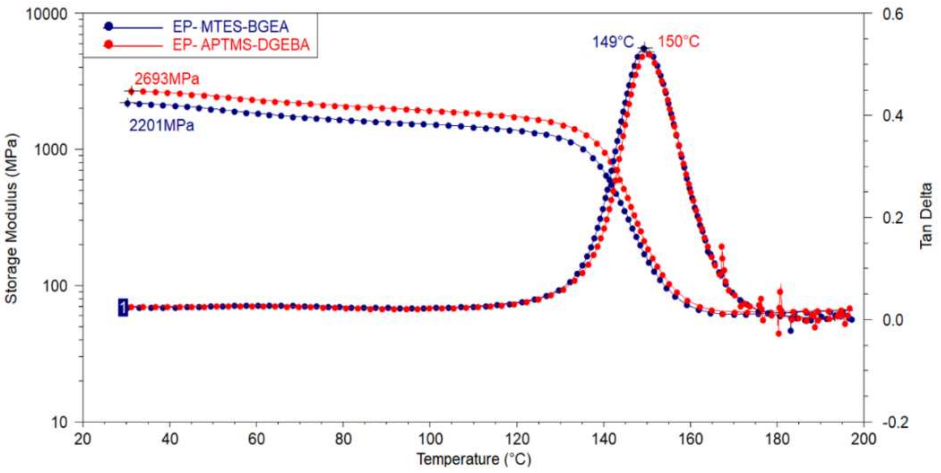

Figure 1. DMA curves of EP-MTES-BGEA and EP-APTMS-DGEBA composites: storage modulus and Tan δ.

The results of the 3-points bending tests are summarized in fig. 2. The behaviour of the resin sample is elastic with low plastic deformation. For composites, the behaviour is elastic fragile with a deformation and a tensile strength much lower than those of the resin alone (fig. 2a and 2b). The elastic modulus of composites is superior to that of the pure resin because the presence of fibres limits the elastic deformation of the matrix. Comparing the mean values, it seems that the EP-APTMS-DGEBA composite is more resistant in transverse mode, which could reveal a better charge transfer between the matrix and the fibres sized with the reactive system (fig.2c). Nevertheless, the deviation is too high to draw unambiguous conclusions. The experiments should be improved to increase the test sensitivity and clearly discriminate both systems.

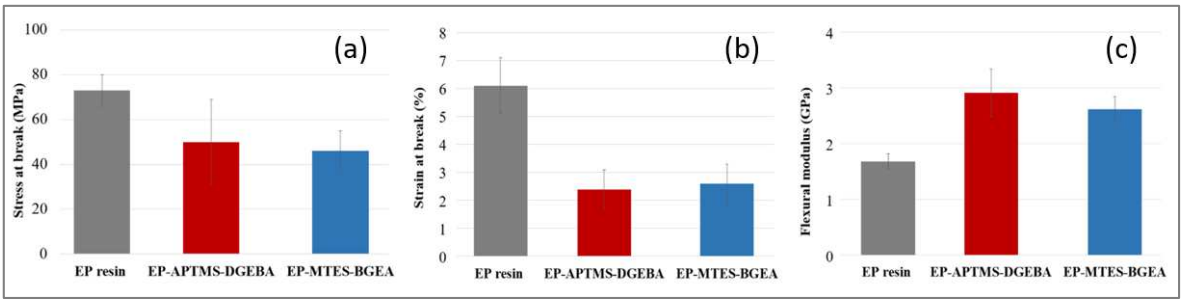

Figure 2. Mechanical properties of resin and composites obtained by 3-point bending test. (a) stress at break (MPa), (b) strain at break (%), (c) flexural modulus (GPa).

3.2. Interfacial adhesion by microfractography analysis

Fig. 3 shows SEM microfractography of the failure regions for the epoxy composites elaborated with the reactive (APTMS-DGEBA) and the non-reactive (MTES-BGEA) fibre sizings. The EP-APTMS-DGEBA shows substantially more epoxy remaining on the fibre surface, while the EP-MTES-BGEA sample shows a cleaner fibre surface. The silane with amino groups can react with the film former, and in the other hand, silanols create Si-O-Si siloxane bonds (covalent bonds) or hydrogen bonds with silanols on the glass fibres [18,19]. MTES-BGEA is less reactive or inactive to the resin even if it has hydroxyl groups which can create hydrogen bonds, but it is not enough to maintain the system and to obtain a good adhesion. The epoxide rings of BGEA are already neutralized so it cannot react. Fibres and matrix can only be linked by hydrogen bonds and Van Der Waals interactions. This suggests a higher probability for adhesive failure for EP-MTES-BGEA system than in the case of EP-APTMS-DGEBA system. It is consistent with the fact that BGEA is non-reactive with both the resin matrix and MTES coupling agent.

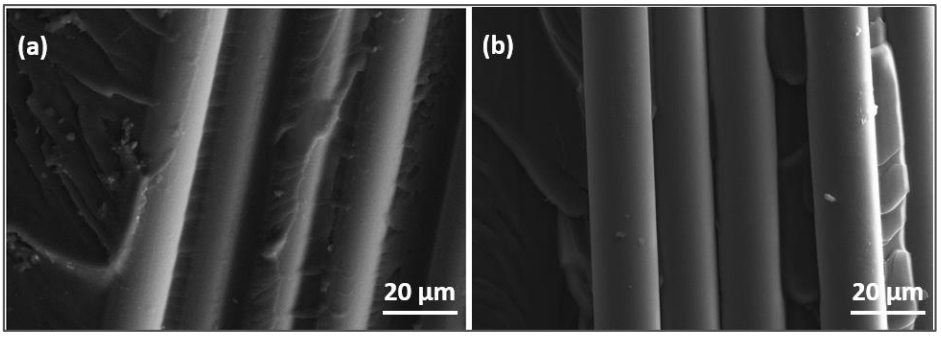

Figure 3. SEM microfractography of epoxy composites reinforced with (a) APTMS-DGEBA sized fibres, (b) MTES-BGEA sized fibres.

3.3. Pull-out and fragmentation micromechanical tests

Fig. 4 shows the curves obtained by the fragmentation tests and represents the normalized stress (MPa) as a function of strain (%). In order to compare the results, the stress is divided by the average number of fibres in each system. For these experiments, the maximum force of the cell-force was reached before the sample fracture. As observed for the whole curves and whatever the strain level, the values of the normalized stress of the APTMS-DGEBA specimens are twice higher than those of MTES-BGEA ones. This significant increase in the normalized stress reflects a more efficient load transfer from the matrix to the fibre, due to a higher adhesion when fibres are sized with the reactive system.

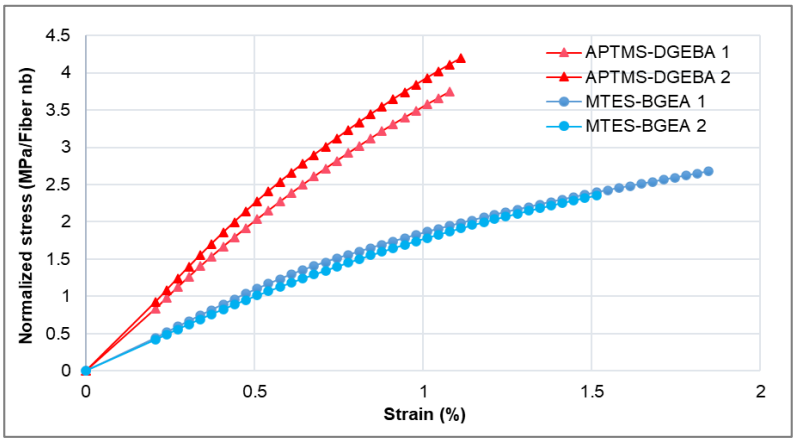

Figure 4. Normalized stress versus the strain in the case of APTMS-DGEBA and MTES-BGEA systems during fragmentation test.

In the case of the non-reactive sizing, the matrix and the fibres can be deformed almost independently. The reinforcement is consequently more limited in that case. A non-linear behaviour is visible in each case beyond 0.5-1 % of strain. It can result from the beginning of fibre fracture. Moreover, at that strain, stress gradients are generated in interfacial areas due to the important difference between the Young modulus of fibres and epoxy matrix.

The fig. 5 shows the results of pull-out test for both embedded sized fibres. The average fibres number was respectively 5 and 10 for APTMS-DGEBA and MTES-BGEA systems. To compare both configurations, the forces were normalised by the number of fibres. The length of embedded fibres was not fully optimized due to the flow of the resin from the drop to the fibres by capillarity. Some fibres could consequently break before pulling out the resin. However, and despite the dispersion, a difference between the two systems is clearly noticeable. The curves show an increasing slope for both systems attributed to the free fibres alignment before reaching the elastic strain and the interfacial shearing [16]. Discontinuities are observed on MTES-BGEA curves around 1.4 % of strain and the normalized force values for MTES-BGEA are much lower than APTMS-DGEBA ones over the whole curve. The results are consistent with the fragmentation results.

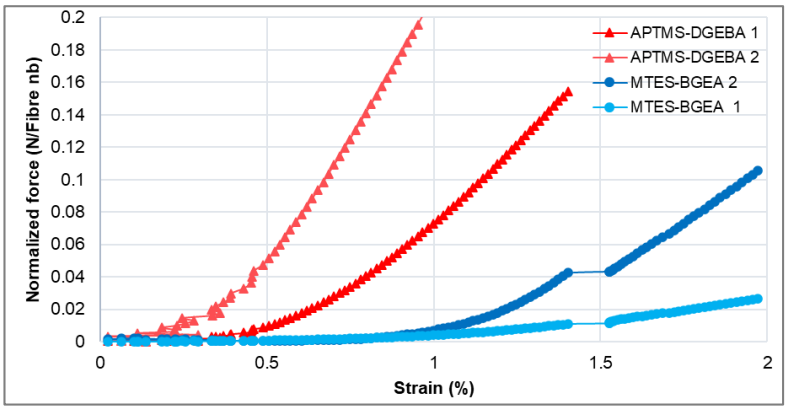

Figure 5. Normalized force versus the strain in the case of APTMS-DGEBA and MTES-BGEA systems during pull-out test.

Both fragmentation and pull-out tests show up the higher interfacial strength obtained with APTMS-DGEBA system compared to MTES-BGEA system due to a better load transfer between the matrix and the sized fibres.

3.4. Interphase properties at nanomechanical scale

To accurate information about the glass fibre/polymer matrix interface at the nanometer scale, AFM observations were performed on the interface regions. In fig. 6 the most representative mechanical maps obtained for the EP-APTMS-DGEBA and EP-MTES-BGEA systems are presented. Section analysis profiles of the modulus are also shown. In the case of composite reinforced with APTMS-DGEBA sized fibres (fig. 6a), the AFM nanomechanical analysis shows a clearly defined interface between the fibre and the matrix. A deep observation of the DMT modulus scans reveals the presence of some areas around the fibres with low elastic modulus, which correspond to interphase zones. These lasts have a width of around 200 nm with modulus values around 2.5 GPa compared to 3.5 GPa in the matrix beyond 1 µm from fibre.

In the case of fibres sized with MTES and BGEA, referred to as non-reactive system, the contrast in modulus values between the resin and the fibres is lower than for the reactive system. Moreover, the interface is not always clearly visible. It indicates that the fibres may be recovered by the resin during the cross-section polishing. When detected, the interphase width can reach up to around 200 nm with a modulus value around 2.5 GPa. The gap between the interphase modulus and the matrix modulus is lower than that observed in the reactive system. This can result from the spreading of the resin on fibres, which partly hinders the interphase response.

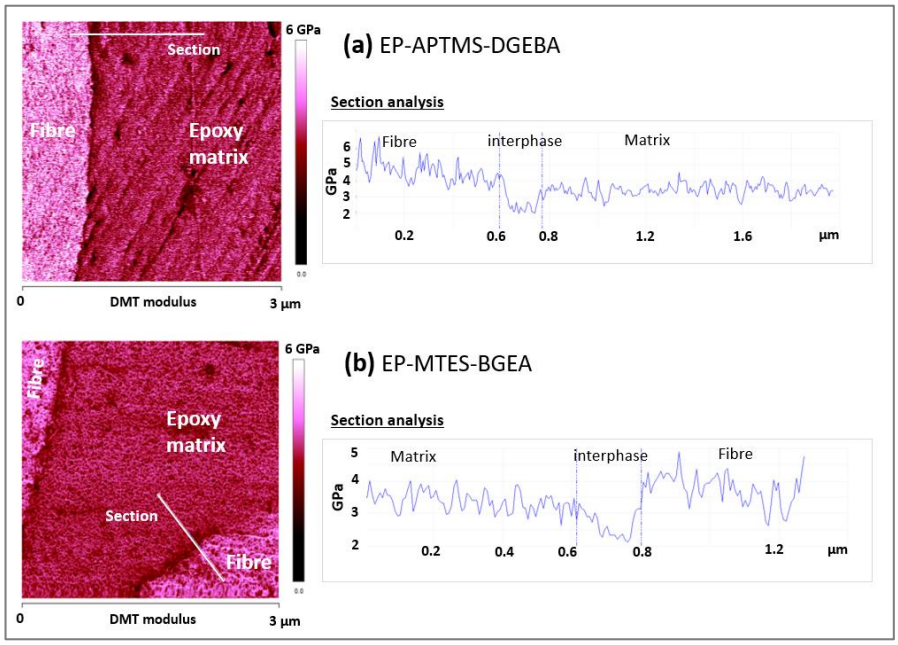

Figure 6. DMT modulus maps and section analysis obtained for composite reinforced with (a) APTMS-DGEBA reactive sized fibres, (b) MTES-BGEA non-reactive sized fibres. The section's analysis shows the variation of the E' around the fibres.

Even the reactivity character of the APTMS and DGEBA film former, an interphase zone has been probed for this system. The coupling agent creates covalent bonds between the fibre and the matrix. It reacts with the epoxy groups of the film former and the matrix pre-polymer. While for the non-reactive sizing system, the cohesion between the matrix and the fibres is poor which results in the spreading of the matrix on fibres. Despite this phenomenon, an interphase is also observed. In that case, it can result from plasticizing effects of the non-reactive BGEA which diffuses inside the matrix at fibre vicinity during the composite elaboration. The matrix modulus value beyond 1 µm from fibre surface are similar between the two systems, which is consistent with DMA results.

  doi:10.5075/epfl-298799_978-2-9701614-0-0

4. Conclusion

The objective of this work was to correlate the impact of two different sizings on the adhesion and the interfacial properties between an epoxy-based organic matrix and glass fibres. The control of the interfacial properties is determinant in glass fibre-reinforced composite materials. The characterization at macroscale using DMA and 3-points bending tests does not clearly show the influence of the sizing chemistry on the interfacial properties of the glass fibre-reinforced epoxy composites. However, the experiments at microscale using pull-out and fragmentation tests revealed the sizing's influence on adhesion and charge transfer at the matrix/fibre interface. The results of two micromechanical tests showed the same trends and were consistent with microfractography SEM images of the two composite systems. The adhesion was more important for composites with APTMS-DGEBA sizing due to the affinity and the creation of covalent bond with matrix. The MTES-BGEA sizing decreased the adhesion and limited the charge transfer from matrix to fibres. Interestingly, the AFM experiments in nano-mechanics mode were a powerful tool to probe the presence of interphase zones at the vicinity of the fibres. The detected interphases have thickness of about 200 nm with an elastic modulus value less than the matrix bulk.

Acknowledgments

The authors acknowledge the financial support ANBG (Agence Nationale des Bourses du Gabon).

5. References

1. Thomason JL. The interface region in glass fibre-reinforced epoxy resin composites: 1. Sample preparation, void content and interfacial strength. Composites 1995;26:467–75.
2. Drzal LT, Rich MJ, Lloyd PF. Adhesion of Graphite Fibers to Epoxy Matrices: I. The Role of Fiber Surface Treatment. J Adhes 1983;16:1–30.
3. Dong Y, Zhu Y, Zhao Y, Liu F, Wang E, Fu Y. Enhance interfacial properties of glass fiber/epoxy composites with environment-friendly water-based hybrid sizing agent. Compos Part Appl Sci Manuf 2017;102:357–67.
4. Thomason JL, Nagel U, Yang L, Bryce D. A study of the thermal degradation of glass fibre sizings at composite processing temperatures. Compos Part Appl Sci Manuf 2019;121:56–63.
5. Joliff Y, Belec L, Heman MB, Chailan JF. Experimental, analytical and numerical study of water diffusion in unidirectional composite materials – Interphase impact. Comput Mater Sci 2012;64:141–5.
6. Gao S-L, Mäder E. Characterisation of interphase nanoscale property variations in glass fibre reinforced polypropylene and epoxy resin composites. Compos Part Appl Sci Manuf 2002;33:559–76.
7. Mäder E, Moos E, Karger-Kocsis J. Role of film formers in glass fibre reinforced polypropylene — new insights and relation to mechanical properties. Compos Part Appl Sci Manuf 2001;32:631–9.
8. Brodowsky HM, Jenschke W, Mäder E. Characterization of interphase properties: Microfatigue of single fibre model composites. Compos Part Appl Sci Manuf 2010;41:1579–86.
9. Cross WM, Kjerengtroen L, Kallar JJ. Interphase variation in silane-treated glass-fiber-reinforced epoxy composites. J Adhes Sci Technol 2005;19:279–90.
10. Plonka R, Mäder E, Gao SL, Bellmann C, Dutschk V, Zhandarov S. Adhesion of epoxy/glass fibre composites influenced by aging effects on sizings. Compos Part Appl Sci Manuf 2004;35:1207–16.

11. VanLandingham MR, Dagastine RR, Eduljee RF, McCullough RL, Gillespie JW. Characterization of nanoscale property variations in polymer composite systems: 1. Experimental results. Compos Part Appl Sci Manuf 1999;30:75–83.
12. Karger-Kocsis J, Mahmood H, Pegoretti A. Recent advances in fiber/matrix interphase engineering for polymer composites. Prog Mater Sci 2015;73:1–43.
13. Cech V, Palesch E, Lukes J. The glass fiber–polymer matrix interface/interphase characterized by nanoscale imaging techniques. Compos Sci Technol 2013;83:22–6.
14. Derjaguin BV, Muller VM, Toporov YuP. Effect of contact deformations on the adhesion of particles. Prog Surf Sci 1994;45:131–43.
15. Sader JE, Sanelli JA, Adamson BD, Monty JP, Wei X, Crawford SA, et al. Spring constant calibration of atomic force microscope cantilevers of arbitrary shape. Rev Sci Instrum 2012;83:103705.
16. Tanaka K, Minoshima K, Grela W, Komai K. Characterization of the aramid/epoxy interfacial properties by means of pull-out test and influence of water absorption. Compos Sci Technol 2002;62:2169–77.
17. Wang Z, Yang B, Xian G, Tian Z, Weng J, Zhang F, et al. An effective method to improve the interfacial shear strength in GF/CF reinforced epoxy composites characterized by fiber pull-out test. Compos Commun 2020;19:168–72.
18. Belec L, Nguyen TH, Nguyen DL, Chailan JF. Comparative effects of humid tropical weathering and artificial ageing on a model composite properties from nano- to macro-scale. Compos Part Appl Sci Manuf 2015;68:235–41.
19. Gabet Y. Study and optimisation of fibre-polymer matrix interfaces of thermoplastic-based structural composites. PhD thesis, Univ Claude Bernard Lyon 1 2018:209.

  doi:10.5075/epfl-298799_978-2-9701614-0-0

OPTIMISATION OF ACID DIGESTION CONDITIONS FOR VOLUME FRACTION MEASUREMENTS OF HARD TO DIGEST FIBRE-REINFORCED POLYMER COMPOSITES

Duncan Edser [a], Rory Pemberton [a], Michael Gower [a]

a: National Physical Laboratory – Duncan.Edser@npl.co.uk

Acid digestion is a widely used method for determining matrix, fibre and void content of fibre-reinforced polymer (FRP) composites. Current test standards governing the use of these methods prescribe, for some polymer systems, particularly hazardous chemicals including sulphuric acid and hydrogen peroxide. To reduce the health and safety risks associated with the measurement, it would be beneficial for users of these standards to conduct digestion using nitric acid only, being a far safer chemical to use. This paper reports on methods developed to perform successful digestion measurements on composite systems incorporating phenolic, cyanate ester and polyfurfuryl alcohol polymer matrices using nitric acid only and digestion conditions currently outside the recommendations of ISO and ASTM test standards. These materials were chosen as systems known to be particularly difficult to digest without attacking the fibres. The methods have been validated by characterising the appearance of residual fibres from the digestion process using scanning electron microscopy (SEM).

Keywords: Microwave-Assisted Acid Digestion; Fibre Volume Content; Void Content; Quality Assessment

1. Introduction

Fibre volume fraction and void content of fibre-reinforced polymer (FRP) composites are important characteristics influencing material performance and extensively used in material analysis, as input properties for modelling alongside manufacturing quality control [1, 2]. The acid digestion method, standardised in ISO 14127:2008 [3] and ASTM D3171-15 [4], is one of the techniques most widely used by industry to measure volume fraction properties of carbon fibre-reinforced polymers (CFRP). The method involves removing the polymer matrix phase of a composite specimen through digestion in acid to leave the reinforcing fibres only. Fibre volume fraction and void content are calculated using the constituent polymer and fibre densities, the initial mass and density of the composite specimen and the mass of the fibres following matrix removal.

Several safety precautions require consideration when carrying out the technique. For composites incorporating common epoxy matrices, the method can be conducted in a reasonably safe manner as polymer digestion is possible using concentrated nitric acid which has relatively easy to follow control measures. Different polymer types however (e.g. phenolic and cyanate ester) typically require more hazardous reagents to achieve full matrix digestion with current standards recommending mixtures including sulphuric acid and hydrogen peroxide. Due to the health and safety risks associated with the use, storage, and disposal of these mixtures there is a desire to achieve digestion of these polymer types with nitric acid only. Whilst this approach reduces health and safety risks, omitting such reagents can inhibit the digestion process, putting more emphasis on developing optimum digestion conditions for a given

  doi:10.5075/epfl-298799_978-2-9701614-0-0

material type. This is particularly important considering the method's assumption that the polymer matrix is fully digested by the acid without attacking and removing material from the reinforcing fibre. Regions of undigested polymer or removed fibre from acid attack will introduce errors in the measurement with the potential to over - or under - estimate fibre volume fraction and void content.

Currently there is little guidance available on how to validate that digestion conditions are appropriately digesting the composite. This paper reports on work carried out to develop and validate digestion conditions using nitric acid only for polymers where this is not currently specified in existing standards. In particular, the use of scanning electron microscopy (SEM) is employed to assess the visual characteristics of residual fibres following digestion to validate conditions have not attacked the reinforcing fibres or left regions of undigested polymer.

2. Experimental

2.1 Materials and Specimen Preparation

This work has investigated acid digestion of CFRP systems incorporating phenolic, cyanate ester and polyfurfuryl alcohol polymer matrices. These have been chosen due to previous difficulty encountered when attempting to fully digest the polymer matrix without attacking the reinforcing fibre using nitric acid only. Details of the materials including cured polymer density and fibre density were provided by the material suppliers and are given in Table 1. Density values were taken from technical data sheets due to measured values of the actual constituent densities not being available. Due to confidentiality agreements, manufacturing processing conditions have been withheld. Specimens for digestion (~1 g) were machined from supplied material using a CompCut 500 composite plate saw and dried to constant mass at 105°C before testing. Due to difficulty in digesting cyanate ester, specimens had to be reduced to ~0.5 g.

Table 1: CFRP systems investigated

Composite System	Polymer Matrix	Polymer Density (g/cm^3)	Fibre Density (g/cm^3)
Solvay TM80S-NS (pre-preg)	Phenolic	1.26	1.76
Cytec MTM 110 (polymer) Tenax HTA40 E13 (fibre)	Cyanate ester	1.28	1.76
Evopreg PFC502-C650T (pre-preg)	Polyfurfuryl alcohol	1.20	1.80

2.2 Volume Fraction by Microwave-Assisted Acid Digestion

Acid digestion was undertaken in general accordance with the procedures described in ISO 14127:2008, Method A, Procedure 2 [3] and ASTM D3171-15, Procedure F [4]. Before digestion, the initial mass and density of each specimen was determined in accordance with the immersion method described in ISO 1183-1:2019, Method A [5]. Digestion was carried out using 70% concentrated nitric acid (HNO_3) in an Ethos Up Milestone microwave digester supplied by Analytix Ltd (Boldon, UK). Specimens were placed inside vessels with the chosen acid profile

(acid type, quantity, and mixing ratio) and ramped to reach the set digestion temperature within 10 mins. Temperature was maintained to ± 2°C by automatic adjustment of the microwave output power which was limited to a maximum of 800 W. Following digestion, the contents of the vessel were cooled to ~65°C and the reinforcing fibres separated from the acid solution using a vacuum pump to pull the acid and digestion residue through a pre-weighed filter. The residual fibres were washed several times through the filter using deionised water and acetone before being dried to constant mass at 105°C. All mass measurements were made to 0.1 mg using a calibrated Mettler Toledo X105 analytical balance. The fibre volume fraction (V_f) was subsequently calculated using the mass of the fibres following digestion (M_f), the mass of the initial specimen (M_i), constituent fibre density (ρ_f) and the density of the composite (ρ_c):

$$V_f = \frac{M_f}{M_i}\frac{\rho_c}{\rho_f}\ [\times 100] \quad (1)$$

Digestion parameters including acid profile, digestion time and temperature were varied during the experiments to achieve successful matrix removal. Once an optimised set of digestion parameters had been established, (see Section 2.3) five repeats at those conditions were carried out to assess repeatability.

2.3 Scanning Electron Microscopy

Scanning electron microscopy (SEM) was used to validate digestion parameters by visually assessing the condition of residual fibres and checking for either fibre attack or regions of undigested polymer. SEM images were taken using either the InLens or SE2 detector in a Zeiss Supra SEM at an accelerating voltage of 2.5 or 5.0 kV and a 20 µm aperture.

3. Results and Discussion

3.1 Digestion Using Concentrated Nitric Acid (70% HNO_3)

Initial digestion runs evaluated typical conditions when digesting with nitric acid (HNO_3) as recommended in ISO 14127:2008 [3] and ASTM D3171-15 [4]. Specimens were digested in 20 ml of 70% concentrated HNO_3 for 30 mins at temperatures between 120 and 160°C. Previous studies [6] had shown temperature to be the dominant factor influencing digestion, so was initially chosen as the main variable.

Figure 1 shows SEM micrographs taken of the residual fibres from digesting phenolic composite specimens in 70% concentrated HNO_3 for 30 mins at 120 and 160°C. At these two ends of the temperature range, evidence of both undigested polymer and fibre attack were observed. Whilst the bulk of the polymer resin has been removed at 120°C (Figure 1(a)), a 'stained' appearance was noted on the surface of some of the fibres indicating fibre attack. At the higher digestion temperature of 160°C (Figure 1(b)) further indication of fibre attack is present, observed as a flaky appearance of the fibre surface where material has been removed by the acid. Even at these higher temperatures this micrograph also shows regions of undigested polymer present amongst the fibres. These regions show up as high contrast areas that result from the 'charging' of the polymer that occurs in the SEM due to the non-conductive nature of the polymer [7]. These results show that using the recommended acid profile (20 ml of 70% HNO_3), no temperature window exists in which the material can be optimally digested. Similar

  doi:10.5075/epfl-298799_978-2-9701614-0-0

observations were seen when analysing cyanate ester and polyfurfuryl alcohol under these conditions.

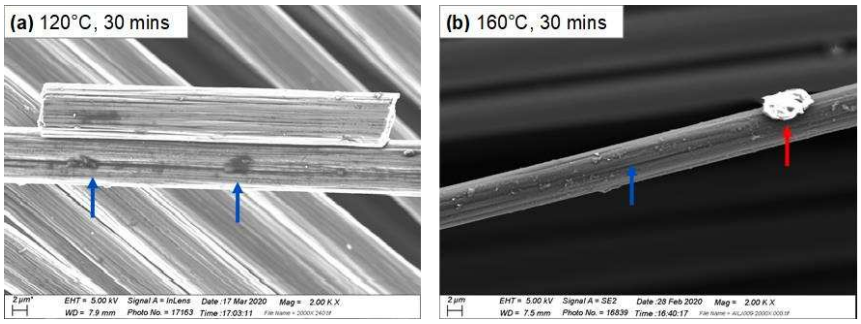

Figure 1 – SEM micrographs of the residual fibres from digestion of phenolic composite after 30 mins using 70% concentrated HNO_3 at (a) 120°C, and (b) 160°C. Blue and red arrows indicating attacked fibre and undigested polymer, respectively.

3.2 Digestion Using Diluted Nitric Acid (35% HNO_3)

The results using 70% concentrated HNO_3 indicated digestion conditions were too aggressive and a more controlled treatment of the specimen was required to remove the polymer matrix without attacking the fibres. To achieve better control, digestions were undertaken by diluting 70% HNO_3 with deionised water at a 1:1 ratio, effectively reducing the acid concentration to 35%. Specimens of all material types were digested in a mixture of 5 ml HNO_3 and 5 ml deionised water over a range of time and temperatures and the residual fibres assessed under SEM.

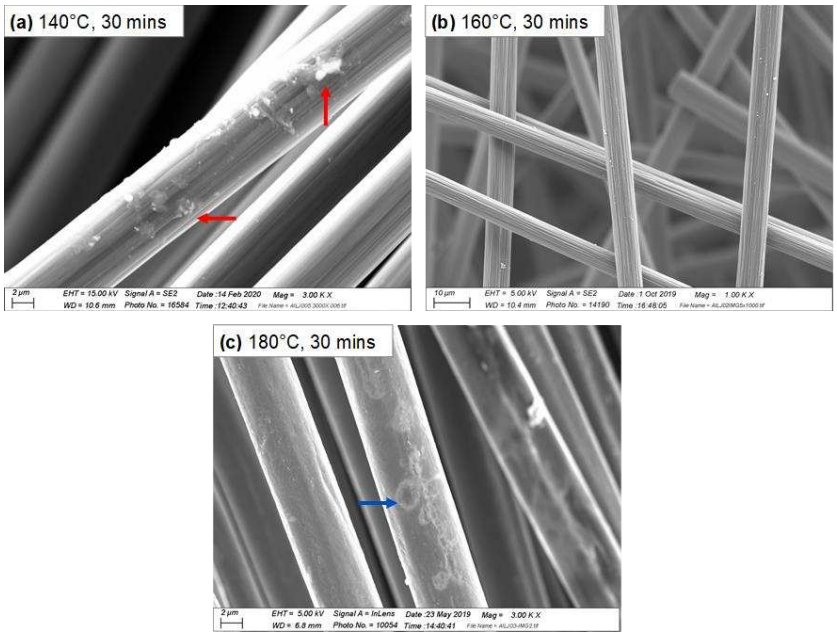

Figure 2 – SEM micrographs of the residual fibres from digesting phenolic composite for 30 mins using 35% concentrated HNO_3 at (a) 140°C, (b) 160°C, and (c) 180°C. Blue and red arrows indicating attacked fibre and undigested polymer, respectively.

SEM micrographs of the residual fibres following digestion for 30 mins using 35% HNO_3 for composite systems containing phenolic, polyfurfuryl alcohol and cyanate ester are shown in Figures 2, 3 and 4, respectively. Figure 2 shows the evolution of residual fibre condition with

changing digestion temperature for the phenolic composite. At 140°C regions of undigested polymer can be observed on the fibre surface (Figure 2(a)). As the temperature was increased to 160°C the acid has removed all the polymer phase without affecting the fibre condition (Figure 2(b)). Some very fine debris is observed and whilst it is unknown if this is undigested polymer or other constituents, such as a filler, it is assumed these will have little effect on calculated values of fibre volume fraction. On increasing digestion temperature further to 180°C, evidence of acid starting to attack the fibre is observed from the stained appearance on the fibre surface. In addition, the striations that can be observed on the clean fibres at 160°C are not present, further indicating removal of fibre material. Similar observations were seen for polyfurfuryl alcohol, although complete removal of the polymer matrix was possible at lower temperatures. Only at 100°C (Figure 3(a)) were some small regions of undigested polymer seen.

In contrast, cyanate ester specimens presented greater difficulty in achieving complete polymer digestion without fibre attack despite reducing the specimen size from 1.0 to 0.5 g. Figure 4(a) shows the residual fibres after digestion at 160°C and whilst these appear clean, large macroscopic clumps of undigested polymer were present in the filter from the filtration process following digestion. As with phenolic and polyfurfuryl alcohol specimens, increasing digestion temperature above 160°C showed evidence of fibre attack (Figure 4(b)). To achieve complete matrix removal for cyanate ester specimens, further trials were carried out increasing the digestion time to 60 mins. Complete digestion with no observations of undigested polymer was found to be possible at 160°C as evidenced in Figure 5(b).

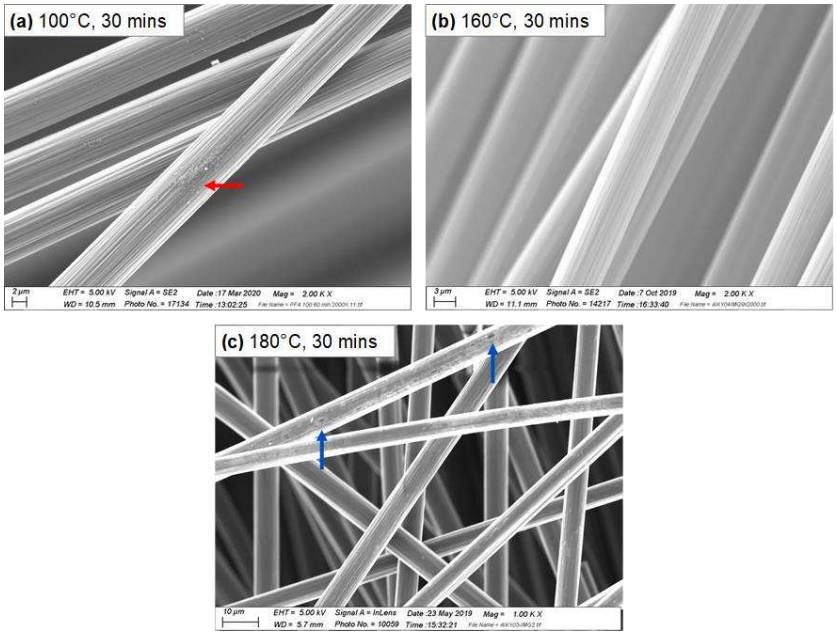

Figure 3 – SEM micrographs of the residual fibres from digesting polyfurfuryl alcohol composite for 30 mins using 35% concentrated HNO_3 at (a) 100°C, (b) 160°C, and (c) 180°C. Blue and red arrows indicating attacked fibre and undigested polymer respectively.

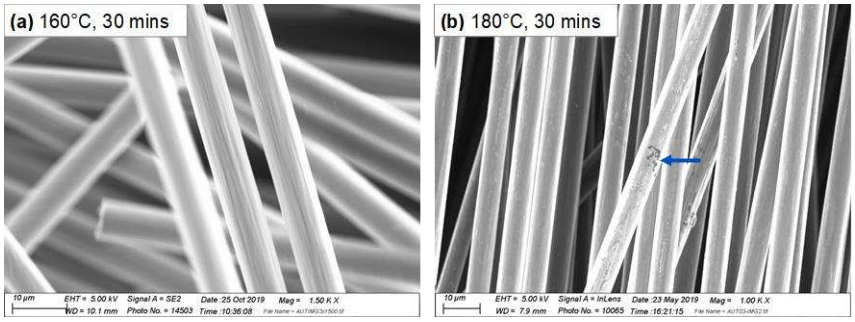

Figure 4 – SEM micrographs of the residual fibres from digesting cyanate ester composite for 30 mins using 35% concentrated HNO_3 at (a) 160°C, and (b) 180°C. Blue and red arrows indicating attacked fibre and undigested polymer respectively.

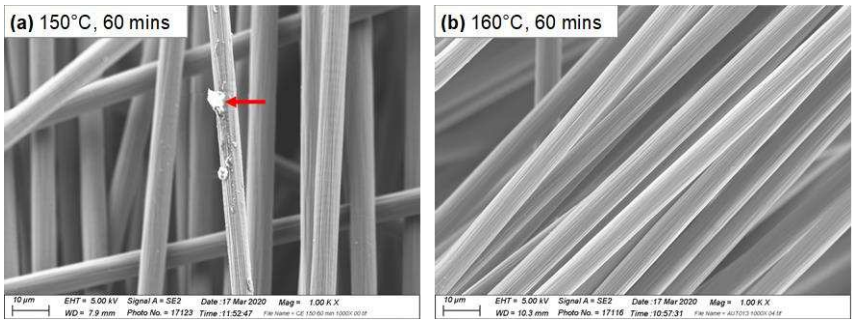

Figure 5 – SEM micrographs of the residual fibres from digesting cyanate ester composite for 60 mins using 35% concentrated HNO_3 at (a) 150°C, and (b) 160°C. Red arrows indicating undigested polymer.

Digestions at 160°C for 60 mins were also carried out for the phenolic and polyfurfuryl alcohol materials to assess the influence of extended digestion time on these materials. Figures 6 shows micrographs for the residual fibres following digestion for all materials at 160°C for 60 mins. These show that increasing digestion time at 160°C does not appear to further initiate fibre attack. Interestingly, although the different materials investigated use different grades of carbon fibre, the evidence from all SEM micrographs indicate fibre attack is only initiated with this acid profile at digestion temperatures above 160°C.

The analysis of residual fibres with SEM has indicated that polymer digestion with nitric acid only is possible for composites comprising of a range of different matrices as well as epoxy. The digestion conditions shown to be successful are currently outside those recommended in ISO 14127:2008 [3] and ASTM D3171-15 [4]. It is suspected that this has been achieved by creating a more controlled digestion of the material. By reducing the HNO_3 concentration the polarity of the acid mixture is lowered enabling slower microwave absorption during heating. This, combined with the weaker acid reducing pressure inside the reaction vessel, would result in a more controlled, less aggressive digestion process, enabling the polymer to become fully digested without fibre attack.

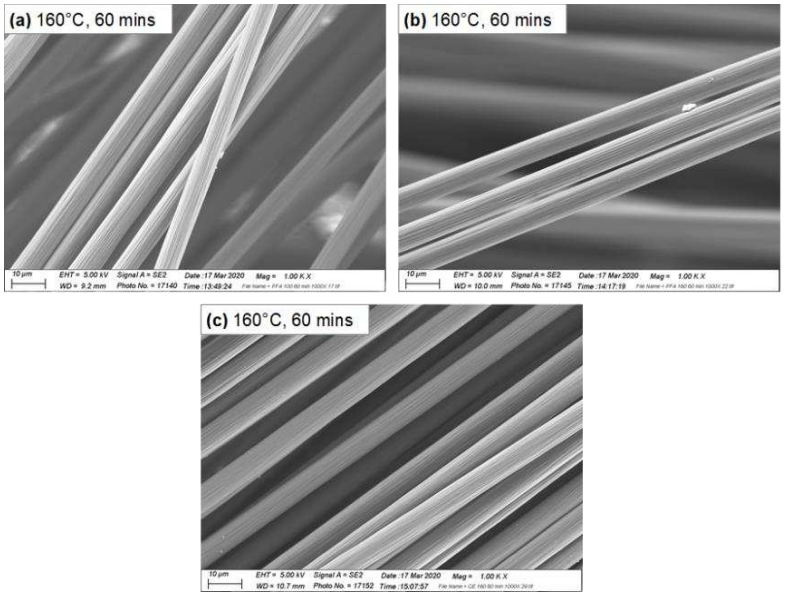

Figure 6 – SEM micrographs of the residual fibres from digesting (a) phenolic, (b) polyfurfuryl alcohol, and (c) cyanate ester composites for 60 mins using 35% concentrated HNO_3 at 160°C.

3.3 Fibre Volume Fraction Measurements

To further validate digestion conditions, five repeat digestions at 160°C for 60 mins were carried out on all materials. The results for calculated fibre volume fraction (V_f) are given in Table 2. Values for void content (V_v) have not been reported due to the high uncertainty of the theoretical values for polymer density used to calculate V_v leading to erroneous values. Had more accurate polymer density values been measured or known, V_v could have been easily derived. The high level of repeatability observed from the low coefficients of variation (CV) further indicate optimal digestion. Large variability would be expected if either under- or over-digestion was present. The higher CV for cyanate ester specimens is likely a result of these specimens being of smaller volume (0.5 g) and therefore individual specimens potentially encompassing different sections of the unit cell of the composite.

Table 2 – Statistics for fibre volume fraction (V_f) for each composite determined from 5 repeat digestions

Polymer Matrix	Mean, V_f (%)	Standard Deviation, V_f (%)	CV, (%)
Phenolic	56.4	0.8	1.38
Polyfurfuryl Alcohol	55.4	0.7	1.28
Cyanate Ester	54.4	1.9	3.46

4. Conclusions and Further Work

This work has established methods for carrying out acid digestion using nitric acid only on materials where this is not currently stipulated in standards. By omitting the use of hazardous reagents such as hydrogen peroxide and sulphuric acid, the developed methods significantly reduce the health and safety risks associated with this measurement. Further, the digestion conditions established have included temperatures and times outside of those currently recommended within ISO 14127:2008 [3] and ASTM D3171-15 [4]. Validation of digestion

conditions was conducted through characterising the appearance of undigested polymer and attacked fibres in the residual material from digestion. These visual characteristics are of use for validating digestion conditions on other materials and where alternative digestion systems are used.

An interlaboratory study including other polymer types for which hazardous reagents are recommended would further confirm the methodologies outlined within this measurement note. Such an investigation could also establish the repeatability and reproducibility of the method required for standardisation.

Acknowledgements

The work reported in this Measurement Note was carried out by NPL as part of the National Measurement System (NMS) programme funded by the United Kingdom Department of Business, Energy and Industrial Strategy (BEIS).

The authors acknowledge contributions to the work from Mr Duncan Rowe at Analytix Ltd (Boldon, UK). The authors would also like to express their gratitude to MBDA UK Ltd., Attwater & Sons Ltd. and Composites Evolution Ltd. for supplying the materials.

References

[1] He H.W., Huang W., and Gao, H. Comparison of four methods for determining fiber content of carbon/epoxy composites. Int. J. Polym. Ch., 2016; 21(3): 251-258

[2] Ghiorse S.R. A comparison of void measurement methods for carbon/epoxy composites. U.S. Army Materials Technology Laboratory. Report number: MTL TR 91-13; 1991

[3] BS ISO 14127:2008. Carbon-fibre-reinforced composites – Determination of the resin, fibre and void contents.

[4] ASTM D3171-15. Standard Test Methods for Constituent Content of Composite Materials.

[5] BS EN ISO 1183-1:2019. Plastics – Methods for determining the density of non-cellular plastics. Part 1: Immersion method, liquid pycnometer method and titration method.

[6] Hassan M.H., Othman A.R., and Kamaruddin S. The use of response surface methodology (RSM) to optimize the acid digestion parameters in fiber volume fraction test of aircraft composite structures. Int. J. Adv. Manuf. Tech., 2017; 90: 3739-3748.

[7] Postek M.T., and Vladar A.E. Does Your SEM Really Tell the Truth? – How Would You Know? Part 4: Charging and its Mitigation. Proc. SPIE Int. Soc. Opt. Eng., 2015; 9636.

  doi:10.5075/epfl-298799_978-2-9701614-0-0

MECHANICAL PROPERTIES OF THE EPOXY RESIN AND CARBON FIBRE-REINFORCED COMPOSITES MODIFIED BY CORE-SHELL RUBBER PARTICLES

Tatjana Glaskova-Kuzmina[a], Jevgenijs Sevcenko[a], Leons Stankevics[a], Sergejs Tarasovs[a],

Vladimir Špaček[b], and Andrey Aniskevich[a]

a: Institute for Mechanics of Materials, University of Latvia, Riga, Latvia, email: Tatjana.Glaskova-Kuzmina@lu.lv
b: SYNPO, Pardubice, Czech Republic

Abstract: *The study aimed to evaluate how tensile properties and fracture toughness of the epoxy resin change as a function of core-shell rubber (CSR) particle filler content (0-6 wt.%). Three additives, i.e., ACE MX series 125, 156, and 960 containing CSR particle filler were added to CHS Epoxy 582. It was found that the effect of ACE MX additives on the tensile properties of the epoxy resin was significant. The tensile strength and elastic modulus were decreased by 10-20% but fracture toughness was increased by approx. 60-100 % at the highest CSR content. No significant difference in the fracture toughness among the additives was revealed proving that smaller CSR particles were the same effective as bigger ones. Though, in general ACE MX 156 showed the highest improvement of fracture toughness which was approx. 108% at CSR content 4 wt.%.*

Keywords: epoxy; core-shell rubber particles; tensile properties; fracture toughness

1. Introduction

Epoxy polymers are widely applied as matrices in composite technology. They are characterized by the relatively high elastic modulus and tensile strength, low creep and good performance at elevated temperatures [1]. Though the structure of highly crosslinked thermosetting polymers results in rather high brittleness with poor resistance to crack initiation and propagation [2].

To enhance their toughness, epoxy resins can be mixed with core-shell rubber (CSR) particles consisting of a soft rubbery core and a hard shell around it. Mostly they are produced by emulsion polymerization and further added to epoxy resins. Thus, in contrast to phase-separating rubbers, it is possible to control the particle size by changing the core and shell diameters [3]. The shell material of CSR particles should be compatible with the epoxy polymers, and therefore, typically poly (methyl methacrylate) (PMMA) is preferred to be used. The materials for the core include butadiene, siloxane and acrylate polyurethane [4, 5].

The addition of CSR particles was found to have a detrimental effect on tensile properties of the epoxy resin (DGEBA) and no effect on its glass transition temperature at the same time [2]. The elastic modulus and tensile strength of the epoxy were reduced by 27 and 36%, accordingly, for the 15 wt.% content of CSR. Nevertheless, the improvement of about 550% for the fracture energy was defined for the same composition of CSR filler particles. Similar results were obtained for the epoxy filled with CSR particles from 0 to 38 vol.%. The glass transition temperature and Poisson's ratio were gradually increased while both tensile and compressive properties of CSR-modified composites were significantly decreased which was attributed to the lower Young's modulus and higher Poisson's ratio of rubber [6]. The toughening mechanisms

  doi:10.5075/epfl-298799_978-2-9701614-0-0

such as shear band yielding, core to shell debonding and plastic void growth were defined by using SEM of fracture surfaces and analytical models [2, 6].

Generally, both rigid and soft particles were found to improve the fracture toughness of epoxy [7, 8]. The rigid particles toughen epoxy through crack pinning, crack deflection/bifurcation effects, whereas the toughening mechanisms of the soft particles are filler debonding, and the subsequent void growth as well as the matrix shear band.

The aim of the work was to evaluate how tensile properties and fracture toughness of the epoxy change as a function of CSR particle filler content (0-6 wt.%) for three different types of CSR particles. The most effective composition will be further used to manufacture carbon-fibre reinforced composite and evaluate the effect of CSR particles on its interlaminar fracture toughness.

2. Materials and Methods

2.1 Materials

The investigated materials were based on CHS-Epoxy 582 (Spolchemie, Czech Republic) [9], which is a diglycidyl ether of bisphenol A having an epoxide equivalent weight (EEW) of 165-173 g/mol. It is recommended for the use in composites, adhesives, wind energy, construction, electronics, and corrosive coatings. The hardener was Telalit 0420 (Spolchemie, Czech Republic) which is a cycloaliphatic amine [10]. It was used in the ratio of 100:25 to cure the epoxy resin.

Three types of CSR particles characterized by different particle size and material were used. These were ACE MX series additives 125, 156, and 960 supplied by Kaneka (Belgium). The composition and properties of the CSR particles are provided in Table 1, but the photo of all mixtures is given in Figure 1. Each additive contains a specific CSR type dispersed in the epoxy with concentration of 25 wt.% in DGEBA. The shell material for all CSR particle types was PMMA, EEW for all of them was 243 g/mol, and the density was 1.1 g/cm^3 [11]. Four different compositions for each CSR particle type were studied for the epoxy at filler fraction 0, 2, 4, and 6 wt.%.

Figure 1. 25 wt.% concentrate of CSR particles ACE MX-125, MX-156 and MX-960 in the epoxy.

Table 1: CSR type and mass fraction dispersed in epoxy [11].

Additive name	Core material	CSR size [nm]
ACE MX-125	Styrene butadiene	100
ACE MX-156	Polybutadiene	100
ACE MX-960	Siloxane	300

  doi:10.5075/epfl-298799_978-2-9701614-0-0

2.2 Preparation of the Test Samples

To manufacture pure epoxy samples, the epoxy resin was manually mixed with the hardener for approx. 10 minutes. After it the mixture was degassed using the vacuum pump. For CSR-modified epoxy resin, certain content of CSR particles was added to the epoxy and manually mixed, degassed, and then mixed with the hardener for approx. 10 min. After the degassing all mixtures were poured into silicon moulds. According to supplier recommendations [9], all samples were cured in the moulds overnight at room temperature, then 2 h at 60 °C, 1 h at 80 °C, and 1 h at 120 °C. After curing, the samples were measured and sanded to get rid of imperfections.

The silicon moulds were produced on-site according to standards for the determination of tensile properties [12, 13] and fracture toughness [14]. Thus, dog-bone samples and tapered double cantilever beam (TDCB) samples (as shown in Figure 2) were manufactured at a quantity of at least 5 samples for each test and CSR particle type, and each filler content. No agglomeration of CSR particles was observed by optical microscope Olympus BX51.

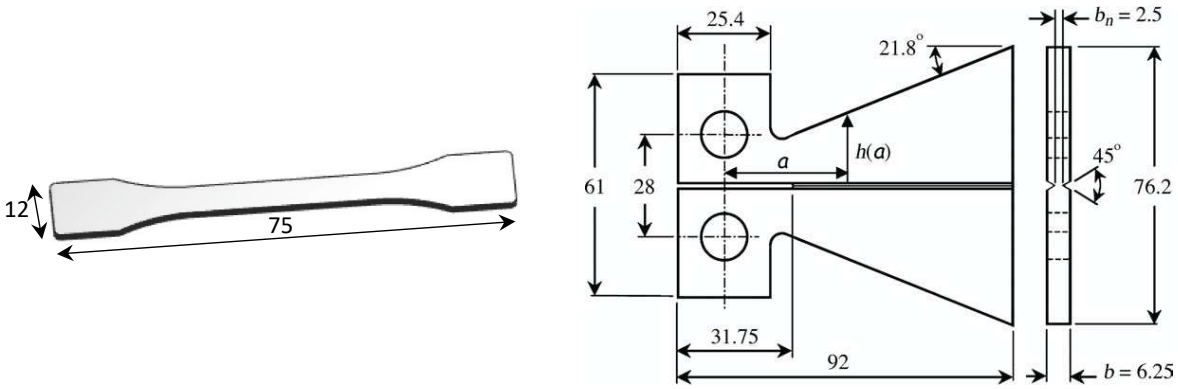

Figure 2. Scheme of dog-bone (a) and TDCB samples (b) (the dimensions are given in mm).

2.3 Tensile Tests

Quasi-static tensile tests were performed for the test specimens with different CSR content using Zwick 2.5 universal testing machine with a crosshead speed of 2 mm/min at room temperature. Tensile strength was defined as the maximal achieved value of stress in the specimen, and the elastic modulus was calculated from the slope of a secant line between 0.05 and 0.25% strain on a stress-strain plot by using equation:

$$E = \frac{\sigma_2 - \sigma_1}{\varepsilon_2 - \varepsilon_1}, \quad (1)$$

ε_1 and ε_2, σ_1 and σ_2 are corresponding strains and stresses, respectively.

Five test samples per each CSR type and content were tested, and the values given correspond to their arithmetic mean value.

2.4 Fracture Toughness Testing

The correct measurement of the stress intensity factor (SIF) requires a specimen with a sharp pre-crack. TDCB specimens which were made in the silicone moulds had an initial notch with 1 mm width and a round end, which may substantially increase the apparent fracture toughness of the material. The initial pre-crack of 2-5 mm length was created in the specimen before testing

  doi:10.5075/epfl-298799_978-2-9701614-0-0

by the sharp knife strike. In addition, side grooves of the depth approx. 1.875 mm were provided to avoid crack deflection and to maintain the crack path along the midplane of the specimens [14]. The tests were conducted on Zwick 2.5 universal testing machine at room temperature of 22 °C with a constant displacement rate of 1 mm/min. SIF was calculated using Mode I load for a crack length <20 mm within constant SIF region.

The SIF value for the non-grooved specimen can be calculated using the following expression:

$$K_{ng} = 2P_c \frac{\sqrt{m}}{b}, \quad (2)$$

where P_c is the critical load, b is the width of the specimen and m is a geometrical parameter, which for the specimen of the considered geometry equals 0.6 mm^{-1}. For the specimen with grooves, the expression for the SIF should be modified as

$$K_g = K_{ng} \left(\frac{b}{b_n}\right)^x, \quad (3)$$

where b_n is the reduced width of the specimen at the grooves' location, and the value of the exponent was determined from a series of three-dimensional finite element simulations with grooves of different length.

2.5 Density Measurements

The density of all samples was determined at room temperature (22 °C) by using hydrostatic weighing in isopropyl alcohol and Mettler Toledo XS205DU balance with a precision of ± 0.05 mg. First, the density of isopropyl alcohol was determined by using a sinker of known volume 10 cm^3. Then the mass of the samples was registered in air (m_a) and in the liquid of known density (m_l). The density of the samples was determined by the formula:

$$\rho = \frac{m_a}{m_a - m_l}(\rho_l - \rho_a) + \rho_a, \quad (4)$$

where ρ_l and ρ_a is the density of the liquid (0.785 g/cm^3 for isopropyl alcohol) and of the air (0.0012 g/cm^3 for air).

3. Results

3.1 Density and Porosity

The experimental results for density are provided in Figure 2. It obvious that the addition of all types of CSR particles resulted in the decrease of the density for CSR-modified epoxy. It is possible to estimate the density of the composite by using mixture rule

$$\rho_c = \rho_f \times v_f + \rho_m \times (1 - v_f), \quad (5)$$

where ρ_f and $\rho_m$is the density of the filler (CSR particles) and polymer matrix (epoxy), but $v_f$is the volume fraction of filler, accordingly. The density of the epoxy was experimentally found to be 1.159 ± 0.002 g/cm^3. Considering the known density of 25%-CSR-modified epoxy of 1.1 g/cm^3 [11], the density of CSR particles was found to be 0.91 g/cm^3 [2].

The volume fraction of filler was obtained from the equation [15]:

$$v_f = \frac{\rho_m \times c_f}{\rho_m \times c_f + \rho_f \times (1 - c_f)}, \quad (6)$$

  doi:10.5075/epfl-298799_978-2-9701614-0-0

where c_f is the weight fraction of the filler.

According to Figure 3, the mixture rule (Eq. (5)) provided an overestimated evaluation for the density of all CSR-modified epoxy materials. Therefore, the efforts were being made to evaluate the density of the composites by adding additional phase such as air filled pores which could exist in the composites and as a result could lower the density:

$$\rho_c = \rho_f \times v_f + \rho_p \times v_p + \rho_m \times (1 - v_f - v_p), \quad (7)$$

where ρ_p is the density of the air and v_p is the volume fraction of pores in the composites.

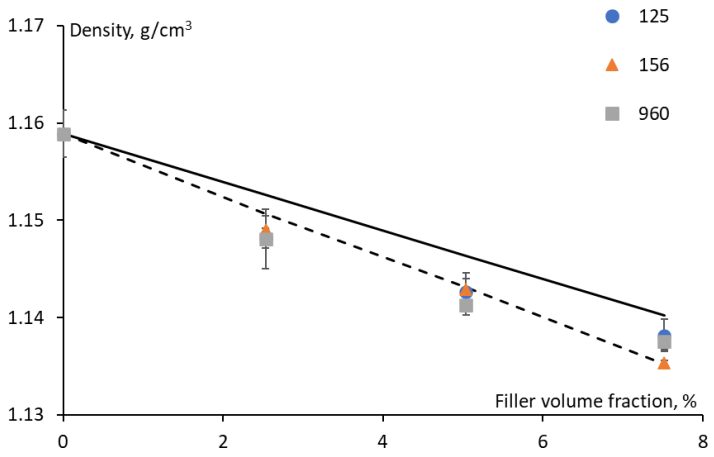

Figure 3. Density of the epoxy filled with CSR particles (indicated on the graph) vs. filler volume fraction (symbols – experimental data, solid and dashed lines – evaluation by Eq. (5) and Eq. (7), accordingly.

Thus, from Eq. (7) the volume fraction of the pores was obtained by the following expression:

$$v_p = \frac{v_f \times (\rho_f - \rho_m) + \rho_m - \rho_c}{\rho_m - \rho_p}, \quad (8)$$

The results for the volume fraction of the pores were not significant for all materials and were approx. 2 vol. %. This value was considered in further calculations of the elastic modulus of CSR-modified epoxy.

3.2 Tensile properties

The representative stress-strain curves for the neat and CSR-modified epoxy with ACE MX-125 are provided in Figure 4a. Similar results were obtained for the other additives. As it was expected the addition of CSR particles diminished the tensile properties such as elastic modulus and tensile strength and led to the increase of maximal deformation. According to Figure 4b the elastic modulus of all studied materials significantly decreased with increasing CSR content. The elastic modulus of 1.99 ± 0.04 GPa was found for unmodified epoxy. Generally, it had the lowest value for ACE MX-960 at all filler fractions which could be attributed to lower effective stiffness of particles due to the highest CSR size in comparison with the other additives (see Table 1) [2]. The tensile strength of the epoxy (73 ± 3 MPa) decreased by approx. 10-20% with the addition of CSR particles. Again, slightly lower tensile strengths were found for ACE MX-960 in comparison to the other CSR particles. It could be noted from Figure 4a that the maximal deformation increased (from 4.9 ± 0.6% till 7.2 ± 0.5%) with the increase of CSR content revealing

  doi:10.5075/epfl-298799_978-2-9701614-0-0

plasticization/softening effect resulted from the inclusion of softer filler particles in a brittle matrix.

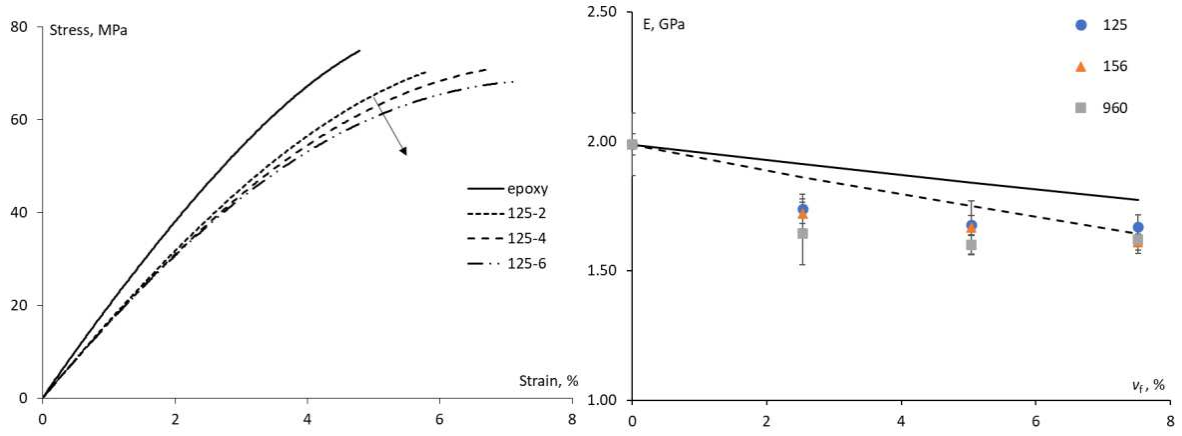

(a) (b)

Figure 4. Representative stress-strain curves for the epoxy and epoxy modified with ACE MX-125 at different filler fractions indicated on the graph (a) and elastic modulus vs. volume fraction of filler (dots -experimental results for different CSR particles, solid and dashed lines – evaluation by Eq. (9) without consideration of the pores and with the pores, accordingly) (b).

Different analytical models, e.g., Halpin-Tsai [2], Lewis-Nielsen [2, 6] and Mori-Tanaka [6] were applied to describe the reduction of the elastic modulus of the epoxy filled with CSR particles. In this work, Hansen model [16, 17] considering spherical particles embedded in spherical shells of matrix was used. Thus, the elastic modulus of the composite filled with CSR particles could be estimated by using following formula:

$$E_c = \frac{(1-v_f)+(1+v_f)E_f/E_m}{(1+v_f)+(1-v_f)E_f/E_m} \times E_m, \quad (9)$$

where E_f and E_m is the elastic modulus of the filler (CSR particles) and the epoxy matrix, accordingly. The effective elastic modulus of CSR particles was equal to 4 MPa [2], thus resulting in a decrease of the elastic modulus of the composite with the increase of filler volume fraction. The porosity was also considered by adding volume fraction of the pores (0.77-2.00 vol.%) to the overall filler content. The results of evaluation by Eq. (9) are shown in Figure 4b. Generally, at higher filler contents Hansen model allowed to predict the reduction of the elastic modulus by approx. 20% due to addition of soft CSR particles to the epoxy resin.

3.3 Fracture toughness

The fracture toughness of the unmodified epoxy was experimentally found to be 0.83 ± 0.07 MPa·m$^{1/2}$ which is slightly lower than the values reported in the literature for the epoxy resins [6, 7]. As seen from Figure 5 the addition of CSR particles resulted in a steady increase of the fracture toughness for all three types of the additives. No significant difference in the fracture toughness among the additives was revealed proving that smaller CSR particles were the same effective as bigger CSR particle. Though, in general ACE MX 156 showed the highest improvement of fracture toughness which was approx. 108% at CSR content 4 wt.%. The optimum rubber content beyond which fracture toughness does not improve was reported by many authors in the literature [6, 18]. In this work, according to Figure 5 the optimum CSR particle content could be estimated as 4 wt.% for all additives. Of course, this result is only

  doi:10.5075/epfl-298799_978-2-9701614-0-0

relevant for certain dispersion conditions of CSR particles in the epoxy since. Nevertheless, the manual mixing of CSR particles in the epoxy resulted in noticeable improvement of the fracture toughness. Also, low fraction of pores that was indirectly estimated from density measurements reveals sufficient quality of the manufactured samples.

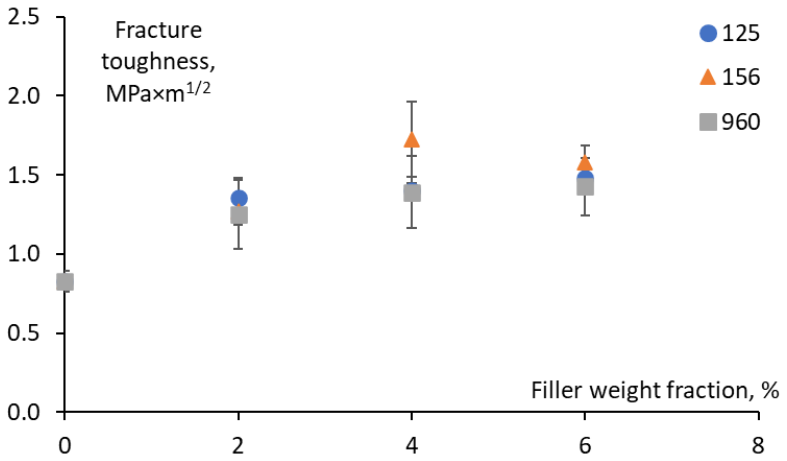

Figure 5. Fracture toughness for the epoxy and epoxy modified with ACE MX-125, 156, and 960 at different filler fractions (indicated on the graph).

4. Conclusions

The epoxy resin was modified by the addition of three different types of CSR particles at different content. The addition of relatively soft CSR particles led to the slight decrease in density, and significant decrease in elastic modulus and tensile strength. The reduction of the elastic modulus was described by Hansen model, and good agreement was found at high filler content.

Nevertheless, it was testified that the fracture toughness of the epoxy could be significantly improved by the addition of all investigated types of CSR. Optimum CSR particle content was found to be 4 wt. % for all CSR particle types. No significant difference in the fracture toughness among the additives was revealed proving that smaller CSR particles were the same effective as bigger CSR particle. Though, in general ACE MX 156 showed the highest improvement of fracture toughness which was approx. 108% at CSR content 4 wt.%.

Possible combination of rigid and soft particles could be a compromise to simultaneously improve both tensile properties and fracture toughness, which cannot be achieved by the single-phase particles independently.

Acknowledgements

This research was funded by M-Era.Net project MERF “Matrix for carbon reinforced epoxy laminates with reduced flammability” grant No. 1.1.1.5/ERANET/20/04 from Latvian State Education Development Agency.

References

1. Guedes RM Creep and fatigue in polymer matrix composites, 2nd ed., Elsevier, ch. 4. Effect of moisture on elastic and viscoelastic properties of fibre reinforced plastics: retrospective and

current trends by Aniskevich A. and Glaskova-Kuzmina T., Woodhead Publishing, p. 83-120 (586 p.). 2019.
2. Giannakopoulos G, Masania K, Taylor A.C. Toughening of epoxy using core-shell particles. Journal of Material Science 2011; 46:327-338.
3. Day RJ, Lovell PA, Wazzan AA. Thermal and mechanical characterization of epoxy resins toughened using preformed particles. Polymer International 2001; 50 (8): 849-857.
4. Qian JY, Pearson RA, Dimonie VL, El-Aasser MS. Synthesis and application of core–shell particles as toughening agents for epoxies. Journal of Applied Polymer Science 1995; 58 (2): 439-448.
5. Shen J, Zhang Y, Qiu J, Kuang J. Core-shell particles with an acrylate polyurethane core as tougheners for epoxy resins. Journal of Materials Science 2004; 39: 6383–6384.
6. Quan D, Ivankovic A. Effect of core-shell rubber (CSR) nano-particles on mechanical properties and fracture toughness of an epoxy polymer. Polymer 2015; 66 (1): 16-28.
7. Tang LCh, Zhang H, Sprenger S, Ye L, Zhang Z. Fracture mechanisms of epoxy-based ternary composites filled with rigid-soft particles. Composites Science and Technology 2012; 72 (5): 558-565.
8. Dadfar MR, Ghadami F. Effect of rubber modification on fracture toughness properties of glass reinforced hot cured epoxy composites. Materials and Design 2013; 47: 16-20.
9. Material datasheet for CHS-Epoxy 582 by Spolchemie (Czech Republic), https://www.spolchemie.cz/en/product.chs-epoxy-582/?msclkid=77435be2bb3011ec852121a4067dc4ca, accessed on 13.04.2022.
10. Material datasheet for Telalit 0420 by Spolchemie (Czech Republic), https://www.spolchemie.cz/en/product.telalit-0420/?msclkid=2065552fbb3111ec82d92b19f5b9d09c, accessed on 13.04.2022.
11. Material datasheet for ACE MX-125, ACE MX-156, and ACE MX-960 by Kaneka (Belgium), https://www.kaneka.be/sites/default/files/uploads/brochures/MX/Kaneka-leaflet-Kane-Ace-Product-properties.pdf?msclkid=a2acc2d9bb3311ecb184043310b58907, accessed on 13.04.2022.
12. ISO 527-1 (2012) Plastics — Determination of tensile properties-part 1: General principles. ISO, Geneva.
13. ISO 527-2 (2012) Plastics — Determination of tensile properties-part 2: Test conditions for moulding and extrusion plastics. ISO, Geneva.
14. Beres W, Ashok KK, Thambraj R. A tapered double-cantilever-beam specimen designed for constant-K testing at elevated temperatures. Journal of Testing and Evaluation 1997; 25 (6): 536-542.
15. Glaskova-Kuzmina T, Zotti A, Borriello A, Zarrelli M, Aniskevich A. Basalt fibre composite with carbon nanomodified epoxy matrix under hydrothermal ageing. Polymers 2021; 13 (4), 532.
16. Hansen TC. Influence of aggregate and voids on modulus of elasticity of concrete, cement mortar, and cement paste. International Concrete Abstracts Portal 1965; 62 (2): 193-216.
17. Yoshitake I, Rajabipour F, Mimura Y, Scanlon A. A prediction method of tensile Young's modulus of concrete at early age. Advances in Civil Engineering 2012, 391214.
18. Becu L, Maazouz A, Sautereau H., Gerard JF. Fracture behavior of epoxy polymers modified with core-shell rubber particles. Journal of Applied Polymer Science 1997; 65: 2419–2431.

  doi:10.5075/epfl-298799_978-2-9701614-0-0

ON THE EXPERIMENTAL AND NUMERICAL CHARACTERISATION OF UNCURED PREPREG COMPOSITE

David, Aveiga[a], Mario, Rueda[a], David, Garoz[a], Carlos, González[ab]

a: IMDEA Materials Institute – jorgedavid.aveiga@imdea.org
b: ETSI Caminos Canales y Puertos – Polytechnic University of Madrid

Abstract: *Pre-impregnated composite plies have the potential to be shaped into high-performance structural components through processes like Thermoforming manufacturing. The process conditions affect the mechanisation and moulding of these prepreg plies and could lead to undesired defects like out-of-plane wrinkles. An essential aspect to avoid part imperfections during the thermoforming is understanding how the prepreg will respond to the mechanical demands. A complete experimental characterisation was achieved concerning the difficulties reported in the literature due to the presence of viscoelasticity and the irregular bonds between the plies. The experimental campaign consisted of tests at several strain rates and temperatures. A new method is proposed to produce coupons that have cured tabs zone with the central part of the coupon without being cured. The values of uncured ply properties and the modelling approach were validated using benchmark tests. The validity is checked by comparing the experimental response with the predictions of the numerical model.*

Keywords: Prepreg; Viscoelasticity; Material Characterisation; Thermoforming.

1. Introduction

Structures designs in the aeronautical industry increased the employment of pre-impregnated (prepregs) thermoset/thermoplastic composites. Since this material has an incomplete cured resin, which is very malleable, the part production is usually referred to manufacturing systems like hot plate press, vacuum infusion, sheet moulding compound and thermoforming. The knowledge about the interaction between material and process parameters is essential to achieve the best outcome from the manufacturing process selected.

Moulding a composite laminate part is a process that involves a number of discontinuities or undesired defects like in-plane or out-of-plane wrinkles, non-uniform thickness and fibres buckling. These defects are stress concentrators that will affect the lifespan of our structure (1)(2). In order to produce a very refined component, the mechanical response of prepreg composite in an uncured state needs to be characterised and modelled.

There is vast information regarding the mechanical behaviour of prepreg laminates with a cured state of the resin, but regarding uncured prepregs, the scenario is not defined and is full of uncertainness. The viscoelastic behaviour present in prepregs (3) makes it unable to use the standards methods designed for composite materials. Especially when heat is introduced in the process, the resin becomes more fluid, allowing the plies to slide between them, producing a miscalculation of the stress. This problem has been reported in the literature, and different

  doi:10.5075/epfl-298799_978-2-9701614-0-0

alternatives have been proposed (4)(5). However, there is no consistency between the methods, or the setup is not feasible.

A practical solution is proposed that allows using the standard methods without miscalculating the stress resistance, and the repeatability of the test is constant even when varying the cross-section of the coupons. This methodology was employed to calculate all the principal stress resistances necessary to characterise a composite laminate. In this work, the setup for this method is shown. We validate the result by comparing test results between coupons produced with or without this procedure.

2. Sample Production Procedure and Material Characteristics

HexPly® AS4/8552 UD prepreg composite sheets were employed to build the laminates. Hexcel® fabricates this material with a nominal fibre volume of 57.42% embedded with a thermoset resin with a density of 1.3 g/cm^3.

The prepreg plies are stacked to the desired sequence, and the coupons are cut according to the ASTM D3039 standard method recommendations. Before testing, the samples are placed over a “partial curing” plate, as seen in Figure 1:

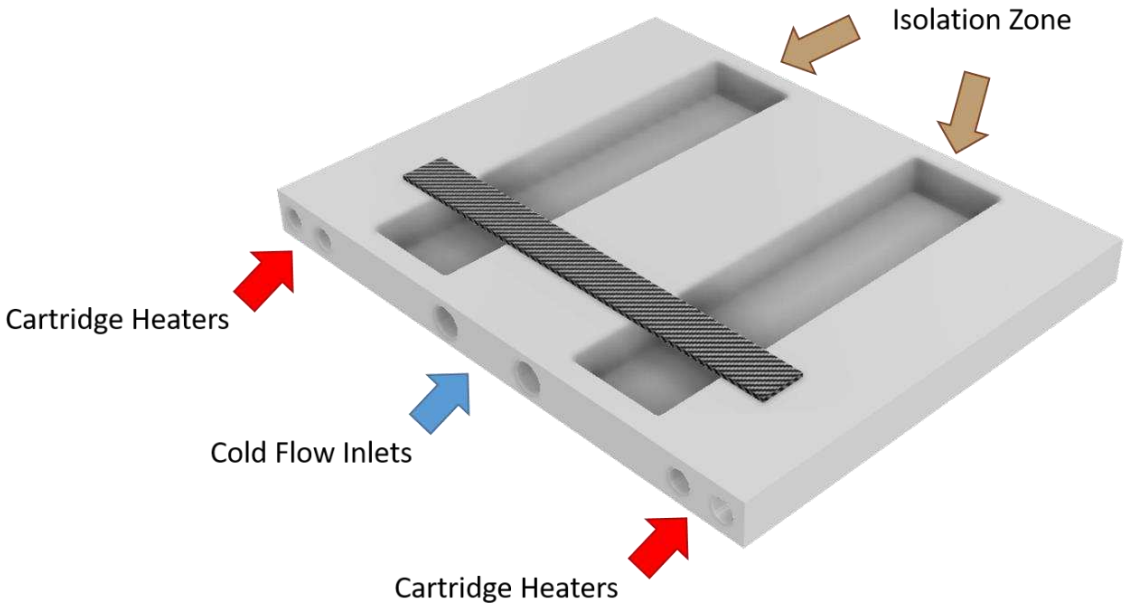

Figure 1. Partial Curing Plate.

This rectangular plate will allow curing of the ends of the samples creating a tab zone of 20x20 mm, which corresponds to the grip area of the testing machine clamps. The plate has six ducts that go all through the plate and allow to insert of four cartridge heaters at the ends of the plate,

  doi:10.5075/epfl-298799_978-2-9701614-0-0

which are denominated as the curing zones, and two ducts at the central part of the plate where a constant cold flow will keep this not curing zone cold and therefore the sample will not cure. Between these zones, there are two sockets where a thermal insulator material will be inserted to reduce heat transfer. The partial curing process consists of heating the ends of the sample at 100 °C and cooling the centre to keep it under 20°C. A vacuum bag system should be employed during the whole process to reduce the void content. After 6 to 8 hours with these conditions, a sample with cured tabs and fresh material in the middle is obtained.

The dimensions of the plate can be adapted according to the sample dimensions required, but it is essential to consider that the distance between the hot and the cold zone will affect the heat transfer and, therefore, the temperature balance over the plate. Another detail about this procedure is that the curing time has an impact on the curing grade of the samples since carbon fibres and other types of fibres are heat conductors. Thus, there is a heat gradient from the end of the sample to the centre, causing different curing grades along the sample that can affect the stress resistance. To avoid any problems regarding this effect, we recommend using the same curing time for all the sample production.

3. Experimental Test and Partial Results

The tests performed in order to validate the partial cure process consist of laminates with a stacking sequence of $[\pm 45]_{ns}$ .Which is a symmetric laminate that, in our case, we considered 8 and 16 plies. A tensile test was performed with samples that possessed cured tabs and samples without curing. The test was performed at room temperature (RT=22°C) with a 0.5 mm/min strain rate for both cases. Figure 2 and Figure 3 illustrate the results, respectively:

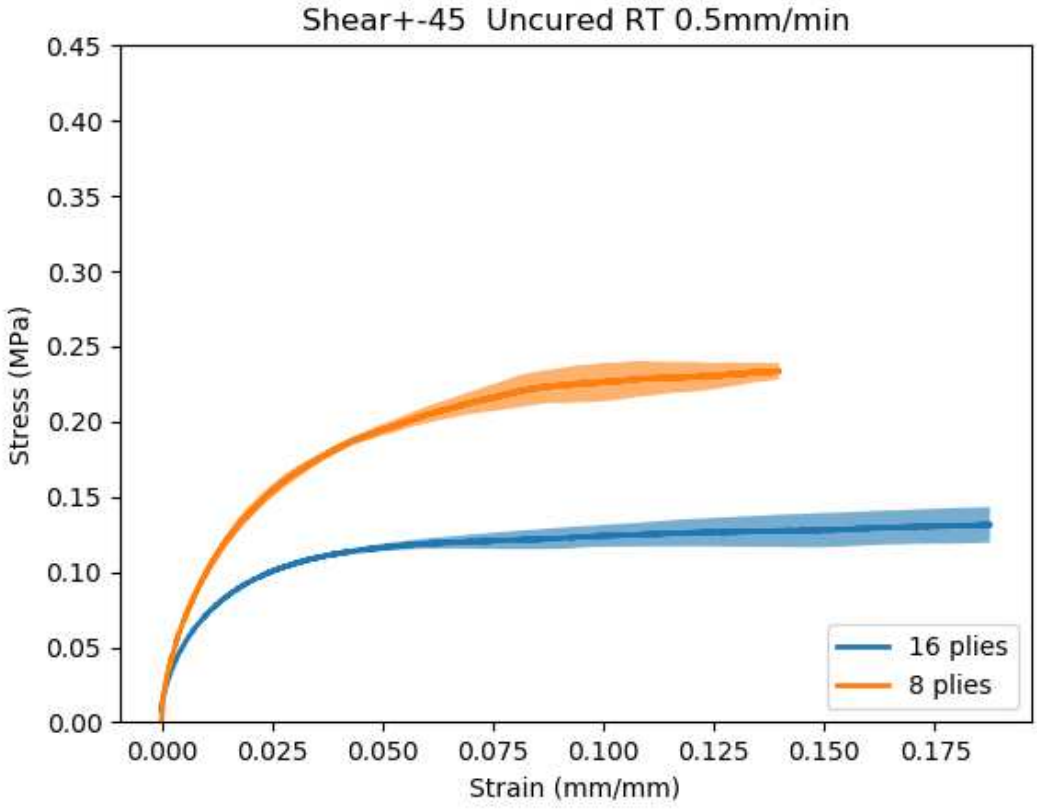

Figure 2. Tensile Shear Test using samples with 8 and 16 plies without cured tabs.

For this first case, we can realise that increasing the thickness will reduce the stress resistance. This effect was observed for this case and for all the fibre directions considered. A simply explanation could be that a poor bond exists between the plies, and at a specific load, the plies will slide between each other, and the load supported will correspond only to the plies in contact with the testing machine clamps while the plies in the middle will not support any load. The stress calculated decreases with increasing thickness since a lower load is sustained and a more extensive cross-sectional area exists.

Another way to prove this effect is to check the strain distribution over the sample. In a regular tensile test, we expect a region where the strain is concentrated (centre of the sample). However, in an uncured prepreg sample, this region does not exist and what we observe is that different strain concentration points appear and disappear during the tensile test (Figure 4a).

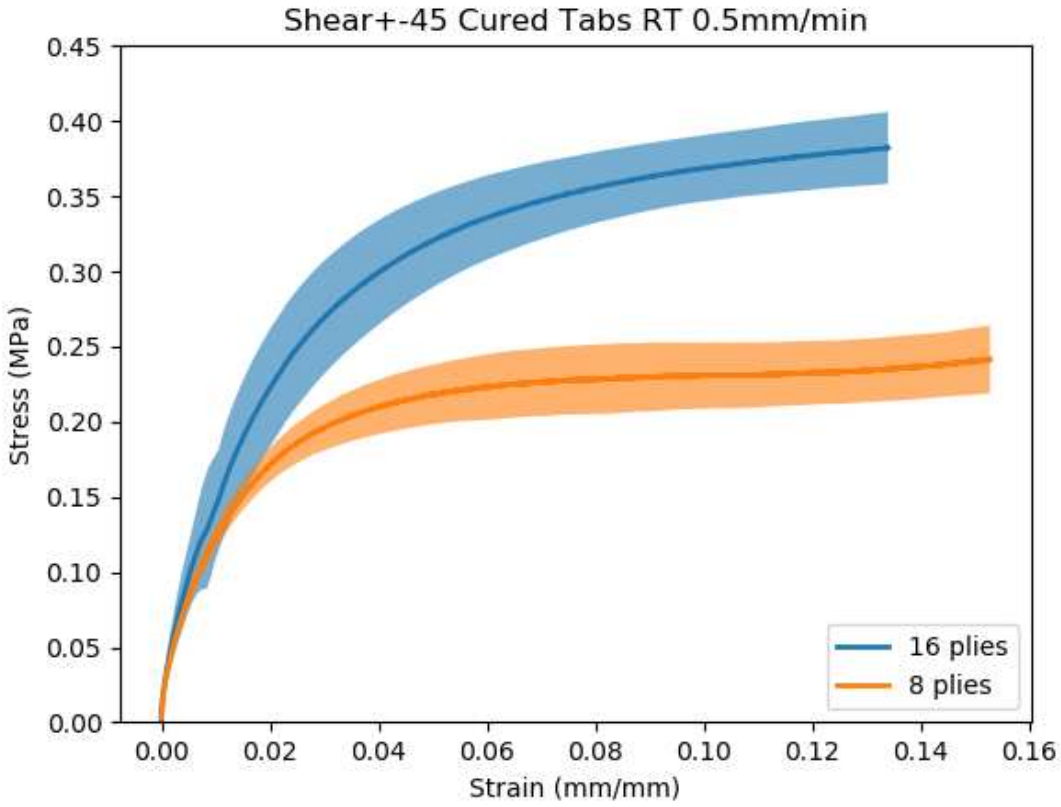

Figure 3. Tensile Shear Test using samples with 8 and 16 plies with cured tabs.

Curing the tabs will guarantee that the load is transmitted to all the plies. Therefore, the stress measured does not decrease with an increasing number of plies. In an ideal scenario, we should expect the same stress resistance value independent of the dimensions of the cross-section. However, we should keep in mind that an uncured prepreg laminate might present inconsistencies like fibre rotation during the loading (6), and the interaction between the plies (7) will cause a difference in the expected result. The calculated stress should not decrease in any hypothesis while increasing the ply number. Thus, we consider that our proposal solves load transfer problems through the thickness in uncured prepreg laminates. Additionally, as the temperature increases, these inconsistencies have less impact on the final result.

  doi:10.5075/epfl-298799_978-2-9701614-0-0

In counterpart to the previous case, when we cure the tabs, we will observe a strain concentration region just in the middle of the sample (Figure 4b).

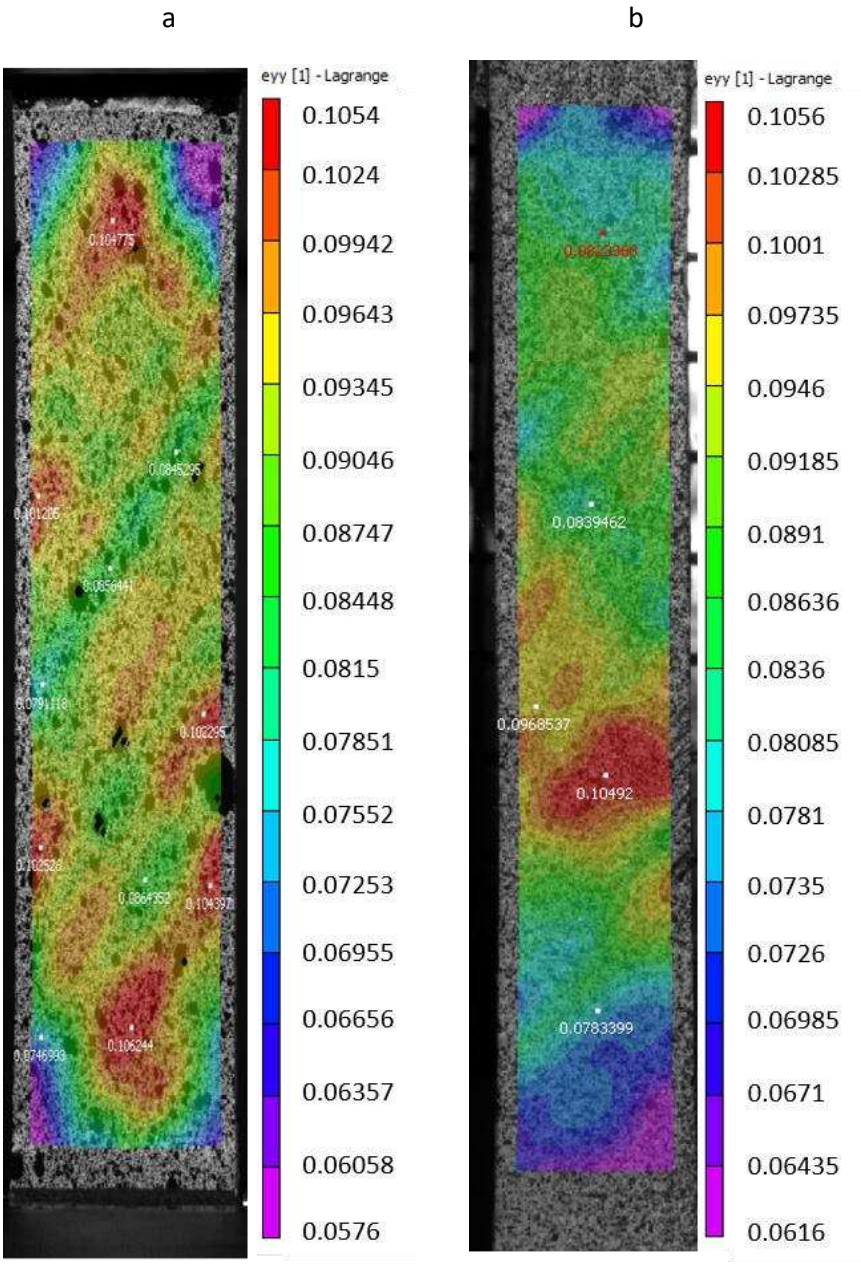

Figure 4. Strain distribution at 10% of strain. a) Uncured prepreg sample b) Cured tab sample.

4. Conclusions

A sample production process was proposed to solve the problem of load transfer through the thickness in uncured prepreg laminates. It was previously observed that if a tensile test is performed with uncured samples, the external plies of the laminate are the only plies supporting the load, causing miscalculations of the stress resistance. Curing the tabs following the procedures explained above will guarantee that all the plies in the laminate will be loaded, and

  doi:10.5075/epfl-298799_978-2-9701614-0-0

the stress resistance calculated has a more accurate value. In the meantime, we performed a set of experimental tests to supply a material model that relayed excellent outcomes when used in the simulation.

5. References

1. Potter K, Khan B, Wisnom M, Bell T, Stevens J. Variability, fibre waviness and misalignment in the determination of the properties of composite materials and structures. Compos Part A Appl Sci Manuf. 2008;39(9):1343–54.

2. Wang L, Xu P, Peng X, Zhao K, Wei R. Characterization of inter-ply slipping behaviors in hot diaphragm preforming: Experiments and modelling. Compos Part A Appl Sci Manuf [Internet]. 2019;121(September 2018):28–35. Available from: https://doi.org/10.1016/j.compositesa.2019.03.012

3. Alshahrani H, Hojjati M. Bending behavior of multilayered textile composite prepregs: Experiment and finite element modeling. Mater Des [Internet]. 2017;124:211–24. Available from: http://dx.doi.org/10.1016/j.matdes.2017.03.077

4. Heller K, Hallmannseder M, Colin D, Kind K, Drechsler K. Comparing Test Methods for the Intra-ply Shear Properties of Uncured Prepreg Tapes. Sci Eng Compos Mater. 2020;27(1):89–96.

5. Wang Y, Chea MK, Belnoue JPH, Kratz J, Ivanov DS, Hallett SR. Experimental characterisation of the in-plane shear behaviour of UD thermoset prepregs under processing conditions. Compos Part A Appl Sci Manuf. 2020;133(October 2019).

6. Miao C, Fernando D, Zhou H, Wilson P, Heitzmann M. Behaviour of hybrid glass fibre-reinforced polymer and timber composite laminates under shear loading: Importance of fibre rotation. Compos Struct [Internet]. 2022;287(January 2021):115304. Available from: https://doi.org/10.1016/j.compstruct.2022.115304

7. Åkermo M, Larberg YR, Sjölander J, Hallander P. Influence of interply friction on the forming of stacked UD prepreg. ICCM Int Conf Compos Mater. 2013;2013-July:919–28.

  doi:10.5075/epfl-298799_978-2-9701614-0-0

IDENTIFYING MICROSTRUCTURAL FEATURES IN UNIDIRECTIONAL COMPOSITE TAPES

Nico Katuin[a,b], Daniël Peeters[a] and Clemens Dransfeld[a]

a: Delft University of Technology, Department of Aerospace Structures and Materials, Delft, The Netherlands – c.a.dransfeld@tudelft.nl
b: Current address: Boikon B.V., Leek, The Netherlands

Abstract: *The microstructure of composites has a strong impact on their performance and processability. It influences the structural performance and fatigue life when architected into thin ply composites. The microstructure is also affected by processing conditions, respectively recursively affects processability as observed in the deconsolidation or intimate contact formation during laser assisted tape laying. This work presents a novel approach to identify microstructural features. This is achieved by Voronoi tessellation-based evaluation of the fibre volume content on cross-sectional micrographs, considering the matrix boundary. The method was applied on unidirectional tape samples with characteristic processing history. It is shown to be robust, it is suitable to be automated and has the potential to be expanded into 3d imaging techniques. It offers the possibility to discriminate specific microstructural features and to relate them to processing behaviour.*

Keywords: Unidirectional composites; Microstructure; Imaging; Voronoi

1. Introduction

Carbon fibre reinforced polymer composites have outstanding properties at low weight. They contribute to the sustainability of air transport, automotive and energy sector. Especially when exploiting their anisotropy in the unidirectional configuration, they outperform most engineering materials in specific stiffness or weight. The engineering and processing properties of unidirectional materials are most commonly derived from homogenization approaches, which assume a perfect regular distribution of the fibre in the matrix. However their processing history, from carbon fibre rovings to finished parts affects their microstructural arrangement and homogeneity. Amacher [1] observed that unidirectional composites, when spread to very thin plies, impact the microstructural homogeneity of the resulting unidirectional laminate resulting in an increase of compression strength of up to 24%. Also in processing, Schuler [2] observed that transverse squeeze flow, an essential behaviour for intimate contact formation [3], is affected by inhomogeneity in fibre distributions. Although the relation between microstructure and resulting properties is undeniable, its correlation has been primarily qualitative.

This work aims to develop quantitative analysis methods for unidirectional composite tapes based on optical cross-sectional microscopy. Using fibre centre identification through image processing, computer vision, and Voronoi tessellation, various quantitative evaluations have been explored and correlated to the processing behaviour.

  doi:10.5075/epfl-298799_978-2-9701614-0-0

2. Method

The basic approach of cross-sectional microscopy of unidirectional composites has been previously explored by Zangenberg et al. [4]: by identification of fibre centres, a Voronoi tessellation of the cross-section is achieved, where every cell with an area A_v contains an individual fibre with a cross section area A_f. We can therefore express the Voronoi-based local fibre volume content V_{fv} at the resolution of a single fibre.

$$\mathrm{V_{fv}} = \frac{\mathrm{A_f}}{\mathrm{A_v}} \tag{1}$$

To process larger microstructures, an adapted, numerically efficient methodology is presented based on the open-source Python library OpenCV [5]. The complete commented code is available on GitHub and archived in Zenodo [6]. Images were taken from embedded samples of carbon fibre unidirectional tapes with a polyaryletherketone matrix. The images were captured with a Keyence VK-X1000 laser scanning confocal microscope in the optical mode using a 50x magnification and coaxial lighting. This corresponded to a pixel resolution of about 1/20th of a fibre diameter. Using the embedded stitching capability, images with 17000 x 700 pixels of large tape cross-sections were assembled.

The image processing consisted of four main steps : (1) fibre centre detection, (2) identification of individual fibre diameters, (3) detection of the outer boundary, followed by (4) Voronoi tesselation taking into account these boundaries.

The images were processed through mean shift segmentation, blurring and thresholding (*Figure 1*). Applying Euclidian distance mapping in combination with an 8-connectivity watershed allowed to discriminate individual fibres, also in densely packed situations, as seen in *Figure 2*. Furthermore, proximity analysis based on the nominal fibre diameter allowed to merge overlapping interpretations.

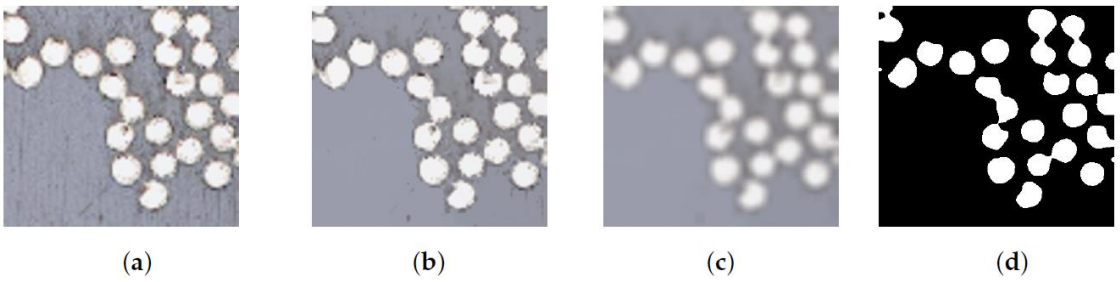

Figure 1. Image processing steps (a) original, (b) mean shift segmentation, (c) blurring, (d) thresholding, (from [7])

Based on previously computed fibre centres, the fibre radius was determined in four directions based on greyscale thresholding as illustrated in Figure 3. Other authors use the circle Hough Transform [8] for the fibre centre and fibre diameter feature extraction, which comes, compared to this method, at high cost of computation and storage compared to the presented methods.

The outmost Voronoi cells of a finite number of fibre centres have, per definition, an infinite size; therefore, the matrix boundary of the tape sample was digitized into a polygon to cap the perimeter Voronoi cells (Figure 4) for dedicated analyses.

  doi:10.5075/epfl-298799_978-2-9701614-0-0

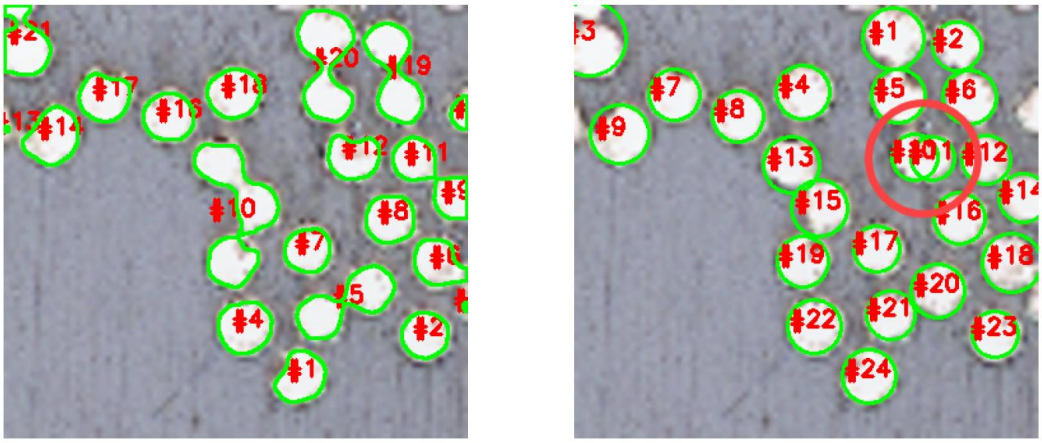

Figure 2. Definition of fibre contours (a) without and (b) with 8-connectivity watershed, (from [7])

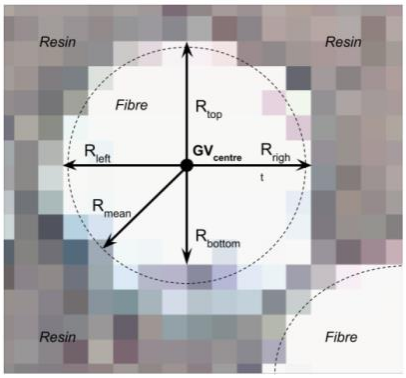

Figure 3. Definition of mean fibre radius based on grey scale evaluation in 4 directions (from [7])

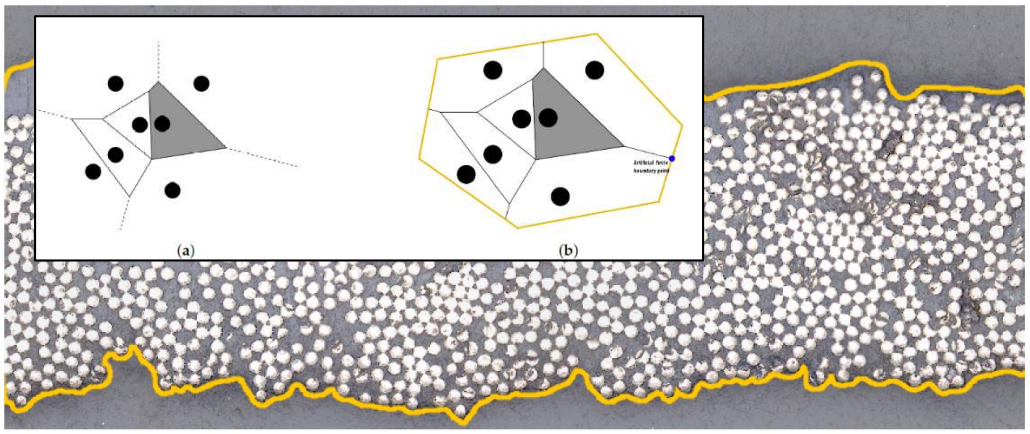

Figure 4. Tape boundary represented as polygon, trimming the infinite boundary Voronoi cells (a) to finite size (b) (from [7], modified)

3. Results

To assess the method, three unidirectional tapes, further referred to as A, B and C, made with different spreading and impregnation techniques [9, 10] were imaged, segmented and analysed. Next to analysing the fibre volume content over the entire cross-section, the V_{fv} was also

  doi:10.5075/epfl-298799_978-2-9701614-0-0

homogenized for a through thickness evaluation and for dedicated analysis of the outmost upper and lower boundary elements, as illustrated in Figure 5. In some cases, in highly compacted areas, due to imaging inaccuracies, the evaluation of V_{fv} could yield values greater than one, when $A_f \geq A_v$. These cells were flagged red for clarity and removed from the analyis.

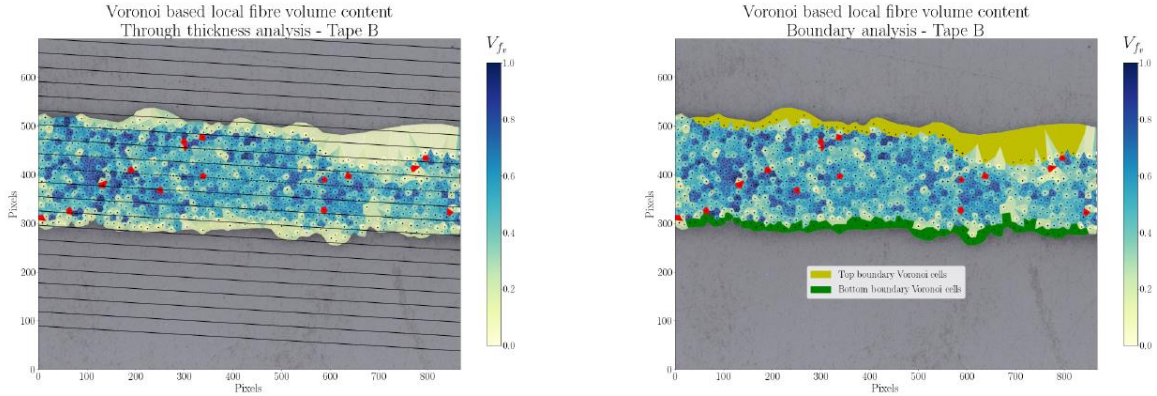

Figure 5. (a) Through thickness segmentation of tape in about 8-10 segments, (b) identification of top and bottom surface cells for specific analyses, (example from tape B, taken from [7])

The V_{fv} plots of the different tapes shown in *Figure 6* to *Figure 8* reveal distinct differences between the different tapes. The through-thickness analyses shown in *Figure 9*, reveal distinct edge-core morphologies for tape A and B. This is also confirmed in the histograms shown in Figure 10, again tapes A and B show contrasting V_{fv} distributions at the surface in terms of median and skewness.

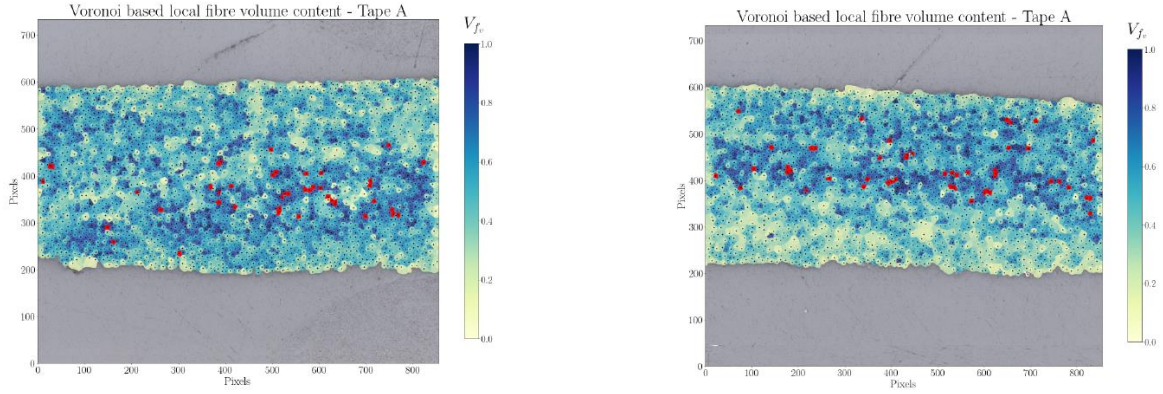

Figure 6. V_{fv} analyses of two characteristic sections from tape A [7]

  doi:10.5075/epfl-298799_978-2-9701614-0-0

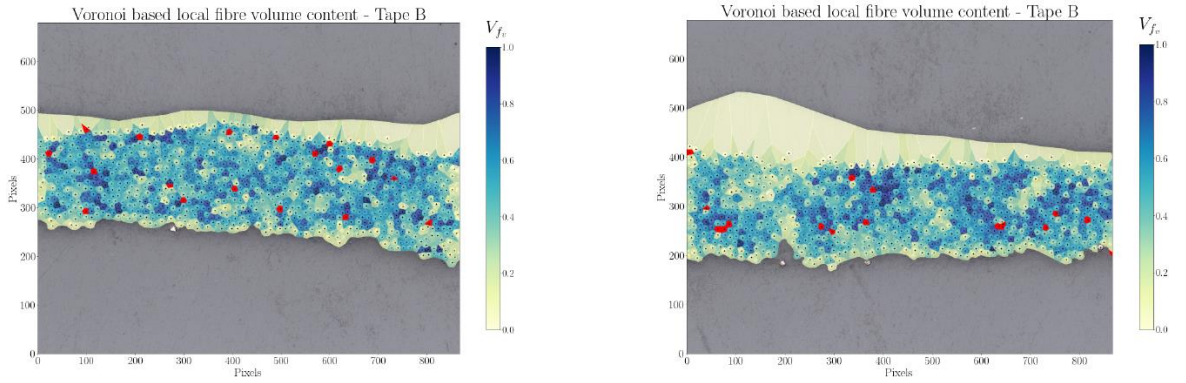

Figure 7. V_{fv} analyses of two characteristic sections from tape B [7]

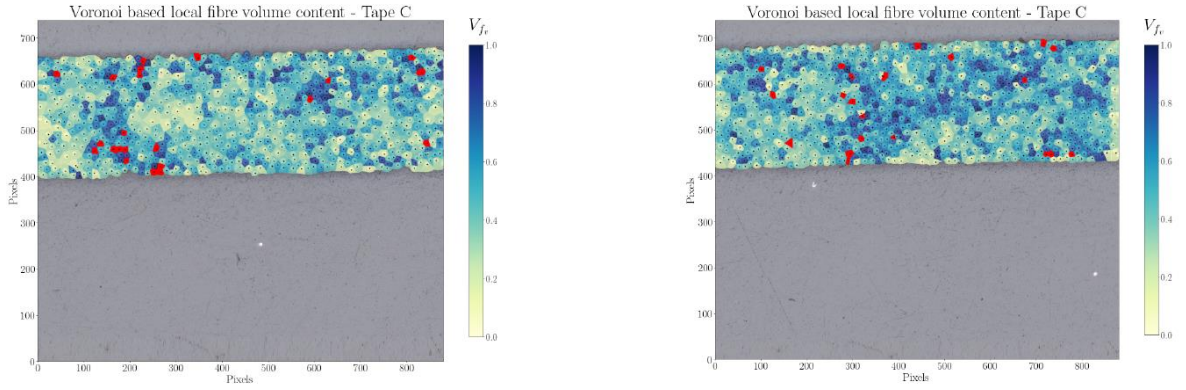

Figure 8. V_{fv} analyses of two characteristic sections from tape C [7]

4. Conclusion

This work presents a novel approach to identifying microstructural features, based on single fibre identification in cross-sectional micrographs, considering the matrix boundary. The authors have investigated the robustness of the methods in depth [7]. The methods reveal characteristic microstructural features of the fibre distribution, which can be further spatially or statistically quantified and related to processing properties. Ultimately, these can be expanded to the 3rd dimension and will serve to develop representative volume elements. The observation of tape manufacturing-related edge core effects does also relate to other microstructural features of the fibre architecture, which has recently been confirmed by Gomarasca et al [11].

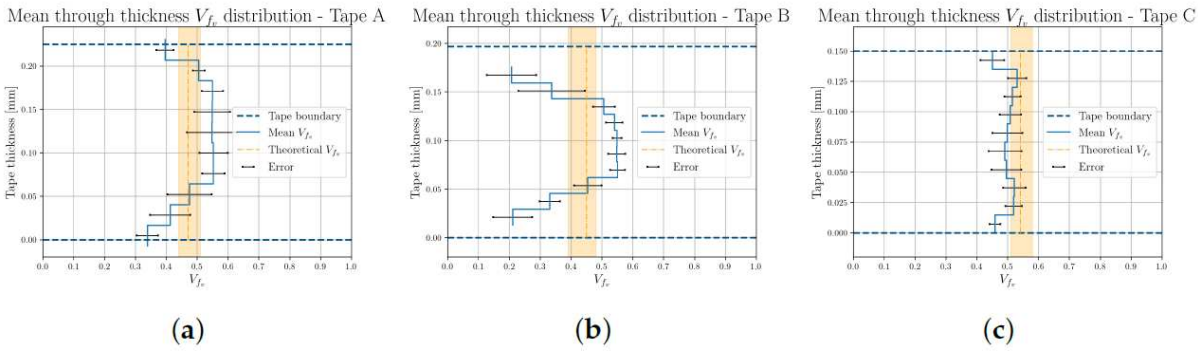

Figure 9. Through thickness evolution of V_{fv} for tapes A, B and C (from [7])

  doi:10.5075/epfl-298799_978-2-9701614-0-0

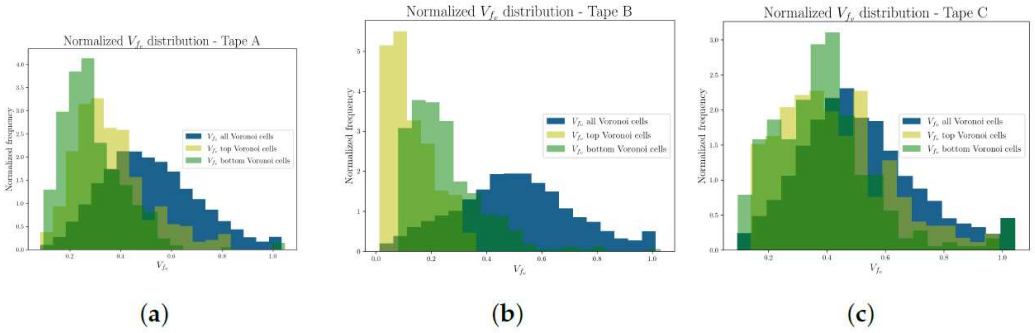

Figure 10. V_{fv} for the entire tape compared to the top and bottom surface for tapes A, B and C (from [7])

5. References

[1] R. Amacher, J. Cugnoni, J. Botsis, L. Sorensen, W. Smith, and C. Dransfeld, "Thin ply composites: Experimental characterization and modeling of size-effects," *Composites Science and Technology,* vol. 101, no. 0, pp. 121-132, 9/12/ 2014.

[2] S. F. Shuler and S. G. Advani, "Transverse squeeze flow of concentrated aligned fibers in viscous fluids," *Journal of Non-Newtonian Fluid Mechanics,* vol. 65, no. 1, pp. 47-74, 1996/07/01/ 1996.

[3] O. Çelik, D. Peeters, C. Dransfeld, and J. Teuwen, "Intimate contact development during laser assisted fiber placement: Microstructure and effect of process parameters," *Composites Part A: Applied Science and Manufacturing,* vol. 134, p. 105888, 2020/07/01/ 2020.

[4] J. Zangenberg, J. B. Larsen, R. C. Østergaard, and P. Brøndsted, "Methodology for characterisation of glass fibre composite architecture," *Plastics, Rubber and Composites,* Conference Paper vol. 41, no. 4-5, pp. 187-193, 2012.

[5] G. Bradski and A. Kaehler, *Learning OpenCV: Computer vision with the OpenCV library*. " O'Reilly Media, Inc.", 2008.

[6] N. Katuin and C. Dransfeld, "UD Microstructural characterisation," no. v1.0. doi: 10.5281/zenodo.5517774

[7] N. Katuin, D. M. J. Peeters, and C. A. Dransfeld, "Method for the Microstructural Characterisation of Unidirectional Composite Tapes," *Journal of Composites Science,* vol. 5, no. 10, p. 275, 2021.

[8] J. Illingworth and J. Kittler, "A survey of the hough transform," *Computer Vision, Graphics, and Image Processing,* vol. 44, no. 1, pp. 87-116, 1988/10/01/ 1988.

[9] K. K. C. Ho, S. R. Shamsuddin, S. Riaz, S. Lamorinere, M. Q. Tran, A. Javaid, and A. Bismarck, "Wet impregnation as route to unidirectional carbon fibre reinforced thermoplastic composites manufacturing," *Plastics, Rubber and Composites,* vol. 40, no. 2, pp. 100-107, 2011/03/01 2011.

[10] C. Hopmann, E. Wilms, C. Beste, D. Schneider, K. Fischer, and S. Stender, "Investigation of the influence of melt-impregnation parameters on the morphology of thermoplastic UD-tapes and a method for quantifying the same," *Journal of Thermoplastic Composite Materials,* p. 0892705719864624, 2019.

[11] S. Gomarasca, D. M. J. Peeters, B. Atli-Veltin, and C. Dransfeld, "Characterising microstructural organisation in unidirectional composites," *Composites Science and Technology,* vol. 215, p. 109030, 2021/10/20/ 2021.

  doi:10.5075/epfl-298799_978-2-9701614-0-0

EXPERIMENTAL STUDY OF OFF-AXIS COMPOSITE LAMINATES SUBJECTED TO DYNAMIC COMPRESSION: THE OPEN HOLE EFFECT

J.M. Rodríguez Sereno, J. Pernas-Sánchez, J.A. Artero-Guerrero, J. López-Puente [a]

a: Department of Continuum Mechanics and Structural Analysis, University Carlos III of Madrid– jpernas@ing.uc3m.es

Abstract: *The Strain Rate dependency of mechanical properties and the failure envelopes for woven CFRP under combined in-plane shear and compressive loading have been analyzed experimentally by quasi-static and dynamic tests. An analytical off-axis failure envelope is obtained by the Maximum Stress Criterion. The increment of the mechanical properties and the evolution of the failure envelope with the increment of the strain rate is studied. The dynamic response is obtained using the Split Hopkinson Pressure Bar under high strain rates (up to 300/s). Moreover, the effect of the stress concentration in compression loading is analyzed by the Open Hole Compression specimens under quasi-static and dynamic loading. The off-axis compressive strengths, rate dependency and damage mechanisms in Open Hole Compression experiments exhibit similar behavior than the previous experiments. The decrements of the compression strength in Open Hole Compression specimens at the same strain rate seems to be related to the area ratio in the damage initiation zone, but not the stress concentrations.*

Keywords: Strain Rate; Split Hopkinson Pressure Bar; Open Hole Compression: Woven fabric carbon composite

1. Introduction

Composite laminates are extensively used in aircraft industry and engineering applications due to their high ratio between mechanical properties and density. In fact, composites in aircraft industry have achieved 50% in terms of weight. However, when subjected to transversal loads such as those generated by impact, unidirectional laminates present large delamination areas. Woven Fabric laminates, although possessing lower mechanical properties in the fiber direction, they exhibit lower delamination areas and higher fracture toughness and impact tolerance.

There is little available information regarding the behavior of plain weave composites at high strain rates. Even that woven composites exhibit an increment of mechanical properties proportional to the loading rate, the research community has not yet agreed to find a solid methodology to describe the impact response.

An experimental study has been performed to describe the behavior of a plain woven CFRP composite in longitudinal, transverse and off-axis compression, at three different strain rate levels (1x103 s-1, 150 s-1 and 300 s-1). Digital Image Correlation (DIC) has been used to obtain the true stress-strain response. Moreover, Open Hole Compression tests have been set up at different rate levels to analyze the open hole effect in specimens loaded in longitudinal and off-axis compression.

  doi:10.5075/epfl-298799_978-2-9701614-0-0

The material system used for this study is a carbon/epoxy preimpregnated AS4-8552-AGP193 plain weave fabric. AGP193-PW represents a perfect balanced woven composite (equal number of fibers in warp and weft direction). To obtain a nominal panel thickness of 4 mm at a given cured ply thickness of 0.2 mm, a layup of [0]20 was chosen.

Quasi-static compression tests on woven CFRP specimens were performed by means of an INSTRON 8516 (100KN). The compression load was applied along the longer direction, with a constant velocity of 1.25 mm/min. Since the nominal specimen length is 20mm the quasi-static strain rate is 1x103 s-1. The experiments were recorded by means of a Basler acA2440 Camera with a resolution of 2404x2056 pixel2. The acquisition rate was configured at 5 fps, whit a shutter speed of 1/5,000 s. VIC-2D software was implemented to obtain the strain field. The DIC pattern was performed implementing the Water-Slide Paper Technique in order to ensure repeatability and accuracy in the strain analysis.

Intermediate and high-rate compression tests were performed using a Split Hopkinson Pressure Bar System. The striker, incident, and transmitted bars, which are made of steel, have a length of 0.5m, 2.6m and 1.4m respectively, using the same diameter (22mm) to balance the impedance. Different sizes for a circled-section copper pulse shaper were used depending on the fiber orientation to ensure a constant strain rate along the dynamic loading. Strain gauges were connected to a Digital Oscilloscope RTB2004 with a frequency of acquisition of 41.7 MHz. A Photron SA-Z high speed camera was used to record the experiments at both loading rates, using a frequency of acquisition of 200,000 fps, with a shutter speed of 1/800,000 s, being able to record a pixel size of 364x160 pixel2. The high-speed camera pictures were imported to the VIC-2D software to analyze the strain field. As explained in QS Set-Up, the DIC pattern was implemented using the Water-Slide Paper Technique, giving us a better understanding of the strains in the CFRP fragment along the experiment.

Quasi-static off-axis experiments allowed us to analyze the material failure envelope. SHPB experiments have given us a better understanding about the strain rate dependency of the woven CFRP, both for mechanical properties and failure envelope. Finally, the open hole compression tests were important to analyze the influence of the stress and strain concentration in dynamic tests.

Figure 1 shows the results of the experiments and the envelope of failure obtained, it is shown how the dynamic effect could be observed in the increasing trend of the strength failure envelope.

  doi:10.5075/epfl-298799_978-2-9701614-0-0

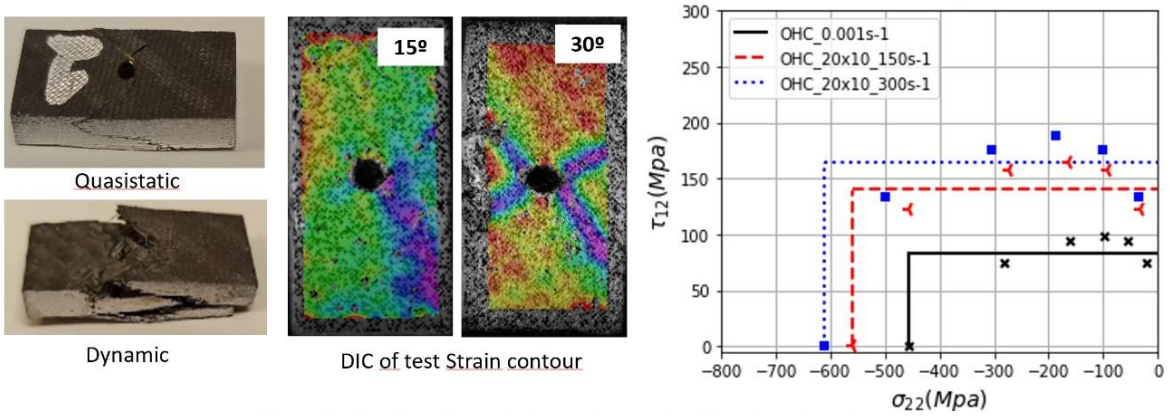

Figure 1. Results of open hole experiments at different strain rates

Acknowledgements

This project has received funding from the Clean Sky 2 Joint Undertaking (JU) under grant agreement No. 886519. The JU receives support from the European Union's Horizon 2020 research and innovation program and the Clean Sky 2 JU members other than the Union.

2. References

1. H. Koerber, J. Xavier, y P. P. Camanho, «High strain rate characterisation of unidirectional carbon-epoxy IM7-8552 in transverse compression and in-plane shear using digital image correlation», Mech. Mater., vol. 42, n.o 11, pp. 1004-1019, nov. 2010, doi: 10.1016/j.mechmat.2010.09.003.
2. Martín-Montal, Jordi, Jesus Pernas-Sánchez, y David Varas. «Experimental Characterization Framework for SLA Additive Manufacturing Materials». *Polymers* 13, n.º 7 (enero de 2021): 1147. https://doi.org/10.3390/polym13071147
3. López-Puente, J., y S. Li. «Analysis of Strain Rate Sensitivity of Carbon/Epoxy Woven Composites». *International Journal of Impact Engineering*, Advances in Impact Mechanics in Honour of Professor Steve Reid, 48 (1 de octubre de 2012): 54-64. https://doi.org/10.1016/j.ijimpeng.2011.05.008.

  doi:10.5075/epfl-298799_978-2-9701614-0-0

LIGHT-WEIGHT NEW GENERATION OF GRAPHENE/POLYMER NANOCOMPOSITES FOR HYDROGEN STORAGE

Mufeng Liu[a], Kailing Lin[a], Mingyu Zhou[a], Ian A. Kinloch[a]

a: National Graphene Institute, Henry Royce Institute and Department of Materials, School of Natural Sciences, The University of Manchester, Oxford Road, Manchester M13 9PL, UK– mufeng.liu@manchester.ac.uk

Abstract: *Polypropylene is one of the most widely-applied materials for automobile industries, and graphene-related materials have shown extraordinary properties in gas barrier, owing to its unique 2 dimensional geometry and high aspect ratio. Herein, we have incorporated graphene-related materials into a high-molecular-weight polypropylene, aiming at developing vessels for hydrogen storage. We have compared two different types of fillers AVA 0312 (reduced graphene oxide developed Avanzare) and BeD-graphene (graphene nanoplatelets developed by BeDimensional). The surface area of the two nanomaterials was determined by the BET test, which showed that the AVA0312 possesses significantly higher surface area than BeD-graphene. The hydrogen permeability of the materials was effectively reduced by the addition of graphene-based fillers. Overall, the experimental results show a promise of the light-weight, low-cost and easily-prepared polypropylene/graphene nanocomposites to be developed for the next generation hydrogen storage for transportation industry.*

Keywords: graphene; nanocomposites; hydrogen storage; polymer;

1. Introduction

The challenge of global climate change demands green energy consumption for automobile and other types of transportation. An ideal option is to use hydrogen to replace fossil fuels as an energy source, which requires new generation of light-weight materials with excellent hydrogen barrier properties. Polypropylene has been the most widely applied material for automobile industries. Graphene-related materials have shown extraordinary properties in gas barrier, owing to its unique two dimensional geometry and high aspect ratio [1].

Herein, we have incorporated graphene-related materials into a high-molecular-weight polypropylene, aiming at developing vessels for hydrogen storage. We have compared two different types of fillers AVA 0312 (reduced graphene oxide developed Avanzare) and BeD-graphene (graphene nanoplatelets developed by BeDimensional). The composition of the two nanoparticles was checked by XPS, confirming low oxygen content of both fillers. The surface area of the two nanomaterials was determined by the BET test, which showed that the AVA0312 possesses significantly higher surface area than BeD-graphene. The GRM-reinforced polypropylene nanocomposites was successfully prepared by melt mixing and hot press. The actual filler content was checked by thermogravimetric analysis (TGA). The crystallinity of the materials was measured by differential scanning calorimetry (DSC), suggesting the increase of crystallinity of the polypropylene with increasing filler content. The nanoscale morphology of the nanocomposites was examined by transmission electron microscopy (TEM), indicating the graphene substances were well-dispersed in the polymer matrix. We evaluated the hydrogen

  doi:10.5075/epfl-298799_978-2-9701614-0-0

permeability of the materials using a locally-made permeability rig [2]. The hydrogen permeability of the materials was effectively reduced by the addition of graphene-based fillers. The results indicated higher efficiency of improving the gas barrier properties for the reduced graphene oxide than the graphene nanoplatelets, possibly owing to the higher surface area of the AVA0312 that was confirmed by the BET test. Overall, the experimental results show a promise of the light-weight, low-cost and easily-prepared polypropylene/graphene nanocomposites to be developed for the next generation hydrogen storage for transportation industry.

2. Experimental method

2.1 Materials and preparation

Reduced graphene oxide (coded as AVA-0312) was provided by Avanzare Ltd and used as received. Graphene nanoplatelets (BeDimensional) was provided by BeDimensional and used as received. The polypropylene (Mw~) granule pellets was purchased from Sigma-Alderich and used as received.

The nanocomposite sample were prepared by melt mixing in an internal mixer, followed by compression molding. The melt mixing took place at 190 °C at 70 rpm for 5 minutes. The weight percentage of AVA-0312 filler was 0.5, 1, 1.5 and 2.5 wt%, while the loading of BeDimensional GNP was 1, 2.5, 5, and 10 wt%. The samples throughout the manuscript are coded as the composition of the materials and the weight percentage of the filler. For example, PP-BeD10 stands for the PP and BeDdimensional mixture where '10' means the nominal weight fraction of the filler is 10 wt%.

The compression molding was conducted at a hydraulic pressure of 30 bars for 5 minutes followed by a fast water cooling to the room temperature, while the pressure was kept at 30 bars during the cooling procedure. The thickness of the compression molded sheets was around 1 mm, controlled by the mold. The samples were then stamped into disc shape with a diameter around 10 mm for the gas permeability testing.

2.2 Characterizations

X-ray Photoelectron Spectroscopy (XPS) was carried out to determine the elemental compositions of the fillers, using an Axis Ultra Hybrid spectrometer (Kratos Analytical, Manchester, United Kingdom) with monochromated Al Kα radiation (1486.6 eV, 10 mA emission at 150 W, spot size 300 x 700 µm) with a base vacuum pressure of ~5×10^{-9} mbar. Charge neutralisation was achieved using a filament. Binding energy scale calibration was performed using C-C in the C 1s photoelectron peak at 285 eV. Analysis and curve fitting was performed using Voigt-approximation peaks using CasaXPS.

The specific surface area was determined by N_2 adsorption at 77 K with BET (Brunauer, Emmett and Teller) method using Quadrasorb EVO surface area and pore size analyzer.

The actual filler loadings of the samples were checked by Jupiter STA 449 thermogravimetric analyzer (TGA) from room temperature to 800 °C in an atmosphere of N_2 at a heating rate of 10 °C/min. The equipment was employed to investigate the melting and crystallization behavior. Samples of about 10 mg were heated, cooled and re-heated between 30°C and 200°C using a heating/cooling rate of 10 °C/min, under a nitrogen flow of 50 ml/min.

A FEI Tecnai G2 20 (LaB6) transmission electron microscope (TEM) was employed to examine the nanoscale morphology of the nanocomposites, which was operated at an acceleration voltage of 200 kV. Thin sections of the samples (neat PP and highest loadings of the nanocomposites) with a thickness of 80 nm were prepared using a diamond knife mounted on an ultramicrotome. The cutting procedure was performed at room temperature at the out-of-plane direction of the compression molded sheets.

The hydrogen (H_2) permeability was measured using a differential pressure testing system (Fig.1), in accordance with standard BS ISO 15105-1:2007. The gas permeability (P) was determined by the following equation [2]:

$$P = \frac{V_{LP}}{R \times T_K \times p_{HP} \times A} \times \frac{dp_{LP}}{dt} \times h \quad (1)$$

where V_{LP} is the volume of the low-pressure chamber, R is the gas constant $8.31 \times 10^3\ J \cdot K^{-1} \cdot mol^{-1}$), T_K is the thermodynamic temperature, p_{HP} is the pressure of the high-pressure chamber, A is the transmission area of the specimen, dp_{LP}/dt is the pressure change per unit time of the low-pressure chamber and h is the thickness of the specimen.

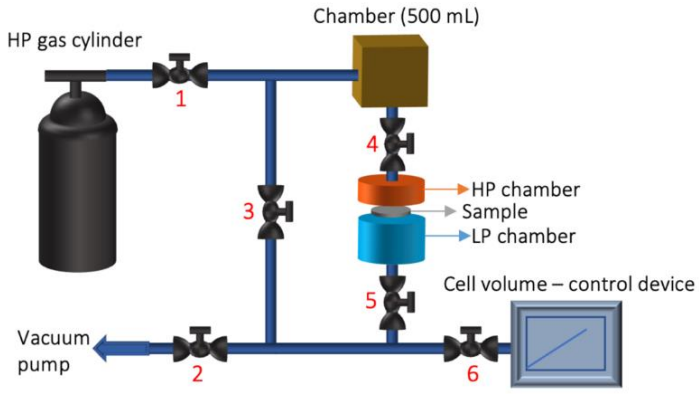

Figure 1. Schematic diagram of the H_2 gas permeability rig, numbers 1-6 refer to the valves; HP and LP stand for high pressure and low pressure, respectively.

3. Result and discussion

3.1 Analytical characterizations

Regarding the neat fillers, elemental analysis was performed using XPS, in order to check the oxygen ratio and other possible elements that might be presented in the fillers. The surface area of the two graphene-based nanomaterials was also determined using BET. The results can be seen in Table 1. It was found that both nanofillers contain low oxygen ratios. The BeD graphene possesses low content of nitrogen while AVA 0312 contains very low ratio of sulphur. The BET surface area of BeD (~6.5 m^2/g) has shown significant lower value than AVA 0312 (137.2 m^2/g). This factor is particularly crucial in determining the end properties of the nanocomposites [3]. The difference of the H_2 permeability will be discussed in the latter section.

  doi:10.5075/epfl-298799_978-2-9701614-0-0

Table 1: Results of elemental ratio and BET surface area of the neat filler.

Filler	Element (%)	BET surface area (m^2/g)
BeD	C (96.34), O (2.46), N (1.21)	6.5
AVA	C (96.22), O (3.64), S (0.14)	137.2

With respect to the molded samples of the nanocomposites, the actual loadings of the fillers were checked by TGA, and the crystallinity of the PP/graphene nanocomposites was determined by DSC. The results can be seen in Table 2. It can be found that the actual mass fraction of the filler is quite close to the nominal weight percentage that was mixed into the polymer. The volume fractions of the filler were then calculated by the equation,

$$V_f = \frac{w_f \rho_m}{w_f \rho_m + (1 - w_f)\rho_f} \quad (2)$$

where w_f is the mass fraction of the filler, ρ_m (=0.905 g/cm^3) and ρ_f (=2.2 g/cm^3) are the densities of the matrix and the filler, respectively.

The enthalpy of melting of all samples was measured by DSC, in order to calculate the crystallinity of the nanocomposites. The crystallinity of the samples is given by,

$$X_c = \Delta H_f / \Delta H_{f0} \times 100\% \quad (3)$$

where ΔH_f is enthalpy of fusion of the sample and ΔH_{f0} is the enthalpy of fusion of 100% crystalline isotactic PP (170 J/g [4]). It was shown that the addition of the graphene increased the crystallinity of PP in general. However, the increase of the crystallinity by addition of BeD graphene was more related to the filler loadings, while the addition of AVA graphene increased the crystallinity of PP by approximately 7% but did increase gradually with increasing filler loadings.

  doi:10.5075/epfl-298799_978-2-9701614-0-0

Table 2: Mass fraction, volume fraction, enthalpy of melting and crystallinity obtained and calculated from the results of TGA and DSC.

Sample	Mass fraction of the filler (%)	Volume fraction of the filler (%)	Enthalpy of melting (J/g)	Crystallinity (%)
PP	0	0	82.8	48.7
PP-BeD1	0.45 ± 0.08	0.18 ± 0.04	90.9	53.5
PP-BeD2.5	2.64 ± 0.08	1.10 ± 0.04	93.5	55.0
PP-BeD5	4.02 ± 0.06	1.68 ± 0.03	94.7	55.7
PP-BeD10	10.64 ± 0.08	4.64 ± 0.04	106.6	62.7
PP-AVA0.5	0.36 ± 0.06	0.18 ± 0.03	82.8	55.4
PP-AVA1	0.76 ± 0.11	0.36 ± 0.05	94.1	55.2
PP-AVA1	0.94 ± 0.06	0.49 ± 0.03	93.9	55.9
PP-AVA2.5	1.83 ± 0.06	0.90 ± 0.03	95.0	52.1

3.2 Microstructure

The microstructure of the neat polymer and the highest loadings of the two nanocomposites was examined by TEM that are shown in Fig.2. It can be seen that the AVA graphene displayed a significantly more homogeneous dispersion than BeD graphene, which could contribute to a better efficiency of gas barrier improvement.

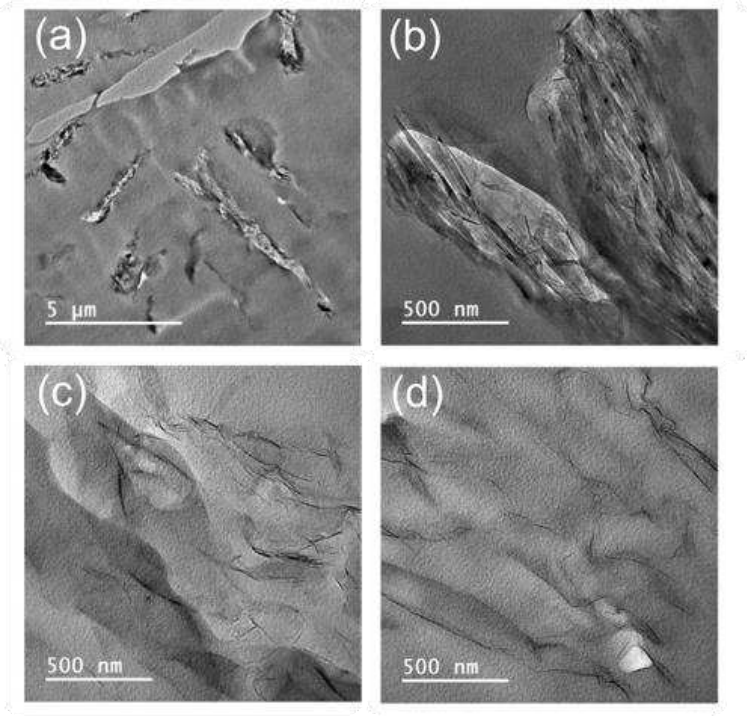

Figure 2. TEM images of (a, b) PP-BeD10 and (c, d) PP-AVA2.5.

  doi:10.5075/epfl-298799_978-2-9701614-0-0

3.3 Gas permeability

The gas permeability was measured by a homemade permeability rig that was shown in Fig.1. The permeability of H_2 of all samples was in the order of ~10^{-15} mol.m/(m^2.s.Pa), which is consistent with the data in literature for polymers [5]. It can be seen that the addition of both fillers contributed to a reduction in the H_2 permeability. The mechanism of the reduction of the permeability of H_2 can be explained by the increased tortuosity of the path that the gas molecules had to travel due to the addition of the 2D materials. Herein, we use a well-known Nielsen's model to fit the data as can be seen in both figures. The permeability of the 2D materials filled nanocomposites (P_c) is given by [6],

$$P_c = P_m \cdot \frac{1-V_f}{1+\frac{s}{2}\cdot V_f} \quad (4)$$

where P_m is the permeability of the neat matrix, s is the aspect ratio of the filler and V_f is the volume fraction of the filler. The tortuosity factor is $(1+\frac{s}{2}\cdot V_f)$, based on Nielsen's model [6]. It should be noted that the Nielsen's model employed here describes a specific ideal case, which should be the lower bound of the permeability of a filled composite. In the figure, therefore, we quoted Nielsen aspect ratio (s_N), emphasizing that the values of the aspect ratio here was the ones that fitted by the model, which should be differentiated from the actual aspect ratio of the filler. We can see that the improvement of H_2 barrier properties by AVA graphene indicated a significantly higher efficiency than that of BeD graphene, possibly due to their better dispersion in nanoscale. The Nielsen aspect ratio given by eq.(4) was ~170 for AVA graphene and approximately 10 times higher than BeD graphene (only ~18). Hence, we can summarize that the AVA0312 (rGO-based graphene) performed better than BeD (graphene nanoplatelets (GNP)-based graphene). The main difference that we have characterized between these two nanomaterials was the BET surface area. It can be concluded that the neat graphene with higher surface area may result in better gas barrier improvement.

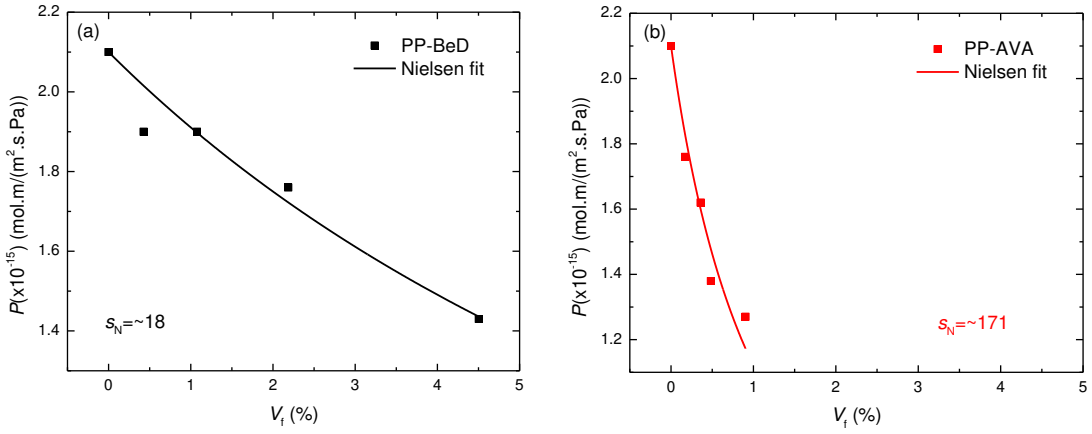

Figure 3. H_2 Permeability of (a) PP-BeD samples and (b) PP-AVA samples. The results of both samples were fitted by Nielsen's model, giving an aspect ratio of BeD graphene of ~18 and that of AVA graphene of ~171.

  doi:10.5075/epfl-298799_978-2-9701614-0-0

4. Conclusion

Polypropylene/graphene nanocomposites were successfully prepared by melt mixing and molded by hot press. The actual loadings of the fillers were consistent with the nominal loadings that were added. The characterization of the graphene-based materials indicated that the main difference between the neat fillers is their surface area, where AVA graphene displayed much higher value of BET than BeD graphene, which is possibly due to their preparation routes (AVA is rGO, while BeD is graphene nanoplatelets). The addition of both graphene products increased the crystallinity of PP. The TEM images have successfully shown the difference of the nanostructure of the nanocomposites between the two samples. The BeD has shown a micro-scale dispersion while the AVA displayed a nanoscale dispersion in the polymer. The different level of dispersion was found to determine the H_2 permeability of the nanocomposites. AVA0312 graphene has shown a significantly higher efficiency in the improvement of H_2 barrier properties than BeD graphene. The key factor determining the gas barrier improvement was believed to be the surface area and the degree of dispersion of the filler. Higher surface area and better dispersion of the 2D materials gives rise to a higher value of effective aspect ratio modelled by Nielsen's model. Overall, graphene-based polymer shows a promise in fabrication of liners for gas vessel, which could be developed into the next generation of hydrogen storage.

Acknowledgements

The authors acknowledge the support from "Graphene Core 3" GA: 881603 which are implemented under the EU-Horizon 2020 Research & Innovation Actions (RIA) and are financially supported by EC-financed parts of the Graphene Flagship. Ian A. Kinloch also acknowledges the Royal Academy of Engineering and Morgan Advanced Materials. All research data supporting this publication are available within this publication.

5. References

1. Papageorgiou, D. G.; Kinloch, I. A.; Young, R. J., Mechanical properties of graphene and graphene-based nanocomposites. *Progress in Materials Science* **2017,** *90*, 75-127.
2. Liu, M.; Cataldi, P.; Young, R. J.; Papageorgiou, D. G.; Kinloch, I. A., High-performance fluoroelastomer-graphene nanocomposites for advanced sealing applications. *Composites Science and Technology* **2021,** *202*, 108592.
3. Kovtun, A.; Treossi, E.; Mirotta, N.; Scidà, A.; Liscio, A.; Christian, M.; Valorosi, F.; Boschi, A.; Young, R. J.; Galiotis, C.; Kinloch, I. A.; Morandi, V.; Palermo, V., Benchmarking of graphene-based materials: real commercial products versus ideal graphene. *2D Materials* **2019,** *6* (2), 025006.
4. Lanyi, F. J.; Wenzke, N.; Kaschta, J.; Schubert, D. W., On the Determination of the Enthalpy of Fusion of α-Crystalline Isotactic Polypropylene Using Differential Scanning Calorimetry, X-Ray Diffraction, and Fourier-Transform Infrared Spectroscopy: An Old Story Revisited. *Advanced Engineering Materials* **2020,** *22* (9), 1900796.
5. Su, Y.; Lv, H.; Zhou, W.; Zhang, C., Review of the Hydrogen Permeability of the Liner Material of Type IV On-Board Hydrogen Storage Tank. *World Electric Vehicle Journal* **2021,** *12* (3), 130.
6. Nielsen, L. E., Models for the Permeability of Filled Polymer Systems. *Journal of Macromolecular Science: Part A - Chemistry* **1967,** *1* (5), 929-942.

EXPERIMENTAL AND NUMERICAL VALIDATION OF AN INTER-PLY FRICTION MODEL FOR THERMOSET BASED FIBRE METAL LAMINATE UNDER HOT-PRESSING CONDITIONS

Shichen Liu[1*], Jos Sinke[1], Clemens Dransfeld[1]

[1]Aerospace Manufacturing Technologies Group, Faculty of Aerospace Engineering, Delft University of Technology, Delft, The Netherlands

*Presenting Author: S.Liu-7@tudelft.nl

Abstract: *Hot-pressing can be an attractive fabrication method that enables the forming of hybrid materials like thermoset based fibre metal laminates. However, the process simulation on press forming requires accurate material characterization and boundary conditions to facilitate part design for a defect-free component. In order to improve the overall predictive simulation quality, the inter-ply sliding at metal-prepreg interfaces which is one of the critical deformation mechanisms is considered. An inter-ply friction model has been established using an experimental friction test apparatus and the effect of slip rate, normal force and temperature is taken into consideration. To validate the proposed friction model, a comparative study between results obtained from the numerical model and the experimental ones is carried out. The research demonstrates that the inter-ply friction model can be a valuable building block for the finite element simulation of the hot-pressing process for thermoset based fibre metal laminates.*

Keywords: Fibre metal laminates (FMLs); Inter-ply friction; Hot-pressing; Numerical simulation

1. Introduction

Fiber metal laminates are lightweight composites made by alternative layers of fibre reinforced materials and metal alloy sheets. The hybrid structures can be used for different properties using various constituents and the combination has superior performance over their individual layers [1,2]. Conventional approaches like lay-up techniques and autoclaves can only manufacture FML parts with a relatively simple shape, having large radiuses like aircraft fuselages. The main reason is that the deformability of the hybrid laminates is limited by the small failure strain of the fibres and the failure modes of the laminates [3]. Therefore, this research puts forward a methodology which combines hot-pressing and subsequent curing process in one cycle using the same mould to achieve better performance without the occurrence of fractures, wrinkles or other possible defects [4,5]. The proposed hot-pressing process is shown in Fig.1. Prior to the hot-pressing and curing steps, the uncured laminate is stacked and pre-heated which decreases the resin viscosity and eases the deformation of the prepreg, in particular inter-ply friction. However, temperature and time are two critical factors that need to be carefully controlled as the initiation of epoxy resin cure would increase the stiffness of the prepreg and constrain deformation. The process combines sheet metal forming and composite forming technologies for manufacturing the final product without losing much mechanical performance. Therefore, both the deformation modes of these two materials should be considered in order to improve the formability of the fibre metal laminates. The metal sheets are usually deformed into 3D shapes by bending and in-plane plastic deformation, while the deformation of fibre prepregs is achieved by allowing the

  doi:10.5075/epfl-298799_978-2-9701614-0-0

individual layers to deform through intra-ply shear within the prepregs and inter-ply sliding in-between the metal sheets and prepregs.

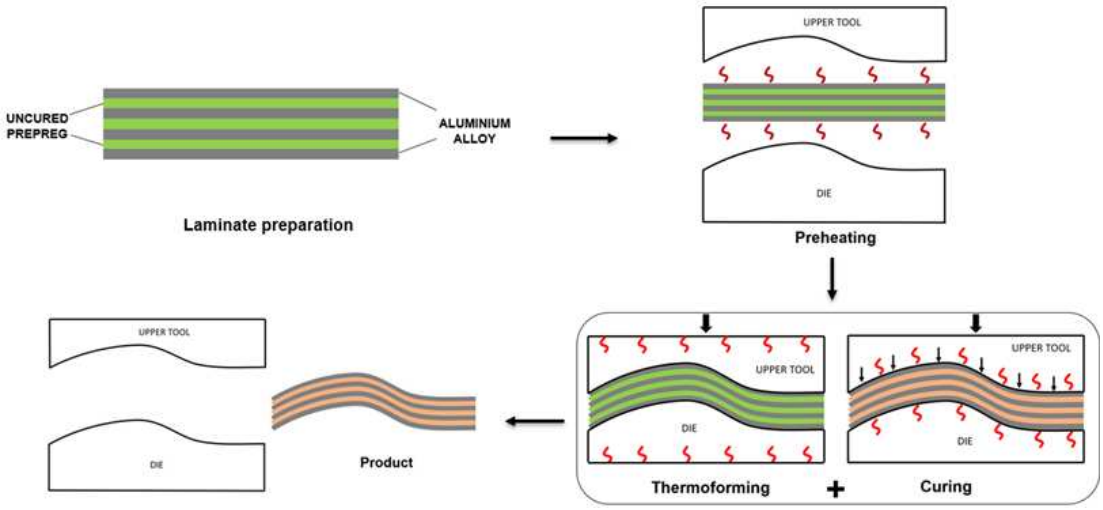

Figure 1. Proposed hot-pressing process of thermoset based fibre metal laminate manufacturing

The finite element modelling of fibre metal laminates can be approached mainly in three ways: micro-level, meso-level and macro-level. For the micro-level approach, individual materials are differentiated in the model consisting of fibres and matrix. This is the most complex but realistic approach as it requires partitioning the model into different pieces [6]. The meso-level approach regards the laminate as a system of independent layers with specific homogenized mechanical properties. This approach results in an effective modelling for all type of hybrid laminates as it requires relatively limited number of elements. Although there are some simplifications which skips the issue of layer boundary conditions, it would not affect the laminate performance unless delamination or other failure phenomena occur [7,8]. The macro-level approach describes the entire hybrid laminate as a homogenized material with anisotropic properties. This approach can be described as a simple generalization since only a few engineering constants are needed. The biggest problem for this method is to obtain the data of the homogenized material as the replacement for the hybrid laminate. One of the possible solutions is the application of Classical Laminate Theory which enables the description of their behaviour under external loads based on the engineering constants, representing membrane, bending and coupling behaviour, or by the uniaxial tensile test of the specimen in order to obtain the constant data in the theory [9,10]. Moreover, process simulation of the hot-pressing of fibre metal laminates requires an accurate mathematical description of the main deformation mechanisms such as intra-ply shear, inter-ply sliding as well as bending [11]. None of these mechanisms is negligible or dominant, as the laminate deformability is supposed to be a result of a delicate balance among them [12]. Therefore, more advanced material constitutive models and boundary conditions of each deformation mechanisms are required to improve the predictive quality for manufacturing.

This research aims to develop a homogenized meso-level model for inter-ply friction in the hot-pressing process and implement it into numerical software Abaqus for validation. The inter-ply friction mechanism at the metal-prepreg interfaces of glass fibre reinforced aluminium laminate (GLARE) is investigated experimentally. Then, the meso-level approach coupled with the friction contact model for numerical simulation is established. As the current frictional models neglect the effect of any transient which greatly influence the predictive quality [13,14], a static-kinetic

  doi:10.5075/epfl-298799_978-2-9701614-0-0

exponential decay equation is used to model the transition from static to kinetic friction under different conditions such as temperature, sliding rate and normal force in order to include the initial transient response into the inter-ply friction model. The coefficients of static and kinetic friction are obtained by a novel experimental friction test as the values are key indicators of the initial and steady transient response. To validate the ability of the proposed friction models for replicating the response of the inter-ply friction test, numerical software ABAQUS which allows for the implementation of user-defined frictional behaviour via a subroutine is applied. Also, the results of the stress-displacement response are analysed and compared with the commonly used cohesive zone model and penalty friction model with steady response. The establishment of the inter-ply friction model provides deep insights into the underlying deformation mechanism of fibre metal laminate under various hot-pressing conditions.

2. Materials and methods

The hybrid material involved in this work was the aerospace graded fibre metal laminate named as GLARE-glass fibre reinforced aluminium laminate. The experimental sample presented in Fig.2 consists of three layers of 0.5-mm thick 2024-T3 aluminium sheets and two layers of glass fibre reinforced prepreg S2-glass/FM-94 epoxy. Each fibre layer included two unidirectional prepreg plies with a nominal thickness of 0.18 mm. The unidirectional fibre ply oriented at zero direction corresponded with the rolling direction of the aluminium sheet. Prior to assembling, aluminium surface was pre-treated with chromic acid anodizing and BR 127 primer for corrosion protection [15-17] since the surface treatment has a great influence on the friction studied in the research.

In this work, an inter-ply friction test was chosen as the experimental procedure. It was designed by modifying the ASTM D3528 standard which is used to determine the shear strengths of adhesives for bonded metals [18]. The schematic diagram and dimension for the test sample is presented in Fig.2 and the normal force is applied on top and bottom layers by a clamping loadcell. Besides, the preheat temperature inside the chamber and the sliding rate for pull-out can be set through manual input. The friction test apparatus which allows for testing at various conditions, was designed for the measurement of inter-ply friction coefficient at metal-prepreg interface. Instead of bonding and curing through standard autoclave cycle, the uncured prepreg layer could slide along the pre-treated aluminium sheet under specific normal loads. The heated resin was not only the matrix material of the resulting prepreg but also acted as a lubricant when the prepreg slides between two metal plates. To investigate the effects of different parameters on the friction coefficient at the metal-prepreg interface, a set of values were chosen in Table 1. Experiments were conducted varying two parameters at a time while keeping the other at their baseline values.

Table 1: Test parameters used for inter-ply friction tests .

Parameter	Baseline value	Additional values investigated
Normal force (N)	500	100,200,300,600,1000
Sliding rate (mm/min)	10	5,15,20,30,40
Temperature (℃)	23	40,60,80,100,120

  doi:10.5075/epfl-298799_978-2-9701614-0-0

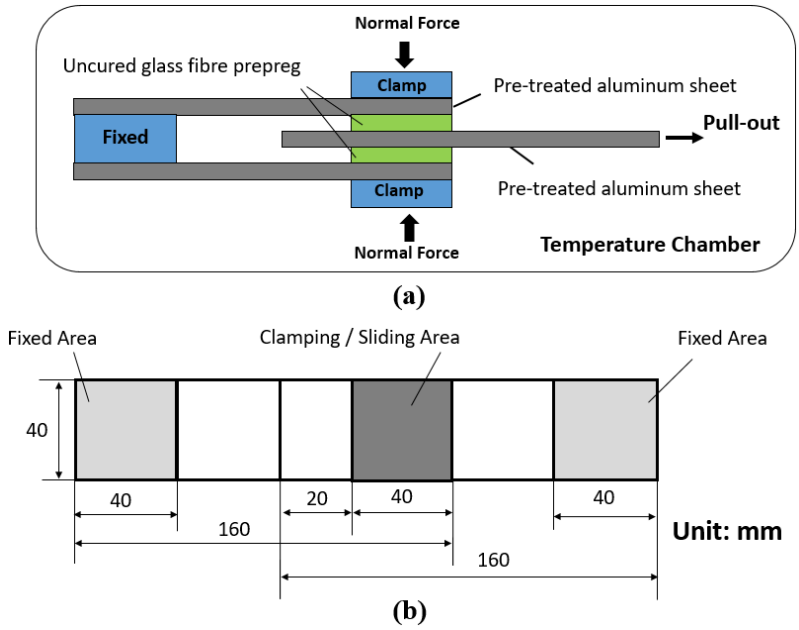

Figure 2. Schematic diagram (a) and dimension (b) for the designed inter-ply friction test

For the numerical verification, a finite element model of the experimental friction setup was done with Abaqus. The finite element model shown in Fig.3 includes two outer aluminium sheets fixed at one end and a middle aluminium sheet pulled out from the other end, together with two alternating glass fibre prepreg layers. A normal force was applied on the outer aluminium surfaces and the sizes as well as thicknesses were the same as the experimental setups. To simplify the setup and reduce computation time, the two material constituents were modelled as deformable bodies with four-node bilinear plane stress quadrilateral elements (CPS4R) and with a mesh size of 1 mm. Such laminate model was represented in the composite layup module where all layers and material parameters like orientation, thickness, property and relative location was defined. The inter-ply friction model used a static-kinetic exponential decay equation to simulate surface to surface contact instead of constant friction coefficient value. Values of static and kinetic friction coefficient were obtained by an experimental friction test and the decay constant was calculated to best fit the experimental data points [19]. A cohesive zone model with contact elements was compared for validation. The interface properties of the cohesive layers were gathered from literatures and the interfacial delamination can be modelled based on cohesive law by adopting a softening relationship between traction and separation [20].

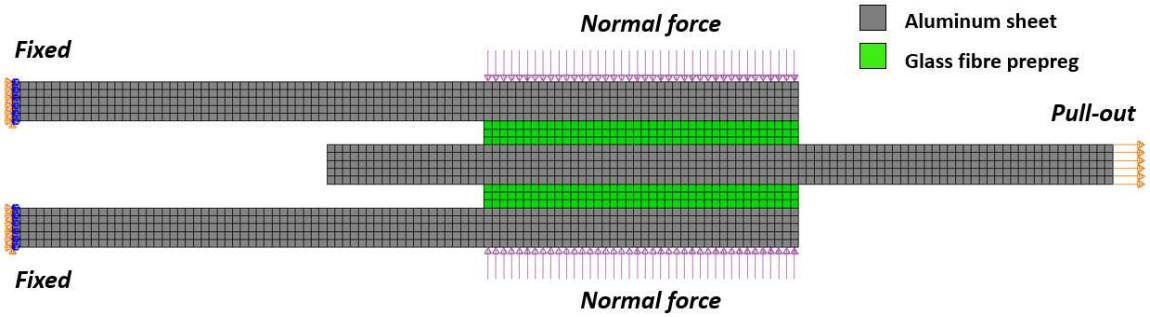

Figure 3. Finite element model for the inter-ply friction test of fibre metal laminates

  doi:10.5075/epfl-298799_978-2-9701614-0-0

3. Results and discussion

3.1 Numerical implementation of experimental results

For the inter-ply friction behaviour, the graph of Fig.4 validated that the numerical model can capture a peak state as it was associated with the static friction and a steady sliding state for the kinetic friction. Both results revealed that friction coefficient increases with the increasing sliding rate and this relationship suggested that the friction was characterised by the Newtonian shearing of the epoxy matrix where shear stresses increase with the increasing shear rate. In contrast, the friction decreases with the increasing normal force and explanation can be that at low normal forces, interface between the fibre reinforced prepreg and aluminium sheet has a relatively rough surface contact with high asperities. While higher normal force can result in the resin percolation as well as a better film of slippage, and thus decrease the friction coefficients. Fig.4(b) revealed that the static and kinetic friction coefficients decrease as the test temperature increases from the temperature of 40℃ to 120℃. The reason for that is mainly due to the lower viscosity and increased lubrication as resin squeezing out when the temperature increases. More details can be found in reference [19]. The Fig.4 also showed that static friction coefficient and onset sliding displacement obtained from the model does not correspond exactly to the experimental data, and the model observed a steady kinetic friction at the early stage of displacement while the experimental coefficient of friction continues to drop slightly. This small difference can be ignored due to the inevitable experimental errors and the numerical model can thus be regarded as a good solution to predict the inter-ply friction accounting for the variations in sliding rate, normal force and temperature of the preformed fibre metal laminates.

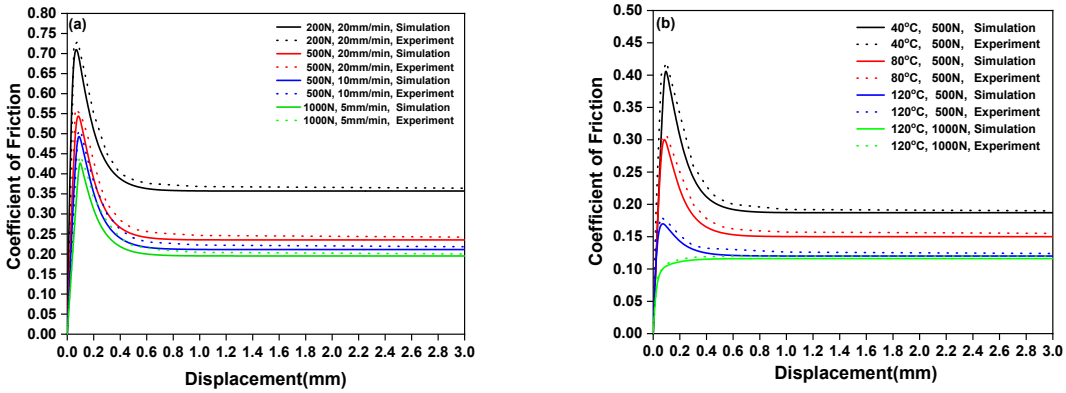

Figure 4. Comparison between numerical and experimental results for inter-ply friction of fibre metal laminates: (a) At room temperature 23 ℃; (b) At sliding rate 10 mm/min

3.2 Comparison with other numerical models

To further validate the accurate response of the applied static-kinetic friction model, two other numerical models for simulating the inter-ply contact behaviour were compared. The stress and displacement curves for the three models under specific conditions are presented in Fig.5. The penalty friction model was set at a steady friction coefficient value of 0.2 and a normal force of 500N, while the cohesive zone model was performed with the shear stiffness of 10^5 MPa/mm, maximum shear strength of 50 MPa and fracture toughness of 0.2 N/mm. It was obviously seen from the figure that the value of stress for the cohesive zone model during the sliding period is

not in the same order of magnitude as the other two friction models, and the maximum stress is reached at a smaller displacement. This is because the cohesive zone model is essentially equivalent to tie constraint where the initial slide of aluminium sheet causes the layer separation or even fracture with extremely high shear stress. Fig.6(a) shows the delamination at the metal-prepreg interfaces when the cohesive zone model was applied. This failure mode may limit the deformability of fibre metal laminate as it was more like a cured sample. Therefore, the cohesive zone model was not suitable to simulate the inter-ply contact at various hot-pressing conditions. As for the penalty friction model, there is no difference in the steady sliding state compared with the static-kinetic friction model even though stress concentration occurs in the initial sliding area (Fig.6(b)). However, the initial transient response behaved differently where no obvious static state was found. This was more likely to occur at higher temperature with lower resin viscosity shown in the inter-ply friction tests. Therefore, the penalty friction model was inappropriate for simulating the inter-ply sliding behaviour under all the hot-pressing conditions. After comparing with the two numerical models, the static-kinetic friction model was proved to be the best-fit to accurately model the inter-ply friction of fibre metal laminate in actual hot-pressing process.

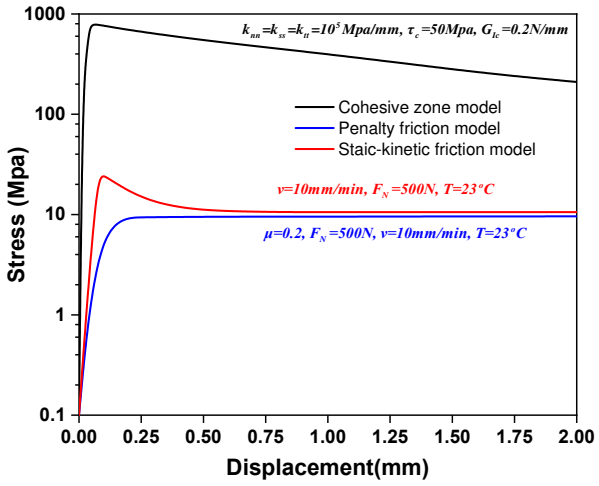

Figure 5. Comparison of three numerical models at the metal-prepreg interface

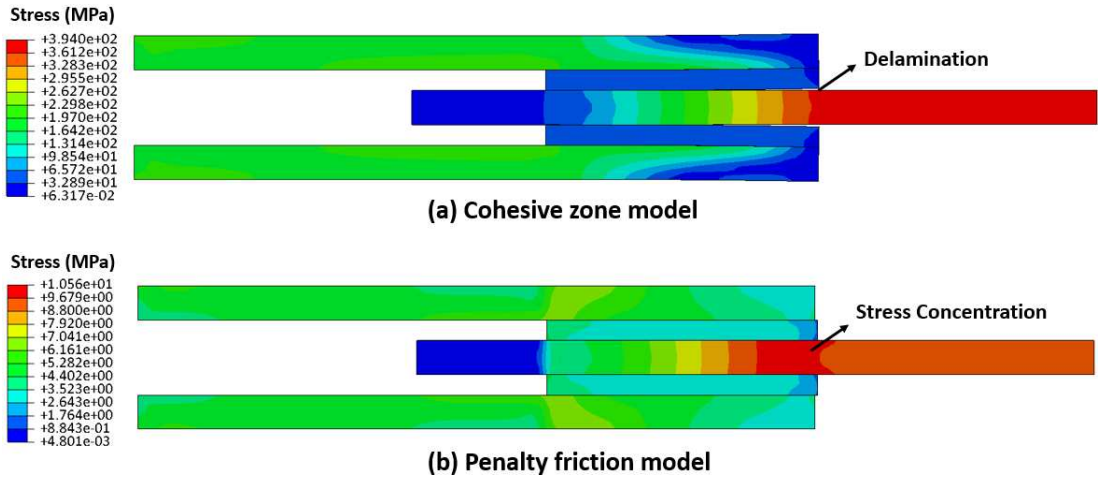

Figure 6. Numerical results of two different contact models at the displacement of 1 mm

4. Conclusion

In the present work, the friction coefficient at metal-prepreg interfaces for fibre metal laminate under various hot-pressing conditions was measured using a novel friction-test apparatus. A static-kinetic friction model for the prediction of the inter-ply friction behaviour of fibre metal laminate was established and validated. The proposed model was able to predict initial transient response and transition from static to kinetic friction under different parameters such as sliding rate, temperature and normal force. The friction coefficient-displacement trends predicted by the numerical model correlated well to those determined through experimental test. Moreover, two other numerical models for simulating the inter-ply contact of fibre metal laminates were proposed. The cohesive zone model was proved to be insufficient as the shear stress was too high and delamination was prone to occur. The penalty friction model can model the kinetic friction during the steady sliding state, while the initial transient response was neglected thus cannot be applied under all hot-pressing conditions. As a result, the inter-ply friction model can be a valuable building block for the finite element simulation of the hot-pressing process for thermoset based fibre metal laminates.

Acknowledgements

The presenting author would like to thank the financial supports of China Scholarship Council (No.201906040174).

5. References

1. Asundi A, Choi AYN. Fiber metal laminates: An advanced material for future aircraft. J Mater Process Technol. 1997;63(1-3):384-394.
2. Sinmazçelik T, Avcu E, Bora MÖ, Çoban O. A review: Fibre metal laminates, background, bonding types and applied test methods. Mater Des. 2011;32(7):3671-3685.
3. Sinke J. Manufacturing of GLARE Parts and Structures. Appl Compos Mater. 2003;10(4-5):293-305.
4. Sinke J. Feasibility of tailoring of press formed thermoplastic composite parts. AIP Conf Proc. May, 2018.
5. Ersoy N, Potter K, Wisnom MR, Clegg MJ. An experimental method to study the frictional processes during composites manufacturing. Compos Part A Appl Sci Manuf. 2005;36(11):1536-1544.
6. P. Linde, J. Pleitner, H. de Boer, and C. Carmone. Modelling and Simulation of Fibre Metal Laminates. ABAQUS Users Conf, pp. 421–439, 2004.
7. Soltani P, Keikhosravy M, Oskouei RH, Soutis C. Studying the tensile behaviour of GLARE laminates: A finite element modelling approach. Appl Compos Mater. 2011;18(4):271-282.
8. Zal V, Moslemi Naeini H, Sinke J, Abouhamzeh M, Benedictus R. A new procedure for Finite Element simulation of forming process of non-homogeneous composite laminates and FMLs. Compos Struct. 2017;163:444-453.
9. Boisse P, Buet K, Gasser A, Launay J. Meso/macro-mechanical behaviour of textile reinforcements for thin composites. Compos Sci Technol. 2001;61(3):395-401.
10. Smolnicki M, Stabla P. Finite element method analysis of fibre-metal laminates considering different approaches to material model. SN Appl Sci. 2019;1(5):1-7.
11. Haanappel SP. Forming of UD Fibre Reinforced Thermoplastics. Univeristy of Twente, 2013.

  doi:10.5075/epfl-298799_978-2-9701614-0-0

12. Sachs U, Akkerman R, Fetfatsidis K. Characterization of the dynamic friction of woven fabrics: Experimental methods and benchmark results. Compos Part A Appl Sci Manuf. 2014;67:289-298.
13. Mosse L, Compston P, Cantwell WJ, Cardew-Hall M, Kalyanasundaram S. The development of a finite element model for simulating the stamp forming of fibre-metal laminates. Compos Struct. 2006;75(1-4):298-304
14. Jauffrès D, Sherwood JA, Morris CD, Chen J. Discrete mesoscopic modeling for the simulation of woven-fabric reinforcement forming. Int J Mater Form. 2010;3:1205-1216.
15. Sun L. Thermal Rheological Analysis of Cure Process of Epoxy Prepeg. Dep Chem Eng. 2002;PhD:127.
16. Solvay Adhesive Materials. Technical Data Sheet for FM-94 Film Adhesive. https://www.solvay.com/en/product/fm-94#product-documents.
17. R. Geissberger, J. Maldonado, C. Dransfeld, and K. Masania. Rheological modelling of thermoset composite processing. Compos. Part B Eng, 2017 ; 124, pp. 182–189.
18. ASTM International. D3528-96 Standard Test Method for Strength Properties of Double Lap Shear Adhesive Joints by. Am Soc Test Mater. 2016;96.
19. Liu S, Sinke J, Dransfeld C. An inter-ply friction model for thermoset based fibre metal laminate in a hot-pressing process. Compos Part B Eng. 2021;227:109400.
20. Ahmad SM, Kawashita LF, Featherston CA. A modified cohesive zone model for fatigue delamination in adhesive joints: Numerical and experimental investigations. Compos Struct. 2019;225:111114.

  doi:10.5075/epfl-298799_978-2-9701614-0-0

THERMOMECHANICAL CHARACTERIZATION OF 3D INTERLOCK CARBON COMPOSITES

Libor, Navrátil[a], Yann, Marco[a], Vincent, Le Saux[a], Sylvain, Leclercq[b], Nicolas, Carrere[a]

a: ENSTA Bretagne, IRDL, UMR CNRS 6027
2, rue François Verny
29806 Brest, France – libor.navratil@ensta-bretagne.org
b: Safran Landing systems, Vélizy-Villacoublay, France

Abstract: *This study deals with an interlock woven composite and aims at providing a better understanding of the dissipative mechanisms activated under cyclic loadings that are applied during heat build-up experiments. The instrumentation of these experiments relies mostly on infrared thermometry and a special focus is put on the post-processing of the thermal measurements as the results of this post-processing can guide the identification of the dissipative mechanisms. Moreover, the experimentally obtained dissipated energy fields can be compared to numerical results in order to identify the dissipation sources related to the inelastic behaviour of the resin.*

Keywords: woven composites ; thermomechanical characterization ; heat build-up

1. Introduction

The broad implementation of composite materials in aircraft structures is the result of their excellent specific strength and specific stiffness properties. In industrial applications, woven or textile composites have been gaining popularity since they lack some drawbacks found in commonly used laminated composites: a low damage resistance or poor out-of-plane properties [1]. With this objective in mind, this study focusses on a three-dimensional woven composite with an organic matrix that was developed for research purposes by the Safran group. The presented thermomechanical characterization is based on analyses of the heat build-up phenomenon occurring under cyclic loadings. This phenomenon is often investigated in approaches that aim at accelerating the characterization of the fatigue properties [2-3]. Nevertheless, in order to achieve this goal, the relation between the thermomechanical signature and the dissipative mechanisms activated under cyclic loadings must be described.

2. Damage scenario of woven composites

In the case of woven composites, the damage scenario is complex due to the complex microstructure and involves several phenomena: matrix cracking, inter-yarn and intra-yarn cracking, inter-ply and intra-ply delamination (Figure 1a) [4-5]. The present work focusses mainly on the early damage occurring under relatively low loadings leading to long fatigue lifetimes. The complex damage scenario implies a large number of dissipative mechanisms, which can include viscoelasticity, plasticity, damage, etc.

3. Identification of dissipation mechanisms from thermal measurements

In order to identify the dissipative mechanisms activated under cyclic loadings, the infrared thermometry is employed. The latter gives access to temperature fields on the sample's surface

  doi:10.5075/epfl-298799_978-2-9701614-0-0

that can be submitted to further post-processing. Figure 1b illustrates a thermoelastic coupling field obtained on the front face of a tested specimen. It appears that the implemented post-processing methods enable a fine description of the thermomechanical response on the meso-scale level. Other examples of these experimentally obtained fields include dissipated energy fields, thermal event maps or 2×f amplitude maps [6-7].

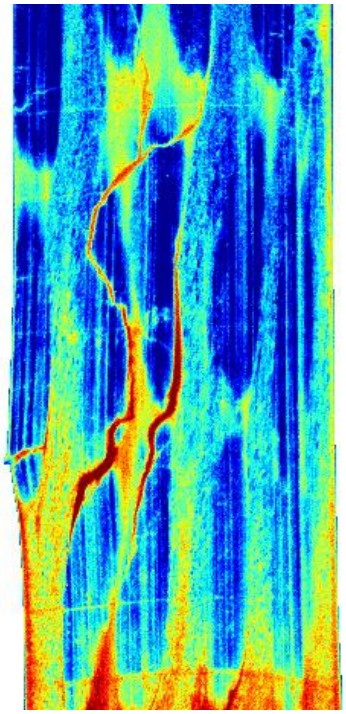

Figure 1a: Cracks apparition observed by infrared camera

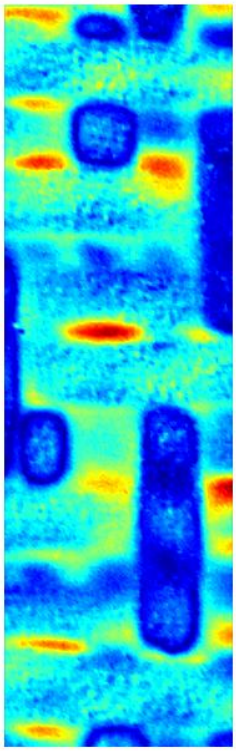

Figure 1b: Thermoelastic cartography obtained from thermal measurement

4. Description of dissipation mechanisms based on simulation/experiment comparisons

As mentioned previously, the analyses of these experimentally obtained fields can be used to guide the identification process of the dissipated mechanisms. Another use of these fields is to provide an experimental database that can be compared to the results obtained by means of constitutive modelling [8-9]. These comparisons can be used to validate the behaviour laws used at the meso-scale level or can further refine the description of the dissipation scenario. This is done by comparing the numerical and experimental dissipation under relatively low cyclic loadings. These simulation/experiment comparisons show that as long as the specimen is free of damage, the major dissipation source results from the inelastic behaviour of the resin [10].

5. Conclusion

Studies investigating dissipative mechanisms activated under cyclic loadings have been gaining popularity as a detailed description of the dissipation scenario can pave the way for fatigue life

  doi:10.5075/epfl-298799_978-2-9701614-0-0

predictions. However, the complex architecture of woven composites leads to the activation of a relatively large number of dissipative mechanisms. In order to identify these dissipative phenomena, two strategies are being presented. The first one makes use of the information provided by full-field temperature measurements and proposes post-processing methods that highlight the creation of cracks on the observed surface. The second one compares the experimental and numerical energy dissipated under cyclic loadings in order to identify the dissipation sources related to the inelastic behaviour of the composite resin.

Acknowledgements

The research presented in this article was funded by the Safran Group, France. Safran Tech-Composites Platform is acknowledged for the manufacturing of the samples used in this study. The authors would also like to thank the French ANRT Agency for its financial support (CIFRE n°2017/1 456)

6. References

1. Irving PE, Soutis C. Polymer Composites in the Aerospace Industry. Woodhead Publishing. 2015.
2. Meneghetti G, Quaresimin M. Fatigue strength assessment of a short fiber composite based on the specific heat dissipation. Composites Part B: Engineering 2011; 42: 217–225.
3. Jégou L, Marco Y, Le Saux V, et al. Fast prediction of the Wöhler curve from heat build-up measurements on short fiber reinforced plastic. International Journal of Fatigue 2012; 259–267
4. Schneider J, Aboura Z, Khellil K, et al. Contribution of damage mechanisms comprehension of interlock-reinforced composite materials. 13th European Conference on Composite Materials (ECCM-13) 2008; Stockholm
5. Tsai K, Chiu C and Wu T. Fatigue behavior of 3D multi-layer angle interlock woven composite plates. Composite science and technology 2000; 60: 241–248
6. Navrátil L, Le Saux V, Marco Y, et al. Understanding the damage mechanisms in 3D layer-to-layer woven composites from thermal and acoustic measurements. Journal of Composite Materials 2022
7. Navrátil L, Le Saux V, Leclercq S, et al. Infrared Image Processing to Guide the Identification of Damage and Dissipative Mechanisms in 3D Layer-to-Layer Woven Composites. Applied Composite Materials 2022
8. Lomov SV, Ivanov DS, Verpoest I, et al. Meso-FE modelling of textile composites: Road map, data flow and algorithms. Composite science and technology 2007; 67: 1870-1891
9. Stig F, Hallström S. A modelling framework for composites containing 3D reinforcement. Composite Structures 2012; 94: 2895-2901
10. Navrátil L, Carrere N, Le Saux V, et al. On the ability of a viscoelastic model to predict the average energy dissipated by a 3D layer-to-layer composite under cyclic loadings. Article in preparation 2022.

  doi:10.5075/epfl-298799_978-2-9701614-0-0

PERMANENT DEFORMATION, STIFFNESS DEGRADATION AND STRENGTH OF OPEN HOLE GLASS/PA6 UD THERMOPLASTIC COMPOSITE IN TENSION AND COMPRESSION

Ruben Sevenois[a], Wim Van Paepegem[a]

a: Department of Materials, Textiles and Chemical Engineering, Faculty of Engineering and Architecture, Ghent University, Technologiepark Zwijnaarde 46, B-9052 Zwijnaarde, Belgium

Abstract: *The permanent deformation, stiffness degradation and strength of UD Glass/PA6 coupons with an open hole under tension and compression loading is investigated. 3 layups: $[0/90]_{5s}$ and $[+45/-45]_{5s}$ and $[+45/0/-45/90]_{3s}$ were tested. The specimen shape was rectangular with a width of 36 mm and a hole size of 6 mm, according to ASTM D5766. Both monotonic loading as well as Loading-Unloading-Reloading tests were executed. This, together with a measure of the full field strain of the sample (using Digital Image Correlation) allowed to identify the general sample strength as well as identify several regions where permanent deformation and damage occurred.*

Keywords: open hole; thermoplastic; Experimental; Digital Image Correlation

1. Introduction

While for Thermoset Fibre Reinforced Polymers (TS FRP) [1–3] detailed studies about the failure behaviour in the presence of stress concentrations exist, they seem to be absent for Thermoplastic Fibre Reinforced Polymers (TP FRP). Also, there is an increasing interest for advanced material models which are able to predict the nonlinear behaviour of TP-FRP. For an in-depth validation of such material models detailed information is required about the strain field evolution during the loading process. In addition, knowledge of the quantitative evolution of specimen stiffness and permanent strain, which may be caused by a combination of damage phenomena including matrix cracking and plastic deformation, fiber failure, fiber-matrix debonding and delaminations is crucial input for such numerical models.

In this work UD Glass/PA6 laminates with an open hole are subjected to tension (OHT) and compression (OHC) loading. Both monotonic and Loading-Unloading-Reloading (LUR) tests were executed to identify the evolution of specimen stiffness and the development of permanent strain on the specimen surface.

2. Methodology

Laminated plates were hot pressed with TenCate CETEX UD glass/nylon-6 from Ten Cate Advanced Composites B.V. Laminated plates with layup $[0/90]_{5s}$ and $[+45/-45]_{5s}$ were produced from which rectangular specimens were cut using water jet cutting. Afterwards a central hole with diameter 6 mm, to avoid damage to the hole edges, was milled from the composite coupons. *Figure **1*** shows the specimen dimensions. The specimens with 250 mm length were used for tensile tests. The specimens with 150 mm length were used for compressive tests. A summary of the test program is given in *Table **1***.

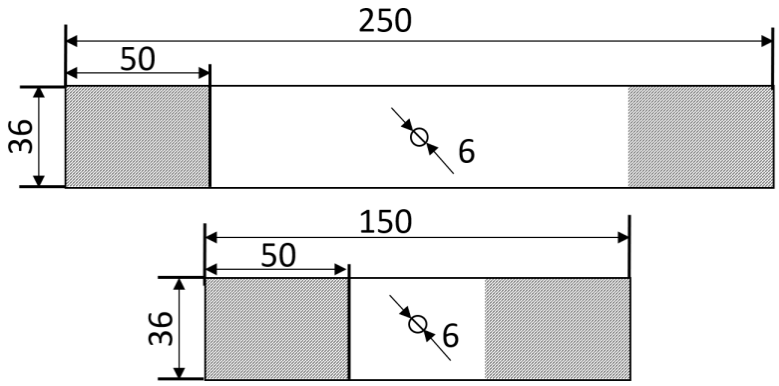

Figure 1: Specimen shapes. Top: tensile specimen. Bottom: compression specimen. The grey area is the clamped area

The specimens were tested on a 100 kN hydraulic Instron uniaxial test bench. The clamps of the machine were aligned before testing to ensure proper load introduction. The specimens were inserted over the full clamp length. Thus, the effective gauge length was 150 mm and 50 mm for, respectively, the tensile and compressive specimens. Both monotonic loading until failure as well as Loading Unloading Reloading (LUR) tests were executed. In the LUR tests consecutive reloadings were done at approximately 25%, 35%, 50%, 65% and 85% of the static strength after which the specimen was loaded until fracture.

The strain on the sample surface was measured using 3D Digital Image Correlation (DIC). For this the specimen surface was first painted with white, water based, acrylic airbrush paint. This type of paint adheres well to the surface while it does not form a film. The latter ensures that, when large deformations occur, the paint does not detaches or peels from the specimen surface. The 3D DIC system consisted of a custom setup with 2 Pointgrey cameras with 5MP resolution. The images were calibrated and analysed using the software VIC-3D from Correlated Solutions.

Table 1: Overview of specimens and load type

Load type	Layup	Length [mm]	Width [mm]	Thickness [mm]	Hole diameter [mm]	Actuator. Speed [mm/min.]
Monotonic tensile LUR Tensile	$[0/90]_{5S}$	250	36	5.2	6	2
	$[+45/-45]_{5S}$	250	36	5.2	6	2
	$[+45/0/-45/90]_{3s}$	250	36	6.2	6	2
Monotonic compression LUR Compression	$[0/90]_{5S}$	150	36	5.2	6	0.5-0.6
	$[+45/-45]_{5S}$	150	36	5.2	6	0.5-0.6
	$[+45/0/-45/90]_{3s}$	150	36	6.2	6	0.5-0.6

From the testdata several aspects such as the observed failure phenomena, the general stress-strain behaviour, the development of permanent strain and apparent damage (sample stiffness reduction) is investigated. For the global specimen stress-strain behaviour, the nominal stress,

σ_{nom}. , is calculated by dividing the force from the load cell with the initial cross sectional area at the maximum hole width as shown in Equation 1.

$$\sigma_{nom} = \frac{F}{(w - d) * t}$$

Equation 1

In Equation 1, F is the force from the load cell, w is the sample width, t is the sample thickness and d is the hole diameter. The global sample strain is defined as the engineering strain between two points located close to the clamps, as indicated in *Figure 2*. Due to the presence of the hole, the authors stress that the forthcoming stress-strain curves of these experiments indicate specimen behaviour and not intrinsic material behaviour.

An example of the global stress-strain behaviour for a LUR-OHT test with layup $[+45/-45]_{5s}$ is shown in Figure 2. One can clearly see the development of permanent strain after each loading cycle. Furthermore, the specimen stiffness is defined as the slope between consecutive maximum and minimum loads in an unloading-reloading cycle. This is indicated by the straight black lines.

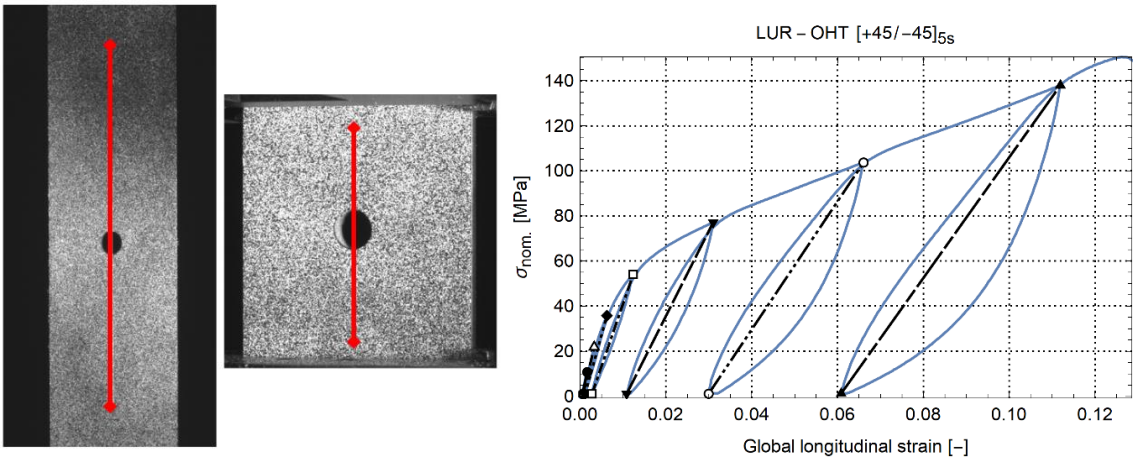

Figure 2: Global sample strain gauge for tension (left) and compression (right) specimen, b) Nominal stress- global strain of an open hole sample with layup $[+45/-45]_{5s}$ under tension load.

3. Results and Discussion

In this section the global specimen stress-strain behaviour is discussed in Section 3.1. Then, in Section 3.2 the observed failure type for each type is discussed. This is followed by a discussion about the development of permanent strain and damage in Section 3.3.

3.1 Nominal stress – global strain

The nominal stress - global strain of the experiments is shown in Figure 3. The result for each layup is represented by a different colour. For the results of samples with the same layup, different dashing is used.

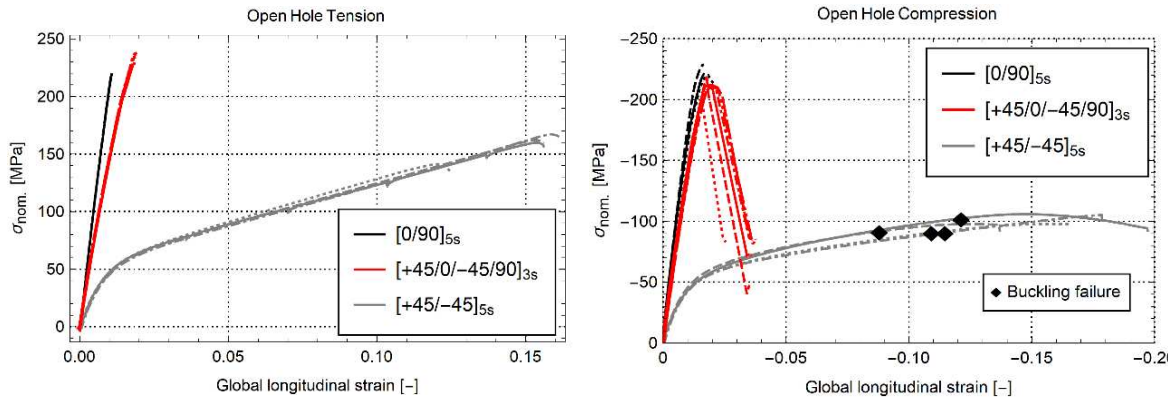

(a) (b)

Figure 3: Nominal stress vs global strain of samples subjected to monotonic loading until failure. a) OHT, b) OHC

The cases for OHT are shown in Figure 3a. The coupons with layup $[0/90]_{5s}$ and $[+45/0/-45/90]_{3s}$ show quasi-linear behaviour up to sudden failure at about 220 MPa. The coupon with layup $[+45/-45]_{5s}$ initially shows linear behaviour and becomes nonlinear at 1% strain. A failure strain of about 12-15% is observed with a failure load of about 150 MPa. These failure strains are significantly higher than for the other specimens because the +45/-45 plies are primarily loaded in shear, which illustrates the large deformation capability of the PA6 matrix. Remarkable is that the OHT strength of the QI laminate is higher than the OHT strength of the coupon with layup $[0/90]_{5s}$. This is caused by the high OHT strength of the +45/-45 plies in the QI laminate.

The data for OHC are shown in Figure 3b. Similar to tension, layups $[0/90]_{5s}$ and $[+45/0/-45/90]_{3s}$ show quasi-linear behaviour up to failure. A small non-linear region is present close to final failure. After kinking at maximum load the QI samples were still able to carry about 35% of the maximum strength at -75 MPa. The curves for layup $[+45/-45]_{5s}$ are non-linear. A notable difference is that buckling occurs at about -90 MPa, as indicated by the black diamonds. The end of the curves for $[+45/0-45/90]_{3s}$ and $[+45/-45]_{5s}$ do not indicate specimen failure. The specimens were removed after, respectively, kinking and buckling to protect the load cell of the machine and preserve the crosshead alignment. Yet, the specimens could still have been compressed further.

3.2 Failure observations

For each of the six combinations of load (tensile and compressive) and layup ($[0/90]_{5s}$ and $[+45/-45]_{5s}$, $[+45/0/-45/90]_{3s}$) different failure phenomena were observed.

Figure 4 shows images of typical failure behaviour of the samples with layup $[0/90]_{5s}$ under, respectively, tensile and compressive load. OHT failure of the samples with layup $[0/90]_{5s}$ shows no indication of growing cracks up till sudden failure. Despite the sudden breakage large symmetrical cracks appear from the sides of the holes and span almost the entire width of the sample. At the sides of the specimen a number of fibers are still bridging over the crack, effectively holding both specimen halves together. Although this connection is weak, it indicates that next to fibre breakage also fibre pull-out is an important damage phenomenon. OHC failure of the samples with layup $[0/90]_{5s}$ show relatively sudden kinking failure. Just before failure initial localized kinking can be observed originating from the hole edge. This is very difficult to

see visually, however, they can be spotted with the DIC strain field through a local strain concentration, or local correlation failure of the strain field.

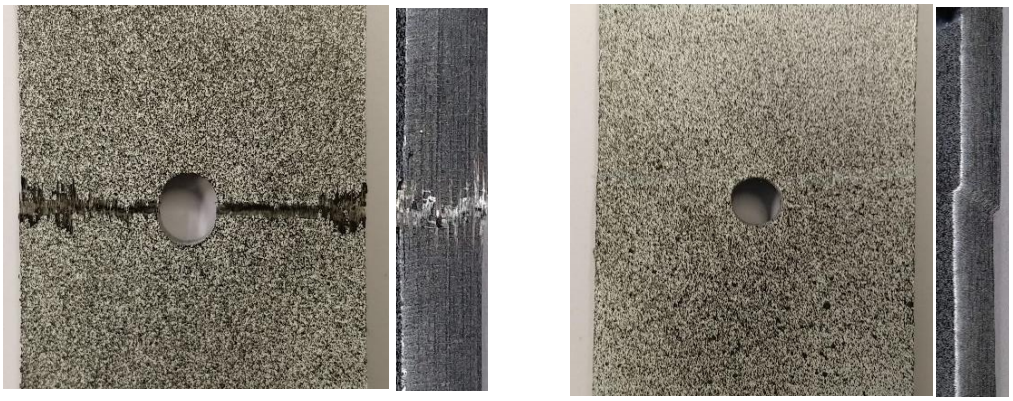

a) b)

Figure 4: Front and side view of ultimate failure of Glass/PA6 laminate, layup $[0/90]_{5s}$, with 6 mm diameter hole in a) tension, b) compression

For the samples with layup $[+45/-45]_{5s}$ both tensile and compressive loading showed large non-linear behaviour before failure. Figure 5 shows typical observations under, respectively, tensile and compressive loading. OHT failure for layup $[+45/-45]_{5s}$, Figure 5a, shows a combination of crack growth and ductile failure. Before failure multiple cracks develop at the hole edge. However, note that not all cracks necessarily grow to cause final failure. In Figure **5**a, a crack is indicated with a red circle. Although this crack appears to be the largest before failure, the crack causing load bearing failure occurs from a different location. OHC failure for layup $[+45/-45]_{5s}$, Figure **5**b **Error! Reference source not found.**, could not be achieved. The samples showed very high nonlinear deformation before eventually buckling at about 90-100 MPa σ_{nom}, Figure 3b. This shows the very high sample deformation which could be observed. After the occurrence of buckling, samples were unloaded and removed.

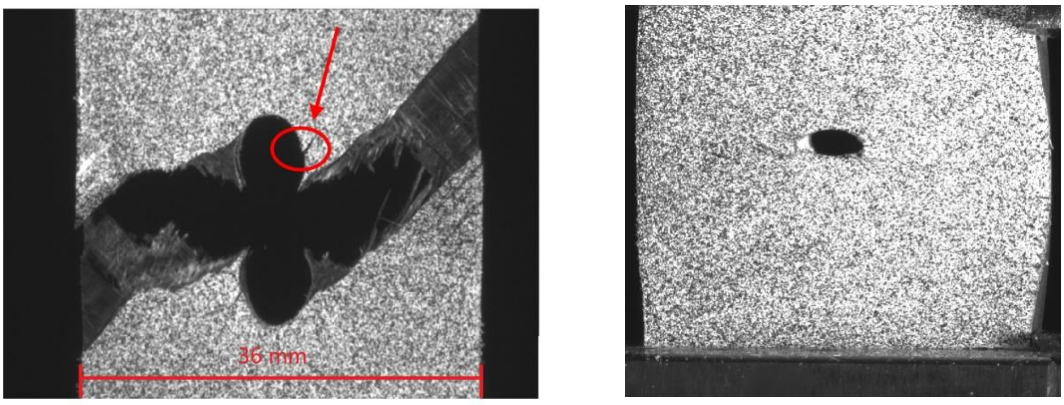

(**a**) (**b**)

Figure 5: Failure for laminate $[+45/-45]_{5s}$ a) tensile, b) compressive

Figure 6 shows the tensile and compressive failure for specimen with layup $[+45/0/-45/90]_{3s}$. For the tensile case, cracks develop along the +45 fibre direction of the top ply. These grow from the hole edge towards the edges of the sample until final failure. The specimen fails in a brittle way due to the presence of the 0 degree plies. The [0] plies show fibre pull-out with delamination, [90] plies show matrix cracking and the [45] plies failed in the typical shear-out

389/1211 ©2022 Sevenois et al. doi:10.5075/epfl-298799_978-2-9701614-0-0 published under CC BY-NC 4.0 license

failure. Similar to $[0/90]_{5s}$; the compressive failure of $[+45/0/-45/90]_{3s}$ occurs in the form of kinking, Figure 6b. Buckling was not observed during loading. It is noted, however, that the specimens do not fracture in two pieces as seen from the side view. The delamination damage is contained within the kinking zone. The combination of plies in all three primary directions is able to keep the plies from both sides of the specimen connected and attached, even after severe kink deformation. This allows the specimen to carry load after initial failure.

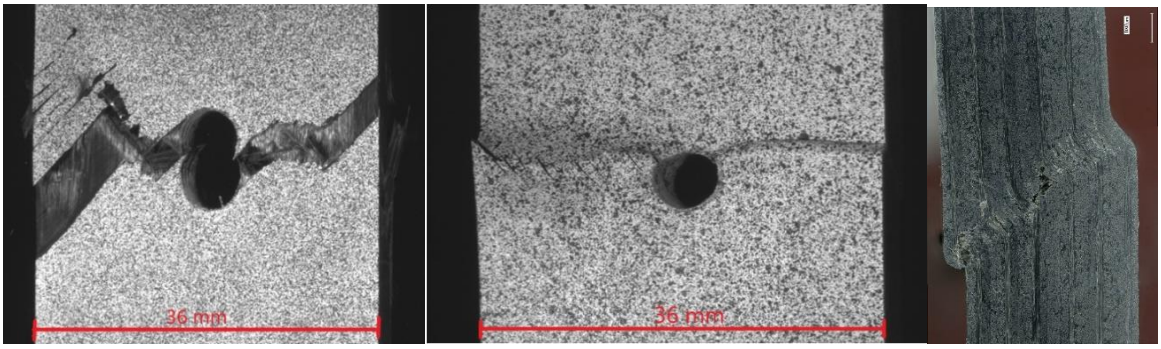

a) b)

Figure 6: Failure for laminate $[+45/0/-45/90]_{3s}$ a) tensile, b) compressive + side view

3.3 Stiffness and permanent strain evolution

Figure 7 shows the evolution of permanent strain and modulus of the specimen with layup $[+45/-45]_{5s}$. In the figures, the same symbols are used for the same test. The datapoints in gray occurred after buckling. A large amount of permanent strain occurs, and the elastic modulus reduces with each load cycle up to about 30% of the original modulus for tension, and 40% (before buckling) for compression. Between tensile and compression loading the evolution of permanent strain is similar, the evolution of specimen elastic modulus is less steep for compression.

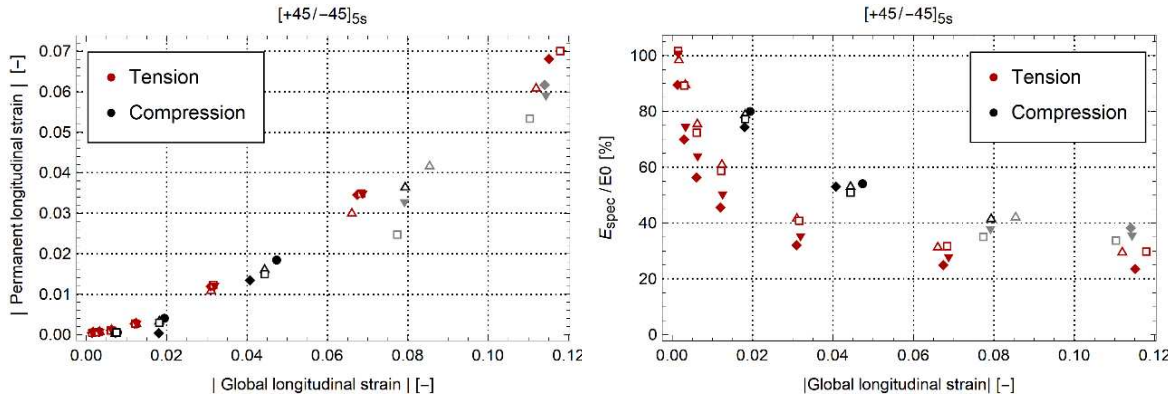

a) b)

Figure 7: a) Permanent strain and b) evolution of normalized elastic modulus for $[+45/-45]_{5s}$. Datapoints in gray are measured after buckling.

Figure 8 shows the evolution of longitudinal permanent strain and elastic modulus for $[0/90]_{5s}$ and $[+45/0/-45/90]_{3s}$. Though the nominal stress- global strain curve is quasi-linear, both layups show a small evolution in global permanent strain with a modulus reduction of about 20%. This suggests that, at least locally, some damage and plasticity occurs in the specimen volume. Similar evolutions are shown between tension, compression, and per layup. Note the initially

390/1211 ©2022 Sevenois et al. doi:10.5075/epfl-298799_978-2-9701614-0-0 published under CC BY-NC 4.0 license

higher elastic modulus after the first unloading cycle in the compression data of Figure 8b. This is caused by variability in strain measurement at small strain magnitude. Despite this, both elastic modulus evolution and permanent strain evolution are similar for tension and compression.

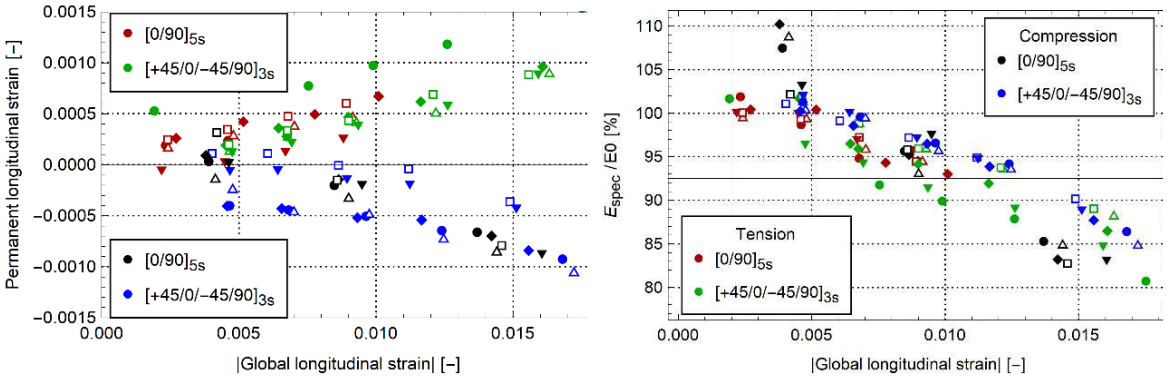

a) b)

Figure 8: a) Permanent strain and b) normalized elastic modulus for $[0/90]_{5s}$ and $[+45/0/-45/90]_{3s}$.

Figure 9 shows the longitudinal strain on the specimen surface for the layup $[+45/-45]_{5s}$ and $[0/90]_{5s}$ at unloading after either the last load cycle or just before buckling. For the samples with layup $[+45/-45]_{5s}$ X-shaped shear bands with high permanent strain develop. These meet at the side of the hole. This is illustrated in Figure 9a for the tensile case where the longitudinal strain is positive. For compression the longitudinal strain has the same shape, yet with negative sign. For the samples with layup $[0/90]_{5s}$, Figure 9b, a region of nearly zero longitudinal strain occurs above and below the hole center. To the left and right of the hole a local region with permanent strain occurs. For the compressive case the pattern is similar. The region with larger permanent strain is limited to the immediate vicinity of the hole. The permanent strain pattern for the QI layup shows a combination of the patterns from the $[0/90]_{5s}$ and $[+45/-45]_{5s}$ laminates.

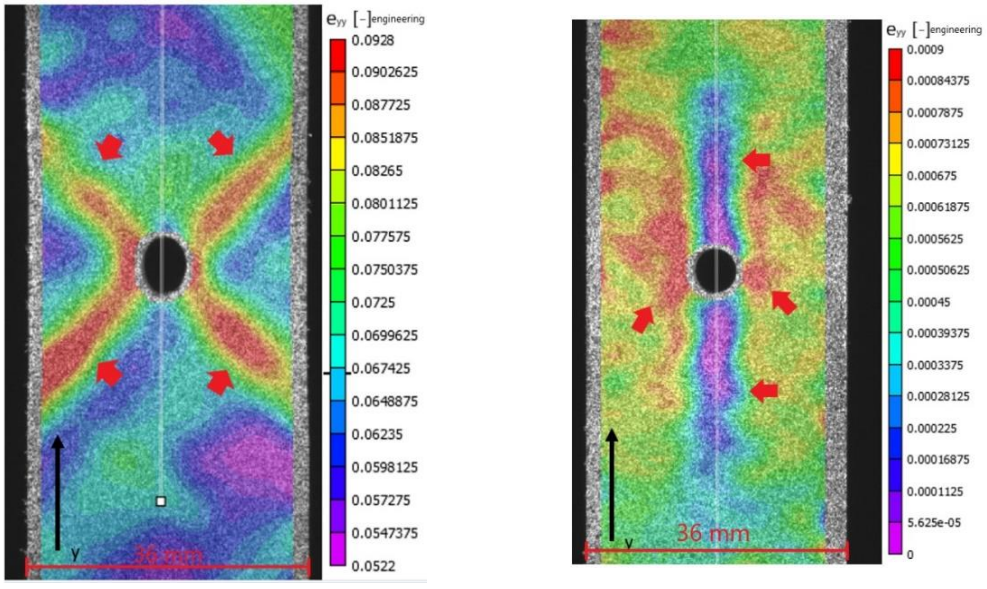

a) b)

Figure 9: Permanent strain developed after unloading specimen a) LUR-OHT with layup $[+45/-45]_{5s}$ and b) $[0/90]_{5s}$after the highest loading cycle before failure

391/1211 ©2022 Sevenois et al. doi:10.5075/epfl-298799_978-2-9701614-0-0 published under CC BY-NC 4.0 license

4. Conclusion

In this work Open Hole Tension and Open Hole Compression tests were executed on three laminates from UD Glass/PA6 material. The laminates tested are $[0/90]_{5s}$, $[+45/-45]_{5s}$ and $[+45/0/-45/90]_{3s}$. Both monotonic and Loading-Unloading-Reloading experiments were executed. This allowed to identify global specimen behaviour, the development of permanent strain, and evolution of specimen elastic modulus until final failure.

The experimental results show the significant nonlinear behaviour of Open Hole specimens made from thermoplastic fibre reinforced materials under both tensile and compressive loading. The specimens with layup $[+45/-45]_{5s}$ showed similar behaviour under both tension and compression. A degradation of the specimen elastic modulus up to 70% and permanent longitudinal strain of 7% is seen. The specimens with layup $[0/90]_{5s}$ and $[+45/0/-45/90]_{3s}$ show a maximum reduction of about 20% in elastic modulus. A very small amount of 0.1 % permanent longitudinal strain is noted.

The availability of the entire strain field on the sample surface throughout the test can be used to verify and validate finite element simulations of open hole tests for this material. A remarkable observation is that, while the evolution of global permanent strain and elastic modulus reduction between the tensile and compressive load cases is quite similar, the distribution of permanent strain development can be different. This indicates the necessity to include full field strain measurements, as well as both tensile as compressive loading, in future experimental programs on composite mechanical behaviour.

Acknowledgements

This research was funded by Research Foundation Flanders FWO, grant number 12R3221N.

References

[1] Clay SB, Knoth PM. Experimental results of quasi-static testing for calibration and validation of composite progressive damage analysis methods. J Compos Mater 2016;0:1–21. https://doi.org/10.1177/0021998316670132.

[2] Hinton M, Kaddour a. Triaxial test results for fibre-reinforced composites: The Second World-Wide Failure Exercise benchmark data. J Compos Mater 2012. https://doi.org/10.1177/0021998312459782.

[3] Kaddour AS, Hinton MJ, Smith PA, Li S. Mechanical properties and details of composite laminates for the test cases used in the third world-wide failure exercise. J Compos Mater 2013;47:2427–42. https://doi.org/10.1177/0021998313499477.

COMPOSITE PREPREGS TACK CHANGE ALONG THE PROCESS CHAIN

Nils, Siemen [a], Klaus, Heller [b]

a-b: of Carbon Composites, TUM Department of Mechanical Engineering, Technical University of Munich, Boltzmannstr. 15, 85748 Garching, Germany
a: E-Mail: nils.siemen@tum.de

Abstract: *The tack of uncured prepreg is recognized as being one of the most important material properties. It is well known that in automated lay-up process, tack affects production rate and the component quality. Most studies have focused in which extent process parameters and environmental parameters influence the tack properties without considering the material composition. Therefore, the aim of our work is to determine how the material manufacturing affects the tack of the prepregs. We investigated five different pre-impregnated materials at different process parameters and environmental conditions. The materials differ with regard to resin content, resin viscosity and semi-finished product types (towpreg and prepreg). Overall, our results show that material properties, as resin content, resin viscosity or type of semi-finished product influence the tack. For example, increasing the resin content by 5 % leads almost to a 100 % increase in tack. It was also found that the impact of process parameters and environmental conditions on the tack properties is affected by the material configurations. We have obtained comprehensive results proving that it is possible to configure the tack properties during material development and production. By this, the tack characteristics can be specifically adapted to the requirements of the corresponding application, for example the automated fiber placement (AFP)-process. Furthermore, the testing procedure can be used for quantification at an early stage in the material development process and consequently enable resource-efficient material development.*

Keywords: tack; automated fiber placement; prepreg; towpreg; material characterization

1. Introduction

The increasing demands from the public and governing bodies, to reduce energetic resource and emissions, requires technological solutions. Fiber-reinforced materials have a higher weight-specific stiffness and strength than metals and thereby offer a high potential for lightweight construction. For this reason, they are used in variety applications, especially in the aircraft industry [1]. Automated fiber placement (AFP) is an established manufacturing process in the aerospace industry for composite lightweight structures [2]. The AFP laying head, moved by a robotic system, can simultaneously lay down several pre-impregnated tapes on a tool surface [2]. The interaction between the process and the uncured material properties of the prepreg tapes plays an important role [3]. One material property is the tack, which can be described as the resistance of the pre-impregnated fibers to be separated from the substrate/tool surface [4]. Especially, an inadequate tack of the prepreg tapes might increase lay-up defects, which reduce the productivity of the process and the quality of the end products [3–5].

A growing body of literature has investigated experimental set-ups, to determine the tack of prepregs. The most well-known set ups are the probe tack test and the peel test [3–22]. There is a considerable amount of literature on investigations, how process parameters,

  doi:10.5075/epfl-298799_978-2-9701614-0-0

environmental parameters and material parameters influence the tack of prepregs and towpregs [3–13, 15–22].

In literature, there are many examples of investigations of the influence of resin content on tack properties [12, 13, 15, 16, 18, 20]. Most studies have only focused on examining woven prepregs or glass fiber prepregs [15, 16, 18]. Crossley et al. [10] mention that, fiber architecture and fiber type has an influence on tack characteristics, so the results might not be transferable to unidirectional carbon fiber prepregs. In their analysis of the influence of resin content on tack, Edwin et al. [20] change other material parameters besides resin content in their experimental design, so that the influence of resin content cannot be clearly recognized. Hayes and Seferis [13] measured the influence of impregnation parameters in the production of unidirectional carbon fiber prepregs on the tack and the resin content, but did not correlate the results directly with each other. Moreover, the tack between the prepreg layers was measured. Several studies found that the tack between prepreg layers is significantly higher than the tack between prepreg and steel [7, 22]. Therefore, the results of Hayes and Seferis cannot be transferred to the lay-up of a prepreg on a steel surface.

Previous work has focused on the tack behavior of uncured prepregs [3–7, 9–13, 15–22]. The investigation of towpreg materials with regard to the tack was only carried out by Rao et. al. [8]. However, there is still a need to analyze the effect of the semi-finished product in terms of the tack behavior. A number of studies reported the fiber architecture effect the tack [10, 20]. It can thus be suggested that the semi-finished product type has an influence on the tack.

Many publications have studied the viscoelastic behavior of prepregs and the resulting relevance to tack properties [4, 7–11, 21, 22]. In this context, rheological measurements have been carried out simultaneously with the tack measurements under changing process and environmental parameters [8, 9, 22]. Nevertheless, no information has yet been found on how the selection of high or low viscosity resins in the production of prepregs or towpregs affects the tack characteristics.

Consequently, we have addressed the research question of whether and how material parameters must be set during the production of pre-impregnated tapes in order to influence the tack properties in the AFP processing area in a targeted manner. We decided that a suitable approach for this investigation is to evaluate materials that only differ in one material property. Only change one factor at a time allowed us to analyze the clear impact of resin content, viscosity of the resins and type of semi-finished product on the tack. We characterize the tack behavior of these materials with the novel test bench "TUM peel tack test", which offers the possibility to lay down the pre-impregnated tapes with an AFP laying head and then perform out a peel test. In this approach we are able to vary the AFP-parameters like lay-up speed, compaction force and infrared (IR) lamp power. This enables us to carry out a full-factorial test design in a realistic industrial processing condition. The influence of the environmental parameters is represented by variation of the aging time of the different materials at defined climatic conditions. In the AFP-Process, it is important that the first ply, which is lay-up on a steel tool, has sufficient tack during placement to prevent slippage or displacement during the rest of the process [19]. Therefore, we decided to investigated this “worst-case-scenario” the tack between steel surface and pre-impregnated tape.

  doi:10.5075/epfl-298799_978-2-9701614-0-0

2. Materials and Methods

2.1 Materials

The materials in Table 1 were tested with regard to their tack. Ref. serves as a commercially available reference prepreg system. P_lv_35 to T_lv_33 are development materials and were specially provided for this series of tests. Due to non-disclosure agreements, the exact material designation and composition may not be described.

Table 1: Specifications of the tested pre-impregnated unidirectional tapes

Reference	Type of semi-finished product	Fiber type	Resin type	Resin content [%]	Areal Weight [g/m²]
Ref.	Prepreg	HTS Carbon fiber	Commercially available resin	40	440
P_lv_35	Prepreg	Carbon fiber	Low viscosity resin	35	406
P_lv_40	Prepreg	Carbon fiber		40	440
P_hv_35	Prepreg	Carbon fiber	High viscosity resin	35	406
T_lv_33	Towpreg	Carbon fiber	Low viscosity resin	33	361

2.2 Tack measurement

The peel tack of the individual materials was investigated fully factorially with the following test configuration in Table 2.

Table 2: Test configuration for the determination of the peel tack

Parameter category	Parameter	Unit	Tested settings
Environmental parameters	Aging time	[d]	1; 15; 30
Process parameters	Lay-Up speed	[m/s]	0.06; 0.08
	Lamp power	[W]	315; 420
	Compaction force	[N]	100; 400

The samples were aged in an industrial manufacturing facility at a relative humidity of 40% and temperature of 21 °C. Three replicates were performed for each of the 24 settings, so that a total of 360 tests were carried out.

As shown in the left part of Figure 1, the “TUM peel tack test” bench was installed directly next to the AFP unit of the Technical University of Munich. The base plate with a template for the specimen holder was fixed on the AFP tool table. The AFP machine processes 1/8" (3.175mm) wide slit-tapes. Since slit tapes were not available for the various materials, the samples were manually applied to the specimen holder as shown in Figure 1 on the right. Therefore, the prepregs were cut to 25mmx350mm samples by a CNC cutter. The 12.7 mm wide towpreg was

  doi:10.5075/epfl-298799_978-2-9701614-0-0

controlled unwound from the spool and cut to a length of 350 mm. A release film was placed between the specimen and the specimen holder in the back area of the specimen holder. In order to simulate the lay-up process, the laying head was then moved over the specimen under defined process conditions as shown in Table 2.

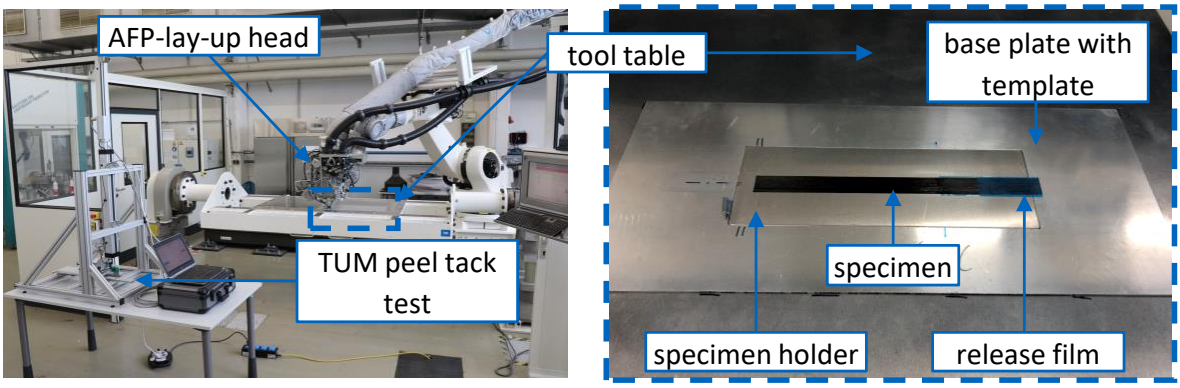

Figure 1: Test set-up (left) and depositing of samples (right) for performing the "TUM peel tack test" adapted from [3]

After this step the specimen holder was removed and inserted into the test bench. Thereby, the specimen was fixed in the clamping jig as shown on the left side of Figure 2. The specimen is then peeled off at 5 mm/s.

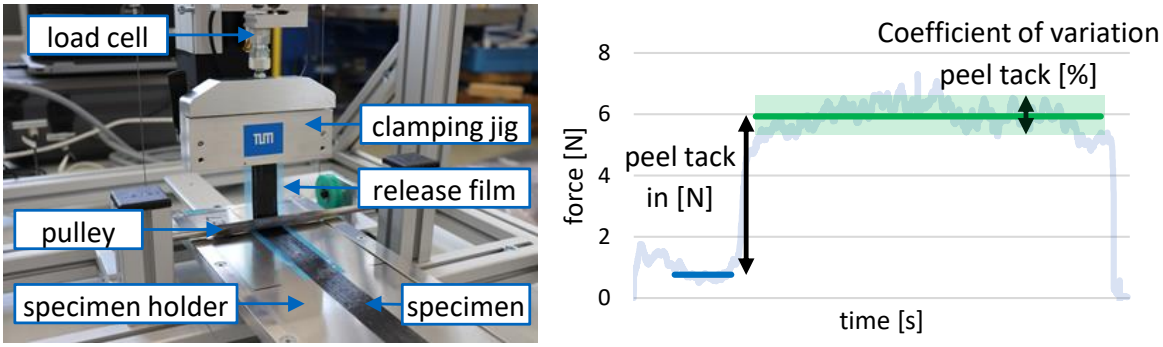

Figure 2: Execution (left) and presentation of results (right) of the "TUM peel tack test" adapted from [3]

The load cell measures the required force over time, as shown in the Figure 2 on the right. In the area where the specimen is placed on the release film, only the material stiffness of the specimen is measured. In the remaining area, where the specimen was applied directly to the specimen holder, the tack is measured in addition to the material stiffness. The difference between the two areas is the tack [3, 14]. In addition, for every peel test the coefficient of variation (CV) of the tack along the specimen was determined.

3. Results and Discussion

The results of the measurement of the different materials is summarized in Figure 3. The peel tack is given in N/mm as a function of the specimen width. The results show that by varying the material configurations of pre-impregnated tapes, the peel tack can be influenced in a targeted manner. The tack values of a standard materials such as Ref. can be exceeded. However, it can be seen that the standard material has lower CV of peel tack.

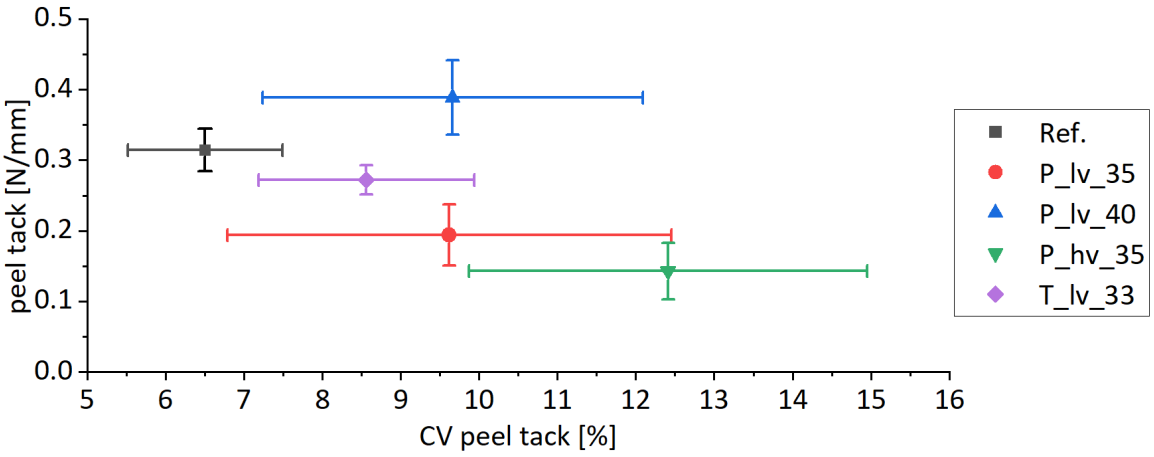

Figure 3: Averaged results and standard derivations over all settings of the peel tack and coefficient of variation (CV) of the tack in relation to the materials

The correlation between P_lv_35 and P_lv_40 describe the influence of the resin content on the tack behaviour of prepregs. An increase in resin content by 5% leads to an increase in tack by 100% and does not impact the CV of the peel tack. A possible explanation for the increase in peel tack could be that more resin is in the interface and improves the adhesion between the bonding partners. Our results are in line with the findings of Hayes and Seferis [13]. P_lv_35 has a viscosity in the temperature range of the AFP process 10 times lower than that of P_hv_35. The low viscosity leads to an increase by 26 % in the peel tack and a decrease by 29% in the CV of the peel tack. The main reason for this behavior may be that the low viscosity has led to better wetting on the specimen holder, which increases the peel tack. Figure 3 also shows that the towpreg (T_lv_33) with the same material combination as the prepreg has a 40% higher peel tack and 11 % less CV of peel tack than the prepreg (P_lv_35). These results can be explained in part by the different manufacturing processes of the semi-finished product types.

In order to investigate how the material parameters influence the processing in the AFP processing area, the results of the tack measurements of the individual materials as a function of the environmental and process parameters are shown in Figure 4 and Figure 5.

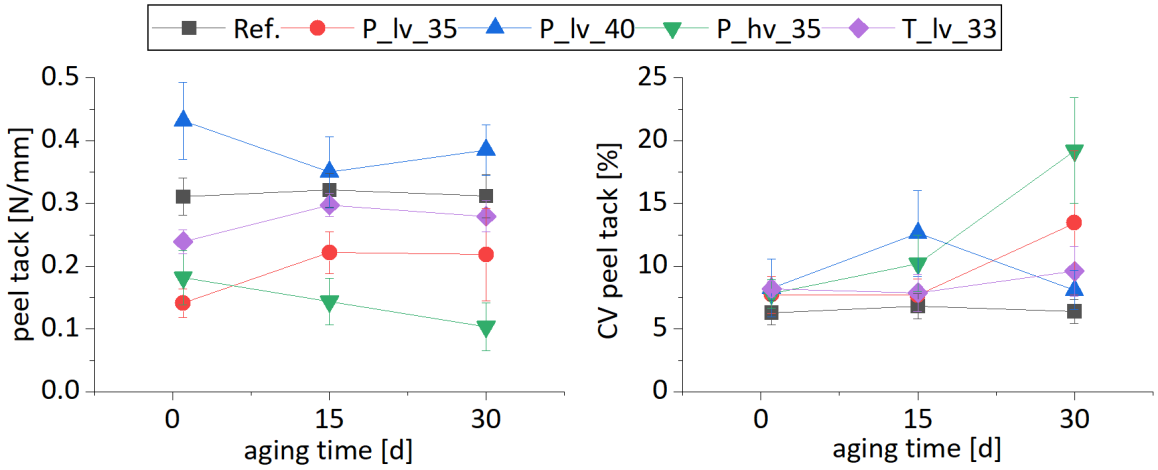

Figure 4 Results of the peel tack (left) and the coefficient of variation (CV) of peel tack (right) of the materials in relation to the aging time

With respect to the lamp power shown in Figure 5, its variation has no influence on the tack measurements. An explanation for this behaviour is the tape is only heated on the surface when the samples are applied by hand. The area between the tape and the substrate is not heated, as is the case with AFP placement. As can be seen in the plots in Figure 5 the results of the CV of peel tack as a function of the lay-up speed, compaction force and lamp power have high standard deviation , so these parameters have no significantly influence. Therefore, these results are not taken into account here.

It can be clearly seen that the tack properties of Ref. are barely influenced by environmental and process parameters and has no significiant change in values in the AFP process area. P_lv_35 and P_lv_40 show oppostive behaviour depending on aging time and lay-up speed. With a low resin content, both the peel tack and the CV of peel tack increase with aging time. With a higher resin content, there is a decrease in peel tack and a peak of the CV of peel tack at the aging time of 15 days. The peel tacks show a decrease for P_lv_35 and no influence for P_lv_40 with an increase of the lay-up speed. These oppositve behaviour may be can explained by the adhesive and cohesive mechanisms, which take a role in the tack of the prepreg [4]. Cohesive failure has been noticed more frequently at P_lv_40 during testing. The change in the interaction between adhesive and cohesive failure could have an influence on the different dependence of peel tack and CV of peel tack on lay-up speed and aging time. Regardless of the resin content, both materials show a low gradient in peel tack with increasing compaction pressure.

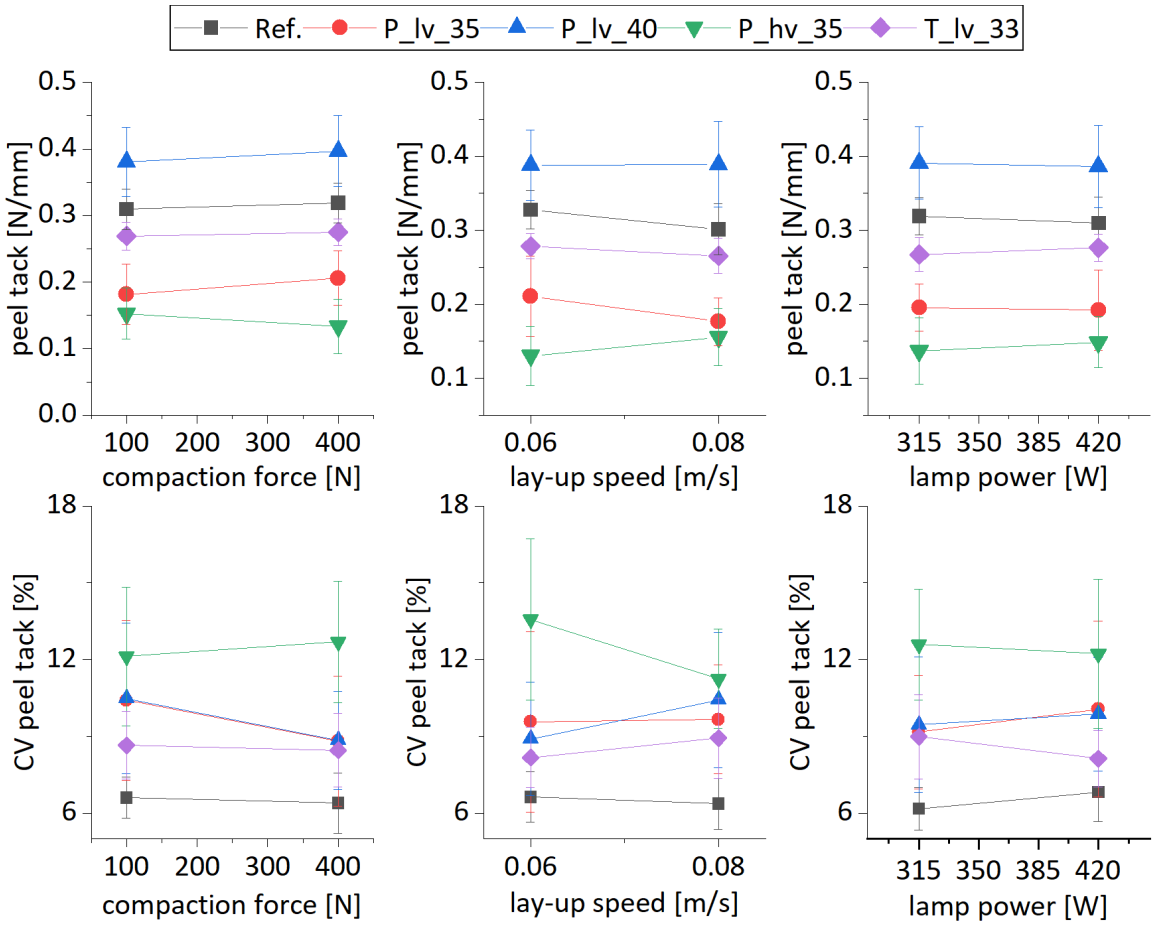

Figure 5: Results of the peel tack (above) and the coefficient of variation (CV) of peel tack of the materials in relation compaction force (left) and lay-up speed (middle) and lamp power (right)

The viscosity of the resin system influences the dependence of the peel tack on the environment and process parameters. For prepreg with high viscosity resin, a decrease in peel tack with increased compaction pressure and reduced speed can be seen. The opposite is true for prepregs with low viscosity resin. The reason for this result is still not entirely clear. Possibly, the toughness of the resins influences the kinematics of the prepregs in the process, which in turn influences the tack properties. The dependence of the peel tack on the aging time also change due to the resin viscosity. For P_lv_35 an increase in peel tack with aging time is to be expected. For P_lv_40 the opposite is the case. The CV of peel tack increase for low and high resin viscosity. Towpregs and prepregs with the same material combination demonstrate the same correlations between peel tack and CV of peel tack to the parameters ageing time, compaction pressure and lay-up speed.

4. Conclusion

By adjusting the material parameters during the production of pre-impregnated tapes, the tack behaviour in the AFP process area can be influenced directly. In conclusion, these findings suggest that by increasing the resin content, selecting low viscosity resins, and using towpregs instead of prepregs, the peel tack can be increased. Accurate results were obtained in this manuscript, which shows that the different material configurations influence the dependence of the tack behaviour on the enviromental and process parameters. The present findings help to adapt the materials directly to the processing requirements in order to achieve the highest possible productivity and quality. Therefore, further work with the aim of idendifying the machine-specific tack area where the fewest machine stops and lay-up errors occur, is reguired.

Acknowledgements

This work was funded by the Bavarian Ministry of Economic Affairs, Regional Development and Energy as part of the project "Automated Composite Sandwich Lay-Up System (MAI ACoSaLUS)" (No. LABAY 113E). We gratefully acknowledge the help provided by SGL Technologies GmbH, Meitingen for the constructive comments and for providing the test materials. We also thank GKN Aerospace Deutschland GmbH, Munich for the ongoing collaboration and the possibility of aging the test materials in your facilities.

5. References

1. Heinecke F, Willberg C. Manufacturing-Induced Imperfections in Composite Parts Manufactured via Automated Fiber Placement. J. Compos. Sci. 2019;3:56.
2. Brasington A, Sacco C, Halbritter J, Wehbe R, Harik R. Automated fiber placement: A review of history, current technologies, and future paths forward. Composites Part C: Open Access. 2021;6:100182.
3. Heller, K., Colin, D., Drechsler, K. Quantifying the Influence of Out-time on Prepreg Material Properties and Out-of-plane Steering Defects during Automated Fiber Placement. Frontiers in Materials. 2022.
4. Budelmann D, Schmidt C, Meiners D. Prepreg tack: A review of mechanisms, measurement, and manufacturing implication. Polym Compos. 2020;41:3440–58.
5. Beakou A, Cano M, Le Cam J-B, Verney V. Modelling slit tape buckling during automated prepreg manufacturing: A local approach. Composite Structures. 2011;93:2628–35.

  doi:10.5075/epfl-298799_978-2-9701614-0-0

6. Belhaj M, Dodangeh A, Hojjati M. Experimental investigation of prepreg tackiness in automated fiber placement. Composite Structures. 2021;262:113602.
7. Endruweit A, Choong GY, Ghose S, Johnson BA, Younkin DR, Warrior NA, Focatiis DS de. Characterisation of tack for uni-directional prepreg tape employing a continuous application-and-peel test method. Composites Part A: Applied Science and Manufacturing. 2018;114:295–306.
8. Rao S, Umer R, Thomas J, Cantwell WJ. Investigation of peel resistance during the fibre placement process. Journal of Reinforced Plastics and Composites. 2016;35:275–86.
9. Crossley RJ, Schubel PJ, Focatiis D de. Time–temperature equivalence in the tack and dynamic stiffness of polymer prepreg and its application to automated composites manufacturing. Composites Part A: Applied Science and Manufacturing. 2013;52:126–33.
10. Crossley RJ, Schubel PJ, Warrior NA. The experimental determination of prepreg tack and dynamic stiffness. Composites Part A: Applied Science and Manufacturing. 2012;43:423–34.
11. Rajaei M, Beheshty MH, Hayaty M. Preparation and Processing Characterization of Glass/Phenolic Prepregs. Polymers and Polymer Composites. 2011;19:789–96.
12. Dubois O, Le Cam J-B, Béakou A. Experimental Analysis of Prepreg Tack. Exp Mech. 2010;50:599–606.
13. Hayes BS, Seferis JC, Chen JS. Development and hot-melt impregnation of a model controlled flow prepreg system. Polym Compos. 1996;17:730–42.
14. Klaus Heller, Simon Seyfferth, Kalle Kind, Klaus Drechsler, editor. A Post Lay-up Tack Peel Test for Aerospace Grade Prepreg Tapes; 2020.
15. Popp A, Klostermann D, Chartoff R. Correlation of prepreg tack with process perfirmance in laminated object manufacturing. In: Bridging the centruies wirth SAMPE´s materials and processing technology. p. 90–103.
16. Putnam JW, Seferis JC, Pelton T, Wilhelm M. Perceptions of Prepreg Tack for Manufacturability in Relation to Experimental Measures. Science and Engineering of Composite Materials. 1995;4:55.
17. Ahn KJ, Seferis JC, Pelton T, Wilhelm M. Analysis and characterization of prepreg tack. Polym Compos. 1992;13:197–206.
18. Cole KC, Noël D, Hechler J-J, Cielo P, Krapez J-C, Chouliotis A, Overbury KC. Room-temperature aging of Narmco 5208 carbon-epoxy prepreg. Part II: Physical, mechanical, and nondestructive characterization. Polym Compos. 1991;12:203–12.
19. Chinh D. Nguyen, Dominik Delisle. FIRST PLY TACK OF AN AUTOMATED FIBRE PLACEMENT PROCESS – INFLUENCE OF HEATABALE MOULD SURFACE, RELEASE FILMS AND PROCESS PARAMETERS. SAMPE Europe Conference. 2017.
20. Edwin J. Smith, Cecile Grubb, John Misasi, and Nicole Larson, editor. Developing a Procedure for Prepreg Tack Characterization; September 23, 2019.
21. Banks R, Mouritz AP, John S, Coman F, Paton R. Development of a new structural prepreg: Characterisation of handling, drape and tack properties. Composite Structures. 2004;66:169–74.
22. Budelmann D, Detampel H, Schmidt C, Meiners D. Interaction of process parameters and material properties with regard to prepreg tack in automated lay-up and draping processes. Composites Part A: Applied Science and Manufacturing. 2019;117:308–16.

SURFACE ENERGY DETERMINATION OF PARTICLES USED AS FILLERS IN POLYMERS: APPLICATION TO LIGNIN/PLA COMPOSITES

Valentin Carretier[a], Monica Francesca Pucci[b], Clement Lacoste[a], Arnaud Regazzi[b], José-Marie Lopez-Cuesta[a]

a: Polymers Composites and Hybrids (PCH), IMT Mines Ales, Ales, France
b: LMGC, IMT Mines Ales, Univ Montpellier, CNRS, Ales, France – monica.pucci@mines-ales.fr

Abstract: *This study has the aim to propose a new simple method to determine the surface energy components of particles used as fillers in polymers. An experimental protocol coupled to a modified Jurin law is proposed. This protocol was applied to lignin particles used as reinforcement in polylactic acid (PLA). Some treatments were performed on lignin to improve the adhesion with PLA and the modifications due to the treatments were characterized. The originality of this method was to extend the theory of Jurin to porous media and compare it to the well-known theory of Washburn. Results showed that the Washburn theory had some limits for the application to these materials, since some hypotheses were not respected or no longer valid. Reliable surface energy and components of untreated and treated lignin were obtained revealing the efficiency of the proposed method.*

Keywords: *Capillary wicking; interface; surface energy; lignin; biocomposite.*

1. Introduction

The addition of some biofillers like lignocellulosic biomass is an effective way to improve polylactic acid (PLA) properties and to extend its range of applications. Lignin, in powder form, has a wide set of applications as filler in composites, such as UV blocker, antioxydant, charring agent in flame retardancy, mechanical reinforcement or surfactant [1]. However, the strong polar nature of lignin, due to the presence of hydroxyl groups, makes it incompatible with the non-polar PLA matrix, resulting in a poor interfacial filler-matrix adhesion. Acetylation and phosphorylation are two lignin chemical modifications used to enhance the mechanical and thermal properties of lignin/PLA composites respectively. These properties are strongly related with the interfacial adhesion between fillers and PLA [2].

To characterize the interfacial adhesion, the determination of lignin and PLA surface energy components is required. Surface energy is an intrinsic property of each liquid and solid material and, for a solid, it is obtained by means of equilibrium contact angle measurements. However, for powders assumed as porous media more issues arise, notably due to the imbibition of the liquid into the medium. An apparent contact angle can be obtained using wicking tests and the well-known modified Washburn equation for porous materials. However this method, that theoretically allows the determination of apparent advancing contact angles, does not always give reliable results due to the Washburn hypotheses that are not respected or no longer valid (typically the non-linearity of wicking curves for which apparent advancing contact angles could not be obtained).

A new simple method using a modified Jurin law for porous media is proposed here in order to determine reliable apparent equilibrium contact angles and obtain surface energy of fillers [3].

  doi:10.5075/epfl-298799_978-2-9701614-0-0

An experimental protocol based on capillary wicking and coupled to the modified Jurin law was set and applied to lignin particles used as reinforcement in PLA. Some treatments were performed on lignin to improve the adhesion with PLA and the modifications due to the treatments were characterized. Reliable surface energy and dispersive and polar components of untreated and treated lignin were obtained revealing the efficiency of the proposed method. Lignins were then used as reinforcements for PLA. The microstructure of the biocomposites was characterized to highlight the modification of adhesion at the filler/matrix interface due to the modification of fillers surface properties [3]. This characterization will be discussed during the oral presentation.

2. Materials and Methods

2.1 Materials

The lignin used in this study is an alkali lignin supplied by TCI (Tokyo, Japan). This was named untreated or reference lignin (Ref-Lig). The content of methoxyl group is between 10 and 12 % and the median particle diameter is around 50 µm. For the surface energy determination, four liquids were tested with lignin. Table 1 shows density ρ, dynamic viscosity η, surface tension γ_L and dispersive γ_L^D and polar γ_L^P components for each liquid at standard conditions [4]. The n-Hexane (99 % pure and supplied by Chem-Lab) was used as totally wetting liquid. The water and the ethylene glycol (99.5 % pure and supplied by Chem-Lab) were used because of their polarity. The lactic acid (90 % pure, supplied by Sigma-Aldrich), was used expecting to have similar wetting properties of PLA. Dynamic viscosity of lactic acid was measured using a AR2000ex rheometer (TA Instrument) with a coaxial cylinder system. Surface tension and dispersive and polar components were determined using a K100SF tensiometer (Krüss) and performing a three-step procedure detailed in a previous work [5]. As expected, lactic acid was found to have a quasi-totally dispersive nature, with dispersive and polar components very close to ones of PLA [6].

Table 1: Test liquids properties at 20°C.

Liquid	ρ (g/cm3)	η (mPa.s)	γ_L (mN/m)	γ_L^P (mN/m)	γ_L^D (mN/m)
n-Hexane	0.659	0.32	18.4	0.0	18.4
Water	0.998	1.00	72.8	51.0	21.8
Ethylene gl.	1.113	21.81	48.0	19.0	29.0
Lactic acid	1.248	69.01 ± 1.01	42.2 ± 0.1	4.5 ± 0.4	37.7 ± 0.3

2.2 Lignin treatments

The chemical treatment of acetylation was performed on lignin using an adapted protocol from the literature [7]. A volume of 250 mL of acetic anhydride was introduced in a 500 mL round-bottomed flask and equilibrated at 65°C with reflux. After that, 1 mL of 1-methylimidazole working as catalyst was added. A mass of 40 g of alkali lignin was added slowly in the flask. The mixture was equilibrated at 65°C for 24 h. The reaction was stopped by introducing the mixture in 1.5 L of cold deionized water. Then the treated lignin was separated from the reaction mixture

  doi:10.5075/epfl-298799_978-2-9701614-0-0

by centrifugation (Hettich, Rotina 380). The lignin was washed from 3 to 5 times with deionized water in order to obtain a neutral pH (to remove acid residues). Then the lignin was dried in an oven at 80°C for 24 h. The treated lignin was named acetylated lignin (or Ac-Lig).

The phosphorylation treatment was also adapted from the literature [8]. A 60 % phosphoric acid was prepared using 85 % phosphoric acid and deionized water. The phosphoric acid was poured in a round-bottomed flask and stabilized at 80°C with reflux. Then 12.5 g of urea were slowly added to the acid. The mixture was put under agitation. When the urea was fully dissolved, 25 g of alkali lignin were slowly added to the mixture under vigorous agitation. After 1 h of reaction the mixture was dried in an oven at 70°C overnight, then it was heated at 150°C during 2 h for the thermal curing. After that, the lignin was cooled at room temperature and washed with ethanol using centrifugation. Finally, the treated lignin was dried at 80°C overnight. This lignin was named phosphorylated lignin (or P-Lig).

After both treatments, treated lignins were manually ground using an agate pestle and mortar set due to the agglomerates created during the chemical modifications. Thermogravimetric analysis (TGA), infrared spectroscopy (FTIR) characterizations and scanning electron microscopy (SEM) observations showed the effectiveness of both treatments on lignin.

2.3 Lignin surface energy characterization

Using more than two liquids with known surface tensions (γ_L) and components (γ_L^D, γ_L^P) for contact angle measurements, the dispersive and polar components (γ_S^D, γ_S^P) of solid surface energy (γ_S) can be determined via a linear form of the Owens-Wendt equation [5]:

$$\frac{\gamma_L(1+\cos\theta_e)}{2(\gamma_L^D)^{0.5}} = (\gamma_S^P)^{0.5}\frac{(\gamma_L^P)^{0.5}}{(\gamma_L^D)^{0.5}} + (\gamma_S^D)^{0.5} \quad (1)$$

It is important to point out that for surface energy determination, equilibrium contact angles (θ_e) are defined in Eq. 1, which might be significantly different from the advancing contact angles.

Advancing contact angles are defined in the well-known Washburn equation. This equation, originally describing the capillary rise in a tube, has been extended to describe the capillary wicking into porous media packed in a cylindrical column and assumed as capillary tube arrangements:

$$m(t)^2 = \left[\frac{(c\bar{r})\cdot\varepsilon\cdot(\pi R^2)^2}{2}\right]\frac{\rho^2\cdot\gamma_L\cdot cos\theta_a}{\eta}t \quad (2)$$

where $m(t)^2$ is the squared mass gained during the liquid rise, c is a parameter inversely proportional to the tortuosity and $\bar{r}$ is the mean capillary radius. The $c\bar{r}$ is defined as a geometric factor. R is the inner radius of the column (or the cylindrical sample holder), ε is the porosity of the medium and θ_a is the apparent advancing contact angle, representative of the interaction between the liquid and the porous medium during the capillary rise.

Generally, the capillary rise in a tube is stopped when the capillary force is balanced by the liquid weight in the tube. From this equilibrium, the well-known Jurin law defines the equilibrium height achieved by the liquid. An extension of the Jurin law for porous media packed in a column is proposed here. The Jurin law has been expressed as a function of the liquid mass at the

  doi:10.5075/epfl-298799_978-2-9701614-0-0

equilibrium (m_{eq}) and modified for powders or porous media packed in a cylindrical sample holder [3] as follows:

$$m_{eq} = \frac{2 \cdot \gamma_L \cdot \cos(\theta e)}{(c\bar{r}) \cdot g} \varepsilon \cdot (\pi R^2) \quad (3)$$

where g is the gravitational acceleration and θ_e is here an apparent equilibrium contact angle, representative of the liquid/porous medium interaction at equilibrium. The benefit and the originality of using this approach consist in taking advantage of the recorded equilibrium mass achieved after capillary wicking to obtain an apparent equilibrium contact angle.

The dynamic test of capillary wicking was carried out using a K100SF tensiometer (Krüss, Germany). The K100SF is provided with an electronic microbalance (resolution of 10^{-7} g) where the sample holder containing the porous medium is clamped (Figure 1A). The sample holder consists of a hollow cylinder with an inner radius of 4.6 mm and a graduated height of 20 mm (Figure 2B). The lignin was inserted in the sample holder in order to achieve a filled height of 10 mm. Knowing the density of each type of lignin (measured by the pycnometer) and the sample-holder volume that had to be filled, the lignin mass was determined in order to set the same powder volume fraction Vp for each test and lignin. A Vp of 45% (resulting in a porosity of 55%) was then chosen for all wicking tests.

Wicking tests were carried out with reference, acetylated and phosphorylated lignins using n-Hexane, water, ethylene glycol and lactic acid. All tests were performed in standard conditions. Both modified Washburn equation (Eq. 2) and Jurin law (Eq. 3) were applied for these experiments in order to characterize the $c\bar{r}$ and the contact angles corresponding to each theory.

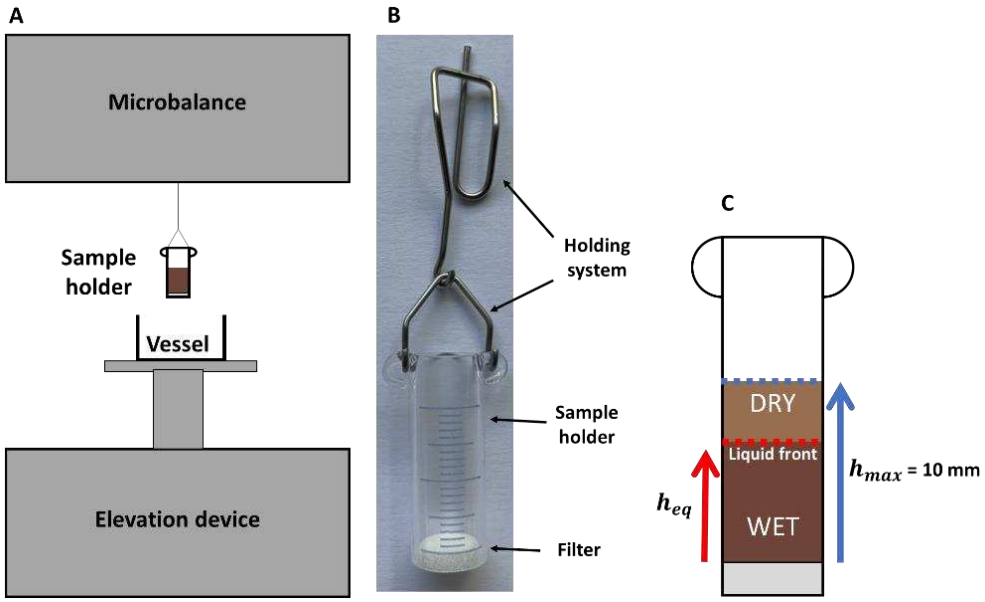

Figure 1. Capillary wicking: A) experimental set-up B) sample holder C) wicking representation.

An example of experimental curve is given in Figure 2 for the reference lignin with n-Hexane. The Washburn equation is verified if the curves recorded by the tensiometer during capillary wicking (m^2 vs t) have a linear trend. Firstly, n-Hexane is used as totally wetting test liquid (cos θ is approximated to 1) which allows the determination of $c\bar{r}$ from fit of the experimental

wicking curve with Eq. 2, as shown in Figure 2. In the same way, once $c\bar{r}$ is known, the linear fit of wicking curve with other liquids can be used to determine the apparent advancing contact angles (θ_a).

It is now interesting to observe that the curve in Figure 2 reaches an equilibrium weight (m_{eq}) due to the saturation of the porous medium by the test liquid. As for the Washburn approach, also for the Jurin law application, the squared equilibrium mass (m^2_{eq}) obtained with n-Hexane was used for the calculation of the $c\bar{r}$. Afterwards, the m^2_{eq} obtained with the other test liquids were used to determine the apparent equilibrium contact angles (θ_e).

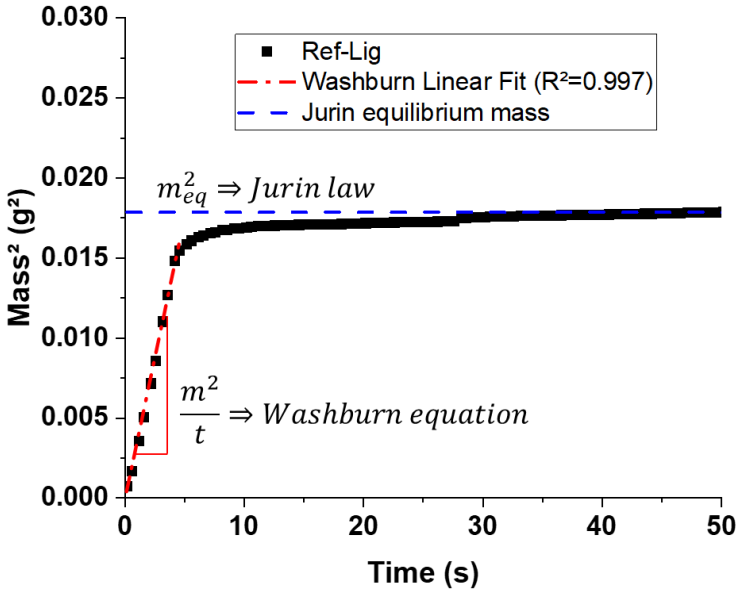

Figure 2. Washburn linear fit of experimental test of reference lignin with n-Hexane and Jurin squared equilibrium mass.

3. Results and discussion

3.1 Characterization of morphological and wetting parameters

Five tests were firstly performed with n-Hexane (Figure 3) in order to determine the $c\bar{r}$ for each lignin. It is possible to observe that the curves show a rapid wicking (less than 10 s) for untreated and treated lignins. All the samples were fully wetted showing a linear trend of wicking and the squared equilibrium mass was in a range between 0.0125 and 0.030 g² for all lignins. The slope of the curve (m^2/t) and the equilibrium mass (m_{eq}) were then used for the respective calculation of $c\bar{r}$ based on Washburn and Jurin equations.

Using the respective $c\bar{r}$, the determination of the contact angles was made applying both Washburn and Jurin approaches with the other test liquids, according to the experimental procedure.

Figure 4 shows wicking curves obtained for all lignins with ethylene glycol and photos of one sample per lignin after the test. One can observe that wicking kinetics were very different as a function of lignin. However, no curves showed a linear trend and then the Washburn equation could not be applied to determine the advancing contact angles. This was probably due to a

  doi:10.5075/epfl-298799_978-2-9701614-0-0

change in morphology occurring when the liquid is in contact with the lignin and then Washburn hypotheses (with a constant $c\bar{r}$) are not valid [9]. This interaction between lignin and ethylene glycol was observed in the literature and here, it causes a slight decrease of mass before achieving the equilibrium. Moreover, it is important to observe that the liquid reached different equilibrium heights depending on the lignin type. Using the Jurin approach, different apparent equilibrium contact angles were then found.

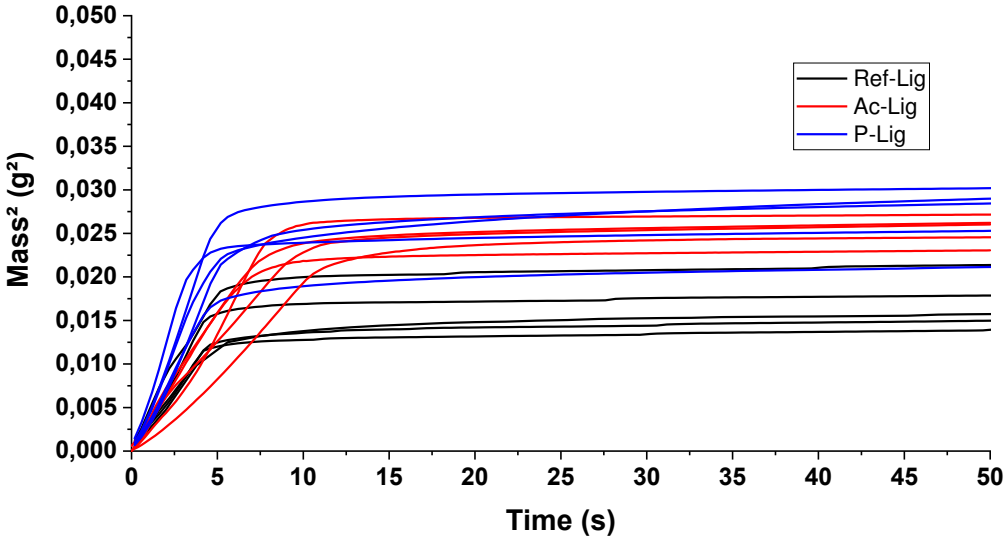

Figure 3. Wicking curves with n-Hexane for Ref-Lig, Ac-Lig, P-Lig.

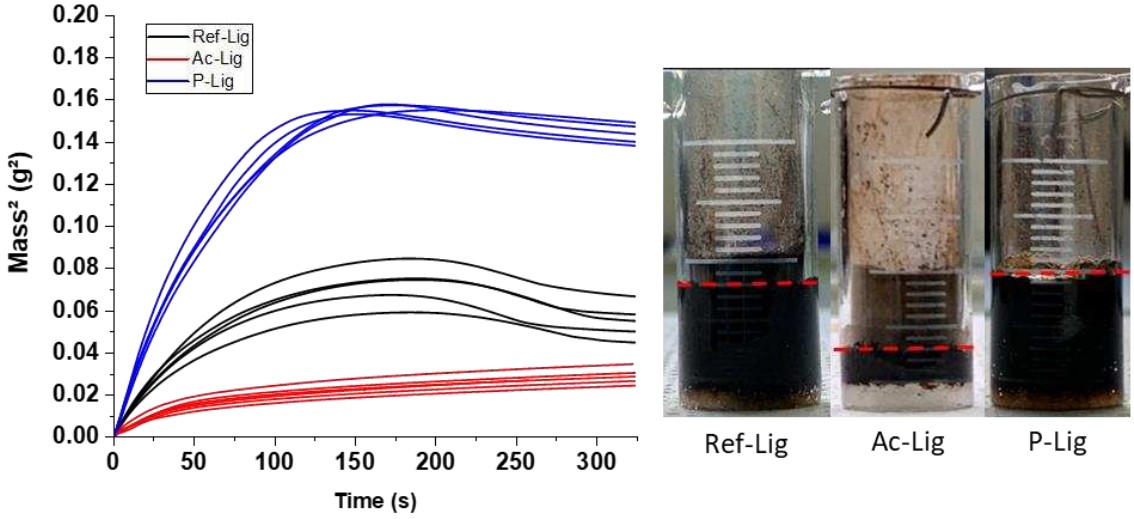

Figure 4. Wicking curves with ethylene glycol for Ref-Lig, Ac-Lig, P-Lig and respective liquid equilibrium heights (dash lines in red).

All equilibrium contact angles obtained applying the Jurin approach were then used to determine the surface energy and the dispersive and polar components of lignins.

  doi:10.5075/epfl-298799_978-2-9701614-0-0 published under CC BY-NC 4.0 license

3.2 Determination of lignin surface energy

The determination of lignin surface energy and their dispersive and polar components was possible using the Eq.1 and the apparent equilibrium contact angles obtained via the modified Jurin approach for porous media. Results are shown in Table 2.

Table 2: Surface energy and components of the different lignins.

	Ref-Lig	Ac-Lig	P-Lig
γ_S^D (mN/m)	13.60 ± 0.18	11.64 ± 0.14	23.31 ± 0.34
γ_S^P (mN/m)	39.25 ± 2.85	29.17 ± 1.36	17.88 ± 1.42
γ_S (mN/m)	52.85 ± 3.03	40.81 ± 1. 50	41.19 ± 1.76

Ref-Lig was found to have the highest surface energy (γ_s = 52.85 ± 3.03 mN/m) with a very high polar component (39.25 ± 2.85 mN/m). In the literature, Notley et al. [10] found a quite similar surface energy (57.1 mN/m) for a kraft lignin film using contact angles determined with a goniometer. Even if the two methods and the material form are different, the surface energies were close. However, the dispersive and polar components were not similar. The Ref-Lig is more polar that the Ac-Lig and the P-Lig, probably due to the OH and the Na+ content. The Ac-Lig (γ_s = 40.81 ± 1.50 mN/ m) and the P-Lig (γ_s = 41.19 ± 1.76 mN/m) have a lower surface energy with a widely reduced polar component. This is consistent with the fact that the chemical treatments removed a part of Na and grafting new functional groups on hydroxyl sites. Due to the effectiveness of treatments, the lignin clearly lost a large part of polar components. Reducing the polarity of lignin should have a beneficial effect on the adhesion with PLA that is known as a hydrophobic matrix [6]. P-Lig showed the lowest polar component (17.88 ± 1.42 mN/m) and, in addition, an increase of the dispersive component compared to Ref-Lig and Ac-Lig. This is due to the addition of phosphorus, which has a heavier electron cloud and facilitates instantaneous dipolar moments formation [11].

4. Conclusion

Surface energy results were found to be consistent with the literature and with lignins characterizations. This proves that the modified Jurin approach coupled to an adapted experimental procedure for powders and porous media can be an effective and simple solution to determine suitable surface energy of these materials. Another interesting result is that the phosphorylation, known to be efficient for improving thermal stability of composites, could be also promising to improve the adhesion at the lignin/PLA interface compared to the acetylation, which is already known as an efficient treatment for this aim. Knowing filler surface energy components is also relevant to determine the work of adhesion between the filler and the matrix. For PLA matrix, surface tension components should be determined at the molten state [12, 13]. However, as a first approximation, lactic acid dispersive and polar components could be used to calculate the work of adhesion. All these aspects will be discussed during the oral session. Further studies about the enhancement of interface adhesion and the mechanical behavior of this interface represent the perspectives of this work.

  doi:10.5075/epfl-298799_978-2-9701614-0-0

Acknowledgements

The authors thank J.C. Roux of IMT Mines Alès for his help to conduct the SEM characterizations.

5. References

1. A. Duval and M. Lawoko, "A review on lignin-based polymeric, micro- and nano-structured materials," *React. Funct. Polym.*, vol. 85, pp. 78–96, 2014.
2. J. Guo, X. Chen, J. Wang, Y. He, H. Xie, and Q. Zheng, "The influence of compatibility on the structure and properties of PLA/lignin biocomposites by chemical modification," *Polymers*, vol. 12, no. 1, 2020.
3. V. Carretier, M. F. Pucci, C. Lacoste, A. Regazzi and J. M. Lopez-Cuesta, "An efficient solution to determine surface energy of powders and porous media: application to untreated and treated lignin," *Applied Surface Science,* vol. 579, 152159, 2022.
4. W. Wu, R. F. J. Giese, and C. J. van Oss, "Evaluation of the Lifshitz-van der Waals/Acid-Base Approach To Determine Surface Tension Components," *Langmuir*, vol. 11, no. 1, pp. 379–382, 1995.
5. M. F. Pucci, P. J. Liotier, and S. Drapier, "Tensiometric method to reliably assess wetting properties of single fibers with resins: Validation on cellulosic reinforcements for composites," *Colloids Surfaces A Physicochem. Eng. Asp.*, vol. 512, pp. 26–33, 2017.
6. L. Jeantet, A. Regazzi, A. Taguet, M. F. Pucci, A. S. Caro, and J. C. Quantin, "Biopolymer blends for mechanical property gradient 3d printed parts," *Express Polym. Lett.*, vol. 15, no. 2, pp. 137–152, 2021.
7. S. C. Fox and A. G. Mcdonald, "Chemical and Thermal Characterization of Three Industrial Lignins and Their Corresponding Lignin Esters," *BioResources*, vol. 5, no. 2, pp. 990–1009, 2010.
8. Y. Guo, C. Cheng, T. Huo, Y. Ren, and X. Liu, "Highly effective flame retardant lignin/polyacrylonitrile composite prepared via solution blending and phosphorylation," *Polym. Degrad. Stab.*, vol. 181, 109362, 2020.
9. H. N. Vo, M. F. Pucci, S. Corn, N. Le Moigne, W. Garat, S. Drapier and P. J. Liotier, "Capillary wicking in bio-based reinforcements undergoing swelling – Dual scale consideration of porous medium," *Compos. Part A Appl. Sci. Manuf.* vol. 134, 105893, 2020.
10. S. M. Notley and M. Norgren, "Surface energy and wettability of spin-coated thin films of lignin isolated from wood," *Langmuir*, vol. 26, no. 8, pp. 5484–5490, 2010.
11. J. M. Douillard, F. Salles, M. Henry, H. Malandrini, and F. Clauss, "Surface energy of talc and chlorite: Comparison between electronegativity calculation and immersion results," *J. Colloid Interface Sci.*, vol. 305, no. 2, pp. 352–360, 2007.
12. M.F. Pucci, B. Duchemin, M. Gomina and J. Bréard, "Temperature effect on dynamic wetting of cellulosic substrates by molten polymers for composite processing" *Compos. Part A Appl. Sci. Manuf.* vol. 114 pp. 307-315, 2018.
13. M.F. Pucci, B. Duchemin, M. Gomina and J. Bréard, "Dynamic wetting of molten polymers on cellulosic substrates: model prediction for total and partial wetting" *Frontiers in Materials*: vol 7: 143, 2020.

  doi:10.5075/epfl-298799_978-2-9701614-0-0

SIMULATING PID FOR CURING IN A DIAPHRAGM FORMING STATION

Franz, Maier[a], Joachim Osterberger[a], Florian Silber[a], Roland Hinterhölzl[a]

a: University of Applied Sciences Upper Austria – franz.maier@fh-wels.at

Abstract: *We describe the material characterization required to model curing and the resulting process induced deformations for a low temperature epoxy UD prepreg. This includes the cure kinetics, cure shrinkage, coefficient of thermal expansion and modulus-development. Material data was fit to models with python scripts. Curing experiments with multiple lay-ups were performed in a diaphragm forming station on aluminum tool equipped with heating cartiges. The process was modeled in Abaqus with the Compro plug-in. High-resolution 3D laser scans of manufactured parts were compared with the predicted process induced deformations and good agreement was observed.*

Keywords: process induced deformations, process simulation, diaphragm forming, epoxy, UD prepreg

1. Introduction

Finite element (FE) based process simulations became a viable tool to simulate the draping behavior, cure kinetics and the resulting process induced deformations (PID) of carbon fiber reinforced polymer (CFRP) components [1]. Simulation approaches either aim to incorporate a variety of relevant, individually characterized mechanisms [2] or rely on carefully calibrated phenomenological assumptions [3]. A full process simulation allows for a detailed investigation and virtual optimization, but it does require substantial experimental and computational effort. The phenomenological approach can provide reasonably accurate PID simulations comparably fast, but results are typically specific to certain processing-conditions and material lay-ups and cannot be generalized. In this paper we describe a full characterization of a low-temperature epoxy-prepreg and include it in the material library of the commercially available process simulation toolbox Compro (Convergent). Simulation results are compared against parts draped and cured in a diaphragm forming station.

2. Methods

We used the low temperature UD prepreg HexPly M79/34%/UD300/CHS with an isothermal curing temperature of 70°C to 120°C and curing time of $\leq$480 min and $\leq$60 min, respectively and 0.5-5 bar pressure, according to the data sheet. These conditions allow for out-of-autoclave curing, realized as modified diaphragm forming station setup. The corresponding process model was set-up in Abaqus 2019 with the Compro plug-in.

2.1 Material Characterization and Modelling

Compro follows the Cure Hardening Instantaneously Linear Elastic (CHILE) approach [4] and the material properties evolve as a function of a monotonically increasing degree of cure (DOC). The models are described in detail in [5] and are only briefly described below.

2.1.1 Cure Kinetics

Utilizing a DSC 3 (Mettler Toledo) we measured the heat flow at either constant curing temperatures, i.e., isothermal at 100,110 and 120°C, or at constant heating rates, i.e., dynamic,

  doi:10.5075/epfl-298799_978-2-9701614-0-0

with 0.5, 2, 5, 10, 15 and 20°C/min, representing the thermal conditions occurring during processing. Specimen of 6.5.mg ± 1 mg where weighted and placed in an aluminium crucible. A Arhenius-type cure kinetics model developed by [6] (CK Model 5 in Compro), used for the (Hexcel 8552 expoxy resin) was used to model the experimental data:

$$\dot{\alpha} = K_1(1-\alpha)^l + K_2\alpha^m(1-\alpha)^n, K_i = A_i e^{\frac{\Delta E_i}{RT}}, \quad (1)$$

where K_1 and K_2 are the rate constants, α is the degree of cure, l, m and n are fitting parameter, A is the pre-exponential factor, E is the activation energy, R is the universal gas constant, and T is the absolute temperature.

2.1.2 Cure Shrinkage

A plate-plate rheometer (MCR302, Anton Paar), where the gap distance was measured during curing while a constant force (F = 0.1 N) was maintained [7], was used to measure the cure shrinkage of the neat resin at 120°C. The measured strain was fit to linear cure shrinkage strain:

$$\varepsilon_L = ((1+\nu)\left(\frac{\nu}{1-\nu}\right)+1)^{-1}\left(\frac{h-h_0}{h_0}\right), \quad (2)$$

where the Poisson's ratio ν = 0.35, h_0 is the initial gap distance and h is the current gap. It was converted to a volumetric shrinkage strain:

$$\varepsilon_V = (\varepsilon_L + 1)^3 - 1 \quad (3)$$

The experimental setup necessitates a minimal detectable force response and cannot detect the cure shrinkage before gelation. To account for the shrinkage in this range of the process the measured data was linearly extrapolated.

2.1.3 Coefficient of Thermal Expansion (CTE)

A 12M Aramis DIC system (GOM), was used to measure the longitudinal and transversal strain during heating of a speckled specimen positioned on a heating plate. Temperature was recorded using a thermocouple. For the thermal expansion of the laminate in fibre direction a CTE_1 value of 0.5*10^{-6}K^{-1} was found in the literature [8]. To model the changing CTE with progressing DOC a biliniear approach, with a linear CTE below and above the T_g, was used [9]. Thus, two experiments, one with an uncured and one with a cured specimen were conducted. The material behavior was modelled with a lumped CTE model:

$$\mathrm{CTE}_{22} = \mathrm{CTE}_{22\mathrm{Nom}} + \mathrm{CTE}_{22\mathrm{TF}}(T - \mathrm{CTE}_{\mathrm{T0}}) + \mathrm{CTE}_{22\mathrm{AF}}(\alpha - \mathrm{CTE}_{\mathrm{AL0}})$$
$$\mathrm{CTE}_{11} = \mathrm{CTE}_{11\mathrm{Nom}} + \mathrm{CTE}_{11\mathrm{TF}}(T - \mathrm{CTE}_{\mathrm{T0}}) + \mathrm{CTE}_{11\mathrm{AF}}(\alpha - \mathrm{CTE}_{\mathrm{AL0}}) \quad (4)$$

$\mathrm{CTE}_{22\mathrm{Nom}}$ is the thermal expansion coefficient of the uncured material ($\triangleq \mathrm{CTE}_{22\mathrm{uncured}}$), $\mathrm{CTE}_{22\mathrm{Af}}$ ($\triangleq \mathrm{CTE}_{22\mathrm{cured}}$ - $\mathrm{CTE}_{22\mathrm{uncured}}$) and $\mathrm{CTE}_{22\mathrm{Tf}}$ are fitting parameters, $\mathrm{CTE}_{\mathrm{T0}}$ and $\mathrm{CTE}_{\mathrm{AL0}}$ are the initial temperature and initial degree of cure, T is the current temperature and α is the current degree of cure.

2.1.4 Modulus Development

The elastic modulus of the neat M-79 resin was determined with an oscillating rheometer (MCR 302, Anton Paar) with a frequency of 10 rad/s at a maximum strain of 25% and a gap

  doi:10.5075/epfl-298799_978-2-9701614-0-0

distance of 1 mm. Experiments at 100°C and 120°C were considered for model fitting. The storage modulus of the resin was fitted to (RM2 in Compro) [2]:

$$E_r' = E_r^0 + \frac{(T^* - T_{C1}^*)}{(T_{C2}^* - T_{C1}^*)}(E_r^\infty - E_r^0), T_{C1}^* < T^* < T_{C2}^* \quad (5)$$

and set to $E_r^0 = E_r^\infty/1000$ below glass transtion and $E_r^\infty = 7200$ MPa for the fully cured resin (determined with Chami's rules of mixtures). The Temperature T^* and the lower and upper bound for glass transition Temperatures T_{C1}^* and T_{C2}^* are determined with rules of mixtures. Then the final resin modulus was determined as:

$$E_r = E_r'[1 + a_{Er}(T - T_0)] \quad (6)$$

2.2 Diaphragm Forming and Curing

For this study we combined a diaphragm forming station (Langzauner) with a heated tool (Fig. 1 a), allowing us to cure prepregs immediately after draping, without moving the tooling after draping (Fig. 1 b). The prepreg was draped and in a subsequent step the membrane was raised and a peel ply and breather cloth were placed. Heating was realized by drilling holes in the tooling and placing 6 heating cartridges with a total of 1800W, allowing us to reach 120°C within 10 minutes. This temperature was then held for 45 min to completely cure the part. Cooling was accelerated by blowing compressed air through the foundation of the tooling (c.f. Silicon tubing indicated by the red arrow in Fig. 1 a).

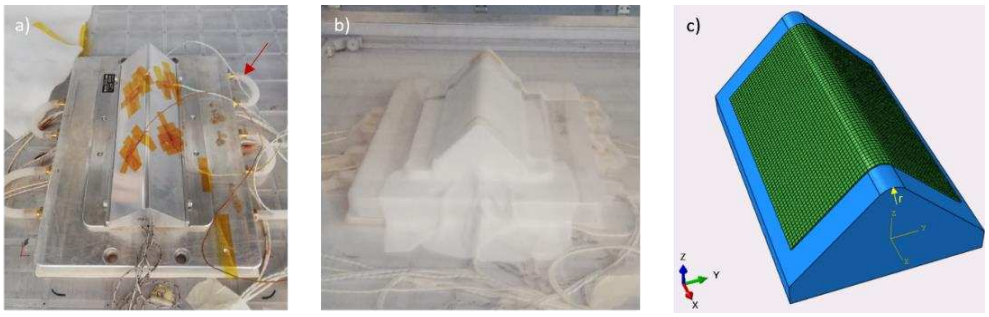

Figure 1:a) Tool with thermocouples, heating cartiges and cooling (red arrow); b) setup during curing; c) FEM modell

2.3 Process Model and Comparison with Experiment

The curing and PID simulation were implemented in Abaqus CAE (2019) with the Compro (Convergent) plug-in. A simple L-shaped geometry (Fig. 1 c)) with a radius of 6.4 mm and multiple lay-ups ([0-0-0], [0-0-90], [0-90], [0-90-90]) were realized. The temperature profile for the curing simulation was measured in a preliminary experiment with multiple thermocouples placed at the surface (Fig. 1 a) and implemented as amplitude. The pressure amplitude was modelled according to the setting by the system. The laminate is meshed with quadratic brick elements (C3D20). The manufactured parts were scanned with a 3D-Laser scanner (RS-6, Hexagon) and compared to the predicted geometry within Geomgaic Control-X. Experiment and Simulation were aligned using a best-fit algorithm. Maximum, minimum, and average values for the deviation as well the Spring-in in the center and the periphery of each part were extracted.

  doi:10.5075/epfl-298799_978-2-9701614-0-0

3. Results

3.1 Material Characterization and Modelling

3.1.1 Cure Kinetic

Heating rates 2-20K/min resulted in insuffcient curing and an inconsisten heat of reaction an had to be discarded for modelling (Fig. 2 a). This appears to be a characteristic of the resisn where diffusion is prohibitet at high curing rates. This problem did not arise at 0.5K/min (Fig. 2 b) and during the isothermal experiments (Fig. 2 c), where a heat of reaction of 80 J/g was determined, matching the data sheet. The fitted models are showin in Fig. 3 and model parameters are summarized in Table 1.

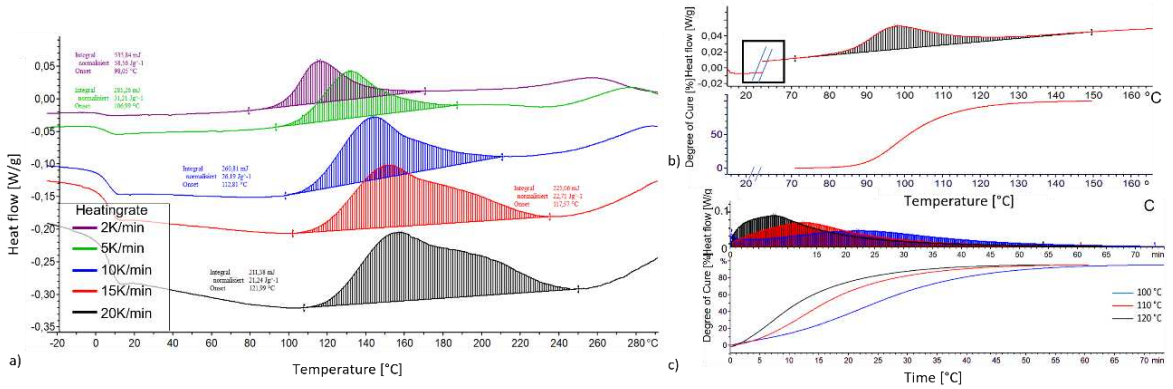

Figure 2: a) Recorded heat flow during dynamic DSC runs with inconsistent heat of reaction; b) dynamic DSC run at 0.5K/min with consistent heat of reaction. The box indicates a cut of the x-axis; c) the isothermal DSC experiments.

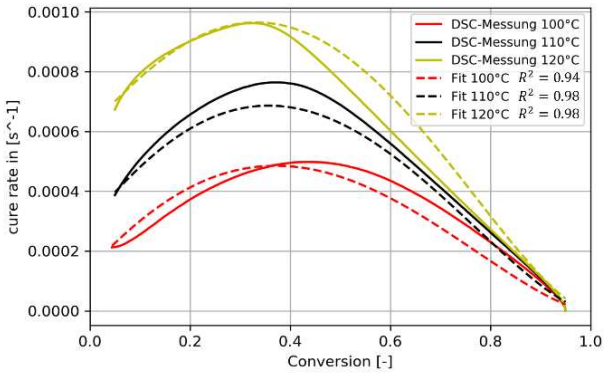

Figure 2: Isothermal DSC experiments and model fits.

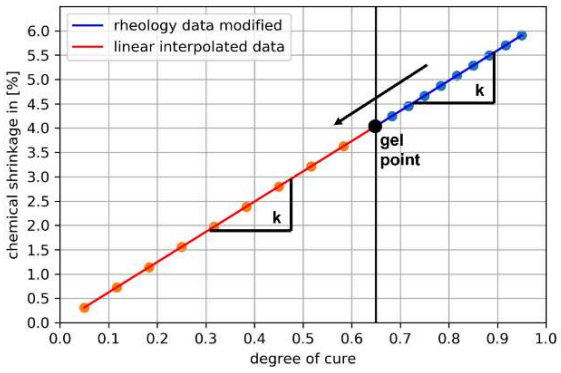

Figure 4: Linear cure shrinkage

3.1.2 Cure Shrinkage

The cure shrinkage strain determined at 120°C is shown in Fig. 4. A total volumetric shrinkage strain of 5.9% at a conversion rate of 95% was determined, resulting in a linear coefficient A = 0.0621.

3.1.3 Coefficient of Thermal Expansion

The recess and subsequent increasing of the curve could also be an indicator, that the material was not fully cured. Results are shown in Fig. 5.

  doi:10.5075/epfl-298799_978-2-9701614-0-0

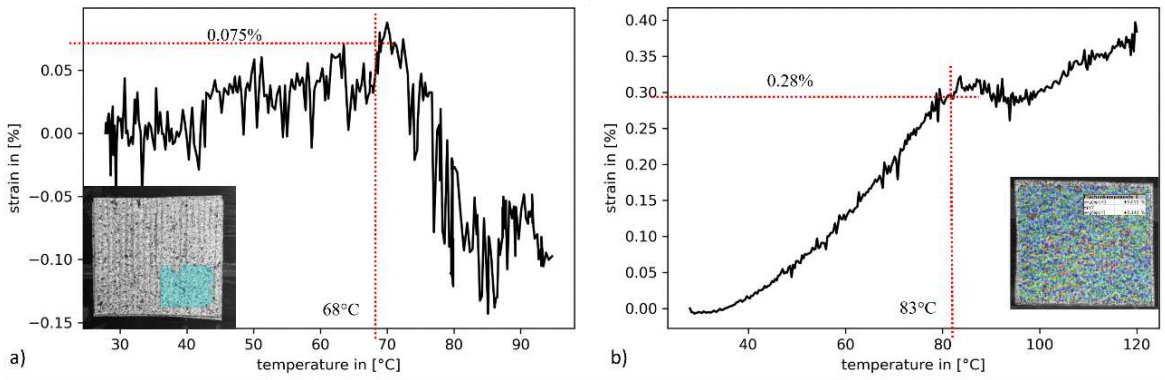

Figure 3: Thermal expansion measured with DIC for a) uncured and b) cured specimen

A $CTE_{22uncured}$ of $1.74*10^{-5}$ K^{-1} at $\varepsilon = 0.075\%$ and ΔT of 43°C (from 25°C to 68°C) and a $CTE_{22cured}$ of $4.8*10^{-5}$ K^{-1} at ε = 0.28% and a ΔT of 58°C (25°C to 83°C) were considered for parameter fitting. The resulting fitting parameter for the lumped model are summarized in Table 1.

Table 1: Model Parameter for Compro

Model Parameter	Cure Kinetics
E1	88586.362
E2	39144.5
A1	366232451.3
A2	834.153
m	1.039
n	1.600
l	4.812

Model Parameter	Modulus Development
E_r^0	5.923E+06 Pa
E_r^∞	5.923E+09 Pa
$T^*_{C1_a}$	222.3097°C
$T^*_{C1_b}$	0 1/°C
T^*_{C2}	309.334 K
T_{ga}	276 K
T_{gb}	463 K
T_0	20°C
a_{Er}	0 1/K

Model Parameter	Lumped CTE
CTE_{11Nom}	0.5E-06 K^{-1}
CTE_{11TF}	0.00
CTE_{11AF}	0.00
CTE_{22Nom}	1.74E-05 K^{-1}
CTE_{22TF}	0.00
CTE_{22AF}	3.06E-05 K^{-1}
CTE_{T0}	30.00°C
CTE_{AL0}	0.05

3.1.4 Modulus Development

The loss and storage modulus for the neat resin at 120°C are show in Fig. 6 a) and the corresponding model fit of the response after the onset of cure in Fig. 6 b). Material parameters are summarized in Table 1.

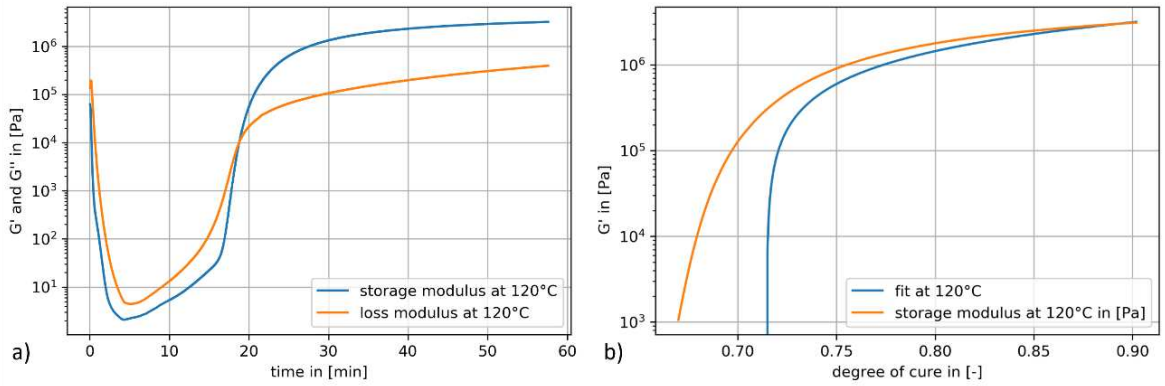

Figure 4: a) Storage and loss modulus from oscillation rheometer experiments and b) corresponding fit for the modulus after the onset of curing at 120°C

3.2 Process Model and Comparison with Experiment

Figure 7 shows representative parts for each lay-up and the corresponding deviation from the 3D comparison. The average deviation is very low due to the best-fit alignment procedure. More importantly we see that the absolute deviation (min or max) is reasonably low, i.e. for all investigated lay-ups. The biggest deviation between simulation and experiment was found for the unsymmetric lay-up [0-0-90], where the very tips of each corner showed absolute values up to 1.5 mm. The overall deformation of the part is inhomogeneous because of simultaneous spring-in and warpage and thus, is challenging to assess. Comparison with an ideal 90° angle showed a deviation of approx. 6.5mm. The average spring-in across in the center and periphery was predicted within 2.32° for the [0-0-90] lay-up und <1° for the remaining lay-ups.

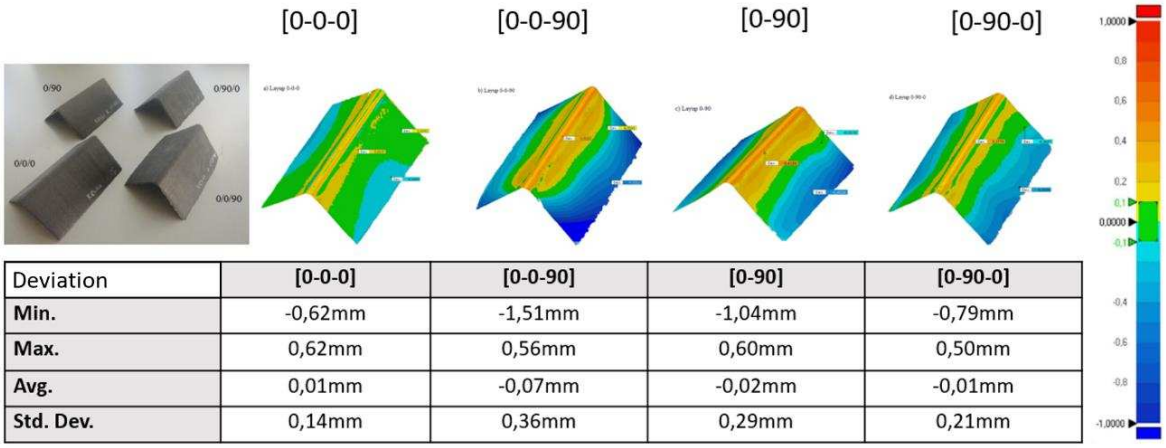

Deviation	[0-0-0]	[0-0-90]	[0-90]	[0-90-0]
Min.	-0,62mm	-1,51mm	-1,04mm	-0,79mm
Max.	0,62mm	0,56mm	0,60mm	0,50mm
Avg.	0,01mm	-0,07mm	-0,02mm	-0,01mm
Std. Dev.	0,14mm	0,36mm	0,29mm	0,21mm

Figure 5: Comparison of predicted PID and Experiments.

	Spring-In									
	MP1			MP2			MP3			Mean Dev.
	Exp.	Sim.	Δ in Grad	Exp.	Sim.	Δ in Grad	Exp.	Sim.	Δ in Grad	
[0-0-0]	0,45°	0,10°	-0,35°	0,71°	-0,19°	-0,9°	0,45°	0,25°	-0,2°	**-0,48°**
[0-0-90]	1,15°	-1,08°	-2,24°	-2,14°	-3,92°	-1,78°	2,55°	-0,41°	-2,95°	**-2,32°**
[0-90]	-4,89°	-5,34°	-0,45°	-5,51°	-6,37°	-0,86°	-4,61°	-5,77°	-1,17°	**-0,83°**
[0-90-0]	0,64°	-0,06°	-0,69°	0,77°	-0,32°	-1,09°	0,82°	-0,08°	-0,91°	**-0,9°**

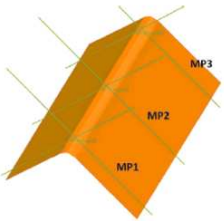

Figure 6: Comparison of predicted and experimentally determined spring-in.

4. Discussion

The presented material characterization allowed for concise modelling of the material behavior for curing and subsequent PID simulations with Abaqus and the Compro plug-in. Overall good agreement between the selected models and the experimental data was achieved for the investigated processing conditions. However, higher heating rates, as desirable for industrial applications could not be accurately depicted with the selected model. A model capable of capturing the diffusion phenomenon should be considered to improve the applicability. We did not consider the formation of gradients in the fiber volume fraction due to resin flow and bleeding before the onset of curing. This mechanism requires the characterization of the viscosity with advancing degree of cure and could be implemented in Compro (flow-compaction). However, because of the relatively short curing time, the moderate pressure, and the thin laminates, we deemed this aspect negligible.

  doi:10.5075/epfl-298799_978-2-9701614-0-0

While we performed a preforming step with the diaphragm forming station, we did not include this step in the simulation. Potential residual stresses due to draping are therefore not considered. In our experiments we found that initial manufacturing defects, especially fiber bridging and folds tend to disappear once the material is heated. The originally tacky material softens significantly and allows for relative movement of the laminate and tooling, allowing a relaxation of residual stresses and manufacturing defects.

Our approach to create 3D scans of the experiments allows for a thorough comparison, bypassing the challenge of locally comparing complex shapes showing superimposed signs of warpage and spring-in. However, so far only a simple geometry with no initial defects is successfully compared using the 3D Laser scans. Comparing more complex geometries necessitates to model the complete process chain from preforming to curing and is the subject of ongoing investigations.

Currently only thin laminates up to four layers are being investigated to ensure good drapability of the stacks. Expanding the setup to thicker laminates and carefully assessing the laminate quality is the topic of an ongoing project. However, due to the lack of structural stability PID's are typically more pronounced in thinner laminates, making them an ideal target to validate PID simulations. We could observe that warpage was generally overestimated. One potential explanation could be an insufficient modelling of the tool-part interaction, a major driver of warpage. Therefore, the frictional properties of the laminate with increasing temperature and degree of cure must be thoroughly characterized. Additionally, predictions were more accurate for symmetric lay-ups, indicating that modelling the bending-extension interaction should be improved.

The validation results show that the curing process within the diaphragm forming station is generally well predicted by the simulation and that diaphragm forming with prepregs is not inevitable only a preforming step but can also be expanded for direct out of autoclave part production.

Acknowledgements

We thank our funding source, the Austrian Research Promotion Agency (FFG) for supporting us in the project ProSim (866878).

References

1. Baran, I., Cinar, K., Ersoy, N., Akkerman, R., and Hattel, J. H. (2017). "A Review on the Mechanical Modeling of Composite Manufacturing Processes." *Archives of Computational Methods in Engineering*, Springer Netherlands, 24(2), 365–395.
2. Johnston, A. a. (1997). "An integrated model of the development of process-induced deformation in autoclave processing of composite structures." University of British Columbia, (April), 1–367.
3. Kappel, E., Stefaniak, D., and Fernlund, G. (2015). "Predicting process-induced distortions in composite manufacturing - A pheno-numerical simulation strategy." Composite Structures, Elsevier Ltd, 120, 98–106.
4. Johnston, A., Vaziri, R., and Poursartip, A. (2001). "A plane strain model for process-induced deformation of laminated composite structures." Journal of Composite Materials, 35(16), 1435–1469.

  doi:10.5075/epfl-298799_978-2-9701614-0-0

5. Convergent Manufacturing Technologies Inc. (2018). “CCA Material Constitutive Model Documentation.”
6. S.N. Lee, M.T. Chiu, and H.S. Lin, Kinetic Model for the Curing Reaction of a Tetraglycidyl Diamino Diphenyl, Methane/Diamino Diphenyl Sulfone (TGDDM/DDS) Epoxy Resin System, Polymer Engineering and Science 32(15), 1992, pp. 1037-1046.
7. Haider, M., Hubert, P., and Lessard, L. (2007). “Cure shrinkage characterization and modeling of a polyester resin containing low profile additives.” Composites Part A: Applied Science and Manufacturing, 38(3), 994–1009.
8. Meschut, G., Mayer, B., Brede, M., Jäger, H., and Melz, T. (2020). FAT-Schriftenreihe 326.
9. Menard, K., and Cassel, B. (2013). “Basics of Thermomechanical Analysis with TMA 4000.” 1–4.

  doi:10.5075/epfl-298799_978-2-9701614-0-0

A CASSETTE-LIKE PEELING TEST SYSTEM FOR EVALUATING THE DELAMINATION RESISTANCE OF SOFT-TO-RIGID BONDING ASSEMBLIES

Xiaole, Li, Gilles, Lubineau

Email: xiaole.li@kaust.edu.sa (Xiaole Li), gilles.lubineau@kaust.edu.sa (Gilles Lubineau)

Mechanics of Composites For Energy and Mobility Lab, Mechanical Engineering Program, Physical Science and Engineering Division, King Abdullah University of Science and Technology (KAUST), Thuwal 23955-6900, Kingdom of Saudi Arabia

Abstract: *We develop a cassette-like peeling system for measuring fracture toughness of bonding assemblies composed of a soft film and a relatively rigid substrate. The system adopts a tensile load to drive the rotation of a cassette-like spool so as to peel the soft film, which facilitates its accommodation into universal testers. With this system, we maintain a self-similar fracture process zone and a stationary peeling front during peeling. Moreover, this simple-yet - versatile peeling configuration is naturally suitable for the evaluation of the delamination resistance of curved specimens, like those composite pipes manufactured by filament winding. A comprehensive validation is carried out by comparing the results of peeling a Kapton® tape and a hypereleastic film by using the developed peeling system and the conventional system. Featuring with the versatility and ease-to-use characteristic, the cassette-like peeling system has a potential to promote the next generation of peeling test standards.*

Keywords: Peeling test; Soft film bonding; Adhesion; Delamination resistance

1. Introduction

Different test methods can be employed for measuring the fracture toughness of bonded assemblies. Some representative are the double cantilever beam test, the compact tension and the peeling test. Among the existing test methods, the peeling test is a common practice to evaluate the adhesion of flexible-to-flexible and flexible-to-rigid bonded assemblies, usually by tensile. For a peeling test, we should maintain a self-similar fracture process zone throughout the peeling process. To achieve this, different test-setups are developed, e.g., the T-peel test, Floating roller test and Climbing drum test, etc [1]. These peeling test configurations have found their applications in evaluating toughness of specific flexible-to-flexible and flexible-to-rigid bonded assemblies. In most cases, the implementation of such tests is tedious, and a synchronizing motion of specimen substrate (the rigid part) with the peeling displacement needs to be applied to maintain the peeling angle. However, when evaluating soft-to-rigid assemblies, all the existing peeling test standards will fail to measure the accurate toughness due to the considerate stretching of peeled film under the peeling load. Recently, a double drum peel test was developed to measure the delamination resistance of curved composite structures [2].

The test shown in Figure 1 shows the limitation of the conventional peeling test in evaluating a soft-to-rigid bonding assembly. We peeled a sis thin film that is bonded to an aluminum substrate. The supposed peeling angle is θ_0=60° as shown by the initial state of the test setup. With the load increases, the soft film experienced elastic elongation without crack propagation. Because of the synchronized movements of peeling head and the specimen, the elongation of peeling arm led to a misalignment between the peeling head and crack tip, such that a changing

  doi:10.5075/epfl-298799_978-2-9701614-0-0 published under CC BY-NC 4.0 license

peeling angle θ'. This misalignment generally occurs when peeling any materials using the conventional approach. When peeling a soft film with high stretchablity, this misalignment will be significant due to the extensive tensile deformation of the film, as shown in Figure 1. This will produces an inaccurate measurement of peeling force due to the continuously changing peeling angle.

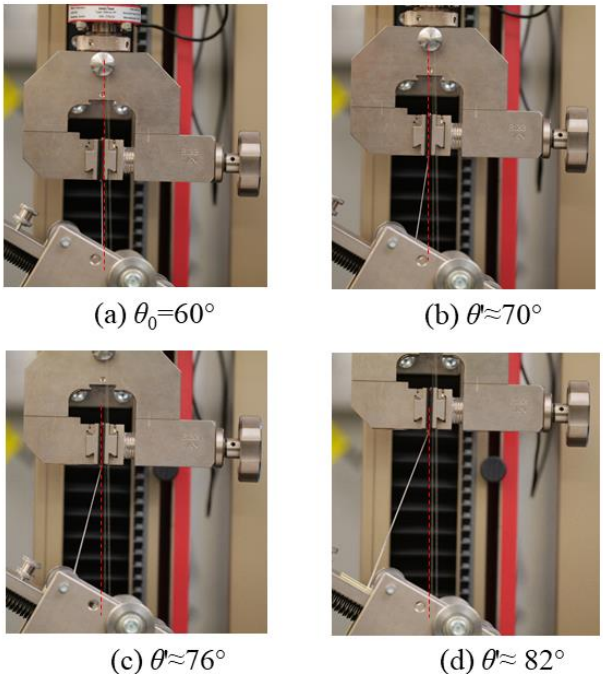

Figure 1. Peeling a soft film with the conventional peeling test method (TH50+SW1, Grip Engineering Inc.*).*

To have an objective evaluation of the adhesion quality of soft-to-rigid bonding assemblies, the present work aims at developing a novel peeling test system that facilitates the test of peeling a soft film.

2. Cassette-like peeling system

Similar with the conventional peeling method, we adopt tensile load to drive the crack propagation, ensuring the system's compatibility with most universal testers. Inspired by working process of audio cassette and the double drum peel test [2], the specimen is designed to be pie-shaped, achieving a cassette-like peeling process. The concept of the cassette-like peeling system is shown in Figure 2a, a reverse torque is applied on the cassette spool to balance the torque induced by the off-axial peeling load when the peeling angle is smaller than 90°. In this case that the interface is with uniform fracture properties, i.e. a constant fracture toughness, the applied peeling force and the reverse torque should not change during peeling process. As long as the proper load is applied, the peeling angle is only dependent on the horizontal distance between the axle of spool and the crack tip. The rendered prototype is shown in Figure 2b based on the cassette-like peeling concept. The reverse torque is applied via a suspended counterweight sagging tangential to the coaxial spool with the radius *R*. The magnitude of the torque can be adjusted by changing the suspended counterweight sagging tangential to the coaxial spool to ensure the peeling film is always vertical to the platform. In so doing, the peeling angle will be always the supposed one.

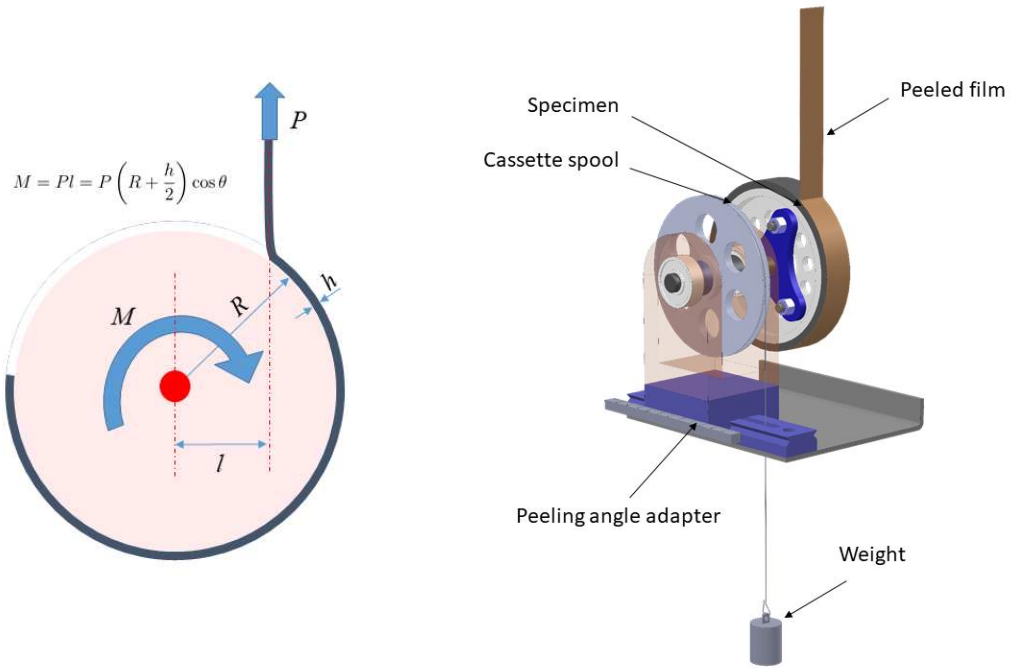

Figure 2. The cassette-like peeling concept and the rendered peeling test system to realize this concept.

Figure 3 shows the cassette-like peeling test apparatus manufactured in house. The spool was made from a very light Al alloy to reduce the effect of inertia on the test. The axle was based on a platform fitted to a slide rail. We accommodate the manufactured cassette-like peeling system into the Zwick/Roell universal testing machine as shown in Figure 3. A laser pointer connecting to the gripper of peeling film is installed. In the initial stage of establishing steady crack, the trial reverse torque is adjusted by changing the counterweights to ensure the peeling arm is perpendicular to the base platform, the alignment of the film is diagnosed by the laser pointer. Once the peeling film is perfectly vertical indicated by the positioning laser line, the expected peeling angle is achieved. We notice that, in this system, the peeling angle is adjusted by changing the position of the cassette spool along the sliding rail.

Figure 3. The prototype of the cassette-like peeling system.

  doi:10.5075/epfl-298799_978-2-9701614-0-0

3. Validation of the cassette-like peeling system

3.1 tape test

We carried out the tape peeling tests. Specifically, we peeled an almost inextensible Kapton® tape with a width of 20 mmm using both the conventional peeling system and the cassette-like peeling system. It is, as demonstrated by the 60° peeling tests result and 90 peeling test results in Figure 4, that in the case of peeling without considerate elongation, the developed cassette-like peeling system perform equally well with the commercially available conventional peeling test system. The oscillation of the peeling force in 60° peeling is induced by the operation of adjusting the reverse torque at the initial stage, afterwards, the film kept vertical and achieve a stable crack propagation with constant peeling angle.

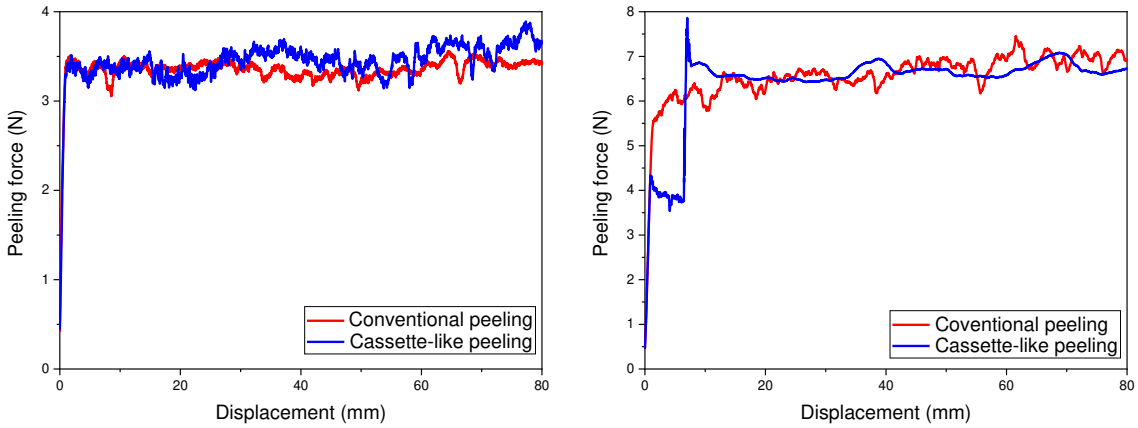

(a) 90 degree peeling *(b) 60 degree peeling*

Figure 4. The tape test results.

3.2 Energy balance analysis of peeling a soft film

Considering all the possible sources of energy dissipation, the Griffith's energy criterion can be written as:

$$G_c + \frac{1}{b}\left(\frac{\mathrm{d}U_{ft}}{\mathrm{d}a} + \frac{\mathrm{d}U_{fb}}{\mathrm{d}a} + \frac{\mathrm{d}U_{\mathrm{loss}}}{\mathrm{d}a}\right) = -\frac{\partial \Pi}{b\partial a} = \frac{1}{b}\left(\frac{\mathrm{d}U_{ext}}{\mathrm{d}a} - \frac{\mathrm{d}U_{e}}{\mathrm{d}a}\right) \tag{1}$$

where Π is the total potential of the peeling system, a is the crack length, U_{ext} is the external work, U_e is the stored tensile strain energy, U_{ft} and U_{fb} are the energy dissipation caused by film tension and film bending, respectively, and U_{loss} is the energy loss because of friction, material inertia and etc. In the case that the thickness of the peeling film (h) is negligible compared to R, we can derive G_c according to the Griffith energy balance theory [3]:

$$G_c = \frac{P}{b}(1-\cos\theta) + \frac{P}{b}(\lambda - 1) - h\int_0^{\lambda} \sigma_e \cdot \mathrm{d}\lambda \tag{2}$$

where P is the peeling force, θ is the peeling angle and σ_e is the nominal stress carried by the film and λ is the stretch ratio of the film. It should be noticed that we ignored the energy loss of system and assumed a zero bending stiffness of the film (this is generally true for flexible films).

  doi:10.5075/epfl-298799_978-2-9701614-0-0

Clearly, in the case that the term $\frac{P}{b}(\lambda-1)-h\int_0^{\lambda}\sigma_e\cdot\mathrm{d}\lambda$, i.e., the complementary strain energy per cross-section area (reference configuration) under tension, is negligible compared to the magnitude of G_c, above calculation of the critical fracture energy release rates G_c is identical with Kendall's classical peeling equation [4]. This is the case where we peeled a Kapton® tape. When peeling a film made of soft materials, e.g. rubber, the film is with high stretchability. Thus the tensile force imposed on the peeled arm during peeling process may lead to large deformation, which results in considerable complementary energy density. In this case, Kendall's classical peeling equation will produce an underestimated G_c. Therefore, it is of importance to consider the energy consumption caused by the tensile deformation of the soft film in the case of analysing the response of peeling a soft film off rigid substrates.

3.3 Results of peeling a soft film

As indicate by eq(2), the prerequisite that we derive a measurement of G_c based on peeling test results is that we are able to quantify the complementary energy density data of the peeled film. Here we performed a uniaxial test to collect the data for complementary energy density. The specimen for tensile test is made of Polystyrene-block-polyisoprene-block-polystyrene (SIS) that will soon be used to fabricate the bonding specimen of soft-to-rigid assemblies. Since the SIS used for tensile tests and peeling tests are both unconditioned, the energy consumption from tensile deformation is composed of the elastic energy stored in the system and the dissipation due to the Mullins' effect. We adopt the nominal stress σ_e to present the experimental data of the tensile test. With the σ_e versus λ data for the loading process of the tensile test, we may get, with a numerical integration scheme, the complementary energy density as a function of nominal tensile stress as shown in Figure 5.

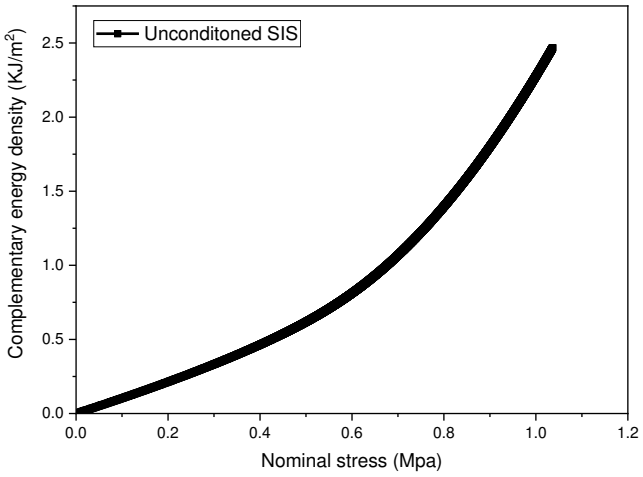

Figure 5. Complementary energy density of SIS as a function of tensile nominal stress.

Using the cassette-like peeling system, we performed the tests of peeling a SIS film from metal substrate with different peeling angles. The peeling force responses are shown in Figure 6. The delamination speed was controlled to be ~ 4 mm/min to eliminate the effect of the delamination speed on the measured G_c. The climbing regime of the curves indicates the process of establishment of steady crack propagation. The random jumps and oscillations observed in

the force responses correspond to the adjustment of the reverse torque to maintain the alignment of the peeled film, followed by a steady force-displacement response for all four tests. A stable peeling force was observed in this steady peeling process.

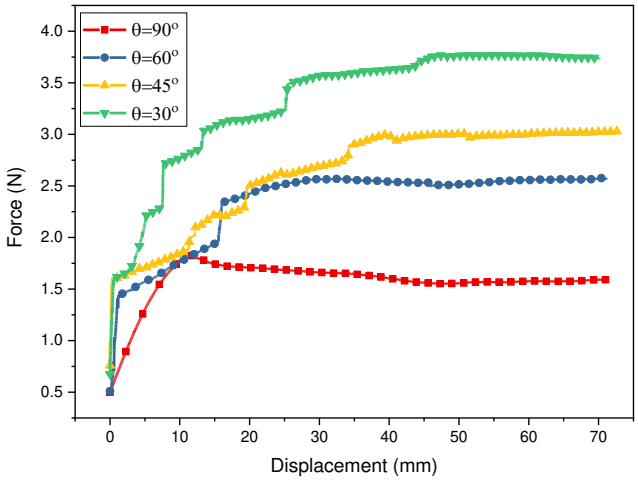

Figure 6. Peeling force responses obtained by cassette-like peeling system.

Substitute the steady peeling force and the complementary energy density value corresponding to the nominal stress experienced by the peeled film in the four tests, we derive, using eq(2), the G_c measured, as presented in Table 1. It is interesting to see that the fracture energy of soft-to-rigid bonding assemblies shows a negative correlation of peeling angle. This is possibly due to the fact that the scale of fibrils within fracture process zone is different for soft-to-rigid debonding under different fracture mode.

Table 1: G_c measurement for SIS/metal bonding system under different peeling angles.

Peeling angle (°)	30	45	60	90
G_c (KJ/m^2)	0.2473	0.2212	0.2093	0.1691

4. References

1. Kawashita LF, Moore DR, Williams JG. Comparison of peel tests for metal–polymer laminates for aerospace applications. Journal of Adhesion. 2005 Jun 1;81(6):561-86.
2. Daghia F, Cluzel C, Hébrard L, Churlaud F, Courtemanche B. The Double Drum Peel (DDP) test: a new concept to evaluate the delamination fracture toughness of cylindrical laminates. Composites Part A: Applied Science and Manufacturing. 2018 Oct 1;113:83-94.
3. Li X, Tao R, Xin Y, Lubineau G. Cassette-like peeling system for testing the adhesion of soft-to-rigid assemblies. Submitted to IJSS. 2022.
4. Kendall K. Thin-film peeling-the elastic term. Journal of Physics D: Applied Physics. 1975 Sep 11;8(13):1449.

  doi:10.5075/epfl-298799_978-2-9701614-0-0

INFLUENCE OF THE TRIGGER GEOMETRY ON THE CRASH BEHAVIOR OF A CARBON FIBER LAMINATE

Lorenzo Vigna[a], Andrea Calzolari[b], Giuseppe Galizia[b], Giovanni Belingardi[a],

Davide Salvatore Paolino[a]

a: Department of Mechanical and Aerospace Engineering, Politecnico di Torino, Turin, Italy – email: lorenzo_vigna@polito.it
b: ITW Test And Measurement Italia S.r.l. - Instron CEAST Division, Pianezza (TO), Italy

Abstract: *Fiber reinforced plastics are employed in structures for crashworthiness applications thanks to their high Specific Energy Absorption (SEA), which permits a significant reduction of weight and noxious vehicle emissions. In these structures it is important to have a geometric feature, known as failure trigger, to locally reduce the strength and initiate a stable crash failure avoiding excessive peak forces and instabilities. This is of particular importance for specimens dedicated to material characterization. In this study, triggers of six different geometries were machined on flat specimens made of carbon fiber reinforced epoxy. Crash tests were performed using a fixture developed to avoid the buckling of the plate loaded in the in-plane direction in quasi-static and impact loading conditions. Test results showed a strong effect of the trigger in the first part of the load-displacement curve (failure initialization). No effect was found in the steady crash region, where the force was approximately constant in all the tests. No significant influence of the trigger type was therefore detected on the SEA evaluation.*

Keywords: Crashworthiness; Specific Energy Absorption; Failure trigger; Carbon fiber; Impact testing.

1. Introduction

Since their first appearance, fiber reinforced composites have been used in primary structures of vehicles in substitution of metals for lightweighting purposes. This was allowed by their excellent mechanical properties combined with low density, and composites are widely recognized as the best choice for high performance application where high strength and low density are required. Today, substitution of metals with composites is considered one of the most effective ways to reduce the weight of vehicles in order to achieve efficiency and sustainability goals [1].

Crashworthiness is an important characteristic of every vehicle because it is not possible to completely exclude the occurrence of incidents during its life. To protect the passengers in case of crashes, it is common practice to include in the primary structure of vehicles some elements, typically known as crash boxes or crash absorbers, whose task is to absorb kinetic energy in a controlled manner so to achieve a constant deceleration of the vehicle and avoid high peak forces that could cause injuries for the passengers [2]. These structures are designed to have the failure starting in a specific area and propagating to the rest of the structure in a steady and progressive way. The failure should progressively involve all the material of the crash box to absorb a high amount of energy and avoid localized failures (e.g. buckling) that cause lower energy absorption. The steady progressive failure can be initiated by the geometry (e.g.,

  doi:10.5075/epfl-298799_978-2-9701614-0-0

a conical structure will start failing from the vertex, where the stress is maximum with same load) or by specific geometric features, known as failure triggers, that weaken a part of the structure to ensure the failure initializing from that point. Once the failure is triggered in a specific area, in a well-designed crash absorber the failure propagates progressively to the rest of the material. While the geometry itself initiates the failure in most crash absorbers, the use of a failure trigger is extremely important when testing material coupons to obtain the same failure mode that occurs in the real component.

Several different triggers have been proposed in the literature and applied to different kinds of specimens. The simplest trigger consists of a chamfer that reduces the thickness of the laminate. With this trigger the crash force grows rapidly up to a peak, then stabilizes to a lower value when the steady crash propagation condition is reached. The chamfer angle is influent on the peak force [3]. The chamfer is typically machined, but a similar effect can be obtained with a progressive reduction of the laminate thickness, reducing the number of layers [4]. Other geometries found in literature require some cuts in the direction of the laminate, like V-shaped trigger [5,6], sawtooth trigger [7–9] or cuts with different geometries [10,11]. A different way of inducing the desired failure mode on the material consists of an external device that forces the flow of crashed material in the wanted direction [12,13]. Some of these trigger configurations may modify the failure mode of the material, and consequently the energy absorption.

The aim of the present paper is to present some of the results of an experimental campaign developed to evaluate the effect of different trigger types on a crashworthiness test carried out on flat specimens for the evaluation of the Specific Energy Absorption (SEA) of the composite material. The force-displacement curves and SEA values obtained with six different trigger geometries were compared to find the most adequate for material crashworthiness characterization on flat panels. Tests were carried out on a carbon fiber laminate using an anti-buckling fixture to support the specimen during the test, as proposed in the literature[7–9,14]. Tests were run in impact conditions using a drop tower testing machine and in quasi-static conditions to detect a possible effect of the strain rate.

2. Materials and methods

Specimens having six different trigger types were produced using the same Microtex GG630 prepreg (carbon fiber 2x2 twill fabric coated with E3-150 epoxy resin, resin content 33% in volume) by the company Carbon Mind. All the specimens had rectangular shape with dimensions 100x150 mm and were obtained by milling from larger plates made of four layers for a total thickness of 2.65 mm. Each specimen type had a different failure trigger on the shorter edge, as depicted in Fig. 1. Four trigger geometries were realized during the specimens cutting process:

- trigger A (Fig. 1a): saw-tooth trigger with depth 2.5 mm and step 5 mm,
- trigger B (Fig. 1b): saw-tooth trigger with depth 5 mm and step 5 mm,
- trigger C (Fig. 1c): saw-tooth trigger with depth 10 mm and step 5 mm,
- trigger D (Fig. 1d): two large triangles (with width of 50 mm) machined with depth 10 mm.

Triggers E and F were realized during the layup process:

  doi:10.5075/epfl-298799_978-2-9701614-0-0

- trigger E (Fig. 1e): a 5 mm deep delamination at the mid plane of the laminate was created including a thin polytetrafluoroethylene (PTFE) layer during the layup process, that prevented the bonding between the second and the third layers,
- trigger F (Fig. 1f): the thickness of the laminate was reduced from four to two layers for a depth of 5 mm. In the trigger area, the first and fourth layers were removed to preserve the symmetry with respect to the mid plane of the laminate.

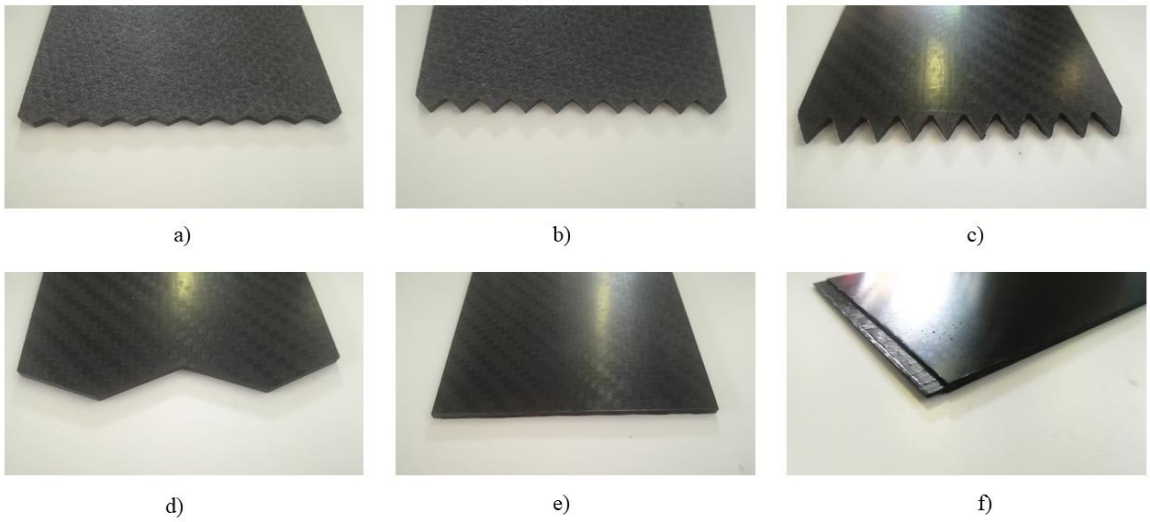

Figure 1. Different triggers tested in this study: a) triangular saw-tooth with depth of 2.5 mm; b) triangular saw-tooth with depth of 5 mm; c) triangular saw-tooth with depth of 10 mm; d) two large triangles with depth of 10 mm; e) internal notch created positioning a thin PTFE layer at the mid plane of the laminate for a depth of 5 mm; f) reduction of the thickness of the laminate from four to two layers for a depth of 5 mm.

Crashworthiness tests were performed using a testing fixture optimized for impact testing and avoiding buckling of the specimen [15]. The specimen was vertically positioned and supported by six vertical columns (three for each side of the specimen) to avoid its buckling (Fig. 2a). The failure trigger was positioned in contact with a horizontal steel plate that represents the surface against which the failure happens. The lower part of the specimen was left laterally unsupported for a height of 5 mm to allow material failure and fronds formation. A clamping system provided a controlled force of 4 kN and its effect in terms of energy absorption due to friction was minimized applying a PTFE solid lubricant to the supporting columns [16]. The load was applied on the top of the specimen by means of a flat disk connected to the falling mass in the case of impact test or to the upper grip of the universal testing machine in quasi-static tests. Impact tests were performed with an Instron 9450 drop tower using an impact energy of 800 J, an impact velocity of 7 m/s and a drop mass of 32.89 kg. The crash force was measured using an instrumented striker with a load cell characterized by maximum load capacity of 222 kN and sampled at a frequency of 1 MHz. The displacement and energy absorption were calculated from the integration of the force signal. Quasi static tests were performed with an Instron 8801 hydraulic universal testing machine at a constant speed of 10 mm/min. The load was acquired using a load cell with maximum load capacity of 100 kN, while the displacement of the impactor was measured by an LVDT sensor. From load-displacement curves, the SEA was calculated from Eq. (1):

  doi:10.5075/epfl-298799_978-2-9701614-0-0

$$SEA = \frac{E_a}{m} \quad (1)$$

where E_a is the energy absorbed and m the specimen crashed mass, calculated considering the density and the volume of crashed material. The absorbed energy corresponds to the area below the force-displacement curve in the displacement range between 20 mm and 40 mm and the volume of crashed material is considered in the same displacement range. The first 20 mm of the curve were neglected to avoid the influence of the failure initialization induced by the trigger, while 40 mm is the maximum displacement achieved during quasi-static tests. Further details regarding this aspect are provided in the next clause. Two repetitions of the quasi-static tests and three repetitions of the dynamic tests were performed.

3. Test results

Under both the quasi-static and impact compression loads the specimens showed a splaying failure mode (Fig. 2b).

a) b)

Figure 2. a) Testing fixture for impact and quasi-static compression test. The flat disk (insert) that applies load is also shown. b) Carbon fiber/epoxy specimen after crashworthiness test.

The energy is absorbed by the material due to delamination, debris formation, matrix and fibers cracking and bending of layers. Typical force-displacement curves acquired during quasi-static and dynamic tests are plotted in Fig. 3 and in Fig. 4, respectively. All curves are characterized by a growth of the force value from zero (first contact with the flat disk visible in Fig. 2a) to a peak that corresponds to the initiation of the failure on the full cross section of the specimen (end of the trigger). The height and position of the peak on the force-displacement curve depend on the trigger geometry. After the peak, the crash force reduces to an approximately constant level due to the stabilization of the failure process, that steadily progresses. Oscillations of the force signal and scatter of results are typical of crashworthiness tests because of the natural presence of defects in the material that can influence the crash force. As visible in Fig. 3, the load-displacement curves obtained in quasi-static conditions can be divided in three phases:

  doi:10.5075/epfl-298799_978-2-9701614-0-0

- From 0 mm to 10 mm the behavior is strongly characterized by the trigger geometry.
- From 10 mm to 20 mm the force reduces due to the crash front development.
- After 20 mm the force stabilizes, and the behavior becomes very similar in all the curves.

The effect of the different trigger geometries is easily visible in the first 10 mm of the force-displacement curve:

- Specimens with saw-tooth trigger (A, B and C) show a growth of the force up to the peak due to the progressive increment of the cross section. The slope of the curve and the height and position of the peak are related to the depth of the sawtooth geometry.
- Specimens with trigger D, with two 10 mm deep large triangles, have a behavior very similar to trigger C due to the similar shape and same trigger depth.
- Specimens with trigger E, having an artificially created internal notch, shows a high initial peak due to the absence of a cross section reduction in the trigger area, then force drops to a steady-state value.
- Specimen with trigger F, having a thickness reduction, presents a first peak followed by a steady state force of about 12 kN due to the failure of the part of specimen with lower thickness, then a second peak followed by some oscillations and a stabilization of the force after about 20 mm.

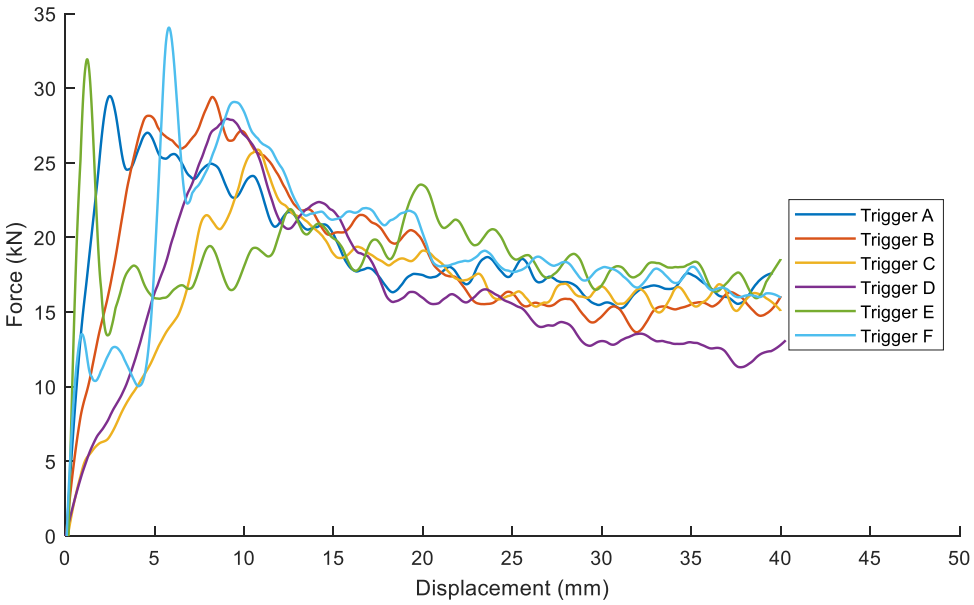

Figure 3. Typical filtered force-displacement curves acquired during quasi-static tests.

Similar considerations can be drawn from impact tests (Fig. 4):

- From zero to 10 mm the effect of the different trigger geometries is strongly visible in the different raising trend of the force signal.
- After 10 mm a steady state force level is achieved.

The main difference with quasi-static tests is the absence of the decrease phase of the force value before reaching the steady state condition. This is probably due to the faster development of the crash front which is facilitated by the higher strain rate and vibrations induced by the impact.

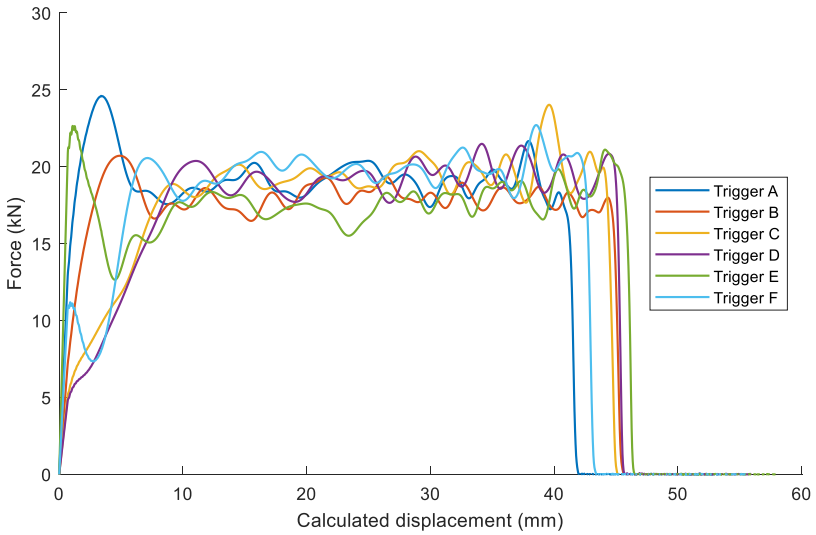

Figure 4. Typical filtered force-displacement curves acquired during impact tests.

A clear effect of the trigger geometry and of the testing condition on the peak force is visible in Fig. 5a), that considers unfiltered data as the choice of the filter is consistently influent on the peak force. The trigger geometry causes high peak forces specially on triggers E and F, due to the absence of a gradual cross section reduction that causes smooth increase of the crash force. The situation is different with the triangular saw tooth triggers A, B, C and D, where the progressive increase of the cross section causes a smoother increase of the force signal and a lower peak force. In case of a deeper sawtooth trigger, the force increment is smoother and the peak force is lower. The peak force in dynamic conditions is typically higher because of high frequency vibrations of the force signal excited by the impact (not visible in Fig. 4 due to filtering) and summed to the crash force given by the material. These are essentially axial vibrations in the impact mass that are captured by the load cell and have been filtered in Fig. 4 to allow a better comprehension of the plot. The amplitude of vibrations increases if the load is applied in a more sudden way to the specimen (i.e., if the cross section of the specimen increases rapidly and consequently the initial slope of the force-displacement curve increases).

The SEA of the material was calculated to find possible differences caused by the trigger geometry. The unfiltered curves were used for calculation because the filter does not affect the SEA value. The performed analysis considered the part of the force-displacement curve between 20 mm and 40 mm, as it is necessary to consider a part of the crash curve in which the failure mode is steady, and the force is approximately constant. The average SEA values obtained from quasi-static and impact tests are reported in Fig. 5b, where no clear trends or differences between triggers appear. More in details:

- Specimens A, B, and C have very similar SEA values both in quasi-static and dynamic conditions; in average, dynamic SEA results higher than quasi-static SEA.
- Specimen D presents the higher dynamic SEA and the lowest quasi-static SEA; this important difference between the two loading conditions does not find confirmation in the other specimen types and thus can be considered as due to the trigger geometry D.
- Specimen E and F showed high scatters, particularly in quasi-static tests, but results aligned with specimens A, B and C.

  doi:10.5075/epfl-298799_978-2-9701614-0-0

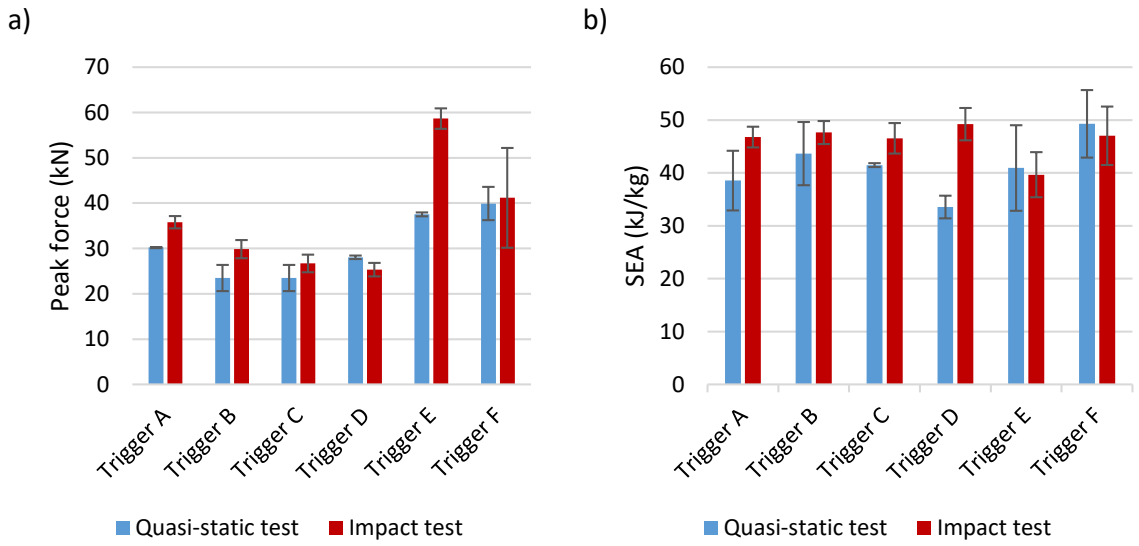

Figure 5. Quasi-static and dynamic test results: a) Peak force from unfiltered curves; b) SEA calculated from unfiltered curves in the range of displacement between 20 mm and 40 mm.

Considering all the performed tests, dynamic SEA value is typically higher than the quasi-static one. An ANOVA test considering as parameters the trigger geometry and the testing condition indicated a significant effect of the testing speed (p-value 0.006) and no significant effect of the trigger geometry (p-value 0.135).

4. Conclusions

Crashworthiness tests carried out on carbon fiber flat plates showed an effect of the trigger geometry in the first part of the force-displacement curve, with non-negligible variations of the peak force. This effect is more evident in impact tests, that cause an increase of peak forces. Results showed that the smoother is the transition from the first contact with the impactor to the failure of the full cross section of the specimen, the lower is the peak force. A smooth transition can be obtained with a saw tooth trigger that causes a reduction of the cross section of the specimen, and consequently lower initial force. High peak forces in impact tests generally lead to vibrations of the specimen and in the experimental apparatus that are acquired and visible in the acquired experimental curve, and this could affect the evaluation of the performance of the material. When designing a crash absorber, it is important to have a progressive increment of the cross section to avoid excessive peak forces that can cause injuries for the passengers. A saw-tooth geometry demonstrated to be a more effective way to reduce the peak force if compared with a thickness reduction or with a specimen having internal notch obtained with a PTFE layer.

The analysis of the stable crash region of the force-displacement curve allowed to measure the SEA of the different specimens. Due to a certain scatter of experimental results, which is typical of crashworthiness tests, it was not possible to state that the trigger geometry affects the SEA of the material for most of the triggers taken in consideration. Only trigger D (two large triangles with 10 mm depth) shows a peculiar result, with dynamic SEA considerably higher than quasi-static SEA. This effect could be due to a lower effectiveness to trigger the splaying failure in quasi-static testing, while dynamic results are well aligned with the results on other triggers. Dynamic SEA resulted on average 12% higher than quasi-static SEA.

  doi:10.5075/epfl-298799_978-2-9701614-0-0

In conclusion, all the tested trigger geometries, except for trigger D, can be effectively used for an in-plane crashworthiness test on flat panels. Specimens E and F caused high peak forces both in quasi-static and dynamic conditions because of the sudden load increase. A saw tooth trigger is then the best choice for this kind of test because of the simple manufacturing process and the possibility to avoid high peak forces choosing a saw tooth geometry with sufficient depth.

5. References

1. Lukaszewicz DH-JA. Automotive Composite Structures for Crashworthiness. In: Elmarakbi A, editor. Advanced Composite Materials for Automotive Applications: Structural Integrity and Crashworthiness. Chichester, UK: John Wiley & Sons, Ltd; 2013. p. 99–127.
2. CMH-17. Crashworthiness and Energy Management. In: Composite Materials Handbook (CMH-17). 2012.
3. Sigalas I, Kumosa M, Hull D. Trigger mechanisms in energy-absorbing glass cloth/epoxy tubes. Compos Sci Technol. 1991;40(3):265–87.
4. Thuis HGSJ, Metz VH. The influence of trigger configurations and laminate lay-up on the failure mode of composite crush cylinders. Compos Struct. 1994;28(2):131–7.
5. Ueda M, Anzai S, Kubo T. Progressive crushing of a unidirectional CFRP plate with V-shaped trigger. Adv Compos Mater. 2015;24(1):85–95.
6. Dalli D, Varandas LF, Catalanotti G, Foster S, Falzon BG. Assessing the current modelling approach for predicting the crashworthiness of Formula One composite structures. Compos Part B Eng. 2020;201(July).
7. Lavoie JA, Morton J. Design and Application of a Quasistatic Crush Test Fixture for Investigating Scale Effects in Energy Absorbing Composite Plates. NASA Contractor Report 4526. 1993.
8. Feraboli P. Development of a Modified Flat-plate Test Specimen and Fixture for Composite Materials Crush Energy Absorption. J Compos Mater. 2009;43(19):1967–90.
9. Babaei I, Garg R, Vigna L, Paolino DS, Belingardi G, Cascone L, et al. Newly Developed Anti-Buckling Fixture to Assess the In-Plane Crashworthiness of Flat Composite Specimens. Appl Sci. 2020 Nov 3;10(21):77-97.
10. Czaplicki MJ, Robertson RE, Thornton PH. Comparison of bevel and tulip triggered pultruded tubes for energy absorption. Compos Sci Technol. 1991;40(1):31–46.
11. Jiménez MA, Miravete A, Larrodé E, Revuelta D. Effect of trigger geometry on energy absorption in composite profiles. Compos Struct. 2000;48(1):107–11.
12. Siromani D, Henderson G, Mikita D, Mirarchi K, Park R, Smolko J, et al. Composites : Part A An experimental study on the effect of failure trigger mechanisms on the energy absorption capability of CFRP tubes under axial compression. Compos PART A. 2014;64:25–35.
13. Chambe JE, Bouvet C, Dorival O, Rivallant S, Ferrero JF. Effects of dynamics and trigger on energy absorption of composite tubes during axial crushing. Int J Crashworthiness. 2020;26(5):549–67.
14. Cauchi Savona S, Hogg PJ. Effect of fracture toughness properties on the crushing of flat composite plates. Compos Sci Technol. 2006;66(13):2317–28.
15. Vigna L, Babaei I, Garg R, Belingardi G, Paolino DS, Calzolari A, et al. An innovative fixture for testing the crashworthiness of composite materials. Frat ed Integrità Strutt. 2021;15(55):76–87.
16. Vigna L, Calzolari A, Galizia G, Belingardi G, Paolino DS. Effect of friction on a crashworthiness test of flat composite plates. Forces Mech. 2022;6.

  doi:10.5075/epfl-298799_978-2-9701614-0-0

RESIDUAL STRESS AND STRAIN IN RAPIDLY CURED COMPOSITES

Benjamin, Seers[a], Rachel, Tomlinson[a], Patrick, Fairclough[a]

a: Department of Mechanical Engineering University of Sheffield – bseers1@sheffield.ac.uk

Abstract: *In this work a preliminary investigation into the feasibility of using embedded optical fibres with Fibre Bragg Gratings (FBG) to monitor residual strain in rapidly curing composites is undertaken. Curing times of 1-8 minutes are achieved by hot-pressing prepreg unidirectional composites with specialized thermosetting resin matrices. Residual strain is then monitored using embedded FBG's and the results are analyses qualitatively to investigate the dominant mechanisms in the formation of residual stress in rapidly cured composites. Then, transverse three-point bending tests are conducted to determine the effect of thickness and cure temperature on laminate bending strength. It was found that bending strength increased with curing temperature and was not affected by laminate thickness.*

Keywords: Composites; Residual strain; Rapid curing; FBG sensor

1. Introduction

Carbon fibre reinforced plastics are becoming more and more popular in the aerospace and automotive industries due to their high specific strength and stiffness. However, one major drawback of more traditional composite manufacturing techniques is that they have very long processing times. This is primarily due to the need to slowly increase and decrease the processing temperature to avoid residual stress formation and warpage after cure. In recent years, rapidly cured resins have been developed to reduce the processing time required to cure parts. However, the effect of shorter processing times on residual stress formation is still not well understood and if these manufacturing techniques are to be adopted for structural applications this gap in knowledge must be addressed. Therefore, this research aims to investigate ways in which to evaluate residual stress in fast curing composites and to determine the effect that residual stress has on the mechanical performance of the finial composite part. In this work, the applicability of the use of embedded optical fibres with Fibre Bragg Gratings (FBGs) in fast-curing composite systems for the measurement of residual strain is investigated.

Advances in embedded sensors technologies have proven very promising for the more widespread adoption of residual stress monitoring in composites [1][2]. Embedding FBG's into a laminate before cure allows for an insight into the internal strain state of the composite laminate during cure and while analysing the structural performance during subsequent testing. In this work, residual stress fields within the laminate are manipulated by altering curing temperature and laminate thickness. Transverse flexural testing is then used to investigate the effect of varying levels of residual stress on the matrix dominated bending response of the laminate.

  doi:10.5075/epfl-298799_978-2-9701614-0-0

Materials and method

An optical fibre consists of a glass core, a cladding layer with a lower refractive index than that of the core and a coating layer to aid adhesion and give strength. Light is passed through the core and is totally internally reflected by the cladding due to its lower refractive index. An FBG is fabricated by using a UV laser to periodically etch the surface of the core of an optical fibre resulting in a periodic variation in the refractive index of the core in the etched area. When light is passed through the etched area, or 'grating', a specific wavelength of light known as the Bragg wavelength, λ_B is reflected by the grating which is a function of the grating spacing, Λ and the effective refractive index of the core, η_{eff} as described by Equation (1). This is then detected by an interrogator unit connected to the end of the fibre and wavelength of the reflected spectra can be measured.

$$\lambda_B = 2\eta_{eff}\Lambda \quad (1)$$

If a strain is then applied to the FBG or it experiences a temperature change, T then the grating spacing changes and the reflected Bragg wavelength changes accordingly. Strain can be split into two components, mechanical strain, ε_z and thermal strain which is caused by a temperature change ΔT. Applying corresponding sensitivity factors S_ε and S_T, this relation can be expressed by Equation (2).

$$\Delta\lambda_B = S_\varepsilon\varepsilon_z + S_T\Delta T \quad (2)$$

The fibres used in these experiments were obtained from FBGS and have reported sensitivity values of 7.8 με-1 ×10-7 and 6.5 K-1 ×10-6 for S_ε and S_T respectively (1). From Equation (2) it can be seen that both temperature variations and mechanical strain cause a shift in the Bragg wavelength. Therefore, when using FBG's to monitor cure in composite laminates it is critical to be able to separate these two components so that the actual mechanical strain due to resin thermal expansion and shrinkage is known and the contribution of the thermal expansion of the optical fibre is discretised. This can be done by measuring the temperature at the FBG and then removing this term from equation (2). In this work, temperature monitoring is done with a simple k-type thermocouple.

FBGS low bend loss fibres with a cladding diameter of Ø125 µm and an ORMOCER coated fibre with a diameter of 195 µm have been used. With a nominal Bragg wavelength of 1550 nm and a grating length of 1 mm. From initial studies it was found that a short grating length reduced peak splitting of the reflected spectra, leading to a more accurate strain response measurement. These are paired with a SmartFibres SmartScope interrogator unit which operates in a wavelength rage of 1528 nm to 1568 nm, a scan frequency of 5 Hz and a wavelength resolution of 0.2 pm.

Rapid curing strain measurement tests used 150x150 mm $[0]_n$ prepreg laminates, where n was varied to achieve various thicknesses. Fibres were embedded transverse to the fibre direction at the first ply in the laminate and at the mid-thickness ply to measure the transverse matrix residual strain during cure at the outer and inner thicknesses of the laminate. The fibre gratings were placed in the in-plane centre of the laminate and the optical fibre continued to the edge of the laminate, thereby leaving a 75 mm "tail" of optical fibre after the grating. A Ø 0.5 mm

PTFE tube was placed around the fibre optic cable at the point where it enters the laminate to provide some mechanical support as initial tests had shown this to be an area prone to failure. K-type thermocouples were placed approximately 20 mm away from the embedded grating on the same ply as the gratings to allow for a representative temperature reading and to not affect the strain measurement taken by the grating. A metal retaining "collar" with the same thickness as that of the final cured laminate is then placed around the laminate stack before being hot pressed to control the laminate shape and thickness. The embedded sensor layup is shown in Figure 1.

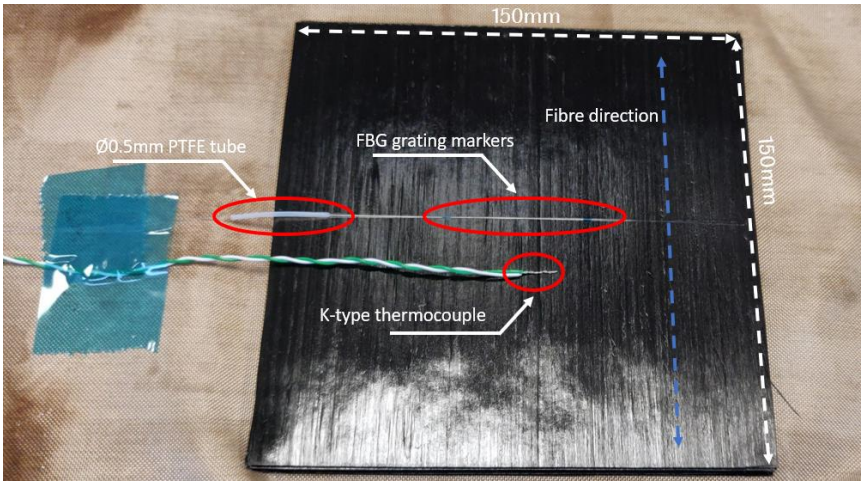

Figure 1: Embedded sensor for residual strain measurement setup at mid-thickness

After some preliminary tests were carried out a standard mythology was adopted. To investigate both the effect of thickness and curing temperature on residual strain, two extremes were chosen for thickness and temperature to better highlight these effects. For thickness, samples were designated as either "thick" or "thin" with 6.35 mm and 2 mm laminates respectively. For cure temperature, "cool" and "hot" conditions were used which were cure temperatures of 140 °C and 180 °C respectively with cure times altered accordingly to achieve full cure. The full experimental specifications are outlined in Table 1.

Table 1: Residual strain experiment specifications

Test	No. plies	Thickness (mm)	Cure temperature (°C)	Cure time (min)
Cool_thin	11	2	140	8
Cool_thick	35	6.35	140	8
Hot_thin	11	2	180	1
Hot_thick	35	6.35	180	1

2. Residual strain results

As the resin matrix is liquid and E''>>E' before α_{gel} then all strain that occurs before α_{gel} does not contribute to residual stress as it is dissipated viscously. Therefore, to gain a meaningful insight into the effect of residual strain on the residual stress state of the laminate, the measured strain is zeroed at α_{gel}. In this work this is defined as the point at which strain begins to be developed as measured by the embedded FBG. An example experiment, Cool_thin, is

shown in Figure 2 with its corresponding temperature data so important points can be identified.

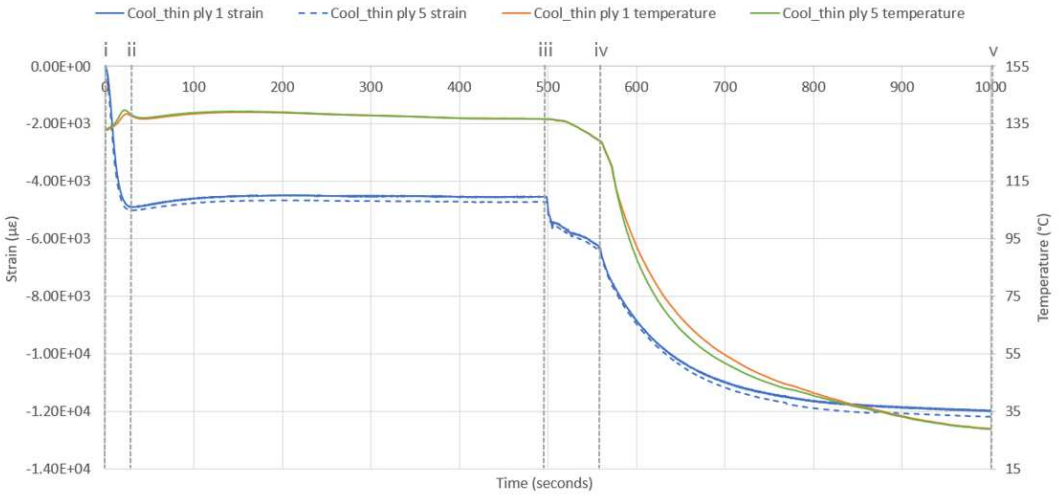

Figure 2: Cool_thin embedded strain and temperature data, strain zeroed at α_{gel}.

Figure 2 clearly shows the development of transverse residual strain during cure, with both chemical shrinkage and thermal effects clearly visible. Chemical shrinkage occurring during the polymerization of the resin matrix between i-ii. An isothermal holding phase between ii-iii to ensure full cure of the laminate. Then, the compressive thermal strain being applied when the temperature is dropped after removal from the hot press, iii-v. Where iii is the point at which the hot press is opened and iv is when the laminate is removed from the hot press. Results from all of the experiments outlined in Table 1 are presented in Figure 3. It should be noted that there is no data available for the mid-thickness hot_thick sample as during cure the reflected Bragg wavelength peak exceeded the dynamic range of the SmartScope due to high levels of strain and was therefore unable to be recorded.

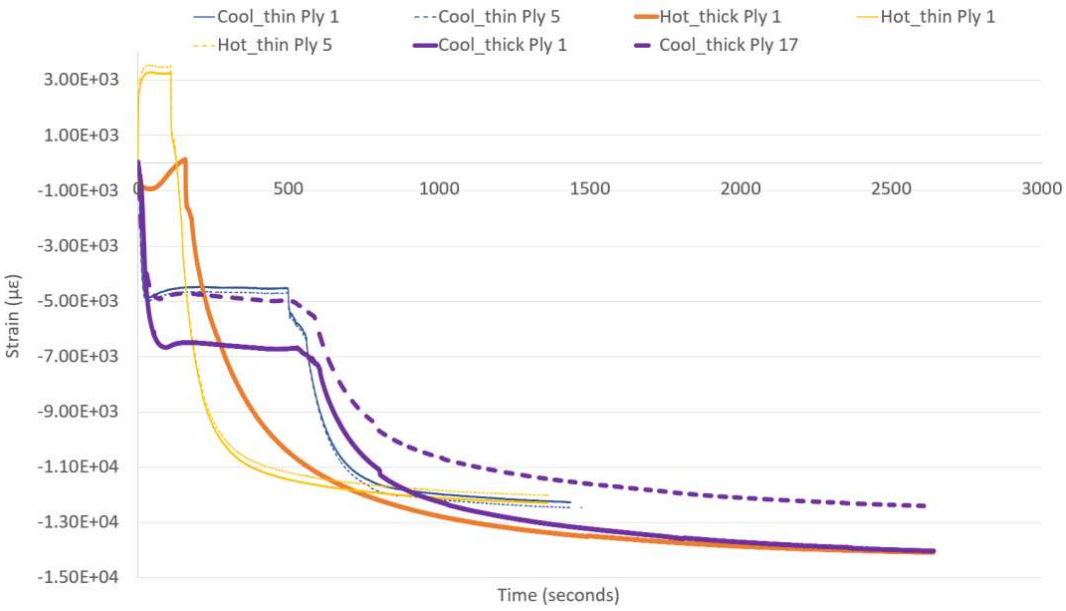

Figure 3: Embedded strain data, zeroed at α_{gel} for time 0-4000 seconds

  doi:10.5075/epfl-298799_978-2-9701614-0-0

Examining the full strain history for all the laminates tested in Figure 3, several key features are apparent. Firstly, for the laminates tested the total final residual strain is independent of cure temperature and only depends on laminate thickness with the thicker laminates resulting in higher levels of compressive residual strain. The final total residual strain for all thermal histories, laminate thicknesses and sensor locations is broadly similar across all cases. With the largest deviation from the average being approximately an 11% difference in total strain.

From Figure 3 we can see that the apparent compressive chemical shrinkage strain (points i-ii in Figure 2) that occurs after gelation of the "hot" samples is less than that of the "cool" samples. Indeed, the apparent chemical shrinkage strain of the hot_thin samples is positive. However, this is not the true chemical shrinkage strain of the resin matrix as this is caused by the polymerization of the resin matrix it is independent of the cure condition assuming it has been fully cured. This is due to gelation of the resin matrix occurring before the cure temperature of the laminate has been reached. Therefore, the tensile thermal expansion of the resin is greater than the compressive chemical shrinkage during the initial parts of the curing cycle. Whereas, for the cool condition the temperature remains relatively constant after gelation so the compressive chemical shrinkage strain can be fully seen. The result of this is that the final total residual strain of hot and cool laminates is similar even though the thermal contribution of strain during the cooling phase is significantly higher for the hot cure condition. However, it is important to note that this does not mean the final residual stress state of the laminates is similar. In the case of the hot laminates the majority of the strain developed during cure comes after the resin has fully developed it's stiffness (E' >> E'') during the cooling phase of the cure cycle. Whilst a significant proportion of the strain developed in the "cool cure" condition laminates is developed early in the cure cycle, right after gelation. Here, the storage modulus of the resin is much lower and as such the resultant residual stress will be much lower for the same given strain. This is because the much of the energy imparted into the resin system from thermal expansion and chemical shrinkage is dissipated viscously as E'' is not negligible at this stage of the cure. In the thick samples the difference between the onset of gelation between the outer and inner plies is greater than that of the thin samples. This is caused by the large temperature gradient through the thickness of the laminate seen in the thicker samples. This causes the outer plies of the laminate to cure sooner than the internal ones, setting up an uneven cure gradient through the laminate thickness. This is further exacerbated by the higher temperature used in the hot cure condition.

Additionally, the average total final residual strain is approximately -14,000 με (or -1.4%) which is significantly higher than the final strain seen for slower curing laminates found in the literature. For example, Minakuchi et al (2) measured a final mid-thickness in-plain strain of -2850 με with a 100x100x7.5 mm UD laminate cured at 90 ℃ for 5 hours. While Qi et al (3) found a final residual strain of -5183 με with a 200x200x2.5 mm UD laminate cured at 80 ℃ for 10 minutes and then 100 ℃ for an additional 20 minutes. However, it should be noted that strain was not zeroed at gelation for this testing, so the true value of residual strain is likely to be lower. Again, Hu et al (4) found a total final residual strain of approximately -7500 με using a 110x110x10 mm UD laminate with a cure schedule of 130 ℃ for 60 minutes and then an additional 3.5 hours at 180 ℃. While it is evident that the experiments seen in the literature

  doi:10.5075/epfl-298799_978-2-9701614-0-0

have used a variety of experimental methodologies and as such cannot be directly compared, they do still allow for two key observations to be made. First, the experiments conducted in this work use cure times one or two orders of magnitude smaller than that seen in the literature. Thus, this current work gives us a unique insight into the residual strain history of very fast curing laminates. Second, these rapid curing conditions have resulted in very large levels of transverse residual strain to be developed within the laminate, both in the mid-thickness and outer edges.

3. Transverse three-point bending results

To investigate the effect of various residual stress conditions on the matrix dominated transverse bending response, transverse three-point bending tests were conducted on samples with a variety of cure states and thicknesses. Samples with a span to support ratio of 8:1 were waterjet cut out of from the panels created during the fast curing residual strain experiments. The results of the transverse three-point bending tests are shown graphically in Figure 4.

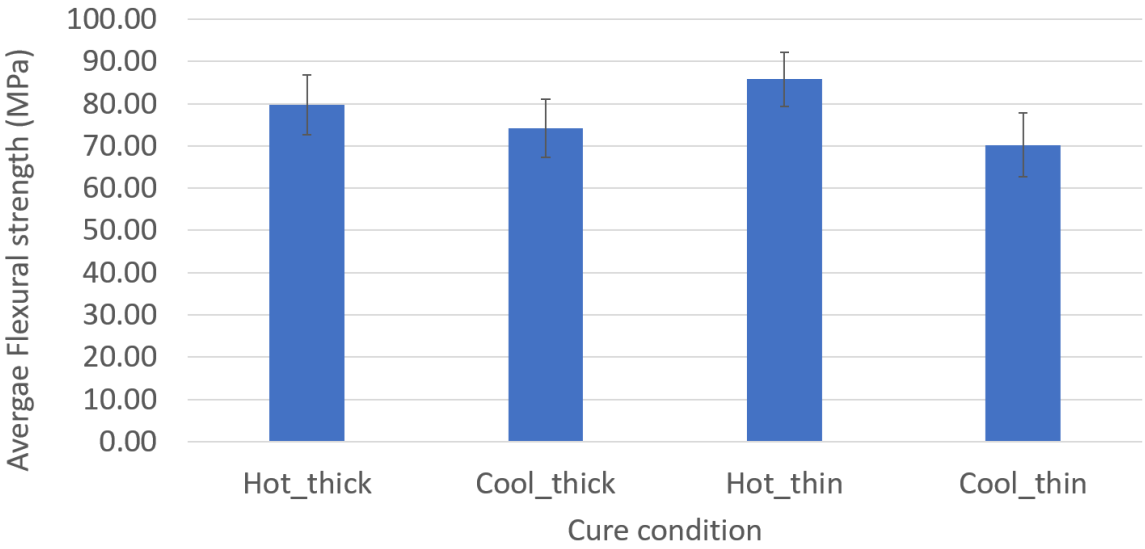

Figure 4: Average flexural strength of three-point bending specimens with varying cure conditions

On first examination of the transverse three-point bending results presented in Figure 4 it is difficult to identify many clear trends. However, by applying an unpaired two-tailed t-tests it is possible to identify two key trends. Here, a t-test is applied to test the null hypothesis that the difference between the two groups is not statistically significant. A 95% confidence interval is used to determine whether the null hypothesis has been met. The results of this statistical analysis are shown in Table 2.

  doi:10.5075/epfl-298799_978-2-9701614-0-0

Table 2: P-test of transverse three-point bending samples

Test	P-value	Null hypothesis
Cool_thin vs Cool_thick	0.1579	Accepted
Hot_thin vs Hot_thick	0.0797	Accepted
Cool_thin vs Hot_thin	0.0002	Rejected
Cool_thick vs Hot_thick	0.0367	Rejected

Now, it is possible to see that changing the thickness of the samples does not change the average flexural strength of the laminate by a statistically significant amount. Whilst increasing the cure temperature of the laminate increases the average flexural strength. This additional transverse flexural strength is indicative of the samples cured at higher temperatures having higher levels of compressive residual stress on the outer edges of the laminates. Therefore, there is an additional compressive load that needs to be overcome before a tensile load is applied to the outer tensile surface of the bending specimen. Thus, leading to a higher failure load and higher apparent flexural strength.

4. Conclusion and future work

In conclusion, this work has shown the applicability of FBG sensors to measuring residual strain in very rapidly curing composites. A qualitive analysis of various mechanisms of residual strain development in fast curing composites has been given. It was found that for the laminates tested, the final resultant strain was independent of curing temperature and only depended on laminate thickness. However, the laminates cured at higher temperatures had the majority of their residual strain form in the latter stages of the laminate cure when the modulus of the resin matrix was also high. This suggests higher levels of residual stress are present in the laminates cured at higher temperatures. Subsequent transverse three-point bending tests confirmed that laminate bending strength was only dependent on cure temperature and not laminate thickness. This is hypothesized to be a result of higher levels of compressive residual stress on the outer edges of the laminates cured at higher temperatures.

Future work is to utilize in-situ resin modulus monitoring with tailed FBG sets, as outlined in works by Minakuchi et al (2)(5)(6) and Hu et al (7). This will allow for real time measurements of the cure state of the laminate which will subsequently be used to analyze the residual stress state of that laminate. This technique is particularly useful for this work as traditional rheological techniques, and then subsequent associated inferences about cure state, become difficult to apply in resin systems that cure so rapidly. This will offer a unique insight into the suitability of rapidly cured composites in structurally critical applications.

Acknowledgements

The authors would like to acknowledge Solvay Group, for providing materials and funding, also the EPSRC for funding via the CDT in Polymers, Soft Matter and Colloids EP/L016281/1.

5. References

1. FBGS - Draw Tower Gratings in low bend loss fiber. [Internet]. [cited 2020 May 20].

Available from: https://fbgs.com/components/draw-tower-gratings-dtgs/

2. Minakuchi S, Niwa S, Takagaki K, Takeda N. Composite cure simulation scheme fully integrating internal strain measurement. Compos Part A [Internet]. 2016 [cited 2020 Jul 27];84:53–63. Available from: http://dx.doi.org/10.1016/j.compositesa.2016.01.001

3. Qi Y, Jiang D, Ju S, Zhang J. Investigation of strain history in fast and conventional curing epoxy matrix composites by FBGs. Compos Sci Technol [Internet]. 2018 May 3 [cited 2018 Oct 12];159:18–24. Available from: https://www.sciencedirect.com/science/article/pii/S0266353817321218

4. Hu H, Cao D, Pavier M, Zhong Y, Zu L, Liu L, et al. Investigation of non-uniform gelation effects on residual stresses of thick laminates based on tailed FBG sensor. Compos Struct. 2018;202:1361–72.

5. Minakuchi S. In situ characterization of direction-dependent cure-induced shrinkage in thermoset composite laminates with fiber-optic sensors embedded in through-thickness and in-plane directions. Compos Mater [Internet]. 2015 [cited 2019 Oct 8];49:1021–34. Available from: https://journals.sagepub.com/doi/pdf/10.1177/0021998314528735

6. Tsukada T, Minakuchi S, Takeda N. Identification of process-induced residual stress/strain distribution in thick thermoplastic composites based on in situ strain monitoring using optical fiber sensors. Compos Mater. 2019;53(24):3445–58.

7. Hu H, Li S, Wang J, Zu L, Cao D, Zhong Y. Monitoring the gelation and effective chemical shrinkage of composite curing process with a novel FBG approach. Compos Struct. 2017 Sep 15;176:187–94.

MEASUREMENT OF DAMAGE GROWTH IN ULTRASONIC SPOT WELDED JOINTS

Eva Smeets[a], Calvin Rans[a], René Alderliesten[a], Saullo Castro[b], Irene F. Villegas[b]*

a: Structural Integrity & Composites Group, Aerospace Structural & Materials, Delft University of Technology, Delft, the Netherlands
b: Aerospace Structures & Computational Mechanics Group, Aerospace Structural & Materials, Delft University of Technology, Delft, the Netherlands
* Corresponding author's email: e.t.b.smeets@tudelft.nl

Abstract: *Ultrasonic spot welding is a joining technique for thermoplastic composites with great potential regarding processing speed and cost. To investigate the damage tolerance and possible inherent damage arresting behavior of multi-spot welded joints, a technique is necessary to measure damage growth in the joints under cyclic loading. Visual inspection is not possible because the damage is not located on the outside surface and conventional techniques such as C-scan are not practical during a fatigue test because the specimen would have to be removed from the setup. This paper details a methodology for quantifying damage growth rates in single-spot welded joints using surface strain measurements made by Digital Image Correlation. This represents the first step towards developing a methodology for quantifying damage progression behavior in complex multi-spot welded joints.*

Keywords: damage growth; ultrasonic spot welding; thermoplastic composites; Digital Image Correlation (DIC), fatigue

1 Introduction

Thermoplastic composites present the opportunity to use fusion bonding, or welding, as a joining technique instead of mechanical fastening or adhesive bonding. Fusion bonding is particularly interesting to the aerospace industry since it is fast and cost-effective [1, 2], and eliminates many surface preparation and process control needs related to adhesive bonding [3]. The specific fusion bonding technique of ultrasonic welding provides an additional opportunity for structural joints with the possibility to tailor the damage tolerance and progressive failure behavior. The damage in these ultrasonically welded joints is confined to the welded region rather than growing through the adherends [4]. This means that the individual weld locations in a spot welded joint contain the growth of discrete damage sources, and the progression of damage to adjacent welds requires a new damage initiation event. To investigate and exploit this possibility, however, a robust methodology for quantifying the damage progression behavior in these joints is required.

Monitoring damage progression in an ultrasonically spot welded joint is hampered by the very feature of damage growth that we would like to exploit – damage growth is contained between the adherends. The study in this paper is limited to circular spot welds at the center of the specimen, which are not visible from the outside. Thus, direct observations of the damage growth are not possible. Non-destructive testing techniques such as C-scan can provide information about damage shape and size, however, this technique becomes less practical for continuous monitoring of damage progression during a fatigue test due to the

need to remove the specimen from the testing machine for inspection. This paper investigates an alternative indirect approach to monitoring the damage progression behavior using surface strains measured with the Digital Image Correlation technique (DIC). This technique has quickly become a staple measurement technique in laboratories for strain measurement but has also been successfully used in past studies for monitoring hidden interface damages. This paper will specifically look at the advantages and challenges of applying it on ultrasonically spot-welded joints.

2 Methodology

This study aims to investigate the suitability of using DIC as a quantitative method for indirectly monitoring damage progression behavior in ultrasonically spot-welded joints. To carry this out, displacement-controlled fatigue tests of single lap shear joints with a single spot weld (similar to previous studies by Choudhary and Villegas [5]) are conducted. The dimensions of the test specimens are shown in

Figure 1, the loading is applied in the horizontal direction. The lay-up of the adherends is $[0/135/90/135/45/135]_s$ and the ply material is carbon fiber with LMPAEK resin. Fatigue testing is conducted using a displacement associated with 80% of the B-basis static strength of 10 single-spot welded specimens, with a loading ratio of 0.2 and testing frequency of 5 Hz. As the focus of this paper is to examine the damage monitoring potential of DIC, the remainder of the methodology section focusses on describing the measurement and data processing methods used in the study.

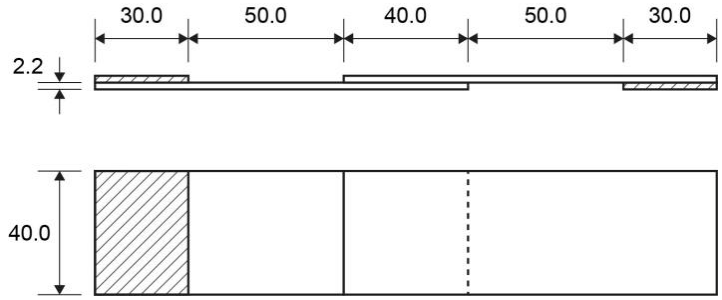

Figure 1. Dimensions in [mm] of the single lap shear specimens.

2.1 Experimental measurements

During the fatigue tests, the reaction force in the specimens is recorded by the testing machine with a peak-valley detection so that the maximum and minimum force in each cycle is registered. At every 50th cycle, a two second dwell at the maximum displacement is programmed to facilitate image capturing with two stereoscopic camera pairs for DIC measurements. The two pairs of cameras each consisting of two Grasshopper 3 (model: GS3-U3-23S6C-C) cameras are used to monitor the front and back side of the specimen. The cameras at the front of the specimen have a 50 mm lens and the ones at the back have a 28 mm lens. However, the cameras on both sides are positioned such that they have a similar field of view that maximizes the overlap region of the specimen.

2.2 Data processing

The DIC images are first processed with the Vic-3D 8 software [6] to correlate the stereo images and obtain the local displacement in all three directions. From this displacement field, a virtual extensometer can be defined to track the global compliance change of the specimen and the displacement field is converted to a strain field using a Lagrangian finite strain formulation.

Once the strains in the two principal directions (ε_{xx} and ε_{yy}) are obtained, the data is smoothed using Arbocz [7] half-wave cosine function, which can be written as:

$$f = \sum_{j=0}^{n} \sum_{i=0}^{m} cos\left(\frac{i\pi x}{L}\right)\left(A_{ij}\, cos(j\theta) + B_{ij}\, sin(j\theta)\right) \quad (1)$$

where A_{ij} and B_{ij} are the amplitudes of the corresponding shape functions. The first partial derivative $\partial f/\partial y$ is:

$$\frac{\partial f}{\partial y} = \sum_{j=0}^{n} \sum_{i=0}^{m} cos\left(\frac{i\pi x}{L}\right) j\left(-A_{ij}\, sin(j\theta) + B_{ij}\, cos(j\theta)\right) \quad (2)$$

The coefficients A_{ij} and B_{ij} are calculated based on measured data using for example a linear least-squares algorithm. In theory, m and n can be chosen for any desired accuracy, but in practice the least-squares algorithms require a high amount of computer memory that limits the maximum values for m and n. In the present work, the diccp Python module version 0.1.7 [8, 9] is used to determine the A_{ij} and B_{ij} coefficients.

Once the noise is filtered from the experimental data by excluding the high frequency terms from the half-wave cosine formulation, a five step process is followed:

1. Choose 5 vertical probing lines along the surface of the overlap (Figure 2 a and b). The data is transformed such that both sides of the specimen use the same coordinate system. The choice to use 5 probing lines was made to provide enough detailed information while not using too much computational power during the processing of the data.
2. Extract the data along the probing lines (Figure 2c).
3. Find local minima and maxima on the 5 probing lines on both sides of the specimen using the partial derivative $\partial f/\partial y$ (Figure 2c). The data from both sides is combined to get a complete view of the damage state. On the front side the data from the top half of the overlap is used and on the back side the data from the bottom half is used.
4. Figure 2d shows that the false positives are located outside of the weld boundary and at the centerline of the weld. These false positives are removed from the calculations. This is done by first identifying which points are located within the initial boundary of the weld and afterwards removing the points that are not the outer two points on each probing line, thus removing the false positives around the centerline.
5. Determine weld area by summing the areas of the 5 probing lines as shown in Figure 3. The damage is represented as a percentage of the initial weld area.

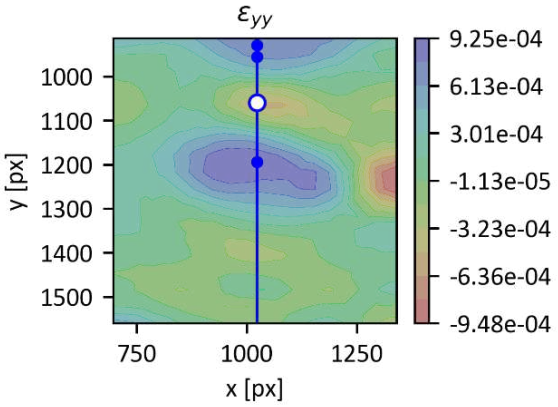

a. *Surface plot with a single probing line and extracted points on the front of the specimen.*

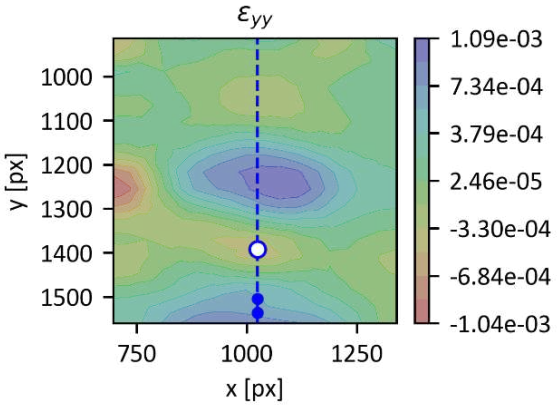

b. Surface plot with a single probing line and extracted points on the back of the specimen.

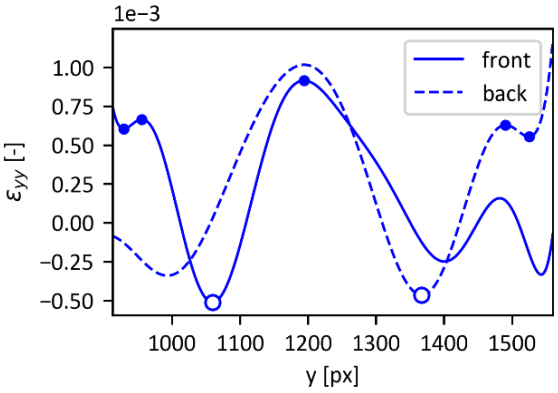

c. Line plots of the center probing lines on the front and the back of the specimen.

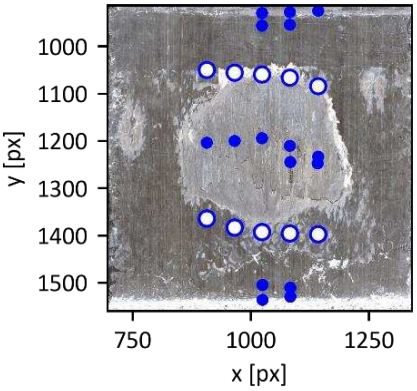

d. Fracture surface with the locations of the extracted points

Figure 2. Processing the DIC data. Points on the weld edge are indicated with open dots ○, false positives with closed dots ●.

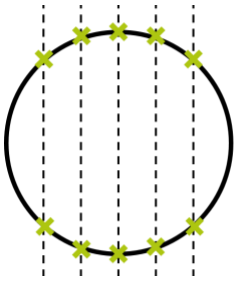

a. Estimated weld height based on each probing line.

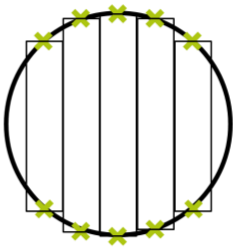

b. Estimated weld area based on each probing line.

Figure 3. Weld area estimation based on extracted weld edges.

These steps are performed for each DIC data point so that the damage progression through the fatigue life can be plotted. The data is then smoothed with the incremental polynomial method from the ASTM standard E647 [10] to calculate the damage growth rate.

3 Results

Figure 4 shows the fracture surface for two of the test specimens. The weld location is determined using the previously described methodology for four different moments during the fatigue life of the specimens.

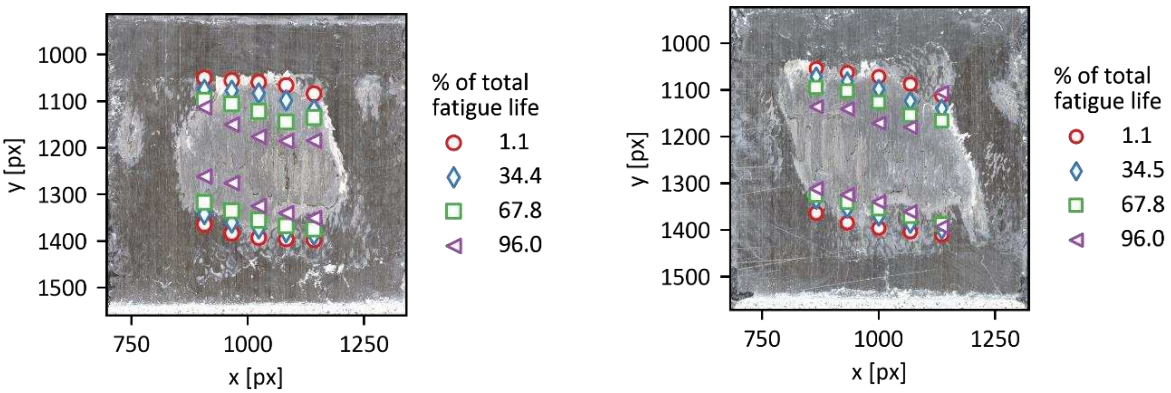

a. Extraction for test specimen 1. *b. Extraction for test specimen 2.*

Figure 4. Extracted weld edges for two different specimens at four moments during the fatigue life.

The damage evolution through the whole fatigue life is determined by performing the post-processing steps for every DIC measurement point. The result for the same two specimens can be seen in Figure 5. The smoothed result of the incremental polynomial method from the ASTM standard E647 [10] is also included.

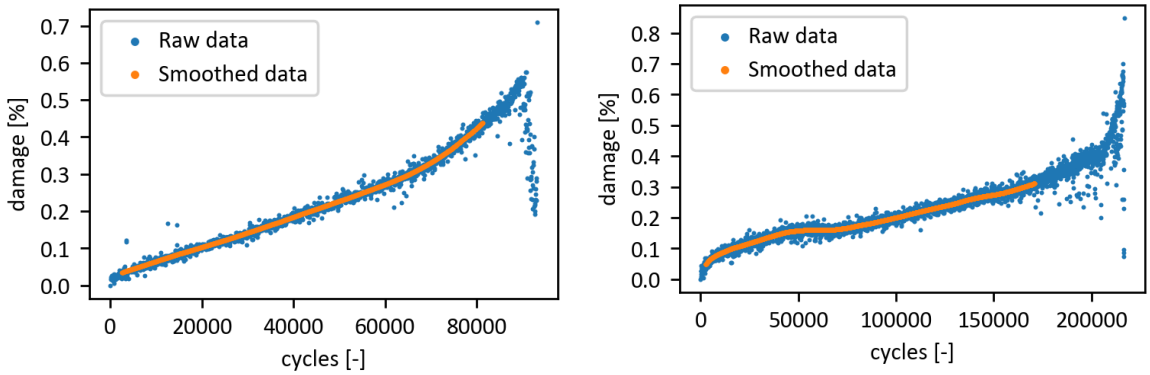

a. Damage evolution for test specimen 1. *b. Damage evolution for test specimen 2.*

Figure 5. Damage evolution through the fatigue life for two different test specimens.

4 Discussion

The raw strain data obtained from the DIC is fitted with a half-cosine Fourier fitting to filter the noise and obtain continuous functions. Figure 6 shows the strain in vertical direction over the center of the overlap fitted with two different numbers of coefficients. An increasing number of coefficients leads to the inclusion of higher frequency components. Therefore, the fitted function approaches the raw data with more accuracy, but more noise is included as well. A total of 6 coefficients was chosen to proceed with the analysis.

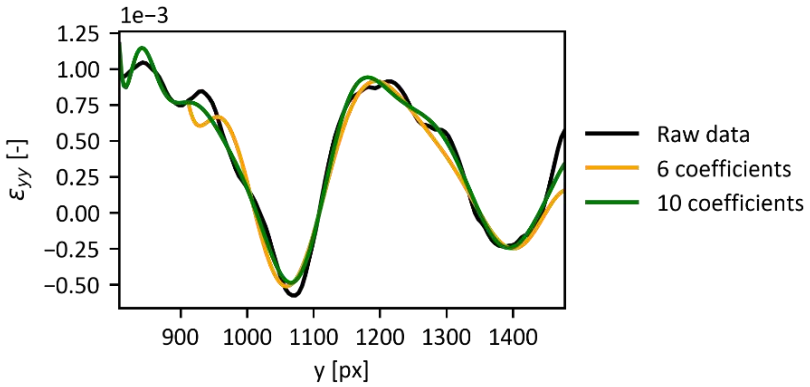

Figure 6. Half-cosine Fourier fitting of the raw DIC data with different numbers of coefficients

The information from the DIC measurements on both sides of the specimens is combined to get a full view of the overlap area, relying on the assumption that the growth of damage occurs from both sides of the centerline and does not cross the centerline of the overlap from either side. This assumption only has a small effect on the estimated damage percentage in single spot joints if there are no secondary welds. After the measurements are combined, the false positives are filtered from the extracted points by finding the two most outer points on each probing line within the weld area.

The comparison of the extracted points and the fracture surface in Figure 4 shows that the actual physical weld size is overestimated, which is especially visible when comparing the extraction at the start of the fatigue life to the complete fracture surface. When comparing the extraction at the end of the fatigue life, this comparison shows that large damages are difficult to extract, herein attributed to the fact that secondary bending is dominant when the damage has grown to most of the initial weld area.

Figure 5 shows the extracted weld area of two different specimens through their whole fatigue life. Since this data is oversampled, it is smoothed using the incremental polynomial technique as described in the ASTM standard E647 [10]. Figure 7 shows the comparison of the damage percentage after the smoothing and the compliance during the fatigue life and Figure 8**Error! Reference source not found.** shows the damage growth rate and the change in compliance. Both graphs show a good comparison between the global compliance in the specimen and the damage in the weld.

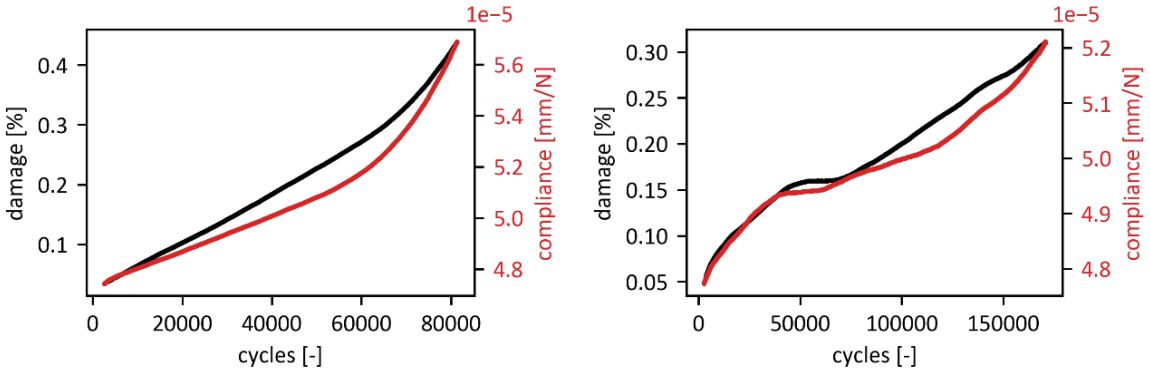

a. Damage evolution for test specimen 1 *b. Damage evolution for test specimen 2*

Figure 7. Damage evolution and compliance for the two same specimens during the fatigue life.

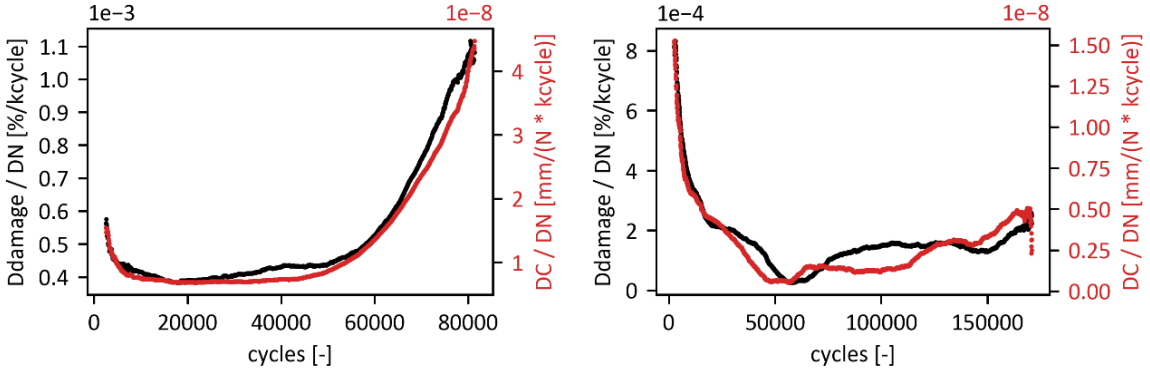

a. Damage growth rate for test specimen 1 *b. Damage growth rate for test specimen 2*

Figure 8. Damage growth rate and change of compliance versus number of cycles.

While the overall evolution of the damage is well captured, small deviations can be observed in the comparison with the global compliance (in Figure 7), specifically in the middle of the fatigue life. These differences can be attributed to damage growth in the horizontal direction. Note that the proposed method only captures growth in the direction of the loading, since the features in the other direction are too small to be captured.

Some remarks can be made regarding the expansion of this method to the analysis of multi-spot joints. First, the assumption in the combination of the measurement data, that the damage only grows on either side of the centerline, does not always hold. For example, if several spots are aligned in the direction of loading, the damage might only grow on one side of the overlap and the spots are not located in the center of the specimens. Second, in this method two points are chosen on every probing line, making it difficult to know when a weld is fully damaged. In the current test, this is not crucial information because the joints only consist of a single weld, therefore joint failure and spot failure are identical. However, in the case of multi-spot specimens, this is much more relevant information, for instance to be able to determine the sequence of failure since the failure of a single spot in the configuration does not immediately mean that the complete joint also failed. Both considerations must be addressed in the future testing campaign, when a series of multi-spot specimens with different configurations will be tested in experiments that are similar to those described in the present paper.

  doi:10.5075/epfl-298799_978-2-9701614-0-0

5 Conclusion

This paper discussed the characterization of damage growth in ultrasonically spot welded joints with use of surface strain measured by a Digital Image Correlation (DIC) system. The raw DIC data was first filtered with a half-cosine Fourier function with six coefficients. The resulting continuous functions were used to locate the local minima and maxima of the strain in vertical direction. After filtering out false positives, a view of the damage state was obtained.

After the test was completed, the fracture surface could be observed and compared to the extracted points at different moments, showing that the exact physical weld area cannot be captured with great accuracy.

When the extraction procedure was performed on every measurement point, a damage growth curve was obtained. The comparison of the damage percentage and the specimen compliance as well as the change in damage and change in compliance over the course of the fatigue life showed that a good representation of the damage evolution was obtained. Small deviations could be observed between the damage and compliance results, which were attributed to a growth of the damage in the horizontal direction, that was not captured with the current method.

It is concluded that the proposed method does allow to measure and observe the evolution of the damage growth in an ultrasonically spot welded joint. However, one should always keep in mind that the proposed damage detection methodology consists of an indirect measurement that still requires further validation against direct damage detection methods such as C-scan measurements.

6 References

1. Villegas IF, Moser L, Yousefpour A, Mitschang P, Bersee HEN. Process and performance evaluation of ultrasonic, induction and resistance welding of advanced thermoplastic composites. Journal of Thermoplastic Composite Materials. 2012;26(8):1007-24.
2. Grewell D, Benatar A. Welding of plastics: Fundamentals and new developments. International Polymer Processing. 2007;22(1):43-60.
3. Villegas IF, Bersee HEN. Ultrasonic welding of advanced thermoplastic composites: An investigation on energy-directing surfaces. Advances in Polymer Technology. 2010;29(2):112-21.
4. Zhao T, Palardy G, Villegas IF, Rans C, Martinez M, Benedictus R. Mechanical behaviour of thermoplastic composites spot-welded and mechanically fastened joints: A preliminary comparison. Composites Part B: Engineering. 2017;112:224-34.
5. Choudhary A, Fernandez I. Robotic sequential ultrasonic welding of thermoplastic composites: process development and testing. American Society for Composites 2021: Destech Publications, Inc.; 2021.
6. Correlated Solutions. Vic-3D 8. Available from: https://correlatedsolutions.eu/software/vic-software/.
7. Arbocz J. The imperfection data bank, a mean to obtain realistic buckling loads. Journal of Applied Mechanics. 1982:535-67.
8. Castro SGP. Digital Image Correlation Post Processing module Version 0.1.7. Available from: https://pypi.org/project/dicpp/0.1.7/.

9. Castro SGP, Almeida Jr JHS, St-Pierre L, Wang Z. Measuring geometric imperfections of variable–angle filament–wound cylinders with a simple digital image correlation setup. Composite Structures. 2021;276:114497.
10. ASTM Standard E647, 2016, "Standard Test Method for Measurement of Fatigue Crack Growth Rates", ASTM International, West Conshohocken, PA, 1978, DOI:10.1520/E0647-15E01, www.astm.org

COMPARISON OF PULSED, PULSE-PHASE, LOCK-IN AND STANDARD DEVIATION THERMOGRAPHY TECHNIQUES FOR NONDESTRUCTIVE EVALUATION OF COMPOSITE MATERIALS.

Angelos, Ntaflos[a]*, Arsenios Gkourras*[a]*, Leonidas N. Gergidis*[a]*, Alkiviadis S. Paipetis*[a]*.*

a: Department of Materials Science and Engineering, University of Ioannina, 45110 Greece.
A.ntaflos@uoi.gr

Abstract:

IR Thermography is a versatile nondestructive evaluation tool for fast determination of defect depth, geometry, and size in composite materials. Four thermographic techniques are evaluated for their fast and reliable inspection of impact damage on unidirectional carbon fibre reinforced plastics. Pulse Thermography (PT), Lock-In Thermography (LIT), Pulse-Phase Thermography (PPT) and a new novel post-processing method was assessed based on the Standard Deviation (SD) of the temperature rise compared to the mean value of the thermographic stack. The results presented make SD a low-cost alternative to the other methods presented here, capable of detecting with high resolution surface damage from impact testing.

Keywords: Thermography; Standard Deviation; composite materials; image processing.

1. Introduction

Composite materials are currently a major percentage of materials used in most advanced industries due to their tailor made properties and low weight ratio.(1) Thermographic inspection has been used widely in a variety of fields, from structural health monitoring and cultural heritage to medical applications, due to its relatively fast and reliable results.(2) Infrared Thermography for composite evaluation basically requires the material having uniform thermal characteristics, where thermal anomalies created by defects or impurities change the signature compared to the sound material. Infrared thermal images are generally noisy and have low signal to noise ratio, that is why various image and data processing techniques are used to enhance the acquired thermograms. The main objective of image processing techniques is the detection of anomalous areas and the extraction of defect features. For image enhancement purposes various algorithms like contrast stretching, histogram equalization, etc. can be used. Intense research is being conducted to develop techniques that allow deeper probing, better spatial resolution, and higher noise reduction for more accurate results.(3) Four thermographic techniques will be evaluated for their fast and reliable inspection. Pulse Thermography (PT), where a short duration pulse excites the material and a measurement of the surface temperature over time is performed.(4) Lock-In Thermography (LIT) in which the material is excited with a wave of modulated frequency, the term lock-in refers to the necessity of monitoring the time dependence between the output signal and the reference input signal to extract amplitude and phase images from the data.(5) Pulse-Phase Thermography (PPT) which was proposed by Maldague et al.(6) and combines the procedure of PT with the data analysis of LIT and an image processing computational methodology that incorporates fast and novel data analysis techniques, based on the Standard Deviation of the temperature from the mean value

  doi:10.5075/epfl-298799_978-2-9701614-0-0

of an IR image sequence, produced by applying a thermal excitation.Damage caused by low velocity impacts is of particular interest in the aircraft industry. In this work, CFRP composites (150 x 100 mm) of 2.75 mm thickness, 10 ply unidirectional were manufactured with vacuum infusion. The CFRP underwent impact damage and were evaluated post-impact with the thermographic techniques mentioned above and with ultrasonic C-Scan inspection to evaluate the results.

2. Equipment & Materials

2.1 Equipment

IR Camera based testing was done in reflection mode with a FLIR A6751 thermal imaging camera, with a frame rate up to 125 Hz, temperature resolution 0.1 K and a (640 x 512) image resolution, connected to a computer with the appropriate software by Teledyne-Flir to extract the thermogram stack as a series of 32-bit tiff. formated images. A Tektronix AFG3052C Function generator and two 1000W Halogen Lamps were used to complete the set-up requirements. The specimens were placed at a single meter distance from the camera and the lamps. For the purposes of this study, the camera had a set frame rate of 20Hz. Impact damage was done with an Instron Ceast 9340. A falling weight impactor with a hemispherical 16 mm radius head was used to apply impacts of controlled energy. C-scan with Dolphicam2 by Dolphitech was performed to access the damage and correlate the results. For the purposes of this study a digital imaging methodology has been developed to process thermal images utilizing various techniques used for thermal imaging. The main computational tool adopted in the present research study was the open computer vision (OpenCV) library that finds applications in areas such as facial recognition, motion tracking and image segmentation (7). The programming language Python (8) was chosen for the in-house software development due to the simplicity, versatility and compatibility with other computational tools and libraries.

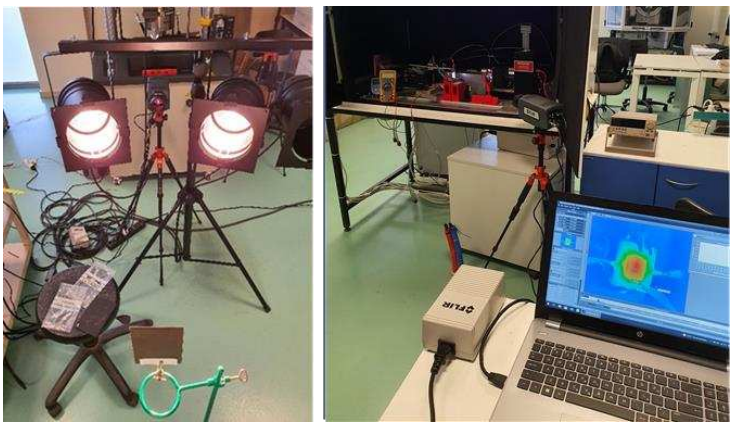

Figure 1: Thermography equipment set-up.

2.2 Materials

CFRPs were created with an Araldite LY5052 Epoxy and an Aradur 5052 hardener matrix with a 100:38 ratio and carbon fibre with 300g/m^2 weight was provided from FIBERMAX GR. Composite with ply orientation of $[0]_{10}$ was made using Vacuum resin infusion. The composite was cured for 24 hours under vacuum in environmental temperature.

  doi:10.5075/epfl-298799_978-2-9701614-0-0

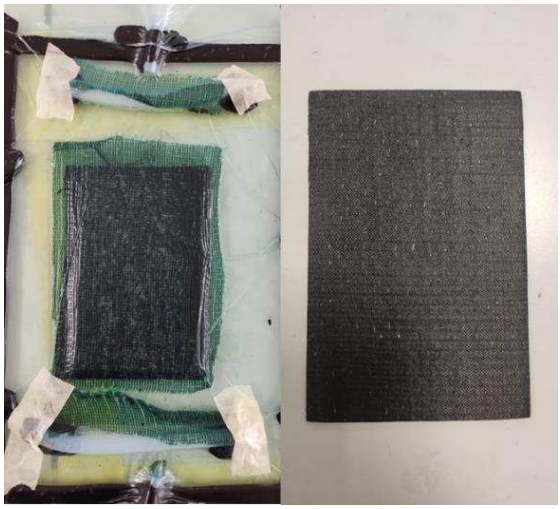

Figure 2: Specimen during the Vacuum Infusion and final product

2.3 Methodology

2.3.1. Lock-In Thermography

Sin/Cos Correlation and the 4 bucket method are some of the most common algorithms used, were information of each pixel of the image is processed as if it were fed into a lock-in amplifier. (9) The digital lock-in correlation procedure consists in multiplying the incoming IR images by a set of weighting factors and summing up the results in a frame storage.(10) The specimen undergone 3 heating cycles, with a sinusoidal wave of 0.2Hz frequency.

2.3.2 Pulse Phase Thermography

Pulse-Phase Thermography (PPT) follows the procedure of Pulse Thermography combined with the ability to extract information about phase difference and amplitude, like LIT. It is based on the thermal decay following a pulse stimulation and the sequence of infrared images are processed with a Discrete Fourier Transform (DFT).(11) A single pulse of 0.2Hz frequency excited the specimen.

2.3.3 Standard Deviation Technique

In this study we propose an image processing methodology that incorporates fast and novel data analysis techniques based on the SD of the temperature from the mean value of an IR image sequence produced by applying a thermal pulse.

2.3.4 Drop Weight Impact.

The sample dimensions were 150 mm x 100 mm x 2.75 mm and drop weight impact was done with an Instron Ceast 9340. The drop weight impact test was performed for all composite materials produced with the same impact energy of 20 J. Due to the nature of the inspection, the test didn’t adhere to any international standards.

2.3.5 C-Scan Inspection

  doi:10.5075/epfl-298799_978-2-9701614-0-0

Ultrasonic C-Scan inspection was performed with the Dolphicam2 by Dolphitech and a 3.5Mhz transducer to evaluate the defect geometry and depth and be compared with the thermographic data. The equipment was calibrated for 3 mm thick materials. For clearer visual inspection thresholding “gates” were added to reduce ultrasonic pulse reflections in the upper layers.

3. Results

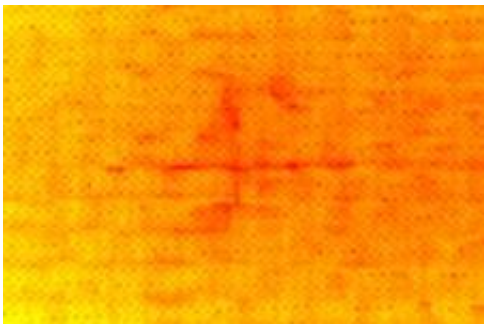

Figure 3: Single Frame extracted from Pulse thermography data. Pulse duration was 5 sec.

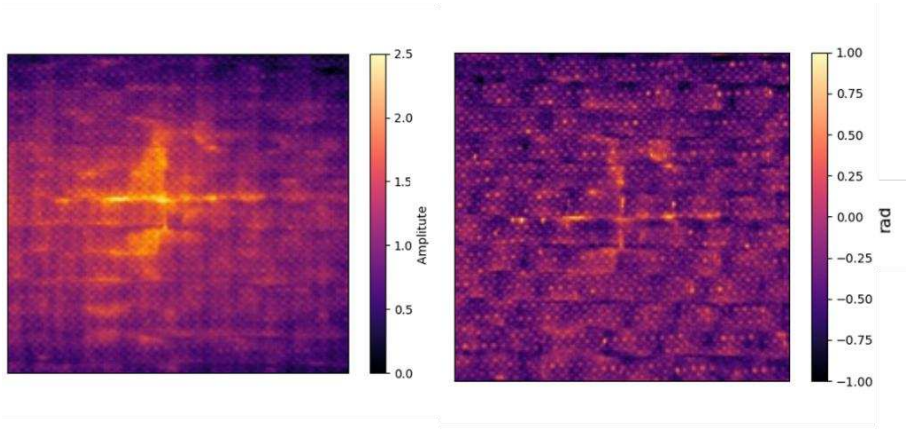

Figure 4: Digital Lock-In correlation procedure at 0.2hz, Amplitude (left), Phase (right).

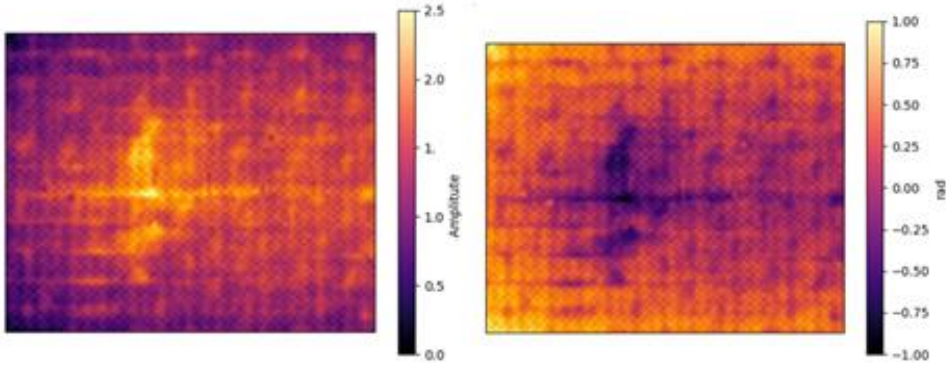

Figure 5: Pulse Phase 0.2Hz, Amplitude (Left), Phase (right)

  doi:10.5075/epfl-298799_978-2-9701614-0-0

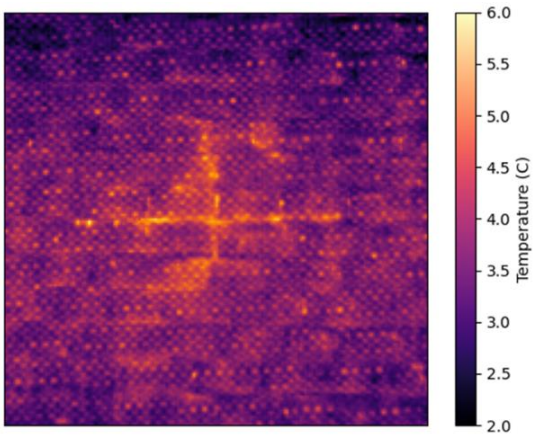

Figure 6: Standard Deviation results at 0.2 hz frequency.

The deviation from the average temperature of the specimen post-heating becomes higher the closer you get to the impact point due to anomalous heating created by the differences of the thermal properties of the defected area. The aforementioned produces a clear hot-spot image of the defect shape that agrees with the results of the established methods above. Showing, similar results but without the need of expensive equipment and expertise. Since SD method isn't wildly used, efficiency protocols haven't been established or proposed, many factors must still be considered, contrast evaluation, correct frame selection, time-defect depth correlation, maximum visible depth, and similar parameters necessary for any thermographic technique. This technique could prove to be a valuable tool for fast inspection services, or even for portable applications.

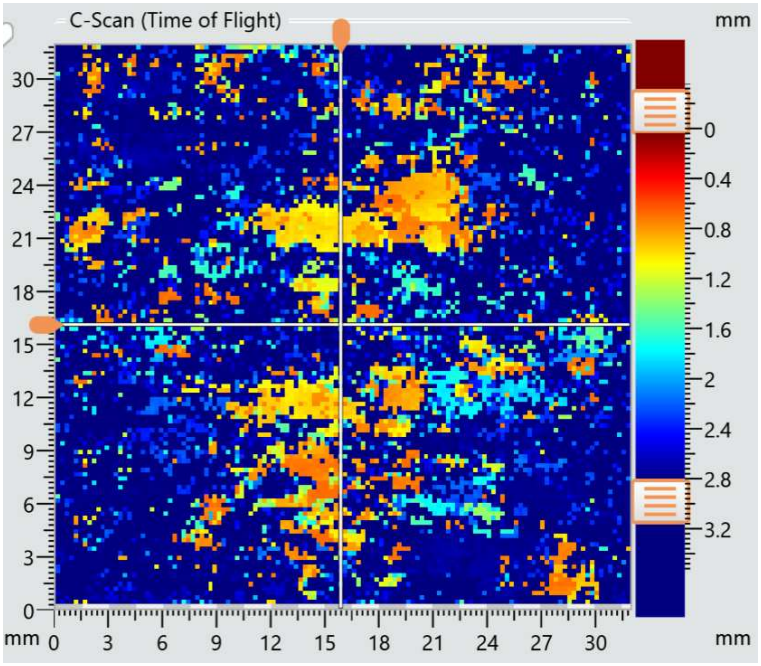

Figure 7: C-scan inspection. The defected area is located around 1 mm in depth.

Comparing the results of both thermography and C-scan, we can correlate the damage to the anomalous areas and examine the damage with respect to depth. Taking a slice by "gating" the

  doi:10.5075/epfl-298799_978-2-9701614-0-0

signal, the majority of the damage is revealed to be between plies 4 and 5, around 1 mm in depth, in a geometry that agrees with the results of our thermographic data.

Acknowledgements

This research has been co-financed by the European Union and Greek national funds through the Operational Program Competitiveness, Entrepreneurship, and Innovation, under the call RESEARCH – CREATE – INNOVATE (project code: AIOLOS T2EDK-02971).

4. References

1. P. Bagavac. Lock-in thermography image procesing. HDKBR INFO Mag. 2016;6(1):7.
2. Ibarra-Castanedo C, Maldague XP V. Handbook of Technical Diagnostics. Handbook of Technical Diagnostics. 2013.
3. Bagavathiappan S, Lahiri BB, Saravanan T, Philip J, Jayakumar T. Infrared thermography for condition monitoring - A review. Infrared Phys Technol. 2013;60:35–55.
4. Subbarao G V., Mulaveesala R. Quadratic frequency modulated thermal wave imaging for non-destructive testing. Prog Electromagn Res M. 2012;26(June):11–22.
5. Montanini R, Freni F. Non-destructive evaluation of thick glass fiber-reinforced composites by means of optically excited lock-in thermography. Compos Part A Appl Sci Manuf. 2012;43(11):2075–82.
6. Maldague X, Marinetti S. Pulse phase infrared thermography. J Appl Phys. 1996;79(5):2694–8.
7. Bradski G. Dr. Dobb's Journal of Software Tools. 2000. 120–125 p.
8. M. Pilgrim SW. Dive into Python 3. 2009.
9. Breitenstein O, Warta W, Schubert MC. Lock-in Thermography. Second. Springer; 2000. 101–147 p.
10. Huth S, Breitenstein O, Huber AD-PD, Dantz D, Lambert UDD-M, Altmann F. Lock-In IR-Thermography A Novel Tool for Material and Device Characterization. Solid State Phenom. 2001;82–84:741–6.
11. Ibarra-Castanedo C, Maldague X. Pulsed phase thermography reviewed. Quant Infrared Thermogr J. 2004;1(1):47–70.

  doi:10.5075/epfl-298799_978-2-9701614-0-0

SURFACE AND SUBSURFACE DAMAGE ASSESSMENT OF MULTI-DIRECTIONAL COMPOSITE LAMINATES UTILIZING A FULL FIELD IMAGING TECHNIQUE

R. Ruiz-Iglesias[1], G. Ólafsson[2], O.T. Thomsen[3] and J.M. Dulieu-Barton[4]

[1-4]Bristol Composites Institute (BCI), School of Civil, Aerospace and Mechanical Engineering, University of Bristol, Bristol BS8 1TR, UK - rafael.ruiziglesias@bristol.ac.uk

Thermoelastic Stress Analysis (TSA) is a full-field infra-red imaging technique which has traditionally been used to infer the stress state on the surface of a component undergoing cyclic load. It has been recently demonstrated that the subsurface thermoelastic response can be obtained at low loading frequencies where adiabatic conditions break down and through thickness heat diffusion can occur. Digital Image Correlation (DIC) is a full-field surface measurement technique which employs white light imaging to track changes in contrast to obtain the material surface displacements and strains. Since DIC relies on the laminate surface kinematics and consequently is independent of heat diffusion the laminate surface thermoelastic response under adiabatic conditions can be derived from the measured DIC strains. Hence, there is a possibility that by subtracting the surface response derived from the DIC, from the measured thermoelastic response, subsurface damage could be revealed. This proposition is explored for CFRP (IM7/8552) multidirectional strip specimens subjected to uniaxial tension loading.

Keywords: Thermoelastic Stress Analysis (TSA); Digital Image Correlation (DIC); Experimental mechanics; Damage; Laminated composites.

1. Introduction

Thermoelastic Stress Analysis (TSA) is a non-contact full-field technique that utilises infra-red imaging. The technique is based on the measurement of a small temperature changes on the surface of a component that occur when it is cyclically loaded. The temperature change occurs under elastic loading conditions as a result of the relationship between mechanically deformation and the generated thermal energy [1]. Temperature variations are captured using a sensitive infra-red detector, which can then be related to the stress changes on the surface of a component. The correlation between temperature change and the stresses was established in [2] for orthotropic composite materials as:

$$\Delta T = \frac{-T_0}{\rho C_p}(\alpha_1 \Delta\sigma_1 + \alpha_2 \Delta\sigma_2) \quad (1)$$

where ΔT is defined as the temperature change (peak-to-peak temperature change) or the thermoelastic response, T_0 is the material surface temperature, ρ is the density, C_p is the specific heat capacity, α_1 and α_2 are the coefficients of linear thermal expansion in the principal material directions and $\Delta\sigma_1$ and $\Delta\sigma_2$ are the stress changes in the principal material directions. It is important to note that $\alpha_6 = 0$ in the principal material directions and hence $\Delta\sigma_6$ is not required in the formulation of equation (1).

  doi:10.5075/epfl-298799_978-2-9701614-0-0

Equation (1) is valid only if ΔT occurs under isentropic conditions. In the context of the present work this means no heat transfer occurs, i.e. adiabatic conditions are achieved by cyclically loading at a sufficiently high rate to limit heat diffusion. If adiabatic conditions are not achieved, then the surface response measured by the infra-red detector will include the subsurface response. If the surface response according to equation (1) can be removed from the overall response, then TSA offers a means of assessing subsurface features and defects. To derive the surface response, it is proposed that Digital Image Correlation (DIC) is used. DIC is also a full-field non-contact imaging technique that can provide surface deformation and strains from a component under load. DIC is a kinematic technique, which tracks the movement of a speckle pattern applied on the material surface to calculate displacements [3, 4] so the strain field can be determined by differentiation of the displacements. DIC has been used over a wide measurement range from microscale [5] to macroscale [6]. However, this technique is limited to surface measurement and thus achieving an optimum combination with TSA is essential for detecting surface and subsurface damage. Combining TSA and DIC offers the opportunity to create a new tool for assessment of subsurface features in composite materials.

Many previous studies [7–12] have investigated the nature of the thermoelastic response from laminated composites and have demonstrated that the heat transfer is driven by the stress induced temperature change from ply to ply and the loading frequency. To assess the effect of any subsurface damage or features, it is necessary to understand the nature of the thermoelastic response for a particular laminate, as the thickness of any surface resin layer and the fibre volume fraction all play a role in the surface temperature change.

To determine the heat transfer effect on the thermoelastic response, a comparison between the measured ΔT (obtained from TSA) was made in [11] with a calculated value determined from the measured strains (obtained with DIC using a lock-in approach described in [13]). The theoretical assumptions presented in the previous research were drawn together and three models were suggested for the source of ΔT in an undamaged multidirectional laminate:

- The resin rich layer model, where ΔT results from the surface resin alone, which is considered to be as an isotropic material that is thermally isolated from the laminate stack (i.e. a strain witness [9, 10]).
- The surface ply model, where the surface ply is treated as an isolated ply and any heat transfer effects are neglected.
- The global laminate model, where ΔT results from the entire material, i.e. homogenized through the thickness of the laminated plate.

Using this methodology and assumptions enables a comparison of the models with TSA results and hence identifying the source of thermoelastic response. The study presented in [11] demonstrated that CFRP (IM7/8552) $[90,0]_{3S}$ and $[0,90]_{3S}$ laminated coupons revealed different sources of thermoelastic response at different loading frequencies (3.1 to 40.1 Hz), concluding that adiabatic conditions were not met at low loading frequencies, thereby enabling the acquisition of subsurface information. Combining this with a theory developed in [14], could provide a basis of using TSA to evaluate damage in composite materials. Although improvements have been made in laminate failure theories and new ones have emerged (e.g. Puck2D and LaRC03), there is an urgent need for improved damage detection techniques particularly in the service environment to extend life and reduce maintenance costs of high value composite

  doi:10.5075/epfl-298799_978-2-9701614-0-0

assets. The work presented here provides the initial steps to determine damage parameters based on TSA.

2. Materials and Methodology

2.1 Laminated coupons and material properties

CFRP (IM7/8552) pre-preg panels were manufactured in an autoclave according to the recommended cure cycle in the supplier's data sheet. Strip specimens used in this study were cut from the panels to the dimensions specified in Table 1.

Table 1. Laminated coupons dimensions.

Coupon Layup	CFRP (IM7/8552)		
	Length (mm)	Width (mm)	Thickness (mm)
$[90,0]_{3s}$	220	25	1.527

As the resin rich layer performs a critical role in the thermoelastic response of the material, both the volume fraction and the thickness of the resin rich layer were obtained from micrographs. The lamina properties were obtained from literature [11, 15]. The overall laminate properties and estimates of First Ply Failure (FPF) and ultimate failure were obtained using Classical Laminate Theory (CLT) inbuilt in the ESAComp software provided by Altair.

2.2 Experimental methodology

Phase 1 of the experiments commenced with an inspection of the undamaged $[90,0]_{3S}$ coupons by cyclically loading (below the first ply failure load) using the combined both TSA and DIC described in [11] to determine the nature of the thermoelastic response. As the FPF stress of the laminated coupon was calculated to be 542.60 MPa (for the 90° ply), a cyclic stress of 162.66 ± 141.33 MPa was applied to avoid any chance of failure. Phase 2 consisted of applying uniaxial tensile loading ramps to gradually increase the load applied and hence incrementally damage the specimen. In each ramp the maximum load applied was equivalent to 54%, 65% and 76% up to 87% of the UTS (last damage step for the $[90,0]_{3S}$ strips). After each loading ramp the load was reduced, and an inspection phase was carried out using cyclic loading at the same level as phase 1 to characterise damage induced during the quasi-static loading but minimising damage propagation. During each inspection, the specimens were subjected to cyclic uniaxial tension at a range of different loading frequencies (3.1 to 20.1 Hz) to obtain the different thermodynamic conditions. At high frequencies (≈ 20 Hz) adiabatic conditions are approached as determined in [11]; at lower frequencies through thickness heat conduction occurs. This phenomena offers an opportunity for the detection of subsurface features such as damage.

During the inspection phase TSA was performed using a fast Telops M3K camera and DIC were performed using two 12MPx polarized monochrome cameras with progressive scan CMOS sensors (BFS-U3-51S5P-C USB 3.1 Blackfly®). The thermal data were firstly processed to compensate for motion by tracking circular fiducial markers specifically selected to have a different emissivity to the specimens. The image series captured by the white light cameras was

  doi:10.5075/epfl-298799_978-2-9701614-0-0

processed using MatchID DIC software. Strains were obtained for each image captured relative to the first image in the image series. The strain data were then processed using a lock-in process to obtain the magnitude of the strain [7]. The fiducial markers were further used to align the strain magnitude image from the DIC and the ΔT image from the TSA to a common datum. Then the data were interpolated to an identical coordinate systems equivalent to that of the lower resolution DIC image coordinate system allowing a pointwise comparison between TSA and DIC.

3. Results and Discussion

To highlight the importance of the motion compensation procedure, the full field thermoelastic response before and after applying motion compensation is shown in Figure 1 for the specimen with a damage level of 76% of the UTS. The uncompenated image on the left of Figure 1 shows significant image blurring most evident in the non-circular shape of the fiducial markers. The image on the right of Figure 1 clearly shows regions of much greater response (and hence stress) which is emanating from the intact 0° subsurface ply. The regions of lower response are the 90° surface ply that is unable to carry any stress due to the damage.

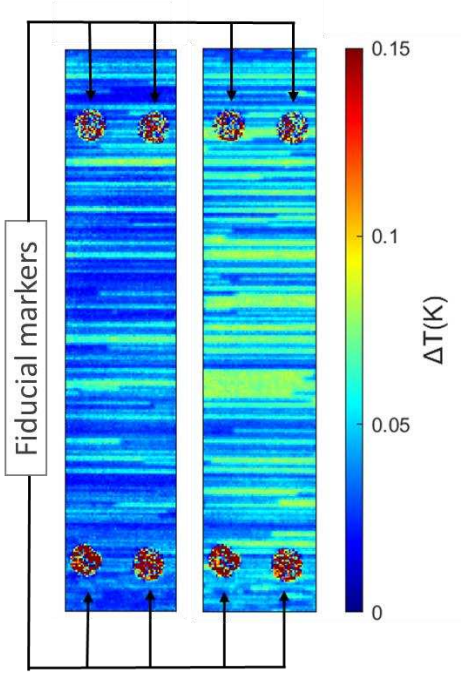

Figure 1. Thermoelastic response of damaged $[90,0]_{3S}$ specimen before (left) and after (right) motion compensation.

The full-field thermoelastic response images of the $[90,0]_{3S}$ coupons corresponding to undamaged and damaged states at different loading frequencies are shown in Figure 2. The images shown in Figure 2a display the undamaged laminate thermoelastic response in its normalised form: $\Delta T/T_0$. This has been done to account for any surface temperature changes due to the damage evolution. At low frequencies (where non-adiabatic conditions prevail), the thermoelastic response approximates a homogenised laminate response as heat transfer occurs from one ply to its adjacent ply/plies. At high frequencies (and as adiabatic conditions are met), the response tends toward the surface ply response. This phenomenon is explained because of the ply configuration: the 90° ply is on the surface, the stress induced temperature change in the subsurface ply (0°) is less and as a result the heat will transfer from the surface ply to the

  doi:10.5075/epfl-298799_978-2-9701614-0-0

subsurface at low loading frequencies. As the loading frequency increases the thermal diffusion length decreases, as there is less time for heat transfer and the system becomes more adiabatic. The full field thermoelastic response observed for the undamaged laminate at lower frequencies (3.1 Hz and 5.1 Hz) reveal vertical lines which correspond to the subsurface (0°) thermoelastic response (fibre direction) and horizontal thin lines corresponding to the surface (90°) ply.

As the CLT predicted, the FPF of the cross-ply laminate occurred at 54% of the UTS of the laminate in the 90° plies. As the load was increased more damage propagated in the surface ply which means it is unable to carry stress, so its stress induced temperature change decreases. Figure 2b shows the thermoelastic response of the specimen after 76% of the UTS of the laminate had been experienced. Here, the thermoelastic response clearly decreases with loading frequency. This is because heat is being transferred from the intact subsurface ply at lower frequencies and at higher loading frequencies the thermoelastic response reduces as a result of the inability of the surface ply to carry stress. Further analysis is required but clearly at the higher loading frequency the response from the subsurface ply is evident through the horizontal cracks in the surface ply. More interestingly are the regions of higher response in the subsurface cracks indicated by the red horizonal lines in Figure 2b at the lower loading frequencies. This points to an influence from the 3rd (90°) ply in the stack, which is transferring heat into the 0° ply and suggests it is still able to carry stress, indicating an increased strength possibly due to the constrained layer effect.

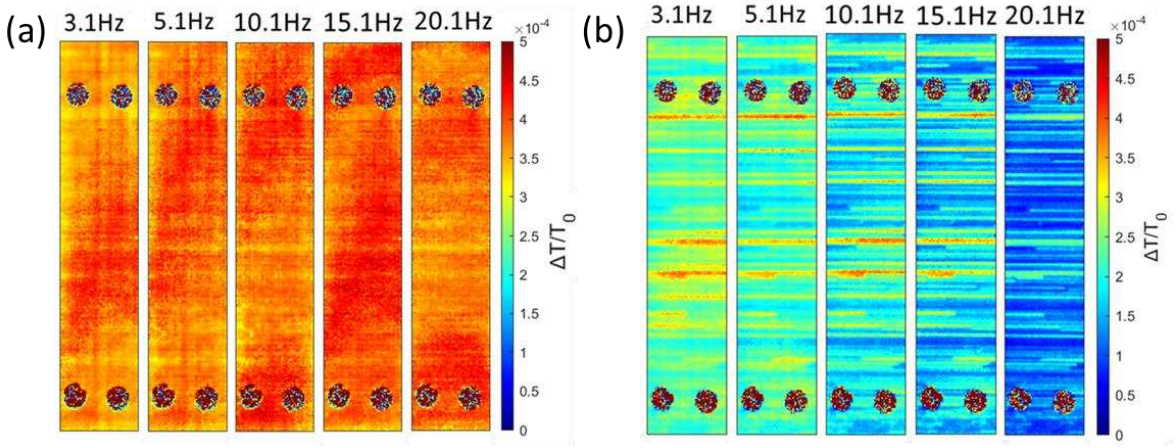

Figure 2. Full-field normalized thermoelastic response of CFRP IM7/8552 $[90,0]_{3S}$ laminates at different loading frequencies (3.1 – 20.1 Hz) after reaching (a) 32% of the UTS (b) 76% of the UTS.

4. Conclusions

It has been shown that it is possible to identify damage in the surface ply of a CFRP laminate using TSA. The identification of the damage was greatly improved by implementing a motion compensation procedure on the thermal images. More importantly it was shown that, as a consequence of the damage, the thermoelastic response changed considerably as the loading frequency increased. This is because the different thermal conditions imposed by the damage modifies the heat transfer in the specimen. Clearly further work is required, but the results presented here, demonstrate clearly the proposition of being able to identify subsurface damage in a component undergoing fatigue loading during the test. The possibility of damage assessment and creating a damage parameter will be the focus of future work.

  doi:10.5075/epfl-298799_978-2-9701614-0-0

Acknowledgements

The authors are grateful to Dr Irene Jimenez-Fortunato for the support and training received in relation to TSA, DIC and data processing. The research presented was supported by the EPSRC Programme Grant 'Certification for Design – Reshaping the Testing Pyramid' (CerTest, EP/S017038/1). The support received is gratefully acknowledged.

5. References

1. Zaoui A, Stolz C (2001) Elasticity: Thermodynamic Treatment. In: Encyclopedia of Materials: Science and Technology. Elsevier, pp 2445–2448
2. Stanley P, Chan WK (1985) Quantitative stress analysis by means of the thermoelastic effect. The Journal of Strain Analysis for Engineering Design 20:129–137
3. Hild F, Roux S (2012) Chapter 5: Digital Image Correlation. Optical Methods for Solid Mechanics: A Full-Field Approach
4. Chu TC, Ranson WF, Sutton MA (1985) Applications of digital-image-correlation techniques to experimental mechanics. Experimental Mechanics 25:232–244
5. Canal LP, González C, Molina-Aldareguía JM, Segurado J, Llorca J (2012) Application of digital image correlation at the microscale in fiber-reinforced composites. In: Composites Part A: Applied Science and Manufacturing. pp 1630–1638
6. Giancane S, Nobile R, Panella F, Dattoma V (2010) Damage evolution of composite laminates with digital image correlation. Key Engineering Materials 452–453:377–380
7. Frühmann RK, Sambasivam S, Dulieu-Barton J, Quinn S (2008) Material properties for quantitative thermoelastic stress analysis of composite structures. pp 99–104
8. Sambasivam S, Quinn S, Dulieu-Barton J (2009) Identification of the source of the thermoelastic response from orthotropic laminated composites. ICCM International Conferences on Composite Materials
9. Emery TR, Dulieu-Barton JM, Earl JS, Cunningham PR (2008) A generalised approach to the calibration of orthotropic materials for thermoelastic stress analysis. Composites Science and Technology 68:743–752
10. Pitarresi G, Found MS, Patterson EA (2005) An investigation of the influence of macroscopic heterogeneity on the thermoelastic response of fibre reinforced plastics. Composites Science and Technology 65:269–280
11. Jiménez-Fortunato I, Bull DJ, Thomsen OT, Dulieu-Barton JM (2021) On the source of the thermoelastic response from orthotropic fibre reinforced composite laminates. Composites Part A: Applied Science and Manufacturing 149:1–15
12. Wong A (1991) A non-adiabatic thermoelastic theory for composite laminates. Journal of Physics and Chemistry of Solids 52:483–494

  doi:10.5075/epfl-298799_978-2-9701614-0-0

13. Fruehmann RK, Dulieu-Barton JM, Quinn S, Tyler JP (2015) The use of a lock-in amplifier to apply digital image correlation to cyclically loaded components. Optics and Lasers in Engineering 68:149–159

14. Zhang D, Sandor B (1990) A thermoelasticity theory for damage in anisotropic materials. Fatigue & Fracture of Engineering Materials and Structures 13:497–509

15. Saad MT, Miller SG, Marunda T (2014) Thermal characterization of IM7/8552-1 carbon-epoxy composites. In: International Mechanical Engineering Congress and Exposition. American Society of Mechanical Engineers, pp 1–8

  doi:10.5075/epfl-298799_978-2-9701614-0-0

MULTIMODAL NDT MONITORING OF TEXTILE REINFORCED CEMENTITIOUS COMPOSITE SANDWICH BEAMS IN BENDING

Nicolas Ospitia[a,b], Eleni Tsangouri[a], Ali Pourkazemi[b], Johan H. Stiens[b], Dimitrios G. Aggelis[a]

a: Department of Mechanics of Materials and Constructions (MeMC), Faculty of Engineering, Vrije Universiteit Brussel (VUB), Brussels, Belgium. Nicolas.ospitia.patino@vub.be
b: Department of Electronics and Informatics (ETRO), Faculty of Engineering, Vrije Universiteit Brussel (VUB), Brussels, Belgium

Abstract: *Textile Reinforced Cementitious (TRC) sandwich technology generate lightweight elements with satisfactory loadbearing capacity. The non-corrosive nature of the textiles allows for concrete cover reductions, and therefore energy savings and lower carbon emissions when compared to a steel reinforced concrete sandwich, or steel reinforced concrete elements. However, due to its composite nature, TRC sandwich elements have a complex damage behavior, and bad interlaminar bond, might cause premature debonding, and drastically reduce the loadbearing capacity of the composite. Non-Destructive Testing (NDT) Techniques allow to inspect and monitor structural elements without affecting their behavior. In this study, MMW Spectrometry, Acoustic Emission, and Digital Image Correlation are used simultaneously to monitor quasi static four-point bending tests of TRC sandwich panels, and similar elements with an artificially destroyed interlaminar bond.*

Keywords: TRC sandwich; Damage monitoring; Acoustic Emission; MMW Spectrometry; Digital Image Correlation.

1. Introduction

Concrete sandwiches are constituted of two cementitious facings, and a thermal and acoustic insulating core. This technology has proven to be more advantageous than traditional steel rebars reinforced concrete by optimally utilizing the material where it is needed increasing the moment of inertia [1]. Reinforced concrete has been widely used as a facing material, however, to avoid corrosion of steel, the thickness of the concrete cover increases, not allowing for slender sections, compromising the lightweight nature of the sandwich element. Recently, Textile Reinforced Cementitious (TRC) composites have been proposed as an alternative facing material, allowing for slender, free-form, non-corrosive, and lightweight structural elements. The mechanical behavior of TRC's [2]–[4] , as well as TRC sandwiches [5]–[12] have been widely investigated.

Despite the clear advantages of TRC sandwich technology, its composite nature, and its thin-wall facings, renders the failure mechanisms quite complex, since a weak interlaminar bond can lead to premature debonding and substantially reduces the loadbearing capacity [13].

An early, and periodic non-destructive (NDT) inspection of the TRC sandwich is necessary to ensure long-term structural efficiency. Previous studies show that premature debonding can successfully be detected and tracked by Acoustic Emission (AE) and Digital Image Correlation (DIC) [14].

  doi:10.5075/epfl-298799_978-2-9701614-0-0

In this study, TRC sandwich beams with an artificially weak interlaminar bond, and reference ones are subjected to four-point bending and monitored by AE, DIC, and for the first time by Millimeter Wave Spectrometry (MMW-S).

Results show a good consensus between techniques and exhibit complementarity. DIC successfully tracks the cracks formation and interfacial debonding at the surface, while AE provides characterization and localization of internal cracks with very high sensitivity, allowing to predict the failure mode and progress. Furthermore, MMW-S follows the loading and shows sensitivity to delamination, matrix, and core deterioration in the area of applied load, and the wide range of frequencies of the technique allows to extract information at different scales.

2. Materials and methods

2.1 Materials

Along this study, five reference TRC sandwich beams, and two with an artificially destroyed lower interlaminar bond were tested. The two TRC skins were cast directly on the 100 mm thick extruded polystyrene, with a surface "waffled" pattern to improve the bonding with the TRC facings and cured for 24 hours. Then they were turned around, and the second TRC facing was cast. The cementitious matrix of the TRC was reinforced with AR-Glass SITgrid200 [15]. All samples were covered by plastic foil for better curing for at least 28 days.

The cementitious matrix composition is summarized in Table 1.

Table 1: Cementitious matrix composition

	Ratio
CEM I 52.5 N Strong [ref CEM]	1
Water	0.45
River sand	2
Superplasticizer	0.5%

The lower interlaminar bond of two TRC sandwich was artificially destroyed by applying a thin layer of oil in the area that corresponds with the maximum bending moment (see figure 1).

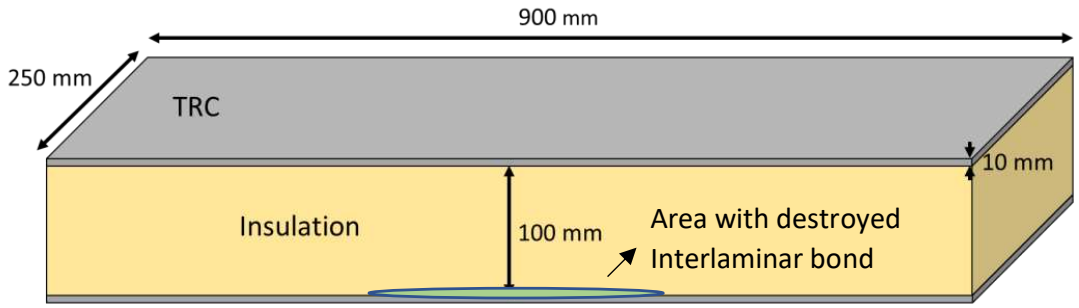

Figure 1. Geometry TRC sandwich samples

  doi:10.5075/epfl-298799_978-2-9701614-0-0

All samples were tested under quasi-static four-point-bending with a loading rate of 2 mm/min.

2.2 MMW Spectrometry

For this study, two Ka-Band Spot-Focusing Lens Antennas [16] with 10 cm of focal length, and 5 cm of spot size were used to couple the EM waves from the ruggedized 14RKFK50-1.0 cables into a free-space radiation. An Anritsu Vector Network Analyzer (VNA) MS46122B was used, with a capacity to operate from 10 MHz to 43 GHz. The selected frequency band was 26-42 GHz, with 201 spectral points, and a sampling rate of 0.33 pictures/second. As seen in Figure 3, the two antennas were focusing on the central area of the beam, where the highest bending moment is expected. Additionally, the whole MMW-S setup was fixed with the frame, to follow the vertical displacement during the test.

2.3 Acoustic Emission

The AE monitoring was performed with eight sensors resonant at 150 kHz. Two on the compressive TRC facing, and six in the bottom tensile TRC facing, where more activity is expected (for sensor placement, see Figure 2). Vaseline was used as coupling between the sensors and the samples. Additional technical details of the AE setup are shown in Table 1.

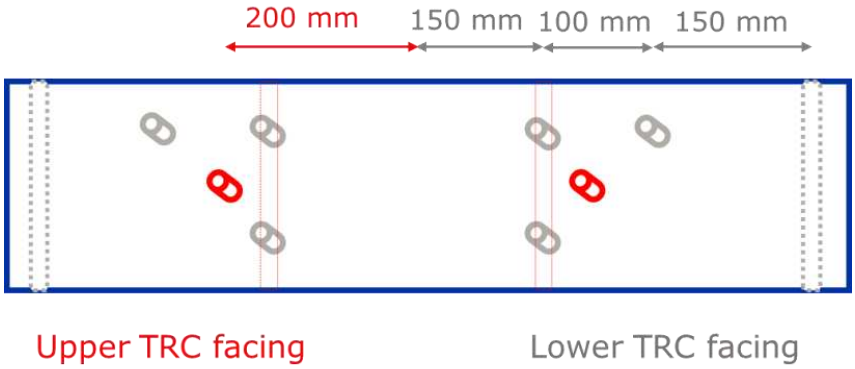

Figure 2. Acoustic Emission setup

Table 1: AE experimental details.

Transducer	Sampling rate	Pre-amplification	Wave Velocity
R15	10 MHz	40 dB	3000 m/s

2.4 Digital Image Correlation

The DIC setup (see Figure 3) consisted of two high resolution cameras (2546x2048 pixels) with focal lenses of 8 mm and a measuring frequency of 0.33 pictures/sec, that were used to measure strains and displacement of the TRC sandwich panels subjected to quasi-static four-point-bending.

  doi:10.5075/epfl-298799_978-2-9701614-0-0

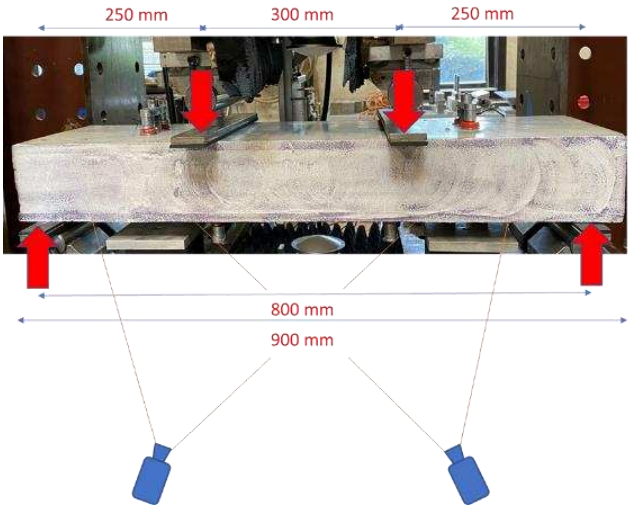

Figure 3. MMW-S and DIC setup

3. Results

In this section, the results are analyzed from the MMW-S and AE point of view, corroborated with DIC.

Figure 4 shows the load vs. vertical displacement of both a reference TRC sandwich beam, and one with a artificially destroyed bond. It is clear that by destroying the lower interlaminar bond, the loadbearing capacity of the specimen is reduced more than 50%.

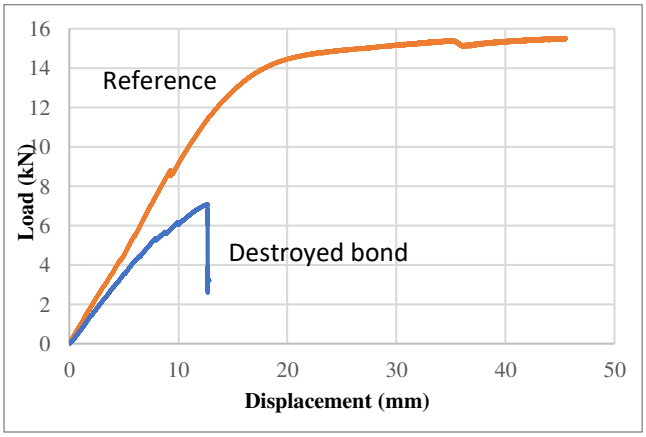

Figure 4. Load vs. displacement for a representative reference sample, and with an artificially destroyed bond.

3.1. MMW Spectrometry

Figure 5a shows the average transmission magnitude for a frequency band of 26-38.4 GHz of a representative reference TRC sandwich. A first look evidences its sensitivity to crack opening, following a similar behavior to the load, increasing until a vertical displacement of 15 mm, and a stabilization around 17 mm. Additionally, Figure 5a shows the crack opening evolution for a central crack in the tensile TRC facing for the same specimen. The similarities of the crack evolution, and the average magnitude of S21 evidence that EM waves are especially sensitive to vertical crack openings in the Area of Interest (AOI). Figure 5b illustrates an EM wave propagating through a typical tensile crack. From this schematic representation, it is clear that

  doi:10.5075/epfl-298799_978-2-9701614-0-0 published under CC BY-NC 4.0 license

the wave is less attenuated with these kind of tensile cracks, specially taking into account that the TRC facings, by having higher permittivity, have more influence in the transmission of the EM wave than the insulation, that has a permittivity close to the one of air.

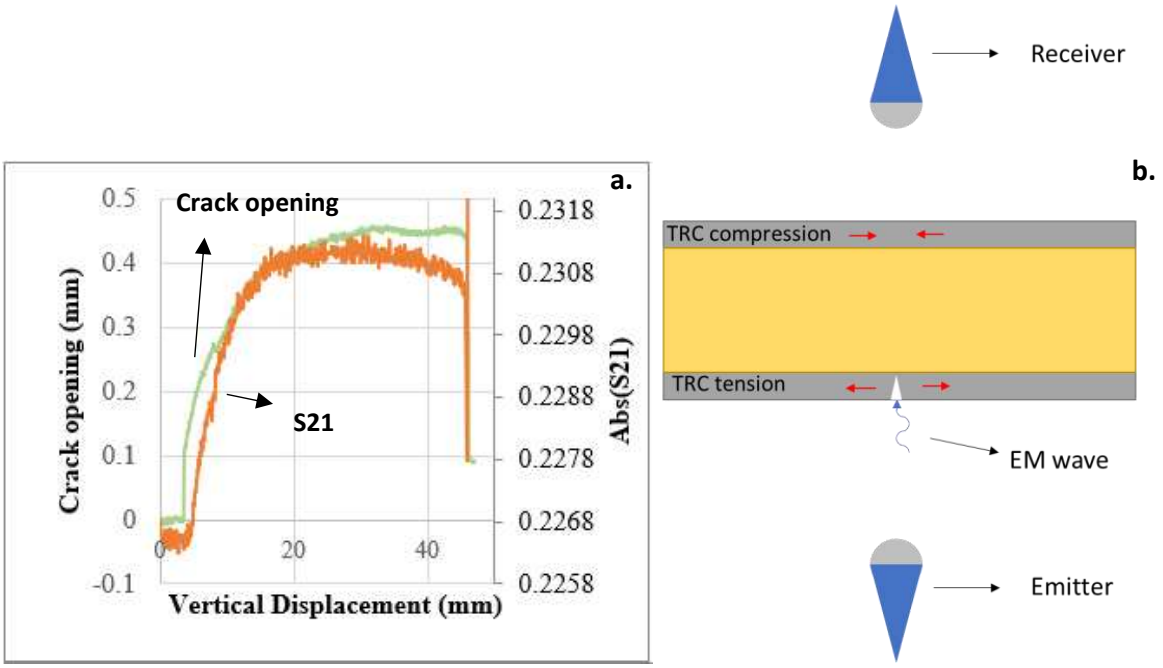

Figure 5. MMW-S a) average transmission abs(S21) and crack opening (in the AOI of the lower TRC facing) vs vertical displacement and b) Illustration of crack opening and transmission of EM waves.

3.2. Acoustic Emission

Figure 6a shows the AE hits for both the reference sample, and the one with a destroyed lower interlaminar bond. Results show big differences in the initial AE activity, evidenced in the amount of hits, and the AE characteristics. The reference sample reached 12000 hits at 2 mm of vertical displacement, while the sample with destroyed lower interlaminar bond did not reach 700 hits. Additionally, the AE characteristics are different for both samples. The reference had higher frequency content, as measured by the "average frequency", AF in time domain and lower RA value (defined as the rise time over the amplitude of the waveform) [17] than the one with destroyed interlaminar bond. This suggests that the reference sample presents more tensile related activity (such as matrix cracking), while the lack of bond of the other sample, triggers more debonding activity. Figure 6c shows the vertical strain of a sample with destroyed interlaminar bond evidencing that the early activity was mainly attributed to debonding phenomena, demonstrated by the shear strain map shown in Figure 6d.

  doi:10.5075/epfl-298799_978-2-9701614-0-0

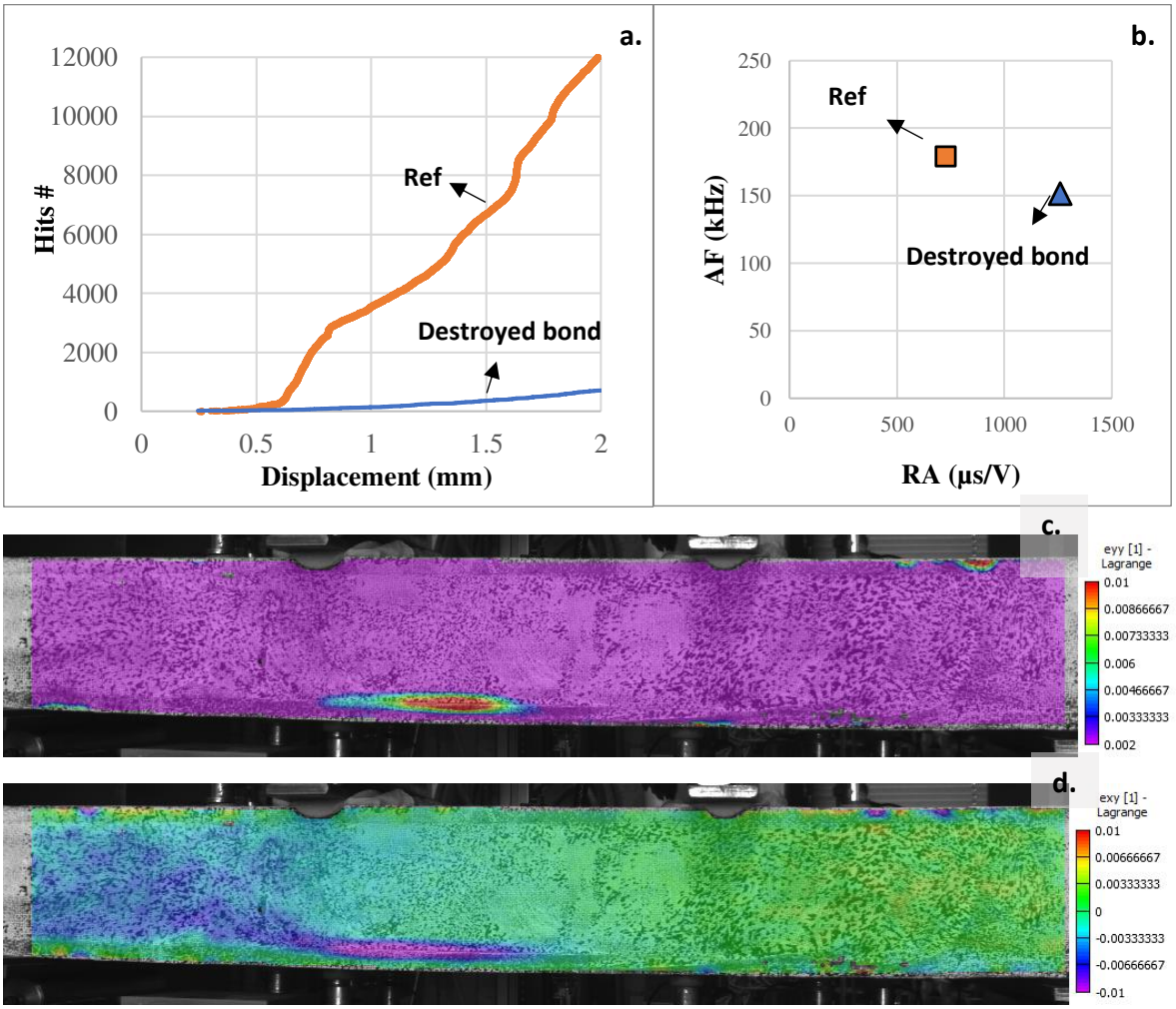

Figure 6. a) AE hits and b) AF vs RA value for very early load (less than 25% of the maximum) c) Vertical Strain and d) shear strain (ε_{xy}) at very early load obtained from DIC

Conclusions

The damage produced by 4 Point bending in TRC sandwich beams was monitored and characterized by optical, electromagnetic, and elastic wave-based NDTs. Additionally, TRC beams with an artificially weak interlaminar bond were tested and results were compared to allow for possible predictions at low load conditions. Results showed that a local weak interlaminar bond reduced the ultimate load more than 50%. Moreover, the information obtained from AE, DIC and MMW Spectrometry show high sensitivity to the test, and compatibility between each other. AE parameters allowed to characterize damage and proved useful as a tool to predict premature debonding. MMW showed sensitivity to damage, following closely the crack opening. Finally, DIC allowed to monitor surface strain maps, and measuring crack openings, that complements and validates AE and MMW data.

Acknowledgements

The authors acknowledge the Fonds Wetenschappelijk Onderzoek-Vlaanderen, FWO for the grants G.0337.19.N, and 12J7720 N), Vrije Universiteit Brussel (VUB) through the SRP-project

  doi:10.5075/epfl-298799_978-2-9701614-0-0

M3D2, the ETRO-IOF project IOF3016, the OZR-VUB for the OZR3251 Medium scale measurement infrastructure project related to Vector network analyzers. Innoviris-Brussels through the D-Stream project BRGRD32, and Differential Smooth Transient Radar Method, BRGSOIB5, TRM4aSF.

4. References

[1] R. O'Hegarty and O. Kinnane, "Review of precast concrete sandwich panels and their innovations," *Construction and Building Materials*, vol. 233, p. 117145, 2020, doi: 10.1016/j.conbuildmat.2019.117145.

[2] A. Peled, B. Mobasher, and A. Bentur, *Textile Reinforced Concrete*, vol. 19. CRC Press Taylor & Francis Group, 2017. doi: 10.1017/CBO9781107415324.004.

[3] Wolfgang Brameshuber, *Textile Reinforced Concrete - Report 36 - RILEM*. RILEM Publications S.A.R.L., 2006.

[4] J. Hegger, N. Will, O. Bruckermann, and S. Voss, "Load-bearing behaviour and simulation of textile reinforced concrete," *Materials and Structures/Materiaux et Constructions*, vol. 39, no. 292, pp. 765–776, 2006, doi: 10.1617/s11527-005-9039-y.

[5] J. Vervloet *et al.*, "Experimental investigation of the buckling behaviour of Textile Reinforced Cement sandwich panels with varying face thickness using Digital Image Correlation," *Construction and Building Materials*, vol. 194, pp. 24–31, 2019, doi: 10.1016/j.conbuildmat.2018.11.015.

[6] J. Vervloet *et al.*, "Validation of a numerical bending model for sandwich beams with textile-reinforced cement faces by means of digital image correlation," *Applied Sciences (Switzerland)*, vol. 9, no. 6, 2019, doi: 10.3390/app9061253.

[7] J. Vervloet *et al.*, "Experimental and numerical evaluation of textile reinforced cement (TRC) sandwich walls in compression: A geometrical study," *Construction and Building Materials*, vol. 240, p. 117904, 2020, doi: 10.1016/j.conbuildmat.2019.117904.

[8] M. de Munck *et al.*, "Fatigue behaviour of textile reinforced cementitious composites and their application in sandwich elements," *Applied Sciences (Switzerland)*, vol. 9, no. 7, 2019, doi: 10.3390/app9071293.

[9] J. Hegger *et al.*, "Sandwich panels made of TRC and discrete and continuous connectors," *International RILEM Conference on Material Science*, vol. I, pp. 381–392, 2010.

[10] A. Junes and A. Si Larbi, "An indirect non-linear approach for the analysis of sandwich panels with TRC facings," *Construction and Building Materials*, vol. 112, pp. 406–415, 2016, doi: 10.1016/j.conbuildmat.2016.02.190.

[11] I. G. Colombo, M. Colombo, and M. di Prisco, "Precast TRC sandwich panels for energy retrofitting of existing residential buildings: full-scale testing and modelling," *Materials and Structures/Materiaux et Constructions*, vol. 52, no. 5, pp. 1–16, 2019, doi: 10.1617/s11527-019-1406-1.

[12] A. Shams, M. Horstmann, and J. Hegger, “Experimental investigations on textile-reinforced concrete (TRC) sandwich sections,” *Composite Structures*, vol. 118, no. 1, pp. 643–653, 2014, doi: 10.1016/j.compstruct.2014.07.056.

[13] A. Shams, A. Stark, F. Hoogen, J. Hegger, and H. Schneider, “Innovative sandwich structures made of high performance concrete and foamed polyurethane,” *Composite Structures*, vol. 121, pp. 271–279, 2015, doi: 10.1016/j.compstruct.2014.11.026.

[14] E. Tsangouri, H. Ismail, M. de Munck, D. G. Aggelis, and T. Tysmans, “Reveal of internal, early-load interfacial debonding on cement textile-reinforced sandwich insulated panels,” *Applied Sciences (Switzerland)*, vol. 11, no. 2, pp. 1–15, Jan. 2021, doi: 10.3390/app11020879.

[15] v. FRAAS solutions in textile, “Datenblatt : SITgrid200,” *www.solutions-in-textile.com*, p. 1, 2017.

[16] I. SAGE Millimeter, “SAQ-333039-28-S1,” 2018. https://www.eravant.com/26-5-to-40-ghz-3-94-focal-length-1-2-spot-size-wr-28-ka-band-spot-focusing-lens-antenna (accessed Apr. 06, 2022).

[17] RILEM Technical Committee (Masayasu Ohtsu). Recommendation of RILEM TC 212-ACD: acoustic emission and related NDE techniques for crack detection and damage evaluation in concrete*. Mater Struct 43, 1187–1189 (2010). https://doi.org/10.1617/s11527-010-9640-6

  doi:10.5075/epfl-298799_978-2-9701614-0-0

SHEAROGRAPHY NON-DESTRUCTIVE TESTING OF A COMPOSITE SHIP HULL SECTION SUBJECTED TO MULTIPLE IMPACTS

Nan Tao[a], Andrei G. Anisimov[a], Marcel Elenbaas[b], Roger M. Groves[a]*

a: TU Delft Structural Integrity & Composites
b: Damen Shipyards
*n.tao@tudelft.nl

Abstract: *The use of thick composites and sandwich structures is increasing rapidly in diverse industries. Nevertheless, due to extreme loads such as impact and blast, various defects tend to occur in thick composites that can degrade the structural integrity severely. Hence, it is important to advance non-destructive testing (NDT) towards composite structures of significant thickness. The objective of this study is to perform shearography NDT of a composite ship hull section which has been multiple impacts in the RAMSSES project. In this paper, experimental results on the inspection of the large-scale composite structure are reported. Different loading scenarios including step heating and mechanical loading were performed for shearography NDT. A comparison between thermal loading and mechanical loading on thick composite inspection with shearography is presented. Here we aim at bringing the shearography technique out of the laboratory and extending its applications to composites with a thickness of more than 50 mm.*

Keywords: thick composite inspection; shearography NDT; composite ship hull section; multiple impacts; thermal and mechanical loading

1. Introduction

Owing to the remarkable advantages of lightweight and superior material properties, composite materials are seeing widespread applications in various industrial sectors [1–4]. Initially, these materials were mainly used in thin structures, but in recent years the use of thick composites and sandwich structures has increased rapidly in the marine sector (e.g. decks and hulls) [1] and in wind energy (e.g. wind turbine blades) [3,4]. Particularly, sandwich structures consisting of glass-fiber laminate skins bonded to a foam core are attractive in the marine sector due to their resistance to corrosion and underwater shocks and cost-effectiveness [5]. Those marine composites tend to have significant thicknesses (e.g. 50-200 mm) and to be large-scale (e.g. up to 85 m in length). Nevertheless, they are susceptible to extreme loads such as impacts or blasts that can result in various defects including delaminations, core debonding, and fiber breakage. The presence of those defects can degrade material properties and structural integrity severely. Hence, it is important to advance non-destructive testing (NDT) towards composite structures of significant thickness.

Some well-known NDT techniques, including ultrasonic testing and thermography, are difficult to be implemented for thick composite inspection. For ultrasonic testing, the problems of attenuation [3,4] and practical coupling issues with high surface roughness are significant. For thermography, it is difficult to heat evenly a large structure and to avoid rapid heat dissipation in thick composites [3,4]. Among the various NDT methods, shearography [6,7] is an optical NDT method that offers many advantages such as full-field and non-contact measurement. It reveals

  doi:10.5075/epfl-298799_978-2-9701614-0-0

defects by comparing two states of deformation of a test object. By applying a suitable loading, the defects can be revealed by looking for defect-induced anomalies in fringe maps or phase maps that can be related to surface strain components. It is possible to improve the sensitivity of shearography for defect detection by selecting suitable loading methods [8]. In shearography NDT, thermal loading is commonly used because of the advantages of versatility, non-contact, and low cost. Nevertheless, studies on the efficacy of mechanical loading on defect detection are rarely reported [9]. Our previous work with a 51 mm thick marine laminate [10] showed that defects at 5 to 20 mm depth can be detected successfully using shearography with thermal loading. Here we aim at bringing this technique out of the laboratory and extending shearography applications to large-scale composites with a thickness of more than 50 mm.

The objective of this study is to perform shearography NDT of a large-scale thick composite structure, specifically a composite ship hull section which had been subjected to multiple impacts. Different loading scenarios including step heating as well as mechanical loading were performed for shearography NDT. Section 2 describes the tested composite hull section and the shearography inspection system. Section 3 presents experimental inspection results of the large-scale composite structure. A comparison between thermal loading and mechanical loading on thick composite inspection with shearography is given in section 3 as well. The conclusions are given in section 4.

2. Shearography inspection system for the composite ship hull section

An overview of the composite ship hull section is shown in Fig. 1. The dimensions are about 6 meters in height and 2.3 meters in width. The structure is made from FRP laminate skins and foam cores. The composite ship hull section is a RAMSSES demonstrator [11,12] at Damen Shipyards. Before shearography inspection, multiple impact tests (https://vimeo.com/522716506) surpassing helicopter emergency landing loads have been performed on the hull shell and its composite helicopter deck for proving the resilience of composites to harsh marine environments. The impacted area on the hull shell is shown in Fig. 1(c).

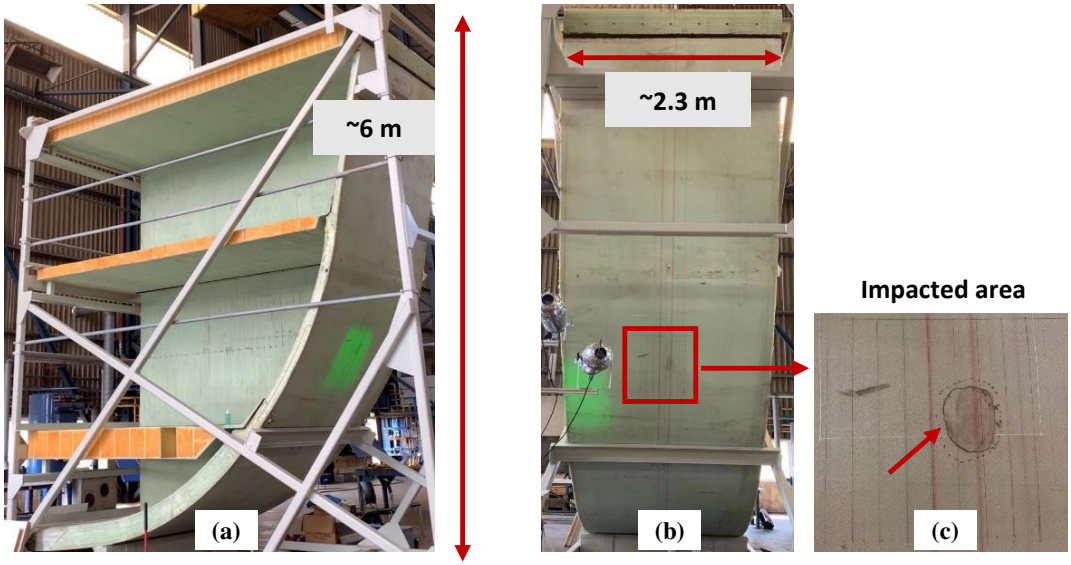

Figure 1 The composite ship hull section at Damen Shipyards: (a) Overall view. (b) Front view. (c) The area with multiple impacts on the hull shell.

In this study, shearography was used to perform NDT of the large-scale composite ship hull section. Its theory and operation principle are well reported in [6,7,9]. For this experiment, the shearography instrument [Fig. 2(a)] was adopted to measure the out-of-plane displacement derivative in a location where defect-induced deformation is expected to be high. Both thermal and mechanical loadings were applied for shearography NDT to evaluate their corresponding efficacies in defect detection.

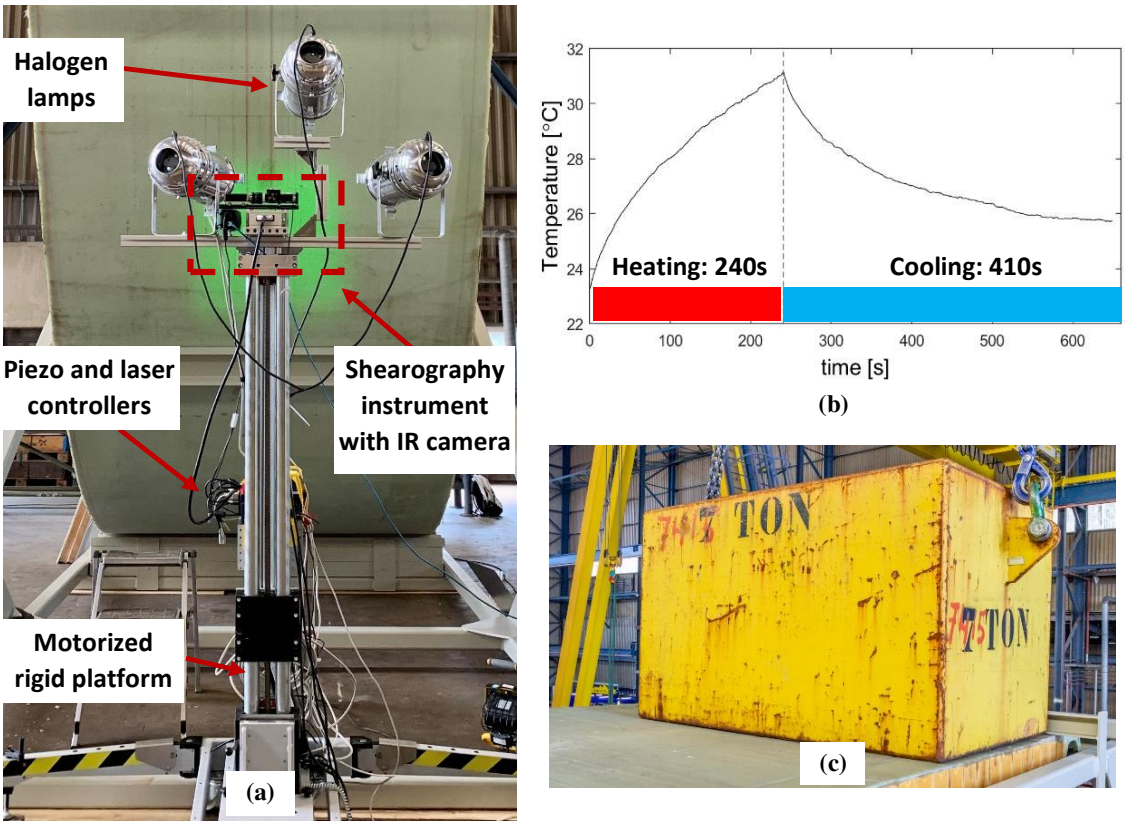

Figure 2 Testing campaign at Damen Shipyards: (a) Experimental inspection system. (b) Average temperature profile from thermal loading. (c) Applying mechanical loading.

The hull shell was illuminated with a Torus 532 laser source (optical power of 500 mW and wavelength of 532 nm) through a beam expander [Fig. 2(a)]. The formed speckle image was captured by a Pilot piA2400 camera with Linos MeVis-C 1.6/25 imaging lens and a Thorlabs bandpass filter through a Michelson interferometer. A piezo-electric actuator PSH 4z from Piezosystem Jena was used to enable temporal phase-shifting (three-step, 2.8 s per phase-shifting cycle). The shearing distance is about 9 mm (~34 pixels) in the vertical direction, which was determined experimentally to produce reliable phase maps for defect detection. During the testing, the shearography instrument was fixed on a motorized rigid platform. By adjusting the rigid platform, scanning in both horizontal and vertical directions can be achieved, enabling a large-area inspection.

Thermal loading was performed by three halogen lamps, each operating at full electrical power (1000W) [Fig. 2(a)]. During heating and cooling, the surface temperature of the hull shell was monitored with a FLIR A655 thermal infrared (IR) camera. The fields of view (FOVs) were inspected by repeating the same thermal loading [Fig. 2(b), 240s of heating], while the average temperature increase of the heated area was about 8 ℃. Mechanical loading was done by

placing a 7-ton metal block on the structure [Fig.2(c)], which corresponds to the landing of a medium-sized helicopter.

3. Results and discussions

3.1 Shearography inspection results

The experimental results with thermal loading are shown in Fig. 3. A total area of about 1500×900 mm^2 was inspected by stitching six FOVs of 600×600 mm^2 [Fig. 3(a), 2 in the vertical direction by 3 in the horizontal with about 20% overlap for stitching]. Phase-shifted sets of speckle images were captured continuously during cooling. All sets of the recorded images were analyzed and stitched together to produce built-up phase maps of the whole area [Fig. 3(b)] that represent the evolution of the surface out-of-plane strain during cooling. The resultant phase map was further processed to obtain the compensated phase map [Fig. 3(c)], where the defect-induced deformation was extracted [10]. This compensated phase map reports the presence of damage in the structure. The stitching process can be further improved by considering the shape of the surface, the positions of the camera and the laser [13]. The damage in the impacted region is not obvious, this can be because its position is close to the edge of the FOVs no.5 and no.6, which makes it difficult to extract actual defect deformation.

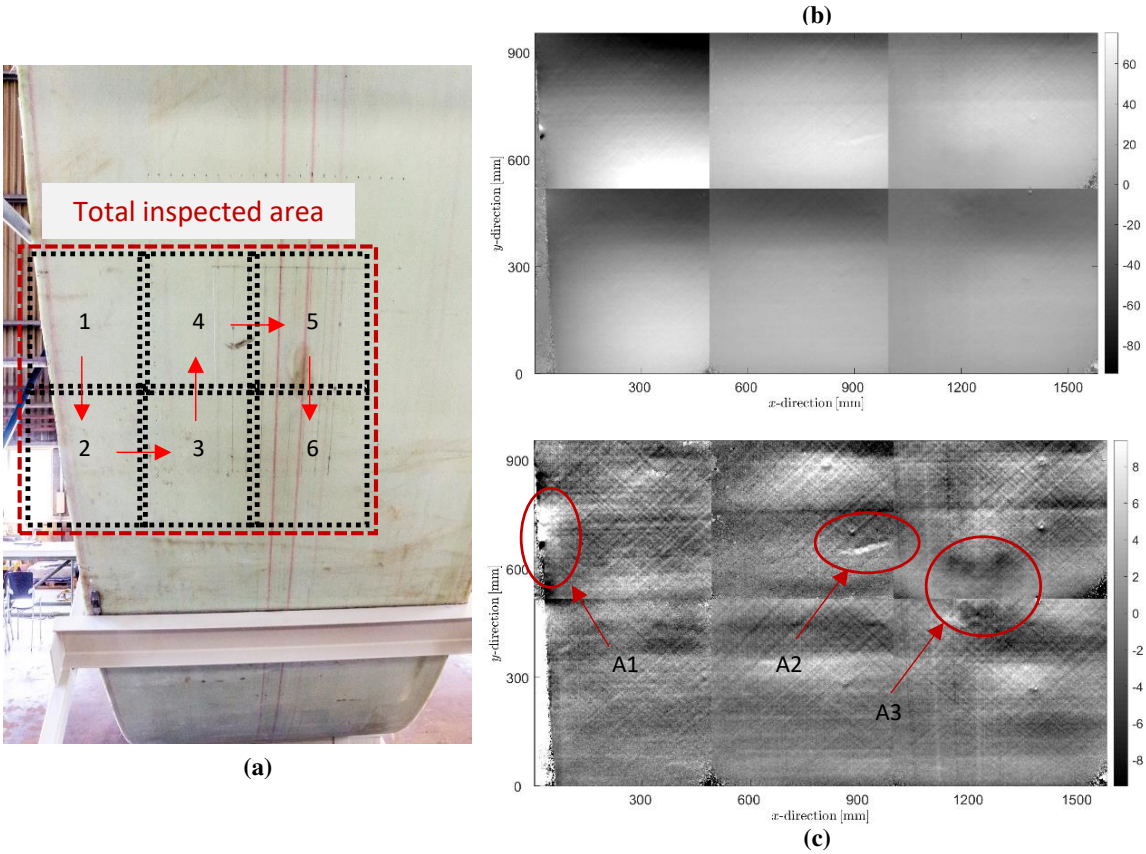

Figure 3 Stitched inspection results for six FOVs with thermal loading: (a) Total inspected area (FOVs no. 1-6). (b) Origin phase map. (c) Compensated phase map, A1 - skin-to-core debonding, A2 - heat damage, A3 - impact damage of interest. [Unit of phase is radian]

The results of the detailed inspection of the impacted area are shown in Fig. 4. Both thermal loading and mechanical loading were applied for shearography NDT. The compensated phase maps with thermal and mechanical loadings are shown in Figs. 4(b) and 4(c), respectively. The

impact damage (shown as strain anomalies in compensated phase maps) was detected successfully from both thermal and mechanical loadings in the same region, which indicates the reliability of shearography. These strain anomalies are expected to be due to delaminations and potential skin-to-core debonding in the thick structure.

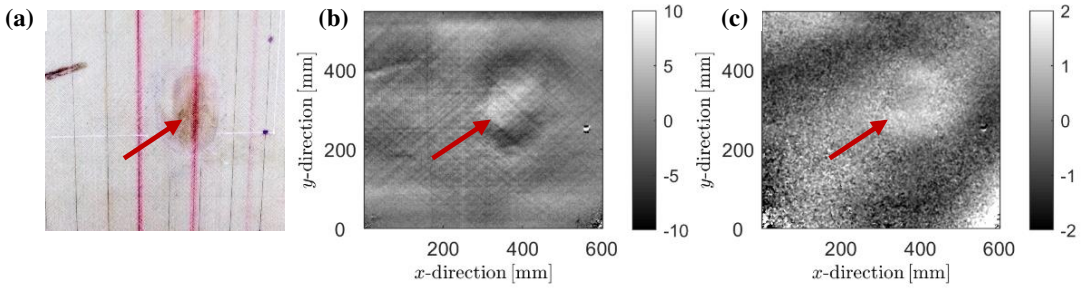

Figure 4 Detailed inspection of the impact region (a) The inspection area with multiple impacts. (b) The compensated phase map with thermal loading. (c) The compensated phase map with mechanical loading. [Unit of phase is radian]

3.2 Discussion

The principle of shearography NDT relies on deformation changes of the test object surface. Therefore developing shearography NDT operation eventually becomes developing a suitable method of loading to deform the object that can reveal defects [9].

For thermal loading, it is easy to apply, and loading parameters such as intensity and time of heating are easy to control. Uniform heating can be useful to inspect a large structure. Nevertheless when inspecting deep defects, e.g. deeper than 20 mm, more time is required for heat to propagate (tens of minutes). It can be noted that heating lamps can cause hot airflow during heating and cooling which should be treated carefully in experiments.

For mechanical loading, it is possible to reveal critical defects only and to avoid trivial defects if the test object is loaded in a similar stress state to the actual working load in-service [9]. One possible advantage can be fast measurement time as heat propagation is not needed. However, the deformation of the test object is difficult to estimate in experiments. Suitable loading increments need to be determined for shearography. The loading process usually introduces large rigid body movements that may cause unfavorable speckle decorrelation in shearography. This was observed during the inspection. The unloading process is found to be acceptable in experiments for producing reliable phase maps. The challenge is to develop an adequate mechanical loading scenario to obtain the detectable defect-induced strain. For this, prior numerical modelling can be done to give an estimation of the needed load for expected critical defects.

4. Conclusions

This experimental study of the composite hull section demonstrates that shearography can be a suitable NDT technique for large-scale composite structures of significant thickness up to 50 to 200 mm. Both thermal and mechanical loadings were evaluated for shearography NDT. Compensated phase maps from the two loadings both identified the presence of impact damage successfully. Uniform heating can be useful for inspecting a large structure with shearography, however significant time, e.g., 10 to 20 minutes, can be needed for heat to propagate when inspecting deep defects. Mechanical loading is possible to reveal critical defects directly and fast

  doi:10.5075/epfl-298799_978-2-9701614-0-0

in speed, nevertheless, one precaution is to avoid excessive rigid body movements. Future work can be to determine suitable mechanical loading increments for shearography and to study the detection capability of shearography with mechanical loading.

Acknowledgements

Access to the composite ship hull section subjected to multiple impacts is provided by the partners of the European Innovation Action RAMSSES project. This research was supported by the Operationeel Programma Zuid-Nederland (Op-Zuid) Project as part of the Dutch Composite Maintenance Centre (DCMC), supported by the Europees Fonds voor Regionale Ontwikkeling (EFRO) and the North Brabant province of the Netherlands.

5. References

1. Greene E. Inspection techniques for marine composite construction and NDE. Report No SSC-463, United States Ship Structure Committee, Washington, DC 2012.
2. Groves RM. Inspection and Monitoring of Composite Aircraft Structures. In: Beaumont PWR, Zweben CH, editors. Comprehensive Composite Materials II, Oxford: Elsevier; 2018, p. 300–11.
3. Ibrahim ME. Nondestructive evaluation of thick-section composites and sandwich structures: A review. Composites Part A: Applied Science and Manufacturing 2014;64:36–48.
4. Nsengiyumva W, Zhong S, Lin J, Zhang Q, Zhong J, Huang Y. Advances, limitations and prospects of nondestructive testing and evaluation of thick composites and sandwich structures: A state-of-the-art review. Composite Structures 2021;256:112951.
5. Tran P, Ghazlan A, Nguyen TP, Gravina R. Experimental and theoretical damage assessment in advanced marine composites. In: Pemberton R, Summerscales J, Graham-Jones J, editors. Marine Composites, Woodhead Publishing; 2019, p. 55–84.
6. Steinchen W, Yang L. Digital shearography: theory and application of digital speckle pattern shearing interferometry. vol. 100. CCH; 2003.
7. Francis D, Tatam RP, Groves RM. Shearography technology and applications: a review. Measurement Science and Technology 2010;21:102001.
8. Jiang H, Ma Y, Dai M, Dai X, Yang F, He X. Panoramic dual-directional shearography assisted by a bi-mirror. Appl Opt 2020;59:5812–20.
9. Hung YY. Shearography for non-destructive evaluation of composite structures. Optics and Lasers in Engineering 1996;24:161–82.
10. Tao N, Anisimov AG, Groves RM. Shearography non-destructive testing of thick GFRP laminates: Numerical and experimental study on defect detection with thermal loading. Composite Structures 2022;282:115008.
11. Cau C, Krause M, Roland F. RAMSSES--Realisation and Demonstration of Advanced Material Solutions for Sustainable and Efficient Ships. Proceedings of 7th Transport Research Arena TRA 2018 2018.
12. Paboeuf S, de Bruijn A, Evegren F, Krause M, Elenbaas M. A “Fast Track to Approval” Process for Innovative Maritime Solutions. In: Okada T, Suzuki K, Kawamura Y, editors. Practical Design of Ships and Other Floating Structures, Singapore: Springer Singapore; 2021, p. 51–63.
13. Anisimov AG, Serikova MG, Groves RM. 3D shape shearography technique for surface strain measurement of free-form objects. Appl Opt 2019;58:498–508.

  doi:10.5075/epfl-298799_978-2-9701614-0-0

ASSESSMENT OF COMPLEX STRUCTUAL SCALE COMPOSTE STRUCTURES BY THERMOELASTIC STRESS ANALYSIS (TSA) ADAPTED FOR 3D PERSPECTIVE IMAGING.

G. Ólafsson[1], O.T. Thomsen[1] and J.M. Dulieu-Barton[1]

[1]Bristol Composites Institute (BCI), School of Civil, Aerospace, and Mechanical Engineering, University of Bristol, Bristol BS8 1TR, UK – geir.olafsson@bristol.ac.uk

Thermoelastic Stress Analysis (TSA) is unique in its ability to provide rich full field data describing stress distributions across a large field of view. Such data is invaluable for the evaluation of structures and for the validation of numerical models. Hitherto a key limitation of thermographic methods is that data output is in a 2D array, whereas most structures, and models of structures are 3D. Where model validation is concerned, this significantly limits the ability for point-by-point comparisons between models and experimental data. Hence, the paper presents a novel method of obtaining 3D point cloud output data based on principles developed for machine vision (white light) imaging applications. The proposed method uses a bespoke calibration plate designed to be visible in the infra-red spectrum to perform stereo calibration of two nominally identical thermal cameras. Data is then processed and projected onto a 3D model of the structure whereby direct point wise comparisons could be made to a numerical model which would be based on the same geometry. The paper presents work carried out to develop the calibration plate, and a simple proof of concept. Finally, the procedure is applied to a carbon fibre reinforced epoxy C-spar structure, designed to be representative of structural features found in many aerospace applications.

Keywords: Thermoelastic Stress Analysis (TSA); Thermography; Experimental mechanics; Laminated composites; Model Validation.

1. Introduction

Finite Element Analysis (FEA) offers a convenient means to analyse structures and components. However, if confidence is to be placed in such models, it is imperative that they are appropriately experimentally validated. Traditional experimental validation campaigns use sensors, e.g. strain gauges to provide data for comparison to FEA. These sensors typically provide only point measurements, and judicious placement of strain gauges is crucial if useful validation data is to be obtained. Moreover, such localised measurements do not necessarily validate numerical models since they provide no information pertaining to the rest of the component. In contrast, TSA is a quantitative [1] full field measurement technique based on thermal imaging that provides thousands of temperature measurements across a field of view, that can be used to infer the distribution of stress in a component [2]. Hence, TSA provides spatially and temporally rich data with significant potential for model validation. Moreover, TSA is unique in its capability to provide quantitative information related to stress distributions, as opposed to displacement and strains obtained from other full field strain measurement methods such as digital image

  doi:10.5075/epfl-298799_978-2-9701614-0-0

correlation (DIC). TSA relates temperature changes, caused by a transient, usually cyclic, loading to changes in principal stresses in an orthotropic laminate by

$$\Delta T = \frac{-T_0}{\rho C_p}(\alpha_1 \Delta\sigma_1 + \alpha_2 \Delta\sigma_2) \quad (1)$$

where ΔT is change in temperature, T_0 is the mean surface temperature, ρ is density, C_p is specific heat. α_i is the thermal coefficient of expansion, and σ_i where the indices are the principal material directions.

When TSA is combined with other techniques such as DIC, the stress values can be combined with the strains and provide indications of the changing material properties and redistribution of the component's load carrying capacity and hence evolving damage. However, thermal cameras capture data on a 2D sensor array, whereas FE models often are generated to capture the 3D nature of components and structures. To date, model validation studies that utilise TSA have mainly focussed on planar specimens or surfaces, where 2D comparisons can be readily made. Yet real structures and components are rarely 2D, and often exhibit significant curvatures, e.g. leading edges of aeroplane wings. Using a single infrared camera to capture data for validation purposes from a curved surface results in perspective effects that skew and distort the view of the surface. Although, it is possible to map points onto a 3D surface, a great deal of interpretation is required to account for lens distortion and perspective effects. To improve the accuracy of imaging curved surface a new approach is proposed that utilises aspects of machine vision. Two infra-red (IR) cameras are used to capture thermal images using which are stereo calibrated in order to perceive depth and reconstruct curved surfaces enabling a 3D point cloud which can then be integrated with complex 3D models. The paper describes the design of a suitable experimental setup for stereo vision in IR, including the production of a suitable calibration plate. Results of validation work carried out on a cylindrical specimens are then presented showing a point cloud capturing 160 degree arc of the cylinder. Preliminary work describing a demonstration of the technique C-shaped spar specimen is then presented.

2. Proof of Concept

A simple experiment was devised using a cylindrial specimen to which the the point cloud methodology could be appied. The initial step in the work was the design and manufacture of a suitable calibration plate. Calibration plates are used in machine vision for two purposes, first to estimate intrinsic parameters which capture effects such as lens distortion, and secondly the extrinsic parameters such as relative positions between the stereo cameras, and between the cameras and the specimen [3]. As such several design criteria were specified for the calibration plate. It must be flat, and be marked with a regular pattern that is clearly distinguishable in thermal images. The solution developed was to print a checkerboard pattern onto aluminium plates using an industrial printer. The pattern is used in many machine vision approaches, and while other patterns can be used, the checkerboard pattern was selected primarily for its compatibility with the machine vision toolbox in Matlab which was used for all processing presented in the paper. The manufactured calibration plate was a rectangular plate where the

  doi:10.5075/epfl-298799_978-2-9701614-0-0

emissivity varied between the bare aluminium surface (low emissivity) and areas with printed pattern that exhibited higher surface emissivity.

Two Infratec Variocam HD cameras were placed side by side, each on a separate tripod with overlapping field of view, with a stereo angle of approximately 25 degrees. Figure 1 shows an image of the calibration plate, where the thermal contrast is evident. As the contrast between bare and printed areas was not sufficient to ensure accurate calibrations at room temperature, a heat pad was bonded to the rear surface of the plate to increase contrast. Contrast improved significantly when surface temperatures exceeded approximately 30 degrees Celsius.

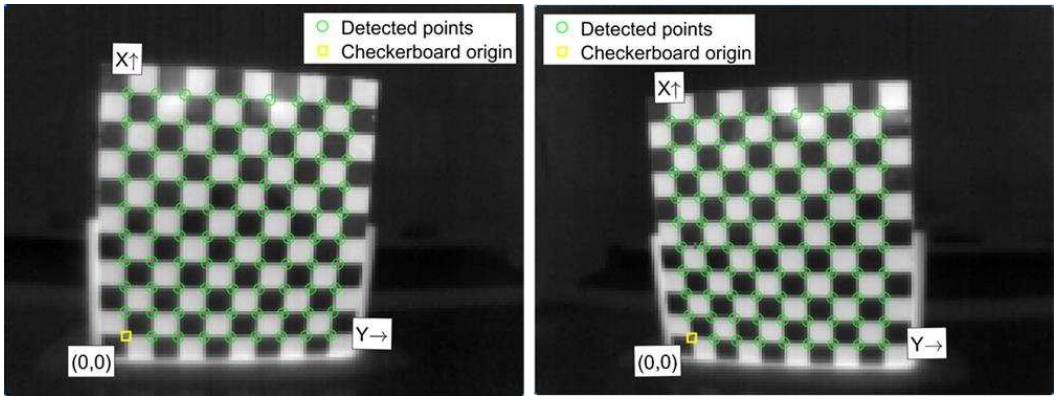

Figure 1: Bespoke thermal calibration plate

The calibration plate was then placed in front of the cylindrical specimen (a beverage can) and 10 unique sets of calibration images recorded i.e. one image on each camera per set for a total of 20 images. The calibration plate was moved slightly between each image set provide extra information for the calibration processing thus improving calibration accuracy. The calibration plate was removed, and hot water poured into the specimen to increase its temperature. A random pattern was applied to the surface of the specimen using small rectangular pieces of tape. This provided unique shapes that were visible in the thermal data that could test the ability of the processing to project data accurately without causing excessive distortion. Thermal data was acquired using both cameras. Triggering was achieved manually since the thermal distribution was stationary and hence timing of image acquisition was not crucial. A model of the specimen was imported into Matlab using the STL Import toolbox. Stereo calibration was performed using the machine vision toolbox in Matlab. The thermal data was then imported into Matalb and projected onto the STL geometry using the machine vision toolbox functions. Figure 2 shows that the thermal data was successfully projected onto the geometry, and the rectangular features added to the specimens are well defined and accurately captured without perspective effects. An additional advantage of using the calibration procedure is that lens distortions are accounted for in the intrinsic calibration process. Results of the calibration showed significant lens distortion relative to white light lenses, an effect which is rarely accounted for in thermographic imaging.

  doi:10.5075/epfl-298799_978-2-9701614-0-0

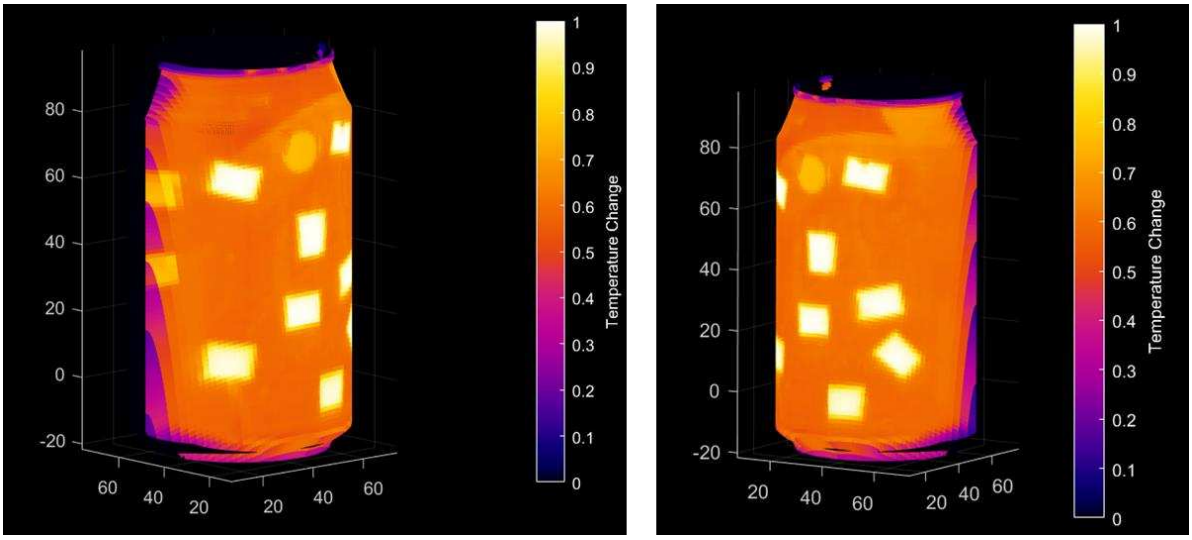

Figure 2: Projected normalised thermal data showing random rectangular pattern on cylindrical specimens

3. Application to Complex Geometry

Following the proof of concept a second test campaign was conducted, designed to apply the previously developed methodology to a more complex geometry, which is also representative of real aerospace structures. A common feature in many aerospace applications is either a box or c-shaped spar which is used to accommodate either compressive or bending stresses. To achieve a realistic loading scenario for the c-spar a compression loading was considered, which for the purposes of the application of TSA was achieved in a servo-hydraulic test machine. The c-spar was manufactured as described in [4] using 24 plies of AS4 8552 pre-preg plies in quasi-isotropic lay up $[(45/0/-45/90)_3]_s$. The laminate was laid up flat and then formed onto a mould tool at 60°C using continuous vacuum bag debulking during the cure cycle. The dimensions of the tool are given in Figure 3 (a), whereby a taper was included in the mid section of the spar. The taper was applied to both the web and flanges of the spar to create a gauge section where the highest stresses would develop and to encourage buckling failure modes over compressive failure of the composite at the edges. At both the flange and web sections of the c-spar, a 1:20 ramp was used to create the tapered region. Post manufacture, the c-spar was machined to trim all edges to improve tolerances and part finish, resulting in an overall length of 450 mm and a flange width of 55 mm, presented in Figure 3 (b).

  doi:10.5075/epfl-298799_978-2-9701614-0-0

a) Male tool geometry

b) Schematic of C-spar overall geometry after machining

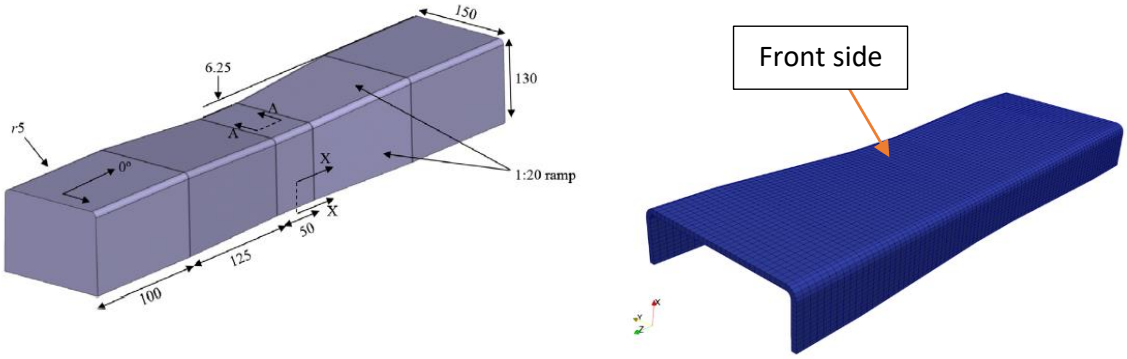

Figure 3: C-Spar Specimen Dimensions from [4]

To further prevent compressive failures, brooming, and to achieve good alignment, each end of the c-spar was constrained using machined steel end caps. The end caps were manufactured using 25 mm thick plate with a 15 mm deep groove machined to match the geometry of the c-spar cross section with a 3 mm clearance designed around the c-spar shown in Figure 4 (a). The end caps were also designed to include a central hole which was aligned with the c-spar neutral axis to aid alignment into the test machine. To mount the end caps, an alignment jig was used to hold the c-spar perpendicular to the end cap. Araldite 2011 adhesive was used to bond the end cap to the c-spar as shown in Figure 4 (b). After curing, the bonded end cap was moved to the servo hydraulic test machine which was used to test the specimens. Compression platens were designed to have a central drilled and tapped hole to interface with the hole in the end caps. An M8 bolt was used to suspend the previously bonded end cap and c-spar perpendicular to the test frame. The hydraulic actuator was lowered to its lowest position so it would remain stationary even if hydraulic power was lost. The cross head was then lowered to mount the lower end of the c-spar into the end cap where more Araldite 2011 adhesive was used to adhesively bond the c-spar to the lower end cap. This procedure ensured that the end caps were precisely aligned to the test machine to minimise misalignment during loading.

a) End cap design

b) C-spar bonded into end cap

Figure 4: End cap design

  doi:10.5075/epfl-298799_978-2-9701614-0-0 published under CC BY-NC 4.0 license

The final test configuration is shown in Figure 5, showing two end caps bonded to the c-spar, mounted in the hydraulic test machine. Two Infratec Variocam HD cameras were positioned in front of the test specimen. The same calibration procedure as described above was applied to the c-spar, whereby images were acquired by both cameras of the calibration plate at 10 different angles. Thermal data was acquired at frame rate of 30 Hz using both cameras, of the c-spar subjected to cyclic loading at 10 kN +/- 8 kN at 3.1 Hz loading frequency.

Figure 5: C-spar mounted in hydraulic test machine

4. Results

The thermal data from each camera was initially processed using least squares fitting to a sine wave [5] to obtain the small thermoelastic temperature change, ΔT, given in equation (1), to provide a single image corresponding to the sensors in the 2D detector array. The two sets of image data were imported into Matlab, alongside the calibration images recorded. The machine vision tool box was used to project the thermal data onto 3D point cloud. Figure 6 shows an example ΔT image from this test campaign. The data pertains to an experiment intentionally carried out at non-adiabatic conditions (3.1 Hz loading frequency) in a procedure based on [6], which revealed substantial subsurface wrinkle defects, not visually apparent from the surface.

  doi:10.5075/epfl-298799_978-2-9701614-0-0

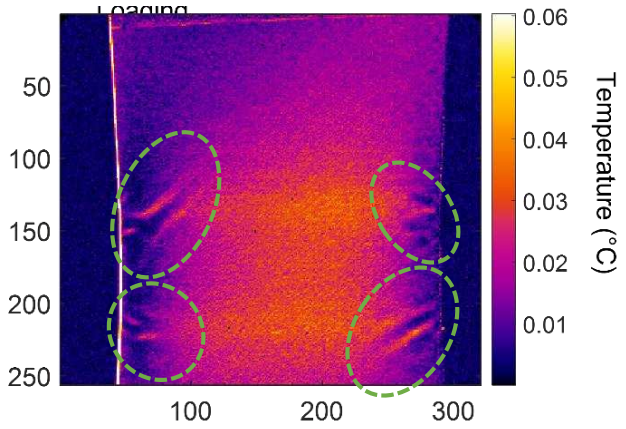

Figure 6: Typical ΔT image obtained from the web of the C-spar gauge section as seen from the front. Subsurface wrinkles highlighted in green.

5. Conclusions

A bespoke calibration plate has been designed to enable stereo calibration of two thermal cameras. A procedure has been developed and a proof of concept test carried out on a cylindrical test specimen whereby thermal data acquired from two cameras is projected onto a 3D point cloud using Matlab. The methodology has been applied to a realistic structural component demonstrating how TSA can be performed on 3D geometry to obtain point cloud data which could enable point by point comparisons to 3D numerical models. The work makes a significant step towards high fidelity modelling by enabling better use of full field thermoelastic data for the validation of 3D numerical models.

Acknowledgements

The research presented was supported by the EPSRC Programme Grant 'Certification for Design – Reshaping the Testing Pyramid' (CerTest, EP/S017038/1). The support received is gratefully acknowledged. As part of this project, the c-spar test specimens were provided by Professor Richard Butler and Dr Andrew Rhead of the University of Bath.

References

[1] P. Stanley and W. K. Chan, "Quantitative stress analysis by means of the thermoelastic effect," *J. Strain Anal. Eng. Des.*, vol. 20, no. 3, pp. 129–137, 1985, doi: 10.1243/03093247V203129.

[2] G. Pitarresi, R. Cappello, and G. Catalanotti, "Quantitative thermoelastic stress analysis by means of low-cost setups," *Opt. Lasers Eng.*, vol. 134, no. April, 2020, doi: 10.1016/j.optlaseng.2020.106158.

[3] Z. Zhang, "A flexible new technique for camera calibration," *IEEE Trans. Pattern Anal. Mach. Intell.*, vol. 22, no. 11, pp. 1330–1334, 2000, doi: 10.1109/34.888718.

[4] K. J. Johnson, R. Butler, E. G. Loukaides, C. Scarth, and A. T. Rhead, “Stacking sequence selection for defect-free forming of uni-directional ply laminates,” *Compos. Sci. Technol.*, vol. 171, no. October 2018, pp. 34–43, 2019, doi: 10.1016/j.compscitech.2018.11.048.

[5] J. E. Thatcher, D. A. Crump, C. Devivier, P. B. S. Bailey, and J. M. Dulieu-Barton, “Low cost infrared thermography for automated crack monitoring in fatigue testing,” *Opt. Lasers Eng.*, vol. 126, no. May 2019, p. 105914, 2020, doi: 10.1016/j.optlaseng.2019.105914.

[6] I. Jimenez-Fortunato, D. J. Bull, O. T. Thomsen, and J. M. Dulieu-Barton, “On the source of the thermoelastic response from orthotropic fibre reinforced composite laminates,” vol. 149, no. June, 2021, doi: 10.1016/j.compositesa.2021.106515.

ASSESSING POROSITY MORPHOLOGY IN COMPOSITE MATERIALS BY ANALYSIS OF FREQUENCY RESPONSE

Juan-Ignacio Caballero-Garzon[a], Guillermo Cosarinsky[b], Jorge Camacho[b], Ernestina[c] Menasalvas, Consuelo Gonzalo-Martin[c], Federico Sket[d], C. González[a].

a: Universidad Politécnica de Madrid, Escuela Técnica Superior de Caminos, canales y puertos., 28040 Madrid Spain – juanignacio.caballero@upm.es
b: Ultrasound Systems and Technology Group (GSTU), institute for Physical and Information Technologies (ITEFI), Spanish National Research Council (CSIC), c/Serrano 144, 28006 Madrid, Spain
c: Universidad Politécnica de Madrid, Centro de Tecnología Biomédica, 28223 Pozuelo de Alarcón, Madrid, Spain.
d: IMDEA Materials, C/Eric Kandel 2, 28906, Getafe Madrid, Spain.

Abstract: *Nowadays the aerospace and energetic industries use ultrasonic non-destructive testing (NDT) to assess the presence of porosity in composite material parts. Ultrasonic testing is the most used technique due to its cost and easy use. The attenuation of the sound waves in the propagation through the composite thickness has been related to the void volume fraction. However, ultrasonics alone does not allow the prediction of the porosity level for any material. This is partly due to the impact that the voids morphology attributes like shape, size, and distribution have on the estimation. To date, ultrasonic testing cannot measure or identify these attributes. Instead, X-ray computed tomography (XCT) provides high resolution 3D images. It enables the digital reconstruction of voids. XCT is not suitable to be used in service due to the limitations of the inspection in size and time. The relation of XCT to ultrasonic signals could boost the discovery of new features to characterize the voids morphology. Even though ultrasonic dates to the 70's in composite materials, its research has been focused mostly on the analysis of the attenuation of the A-scan. We propose to compare the XCT volume to the ultrasonic signals obtained by phased array, using frequency domain analysis to inspect the signal behaviour in porosity areas. The experimentation was carried out on two coupons of different carbon fiber reinforced polymers. They were inspected at 10 MHz and XCT. It was validated that different morphologies of voids were present. Results show different patterns in the frequency analysis*

Keywords: NDT, porosity, ultrasounds, XCT, composites

1. Introduction

The presence of porosity is the main manufacturing defect in composite materials. It endangers the properties of the components and, therefore, inspections need to be performed to guarantee the quality of materials. The most used non-destructive technique is ultrasonic testing due to its easiness and speed. However, even though ultrasonic testing traces back to the seventies, its use for porosity assessment is still a challenge.

Ultrasonic testing consists of the propagation of an ultrasound wave through the material. There is a relationship between the attenuation of the sound wave and the present volumetric fraction of porosity [1]. Several models such as bilinear or exponential relationships have been

  doi:10.5075/epfl-298799_978-2-9701614-0-0

suggested. [2] [3]. Nevertheless, there is not a unique model to assess porosity for any kind of composite material. [4]. All mentioned studies have pointed to the relevance of porosity properties such as size, shape, and distribution as the main limitation in the estimation of the void volume fraction. Unfortunately, no ultrasonic methodology can estimate these characteristics.

Possible solutions may come from inspecting with different equipment. The use of phased arrays (PAUT) systems could improve the information regarding porosity details because it enables the finding of smaller defects and a better signal-to-noise ratio. [5]. They are also more suitable for thicker and larger parts or when access to only one side is needed. [6].

Other signal analyses may contribute to the determination of void characteristics. One option consists in the analysis of the frequency domain. [7]. Chen et al. showed that if the transducer frequency is equivalent to the resonant frequency of the composite, the center frequency of the backscattered echoes diminishes with the increasing quantity of porosity. They also developed an identification and location method. However, the effect of different void sizes in the distribution of the frequency domain was not studied.

In conclusion, there is an opportunity in the assessment of porosity characteristics by using phased arrays and analysis in the frequency domain. Due to the complexity of the propagation of ultrasound in composite materials, it is common to verify the results through other methodologies. In this regard, X-ray computed tomography enables to generate 3D volumes with very high resolution. It can provide a 3D volume of the porosity present in the interior of the composite materials. Therefore, XCT porosity results can be used as ground truth to the discussion of the results.

The goal of this work is to analyze the response in the frequency domain for two different carbon fiber reinforced polymers (CFRP) to find patterns related to porosity morphology. Ultrasonic tests were performed using a phased array of center frequency equal to 10 MHz. The samples were inspected by X-ray computed tomography to obtain a 3D reconstruction of the porosity. A comparison between the frequency domain and the projection of the porosity is performed. It was found that frequency distribution was relevant to locating the horizontal channels and the better determination of dispersed and clustered porosity.

2. Experimental testing and materials

Two coupons of sizes approximately 150x40x5 mm were the subject of study, each of them obtained from two carbon fiber reinforced polymers (CFRP). Both materials were thermoset resins. The manufacturing methods were different, material one was manufactured out of autoclave, while material two was obtained by automatic fiber placement (AFP). Both processes were carried out far from the optimal parameters to induce the creation of porosity.

Ultrasonic testing was performed in pulse-echo mode using a linear transducer array with 128 elements and a central frequency of 10MHz. In this modality, the transducer receives one echo when propagating in water, and three echoes when the propagation occurs in the CFRP. The inspection sweep direction was parallel to the longest axis of the coupons. To obtain the whole coupon inspected two sweeps were needed. The two parts were concatenated afterward.

The coupons were inspected by X-ray computed tomography with a voxel resolution equal approximately to 20 um. The porosity was segmented by image processing methods. At the end of the process, a binary volume is obtained for each coupon. Void voxels are represented in white (pixel value equal to 1) while the matrix is black (pixel equal to 0). An illustration of the outcome for one slice is in figure 2.

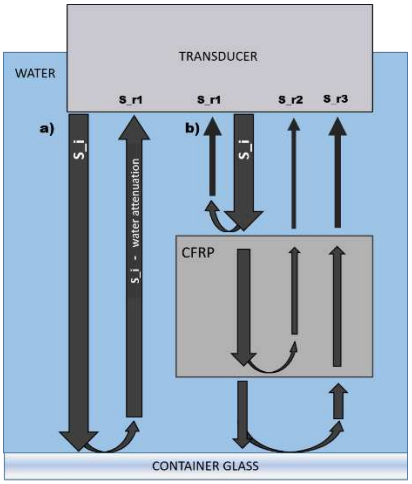

Figure 1: Calibration of ultrasonic testing

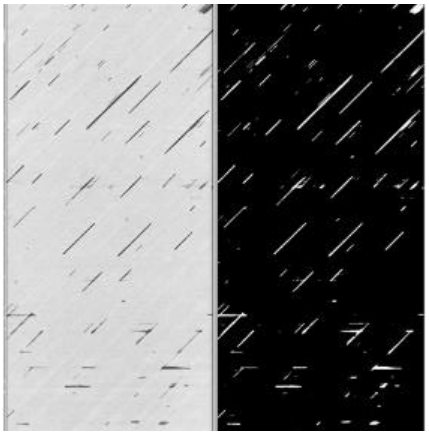

Figure 2 : Example of segmentation of the voids

3. Frequency domain analysis

As it was mentioned in the introduction, the study aims at finding patterns in the behavior of the signals in the frequency domain that could lead to differentiate porosity characteristics such as size, shape, and distribution. In this regard, the analysis of the backscattered echoes and the backwall-echo are explored.

The ultrasound volumes were aligned based on the maximum peak in the radio-frequency. Two thresholds were used to define a window of backscattered echoes, all points outside the window were set to 0. Then the FFT was performed for each signal.

To analyze the back-wall echo, again all signals were aligned as in the backscattered analysis. Then a signal in a centered only water region was selected. A window was set to segment the echo at the bottom of the tank and its FFT was obtained. This signal was used as the reference signal of the transducer frequency distribution. After that, all back-wall echoes were segmented and their FFT was obtained. Finally, the FFT of every back-wall echo is divided by the reference signal. A linear model was fit in part of the domain, and its slope value was plotted.

4. Results

4.1 Coupon of material 1.

It was found a good relationship between the attenuation C-scan and the projection of binary volume of the X-ray computed tomography. The voids tend to form long ellipsoids or large plain plates. Also, there were some small voids dispersed in all the coupon.

  doi:10.5075/epfl-298799_978-2-9701614-0-0

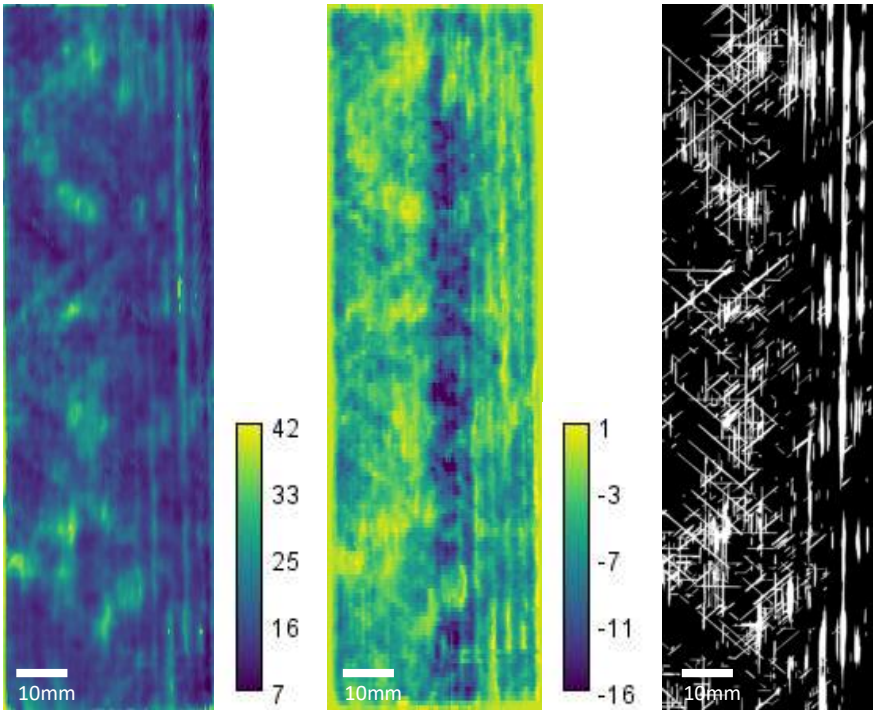

Figure 3 : (left) Attenuation C-scan, slope-value image, and XCT projection (right) for coupon one.

The volume of the FFT of the backscattered echoes was manually compared with the projection of binary void volume from the XCT. On the one hand, it was checked not all peaks correspond to void regions, for example, the figure 4. On the other hand, at the higher frequencies, it was found the closest relation to the attenuation C-scan.

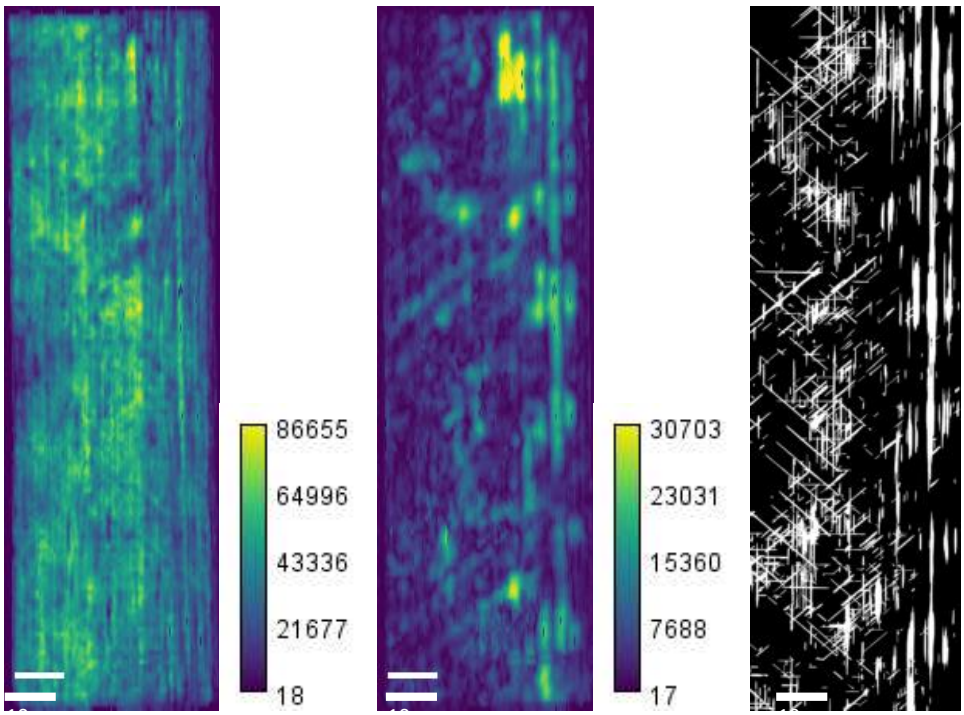

Figure 4 : (left) Maximum peak in the backscattered FFT volume, slice at ≈12.5MHz, and XCT projection (right) for coupon one.

  doi:10.5075/epfl-298799_978-2-9701614-0-0

In the analysis of the back-wall echoes, it was found two clear behaviors between areas with porosity and areas of no-porosity. In the figure 5, the top graph represents the distribution in the frequency domain of the transducer measured in a centered only water region. The left graph is an example of a signal in a non-porosity area. The right graph is an example of the signal for a region with porosity. A linear model was fit in the range [7,10], the value of the slope forms the image of figure 3. Despite the high contrast in the middle section of the image, it correlates well to the attenuation C-scan and the XCT.

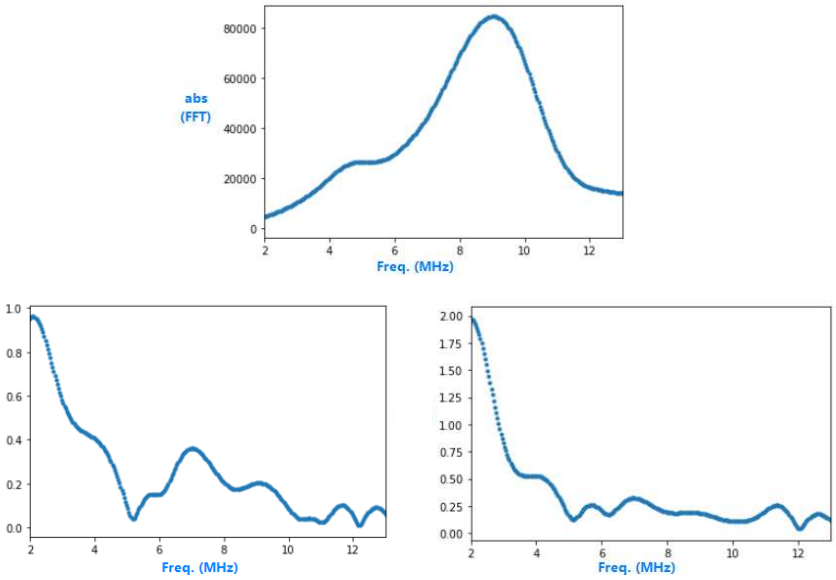

Figure 5 : (top) Reference FFT in water propagation, (left) sample signal of frequencies distribution in a non-porosity area, (right) sample signal of frequencies distribution in a porosity area.

In the FFT volume for the backwall-echoes, it was found that the two local peaks were highly correlated to the attenuation C-scan. The image corresponding to higher frequencies seems to count with more contrast than the other one.

4.2 Coupon of material 2.

In this case, it was also found a good relationship between the attenuation C-scan and the projection of binary volume of the X-ray computed tomography. This coupon presents a different void morphology. The voids tend to form be small, spherical, and be dispersed or concentrated in clusters. The long, thin, vertical, and horizontal channels are a byproduct of the step of the automatic fiber placement machine. This indeed explains its regularity.

The volume of the FFT of the backscattered echoes was manually compared with the projection of binary void volume from the XCT. As in coupon one, the frequency corresponding to the maximum peak could not be related to the porosity, illustrated by figure 8. It was not found a frequency that could be easily related to the porosity projection of the XCT. Furthermore, it was not possible to find any frequency where the horizontal nor the vertical channels could be found.

  doi:10.5075/epfl-298799_978-2-9701614-0-0

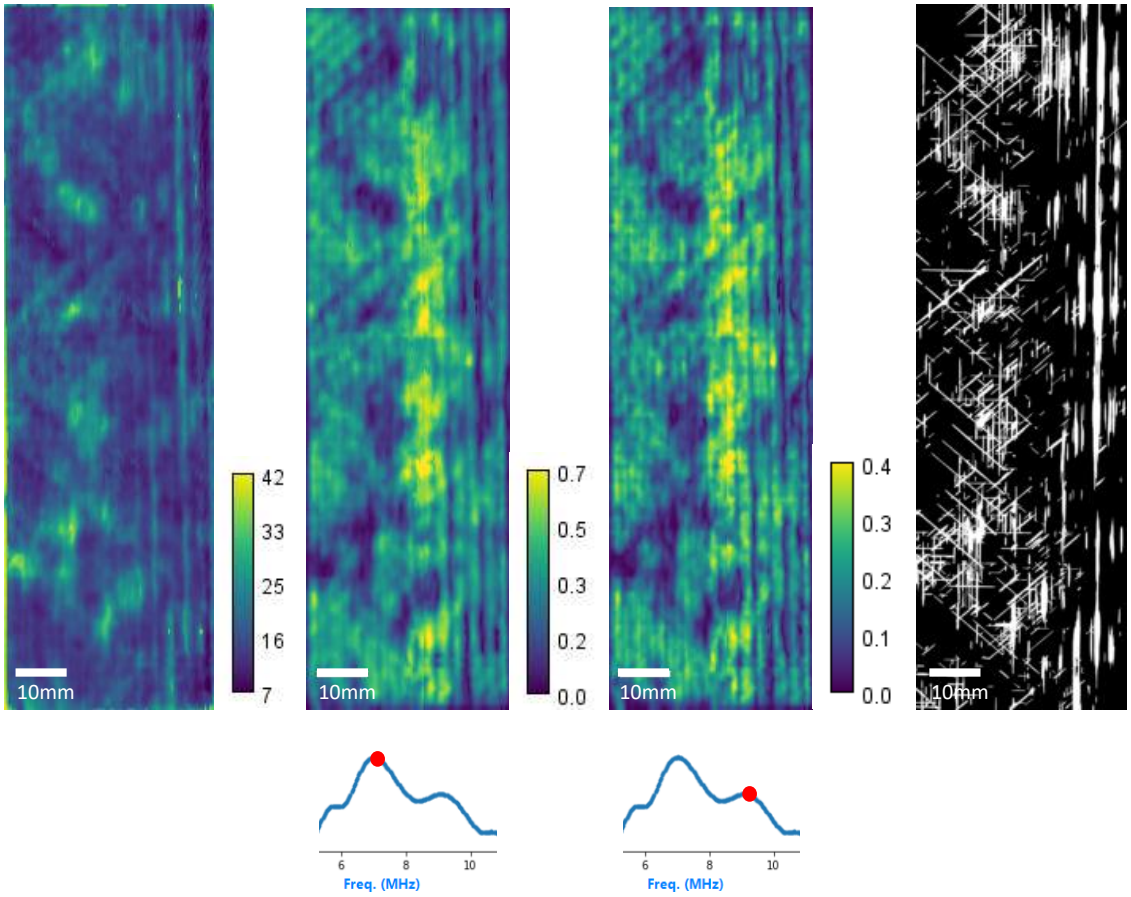

Figure 6 : (left) Attenuation C-scan, slice correspondent to the first in the frequency (≈7MHz), slice correspondent to the first in the frequency (≈9MHz), and XCT projection (right) for the coupon one.

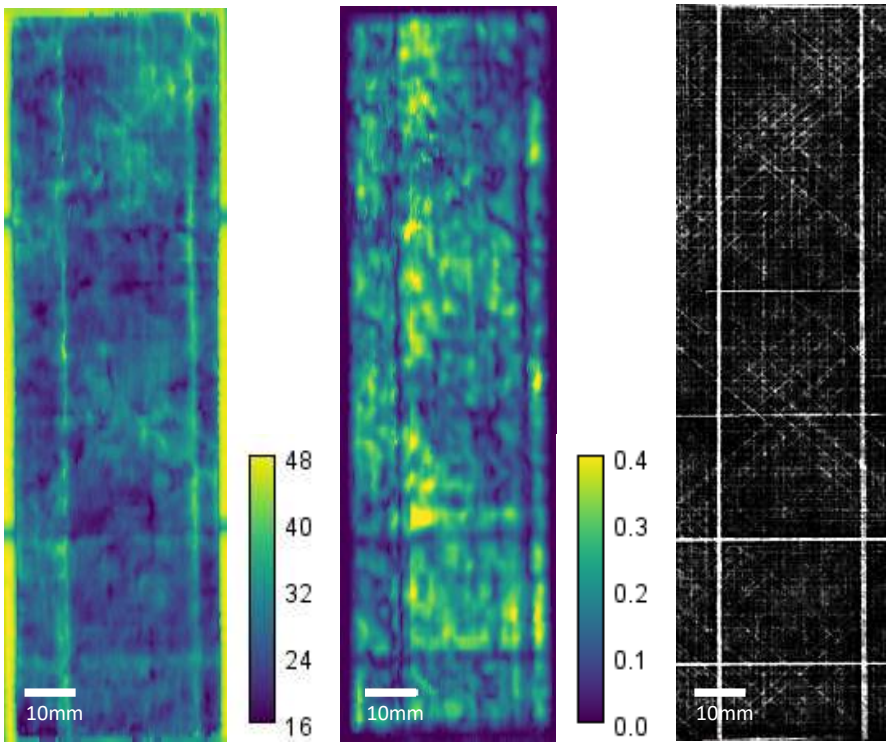

Figure 7 : (left) Attenuation C-scan, slope-value image, and XCT projection (right) for coupon two.

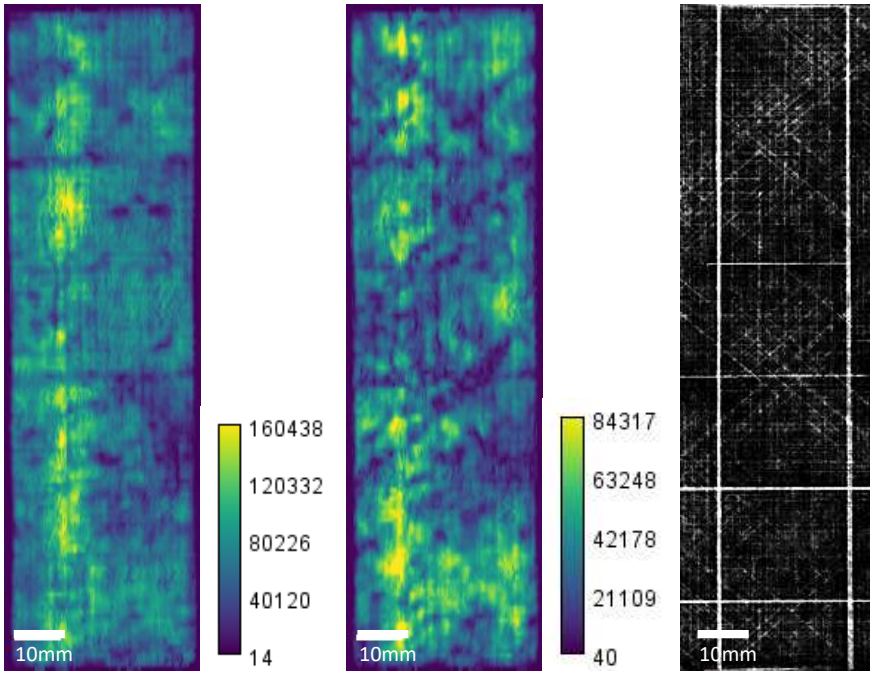

Figure 8 : (left) Maximum peak in the backscattered FFT volume, slice at ≈9.5 MHz, and XCT projection (right) for coupon two.

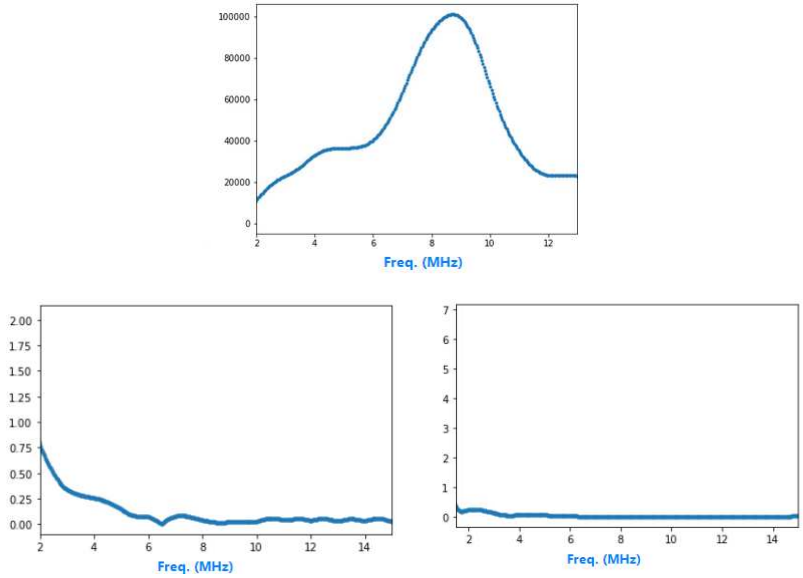

Figure 9 : (top) Reference FFT in water propagation, (left) sample signal of frequencies distribution in a non-porosity area, (right) sample signal of frequencies distribution in a porosity area for coupon two.

It was not possible to find a region not affected to some degree by porosity. The reference FFT signal was very similar to the one obtained in the test of coupon one. In the figure 9, the top graph represents the distribution in the frequency domain of the transducer measured in a centered only water region. The left graph is an example of a signal in a low-porosity area. The right graph is an example of the signal for a region with porosity. A linear model was fit in the range [7,10], the value of the slope forms the image of figure 7. These materials and their porosity made most of the frequency spectrum be in very low levels, under a 0.25 of the ratio of the FFT reference signal. Furthermore, above the 7.5-8 MHz it was close to being white noise and no pattern was found. Images near the 4 MHz and 7 MHz in the average signal of the volume

  doi:10.5075/epfl-298799_978-2-9701614-0-0

were highly correlated to the attenuation C-scan and the XCT projection, figure 10. It was not found a frequency that could be exclusively linked to the horizontal or vertical channels, clusters of small voids behaved similarly.

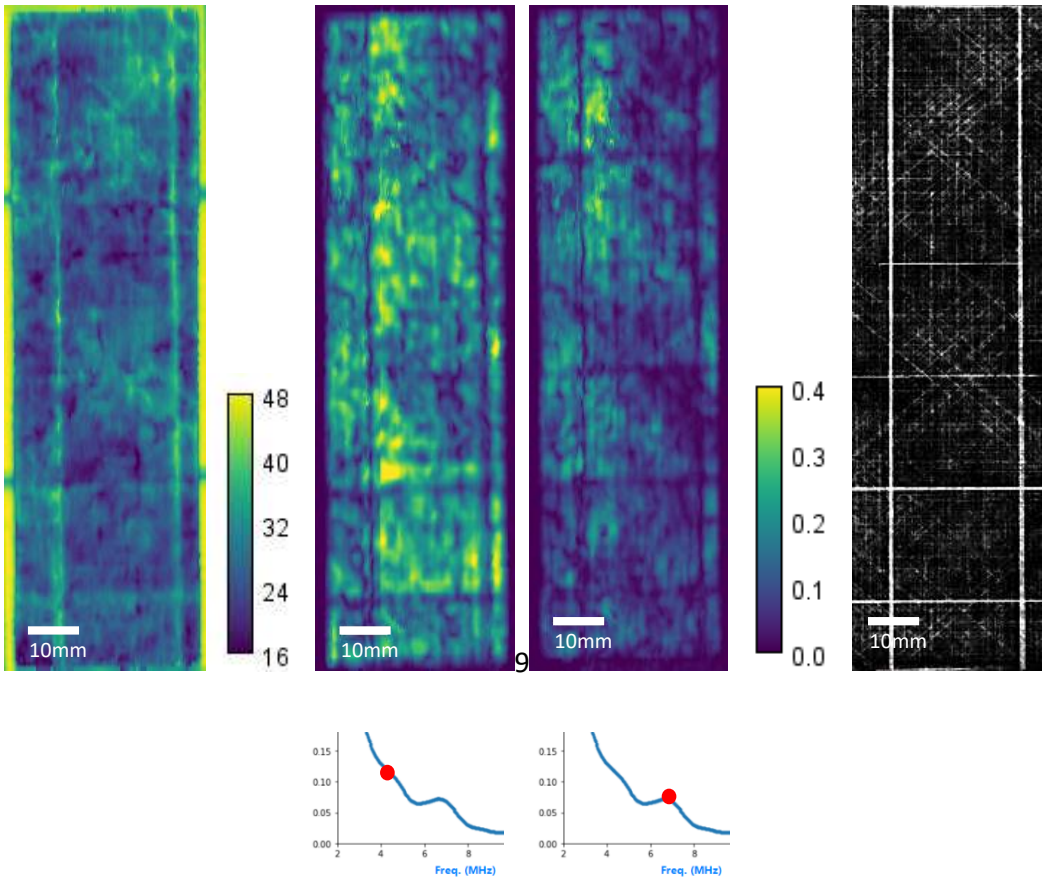

Figure 10 : (left) Attenuation C-scan, slice correspondent to the first in the frequency (≈7MHz), slice correspondent to the first in the frequency (≈9MHz), and XCT projection (right) for the coupon one.

5. Discussion

The goal of this work was to analyze the response in the frequency domain for two different carbon fiber reinforced polymers (CFRP) to find patterns related to porosity morphology. The first coupon presented long, large, cylindrical voids and some thin plates. Coupon two presented large, thin vertical and horizontal channels and small, spherical voids that could be dispersed in a region or they could form clusters.

It was verified for both coupons that the attenuation C-scan was highly correlated to the XCT binary void projection. The analysis in the frequency domain was performed in the backscattered echoes and the back-wall echoes. The maximum peak of the FFT of the backscattered echoes did not correlate well to the attenuation C-scan nor the XCT projection for both coupons. A possible explanation maybe that is the resonance frequency of the matrix. It was noted that the behavior of the Fourier domain is different for each coupon. On the one hand, the coupon one with large cylindrical voids showed patterns in high frequencies (12.5 MHz as the one shown in figure 4). On the other hand, coupon two with small spherical porosity had frequencies above 8.5 MHz almost entirely attenuated.

The FFT of the backwall-echoes local peaks: coupon one at 7 and 9 MHz approximately, coupon two one peak at approximately 7 MHz. At those values of frequency, the images were highly correlated to the XCT projection. Despite no direct and simple pattern was found in the frequencies distribution that enables to make a difference between certain voids morphology, i.e. the plain plates and cylindrical voids, nor the thin channels and the clustered voids, certainly, the analysis of frequency images makes clearer the presence of horizontal channels, the location of dispersed porosity, and the disposition of angled clustered of voids than the attenuation C-scan in coupon two. Coupon one provides a coarser illustration of the porosity, that could help to establish its shape and size from the ultrasounds data alone.

6. Conclusion and future work

Two coupons of carbon fiber reinforced polymers were tested by the phased array at 10MHz and X-ray computed tomography. Each of them presented different porosity morphology and the goal of this work was to analyze the response in the frequency domain to find patterns related to the porosity morphology. The analysis focused on comparing the backscattered and back-wall frequencies to the XCT projection of the voids. It was checked that at higher frequencies (approx. 12.5MHz) large cylindrical voids could be visualized in the FFT signals, while it was not possible for the small porosity. Although, the matrix plays an important role in the frequency distribution and more research would be needed. The FFT of the back-wall echoes was useful for the better determination of horizontal channels, distinguishing regions of average attenuation due to dispersed porosity, and determination of regions of clustered voids. However, the patterns are not simple, this could open the door to machine learning analysis. The fusion of attenuation information and FFT could lead to void morphology classification systems and better estimations of the void content.

7. References

1. Stone DEW, Clarke B. Ultrasonic attenuation as a measure of void content in carbon-fibre reinforced plastics. Non-Destructive Testing. 1975 Jun;8(3):137–45.
2. Lin L, Luo M, Tian H. Experimental investigation on porosity of carbon fiber-reinforced composite using ultrasonic attenuation coefficient. 2008;9.7.
3. Ding S, Jin S, Luo Z, Liu H, Chen J, Lin L, et al. Investigations on relationship between porosity and ultrasonic attenuation coefficient in CFRP laminates based on RMVM. :9.4.
4. Smith RA, Nelson LJ, Mienczakowski MJ, Wilcox PD. Ultrasonic Analytic-Signal Responses From Polymer-Matrix Composite Laminates. IEEE Trans Ultrason, Ferroelect, Freq Contr. 2018 Feb;65(2):231–43.
5. Taheri H, Hassen AA. Nondestructive Ultrasonic Inspection of Composite Materials: A Comparative Advantage of Phased Array Ultrasonic. Applied Sciences. 2019 Apr 19;9(8):1628.
6. Rus J, Gustschin A, Mooshofer H, Grager J-C, Bente K, Gaal M, et al. Qualitative comparison of non-destructive methods for inspection of carbon fiber-reinforced polymer laminates. Journal of Composite Materials. 2020 Nov;54(27):4325–37.2.
7. Chen Y, Yang C, Zhou X, Li Z, Zheng H. CFRP voids 3D identification and location method based on the process of backscattered signal. J Wuhan Univ Technol-Mat Sci Edit. 2016 Feb;31(1):172–7.

APPLICATION OF MACHINE LEARNING METHODS ON THE DEFECT DETECTION IN SHEAROGRAPHIC IMAGES

Christian, Düreth[a], Andreas, Hornig[a], Ilja, Koch[a], Maik, Gude[a]
a: Institute of Lightweight Engineering and Polymer Technology, TU Dresden, Dresden, Germany – christian.duereth@tu-dresden.de

Abstract: *Defect detection in primary composite lightweight structures is a major ongoing challenge in terms of reliability, rapidity, and accuracy for a secure operational life-cycle. Shearography is a full-field and material independent non-destructive testing method. Despite its major suitability for large composite components, this method still requires specialists to reliably identify the defect patterns. Modern algorithms in terms of machine learning have gained huge popularity and provide the ability to outperform conventional algorithms, especially in image analysis. Hence, an object detection model based on convolutional neural networks has been implemented and applied to shearographic images of different composite specimens. Concluding, the model performs with a considerable high accuracy considering the medium sized and manually labeled dataset.*

Keywords: shearography; non-destructive testing; composite; machine learning

1. Introduction

The increasing demand for composite materials in the aviation, space, and automotive industry as well as in new advanced storage technologies for hydrogen requires rapid, reliable, and accurate methods for quality assurance and component inspection. Shearography, a full-field and material independent non-destructive testing (NDT) method is predestined for defect detection in large composite components e.g. wings, fuselages manufactured from carbon or glass fiber reinforced plastics (GFRP , CFRP) [1, 2]. Currently, (human) expert knowledge is still required to detect defects based on additional inherent material information, e.g. ply drops or weave pattern [3]. Conventional algorithms, which can support in a semi-automatic manner, are based on a heuristic threshold analysis. Thus, approaches based on machine learning algorithms gain increasing attention and already outperform bespoke conventional algorithms [4, 5].

In this work, a machine learning approach is applied to shearographic images containing different kinds of defect patterns and characteristics. The object detection framework *faster R-CNN*, which is based on convolutional neural networks (CNN), has been implemented in Python using the PyTorch library [6]. This implementation uses the pretrained *ResNet-50* as a backbone for feature extraction and classification tasks [7]. The transfer learning training was performed on a high-performance cluster of the TU Dresden. To determine the accuracy of the model the common evaluation method (COCO [8]) was applied on an unknown dataset.

2. Experimental Methods

2.1 Principals of Shearography

Shearography, also known as electronic speckle pattern interferometry (ESPI), is a coherent laser measuring technique based on phase shifting and interferometry. Fig. 1 a) illustrates the typical test setup for temporal phase shifting shearography, which consists of a coherent laser source and an optical measurement unit [1, 9–11]. Emitted coherent and expanded laser light is

  doi:10.5075/epfl-298799_978-2-9701614-0-0

refracted from the test object surface to optical measurement unit. The illuminated rough surface, thereby, creates a speckle pattern, that is acquired by the charge-coupled device (CCD) sensor in the optical measurement unit [12]. By utilizing a modified Michelson interferometer as a shearing device, the intensities of two points (P_1 and P_2) in the distance of the shear amount δ_x are combined at a single point and pixel on the CCD ($P_1 \cup P_2$), respectively. Thereby, the shear amount is proportional to the shear angle $\alpha_s/2$, the tilting angle of the shear mirror [9]. To measure the phase φ of the two rays from P_1 and P_2 temporal phase shifting is used. In this type of temporal phase shifting, four speckle images are recorded, between each a piezo generates a denoted phase shift of multiples of $\pi/2$ for each image. Finally, φ is calculated according to the four-bucket algorithm [10].

For defect detection purposes two or multiple φ-images are recorded at an unloaded or reference state and a loaded state to measure local discontinuities, caused by underlying defects and voids, respectively (cf. Fig. 1 a)). A variety of excitation methods are possible, thermal loads are the most common [11].These φ-images are subtracted, as shown in Fig. 1 b), to calculate the phase difference $\Delta\varphi$ of two different states. Thereby, $\Delta\varphi$ represents values between $-\pi/2$ to $\pi/2$. After demodulation of $\Delta\varphi$ the so called shearogram is obtained, with its characteristic butterfly pattern, shown in Fig. 1 b), for a round shaped underlying defect [1, 9, 10]. These kinds of patterns are the features the defect detection should be able to detect. Furthermore, to distinguish damage specific patterns from similar patterns caused by other inhomogeneities such as e.g., weave patterns or ply drops.

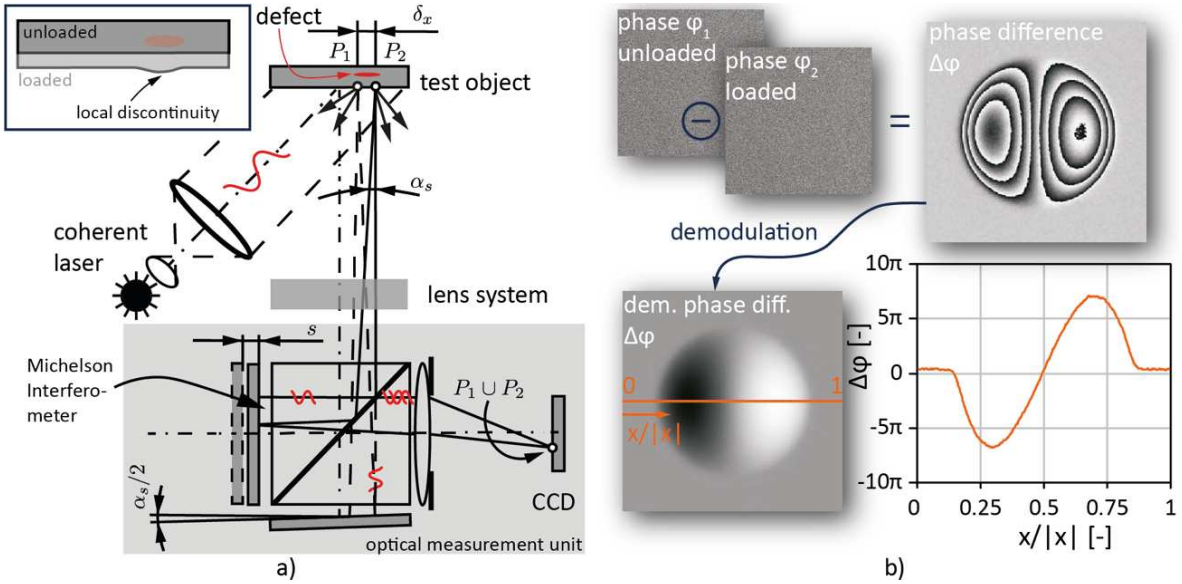

Figure 1. Principal of temporal phase shifting shearography: a) test setup and ray paths of coherent light [9]*; b) illustration of shearographic measurement results* [10]

2.2 Specimens

Two different specimen classes have been chosen for creating the detection network's dataset. The first one contains specimens with defects of defined geometry, as shown in Fig. 2. Three CRFP specimens were manufactured featuring different dimensions, drilling patterns, and thicknesses according to Fig. 2 a) – c). The second class features GFRP specimens with defects of undefined geometry. Four specimens with impact damage and two specimens with manufacturing induced dry spots are chosen. Specimens with impact damage were subjected to varying impact energies [13]. The specimens with dry spots were manufactured by a procedure

  doi:10.5075/epfl-298799_978-2-9701614-0-0

utilizing different amounts of ammonium hydrogen carbonate (NH_4HCO_3) to create dry spots and voids, respectively. The process is described and specimens are illustrated in [13].

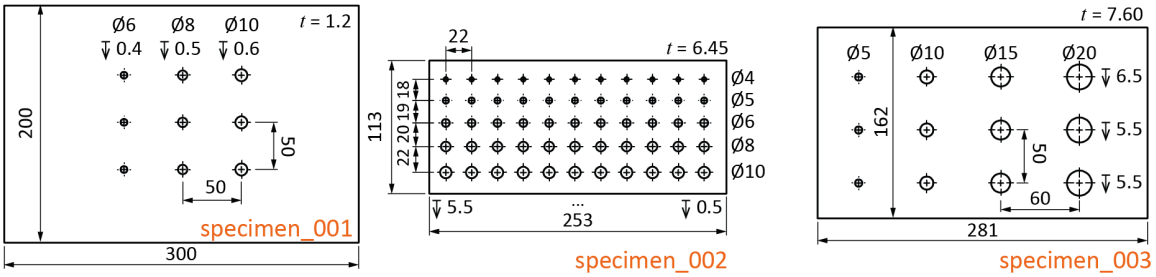

Figure 2. Illustration of specimens with defects of defined geometry: a) specimen_001; b) specimen_002; c) specimen_003

2.3 Experimental Setup

Experiments were carried on a SE3 shearography system from isi-sys GmbH. It is equipped with a 5 MPx (2452 x 2052 Px) CCD-Sensor and a 500 mW LED laser array (wavelength λ = 658 nm). Loading of the test objects was realized using a halogen radiator (1.2 kW). All specimens were excited with a ΔT of 2 K measured at the top surface and examined with different shear angles and amounts, respectively. The range varied from 10 to 40 kSt in 5 kst increments in both directions for the piezo, which corresponds to a spatial resolution range of 2.63 to 6.98 mm shear amount δ_x and δ_y for a working distance of 833 mm.

2.4 Experimental Results

In the following, a comprehensive summary of the experimental results is provided. The entire dataset can be found in the ShearDetect dataset [14]. As an example, Fig. 3 a) illustrates the shearograms of specimen_001 (cf. Fig. 2 a)) for different shear amounts δ_x. Additionally, the defect patterns are highlighted on the extraction path. The $\Delta\varphi$-values of different measurements with increasing δ_x are compared in Fig. 3 b) (in 8-bit grayscale values). Thereby it can be determined that the weave pattern has a significant influence on the shearogram and represents a similar pattern as any defect for any δ_x compared. Hence, especially for fiber reinforced plastics the necessity of modern detection algorithms are existent to guarantee a reliable and user independent defect detection.

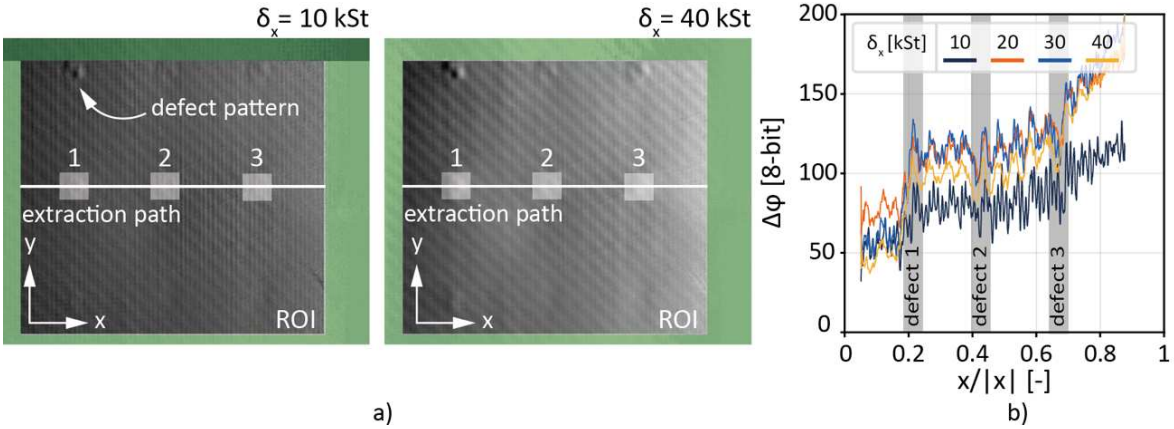

Figure 3. Exemplary illustration of a) measurement results for different δ_x and b) $\Delta\varphi$- values of path extraction for different δ_x and highlighting of defect areas (specimen_001)

  doi:10.5075/epfl-298799_978-2-9701614-0-0

3. Machine Learning Methods

3.1 Object Detection Network

A robust defect detection framework for shearographic images based on machine learning algorithms has been achieved by training the object detection framework *faster R-CNN* [6]. Fig. 4 illustrates the network architecture of the CNN with a region proposal network (RPN). An input image is firstly analyzed regarding significant features by the CNN-backbone *ResNet-50* [7]. This CNN is a residual network with 50 CNN-layers clustered into 19 sequential residual blocks. A residual block or "*deep residual learning"* uses so-called "shortcut connections". It has the main advantage that this network still increase in accuracy due to the greatly increased depths of the network. Back-propagation algorithms such as stochastic gradient-descent or adaptive moment estimation (ADAM) can optimize more sufficiently [7, 15].

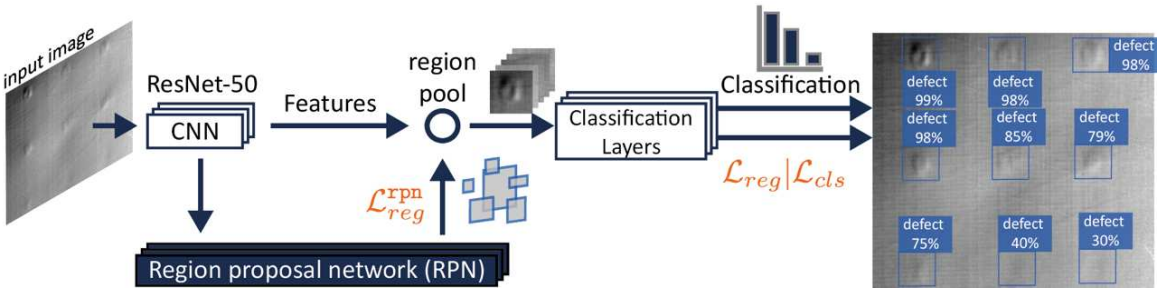

Figure 4. Schematic network architecture of faster R-CNN an object detection framework [6]

These extracted features maps are furthermore processed by the RPN. In the *faster R-CNN* approach anchor boxes are utilized to efficiently predict region proposals with a wide range of scales and aspect ratios [6]. These anchor boxes are a set of possible sizes of bounding boxes that match to feature maps. The best predictions of anchor boxes are furthermore treated as region proposals and pooled and classified by the CNN's backbone [16]. The result of each object detection is a four variables vector (coordinates of upper left and lower right corner of bounding box: $[x_1, y_1, x_2, y_2]$), a class ("specimen" or "defect"), and a corresponding probability of each bounding box, as Fig. 5 illustrates. The backbone *ResNet-50* was downloaded as a pretrained model on "COCO train 2017" to perform transfer learning with the dataset [8, 17, 18].

In this paper the object detection framework is implemented in Python using the machine learning library Pytorch 1.11 [17]. The implementation and the trained model is available in [18] and [19] respectively. This implementation has 41,309,426 parameters including 41,087,026 trainable parameters. For a batch size of 30 and an input size of 2452 x 2052 x 1 the network needs an estimated total size of 35.5 GB free RAM. A detailed summary of the characteristics can be found in [18].

3.2 Loss-functions ($\mathcal{L}$)

For training the deep learning model it must be minimized by the chosen optimizer to the following objective function Eq. 1 [6]:

$$\mathcal{L}(\{p_i\},\{t_i\}) = \sum_i \mathcal{L}_{cls}(p_i, p_i^*) + \sum_i p_i^* \mathcal{L}_{reg}(t_i, t_i^*) \quad (1)$$

The so-called loss-function $\mathcal{L}$ consists of two parts, the classification loss $\mathcal{L}_{cls}$ and the regression loss $\mathcal{L}_{\mathrm{reg}}$. The subscript index i denotes the index of an anchor in a mini-batch, p_i is the probability of the anchor of being an object. The upper script .* denotes the ground-truth label, where p_i^* is 1 if the anchor is positive and vice versa. Hence, the classification loss $\mathcal{L}_{cls}$ is the

logarithmic loss of object and not object. This is represented in the following equation by the binary cross entropy [17]:

$$\mathcal{L}_{cls}(p_i, p_i^*) = -p_i^* \log p_i - (1 - p_i^*) \log(1 - p_i) \quad (2)$$

The variable t_i is a four parameterized coordinates vector representing the location of the predicted bounding box (object). The parameterization is according the following equations [6]:

$$t_x = (x - x_a) / w_a;\ t_y = (y - y_a)/h_a;\ t_w = \log(w/w_a);\ t_h = \log(h/h_a) \quad (3)$$

Thereby, x, y, w and h are the boxes' center coordinates and their width and height. Variables x, x_a and x^* denotes the predicted box, anchor box and ground-truth box, respectively (analog for y, w and h). The bounding box regression loss was defined in [20] as a robust smooth_{L_1} loss according to the following equation

$$\mathcal{L}_{reg}(t, t_i^*) = \sum_{k \in \{x,y,w,h\}} \mathrm{smooth}_{L1}(t_k - t_k^*), \quad (4)$$

whereas the loss is the sum of the four parameter according to Eq. 3 [17, 20]:

$$\mathrm{smooth}_{L1}(t_k - t_k^*) = \begin{cases} 0{,}5\ (t_k - t_k^*)^2 & \forall\ |t_k - t_k^*| < 1 \\ |t_k - t_k^*| - 0.5 & \text{otherwise} \end{cases} \quad (5)$$

The calculation points in the network for the classification and regression loss are highlighted in Fig. 5. Additionally, the regression loss $\mathcal{L}_{reg}^{\mathrm{rpn}}$ of the region proposal network is calculated and tracked during training. This can give better feedback of the training process.

3.3 Dataset

The dataset to train, validate and test the model was created with *Labelbox*, an open-source online Toolbox for data labeling [21]. Thereby, the experimental data was annotated with the ground truth bounding boxes for each defect manually. The labeled data of specimen_001 to _003 and _006 to _009 was randomly split into the training and validation set by the ratio 80 % and 20 %, respectively. The test set only includes the specimens_004 and _005. Hence, the model will be evaluated on unknown data to test its reliability. The dataset is available in [14].

3.4 Data Augmentation

Data augmentation is a common method to increase both size and diversity of labels training set to prevent overfitting in deep learning models and to improve the performance [22]. This is achieved by leveraging input transformations that preserve corresponding output labels. In this implementation the open-source library *Albumentations* [22] was utilized for data augmentation of the training set. The following transforms have been applied randomly to all images of the training set: random rotation of an image by 90 degrees zero or more times, random change of brightness & contrast and random perspective transform with horizontal flip.

3.5 Optimizer and Training Schedule

To minimize the stochastic objective loss function $\mathcal{L}$ (Eq. (1)) the gradient based optimizer ADAM has been incorporated in this implementation of *faster R-CNN* [15]. ADAM is a simple and computationally efficient algorithm for machine learning problems with large datasets and/ or high dimensional parameter spaces [15]. Additional advantages of ADAM are its straightforward implementation by the PyTorch library [17] and low memory requirements.

The commonly static learning rate, a tuning parameter that determines the step size of each iteration while minimizing the objective loss function $\mathcal{L}$ [23], is modified by an approach based on a restart technique presented in [24]. Those warm restart techniques gain popularity in

  doi:10.5075/epfl-298799_978-2-9701614-0-0

gradient-based optimization due to improved convergence behavior and performance. Warm restarts are considered as adjustments to learning rate whilst on going iteration. Thereby, this implementation uses the cosine annealing schedule according to the following equation for the current learning rate η_t within the i-th iteration [17, 24] (cf. Fig. 6 a)):

$$\eta_t = \eta_{min}^i + \frac{1}{2}\left(\eta_{max}^i - \eta_{min}^i\right)\left(1 + \cos\left(\frac{T_{cur}}{T_{max}}\pi\right)\right), \tag{6}$$

where η_{min}^i and η_{max}^i are the lower and upper limits of η_t, T_{cur} is the current iteration, and T_{max} is the period of iterations for every restart. Thereby, an epoch describes the sum of i-iterations that a dataset needs to pass one time forward and backward through an CNN for gradient calculation according to its mini-batch size [23]. The following training parameters have been chosen: epochs = 100, batch size = 30, η_{max} = 1E-2, η_{max} = 1E-3 and T_{max} = 33.
The training was conducted on the high-performance computing cluster of the TU Dresden. The GPU Nvidia® A100 SXM with 40GB dedicated VRAM guaranteed a large batch size of 30 images (≈ 35GB VRAM) and consequently speeded up training times.

3.6 Evaluation Methods

For evaluation of the model performance and accuracy the common objects in context (COCO) evaluation method API from Microsoft® was implemented [8]. To determine whether a predicted bounding box is true positive TP or false positive FP the metric intersection over union IoU is used:

$$\mathrm{IoU} = \frac{A_{\mathrm{pred}} \cap A_{\mathrm{gTruth}}}{A_{\mathrm{pred}} \cup A_{\mathrm{gTruth}}}, \tag{7}$$

where A is the area of the bounding box of the prediction (pred) and ground truth (gTruth), respectively. This portion of intersection is compared to different IoU-thresholds to distinguish between TP and FP. A commonly used threshold is 50 %, additionally the COCO-evaluation takes the range from 50 to 95 % in 5 % increments into account for comparison, especially for the average recall. Consequently, the recall r and the precision p to quantify the model accuracy are computed as following:

$$\mathrm{r} = \frac{\sum \mathrm{TP}}{\sum \mathrm{TP} \cup \sum \mathrm{FN}} = \frac{\sum \mathrm{TP}}{\sum \mathrm{gTruths}}; \qquad \mathrm{p} = \frac{\sum \mathrm{TP}}{\sum \mathrm{TP} \cup \sum \mathrm{FP}} = \frac{\sum \mathrm{TP}}{\sum \mathrm{predictions}}, \tag{8}$$

The average precision AP is calculated by the sum of the maximal values of p(r) in 11 equally spaced intervals for each selected IoU:

$$\mathrm{AP} = \frac{1}{11} \sum_{\mathrm{r} \in \{0,.1,\ldots,1\}} \hat{\mathrm{p}}(\mathrm{r}) \quad \text{with} \quad \hat{\mathrm{p}}(\mathrm{r}) = \max_{\tilde{\mathrm{r}}:\tilde{\mathrm{r}} \le \mathrm{r}} \mathrm{p}(\mathrm{r}). \tag{9}$$

More important in terms of a reliable defect detection is the metric average recall AR that is calculated as following in dependence of the IoU-range 0.5 to 0.95 [23]:

$$\mathrm{AR} = 2 \int_{0.5}^{0.95} \mathrm{r}(\mathrm{IoU}) d\mathrm{IoU}. \tag{9}$$

The mean average precision (mAP) and recall (mAR) are basically the mean values of AR and AP, respectively, across all individual classes.

  doi:10.5075/epfl-298799_978-2-9701614-0-0

3.3 Results

The training of 100 epochs with a batch size of 30 images per iteration of the ShearDetect model (available in [19]) on the A100 SXM GPU was with 7.7194 s / iteration sufficiently fast. Due to the implementation of mixed precision training the memory consumption decreased to 27,427 MB (26.8 GB) per batch. This method sets automatically the gradient calculation in the forward/backward pass of the model to either 16 or 32 bit floating precision, where necessary [17]. Overall, the training with integrated validation and testing each epoch took 2 h 22 min.

During training the learning rate η_t and the losses have been tracked for the training and validation set. Fig. 6 illustrates the median and standard deviation values per epoch per 9 and 3 iterations, respectively. Fig. 5 a) shows a rapidly decreasing $\mathcal{L}$ in the first epochs and slowly decreasing and converging values with a short increase between the epochs 20 to 40. Fig 5 b) and c) illustrates that behavior separately for $\mathcal{L}_{reg}$ and $\mathcal{L}_{cls}$. Noticeably, whilst $\mathcal{L}_{reg}$ increased from epoch 20 to 40 $\mathcal{L}_{reg}^{\mathrm{rpn}}$ decreased over all epochs. Hence, the RPN might provide sufficient region proposals to the region pool and classification layers (cf. Fig. 4 a)), but they might be misinterpreted. This behavior should be further investigated.

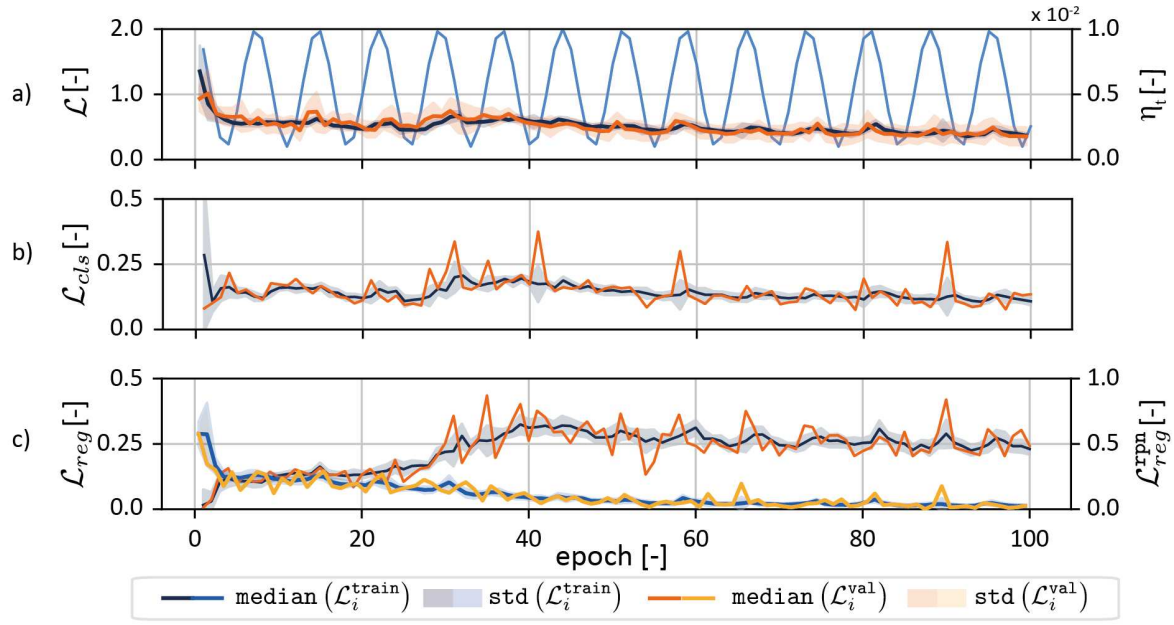

Figure 5. Illustration of median and standard deviation per epoch for a) overall loss $\mathcal{L}$ and learning rate η_t ,b) classification loss $\mathcal{L}_{cls}$ and c) regression loss for whole model $\mathcal{L}_{reg}$ and RPN $\mathcal{L}_{reg}^{rpn}$ for training set and validation set

Nevertheless, the bespoke loss increasing effect seems not to affect the evaluation metrics `mAP` and `mAR` of the shear detect model. Fig 6 a) and b) illustrates the floating median ($\mathtt{m}_{10}$) and standard deviation ($\mathtt{std}_{10}$) over 10 epochs for `mAP` and `mAR` of the test set and the discrete values for the validation set every 10th epoch. Noticeably, the metrics indicate a major increase at the epochs 20 to 50 until `mAP` and `mAR` converge to their certain value. After 100 epochs the following evaluation metrics could be obtained (values for the validation set are in brackets for better comparability): `mAP(IoU = 0.5)` = **0.806** (0.964), `mAP(IoU=.5:.95)` = **0.447** (0.683) and `mAR(IoU=.5:.95)` = **0.511** (0.721). These values indicate that the model conceives for the validation set, for data that is similar to the training set, and still has considerable performance on unknown data.

  doi:10.5075/epfl-298799_978-2-9701614-0-0

Furthermore, Fig. 6 b) illustrates and compares the precision-recall curves dependent on the IoU-range (.5:.8) for the class "defect" of the validation and test set. The main difference of the evaluation is that the model indicates a higher FP-rate on the test set. Hence, the precision decreases quite rapidly. However, a more profound examination on the testing results revealed that the data set features some human bias, as shown in Fig 6 c). There, the model predicts with 91.2% probability a defect that was not marked during manual labeling but is obviously present during X-ray examination. Hence, methods to create a better and reliable data set should be elaborated, to gain better performance of the model.

Lastly, it should be mentioned that the model performs on a A100 SXM with 0.0235 s, on a standard Quadro P4000 with 0.1550 s and on a CPU i7@860 with 22.7593 s per frame of the size 2452 x 2052 Px (8-bit). GPU-acceleration is highly recommended for training and evaluation.

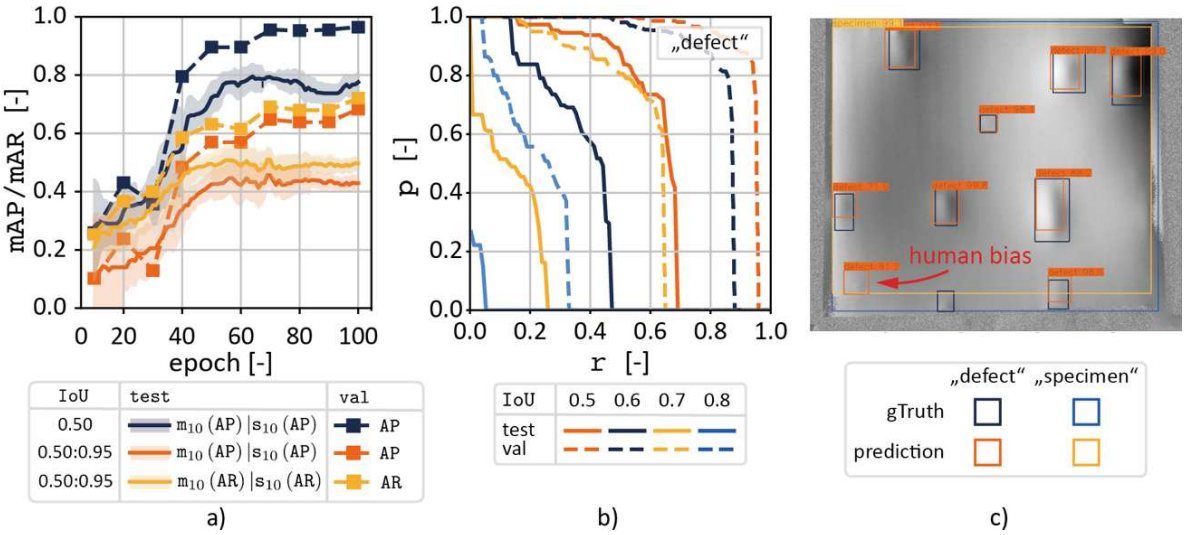

Figure 6. Illustration of a) median and standard deviation per epoch for mAP and mAR of the test and validation set and b) precision-recall curves for "defect" and IoU-range c) exemplary result for specimem_004

4. Conclusion

In this work, shearographic examinations of different specimens are conducted with temporal phase shifting method to create a large data set. Thereby, different shear angles and amounts have been considered to increase the diversity of the dataset. This data set has been used to train, validate, and test a machine learning model based on a CNN with the *faster R-CNN* region proposal network and the pretrained ResNet-50 as backbone. Via transfer learning the model was optimized using the ADAM optimizer and training rate scheduler on the dataset of shearographic images. Using the COCO evaluation method, the model preformed with a considerable mean average precision of 47.7 % and a mean average recall of 51.1 % on an unknown dataset for the intersection over union rage from 50 to 95 %. It emerged that the relative low accuracy occurred from a high false positive rate, due to human labeling bias. Consequently, further studies and methods have to be elaborated to decrease the impact of manual annotations.

  doi:10.5075/epfl-298799_978-2-9701614-0-0

Acknowledgements

This work was supported by the German Federal Ministry of Education and Research (BMBF, 01/S18026A-F) by funding the competence center for Big Data and AI "ScaDS.AI Dresden/Leipzig".

We thank the Center for Information Services and High-Performance Computing (ZIH) at TU Dresden for generous allocations of compute resources.

References

1. Steinchen W, Yang L (2003) Digital shearography: theory and application of digital Speckle pattern shearing interferometry. SPIE Optical Engineering Press, Bellingham, Wash.
2. Francis D (2013) Non-destructive evaluation (NDE) of composites: introduction to shearography. In: Non-Destr. Eval. NDE Polym. Matrix Compos. Elsevier, pp 56–83
3. Vandenrijt J-F, Georges M (2014) Automated Defect Detection Algorithm Applied to Shearography in Composites. In: Osten W (ed) Fringe 2013. Springer Berlin Heidelberg, Berlin, Heidelberg, pp 237–240
4. Scholz V, Winkler P, Hornig A, Gude M, Filippatos A (2021) Structural Damage Identification of Composite Rotors Based on Fully Connected Neural Networks and Convolutional Neural Networks. Sensors 21:2005
5. Hauffe A, Hähnel F, Wolf K (2020) Comparison of algorithms to quantify the damaged area in CFRP ultrasonic scans. Compos Struct 235:111791
6. Ren S, He K, Girshick R, Sun J (2015) Faster R-CNN: Towards Real-Time Object Detection with Region Proposal Networks. ArXiv150601497 Cs
7. He K, Zhang X, Ren S, Sun J (2015) Deep Residual Learning for Image Recognition. ArXiv151203385 Cs
8. Lin T-Y, Maire M, Belongie S, Bourdev L, Girshick R, Hays J, Perona P, Ramanan D, Zitnick CL, Dollár P (2015) Microsoft COCO: Common Objects in Context. ArXiv14050312 Cs
9. Mäckel P (2001) Grundlagen zur Entwicklung und Anwendung eines modularen Speckle Shearografiesystems zur Absolutmessung von mechanischen Größen an Freifromflächen. Universität Kassel
10. Menner P (2013) Zerstörungsfreie Prüfung von modernen Werkstoffen mit dynamischen Shearografie-Verfahren. Universität Stuttgart
11. Steinchen W, Yang LX, Kupfer G (1997) Digital Shearography for Nondestructive Testing and Vibration Analysis. Exp Tech 21:20–23
12. Anisimov AG, Groves RM (2015) 3D shape shearography with integrated structured light projection for strain inspection of curved objects. In: Lehmann P, Osten W, Albertazzi Gonçalves A (eds). Munich, Germany, p 952517
13. Pfeffer P, Düreth C, Giovanni S, Just G, Koch I, Jäger H, Hochrein T, Bastian M (2020) Automatisierte Shearografie - Zerstörungsfreie Prüfung mittels automatisierter Shearografie zur bedienerunabhängigen Fehlerdetektion in Faserverbundkunststoffstrukturen. Shaker (Verlag)
14. Düreth C (2022) ShearDetect - Dataset (Version 1.1). Zenodo. https://doi.org/10.5281/zenodo.6463119
15. Kingma DP, Ba J (2017) Adam: A Method for Stochastic Optimization. ArXiv14126980 Cs
16. Zhao Z-Q, Zheng P, Xu S, Wu X (2019) Object Detection with Deep Learning: A Review. ArXiv180705511 Cs
17. (2022) PyTorch documentation - Pytorch 1.11 documentation. In: PyTorch Doc. - Pytorch 111 Doc. https://pytorch.org/docs/stable/index.html.

  doi:10.5075/epfl-298799_978-2-9701614-0-0

18. Düreth C (2022) ShearDetect (Software). https://github.com/ILKGit/ShearDetect.
19. Düreth C (2022) ShearDetect - pretrained model (Version 1). Zenodo. https://doi.org/doi.org/10.5281/zenodo.6504390
20. Girshick R (2015) Fast R-CNN. ArXiv150408083 Cs
21. (2022) Labelbox: the leading training data platform for data labeling. https://labelbox.com.
22. Buslaev A, Iglovikov VI, Khvedchenya E, Parinov A, Druzhinin M, Kalinin AA (2020) Albumentations: Fast and Flexible Image Augmentations. Information 11:125
23. Goodfellow I, Bengio Y, Courville A (2016) Deep Learning. MIT Press
24. Loshchilov I, Hutter F (2017) SGDR: Stochastic Gradient Descent with Warm Restarts. ArXiv160803983 Cs Math

  doi:10.5075/epfl-298799_978-2-9701614-0-0

TERMINATION CRITERIA FOR FATIGUE TESTS OF CONTINUOUS FIBER REINFORCED POLYMERS

Maria Gfrerrer[a], Johannes Wiener[a], Christian Schneider[b], Andreas J. Brunner[c†], Gerald Pinter[a]

a: Montanuniversität Leoben, Materials Science and Testing of Polymers, Leoben, Austria – maria.gfrerrer@unileoben.ac.at
b: Exel Composites GmbH, R&D, Kapfenberg, Austria
c: Empa, Swiss Federal Laboratories for Materials Science and Technology, Dübendorf, Switzerland
†: Retired Scientist

Abstract*: The aim of this work is to find termination criteria for fatigue tests of continuous fiber reinforced polymers, which reliably predict end of life. For this purpose, Young's modulus, dissipated energy and acoustic emission events are monitored during fatigue testing of a ±60° and a ±75° glass-fiber reinforced epoxy laminate. Results show that the expected growth rate of damage events occurring at the end of lifetime is not necessarily reflected in a significant decrease of stiffness. However, material degradation at this stage is indicated by the dissipation of energy and a higher rate of detected acoustic emission events.*

Keywords: glass-fiber reinforced polymers; fatigue; termination criteria; non-destructive testing; acoustic emission

1. Introduction

Due to their outstanding weight-specific properties, in particular strength and stiffness, fiber reinforced polymers (FRPs) are widely used in high-performance structures for the aerospace, automotive or wind energy sector. Especially in those areas of application, unexpected property degradation or component failure can lead to catastrophic consequences. Hence, to ensure safe material use, characterization of fatigue behavior of FRPs is essential [1, 2].

The most common way to describe fatigue behavior of materials are S/N-curves, also referred to as Wöhler lines. They represent the maximum bearable number of cycles at certain stress or strain amplitude levels until a predefined termination criterion is reached [3–5]. Since S/N-curves assess fatigue life by a single event, commonly specimen fracture, they do not yield any information about the occurring damage mechanisms and the resulting property degradation.

The theory of fracture mechanics takes the mechanisms of crack initiation and propagation into account. It is well established for life-time estimations of metallic components, where usually one single crack dominates fatigue behavior. This is not the case for composites, since this material class usually fails due to the accumulation of damage from several mechanisms and not because of a single crack [6].

Another approach describing composite fatigue is based on the change of stiffness due to progressing material damage. As already mentioned, there is a series of complex damage mechanisms occurring in FRPs during fatigue. In the first 10 to 15 % of fatigue life, the

  doi:10.5075/epfl-298799_978-2-9701614-0-0

dominating mechanism is matrix cracking in off-axis plies resulting in a significant stiffness reduction. Coalescence of matrix cracks at the interface of two adjacent plies can lead to delaminations as a further consequence. The terminating damage event usually is large-scale fiber failure of the fibers aligned closest to the principal loading direction. All those mechanisms contribute to the stiffness degradation to different extent depending on layup and loading situation. For most composite structures a certain decrease in stiffness is inadmissible for the application and therefore defines fatigue life [3, 1].

Damage progression also manifests in dissipation of energy, which is reflected by the increasing area inside the hysteresis loop under cyclic loading. Due to internal friction between unbounded regions in the matrix or between fiber and matrix heat is generated. Thus, one portion of the input mechanical energy is released in the form of heat [3]. Another part of the energy may be released in the form of elastic stress waves if microstructural changes occur in the material. Such phenomena are referred to as acoustic emissions and can be detected by piezo-electric sensors [7, 8].

In this work Young's modulus, dissipated energy and acoustic emission (AE) activity are monitored during fatigue tests of glass-fiber reinforced polymers with two different layups: ±60° and ±75°. An attempt is made to assess the measured parameters in terms of their suitability to monitor structural health and in further consequence to define criteria terminating fatigue life of continuous FRPs.

2. Experimental

2.1 Material and specimen preparation

Specimens are manufactured from an unidirectional glass fiber fabric and an epoxy resin as matrix material with a fiber volume content of approximately 40 %. The fabric is of type 92145 by Porcher Industries Germany GmbH (Erbach, Germany) with an areal weight of 220 g/m^2 and 10 % weft yarn referring to the total fabric mass. The matrix contains a resin of type EPIKOTE™ MGS® LR160 and a curing agent of type EPIKURE™ MGS® LR160 both by Lange + Ritter GmbH (Gerlingen, Germany). The mixing ratio of resin to curing agent is 4:1 (weight proportion). Matrix and fabric are cured at a temperature of 80 °C and a pressure of 1 MPa for 3 hours. Subsequently all specimens are post-cured at 80 °C for 15 hours. Each specimen consists of 12 layers, which are symmetrically arranged. The layup is $(-\theta_3, +\theta_3)_s$ with θ being 60° and 75°. The specimen geometry is 200x20x2.6 mm^3 with shafted aluminum tabs of 1 mm thickness and a gauge length of 100 mm, as shown in Figure 1. Additionally, a speckle pattern is applied to the specimens, which is necessary for the evaluation of Young's modulus with digital image correlation (DIC), as will be described in the following sections.

  doi:10.5075/epfl-298799_978-2-9701614-0-0

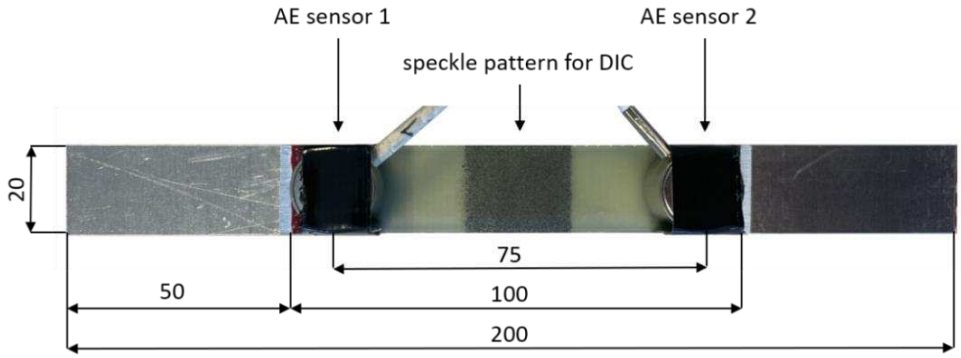

Figure 1: Specimen with WD sensors and speckle pattern for DIC (dimensions in mm).

2.2 Testing equipment

The fatigue tests were performed on a servo-hydraulic testing machine of the model 322.31 by MTS Systems Corporations (Minnesota, USA) equipped with a 250 kN load cell. For DIC the software MercuryRT 2.8 by Sobriety Mercury d.o.o. (Blaneská, Czech Republic) in combination with a high-resolution camera of type Prosilica GT6600 by Allied Vision (Stadtroda, Germany) is used. The AE system is by MISTRAS Group Inc. (Princeton Junction, USA). Two broad band (WD) sensors are mounted to the specimen with fabric tape at a distance of 75 mm (see Figure 1). Silicone free vacuum grease is used as coupling medium between specimen surface and sensors. Each sensor is connected to a 2/4/6 preamplifier with a gain of 40 dB and a 20 - 1000 kHz bandpass filter. For AE data acquisition and evaluation, the software AEwin™ by MISTRAS Group Inc. is used.

2.3 Testing procedure and parameters

The testing procedure is adapted from the one proposed by Brunbauer et al. [9]. Thereby, the fatigue tests are interrupted at certain intervals and quasi-static tensile tests are performed in between to be able to determine the change of static Young' modulus during the experiment. For this purpose, every 100 N during the tensile test a picture of the speckle pattern on the specimen is recorded and subsequently evaluated with DIC. Tensile tests are conducted with a testing speed of 0.5 mm/min and are stopped before reaching the maximum stress level σ_{max} of the cyclic loading blocks. The cyclic loading blocks are implemented with a testing frequency f of 5 Hz and an R-ratio of 0.1. Tests were performed at various σ_{max} levels for each layup. In this contribution two representative experiments are discussed: For the ±60° laminate an experiment with a σ_{max} of 38.6 MPa and for the ±75° laminate an experiment with a σ_{max} of 31.6 MPa is presented. Dissipated energy is calculated directly from the machine data and corresponds to the area inside the hysteresis loop. The testing procedure is schematically shown in Figure 2. While the fatigue blocks are conducted in load controlled mode, the tensile tests are performed in displacement control.

  doi:10.5075/epfl-298799_978-2-9701614-0-0

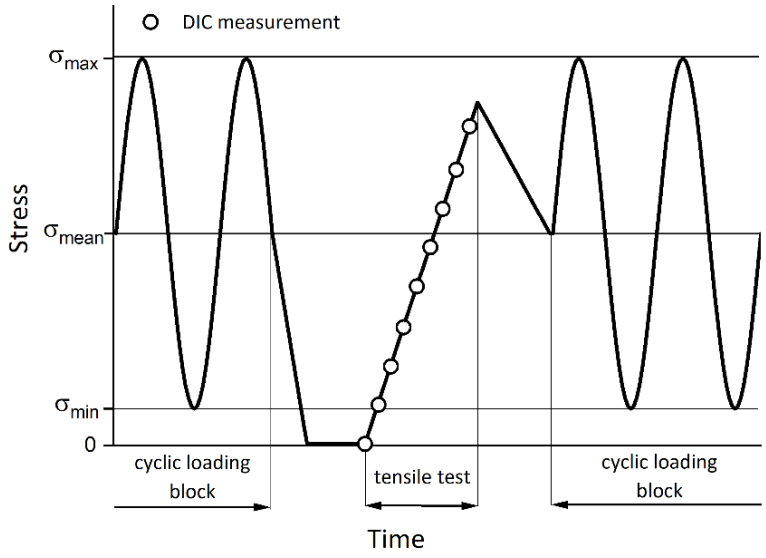

Figure 2: Schematic testing procedure for fatigue tests (load control, R-ratio 0.1) with quasi-static tensile tests between fatigue load blocks, the circles indicate stress levels for DIC measurements for the determination of Young's modulus.

For AE data acquisition a sampling rate of 5 MHz is used. The threshold is set to 40 dB_{AE} and the following AE timing parameters are chosen:

- Peak definition time (PDT): 50 µs
- Hit definition time (HDT): 100 µs
- Hit lockout time (HLT): 300 µs

If a detected AE signal, also called “hit”, is recorded at least at two sensors within a certain time interval (depending on the wave speed in the specimen and the distance of the respective sensors) it is referred to as an AE event [7]. For the interpretation of the AE data only events occurring in between the two sensors are considered, in order to eliminate “hits” originating from outside the region of interest to a great extent.

3. Results and discussion

In the following two sections, the results of the fatigue tests of the ±60° and ±75° layups are presented. Young’s modulus and dissipated energy are shown relative to their initial values. The fatigue life in % refers to the point of specimen rupture (final material failure). Subsequently the measured parameters are discussed with regard to their qualification to monitor structural health and how this can be used to define termination criteria.

3.1 Fatigue test results of ±60° laminate

Figure 3 shows relative Young’s modulus, relative dissipated energy and cumulative AE events during fatigue life of a ±60° laminate. Final material failure for this representative specimen occurred at 204'761 cycles. In the beginning, a rapid decrease of Young’s modulus can be observed. It declines to 55 % of the initial value already within the first 15 % of fatigue life. During the remaining 85 %, Young’s modulus decreases with a much smaller rate to 45 % at the end of life. Only a slightly higher decrease rate of Young’s modulus can be observed close to final

  doi:10.5075/epfl-298799_978-2-9701614-0-0

material failure. Contrary to Young's modulus, dissipated energy shows a recognizable increase within the first 15 % of fatigue life. Both of these observations probably can be attributed to matrix cracking, which is the dominating damage mechanism at this early stage of fatigue life [1]. This fast increase is followed by a section, in which dissipated energy increases more slowly. Shortly before failure, at approximately 85 % of fatigue life, dissipated energy strongly increases again, indicating increased inner friction due to a growing accumulation of damage. At this stage typical damage mechanisms occurring are delamination or fiber breaking [1]. Considering the cumulative AE events, there are two sections, showing a higher slope. One is located between 50 and 60 % of fatigue life. However, no noticeable changes of Young's modulus or dissipated energy can be observed in this period. Additional non-destructive methods, e.g. computed tomography or thermography, to monitor the condition of the specimen are necessary to assess the cause for this increase. The second section showing a higher increase rate starts shortly before specimen rupture at around 90 % of fatigue life. Similar to the progression of dissipated energy at this stage, the increase in AE events can be attributed to a higher rate of damage occurring just before specimen rupture.

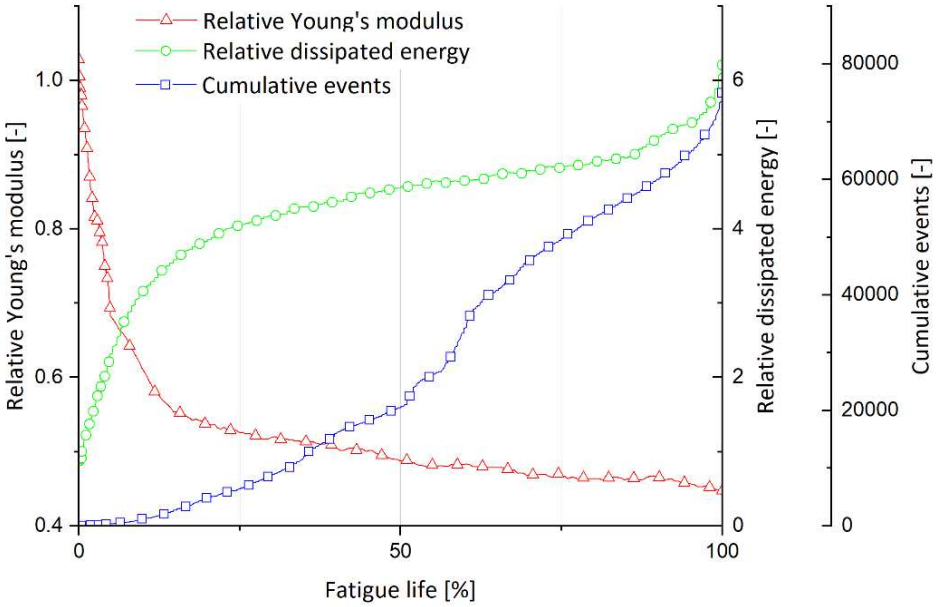

Figure 3: Relative Young's modulus, relative dissipated energy and cumulative AE events during fatigue life of a ±60° glass-fiber reinforced epoxy resin (σ_{max} = 38.6 MPa, R = 0.1, f = 5 Hz).

3.2 Fatigue test results of ±75° laminate

The monitored parameters during the fatigue test of the representative ±75° laminate are presented in Figure 4. After 353'959 cycles the specimen failed. Just as with the ±60° laminate, Young's modulus declines rapidly at the beginning, in this case to 58 % of the intact specimen within the first 15 % of fatigue life. This is again followed by a section with a smaller decrease rate. As for the ±60° laminate, a slightly higher decrease rate can be noticed close to final failure. Young's modulus at the end of fatigue life amounts to 46 % of the initial value. Dissipated energy also shows the same trend as already monitored for the first laminate. After a high increase rate at the beginning, there is a section with a slower steady increase. At around 80 % of fatigue life a slightly higher increase can be observed. Approximately at the same time AE events are detected with a higher rate, reflecting the increasing amount of damage leading to specimen

  doi:10.5075/epfl-298799_978-2-9701614-0-0

rupture shortly thereafter. A sudden increase in AE events can be observed at around 10 % of fatigue life. As already mentioned in section 3.1 additional non-destructive methods are necessary to determine the origin.

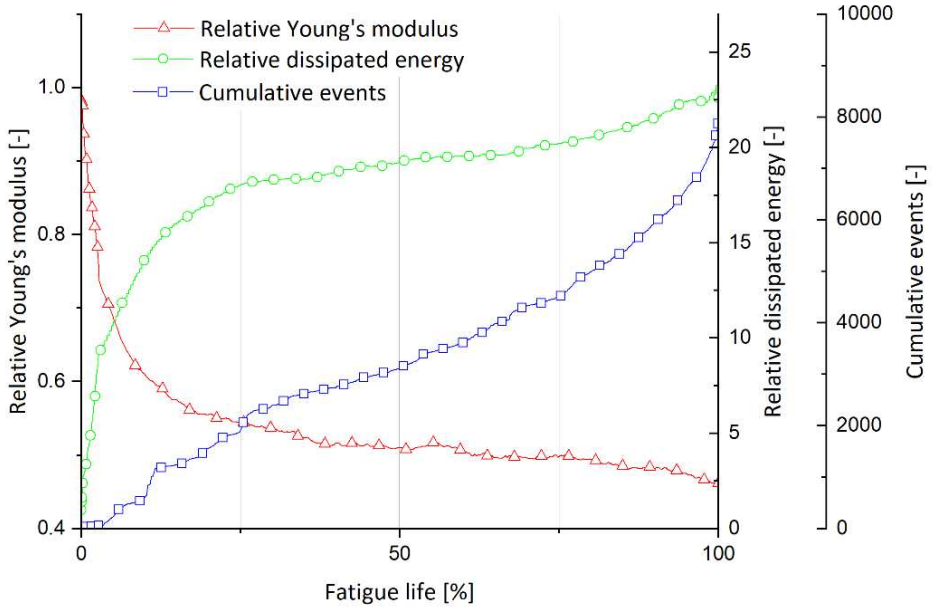

Figure 4: Relative Young's modulus, relative dissipated energy and cumulative AE events during fatigue life of a ±75° glass-fiber reinforced epoxy resin (σ_{max} = 31.6 MPa, R = 0.1, f = 5 Hz).

3.3 Termination criteria

For both laminates tested, Young's modulus severely declines within the first 15 % of fatigue life. This observation can be attributed to the mechanism of matrix cracking, which typically occurs at this stage of fatigue life in laminates with off-axis plies [1]. Young's modulus subsequently slowly decreases until final failure. Shortly before specimen rupture, it decreases with a slightly higher rate. However, since this change is so small, it is difficult to predict specimen failure considering the progression of Young's modulus exclusively. Nevertheless, some applications require a certain stiffness in order to ensure proper performance. Therefore, fatigue life can always be determined by a certain limit of the decrease of Young's modulus.

Dissipated energy is much more sensitive towards the specimen's end of life. The higher increase rate in the section before final failure represents a potential termination criterion, which can be applied to both tested laminates. For the ±60° laminate it is around 85 % and for the ±75° laminate at around 80 % of fatigue life, leaving enough time to exchange damaged components before fracture.

The method of AE proves its applicability for monitoring the structural health of laminates. For both laminates tested, an increasing number of AE events is detected before final material failure. Nevertheless, fatigue life cannot be predicted by this observation since there are other regions showing a higher detection rate at an earlier stage of fatigue life as well.

  doi:10.5075/epfl-298799_978-2-9701614-0-0

4. Conclusion

The purpose of this work was to find termination criteria for fatigue tests of continuous FRPs, reliably predicting end of life at an early stage. Young's modulus, dissipated energy and cumulative AE events were monitored during fatigue tests of glass-fiber reinforced epoxy laminates with two different layups of $(-\theta_3, +\theta_3)_s$ with θ being 60° and 75°. In order to determine classic Young's modulus, the fatigue tests were interrupted in regular intervals and quasi-static tensile tests were conducted between the cyclic loading blocks.

Results show that Young's modulus exhibits the highest decrease within the first 15 % of fatigue life. It amounts to approximately 80 % of total stiffness loss. The remaining 20 % stiffness loss occur steadily during the rest of life. Besides a minimally higher decrease rate, there is no significant warning for the occurrence of failure. Dissipated energy on the contrary is more sensitive towards the end of life. It shows a higher increase rate between 80 and 85 % of fatigue life, which may be used as termination criterion. Needless to say, fatigue life for certain applications can already be terminated at an earlier stage by a function-critical stiffness loss. The higher rate of damage occurring near the end of the experiment is reflected in the curve of cumulative AE events as well, which exhibits a higher detection rate at this period. Other regions during fatigue life showing a higher detection rate as well need to be investigated in more detail in order to assess their origin.

An approach for prospective interpretations of AE data would be the evaluation of other features of the signals, e.g. the absolute energy. This parameter has potential for being a sensitive indicator for changes occurring in the material due to damage accumulation, since recorded signals are not only counted, but also weighted by their intensity.

5. References

1. Reifsnider KL, editor. Fatigue of composite materials. Amsterdam, New York: Elsevier; 1991.
2. Schürmann H. Konstruieren mit Faser-Kunststoff-Verbunden. 2. bearb. u. erw. Aufl. Berlin, Heidelberg: Springer Berlin Heidelberg; 2007.
3. Vassilopoulos A, editor. Fatigue Life Prediction of Composites and Composite Structures. 2nd ed. Duxford, United Kingdom: Elsevier; 2020.
4. Haibach E. Betriebsfestigkeit: Verfahren und Daten zur Bauteilberechnung. 3rd ed. Berlin, Heidelberg: Springer Berlin Heidelberg; 2006.
5. Radaj D, Vormwald M. Ermüdungsfestigkeit. Berlin, Heidelberg: Springer Berlin Heidelberg; 2007.
6. Rösler J, Bäker M, Harders H. Mechanisches Verhalten der Werkstoffe. 3., durchgesehene und korrigierte Auflage. Wiesbaden: Vieweg+Teubner Verlag / GWV Fachverlage GmbH, Wiesbaden; 2008.
7. Sause MGR. In Situ Monitoring of Fiber-Reinforced Composites: Theory, Basic Concepts, Methods, and Applications. Cham: Springer International Publishing AG; 2016.
8. Unnorsson R. Hit Detection and Determination in AE Bursts. In: Sikorski W, editor. Acoustic Emission - Research and Applications. InTech; 2013.
9. Brunbauer J, Arbeiter F, Stelzer S, Pinter G. Stiffness Based Fatigue Characterisation of CFRP. Advanced Materials Research 2014; 891-892:166–71.

  doi:10.5075/epfl-298799_978-2-9701614-0-0

WEAK BOND DETECTION IN SINGLE-LAP SHEAR BONDS BY EVALUATING VIBROACOUSTIC MODULATIONS WITH ARTIFICIAL NEURAL NETWORKS

Benjamin Boll[a], Erik Willmann[a], Bodo Fiedler[a], Robert Horst Meissner[a,b]

a: Institute of Polymers and Composites, Hamburg University of Technology, Hamburg
b: Institute of Surface Science, Helmholtz-Zentrum Hereon, Geesthacht, Germany
*benjamin.boll@tuhh.de

Abstract: *Adhesive bonding is an essential method for joining composite materials. However, the occurrence of contaminations, resulting in a not detectable weakened adhesion, persists. This study aims to uncover weak bonds with the vibroacoustic modulation method, a nonlinear ultrasonic testing method, where ultrasonic guided waves are modulated by a simultaneously applied, high amplitude pump wave. Afterwards, the measurements are evaluated by a deep learning approach. A previous dataset of 40 single-lap shear specimens (ASTM D5868-01), in which artificial interfaces in the form of circular PTFE films or release agent contaminations were introduced, was extended by a second dataset with 14 specimens of a different laminate to evaluate the robustness and transferability of the method. The proposed neural network approach can reliably recognize the bonding flaws in the training dataset and even has high accuracies on the transfer dataset, demonstrating the tremendous potential for the nondestructive evaluation of adhesive joints.*

Keywords: Composites; Weak bonds; Nondestructive Testing; Vibroacoustic Modulation; Artificial Neural Networks

1. Introduction

The application of fiber-reinforced composites for primary structures is widely adopted due to their high specific strength, corrosion resistance, and fatigue properties. Nevertheless, the lightweight potential for bonding composite structures is not fully exploited since the traditional bonding with bolts or rivets introduces substantial stress concentrations around the fastener and, therefore, requires a thickened material [1]. Adhesive bonding overcomes these difficulties due to the homogeneous stress concentration in the bonding area [1,2]. However, even with highly automated processes, contaminations persist, resulting in areas of weekend adhesion. Since the weakened bond arises from a changed chemical interaction, magnitudes smaller than ultrasonic wavelengths [3], they are hard or even impossible to detect with conventional nondestructive testing. The significant reduction of bond strength, coupled with the inability to detect these defects, poses a severe threat to structural safety and limits the lightweight and application potential [2,4].

Numerous studies have been published where weak bonds are created artificially either by contaminating the adherent's surface [5–7] or by introducing a non-adhesive film [5,8–10]. While the non-adhesive film is detectable by several NDT methods [5,6,8], the release agent contamination resembles reality much closer [11] and is more challenging to detect. To the author's knowledge, there is no method capable of reliably detecting areas of reduced adhesion, preventing the application of adhesives as the main bonding method in primary structures [1,4,12,13]. In this regard, applying nonlinear ultrasonic methods has shown promising results

  doi:10.5075/epfl-298799_978-2-9701614-0-0

in the literature. The vibroacoustic modulation (VAM)—which combines nonlinear ultrasonic measurements with a simultaneously introduced vibration— has shown a superior sensitivity to damages already on other specimen types [6,14–16].

Our prior work [17] showed the ability to detect weak bonds in single lap shear specimens. An artificial neural network evaluated the VAM measurements to classify the bonding state. This combination has proven superior to the traditional VAM evaluation based on a damage index. In recent VAM-related works, the nonlinear modulation—indicating the damage—is divided into amplitude and phase modulation. In this work, we quantify whether—based on our extended dataset—a weak bond detection, evaluating only these modulation values results in precise predictions as well. Furthermore, the transferability and robustness of the old and newly trained ANNs are evaluated on the newly manufactured specimen with a different laminate layup.

2. Introduction

2.1 Specimen manufacturing

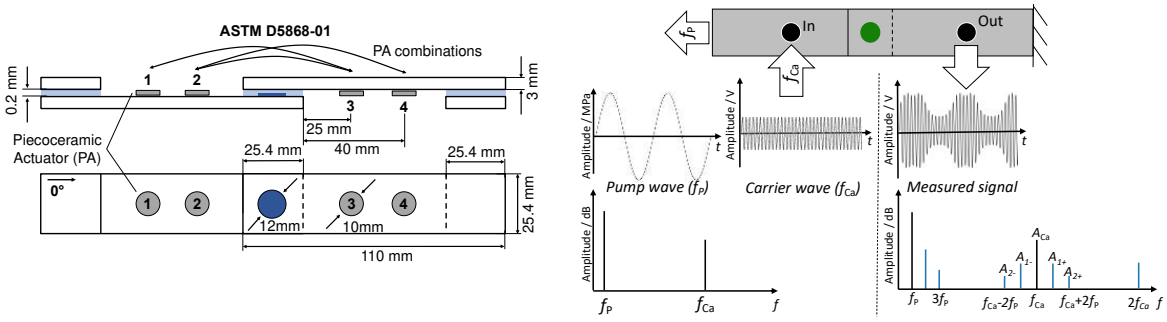

Figure 1. Dimensions of the tested specimen (left). The gray disks illustrate the different positions of the piezoceramic actuators. Illustration of VAM (right), where the excitation signals on the left result in the modulated signal with higher harmonics and sidebands (adapted [17]*).*

Additionally to the 40 original specimens (details in [17]), 14 specimens were manufactured according to the same procedure but with a different laminate layup. In contrast to the 3mm $[0_4]$s glass fiber laminate, the new specimens were made from a 3 mm thick adherent with a $[0,\pm45_3]_s$ layup. The same E-glass fibers and the low-viscosity epoxy system (RIMH135 with RIMR137 from Hexion) have been used. The single-lap joints are produced in a secondary-bonding process with the 2C-epoxy adhesive (Sika-Power-1280). The dimensions follow the ASTM D5868-01, as shown in Figure 1 (left). Prior to the bonding process, seven specimens were contaminated with a release agent (RA) (Mikon W-64+ from Münch Chemie) in a circular area (d=12 mm), creating nondetectable weak bonds in ultrasonic C-Scans. Since the PTFE intrusions are detectable with VAM [6,17] and traditional testing methods (e.g. ultrasonic testing), only the RA and pristine specimens were newly manufactured and compared.

2.2 Vibroacoustic modulation method

The vibroacoustic modulation (VAM) is an active nonlinear ultrasonic method for nondestructive testing. It utilizes the modulation of two sinusoidal frequencies. The *pump wave* has a low-frequency f_P but high amplitude to alter the stress state in the specimen, especially around defects. The *probe wave* with the high-frequency f_Ca acts as a carrier for the modulated signal

  doi:10.5075/epfl-298799_978-2-9701614-0-0

[14]. Damages (initial defects, i.e., discontinuities, surfaces, interfaces, etc.) and presumably the weak bonds of this work result in a nonlinear modulation of the carrier [15–17].

Traditionally, VAM is evaluated by calculating the frequency domain from the steady-state signal with the Fast Fourier transform (FFT). The nonlinear behavior of the specimen results in a superposition of several dominating frequencies. They can be attributed to the unmodulated frequencies at f_{P} and f_{Ca}, the higher harmonics due to the modulation $(nf_{\mathrm{P}} \wedge nf_{\mathrm{Ca}} \mid n \in \mathbb{N})$, and sidebands around the carrier frequency $(f_{\mathrm{Ca}} \pm nf_{\mathrm{P}} \mid n \in \mathbb{N})$ [14] as shown in Figure 1 (right). For evaluation, a representative value such as the Modulation Index (MI) is calculated from the amplitudes of the carrier signal and first sidebands denoted as A [18,19].

$$MI = 20 \cdot log_{10}\left(\frac{A_{1+}+A_{1-}}{2 \cdot A_{\mathrm{Ca}}}\right) \quad (1)$$

In recent works, the separation in amplitude modulation (AM) and phase modulation (PM) was shown to be beneficial and attributed to different types of damage, which in turn increased the sensitivity of VAM. This separation was proposed by methods like the Hilbert-transform [20], the Hilbert-Huang-transform [21], the In-phase/Quadrature Homodyne Separation (IQHS) [22], and the short-time Fourier-transform (STFT) [23]. Since the STFT provides a significant advantage of the lowest computational cost, which is beneficial for the real-world application in sensor networks, in the following we analyze whether it could be used for weak bond detection.

Most works analyze the development of the MI over the specimen lifetime, where the first measurement is defined as a baseline. However, comparing measurements from different specimens leads to severe differences in signal strength and initial modulation, making evaluations a complex endeavor. Hence, as presented later, the data-driven analysis proves beneficial for such complex and highly correlated input data.

2.3 Experimental setup

To have similar conditions for all measurements, all vibroacoustic measurements were performed on a servo-hydraulic testing machine (Instron 8801 with a max. load capacity of 63 kN). The pumping frequency was chosen as 5 Hz with an amplitude of 11 MPa and a stress ratio of $R = 0.1$ due to limitations on the hydraulic valve of the machine and the tensile strength of the specimen. The high-frequency ultrasonic vibration was introduced by piezoceramic actuator disks (PI-Ceramics 10 x 2mm) attached to the specimen with double-sided tape (Tesa 56172). A NI-USB 6366 (National Instruments) with a sampling rate of 2 MS/s was used for the excitation and monitoring of the piezoceramics. The generated sine was amplified to 12 $V_{pp,}$ and 39 equidistant measurements in a range of 200 kHz <f_{Ca}< 220 kHz and a duration of 2 s were acquired. Furthermore, as shown in Figure 1, the signal path between actuating and receiving piezoceramic was alternated, resulting in a total of 234 VAM samples per specimen (39 frequencies, three pathways, two directions).

2.4 Machine Learning Application

As preprocessing, the transient regime (first 0.4 ms) of all measurements was removed. The remaining signal (1.996 s) was multiplied with a Hanning window function and afterwards transformed with a fast Fourier transformation (FFT) into the frequency domain. This procedure resulted in a reduction of spectral leakage and clearly pronounced sideband peaks in the frequency domain. For each specimen j, the amplitude of the sidebands $A_{j,i\pm}$ and the carrier

  doi:10.5075/epfl-298799_978-2-9701614-0-0

amplitude $A_{j,\mathrm{Ca}}$ are stored in a data matrix denoted as $\mathbf{X_{SB}}$ for the initial and $\mathbf{X_{Transf}}$ for the newly manufactured specimen. The bonding type is stored as the label for the classification in vectors denoted as $\boldsymbol{y}$ and $\boldsymbol{y}_{\mathbf{Transf}}$. All amplitudes in dB-scale were normalized so that the mean value was set to zero and the standard deviation equals one (Z-score normalization). This normalization was calculated for the training set and adapted for the validation set and $\mathbf{X_{SB}}$. For a second dataset $\mathbf{X_{APM}}$, the amplitude modulation $\mathrm{m_{j,A}}$ and phase modulation $\mathrm{m_{j,P}}$ were calculated based on the STFT [23].

The defect detection is implemented as a classification problem in TensorFlow. The optimal network architecture for the dataset $\mathbf{X_{SB}}$ was determined in a randomized grid search as described in [17]. Here, the number of used sidebands as ANN-input, the frequency range, and the signal path of the measurements were permuted to identify whether some frequencies or placements of the piezoceramics resulted in more precise predictions. These results are compared to a smaller network (ANN 2) with 16 neurons in one hidden layer (2-16-3 neurons) trained on $\mathbf{X_{APM}}$.

All models were evaluated by calculating the accuracy of each prediction, which is defined as $\mathrm{accuracy}(\boldsymbol{y}, \hat{\boldsymbol{y}}) = \frac{1}{n}\sum_{i=1}^{n} 1_{\boldsymbol{y}_i}(\hat{\boldsymbol{y}}_i)$ where n is the number of samples, $\hat{\boldsymbol{y}}_i$ is the predicted label of the i-th sample, $\boldsymbol{y}_i$ is corresponding true label, and $1_{\boldsymbol{y}_i}(\hat{\boldsymbol{y}}_i)$ is the indicator function which returns one if both match and zero otherwise.

Since the dataset is rather small for the training of deep ANNs, the dataset splitting in the training set (80%) and validation set (20%) influences the result. Therefore, every shown result from an ANN is the mean of 10 randomized splits. In every split, all measurements of a specimen are either in the test or validation set, as this has been shown to increase the reliability of the results [17].

3. Results and Discussion

3.1 Vibroacoustic measurements

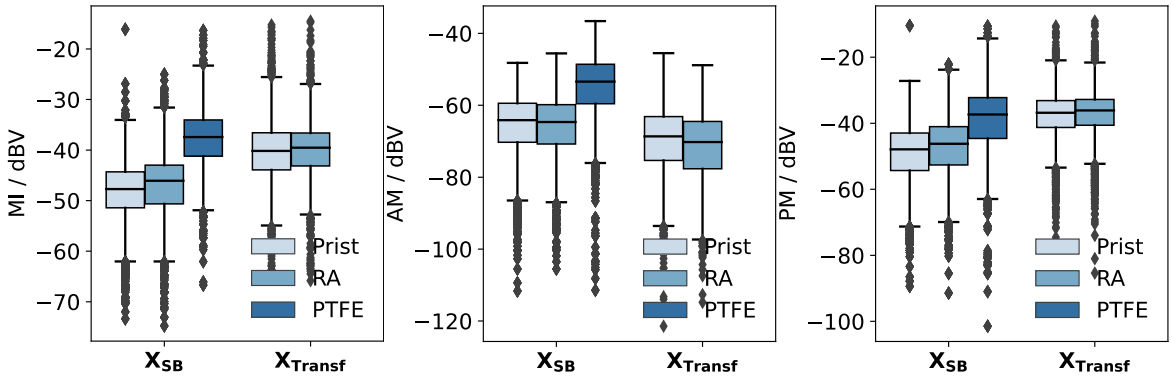

Figure 2. Boxplots for the Modulation index (left), amplitude modulation (middle) and phase modulation (right).

The vibroacoustic measurements are typically evaluated by calculating the "traditional" MI, as shown in Figure 2 (left). Here, the MI is plotted for the 239 measurements of all specimens in a boxplot. Indicated by the median value (line inside each box), a differentiation of the PTFE specimen of $\mathbf{X_{SB}}$ is possible even though the standard deviation and interquartile range are relatively high. However, the release agent specimen cannot be differentiated from the pristine

  doi:10.5075/epfl-298799_978-2-9701614-0-0 published under CC BY-NC 4.0 license

specimens based on the MI. The mean MI of the new dataset $\mathbf{X_{Transf}}$ is significantly higher compared to $\mathbf{X_{SB}}$ and closer to the mean of the PTFE specimens, underlining the importance of more values to be analyzed.

Therefore, also the values of the amplitude and phase modulation calculated with the STFT are presented. For both values, the modulation of the PTFE specimen is the highest. However, the mean AM of the RA specimens is slightly lower and the mean PM is marginally higher compared to pristine specimens. However, both differences are negligibly compared to standard deviation.

3.2 Adhesive Bonding Classification

To outperform the bond differentiation based on a pure MI evaluation or other indices, shown in the previous chapter, more sophisticated data-driven methods were applied to predict the bonding. As described in the methods section, we have created two datasets from the measurements, where $\mathbf{X_{SB}}$ contains the normalized sideband values and $\mathbf{X_{APM}}$ contains the calculated AM and PM value of the signal obtained with the STFT transform. Since the measured frequency range is rather big, the ANNs were trained on subsets of 5 neighboring frequencies of one piezo combination. The most precise results of the 10-fold cross-validation are shown in Figure 3. Note that the used carrier frequency ranges overlap. Hence, each point represents the highest achieved accuracy of a frequency obtained for training an ANN with input data from a certain frequency range.

The ANNs trained on the actual sideband values ($\mathbf{X_{SB}}$) were able to predict the bonding type reliably. The differentiation between the three classes of specimens is possible with an accuracy of 93.4 % if the frequency range of 202.5 − 204.5 kHz and the number of five sidebands on both sides and the carrier are used (as marked with the red circles). As discussed in [17], the accuracy of the prediction depends on the number of sidebands used as input for the ANN. Less evaluated sidebands result in lower accuracies due to less information as ANN input. However, a high number of used sidebands results in the ANN overfitting the existing noise. Hence, this number has to be chosen carefully. Furthermore, the accuracy is also dependent on the placement of the piezoceramic. The asymmetric combinations (P1–P3 and P2–P4) result in high accuracy and strong frequency dependence compared to the symmetric layout (P2–P3). This might be an effect of the distance to the bond, the signal path length, or more generally the resulting eigenmodes of the specimen.

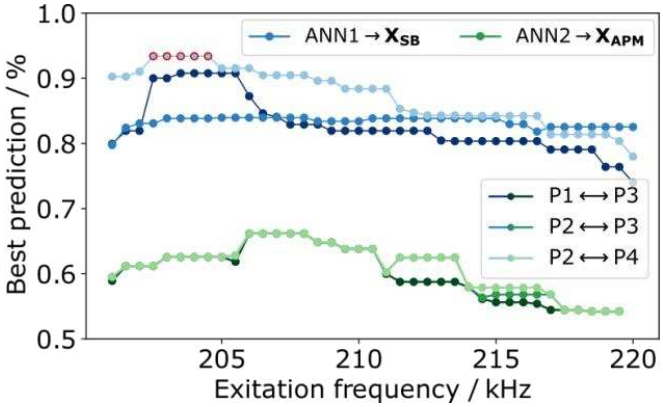

Figure 3. Comparison of the maximal achieved bond line defect classification for different signal pathways between the piezoceramics and probe frequencies. Compared are the results for the ANNs trained on $\mathbf{X_{SB}}$ and $\mathbf{X_{APM}}$.

  doi:10.5075/epfl-298799_978-2-9701614-0-0

When training the ANNs solely on the AM and PM values ($\boldsymbol{X_{APM}}$) extracted by the STFT, the accuracy of the prediction is less accurate compared to the networks trained on the peak values. Only a maximal accuracy of 67 % was reached with a maximal value around 206-208 kHz. Comparable to the prior results, a dependency on the utilized frequency range is observable as well. Nevertheless, the precision of the different piezo combinations is mostly similar. This significantly worse behavior can have a variety of reasons. Most importantly, the STFT is based on the assumption of a perfect sinusoidal modulation, which might be close but not exactly the predominant stress-strain response of the specimens. Furthermore, the STFT evaluates only frequency components of f_{P} and f_{Ca}. However, as many publications describe, higher harmonics also occur as a nonlinear response to damages. Since VAM is evaluated at the steady state of the vibration, these higher harmonics are also reflected many times in the specimen and, in turn, contribute to the higher-order sidebands as well. For example, the first harmonic at 10 Hz would contribute to the second, fourth, and sixth sidebands, the second harmonic in the third and sixth. These contributions are not taken into account by the STFT. Finally, the networks applied on $\mathbf{X_{APM}}$ are smaller compared to $\mathbf{X_{SB}}$ since patterns in two input values are much easier to detect and bigger networks overfit the data resulting in even worse results.

Interestingly, interchanging the left and right sidebands of the $\mathbf{X_{SB}}$ evaluation dataset results in a mean accuracy decrease of around 28 %. This underlines the relevance of the asymmetries in the sideband peaks and results in a similar accuracy comparable to the AM and PM ANN training ($\mathbf{X_{APM}}$), which—as an approximation—does not take all frequency components into account.

3.3 Transfer of trained models to the new dataset

Based on the most accurate prediction of $\mathbf{X_{SB}}$ (piezo combination P2–P4, the frequency range of 202.5 − 204.5 kHz, amplitudes of 5 sidebands to each side and of the carrier as input, marked as red circles in Figure 3), 50 new ANNs have been trained and saved with randomized splits into test and training data of $\mathbf{X_{SB}}$ to evaluate whether the "learned" patterns are universal and also applicable to the specimen with a changed laminate layup in $\mathbf{X_{Transf}}$. The number of trained networks is increased compared to the prior results to further test the robustness. These networks reach a mean accuracy of 92,5 %, which is 0.9 % below the results from the previous chapter due to statistical reasons of the small dataset, but still underlining the good agreement.

These networks were now used to predict the bonding state of $\mathbf{X_{Transf}}$. The combined predictions are shown in Figure 4 in a confusion matrix. Note that no PTFE specimens have been tested, resulting in only two rows. However, the networks were trained as ternary classification and misclassified a marginal percentage of samples as PTFE specimens, as shown in the left column.

The upper-middle and lower-right boxes represent the percentage of correct predictions, while the other indicates the wrong predictions. In total, an accuracy of 72.9 % was achieved. However, the confusion matrix indicates that the networks tend to classify specimens as contaminated, resulting in higher accuracy for the release agent specimen than the pristine ones. This could stem from the lower stiffness and therefore changed wave propagation of the new composite layup. Furthermore, the high count of fibers in a $\pm$45° direction influences the Lamb waves. As discussed by [24], a continuous mode conversation (S to A mode) occurs in composites made with twill fabric and possibly other layups. These factors eventually change

  doi:10.5075/epfl-298799_978-2-9701614-0-0

the measured signal, resulting in slight changes in the modulation, which probably explain the near 20% reduction in accuracy.

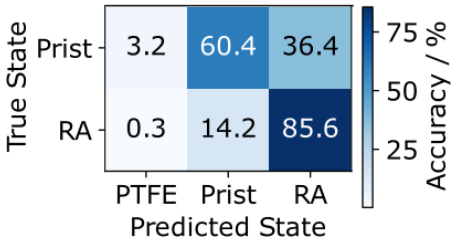

Figure 4. Confusion matrix of the 50-fold prediction of X_{Transf} with ANNs trained on $\mathbf{X_{SB}}$.

4. Conclusion

The evaluation of the vibroacoustic measurements with a machine learning approach, as presented in this work, has shown promising capabilities for detecting a reduced adhesion by release agent contaminations (or more general weak bonds). The results indicate that the nonlinear modulation of ultrasonic waves can detect defects or adhesive properties in the interface between adhesive and substrate [19], although the wavelength is in the cm range and, therefore, considerably larger than the adhesive layer thickness. The enhanced sensitivity is most likely related to the interaction of the cyclic stress change in the bond by the high-stress pump frequency and the Lamb-wave characteristics. Larger contaminated regions are likely to boost the signal's nonlinear amplitudes, improving ANN accuracy, although contaminations smaller than the Lamb wavelength may be more difficult to detect.

However, just training a network on the extracted values of amplitude and phase modulation results in a severe decrease in the reached accuracy. This decrease indicates that the information in the sideband amplitudes and the carrier are not completely included in the STFT calculations. For example, interchanging the inputs of the most accurate ANN trained on $\mathbf{X_{SB}}$ by swapping left and right sidebands results as well in an average decrease in classification accuracy of 28 %, which is in the range of the predictions on $\mathbf{X_{Transf}}$.

Predicting the contamination of specimens with the same dimensions but different layup shows a decrease in accuracy as well. Presumably, the changes in the laminate structure result in altered wave propagations and further effects like a continuous mode conversation of the lamb waves. Despite these effects, the ANNs trained on $\mathbf{X_{SB}}$ were still able to predict the bonding state of $\mathbf{X_{Transf}}$ reasonably well with a more reliable detection of contaminated specimens (86 %) while misclassifying roughly 40 % of the pristine specimens.

To conclude, this supervised ANN approach is suitable for analyzing similar specimens, e.g., in mass productions. Hence, the change in specimen dimensions, design, or manufacturing reduces prediction quality. However, the examined specimen with the different laminate could be classified with an accuracy far beyond a random guess.

5. References

1. Breuer. Commercial aircraft composite technology. Commercial Aircraft Composite Technology. 2016. 1–257 p.
2. Ehrhart, Valeske, Muller, Bockenheimer. Methods for the Quality Assessment of Adhesive Bonded CFRP Structures - A Resumé. AIP Conf Proc. 2010;44(3):1–8.

  doi:10.5075/epfl-298799_978-2-9701614-0-0

3. Brotherhood, Drinkwater, Dixon. The detectability of kissing bonds in adhesive joints using ultrasonic techniques. Ultrasonics. 2003;41(7):521–9.
4. Schmid Fuertes, Kruse, Körwien, Geistbeck. Bonding of CFRP primary aerospace structures - Discussion of the certification boundary conditions and related technology fields addressing the needs for development. Compos Interfaces. 2015;22(8):795–808.
5. Wood, Charlton, Yan. Ultrasonic evaluation of artificial kissing bonds in CFRP composites. e-Journal Nondestruct Test. 2014;19(12):1–10.
6. Chen, Soh, Lee, Tay, Tan. A vibro-acoustic modulation method for the detection of delamination and kissing bond in composites. J Compos Mater. 2016;50(22):3089–104.
7. Nagy. Ultrasonic classification of imperfect interfaces. J Nondestruct Eval. 1992;11(3–4):127–39.
8. Jairaja, Naik. Weak bond effects in adhesively bonded joints between the dissimilar adherends. J Adhes. 2019;00(00):1–23.
9. Ren, Lissenden. Ultrasonic guided wave inspection of adhesive bonds between composite laminates. Int J Adhes Adhes. 2013;45:59–68.
10. Heidarpour, Farahani, Ghabezi. Experimental investigation of the effects of adhesive defects on the single lap joint strength. Int J Adhes Adhes. 2018;80:128–32.
11. Harder, Florian. Localised Weak Bonds in Scarf Bonded CFRP Repairs - A Study of the Size and Location Dependence under Consideration of Hot-Wet Conditioning. 2019;
12. Heilmann. Qualitätskontrolle von Reparaturklebungen an Faserverbundstrukturen durch vollflächige Festigkeitsprüfung. 2020;
13. U.S. Department of Transportation. Federal Aviation Administration, Federal Aviation Administration. Advisory Circular Advisory Circular. Aviation. 2012;1(AC 25.1529-1A):1–2.
14. Pieczonka, Klepka, Martowicz, Staszewski. Nonlinear vibroacoustic wave modulations for structural damage detection: an overview. Opt Eng. 2015;55(1):011005.
15. Lim, Sohn. Necessary conditions for nonlinear ultrasonic modulation generation given a localized fatigue crack in a plate-like structure. Materials (Basel). 2017;10(3).
16. Pieczonka, Klepka, Dziedziech, Broda, Packo, Martowicz, et al. Nonlinear acoustics for structural health monitoring - Classical vs. non-classical approaches. 8th Eur Work Struct Heal Monit EWSHM 2016. 2016;1(July):1–12.
17. Boll, Willmann, Fiedler, Meißner. Weak adhesion detection – Enhancing the analysis of vibroacoustic modulation by machine learning. Compos Struct. 2021;273.
18. Zagrai, Donskoy, Chudnovsky, Golovin. Micro-and macroscale damage detection using the nonlinear acoustic vibro-modulation technique. Res Nondestruct Eval. 2008;19(2):104–28.
19. Dorendorf, Lalkovski, Rutner. Physical explanation for vibro-acoustic modulation due to local and global nonlinearities in a structure and its experimental and numerical validation. J Sound Vib. 2022;116885.
20. Ooijevaar, Rogge, Loendersloot, Warnet, Akkerman, Tinga. Vibro-acoustic modulation–based damage identification in a composite skin–stiffener structure. Struct Heal Monit. 2016;15(4):458–72.
21. Hu, Staszewski, Hu, Jenal, Qin. Crack detection using nonlinear acoustics and piezoceramic transducers-instantaneous amplitude and frequency analysis. Smart Mater Struct. 2010;19(6).
22. Donskoy, Ramezani. Separation of amplitude and frequency modulations in Vibro-Acoustic Modulation Nondestructive Testing Method. 2018;045002:045002.
23. Oppermann, Dorendorf, Rutner, Renner. Nonlinear modulation with low-power sensor networks using undersampling. Struct Heal Monit. 2021;(January).
24. Mook, Willberg, Gabbert, Pohl. Konversion von Lambwellen in CFK-Platten. DACH-Tagung der Dtsch Österreichischen und Schweizerischen Gesellschaft für Zerstürungsfreie Prüfung, 17-1992012 Graz. 2012;BB 136-CD:1–9.

  doi:10.5075/epfl-298799_978-2-9701614-0-0

A COMPUTATIONAL STUDY OF ACOUSTIC EMISSION DUE TO FIBER BREAK AND FIBER MATRIX DEBONDING IN MODEL COMPOSITE

Zeina Hamam[a], Nathalie Godin[a], Claudio Fusco[a], Aurélien Doitrand[a] and Thomas Monnier[b]
a: INSA de Lyon, Univ. Lyon, MATEIS UMR 5510, F-69621 Villeurbanne, France
b: INSA-Lyon, Univ. Lyon, LVA EA677, F-69621 Villeurbanne, France;
nathalie.godin@insa-lyon.fr

Abstract: *This work presents a computational analysis of AE waveforms resulting from fiber break and fiber/matrix debonding in a model composite with a single carbon fiber. In this study, Finite Elements Modeling (FEM) is used to simulate AE signals due to fiber break and fiber/matrix debonding in a model carbon fiber composite. A specimen made of a single carbon fiber and epoxy matrix is tested to experimentally validate the simulated fiber break AE signals. The comparison of the AE signals from a validated fiber break simulation to the AE signals obtained from fiber/matrix debonding (with several models) and fiber break obtained in several media allows to discuss the capability to detect and identify each source.*

Keywords: acoustic emission, composite, modelling, sensor effect, F/M debonding.

1. Introduction

Composite materials exhibit different damage mechanisms such as matrix cracking, fiber break, fiber/matrix debonding and delamination. Real-time monitoring of composite damage may be carried out using Acoustic Emission (AE) [1-2]. A main advantage of AE is the possibility to detect damage in-situ even at an early stage in a nondestructive manner. However, the main difficulty consists in establishing a robust link between the different damage mechanisms and the signals acquired by the sensors. AE signals depend on several distinct factors: the damage source, the specimen geometry, the material properties and the type of sensor and instrumentation. Modeling and numerical simulations of AE appear as a promising way to establish a quantitative link between AE signal and source [3-6]. Giordano *et al.* [3] developed a model for AE wave propagation based on the ray theory, applied in plates with viscoelastic properties. Numerical methods were then used to simulate the sources of AE. Dietzhausen *et al.* [4] investigated the dynamic behavior due to a single glass fiber break in a polymer matrix using FEM and carried out parametric studies with different matrix material behaviors (elastic, nonlinear elastic and elastic-plastic model) and various fiber positions in the thickness of the specimen. Sause *et al.* [6] simulated the AE sources in a composite material using FEM applying a multiscale approach. They also considered the different elements of the acquisition chain, thus enabling a comparison between the signals obtained numerically and experimentally. Such a quantitative comparison cannot be achieved without accounting for the transfer function of the sensor, which can be obtained either from the analytical reciprocity method [7] or from multi-physics simulations reproducing the interface between the sensor and the material [8].

In this study, a specimen made of a single carbon fiber and epoxy matrix [9-10] is used to experimentally obtain the fiber break AE signals and to validate the model. A good agreement in both time and frequency domains between numerical and experimental AE signals from fiber break [9] is obtained. The objective of this study is to extend the proposed model to account for

  doi:10.5075/epfl-298799_978-2-9701614-0-0

both fiber break and fiber/matrix debonding as well as to identify the main parameters that influence the acoustic emission signatures and to discuss the detectability of the sources [10].

2. Experimental procedure and numerical simulation.

2.1 Sample and AE monitoring

The specimen is made of a single long carbon fiber T700 embedded in epoxy matrix. The dimensions of the specimen are shown in Figure 1a. Concerning the AE system, nano30 piezoelectric transducers are used. The distance between each couple of sensors is 40 mm. All recorded signals are filtered in the [20 - 1200] kHz bandwidth. The Single Fiber Fragmentation Test (SFFT) is applied on single fiber composite in axial direction, in order to create fiber breakage.

2.2 Fiber break and fiber/matrix debonding simulation

A 3D FE model of the single fiber specimen is set up using Abaqus™ Standard. The fiber and matrix behaviors are considered linear, elastic and isotropic. The simulated first fiber break is located at the position denoted P2 and 0.5 mm from the top surface (Figure 1c). The nodes lying on the fracture plane are doubled so as to enable the surface separation at this location. Several cases of debonding between the epoxy matrix and the fiber are studied. It should be pointed out that debonding is assumed to occur at the same applied load as the one applied for the fiber break (Figure 1). Figure 2 shows different kinetics of debonding for the model A, B, C and D. The waveforms (out-of-plane velocity v_z) are calculated on several nodes from the epicenter of the source to the boundaries of the gauge length on the top surface (Figure 1c).

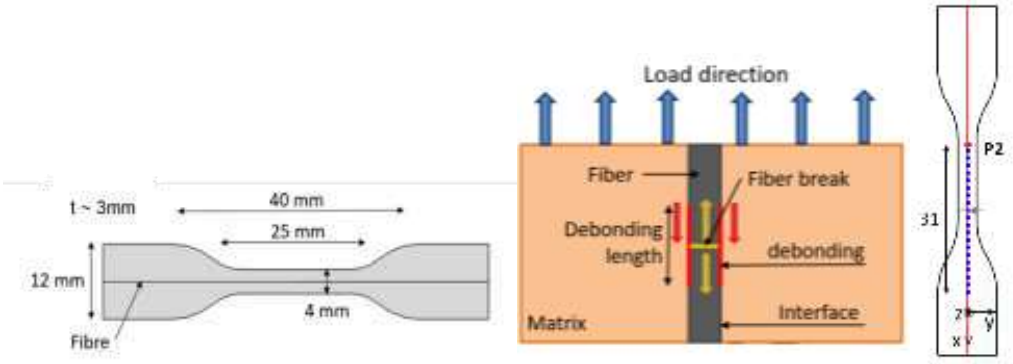

a) b) c)

Figure 1. Schematic representation of the specimen (t : thickness) (b) Position of the simulated fiber break and fiber/matrix debonding, c) position of the source (P2) and position of the simulated signal (blue points).

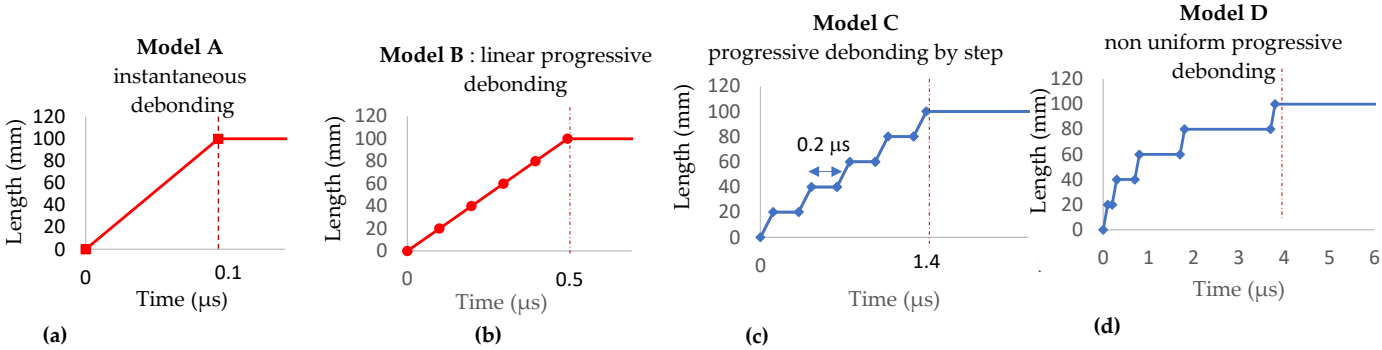

Figure 2. Variation of debonding length as a function of time. (a) Model A: instantaneous debonding, (b) Model B: linear progressive debonding, (c) Model C: uniform progressive debonding by step and (d) Model D: non-uniform progressive debonding by step.

The influence of the surrounding medium on the AE signature due to fiber break is also investigated. The properties of the matrix material are chosen in order to simulate different materials [10] such as polymers (PPMA) or ceramics (SiC or carbone). The values are reported in table 1. The comparison between the different matrices cannot be established based on the same imposed force because of the stiffness differences. Therefore, the imposed force was adapted to ensure the same 2.5% fiber failure strain.

Table 1. Set of material properties used for FE simulation for several surrounding media.

Matrix	Young's modulus (GPa)	Poisson's ratio	Density (kg/m^3)	Rayleigh parameters	
				α_R (s^{-1})	β_R (s)
DGEBD-3DCM	1.41	0.38	1034	50 000	10^{-8}
PMMA	6.2	0.32	1160	1000	10^{-10}
Carbone	35	0.22	2200	10 000	3×10^{-9}
SiC	350	0.2	3150	10 000	4×10^{-10}

2.3 Sensors simulation and extracted descriptors

Two types of sensors are considered in the modeling part: a perfect virtual point-contact sensor and resonant sensors. The details for the sensor modelling are given in [9-10]. The simulated signals are analyzed in time and frequency domain. The main features to be investigated are amplitude or energy, frequency centroid (FC), peak frequency (PF) and the partial powers, denoted PPi. PPi evaluate the frequency distribution in the signal. They represent the percentage of energy contained in separate frequency intervals. For the nano30 sensor, the intervals are the following, PP1 [0–125 kHz], PP2 [125–250 kHz], PP3 [250–450 kHz] and PP4 [450–1200 kHz]. Additionally, the roll-off frequency is also investigated. The interval [0-froll-off] contained 95% of the energy of the complete spectrum.

3. Results and discussion

  doi:10.5075/epfl-298799_978-2-9701614-0-0

The experimental signals and the simulated signals are presented in order to show the validation of the modeling approach before expanding this numerical investigation to different media and different damage mechanisms. Figure 3a shows the direct comparison between experimental signals and simulated signals resulting from fiber break in time domain. Figure 3b shows the evolution of two features (amplitude and frequency centroid) versus the distance of propagation for the experimental data and the simulated data. We observed a good agreement. Accordingly, we can use this simulation to extrapolate the signal recorded in several surrounding media.

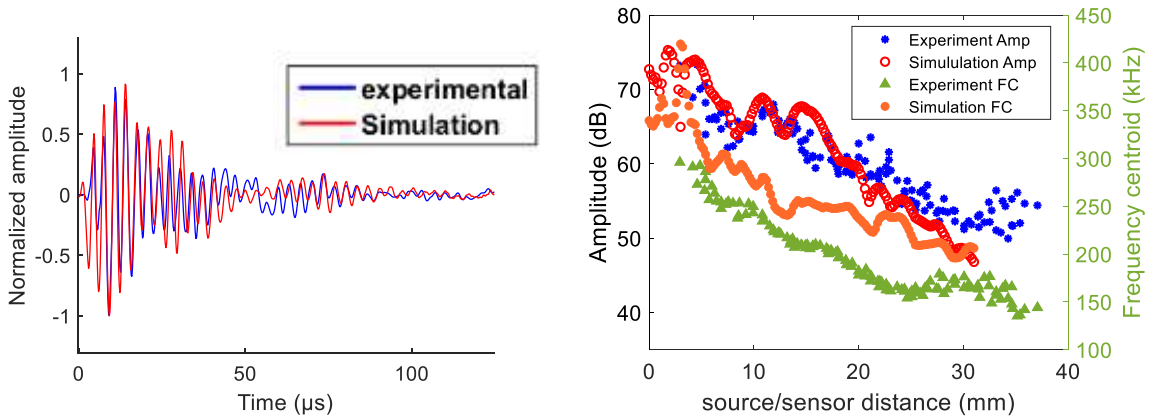

a) *b)*

Figure 3. a) Comparison between simulated and experimental data obtained with nano 30 sensor (distance source/sensor 12 mm) b) *Amplitude and roll-off frequency vs. source/sensor distance for experimental signals and numerical signals with nano30 sensors.*

The effects of the medium on the AE signature of a fiber break are summarized in Figure 4a and Figure 4b. The dispersion modes depend on the mechanical properties of the matrix (e.g. Young's modulus, density). The dispersion modes detected in polymer materials are much more numerous than in a ceramic material over the same frequency range up to 1 MHz. The viscoelastic nature of polymer materials significantly attenuated the frequency compared to ceramic materials. Young's modulus plays an important role in the energy content of the signals. The higher the Young's modulus, the lower the energy content of the signals. This simulation confirmed the impossibility to obtain a universal signature for the same fiber break in several media. Our study shows that it is not possible to generalize the results of a fiber break signature (amplitude and frequency content) to all composite materials. Therefore, it is necessary to treat each medium independently.

We can now use the model to compare the fiber breakage and fiber/matrix debonding. The amplitude of the signals resulting from debonding and recorded with a perfect sensor is much smaller than that from fiber break, even when the size of the debonding was large (Figure 5). On the other hand, instantaneous debonding and fiber break had very similar centroid frequencies with perfect sensor. Debonding also generated high-frequency waves but did not excite the same modes as did fiber break in the near field. Fiber break rather excited the fundamental anti-symmetric mode at low frequencies (Figure 6). For F/M debonding we can notice excited modes with higher order.

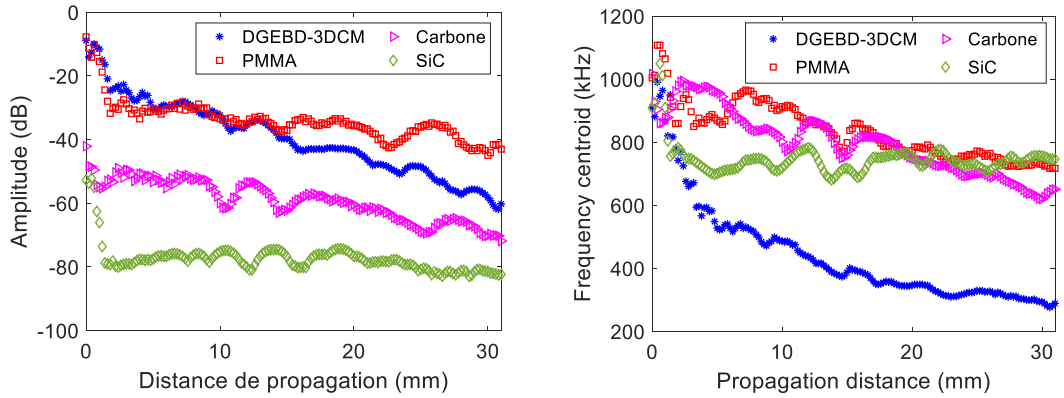

a) b)

Figure. 4. Variation of amplitude a) and frequency centroid b) as a function of distance of propagation for the simulated acoustic emission signature of fiber break in several surrounding media (perfect sensor).

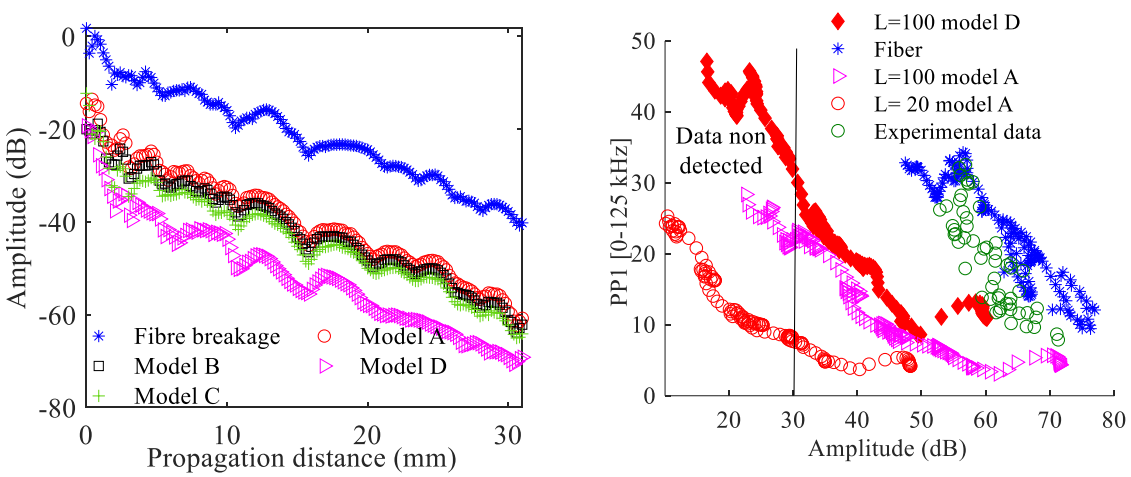

a) b)

Figure 5. a) Evolution of the amplitude versus propagation distance for simulated F/M debonding (L=100 µm) and Fiber break (perfect sensor) b) Variation of Partial Power PP1 [0–125 kHz] as a function of amplitude obtained with nano 30 sensor for several simulated sources. The experimental data are also reported. The acquisition threshold is equal to 30 dB.

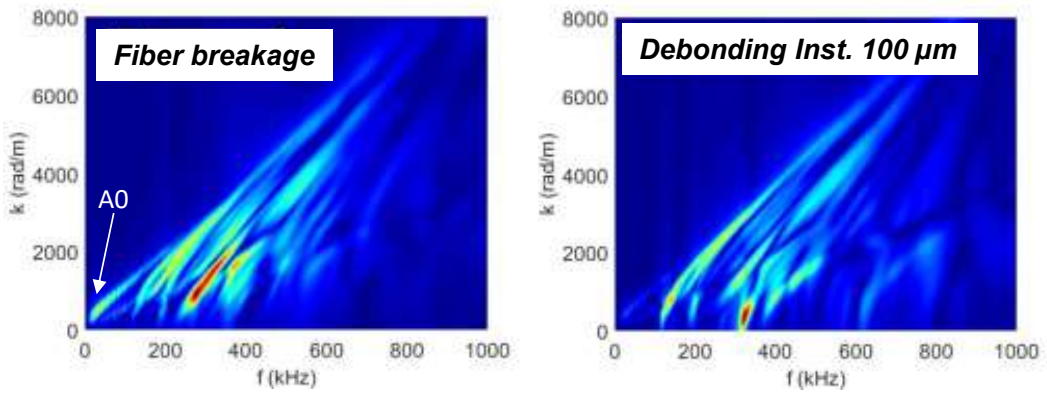

a) *b)*

Figure 6. Simulated dispersion curves (wavenumber k versus frequency f) via 2D-FFT of signals due to a) fiber break, b) debonding model A - L=100 μm and recorded along a straight line on the top surface of numerical specimen without sensor effect.

The acoustic signature for debonding is mostly affected by the debonding conditions (instantaneous debonding or progressive debonding). The signals obtained with progressive debonding have lower amplitude and frequency (Figure 5a). For instantaneous debonding for different lengths, the amplitude is affected more than the frequency content (Figure 5b).

Comparison of the results associated with the perfect virtual point sensor and those associated with the nano30 sensor shows that the differences between the amplitudes of the fiber breakage signals and those associated with the F/M debonding slightly increase. Nevertheless, the response of the nano30 sensor modified the frequency barycenter level compared to the perfect virtual point sensor. The frequency centroid values associated with instantaneous debonding, linear progressive debonding, and step progressive debonding are higher than those of fiber breakage, whereas without the sensor effect, they were almost at the same level.

The combination of the sensor effect and the acquisition threshold makes it possible to define the detectability of the source according to its nature and size. The notion of detectability of the source is rarely considered for the labeling of clusters. Moreover, if we assumed a detection threshold of 30 dB, which is often experimentally chosen, the simulation showed a very low detection of 20 µm debonding as well as 100 µm debonding with Model D. On the other hand, for the fiber break for this propagation distance, the detection rate was 100%. This result confirms that all the damage mechanisms observed from microscopy may not always be detected depending on the position of the sensor. Numerical simulation of AE offers the ability to evaluate whether a damage mechanism occurring in the specimen may be detected by the AE system or not.

Finally, in the last part we consider the combination of the 2 damage modes. We model in the following part these two combined damage modes by considering that fiber breakage and debonding are created simultaneously at the same position. The signals from these two damage modes are calculated over a distance of 31 mm and are then summed for each sensor position. The presented signals are calculated for a virtual perfect sensor. In the amplitude / frequency centroid plane, the combined damage is compared to the debonding damage and the fiber breakage. The evolution of the combined damage and the fiber breakage are superimposed because of the difference in magnitude between the amplitude of the debonding and the fiber break (Figure 7a). The AE signature due to the combined damage is dominated by the one of the fiber breakages. These results show that we cannot distinguish the signals from fiber breakage from those obtained with the two simultaneous damage modes. However, debonding can be distinguished from the fiber breakage in particular by the amplitude and the frequency content. Even if the frequency centroid is equivalent for different damage types, the interfacial debonding can be separated from the other damage modes in an amplitude/partial power plane (Figure 7b).

  doi:10.5075/epfl-298799_978-2-9701614-0-0

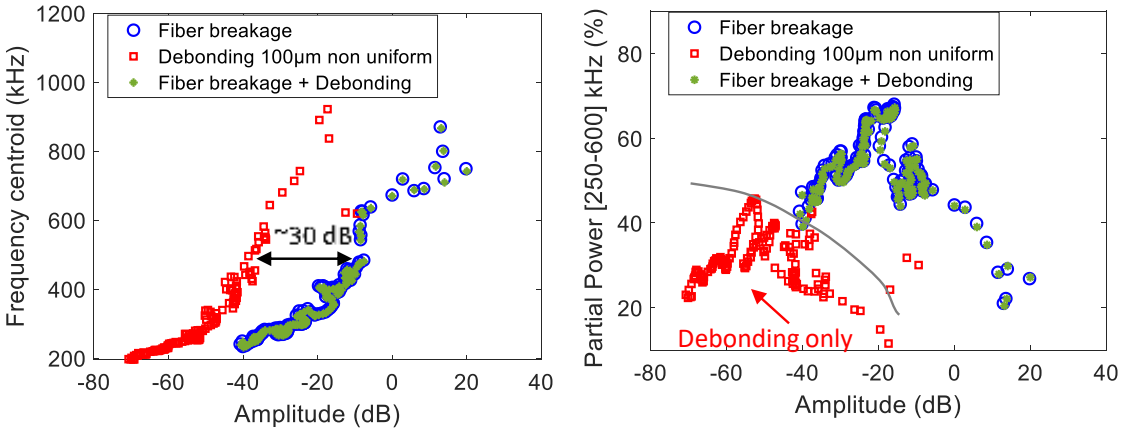

a) b)

Figure 7. a) Frequency centroid versus amplitude, b) PP3 [250-600] kHz versus amplitude. Simulation with perfect sensor for fiber break, fiber/matrix debonding (model D - L = 100 µm) and combined fiber break and debonding.

4. Conclusion

A numerical model of the carbon fiber failure embedded in an epoxy matrix is established. This numerical model is validated by comparison with the experimental results. A parametric study is carried out in order to identify the effect of the propagation medium on the acoustic signature. An extension of this numerical model is also proposed in order to simulate the interfacial fiber / matrix debonding. These numerical AE signals can be used in addition to experimental data to build libraries for life prediction approaches, based on machine learning methods within a PHM (Prognosis Heath Management) approach.

References

1. Sause, M. In Situ Monitoring of Fiber-Reinforced Composites: Theory, Basic Concepts, Methods, and Applications; Springer Series in Materials Science; Springer: Berlin/Heidelberg, Germany, 2016; Volume 242.
2. Godin, N.; Reynaud, P.; Fantozzi, G. Acoustic Emission and Durability of Composites Materials; John Wiley & Sons: Hoboken, NJ, USA, 2018; ISBN: 9781786300195.
3. Giordano, M.; Condelli, L.; Nicolais, L. Acoustic emission wave propagation in a viscoelastic plate. Compos. Sci. Technol. 1999, 59, 1735-1743.
4. Dietzhausen, H.; Dong, M.; Schmauder, S. Numerical simulation of acoustic emission in fiber reinforced polymers. Comput. Mater. Sci. 1998, 13, 23-30.
5. Zelenyak, A.M.; Schorer, N.; Sause, M.G.R. Modeling of ultrasonic wave propagation in composite laminates with realistic discontinuity representation. Ultrasonics 2018, 83, 103-113.
6. Sause, M.G.R.; Horn, S. Simulation of acoustic emission in planar carbon fiber reinforced plastic specimens. J. Nondestruct. Eval. 2010, 29, 123-142.
7. Dia, S.; Monnier, T.; Godin, N.; Zhang, F. Primary Calibration of Acoustic Emission Sensors by the Method of Reciprocity, Theoretical and Experimental Considerations. J. Acoust. Emiss. 2012, 30, 152-166.

  doi:10.5075/epfl-298799_978-2-9701614-0-0

8. Zhang, L.; Yalcinkaya, H.; Ozevim, D. Numerical approach to absolute calibration of piezoelectric acoustic emission sensors using multiphysics simulations. Sens. Actuators A 2017, 256, 12-23.
9. Hamam, Z.; Godin, N.; Fusco, C.; Monnier, T. Modelling of Acoustic Emission Signals Due to Fiber Break in a Model Composite Carbon/Epoxy: Experimental Validation and Parametric Study. Appl. Sci. 2019, 9, 5124.
10. Hamam Z., Godin N., Fusco C., Doitrand A., Monnier T. Acoustic Emission Signal Due to Fiber Break and Fiber Matrix Debonding in Model Composite: A Computational Study. Appl. Sci. 2021, 11, 8406.

  doi:10.5075/epfl-298799_978-2-9701614-0-0

NON-DESTRUCTIVE MEASUREMENT OF CONDUCTIVITY OF ORIENTED SILVER NANOWIRES-POLYDIMETHYLSILOXANE COMPOSITES VIA TERAHERTZ TIME DOMAIN SPECTROSCOPY

Dong-woon, Park[a], Young-min Joo[a], and Hak-sung, Kim[a]

a: Department of Mechanical Convergence Engineering, Hanyang University, 222, Wangsimni-ro, Seongdong-gu, Seoul, Republic of Korea – dongwoon902@gmail.com
b: Institute of Nano Science and Technology, Hanyang University, 222, Wangsimni-ro, Seongdong-gu, Seoul, Republic of Korea

Abstract: *Due to their versatility, stretchable and transparent electrodes with metallic nanowires (NWs) have been used in various electronic fields of wearable and stretchable devices, such as light-emitting diodes and displays. Orienting the AgNWs on the transparent substrate can overcome the limitation of a trade-off between the optical transmittance and electrical conductivity observed at the electrodes of AgNWs with random distribution.*

In this study, the dip-coating method was used to coat and align the AgNWs on polydimethylsiloxane (PDMS) substrates according to a coating speed. From microscopy analysis, it was observed that the AgNWs on the PDMS substrate were well coated and aligned as intended. Additionally, the degree of AgNWs alignment according to coating speed was investigated by measuring birefringence characteristics of AgNWs/PDMS composites using terahertz time-domain spectroscopy. From the measurement result, the distribution of AgNWs on the PDMS substrate can be confirmed using the terahertz inspection method.

Keywords: Terahertz wave; Ag Nanowires-Polydimethylsiloxane composites; conductivity; alignment; Birefringence

1. Introduction

The implementation of thin films with transparent conductive material on flexible substrates has led to the development of highly efficient sensors in recent years [1, 2]. The transparent thin film was used for displays, solar cells, flexible devices, and touch screen panels. Devices with thin film have advantages, including low cost, ease of manufacturing, and choice of substrate material [3, 4].

There are candidates for transparent-electrode materials such as Indium tin oxide (ITO), single/multi-walled carbon nanotubes (CNTs), graphene, and metallic nanowires (NWs) [5, 6, 7]. The ITO widely used for transparent electrodes requires careful fabrication and is vulnerable to cracking due to its brittle nature [8]. CNTs and graphene have advantages for high-performance transparent electrodes. However, it has a trade-off between its optical transparency and resistance property. To improve the conductivity of the electrode, the amount of CNTs and graphene in the electrode should be increased [9]. Metallic NWs are good candidates to be applied as transparent and flexible electrodes since they show high electrical conductivity and mechanical flexibility [10]. The mesh network of NWs can exhibit consistent conductivity even at a 100% stretched substrate [11].

  doi:10.5075/epfl-298799_978-2-9701614-0-0

In recent research, the metallic NWs were coated on the substrate by aligning them to improve the flexible and stretching properties of the transparent conductive electrode [12, 13]. By orienting the metallic NWs, an additional effect can be obtained which overcomes the trade-off between optical transmittance and electrical conductivity in randomly distributed NWs at electrodes [14].

The electrical conductivity of the transparent conductive electrodes is inspected to ensure their performance. The conductivity has been measured using traditional methods such as four-point probe measurement and the eddy current method. These methods are not ineffective for inspecting the reliability of the transparent conductivity electrode in mass production. The four-point probe method requires mechanical contact between probe tips and electrode, which would lead to damage to the electrode [15]. Due to the edge effect as an inherent characteristic of the eddy current, it has a limit on the inspectable area of transparent conductive electrodes on substrates, which would reduce the inspection reliability and the usable area of the transparent conductive electrode [16].

On the other hand, the conductive measurement methods using electro-magnetic waves can inspect the electrical properties of the transparent electrode in a non-contact manner and with high resolution [17]. Among electro-magnetic waves, the terahertz (THz) wave technique has been widely used for the following reasons: The THz waves with a low energy band are harmless to the human body and do not cause electrical and mechanical damage to the electrodes [18]. In addition, it can be used for roll-to-roll production with a fast inspection time. Also, THz waves have the characteristics of penetrating non-metallic materials and reflecting metallic materials.

In this study, a terahertz time domain spectroscopy (THz-TDS) technique was used to investigate the conductivity and degree of distribution of AgNWs on a polydimethylsiloxane (PDMS) substrate as shown in Fig. 1. The relation between the reflection behavior of THz wave and the conductivity of the oriented AgNWs on the PDMS substrate was analyzed according to the coating speed. Additionally, the birefringence characteristics of the AgNWs/PDMS composites were obtained from horizontal and perpendicular measurements with the orientation of the AgNWs. Based on the result, the orienting distribution of the AgNWs was confirmed according to coating condition.

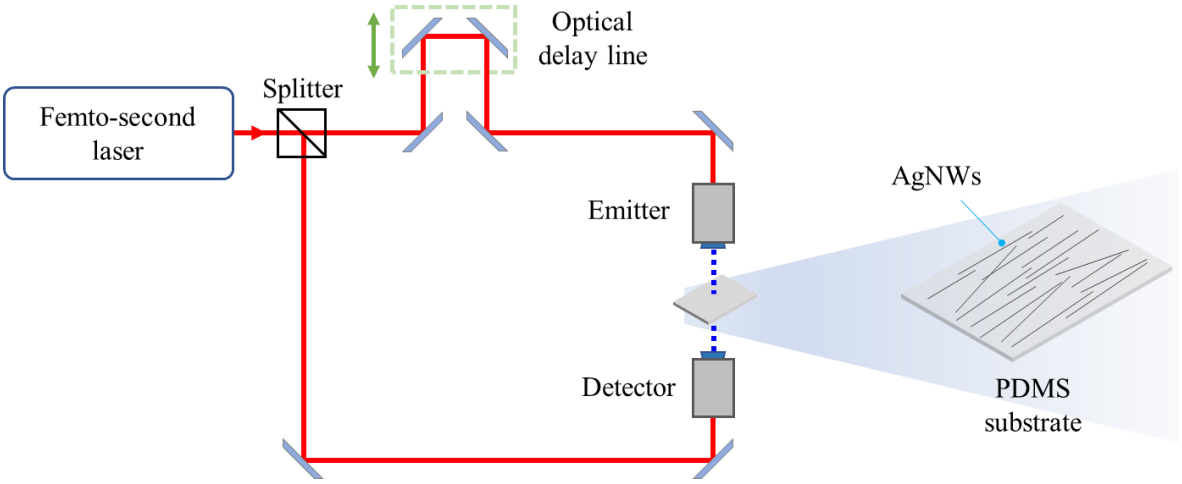

Fig. 1 Schematic for inspecting the transparent electrode with oriented AgNWs via transmission mode terahertz time domain spectroscopy

2. Experiment

2.1 Sample preparation

The fabrication process of the AgNWs/PDMS composites is depicted through four steps as shown in Figure 2. In this study, poly-di-methyl-siloxane (PDMS) solution was used as a substrate. The PDMS solution (SYLGARD 184) was provided by Dow Chemical (USA), while the 0.5wt% silver nanowires-IPA dispersion solution (Flexiowire2020c) was provided by SG Flexio Co., Ltd (South Korea). A mixture (v/v, 10:1) of PDMS solution and hardener was mechanically stirred for 10 min, and poured into molds with 1.0 mm of engrave as shown in Figure 2(a). The curing process was performed for 24 hours at 75 °C. After demolding the PDMS substrate, the PDMS substrate with 1 mm of thickness was attached to a slide glass to prevent the coating of AgNWs on both sides of the substrate as shown in Figure 2(b). After that, the PDMS/slide glass specimen was dipped in the 0.1% AgNWs-IPA dispersion solution and pulled up at 0.5-3.0 mm/s as shown in Figure 2(c). As shown in Figure 2(d), a shear force induced by relative movement between the AgNWs-IPA solution and the substrate allows AgNWs to be coated on the PDMS substrate parallel to the movement.

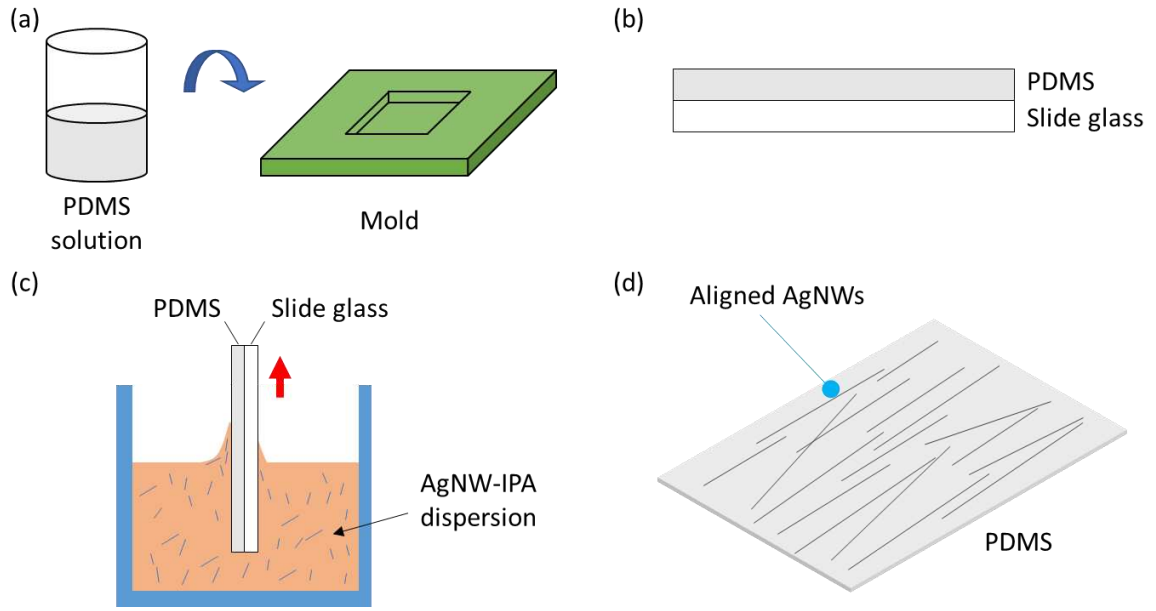

Figure 2. Schematic diagram of fabricating AgNWs film on PDMS substrate

2.2 Characteristics

In this study, a commercial terahertz time domain spectroscopy (THz-TDS) system (FiCO™, Zomega Terahertz Corp.) was used to investigate the optical and electrical properties of the AgNWs/PDMS composites as shown in Figure 1. The THz-TDS system is composed of an emitter module, a detector module, an optical delay line, and a femto-second layer module. The emitted THz signals have a frequency spectrum of 0.1-3.0 THz, in which the signal-to-noise (SNR) ratio is over 60 dB. For measuring THz signals, the transmission mode of the THz system was used where the emitter and detector module were aligned on a line, and the AgNWs/PDMS composites were vertically placed on the THz beam. To measure the birefringence according to alignment of AgNWs, the polarized THz signals were irradiated onto the sample perpendicular and parallel to the orientation of the AgNWs as shown in Figure 3.

  doi:10.5075/epfl-298799_978-2-9701614-0-0

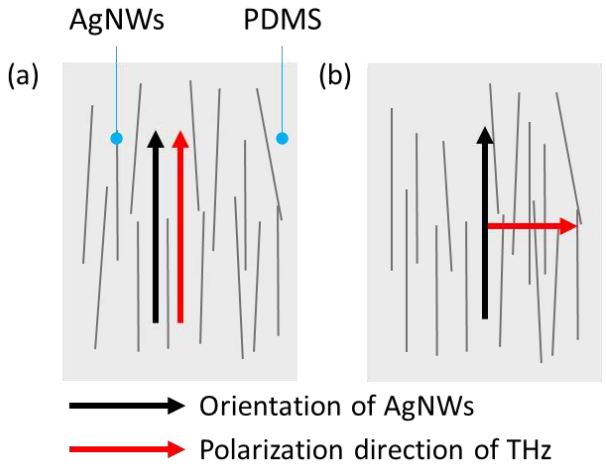

Figure 3. Schematic diagram for birefringence measurement: polarization direction of THz angle (a) perpendicular and (b) parallel to the orientation of the AgNWs

3. Result and Discussion

3.1 Coverage density and sheet resistance

When the PDMS substrate was pulled up, the AgNWs were aligned and coated by the shear force, which was induced by the relative movement between the solution and the substrate. As shown in Figure 4 (a), it can be observed that the AgNWs were well aligned in the direction of coating movement when the coating speed was 0.5 mm/s. The coverage densities of AgNWs on PDMS were measured according to the coating speed of 0.5-3.0 mm/s using microscopy images and image segmentation in MATLAB (R2021b, MathWorks). As shown in Figure 4 (b), it was confirmed that the coverage density was affected by the coating speed because the slow movement of pulling up allows the silver nanowire to attach better to the PDMS substrate. Therefore, as the coating speed was increased, the coverage density was gradually decreased. Accordingly, a high coverage density was found to have a relation with the increase of reflection ratio of terahertz waves and the decrease of the sheet resistances.

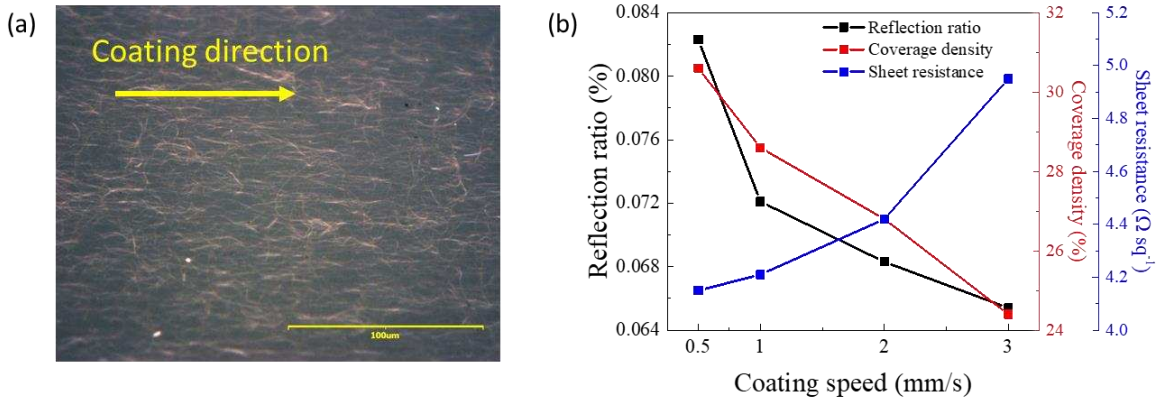

Figure 4. (a) Microscopy image for calculating the coverage density of AgNWs at the coating speed of 0.5 mm/s and (b) Measurement results of the coverage density and sheet resistance of AgNWs/PDMS composites according to the coating speed

  doi:10.5075/epfl-298799_978-2-9701614-0-0

3.2 Effect of alignment distribution on birefringence

In this study, the influence of the AgNWs alignment degree on the optical properties was investigated by birefringence. Figure 5 (a) shows a comparison of THz wave measurement results parallel and perpendicular to the polarization direction of THz waves. The peak time of THz waves parallel to the AgNWs was more delayed than those perpendicular to the AgNWs when the coating speed was 0.5 mm/s. Since the thickness of the sample was the same by measuring the same point, the angle between the polarization of the AgNW and the terahertz wave affected the time delay. The refractive index ($\bar{n}_s(\omega) = n_s - i\kappa_s$) of AgNWs/PDMS composites with a thickness of *d* can be calculated by phase difference ($\varphi(\omega)$), which was extracted from the fast Fourier transformation of reference and sample THz signals as below,

$$n_s(\omega) = \varphi(\omega) \cdot \frac{c}{\omega \cdot d} + 1 \quad (1)$$

where c and ω are the speed of THz waves and the anglur frequency of THz waves, respectively. Figure 5 (b) shows the refractive index extracted from parallel and perpendicular measurements when the coating speed was 0.5 mm/s. Over the frequency range of 0.4–2.0 THz, the parallel refractive index was higher than the perpendicular refractive index. This means that the AgNWs parallel to the polarization direction of THz waves have an effect on THz waves propagating slowly. In other words, the aligned AgNWs/PDMS composites have the characteristics of a birefringence material.

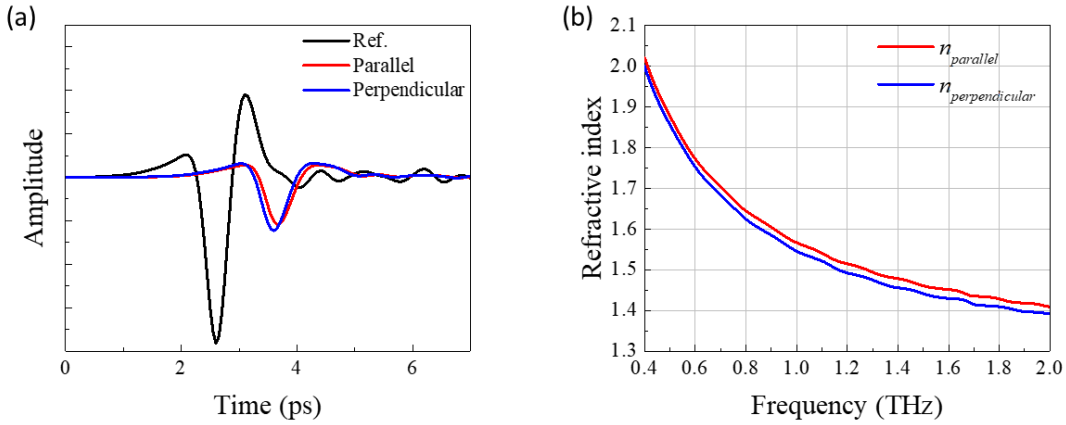

Figure 5. Comparing results of terahertz wave measurements parallel and perpendicular to AgNWs alignment when the coating speed was 0.5 mm/s : (a) THz waveform in time-domain and (b) refractive index in frequency-domain

The birefrigence Δn_s was calculated by difference of refractive index between parallel ($n_{s,par}$) and perperndicular ($n_{s,per}$) measurement as below,

$$\Delta n_s(\omega) = n_{s,par} - n_{s,per} \quad (2)$$

From the study [13], the coating speed of AgNWs would affect the degree of alignment distribution due to the shear force. When the coating speed is slow, the AgNWs are provided sufficient time to be aligned parallel to the coating dicrection. As shown in Table 1, the birefringence phenomenon can be observed at all cases of coating speed and the birefringence phenomenon stand out at slower coating speed due to the well aligned AgNWs.

  doi:10.5075/epfl-298799_978-2-9701614-0-0

Table 1: The calculation results of birefringence characteristics of the AgNWs/PDMS composites

Coating speed (mm/s)	Birefringence (0.8 THz)	Birefringence (1.2 THz)
0.5	0.0201	0.0226
1	0.0107	0.0119
2	0.0074	0.0085
3	0.0036	0.0039

4. Conclusion

In this study, the AgNWs were coated on the PDMS substrate using the dip-coating process to align the AgNWs in the direction. The range of coverage density was about 24–32% according to the coating speed. It was confirmed that the coating speed affects the coverage density of the AgNWs and the resistance of the electrode due to the shear force between the substrate and the solution. Additionally, the degree of AgNWs alignment can be affected by the coating speed. This can be confirmed by the birefringence of AgNWs/PDMS composites using non-destructive evaluation of the pulsed THz system. It is expected that the coverage density related to the electrical conductivity as well as the degree of alignment of the AgNWs can be inspected using THz-TDS. Therefore, THz wave inspection technique can be applied to roll-to-roll manufacturing due to its characteristics including non-contact, fast inspection time, and safety.

5. Acknowledgements

This research was supported by the BK21 FOUR (Fostering Outstanding Universities for Research) project of the National Research Foundation of Korea Grant. This research was also supported by a National Research Foundation of Korea (NRF) grant funded by the Korean Government (MEST) (2021M2E6A1084690, Solution development for non-destructive evaluation challenge based on data science).

6. References

1. Naghdi S, Rhee KY, Hui D, Park SJ. A review of conductive metal nanomaterials as conductive, transparent, and flexible coatings, thin films, and conductive fillers: Different deposition methods and applications. Coatings. 2018; 8(8):278.
2. Abdulhameed A, Wahab NZA, Mohtar MN, Hamidon MN, Shafie S, Halin IA. Methods and applications of electrical conductivity enhancement of materials using carbon nanotubes. Journal of Electronic Materials. 2021; 50(6):3207-21.
3. Sajid S, Elseman AM, Huang H, Ji J, Dou S, Jiang H, Liu X, Wei D, Cui P, Li M. Breakthroughs in NiOx-HTMs towards stable, low-cost and efficient perovskite solar cells. Nano Energy. 2018; 51:408-24.
4. Wang T, Wang M, Fu L, Duan Z, Chen Y, Hou X, Wu Y, Li S, Guo L, Kang R. Enhanced thermal conductivity of polyimide composites with boron nitride nanosheets. Scientific reports. 2018; 8(1):1-8.

  doi:10.5075/epfl-298799_978-2-9701614-0-0

5. Azani MR, Hassanpour A, Torres T. Benefits, problems, and solutions of silver nanowire transparent conductive electrodes in indium tin oxide (ITO)-free flexible solar cells. Advanced Energy Materials. 2020; 10(48):2002536.
6. Wang Y, Kong X, Gao J, Gong M, Lin X, Zhang L, Guo M, Wang D. Customizable Stretchable Transparent Electrodes Based on AgNW/CNT Hybrids via Tailoring Sizes of Building Blocks. ACS Applied Electronic Materials. 2022.
7. Zhu Y, Deng Y, Yi P, Peng L, Lai X, Lin Z. Flexible transparent electrodes based on silver nanowires: Material synthesis, fabrication, performance, and applications. Advanced Materials Technologies. 2019; 4(10):1900413.
8. Bi YG, Liu YF, Zhang XL, Yin D, Wang WQ, Feng J, Sun HB. Ultrathin metal films as the transparent electrode in ITO-free organic optoelectronic devices. Advanced Optical Materials. 2019; 7(6):1800778.
9. Kim B-J, Han S-H, Park J-S. Sheet resistance, transmittance, and chromatic property of CNTs coated with PEDOT: PSS films for transparent electrodes of touch screen panels. Thin Solid Films. 2014; 572:68-72.
10. Han J, Yang J, Gao W, Bai H. Ice-Templated, Large-Area Silver Nanowire Pattern for Flexible Transparent Electrode. Advanced Functional Materials. 2021; 31(16):2010155.
11. Liu H-S, Pan B-C, Liou G-S. Highly transparent AgNW/PDMS stretchable electrodes for elastomeric electrochromic devices. Nanoscale. 2017; 9(7):2633-9.
12. Dong J, Abukhdeir NM, Goldthorpe IA. Simple assembly of long nanowires through substrate stretching. Nanotechnology. 2015; 26(48):485302.
13. Lee J, Sun F, Lee J. Fabrication of large area flexible and highly transparent film by a simple Ag nanowire alignment. Journal of Experimental Nanoscience. 2013; 8(2):130-7.
14. Cho S, Kang S, Pandya A, Shanker R, Khan Z, Lee Y, Park J, Craig SL, Ko H. Large-area cross-aligned silver nanowire electrodes for flexible, transparent, and force-sensitive mechanochromic touch screens. ACS nano. 2017; 11(4):4346-57.
15. Park S-H, Chung W-H, Kim H-S. Non-contact measurement of the electrical conductivity and coverage density of silver nanowires for transparent electrodes using Terahertz spectroscopy. Measurement Science and Technology. 2016; 28(2):025001.
16. Xie Y, Li J, Tao Y, Wang S, Yin W, Xu L. Edge Effect Analysis and Edge Defect Detection of Titanium Alloy Based on Eddy Current Testing. Applied Sciences. 2020; 10(24):8796.
17. Park D-W, Oh G-H, Kim D-J, Kim H-S. In-situ thickness measurement of epoxy molding compound in semiconductor package products using a Terahertz-Time of Flight System. NDT & E International. 2019; 105:11-8.
18. Park D-W, Oh G-H, Kim H-S. Predicting the stacking sequence of E-glass fiber reinforced polymer (GFRP) epoxy composite using terahertz time-domain spectroscopy (THz-TDS) system. Composites Part B: Engineering. 2019; 177:107385.

NON-DESTRUCTIVE TESTING OF CARBON FIBER NONWOVEN USING NOVEL ANISOTROPIC EDDY CURRENT ANALYSIS

Bernhard Leitner[a], Lisa Machuj, Artos Gläser, Frank Manis, Georg Stegschuster[b], Richard Kupke[c]

a: Fraunhofer IGCV – bernhard.leitner@igcv.fraunhofer.de
b: Institut für Textiltechnik Augsburg gemeinnützige GmbH
c: SURAGUS GmbH – Sensors and Instruments

Abstract: *With an exponentially growing Carbon Fiber (CF) market the recycling of those material gains traction quickly. One way is to reuse the reclaimed CF as nonwoven in semi-finished products. In this study an eddy current testing method is investigated for the characterization of the properties of a CF-nonwoven. A novel anisotropic sensor is used to evaluate the orientation of the carbon fibers in the nonwoven. In addition, the fiber areal weight (FAW) and the fiber volume content (FVC) of the CF-nonwoven mixed with thermoplastic fibers (TF) was measured. The measured orientation of the CF in the nonwoven, was validated via mechanical testing after consolidation and showed good correlation. The results obtained by eddy current testing for the FAW measured as nonwoven was deviating 6,5%. Furthermore the CF volume content of the nonwoven containing CF and TF can be determined with about 4,7 % deviation with eddy current testing.*

Keywords: Recycling; Carbon Fibers; Nonwoven; Eddy-current; NDT

1. Introduction

Eddy current testing is widely used in the field of carbon fiber reinforced plastics (CFRP), but only in the case of continuous fiber reinforced materials, which means for CFRPs, they are made of virgin carbon fibers [1-3]. Since the recycling of carbon fibers gains more and more importance due to rising usage of CFRP not only the non-destructive testing of the first lifecycle products is necessary but also the non-destructive testing of second lifecycle products is progressively needed [4,5]. These products made of recycled carbon fibers (rCF) are often made from nonwoven material, which can contain either only rCF as a 100% rCF product or also a thermoplastic component, usually as a thermoplastic fiber [6-8]. A typical process to consolidate hybrid nonwoven material to CFRPs is hot pressing. A 100% rCF nonwoven is normally infiltrated by a thermoset resin and then hardened in a RTM process or similar ones like wet compression moulding. The aim of this study is to show the potential of eddy current testing for CF-nonwoven in terms of measuring the fiber areal weight, the fiber volume content and the orientation of the carbon fibers in the nonwoven. Those three characteristics of a nonwoven are very important for the resulting mechanical properties of the consolidated CFRP. Measuring and regulating the three parameters during nonwoven production has a huge potential to increase the quality of the semi-finished product. In this study the feasibility of this method is investigated by using a novel anisotropic eddy current sensor at lab scale.

  doi:10.5075/epfl-298799_978-2-9701614-0-0

2. Materials and methods

The eddy current device used for the main measurements of the presented article is EddyCus® CF lab 4040 with the related software EddyCus® CF lab Control by the company SURAGUS GmbH, Dresden, Germany. The device includes two coils in a transmission arrangement. The coils themselves are oriented, meaning focused, with higher sensitivity along the x axis. This enables the determination of fiber orientation. The applied frequency is located between 5 and 30 MHz. The detected eddy current signal can be translated as the relative amount of carbon fibers. The eddy current measurement was conducted at, 4x4 grid, in total 16 points per nonwoven specimen. At each of these locations, four angles were measured. The eddy current signal in 0°, 45°, 90° and 135°. This was done by manual rotating the specimen between the sensors. For each of these points the orientation of the fibers was calculated by dividing the 0°-value by the 90°-value. This leads to the orientation ratio, often called MD/CD-ratio (machine direction/cross direction). The MD/CD-ratio is commonly used to describe nonwoven orientation. Besides calculating the orientation-value at each point, the mean value from all four measured angles was calculated to get a reliable value for the amount of carbon fiber in the nonwoven at each measured spot. Furthermore, to verify the orientation measurement via eddy current testing, a mechanical characterization via four-point bending of CFRP-plates was conducted.

For pre-tests a virgin carbon-fiber uni-directional (UD)-textile from the company SGL Carbon, Meitingen, Germany, with the tradename Udo UD CS 300/300 was used with an areal weight of 300 g/m². The carbon fiber nonwoven used in this study were produced by Institut für Textiltechnik Augsburg gGmbH (ITA Augsburg), Augsburg, Germany. The materials were made of 100 % carbon fiber as well as mixtures of carbon fibers with thermoplastic fibers as either polyamide 6 (PA6) fibers or polyethylenterephtalate (PET) fibers. Therefore the carbon fiber CarboNXT chopped 60.000 NP5 R from the company Mitsubishi Chemical Advanced Materials, Wischhafen, Germany, was used, which origins from cut-off waste and has the mechanical properties of a high tenacity carbon fiber. These cut-off CFs were used for the 100% rCF-nonwoven and hybrid nonwovens containing polyamide 6 P300 from EMS Chemie AG, Dormat/Ens, Switzerland, or PET T290 by the Trevira GmbH, Bobingen, Germany. For the PET containing nonwoven the rCF-volume content was varied between 20 % and 30 % with three different types of nonwoven containing either 20%, 25% or 30% carbon fibers. For orientation measurements a hybrid nonwoven made with the pyrolysed carbon fiber Carbiso C SM45R by ELG Carbon Fiber Ltd., Coseley, UK and P300 PA6-fibers was used. The rCF volume content of this used hybrid nonwoven was 30%. The used thermoplastic fibers are shown in *Table 1*.

Table 1. Thermoplastic fibers and their textile properties.

Type	Length [mm]	Fineness [dtex]	Crimp [B/cm]	Code
P300	40	1.7	8	P300
TREVIRA® 290	60	6.7	4	T290

  doi:10.5075/epfl-298799_978-2-9701614-0-0

3. Results

3.1 Pre-Tests with UD-Material

First the sensitivity of the novel eddy current sensor on orientated carbon fibers is investigated, by measuring unidirectional fabrics. The measurement setup is shown in *Figure 1* on the left side. On the right side, the dependency of the measured eddy current signal on the fiber areal weight is shown.

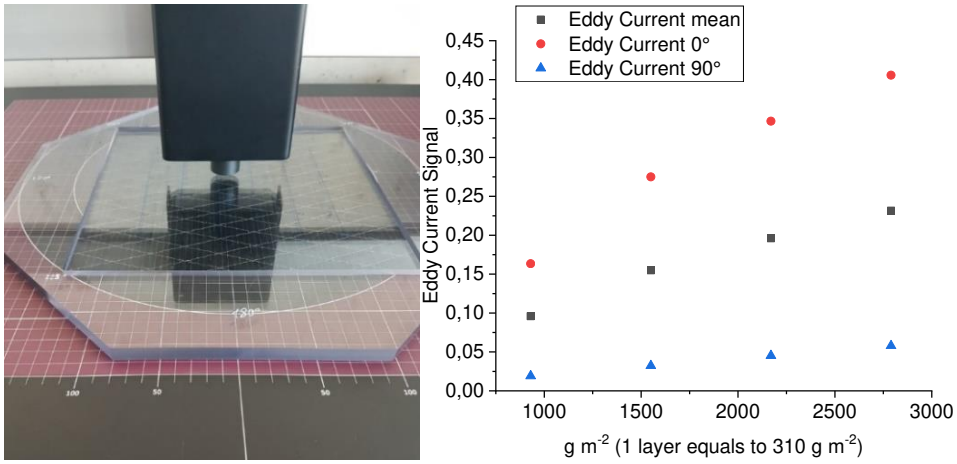

Figure 1. Measurements of carbon fiber UD-layers show that the sensor is sensitive to the fiber orientation and to the fiber areal weight.

Figure 2 shows the polar-diagram of the UD-fabric on the left side and a polar diagram of a slightly orientated nonwoven made of rCF and PA6-fibers. By the measurement of different amounts of UD-fabric layers it is demonstrated that on one hand the eddy current signal increases with more carbon fibers and on the other hand the eddy current value in 0° orientation of the sensor to the UD layers is highest and in 90° orientation lowest. This shows the potential of the sensor to measure the carbon fiber orientation.

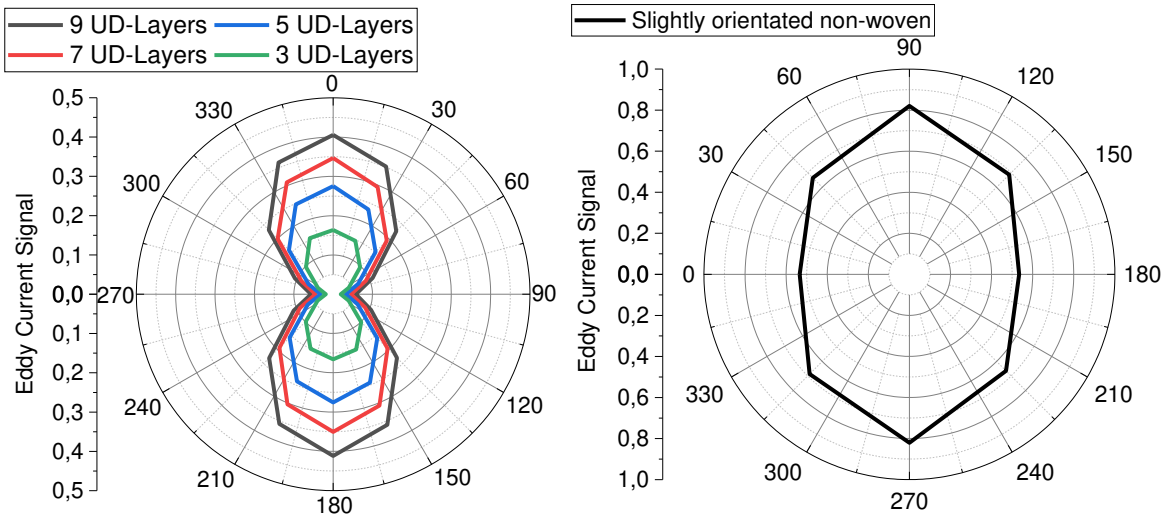

Figure 2. On the left an eddy-current orientation measurement at UD-layers of a carbon fiber fabric is shown. On the right an orientation measurement of a slightly orientated hybrid-nonwoven made of rCF and PA6-fibers.

When measuring a slightly orientated nonwoven, it can be noticed that the CF-orientation in 0° is higher than in 90° orientation. Measuring the orientation of carbon fibers and the carbon fiber areal weight by this eddy current sensor in nonwovens are further investigated in the following chapters.

3.2 Fiber areal weight determination of 100% rCF-nonwoven (cut-off waste)

To verify the usability of the sensor for determining the carbon fiber areal weight of nonwoven for e.g. quality control in a textile production line the following investigation is conducted. There are nonwoven made of 100% rCF tested with areal weights ranging from 150 to 750 g/m². A linear model is used for creating an equation to determine the fiber areal weight of samples by using the measured eddy current signal. This can be seen in Figure 3. It was found that the fiber areal weight of test samples can be determined with an accuracy of on average 6,5 % by using the linear model. The single values are visible in *Table 1*.

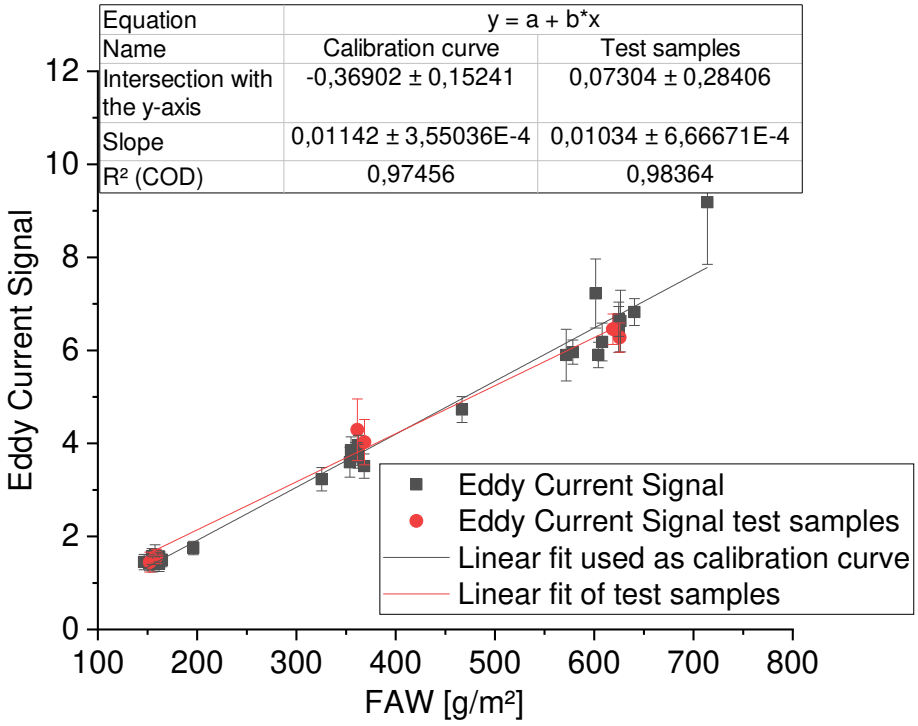

Figure 3. Dependency of eddy current signal on the carbon fiber areal weight of nonwoven.

Table 1. Weighed values, calculated values and values for the deviation of the used test samples.

ID number	Weighed fiber areal weight [g/m²]	Calculated fiber areal weight [g/m²]	Deviation [%]
1	152,3	159,3	4,6
2	159,2	170,0	6,8
3	361,4	409,0	13,2
4	368,6	385,6	4,6
5	618,8	598,7	3,2
6	625,6	582,9	6,8

Differences in the weighed and calculated values might be caused by inhomogeneities of the nonwoven material, overall there is a good correlation between weighed and calculated values.

3.3 Carbon fiber volume content determination of mixed nonwoven made of rCF (cut-off waste) and PET

Often there are hybrid nonwove made of carbon fibers and plastic fibers and a quality control of those during production is necessary. Therefore here the carbon fiber volume content (FVC) is evaluated and measured with the eddy current sensor. After the eddy current measurement nonwovens are pyrolysed to determine the amount of rCF and the FAW of the rCF in the hybrid nonwoven. The pyrolysis basically burns of the PET and leave the CF blank. In order to obtain the FVC, one simply has to weigh the nonwoven before and the remaining CF after pyrolysis. By converting the fiber areal weight of PET and rCF with the help of the densities of both materials like shown in Eq. 1 the fiber volume (FV) per m² is obtained. By dividing the FV per m² for rCF by the FV per m² of both rCF and PET the FVC is obtained.

$$FV\ per\ m^2 = \frac{FAW}{\rho} \tag{1}$$

The next *Figure 4* shows the fiber areal weight of the nonwoven after pyrolysis, so the FAW of the CF in the nonwoven. This means by using the shown calibration curve the fiber volume content of the carbon fibers can be determined just by measuring the eddy-current signal of the nonwoven and their weight, containing both, thermoplastic and carbon fibers, the results are shown in *Table 2*, the calculated values are obtained with the help of the calibration curve and compared to the values obtained by pyrolysis. The deviation of the calculated rCF-volume content from the rCF-volume content obtained by pyrolysis of the test samples is in average 4,7%.

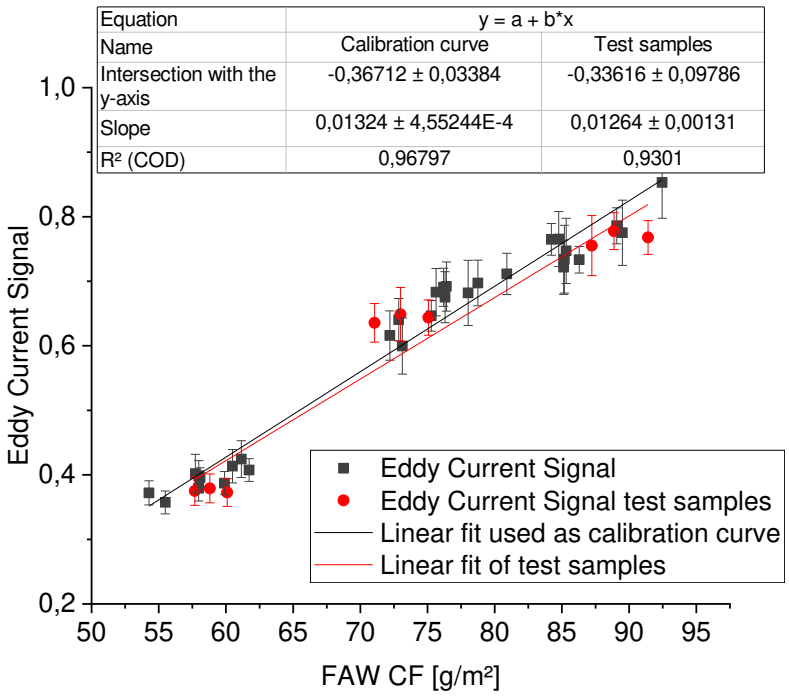

Figure 4. Dependency of eddy current signal of the carbon fiber areal weight of hybrid nonwoven.

Table 2: Determined FVC values by pyrolysis, calculated values FVC by eddy-current measurement and values for the deviation of the used test samples.

ID num-ber	FV per m²-PET obtained by pyrolysis [cm³/m²]	FV per m²-rCF obtained by pyrolysis [cm³/m²]	FV per m²-PET obtained by eddy current testing [cm³/m²]	FV per m²-rCF obtained by eddy current testing [cm³/m²]	FVC-CF obtained by pyrolysis [%]	FVC-CF obtained by eddy current testing [%]	Deviation [%]
1	142,33	32,41	143,51	31,49	18,55	18,00	2,97
2	144,18	33,03	145,95	31,66	18,64	17,83	4,37
3	139,48	33,76	142,54	31,39	19,49	18,05	7,40
4	114,91	39,92	111,52	42,55	25,78	27,62	7,11
5	121,51	42,17	120,58	42,89	25,77	26,24	1,83
6	116,43	41,01	113,72	43,11	26,05	27,49	5,52
7	114,06	49,93	115,80	48,58	30,45	29,55	2,94
8	112,02	51,35	116,14	48,16	31,43	29,31	6,75
9	111,34	49,00	113,11	47,62	30,56	29,63	3,05

The measurement of the FVC of the rCF in the hybrid nonwoven with the eddy-current sensor is very promising and shows just slight deviation from the value obtained by pyrolysis and weighing of the samples.

3.4 Measurement of carbon fiber orientation in CFRPs made of rCF and PA6

To verify the measurement of the carbon fiber orientation in the rCF-PA6 nonwoven by eddy current testing two different CFRP plates were hot pressed and mechanically characterized via four-point bending tests. Besides mechanical tests, the unpressed nonwoven and the hot pressed CFRP were characterized with the eddy-current sensor. All tests are conducted at the same spot on the nonwoven and respectively the CFRP, in order to ensure that both methods are used at identical locations. The mechanical tests are conducted at octagon-shaped samples shown in *Figure 5*. They were only bend within the linear elastic part of the bending curve, to ensure the parts integrity for all four directions (0°, 45°, 90° and 135°), so that the youngs modulus ca be used for the evaluation of the bending tests. This means that the octagon samples are not tested until failure. The anisotropic plate 1 and the isotropic plate 2 are made of 10 nonwoven samples for each plate, which are hot-pressed to make a 2 mm thick consolidated CFRP. The only difference between both plates is, that the slightly orientated nonwoven is always stacked in the same direction for plate 1 but for plate 2 every second layer is rotated by 90 degrees to achieve an isotropic CFRP.

Figure 5 : Octagon test sample (left), stacking order for plate 1 and 2 (middle and right).

The results show that the orientation of the fibers in the nonwoven is correctly predicted by the eddy current sensor. The measurement of the orientation of the fibers in the unpressed condition with eddy current sensor is very similar to the mechanically determined orientation of the fibers, see *Figure 6* and *Figure 7*. The eddy current measurement at the pressed CRRPs shows nevertheless the same orientation direction for the carbon fibers compared to the mechanical investigation but with a smaller ratio. The reason could be the pressed form, which results in more electrical connections points of the same amount of fibers. Hence, the electrical resistance for hot-pressed parts is generally lower than for unpressed nonwovens. Hence, this leads to a lower MD/CD-ratio. The isotropic plate shows that the eddy current measurement of both plate and nonwoven is very similar to the mechanical characterization.

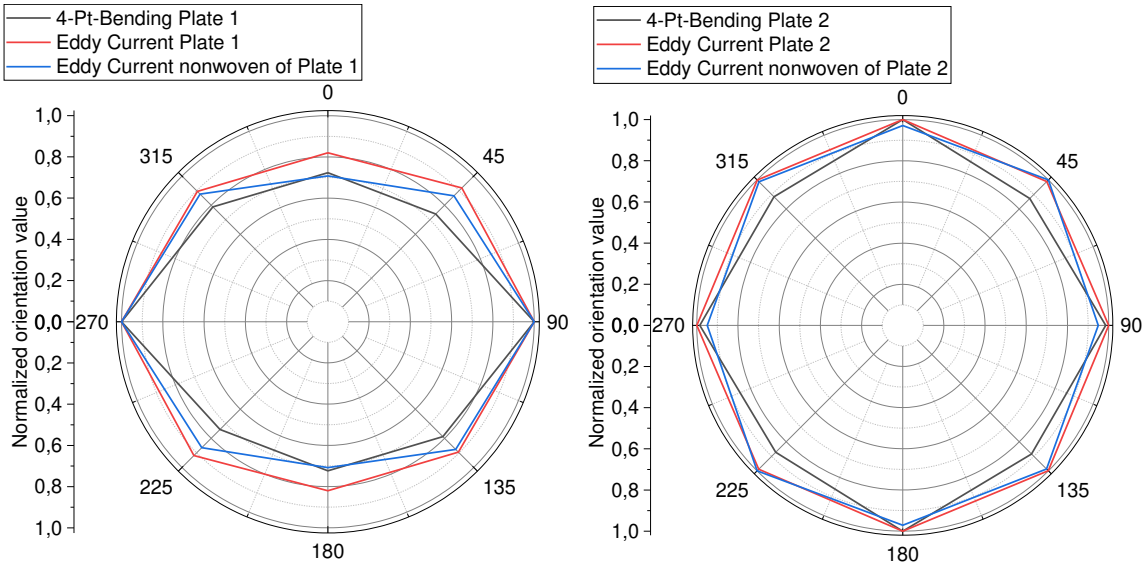

Figure 6 : Polar diagram of orientation measurements determined by bending test and eddy current test of plate 1 (left) and plate 2 (right)

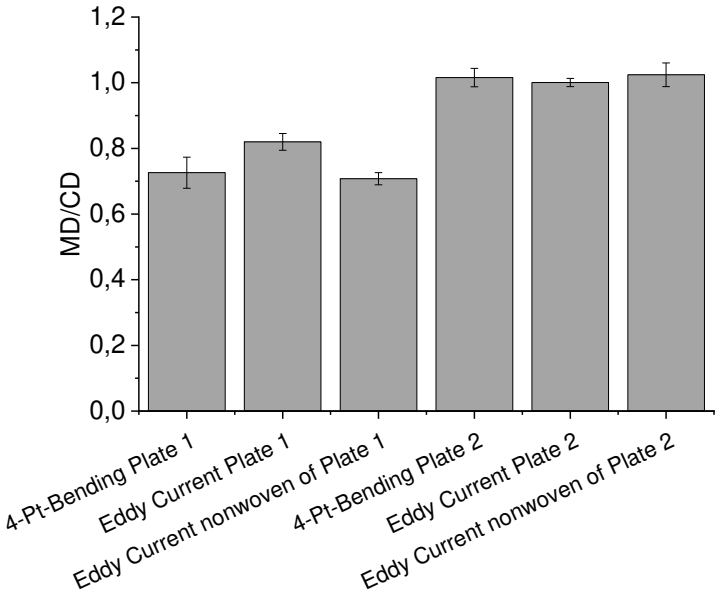

Figure 7 : MD/CD ratios of plate 1 (left) and plate 2 (right) determined by bending test and eddy current test.

  doi:10.5075/epfl-298799_978-2-9701614-0-0

4. Conclusion

The results demonstrate the potential of the eddy current characterization for rCF-nonwoven as semi-finished products. The fiber areal weight and the fiber volume content can be measured with low deviation from the real value, when using the SURAGUS eddy current sensor of the company Suragus GmbH, Dresden. As a next step the measurement of both values should be done during production of a nonwoven. For example a carding or wet-laying process. Also, the measurement of the fiber orientation in the nonwoven and in the CFRP was confirmed via mechanical testing. Being able to measure the orientation – a key quality parameter - in early production steps allows to influence and monitor this values. The orientation plays a significant role for the mechanical performance of CFRP made from semi-finished rCF products.

Acknowledgements

The results were obtained from the project "IZI-Direct - Innovative non-destructive method for inline characterization and quality assurance of discontinuous recycled carbon fiber semi-finished products" (funding code 033RK057B), which is funded by the Federal Ministry of Education and Research (BMBF) of Germany.

5. References

1. Heuer, H.; Schulze, M.; Pooch, M.; Gäbler, S.; Nocke, A.; Bardl, G. et al. Review on quality assurance along the CFRP value chain – Non-destructive testing of fabrics, preforms and CFRP by HF radio wave techniques. Composites Part B: Engineering 2015 ; 77:494-501.
2. Khan, Adnan Maroof; Bardl, Georg; Nocke, Andreas; Cherif, Chokri. Quality analysis of 2D and 3D-draped carbon preforms by eddy current scanning. Composites Part B: Engineering 2019; 176 :107-110.
3. Mook, Gerhard; Lange, Rolf; Koeser, Ole. Non-destructive characterisation of carbon-fiber-reinforced plastics by means of eddy-currents. Composites Science and Technology 2001; 61:865-873.
4. Bledzki AK, Seidlitz H, Goracy K, Urbaniak M, Rösch JJ. Recycling of Carbon Fiber Reinforced Composite Polymers-Review-Part 1: Volume of Production, Recycling Technologies, Legislative Aspects. Polymers 2021; 13:300.
5. Bledzki AK, Seidlitz H, Krenz J, Goracy K, Urbaniak M, Rösch JJ. Recycling of Carbon Fiber Reinforced Composite Polymers-Review-Part 2: Recovery and Application of Recycled Carbon Fibers. Polymers 2020; 12:3003.
6. Wölling J, Schmieg M, Manis F, Drechsler K. Nonwovens from Recycled Carbon Fibers – Comparison of Processing Technologies. Procedia CIRP 2017; 66:271–6.
7. Manis F, Stegschuster G, Wölling J, Schlichter S. Influences on Textile and Mechanical Properties of Recycled Carbon Fiber Nonwovens Produced by Carding. J. Compos. Sci. 2021; 5:209.
8. Sauer M, Feil J, Manis F, Betz T, Drechsler K. Thermoplastic Multi-Material Nonwovens from Recycled Carbon Fibers Using Wet-Laying Technology. KEM 2019; 809:210–6.

  doi:10.5075/epfl-298799_978-2-9701614-0-0

SELF-POWERED STRUCTURAL HEALTH MONITORING OF NOVEL THERMOELECTRIC ENERGY HARVESTING GFRP COMPOSITES

Lampros Koutsotolis[a], George Karalis[a], Kyriaki Tsirka[a], Alkiviadis S. Paipetis[a]

a: Composite and Smart Materials Laboratory, Department of Materials Science and Engineering, University of Ioannina, GR-45110, Ioannina, Greece
l.koutsotolis@uoi.gr

Abstract: *In this study a new approach regarding Structural Health Monitoring (SHM) of composite materials is investigated since a Thermoelectric Generator (TEG) is utilized as a strain/damage sensor. To this end p- and n-dopped CNT inks were printed with the appropriate architecture onto a glass fiber substrate, that was then incorporated as the top ply lamina of a Glass Fiber Reinforced Polymer (GFRP) laminate. Specimens were extracted and subsequently tested under static and dynamic loading, while concurrently their electrical resistance change was measured. Identical mechanical tests were carried out, this time however the generated electrical current was measured. Results revealed that both monitored parameters, namely the resistance and the current, provide information about the structural integrity of the composite, thus making a step towards autonomous SHM*

Keywords: Energy harvesting; SHM; Sensing

1. Introduction

During the last decades, the use of composite materials has rapidly increased in various critical applications, replacing metals to a certain degree. Composites, offer higher specific strength, superior fatigue behavior, and tailorable mechanical properties, hence making them attractive in specific industries such as aerospace. [1] However, their complex nature in combination with the multiplicity of damage mechanisms that they display [2] calls for the development of reliable methods to monitor their structural integrity. SHM in comparison with traditional Non-Destructive Evaluation (NDE) methods is capable of providing continuous and real-time information about the structural health of materials [3]. The goal of such a monitoring system is to make structures safer, while in parallel minimizing their maintenance cost [4].

With the ever-increasing use of composite materials, along with the increasingly significant energy consumption problem it is of great importance to develop appropriate SHM techniques, requiring neither external sensors nor an external power supply to function. A well-established method to detect and characterize damage in electrically conductive composites is the Electrical Resistance Change Method (ERCM). Considering that an inherent property of the material is measured, the ERCM falls under the scope of self-sensing. When monitoring the resistance change, strain manifests itself as a linear increase, while resistance increases in a stepwise manner when damage occurs. [5-7].

The ERCM can also be applied to appropriate modified GFRPs that are normally not conductive but can be rendered as such with the addition of electrically conductive nonofillers, such as Carbon NanoTubes (CNTs) [8-9]. Alternatively, a conductive path printed or deposited onto the material could serve as a strain and damage sensor [10-11].

  doi:10.5075/epfl-298799_978-2-9701614-0-0

Apart from SHM another significant problem that modern constructions face is that of energy consumption, as large amounts of energy is dissipated as heat. A possible solution to this may provide the thermoelectric (TE) effect, where temperature difference is directly converted into electric voltage. A composite endowed with the functionality of thermal energy harvesting could alleviate the energy loss problem, making as a consequence structures environmentally and economically more viable. Several recent studies have reported on such multifunctional composites [12-14]. Regarding the materials comprising the TEGs there are many options such as PEDOT [15], but more recently CNTs, being inherently multifunctional, were employed in order to fabricate generators [16-18]. When combining the functionalities of SHM and energy harvesting that the CNTs bestow upon composites with their primary load-bearing purpose smart of multifunctional materials emerge.

Taking the above into consideration, the scope of this study was to utilize the two aforementioned functionalities that specifically engineered composites can offer. Therefore, dopped CNT inks were printed with the appropriate architecture onto the surface of glass fiber fabrics. Subsequently these fabrics were laminated as the top-ply lamina of cross-ply composites. Afterwards tensile specimens were cut from the plates. The TEG-enabled GFRP specimens were subjected to tensile and fatigue testing. Firstly, the efficiency of the TEGs was measured at specific load cycle intervals, in order to assess damage accumulation and its subsequent effect in energy harvesting. Then the whole process took place on-line, meaning that a real-time and continuous monitoring of the TEGs' behavior was carried out. This was implemented in two distinct ways. The first one was by employing the ERCM and measuring the change in the electrical resistance of the TEGs. The second manner, and here lies the innovation of this study, was by measuring the electrical current generated by the TEGs upon being exposed to a constant temperature difference. Thereby the procedure was zero-biased, since no external voltage was applied but the material itself provided the electrical current that was to be measured.

2. Experimental Section

2.1 TEG printing and laminate manufacturing

The materials and process to prepare the p-and n-doped CNTs thermoelectric inks can be found in [19]. After preparation the inks were appropriately deposited by hand onto a unidirectional glass fiber substrate obtained from Fibermax (Greece). The printing process took place on a hot plate for the inks to dry and was assisted with a vinyl mask. The architecture of the TEG involved alternating p- and n-type thermoelectric legs, electrically connected in series and thermally in parallel. This architecture is described in detail in [18] and has the potential of high-power outputs since the contact resistance between thermoelectric elements is minimized [17]. Then the TEGs were incorporated into cross-ply GFRP laminates with $[90/0]_{2s}$ layup. The fabrics bearing the TEGs were then used as a top ply lamina, so that the mechanical performance of the composites would not be affected [20]. The manufacturing of the composites was carried out by hand using the Araldite LY5052 resin system acquired from Huntsman Advanced Materials (Switzerland). After layup the laminates were positioned in to a hot press and cured for 24 hours at 25 ^{o}C, followed by a 4 hour post-curing at 100 ^{o}C under 3 MPa applied pressure. Tensile and fatigue specimens of 240x35x2 mm^3 were extracted from the laminate on which GFRP tabs were attached. The specimens tested at fatigue loading had their edges polished. As electrical measurements were afterwards to be carried out cooper wires were attached to the two edges

  doi:10.5075/epfl-298799_978-2-9701614-0-0

of the TEGs with the RS Pro conductive silver paste (UK). The TEG printing and composites manufacturing procedure is depicted in Figure 1.

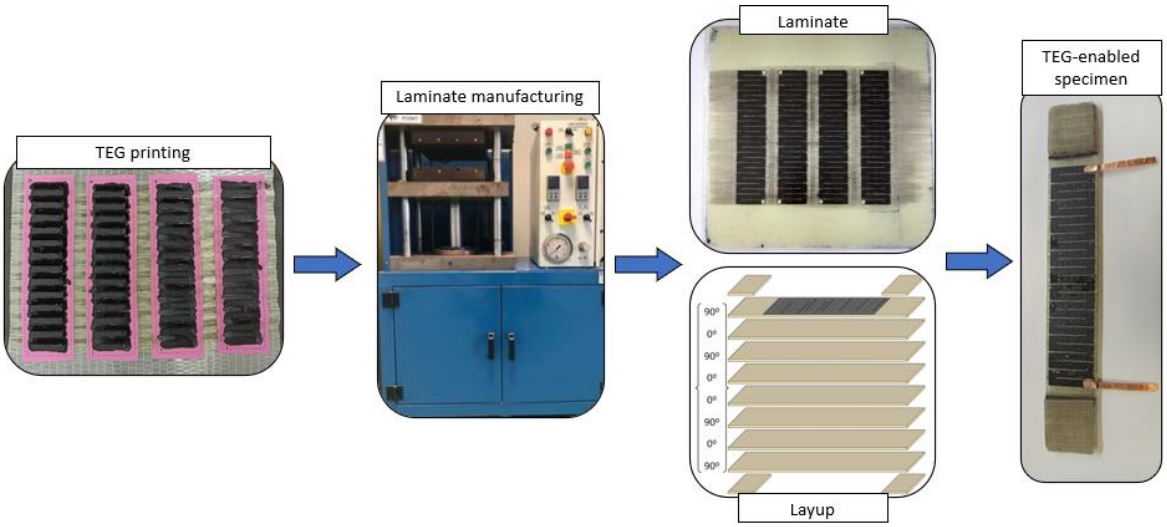

Figure 1: TEG printing and specimen manufacturing process.

2.2 Mechanical testing and TEG output degradation

Monotonic tensile testing was conducted according to ASTM D3039 on an Instron 8800 Universal Testing Machine equipped with a 100kN loadcell to define the ultimate tensile strength σ_t, the fracture strain ε_t and the elastic modulus. Five specimens were used, whereas testing was performed at a constant displacement rate of 2 mm/min.

Tension-tension fatigue loading was conducted on the same testing machine as per ASTM D3479. The load ratio R was set at 0.1 and a frequency of 5 Hz was used. Two different scenarios were investigated. More precisely, in the first one a TEG-enabled specimen was subjected to low stress, i.e., 20% of σ_t so as not to induce mechanical degradation, while the second specimen was tested under a stress equal to the 40% of σ_t. The thermoelectric characteristics of the specimens, namely the internal resistance R_{TEG}, the produced voltage V_{TEG}, and the generated current I_{SC} were measured prior to testing under an applied temperature difference of 75 ^oC. Every 5000 cycles the specimens were unmounted from the testing machine and had their output characteristics measured again. This was done in order to assess the degradation that dynamic loading induces to the thermoelectric performance of the material.

To carry out the thermoelectric measurements a longitudinal side of the TEG was placed onto a hot plate operating at 100 ^oC, while the remaining part was positioned on a cool metal block to achieve the desired temperature difference of 75 ^oC. For the electrical measurements the Agilent 34401A6½ digital multimeter was utilized, employing the two-probe method.

2.3 On-line monitoring

In order to exploit the printed TEG to achieve stain and damage sensing, electrical measurements were carried out during mechanical testing. This was achieved with two different approaches. Initially the ERCM was applied, and the internal resistance was measured. The second approach took it a step further as the generated current was measured. In this way, zero-biased measurements were performed since the sensor was powered up by the harvested

  doi:10.5075/epfl-298799_978-2-9701614-0-0

energy. To perform this a metallic thermal heater was attached onto a longitudinal side of the TEG and was thermally activated via the Joule effect. For online monitoring the specimens were subjected to tensile and fatigue loading of 3 Hz and $\sigma = 0.6\sigma_t$, while their electrical characteristics were measured in real time. The whole procedure is summarized in Figure 2.

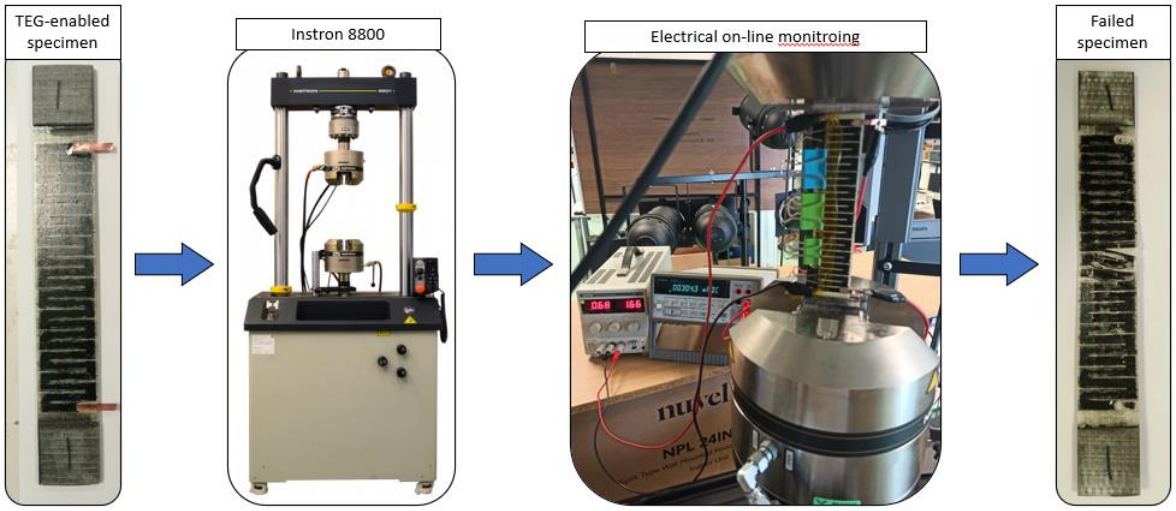

Figure 2: Schematic diagram of electrical SHM performed on TEG-enabled specimens.

3. Results and Discussion

3.1 Mechanical testing and TEG output degradation

Specimens failed at 418.57 ± 6.25 MPa, corresponding to a 3.45 ± 0.04 % strain, while the elastic modulus of the material was 17.0 ± 0.1 GPa. The effect that the application of dynamic mechanical loading had on the output characteristic of the specimens is presented in Table 1.

Table 1: Thermoelectric output performance at specific fatigue cycle intervals.

Stress level	Cycles	R_{TEG} (Ohm)	V_{TEG} (mV)	I_{SC} (μA)
20%	0	200	41	258
	5000	200	42	258
	10000	198	42	258
	15000	198	41	257
	20000	192	38	220
	25000	195	37.5	222
40%	0	203	44.5	274
	5000	204	44	251
	10000	206	37.9	217
	15000	215	40.1	223
	15977	∞	0	0

It is observed that testing at 20% of σ_t did not result in specimen failure up to the 25000 cycles, while the application of a 40% stress level led to complete failure of the specimen at 15977 cycles. As cracks due to fatigue occur and propagate [21] the TE performance is adversely affected. In more detail, the material degradation resulted in an increase in the internal resistance R_{TEG}. Contrariwise both the generated voltage V_{TEG} and the current I_{SC} decreased with

  doi:10.5075/epfl-298799_978-2-9701614-0-0

damage accumulation. These findings can be clearly distinguished in the loading scenario of 40%, where the material ultimately failed. Such behavior was on the contrary barely observed with the low stress level, where the R_{TEG} remained practically constant, and the output characteristics decreased only slightly. This was to be expected since the applied stress remained low enough to induce only small damage if any at all. With ultimate failure of the tested specimen came a total disruption of the conductive path, therefore their electrical resistance reached an infinite value, while the current dropped to zero.

3.1 On-line monitoring

Figure 3 depicts the stress-strain curve of the specimen under tension in conjunction with the relative resistance change $\Delta R/R_o$ of the TEG. From the diagram it becomes clear that the printed TEG has the potential to act as a strain/damage sensor to fulfil SHM purposes. This is feasible due to the relative high conductivity of the printed path. Furthermore, because the TEG was incorporated into the composite it followed its deformation. As a result, electrical resistance provided information about both the strain and the damage that occurred. As the specimen was deformed due to tensile loading and its length increased, the length of the conductive path also increased, resulting in a rise in electrical resistance. At the moment of fracture, the conductive path was disrupted resulting in an abrupt resistance increase [5, 9]. It is mentioned here that the information about the structural integrity refer only to the damage developed in the outer lamina since the measured conductive path was located there. Therefore, damage occurring into the material such as delaminations could not be detected. From the joined diagram it can be deduced that prior to final failure the conductive path experienced no other damage.

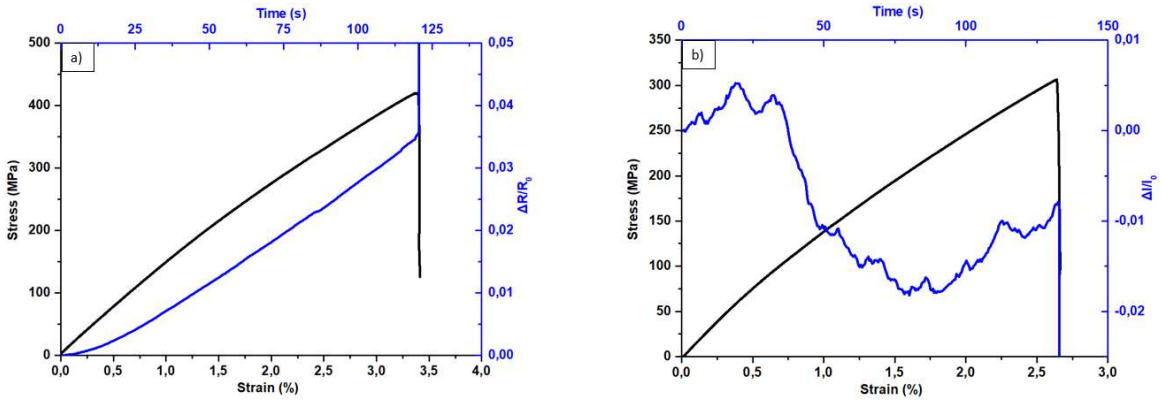

Figure 3: Stress-strain curves of the TEG-enabled specimen during tensile testing coupled with electrical measurements. a) Relative resistance change. b) Relative change of the generated current.

In Figure 3 b the stress-strain curve is plotted together with the relative change of the generated electrical current $\Delta I/I_o$. The expected behavior would be a linear decrease in current, being inversely proportional to the R_{TEG}. Additionnaly it should be further affected by the structural condition of the TEG due to accumulated damage. Moreover, the generated voltage strongly depends on the applied temperature difference [13]. Therefore, even minor temperature fluctuations can lead to current changes larger than the ones deriving from the change of the electrical resistance. In Figure 3b a decrease in the relative current change can be partially recognized. Only an area within the middle of the diagram decreases, while the two outer parts are characterized by an increase of the generated current. This owns probably to the fluctuation

  doi:10.5075/epfl-298799_978-2-9701614-0-0

of the thermal difference generating the current. Consequently, only a part of the curve reliably reflects the structural condition of the material. The small fluctuations that are present in the curve are attributed to the random small oscillations of the applied ΔT. It is noted that these temperature oscillations could not be avoided, since the TEG was heated in real time with an externally applied heater the temperature of which was not strictly controlled. Finally, at specimen breakage the generated current dropped to zero as the conductive path existed no more. Therefore, with this approach it was possible to detect the final failure of the material via a zero-biased electrical method. The strain monitoring on the other hand is as discussed not so reliable due to high sensitivity on temperature difference.

The electrical response of the TEG during fatigue testing is depicted in Figure 4. The diagram in Figure 4a illustrates the overall change in resistance throughout the test, namely from the initial preloading stage to the final failure. The load level of 60% was chosen in order to allow for a relative slow damage accumulation that could be easily monitored. Initially, a sharp linear increase in resistance was observed, corresponding to the deformation of the material during preloading. Then as the specimen was subjected to dynamic loading the resistance showed a linear increase with a much smaller slope than the preloading area. This small but steady increase in resistance is related to microdamage accumulation and stiffness loss [7, 21]. As previously, final failure was manifested by a stepwise increase in resistance at the end of the curve. Looking at the magnified image in Figure 4a, it is seen that the electrical resistance closely follows the deformation of the specimen. In summary, the relative change in electrical resistance during dynamic loading proved a sensitive and reliable index of the material's structural integrity, providing information about strain, damage accumulation and final failure.

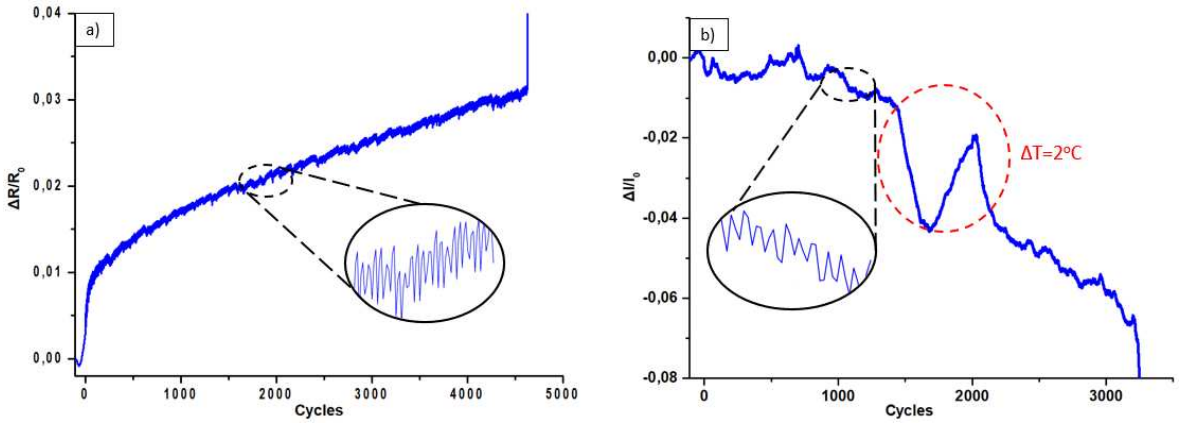

Figure 4: Electrical behavior of the TEG-enabled specimen during fatigue loading. a) Relative resistance change. b) Relative change of the generated current.

Figure 4 b illustrates the relative change in the generated electric current $\Delta I/I_o$ by means of thermal energy harvesting during fatigue loading. As seen, the generated current gradually decreased, displaying an almost linear behavior. This reduction corresponded not only to the increase in the internal resistance (Figure a) but to a possible drop of the TEG's efficiency as well. Both of these phenomena were owing to the microdamage accumulation during fatigue. The zoomed part of the curve shows that the values of the current followed the oscillations of the applied stress, thus serve as strain sensor. It can also be noticed that the current values deviate from this behavior at an area around 1500 cycles, marked with a red cycle and accompanied by the indication ΔT = 2 °C, where a distinguishable oscillation exists. This temperature difference

  doi:10.5075/epfl-298799_978-2-9701614-0-0

originated from turning off and then on again the air-condition, while the room temperature was measured. This was purposely done in order to confirm the previous findings. It is therefore concluded that even a small change in the applied ΔT has a stronger effect on the generated current than the changes in resistance due to damage. This means that for TEG to operate as a self-powered SHM sensor, a constant applied temperature difference is of outmost importance.

4. Conclusion

The objective of this work was to explore the possibility of utilizing a TEG incorporated into a composite material to achieve SHM. For this reason, initially the ERCM was employed, and the internal resistance of the printed TEG was measured online. Results that arose from both static and dynamic loading showed that the relative change in the internal resistance is directly related to its structural integrity. The strain of the material was demonstrated as a linear increase in the resistance while final failure of the material was accompanied by an abrupt increase. The next step, being the novelty of this study was to monitor the generated current instead of the electric resistance to accomplish strain and damage sensing. In this case, deformation was manifested as a decrease in the generated current whereas at final failure the current became zero. Although, recordings of electrical resistance provided reliable results, the utilization of the current as a strain/damage index was strongly dependent on external factors, namely the applied temperature difference, the effect of which is dominant. Therefore, a stable ΔT would be a prerequisite in order to implement this approach to real structures. However, it offers the significant advantage that the energy harvested via the thermoelectric effect was used to power up the method, thus laying the foundations to future autonomous SHM.

Acknowledgements

This research has been co-financed by the European Union and Greek national funds through the EPAnEK 2014-2020 Operational Programme Competitiveness, Entrepreneurship and Innovation, under the call RESEARCH – CREATE – INNOVATE (project code: T1EDK 03480).

References

1. Towsyfan H, Biguri A, Boardman R, Blumensath T. Successes and challenges in non-destructive testing of aircraft composite structures. Chinese J Aeronaut. 2020;33(3):771–91.
2. Clyne TW, Hull D. An Introduction to Composite Materials. An Introduction to Composite Materials. 2019.
3. García Márquez FP, Peco Chacón AM. A review of non-destructive testing on wind turbines blades. Renew Energy. 2020;161:998–1010.
4. Crane RL. Introduction to structural health monitoring. Compr Compos Mater II. 2017;(March):355–7.
5. Schulte K, Baron C. Load and failure analyses of CFRP laminates by means of electrical resistivity measurements. 1989;36:63–76.
6. Todoroki A, Yoshida J. Electrical resistance change of unidirectional CFRP due to applied load. JSME Int Journal, Ser A Solid Mech Mater Eng. 2004;47(3):357–64.
7. Vavouliotis A, Paipetis A, Kostopoulos V. On the fatigue life prediction of CFRP laminates using the Electrical Resistance Change method. Compos Sci Technol. 2011;71(5):630–42.
8. Thostenson ET, Chou TW. Carbon nanotube networks: Sensing of distributed strain and damage for life prediction and self healing. Adv Mater. 2006;18(21):2837–41.

  doi:10.5075/epfl-298799_978-2-9701614-0-0

9. Grammatikos SA, Gkikas G, Paipetis A. Monitoring strain and damage in multi-phase composite materials using electrical resistance methods. Smart Sens Phenomena, Technol Networks, Syst 2011. 2011;7982:79820K.
10. Kang I, Schulz MJ, Kim JH, Shanov V, Shi D. A carbon nanotube strain sensor for structural health monitoring. Smart Mater Struct. 2006;15(3):737–48.
11. Rein MD, Breuer O, Wagner HD. Sensors and sensitivity: Carbon nanotube buckypaper films as strain sensing devices. Compos Sci Technol. 2011;71(3):373–81.
12. Karalis G, Mytafides CK, Tzounis L, Paipetis AS, Barkoula NM. An approach toward the realization of a through-thickness glass fiber/epoxy thermoelectric generator. Materials (Basel). 2021;14(9).
13. Karalis G, Tzounis L, Lambrou E, Gergidis LN, Paipetis AS. A carbon fiber thermoelectric generator integrated as a lamina within an 8-ply laminate epoxy composite: Efficient thermal energy harvesting by advanced structural materials. Appl Energy. 2019;253(July).
14. Chung DDL. Thermoelectric polymer-matrix structural and nonstructural composite materials. Adv Ind Eng Polym Res. 2018;1(1):61–5.
15. Zhang K, Qiu J, Wang S. Thermoelectric properties of PEDOT nanowire/PEDOT hybrids. Nanoscale. 2016;8(15):8033–41.
16. Choi J, Jung Y, Dun C, Park KT, Gordon MP, Haas K, et al. High-Performance, Wearable Thermoelectric Generator Based on a Highly Aligned Carbon Nanotube Sheet. ACS Appl Energy Mater. 2020;3(1):1199–206.
17. Wu B, Guo Y, Hou C, Zhang Q, Li Y, Wang H. From carbon nanotubes to highly adaptive and flexible high-performance thermoelectric generators. Nano Energy. 2021;89(June).
18. Mytafides CK, Tzounis L, Karalis G, Formanek P, Paipetis AS. High-Power All-Carbon Fully Printed and Wearable SWCNT-Based Organic Thermoelectric Generator. ACS Appl Mater Interfaces. 2021;13(9):11151–65.
19. Karalis G, Tzounis L, Tsirka K, Mytafides CK, Voudouris Itskaras A, Liebscher M, et al. Advanced Glass Fiber Polymer Composite Laminate Operating as a Thermoelectric Generator: A Structural Device for Micropower Generation and Potential Large-Scale Thermal Energy Harvesting. ACS Appl Mater Interfaces. 2021;13(20):24138–53.
20. Karalis G, Tsirka K, Tzounis L, Mytafides C, Koutsotolis L, Paipetis AS. Epoxy/glass fiber nanostructured p- and n-type thermoelectric enabled model composite interphases. Appl Sci. 2020;10(15).
21. Carraro PA, Maragoni L, Quaresimin M. Characterisation and analysis of transverse crack-induced delamination in cross-ply composite laminates under fatigue loadings. Int J Fatigue. 2019;129(August).

  doi:10.5075/epfl-298799_978-2-9701614-0-0

NON-DESTRUCTIVE DETECTION OF MICRO DELAMINATION IN GLASS FIBER REINFORCED POLYMER COMPOSITES USING TERAHERTZ WAVE WITH CONVOLUTION NEURAL NETWORK

Heon-Su, Kim[a], Dong-Woon, Park[a], Sang-Il Kim[a], and Hak-Sung, Kim[a,b]

a: Department of Mechanical Convergence Engineering, Hanyang University, 222, Wangsimni-ro, Seongdong-gu, Seoul, Republic of Korea – khsu0212@gmail.com
b: Institute of Nano Science and Technology, Hanyang University, 222, Wangsimni-ro, Seongdong-gu, Seoul, Republic of Korea

Abstract: *The algorithm for detecting micro-delamination inside the glass fiber reinforced polymer (GFRP) was studied by training the terahertz (THz) signal based on the convolutional neural network (CNN). THz signals with respect to the thickness of delamination in GFRP specimens were obtained through the reflection mode of the Terahertz Time-Domain Spectroscopy (THz-TDS) system. Peaks of the THz signal reflected from the top surface,* micro-*delamination, and the bottom surface of the GFRP specimens were classified, respectively. Then, after transforming 1D-THz signals to 2D-spectrograms through Short-Term Fourier Transform (STFT), the THz signals were trained through a CNN. Based on this, the probability map that can predict the thickness of micro-delamination from the THz signal was derived. As a result, the thickness of micro-delamination could be successfully predicted.*

Keywords: Composites; Delamination; Non-destructive Evaluation; Terahertz; Convolutional Neural Network

1. Introduction

Glass fiber reinforced polymer (GFRP) has characteristics of light weight and superior mechanical properties, making them a popular material in the fields of automobiles, aviation, space, and so on [1]. The structures of composite materials have been suffered from delamination and debonding interfaces, which can deteriorate their strength and stiffness. Many studies have been conducted to inspect the delamination in the GFRP composites via non-destructive evaluation (NDE) methods [2,3]. Among them, the NDE method using terahertz waves is effective for inspecting the delamination of the GFRP composites due to their characteristics [4,5]; The THz waves can straightly transmit non-metallic materials without a medium such as a gel. Additionally, the THz waves are non-ionizing and harmless to the human body. The delamination can be analyzed using the separately detected signals at each interface. However, since the wavelength of the THz signal is in the millimeter range, superposition between signals occurs in micro-scale delamination. This makes it difficult to determine the depth and thickness of the micro delamination in the GFRP composites.

  doi:10.5075/epfl-298799_978-2-9701614-0-0

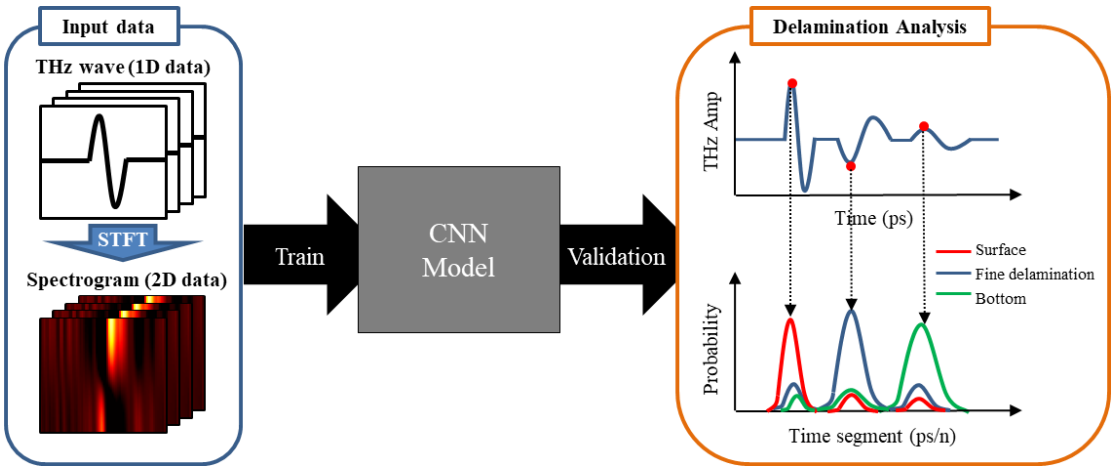

Figure 1. Schematic of delamination analysis through CNN based THz signal learning

By analyzing the superposed THz signals, a technique for detecting the depth and thickness of micro delamination in the GFRP composites was developed through the convolutional neural network (CNN) algorithm as shown in Figure 1. First, THz signals measured at each delamination in GFRP composites were measured through the reflection mode of terahertz time-domain spectroscopy (THz-TDS). The peak times of the THz signal reflected from the surface, fine delamination, and the bottom of the GFRP composites were labeled for CNN training. By using short-term Fourier transform (STFT), the 1D-type THz signals were transformed into 2D images. Then, the images were learned through the CNN algorithm which can classify the THz signals into the trained labels. To verify the CNN algorithm, the THz signals were segmented every 0.055 ps with 12 ps intervals for CNN classification. From the CNN classification results, a probability distribution of trained labels for each segmented signal was derived. As a result, the THz signals according to the depth and thickness of micro delamination can be successfully identified.

2. Experiments

2.1 Sample preparation

The GFRP was manufactured by laminating 4 sheets of UD prepreg (UGN160B, SK Chemical) in one direction and then using the vacuum bagging method. The laminated prepregs were subjected to a pressure of 0.6 MPa and cured under the temperature condition as shown in Figure 2(a). The thickness of the fabricated GFRP plate was 0.5 mm. To measure the THz superposed signal generated from micro-delamination, thin films of 25, 50, 75, 110 um thickness were inserted between two GFRP plates as shown in Figure 2(b).

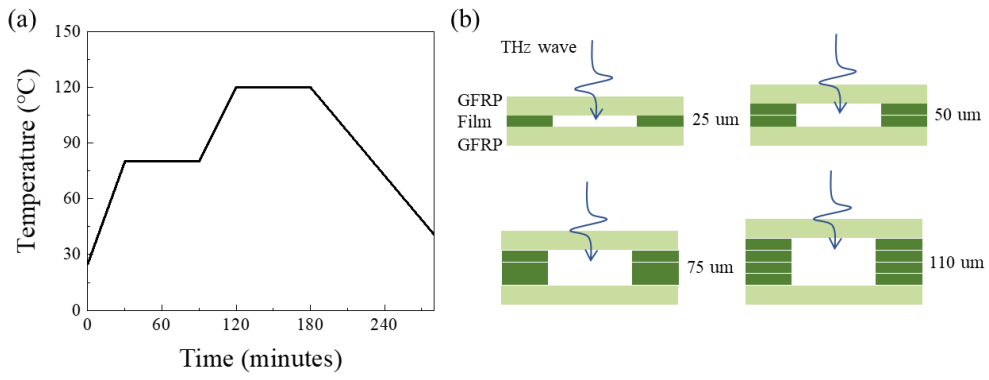

  doi:10.5075/epfl-298799_978-2-9701614-0-0

Figure 2. (a) Curing temperature of the GFRP prepreg (b) The GFRP specimens with micro-delamination (25, 50, 75, 110 um)

2.2 THz-TDS system

A terahertz time-domain spectroscopy (THz-TDS) system was used for signal measurement in micro-delamination of the GFRP. The THz-TDS system used in this study (FiCOTM, Zomega Terahertz Corp.) consists of a femtosecond laser module, a THz emitter module, a THz detector module, and optical instruments. In addition, it has a frequency range of 0.1-3.0 THz, a frequency resolution of 11 GHz, a time resolution of 55 fs, and a signal-to-noise ratio (SNR) of 60 dB. When measuring the THz signal with respect to the size of the micro-delamination inside the GFRP, the signal was measured using a reflection mode having an incident angle of zero degrees.

2.3 Convolutional Neural Network

For the CNN structure, a simple structure consisting of two convolution, max-pooling layers, and one dense layer was used. The rectified linear unit (ReLU) activation function was applied to each layer, and SoftMax was applied to the output layer. Since there are many classes to be classified, categorical cross-entropy, which enables multiple classifications, was applied as a loss function. For learning, 100 data for each micro-delamination were measured. The class for learning was divided into peaks reflected from the top surface, from the bottom surface, and peaks superposed from the micro-delamination. The classes of the superposed signals were divided into thicknesses of 25, 50, 75, and 110 um. Also, a class of noise signals was added to increase the learning accuracy.

For learning, the THz signals were segmented into 12 ps ranges based on the peak positions of each class. In addition, signals above 1 THz were filtered to improve learning accuracy. Then, a 2D spectrogram was derived through short-term Fourier transform (STFT) for a 1D THz signal since the CNN model is trained based on 2D image data. The STFT equation is as follows.

$$\boldsymbol{STFT}\{\boldsymbol{x}(\boldsymbol{t})\}(\boldsymbol{\tau},\boldsymbol{\omega}) \equiv \boldsymbol{X}(\boldsymbol{\tau},\boldsymbol{\omega}) = \int_{-\infty}^{\infty} \boldsymbol{x}(\boldsymbol{t})\boldsymbol{w}(\boldsymbol{t}-\boldsymbol{\tau})\boldsymbol{e}^{-\boldsymbol{i}\boldsymbol{\omega}\boldsymbol{t}}\boldsymbol{dt} \quad (1)$$

where $w(\tau)$ is the Hann window function, $x(t)$ is the signal to be transformed, $\mathrm{X}(\tau, \omega)$ is the Fourier transform of $x(t)w(t-\tau)$, ω is the frequency, and t, τ are the time axis. The function to be transformed ($x(t)$) is multiplied by a window function $w(\tau)$ which is non-zero for only a short period of time. The Fourier transform of the resulting signal is taken as the window is slid along the time axis, resulting in a two-dimensional representation of the signal. As a result, the CNN model was trained using the transformed spectrograms.

When classifying the signal, a window of the same range as the data used for learning (12 ps) was created, and the window was shifted by 0.055 ps from the beginning of the THz signal. Then, the probability map for the THz signal was derived by extracting the class probability of the signal corresponding to each window position. Since truncated forms of signals are generated as the window moves, the CNN model was trained by separately adding classes of truncated signals to reduce the error due to untrained data.

3. Results and Discussions

3.1 THz signals with respect to micro-delamination

  doi:10.5075/epfl-298799_978-2-9701614-0-0

Figure 3(a) shows the measurement results of THz signals with respect to the thickness of the micro-delamination for the GFRP. The first peaks in the signals are the fastest detected peak among the THz detection signal, which represents the signal reflected from the top surface of the specimen. It can be confirmed that the peaks were detected more quickly as the thickness of the micro-delamination increased as shown in Figure 3(b). This is because the optical path of the THz signal is different since there is a difference in the height of the entire specimens as much as the difference in the thickness of the micro-delamination. On the other hand, it was confirmed that the peak positions were the same regardless of the thickness of the micro-delamination in the signals reflected from the bottom surface as shown in Figure 3(d). This is because, although there is a difference in the height of the specimens, the overall optical paths of the signals reflected from the bottom are the same. Figure 3(c) shows the THz superposed signals reflected at the micro-delamination, and it was confirmed that the shapes of the THz superposed signals for each thickness of the micro-delamination were different. Among them, several trends can be confirmed. As the thickness of the micro-delamination increased, the intensity of the THz superposed signal gradually increased. Also, the peak of the superposed signals with thicker delamination was detected later. This is because the degree of superposition gradually decreased as the thickness of the micro-delamination increased.

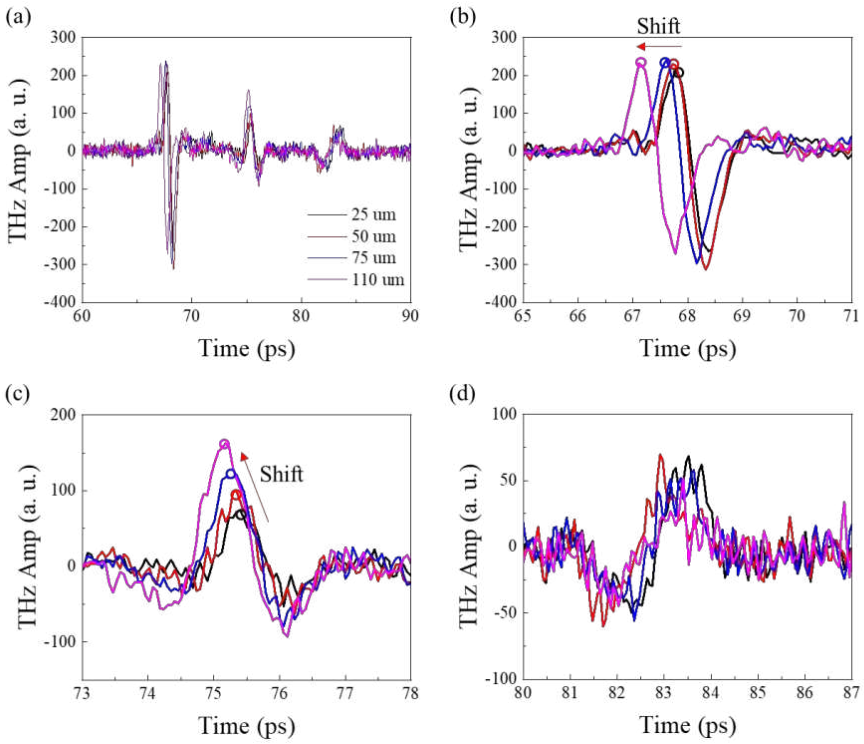

Figure 3. (a) THz signals measured by reflection mode with respect to the micro-delamination, and the magnification of the signals (b) reflected from the top surface, (c) reflected from micro-delamination, and (d) reflected from the bottom surface of the GFRP specimens

As described above, it has been confirmed that the intensity and the detection time of the THz superposed signals change with respect to the thickness of the micro-delamination. But the exact thickness of the delamination cannot be determined from the shape of the superposed signal alone. Therefore, the probability map of the THz signal was derived through the CNN model.

  doi:10.5075/epfl-298799_978-2-9701614-0-0

3.2 Probability map

The probability maps of the THz signals measured with respect to the micro-delamination were derived through the trained CNN algorithm for each signal type as shown in Figure 4. In the top and bottom surface signals, it was confirmed that the peak positions were accurately pointed to in the probability map. Also, the positions of the superposed signals could be determined in the probability map, and even the thicknesses of the micro-delamination could be determined through the class in the probability maps. In the case of the superposed signals, only the presence or absence of superposed signals could be determined using only the shapes of the THz signals. However, the CNN algorithm trained the shapes of the signals that change due to superposition, and as a result, the superposed signals could be analyzed more intuitively through the probability maps.

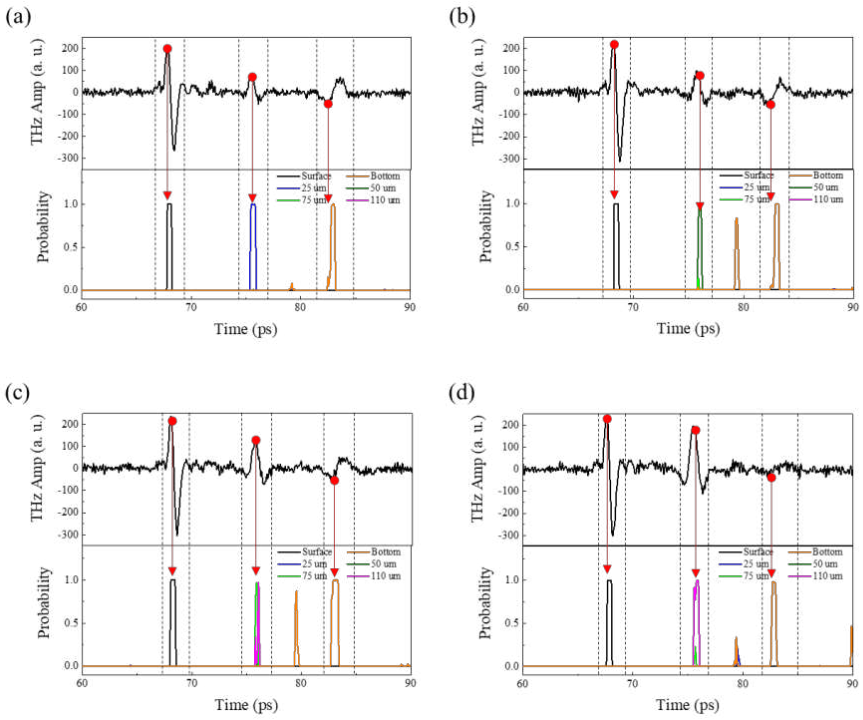

Figure 4. probability maps of the THz signals measured with respect to the micro-delamination; (a) 25 um, (b) 50 um, (c) 75 um, and (d) 110 um

4. Conclusion

In this study, the THz signals including the superposition of the signals were trained through the convolutional neural network (CNN) to analyze depth and thickness of the micro-delamination inside the GFRP. The GFRP specimens with 25, 50, 75, 110 um delamination were prepared, and THz signals were measured through the reflection mode. It was confirmed that the larger the delamination thickness, the weaker the superposition of the signals, which increased the amplitude and decreased the peak detection time of the superposed signal. Based on the measured THz signals, the signals were classified into the peaks reflected from the top surface, micro-delamination (superposed signals), and the bottom surface. Also, the classes for the noise signals and signals with truncated form were added. Then, the THz signals were transformed into 2D spectrograms through the STFT and trained through the CNN algorithm. After training, the probability maps of the THz signals with respect to the micro-delamination were derived

  doi:10.5075/epfl-298799_978-2-9701614-0-0 published under CC BY-NC 4.0 license

through the CNN classification. Consequently, from the probability maps, it was possible to determine the peaks of the signals reflected from the top surface, the bottom surface, and the micro-delamination, as well as the thickness of the micro-delamination.

Acknowledgments

This work was supported by a grant from the Human Resources Development program (no. 20204010600090)of the Korea Institute of Energy Technology Evaluation and Planning (KETEP), funded by the Ministry of Trade, Industry, and Energy of the Korean Government. This research was also supported by a National Research Foundation of Korea (NRF) grant funded by the Korean Government (MEST) (2021M2E6A1084690).

5. References

1. PALANIKUMAR, K.; PRAKASH, S.; SHANMUGAM, K. Evaluation of delamination in drilling GFRP composites. Materials and Manufacturing Processes, 2008, 23.8: 858-864.
2. YANG, Ryan SH, et al. An automated ultrasonic inspection approach for flip chip solder joint assessment. Microelectronics Reliability, 2012, 52.12: 2995-3001.
3. WANG, Fuliang; WANG, Feng. Void detection in TSVs with X-ray image multithreshold segmentation and artificial neural networks. IEEE Transactions on Components, Packaging and Manufacturing Technology, 2014, 4.7: 1245-1250.
4. KIM, Do-Hyoung, et al. Nondestructive evaluation of hidden damages in glass fiber reinforced plastic by using the terahertz spectroscopy. International Journal of Precision Engineering and Manufacturing-Green Technology, 2017, 4.2: 211-219.
5. RYU, Chung-Hyeon, et al. Nondestructive evaluation of hidden multi-delamination in a glass-fiber-reinforced plastic composite using terahertz spectroscopy. Composite Structures, 2016, 156: 338-347.

  doi:10.5075/epfl-298799_978-2-9701614-0-0

NON-DESTRUCTIVE EVALUATION FOR CRYSTALLINITY AND MOISTURE CONTENT OF POLYETHYLENE TEREPHTHALATE USING TERAHERTZ WAVE

Sang-Il, Kim[a], Dong-Woon, Park[a], Heon-Su, Kim[a] and Hak-Sung, Kim [a,b]

a: Department of Mechanical Convergence Engineering, Hanyang University, 222, Wangsimni-ro, Seongdong-gu, Seoul, Republic of Korea
b: Institute of Nano Science and Technology, Hanyang University, 222, Wangsimni-ro, Seongdong-gu, Seoul, Republic of Korea

Abstract: *In this study, a terahertz time-domain spectroscopy (THz-TDS) system was used to analyze the crystallinity and moisture content of polyethylene terephthalate (PET). The crystallinity of the PET specimen was analyzed by differential scanning calorimetry (DSC), and the moisture content of the PET specimen was measured by an electronic scale. The complex refractive index with respect to the crystallinity and moisture content of the PET was obtained using the transmission mode of the THz-TDS system. As the crystallinity of the PET increased, the refractive index was increased due to the increased polymer density. In addition, as the moisture content of the PET increased, the refractive index increased since the moisture absorbed the THz signal. Consequently, it was confirmed that the crystallinity and moisture content of the PET can be successfully analyzed by THz signals.*

Keywords: terahertz; polymer; non-destructive evaluation; moisture; crystallinity

1. Introduction

Polyethylene terephthalate (PET) has been used in various industries such as automobiles, electronics, and construction due to its characteristics of lightweight and electrical insulating properties. Since the mechanical properties of PET are affected by crystallinity and moisture content, a non-destructive evaluation (NDE) method for inspecting the crystallinity and moisture content of PET is required in the industry to ensure reliability [1, 2]. Currently, differential scanning calorimeter (DSC) and X-ray diffraction (XRD) methods have been used to measure the crystallinity of the polymer. However, the DSC method destroys a sample, and the XRD method generates dangerous X-ray radiation for the human body. Also, these methods are impossible to inspect in real-time because they require a long time to measure. For measuring the moisture content, the weight of the specimen is measured, which is also too much time consuming process. On the other hand, the NDE method using a terahertz (THz) wave has characteristics of fast inspection time and straightness without a medium. Furthermore, the THz waves are safe for the human body due to their low energy level. In addition, the THz waves are sensitive to moisture with dielectric relaxation [3].

In this study, the relationship between the THz waves and the crystallinity/moisture content of the PET was investigated via terahertz time-domain spectroscopy (THz-TDS). The THz signals transmitted through the PET specimens were measured according to their crystallinity and moisture content. The crystallinity and moisture content of the PET specimen were confirmed using the DSC and the electronic scale, respectively. Then, the THz signals were measured with respect to the crystallinity and moisture content and the refractive index was derived to analyze the relationship between the THz waves and the crystallinity/moisture content.

  doi:10.5075/epfl-298799_978-2-9701614-0-0

2. Experiment

2.1 Sample preparation

The PET specimens were fabricated using twenty-two PET (SKC Co., South Korea) films with a thickness of 50 um. The stacked PET films were hot-press molded at 0.2 MPa with 300 °C. After the hot press molding, the cooling rate was controlled to fabricate specimens with different crystallinities by fast cooling (100 °C/min) and slow cooling (2 °C/min) conditions as shown in Figure 1. The specimen fabricated by fast cooling forms an amorphous structure, which is the polymer chain combined irregularly, since the polymer chain does not have enough time to be regularly bonded due to the fast cooling rate. On the other hand, the specimen fabricated by slow cooling forms a crystalline structure in which the polymer chain is combined regularly since the polymer chain has enough time to be combined regularly due to the slow cooling rate.

To prepare specimens with different moisture contents, a water absorption test was conducted. The PET specimens were immersed in distilled water at room temperature for 1, 3, and 7 days, and the increase in weight of specimens due to water absorption was measured using an electronic scale.

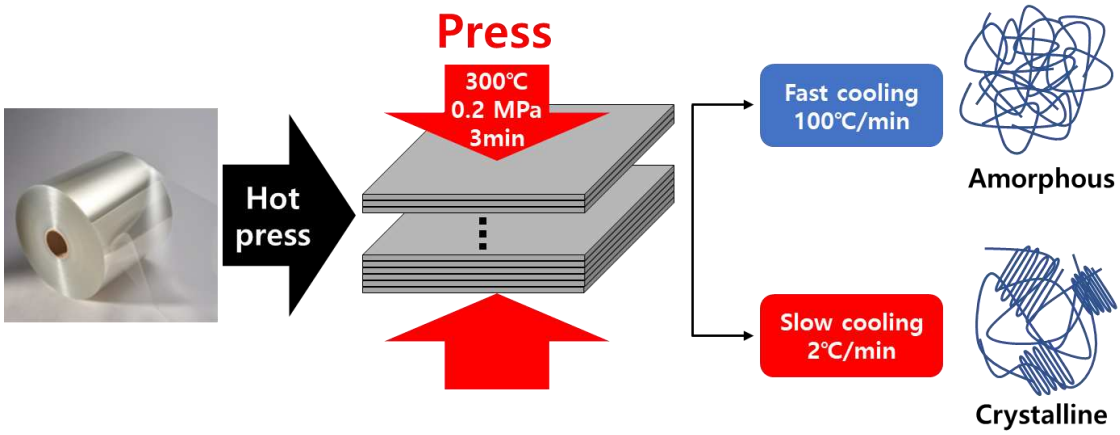

Figure 1. A schematic diagram of the process for amorphous and crystalline specimens.

2.2 Differential Scanning Calorimeter (DSC)

The crystallinities of the PET specimens were measured using the DSC. The DSC (SDT Q600, Auto-DSCQ20 System, TA Instruments) inspection method was performed with a heating rate of 10 °C/min from a temperature of 25 °C to 297 °C. By calculating the melting enthalpy and crystallization enthalpy of the PET specimen (Equation (1)), the crystallinity (K) of the PET specimen can be calculated using Equation (2) ([4]).

$$\Delta H_m(T_2) - \Delta H_m(T_1) = \int \Delta C_p dT \tag{1}$$

$$K = \frac{\Delta H_m - \Delta H_c}{\Delta H_{lit}} \tag{2}$$

where, ΔH_m, ΔH_c, and ΔH_{lit} were the melting enthalpy, crystallization enthalpy, and enthalpy of melting for 100% crystalline (140J/g), respectively [3].

  doi:10.5075/epfl-298799_978-2-9701614-0-0

2.3 THz non-destructive inspection

The terahertz time-domain spectroscopy (THz-TDS) system was used for inspecting the crystallinity and moisture content of the PET specimen. The THz-TDS system (FiCOTM, Zomega Terahertz Corp.) consists of a femtosecond laser module, a THz emitter module, a THz detector module, and an optical module, e.g., lenses, beam splitters, and reflectors, as shown in Figure 2. The THz-TDS system has a frequency range of 0.1 to 3.0 THz, a frequency resolution of 11 GHz, a time resolution of 55 fs, and a signal-to-noise ratio of 60 dB. The emitter and detector module of the THz system were set to transmission mode, which is coaxially aligned with a specimen between them.

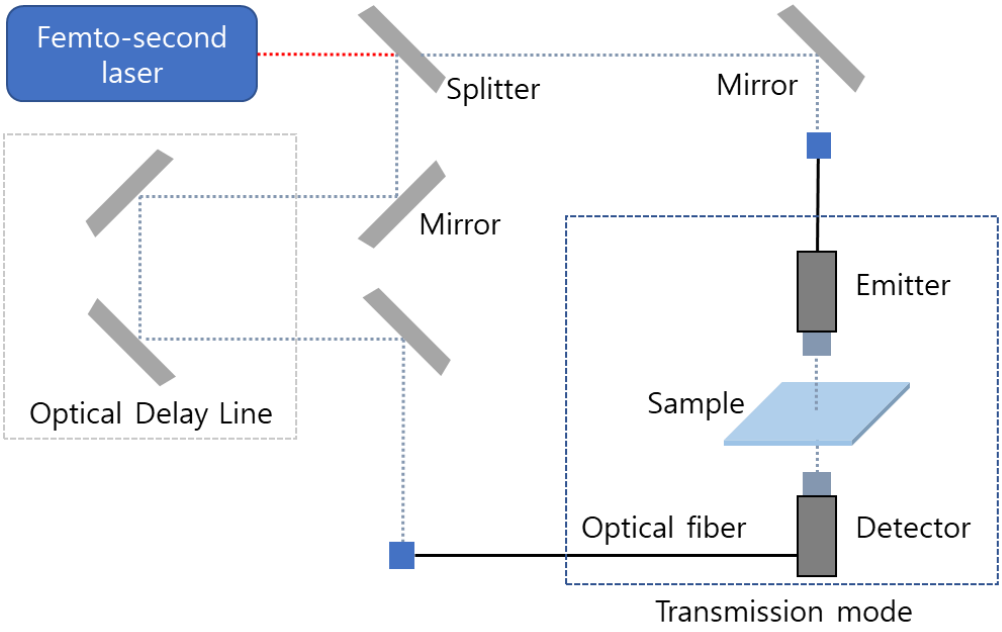

Figure 2. Schematic diagram of the optical equipment constituting the THz-TDS system.

3. Theory

The complex refractive index ($\tilde{n}_s$), which is the electromagnetic property of the specimen, can be derived by measuring reference (transmitted air) and sample (transmitted specimen) signals in transmission mode. The complex refractive index is comprised of the refractive index (n_s) and the extinction coefficient (k_s) as the following equation (Equation (3))

$$\tilde{n}_s(\omega) = n_s(\omega) - ik_s(\omega) \tag{3}$$

The refractive index and the extinction coefficient were described by the phase difference (∅(ω)) between the reference and the sample signal and the magnitude ratio of the reference signal to the sample signal (ρ(ω)) in the frequency domain as shown in Equation (4) and (5).

$$n_s(\omega) = \emptyset(\omega) \times \frac{c}{\omega \cdot d} + n_{air} \tag{4}$$

  doi:10.5075/epfl-298799_978-2-9701614-0-0

$$k_s(\omega) = \ln\left(\frac{4n_s(\omega)}{\rho(\omega)\cdot(n_s(\omega)+1)^2}\right) \times \frac{c}{\omega \cdot d} \quad (5)$$

where, ω is the angular frequency, c is the speed of light, d is the thickness of the specimen, and n_{air} is the refractive index of air.

In this study, the refractive index, which is the real part of the complex refractive index, was used to analyze the crystallinity and moisture content of the PET specimen. This was because the refractive index changes sensitively with the polymer structure and moisture condition ([5], [6]).

4. Results and discussions

4.1 Crystallinity

Figure 3(a) shows the results of the DSC with respect to the crystallinity of the PET specimen. By using Equation (2), the crystallinities of the amorphous and crystalline specimen were calculated as 14.31% and 41.45%, respectively. The PET specimens were well fabricated with different crystallinities by controlling the cooling rate.

The THz signals were measured with respect to the crystallinity using transmission mode. The THz signals were converted to the frequency domain using a fast Fourier transform (FFT). Then, the refractive index was calculated using Equation (4) and is depicted in Figure 3(b). From Figure 3(b), it was confirmed that the refractive index differed with respect to the crystallinity of the PET specimen. This is because the density of the polymer structure increased as the crystallinity increased [7]. As a result, the refractive index of the crystalline specimen was higher than the amorphous specimen due to the higher density. Based on this result, the refractive index of the PET specimen with respect to the moisture absorption time was compared in the 0.3 THz frequency range. This is because the 0.3 THz frequency range responded most sensitively to changes in the crystallinity and moisture content of the PET specimen.

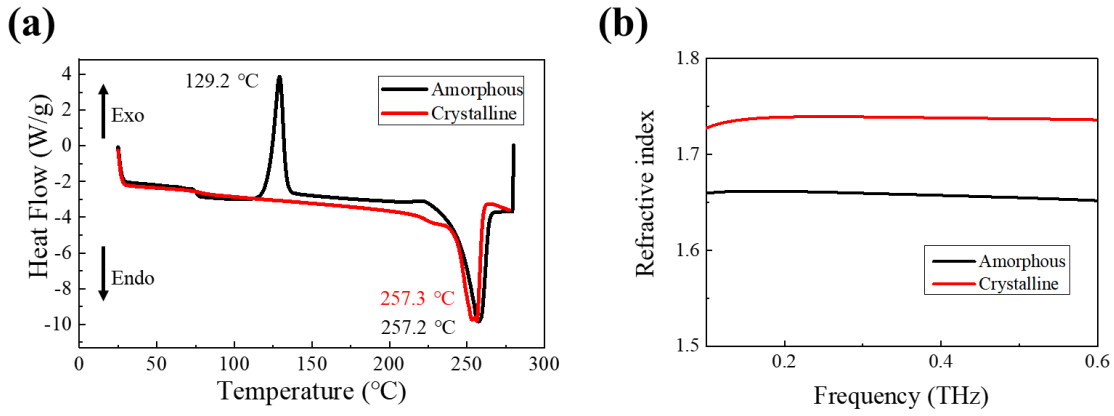

Figure 3. Characterization of PET specimen with respect to the crystallinity using (a) DSC and (b) refractive index

4.2 Moisture content

Figure 4(a) shows the weight increases with respect to crystallinities during water absorption time in the distilled water. From Figure 4(a), it was confirmed that the moisture absorption of

the PET specimen differed with the crystallinity. Since the PET specimen has a different density depending on the degree of crystallinity, the amorphous specimen with a low density absorbs more moisture than the crystalline specimen with a high density.

Figure 4(b) shows the refractive index with respect to the moisture content of the PET specimens. The refractive index of amorphous and crystalline PET specimens was increased during the moisture absorption. This is because the moisture in the PET specimen absorbed the THz electromagnetic wave with the dielectric relaxation in the terahertz region [8]. Therefore, the increased moisture content in the PET specimens increased the refractive index of the PET specimens as shown in Figure 4(b).

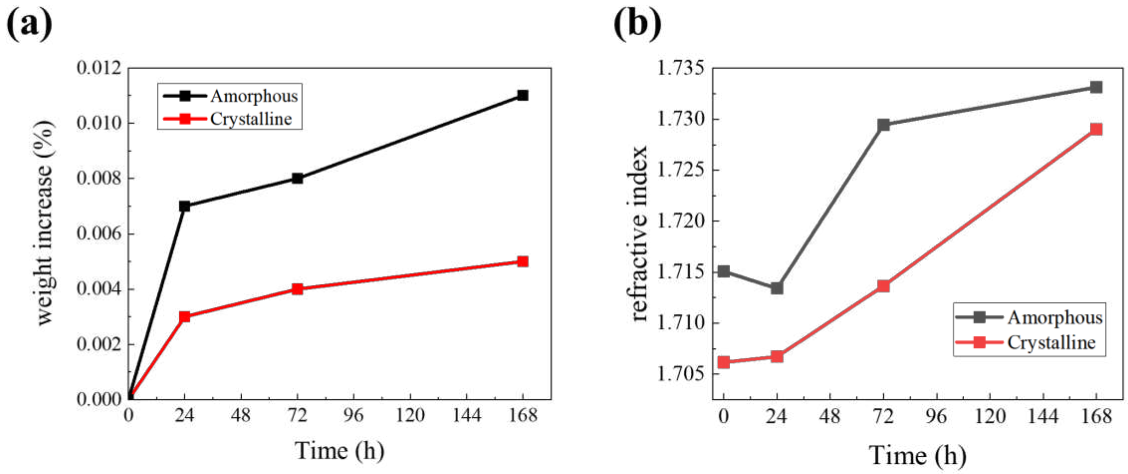

Figure 4. Characterization of PET specimen with respect to absorption time using (a) electronic scale and (b) refractive index

Conclusion

In this research, the THz-TDS system was used to analyze the relationship between the THz waves and the crystallinity/moisture content of the PET. The different crystallinity PET specimens were fabricated by controlling the cooling rate, and the crystallinity was confirmed by the DSC. Then, the PET specimens with respect to the crystallinities were submerged into the distilled water chamber, and the moisture content of the PET specimen was measured by the electronic scale. Using the THz-TDS transmission mode, the refractive index of the PET specimen was derived with respect to the crystallinity and moisture content. As the crystallinity of the PET specimen increased, the refractive index of the specimen was also increased because the density was increased. In addition, the refractive index was increased as the moisture content increased due to the moisture absorbing the THz signal. As a result, it was confirmed that the crystallinity and moisture content of the PET specimen can be monitored using the THz-TDS system in a non-destructive and non-contact method.

Acknowledgements

  doi:10.5075/epfl-298799_978-2-9701614-0-0

This work was supported by Korea Institute of Energy Technology Evaluation and Planning(KETEP) grant funded by the Korea government(MOTIE)(20202020800360, Innovative Energy Remodeling Total Technologies(M&V, Design, Package Solutions, and Testing & Verifications Technologies) for the Aging Public Buildings). This work was also supported by Korea Institute of Energy Technology Evaluation and Planning(KETEP) grant funded by the Korea government(MOTIE)(20212020800090, Development and Demonstration of Energy-Efficiency Enhanced Technology for Temperature-Controlled Transportation and Logistics Center). This research was also supported by the BK21 FOUR (Fostering Outstanding Universities for Research) project of the National Research Foundation of Korea Grant.

5. References

1. Demirel B, Yaraş A, Elçiçek H. Crystallization behavior of PET materials. (2011).
2. Jabarin SA, Lofgren EAJPE, Science. Effects of water absorption on physical properties and degree of molecular orientation of poly (ethylene terephthalate). 26, 620-625 (1986).
3. Rønne C, Åstrand P-O, Keiding SRJPrl. THz spectroscopy of liquid H 2 O and D 2 O. 82 (1999).
4. Um, Hui-Jin, et al. "Effect of crystallinity on the mechanical behavior of carbon fiber reinforced polyethylene-terephthalate (CF/PET) composites considering temperature conditions." *Composites Science and Technology* 207 (2021): 108745.
5. Strachan, Clare J., et al. "Using terahertz pulsed spectroscopy to quantify pharmaceutical polymorphism and crystallinity." *Journal of pharmaceutical sciences* 94.4 (2005): 837-846.
6. Jördens, C., et al. "Investigation of the water absorption in polyamide and wood plastic composite by terahertz time-domain spectroscopy." *Polymer Testing* 29.2 (2010): 209-215.
7. X-Ray Determination of Crystallinity in Poly (ethylene Terephthalate), D. E. BOSLEY, JOURNAL OF APPLIED POLYMER SCIENCE, 1964
8. Rønne C, Åstrand P-O, Keiding SRJPrl. THz spectroscopy of liquid H 2 O and D 2 O. 82, 2888 (1999).

  doi:10.5075/epfl-298799_978-2-9701614-0-0

CHARACTERISATION OF EXPERIMENTAL LAMB WAVES PROPAGATION IN CFRP LAMINATES WITH THE METHOD OF WAVELET TRANSFORM

Lea A. C. Lecointre[a], Ryo Higuchi[a], Tomohiro Yokozeki[a], Shota Tonegawa[b], Masakatsu Mita[b], Naoki Hosoya[b], Shin-ichi Takeda[c]

a: The University of Tokyo – lea.lecointre.jp@gmail.com
b: Shibaura Institute of Technology
c: Japan Aerospace Exploration Agency (JAXA)

Abstract: *The use of Ultrasonic guided waves such as Lamb Waves has been identified in the last decades as a promising Non-Destructive Testing (NDT) method for defects detection in composites. However, their propagation is complex, especially in Carbon Fiber Reinforced Plastics (CFRP) which are widely used for aerospace structures. Moreover, analyzing the Lamb Waves propagation requires to develop an efficient Signal Processing method to interpret the waves characteristics. In this study, a Signal Processing method using the Wavelet Transform allows to analyze several features of the propagated Lamb Wave: the amplitude, the frequency and the propagation velocity. This study also investigates how these waves features are impacted by different sample parameters such as the thickness, the anisotropy or the presence of delamination.*

Keywords: Non-Destructive Testing ; Lamb Waves ; Ultrasonic Testing ; Wave propagation

1. Introduction

Carbon Fibers Reinforced Plastics (CFRP) are increasingly used in the aerospace industry due to their high strength performance and low weight. However, CFRP are anisotropic and susceptible to specific internal defects or damages. Therefore, the use of very efficient Non-Destructive Testing (NDT) method is necessary at every step of the life cycle of CFRP aerospace structures, from the manufacturing to the maintenance.

One of the most widely used NDT method is the Ultrasonic Testing (UT), which consists in analyzing the propagation of waves through the structures in order to detect irregularities which can be caused by the presence of internal defects. In the last decades a type of UT using guided waves such as Lamb Waves has been attracting more and more interest. Whereas the classic UT methods need complete scanning of the structure, the Lamb Waves can propagate through wide areas, which gives the perspective of a drastic reduction of the time of control. However, the use of Lamb Waves for NDT requires deep investigation in order to fully understand all the complex phenomena which occur during the propagation, and in order to develop efficient Signal Processing method for the measurement and interpretation of the propagated wave signals.

This study proposes an innovative Signal Processing method using the Wavelet Transform. This Signal Processing method allows to convert the measurement of surface out-of-plane displacements into useful information about several characteristics of the propagated wave: the amplitude, the frequency bandwidth and the propagation velocity. Afterwards, the study also investigates the effect of different sample parameters on these propagated wave characteristics. The parameters investigated are the plate thickness, the direction of propagation, the presence of a thickness change and the presence of delamination.

  doi:10.5075/epfl-298799_978-2-9701614-0-0

2. The Theory of Lamb Waves Propagation

In the early 20th century, a type of elastic waves propagating in plate-like structures over relatively long distances has been identified. These waves, called Lamb Waves, are one of the most promising perspectives for the improvement of UT. However, deep studies of Lamb Waves propagation principles and functional set-up still must be performed in order to master this method and to implement it for industrial NDT.

Lamb Waves mostly propagate with two different modes. The Antisymmetric mode (A mode) consists in an out-of-plane displacement of the particles. The Symmetric mode (S mode) consists in an in-plane displacement of the particles. Several A mode and S mode can coexist during a Lamb Waves propagation. In this case, the modes are named A_n and S_n with $n = 0, 1, 2, 3 \ldots$ The resolution of Lamb Waves propagation equations [1] allows to obtain the dispersion curves, which show the evolution of the group and phase velocity with the wave frequency. The resolution can only be performed with numerical methods. In this study, a simulation tool called GUIGUW has been used in order to obtain the theoretical dispersion curves in the experimental condition. The theoretical dispersion curves obtained are shown in figure 1.

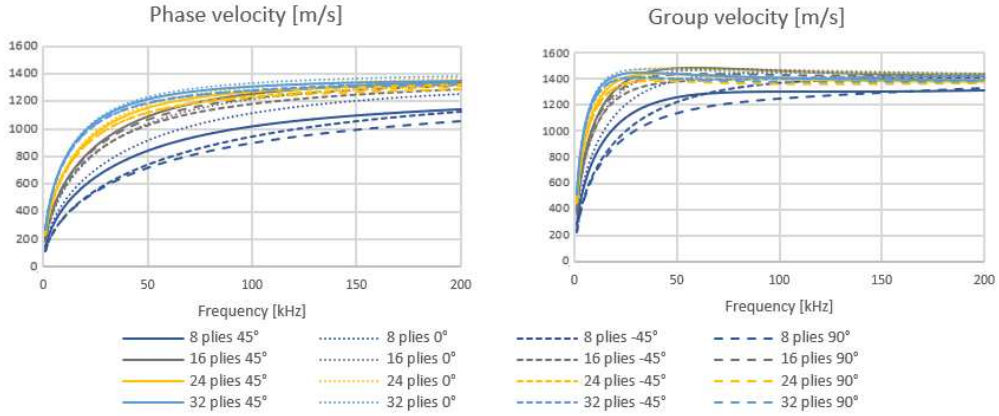

Figure 1: Theoretical group and phase velocity dispersion curves calculated from GUIGUW software

The NDT with Lamb Waves can be decomposed into four main steps. The first step is the excitation of the wave, which is generally performed with Piezoelectric Transducers (PZT) or Air-Coupled Transducers (ACT) [2, 3]. The second step is the propagation of Lamb Waves through the intact or defected material, which is an important topic of research nowadays, particularly with the use of Finite Element Method (FEM) simulation [4, 5] . The third step is the reception of the response signal from the controlled structure. The typical methods for this signal reception are PZT, ACT or Single-Laser-Doppler Vibrometers (SLDV) [2, 3, 6]. Finally, the fourth step is the step of signal processing. This step consists in treating the response signal measured at the third step in order to transform these signals into understandable information for the control of the structure (thickness measurement, defect detection, etc.) [7]

3. Experimental set-up

In this experiment, some CFRP samples are used in order to calibrate a Lamb Waves NDT process including non-contact excitation and reception methods and a signal processing technique using the Wavelet Transform. The use of the Wavelet Transform is investigated due to the ability of this technique to obtain information about several features of the propagated wave: the frequency, the wave amplitude and the group velocity. The calibrated method using the Wavelet

  doi:10.5075/epfl-298799_978-2-9701614-0-0

Transform is then used to characterize the Lamb Waves propagating into plates with different parameters (thickness, geometry, delamination, etc.) in order to observe the effect of these parameters on the waves features and to identify the most promising features for defects detection.

A total of eight samples is used is the current study. The table 1 and the figure 2 describe the experimental samples.

Table 1: Experimental samples description:

Sample denomination	Number of plies	Thickness [mm]	Size [mm]	Lay-up	Condition
LW-08-00-00	8	1,6	450x450	[45/0/-45/90]s	Healthy, flat
LW-16-00-00	16	3,2	450x450	[45/0/-45/90]2s	Healthy, flat
LW-24-00-00	24	4,8	450x450	[45/0/-45/90]3s	Healthy, flat
LW-32-00-00	32	6,4	300x300	[45/0/-45/90]4s	Healthy, flat
LW-08-08-00	8 16*	1,6 3,2*	450x450	[45/0/-45/90]s [45/0/-45/90]2s*	Healthy, stiffened
LW-08-08-50C	8 16*	1,6 3,2*	450x450	[45/0/-45/90]s [45/0/-45/90]2s*	Delaminated, stiffened
LW-08-08-50S	8 16*	1,6 3,2*	450x450	[45/0/-45/90]s [45/0/-45/90]2s*	Delaminated, stiffened
LW-08-08-75S	8 16*	1,6 3,2*	450x450	[45/0/-45/90]s [45/0/-45/90]2s*	Delaminated, stiffened

*At the stiffened zone

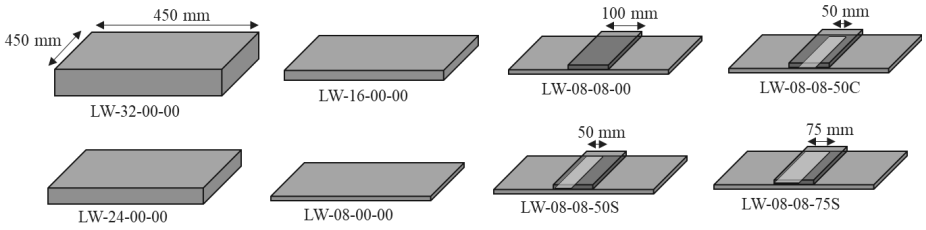

Figure 2: Experimental samples geometry (grey color represents CFRP, white color represents delamination)

In this experiment, a fully non-contact excitation and reception of Lamb Waves is implemented. The excitation of Lamb Waves is performed with a Laser-Induced Plasma (LIP) shock wave. The concentration of a high pulse laser a few centimeters on top of the surface of the controlled sample generates a shock wave which, when propagating in the air, encounters the surface of the sample, resulting in the excitation of Lamb Waves through the material. This method of Lamb Waves excitation has been developed and calibrated by Pr. Hosoya et al. [8 – 10]

The measurement of response signal is performed with a SLDV which measures exclusively the out-of-plane displacement of particles on the surface of the sample, corresponding therefore to the A mode propagation.

Two different SLDV scanning were implemented. The Area-method consists in scanning all points in a 200x200 mm area centered on the sample surface with a step of 2 mm, corresponding to 10201 points in total. The particle displacement at each point is measured during 800 µs. The Line-method consists in scanning all points in a 300 mm or 400 mm line in a chosen direction (45°, 0°, -45° or 90° following the different fibers directions in the sample). The step is 2 mm and the measurement duration is 800 µs. This corresponds to 151 points for 300 mm line and 201 points for a 400 mm line. The experimental results therefore take the form of a matrix containing the particle displacement versus time for every scanned point. (Figure 3b and c)

  doi:10.5075/epfl-298799_978-2-9701614-0-0

4. Experimental data analysis method

4.1. Principles of Signal Processing and the Wavelet Transform

After the raw experimental data is obtained from experiment, it is necessary to process this data, which takes the form of a matrix of signals, in order to obtain the relevant information. This analysis generally consists in one or several steps of signal processing.

In this study, a method of signal processing called the Wavelet Transform is used. The Wavelet Transform is a type of signal processing in which a signal is decomposed as a matrix of coefficients, called the Coefficients of Wavelet Transform (Cwt). The principle is to scan the full signal with a chosen mother wavelet in the time domain and in the frequency domain. The Cwt therefore reflects the concordance of the signal with the mother wavelet at each parameter. The matrix of calculated Cwt can then be visualised as a colour cartography with time as x-axis (from the values of τ), the frequency as y-axis (from the values of s) and Cwt amplitude as colour scale (representing the amplitude of the signal) (Figure 3a)

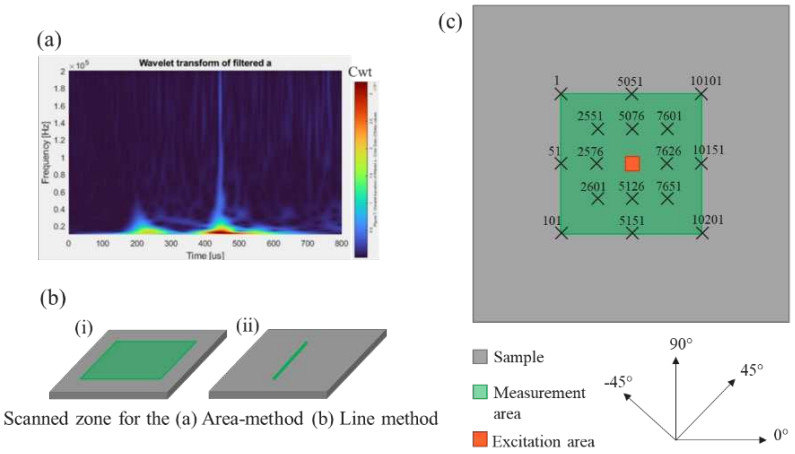

Figure 3: (a) Example of Wavelet Transform figure. The first peak represents the Lamb Wave peak. The second peak represents the Shock Wave peak. (b) Description of the scanned zone for the Area-method and Line-method, (c) Mapping of the analysis points for the Area-method

4.2. Step-by-step analysis method

In the current study, the Wavelet Transform figures have been calculated at several points on the surface of the experimental samples, in order to observe the evolution of the wave amplitude, the wave frequency and the wave velocity during the propagation. The points selected at which the wavelet transform is performed have been chosen to follow the different fiber directions in the samples for the Area-method, or points along the line for the Line-method.

After the wavelet transform figures are obtained at each point, the values of frequency-bandwidth, Cwt amplitude and Time-of-Arrival of the Lamb Wave peak are recorded and compared. The Time-of-Arrival data allow to calculate the group velocity, knowing the distance between every analysed point. With this data, a comparison is performed in order to observe the influence of the plate thickness, the direction of propagation (anisotropy of the sample), the change of geometry and the presence of delamination on the wave features obtained from analysis of the wavelet transform figures. These comparisons are presented in section 5.

  doi:10.5075/epfl-298799_978-2-9701614-0-0

5. Experimental results

5.1. Effect of the plate thickness

For comparing the wave propagation for different sample thicknesses, the samples LW-08-00-00, LW-16-00-00, LW-24-00-00 and LW-32-00-00, which correspond to flat healthy samples with respectively 8, 16, 24 and 32 plies, are used. (Figure 2)

The comparison of the amplitude of Cwt at the Lamb Wave peak of every figure shows that the amplitude decreases very quickly with the increasing of thickness. Also, whereas the Cwt amplitude at the 8-ply sample shows relatively high variation for different points at different zones, and reflecting different directions of propagation, the Cwt amplitude gets more stable when the number of plies increases. (Figure 4a)

The analysis of the evolution of the frequency bandwidth, which is observed by measuring the height of the visible Lamb Wave peak on the Wavelet Transform figure (Figure 3a) shows also a neat decrease of the frequency bandwidth for thicker samples. The frequencies which are lost for thicker samples are the high frequencies (the Lamb Waves peaks appear shorter). The analysis also shown that the frequency bandwidth decreases with increasing distance of the measurement point from the excitation point. Again, the lost frequencies during the propagation are the highest frequencies. (Figure 4c)

The analysis of Time-Of-Arrival observable on the x-axis of the Wavelet Transform figures at all visible frequencies for each peak allowed to build some experimental dispersion curves of the experimental group velocities measured. These experimental dispersion curves show a velocity around 1000 to 1500 m/s with an increasing of the group velocity with the increase of thickness and with the frequency. This is concordant with the theoretical dispersion curves. (Figures 4b and 1)

Therefore, it is observed that the thickness of the plate influences importantly the Lamb Wave propagation on all the calculated features: the wave amplitude, reflected by the Cwt amplitude, the frequency bandwidth and the group velocity.

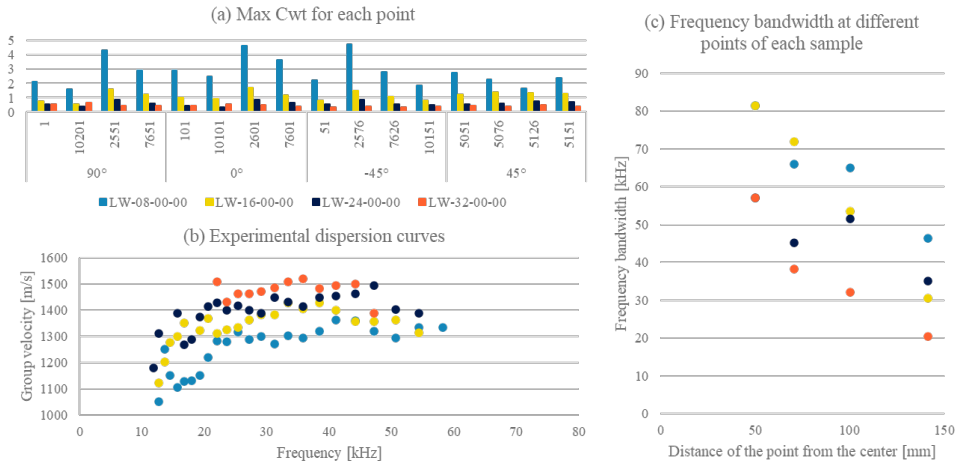

Figure 4: Experimental results for the effect of thickness on wave propagation
(a) Study of the wave amplitude (b) Study of the group velocity (c) Study of the frequency bandwidth

  doi:10.5075/epfl-298799_978-2-9701614-0-0

5.2. Effect of the material anisotropy

A comparison of the samples LW-08-00-00, LW-16-00-00, LW-24-00-00, LW-32-00-00, LW-08-08-00 and LW-08-08-50C allows to compare the wave features in different directions of propagation for flat and stiffened samples. (see figure 2)

The group velocity was calculated at several points of every direction for every sample, and then averaged to obtain a main group velocity of the Lamb Wave beam in every fiber direction (0°, 90°, 45° and -45°). The results shown that the group velocity was highly influenced by anisotropy for 8-ply samples with and without stiffener, whereas it is more stable in every direction for thicker samples. The exception is the 32-ply samples at which the variability of calculated group velocity was higher, resulting is less reliable values. This was due to the low amplitude of the Lamb Wave peak on the Wavelet Transform figure at 32 plies which makes the measurement of the exact Time-Of-Arrival of the wave more difficult. It has also been observed that for every sample except the LW-08-08-50C, the group velocity at 45°, which corresponds to the direction of the top and bottom fibers was higher than in other directions. (see figure 5)

However, no important influence of the direction of propagation was observed for the frequency bandwidth nor the Cwt amplitude.

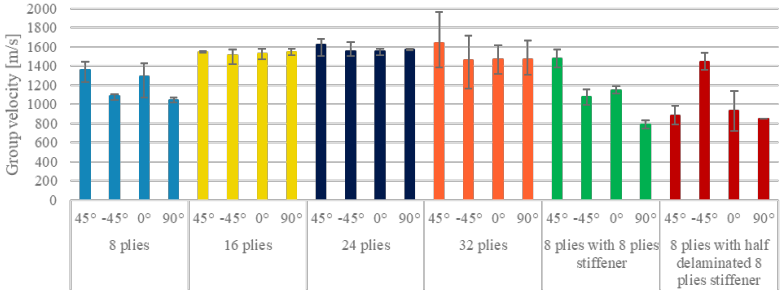

Figure 5: Comparison of the experimental main group velocities of the Lamb Wave beam for each direction

5.3. Effect of stiffener and delamination

Finally, for observing the effect of delamination at stiffened zone, a comparison of signals measured with the Line-method in the 90° direction in two different ways was performed on the LW-08-08-00 and the LW-08-08-75S samples. (Figure 2 and 6)

The analysis of the Cwt amplitude and the frequency bandwidth evolution along the line allowed to notice that there is a decrease of amplitude after crossing the stiffener, which is generally more important for delaminated sample, especially for the Cwt amplitude. (Figure 6)

Experimental dispersion curves have also been calculated from the experimental results measured on the different points of the signal line, with a differentiation of three propagation zones: zone 1 which corresponds to the delaminated 16-ply zone, zone 2 which corresponds to the 16-ply healthy zone and zone 3 which corresponds to the 8-ply healthy zone. The dispersion curves shown some high velocity values only in zone 2, which corresponds to the thicker zone. Some values of low velocities are also observed for a few points at the zone 1 (delamination). Therefore, it is observed that the presence of delamination, which can affect the group velocity, the Cwt amplitude and the frequency bandwidth, can be detected by the use of the Wavelet Transform. However, it seems that the results are disturbed by the presence of wave modes travelling in healthy zones or reflected. (Figure 7)

  doi:10.5075/epfl-298799_978-2-9701614-0-0

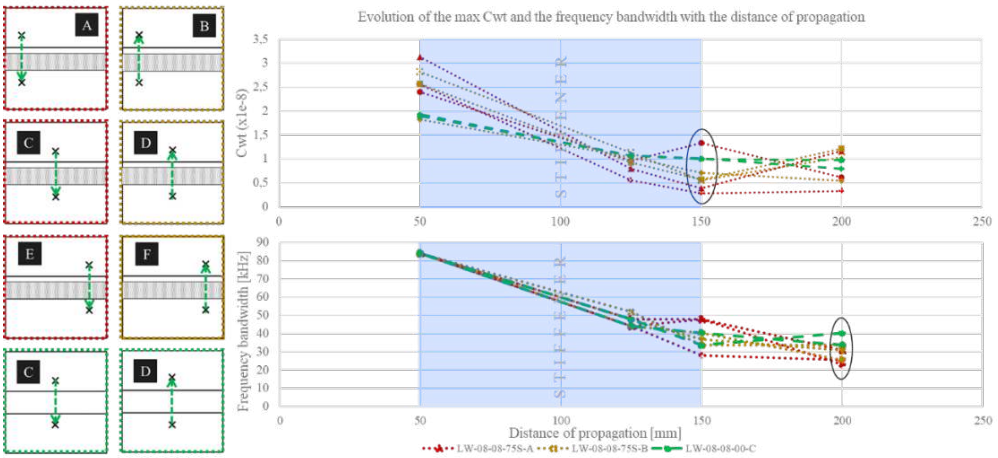

Figure 6: Signals compared for the stiffened delaminated zone analysis.

Figure 7: Experimental dispersion curves calculated from the experimental propagation, with differentiation of three different zones of propagation

6. Conclusion and perspectives

In this study, a signal processing method of experimental Lamb Wave propagation signals using the Wavelet Transform is proposed and used for characterizing some Lamb Wave propagation under different plate and propagation parameters. The method with the Wavelet Transform allowed to observe different features of the experimental propagating waves: the wave amplitude, reflected by the Coefficient of Wavelet Transform amplitude, the wave frequency bandwidth which can be easily observed on the Wavelet Transform figure as the Lamb Wave peak and the group velocity which is calculated by comparing different time of arrival of the Lamb Wave at different points of the plate surface with known distance.

The application of this method for comparing experimental Lamb Wave propagations under different plates parameters allowed to obtain some characteristics of the Lamb Wave propagation in CFRP. The thickness of the plate influences highly the Lamb Wave beam amplitude, frequency bandwidth and group velocity, which is relevant with the Rayleigh-Lamb equation theory. The direction of propagation shown especially influence on the group velocity for thin samples, whereas on thicker samples the group velocity reached stable values in every direction, which is due to the change of general stiffness of the plate with increasing number of

  doi:10.5075/epfl-298799_978-2-9701614-0-0

plies. The change of geometry and the presence of delamination shown only a small effect on the wave amplitude and the wave frequency and was difficult to observe for the wave velocity. This is probably due to the presence of interferences due to the more complex geometry. The method with the Wavelet Transform may therefore be improved by filtering the signals created by the delamination and the stiffener from the signals in healthy zones.

Acknowledgements

The authors acknowledge Japan Society for the Promotion of Science for the financial support of this project(Grant-in-Aid for Scientific Research, 22H01692).

References

[1] Ultrasonic Guided Waves in Solid Media, J. L. Rose, *Cambridge 2014*

[2] Damage Detection in Composite Materials using Lamb Waves Methods, Seth S Kessler, S Mark Spearing, Constantinos Soutis, *Smart Materials and Structures 11 (2002)*

[3] The generation, propagation, and detection of Lamb waves in plates using air-coupled ultrasonic transducers, M. Castaings, P. Cawley, *The Journal of the Acoustical Society of America 100 (1996)*

[4] Numerical Simulation of the Lamb Waves Propagation in impacted CFRP laminate, A. De Luca, Z. Sharif-Khodaei, M. H. Aliabadi, F. Caputo, *Procedia Engineering 167 (2006)*

[5] Simulation of Lamb Waves propagation for the Characterization of complex Structures, Agostini V., Delsanto P. P., Genesio I., Olivero D., *IEEE Transactions on Ultrasonics, Ferroelectrics, and Frequency control, vol. 5° No 4 April 2003*

[6] Damage detection in composite panels based on mode-converted Lamb waves sensed using 3D laser scanning vibrometer, Łukasz Pieczonka, Łukasz Ambroziński, Wiesław J.Staszewski, David Barnoncel, Patrick Pérès, *Optics and Lasers in Engineering, Volume 99, December 2017, Pages 80-87*

[7] Comparison Studies of full Wavefield Signal Processing for Crack Detection, W. Ostachowickz, M. Radzienski, P. Kudela, *International Journal for Experimental Mechanics, Strain 50, 2014*

[8] Non-contact and non-destructive Lamb wave generation using laser-induced plasma shock wave, Naoki Hosoya, Atsushi Yoshinaga, Atsushi Kanda, Itsuro Kajiwara, *International Journal of Mechanical Sciences 140 (2018) 486–492*

[9] Defect Detection of Concrete in Infrastructure based on Rayleigh Wave Propagation generated by Laser-induced Plasma Shock Waves, Sho Wakata, Naoki Hosoya, Noboru Hasegawa, Masaharu Nishikino, *International Journal of Mechanical Sciences 218 (2022)*

[10] Measurements of S0 mode Lamb Waves using a high-speed polarization Camera to detect Damage in transparent Materials during non-contact Excitation based on a Laser-induced Plasma Shock Wave, Naoki Hosoya, Tsubasa Katsumata, Itsuro Kajiwara, Takashi Onuma, Atsushi Kanda, *Optics and Lasers in Engineering 148 (2022)*

  doi:10.5075/epfl-298799_978-2-9701614-0-0

APPLICATIONS OF RAMAN SPECTROSCOPY ON CARBON-BASED COMPOSITES

Zheling Li[a], Libo Deng[b], Ian A. Kinloch[a], Robert J. Young[a]

a: National Graphene Institute/Department of Materials, The University of Manchester, Manchester M13 9PL, UK – zheling.li@manchester.ac.uk
b: College of Chemistry and Environmental Engineering, Shenzhen University, Shenzhen, 518060, China

Abstract: *Composites are indispensable modern structural and functional materials with wide applications. The carbon material family, including graphene, carbon nanotubes and carbon fibres, plays an important role in reinforcing various applications. It emphasized the crucial role of understanding what mechanisms govern the reinforcement. The properties of carbon-based bulk composites have been studied extensively, however these properties are ultimately determined by the structure, interfaces and processes at micro- and nano-scale. Thus it is important for techniques to be developed to study individual phases at this scale. As an analytical tool, Raman spectroscopy has found wide applications covering polymers, ceramics and inorganics. Fundamental theories have been well established on different forms of carbon materials. In this paper, applications of Raman spectroscopy will be reviewed for NDT investigation of individual carbon filler in composites and their interaction. It can be used to quantify the features that are crucial for composite applications from microscale to bulk scale.*

Keywords: Raman spectroscopy; carbon; composites

1. Introduction

The first report of the Raman spectrum of graphite was in the 1970 paper of Tuinstra and Koenig [1], following a presentation at the American Physical Society (APS) Meeting in 1969, which was apparently received with considerable scepticism. After all, it was known at the time that Raman scattering was a relatively weak phenomenon and that graphitic carbon was a very strong absorber of light; carbon black, for example, was a well-established black pigment. Following the pioneering work of Tuinstra and Koenig upon the Raman spectra of graphite and CFs in 1970 [1, 2], there was initially a trickle of papers published reporting the Raman spectra of different forms of graphitic carbon [3] and glass carbon [4].

Subsequent research upon carbon materials has been greatly facilitated through the development of improved hardware in the form of Raman microscopes that are essentially Raman spectrometers combined with optical microscopes. People had been experimenting with using lenses to focus the laser beam in order to obtain local spectroscopic information but this was found to be relatively inefficient. In Raman microscopes, the spatial resolution (radius of laser spot size) is diffraction limited ~0.61λ/NA (NA is the numeric aperture of objective and λ is

  doi:10.5075/epfl-298799_978-2-9701614-0-0

the wavelength of excitation laser). It is estimated to be ~0.5 μm but ~1 μm is a more practical value. The spatial resolution has been significantly improved to <100 nm or even at single cell level, by the recent development of SERS, TERS and shell-isolated nanoparticle-enhanced Raman spectroscopy. The resolution along Z direction depends on the transparency of specimen and the laser penetration depth, usually in the order of tens of nm. Thanks to the polarised nature of lasers, information upon anisotropy of specimens can also be extracted.

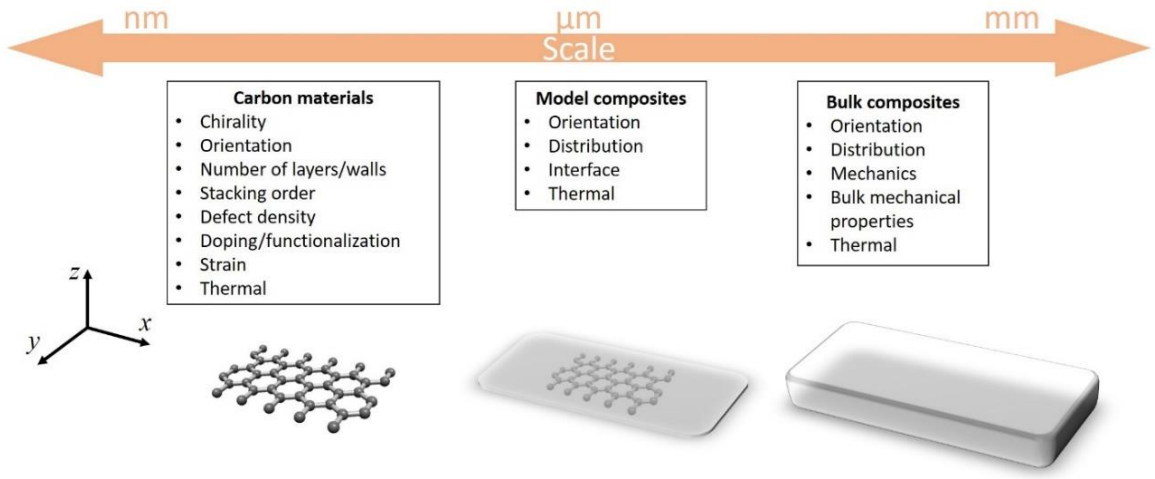

Figure 1 Multiscale applications of Raman on various properties.

Raman spectroscopy has now become an important NDT tool to characterize carbon materials and their composites with high resolution, particularly to enable the interaction between a carbon filler and matrix to be studied from a fundamental perspective. This sheds light on the application of Raman spectroscopy for bulk carbon-material based composites, to understand bulk properties through a microscale interpretation (*Figure 1*). Overall, the development of Raman spectroscopy has offered the opportunity to study many different aspects of carbon materials and their composites: (1) multiscale from nanometer to millimeter scale, covering everything from neat filler to bulk composites, (2) various features such as strain, doping and thermal properties (*Figure 1*).

2. Interfacial Mechanics and Model Composites

A crucial application of Raman spectroscopy is for model composites, in order to investigate structure-property relations *in-situ* and interfacial micromechanics at the single filler level [5, 6]. This has been achieved primarily through the correlation between local strain filler and its Raman band position. One important question that need to be answered with nanofillers such as graphene and CNTs was could they be analysed by using conventional continuum mechanics, or did new nano-mechanics theories need to be developed? It will be shown that Raman spectroscopy has now enabled this question to be answered.

In the following it will be reviewed how these can be demonstrated and quantified by the combination of Raman and model composites with a mapping process can be carried. Ideally model composites refer to modelized structure, where single or well-defined number of fillers are embedded in matrix in assemble to the structure of a bulk composite, but the terminology is also used if fillers are simply supported on substrate. There are several typical forms of model composites to be used for fragmentation test, microdroplet test, push-out test and pull-out test

  doi:10.5075/epfl-298799_978-2-9701614-0-0

[7]. The choice mainly depends on different geometry and size of carbon fillers. Generally, the Raman D, G and 2D downshift with strain with reference shift rates of about -30, -30 and -60 cm^{-1}/% strain in uniaxial tension [8]. However, these are the ideal reference values that can be affected by intrinsic properties such as defects, grain boundaries, wrinkles and other nanoscale inhomogeneity [9, 10] which does not reflect the true interaction between graphene and matrix. Hence the experimentally measured band shift is usually used as practical calibrations instead.

2.1 Graphene model composites

Although chronologically the most recent form of carbon to be studied, it is scientifically logical to discuss graphene first, as it is the building block of all the graphitic carbon fillers. A key milestone was reported by Gong et al. [11] where they sandwiched monolayer graphene by two polymer layers on a PMMA substrate and subjected it to tension. Again the value of $d\omega_{2D}/d\varepsilon$ was used to calibrate the strain, but a mapping process was conducted to reveal the strain distribution across the graphene flake. It was found that the strain distribution follows a shape that could be described using the well-established continuum mechanics 'shear-lag' model modified for 2D fillers [11]:

$$\varepsilon_g=\varepsilon_m\left[1-\frac{\cosh\left(ns\frac{x}{l}\right)}{\cosh\left(\frac{ns}{2}\right)}\right] \text{ where } n=\sqrt{\frac{2G_m}{E_g}\left(\frac{t}{T_{RVE}}\right)} \tag{11}$$

This study confirmed that graphene, even as a nanomaterial with one-atomic thickness, still obeys the continuum mechanics. The strain distribution obtained can be further derived to the distribution of interfacial shear stress using force balance approach in the shear-lag analysis [11, 12]. The interfacial failure at the graphene edge is just one of failure mechanisms found in graphene composites. Failure also occurs when the applied strain is greater than the fracture strain of the graphene [13], or the yield strain of matrix [14].

2.2 Carbon nanotube model composites

Similar work has also been carried out on CNTs. It typically involves CNTs suspended over trenches, which are the subjected to uniaxial strain [15]. Gao et al. [16] stretched SWNTs suspended over a trenched PDMS substrate. Values of $d\omega_G/d\varepsilon$ as large as -30 cm^{-1}/% were obtained, similar to the theoretical value [8], without the occurrence of slippage on the PDMS substrate. This indirectly shows good interfacial stress transfer as well as strong interfacial adhesion for SWNT/PDMS composites. Another form of CNT model composite is electrospun fibres incorporating isolated CNTs [17]. SWNTs with different chirality show quite different values of $d\omega_{2D}/d\varepsilon$ [16, 17]. This implies chirality-dependent interfacial stress transfer for different CNT species in electrospun fibre that could facilitate the application of CNTs in composites, strain sensors and devices. Unfortunately due to the practical difficulty in resolving the individual SWNTs optically, their strain distributions when subjected to deformation have not been revealed. Considering this, CNT bundles can be used instead, with an extra length factor η_l and orientation parameter η_o having to be taken into consideration to interpret the micromechanics.

2.3 Carbon fibre model composites

Investigations of the micromechanicas of CF model composites using Raman spectroscopy precede to those of graphene and CNT. Melanitis et al. [18] used Raman spectroscopy to map

  doi:10.5075/epfl-298799_978-2-9701614-0-0 published under CC BY-NC 4.0 license

the strain distribution of a high modulus CF embedded in an epoxy matrix. When the applied strain is at a low level ~0.6%, the strain increases from both ends towards the centre and eventually plateaus, similar to the behaviour of graphene [11, 14]. This observation experimentally validated the classical shear-lag model for 1D rod fillers [19-21]. Derivation of the axial strain distribution using force balance approach gives the distribution of τ_i to be directly estimated [18, 22].

3. Applications in Carbon-based Bulk Composites

The application of Raman on model composites enables the micromechanics to be studied at the single filler particle scale. However, their performance can be significantly different when they are used on the bulk scale, due to issues such as agglomeration, spatial orientation and morphology etc. Fortunately, those phenomena and their correlation, can all be studied by the use of Raman *in-situ* (*Figure 2*). In bulk composites many carbon fillers can be studied statistically and then the performance of the whole nanocomposite can be modelled. This fills the gap between the nanoscale measurement (usually by AFM or simulation) and bulk scale measurement (usually by mechanical testing) [23]. It also enables Raman spectroscopy to be a powerful NDT technique to sense crucial parameters such as filler damage during the production of composites.

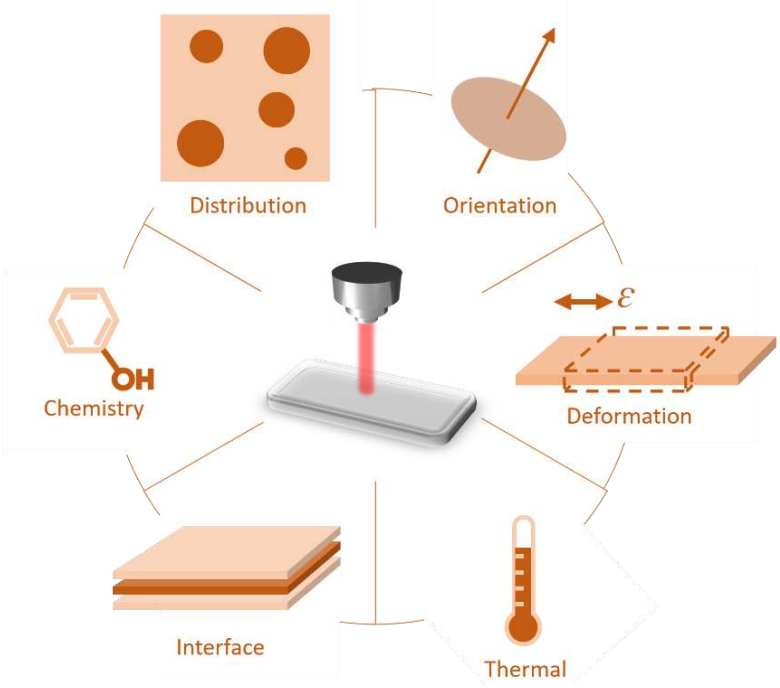

Figure 2 Applications of Raman spectroscopy in carbon-based composites.

1. References

1. Tuinstra F, Koenig JL. Raman Spectrum of Graphite. The Journal of Chemical Physics 1970; 53: 1126-1130.
2. Tuinstra F, Koenig JL. Characterization of Graphitic Fiber Surfaces with Raman Spectroscopy. Journal of Composite Materials 1970; 4: 492-499.

3. Nakamizo M, Kammereck R, Walker PL. Laser Raman Studies on Carbons. Carbon 1974; 12: 259-267.
4. Nathan MI, Smith JE, Tu KN. Raman spectra of glassy carbon. Journal of Applied Physics 1974; 45: 2370.
5. Kumar A, Sharma K, Dixit AR. Carbon nanotube- and graphene-reinforced multiphase polymeric composites: review on their properties and applications. Journal of Materials Science 2020; 55: 2682-2724.
6. Sun X, Huang C, Wang L, Liang L, Cheng Y, Fei W, Li Y. Recent Progress in Graphene/Polymer Nanocomposites. Advanced Materials 2021; 33: 2001105.
7. Piggott MR. Why interface testing by single-fibre methods can be misleading. Composites Science and Technology 1997; 57: 965-974.
8. Mohiuddin TMG, Lombardo A, Nair RR, Bonetti A, Savini G, Jalil R, Bonini N, Basko DM, Galiotis C, Marzari N, Novoselov KS, Geim AK, Ferrari AC. Uniaxial strain in graphene by Raman spectroscopy: G peak splitting, Gr\"uneisen parameters, and sample orientation. Physical Review B 2009; 79: 205433.
9. Xu C, Yao Q, Du H, Hong C, Xue T, Kang Y, Li Q. Abnormal Raman Characteristics of Graphene Originating from Contact Interface Inhomogeneity. ACS Applied Materials & Interfaces 2021; 13: 22040-22046.
10. Anagnostopoulos G, Paterakis G, Polyzos I, Pappas P-N, Kouroupis-Agalou K, Mirotta N, Scidà A, Palermo V, Parthenios J, Papagelis K, Galiotis C. Strain Engineering in Highly Wrinkled CVD Graphene/Epoxy Systems. ACS Applied Materials & Interfaces 2018; 10: 43192-43202.
11. Gong L, Kinloch IA, Young RJ, Riaz I, Jalil R, Novoselov KS. Interfacial Stress Transfer in a Graphene Monolayer Nanocomposite. Advanced Materials 2010; 22: 2694-2697.
12. Gong L, Young RJ, Kinloch IA, Riaz I, Jalil R, Novoselov KS. Optimizing the Reinforcement of Polymer-Based Nanocomposites by Graphene. ACS Nano 2012; 6: 2086-2095.
13. Zhao X, Papageorgiou DG, Zhu L, Ding F, Young RJ. The strength of mechanically-exfoliated monolayer graphene deformed on a rigid polymer substrate. Nanoscale 2019; 11: 14339-14353.
14. Liu M, Li Z, Zhao X, Young RJ, Kinloch IA. Fundamental Insights into Graphene Strain Sensing. Nano Letters 2021; 21: 833-839.
15. An J, Zhan Z, Sun G, Mohan HKSV, Zhou J, Kim Y-J, Zheng L. Direct Preparation of Carbon Nanotube Intramolecular Junctions on Structured Substrates. Scientific Reports 2016; 6: 38032.
16. Gao B, Jiang L, Ling X, Zhang J, Liu Z. Chirality-Dependent Raman Frequency Variation of Single-Walled Carbon Nanotubes under Uniaxial Strain. The Journal of Physical Chemistry C 2008; 112: 20123-20125.
17. Deng L, Young RJ, Sun R, Zhang G, Lu DD, Li H, Eichhorn SJ. Unique Identification of Single-Walled Carbon Nanotubes in Electrospun Fibers. The Journal of Physical Chemistry C 2014; 118: 24025-24033.
18. Melanitis N, Galiotis C, Tetlow PL, Davies CKL. Monitoring the micromechanics of reinforcement in carbon fibre/epoxy resin systems. Journal of Materials Science 1993; 28: 1648-1654.
19. Cox HL. The elasticity and strength of paper and other fibrous materials. British Journal of Applied Physics 1952; 3: 72-79.
20. Nairn JA. On the use of shear-lag methods for analysis of stress transfer in unidirectional composites. Mechanics of Materials 1997; 26: 63-80.
21. Galiotis C, Paipetis A. Definition and measurement of the shear-lag parameter, β, as an index of the stress transfer efficiency in polymer composites. Journal of Materials Science 1998; 33: 1137-1143.
22. Huang Y, Young RJ. Interfacial micromechanics in thermoplastic and thermosetting matrix carbon fibre composites. Composites Part A: Applied Science and Manufacturing 1996; 27: 973-980.

23. Xu C, Xue T, Guo J, Qin Q, Wu S, Song H, Xie H. An experimental investigation on the mechanical properties of the interface between large-sized graphene and a flexible substrate. Journal of Applied Physics 2015; 117: 164301.

  doi:10.5075/epfl-298799_978-2-9701614-0-0

MEASUREMENT OF ELECTRICAL CONDUCTIVITY AND PERCOLATION THRESHOLD OF MULTI-WALLED CARBON NANOTUBE/EPOXY COMPOSITES USING TERAHERTZ TIME DOMAIN SPECTROSCOPY

You-gwon Kim[1*], Dong-woon Park[1], and Hak-Sung Kim[1, 2]

a: Department of Mechanical Convergence Engineering, Hanyang University, 222 Wangsimni-ro, Seongdog-gu, Seoul, Republic of Korea
b: Institute of Nano Science and Technology, Hanyang University, 222, Wangsimni-ro, Seoungdong-gu, Seoul, Republic of Korea
*Email: yougwon1@gmail.com

Abstract: Due to superior electrical and mechanical properties of carbon nanotubes (CNT), CNT/epoxy composites have been widely used in various fields such as sensors, automobiles, and aerospace. Accurate measurement of the conductivity is important to reduce manufacturing costs. In this work, terahertz time domain spectroscopy (THz-TDS) from 0.1 to 3.0 THz was used to measure the conductivity of the MWCNT/epoxy composites with different CNT contents. The absorption behavior of THz waves in CNT/epoxy was investigated according to the MWCNT contents. It can be found that the optical properties including the extinction coefficient and the absorption coefficient were affected by the contents of the MWCNTs.

Keywords: Electrical conductivity; Carbon-nanotube; Terahertz time-domain spectroscopy

1. Introduction

In recent years, conductive epoxy composites have attracted much attention from researchers worldwide because of their excellent strength and good processing conditions. Also, the conductive epoxy composites have various applications, including sensor, antennas, electromagnetic shielding, automobiles, and aerospace [1]. However, the conductive epoxy composites have limitations in these fields due to their low electrical conductivity and high percolation thresholds. One approach to overcome these limitations is to add the carbon-nanotubes (CNT) with the epoxy resin. Many studies have been performed on the electrical conductivity of CNT composites [2, 3, 4]. Epoxy composites containing multi-walled carbon nanotube (MWCNT) have advantage of high electrical conductivity and low percolation threshold by forming conductive pathways of filler particles.

Non-destructive testing of electrical conductivity is essential because the damage of nanoparticle structure affects the electrical properties of CNT [5]. Additionally, predicting the percolation threshold of MWCNT content can increase manufacturing efficiency in terms of price and conductivity. For manufacturing the conductive composites, the evaluation of electrical conductivity in non-contact has been required to improve the reliability of product and yield of process.

In recent studies, the electrical properties of the CNT/polymer composites were investigated using the X-ray diffraction (XRD) method [6]. However, the XRD method is not practical in field, because the XRD method has several fatal problems such as generating dangerous radiation on

  doi:10.5075/epfl-298799_978-2-9701614-0-0

the human body and long measurement time. On the other hand, terahertz (THz) radiation can complement these problems. The THz radiation method has advantage of non-invasive, fast inspection time and non-destructive characterization techniques for the electrical properties of composites [7].

The purpose of this paper is to investigate the relation between optical properties and electrical conductivity of MWCNT/epoxy composites using the pulsed THz system as shown Fig.1. The amplitude and phase information of the composites were obtained using the pulsed THz system. From these data, the optical properties of MWCNT/epoxy composites were extracted in 0.2–1.0 THz according to MWCNT content. Based on the results, the electrical conductivities of MWCNT/epoxy composites were analyzed with optical properties based on effect of CNT on epoxy composite.

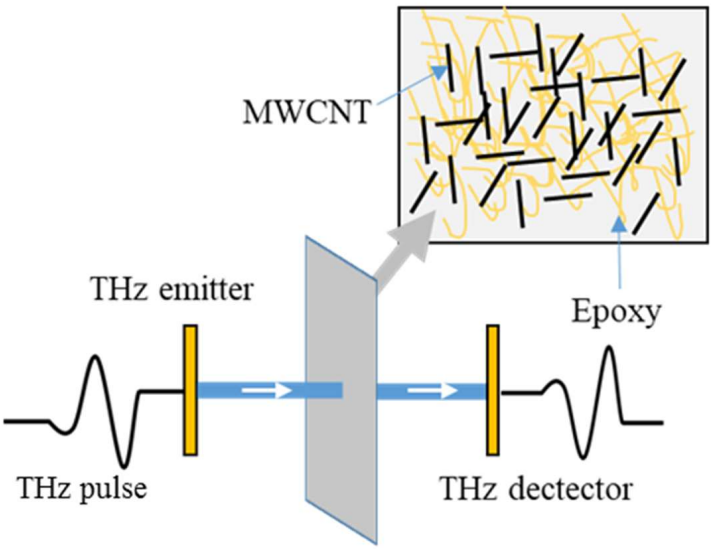

Figure 1. Schematics of inspecting CNT/epoxy composites using the pulsed THz waves

2. Experiment

2.1 Functionalization of MWCNT

The multi-walled carbon nanotube (MWCNT) provided by Hanwha Solution Chemical Division is the CNT-P type. To promote the dispersion of MWCNT in epoxy, the functionalization of MWCNT was performed with an acid solution, which modified CNT-P to CNT-COOH. The CNT-P (0.15 g) was added to 40 ml of a mixture (v/v, 3/1) of sulfuric acid (8 M) and nitric acid (8 M). The mixture was then magenetically stirred for 6 hours at room temperature [8]. Through a vacuum filtration, the mixture was washed with distilled water until pH 7. After that, the CNT-COOH was dried in an oven for 24 h at 80 °C.

2.2 Sample preparation

The prepared CNT-COOH was added to a solution with a mixture of ethanol and toluene, and the solution mixture with CNT was sonificated for 2 hours at room temperature. Afterwards, the required amount of epoxy resin (KFR-120, Kukdo Chemical) was added to the solution mixture. The dispersion of MWCNT was conducted by magnetically stirring for 60 min at room temperature and sonicating for 60 min at 60 °C. After that, to obtain pure MWCNT/epoxy resin,

  doi:10.5075/epfl-298799_978-2-9701614-0-0

the mixture was placed in an air circulation oven for 24 hours at 100 °C to evaporate the ethanol and toluene. The hardener (KFH-160, Kukdo Chemical) was added in a ratio of 10:3 (epoxy:hardener). The mixture was mechanically stirred for 10 min. The MWCNT/epoxy composites was poured into silicon rubber molds and placed in an oven at 80 °C for 24 hours for curing.

2.3 THz inspection system

The time-domain THz signals of the prepared MWCNT/epoxy composites were measured using the pulsed THz system (FiCOTM, Zomega Terahertz Corp.) as shown in Fig 2. The THz system consists of a THz emittor, a detector, an optical instrument, and a femtosecond laser module as shown in Fig 2(a). The frequency range of THz pulse is 0.10–3.0 THz, and the signal-to-noise ratio (SNR) is 50 dB as shown in Fig 2(b). The transmission mode with a zero-incidence angle was used to derive the complex refractive index.

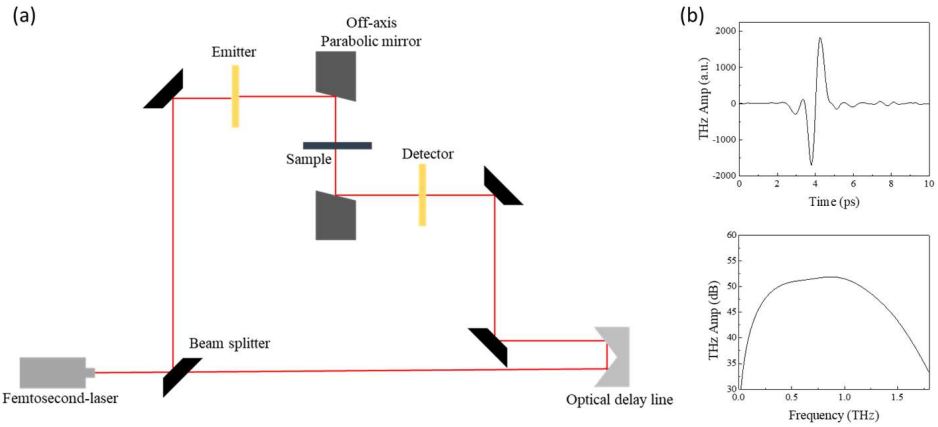

Figure 2. (a) Schematic diagram of THz-TDS system and (b) THz signals in time-domain and Frequency domain

3. Theory

The complex refractive index of the MWCNT/epoxy composites can be calculated by the THz signal difference between the reference signal ($E_{ref}(t)$) and the sample singals ($E_s(t)$), which are time-dependent data as shown in Fig. 3 [9].

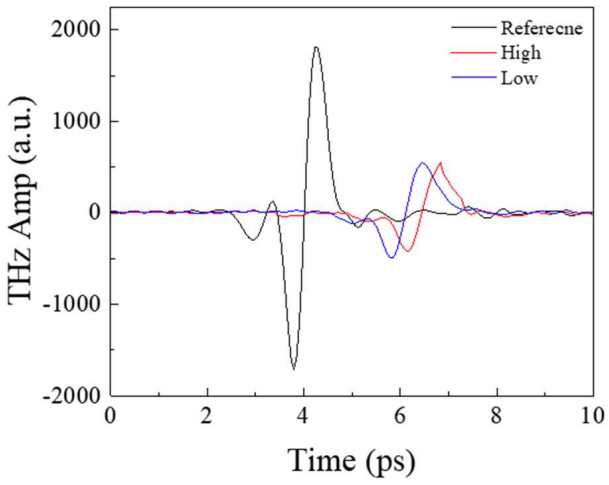

Figure 3. The waveform of THz signals passing air (reference) and MWCNT/epoxy composites

By using fast Fouier transform (FFT), the magnitude ratio ($A(\omega)$) and the phase difference ($\varphi(\omega)$) can be described in the frequency domain as below,

$$\frac{\bar{E}_s(\omega)}{\bar{E}_{ref}(\omega)} = A(\omega) \cdot e^{-i\ (\omega)} \quad (1)$$

where ω is the angular frequency. The bar notation denotes the complex quantities. The complex refractive index is a complex number composed of real and imaginary parts, which can be described as

$$\bar{n}_s(\omega) = n_s - i\kappa_s \quad (2)$$

where n_s and κ_s are the refractive index and extinction coefficient, respectively. The refractive index is related to the refraction of signals, while extinction coefficient is related to the absorption of signals, respectively. The complex refractive index can be calculated using the values extracted in Eq. (1) as below,

$$n_s(\omega) = \varphi(\omega) \cdot \frac{c}{\omega \cdot d} + 1 \quad (3)$$

$$\kappa_s(\omega) = \ln\left(\frac{4 \cdot n_s(\omega)}{A(\omega) \cdot (n_s(\omega)+1)^2}\right) \cdot \frac{c}{\omega \cdot d} \quad (4)$$

where *d* and *c* are the thickness of the sample and speed of THz signals in air, respectively. From the extinction coefficient, The absorption coefficient (α_s) is calculated as following,

$$\alpha_s(\omega) = \frac{2\omega\kappa_s}{c} \quad (5)$$

From the THz signal and Eq. (3)-(5), the optical properties of MWCNT/epoxy composites can be calculated according to MWCNT content.

4. Result and discussion

4.1 DC Conductivity

The electrical conductivity of MWCNT/epoxy composites was affected by amount of carbon nanotubes. By manufacturing the copper electrode on a surface of sample as shown in Fig. 4 (a), the resistance was measured using the multimeter with respect to high and low MWCNT contents. As shown in Fig. 4(b), the DC conductivities can be calculated using measured resistance as below Eq. (6)

$$\sigma = \frac{d}{RA}\ , \quad (6)$$

where R, d, and A are the measured resistance, the distance between the electrodes of the sample, and the area of the face of sample in contact with the electrode, respectively.

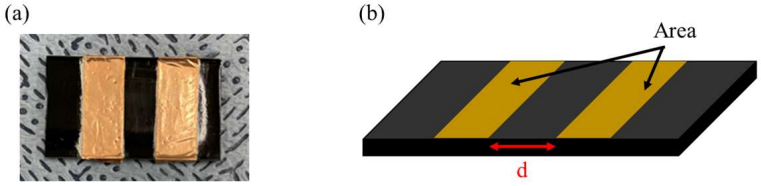

Figure 4. (a) Sample of MWCNT/epoxy composites with copper electrodes (b) schematics of sample

The electrical properties of sample with different amounts of CNT in the MWCNT/epoxy composites are summarized in Table 1. The electrical resistance was measured at 15.4 X 10^6 Ω in high MWCNT/epoxy composites and 20.1 X 10^6 Ω in low MWCNT/epoxy composites, respectively. The electrical properties such as conductivity and resistivity were calculated using the measured electrical resistance. It was observed that the electrical conductivity was increased because the contact resistance was decreased.

Table 1: Electrical properties by the content of MWCNT/epoxy composites.

MWCNT content	Resistance (Ω)	Resistivity (Ω·cm)	Conductivity (S/cm)
High	15.4×10^6	5.5×10^5	1.8×10^{-6}
Low	20.1×10^6	7.1×10^5	1.4×10^{-6}

4.2 Extinction and absorption coefficient

The two types of specimens of MWCNT/epoxy composites and epoxy resin were investigated using the transmission mode of THz pulsed system. The extinction coefficient and the absorption coefficient were calculated from the pulsed THz system using Eq. (2)-(5), and these results were plotted in Fig. 5, respectively. The epoxy containing CNT and the pure epoxy showed a clear difference in the range of 0.4-1.2 THz. The CNT content and optical properties were highly correlated, indicating that the THz spectroscopy was very suitable for measuring relative changes in the CNT content. The sample with the high MWCNT content showed the higher extinction coefficient and absorption coefficient than other samples. It is showed extinction coefficient and absorption coefficient tend to increase as the content of CNT increases due to absorbance property of CNT. From this tendency, the THz pulsed system can predict conductivity through an increase in CNT content in epoxy resin, which will also enable prediction of percolation thresholds.

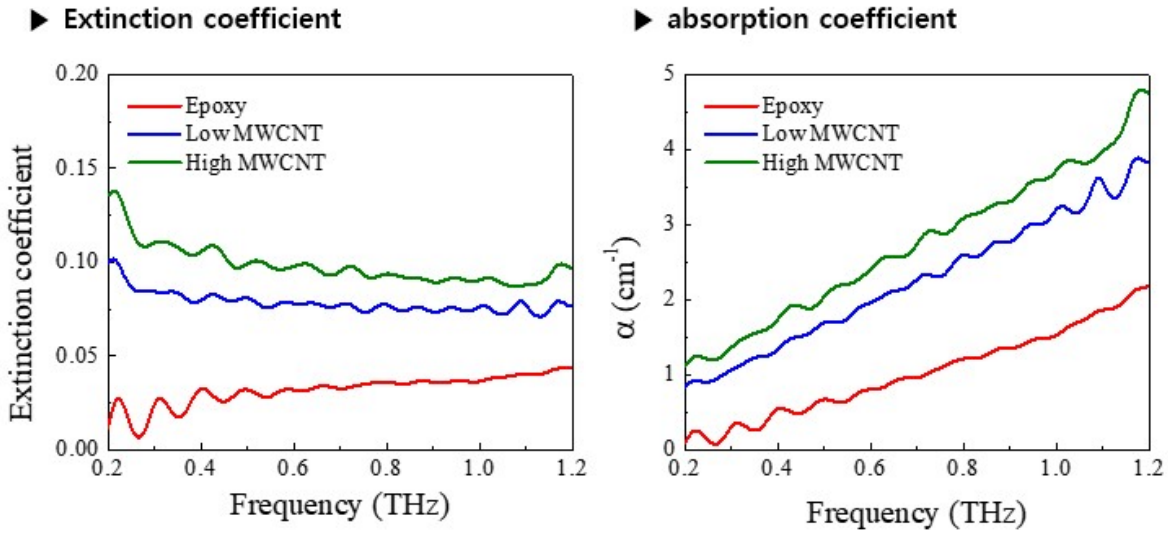

Figure 5. Extinction coefficient and absorption coefficient on the THz waveform at Frequency band for weight fractions of MWCNT/epoxy composites sample and the epoxy resin

5. Conclusion

The effect of CNT on the electrical properties of epoxy composites was investigated based on the transmission mode of the THz pulsed system. Two types of specimens prepared according to the amount of MWCNT in the epoxy resin were measured for electrical properties such as conductivity and resistivity. It was confirmed that as the CNT content in the epoxy composites increased, the resistance decreased and the conductivity increased because of the conductive pathway. From the THz measurement, these effects could also be confirmed by comparing extinction and absorption coefficient. The higher the amount of CNT, the higher the extinction coefficient and the absorption coefficient. As a result of this study, it is expected that this conductivity measurement method can be predicted using the pulsed THz system.

Acknowledgements

This work was supported by the Korea Institute of Energy Technology Evaluation and Planning(KETEP) and the Ministry of Trade, Industry & Energy(MOTIE) of the Republic of Korea (No. 20206910100160). This research was also supported by a National Research Foundation of Korea (NRF) grant funded by the Korean Government (MEST) (2021M2E6A1084690, Solution development for non-destructive evaluation challenge based on data science).

4. References

1. Jinrui Huang, Fabrication of a highly tough, strong, and stiff CNT/epoxy conductive composites with an ultralow percolation threshold self-assembly, Nanjing Forestry University, 2019
2. Piyush R. Thakre, Electrical and Mechanical Properties of Carbon Nanotube-Epoxy Nanocomposites, Aerospace engineering. Texas University, 2009
3. Yoon jin Kim, Taek Sun Shin, Hyung Do Choi, Jong Hwa Kwon, Electrical conductivity of chemically modified multiwalled carbon nanotube/epoxy composites, Korea University, 2004
4. Frank Gardea, Dimitris C. Lagoudas, Characterization of electrical and thermal properties of carbon nanotube/epoxy composites, Department of Aerospace Engineering, Texas University, 2013
5. Fred Fagergrn, Shane Sypherd, Mechanical Engineering, Brigham Young University, Using non-destructive testing to predict bending modulus of carbon infiltratedcarbon nanotubes
6. Iman Taraghi, et al “X-ray and terahertz imaging as non-destructive techniques for defects detection in nanocomposites foam-core sandwich panels containing carbon nanotubes”, Polymer Testing (2019), 0142-9418
7. Weihao Ma, et al “Application of Terahertz Time-Domain Spectroscopy in Characterizing Thin Metal Film–Substrate Structures”, Trancations on terahertz science and technology (2020), 2156-342X
8. Ji-Hoon Lee, Kyong Yop Rhee, Soo Jin Park, Silane modification of carbon nanotubes and its effects on the material properties of carbon/CNT/epoxy three-phase composites, Inha University, 2011
9. Heon-Su Kim, Dong-Woon Park, Hak-Sung Kim, Non-destructive evaluation of cement hydration with pulsed and continuous Terahertz electro-magnetic waves, Hanyang University, 2020

  doi:10.5075/epfl-298799_978-2-9701614-0-0

NON-DESTRUCTIVE EVALUATION OF INTERFACIALLY ENGINEERED COMPOSITES

Gábor Szebényi[a,b], Viktor Hliva[a], Balázs Magyar[a]
a: Department of Polymer Engineering, Faculty of Mechanical Engineering, Budapest University of Technology and Economics, Budapest, Hungary, szebenyi@pt.bme.hu
b: MTA-BME Lendület Lightweight Polymer Composites Research Group, Műegyetem rkp. 3., H-1111 Budapest, Hungary

Abstract: *In this paper, we investigated the pseudo-ductile behavior of carbon fibre reinforced polymer composites via compression after impact (CAI) testing with a new method to analyze the occurring deformation zone. The pseudo-ductile behavior appears due to the engineered semi-IPN structure, which is formed at the interface between the fibres and resin by a printed inter-layer. Thus, the semi-IPN (interpenetrating network) structure locally weakened the interfacial shear, which slowed down the crack propagation during load. After the initial impact to create delamination, CAI tests were carried out. We 3D scanned the specimens' on both sides after the compression. With the created surface models, the occurring differences can be analyzed to determine the dominant damage mode.*

Keywords: pseudo-ductile composite, 3D scan, semi-IPN

1. Introduction

The use of high-performance carbon fibre reinforced polymer (CFRP) materials is unavoidable in applications requiring low weight and high strength. Composites appeared at the dawn of history, as these materials can be used to combine different material properties, even with several families of materials. The word "compositus" refers to complexity [1], which is the Latin original of the term composite, meaning to put it together. The proliferation of modern polymer composites has been greatly fueled by the emergence of weight reduction needs, which have highlighted the hypothesis that the design of load-bearing fibers in the direction of load can significantly decrease the density of the part [2]. The advancement of carbon fibre composites is inevitable in today's modern world. A 2018 study also shows wellthat the demand for use shows an extremely high, steadily increasing trend [3].

Even though their spread is limited by their lack of ductile behavior. Ductility is the resistance of the material against crack propagation. It can also be described as the energy-absorbing ability of the material. In the case of carbon fiber reinforced thermoset matrix composites, the ductile behavior is not typical; in most cases, brittle failure occurs during damage. With the development of ductility, the reliability of these systems can be increased. In the case of carbon fibre-reinforced epoxy composites, it is essential to introduce the term pseudo-ductility. The pseudo-ductility refers to the appearance of a non-linear characteristic, but this is not due to plastic deformation but to the appearance of gradual damage [4, 5].

There are already several methods to increase ductile behavior. The methods can be divided into several groups according to which composite component has been altered. On the

  doi:10.5075/epfl-298799_978-2-9701614-0-0

reinforcement side, mostly hybrid reinforcements were used to achieve pseudo-ductility. The energy absorption capacity of the system can be increased by combining the carbon fibres with higher deformation capacity fibres [6-8]. This gives the system additional deformation capability even when the carbon fibres are torn under load. From the matrix side, the ductile behaviour can be achieved with different additives. In most cases, the matrix was associated with rubber or thermoplastic additives that locally increase the ductility of the system [9-11].

Non-destructive testing of composites is a hot topic because proper structural health monitoring is necessary for safety-critical applications. The failure of composites is a complex process of the progression and multiplication of minor local damages leading to total failure. When the failure zones can only be detected when the level of structural damage is critical, a test is not considered non-destructive anymore. All NDT methods have limitations, size, applicability in field measurement, a required special treatment, or slight damage to the structure.

In our research, we present a 3D scan-based test method, which is capable of detecting damage at an early stage and applying it to an exceptional kind of composite sample, which is interracially engineered to have pseudo-ductile properties. Our method uses 3D printing of polycaprolactone (PCL) interlaminar layers to create locally weakened fibre-matrix adhesion zones in carbon fibre (CF) - epoxy (EP) composites [12-14] . During the loading of these structures, delamination is created at the printed pattern locations, and with a slight loss in strength, the structure shows a pseudo-ductile failure with improved strain at break values and pseudo-ductile plateaus.

2. Experimental

2.1 Materials

We used IPOX ER 1010 (IPOX Chemicals Kft., Budapest, Hungary) DGEBA-based epoxy resin (EP) as the matrix of the composite laminates, with IPOX MH 3111 anhydride-based curing agent. The mixing weight ratio was 100:75, according to the producer's recommendation. We cured the resin at 90°C for 3 hours. Fibre reinforcement was PX35FBUD0300 (Zoltek Zrt., Nyergesújfalu, Hungary) unidirectional carbon weave (309 g/m^2 surface weight), consisting of Panex35 50k rovings. For the 3D printed interface, we selected eMorph175N05 (Shenzhen Esun Industrial Co. Ltd., Shenzhen, China) PCL filament. We chose PCL because it is soluble in the matrix, it is easier to process than other thermoplastic additives due to its lower melting temperature, and because it is a biomaterial, so it is not harmful to the environment, unlike many high-performance additives. The diameter of the filament was 1.75 mm (melting temperature, Tm = 60 °C, print temperature: >80 °C). The manufacturing process and the inter-layer design (Figure 1., Table 1) are similar to in the structure presented in our previous paper [13].

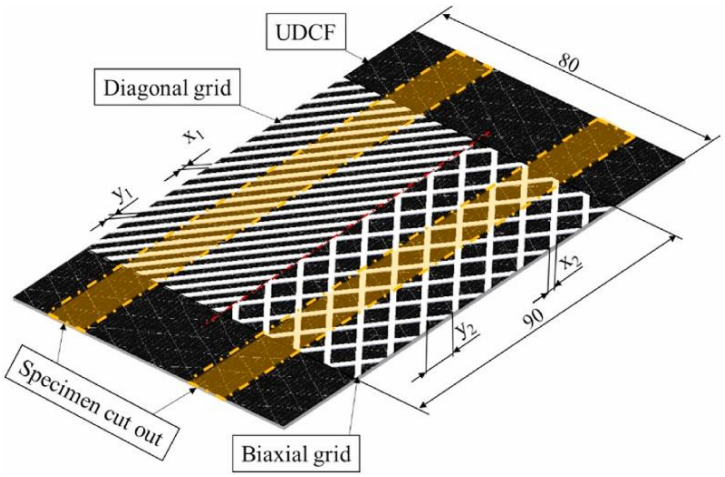

Figure 1. Printed inter-layers on the surface of UD carbon fibre [13]

Table 1: Design parameters of the inter-layer patterns [13]

Surface filling (SF) [%]	Diagonal		Biaxial	
	x1 (Line thickness) [mm]	y1 (Distance) [mm]	x2 (Line thickness) [mm]	y2 (Distance) [mm]
12.5	0.5	3.5	0.5	8.0
25.0	1.0	3.0	1.0	6.9
37.5	1.5	2.5	1.5	5.7
50.0	2.0	2.0	2.0	4.6
62.5	2.5	1.5	2.5	3.4
75.0	3.0	1.0	3.0	2.3
87.5	3.5	0.5	3.5	1.1
100.0	4.0	0.0	4.0	0.0

2.2 Initial delamination

The mechanical properties of the composites are significantly affected by the inherent damage in the material. Prior to the CAI measurements, the exposed specimens were subjected to impact by a hemispherical dart impactor to achieve a certain level of delamination in the specimens. The dimensions of the specimens were 80x80x2 mm, and we exposed them to an impact of 20 J. At this value, only delamination occurs, without complete failure of the specimen.

2.3 Compression after impact

During the CAI test, we examined the change in the pseudo-ductile properties of the composite specimens. After creating the initial defect, the specimens were subjected to a compression test.

We used a Mercury Monet 3D two-camera DIC to follow the deformation of the specimens in 3D, as well as the whole process of the failure (Figure 2 a; b).

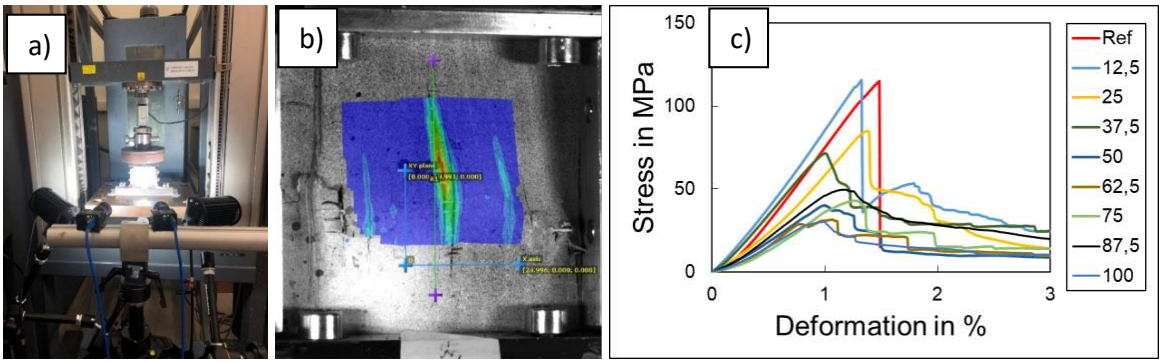

Figure 2. a) Arrangement during the CAI test; b) DIC recording of a compressed specimen; c) Compression curves at different surface filling

Based on the compressive stress-strain curves (Figure 2 c), the reference samples and the samples with a low PCL ratio reached the highest compressive strength values, and by increasing the PCL content, stress values dropped significantly. In the case of deformations related to maximal stress values, higher deformation values can be observed for samples with a lower surface filling ratio. As the proportion of PCL increases, the curves become more and more flattened; here, we can speak of a more gradual failure (more ductile behavior) than in the case of reference samples, where a brittle failure appeared. Based on the specific absorbed energy (SAE) the application of a small percentage of PCL increased the energy values (Figure 3).

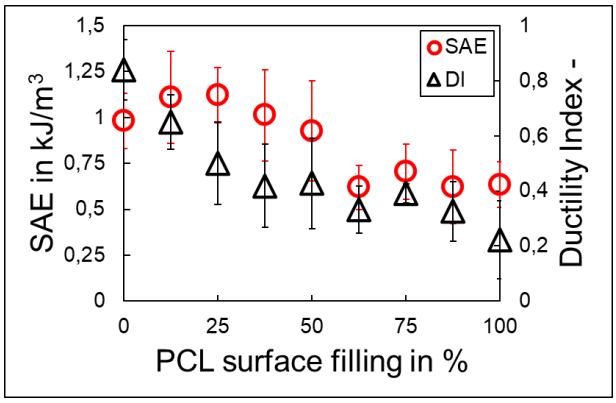

Figure 3. Ductility results at compression after impact test at different surface filling content

This increase is due to the fact that the compressive strength and deformation values of the samples with low PCL content have not yet decreased significantly, but the elongated failure behavior has already appeared at low PCL content already. Above 50% of PCL, the absorbed energy started to decrease. The decreasing tendency appeared due to the decreasing stress values as well, resulting in less area under the curve.

As PCL proportion increased, the ductility index decreased, i.e., more ductile behavior was observed than in the reference samples (which were close to 1 value). For samples with a high surface area filling, the values show more ductile behavior. In the case of the reference samples, we can speak of brittle fracture, i.e., after the cracking started, the material was no longer able to absorb energy. For samples with a high PCL ratio, a more ductile failure occurred, resulting in

a significant amount of energy being absorbed even after crack initiation. This can be explained by the fact that when the crack path intersected with the PCL zones, the propagation slowed down, thanks to the altered interfacial shear strength [12]. In the case of specimens with a high PCL, the crack reached the locally modified zones more often, thus, the specimen was able to deform more, thus achieving a more pseudo-ductile behavior.

2.4 Evaluation of the deformation zone

To evaluate the deformation zone, we 3D scanned the compressed specimens' on both sides. We took 4-5 recordings of a specimen in order to get an accurate picture of it. We used GOM ATOS Core 5M to 3D scan the specimens. Using the point cloud generated by the GOM InspectSuit 2020 program, we fitted the surface on them in MatLab (Figure 4).

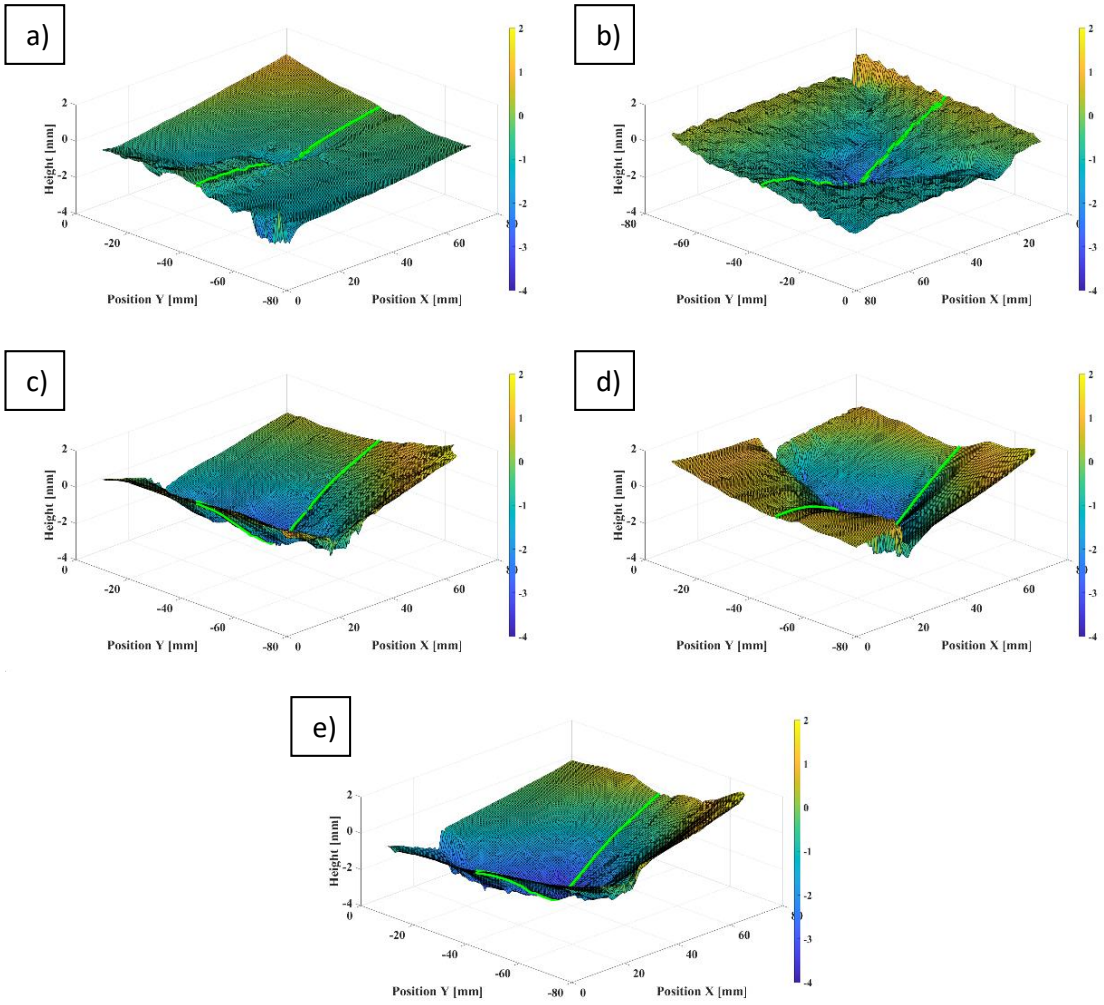

Figure 4. Fitted deformed surfaces after compression with the midplane line which evaluated in MatLab; a) Reference; b) 25% PCL; c) 50% PCL; d) 75% PCL; e) 100% PCL

In order to examine the deformations, the front and back of the specimens after the compression test were compared, which are illustrated in Figure 5. The green lines show the front surface and the yellow lines the back surface of the compressed specimens. The lines were located in the centre of the surface of the specimens, parallel to the direction of the fibres and perpendicular to one side. We placed the lines on top of each other, assuming the same specimen thickness to better illustrate the differences between the surfaces (Figure 5).

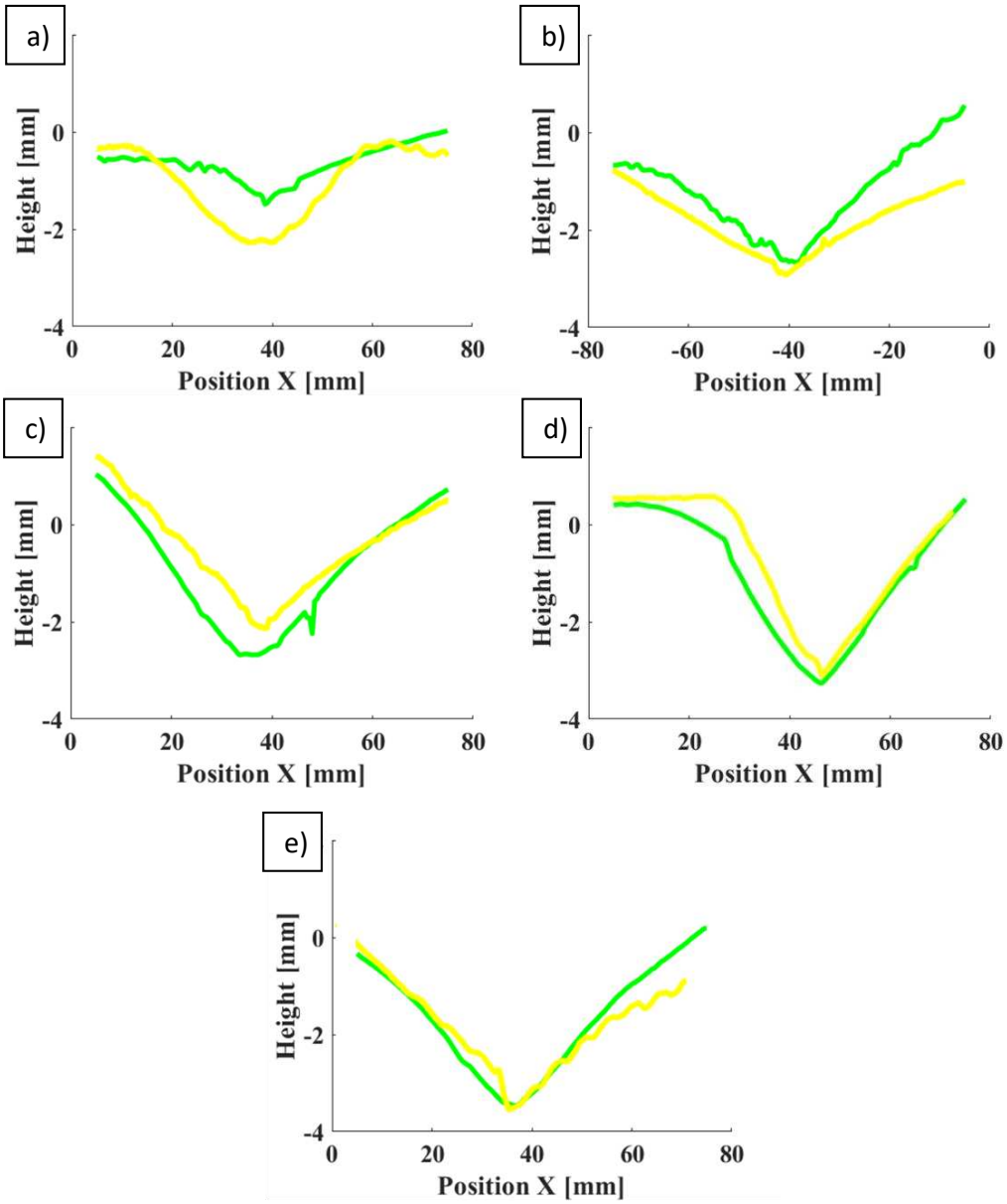

Figure 5. Midplane deformation at CAI where green line is the front plane, yellow line is the back plane; a) Reference; b) 25% PCL; c) 50% PCL; d) 75% PCL; e) 100% PCL

The comparisons show that as the PCL increases, the curves become more and more aligned. Delamination failure may occur for samples with a low PCL ratio, which explains the difference between the stress-deformation curves, especially for reference samples where there is a millimeter difference between the two curves. In the case of samples with a higher PCL percentage, we can speak of fibre breakage so that the contact surfaces did not separate to the same extent during delamination as during delamination, so the curves fell more on top of each other. At high PCL content the structural integrity of the specimens remained.

3. Conclusions

We performed compression after impact tests on interface-modified (which inter-layer formed semi-IPN structure) composite samples. A more ductile behavior appeared with increasing the concentration of the interlayer material. The interfacial adhesion has been changed locally, and the shear strength has also increased with the help of the thermoplastic material. A 3D scanning

  doi:10.5075/epfl-298799_978-2-9701614-0-0

procedure was used to observe the deformation zone, in which the front and back sides of the specimens were analyzed in a MatLab environment. The characteristic failure can be determined from the formed deformation fields. The structural integrity in the case of reference samples disappeared after the load was unapplied, which also appeared on the line diagrams. In the case of the modified samples, the layers could work together until the load ceased and no layer separation occurred. Due to the long-term cooperation of the layers, a more ductile behavior appeared during the damage process.

Acknowledgements

The research reported in this paper and carried out at BME has been supported by the NRDI Fund (TKP2020 IES, Grant No. BME-IE-NAT) based on the charter of bolster issued by the NRDI Office under the auspices of the Ministry for Innovation and Technology. The research has also been supported by the NRDI Office (NKFIH FK 124352 and FK 131882).

4. References

1. *Online Etymology Dictionary.* 2020.
2. McGarry, F.J., *Polymer Composites.* Annual Review of Materials Science, 1994. **24**(1): p. 63-82.
3. Witten, E., et al., *Composites Market Report.* Industrievereinigung Verstärkte Kunststoffe, 2018.
4. Fuller, J.D. and M.R. Wisnom, *Ductility and pseudo-ductility of thin ply angle-ply CFRP laminates under quasi-static cyclic loading.* Composites Part A: Applied Science and Manufacturing, 2018. **107**: p. 31-38.
5. Fuller, J.D., M. Jalalvand, and M.R. Wisnom, *Combining fibre rotation and fragmentation to achieve pseudo-ductile CFRP laminates.* Composite Structures, 2016. **142**: p. 155-166.
6. Yu, H., et al., *Pseudo-ductility in intermingled carbon/glass hybrid composites with highly aligned discontinuous fibres.* Composites Part A: Applied Science and Manufacturing, 2015. **73**: p. 35-44.
7. Finley, J., et al., *Exploring the pseudo-ductility of aligned hybrid discontinuous composites using controlled fibre-type arrangements.* Composites Part A: Applied Science and Manufacturing, 2017. **107**.
8. Tepfers, R., et al., *Ductility of nonmetallic hybrid fiber composite reinforcement for concrete.* Mechanics of Composite Materials - MECH COMPOSITE MATER-ENGL TR, 1996. **32**: p. 113-121.
9. Hodgkin, J.H., G.P. Simon, and R.J. Varley, *Thermoplastic toughening of epoxy resins: a critical review.* Polymers for Advanced Technologies, 1998. **9**(1): p. 3-10.
10. Pearson, R.A. and A.F. Yee, *Toughening mechanisms in thermoplastic-modified epoxies: 1. Modification using poly(phenylene oxide).* Polymer, 1993. **34**(17): p. 3658-3670.
11. Pearson, R.A. and A.F. Yee, *Influence of particle size and particle size distribution on toughening mechanisms in rubber-modified epoxies.* Journal of Materials Science, 1991. **26**(14): p. 3828-3844.
12. Szebényi, G., B. Magyar, and T. Czigany, *Achieving Pseudo-Ductile Behavior of Carbon Fiber Reinforced Polymer Composites via Interfacial Engineering.* Advanced Engineering Materials, 2021. **23**(2): p. 2000822.
13. Magyar, B., T. Czigany, and G. Szebényi, *Metal-alike polymer composites: The effect of inter-layer content on the pseudo-ductile behaviour of carbon fibre/epoxy resin materials.* Composites Science and Technology, 2021. **215**: p. 109002.

14. Szebényi, G., et al., *3D printing-assisted interphase engineering of polymer composites.* Concept and feasibility, 2017. **11**(7): p. 525-530.

DEVELOPMENT OF A NEW METHODOLOGY FOR AUTOMATED QUANTIFICATION OF IMPACT INDUCED DAMAGE PATTERN IN CFRP MEASURED BY IRT AND X-RAY RADIOGRAPHY

Yagdjian[a], Harutyun; Vogtmann[b], Julia; Gurka, Martin

a: Harutyun.Yagdjian@ivw.uni-kl.de
b: Julia.Vogtmann@ivw.uni-kl.de

Abstract: *In this research paper, we present a sensitive algorithm for automatic quantification of the lateral extent of impact-related damages in carbon fibre reinforced plastic (CFRP) measured by imaging non-destructive (NDT) test methods. We compare our method with known state-of-the-art methods for contour detection using X-ray radiography and IR thermography images. In order to identify the real damaged area, micrographs of polished cross-sections were used as reference. The algorithm for contour detection proposed by us provides a very good alternative with high accuracy and sensitivity, especially for X-ray radiography or IR thermography images with low signal to noise ratio.*

Keywords: Contour detection, Automated defect quantification, X-ray radiography, IR thermography, Impact damage

1. Introduction

The detection and quantification of low-velocity impact damage in CFRP is highly relevant for the development and service use of CFRP applications as it occurs frequently and causes a complicated, sometimes hard to detect damage pattern.[1] NDT test methods such as ultrasonic inspection (US), IR thermography (IRT) - and in laboratory environment X-ray radiography and X-ray computed tomography (CT) - are state of the art methods for the characterization of such damages.[2] Contour detection algorithms, such as Canny Edge, Active contour model (snake model), threshold based, histogram based etc. are used to separate the region of interest (ROI) before binarization and quantification.[3] Because of the inherently low contrast in IRT[4] or X-ray[5] images of impact damages in CFRP and the combination of different damage modes, such as fibre breaking, fibre-matrix detachments and delamination of the individual layers[4,6], the automated evaluation and quantification is especially challenging.

In this research, we propose a new algorithm for automated quantification of such images, based on the analysis of the information content in the image rather than on previously detected contour lines to provide a basis for the automated evaluation of data derived by NDT test methods with constantly evolving capabilities such as higher resolution and faster tracking, resulting in a large amount of data.

It is based on approaches adapted from the analysis of acoustic emission (AE) signals, namely the Akaike information criterion (AIC)[7,8], the short-term average/long-term average (STA/LTA) ratio technique[9] and the spectral power density (PSD) analysis method[10]. It was tested on a dataset acquired with X-ray radiography and IRT from the same CFRP samples which were low-

  doi:10.5075/epfl-298799_978-2-9701614-0-0

velocity impacted with different impact energies (10J, 7J, 5J) in a drop tower setup as described in[11]. Additionally, we calibrated our results with data obtained by high-resolution CT and microscopy of polished cross sections.

2. Methods

2.1 Impact testing

The dimension of the specimens were 600 × 600mm^2, with a thickness of 1.70 ± 0.01mm, cut out from plates with a layup of (45/-45/45/-45/90/0/90)s, fabricated from unidirectional prepreg (Solvay Cycom 977-2-35-12kHTS-134-1500, consisting of carbon fibre Teijin Tenax HTS40 and epoxy resin Cycom 977-2). The sheets were cured in an autoclave (pressure <0.1 mbar) at 180◦C and 7bar for 3h. The plates were subjected to impact loading using a drop tower setup according to DIN EN 6038 and AITM1-0010. A circular impactor with a diameter of 16 mm and a total mass of 4.74kg was used. The impact force was recorded using a 100kN load cell. Further details are described in[11].

2.2 Infrared thermography

IRT is considered an effective method for evaluating impact damage and is therefore often used to detect the damage area after impact. IRT´s advantages are contactless, direct imaging at high speed, good resolution and sensitivity.[12]

Offline pulse-phase thermography (PPT) was performed in reflection geometry as described in[11]. The surface temperature was measured with an IR camera (Image IR9410 BI S, InfraTec GmbH, Dresden, Germany) having a thermal sensitivity of < 0.20mK. A telephoto lens with f = 50mm was used at a distance to the sample of 1320mm. The image sensor of the camera has 1280 × 1024 px and the geometric resolution was set to 0.211 mm/px, referring to the outer edges of the sample. The acquisition rate SR was set to 180 Hz and the acquisition duration to 30s with a pretrigger of 0.1s (18 frames).

2.3 X-ray radiography/CT

X-ray radiography combined with a contrast agent is a fast and easy tracking method for inner delamination. To determine whether X-ray projections are showing the real damage area in addition, a high-resolution volume scan with the same device was made and compared with optical microscopy on micrographs of polished cross sections.

The projections and the high-resolution CT volume scan were taken with a micro-focussed X-ray CT (Zeiss Versa 520). To enhance contrast, the samples were previously immersed for 24 hours in a contrast agent solution consisting of 250g zinc iodide in 80ml distilled water and 80ml isopropyl alcohol with 1ml wetting agent (Tetenal Mirasol 2000) at room temperature for 24 hours. Projections were averaged from 10 single frames acquired with an accelerating voltage of 40kV, a beam power of 3W, exposure time of 3s and a geometric resolution of 0.019 mm/px. To account for the laterally non-uniform emission profile of the X-ray source and sensitivity of the detector, a reference image was subtracted. For the determination of the damage area, the absorption image was used. The volume scan was done with an accelerating voltage of 50kV, a

beam power of 4W, an exposure time of 0.15s with averaging 20 single frames per projection and a resolution of 0.025 mm/px.

2.4 Data processing

The defect detection algorithm developed in this research is based on considering any line in the image as spatial 1D-dataset and used the adapted event detection algorithms of AE to identify the defect contour or rather the defect area. Briefly about three different AE-algorithms are used:

(a) AIC: The concept formulated by Hirotugu Akaike - Akaike Information Criterion (AIC)[7], originally introduced for the purpose of statistical identification, was established by Maeda[8] for signal onset detection in seismic data analysis[8] and since then is one of the widely used methods in acoustic signal processing. The idea is to compare the entropy of the given dataset which includes stochastic noise and signal itself. Each point in time (in our case each spatial point) divides the dataset into two windows whose variances are calculated. Usually, the global minimum of AIC, which is calculated for each time (or spatial) point using equation (1), is assumed as the start of the signal.

$$AIC(t_i) = t_i \cdot \log\left(\sigma_{1,i}^2\right) + (t_N - t_i - 1) \cdot \log\left(\sigma_{i,N}^2\right) \quad i \in [1, N] \tag{1}$$

where $\sigma_N^2 = \frac{1}{N}\sum_{j=1}^{N}(x_i - \bar{x})^2$.

For a better adjustment on our goals, we also consider local minima and their heights which may appear before global ones. Local height (if it exists) comparison to global allows threshold introduction and thus better control of the procedure.

(b) STA/LTA: By this approach, the dataset is divided into two consecutive short and long windows at each point in time (or in our case space). For each window, using the characteristic function - f, corresponding mean values STA and LTA are calculated. The ratio between mean values as given by equation (2) is used as a criterion for determining the onset of the signal. The onset of the signal is considered at the moment when the amplitude of the calculated ratio exceeds a previously set threshold value.

$$\left(\frac{STA}{LTA}\right)_i = \frac{\frac{1}{N_S}\sum_{j=i-N_S}^{i} f(x_j)}{\frac{1}{N_L}\sum_{j=i}^{i+N_L} f(x_j)} \tag{2}$$

(c) PSD: We modified and employed the event detection method of the PSD technique introduced by Vaezi & Van der Baan[10]. The main idea is to compare estimated power spectral densities $PSD_n^t(f)$ for each segment of the data set with mean power spectral densities $\overline{PSD}(f)$ calculated by the Welch method[13] using a Hann window. In this research the classic (global minimum) AIC method on the calculated average version of the PSD ($\Lambda(t)$) according to equation (3) is used to detect the outer contour of the damage area.

$$\Lambda(t) = \frac{\sum_f u_t(f)}{N_f} \quad \text{where } u_t(f) = \frac{\Delta PSD_n^t(f)}{\sigma(f)},\ \Delta PSD_n^t(f) = PSD_n^t(f) - \overline{PSD}(f) \tag{3}$$

Returning to the defect contour search, summation of 2D dataset elements (image) over the horizontal and vertical axis supply two new 1D datasets. On both of them (in forward and

  doi:10.5075/epfl-298799_978-2-9701614-0-0

backward direction), the described technique was applied to determine the region of interest (ROI) where the defect is approximately located. According to the characteristics of the specimen, it can be expected that the defect has centro-symmetry with respect to the position of impact. Based on these characteristics, it can be assumed that the center of the ROI is more likely located within the defect. Moreover, “all lines" (1D datasets) crossing the center point are used and the same approach is applied to find the points of the damage contours. Once the contour of the defect has been identified, standard algorithms are used to fill the area inside prior to binarization (cv2.fillConvexPoly from OpenCV Python module) and quantitative determination of the damage area. Another important aspect is the presence of noise or/and very small defects in the image that can affect the algorithm. At the beginning, to reduce the influence of noise, a two-dimensional median filter (e.g. scipy.ndimage.median_filter) can be applied to the data. Additionally, a density-based spatial clustering of applications with noise (DBSCAN) algorithm[14] was adapted to filter the contour points found before they are used to determine the damage area.

3. Results and Discussion

At first, the algorithm was tested on X-ray absorption and PPT images of 8 CFRP plates after low-velocity impact testing with different impact energy (5J, 7J, 10J)[11]. To ensure the automation of the process, the control parameters optimized for each algorithm and the DBSCAN clustering filter were determined in advance and then applied for the evaluation of all 8 images. When comparing the results qualitatively, the AIC method showed the best results for X-ray radiography images (Figure. 1). Because of this, it was selected for further comparison with standard methods.

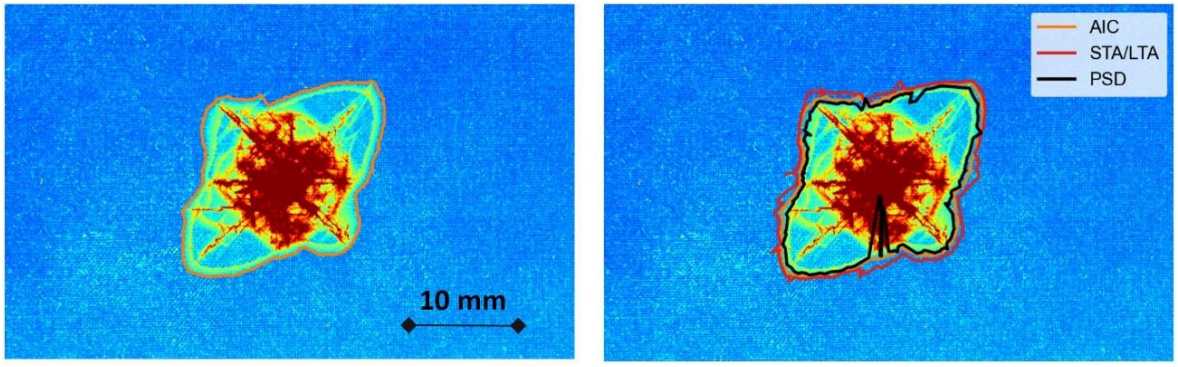

Figure 1 : Comparison of automated contour search with three different AE-algorithms applied to a X-ray absorption image (right). The best result was found with the AIC method (left).

For comparison, four widely used algorithms have been considered (Canny Edge, Active contour model (snake model), Threshold based and Histogram based contour detection algorithms), all implemented in the Python modules *cv2* and *skimage*. These standard algorithms usually consist of several steps which include, among others, noise reduction using different filters. It should be noted that for specific tasks/cases it is not always possible to set the control parameters in such a way that all images can be processed automatically with best results. Therefore, in order to obtain comparable results, we adapted these parameters to each image individually for all methods so that automated processing was not possible. Only the histogram-based method

  doi:10.5075/epfl-298799_978-2-9701614-0-0

provided good results automatically (Figure 2 left). Qualitative and quantitative comparison shows comparable results between the histogram based method and ours (Figure. 2 right / Table 1).

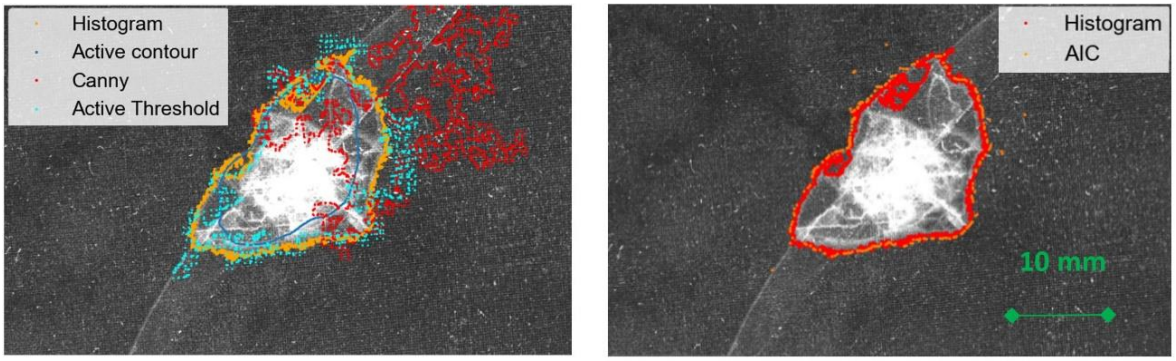

Figure 2 : Comparison of contour search standard algorithms (left) and the best results with our method (right) applied to an X-ray absorption image.

Table 1: Comparison of the detected defect area [pixel] with standard methods considered in this research for all investigated specimens

Impact energy	defect area [pixel]				
	Our method	Histogram	Canny	Active Threshold	Active contour (snake model)
10 J	987336	971407	902769	505901	729869
10 J	1288824	1197471	784828	777117	1169354
7 J	823221	755920	534223	374781	701305
10 J	1269945	1375604	1335989	1239727	986590
7 J	756747	702732	636110	728488	462809
5 J	530678	487615	739387	170665	403869
5 J	503124	474341	629743	2336919	683469
7 J	913959	1067947	1034743	570272	1013625

In contrast, when examining IRT images, the PSD-based contour search algorithm showed better results than the others (Figure 3 above). The standard methods (Histogram based, Canny Edge, Adaptive Threshold) delivered more or less good results. Despite the fact that in many cases the damage contours found in the comparison above can be qualified as good by visual inspection, the question remains open: How well do these automatically detected contours reflect the real damaged area? To answer this question and to set the basis for a calibration of the NDT test methods investigated, here selected specimens were examined further. Firstly, high-resolution X-ray CT scans were acquired from which the 3D volume of the specimen was reconstructed. Secondly, polished cross sections of selected specimens were prepared with 1mm increment across the lateral extension of the defect and examined with optical microscopy. As an example,

  doi:10.5075/epfl-298799_978-2-9701614-0-0

the cross section image from optical microscopy is compared with the corresponding cross section derived from the reconstructed X-ray CT scan in Figure 4. The exact location of the cross section is shown in the left-hand side of Figure 4. The lateral extension of the impact damage in different depths can be seen in both images similarly.

But the comparison of both images reveals that the contrast agent has not penetrated into the delamination cracks entirely. Due to capillary forces, a small volume at the outer edge was left out. Thorough examination of the X-ray absorption images (Figure 4, left) displays the area penetrated by the contrast agent well, but some shadows can also be seen at the outer border. Further, more quantitative investigations have to be carried out to determine whether such shadows are caused by contrast agent or by the impact damage itself. A quantitative comparison of the total length of the damage at the position of the cross section as marked in Figure 4 (left) leads to very similar results. The cross section depicted in Figure 4 can be assumed to be representative.

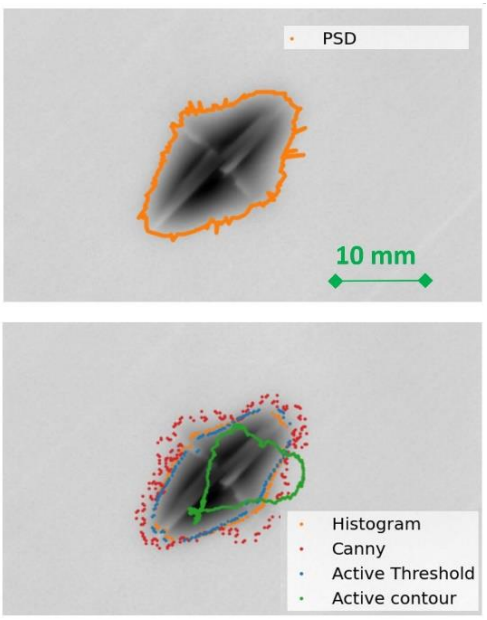

Figure 3 : Representative phase image of PPT of the impact specimen and associated contour search results using standard methods (below) and ours (above).

The length obtained from the optical microscopy micrograph and from the CT section are 10.01mm and 10.13mm, respectively. From the automated determination of the defect size from the 2D image derived by X-ray absorption image a length of approx. 10.16mm can be found.

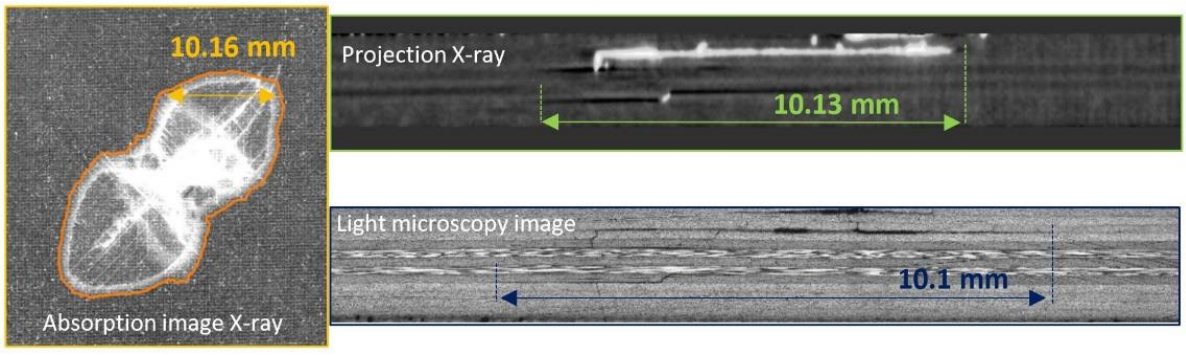

Figure 4: Qualitative comparison and quantitative measurement of damage size from three test methods : X-ray radiography absorption image (left), cross section derived from reconstructed X-ray CT scan (right- above) & light microscopy image of polished cross section (right-below) and contour search using our method.

  doi:10.5075/epfl-298799_978-2-9701614-0-0

4. Conclusion

The algorithm for automated contour detection we proposed is a good alternative to the well-established standard algorithms for image processing. Its main advantages are the high sensitivity and accuracy, especially for images with low signal-to-noise-ratio, derived by X-ray radiography, X-ray CT scan or infrared thermography. In addition, the possibility to adapt the threshold for damage contour detection to a certain method or group of specimen proved useful for the investigation of low-velocity impact damage in CFRP.

For a precise calibration for automated quantification, some additional research should be carried out to resolve the issues arising from the usage of a contrast agent for X-ray imaging. There is also great potential for an optimized implementation in Python to speed up the computations.

5. References

(1) Maierhofer, C.; Krankenhagen, R.; Röllig, M. Application of Thermographic Testing for the Characterization of Impact Damage during and after Impact Load. *Composites Part B: Engineering* **2019**, *173*, 106899. https://doi.org/10.1016/j.compositesb.2019.106899.

(2) Towsyfyan, H.; Biguri, A.; Boardman, R.; Blumensath, T. Successes and Challenges in Non-Destructive Testing of Aircraft Composite Structures. *Chinese Journal of Aeronautics* **2020**, *33* (3), 771–791. https://doi.org/10.1016/j.cja.2019.09.017.

(3) Gong, X.-Y.; Su, H.; Xu, D.; Zhang, Z.; Shen, F.; Yang, H.-B. An Overview of Contour Detection Approaches. *International Journal of Automation and Computing* **2018**, *15*, 1–17. https://doi.org/10.1007/s11633-018-1117-z.

(4) Sause, M. G. R. *In Situ Monitoring of Fiber-Reinforced Composites: Theory, Basic Concepts, Methods, and Applications*; Springer series in materials science; Springer, 2016.

(5) Popow, V.; Gurka, M. Full Factorial Analysis of the Accuracy of Automated Quantification of Hidden Defects in an Anisotropic Carbon Fibre Reinforced Composite Shell Using Pulse Phase Thermography. *NDT & E International* **2020**, *116*, 102359. https://doi.org/10.1016/j.ndteint.2020.102359.

(6) Léonard, F.; Stein, J.; Soutis, C.; Withers, P. J. The Quantification of Impact Damage Distribution in Composite Laminates by Analysis of X-Ray Computed Tomograms. *Composites Science and Technology* **2017**, *152*, 139–148. https://doi.org/10.1016/j.compscitech.2017.08.034.

(7) Akaike, H. Markovian Representation of Stochastic Processes and Its Application to the Analysis of Autoregressive Moving Average Processes. *Ann Inst Stat Math* **1974**, *26* (1), 363–387. https://doi.org/10.1007/BF02479833.

(8) Maeda N. A Method for Reading and Checking Phase Time in Auto-Processing System of Seismic Wave Data. *Zisin (Journal of the Seismological Society of Japan. 2nd ser.)* **1985**, *38* (3), 365–379. https://doi.org/10.4294/zisin1948.38.3_365.

(9) Vaezi, Y.; Van der Baan, M. Comparison of the STA/LTA and Power Spectral Density Methods for Microseismic Event Detection. *Geophys. J. Int.* **2015**, *203* (3), 1896–1908. https://doi.org/10.1093/gji/ggv419.

(10) Vaezi, Y.; van der Baan, M. Analysis of Instrument Self-Noise and Microseismic Event Detection Using Power Spectral Density Estimates. *Geophysical Journal International* **2014**, *197* (2), 1076–1089. https://doi.org/10.1093/gji/ggu036.

(11) Popow, V.; Vogtmann, J.; Gurka, M. In-Situ Characterization of Impact Damage in Carbon Fibre Reinforced Polymers Using Infrared Thermography. *Infrared Physics & Technology* **2022**, *122*, 104074. https://doi.org/10.1016/j.infrared.2022.104074.
(12) Busse, G.; Wu, D.; Karpen W. Thermal Wave Imaging with Phase Sensitive Modulated Thermography. *Journal of Applied Physics:* **1992**, *71* (8).
(13) Welch, P. The Use of Fast Fourier Transform for the Estimation of Power Spectra: A Method Based on Time Averaging over Short, Modified Periodograms. *IEEE Trans. Audio Electroacoust.* **1967**, *15* (2), 70–73. https://doi.org/10.1109/TAU.1967.1161901.
(14) Schubert, E.; Sander, J.; Ester, M.; Kriegel, H. P.; Xu, X. DBSCAN Revisited, Revisited: Why and How You Should (Still) Use DBSCAN. *ACM Trans. Database Syst.* **2017**, *42* (3), 1–21. https://doi.org/10.1145/3068335.

INVESTIGATION OF BAMBOO NODES INTERNAL STRUCTURE WITH X-RAY MICRO-CT IMAGING

Judith Gouin[a,b], Pascal Turberg[b,c], Anastasios P. Vassilopoulos[a]

a: Composite Construction Laboratory (CCLab), Ecole Polytechnique Fédérale de Lausanne (EPFL), 1015 Lausanne, Switzerland – judith.gouin@epfl.ch
b: Plant Ecology Research laboratory (PERL), Ecole Polytechnique Fédérale de Lausanne (EPFL), 1015 Lausanne, Switzerland
c: WSL Swiss Federal Institute for Forest, Snow and Landscape Research, Site Lausanne, Switzerland

Abstract: *This study presents the 3D characterization of the nodal region of an Arundinaria amabilis bamboo using X-ray micro-computed tomography imaging (µCT). The complex pattern of vascular bundles across the node was identified, and the sample was characterized regarding the relative volumes of parenchyma and sclerenchyma tissues. The results show that the node witnesses the development of radial and tangential vascular bundles, forming a net-like pattern. Some specific nodal structures ("splitting bundles") were also identified: regularly distributed around the culm, they split below the diaphragm between bundles crossing radially into the diaphragm and others deviating to the outer side of the culm. Finally, the volumetric fraction of lignified sclerenchyma tissue reaches a minimum at the location of the node. In addition, the µCT technique was used to build a discretized model of an internodal part of the bamboo sample, thus allowing to recreate the real 3D structure of the composite material and showcasing the potential of µCT imaging for finite element analysis.*

Keywords: Bamboo node; X-ray microtomography; 3D reconstruction; Vascular bundles; Finite-element model

1. Introduction

Bamboo is a sustainable, fast-growing and resistant material used in the construction industry in recent years, as an environmentally friendly alternative to more traditional and polluting construction materials. A bamboo culm is composed of an alternation of hollow internodes and solid nodes [1] and consists of vascular bundles embedded in parenchyma ground tissue. Bamboo is considered a natural composite, and its morphological structure directly influences its mechanical properties. The vascular bundles are responsible for the transport of water and nutrients within the culm and are themselves composed of xylem and phloem vessels surrounded by protective fiber sheaths made of sclerenchyma tissue. The sclerenchyma fibers are dense and provide strength and stiffness to the bamboo culm [2] while the parenchyma ground tissue behaves like a foam and distributes the local stresses to the whole structure as a matrix [3,4].

The structure of internodes is today well understood; the vascular bundles are longitudinally arranged in internodes and their distribution follows a radial density gradient. The morphological structure of bamboo nodes – controlling the mechanical properties - is however more complex and has been less studied. Research on bamboo nodes began in the 1960s [6], relying mainly on optical microscopy. Using enlarged images of longitudinal and transverse

  doi:10.5075/epfl-298799_978-2-9701614-0-0

sections, [7] studied the anatomical characteristics of vascular bundles in bamboo nodes, while [8] reconstructed by hand the complex 3D structure of a node, showing that bamboo nodes witness an intensive fusion and separation of conducting cells as well as vascular bundles deviating from their longitudinal path and passing horizontally through the diaphragm.

2D visualization methods remain limited since they require complex and sometimes damaging preparations of the samples. In recent years, several studies have turned to the high-resolution and non-invasive technique of X-ray microtomography (µCT) to better understand the internal structure of bamboo nodes through 3D reconstruction [10-14]. However, among those, only [14] investigated the structure of a simple node (without any type of branching) through 3D reconstruction which provided a general view of the fibers' connectivity but didn't discuss the effect the fibers have on the node's performance. Indeed, there is to this day no consensus on the mechanical properties of bamboo nodes and the research on this topic remains quite sparse and often contradictory, nodes being seen either as weak points in the culm or helping to strengthen it [9, 15-16].

The main goal of this work is to isolate the path of individual fibers in a bamboo node to better understand the behavior of the vascular bundles in the node and how it affects the mechanical properties of bamboo nodes. With this view in mind, this study is also investigating the potential of µCT imaging for building a finite-element model of the node. Such model based on the real 3-dimensional geometry of the node would indeed allow to perform numerical simulations that could be of critical interest for the understanding of the node behavior. An FE model of a node is built following a simple procedure based on an automatic threshold.

2. Materials and methods

2.1 Material

Samples of *Arundinaria amabilis* bamboo were purchased from www.bambushandel-condam.de. A section of the culm of 21 mm in height, with an external diameter of 26 mm and internal diameter of 17mm, was selected for µCT scanning. The node was positioned at the center of the scanned sample.

2.2 X-ray computed microtomography

The µCT imaging technique is based on the attenuation of the X-ray radiation by the scanned material. It thus allows to detect materials that attenuate the radiations differently. In the case of bamboo, dense fibers tend to attenuate a lot the X-rays, while the softer and more porous parenchyma attenuates less. As for the conducting vessels, they do not attenuate at all X-rays. µCT imaging therefore allows to detect the three main components of a bamboo culm: parenchyma, fibers and conducting vessels. The sample was scanned using an Ultratom X-ray imaging system from RX solutions. The following scan parameters were used: X-ray source voltage of 45 kV, current of 311 µA, and averaging over 6 pictures. The images were acquired at a rate of 2.5 pictures/second and a total of 1632 projections were used. A resulting voxel size of 0.0143 µm was obtained.

2.3 Image processing

Images were processed and analyzed using the AVIZO 3D software (2021.1 version). The slices were combined and reconstructed from the projections with a non-iterative filtered backprojection algorithm and exported as a stack of TIFF images. A total of 1509 slices was obtained. The original TIFF stack was denoised using the non-local means denoising filter of

  doi:10.5075/epfl-298799_978-2-9701614-0-0

AVIZO 3D. The automatic threshold function of AVIZO 3D was then used to segment the different tissues from one another: fibers, parenchyma and conducting vessels (Figure 2). The volumetric content of the different components was then computed for the whole sample as well as for each transverse slice.

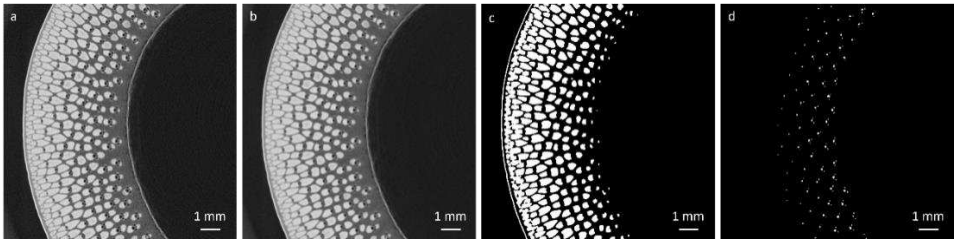

Figure 2. Image processing of the µCT stack. (a) Detail of an original transverse µCT section. Color scale: densest and most attenuating materials (fibers) in white to least attenuating materials (voids) in black. (b) After denoising with a non-local means filter. (c) Binary mask of the fibers after segmentation. (d) Binary mask of the conducting vessels after segmentation.

2.4 Finite-element model

Once the segmentation of the different components of the culm was performed, an attempt was made at meshing the structure. The goal was to obtain a finite-element model that could be exported to ABAQUS software for further numerical simulations. To ease the meshing, the structure was simplified by considering only the parenchyma and the fibers: the conducting vessels, which represent no more than a few percent of the culm in terms of volume, were included in the parenchyma segmentation. Two approaches were followed to develop the finite-element model. The first one was based on the generation of a surface mesh using the AVIZO 3D *"Generate surface"* function. The generated surface was then exported as an .STL file into the open-source software Meshmixer, where the mesh was repaired and simplified. Finally, the open-source software Gmsh was used to compute the final solid mesh from the surface mesh. An alternative approach was also implemented using the X-Wind meshing module of AVIZO 3D, which allows to directly compute a solid mesh based on a given segmentation.

3. Results and discussions

3.1 Morphological analysis of the node

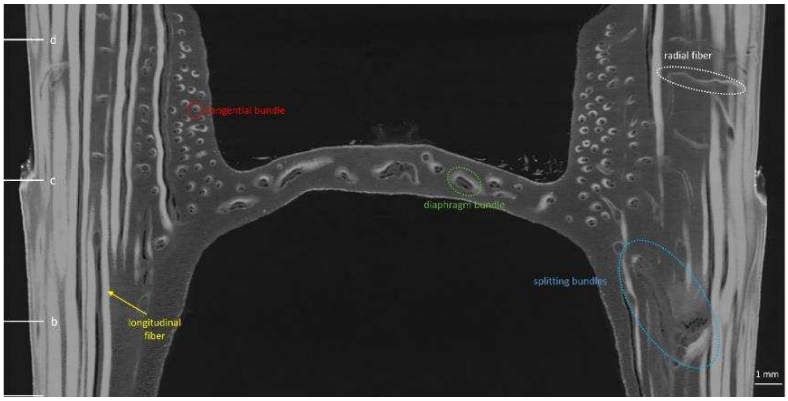

Figure 3. Longitudinal view of the node and identification of different types of vascular bundles.

The general morphology of an *Arundinaria amabilis* bamboo node can be seen in Figure 3. On the transverse sections (Fig. 4 and 5) the different components of the culm can be well

distinguished: the parenchyma and the vascular bundles consisting of the sclerenchyma fibers and the conducting vessels. The morphological characteristics of fibers and vascular bundles in the node can be identified on the longitudinal and transverse section views of Figures 3 to 5.

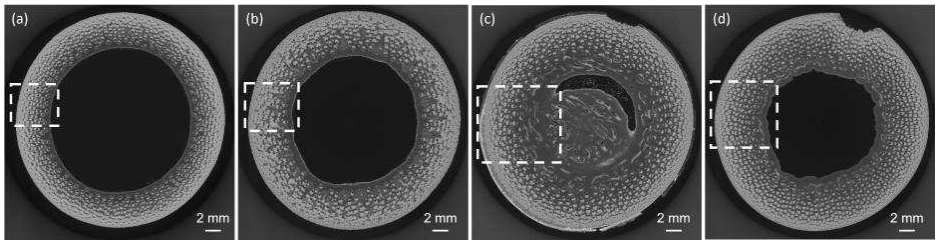

Figure 4. Transverse views at different locations of the culm. (a) at the bottom. (b) below the diaphragm. (c) at the sheath scar and diaphragm position. (d) above the diaphragm.

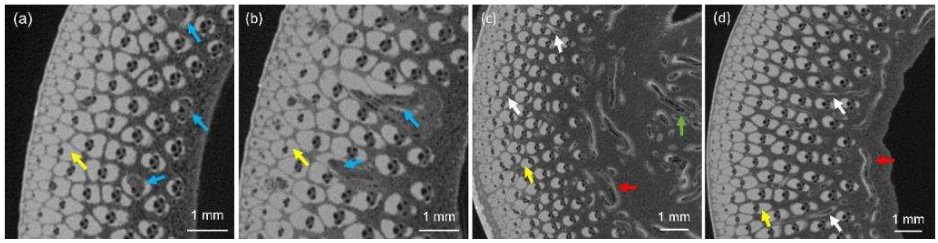

Figure 5. (a to d) Close-up of the transverse slices of Fig. 4. Longitudinal fibers (yellow arrows), splitting bundles (blue arrows), tangential bundles (red arrows), radial fibers (white arrows), diaphragm bundle (green arrow).

At the bottom of the node (Fig. 5a) all the fibers have a longitudinal orientation. Closer to the node, the thickness of the culm increases, and the vascular bundles tend to lose completely their lateral fiber sheaths, while the two polar sheaths of the bundles increase in size and become rounder, as had already been noticed by [7] and [9]. Some peculiar layout also begins to appear, called "splitting bundles" in this manuscript. The "splitting bundles" are originally located on the inner layer of the culm and regularly distributed on its circumference (Fig. 5a, blue arrows). They first begin to dilate (Fig. 5a, blue arrows), before splitting below the diaphragm into several bundles (Fig. 5b, blue arrows): some will deviate radially of a few millimeters towards the outer side of the culm before regaining a longitudinal orientation, while another bundle will develop towards the center of the culm and cross into the diaphragm (Fig. 3). That specific type of "splitting bundles" had not been analyzed by [14] but can however be detected on the µCT node images shown in that paper. Those bundles seem to be a critical element for the transverse transport of water and nutrients in the culm.

The bundles that cross into the diaphragm mostly have a horizontal orientation (Fig. 3 and 5, green arrows). Unlike the longitudinal vascular bundles of the culm which have large fiber sheaths and small conducting vessels, the diaphragm bundles are mainly composed of conducting elements only surrounded by a thin layer of sclerenchyma tissues. Above the node, many small tangential vascular bundles that turn and twist forming a ring around the culm can be detected; an observation that agrees with previous observations by [1][11][12]. Thin fibers developing radially can also be observed above the diaphragm of the node (Fig. 3 and 5, white arrows) that originate by branching from the main longitudinal fibers. Above the node, the combination of radial, tangential and longitudinal bundles creates a three-dimensional

interwoven net of fibers [9][14]. When moving away from the node, the longitudinal fibers regain their original elongated shape and lateral sheaths appear again.

An automatic segmentation of the sample was also performed, enabling the visualization of the global pattern of vascular bundles (fibers and conducting vessels) in the node (Fig. 6). The ring of tangential and radial fibers above the node can be well identified on Fig.6a., and the pattern of "splitting bundles" joining the diaphragm from the inner side of the culm can be noticed on Fig.6b. Concerning the conducting vessels, Figs.6c. and 6d. show that they remain mostly longitudinal, except near the diaphragm where tangential vessels appear in the inner side of the culm, as well as vessels crossing horizontally the diaphragm. In general, a high connectivity between the vascular bundles can be observed especially in the diaphragm and in the inner layer of the culm, which is consistent with the findings of [14] and [7], who first noticed that an "intensive fusion and re-separation" of vascular bundles occurs in the node. Through the fusion of vascular bundles in the diaphragm, most conducting vessels can cross from one side of the culm to the other, as is shown in Figure 6d.

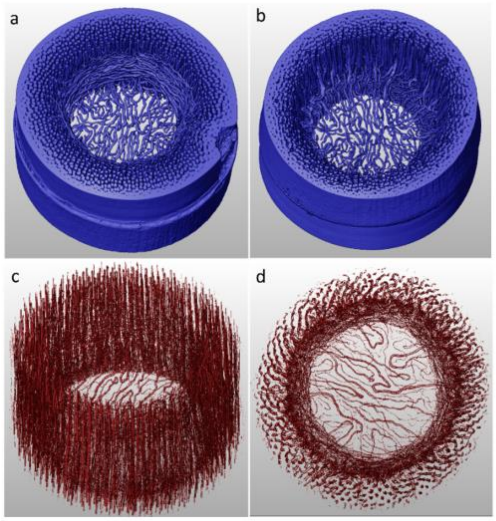

Figure 6. (a) Segmentation of the fibers, top side view. (b) Segmentation of the fibers, bottom side view. (c) Segmentation of the conducting vessels, top side view. (d)

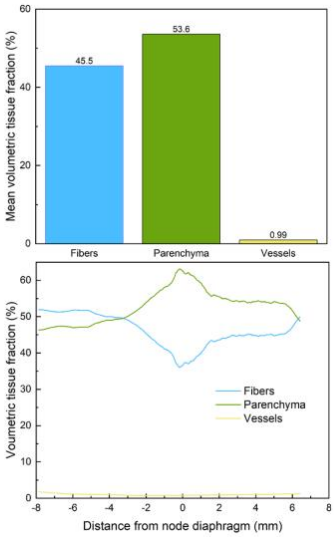

Figure 7. (top) Mean tissue fractions over the whole sample. (bottom) Distribution across the node.

Using this segmentation, the volumetric fraction of fibers, vessels and parenchyma could directly be computed at different positions of the culm (Fig. 7). The mean volumetric fractions over the whole node were also computed: the sample is composed of 53.6% parenchyma, 45.5% fibers and 0.99% conducting vessels. Those fractions differ quite significantly from what had been found by [14], who reported a smaller content of fibers and larger amount of conducting vessels. This discrepancy could however be explained by the different species of bamboo used as well as the uncertainty of measurement due to the segmentation. The profile of fiber content across the node seems however to corroborate the trend observed by [14]. Starting from below the node, the fiber content decreases as the culm thickens and reaches a minimum of 36% at the location of the diaphragm. Above the node, where the ring of tangential bundles is present and the culm remains thick, the fiber content stagnates at 45%, before regaining its internodal value of about 51%. This shows that for *Arundinaria amabilis bamboos*, nodes have a lower fiber

  doi:10.5075/epfl-298799_978-2-9701614-0-0

content than internodes, despite the apparition of horizontal bundles and the coarser fibers in the node.

The X-ray microtomography that was performed in the frame of this work allowed the detailed analysis of the morphology of an *Arundinaria amabilis* bamboo node. Specific characteristics of the node were identified and clearly visualized for the first time, such as the splitting bundles, the diaphragm structure, and the interwoven net of tangential, radial and longitudinal bundles above the diaphragm. From a biological perspective, this analysis confirms the important role of the node for the transport of water and nutrients [1]: the splitting bundles as well as the high connectivity of the vascular bundles in the diaphragm allow water and nutrients to be transported along the whole culm, longitudinally as well as transversely. Concerning the mechanical properties of the node however, it is hard to reach conclusions based solely on this morphological analysis. On the one hand, the deviations undergone by the longitudinal fibers and especially the splitting bundles, combined with the low fiber content of the node, could be an indicator for the weakness of the node and its low tensile strength [15, 16]. On the other hand, the interweaving fibers above the diaphragm could strengthen the node and make it more resistant to crack propagation [9]. In this context, using µCT to build a finite-element model of the node to perform numerical simulations could be particularly interesting.

3.2 Finite element discretization

The building of a finite-element model of the node based on the segmentation of the µCT image stack was attempted. To simplify the complex geometry of the node, only the fibers and the parenchyma were segmented and considered for the creation of the mesh. It was chosen to neglect the conducting vessels since they only make up a few percent of the total volume of the node. As mentioned in the introduction, [4] and [13] already succeeded in meshing respectively a small internode sample of 2x2 mm and a branching node of about 2 mm in diameter and 8 mm in height.

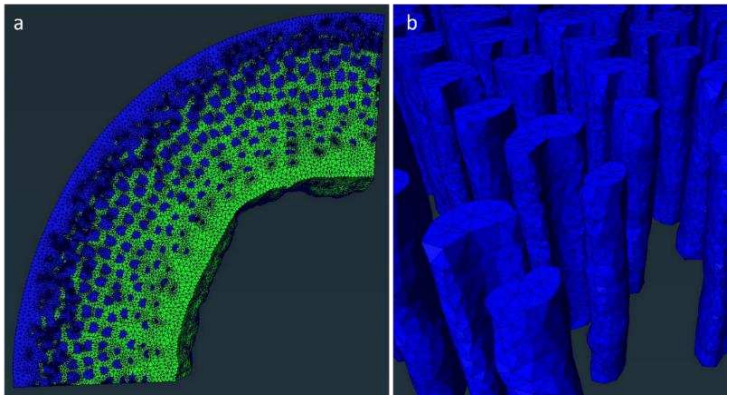

Figure 8. Finite-element model of a part of the culm using the X-Wind module of AVIZO 3D. (a) Meshed sample. Parenchyma in green and fibers in blue. (b) Close-up of the fibers' mesh.

However, the structure of the node investigated in this work is very different from the structure analyzed by Palombini et al. and its size is much bigger (an order of magnitude). Therefore, the manual segmentation method used by Palombini et al., which, although it is very time consuming, allows a clean segmentation and a relatively easy meshing, could not be used in this case. An attempt was therefore made at finding a way to build a mesh of the node using only an automatic threshold segmentation of the fibers.

  doi:10.5075/epfl-298799_978-2-9701614-0-0

Several difficulties were encountered. Initially, to obtain a clean segmentation of the fibers, the µCT images need to be well contrasted and the level of contrast should be uniform over the whole sample. Also, a high resolution is required, which can be a limitation when the scanned sample is big. For example, in this case, the fibers located on the outer side of the culm could not be segmented separately because of a lack of resolution. Finally, due to the complexity of the structure around and in the node, with thin fibers that merge and separate randomly, the resulting surfaces are complicated and make the computation of the mesh very heavy and prone to errors.

Since the meshing of the node proved difficult, an attempt was made at modeling a simpler and smaller part of the culm located above the node, were most of the fibers are oriented longitudinally. The sample considered consists of a quarter of the culm (diameter of 27 mm) of height 1.43 mm. The segmentation was made with an automatic threshold. As mentioned in Section 2.4, two approaches were followed to obtain a good meshing of the structure. The first approach consists of triangulating the surface of the structure using the "Generate surface" function of AVIZO 3D and exporting the resulting surface mesh to Meshmixer for repairing and remeshing operations. Using this repaired and remeshed surface, the final 3D finite-element model can be built using Gmsh. However, this method is not optimal, due to the complication of using different interfaces and the difficulty of repairing the errors generated when creating the surface mesh with AVIZO 3D. The second approach used the X-Wind meshing module of AVIZO 3D, which automatically builds the 3D mesh based on the provided segmentation without having to first create a triangulated surface. This approach resulted in a mesh composed of about 1’400’000 tetrahedrons for both the parenchyma and sclerenchyma (Fig. 8), which remains a reasonable number from a computational point of view while allowing to retain enough details regarding the geometry of the structure. This second approach proved to be efficient and more straightforward than the first one.

Using an automatic threshold segmentation of a µCT scan, a finite-element model for a relatively big internode sample of the culm has been built here. However, the more complex structure of the fibers in the node could not be modeled using this simple procedure since the computation of the mesh quickly became too heavy. Such a model would indeed require a higher scanning resolution as well as a relatively clean segmentation of the fibers, thus avoiding the need to mesh overly complex surfaces.

Conclusions

This study aimed at better understanding the morphological structure of a bamboo node using X-ray microtomography, focusing on investigating the influence of the vascular bundles' layout in the node on the node's mechanical properties. In this context, the potential of µCT for building a finite-element model of the node was also explored. Specific characteristics of the node were identified and clearly visualized for the first time, such as the "splitting bundles", the diaphragm structure and the interwoven net of tangential, radial, and longitudinal bundles above the diaphragm.

From a biological point of view, the existence of splitting bundles and the high connectivity of the vascular elements in the diaphragm seem to indicate that one of the primary roles of bamboo nodes is to allow the transverse transportation of water and nutrients in the culm. Regarding the node's mechanical performance however, the deviations undergone by the longitudinal fibers as well as the low fiber content in the node might indicate that nodes are

  doi:10.5075/epfl-298799_978-2-9701614-0-0

weak points in a bamboo culm, in line with the findings of [15][16]. The net of interweaved bundles identified above the node could in this case be viewed as an attempt to reinforce a weak but essential component of the bamboo culm, since it has been show that the net-like pattern of the node increases its fracture toughness [16].

This study also showed that if the µCT technique has a great potential for meshing large portions of the culm, it reaches its limitations when attempting to mesh more complex structures such as the center of the node, based on a simple threshold segmentation. Once a way to model the node is found, a combination of finite-element analysis and mechanical tests could help conclude on the mechanical strength and properties of bamboo nodes.

Acknowledgements

We thank Gary Perrenoud for micro-CT measurements at the EPFL Platform for X-Ray Radioscopy and Tomography (PIXE). This work was supported through an ENAC Exploratory grant 2018/2020 in the frame of the “New plant-based composite materials” project.

1. References

1. Liese, W. (1998). The anatomy of bamboo culms, volume 18. Brill.
2. Amada, S., Munekata, T., Nagase, et al. (1996). The mechanical structures of bamboos in viewpoint of functionally gradient and composite materials. J Comp Mat, 30(7):800–819.
3. Dixon, P. G. and Gibson, L. J. (2014). The structure and mechanics of moso bamboo material. Journal of the Royal Society Interface, 11(99):20140321.
4. Palombini, F. L., et al. (2016). Bionics and design: 3d microstructural characterization and numerical analysis of bamboo based on x-ray microtomography. Mat Char, 120:357–368.
5. Obataya, E., et al. (2007). Bending characteristics of bamboo (phyllostachys pubescens) with respect to its fiber–foam composite structure. Wood sci technol, 41(5):385–400.
6. Lee, C. et al. (1960). Anatomical studies of some chinese bamboos. J Integ Plant Biol, 9(1).
7. Grosser, D. and Liese, W. (1971). On the anatomy of asian bamboos, with special reference to their vascular bundles. Wood Science and technology, 5(4):290–312.
8. Ding, Y. and Liese, W. (1995). On the nodal structure of bamboo. Bamboo Res, 14:24–32.
9. Chen, G. and Luo, H. (2020). Effects of node with discontinuous hierarchical fibers on the tensile fracture behaviors of natural bamboo. Sust Mat Technol, 26:e00228.
10. Huang, P., Chang, W.-S., Ansell, M. P., et al. (2015). Density distribution profile for internodes and nodes of phyllostachys edulis (moso bamboo) by computer tomography scanning. Construction and Building Materials, 93:197–204.
11. Peng, G., Jiang, Z., Fei, B., et al. (2014). Detection of complex vascular system in bamboo node by x-ray µct imaging technique. Holzforschung, 68(2):223–227.
12. Xiang, E., Yang, S., Cao, et al. (2021). Visualizing complex anatomical structure in bamboo nodes based on x-ray microtomography. J. Renew Mater, 9(9):1531.
13. Palombini, F. L., Nogueira, F. M., Kindlein, W., et al. (2020). Biomimetic systems and design in the 3d characterization of the complex vascular system of bamboo node based on x-ray microtomography and finite element analysis. Journal of Materials Research, 35(8):842–854.
14. Li, S., Yang, S., Shang, L., Liu, X., et al. (2021). 3d visualization of bamboo node’s vascular bundle. Forests, 12(12):1799.
15. Shao, Z., Zhou, L., Liu, Y., et al. (2010). Differences in structure and strength between internode and node sections of moso bamboo. J of Tropical Forest Science, pages 133–138.
16. Taylor, D., Kinane, B., Sweeney, C., et al. (2015). The biomechanics of bamboo: investigating the role of the nodes. Wood science and technology, 49(2):345–357.

  doi:10.5075/epfl-298799_978-2-9701614-0-0

MODE I CRACK PATH TRANSITIONS IN UNIDIRECTIONAL CARBON FIBRE COMPOSITES ANALYSED USING IN SITU 3D COMPUTED TOMOGRAPHY AND THE EXTENDED FINITE ELEMENT METHOD

Keiran Ball[a], Yeajin Lee[a], Carolina Furtado[b], Albertino Arteiro[c], Palak Patel[b], Marta Majkut[d], Lukas Helfen[e], Brian L. Wardle[b], Mark Mavrogordato[a], Ian Sinclair[a], Mark Spearing[a]

a: University of Southampton, Southampton, UK – k.ball@soton.ac.uk
b: Massachusetts Institute of Technology, Cambridge, MA, USA
c: University of Porto, Porto, Portugal
d: European Synchrotron Radiation Facility, Grenoble, France
e: Institut Laue-Langevin, Grenoble, France

Abstract: *Synchrotron Radiation Computed Tomography has been used to make time-series observations of crack transition in a particle toughened unidirectional carbon fibre reinforced polymer composite system during an in situ wedge opening Mode I delamination test. Furthermore, a finite element model combining both cohesive elements and the eXtended Finite Element Method has been used to explore factors contributing to crack transition. The synchrotron data reveals features such as tow gaps and resin pockets, which could be significant in crack transition A lateral crack transition to the ply was observed suggesting the need for three-dimensional analysis of the crack transition problem. The finite element modelling suggests variation in interlayer thickness is critical in crack transition where a thicker more uniform interlayer favoured crack propagation in the interlayer, whereas variability in the interlayer results in transition of the crack to the fibre interface and ply region of the composite around the thinnest regions.*

Keywords: Synchrotron Radiation Computed Tomography; Carbon Fibre Reinforced Polymer Composites; eXtended Finite Element Method; Delamination; Crack transition

1. Introduction

Predicting and controlling the delamination behaviour of carbon fibre reinforced polymer (CFRP) composites remains a challenge due to the interplay of various local damage response mechanisms. Toughened matrix interlayers are widely reported to increase laminate toughness and reduce residual damage under impact [1-5]. There are several reported delamination pathways during tensile opening (Mode I) of an interlayer toughened CFRP, such as in the toughened interlayer, the interlayer-fibre interface and the intralayer [3, 6, 7]. Experimental interrogation of factors impacting coupon scale delamination resistance, such as relative interface strengths, crack shielding mechanisms, and variability in interlayer architecture, is potentially complex. For this reason, a combined experimental and modelling study is employed to analyse factors impacting crack transitions and the potential knock-on effect on material toughness. In this work, a Double Cantilever Beam (DCB) specimen, representative of standard test coupons, has been used to investigate mesoscale damage mechanisms, complementing previous experimental observations obtained via micro-focus X-ray computed tomography (laboratory CT) and Synchrotron Radiation Computed Tomography (SRCT) of sub-sized samples [8]. Applying a combined cohesive element and eXtended finite element methods (XFEM) allows for such failure to be analysed in terms of interactions between geometrical and material variables. These variables include three-dimensional interlayer morphology, and relative

  doi:10.5075/epfl-298799_978-2-9701614-0-0

cohesive properties of the material phases and interfaces. This work assesses delamination paths in constant thickness and varying thickness interlayer models (related to CT measured morphology) across a range of cohesive strength properties.

2. Materials and Methods

A proprietary particle toughened CFRP was supplied by the Cytec Solvay Group, cured via a standard aerospace autoclave cure cycle. DCB samples were prepared, conforming to ASTM D 5528 – 01 and consisted of a 26-ply unidirectional layup with a 25 mm wide, 40 µm thick, polytetrafluoroethylene (PTFE) insert placed at the mid-plane in order to control the initiation of fracture. Specimens were a standard size of 254 mm in length and 25 x 5 mm cross-section. Secondary phase particles were initially dispersed in the interlayer at a *Vf* (volume fraction) of 13%.

For *in situ* visualisations of crack growth, specimens were delaminated using a wedge opening rig based on the rig used for *in situ* experiments by Borstnar *et al.* [9]. The device drove a wedge into the midplane of the specimen, pushing the cantilever arms apart and growing the crack. The loading was carefully controlled using a screw mechanism facilitating stable crack growth. The specimens were imaged after a load step was applied to propagate the crack and then a second time after the second load step.

2.1 Synchrotron Radiation Computed Tomography

Phase-sensitive synchrotron X-ray computed tomography was carried out at the European Synchrotron Radiation Facility (ESRF) using beamline ID 19, Grenoble, France. The sample to be scanned was placed and secured to the rotate stage in the *in situ* loading rig described above. The sample was scanned at a voxel resolution of 0.65 µm, giving a field of view (FOV) per scan of 1.664 x 1.404 mm using a 2560 x 2160 pixel camera.

A beam energy of 19 keV was used for tomographic imaging. The exposure time of the beam was 30 ms, and five thousand projections were taken for a 180^{o} rotation, allowing for region of interest (ROI) "padding" to reduce artefacts caused by scanning a small area of the sample [10]. In addition, the detector was placed after a propagation distance of 55 mm with respect to the sample to allow a distinction between similarly attenuating material features using phase-enhanced contrast in the edge-detection regime [11]. The data was reconstructed using in-house software pyHST (High-Speed Tomography in a Python^{TM} version) [12].

3. Finite Element Model Description

The Hexcel IM7/8552 material system's properties were used for the DCB test finite element model. This is an intermediate modulus fibre and particle toughened epoxy resin system comparable to the material used in the experimental part of the study. This material was used because its mechanical properties are widely available and were used in the third worldwide failure exercise [13]. Model material properties are shown in Table 1. A coupon scale specimen has been modelled and captures the first five millimetres of crack propagation to assess the transition of the crack from the toughened interlayer to the ply of the composite, as shown in Figure 1a.

Figure 1b refers to the discretisation of the ROI. Cohesive elements have been used to model the crack propagation through the centre of the interlayer using the maximum stress criterion.

  doi:10.5075/epfl-298799_978-2-9701614-0-0

The solid elements adjacent to the cohesive elements of the interlayer have been enriched using the eXtended Finite Elements Method (XFEM) to allow for coalescence of the various layers of potential delamination paths. A simple power-law criterion (exponent n = 1) was used to determine crack propagation, similar to that used by Yang *et al*. [14]. The cohesive element layers on either side of the interlayer represent the interface between the interlayer and the first layer of fibres, similar to the method used for microscale simulations by Borstnar *et al*. [6]. The second set of cohesive layers represents the fibre-matrix interface layer, three fibre diameters into the adjacent ply region, and lies between the bulk ply region and the XFEM enriched thin ply region. The stiffness of the cohesive layers is in line with values used previously in the literature [15]. A simple quadratic stress initiation criterion is used to determine delamination onset and a simple power-law to model crack propagation. The enriched ply region allows for transverse intralaminar cracking through the ply and hence coalescence through the fibre layer and uses the transverse tensile strength of the composite in the quadratic failure criterion to model damage onset.

The interlayer architecture varies between models. Five models are presented in this work consisting of three constant thickness interlayer geometries and two varying thickness models reported in Table 1. The varying geometry case (Model 4), which varies from 'thick', 0.08 mm to 'thin', 0.01 mm, in a sinusoidal manner, is shown in Figure 1c and has a period of 2 mm across the 10 mm width of the symmetric model. This parameterisation represents an extreme case arising from measurements of the thickest and thinnest regions taken from a sample of the same materials system used in the experimental part of the study. Model 1 represents the constant thickness model for the thinnest measured interlayer thickness; model 2 the median interlayer thickness (as the data is not normally distributed); in model 3 the variation represents 95% of the data measured, so excluding extreme values; model 4 was described above; and model 5 represents the constant thickness case for the thickest interlayer section measured. Variations in interlayer thickness have previously been termed tow-aligned resin pockets (TARPs) and have been analysed and quantified for aerospace grade unidirectional composite systems by Fritz *et al. [16].* By using automated objective algorithms to process three-dimensional computed tomography images periodic TARPs with thicknesses typically 2–3X greater than the average interlayer thickness were observed. The sinusoidal parameterisation is a simplification of the varying interlayer observed in CT datasets (not presented in this work), and allows for direct verification of the impact the interlayer variation has on crack transition, while being able to maintain a good quality mesh in that region .

This modelling aims to evaluate the relative importance of: interlayer thickness, initiation stress, and strain energy release rates in determining crack path transition.

  doi:10.5075/epfl-298799_978-2-9701614-0-0

Table 1 Material and geometric properties for Hexcel IM7/8552 toughened epoxy resin system. Unless stated otherwise all mechanical properties are taken from WWFE III [13], and geometric properties based on a standard sized DCB test coupons.

Cohesive Element Interfacial Properties			**Bulk Material Properties**		
Properties	**Fibre Interfacial Region**	**Interlayer Interfacial Region**	**Properties**	**Interlayer**	**Ply**
$K_1 = K_2 = K_3$ (N/mm³)	5,000,000*	2,300,000*	E_{11} (MPa)	4,080	165,000
$\Gamma_{IC}^{Interface}$ (N/mm)	0.2	0.3	E_{22} (MPa)	4,080	9,000
$\Gamma_{IIC}^{Interface} = \Gamma_{IIIC}^{Interface}$ (N/mm)	0.8	0.8	E_{33} (MPa)	4,080	9,000
$\sigma_{Normal}^{Interface}$ (MPa)	56.7 – 69.3	63	G_{12} (MPa)	1,478	5,600
$\sigma_{Transverse}^{Interface}$ (MPa)	73	63	G_{13} (MPa)	1,478	5,600
$\sigma_{Shear\ In-plane}^{Interface}$ (MPa)	90	57	G_{23} (MPa)	1,478	2,800
$\sigma_{Shear\ Transverse}^{Interface}$ (MPa)	90	57	$\upsilon_{12} = \upsilon_{13}$	0.38	0.34
$\sigma_{Shear\ Through-thickness}^{Interface}$ (MPa)	57	57	υ_{23}	0.38	0.5

Geometric Properties					
Length (*L*)	150 mm	Width (*B*)	20 mm	Thickness (*2h*)	3 mm
Initial Delamination Length (a_0)	50 mm	Region of Interest (L_{ROI})	5 mm	Ply Thickness	0.18 mm

Interlayer Geometric Properties			
Model Number	Minimum Thickness	Maximum Thickness	Mean Thickness
1	Constant	Constant	0.0100 mm
2	Constant	Constant	0.0260 mm
3	0.0150 mm	0.0500 mm	0.0325 mm
4	0.010 mm	0.0800 mm	0.0450 mm
5	Constant	Constant	0.0800 mm

*Values calculated using the method proposed by Turon *et al. [15].*

  doi:10.5075/epfl-298799_978-2-9701614-0-0

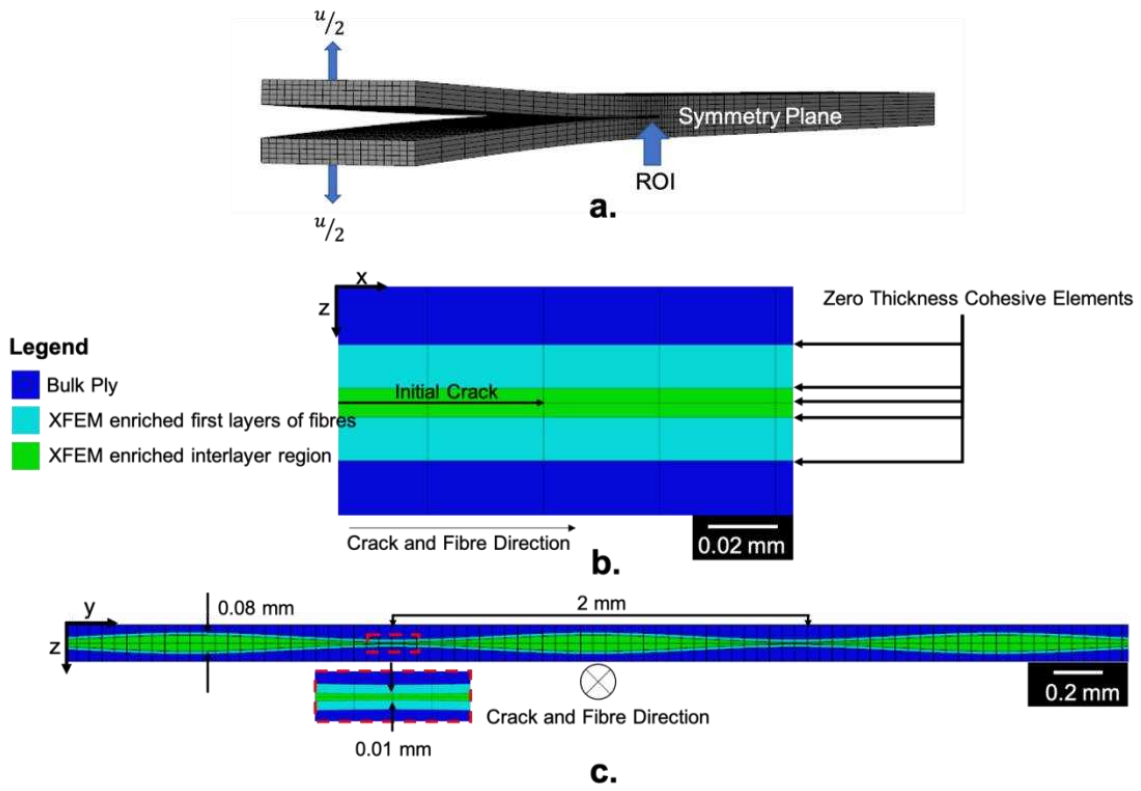

Figure 1 Model geometry, boundary conditions and discretisation. 1a. Overview of the whole model showing loading and symmetry condition. 1b. A detailed view of the ROI shows the central XFEM enriched interlayer region, zero-thickness cohesive element layers on either side representing the interlayer-fibre interface. The first layers of fibres are also enriched using the XFEM. Another zero-thickness layer of cohesive interface elements three fibres deep into the ply between the bulk ply and enriched region model intralaminar delamination. 1c. Cross-section of ROI with crack and fibres going into the page. The thickness of the interlayer varies in a sinusoidal manner from 'thick' to 'thin'.

4. Results

4.1 Synchrotron Radiation Computed Tomography

Both the crack and fibres in Figure 2 are going into the page. Figure 2a shows the scanned region near the crack tip after the initial crack propagation. The layers of the composite can be seen with the ply region containing the fibres and the resin-rich, particle toughened interlayer between them. After the first load step, the crack remains entirely within the interlayer for the field of view shown. In the second load step shown in Figure 2b, the crack has bifurcated laterally into the ply. However, there is still a continuity of the crack within the interlayer. After applying the final load step in Figure 2c, the crack that had laterally propagated into the ply can be seen to have coalesced with the crack in the interlayer. The cross-sections of individual fibres can be seen in the crack opening within the ply, which could indicate oblique fibre bridging. It is also noteworthy that the crack has bifurcated on the right-hand side of the image and is propagating on both sides of the particle toughened interlayer.

  doi:10.5075/epfl-298799_978-2-9701614-0-0

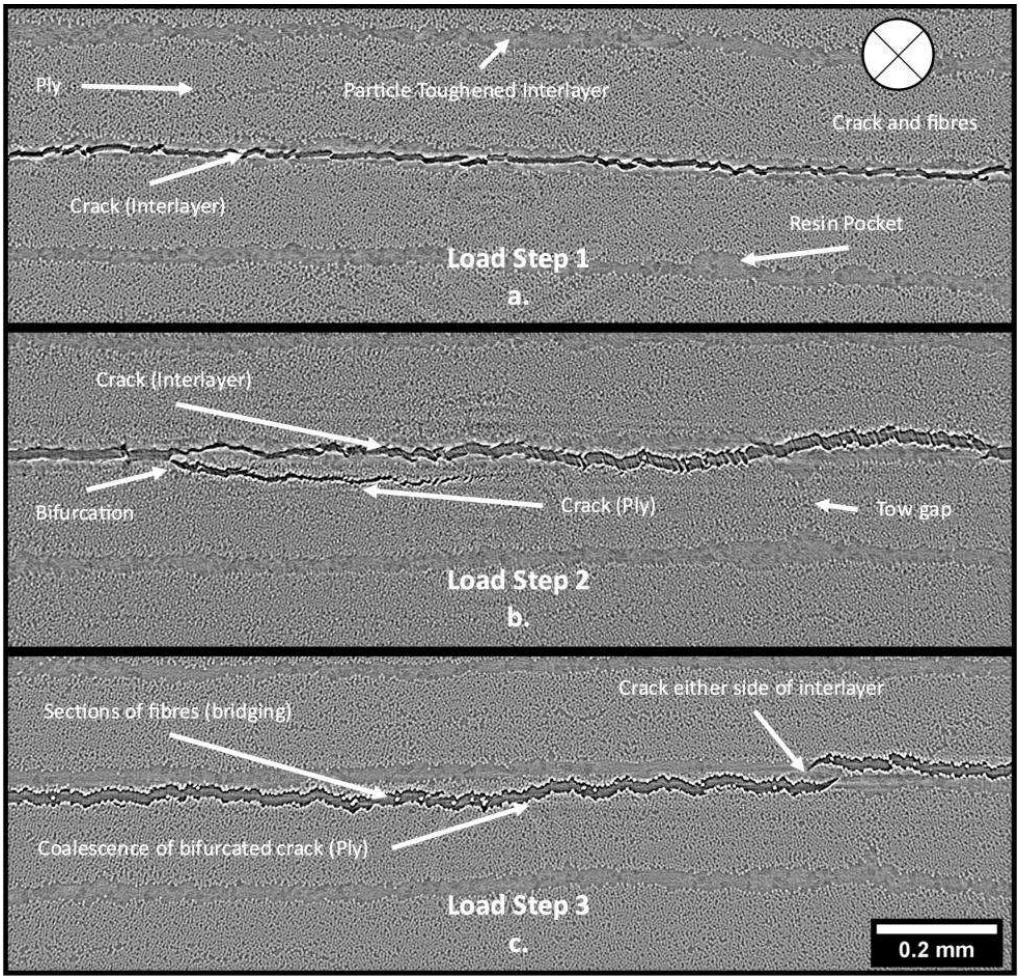

Figure 2 SRCT load step series of scan stack slices. 2a. Scan around the crack tip after the first load step. The crack is in the particle toughened interlayer. 2 b. After the second load step, the crack can be seen to be making a transition laterally from the interlayer to the ply. 2c. In the final load step where the laterally extended crack seen in load step 2 has coalesced with the crack on the interlayer-fibre interface, and the crack can be seen to be propagating on either side of the interlayer. The crack and fibres are going into the page.

4.2 Finite Element Modelling

The proportion of the fully developed crack (as defined by the cohesive traction reaching 0) in each cohesive layer of the model is shown in *Figure 3*. The proportion of the crack in each layer was calculated by adding the number of fully degraded elements and calculating the proportion from each set. Each model has been compared at the same load point opening displacement. There is a positive correlation between mean interlayer thickness and the proportion of the crack which remains in the interlayer. The thinnest constant thickness model sees the highest area fraction of crack transition, whereas the thickest constant thickness model sees no crack transition away from the interlayer. Model 4 is the varying geometry model shown in *Figure 1*c. The crack transition occurs in the vicinity near the thinner regions. Further, the analysis also showed that the transition regions under stochastic conditions were biased to the thin regions' coordinates compared to the constant thickness. This suggests that the presence of variations in the interlayer, which can be attributed to various means such as tow gaps and toughening

  doi:10.5075/epfl-298799_978-2-9701614-0-0

particle depleted regions, will directly impact the delamination path. Therefore, the interlayer should be as uniform as possible to reduce the probability of crack transition.

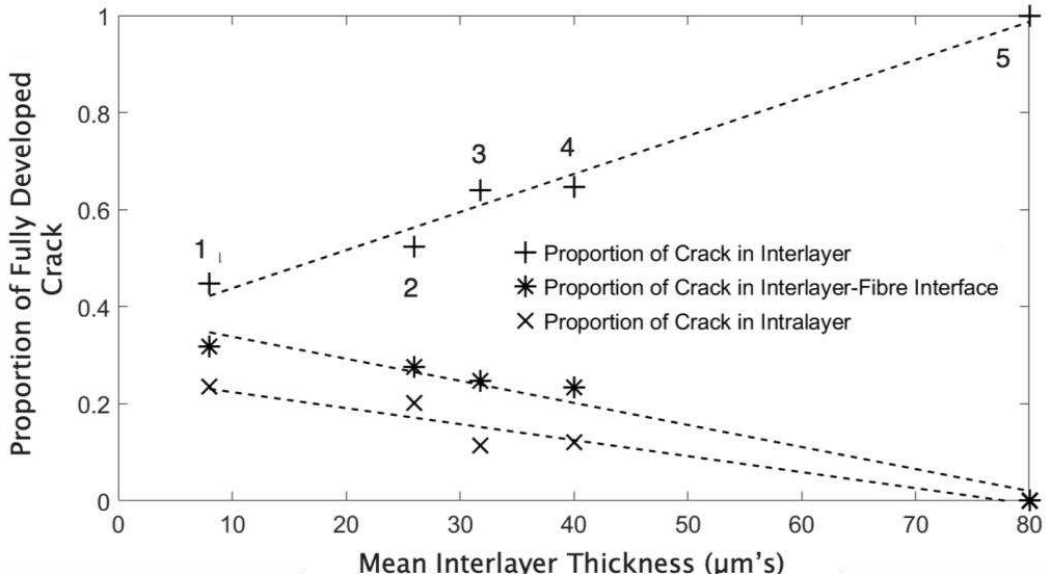

Figure 3 The proportion of a fully developed crack in the cohesive layers of the model as a function of mean interlayer thickness.

5. Conclusions

This work demonstrates the significance of monitoring crack path transition in three dimensions. It can be seen that not only do crack transitions occur in the plane of the crack, as commonly reported in the literature, but also out of the plane of the crack. This transition suggests that the architecture of the toughened interlayer region could be significant in determining whether a crack transitions to the ply region of the laminate. The finite element modelling suggests that the thickness and uniformity of the interlayer play a significant role in crack path transition as thinner regions create greater competition between potential delamination paths. Furthermore, features that could distort the interlayer thickness, such as tow gaps and sparsity of toughening particles, can cause local transition regions, which could have a further impact on the toughness of the materials system due to the damage response being due to fibre toughening mechanisms as opposed to interlayer and particle toughening mechanisms.

Further work is required to link the micro-scale crack path transition observations to the toughness response of a standard size test sample. Furthermore, although it has been demonstrated that thicker and more uniform interlayer geometries provide a more desirable crack propagation path in the context of this work, the consequences of this on real material toughness have not been explored.

Acknowledgements

The authors gratefully acknowledge contributions from the Cytec Solvay Group for their sponsorship, supply of materials, and technical support. The authors would also like to recognise the support provided by the ESRF where the SRCT experiments were performed on beamline ID19 under DOI 10.15151/ESRF-ES-569733595.

6. References

1. Bull DJ, Spearing SM, Sinclair I, Helfen L. Three-dimensional assessment of low velocity impact damage in particle toughened composite laminates using micro-focus X-ray computed tomography and synchrotron radiation laminography. Compos Pt A-Appl Sci Manuf. 2013;52:62-9.
2. Bull DJ, Scott AE, Spearing SM, Sinclair I. The influence of toughening-particles in CFRPs on low velocity impact damage resistance performance. Composites Part A: Applied Science and Manufacturing. 2014;58:47-55.
3. Borstnar G, Mavrogordato MN, Helfen L, Sinclair I, Spearing SM. Interlaminar fracture micro-mechanisms in toughened carbon fibre reinforced plastics investigated via synchrotron radiation computed tomography and laminography. Composites Part A: Applied Science and Manufacturing. 2015;71:176-83.
4. Bull DJ, Spearing SM, Sinclair I. Investigation of the response to low velocity impact and quasi-static indentation loading of particle-toughened carbon-fibre composite materials. Composites Part A: Applied Science and Manufacturing. 2015;74:38-46.
5. Walker L, Sohn M-S, Hu X-Z. Improving impact resistance of carbon-fibre composites through interlaminar reinforcement. Composites Part A: Applied Science and Manufacturing. 2002;33(6):893-902.
6. Borstnar G, Mavrogordato MN, Yang QD, Sinclair I, Spearing SM. Crack path simulation in a particle-toughened interlayer within a polymer composite laminate. Composites Science and Technology. 2016;133:89-96.
7. Xie Y, Koslowski M. Numerical simulations of inter-laminar fracture in particle-toughened carbon fiber reinforced composites. Composites Part A: Applied Science and Manufacturing. 2017;92:62-9.
8. Borstnar G. Micro-mechanical contributions to interlaminar toughness in particle-toughened CFRPs [Doctoral]: University of Southampton; 2016.
9. Borstnar G, Gillard F, Mavrogordato MN, Sinclair I, Spearing SM. Three-dimensional deformation mapping of Mode I interlaminar crack extension in particle-toughened interlayers. Acta Materialia. 2016;103:63-70.
10. Kyrieleis A, Titarenko V, Ibison M, Connolley T, Withers PJ. Region-of-interest tomography using filtered backprojection: assessing the practical limits. J Microsc (UK). 2011;241(1):69-82.
11. Cloetens P, Pateyron-Salomé M, Buffière JY, Peix G, Baruchel J, Peyrin F, et al. Observation of microstructure and damage in materials by phase sensitive radiography and tomography. Journal of Applied Physics. 1997;81(9):5878-86.
12. Mirone A, Brun E, Gouillart E, Tafforeau P, Kieffer J. The PyHST2 hybrid distributed code for high speed tomographic reconstruction with iterative reconstruction and a priori knowledge capabilities. Nuclear Instruments and Methods in Physics Research Section B: Beam Interactions with Materials and Atoms. 2014;324:41-8.
13. Kaddour AS, Hinton MJ, Smith PA, Li S. The background to the third world-wide failure exercise. J Compos Mater (USA). 2013;47(20-21):2417-26.
14. Yang Q, Cox B. Cohesive models for damage evolution in laminated composites. International Journal of Fracture. 2005;133(2):107-37.
15. Turon A, Dávila CG, Camanho PP, Costa J. An engineering solution for mesh size effects in the simulation of delamination using cohesive zone models. Eng Fract Mech. 2007;74(10):1665-82.
16. Fritz NK, Kopp R, Nason AK, Ni X, Lee J, Stein IY, et al. New interlaminar features and void distributions in advanced aerospace-grade composites revealed via automated algorithms using micro-computed tomography. Composites Science and Technology. 2020;193:108132.

  doi:10.5075/epfl-298799_978-2-9701614-0-0

FIBRE STRESS CONCENTRATORS CAUSED BY FIBRE ENDS IN SHORT ALIGNED GLASS FIBRE COMPOSITES

Camilo, Rojas G.[a], Joël, Cugnoni[b], Stepan, Lomov[a], Yentl, Swolfs[a]

a: Department of Materials Engineering, KU Leuven, Leuven,3000, Belgium, Email: camilo.rojas@kuleuven.be
b: School of Management and Engineering Vaud, University of Applied Sciences and Arts Western (HES-SO), Switzerland

Abstract: *One of the common assumptions when predicting the strength of composite materials is that fibres are ideally parallel to each other. Although progress has been made to use real microstructures in models* [1]*, they introduce unverified assumptions. When variables that do not depend on real parameters are introduced, it becomes unrealistic to explain the correlation between the microstructure and the results. In the present work, we use a real microstructure digital twin model to evaluate the effect of fibre ends on local stress concentration factors. Using 3D finite element models to compare ideally unidirectional composites and the digital twin, we found differences in the local stress concentration factor of up to 25%. The real microstructure has a higher local stress concentration factor than the ideal one, but it will change through the loading of the models.*

Keywords: Discontinuous composites; Local stress concentrator; Aligned composites

1. Introduction

The demand for carbon fibre-reinforced polymer composites has increased over the last decade from 51,000 to 141,500 tons [2]. With the increase in demand for composites also comes an increase in the waste generated, which amounts to 40% of the original raw material [3]. The high percentage of wasted material and a composite market valuation of 48.7 billion USD [4] in 2020, incentivises us to find ways of recycling and exploiting composite materials.

The desired properties of fibre-reinforced composites are primarily on the direction of the fibres. The narrower we can make the fibre orientation distribution, the better mechanical properties can be achieved. To create a material with preferential orientation, processes such as HiPerDiF [5] can use discontinuous recycled fibres, although the microstructure is not the same as a unidirectional composite. It's different because it has a higher variation in fibre orientation and more common discontinuities in the form of fibre ends [5].

There has been a steady progression in understanding the failure process of unidirectional composites: from using 1D models to explain the contribution of the matrix transferring the shear loads (shear-lag) [6] to 3D models that use quasi-random 2D extruded microstructures to evaluate unidirectional composites failure development and strength [7]. It is agreed that once a fibre has broken, neighbouring fibres are loaded higher than distant fibres, and the magnitude of the overloading affects the way failure develops. Batdorf and Ghaffarian [8] argued that variable inter-fibre distancing affected the stress redistribution around a discontinuity. This leads to variable stress concentration factors that depend on the microstructure of the composite. Later works [9] have shown the variation of distance and stress concentration factors for idealised 3D microstructures.

  doi:10.5075/epfl-298799_978-2-9701614-0-0

For unidirectional composites, it has been accepted that the cross-section microstructure is stable throughout the length of analysis. The same is not true for discontinuous aligned composites, as **Error! Reference source not found.**fibres not only change neighbours throughout their length, but discontinuities are also more frequent, particularly fibre ends.

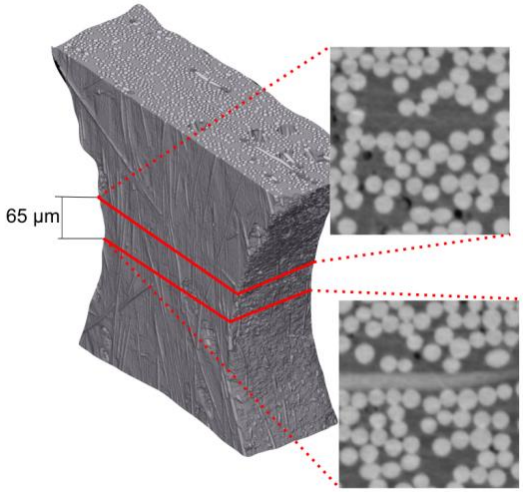

Figure 1 Cross-sectional slices of the same region 65 µm apart, horizontal fibre appears, fibres move, change neighbours. showing the variability in the 3D microstructure.

We present in this paper the results of 3D finite element models, using the real microstructure as a base to generate a digital twin. With the results of the model, we provide an interpretation of the difference between “average” stress concentration factors and “local” stress concentration factors. We will also compare how the local stress concentration varies in the digital twin versus a unidirectional idealised counterpart for the same microstructure.

2. Description of the model

First, we took a synchrotron x-ray computed tomography scan of our discontinuous aligned composite at the Paul Scherrer Institute. The samples were manufactured from HYBON 2026 glass fibres and Sicomin SR8500 epoxy matrix using the HiPerDiF manufacturing method. More details about the sample and method can be found in [5]. With the fibre break development registered for every loading step in the synchrotron x-ray computed tomography scans, Figure 2.a, we selected one region of interest that presented a fibre break adjacent to a fibre end, Figure 2.b-c. The cubic region of interest has a volume of 7415 μm^3 and a fibre volume fraction of 38%.

Second, we extract the microstructure using the cylinder template method proposed by Weber et al [10] and Rigor et al [11] that is currently implemented in Avizo®. This allows us to extract the fibre positions in the volume. Since modelling the full volume exceeds the computational capabilities at our disposal, we approached it as a combined master volume model and region of interest sub-model.

The master volume model mechanical properties consist of those that come from the constituents’ characterisation. Using the rules of mixtures to calculate equivalent unidirectional plies and classical laminate theory to compensate for the in-plane orientation.

  doi:10.5075/epfl-298799_978-2-9701614-0-0

We calculated the average orientation and equivalent ply thickness discretising the in-plane orientation distribution into 10 bins of equivalent probability.

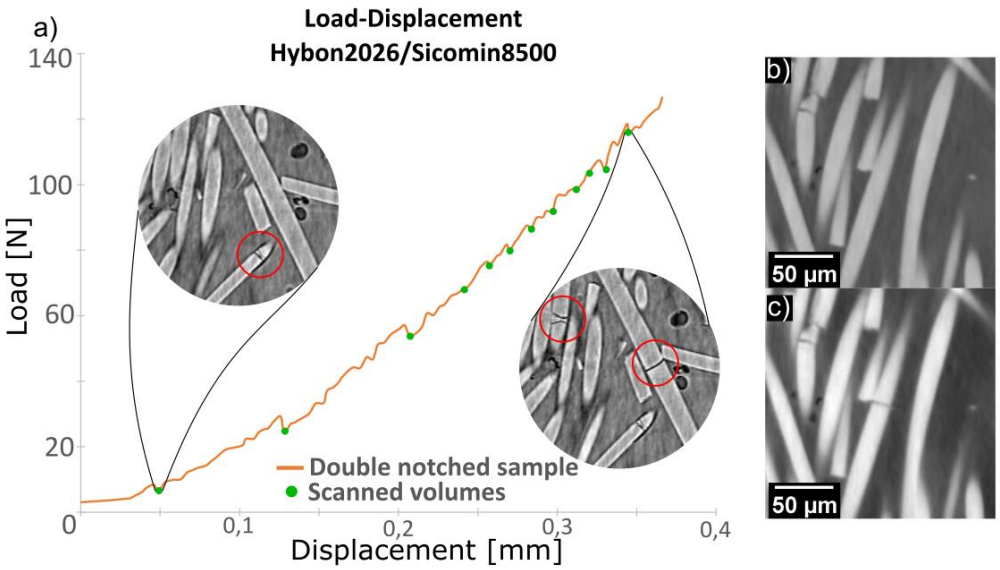

Figure 2 Region of interest selection a) Hold at displacement scanned volumes (adapted from [5]*), b) region of interest before fibre break, and c) region of interest after fibre break.*

We applied controlled displacement to the master volume to match the load measured in the experiments. Since our region of interest does not have a repetitive structure or boundary, we used the master volume model to generate boundary conditions like the ones expected for our region of interest sub-model, Figure 3.a. In the surroundings of the discontinuity in the region of interest, elements of 1/20th the size of remote elements were used to capture with sufficient detail the local stress concentration factor. The overall dimensions of the master volume model are 1.2x0.4x1.1 mm and the dimensions of the region of interest sub-model are 0.16x0.16x0.16 mm. The number of elements on each model was 1.376.513 and 994.578 respectively, using only quadratic tetrahedral (C3D10) elements. In total, 102 fibres were modelled in the digital twin.

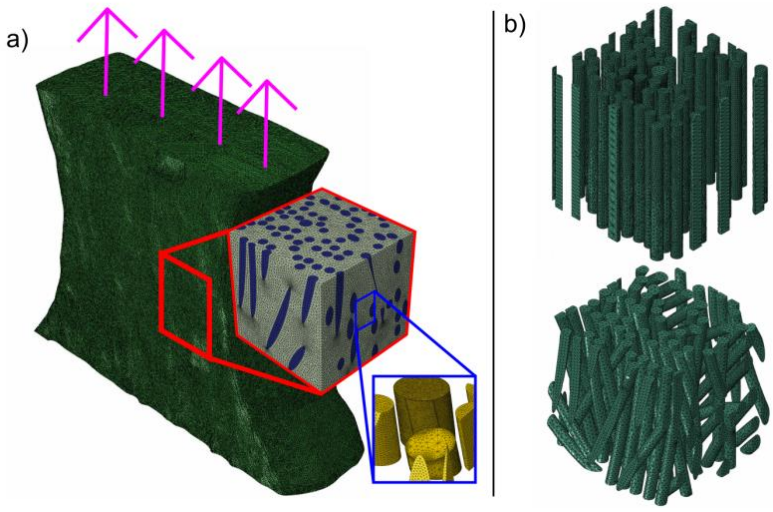

Figure 3 Finite element models details a) Master volume and sub-model b) Idealised and digital twin sub-models

Although the diameter varies from fibre to fibre, we assumed that every fibre had the same radius (6.5 µm), except for the broken fibre and the fibre end. These fibres had a diameter of respectively 7.2 and 8.2 µm. One of the simplifications in the model is the use of a minimum surface-to-surface distance. This is to avoid the instabilities that come with modelling contact between fibres. This distance between the broken fibre and the fibre end is 0.9 µm in the digital twin model.

To generate the ideal unidirectional microstructure, the critical cross section where the fibre end and the broken fibre are localised is used to identify the fibre axis locations (centres of fibre section). Then the individual fibres are generated by extrusion using the identified fibre centres. Special care was taken to maintain the inter-fibre distance for the broken fibre and the fibre end of interest. The difference in both models is shown in Figure 3.b. In the idealised model we only have 70 fibres, compared to 102 in the digital twin, since not every fibre is present in our critical cross-section. The fibre volume fraction changes from 38% in the digital twin to 30% in the idealised unidirectional model.

The stress concentration factor was defined as the relative difference between the average stress in a certain cross-section and the average remote stress. However, the localised stress nearest to the discontinuity can be significantly higher than that of the average of the cross-section. To differentiate both the localised stress and the average cross-section stress, we propose to use the local stress concentration factor (LSCF). To evaluate the LSCF first we calculate the average stress and maximum stress in a cylinder of length "s" that has the same diameter as the fibre and follows the central axis of the fibre, *Figure* 4. We define the LSCF as the difference between the average cross-section stress in the fibre $\sigma_{s,\,avg}$ and the maximum stress in the same region $\sigma_{s,\,max}$:

$$LSCF = \frac{\sigma_{s,max} - \sigma_{s,avg}}{\sigma_{s,avg}} x100 \quad (1)$$

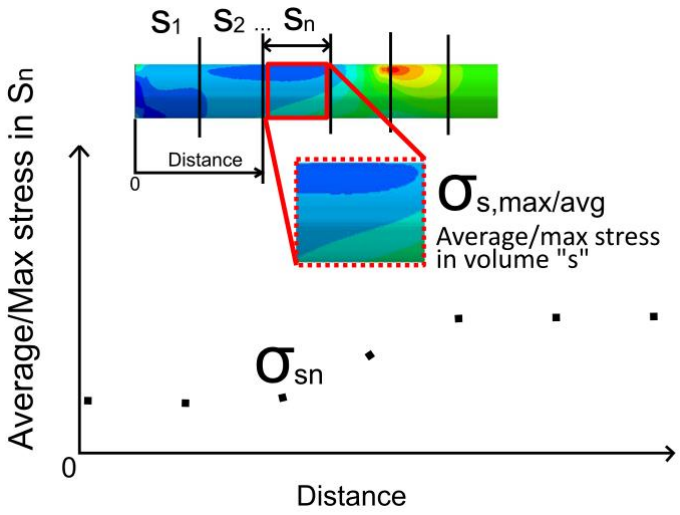

Figure 4 Volumetric averaging and Max in the fibre path to calculate the local stress concentration factor

3. Results and discussion

We used the mechanical properties reported in [12] for the glass fibres (stiffness of 92 GPa and Poisson's ratio of 0.3). The matrix is modelled with plastic-elastic matrix behaviour as reported

  doi:10.5075/epfl-298799_978-2-9701614-0-0

in [13] (stiffness of 3.4 GPa and Poisson's ratio of 0.4). On the experimental results, we cannot pinpoint the force at which the fibre break happens in our region of interest. We can, however, have a window from the last scan where there was no break to the next scan where the break is present. This is respectively 53 and 65 N. We will analyse the results at a load of 53 N in our plots, and refer to it as fibre break force.

Glass fibres fail as brittle materials, we will use the maximum principal stress as the measure for the stress concentration and stress average throughout our analysis. It is to be noted that the maximum principal stress aligns almost perfectly with the fibre axis in our current case. We should take care to analyse this in more detail for future research.

In both models, we find a local maximum principal stress that reaches a peak before the growth of a plastic band in the matrix. After the onset of the plastic band, the peak spreads out over a large distance, see Figure 5. These transitions happen just below 50% of the fibre break force. In the digital twin model, more abnormalities are present on the fibre edges, Figure 5.a. We associate this with edge effects that are inherent to the sub-modelling approach we used. Nevertheless we consider these abnormalities far enough from the region of interest, as we can still see a stabilisation before reaching the discontinuity.

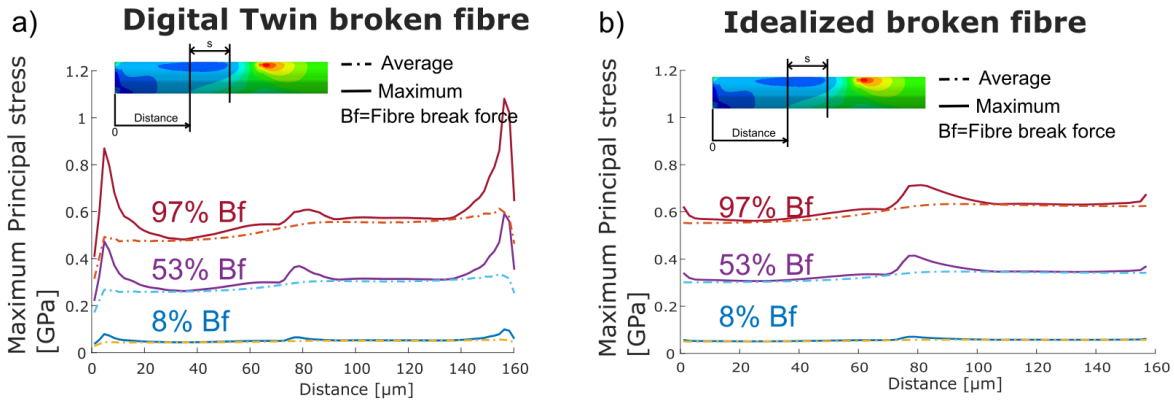

Figure 5 Broken fibre max. principal stress state a) Digital twin b) Idealised unidirectional.

Looking at the beginning and end of the broken fibre in Figure 5, the abnormalities around the edges are of a smaller scale on the idealised unidirectional model than on the digital twin. Again, we associate this edge effects with the difference in homogeneity of the microstructures near the boundaries. Looking at the average maximum principal stress before and after the fibre end location (80µm), there is a step-like increase in the average maximum principal stress for both models. In the idealised model, we can attribute this to the change in fibre volume fraction along the fibre, the fibre end is located at 80 µm. Since there are less fibres to carry the same load, we expect the neighbouring fibres taking on more load. The same cannot be said about the digital twin model, as the fibre volume fraction across the loading direction changes from slice to slice with an overall positive trend, see Figure 6.a.

  doi:10.5075/epfl-298799_978-2-9701614-0-0

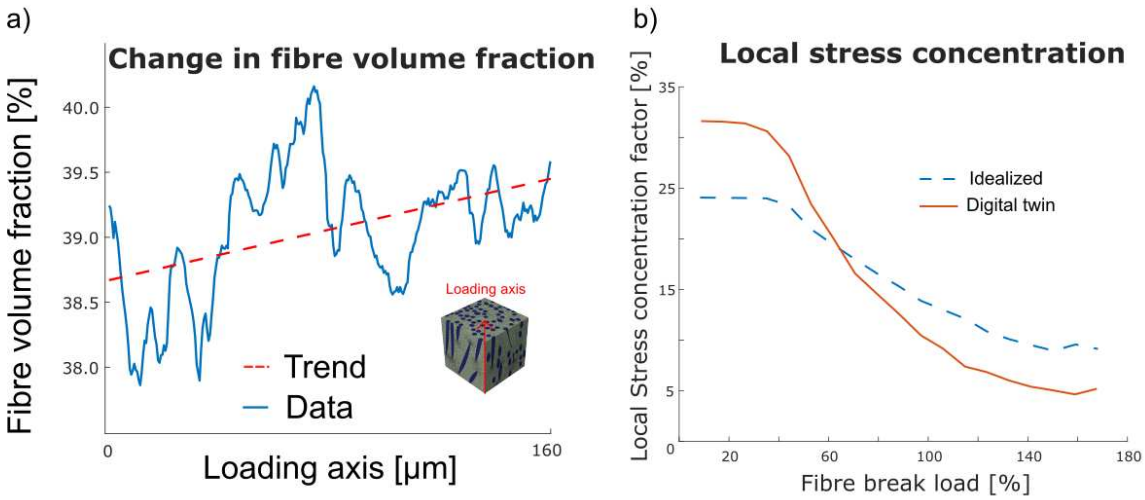

Figure 6 a) Fibre volume fraction through change through the loading axis b) Local stress concentration factor evolution while loading.

When we compare the local stress concentration factor, between the idealised and digital twin models, a local stress concentration factor difference of 25% is observed before the onset of the plastic zone. As the load progresses, the local stress concentration factor diminishes faster for the digital twin than for the idealised model. The stress concentration factor differences shown in Figure 6.b highlight the overall importance of the microstructure on such results. Indeed, the local stress concentration factor is up to 32% higher than the average stress for the equivalent cross-section in the case of the digital twin, and up to 24% higher for the idealised case.

It is also noted that in both microstructures, the stress concentration factor decreases with applied load due to plastic band developments. However, as plastic strain band development is a complex 3D mechanism, its effect on the stress concentration factor strongly depends on the microstructure. As shown in Figure 6b, it appears that stress redistribution by plasticity, denoted by the reduction of the stress concentration factor, is more effective in the “real” microstructure than in the idealized unidirectional configuration.

4. Conclusions

There is a significant difference in the local stress concentration factor for idealised and realistic models. This difference is clearly the role of the microstructure in composites. The use of local stress concentration factors helps us to understand where the highly stressed fibres might fail when longer models are not possible. This enables an analysis when the stress state of the fibre cannot be assumed to reach a steady state.

As other authors have noted, having a higher local stress concentration factor that is on top of the average cross-section stress concentration factor will affect composite strength predictions. And with up to 25% difference, it should be accounted for in future strength models. With these models where the stress state across a fibre cross-section changes up to 32%, remarks the importance of finding a volumetric strength distribution for fibres.

With realistic digital twin models, microstructural assumptions are reduced, and the effectiveness of the local stress concentration factor is validated when compared with

  doi:10.5075/epfl-298799_978-2-9701614-0-0

idealised unidirectional models. Future work should address what the implications are for strength models and digital twins of unidirectional composites.

Acknowledgements

The research leading to these results has been performed within the framework of the HyFiSyn project and has received funding from the European Union's Horizon 2020 research and innovation program under the Marie Skłodowska-Curie grant agreement No 765881.

We acknowledge the Paul Scherrer Institute, Villigen, Switzerland for the provision of synchrotron radiation beamtime at the TOMCAT beamline X02DA of the SLS and would like to thank Christian Schlepütz for his assistance.

5. References

[1] Catalanotti G, Sebaey TA. An algorithm for the generation of three-dimensional statistically Representative Volume Elements of unidirectional fibre-reinforced plastics: Focusing on the fibres waviness. *Composite Structures*; 227. Epub ahead of print November 1, 2019. DOI: 10.1016/j.compstruct.2019.111272.

[2] Sauer M. *Composites Market Report 2019: The global CF and CC Market 2019, Market developments, Trends, outlook and challenges-published short version*. 2019.

[3] Pickering SJ, Turner TA, Meng F, et al. Developments in the fluidised bed process for fibre recovery from thermoset composites. In: CAMX 2015 (ed) *2nd Annual Composites and Advanced Materials Expo*. Dallas, 2015.

[4] Meng F, Olivetti EA, Zhao Y, et al. Comparing Life Cycle Energy and Global Warming Potential of Carbon Fiber Composite Recycling Technologies and Waste Management Options. *ACS Sustainable Chemistry and Engineering* 2018; 6: 9854–9865.

[5] Rojas CA, Schöberl E, Longana ML, et al. Microstructural correlations in short-aligned glass fiber composites. In: *Proceedings of the American Society for Composites—Thirty-Sixth Technical Conference on Composite Materials*. 2021.

[6] Hedgepeth JM. *STRESS CONCENTRATIONS IN FILAMENTARY STRUCTURES*. Washington, May 1961.

[7] Breite C, Melnikov A, Turon A, et al. Blind benchmarking of seven longitudinal tensile failure models for two virtual unidirectional composites. *Composites Science and Technology*; 202. Epub ahead of print January 20, 2021. DOI: 10.1016/j.compscitech.2020.108555.

[8] Batdorf SB, Ghaffarian R. *Size effect and strength variability of unidirectional composites*. 1984.

[9] Swolfs Y, Gorbatikh L, Romanov V, et al. Stress concentrations in an impregnated fibre bundle with random fibre packing. *Composites Science and Technology* 2013; 74: 113–120.

  doi:10.5075/epfl-298799_978-2-9701614-0-0

[10] Weber B, Greenan G, Prohaska S, et al. Automated tracing of microtubules in electron tomograms of plastic embedded samples of Caenorhabditis elegans embryos. *Journal of Structural Biology* 2012; 178: 129–138.

[11] Rigort A, Günther D, Hegerl R, et al. Automated segmentation of electron tomograms for a quantitative description of actin filament networks. *Journal of Structural Biology* 2012; 177: 135–144.

[12] Mesquita F, Bucknell S, Leray Y, et al. Single carbon and glass fibre properties characterised using large data sets obtained through automated single fibre tensile testing. *Composites Part A: Applied Science and Manufacturing*; 145. Epub ahead of print June 1, 2021. DOI: 10.1016/j.compositesa.2021.106389.

[13] Breite C. *Aligning fibre break models for composites with observable micro-scale material behaviour*. PhD Thesis, KULeuven, 2021.

Detailed Micro Computed Tomography Investigation of Damage Progression in Notched CFRP Specimens

Ofir Shor[a*], David Mollenhauer[b], Tamas Rev[c], Tzachi Nachman[a] , Daniel Rittel[c], Ido Simon[a]

a: Rafael Advanced Defense Systems LTD, Israel (ofirso@rafael.co.il)
b: US Air Force Research Laboratory, USA
c: Technion Israel Institute of Technology, Israel
* Corresponding author (ofirso@rafael.co.il)

Abstract: This work is part of an in-depth study investigating ply sequence, material architecture, and size effects on damage progression in notched carbon fiber reinforced polymer (CFRP) specimens under tensile and compressive loads. Tensile loading is applied to notched specimens having different ply sequences manufactured using unidirectional Hexply M21 prepreg (M21/34%/UD194/IMA-12k) and woven Hexply AS4C/M21 2-by-2 twill fabric prepreg. Microcomputed tomography allows investigating the effect of the weave microstructure on damage propagation and is compared to damage progression in laminates manufactured using unidirectional plies.

Keywords: Micro-computed tomography; Damage propagation; Unidirectional; Woven; Over Height Compact Tension

1. Introduction

Micro-Computed Tomography (µCT) is a non-destructive inspection technique that allows detailed three-dimensional inspection of composite samples, revealing the internal microstructure of the material. The application of this method to composite-related research is increasing, mainly due to the improvement of imaging capabilities and computing power required for the analysis of scanned volumes. Garcea et al. [1] reviewed the technical aspects related to µCT imaging of composites. Rashidi et al. [2] performed a parametric study of results obtained using µCT when applied to carbon fabric composites. The method has numerous applications related to composite materials, from static to dynamic and fatigue loading (Gu et al. [3], Cinar et al. [4], Qiao et al. [5]), as well as in-situ testing at room and elevated temperatures (Cornet et al. [6], Forna-Kreutzer et al. [7]). The method can be applied to detect manufacturing defects in composites - Mehdikhani et al. [8] applied µCT to characterize voids in multidirectional carbon fiber/epoxy composite laminates with different stacking sequences. In this work, µCT is used to investigate damage propagation in Overheight Compact Tension specimens following tensile loading to reveal the dominant fracture mechanisms that govern the mechanical behavior observed in the experiments.

  doi:10.5075/epfl-298799_978-2-9701614-0-0

2. Experimental

Overheight Compact Tension (OCT) specimens are often used for the investigation of intralaminar damaged growth within composite specimens due to the relatively controlled manner of damage growth in this specimen geometry (Kongshavn et al. [9]). In this study, OCT specimens were manufactured using a unidirectional M21/34%/UD194/IMA-12k and a twill weave AS4C/M21 carbon/epoxy prepregs supplied by Hexcel. OCT Specimens, with a geometry described in Figure 1, were cut using a water jet cutting system from plates cured in an autoclave using a 180 °C cure cycle profile recommended by Hexcel. Table 1 lists the various ply sequences investigated in this study and the naming designations for each configuration. To examine the effect of material architecture on damage propagation, ply sequence from the unidirectional, and woven material architecture was chosen. Each ply sequence based on a woven material architecture was represented by an equivalent ply sequence based on a unidirectional material architecture.

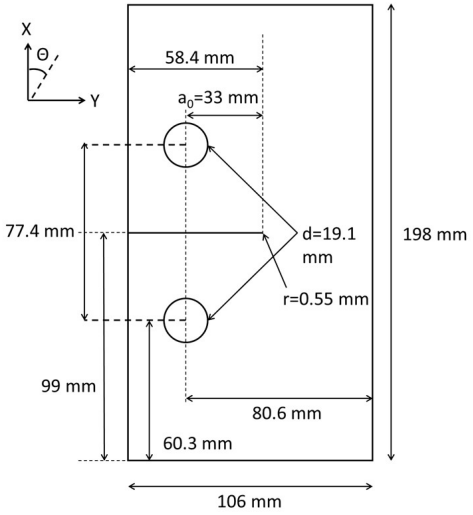

Figure 1 – Nominal geometry of an OCT specimen

Table 1. Summary of OCT specimen configurations

Lay-up configuration	Material architecture	
	Woven	Unidirectional (UD)
'Hard'	$[90/0]_{4s}$	$[90/0]_{6s}$
'Soft'	$[45/-45]_{4s}$	$[45/-45]_{6s}$
Quasi-isotropic (QI)	$[45/0/-45/90]_{2s}$	$[45/-45/0/90]_{3s}$

Tensile experiments were carried out using an Instron electromechanical testing machine. The load was applied to the specimens through two pins inserted into holes located from both sides of an initial artificial crack within the specimen. During the experiment, the load and displacements are monitored. Specimens were tested to complete failure and selected points

along the load profile to allow microcomputed tomography inspection. A detailed description of the experimental setup, experimental results, and microcomputed tomography findings obtained from this study, are brought in a separate paper. Only limited results are presented here.

3. Micro Computed Tomography

To investigate the damage propagation within the specimens, µCT scans were carried out using Zeiss Xradia 620 Versa X-ray µCT system, with an interior shown in *Figure 2*. The system includes a closed 160 KV X-rays source (1) generating X-rays at power levels ranging from 3 to 20 watts, transmitted toward the positive global Z direction. An automatic filter wheel (2) allows selecting a wide range of filters. The X-rays pass through the specimen (3) mounted on a specimen holder (4), rotating around an axis parallel to the global Y-axis. The system allows various means of X-ray detection: a CCD camera (5) allows using a selection of optical objectives: a 0.4x objective is shown in (6), as well as a turret consisting of 4x, 10x, and 20x objectives (7). In addition, a 4-megapixel flat panel detector (8) is available, shown here in a retracted position. When the flat panel is used for data acquisition, the optical detector assembly (5,6,7) is moved toward the positive Z-axis direction, and the flat panel is moved toward the X-ray beam (negative X direction). A zinc-iodide dye penetrant solution was used in selected scans to enhance the contrast of cracks with respect to the undamaged volume of material.

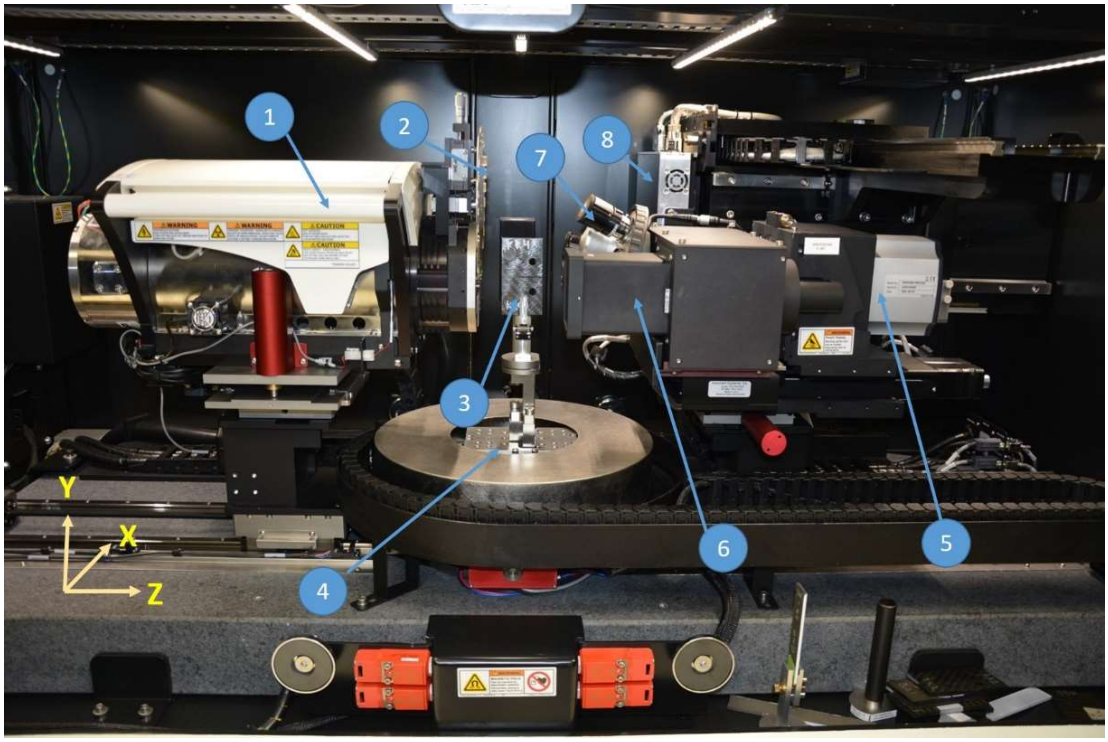

Figure 2 – Interior of the Zeiss Xradia 620 Versa µCT system

  doi:10.5075/epfl-298799_978-2-9701614-0-0

3.1 Material Architecture Effects

A typical µCT scan of 0° ply in a QI specimen soaked in a dye penetrant solution for 48 hours is shown in Figure 3. The scan was performed using 100 KkVand 14 watts power setting aandLE2 filter. The images were captured using a flat panel detector with an exposure time of 0.12 seconds per projection. A full scan consisted of 2,401 projections, yielding a voxel size of 13 µm. The crack, propagating toward the x_1 direction, is visible, as well as a large number of matrix cracks that grow parallel to the fiber direction (x_2).

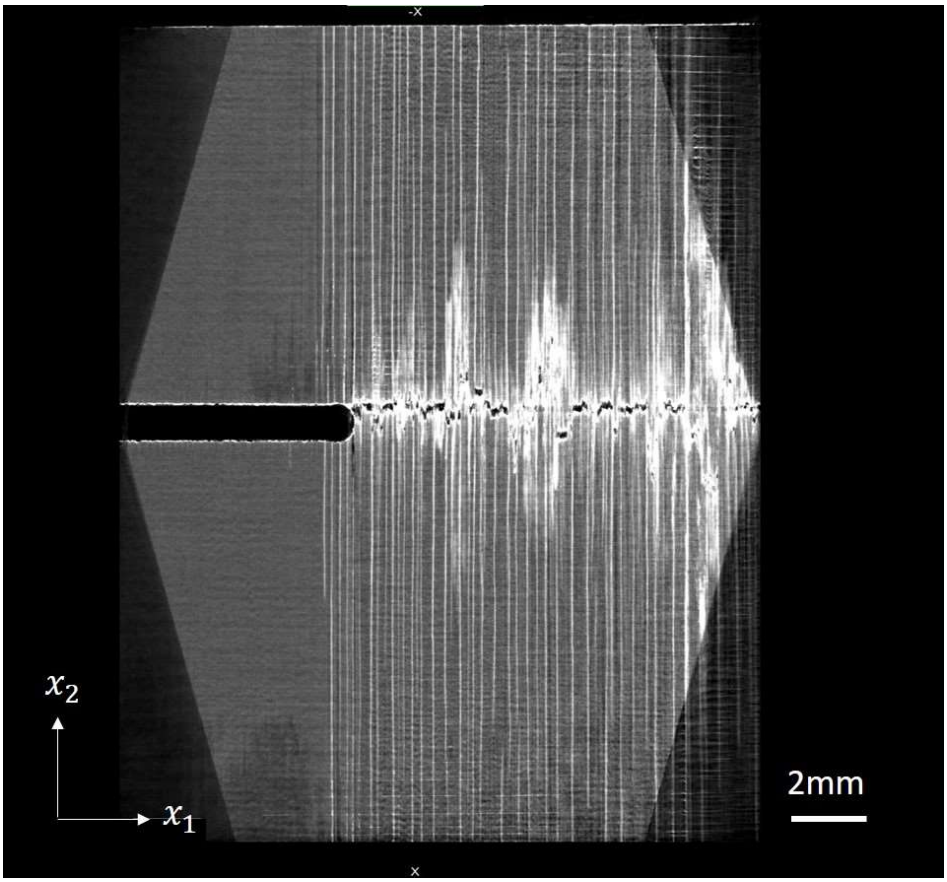

Figure 3 - µCT scan result showing a cross-section of a 0° ply in a QI layup OCT specimen manufactured using a unidirectional material, soaked in a dye penetrant solution before the scan. The scan was performed using a flat panel detector, yielding a voxel size of 13 µm

A µCT image of a QI specimen manufactured using the woven material is shown in Figure 4. Here, too, the scan was performed using 100 kV and a power setting of 14 watts, and a LE2 filter. The images were captured using a flat panel detector with an exposure time of 0.12 seconds per projection. This scan reveals the dramatic difference in damage observed in UD and woven-based OCTs tested. While the damage in the woven-based OCT was limited to a narrow band around the main crack, damage in unidirectional based OCT specimens spread across a broad region of the coupon with vast matrix cracking present far from the primary fiber fracture path.

  doi:10.5075/epfl-298799_978-2-9701614-0-0

This behavior affects the energy absorbed during crack growth, but its detailed description is beyond the scope of this paper, and is discussed in more detail in a separate paper.

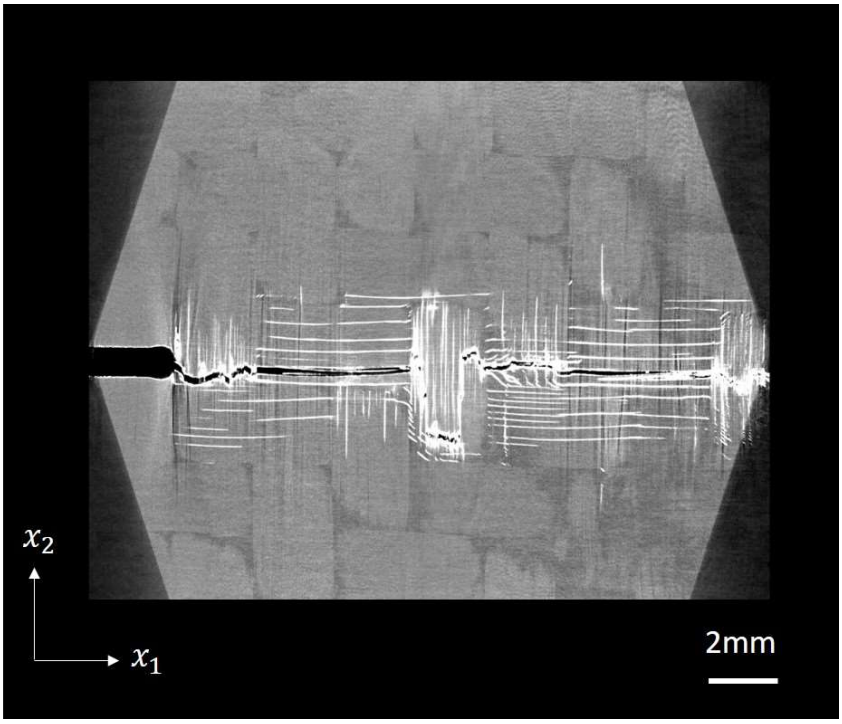

Figure 4 – A µCT scan results showing a cross-section of a $0^\circ/90^\circ$ ply in a QI layup OCT specimen manufactured using a woven material, soaked in a dye penetrant solution before the scan. The scan was performed using a flat panel detector, yielding a voxel size of 13 µm

Figure 5 shows a comparison of µCT cross-sections of the unidirectional (top image) and woven (bottom image) based OCT QI specimens, loaded to complete failure. Here, the crack propagates toward the right side (x_1) direction, and the out-of-plane direction is oriented toward the x_3 axis. Opposed to the results brought in Figure 3 and Figure 4, these scans were performed without a dye penetrant, allowing more details to be captured within the laminate plies, with the drawback of lower contrast between the matrix cracks and the undamaged material. Images were captured using the flat panel detector, 2,401 projections and 0.15 second exposure time per projection, and X-ray source settings of 100 kV, 14 watts. It can be seen in *Figure 5* that the damage in the OCT specimen fabricated using a woven material is more localized in the through-thickness direction compared to damage developed in the OCT specimen manufactured using the unidirectional material architecture. Delamination was present in almost all of the interfaces in the unidirectional-based OCT. In the woven-based OCT, delamination was locally present mainly at the interfaces close to the laminate's surface and only along a small number of fiber bundles.

  doi:10.5075/epfl-298799_978-2-9701614-0-0

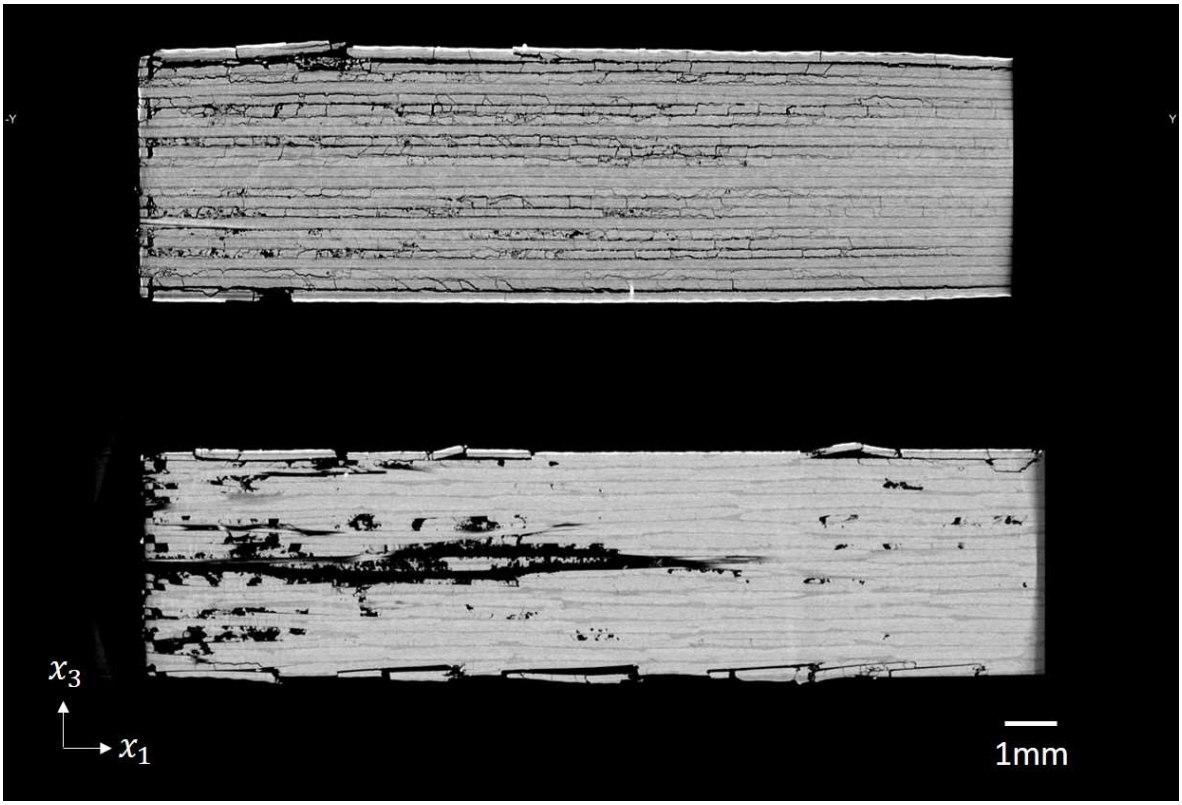

Figure 5 - A comparison between µCT cross-sections of QI OCT specimens manufactured using unidirectional (top) and woven material (bottom), with a voxel size of 13 µm. The specimens were loaded to complete failure, with the crack propagating toward the x_1 direction. The specimen's out-of-plane direction is oriented toward the x_3 axis

3.2 High Aspect Ratio Tomography

The Zeiss Xradia 620 Versa system allows two different scanning techniques for scanning high aspect ratio specimens, typical of composite laminates. The first approach allows optimizing the scan time for high aspect ratio specimens. The projections are captured using varying exposure times, where longer exposure times are applied to images taken along the longer dimension of the specimen, and shorter exposure times are applied to images taken along the shorter direction of the specimen. This way, the exposure time is set such that sufficient information is obtained at each specimen angle without sacrificing a longer exposure time for images taken along the short direction of the specimen. The application of this method can dramatically reduce the scan time without sacrificing the tomography image quality.

In addition, the system features an option to apply varying angular resolution during the scan. Using this method, the specimen rotation angles between every projection are varied and become smaller at angles where the specimen is oriented in the longest direction with respect to the X-ray beam. The effect of this high aspect ratio tomography (HART) algorithm is demonstrated in Figure 6. The left image is a through-thickness cross-section of the OCT specimen, with the through-thickness direction oriented along the x_3 direction. The left image is taken from a scan performed without applying the HART algorithm. Noise is visible in the air

  doi:10.5075/epfl-298799_978-2-9701614-0-0

volume surrounding the sample, and the contrast is relatively low within the specimen's cross-section. The image on the right is taken from a can in which the HART algorithm is applied. Here, the noise level in the air surrounding the specimen is reduced, and the plies within the laminate cross-section are better visualized. In addition, less noise is present within the laminate itself.

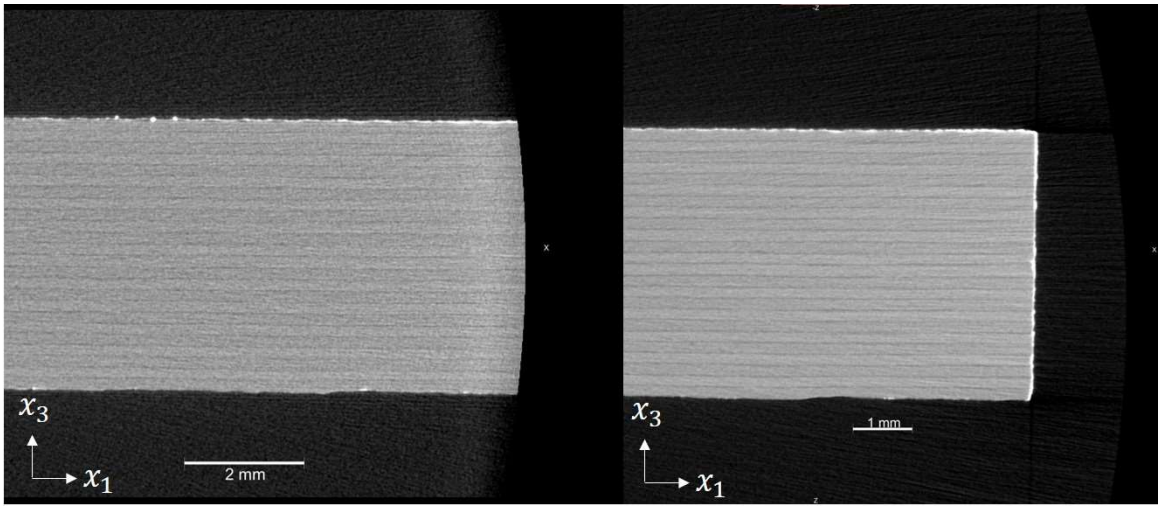

Figure 6 – A cross-section in a µCT scan performed without (left) and with (right) High Aspect-Ratio Tomography (HART) algorithm. The out-of-plane direction of the specimen is aligned along the x_3 direction.

4. Conclusions

Overheight Compact Tension specimens are manufactured using woven and unidirectional material architectures and loaded to complete failure. µCT investigation demonstrates the difference in damage developed within these two material architectures. While damage developed in woven laminates was localized to a narrow band around the main crack with minor delamination damage, damage in a unidirectional laminate spread across the specimen while exhibiting many matrix cracks and extensive delamination. This behavior can potentially affect the energy consumed during the fracture process and is discussed in a separate detailed paper.

An algorithm intended for scanning high aspect ratio specimens allows for better results during the scan, reducing the noise in the air region around the sample and the signal-to-noise ratio within the laminate.

Acknowledgments

This work was funded by Rafael Advanced Defense Systems LTD in collaboration with Technion Israel Institute of Technology and the US Air Force Research Laboratory (AFRL). Furthermore, the authors would like to acknowledge the Dynamic Fracture Laboratory at Technion and Ido Simon for their contribution.

  doi:10.5075/epfl-298799_978-2-9701614-0-0

References

1. Garcea S.C., Wang Y, Withers P.J. X-ray computed tomography of polymer composites. Composites Science and Technology 2018; 156:305-319
2. Rashidi A, Olfatbakhsh T, Crawford B, Milani A. A review of current challenges and case study toward optimizing micro-computed X-ray tomography of carbon fabric composites. Materials 2020; 13
3. Gu Y, Zhang D, Zhang Z, Sun J, Yue S, Li, G, Qian K. Torsion damage mechanisms analysis of two-dimensional braided composite tubes with digital image correction and X-ray micro-computed tomography. Composite Structures 2021; 256
4. Cinar K, Guven I, Oz F, Ersoy N. Quantifying the delamination of L-shaped composite laminates under low velocity impact using x-ray computed tomography. 33rd Technical Conference of the American Society for Composites 2018; 1: 561 – 576
5. Yao Q, Salviato M. Micro-Computed Tomography Analysis of Damage in Notched Composite Laminates Under Multi-Axial Fatigue. ArXiv 2019
6. Cornet A, Eastwood, D.S, Bourne, N.K., Mummery, P.M., Cady, C.M., Rau, C. Advances on mode I fracture testing in brittle and quasi-brittle materials with X-ray tomography. Proceedings of AIP Conference 2020; 2272
7. Forna-Kreutzer J, Paul J, Barnard H, Pirzada Talha J, Ritchie R.O, Liu D. Full-field characterisation of oxide-oxide ceramic-matrix composites using X-ray computed micro-tomography and digital volume correlation under load at high temperatures. Materials and Design 2021; 208
8. Mehdikhani M, Straumit I, Gorbatikh L, Lomov S.V. Detailed characterization of voids in multidirectional carbon fiber/epoxy composite laminates using X-ray micro-computed tomography. Composites Part A: Applied Science and Manufacturing 2019; 125
9. Kongshavn I, Poursartip A. Experimental investigation of a strain-softening approach to predicting failure in notched fibre-reinforced composite laminates. Composite Science and Technology 1999;59:29–40.

  doi:10.5075/epfl-298799_978-2-9701614-0-0

ANALYSIS OF VOIDS IN FILAMENT WOUND COMPOSITES USING A MACHINE-LEARNING BASED SEGMENTATION TOOL

Shailee, Upadhyay[a,d], Abraham, Smith[b], Dirk, Vandepitte[c], Stepan V., Lomov[a], Yentl, Swolfs[a], Mahoor, Mehdikhani [a]

a: Department of Materials Engineering, KU Leuven – shailee.upadhyay@kuleuven.be
b: Department of Computer Science, University of Copenhagen
c: Department of Mechanical Engineering, KU Leuven
d: SIM vzw, Technologiepark 48, 9052 Zwijnaarde, Belgium

Abstract: *Filament wound composites (FWC), typically used for high-strength applications, are prone to high void content, large void sizes as well as complex void geometries as a function of the manufacturing and design conditions. Voids in composites have a detrimental effect on their thermo-mechanical performance, governed by void characteristics. This makes accurate characterisation of voids in FWC vital for analysing their performance. Recently, micro-computed tomography has been widely used for this purpose. Several techniques have been proposed for segmentation of voids in the resulting tomograms. In this paper, a conventional grayscale thresholding technique is compared with an advanced machine learning-based segmentation technique, with respect to quantification of void characteristics in FWCs. The causes for error in grayscale thresholding are discussed and possible use cases of both techniques are highlighted based on the accuracy of the obtained characteristics and the application of the derived data.*

Keywords: Filament wound composites; Voids; Grayscale thresholding; Machine learning

1. Introduction

Filament winding is primarily used for manufacturing of axisymmetric, high strength composite parts such as pressure vessels as it allows usage of long unidirectional fibres. However, due to low-tension winding, filament wound composites (FWC) suffer from high void content and complexity depending on process parameters which lead to deterioration of part strength[1,2]. The influence of sizes and shapes of voids become more detrimental to the composite performance with increased void content. They can serve as crack initiation sites based on their characteristics [3–5] . Therefore, accurate void characterisation is crucial for the optimisation of FWC microstructure.

Numerous techniques have been developed for characterization of voids, among which X-ray micro-computed tomography is the most advanced and accurate one that provides 3D data on voids characteristics. To obtain quantitative information regarding voids from tomography results, the voids need to be segmented. Several techniques and software tools have been utilised to segment voids in 3D volumes [5]. The most common and simplistic method is grayscale thresholding, either global or local, in which a threshold value is chosen based on the gray value of the void in the image. The segmentation techniques are highly sensitive to image resolution, contrast, noise and artifacts. To enable grayscale thresholding for noisy images, appropriate denoising filters need to be applied [6,7].

  doi:10.5075/epfl-298799_978-2-9701614-0-0

In recent years, machine learning (ML) based techniques have emerged as a powerful tool for image analysis. For composites, ML techniques such as Weka segmentation, fuzzy reasoning and deep learning have been successfully used for segmentation of features of interest [8,9]. However, these have been primarily applied on 2D optical micrographs of composites with low void content and complexity. Although more accurate, they have been found to be time-consuming compared to the conventional methods.

The accuracy of the measured void characteristics is directly dependent on the accuracy of the segmentation quality. To enable the selection of an appropriate segmentation method, the difference between conventional methods and more advanced ML-based segmentation methods needs to be understood quantitatively.

In the present paper, the conventional grayscale thresholding and an ML-based segmentation technique for void segmentation in 3D images of FWCs are compared in terms of segmentation quality and the differences are quantified. The image processing requirements of both techniques are briefly discussed, and a comparison of void characteristics (void count, void fraction and void distribution and size) obtained from both techniques is discussed for a 2D slice and a 3D volume.

2. Methodology

The sample of dimension 1.8 (length) x 0.8 (thickness) x 1.4 (width) mm was cut from a CF/epoxy unidirectional FWC cylinder. The cylinder was manufactured by Plastic Omnium under the RELFICOM project. The scans were performed using a TeScan UniTom HR µCT system at a voxel size of 0.8 microns, at voltage and power of 60kV and 1.5W respectively. Overall, 1800 projections were taken in one scan to obtain the volumetric dataset in about 120 minutes.

For grayscale thresholding, we used the built-in algorithms in FIJI ImageJ [10] software. The Gaussian blur noise filter was applied to enable grouping of pixel gray values. The thresholding methodology was chosen iteratively from the built-in global and local thresholding algorithms. In the present analysis, the Otsu technique (global) and adaptive local thresholding technique (local) provided satisfactory results.

For machine learning-based segmentation, we used RootPainter [11]. RootPainter enables rapid training of deep neural networks for image segmentation via corrective-annotation with a graphical user interface. RootPainter has been used successfully for the segmentation of biological images [12–15].

The 2D measurements were made using ImageJ software. For comparison of 3D features, a void analysis was performed on VoxTex software [16], which enables fitting an ellipsoid of equivalent volume in place of voids in segmented datasets.

3. Algorithm implementation

When implementing both the grayscale thresholding with ImageJ and the ML-based segmentation with RootPainter, certain steps were followed for all datasets. Figure 1 illustrates the process-flow for segmentation using the two methodologies.

  doi:10.5075/epfl-298799_978-2-9701614-0-0

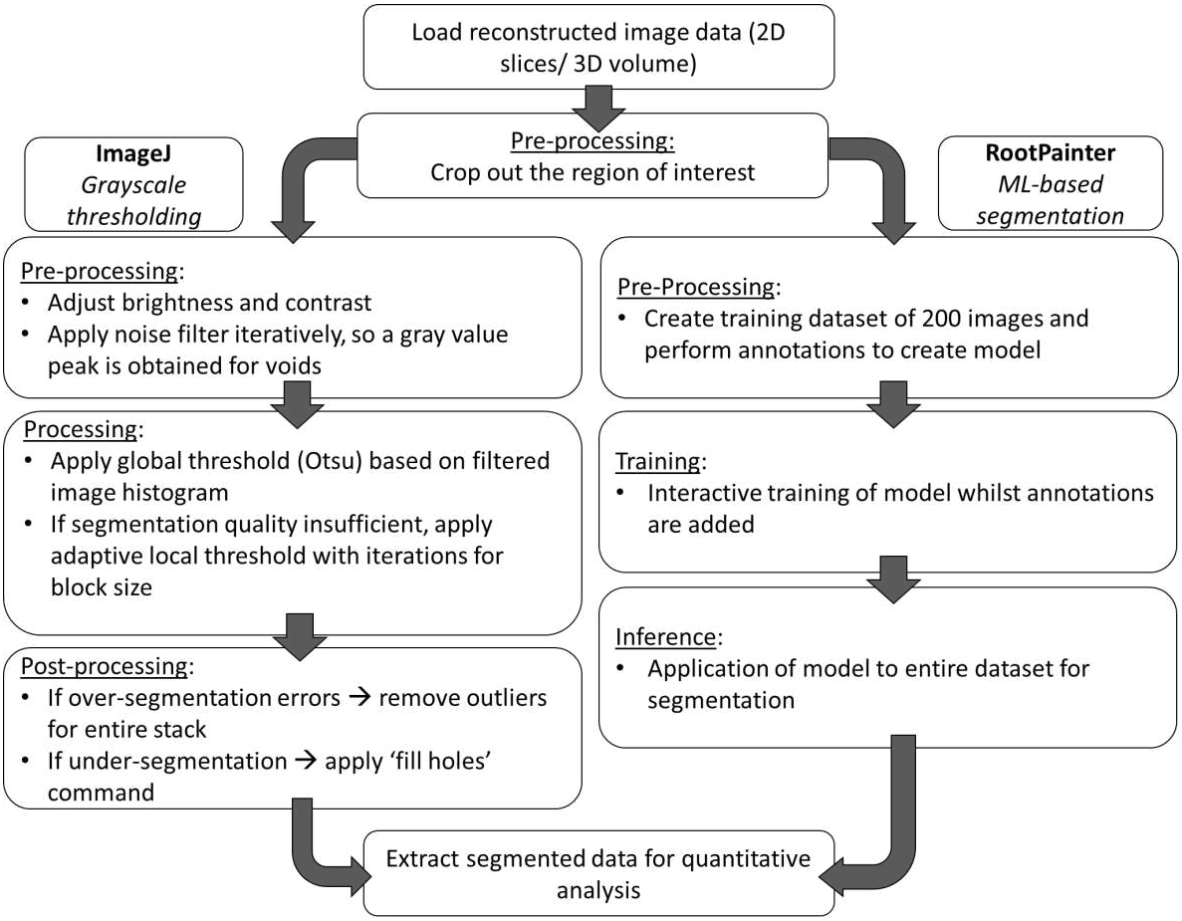

Figure 1: Segmentation process-flow.

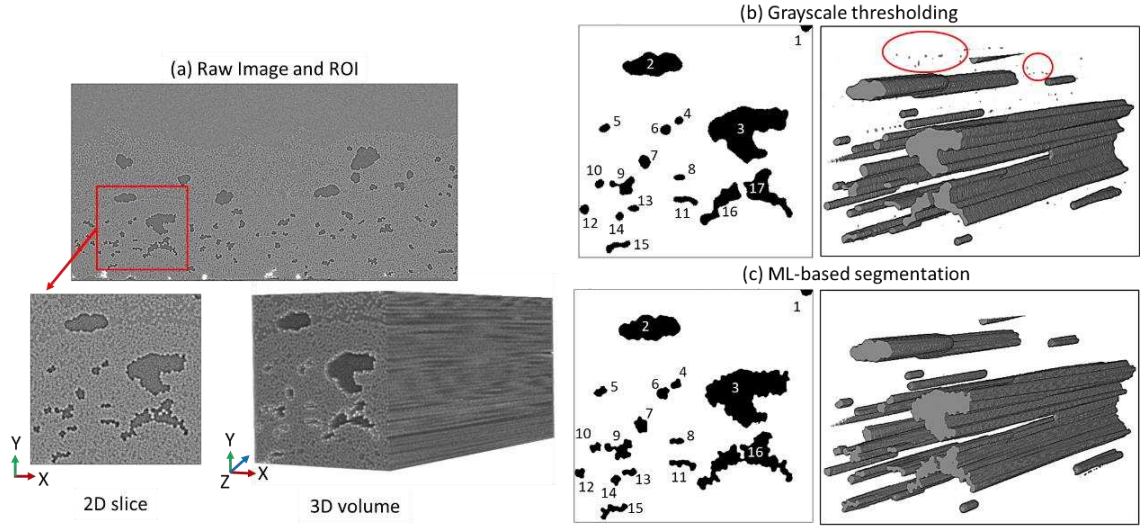

Figure 2: (a) ROI for void analysis; 2D slice with void labels and 3D volume segmented with (b) Grayscale thresholding and (c) ML-based segmentation

  doi:10.5075/epfl-298799_978-2-9701614-0-0 published under CC BY-NC 4.0 license

4. Results and discussions

For ease of validation, segmentation algorithms were applied to a Region of Interest (ROI) of dimensions 0.4x0.4x0.75 mm, as shown in Figure 2a.The ROI represents typical microstructure of FWC with large inter-layer and inter-tow voids and small intra-tow voids.

The segmentation results are shown in Figure 2b and 2c. Visually, the ML-based segmentation appeared more accurate in both the 2D slice and 3D volume. For quantitative analysis of void characteristics, a one-to-one analysis was made for the 2D slice (see labels in Figure 2b and 2c) and a volumetric range based analysis was done for 3D volume. It should be noted that the grayscale thresholding volume shows some 'specks' (encircled in Figure 2a) due to over-segmentation i.e. misidentification of non-void region as void. Their effect was minimised by only considering voids with volume over 5µm³ for analysis.

4.1 Void count and void fraction

The void fraction and void count are the basic global parameters obtained during void analysis. Figure 3a shows the difference between void count obtained for the two techniques for both 2D and 3D data:

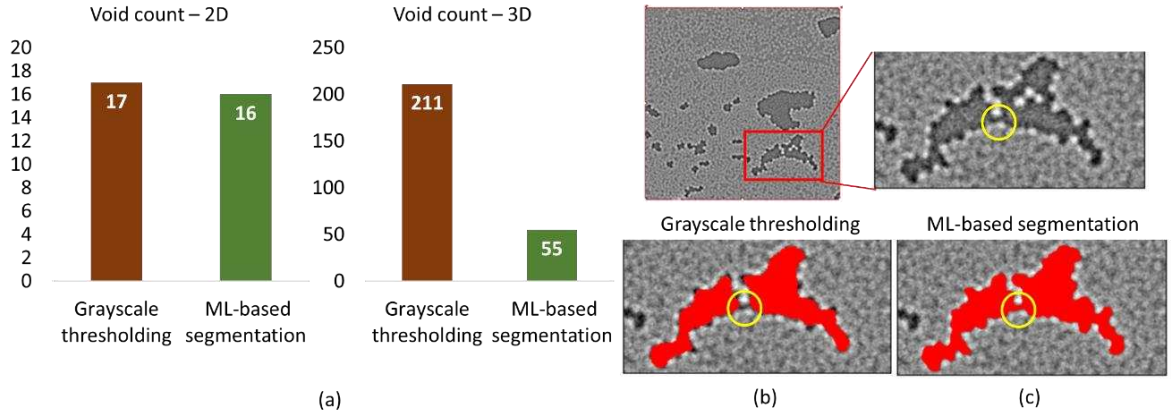

Figure 3: (a) Void count in 2D and 3D segmentations, and (b) splitting of void in grayscale thresholding image.

The grayscale thresholding finds one more void than the ML-based segmented image for 2D analysis. The void shown in Figure 3b is wrongly identified as two voids in the grayscale thresholding due to edge distortion caused by the noise reduction filter or post-processing operations. For complex void shapes, the edge distortion can lead to splitting of void into two or more parts. The ML-based segmentation could more accurately depict the void shape as training and inference was performed on the raw unfiltered image, and the algorithm does not work only based on the gray level. In the 3D volume, this effect was compounded with the void count in grayscale thresholding being 4 times larger than the void count from the ML-based segmentation.

The void volume fraction comparison is shown in Figure 4. The values are found to be comparable for both techniques, although slightly larger for the ML approach. This implies that the edge distortion and splitting of voids does not significantly affect the determination of the overall void content.

  doi:10.5075/epfl-298799_978-2-9701614-0-0

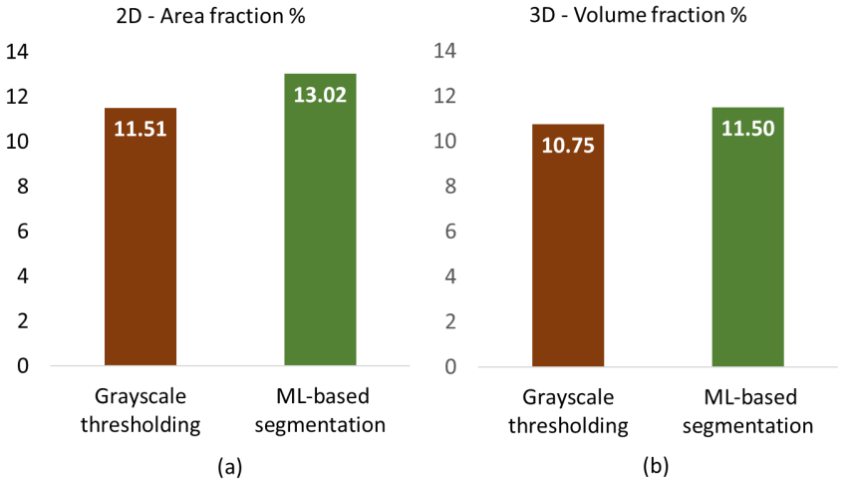

Figure 4: Void fraction for (a) 2D slice, (b) 3D volume

4.2 Void distribution

For analysis in 2D, the centroids are plotted in Figure 5a for the voids labels shown in Figure 2b and 2c.

If the void is identified by both techniques without splitting, the void centroid position is similar according to both techniques. However, the split void appears as two voids in the thresholding results, which could lead to false conclusions (encircled in Figure 5a).

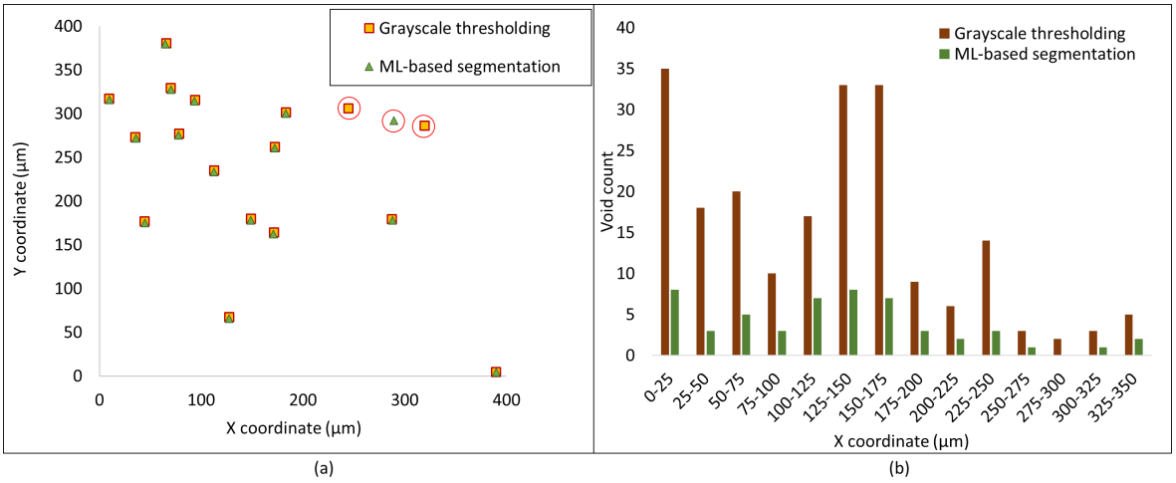

Figure 5: Comparison of void location (a) Centroid of each void in 2D slice (b) Void count along scan horizontal axis in 3D volume.

In the 3D volume, the number of voids along the horizontal axis of the scan (Figure 5b) reveals that although the number of voids is different for the two techniques, the trend of void distribution along this axis remains similar as split voids lie fairly close to each other.

4.3 Void size

For size analysis in the 2D slice, the area of each void is evaluated. Although the overall void area fraction is comparable between the two techniques, Figure 6a shows high variation between individual void sizes.

  doi:10.5075/epfl-298799_978-2-9701614-0-0

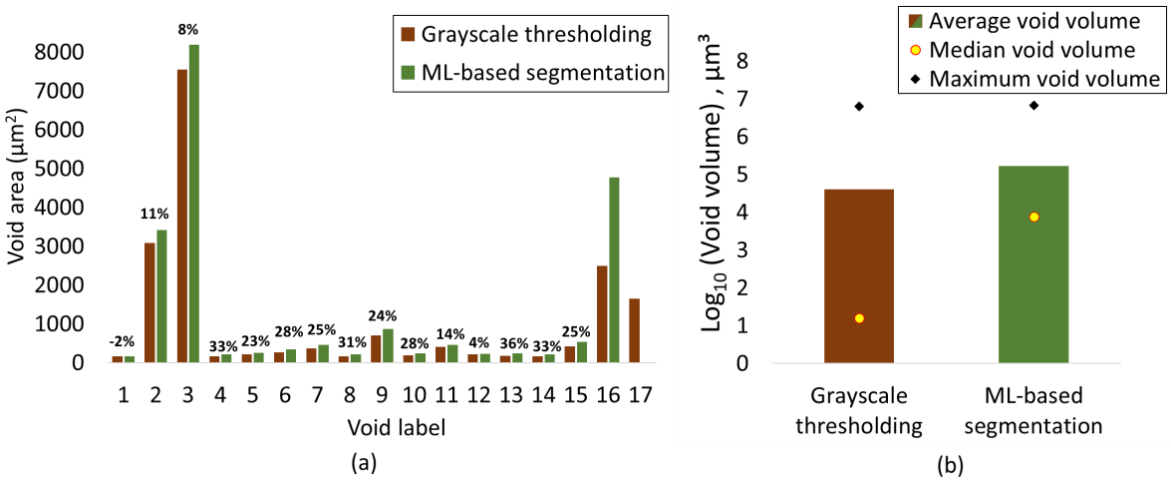

Figure 6: Void size comparison (a) Area of voids in 2D slice and % change in void area from grayscale- thresholding to ML-based segmentation (b) Void volume comparison in 3D

The smaller voids show higher variation as can be seen, due to the large relative difference in area measured by grayscale thresholding and ML-based segmentation. It should be noted that a one-to-one comparison for the split void is not possible. For void size comparison in the 3D volume, the logarithm of the void volume is plotted in Figure 6b. The average void volume is found to be almost 4 times lower for grayscale thresholding, which corresponds to the 4-fold increase in void count. This indicates the an excessive splitting of the voids as well as the presence of some over-segmented regions (volume > 5µm³) by grayscale thresholding. The low median value for grayscale thresholding also supports this observation. The effect of edge distortion noted for the void area in 2D slice also gets compounded over the volume, contributing to the decreased void volume in grayscale thresholding. These values obtained for grayscale thresholding may lead to false conclusions regarding average void characteristics, and can significantly affect local property analysis. Interestingly, the maximum detected void size is almost similar for both methods.

5. Conclusions

A filament wound composite sample with a high void fraction with varying shape complexity was segmented using a traditional grayscale thresholding and an advanced ML-based segmentation technique. The results were compared quantitatively for void characteristics at 2D and 3D cases. The following conclusions can be made based on the analysis:

1. Grayscale thresholding requires iterative pre-processing and post-processing steps, which may lead to edge distortion in voids causing mischaracterisation of void parameters. ML-based segmentation can be done directly on raw images. The iterative nature of grayscale thresholding also increases the possibility of human error during segmentation.
2. The overall void area and volume fractions as well as location (for the voids which do not split) are comparable for both techniques.
3. Due to edge distortion, complex voids may split affecting the location, shape, size and spatial distribution of voids in grayscale thresholding. These effects were more

  doi:10.5075/epfl-298799_978-2-9701614-0-0

prominent for small voids or complex-shape voids. Simple-shape voids were not found to be significantly affected.

4. The grayscale thresholding method was found to be sufficient for analysis of overall void content, simple-shape voids in small datasets. ML-based segmentation outperforms grayscale thresholding for complex void shapes, accurate individual void characterisation and large datasets.

Acknowledgment

The authors gratefully acknowledge SIM (Strategic Initiative Materials in Flanders) and VLAIO (Flanders Agency for Innovation & Entrepreneurship) for their support of the SBO project RELFICOM, within the SIM Nanoforce Program. . M. Mehdikhani would like to acknowledge his FWO Postdoc Fellowship, project ToughImage (1263421N).

6. References

1. Ellul B, Camilleri D. The influence of manufacturing variances on the progressive failure of filament wound cylindrical pressure vessels. Composite Structures. 2015;133:853–62.

2. Cohen D. Influence of filament winding parameters on composite vessel quality and strength. Composites Part A: Applied Science and Manufacturing. 1997;28(12):1035–47.

3. Hyde A, He J, Cui X, Lua J, Liu L. Effects of microvoids on strength of unidirectional fiber-reinforced composite materials. Composites Part B: Engineering. 2020;187(October 2019):107844.

4. Wang M, Zhang P, Fei Q, Guo F. Computational evaluation of the effects of void on the transverse tensile strengths of unidirectional composites considering thermal residual stress. Composite Structures. 2019;227(May):111287.

5. Mehdikhani M, Gorbatikh L, Verpoest I, Lomov S V. Voids in fiber-reinforced polymer composites: A review on their formation, characteristics, and effects on mechanical performance. Journal of Composite Materials. 2019;53(12):1579–669.

6. Rashidi A, Olfatbakhsh T, Crawford B, Milani AS. A review of current challenges and case study toward optimizing micro-computed X-ray tomography of carbon fabric composites. Materials. 2020;13(16).

7. Nichele L, Persichetti V, Lucidi M, Cincotti G. Quantitative evaluation of ImageJ thresholding algorithms for microbial cell counting. OSA Continuum. 2020;3(6):1417.

8. Luo L, Zhang B, Lei Y, Zhang G, Zhang Z, Meng B, et al. Identification of voids and interlaminar shear strengths of polymer-matrix composites by optical microscopy experiment and deep learning methodology. Polymers for Advanced Technologies. 2021;32(4):1853–65.

9. Dominguez JA, Tate LC, Wright MC, Caraccio A. Fuzzy reasoning to more accurately determine void areas on optical micrographs of composite structures. Applied Composite Materials. 2013;20(6):1125–34.

  doi:10.5075/epfl-298799_978-2-9701614-0-0

10. Schneider CA, Rasband WS, Eliceiri KW. HISTORICAL commentary NIH Image to ImageJ : 25 years of image analysis. Nature Methods. 2012;9(7):671–5.

11. Smith AG, Han E, Petersen J, Olsen NAF, Giese C, Athmann M, et al. RootPainter: Deep Learning Segmentation of Biological Images with Corrective Annotation. bioRxiv. 2020;

12. Han E, Smith AG, Kemper R, White R, Kirkegaard JA, Thorup-Kristensen K, et al. Digging roots is easier with AI. Journal of Experimental Botany. 2021;72(13):4680–90.

13. Alonso-crespo IM, Weidlich EWA, Temperton VM, Delory BM. Assembly history modulates vertical root distribution in a grassland experiment. 2021;

14. Clément C, Sleiderink J, Svane SF, Smith AG, Diamantopoulos E, Desbrøll DB, et al. Comparing the deep root growth and water uptake of intermediate wheatgrass (Kernza®) to alfalfa. Plant and Soil. 2022;(0123456789).

15. Denison RF. Legume-imposed selection for more-efficient symbiotic rhizobia. Proceedings of the National Academy of Sciences of the United States of America. 2021;118(22):22–4.

16. Mehdikhani M, Straumit I, Gorbatikh L, Lomov S V. Detailed characterization of voids in multidirectional carbon fiber/epoxy composite laminates using X-ray micro-computed tomography. Composites Part A: Applied Science and Manufacturing. 2019;125(January):105532.

THE ROLE OF MATRIX BOUNDARY IN THE MICROSTRUCTURE OF UNIDIRECTIONAL COMPOSITES

Silvia Gomarasca[a], Daniël Peeters[a], Bilim Atli-Veltin[a,b], Joris Markenstein[c], Hans Luinge[c], Clemens Dransfeld[a]

a: Delft University of Technology, Department of Aerospace Structures and Materials, Delft, Netherlands – s.gomarasca@tudelft.nl
b: Nederlandse Organisatie voor Toegepast Natuurwetenschappelijk Onderzoek (TNO), Delft, Netherlands
c: Toray Advanced Composites, Nijverdal, Netherlands

Abstract: *Finding new ways to evaluate the microstructural characteristics and their effect on macroscopic properties such as permeability and mechanical performance is of increasing interest for fibre reinforced polymer composites. The three-dimensional variability of microstructural features is not fully understood and its effect on macroscale properties is not well established, and so far mostly analysed at a phenomenological level. In order to achieve a more complete definition of the unidirectional composites domain, an understanding of matrix-based features and their interrelation with fibre architecture descriptors is needed. We introduced in recent work a method based on X-ray Computed Tomography for the quantification of fibre-architecture descriptors at an increasing level of complexity. To expand the methodology, this work accounts for matrix-based phenomena such as tape boundary variability and distribution of voids.*

Keywords: Microstructure; Unidirectional Composites; X-ray Computed Tomography; Matrix boundary; Voids.

1. Introduction

Finding new ways to evaluate the microstructural characteristics and their effect on macroscopic properties such as permeability and mechanical performance [1,2] is of increasing interest for fibre reinforced polymer composites. 3D imaging techniques have been receiving increasing interest in evaluating fibre architectures, void distribution and damage formation [3–5]. However, the variability of microstructural features at a three-dimensional level is not fully understood. Its effect on macroscale properties is not well established, and mostly analysed at a phenomenological level [6].

We introduced in recent work a method based on X-ray Computed Tomography for the three-dimensional description of the fibrous microstructure of unidirectional tapes at a single fibre level [7]. Three metrics are introduced in the work to describe the increasing level of complexity in the microstructural organization, from a single fibre path level with differential tortuosity, over group behaviour with collective motion, to fibre network connectivity with the length of neighbourhood. These descriptors and their interdependence highlight local effects like edge-core segregation in microstructural characteristics.

However, to achieve a complete definition of the unidirectional tape domain, capturing matrix-based features such as tape boundary and void distribution is crucial to characterize its properties [8,9]. In particular, recent studies relate the effects of surface resin-rich layers in

  doi:10.5075/epfl-298799_978-2-9701614-0-0

unidirectional tapes to their processability [10,11]. The interrelation between matrix and fibre descriptors will also help generate further insight into microstructure formation, properties and quality assessment.

In this work, we expand the methodology we have recently developed [7] by inter-relating fibre and matrix descriptors: fibre differential tortuosity, to matrix-based characteristics such as tape boundary variability, and void distribution and morphology. The approach is showcased on a unidirectional composite tape.

2. Methodology

To define a data processing method to characterise matrix-based features such as tape surface variability, void distribution and void morphology at a 3D level, the local tape boundary and internal void locations were extracted via image analysis methods. The workflow is showcased with the study of a unidirectional fibre-reinforced tape analysed via X-ray micro-computed tomography. The composite tape studied is an experimental thermoplastic tape reinforced with unidirectional standard modulus carbon fibres manufactured by Toray Advanced Composites.

2.1 X-ray computed tomography

A X-ray micro computed tomography scan was conducted with a Zeiss Xradia 520 Versa machine, at a voxel size of 0.7788 µm, with a resulting tape cross-section width of 1200 µm. A representative cross-section is shown in Figure 1a. The volume was acquired with a voltage of 70 kV, power of 5 W, and exposure time of 7 s. Of the acquired volume, a length of 800 µm in the fibre direction was considered for the analysis.

2.2 Segmentation of the microstructural features

The scan volume was processed via Fiji plugins to extract the features of interest [12]. The focus was to highlight matrix-based features such as tape contour and voids distribution, and fibre positions through the volume. Prior to feature extraction, volume tilt was corrected via re-slicing and manual alignment with the main fibre direction. A data reduction scheme was then applied where one slice every five in the tape length direction was used, resulting in a ‘stretched’ voxel having dimensions of 0.78 µm by 0.78 µm in the plane perpendicular to the principal fibre direction and 3.9 µm in the primary fibre alignment (longitudinal) direction.

The workflow for the extraction of matrix features is described in Figure 1. Fibres were segmented via Trainable Weka segmentation [13] with a result as in Figure 1b. Tape surface and air were segmented in a second step via the same method, resulting in the map of Figure 1c. Thresholding followed by morphological filtering (opening and closing with a spherical structuring element of 2 pxl in diameter) were then applied to reduce the noise in the segmented volume. Area filtering was conducted on the connected components of the tape to remove segmentation artefacts outside the tape region, resulting in a binary output, shown in Figure 1c. The contour of the remaining connected components was then evaluated (Figure 1d) and merged to identify the local boundary of the tape at each cross-section, as in Figure 1e. The local boundary was then used as a mask to isolate the internal voids from the surrounding air, as shown in Figure 1f.

  doi:10.5075/epfl-298799_978-2-9701614-0-0

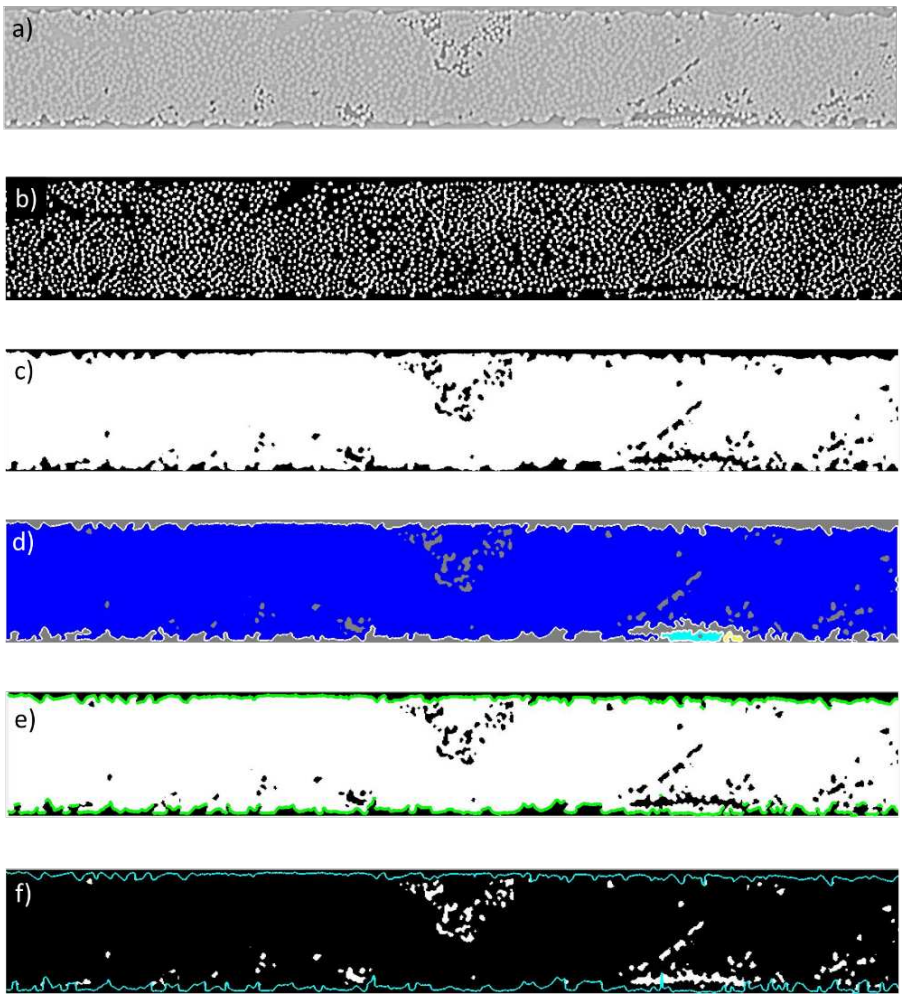

Figure 1. Workflow for tape analysis a) tape cross-section b) segmented fibres, highlighted in white c) tape matrix and fibres (white) and air (black) as obtained after segmentation, thresholding, morphological operations and area filtering d) boundary detection for each connected component, consisting in this case of three regions, labelled respectively in blue, cyan and yellow e) resulting tape boundary of the cross-section, highlighted in green f) internal voids highlighted in white, within the tape boundary in cyan.

2.3 Determination of the microstructural descriptors

2.3.1 Fibres

Fibre paths reconstruction and analysis were conducted as a variation of the methodology described in previous work [7]. Individual fibre path reconstruction was performed by TrackMate [14]**.** A smoothing length of five times the fibre diameter was used to post-process the fibre tracks before the calculation of the parameters. Differential tortuosity was used as a microstructural descriptor of the unidirectional fibre architecture, as defined in our previous work [7]. The parameter is calculated for each fibre:

$$\tau^d = \frac{L - L_o}{L_o} \quad (1)$$

where L is the total detected length of the fibre, and L_o is the perpendicular distance between the two outer sections analysed.

  doi:10.5075/epfl-298799_978-2-9701614-0-0

The parameter quantifies the cumulative local misalignment of fibre paths and can provide a first indication of the local disorder in the fibre arrangement. The tortuosity values were then interpolated at the voxel locations to obtain a 2D homogenised distribution.

2.3.2 Tape boundary

The tape surface variability was determined as local elevation compared to the mean coordinate of the upper and lower boundaries. The range of elevation was then determined for each pixel along the tape width as the difference between the maximum and minimum values. A smoothing length equal to two fibre diameters (15 µm) was used to reduce the noise of the range profile. The surface elevation range was related to the mean logarithm of differential tortuosity at the same voxel locations.

2.3.3 Voids

Voids with the size of a unit voxel were filtered out as noise, while the remaining voids were further analysed in terms of their size, aspect ratio and spatial distribution. The 2D histogram of the distribution of voids over the cross-section was used to map the local void accumulation, defined as the product of the histogram bin-count for each cross-sectional location and the voxel size along the primary fibre alignment direction. The void accumulation was then related to the logarithm of differential tortuosity.

3. Results and discussion

In this section, the results of the analysis of fibre differential tortuosity, and of tape boundary variability and voids are provided and discussed.

3.1 Differential tortuosity

The map of the logarithm of differential tortuosity is reported in Figure 2. The values reported are a homogenization of the values determined in the length of observation considered of 800 µm. The parameter varies along the cross-section. Corridors generated by high tortuosity fibres are highlighted in Figure 2 with dashed yellow lines and are observed along the bottom tape surface, running from the bottom to the top side of the cross-section. Darker regions of lower tortuosity, where fibres are more aligned, are present in-between higher tortuosity regions.

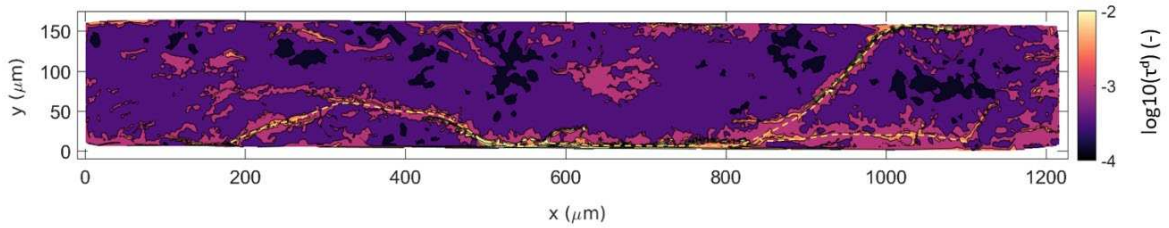

Figure 2. Map of the logarithm of differential tortuosity. High tortuosity corridors are highlighted with a yellow dashed line.

3.2 Tape boundary

Local topology changes in terms of elevation were determined for top and bottom surfaces, as shown in Figure 3a-b. The surface variability shows an overall tendency to align in the fibre direction, with local surface misalignments from the longitudinal direction. The comparison

  doi:10.5075/epfl-298799_978-2-9701614-0-0

between the range of the surface elevation and the logarithm of differential tortuosity at the tape edge is reported in Figure 3c for both top and bottom tape surfaces. The results suggest a positive correlation between the standard deviation of elevation and the logarithm of differential tortuosity.

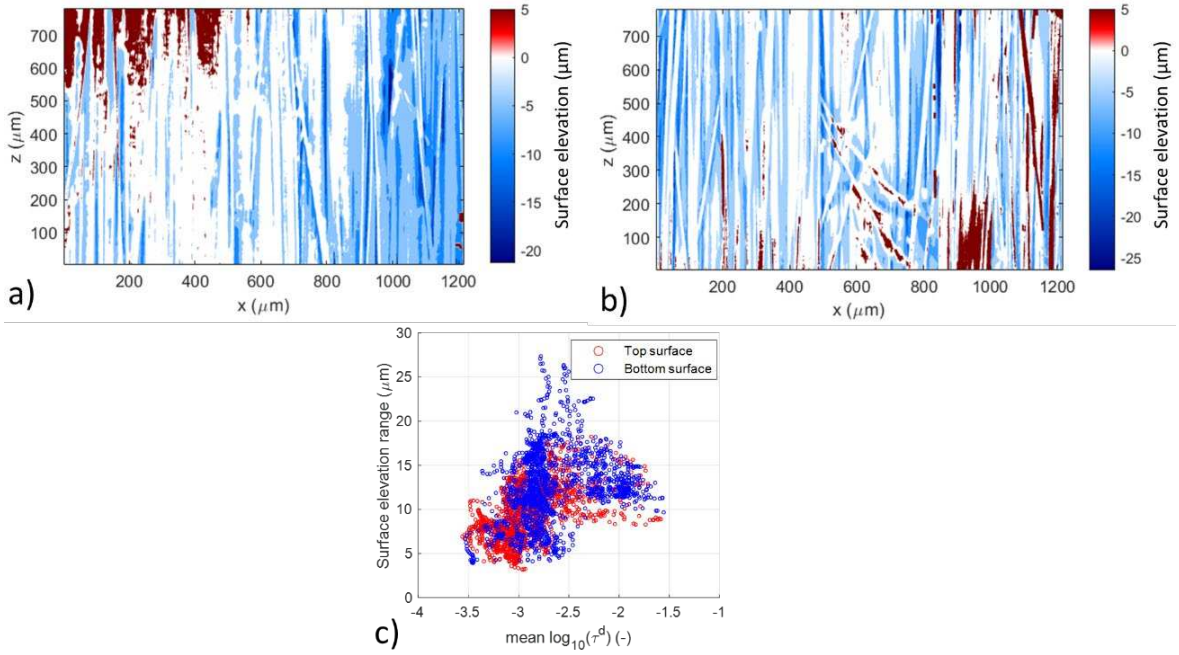

Figure 3. Surface elevation maps for a) top and b) bottom tape boundary; c) comparison of the surface elevation range calculated along the tape width and the correspondent values of the logarithm of differential tortuosity.

Surface variability effects are relevant to the understanding of the processability of unidirectional tapes [8]. Relating 3D surface variability and the underlying fibre architecture enables the extraction of surface fibre architecture information from the surface topology, potentially allowing the extraction of surface features during in-line monitoring. Approaches based on local fibre misalignment have been applied in the literature to estimate fibre alignment in composites from 2D micrographs [15], however 3D analysis of surface topology in relationship to underlying measured fibre tortuosity at the surface has not been reported for the study of unidirectional tapes to the authors' knowledge. The differential tortuosity map in Figure 2 shows corridors of higher tortuosity, which are both located along the bottom surface and running from the bottom-left to the top-right of the cross-section. Similar locations of surface elevation misalignment from the longitudinal direction can be located in Figure 3b. By comparing the surface elevation range to the tortuosity of the fibre architecture close to the boundary, it was possible to observe a positive correlation between the two, as shown in Figure 3c. The extent of the correlation between tape surface variability and fibre microstructure is expected to depend on the presence of resin-rich regions at the tape surface, which is minimal in this tape, as observed in Figure 1a.

3.3 Voids

The morphology and spatial distribution of voids was quantified via connected region analysis on the internal voids identified as in Section 2.2.1. Figure 4a shows a 3D representation of the distribution of the voids. The distribution of the voids aspect ratio between the longitudinal

  doi:10.5075/epfl-298799_978-2-9701614-0-0

dimension and the major cross-sectional dimension has been reported in Figure 4b, showing a tendency to void elongation in the longitudinal direction (values greater than 1). The void size distribution is shown in Figure 4c and spans over six orders of magnitude. The voids appear to be interfacial at a qualitative observation, being located at the fibre-matrix interface.

Since the voids tend to align along the fibre direction, their 2D accumulation for each location in the cross-section was considered, as reported in Figure 5a. The voids do not appear to be homogeneously distributed, but they seem to cluster in discrete regions. While low accumulation lengths were neglected, the cross-sectional void distribution for accumulation lengths greater than 100 µm was related to the logarithm of differential tortuosity. The mean logarithm of differential tortuosity was considered as a threshold for comparison. The regions where the logarithm of differential tortuosity is greater than its mean value are highlighted in yellow in Figure 5b. The histogram of Figure 5c reports the probability of void accumulation above and below the mean value of differential tortuosity and shows a greater probability of high void accumulation for high tortuosity values.

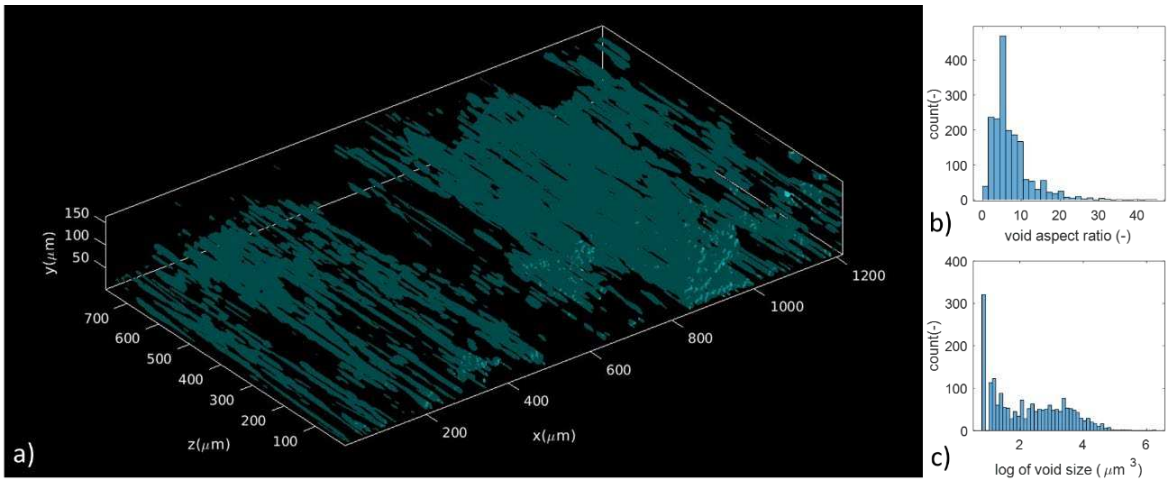

Figure 4. a) 3D representation of the internal void distribution in the scan volume. Statistics for the detected voids b) histogram of the aspect ratio of voids c) histogram of the distribution of the size of voids.

The sample considered shows interfacial voids between fibres and resin [16] elongated in the fibre length direction, as shown in Figure 4b, which is commonly observed in literature for UD composites [5,17]. Their presence might be attributed to incomplete impregnation. The comparison of the cross-sectional variability of voids and tortuosity of Figure 5c suggests that regions with high tortuosity have a higher probability of increased void formation. This might be related to hindering of the resin flow during impregnation. Conversely, regions with lower tortuosity, where fibre paths deviate less from the nominal alignment, show lower probability of voids presence.

4. Conclusion

A unidirectional composite tape was analysed accounting for both fibre-based descriptors, and matrix-based characteristics. The higher presence of defects in the development-grade material used compared to commercial grade tapes provides an opportunity to investigate links between tape boundary variability and void distribution to fibre-based descriptors such as differential tortuosity. The approach outlined in this work was able to describe the 3D microstructure at

  doi:10.5075/epfl-298799_978-2-9701614-0-0

both fibre and matrix level in unidirectional composite tapes. Future work should further investigate these emerging relationships in their broader application to unidirectional tapes and composites.

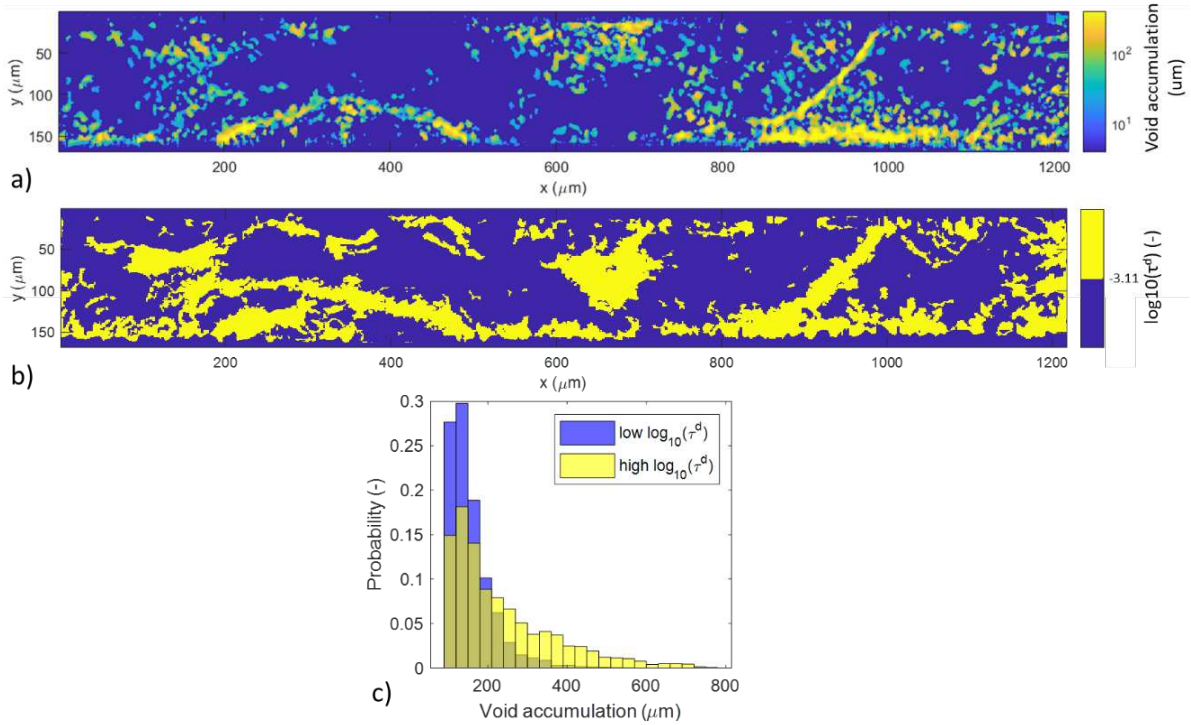

Figure 5. a) 2D histogram of the voids distribution in the cross-section b) map which highlights in yellow the regions where the logarithm of differential tortuosity is greater than its mean value c) histogram of the void accumulation for high value of the logarithm of differential tortuosity (above the mean value) and for low values (below the mean value).

Acknowledgements

The authors would like to acknowledge Naturalis Biodiversity Centre (Leiden, Netherlands) for conducting the X-ray computed tomography measurements, and Onur Yüksel (Aerospace Manufacturing Technologies group, Delft University of Technology, Delft, Netherlands) for the valuable discussions.

5. References

1. Gommer F, Wedgwood KCA, Brown LP. Composites : Part A Stochastic reconstruction of filament paths in fibre bundles based on two-dimensional input data. Compos PART A. 2015;76:262–71.
2. Gommer F, Endruweit A, Long AC. Quantification of micro-scale variability in fibre bundles. Compos Part A Appl Sci Manuf. 2016;87(January):131–7.
3. Emerson MJ, Wang Y, Withers PJ, Conradsen K, Dahl AB, Dahl VA. Quantifying fibre reorientation during axial compression of a composite through time-lapse X-ray imaging and individual fibre tracking. Compos Sci Technol. 2018;168(August):47–54.
4. Mehdikhani M, Breite C, Swolfs Y, Wevers M, Lomov S V., Gorbatikh L. Combining digital image correlation with X-ray computed tomography for characterization of fiber orientation in unidirectional composites. Compos Part A Appl Sci Manuf.

  doi:10.5075/epfl-298799_978-2-9701614-0-0

2021;142(September 2020):106234.
5. Mehdikhani M, Gorbatikh L, Verpoest I, Lomov S V. Voids in fiber-reinforced polymer composites: A review on their formation, characteristics, and effects on mechanical performance. J Compos Mater. 2019;53(12):1579–669.
6. Krämer ETM, Grouve WJB, Koussios S, Warnet LL, Akkerman R. Real-time observation of waviness formation during C/PEEK consolidation. Compos Part A Appl Sci Manuf [Internet]. 2020;133(January):105872.
7. Gomarasca S, Peeters DMJ, Atli-Veltin B, Dransfeld C. Characterising microstructural organisation in unidirectional composites. Compos Sci Technol. 2021;215(July):109030.
8. Çelik O, Peeters D, Dransfeld C, Teuwen J. Intimate contact development during laser assisted fiber placement: Microstructure and effect of process parameters. Compos Part A Appl Sci Manuf. 2020;134(February):105888.
9. Hapke J, Gehrig F, Huber N, Schulte K, Lilleodden ET. Compressive failure of UD-CFRP containing void defects: In situ SEM microanalysis. Compos Sci Technol. 2011;71(9):1242–9.
10. Katuin N, Peeters DMJ, Dransfeld CA. Method for the microstructural characterisation of unidirectional composite tapes. J Compos Sci. 2021;5(10).
11. Çelik O, Peeters D, Dransfeld C, Teuwen J. Intimate contact development during laser assisted fiber placement: Microstructure and effect of process parameters. Compos Part A Appl Sci Manuf. 2020;134(December 2019):105888.
12. Schindelin J, Arganda-Carreras I, Frise E, Kaynig V, Longair M, Pietzsch T, Preibisch S, Rueden C, Saalfeld S, Schmid B, Tinevez JY, White DJ, Hartenstein V, Eliceiri K, Tomancak P, Cardona A. Fiji: An open-source platform for biological-image analysis. Nat Methods. 2012;9(7):676–82.
13. Arganda-Carreras I, Kaynig V, Rueden C, Eliceiri KW, Schindelin J, Cardona A, Seung HS. Trainable Weka Segmentation: A machine learning tool for microscopy pixel classification. Bioinformatics. 2017;33(15):2424–6.
14. Tinevez JY, Perry N, Schindelin J, Hoopes GM, Reynolds GD, Laplantine E, Bednarek SY, Shorte SL, Eliceiri KW. TrackMate: An open and extensible platform for single-particle tracking. Methods. 2017;115:80–90.
15. Raimondi L, Brugo TM, Zucchelli A. Fiber misalignment analysis in PCM-UD composite materials by Full Field Nodal Method. Compos Part C Open Access. 2021;5(May):100151.
16. Çelik M, Noble T, Jorge F, Jian R, Br MÓ, Robert C. Influence of Line Processing Parameters on Properties of Carbon Fibre Epoxy Towpreg. J. Compos. Sci 2022;*6*(3):75
17. Comer AJ, Ray D, Obande WO, Jones D, Lyons J, Rosca I, Higgins RMO, Mccarthy MA. Composites : Part A Mechanical characterisation of carbon fibre – PEEK manufactured by laser-assisted automated-tape-placement and autoclave. Compos PART A. 2015;69:10–20.

DETAILED MICROSTRUCTURE CHARACTERISATION OF 3D PRINTED CARBON-FIBRE/PEEK USING X-RAY COMPUTED TOMOGRAPHY

Silvano Sommacal[a], John Holmes[a], Alexander Matschinski[b], Klaus Drechsler[b], Paul Compston[a]*

a: ARC Training Centre for Automated Manufacture of Advanced Composites, Australian National University, Acton, ACT 2601, Australia – Silvano.Sommacal@anu.edu.au
b: Chair of Carbon Composites, Department of Aerospace and Geodesy, Technical University of Munich, 85748 Garching, Germany

Abstract: *Extrusion-based processes offer the possibility of producing carbon fibre reinforced composite (CFRC) components for lightweight construction of virtually any size and shape. However, many challenges still need to be addressed before their widespread adoption. Chief amongst them is the presence of defects and the material's anisotropic and heterogeneous internal structure. In this study, X-ray micro-computed tomography (micro-CT) has been utilised to analyse, characterise and compare two suites of five 3D printed short CF/PEEK samples and the two commercial feedstock materials used to produce them. Main material constituents (fibres, matrix, voids) have been identified and segmented, their distribution mapped and visualised in 3D and respective volume fractions quantified. Voids have been individually labelled and their key geometrical characteristics extracted and analysed. Similarly, preferential fibre orientation has been measured. Furthermore, the effect of key 3D printing parameters on samples' microstructure has been assessed.*

Keywords: Fused Filament Fabrication (FFF); Short carbon fibre reinforced composite (CFRC); Micro-computed tomography (micro-CT); Microstructure characterisation

1. Introduction

Additive manufacturing (AM) is increasingly used in many industries for spare parts, small series production, and tooling (1). For non-metallic materials, under the generic AM term, several different processes exist; among them, extrusion-based fused filament fabrication (FFF) has become increasingly popular as the 3D printing technology that can produce components for lightweight construction of virtually any shape and size (2). In addition, FFF offers the possibility of printing high-performance polymer materials such as polyetheretherketone (PEEK), which has already proven of great interest, for instance, in the medical engineering (3) and space (4) fields. Furthermore, the addition of carbon fibres, continuous or short, can improve the mechanical properties of 3D printed PEEK components (5).

However, the overall quality and measured mechanical properties of FFF printed composites, especially when reinforced with carbon fibres, are still below expectations (6). The presence of voids linked to both feedstock material quality and printing process parameters can severely compromise the expected performance of the final product (7). In addition, the process-induced preferential orientation of fibres and their uneven distribution throughout the matrix cause anisotropy in the printed component, which along with potential fibre damage, affects its mechanical properties (8, 9). Understanding the characteristic geometry and shape of these defects as well as their spatial distribution within the three-dimensional material

  doi:10.5075/epfl-298799_978-2-9701614-0-0

microstructure, can provide valuable insight into the origin of their formation and enable optimisation of the fabrication process. In recent years, X-ray micro-computed tomography (micro-CT) has proven an ideal non-destructive imaging technique to provide very accurate structural 3D information, allowing for voids and other manufacturing defects to be characterised in detailed and quantified (10–12) and their influence and impact on materials' mechanical properties be better understood (7, 13).

In this work, we used X-ray micro-CT to acquire high-resolution volume data on ten printed short CF/PEEK samples and two commercial feedstock filaments. Subsequently, we extract detailed geometrical characteristics of voids and fibres, such as size, shape, orientation, 3D distribution and volume fraction for all specimens. Finally, the effect of key 3D printing parameters on the sample's voids/fibres content and distribution is assessed.

2. Experimental

2.1 Materials

The feedstock fused filament material utilised in this work is PEEK polymer containing randomly distributed short carbon fibres (SCF). It comprises of Victrex (30 wt% of SCF, 450CA30 grade, trade name: TECAFIL PEEK CF30 black, sample name: *Feed Vx*) and Lehmann & Voss & Co. KG (10 wt% of SCF, trade name: LUVOCOM® 3F PEEK CF 9676 BK, sample name: *Feed L&V*). Samples were printed following the procedure described in (11). Printer settings used and samples names are summarised in Table 1.

2.2 Sample preparation and image acquisition

All images utilised for this work have been acquired on a HeliScan™ micro-CT instrument equipped with a flat-panel detector with 3040 x 3040 pixels and a micro-focus X-ray source of 60 kV hosted at the ANU CT laboratory that utilises helical scanning (14), space-filling trajectory (15) and iterative reconstruction (16) technologies. Original dimensions and shape of both the feedstock material (cylinder, ~1.75 mm diameter) and 3D printed sample (prism, ~2 x 2 mm cross-section) were ideal for micro-CT imaging, and the only preparation required was to cut them into pieces of similar size (see Table 1). Individual image acquisition time was ~10 hours, while scanning resolution (i.e. voxel size) is given in Table 1.

Table 1 : Feedstock filaments and 3D printed samples names, printer settings, dimensions and image scanning resolution; where [a] mm, [b] °C, [c] µm.

	Feed Vx	*Feed L&V*	*H200 Vx*	*H200 L&V*	*M1 Vx*	*M1 L&V*	*Ref Vx*	*Ref L&V*	*T450 Vx*	*T390 L&V*	*W600 Vx*	*W600 L&V*
Layer Height[a]	NA	NA	0.2	0.2	0.1	0.1	0.1	0.1	0.1	0.1	0.1	0.1
Layer Width[a]	NA	NA	0.4	0.4	0.4	0.4	0.4	0.4	0.4	0.4	0.6	0.6
Extr. Temp.[b]	NA	NA	510	510	510	510	510	510	450	390	510	510
Extr. Mult.	NA	NA	0.95	0.95	1.0	1.0	0.95	0.95	0.95	0.95	0.95	0.95
Diameter/ Cross Sect.[a]	1.68	1.81	1.73 x 1.73	1.79 x 1.46	1.77 x 1.77	1.80 x 1.80	1.73 x 1.73	1.79 x 1.79	1.78 x 1.78	1.80 x 1.85	1.78 x 1.7	1.80 x 1.88
Length[a]	4.50	4.51	4.33	4.47	4.44	4.50	4.33	4.47	4.44	4.50	4.44	4.50
Voxel size[c]	1.2008	1.2017	1.5750	1.6269	1.6140	1.6362	1.5731	1.6265	1.6147	1.6380	1.6137	1.6368

2.3 Image processing and analysis

Image processing and quantitative analysis were carried out using the ANU software tool Mango. Images were first spatially re-aligned with respect to the Cartesian axis (X, Y, Z) such that Z corresponds to the filament pulling direction (feedstock samples) and to the direction parallel to both the mould plate and printing direction (printed samples); X and Y are both perpendicular to the pulling direction for the feedstock filaments, while for the printed samples, X is parallel to mould plate, perpendicular to printing direction and Y is perpendicular to both mould plate and printing direction. Image segmentation was then performed using the method developed by Sheppard et al. (14). The fibre segmentation analysis was guided by prior compositional information available on the feedstock material. Since carbon fibre weight % content and density values of both matrix and fibres are known, using equations 3.8 and 3.11 from (17) and considering samples' segmented void content, the average fibre content expressed as volume % can also be calculated. At the end of the segmentation process, material's constituents were partitioned into separate volume segments. All segmented voids were then individually labelled and their dimensional properties extracted for geometric characterisation and analysis. Voids smaller than 200 voxels were excluded from the analysis as too small to provide meaningful geometric characteristics. Ellipsoids were fitted to each void, then axis lengths and orientation were extracted, and MATLAB® was used to calculate the mean, standard deviation and sometimes minimum, maximum, and median values of void size and selected geometric properties. Several derived characteristics were calculated, among them elongation and roundness as defined in (10). The orientation of the voids is determined by the absolute components of the axis unit vector for each Cartesian axis. The segmented fibre phase of all specimens was analysed using the ImageJ plugin OrientationJ on subsamples of four-hundred voxels thickness and entire diameter/cross-section from the middle of the samples. The distribution of fibre orientations both within, and out of, the print plane was measured and the average fibre angle deviation from the principal fibre direction in each plane was found.

3. Results and discussion

The image segmentation results are summarised in Table 2. Void, resin and fibres distribution were mapped in 3D, and respective content profiles were created by extracting and plotting slice by slice content in the X-Y combined and Z (feedstock filaments), X, Y and Z directions (3D printed samples) (examples are provided in Figure 1 and Figure 2). Furthermore, for all the 3D printed samples, interconnected voids within the material microstructure were identified and segmented, their amount quantified (Table 2), and their distribution mapped and visualised in 3D (one example is provided in Figure 2). From the Label images, void size profiles were created (Figure 2), and void size distributions extracted and plotted (Figure 3). Furthermore, key void characteristics were extracted and summarised (Table 3). From the segmented fibre phase, fibre misalignment was measured, plotted and visualised in 3D (Figure 4 and Figure 5).

Table 2: Image segmentation results in volume %

	Feed Vx	*Feed L&V*	*H200 Vx*	*H200 L&V*	*M1 Vx*	*M1 L&V*	*Ref Vx*	*Ref L&V*	*T450 Vx*	*T390 L&V*	*W600 Vx*	*W600 L&V*
Voids	19.4	19.7	21.1	24.4[a]	17.3	18.5	19.0	18.7	21.8	28.5	15.0	20.1
Voids[b]	NA[c]	NA[c]	65.6	56.6	61.4	9.9[d]	81.4	52.1	83.4	51.5	42.5	NA[c]
Resin	61.7	74.4	59.9	64.6	63.3	75.2	61.7	75.2	59.5	66.2	64.8	73.8
Fibres	18.9	5.9	19.0	5.2	19.4	6.2	19.4	6.0	18.7	5.2	20.2	6.1
Fibres[e]	19.1	6.0	18.7	5.2	19.6	6.1	19.2	6.1	18.6	5.3	20.2	6.0

HD	NA	<0.1	NA	<0.1	NA	<0.1	NA	0.1	NA	<0.1	NA	<0.1

[a] additional single large void of 5.7% volume segmented separately as it does not belong to the sample main void phase; [b] % of the total voids interconnected to form a single large cluster; [c] large clusters of interconnected voids not identified; [d] a second large cluster 7.0% of the total void volume identified; [e] calculated fibre content value.

3.1 Void analysis: feedstock filaments

Void segmentation results show that the total void content is very similar for the two filaments, while the total void number differs greatly. This implies that the microstructure of the two filaments must be characterised by distinctly diverse void populations. This is reflected in the void average and median size values of the two samples, which are about seven and four times, respectively, higher for *Feed L&V*. Differences among the samples' microstructures are also clearly captured by the plots of Figure 3, which show that despite both samples containing a large number of small voids, the actual void size distribution differs, in particular for the larger voids population that accounts for most of the measured porosity. Some geometric characteristics highlight key differences in void shapes, with mean void elongation and axis L values about four to five times higher for *Feed L&V*. On the other hand, our data also identifies interesting similarities between the two samples. For both filaments, X-Y profiles show that average void content and size increase towards the centre of the samples, mean roundness values are similar, while mean void orientation values (axis Lz) indicate that in both, voids are primarily oriented along Z, although this is more evident for *Feed L&V* than *Feed Victrex*.

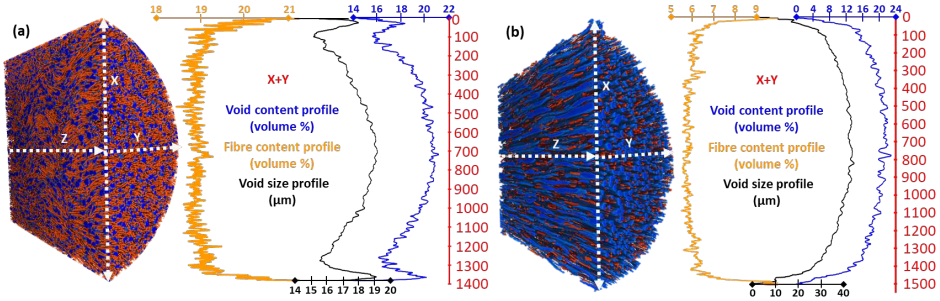

Figure 1. (a) left: 3D visualisation of segmented image of Feed Vx filament: voids (blue), fibres (orange), resin transparent; right: Feed Vx void and fibre content, void size profiles for combined X-Y directions; (b) same for Feed L&V; white dotted arrows show direction of X, Y, Z axis.

3.2 Void analysis: 3D printed samples

Void segmentation data have been obtained, void content and size profiles created for the ten printed samples over more than six million voids; void geometric characteristics have been extracted for about one million eight hundred thousand voids. However, only the main findings will be reported here due to length constraints. Void segmentation results show that all samples, independent of the printing settings, still have a high void content, higher or lower than the parent filament. The percentage of voids interconnected shows that despite samples in the two series having very comparable void contents, voids within samples of the *Vx Series* are in general much more interconnected than for the *L&V Series*. Void main geometric characteristics show that samples within each series are characterised by quite different void populations, with void size mean and average values, in particular, varying noticeably among samples. Mean elongation and axis L values are also quite different for samples within and between series and void size distribution plots can capture microstructural differences among samples, like for instance in the case of *M1 Vx* and *M1 L&V*. At the same time, void main geometric characteristics highlight

some similarities and common trends between samples of different series printed using same (or almost same) settings, suggesting that the different printing parameters affect the material microstructure differently. In both series, for instance, *T450 Vx* and *T390 L&V* are the samples with the highest values of void mean and median size, axis L and axis Lz, while mean elongation value is the highest in the series for *T450 Vx*, second highest for *T390 L&V*. In all samples the axis Lz value is the highest with a value on average around 0.9, indicating that the primary void orientation is always strongly aligned with the printed direction.

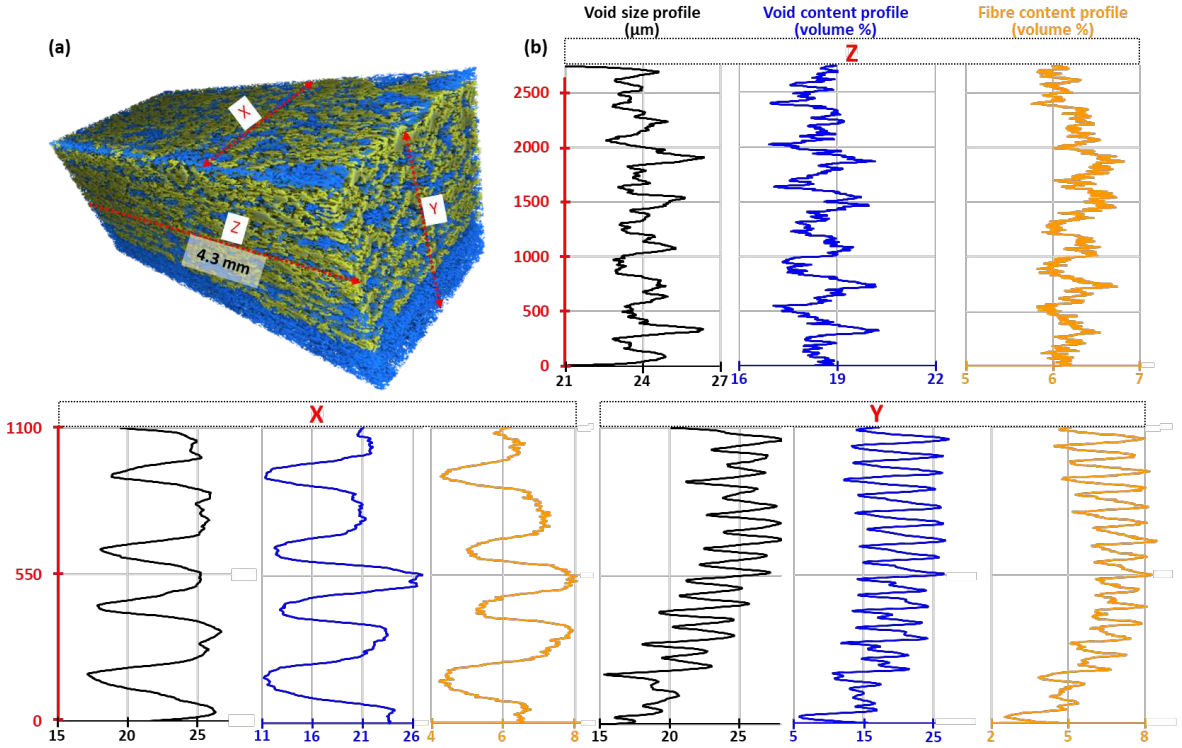

Figure 2. (a) 3D visualisation of segmented image of entire H200 Vx sample showing in yellow / green interconnected voids, blue the rest of the voids, with resin and fibres set transparent; (b) slice by slice position (red axis) X, Y, Z void and fibre content, void size profiles for M1 L&V.

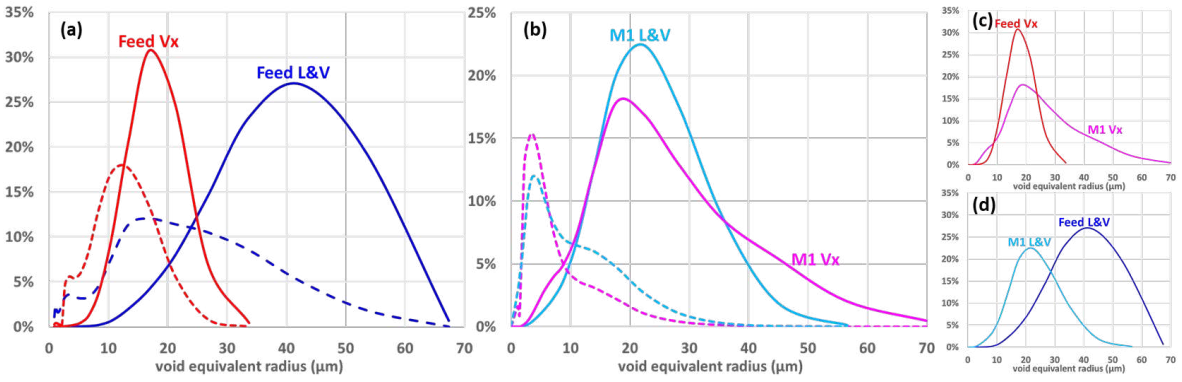

Figure 3. Void size distribution plots for (a) Feed Vx and Feed L&V, (b) M1 Vx and M1 L&V, (c) Feed Vx and M1 Vx, (d) Feed L&V and M1 L&V, where dotted lines display the normalised total amount of voids with a given radius, continuous lines the normalised amount of porosity.

The effect of the layer-by-layer depositional printing process is very clearly highlighted by the void content and size distribution plots (in Figure 2), particularly in the Y direction. For all the printed samples, these plots show that voids are strongly preferentially aligned in planes parallel to the mould plate, giving the samples an alternating low/high-void content layered structure.

In all samples, average void content is low within the bottom planes, which correspond to the portion of the sample near the build plate surface, then it progressively increases, reaching its highest value near to, or at, the top surface. This trend is, however, more defined within the *Vx Series,* suggesting the *Vx* samples generally have a far more heterogeneous void distribution and anisotropic structure than the *L&V* series. These plots provide an accurate qualitative and quantitative description of the 3D void distribution and could be used to further explore and identify relationships between the printing settings and the resulting samples' architecture.

Table 3 : Summary of void main geometric characteristics for the Victrex and L&V Series

Vx Series[a]	**FeedVx**	**H200Vx**	**M1Vx**	**RefVx**	**T450Vx**	**W600Vx**
Size (voxels)	5883 ± 7017	3333 ± 13822	2475 ± 6789	4066 ± 16213	4044 ± 9470	1945 ± 4440
Size (μm^3)	10186 ± 12148 (346, 190547) [b]5873	13022 ± 54005 (781, 9010140) [b]4153	10404 ± 28544 (841, 1680705) [b]2808	15826 ± 63110 (779, 7995912) [b]3745	17023 ± 39866 (842, 1430463) [b]4614	8175 ± 18658 (840, 1560069) [b]2807
Number*	220611	674124	825037	455010	649853	852449
Number	186732	203946	219149	150700	173659	240337
% > 200[c]	99.6	97.0	94.6	97.5	96.9	93.7
Axis L (µm)	22.2 ± 10.6	29.0 ± 18.2	27.1 ± 17.9	27.6 ± 18.1	33.8 ± 22.2	25.9 ± 17.3
Axis I (µm)	12.0 ± 4.95	13.4 ± 8.24	12.0 ± 7.66	12.6 ± 8.32	13.8 ± 8.89	12.0 ± 7.21
Axis S (µm)	7.99 ± 3.53	8.04 ± 5.11	7.23 ± 4.49	7.94 ± 5.26	8.44 ± 5.52	7.24 ± 4.07
Elongation	2.31 ± 0.929	2.86 ± 1.25	2.95 ± 1.30	2.81 ± 1.19	3.21 ± 1.40	2.77 ± 1.24
Roundness	1.59 ± 0.489	1.73 ± 0.519	1.70 ± 0.498	1.62 ± 0.454	1.70 ± 0.502	1.70 ± 0.492
Axis L_z	0.897 ± 0.163	0.872 ± 0.192	0.899 ± 0.168	0.898 ± 0.172	0.932 ± 0.130	0.866 ± 0.201
L&V Series[a]	**FeedL&V**	**H200L&V**	**M1L&V**	**RefL&V**	**T390L&V**	**W600L&V**
Size (voxels)	41788 ± 69361	5298 ± 14550	3285 ± 6055	4869 ± 10137	6963 ± 12544	3369 ± 5124
Size (μm^3)	72516 ± 120363 (347, 1320367) [b]23640	22814 ± 62653 (861, 4894450) [b]7264	14389 ± 26522 (876, 781682) [b]5116	20950 ± 43622 (861, 1138277) [b]6154	30604 ± 55134 (879, 1036155) [b]9551	14774 ± 22473 (877, 716354) [b]6631
Number*	32883	535751	620254	422785	525160	714506
Number	26571	122897	182914	114510	139257	199573
% > 200[c]	90.0%	98.9%	97.7	98.4	99.1	98.1
Axis L (µm)	104. ± 72.1	30.3 ± 18.8	27.1 ± 16.5	32.1 ± 20.4	35.3 ± 22.8	25.4 ± 14.4
Axis I (µm)	14.2 ± 7.93	15.9 ± 9.64	13.5 ± 7.73	14.4 ± 8.91	16.2 ± 9.78	13.9 ± 7.03
Axis S (µm)	8.64 ± 4.85	9.28 ± 6.05	7.94 ± 4.52	8.40 ± 5.39	9.73 ± 6.10	8.75 ± 4.49
Elongation	9.10 ± 4.49	2.60 ± 1.24	2.70 ± 1.36	3.05 ± 1.55	3.02 ± 1.76	2.40 ± 1.21
Roundness	1.76 ± 0.649	1.81 ± 0.597	1.78 ± 0.606	1.80 ± 0.600	1.78 ± 0.658	1.68 ± 0.565
Axis L_z	0.986 ± 0.0669	0.777 ± 0.259	0.881 ± 0.189	0.910 ± 0.164	0.920 ± 0.154	0.840 ± 0.223

[a] data for voids larger than 200 voxels denoted as: Mean ± Standard deviation (min, max); [b] median size values;
[c] relative volume % relative of voids > 200 voxels; * includes voids < 200 voids

3.3 Fibre analysis: feedstock filaments and 3D printed samples

Segmented fibre contents are very close to the calculated ones, which provides a reasonable degree of confidence in the overall fibre phase identification accuracy. As seen with void analysis, X, Y, and Z fibre profiles accurately describe the 3D fibre distribution within each filament and printed sample microstructure. For the printed samples, fibre content plots in the Y direction again clearly identify the material layered structure, a direct consequence of the depositional nature of the printing process. These plots also show that, similarly to the void, the fibre content too is usually lower near the mould plate and gradually increases towards the top surface, a trend that is observed in nearly all samples with the noticeable exceptions of *T450 Vx* and *T390 L&V* where it is highest around mid-thickness and then decreases again towards the top. By plotting X, Y and Z fibre and void content profiles next to each other, there is a very close void-fibre relationship showing that within the layered microstructure, layers with higher void content also have higher fibre content and vice versa. This close relationship has been verified in all printed samples of both series, independently from the individual samples' fibre/void content. On the other hand, the same relationship is not found in the feedstock filaments where X-Y combined and Z content profiles suggest that void and fibre distribution within the material

microstructure are not closely linked. As a result, it can be assumed that the void-fibre association in the printed sample is another direct consequence of the printing process. Fibre orientation also reveals that fibres are aligned parallel to the pulling direction within the filaments, particularly in *Feed L&V* where the fibre angle misalignment is smaller than *Feed Vx* (Figure 4 a, b). After printing, fibres become strongly aligned parallel to the printing direction (Figure 4 c, d). However, while fibre misalignment decreases with printing for *Vx* specimens, it increases for *L&V* specimens (Figure 5). This is possibly due to the lower fibre fraction or the drastic change in microstructure between *L&V* filament and printed samples, caused by the radical size and shape change of the larger void population, which is a direct consequence of the printing process. Furthermore, Figure 5 shows there is more misalignment to the primary fibre angle in the printing plane compared to out-of-plane for both materials, though this is especially evident for *L&V*, which can be related to the layer-by-layer depositional nature of the printing process. Therefore, in addition to the evident anisotropy with the Z printing direction, there is also anisotropy transverse to it in X and Y, which implies anisotropic mechanical properties.

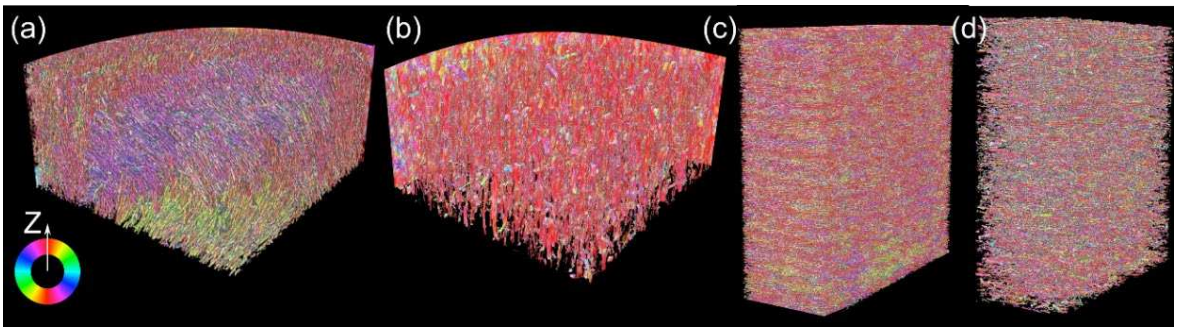

Figure 4. 3D visualisations of fibre misalignment respect to filament pulling direction for Feed Vx (a) and Feed L&V (b), to sample printing direction for W600 Vx (c) and W600 L&V (d).

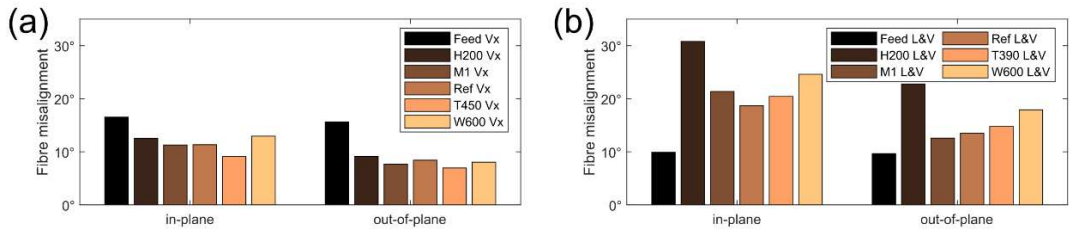

Figure 5. Fibre misalignment plots from principal direction for Vx (a) and L&V (b) Series.

4. Conclusions

Image analysis showed that both feedstock filaments contain a large number of voids (~19.5%) that were not removed by the printing process, and varying key printing parameters only marginally affected the overall samples' void content (15% to 28.5%). Moreover, the depositional nature of the printing process has a dramatic effect on the samples' microstructure. All printed samples displayed a distinctive layered structure, where layers with high/low void /fibre content regularly alternate (Figure 2). Furthermore, both voids and fibres are preferentially aligned, with fibres within ~10° (*Vx*) and ~20° (*L&V*) of the printing direction and void's Lz component ~0.9 for most specimens. Therefore, printed samples have a strongly anisotropic structure and detailed microstructure characterisations as provided here can form the basis for modelling/understanding directional differences in their mechanical performance.

Acknowledgements*: ARC Training Centre for Automated Manufacture of Advanced Composites (IC160100040), ANU CTLab, and ANU National Computational Infrastructure.*

  doi:10.5075/epfl-298799_978-2-9701614-0-0

5. References

1. Bromberg J, Kelly R. Additive manufacturing: A long-term game changer for manufacturers; 2018. Available from: URL: https://www.mckinsey.com/business-functions/operations/our-insights/additive-manufacturing-a-long-term-game-changer-for-manufacturers.

2. Türk D-A, Kussmaul R, Zogg M, Klahn C, Leutenecker-Twelsiek B, Meboldt M. Composites Part Production with Additive Manufacturing Technologies. Procedia CIRP 2017; 66:306–11.

3. Haleem A, Javaid M. Polyether ether ketone (PEEK) and its 3D printed implants applications in medical field: An overview. Clinical Epidemiology and Global Health 2019; 7(4):571–7.

4. Rinaldi M, Cecchini F, Pigliaru L, Ghidini T, Lumaca F, Nanni F. Additive Manufacturing of Polyether Ether Ketone (PEEK) for Space Applications: A Nanosat Polymeric Structure. Polymers (Basel) 2020; 13(1).

5. Luo M, Tian X, Shang J, Zhu W, Li D, Qin Y. Impregnation and interlayer bonding behaviours of 3D-printed continuous carbon-fiber-reinforced poly-ether-ether-ketone composites. Composites Part A: Applied Science and Manufacturing 2019; 121:130–8.

6. Pratama J, Cahyono SI, Suyitno S, Muflikhun MA, Salim UA, Mahardika M et al. A Review on Reinforcement Methods for Polymeric Materials Processed Using Fused Filament Fabrication (FFF). Polymers (Basel) 2021; 13(22).

7. Dong C. Effects of Process-Induced Voids on the Properties of Fibre Reinforced Composites. Journal of Materials Science & Technology 2016; 32(7):597–604.

8. Mulholland T, Goris S, Boxleitner J, Osswald T, Rudolph N. Process-Induced Fiber Orientation in Fused Filament Fabrication. J. Compos. Sci. 2018; 2(3):45.

9. Matschinski A, Ziegler P, Abstreiter T, Wolf T, Drechsler K. Fiber Formation of Printed Carbon Fiber/Poly (Ether Ether Ketone) with Different Nozzle Shapes. Polym Int 2021; 70(8):1109–17.

10. Mehdikhani M, Straumit I, Gorbatikh L, Lomov SV. Detailed characterization of voids in multidirectional carbon fiber/epoxy composite laminates using X-ray micro-computed tomography. Composites Part A: Applied Science and Manufacturing 2019; 125:105532.

11. Sommacal S, Matschinski A, Drechsler K, Compston P. Characterisation of void and fiber distribution in 3D printed carbon-fiber/PEEK using X-ray computed tomography. Composites Part A: Applied Science and Manufacturing 2021; 149:106487.

12. Holmes J, Sommacal S, Das R, Stachurski Z, Compston P. Characterisation of off-axis tensile behaviour and mesoscale deformation of woven carbon-fibre/PEEK using digital image correlation and X-ray computed tomography. Composites Part B: Engineering 2022; 229:109448.

13. Wang X, Zhao L, Fuh JYH, Lee HP. Effect of Porosity on Mechanical Properties of 3D Printed Polymers: Experiments and Micromechanical Modeling Based on X-ray Computed Tomography Analysis. Polymers (Basel) 2019; 11(7).

14. Sheppard A, Latham S, Middleton J, Kingston A, Myers G, Varslot T et al. Techniques in helical scanning, dynamic imaging and image segmentation for improved quantitative analysis with X-ray micro-CT. Nuclear Instruments and Methods in Physics Research Section B: Beam Interactions with Materials and Atoms 2014; 324:49–56.

15. Kingston AM, Myers GR, Latham SJ, Recur B, Li H, Sheppard AP. Space-Filling X-Ray Source Trajectories for Efficient Scanning in Large-Angle Cone-Beam Computed Tomography. IEEE Trans. Comput. Imaging 2018; 4(3):447–58.

16. Myers GR, Kingston AM, Latham SJ, Recur B, Li T, Turner ML et al. Rapidly converging multigrid reconstruction of cone-beam tomographic data. In: Developments in X-Ray Tomography X. SPIE; 2016. 99671M (SPIE Proceedings).

17. Gibson RF. Principles of composite material mechanics. 3. ed. Boca Raton, Fla. [u.a.]: CRC Press; 2016. (Mechanical engineering; vol 218).

MICRO-COMPUTED TOMOGRAPHY FOR MESOSCALE ANALYSIS OF WOVEN FIBRE-REINFORCED COMPOSITES

John Holmes[a], Silvano Sommacal[a], Raj Das[b], Zbigniew Stachurski[c], Paul Compston[a]*

a: ARC Training Centre for Automated Manufacture of Advanced Composites, Australian National University, Acton, ACT 2601, Australia – John.Holmes@anu.edu.au
b: Aerospace Engineering and Aviation, RMIT University, Melbourne, VIC 3000, Australia
c: School of Engineering, Australian National University, Acton, ACT 2601, Australia

Abstract: *The heterogeneous deformation and damage behaviour of woven composites benefits from advanced characterisation techniques, including micro-computed tomography (micro-CT). This paper uses high-resolution micro-CT images of a woven carbon fibre/polyetheretherketone (C/PEEK) laminate to compare with digital image correlation (DIC) during experimental loading and to provide the architecture for an accurate mesoscale numerical model. The mesh for the finite element model is created from the segmented phases (fibre tows, matrix, and voids) of the micro-CT volume. The combined experimental and numerical approach provides detailed insights into how defects and architectural variations, such as voids and layer alignment, influence the 3D deformation and damage development.*

Keywords: Digital image correlation (DIC); Digital material twins; Finite element analysis (FEA); Micro-computed tomography (micro-CT); Woven thermoplastic composites

1. Introduction

Understanding the mesoscale deformation and damage development of woven fibre-reinforced composites is crucial for their increased adoption. Specifically, woven thermoplastic composites are becoming increasingly popular in the automotive and aerospace sectors [1,2], but more work is needed to characterise their local and heterogeneous behaviour. Advanced experimental characterisation, in the form of micro-CT, can provide insight into experimental surface deformation observations and inputs into architecturally-accurate numerical models.

Digital image correlation (DIC) has become a standard technique for in-situ observation and measurement of mesoscale deformation of woven composites, including strain [3–5], topography [6–8], and damage development [9–11]. However, as a surface-based technique, DIC provides limited information on the relationship between the observed surface deformation and the underlying internal structure of the woven composite. Micro-CT provides a solution to accurately reveal the 3D internal architecture of woven composites and is being increasingly used to examine defects, architectural variance and damage development (cracking and delamination) [12,13]. However, in-situ micro-CT testing can be time-consuming, and specimen size is limited, suggesting benefits may exist by combining a single ex-situ micro-CT scan with other characterisation methods such as DIC.

Micro-CT can also benefit numerical simulations by enabling the creation of digital material twins with accurate architecture [14,15]. There has been significant recent research on creating models from CT of woven composites, primarily focusing on the segmentation of material phases [16–18]. These models capture actual architectural variations and defects, such as voids

  doi:10.5075/epfl-298799_978-2-9701614-0-0

and complex changes in yarn cross-section, which idealised computer-generated models are not constructed for. While many aforementioned works treat the simulation in isolation or with limited comparison to experimental results, there are benefits to using both the mesoscale experimental and the numerical results to better elucidate the underlying behaviour.

In this work, micro-CT is used along with DIC to provide insight into the observed surface behaviour of a woven thermoplastic composite. In parallel, micro-CT is used to construct authentic 3D architecture for creating accurate mesoscale numerical models, a digital material twin, which can then be analysed along with the experimental results.

2. Experimental

2.1 Material and methods

Material: A high-performance four-layer plain woven carbon fibre/polyetheretherketone (C/PEEK) laminate is used in this study. It is consolidated from a Pipreg® fabric (Porcher Industries) with powder impregnation and a double belt press. The laminate has a thickness of 1 mm, a fibre volume fraction of 50% and tow width of about 2 mm. The microstructure of the material varies as the random shifting between layers during manufacture can result in aligned, nested or balanced architecture for pairs of adjacent layers in each consolidated sheet.

Specimen: Three specimens were cut using a waterjet; their design is shown in Fig. 1a. The curved specimen design concentrates deformation into an observable region and eliminates the need for gluing end tabs to the specimen to prevent failure in the grips. The full specifications for the specimen are given in Fig. 1a where the hatched region is gripped during loading.

Testing: Tensile tests were conducted until failure at a rate of 2 mm/min on a hydraulic 25 kN INSTRON® (model 8874). A stereo DIC system (ARAMIS® version 6.3) that observed one side of the specimen enabled the characterisation of surface deformation. A random black and white pattern was applied on the specimen with spray paint prior to testing to ensure displacement tracking. A small measuring volume of 45 mm x 40 mm with a 25 mm depth allowed high accuracy displacement and strain measurement for mesoscale deformation. Camera sensors of 2448 x 2048 pixels resulted in approximately 51 pixels/mm resolution. Fig. 1b shows subsets of 15 x 15 pixels (290 µm) with a step size of 5 pixels (95 µm), allowing correlation and tracking of point displacements. The random noise inherent in the imaging process and the resultant error in displacements and strains were determined from an initial series of images before loading, as previously described [6,19]. Displacement accuracy was found to be on average ± 0.29 µm for in-plane, and ± 1.35 µm for out-of-plane and strain accuracy was similarly quantified as ± 0.17% for εx and εy and ± 0.14% for εxy. Data was then exported to MATLAB® for strain and topography visualisation, using a previously defined technique [6,7] and comparison with micro-CT.

Micro-CT: Post-test X-ray micro-computed tomography (micro-CT) allowed characterisation of the 3D weave layer alignment and void defects. The specimens were imaged using a HeliScan™ micro-CT instrument hosted at the ANU CTLab with 60kV, 100 µA X-ray source [20]. An 8 mm x 16 mm wide central section was imaged for each specimen. This size encompassed several unit cells, see Fig. 1c, while achieving a scanning resolution of 4.2 µm/voxel, below the 7 µm fibre diameter. Radioscopic projections were taken with a 3040 x 3040 detector and subsequently reconstructed into the 3D 16-bit greyscale volume using a proprietary ANU reconstruction algorithm [21]. Fibre orientation analysis and visualisation were accomplished using

OrientationJ, an ImageJ plugin [22]. Further processing and segmentation of the CT image for numerical analysis are described in section 3.1.

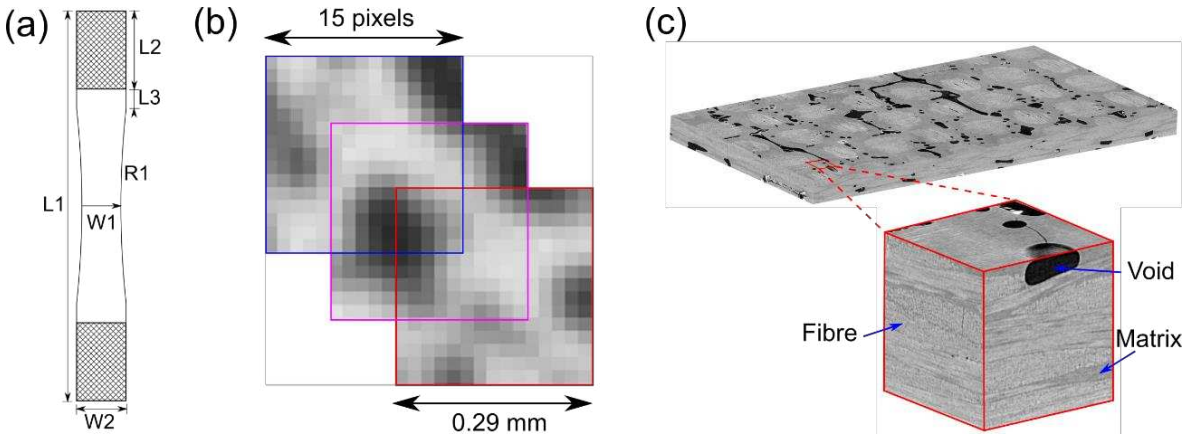

Figure 1. Specimen and testing, (a) specimen design in mm: L1 = 200, L2 = 40, W1 = 20, W2 = 25.4, R1 = 464.31, (b) DIC subsets showing pixel size in relation to speckle, and (c) micro-CT tomogram images with the matrix, fibre and void phases.

2.2 Results and discussion

The observed surface deformation, topography and strain are closely linked to the underlying weave architecture observed with micro-CT. Greater alignment of the two layers directly below the painted DIC surface in Fig. 2i induces larger topographical change and local strain gradients during loading. This is in contrast to the balanced (shifted by 1 tow width) and nested (shifted by around half a tow) architectures of Fig. 2ii and Fig. 2iii, respectively. The mechanism behind the topographical change is the straightening of fibres orientated with the direction of loading, which forces transverse weave tows above them out of the surface. If the second layer is aligned with the first, this topographical movement is synchronised, while if it is overlapping or entirely shifted, also called balanced or mirrored, this movement is resisted by the second layer. A related study further explores these phenomena and includes results for off-axis testing with these aligned, nested, and balanced architectures [23].

In addition to helping explain the surface deformation heterogeneity, micro-CT results can also significantly characterise the internal microstructure. Fibre orientation measurements can show local variation and overall consistency. In-plane orientations vary by less than 10 degrees from the primary warp and weft directions with under 5-degree deviation typical. Out-of-plane orientation varying with the weave crimp is characterised at a maximum typical angle of 9.5°. Similarly, void location, volume, and orientation can also be determined. The void volume fraction is 3.8% for i., 0.1% for ii., and 3.3% for iii. Fig. 3c shows voids tend to be located in the inter-tow matrix rich regions, especially at tow intersections. Both globular and elongated voids are observed with the more spherical geometries typical at tow intersections and the elongated voids running parallel to the tows in i. and iii. While these voids have little observed impact on tensile properties of the stiff carbon fibres, probably due to their inter-tow location and surrounding thermoplastic matrix ductility, they may have a more significant influence on other properties such as inter-laminar shear and delamination.

  doi:10.5075/epfl-298799_978-2-9701614-0-0

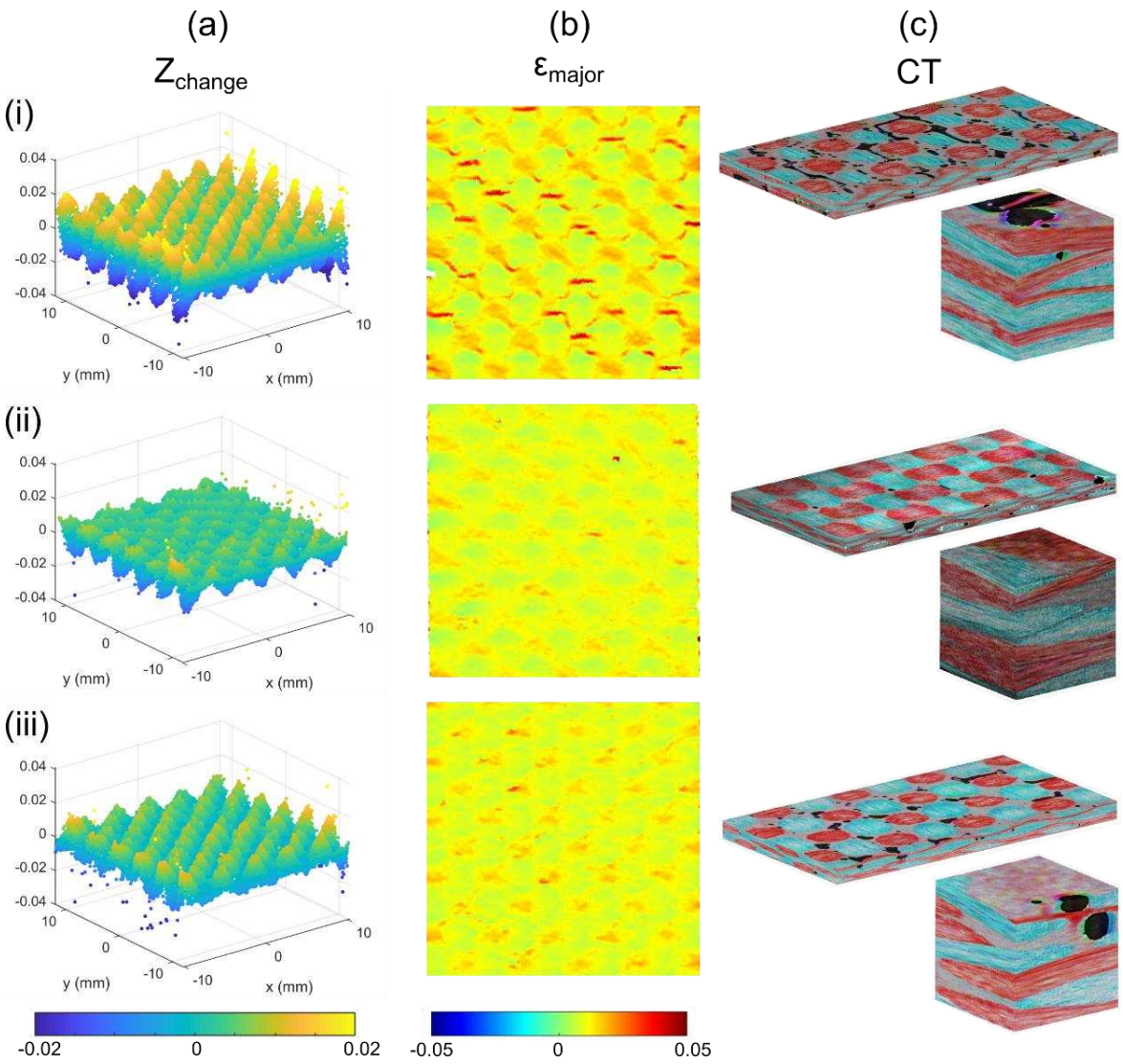

Figure 2. Experimental results, (a) Z_{change} topography (mm), (b) Major principal strain, and (c) micro-CT with fibre orientation analysis and voids visible for specimens (i-iii). Note (c) shows unpainted side of volume to better show voids. Additional off-axis results are published in [23].

3. Numerical

3.1 Method

Conversion of micro-CT greyscale tomogram images into a mesh for finite element analysis is non-trivial. It is especially challenging for C/PEEK as there is little greyscale differentiation between the phases as shown in Fig. 3a. Therefore, this preliminary study primarily focused on converting the micro-CT data into accurate and usable meshes for simulation.

Segmentation: Initial image segmentation of fibre bundles, voids and matrix was conducted using Mango software [20,24]. Before segmentation, the low-intensity contrast between carbon fibre and PEEK matrix was enhanced by applying a proprietary de-noise filter on the original tomogram image based on the Non-Local Means algorithm, resulting in distinct peaks for the two phases of the greyscale histogram. Image segmentation of fibres and matrix was subsequently carried out in Mango using the technique described in [24]. The segmentation method combines greyscale intensity, gradient, and surface morphology and uses a bottom-up

  doi:10.5075/epfl-298799_978-2-9701614-0-0

watershed filling scheme. The higher contrast of the voids to the matrix and fibres makes their segmentation comparatively more straightforward. Warp and weft tows are subsequently separated into two distinct phases exploiting their different texture and geometric orientation.

While this initial segmentation is suitable for visualising and quantifying phase volume, it is not yet adequate for simulation. Rough geometric transitions between fibre tows and the surrounding matrix and phase inclusions, such as matrix and thin elongated voids in fibre tows, result in small and complex geometric features. Attempting to mesh this geometry lacks practicality due to the large number of elements due to the high mesh refinement to match the geometrical contour. The solution is to remove small inclusions and smooth the phase boundaries through a combination of eroding and dilating operations. The resulting segmentation is now suitable for meshing. Specimen i., with and without the void phase, is used to demonstrate the procedure for the remainder of the process, see Fig. 3b and c.

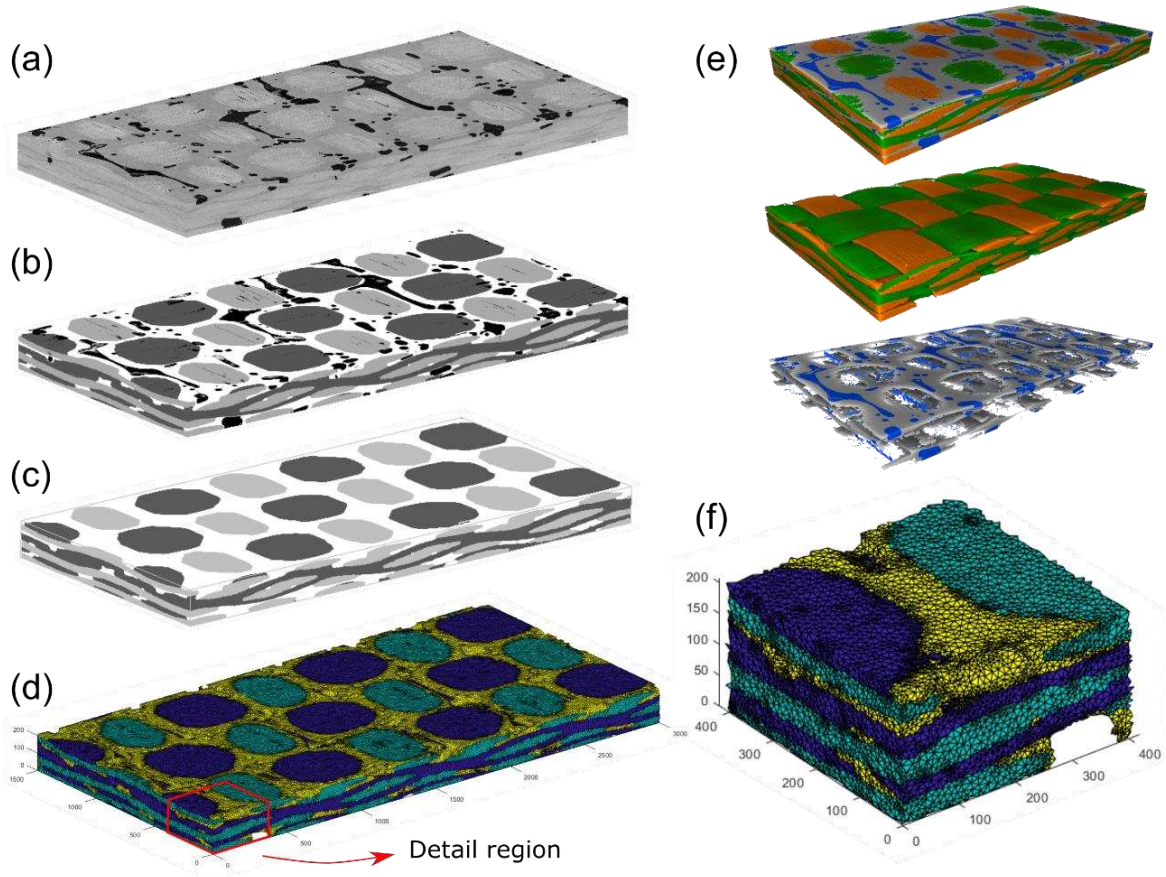

Figure 3. Numerical method, (a) Original tomogram for a region 3 x 6 tows, (b) smoothed segmented region with voids, (c) smoothed segmented region without voids, (d) FEA mesh, (e) 3D visualisation of phases for the specimen, and (f) detail of FEA mesh.

Meshing: For the woven composite architecture, a high-quality mesh needs to suitably capture the contours of the weave without producing either excessive element number or highly distorted elements. For this reason, a tetrahedral mesh was found to be optimal and robustly conformed to the geometry. Iso2Mesh [26], an open-source package, which runs in MATLAB®, was used to mesh the specimens. The segmentation produced images with discrete grey-level

  doi:10.5075/epfl-298799_978-2-9701614-0-0 published under CC BY-NC 4.0 license

values recognised by Iso2Mesh. A distance bound of 2 voxels allowed a small amount of leeway (8.4 µm) at phase boundaries, relaxing the need for mesh refinement. A maximum 100 voxel node distance for element size was used. The final mesh of tetrahedral elements for specimen i. had 1782931 elements without voids and 2213287 elements with voids included in the segmentation (see Fig. 3d and f). The resulting models of C3D4 elements took less than 30 minutes to run using Abaqus 6.14 on an 8 core 17-9700 CPU at 4.5 GHz. The mesh sensitivity was determined by reducing the distance bound to 1.5 voxels, thereby increasing the element count by about 50%. The resulting change in Z displacement was within 6%, with the most significant differences being near small geometric features such as voids, and therefore the mesh size was found to be satisfactory for this mesoscale study of behaviour.

Material properties: Basic properties for woven C/PEEK were used. Fibre and matrix properties were taken from previous testing and datasheets [6] and the determined tow properties were: E1 = 138 GPa, E2 = E3 = 10.2 GPa, G12 = 5.7 GPa. Orthogonal material orientations are used, but local fibre orientations could be mapped to individual elements in future work, greatly improving the accuracy of the simulation. Similarly, various failure criteria could be added to the matrix and fibre tows to investigate damage progression.

Boundary conditions: As with the material properties, simplified boundary conditions were also used. One side of the specimen was fixed, and the other had a tensile displacement applied while fixed in transverse directions. A deformation of 1% strain in 20 increments was applied to the specimens, and the displacement, strain and stress evolution were recorded.

3.2 Results and discussion

The numerical model reveals how weave layer alignment and voids influence the deformation response. Matching experimental results, topographical high points in Fig. 4 coincide with transverse tows. Moreover, the shifted lower ply layers induce continuous ridges and valleys rather than the checkerboard pattern that an idealised architecture without nesting would produce [6]. Fig. 4b, with voids included, shows similar behaviour but more significant topographical change. This change would suggest that the 3.8% void volume, in this case, noticeably reduces the restriction on out-of-plane topographical movement even at 1% global strain. The models also show that topographical behaviour is not separated into ply layers but transfers through the whole thickness, which cannot be ascertained from surface observation alone. The ability to see through-thickness behaviour in the simulation and compare the surface to experiments highlights the benefits that micro-CT can bring for an integrated characterisation of behaviour.

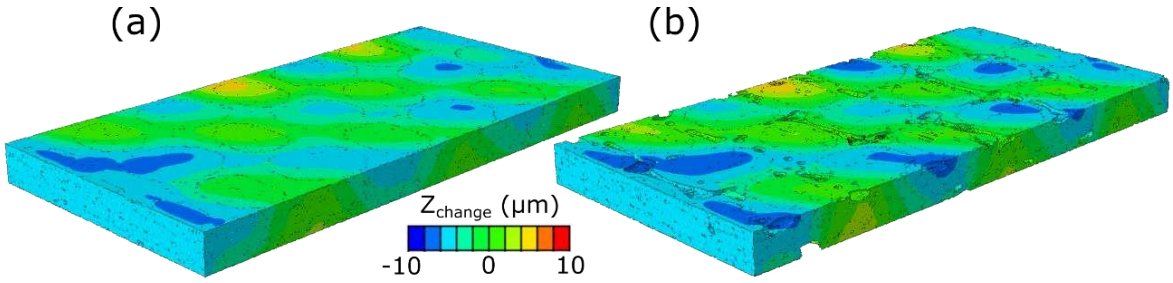

Figure 4. FEA results for displacement in Z through-thickness for (a) specimen with voids removed and (b) the same specimen with voids included.

4. Conclusions

Micro-CT has revealed a close link between the 3D microstructure and mesoscale surface deformation. Differences in strain and topography can be explained by variations in the layer alignment of the weave. Moreover, segmented and processed micro-CT images provide the basis for creating simulations with realistic tow architecture and locations of void defects. These simulations can then provide additional insight into the 3D strain state as well as further reveal the mechanisms behind the experimentally observed behaviour. From this preliminary study, there is significant potential to improve these digital material twins for simulation, and many insights can be gained by using a combined experimental (DIC) and simulation-based approach.

Acknowledgements

This project was in part conducted within the ARC Training Centre for Automated Manufacture of Advanced Composites (IC160100040), supported by the Commonwealth of Australia under the Australian Research Council's Industrial Transformation Research Program. The support of the Australian Government Research Training Program (RTP) Scholarship (John Holmes) is also acknowledged. The authors would also like to t the personnel involved with the ANU X-ray Computed Tomography laboratory (CTLab) for technical support and the ANU Supercomputer Facility and National Computational Infrastructure (NCI) for computing time.

Author Contribution

John Holmes: Conceptualisation, Investigation, Visualisation, Writing – Original Draft. *Silvano Sommacal*: Supervision, Visualisation, Writing - Review & Editing. *Raj Das*: Supervision, Writing - Review & Editing. *Zbigniew Stachurski*: Supervision, Writing - Review & Editing. *Paul Compston*: Conceptualisation, Funding Acquisition, Supervision, Writing - Review & Editing.

5. References

1. Long AC, Clifford MJ. Composite forming mechanisms and materials characterisation. In: Long AC, editor. Composites Forming Technologies. Elsevier Ltd; 2007. p. 1–21.
2. Zheng B, Gao X, Li M, Deng T, Huang Z, Zhou H, et al. Formability and Failure Mechanisms of Woven CF/PEEK Composite Sheet in Solid-State Thermoforming. Polymers (Basel). 2019;11(6):966.
3. Koohbor B, Ravindran S, Kidane A. Experimental determination of Representative Volume Element (RVE) size in woven composites. Opt Lasers Eng. 2017;90:59–71.
4. Holmes J, Vlandis G, Stachurski Z, Das R, Compston P. Failure behaviour in woven thermoplastic composites subjected to various deformation modes. Compos Part A Appl Sci Manuf. 2021;146:106410.
5. Doitrand A, Fagiano C, Leroy F-H, Mavel A, Hirsekorn M. On the influence of fabric layer shifts on the strain distributions in a multi-layer woven composite. Compos Struct. 2016;145:15–25.
6. Holmes J, Hafiz Y, Stachurski Z, Das R, Kalyanasundaram S. Surface topography evolution of woven thermoplastic composites under deformation. Compos Part B Eng. 2020;188:107880.
7. Holmes J, Das R, Stachurski Z, Compston P. 3D topographical analysis for defect detection during loading of woven thermoplastic composites. Compos Commun. 2022;29:100991.
8. Rossol MN, Rajan VP, Zok FW. Effects of weave architecture on mechanical response of

  doi:10.5075/epfl-298799_978-2-9701614-0-0

2D ceramic composites. Compos Part A Appl Sci Manuf. 2015;74:141–52.
9. Holmes J, Sommacal S, Stachurski Z, Das R, Compston P. Digital image and volume correlation with X-ray micro-computed tomography for deformation and damage characterisation of woven fibre-reinforced composites. Compos Struct. 2021;279:114775.
10. Sun G, Kong X, Wang Z, Luo Q, Li Q. Experimental investigation into stamping of woven CF/PP laminates: Influences of molding temperature on thermal, mesoscopic and macroscopic properties. Compos Struct. 2021;263:113507.
11. Mehdikhani M, Steensels E, Standaert A, Vallons KAM, Gorbatikh L, Lomov S V. Multi-scale digital image correlation for detection and quantification of matrix cracks in carbon fiber composite laminates in the absence and presence of voids controlled by the cure cycle. Compos Part B Eng. 2018 Dec 1;154:138–47.
12. Garcea SC, Wang Y, Withers PJ. X-ray computed tomography of polymer composites. Compos Sci Technol. 2018;156:305–19.
13. Zeng Q, Sun L, Ge J, Wu W, Liang J, Fang D. Damage characterization and numerical simulation of shear experiment of plain woven glass-fiber reinforced composites based on 3D geometric reconstruction. Compos Struct. 2020;233:111746.
14. Naresh K, Khan KA, Umer R, Cantwell WJ. The use of X-ray computed tomography for design and process modeling of aerospace composites: A review. Mater Des. 2020;190:108553.
15. Maire E, Withers PJ. Quantitative X-ray tomography. Int Mater Rev. 2014;59:1–43.
16. Huang W, Xu R, Yang J, Huang Q, Hu H. Data-driven multiscale simulation of FRP based on material twins. Compos Struct. 2021;256:113013.
17. Sinchuk Y, Kibleur P, Aelterman J, Boone MN, Paepegem W Van. Geometrical and deep learning approaches for instance segmentation of CFRP fiber bundles in textile composites. Compos Struct. 2021;277:114626.
18. Ali MA, Guan Q, Umer R, Cantwell WJ, Zhang T. Efficient processing of µCT images using deep learning tools for generating digital material twins of woven fabrics. Compos Sci Technol. 2022;217:109091.
19. Holmes J, Das R, Stachurski Z, Compston P, Kalyanasundaram S. Development of an S-specimen geometry for shear testing of woven thermoplastic composites. Compos Part B. 2020;203:108485.
20. Sommacal S, Matschinski A, Drechsler K, Compston P. Characterisation of void and fiber distribution in 3D printed carbon-fiber/PEEK using X-ray computed tomography. Compos Part A Appl Sci Manuf. 2021;149:106487.
21. Myers GR, Kingston AM, Latham SJ, Recur B, Li T, Turner ML, et al. Rapidly converging multigrid reconstruction of cone-beam tomographic data. In: Developments in X-Ray Tomography X. 2016. p. 99671M.
22. Püspöki Z, Storath M, Sage D, Unser M. Transforms and Operators for Directional Bioimage Analysis: A Survey. In: Advances in Anatomy Embryology and Cell Biology. 2016. p. 69–93.
23. Holmes J, Sommacal S, Das R, Stachurski Z, Compston P. Characterisation of off-axis tensile behaviour and mesoscale deformation of woven carbon-fibre/PEEK using digital image correlation and X-ray computed tomography. Compos Part B Eng. 2022;229:109448.
24. Sheppard A, Latham S, Middleton J, Kingston A, Myers G, Varslot T, et al. Techniques in helical scanning, dynamic imaging and image segmentation for improved quantitative analysis with X-ray micro-CT. Nucl Instruments Methods Phys Res Sect B Beam Interact with Mater Atoms. 2014;324:49–56.

MICROSCALE 3D STRAIN MAPPING AT FIBER-MATRIX INTERFACE USING SYNCHROTRON COMPUTED TOMOGRAPHY AND DIGITAL VOLUME CORRELATION

Mahoor, Mehdikhani[a], Sina, AhmadvashAghbash[a], Babak, Fazlali[a], Yentl, Swolfs[a]

a: KU Leuven, Department of Materials Engineering, Kasteelpark Arenberg 44 - bus 2450, Leuven, Belgium – mahoor.mehdikhani@kuleuven.be

Abstract: *Although many analytical and some numerical models have been developed to predict the interface stress/strain state, experimental evidence to verify them is scarce. In the current study, we combine synchrotron computed tomography with Digital Volume Correlation (DVC) to acquire, for the first time, 3D strain maps around a glass fiber embedded in epoxy and loaded in-situ in tension. DVC requires a volumetric speckle pattern inside the material, which in this study is achieved by a barium titanate nano-powder. The resulting axial DVC strain map shows a localization at the fiber break, due to the local opening of the break, and higher strain values in the matrix in the vicinity of the fiber break, which diminishes further away from the break. The resulting shear strain has a symmetric distribution at the sides of the fiber with regard to the fiber break. This analysis allows for the definition of real values of strain recovery length.*

Keywords: Digital volume correlation; Synchrotron computed tomography; Debonding; Single-fiber test

1. Introduction

Fiber-reinforced composites are known for their superior mechanical properties combined with low density and a high degree of design freedom. Load transfer between fiber and matrix is crucial for the mechanical behavior of these composites. This load transfer takes place through the fiber-matrix interface, and thus, the interfacial stress/strain state has been a point of interest since the very early days of composites. This becomes vital for longitudinal behavior of composites, especially when the fiber breaks, and the stress/strain state is locally disturbed at the break site. Numerous models have been proposed for representation of the interface stress state, starting from the analytical Cox's shear-lag [1] and Kelly-Tyson's shear-sliding [2] approaches to more recent numerical models accounting for different phenomena present at the interface during debonding (e.g. [3]). However, little experimental investigation on the stress/strain state at the interface has been performed, which makes validation of the proposed models difficult. This is primarily due to the fiber being embedded in the (opaque) bulk matrix, the very small scale of the region of interest, and the need for accurate stress/strain quantification techniques.

2D investigations of debonding have been conducted on Single-Fiber Fragmentation Tests (SFFTs) using in-situ optical microscopy with polarized light [4, 5]. This allows detection of the birefringence phenomenon (photoelastic pattern) occurring at the fiber break site. Although it is experimentally rather easy to perform, this approach does not provide a very accurate measurement of the extent of the debond and is limited to 2D information. Another technique for stress analysis characterization during SFFT is Raman spectroscopy [6, 7]. Based on the stress

  doi:10.5075/epfl-298799_978-2-9701614-0-0

dependency of certain vibrational modes of the fibers, Raman can measure the fiber stress along its axis, a stress profile which displays the stress magnitude at the fiber break, debonding, and recovery regions. Nevertheless, Raman spectroscopy needs special measurement tools, does not work on glass fibres, and provides no information on the matrix stress state in the vicinity of the fiber.

More recently, X-ray micro-Computed Tomography (micro-CT) enables 3D imaging of the microstructure of composite materials and possibly of its evolution during mechanical loading. A few studies have employed micro-CT for in-situ debonding analysis in composites. Mode I debonding of a single glass fiber from epoxy was evaluated with in-situ micro-CT in [8]. Although the results were very interesting, the studied glass fiber had a significantly larger diameter than the typical glass fibers, and the debond length was measured visually in the CT images, which is feasible only when the debonding is in opening mode. In a more recent study [9], interface debonding and in-resin crack initiation and propagation in a carbon fiber-epoxy composite were looked at with nanoscale in-situ synchrotron micro-CT. Similarly, the opening mode of the loading allowed visual analysis of the crack in the CT results. To the authors' best knowledge, no 3D studies of fiber-matrix debonding in longitudinal loading have been carried out.

In the current study, we apply tensile loading to a single glass fiber-epoxy specimen and monitor the fiber break and the consequent phenomena via in-situ synchrotron micro-CT. To quantify the deformation around the fiber break, Digital Volume Correlation (DVC) is used. DVC works based on tracking the greyscale pattern in consecutive 3D images of deformation, for which a volumetric speckle pattern inside the material is needed [10]. We use a nano-powder to create the speckle pattern. This allows microscale strain measurement around the glass fiber after it breaks.

2. Materials and Methods

2.1 Specimen Preparation

A silicone mold was made to produce double-notched single-fiber specimens with a nominal notch cross-section of 1 × 1 mm^2. Individual fibers were extracted from a fiber bundle (HYBON 2026 glass fiber), and placed in the silicone mold, guided by the slots on both side of the mold. They were loaded in the mold by hanging on them a weight of 15.4 g to keep them straight during manufacturing. The fibers were then fixed to the substrate using two glue droplets (Bison 2-component epoxy adhesive) on both sides.

To create the required speckle pattern for the DVC, the commercially available tetragonal barium titanate particles with nominal mean size of 400 nm (US Research Nanomaterials Inc., Houston, TX, USA) was used. The powder was mixed in a SR8500/KTA313 dual-component epoxy (Sicomin, Châteauneufles-Martigues, France) before curing and dispersed using sonication. The volume fraction was set to 3 vol%. To remove the entrapped air from the resin mixture, it was degassed for 10 min in a vacuum oven, injected into the mold using a syringe, and again degassed in two sets of 5 min. The cure cycle, in line with the manufacturer's recommendation, was as follows. The oven was preheated to heat up the specimen at the dwell temperature of 70 °C for 60 min with 0% ventilation. Then, the temperature was increased in steps of 10 °C until 120°C was reached, with holding at each step for 10 min. Finally, after 90 mins at 120°C, the temperature is lowered to room temperature.

2.2 Mechanical loading and in-situ synchrotron micro-CT

Tensile tests were performed with a CT500 loading rig (Deben Ltd., UK) with a Perspex (PMMA) protective tube (Figure 1), which is designed for mechanical loading with in-situ micro-CT. Loading was applied with a displacement rate of 0.2 mm/min and was interrupted at certain displacements for in-situ scanning. To alleviate potential effects of specimen relaxation during the stops, scanning was started after a slight (~10%) reduction in load, at each step. The experiments were carried out on the TOMCAT beamline at the Swiss Light Source (SLS), Paul Scherrer Institute (PSI), Villigen, Switzerland.

The scans were acquired with 1500 projections spread over 180° and an exposure time of 80 ms per projection, leading to a total scan time of 2 min. A polychromatic (white) beam with an energy of 15 keV was used. The specimen-to-detector distance was set to 30 mm, and the voxel size of was 650 nm. A pco.edge detector was used. The scans were reconstructed using the in-house SLS absorption-based (Gridrec) algorithm [11].

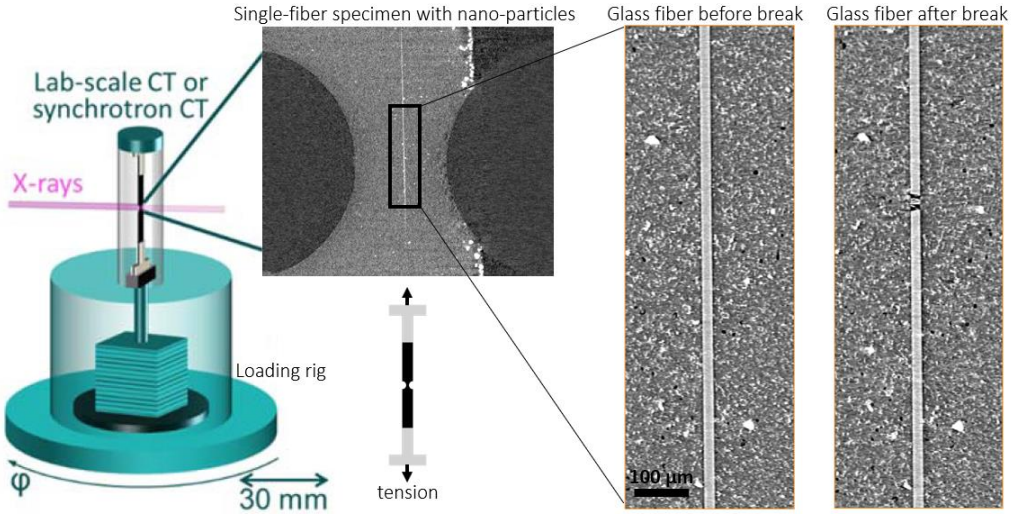

Figure 1. Loading setup for in-situ imaging of composite specimens for DVC analysis and 2D slices of the glass fiber before and after a break.

2.3 Digital volume correlation

DVC is an image-processing technique for quantification of deformation in 3D images taken in situ from a deforming material. DVC uses the changes occurring in the greyscale pattern of the images due to deformation. Thus, a random speckle pattern is required, which can be taken as the natural texture of the material or, in the absence of a distinct texture, created artificially (like in the current study).

The Avizo 2019 software is used for application of DVC in this study, which can be performed in two ways: subset based (local) or Finite-Element (FE) based (global). Subset-based DVC is conducted using a coarse cubic mesh and provides a rough estimation of strain at a low computational cost, but it is less accurate and does not result in a continuous displacement field. On the contrary, finite-element-based DVC, using a fine tetrahedral mesh, ensures continuity of the displacement results, which are much more accurate, but of course, computationally more expensive to reach [10]. Two 3D images, from before and after the fiber break, are imported in Avizo. They are registered (overlaid on top of each other) and cropped to a suitable size for the

region of interest. Subset-based DVC is performed with a subset size of 48 px (31.2 µm). The resulting displacement field is used as an initial guess for a finite-element DVC with a 20-px (13 µm) mesh. The mesh size relative to the fiber dimensions can be noted in Figure 2.

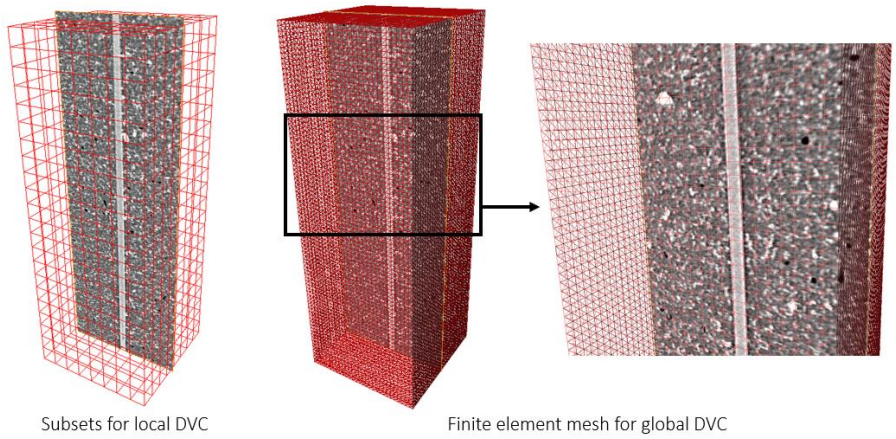

Figure 2. The subsets and finite-element mesh for local and global DVC, respectively, for the selected region of interest around the single fiber

3. Results and discussion

3.1 Miro-scale displacement and strain fields

3D longitudinal and shear strain fields were acquired using DVC. For ease of visualization, 2D slices of these fields along the fiber are shown in Figure 3. These results yield some strain localization around the fiber break. The longitudinal strain field shows a very large strain localization (red) on the break site, which corresponds to the opening of the break and is not really due to a material deformation. However, the relatively high strain (yellow) in the matrix around the fiber break corresponds to the local deformation of the matrix in that region to comply with the fiber break opening. The shear strain map displays more interesting results. Localizations of shear strain occurs around the fiber break. These localizations tend to follow a symmetric (butterfly) pattern with regard to the fiber break plane (Figure 3). They also correspond to the local deformation of the matrix at the interface near the fiber break.

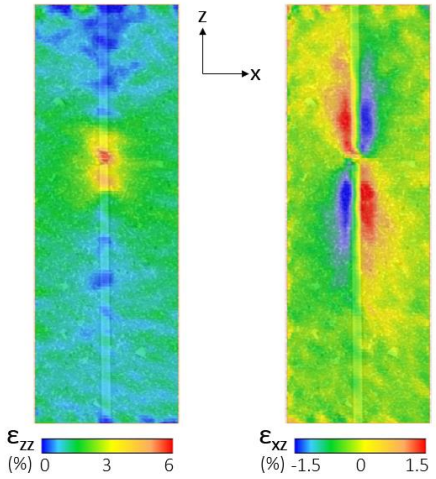

Figure 3. DVC resulting (axial ε_{zz} and shear ε_{xz}) strain maps (FE-based) shown on a 2D slice along the fiber.

3.2 Strain profiles along the fiber

To analyze the results more quantitatively, strain profiles are extracted along two lines on the left and right side of the fiber. The strain profiles, confirming the symmetric shear strain around the break, provide an estimation of the ineffective length, yielding values of ~ 150 µm. This measurement may be sensitive to the mesh size, which needs to be evaluated further.

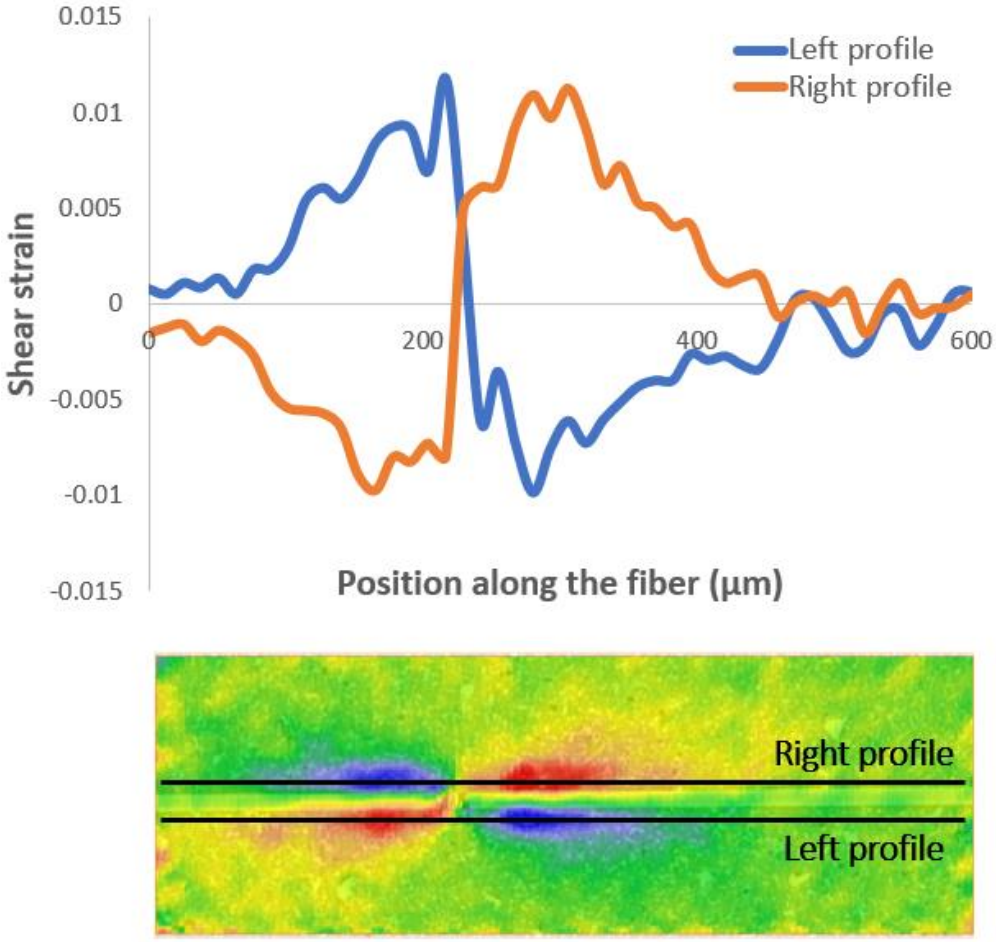

Figure 4. Shear strain profiles along two lines on the left and right side of the fiber (rotated 90°).

4. Conclusions

A methodology for microscale characterization of strain at the fiber-matrix interface nearby a fiber break is developed. It combines in-situ synchrotron tomography of a single-fiber specimen under axial tension with digital volume correlation. The resulting strain fields show localization at the fiber break site, which can be used for characterization of the microscale properties. This asks for a finite-element model to back-calculate the properties from the resulting strains. The ineffective length can be identified using the strain profiles along the fiber. For this, a mesh sensitivity analysis needs to be performed to evaluate the effect of the global DVC mesh size on the resulting ineffective length. Moreover, fiber-matrix debonding characterization may be feasible with further refinement of the mesh.

  doi:10.5075/epfl-298799_978-2-9701614-0-0

Acknowledgements

The research leading to these results has been done within the framework of the HyFiSyn project and has received funding from the European Union's Horizon 2020 research and innovation programme under the Marie Skłodowska-Curie grant agreement No 765881. M. Mehdikhani would like to acknowledge his FWO Postdoc Fellowship, project ToughImage (1263421N).

5. References

1. Cox HL. The elasticity and strength of paper and other fibrous materials. British Journal of Applied Physics 1952; 3:72-79.
2. Kelly A, Tyson WR. Tensile properties of fibre reinforced metals: copper/tungsten and copper/molybdenum. Journal of the Mechanics and Physics of Solids 1965; 13:329-350.
3. Ahmadvashaghbash S, Breite C, Mehdikhani M, Swolfs Y. Longitudinal debonding in unidirectional fibre-reinforced composites: Numerical analysis of the effect of interfacial properties. Composites Science and Technology 2021; 109117.
4. Kim BW, Nairn JA. Observations of Fiber Fracture and Interfacial Debonding Phenomena Using the Fragmentation Test in Single Fiber Composites. Journal of Composite Materials, 2002; 36:1825-1858.
5. Ma T, Liu L, Wang C. Interfacial shear strength of opaque resin/carbon fiber based on mapping from energy dispersive X-ray spectroscopy. Polymer Composites 2020; 41:2134-2144.
6. Huang Y, Young RJ. Analysis of the fragmentation test for carbon-fibre/epoxy model composites by means of Raman spectroscopy. Composites Science and Technology 1994; 52:505-517.
7. Zhu M, Wang Y, Wang C, Chen F, Liu Q. An improved analytical model for inversely determining multiple interfacial parameters from single fiber micro-Raman and fragmentation tests. Composites Science and Technology 2021; 108983.
8. Martyniuk K, Sørensen BF, Modregger P, Lauridsen EM. 3D in situ observations of glass fibre/matrix interfacial debonding. Composites Part A: Applied Science and Manufacturing 2013; 55:63-73.
9. Watanabe T, Takeichi Y, Niwa Y, Hojo M, Kimura M. Nanoscale in situ observations of crack initiation and propagation in carbon fiber-epoxy composites using synchrotron radiation X-ray computed tomography. Composites Science and Technology 2020; 197:108244.
10. Mehdikhani M, Breite C, Swolfs Y, Soete J, Wevers M, Lomov SV, Gorbatikh L. Digital volume correlation for meso/micro in-situ damage analysis in carbon fiber reinforced composites. Composites Science and Technology 2021; 213:108944.
11. Marone F, Stampanoni M. Regridding reconstruction algorithm for real-time tomographic imaging. Journal of synchrotron radiation 2012; 19:1029-37.

  doi:10.5075/epfl-298799_978-2-9701614-0-0

ELECTRICAL IMPEDANCE TOMOGRAPHY FOR DAMAGE DETECTION AND LOCALIZATION ON CARBON FIBRE REINFORCED POLYMER COMPOSITES

Helena, Rocha[a, b], Christophe, Fernandes[c], Nelson, Ferreira[c], Ugo, Lafont[d], João P., Nunes[a]

a: Institute for Polymers and Composites, University of Minho, Guimarães, Portugal – helenarocha@dep.uminho.pt
b: PIEP – Innovation in Polymer Engineering, Guimarães, Portugal
c: Stratosphere, Guimarães, Portugal
d: European Space Agency, Noordwijk, The Netherlands

Abstract: *Electrical impedance tomography (EIT) is being developed as promising non-intrusive technology for damage detection in conductive fibre reinforced polymers (FRP) composites. This work assessed EIT and one-step difference Gaussian-Newton algorithm to detect different damages in CFRP laminates, including through-thickness holes and impact damage of different severities. Two layup laminates were studied: quasi-isotropic [0/45/90/-45]s and unbalanced [0/0/45/90/-45]s. Each laminate configuration was subjected to three levels of impact energy. Through-thickness holes with diameters as small as 2 mm were detected. The LVI on unbalanced specimens created elongated shaped damages, which were observed through EIT and ultrasonic C-scan. Differently, the ultrasonic C-scan inspections revealed circular shaped damages on the centre of the quasi-isotropic specimens, while EIT could not reveal a well-defined damage shape. Yet, the presence of damage was observed in the centre of the specimens by EIT. Although EIT overestimated the damaged area, it was highly sensitive to the imposed damages.*

Keywords: Carbon Fibre Reinforced Polymer Composite; Electrical Impedance Tomography; Impact Damage Detection; Barely Visible Impact Damage; Through-thickness hole

1. Introduction

The performance of FRP composites is particularly affected by the presence of barely visible impact damage, produced by low velocity impacts (LVI) (1). Several approaches for impact damage detection and localization on composites are addressed in the literature. Although various types of sensors have been already embedded in composite structures for damage detection, like optical fibre-based and piezoelectric ones, their presence may affect the mechanical performance of such structures (2). Alternatively, as electrical impedance tomography (EIT) technique uses surface electrodes instead of invasive sensors, their use does not affect the performance of composites (3). Electrodes are mounted on the boundary of an electrically conductive composite, such as carbon fibre reinforced polymer (CFRP) composites or composites with conductive particles modified matrices (4–7). Current is injected though a pair of electrodes, and resultant voltages in the following pairs are measured (3). This allows to construct tomographic images of the distribution of spatial electrical conductivity. Despite the reduced spatial resolution, EIT can detect subtle conductivity variations when damages like cracks or delaminations disrupt the conductive network (8). Yet, the EIT technology remains at low TRL regarding monitoring of anisotropic materials such as composites, in contrast to conductive anisotropic materials like metals.

  doi:10.5075/epfl-298799_978-2-9701614-0-0

Algorithms for reconstruction of static electrical impedance tomography images may lead to measurement errors, due to the higher sensitivity of EIT to changes in the boundary proximity than within the sample. A slight error on electrode positioning may generate similar voltage measurements to those of a severe inhomogeneity in the middle of a specimen. Alternatively, algorithms for dynamic imaging reconstruction avoid this limitation of static EIT. In dynamic EIT reconstruction, the conductivity image at time instant t_2 is determined by the difference of voltage v_2, at t_2, and of the prior measured voltage v_1 at time instant t_1 (9). Thus, the EIT voltage difference, *y*, can be calculated resorting to Eq. (1) (10).

$$[y]_i = [v_2]_i - [v_1]_i \tag{1}$$

The medium conductivity is modelled using a finite element model, comprising n_N elements, which are represented by the vector of conductivity $\sigma \in \mathbb{R}^{n_N}$. The difference EIT can also be obtained through the conductivity change vector, *x,* given by the difference of conductivity distribution σ_2, at t_2, and the conductivity distribution σ_1, at t_1, as stated in Eq. 2 (10).

$$x = \sigma_2 - \sigma_1 \tag{2}$$

To obtain the boundary voltage data from the measured reference conductivity, and solve the forward problem in the difference EIT methodology, the linear Eq. 3 is applied (10).

$$y = Jx + n \tag{3}$$

being *J* the Jacobian matrix and *n* the measurement noise.

This work used a one-step difference Gaussian-Newton (GN) algorithm to solve the inverse problem of EIT and to construct the EIT images. The conductivity can be promptly calculated as a linear matrix, facilitating real-time EIT image reconstruction. The one-step GN algorithm searches for the minimized solution $\hat{x}$, given by the minimized sum of quadratic norms, as presented in Eq. 4 (10).

$$\|y - J\hat{x}\|^2_{\sum n^{-1}} + \|x - x^0\|^2_{\sum x^{-1}} \tag{4}$$

where x^0 is the anticipated conductivity changes in the element, being null for difference EIT, $\sum_n$ is the covariance matrix of *n* and $\sum_x$ is the projected image covariance.

A one-step linearized inverse solution is given in Eq. 5 (10).

$$\hat{x} = (J^T W J + \lambda^2 R)^{-1} J^T W y \tag{5}$$

being *W* and *R* heuristically calculated, as presented in Eq. 6 and 7, respectively, *R* the regularization matrix, and λ the hyperparameter, calculated through Eq. 8.

$$W = \sigma_n^2 \sum n^{-1} \tag{6}$$

$$R = \sigma_x^2 \sum x^{-1} \tag{7}$$

$$\lambda = \frac{\sigma_n}{\sigma_x} \tag{8}$$

where σ_n is the average amplitude of *n* and σ_x is the initial conductivity change.

This work explored EIT technique with one-step difference GN algorithm to detect different damages in CFRP laminates, namely through-thickness holes, and impact damage of different

  doi:10.5075/epfl-298799_978-2-9701614-0-0

severities. Two layup configurations were produced and evaluated: a quasi-isotropic configuration, believed to present a more isotropic-like behaviour and an unbalanced configuration, believed to present a more anisotropic-like behaviour. Each laminate configuration was subjected to three levels of impact energy drilled with fully through-thickness holes. Ultrasonic C-scan inspections were undertaken for comparison and validation of EIT.

2. Materials and Experimental Techniques

2.1. CFRP Laminates

CFRP laminates were made of epoxy, composed of Biresin® CR83 resin and CH83-6 hardener (Sika AG, Switzerland) mixed in a proportion of 100/30 wt%, respectively, and unidirectional carbon fibre fabric, 350UT (Toray Industries, Inc., Japan), with an areal weight of 340 g/m2. The laminates were produced with two different layup configurations: a quasi-isotropic laminate with 8 layers, [0/45/90/ 45]s, and an unbalanced laminate with 10 layers, [0/0/45/90/ 45]s.

The CFRP plates, measuring about 500 mm x 700 mm, were manufactured by vacuum assisted resin infusion (VARI). The laminates were initially left to cure at room temperature, under vacuum, for approximately 40 hours and then, post cured at 70 °C for around 8 hours at ambient pressure. The cured composite plates were cut into specimens of approximately 150 x 100 mm, according to ASTM D7136 standard, for impact testing.

2.3. Production of damage in the CFRP plates

Through-thickness holes were drilled on the CFRP specimens. The locations of the two through-thickness holes are represented by the red dots A and B in Figure 1. Hole A was firstly created having an initial 2 mm diameter, being later expanded to 4.5 and 6 mm. With hole A having a 6 mm diameter, hole B was then drilled following the same diameter increments as hole A. EIT imaging was recorded between each drilling step for diameter increase.

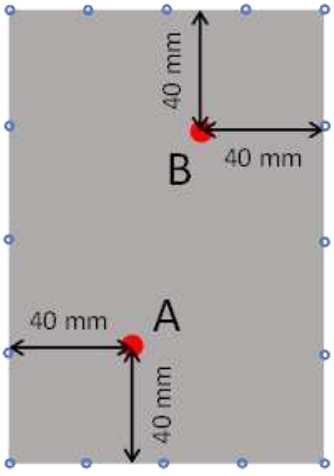

Figure 1. Red dots A and B indicate the location of the through-thickness holes

A drop-weight impact testing setup was used to produce impact damages. Distinct degrees of damage severity (unnoticed damage, barely visible damage, and severe damage) were enforced in the laminates. Different impact energies had to be employed on the distinct laminates to generate damages of equivalent severity, since the different layup configurations result in distinctive impact resistance. The quasi-isotropic and the unbalanced specimens were exposed

to impact energies of 20.0, 30.0 and 49.5 J and 15.0, 30.0 and 49.5 J, respectively. Each condition was replicated in three specimens. Drop-weight impact testing was conducted on the Fractovis Plus equipment from CEAST, with a 20 mm diameter hemispheric head impactor, with a mass of 5.045 kg. The vertical position of the impactor was adjusted between 305 and 1000 mm, producing the different levels of impact energy. Tests were conducted according to ASTM D7136 standard.

2.4. Damage Inspection

Each specimen, of 150 mm x 100 mm, had sixteen electrodes applied on its boundary for EIT analysis. The location of the electrodes is schematically represented by the blue circles in Figure 1 and it can be seen in Figure 2 (b) and (c). The EIT equipment, developed at Stratosphere company, comprised a power supply (XPH 35-4D Dual DC – Sorensen), a digital multimeter (2100 – Keithley) and a type-k thermocouple (see Figure 2 (a)). It was used the adjacent current injection method, where current is injected in one pair of adjacent electrodes and resultant voltages on all following adjacent electrodes pairs are measured. The inverse EIT problem was solved with one-step difference GN algorithm for image reconstruction. A λ of 1 was utilized for image reconstruction. Each specimen was analysed prior to damage creation to serve as reference baseline for EIT image reconstruction.

(a) (b) (c)

Figure 2. (a) EIT equipment; (b) specimens with 16 boundary electrodes being analysed and (c) detailed of a boundary electrode

Non-destructive ultrasonic C-scan inspections were performed on impacted specimens to provide a comparison and validate the EIT images. The ultrasonic C-scan inspections were carried out in an Omni Scan Sx – Olympus, using a 0.5 MHz M2008 probe. A two-axis encoder, with 1.0 mm and 3mm resolution in the axis along the specimens length and width, respectively, was used.

3. Results and discussion

Figure 3 and Figure 4 show the EIT reconstruction images of the quasi-isotropic and unbalanced specimen, respectively, with drilled holes A and B with progressive larger diameters. A decrease of electrical conductivity (darker blue) is observable in the bottom area of Figure 3 and Figure 4 (a), (b) and (c), showing larger and darker blue areas as the holes diameters are increased. Similarly, the production and diameter increase of hole B induced larger and darker blue areas in the top of Figure 3 and Figure 4 (d), (e) and (f). The created damages induced an electrical interference in the region close to the boundary electrodes. Nevertheless, the employed EIT method was sensitive to the presence of the smallest 2 mm diameter through-thickness hole.

  doi:10.5075/epfl-298799_978-2-9701614-0-0

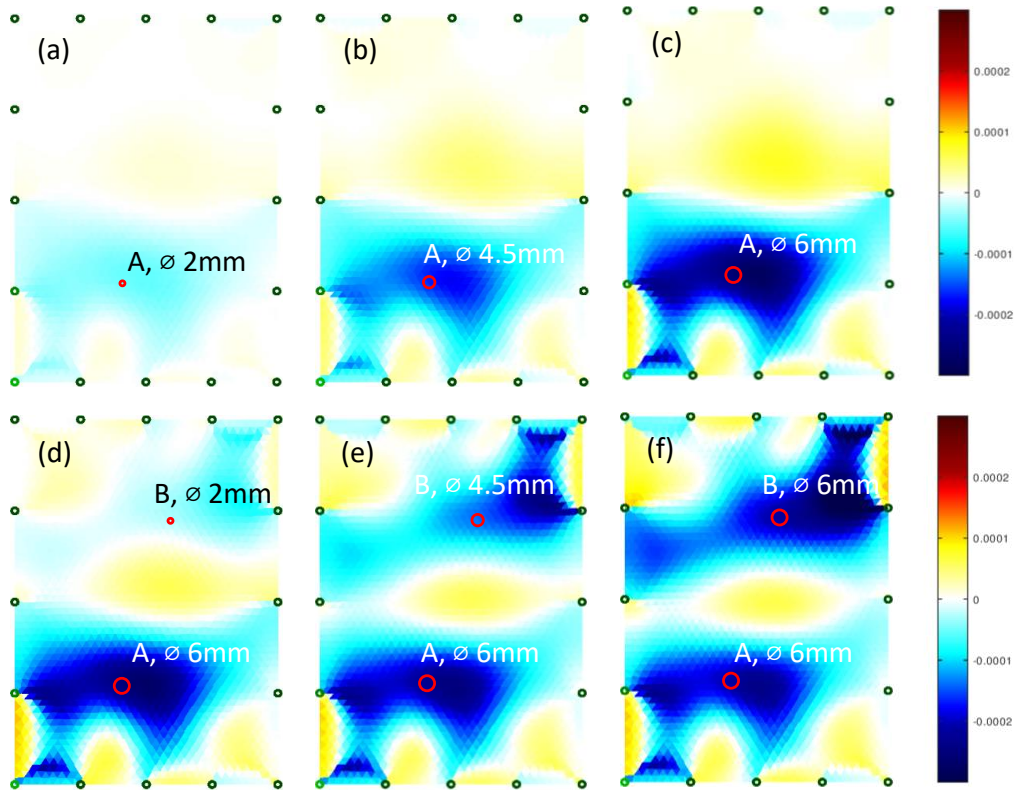

Figure 3. EIT images of a drilled quasi-isotropic specimen with through-thickness holes A and B having different diameters: (a) A: 2 mm, B: non-existent; (b) A: 4.5 mm, B: non-existent; (c) A: 6 mm, B: non-existent; (d) A: 6 mm, B: 2 mm; (e) A: 6 mm, B: 4.5 mm; (f) A: 6 mm, B: 6 mm. The green dots indicate the locations of the electrodes

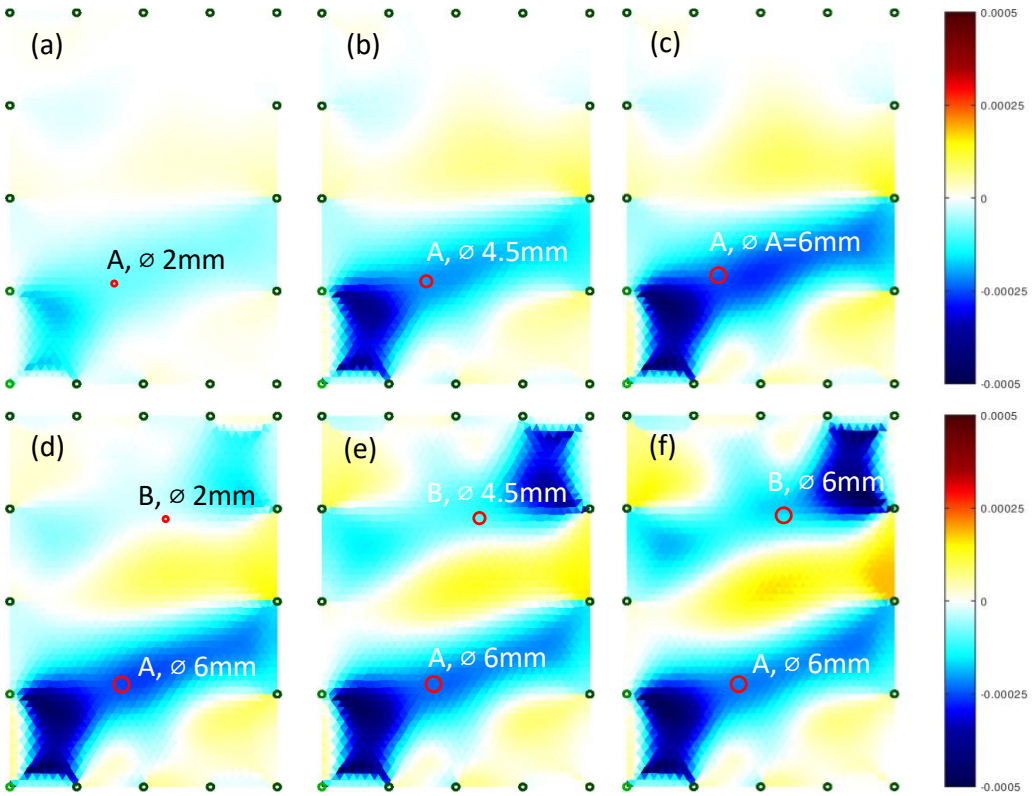

Figure 4. EIT images of a drilled unbalanced specimen with through-thickness holes A and B having different diameters: (a) A: 2 mm, B: non-existent; (b) A: 4.5 mm, B: non-existent; (c) A: 6 mm, B: non-existent; (d) A: 6 mm, B: 2 mm; (e) A: 6 mm, B: 4.5 mm; (f) A: 6 mm, B: 6 mm. The green dots indicate the locations of the electrodes

  doi:10.5075/epfl-298799_978-2-9701614-0-0

The impact events produced different damage shapes on the two laminates of different configuration. Contrary to the expectations, the quasi-isotropic specimens revealed an increase of electrical conductivity in the central region of the specimens, with undefined shape of damage (top of Figure 5). Contrarily, the unbalanced laminates (top of Figure 6) showed elongated "peanut" shaped damages (11), where a decrease of electrical conductivity can be seen. The ultrasonic inspections (bottom of Figure 5 and 6) verified the damage shapes created in the impacted laminates, where the EIT of unbalanced laminates overestimates the delamination areas in about 1.4 to 2 times.

It was expected that EIT would locate damage with improved accuracy in the quasi-isotropic laminate. Yet, the opposite was verified, which might be explained by the higher number of layers at 0°, yielding an improved path for electrical conduction in the unbalanced specimens.

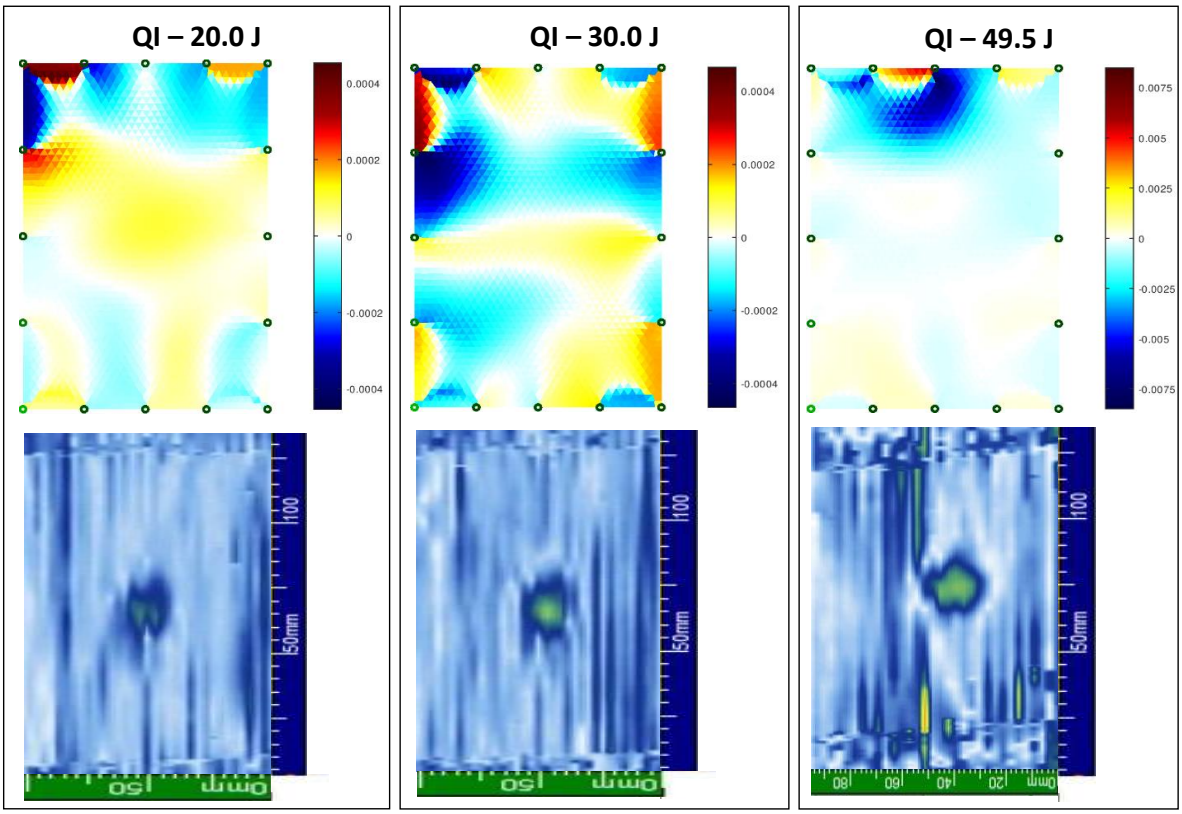

Figure 5. (top) EIT images and (bottom) ultrasonic C-scan inspection images of quasi-isotropic specimens damaged by Impacts of different energies: (left) 20.0J, (middle) 30.0 J, and (right) 49.5 J

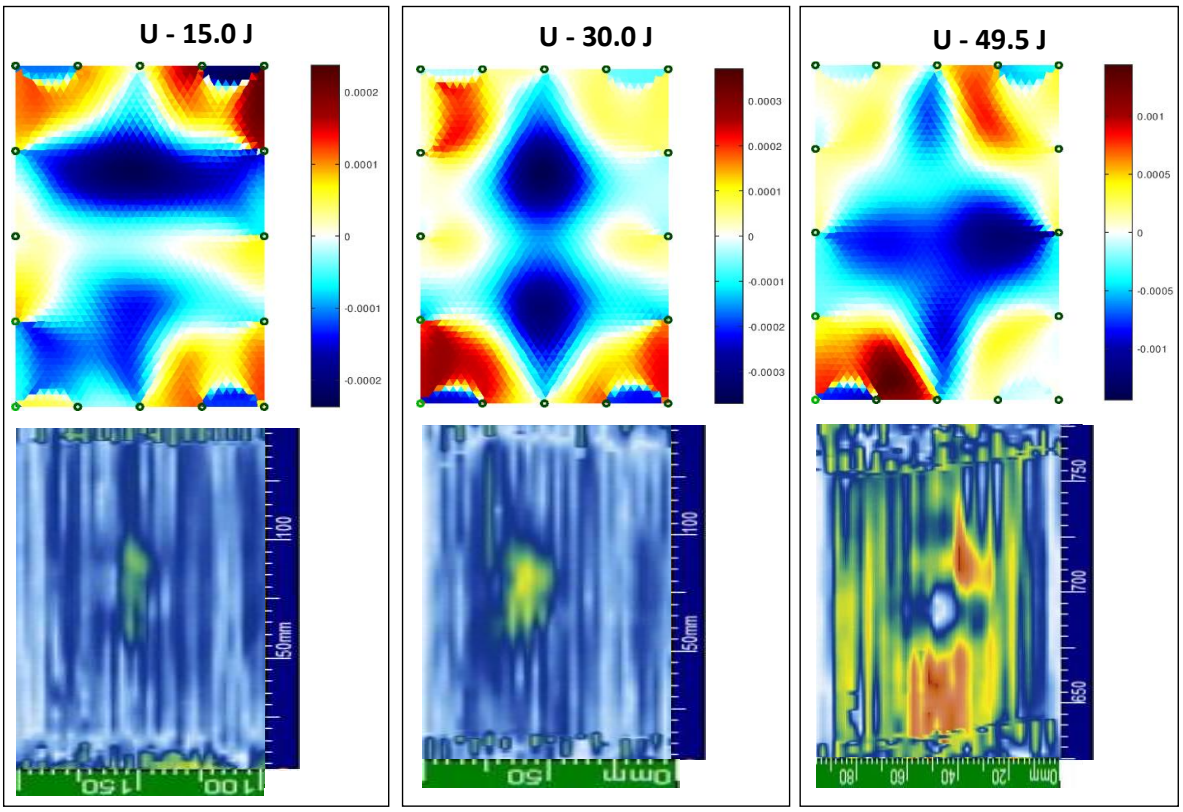

Figure 6. (top) EIT images and (bottom) ultrasonic C-scan inspection images of unbalanced specimens damaged by Impacts of different energies: (left) 15.0J, (middle) 30.0 J, and (right) 49.5 J

4. Conclusions

EIT with a one-step GN algorithm was evaluated for damage detection in CFRP composites. Different damage types were produced in the CFRP laminates: through-thickness holes and impact damage produced by impact testing with three levels of impact energy. CFRP plates with two distinct layup configurations (a quasi-isotropic and an unbalanced configuration) were manufactured by VARI process.

EIT was sensitive to through-thickness holes as little as 2 mm and showed progressively larger areas of decreased electrical conductivity, as the holes diameter increased.

The impacts on unbalanced specimens resulted on elongated shaped damages, “peanut” shape-like damage, which were observable by both EIT and ultrasonic C-scan inspections. The ultrasonic C-scan inspections revealed circular shaped damages in the impacted quasi-isotropic specimens, while the EIT images could not reveal a defined damage shape. Yet changes of electrical conductivity are visible in the specimens centre. Generally, the EIT technique overestimate the damaged area.

Acknowledgements

The authors would like to acknowledge the support of the European Regional Development Fund [grant number NORTE-01-0145-FEDER-000015]; and of the European Space Agency [Network/Partnering Initiative Program - ESA Contract 4000123315].

5. References

1. Giurgiutiu V. SHM of Aerospace Composites – Challenges and Opportunities. CAMX Conf Proc. 2015;1–15.

2. Ramakrishnan M, Rajan G, Semenova Y, Farrell G. Overview of Fiber Optic Sensor Technologies for Strain/Temperature Sensing Applications in Composite Materials. Sensors [Internet]. 2016;16(1):99. Available from: http://www.mdpi.com/1424-8220/16/1/99

3. Loyola BR, Saponara V La, Loh KJ, Briggs TM, Bryan GO, Skinner JL. Spatial Sensing Using Electrical Impedance Tomography. IEEE Sens J. 2013;13(6):2357–67.

4. Nonn S, Schagerl M, Zhao Y, Gschossmann S, Kralovec C. Application of electrical impedance tomography to an anisotropic carbon fiber-reinforced polymer composite laminate for damage localization. Compos Sci Technol [Internet]. 2018;160:231–6. Available from: https://doi.org/10.1016/j.compscitech.2018.03.031

5. Cagáň J, Pelant J, Kyncl M, Kadlec M, Michalcová L. Damage detection in carbon fiber–reinforced polymer composite via electrical resistance tomography with Gaussian anisotropic regularization. Struct Heal Monit. 2019;18(5–6).

6. Tallman TN, Gungor S, Wang KW, Bakis CE. Damage detection via electrical impedance tomography in glass fiber/epoxy laminates with carbon black filler. Struct Heal Monit. 2015;14(1):100–9.

7. Thomas AJ, Kim JJ, Tallman TN, Bakis CE. Damage detection in self-sensing composite tubes via electrical impedance tomography. Compos Part B Eng [Internet]. 2019;177(107276). Available from: https://doi.org/10.1016/j.compositesb.2019.107276

8. Cagáň J, Michalcová L. Impact Damage Detection in CFRP Composite via Electrical Resistance Tomography by Means of Statistical Processing. J Nondestruct Eval. 2020;39(2).

9. Adler A, Guardo R. Electrical impedance tomography: Regularized imaging and contrast detection. IEEE Trans Med Imaging. 1996;15(2):170–9.

10. Adler A, Dai T, Lionheart WRB. Temporal image reconstruction in electrical impedance tomography. Physiol Meas. 2007;28(7).

11. Abrate S. Impact on Composite Structures. Cambridge University Press; 1998.

Composites Meet Sustainability – Proceedings of the 20th European Conference on Composite Materials,
ECCM20. 26-30 June, 2022, Lausanne, Switzerland

CREATION OF DIGITAL MATERIAL TWIN (DMT) GEOMETRIC MODELS OF HIGH PERFORMANCE COMPOSITES BASED ON X-RAY MICROTOMOGRAPHY

F. Trochu [a], B. Yang [a,b], J. Wang [b], C. Béguin [a], P. Causse [c]

a: Department of Mechanical Engineering, Research Centre for High Performance Polymer and Composite Systems (CREPEC), Polytechnique Montréal, 2900 Boulevard Edouard-Montpetit, Montréal, (Québec), H3T 1J4, Canada; Email: trochu@polymtl.ca
b: Wuhan University of Technology, Wuhan, Hubei, China
c: Department of Mechanical Engineering, Ecole de Technologie Supérieure (ETS),
1100, rue Notre-Dame Ouest Montréal (Qc), H3C 1K3, Canada.

Abstract: *Numerical simulation is crucial to study the multi-scale formation of defects and failure mechanisms in fiber-reinforced composites. It allows establishing important connections between the mesoscopic structure and their macroscopic properties. The analysis reliability depends strongly on the accuracy of the geometrical model describing the architecture of reinforcements. This paper establishes a new approach to creating mesoscopic models containing matrix and reinforcement from three-dimensional images obtained by microcomputed tomography. The method follows three main stages: (1) extracting the geometric features of the scanned object; (2) evaluating the direction and local variability of fiber tows; and (3) geometric modeling of the dual-scale porosity of the textile. A new multi-objective optimization algorithm is proposed to quantitatively evaluate and control the model accuracy. Results show that the reconstructed geometry is consistent with the scanned image. Besides, the performance evaluation confirms that the modeling software based on the proposed method is reliable and efficient.*

Keywords: Composites; Textile reinforcement; Digital Material Twin; Microcomputed tomography

1. Introduction

Engineering textiles are used as fibrous reinforcements in high performance polymer composites. The mechanical and flow properties of continuous fiber composites depend on their dual-scale porous structure. Depending on the flow front velocity during fabrication by Liquid Composite Molding (LPM), long and elongated microscopic open spaces (micropores) may appear between the filaments of fiber tows, or up to two orders of magnitude larger mesoscopic spaces (mesopores) can be created between yarns. Because of this complex material structure and intrinsic material variability of reinforcement textiles, numerical predictions are not easy.

X-ray micro-tomography (micro-CT) is widely used to provide detailed information on the mesoscopic geometric structure of continuous fiber composites [1]. For instance, Madra et al. [2] and Vilà et al. [3] investigated the size, and distribution of voids in composites quantitatively using micro-CT. However, the direct generation of numerical models from 3D image sequences still faces many challenges. Madra et al. [4] among the first creating micro-CT image-based geometrical models of reinforcements. Huang [1] introduced the concept of *Micro-CT Added Modelling*. However, these models cannot be used for numerical simulation directly due to the lack of necessary information such as fiber volume content and element orientation. Several

  doi:10.5075/epfl-298799_978-2-9701614-0-0

new approaches [5, 6] for image-based model reconstruction have been reported since then. However, an approach that can simultaneously achieve data preprocessing, model precision control, and a relatively simple process is still engaging.

A new approach is presented to construct detailed geometric vector models of engineering textiles from micro-CT three-dimensional (3D) raster images. These models are called "*Digital Material Twins*" (DMT) because they possess three distinctive features: (1) they represent the intrinsic variability of the reinforcement; (2) their accuracy can be evaluated and controlled; (3) computer simulations can be performed to predict mechanical and flow behaviors. Although the scope of this article is limited to the various issues connected with the creation of DMT models, the ultimate goal will be to show how accounting for material variability turns out to be a critical factor improve the reliability of numerical predictions.

This new and general methodology is applied to create the DMT models of a 3D woven fabric by introducing a kernel density based approach to preprocess the extracted pointwise description of textile architecture. The morphological accuracy of the reconstructed DMTs is compared to the original micro-CT image. The anisotropic direction of fiber tow and local tow porosity are evaluated to complete the models, thus making them be ready for numerical simulation. Besides, the performance evaluation confirms that the modeling software based on the proposed method is reliable and efficient.

2. Material and micro-CT characterization

A 3D orthogonal woven glass textile of areal density 3250 g/m^2, TG96N, from Texonic Inc. was used to develop the micro-CT image based DMT creation methodology. It consists of three different glass yarns: straight in-plane warp and weft yarns are orthogonal and bound together by the waved binder yarns (see Figure 1).

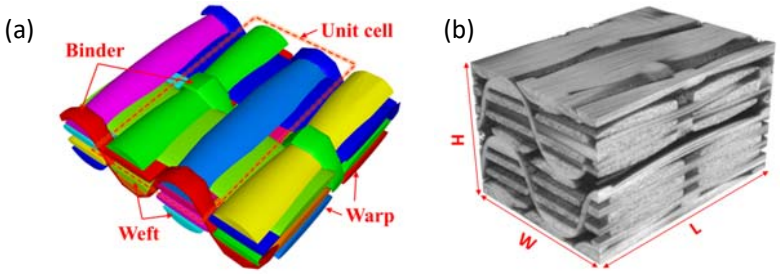

Figure 1. The structure of 3D orthogonal glass woven textile TG96N from Texonic [7]. (a) woven pattern, and (b) volume rendering of X-ray micro-CT results.

Nikon XT H 225 available at the *École de Technologie Supérieure* in Montreal was used to carry out the observations with a voxel size of 22^3 µm^3. The size of the *Region of Interest* (ROI) shown in Figure 1b is $8.8\ \text{mm} \times 6.27\ \text{mm} \times 5.17\ \text{mm}$ ($L \times W \times H$), which contains two unit cells. To maximize the field of view, the resolution is lower than other investigations which focused at high resolution. This compromise is deemed necessary to create geometric models that represent the actual variability of real fibrous reinforcements. More discussions on this particular issue can be found in [8]. The fiber volume fraction of the specimen is 57 %.

A semi-automatic segmentation method was implemented in *ImageJ* software [9] to obtain data for the 3D reconstruction of the ROI from the scanned 3D voxel images. It consists of three steps: (1) manual segmentation of key slices; (2) mathematical morphology interpolation between key

  doi:10.5075/epfl-298799_978-2-9701614-0-0

slices; (3) interactive manual correction of tow contours. Different interpolation functions were used depending on the trajectory of fiber tows. The segmented 3D point cloud data gives separated data point representations of fiber tow contours that will then be available for data preprocessing, 3D surface rendering and local variability extraction. It is particularly important as it governs the ability of DMTs to represent effectively the fiber tow architecture, and hence their further use in computer simulations.

3. Surface representation of fiber tow

3.1 Parametric representation of fiber tow profiles

(1) Parametrization

To reduce complexity, the parametric representation will always be carried out in a 2D plane as shown in Figure 2. The normalized Euclidean distance t_i of fiber tow contour pixels with respect to the initial position in a cross-sectional profile is defined by Eq. (1), where *N* is the number of pixel positions defining the contour and $\sum l_i$ denotes the distances between pixel i and the initial position as indicated by the blue dashed line:

$$t_i = \frac{\sum_{i=1}^{i} l_i}{Perimeter}; \quad \begin{cases} i \leq N \\ t \in [0,\ 1] \end{cases} \tag{1}$$

Thus, the position of pixels i can be denoted as $P[x(t_i), y(t_i)]$. This parametric approach allows analyzing statistically the distribution of pixels on the fiber tow surface and express as a parametric function. Angular position is not used as a parameter because of its inability to describe concave profiles, which are very common in fiber bundles.

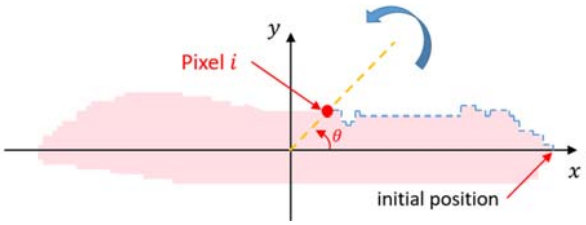

Figure 2. Normalized distance t_i and angular position θ for pixel position description

(2) Parametric representation by kriging

Parametric curve kriging is used to create parametric functions for the fiber tow surface. The pixel coordinates of the cross-sectional profile of fiber bundles can be represented in a 2D plane by a sequence of data points $[x(t_i), y(t_i)]$ for $1 \leq i \leq N$ as a function of the normalized distance t:

$$\begin{cases} x(t) = a_0^x + a_1^x \cdot t + a_2^x \cdot t^2 + \sum_{i=1}^{N} b_i^x \cdot K(|t - t_i|) \\ y(t) = a_0^y + a_1^y \cdot t + a_2^y \cdot t^2 + \sum_{i=1}^{N} b_i^y \cdot K(|t - t_i|) \end{cases} \tag{2}$$

In this kriging model, a quadratic drift is used together with a generalized covariance $K(|t - t_i|)$ which can be linear, logarithmic or cubic [10], depending on the shape of fiber tow trajectory. Note that the kriged function Eq. (2) passes through the measured points as it is the best linear

  doi:10.5075/epfl-298799_978-2-9701614-0-0

unbiased estimator of a random variable. This allows accurate representation of the profiles. Besides, it is also continuous and differentiable, which is important for the derivation of the yarn tangent when we applied kriging method to fiber tow trajectory.

3.2 Density based point cloud processing

In order to preserve the shape of fiber tows accurately while removing redundant data to compress and smooth the fiber tow surface, knowledge of the pixel distribution is required. *Kernel Density Estimation* (KDE) is a non-parametric way to estimate an unknown probability density function $\hat{f}_h(x)$ of a random variable. The estimated distribution density $\hat{f}_h(x)$ writes as follows:

$$\hat{f}_h(x) = \frac{1}{N}\sum_{i=1}^{N} K_h(x - x_i) = \frac{1}{N\,h}\sum_{i=1}^{N} K\left(\frac{x - x_i}{h}\right) \tag{3}$$

where $h > 0$ is a smoothing parameter called the *bandwidth* and N the total number of pixels, namely here the pixel positions in the contour. The kernel function $K_h(x - x_i)$ is the probability density estimator. As in kriging, the kernel function is used to put more weight on the data close to the observed one. The Gaussian kernel function chosen in this work is:

$$K_h(x - x_i) = \frac{1}{\sqrt{2\pi}h} e^{-\frac{(x-x_i)^2}{2h^2}} \tag{4}$$

where x is the pixel under consideration, and x_i is a pixel from the dataset describing a fiber tow. The application of the KDE method is illustrated by applying to the point dataset of a weft fiber tow segmented from the micro-CT images. The results is shown in Figure 3. The extrema of estimated probability density functions give the normalized distance of feature pixels that are most important to describe a fiber tow contour (see Figure 3a). Combining with kriging functions, the new point cloud dataset can be generated and visualized by Figure 3b. It is referred as Global KDE because the probability density estimation method was applied to the point cloud dataset of the entire fiber bundle.

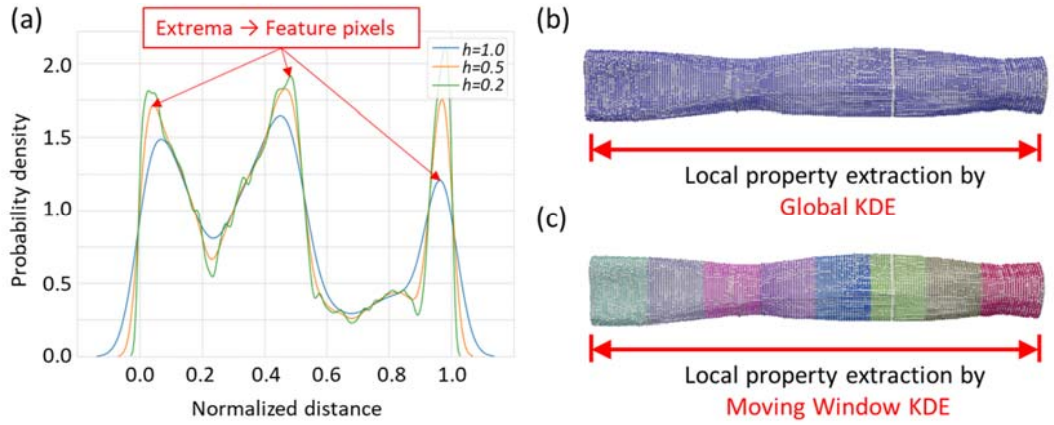

Figure 3. (a) Feature pixel extraction using Kernel Density Estimator (KDE) *and the point cloud representation of fiber tow surface generated by parametric kriging with the feature pixels extracted by (b) global KDE and (c) Moving Window KDE (MW-KDE).*

  doi:10.5075/epfl-298799_978-2-9701614-0-0

On the basis of standard KDE method, a *Moving Window* KDE approach is proposed to improve the quality of data processing. As illustrated in Figure 3c, the probability density function is estimated inside fixed-length windows (8 windows in this case) along the longitudinal direction of fiber tows instead of a whole fiber tow. Therefore, several collections of localized feature pixels could be extracted rather than the same for all the cross-sections in a fiber tow.

3.3 Accuracy evaluation

As shown in Figure 4a, the weft tow models (red) obtained from the global or moving window KDE approaches are superposed on the original image stack (gray, matrix hidden) to evaluate its accuracy. The bandwidth value is varied to achieve the 30, 50 and 100 extrema (feature pixels) in each case. The visible differences are circled using ellipses, which shows qualitatively that the error is minimized for a larger number of feature pixels describing the profile. Thus, the accuracy could be controlled easily. Besides, less error is detected in the model generated by MW-KDE in case C in Figure 4a than in case B, although both cases used 50 feature pixels to describe the tow profiles. A quantitative evaluation is carried out for the cross-sectional area, width and height of fiber tow contours as shown in Figure 4b. The relative error is the ratio of the deviation of the considered property to the same property obtained from the original image stack. The relative error is always less than 4% for all the cases considered. This shows that the model accurately represents the original geometry with a controlled accuracy. Besides, the accuracy analysis confirms that the MW-KDE approach shows a significant advantage over global KDE.

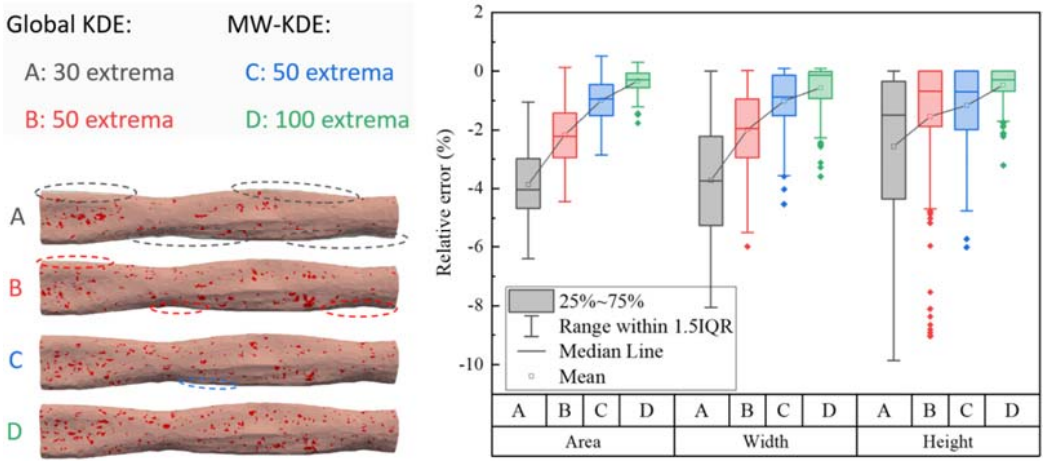

Figure 4. Accuracy evaluation of DMT model (red) by superposing to the reference fiber tow structure (gray) (a) and by key geometric features (b).

4. Microscopic property extraction

A DMT model can be used for efficient manufacturing or mechanical simulations because it reflects the variability of microscopic properties in actual reinforcements. Among other features, the two most important ones are fiber orientation and fiber volume fraction.

4.1 Fiber orientation

Fiber tows are not necessarily straight, depending on the weave patterns. However, only scalar information can be obtained directly from micro-CT images. In this work, the fiber orientation

  doi:10.5075/epfl-298799_978-2-9701614-0-0

was obtained in three steps: (1) extract the central line using the image skeleton algorithm implemented in *ImageJ;* (2) sort the points and apply curve kriging with nugget effect to smooth the central line; (3) The tangent of the central line can be derived immediately from the kriging expression, which is continuous and differentiable. The smoothed central line and the orientation vectors are shown in Figure 5. Note that the central line obtained by the skeleton method may exhibit several branches, which have to be removed.

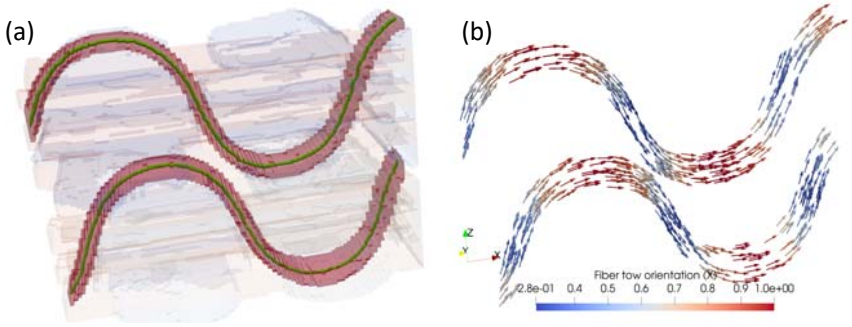

Figure 5. Fiber orientation: (a) smoothed central lines of two binders and (b) and the corresponding glyph rendered using the x-component of the unit direction vector

4.2 Local fiber volume fraction V_f^{cs}

For fiber tows with waviness, the cross-section that parallels the plane of the micro-CT image slices cannot be used to determine V_f^{cs}. Hence, we have to identify the perpendicular cross-sections to the central line first, as shown in Figure 6. The ray-tracing technique is implemented to fulfill this purpose. The local fiber volume fraction is calculated by:

$$V_f^{cs} = \frac{A_f}{A_t^i} \tag{5}$$

where A_f is the total fiber area of a tow cross-section, and A_t^i is the area of cross-section i.

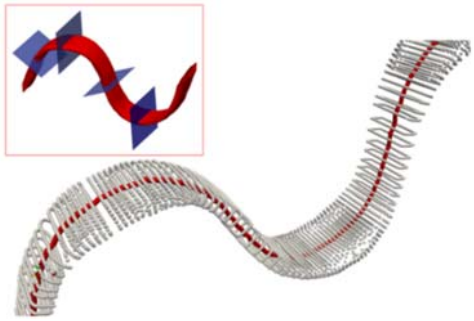

Figure 6. The cross-sections perpendicular to the central line are determined by ray tracing

5 Result and discussion

5.1 *Digital Material Twin* model

The *Digital Material Twin* (DMT) geometric model created by the proposed method is given in Figure 7a. Note that the matrix is hidden for better visualization of the reinforcement. Figure 7b gives the glyph representation of fiber orientations rendered using the x-component of the unit

  doi:10.5075/epfl-298799_978-2-9701614-0-0

direction vector, which is consistent with the woven pattern of the fabric considered. The local fiber volume fraction distribution of two binders and the unit cells are given in Figure 7c and Figure 7d. The local fiber volume fraction ranges from 54% to 89%, reaching a maximum where fiber tows meet.

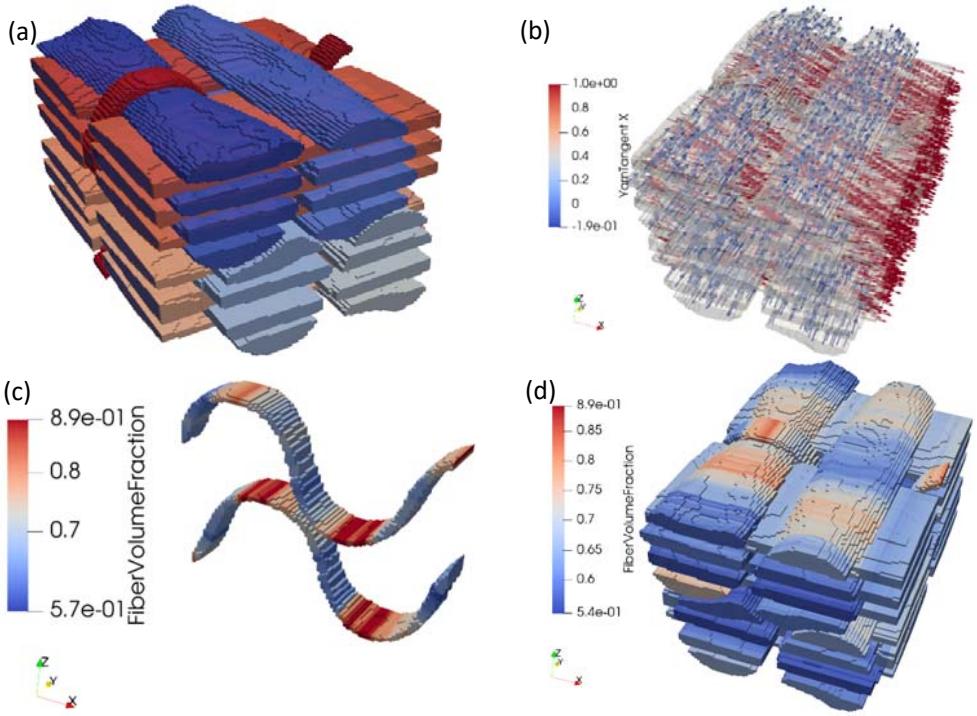

Figure 7. Incorporating microscale information to the DMT model: (a) DMT model with fiber yarns labeled separately; (b) fiber orientation distribution and local fiber volume fraction distribution of (c) the binders, and (d) the unit cells.

5.2 Computational efficiency

The workflow mentioned above for DMT creation was programmed in Python. The code efficiency tested for a mesh containing 1 million hexahedral elements is shown in Table 1. The processor used is Intel® Core™ i7-7700HQ with 4 physical cores, and the RAM is 16 GB. The test shows that the computational time to obtain the mesh, including data reading, geometric feature extraction, digital twin model reconstruction and data writing, does not exceed 20 minutes. Since the above tests are all performed under a single thread, the modeling time should be reduced dramatically in parallel processing.

Table 1: Code efficiency tested for a mesh containing 1 million hexahedral elements.

File format	Mesh file size [MB]	Reading speed [s]	Geometric feature analysis [min]	Mesh reconstruction	Writing speed [s]
ASCII	105	5	3	15 min	8
Binary	16	0.5			3

  doi:10.5075/epfl-298799_978-2-9701614-0-0

6. Conclusion

A new approach to create mesoscopic *Digital Material Twin* (DMT) models containing matrix and reinforcement from a three-dimensional micro-CT image is established. A multi-objective optimization algorithm, based on the newly proposed Moving Window Kernel Density Estimator (MW-KDE), is implemented to quantitatively evaluate and control model accuracy. This new and general methodology is applied to create DMT models of a 3D woven fabric. The morphological accuracy of the reconstructed geometry is consistent with the original micro-CT scanned image.

The DMT model contains detailed information on the anisotropic directions and local porosity of fiber tows, thus making them ready for numerical simulation. The first parameter is derived from the trajectory of fiber tows, and the second one was obtained by combining the trajectory information with a ray-tracing technique. This ensures the suitability of this approach for fiber tows either with or without waviness. Besides, an implementation in Python allows taking full advantage of the large dataset acquired by micro-CT. The performance evaluation confirms that the modeling software is reliable and efficient. By performing computer analysis to predict mechanical and flow behaviors, the creation of a virtual laboratory can be contemplated.

Acknowledgements

Authors would like to thank W. Huang from Wuhan University of Technology for his advice on image processing, Prof. V. Brailovski for access to the X-ray microtomograph at École de Technologie Supérieure (ETS), Montreal and NSERC, FNR-Luxembourg for financial support.

References

1. Huang W, Causse P, Brailovski V, Hu H, Trochu F. Reconstruction of mesostructural material twin models of engineering textiles based on Micro-CT Aided Geometric Modeling. Composites Part A: Applied Science and Manufacturing. 2019;124(June).
2. Madra A, Hajj NE, Benzeggagh M. X-ray microtomography applications for quantitative and qualitative analysis of porosity in woven glass fiber reinforced thermoplastic. Composites Science and Technology. 2014;95:50-8.
3. Vilà J, Sket F, Wilde F, Requena G, González C, Llorca J. An in situ investigation of microscopic infusion and void transport during vacuum-assisted infiltration by means of X-ray computed tomography. Composites Science and Technology. 2015;119:12-9.
4. Madra A, Breitkopf P, Rassineux A, Trochu F. Image-based model reconstruction and meshing of woven reinforcements in composites. International Journal for Numerical Methods in Engineering. 2017;112(9):1235-52.
5. Wintiba B, Vasiukov D, Panier S, Lomov SV, Ehab Moustafa Kamel K, Massart TJ. Automated reconstruction and conformal discretization of 3D woven composite CT scans with local fiber volume fraction control. Composite Structures. 2020;248:112438.
6. Rassineux A. Robust conformal adaptive meshing of complex textile composites unit cells. Composite Structures. 2022;279:114740.
7. Karaki M, Hallal A, Younes R, Trochu F, Lafon P. In-plane permeability prediction model for non-crimp and 3D orthogonal fabrics. Journal of the Textile Institute. 2018;109(8):1110-26.
8. Hilal S. Caractérisation par microtomographie de la mésostructure des renforts fibreux pour la fabrication de composites. Montreal: École Polytechnique de Montréal; 2018.
9. Ferreira T, Rasb W. ImageJ user guide: IJ 1.46 r. 2012.
10. Trochu F. A Contouring Program Based on Dual Kriging Interpolation. Engineering with Computers. 1993;9(3):160-77.

  doi:10.5075/epfl-298799_978-2-9701614-0-0

EVALUATION OF POROSITY IN OUT-OF-AUTOCLAVE CURED CFRP LAMINATES USING THROUGH-TRANSMISSION ULTRASOUND AND X-RAY MICROTOMOGRAPHY

J. Sun [a], O. Inal [a], M. Turski [b], P. Potluri [a] and *K.B. Katnam [c]*

a: Department of Materials, University of Manchester, M13 9PL, Manchester, UK – jingjing.sun@manchester.ac.uk
b: R&T Propound Project Team, Safran Nacelles, BB10 2TQ, Burnley, UK
c: Department of Mechanical, Aerospace and Civil Engineering, University of Manchester, M13 9PL, Manchester, UK

Abstract: *Voids in composite laminates can influence damage initiation, propagation and lead to catastrophic failure. It is therefore important to characterize the morphology and content of voids reliably in order to decide deployment or disposal of a composite component. In this work, thin carbon/epoxy non-crimp-fabric laminates with varying void contents/porosities are manufactured using an out-of-autoclave curing method and then employed to evaluate the robustness of through-transmission ultrasound and X-ray Computed Tomography (micro-CT) scans. The porosity post-processed using a micro-CT 'ambient occlusion' strategy is compared with the volumes captured by an Otsu's grayscale thresholding strategy and the standard acid digestion test. The micro-CT results show that the occlusion method captures the volume of enclosed and open (i.e. near/at laminate surface) voids and thus provides a more comprehensive assessment of voids content and their morphology. The results show a good correlation between ultrasound attenuation and the porosities measured from micro-CT and acid digestion methods.*

Keywords: Manufacturing defects; porosity; non-crimp fabric laminates; through-transmisson ultrasound; X-ray micro-tomography.

1. Introduction

Manufacturing process induced defects such as voids or air bubbles appearing in composite laminates can influence damage initiation and also lead to catastrophic failure [1]. Industrial composite components are often classified as 'use as is', 'use with restriction' or 'discard' based on quantitative assessment of void volume fractions. It is therefore important to detect voids and assess void content in composite structures, preferably using semi- or non-destructive methods. However, the robustness of existing evaluation methods for assessing various void morphologies, for instance, open voids at/near laminate surface or closed voids inside laminae, remains a question.

This paper combines three techniques, viz. through-transmission ultrasound (non-destructive) and X-ray microtomography (semi-destructive) and acid digestion (destructive) methods, to analyse voids in thin carbon/epoxy non-crimp fabric laminates. Ultrasonic C-scans have been widely used to qualitatively evaluate volumes of porosities in industrial composite components based on a linear relation between ultrasound attenuation and the increase in void content [2]. X-ray micro-CT technique allows the visualization of voids formed in heterogeneous composite architectures and their morphologies, in both 3D and 2D formats. The development of micro-CT image post-processing algorithms allows voids with complex geometries to be distinguished and

  doi:10.5075/epfl-298799_978-2-9701614-0-0

quantified from the scanned material volume. Acid digestion of miniature specimens captured from composite structures have been used to determine voids volume fractions based on the Archimedes' theory.

2. Manufacturing and Materials

Carbon fibre reinforced polymer (CFRP) laminates containing average volume fractions of porosities in a range of 0% to 5% were manufactured using vacuum assisted resin infusion (an out-of-autoclave cure) method. The laminates were manufactured with two plies of tri-axial non-crimp fabrics (NCFs) and RTM6 epoxy resin. The stacking sequence of the laminate is $[\pm 60/0]_s$. The fibre tows in the tri-axial fabrics are packed with polyester stitching yarns.

Porosities in the laminates were generated using a novel bag-venting strategy mimicking the leakage of vacuum bags designed with a special arrangement of consumable materials. The bags were vented at predetermined gauge pressures for certain durations in order to introduce air bubbles into the bag. The volumes of air bubbles entrapped in the impregnated fabrics were adjusted by consolidating the vented bags at various vacuum pressures. The laminates were pre-cured at 120 °C for 5 hours followed by a post-cure at 180 °C for 2 hours. The laminates were then trimmed to 500 × 500 mm^2 prior to the subsequent ultrasonic scans.

3. Experimental procedure

3.1 Ultrasonic scans

Porosities produced in the laminates were initially evaluated in a non-destructive manner according to the point-wise ultrasound attenuations acquired from ultrasound scans. The laminates were scanned with a pair of 5 MHz Midas® probes on a Midas® ultrasound scanning machine in through-transmission mode. The scanning resolution is 250 × 250 μm per pixel. The ultrasonic attenuation images were employed to define the locations of 25 × 25 mm^2 specimens with increasing average ultrasound attenuations. The specimens were cut from the laminates for subsequent X-ray CT scans.

3.2 X-ray CT scans

The specimens were scanned using the Nikon XTEK High Flux Bay X-ray computed tomography device, followed by reconstruction on a Nikon Metrology proprietary CT-Pro 3D software in Henry Moseley X-ray Imaging Facility, University of Manchester. The volumetric scanning resolution was 15^3 µm^3/voxel which can detect voids with a volume of at least 3 times of the scanning resolution, i.e. ~45^3 µm^3/voxel. The parameters associated with micro-CT data acquisition are shown in Table 1.

Table 1: X-ray computed tomography scanning parameters (no filter was used for the scan).

Parametes	Energy [kV]	Current [μA]	Exposure time [ms]	Binning	Projections	Frames per projection	Average Gain
Settings	110	95	1000	1	3179	8	4

  doi:10.5075/epfl-298799_978-2-9701614-0-0

The spatial distribution, size, shape and volume of porosities captured in the 3D tomographs are characterized using an Amira-Avizo software. Voids are segmented from the composite using an Otsu-thresholding-based algorithm implemented by segmenting the grayscale intensities related to carbon fibres, resin, polyester stitching yarns from air bubbles, as shown in Figure 1 (a). It has been widely accepted that the microstructure of voids is closely related to the properties of constituent materials, such as fabric architecture, viscosity of resin and the process parameters associated with the resin infusion, vacuum application and consolidation processes [1]. Some voids appear on the surfaces of porous specimens and are coalesced with the ambient air in the scanning volume. In addition, some large volume voids emerge at the interface between two tri-axial layers and display as hollow spaces mostly enclosed by the composite and at some disclosure points coalesce with the ambient open air, for instance voids found in the bottom tri-axial layer intersecting with the regularly spaced through-thickness polyester stitching yarns, shown in Figure 1 (a). The Otsu-grayscale-thresholding algorithm can detect cavities that define the boundaries of voids completely enclosed by composites, for instance the green region depicted in Figure 1 (b). However, the algorithm is incapable to determine a boundary between the space of an open void buried in material and open air. Instead, it assigns such open voids as ambient air, leading to an underestimation of the overall volume of voids in the material.

This problem is solved by deploying a built-in 'ambient occlusion' computation algorithm [3] in Amira-Avizo- software. This occlusion algorithm not only captures the enclosed voids but also the open ones. The occlusion algorithm is capable to detect the enclosed voids as well as the open ones, shown as the blue and red regions in Figure 1 (c), respectively. The algorithm is implemented by casting rays in all directions from each voxel in all air-filled space in the scanning field. Each voxel is assigned with an ambient occlusion coefficient. Voxels associated with higher ratio of rays reflected back due to hitting on the composite in certain directions is occluded with respect to those directions [3]. Voxels buried in the composite are associated with high ambient occlusion coefficients, whereas low values for those outside the composite. This function facilitates an assessment of the volume of open voids that are crucial to consider especially when the composites are loaded in severe conditions with humidity, ice or significant temperature variations, etc.

The occlusion approach is implemented with the settings recommended by the Amira-Avizo software user's guide [4]. The volumes of enclosed voids captured by the thresholding-based segmentation algorithms and the volumes of the open voids computed by subtracting the enclosed voids volumes from those measurements given by the occlusion algorithms are analyzed in this case.

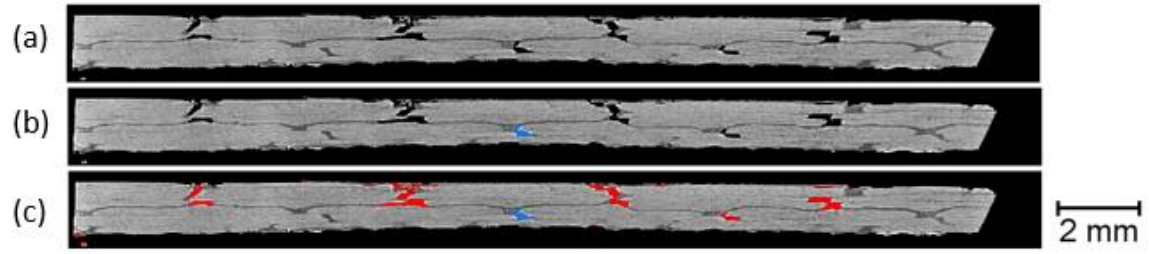

Figure 1. (a) 2D cross-section of an ~1.5 mm thick porous NCF laminate, segmented using (b)the Otsu-grayscale-thresholding algorithm with the enclosed void (highlighted in blue) and

  doi:10.5075/epfl-298799_978-2-9701614-0-0

(c) an ambient-occlusion module capturing both enclosed and open voids (highlighted in red) disclosed to ambient air.

3.3 Acid digestion

Voids contents analyzed by micro-CT are subsequently validated by acid digestion of the specimens performed according to the ASTM D3171-15 (method I) standard. Porosities were computed with the densities of carbon fibre and epoxy resin taken as 1.77 g/cm^3 and 1.148 g/cm^3, respectively. In this case, the density of polyester stitching yarns is assumed as identical to the RTM6 resin, i.e. accounted as a fraction of the matrix system. A standard deviation of $\pm$0.3% is considered for the measurements due to the uncertainty in the densities of fibre, matrix and stitching yarns.

4. Results and discussion

Figure 2 presents the average ultrasound attenuations of eight 25 x 25 x ~1.5 mm (in length/width/thickness) specimens containing porosities in a range of 0% to 4%. The volumes of the enclosed and open voids acquired by post-processing the 3D volumes captured from the CT method, as well as measurements obtained by acid digestion of the specimens are also shown.

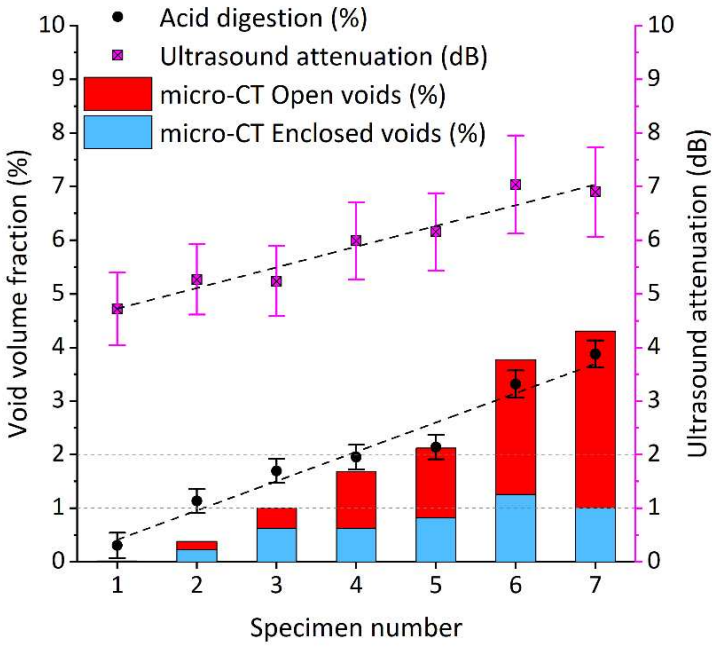

Figure 2. (a) Average ultrasonic attenuation of 25 x 25mm ~1.5 mm thick porous specimens with the volume fractions of enclosed and open voids measured by X-ray micro-CT and acid digestion methods.

Figure 2 shows a generally linear increase in the average ultrasonic attenuation (with a standard deviation of 0.5 dB) with respect to the increased void volume fractions. Results indicate that the ambient occlusion algorithm provides measurements closer to those obtained by the acid digestion method, in contrast with the thresholding-based segmentation algorithm. This is attributed to the occlusion approach encompassing not only the enclosed voids segmented by the Otsu-thresholding algorithm, but also the near-surface open voids. It was found that for an overall volume less than 1%, i.e. specimens 1 to 4, voids are dominated by the enclosed ones. In

terms of specimens 5 to 8 with porosities greater than 1%, open voids account for at least 50% of overall void volumes. As the overall porosity increases further, for instance specimens 7 and 8 (shown in Figure 2), over 75% of voids are exposed to ambient air and the X-ray CT method gives even higher magnitudes than those obtained by acid digestion.

Figure 3 present the 3D volumes of specimens 4, 6 and 7 (shown in Figure 2) post-processed using the ambient occlusion approach, as well as two 2D images captured from representative XZ (highlighted in blue) and YZ (highlighted in yellow) cross-sections. The porosities measured by acid digestion method for specimens 4, 6 and 7 are 1.79%, 2.24% and 3.47% (see Figure 2), respectively. Enclosed and open voids are highlighted in blue and red, respectively. The first 3D volume highlights the open voids formed on spcimens surfaces. These open voids are also depicted in the second 3D volume. The X-ray CT 3D volumes and 2D cross-sections captured from the three samples provide an insight to the distribution and morphological evolution of voids with increased volumes.

The 3D volume shown in Figure 3 (a) presents periodic ellipsoid voids (shown in blue) in the 0° fibre direction, i.e. the X-axis direction. Voids are dominated by enclosed ones for a porosity content of 1.79%. These enclosed voids are formed at the interface between two central 0° sublayers (see the 2D views) and mostly along the periodic gaps between adjacent 0° fibre tows (see the 3D volume). The voids are trapped at the periodic locations where the polyester yarns stitch across the thickness of the fabric, as can be observed from the XZ cross-section. Moreover, a smaller number of enclosed voids are also found to grow along the gaps between the off-axis fibre tows, as shown in the 3D volume and the XZ cross-section. Some spindle-shaped voids initiated from the surface stitches and develop along the off-axis tows are also seen from the 3D volumes. It was noticed that the YZ cross-section (highlighted in green) shows a seemigly-enclosed void at the interface but is shown in red. This is because the void is connected with the ambient on other unselected cross-section(s). For instance, the voids with greater volumes and close to the top-left corner of the 3D volume grow along the through-thickness stitching yarns and eventually develop across the outer $\pm 60^\circ$ sublayers and become a open void in connection with the ambient air. More voids behave in this way were found in specimens 6 and 7 shown in Figure 3 (b) and (c). Moreover, the waviness of the fabrics and the presence of voids lead to significant thickness variation, as depicted in the 2D views.

As the porosity increases to 2.24%, see specimen 6 shown in Figure 3 (b), a greater number of enclosed voids trapped by the stitches are found to elongate along the 0° fibre bundles next to the central interface. The 3D volume shows a small number of triangular enclosed 'platelets' (labelled in the 3D view). The platelets are initially formed at the central $0^\circ/0^\circ$ interface and then migrate to the adjacent $+60^\circ/+60^\circ$ interface along the stitching yarns and eventually exhibit as voids across the interfaces formed by fibres tows in three orientations as highlighted in the YZ cross-section. This 'lateral void migration along a stitching yarn' behaviour is also highlighted in the XZ 2D view, where the void appears at the middle interface is connected with ambient air, i.e. a typical characteristic of large volume voids in NCFs. An increase in the number of voids along the gaps between surface off-axis fibre tows are also observed in this specimen.

As the porosity increases to 3.47% (see specimen 7 shown in Figure 3 (c)), voids formed at the periodic stitching positions in the 0° sublayers expand along the central $0^\circ/0^\circ$ interface and shown as 'platelets' in the 3D view. Some of the periodic platelets join up and become

continuous hollow volumes at the $0^{\circ}/0^{\circ}$ interface as can be seen from the 3D volume and the XZ cross-section. It was noticed that the missing tows resulted in the shallow resin-deprive volumes on specimen surface. These 'dry spots' were mostly not accounted as voids by either acid digestion or the ambient occlusion CT post-processing algorithm.

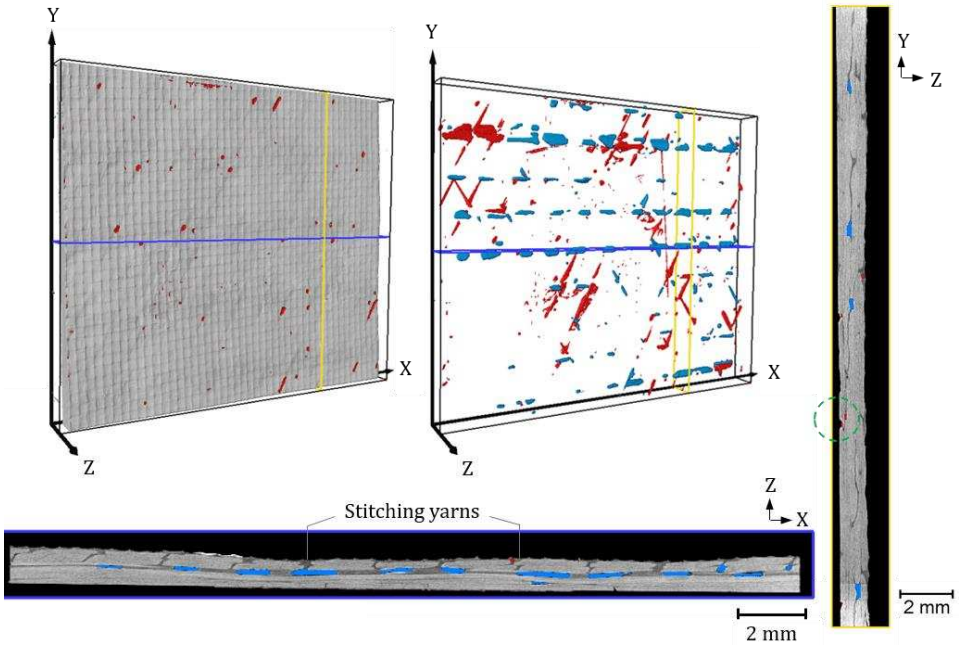

(a)

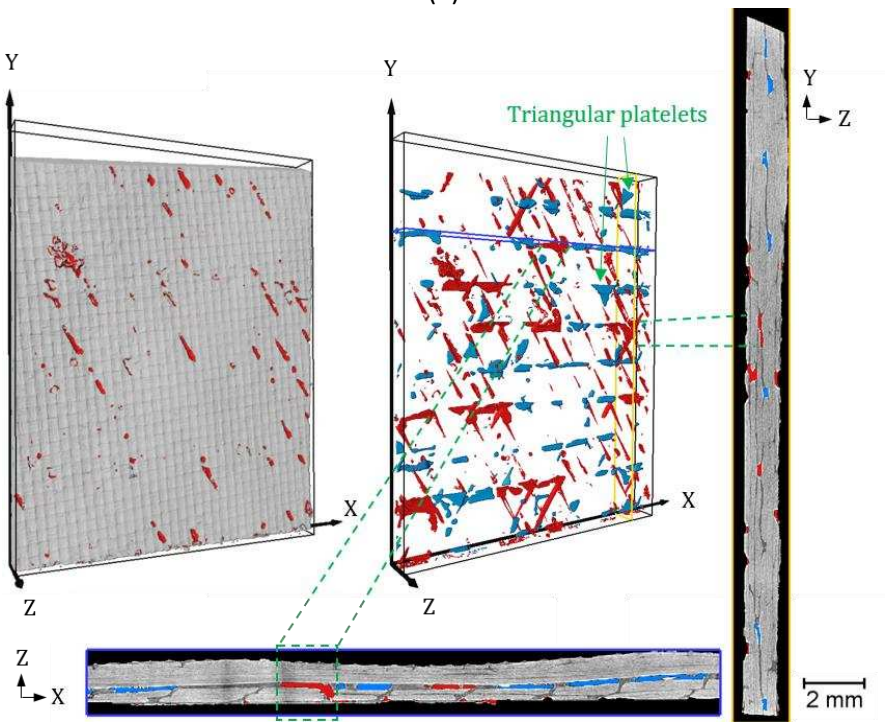

(b)

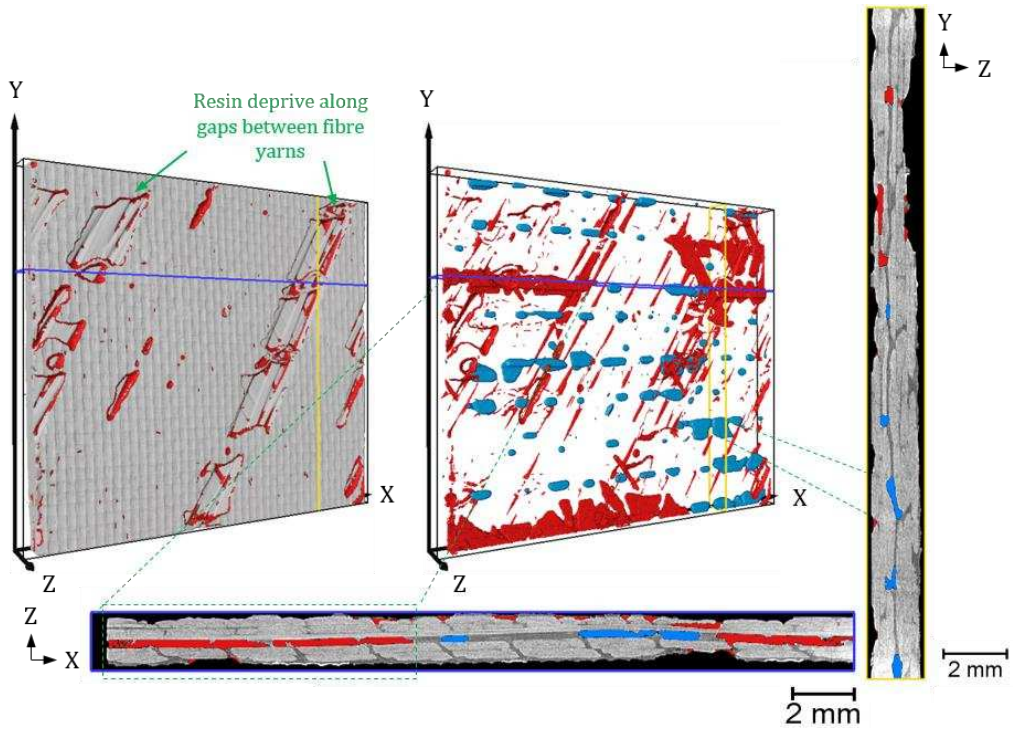

(c)

Figure 3. 3D volumes and 2D cross-sections of 25x25x~1.5 mm (in length/width/thickness) (a) specimen 4 with 1.79% porosities (measured by acid digestion), (b) specimen 6 with 2.24% porosities and (c) specimen 7 with 3.47% porosities post-processed using the ambient occlusion algorithm (the open and enclosed voids are highlighted in blue and red, respectively).

5. Conclusions

This paper evaluated porosities presented in carbon fibre NCF/epoxy laminates containing porosities in a range of 0 to 4%. Porosities generated by mimicking a practical 'leak vacuum bag' scenario using an out-of-autoclave method are assessed globally using an ultrasonic method performed in through-transmission mode. Microstructures and volume fractions of voids in miniature specimens cut from the laminates were analysed by X-ray CT scans. The porosity volumes were then compared with the measurements obtained by acid digestion of the specimens. Based on the obtained results, the follwong conclusions are drawn:

- The average ultrasound attenuation is generally linearly proportional to the volumes of porosities in ~1.5 mm thick miniature carbon fibre NCF/epoxy specimens.
- The 'ambient occlusion' segmentation algorithm provides a more accurate measurement of porosities presented in laminates manufactured with a leak bag, since the method captures both completely enclosed voids and partially buried ones coalescing with ambient air and provide porosity volumes close to those acquired from the acid digestion method;
- The X-ray CT 3D volumes and 2D cross-sections captured from the specimens with increased volumes of porosities indicate that the voids initially appear at the interface of two layers of NCFs are mostly entrapped at the periodic stitching positions in the two central 0° sublayers, as the void volume becomes greater than 2%, the ellipsoid voids elongate along the 0° stitching yarns, or migrate transversely toward the adjacent interfaces between off-axis

  doi:10.5075/epfl-298799_978-2-9701614-0-0

sublayers via the inter-tow empty spaces due to the presence of polyester yarns, forming 'platelets' and even 'hollow tunnels', i.e. a connection of a series of 'platelets'.

Acknowledgements

The authors would like to acknowledge Innovate UK for the financial support (Propound 2), Safran Nacelles (UK) for supplying manufacturing materials, Composite Integration (UK) for supplying a vacuum infusion machine, and Dr Alan Nesbitt and Mr Christopher Cowan (Northwest Composites Centre) for providing technical support. This work was supported by the National Research Facility for Lab X-ray CT (NXCT) through EPSRC grant EP/T02593X/1.

6. References

1. Mehdikhani M, Gorbatikh L, Verpoest I, Lomov S V. Voids in fiber-reinforced polymer composites: A review on their formation, characteristics, and effects on mechanical performance. Journal of Composite Materials 2019; 53:1579–669.
2. Stone DEW, Clarke B. Ultrasonic attenuation as a measure of void content in carbon-fibre reinforced plastics. Non-Destructive Testing 1975.
3. Titschack J, Baum D, Matsuyama K, Boos K, Färber C, Kahl WA, et al. Ambient occlusion – A powerful algorithm to segment shell and skeletal intrapores in computed tomography data. Computers and Geosciences 2018; 115:75–87.
4. User's Guide Avizo Software 2019. https://assets.thermofisher.com/TFS-Assets/MSD/Product-Guides/user-guide-avizo-software-industrial-inspection.pdf [Accessed 4th Mar 2022].

  doi:10.5075/epfl-298799_978-2-9701614-0-0

Coupling rheometry and computed tomography to study the evolution of voids during the consolidation of CF/PEKK composites

Raphaël Arquier[1,], Mario Scheel[2], Timm Weitkamp[2], Ilias Iliopoulos[1], Gilles Régnier[1], Guillaume Miquelard-Garnier[1]*

[1] *Laboratoire PIMM, UMR 8006, Arts et Métiers Institute of Technology, CNRS, Cnam, HESAM Universite, 151 boulevard de l'Hôpital, 75013 Paris, France*
[2] *Synchrotron SOLEIL, L'Orme des Merisiers, BP 48, Saint-Aubin, 91192 Gif-sur-Yvette, France*

*Email : raphael.arquier@ensam.eu

Abstract: One of the manners to optimize the consolidation quality of composites is to understand how the voids present within or between the tapes are reduced. This work proposes to study tomography scanned specimens (unidirectional and cross-ply), obtained from interrupted squeeze flow experiments on rheometer. Results show that inter-ply porosities are rapidly reduced and that the ply-ply interface is more rapidly indistinguishable for UD laminates than cross-ply ones suggesting a good {fiber + matrix} homogenization at the interface. It is also shown that intra-ply voids, surrounded by densely packed fibers are hardly reduced. These porosities limit the consolidation quality, suggesting that an effort in better separating the fibers during the pre-impregnation step is essential for the quality of composites.

Keywords : CF/PEKK composites, Synchrotron radiation, micro-tomography, porosity, consolidation

1. Introduction

Carbon fiber reinforced thermoplastic composites have gained interest over thermoset ones because of their recyclability and weldability, as well as quicker manufacturing processes [1,2]. The Polyaryletherketone (PAEK) family is commonly chosen as the matrix of such composites because of its high service temperature, high oxidation and chemical resistance and good impact properties [3,4]. Specifically, polyetherketoneketone (PEKK) has been developed for its versatility in terms of service and processing temperatures, which can be tuned by varying the terephtaloyl (T) and isophtaloyl (I) isomers ratio, [5,6] as shown in Figure 1.

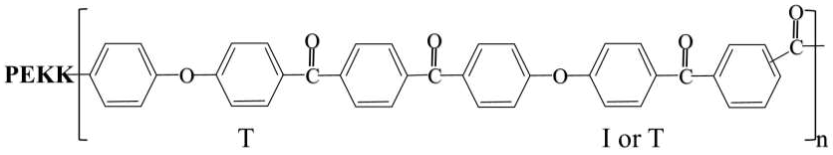

Figure 1: Chemical structure of PEKK

Nevertheless, optimizing the manufacturing of CF/PEKK composites, involving a pre-impregnation step, a placement step and a consolidation one, remains an open area of research. To do so, the rheology of the system responsible for the reduction of voids present within the ply (intra-laminar voids) and between the plies (inter-laminar voids) needs to be better understood. It is then proposed in this study to conduct interrupted squeeze flow experiments on UD (unidirectional) and cross-ply [0/90] CF/PEKK

tapes. The obtained samples are then characterized by high-resolution X-ray micro-computed tomography in order to visualize the microstructural evolution of the composite during consolidation, especially the size, location and shapes of the voids.

2. Materials and methods

2.1. Materials

Continuous (UD) tapes (plies) consist in PEKK with a T/I ratio equal to 70/30 (Arkema) impregnating Hexcel High Strength carbon fibers (Tensile strength ~5 GPa and young modulus ~240 GPa), with a fiber volume content about 60 v% and a thickness close to 200 µm (see a typical optical image of the tape in Figure 2).

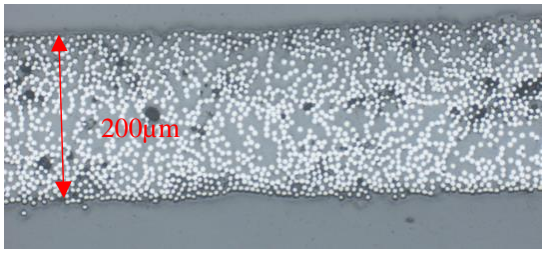

Figure 2: CF/PEKK tapes typical microstructure as observed with an optical microscope (x20). White circles represent the fibers, the grey area is the matrix and the black spots are the initial voids.

2.2. Equipment for squeeze flow experiments

Squeeze flow experiments are conducted on an Anton Paar MCR 502 rheometer with a plan-plan geometry (25 mm) in a constant surface configuration. This means that the samples initially fill all the surface of the plates such that, during all the experiment, the contact surface between the plates and the sample remains constant. The samples are cut into 25 mm diameter disks and then hand-laid up to stack manually UD 8-ply $[0]_8$ and cross-ply $[0/90]_4$ laminates. The laminate is carefully placed on the rheometer at T_1 (above T_g). Then heating occurs until T_2 ($T_2 > T_m$) at a constant force F=1 N to maintain contact between the plates and the sample. After a few minutes at T_2, a controlled ramp of force is applied till a value F_0 is reached (leading to a pressure around 1 bar, such as in VBO process). The force is then kept constant for the duration of the test. The whole procedure is schematized in Figure 3. Interrupted test are conducted where the sample is removed from the rheometer at certain times shown by the blue dots in Figure 3.

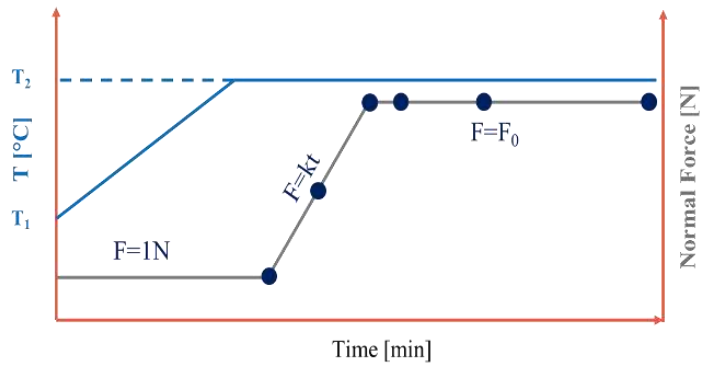

Figure 3: Temperature and normal force profiles of the squeeze flow experiments

2.3. Micro-computed tomography

The samples are cut into bar shape (with a cross section around 1.5 mm x 1.5 mm) using a diamond wire saw and fixed on a sample carrier for tomography measurements. The tomography measurements were made at the Anatomix beamline of Synchrotron SOLEIL [7]. A polychromatic ("white") X-ray beam with a central energy around 10 keV was used. The detector had 2048x2048 pixels; the effective pixel size was 0.65 µm. For each scan, 2000 projections were taken over an angular range of 180 degrees. The reconstructed volumes have a diameter and height of 1.3 mm. After tomographic reconstruction using the standard pipeline at the beamline and the PyHST2 reconstruction software [8], all volumes were post-treated with the ImageJ software [9] to quantitatively characterize the voids size, location and shape.

3. Results and discussion

Through the squeeze flow experiments on the rheometer, one can plot the variation of the laminate thickness as a function of time (Figure 4). The gap rapidly decreases when the force increases and stabilizes after about 15 min.

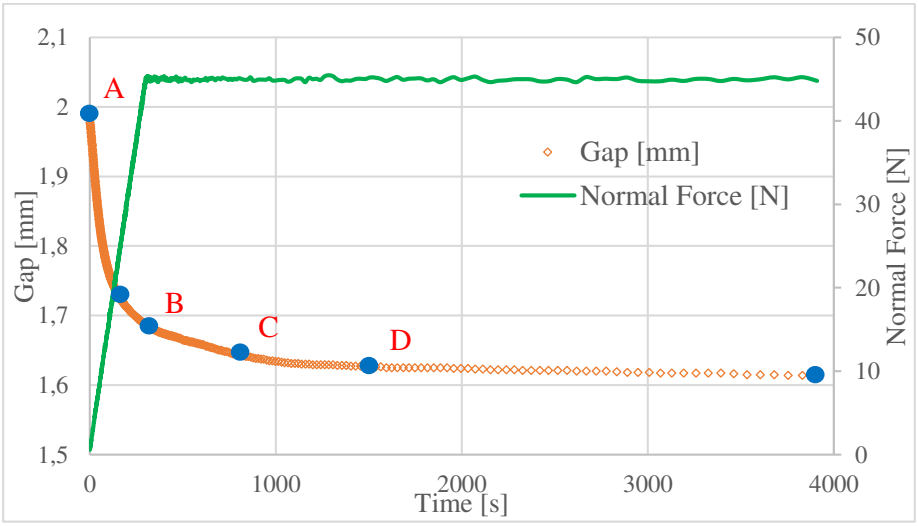

Figure 4: Evolution of the [0/90]$_4$ CF/PEKK laminate during the squeeze flow experiment. The blue dots represent the points where the test is interrupted. Letters A, B, C and D are for the four images shown in Figures 5 and 6

The observed porosities are strongly anisotropic, oriented along the fibers. They decrease in terms of size and quantity when the time of squeeze increases (Figure 5). The large thickness variation observed at the beginning of the experiment is mainly due to the tapes' initial surface roughness, which flatten under compression. Very rapidly, this rough interface between plies disappear and the laminate starts to form a homogeneous composite.

However, the voids present within the tapes remain, even for longer squeeze times (see Figure 5. D). Such porosities appear surrounded by very dense areas of fibers. During the impregnation step, some fibers have not been sufficiently separated leading to a poor matrix impregnation in these areas and the presence of trapped voids. The pressure applied (close to 1 bar) combined with high matrix viscosity cannot enable the filling of these voids in a reasonable squeeze time. Hence, it is suggested here, that, for VBO consolidation, an effort should be done on the homogenization of the {fiber + matrix} repartition.

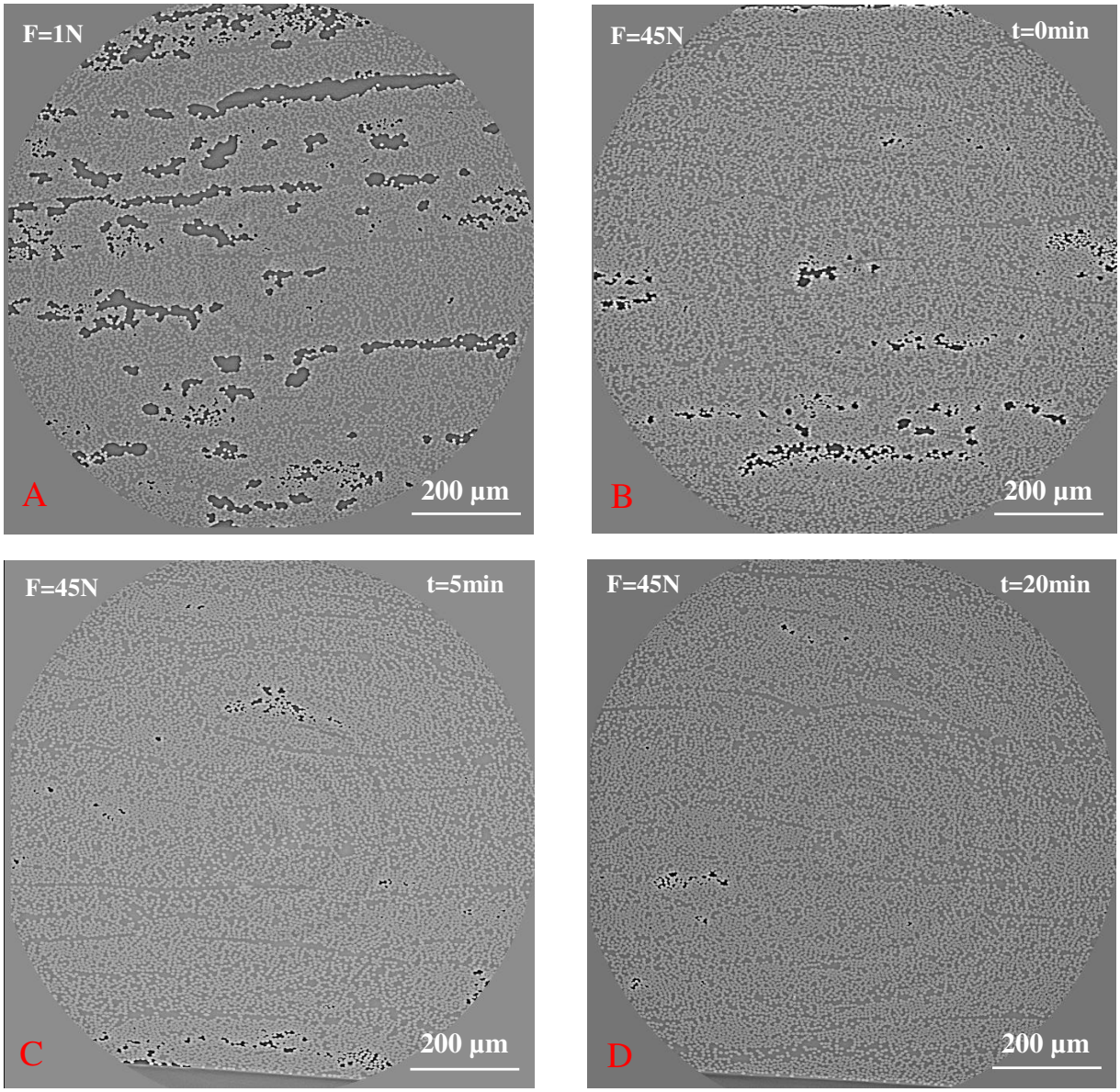

Figure 5: Tomography images, orthogonal to the fibers direction, of the squeezed UD $[0]_8$ laminates for four different moments: A, B, C and D shown in Figure 4.

Quite similar results can be extracted from the tomography measurements on cross-ply [0/90] laminates (Figure 6). As for UD laminates, the voids are progressively reduced; inter-laminar voids seem to disappear faster than intra-laminar ones; porosities trapped are not able filled by the matrix during the time of the experiment.

Nevertheless, contrary to UD laminates, the individual plies can be distinguished late in the process, as shown by the green arrows. This is explained by the fact that cross-ply stacking leads rapidly to fibers blocking, while fibers in the same orientation favor the interpenetration of one ply towards the other.

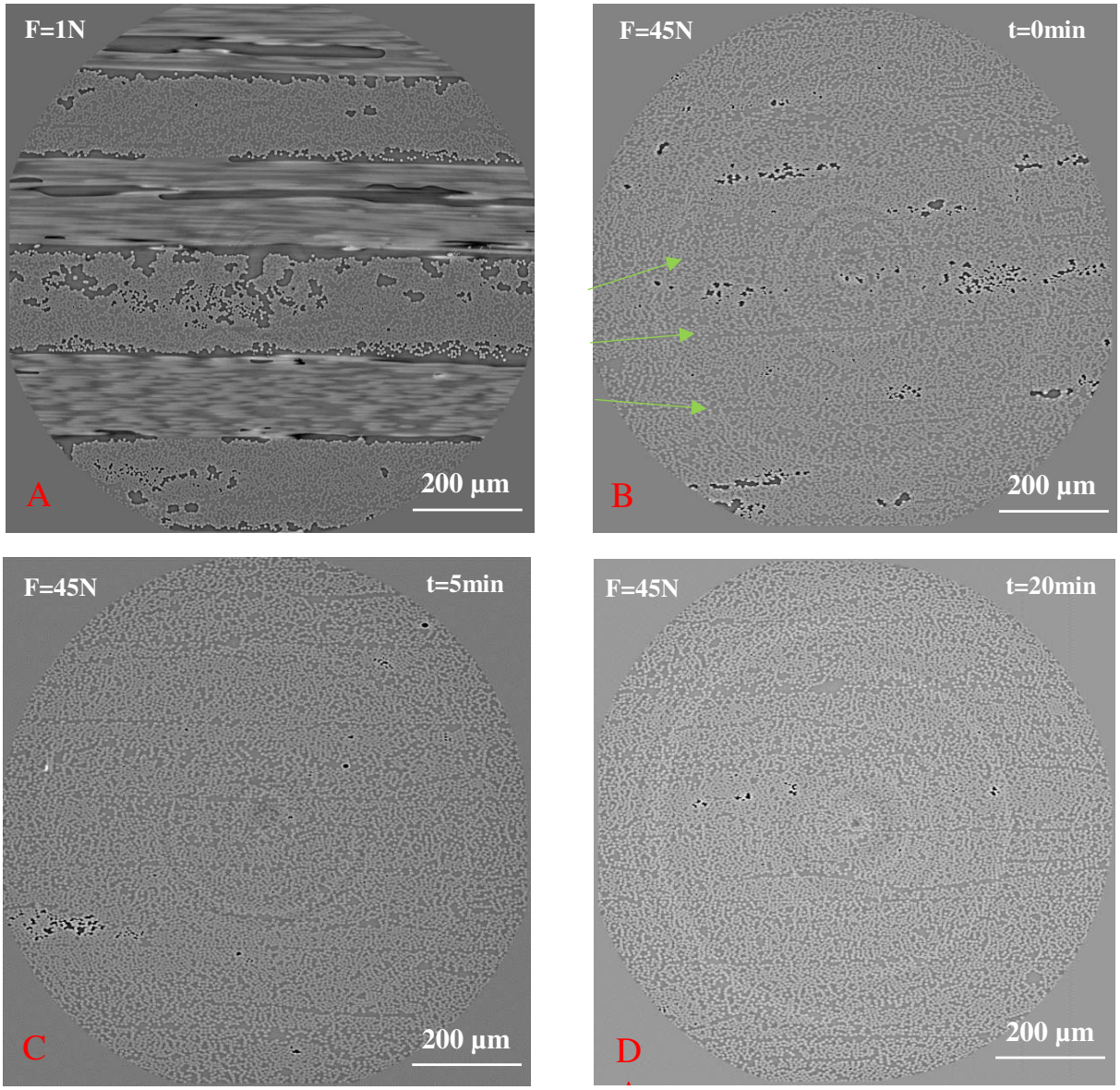

Figure 6: Tomography images of the squeezed cross-ply $[0/90]_4$ laminate for four different moments: A, B, C and D shown in Figure 4. In A, the slice is either parallel to the fibers (plies with lines of fibers) or transverse to the fibers (plies with circular fibers). The view of the three other images (B, C, and D) is either at 45° or -45° towards the fibers, hence the elliptical shape of the fibers in the images.

At the beginning of consolidation, the matrix flows first and fills the inter-laminar voids leading to resin-rich regions at the interface but, with time, local micro movement of fibers lead to a homogenization at the interface in terms of {fibers + matrix} repartition (see Figure 6.C and D).

4. Conclusion

This work studies the evolution of voids during consolidation of CF/PEKK by visualizing tomography scans of UD and [0/90] laminates through interrupted squeeze flow tests. It is observed that inter-ply porosities are rapidly reduced whereas those within the plies, surrounded by high concentrated fibers areas, are much more hardly filled. A progressive homogenization in terms of {fibers + matrix} repartition at the ply-ply interface is also highlighted for the cross-ply [0/90] laminates.

5. Acknowledgments

The work presented here is developed under HAICoPAS framework, a PSPC (Projet de Recherche et Dévelopement structurant pour la compétitivité) project. BPI France is acknowledged for funding Raphaël ARQUIER's PhD thesis (Projet number: PSPC.AAP-7.0_HAICoPAS). Hexcel and Arkema, and more specifically Lucien FIORE, Stéphanie LAMBOUR, Nicolas CADORIN, Mayeul DUCROT, Michel GLOTIN, Henri-Alexandre CAYZAC, Yves DEYRAIL and Sylvie GIRAULT are thanked for fruitful discussions. Industrial Chair Arkema (Arkema/CNTS-ENSAM-Cnam) is acknowledged for support.

The authors thank Synchrotron Soleil for the ANATOMIX beamline time (proposal n° 20210363). ANATOMIX is an Equipment of Excellence (EQUIPEX) funded by the *Investments for the Future* program of the French National Research Agency (ANR), project *NanoimagesX*, grant no. ANR-11-EQPX-0031.

6. References

[1] Clyne TW, Hull D. An Introduction to Composite Materials. Second Edi. In: Cambridge Solid State Science Series; 2019.

[2] Vaidya UK, Chawla KK. Processing of fibre reinforced thermoplastic composites. Int Mater Rev 2008;53:185–218. https://doi.org/10.1179/174328008X325223.

[3] Choupin T, Fayolle B, Régnier G, Paris C, Cinquin J, Brulé B. Isothermal crystallization kinetic modeling of poly(etherketoneketone) (PEKK) copolymer. Polymer (Guildf) 2017;111:73–82. https://doi.org/10.1016/j.polymer.2017.01.033.

[4] Choupin T, Fayolle B, Régnier G, Paris C, Cinquin J. A more reliable DSC-based methodology to study crystallization kinetics : Application to poly (ether ketone ketone) (PEKK) copolymers. Polymer (Guildf) 2019;155:109–15. https://doi.org/10.1016/j.polymer.2018.08.060.

[5] Choupin T, Debertrand L, Fayolle B, Régnier G, Paris C, Cinquin J, et al. Influence of thermal history on the mechanical properties of poly(ether ketone ketone) copolymers. Polym Cryst 2019;2:1–8. https://doi.org/10.1002/pcr2.10086.

[6] Veazey D, Hsu T, Gomez ED. Next generation high-performance carbon fiber thermoplastic composites based on polyaryletherketones. J Appl Polym Sci 2017;134:19–21. https://doi.org/10.1002/app.44441.

[7] Weitkamp T, Scheel M, Giorgetta J, Joyet V, Le Roux V, Cauchon G, et al. The tomography beamline ANATOMIX at Synchrotron SOLEIL. J Phys Conf Ser 2017;849:012037. https://doi.org/10.1088/1742-6596/849/1/012037.

[8] Mirone A, Brun E, Gouillart E, Tafforeau P, Kieffer J. The PyHST2 hybrid distributed code for high speed tomographic reconstruction with iterative reconstruction and a priori knowledge capabilities. Nucl Instruments Methods Phys Res Sect B Beam Interact with Mater Atoms 2014;324:41–8. https://doi.org/10.1016/j.nimb.2013.09.030.

[9] Schneider CA, Rasband WS, Eliceiri KW. NIH Image to ImageJ: 25 years of image analysis. Nat Methods 2012;9:671–5. https://doi.org/10.1038/nmeth.2089.

TRANSLAMINAR FRACTURE OF THIN-PLY COMPOSITES: A NOVEL DESIGN FOR 4D SYNCHROTRON COMPUTED TOMOGRAPHY

Sina, AhmadvashAghbash[a], Mahoor, Mehdikhani[a], Yentl, Swolfs[a]

a: Department of Materials Engineering, KU Leuven, Kasteelpark Arenberg 44 bus 2450, Belgium – *sina.ahmadvashaghbash@kuleuven.be*

Abstract: *A novel design of compact tension specimen, allowing for 4D synchrotron radiation computed tomography, is developed and used, for the first time, to characterise the translaminar fracture of thin-ply composites at the microscale. The mini compact tension specimens are manufactured with thin-ply carbon-epoxy prepregs in $[90_2/0/90_2/0/90_2/0/90_2]$ lay-up configuration. Afterwards, software tools for the training of deep neural networks are employed to segment the acquired images and build a 3D visualisation of the progressive crack. The results reveal advancing crack fronts in the 90° plies and lagging fronts in the 0° plies.*

Keywords: Translaminar fracture; synchrotron radiation computed tomography; thin-ply composites; deep learning.

1. Introduction

The fracture behaviour of laminated fibre-reinforced polymers (FRPs) can be classified into three types. The intralaminar and interlaminar fracture, where the crack propagates parallel to the fibre direction, have been examined comprehensively in the literature. The interest in the third type, translaminar fracture, has grown in the last 15 years despite being an important failure type as it governs the damage tolerance and notch sensitivity of a fibre-reinforced composite [1]. The translaminar fracture toughness is the toughness associated with a crack propagating perpendicular to the fibre direction, thus fracturing the fibres.

In conventional brittle fibre composites, such as carbon and glass fibre composites, the main energy dissipating mechanisms during translaminar fracture are fibre-matrix debonding and fibre pull-out. The visual examination of the translaminar fracture surface of carbon fibre reinforced laminates (fracture surface associated with the tensile failure of the fibres), reportedly, reveals a hierarchical organization of fibre pull-outs, where single fibres are pulled out of small bundles, which in turn are pulled out of larger bundles [2,3]. However, the majority of these observations are limited to the fracture surface of a post-mortem specimen, which cannot reveal all details of the in-situ failure mechanisms.

This study aims to design a new compact tension specimen that, in addition to being geometrically suitable for 4D synchrotron radiation computed tomography (SRCT), can yield stable crack propagation. This design will allow observing the translaminar failure mechanisms in thin-ply composites in more detail and provide more insight than what the frequently used post-mortem analyses can achieve.

2. Specimen Design

The translaminar fracture cannot be tested on unidirectional laminates, since the specimens would fail in shear rather than yielding propagation of the crack across the fibres. Therefore,

  doi:10.5075/epfl-298799_978-2-9701614-0-0

cross-ply laminates are used. A composite panel made of HS40 fibres and ThinPregTM 736LT resin with a nominal thickness of 50.8 μm and lay-up of $[90_2/0/90_2/0/90_2/0/90_2]$ was manufactured in an autoclave. Subsequently, the panel was water-jet cut to the 3 proposed compact tension specimens designs for 4D SRCT, as shown in Figure 1. The first design is based on the doubly-tapered compact tension [4], the second, Pac-Man, is inspired by the curved compact tension specimen [5], and the last design, entitled mini-protruded, is proposed to increase the crack propagation stability and capture the plateau region on the R-curve (energy release rate vs. the crack extension length).

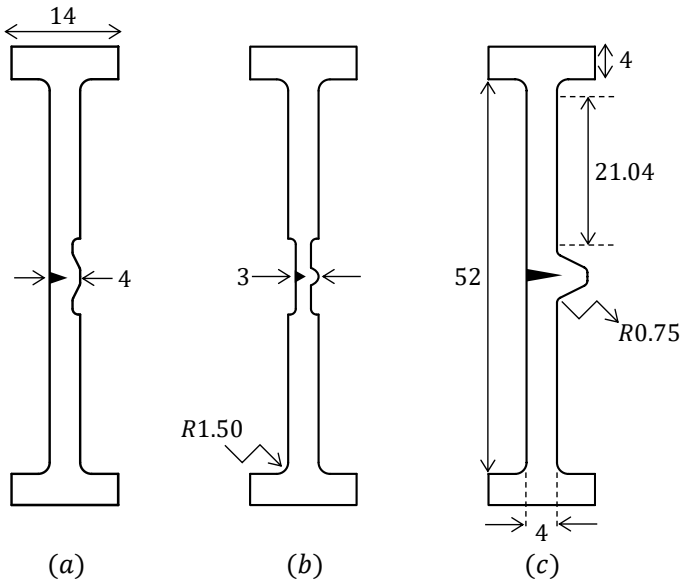

Figure 1. Schematics of the three proposed specimen designs: (a) mini-doubly-tapered, (b) Pac-Man, and (c) mini-protruded compact tension specimens (values are in mm).

3. Synchrotron Radiation Computed Tomography

SRCT uses synchrotron light to perform computed tomography (CT) scans. It consists of highly coherent, parallel X-rays, which yield SRCT radiographs with better clarity and contrast than radiographs obtained via lab-scale CT scanners. This special X-ray radiation is created by undulating and bending electron paths inside the synchrotron storage ring using strong magnets. Electrons are continuously supplied by a particle accelerator in the centre of the synchrotron. After traversing the specimen in the field of view, the synchrotron light is turned into visible light using a scintillator and captured using a camera with magnifying optics [6].

The versatile and lightweight (1 kg) Deben CT500 in-situ testing stage is suitable for mounting on most µCT systems. The adaptable tube length and in-house redesigned tensile jaws, combined with the motor speed range of 0.1 mm/min to 1.0 mm/min, allow testing samples of variable length and shape and performing in-situ imaging of how materials behave under different loading conditions. Figure 2 illustrates the mini-protruded compact tension specimen with a 4 mm pre-crack mounted in the rig.

The experiments were carried out under continuous loading and scanning condition using the ultra-fast SRCT at the TOMCAT beamline of the Swiss Light Source (SLS) at the Paul Scherrer Institut (PSI) in Villigen, Switzerland. In the conducted experiments, a voxel size of 800 nm was achieved. The GigaFRoST camera was employed as the detector, and a polychromatic beam with an energy of 24 keV was used. The scans were reconstructed using the SLS in-house absorption-

based algorithm (Gridrec) [7] for the critical points during the test (before and after a load drop, see Figure 3a). Figure 3 shows the load-displacement curves obtained for all three designs, revealing that only the mini-protruded design yields stable crack propagation and the other two designs displayed sudden failure.

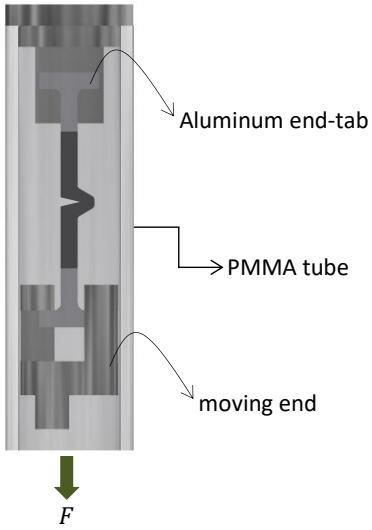

Figure 2. Schematics of the mini-protruded compact tension specimen mounted in tensile jaws.

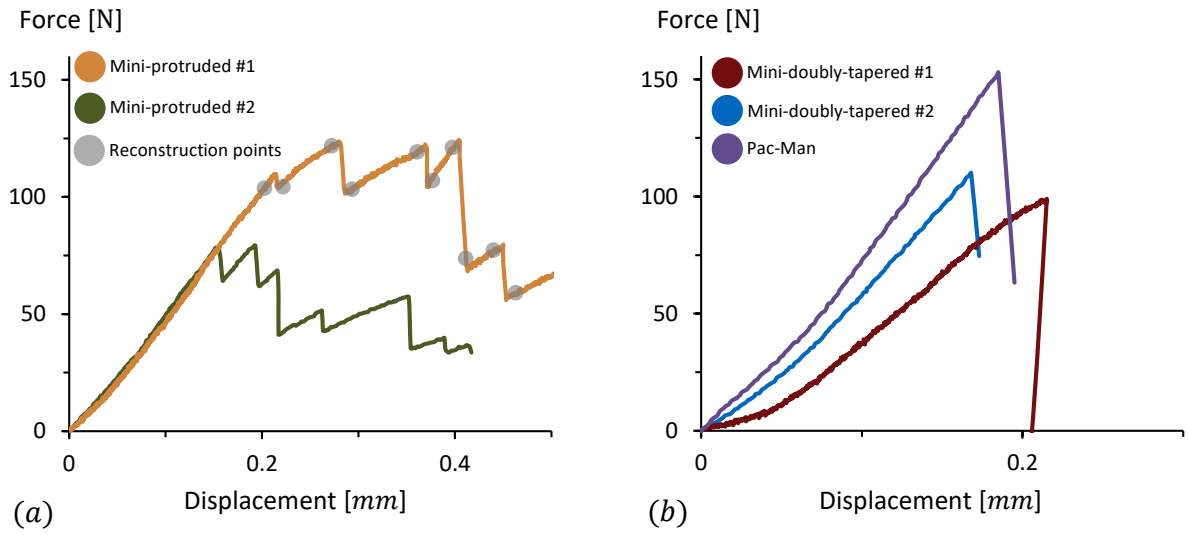

Figure 3. Force-displacement curves form the experiments: (a) successful tests from 2 mini-protruded specimens with 4 mm pre-crack, and (b) 3 unsuccessful tests based on the other two suggested designs (grey dots on the mini-protruded #1 are the critical points that have been selected for the volume reconstruction and further analysis).

4. Image Analysis

Following the reconstructions, the analysis of the 3D rendered volumes (Figure 4) and 2D slices (Figure 5), using any image processing software (such as Avizo), indicates the in-situ shape of the pulled-out fibre bundles in the 0° plies and dissimilar crack front advancements in the 0° and 90° plies. Initially, RootPainter [8], a GUI-based segmentation tool, based on rapid training of deep neural networks, was used to segment the crack volume in the acquired tomograms.

RootPainter allows both fully-automatic and semi-automatic image segmentation. Similarly, Dragonfly, as an advanced analysis and visualization software, includes deep learning segmentation algorithms. This tool is user-friendlier than RootPainter. Succeeding the training procedures, Figure 6 shows the results of segmentation carried out via both software. Initial analysis proves that the segmentation can visualise and isolate the crack development per volume and can be used to approximate the in-situ shape of the pulled-out fibre bundles. These observations can further enrich the existing analytical or finite element models for the translaminar fracture in FRPs.

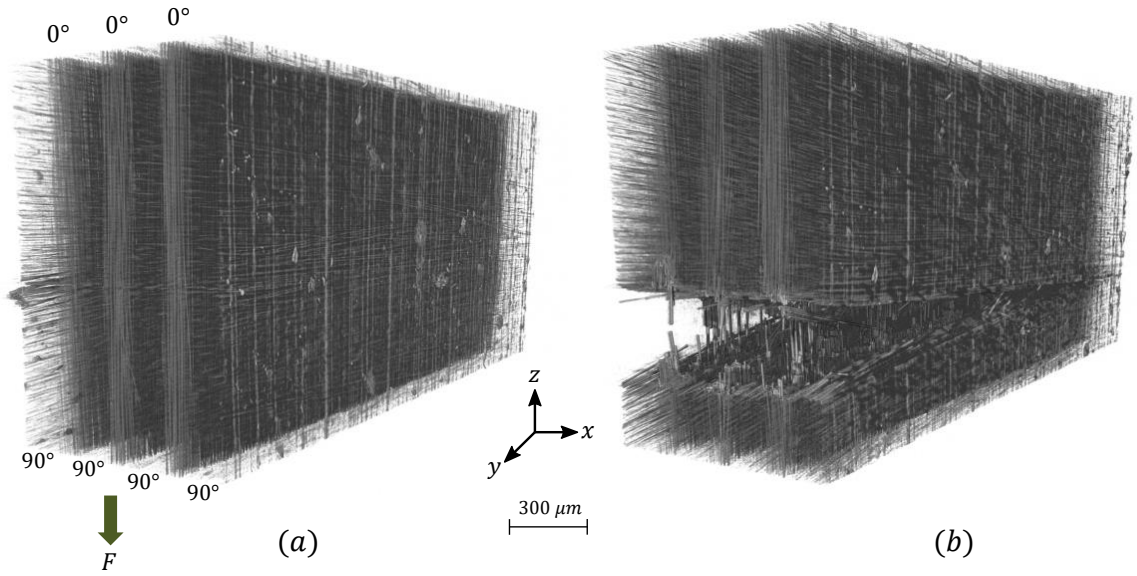

Figure 4. 3D Volume rendering of (a) the first, and (b) the last load step of a mini-protruded compact tension specimen.

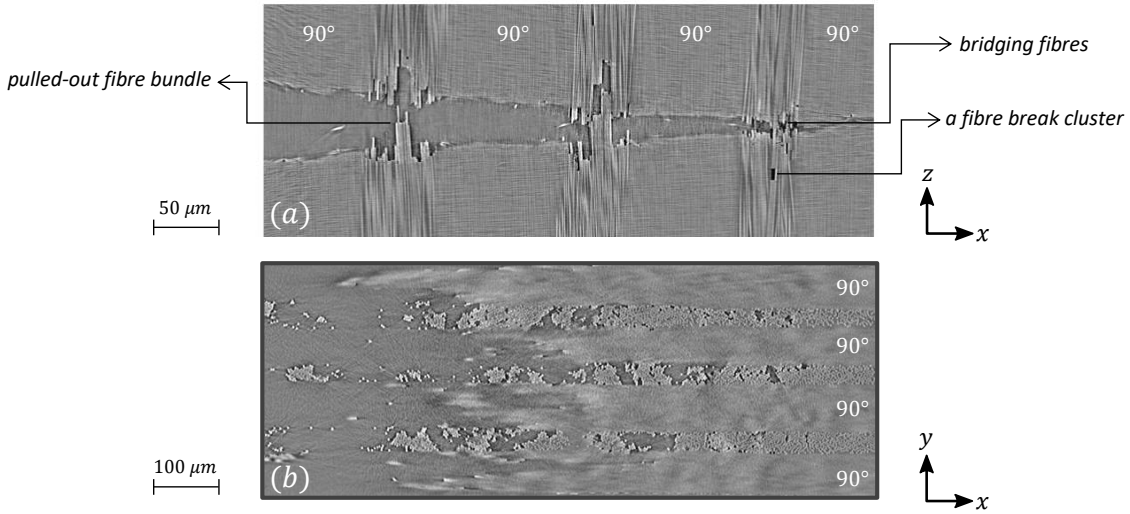

Figure 5. 2D slices of the last load step of a mini-protruded compact tension specimen indicating (a) the shape of the pulled-out fibre bundles and possible fibre break clusters, and (b) advancing crack fronts in the 90° and lagging crack fronts in the 0° plies.

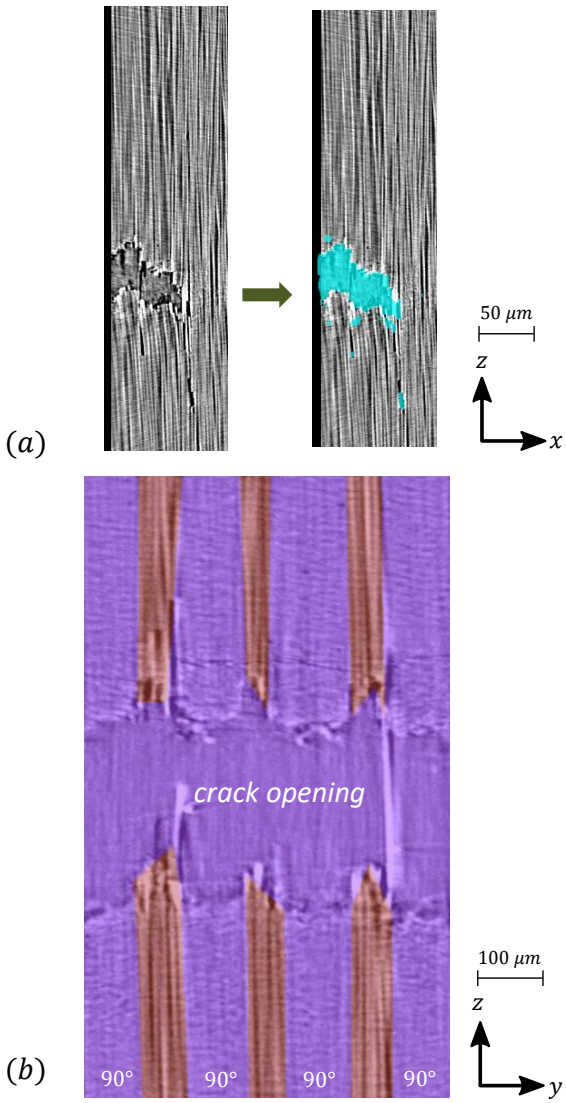

Figure 6. Image segmentation results: (a) example input and segmentation output showing the segmented crack in a fractured region of a 0° ply via RootPainter, and (b) the segmented 0° plies providing the shape of the pulled-out fibre bundles via Dragonfly software.

5. Conclusions

Three proposed mini compact tension specimen prototypes, allowing for 4D synchrotron radiation computed tomography, were investigated for their competence in characterising the translaminar fracture of thin-ply composites at the microscale. Among the proposed designs, the mini-protruded design, with a pre-crack half its length, results in stable crack propagation. The 2D slices reveal advancing crack fronts in the 90° plies and lagging fronts in the 0° plies on the laminate fracture surface. Using deep learning image segmentation software tools, the acquired images are segmented to yield a 3D visualisation of the progressive crack and the shape of the pulled-out fibre bundles. Further extensions to the current work may include assessing the 0° ply-block thickness effect on the developed failure mechanisms. This study has significant implications for the development of analytical and numerical damage propagation models used for design and damage-tolerance analysis.

  doi:10.5075/epfl-298799_978-2-9701614-0-0

Acknowledgements

The research leading to these results has been done within the framework of HyFiSyn project and has received funding from the European Union's Horizon 2020 research and innovation programme under the Marie Skłodowska-Curie grant agreement No. 765881. M. Mehdikhani would like to acknowledge his FWO Postdoc Fellowship, project ToughImage (1263421N).

6. References

1. Geboes Y, Katalagarianakis A, Soete J, Ivens J, Swolfs Y. The translaminar fracture toughness of high-performance polymer fibre composites and their carbon fibre hybrids. Composites Science and Technology 2022; 221.

2. Pinho ST, Robinson P, Iannucci L. Fracture toughness of the tensile and compressive fibre failure modes in laminated composites. Composites Science and Technology 2006; 66:2069–2079.

3. Laffan MJ, Pinho ST, Robinson P, Iannucci L. Measurement of the in situ ply fracture toughness associated with mode I fibre tensile failure in FRP. Part I: Data reduction. Composites Science and Technology 2010; 70:606–613.

4. Blanco N, Trias D, Pinho ST, Robinson P. Intralaminar fracture toughness characterisation of woven composite laminates. Part I: Design and analysis of a compact tension (CT) specimen. Engineering Fracture Mechanics 2014; 131:349–360.

5. Katafiasz TJ, Iannucci L, Greenhalgh ES. Development of a novel compact tension specimen to mitigate premature compression and buckling failure modes within fibre hybrid epoxy composites. Composite Structures 2019; 207:93–107.

6. Breite C. Aligning Fibre Break Models for Composites with the Observable Micro-Scale Material Behaviour (PhD Thesis) 2020; KU Leuven.

7. Marone F, Stampanoni M. Regridding reconstruction algorithm for real-time tomographic imaging. Journal of Synchrotron Radiation 2012; 19:1029–1037.

8. Smith AG, Han E, Petersen J, Olsen NAF, Giese C, Athmann M, Dresbøll DB, Thorup-Kristensen K. RootPainter: Deep Learning Segmentation of Biological Images with Corrective Annotation. *bioRxiv* 2020; 1–16.

DEVELOPMENT OF THE ASTM D8336 21: STANDARD TEST METHOD FOR CHARACTERIZING TACK OF PREPREGS USING A CONTINUOUS APPLICATION AND PEEL PROCEDURE

Davide S.A. De Focatiis, Gabriel Y.H. Choong, Adam Joesbury and Andreas Endruweit

Faculty of Engineering, University of Nottingham, UK – davide.defocatiis@nottingham.ac.uk

Abstract: *An ASTM standard test method for the characterisation of prepreg tack was recently approved based on research undertaken over the past decade. In this method, a prepreg is applied to a substrate under controlled rolling pressure and immediately peeled off at a controlled rate and temperature using a custom fixture. The method caters for measurement of ply-to-tool and ply-to-ply tack, and, through the use of time-temperature superposition, a tack mastercurve can be constructed to identify peak tack at the transition between adhesive and cohesive failure of the formed bond. This paper provides an overview of the underlying research and discusses the process of successfully passing an ASTM ballot. Currently a team of 12 industrial partners and research institutions are undertaking a round-robin exercise required to prove the usefulness of the standard in terms of lab-to-lab repeatability and reproducibility of experimental data. Some insights into this process are also discussed.*

Keywords: Adhesive tack; time-temperature superposition; standardization; prepreg; peel.

1. Introduction

Automated Material Placement (AMP) processes, including Automated Tape Laying and Automated Fibre Placement, are commonly used in the manufacture of large composite components, particularly, but not exclusively, in the aerospace sector. In these processes, layers of prepreg tape are applied to the surface of a tool or to previously deposited layers of tape at controlled orientations to form a laminate. Prepregs are commonly made from carbon fibre impregnated with a partially cured viscoelastic thermosetting resin. In order to prevent the formation of defects such as wrinkling or bridging due to the presence of axial forces in the prepreg tape, a sufficient level of both prepreg-to-tool and prepreg-to-prepreg adhesion (tack) is necessary which prevents debonding at the interfaces. Although the laminate will undergo further processing stages after lay-up (typically, consolidation and curing in an autoclave), defects formed during the lay-up phase may have a detrimental effect on the achievable quality of the finished composite component.

As the lay-up quality is related to the level of tack between the prepreg and either the tool surface or the surface of an adjacent prepreg layer, tack has an effect on the product properties. The experimental characterisation of prepreg tack is therefore a prerequisite for the understanding of the behaviour of a prepreg during processing, and for the selection of appropriate process parameters to obtain optimum lay-up performance. A recent comprehensive review covers the mechanisms of tack and the broad range of associated measurement methods [1], many of which are based on techniques from the pressure sensitive adhesives literature, and not always easy to apply or interpret with respect to prepregs. In the late 2000s, Crossley et al. developed a simple experimental technique specifically for the

  doi:10.5075/epfl-298799_978-2-9701614-0-0

measurement of prepreg-to-tool tack under conditions mimicking AMP processes [2]. Following initial studies, the design of the experimental fixture and the method for processing and interpretation of the acquired data have been refined, and the effects of a wide range of parameters have been further studied [3]. Aiming at consistency of data in industrial supply chains, this eventually led to the formulation of an ASTM standard, namely D8336 21: Standard Test Method for Characterising Tack of Prepregs Using a Continuous Application and Peel Procedure [4], which was approved in March 2021. This paper provides an overview of the test method detailed in the standard and of the issues encountered during the process of developing the ASTM standard.

2. The test method

2.1 Basic principle and test fixture

The continuous application-and-peel method for prepreg tack testing has been previously explained in detail by Crossley et al. [2], and only a brief overview is given here. In this context, tack between a prepreg specimen and a rigid substrate is defined quantitatively as the force required to peel the prepreg from the substrate at a given specimen width, peel speed and temperature. Rectangular prepreg specimens are laid up on rectangular steel substrates without applying any compaction pressure. The substrates with specimens are then loaded into a custom test fixture comprising two pairs of rigid rollers. The first pair of rollers provides guidance, while the second pair consists of the top, fixed peel roller, and the bottom compaction roller. The latter is designed to move vertically to apply a normal force on the substrate, pressing the prepreg against the peel roller at a known compaction force, achieved through springs of adjustable length. The entire assembly is mounted on the base of a Universal Testing Machine. One end of the prepreg specimen is attached to the moving cross-head and load cell of the test machine via a custom material clamp, by bending the specimen around the peel roller (upwards) towards the clamp.

During a tack test, the cross-head moves vertically away from the fixture at a constant speed, pulling the specimen assembly through the rollers in a horizontal direction, as shown in Figure 1. This results in the prepreg being bonded to and immediately peeled from the substrate in a single continuous motion at a peel rate corresponding to the speed of the cross-head. The tack force is derived from the force measured at the load cell, recorded as a function of the cross-head displacement. In order to do this, a section of the prepreg is prevented from adhering to the substrate (and thus peeling with no force) using a separating film at the interface. The measured average force required to pull the assembly through the fixture in this region, denoted as phase 1, records dissipative effects arising from friction and bending the prepreg only. It is subtracted from the measured average force required to pull the assembly in the following region, denoted as phase 2. In this second phase, the force is determined by the adhesion of the prepreg to the substrate, but is also affected by the same dissipative effects as phase 1.

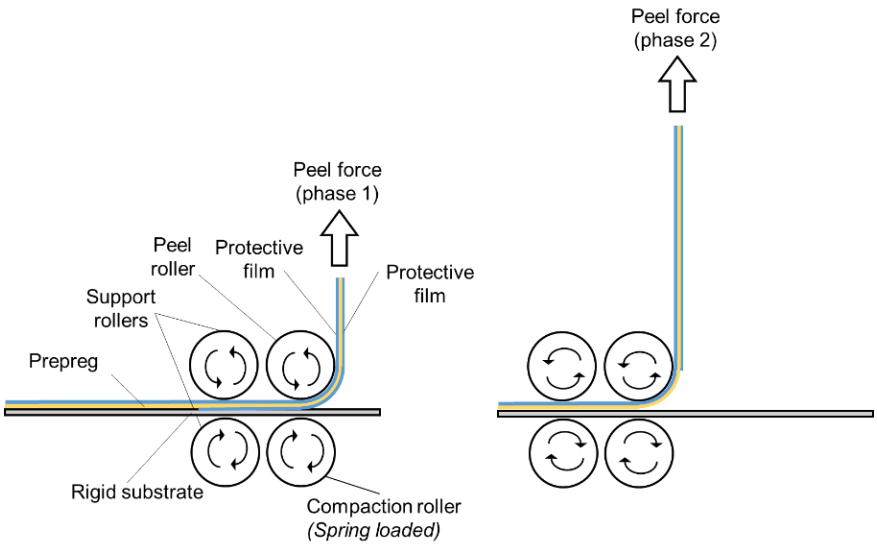

Figure 1. Schematic of a prepreg-to-tool tack test during the two phases of measurement. Protective film separates prepreg and substrate in phase 1, while interface between prepreg and substrate can form in phase 2.

The test method was later extended to allow tack to be measured for material combinations other than prepreg-to-tool, most notably prepreg-to-prepreg. This is achieved by bonding a flat layer of uncured prepreg to the metal substrate using a standard pressure-sensitive adhesive, and using this combined assembly as the substrate [3]. The test fixture was also modified to allow the rigid peel roller to be swapped for a compliant one with properties akin to rollers on industrial AMP machinery.

The entire tack testing fixture and material clamp can be enclosed in an environmental chamber, as shown in Figure 2a. This allows experiments to be conducted at different temperatures as well as different feed rates, which is necessary to explore the effect of viscoelastic resin properties on tack.

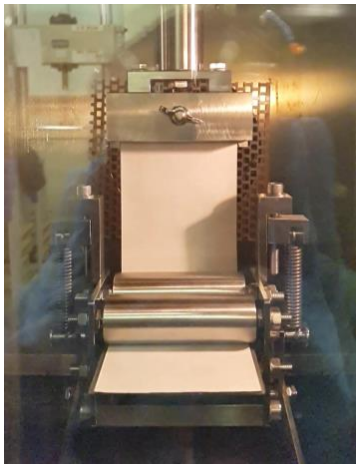

(a)

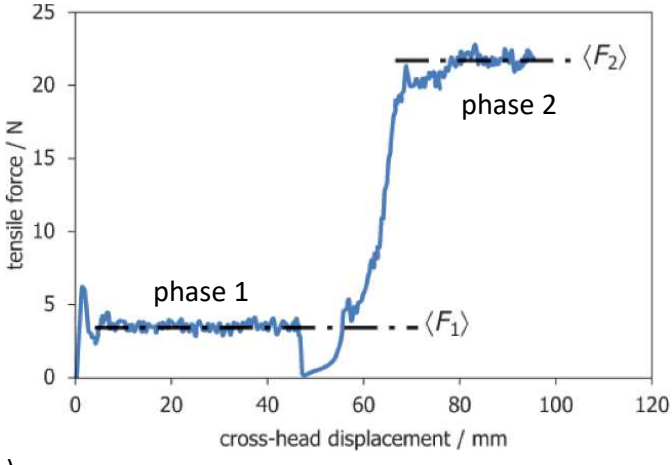

(b)

Figure 2. (a) The fixture inside an environmental chamber loaded with a prepreg specimen and ready for a test to begin; (b) representative force data as a function of the displacement recorded during a tack test.

2.2 Data processing

An example of the force as a function of the cross-head displacement, measured during a tack test, is shown in Fig. 2b. The first part of the curve corresponds to the dissipative effects arising from friction and bending the prepreg, which is characterised by an average value, $\langle F_1 \rangle$. In the second part, the force required to overcome the adhesion between the prepreg and the substrate is recorded in addition to the force arising from dissipative effects. This force has an average value, $\langle F_2 \rangle$. The difference between the two average values of force, $\langle F_2 \rangle$ - $\langle F_1 \rangle$, is reported as the tack of the prepreg

- on a defined surface,
- at a defined compaction pressure,
- at a defined temperature,
- and a defined peel rate.

Typically, tack tests for any prepreg are conducted at multiple combinations of peel rate and temperature (at a given compaction pressure). The example in Figure 3 shows the measured tack force as a function of the feed rate (which is identical to the peel rate) at different test temperatures. Here, prepreg-to-prepreg tack was measured. It is observed that, at low test temperatures (20 °C and 30 °C), a maximum in tack occurs at low feed rates. With increasing measurement temperature, the maximum in tack moves to higher feed rates (at 40 °C and 50 °C). Tack levels in a given range of rates increase with increasing temperature (20 °C and 30 °C) and then decrease again as the temperature increased further (40 °C to 50 °C). These observations are a reflection of the viscoelastic behaviour of the resin in the prepreg.

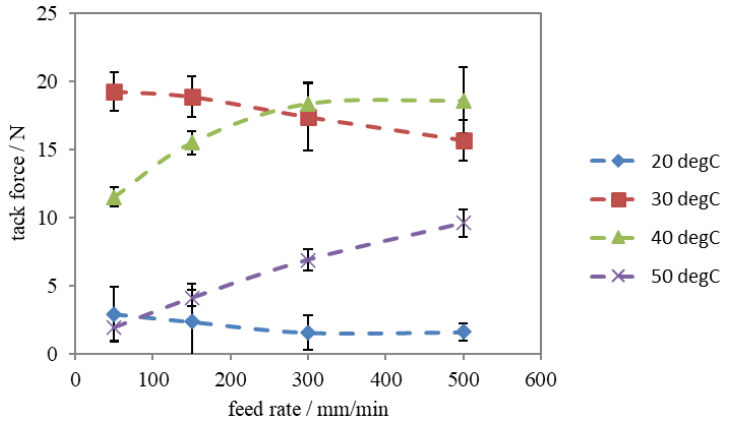

Figure 3. Example data for the tack force as a function of the feed rate, measured at different test temperatures [3].

2.3 Tack mastercurves

For a set of tack values acquired at different temperatures and rates, the principle of time-temperature-superposition (TTS) is applicable. This implies that the tack (i.e. a force) measured at a known test temperature and feed rate is equivalent to tack at an arbitrary reference temperature and a shifted feed rate, which is calculated from the rate and temperature of the test, the reference temperature and time-temperature shift parameters relating to the resin properties [5]. These parameters can be determined from rheological experiments on the resin used in the prepreg.

Figure 4 shows the same data plotted in Figure 3, but now the rates have been shifted to a reference temperature of 20 °C using TTS. The figure shows that data points acquired at all test temperatures lie on a curve (considering the uncertainty in determining each individual data point), which can be approximated by a Gaussian. To the left of the maximum of the Gaussian, i.e. at lower feed rates, tack is limited by cohesive failure in bonds formed between the prepreg and the substrate. During a test long drawn-out resin threads may be observed at the interface ("fibrillation"). To the right of the maximum of the curve, i.e. at higher feed rates, tack is dominated by adhesive failure, and minimal or no formation of resin threads is observed between the surfaces. At different temperatures, the maximum in the Gaussian will occur at different (shifted) rates.

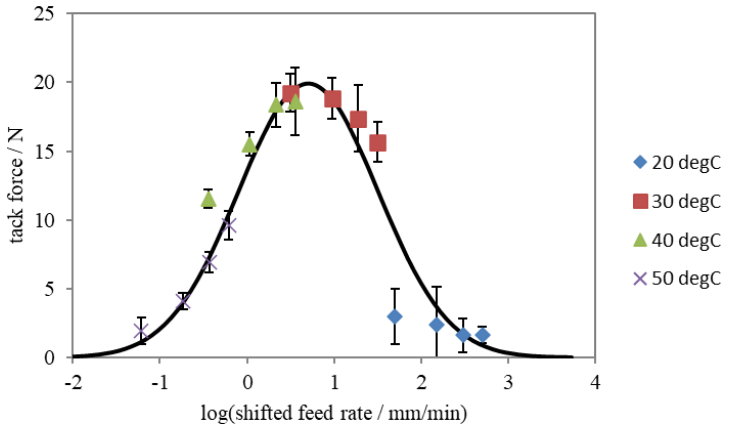

Figure 4. The same data as in Figure 3. Here, all feed rates are shifted to a reference temperature of 20 °C.

Application of TTS enables tack data acquired at different temperatures to be interpreted in terms of a broader range of feed rates than can be explored using a screw-driven testing machine. Hence, the procedure is able to provide insight into the applicability of the tack test to deposition rates relevant to industrial AMP processes (of the order of 1 m/s).

3. The ASTM standardization process

3.1 Motivation

Data obtained using the method described above were found useful for optimisation of process parameters in the manufacture of aerospace composite components. In particular, using experimental data to find combinations of temperature and rate to achieve optimum tack levels is of high practical relevance. It has been demonstrated by Smith et al. [6] that tack process maps can be created, which are easy to use in an industrial setting for looking up the parameters for the desired tack level.

In an industry-driven effort to guarantee consistency of relevant tack data in supply chains, it was attempted to turn the test method into a standard. This will allow interested parties to set up their own tack testing facility and conduct the tests. A working group for formulating the standard was established from members of academia, prepreg manufacturers and end users.

  doi:10.5075/epfl-298799_978-2-9701614-0-0

3.2 Approach

In formulating the standard, it is to be considered that this is not an academic document, but effectively a manual for setting up and conducting the tests. In the document, a brief summary of the method is followed by a statement of the significance of the standard. The test fixture itself needs accurate description and definition. The process of writing the standard led the authors to consider specific decisions with respect to the design of the test fixture, and the extent to which these were necessary for a standard. This led to a somewhat simplified version of the original design of the test fixture, which was described in some detail in a manner not dissimilar to descriptions found in patents. The description of the fixture focuses on the critical components and is detailed enough to allow the fixture to be reproduced (Figure 5). Following a statement on calibration (of the compaction springs), the procedure for tack testing is described in detail, and the data reduction method is explained. The information to be included in a test report is also listed.

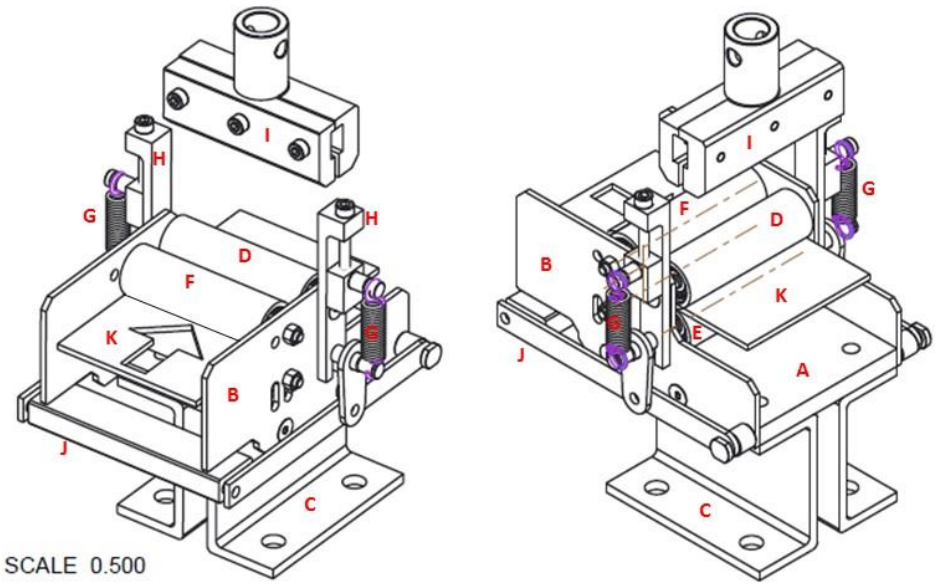

Figure 5. Test fixture of the type detailed in the standard. A: base plate; B: side plates; C: connection to Universal Testing Machine; D: peel roller; E: compaction roller; F guide rollers; G: compaction springs; H: jacking screws (to adjust compaction load); I: material clamp; J: spreader bar (for material loading); K: rigid substrate.

3.3 Adaptation of test method

In many respects the standard mirrors the test procedures used in the work discussed in earlier publications, but the need for results to be reproducible across laboratories requires prescription of many aspects. The design of the test fixture is one area in which the standard attempts to prescribe everything that is essential to achieving reproducible test results, but acknowledges that this may be done, for example, using different Universal Testing Machines.

The analysis of the data is one area in which the standard needed to be more prescriptive than earlier publications, for instance in the calculation of the average forces from the test data, and the authors re-analysed existing data using a range of limits in order to establish a set of limits appropriate for the specific dimensions of test specimens prescribed in the standard.

  doi:10.5075/epfl-298799_978-2-9701614-0-0

3.4 Balloting process

The draft standard was submitted for balloting to the relevant ASTM sub-committee (here: Subcommittee D30.03 on Constituent/Precursor Properties for composites). In a second stage (after approval at the sub-committee stage) it was submitted to the relevant committee (here: Committee D30 on Composite Materials). The balloting process is much like the reviewing process of an academic journal article except that the number of reviewers is substantially larger. The members are mainly from industry, but also from test laboratories, (US) government organisations and academia. ASTM is a full consensus organization, and ballot items must be agreed upon by all voters. This means that any issues or concerns raised through negative votes must be resolved to the satisfaction of the voter.

The draft standard was proposed to the committee by a member of the working group, together with a brief rationale. In the first ballot, seven members of the ASTM sub-committee voted. All concerns and requests for added information and changes expressed in the votes had to be addressed to the satisfaction of the voters. Unlike in the review process for a journal article, the identities of the voters are known, and the revision process can involve discussion with the voters.

After the revised draft was accepted by all voters at sub-committee level, it was submitted for the main ballot at committee level, where 15 members voted. All requests and suggestions needed to be addressed prior to a second vote by the same committee. In the second vote, 10 voters (not necessarily identical to the voters in the first round) again submitted comments and suggestions. After resolving the remaining issues raised in the vote, the committee approved the standard. The process took approximately one year, with the sub-committee ballot in February 2020, the main committee first ballot in June 2020 and the reballot in December 2020.

3.5 Round-robin exercise

Currently, a team of 12 partners from multiple industry sectors and from research organisations and academia are undertaking a tack testing round-robin exercise. The scope of this exercise is testing of two different commercial prepreg materials at different combinations of temperature and rate. This testing campaign is required to prove the usefulness of the standard in terms of lab-to-lab repeatability and reproducibility of experimental data. Another aim is to understand whether corrections or additions need to be made to the standard. The round-robin exercise is expected to conclude in 2022.

4. Conclusions

This paper has described the research and processes that have led to the establishment of a recently approved ASTM standard test method for the characterisation of prepreg tack. The method involves the peel of a prepreg from a substrate under controlled application pressure, peel rate and temperature using a custom fixture, and allows measurement of ply-to-tool and ply-to-ply tack. Additionally, using time-temperature superposition, tack mastercurves can be constructed to identify peak tack at the transition between adhesive and cohesive failure. The process of writing and submitting a draft standard, and the subsequent ballots and revisions have been described. At present a round-robin test exercise is in progress involving 12 industry and research partners.

5. Acknowledgements

The authors acknowledge the contributions of Sayata Ghose, Brice Johnson, Charles Park, and Adam Sawicki of The Boeing Company for sponsoring the ASTM ballot for this standard and for contributing to its development, and of Damon Call and Sam Tollefsen of Toray Composite Materials America Inc. for contributing to the development of the standard.

6. References

1. Budelmann D, Schmidt C, Meiners D. Prepreg tack: A review of mechanisms, measurement, and manufacturing implication. Polymer Composites 2020; 41:3440–3458.
2. Crossley RJ, Schubel PJ, Warrior NA. The experimental determination of prepreg tack and dynamic stiffness. Composites Part A - Applied Science 2012; 43(3): 423–434.
3. Endruweit A, Choong GYH Ghose S, Johnson BA, Younkin DR, Warrior NA and De Focatiis DSA. Characterisation of tack for uni-directional prepreg tape employing a continuous application-and-peel test method. Composites Part A: Applied Science and Manufacturing, 2018; 114:295-306.
4. ASTM Standard D8336-21 (2021), Standard Test Method for Characterizing Tack of Prepregs Using a Continuous Application-and-Peel Procedure, ASTM International, DOI: 10.1520/D8336-21, www.astm.org.
5. Crossley RJ, Schubel PJ, De Focatiis DSA. Time-temperature equivalence in the tack and dynamic stiffness of polymer prepreg and its application to automated composites manufacturing. Composites Part A: Applied Science and Manufacturing, 2013; 52:126-133.
6. Smith AW, Endruweit A, Choong GYH, De Focatiis DSA and Hubert P. Adaptation of material deposition parameters to account for out-time effects on prepreg tack. Composites Part A: Applied Science and Manufacturing, 2020; 133:105835.

COMPARING LOCAL FIBER ANGLES FROM DRAPING EXPERIMENTS TO SIMULATIONS

Sophia, Keller[a], Franz, Maier[a], Joachim, Osterberger[a], Roland Markus, Hinterhölzl[a]

a: Research Group of Lightweight Design and Composite Materials, University of Applied Sciences Upper Austria, Wels, Austria – sophia.keller@fh-wels.at

Abstract: *The mechanical performance of fiber reinforced composite components strongly depends on the fiber orientation. In order to determine the performance of a part as-built, the deviation of the fiber orientation from the intended configuration (as-designed) is crucial. Within this study, a method to compare local fiber orientations in manufactured components with draping simulation results was developed for unidirectional (UD) carbon laminas. The developed algorithm was tested on a plane plate geometry and a 3D double sine geometry. The resulting fiber angle deviations showed that the method enables a robust way for comparing local fiber orientations of manufactured parts and simulation results.*

Keywords: draping simulation; process simulation; fiber orientations; carbon fiber reinforced plastics; fiber angle measurements

1. Introduction

By forming any kind of semi-finished composite into a complex 3D shape, the fibers usually experience changes in orientation. The fiber orientation, however, is crucial for the mechanical properties of the composite component. Slight deviations in local fiber orientations within a manufactured part compared to the ideal (as-designed) component can cause considerable losses in the mechanical performance. However, with a precise prediction of local fiber angle deviations within a component, the mechanical performance of the manufactured component can be assessed adequately.

There are various established methods to determine local fiber orientations of manufactured carbon-fiber reinforced plastics (CFRP). One method that allows to assess fiber orientations throughout a ply stack is the computer tomography (CT) [1]. It offers a high level of detail, however, typically requires a strong contrast in X-ray absorption of fiber and matrix. Additionally, the low scanning speeds result in a high time consumption and thus, high costs for individual scans. If the analysis of the surface is sufficient, less expensive methods, e.g. the Eddy current method [2], should be preferred. This method is based on the principle of electrical conductivity to obtain information of the fiber orientations. However, it is therefore restricted to conductive fibers, i.e. carbon fibers, and not applicable to e.g. glass or aramid fibers. An approach accessible for arbitrary fiber types is implemented in the APODIUS Vision Sensor [3], which uses the refractive properties of the component's surface. The method used for this study was the photometric stereo (PS) technology, utilized by the FScan device developed by PROFACTOR [4]. Thereby, multiple images of the component surface are taken under different lighting conditions and superimposed, revealing information about the azimuthal properties of the scanned section. The comparison of this data to numerical results, however, still poses challenges. Different solution approaches can be found in literature. Margossian [5] and Leutz

  doi:10.5075/epfl-298799_978-2-9701614-0-0

[6] used a MATLAB routine to compare local material orientations for selected regions on the tool surfaces. Another approach using grid strain analysis to evaluate local fiber orientations within a draped component is shown in [7]. Those approaches, however, either are marker based (using grid analysis) or limited to small regions of interest. In order to assess the influence of the fiber orientations on the mechanical performance, it is important that the evaluation covers the entire part rather than being constrained to small regions of interest. The presented approach allows a fiber angle evaluation of the entire component surface using marker-less methods for data generation.

2. Methods

2.1 Data acquisition

The algorithm was developed and tested with a simple geometry, i.e. a plane CF-Epoxy (CF-EP) plate with a layup of $[0°]_4$, and was then expanded onto a more complex double sine geometry. The double sine geometry was manufactured in a diaphragm draping process using a $[0°]_3$ layup. We used the low temperature curing UD epoxy prepreg HexPly M79/45%/UD300/CHS.

2.1.1 Draping simulations

For the double sine geometry, the diaphragm forming process was modeled in Abaqus/CAE using the built-in *Fabric* material model for the laminate [8]. A detailed description of the simulation setup can be found in [9]. Figure 1 shows the simulated geometry, draped onto the double sine tool (the 0° direction coincides with the global x-direction).

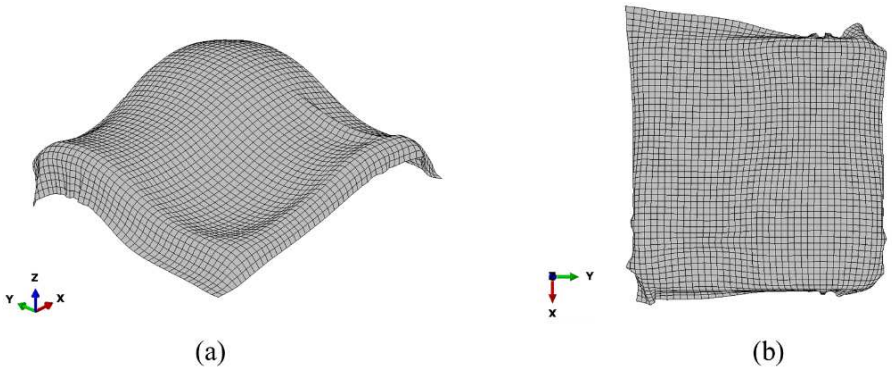

Figure 1. (a) Isometric and (b) top view of the resulting output geometry from the draping simulation

Local coordinate systems at each element integration point in vector form, where the x- and y-directions correspond to the local fiber directions, can be exported from Abaqus. For a UD lamina, the x-direction of the local coordinate system represents the fiber orientation. Simulations were conducted using S4 elements, with four integration points and thus four orientation vectors. The plate was compared to a reference line indicating the 0° direction rather than a process simulation result.

2.1.2 Experimental data

Figure 2a shows the plate geometry used for generating experimental fiber orientation data. With this simple geometry we set up and verified the correct functionality of the implemented algorithm. The experimental data for the double sine geometry was generated by draping a $[0°]_3$

stack onto the tool using a diaphragm forming press (Langzauner). An exemplary draping result of a single 0° ply is shown in Figure 2b.

(a) (b)

Figure 2. (a) Top view of the $[0°]_4$ CFEP-plate (fixed on three points for the FScan) and (b) manufactured double sine geometry with plasticine markers

The geometries were scanned using the FScan sensor (Profactor) mounted on a six-axis Fanuc robot (CR-35*i*A). For calibration purposes, plasticine markers were attached to the double sine geometry (see Figure 2b). Using custom software provided by Profactor, the robot path was planned on a .stl file of the geometries. The flat plate was drawn in Abaqus and exported as .stl file. For the double sine geometry, two steps were conducted before planning the robot path: first, the manufactured geometry was scanned using a laser scanner (Hexagon Absolute Arm 8520 with RS6). Then, an .stl file of the simulation result (Figure 1) was aligned with the scanned manufactured geometry. The aligned simulation result was used for planning the robot path in order to receive a good mesh quality. To ensure good agreement of simulation result and manufactured geometry, the components were compared using Control X (Geomagic). Occurring deviations between scan and draping simulation were within the positioning tolerance of the FScan sensor, i.e. less than 10 mm. That way, the planned robot path ensured reliable scanning results that were repeatable and could be automatized. The fiber orientation data generated by the FScan sensor is exported as a point cloud of tangential vectors parallel to the local fiber directions (as a hdf5-file). The number of exported points and the density of the point cloud is determined by the element size of the .stl mesh. Since the .stl mesh consists of triangular elements while the draping simulations required rectangular shell-elements, an algorithm for mapping and comparing results was needed.

2.2 Algorithm for comparing fiber orientations of different datasets

There are two obstacles that prohibit a direct comparison between the tangential vectors gained from simulation and experiment: besides the discretization disparity of the meshes, all gathered vectors are described in 3D space. However, at present there are no readily available methods for comparing 3D vectors with each other to obtain scalar deviation values that could indicate the draping quality. The developed algorithm written in PYTHON therefore consists of two parts. First, scalar fiber angles are determined from the source data and second, two datasets with a different discretization are mapped onto a common base, to enable a direct comparison.

2.2.1 Fiber angle determination

The fiber angle determination algorithm was developed to calculate a scalar value for the angle between a reference vector (representing the 0° direction) and the tangential vector of each evaluation point. A schematic sketch of the concept is shown in the following figure:

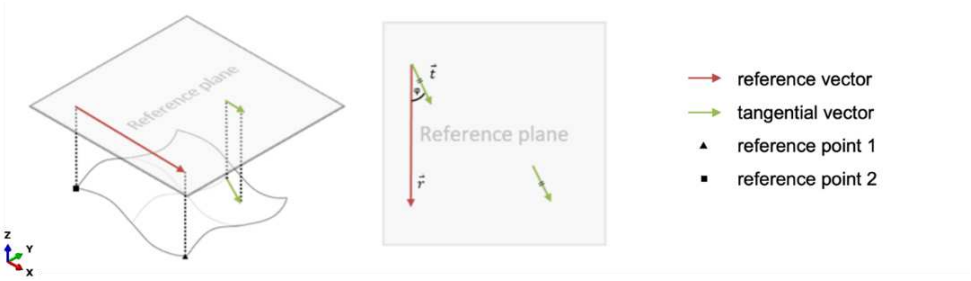

Figure 3. Schematic sketch of the scalar angle calculation

Both, the direction vectors as well as the reference vector are projected onto a reference plane using orthogonal projection. The reference plane thereby lies in a certain distance above the component parallel to the global xy-plane, which is parallel to the base plate of the double sine tool. Using the generalized law of cosines (see Eq. (1)), a scalar angle φ between the projected tangential vectors $\vec{t}$ and the projected reference vector $\vec{r}$ is calculated:

$$\varphi = \arccos\left(\frac{\vec{r}\cdot\vec{t}}{|\vec{r}|\cdot|\vec{t}|}\right). \tag{1}$$

By reducing the 3D vectors to a scalar angle between projected vectors, the output becomes dependent on the local element incline. However, by comparing two datasets with the same initial geometry (i.e. comparing experimental and numerical results), the influence of local element inclines is identical for both datasets and a measure of fiber angle deviations is received. Note that this evaluation method was applied for each integration point of the simulation mesh. To receive one value per element, which could then be compared to the FScan data, the mean value per element was assigned to the center point of the element.

2.2.2 Mapping the datasets

To deal with the discretization disparity between the datasets, an algorithm that maps the FScan data onto the typically coarser FE mesh was developed. The mapping method implemented within this algorithm is a slight modification of the nearest-neighbor method (with the Euclidian distance as clearance). The nearest-neighbor method calculates the distances between a fixed point and multiple points of a point set to determine the closest point to the fixed point. When using this method for mapping the FScan data onto the FE mesh, exactly one point from FScan would be assigned to a FE mesh center point. There is typically a higher density of FScan points than of FE mesh center points. This implies that multiple FScan points should be considered for the assignment to a single FE mesh point. This was done by slightly modifying the nearest-neighbor method by introducing a distance criterion. The mapping procedure thereby follows the following steps: first, the center point coordinates of each element are calculated. Then, the modified nearest-neighbor method is applied on the center points and the FScan point cloud. All FScan points, which lie in the “immediate vicinity” of the center point are then matched with the corresponding element. The immediate vicinity is defined by a spherical area around the center point of each element with the distance criterion being the radius of the sphere. For the

  doi:10.5075/epfl-298799_978-2-9701614-0-0

evaluations, this radius was chosen as the half diagonal of a representative FE-mesh element, to make sure that the majority of FScan points is considered. To obtain a fiber angle deviation value, the mean value of the FScan points assigned to an element is compared to the FE results of the respective element. This working principle is illustrated in the following figure on a component with 4 elements in total:

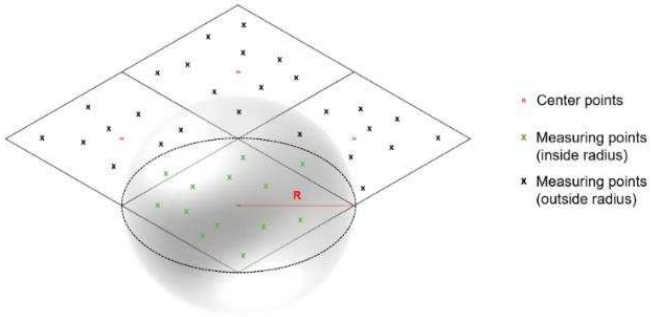

Figure 4: Schematic sketch of the principle of the averaging algorithm

3. Results

3.1 Fiber Angle Evaluation for the Simple Plate

For the evaluation of the simple plate geometry, only the first part of the evaluation algorithm (section 2.2.1) was used. Assuming that all fibers run parallel to the global 0° direction, the reference line (displayed as a red line in Figure 5a) was chosen between two calibration points. That way, all scalar fiber orientations could be determined relative to that line to receive absolute deviations from that line. Figure 5a shows the resulting deviation field relative to the reference line. The corresponding (aligned) histogram of the fiber angle deviations is shown in orange in Figure 5b.

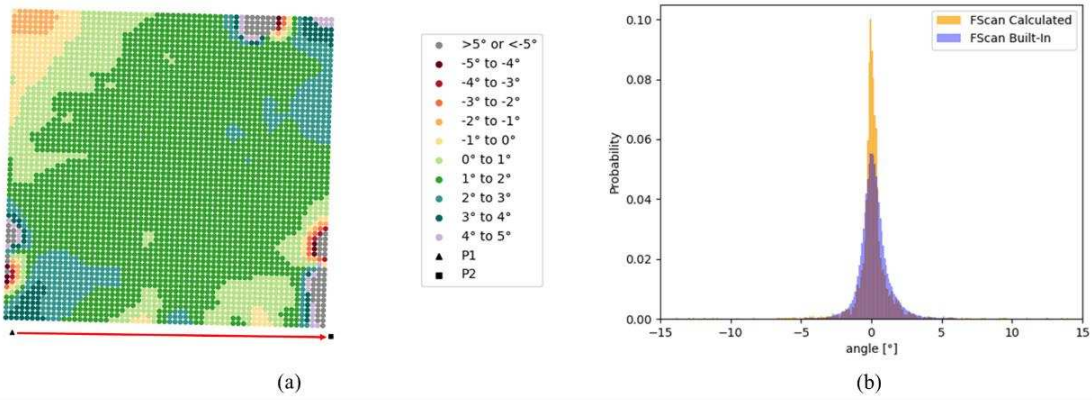

Figure 5. (a) Resulting deviation field with the chosen reference line and (b) aligned histograms of the resulting fiber angle deviations (orange) and the despeckled azimuthal images provided by the FScan software (blue)

The majority of data points (approx. 65 %) shows deviations between 1 and 2° (i.e. the dark green area). Therefore, it can be stated that the reference line deviates by 1 to 2° from the main fiber direction of the plate. However, the light green regions (i.e. deviations between 0 and 1°) as well as the light blue regions (i.e. deviations between 2 and 3°) also occupy a significant area

of the plate (approx. 23 % of the data points). The grey areas (i.e. deviations above 5° and below -5°) mainly occur at boundary areas and in near proximity of fixation points. Those areas can therefore be neglected for the evaluation. In general, the fibers tend to deviate more towards the upper left corner of the plate. For validation purposes, the distribution of the calculated fiber angles was compared to a histogram of the despeckled raw azimuthal images provided by the FScan software (see Figure 5b). Therefor, the main fiber direction of each histogram was aligned with 0°. Since the fiber angle distributions are quite similar for both histograms, it can be stated that the algorithm provides reliable results for the fiber angle deviations.

3.2 Fiber angle evaluation for the double sine geometry

For the evaluation of the double sine geometry, the full algorithm of section 2.2 was used. The reference line was defined between two calibration points of the experimental setup (see red line in the $[0°]_3$ draping result in Figure 6). Note that the image for Figure 6 was taken after removing the plasticine markers to prepare the component for the FScan. To ensure a valid comparison of the datasets, the simulation results were evaluated using the same reference vector as the evaluation of the manufactured double sine.

Figure 6. Reference line definition for the double sine geometry

The experimental and numerical results for the projected scalar angles were analyzed separately before they were compared to each other. The results of the individual evaluations are shown in Figure 7. Note that the wrinkle in the bottom left corner of the simulation result did not occur in the experimental result. Therefore, the affected elements were not captured by the FScan and are colored grey, which indicates elements that are excluded from the evaluation.

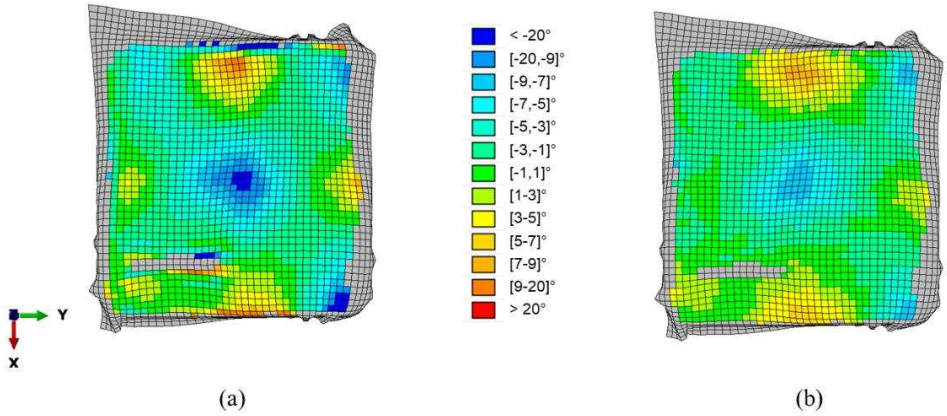

Figure 7. Separate evaluations of the projected fiber angles for the (a) simulation results and the (b) FScan result mapped onto the FE mesh

A distinct pattern is apparent in Figure 7a, where the middle as well as the mid-length of the four edges are polarizing locations with a high difference to the orientation of the reference line. This pattern (which is less dominant in Figure 7b) indicates the error that is made by projecting the tangential vectors within the elements of different inclines onto a 2D reference plane because the pattern corresponds to the gradient of a double sine geometry. However, since the local incline of the elements is identical for the simulation and the FScan result, it can be assumed that the error is canceled out within a direct comparison, provided that the inclination is not too steep. Figure 8 shows the deviation of the projected and actual angle, dependent on the inclination of the base to the projection plane. A critical inclination of about 30°, considering 0° laminas, was determined.

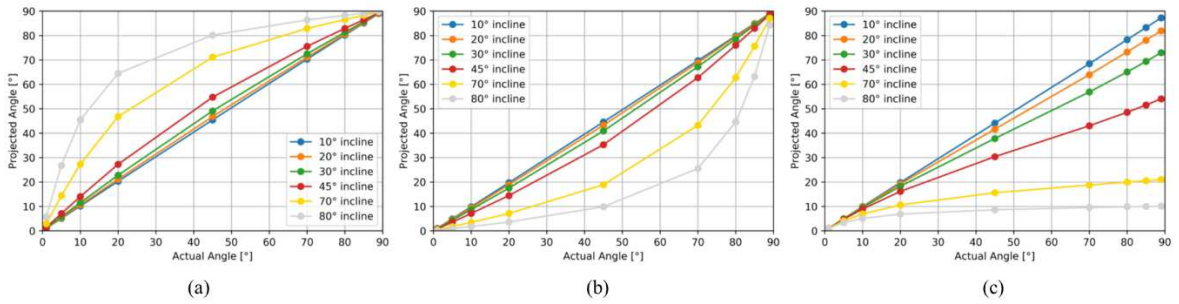

Figure 8. Projection error for (a) an incline in 0° direction, (b) an incline in 90° direction and (c) a combined incline in 0° and 90° direction

The incline of the double sine geometry at the steepest points (in the center of the geometry) is about 29°. Therefore, the algorithm provides reliable data for the double sine geometry. Figure 9 shows the deviation plot, i.e. the difference between Figure 7a and b, and the manufactured geometry.

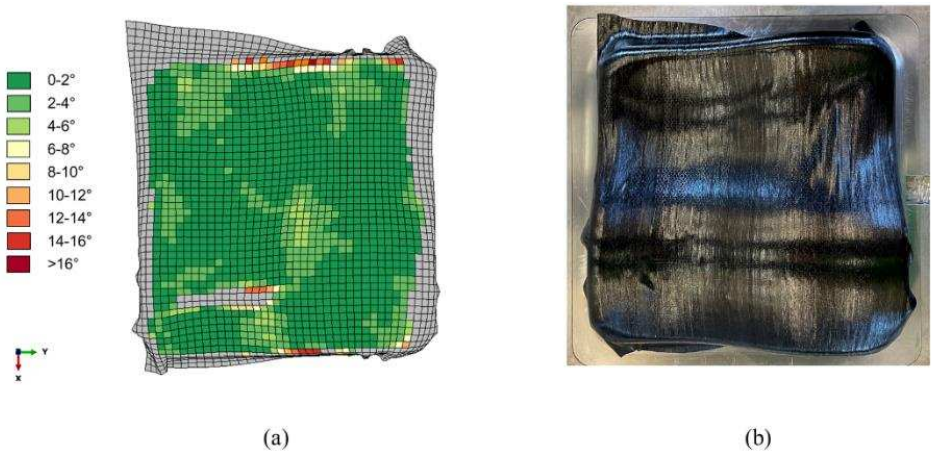

Figure 9. (a) Deviations between simulation and FScan result and (b) manufactured part

Most elements exhibit a deviation value of about 0-2°. Some areas exhibit slightly increased deviation values, most likely caused by geometrical features such as wrinkles. Fiber angle deviations above 6° solely occur at the edge of the wrinkle and the edge of the evaluation field. This indicates that simulation and experiment are in good agreement.

  doi:10.5075/epfl-298799_978-2-9701614-0-0

4. Conclusion

The method developed within this study provides a robust way to compare fiber orientations of manufactured components to numerically derived fiber orientations. The algorithm works best for plane geometries because for those components there is no influence of the vector projection on the result. Provided that the measured component does not exhibit overly steep inclines, the method is also valid for more complex components. For non-planar geometries, however, it must be emphasized, that the resulting scalar angles are relative values, not absolute ones. This means, that the resulting scalar orientations cannot be readily used as input for the orientation in subsequent simulations. For future studies, the algorithm could be enhanced by implementing geometric gradient information to compensate the error made by the projection onto a 2D plane.

Acknowledgements

We gratefully acknowledge the financial support of the Austrian Research Promotion Agency (FFG) under the 7th "Coin Aufbau" Program in the scope of the project ProSim (Grant No. 866878).

5. References

1. Sabuncuoglu B, Tanabi H, Soete J, Lomov SV. Micro-CT analysis of deviations in fiber orientation and composite stiffness near the microvascular channels embedded in glass-fiber reinforced composites. *Composite Structures.* 2020; 237: 1-17.
2. Bardl G, Nocke A, Cherif C, Pooch M, Schulze M, Heuer H, Schiller M, Kupke R, Klein M. Automated detection of yarn orientation in 3D-draped carbon fiber fabrics and preforms from eddy current. *Composites Part B: Engineering*. 2016; 132: 49-60.
3. Malhan RK, Shembekar AV, Kabir AM, Bhatt PM, Shah B, Zanio S, Nutt S, Gupta SK. Automated planning for robotic layup of composite prepreg. *Robotics and Computer Integrated Manufacturing*. 2020; 67: 1-27.
4. Zambal S, Palfinger W, Stöger M, Eitzinger C. Accurate fibre orientation measurement for carbon fibre surfaces. Pattern Recognition. 2014; 48: 3324-3332.
5. Margossian A. *Forming of tailored thermoplastic composite blanks: material characterization, simulation and validation*. Germany: Technical University of Munich; 2017.
6. Leutz DM. Forming simulation of AFP material layups: Material characterization, simulation and validation. Germany: Technical University of Munich; 2016.
7. Chen S, McGregor OPL, Harper LT, Endruweit A, Elsmore MT, Warrior NA. Defect formation during preforming of a bi-axial non-crimp fabric with a pillar stitch pattern. *Composites Part A: Applied Science and Manufacturing*. 2016; 91: 156-167.
8. ABAQUS, Inc. *ABAQUS/Standard Theory Manual*, Version 6.8. USA: Dassault Systèmes Simulia Corp; 2008.
9. Osterberger J, Maier F, Hinterhölzl RM. Process Modelling of Diaphragm Forming with UD Semi-finished prepregs. *Conference Proceeding at SAME Europe*. 2020.

  doi:10.5075/epfl-298799_978-2-9701614-0-0

EXPERIMENTAL CHARACTERIZATION OF TRANSVERSE FABRIC COMPRESSIBILITY BY MEANS OF IN-SITU-IMPREGNATION

Marcel, Bender[a], Ewald, Fauster[a]

[a] Montanuniversität Leoben, Processing of Composites Group,
Otto Glöckel-Strasse 2, 8700 Leoben, Austria – ewald.fauster@unileoben.ac.at

Abstract: *A novel test rig is presented for experimental characterization of transverse compressibility of reinforcing fabrics. The test rig allows for in-situ-saturation of samples under transverse load and thus, for experimental characterization of dry and wet compressibility of the materials in a single test. The work introduces the novel test rig as well as a novel test configuration with (i) closing, (ii) holding, (iii) fluid injection, (iv) holding and (v) opening stages together with the resulting sample response in terms of (i) compression, (ii) dry relaxation, (iii) impregnation, (iv) wet relaxation and (v) decompression. First results on two Glass fiber based materials, a woven fabric and a non-crimp fabric, are presented and discussed.*

Keywords: transverse fabric compressibility; experimental characterization; ex-ante saturation; in-situ saturation

1. Introduction

In liquid composite molding (LCM), dry fibrous preforms consisting of reinforcing fabric layers are impregnated by viscous fluids, in particular chemically reactive resin systems. The impregnation quality is of crucial importance for the mechanical performance of the resulting composite part. Thus, impregnation mechanisms and the most relevant preform properties have been scientifically investigated in the past decades. In particular, in-plane as well as out-of-plane preform permeability as well as transverse preform compressibility were studied on a theoretical and experimental basis, respectively (1–5). Transverse preform compressibility of fibrous preforms shows viscoelastic properties and is a phenomenologically complex process due to the superposition of: (i) cross-sectional fiber bundle deformation, (ii) longitudinal fiber bundle flattening, (iii) fiber bundle bending deformation, (iv) cross-sectional void condensation and (v) nesting between fabric layers (6). As a result, transverse preform compressibility is affected by a number of material and test parameters, most importantly: (i) the number of fabric layers, (ii) the number of load cycles, (iii) the level of compressive speed, (iv) the experimental test configuration and (v) the state of preform saturation (dry/wet).

Figure 1 shows an overview of the most frequently used experimental test configurations in terms of schematic plots of compressive load F and sample thickness h over experimental time t. For resin transfer molding (RTM), the loading/relaxation/unloading configuration is of particular relevance. There, the preform is transversely compacted until a certain height is reached, when the RTM mold is closed, and subsequently held at constant height, which allows stress relaxing effects to take place. The research group authoring the paper at hand participated in a recently published international benchmark exercise (IBE) on experimental characterization of transverse compaction of reinforcing fabrics (5), listed with ID no. 1 in the list of participants provided in Table 1 of that paper. There, a test configuration with the following conditions was

  doi:10.5075/epfl-298799_978-2-9701614-0-0

prescribed: (i) constant speed loading at 1 mm/min until a sample height of 3 mm was reached, (ii) relaxation at that constant sample height and (iii) constant speed unloading at 1 mm/min. A woven fabric as well as a non-crimp fabric was characterized by 26 research institutions worldwide in dry and wet conditions, respectively. Compression of wet samples leads to significantly lower compaction pressure compared to compression of dry samples due to lubrication effects (5).

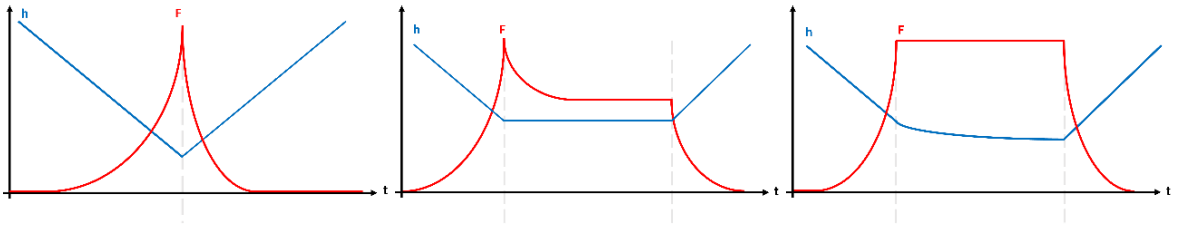

Figure 1 : Schematics of typical test methods for experimental characterization of transverse preform compressibility: loading/unloading (left), loading/relaxation/unloading (center) and loading/creeping/unloading (right).

For studying wet compressibility in that IBE, a guideline specifying ex-ante saturation of the fabric samples in a fluid bath followed by dripping of excessive fluid and subsequent testing was provided. Thus, during compression of the fully wetted samples, squeeze flow effects occur. These not only impact the compressive load readings, the conditions are actually not perfectly representative for RTM. There, the saturation takes place while the preform is under transverse compressive load and thus, Darcy fluid flow is dominant (7, 8).

The work at hand presents a novel test rig for experimental characterization of wet compressibility involving in-situ saturation of the fabric samples: At first, the samples are compressed in dry state according to a loading/relaxation test configuration and subsequently impregnated with the test fluid through an injection gate central to the sample under load (see Figure 2).

A new test configuration with loading/dry relaxation/wet relaxation/unloading stages is proposed. This allows for experimental characterization of compressibility properties at conditions directly comparable to those of RTM. Moreover, dry as well as wet compressibility characteristics can be determined from a single experiment, which minimizes experimental time as well as material usage. In addition, data comparability will be improved by reducing the influence of manual handling and varying sample properties.

2. Experimental Work

2.1 Test Equipment

The novel test rig is mounted to a universal testing machine (UTM) with a maximum load capacity of 250 kN and a load cell capacity of 30 kN. The fabric samples are applied to a base platen, which is moved in upwards direction by the crosshead in order to compress the samples against a metal stamp (100 mm in diameter). A linear variable differential transformer (LVDT) is mounted closely to the stamp and measures the distance between base plate and stamp, i.e. the sample thickness, during the experiment. In addition, the distance readings are used for precise motion control of the UTM. As shown in Figure 2 (left), the setup is equipped with four additional LVDT, whose readings can be processed to identify unwanted tilting of the

compression platens. Moreover, two heating mandrels and corresponding isolation sleeves are provided, allowing for tests at elevated temperature levels. The base platen shows a central injection gate for in-situ-saturation of the samples under test. The fluid is provided over a channel in the base plate as shown in Figure 2 (right).

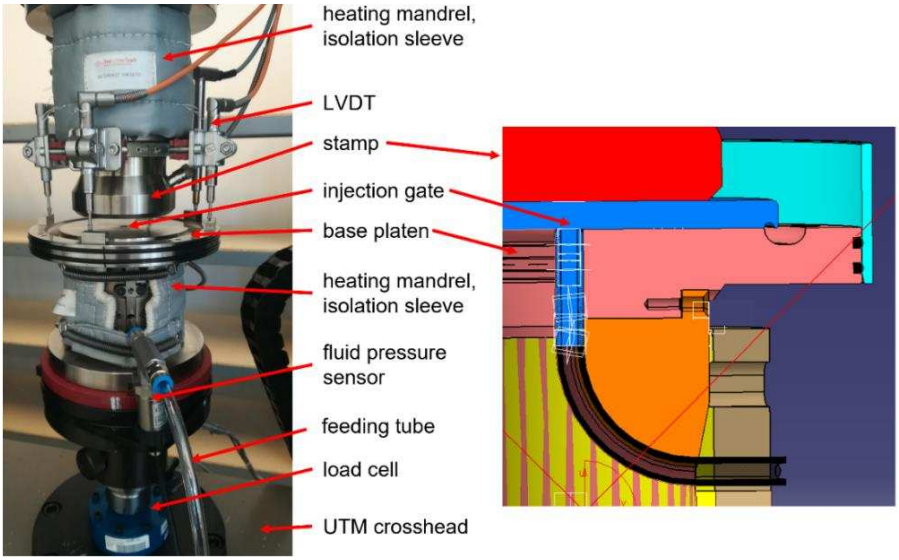

Figure 2: Novel test rig for experimental characterization of fabric compressibility with optional in-situ saturation (left). CAD drawing emphasizing the fluid channel in the base plate (right).

The fluid is kept in a standard pressure pot, which is loaded by compressed air to a desired pressure level by means of a pressure control valve. The feeding line is equipped with a ball valve, a fluid temperature sensor and a fluid pressure sensor. The latter is mounted closely to the point of fluid entrance into the base plate. All of the sensors (four LVDT, fluid temperature and pressure) and actuators (two heating mandrels, pressure control valve and ball valve) are connected to an industrial PLC, which in turn is communicating with a Labview application specifically implemented for temperature control as well as data visualization and archiving. With in-situ-saturation of the samples under test, the setup allows for experiments in a loading/dry relaxation/wet relaxation/unloading configuration as visualized in Figure 3.

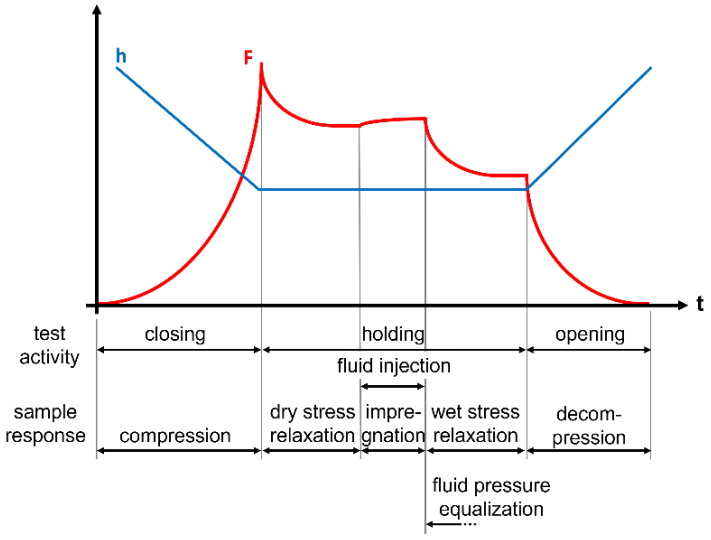

Figure 3: Schematic of a test procedure involving in-situ saturation of the sample under test.

2.2 Materials

In the present work, two different Glass fiber based fabrics were tested:

- A biaxial non-crimp fabric (NCF), Saertex X-E-444, with a nominal areal weight of 0.444 kg/m² (fiber bundles in +45° and −45° direction, respectively, with 217 g/m² each; stabilization yarns in 0° and 90°, respectively, with 2 g/m² each and a polyester stitching yarn with 6 g/m²).
- A 2/2 twill weave woven fabric (WF), Hexcel Hexforce 1202, with a nominal areal weight of 0.290 kg/m² and a slightly unbalanced internal construction in warp (7 yarns/cm) and weft (7.2 picks/cm) direction, respectively.

The materials were chosen due to their commercial availability as well as the accessibility of reference data, as they were both extensively tested in the recently published IBE (5) as mentioned above. For the tests on wet samples presented in this paper, Dow Corning XIAMETER PMX-200 silicone oil (dynamic viscosity of about 0.1 Pas at room temperature) was used as test fluid.

2.3 Experimental Design

In order to ensure comparability with the results obtained in the IBE test series (5), their experiments were initially repeated with samples of recent material batches. In particular, ex-ante-saturated samples of the two materials were tested with five repeats. In addition, five samples of the recent material batches were tested following the novel test procedure, i.e. in a loading/dry relaxation/wet relaxation/unloading configuration. Table 1 shows an overview of the experimental design.

Table 1: Overview of experimental design with number of repeats in each test configuration.

sample saturation state	IBE test series (5) (material batches from 2017)	novel test series (material batches from 2021)
dry	5	-
wet (ex-ante)	5	5
dry & wet (in-situ)	-	5

While the experiments of the novel test series were conducted with the test rig described in Section 2.1, the experiments for the IBE test series (5) were run with a former version of the test rig. As far as relevant for the work at hand, the major differences between the test rig versions are: (i) the diameter of the metal stamp (50 mm in the former setup, 100 mm in the novel setup), (ii) the shape and dimensions of the fabric samples (square, side length 60 mm, in the IBE test series and round, diameter 120 mm, in the novel test series) and (iii) the option for in-situ-saturation in the novel setup.

3. Results and Discussion

3.1 Comparison of Results from Ex-Ante-Saturated Samples

At first, the results obtained with the novel test rig are compared with those found in the IBE test series (5). Figure 4 shows compaction pressure characteristics of ex-ante saturated samples of the Saertex NCF material in terms of average data and min/max envelopes. While the maximum compaction pressure, p_{max}, is higher for the novel test series, the final compaction pressure at the end of the holding phase, p_{hold}, is lower. The disagreements might be attributed to the different dimensions of samples and stamp, respectively, as well as the different material batches in the two test series. However, the effects will be studied in future works in more detail in order to quantify the particular contributions.

In order to rank the magnitude of the differences, average and standard deviation data of p_{max} and p_{hold}, respectively, are visualized in Figure 4 for the two test series as well as for the overall results of the IBE by means of statistical error bars. As can be seen, the error bar for p_{max} found in the novel test series is overlapping with that from the IBE test series, however, it is outside the error bar of the overall IBE results. For p_{hold}, the error bars of the results for the material batches from 2017 and 2021 are both within the error bar of the overall IBE results. In fact, the average value of p_{hold} found for the novel test series agrees very well with the corresponding value found for the overall IBE results. The standard deviation values found for the material batches from 2017 and 2021 are well comparable. Thus, the results of the test series being compared are considered as generally in good agreement.

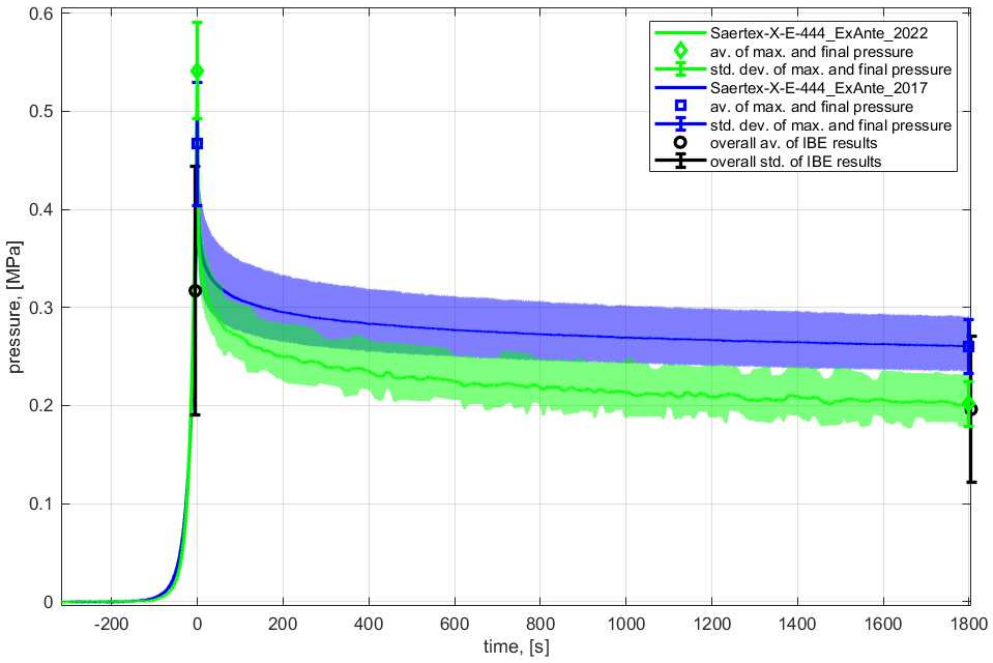

Figure 4: Comparison of compaction pressure data collected in the IBE test series and the test series with the novel test rig on the Saertex NCF.

The results obtained in the tests of the Hexcel WF material reveal similar findings, however these are omitted here due to length restrictions for the manuscript.

3.2 Results from Novel Test Method with In-Situ-Saturation

In Figure 5, normalized compaction pressure characteristics are shown from an exemplarily chosen test of the Saertex NCF material. In addition, the normalized fluid injection pressure characteristics are visualized in order to highlight the phase of fluid injection, i.e. in-situ-saturation of the sample under test. In fact, the normalized pressure characteristics allow for a clear separation of the (i) compression, (ii) dry relaxation, (iii) impregnation, (iv) wet relaxation and (v) decompression phases of the test as discussed in Section 2.1. The duration of both, dry and wet relaxation, were prescribed with 30 minutes.

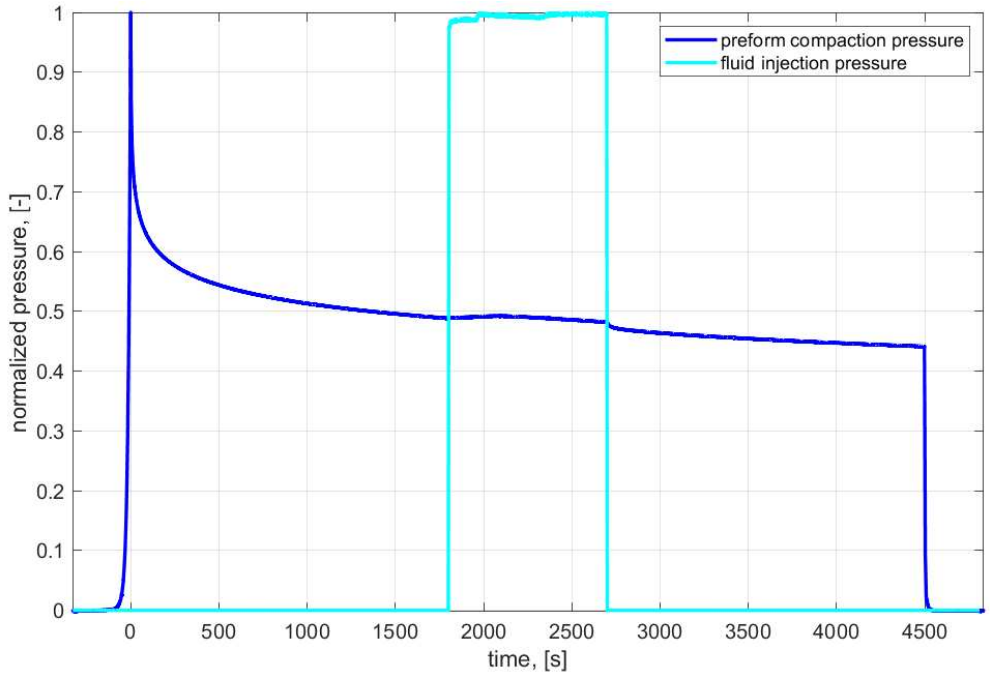

Figure 5: Normalized sample compaction pressure and normalized fluid injection pressure over experimental time for the novel test method involving in-situ saturation: Example data chosen from a test on the Saertex NCF material.

In the phase of fluid injection, the pressure data shows contributions from the preform compaction as well as the test fluid saturating the sample: While the contribution of the test fluid is increasing with time as a result of the progressing flow front, the contribution of the preform compaction is decreasing due to lubrication effects. For the data shown in Figure 5, these two effects are in a similar range, which is a result of (i) the chosen level of fluid injection pressure and (ii) the low level of stress relaxation inherent to the Saertex NCF material. As derived from data reported in the IBE (5), the degree of stress reduction due to lubrication expressed as:

$$d_{lubrication} = 1 - \frac{p_{hold,wet}}{p_{hold,dry}}, \quad (1)$$

is less than 15 % for the Saertex NCF material. The reason is given by the limited ability of the NCF material for fiber bundle bending deformation, cross-sectional void condensation and nesting between fabric layers as a result of its internal architecture.

For the Hexcel WF material, however, stress reduction due to lubrication is as much as 45 % as derived from data reported in the IBE (5). This can be clearly seen in Figure 6, which shows normalized compaction pressure characteristics from an exemplarily chosen test of the Hexcel

WF material. During fluid injection, the pressure data is decreasing significantly, which indicates the lubrication effect dominating over the contribution from fluid injection.

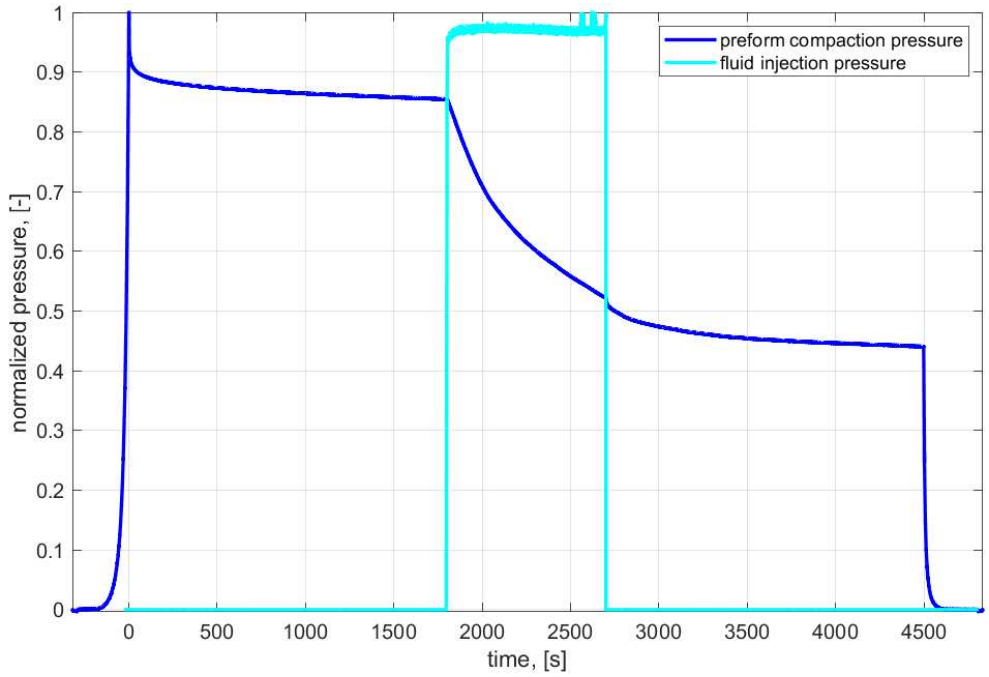

Figure 6: Normalized sample compaction pressure and normalized fluid injection pressure over experimental time for the novel test method involving in-situ saturation: Example data chosen from a test on the Hexcel WF material.

Fluid injection was stopped in all tests as soon as fluid was visually observable around the sample indicating complete sample impregnation. For the chosen level of fluid injection pressure, which is still part of a parameter study for this novel test method, impregnation time was typically less than 15 minutes. The subsequent phase of wet relaxation is initially superimposed by fluid pressure equalization. This effect is expected to be short in time compared to the duration of wet relaxation (30 minutes), however, will be subject of future research activities. Anyway, the level of compaction pressure at the end of the wet relaxation stage, $p_{hold,wet}$, is expected to be well comparable to the corresponding entity determined from tests on ex-ante-saturated samples.

3.2 Comparison of Results from Different Saturation Methods

According to the experimental plan specified in Table 1, the parameters p_{max} and $p_{hold,dry}$ can be compared for the results of (i) the IBE test series on dry samples and (ii) the novel test series. In addition, the parameter $p_{hold,wet}$ can be compared for the results of (i) the IBE test series on ex-ante-saturated samples, (ii) the novel test series on ex-ante-saturated samples and (iii) the novel test series with in-situ-saturation. Finally, this allows for a comparison of the 'lubrication degree', $d_{lubrication}$, i.e. the degree of stress relaxation due to lubrication according to Equation (1).

Although details of these comparisons need to be omitted here due to length restrictions for the manuscript, the 'lubrication degree' shows well comparable results: For the Saertex NCF material, it was found with 13.90 % in the IBE test series and 9.63 % in the novel test series. For the Hexcel WF material, it was found with 51.42 % in the IBE test series and 47.14 % in the novel test series.

4. Summary and Conclusions

The paper at hand proposes a novel test rig for experimental characterization of transverse compressibility of reinforcing fabrics. The test rig allows for in-situ-saturation of samples under transverse load and thus, for experimental characterization of dry and wet compressibility of the materials in a single test. The work introduces the novel test rig as well as a novel test configuration with (i) compression, (ii) holding, (iii) fluid injection, (iv) holding and (v) decompression stages together with the resulting sample response in terms of transverse compaction pressure characteristics. First results on two Glass fiber based fabrics, well-known from a recent IBE, are very promising in terms of comparability of the resulting parameters, p_{max}, $p_{hold,dry}$ and $p_{hold,wet}$.

Future research activities will concentrate on mathematical modelling of the fluid pressure field developing in the sample under test according to Darcy flow mechanisms as well as the duration of fluid pressure equalization after stopping fluid injection. In addition, the influence of the type of test fluid used for the tests will be investigated. Moreover, the two fabric materials tested in this work will be studied in more comprehensive test series.

Acknowledgements

The test rig and associated research work was publicly funded in the frame of projects 'MoVeTech' and 'Evolution#4', both administered in the Austrian research program 'Take Off' of the Austrian Federal Ministry for Climate Action, Environment, Energy, Mobility, Innovation and Technology, which is greatly acknowledged.

References

1. Robitaille F, Gauvin R. Compaction of textile reinforcements for composites manufacturing. I: Review of experimental results. Polymer Composites 1998; 19(2):198–216.

2. Robitaille F, Gauvin R. Compaction of textile reinforcements for composites manufacturing. II: Compaction and relaxation of dry and H2O-saturated woven reinforcements. Polymer Composites 1998; 19(5):543–57.

3. Robitaille F, Gauvin R. Compaction of textile reinforcements for composites manufacturing. III: Reorganization of the fiber network. Polymer Composites 1999; 20(1):48–61.

4. Potluri P, Sagar TV. Compaction modelling of textile preforms for composite structures. Composite Structures 2008; 86(1-3):177–85.

5. Yong A, Aktas A, May D, Endruweit A, Lomov SV, Advani S et al. Experimental characterisation of textile compaction response: A benchmark exercise. Composites Part A: Applied Science and Manufacturing 2021; 142.

6. Grieser T, Mitschang P. Investigation of the compaction behavior of carbon fiber NCF for continuous preforming processes. Polymer Composites 2017; 38(11):2609–25.

7. Advani SG, Sozer EM. Process modeling in composites manufacturing. 2nd ed. Boca Raton, FL: CRC Press; 2011.

8. Bear J. Dynamics of fluids in porous media. New York: Dover; 1988.

  doi:10.5075/epfl-298799_978-2-9701614-0-0

MEASUREMENT OF TEXTILE COMPACTION RESPONSE AND OUT-OF-PLANE PERMEABILITY: 2ND INTERNATIONAL BENCHMARKING EXERCISE

Ana X. H. Yong[a], Jamin D. S. Vincent[a]

a: National Physical Laboratory, Hampton Road, Teddington, Middlesex, TW11 0LW, United Kingdom. Email: ana.yong@npl.co.uk

Abstract: *The manufacture of composite materials by Liquid Composite Moulding (LCM) processes is dependent upon the infiltration of a dry fibre preform by a liquid resin. These manufacturing processes can be supported by the characterisation of the preform through measurement of its permeability and compaction response. These measurements are often used to inform the design of the manufacturing process as input parameters for process simulation.*

Previous benchmarks have been carried out to measure the in-plane permeability, out-of-plane permeability, and textile compaction response. This paper presents the results of the second round of benchmark exercises which were launched in 2021. This second round of benchmarking included 33 international participants for each exercise. The aim of this ongoing work is to assess the reproducibility of results and ultimately provide recommendations that lead towards a standardised test procedure.

Keywords: Permeability; compressibility; resin injection; resin flow; process monitoring

1. Introduction

Liquid Composite Moulding (LCM) processes can be described by the injection of a liquid resin into a dry fibre textile within a mould of the desired shape. It is important for the success of this process that the dry fibre be completely saturated with resin prior to cure and demoulding. To support these methods of manufacturing a polymer matrix composite part, it is good practice for the permeability of the dry fabric to be measured to understand the behaviour of the resin flow during injection.

The permeability of a dry fibre reinforcement is typically measured in the in-plane (x and y) direction and out-of-plane (z) directions separately. These measurements can provide important information as standalone values, or more valuably as data inputs to manufacturing process simulations. Measurement of the in-plane and out-of-plane permeability has been the subject of a collaborative international effort to standardise these techniques through iterative benchmarking exercises [1-5]. Following the third international benchmark exercise, measurement of the in-plane permeability has progressed to a draft ISO standard. The first out-of-plane benchmarking exercise was completed in 2021 and resulted in several recommendations to refine the test procedure, aimed at improving the reproducibility of these measurements across sites. These recommendations formed the basis of the test procedure used in the second international benchmarking exercise.

  doi:10.5075/epfl-298799_978-2-9701614-0-0

In addition to measurement of the permeability, it is pertinent to characterise the behaviour of the dry textile under compression. Understanding the compaction pressure not only provides information on the achievable volume fraction or the pressure exerted on the tool but has a direct relationship to the permeability of the fabric, whereby the permeability of the fabric is reduced with increasing compaction. Following the example of the permeability measurement benchmarking exercises, an international benchmarking exercise for measuring the textile compaction response was carried out in parallel to the first out-of-plane permeability measurement and third in-plane permeability measurement exercises and completed in 2021. Despite the simplicity of the test, a high variability (38-50% coefficient of variation) was found between participants. In parallel to the out-of-plane permeability measurement benchmarking exercise, the recommendations from the first textile compaction benchmark have been used to create an updated test procedure for a second round of benchmarking.

These two new benchmarking exercises have been coordinated by the National Physical Laboratory with the support of a steering committee from the University of Nottingham, KU Leuven, University of Delaware, McGill University and the Insitut für Verbundwerkstoffe. In total, 33 participants from 15 countries are taking part and are listed in Table 1. The latest findings from these two benchmarking exercises are presented in this paper.

Table 1: List of participants

IMT Mines Albi (France)	University of Nantes (France)
TENSYL (France)	University of Nottingham (UK)
University of Auckland (New Zealand)	National Physical Laboratory (UK)
Brigham Young University (USA)	Orleans University (France)
TU Delft (Netherlands)	University of Reims (France)
Ecole Polytechnique Federale de Lausanne (Switzerland)	Centre Technologique En Aérospatiale (Canada)
Nanyang Technological University (Singapore)	University of Applied Sciences and Arts Northwestern Switzerland (Switzerland)
Institut de Soudure Groupe (France)	Sabanci University (Turkey)
ITAINNOVA (Spain)	University Stuttgart (Germany)
Institut fur Verbundwerkstoffe GmbH (Germany)	Skolkovo Institute of Science and Technology (Russia)
Khalifa University of Science and Technology (UAE)	Advanced Manufacturing Research Centre (UK)
KOC University (Turkey)	Warwick University (UK)
Montanuniversitat Leoben (Austria)	Caen-Normandy University (France)
KU Leuven (Belgium)	University of Valencia (Spain)
IMT Lille Douai (France)	Jean Monnet University (France)
McGill University (Canada)	IMT Mines-Ales (France)
Technische Universitat Munchen (Germany)	

  doi:10.5075/epfl-298799_978-2-9701614-0-0

2. Materials

2.1 Figures and Tables

All participants used the same materials for these two benchmarking activities. The fabric used in these benchmark exercises was a ±45° biaxial E-glass fibre non-crimp fabric with areal weight 444 g/m^2, supplied by Saertex. This fabric was nominally the same as the fabric used in the first benchmarking exercises, which was characterised by May et al. [3]. It was noted, however, that the batch used in this new round of benchmarking was visibly different to the batch used previously. The new batch was therefore characterised at KU Leuven and shown in Figure 1.

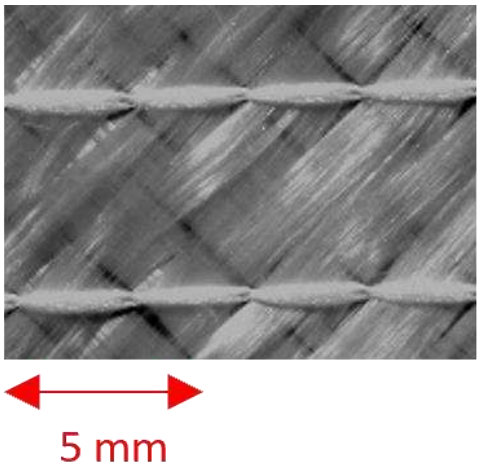

Figure 1. Image of the non-crimp fabric used in these benchmarking exercises

Participants were instructed to use the same silicone fluid in these benchmarking exercises as in the previous, Dow Corning XIAMETER PMX-200 100 cs silicone fluid. Participants carried out viscosity measurements on the model fluid at their site and no procedure was set, however the option was given for a secondary viscosity measurement at the National Physical Laboratory for benchmarking purposes.

3. Experimental Methods

3.1 Out-of-plane permeability measurement

The test method for this benchmark was limited to the 1D test setup, as this was found to be the most used setup in the first benchmark exercise. Limiting variations in test setup in turn limits the degrees of freedom of the test and enables more meaningful statistical analysis of the data returned by participants. The pressure differential between the inlet and outlet was limited to the range 100 – 200 MPa. The target volume fractions were 45%, 50% and 55%. The number of layers of fabric in each specimen stack was not fixed but limited to a range (10-20 layers) nor was the cavity height used to achieve these V_f prescribed, to account for the variety of closing mechanisms implemented by participants to set the cavity height. Figure 2 shows three different closing mechanisms used to set the cavity height.

  doi:10.5075/epfl-298799_978-2-9701614-0-0

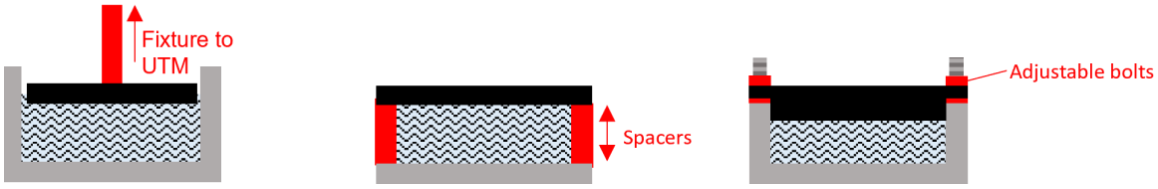

Figure 2. Schematic showing methods to set the cavity height in a 1D out-of-plane permeability test setup using a) Universal Test Machine (UTM) displacement; b) spacers and c) bolts

3.2 Textile compaction characterisation

The number of layers in each specimen stack and test profile for this compression test was fixed at ten for all participants to directly measure the variability in compaction pressure at a known V_f. Participants were instructed to use a closing speed of 1 mm/min to a plate distance of 3 mm, followed by an opening speed of 1 mm/min. In addition, participants carried out compliance measurements at the beginning and end of each test series (wet and dry). In addition to measuring the compliance, it was mandatory for all participants to include at least one direct displacement measurement. The parallelism of the platens was assessed using pressure-sensitive film.

Tests were carried out on both dry fabric stacks and wet fabric stacks which had been saturated for 15 minutes in silicone oil and drained for a further 15 minutes prior to test.

4. Results

4.1 Out-of-plane permeability measurement

The first set of results has been returned and the results are given in Table 2. This participant was able to successfully follow the test procedure that was updated following the outcomes of the first benchmark exercise to include restrictions that would seek to minimise the variability in measured permeability between participants. This first set of results shows that the coefficient of variation increases with decreasing volume fraction, which agrees with the effect seen in the first benchmark exercise [5].

Table 2: First results of the out-of-plane permeability measurement exercise

Volume fraction (av.)	Permeability (av.)	Coefficient of variation
0.46	1.30×10^{-12} m^2	0.12%
0.51	7.14×10^{-13} m^2	0.08%
0.55	4.98×10^{-13} m^2	0.07%

4.2 Textile compaction response

Six participants have returned the results of the compaction benchmarking exercise. All of the participants carried out testing using circular platens larger than the specimen. Five of the participants used both machine displacement and at least one LVDT to measure the thickness

  doi:10.5075/epfl-298799_978-2-9701614-0-0

(distance between platens). One participant used a point-tracking algorithm which interpreted images taken of a precision ruler.

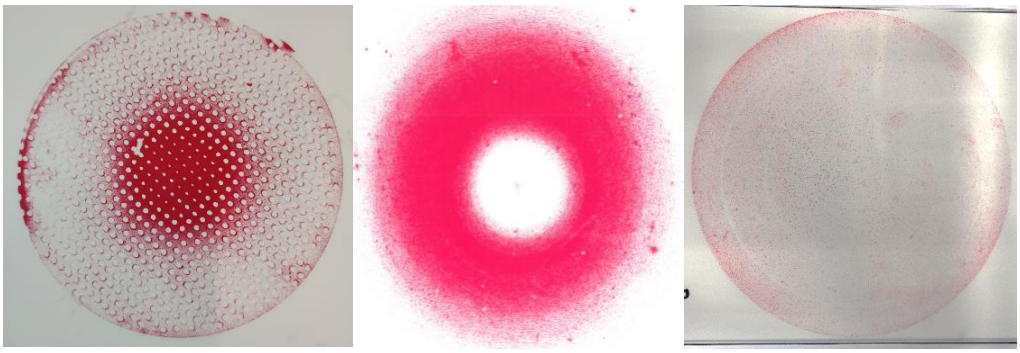

Figure 3. Images of the pressure paper prints used to assess platen parallelism

Three of the participants used pressure sensitive film to assess the parallelism of the platens. Figure 3 shows the resulting images. The intensity of the colour on the pressure-sensitive film corresponds directly to the pressure exerted on the surface of the platen. All three images show the even spread of colour that would be expected from well-aligned platens.

All participants carried out compliance measurements before and after each test series. Representative graphs are given in Figure 4.

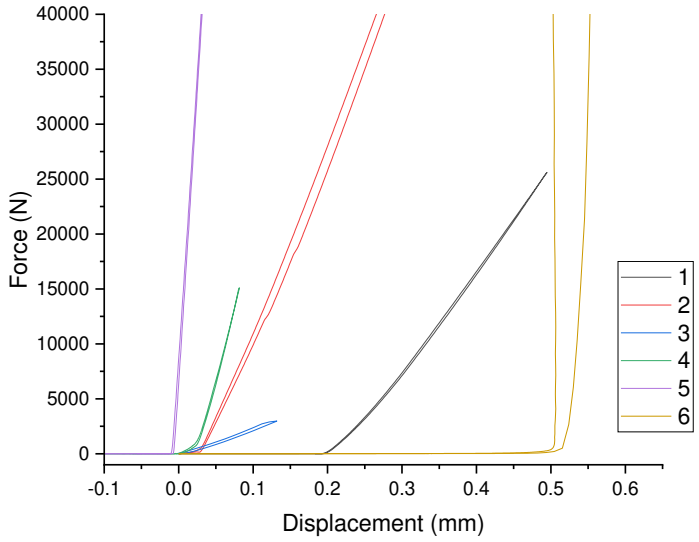

Figure 4. Compliance measurements carried out prior to testing

The results returned to date are given in the graph Figure 5 and Figure 6, which show the maximum pressure at the target thickness of 3 mm. Following the aims of this work to assess the reproducibility of these measurements, the coefficient of variation (c.v.) between participant data was calculated (the coefficient of variation has been used to quantify the scatter). The c.v. for the dry and wet tests was 60% and 49%, respectively. At each site the c.v. ranged from 0.5% to 10% for the dry tests and 1.5% to 13% for the wet tests. In the previous

  doi:10.5075/epfl-298799_978-2-9701614-0-0

benchmark, the coefficient of variation between 26 participants was 38-40% for tests carried out on nominally the same non-crimp fabric.

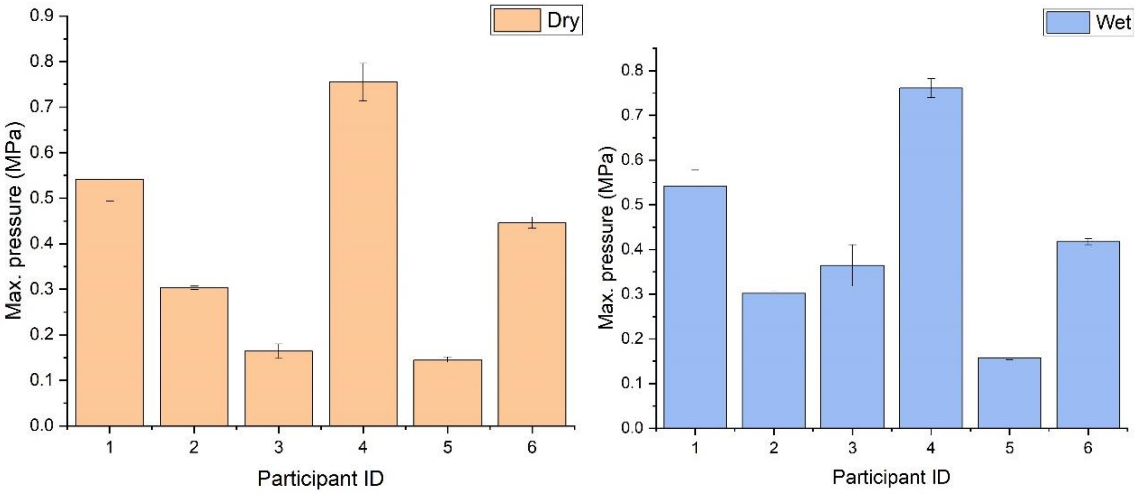

Figure 5. Maximum pressure values for a) dry tests and b) wet tests

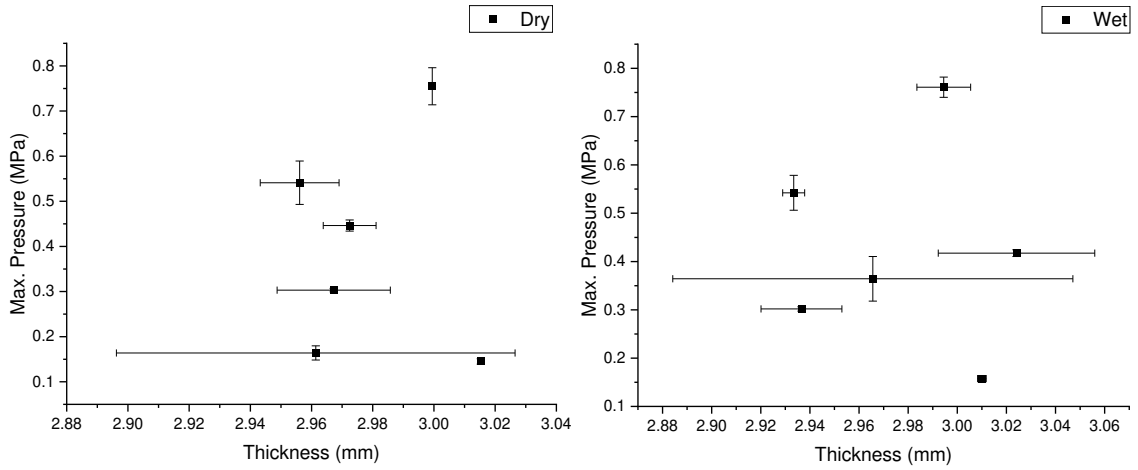

Figure 5. Scatter showing the thickness at maximum pressure for a) dry tests and b) wet tests

5. Conclusions

Two benchmark studies are being carried out using test procedures that have been refined following recommendations given in previous work [4], [5]. The new test procedures introduced limitations to the test setup and test method. Early results presented in this paper show that participants have complied with these two new test procedures without difficulty, which will be an essential component to the eventual standardisation of these test methods.

It has not yet been possible to assess the variation in data between participants for the out-of-plane permeability exercise, however the data returned by one participant show a high degree of repeatability (0.07-0.12% c.v.) following this new test procedure.

  doi:10.5075/epfl-298799_978-2-9701614-0-0

The data returned for the measurement of compaction response show a coefficient of variation at each site of between 0.5% to 13%, however a coefficient of variation between sites of between 49% and 60% for the wet and dry tests, respectively. Further analysis will need to be carried out upon return of the data from all 33 participants in order to isolate the main sources of variation in these tests and provide updated recommendations to the best-practice test procedure.

Acknowledgements

The authors of this paper would like to kindly acknowledge the support of Saertex GmBH by providing the fabric used in this study free of charge. The ongoing contributions of the steering committee and participants are also kindly acknowledged.

6. References

1. Arbter R, Beraud JM, Binetruy C, Bizet L, Bréard J, Comas-Cardona S, Demaria C, et al. Experimental determination of the permeability of textiles: a benchmark exercise. Compos Part A-Appl S, 2011, 42(9):1157-1168.

2. Vernet N, Ruiz E, Advani S, Alms JB, Aubert M, et al. Experimental determination of the permeability of engineering textiles: Benchmark II. Compos Part A-Appl S, 2014, 61:172-184.

3. May D, Aktas A, Advani SG, Endruweit A, Fauster E, Lomov SV, Long A, Mitschang P, et al. In-plane permeability characterization of engineering textiles based on radial flow experiments: a benchmark exercise. Compos Part A-Appl S, 2019, 121:100-114.

4. Yong AXH, Aktas A, May D, Endruweit A, Lomov SV, Advani S, Hubert P, et al. Experimental characterisation of textile compaction response: a benchmark exercise. Composites Part A-Appl S 2021; 142:106243

5. Yong AXH, Aktas A, May D, Endruweit A, Advani S, et al. Out-of-plane permeability measurement for reinforcement textiles: a benchmark exercise. Compos Part A-Appl S 2021; 148:106480.

  doi:10.5075/epfl-298799_978-2-9701614-0-0

DETERMINATION OF A RACETRACKING PASS-FAIL CRITERION FOR EDGE FLOW PERMEABILITY MEASUREMENT

Andrew George[a], Mack Huntsman[a], Arjen Koorevaar[b], Ewald Fauster[c], David May[d]

a: Brigham Young University – andy_george@byu.edu
b: POLYWORX
c: Montanuniversität Leoben
d: Leibniz-Institut für Verbundwerkstoffe GmbH

Abstract: *A unique disadvantage to one-dimensional flow permeability measurement is its sensitivity to flow race-tracking. This usually causes an over-estimation of the measured permeability, but the magnitude of this error is difficult to determine. There currently exists no clear pass-fail criterion for such a permeability test, i.e. how to know when race-tracking caused too much error. This study reports the results of an ISO task force assigned to remedy this. An extensive series of virtual one-dimensional flow experiments was performed using flow simulation, varying the race-tracking channel width as well as several other experimental parameters. The magnitude of race-tracking error in each test was evaluated as the ratio between the measured- and true-permeability. Several candidates for pass-fail criteria were evaluated by comparing them against this ratio. A simple comparison between the flow front positions at the sample edges and middle proved to be an effective correlation to the race-tracking error magnitude.*

Keywords: permeability; racetracking; liquid composite moulding, flow simulation

1. Introduction

A common phenomenon observed in one-dimensional flow is so-called “race-tracking” (RT). This term refers to the preferential flow of the matrix fluid along a path of less resistance, i.e., any path with higher porosity, than the bulk reinforcement. This causes the flow front shape to deviate from a uniform progression, with regions of faster and slower flow [1-3]. Such edgewise RT is often detrimental to processing, as it may result in excessive resin bleeding or dry spots due to sealing off vent-gates with resin flow before the entire reinforcement has been filled [4]. RT is also detrimental during permeability measurement. The high-porosity edge-flow leads to faster filling than what is representative of the reinforcement. This causes an over-estimation of the measured permeability value [5,6]. This magnitude of RT-induced measurement error can be difficult to determine, as it requires both evaluation of the permeability in RT-effected tests, and some way to evaluate the permeability free of such RT. The latter can be done by either: 1) comparison with radial testing results (free of edge-wise RT), 2) several measurements to determine a minimum permeability approximating an RT-free test [3,5], or 3) carefully sealing the edges with a filler before the infusion test [6].

There currently exists no clear pass-fail criterion in the literature, for such a permeability test, i.e., how to know when the data from a particular permeability test must be rejected due to too much RT. Within a broader work to develop an ISO standard for permeability measurement, a

  doi:10.5075/epfl-298799_978-2-9701614-0-0

task force was organized to determine a pass-fail criterion for such RT-induced error. This study reports the results of that task force.

A series of virtual one-dimensional flow experiments was performed by flow simulation, varying the RT channel width along the peripheral edge of the reinforcement. The experiments were repeated with intermittent start / end of the channel, multiple channels, and over-compressed edges, as well as with varied flow orientation angle, sample width and sample length. For each virtual test, the magnitude of RT error that would result during such a permeability test was calculated as the "permeability ratio" between K_M, the permeability as would be measured from that simulated flow experiment by various measurement methods, and K_T, the true reinforcement permeability as input into the simulation.

2. Methodology

2.1 Flow Simulation

A commercial CV-FEM flow simulation package (RTM-Worx) was used for the virtual flow experiments. In all cases the simulation rendered in-plane flow through a rectangular sample with a fluid inlet along the one of the four edges. The average element size was approximately 10 mm. A SALT script was prepared which allows for quick specification of the experimental parameters. The script then calls the flow simulation solver with these parameters. The SALT script includes an algorithm which calculates all the x,y point locations of where the flow front intersects the element edges and tabulates all of these point locations for each time step.

2.2 Permeability Measurement

The apparent permeability K_M represents what the measured permeability would be for this test. The length between the inlet and the flow front, x, is taken from the simulation data, for each time, t. K_M was determined for each test by the traditional linear interpolation of $x^2(t)$. Three different variants of x were used: 1) x_{mid}, at the middle of the sample width W, 2) x_{avg}, the mean location of the flow front, and 3) x_{min}, the minimum location of the flow front. The middle point is by far the easiest of the three options and works with a single linear flow sensor placed along the middle of the mold. x_{mid} will be used for the error calculations throughout this paper.

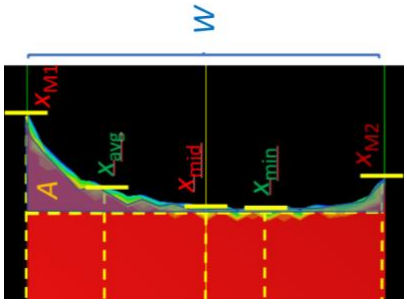

Figure 1. Example flow front image showing various flow front position measurements, sample width W, and racetracking area A.

2.3 RT Metrics

Several metrics of RT magnitude were evaluated as candidates for pass-fail criteria (refer to Figure 1):

  doi:10.5075/epfl-298799_978-2-9701614-0-0

1. "CX" = $(x_M - x_{min})/x_{min}$, where x_M is the max flow front length, either x_{M1} or x_{M2}
2. "CW" = $(x_M - x_{min})/W$
3. "CW2" = $[(x_{M1} + x_{M2} - 2x_{mid})]/2W$
4. "CA" = A/W, where A is the area bounded by x_{min} and the flow front
5. "CL" = Linearity (RMSE) of x_{mid}^2 as a function of the time, for all (x_{mid},t) data
6. "CM" = $|M/K_M|$, M=slope of $K_M(t)$, where K_M is evaluated from the velocity.
7. "CSxt" = Surface fit quality (RMSE) of $x=M(t^{1/2})+B$ for all (x,t) data.
8. "CSxyt" = Surface fit quality (RMSE) of $x=M(t^{1/2})+B+Cy$, where y is along W.

3. Results

3.1 Single RT Channel Diameter

The first tests were made with a nominal sample length (L) and W, and isotropic K, of 600 mm, 200 mm and $1{\cdot}10^{-10}$ m^2 respectively. A single continuous RT channel was simulated along one edge and repeated with progressively greater diameters (D). Figure 2 shows the RT error for K_M measured by all three positions (Figure 1). The resulting error is approximately equal when measured with x_{avg} and x_{mid}. An inflection point is seen in x_{min} and it decreases to no error at high D, as the simulation ends when the flow first reaches the vent, and the RT flow-front hasn't completely developed yet for high D.

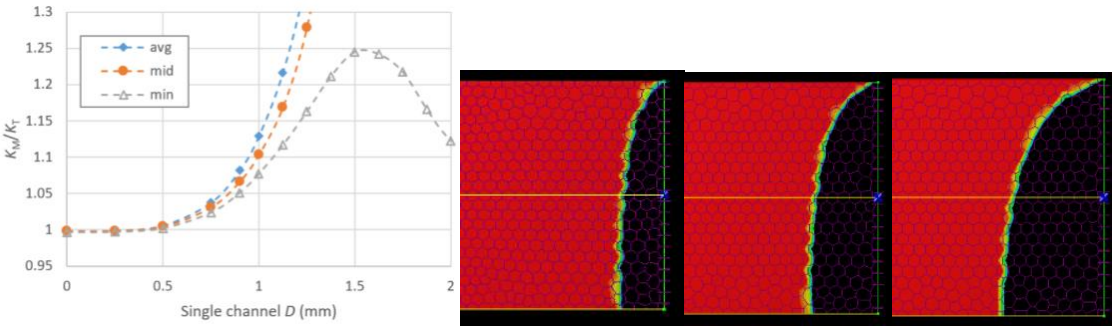

Figure 2. Error ratio for single-sided RT channel D variation (left), and comparison of flow-front for (left-to-right) D=0.9 mm (7% error), 1.0 mm (10% error) and 1.125 mm (17% error).

Figure 2 also shows the flow front shape resulting from select channel diameters. From industrial practice, an edge channel of 1mm diameter causes approximately the same degree of flow front perturbation seen in the average RTM-manufactured part, resulting in a 10% over-estimation of K. With special care devoted to edge cutting for a K test, less RT effect should be feasible. Thus this 10% error (K_M/K_T) was taken as a pass-fail threshold.

Figure 3 shows the various criteria candidates for these simulations with varying channel D. All the criteria seem to be sensitive to the RT error, with a continually positive correlation for this range in error. Any of these metrics would work as a pass-fail criterion; if 10% error is used as the threshold, then each gives a maximum number, beyond which the test is considered a failure due to excessive RT.

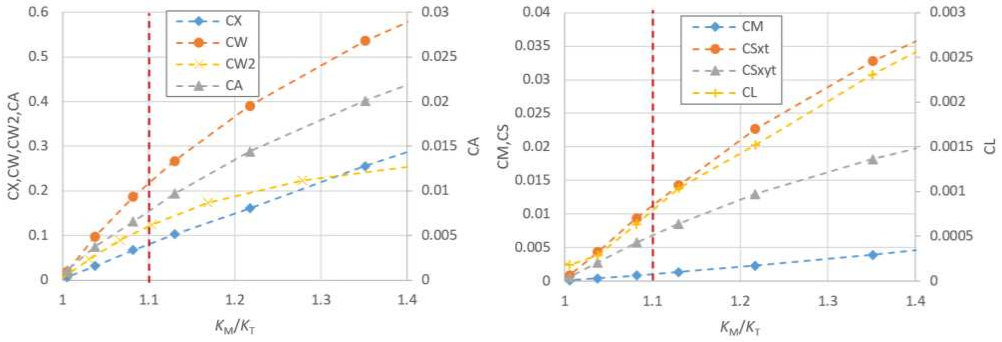

Figure 3. Error-metrics correlation for single channel RT of varying diameter. Red dashed line indicates 10% error threshold.

3.2 Multiple RT Channels

The next set of virtual tests was run with the parameters as the preceding scenario, but with RT channels on both sides of the reinforcement. Holding everything else equal, the resulting error K_M/K_T for both RT sides is double what it is with only one RT side. Figure 4 shows the error for a 1 mm channel on the top side (D_{top}), with varying diameters from 0 to 1 for the bottom channel (D_{bot}); the error rises exponentially as the bottom channel increases in size. This is where most of the criteria prove to be unsuitable (Figure 4). Only CW2, CSxyt, and CL show a positive correlation with the increasing error from the second RT channel. The solid lines in Figure 4 repeat the metric-error correlation from the single channel tests (Figure 3) and show a good match between the correlation for single and double channels for these three metrics. Note that dual-sided RT (both edges) is a common occurrence; the chosen criteria must show a positive correlation with increased error compared to that from only one side RT. This disqualifies all the other criteria.

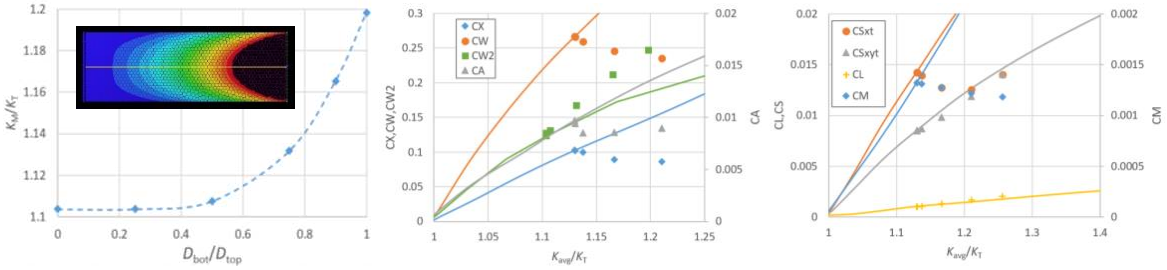

Figure 4. Error-metrics correlation for top 1mm channel with varying bottom channel D.

3.3 Intermittent RT Channels

The next simulated case was an intermittent channel, specifically where there is no RT for an initial duration of the experiment, and a single-sided RT channel then begins. A series of virtual experiments was made for various positions along the top edge length where a 1.5 mm RT channel begins. The error ratios (Figure 5) again support the use of x_{mid}, demonstrating a lower error for x_{mid} compared with x_{avg} based K measurements, and an inflection point in the x_{min}-based measurement.

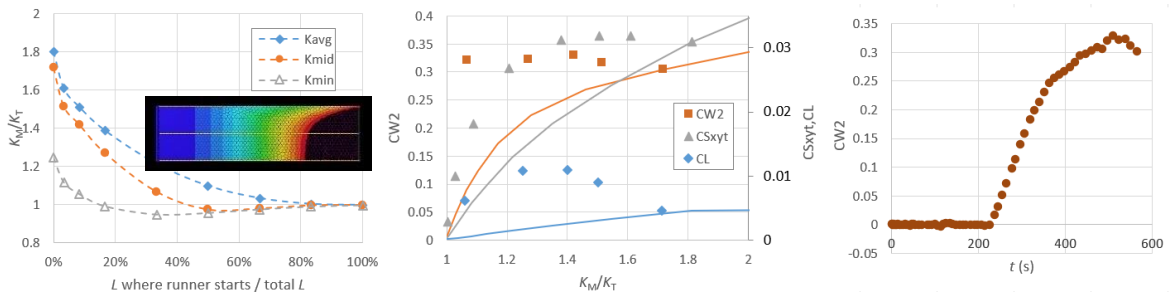

Figure 5. Delayed start of RT: error ratio (left), candidate metrics (center), and CW2 metric as a function of time during one of these tests.

The remaining RT metric candidates are also shown in Figure 5. Again, solid lines denote the continuous single channel correlations from Figure 3. There seems to be an inflection point between 20 and 60% error for all three. In all three cases, the error is higher than it would be with a continuous channel. The CW2 metric is the only one of the three remaining metrics to be evaluated at each time step instead of a fit to all the time steps. This allows the operator to monitor the metric to watch for when it increases above the failure threshold. This is clearly seen in the right-most graph in Figure 5, where the 1.5 mm channel begins at about 225 s into the experiment. All the data before this could still be used (salvaged), and the RT-affected data afterwards thrown out.

3.4 Slow-tracking

When an edge is over-compressed, the opposite of RT, slow-tracking, may occur. Slow-tracking in essence makes the bulk preform the RT region or path of least resistance, thus the slower edges have little effect on the bulk flow. These virtual tests were repeated with one side having a traditional RT channel, and the other side a slow-track channel, but the results were nearly identical to the single channel RT results, as if the slow-track channel didn't exist. This scenario has little effect on either the permeability measurement error or the metric candidates.

3.5 Nonrectilinear flow

If the orientation of the permeability tensor is not already known to lie along either the warp or the weft directions of the reinforcement, then three flow orientations must be tested: 0°, 90°, and 45° (bias). If the permeability is highly anisotropic, the flow front in such a bias flow test will appear diagonal to the sample edges. This will affect the RT criteria, even in the absence of any actual edgewise RT. A virtual test was run with a severe 5:1 anisotropy, without RT, yet still caused a 10% over-estimation in the permeability measurement, similar to a 1 mm RT channel. A wide sample is normally assumed to be beneficial in *K* measurement to mitigate the effects of edge RT. But in this unique scenario of anisotropy and bias direction flow, increasing the width exacerbates the inlet shape inaccuracy and increases the measurement error. A more typical maximum anisotropy for multiaxial reinforcements is about 2, for which the maximum error from bias direction flow for *W*=400 mm is only 4%.

The error and metric candidate correlation during bias flow testing is outside of the scope of this paper due to its complexity. By an approximation, the two rotation scenarios above resemble single- or dual-sided RT, and thus the failure criteria for other scenarios should be similar for this case. However, the CL criteria for this scenario showed negative correlations with permeability

error, up through 50% error. This is only for highly anisotropic materials, in a bias flow test, with RT.

3.6 Length

Another series of tests was done with varying the sample length *L* from 100 to 2,000 mm, holding all else constant (*W* = 200 mm, warp direction flow). This was repeated for a single top-side RT channel of 1.0- and 1.5-mm diameter. This was the first case where K measurement showed a significant difference between x_{avg}- and x_{mid}-based measurement (Figure 6). The middle of the flow-front is unaffected at first by edge-RT, then eventually "pulled" along, thus an increasing error with greater *L*. The error in measurement levels off at around 400 mm and converges with the x_{avg} method. This suggests that shorter length allows less error from RT, but it's commonly accepted that a minimum length is desired to allow the flow front to develop. Ideally, the error is not a function of *L* or the measurement method, and this only occurs for higher *L*. This is demonstrated in the right-most graph in Figure 6, showing the error-CW2 correlation for 300, 400, and 600 mm sample lengths with a 1 mm channel. There is little difference between the latter two *L*'s. At progressively shorter *L*, the CW2 threshold for 10% error increases. In practice, the fail-criteria for a 600 mm test (CW2>0.12) would still result in a failed test for a 300 mm test. The chance for a false-negative increases exponentially for any *L* under 300 mm. Very high *L* (> 600 mm) slightly shifts the correlation curve to the right, and risks greater capillary pressure effects due to slower resin flow at the end of a long sample. Thus a range of 300-600 mm seems appropriate.

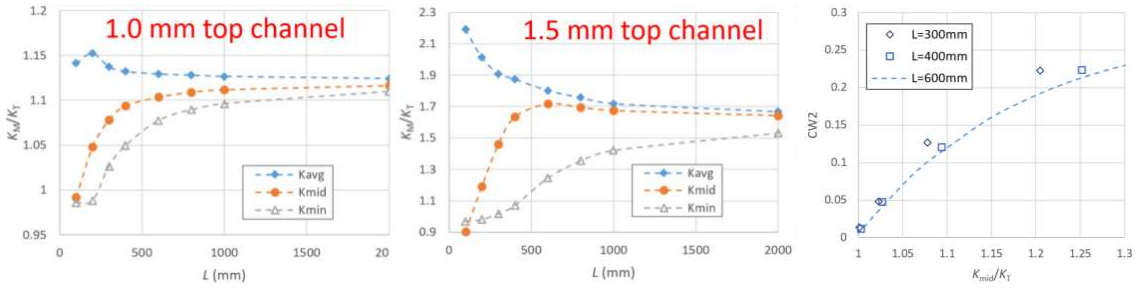

Figure 6. Error ratio for varying L, for a top RT channel of 1.0 mm (left) and 1.5 mm (middle), and CW2 metric correlation (right).

3.7 Width

For warp/weft direction infusions, the sample width *W* is a simpler relationship. Greater W mitigates the error by any measurement method. This is shown in Figure 7 for three different channel diameters. More sample width "dilutes" the edge effects by having more bulk reinforcement to flow through. The benefits (in reduced error) decrease with the size of the channel, and with increasing *W*. Mold deflection becomes a greater challenge with high *W* as well. As mentioned above, increasing *W* actually causes higher error for bias direction flow tests. Thus a middle-ground value of 150 mm is recommended.

  doi:10.5075/epfl-298799_978-2-9701614-0-0

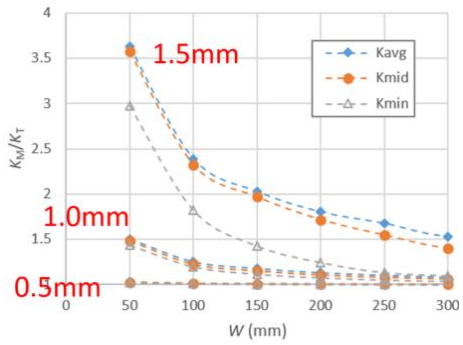

Figure 7. Error ratio for varying W, for a three top RT channel D's.

3.8 Criteria Robustness

The two candidate metrics for RT pass-fail criteria, which seemed to work reasonably throughout all these scenarios are CW2 and CSxyt. The surface fit, CSxyt, is a robust method, where point-to-point difference are mitigated by averaging from the extensive data set. But the requirement for many data points is its greatest weakness. These virtual tests were performed with approximately 100 time steps for each virtual infusion, and 50 *x*,*y* points along the flow front at each time step. This high resolution of data sampling would require significant imaging capability and extensive image analysis and would be difficult to do in practice. The RMSE (fit quality) of the CSxyt metric is highly sensitive to the total number of data points, and a nonlinear relationship. How this would affect the CSxyt metric's correlation to the RT error ratio is difficult to model. This essentially excludes the possibility to work with flow sensors instead of optical tracking. That CSxyt-to-error correlation also proved to be highly sensitive to the sample width and anisotropy.

For simplicity's sake, and to allow a non-optical system, the CW2 metric was recommended to the ISO committee. This proved to be less sensitive to the test parameters compared with CSxyt and relies on only three measurements for each time step, allowing either optical visualization or a simple three-line array of sensors. The CW2 threshold for a particular error is not significantly affected by: *K*, channel size, single or double channel, number of sides affected, or the number of measurements.

To adjust the CW2 threshold for anisotropy and length, the CW2 number representing 5% and 10% error was plotted for the various scenarios in Figure 8. The anisotropy here represents the ratio of *K* in the flow direction, to *K* transverse to that direction, whatever those are for the particular flow test. Logarithmic fits of $y=A\cdot\ln(x)+B$ worked well with the data. As the slope constant *A* seems fairly uniform, this was approximated as a constant, taken as the average, thus $A = 60$ for both error values. The intercept, *B* is more sensitive to *L*. The values of *B* were adjusted to fit better with A=60, and then fit to their own linear model as a function of *L* (right-side of Figure 8). This allows an approximate adjustment of the pass-fail criteria for any anisotropy of 0.6 to 5, and any *L* from 300 to 600 mm.

  doi:10.5075/epfl-298799_978-2-9701614-0-0

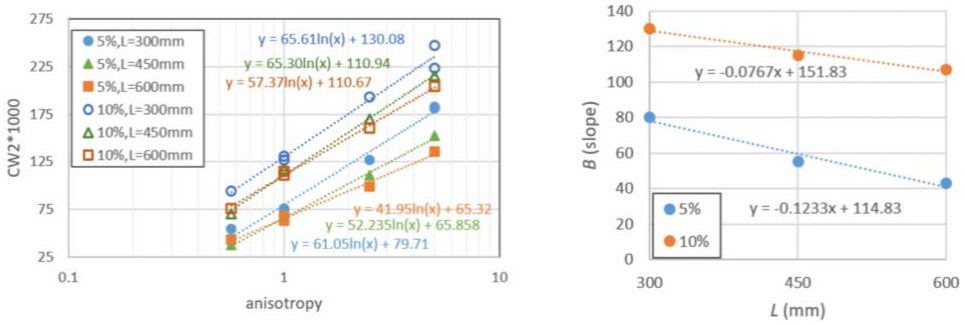

Figure 8 – CW2 threshold for 5% error and 10% error, for various anisotropy and L (left), and relationship (right) between L and the y-intercept (in the left graph).

To adjust for different sample widths, the threshold CW2 value for 5% and 10% error was determined for W = 100, 150, and 200 mm, for high and low isotropic K values, and a set L=300 mm. The threshold CW2 was nearly identical for both K values and error tolerances, but a linear relationship with the sample width, CW2(W)/CW2(W=150mm) = 0.41·(W/150mm)+0.61. This adjustment works for L=300 and anisotropy α=1, but not so well for other L and α, resulting in differences of up to 50% in the CW2 threshold. For this reason, the sample W was prescribed to 150 mm.

4. Conclusions (Pass-Fail Criteria Recommendation)

The recommended RT pass-fail criteria for unidirectional K measurement is as follows. For a sample of L = 300 to 600 and set W = 150 mm, the operator measures (x_{M1}, x_{M2}, x_{mid}) at various values of time t during the flow test, then calculates CW2 (= $[(x_{M1}+ x_{M2}- 2x_{mid})]/2W$) for each t. For a 10% error limit, the CW2 pass/fail threshold is calculated as $0.06\cdot\ln(\alpha) - 0.077 m^{-1}\cdot L + 0.152$. If at any point during the infusion the CW2 value exceeds this threshold, then any subsequent data is rejected.

5. References

1. Bickerton S, Advani SG. Characterization and modeling of race-tracking in liquid composite molding processes. Composites Science and Technology 1999; 59:2215–29.
2. Lundström TS, Toll S, Håkanson JM. Measurements of the permeability tensor of compressed fibre beds. Transport in Porous Media 2002; 47:363-80.
3. Devillard M, et al. On-line characterization of bulk permeability and racetracking during the filling stage in resin transfer molding process. Journal of Composite Materials 2003; 37:1525–41.
4. Siddig NA, et al. A new methodology for race-tracking detection and criticality in resin transfer molding process using pressure sensors. Journal of Composite Materials 2018; 52:4087-103.
5. Lawrence JM, et al. Characterization of preform permeability in the presence of race tracking. Composites Part A 2004; 35:1393-1405.
6. Berg DC, et al. Influence of inaccuracies in permeability measurements. ECCM 2014.

  doi:10.5075/epfl-298799_978-2-9701614-0-0

FIRST INSIGHTS FROM THE VIRTUAL PERMEABILITY BENCHMARK ON A FIBROUS MICROSTRUCTURE

Tim Schmidt[a], Elena Syerko[b], David May[a], Christophe Binetruy[b], Luisa Silva[b], Stepan V. Lomov[c], Suresh G. Advani[d]

a: Leibniz-Institut für Verbundwerkstoffe GmbH, Erwin-Schroedinger-Straße 58, 67663 Kaiserslautern, Germany – tim.schmidt@ivw.uni-kl.de,
b: Ecole Centrale de Nantes, Research Institute in Civil Engineering and Mechanics (GeM), UMR CNRS 6183, 1 Rue de la Noë, 44321 Nantes, France – elena.syerko@ec-nantes.fr
c: KU Leuven, Department of Materials Engineering, Kasteelpark Arenberg 44, 3001 Leuven, Belgium
d: University of Delaware, Department of Mechanical Engineering, 126 Spencer Lab, DE 19716 Newark, USA

Abstract: *Permeability is a key parameter to predict the impregnation of fibrous structures by resin. Numerical permeability prediction (NPP) is becoming more and more important, but the number of influencing parameters for NPP is enormous and many seem to have a considerable impact. The Virtual permeability benchmark was launched to get an overview of methods used by researchers and possible sources of variation. The approach was to send a segmented 2D-image stack and a corresponding 3D-volume of a fibrous microstructure to 16 participants, in order to calculate the permeability tensor and fill out a questionnaire about their methodology. This provides a holistic image of the procedures for NPP and allows identification of differences between the methods and hence sources of variation. The benchmark showed, for instance, that the deviation range of the axial permeability was much smaller than that of the permeabilities transverse to the fiber direction.*

Keywords: Numerical calculation, Permeability, Benchmark, Image-based computation, Impregnation

1. Introduction

Liquid Composite Molding (LCM) processes are widely applied to manufacture various components made of fiber reinforced polymer composites. In LCM, dry fiber structures (usually technical textiles) are impregnated with a resin system. When designing LCM processes, it must be ensured that full impregnation is reliably reached and for this task numerical filling simulations are used to predict the filling pattern. However, filling simulations can only be as good as their input parameters, especially those characterizing the material behavior. A key material property in this context is the permeability, which quantifies the resistance of the fiber structure to the resin flow. This permeability can be determined experimentally, but is very elaborate and time consuming and shows considerable variation [1, 2]. Numerical permeability prediction (NPP) has great potential in this context, as extensive parameter studies can be carried out quite easily, which would not be feasible experimentally, either for economic reasons or also for technical reasons. However, virtual permeability prediction also involves several challenges, especially due to the complex fiber structure, with multiscale pore structure

  doi:10.5075/epfl-298799_978-2-9701614-0-0

(Figure 1) and extensive structural variations. In addition, today there is a multitude of applied methods and boundary conditions for the NPP, presumably leading to differing results.

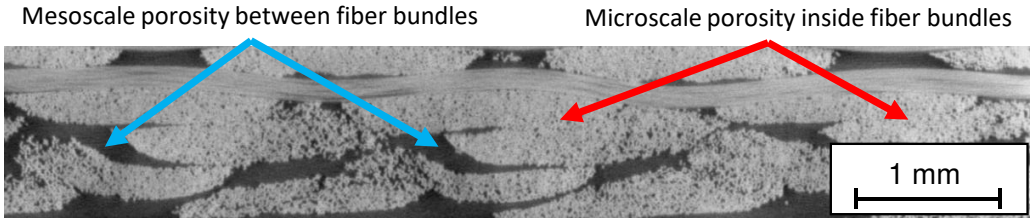

Figure 1. Cross section through a textile showing the multiscale porosity between and inside the fiber bundles

Due to the multiscale porosity, it is convenient to use multiscale approaches for virtual permeability prediction, i. e. simulation of flows within fiber bundles separately from flow between them. A distinction is therefore made between the microscale (fiber level, µm-range) within fiber bundles, the mesoscale (textile level, mm-range) and the macroscale (component level, m-range). For the prediction of permeability, micro- and mesoscale are relevant, and can be averaged and then used on the macro scale for the filling simulations.

The target of the presented work was to benchmark methods and techniques applied around the world for virtual permeability prediction. In the first step, presented in this paper, the focus was solely on the microscale. Therefore, the basic idea was to send out segmented images of the microstructure of a textile reinforced polymer at the scale of fiber bundles. Based on these images, the participants embarked on the task to calculate the permeability tensor and to fill out a detailed questionnaire about the numerical method and boundary conditions they used. This benchmark was organized by Ecole Centrale de Nantes, Research Institute in Civil Engineering and Mechanics (GeM, Nantes, France) and Leibniz-Institut für Verbundwerkstoffe GmbH (IVW, Kaiserslautern, Germany), and supported by Fraunhofer Institute for Industrial Mathematics (Germany), KU Leuven (Belgium), High Performance Computing Institute (ICI, Nantes, France), and University of Delaware (USA) as members of the Advisory Board. Table I lists the 16 research groups that participated in the virtual permeability benchmark exercise.

2. Materials & Methods

With the aim of providing the participants with a realistic fiber structure model, a plate was made from a glass fiber fabric and epoxy resin via the RTM process. In the sample plate, with a size of 465 x 465 mm² and thickness of 3.0 mm, 14 equally oriented layers of the glass fiber fabric Hexcel HexForce 01102 1000 TF970 were placed. This results in fiber volume content (FVC) of 54% within the plate, which will allow one to investigate a more pronounced multi-scale character of flow through the textile. The epoxy resin system Hexion EPIKOTETM Resin MGSTM RIMR 935 with EPIKURETM Curing Agent MGSTM RIMH 936 was used for impregnation. The Hexcel glass fiber twill weave 2/2 is a balanced fabric (weight distribution: 50% warp and 50% weft) with a nominal weight of 295 g/m2. The fiber bundles in the textile consist of three EC9 68 glass fiber yarns twisted in a tow (40 twist/m) in warp and weft directions. The fiber bundles with a linear density of 68 g per 1000 m consists of continuous filaments of electrical glass (E-glass) with a theoretical diameter of 9 µm. Variation of filament diameters between 7.5 - 9.3 µm was further determined from cross-sectional micrographs. A sample was extracted from the plate and scanned in a X-ray microscope.

  doi:10.5075/epfl-298799_978-2-9701614-0-0

Table 1: List of participants

Institution / Department	Participant
École Polytechnique Fédérale de Lausanne / Laboratory for Processing of Advanced Composites (LPAC) Université Grenoble Alpes – CNRS / Laboratory Soils, Solids, Structures, Risks (3SR Lab)	Veronique Michaud, Baris Caglar, Guillaume Broggi, Laurent Orgéas, Sabine Rolland du Roscoat
Ferdowsi University of Mashhad National University of Singapore RISE Research Institute of Sweden	Naser Asiaban, Masoud Tahani, Mohammad Rouhi
Fraunhofer Institute for Industrial Mathematics (ITWM)	Stefan Rief, Katja Schladitz
Ecole Centrale de Nantes / High Performance Computing Institute	Luisa Rocha da Silva, Hughes Digonnet, Nesrine Aissa
IMT Lille Douai, Centre for Materials and Processes	Modesar Shakoor, Chung Hae Park
University of Stuttgart / Institute of Aircraft Design	Jörg Dittmann, Peter Middendorf
Khalifa University of Science and Technology	Muhammad A. Ali, Rehan Umer
KU Leuven / Department of Materials Engineering, Composite Materials Group	Roman Kandinskii, Yentl Swolfs, Stepan V. Lomov
Leibniz-Institut für Verbundwerkstoffe GmbH	Tim Schmidt, David May
Ecole des Mines de Saint-Etienne – CNRS / LGF	Nicolas Moulin, Julien Bruchon, Sylvain Drapier
Ecole Centrale de Nantes - CNRS / Research Institute in Civil Engineering and Mechanics (GeM)	Elena Syerko, Adrien Leygue, Christophe Binetruy
Siemens Industry Software NV	Oxana Shishkina, Paula Martinez, Kristof Vanclooster
Skolkovo Institute of Science and Technology / Center for Design, Manufacturing and Materials	Biltu Mahato, Iskander S. Akhatov, Sergey G. Abaimov
Skolkovo Institute of Science and Technology / Center for Design, Manufacturing and Materials	Ruslan Vorobyev, Ivan Sergeichev, Iskander S. Akhatov
TENSYL	Alexandre Guilloux
University of Nottingham / Composites Research Group, Faculty of Engineering	Mikhail Matveev, Andreas Endruweit

Scanning & Segmentation

In order to achieve the resolution and contrast between the scanned materials to be as high as possible, a small cut-out of 1 x 1 x 3 mm^3 was prepared. This was done with a precision cutter under permanent cooling in order not to affect the structure due to the heat input into the sample. The 3D scan was performed by using the X-ray Microscope Zeiss Xradia 520 Versa 3D at IVW. The sample was scanned with a voxel size of 0.521 μm^3 (Figure 2). A voxel is a uniform cubic element, comparable to a pixel in 2D-images. From the scanned volume, a subvolume (Region of interest) of 1003 x 124 x 973 voxels (523 x 65 x 507 μm^3) was extracted from a single fiber bundle covering the bundle height and containing about 400 fibers. Here, the subvolume of the scan is referred to as a microscale volume (MSV). Since a segmentation by conventional thresholding techniques can lead to false inter-fiber ''bridges'' that can have a significant impact on the permeability predictions, the segmentation of the MSV was performed at ECN via the

  doi:10.5075/epfl-298799_978-2-9701614-0-0

following steps (figure 2): a Hough transformation was applied to each 2D-slice of the volume separately in the first step to detect each fiber center and its circular cross section. In the second step, the single fibers were labeled and their paths through-out the slices were identified using the closest neighbor algorithm. In the third step, a 3D-smoothing of the fiber paths was performed over the volume by local regression using weighted linear least squares and a 1st degree polynomial model. This workflow led to a volume with two phases: fibers (white) and pores (black). The fiber fraction of the 2D slices varied between 54% and 59% along the fiber direction. Varying FVC within the fiber bundles in the textile results from the fabric architecture, wherein the fiber bundles intersect and are locally more or less compacted. Over the entire MSV, the average FVC was 56.46%.

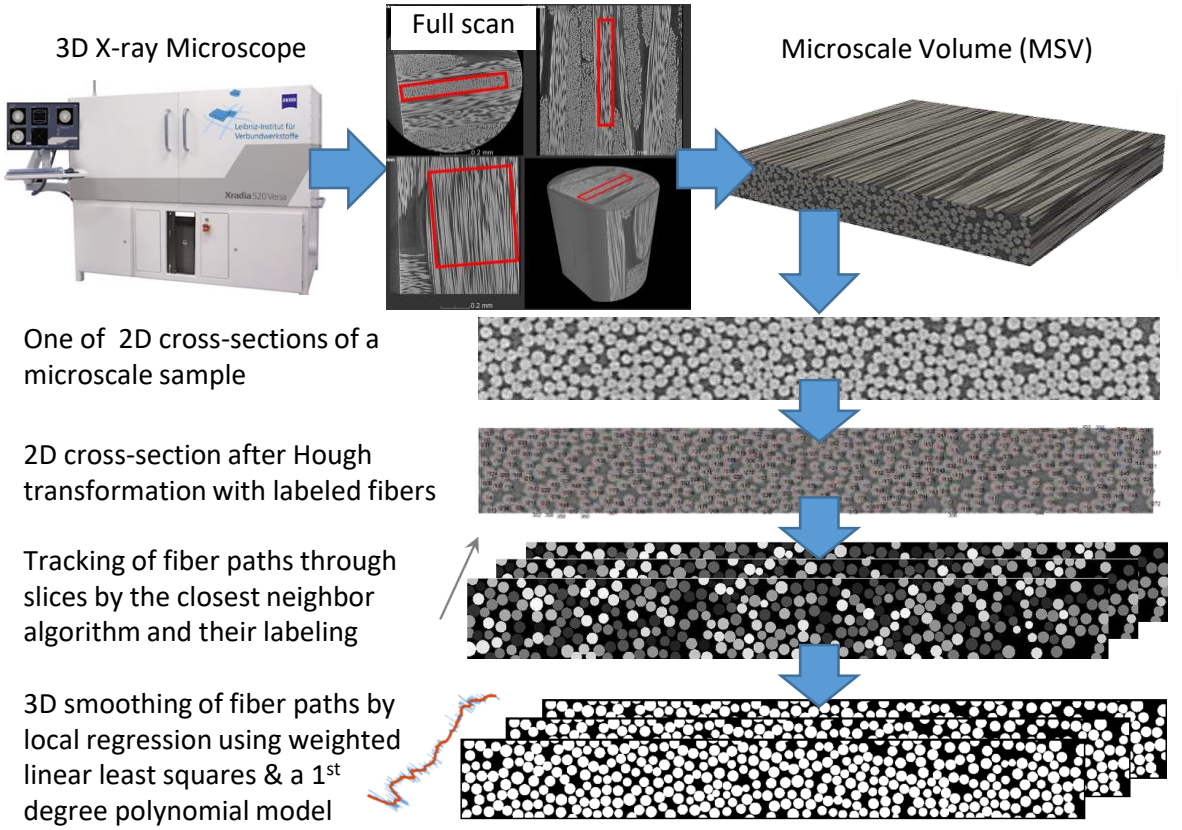

Figure 2: From 3D-Scan of a cut-out to the segmented MSV

Data Set & Task Definition

A data package consisting of the guidelines, the MSV segmented and not segmented as a 3D-raw-file and in form of a stack of 973 2D-images was sent to all participants. The guidelines contained a description of the task as well as a questionnaire for the description of the applied methodology and for the determined results. The mandatory task for all participants was to calculate the permeability tensor based on the segmented MSV and to fill out the questionnaire. There were no further limitations regarding the permeability determination, participants could freely choose the methods they find most promising given their available computational capacity. The model could also be reduced in size or subdivided into subvolumes. Further optional tasks were the prediction of the permeability tensor based on a self-segmented MSV or using analytical methods. Table 2 gives an overview of the methods used for the mandatory task by the 16 participants.

  doi:10.5075/epfl-298799_978-2-9701614-0-0

Table 2: Methods used for the numerical calculation of the permeability of the segmented MSV

Participants	Numerical approximation	Discretization	Flow model	2D or 3D formulation	Physical variables	Model size in voxel	FVC in %
1	FVM	Voxel-based	Stokes	3D	SIMPLE	1003x973x124 0.521 µm³	56.46
2	FEM	Geometry-based	Navier-Stokes	2D	mixed velocity-pressure	10 2D slices of 1003x124 0.521 µm³	56.73, 58.54
3	FVM	Voxel-based	Navier-Stokes	3D	mixed velocity-pressure	1800x180x200/ 0.2605 µm x 2.605 µm x 0.2605 µm	57.00
4	CVFEM	Voxel-based	Navier-Stokes	3D	mixed velocity-pressure	10 sub-volumes of ≈ 1003x100x124 for Kxx, Kzz 0.521 µm³	56.47
5	FVM	Voxel-based / LIR	Stokes	3D	mixed velocity-pressure	10 sub-volumes ≈100x973x124 for Kyy 0.521 µm³	56.46
6	FEM	Geometry-based	Stokes	2D	mixed velocity-pressure	1003x973x124 0.521 µm³	55.87
7	FVM	Geometry-based	Navier-Stokes	3D	SIMPLE	973 2D slices of 1003x124 0.521 µm³	59.87
8	FDM	Voxel-based	Stokes	3D	mixed velocity-pressure	1003x973x124 0.521 µm³	57.16
9	FVM	Geometry-based	Stokes	3D	mixed velocity-pressure	972x972x108: 648 sub-volumes of 54x54x54 0.521 µm³	56.36 (46.96 – 60.84)
10	FEM	Voxel-based	Stokes	3D	pseudo-compressibility (penalization)	16 sub-volumes of ≈251x243x124/ 0.521 µm³	56.46 (46.49 – 61.81)
11	FVM	Geometry-based	Navier-Stokes	3D	mixed velocity-pressure	64 sub-volumes of ≈126x122x124/ 0.521 µm³	58.69
12	FVM	Voxel-based / LIR	Stokes	3D	SIMPLE	1003x679x124 ≈0.7368 µm³	56.46
13	FVM	Geometry-based	Navier-Stokes	3D	mixed velocity-pressure	1003x973x124 0.521 µm³	59.54
14	FEM	Geometry-based	Stokes	2D	mixed velocity-pressure	124x192x124 0.521 µm³	56.40
15	FEM	Geometry-based	Stokes	3D	mixed velocity-pressure	973 2D slices of 1003x124 0.521 µm³	56.46
16	FVM	Voxel-based / LIR	Stokes	3D	mixed velocity-pressure	1003x973x124 0.521 µm³	56.46

The majority of participants used the finite volume method (FVM) for the numerical resolution; participant #8 used the finite difference method (FDM) whereas participant #4 applied the finite-element control-volume method (CVFEM), and the rest used the finite element method (FEM). The discretization used is geometry-based or voxel-based for half of the participants,

respectively. Similarly, an almost equal number of contributions can be seen for the Stokes and Navier-Stokes flow models. Three participants #2, #6, and #14 performed the calculations in 2D on the cross-sectional slices perpendicular to fiber direction. Five participants #4, #8, #9, #10, and #16 divided the 3D model into 10 to 648 sub-volumes for calculation and averaged the respective permeability results to one final tensor. Not using the entire model affects the FVC for each calculation, since it varies locally in the fiber bundle. Thus, values between 46.49% and 61.81% FVC can be found in Table 2. An interesting fact here is, that out of the 16 participants, there were no two participants who used exactly the same methods and boundary conditions.

3. Results

In total, 16 benchmark participants submitted 49 results. Each of these participants calculated the permeability tensor (or diagonal components) based on the segmented model. In addition, two participants provided three analytically calculated results and seven other participants provided between one and 21 additional numerically calculated results for self-segmented models, sub-volumes, different solver, different boundary conditions and different convergence criteria for the numerical calculation. A first overview of the results was already given at the 36th Technical Conference of the ASC [3]. An overview of all 49 results is presented in Figure 4 (left), showing significant variation.

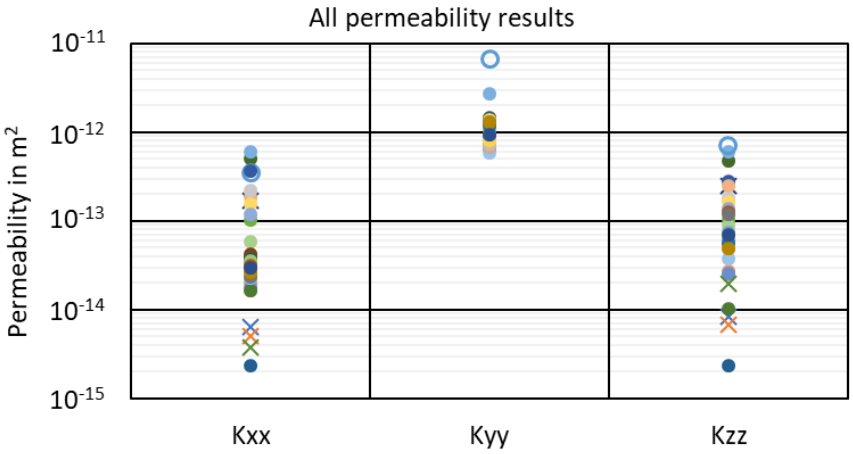

Figure 4: Overview of all results: Kxx & Kzz (transverse) and Kyy (axial) - In the diagram the 2D results are marked as cross and #11 only with the outline

The coefficients of variation are 80% in fiber direction (Kyy), and 162% (Kxx), respectively 130% (Kzz) transverse to the fiber direction. This clearly underlines the significance of this benchmark study. Model meshing, cropping etc. can lead to substantial variation in the FVC, which is known to be one of the most influencing parameters on the permeability. But the data scatter in the two diagrams in Figure 5 implies, that there must be more sources of variation. In these diagrams the permeability is plotted over the FVC. Usually, a correlation between the fiber volume content and the permeability is expected, which is absent for the transverse permeability values, and can be partially followed for the axial permeability. In principle, these are plausible results, since the axial permeability (fiber direction - Kyy) are higher with a mean value (MV) of 1.45×10^{-12} m^2 than the transverse permeability (transverse to the fiber – Kxx and Kzz). Furthermore, the transverse permeability components are quite close together: MV for Kxx: 1.06×10^{-13} m^2 and MV for Kzz: 1.41×10^{-13} m^2. When excluding the results of participant #11 as an obvious outlier, as well as the results of #2, #6 and #14 since they performed the calculations

  doi:10.5075/epfl-298799_978-2-9701614-0-0

in 2D, the transverse permeability scatters over two orders of magnitude while the CV of the axial permeability decreases by a value of 25%. Significantly higher permeability of participant #11 is due to the fact that, firstly, the indicated domain dimensions (resolution) were not respected – the used volume was bigger, and, secondly, it was generated by extrusion of one taken from a 2D cross-section, and thus did not include fibers misalignment.

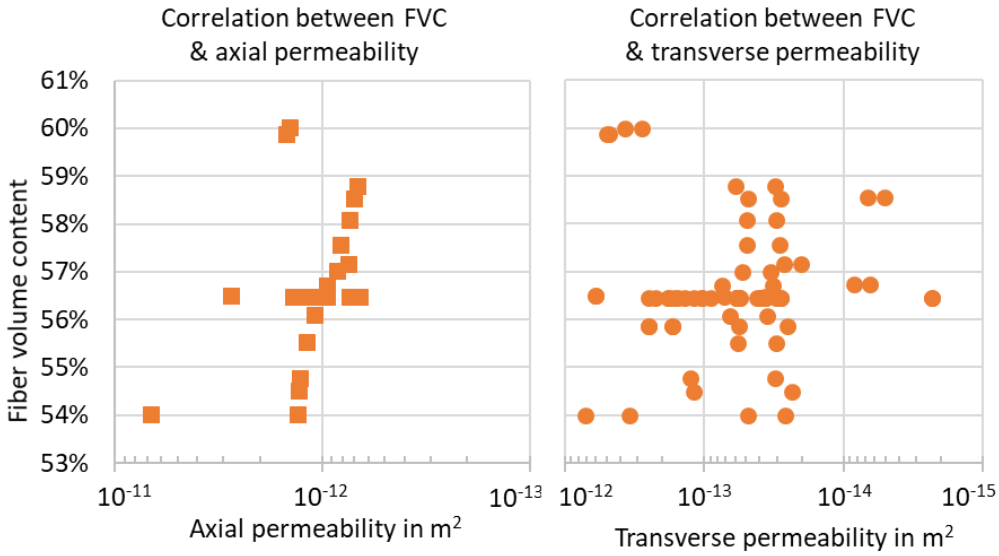

Figure 5: Correlation between FVC and permeability of all results – Diagram axial permeability without 2D results

Despite working with an already segmented model volume, such deviations from the actual FVC of the complete sample can result from cropping or the domain meshing. A CV of 25% is close to experimental permeability determination variations, as has been shown in experimental permeability benchmark studies [1, 2]. Further significant sources of variation could be identified, but as many variations superimpose, additional investigation of the results is necessary to get a clear understanding on the effect of different parameters and their cross-correlations. However so far, the results indicate a significant impact of the following simulation parameters:

- Model size, averaging of sub-volume results
- Meshing
- Boundary conditions in flow and tangential directions
- Numerical approximation method
- Flow formulation (Stokes or Navier-Stokes equation)
- Physical variables formulation used for computation
- 2D vs. 3D formulations

4. Second stage of the virtual permeability benchmark

The second stage of the Virtual Permeability Benchmark will be concerned with the mesoscale or textile level. The same principle will be applied: The participants will be provided with segmented images of the woven structure of a textile composite (see figure 6). Based on these images, the participants will be asked to calculate the permeability tensor based on the mesoscale simulations and to fill out a detailed questionnaire about the methods used. At the mesoscopic scale, the additional point as opposed to the micro-scale benchmark stage will be to assign a specified microscale permeability to the fiber bundles. In the scanned images at this

  doi:10.5075/epfl-298799_978-2-9701614-0-0

scale the fiber bundles appear as a continuum since the scanning was done with a resolution of eight µm, which does not allow one to distinguish fibers, but allows one to create a larger scan that includes a sufficiently large section of the textile. In order to account for the orientation of the microscale permeability tensor, the textile was segmented into two groups: fiber bundles in 0° direction (warp) and fiber bundles in 90° direction (weft). An additional map of local orientations is provided to also provide the information of the out-of-plane fiber undulation. Again, the objective is to benchmark the methods and tools used worldwide for determining permeability at the textile level, possibly taking into account the multiscale flow character.

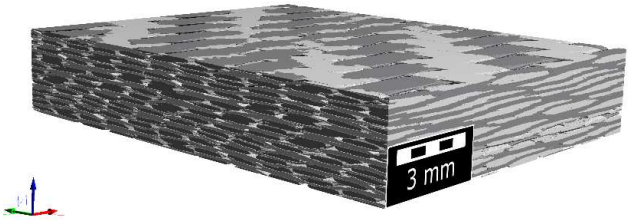

Figure 6: Segmented mesoscale scan for the second stage of the benchmark

5. Conclusion

Even on this comparatively simple microscale structure of unidirectional fibers, the results were found to scatter considerably over two orders of magnitude based on the methodology and methods used by the participants. It should be noted that a significant source of variation - image processing - was eliminated by providing segmented images stacks. The fact that such a scattering of permeability values nevertheless occurs shows the importance of this benchmark study. After the first stage of the benchmark one may expect that at the mesoscale level the variation can be even higher due to more complex structure and more options in terms of numerical modeling. The data package for the second stage (mesoscale benchmark) is prepared. In order to reduce the variation in the results of the second benchmark stage, recommendations and adjustments to the guidelines for numerical permeability prediction are formulated based on the microscale results. Also, the intention is to minimize superposition of sources of variation, so that a more quantitative analysis is possible. Through these efforts, the benchmark studies are intended to increase confidence in numerical permeability prediction and develop sound methodological guidance in the future.

Acknowledgment

We would like to thank all participants of the first microscale stage of the benchmark study and hope for numerous participants in the second stage, the mesoscale benchmark study.

6. References

1. Yong AXH, Aktas A, May D, et al. Experimental characterization of textile compaction response: A benchmark exercise. Composite Part A: Applied Science Manufacturing. 2021. https://doi.org/10.1016/j.compositesa.2021.106480
2. May D, Aktas A, Advani SG, et al. In-plane permeability characterization of engineering textiles based on radial flow experiments: A benchmark exercise. Composite Part A: Applied Science Manufacturing. 2019. https://doi.org/10.1016/j.compositesa.2019.03.006
3. May D, Syerko E, Schmidt T, Binetruy C, et al. Benchmarking virtual permeability predictions of real fibrous microstructure. Proceedings of the American Society for Composites 36th Technical Conference 2021; 2123-2132.

  doi:10.5075/epfl-298799_978-2-9701614-0-0

FAILURE OF COMPOSITE LAMINATES UNDER FATIGUE LOADING: A FOCUS ON THE EFFECT OF MATRIX DAMAGE ON RESIDUAL STRENGTH

Christophe Bois [a], Christian Hochard[b], Noël Lahellec[b], Olivier Montagnier[b,c], Jean-Christophe Wahl[a]

a: Bordeaux University, Institut de Mécanique et d'Ingénierie de Bordeaux, CNRS, Esplanade des Arts et Métiers, 33400 Talence, France, christophe.bois@u-bordeaux.fr
b: Aix-Marseille University, CNRS, Centrale Marseille, LMA, 4 impasse Nikola Tesla 13453 Marseille, France
c: Centre de Recherche de l'Armée de l'Air, École de l'air, B.A. 701, 13661 Salon-Air, France

Abstract: *Predictive models for fatigue life and residual strength of composite laminates are generally expressed as a function of the number of cycles applied to a given laminate sequence. Phenomenological laws deduced from tests are therefore loading dependent and identifying a relevant model for various loading conditions and stacking sequences requires expensive testing procedure. Ply scale models based on damage mechanics makes it possible to overcome this limitation. In these models, stiffness loss due to damage is represented by internal variables. However, in most of applications, the final failure of the structure is not related to stiffness loss but to the strength in fibre direction. Fibre-matrix decohesion and matrix cracks reduce the capacity of the matrix to transfer loads between fibres. These damages therefore reduce the material strength in fibre direction. This paper present specific testing procedures used to highlight this phenomenon and several results obtained for various material.*

Keywords: fatigue damage; residual strength; multiaxial loading; ply scale model

1. Introduction

Residual strength in composite laminates after fatigue loading has been studied for decades. Predictive models are generally expressed as a function of the number of cycles applied to a given laminate sequence subjected to a given loading. Phenomenological laws deduced from tests are therefore loading dependent and identifying a relevant model for various loading condition of a given laminate requires long testing campaigns.

To overcome this difficulty, some authors have proposed ply scale models based on damage mechanics. In these models, stiffness loss and residual strains due to matrix damage is represented by internal variables. However, in most of applications, the final failure (maximal load) of the structure is not related to stiffness loss but to the strength in fibre direction. Actually, after fatigue loading, the residual static load that the material could support will be less than the load it was able to support before fatigue loading. This phenomenon is mainly explained by the fact that once fibre-matrix decohesion and matrix cracks develop, matrix progressively loses its capacity to transfer loads between all the fibres. As soon as loads cannot be distributed between fibres, deviations in material configuration make some fibres more loaded than others and early progressive fibre failures will result in a decrease in its strength.

In this paper specific testing procedures developed by LMA Marseille and I2M Bordeaux research teams to highlight and quantify the effect of matrix and fiber matrix interface damage

on strength in fiber direction are described. Results on both residual tensile and compressive strength for different materials are then presented and analyzed.

For more details on the different studies summarized in this paper, the reader could refer to numerous publications quote in this paper.

2. Experimental procedure

2.1 Multi-axial test on tubes

The test procedure consists in generating a fatigue shear loading on a $[0]_n$ tube by applying a torsion torque. Several numbers of cycles were selected in order to generate various level of damage. Then, a tensile or compressive load was applied to evaluate the residual strength in fibre direction according to the level of matrix damage. The tube shape was studied so that the strain field was homogeneous in the central area [1,2]. An example of the geometry of a specimen for a glass epoxy laminate made of unbalanced woven plies is represented on Figure 2.

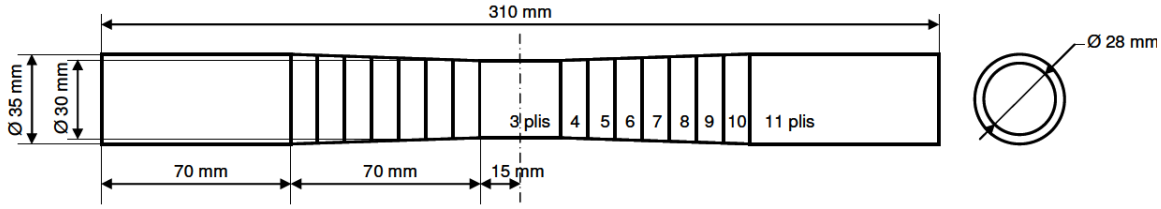

Figure 1. Tube shape for multi-axial tests [1]

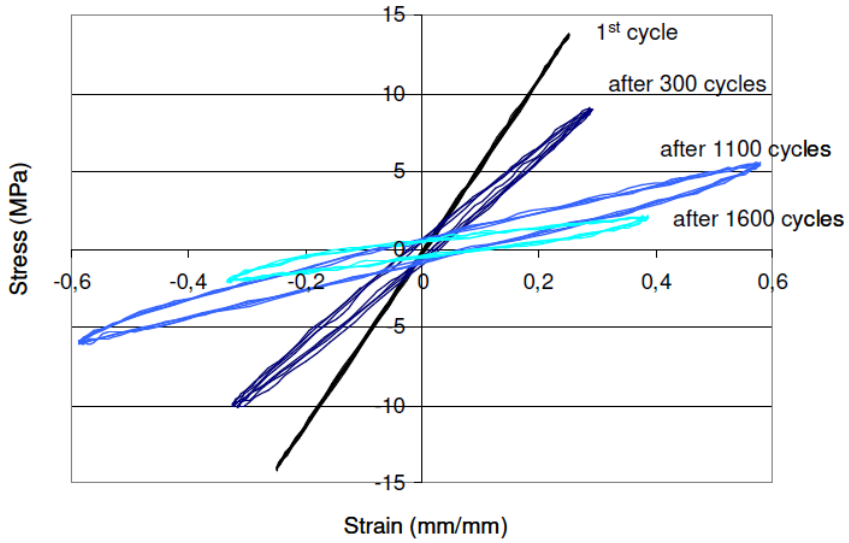

Figure 2. Stress strain curves for different numbers of fatigue cycles obtained for an unbalanced woven glass epoxy laminate $[0]_n$ *on tube specimen subjected to torsion loading* [1]

2.2 Multi-axial test sequence from wide plates

The test procedure consists in applying a fatigue tensile load on wide plates made of $[\pm 45]_{ns}$, $[0/90]_{ns}$ unidirectional plies or $[90]_n$ woven plies in order to extract several $[0/90]_{ns}$ or $[0]_n$ samples to evaluate the residual strength in fibre direction. As for tube specimens, several numbers of tension-tension fatigue cycles were selected in order to generate various level of damage as shown on Figure 3. $[0/90]_{ns}$ or $[0]_n$ samples are extracted by water jet cutting as illustrated on Figure 4 and Figure 5. $[\pm 45]_{ns}$ plates are cut along 45° direction, while $[0/90]_{ns}$ and $[90]_n$ plates are cut along 90° direction. The presence of fibres in weft direction (loading direction for wide plate) for $[90]_n$ plates made of woven plies allows carrying a high load giving the possibility to generate diffuse transverse cracks. In the case of a laminate $[90]_n$ made of UD plies, a load perpendicular to the fibres would result in immediate failure of the specimen after the on-set of the first transverse crack. With this test procedure, UD plies have to be damaged using $[0/90]_{ns}$ stacking sequence in order to obtain numerous transverse cracks in 90° plies.

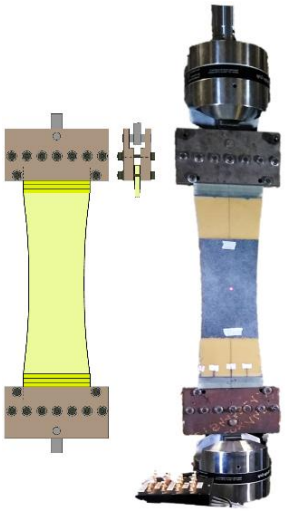

Figure 3. Fatigue test on wide specimen using dedicated clamping fixture

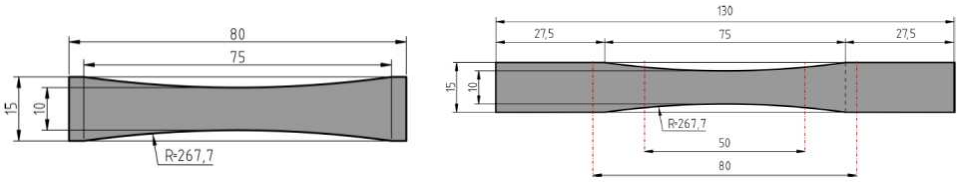

(a) (b)

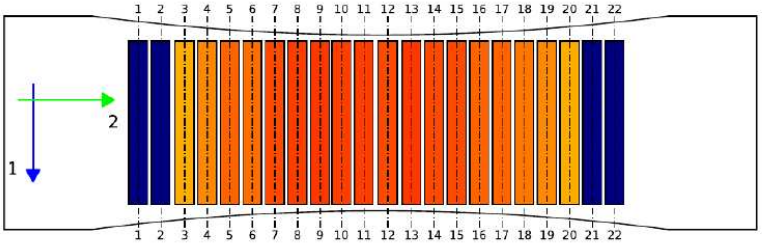

Samples	1	2	3	4	5	6	7	8	9	10	11	12	13	14	15	16	17	18	19	20	21	22
Damage	0	0	74	78	82	81	85	86	87	86	86	85	87	85	85	82	82	80	78	74	0	0

(c)

Figure 4. (a) hourglass sample for compression test, (b) hourglass sample for 4 points bending test, (c) wide $[90]_{14}$ plate made of unbalanced woven plies *with cutting diagram for sample extraction (color and table give the expected level of damage for each specimen)*

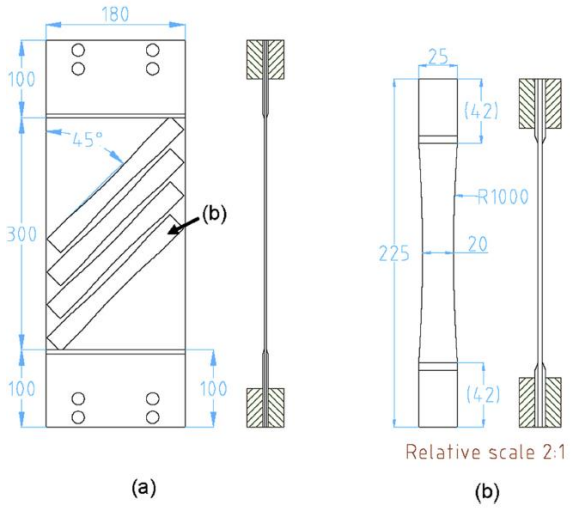

Figure 5. (a) wide $[\pm 45]_{2s}$ plate made of UD plies with cutting diagram for sample extraction, (b) hourglass sample for tensile test

Both tensile and compressive residual strength can be evaluated using this procedure. All extracted specimens include a decrease of their width in gage area in order to prevent failure close to the tabs. For compressive residual strength, short hourglass samples as illustrated on Figure 4(a) are tested with the help of an anti-buckling fixture conform to ASTM D695. For tensile residual strength, for glass fibres either hourglass samples for tensile test (see Figure 5(b)) or 4 points bending samples (see Figure 4(b)) can be used. Indeed, for glass fibres, since the tensile strength is lower than the compressive strength, 4 points bending specimens failure occurs in the tension side. For carbon fibres, tensile residual strength measurement requires samples dedicated to tensile test (see Figure 5(b)). Strain gauges are bonded on the two sides of each specimen in the gage area.

3. Results

3.1 Evaluation of the damage level

The evaluation of the damage level relies on the stiffness loss. However, fibre-matrix decohesion and matrix cracks generate numerous phenomena and complex stress strain curves including residual strain and hysteresis loops during unloading reloading cycles especially under shear loadings. The loss of stiffness at laminate scale can be measured as the loss in the secant stiffness during these loops, to reduce viscous effects this loss of secant stiffness is measured during unloading reloading cycles at low loading velocity realised between fatigue cycles. Digital Image Correlation (DIC) is used to evaluate the strain field on wide plate specimen. Due to the large width of plate specimen, the damage level is quite non-uniform throughout the specimen. FE analysis including damage model [3,4] may then be used to evaluate the actual damage level of each specimen.

3.2 Effect of damage on residual tensile strength

A first experimental result obtained using multiaxial test on tubes (see Figure 1) made of unbalanced woven glass epoxy plies is presented in Figure 6 [5,6]. The evolution of residual strength in fibre direction according to the level of matrix damage is clearly demonstrated. The trend presented above was corroborated by [7] on an other reinforcement type with the

procedure based on wide $[\pm 45]_{2s}$ plate (Figure 6). Results obtained for an unidirectional glass epoxy ply are presented on Figure 7.

For a low level of damage, no significant strength change is highlighted, but as soon as the level of damage become greater than a particular value, the strength decreases sharply up to approximatively 50%. A test performed at a temperature close to the glass transition temperature gives a strength similar to the one obtained with a high level of damage. This confirms that damage suppress the ability of matrix to distribute stresses between fibres. The damage threshold leading to the strength drop seems depending on the reinforcement type since in these two studies the damage is introduced by shear loading. However, torsion loading makes it possible to apply a symmetrical loading which prevents the development of residual strain. As displayed on Figures 6 and 7, progressive or sharp phenomenological law can be proposed to represent that evolution in a predictive model.

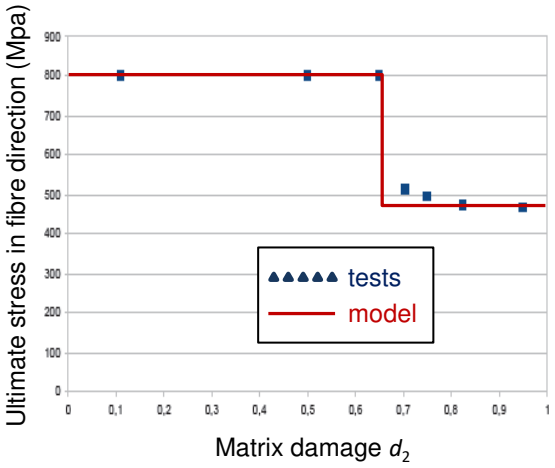

Figure 6. Residual tensile strength of unbalanced woven glass epoxy ply in fibre direction as a function of shear damage obtained with tube procedure [5]

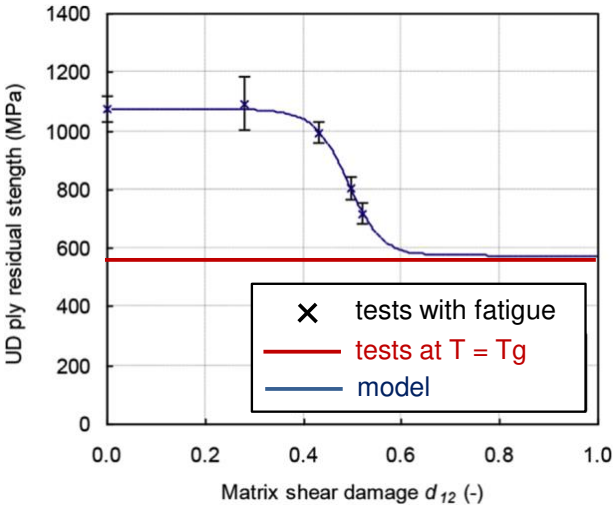

Figure 7. Residual tensile strength of UD glass epoxy ply in fibre direction as a function of shear damage obtained with wide plate procedure *[7,8]*

More recently, [9] used the procedure based on wide $[90]_{14}$ plate (Figure 4) and 4 points bending tests to study an unbalanced woven ply with 17% of fibres in weft direction (loading direction of the wide plate). Results shows that the strength drop occurs for a virtual matrix damage level in warp direction close to 0.8. For the definition of the virtual matrix damage, refer to [3,10]. The effect of reinforcement type, strain gradient introduced in bending test and the loading type used to generate damage can explain change of the damage threshold leading to the strength drop.

3.3 Effect of damage on residual compressive strength

Eyer et al. proposes to use multiaxial test on tubes in order to get the residual compressive strength after shear damage on balanced woven carbon/epoxy [2]. Results presented in Figure 8 show a progressive loss (quasi linear evolution) of the ultimate compressive strain up to a very low value when the level of damage become close to 1.

In the same study mentioned in previous section, Cocchi et al. used short hourglass samples extracted from damaged wide $[90]_{14}$ plate to identify the residual compressive strength of an unbalanced woven ply [9,10]. The virtual damage level of specimens is close to 0.8. The trend presented in Figure 9 is quite different. The strength loss is around 11% in spite of the high damage level.

As for residual tensile strength, the difference can be explained first by the difference between the two materials (unbalanced glass epoxy fabric vs. balanced carbon epoxy) and also the different damaging techniques used. Indeed, cracks generated by shear or transverse loading are different influencing in different ways the compression strength which is governed by a complex micro-buckling process.

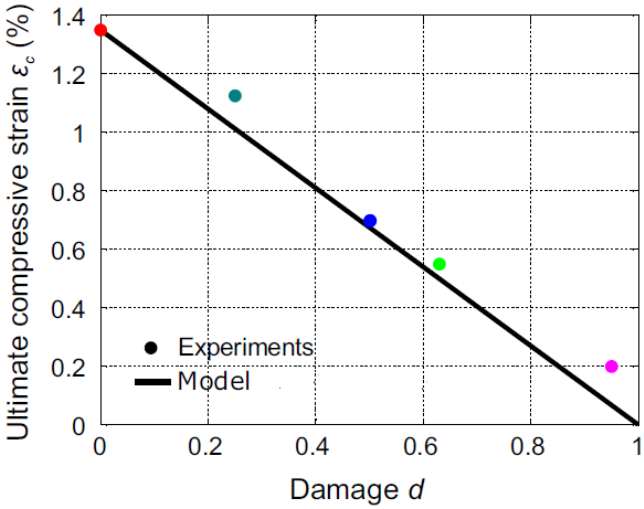

Figure 8. Residual compressive strength of balanced woven carbon epoxy ply in fibre direction as a function of shear damage obtained with tube procedure [10]

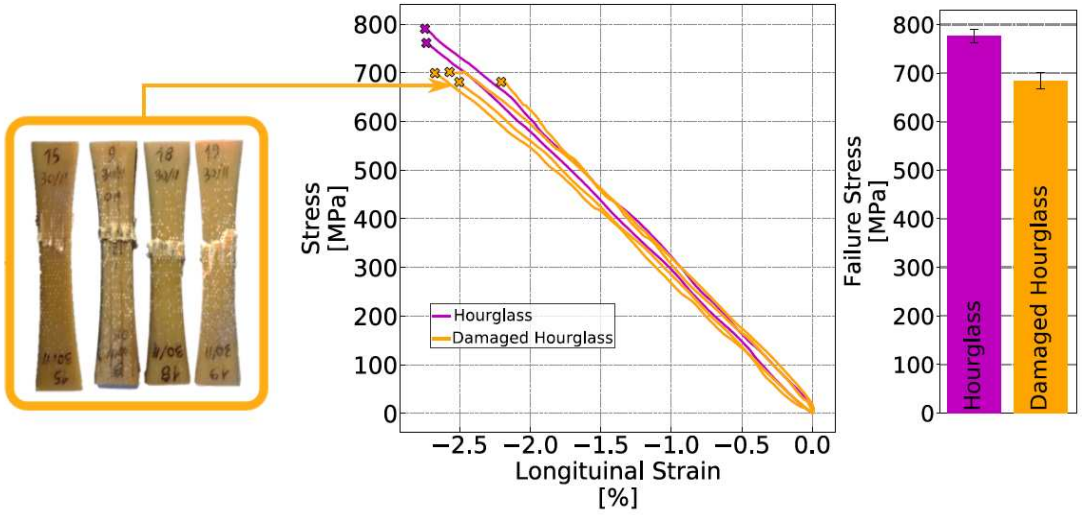

Figure 9. Residual compressive strength of unbalanced woven glass epoxy ply in fibre direction as a function of transverse damage obtained with wide plate procedure [9]

3. Conclusion

Two different testing procedures are proposed to introduce matrix and fibre matrix decohesion damage on composite laminates before evaluating their residual tensile and compressive strength in fibre direction. Similar trends are found for different materials for the two procedures concerning tensile residual strength. As soon as the level of damage become greater than a given treshold, the strength decreases sharply. The damage treshold seems depending on the reinforcement type. Trends on residual compressive strength differ for the two studied materials. Currently, this difference can be assigned to several reasons, among them, the most significant are the role of reinforcemnt type (UD or fabric), fibre type (glass or carbon), matrix grade and the loading type used to generate damage (shear or transverse).

Performing tests at different temperatures is a relevant and complementary way to study the influence of matrix state on strength in fibre direction [7,9,10,12]. Our future works aim at confronting the effect of damage and temperature by developing dedicated experimental protocols and micromechanical models.

4. References

[1] Hochard C, Miot S, Lahellec N. Rupture en fatigue de structures en composite stratifié. 17ème Journ Natl Sur Matér Compos. Poitiers; 2011.

[2] Eyer G, Montagnier O, Hochard C, et al. Effect of matrix damage on compressive strength in the fiber direction for laminated composites. Compos Part Appl Sci Manuf. 2017;94:86–92.

[3] Hochard Ch, Thollon Y. A generalized damage model for woven ply laminates under static and fatigue loading conditions. Int J Fatigue. 2010;32:158–165.

[4] Caous D, Bois C, Wahl J-C, et al. Toward composite wind turbine blade fatigue life assessment using ply scale damage model. 7th Int Conf Fatigue Des Fatigue Des. Senlis, France; 2017.

[5] Hochard C, Thollon Y. Comportement à rupture dans le sens fibres de FRP sous chargement statique et de fatigue. JNC16 Toulouse. 2009;1–6.

[6] Hochard C, Miot S, Lahellec N. Rupture en fatigue de structures en composite stratifié. 17ème Journ Natl Sur Matér Compos. Poitiers; 2011.

[7] Caous D, Bois C, Wahl J-C, et al. A method to determine composite material residual tensile strength in the fibre direction as a function of the matrix damage state after fatigue loading. Compos Part B Eng. 2017;127:15–25.

[8] Caous D. Rôle de l'endommagement sur la durée de vie en fatigue des matériaux composites stratifiés : application au domaine éolien. Arts et Metiers ParisTech; 2017.

[9] Cocchi A. Analyse du comportement en compression sens fibre de structures composites stratifiées en présence de dégradation matricielle et concentrations de contraintes [Internet] [These en préparation]. Aix-Marseille; 2020 [cited 2021 Sep 7]. Available from: http://www.theses.fr/s186752.

[10] A. Cocchi, O. Montagnier and C. Hochard, "Study of hourglass-shaped specimens for the analysis of compression behaviour in fibre direction of FRP composites using compression and four-point bending tests," *Composites Part A: Applied Science and Manufacturing,* p. 144, 2021

[11] Miot S, Hochard Ch, Lahellec N. A non-local criterion for modelling unbalanced woven ply laminates with stress concentrations. Compos Struct. 2010;92:1574–1580.

[12] Boissin E, Bois C, Wahl J-C, et al. Effect of temperature on damage mechanisms and mechanical behaviour of an acrylic-thermoplastic-matrix and glass-fibre-reinforced composite. J Compos Mater. 2020;54:4269–4282.

GLOBAL SENSITIVITY ANALYSIS OF AN S-N CURVE-BASED FATIGUE COHESIVE ZONE MODEL AND VALIDATION THROUGH A BENCHMARK TEST

I. Leciñana[a-b], J. Zurbitu[a], J. Renart[b], Albert Turon[b] and Laura Carreras[b]

a: IKERLAN Technology Research Centre, Basque Research and Technology Alliance (BRTA), Spain (Arrasate, ES) – ilecinana@ikerlan.es
b: Analysis and Advanced Materials for Structural Design (AMADE), University of Girona, Spain

Abstract: *A fatigue CZM model recently proposed in the literature has been implemented as a user defined UMAT subroutine for Abaqus Standard. The fatigue damage accumulation function is based on S-N curves. Its main advantage is that the formulation is only dependant on the local displacement jumps at the interface. This allows a direct implementation of the model to 3D structures with arbitrary shaped crack fronts. The impact of the input parameters in the fatigue response of the model is analysed by a global sensitivity analysis. The predictive capabilities of the model are validated by means of a benchmark test. The obtained results are discussed and compared against those obtained with a Paris law-based fatigue CZM and some key points for improvement are identified.*

Keywords: Cohesive Zone Models; Fatigue; Fracture; Sensitivity; Benchmark

1. Introduction

Efficient predictive tools that can deal with fatigue delamination are of great value during design and certification processes. Among different approaches, cohesive zone models (CZM) highlight as the best candidates due to computational efficiency, consistency to predict quasi-static delamination, and capacity to model the fracture mechanism acting in the fracture process zone (FPZ). However, there still is controversy regarding how to model fatigue loading with cohesive zone models.

The most extended approaches rely on Paris law-like crack growth equations, where the fatigue inputs of the model are experimentally determined from delamination tests [1,2]. The main challenge of these models is that the experimental fatigue delamination data is reduced following a global scheme, taking into account the global load and displacement of the specimen. On the contrary, CZM are based on local interface tractions and separations, and therefore, the Paris law constants cannot be integrated in the CZM in a straightforward way. This causes many fatigue cohesive zone models (FCZM) in literature to struggle when facing delamination in complex 3D structures [2]. In this context, Carreras *et al*. [3,4] introduced a global computation scheme to build a Paris law based fatigue CZM able to predict delamination in structures with non-negligible FPZ and arbitrary shaped crack fronts [5].

Alternatively, fatigue models based on experimental tests that better fit the local nature of the CZM are starting to emerge. These approaches understand the fatigue delamination process as a consecution of fatigue onset of different material points. Therefore, both fatigue onset and fatigue crack growth can be modeled at an integration point level. In this context, Dávila *et al*.

  doi:10.5075/epfl-298799_978-2-9701614-0-0

developed a model based on S-N curves [6,7], which is able to model fatigue onset and crack propagation under different load ratios and mode mixites. Due to the novelty of this approach, more work must be done to get a better understanding on its limitations, predictive capabilities, and comparison with the models based on Paris law based FCZM.

In the present work, the influence of the input parameters in the fatigue response of the S-N curve based CF20 FCZM presented by Dávila *et al*. [7] is compared against the Paris law based FCZM developed by Carreras *et al*. [3,4]. Additionally, the ability to reproduce fatigue delamination in DCB specimens is demonstrated with both models, and finally the predictive capabilities of the CF20 model are validated against the R-DCB benchmark test specimen presented in [5].

2. Constitutive models: static and fatigue cohesive zone models

Two different constitutive models were used. On one hand the S-N curve based CF20 fatigue CZM presented by Dávila *et al*. [7] was implemented on the static CZM formulated by Turon *et al*. [8] as an UMAT subroutine. The fatigue damage accumulation function is defined by the local displacement jumps λ and semi-empirical properties derived from S-N curves:

$$\frac{dD}{dN} = \frac{1}{\gamma}\frac{(1-D)^{\beta-p}}{E^{\beta}(p+1)}\left(\frac{\lambda}{\lambda^*}\right)^{\beta} \tag{1}$$

where D is the damage variable, γ is the number of cycles at which infinite life is considered, and E is the endurance limit at a given stress ratio R and mode-mixity B, which can be related to the relative endurance ε (R=-1, B=0) with the Goodman relation:

$$E = \frac{2C_L\varepsilon}{C_L\varepsilon+1+(C_L\varepsilon-1)R} \tag{2}$$

where $C_L = 1 - 0.42\,B$, β is the slope of the S-N curve and is defined by:

$$\beta = \frac{-7\eta}{log\ E} \tag{3}$$

where η is a "brittleness" parameter that can account for the low-cycle bulge exhibited by some materials. The exponent p does not affect the S-N curve definition. Instead, it has a direct impact on the calculated C coefficient in the Paris law.

On the other hand, the Paris law-based FCZM developed by Carreras *et al*. was used as an UEL subroutine. The fatigue damage accumulation is related to the fatigue crack growth $\frac{da}{dN}$ as a function of the mode mixity B and the equivalent one-dimensional displacement jump λ:

$$\frac{dD}{dN} = \left(\frac{\partial D}{\partial B}\frac{\partial B}{\partial a} + \frac{\partial D}{\partial \lambda}\frac{\partial \lambda}{\partial a}\right)\frac{da}{dN} \tag{4}$$

by applying the chain rule. Crack growth rate is related to the strain energy release rate:

$$\frac{da}{dN} = C\left(\frac{G_{\max}(1-R)}{G_{IC}}\right)^{m} \tag{5}$$

which is computed globally using the damage growth driving direction [3] and the mode-decomposed energy release rate [4] tools. Where m and C are the Paris law coefficients.

3. Case studies

A parametric simulation of a DCB specimen was used to perform a sensitivity analysis of the FCZ models defined in Section 2. Then, the capabilities of the CF20 model to predict fatigue crack growth in 3D structures were demonstrated by simulating the R-DCB benchmark test specimen presented in [5].

The unidirectional CFRP laminate characterized in [9] was used in the simulations. The DCB tests were modelled as specified in Table 1.

Table 1: Numerical modelling of DCB specimens.

	CF20 (7)		**Carreras *et al.*** (3)**,** (4)	
Property	**Value**	**Units**	**Value**	**Units**
K_I: Mode I penalty stiffness	1E5	MPa/mm	1E5	MPa/mm
Δd_t: Fatigue damage target per equilibrium iteration	1E-2	-	0.3	mm
l_e: Cohesive element length	0.1	mm	0.3	mm
Elements in sub-laminate thickness	8		3	
Solver	Newton – Raphson NLGEOM static		Newton – Raphson NLGEOM static	
Element type in beams	CPE4 (Abaqus 6.14-2)		C3D8I (Abaqus 6.14-2)	
Cohesive element	COH2D4 + UMAT subroutine		UEL subroutine	

The R-DCB benchmark specimen tested in [10] (Figure 1) and simulated with the Carreras´ *et al.* formulation in [5] (Figure 1) was modeled as specified in Table 2:

Table 2: Numerical modelling of the R-DCB specimen.

Property	**Value**	**Units**
K_I: Mode I penalty stiffness	1E5	MPa/mm
Δd_t: Fatigue damage target per equilibrium iteration	1E-2	-
l_e: Cohesive element length	0.36	mm
Elements in sub-laminate thickness	4	
Solver	Newton – Raphson NLGEOM	
Element type in beams	SC8R (Abaqus 6.14-2)	
Cohesive element	COH2D4 + UMAT subroutine	

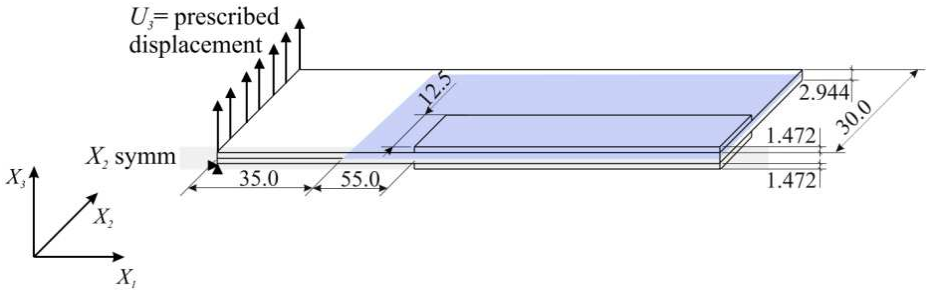

Figure 1. Sketch of the partially reinforced DCB specimen [mm][10]. Only half of the specimen is represented in Figure 5.

4. Sensitivity analysis

To analyze the influence of the cohesive law shape, the fatigue properties, and other numerical parameters in the fatigue response of the model, a global sensitivity analysis was performed using Morris´ method [11]. Morris´ method was chosen because it gives the most reliable information at a low computational cost. Input parameter values are changed one at a time, describing trajectories based on a space filling algorithm. It can qualitatively measure the influence and non-linearity of each parameter even in non-linear and non-monotonic models.

The input parameters and the ranges that were considered in the analysis are defined in Table 3. The mode I penalty stiffness K_I, the static strength τ_{I0}, and toughness G_{IC} define the cohesive law shape. The mode I Paris law coefficient C_I and exponent m_I are the fatigue parameters needed in Carreras´ *et al*. model [5]. The brittleness factor η, the relative endurance limit for fully reversed axial loading ε, the nondimensional material dependent coefficient p and exponent β are the fatigue parameters in the CF 20 model [12]. The maximum damage increment per equilibrium iteration Δd_{max} and mesh size l are the other numerical parameters considered in the analysis. To make the results of the two models comparable, proportionality was maintained when defining the ranges of the input parameters in Table 3.

The influence of the model parameters in the fatigue onset was evaluated by the change in the fitting parameters O_A and O_B in the equation:

$$\frac{d}{F} = O_A N^{O_B} \tag{6}$$

through the interval $N = [0 – N_{0.05}]$, cycles where $N_{0.05}$ is the cycle at which the compliance of the specimen has increased a 5 %. d and F are the displacement and reaction force at the loading point of the specimen. The influence in the fatigue crack growth was determined by the change in the Paris law coefficient C and exponent m defined by Eq. 5.

Table 3: Morris´ sensitivity analysis.

CF20 [8]			Carreras et al. [3-5]		
Property	**Range**	**Units**	**Property**	**Range**	**Units**
Δd_{max}	5E-3 – 1E-2	-	Δd_{max}	0.15 – 0.3	mm
l	0.04 – 0.1	mm	l	0.12 – 0.3	mm
K_I	1E5 – 1E6	MPa/mm	K_I	5E4 – 1E5	MPa/mm
τ_{I0}	24 – 36	MPa	τ_{I0}	24 – 36	MPa
G_{IC}	0.244 – 0.366	N/mm	G_{IC}	0.244 – 0.366	N/mm
η	0.80 – 0.99	-	m_I	6.712 – 10.068	-
ε	0.16 – 0.24	-	C_I	5.16E-2 – 7.74E-2	mm/cycle
p	β-1.5 – β+1.5	-			

The influence of the input parameters in the fatigue crack growth is shown in Figure 2. The absolute of the mean elementary effect μ^* gives a measure of the influence of each parameter in the output, while the standard deviation of the elementary effect σ indicates the non-linearity of the response and the higher order interactions with other parameters. It is worth mentioning that the Morris´ analysis only provides qualitative information and therefore the results cannot be proportionally compared between parameters nor models.

  doi:10.5075/epfl-298799_978-2-9701614-0-0

In both FCZ models the fatigue crack growth is governed by its respective fatigue parameters. However, the response of the CF20 model is directly influenced by the static cohesive law (τ_{I0} and G_{IC}) and by its interactions with the fatigue parameters (figures 2 a and b and Figure 3). On the contrary, fatigue delamination in Carreras´ *et al*. model is only dependent on the fatigue parameters (figures 2 a and b). Fatigue onset was only analyzed with the CF20 formulation because Paris law-based models do not have the capability to control the damage initiation. Similarly to the fatigue crack growth response, in the case of fatigue onset, fatigue and static parameters have significant influence in the CF20 model.

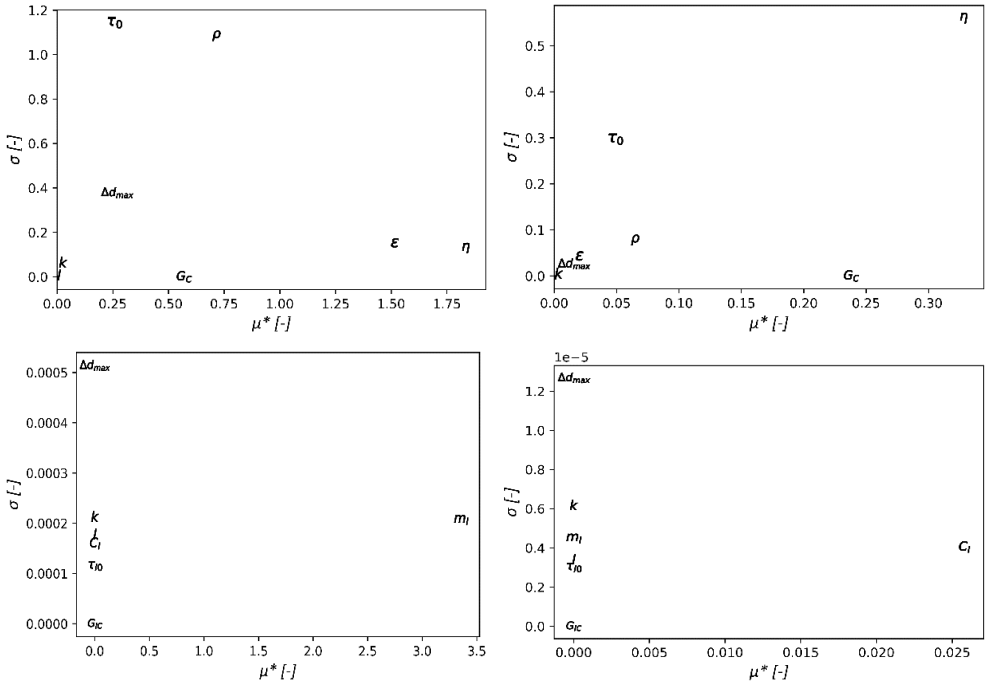

Figure 2. Morris´ analysis results for: a) CF20 model, Paris law exponent m. b) CF20 model, Paris law coefficient C. c) Carreras et al. model, Paris law exponent m. d) Carreras et al. model, Paris law coefficient C.

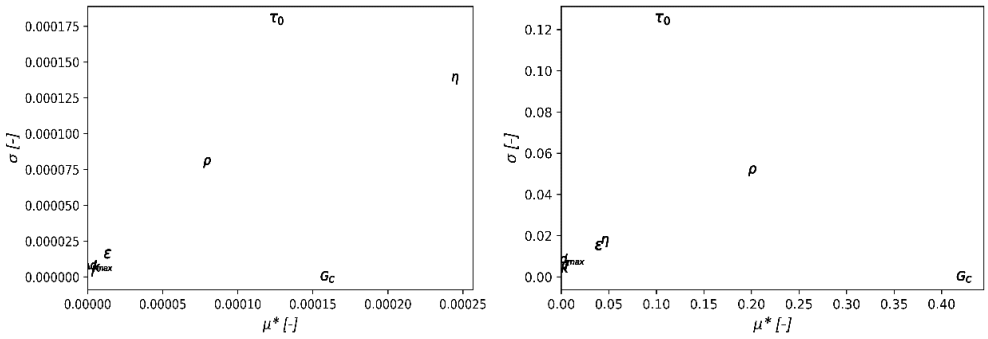

Figure 3. Morris´ analysis results for: a) CF20 model, fatigue onset exponent O_B. b) CF20 model, fatigue onset exponent O_B.

5. Verification of the constitutive models

DCB specimen case study was used to verify the capability of the formulations to model fatigue loading. Experimental fatigue delamination data of [9] was fitted to eq. 2 resulting in experimental Paris coefficients of m_I = 8.26 and C_I = 5.1E-2.

  doi:10.5075/epfl-298799_978-2-9701614-0-0

Obtained fatigue crack growth curves for d_{max} = 5 mm and R = 0.1 are ploted in Figure 4 and numerical Paris coefficients are gathered in Table 4. As expected, Carreras *et al.* model yields the same Paris coefficients as it has been fed with.

A first run of CF20 model with the recommended fatigue coefficient values proposed in [7] resulted in significantly deviated Paris law (Table 4, CF20_run1). This result is consistent with the sensitivity analysis in section 4, since the CF20 fatigue response is coupled with the cohesive law shape, while the static behavior of a material may be independent of its fatigue response. Therefore, in the authors´ opinion, before the CF20 model can be used as predictive tool for 3D structures, the fatigue parameters must be determined considering the experimental static and fatigue response of the material. To do so, characterization tests can be simulated looking for numerical-experimental correlation.

Table 4: Fatigue input parameters and results of DCB specimen simulations.

Model	Fatigue input parameters			Numerical Paris coefficients	
				m_I [-] (error)	C [mm/cycle] (error)
CF20_run1	$\varepsilon = 0.2$	$p = \beta$	$\eta = 0.95$	7.53 (8.8%)	8.9E-2 (74.5%)
CF20_run2	$\varepsilon = 0.245$	$p = \beta + 0.75$	$\eta = 0.89$	8.16 (1.1%)	5.5E-2 (7.8%)
Carreras *et al.*	$m_I = 8.26$	C_I = 5.1E-2		8.26 (0%)	5.1E-2 (0%)

After an iterative process, an acceptable correlation between experimental and numerical Paris law was achieved (Table 4, CF20_run2), and the low cycle "bulge" was also captured (Figure 4). The ability of CF20 to control the low and high cycle fatigue independently constitutes an interesting advantage over Carreras *et al.* model. It must be highlighted that the iterative process could have been continued and the correlation improved.

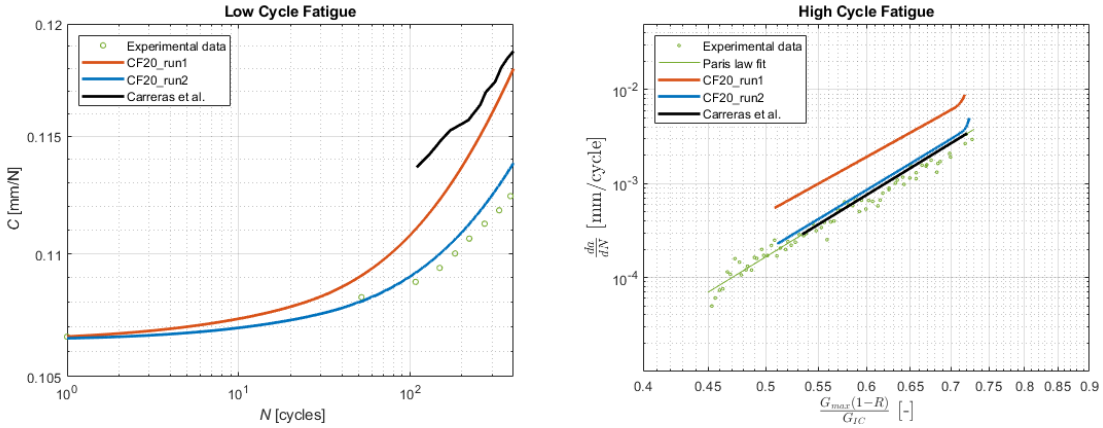

Figure 4. DCB specimen fatigue simulation: a) Damage onset. b) Delamination.

6. Validation of CF20 model

R-DCB benchmark specimen was simulated at d_{max} = 10 mm and R = 0.1 to validate the predictive capabilities of the CF20 FCZM. Obtained results were compared against the results of Carreras *et al*. model presented in [5]. As demonstrated in Figure 5, the local formulation of CF20 model can predict fatigue delamination even in crack-front-shape changing 3D structures, where the material points in the FPZ get damaged at different rates. Also, it is confirmed that fatigue

parameters must be calibrated by simulating material characterization tests before using CF20 as a predictive tool.

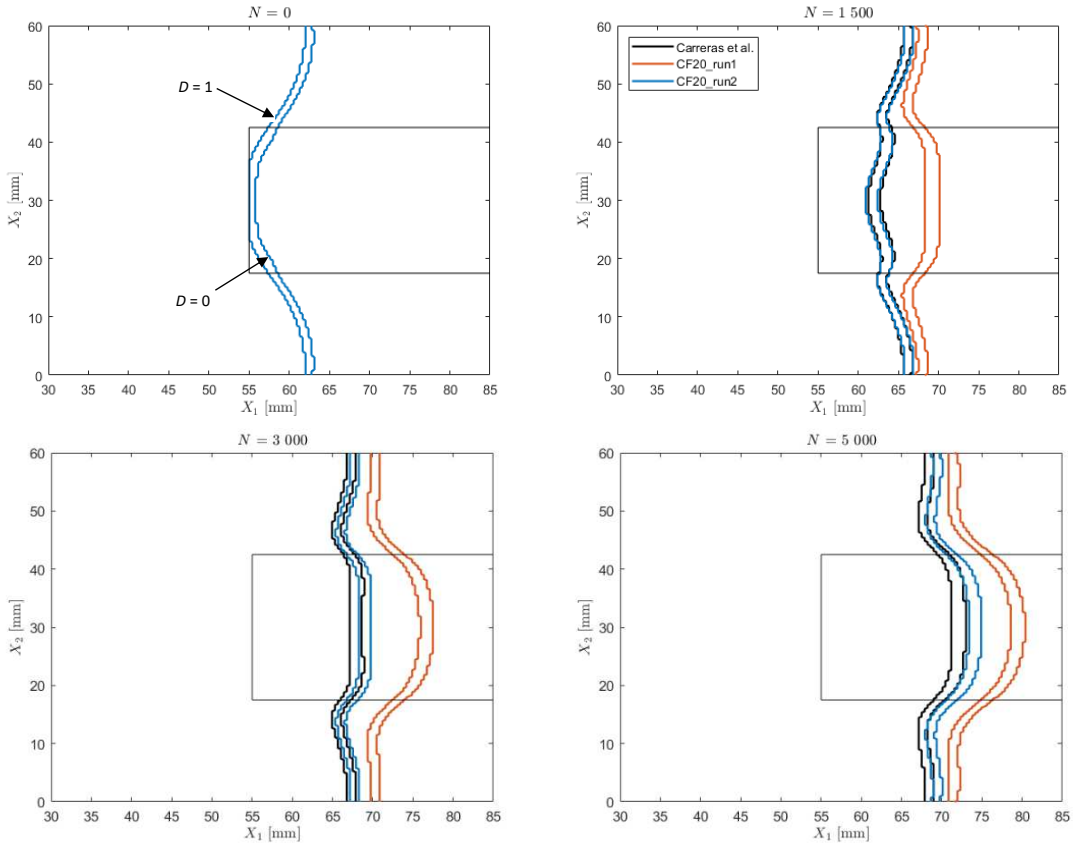

Figure 5. R-DCB benchmark specimen simulation.

7. Conclusions and future lines

The predictive capabilities of the S-N based and locally formulated FCZM presented by Dávila *et al*. [7] was validated through the simulation of the R-DCB specimen presented in [5].

Additionally, this work has brought the opportunity to compare two state-of-the-art FCZM. The fatigue response of the Paris law based global model presented by Carreras *et al*. [3,4] is only dependent on its input fatigue properties and therefore it can be directly used as a predictive tool. However, since it is only fitted with Paris law coefficients, the low cycle fatigue cannot be independently controlled from the high cycle fatigue. Also, its global formulation makes it computationally less efficient if compared to a local model.

On the other hand, it has been proved that the S-N based and locally formulated FCZM presented by Dávila *et al*. [7] is an excellent candidate to model both low and high cycle fatigue efficiently. However, its main drawback is that the fatigue behaviour is conditioned by both input fatigue parameters and static cohesive law shape. Consequently, a fatigue parameter determination process must be done by simulating characterization tests before using the model as predictive tool for real structures. According to [7], once calibrated, the model can account for *R*-curve, mode mixity, *R*-ratio and scale effects. Even if an iterative correlation process was performed in the present work, the authors consider that developing a robust fatigue parameter

determination process can be of great interest for the future use of the CF20 model as a predictive tool.

Acknowledgements

To Carlos Dávila for the valuable conversations. To Aravind Sasikumar for the shared insight into the Morris analysis.

8. References

1. Turon A, Costa J, Camanho PP, Dávila CG. Simulation of delamination in composites under high-cycle fatigue. Compos Part A Appl Sci Manuf. 2007;38(11):2270–82.

2. Bak BL V, Turon A, Lindgaard E, Lund E. A Benchmark Study of Simulation Methods for High-Cycle Fatigue-Driven Delamination Based on Cohesive Zone Models. Compos Struct [Internet]. 2016.

3. Carreras L, Bak BLV, Turon A, Renart J, Lindgaard E. Point-wise evaluation of the growth driving direction for arbitrarily shaped delamination fronts using cohesive elements. Eur J Mech A/Solids [Internet]. 2018;72(October 2017):464–82.

4. Carreras L, Lindgaard E, Renart J, Bak BLV, Turon A. An evaluation of mode-decomposed energy release rates for arbitrarily shaped delamination fronts using cohesive elements. Comput Methods Appl Mech Eng [Internet]. 2019;347:218–37.

5. Carreras L, Turon A, Bak BLV, Lindgaard E, Renart J, Martin de la Escalera F, et al. A simulation method for fatigue-driven delamination in layered structures involving non-negligible fracture process zones and arbitrarily shaped crack fronts. Compos Part A Appl Sci Manuf [Internet]. 2019;122(January):107–19.

6. Dávila CG. From S-N to the Paris law with a new mixed-mode cohesive fatigue model for delamination in composites. Theor Appl Fract Mech . 2020.

7. Dávila CG, Rose CA, Murri GB, Jackson WC, Johnston WM. Evaluation of fatigue damage accumulation functions for delamination initiation and propagation. Nasa/Tp–2020-220584. 2020;(April).

8. Turon A, González E V, Sarrado C, Guillamet G, Maimí P. Accurate simulation of delamination under mixed-mode loading using a cohesive model with a mode-dependent penalty sti ff ness. Compos Struct [Internet]. 2018;184(October 2017)

9. Renart J, Budhe S, Carreras L, Mayugo JA, Costa J. A new testing device to simultaneously measure the mode I fatigue delamination behavior of a batch of specimens. Int J Fatigue [Internet]. 2018;116:275–83

10. Carreras L, Renart J, Turon A, Costa J, Bak BLV, Lindgaard E, et al. A benchmark test for validating 3D simulation methods for delamination growth under quasi-static and fatigue loading. Compos Struct [Internet]. 2019;210(October 2018)

11. Morris MD. Factorial sampling plans for preliminary computational experiments. Technometrics. 1991;33(2):161–74.

12. Allegri G, Wisnom MR. A non-linear damage evolution model for mode II fatigue delamination onset and growth. Int J Fatigue [Internet]. 2012;43:226–34.

FATIGUE LIFE STUDY OF LAMINATED COMPOSITES CARBON-EPOXY MANUFACTURED FROM UNIDIRECTIONAL PLIES AND 2D-WOVEN PLIES COMBINING THERMO-MECHANICAL ANALYSIS AND A RESIDUAL STRENGTH MODEL

*K. DEMILLY[a, b, *], Y. MARCO[b], V. LE SAUX[b],*

G. DOLO[a], E. BILLAUDEAU[a], Y. PANNIER[c], M. RIOU[a, d],

N. CARRERE[b]

a : Naval Group, Technocampus Ocean, Rue de L'Halbrane, 44340 Bouguenais, France
b : ENSTA Bretagne, UMR CNRS 6027, IRDL, F-29200 Brest, France
c : ISAE-ENSMA - UPR CNRS 3346, Institut P', 86360 Chasseneuil-du-Poitou, France
d : Université de Nantes, 44000 Nantes, France

*kilian.demilly@ensta-bretagne.org

Abstract: *Long-term durability under repeated mechanical loading is a major criterion for design of composite structures. The development of a fatigue criterion faces two major difficulties: (i) the proposal of a load/life curve (S-N curve) describing the natural dispersion of the fatigue tests and (ii) the duration of these tests.*

The goal of the study is to combine the Sendeckyj's approach based on a so-called residual strength that fits S-N curve and associates a failure probability [1], and a self-heating-based method that estimate a mean S-N curve from the thermal dissipation, determined from temperature measurements on a single sample [2]. The fatigue lifetime for high cycles loading is estimated by the heat-build up protocol. Quasi-static tests and a few fatigue tests are used to estimate the failure distribution based on a two-parameters Weibull model.

Keywords: Composite; Fatigue; Self-Heating; Residual Strength

1. Introduction

This Fatigue campaign is widely used to characterize long-term durability of materials and develop a fatigue criterion as it is a major concern in the design of structures. Such a campaign faces two difficulties: the natural scattering of fatigue tests that need to be considered in the estimation of the load/life curve (S-N curve) in order to get a sufficient degree of confidence in the estimation; and the duration and cost of these tests due to the determination of this natural scattering and the high cycles lifetime part. First, this study will present the Sendeckyj's approach as a solution to associate a failure probability to the S-N curve using a so-called residual strength. Then, the self-heating-based method will be presented as a solution to obtain a fast estimation of the mean S-N curve by using a single specimen. Finally, the combination of both methods to obtain a fast estimation of the S-N curve associated to a failure probability will be considered.

  doi:10.5075/epfl-298799_978-2-9701614-0-0

2. Material

The material used in this study is a carbon-epoxy laminated composite. This laminate is composed of unidirectional and 2D-woven plies. Composite plates, made of pre-impregned plies, have been assembled by the author and cured under autoclave cycle.

Specimens of 250 mm x 25 mm x 3.6mm have been drawn in a bigger plate. Theses dimensions have been chosen according to the standard ASTM - D 3039-D 3039M [3]. As the specimen obtained were too thin, tabs of 50 mm have been bonded to the specimens on each side and at each end in order to have a higher thickness so the testing machine could grab the specimen. Thus, the gage length of the specimen is 150 mm.

3. Sendeckyj's approach

In order to estimate a S-N curve describing the natural scattering of the fatigue tests, Sendeckyj proposed an approach based on a so-called residual strength that fits S-N curve and associates a failure probability [1].

The Sendeckyj's approach is based on the evolution of the composite's strength (residual strength) during a cyclic loading. By assuming that the mechanisms responsible of the dispersion are the same for quasi-static and fatigue tests, a S-N curve can be estimated and associated to a failure probability [1]. The procedure to identify this model requires both quasi-static and fatigue tests. The S-N curve obtained is valid for a particular loading frequency and a particular loading ratio. Beyond the failure probability, another benefit of the Sendeckyj's approach is the estimation of the fatigue lifetime for a wide lifetime range: from quasi-static loading to high cycles loading.

Nevertheless, this fatigue campaign could be large and time consuming to be trustworthy enough, particularly if fatigue lifetime for high cycles loading is seek in the study.

4. Self-heating-based method

A solution to decrease the duration of the tests consists in using a self-heating-based method. The heat-build up protocol consists in submitting the sample to a sequence of cyclic loading steps defined by a fixed stress ratio and an increasing peak stress value. Its objective is to determine the relation between the cyclic dissipated energy and the applied stress thanks to thermal measurements [2-4]. The dissipated energy during a cycle is related to the evolution of the temperature thanks to the heat equation. Under some assumptions (not recalled here for sake of consistency) including adiabaticity, it is possible to show that the energy dissipated per cycle is proportional to the rate of temperature rise determined during a few numbers of cycles.

The curve representing the evolution of the dissipated energy with the maximum stress applied in a specific block is called the self-heating curve. It has been shown that this self-heating curve can be divided into 3 distinct zones for composites materials [4]. The first zone corresponds to a very low dissipation. In the second zone other mechanisms are involved and a high increase of dissipation can be observed. The stress corresponding to the transition between these two zones is usually arbitrarily related to a fatigue lifetime of 10^6 cycles to failure. This value of 10^6 cycles to failure has been verified on a large range of polymer-based matrix materials [2-4].

  doi:10.5075/epfl-298799_978-2-9701614-0-0

The last bloc is ran to failure in order to obtain a couple of [dissipation; number of cycles to failure]. Finally, the S-N curve can be estimated thanks to an energetic criterion of the fatigue lifetime of the Basquin type.

Thus, this method reduces drastically the duration of the fatigue tests campaign. However, neither the associated scattering nor the low cycle fatigue part can be estimated without further developments.

5. Conclusion and Perspectives

Finally, with self-heating-based method, the stress corresponding to the transition between the two first zones and related to 10^6 cycles (red point in the Figure 1) seems consistent in comparison with fatigue data (blue points). Therefore, it seems reasonable to combine both approaches. Quasi-static tests are used to identify the scattering. Few fatigue tests for low cycle fatigue loading are performed and the high cycle fatigue results necessary to identify the model are replaced by the estimation of the stress at 10^6 cycles estimated by the self-heating curve. By doing so, the identification of the S-N curve and the related dispersion should be possible in a short amount of time with a limited number of specimens. Moreover, the self-heating method estimates a fatigue point for high cycle loading based on the global response of the material and not by the failure of specimen because of a defect. Thus, the natural scattering obtained for the fatigue data estimated for each specimen tested by self-heating method should be really lower than the one of a classical fatigue campaign.

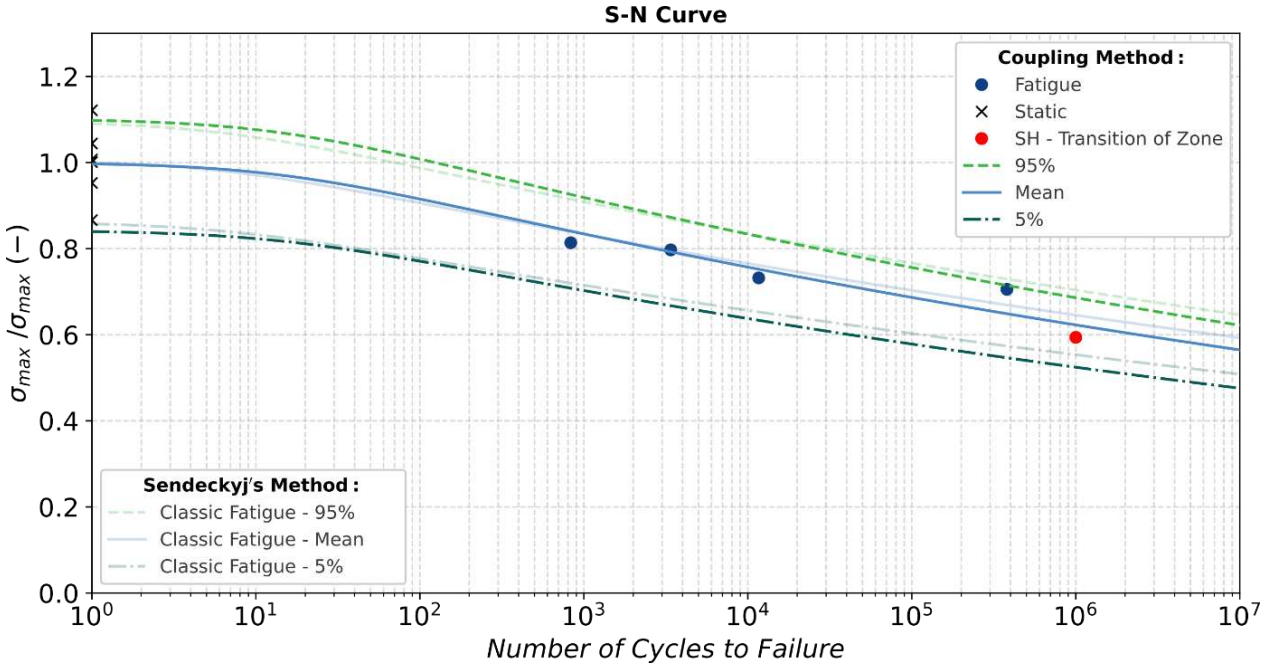

Figure 1: S-N curve of the laminated composites obtained by combining the Sendeckyj's approach and the self-heating-based method

6. Acknowledgements

A part of this study belongs to the "Self-Heating" ANR - Safran - Naval Group research chair (Grant # ANR-20-CHIN-0002) involving Safran Companies, Naval Group, ENSTA Bretagne (IRDL) and Institut Pprime.

  doi:10.5075/epfl-298799_978-2-9701614-0-0

7. References

1. Sendeckyj GP. Life prediction for resin-matrix composite materials. In Fatigue of composite materials (519 p), edited by K.L. Reifsnider 1990:431-483.
2. Leveuf L, Marco Y, Le Saux V, Navrátil L, Leclercq S, .Olhagaray J. Fast screening of the fatigue properties of thermoplastics reinforced with short carbon fibers based on thermal measurements, Polym. Test. 2018;68:19-26.
3. ASTM - D 3039-D 3039M, Standard Test Method for Tensile Properties of Polymer Matrix Composite Materials.
4. Marco Y, Rajic N, Bitton D, Brooks C, Le Saux V. Thermographic investigations on the fatigue properties of carbon fibers laminated composites for airframe applications: from coupon level to in-situ diagnosis. MATERIAUX, Strasbourg, 2018.

  doi:10.5075/epfl-298799_978-2-9701614-0-0

FATIGUE DAMAGE AND LIFE PREDICTION OF UNIDIRECTIONAL COMPOSITES IN TENSION-TENSION LOADING

Babak, Fazlali, Stepan, V. Lomov, Yentl, Swolfs

Department of Materials Engineering, KU Leuven, Kasteelpark Arenberg 44 box 2450, 3001 Leuven, Belgium – Babak.fazlali@gmail.com

Abstract: *The fatigue behavior of unidirectional (UD) composites is essential to simulate the behavior of complex composite laminates. A fatigue fiber break model [1] takes into account the stress distribution due to fiber breakage and fiber-matrix debonding, including effects of local volume fraction on the stress recovery of broken fibers and on stress concentrations in the nearby fibers. The Palmgren-Miner rule accounts for the damage accumulation due to varying stress. The present work investigates the concurrent role of fiber fatigue and fiber-matrix debond fatigue growth.*

Keywords: Fatigue damage progression; Fiber-matrix debond growth; Unidirectional; Weibull, Cluster development

1. Introduction

Fatigue failure is one of the most common failure modes of in-service structures(1). The fatigue related design of composites structures is mostly experimental based at macro- or full-scale level due to a lack of comprehensive models to predict the behavior of composite structures in fatigue. The complexity of damage mechanics and anisotropic nature of composites hinder reliably prediction of the fatigue behavior. In laminated composites, failure of 0° plies often controls the failure of the composites (2). Therefore, it is important to study and understand the behavior of 0° UD composites. The available micromechanical models in the literature are mostly limited to one or two damage mechanisms to simulate UD laminates behavior in fatigue (3,4). However, a combination of different damage mechanisms control the behavior of UD composites. Therefore, a first step to go beyond this boarder is establishing a model to simulate the behavior of UD composites by considering different damage mechanisms in fatigue.

Fig. 1 shows the damage progression of UD composites in tension-tension fatigue. Fiber breakage is the first damage mechanism which is happens to the weakest fibers (5). Matrix cracking, matrix plasticity and fiber-matrix debonding could appear around a broken fiber (6). Fibers in the vicinity of a broken fiber experience stress concentration which increases the possibility of having a cluster of breaks. By increasing the number of cycles, the cluster density increases owing to the fiber-matrix debond growth and fiber fatigue. In later stage, larger clusters appear where isolated clusters connect to each other by longitudinal splitting. Finally, one of the clusters reaches the critical state and causes fatigue failure.

  doi:10.5075/epfl-298799_978-2-9701614-0-0

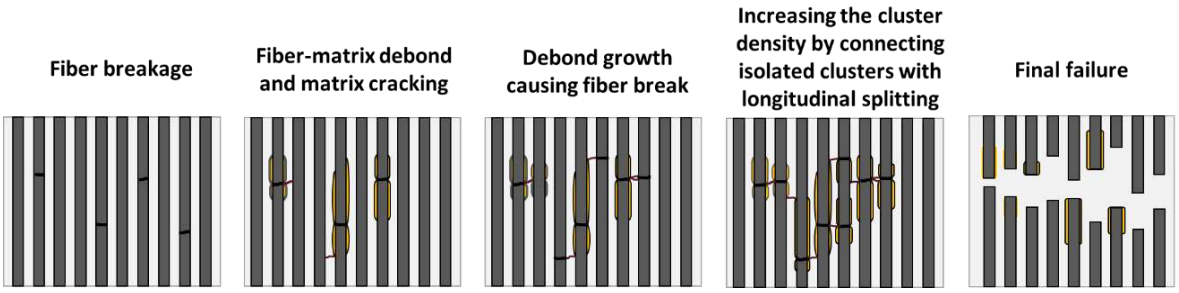

Figure 1. Damage progression in UD composites

Fatigue behavior of UD composites were mostly studied by considering fiber-matrix debond growth as the only damage mechanisms. Alves and Pimenta (3) proposed a hierarchical model to predict the fatigue life of UD composites. The fiber-matrix debond grows as the only damage mechanism and is governed by Paris-Erdogan law. The constant parameters of Paris-Erdogan law were back calculated from the S-N data rather than the actual test data. They considered an unrealistic constant stress concentration of 2 on the fibers in the vicinity of broken fiber. This assumption has a significant effect on fiber break development and hence fatigue life.

Sørensen and Goutianos (4) proposed a micromechanical model to predict the fatigue limit of UD composites. They introduced a critical length for debond growth where the tip of the debond crack experiences sticking friction and cannot grow any further. The fatigue limit was defined when none of the 6 fibers in the vicinity of a broken fiber in a hexagonal packing fails due to stress concentration as a result of debonding. Since the isolated fiber break could happen at any loading levels, this model could overestimate the fatigue life. Sørensen (7) also proposed a critical damage state to define the fatigue life of UD composites where the isolated fracture surfaces connect to each other by longitudinal splitting and approach final failure. In both of their models, they provide a criterion to define the critical state rather than how to reach that state. Recently, Sørensen et al. (8) proposed a model by combining both their previous models to predict the fatigue life of UD composites. The model, however, does not consider other important damage mechanism such as fiber fatigue.

Hiremath et al. (9) proposed a model to consider fiber fatigue evolution as the only damage mechanism under tension-tension fatigue. They investigated the sensitivity of fiber break density and used the Palmgren-Miner rule to calculate the remaining fatigue life. Their model did not account for stress concentrations on the fibers in the vicinity of broken fiber and hence the model could be overestimated. Qian et al. (10) proposed a multiscale fatigue model with a three-step geometrical up-scaling process. They considered the fiber fatigue as the main damage mechanism in a unit cell containing 7 and 45 fibers scaling up to a unit cell with cross-section of 1 mm^2 and then 15 mm^2 to predict the failure of coupon specimens. However, their model only accounted for the stress concentration due to fiber breaks, ignoring other main damage mechanisms, such as fiber-matrix debond growth, and therefore yielded overestimated predictions.

To overcome the limitation of available models in simulating tension-tension behavior of UD composite, the current work considers: 1) comprehensive damage mechanisms 2) random fiber packing 3) the effect of fiber volume fraction on stress redistribution around broken fiber. The fiber-matrix debond growth is governed by Paris-Erdogan law and limited to a critical length. The proposed fiber break model simulates the stress distribution around a fiber break influenced

by local fiber volume fraction and debond length. The Palmgren-Miner rule is utilized to account for the varying of stress caused by fiber break and fiber-matrix debond growth on remaining fatigue life. S-N curve and cluster density progression are calculated and assessed for each damage mechanisms as well as synergy between them.

2. Model description

A fiber break model (11) is further developed to predict the fatigue damage development and fatigue life of UD composites in tension-tension loading. A unit cell with random packing including 3200 fibers was created. The size of the unit cell is 0.5 mm x 0.5 mm x 5mm. The simulation were performed for UD T700/epoxy and the input data used in the model were summarized in (11).

The fatigue simulation is performed in two steps. The first step is a quasi-static loading where the strain incrementally applied until reaching the maximum applied stress. After that, the cyclic loading starts. A cycle jump method is used to reduce the computational time.

In the first step, each fiber in the unit cell is divided into elements and strength is randomly assigned to each element by a unimodal Weibull distribution. After strain incrementation, the stress in each element is calculated and compared to its assigned strength. A fiber break happens when the stress in each element exceeds the element strength. Based on experimental data (12), a 14 μm constant debonding is imposed on broken fiber. Then, the stress will be updated around broken fiber based on a series of FE simulations with different random packing RVEs (13). The stress redistribution depends on radial and axial distance from broken fiber, debond length and local volume fraction. The stress concentration on the fibers in the vicinity of broken fiber is averaged over the cross-section. This extra load on nearby fibers may cause new fiber breaks and hence new clusters of fibre breaks. After reaching the maximum applied stress, the cyclic loading starts. A fatigue cycle jump is used to simulate fatigue loading in which the size changes with the progression of fatigue loading (11). The fiber matrix debonds grows based on Paris-Erdogan law where the corresponding constant parameters are defined using experimental data (12). The composite failure will happen when the number of fiber breaks increases unstably.

3. Results

Fig. 1a shows the predicted results of damage progression. The damage progression is predicted for three different variants of assumed fatigue behavior: 1) debond growth only 2) fiber fatigue only 3) both debond growth and fiber fatigue. The development of fiber break density in the case of considering debond growth only is limited and will come to a halt. A higher number of fiber breaks are predicted with considering fiber fatigue on its own; however, the fiber breaks are mostly isolated and the level of clusters is limited to 2-3. The fatigue failure of composite occurs at a lower number of cycles when both damage mechanisms are considered. Fig. 1b shows the S-N relationship of UD composites for different assumed behavior. The effect of fiber fatigue on fatigue life is significant as increasing fiber fatigue from 10% to 25% will decrease the fatigue life by about 3 orders of magnitude. Fig. 1 also reveals that ignoring either one of the main damage mechanism will lead to overpredicted fatigue life.

  doi:10.5075/epfl-298799_978-2-9701614-0-0

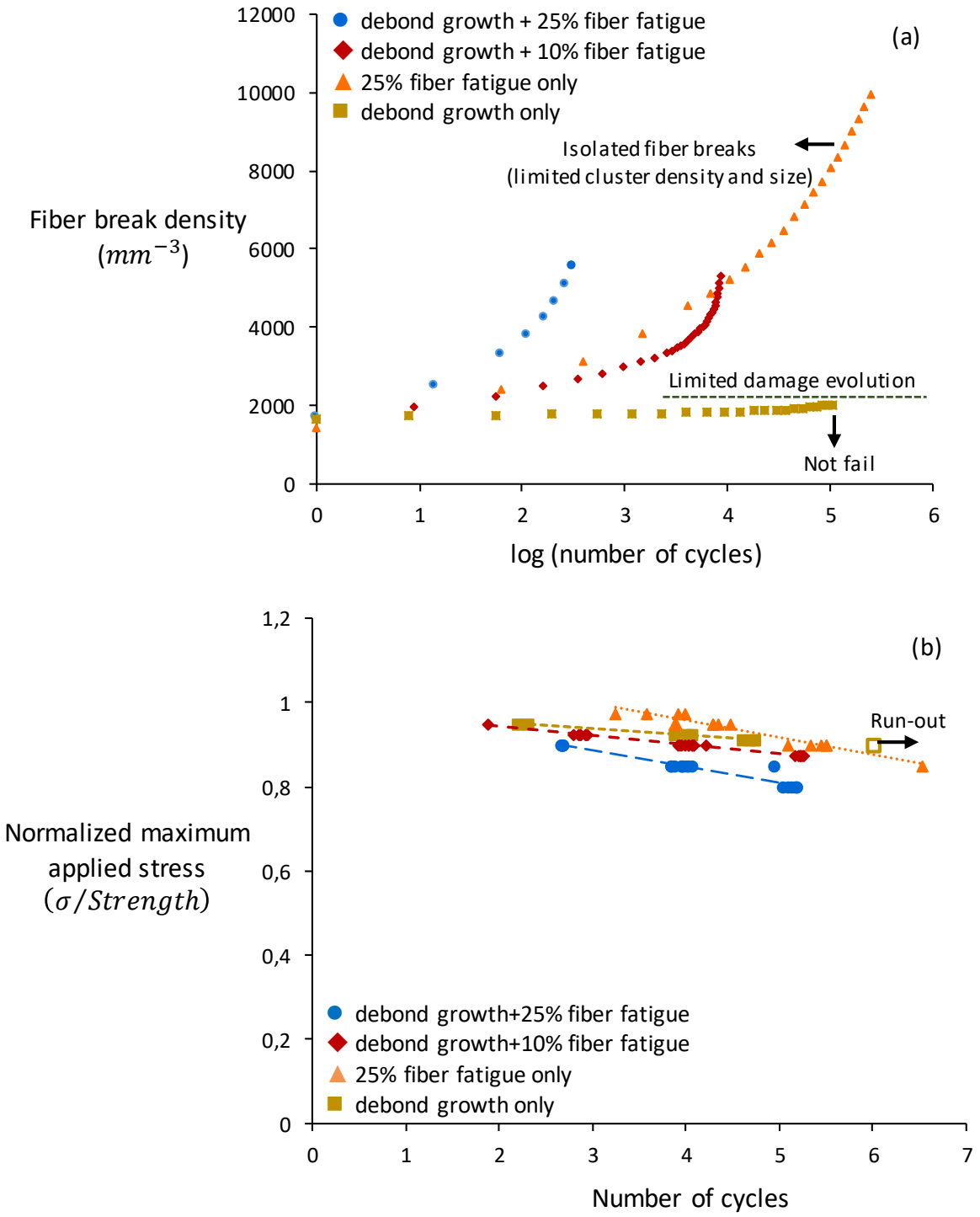

Fig. 1: Predicted results of UD T700/epoxy laminate in tension-tension loading: a) fiber break development at stress level of 90% of ultimate tensile strength, and b) S-N data. R = 0.1, fibre volume fraction=50%.

4. Conclusion

Fatigue damage and fatigue life of unidirectional composites are predicted by considering comprehensive damage mechanisms. The effect of debond length and local

volume fraction on stress redistribution around broken fiber are considered. The results of this study reveal that:

- The fiber break density increases fast in fatigue loading, an orders of magnitude over the static loading (first cycle).
- Ignoring either fiber fatigue or debond growth leads to a limited cluster density and an overestimated fatigue life by about one to two orders of magnitude.

Comparison of the fatigue damage progression to synchrotron computed tomography data is ongoing.

Acknowledgements

This research was performed within the framework of the HyFiSyn project and has received funding from the European Union's Horizon 2020 research and innovation programme under the Marie Skłodowska-Curie grant agreement No 765881.

5. References

1. Swolfs Y, Fazlali B, Melnikov A, Mesquita F, Feyen V, Breite C, et al. State-of-the-art models for mechanical performance of carbon-glass hybrid composites in wind turbine blades. IOP Conf Ser Mater Sci Eng. 2020;942(1):1–15.
2. Swolfs Y, Verpoest I, Gorbatikh L. A review of input data and modelling assumptions in longitudinal strength models for unidirectional fibre-reinforced composites. Compos Struct [Internet]. 2016;150:153–72.
3. Alves M, Pimenta S. A computationally-efficient micromechanical model for the fatigue life of unidirectional composites under tension-tension loading. Int J Fatigue. 2018;116(May):677–90.
4. Sørensen BF, Goutianos S. Micromechanical model for prediction of the fatigue limit for unidirectional fibre composites. Mech Mater. 2019;131(January):169–87.
5. Gamstedt EK. Effects of debonding and fiber strength distribution on fatigue-damage propagation in carbon fiber-reinforced epoxy. J Appl Polym Sci. 2000;76(4):457–74.
6. Castro O, Carraro PA, Maragoni L, Quaresimin M. Fatigue damage evolution in unidirectional glass/epoxy composites under a cyclic load. Polym Test [Internet]. 2019;74(November 2018):216–24.
7. Sørensen BF. The critical damage state controlling the tension-tension fatigue life of unidirectional fibre composites. Compos Sci Technol [Internet]. 2019;172(November 2018):172–81.
8. Sørensen BF, Goutianos S, Mikkelsen LP, Fæster S. Fatigue damage growth and fatigue life of unidirectional composites. 2020;1–15.
9. Hiremath CP, Senthilnathan K, Naik NK, Guha A, Tewari A. Mechanistic model for fiber crack density prediction in cyclically loaded carbon fiber-reinforced polymer during the damage initiation phase. J Compos Mater. 2019;53(8):993–1004.
10. Qian C, Westphal T, Nijssen RPL. Micro-mechanical fatigue modelling of unidirectional

  doi:10.5075/epfl-298799_978-2-9701614-0-0

glass fibre reinforced polymer composites. Comput Mater Sci [Internet]. 2013;69:62–72.

11. Fazlali B, Lomov S V., Swolfs Y. Fiber break model for tension-tension fatigue of unidirectional composites. Compos Part B Eng. 2021;220(April).

12. Pupurs A, Goutianos S, Brondsted P, Varna J. Interface debond crack growth in tension-tension cyclic loading of single fiber polymer composites. Compos Part A Appl Sci Manuf [Internet]. 2013;44(1):86–94.

13. Ahmadvashaghbash S; Fazlali B; Mehdikhani M; Swolfs Y. Finite Element Analysis of the Effect of Longitudinal Debonding on Stress Redistributions around Fibre Breaks in Randomly Packed Fibres. under reviwe.

  doi:10.5075/epfl-298799_978-2-9701614-0-0

FATIGUE RESPONSE OF CARBON/EPOXY LAMINATES UNDER MULTIAXIAL STRESSES FOR DIFFERENT LAY-UP PARAMETERS

Kalliopi-Artemi, Kalteremidou[a], Danny, Van Hemelrijck[a], Lincy, Pyl[a]

a: Department of Mechanics of Materials and Constructions, Vrije Universiteit Brussel (VUB), Pleinlaan 2, 1050 Brussels, Belgium – Kalliopi-Artemi.Kalteremidou@vub.be

Abstract: *The inherent anisotropy of composites complicates their damage response. The influence of multiaxiality is not thoroughly understood due to obstacles related to damage monitoring during loading. In this study, the response of carbon/epoxy laminates under fatigue is examined through in-situ microscopic observations.* $[0^o/\vartheta]_{2s}$, $[0^o/\vartheta/0^o/-\vartheta]_s$ *and* $[0^o/\vartheta/-\vartheta]_{2s}$ *laminates with two off-axis angles, namely 30 and 60 degrees, are tested under fatigue. By varying the orientation of off-axis layers, the impact of multiaxiality on the mechanical and damage response is evaluated. Furthermore, balanced and unbalanced laminates are compared, considering the limited information for the latter. The influence of the number of off-axis layers is finally assessed. The fatigue response is evaluated both from the mechanical and the damage point of view. Significant conclusions are drawn, especially for the benefits of unbalanced laminates and the impact of shear stresses, allowing utilization of the data for the establishment of reliable fatigue models.*

Keywords: Multiaxial fatigue; Damage accumulation; Fatigue crack growth; Unbalanced laminates

1. Introduction

Understanding the behavior of composite materials under multiaxial dynamic loads is essential in order to design high-performance materials and to develop physically based models suitable to predict the fatigue life and damage. A quite detailed review on the multiaxial fatigue investigation of composite materials is given by Quaresimin [1]. According to this review, multiaxial studies on composites are still limited and dedicated experimental campaigns have to be performed in order to understand in depth how different multiaxial conditions influence the fatigue damage process. The majority of the fatigue experimental works in composites concern common unidirectional (UD) or cross-ply lay-ups in which nearly uniaxial stress states are developed and the multiaxiality is not taken into account. On the contrary, in cases where multiaxiality is indeed considered, damage studies are limited either to damage initiation or to damage propagation, therefore detailed damage sequences and their correlation with generic stress states are hardly reported [2]. Especially elaborate damage studies in Carbon Fiber Reinforced Polymers (CFRPs) when different multiaxial stress states occur are rarely found. Flat laminates consisting of off-axis plies have been indicatively examined in [3,4]. However, the fatigue response of the composites in the majority of these cases has been studied only in terms of S-N curves or stiffness degradation measurements and detailed damage monitoring is not reported. Damage measurements in laminates under multiaxial loading are very limited in literature. May et al. [5] examined for instance the matrix cracking initiation during fatigue in CFRP $[(0^o)_2/(90^o)_4]_s$ and $[(0^o)_2/(60^o)_4]_s$ laminates using X-rays and Acoustic Emission. However, detailed damage monitoring throughout the total material life is not reported. Quaresimin et al.

  doi:10.5075/epfl-298799_978-2-9701614-0-0

[6] compared the damage initiation and propagation in Glass Fiber Reinforced Polymer (GFRP) tubular and flat specimens when the same multiaxial stresses were developed. However, also in this case, only matrix cracking phenomena are reported and correlated with the developing multiaxial stresses. Moreover, their approach is restricted to GFRPs because of the transparency of the glass fibers allowing damage monitoring by fixing the proper lightning conditions. Thus, the need to study the fatigue damage response of CFRP laminates under multiaxial stresses has been made clear through the lack of existing literature in polymer composites.

Multiaxiality in composites can be applied in two ways; internally and externally. The internal multiaxiality in composites arises from their inherent anisotropy. This means that even under simple uniaxial loading of flat laminates, multiaxiality can be developed in off-axis plies, i.e. in plies where the fibers are not parallel to the loading direction. The free edges of the coupons are sometimes considered a drawback due to the nucleation of high interlaminar stresses leading to delaminations. However, in the majority of real applications, flat laminates are used consisting of free edges. Thus, knowledge of the impact of multiaxial stress conditions on the fatigue damage initiation and growth in such geometries is of great importance. To that end, an extensive fatigue testing campaign is described in this work. The effect of multiaxiality is primarily investigated. 8-ply laminates including off-axis layers with an orientation equal to 30^o or 60^o are tested to establish different multiaxial stress states and to examine the influence of shear on the fatigue behavior. Furthermore, balanced laminates are compared with unbalanced lay-ups having the same off-axis layers. A beneficial response of the unbalanced laminates was identified during a quasi-static study of the considered laminates in a previous work of the authors [7]. The potential of an improved fatigue response is therefore evaluated in the current study. The impact of the number of the off-axis layers is also examined by testing 12-ply laminates including eight instead of four off-axis plies. The fatigue response is evaluated both from the mechanical aspect and from the damage point of view. Significant differences are observed, allowing utilization of the obtained data as important input for the establishment of reliable fatigue damage models [8].

2. Materials and methods

The material employed in the present study is TR 360E250S pre-preg CFRP in the form of flat laminates, manufactured by Mitsubishi Chemical Corporation and Honda R&D Co., Ltd. (Tokyo, Japan). Six angle-ply flat laminates were tested. $[0^o/\theta]_{2s}$ unbalanced laminates were initially chosen for two different θ values to account for dissimilar multiaxiality in the off-axis layers. Secondly, $[0^o/\theta/0^o/-\theta]_s$ balanced laminates with the same θ values were tested. Finally, 12-ply $[0^o/\theta/-\theta]_{2s}$ laminates were assessed to examine the influence of the number of off-axis layers on the mechanical response. The off-axis angle values θ were chosen based on calculations using the Classical Laminate Theory (CLT). Considering that most failure criteria make use of stresses and strains in the material coordinate system, it was decided to choose the angle of the off-axis layers based on the biaxiality ratio λ_{12}, which expresses the relation between the normal and shear stresses in the principal directions [1], defined as $\lambda_{12}=\tau_{12}/\sigma_{22}$. To obtain a different multiaxial condition, two angles were chosen based on the λ_{12} ratio, namely 30 and 60 degrees. It can be calculated from the CLT that in the $[0^o/\theta]_{2s}$ lay-up the λ_{12} ratio is equal to 2.02 for $\theta=30^o$, whereas in the 60^o layers it equals 0.64. These values depict that in the $[0^o/30^o]_{2s}$ laminates, the shear stresses τ_{12} are dominant in the off-axis plies while the transverse stresses σ_{22} represent the highest stress component in the 60^o layers of the $[0^o/60^o]_{2s}$ laminates. The dimensions of the

tested specimens were defined based on [9]. All samples had a total length equal to 250 mm and a width of 25 mm. The thickness of the 8-ply laminates was equal to 1.83 mm on average, whereas for the 12-ply laminates it equalled 2.74 mm.

An MTS fatigue testing system was used for the experimental campaign. Constant amplitude load-controlled fatigue tests at a frequency of 3 Hz were performed for all considered laminates. Initially, continuous fatigue was applied to all specimens until catastrophic failure occurred or until the fixed run-out value was reached. Three maximum fatigue stress levels σ_{max} were applied corresponding to 70%, 80% and 90% of the respective ultimate strength σ_{ult} for each laminate. The R-ratio was equal to 0.1 while the run-out value was set to one million cycles. Based on the continuous tests and the total number of cycles to failure N_f for each case, interrupted fatigue tests were then performed to assess the microscopic through-thickness damage evolution at certain fatigue intervals. An optical microscope was used for in-situ through-thickness monitoring of the fracture patterns during the interrupted tests. By keeping the specimens tensioned, through-thickness damage observations on their free edge were performed along their gauge length. The advantage of this set-up is that load is still applied to the specimens during the observations, therefore occurring cracks are still open and visible, in contrast to the cases in which only post-monitoring is performed. The microscope used was an MZ125 stereomicroscope by Leica Microsystems. A Digital Image Correlation system by Correlated Solutions was also used for strain measurements. The testing set-up is depicted in Figure 1.

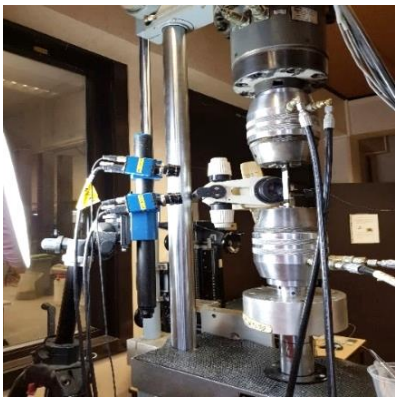

Figure 1. Experimental set-up

3. Results and discussion

3.1 S-N_f data

In Figure 2 the S-N_f data for the unbalanced laminates are initially plotted. On the x-axis the cycles to failure N_f are plotted on a logarithmic scale. On the y-axis the σ_{max} values are plotted on a linear scale. The filled data points mean that N_f was less than 10^6 cycles, whereas the unfilled ones indicate run-outs. It can be noticed that the $[0^o/60^o]_{2s}$ laminates lead to a generally better fatigue behaviour in terms of the cycles to final failure than the $[0^o/30^o]_{2s}$ laminates. Run-outs are observed in both cases when the maximum fatigue stress is equal to 60% of σ_{ult}. This can be explained by the fact that carbon/epoxy laminates are quite fatigue resistant. This means that any difference in the fatigue behaviour will be revealed only at high fatigue loads, explaining thus the choice of the high stress levels for the fatigue experimental campaign. It can be seen that the $[0^o/60^o]_{2s}$ laminates lead to run-out even for σ_{max} equal to 70% of σ_{ult}, whereas this is not the case for the $[0^o/30^o]_{2s}$ laminates which fail after 3-7*10^5 cycles. This difference is also

  doi:10.5075/epfl-298799_978-2-9701614-0-0

obvious when the maximum fatigue stress equals 80% of σ_{ult}. This behaviour is inversed for the very high fatigue loads with σ_{max} equalling 90% of σ_{ult}. In this case both laminates lead to fatigue lives of some thousands of cycles, with the $[0^o/60^o]_{2s}$ laminates being characterised by relatively fewer cycles to failure. As a first conclusion, it can be assumed that the high shear stresses in the off-axis layers of the $[0^o/30^o]_{2s}$ laminates lead to quicker degradation of the material and consequently to lower fatigue life. The oppositeness for the very high fatigue loads can be attributed to the high matrix crack densities occurring in the $[0^o/60^o]_{2s}$ laminates, leading in this case more quickly to catastrophic failure, without though significant differences in the N_f values.

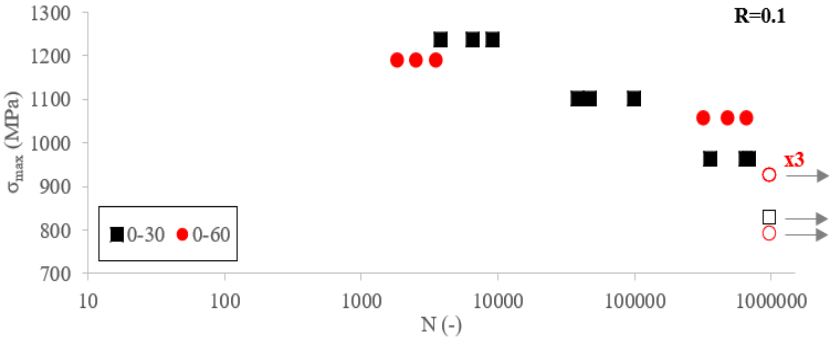

Figure 2. S-N_f data of $[0^o/30^o]_{2s}$ and $[0^o/60^o]_{2s}$ laminates

To confirm the previous results, in Figure 3 the S-N_f data for the $[0^o/\theta/0^o/-\theta]_s$ laminates are plotted. In this case the influence of the different multiaxial stresses is much more obvious. The balanced $[0^o/60^o/0^o/-60^o]_s$ laminates lead to significantly better fatigue response than the $[0^o/30^o/0^o/-30^o]_s$ laminates. Both lead to run-out when σ_{max} equals 60% of σ_{ult}. However, the $[0^o/60^o/0^o/-60^o]_s$ laminates lead then always to higher fatigue life for all stress levels, even if σ_{max} is similar in both cases. This is also confirmed from Figure 4 plotting the S-N_f data for the thicker $[0^o/\theta/-\theta]_{2s}$ laminates. Also in this case, the shear-dominated $[0^o/30^o/-30^o]_{2s}$ laminates are characterised by lower fatigue lives than the $[0^o/60^o/-60^o]_{2s}$ laminates. Apart from the 60% maximum fatigue stress case, at which both laminates lead to run-out, for the rest of the stress levels the $[0^o/60^o/-60^o]_{2s}$ laminates fail always after a higher number of cycles.

Comparing from Figures 2 and 3 the unbalanced with the balanced laminates in terms of their fatigue life, the potential of the first ones is revealed. For all stress cases, the unbalanced laminates fail after a higher number of cycles. Indicatively, for the 90% case a big difference appears between the $[0^o/30^o]_{2s}$ and $[0^o/30^o/0^o/-30^o]_s$ laminates, with the first ones failing after some thousands of cycles, while the latter ones only survive for some dozens of cycles. These findings agree with the results obtained after analysis of static tests [7], showing that unbalanced laminates can perform better than balanced ones, delaying the onset and propagation of damage. Trying to explain the influence of the number of the off-axis layers on the fatigue response of the material by comparing Figures 3 and 4, the impact is more obvious for the 60° angle case. If the 8-ply $[0^o/60^o/0^o/-60^o]_s$ laminates are compared with the 12-ply $[0^o/60^o/-60^o]_{2s}$ laminates, it is obvious that the last ones have a worse fatigue behaviour, leading to 3 times lower fatigue lives on average for the 80% and 90% stress cases. The influence is smaller for the 30° off-axis angle, with the $[0^o/30^o/-30^o]_{2s}$ laminates leading to similar fatigue lives with the $[0^o/30^o/0^o/-30^o]_s$ laminates. This could be related to the multiple interfaces in the 12-ply lay-up which accumulate the damage at independent regions without crucial propagation, as will be discussed later.

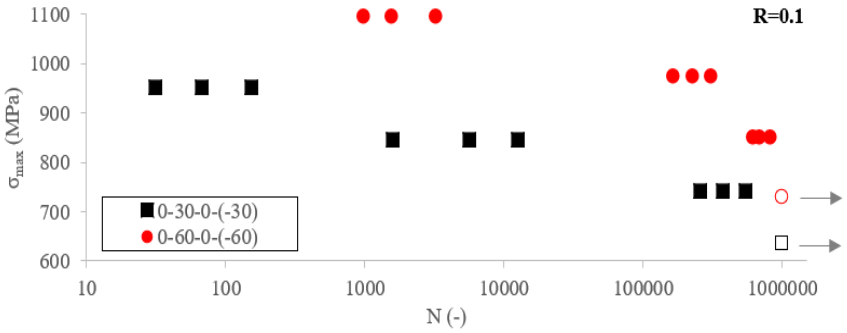

Figure 3. S-N_f data of $[0^o/30^o/0^o/-30^o]_s$ and $[0^o/60^o/0^o/-60^o]_s$ laminates

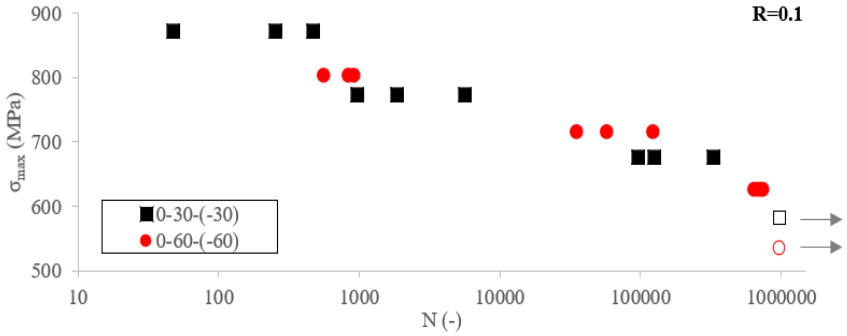

Figure 4. S-N_f data of $[0^o/30^o/-30^o]_{2s}$ and $[0^o/60^o/-60^o]_{2s}$ laminates

3.2 Damage process investigation

The analysis will start with the laminates with 60° layers, in which the domination of the transverse stresses triggers more directly the initiation of matrix cracks. In these laminates, matrix cracking of all off-axis layers along the total gauge length was always the primary damage mode occurring. In Figure 5 the average evolution of the measured matrix crack density versus the number of cycles N is plotted for the unbalanced $[0^o/60^o]_{2s}$ laminates. A distinction between the cracks in the thick layer (middle pair of 60° layers), represented by the blue curves, and the thin single 60° layers, corresponding to the orange lines, is made. It is obvious that matrix cracks initiate with a high rate from the first cycles saturating as the test continues. Increasing the fatigue stress level leads to higher matrix crack density and greater densities are observed in the thin off-axis plies. It is also notable that the highest the σ_{max}, the quickest the crack saturation occurs whereas the rate is smaller for lower stress levels. To demonstrate the delamination behaviour in the $[0^o/60^o]_{2s}$ laminates, in Figure 6 the average delamination crack growth versus N is plotted. A differentiation between the delaminations along the interfaces of the outer 0° layers and the adjacent 60° layers at both sides of the laminate is done (blue and orange curves). It is apparent that the initiation of delaminations is delayed and the crack growth rate is decreased when the stress level drops. Based on the damage observations on the $[0^o/60^o]_{2s}$ laminates it can be concluded that predictions for the initiation of interlaminar delaminations can be accomplished, based on measurements of the matrix crack density in the off-axis layers. Stemming from empirical observations, it was noticed that for all fatigue testing conditions, delaminations appeared when the matrix crack density in the off-axis layers reached a saturation level or else when the Critical Damage State (CDS) was exceeded.

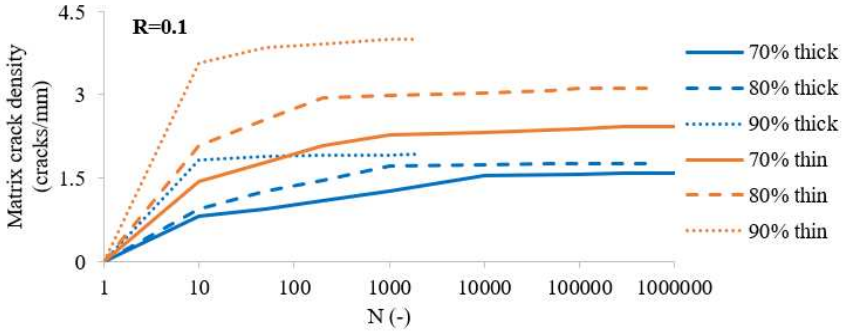

Figure 5. Matrix crack density versus N in $[0^o/60^o]_{2s}$ laminates

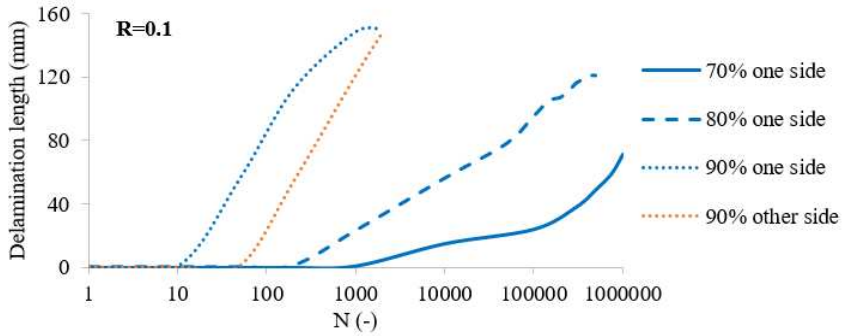

Figure 6. Delamination crack growth versus N in $[0^o/60^o]_{2s}$ laminates

When comparing the crack densities between the balanced and the unbalanced laminates, one important difference was observed, which is that for the same σ_{max} level the saturation of the matrix cracks occurs earlier in the balanced laminates, meaning that the crack rate is significantly higher in this case. This is quite significant since, as discussed previously, the saturation of the cracks is directly linked to the initiation and propagation of interlaminar delaminations. Indeed, also in the case of the balanced laminates, the saturation criterion applies. Delaminations initiated earlier than in the unbalanced lay-up for the same stress level. Moreover, the extent of damage was more detrimental in the $[0^o/60^o/0^o/-60^o]_s$ laminates compared to the $[0^o/60^o]_{2s}$ ones. Regarding the 12-ply laminates, increasing the number of the off-axis layers resulted in notably higher matrix crack densities in all off-axis layers. It was also remarkable that the crack density saturated rapidly in the 12-ply laminates, corresponding to a high cracking rate.

Regarding the shear-dominated $[0^o/30^o]_{2s}$ laminates, it was observed that in all test cases delaminations were developed at the edge of the laminate when a certain matrix crack density in the middle thick layer was reached. In all cases, soon after the nucleation of delaminations, matrix cracks in both thin 30° layers were observed. However, it should be highlighted that the thin off-axis layers were not immediately cracked along the total gauge length. Initial matrix cracks appeared always close to the tip of the formed delamination in both off-axis layers and new ones kept on nucleating afterwards along the layer length. However, the total length was always cracked before delamination at the opposite laminate side was evident. Furthermore, it is notable that contrary to the $[0^o/60^o]_{2s}$ laminates, the matrix crack density kept increasing after the propagation of delaminations in the $[0^o/30^o]_{2s}$ laminates. Therefore, the matrix cracking saturation criterion for the nucleation of delaminations does not apply for the last case. This shows that the damage conditions that suffice for the initiation of delaminations in the $[0^o/30^o]_{2s}$

laminates are much more limited compared to the $[0^o/60^o]_{2s}$ laminates. A significantly lower CDS and thus a considerably limited generated energy are enough for delaminations to appear due to the high shear stresses in the laminas. On the other hand, despite the fact that high matrix crack densities appear in the $[0^o/60^o]_{2s}$ laminates, delaminations are delayed, indicating a certain sensitivity of the material for the appearance of delaminations when shear is dominant. Also in the case of the 30° off-axis angle, it was noticed that the balanced laminates were significantly more deteriorated compared to the unbalanced laminates for the same number of cycles and the same stress level. Regarding the 12-ply $[0^o/30^o/-30^o]_{2s}$ laminates, it was characteristic that in many cases a full deterioration of one region was suddenly observed, consisting of multiple matrix cracks and delaminations along a limited length of maximum 10 mm. Due to the multiple interfaces along the laminate thickness, these fracture phenomena saturated immediately.

Characteristic microscopy images of the balanced 8-ply laminates are shown in Figure 7 after 50 and 200 fatigue cycles, indicating major differences between the laminates with 30° and 60° layers and pinpointing the detrimental effect of shear on the appearance of delaminations.

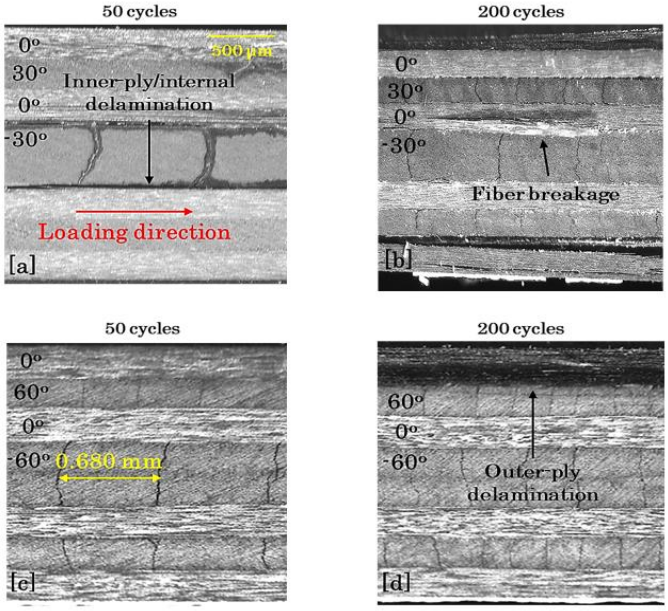

Figure 7. Damage in $[0^o/30^o/0^o/-30^o]_s$ (top) and $[0^o/60^o/0^o/-60^o]_s$ laminates (bottom) after 50 and 200 cycles for $\sigma_{max}=0.8*\sigma_{ult}$

4. Conclusions

The effect of multiaxiality, a comparison between balanced and unbalanced laminates and the impact of the number of off-axis layers on the tension-tension fatigue response were demonstrated in this work by testing angle-ply CFRP laminates for two different off-axis angles. The impact of shear was clearly indicated with laminates consisting of 30° off-axis plies leading to lower N_f values. A much better performance was observed for the first time for the unbalanced laminates having the same off-axis angle and being tested under the same fatigue conditions as the balanced ones. All findings were confirmed by studying the progressive damage development during fatigue. Specifically, for the laminates with 60° off-axis plies, matrix cracks appeared in all off-axis layers during the very first fatigue cycles. Moreover, a saturation criterion applied, indicating that when the transverse stresses determine the damage process,

interlaminar delaminations during fatigue loading occur only after a certain saturation of the matrix cracks has been reached. The CDS was reached quite earlier in the balanced lay-up. Significantly higher matrix crack densities were acquired for the 12-ply laminates, showing a certain impact of the number of off-axis plies on the fatigue response. On the contrary, the damage response was different in the shear-dominated laminates. Only when the crack density reached a certain value in the middle thick layer, delaminations and matrix cracks in the thin off-axis layers initiated. The crack density limit, after which delaminations started occurring in the laminate, was quite smaller for the balanced laminates, indicating a lower fracture toughness.

Acknowledgements

The work leading to this publication has been partially funded by the SBO project “M3Strength”, which fits in the MacroModelMat (M3) research program, coordinated by Siemens (Siemens Digital Industries Software, Belgium) and funded by SIM (Strategic Initiative Materials in Flanders) and VLAIO (Flanders Innovation & Entrepreneurship Agency). The authors gratefully acknowledge the material suppliers Mitsubishi Chemical Corporation and Honda R&D Co., Ltd. and would like to thank the financial support of the Fonds Wetenschappelijk Onderzoek (FWO) research program “Multi-scale modelling and characterisation of fatigue damage in unidirectionally reinforced polymer composites under multiaxial and variable-amplitude loading” (G.0090.15).

References

1. Quaresimin M. 50th anniversary article: Multiaxial fatigue testing of composites: From the pioneers to future directions. Strain 2015; 51(1):16-29.
2. Hinton M, Kaddour AS, Soden PD. Failure criteria in fibre reinforced polymer composites: The world-wide failure exercise. Elsevier. 2004.
3. Philippidis TP, Vassilopoulos AP. Fatigue of composite laminates under off-axis loading. International Journal of Fatigue 1999; 21(3):253-262.
4. Kawai M, Suda H. Effects of non-negative mean stress on the off-axis fatigue behavior of unidirectional carbon/epoxy composites at room temperature. Journal of Composite Materials 2004; 38(10):833-854.
5. May M, Pullin R, Eaton M, Featherston C, Hallett SR. An advanced model for initiation and propagation of damage under fatigue loading - Part II: Matrix cracking validation cases. Composite Structures 2011; 93(9):2350-2357.
6. Quaresimin M, Carraro PA, Mikkelsen LP, Lucato N, Vivian L, Brøndsted P, Sørensen BF, Varna J, Talreja R. Reprint of: Damage evolution under cyclic multiaxial stress state: A comparative analysis between glass/epoxy laminates and tubes. Composites Part B-Engineering 2014; 65: 2-10.
7. Kalteremidou KA, Hajikazemi M, Van Paepegem W, Van Hemelrijck D, Pyl L. Effect of multiaxiality, stacking sequence and number of off-axis layers on the mechanical response and damage sequence of carbon/epoxy composite laminates under static loading. Composites Science and Technology 2020; 190:108044.
8. Kalteremidou KA, Van Hemelrijck D, Pyl L. The influence of different lay-up parameters on the fatigue response of carbon/epoxy laminates under internal multiaxial stress states. Materials 2021; 14(24):7494.
9. D3039, Standard test method for tensile properties of polymer matrix composite materials. ASTM. 2008.

  doi:10.5075/epfl-298799_978-2-9701614-0-0

CREEP-FATIGUE INTERACTION DAMAGE MODEL FOR GFRP LAMINATES BASED ON THERMODYNAMICS

Seyed Shayan Khalooei Tafti , Anastasios P. Vassilopoulos

Composite Construction Laboratory (CCLab), École Polytechnique Fédérale de Lausanne, Lausanne, CH (shayan.khalooei@epfl.ch)

Abstract: *In this study, the fatigue behavior of FRP composites is analyzed based on the thermodynamics theory. An analytical model based on the thermodynamics of the irreversible process is utilized to evaluate the long-term behavior of the FRP composite laminates. The advantage of the proposed model is that it considers both time-dependent and cycle-dependent behaviors interacting during fatigue loading, by assuming the accumulated entropy generation at failure as a metric for assessing the fatigue life. In the developed model, the accumulated entropy generated from dissipated hysteresis energy and the corresponding damage energy resulting from that is attributed to the cycle-dependent fatigue damage. Moreover, due to the viscoelastic nature of polymer matrix composites, the time-dependent behavior participates even in constant amplitude fatigue loading with non-zero mean stress. Therefore, due to the energy stored in the material resulting from viscoelastic deformation (dissipated at failure), the corresponding entropy generation is considered to quantify the damage resulting from time-dependent behavior. The results of constant amplitude fatigue tests for GFRP composite laminates are used to evaluate the model's performance and quantify creep and fatigue damage contribution to the failure depending on the stress level and the stress ratio.*

Keywords: Fatigue, Composites, Creep-fatigue interaction; Thermodynamics theory; Fatigue Failure.

1. Introduction

The degradation of the material under loading is usually interpreted as the result of irreversible thermodynamic processes that disorder the material under loading [1]. Accordingly, entropy, the fundamental thermodynamic parameter characterized by disorder, can provide a reliable measure of material degradation [2,3]. Therefore, thermodynamics-based fatigue damage models have recently been developed to analyze and predict the fatigue behavior of different materials. By applying the first and second laws of thermodynamics, entropy generation-based models can be proposed to evaluate the fatigue behavior considering all the dissipation processes involved during fatigue loading.

Naderi et al. [1-3] firstly investigated the metals' low-cycle fatigue degradation using the entropy generation approach. Entropy generation was calculated using the hysteresis loop obtained during fatigue testing. It has been shown that a constant amount of entropy is generated and accumulated up to the failure under fatigue loading, called fracture fatigue entropy (FFE), [1,2,4]. Besides, it has been proposed that FFE is independent of loading amplitude, frequency,

  doi:10.5075/epfl-298799_978-2-9701614-0-0

and testing conditions. Naderi and Khonsari extended the application of the entropy generation model to analyze the FRP composite laminates' fatigue behavior [5], showing that the accumulation of entropy generation was an efficient measure for evaluating the fatigue life of composite laminates under cyclic loading, despite neglecting damage energy in FFE calculation [5]. In another study, they improved the analysis by also considering the damage energy for calculating the FFE and achieving better agreement with experimental data [6].

The present work aims to extend the thermodynamics-based analysis to include also the time-dependent behavior of FRP composites, i.e., the creep deformation under fatigue loading, to calculate FFE. Therefore, both hysteresis energy and damage energy, calculated using the first thermodynamics law, are considered for fatigue behavior analysis. Since the FRP composite materials would undergo creep deformation even under constant amplitude cyclic loading, a new methodology is presented to consider time-dependent behavior and its contribution to the failure. Thus, the second law of thermodynamics is modified compared to the literature to include the mechanical work done and stored in the material due to viscoelastic deformation. This time-dependent deformation causes an amount of work which could be stored in the material through primary and secondary stages of creep deformation. Although this work is stored in the material during loading, it will be dissipated at the failure in the tertiary stage of creep, causing entropy generation. Therefore, the entropy generation due to creep deformation can be estimated and compared with the entropy generation resulting from fatigue damage. As a result, the contribution of fatigue damage and creep deformation to fatigue failure can be evaluated for different loading conditions. The constant amplitude fatigue tests for different stress levels and *R*=0.1 of GFRP laminates reported in [7] are used to validate the proposed analysis in this work. Besides, the limited results obtained for the same material and *R*=0.5 [8] are used in the last part for comparison.

2. Thermodynamics-based creep-fatigue model

According to the mentioned literature on this topic, the specimen's gauge section between grips under fatigue loading can be considered as a system that can be studied thermodynamically. The mechanical energy inserted into the system in each cycle under fatigue loading can be obtained by calculating the area of the hysteresis loops [6]. According to the different energy dissipation processes involved during fatigue loading, the energy balance, as presented in Eq. (1), holds as a result of applying the first law of thermodynamics. Therefore, the mechanical energy input, which is called hysteresis energy (H), can be divided into volumetric heat dissipated energy ($E_{Heat\ dissipation}$), the energy associated with thermal capacity ($E_{Thermal\ capacity}$), and the energy consumed by fatigue damage ($E_{Fatigue\ damage}$) [6]. The thermal capacity energy is responsible for energy stored in the material resulting from the self-heating temperature rise of the specimen under cyclic loading. The damage energy is associated with the energy consumed for initiation and propagation of the different damage modes resulting from fatigue loading. The heat can be dissipated from the specimen (system) to the surrounding through convection, conduction, and radiation, as presented in Eq. (2), [6].

$$H = E_{Thermal\ capacity} + E_{Heat\ dissipation} + E_{Fatigue\ damage} \quad (1)$$

  doi:10.5075/epfl-298799_978-2-9701614-0-0

$$E_{Heat\ dissipation} = E_{convection} + E_{radiation} + E_{conduction} \quad (2)$$

Based on the energy balance equation resulted, the energy consumed to initiate and propagate fatigue damage during loading can be calculated. Besides the measurements of hysteresis loops (H), the terms representing the thermal capacity and heat dissipation energies should be estimated. Using the definition of thermal capacity, Eq. (3) can be adopted, where ρ is the density, c is the specific heat, T_s is the specimen's temperature, and t represents time. According to Eq. (4), the energy due to heat dissipation can also be estimated using the basic equations in thermodynamics theory for convection, radiation, and conduction processes. In Eq. (4), h is the convection heat transfer coefficient, T_s and T_a are specimen and ambient temperatures, e represents the surface emissivity, β is the Stefan–Boltzmann constant, k is the thermal conductivity coefficient of the GFRP laminate, $\frac{\Delta T}{\Delta z}$ is the temperature gradient between the ends of the specimen and the grips, V is the volume of the gage section, and finally, A_s and A_c are surface and cross-sectional area of the gage section (for conduction), respectively [6].

$$E_{Thermal\ capacity} = \rho c \frac{\partial T_s}{\partial t} \quad (3)$$

$$E_{Heat\ dissipation} = h(T_s - T_a)\frac{A_s}{V} + e\beta(T_s^4 - T_a^4)\frac{A_s}{V} + 2k\frac{\Delta T}{\Delta z}\frac{A_c}{V} \quad (4)$$

Based on thermodynamics theory, the variation of entropy of a system (dS) is the summation of two components according to Eq. (4).

$$dS = d_i S + d_e S \quad (5)$$

where $d_e S$ represents the entropy exchanging between the system and the surroundings and $d_i S$ is the entropy generation within the specimen, which must be non-negative, according to the second law of thermodynamics. Corresponding to the different energy dissipation processes mentioned, the entropy generation rate is the sum of entropy generation due to mechanical input ($S_{mechanical}$), internal variables evolutions or fatigue damage (S_{damage}), and heat dissipation (S_{heat}) as presented in Eq. (6) [6].

$$S = S_{mechanical} + S_{damage} + S_{heat} \quad (6)$$

Considering Eq. (6), the first term represents the work done on the system resulting from the inelastic deformation of the material. This term can be estimated based on hysteresis energy dissipation. However, apart from the cyclic inelastic deformation, the time-dependent deformation of GFRP composite laminates, i.e., the creep deformation under mean stress during cyclic loading, should be considered in the analysis. Therefore, the work done on the system due to this viscoelastic behavior is regarded as the contribution of the time-dependent behavior to failure. This part of the energy is stored in the material during the loading, which would be released and dissipated at the time of failure. Therefore, the entropy generation due to inelastic deformation is comprised of a component related to the hysteresis energy dissipation (H), another one attributed to the work done due to creep (W_{creep}) and other components related to the entropy generation of the internal variable evolution due to damage energy (E_{damage}), and the thermal dissipation due to heat conduction (E_{heat}) according to Eq. (3). However, many

  doi:10.5075/epfl-298799_978-2-9701614-0-0

works in the literature showed that entropy generation due to heat conduction is often negligible during a fatigue process [6], so Eq. (6) is derived for the total entropy generation.

$$S = \left(\frac{H}{T} + \frac{W_{creep}}{T}\right) + \frac{E_{damage}}{T} \tag{7}$$

The accumulation of entropy at the failure ($S_{acc.}$) is obtained by integration of Eq. (7), as derived in Eq. (8).

$$FFE = S_{acc.} = \int_0^{t_f} \left(\left(\frac{H}{T} + \frac{W_{creep}}{T}\right) + \frac{E_{damage}}{T}\right) dt \tag{8}$$

Eqs. (4) and (5) assert that the degradation and damage process in a composite laminate is a function of the temperature evolution, the damage energy, the hysteresis energy, as well as the creep energy. In the previous works, it has been shown that a large amount of hysteresis energy (50–70%) is directly responsible for creating damage in FRP composites [6]. In this work, we consider an additional term, namely the energy associated with creep deformation. In the following section, three sources of entropy generation (hysteresis energy, creep energy, and damage energy), as well as the accumulated entropy generation resulting from them, are considered to assess degradation in the GFRP composite laminate.

3. Results and discussions

As mentioned above, the constant amplitude fatigue test results reported in [7] and [8] are used for angle-ply GFRP laminates under *R*=0.1 and *R*=0.5, respectively. For the thermodynamics analysis, hysteresis areas are calculated based on strain measurements obtained by a video-extensometer. Temperature evolution recorded by the thermal camera has been used for heat dissipation analysis. Table 1 shows the thermal conductivity, surface emissivity, density, and specific heat coefficient of angle-ply GFRP laminates and also the fatigue testing ambient temperature.

Table 1: Thermal properties of angle-ply GFRP laminates and fatigue test temperature

$k_{45}(Wm^{-1}K^{-1})$	e	$\rho(kgm^{-3})$	$c(JkgK^{-1})$	$T_a(k)$
0.24	0.9	1800	1400	293

The results of dissipation analysis based on the first law of thermodynamics are obtained and presented in Figure 1 for two different stress levels and R=0.1. The assumptions considered in heat dissipation analysis include constant thermal properties with respect to the temperature and fatigue damage, the isothermal surface temperature of the gage section, which linearly varies from the end of the gage section to the grips (for conduction), and finally constant ambient temperature [6]. Therefore, the heat dissipation energy through convection, conduction, and radiation is estimated according to Eq. (4) and the properties reported in Table 1. Using the thermal capacity energy estimation (Eq. (3)) and the energy balance equation (Eq. (1)), the energy corresponding to the fatigue damage can be obtained by subtracting the energy associated to the thermal capacity and the heat dissipation from the hysteresis energy. The evolution of each term presented in the energy balance equation as a function of the normalized number of fatigue cycles (with respect to the fatigue life) is shown in Figure 1.

  doi:10.5075/epfl-298799_978-2-9701614-0-0

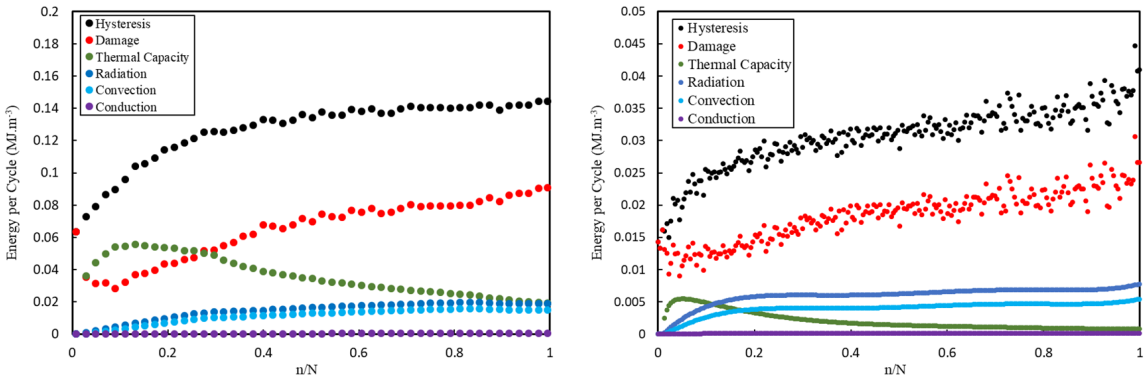

Figure 1. Energy dissipation analysis for R=0.1 and two maximum stress levels of (a) 70 MPa and (b) 58 MPa

According to Figure 1, radiation and convection are the dominant heat dissipation processes compared to conduction for both stress levels. The dissipation of heat is negligible in the early fatigue cycles, and most of the mechanical input (hysteresis energy) is allocated to increasing the temperature of the laminate. With increasing loading cycles, the energy associated with the thermal capacity decreases, as the material is allowed to dissipate energy through different heat processes, and finally reaches a steady state for the higher stress level, while it almost vanishes at lower stress. Conversely, during the initial cycles, the damage energy increases, resulting from the initiation of matrix micro-cracks in the laminate. As shown in Figure 1, more cyclic hysteresis energy and consequently more thermal capacity and damage energy can be observed for a higher stress level compared to the lower one.

The hysteresis energy, fatigue damage energy, and temperature profile are utilized to calculate the cyclic and accumulated entropy generation corresponding to hysteresis and damage energies based on Eqs. (7) and (8). The results of cyclic entropy generation for the same tests discussed earlier are plotted in Figure 2. The total cyclic entropy is the summation of the cyclic damage and the hysteresis entropy generation. The results show that the cyclic hysteresis entropy generation is increasing with fatigue cycles, as well as the cyclic damage entropy generation, except from a slight decrease during the early cycles due to the temperature rise under loading. The other component of the entropy generation resulting from the viscoelastic behavior is included for the estimation of the accumulated entropy generation. The mean stress evolution resulting from the creep behavior and that from the cyclic loading is used for the calculation of the creep energy storage. The resulting energy, which will be released at failure, is used to estimate the accumulated entropy generation due to creep deformation. The accumulated entropy generation due to hysteresis, fatigue damage, creep deformation, and the summation of all components is presented in Figure 4. The results show that the damage energy dissipated by different damage mechanisms resulting from fatigue loading is not negligible and can reach up to roughly 50% of the total accumulated entropy. Therefore, the total accumulated entropy can explain the long-term behavior of material more efficiently, considering all dissipation processes involved during loading and considering both creep and fatigue behaviors.

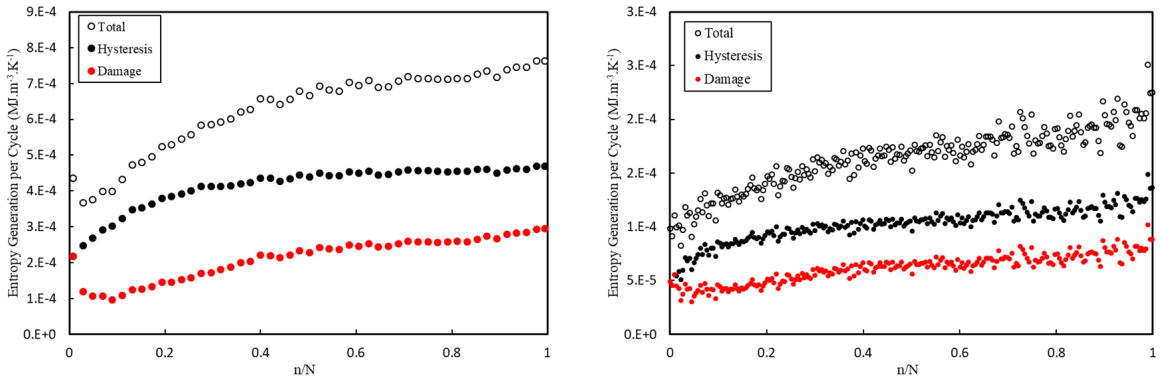

Figure 2. The cyclic entropy generation for R=0.1 and two maximum stress levels of (a) 70 MPa and (b) 58 MPa

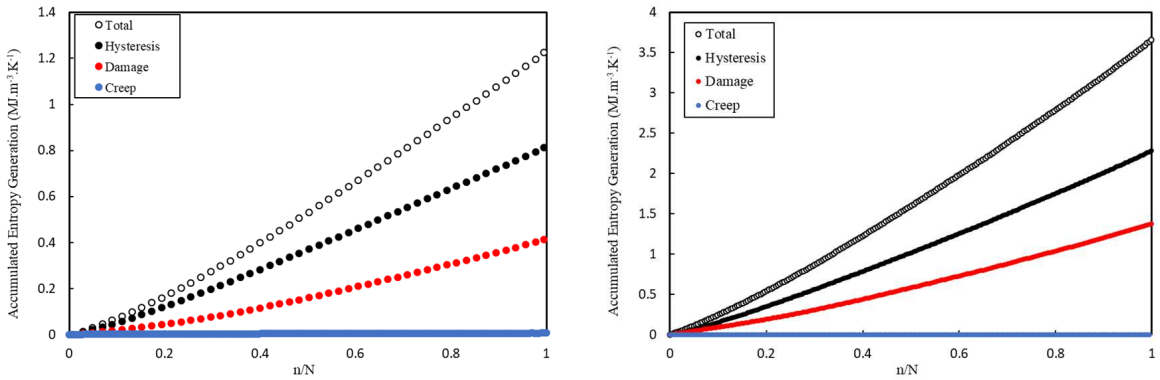

Figure 3. The accumulated entropy generation for R=0.1 and two maximum stress levels of (a) 70 MPa and (b) 58 MPa

As depicted in Figure 3, the entropy generation due to creep deformation is negligible compared to the fatigue damage as expected since the *R*-ratio is low (R=0.1). For further evaluation, as shown in Figure 4-(a), the entropy generation per cycle is presented for all the specimens tested under *R*=0.1 with various maximum stress levels. For higher stress levels, the entropy generation per cycle is higher, resulting from more damage and hysteresis energy. However, according to Figure 4-(b), the accumulated entropy generation for lower stress levels is much more than that generated at higher stress levels showing a more severe damage state in these specimens at failure. This behavior can be explained by considering the fact that at lower stress levels, the material under cyclic loading could tolerate more damage, more evenly distributed through the specimen. Conversely, the damage grows more rapidly for higher stress levels and would concentrate in some parts of the specimen up to failure [7]. Therefore, the conventional consideration of constant entropy generation for different stress levels is not accurate enough. The different material damage states at failure could explain this dependency of entropy generation on stress levels. Also, as depicted in Figure 4-(c), the normalized accumulated entropy generation is a linear function of the normalized fatigue life which could be simply formulated and proposed as a failure criterion for fatigue life prediction. According to Figure 4-

(d), the results obtained for all fatigue tests of *R*=0.1 are presented in comparison with the limited results provided for *R*=0.5. The evolution of the total accumulated entropy generation (black) and the contribution of creep (blue) and fatigue damage (red) are depicted with respect to the maximum stress level for both *R*-ratios of 0.1 (circle) and 0.5 (triangle). The accumulated entropy generation shows an exponential dependency to stress levels, indicating different damage states at the failure for different stress levels. Based on the results, the proposed entropy-based model can effectively quantify the contribution of fatigue damage and creep deformation to the final fatigue failure of GFRP composite laminates. The dependency of the creep and fatigue accumulated entropy generation on the stress level shows more contribution of creep compared to the fatigue damage for higher stress levels. Moreover, both trends show the convergence when stress level approaches the ultimate tensile stress (UTS), which could help interpreting different damage progress and failure modes resulting from different types of loading (fatigue, creep, and quasi-static loadings).

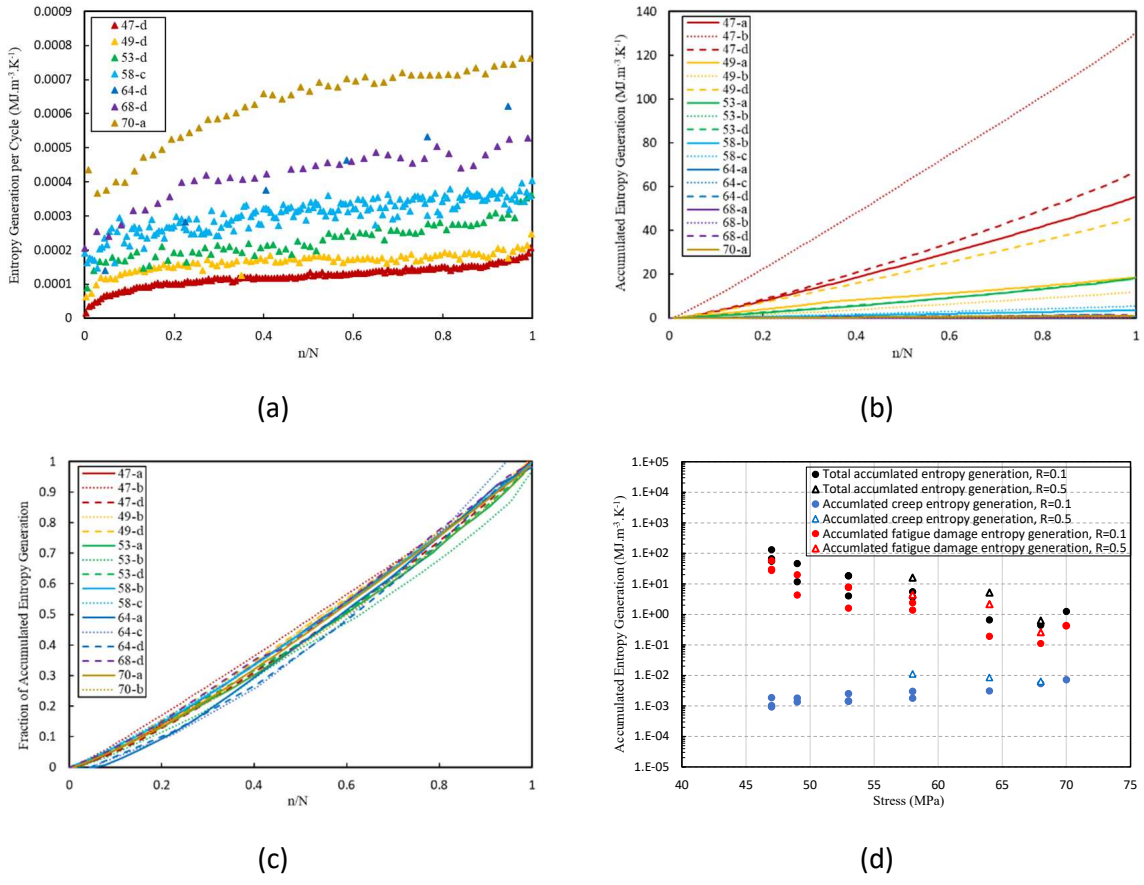

Figure 4. The result of cyclic and accumulated entropy generation for various maximum stress levels (a) Cyclic entropy generation, (b) Accumulated entropy generation, (c) Normalized accumulated entropy generation, (d) Accumulated entropy generation due to creep and fatigue damage for R=0.1 and 0.5.

4. Conclusions

A thermodynamics-based damage model was proposed to evaluate the contribution of creep and fatigue damage in angle ply laminates under cyclic loading. The energy associated with

fatigue damage was obtained using the energy balance equation by applying the first law of thermodynamics. The creep contribution was evaluated by considering the mean strain evolution under mean stress and calculating the corresponding energy storage in the material. The stored energy will be dissipated at failure and causing the entropy generation due to creep behavior. The cyclic and accumulated entropy generation resulting from the different energy dissipation processes during loading was estimated as the metric for evaluating the FRP composite laminates. Therefore, the entropy generation due to hysteresis, fatigue damage, and creep energy were used to obtain the total accumulated entropy at failure. The fatigue tests for angle-ply GFRP laminates under R=0.1 and 0.5 were used to evaluate the performance of the model to interpret the degradation of FRP composite materials caused by creep and fatigue damage. By comparing the accumulated entropy generation results for low and high stress levels, it can be realized that contribution of creep entropy generation is much more at higher stress levels than at lower stress for both R-ratios. Therefore, entropy generation can be considered as a measure for the dependency of creep entropy on stress level for contribution to failure. Although the results show more contribution of creep damage for R=0.5 compared to R=0.1, the material's behavior and the failure were still dominated by the fatigue damage in both cases. This analysis should be applied for more CA fatigue tests under higher R-ratios to futher evaluate the performance of the suggested model by considering both fatigue and creep behaviors.

Acknowledgments

The authors wish to acknowledge the support and funding of this research by the Swiss National Science Foundation (Grant No. 200020_185005).

5. References

1. Naderi M, Khonsari MM. Real-time fatigue life monitoring based on thermodynamic entropy. 2010 Jun 14;10(2):189–97.
2. Naderi M, Khonsari MM. An experimental approach to low-cycle fatigue damage based on thermodynamic entropy. Int J Solids Struct. 2010 Mar 15;47(6):875–80.
3. Naderi M, Amiri M, Khonsari MM. On the thermodynamic entropy of fatigue fracture. Proc R Soc A Math Phys Eng Sci. 2010;466114:423–38.
4. Liakat M, Khonsari MM. Rapid estimation of fatigue entropy and toughness in metals. Mater Des. 2014 Oct 1;62:149–57.
5. Naderi M, Khonsari MM. Thermodynamic analysis of fatigue failure in a composite laminate. Mech Mater. 2012 Mar 1;46:113–22.
6. Naderi M, Khonsari MM. On the role of damage energy in the fatigue degradation characterization of a composite laminate. Compos Part B Eng. 2013 Feb 1;45(1):528–37.
7. Movahedi-Rad AV, Keller T, Vassilopoulos AP. Fatigue damage in angle-ply GFRP laminates under tension-tension fatigue. Int J Fatigue. 2018 Apr 1;109:60–9.
8. Movahedi-Rad AV, Keller T, Vassilopoulos AP. Stress ratio effect on tension-tension fatigue behavior of angle-ply GFRP laminates. Int J Fatigue. 2019 Sep 1;126:103–11.

  doi:10.5075/epfl-298799_978-2-9701614-0-0

LIFE TIME ESTIMATION OF 3D-PRINTED CONTINUOUS FIBER REINFORCED PARTS UNDER FATIGUE LOADING

Andreas Primetzhofer[a], Sandra Petermann[b], Renaud Dietsch[c], Jürgen Leßlhumer[d], Florian Arbeiter[b] and Gerald Pinter[b]

a: Polymer Competence Center Leoben GmbH; Roseggerstrasse 12, 8700 Leoben, Austria,
e-mail: Andreas.Primetzhofer@gmx.at
b: Materials Science and Testing of Polymers, Montanuniversitaet Leoben, Otto Gloeckel-Strasse 2, 8700 Leoben, Austria,
e-mail: Gerald.Pinter@unileoben.ac.at
c: SinusPro GmbH, Conrad-von-Hötzendorf-Strasse 127, 8010 Graz, Austria
d: Kompetenzzentrum Holz GmbH (Wood K plus), Altenbergerstrasse 69, 4040, Linz, Austria

Abstract: *Increasing requirements with regard to emission reduction, material utilization and light weight lead to an increasing usage of 3D-printed structures. Especially for highly loaded parts, the use of fiber reinforced materials is of high interest. To use reinforced materials in structural applications efficiently, even under complex load conditions, it is indispensable to predict their mechanical behavior and in particular the fatigue behavior in an early stage of the development process. Since fiber reinforced 3D-printed materials are highly inhomogeneous and anisotropic, the local micro structure plays an important role. Especially temperature history and orientation influence the material behavior significantly. Therefore, a study to consider these aspects in a well-known simulation chain is presented in this work. Fatigue tests were performed to analyze the influence of process parameters and fiber orientation. Based on the material tests, models were developed to describe the effects of the deposition path and welding temperature.*

Keywords: fatigue life; additive manufacturing; 3D-printed parts; temperature history; continuous fiber reinforcement

1. Introduction

Material extrusion-based additive manufacturing (AM) also known as fused filament fabrication (FFF) or 3D-printing has become increasingly important in many areas in recent years. By now it's a more or less established technology. Despite the high potential of this process, its use is mostly focused on prototyping and the home sector, which is partly due to a lack of knowledge regarding final properties. Furthermore, high strength and stiffness values are necessary for the application in structural applications. Thus, fiber-reinforced materials are increasingly being used. However, fiber reinforced materials place higher demands on the printing process. This in turn increases the necessity of reliable property predictions even more.

In order to be able to transfer and apply life time estimation on components, the entire process must be mapped as a "digital twin" using advanced simulation methods. This twinning procedure starts with the melting of the material in the nozzle of the 3D printer and ends with the mechanical properties of the sample or component. In the end, users are able to analyze components, predict their properties and optimize them before going into actual printing. Similarly, an end-to-end simulation method (*Figure 1*) has been successfully developed and established in the past for the prediction of injection molded short fiber reinforced materials. A

  doi:10.5075/epfl-298799_978-2-9701614-0-0

comprehensive description of the method can be found in [1]. While there are mature routines regarding testing [2], [3] and simulation requirements [4] as available for injection molding, there are just a few for materials manufactured using AM. Existing customized tools for describing the process history of AM have so far been used for the prediction of shrinkage, warpage and stresses. The only missing link to meet the needs of the industry, and the clear goal of this work, is to combine the two available technologies in order to guarantee part performance over the entire or designated life time.

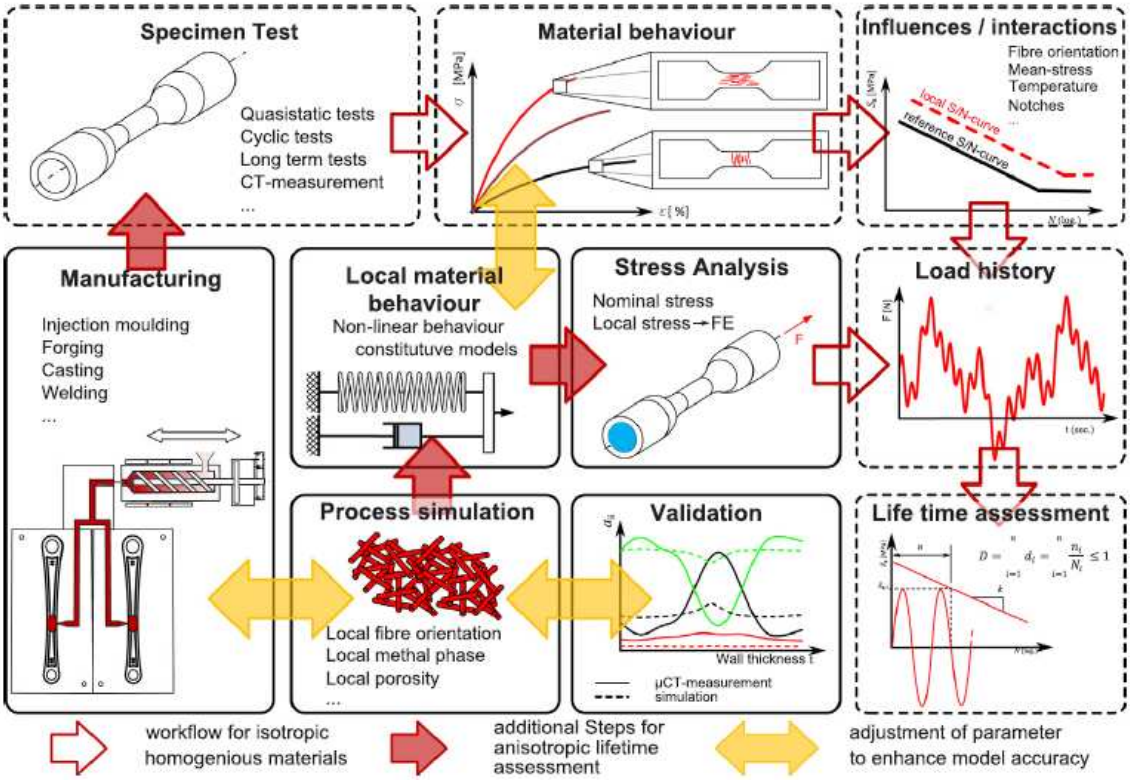

Figure 1. Scheme of a simulation chain to cover local effects [1]

As depicted in Figure 1, the actual material behavior strongly depends on the manufacturing process itself. During processing the material's micro structure is formed, which has a direct influence on local properties, such as the strength of the material. This especially applies for the local orientation of fibers and the local temperature. For this study, the essential input parameters of endless fiber reinforced AM components are identified and put into the evaluation routine shown in *Figure 1* and described in detail in [3], [5].

2. Materials and methods

2.1 Materials

The investigated matrix material was PLA Luminy® L175 (TotalEnergies Corbion, The Netherlands), which is a homopolymer and has a glass transition temperature of approx. 60°C. Natural flax fibers were used as reinforcement material. This matrix/fiber combination was utilized to produce endless-fiber reinforced filaments, which were further processed during 3D-printing.

Viscosity curves of the matrix material were measured by cone-plate rheometry on the modular Compact Rheometer MCR 501 (Anton Paar GmbH, Austria) at temperatures of 190, 220 and

  doi:10.5075/epfl-298799_978-2-9701614-0-0

250°C. The temperature-dependent measurement was performed on Ø25 mm samples, which were punched from 2 mm plates. The viscosity measurements were then used to evaluate the activation energy ΔU (86.14 kJ/mol), which in turn is used to calculate the horizontal temperature shift factor a_T according to the Arrhenius equation

$$a_T(T) = \exp\left[\frac{\Delta U}{R}\left(\frac{1}{T} - \frac{1}{T_{ref}}\right)\right] \quad (1)$$

with R being the molar gas constant, T the actual temperature and T_{ref} the reference temperature (T_{ref} = 190°C). This shift factor function is further used to evaluate the effective weld time during 3D-printing, which is described in section 3.

2.2 Specimen dimensions and manufacturing

Firstly, boxes with dimensions of (180x180x80) mm³ (Figure 2 a) were printed on an Original Prusa i3 MK3S (Prusa Research, Czech Republic) using neat PLA. The printer was equipped with a steel nozzle with a diameter of 0.6 mm. The slicing was performed with the PrusaSlicer 2.1.0 (Prusa Research, Czech Republic) using spiral vase mode. Per print, one box was manufactured. The extrusion width was set to 0.675 mm and the extrusion multiplier to 1.0. The build platform was PEI-coated and heated to 60°C. The printing speed was 40 mm/s, and 20 mm/s for the first layer. The layer thickness was 0.25 mm; the first layer thickness 0.2 mm. The boxes were printed using five different nozzle temperatures: 180, 190, 210, 230 and 250°C. This is necessary to evaluate the temperature-dependent strength of the material. Furthermore, the boxes were only consisting of a single deposited strand per layer and dumbbell specimens were cut-out of the boxes in a way that the load acts perpendicular to the strands. By doing so the weld strength can be examined directly. When samples were produced from the 180°C boxes, it was found that the print quality was insufficient. Thus, this temperature was not used for further evaluations.

In order to describe the influence of flax fiber reinforcement and fiber orientation, (100x100x4) mm³ plates were unidirectionally printed with flax-fiber reinforced PLA. The same printing conditions and configuration described above were applied, whereby a nozzle temperature of 210°C was used (Figure 2 b). Rectangular specimens ((10x100x4) mm³) were cut from the plate using a diamond saw in the direction of (UD0) and perpendicular to (UD90) the fiber orientation.

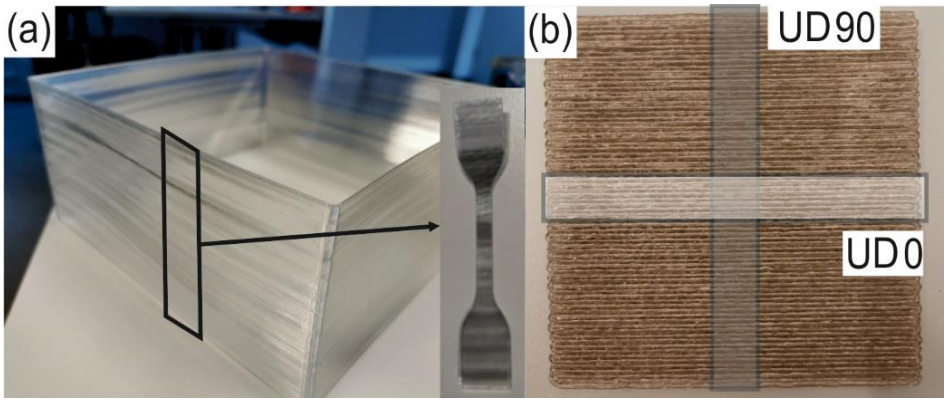

Figure 2. Printed PLA box and specimen for mechanical testing (a) as well as printed flax fiber reinforced PLA plate and UD0 / UD90 specimens (b)

2.3 Fatigue tests

  doi:10.5075/epfl-298799_978-2-9701614-0-0

Force controlled tests were performed on an electrodynamic testing machine ElectroPlusTM E3000 Linear-Torsion (Instron, US). The machine was equipped with a 3 kN load cell. All tests were performed at a constant temperature of 23°C and relative humidity of 50 %. During the whole test the temperature was monitored by a non-contact infrared sensor to check for hysteretic heating. A sinusoidal load with constant frequency of f = 5 Hz was used. Stress levels were defined to achieve a range of cycles to failure from $N = 10^4$ to $N = 10^6$. The total specimen separation, or exceeding a number of cycles of $N = 10^6$, were set as the abort criteria. For the temperature dependent tests on the pure matrix material, a load ratio ($R = F_{min}/F_{max}$) of 0.1 was applied to prevent buckling since only very thin specimens were used. In the case of fiber reinforced PLA, tests with R values of 0.1 as well as -1 were performed since data from different load cases are required for the life time estimation. The clamping length was set as 42 mm for R = 0.1 and reduced to 10 mm for R = -1 to avoid buckling. After the fatigue tests, the respective fracture surfaces (A) were evaluated with a SZX12 (Olympus, Germany) stereo-microscope under reflected light. The measured surface is used to calculate the fatigue limit S_a at $N = 10^6$ cycles to failure.

3. Process simulation

As mentioned in section 1, the life time assessment of short fiber reinforced polymers can be done by the concept of local S/N-curves. However, to be able to predict the life time of 3D-printed parts some extensions to the simulation approach, shown in *Figure 1*, have to be implemented. **Erreur ! Source du renvoi introuvable.** shows the principal approach to consider local orientation and thermal history for an AM process simulation.

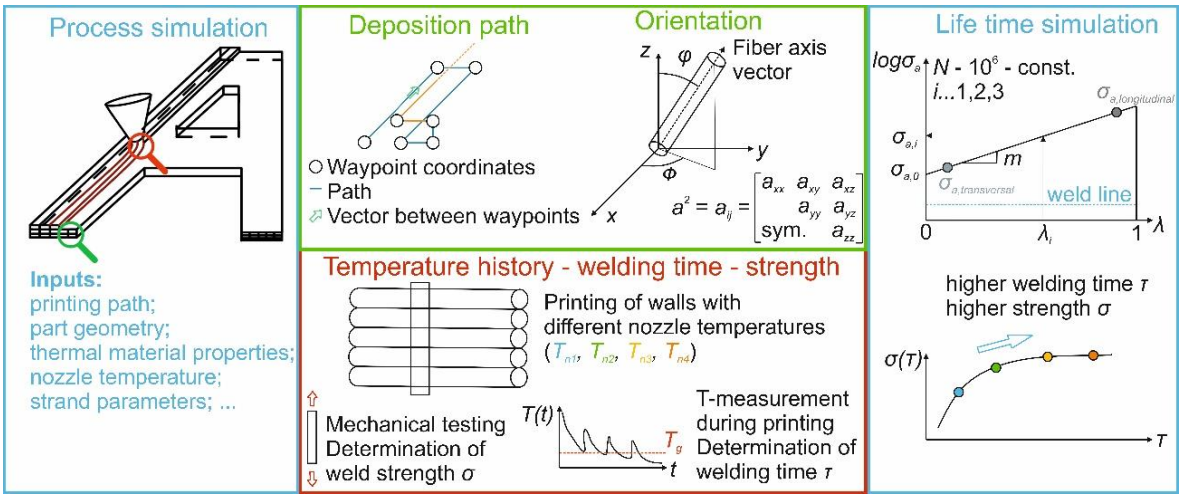

Figure 3. Scheme of necessary extensions for simulation chain

First and foremost, the local orientation must be considered, as it has a great influence on the mechanical performance. To do so the local deposition path should be transferred to a local orientation. Therefore, a second order tensor according to Eq. 2 can be used. First the vector between two waypoints is calculated, which defines the orientation between two waypoints. This orientation is subsequently transformed into the second order tensor using general algebra. In the final step, the orientation is applied to each element of the finite element mesh along the path between two waypoints.

  doi:10.5075/epfl-298799_978-2-9701614-0-0

$$a^2 = a_{ij} = \begin{matrix} a_{xx} & a_{xy} & a_{xz} \\ & a_{yy} & a_{yz} \\ sym. & & a_{zz} \end{matrix} \quad (2)$$

In a second step, the local welding temperature has to be considered since it has a great impact on the local material behavior. Therefore, the temperature history is stored for each node in the finite element mesh over all time steps. This leads to a continuous time-temperature history for each node from the first heating until the final temperature. From literature it is well known that the strength of 3D-printed materials depends strongly on the amount of interlayer bonding [6], which is directly connected to the molecular mobility. Hence, the glass transition temperature is set as the lower limit. To account for the highly non-isothermal welding process, an effective isothermal weld time (t_w), based on a time-temperature superposition principle, is calculated by evaluating the area under the remaining temperature-time curve and weighting it with the temperature shift factor [7]. **Erreur ! Source du renvoi introuvable.** shows the model of a 3D-printed wall and the temperature profile for three representative nodes.

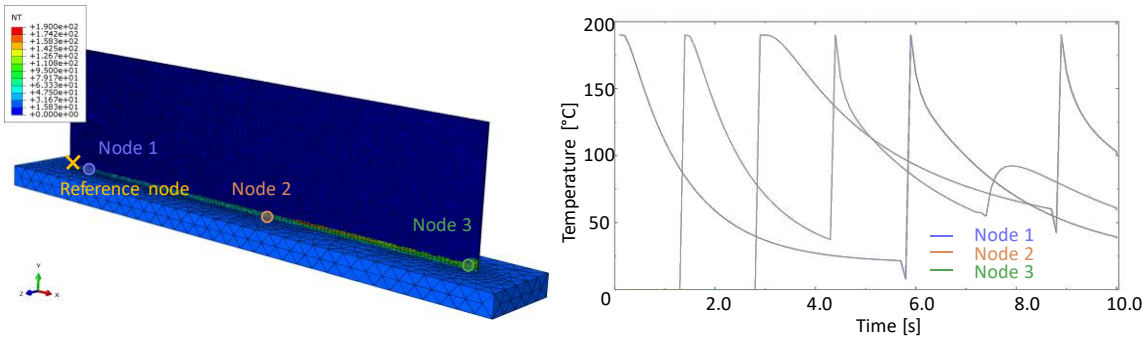

Figure 4. Local temperature evolution from a FE-model of a 3D-printed wall for three representative nodes

4. Material models

Based on the fatigue tests, material models to describe the influence of thermal history and orientation were derived. As mentioned before, tests on reinforced specimens, oriented transversal (UD90) and longitudinal (UD0) to the printing directions, were performed to describe the orientation influence. The fatigue limit S_a at $N = 10^6$ cycles to failure is then plotted against the first eigenvalue λ of the second order tensor a_{ij}, which is 0 for transversal and 1 for longitudinal oriented specimens. The relationship between S_a and λ is described by an exponential approach according to [8]:

$$S_a(\lambda) = exp^{(m*\lambda)} \quad (3)$$

Since mainly the matrix is influenced from the different processing temperatures due to enhanced molecular movement with increased temperature (temperature influence on natural fibers neglectable), the study on thermal history was performed on unreinforced PLA. To describe the influence of the nozzle temperature on the fatigue behavior, the bearable fatigue strength is plotted against the effective isothermal weld time t_W. For the determination of t_W for all investigated temperatures, the temperature history of one representative reference node is chosen in the simulation shown in **Erreur ! Source du renvoi introuvable.**. Since most of the welding took place during the first heating run, only the first heating cycle was used for calculation of t_W. As the simulation is just available for 190°C at the moment, temperature

histories were shifted to higher starting temperatures for comparison. Once simulation of higher temperatures is available, t_w will be recalculated. In Figure 5 a, the temperature profiles for all four printing temperatures are plotted. All curves were cut off by the T_g at 60°C (Limit). In the next step the temperature dependent horizontal temperature shift factor was evaluated for each temperature profile according to Eq. 1 and plotted reciprocally (Figure 5 b). This factor is used to relate welding temperatures with effective welding times [7].

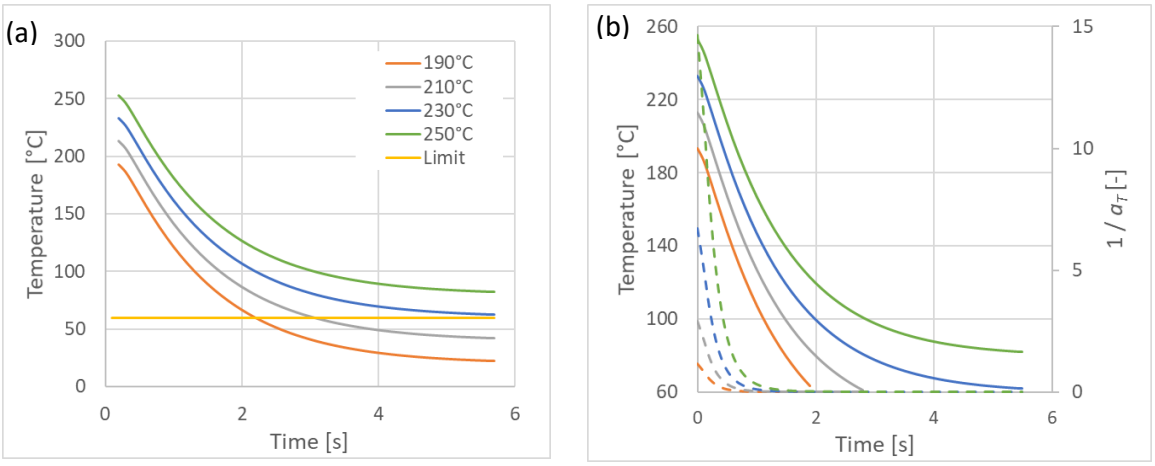

Figure 5. Temperature history at reference node for four printing temperatures (a) and limited temperature profiles in comparison to weighting with the temperature shift factor a_T (dashed lines) (b)

The areas under the temperature profiles weighted by $1/a_T$ were then approximated with trapezoids in an interval of 0.1 s. The effective isothermal weld time of each curve was calculated by adding up the individual areas. Subsequently, the effective isothermal weld time can be correlated with results from fatigue testing, which are currently still under evaluation.

5. Lifetime estimation

Following the approach shown in *Figure 1*, a dataset including all relevant material data and models has to be derived from the material tests. A detailed description of dataset determination and model calibration for fatigue life time estimation is given in [2] and [9]. Further material models, boundary conditions and loading have to be applied in a FE-analysis to calculate the resulting stress field. Once this is done, the stress results and material data sets can be loaded in a life time estimation tool, in this case FEMFAT®.

6. Summary & Outlook

Fatigue tests were performed on 3D-printed PLA specimens manufactured with different printing temperatures in order to evaluate the effect of thermal history on the fatigue weld strength. Furthermore, endless-flax-fiber reinforced PLA was tested longitudinal and transversal to the printing/fiber direction to describe the influence of fiber orientation. Based on the test results, a temperature and orientation dependent model was derived. In parallel, a thermo-mechanical coupled process simulation is conducted for defined printing parameters. From this, a model parameter, the effective isothermal welding time, was evaluated. This was done by calculating the area under the temperature history developing during process simulation and weighting by the temperature shift factor. Based on this model and especially on the effective

  doi:10.5075/epfl-298799_978-2-9701614-0-0

welding time (t_w), it is possible to determine the mechanical behavior for each node in a part volume.

In order to further calibrate the temperature model different printing conditions will be validated via thermocouples in the future. Once fatigue tests are finalized, a data-set will be derived in the next step for use in the life time assessment software FEMFAT®. Once date-sets are available and calibrated on specimen level, the presented approach will be validated on component level.

Acknowledgement

This research was performed within the project eFAM4Ind (877409) which is funded by the Austrian funding agency association (FFG) and the federal ministry of climate action, environment, energy, mobility innovation and technology (BMK). The research work of this paper was performed at the Polymer Competence Center Leoben GmbH (PCCL) in collaboration with the Chair of Materials Science and Testing of Polymers at the Montanuniversiaet Leoben within the framework of the PdZ-program with contribution by Wood K plus, SinusPro GmbH and Head GmbH. The PCCL is founded by the Austrian Government and the State Governments of Styria, Lower and Upper Austria.

7. References

1. Primetzhofer A, Stadler G, Pinter G, Grün F, Lifetime assessment of anisotropic materials by the example short fibre reinforced plastic. International Journal of Fatigue 120 (2019); pp. 294–302.
2. Primetzhofer A, Stadler G, Pinter G, Grün F, Data set determination for lifetime assessment of short fibre reinforced polymers. Journal of Plastics Technology (2019) 15.
3. Primetzhofer A, Stadler G, Pinter G, Grün F, Applicability of Strain Controlled Cyclic Tests for Short Fibre Reinforced Polymers. Materials Sciences and Applications 10 (2019) 08; pp. 568–583.
4. Guster C, Pinter G, Mösenbacher A and Eichlseder W, Evaluation of a Simulation Process for Fatigue Life Calculation of Short Fibre Reinforced Plastic Components. Procedia Engineering 10 (2011) 0, pp. 2104–2109.
5. Mösenbacher A, Brunbauer J, Pichler PF, Guster C et al. Modeling and validation of fatigue life calculation method for short fibre reinforced injection moulded parts. In 16th European Conference of Composite Materials (ECCM Ed.), 2014.
6. Striemann P, Huelsbusch D, Niedermeier M, Walther F, Application-oriented assessment of the interlayer tensile strength of additively manufactured polymers. Additive Manufacturing 46 (2021), p. 102095.
7. Seppala J E, Hoon Han S, Hillgartner K E, Davis C S, Migler K B, Weld formation during material extrusion additive manufacturing. Soft Matter 38 (2017).
8. Gaier C, Fischmeister S, Maier J, Pinter G, Fatigue Analysis of Continuously Carbon Fiber Reinforced Laminates, SAE International Journal of Engines 10 (2017) 2, pp. 305–315.
9. Primetzhofer A, Stadler G, Pinter G, Grün F, Model Calibration and Data Set Determination Considering the Local Micro-Structure for Short Fiber Reinforced Polymers. Journal of Composites Science 5 (2021) 2, p. 40.

  doi:10.5075/epfl-298799_978-2-9701614-0-0

FATIGUE CHARACTERISATION AND MONITORING IN 3D PRINTED SHORT FIBRES REINFORCED POLYAMIDE

Luca M. Martulli[a], Andrea Canegrati[a], Alessandra Panerai[a], Milutin Kostovic[b], Gennaro Rollo[b], Andrea Sorrentino[b], Michele Carboni[a], Andrea Bernasconi[a]

a: Politecnico di Milano, Via La Masa 1, I-20156 Milano, Italy
andrea.bernasconi@polimi.it
b: Polymer, Composites and Biomaterials Institute, National Research Council (CNR), Via Previati 1/E, 23900 Lecco (LC), Italy

Abstract: *3D printed composites are rapidly gaining a growing interest in several industrial sectors. However, for their widespread adoption, it is necessary to characterise their fatigue response. In this work, several 3D printed Onyx specimens were tested under tension-tension fatigue load with two main objectives. The first one was the assessment of different monitoring techniques for the fatigue damage evolution in the Onyx specimens. It was observed that the strain calculations from the machine crosshead displacement led to better results than strains from digital image correlation or extensometers. The second objective was the characterisation of the fatigue response of the Onyx specimens: SEM fractography was able to identify the fatigue damage initiation and propagation regions. Moreover, modulus and temperature trends were observed to assume a non-monotonic trend, which is unusual for composites. It was thus suggested that these quantities can be potential indicators of the fatigue damage in the specimens.*

Keywords: Short fibres; fatigue; 3D printed; damage monitoring; experimental mechanics.

1. Introduction

Fused filament fabrication (FFF), or fused deposition modelling, is one of the most popular additive manufacturing techniques for polymeric composites. Academic and industrial interest for FFF has recently increased, since this technology allows cheap manufacturing of light parts with complex geometries. Several studies have investigated the effects of the manufacturing parameters on the static behaviour of 3D printed composites [1]. Among these parameters, printing orientation has a high influence on the stiffness and strength, as it coincides with the fibre orientation [1].

A few works have also investigated the fatigue response of 3D printed polymers [2] and continuous fibre reinforced polymers [3,4]. However, there is a striking lack of works investigating the fatigue performance of 3D printed short fibres reinforced composites. The topic is of great relevance considering the fast spread of materials like Onyx, a micro-carbon fibres reinforced polyamide developed by Markforged [5]. Moreover, Onyx and similar materials are also frequently used as matrix for continuous fibre reinforced polymers [3]: this makes the characterisation and understanding of their fatigue response even more critical, as it may affect also the higher performing continuous fibres composites.

Given the importance of the topic, this work aims to evaluate different fatigue testing and fatigue damage monitoring techniques in 3D printed short fibres reinforced polymers. The work was performed on Onyx specimens, whose fatigue behaviour was therefore also studied.

  doi:10.5075/epfl-298799_978-2-9701614-0-0

Evaluating the possible monitoring techniques and establishing a proper one for 3D printed short fibres polymers will set the basis for future fatigue characterisations of 3D printed polymers and composites.

2. Materials and methods

2.1 Specimens fabrication

All test specimens were additively manufactured in Onyx with a FFF printer, namely the Markforged Onyx Pro. The layer height and filament width were 0.1 mm and 0.4 mm, respectively.

Since it was not possible to print unidirectional specimens, the specimens were fabricated by alternating layers with a 0° orientation and with a 90° orientation with respect to the longitudinal axis. Moreover, the printer also imposed a contour shell made of two concentric Onyx rings around the specimens. Overall, the final specimens' dimensions were 140 mm x 30 mm x 3.2 mm.

Onyx end tabs were printed to be bonded to the specimens. These tabs had dimensions of 40 mm x 30 mm x 2 mm. A commercially available bicomponent epoxy glue was used for their bonding. As a result, the gauge length of each specimen was 60 mm.

A fatigue test campaign requires the knowledge of the static properties of the analysed specimens. A static characterisation was performed by the authors in another study [6], but the data useful for this study are reported in Table 1.

Table 1 : Static properties of the Onyx specimens with a 0°/90° orientation from the static characterisation of [6]

Young's modulus (MPa)	Ultimate tensile stress (MPa)	Strain at failure (%)
967	23.7	11.8

2.2 Fatigue tests and monitoring techniques

Load-controlled cyclic tests were performed according to the ASTM D3479 standard [7]. The machine used was an MTS Landmark Stigma, equipped with a 100 kN load cell. The cyclic frequency was set to 2 Hz. The machine was set to acquire data for the first 100 cycles, then for every 10 cycles between 10^2 and 10^3 cycles, for every 100 cycles between 10^3 and 10^4 cycles and so on. Specimens that did not fail within one million cycles were considered runouts. R-ratio of minimum to maximum load was R=0.1. Crosshead displacement was available for all tested specimens.

To evaluate different monitoring techniques, the specimens were equipped with several instruments. All the adopted techniques per each specimen are reported in Table 2, while each technique is described below.

An MTS extensometer with a 20 mm gauge length was used for some specimens (EXT in Table 2). The acquisition rate was 200 Hz. Extensometer data were acquired together with all the other tests data (e.g. load, displacement) in the same data file created by the test control software.

  doi:10.5075/epfl-298799_978-2-9701614-0-0

Digital Image Correlation (DIC in Table 2 and the rest of the paper) was also considered for some specimens. In particular, one of the surfaces of these specimens was spray painted with a white paint and then a black speckle was applied. The image acquisition was performed with a full frame Canon EOS-RP camera equipped with a Canon RF 85 mm F2 macro IS lens. The camera was mounted on a tripod and a remote control was used to acquire the pictures. The load history of these specimens was adjusted to allow image acquisition. In particular, at fixed number of cycles, tests were interrupted, and static load ramps were performed, ranging from 0 kN to the maximum applied level of fatigue load, at an applied speed of 5 mm/min. Load was then held, and a picture was taken at this maximum load. The load was then set back to zero and cycling could continue. These ramps were performed:

- every 20 cycles in the first 200 cycles;
- every 100 cycles from cycle 200 to cycle 10^3;
- every 200 cycles from cycle 10^3 to cycle 10^4;
- every 250 cycles from cycle 10^4 to cycle $7 \cdot 10^4$;
- every 10^3 cycles from cycle $7 \cdot 10^4$ to cycle 10^5;
- every $2 \cdot 10^3$ cycles from cycle 10^5 until the end.

GOM Correlate was used to post-process the images.

Finally, some specimens were also equipped with a PT100 thermo-resistance (TEMP in Table 2) pressed with a clip on the analysed specimens. This device measured the temperature fluctuations in the specimens due to the cyclic loading. The tests were performed in a controlled environment, so that environmental conditions did not play a significant role in these measurements.

Table 2: Monitoring techniques adopted for each tested specimen.

Specimen number	Load level (% of UTS)	Monitoring techniques	Cycles to failure
1	85%	EXT	246
2	85%	DIC	265
3	70%	EXT	234074
4	70%	EXT	26740
5	70%	EXT	220572
6	70%	EXT + TEMP	160081
7	70%	DIC	241334
8	60%	EXT + TEMP	Runout

2.3 Microscopy

The fracture surface of four specimens, two EXT and two DIC, was observed on a Zeiss EVO 50XVP Scanning Electron Microscope (SEM). Due to their length, the specimens were cut to fit into the SEM. A minimum distance of 10 mm between the cut and the fracture surface was

  doi:10.5075/epfl-298799_978-2-9701614-0-0

maintained to avoid altering the fracture features. A gold coating was applied prior to the scanning. Moreover, a ZEISS Stereo Discovery V12 microscope was also used in the analysis.

3. Results and discussion

3.1 Fatigue response of Onyx specimens

Figure 1 shows the results of the specimens tested with the different monitoring techniques. The figure is meant as an overview of the tests results: since the specimens featured different measuring equipment (extensometers, DIC, etc.), results cannot be used to derive a stress-number of cycles relationship useful for the durability of the material.

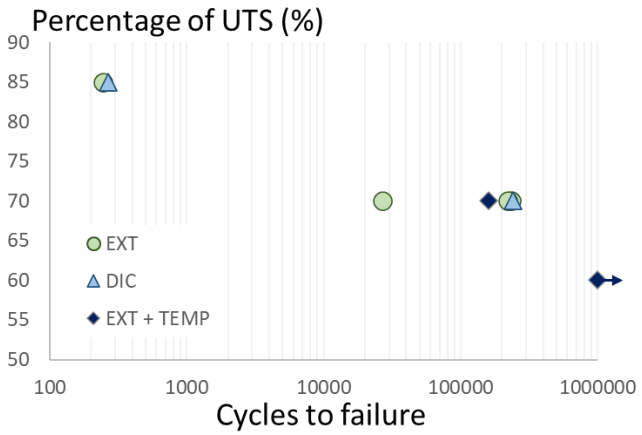

Figure 1: Results of the different fatigue tests

Nevertheless, valuable information was obtained on the fatigue failure behaviour of the tested specimens. In particular, the SEM fractography of the analysed specimens revealed the presence of two different micro-mechanical behaviours in the same fracture surface: a micro-ductile and a micro-brittle failure behaviour. The entire cross-section of specimen 7 is shown in Figure 2a, as an example, with close-ups on micro-brittle and micro-ductile region shown respectively in Figure 2b and Figure 2c. As shown, the micro-ductile fractured surface is identifiable by the presence of high plastic deformation, with strong presence of polymeric “filaments”; on the other hand, the micro-brittle fractured surface presents significantly lower deformation. Using DIC, the strain distribution along the fracture surface at 99.4% of the specimen’s life was obtained and reported in Figure 2a. As shown, the region with the higher strain corresponds to the micro-ductile region in the fracture surface. It seems likely that, in this area, fatigue damage nucleated and propagated, as it is the case for injection moulded composites [9]. Fatigue damage thus seems to occur in a ductile fashion. Once the remaining cross section can no longer sustain the applied load, static failure occurs abruptly: this high-strain-rate failure causes the micro-brittleness in the remaining region. This behaviour was also observed under static load conditions [6].

  doi:10.5075/epfl-298799_978-2-9701614-0-0

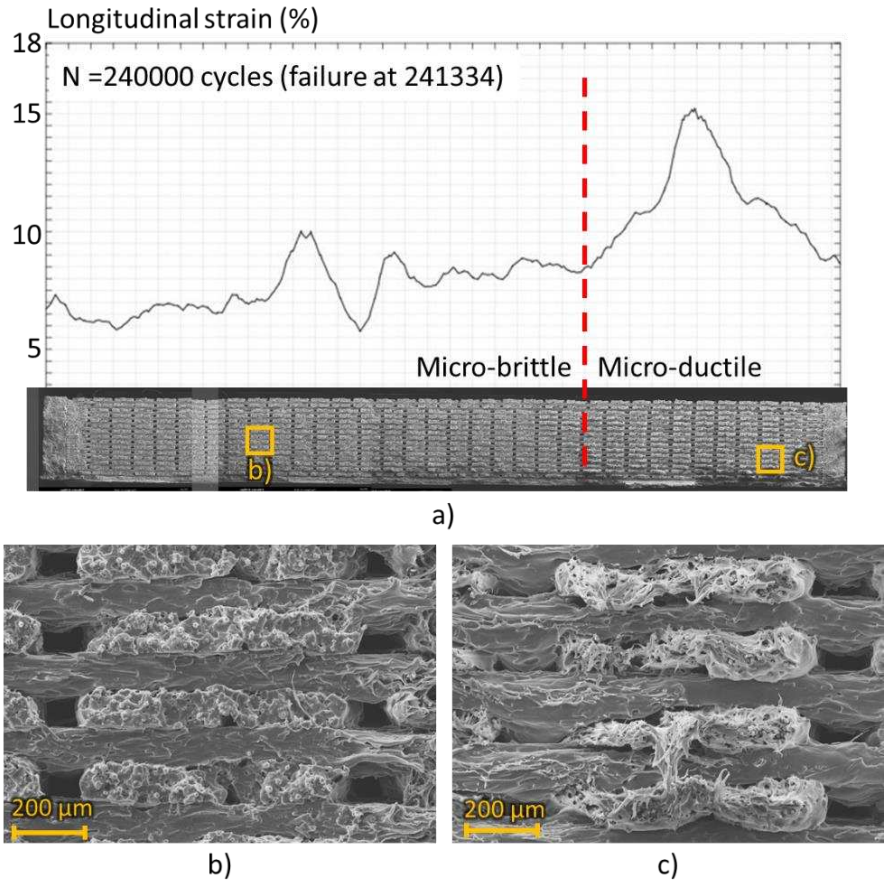

Figure 2: a) Fracture surface of specimen 7 with DIC strain measurement and detail of b) the micro-brittle region and c) the micro-ductile region.

3.2 Displacement and strain measurement during cyclic load

The stiffness evolution during the cyclic load is usually considered an important indicator of the fatigue damage in composite materials [8]. It is therefore crucial to adopt an adequate strain monitoring technique that does not affect the fatigue response of the tested material. In this work, strains were measured or calculated using DIC, extensometer and the crosshead displacement. These techniques are here compared and evaluated.

Figure 3a shows a comparison of the maximum and minimum measured strains via crosshead displacement and extensometer for specimen 3. As shown, the two measurements are initially very close and coherent with each other. However, after several cycles, the two measured trends diverge and are not correlated anymore. This behaviour was observed for all specimens equipped with the extensometer. Considering the accurate initial performance, it is unlikely that this was caused by an intrinsic difference between the two measuring techniques. It is arguable that the crosshead displacement is usually affected by the compliance of the machine itself, and thus often considered an unreliable strain measuring technique. However, in this case the low stiffness of the material (around 1 GPa) makes this error negligible, as confirmed by the initial accurate estimation. More likely, the difference arises when diffused fatigue damage reduces the material stiffness also outside the shorter gauge length of the extensometer. This is also coherent with the lower measured strain by the extensometer. Moreover, Figure 3b shows a microscopic magnification of the region close to the extensometer's arms of one of the

  doi:10.5075/epfl-298799_978-2-9701614-0-0

specimens: as shown, these arms left an imprint on the surface of the specimen. These imprints were observed in all specimens equipped with extensometer; moreover; all these specimens failed very close to these imprints and in the extensometer's arms area. This failure behaviour strongly supports the fact that strain calculated via crosshead displacement is to be preferred to extensometer measurements.

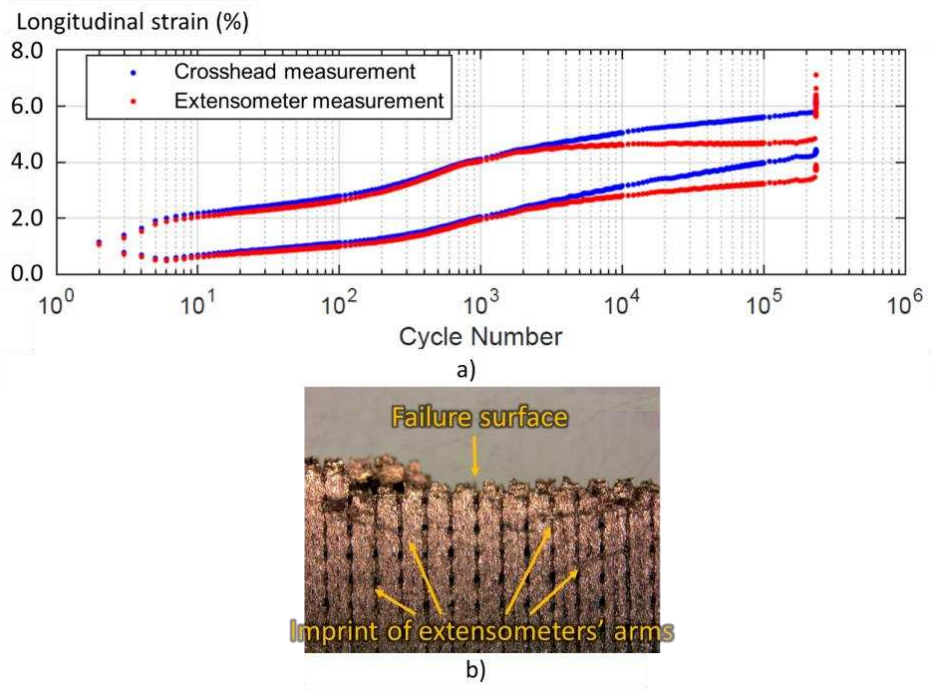

Figure 3: a) Maximum and minimum strain measured by the extensometer and calculated via crosshead displacement for specimen 3 and b) imprints of the extensometers' arms

DIC is not at risk of influencing the local failure behaviour of the specimens, thanks to its contactless nature. However, this technique is affected by two major issues. The first one is the need for a modified load history that includes static ramps for a correct image acquisition. Especially for higher loads (like for specimen 2), the holding time required to acquire the picture was long enough for the material to be subjected to creep. This is shown in Figure 4a, where strain increase is clearly visible in the ramps. This significantly affected the stiffness monitoring, as explained in section 3.3. In addition, the white paint used for the speckle was observed to penetrate several layers of specimen 2. This was observed via SEM of the fracture surface, of which Figure 4b reports a close-up. This likely influenced the fatigue response of the Onyx specimens, although a deeper investigation is required to assess how. While this is not necessarily a consistent phenomenon (it was not observed for specimen 8), the intrinsic discontinuous and porous morphology of 3D printed composite specimens makes this risk non negligible.

Overall, both extensometer and DIC are likely to affect the mechanical performance and/or fatigue failure behaviour of the specimens. Therefore, they both proved to be inadequate measuring techniques for the 3D printed Onyx specimens undergoing fatigue loads. On the other hand, the crosshead displacement led to more reliable strain calculations, also due to the high compliance of the Onyx material.

  doi:10.5075/epfl-298799_978-2-9701614-0-0

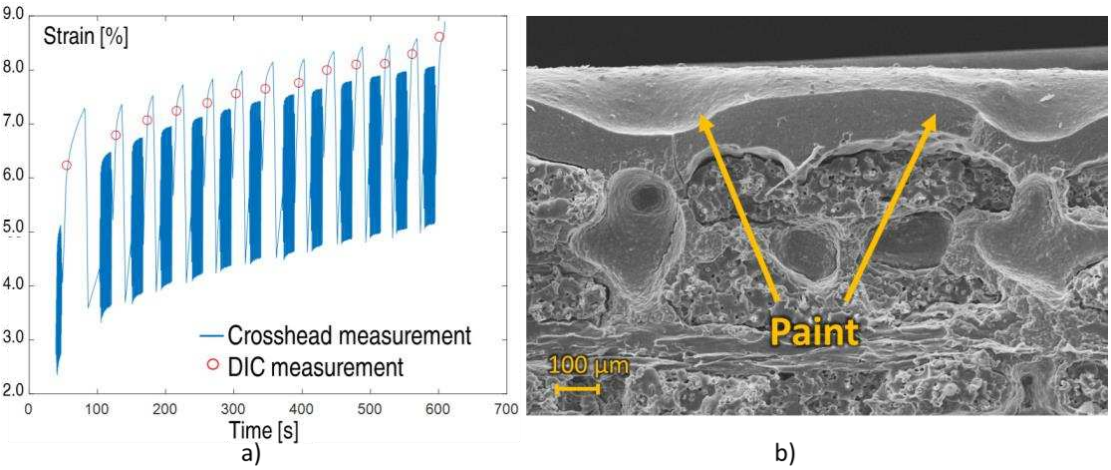

Figure 4: a) DIC and crosshead comparison on specimen 2 and b) detail of the SEM fracture surface of the same specimen

3.3 Modulus and temperature trends

Figure 5a shows the modulus trends for the tested specimens. As explained in section 3.2, these were obtained with the strain calculated via crosshead displacement; moreover, the trends of the specimens on which DIC measurements were performed were heavily affected by the different load history and were thus not included. Interestingly, all moduli do not decrease monotonically due to damage, but start to increase after around 10^3 cycles. A similar trend change is observed in the temperature measured on the specimens. As shown in Figure 5b, the temperature increases due to the cyclic loading until 10^3 cycles, after which it starts to decrease (fluctuations of the measured temperature in the high-cycle part of the load history are attributed to large period fluctuations in the room temperature).

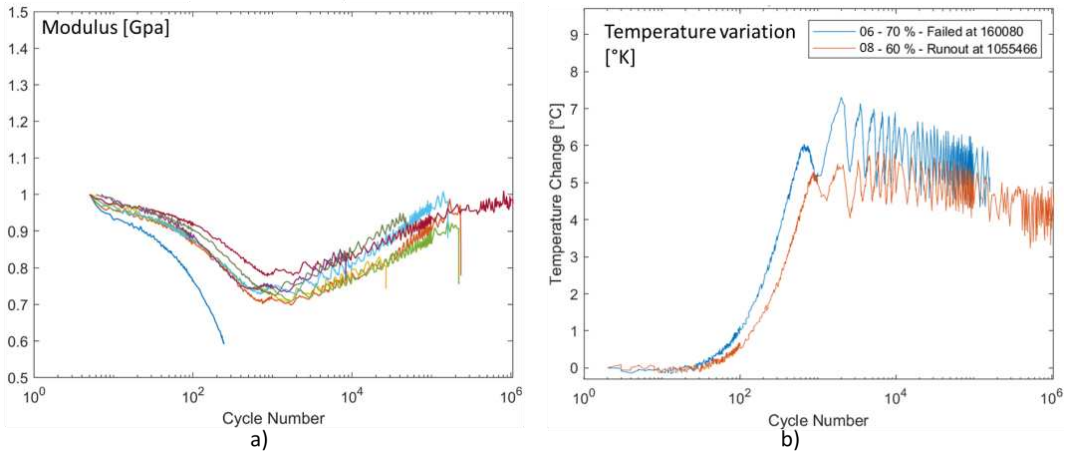

Figure 5: a) Modulus and b) temperature trends

This behaviour is highly unusual for short fibre reinforced composites, that simply show a modulus decrease due to damage [8]. The modulus and temperature trends seem to be highly correlated, although a deeper investigation is necessary to fully understand this correlation. Nevertheless, both the specimens' stiffness and temperature were successfully measured during the tests. The results suggest that these quantities may be used to monitor damage in 3D printed Onyx, although not as straightforwardly as done for injection moulded composites [8].

  doi:10.5075/epfl-298799_978-2-9701614-0-0

4. Conclusions and future works

3D printed Onyx specimens with a 0°/90° raster orientation were tested under tension-tension fatigue load. Several monitoring techniques were adopted for different specimens to assess their applicability to this material. It was shown that both extensometer and DIC likely alter the fatigue response of the Onyx specimens. Therefore, it was suggested to calculate strains from the crosshead displacement of the testing machine. Regarding the fatigue response of the material, fatigue damage initiates and propagates in a micro-ductile manner. This makes it easier to identify the fatigue initiation and propagation regions by SEM fractography. Moreover, the stiffness of the specimens was shown to have a non-monotonic behaviour, with a first decreasing part followed by an increasing one. A strong inverse correlation was found between modulus and specimens' temperature, with the latter increasing and decreasing accordingly. This work is therefore a useful guide for fatigue testing of short fibres 3D printed short fibre reinforced polymers.

Moreover, it also highlighted important open questions regarding the fatigue response of these materials. In particular, the modulus and temperature trends shown by the specimens has still to be fully understood, as well as their relationship. This work thus set some basis for a full characterisation of the fatigue response of 3D printed short fibres reinforced polymers, that will also require the testing of specimens with different raster orientation and under different loading and environmental conditions.

5. References

1. Brenken B, Barocio E, Favaloro A, Kunc V, Byron Pipes R, Fused filament fabrication of fiber-reinforced polymers: a review. Add Man 21, 1-16 (2018).
2. Safai L, Cuellar JS, Smit G, Zadpoor AA, A review of the fatigue behaviour of 3D printed polymers. Additive manufacturing 28, 87-97 (2019).
3. Shanmugan V, Das O, Babu K, Marimuthu U, Veerasimman A, Johnson DJ, Neisiany RE, Hedenqvist MS, Ramakrishna S, Berto F, Fatigue behaviour of FDM-3D printed polymers, polymeric composites and architected cellular materials. Int J Fat 143, 106007 (2021).
4. Pertuz AD, Díaz-Cardona S, González-Estrada OA, Static and fatigue behaviour of continuous fibre reinforced thermoplastic composites manufactured by fused deposition modelling technique, Int J Fat 130, 105275 (2020).
5. Markforged, Onyx datasheet 2020: https://markforged.com/materials/plastics/onyx
6. Canegrati A, Martulli LM, Bolzoni G, Kostovic M, Rollo G, Sorrentino A, Carboni M, Bernasconi A, 3D printed short carbon fibres reinforced polyamide: tensile and compressive characterisation and multiscale failure analysis. 20th European Conference on Composite Materials (ECCM20), 26-30 June 2022, Lausanne (CH).
7. ASTM D3479. Standard Test Method for Tension-Tension Fatigue of Polymer Matrix Composite. vol. 08; 2002.
8. Monte M, Moosbrugger E, Quaresimin M. Influence of temperature and thickness on the off-axis behaviour of short glass fibre reinforced polyamide 6.6 cyclic loading. Compos Part A Appl Sci Manuf 2012;41:136
9. Horst JJ, Spoormaker JL. Mechanisms of fatigue in short glass fiber reinforced polyamide 6. Polym Eng Sci 1996;36:2718–26.

PROGRESSIVE DAMAGE ACCUMULATION PROCESS OF CFRP CROSS-PLY LAMINATES DURING THE EARLY FATIGUE LIFE

Xi,Li[a,b], Rinze,Benedictus[a], Dimitrios,Zarouchas[a,b]

a: Structural Integrity & Composites Group, Aerospace Engineering Faculty, Delft University of Technology
b: Center of Excellence in Artificial Intelligence for structures, prognostics & health management, Aerospace Engineering Faculty, Delft University of Technology – Xi.Li@tudelft.nl

Abstract: *The present work aims at investigating the progressive damage accumulation process of CFRP laminates in an interactive scheme, with a special focus on the early fatigue life where mainly matrix-dominant damage accumulates and stiffness degrades significantly. An in-situ damage monitoring system, containing edge observation, digital image correlation and acoustic emission techniques, was established to characterize and quantify the accumulation of transverse cracks and delamination. Two cross-ply configurations ($[0/90_2]_s$ and $[0_2/90_4]_s$) and different stress levels were involved in the experimental campaign. Dependent crack ratio was proposed to reflect the interaction among transverse cracks, and saturated crack density was used to represent the interactive level between transverse cracks and delamination. Results showed that generation of transverse cracks and their interaction govern the early fatigue damage accumulation of the $[0/90_2]_s$ laminates, while not only the interaction among cracks but also the interaction between both damage mechanisms were observed for the $[0_2/90_4]_s$ laminates.*

Keywords: Delamination; Fatigue damage; Stiffness degradation; Transverse crack

1. Introduction

When subjected to fatigue loading, composite laminates have been recognized to experience a progressive damage accumulation process, which is initially dominant by off-axis cracking, then followed by delamination and finally ended by fiber breakage. Accordingly, a three-stage stiffness degradation is presented in a rapid-slow-rapid manner, and each stage is dominated by one damage mechanism: Stage I - off-axis cracks; Stage II - delamination, Stage III - fiber damage.

Based on this non-interactive damage scheme, a gradual stiffness degradation of 90 plies was performed to reflect the transverse crack evolution of cross-ply laminates within Stage I, which was then terminated by a sudden 90-ply discount when reaching the saturation of transverse cracks in the progressive damage model established by Shokrieh and Taheri-Behrooz [1]. Also, Pakdel and Mohammadi [2,3] regard the moment of the onset of matrix crack saturation as the moment of the initiation of delamination when higher energy is released by the growth of delamination than the multiplication of matrix cracks; then, they formulated a competition criterion considering different damage modes to predict the saturated crack density of laminates.

As extensive efforts have been put on the in-situ damage monitoring through experiments, it is found that multiple mechanisms could coexist and interact in a synergistic or competitive way. For instance, delamination could initiate within Stage I, even before the initiation of off-axis

  doi:10.5075/epfl-298799_978-2-9701614-0-0

cracks [4–6]; both delamination and fiber damage could occur within Stage III which may form either delamination dominant or fiber dominant damage state [7]. Besides the interaction between different damage mechanisms, the interaction within the same damage mechanism, like matrix cracks, could also be significant for laminates [8]. Therefore, an interactive damage scheme, considering the above-mentioned damage interaction, should be proposed for characterizing the progressive damage accumulation process of laminates under fatigue loading.

In view that cross-ply laminates usually show the most of stiffness degradation within Stage I, the focus of present study is their interactive damage accumulation process during the early fatigue life. Around 30 specimens with two ply configurations, $[0/90_2]_s$ and $[0_2/90_4]_s$, were tested under tension-tension fatigue loading at different stress levels. An in-situ damage monitoring system which contains edge observation by digital cameras, digital image correlation and acoustic emission techniques was used to investigate the accumulation of transverse cracks and delamination, the interaction among transverse cracks, and the interaction between transverse cracks and delamination for both ply-configurations.

2. Experimental methods

2.1 Material and specimen design

Unidirectional (UD) Prepreg, named Hexply® F6376C-HTS(12K)-5–35%, with a nominal thickness of 0.125 mm, was used to fabricate cross-ply laminates in the dimension of 250 × 25 mm according to ASTM D3479/D3479M-19 standard [9]. Thick paper tabs were glued on the clamping region of the specimen with a 50 mm length, using cyanoacrylate adhesive. Details about the material properties of UD lamina and manufacturing process can be found in [5,6].

2.2 Test set-up and load conditions

Figure 1 shows the experimental set-up: a 60 kN fatigue machine, two pairs of cameras and acoustic emission sensors. One pair of cameras in the front is to obtain the strain field of the gauge region (~80 mm) using digital image correlation (DIC) methods. Another pair of cameras at left and right sides is to monitor transverse cracks at 90 plies and interlaminar cracks at 0/90 interfaces from the edge view, which was later quantified or localized by an image processing algorithm [10]. Delamination area can be obtained by the area of transverse strain concentration from DIC, which shows the potential to reflect the separation between 0 and 90 plies [5].

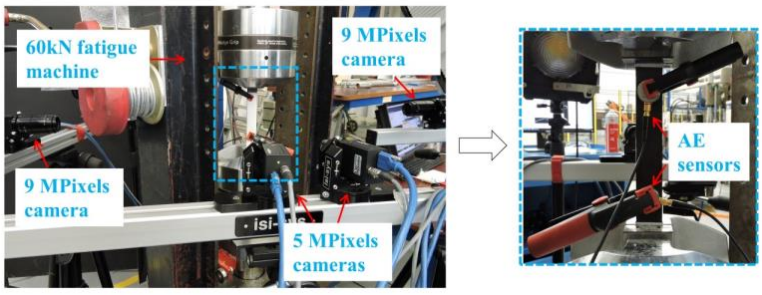

Figure 1. Test set-up.

Cyclic loading with a constant stress amplitude was applied on the specimen with a stress ratio 0.1 and frequency 5 Hz. Every 500 cycles, an unloading-loading tensile ramp in two seconds was performed where the image acquisition of both pairs of cameras was triggered. For the $[0/90_2]_s$

laminates, maximum stress levels at 77%, 70% and 63% of ultimate tensile strength (UTS) were applied, and tests executed till the evolution of transverse cracks reached a saturated state. For the $[0_2/90_4]_s$ laminates, 74%, 70%, 66% and 63% of UTS were selected as the maximum stresses and tests stopped when the stiffness degradation approached the stable phase of the second stage. The run-off of all fatigue tests was set to ~1e6 cycles.

3. Results

3.1 $[0/90_2]_s$ laminate

As shown in Figure 2, almost no delamination was detected at the region between two tabs in comparison with the intact one, according to the C-scan results after tests. Besides, no significant interlaminar cracks were observed from images captured at the edge view. Apparently, thin 90 plies with 0.5 mm thickness restrain the growth of delamination, and transverse cracks were the only dominant damage mechanism in the early fatigue life.

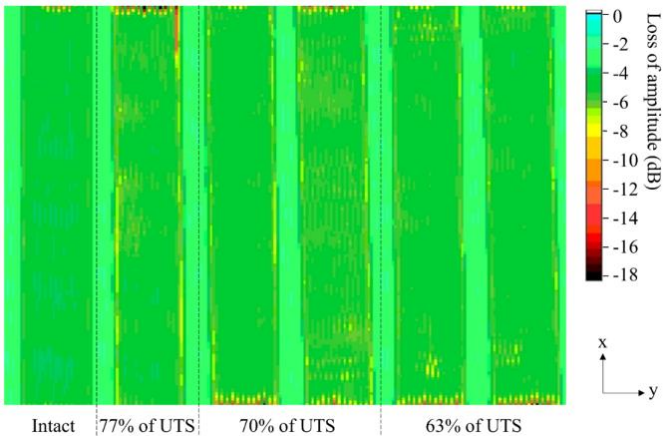

Figure 2. C-scan results for the $[0/90_2]_s$ laminates.

A bi-linear trend of stiffness degradation and crack density as a function of fatigue cycles were observed, as an example of the stress level at the 70% of UTS plotted in Figure 3. A considerable reduction of both the growth rate of crack density and the degrading rate of stiffness occurs when the crack density is relatively high (~ 0.8 mm^{-1}). This phenomenon should be attributed to the significant interaction among transverse cracks that the stress redistribution around prior cracks increased the resistance for the formation of new cracks.

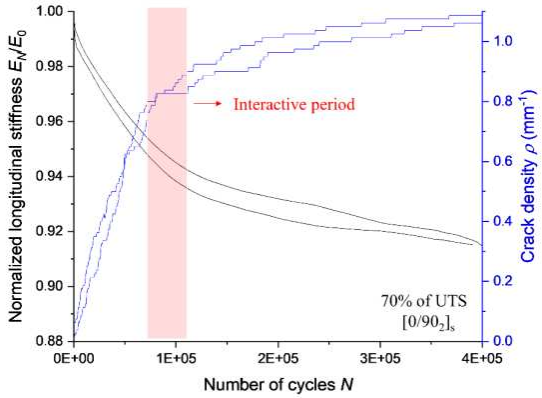

Figure 3. History of stiffness degradation and crack density evolution for the $[0/90_2]_s$ laminates.

3.2 $[0_2/90_4]_s$ laminate

Different form the $[0/90_2]_s$ laminates, significant delamination growth was observed during the early fatigue life of $[0_2/90_4]_s$ laminates. For an example of the specimens which shared a similar stiffness degrading trend at 70% of UTS, Figure 4 presents the accumulation of transverse cracks, delamination growth along edges and within the specimen as a function of fatigue cycles.

Instead of the moment after the saturation of transverse cracks, delamination initiated and started to grow significantly at the very early fatigue life when a low crack density was presented (~0.05 - 0.2 mm^{-1}). The saturation of transverse cracks, known as the characteristic damage state, occurred before the stiffness degradation reached a stable phrase, where the mean value of fatigue cycles at the end of Stage I among specimens is marked as a dash line in Figure 4. At CDS, delamination grew considerably along the edges, while it seldom propagated within the specimens in view that the delamination area is less than 10% (see Figure 4(d)).

From the initiation of delamination to the saturation of transverse cracks, the interactive period occupied about the half of fatigue cycles at Stage I, which shows a remarkable degradation of stiffness. After the saturation of transverse cracks, delamination growth along the edges became slow and gradually approached a fully delaminated state; however, delamination growth with the specimens kept a seemingly linear increase till the end of Stage I.

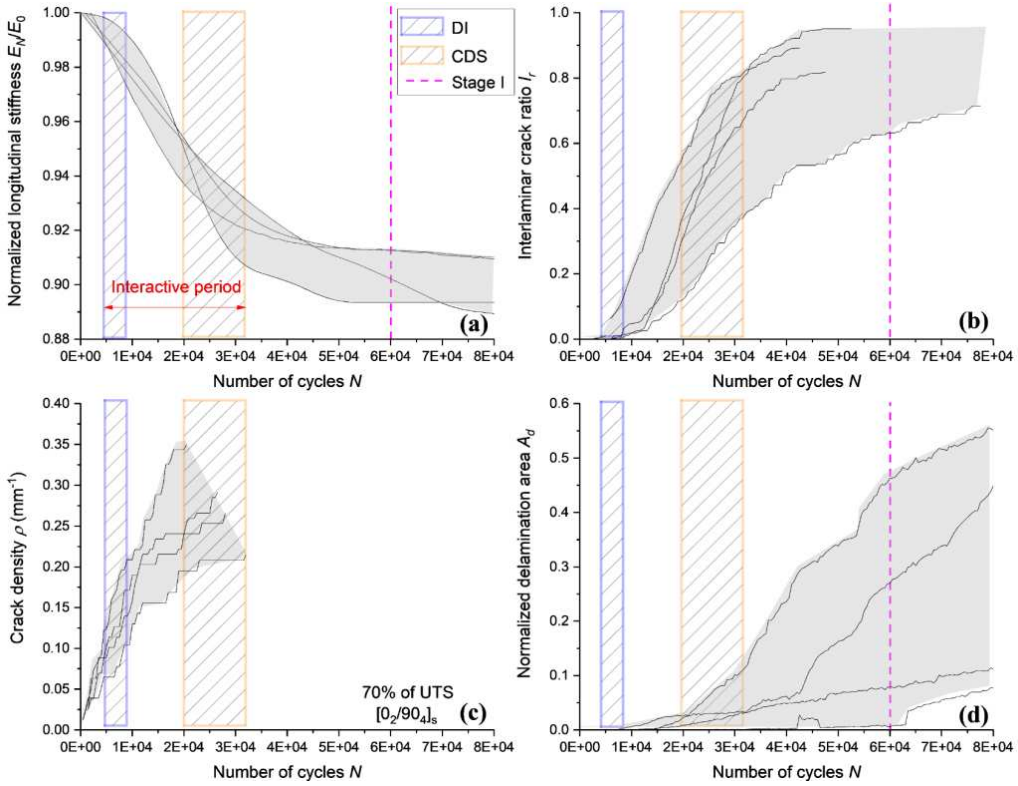

Figure 4. History of stiffness degradation (a), delamination growth along the edge(b), crack density evolution(c) and delamination growth within the specimen (d). (DI - delamination initiation; CDS - characteristic damage state)

4. Discussions

4.1 Interaction between dependent and independent cracks

To investigate the interaction among transverse cracks, dependent and independent cracks are classified by whether they occurred at a stress redistributed region, according to a critical crack spacing from 2D finite element modelling. This model implements two seam creak to simulate the stress sate of cracked region at the maximum cyclic stress, as an example of the $[0/90_2]_s$ laminates shown in Figure 5. By changing the crack spacing *d*, it is found that the axial stress of 90 plies remains the applied level at the middle of two seam cracks when *d* is larger than 2.5 mm and 4.5 mm for the $[0/90_2]_s$ and the $[0_2/90_4]_s$ laminates respectively. Therefore, the minimum or critical crack spacing for a new independent crack to be generated between these two seam cracks should be 2.5/2 = 1.25 mm and 4.5/2 = 2.25 mm at the $[0/90_2]_s$ and the $[0_2/90_4]_s$ laminates respectively.

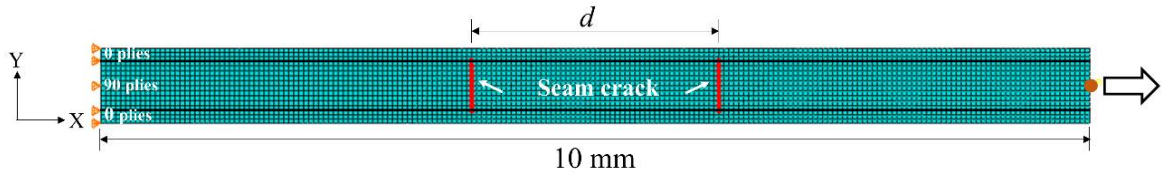

Figure 5. Finite element model for the cracked $[0/90_2]_s$ laminate, including boundary and loading conditions, and geometry dimensions.

After classifying the type of cracks based on the critical crack spacing, the maximum number of independent cracks at CDS for the $[0/90_2]_s$ laminates is about twice of that for the $[0_2/90_4]_s$ laminates. Besides, a dependent crack ratio r_d can be obtained which is the ratio of the maximum number of dependent cracks to the maximum number of independent cracks at CDS. r_d ranges approximately from 1.2 to 1.6 and from 0.1 to 0.7 for the $[0/90_2]_s$ laminates and the $[0_2/90_4]_s$ laminates respectively. This indicates more dependent cracks were generated than the independent cracks for thin 90 plies, as a result of severer interaction among transverse cracks.

4.2 Interaction between transverse cracks and delamination

Competitive relation between transverse crack generation and delamination propagation is found for the $[0_2/90_4]_s$ laminates, as specimens with a low saturated crack density usually presents a larger delamination growth. To further understand interaction between both damage mechanisms, Figure 6 plots delamination growth along the edge when crack density increases.

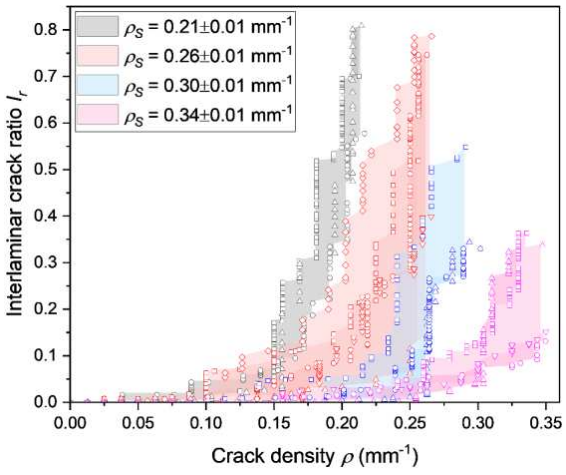

Figure 6. Interlaminar crack ratio (a) & normalised delamination area (b) versus crack density.

In Figure 6, specimens presenting a similar saturated crack density were grouped for all stress levels, and it shows that a faster growth of delamination with the increase of crack density occurs for specimens with a low saturated crack density. This further indicates that saturated crack density can be used to represent the interactive level between transverse cracks and delamination.

5. Conclusions

The progressive damage accumulation process under tension-tension fatigue loading is characterized and investigated for two types of cross-ply laminates, considering the interaction among transverse cracks and interaction between transverse cracks and delamination. The main conclusions are listed as follows:

- Dependent crack ratio can be used to reflect the interaction among transverse cracks, and it is severer at thin 90 plies than thick 90 plies for cross-ply laminates.
- Transverse cracks and delamination interact each other in a competitive way, which is more significant for cross-ply laminates with thick 90 plies; saturated crack density can represent the interactive level between both damage mechanisms.
- An interactive damage scheme is needed for describing the progressive damage accumulation of laminates under fatigue loading.

6. References

1. Shokrieh MM, Taheri-Behrooz F. Progressive fatigue damage modeling of cross-ply laminates, I: Modeling strategy. Journal of Composite Materials. 2010;44(10):1217–31.

2. Pakdel H, Mohammadi B. Characteristic damage state of symmetric laminates subject to uniaxial monotonic-fatigue loading. Engineering Fracture Mechanics. 2018;199(May):86–100.

3. Pakdel H, Mohammadi B. Prediction of outer-ply matrix crack density at saturation in laminates under static and fatigue loading. International Journal of Solids and Structures. 2018;139–140:43–54.

4. Hosoi A, Takamura K, Sato N, Kawada H. Quantitative evaluation of fatigue damage growth in CFRP laminates that changes due to applied stress level. International Journal of Fatigue. 2011;33(6):781–7.

5. Li X, Kupski J, Teixeira De Freitas S, Benedictus R, Zarouchas D. Unfolding the early fatigue damage process for CFRP cross-ply laminates. International Journal of Fatigue. 2020;140(July).

6. Li X, Benedictus R, Zarouchas D. Early Fatigue Damage Accumulation of CFRP Cross-Ply Laminates Considering Size and Stress Level Effects. International Journal of Fatigue. 2022;159(February):106811.

7. D'Amore A, Grassia L. Phenomenological approach to the study of hierarchical damage mechanisms in composite materials subjected to fatigue loadings. Composite Structures. 2017;175:1–6.

8. Glud JA, Dulieu-barton JM, Thomsen OT, Overgaard LCT. Fatigue damage evolution in GFRP laminates with constrained off-axis plies. Composites Part A. 2017;95:359–69.

9. ASTM International. D3479/D3479M-19 Standard Test Method for Tension-Tension Fatigue of Polymer Matrix Composite Materials. West Conshohocken, PA; ASTM International. West Conshohocken, PA; 2019.

10. Li X, Saeedifar M, Benedictus R, Zarouchas D. Damage accumulation analysis of cfrp cross-ply laminates under different tensile loading rates. Composites Part C: Open Access. 2020;1(July).

  doi:10.5075/epfl-298799_978-2-9701614-0-0

TOWARD THE PREDICTION OF THE FATIGUE LIFETIME OF LAMINATED COMPOSITES, USING AN INCREMENTAL DAMAGE MODEL WITH OBSERVABLE VARIABLES

Stacy Patti[a], Myriam Kaminski[a], Frédéric Laurin[a], Jean-François Maire[a], Pere Maimí [b]

a: ONERA, the French Aerospace Lab – stacy.patti@onera.fr
b: AMADE Laboratory, University of Girona

Abstract: *One of the main challenges, which has emerged in the last couple of years for high performances industries, lies in efficiently designing lighter and energy-sufficient structures, while still being competitive by ensuring optimum performances, short lead times, and the necessary level of safety. For these reasons, the use of composite materials has kept increasing, and with it the need for a fatigue lifetime prediction model with a harnessed complexity, which would be able to (i) help cut experimental costs, (ii) reduce design delays and (iii) enable the use of appropriate safety coefficients to avoid oversizing the structures. To answer that need, we propose a damage model able predict, thanks to its incremental formulation, the density of transverse cracks in the different plies of a laminate under complex fatigue loadings.*

Keywords: Fatigue lifetime; laminate; polymer matrix composite; damage model; crack density

1. Introduction

With nearly 50 billion of tons of greenhouse gas emission every year, leading to climate change and threatening an important loss of biodiversity, the environmental stakes have reached a critical point. To maintain the temperature increase below 2°C, reducing the emissions has become a necessity, and with nearly one billion ton of greenhouse gas emitted each year, greener means of aerial transportation are needed.

The aeronautical industry has since been faced with a rising challenge: efficiently making lighter, less consuming structures, with improved performances and increased lifetime, while guarantying their safety and staying competitive on the market.

For this reason, composite materials have been increasingly used, and now make up for about 50% of all materials found in some aircrafts. However, they still lack predictive fatigue damage models, which would require fewer and simpler tests to obtain the same level of information, thus leading to a reduction of experimental costs.

Therefore, we have set ourselves the following objectives: (i) building a model able to describe both static and fatigue behaviors, with a balance between accuracy and complexity to make it an accessible tool in industrial design offices, (ii) validating our approach with available material data, and then (iii) define and carry out an experimental campaign on a new generation of Carbon/Epoxy composite material.

2. Incremental damage model

2.1. Fatigue damage models

  doi:10.5075/epfl-298799_978-2-9701614-0-0

In the literature, two different kinds of fatigue damage models can be found: cyclic ones, driven by the number of cycles, where a counting scheme is usually used to reduce complex irregular loading history into a series of constant amplitude events, and time-based incremental models, where all the cycles of a real loading, however complex, are simulated.

Most models focus first on the prediction of damage for static loadings. They are usually based on continuum damage mechanics, and consider either damage variables defined by their effects on the behavior (1,2), or directly on the measured crack density in each ply (3,4), thus considering an observable damage variable. Then, for the fatigue loading, some models propose modifying material parameters of the static damage evolution law for fatigue loadings as a function of the number of cycles (2), or propose a specific damage evolution law for fatigue loading as a function of cycles, considering for few of them observable damage variables in static and in fatigue (3). However, when it comes to incremental damage model with observable variables, to the best of our knowledge, damage models as proposed in (4) for static loadings, have not been extended to fatigue yet.

By combining observable variables and an incremental formulation, this new kind of fatigue damage model obtained enables the description of real, complex loadings, such as those encountered in the industry, while directly linking the state of damage to the experimental information obtained. We will present this kind of model in the following work.

2.2. The proposed incremental damage model

This model is based on the work initiated by Germain (4), where he proposed a complete mesoscopic modeling dedicated to static loadings, using two observable variables, the mean crack density and the associated length of microdelamination at the cracks' tips. We also worked on the methodology proposed by Angrand (5), where an incremental fatigue damage approach is used for 3D woven composites. The approach proposed here is defined at the unidirectional (UD) ply level in order to predict the fatigue lifetime of laminates with different stacking sequences subjected to both quasi-static or fatigue in-plane loadings. From the behavior law presented in Eq. (1), we define Q^{mat} as the elastic rigidity matrix, and ε^* as the strain taking into account the residual thermal stresses.

$$\sigma = Q^{mat} : \varepsilon^* \quad \text{with } \varepsilon^* = \varepsilon - \varepsilon^{th} \tag{1}$$

Indeed, because the oriented plies have different thermal dilatation coefficients, there is an initial stress state within the laminates' plies, prior to any mechanical loading due to the cooling in the manufacturing process. In order to refine the model's damage onset, this has been taken into account by introducing a thermal strain, of which the expression can be found in Eq. (2). While T represents the test temperature, T_0 is the identified stress free temperature.

$$\varepsilon_{th} = \begin{pmatrix} \alpha_L \\ \alpha_T \\ \alpha_{LT} \end{pmatrix} (T - T_0) \tag{2}$$

The damage onset y^0_{stat} is then further refined by adding a double criterion, taking into account the influence of the ply thickness as well as its position inside the laminate (6,7). A new static damage threshold is therefore defined in strain, as shown below in Eq. (3), according to the so-called *in situ* strength $Y^{is}_{T\varepsilon}$. This implemented double criterion considers that the creation of new

cracks must answer to two different criteria: one formulated in energy, and one expressed in strain. This enables us to obtain different damage thresholds depending on the ply thickness, as it is experimentally observed.

$$y^0_{stat} = \frac{1}{2}\left(Y^{is\,2}_{T\varepsilon} S^0_{22}\right) \quad (3)$$

with $Y^{is}_{T\varepsilon} = \max(\varepsilon^{Re}_{22},\ \varepsilon^{R}_{22})$

$= \max\left(\frac{1}{Q^{mat}_{22}}\sqrt{\frac{8G_{Ic}}{\pi h \Lambda^0_{22}}} - \frac{Q^{mat}_{12}}{Q^{mat}_{22}}\varepsilon^*_{12},\ \varepsilon^R_{22}\right)$ for inner plies,

or $\quad = \max\left(\frac{1}{Q^{mat}_{22}}\sqrt{\frac{4G_{Ic}}{\pi h \Lambda^0_{22}}} - \frac{Q^{mat}_{12}}{Q^{mat}_{22}}\varepsilon^*_{12},\ \varepsilon^R_{22}\right)$ for outer plies

In these equations, G_{Ic} corresponds to the critical energy restitution rate in mode I, and Λ^0_{22} to the inverse of the coefficient Q_{22}.

From there, a damage driving force is defined, as presented in Eq. (4):

$$y = \frac{1}{2}\left(Q^{mat}_{2,2}\varepsilon^{*+2}_2 + a_{66} Q^{mat}_{6,6}\varepsilon^{*+2}_6\right) \quad (4)$$

With ε^{*+} the positive part of the strain inside the ply, as defined in (8), and a_{66} a model parameter to identify in order to enable a coupling with the shear loading.

The static crack density expression proposed by Germain [4] has then been integrated, before being generalized using [5], to obtain the cracking kinetics evolution $\dot{\bar{\rho}}$ presented in Eq. (5).

$$\dot{\bar{\rho}} = f_{stat}(\bar{\rho}) g_{stat}(y) \dot{y}_{max} + f_{cycl}(\bar{\rho}) g_{cycl}(y)[\langle \dot{y} \rangle_+ - \dot{y}_{max}] \quad (5)$$

with $\bar{\rho} = \frac{N_{cracks}}{L_{obs}} * h_{ply}$

where $\bar{\rho}$ is the normalized crack density, defined according to the number of cracks N_{cracks}, the observation length L_{obs} and the ply thickness h_{ply}. It can be noticed that this damage evolution law is written into two different parts. The first one in static is activated whenever $\dot{y}_{max} = \dot{y}$, and has two different functions with three parameters left to identify: $\bar{\rho}_c$, the saturated crack density, and y^c_{stat} and p_{stat}, which are both kinetic parameters found in Eq. (6) and Eq. (7).

The second part in fatigue is activated whenever $\dot{y}_{max} = 0$, and is also made of two different functions, with four parameters to identify: y^0_{cycl}, which is the fatigue damage threshold and needs to be inferior to the static one as observed experimentally, and y^c_{cycl}, p_{cycl} and n_{cycl} which are kinetic parameters found in Eq. (8) and Eq. (9).

Table 1: Damage evolution law's functions

Static	Fatigue
$f_{stat}(\bar{\rho}) = \bar{\rho}_c\left(1 - \frac{\bar{\rho}}{\bar{\rho}_c}\right)$ (6)	$f_{cycl}(\bar{\rho}) = \bar{\rho}_c\left(1 - \frac{\bar{\rho}}{\bar{\rho}_c}\right)^{n_{cycl}}$ (8)
$g_{stat}(y) = \frac{p_{stat}}{2\sqrt{y^c_{stat}\sqrt{y}}}\left\langle \frac{\sqrt{y_{max}} - \sqrt{y^0_{stat}}}{\sqrt{y^c_{stat}}}\right\rangle_+^{p_{stat}-1}$ (7)	$g_{cycl}(y) = \frac{p_{cycl}}{2\sqrt{y^c_{cycl}\sqrt{y}}}\left\langle \frac{\sqrt{y} - \sqrt{y^0_{cycl}}}{\sqrt{y^c_{cycl}}}\right\rangle_+^{p_{cycl}-1}$ (9)

Then, by initially making the assumption that the laminate's behavior is macroscopically linear and that the loading is cyclic with a constant amplitude, we are able to perform an analytic resolution by integration, and to obtain two different crack density expressions from the same damage evolution law: one in static and one in fatigue, as presented below in Eq. (10) and Eq. (11).

$$\bar{\rho}_{stat} = \bar{\rho}_c \left[1 - \exp\left(- \left\langle \frac{\sqrt{y_{max}} - \sqrt{y^0_{stat}}}{\sqrt{y^c_{stat}}} \right\rangle_+^{p_{stat}} \right)\right] \tag{10}$$

$$\bar{\rho}_{cycl}\,(N) = \bar{\rho}_c \left[1 - \left[(n-1)\left(f_{\bar{\rho}_{stat}} + (N-1)I_g\right)\right]^{\frac{1}{1-n}}\right] \tag{11}$$

$$\text{with } f_{\bar{\rho}_{stat}} = \frac{1}{n-1}\left(1 - \frac{\bar{\rho}_{stat}}{\bar{\rho}_c}\right)^{1-n} \text{ and } I_g = \left\langle \frac{\sqrt{y_{max}} - \sqrt{y^0_{cycl}}}{\sqrt{y^c_{cycl}}} \right\rangle_+^{p_{cycl}} \left\langle \frac{\sqrt{y_{min}} - \sqrt{y^0_{cycl}}}{\sqrt{y^c_{cycl}}} \right\rangle_+^{p_{cycl}}$$

This model has been written with the intent of keeping a harnessed complexity, to limit the calculation costs. For this reason, strong hypotheses have been made here for now: we consider that the thermodynamic forces are driven by the total strain, and that the laminate's macroscopic behavior remains linear, which is verified for the majority of materials used today in the aeronautical industry.

2.3. The identification process

To keep the identification process accessible, we have defined two protocols with different optimization tools, one for the static part, and one for the fatigue part. In static, three parameters are left to identify manually on 90° plies, by taking into consideration the crack density value at saturation, the shape of the curve at the onset of damage, and the rate at which the asymptote is reached. This step is then followed by the use of a simplex algorithm, to minimize the distance (RMSE) between the experimental data and the theoretical one. As this method is highly sensitive to local minima, it is only to be used after performing a manual identification. Then, the a_{66} coefficient can be identified on 45° plies by doing an inverse identification of the damage threshold from a tensile test on a quasi-isotropic stacking sequence. Finally, the fatigue part is identified by defining a sweeping range of some parameters, coupled with the use, once again, of a simplex algorithm.

3. The experimental part

3.1. Materials and instrumentation

Two different aeronautical composite materials, made of epoxy resin and continuous carbon fibers, were used: the T700GC/M21 and the IMA/M21ev. The latter presents the particularity of having an increased number of thermoplastic nodulii at the interface to limit delamination.

Both materials were tested in static and in fatigue on an INSTRON machine with a maximal capacity of 100kN. The tests were highly instrumented, using Acoustic Emission sensors, Digital Images Correlation cameras, extensometers and optical microscopy. The latter was used to take

pictures along the specimen's edge during the test at different monitoring level, in order to analyze them later on with an automated crack detection tool (9).

3.2. Tests performed

A first experimental campaign was conducted at ONERA. The quasi-static tensile tests were performed for different monitoring load levels on quasi-isotropic stacking sequences. The fatigue tests were conducted for 100 000 cycles at a frequency of 5 Hz and different load stress ratios, respectively 0,1 and 0,05 for the T700GC/M21 and the IMA/M21ev. Monitoring levels were observed at defined number of cycles, for both the quasi-isotropic and cross-ply laminates tested. The stacking sequences considered in this study are $[45/90/-45/0/45/90/-45/0]_s$ for the quasi-isotropic in T700GC/M21, $[(0/45/90/-45)_2]_s$ and $[(90/-45/0/45)_2]_s$ for the quasi-isotropic in IMA/M21ev, and $[0_2/90_3/0]_s$ for the cross-ply in IMA/M21ev.

4. Results and discussion

4.1. Model's predictive abilities

The model has been able to describe the static results obtained on the T700GC/M21, as well as on the IMA/M21ev, as illustrated below in Figure 1 and Figure 2. The first results obtained in static on different quasi-isotropic stacking sequences of IMA/M21ev showed an unusual behavior for this kind of material: the outer plies did not seem to undergo more damage than inner ones, as can be seen in Figure 2. It can also be seen on Figure 2 that the ply thickness effect has been taken into account, for both the damage threshold and the saturation value, for double and triple 90° plies.

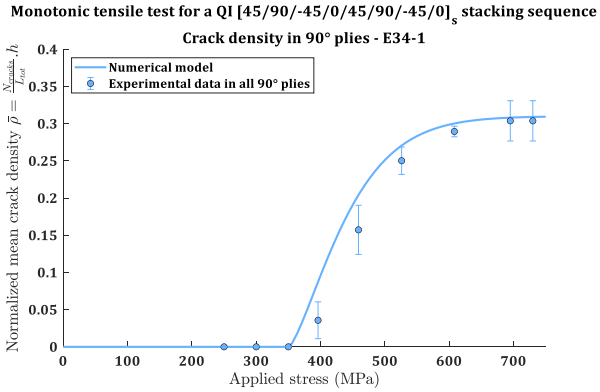

Figure 1: Experimental and numerical results for a quasi-static tensile test on the T700GC/M21 in 90° plies

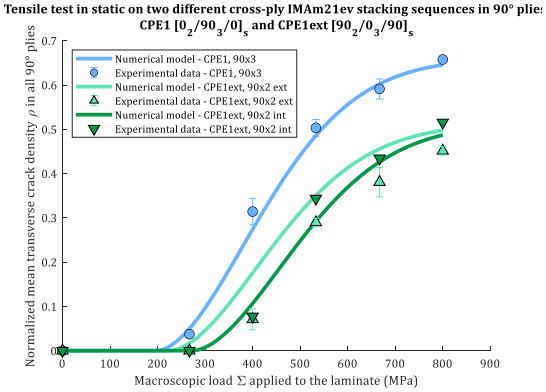

Figure 2: Experimental and numerical results for a tensile test on the IMA/M21ev in 90° double and triple plies

Furthermore, fatigue damage has also been predicted on the T700GC/M21 quasi-isotropic laminate, for different maximum stress levels, even well below the static damage threshold, as can be seen in Figure 3.

  doi:10.5075/epfl-298799_978-2-9701614-0-0

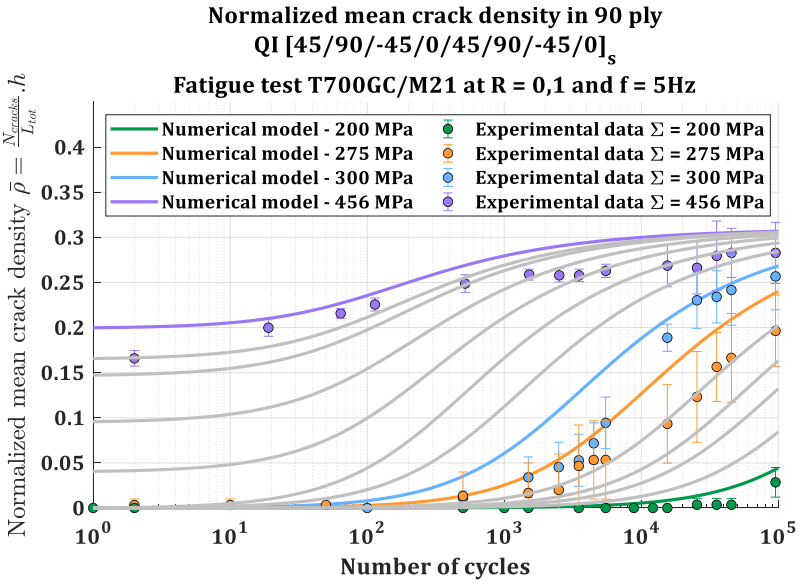

Figure 3: Experimental and numerical results for a fatigue test on the T700GC/M21 in 90° plies, with gray curves as a prediction

Likewise, the model has also been able to describe the state of damage in fatigue of both the 90° and 45° plies of a quasi-isotropic stacking sequence, as shown in **Erreur ! Source du renvoi introuvable.**. From the first experimental campaign conducted, it appears that the specimens have reached a higher saturation value in fatigue than in static, hence their differentiation in those figures. This result will be verified with the next upcoming experimental campaign.

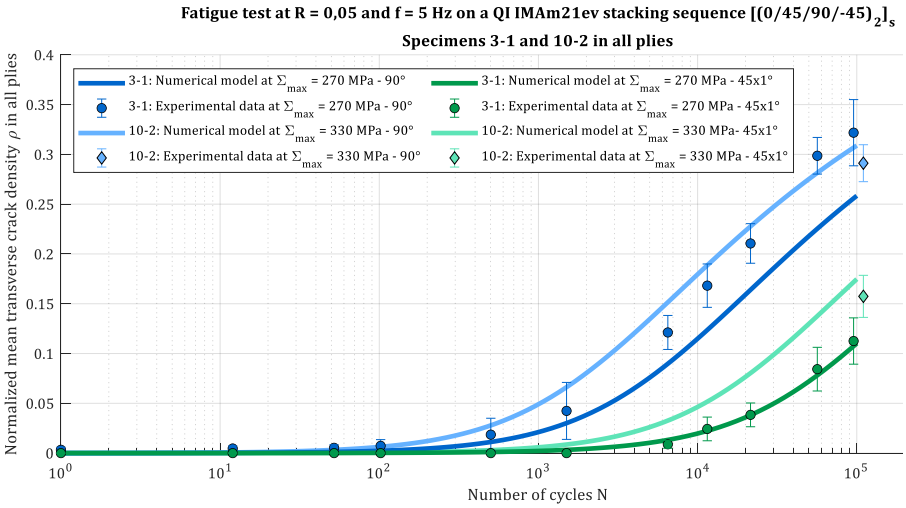

Figure 4:Experimental and numerical results for a fatigue test on the IMA/M21ev in 90 and 45° plies

During post-treatment, all the acoustic emission data have been analyzed, as well as the macroscopic modulus evolution, in order to compare it to the normalized mean crack density throughout the test. The automated crack detection tool has proven to be very relevant in the post-treating process. Overall, this model has proven to be highly efficient to describe constant amplitude fatigue loadings, while keeping a low computational cost (only a few seconds on a laptop).

4.2. Model's limitations

However, some strong hypotheses have been made on this model until now. For instance, we consider that the out-of-plane stresses can be neglected and that the material's behavior is linear. We have also not added the damage effect on the material's behavior yet, nor implemented sources of non-linearity such as viscosity and non-linear elasticity. Those are included in Germain's model [4], and their importance remains to be estimated for the simulation of fatigue tests.

5. Conclusion and perspectives

The model we have proposed here is able to describe both static and fatigue behaviors, while keeping a low complexity and low computational times. It allies both the benefits of an incremental writing with an observable variables formulation: the ability of representing complex loadings, and of directly linking damage to its effect.

It still has some limitations, and work perspectives have been defined to reach our initial objectives: (i) enhancing the model to add the damage effect on the material's behavior, as well as nonlinear phenomena such as viscosity and non-linear elasticity. In a second time, the cumulated damage effect and the mean stress effect will be added, and innovative numerical methods such as the cycle-jump method will be implemented, in order to accelerate the simulation times (10). (ii) Further experimental tests will be conducted to build and validate specific parts of the model, with a second campaign about to begin on a hundred of available specimens, until (iii) it can finally be implemented into a commercial Finite Element code.

6. References

1. Maimí P, Camanho PP, Mayugo JA, Dávila CG. A continuum damage model for composite laminates: Part II – Computational implementation and validation. Mech Mater. 1 oct 2007;39(10):909-19.

2. Thionnet A, Renard J. Meso-macro approach to transverse cracking in laminated composites using Talreja's model. Compos Eng. janv 1993;3(9):851-71.

3. Llobet J, Maimí P, Mayugo JA, Essa Y, Martin de la Escalera F. A fatigue damage and residual strength model for unidirectional carbon/epoxy composites under on-axis tension-tension loadings. Int J Fatigue. 1 oct 2017;103:508-15.

4. Germain J, Rannou J, Laurin F, Martini D. Robust damage prediction of laminated open-hole structures. In: ECCM18 – 18th European Conference on Composite Materials. Athens, Greece; 2018.

5. Angrand L. Modèle d'endommagement incrémental en temps pour la prévision de la durée de vie des composites tissés 3D en fatigue cyclique et en fatigue aléatoire. Université Paris-Saclay; 2016.

6. Camanho PP, Dávila CG, Pinho ST, Iannucci L, Robinson P. Prediction of in situ strengths and matrix cracking in composites under transverse tension and in-plane shear. Compos Part Appl Sci Manuf. 2006;37(2).

7. Dvorak GJ, Laws N. Analysis of Progressive Matrix Cracking In Composite Laminates II. First Ply Failure. J Compos Mater. avr 1987;21(4):309-29.

8. Ju JW. On energy-based coupled elastoplastic damage theories: Constitutive modeling and computational aspects. Int J Solids Struct. 1 janv 1989;25(7):803-33.

9. Nicol M, Laurin F, Hirsekorn M, Maire J-F, Albouy W, Treutenaere S. Modelling the Influence of The Stacking Order on Damage in Laminated Composites. 22 sept 2021;

10. Sally O, Laurin F, Julien C, Desmorat R, Bouillon F. An efficient computational strategy of cycle-jumps dedicated to fatigue of composite structures. Int J Fatigue. 2020;

FATIGUE BEHAVIOUR OF ANGLE-PLY GFRP LAMINATES: EXPERIMENTAL AND ANALYSIS METHODOLOGY TO EVALUATE TIME- AND CYCLE-DEPENDENT PROPERTIES

Seyed Shayan Khalooei Tafti, Anastasios P. Vassilopoulos

Composite Construction Laboratory (CCLab), École Polytechnique Fédérale de Lausanne, Lausanne, CH (shayan.khalooei@epfl.ch)

Abstract: *The tension-tension fatigue behavior of angle-ply GFRP laminate is studied in this work. The main objective is to develop an efficient methodology to obtain time- and cycle-dependent properties considering their interaction. Different aspects of time-dependent deformation on fatigue behavior are discussed. The S-N curves are adjusted according to the true stress state resulting from large creep deformation under fatigue loading. Moreover, the effect of fiber orientation on fatigue stiffness evolution is investigated. A simple analysis is performed to exclude the stiffening effect due to fiber orientation from the monitored fatigue stiffness evolution, which provides the fatigue stiffness evolution due to pure fatigue damage. An experimental methodology is proposed for time-dependent properties to evaluate the effect of fatigue damage on viscoelastic properties. DMA experiments were used to obtain the time-dependent properties of the fatigue-damaged specimen. Finally, this work presents the feasibility of extending the time-temperature superposition principle to time-temperature-fatigue damage superposition, aiming to predict the viscoelastic properties depending on the fatigue damage level.*

Keywords: Fatigue, composites, Creep-fatigue interaction; Residual stiffness; DMA; TTSP.

1. Introduction

Polymer matrix composites are widely used in numerous engineering fields such as aerospace, wind energy, automotive, and civil engineering as a primary component due to their high specific strength and stiffness. Engineering structures experience different loading types, such as creep, fatigue, and impact, during their lifetime. Nowadays, it is widely accepted that FRP composite's long-term behavior should be evaluated for their application in different engineering domains, especially in load-bearing parts of structures. Investigation of FRP composites' fatigue and creep behavior has already been examined since the 1940s, when these materials were firstly introduced in different engineering applications [1, 2]. Since the polymeric matrices possess inherent viscoelastic properties, they are expected to show time-dependent viscoelastic behavior. Therefore, the viscoelastic behavior of polymeric matrices used in structural components can significantly affect FRP composites' failure response under loading. Due to this inherent viscoelastic nature of polymer matrix composite, time-dependent phenomena such as creep, recovery, and relaxation should be considered to evaluate composite laminates' long-term behavior.

In most of the works that already exist in the literature, creep and fatigue behavior have been studied separately for FRP composites' long-term behavior. However, the FRP composite materials undergo time-dependent deformation (creep deformation) even under constant

  doi:10.5075/epfl-298799_978-2-9701614-0-0

amplitude (CA) fatigue loading with non-zero mean stress. Therefore, under fatigue loading, time-dependent behavior would affect the cycle-dependent properties and the 'materials' response, e.g., strength, stiffness, and failure modes. As a result, FRP composites' viscoelastic behavior should be considered for accurate evaluation and prediction of cycle-dependent properties. On the other side, investigation of the effect of fatigue damage on the viscoelastic properties could be more challenging as reported in many works in the literature, i.e., some related research reviewed in [2]. There is a lack of an efficient methodology to investigate the evolution of viscoelastic properties during fatigue loading. The available experimental methodologies to obtain the viscoelastic properties, like those described in [3, 4] suggesting the application of an Interrupted creep-fatigue loading pattern, can affect the fatigue behavior and lifetime of GFRP composites. Therefore, the fatigue life prediction models proposed in the literature, considering the viscoelastic behavior, are developed using the time-dependent properties of undamaged material, directly obtained by conducting creep tests [5].

Based on the challenges discussed above, this work aims to study the fatigue behavior of GFRP composites considering both time- and cycle-dependent behavior as well as their interaction. For this purpose, a robust experimental and analysis methodology is presented to investigate the creep-fatigue interaction under fatigue loading. Angle ply $[\pm 45]_{2s}$ GFRP laminates have been fabricated and used in this work to discuss the presented methodology's performance. Quasi-static experiments have been performed to obtain the GFRP laminate's mechanical properties, i.e., ultimate strength and stiffness, while CA fatigue experiments were performed under different maximum stress levels and three *R*-ratios of 0.1, 0.5, and 0.8 to investigate the material's fatigue performance. The DIC method has been used for strain measurements as well as for studying comparatively the distribution and evolution of the fatigue damage under different loading conditions. The Dynamic Mechanical Analysis (DMA) was used to obtain the viscoelastic properties of damaged material (cut from failed specimen) as well as properties of undamaged ones. The creep master curves were obtained by adopting the time-temperature superposition principle (TTSP) and conducting short-term creep tests at several temperatures [6]. The feasibility of using TTSP on a damaged specimen under fatigue loading was studied based on the limited DMA tests performed and presented in this work. As a result, this work can potentially introduce an extension to the TTSP, the "time-temperature-fatigue damage superposition principle" (TTFDSP). The analysis part is also separated to discuss the evolution of cycle- and time-dependent properties. The effect of relatively large strain resulting from viscoelastic behavior has been addressed for cycle-dependent properties. The effect of fiber-reorientation, which results from the creep deformation, has been also studied. The fiber reorientation during loading was obtained using the DIC measurements for longitudinal and transverse strain. Accordingly, a simple analysis based on the classical laminate theory (CLT) is proposed to exclude the effect of fiber reorientation's stiffness increase [7]. For time-dependent properties, the results obtained by DMA tests on the fatigue-damaged sample were compared to the undamaged one to illustrate the effect of fatigue on viscoelastic properties. In the last part, the DIC results for different stress levels and *R*-ratios are presented to comparatively discuss the damage distribution and evolution for different loading conditions.

  doi:10.5075/epfl-298799_978-2-9701614-0-0

2. Experimental procedure

2.1 Material fabrication and test setup

Unidirectional E-glass fiber fabrics (EC 9-68) with an area density of 425 gr/m^2 and ply thickness of 0.45 mm were impregnated by the low viscosity resin, Biresin® CR83, mixed with the hardener Sika CH83-2, in the ratio of 10:3, to fabricate the $[\pm 45]_{2S}$ GFRP laminates. As depicted in Figure 1-a, the vacuum infusion method was used to fabricate GFRP laminates with dimensions of 40×40 cm^2 using a vacuum pump with a pressure of 0.95 bar. The laminate was kept in the vacuum for 24 hours at laboratory conditions (22±2 °C, 40±10 % RH) and afterward was put in an oven at 70°C for 8 hours for post-curing. Specimens with 250 × 25 mm^2 (length × width) were cut from the laminates by a water-jet cutting machine, and two aluminum tabs with the dimensions of 40 × 25 mm^2 were glued to each specimen end, according to the ASTM D3039. Specimens have been sprayed to make speckle patterns for DIC measurements, as illustrated in Figure 1-b. The Quasi-static and CA fatigue experiments were conducted at an Instron 8800 hydraulic universal testing rig of 100-kN capacity with an accuracy of ±0.01 kN. The test setup for CA fatigue experiments is shown in Figure 1-c. For DIC measurements, a camera Point Grey - Grasshopper3 with a resolution of 2.2 Mpixels and a Fujinon HF35SA-1 35mm F/1.4 lens are used. An infrared (IR) thermal camera with an accuracy of 0.1°C and optical resolution of 160x120 pixels was also employed during the fatigue experiments to record the evolution of the specimen's surface temperature.

2.2 Quasi-static and fatigue Tests

Quasi-static tests have been conducted on several samples to obtain the ultimate tensile strength of material with the same loading rate as fatigue tests. Based on the static results, different maximum stress levels are considered for CA tests. Fatigue tests have been conducted under three *R*-ratios of 0.1, 0.5 and 0.8 considered. The loading rate of 10 kN/sec was chosen to avoid significant self-generated temperature.

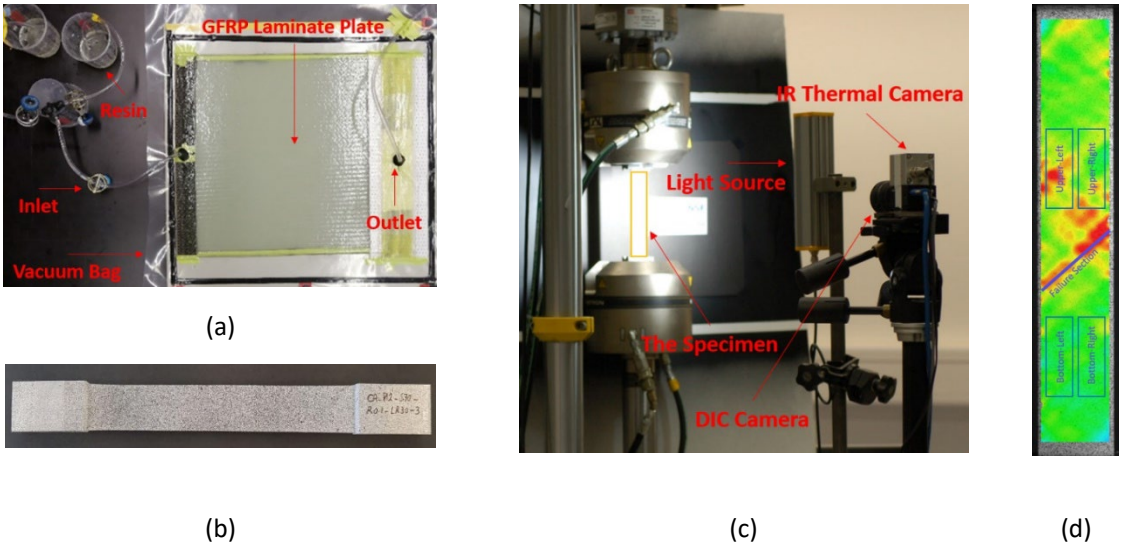

Figure 1. (a) Fabrication Process (Vacuum Infusion), (b) Sprayed specimen for DIC, (c) Fatigue test setup, (d) Cutting sample for DMA tests based on DIC results

2.3 DMA experiments

The DMA experiments were performed using a TA Instruments Q800 dynamic mechanical analyzer to obtain the viscoelastic properties of damaged and undamaged GFRP specimens. The single cantilever fixture has been used for performing the DMA tests. As shown in Figure 1-d, specimens with dimensions of 35.0 × 10.0 mm^2 (length × width) were cut from failed specimens for DMA tests according to the DIC results (to cut samples with different damage states). The creep-recovery tests were carried out for 60 and 120 minutes for each loading part, respectively. In order to apply the TTSP for obtaining the viscoelastic properties, creep-recovery tests were performed in the temperature range of 25–75°C with 10°C intervals. The same testing configuration was considered for the undamaged GFRP specimens to compare the viscoelastic properties.

3. Analysis and discussion

3.1 Cycle-dependent properties

The results of the quasi-static experiments are shown in Figure 2-a. The ultimate tensile strength (UTS) was estimated as 157 ± 9 MPa. The fatigue test results were used to obtain the S-N curves for different *R*-ratios. The S-N curves were obtained by normalizing the maximum stress by the UTS resulting from quasi-static tests to exclude the scattering resulting from the ultimate strength of GFRP laminate. As shown in Figure 2-b, the S-N curves for different *R*-ratio presented with dashed lines and the fatigue experimental data shown by open symbols. As a result of the relatively large deformation of the $[\pm 45]_{2s}$ GFRP laminates under fatigue loading, the level of true stress applied during loading will increase. The effect of the true stress state on S-N curves is investigated by adjusting the stress level based on the strain evolution monitored during loading. The adjusted experimental data are presented by filled symbols and the corresponding S-N curves by solid lines in Figure 2-b. By comparison of S-N curves, it can be realized the underestimation of S-N curves, especially at higher *R*-ratios and stress levels, where creep deformation would be more considerable. As a result, the underestimation of S-N curves can lead to overdesigning of FRP composites' structures. Therefore, it is suggested to consider the true stress levels applying for fatigue tests analysis, i.e., especially to obtain the in-plane shear properties using $[\pm 45]_{2s}$ laminates for designing and also numerical modeling purposes.

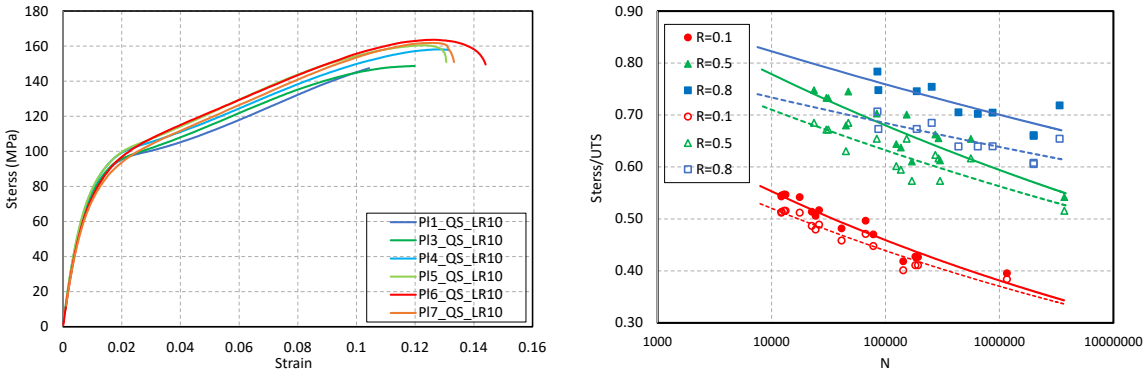

(a) (b)

Figure 2. (a) Stress-strain for same the GFRP laminates fabricated (b) S-N curves for R-ratio of 0.1, 0.5, and 0.8, before (dashed lines and unfilled shapes) and after (solid lines and filled shapes) stress adjustment due to large deformation

In the next step, the effect of fiber reorientation on the evolution of fatigue stiffness during loading has been studied. The fiber reorientation as a result of the cyclic creep (time-dependent deformation) can be estimated from the measurements of the longitudinal and traverse strains. Therefore, the average fiber reorientation in each cycle can be calculated directly by using the DIC measurements for strains in both directions. Based on the results obtained in this work, the fiber reorientation could increase up to 10 degrees for fatigue tests with the *R*-ratio of 0.8. At a higher *R*-ratio and higher maximum stress levels, the material undergoes more creep deformation, and consequently, more fiber reorientation can be experienced. Using the fiber reorientation evolution obtained during fatigue testing, the fatigue stiffness increase due to fiber reorientation can be estimated by CLT. Finally, the normalized fatigue stiffness monitored during the loading can be decomposed to the fatigue stiffness degradation due to fatigue damage and stiffening caused by fiber reorientation. The results of fatigue experiments for high and low maximum stress levels and for *R*-ratio of 0.1, 0.5 and 0.8 are shown in Figure 3. The evolution of normalized fatigue stiffness, degradation due to fatigue damage, and stiffening resulting from fiber reorientation are depicted in black, red, and blue colors, respectively. The selected fatigue tests represented high and low maximum stress levels are compared in Figure 3-a, Figure 3-b, and Figure 3-c for R=0.1, 0.5, and 0.8, respectively. The Fatigue tests reported are named with the stress level ratio (S, maximum stress level/UTS) and *R*-ratio (R). According to Figure 3-c, at a higher *R*-ratio and higher stress level (S0.71_R0.8), more effects of stiffening due to fiber reorientation can be observed. This actually results from more creep deformation, which could increase the stiffness up to 60%.

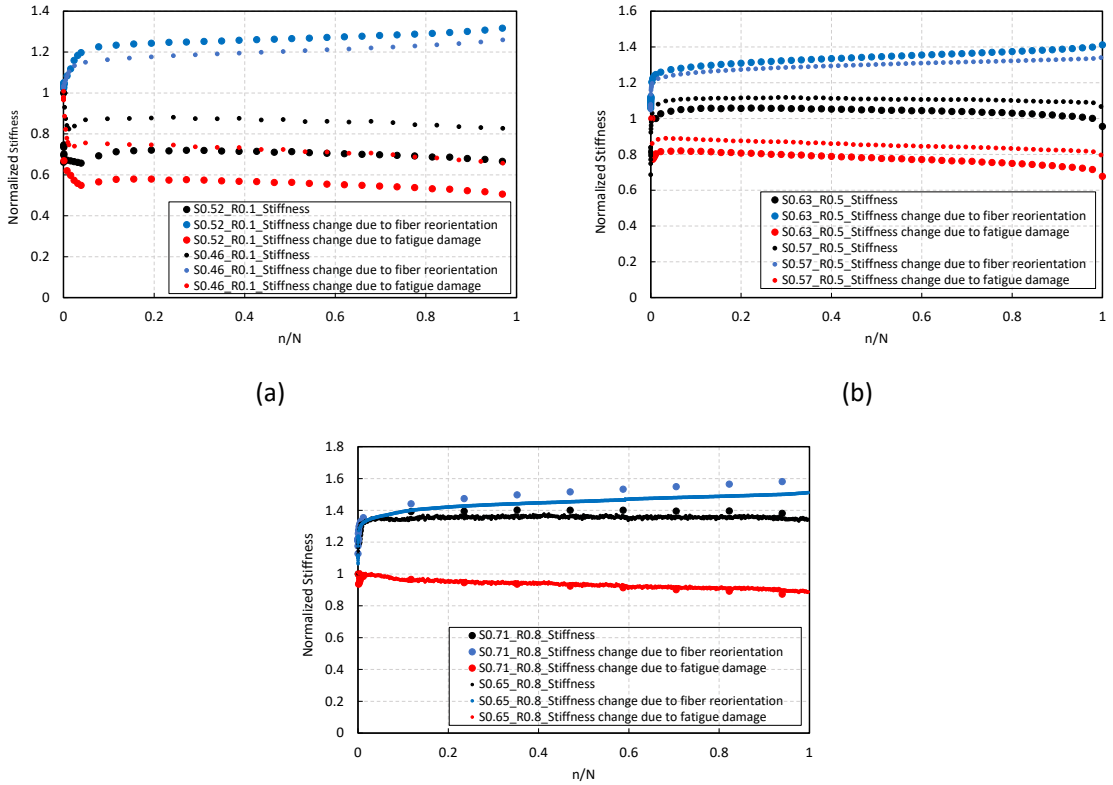

Figure 3. Decomposition of fatigue stiffness evolution due to fiber reorientation and fatigue damage for high and low maximum stress levels at different R-ratio (a) R=0.1, (b) R=0.5, and (c) R=0.8

Considering the fatigue stiffness evolution due to only fatigue damage, the residual stiffness model can be developed to interpret pure fatigue damage evolution. As shown in Figure 3, the stiffness evolution due to fatigue damage is decreasing for all fatigue tests. According to Figure 3-a, at the lower *R*-ratio of 0.1 and at higher stress level (S0.52_R0.1), where fatigue damage dominates the material behavior, the fatigue stiffness decreased, due to fatigue damage, to ca. 50%, while the decrease was less for higher *R*-ratios (See Figs3-b, 3-c), and it almost vanishes for *R*=0.8, where the creep dominates the material behavior.

3.2 Time-dependent properties

The results obtained from DMA experiments conducted on a limited amount of damaged and undamaged specimens. According to Figure 4-a, the creep strain curves were obtained for the undamaged specimen at temperatures in the range of 25–75 °C. The same DMA experimental procedure has been performed on the sample cut from the specimen that failed in the fatigue experiment of "S0.46_R0.1." The result shown in Figure 4-b corresponds to the top-left located sample (cut according to the DIC result in Figure 4-c). The creep strain curves for each damaged and undamaged test have been used to obtain the creep strain master curves using the TTSP. The shift factors have been obtained by adopting the Williams-Landel-Ferry (WLF) model [8]. The results show the feasibility of applying TTSP on damaged GFRP material to obtain the viscoelastic properties depending on the damage level caused during fatigue loading. As shown in Figure 4-c, applying TTSP on a fatigue-damaged specimen provides a smooth master curve to predict creep strain for a longer time period. As seen in Figure 4-c, the creep master curves of the damaged and undamaged specimens are comparable, with the master curve for the damaged material shifted upward at the early stages due to fatigue stiffness degradation, which affects the instantaneous strain. Besides mentioned shifting, the fatigue damage alters the viscoelastic behavior for longer periods, as the master curve diverges more from the one for the undamaged sample. As a result of this observation, extending the TTSP to the time-temperature-fatigue damage superposition principle would be suggested to predict viscoelastic properties depending on the damage level caused during loading. To validate the proposed methodology, more DMA experiments are needed for various fatigue tests performed at different stress levels and *R*-ratios. Finally, it will be possible to establish the novel creep master curves depending on the different loading conditions and the level of fatigue damage. Therefore, the proposed master curve would be used for more accurate modeling and to predict the long-term behavior of FRP composites considering both fatigue damage and creep deformation.

3.3 Damage propagation and failure modes

The DIC measurements were post-processed using the VIC-2D software (from Correlated Solutions, Inc). A field size (160 mm × 25 mm) was defined on each initial image of the samples to capture the specimen's strain field under loading. The most important parameters related to post-processing using DIC software are the subset and step size, as well as the interpolation type. The parameters were tuned effectively, corresponding to the speckle pattern created by spraying.

  doi:10.5075/epfl-298799_978-2-9701614-0-0

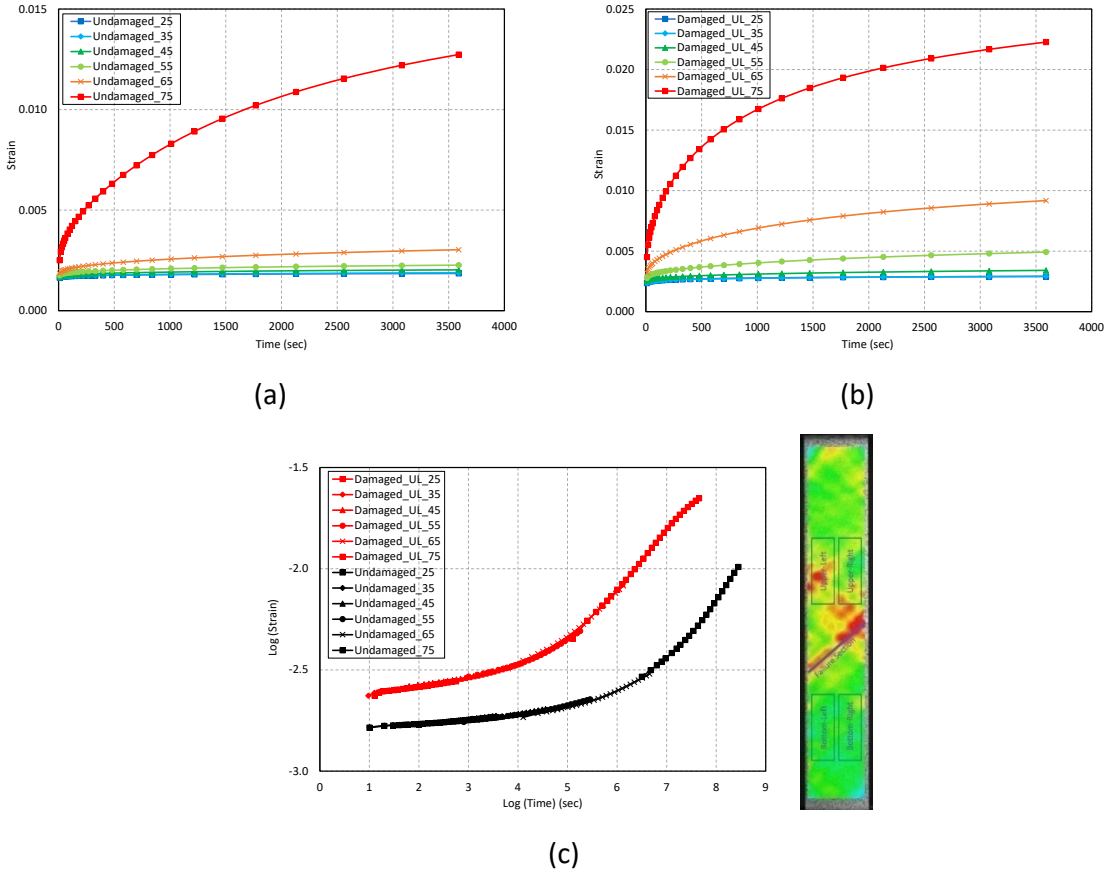

Figure 4. (a) Creep strain curves obtained from creep-recovery tests for temperatures in the range of 25–75 °C on (a) undamaged $[\pm 45]_{2s}$ GFRP, (b) Damaged specimens cut from fatigue test of S0.46_R0.1 (The top-left position in the DIC image), (c) Comparison of creep master curves obtained by TTSP for damaged (S0.46_R0.1, top-left) and undamaged material

As a result of relatively large deformation, the Hencky strain (logarithmic) was used to consider true strain. Finally, the DIC results for longitudinal strain (loading direction) are presented in Figure 5 to qualitatively compare the damage initiation and propagation under different loading conditions. First of all, compared to the IR thermography results, which are not presented here, the DIC method would provide a higher resolution to monitor different damage modes initiated and propagated during the loading. In Figure 5, the longitudinal strain field at different fractions of life is presented for *R*-ratios of 0.1 (top), 0.5 (middle) and 0.8 (bottom). For each *R*-ratio, two test results represent high (left) and low (right) stress levels. By comparing the longitudinal strain distribution, it can be realized that under a lower *R*-ratio (0.1), where fatigue dominates the material behavior, the damage is more concentrated. However, under the *R*-ratio of 0.8 (creep-dominated), the strain distribution and damage distribution are more uniform throughout the specimen. The damage was initiated mainly by matrix cracking at the free edges at the early stages of fatigue loading. In the next stage, the micro-cracks initiated could be propagated parallel to the fiber directions as macro matrix cracks or fiber/matrix debonding. Finally, the propagated damages would mostly lead to delamination and fiber breakage causing the failure of the laminate. Selected images of failure surfaces for different *R*-ratios are presented in Figure 6. The results show different failure modes as fiber breakage, mixed fiber breakage/pull-out, and fiber pull-out for *R*-ratios of 0.1, 0.5 and 0.8, respectively.

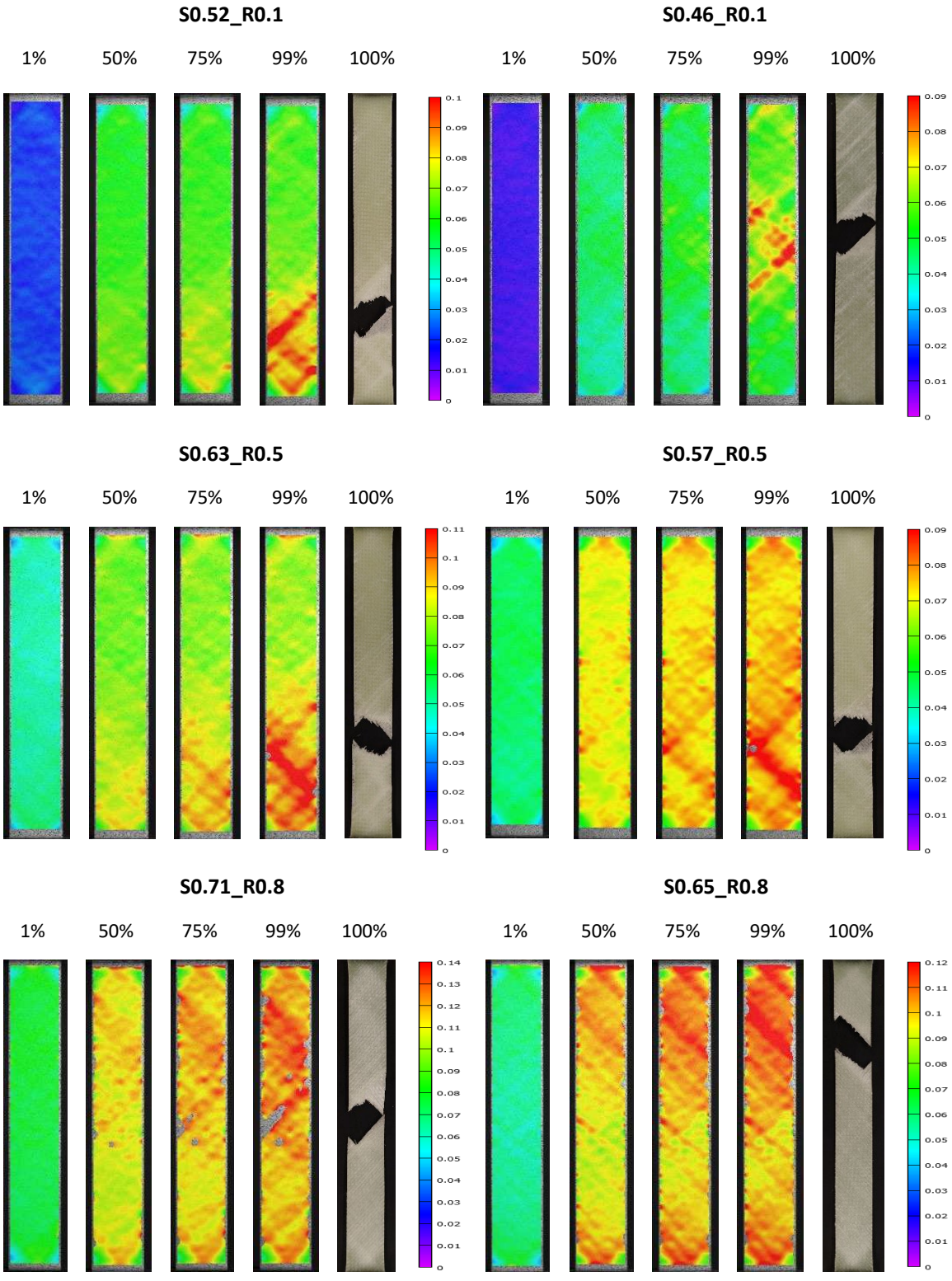

Figure 5. The DIC measurements for longitudinal strain during fatigue tests for R-ratios of 0.1 (top), 0.5 (middle) and 0.8 (bottom), and under high (left) and low (right) stress levels

  doi:10.5075/epfl-298799_978-2-9701614-0-0

(a) S0.52_R0.1: Fiber breakage

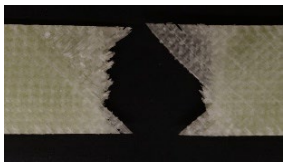

(b) S0.57_R0.5: fiber breakage/pull-out

(c) S0.71_R0.8: Fiber pull-out

Figure 6. The dominant failure modes under different R-ratios: (a) 0.1, (b) 0.5, (c) 0.8

4. Conclusion

The fatigue behavior of angle-ply GFRP laminates was studied considering time- and cycle-dependent behaviors. Different aspects of their interactions under tension-tension CA fatigue loading were addressed. For cycle-dependent properties, it has been shown that the S-N curves were underestimated due to the increasing stress state under fatigue loading, i.e., resulting from large creep deformation, especially for higher *R*-ratio and stress levels. Moreover, the effect of fiber orientation on fatigue stiffness evolution was investigated. A simple analysis was performed to decompose the stiffening effect due to fiber orientation from the fatigue damage stiffness evolution, which provides more accurate residual stiffness models representing the pure fatigue degradation. An experimental methodology using DMA testing was suggested to evaluate the effect of fatigue damage on viscoelastic properties. The results have shown the feasibility of using the time-temperature superposition principle for damaged material, which can provide viscoelastic properties depending on the fatigue damage level. Since limited results were used in this work, the DMA testing should be performed for more damaged specimens under different loading conditions to evaluate the performance of the proposed methodology. Finally, the evolution of DIC measurements and failure surfaces have been discussed for different loading conditions. As a result, it can be concluded that depending on the *R*-ratio, the damage distribution and failure modes could differ, resulting from different inherent behavior of FRP composite materials under creep and fatigue loading.

Acknowledgements

The authors wish to acknowledge the support and funding of this research by the Swiss National Science Foundation (Grant No. 200020_185005).

5. References

1. Anastasios P. Vassilopoulos, Keller T. Fatigue of Fiber-Reinforced Composites. Springer Science & Business Media; 2011.
2. Anastasios P. Vassilopoulos. The history of fiber-reinforced polymer composite laminate fatigue. Int J Fatigue. 2020;134:105512.
3. A. Vahid Movahedi-Rad, Anastasios P. Vassilopoulos, Thomas Keller. Creep effects on tension-tension fatigue behavior of angle-ply GFRP composite laminates. Int J Fatigue. 2019;123:144–56.
4. A. Vahid Movahedi-Rad, Thomas Keller, Anastasios P. Vassilopoulos. Interrupted tension-tension fatigue behavior of angle-ply GFRP composite laminates. Int J Fatigue. 2018 Aug 1;113:377–88.
5. Samareh-Mousavi SS, Taheri-Behrooz F. A novel creep-fatigue stiffness degradation model for composite materials. Compos Struct. 2020 Apr 1;237:111955.
6. Reddy JN. Mechanics of laminated composite plates and shells: theory and analysis. CRC Press; 2003.
7. Williams ML, Landel RF, Ferry JD. The Temperature Dependence of Relaxation Mechanisms in Amorphous Polymers and Other Glass-forming Liquids. J Am Chem Soc. 1955;77(14):3701–7.
8. Povolo F, Fontelos M. Time-temperature superposition principle and scaling behaviour. J Mater Sci 1987 225. 1987 May;22(5):1530–4.

  doi:10.5075/epfl-298799_978-2-9701614-0-0 published under CC BY-NC 4.0 license

Composites Meet Sustainability – Proceedings of the 20th European Conference on Composite Materials,
ECCM20. 26-30 June, 2022, Lausanne, Switzerland

PROBABILISTIC FATIGUE LIFE MODEL OF COMPOSITE LAMINAS UNDER CYCLE LOADING

Guangjian Xiang[a,c], Konstantinos C. Bacharoudis [b], Anastasios P. Vassilopoulos [c],

a: College of mechanics and materials, Hohai University, Nanjing, China – xiangguangjian@hhu.edu.cn
b: Offshore Renewable Energy Catapult, Blyth, NE24 1LZ, UK
c: Composite Construction Laboratory (CCLab), Ecole Polytechnique Fédérale de Lausanne EPFL, Station 16, CH-1015 Lausanne, Switzerland

Abstract: *A probabilistic model for estimating the fatigue life of composite laminas is developed in this paper. Based on the statistical characteristics of the fatigue life (mean value and standard deviation), a linear probabilistic model is proposed along with the statistical uncertainty, which allows for efficiently predicting the distribution of fatigue life at any stress levels for a constant stress ratio. By comparing predicted and experimental results for several composite materials, the proposed model is validated and its accuracy is further evaluated through the use of goodness-of-fit statistical tests. In addition, with a second-order polynomial model, the probabilistic constant life diagrams for different combinations of stress level and stress ratio are developed. Meanwhile, the probabilistic S-N curves for any stress level and stress ratio without experimental measurements are derived, and it is demonstrated that the probabilistic S-N curves agree well with the validation data, which could greatly save the cost of extra fatigue tests.*

Keywords: Fatigue; Composites; Probabilistic modeling; Statistical analysis.

1. Introduction

Fatigue failures occur very often in composite structures [1-3]. A large scatter in the fatigue properties has been observed during experimental investigations on fibrous composite materials [1], [4]. This kind of variability can be attributed to defects induced during manufacture and the inhomogeneity of composite materials. One of the most common approaches to calculate the fatigue strengths is using S-N curves [5, 6], which is a deterministic equation obtained by fitting the measured fatigue life data. Early in 1910, Basquin [7] suggested a power-law equation between fatigue strength and cycles to failure, which is still used by many researchers today. Generally, the fatigue performance of a transversely isotropic composite lamina can be revealed by the S-N curves established in the three principal directions of the materials, which is also an indispensable step in determining the fatigue life of the off-axis lamina [8-9]. Experimental tests on various stress levels are essential to derive the S-N curves, and to further consider the mean stress effect in fatigue life predictions, fatigue data for several R ($R=S_{min}/S_{max}$) values should be measured to construct the well-known constant life diagrams (CLD) [10-12]. However, to cope with the uncertainties introduced in the fatigue properties and derive a rational model of the fatigue life, statistical methods should be applied.

Statistical treatment of the fatigue strength and the developed stresses as random variables is suggested in probabilistic consideration of several fatigue failure criterions [8, 9]. Several stochastic variables, such as the elastic properties of the composite material, the geometrical characteristics and the applied loads, have been defined [13, 14] and introduced in a functional formulation that provides statistical descriptions of the developed stresses, which can be found

  doi:10.5075/epfl-298799_978-2-9701614-0-0

in several works [15, 16]. However, despite a number of probabilistic fatigue life models have been proposed, very few works exist on the formulation of probabilistic CLD and even fewer for the probabilistic modeling of fatigue life with statistical characteristics of experimental data.

To deal with the problem at hand, a parameterization of the statistical characteristics of the fatigue life (mean value and standard deviation) with respect to the stress level *Sa*, and the ratio *R* based on experimental evidence is proposed in this work. Empirical models are developed including the statistical characteristics of fatigue life in closed-form equations, which is able to estimate the distribution of fatigue life for every combination of *Sa* and *R* and obtain probabilistic S-N curves as well as CLD diagrams.

2. Probabilistic fatigue life model

2.1 Linear probabilistic fatigue model

One of the most popular probabilistic models for the fatigue life data is the Lognormal distribution. Assuming that the fatigue life is described by the same type of parametric distribution independently of the applied stress amplitude *Sa* and the ratio *R*, for the Lognormal distribution, the fatigue life model can be written as

$$ln\, N = m + sZ, \tag{1}$$

where *N* is the allowable number of cycles at the stress amplitude *Sa* in a specific ratio *R*, *m* and *s* are the parameters of the Lognormal distribution, and *Z* is a random variable with the standard normal distribution. The mean value, α_1, and standard deviation, α_2, of the allowable number of cycles *N* can be expressed in terms of the parameters *m* and *s* [17]

$$\alpha_1 = e^{m+\frac{s^2}{2}}, \tag{2}$$

$$\alpha_2 = \sqrt{\left(e^{s^2} - 1\right)e^{2m+s^2}}. \tag{3}$$

Due to the limited number of experimental data, statistical uncertainty inserts in the model of Eq. (1). Thus, the variables α_1, α_2 can be thought of as random variables themselves. The interest is mainly focused to express α_1, α_2 (or their statistical characteristics, mean value $E(\alpha_i)$ and standard deviation $D(\alpha_i)$, if statistical uncertainty is considered) by means of simple algebraic equations with respect to the applied stress amplitude *Sa* and ratio *R* based on available experimental data.

For constant ratio *R*, a linear relation between the natural logarithm of α_i and the natural logarithm of the applied stress amplitude *Sa* is assumed as

$$ln\, \alpha_i = E(ln\, \alpha_i) + D(ln\, \alpha_i)Z_i, \quad i = 1,2, \tag{4}$$

where

$$E(ln\, \alpha_i) = c_i\, ln\, S_a + d_i, \quad i = 1,2, \tag{5}$$

where Z_i denotes random variables with the standard normal distribution, c_i and d_i are the regression coefficients. As $ln\alpha_i$ are direct statistical characteristics of testing data, they may be correlated variables. If they are correlated, accordingly the Z_i are also correlated ones with a correlation coefficient ρ.

  doi:10.5075/epfl-298799_978-2-9701614-0-0

Combining Eq. (4) and Eq. (5), we get

$$ln\,\alpha_i = c_i\,ln\,S_a + d_i + D(ln\,\alpha_i)Z_i, \quad i = 1,2, \tag{6}$$

where the term $D(ln\alpha_i)Z_i$ represents the random error accounting for the statistical uncertainty. Both α_1 and α_2 are random variables following the same distribution as N while the random component Z_i represents the statistical uncertainty inserted by the limited number of the experimental data. Ignoring the statistical uncertainty, the Eqs. (4)-(5) are greatly simplified and become

$$ln\,\alpha_i = c_i\,ln\,S_a + d_i, \quad i = 1,2. \tag{7}$$

When the statistical uncertainty is not considered, Eq. (7) can be used to determine the relation between $ln\alpha_i$ and $lnSa$. Once the linear relation is determined, the distribution of the fatigue life can be estimated by inserting Eq. (6) or Eq. (7) into Eqs. (1)-(3).

Through linear regression, we can easily obtain the slope and intercept of the proposed model in Eq. (7) (or Eq. (6) if considering the statistical uncertainty). Thus, for the case that the statistical uncertainty is omitted, the value of α_i for a specific stress level Sa can be directly computed using the proposed linear model, and then the parameters of the distribution can be further obtained. For Lognormal distribution, by solving Eqs. (2)-(3), the parameters m and s can be expressed as functions of α_i

$$m = \ln\left(\frac{\alpha_1^2}{\sqrt{\alpha_1^2+\alpha_2^2}}\right), \tag{8}$$

$$s = \sqrt{\ln\,(1+\frac{\alpha_2^2}{\alpha_1^2})}. \tag{9}$$

Once the parameters of a distribution are determined, the cumulative distribution function (CDF) of the fatigue life N can be thereby obtained.

If the statistical uncertainty is considered, Eq. (6) is used for generating random numbers of α_i. As α_1 and α_2 are correlated variables, a covariance matrix (Cov) is required to generate random samples of α_i

$$Cov = \begin{bmatrix} D(ln\alpha_1)^2 & \rho D(ln\alpha_1)D(ln\alpha_2) \\ \rho D(ln\alpha_1)D(ln\alpha_2) & D(ln\alpha_2)^2 \end{bmatrix}. \tag{10}$$

The value of $D(ln\alpha_i)$ can be determined as the mean error of linear regression for each stress ratio, and the value of ρ can be estimated by bootstrap method. With these values, random samples for [α_1, α_2] with a given size of s_1 are generated. Then the parameters of Lognormal distribution and Weibull distribution corresponding to each pair of α_1 and α_2 are calculated by Eqs. (8)-(10). For each pair of obtained parameters ([m, s]), random numbers in the size of s_2 from the Lognormal distribution are generated with corresponding distribution parameters, which brings a group of random variables with the total size of $s_1 * s_2$. By calculating the mean value and standard deviation of all generated random numbers of N, re-estimation of α_i is achieved on amplified samples where the statistical uncertainty is included. Then the parameters of distribution can be determined following Eqs. (8)-(9), on the basis of estimated values of α_i. In this way, the cumulative distribution function (CDF) of the fatigue life N, where

  doi:10.5075/epfl-298799_978-2-9701614-0-0

the statistical uncertainty is considered, is obtained with calculated values of distribution parameters.

2.2 Probabilistic constant life model

To derive a general probabilistic constant life model, a second-order polynomial model is established to describe each curve in the probabilistic CLD graphs. For constant values of $ln\alpha_i$ (or $E(ln\alpha_i)$ if statistical uncertainty is considered), it can be written as

$$S_a = e_i R^2 + f_i R + g_i,\ i = 1,2, \tag{11}$$

The parameters in Eq. (11) are also assumed to be well described by second-order polynomial models in the following form:

$$\left.\begin{aligned} e_i &= m_i Y^2 + n_i Y + p_i \\ f_i &= s_i Y^2 + t_i Y + r_i \\ g_i &= u_i Y^2 + v_i Y + w_i \end{aligned}\right\},\ i = 1,2. \tag{12}$$

When omitting the statistical uncertainty,

$$Y = ln\alpha_i,\ i = 1,2, \tag{13}$$

and for the case that the statistical uncertainty is considered

$$Y = E(ln\alpha_i),\ i = 1,2. \tag{14}$$

Assuming that N obeys the lognormal distribution, the term $(ln(N)-m)/s$ satisfies the standard normal distribution, which is

$$\frac{\ln(N)-m}{s} \sim N(0,1). \tag{15}$$

By means of the inverse relation of the standard normal cumulative distribution function, the Pth percentile point of fatigue data r can be calculated using the following formula:

$$r = \Phi^{-1}(P) = \frac{\ln(N)-m}{s}, \tag{16}$$

where $\Phi^{-1}(P)$ is the inverse of standard normal distribution for a certain probability P. The distribution parameters m and s can be expressed as functions of the stress level Sa, which are

$$m = F(S_a) = \ln\left(\frac{e^{2(c_1 ln S_a + d_1)}}{\sqrt{e^{2(c_1 ln\ a + d_1)} + e^{2(c_2 ln S_a + d_2)}}}\right), \tag{17}$$

$$s = G(S_a) = \sqrt{\ln(1 + e^{2(c_2 ln\ a + d_2 - c_1 ln\ a - d_2)})}. \tag{18}$$

Substituting Eq.(17) and Eq. (18) into Eq. (16), there is

$$\ln(N) = F(S_a) + G(S_a) * r. \tag{19}$$

For a given value of N and failure probability P, the value of r can be obtained through Eq. (16), and the corresponding stress level Sa can be obtained by solving Eq. (19).

Furthermore, a probabilistic approach is introduced here to derive probabilistic S-N curves for a specific ratio R without experimental measurements including the statistical uncertainty. As the fatigue life N is assumed to satisfy Lognormal distribution, it should be pointed out that the

  doi:10.5075/epfl-298799_978-2-9701614-0-0

distribution parameters *m* and *s* refer to the mean value and standard deviation of a normal distribution which *lnN* satisfies. With the properties of normal distribution, the probabilistic S-N curves can be derived once the distribution parameters *m* and *s* for each stress level are determined. For the case when omitting statistical uncertainty, the values of *m* and *s* can be directly derived once the coefficients of Eq. (12) are obtained through fitting. If the statistical uncertainty is considered, statistical methods proposed in the previous section should be conducted to generate random samples, and the values of *m* and *s* can be determined after re-estimation of α_i.

3. Validation of the proposed model

Experimental data on GFRP multidirectional laminate with a stacking sequence of [90/0/±45/0]S from the DOE/MSU database [18] are used for validation. First, the proposed model was examined on the tension-tension testing data of material DD16 for *R*=0.5, where data in three stress levels are used for fitting. Fig. 1(a) displays linear fitting results of this dataset, and the predicted distribution of fatigue life in the second stress level (marked red in Fig. 1(a)) was plotted in Fig. 1(b). Obviously, almost all the curves in Fig. 1(b) fit well with the experimental data, indicating the proposed model is capable of predicting the fatigue life distribution in the stress level without experimental measurement.

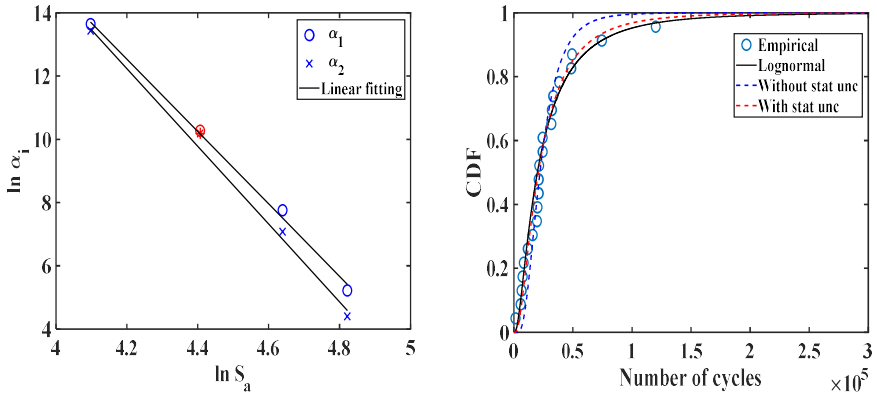

Figure 1. Fitting results on testing data of material DD16 for R=0.5: (a) linear regression results; (b) CDF assuming Lognormal distribution.

Fig. 2 presents the established probabilistic CLD model in and *Sm-Sa* plane. With the proposed second-order polynomial model, the fatigue behavior for any ratio *R* in the range of measured data (e.g., 0.1<*R*<0.9 for this dataset) can be described, and the mean stress effect on the fatigue behavior of the examined material can be reflected as well. Fig. 3 displays the probabilistic S-N curves for *R*=0.8, with the failure probability ranging from 2.28% to 97.72%. As most datapoints fall into the predicted band, the developed P-S-N curves are quite accurate. Besides, when considering statistical uncertainty, the derived S-N curves exhibits more variation and the observed wider range between the upper and lower bonds provides better predictions.

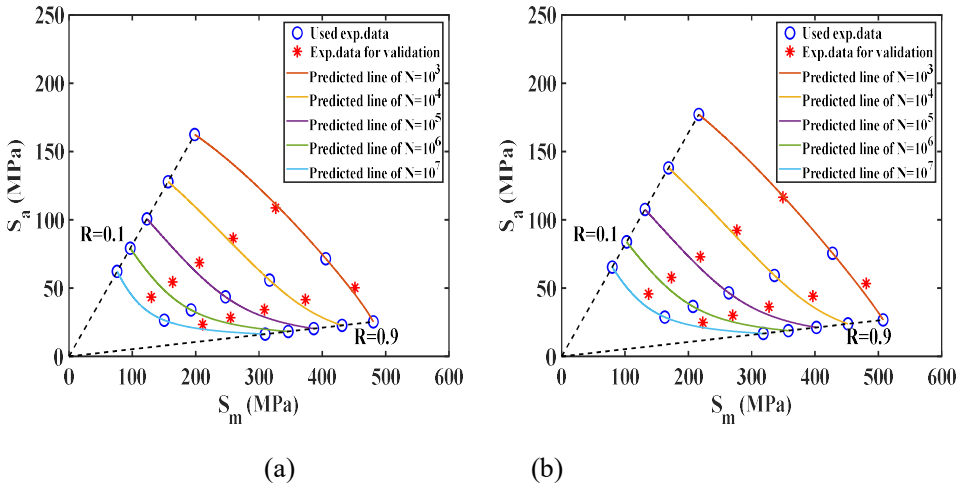

Figure 2 Probabilistic CLD in in Sm- Sa plane of constant N for 0.1<R<0.9 under the failure probability: (a) P=50%; (b) P=90%.

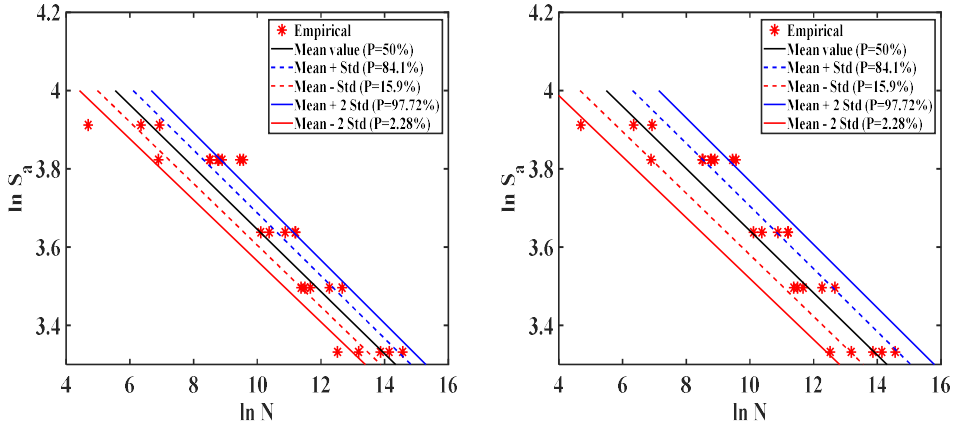

Fig. 3 Probabilistic S-N curves in a ln-ln plot for R=0.8: (a)omitting statistical uncertainty, (b) considering statistical uncertainty.

4. Conclusions

A probabilistic fatigue life model was proposed based on the statistical characteristics (mean value and the standard deviation) of the number of cycles to failure with respect to the applied stress level, *S* and stress ratio, *R*. The results obtained from this study can be summarized as follows:

- The relation between statistical characteristics of experimental data and the applied stress level was well described by the linear model. Statistical procedures of deriving the fatigue life distribution in certain stress level without measured data were suggested based on the proposed linear model, where the statistical uncertainty was included.

- By comparing predicted distributions with experimental data, it was concluded that both the quantity and the quality of used data have an impact on the performance of the proposed model.

  doi:10.5075/epfl-298799_978-2-9701614-0-0

- A probabilistic CLD model was developed without considering the statistical uncertainty, and proved quite successful for the estimation of the fatigue life under a certain failure probability, for different stress levels *Sa* and stress ratio *R* within the range of measured data.

- A probabilistic approach was introduced to develop probabilistic S-N curves for specific *R*-ratios considering the statistical uncertainty. The derived probabilistic S-N curves are well corroborated by the experimental data, while it was shown that the impact of data quantity and quality was reduced when the statistical uncertainty was included.

Acknowledgments

The first author acknowledges the support of the Fundamental Research Funds for the Central Universities (grant no. B220203047), China and the China Scholarship Council (CSC) (grant no.202006710128).

5. References

1. Vassilopoulos AP. The history of fiber-reinforced polymer composite laminate fatigue. International Journal of fatigue, 2020:134;105512
2. Manson SS, Halford GR. Fatigue and durability of structural materials. ASM International (2006)
3. Freudenthal AM. Fatigue mechanisms, fatigue performance and structural integrity. In: Proc air force conference on fatigue and fracture of aircraft structures and materials, AFFDL TR 70-144; 1970.
4. Sarfaraz R, Vassilopoulos AP, Keller T. Experimental investigation and modeling of mean load effect on fatigue behavior of adhesively-bonded pultruded GFRP joints, International Journal of Fatigue, 2012: 44;245-252
5. Sarfaraz R, Vassilopoulos AP, Keller T. A hybrid S-N formulation for fatigue life modeling of composite materials and structures. Composites Part A: Applied Science and Manufacturing 2012;43(3);445-453
6. Sarfaraz R, Vassilopoulos AP, Keller T. Modeling the constant amplitude fatigue behavior of adhesively bonded pultruded GFRP joints, Journal of Adhesion Science and Technology, 2013:27(8);855-878, DOI: 10.1080/01694243.2012.727158
7. Basquin OH. The experimental law of endurance tests. In: Proc ASTM, vol. 10, no. Part II; 1910. p. 625.
8. Philippidis TP, Vassilopoulos AP. Complex stress state effect on fatigue life of GRP laminates. Part II, Theoretical formulation. Int. J. Fatigue 2002; 24(8): 825-30.
9. Philippidis TP, Vassilopoulos AP. Complex stress state effect on fatigue life of GRP laminates. Part I, Experimental. Int. J. Fatigue 2002; 24(8): 813-823.
10. Vassilopoulos AP, Manshadi BD, Keller T. Influence of the constant life diagram formulation on the fatigue life prediction of composite materials. Int J. Fatigue 2009;32(4):659-669
11. Beheshty MH, Harris B. A constant life model of fatigue behavior for carbon fiber composites: the effect of impact damage. Compos Sci Technol, 1998;58(1):9-18
12. Vassilopoulos AP, Manshadi BD, Keller T. Piecewise non-linear constant life diagram formulation for FRP composite materials. Int. J. of Fatigue 2010; 32:1731-38.

13. Joint Committee on Structural Safety. Probabilistic Model Code, 2001(.https://www.jcss-lc.org/jcss-probabilistic-model-code/).
14. Polymer matrix composites: Guidelines for characterization of structural materials. Composite materials handbook, vol. 1. Washington (DC): Department of Defence; 2002 DOD-MIL-HDBK-17-1F.
15. Philippidis TP, Lekou DJ, Aggelis DG. Mechanical property distribution of CFRP filament wound composites. Compos. Struct. 1999; 45: 41-50.
16. Sriramula S, Chryssanthopoulos MK. Quantification of uncertainty modeling in stochastic analysis of FRP composites. Compos. Part A: Appl. Sci. and Manuf. 2009; 40: 1673-84.
17. Montgomery DC, Runger GC. Applied statistics and probability for engineers. Wiley: New York, 2003.
18. Mandell J F, Samborsky D D. DOE/MSU composite material fatigue database[J]. Sandia National Laboratories, SAND97-3002 (online via www. sandia. gov/wind, v. 18, 21st March 2008 Updated), 2010.

Fatigue behavior of continuous-discontinuous sheet molding compounds under application related loading conditions

Miriam Bartkowiak[a,], Melike Kizak[a], Wilfired Liebig[a], Kay André Weidenmann[b]*

a: Karlsruhe Institute of Technology, Institute for Applied Materials – Material Science and Engineering, Kaiserstr. 12, 76131 Karlsruhe, Germany
b: University of Augsburg, Institute for Materials Resource Management, Am Technologiezentrum 8, 86159 Augsburg, Germany
*: Corresponding author. E-mail address: miriam.bartkowiak@kit.edu (M. Bartkowiak)

Abstract: In this work, hybrid sheet molding compound composites consisting of a discontinuous glass fiber-reinforced core and continuous carbon fiber-reinforced face plies were analyzed regarding their bending fatigue behavior at different frequencies and temperatures relevant for automotive applications. While the ultimate flexural strength at fatigue strain rate (UFS^F) of the hybrid composite was only 59 % higher than that of discontinuous SMC, flexural fatigue strength at $3.6 \cdot 10^5$ cycles increased by 260 % due to hybridization. At ambient temperature, fatigue strength of continuous-discontinuous SMC decreased by less than 5 % UFS^F per decade of cycles, whereas that of discontinuous SMC decreased by 10 % UFS^F per decade of cycles. While excellent fatigue properties were determined at ambient temperature, the hybrid composite was sensitive to a temperature increase. This behavior was a result of early kinking of the continuous carbon fiber-reinforced ply on the compression loaded side.

Keywords: Hybrid composites; Fatigue; Sheet Molding Compound; Bending; Effects of Hybridization

1. Introduction

Discontinuous (DiCo) glass fiber-reinforced sheet molding compounds (SMC) are widely used as non-structural and semi-structural components in the automotive industry. However, due to the limited fiber length and a lack of fiber orientation, their mechanical properties are too low for the material to be used as structural components. One approach to increase the mechanical performance of DiCo SMC is locally reinforcing components with load-optimized continuous carbon fiber tape [1]. Preliminary works have shown that such continuous-discontinuous (CoDiCo) sheet molding compounds show excellent mechanical properties under quasi-static loading conditions, especially under bending load [2], with the continuous fiber reinforcement having maximum distance to the neutral axis. Since structural components are usually subject to cyclic loading, it is important to also study the material behavior under fatigue loading. Furthermore, automotive components are loaded at different temperatures with changing frequencies. Unidirectional carbon fiber-reinforced composites are known to be largely insensitive to temperature and frequency changes under tensile load, where the material behavior is mainly fiber-dominated [3,4]. However, a temperature dependence is observed under off-axis loading [3]. The influence of loading frequency on the fatigue behavior of conventional DiCo SMC composites was also found to be minor [5], however, stress-life data show a clear temperature-dependence [6,7]. Whether a hybrid composite combining both types of reinforcement exhibits frequency- and temperature dependent fatigue properties has not yet been investigated.

  doi:10.5075/epfl-298799_978-2-9701614-0-0

In this work, the bending fatigue behavior of hybrid CoDiCo SMC is studied and compared to that of DiCo SMC without continuous reinforcement. The focus is particularly on the effect of temperature and frequency on the stress-life behavior.

2. Materials and Manufacturing

The SMC composites investigated in this study were manufactured at the Fraunhofer Institute of Chemical Technology (Pfinztal, Germany) and consist of a two-step curing unsaturated polyester polyurethane hybrid resin system [8] and either discontinuous glass fiber reinforcement or a hybrid reinforcement with discontinuous glass fibers in the core and unidirectional continuous carbon fibers in the surface layers. Discontinuous SMC was manufactured on a conventional conveyor plant type HM-LB-800 by Schmidt&Heinzmann (Bruchsal, Germany) with a nominal fiber volume content of 26 %. The fiber length was 25.4 mm. The semi-finished product was stored to mature for several days at approximately 30 °C after manufacturing. Continuous semi-finished material with a nominal fiber volume content of 64 % was manufactured by feeding unidirectional carbon fiber non-crimp fabric to the conveyor plant. Additional heating and cooling sections were installed at the end of the manufacturing line to start the first curing reaction by increasing the temperature to 80 °C and then stop the cross-linking by cooling the material to room temperature again. This step was necessary to increase the viscosity of the continuously reinforced semi-finished material, which allowed for better handling and cutting. Both semi-finished materials were cut into sheets, stacked and molded into plaques of 800 mm x 250 mm on a hydraulic press type COMPRESS PLUS DCP-G 3600/3200 AS by Dieffenbacher (Eppingen, Germany) at 125 bar, approximately 145 °C and 112s mold closing time. DiCo SMC was manufactured with 50 % mold coverage. The semi-finished sheet of 400 mm length and 250 mm width were positioned in the center of the mold to enforce a one-dimensional flow during compression molding. The one-dimensional flow resulted in a preferential fiber orientation. Hybrid CoDiCo SMC was molded in one step, by placing one continuous semi-finished sheet into the mold (100 % mold coverage), followed by a stack of discontinuous material (50 % mold coverage) and another continuous sheet (100 % mold coverage). The direction of the continuous carbon fibers corresponded to the direction of flow of the discontinuous material. A schematic of the compression molding process of CoDiCo SMC is depicted in Figure 1.

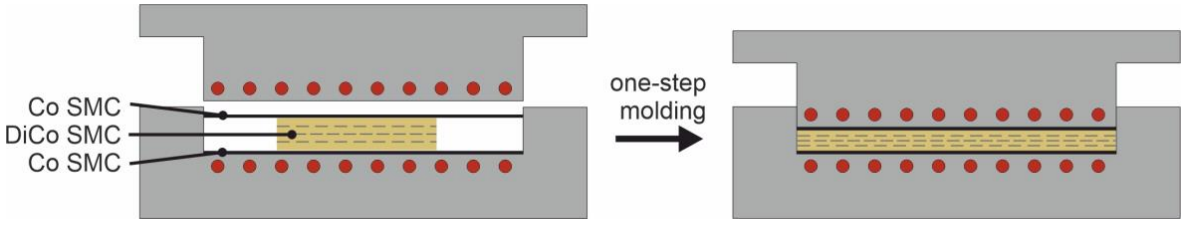

Figure 1 : Manufacturing of CoDiCo SMC plaques in one-step compression molding process. The discontinuous semi-finished material flows in one direction between the two continuous semi-finished plies.

Specimens were extracted from the plaques via waterjet cutting. The thickness of the specimens is depicted in Figure 2. The length was 60 mm and 100 mm for DiCo and CoDiCo SMC, respectively. The width was 15 mm for both materials.

  doi:10.5075/epfl-298799_978-2-9701614-0-0

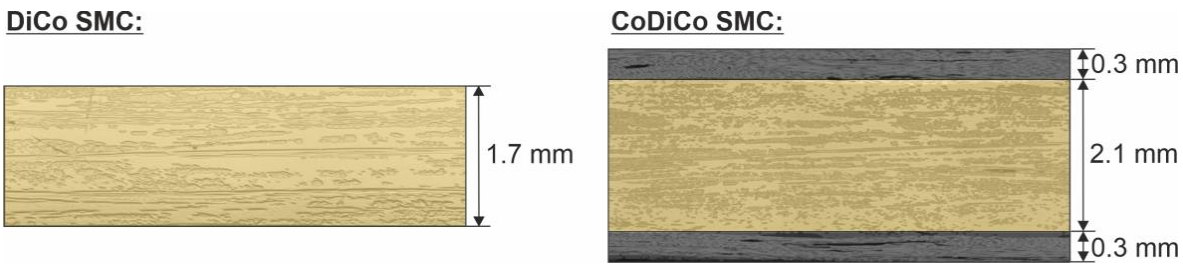

Figure 2: Dimensions of DiCo SMC and CoDiCo SMC specimens.

3. Experimental methods

3-point bending and bending fatigue tests were carried out on an all-electric fatigue test machine type ElectroPuls E3000 by Instron according to ISO 13003 [9] and DIN EN ISO 14125 [10]. The test machine was equipped with a 5 kN load cell. A temperature chamber was installed, which allowed testing at -20 °C, 21 °C and 80 °C. Friction was reduced by applying polytetrafluoroethylene tape onto the lower supports and the loading nose. The span length was 48 mm and 80 mm for DiCo and CoDiCo SMC, respectively. The span lengths were chosen depending on the specimen thicknesses to obtain a constant span-to-thickness ratio of approximately 1:28. Bending tests were carried out under displacement control at fatigue strain rate with a crosshead velocity of 90 mm/s for DiCo SMC and 180 mm/s for the hybrid composite to obtain final failure after around 0.1 s (half a period duration when performing fatigue tests at a frequency of 5 Hz) according to ISO 13003. Bending fatigue tests were carried out under load control with a load ratio of 0.1. The considered loading frequencies were 1 Hz, 5 Hz and 10 Hz. The maximum numbers of cycles was $3.6 \cdot 10^5$, which was due to the size of the liquid nitrogen container that was used for cooling, and due to the long test durations at 1 Hz.

Flexural stresses were determined according to DIN EN ISO 14125 by

$$\sigma = \frac{3FL}{2bh^2} \quad (1)$$

with the force *F*, specimen width *b*, specimen thickness *h* and span length *L*. It should be noted, that the hybrid composite is largely inhomogeneous and the values calculated using Eq. 1 do not represent actual stresses in the plies. These values should only be used to compare the mechanical performance of the different material systems on a macroscopic scale.

4. Results and discussion

4.1 Ultimate flexural strength

The ultimate flexural strength at fatigue strain rate UFS^F of DiCo and CoDiCo SMC are given in Table 1. UFS^F was increased by 76 %, 59 % and 64 % at -20 °C, 21 °C and 80 °C, respectively, due to hybridization.

Table 1: Ultimate flexural strength UFS^F of DiCo and CoDiCo SMC at different temperatures.

	UFS^F (T = -20 °C)	**UFS^F (T = 21 °C)**	**UFS^F (T = 80 °C)**
DiCo SMC	438 MPa ± 60 MPa	425 MPa ± 30 MPa	366 MPa ± 49 MPa
CoDiCo SMC	771 MPa ± 161 MPa	678 MPa ± 81 MPa	602 MPa ± 55 MPa

  doi:10.5075/epfl-298799_978-2-9701614-0-0

4.2 Stress-life data

Stress-life data of DiCo SMC at different temperatures is depicted in Figure 3. The maximum stress is given in MPa on the left y-axis and in percent of UFS^F at 21 °C on the right y-axis. Runouts are marked with arrows and the numbers behind the arrows indicate the number of runouts at -20 °C (blue), 21 °C (yellow) and 80 °C (red). The colored areas are laterally bounded by 10 %- and 90 %-P-S-N curves and shall indicate the scatter range of the data at the different test temperatures.

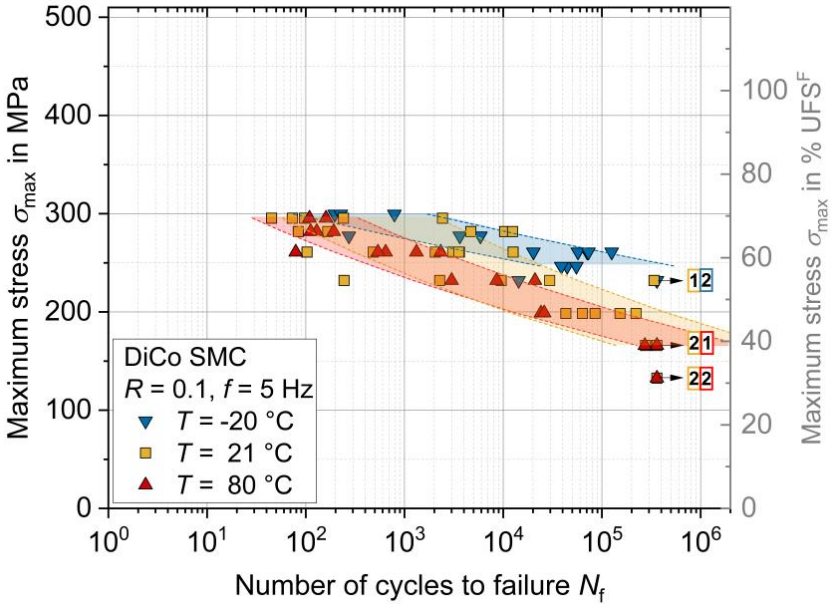

Figure 3: S-N data of DiCo SMC at different temperatures.

The maximum stress, at which no fatigue failure occurred within $3.6 \cdot 10^5$ cycles was 232 MPa (55 % UFS^F) at -20 °C and 132 MPa (31 % UFS^F) at 21 °C and 80 °C. The results at 21 °C and 80 °C are largely similar, with the fatigue strength decreasing by approximately 10 % UFS^F per decade of cycles. The decrease of the fatigue strength per decade of cycles is slightly smaller at -20 °C. The specimens failed due to matrix cracking and pseudo-delamination on the tensile loaded side.

Figure 4 shows the stress-life data of CoDiCo SMC at different temperatures. At 21 °C, fatigue strength decreased by less than 5 % UFS^F per decade of cycles. The material therefore shows a more favorable fatigue behavior than DiCo SMC without continuous reinforcement. However, temperature had a far stronger effect on the fatigue behavior of the hybrid composite than on the fatigue behavior of DiCo SMC. Furthermore, the fatigue behavior of CoDiCo SMC was stronger influenced by temperature than the ultimate flexural strength under monotonic loading. The maximum stress, at which no fatigue failure occurred within $3.6 \cdot 10^5$ cycles was 577 MPa (85 % UFS^F), 475 MPa (70 % UFS^F) and 305 MPa (45 % UFS^F) at -20 °C, 21 °C and 80 °C, respectively. Compared to DiCo SMC, the fatigue strength at $3.6 \cdot 10^5$ cycles has been increased by 149 %, 260 % and 130 % at -20 °C, 21 °C and 80 °C, respectively. The effect of hybridization was therefore higher under fatigue loading than under monotonic loading. The specimens failed due to kinking of the continuous carbon fibers on the compression loaded side. At -20 °C and 21 °C, fracture of the continuous fibers on the tension loaded side followed immediately after the compression loaded ply failed. At 80 °C, the tension loaded ply was still intact after the compression loaded ply failed. However, a stiffness drop of approximately 60 % occurred.

  doi:10.5075/epfl-298799_978-2-9701614-0-0

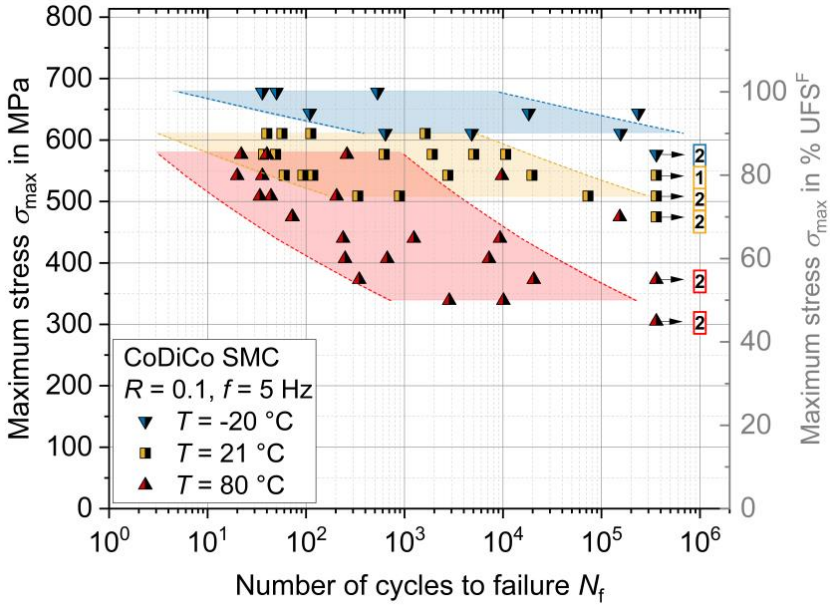

Figure 4: S-N data of CoDiCo SMC at different temperatures.

The influence of frequency on the stress-life data of DiCo and CoDiCo SMC is depicted in Figure 5 and Figure 6, respectively. For both material systems, the fatigue behavior at 1 Hz, 5 Hz and 10 Hz was largely similar. A small effect could be observed in the low cycle fatigue range. One reason for this behavior is the visco-damage behavior of DiCo SMC [11], which results in a higher damage threshold at increased strain rate. This effect is noticeable at short test duration and does not have an effect on the fatigue life in the high cycle fatigue range. It should be noted that the considered frequency range was comparatively small. Especially for the hybrid composite, a frequency dependence is expected at very high frequencies, which would lead to heating of the specimens.

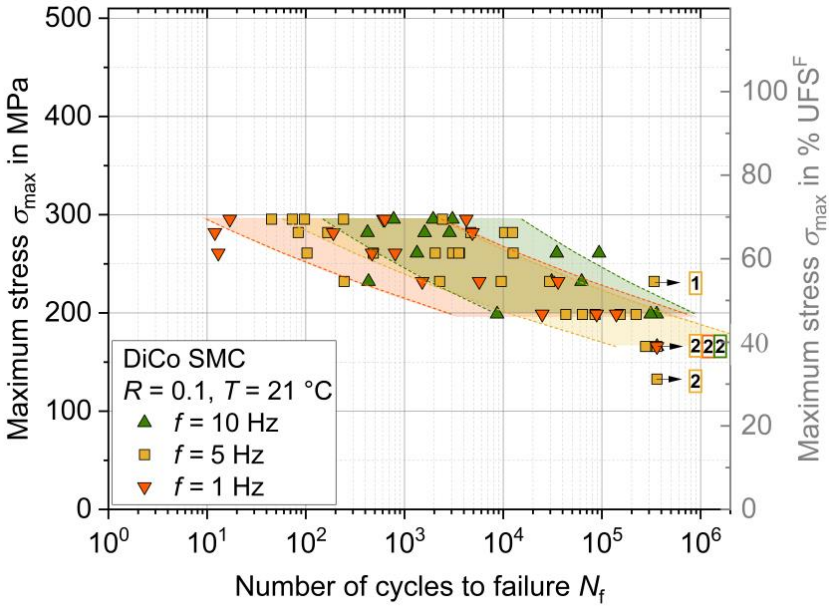

Figure 5: S-N data of DiCo SMC at different loading frequencies.

  doi:10.5075/epfl-298799_978-2-9701614-0-0

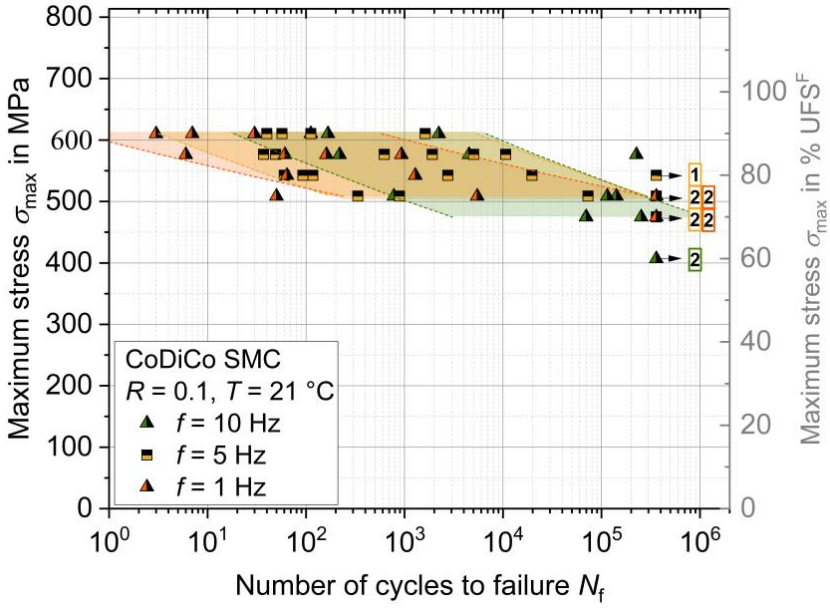

Figure 6: S-N data of CoDiCo SMC at different loading frequencies.

5. Summary and Conclusions

Hybrid CoDiCo SMC showed excellent fatigue properties under bending fatigue load. At a ratio of DiCo glass fiber SMC to continuous carbon fiber SMC of approximately 3:1, the fatigue strength at $3.6 \cdot 10^5$ increased by 260 % compared to DiCo SMC without continuous reinforcement. Positive effects of hybridization were higher under fatigue loading than under monotonic loading. No significant frequency dependence could be observed in the considered range between 1 Hz and 10 Hz for both DiCo and CoDiCo SMC. While the effect of temperature on the fatigue behavior of DiCo SMC was small, the hybrid composite showed a pronounced temperature dependence. This behavior must be considered for potential applications. Since failure of the hybrid composite was characterized by kinking of the continuous carbon fiber ply on the compression loaded side, the influence of temperature is expected to be smaller, if continuous reinforcement is implemented only on the tension loaded side.

6. Acknowledgements

The research documented in this manuscript has been funded by the German Research Foundation (DFG) within the International Research Training Group “Integrated engineering of continuous-discontinuous long fiber reinforced polymer structures” (GRK 2078). The support by the German Research Foundation (DFG) is gratefully acknowledged. The authors also kindly acknowledge the Fraunhofer ICT in Pfinztal, Germany, especially Sergej Ilinzeer, for manufacturing the SMC materials.

7. References

1. Böhlke T, Kärger L, Weidenmann KA, Henning F. Continuous-discontinuous long fiber-reinforced polymer structures: Modeling, characterization and validation. Karlsruhe; 2016. (AFBW AG Composite-Simulation).

2. Trauth A. Characterisation and Modelling of Continuous-Discontinuous Sheet Moulding Compound Composites for Structural Applications. Karlsruhe: KIT Scientific publishing; 2020.
3. Zhou Y, Wang Y, Xia Y, Jeelani S. Tensile behavior of carbon fiber bundles at different strain rates. Materials Letters 2010; 64(3):246–8.
4. Kawai M, Yjima S, Hachinohe A, Takano Y. Off-Axis Fatigue Behavior of Unidirectional Carbon Fiber-Reinforced Composites at Room and High Temperatures. Journal of Composite Materials 2001; 35(7):545–76.
5. Shirinbayan M, Fitoussi J, Meraghni F, Surowiec B, Laribi M, Tcharkhtchi A. Coupled effect of loading frequency and amplitude on the fatigue behavior of advanced sheet molding compound (A-SMC). Journal of Reinforced Plastics and Composites 2017; 36(4):271–82.
6. Denton DL. Mechanical properties characterization of an SMC-R50 Composite. SAE Transactions 1979:2283–94.
7. Tamboura S, Laribi MA, Fitoussi J, Shirinbayan M, Bi RT, Tcharkhtchi A et al. Damage and fatigue life prediction of short fiber reinforced composites submitted to variable temperature loading: Application to Sheet Molding Compound composites. International Journal of Fatigue 2020; 138(4):105676.
8. Bücheler D, Henning F. Hybrid resin improves position and alignment of continuously reinforced prepreg during compression co-molding with sheet molding compound. In: Proceedings of the 17th European Conference on Composite Materials, Munich, Germany; 2016. p. 26–30.
9. ISO 13003. Fibre-reinforced plastics - Determination of fatigue properties under cyclic loading conditions. Geneva, Switzerland: International Organization for Standardization; 2003.
10. DIN EN ISO 14125. Faserverstärkte Kunststoffe - Bestimmung der Biegeeigenschaften. Berlin: Deutsches Institut für Normung e.V., Beuth Verlag GmbH; 2011.
11. Shirinbayan M, Fitoussi J, Meraghni F, Surowiec B, Bocquet M, Tcharkhtchi A. High strain rate visco-damageable behavior of Advanced Sheet Molding Compound (A-SMC) under tension. Composites Part B: Engineering 2015; 82(1):30–41.Mays GC, Hutchinson AR. Adhesives in civil engineering. Cambridge University Press. 1992.

  doi:10.5075/epfl-298799_978-2-9701614-0-0

TENSILE AND FLEXURAL FATIGUE LIVES OF UNIDIRECTIONAL CF/PP COMPOSITES

Taiga Nonaka[a], Masayuki Nakada[b], Yasushi Miyano[b], Yoko Morisawa[b],

Takeharu Isaki[c], Taiki Hirano[c], Kiyoshi Uzawa[b]

a: Graduate School, Kanazawa Institute of Technology
– b1709856@planet.kanazawa-it.ac.jp
b: Materials System Research Laboratory, Kanazawa Institute of Technology
c: Functional Materials Laboratory, Mitsui Chemicals, Inc.

Abstract: *Our proposed accelerated testing methodology (ATM) was applied to the prediction of fatigue strength of unidirectional CF/PP composites (UD-CF/PP) with polypropylene matrix under tension and bending loads. The effects of viscoelastic behavior of matrix resin and repeated loading on the fatigue strength were evaluated. It was found that the fatigue strength of UD-CF/PP showed characteristic behavior depending on the loading direction of tension and bending.*

Keywords: CF/PP; durability; fatigue strength; viscoelasticity; accelerated testing

1. Introduction

Carbon fiber reinforced plastics (CFRP) have been used for primary structural members of airplanes, ships, automobiles, and other vehicles, for which high reliability must be maintained during long-term operation. Therefore, an accelerated testing methodology (ATM) is anticipated strongly for long-term life prediction of CFRP structures exposed to actual environmental temperatures, water, and other influences.

Our earlier reports presented the ATM for predicting the long-term life of CFRP based on the time-temperature superposition principle which holds for matrix resin viscoelasticity [1]. Statistical formulations for scattered time-dependent and temperature-dependent static, creep, and fatigue strengths of CFRP were done based on Christensen's viscoelastic crack kinetics [2].

Recently, Mitsui Chemicals, Inc. has developed a carbon fiber/polypropylene unidirectional sheet (CF/PP UD sheet) using a polyolefin-based sizing agent for carbon fiber. Its effective PP modification provides good compatibility with PP and improves the fiber matrix adhesion. The validity of formulation for the statistical time-dependent and temperature-dependent static and creep strengths was clarified experimentally for tension loading along the longitudinal direction of CF/PP tape. Results clarified that the long-term creep failure time under tension loading can be readily inferred statistically using results obtained from static tests conducted at various temperatures [3].

In this paper, the ATM was applied to the prediction of fatigue strength of unidirectional CF/PP composites (UD-CF/PP) with polypropylene matrix under tension and bending loads. The effects of the number of cycles to failure, temperature, and frequency on the prediction of fatigue strength were evaluated. First, UD-CF/PP tapes and UD-CF/PP laminates made from CF/PP UD sheet as the tension and bending test specimens, respectively. Second, the relaxation moduli of

  doi:10.5075/epfl-298799_978-2-9701614-0-0

the PP matrix resin were measured at various temperatures, and long-term relaxation modulus was obtained based on the time-temperature superposition principle. Third, the static and fatigue strengths were measured under tension and bending loadings at various temperatures. Finally, the viscoelasticity of the matrix resin and the static and fatigue strengths of UD-CF/PP were substituted into the ATM formulation, and the predictions are revealed.

2. Formulations

The formulation of statistical static strength σ_s of CFRP based on the matrix resin viscoelasticity, was presented in an equation in our earlier paper [4], as shown below.

$$\log\sigma_{\mathrm{s}} = \log\sigma_0 + \frac{1}{\alpha}\log[-\ln(1-P_{\mathrm{f}})] + n_{\mathrm{R}}\log\left[\frac{E_{\mathrm{s}}^*(t,T)}{E_{\mathrm{r}}(t_0,T_0)}\right] \tag{1}$$

Therein, P_f signifies the failure probability, t denotes the failure time, t_0 represents the reference time, T stands for the temperature, T_0 stands for the reference temperature, σ_0 and α respectively denote the scale parameter and the shape parameter on the Weibull distribution of static strength. In addition, n_R is the viscoelastic parameter. Therein, E_r and E_s^* respectively represent the relaxation and viscoelastic moduli of matrix resin. The viscoelastic modulus E_s^* for the static load with a constant strain rate is calculated as presented below.

$$E_{\mathrm{s}}^*(t,T) = E_{\mathrm{r}}(t/2\,,T) \tag{2}$$

Statistical creep strength σ_c can be ascertained by shifting the master curve of static strength with log A based on Christensen's theory for viscoelastic crack kinetics [5]. Therefore, the master curve of creep strength can be presented as the following equation [4].

$$\log\sigma_{\mathrm{c}} = \log\sigma_0 + \frac{1}{\alpha}\log[-\ln(1-P_{\mathrm{f}})] + n_{\mathrm{R}}\log\left[\frac{E_{\mathrm{c}}^*(t,T)}{E_{\mathrm{r}}(t_0,T_0)}\right] \tag{3}$$

In this equation, E_c^* represents the viscoelastic modulus for a constant stress.

$$E_{\mathrm{c}}^*(t,T) = E_{\mathrm{s}}^*(At,T) = E_{\mathrm{r}}(At/2\,,T) \tag{4}$$

The shifting amount log A, as ascertained from slope k_R of logarithmic static strength against the logarithmic failure time curve, is calculated using the following equation.

$$\log A = \log\left(1+\frac{1}{k_{\mathrm{R}}}\right), \qquad k_{\mathrm{R}} = n_{\mathrm{R}}m_{\mathrm{R}} \tag{5}$$

Therein, m_R represents the slope of logarithmic relaxation modulus of matrix resin against the logarithmic time curve.

All of parameters for the statistical creep strengths of CFRP shown in Eq. (3) are determined from the viscoelasticity of matrix resin and the statistical static strengths of CFRP and the creep tests are not needed. The failure probability P_f in the case that an arbitrary constant creep stress σ_{c0} is applied at a constant temperature increases monotonically with increasing of the elapsed failure time from Eq. (3) and the scatter of failure time is uniquely determined.

We proposed the formulation of statistical fatigue strength of CFRP, σ_f, based on the matrix resin viscoelasticity, as shown below. The fourth paragraph of right side of this equation is an additional paragraph for considering the damage accumulation by cyclic loading which is determined experimentally

$$\log\sigma_f = \log\sigma_0 + \frac{1}{\alpha}\log[-\ln(1-P_f)] + n_R\log\left[\frac{E_f^*(t,T)}{E_r(t_0,T_0)}\right] - F_f[\log(2N_f)] \quad (6)$$

The viscoelastic modulus E_f^* is calculated using the following equation for the cyclic load for the case in which the stress ratio of the minimum stress/the maximum stress is zero, assuming that the matrix resin deformation in CFRP during cyclic loading is constrained perfectly by carbon fiber rigidity

$$E_f^*(t,T) = \frac{1}{2}\left[E_r\left(\frac{1}{4f},T\right) + E_r\left(\frac{N_f}{f} - \frac{1}{4f},T\right)\right], \quad N_f = ft \quad (7)$$

The fatigue degradation parameter F_f, as a function of the number of cycles to failure N_f, is obtainable by the following polynomial function of $\log(2N_f)$, which is determined based on experimentation

$$F_f[\log(2N_f)] = a[\log(2N_f)] + b[\log(2N_f)]^2 + c[\log(2N_f)]^3 \quad (8)$$

The fatigue strength at N_f = 1/2 is equal to the static strength when failure time t is equal to $1/(2f)$. All of the parameters for the statistical fatigue strengths of CFRP shown in Eq. (6) are determined from the viscoelasticity of matrix resin and the statistical static and fatigue strengths of CFRP. The failure probability P_f in the case that an arbitrary constant maximum stress σ_{fo} is applied at a constant temperature and a constant frequency increases monotonically with increasing of the elapsed failure time or the number of cycles to failure from Eq. (6) and the scatter of failure time is uniquely determined.

3. Testing methods

CF/PP UD sheets with 0.16 mm thick were cut into 2 mm wide and 500 mm long as the tension test specimens. The gage length of tension test specimen is 300 mm. For the bending test, 12 CF/PP UD sheets were stacked to form a 2 mm thick laminate, and then cut into 15 mm wide and 100 mm long specimens. The span of the three-point bending is 80 mm. Both tension and bending tests were performed under various temperatures at a displacement rate of 2 mm/min for static tests and at a frequency of 2 Hz and a stress ratio of 0.1 for fatigue tests.

4. Results and discussion

4.1 Relaxation modulus of matrix resin

Relaxation modulus of polypropylene (PP) was measured at various temperature. Figure 1 shows the long-term relaxation modulus for PP which were obtained by shifting measured data at

various temperatures along the log scale of time and log scale of relaxation modulus until they overlapped each other based on the time-temperature superposition principle. Figure 2 shows the time-temperature shift factor (horizontal shift) and temperature shift factor (vertical shift) for the master curve of relaxation modulus.

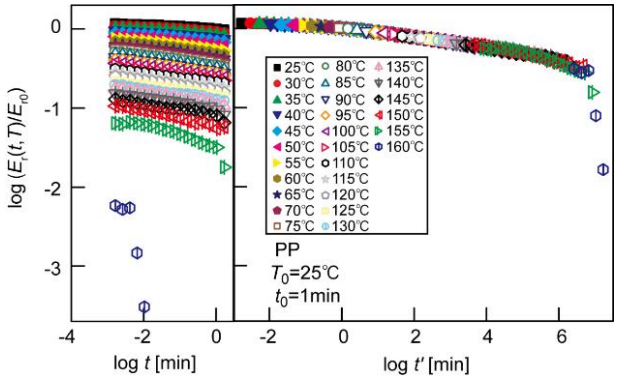

Figure 1. Master curve of relaxation modulus for PP

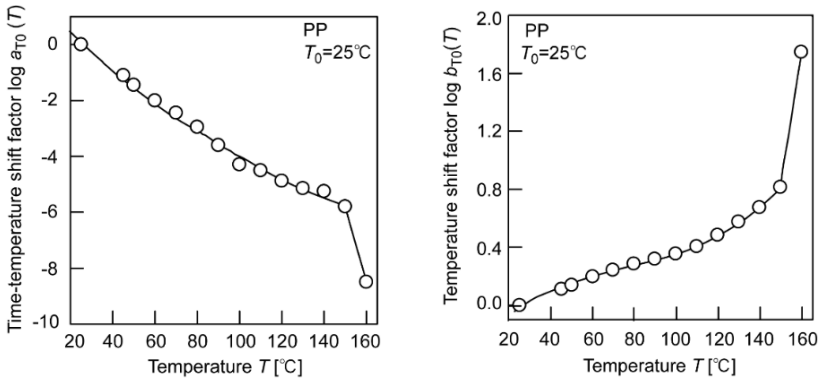

Figure 2. Time-temperature shift factor and temperature shift factor

4.2 Determination of strength parameters of CFRP composites by static tests

Static tension and bending tests for UD-CF/PP were conducted at various temperatures. Figure 3 shows the static strength versus temperature. The static strengths decrease markedly with increasing temperature. The temperature dependence on static strength is different with loading type, tension and bending.

The Weibull distributions for static strength at various temperatures are depicted in Fig.4 for the UD-CF/PP. In this figure, α is the shape parameter and β is the scale parameter. Although the scale parameter decreases according to the temperature rise, the shape parameter maintains an almost constant value for the UD-CF/PP to the temperature rise. Shape parameter α and scale parameter β at temperature T = 25°C in this figure can be inferred as shape parameter α, scale parameter σ_0 of static strength at the reference temperature T_0 = 25°C, and the reference failure time t_0 = 1 min used in Eq. (1).

Figure 5 portrays the dimensionless static strengths of UD-CF/PP σ_s/σ_0 against the dimensionless viscoelastic modulus of PP E_s^*/E_{r0}. The relation of σ_s/σ_0 against E_s^*/E_{r0} can be represented as a straight line with slope of n_R, which is the viscoelastic parameter in Eq. (1). The parameter n_R is different with loading type, tension and bending.

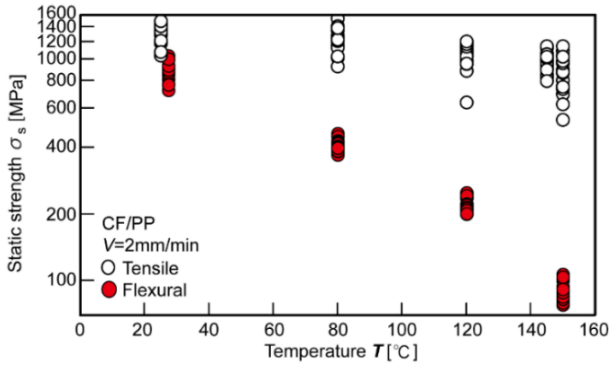

Figure 3. Static strength of UD-CF/PP against temperature

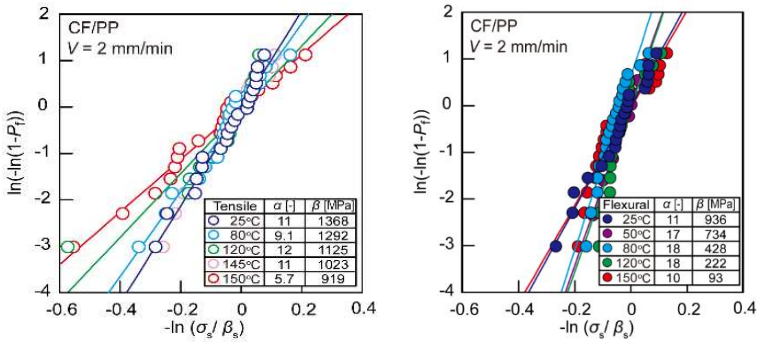

(a) Tension (b) Bending

Figure 4. Weibull distribution for static strength of UD-CF/PP

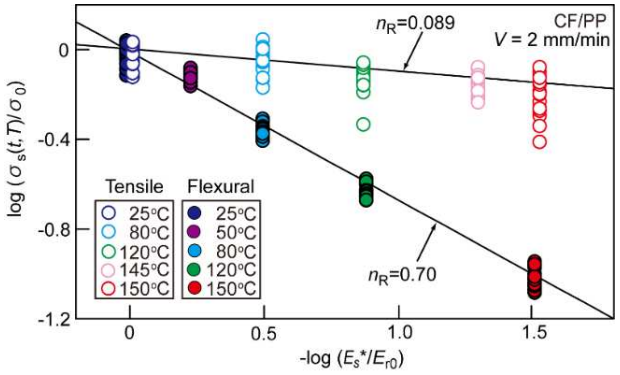

Figure 5. Determination of viscoelastic parameter n_R

  doi:10.5075/epfl-298799_978-2-9701614-0-0

4.3 Fatigue strengths of CF/PP composites

Fatigue tests of UD-CF/PP were conducted for several constant stress levels, at a constant temperature and at a constant frequency, respectively. Figure 6 shows the fatigue strength against number of cycles to failure under tension and bending load. There is no decrease in strength with changes in temperature and frequency under tension load. On the other hand, the strength decreases with changes in temperature and frequency under bending load.

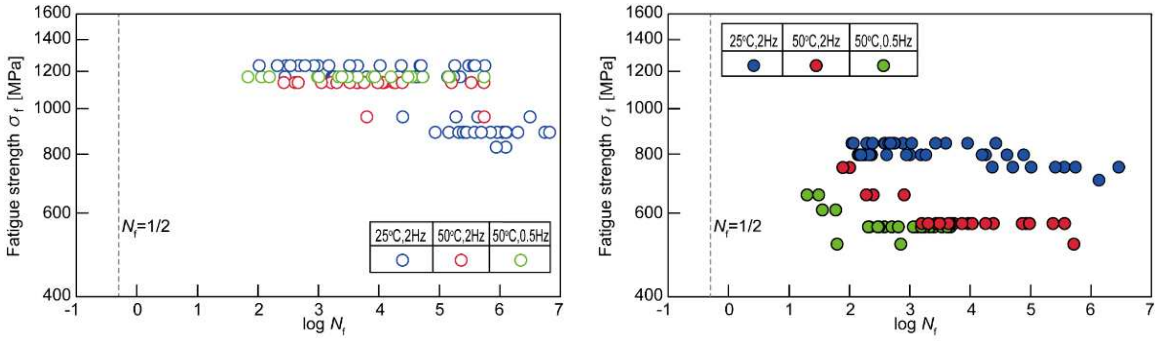

(a) Tension (b) Bending

Figure 6. Fatigue strength against number of cycles to failure of UD-CF/PP

The dimensionless fatigue strength defined by the following equation can be easily derived from Eq. (6).

$$\log S_{\mathrm{f}} = \log\frac{\sigma_{\mathrm{f}}}{\sigma_0} - n_{\mathrm{R}}\log\left[\frac{E_{\mathrm{f}}^{*}(t,T)}{E_{\mathrm{r}}(t_0,T_0)}\right] = \frac{1}{\alpha}\log[-\ln(1-P_{\mathrm{f}})] - F_{\mathrm{f}}[\log(2N_{\mathrm{f}})] \tag{9}$$

This equation means that the relations between the dimensionless fatigue strengths S_{f} and the number of cycles to failure N_{f} obtained by substituting the measured data into the middle side of this equation constitutes the dimensionless statistical S-N master curve shown in the right side of this equation.

Figure 7 presents the relation between the dimensionless fatigue strength S_{f} and the number of cycles to failure N_{f}. This relation clarifies only one curve that is independent of temperature and frequency for tension load. However, for bending load, the dimensionless fatigue strength depends on temperature and frequency.

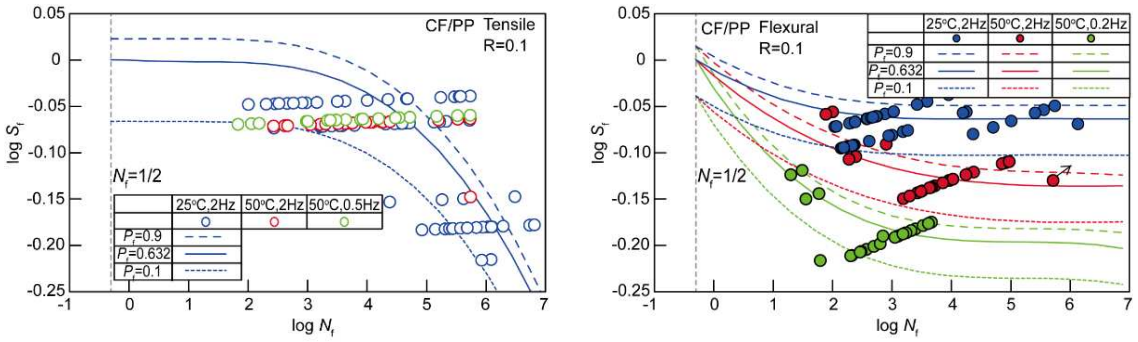

(a) Tension (b) Bending

Figure 7. Non-dimensional fatigue strength against number of cycles to failure of UD-CF/PP

4.4 Prediction of fatigue strength for CF/PP composites

The strength reduction that appears in fatigue strength includes several factors. Figure 8 represents those strength reductions. Strength reduction *A* is attributed to viscoelasticity under tension and bending loadings, while strength reduction *B* is attributed to cyclic loading as obtained from fatigue test results at a test temperature of 25°C and a frequency of 2 Hz. From this figure, it can be found that the effect of viscoelasticity is small under tensile loading and the effect of cyclic loading is large. On the other hand, under bending load, the effect of viscoelasticity is large and the effect of cyclic loading is small. It can be inferred that the difference in strength reduction with loading direction shown in Fig.8 is due to the difference in fracture mechanism. Under tension loading, the failure is the accumulation of fiber breakage, and under bending loading, the failure is triggered by micro-buckling of carbon fibers. By substituting the parameters calculated from each test into Eq (6), the fatigue life at 25°C can be represented as shown in Fig.9.

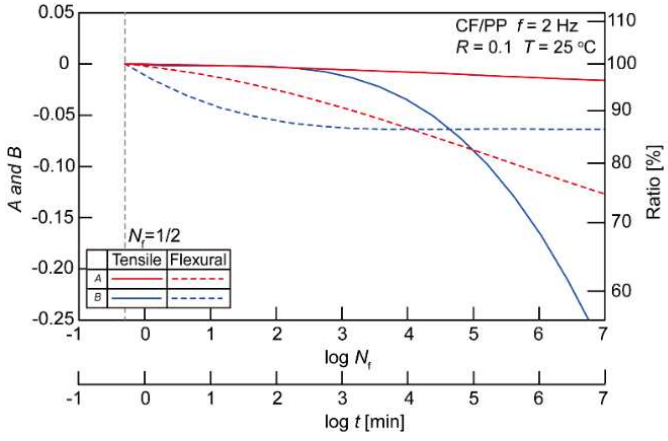

Figure 8. Effects of viscoelasticity and repeated loading on fatigue strength of UD-CF/PP

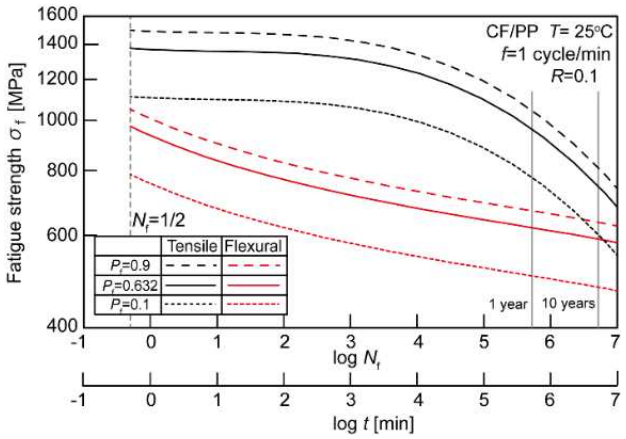

Figure 9. Prediction of fatigue strength of UD-CF/PP

5. Conclusion

In this study, fatigue tests of unidirectional CF/PP composites under tension and bending loadings were conducted to investigate fatigue life prediction of unidirectional CF/PP composites. Long-term fatigue life was determined from the viscoelastic properties of the polypropylene neat resin and the static and fatigue strengths of the unidirectional CF/PP composite. It was found that the fatigue strength of unidirectional CF/PP composites showed characteristic behavior depending on the loading direction in tension and bending due to the fracture mechanism.

References

1. Nakada M and Miyano Y. Advanced accelerated testing methodology for long-term life prediction of CFRP laminates. *J composite Materials* 2015; 49: 163-175.
2. Christensen RM and Miyano Y. Stress Intensity Controlled Kinetic Crack Growth and Stress History Dependent Life Prediction with Statistical Variability. *Int J Fracture* 2006; 137: 77-87.
3. Nakada M, Miyano Y, Morisawa Y, Isaki T, Hirano T and Uzawa K. Statistical life prediction of unidirectional carbon fiber/polypropylene tape under creep tension load. *J Reinforced Plastics and Composites* 2020; 39: 278–284.
4. Miyano Y and Nakada M. Accelerated testing methodology for durability of CFRP, Composites Part B 2020; 191: 107977.
5. Christensen R and Miyano Y. Stress Intensity Controlled Kinetic Crack Growth and Stress History Dependent Life Prediction with Statistical Variability. International Journal of Fracture 2006; 137: 77–87.

  doi:10.5075/epfl-298799_978-2-9701614-0-0

EXPERIMENTAL INVESTIGATION ON FATIGUE DAMAGE GROWTH IN THIN-PLY OPEN-HOLE COMPOSITE LAMINATES UNDER TENSION

Ryoma, Aoki[a], Ryo, Higuchi[b], Tomohiro Yokozeki[c]

a: Department of Aeronautics and Astronautics, The University of Tokyo, Tokyo 113-8656, Japan.
Email: r.aoki@aastr.t.u-tokyo.ac.jp
b: Department of Aeronautics and Astronautics, The University of Tokyo, Tokyo 113-8656, Japan.
c: Department of Aeronautics and Astronautics, The University of Tokyo, Tokyo 113-8656, Japan.

Abstract: *In this study, open-hole tensile fatigue tests are conducted on CFRP laminates with different ply thicknesses (thin- and thick-ply) to investigate the effects of ply thickness. Fatigue tests are conducted at several stress levels, and fatigue damage growth around a circular hole was examined by evaluating the stiffness degradation and observing the internal damage via X-ray radiography. In addition, static tensile tests were conducted on the fatigued specimens to evaluate the effects of the fatigue damage on the residual strength after fatigue. The evaluation of fatigue damage growth and residual strength indicated that the thin-ply composites have suppressed the fatigue damage in the stress concentration region, and maintained the open-hole tensile strength even though the multiple cracks occurred in the circular hole.*

Keywords: Thin-ply composites; Fatigue; Damage observation; Residual strength after fatigue

1. Introduction

In recent years, thin-ply carbon fiber reinforced polymer (CFRP) prepregs manufactured using tow-spreading technology [1] are increasingly investigated as a structural material for future aircraft owing to their ability to improve design flexibility in composite structures. Thinning a single layer of a composite laminate increases the number of layers, facilitating the selection of ply thicknesses and fiber orientations that were previously unavailable, thereby increasing the degree of design freedom. In the future, the combination of thin-ply and automated fiber placement technologies is expected to enable designs with continuously varying ply thicknesses, fiber orientation, and other factors.

Thin-ply CFRP laminates are known to improve non-hole tensile (NHT), non-hole compressive, and open-hole compressive strengths owing to the suppression of cracking and delamination [1–7]. However, studies have reported that the use of thin-ply materials decreases the strength in open-hole tensile (OHT) tests [1,2,4,5,8]. As the impact of ply thickness on damage accumulation (cracks and delamination) and the ultimate strength of laminates is significant, it should be considered for the analysis. Additionally, the effect of ply thickness on fatigue damage growth should be examined because aircraft structures are subjected to cyclic loading during long-term operations. Sihn et al. [1] and Amacher et al. [4] have reported that OHT specimens with thin-ply can effectively suppress damage under fatigue loading. Although the evaluation of the degree of strength loss after fatigue is essential for long-term operations, the residual strength of thin CFRP laminates has not been investigated sufficiently. Therefore, the effect of

  doi:10.5075/epfl-298799_978-2-9701614-0-0

ply thickness on damage propagation under fatigue loading and the residual strength after fatigue requires further analysis.

In this study, fatigue tests were performed on two types of open-hole CFRP laminates with different ply thicknesses to experimentally evaluate the effect of ply thickness on fatigue damage propagation caused by circular holes. Quasi-isotropic (QI) laminates with ply thicknesses of 0.05 and 0.2 mm were subjected to OHT fatigue tests. Internal damage at each fatigue cycle was observed using X-ray radiography to evaluate the effect of ply thickness on the amount of stiffness reduction. Additionally, fatigue tests were performed at several stress levels to compare the crack and delamination propagation under each condition. Residual strength evaluation tests were performed on specimens that did not fail despite the maximum fatigue cycle. Furthermore, quasi-static loading was applied to the specimens to evaluate the effect of fatigue damage in the circular hole on the OHT strength.

2. Open-hole tensile fatigue tests

2.1 Test procedure

Figure 1 shows the schematic of the OHT specimens used in this study: Aluminum tabs 45 mm long and 2 mm thick were used for fatigue tests. As shown in Table 1, the specimens were fabricated using 0.05 mm-thick thin-ply prepregs, and two types of QI laminates with different ply thicknesses of 0.05 mm and 0.2 mm were prepared, as listed in Table 1. Static strengths previously obtained by the authors [8] are also shown in Table 1.

Tensile fatigue tests were performed under load control using the hydraulically driven testing machine Instron 8802. The maximum load of fatigue loading P_{max} is determined by setting the stress level based on the static strength in Table 1. Table 2 summarizes the stress levels and the maximum stresses for the fatigue tests conducted in this study. The stress ratio ($R = P_{min}/P_{max}$) and frequency of the fatigue waveform were set to 0.1 and 5 Hz, respectively. The maximum number of cycles of fatigue loading was set to 500,000 cycles, and fatigue loading was applied until failure or reaching maximum cycles.

Two fatigue tests were conducted at each stress level: one of which was an interrupted test for damage observation, and the other was continuously subjected to fatigue loading up to the maximum cycles. In the interrupted test, the fatigue test was stopped after each predetermined cycle, and then the specimen was unloaded. After the specimen was removed from the testing machine, X-ray images were acquired using a soft X-ray radiography system. A zinc iodide penetrant was inserted into the circular hole of the specimen. After the X-ray images were obtained, the specimens were mounted on the testing machine and subjected to fatigue loading again.

This study evaluates the degradation in laminate stiffness due to accumulated fatigue damage in OHT specimens, and the difference in stiffness reduction with ply thickness is discussed. The stiffness of the laminate to be evaluated is defined as follows, using the maximum and minimum fatigue loads P_{max} and P_{min} and the corresponding displacements δ_{max} and δ_{min}, respectively.

$$\text{Stiffness} = \frac{P_{max} - P_{min}}{\delta_{max} - \delta_{min}} \quad (1)$$

  doi:10.5075/epfl-298799_978-2-9701614-0-0

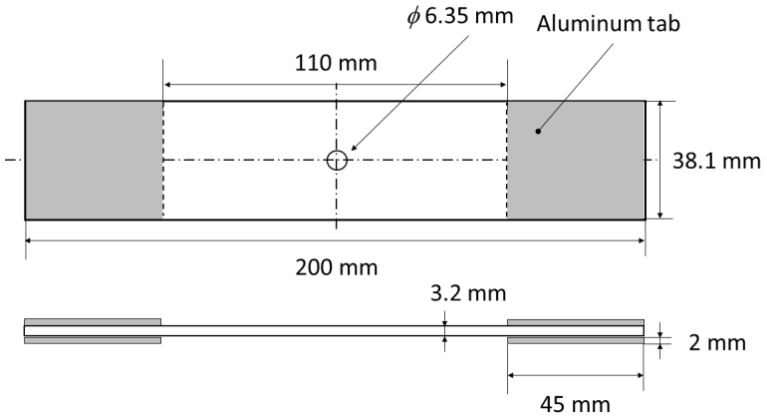

Figure 1. Schematic of open-hole specimen for fatigue tests.

Table 1: Lists of laminate layups: ply thickness and static strength [8].

Type	Layup	Ply thickness [mm]	Static strength [MPa]
QI-1	$[45/0/-45/90]_{8S}$	0.05	490.1
QI-4	$[45_4/0_4/-45_4/90_4]_{2S}$	0.2	532.4

Table 2: Lists of fatigue test conditions.

Type	Target stress level, applied maximum stress		
QI-1	80%, 392 MPa	70%, 343 MPa	50%, 245 MPa
QI-4	80%, 426 MPa	70%, 373 MPa	50%, 266 MPa

2.2 Fatigue test results: Stiffness degradation behavior

The stiffness obtained from the fatigue tests on QI laminates with ply thicknesses of 0.05 mm and 0.2 mm is shown in Figure 2. The stiffness values are plotted as normalized stiffness by the initial stiffness of the first cycle. In the case of laminate QI-1 with a ply thickness of 0.05 mm, stiffness decreased from 50,000 to 100,000 cycles under three stress level conditions, with little decrease in stiffness thereafter. The specimen did not fail by the maximum number of cycles in all conditions, and the amount of stiffness reduction was approximately 5% at the maximum cycles.

In the case of laminate QI-4 with a ply thickness of 0.2 mm, one of the two specimens failed after 350,000 cycles at a stress level of 80%. In the 50% condition, stiffness decreased until 50,000 cycles, and the stiffness degradation was saturated thereafter. Conversely, in the 80% condition, stiffness decreased rapidly up to 100,000 cycles and then decreased slowly thereafter until final failure. The stiffness at the maximum cycles was 30% lower than the initial stiffness in the 70% and 80% conditions. It was confirmed that the stiffness reduction behavior changes significantly with stress level in the case of thick-ply composite laminates.

  doi:10.5075/epfl-298799_978-2-9701614-0-0

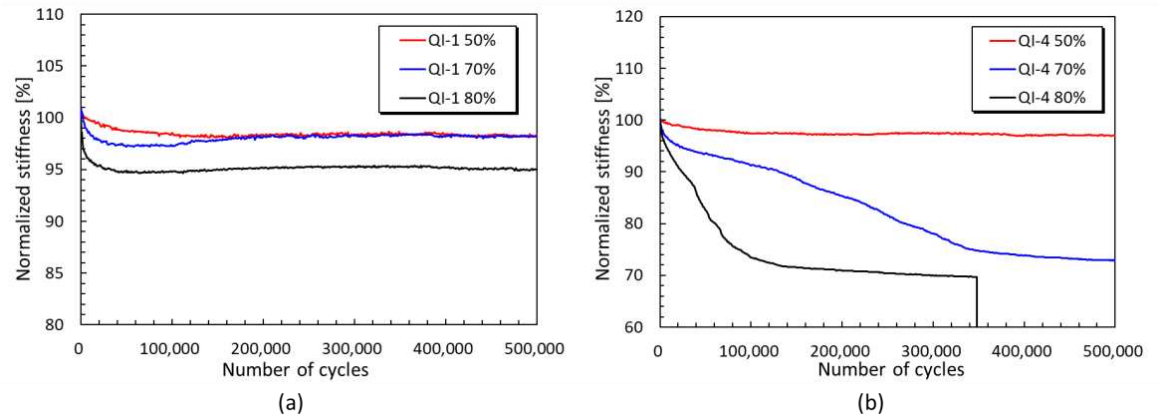

Figure 2. Typical stiffness degradation of open-hole specimens: ply thickness (a) 0.05 mm and (b) 0.2mm.

2.3 Fatigue test results: Damage observation

Figures 3 and 4 depict X-ray images of laminates QI-1 and QI-4, respectively. In the case of a ply thickness of 0.05 mm shown in Figure 3, no cracks or delamination occurred during the first cycle. At 50,000 cycles, multiple cracks occurred in the 90° and ±45°-layers and the 0°-layer splitting also developed. From 50,000 cycles to 500,000 cycles, there was little increase in the number of cracks, with only a slight extension of the cracks occurring at 50,000 cycles, and the cracks were generated only from the edge of the circular hole.

In the case of a ply thickness of 0.2 mm, several 90°-layer cracks were observed from the circular hole during the first cycle. At stress levels of 70% and 80%, ±45°-layer cracks and 0°-layer splitting were also observed to occur significantly. At the 50% stress level, the cracks were distributed in adjacent layers along with the extension of one crack. On the other hand, at the 80% stress level, where the stiffness decreases rapidly by 100,000 cycles, the cracks and delamination propagated to the edges in the width direction at the 50,000 cycles. At maximum cycles, 0°-layer splitting and delamination had propagated from the circular hole to the edges of the specimen, the cracks were almost fully penetrated.

Finally, Figure 5 shows an X-ray image of the entire specimen of laminate QI-4 with a ply thickness of 0.2 mm at the maximum cycles. As shown in the figure, at a stress level of 50%, cracks and delamination originating from the circular hole did not reach the edges of the specimen and remain in the circular hole. In addition to the circular hole, cracks and delamination in the 90-degree layer from the free edge can also be observed. On the other hand, under the 70% and 80% stress level conditions, the cracks and delamination propagated over the entire specimen, indicating that the 0°-layer splitting reaches the tabs of the specimen. In addition to the splitting extending from the circular hole, there were also numerous longitudinal cracks in the 0°-layers. These numerous cracks in the 0°-layers and delamination throughout the specimen were considered to lead to the rapid stiffness reduction observed in Figure 2

  doi:10.5075/epfl-298799_978-2-9701614-0-0

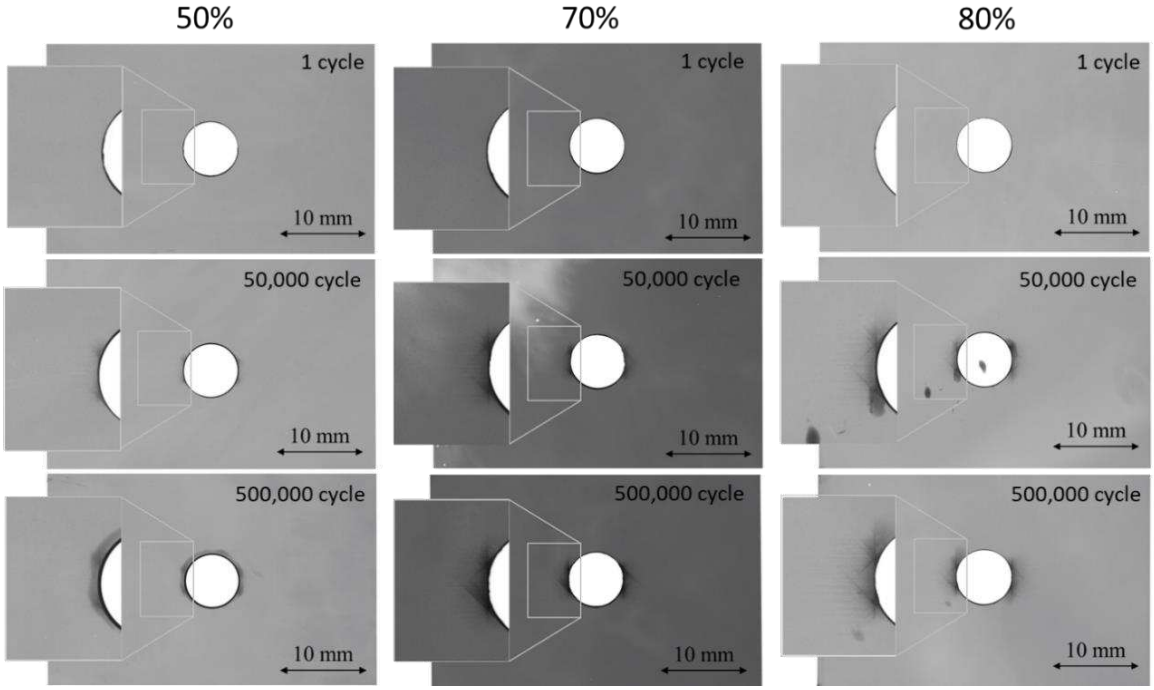

Figure 3. X-ray images of laminate QI-1 at 1, 50,000, and 500,000 cycles under 50%, 70%, and 80% conditions.

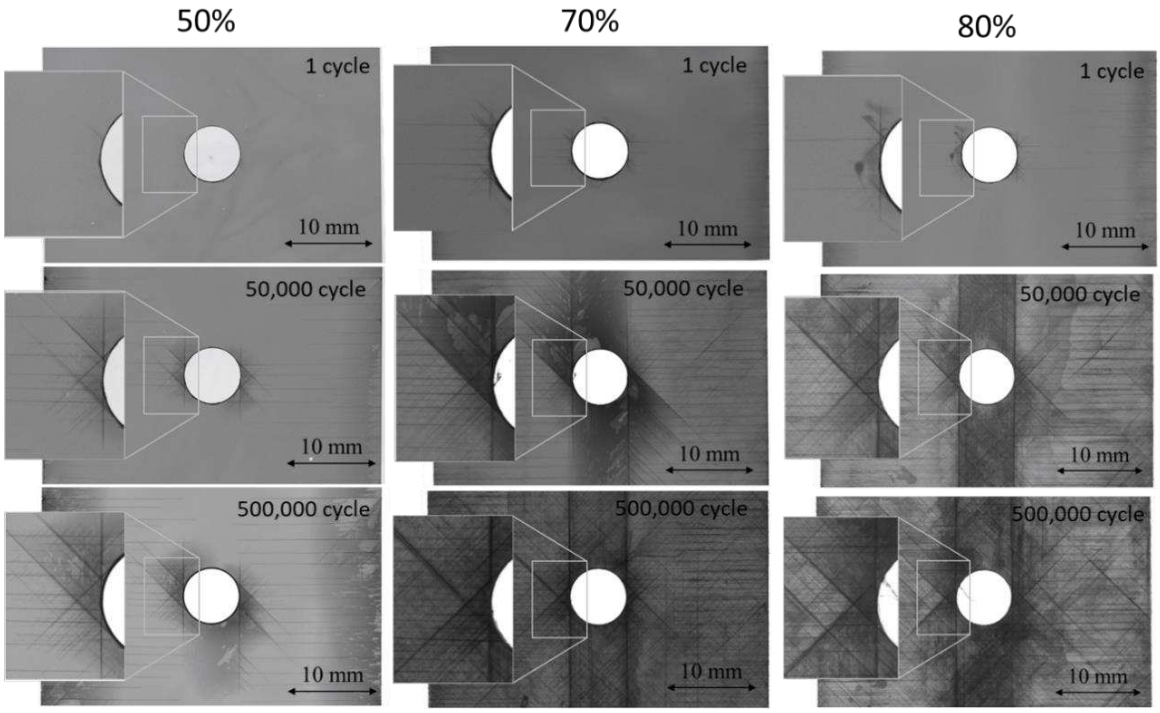

Figure 4. X-ray images of laminate QI-4 at 1, 50,000, and 500,000 cycles under 50%, 70%, and 80% conditions.

  doi:10.5075/epfl-298799_978-2-9701614-0-0

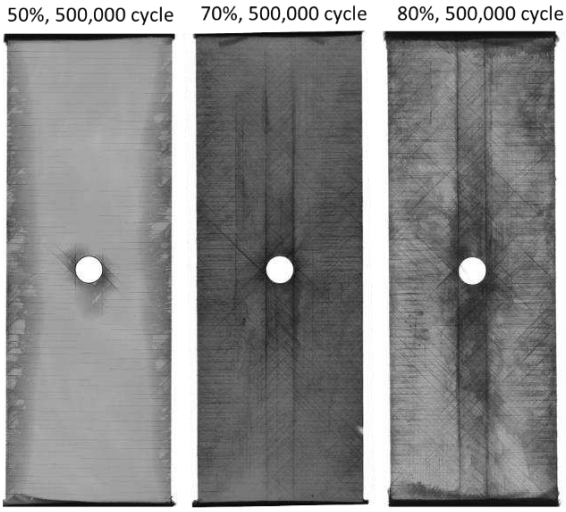

Figure 5. X-ray images of entire specimens of laminate QI-4.

3. Evaluation of residual strength after fatigue

3.1 Test procedure

To evaluate the residual strength after fatigue, the OHT tensile test was conducted in accordance with JIS K7094 [9]. OHT specimens after fatigue testing were subjected to quasi-static tensile loading at a constant displacement rate of 1.0 mm/min until failure using Instron 8802.

3.2 Results and discussion

The residual strength values obtained from the tensile tests on laminates with ply thicknesses of 0.05 mm and 0.2 mm are shown in Figure 6, with the static strength. As shown in Figure 6(a), the residual strength of the laminate with a ply thickness of 0.05 mm was comparable to the static tensile strength at all stress levels after fatigue. The failure mode was a brittle failure without cracks or delamination except at the failed region, which was similar to the static failure without fatigue. These fatigue cracks did not essentially alter the OHT strength or failure modes. Therefore, it is considered that fatigue damage in the circular hole did not have enough effect to alleviate the stress concentration and increase the OHT strength in the thin-ply composites.

In the case of a ply thickness of 0.2 mm, the residual strength after fatigue increased for the 50% stress level condition, was similar for the 70%, and decreased for the 80% condition, compared to the static strength values, as shown in Figure 6(b). The failure mode for the 50% condition was similar to those in the static test: failure with cracks and delamination at the circular hole. However, the entire specimen failed in the 70% and 80% conditions. The residual strength at the 50% stress level exceeding the static strength is presumably the result that the fatigue-induced-cracks relieved the stress concentration in the circular hole. The fatigue cracks propagated further than the cracks just before failure in the static test, resulting in delayed failure and increased OHT strength. Under the 80% stress level condition, cracks on the ±45° and 90°-layers propagated throughout the specimen after the fatigue test, and delamination had developed to the entire specimen, suggesting that almost only the 0° layer was capable of carrying the load. In addition, as shown in Figure 5, many longitudinal cracks in the 0°-layer induced the degradation of the 0°-layer tensile strength after fatigue, which is the reason why the residual strength after fatigue was lower than the static strength.

  doi:10.5075/epfl-298799_978-2-9701614-0-0

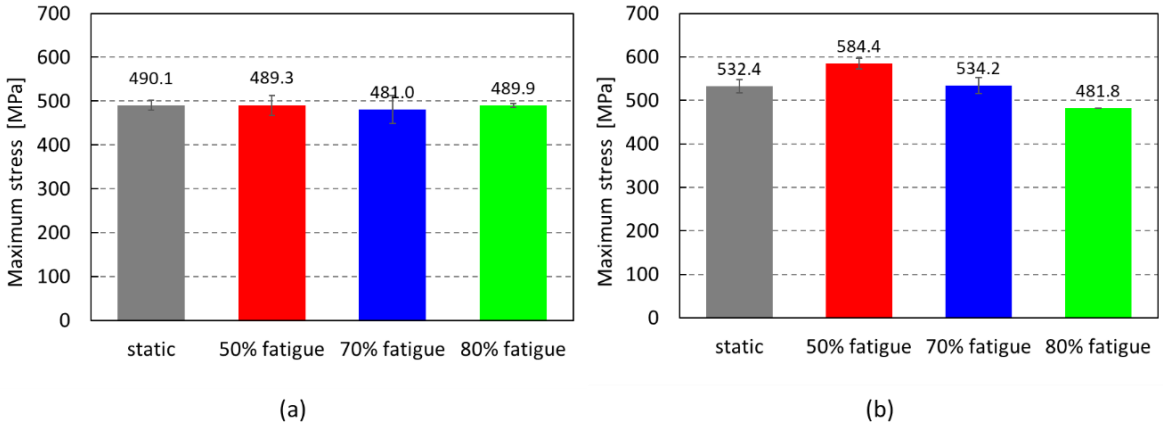

Figure 6. Residual strength after fatigue: (a) laminate QI-1 and (b) QI-4.

4. Concluding remarks

In this study, OHT fatigue tests were conducted on two types of CFRP laminates with different ply thicknesses to experimentally investigate the effect of ply thickness on fatigue damage growth. fatigue tests were performed under three different stress levels to evaluate the stiffness degradation due to fatigue loading, and internal damage was observed by X-ray radiography. The differences in fatigue damage growth due to ply thickness were compared and discussed.

Fatigue test results showed that the thin-ply case (0.05 mm ply thickness) resulted in a stiffness loss of about 5% at the maximum fatigue cycles, even under high-stress level conditions, and that the cracks that occurred were confined to the circular hole. On the other hand, for the thick-ply case (0.2 mm ply thickness), cracks and delamination were observed throughout the specimen under the high-stress level condition, and a significant decrease in stiffness was observed.

Evaluation tests for residual strength after fatigue showed that for the ply thickness of 0.2 mm, the residual strength increased after fatigue at low-stress levels, but decreased after high fatigue loading. In the case of the ply thickness of 0.05 mm, the residual strength was maintained even at high-stress levels, confirming the superiority of thin-ply CFRP in fatigue damage suppression and residual strength properties.

Acknowledgements

This work was carried out under the financial support of JSPS Grant No. 20J13151, and the Japan Science and Technology Agency through the Cross-ministerial Strategic Innovation Promotion Program (SIP) “Materials Integration for Revolutionary Design System of Structural Materials”.

5. References

1. Sihn S, Kim RY, Kawabe K, Tsai SW. Experimental studies of thin-ply laminated composites. Composites Science and Technology 2007;67:996–1008.

  doi:10.5075/epfl-298799_978-2-9701614-0-0

2. Yokozeki T, Aoki Y, Ogasawara T. Experimental characterization of strength and damage resistance properties of thin-ply carbon fiber/toughened epoxy laminates. Composite Structures 2008;82:382–9.
3. Yokozeki T, Kuroda A, Yoshimura A, Ogasawara T, Aoki T. Damage characterization in thin-ply composite laminates under out-of-plane transverse loadings. Composite Structures 2010;93:49–57.
4. Amacher R, Cugnoni J, Botsis J, Sorensen L, Smith W, Dransfeld C. Thin ply composites: Experimental characterization and modeling of size-effects. Composites Science and Technology 2014;101:121–32.
5. Huang C, Ju S, He M, Zheng Q, He Y, Xiao J, et al. Identification of failure modes of composite thin-ply laminates containing circular hole under tension by acoustic emission signals. Composite Structures 2018;206:70–9.
6. Takamoto K, Ogasawara T, Kodama H, Mikami T, Oshima S, Aoki K, et al. Experimental and numerical studies of the open-hole compressive strength of thin-ply CFRP laminates. Composites Part A: Applied Science and Manufacturing 2021;145:106365.
7. Aoki R, Higuchi R, Yokozeki T, Aoki K, Uchiyama S, Ogasawara T. Damage-mechanics mesoscale modeling of composite laminates considering diffuse and discrete ply damages: effects of ply thickness. Composite Structures 2021;277:114609.
8. Aoki R, Higuchi R, Yokozeki T, Aoki K, Uchiyama S, Ogasawara T. Effects of ply thickness and 0°-layer ratio on failure mechanism of open-hole and filled-hole tensile tests of thin-ply composite laminates. Composite Structures 2022;280:114926.
9. JIS K7094. Test method for open-hole tensile strength of carbon fibre reinforced plastic. Tokyo: Japanese Standards Association; 2012.

  doi:10.5075/epfl-298799_978-2-9701614-0-0

INFLUENCE OF VISCOELASTICITY ON FATIGUE BEHAVIOUR OF SHORT FIBRE REINFORCED POLYMERS DEPENDING ON MEAN STRESS AND FIBRE ORIENTATION

Gabriel, Stadler[a], Andreas Primetzhofer[b], Gerald Pinter[a,b], Florian Grün[c]

a: Montanuniversity Leoben - Chair of Materials Science and Testing of Polymers – gabriel.stadler@unileoben.ac.at
b: Polymer Competence Center Leoben
c: Montanuniversity Leoben - Chair of Mechanical Engineering

Abstract: *To realize lightweight vehicles, a wider portfolio of materials is necessary, including different types of short fibre reinforced polymers. These polymers are (depending on the application) high performance polymers, like PEEK, construction polymers, like PPA or standard polymers like PP. All of these materials are exposed to fatigue and static loads during their service life. Since static loads have a main share during a service life, these loads and their influences should be considered in lifetime estimation. To investigate this behaviour, the specimens have been loaded with a sequence of static and fatigue loads. These tests have been performed on short fibre reinforced PP and PEEK to get the influence of viscoelasticity on the fatigue behaviour for different types of polymers, including fibre orientation and mean stress. The results show an influence of the fibre orientation as well as mean stress on the fatigue behaviour depending on the static loads.*

Keywords: fatigue; short fibre reinforced polymers; viscoelasticity; mean stress; fibre orientation

1. Introduction

Changing technologies, like electro mobility offer a lot of possibilities for a novel idea of a vehicle. This idea includes power transmission systems as well as new materials for different applications. But also, combustion engine powered vehicles are need to be improved in the near future. One action for such an optimisation is to build lightweight cars. Therefore, a specific use of materials is necessary. So, a focus is on lightweight materials, like short fibre reinforced polymers and their performance. Especially, a knowledge about the fatigue behaviour is important to estimate a service life under common operational conditions. The fatigue behaviour has been investigated previously and published several times. These investigations dealt mainly with influence factors like, temperature [1], mean stress [2], notches [3] and fibre orientation [4]. However, none of them captured viscoelasticity and the influence on the fatigue behaviour. There are publications available, which treat with the development of the viscoelastic material behaviour during cyclic loading [5, 6]. Since viscoelasticity has also a main influence on the lifetime, this material behaviour should be considered in the lifetime estimation [7].

  doi:10.5075/epfl-298799_978-2-9701614-0-0

2. Test methodology

2.1 Specimens and materials

For these tests, PEEK with 30% of short carbon fibre by weight (VESTAKEEP® 2000 CF30) and PP with 40% of short glass fibre were investigated. These materials were chosen to get mainly the influence of the matrix beneath and above the glass transition temperature. Moreover, different types of fibres were used to increase the gap between these materials in material stiffness and strength. For the PEEK material, bone shaped specimens were milled out of the plates (Figure 1 (left)). So, two different fibre orientations can be captured. For the PP-GF40, a rotating bending specimen was used (Figure 1 (right)). These specimens were produced by injection moulding and were used previously for similar investigations [8, 9] and serve as a reference [7].

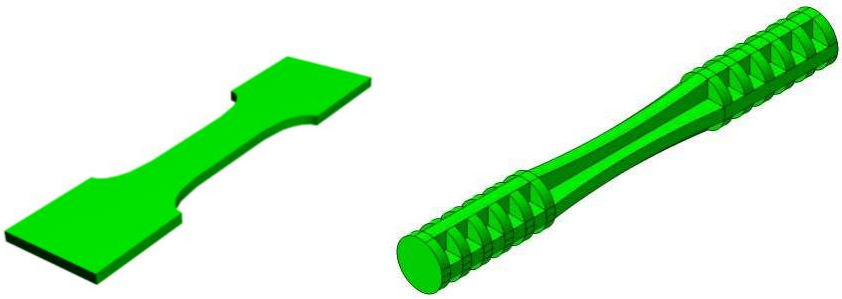

Figure 1. Illustration of short specimen and rotating bending specimen

2.2 Test machines and load sequences

The PP-GF40 specimens were tested on a hydraulic test rig MTS 810 and the PEEK-CF30 specimens on an electrodynamic test rig BOSE AT3550. A temperature of 23°C and a relative humidity of 50% were the ambient conditions for these tests. The load sequence was a combination of cyclic loads at a specific R-ratios and static loads. A schematic load course is shown in Figure 2. The load time was divided into 50% static load and 50% cyclic load. Similar load sequences were used for long fibre reinforced polymers, previously [10]. The frequency for the cyclic part of the load sequence was set to 3Hz for both materials. The static load level was set to the mean or minimum or maximum stress of the cyclic loads.

  doi:10.5075/epfl-298799_978-2-9701614-0-0

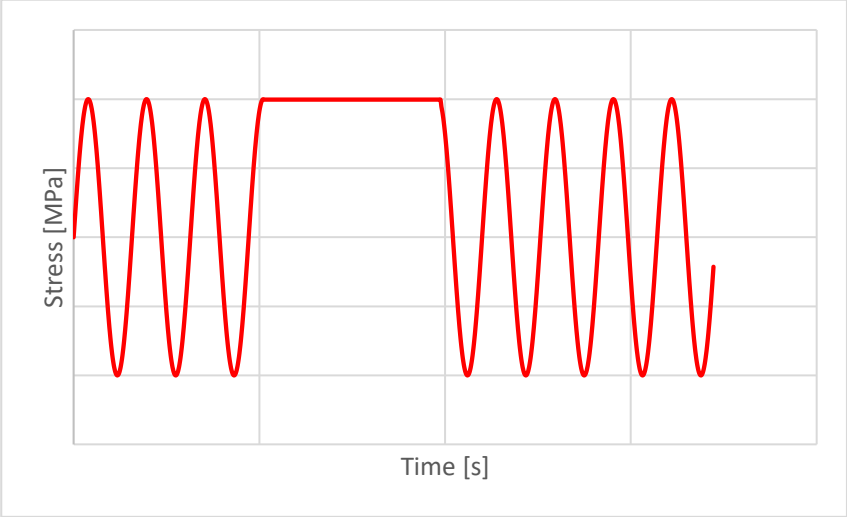

Figure 2. Schematic stress course of combined tests according to [7]

For the investigation of the fibre orientation influence, only one R-ratio was chosen, whereby for mean stress influence, three different stress ratios were tested. The R-ratio is the relationship between the minimum (σ_{min}) and the maximum stress (σ_{max}) of a cyclic load sequence and can be described with equation (1).

$$R = \frac{\sigma_{min}}{\sigma_{max}} \quad (1)$$

The performed test sequences for PP-GF40 including the R-ratios and the constant load level as well as the constant load shares are shown in Table 1.

Table 1: Tests for PP-GF40 at room temperature.

ID	Test type	R-ratio [-]	Constant load shares	Constant load level
1	Fatigue	-1	0%	no constant load
2	Combined	-1	50%	max. load
3	Fatigue	0.1	0%	no constant load
4	Combined	0.1	50%	max. load
5	Combined	0.1	50%	mean. load
6	Combined	0.1	50%	min. load
7	Fatigue	0.5	0%	no constant load
8	Combined	0.5	50%	max. load

A summary of the performed tests on PEEK-CF30 with different fibre orientations are shown in Table 2.

Table 2: Tests sequences for PEEK-CF30 at room temperature

ID	Test type	R-ratio [-]	Constant load shares	Constant load level	Fibre orientation
1	Fatigue	0.1	0%	no constant load	longitudinal
2	Combined	0.1	50%	max. load	longitudinal
3	Fatigue	0.1	0%	no constant load	transversal
4	Combined	0.1	50%	max. load	transversal

This sequence was repeated until a cycle number of $N=10^6$ was reached or failure occured.

3. Results and discussion

3.1 Test results

For PP-GF40 the tests results show a main influence of the mean stress on the fatigue lifetime depending on the static load share. Figure 3 illustrates the influence of the R-ratios and the investigated constant load levels on the resulting S/N-curves. All the results are normalized to the stress at $N=10^6$.

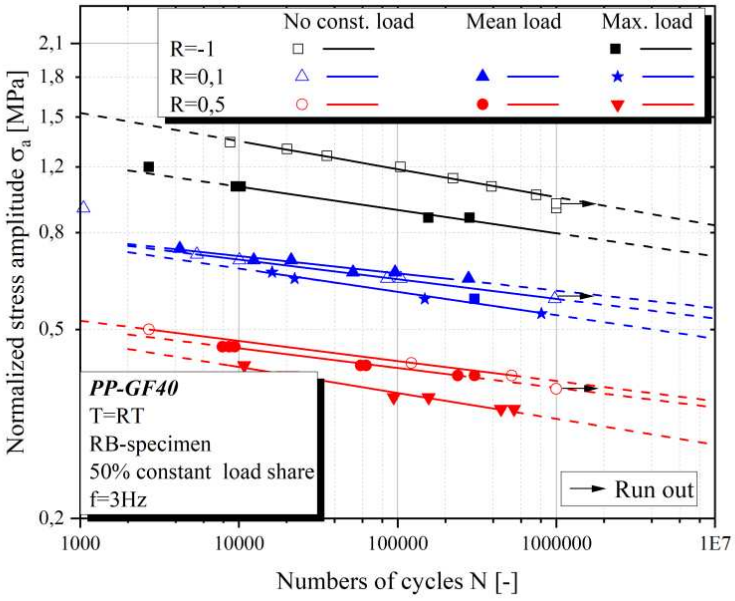

Figure 3. S/N-curves of PP-GF40 at different R-ratios

Moreover, the mean stress influences the effect of constant loads on the resulting lifetime. So, a constant load at maximum stress of the cyclic load reduces the number of bearable stress cycles with an R-ratio of R=-1 by more than a decade. This effect is extenuated with higher R-

ratios and higher load levels. As a result, there is an effect on the slopes of the S/N-curves. The reduction of the lifetime is evoked by creep damage and fatigue. Additionally, the strain of the material increases with the creep load, leading to a higher strain level for each cyclic block compared to pure cyclic load. As a result, the damage from the cyclic load block is increased. This effect is also illustrated in [7]. Further, the effect of constant loads on the mean stress sensitivity has been investigated. The mean stress sensitivity M is calculated with equation (2) and represents the relationship between the stress amplitudes ($\sigma_{a,R=-1}$, $\sigma_{a,R=0.1}$) and the mean stresses ($\sigma_{m,R=-1}$, $\sigma_{m,R=0.1}$) of the stress ratio R=-1 and R=0.1 in that case.

$$M = \frac{\sigma_{a,R=-1} - \sigma_{a,R=0.1}}{\sigma_{m,R=0.1} - \sigma_{m,R=-1}} \qquad (2)$$

It can be shown, that there is hardly any effect of the static loads on the mean stress sensitivity with a maximum load level. Table 3 contains the mean stress sensitivity for pure fatigue and combined loads.

Table 3: Mean stress sensitivity of PP-GF40 at room temperature depending on load sequence

ID number	Test type	Mean stress sensitivity [-]	Constant load shares	Constant load level
1	Fatigue	0.39	0%	no constant load
2	Combined	0.4	50%	max. load

Since the combined tests for R=-1 were just performed at a constant load level of maximum load, only these results are used for the calculation of the mean stress sensitivity. As a consequence, the constant load has the same (reducing) impact on the lifetime for every R-ratio. So, creep failure is getting more dominant with a higher R-ratio at a stress level for bearable number of $N=10^6$ cycles. Figure 4 illustrates the influence of constant loads for the investigated R-ratios in a Haigh diagram for $N=10^6$ cycles.

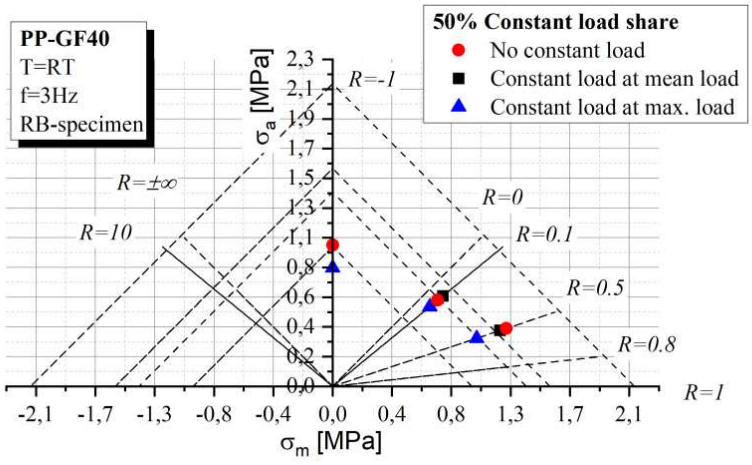

Figure 4. Haigh diagram depending on the load share for $N=10^6$

By observation of the points in the Haigh diagram, it is to recognize that the path of the pure fatigue loads is nearly in a straight line, whereas the course of the maximum constant load points follows the shape of a parabola. This parabola will cut the abscissas at a point, which may be the static strength for $N=10^6$ (The static strength can't be dedicated by definition to a number of bearable load cycles but the time to failure can be calculated with the test frequency).

The tests of the short carbon fibre reinforced PEEK-materials showed a nearly neglectable influence of constant load shares on the S/N-results (Figure 5).

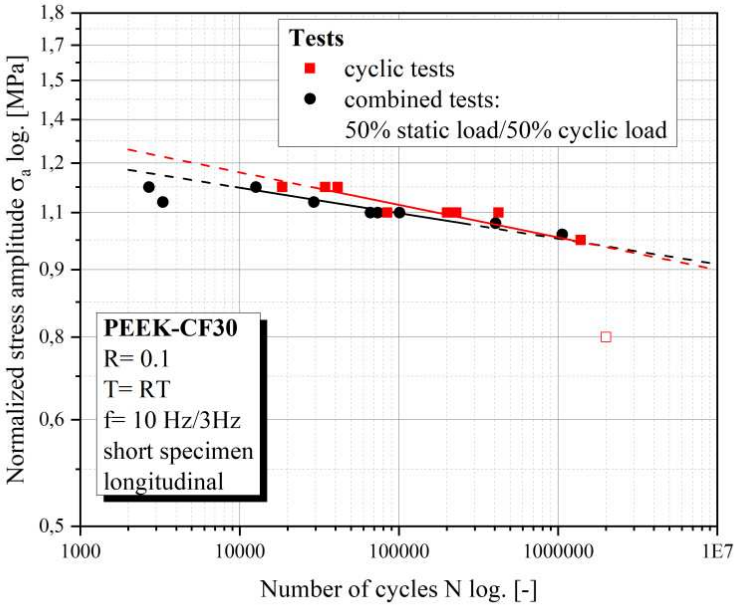

Figure 2. S/N curve PEEK longitudinal constant load at maximum load

There is a small effect on the lifetime with the transversal fibre orientation. Especially at low numbers of cycles, the effect is more pronounced (Figure 6).

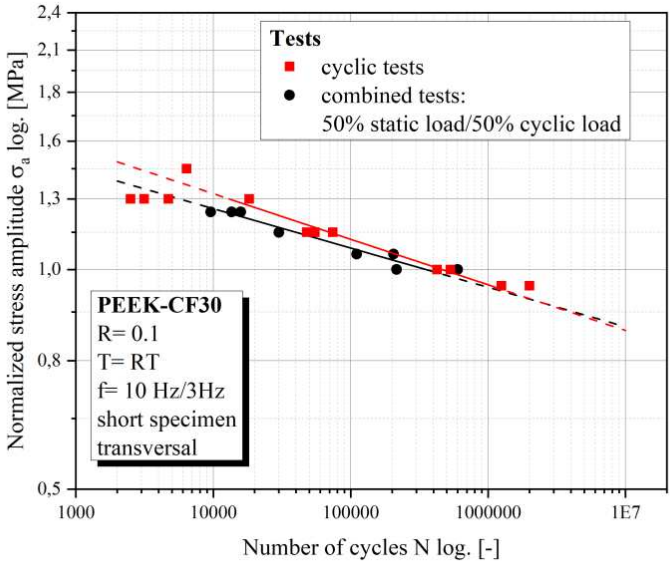

Figure 3. S/N curve PEEK transversal constant load at maximum load

Since the PEEK material is tested beneath the glass transition temperature, the viscoelasticity is much less pronounced compared to PP-GF40, even with a lower fibre content. Therefore, a consideration of the viscoelasticity depends strongly on the matrix material and on the ambient temperature.

4. Summary and outlook

Combined test sequences were used to capture the effect of viscoelasticity on the fatigue behaviour. Additionally, different mean stresses and fibre orientations were investigated to get the effect of these influence factors on the combined test results. The test results show an influence of static loads on the bearable number of cycles. Moreover, the influence is dependent on the static load level. But there is hardly any effect of the static creep load on the mean stress effect. The effect of viscoelasticity is also more pronounced for PP-GF40 compared to PEEK-CF30, where only minor effects could be measured in the specimens with transversal fibre orientation However, the investigated effect depending on the fibre orientation can be shown with PEEK-CF30. The next steps for these investigations are to test the influence of the fibre orientation on PP materials. Additionally, tests with PEEK above the glass transition temperature are necessary to get also information about the behaviour at these temperatures.

Acknowledgements

This research was funded by FFG grant number 854178. The research work of this paper was performed Polymer Competence Center Leoben GmbH (PCCL) in collaboration with the Chair of Mechanical Engineering and the Chair of Science and Testing of Polymers at the Montanuniversitaet of within the framework of the COMET-program of the Austrian Ministry of Traffic, Innovation and Technology with contribution by BOREALIS AG, Brose Fahrzeugteile GmbH & Co. KG, Engineering Center Steyr GmbH (MAGNA Powertrain ECS), Evonik Operations

  doi:10.5075/epfl-298799_978-2-9701614-0-0

GmbH, Hilit AG and Multi Wing international A/S. The PCCL is founded by the Austrian Government and the State Governments of Styria, Lower and Upper Austria.

Literature Cited

1. Mösenbacher A, Guster C. Fatigue behaviour of a short glass fibre reinforced polyamide: Effect of notches and temperature. In: 3nd Fatigue Symposium Leoben. Leoben: Chair of Mechanical Engineering; 2012. p. 152–60.

2. Niesłony A, Böhm M. Mean stress effect correction using constant stress ratio S–N curves. International Journal of Fatigue 2013; 52:49–56.

3. Belmonte E, Monte M de, Hoffmann C-J, Quaresimin M. Damage initiation and evolution in short fiber reinforced polyamide under fatigue loading: Influence of fiber volume fraction. Composites Part B: Engineering 2017; 113:331–41.

4. Bernasconi A, Davoli P, Basile A, Filippi A. Effect of fibre orientation on the fatigue behaviour of a short glass fibre reinforced polyamide-6. International Journal of Fatigue 2007 [cited 2014 Oct 20]; 29(2):199–208. Available from: URL: http://ac.els-cdn.com/S0142112306001484/1-s2.0-S0142112306001484-main.pdf?_tid=6cdb5622-5856-11e4-b4f4-00000aacb35f&acdnat=1413809074_4b68f20402502f7eca1c7b48b53dc501.

5. Zerbe P, Schneider B, Moosbrugger E, Kaliske M. A viscoelastic-viscoplastic-damage model for creep and recovery of a semicrystalline thermoplastic. International Journal of Solids and Structures 2017; 110-111:340–50.

6. Launay A, Maitournam MH, Marco Y, Raoult I, Szmytka F. Cyclic behaviour of short glass fibre reinforced polyamide: Experimental study and constitutive equations. International Journal of Plasticity 2011; 27(8):1267–93.

7. Stadler G, Primetzhofer A, Jerabek M, Pinter G, Grün F. Investigation of the Influence of Viscoelastic Behaviour on the Lifetime of Short Fibre Reinforced Polymers. Polymers (Basel) 2020; 12(12).

8. Mösenbacher A, Guster C, Pinter G, Eichlseder W. Investigation of Concepts Describing the Influence of Stress Concentration on the Fatigue Behaviour of Short Glass Fibre Reinforced Polyamide. In: ECCM 2012 - European Conference of Composite Materials; 2012.

9. Primetzhofer A, Stadler G, Pinter G, Grün F. Lifetime assessment of anisotropic materials by the example short fibre reinforced plastic. International Journal of Fatigue 2018.

10. Movahedi-Rad AV, Eslami G, Keller T. A novel fatigue life prediction methodology based on energy dissipation in viscoelastic materials. International Journal of Fatigue 2021; 152:106457.

  doi:10.5075/epfl-298799_978-2-9701614-0-0

CHARACTERIZATION OF FATIGUE CRACK INITIATION AND PROPAGATION IN THERMOPLASTIC-BASED HYBRID LAMINATES

Selim Mrzljak[a)], Philipp Blickling[a)], Maik Trautmann[b)], Guntram Wagner[b)], Frank Walther[a)]

a: TU Dortmund University, Chair of Materials Test Engineering (WPT),
Baroper Str. 303, D-44227 Dortmund, Germany – selim.mrzljak@tu-dortmund.de

b: Chemnitz University of Technology, Institute of Material Science and Engineering (IWW),
Group of Composites and Material Compounds, Erfenschlager Str. 73, D-09125 Chemnitz,
Germany

Abstract: *Thermoplastic-based hybrid laminates offer the advantage of formability and recyclability, making them particularly attractive for mass production applications. In aircraft applications, hybrid laminates are subjected to notch effects. In this study, the fatigue crack initiation and propagation are investigated with regard to drill hole and double-edge notches using constant amplitude tests. The investigated hybrid laminates consist of 2/1-layer (metal/FRP) and 3/2-layer configurations, containing aluminum alloy AA6082-T4, glass and carbon fiber-reinforced polyamide 6. Electrical resistance measurement and digital image correlation are applied for condition monitoring under fatigue load to characterize the damage behavior. Results show that the applied measurement technologies enable monitoring of the fatigue-induced crack initiation as well as propagation qualitatively and quantitively. The 3/2 configuration with lower metal volume content was affected more by the double-edge notch compared to the 2/1 configuration while showing better fatigue performance overall.*

Keywords: hybrid laminate; thermoplastic; fatigue crack; electrical resistance measurement; DIC

1. Introduction

Hybrid laminates in most cases contain fiber-reinforced polymers (FRP) based on thermoset matrix systems. ARALL (aramid fiber-reinforced epoxy [1]), GLARE (glass fiber-reinforced epoxy, GFRP [2]) and CARALL (carbon fiber-reinforced epoxy, CFRP [3]) are some of the more prominent examples considering aluminum-based laminates, which have proven their fatigue performance [4,5] for applications like the aircraft industry.

Investigations of crack initiation and propagation in hybrid laminates usually rely on electrical measurement of cross-sectional reduction [3,6] or tracking of crack growth using optical measurement devices like cameras [7,8] or microscopes [1,8-10]. Compared to the electrical measurement of crack length, the optical does not rely on the calibration of voltage/crack length relation, can be applied to any specimen geometry, and enables the investigation of multiple cracks at the same time. Disadvantages are the need for optical crack visibility, excluding measurements of hidden layers, and the necessity of a distinguishable pattern for deformation analysis. The accuracy of both, voltage measurement and optical detection, can reach sufficient levels for the discussed tasks with current technology.

For hybrid laminates based on aluminum and thermoset GFRP, like GLARE, many investigations regarding the influence of notches on fatigue properties have been conducted, covering mostly

  doi:10.5075/epfl-298799_978-2-9701614-0-0

drill holes and saw-cuts [7,8,10,11]. In general, for crack growth initiating from notches, progressive development is observed [9], which depending on the applied load and width of the specimen may also contain a linear segment in the beginning. A reliable indicator of unstable crack development can be the crack growth rate [9], which also affects the adjacent delamination. Compared to GFRP-based laminates, CFRP-based ones [3,12,13] can significantly improve the laminate's resilience against crack growth but they suffer from galvanic corrosion.

Thermoplastic-based hybrid laminates, like CAPAAL, offer shaping and shorter consolidation cycle times through thermoforming and enhance recyclability. Only a few results are available for such regarding their mechanical capability [14-16]. The focus of this study lies in analyzing the crack development for notched specimens (drill hole or double-edge notch) based on the stated laminate using electrical resistance measurement and digital image correlation.

2. Materials and experimental methods

2.1 Thermoplastic-based hybrid laminate and specimen

The thermoplastic-based hybrid laminate consists of three laminate components: AA6082-T4 (0.5 mm sheet thickness) sheets and unidirectional glass (GFR-PA6) as well as carbon fiber-reinforced polyamide 6 (CFR-PA6). This improves the laminate's tolerance against aluminum failure [12], while the implementation of GFRP helps prevent direct contact between the carbon and aluminum for increased corrosion resistance, and compensates for the mismatch in thermal expansion coefficient between aluminum and CFRP. A 2/1 and a 3/2 metal-to-FRP layer structure are investigated (Figure 1).

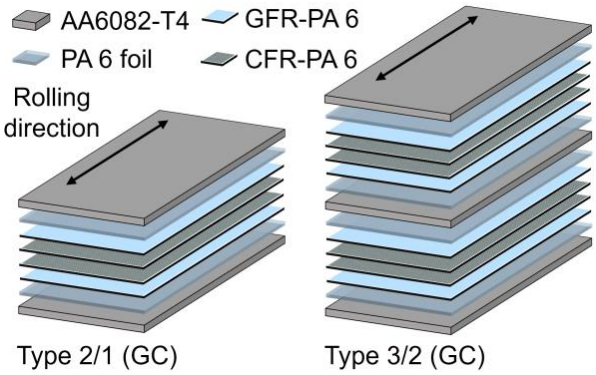

Figure 1. Hybrid laminate structures: (a) 2/1 (GC) with four FRP layers and (b) 3/2 (GC) with 2x four FRP layers between aluminum sheets

The FRP layers are arranged as a symmetrical build-up made of pre-consolidated thermoplastic prepreg tapes, called Ce-Preg® (Cetex Institut gGmbH, Chemnitz, Germany) with a calculated fiber volume fraction of 0.5. The GFR-PA6 consists of two 40 µm thick polyamide 6 (PA6) foils and TURov 4588 (Nippon Electric Glass Co. Ltd., Tokyo, Japan) fibers. The CFR-PA6 contains ZOLTEK PX35 50K (ZOLTEK Corporation, Bridgeton, NJ, USA) fibers.

Table 1 shows a short notation, the composition, and a description for each laminate structure considering the material, quantity, and orientation of the used FRP as well as the included metal. The metal volume content (MVC) describes the volumetric amount of metal using the number of metal layers and layer thickness of the metal and hybrid laminate [16].

  doi:10.5075/epfl-298799_978-2-9701614-0-0

Table 1: Layer structures of thermoplastic-based hybrid laminates made

Short notation	Composition [FRP Orientation]	Description	Thickness (mm)	MVC (%)
2/1 (GC)	Al/GCCG/Al Al/$[0_4^\circ]$/Al	$\left[\mathrm{Al/G}_1^{0^\circ}\mathrm{C}_1^{0^\circ}\right]_\mathrm{S}$	1.64	61
3/2 (GC)	Al/GCCG/Al/GCCG/Al Al/$[0_4^\circ]$/Al/$[0_4^\circ]$/Al	$\left[\mathrm{Al/G}_1^{0^\circ}\mathrm{C}_2^{0^\circ}\mathrm{G}_1^{0^\circ}/\overline{\mathrm{Al}}\right]_\mathrm{S}$	2.78	54

Before laminate consolidation, the aluminum sheet surfaces are mechanically blasted to improve polymer adhesion [15]. The laminate consolidation is carried out by thermal pressing using a laboratory platen press Collin PM300 (Collin Lab & Pilot Solutions GmbH, Maitenbeth, Germany) with a 260 × 260 mm^2 dipping-edge tool. Before processing, the FRP tapes and PA6 foils are dried in an oven at 80 °C for one hour. The consolidation process cycle is described in detail in [15,16]. Specimens based on geometry DIN EN 527-5 type A (Figure 2) are cut out of the laminate sheets using a micro water-jet and the following notches are introduced: a drill hole (hereafter referred to as DH5) and a double-edge notch (hereafter referred to as DEN5), representing the inverse case. Protective tabs are applied in the specimen's clamping area and the surface is speckled with a stochastic pattern for optical deformation measurements.

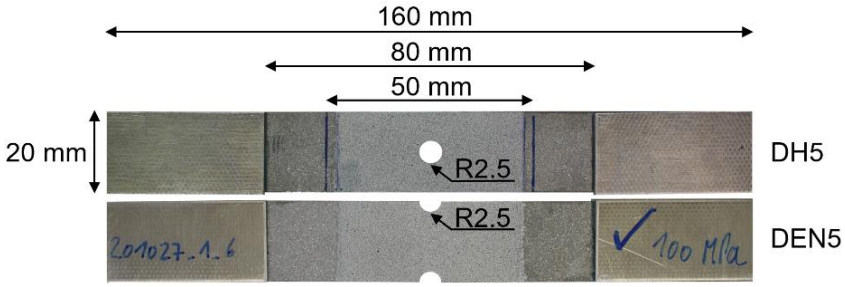

Figure 2. Prepared specimen with speckle pattern for DIC measurement and adhesively bonded protective tabs, showing the central 5 mm drill hole and 2.5 mm radius double-edge notch

2.2 Fatigue testing method and monitoring equipment

Fatigue tests were conducted up to high cycle fatigue regime on a servo-hydraulic testing system EHF-EV50 (Shimadzu Corp., Kyoto, Japan, maximum force F_{max} = ±50 kN). Constant amplitude tests (CAT) were performed under ambient temperature with a sinusoidal load-time function at a stress ratio R = 0.1 (tension/tension loading). The testing frequency was kept at f = 10 Hz and according to ISO 13003 did not increase the specimen temperature significantly.

For condition monitoring using electrical resistance measurement, a high-precision Keithley system (Tektronix Inc., Beaverton, USA) was applied, containing a 2601B source measure unit connected via R232 null modem cable to a 2182A nanovoltmeter. The system was operated in delta mode for the compensation of thermoelectric voltages. To correlate the change in electrical resistance to deformation and damage events a Limess Q400 digital image correlation (DIC) system (Limess Messtechnik und Software GmbH, Krefeld, Germany) was used. For temperature measurements, a Micro-Epsilon TIM 400 thermography camera (Micro-Epsilon Messtechnik GmbH & Co. KG, Ortenburg, Germany) recorded the front aluminum surface

  doi:10.5075/epfl-298799_978-2-9701614-0-0

temperature. Additionally, the machine piston displacement (s) was recorded by a linear variable differential transformer for stress-displacement hysteresis values to reflect on integral damage within the laminate. One used value is the dynamic stiffness (C_{dyn}), representing the change of stress divided through the change of piston displacement: $(\sigma_{max} - \sigma_{min})/(s_{max} - s_{min})$.

The metrology setup for the fatigue investigations is shown in Figure 3a. 3D-DIC measurements for strain analysis on the front aluminum sheet were executed with two 5 Megapixel cameras (optics: Ricoh TV lens FL-CC7528-2M - 75 mm focal length, 10 mm extension tube). For the electrical resistance measurement, 50 mm markers were applied and used for the voltage drop clamp placement (Figure 2a,3b) to ensure reproducible measurement results, and the current in/out clamps were placed adjacent. The clamps were contacted electrically conductive only to the front sheet. Further, a reference target, which underlies the same environmental changes in temperature as the tested specimen, was placed directly to the tested specimen to deduce on the testing and damage induced changes in temperature (Figure 3b).

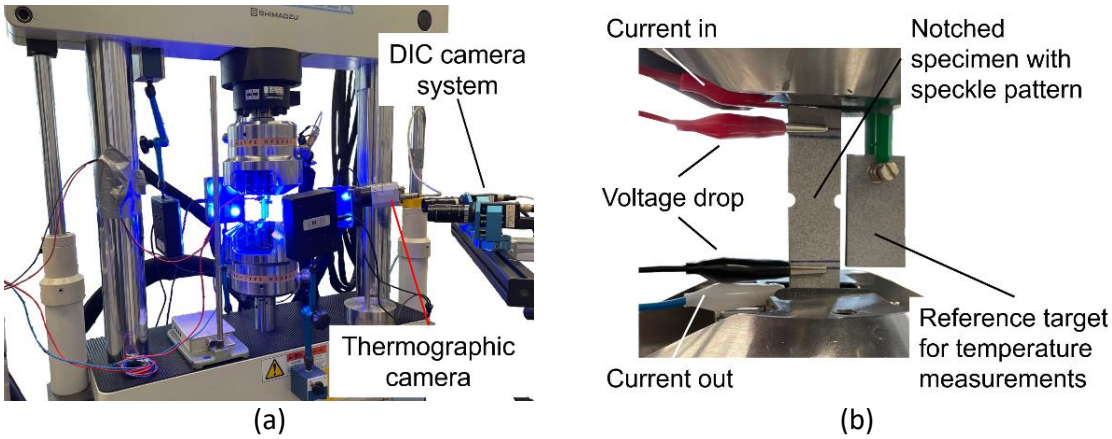

Figure 3. Condition monitoring setup for fatigue testing: (a) servo-hydraulic testing system with front instrumented DIC cameras and thermographic camera; (b) electrically contacted, clamped specimen (DEN5) with reference target for temperature measurements

3. Results

3.1 Condition monitoring during fatigue load

Figure 4 shows the result of a CAT carried out on a 2/1 (GC) DH5 specimen, visualizing the development of electrical resistance, crack growth, change in dynamic stiffness, and temperature for condition monitoring. As expected, a change in electrical resistance is recorded with the initiation of aluminum cracks, which simultaneously lead to a stiffness decrease. No change in temperature, which could affect the material-dependent electrical resistance, was recorded, showing that a suitable testing frequency was chosen for the applied load spectrum. With crack development the electric resistance increases, following a hyperbole function. The progress shows accelerated crack development just before full tear (crack extension until the borders) of the right side of the aluminum sheet, leading to a steep increase in resistance. In the following the crack in the left side of the aluminum sheet develops further, leading to an ultimate resistance increase at tearing. After tearing, no immediate decrease in stiffness is visible, highlighting the good interface capabilities for stress transfer. It should be noted that the stiffness indicates the time of crack initiation, but does not pinpoint further events, rather showing a continuous decrease, making the benefits of the used metrologies obvious.

  doi:10.5075/epfl-298799_978-2-9701614-0-0

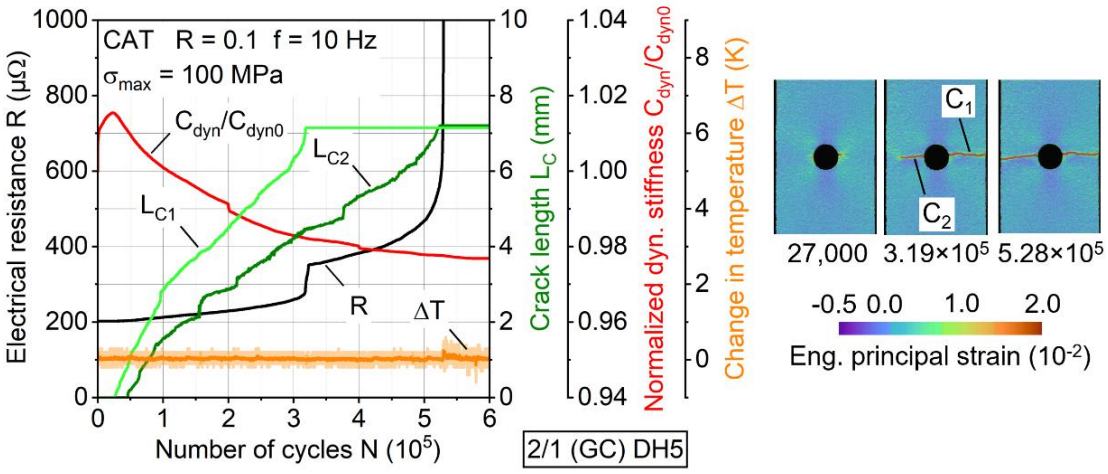

Figure 4. Constant amplitude test for 2/1 (GC) DH5, tested at maximum stress of 100 MPa. Selected states of crack growth are shown in the DIC deformation images.

But the application of electrical resistance measurement for crack detection also has limits. Figure 5 shows the electrical resistance development for CAT with 2/1 (GC) DH5 specimens at several maximum stress levels. Also, DIC deformation images are attached, showing the developed cracks just before the final steep resistance increase. With increasing load, the occurrence of cracks and therefore the electrical resistance changes. At stresses including and above 150 MPa, multiple cracks initiate, leading to a multiplication (150 MPa) or even a change in development (175 and 200 MPa) of the electrical resistance due to multiple parallel developing cracks. A limit value for the change in electrical resistance, until which the conductive capabilities of the hybrid laminate remain, could exemplary be defined as 300 μΩ.

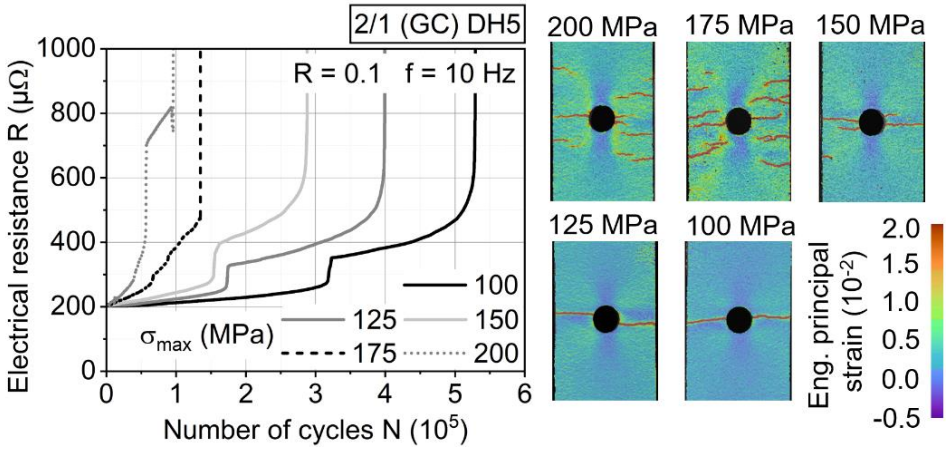

Figure 5. Electrical resistance during constant amplitude tests under varying maximum stresses for 2/1 (GC) DH5. Corresponding states of crack growth before the final pronounced resistance increase are shown in the DIC deformation images.

The influence of notch geometry has to be taken into account since it can affect the measurements immensely (Figure 6). As far as cracks initiate and develop perpendicular to the applied load, the change in resistance is occurring as expected. When cracks pass each other, for example due to lower maximum stress (here 100 instead of 150 MPa) where crack closure does not necessarily occur, the change in resistance takes a different course, and without DIC measurements only estimations regarding the possible crack state can be made.

  doi:10.5075/epfl-298799_978-2-9701614-0-0

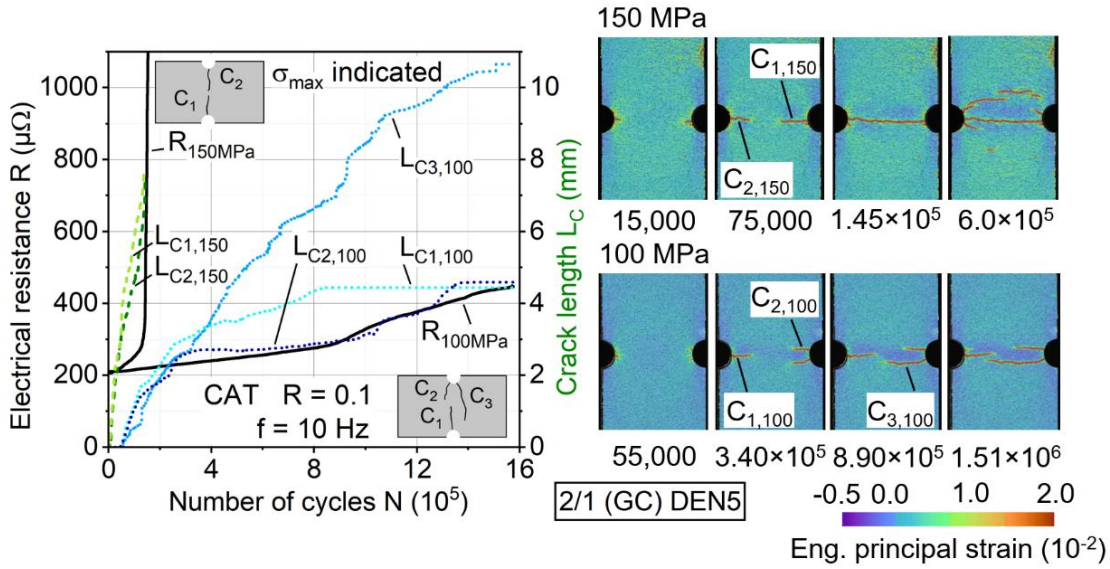

Figure 6. Constant amplitude test for 2/1 (GC) DEN5, tested at maximum stress of 150 and 100 MPa. Selected states of crack growth are shown in the DIC deformation images.

3.2 Influence of notch geometry on fatigue life

The following results regarding crack initiation time and fatigue life until total tear (crack extension until the borders) of the aluminum sheet were determined for the hybrid laminate configurations 2/1 (GC) and 3/2 (GC) and both notch geometries (Figure 7). For detection of first crack initiation, the dynamic stiffness decrease and electrical resistance increase proved to be more viable due to DIC analysis limitations. These include spray pattern quality at the specimen edges, as well as its software recognizability, leading to possible errors considering detection precision. Monitoring the crack propagation, on the other hand, is more accurate using DIC analysis since it enables observation of any local crack formation, rather than the total, which especially for DEN5 is superior and needed to determine when the aluminum cracks reach or surpass each other. If they surpass each other, the number of cycles at the time of surpassing is recorded as the time of the tear. The lifetimes until crack initiation and tear of the front aluminum sheet are shown as circles and triangles. In general, the lifetime until aluminum crack initiation is within a 10 % window of the lifetime until tear of the sheet.

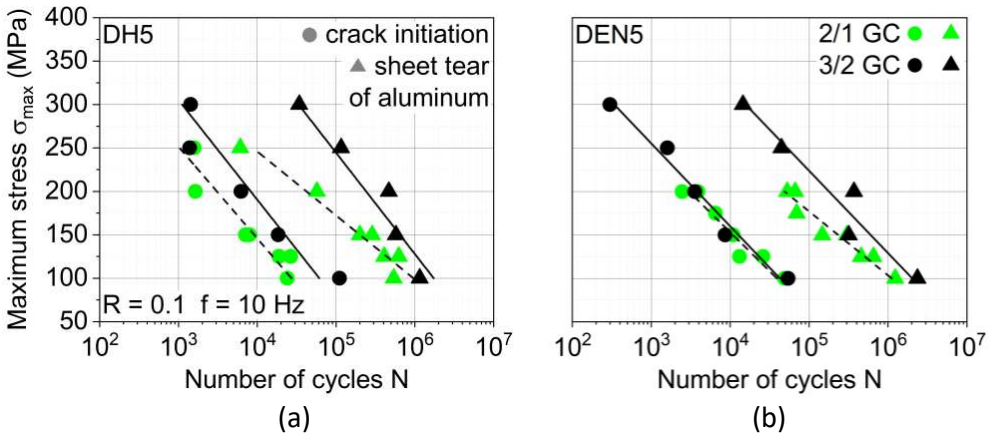

Figure 7. Crack initiation time and lifetime until total tear of the aluminum sheets for the hybrid laminate configurations 2/1 (GC) and 3/2 (GC) with notch geometries DH5 (a) and DEN5 (b).

Correlating to the ultimate fatigue lifetime of all laminate partners [16], tear of the aluminum sheet occurs, in general, later for 3/2 (GC) than for 2/1 (GC), leading to the conclusion of a higher aluminum lifetime with less MVC. This is contradictory to the observations of [11] on aluminum/GFRP-based laminates with similar configurations, where at higher loads the 2/1 configuration yields later aluminum tear than 3/2. Considering the notch geometries, 3/2 (GC) seems to be more affected by DEN5 since the crack initiation in the aluminum sheet is reduced compared to DH5. The performance of 2/1 (GC) between DH5 and DEN5 is comparable.

4. Conclusions and Outlook

The condition monitoring investigations on thermoplastic-based hybrid laminates, made of aluminum alloy AA6082-T4 and unidirectional GFRP and CFRP, showed that during fatigue testing a precise crack state monitoring is possible via electrical resistance measurement, as long as cracks develop as intended by the notch. Higher loads may lead to multiple, and not to the load perpendicular crack initiations, impacting the change in electrical resistance significantly. Here the digital image correlation acquired crack lengths, which can directly be correlated to the change in electrical resistance, are more conclusive.
For the two notch geometries (drill hole and double-edge notch) differences considering monitorability, as well as the impact on fatigue life of the aluminum sheets, were determined. While crack initiation and propagation can be similar for both notch geometries, the double-edge notch cracks tend to pass each other, rather than connect. This leads to a different development of electrical resistance and impedes monitorability with only electrical resistance measurement, while DIC detects the cracks and displacement between them accurately. With regard to crack initiation time and fatigue life until total tear of the aluminum sheet, it was found, that lower metal volume content leads to postponed crack initiation and tear. Further, the investigated 3/2 configuration was affected more by the double-edge notch compared to the 2/1 configuration.

In future investigations the simultaneous monitoring of multiple aluminum sheets, as well as the carbon fibers, should be addressed, enabling a complete monitoring of the laminate and validation of the gathered results. Further, an in-depth study of the hybrid laminate's crack evolution on e.g., a statistical basis, to be able to make accurate load-dependent predictions of the laminate's condition using the electrical resistance alone, is a valuable aspect to be approached.

Acknowledgments

The authors thank the Deutsche Forschungsgemeinschaft (DFG, German Research Foundation) for funding the research project "Mechanism-correlated characterization of the deformation and damage behavior of thermoplastic-based fiber metal laminates for property-oriented process development" - 414332488 (WA 1665/9-1, WA 1672/56-1). Further thanks to Martin Risthaus from Evonic for providing surface treatment.

5. References

1. Kim CW, Oh DJ. Progressive delamination with and without crack propagation in aramid fiber reinforced metal laminates containing a circular notch. Materials Science and Engineering A 2008; 483-484: 251-253. doi: 10.1016/j.msea.2006.10.193

2. Alderliesten RC. Designing for damage tolerance in aerospace: A hybrid material technology. Materials and Design 2015; 66: 421-428. doi: 10.1016/j.matdes.2014.06.068
3. Austin TSP, Singh MM, Gregson PJ, Powell PM. Characterisation of fatigue crack growth and related damage mechanisms in FRP–metal hybrid laminates. Composites Science and Technology 2008; 68: 1399-1412. doi: 10.1016/j.compscitech.2007.11.013
4. Asghar W, Nasir MA, Qayyum F, Shah M, Azeem M, Nauman S, Khushnood S. Investigation of fatigue crack growth rate in CARALL, ARALL and GLARE. Fatigue and Fracture of Engineering Materials and Structures 2017; 40: 1086-1100. doi: 10.1111/ffe.12566
5. Deniz ME, Aydin F. Determination of fatigue life of the unidirectional GFRP/Al hybrid composite laminates. Composites Part B 2019; 166: 580-587. doi: 10.1016/j.compositesb.2019.02.060
6. Tarnowski KM, Nikbin KM, Dean DW, Davies CM. A unified potential drop calibration function for common crack growth specimens. Experimental Mechanics 2018; 58: 1003-1013. doi: 10.1007/s11340-018-0398-z
7. Plokker HM, Khan SU, Alderliesten RC, Benedictus R. Fatigue crack growth in fibre metal laminates under selective variable-amplitude loading. Fatigue & Fracture of Engineering Materials and Structures 2009; 32: 233-248. doi: 10.1111/j.1460-2695.2009.01333.x
8. Huang Y, Liu J, Huang X, Zhang J, Yue G. Delamination and fatigue crack growth behavior in Fiber Metal Laminates (Glare) under single overloads. International Journal of Fatigue 2015; 78: 53-60. doi: 10.1016/j.ijfatigue.2015.04.002
9. Liu Q, Ma J, Kang L, Sun G, Li Q. An experimental study on fatigue characteristics of CFRP-steel hybrid laminates. Materials and Design 2015; 88: 643-650. doi: 10.1016/j.matdes.2015.09.024
10. Wang W, Rans C, Alderliesten RC, Benedictus R. Predicting the influence of discretely notched layers on fatigue crack growth in fibre metal laminates. Engineering Fracture Mechanics 2015; 145: 1-14. doi: 10.1016/j.engfracmech.2015.06.062
11. Meng W, Li Y, Zhang X, Wang Y, Huang X. Analysis and prediction on total fatigue life problems of fiber reinforced metal laminates under two-stage loading. Composite Structures 2020; 237: 111960. doi: 10.1016/j.compstruct.2020.111960
12. Dadej K, Bienas, J. On fatigue stress-cycle curves of carbon, glass and hybrid carbon/glass-reinforced fibre metal laminates. International Journal of Fatigue 2020; 140: 105843. doi: 10.1016/j.ijfatigue.2020.105843
13. Mrzljak S, Schmidt S, Kohl K, Hülsbusch D, Hausmann J, Walther F. Testing procedure for fatigue characterization of steel-CFRP hybrid laminate considering material dependent self-heating. Materials 2021; 14: 3394. doi: 10.3390/ma14123394
14. Zopp C, Dittes A, Nestler D, Scharf I, Kroll L, Lampke T. Quasi-static and fatigue bending behavior of a continuous fiber-reinforced thermoplastic/metal laminate. Composites Part B 2019; 174: 107043. doi: 10.1016/j.compositesb.2019.107043
15. Mrzljak S, Trautmann M, Wagner G, Walther F. Influence of aluminum surface treatment on tensile and fatigue behavior of thermoplastic-based hybrid laminates. Materials 2020; 13: 2080. doi: 10.3390/ma13143080
16. Trautmann M, Mrzljak S, Walther F, Wagner G. Mechanical properties of thermoplastic-based hybrid laminates with regard to layer structure and metal volume content. Metals 2020; 10: 1430. doi: 10.3390/met10111430

MICRO-FATIGUE TEST - A NEW DIMENSION TOWARDS CYCLIC LOAD TEST FOR INTERFACE CHARACTERISATION

Pekka Laurikainen[a], Royson Dsouza[a], Markus Kakkonen[b], Essi Sarlin[a], Mikko Kanerva[a]

a: Materials Science and Environmental Engineering, Tampere University, Finland – pekka.laurikainen@tuni.fi
b: Fibrobotics Oy, Tampere, Finland

Abstract: *The quality of fibre-matrix interphase is commonly characterised via microscale testing methods that show good sensitivity for differences in properties of the interphase. Most approaches focus on quasi-static performance, which while valuable, does not provide all the necessary information needed for characterising the performance of the interphase in real use cases. This paper presents a novel cyclic test approach based on the microbond test concept that provides statistically reliable fatigue data from micro-composite samples. A reasonable throughput is achieved by using relatively high strain rates, which needs to be considered in the analysis. This paper offers insights into the advantages and disadvantages of the approach through comparison with quasi-static experiments. As expected, the results show a clear strain rate dependence but otherwise fit the expected behaviour of a fatigue test. More than 30 droplets were measured per sample for varying number of cycles ranging from 1 to 10^6. Based on the results, the method offers a novel, relatively high throughput approach for dynamic testing of microcomposite samples with applications for studying the dynamic behaviour of the composite interphase.*

Keywords: Micro-scale testing; Interface/Interphase ; Fatigue testing ; Dynamic testing

1. Introduction

Fibre-reinforced composites are only as good as the interfaces as the stress transfer from the matrix to the fibres is crucial for the overall properties. Quasi-static micro composite experiments, such as the pull-out [1] and microbond tests [2], are well established and used to determine the local interfacial parameters such as shear strength and energy release rate of the interface. However, unstable crack propagation is difficult to measure using quasi-static destructive tests and a detailed analysis of the dissipative and non-dissipative energy contributions is not possible. Dynamic tests can reveal these properties and can also provide valuable information on the role of fibre sizing [3]. Despite these advantages, very few studies on fatigue testing of a single fibre/matrix system are available and the behaviour of microcomposite samples in such measurements is therefore not well known. This is likely a result of both the complexity of the test and the uncertainty of the results, the latter a common problem in all fatigue testing.

Cyclic loading with an experimental setup based on the microbond test has been tried only for high stress and low cycles count (up to 20 cycles) [4], which cannot accurately characterise fatigue behaviour of the interface. For efficient life prediction of the interface, the test must be carried out from low to high stress levels and up to a few millions of cycles. More success has

  doi:10.5075/epfl-298799_978-2-9701614-0-0

been documented with a test system utilising cyclic loading in the pull-out method [5]. The method is, however, limited to the measurement of large embedded lengths.

Here, we present an efficient high throughput micro-fatigue test based on the microbond concept that provides force and fibre strain as efficient outputs during the test. This novel test allows droplets with varying embedded lengths to be tested, enabling the collection a large range of data to analyse the fatigue properties of the interface. Multiple droplets are measured from each filament, and an effort is made critically analyse the role of fibre sizing. Each test is performed with a constant peak force for the cyclic loading until the droplet is completely sheared from the fibre. The crack propagation at the interface during cyclic loading and the contributions of dissipative and non-dissipative energies are evaluated.

2. Experimental

The micro-fatigue tests utilised the FIBRObond device (Fibrobotics Oy, Finland) [6]. Data has been collected at different stages of development to evaluate the reproducibility and robustness of the data to variations in parameters and the experimental setup. To enable the high-rate cyclic testing the newest prototype is fitted with a magnetic linear actuator for displacement (δ) during the test. The actuator moves the microtome blades at a rate of 2.0 mm/s with the displacement amplitudes (δ_a) varying based on the embedded length and the desired force (F) level. This results in slight variation of test frequency: between 6 – 10 Hz. This variation should not significantly affect the results. A graphical overview of the device is presented in Figure 1.

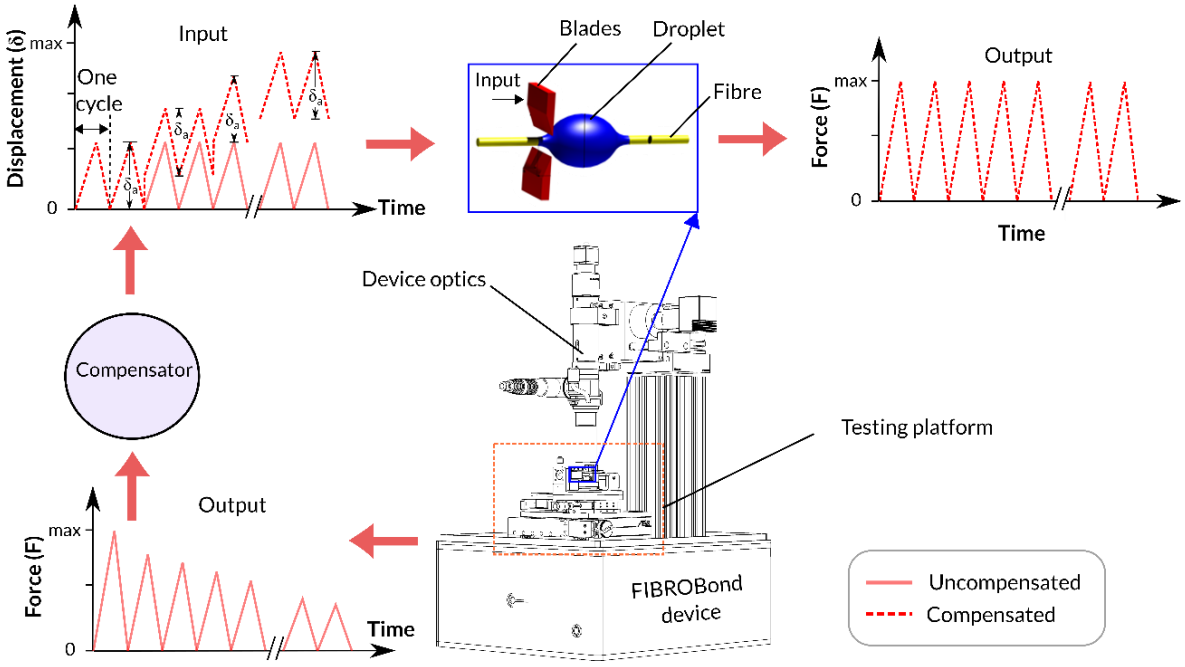

Figure 1. Schematic overview of the experimental setup.

To ensure a steady force (F) level during the test, a compensation algorithm was added to the software. This algorithm monitors changes in peak force (F_{peak}) levels and shifts the zero position of the displacement to incrementally increase the F level to keep it as constant as possible with the starting level. Without such compensations, the F level would change significantly during the test. This phenomenon is mainly attributed to the plastic deformation of

the droplet and the damage propagation at the interphase. The compensation aims to ensure that the loading of the droplet is as constant as possible throughout the test.

The tested samples were studied with scanning electron microscope (SEM, Zeiss ULTRAplus, Germany). Prior to the imaging, they were coated with a thin Pt/Pd layer to ensure their conductivity.

The preliminary testing was done on an old batch of industrially sized E-CR glass fibres with a nominal diameter of 17 µm. A batch of the same fibres was washed in piranha solution to remove the original aged sizing to provide an approximation of an unsized glass fibre sample. Microdroplets were prepared using the resin Araldite LY 5052 and hardener Aradur LY 5052 with a mix ratio of 100:38 (mass/mass). The samples were then cured for 8 hours at 80 °C after the droplet deposition. The droplets were deposited on the fibres with the FIBROdrop system (Fibrobotics Oy, Finland).

3. Results and Discussion

Due to the high sampling rate and long test duration, effective and robust data reduction is key to the analysis and visualization of the experimental data. Figure 3 presents an example of the dataset for a measurement lasting about 2200 loading cycles.

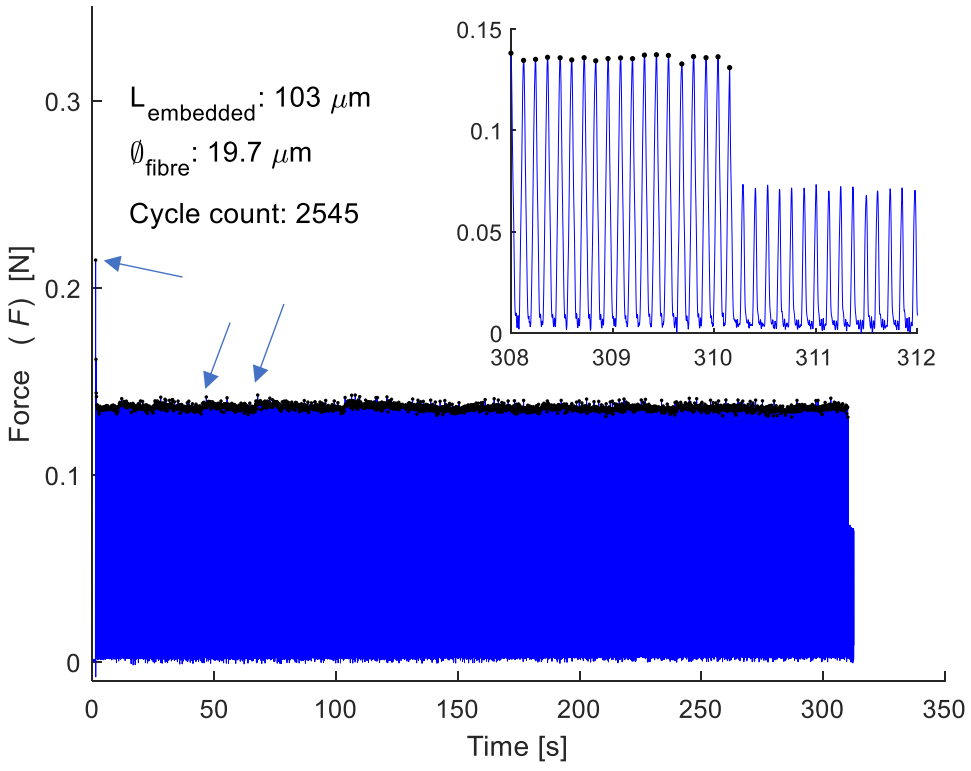

Figure 3. Force data during a micro-fatigue experiment (displacement speed 2.0 mm/s). Compensation events are visible as "steps" in the average F_{peak} and sample debonding is visible as a sudden drop in F_{peak} level. The F_{peak} values for each cycle are highlighted in black. Some notable deviations, from the average F_{peak} level, are highlighted with arrows (see text).

  doi:10.5075/epfl-298799_978-2-9701614-0-0

As seen in Figure 3, the compensation algorithm maintains an even peak load level. The occasional higher peaks arise from noise in the electronics, which affects the average F_{peak}level very little but is worth noting as source of experimental uncertainty. The highest $F_{peak}$is, however, measured with the very first impact and the sudden drop in loading level is due to the plastic deformation of the droplet meniscus. Figure 2 presents an SEM image of the measured droplets. The droplet meniscus area has undergone significant plastic deformation, which highlights the need for the compensations.

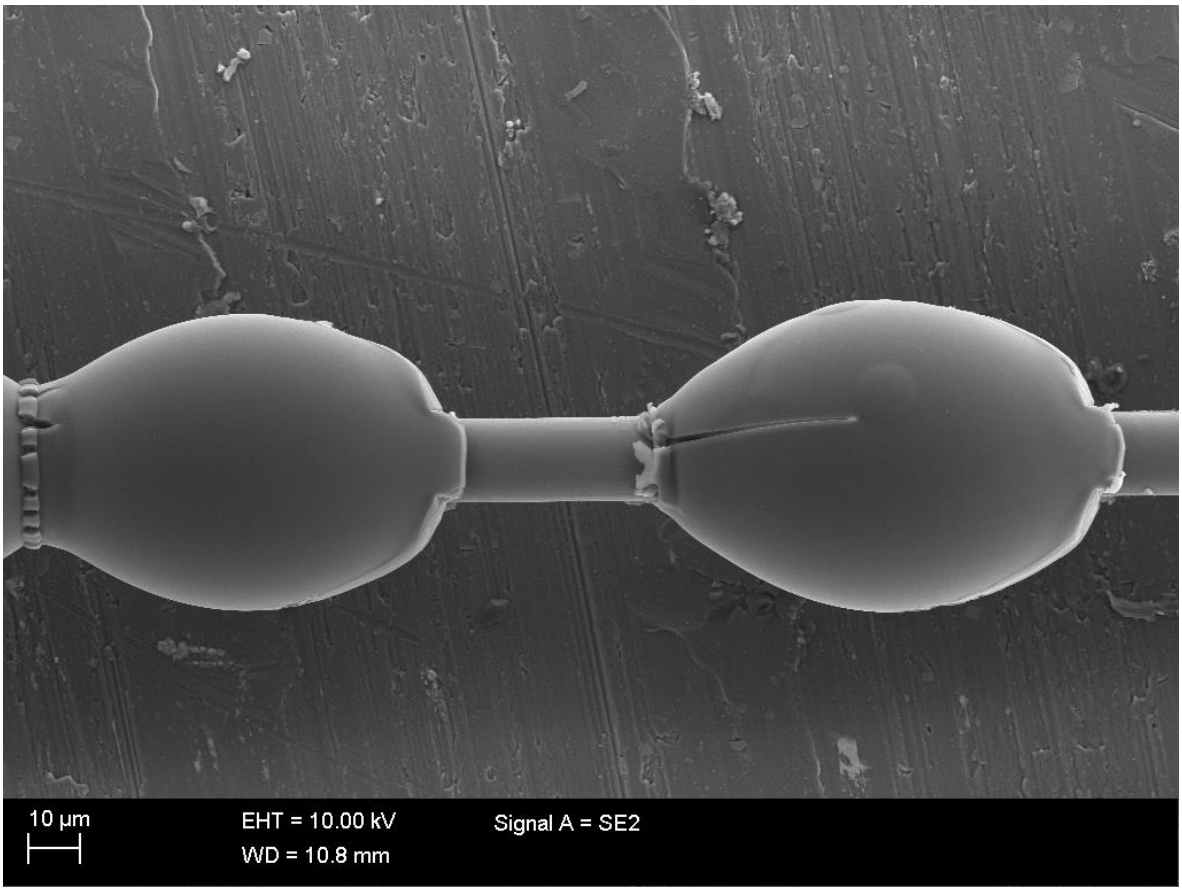

Figure 2. SEM image showing the deformation of the droplets after testing. The microtome blade contact is on the right side of the droplet.

First impacts with significantly higher than the average F values are noted frequently when attempting to measure droplets with higher average F_{peak} levels (i.e., shorter experiments). These experiments also frequently lead to fibre breakages. The main issue is the fact that the loading level was selected with a displacement amplitude (δ_a) guess, aiming for a specific F_{peak} level, that is then used throughout the experiment. To mitigate the problems this causes, the following addition to the functionality was added: the loading level will be selected based on the combination of an initial estimate of δ_a and a target load value. If the loading level based on the initial δ_a does not reach the desired target value or the load peak load values decrease below it due to the early plastic deformation, the δ_a will be adjusted incrementally until the target peak load level is reached. This allows for far more moderate initial $\delta_a$guesses, while still enabling shorter tests (high F_{peak} level) and reducing the risk of fibre breakage.

  doi:10.5075/epfl-298799_978-2-9701614-0-0

The standard output of fatigue testing is an S/N-curve comparing the stress level and number or cycles needed for the sample to break. Figure 4 presents the approximate S/N-curves for the preliminary tests done with the old batch of E-CR fibres and the piranha solution washed fibres, measured with the final experimental setup (*a)* and *b)* respectively). The stress level is an approximation because the droplet dimensions and embedded area can change quite significantly during the test. The stress $S_{approx.}$ is calculated from the average F_{peak} and the initial embedded area.

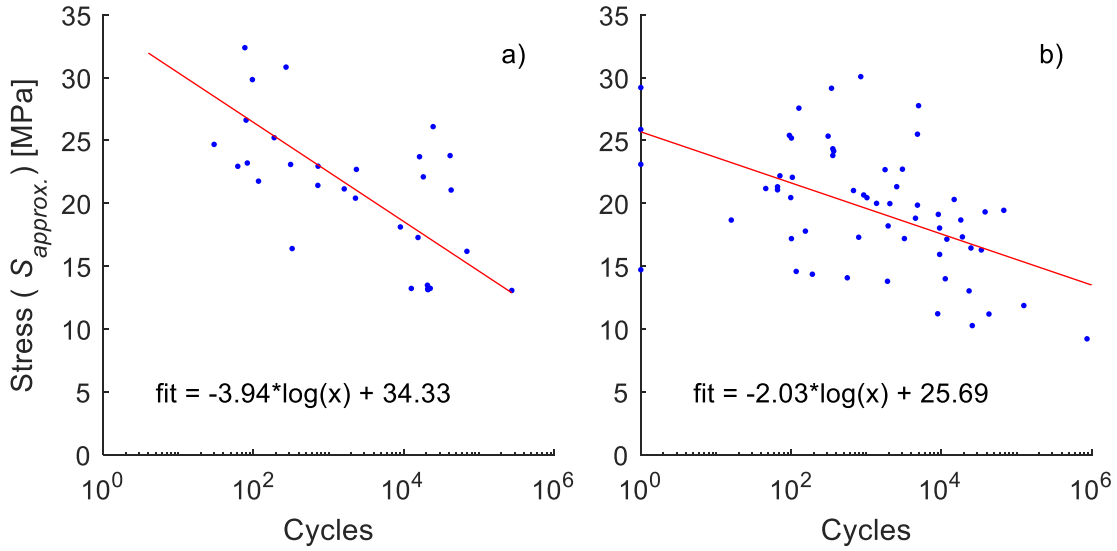

Figure 4. Fatigue test results from a) preliminary tests for old industrially sized glass fibres with crosshead speed set to 1.5 mm/s b) results with the final experimental setup (crosshead speed 2.0 mm/s) for piranha washed fibres with the same resin.

Based on these preliminary results, the fatigue test seems sensitive to changes to the fibre-resin interphase, as expected, and provides valuable information on the behaviour of the interphase not available through quasi-static experimental methods. It is, however, worth noting that the comparison between these presented datasets has significant uncertainty due to the differences in displacement speed and the limited size of the older dataset, which does not extend to low cycle counts. The process of gathering a better dataset for sized fibres is underway and the results are planned for a future publication.

The scatter of the data appears high, but it is comparable to the general trend in fatigue testing i.e., the scatter tends to be quite high even for macroscale testing of homogeneous materials [7]. The testing system seems to therefore provide reliable dynamic test data from a microcomposite system. The major advantages of the method are a relatively high throughput from the high frequency displacement and the ability to measure several droplets from a single filament sample. As an additional note, the experimental setup is identical to the one used for quasi-static microbond experiment [6] and the change from quasi-static to dynamic testing requires only software level operations enabling the collection of comparison data from the same filament sample with both experimental approaches.

  doi:10.5075/epfl-298799_978-2-9701614-0-0

4. Conclusions

In this study, we present a novel experimental approach for dynamic microcomposite testing, which can provide valuable information about interfacial performance that is complementary to the results of well-established microcomposite methods such as the microbond test. Steady force levels are achieved through a compensation algorithm in the measuring software, which is also used to improve the initial $\delta_a$guess to match specific loading levels. The latter is important for the measurement of a suitably wide range in the number of loading cycles from single loading cycles corresponding to high strain rate quasi-static experiments to dynamic tests lasting even over a million loading cycles. The current device fulfils these requirements and a more detailed study on the observable interfacial phenomena is underway.

Acknowledgements

This research is partly funded by the Tampere University Doctoral School and the Jenny and Antti Wihuri foundation (Grant No. 00210182). This work made use of the Tampere Microscopy Center facilities at Tampere University.

5. References

1. Penn LS, Bowler ER. A new approach to surface energy characterization for adhesive performance prediction. Surface and Interface Analysis 1981; 3(4):161-164.
2. Miller B, Muri P, Rebenfeld L. A microbond method for determination of the shear strength of a fiber/resin interface. Composites Science and Technology 1987; 28(1):17-32.
3. Mäder E, Gao S, Plonka R. Static and dynamic properties of single and multi-fiber/epoxy composites modified by sizings. Composites Science and Technology 2007; 67(6):1105-1115.
4. Shin P, Kim J, Baek Y, Park H, Park J. Epoxy Matrix with Adding Dopamine for Improving Mechanical Property and Interfacial Adhesion with Glass Fiber. Composites Research 2019; 32(2):96-101.
5. Brodowsky HM, Jenschke W, Mäder E. Characterization of interphase properties: Microfatigue of single fibre model composites. Composites Part A: Applied Science and Manufacturing 2010; 41(11):1579-1586.
6. Laurikainen P, Kakkonen M, von Essen M, Tanhuanpää O, Kallio P, Sarlin E. Identification and compensation of error sources in the microbond test utilising a reliable high-throughput device. Composites Part A: Applied Science and Manufacturing 2020; 137:105988.
7. Lee Y-L, Pan J, Hathaway RB, Barkley ME. 4.2 The Stress-Life (S-N) and Fatigue Limit Testing. In: Fatigue Testing and Analysis – Theory and Practice 2005. ISBN: 978-0-7506-7719-6.

  doi:10.5075/epfl-298799_978-2-9701614-0-0

FATIGUE BEHAVIOR OF GLASS FIBER REINFORCED COMPOSITE LAMINATES BASED ON RECYCLED PET

Ashwani Kumar, Singh[a], Raman, Bedi[b]

a: Department of Mechanical Engineering, Dr. B R Ambedkar National Institute of Technology Jalandhar, Jalandhar, Punjab 144027, India– ashwanisingh1788@gmail.com
b: Department of Mechanical Engineering, Dr. B R Ambedkar National Institute of Technology Jalandhar, Jalandhar, Punjab 144027, India– bedir@nitj.ac.in

Abstract: *Waste polyethylene terephthalate (PET) in the atmosphere creates an environmental concern. The use of waste PET as a matrix material in composite materials not only lowers material cost but also has a lower environmental impact. For the fabrication of composite laminate, the unsaturated polyester resin (rPET-UPR) is extracted from waste PET through the chemical recycling route (glycolysis). Glass fiber composites of stacking sequence $[0/(\pm45)2/0]_T$ were fabricated with unsaturated polyester resin. Vacuum infusion technique was used for the fabrication of composites. Fatigue tests were performed at the stress ratio of 0.1, where the stress level varied from 45-80% of ultimate tensile strength. The fatigue S-N curve of composite materials fabricated with rPET-UPR was compared with composite materials based on virgin polyester. The results of fatigue tests showed that the fatigue life of composites based on rPET-UPR was lower than that of virgin polyester composites. At low-stress levels, Initially, local damage was observed in composite laminates which is observed to progress gradually and uniformly with increasing number of loading cycles.*

Keywords: Fatigue properties; Glass fiber reinforced composite; Vacuum infusion; Recycled PET.

1. Introduction

Polyethylene terephthalate (PET) is a semicrystalline and transparent thermoplastic having good mechanical properties and chemical resistance, used for making various components especially soft drinks and water bottles [1–3]. The consumption of PET-based products mainly PET bottles increased every year [4]. After the use, the disposal of PET in the atmosphere creates environmental problems as it takes around more than a hundred years to decompose naturally [5,6]. Waste PET in natural weathering does not affect the environment directly. PET has low biodegradability and high resistance to atmospheric degradation. Due to this, a large volume fraction of waste PET in the stream seems as a noxious material [1,7]. Recycling of waste PET is the scientific technique to reduce the detrimental effect on the environment [8,9] [10] and embodied energy [11]. The waste PET is converted into matrix materials for glass fiber reinforced composite materials via chemical (thermosetting matrix) or mechanical recycling (thermoplastics matrix).

The recycled polymer-based composite materials are well suited in numerous engineering and industrial applications such as in aerospace, automotive, construction, etc. [12]. Glass fiber is the most commonly used reinforcement for recycled PET. Generally, glass fiber composite materials based on recycled PET matrix (thermoplastic matrix) are prepared through mechanical

  doi:10.5075/epfl-298799_978-2-9701614-0-0

recycling. In this context, the various research group made an effort on the fabrication of recycled PET based glass fiber composite materials and investigated their properties in terms of tensile [13] [14] [15], flexural [16] [13] [14] [15], impact [13] [14] [15] [16]. Fiber is the major load bearing member of composite materials. Therefore, fiber content affects the mechanical properties of composite materials. Kracalık et al. [17] investigated the rheological, thermal, and mechanical properties of recycled PET-based glass fiber composite. They observed that the tensile strength, tensile modulus, flexural modulus, melt viscosity, and glass transition temperature increased with increasing fiber content. Also, Rezaeian et al. [18] was reported the tensile properties and impact strength of glass fiber recycled PET composites increased with increasing fiber content.

To the best knowledge, there is no work has been performed to investigate the fatigue of composite materials based on recycled PET. This study aims to investigate the fatigue properties of glass fiber reinforced unsaturated polyester based on recycled polyethylene terephthalate. In addition, the fatigue data (S-N curve) were compared to fatigue data (S-N curve) of composite materials based on virgin polyester [19].

2. Fabrication of composites and Experimentation

2.1 Resin extraction

In this study, unsaturated polyester resin was used as a matrix which is prepared from the waste PET through the chemical recycling route. Figure 1 represent the recycling setup for resin extraction from waste PET. The chemical recycling waste PET flakes, DEG, and zinc acetate introduce in the four neck round bottom flask and heated at 210 ^{o}C in oil bath. After completing the glycolysis process, the glycolyzed product, maleic anhydride, phthalic anhydride, and propylene glycol were heated at 210 ^{o}C till the acid value reached to desirable value. Once the acid value reached stopped the reaction and cooled the resin to 90 ^{o}C. Finally, the obtained highly viscous resin were diluted with styrene.

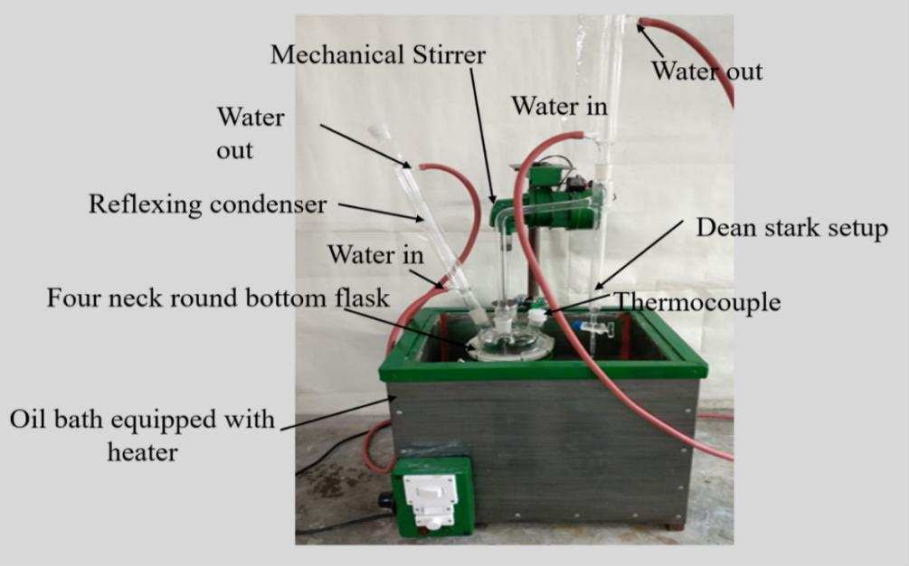

Figure 1 Recycling setup for waste PET.

2.2 Composites fabrication

Four-ply composite laminate of staking sequence $[0/(\pm45)2/0]_T$ were fabricated by using vacuum infusion technic. The specimens for the tensile and fatigue test were cut from the prepared laminate with a diamond cutter as per ASTM D3039/3039M-17 [20] as shown in Figure 2. The edges of specimens were trimmed with silica paper of grit size 600 to abate the probabilities of edge-related failure. Aluminum tabs were glued at end of each specimen by using epoxy bond adhesive to avoid grip failures.

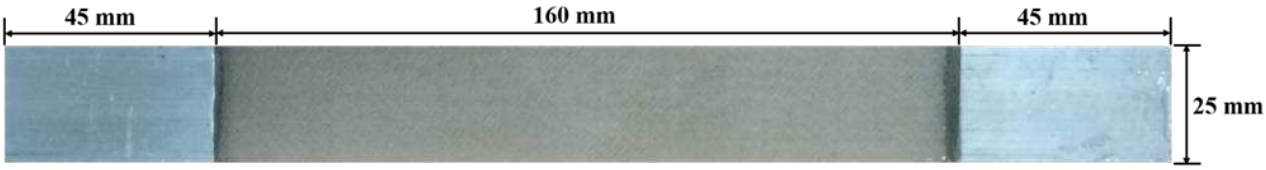

Figure 2 Specimens geometry for Tensile test and Fatigue test

2.3 Testing procedures

The tensile test of prepared specimens was performed on MTS servo-hydraulic universal testing machine (capacity 250 kN) with a crosshead speed of 1 mm/min as per ASTM D3039/3039M-17. Tension-tension fatigue tests were performed as per ASTM D3479/3479M-19 [21] at the stress ratio of 0.1. All the fatigue tests were performed under the load control mode at 5 Hz frequency and five stress levels (45-80% ultimate tensile strength, UTS) using sine wave. For fatigue life prediction of composites, three specimens were tested at five selected stress level. The damage of the composite during the fatigue test was evaluated with a high-resolution camera by placing the LED light source on other side of the specimens.

3. Result and Discussion

3.1 Tensile test

For the fatigue test, four samples that obtained from different fabricated laminate has been tested to examine the ultimate tensile strength of composite laminate. Figure 3 shows the tensile stress-strain curve of composite materials based on rPET tested at cross head speed of 1 mm/min. The ultimate tensile strength of sample 1, sample 2, sample 3, and sample 4 was 289.57 MPa, 264.53 MPa, 304.02 MPa, and 286.58 MPa respectively.

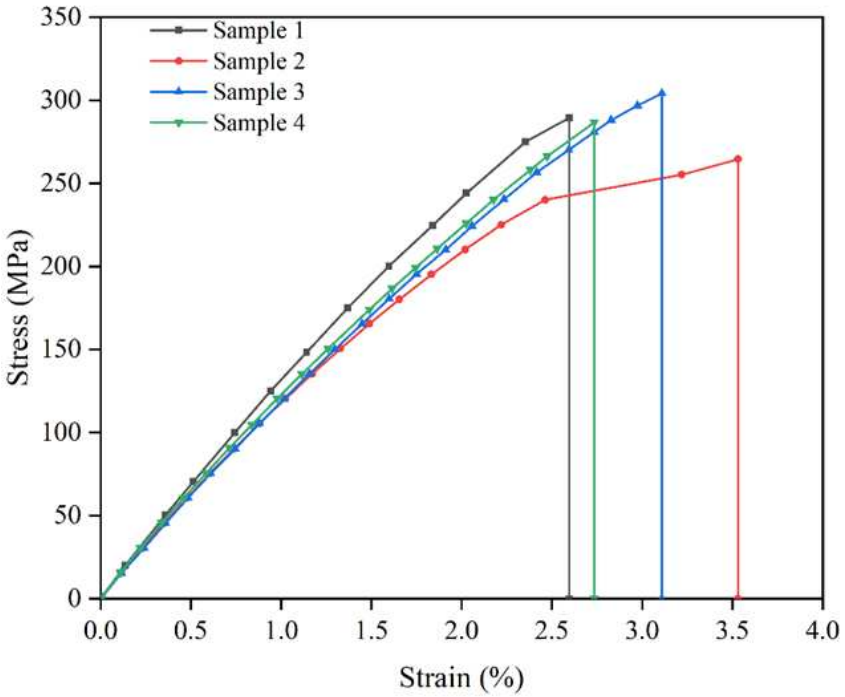

Figure 3 Stress-strain curve of rPET-UPR based composites.

3.2 Fatigue life

Fatigue life or S-N data of composites fabricated with virgin and recycled polyester matrix were plotted on the semilogarithmic scale in terms of normalized maximum stress (σ_{max}/UTS) and the number of cycles to failure (N_f) as shown in Figure 4. The fatigue behavior of composites was modeled with pawer law as follows

$$\sigma_{max} = \sigma_o N^{-1/k} \quad (1)$$

Where σ_o and 1/k are the y-intercept and slope of the S-N curve respectively. The values of these parameters were obtained by linear regression analysis of fatigue data. The estimated values of modeled parameters σ_o and 1/k were given in table 1. From the S-N curve, it was observed that the fatigue life composite materials fabricated with unsaturated polyester based on recycled PET (recycled matrix composites) were less as compared to that of virgin matrix composites. In addition, the slope of the S-N curve trend line of recycled matrix composites was higher as compared to that of virgin matrix composites. This indicate that the fatigue life degradation of recycled matrix-based composite was higher as compared to virgin matrix composite. The lower fatigue life of recycled matrix composites could be attributed to the weak interface and higher degradation of the recycled matrix.

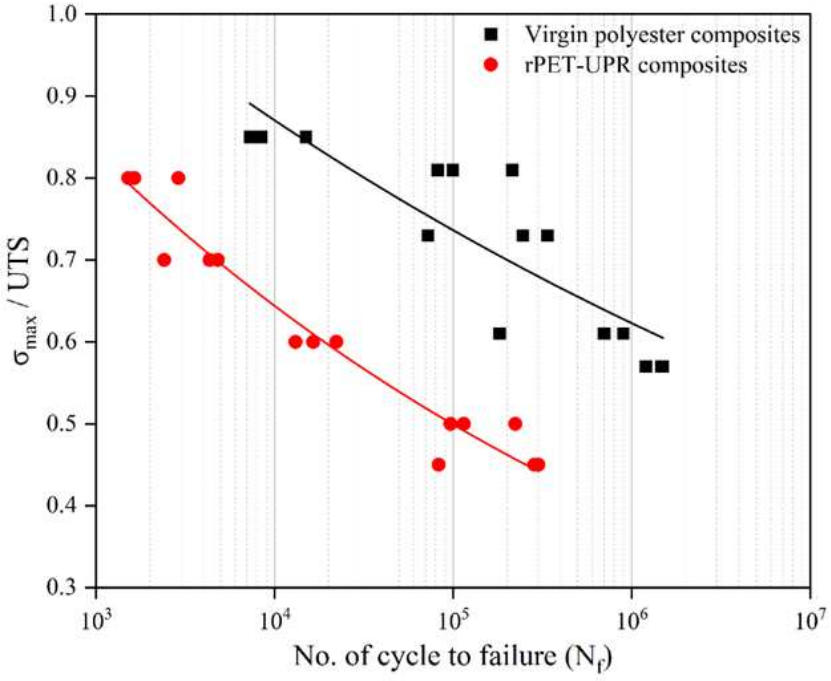

Figure 4 experimental fatigue data and S-N curve of virgin and recycled matrix composites.

3.3 Fatigue damage analysis

Damage development in composite materials is greatly affected by the type of constituent materials, nature of loading, level of loading, etc. The fatigue damage development of rPET-UPR composites at the various fatigue life has been represented in Fig. 4. Where dark regions represent the damage or debonds zone in the sample of their respective number of load cycles. At the initial stage of fatigue loading, local damage was observed (Fig. 5). These local damages were initiated from the edge of the specimens which attributed to the resin deficiency or weak interface at cross overply and increased with increasing the load cycle. It was also noticed that as compared to the high-stress level, the damage zone at low stress level was more uniform as shown in Figure 5a and 5b.

  doi:10.5075/epfl-298799_978-2-9701614-0-0

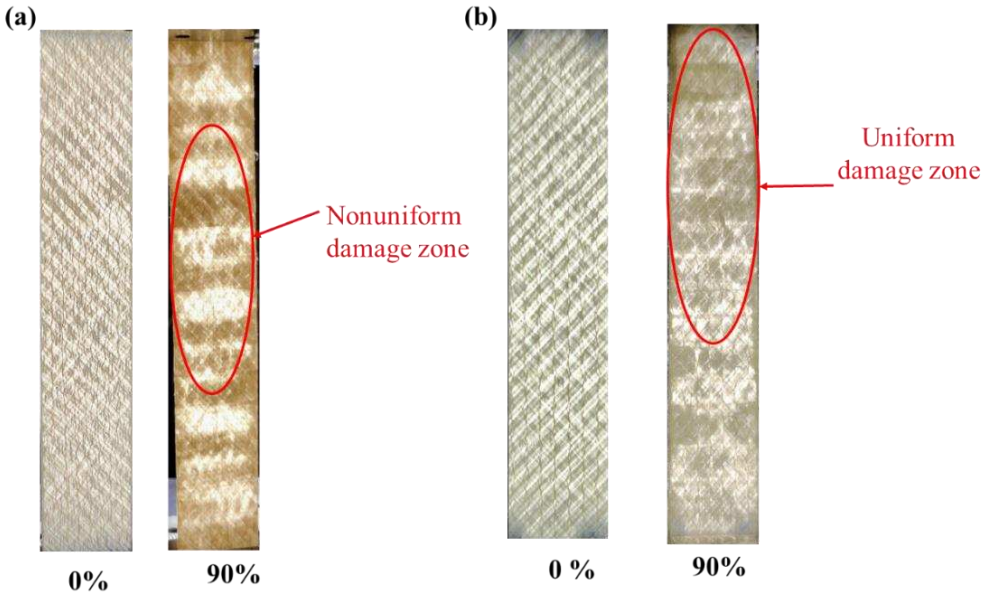

Figure 5 Fatigue damage of tested sample at (a) high stress level (80% of UTS) and (b) low stress level (45% UTS) at various percentages of fatigue life.

4. Conclusion

In this study, the fatigue of rPET based glass fiber composite has been investigated and compared with the virgin polyester matrix composites. For the composite fabrication unsaturated polyester was extracted from the waste PET. The damage development in the composite was examined with the light transmittance technic. The fatigue life of recycled matrix composites materials was lower than that of virgin polyester matrix composites. The fatigue life degradation of recycled matrix composites has higher as compared to virgin matrix composites. As compared to high stress level more uniform damage zone were observed at low-stress levels.

5. References

1. Karayannidis GP, Achilias DS, Sideridou ID, Bikiaris DN. Alkyd resins derived from glycolized waste poly(ethylene terephthalate). Eur Polym J 2005; 41:201–10.
2. Singh AK, Bedi R, Kaith BS. Mechanical properties of composite materials based on waste plastic - a review. Mater Today Proc 2020; 26:1293–301.
3. Torlakoglu A, Güçlü G. Alkyd-amino resins based on waste PET for coating applications. Waste Manag 2009; 29:350–4.
4. Velásquez EJ, Garrido L, Guarda A, Galotto MJ, López de Dicastillo C. Increasing the incorporation of recycled PET on polymeric blends through the reinforcement with commercial nanoclays. Appl Clay Sci 2019; 180:105185.
5. Khoonkari M, Haghighi AH, Sefidbakht Y, Shekoohi K, Ghaderian A. Chemical Recycling of PET Wastes with Different Catalysts. Int J Polym Sci 2015;2015.
6. Liu X, Wen Y, Chen X, Tang T, Mijowska E. Co-etching effect to convert waste polyethylene terephthalate into hierarchical porous carbon toward excellent capacitive energy storage. Sci Total Environ 2020; 723:138055.
7. Paszun D, Spychaj T. Chemical Recycling of Poly(ethylene terephthalate). Ind Eng Chem Res 1997; 36:1373–83.

  doi:10.5075/epfl-298799_978-2-9701614-0-0

8. Shamsi R, Asghari GH, Sadeghi GMM, Nazarpour-Fard H. The Effect of Multiwalled Carbon Nanotube and Crosslinking Degree on Creep–Recovery Behavior of PET Waste Originated-Polyurethanes and Their Nanocomposites. Polym Compos 2017; 39: E1013–E1024.
9. Zhang R, Ma X, Shen X, Zhai Y, Zhang T, Ji C, et al. PET bottles recycling in China: An LCA coupled with LCC case study of blanket production made of waste PET bottles. J Environ Manage 2020; 260:110062.
10. Suh DJ, Park OO, Yoon KH. The properties of unsaturated polyester based on the glycolyzed poly(ethylene terephthalate) with various glycol compositions. Polymer (Guildf) 2000; 41:461–6.
11. Singh AK, Bedi R, Kaith BS. Composite materials based on recycled polyethylene terephthalate and their properties – A comprehensive review. Compos Part B 2021; 219:108928.
12. Abdelhaleem AMM, Megahed M, Saber D. Fatigue behavior of pure polypropylene and recycled polypropylene reinforced with short glass fiber. J Compos Mater 2018; 52:1633–40.
13. Tóth K, Czvikovszky T, Abd-Elhamid M. Radiation-assisted PET recycling using glass fiber reinforcement and reactive additives. Radiat Phys Chem 2004; 69:143–7.
14. F. Ronkay and T. Czigany. Development of composites with recycled PET matrix. Polym Adv Technol 2006; 17:830–4.
15. Novello MV, Carreira LG, Canto LB. Post-consumer polyethylene terephthalate and polyamide 66 blends and corresponding short glass fiber reinforced composites. Mater Res 2014; 17:1285–94.
16. Cantwell WJ. Fracture behavior of glass fiber/recycled PET composites. J Reinf Plast Compos 1999; 18:373–87.
17. Kracalık M, Pospısil L, Slouf M, Mikesova J, Sikora A, Simonık J, et al. Effect of Glass Fibers on Rheology, Thermal and Mechanical Properties of Recycled PET. Polym Compos 2008;29:915–21.
18. Rezaeian I, Jafari SH, Zahedi P, Nouri S. An Investigation on the Rheology, Morphology, Thermal and Mechanical Properties of Recycled Poly (ethylene terephthalate) Reinforced with Modified Short Glass fibers. Polym Compos 2009; 30:993–9.
19. Vassilopoulos AP, Keller Thomas. Fatigue of Fiber-reinforced Composites. Springer Science & Business Media; 2011.
20. ASTM International. ASTM D3039/D3039M Standard Test Method for Tensile Properties of Polymer Matrix Composite Materials. West Conshohocken, PA; ASTM Int 2017.
21. ASTM International. ASTM D3479/D3479M-19 Standard Test Method for Tension-Tension Fatigue of Polymer Matrix Composite Materials. West Conshohocken, PA ASTM Int 2019.

EXPERIMENTAL AND NUMERICAL ANALYSIS OF POST-BUCKLING DELAMINATION OF COMPOSITE PLATE UNDER FATIGUE LOADS

Linge, Liu, Wenli, Liu, Shijun, Guo*

Centre of Excellence for Aeronautics, School of Aerospace, Transport and Manufacturing,
Cranfield University, Cranfield, MK43 0AL, UK
*Corresponding author (wenli.liu@cranfield.ac.uk)

Abstract: *This investigation presents crack growth of composite plates with through-width initial delamination subject to cyclic compression loads. Newly adjusted experimental tests were established to study the post-buckling response of the laminates with single and double embedded delamination, and to determine progressive fatigue failure mechanisms of the post-buckled structures. DIC and a video camera were adopted to measure buckling deformation and crack length. Numerical approaches based on VCCT and CZM procedures were developed to characterise the delamination growth. Fatigue damage growth algorithm was implemented in the CZM model via UMAT. The results of the numerical analysis are compared with experimental results collected, revealing the capabilities and robustness of the proposed numerical model. The study bridged the gap between coupon and structural level in terms of damage tolerant assessment.*

Keywords: Post-buckling; Fatigue; Delamination growth; Modelling

1. Introduction

Composite material has been widely used in aerospace structure for the past decades owing to its superior stiffness-to-weight ratio. But the damage evolution mechanisms of composite are not as well understood as metals, especially under fatigue load. Since compressive loads are more critical than tensile loads, composite plates may easily suffer from buckling particularly for thin-walled structures. For laminates with existed damage, delamination buckling as a local form of buckling, has become a severe phenomenon for such damaged laminates. The local buckling induces a high interlaminate stress at the crack tip that can lead to a propagation of the crack and progressive buckling. This process results in structural instability even catastrophic failure.

Previous research has studied the post-buckling behaviour of skin-stringer debonding for single stringer stiffened panel under static and fatigue loads [1,2]. But phenomenon of delamination buckling has not been clarified in that case. Other studies [3–6] have been carried out under static compression load for structures with single or multiple through-width delaminations in terms of their buckling, post-buckling delamination behaviour and the associated effects of nonlinear deformation. However, fewer studies [7] were performed under fatigue load as it is more complicated due to the complex interaction between nonlinear post-buckling response, different failure modes and accumulation of fatigue damage. Therefore, the investigation of fatigue damage growth in locally post-buckled composite structure is of great importance.

Paris law [8] has been widely used to characterise fatigue crack growth. During the past decades, various numerical techniques have been developed to implement the Paris law into Finite Element (FE) analysis. The Virtual Crack Closure Technique (VCCT), based on the principle of linear elastic fracture mechanics (LEFM), has been exploited by several studies [9–12] to predict

  doi:10.5075/epfl-298799_978-2-9701614-0-0

the fatigue crack growth, showing its validity for specimen-scale and structural components. However, limitation of this technique still exists in coupling with fatigue analysis in geometrically nonlinear domain [13]. In addition, Cohesive Zone Model (CZM) [14–16] has been prominent to simulate fatigue crack growth by utilising interface elements between interlaminate, in association with the Paris law to formulate fatigue damage model.

The aim of this study is to investigate the post-buckling structural behaviour under quasi-static load and delamination propagation under fatigue loading. In this paper, the newly adjusted experiment testing of plates with single or double through-width delamination was established, to achieve on-site continuous measurement of crack growth. Initial embedded through-width delamination with various depths is used to represent critical characteristics of impact damage. Digital Image Correlation (DIC) was used to record out-of-plane buckling deformation of specimens and a video camera was installed near one side of the specimen to allow continuous observation of delamination growth.

2. Test Sample and Experiment

The test samples were made of carbon/epoxy composite material MTC510-T700 prepreg from SHD Composite with a ply thickness of 0.15 mm. The material properties are listed in Table 1. The laminated composite samples were manufactured with a 32-layer quasi-isotropic layup sequence $[90/0/0/90]_{4s.}$ PTFE films (10μm) were inserted as pre-existed through-width delaminations during fabrication. Figure 1 shows the sample dimensions with configuration details listed in Table 2, showing the crack location at different depth across the thickness.

Table 1: Lamina properties of MTC510-T700.

Properties	Value	Unit
Longitudinal Modulus E_1	113	GPa
Transverse Modulus E_2	8.2	GPa
Shear Modulus G_{12}	5	GPa
Poisson's Ratio v_{12}	0.3	
Longitudinal Tensile Strength $0°$	2282	MPa
Transverse Tensile Strength $90°$	1010	MPa
Longitudinal Compressive Strength $0°$	1067	MPa
Transverse Compressive Strength $90°$	558	MPa
In-plane Shear Strength	99	MPa

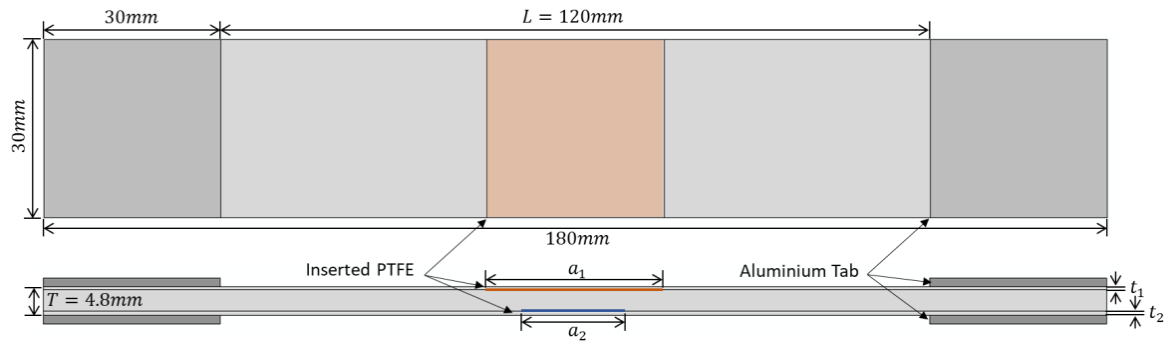

Figure 1. Dimension of samples with through-width delamination

Table 2: Sample configuration and load conditions.

		Group J		Group K	Group L		
Delamination [mm]	a_1 (a_1/L)	30 (25%)		30 (25%)	30 (25%)		
	t_1 (t_1/T)	0.45 (9%)		0.75 (16%)	0.45 (9%)		
	a_2 (a_2/L)	-		-	20 (17%)		
	t_2 (t_1/T)	-		-	0.75 (16%)		
Sample		J1	J2	K1	L1	L2	L3
Test type		Static	Fatigue	Static	Static	Fatigue	Fatigue
Cyclic load	Maximum [kN]	-	17.5	-	-	24.5	26
	Ratio to ultimate load	-	61%	-	-	85%	90%

The experimental tests were performed with two parts using a 100 kN hydraulic-powered Instron 8100 test machine. Quasi-static tests were conducted initially to identify the fatigue load range based on the load-bearing capacity, as well as investigating the buckling and post-buckling behavior of the samples. Secondly, the fatigue tests were performed under an in-plane compression-compression cyclic loading with a 5 Hz frequency and a value of 0.1 was set for the load ratio *R*. The maximum fatigue loads applied with a constant amplitude ranged from 60% to 90% of static ultimate load. The fatigue test was disrupted at regular intervals for DIC and video camera to capture typical damage growth. Fatigue cycles for each sample were run around 300,000 cycles to limit the testing time.

3. Numerical Modelling

The numerical model of plate with embedded delamination was accomplished by the commercial FE package ABAQUS/Standard. The FE models were firstly developed using 2D plain strain element (CPE4R). But due to the restriction of accuracy and the limitation that CPE4R element has brought to the model, 3D models with continuum shell elements (SC8R) were adopted. In the quasi-static analysis, VCCT and CZM procedures were implemented into the FE models respectively to characterise delamination propagation. Figure 2 illustrates a typical delamination buckling model simulated by CZM procedure. The aluminium tab sections were not involved to reduce the total number of elements and computational time. The fixed end has its degrees of freedom fully constrained while the loading end has only its x-direction free. Two layers of cohesive elements (COH3D8) are placed between top and bottom sublaminate.

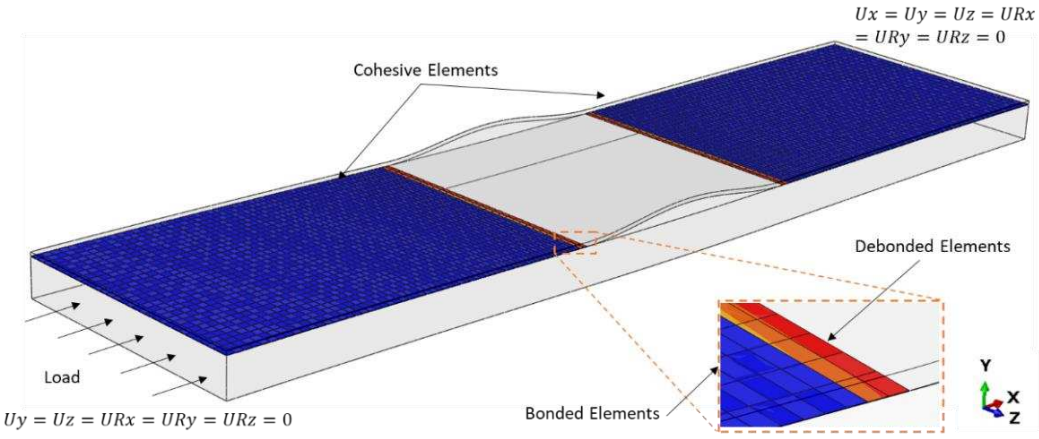

Figure 2. Numerical models of the laminates with through-width delamination

  doi:10.5075/epfl-298799_978-2-9701614-0-0

In the fatigue analysis, the fatigue damage model developed by Turon [14] was adopted, from which the normalized form of Paris Law, as shown in Eq (1), was involved to accommodate the change of mode-mixture in G_c.

$$\frac{da}{dN} = C\left(\frac{\Delta G}{G_c}\right)^m \tag{1}$$

$$log\, C = log\, C_I + \left(\frac{G_{II}}{G_T}\right) log\, C_m + \left(\frac{G_{II}}{G_T}\right)^2 log\, \frac{C_{II}}{C_m C_I} \tag{2}$$

$$m = m_I + m_m \left(\frac{G_{II}}{G_T}\right) + (m_{II} - m_I - m_m)\left(\frac{G_{II}}{G_T}\right)^2 \tag{3}$$

where C and m are mode-ratio dependent fatigue parameters, G_c is the mixed-mode fracture toughness and $\Delta G = G_{\max}(1 - R^2)$. C_{m} and m_{m} are the fatigue parameters under mixed-mode condition, whilst $C_{\mathrm{I}}, m_{\mathrm{I}}, C_{\mathrm{II}}$ and m_{II} are the ones under pure mode conditions. The constant amplitude fatigue loading was introduced via the 'envelope load method' working with cycle jump strategy [17], to reduce the computational time.

4. Results and Discussion

4.1 Quasi-Static Tests and Simulation

Firstly, test results were obtained to exhibit the load-bearing capacity, critical buckling and post-buckling response of the samples under quasi-static compressive load. Figure 3 presents the quasi-static loading history obtained from Sample J1 with the load-displacement curve compared with numerical result. It shows that the linearly increasing load curve was not affected by the local buckling, which indicated it did not lose the load capacity until the occurrence of global buckling at 27.8 kN. The simulation results obtained by both procedures keep consistent with the test results. In addition, the critical buckling loads as well as ultimate load from these three static tests compared with simulation are presented in Table 3. The critical loads from simulation are proved to have a good consistency to the test results. The uncertainties may be mainly resulted from experimental factors, such as the material imperfections from test specimens and some extent of misalignment between the two loading surfaces.

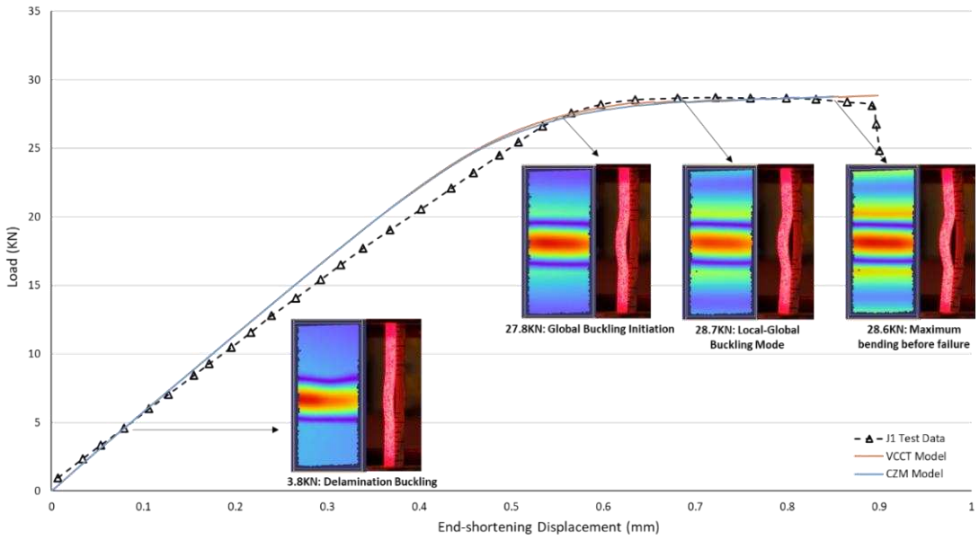

Figure 3. Load curve from J1 static test associated with images of characteristic loads

  doi:10.5075/epfl-298799_978-2-9701614-0-0

Table 3: Loads from static test samples compared with simulation.

Critical Load [kN]		Sample J1	Sample K1	Sample L1
Local buckling	Test	3.8	19.9	4
	Modelling	3.6	18.3	3.5
	Difference	5%	8%	12%
Global buckling	Test	27.2	26.8	26.2
	Modelling	26.2	25	24.5
	Difference	4%	7%	6%
Ultimate load	Test	28.7	27.9	28.7
	Modelling	28.5	25.9	27.6
	Difference	1%	7%	4%

In terms of post-buckling, two mixed-mode post-buckling responses were found, i.e., local-global mixed mode and opening mixed mode. In the local-global mixed-mode response, the plate exhibits initially a local buckling response, while the occurrence of global buckling brings both sublaminates to shift into negative direction. In this mode it is the global buckling that dominates its post-buckling response. However, in the opening mixed mode, the local buckling mode dominates where both sublaminates are deflecting in opposite direction. Figure 4 shows the results of the two specific post-buckling responses. It demonstrates the Samples J1 and L1 which have a thinner top sublaminate (9%) follows the local-global mixed mode while the Sample K1 with thicker top sublaminate (16%) exhibits the opening mixed mode. Moreover, by comparing tests with the modelling results, it is found there is a good agreement in the nonlinear post-buckling deformation.

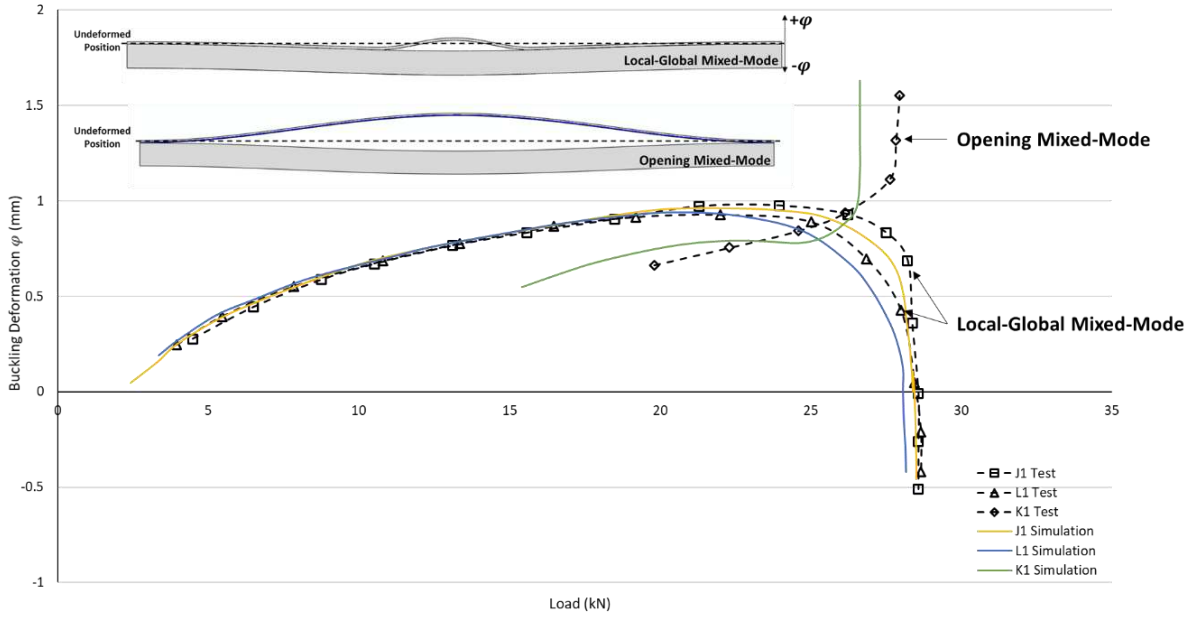

Figure 4. Buckling deformation of static test samples compared with numerical models

  doi:10.5075/epfl-298799_978-2-9701614-0-0

4.2 Fatigue Tests and Simulation

In this section, fatigue test results from three Samples J2, L2 and L3 which have different configurations and various fatigue loads are exhibited and discussed. The fatigue test results are compared with numerical simulations, in terms of measurement of crack length growth and crack growth rate. Figure 5 shows the images captured from video camera and DIC system for Sample J2, it reveals the initial crack grew with respect to fatigue cycles up to 304,000 cycles. The growth of crack and growth rate versus fatigue cycles, as illustrated in Figure 6, are interesting to show that the crack growth rate drops with increasing fatigue cycles. By comparing with numerical results, the numerical models well captured the behaviour of the reduction of crack growth rate, and the predicted results keep consistent with test results.

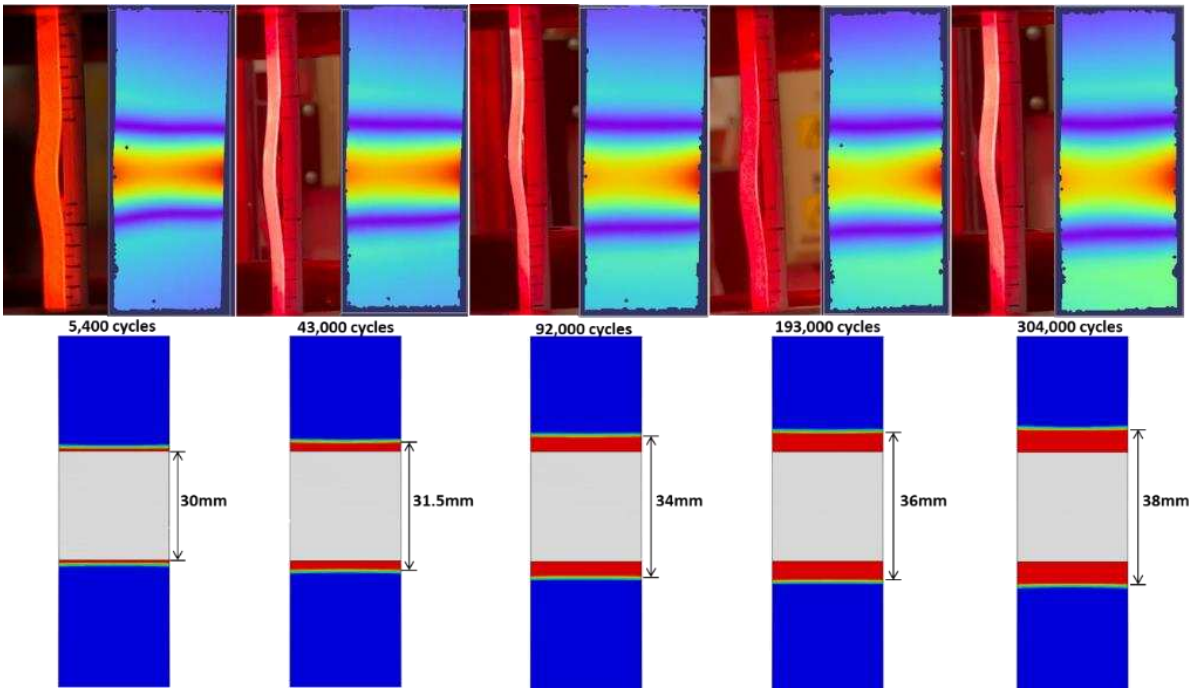

Figure 5. Fatigue delamination growth of J2 sample obtained from DIC and CZM simulation.

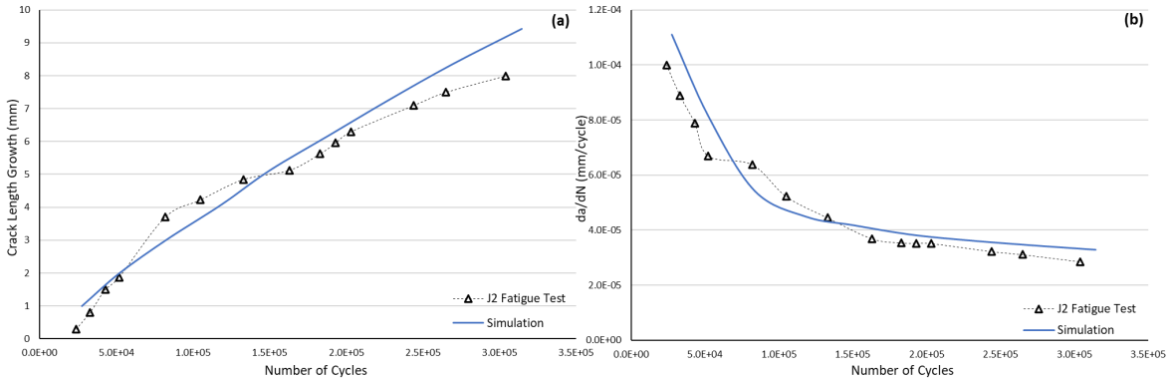

Figure 6. Fatigue crack length growth (a) and crack growth rate da/dN (b) from J2 fatigue test compared with simulation.

Moreover, further comparison was carried out on Sample L2 and L3 fatigue samples which have identical configuration but different fatigue load levels. The fatigue results are compared and expressed in Figure 7. It is interesting to note that both samples have a similar crack growth rate

at initial fatigue stage until 50,000 cycles where the crack growth rate diverts – Sample L3 with 26 kN load level shows a faster growth rate than the L2 sample with 24.5 kN load level. In terms of fatigue life, it can be deducted that the sample with lower fatigue stress level will have a longer fatigue life than that suffered from a higher fatigue stress level. In addition, the second cracks close to the bottom sublaminate from both Sample L2 and L3 have not found buckled out nor propagated, which indicates that the stiffness of the bottom sublaminate is higher than that of the top sublaminate due to the shorter and deeper crack. This means that the fatigue cycles of 200,000 have not made the bottom crack reach the fatigue threshold.

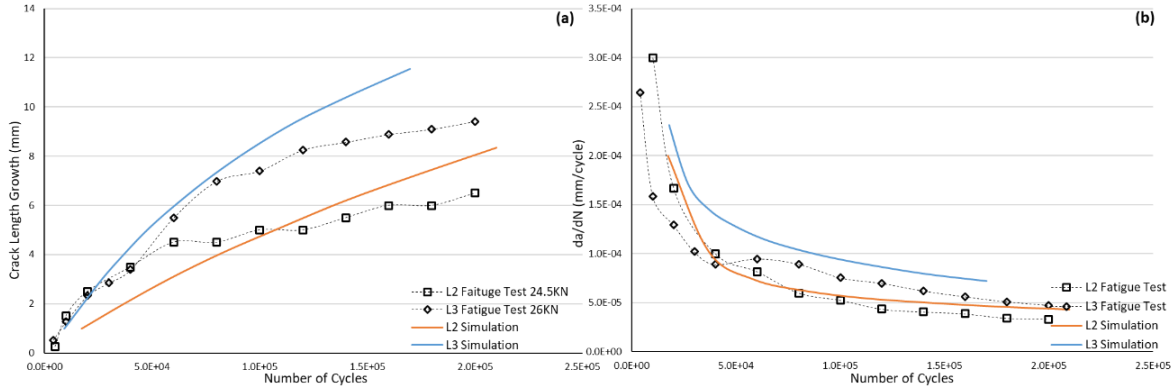

Figure 7. Fatigue crack length growth (a) and crack growth rate da/dN (b) from L2, L3 fatigue test compared with simulation.

5. Conclusions and Future Work

In the paper, the post-buckling response and associated damage growth behavior of composite samples with embedded through-width delamination under post-buckling fatigue load has been experimentally and numerically investigated. Quasi-static and fatigue tests were applied to these samples with different configurations and load levels. Numerical models based on VCCT and CZM approaches were established. The results from numerical analysis have proven to be consistent with the results obtained from the experimental tests, indicating the feasibility and robustness of the numerical model. Two different modes of post-buckling response were found, which are local-global mixed mode and opening mixed mode. Fatigue analysis was developed for the local-global mixed mode to determine the fatigue crack growth. And the robustness of the proposed numerical models was determined. The validity of numerical model could benefit on reducing the number of tests required for design and certification of composite structures.

The current study bridges the gap between coupon and structural level testing and is also considered to contribute on the damage tolerance analysis and relevant post-buckled structure design. Regarding the future work, it is vital to study the effects of different post-buckling mode on the fatigue damage growth behaviour and fatigue life, which is considered to benefit on damage tolerant analysis and optimized design suggestions.

6. References

1. Bisagni C., Vescovini R., Dávila CG. Single-stringer compression specimen for the assessment of damage tolerance of postbuckled structures. Journal of Aircraft. American Institute of Aeronautics and Astronautics; 1 March 2011; 48(2): 495–502.
2. Dávila CG., Bisagni C. Fatigue life and damage tolerance of postbuckled composite stiffened

structures with indentation damage. Journal of Composite Materials. SAGE Publications Ltd STM; 19 June 2017; 52(7): 931–943.
3. Liu PF., Gu ZP., Peng XQ., Zheng JY. Finite element analysis of the influence of cohesive law parameters on the multiple delamination behaviors of composites under compression. Composite Structures. Elsevier; 1 November 2015; 131: 975–986.
4. Köllner A., Kashtalyan M., Guz I., Völlmecke C. On the interaction of delamination buckling and damage growth in cross-ply laminates. International Journal of Solids and Structures. Elsevier Ltd; 1 October 2020; 202: 912–928.
5. Suemasu H., Irie T., Ishikawa T. Buckling and post-buckling behavior of composite plates containing multiple delaminations. Journal of Composite Materials. SAGE Publications Ltd STM; 13 November 2008; 43(2): 191–202.
6. Han SC., Lee SY., Rus G. Postbuckling analysis of laminated composite plates subjected to the combination of in-plane shear, compression and lateral loading. International Journal of Solids and Structures. Pergamon; 1 September 2006; 43(18–19): 5713–5735.
7. Hosseini-Toudeshky H., Saeed Goodarzi M., Mohammadi B. Prediction of through the width delamination growth in post-buckled laminates under fatigue loading using de-cohesive law. Structural Engineering and Mechanics. 10 October 2013; 48(1): 41–56.
8. Paris P., Erdogan F. A critical analysis of crack propagation laws. Journal of Basic Engineering. 1 December 1963; 85(4): 528–533. Available at: DOI:10.1115/1.3656900
9. Krueger R. Development of a benchmark example for delamination fatigue growth prediction. Fatigue Compos. Mater. 2010; 3: 54–73.
10. Krueger R. The virtual crack closure technique for modeling interlaminar failure and delamination in advanced composite materials. Numerical Modelling of Failure in Advanced Composite Materials. Woodhead Publishing; 1 January 2015; : 3–53.
11. Krueger R., Deobald L., Gu H. A benchmark example for delamination growth predictions based on the single leg bending specimen under fatigue loading. Advanced Modeling and Simulation in Engineering Sciences. 2020; 7(1): 11.
12. De Carvalho N V., Mabson GE., Krueger R., Deobald LR. A new approach to model delamination growth in fatigue using the Virtual Crack Closure Technique without re-meshing. Engineering Fracture Mechanics. Elsevier Ltd; 1 December 2019; 222.
13. Bisagni C., Dávila C. Modeling delamination in postbuckled composite structures under static and fatigue loads. 2013.
14. Turon A., Costa J., Camanho PP., Dávila CG. Simulation of delamination in composites under high-cycle fatigue. Composites Part A: Applied Science and Manufacturing. Elsevier; 1 November 2007; 38(11): 2270–2282.
15. Harper PW., Hallett SR. A fatigue degradation law for cohesive interface elements – development and application to composite materials. International Journal of Fatigue. Elsevier; 1 November 2010; 32(11): 1774–1787.
16. Robinson P., Galvanetto U., Tumino D., Bellucci G., Violeau D. Numerical simulation of fatigue-driven delamination using interface elements. International journal for numerical methods in engineering. Wiley Online Library; 2005; 63(13): 1824–1848.
17. Van Paepegem W., Degrieck J. Fatigue degradation modelling of plain woven glass/epoxy composites. Composites Part A: Applied Science and Manufacturing. Elsevier; 1 October 2001; 32(10): 1433–1441.

IMPACT OF CURING ON RESIDUAL STRESSES FORMATION AND FATIGUE BEHAVIOUR OF CARBON/EPOXY LAMINATE COMPOSITES – APPLICATION TO RACING YACHTS

LE PALABE Antoine[1,2], CARRERE Nicolas [2], MARCO Yann [2], KERYVIN Vincent[1]
MARCHANDISE Adrien[3]

[1] Univ. Bretagne Sud, UMR CNRS 6027, IRDL, F-56321 Lorient
[2] ENSTA Bretagne, UMR CNRS 6027, IRDL, F-29200 Brest
[3]AVEL ROBOTICS, F-56100 Lorient

Abstract: *One of the levers to gain in performance of composite structures used for racing yachts (IMOCA, America's Cup) is by a better knowledge between the manufacturing process and the final properties. This study addresses one aspect of this objective. The objective is to study the impact of the manufacturing process on the fatigue behaviour of carbon/epoxy laminate. More precisely, the work aimed at understanding the link between the curing parameters, the residual stresses in the composite laminate and the fatigue behaviour. This work is carried on in collaboration with two companies from the Brittany Sailing Valley dealing with the design and manufacturing of composite parts.*

Keywords: Viscoelasticity; Fatigue; Self-heating; Thermosets; Curing

1. Introduction

In recent years, for the sailing teams involved in yacht racing which have been using more and more laminate composite materials, the fatigue behaviour has become a major issue. Three aspects are at stake: the first one is competitiveness and involves the need of performance and so the lightening of the structures, the second one concerns the security of the sailors and the need to keep them safe during the race especially for transatlantic races or round-the-world races. Finally, reducing the cost of those structures is still an important challenge.

It's in this particular context that this study is made. The idea here is to be able to observe the impact of residuals stresses, in the composite part, on the fatigue lifetime. No matter what the application field is, or the material used, the manufacturing leads to internal residuals stresses that are more or less controlled. In carbon / epoxy laminate composites, it is known that those residual stresses are mainly due to the difference in coefficients of thermal expansion between the matrix and the fibres during the cure. The viscoelastic properties of the matrix tend to relax those residual stresses after the complete cure. To get a better understanding of the complete behaviour, it is important for us to make a characterization from the matrix scale to the composite part scale.

2. Objective and methodology

2.1 Epoxy cure modelling

Thanks to Avel Robotics company, partner of this work, and the literature, it has been noticed that the curing cycle has a major impact on the formation of residuals stresses. Indeed, for a same final state of the resin, the faster the curing is, the higher the level of residual stresses is. An in-house tool to simulate curing cycle has been developed to define different cure cycles that

  doi:10.5075/epfl-298799_978-2-9701614-0-0

lead to a similar final reticulation of the resin. This tool is based on the phenomenological theory developed by KAMAL and SOUROUR (1), then adapted by Fournier (2). This method allows to define two cure cycles extremely different, showed in the Figure 1 : Curing cyclesFigure 1. Those two cycles lead to a curing rate of approximatively 95%. They will be used in the rest of the study to obtain two different states of residual stresses.

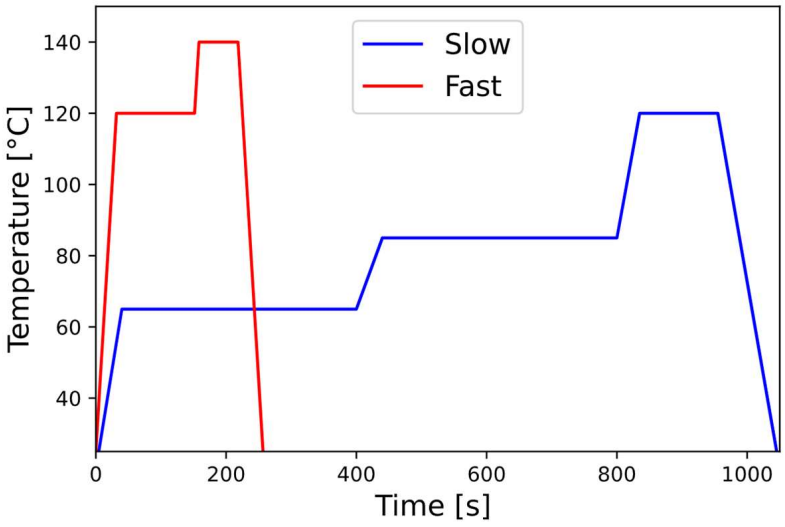

Figure 1 : Curing cycles

2.2 Residual stresses

A lot of methods exist to analyse residual stresses in materials, some of them being usable for composites materials (see (3) for more details). These methods are divided in two main categories: the destructive ones and the non-destructive ones. In the first one we can find methods such as the hole drilling method, the ring-core method and the ply sectioning method. In the second category, there are methods such as optical methods or methods using sensors that are not completely adaptable to composite materials. Between these two categories lies the measurement of curvature method. It is considered as a destructive method because one needs to create an asymmetrical part to measure its out of plane deformation. But one can also consider it as a non-destructive method because one can use a monitoring of the curvature in a long period of time. This last point is interesting in our case because it allows to have an observation of the stress relaxation with time, depending on the temperature of storage. The main drawback of this method is that it is a qualitative observation, and you need a model to have a quantification of the internal stresses.

For the first step of our study the qualitative aspect of this method is sufficient, and a complete modelling will be considered in future works. To create two different parts with two different residual stress states, we used both cycles of cure defined previously on three asymmetrical laminate plate $[90_2{:}0_2]$. Two of them were stored at room temperature and the bending radius was measured from time to time. Figure 2, first, shows the differences of bending radius just after the cure. The slow cycle leads to a bending radius of 532 mm while the fast one leads to 411 mm. Those two measures confirmed that the cycle of cure has a major impact on the formation of residuals stresses. During storage at room temperature, this method allowed us to observe the stress relaxation by noticing a growth in the bending radius. It is still important to notice that for an equivalent time at room temperature, the difference in bending radius still is important.

  doi:10.5075/epfl-298799_978-2-9701614-0-0

The study of (4) showed the importance of temperature on the stress relaxation. Indeed, the closest the part is from his glass transition temperature, the fastest the stress relaxation will be. A point of or study is to do fatigue, so we had to find a solution not to have to manufacture each sample one at the time. We had to validate the hypothesis of non-relaxation at temperature far from glass transition temperature. Figure 2 shows the result obtained for a storage at -18 °C. It shows that the bending radius is constant with the time of storage. That confirms the assumption of non-relaxation at low temperature. So, the sample will be manufactured the same way and stored at -18 °C to ensure a common stress state between the sample from the same part.

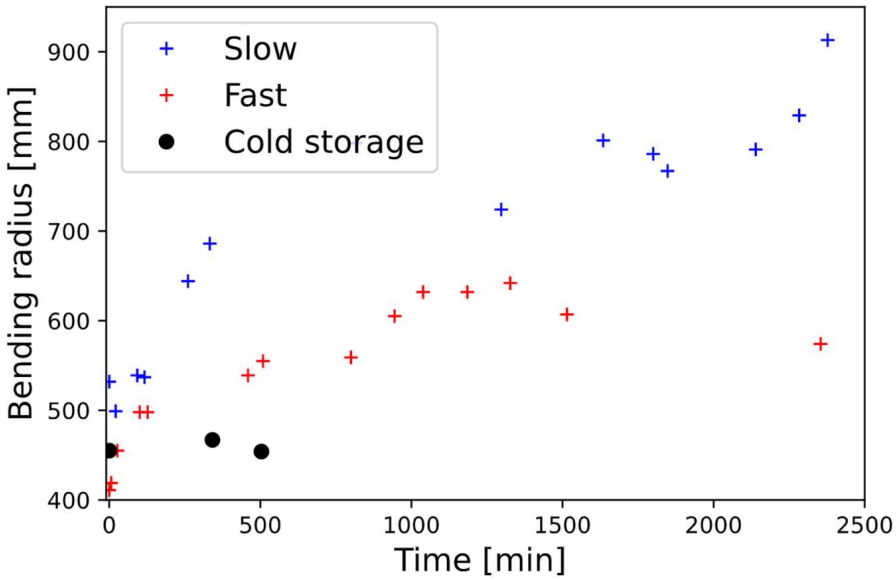

Figure 2 : Evolution of the bending radius at room temperature

2.3 Materials and manufacturing

The epoxy resin used is the epoxy XB3515 developed by HUNTSMAN with a glass transition temperature of 130 °C appropriate for sailing industries. The carbon fibres are the UTS50 reference impregnated by VITECH COMPOSITE. The manufacturing of the plate is made by laying-up unidirectional plies. All the manufacturing is made in AVEL ROBOTICS's factory with controlled temperature and hygrometry. A quality procedure is used to minimize the apparition of porosity, which is a common defect in carbon / epoxy composite material. The expertise of AVEL ROBOTICS allow us to obtain a marginal proportion of porosity. The proportion of porosity is considered as equal in both residual stress state. The curing of the plate is made in an autoclave with temperature control at different strategic places. Four thermocouples are used to ensure the compliance with the thermal instruction. One measures the air temperature, one the temperature of the metallic mould and two the temperature of the plate in the thickness. The laminate stacking used is quasi-isotropic $[0/-45/+45/90]_s$. This particular stacking allows us to have the two plies at $\pm 45°$ one after the other. It is a matter of importance for us to observe easily the impact of residual stresses on delamination. Once the curing is made, the plate are cut, with a waterjet machine, into samples of 250x25 mm^2 with a thickness of 2.5 mm.

  doi:10.5075/epfl-298799_978-2-9701614-0-0

3. Results and discussion

3.3 Monotonic tension

Monotonic tension tests are carried out as a first approach providing information on fracture mode of the samples. Figure 3 and Figure 4 show a good reproducibility both for the low or high residual stress states. It shows a failure stress similar for the two states between 650 and 700MPa. It also shows an abrupt loss of stiffness in the two different states. This is due to the delamination between the two plies at $\pm 45°$. It can be noticed that this drop-in stiffness appears 50 MPa later on the high residual stress state. This demonstrates a first impact of residual stresses on the behaviour of laminate composite. It is now a matter of interest to see if we can see any difference on the fatigue lifetime.

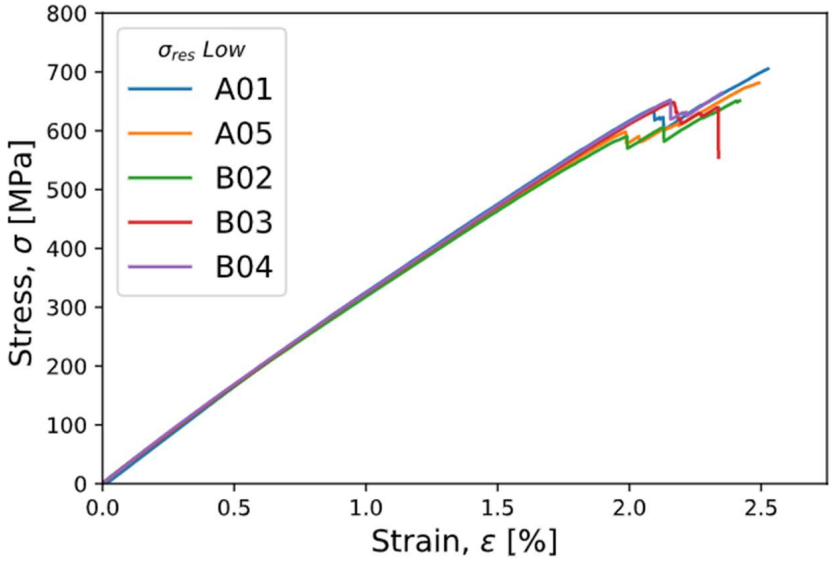

Figure 3 : Monotonic tension on low residual stresses state samples

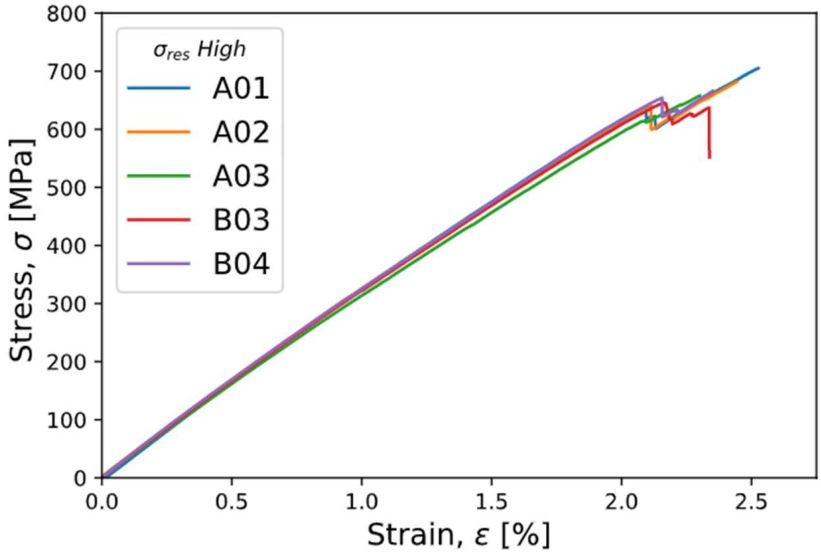

Figure 4 : Monotonic tension on high residual stresses state samples

  doi:10.5075/epfl-298799_978-2-9701614-0-0

3.4 Fatigue and Self-heating

The self-heating method is based on a theory aimed to link the dissipation, caused by a sample subjected to a cyclic solicitation, to damage creation in the part (5). This damage is then linked to a fatigue lifetime. The final objective is to have a rapid prediction. To do so the procedure to follow is quite simple, the point is to perform a series of cyclic loadings and rise the amplitude of stress between each step. In our case, the solicitation mode is tension/tension with a stress ratio R=0.1. Each step is consists in 50 cycles, at a frequency of 2 Hz, and a cooling phase to go back to the equilibrium temperature of the sample.

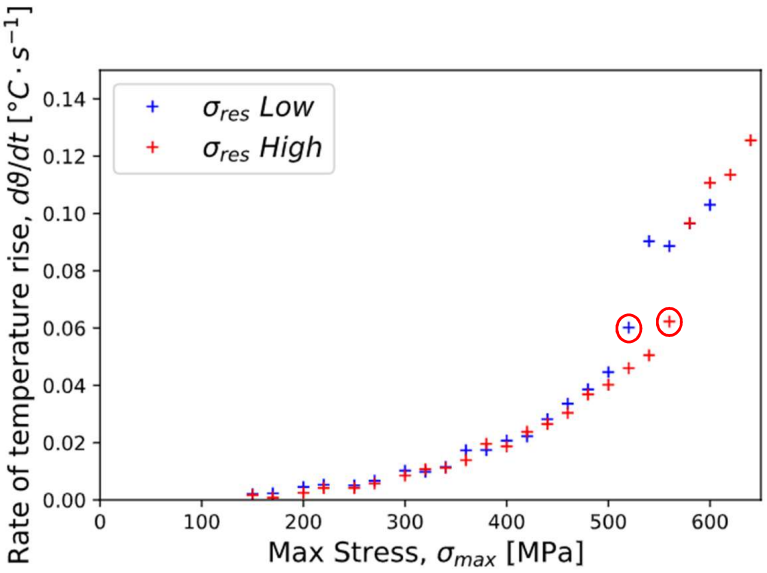

Figure 5 : Comparison of the rate of temperature rise for the different state of residual stresses

The results obtained by this method are shown in Figure 5. The delamination phenomenon is visible as a stabilization of the dissipated heat. It is clearer on the signal obtained for the low residual stress states with a slight diminution of the elevation of temperature between two steps. Again, the delamination appears earlier for the low residual stress state. On Figure 5, the circles indicate the stress at which the delamination have an effect on the dissipation. The self-heating curves will be discussed in more detail during the talk.

3.5 S-N curves

Figure 6 and Figure 7 show the S-N curves for both states of residual stresses. Even if the number of results is limited since other tests are currently being carried out, the tendencies show a slight difference between the two states. Taking a lifetime of 10^6cycles, the approximation made gives a maximal stress of 500 MPa for the low residual stress state, while the one for a high stress state give 430 MPa.

  doi:10.5075/epfl-298799_978-2-9701614-0-0

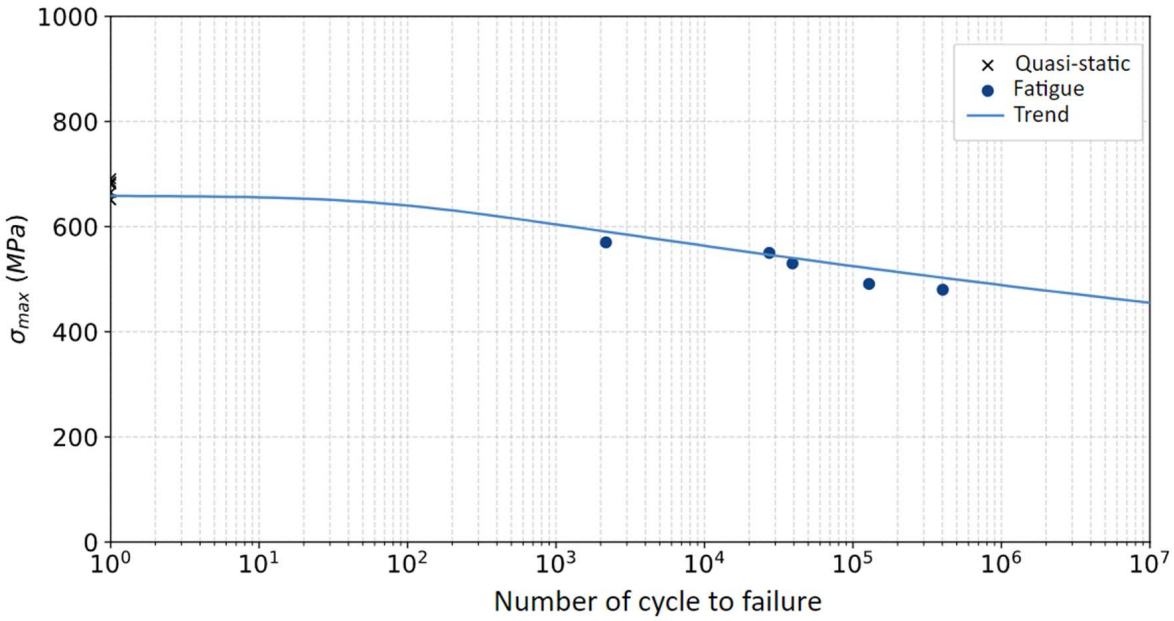

Figure 6 : S-N curve for the low residual stress state

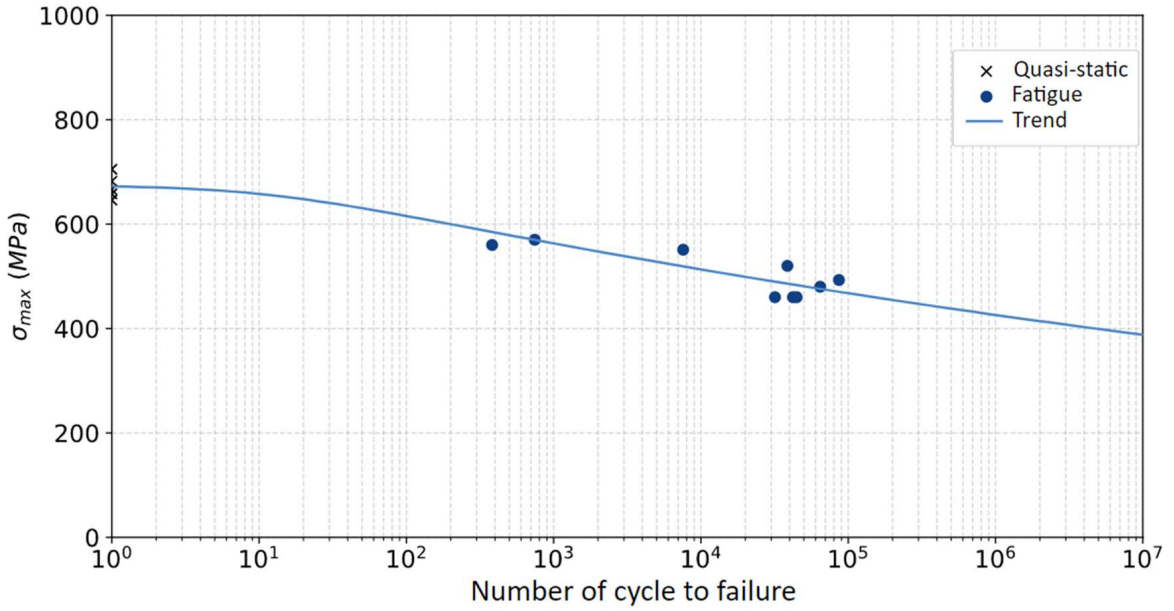

Figure 7 : S-N curve for the high residual stress state

  doi:10.5075/epfl-298799_978-2-9701614-0-0

4. References

1. **KAMAL, M and SOUROUR, S.** *Kinetics and Thermal Characterization of Thermoset Cure.* 1973, POLYMER ENGINEERING AND SCIENCE, JANUARY, 1973, pp. 59-64.

2. **FOURNIER, J., et al.** *Changes in Molecular Dynamics during Bulk Polymerization of an Epoxide-Amine System As Studied by Dielectric Relaxation Spectroscopy.* 1996, Macromolecules, pp. 7097-7107.

3. **SHOKRIEH, M. M.** *Residual stresses in composite material.* s.l. : Woodhead publishing, 2014.

4. **BENAVENTE MIANA, M.** *Visocelastic distortion during manufacturing and post-curing of thermoset composites : characterization and modeling.* ÉCOLE POLYTECHNIQUE DE MONTRÉAL : s.n., 2017.

5. **LEVEUF, Louis, et al.** *Fast screening of the fatigue properties of thermoplastics reinforced with short carbon fibers based on thermal measurements.* 2018, Polymer Testing, pp. 19-26.

  doi:10.5075/epfl-298799_978-2-9701614-0-0

FATIGUE CHARACTERIZATION OF GLASS FIBRE – BIO BASED THERMOSET COMPOSITE INTENDED FOR OFFSHORE RENEWABLE ENERGY APPLICATIONS

Akshay, Hejjaji [a], Alexandre, Portela [a], Anthony, Comer [a]

a: Bernal Institute, School of Engineering, University of Limerick, Limerick, Ireland – akshay.hejjaji@ul.ie

Abstract: *The harsh and corrosive marine environment poses a challenge in terms of efficiency, maintenance and durability of the steel structures used in offshore renewable energy structures. Fiber reinforced composites are a suitable alternative owing to their excellent corrosion resistance. However, the industry refrains from large-scale implementation of composite offshore energy structures due to the lack of understanding about the behaviour of composites. With the aim of filling these research gaps FIBREGY Horizon 2020 EU, funded project was initiated to enable the extensive use of the FRP materials in the next generation of Offshore Wind and Tidal Power (OWTP) structures. In this research, the fatigue behaviour of glass fiber/bio-based thermoset composite is investigated by subjecting the coupons (±45°) to fatigue loading instrumented with thermography, strain gauge and acoustic-emission transducers. In addition to obtaining an S-N curve, the damage induced by fatigue loading is quantified in terms of heat dissipation and acoustic energy for rapid estimation of the fatigue limit using temperature stabilization method.*

Keywords: Glass fiber reinforced composites (GFRP); Fatigue testing; IR Thermography; Acoustic emission.

1. Introduction

The climate change goals have persuaded industries in all sectors to initiate environment centric actions to reduce the carbon footprint of their respective activities. The energy sector in particular is taking strides in this regard by laying emphasis on renewable technology like offshore wind and tidal energy. Offshore wind and tidal energy can contribute significant supply of renewable and clean energy. Offshore wind energy is the most mature technology in terms of development, policies and present and potential installed capacity [1]. While offshore renewable energy has great growth, it is not devoid of challenges. The harsh and corrosive marine environment poses a challenge in terms of efficiency, maintenance and durability of the steel structures, which consequently increase the installation and maintenance costs. The majority of construction material is steel and all of this is subjected to degradation by corrosion, which accounts for 60% of maintenance costs. In addition, the life of these installations is curtailed despite preventive maintenance thus making offshore renewable energy an unfavourable investment [1].

Composites, especially glass fibre reinforced (GFRP) composites can be a suitable alternative to steel, owing to their low cost compared to other composites, high strength to weight ratio and most importantly, corrosion resistance. However, despite such advantages, the industry refrains from the large-scale implementation of composite offshore energy structures due to the lack of

  doi:10.5075/epfl-298799_978-2-9701614-0-0

understanding about the behaviour of such materials under a variety of loading conditions. With the aim of filling these research gaps the FIBREGY Horizon 2020 EU funded project was initiated to enable the extensive use of FRP materials in the next generation of Offshore Wind and Tidal Power (OWTP) structures. As a part of this project, innovative FRP materials, design procedures, guidelines, inspection and monitoring methodologies will be audited and qualified for offshore applications to finally build a real scale prototype for validation. Given that these structures must endure several decades of efficient operation, adequate knowledge in terms of the fatigue behaviour of the materials used is required for the purpose of design and certification, which forms the focus of the present research.

In this study, the behaviour of glass fibre/bio-based InfuGreen 810 GFRP composite under fatigue loading is investigated. GFRP composite test coupons with layup [±45°] are subjected to tension-tension fatigue tests instrumented with infrared thermography, strain gauge and acoustic-emission transducers. The damage induced by fatigue loading is quantified in terms of heat dissipation (specimen temperature from IR camera) and acoustic energy output. The fatigue loading induced damage is quantified from the heat and energy data and is used to estimate the fatigue limit using a fast and innovative temperature stabilisation method. It is important to mention that, the temperature rise due to heat dissipation has been used by several researchers for quicker estimation of the endurance limit by temperature stabilization method without the use of time-consuming Wöhler or S-N curves approach. Initially, this temperature stabilization method was used for metallic materials [2,3], however some studies [4] have successfully adopted this method for composite materials and produced effective results. The S-N curve for the new GFRP material is obtained by performing classical tests and is used to confirm the fatigue limit values obtained by the new method. Finally, the data obtained from tests is used to determine the accuracy of the obtained S-N curve from Miner's rule.

2. Materials and methods

2.1 Composite material

For manufacturing the GFRP laminates glass fiber fabric (unidirectional (UD) non-crimp fabric made from H2026 glass fiber tows, 1182 g/m²) was sourced from Sartex and InfuGreen 810 with SD 8824 hardener, a two-component epoxy system was sourced from Sicomin. InfuGreen 810 is specially formulated for resin transfer processes, such as injection or vacuum infusion, which is produced from 38% of plant origin carbon and thus has a lower environmental impact than standard epoxy systems. Additionally, its low viscosity (750 mPas at 25° C) at ambient temperature enables infusion of large structures at room temperature, which actually is a major requirement for manufacturing OWTP structures. Glass fiber reinforced plastic (GFRP) laminates of size 450 mm × 450 mm were manufactured with 16 plies i.e. $[\pm 45°]_{8s}$ of fabric prepared on a glass mould by vacuum assisted resin transfer moulding (VARTM) at room temperature. The laminate was left to cure at room temperature for 24 hours and later post-cured at 60° C for 16 hours. GFRP test coupons of size 330 mm × 25 mm were extracted from the laminate using abrasive water jet cutting and then tabbed with aluminium using 3M DP 8005 adhesive. Figure 1. represents the dimensions of the test coupons used for the fatigue tests.

  doi:10.5075/epfl-298799_978-2-9701614-0-0

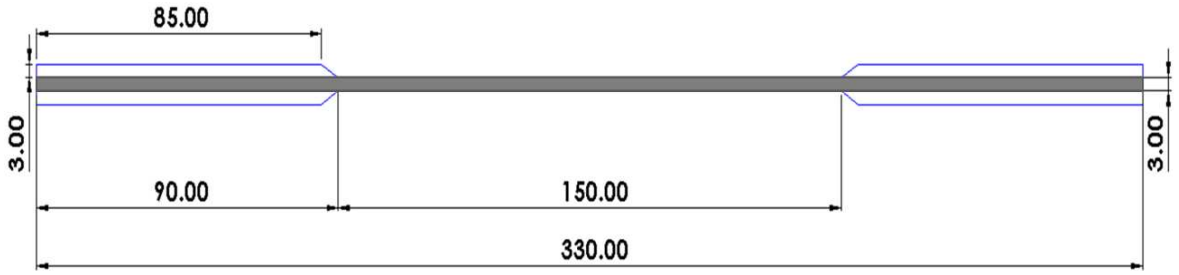

Figure 1. Dimensions of GFRP fatigue test coupons in mm.

2.2 Fatigue tests and instrumentation

S-N Curve tests:

The loading parameters for the tension-tension fatigue tests ware based on the ultimate static tensile strength of the GFRP material. Quasi-static tensile tests were carried out to obtain the ultimate tensile strength. The mechanical tests (static tensile and fatigue loading tests) were performed on a Zwick Roell servo-hydraulic load frame instrumented with 100 kN load cell and an extensometer, in which specimens were held in the test frame using hydraulic grips. The loading rate was 1 mm/min. The average tensile strength (F_{uts}= Load at σ_{uts} (UTS = Ultimate tensile strength) values obtained from three tests was considered for design of tension-tension fatigue tests. The tension-tension fatigue tests were conducted on the same machine used for the static tests instrumented with 100 kN load cell. In addition, multi-instrumentation including, extensometer, infrared thermal camera and acoustic emission transducers and strain gauge was used (cf. Figure 2). The S-N curve was obtained by conducting constant load tension-tension fatigue tests at different levels of σ_{uts} (until failure) where the stress ratio, R was 0.1 and frequency of loading was 8 Hz.

Temperature stabilisation test: The fatigue limit of a material is generally obtained by Whöler curves (stress vs. cycles). These fatigue tests are long and tedious, requiring many specimens and time to obtain a fatigue limit. However, the fatigue limit can also be obtained from the temperature stabilization method by interpolation of two intersecting straight lines of different slopes that fits the stabilization temperature when plotted against the corresponding stress level [2-4]. This method is based on the fact that part of the energy required to start the damage propagation is irreversibly transformed into heat and hence, any deformation and damage in the specimen is followed by an increase in temperature.

To obtain the fatigue limit by this method, load controlled tension-tension stepwise fatigues tests were performed. The test coupons were subjected to 8000 sinusoidal cycles (8 Hz) of tensile-tensile loads (stress ratio R of 0.1 and at room temperature) at 14% of F_{uts}, 21% of F_{uts}, 28% of F_{uts}, 35% of F_{uts}, 42% of F_{uts}, 49% of F_{uts}, 56% of F_{uts} and 63% of F_{uts}. Each load block was separated with a dwell time of 10 min to let the specimens return to room temperature. The tension-tension fatigue test loading protocol is shown in the Figure 3. Three such tests conducted to evaluate the repeatability. An infrared thermal camera Micro Epsilon TIM VGA thermal IMAGER with 33° lens was used to record the temperature of the specimen surface during loading. The thermal data was analysed to estimate the fatigue limit of the specimens using the temperature stabilization method [2-4].

  doi:10.5075/epfl-298799_978-2-9701614-0-0

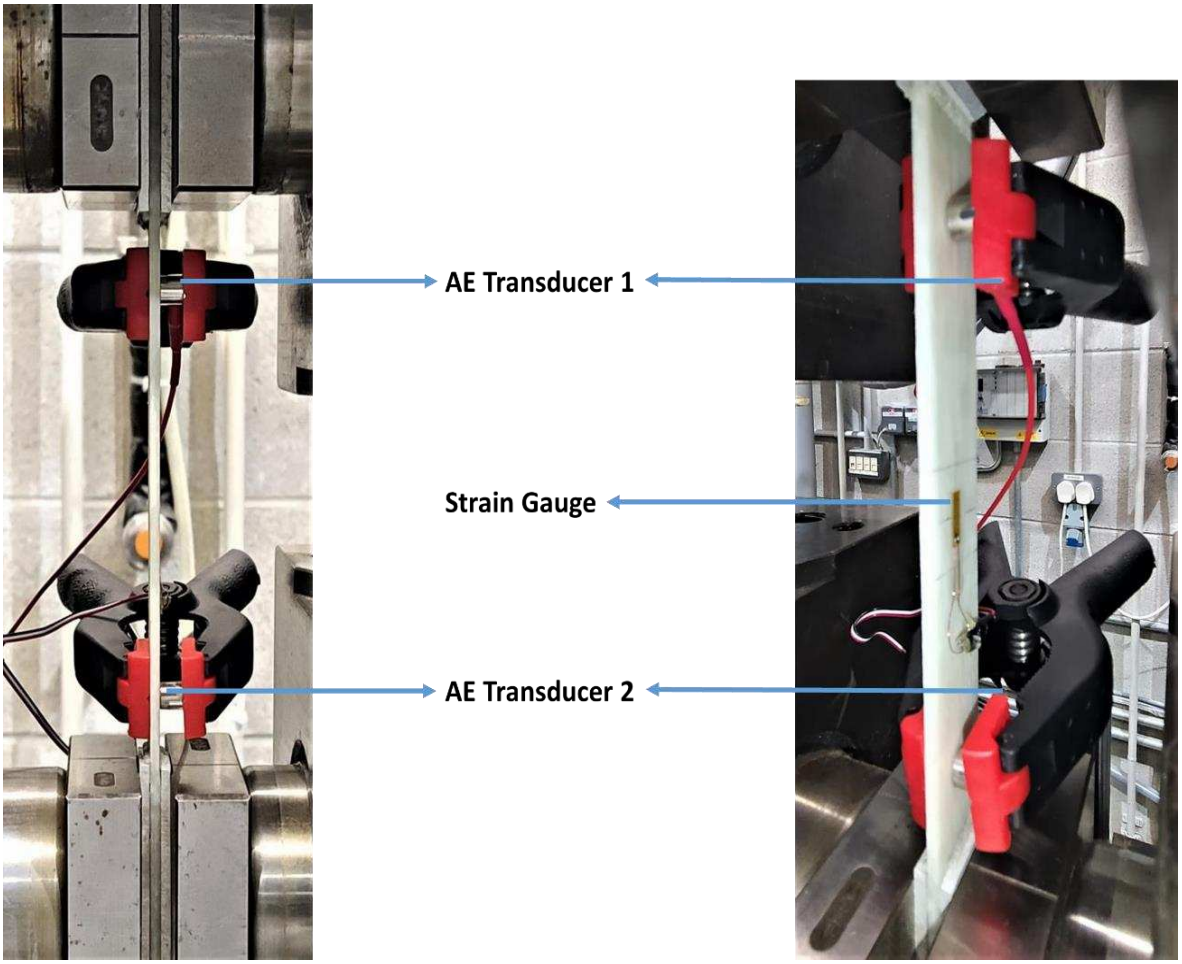

Figure 2. Setup showing instrumentation used for tension-tension fatigue tests

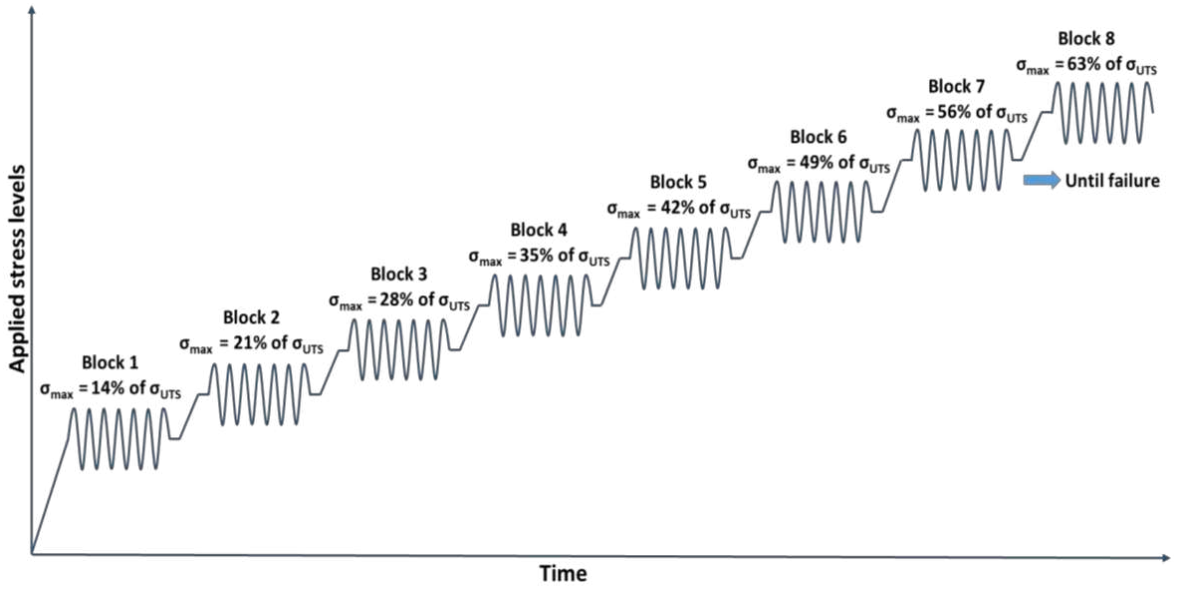

Figure 3. Tension-tension fatigue test loading protocol with R = 0.1 and Frequency = 8 Hz. Tests conducted at room temperature.

  doi:10.5075/epfl-298799_978-2-9701614-0-0

3. Results and discussions

3.1 S-N Curve

The S-N curve of the GFRP material was obtained by conducting constant amplitude load controlled tension-tension fatigue tests. The S-N curve is assumed linear, as the number of tests conducted were limited.

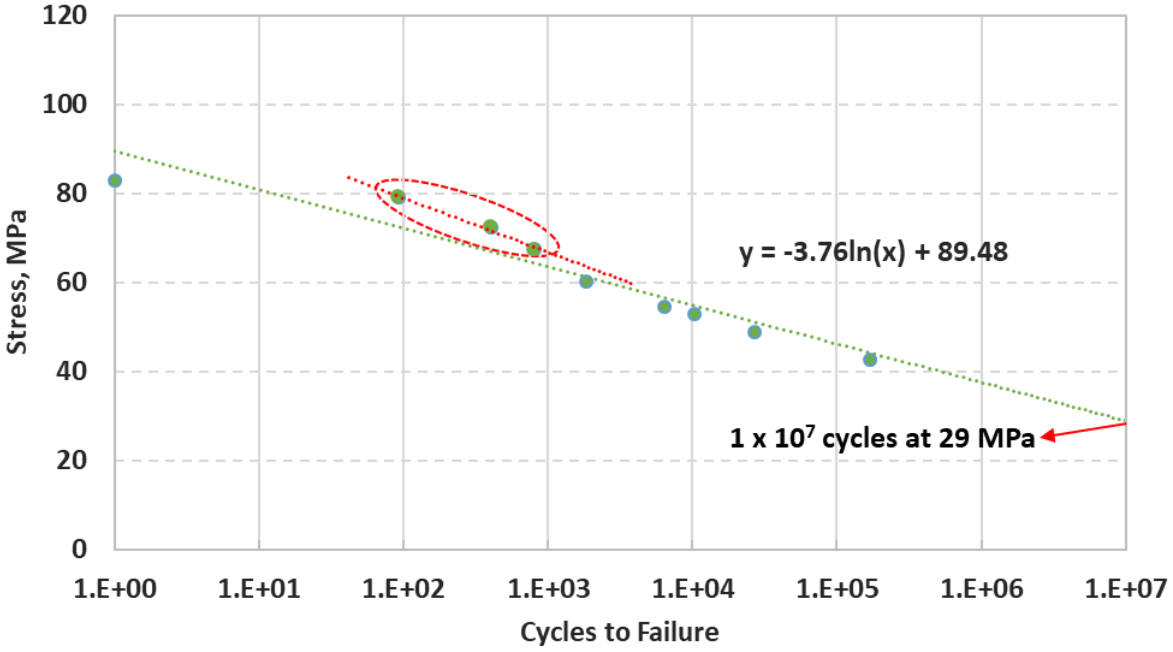

Figure 4. S-N curve of GFRP (GF H2026 – InfuGreen 810)

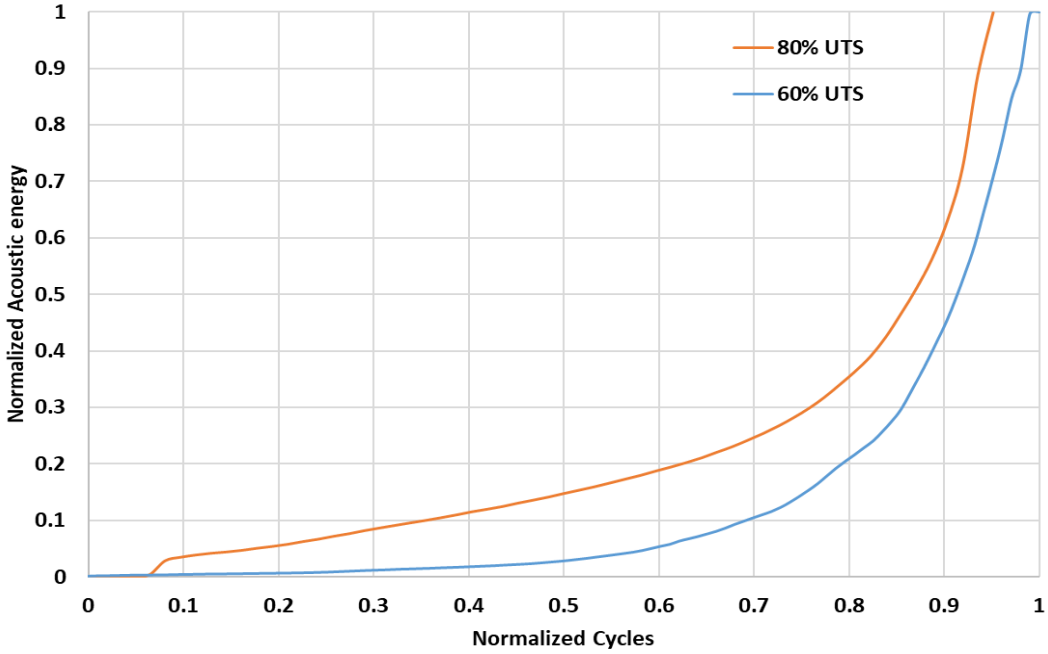

Figure 5. Acoustic energy released due to damage during fatigue loading.

Figure 4 shows the S-N curve for Glass Fiber – InfuGreen 810 GFRP. If we consider the low cycle regime (encircled in red) the slope of the trend line is different from the assumed S-N curve

  doi:10.5075/epfl-298799_978-2-9701614-0-0

(green line). This suggests that the rate of damage accumulation in low cycle regime is different from the high cycle regime. The same can be observed from the acoustic energy. From Figure 5 it can be seen that in low cycle fatigue (80% of UTS) the damage occurs at a higher rate in comparison to high cycle fatigue (60% of UTS) specimen.

3.2 Temperature stabilisation tests

The specimen failure under fatigue loading occurs due to progressive accumulation of damage, leading to total failure. This progression of damage is studied using heat dissipation data (Thermography). During loading, specimen damage occurs by matrix cracks, fiber breaks and crack propagation. These events also give rise to heat dissipation, which increases the specimen temperature [2-4]. Infrared thermography is utilized in this study to measure the temperature evolution on the external surface of the specimen during fatigue loading. The evolution of the rise in the specimen temperature at the end of each load block is presented as a function of the maximum cycle stress applied in each load block (Figure 6). The obtained points can be fitted into two straight lines with different slopes that intersect at a point depicting the fatigue limit. From the Figure 6 it can be found that the fatigue limit of the given specimen is 33.6 MPa. From the S-N curve data (y=-3.76 ln(x) + 89.48) it is found that at 33.6 MPa the specimen can sustain at least 3 X 10^6 cycles. The tests were repeated three times and average fatigue limit was found to be 32.1 MPa. Composite materials do not show a clear fatigue limit like some metals, which can be seen from the obtained S-N curve (Figure 4). Hence, in such cases the stress level, which can sustain 1 x 10^7 cycles, is considered as the fatigue limit. From the S-N curve, the fatigue lime for the GFRP material can be deduced as 29 MPa (cf. Figure 4).

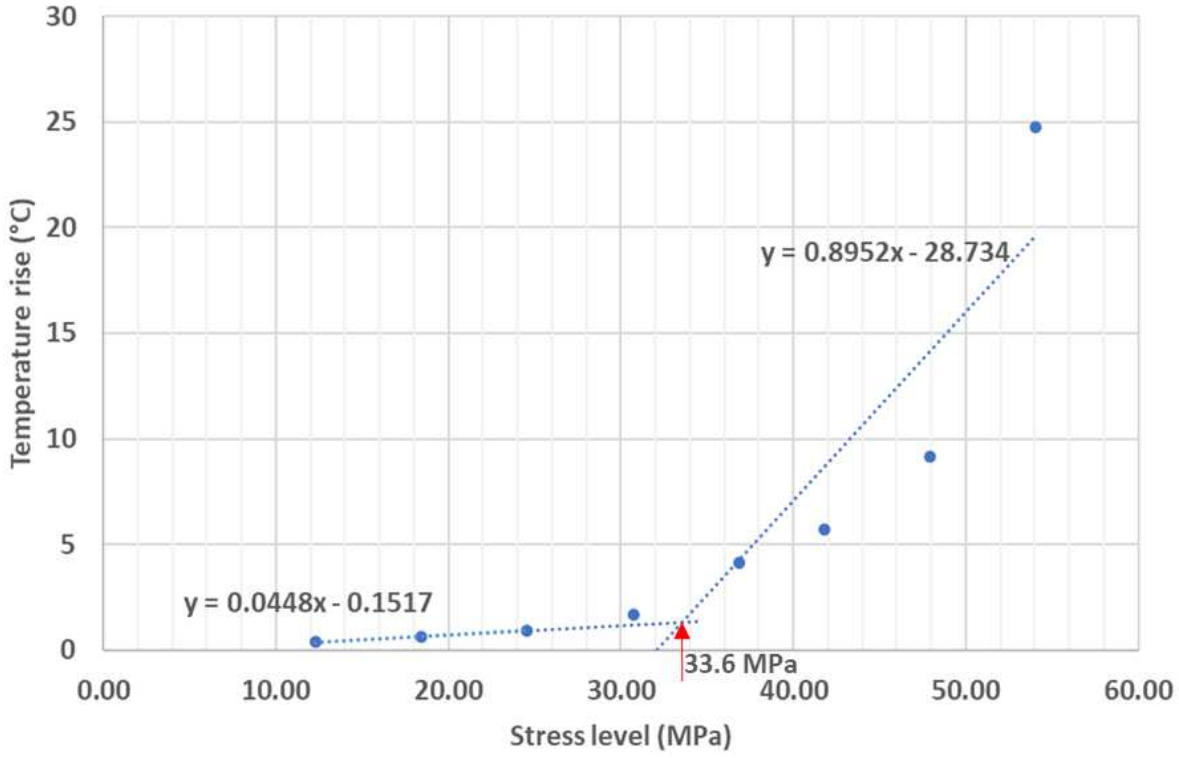

Figure 6. Rise in specimen temperature at end of each block vs. stress level.

  doi:10.5075/epfl-298799_978-2-9701614-0-0 published under CC BY-NC 4.0 license

3.3 Miner's rule

The data obtained from the stepwise tests is used to determine the accuracy of the obtained S-N curve. The Table 1 shows the cumulative damage associated with different stress levels (ratio of actual number of cycles at a particular stress level to the cycles to failure at that stress level) from the stepwise tests. It clearly validates the obtained S-N curve as Miner's sum is close to one.

Table 1: Cumulative damage and Miner's rule.

Stress level (MPa)	Cycles run (n_i)	Cycles to failure (N_i)	Cumulative damage
12.28	8000	40061601	1.997×10^{-04}
18.43	8000	11881746	6.733×10^{-04}
24.57	8000	3530941	2.266×10^{-03}
30.71	8000	1089302	7.344×10^{-03}
36.85	8000	311825	2.566×10^{-02}
41.77	8000	117932	6.784×10^{-02}
47.91	8000	35046	2.283×10^{-01}
54.05	7085	10414	6.803×10^{-01}
		Miner's sum	1.01258

4. Conclusions

Constant load fatigue test were performed on ±45° GFRP samples to characterize its fatigue behaviour and obtain the S-N curve. The fatigue limit (10^7 cycles) was found to be 29 MPa from the S-N curve. Additionally, the fatigue limit of the ±45° GFRP samples was obtained using a rapid method using temperature stabilisation technique, which was found to be 32.1 MPa. The fatigue limit obtained by the rapid method is overestimated by 10%, which is well acceptable given that the method saves time and is economical. Finally, using the S-N curve was validated using the data obtained from stepwise tests by applying Miner's rule.

Acknowledgements

The authors acknowledge and thank the funding received from the European Union's Horizon 2020 Research and Innovation Programme (Grant agreement No. 952966) for the Fibregy project. The authors would also like to thank Adrian McEvoy of the School of Engineering, University of Limerick, for facilitating training and access to the testing facility utilized for this study.

5. References

1. Soukissian T, Karathanasi F, Axaopoulos P. Satellite-Based Offshore wind resource assessment in the Mediterranean Sea. IEEE Journal of Oceanic Engineering 2017; 42, 73–86.

  doi:10.5075/epfl-298799_978-2-9701614-0-0

2. Luong MP. Fatigue limit evaluation of metals using an infrared thermographic technique. Mech Mater 1998; 28:155–63.
3. La Rosa G. Thermographic methodology for rapid determination of the fatigue limit of materials and mechanical components. Int J Fatigue 2000; 22:65–73.
4. Hejjaji A, Zitoune R, Toubal L, Crouzeix L, Collombet L. Influence of controlled depth abrasive water jet milling on the fatigue behavior of carbon/epoxy composites. Composites Part A: Applied Science and Manufacturing 2019: 121:397-410.

  doi:10.5075/epfl-298799_978-2-9701614-0-0

MECHANICAL CHARACTERIZATION OF HIGHLY THERMO-OXIDIZED REINFORCED THERMOPLASTIC AND FATIGUE LIFE PREDICTIONS USING A THROUGH PROCESS MODELING TOOL

Florent, Alexis[a], Sylvie, Castagnet[a], Carole Nadot-Martin[a], Gilles Robert[b], Peggy Havet[c]

a: Institut Pprime CNRS – ISAE-ENSMA - Université de Poitiers, UPR 3346, Département Physique et Mécanique des Matériaux - 1 avenue Clément Ader, F-86962, Futuroscope Chasseneuil, France – florent.alexis@ensma.fr
b: Polytechnyl sas (DOMO Chemicals) - Usine de Belle Etoile, Avenue Albert Ramboz, 69190, France
c: Valeo Thermal Systems - BG Material Laboratory - 8 rue Louis Lormand, 78322, Le Mesnil Saint-Denis, France

Abstract: *The work deals with the fatigue lifetime estimation of Short-Glass-Fiber-Reinforced-Thermoplastics (SGFRP), with a focus on conjugated effects of thermal aging. The material containing 50% (V50) fiber concentration (weight) was aged for 500h at 200°C in air and compared to the same material in Dry-As-Molded (DAM) state. Monotonic and fatigue tests (10Hz, stress-ratio R=0.1) were performed in samples extracted from injected plates and cut along three different orientations to the injection one (0-45-90°) to capture the anisotropy of the skin-core microstructure. Both tests evidenced the stiffening and embrittlement of the Polyamide matrix, with an acuity dependent on the fiber orientation, leading to different fatigue lifetimes' reduction. Fatigue criteria were evaluated based on the different Fatigue-Indicator-Parameters (FIP) obtained from this database. Finally, a Through-Process-Modeling (TPM) tool was used to predict the fatigue lifetimes. To do so, the matrix constitutive behavior was identified from the mid-life hysteresis loops.*

Keywords: Polyamide; Glass fiber; Aging; Fatigue; Simulation

1. Introduction

From an industrial aspect, Short-Glass-Fiber-Reinforced-Thermoplastics (SGFRP) are highly attractive materials and a well-balanced solution to optimize structures of manufactured parts. Thanks to the injection manufacturing process, their mechanical properties can be easily modulated by changes in the final microstructure (skin-core-skin). Moreover, thermoplastics are subjected to many external factors which can impact fatigue behavior such as the stress ratio[1] and loading rate [2]. In addition, conditioning of the materials is also crucial as thermoplastics are sensitive also to their environment. In addition, conditioning of the materials is also crucial as thermoplastics are sensitive also to their environment.

Both short- and long-term effects occur in these materials. The former is linked to quick and reversible mechanisms such as water uptake in humid conditions and material transitions when heated or cooled [3]. When conditioned over longer times, these materials undergo irreversible changes attributed to aging. They are increasingly investigated since severe conditions can lead to premature failure of parts. In addition, these mechanisms are driven by temperature, while composites limits are extended due to the growing temperature requirements of applications. Hence, thermo-oxidative aging in such materials has been studied in the literature for several

  doi:10.5075/epfl-298799_978-2-9701614-0-0

aging temperatures ranging from 37 to 220 °C (for PA6; 6.6 matrices)[4,5]. The main reported effects on the mechanical properties, stiffening, and embrittlement, are mainly consequences of polymer chains' breakage. As reported by many authors, the fiber-matrix adhesion role may be non-negligible. In some cases, tests performed at aging temperature revealed no aging effect while being visible at ambient test temperature [6]. Nevertheless, fatigue tests conducted under high temperatures after severe aging are still lacking in the literature as well as tests generally performed under aging conditions. Hence, in this paper, we propose to study the thermo-oxidative aging effects on the fatigue behavior of a highly-charged polyamide composite.

The first objective is to present the experimental fatigue tests performed at a high aging temperature (200 °C, aged 500 h). On one hand, several cyclic indicators were extracted from stress-strain loops to quantify the aging effects over the cyclic behavior; fatigue lives. The present study focuses on the effect of microstructure on the aging mechanisms. It was motivated by the lack of aging studies for highly filled materials (50%), especially in a fatigue context. Three different orientations with respect to the injection direction (0°, 45°, and 90°) were investigated, at one temperature (200 °C) and one load ratio (R=$\sigma_{min}/\sigma_{max}$=0.1). Specimens were dried before aging to stay consistent with the dry environment induced by such a high temperature.

The second objective is to discuss the performances of fatigue criteria reported in the literature in regard to the results obtained with a predictive Through-Process-Modeling (TPM) tool [7]. This tool is based on the mid-life stabilized Fatigue-Indicator-Parameters (FIP) that can be derived from the experimental hysteresis loops. The herein-faced challenge is the ability to capture a long-term effect (aging) while only simulating a few fatigue cycles as opposed to techniques requiring a complex identification process for the constitutive/damage law [8,9]. This is ultimately done to reduce the extensive cost of a full material characterization that manufacturers are facing when developing new materials.

In the following, Section 2 presents the materials, the experimental procedures (conditioning, aging, and testing), and the numerical methods. Section 3 deals with the fatigue experimental and numerical results (cyclic indicators evolution, fatigue curves, and fatigue life predictions).

2. Materials and Methods

2.1 Materials

The material studied is a composite with a mixed PA6/PA6.6 matrix with 50% wt. of fiber concentration commercialized by Domo Chemicals under the name Technyl® Red A218HPSV50. 340 x 100 x 3 mm^3 rectangular plates were prepared by loading short glass fiber reinforced thermoplastic pellets in an injection molding machine, with the longest dimension being the injection direction. Dogbone-shaped samples (Figure 1a) were extracted following three orientations compared to the injection direction (θ°): 0°, 45°, and 90° (Figure 1b). To ensure tests reliability and homogenous conditions, all samples were dried for 24 h at 80 °C and sealed before testing. These samples are referred to as “unaged” in the following sections. After drying, some samples were aged in an oven at 200 °C under air (natural composition) for 500 h and sealed again shortly after.

  doi:10.5075/epfl-298799_978-2-9701614-0-0

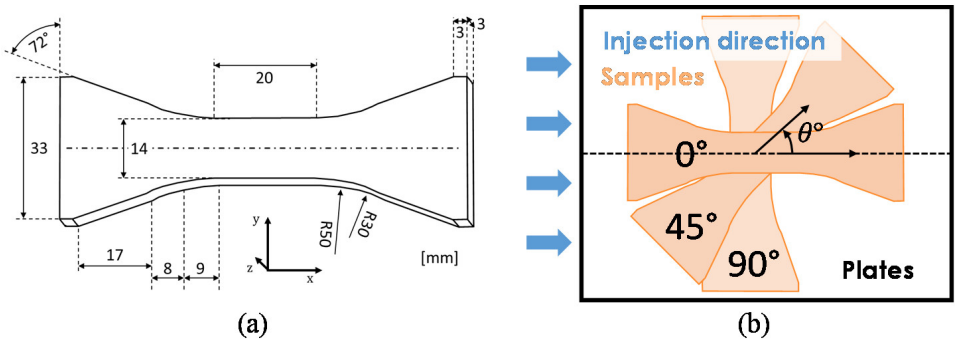

Figure 1. Specimens' specifications: (a) dimensions of the dogbone specimens (mm) and (b) orientation of samples machined out of injected plates comparatively to the injection direction.

2.2 Methods: experimental and numerical

Mechanical tests were performed on a servo-hydraulic Intron® 8802 fatigue testing machine (5 kN load cell) equipped with a climatic chamber heated at the aging temperature (200°C) in air. The temperature was stabilized within one hour of heating (13 °C/min ramp) and tests were performed in series without waiting for the complete cooling of the machine loading train (measured by a thermocouple). Fatigue tests were conducted under load control at a fixed loading ratio (R=$\sigma_{min}/\sigma_{max}$=0.1) in a sinusoidal waveform, a constant amplitude, and a number of cycles to failure (N_f) ranging from 10^3 to 10^6. Before each test, the cross-sections dimensions of the sample were measured and taken into account to calculate the stress level, especially because dimensional changes were observed after aging. The strain evolution was monitored from outside of the climatic chamber, by tracking painted marks on the sample surface. The chosen fatigue frequency was initially set at 10 Hz. The resulting self-heating of the material could be neglected in comparison with the test temperature (200 °C). The FIP considered in the present study are displayed in Figure 2a. Their values were evaluated from the 6th cycle. Data were monitored until the complete failure of the specimens.

For the numerical part, simulations were performed using the Finite Element Method (FEM) in Abaqus® software coupled with Digimat® for the constitutive law. It is a combination of a 4-branches viscoelastic generalized Maxwell model for the matrix and an elastic law for the fibers with the fiber parameters (shape factor, orientation tensor) provided by Domo Chemicals. The law identification was performed with a built-in Dakota® optimization algorithm for the three orientations simultaneously using the mid-life experimental hysteresis loops taken in the range of fatigue lifetimes above $4 \quad 10^5$ cycles. This choice will be discussed in the Results section. The model used for the identification was a Representative Volume Element (RVE) corresponding to a unit-cell of the meshed dogbone with Periodic Boundary Conditions (PBC) (Figure 2b). C3D8 elements were used in both models, with the same number and size distribution through the thickness (Z-axis) to account for the skin-core-skin microstructure. The force or strength required to reach the experimental stress levels was imposed through reference points attached to the mesh nodes for loading in the X direction (C_{11} component). The stress and strain tensor components were homogenized from volume averages over each integration point and element of the mesh, in order to compute the FIP values and compare the numerical-experimental hysteresis loops. Finally, for the dogbone geometry, a virtual extensometer was placed in the gage area to mimic the experimental painted marks.

  doi:10.5075/epfl-298799_978-2-9701614-0-0

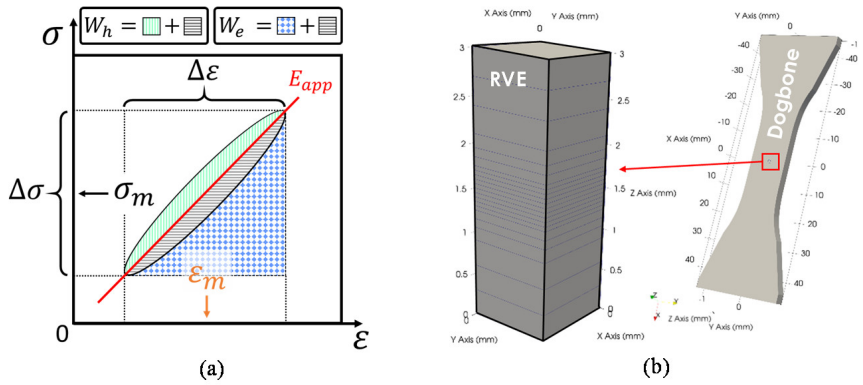

Figure 2. (a) Mechanical quantities employed in the present study for fatigue criteria computation and (b) RVE used for the constitutive law identification.

For confidentiality reasons, all stress-related values were normalized by a common factor whereas all the other quantities were unchanged.

3. Results and discussions

3.1 S-N curves

S-N curves usually plot the fatigue life (N_f) against the imposed stress (σ). The used stress component varies depending on the database. In this study, since only one load ratio is studied, the maximum stress is employed. Values are normalized ($\bar{\sigma}_{max}$) by the same factor whatever the orientation and conditioning.

The S-N curves for every orientation and conditioning are reported in Figure 3a. It is worth mentioning that the same color scheme is used throughout the whole paper. The fatigue data are fitted using log-log regressions under power-law form (see Eq. (1)) and the 95% prediction intervals are drawn only for the unaged composites for clarity reasons. Similar dispersions are observed for the aged materials. It can be observed that thermo-oxidation tends to decrease the slope and increase the intercept which, at a fixed stress level, essentially leads to shorter fatigue life. The amplitude of variations gradually increases with the angle θ°, with the most reduction visible on the 90° specimens. To better grasp the aging effect, ratios of each parameter were computed by dividing the values in the aged state by the unaged ones and reported in Figure 3b.

$FIP = \beta \ \ N_f^{\alpha}$, with α and β being respectively the slope and intercept (1)

Consistently with the results reported in the literature, an increase in rigidity is observed after aging, with more influence visible on the 45° and 90° specimens. A peak value is seen for the former, probably induced by the change of the slope and the vertical shift in stress value. This difference can be explained by the ratio of matrix to fiber sustaining the load, increasing with the orientation. Indeed, the 0° specimens seem to be the least impacted by aging while having most of fibers aligned with the load direction. Tensile tests performed in parallel (not shown here) confirmed that after aging, only the 0 and 45° specimens demonstrated higher values of ultimate tensile stress (UTS). Moreover, multiple damage mechanisms are visible for differently oriented specimens. For instance, as more fibers are aligned perpendicularly to the loading direction, fatigue damage mostly occurs at the interfaces with mechanisms such as debonding and micro-crack propagations [10]. Whereas in the case of 0° specimens, the main mechanisms

  doi:10.5075/epfl-298799_978-2-9701614-0-0 published under CC BY-NC 4.0 license

occur in the matrix with bridges formed between damage markers. The severe aging applied here seems to change the damage appearance order, with matrix-based ones greatly exacerbated. To the author's knowledge, such disparities in aging impact, due to the process-induced microstructure were not reported in the literature. This is undoubtedly related to the fact that very few studies investigate the aging effects in the very same conditions as the initial conditioning.

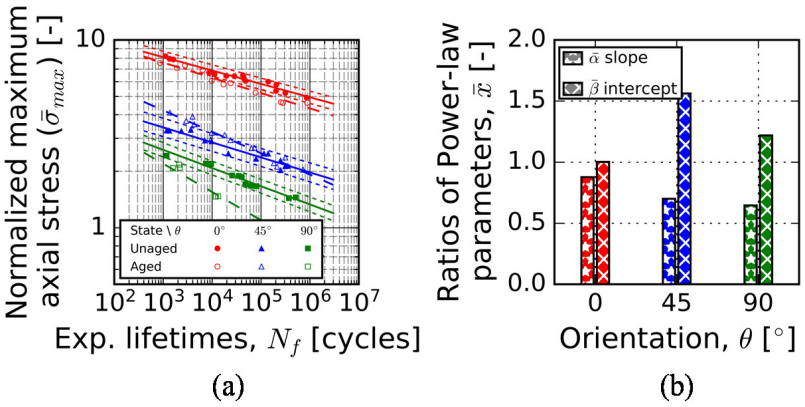

Figure 3. Fatigue results: (a) stress-normalized S-N curves of the unaged and aged materials for every orientation and (b) evolution of slope and intercept power-law parameters as a function of orientation; each quantity after aging if divided by its value in the unaged state.

3.2 Aging impact on cyclic indicators

In a fatigue context, for which several recent criteria are based on a stationary regime (strain increment linked to the ratcheting effect), the aging impact on cyclic indicators must be analyzed thoroughly [11]. Thus, in Figure 4, monitored data such as hysteresis loops (measured at mid-life), and computed energies (see Figure 2a) are plotted against the experimental lifetimes for the 90° specimens. A logarithmic gradient color bar is plotted to precise the fatigue life of each colored data set.

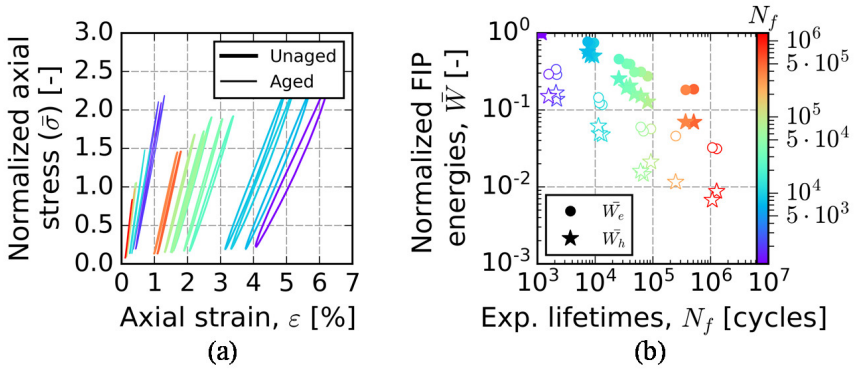

Figure 4. Influence of aging over: (a) stress-normalized hysteresis loops and (b) FIP-normalized values for the 90° specimens for the whole generated database. Fully painted symbols represent the unaged materials whereas empty ones represent aged ones.

Figure 4a shows the normalized stress-strain hysteresis loops measured at mid-life. Hysteresis loops have an asymmetric shape for both conditionings. The loop area, and so the corresponding hysteresis energy density, decreases with the imposed stress amplitudes (Figure 4b). Hence, loops of the longest tests (red color) have near-zero energy compared to shorter tests (blue

  doi:10.5075/epfl-298799_978-2-9701614-0-0 published under CC BY-NC 4.0 license

color; < 10^4 cycles). Similarly, the apparent modulus and the elastic strain energy density are also decreasing. For this orientation, the stress values tend to be positioned at lower levels for the aged specimens at equivalent fatigue lives. Essentially, the closer the S-N curves in both states, the closer the stress amplitudes. Comparatively, the strain amplitudes are heavily decreased whatever the orientation, leading to decreased energy values. Finally, the fatigue curve dispersions appear unchanged after aging. Meaning that the criteria unification ability lies in the criteria itself and not the material conditioning.

3.3 Constitutive law identification

To reduce the computation time, fibers were not directly modeled using a proper distinct meshed phase. Instead, the choice was made to use the Digimat® software to perform the homogenization of the properties at every point of the structure. This way, the cost is greatly diminished since the homogenized stiffness tensor is directly passed to Abaqus®. The matrix law is viscoelastic while for the fiber phase, an elastic one is used. The hypothesis was made of a constant Poisson's ratio (ν=0.45) although in reality, it should depend on time or temperature. The link between the bulk (K) and shear (G) moduli is then constant. Since identification is done from a few cycles only around the mid-life, relaxation times (τ) were chosen in the range of 10^{-4} to 10^{-1} s^{-1} to account for viscoelastic effects. Identification was processed simultaneously for the three orientations. The results for the unaged composite are shown in Figure 5. The criteria used in the objective function (f) computation are the previous energies with the same weights, P_k (see Eq. 2). The algorithm convergence criteria (10^{-7}) automatically stopped the process with the best parameters highlighted (Figure 5b). The results are satisfying, especially for the 45° orientation being centered with the smaller average error (below 5%) and a total average error of 19%. The 0 and 90° stiffness are respectively over- and under-estimated, leading to greater errors.

$$f = \frac{1}{3\ \sum P_k} \sum_{ori=1}^{3} \sum_{k=1}^{2} P_k \quad err_k, \text{ with } err_k \text{ being the co2puted relative error} \tag{2}$$

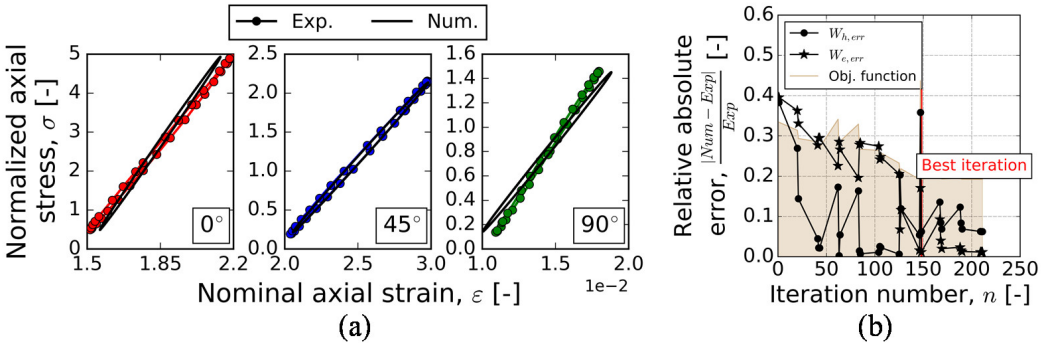

Figure 5. Results of the optimization process for the unaged material: (a) numerical hysteresis loops obtained for the best set of parameters plotted alongside the experimental ones for all orientations and (b) evolution of the relative error for each user-defined criteria and the objective function for the 45° specimens.

3.4 Fatigue life prediction: TPM

Both identified laws (unaged; aged) were used this time in the full geometry. A post-treatment Python® script was used to compute the energies (uniaxial contribution) virtually in a box extracted in the gauge area. Results are reported in Figure 6. An example of the hysteresis energy field of the 45° specimens is also displayed in Figure 6a (red areas correspond to the

  doi:10.5075/epfl-298799_978-2-9701614-0-0 published under CC BY-NC 4.0 license

highest energies). The pink color is used to show the numerical results and experimental data are shown in black color. Predicted lifetimes (N_p) were computed by using the power-law equation (Eq. 1) with the numerical and experimental energies as inputs. The power-law (fatigue criteria) parameters were obtained by identification on either the unaged or the aged data sets of experimental FIP-N curves with all orientations.

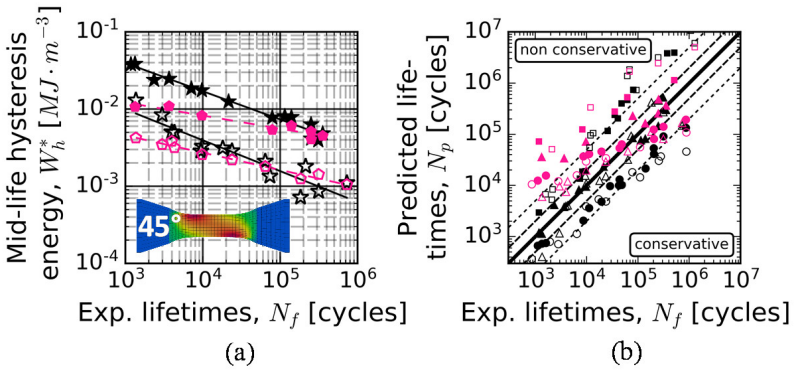

Figure 6. (a) W_h-N curves computed using the mid-life hysteresis loops and (b) predicted lifetimes, N_p, computed with the power-law parameters identified on the whole respective database (unaged-aged with all orientations) versus the experimental lifetimes. Fully painted symbols represent the unaged materials whereas empty ones represent aged ones. Scatter bands of factors 2 and 5 are represented by dashed oblique lines.

Since the identification of the constitutive law was performed using long-term tests, the energy values are accurately estimated for the longest lifetimes (Figure 6a). However, for short lifetimes, the values are underestimated since the law is not fully able to capture the strain sensitivity to much higher imposed stress, leading to lower strain values and less opened hysteresis loops. This leads to a shift of the numerically predicted lifetimes towards the non-conservative domain for short-term tests (Figure 6b). In fact, at so high a temperature, this difference of strain value is certainly attributed to irreversible contributions (among which viscoplasticity) not accounted for by the model. However, since aging is a long-term effect, the identification being performed at a long-time range appears consistent with the often-intended industrial applications (moderate stress where less irreversible changes occur in the material). Nevertheless, the viscoelastic law seems sufficient to capture the discrepancies between the unaged and the aged material at high fatigue lifetimes.

4. Conclusions

The main objective was to study the severe thermo-oxidative aging impact on the fatigue response of a highly-charged SGFRP (50% wt.). Tests were performed on unaged and aged (200 °C, 500h) materials at aging temperature (200°C) for all orientations. The fatigue database was built for one load ratio (R=0.1), one frequency (10 Hz), and FEM simulations were performed using a viscoelastic model and a TPM method. The main results obtained are the following:

- Specimens with fibers mainly oriented towards the loading direction tend to be mechanically less impacted by thermo-oxidative aging;
- Fatigue criteria performances are independent of the specimen conditioning if no major cracks appear during aging, which is the case here: crack propagation only affects the very last stage of fatigue lifetime even after aging (> 90% of N_f);

  doi:10.5075/epfl-298799_978-2-9701614-0-0

- The linear viscoelastic Maxwell model is not able to predict the fatigue lifetimes for tests at high-stress levels or short lifetimes where non-reversible mechanisms are more activated.

Finally, other conditionings or load ratios should be investigated to confirm these results.

Acknowledgements

Pprime Institute gratefully acknowledges «Contrat de Plan Etat - Région Nouvelle-Aquitaine" (CPER) as well as the "Fonds Européen de Développement Régional (FEDER)" for their financial support to the reported work. The authors would like to thank the ANRT (French National Association for Research and Technology) for its financial support via a CIFRE grant. Computations have been performed on the supercomputer facilities of the Mesocentre de calcul SPIN Poitou Charentes.

5. References

1. Zago A, George S. Springer GS. Constant Amplitude Fatigue of Short Glass and Carbon Fiber Reinforced Thermoplastics. Journal of Reinforced Plastics and Composites. 2001;20(7):564-95.
2. Launay A, Maitournam MH, Marco Y, Raoult I, Szmytka F. Cyclic behaviour of short glass fibre reinforced polyamide : Experimental study and constitutive equations. International Journal of Plasticity. 2011;27(8):1267-93.
3. Bergeret A, Pires I, Foulc MP, Abadie B, Ferry L, Crespy A. The hygrothermal behaviour of glass-fibre-reinforced thermoplastic composites : a prediction of the composite lifetime. Polymer Testing. 2001;20(7):753-63.
4. Jia N, Kagan VA. Effects of time and temperature on the tension-tension fatigue behavior of short fiber reinforced polyamides. Polymer Composites. 1998;19(4):408-14.
5. Sang L, Wang C, Wang Y, Wei Z. Thermo-oxidative ageing effect on mechanical properties and morphology of short fibre reinforced polyamide composites – comparison of carbon and glass fibres. RSC Adv. 2017;7(69):43334-44.
6. Rudzinski S, Häussler K, Harnisch Ch, Mäder E, Heinrich G. Glass fibre reinforced polyamide composites: Thermal behaviour of sizings. Composites Part A: Applied Science and Manufacturing. 2011;42(2):157-64.
7. Fouchier N, Nadot-Martin C, Conrado E, Bernasconi A, Castagnet S. Fatigue life assessment of a Short Fibre Reinforced Thermoplastic at high temperature using a Through Process Modelling in a viscoelastic framework. International Journal of Fatigue. 2019;124:236-44.
8. Launay A, Maitournam MH, Marco Y, Raoult I. Multiaxial fatigue models for short glass fibre reinforced polyamide. Part II: Fatigue life estimation. International Journal of Fatigue. 2013;47:390-406.
9. Meraghni F, Nouri H, Bourgeois N, Czarnota C, Lory P. Parameters identification of fatigue damage model for short glass fiber reinforced polyamide (PA6GF30) using digital image correlation. Procedia Engineering. 2011;10:2114-20.
10. Rolland H, Saintier N, Raphael I, Lenoir N, King A, Robert G. Fatigue damage mechanisms of short fiber reinforced PA66 as observed by in-situ synchrotron X-ray microtomography. Composites Part B: Engineering. 2018;143:217-29.
11. Santharam P, Marco Y, Le Saux V, Le Saux M, Robert G, Raoult I, et al. Fatigue criteria for short fiber-reinforced thermoplastic validated over various fiber orientations, load ratios and environmental conditions. International Journal of Fatigue. 2020;135:105574.

  doi:10.5075/epfl-298799_978-2-9701614-0-0

THERMOMECHANICAL ANALYSIS OF THE HIGH CYCLE FATIGUE BEHAVIOR OF A PEEK CF30 UNDER COMPRESSIVE LOADINGS

V. Kwiatkowski[a,b], M. Le Saux[a], V. Le Saux[a], S. Leclercq[b], Y. Marco[a]*

[a] ENSTA Bretagne, UMR CNRS 6027, IRDL, F-29200 Brest, France
[b] Safran Landing Systems, 78140, Vélizy, France

*vanessa.kwiatkowski@ensta-bretagne.org

Abstract: *The assessment of the fatigue life of structures made of short-fiber reinforced thermoplastics is a complex issue due to the non-linear dissipative behavior of the matrix and the heterogeneous distribution of fiber orientations. The aim of this study is to develop an approach for the high cycle fatigue design of PolyEtherEtherKetone reinforced with 30 wt % of short carbon fibers (PEEK CF30), for compressive loadings. This includes the assessment of the ability of the heat build-up technique to predict the fatigue lifetime. To our knowledge, there are no data in the literature for this material and these loading conditions. The results obtained in compression are compared to data obtained in tension. The effects of the loading direction from the injection direction and the load ratio are studied.*

Keywords: Short fiber reinforced thermoplastics; Compression; High cycle fatigue cycles; Self-heating

1. Introduction

Interest in short carbon fiber reinforced thermoplastics is growing in the aerospace industry. Predicting the fatigue behavior of structures made of these materials raises many issues, notably due to the non-linear dissipative mechanical behavior of the matrix and the complex heterogeneous orientation distribution of the fibers, inducing strong anisotropy [1], [2]. This study focuses on PolyEtherEtherKetone reinforced with short carbon fibers (PEEK CF). In some applications, this material is submitted to high cycle fatigue under compression loading. A lot of work has been done on fatigue of short fiber reinforced thermoplastics [1]–[6] but very little for high cycle fatigue and compressive loadings, and even less for PEEK CF. Furthermore, the ability of the heat build-up technique to quickly predict the fatigue lifetime has been demonstrated for short fiber reinforced plastics [7]–[9] but not for the specific conditions of interest here. Heat build-up is the occurrence of a change in temperature of the material under cyclic mechanical loading. The evolution of the dissipated energy determined from the temperature evolution versus the stress amplitude is called the heat build-up curve. This heat build-up curve must then be related to fatigue properties, using an energy-based fatigue criterion [9], [10]

The aim of this study is to develop a fatigue design approach, including rapid characterization by the self-heating method [3], for PEEK CF, for large number of cycles (> 10^6 cycles) and for complex loads in compression.

2. Experimental procedures

  doi:10.5075/epfl-298799_978-2-9701614-0-0

The tested material is a PEEK thermoplastic reinforced with 30% in weight of short carbon fibers. The samples used for compression tests are 5 mm-thick cut from 150 mm x 250 mm injection molded-plates, as shown in Figure 1. They are cut at 0° and 90° from the direction injection. Figure 1 shows the distribution of the fiber orientation through the thickness represented by the components of the second-order orientation tensor obtained by X-ray micro-computed tomography. It is possible to distinguish the core-skin microstructure. The geometry of the samples is presented in Figure 1. The total length of the samples is 140 mm for a 13 mm-long gauge length between the fixtures. The sample width is 13 mm.

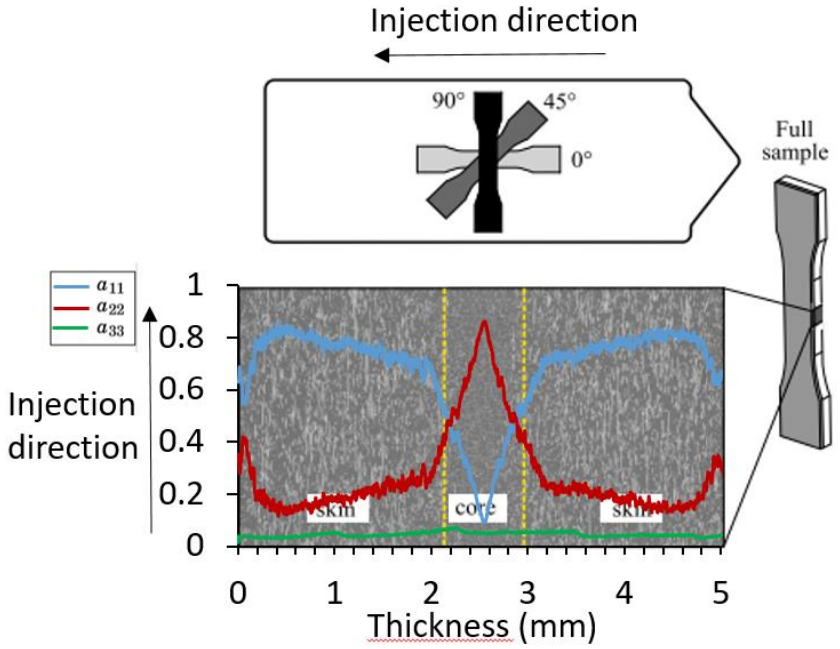

Figure 1 Scheme of samples taken from a plate and the description of the distribution of the fiber orientations through the thickness overlay with an image of the microstructure

The self-heating and the fatigue tests were performed on a MTS servo-hydraulic testing machine with a capacity of 50 kN, at room temperature. The heads of the specimens were clamped with hydraulic jaws leaving a free (gauge) length of 13 mm. The tests were force controlled. The load ratios were set to $R = 10$ (compression-compression) for 0° and 90° samples, and also to $R = 0$ (tension-tension) and $R = -\infty$ (compression-compression) for 0° samples. The loading frequency was $2\,Hz$ or $4\,Hz$. Special attention was paid to the set up to verify the correct alignment of the jaws and the samples with respect to the loading direction. The kinematic fields were measured by image stereo-correlation using a GOM optical cameras system on one side surface (thickness-length plane) of the sample. To do so, a random speckle pattern was applied at the sample surface using spray paints. An InfraTec infrared camera (ImageIR 10300 model) was used to measure the temperature field on the other side surface of the sample, then to determine the dissipated energy. This sample side surface was painted with high emissivity black paint. The self-heating tests were carried out according to the standard protocol [3].The validity of the assumptions on which the method is based has been verified.

3. Results

The difficulty with compression testing is to ensure uniaxiality of the load, *e.g.*, avoid buckling. This was checked for each test from the kinematic fields measured by image stereo-correlation

and the thermo-elastic coupling measured using the infrared camera, on the sample side surfaces (Figure 2).

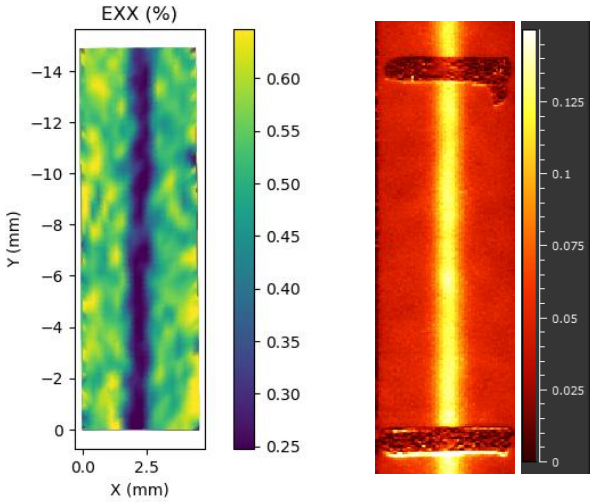

Figure 2 Fields of the transverse strain on one side of the specimen loaded in compression (left) and of the amplitude of the thermoelastic coupling on the other side in °C (right)

Figure 3 shows the results of fatigue tests (N_r is the number of cycles at failure), up to about 10^7 cycles, performed on 0° samples for $R = -\infty$ and for $R = 0$ and the dissipated energies obtained from the heat-build up tests with the same loading frequency. For a given maximal stress in absolute value, the number of cycles at failure is higher in compression than in tension, while the dissipated energy is close. Figure 4 shows the results obtained on 0° and 90° samples for $R = 10$. For a given maximal stress in absolute value, the number of cycles at failure is higher and the dissipated energy if lower for 0° than for 90° samples.

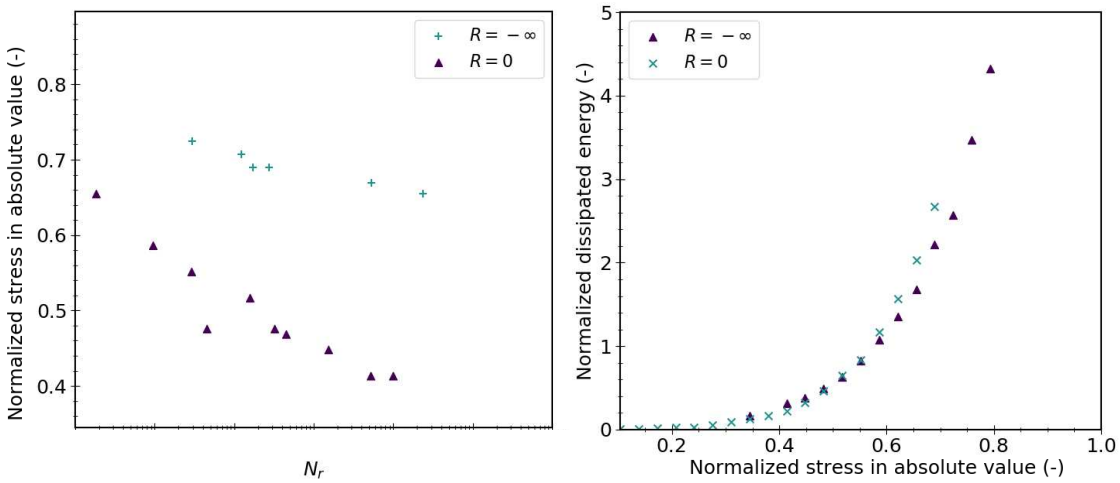

Figure 3 Results of tests performed for 0° samples at R=0 (tension) and R= -∞ with a frequency of 4 Hz: fatigue results (left) and heat build-up curves (right)

The results of the heat-build up tests are analyzed empirically to predict the fatigue life. The approach consists in identifying regimes on the heat build-up curve [3]. Three regimes can be distinguished. The dissipated energy and the fatigue lifetime were related through a power-law criterion:

  doi:10.5075/epfl-298799_978-2-9701614-0-0

$$\Delta^* N_r^b = C \quad (1)$$

with Δ^* the cyclic dissipated energy and b and C two parameters to identify. The parameters of this criterion were determined from the dissipated energy and the number of cycles at failure measured during the last block of the heat-build up test, and from the dissipated energy at the transition between the first and the second regimes, which is arbitrarily assumed to correspond to a lifetime of 10^6 cycles. Then, to predict the Wöhler curves, a mathematical polynomial function was established from heat build-up curves between the dissipated energy and the maximal stress in absolute value. The predictions are compared to experimental data in Figure 5, for 0 and 90° samples, at $R = 10$. The predictions are relatively good and conservative for both sample orientations.

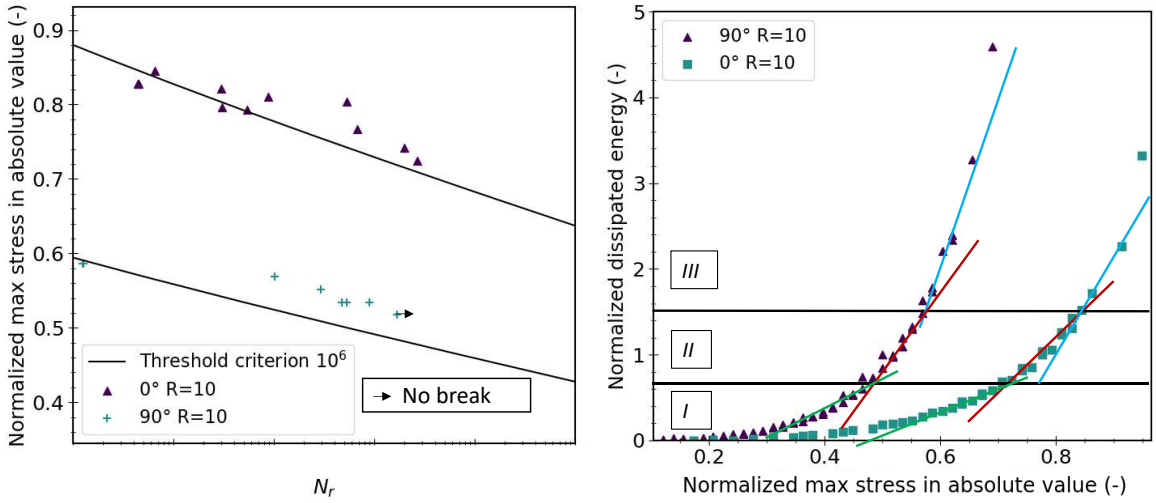

Figure 4 Results obtained for a frequency of 4 Hz on 0° and 90° samples at R=10 (compression): fatigue results (symbols) with the predictions (lines) obtained using an energy-based criterion established using the self-heating method (left); heat build-up curves with the three regimes identified (right)

References

[1] M. Amjadi and A. Fatemi, « Multiaxial fatigue behavior of thermoplastics including mean stress and notch effects: Experiments and modeling », Int. J. Fatigue, vol. 136, p. 105571, juill. 2020

[2] P. Santharam et al., « Fatigue criteria for short fiber-reinforced thermoplastic validated over various fiber orientations, load ratios and environmental conditions », Int. J. Fatigue, vol. 135, p. 105574, juin 2020

[3] L. Leveuf et al., « Fast screening of the fatigue properties of thermoplastics reinforced with short carbon fibers based on thermal measurements », Polym. Test., vol. 68, p. 19-26, 2018.

[4] M. Kawai et al., « Effects of temperature and stress ratio on fatigue life of injection molded short carbon fiber-reinforced polyamide composite », Compos. Part Appl. Sci. Manuf., vol. 98, p. 9-24, juill. 2017

[5] B. Klimkeit et al., « Multiaxial fatigue life assessment for reinforced polymers », Int. J. Fatigue, vol. 33, n° 6, p. 766-780, juin 2011

[6] A. Launay et al., « Multiaxial fatigue models for short glass fiber reinforced polyamide – Part I: Nonlinear anisotropic constitutive behavior for cyclic response », Int. J. Fatigue, vol. 47, p. 382-389, févr. 2013

  doi:10.5075/epfl-298799_978-2-9701614-0-0

[7] Y. Marco et al., « Dissipation analysis in SFRP structural samples: Thermomechanical analysis and comparison to numerical simulations », Int. J. Fatigue, vol. 67, p. 142-150, 2014.
[8] G. Meneghetti and M. Quaresimin, « Fatigue strength assessment of a short fiber composite based on the specific heat dissipation », Compos. Part B Eng., vol. 42, n° 2, p. 217-225, mars 2011
[9] L. Jegou et al., « Thermomechanical identification of a threshold in the cyclic response of "SFRP": Fast identification of the fatigue properties and correlation to microstructural data », ECCM 2012 - Compos. Venice Proc. 15th Eur. Conf. Compos. Mater., juin 2012.
[10] Y. Marco et al., « Prediction of fatigue properties of natural rubber based on the descriptions of the cracks population and of the dissipated energy », Polym. Test., vol. 59, p. 67-74, mai 2017

  doi:10.5075/epfl-298799_978-2-9701614-0-0

Static and fatigue behavior of bonded, bolted and hybrid FRP joints

Lulu Liu[a,b], Xin Wang[b], Zhishen Wu[b], Thomas Keller[a]*

a: Composite Construction Laboratory (CCLab), École Polytechnique Fédérale de Lausanne (EPFL), Lausanne, CH-1015, Switzerland – lulu.liu@epfl.ch
b: Key Laboratory of C & PC Structures Ministry of Education, Southeast University, Nanjing 210096, China – lulu.liu@epfl.ch

Abstract: *An experimental investigation on the static and fatigue behavior of adhesively-bonded, bolted and hybrid bonded/bolted FRP double-lap joints was conducted at EPFL-CCLab. The effects of the adhesive type (stiff or flexible) on the bonded joints and the fiber architecture (uni- or multidirectional) of the adherends on the bolted joints were examined in the static experiments. Both behaviors, static and fatigue, of the hybrid joints, were compared to those of only bonded and only bolted joints of similar dimensions.*

In the static case, bonded joints comprising a flexible acrylic adhesive exhibited a ductile response compared to those with a stiff epoxy adhesive; similarly, as bolted joints with multi-directional fiber architecture did compared to the unidirectional cases. The resistances of the hybrid joints composed of ductile adhesive and adherends with multi-directional fiber architecture corresponded to almost the full summation of the resistances of the bonded and bolted connection parts. The fatigue behavior of hybrid joints was much improved compared to that of only bonded and only bolted joints. The fatigue life of the bonded and hybrid joints was always reached at almost the same ultimate failure displacements. In the hybrid joints, the increase of the adhesive displacements was retarded by the bolts, which extended the fatigue life since more cycles could be sustained to attain the same ultimate failure displacement.

Keywords: bonded joints; bolted joints; hybrid joints; static resistance; fatigue.

1 Introduction

Pultruded fiber-reinforced polymer (FRP) profiles have been the focus of increasing interest as structural members in recent structural engineering applications, such as FRP truss structures or FRP bridge decks, because of their high strength-to-weight ratio, superior mechanical and chemical resistance, and economical industrial production [1]. Since joints are usually the weakest part of load-bearing members, effective joint design is the key to fully utilizing the strength of FRP members [2]. Adhesively-bonded and bolted joints are the two main techniques for connecting FRP members [3]. Adhesively-bonded joints normally exhibit higher stiffness, efficiency, and longer fatigue life [4]; however, bolted joints are easier to assemble and disassemble [5]. To combine the advantages offered by these two joint techniques, hybrid joints, i.e. bonded-bolted joints, have attracted increasing attention in different fields of application [6].

A controversial point of hybrid joints is whether the combined bonded and bolted connections can share the load. In previous studies [7], stiff adhesives were used for hybrid joints and no

  doi:10.5075/epfl-298799_978-2-9701614-0-0

load-sharing was observed, i.e. hybrid joints did not improve the bonded joint resistance. Recently, load sharing between bonded and bolted connections was however achieved by using more flexible adhesives due to large deformations of adhesive [8].

Since the live load-to-weight of FRP structures is often high, particularly in the case of lightweight FRP road bridges subjected to heavy truck loads, the fatigue behavior of such structures, and their joints in particular, represent one of the most important concerns. The fatigue behavior of only bonded and bolted joints have been widely investigated compared to hybrid joints [8,9]. The fatigue life of hybrid joints was the summation of that of the bonded and bolted connections if stiff adhesives were used [9]; however, the life was longer than the summation if flexible adhesives were applied[8].

Although several investigations of hybrid joints have been carried out concerning the static behavior with improved load-sharing, a full summation of the bonded and bolted connection resistances has not yet been achieved and the fatigue behavior of such joints was much less investigated. The aims of the present work were therefore 1) to achieve a full summation of the bonded and bolted connection resistances in hybrid joints by appropriate selection of adhesive and adherend materials, and 2) to characterize the fatigue behavior of hybrid joints, in terms of load-cycle (*F-N*) curves and cyclic displacement variations, and compared to those of only bonded and bolted joints.

The work thus experimentally investigated the static and fatigue behavior of bonded, bolted and hybrid joints. Two different adhesives (a stiff and a flexible one) and two different FRP adherends (with uni- and multidirectional architectures) were selected for hybrid joints to obtain optimum hybrid combinations. Several different load levels were selected for bonded, bolted and hybrid joints for the fatigue experiments to establish the *F-N* curves. The loading frequency for bonded and hybrid joints was varied to maintain the same loading rate for the adhesive. The cyclic-displacement was derived from the load-displacement loops measured during fatigue cycles.

2 Experimental program

The experimental work comprised two main objectives, 1) to investigate the effects of the fiber architecture and adhesive type on the resistance of hybrid joints, to determine the most effective combination; 2) to derive the *F-N* curve of hybrid joints and compare it to those of only bonded and bolted joints of the same dimension.

2.1 Materials

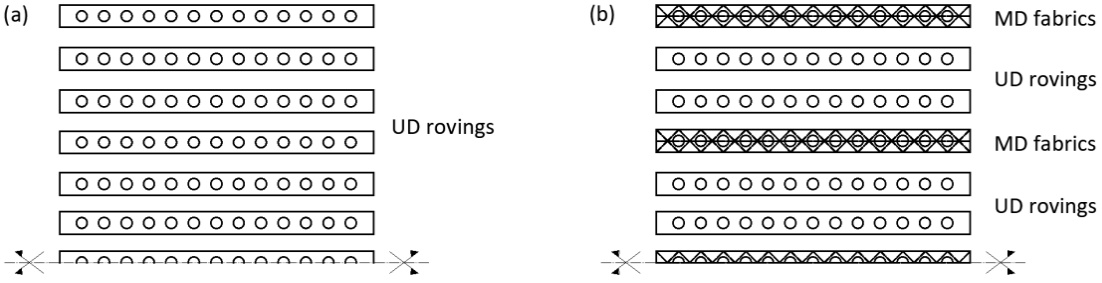

Fig. 1. Fiber architecture of (a) unidirectional, UD and (b) multidirectional, MD adherends.

Basalt-FRP (BFRP) pultruded plates were used as adherends with a thickness of 4.15 mm. Two different fiber architectures were considered, designated UD and MD, as shown in Fig. 1. The total fiber volume fractions were 66% for UD and 68% for MD, individually; the volume fractions in the latter case for different directions of the fiber orientation were 0°/±45°/90°=70/20/10 %. More detailed information can be found in [10]. The basic mechanical properties of BFRP adherends are listed in Table 1.

Stainless steel, 12.9-grade bolts with 1080 MPa yield strength and 1200 MPa ultimate strength were selected. An acrylic adhesive exhibiting high failure strain [11], designated ADP, and an epoxy adhesive with low failure strain [12], indicated EP, were used. The mechanical properties of these two adhesives are listed in Table 1.

Table 1. Mechanical properties of BFRP adherends and adhesives.

Materials	Mechanical properties		
	Tensile strength (MPa)	Tensile modulus (GPa)	Failure elongation (%)
UD adherends	1212 ± 23	51.4 ± 0.9	2.36 ± 0.02
MD adherends	971 ± 25	41.7 ± 1.8	2.33 ± 0.04
ADP adhesive	12 ± 4.3	0.21 ± 0.05	59.8 ± 14.5
EP adhesive	38 ± 2.1	4.6 ± 0.14	0.83 ± 0.13

2.2 Specimen geometry and preparation

Symmetric double-lap joints were considered to minimize the effects of the load eccentricity. The specimen dimensions of the bonded and hybrid joints were derived from the design of the bolted joints with an 8-mm bolt diameter, as shown in Fig. 2. The thickness of the adhesive layer for bonded and hybrid joints was 2 mm. The detailed preparation and fabrication for the joints was reported in [10].

2.3 Experimental set-up and instrumentation

2.3.1 Static experiments

Table 2. Overview of static experiments and results for bonded, bolted and hybrid joints.

Joint type	Specimen denomination	Adherend	Adhesive	Ult. Failure disp. (mm)	Ult. Failure load (kN)
Bonded joints	A-U-E	UD	EP	0.012 ± 0.004	19.3 ± 1.0
	A-U-A	UD	ADP	5.48 ± 0.32	43.7 ± 1.3
Bolted joints	B-U	UD	-	1.56 ± 0.07	11.0 ± 0.2
	B-M	MD	-	9.45 ± 0.21	20.9 ± 0.4
Hybrid joints	H-M-E	MD	EP	9.52 ± 1.47	23.3 ± 1.4
	H-M-A	MD	ADP	5.24 ± 0.13	56.8 ± 3.4

  doi:10.5075/epfl-298799_978-2-9701614-0-0

The static experiments for joints were conducted on a *W+B* 200 kN machine at laboratory temperature (15 ± 5℃). Monotonic tensile loading was applied until the failure of the specimens occurred. A video extensometer camera was used to measure the joint displacements during loading [10]. An overview of the series of static experiments for bonded, bolted and hybrid joints is listed in Table 2. The designation for the joints is as follows: the first term indicates the joint type; the second denotes the fiber architecture of adherends; and the last one represents the adhesive type. Three specimens were examined for each configuration.

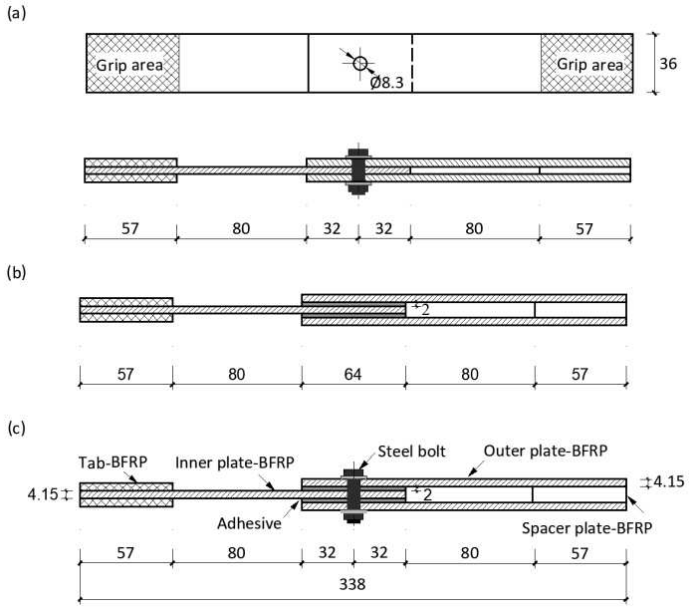

Fig. 2. Joint dimensions: (a) bolted joint; (b) bonded joint; (c) hybrid joint (dimensions in (mm)).

2.3.2 Fatigue experiments

The fatigue experiments were performed according to ASTM D3479 on an Instron 100kN machine. All experiments were conducted under load control, in a sinusoidal loading waveform with constant amplitude and load ratio, $R = F_{min}/F_{max} = 0.1$. A constant fatigue loading rate of 75.6kN/s was selected for the bonded and hybrid joints and a constant loading frequency of 5Hz was determined for the bolted joints. Seven load levels were selected from 8.4 to 29.5 kN for the bonded joints, and six load levels for the bolted joints from 8.4 to 15.8 kN and the hybrid joints from 14.2 to 34.0 kN, respectively, to cover fatigue lives from 10^2 to $2{\cdot}10^6$ cycles. The fatigue loading was applied until failure or up to 2 million cycles.

The load-stroke responses and number of cycles were recorded by the Instron machine. DIC was used to measure the variation of the joint displacements by recording images at 100Hz for specified cycle intervals.

Three specimens were examined at each selected load level and all fatigue experiments were performed in the same air-conditioned laboratory environment (T = 24 ± 2°C, RH = 45 ± 5%) to minimize the effects of ambient temperature changes.

3 Experimental results and discussion

3.1 Static experiments

3.1.1 Bonded joints

The effects of the adhesive type of EP and ADP on the load-displacement responses of the bonded joints are shown in Fig. 3. The EP specimens exhibited a linear and brittle behavior while the ADP specimens showed a bilinear and highly ductile response. Linear elastic behavior was observed up to 64% (on average) of the ultimate failure load, followed by a yield stage and subsequent slight hardening, attributed to the stretching of the molecular chains. In addition, the ultimate failure load of the ADP joints was 2.3x higher (on average) than that of the EP joints.

3.1.2 Bolted joints

The effects of fiber architecture of UD and MD on the load-displacement responses of the bolted joints are shown in Fig. 3. Compared to the UD cases, MD bolted joints exhibited significantly (almost two times) increased ultimate failure loads and much larger deformation capacity, as listed in Table 2. The improved joint behavior was attributed to a change in failure mode from a brittle splitting failure in the UD cases to a progressive bearing failure in the MD joints.

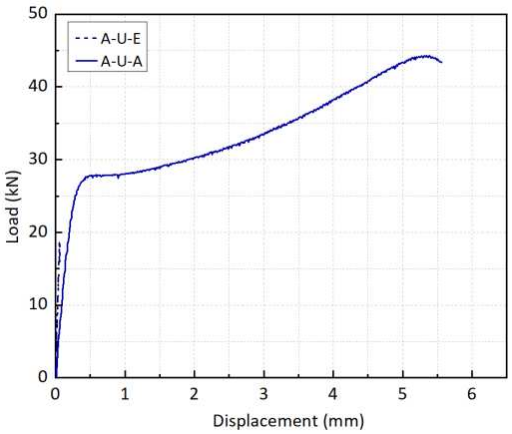

Fig. 3. Load-displacement responses of bonded joints with different adhesives.

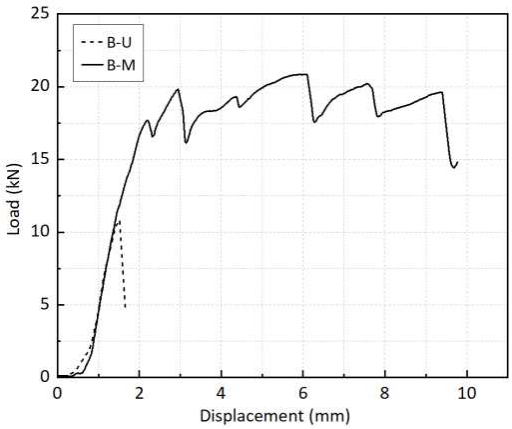

Fig. 4. Load-displacement responses of bolted joints with different fiber architecture.

3.1.3 Hybrid joints

3.1.3.1 MD-EP hybrid joints

The load-displacement response of a typical MD-EP hybrid joint comprising MD adherends and EP adhesive is shown in Fig. 5 and compared with the corresponding MD bolted and EP bonded joints. The hybrid joints exhibited a two-stage behavior, i.e., no load sharing between the bonded and bolted connections occurred. In the first stage, the applied load was only transferred by the adhesive connection due to its much higher stiffness. Subsequently, adhesive failure occurred, and the load dropped to the level of the bolted joint at this displacement. In the second stage, the entire load was transferred by the bolted connection until its ultimate bearing failure with large deformation.

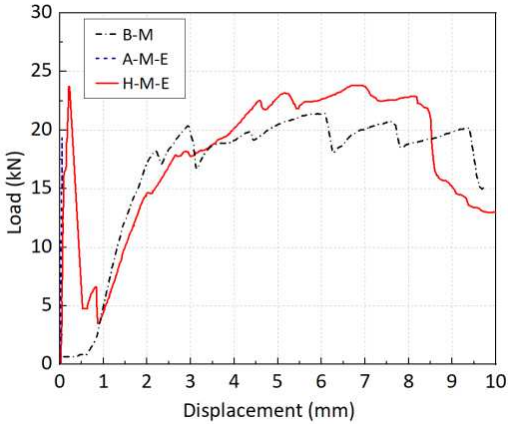

Fig. 5. Load-displacement responses of MD bolted, EP bonded and MD-EP hybrid joints.

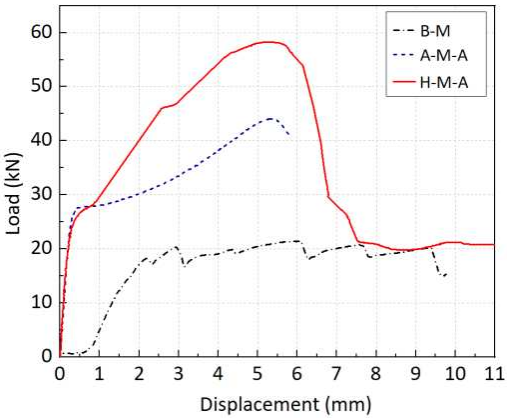

Fig. 6. Load-displacement responses of MD bolted, ADP bonded and MD-ADP hybrid joints.

3.1.3.2 MD-ADP hybrid joints

The load-displacement response of a representative MD-ADP hybrid joint, composed of MD adherends and ADP adhesive, is compared to the responses of MD bolted and ADP bonded joints in Fig. 6. Until the bolted connection was activated, the stiffness of the hybrid joint was governed by the bonded connection, and no load sharing had yet occurred. Subsequently, full load sharing was initiated and continued, and the joint stiffness increased accordingly up to the ultimate failure load, which was almost the summation of the bonded and bolted connection resistances (see mean values in Table 2, -8.7%). After the failure of the adhesive connection, the load dropped to the level of the bolted connection, which continued to sustain the load until its ultimate failure.

3.2 Fatigue experiments

3.2.1 Fatigue life

The fatigue maximum load, F_{max}, against fatigue life, N_f, for bonded, bolted and hybrid joints, on a logarithmic scale, is shown in Fig. 7; a classic power-law relationship, expressed by Eq. (1), was used to fit the *F-N* experimental data:

$$F_{\max} = F_0 N_f^{-k} \tag{1}$$

where F_0 and k are the model parameters obtained from a regression analysis. The model parameters for bonded, bolted and hybrid joints are listed in Table *3*. Specimens survived the 2 million cycles were indicated with a right-facing arrow and were not included in the regression analysis.

The fatigue resistance of the hybrid joints was higher than that of the bonded and bolted joints, and was affected mainly by the bonded connections, as demonstrated by the similar slopes of the *F-N* curves. Bolted joints showed lower fatigue resistance, however, the decreasing rate of the *F-N* curve was much less than in the bonded and hybrid joints.

  doi:10.5075/epfl-298799_978-2-9701614-0-0

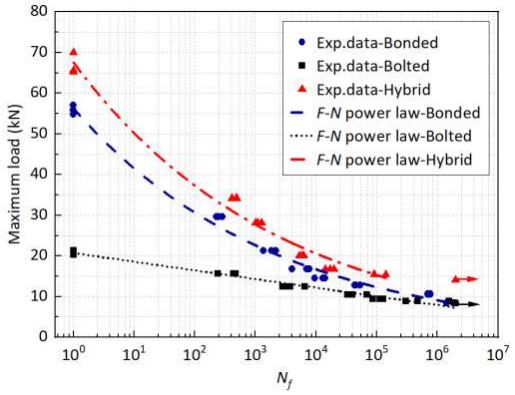

Fig. 7. Experimental fatigue data and fitting F-N curves for bonded, bolted and hybrid joints.

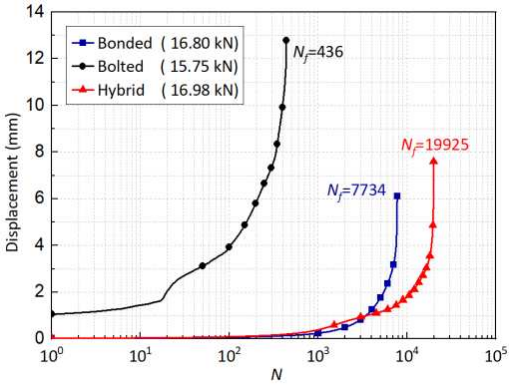

Fig. 8. Cyclic displacements versus normalized number of cycles at a selected load level of 16 kN for bonded, bolted and hybrid joints.

Table 3. Model parameters of F-N fitting curves for bonded, bolted and hybrid joints.

Joint types	F_0	k
Bonded joints	56.32	0.130
Bolted joints	21.28	0.065
Hybrid joints	67.98	0.129

3.2.2 Cyclic displacements

The variation of the cyclic displacements versus the normalized number of cycles during fatigue for bonded, bolted and hybrid joints at a selected load level of 16 kN was compared in Fig. 8. The fatigue life of the hybrid joints was longer than the summation of that of the bonded and bolted joints due to the loading sharing between them. As reported in the previous work [13], all bonded joints failed at a similar failure displacement when the molecular chains were fully stretched. The failure displacement of the hybrid joints was similar to that of the bonded joints, i.e., hybrid joints failed when the failure in the adhesive occurred. However, the increase of displacement of the hybrid joints during fatigue was retarded by the bolts. This limitation extended the fatigue life since more cycles could be sustained to attain the same ultimate failure displacements.

4 Conclusions

An experimental investigation of the static and fatigue behavior of bonded, bolted and hybrid joints was conducted. The effects of fiber architecture and adhesive type on the load-bearing behavior of hybrid joints were investigated to determine the optimum combination. The *F-N* curves for bonded, bolted and hybrid joints were established. The conclusions of this work are summarized as follows:

(1) MD bolted joints significantly increased the joint resistance and deformation capacity compared to the unidirectional cases; ADP bonded joints exhibited a highly ductile response compared to EP cases.

  doi:10.5075/epfl-298799_978-2-9701614-0-0

(2) Hybrid joints comprising EP adhesive failed to achieve load sharing between bonded and bolted connections, however, the resistance of hybrid joints comprising the ADP adhesive corresponded to almost the full summation of the resistances of the bonded and bolted connection parts due to almost equal and large deformation capacities.

(3) The fatigue resistance of hybrid joints comprising the ADP adhesive was much improved compared to that of bonded and bolted joints due to the load sharing behavior; it was mainly dependent on the bonded connections.

(4) Hybrid joints failed at the same displacement as bonded joints. The increase of displacement was retarded by the bolts in the hybrid joints and the fatigue life was thus extended until reaching the same ultimate failure displacement.

5 References

1. Keller T. Recent all-composite and hybrid fibre-reinforced polymer bridges and buildings. Progress in Structural Engineering and Materials. 2001;3(2):132–40.
2. Keller T, Zhou A. Fatigue behavior of adhesively bonded joints composed of pultruded GFRP adherends for civil infrastructure applications. Composites Part A: Applied Science and Manufacturing. 2006;37(8):1119–30.
3. CEN/TC 250. Design of fibre-polymer composite structures. Final draft. 2020;
4. Vassilopoulos AP. Fatigue and Fracture of Adhesively-bonded Composite Joints Behaviour, Simulation and Modelling. UK: Woodhead Publishing; 2015.
5. Girão Coelho AM, Mottram JT. A review of the behaviour and analysis of bolted connections and joints in pultruded fibre reinforced polymers. Materials and Design. 2015;74:86–107.
6. Bodjona K, Lessard L. Hybrid bonded-fastened joints and their application in composite structures: A general review. Journal of Reinforced Plastics and Composites. 2016;35(9):764–81.
7. Lopez-Cruz P, Laliberté J, Lessard L. Investigation of bolted/bonded composite joint behaviour using design of experiments. Composite Structures. 2017;170:192–201.
8. Kelly G. Quasi-static strength and fatigue life of hybrid (bonded/bolted) composite single-lap joints. Composite Structures. 2006;72(1):119–29.
9. Imanaka M, Haraga K, Nishikawa T. Fatigue strength of adhesive/rivet combined lap joints. The Journal of Adhesion. 1995;49(3–4):197–209.
10. Liu L, Wang X, Wu Z, Keller T. Resistance and ductility of FRP composite hybrid joints. Composite Structures. 2020;255:113001.
11. Angelidi M, Vassilopoulos AP, Keller T. Ductility, recovery and strain rate dependency of an acrylic structural adhesive. Construction and Building Materials. 2017;140:184–93.
12. I. M. Foletti A, Sena Cruz J, Vassilopoulos AP. Fabrication and curing conditions effects on the fatigue behavior of a structural adhesive. International Journal of Fatigue. 2020;139(June):105743.
13. Liu L, Wang X, Wu Z, Keller T. Tension-tension fatigue behavior of ductile adhesively-bonded FRP joints. Composite Structures. 2021;268:113925.

EVALUATION OF INTERLAMINAR SHEAR FATIGUE DAMAGE PROGRESSION IN 3D WOVEN COMPOSITES WITH TIME-LAPSE X-RAY COMPUTED TOMOGRAPHY

Leping Wu[a] Prasad Potluri[a], Philip J. Withers[b]

a: Northwest Composites Centre, Department of Materials, School of Natural Sciences, The University of Manchester, M13 9PL, Manchester, UK – leping.wu@manchester.ac.uk
b: Henry Royce Institute, Department of Materials, School of Natural Sciences, The University of Manchester, M13 9PL, Manchester, UK

Abstract: *This research aims to understand the role of Z-binder weave architecture on the interlaminar shear behaviour and corresponding damage progression mechanisms in 3D woven orthogonal composites under cyclic shear loading. Two different structures: 2×1 and 2×2 twill 3D woven orthogonal composites have been investigated under short beam shear fatigue loading. The damage mechanisms have been evaluated by time-lapse X-ray Computed Tomography (CT) at different fatigue life stages. The primary damage mode is the delamination associated with fibre debonding and resin cracks distributed throughout the composites. The Z-binder is influential in delaying delamination propagation because it is subjected to a local tensile loading when the composite is under shear fatigue loading. The 2×2 twill Z-binder configuration provides better fatigue performance in comparison to 2x1 twill.*

Keywords: Textile composites; Fatigue; X-ray Computed Tomography

1. Introduction

In recent decades, three dimensional (3D) woven textile composite materials have been widely applied across a broad range of sectors, including civil engineering, wind energy, aerospace, and vehicle body construction. 3D woven composites offer two main advantages compared with prepreg laminates. The first one is that the mechanical properties can be tailored according to specific requirements with the change of weft, warp and binder architecture. The second is the improved delamination resistance which is achieved by introducing the through-thickness reinforcement. As a result, 3D woven composites demonstrate excellent delamination resistance. This research focuses on Z-binder architecture effects on the interlaminar performance of orthogonal 2×1 and 2×2 twill woven composites subject to cyclic shear loading.

There are many ways to determine the inter-laminar strength and the effect of Z-binder on delamination performance. These include the Mode-I fracture toughness test using a double cantilever beam, the Mode-II fracture test using an end-notched flexure test and the short beam shear (SBS) test. In SBS test, the shortest possible span is used in order to minimise temnsile/compressive stresses due to bending. Further, the interlaminar shear strength is underestimated in this method due to the idealised shear flow equations, which neglect the effect of the concentrated load. In spite of this, the SBS test is a convenient and practical means of comparing the behaviour of different material architectures and analysing their damage mechanisms. The inter-laminar properties and related damage mechanisms are generally investigated postmortem by optical microscopy and SEM or in situ by methods such as digital image correlation (DIC) and X-ray computed tomography (CT).

  doi:10.5075/epfl-298799_978-2-9701614-0-0

It is worth noting that we can change the Z-binder property by changing tow pathways through the preform or the tow density. Increasing Z-binder content has been found to decrease the inter-laminar shear strength and introduce more damage within the composite laminate[1]. The damage was found to be distributed more evenly and regularly within the specimen because the Z-binder arrested the cracks. This damage distribution and the ability to support a more significant load in the post-elastic regime of the load-displacement curve, meant that the 3D woven composites showed a better damage tolerance of than 2D laminates. The presence of Z-binder allowed more damage to initiate under cyclic loading, which reduced the strength of materials in the linear regime, but limited the damage development overall. In contrast, Dehale et al. [2] found that increasing the Z-binder content by changing the tow density, had a negligible effect on the inter-laminar shear strength (~4%) with no significant difference in the failure mechanism during the loading. There is no reported research on the effect of different Z-binder architecture on 3D woven orthogonal composites.

Stitched 3D composites can have a similar structure to 3D woven composites. Recently research has been carried out using X-ray CT to characterise the internal damage of stitched 3D composites under static short beam shear loading [3]. In common with the observations above, damage was found to initiate in the resin-rich area mainly, lowering the elastic limit but improving the damage tolerance. The stitching space forms an enclosed region partitioning the fabric into many cells. Damage occurs within the cells but is restricted inside the cell by the enclosed loop, with the Z-stitch of the enclosed loop suppressing damage propagation across the cells.

To better understand the initiation of damage, crack propagation and damage features of 3D woven composites under fatigue loading, interrupted time-lapse X-ray CT scanning has been applied in this research during cyclic shear loading.

2. Materials and methodology

With the help of an electronic Jacquard loom, the 3D woven fabrics were produced using 12K T700SC 50C untwisted carbon fibre tows as warp and weft yarns. 6K T700SC 50C carbon fibre tows act as Z-binder as shown in Fig 1. The warp is in the x-direction, weft is in the y-direction, and the through-thickness binder is in the z-direction. The tow densities for both the weaves: warp density 11.28/cm, weft density 12.5/cm and z-binder density 2.82/cm. The composite panels were made using Vacuum Assisted Resin Infusion Technique. Using resin burn-off testing, the fibre volume fractions of 2×2 twill and 2×1 twill composites have been found to be 52.79±0.68% and 51.10±0.20%, respectively.

An Instron 8802 has been used to undertake short beam shear testing following the ASTM D2344 for both quasi-static and cyclic fatigue tests. The span has been fixed at 16.5mm. samples are 25mm long and 15mm wide, containing at least one unit cell for the damage analysis. 60% of the Ultimate Failure Stressis applied for the fatigue test conducted at 1 Hz loading frequency. The R ratio is maintained at 0.1, which gives a positive value at the minimum loading point.

  doi:10.5075/epfl-298799_978-2-9701614-0-0

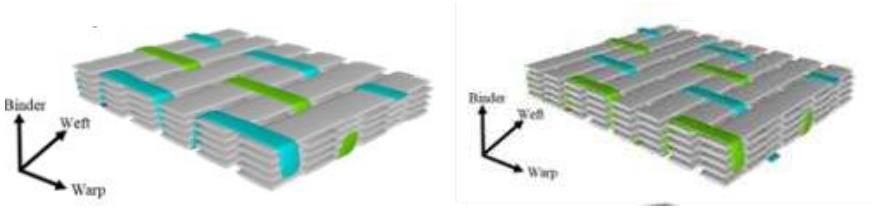

Figure 1. 3D woven preforms with idealised model(Left: 2×1 twill orthogonal structure; Right: 2×2 twill structure). The coloured tows are Z-binder

The CT scanning of the samples have been conducted on a Nikon XTH 225 with an accelerating voltage of 80kV and the current of 80μA respectively. 5013 projections were taken with the rotation of 360° of the sample in equal-angular increments. The exposure time for each projection was 354ms, resulting in a total scanning time of about 2h 36min. To improve the voxel size of the imaging and maintain the whole sample within the field of view, we performed two CT scans side-by-side along the warp direction (x-direction), then stitched two scans together following the method described in [5].

3. Results

3.1 Quasi-static short beam shear test

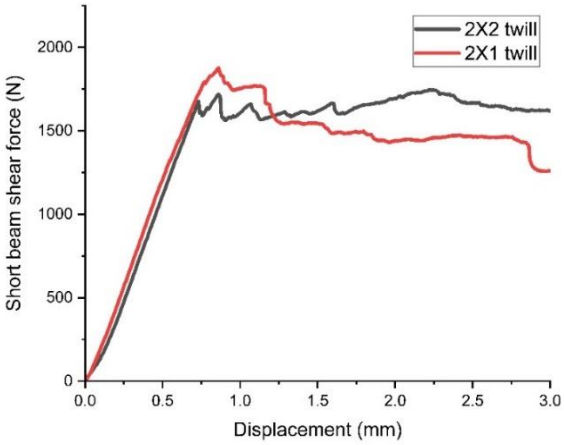

Figure 2(a). The static short beam shear load-displacement curves for two structures

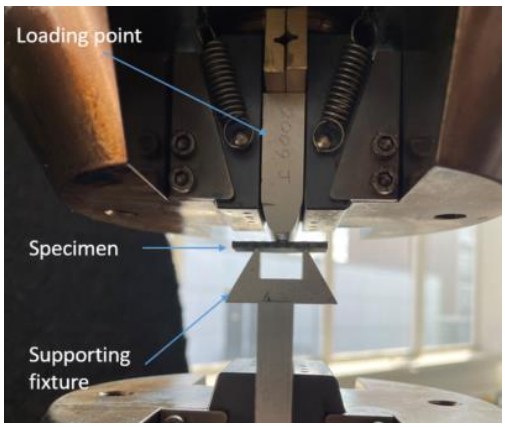

Figure 2(b) the short beam shear testing set-up

  doi:10.5075/epfl-298799_978-2-9701614-0-0 published under CC BY-NC 4.0 license

The load-displacement curves are plotted in figure 2(a) and one of three results are selected from every structure. Firstly, a non-linear region is observed over the first 0-0.5 mm. The composites' response to the increased loading shows a near-linear elastic trend until the shear force reaches the apparent elastic limit. After the peak load, internal damage develops, which significantly affects the inter-laminar response The two samples types show a significant load drop just beyond the peak load. The 2×1 twill structure has a higher maximum failure load.

The shear strength was calculated according to $S=3F_{max}/4bl$[4], where F_{max} is the peak SBS loading force from the load-displacement curve. *b* and *l* are the specimen width and thickness, respectively. The two structures have essentially the same average interlaminar shear strength (ILSS), namely 35.7MPa for the 2×1 twill and 35.8MPa for 2×2 twill, with a standard deviation of 1.nd 1.1 for 2×1 twill structure and 2×2 twill structure. The possible reason is that the two composites have very similar fibre volume fractions and the number of yarn layers, leading to essentially the same shear strength and similar failure mechanisms.

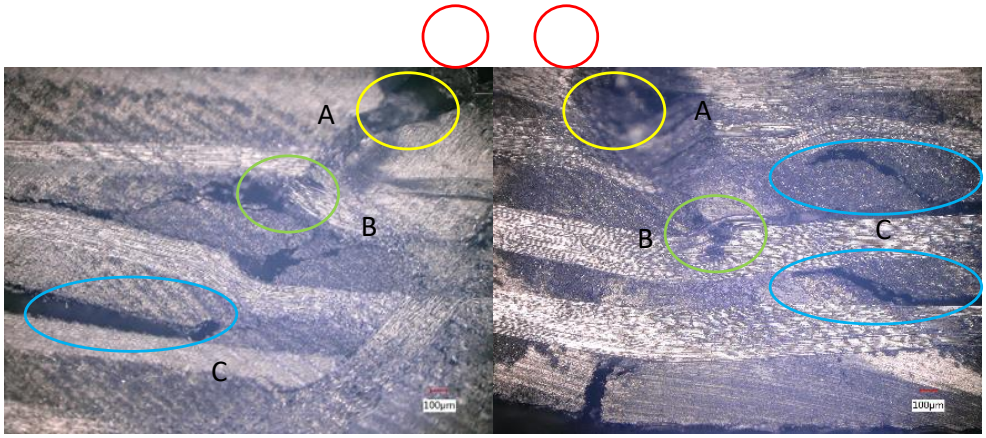

Figure 3. optical microscopy images of Z-binder through-thickness cross-sectional view (left: 2×2 structure; Right: 2×1 structure). Red circles: Loading roller; Yellow circle(A): top surface cracks; Green circle(B): Shear kinking failure; Blue circle(C): delamination

Optical microscopy has been used to investigate the damage features of the failed specimens. Both structures have a similar failure mechanism and damage features. In figure 3, the top of the sample is under compression and the bottom is under tension. Three dominant damage modes are circulated and marked with different colours; local surface compression failure under the loading point (A), fibre tow kinking and pull-out(B), and massive delamination(c). The local surface damage is caused by the strong local stress concentration arising from the loading punch resulting in surface matrix cracking. The cause of shear fibre kinking failure is the fibre tow misalignment and micro-buckling at the particular angle. Delamination is the most extensive damage mechanism, including the fibre tow/matrix delamination and warp/weft tow delamination. The likely delamination propagation pathway is between the binder/matrix region due to the massive shear stress around that area to the resin-rich zone, leading to a severe warp/weft tow delamination. The delamination is arrested by the existence of the next adjacent through-thickness binder yarn. Fibre tow debonding is also evident in combination with the delamination.

  doi:10.5075/epfl-298799_978-2-9701614-0-0

3.1 Fatigue failure under short beam shear testing

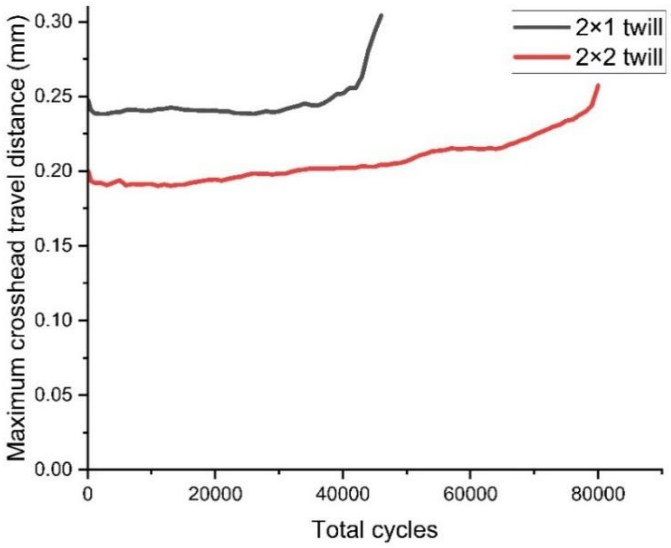

Figure 4 The maximum recorded crosshead movement distance at 60% peak stress level of the static interlaminar shear strength for the two fibre architectures

Figure 4 shows a typical short beam shear cyclic loading crosshead movement distance at every cycle as a function of the total number of cycles. The last point in the diagram corresponds to the stop point for the X-ray CT scanning. Both composites have a slight decrease at the very few cycles. Then a relatively stable stage during 90% of the total cycles. A rapid increase of the displacement occurs close to failure. The 2×2 twill composite has a smaller value than the 2×1 twill structure during the test which means it has relatively higher stiffness and interlaminar shear resistance because the 2×2 has less Z-binder interlacing point and less stress concentration area. The 2×1 twill reaches the rapid increasing point earlier than the 2×2 twill structure, which means the damage develops faster in 2×1 twill composites. A slight increase is observed at the early stage for both structures after the initial drop. It has been reported previously that the kinematic shift of the stress-strain behaviour instead of the shear modulus change during the cycles[6].

3.2.1 The fatigue damage development for the 2×2 twill structure

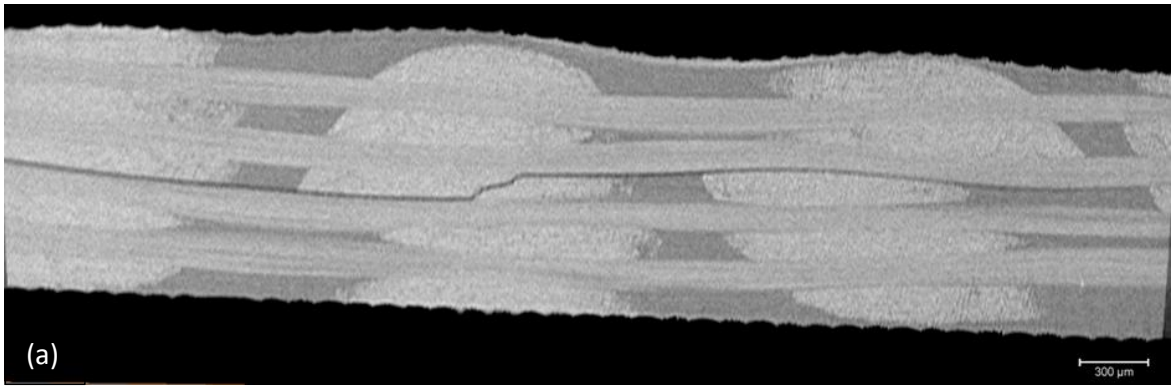

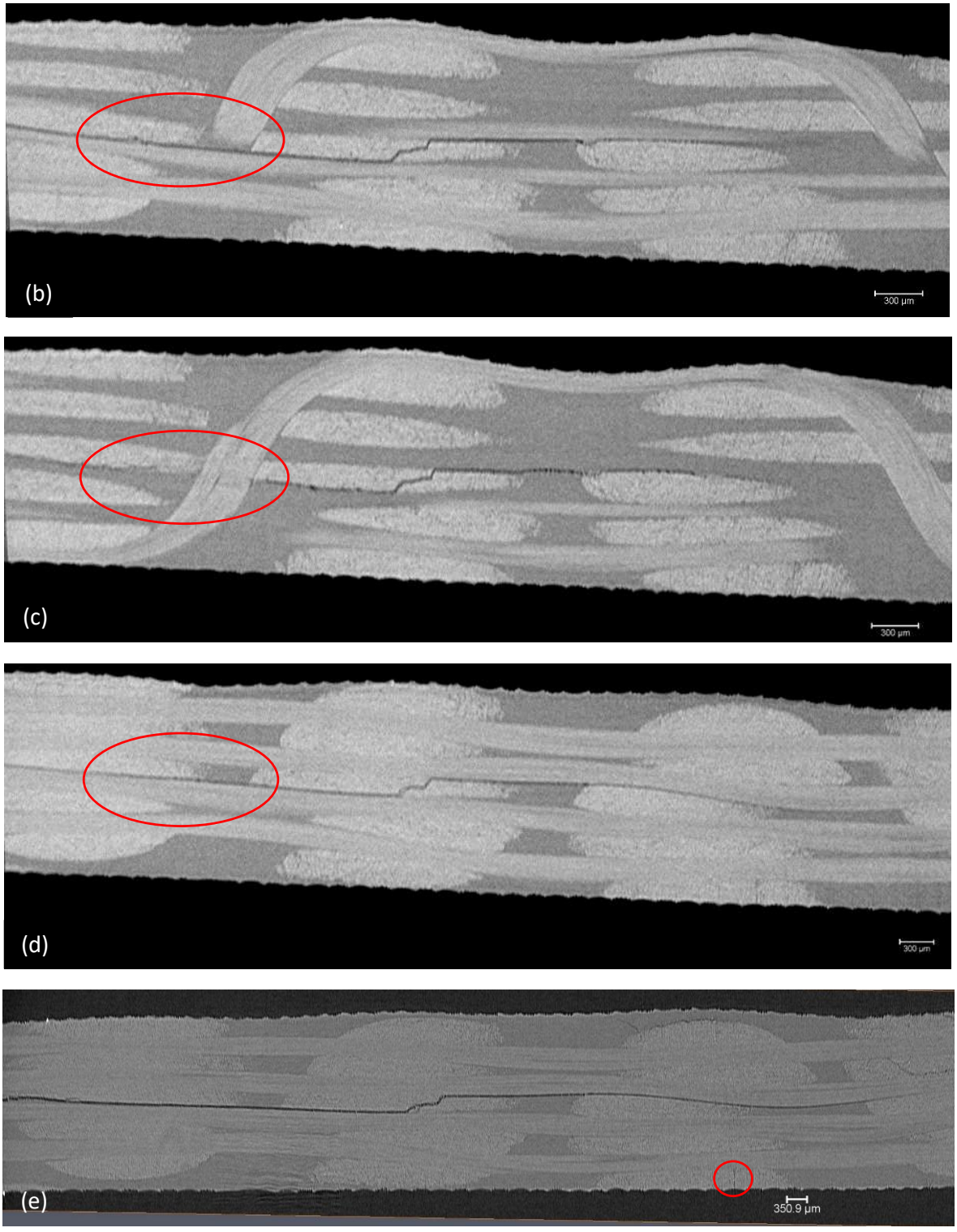

Figure 5 xz virtual cross-sectional X-ray slices for the2×2 twill (Left: the end of sample; Right: the middle of the sample). (a) after80k cycles located in front of the binder, (b) after 80k cycles adjacent to the Z-binder, (c) after80k cycles adjacent to the Z-binder, (d) after80k cycles after the Z binder and (e) the same slice as d) but after 130k cycles.

While short beam shear is a complex failure process comprising at least three damage failure types, delamination is the main reason for the load drop and the stiffness reduction in the fatigue test. Internal delamination is observed at the midplane of the specimen (Figure 5),

  doi:10.5075/epfl-298799_978-2-9701614-0-0

starting from the middle loading area and propagates to the ends of the sample delamination with weft tow debonding. The transverse micro-crack observed in Fig 4(b) possibly develops from the matrix to the fibre/matrix interface. The fibre could be slipped by shear force at the fibre/matrix interface and becomes separated from the matrix.

figure 5(b) to (d) shows how the Z-binder arrests the delamination effectively marked with the red circle. In Figure 5(b), the Z-binder is going to reach the delamination. The damage develops through the y-direction and along the x-direction. In figure 5(c), The Z-binder suppresses the damage progression because the Z-binder is subjected to tension. However, the Z-binder affects damage within a local area and does not arrest delamination along the entire width, as shown in Figure 5(d). Comparing figure 5(d) and (e), with the increasing number of cycles, firstly, the delamination length increases longer towards both ends of the sample. n. Due to the tension effect, a small fibre tow debonding happened at the bottom weft tow shown in figure 5(e) red circle.

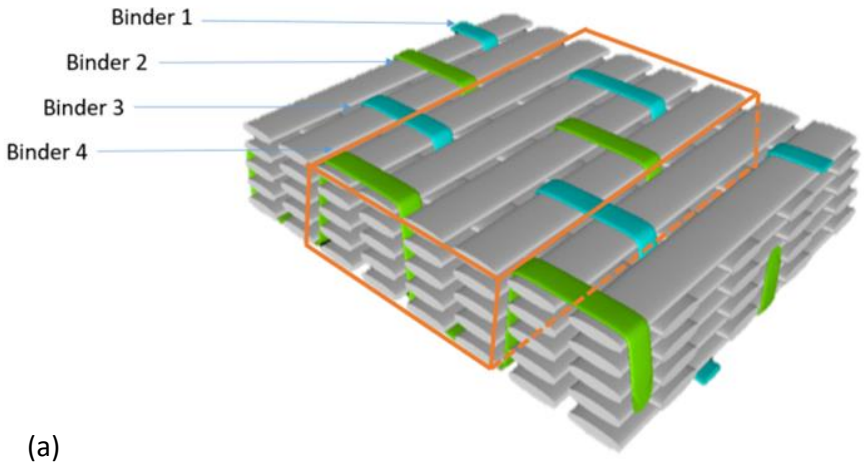

(a)

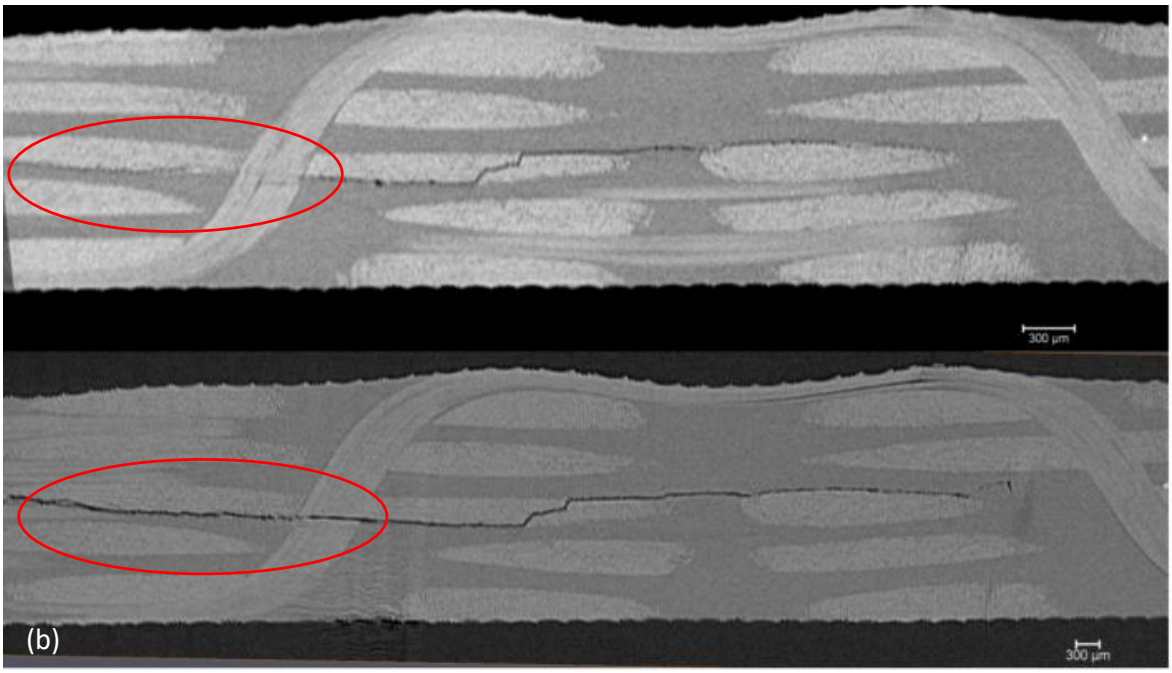

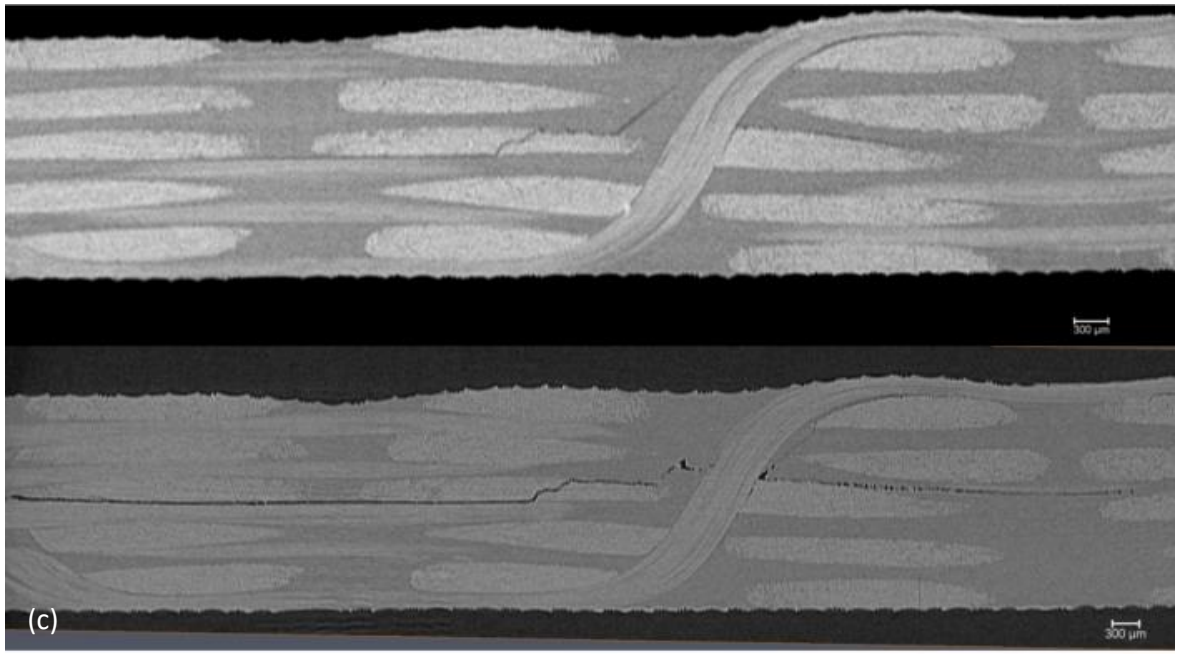

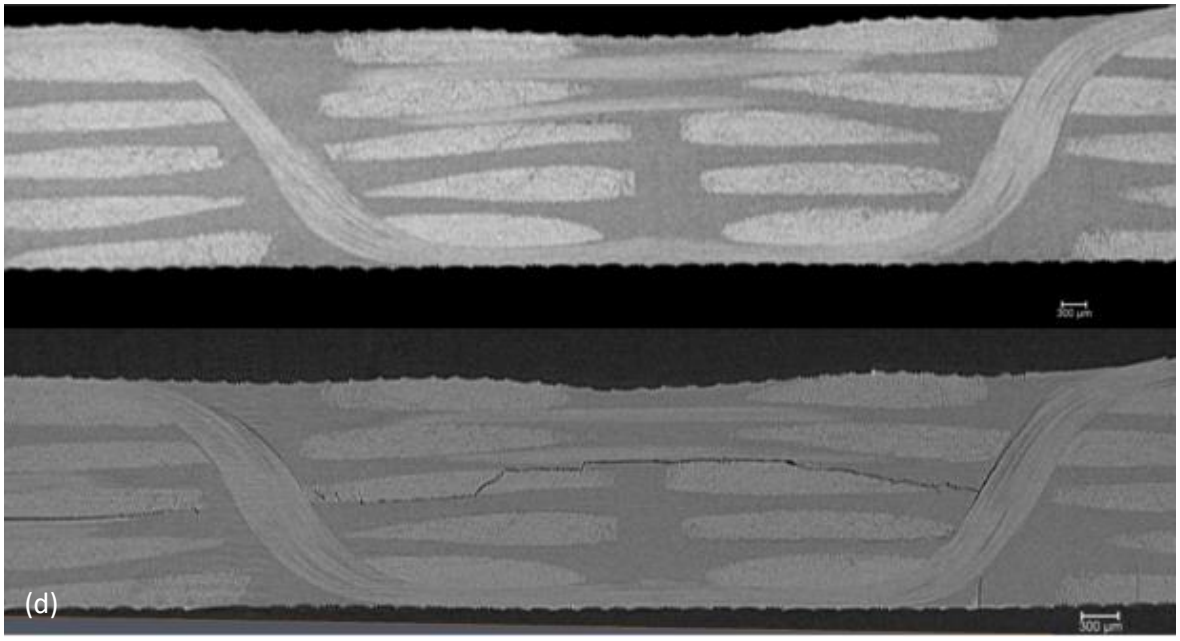

  doi:10.5075/epfl-298799_978-2-9701614-0-0

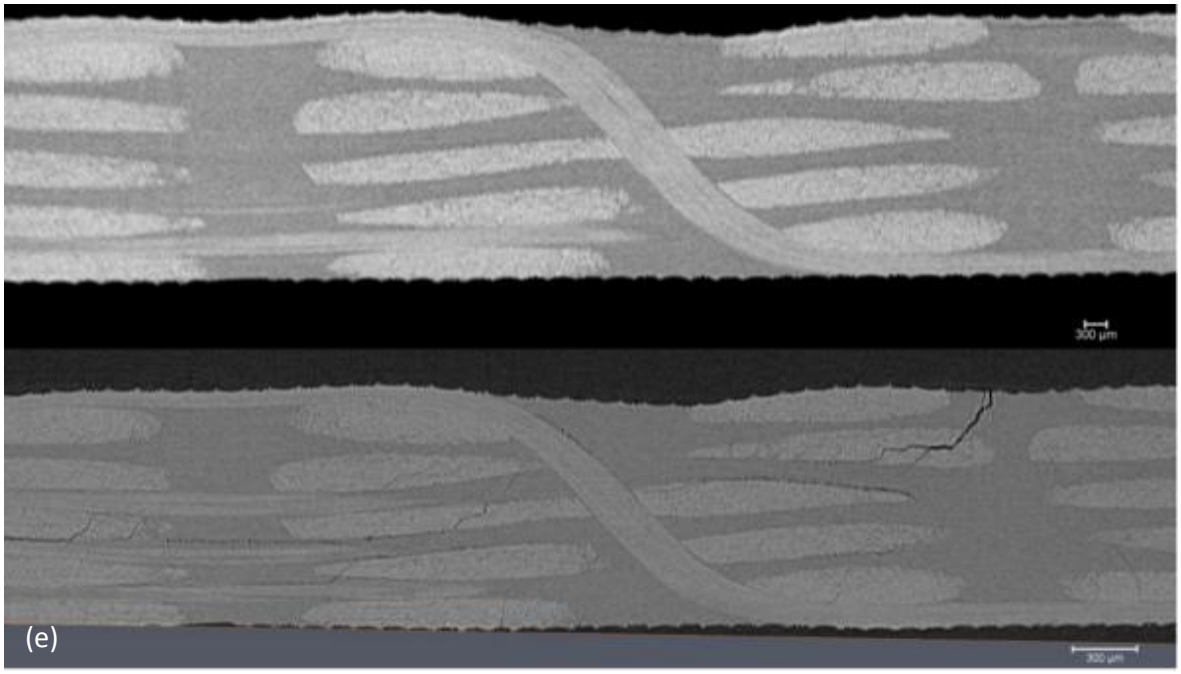

Figure 6 (a) The labelling of the binder and the X-ray CT visualised slices (orange box) for the 2x2 twill xz cross-sectional view of (b) binder 1; (c) binder 2; (d) binder 3; (e) binder 4. (in each case Top: 80k cycles, Bottom: 130k cycles).

If we look at the first Z-binder cross-sectional views after 80k cycles, the Z-binder arrests the delamination and does not fail. Upon further cyclic loading (to 130k cycles), the Z-binder 1 fails under tension, and the delamination propagates until the far end circulated in Figure 6(b). Figure 6(c) shows that Z-binder presents a different morphology and failure mechanism. The delamination develops into a shear crack in the resin-rich area, and the crack stops when it reaches the binder. With the increase of loading, the crack opens and propagates further.

Interestingly, the crack leads to delamination on the other side of the binder, causing delamination under the Z-crown. The possible reason is the Z-binder slipping during the repeated loading as the crack has already been developed in the resin, which causes the Z-binder/matrix debonding. Therefore, the Z-binder may not break and maintain its function. Figure 6(d) shows a similar damage development mechanism to the second binder. A crack is developed after 130k cycles in the resin-rich area because of tensile loading at the bottom of the sample. Another debonding happens within the bottom weft tow, similar to the tensile fatigue failure. in Figure 6(e), a large crack initiates from the top surface after 130k cycles. Due to the repeated compression loading from the top loading point, the crack starts from the resin and propagates deeper. Some mid-plane delamination associated with fibre tow debonding is developed as well, which is happened around the first and second binder after 80k cycles. It happens later because of the sample deformation caused by the stiffness reduction. This deformation leads to an unsmooth surface, and the loading nose may contact this area firstly.

  doi:10.5075/epfl-298799_978-2-9701614-0-0

3.2.2 The fatigue damage development of 2×1 twill

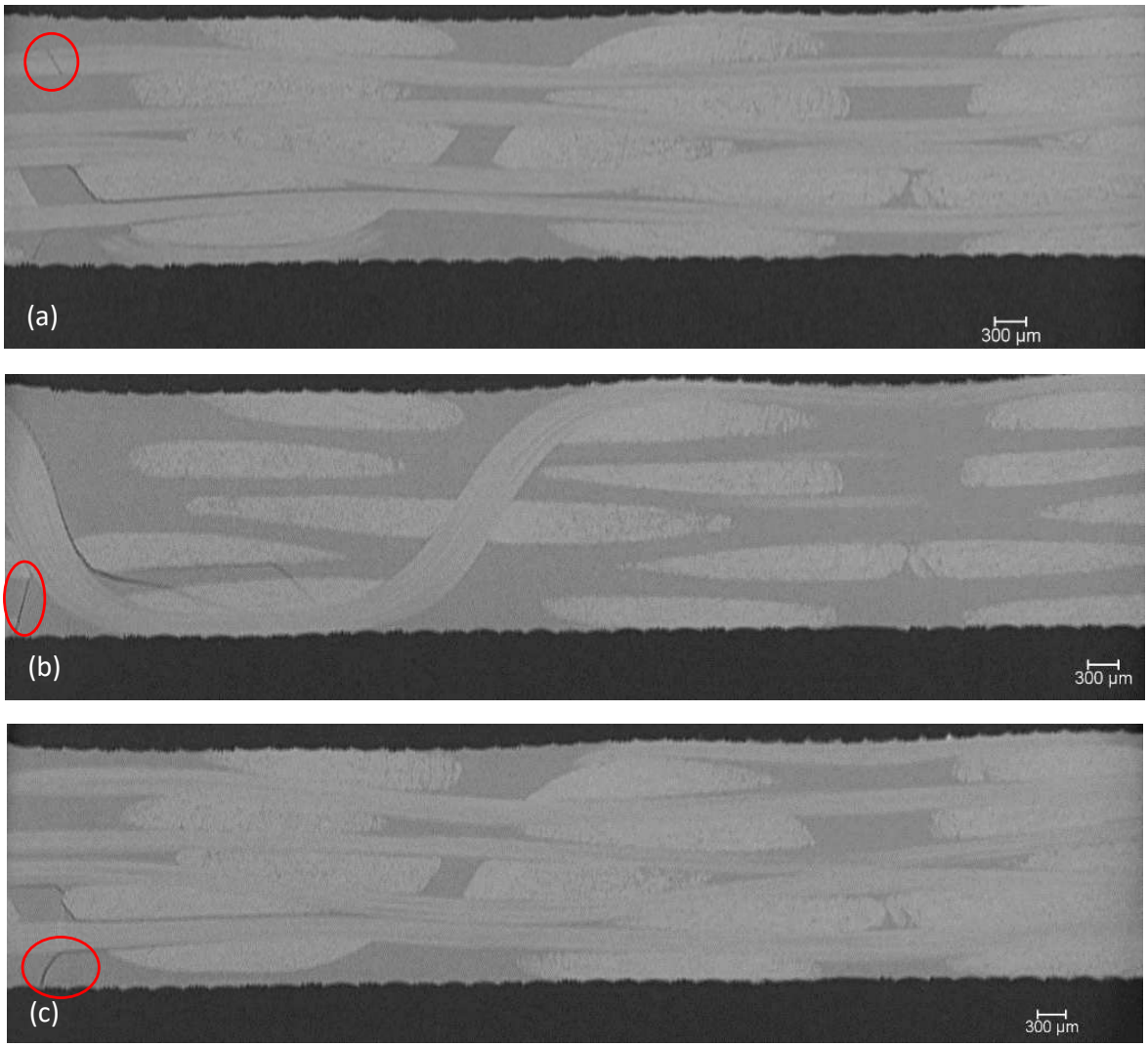

Figure 7 The zx virtual X-ray CT cross-sectional views after 46k cycles for the 2x1 twill composite a) in front of the binder, b) through the Z-binder and c) behind the Z-binder

Comparing Figure 5(a)-(d) and Figure 7(a)-(c), we can see that the damage distribution in the 2×1 twill structure is similar to that for the 2×2 twill structure. Both show delamination at the mid-plane through along the warp direction. The Figure 7(a) red circle shows a rare top warp tow fracture at the early stage of the fatigue life which does not happen in the 2×2 twill structure. This behaviour is yet to be investigated and will be the subject of future research. A resin crack marked in figure 7(b) and (c) initiates from the bottom resin-rich area at the bottom of the sample due to the tensile loading as the shear test is performed in a three-point bending fixture. The tensile loading effect cannot be eliminated completely. The binder stops the further propagation of resin cracks, and it develops as delamination between the bottom warp/weft tow. The propagation direction of the existed delamination is changed and follows the Z-binder/matrix interface extends to the top resin surface leading to a surface resin crack eventually. The tip of the delamination propagates down through the adjacent weft tow resulting in a debonding instead of larger delamination.

  doi:10.5075/epfl-298799_978-2-9701614-0-0

4. Conclusions

Quasi-static and dynamic fatigue short beam shear tests were performed on two 3D woven orthogonal composites. Damage development has been identified and analysed using optical microscopy and X-ray Computed Tomography. Both materials have similar interlaminar shear strength and the shear damage features comprising the delaminations between warp tows, warp tow shear fracture and weft tow debonding. different Z-binder configurations (having the same fibre volume fractions) appear to have similar static shear performance.

The two architectures demonstrate different fatigue responses. The main fatigue damage feature is the internal delamination which is partially arrested by the Z-binder thereby improving the damage tolerance. The shorter Z-binder float length associated with the 2×1 twill gives more interlacing points within the structure, which helps arrest the delamination propagation. On the other hand, some cracks arose in the resin-rich area, reducing the stiffness and introducing more damage. This research shows that the 2×2 twill Z-binder configuration provides better fatigue performance and insight into the interlaminar shear fatigue damage mechanism and the effect of the Z-binder.

Acknowledgements

We would like to thank Mr Stuart Morse from the University of Manchester for help in mechanical testing and Mr Anuj Prajapati from the HMXIF for the X-ray CT imaging processing and analysis. PJW is grateful for the X-ray imaging and analysis facilities within the Henry Moseley X-ray Imaging Facility (HMXIF), which is supported through EPSRC Grant Nos. EP/M010619, EP/K004530, EP/F007906, EP/F001452, EP/I02249X, and EP/F028431 together with the European Research Council grant (CORREL-CT, Grant No. 695638). The HMXIF is part of the National Research Facility for Lab X-ray CT, which is supported through EPSRC grant EP/T02593X/1. LW is grateful for the partial funding from The Armourers & Brasiers' Company.

  doi:10.5075/epfl-298799_978-2-9701614-0-0

5. References

1. Walter TR, Subhash G, Sankar B V., Yen CF. Monotonic and cyclic short beam shear response of 3D woven composites. Compos Sci Technol [Internet]. 2010;70(15):2190–7. Available from: http://dx.doi.org/10.1016/j.compscitech.2010.08.022

2. Dahale M, Neale G, Lupicini R, Cascone L, McGarrigle C, Kelly J, et al. Effect of weave parameters on the mechanical properties of 3D woven glass composites. Compos Struct [Internet]. 2019;223(May):110947. Available from: https://doi.org/10.1016/j.compstruct.2019.110947

3. He Y, Mei M, Wei K, Yang X, Duan S, Han X. Interlaminar shear behaviour and meso damage suppression mechanism of stitched composite under short beam shear using X-ray CT. Compos Sci Technol [Internet]. 2022;218(November 2021):109189. Available from: https://doi.org/10.1016/j.compscitech.2021.109189

4. Zhang D, Liu X, Gu Y, Sun M, Yu S, Zhang Y, et al. Effects of off-axis angle on shear progressive damage of 3D woven composites with X-ray micro-computed tomography. Compos Part A Appl Sci Manuf [Internet]. 2018;115(June):311–20. Available from: https://doi.org/10.1016/j.compositesa.2018.10.007

5. Quinn JP, McIlhagger AT, McIlhagger R. Examination of the failure of 3D woven composites. Compos Part A Appl Sci Manuf. 2008;39(2):273–83.

6. Makeev A. Interlaminar shear fatigue behavior of glass/epoxy and carbon/epoxy composites. Compos Sci Technol [Internet]. 2013;80:93–100. Available from: http://dx.doi.org/10.1016/j.compscitech.2013.03.013

  doi:10.5075/epfl-298799_978-2-9701614-0-0

FATIGUE DELAMINATION GROWTH OF CFRPs MODIFIED WITH ELECTROSPUN BIS-MALEIMIDE RESIN UNDER MODE I REMOTE LOADING CONDITIONS

Athanasios, Kotrotsos[a], Constantinos, Rouvalis[a], Anna, Geitona[a], Vassilis Kostopoulos[a,b,]*

a: Department of Mechanical Engineering and Aeronautics, University of Patras, Patras University Campus, GR-26504 Patras, Greece; – akotrotso@mech.upatras.gr
b: Foundation of Research and Technology, Institute of Chemical Engineering Sciences (FORTH/ICE-HT), Stadiou Str., GR-26504 Patras, Greece;
*: Corresponding author: kostopoulos@mech.upatras.gr; Tel.: +30-2610-969441

Abstract: *In the current work, fatigue life estimation for delamination growth of modified unidirectional (UD) carbon fiber reinforced plastics (CFRPs) with Bis-maleimide (BMI) resin under mode I loading conditions is assessed. More precisely, BMI resin containing or not four layered (4L) graphene nanoplatelets (GNPs) at the amount of 1wt% was integrated locally into the mid-thickness area of high performance CFRPs by solution electrospinning process (SEP) technique. After manufacturing process, reference and modified samples (a) with BMI and (b) with BMI containing GNPs were used for fatigue onset life and propagation tests. All double cantilever beam (DCB) samples were tested under displacement control. During the tests, a travelling microscope was utilized to measure the crack length at the end of precise loading cycles while loads and delamination lengths were recorded at the same time. Based on experimental results, BMI modified CFRPs presented the best resistance to delamination.*

Keywords: CFRPs; Bis-maleimide; Mode I; Fatigue; GNPs

1. Introduction

Fiber reinforced plastics (FRPs) are extensively used in many advanced structures for a wide range of applications. These materials offer high specific strength and modulus, low cost and low weight if compared to traditional metallic ones. Based on literature [1], a major weakness of laminated FRPs is the promotion of delaminations and especially under cyclic loading conditions. Thus, the understanding of the resistance of these materials under interlaminar fracture cyclic loading is of great importance for establishing guidelines for the design of the damage tolerance. Recently, the focus of various researchers has been the enhancement of the fracture behaviour of high performance structural composites. Based on that, a variety of methods have been proposed in the literature (i.e., interleaving, hybridization, stitching, short-fibres, and z-pinning) [2–6]. Interleaving is one of the most spread and effective method for interlaminar fracture toughness properties' enhancement. In [7] Aksoy and Carlsson, incorporated thermoset and thermoplastic type interleaves into composites and it was found that both interleave types have the ability to enhance the interlaminar fracture toughness properties of them to a great extent. Thermoplastic interleaves were found to be more effective than the thermoset ones because of the larger energy-absorbing capability.

Bis-maleimides are a class of materials that present resin type behaviour at ambient conditions while are mendable and present thermoplastic type behaviour beyond its melt point temperature (T_m) [8]. By incorporating this type of materials into composites, have shown to

  doi:10.5075/epfl-298799_978-2-9701614-0-0

considerably enhance the interlaminar fracture toughness properties [9-10] especially when combined with nano-inclusions [11-12]. Addition to them, BMIs are based on special covalent bonding interactions that allow polymer chains to flow upon heating and present self-healing functionality [9-12]. In [9], Kostopoulos et al., achieved to increase the Mode I interlaminar fracture toughness (G_{IC}) by 3.5 times of carbon FRPs by incorporating two BMI prepregs into the mid-thickness area. In [12], Kotrotsos et al., also achieved to enhance the G_{IC} value of CFRPs (almost by 50%) by incorporating a mixture of a BMI material and epoxy in grain form. Recently, the authors achieved to enchance the G_{IC} value of CFRPs by incorporating BMIs in electrospun form, either by solution electrospinning process (SEP) [11] or by melt electro-writing process (MEP) [12] technique.

When delaminations are detected within a composite structure, repair of them must be performed long before the critical length of each delamination or prior the stress at the crack tip to exceed the residual strength of the composite. Models for fatigue life-time prediction as well as for prediction of the remaining life are well established for metallic components. For FRP laminated composites, the development of models for the prediction of the fatigue delamination growth and life-time estimation is also very important together with inspection establishment intervals. FRPs, during fatigue delamination growth present sigmoidal log(da/dN) versus log(G_{Imax}/G_{IR}) curve when plotted. G_{Imax} value represents the energy release rate at maximum stress while G_{IR} is the Mode I delamination instantaneous resistance. The curve is composed by three main regions; the first one represents the threshold, the second one the stable growth while the third one is the region in which the crack propagation becomes unstable up to a catastrophic failure [1].

In the current work, fatigue life-time estimation that is related to delamination growth of UD CFRPs containing BMI resin into the mid-thickness area under Mode I loading conditions is assessed. More precisely, BMI resin containing or not 4L GNPs at the amount of 1 wt% was locally integrated into mid-thickness area of high performance CFRPs by SEP technique. After manufacturing process, reference CFRPs and modified CFRPs containing either BMI resin or nanomodified BMI resin with GNPs were exposed to fatigue crack propagation tests under Mode I loading conditions. The tests were conducted for a predetermined number of 50 k Cycles. During the tests, a travelling microscope was utilized to measure the crack length at the end of precise loading cycles while loads and delamination lengths were also recorded at the same time. From the fitted curves of the propagation data concluded, based on the experimental results, the Paris' law coefficients (m and c) were calculated as well as the da/dN equations representing region II delamination growth were determined.

2. Materials and methods

2.1 Materials

The composite materials which were utilized in the current study were fabricated by using a commercial unidirectional (UD) carbon fibre-epoxy pre-preg tape (identification code: CE-1007 150-38). The commercial pre-preg tape was supplied by SGL Group, Germany. The utilized maleimide oligomers, with approximate molecular weight 1700 Da (BMI-1700) was supplied by Designer Molecules (San Diego, USA). BMI-1700 is hydrophobic, with high decomposition temperature (above 400^{o}C) and it is soluble in most aromatic and aliphatic solvents. The following reactants: furfuryl glycidylether and furfuryl amine which were utilized for trifurane

  doi:10.5075/epfl-298799_978-2-9701614-0-0

(TF) synthesis were purchased from Sigma Aldrich Chemicals (St. Louis, USA). All reagents were used as received and no further purification occurred. Tetrahydrofurane (THF) solvent which played the SEP solvent was supplied by Honeywell Inc. (North Carolina, USA). The obtained GNPs have lateral dimensions of 1–2 μm, average thickness ≤ 4 nm, surface area ≥ 750 m^2/gr and purity ≥ 99% and were supplied by Cheap Tubes Inc., Cambridgeport, USA.

2.2 Electrospinning process and preparation of the modified pre-preg plies

The SHA incorporation was conducted by SEP. The information that is related to the SEP technique and pre-preg plies' modification procedure by SHA is provided in a recent papers by the authors [11, 13] and is not included in this manuscript.

2.3 Composites' manufacturing and quality control

For composites' manufacturing, pre-preg and autoclave technologies have been utilized. Three types of laminated plates with 22 UD pre-pregs were prepared: the reference laminate, and two modified laminates containing pure BMI and BMI with 1 wt% GNPs into their mid-thickness area (5 surface-modified pre-preg plies). During SEP, the deposited BMI resin onto pre-pregs' surface created an "interleaf". Two plates for each material set were manufactured with the following dimensions (270 x 60 x 3) mm^3 that led to 4 DCB samples (2 samples per CFRP plate) having final dimensions of (250 x 25 x 3) mm^3 whose geometry is illustrated in Figure 1 taking into consideration specifications of AITM 1.0005 standard of Airbus [14]. The final fiber volume fraction of all composites (V_f) was calculated to be close to 60±2% without the SHA incorporation to affect the thickness of the final composite. During the manufacturing two polytetrafluoroethylene sheets with 13 μm thickness were positioned in the mid-thickness area to create an artificial pre-crack according to the utilized standard specifications. Following the lamination process, the composites structures were cured in an autoclave. The applied curing profile was 100°C applied temperature, under 4 bars applied pressure for a period of 5 hours. After curing process, all manufactured CFRP plates were ultrasonically scanned, using a physical acoustics corporation UT c-scan system with a 5 MHz transducer.

2.4 Mode I quasi-static and Mode I fatigue testing

Quasi-static Mode I interlaminar fracture toughness tests were performed by using an Instron Universal testing machine equipped with a 5 kN load cell at room temperature (RT) conditions. The tests were performed according to the AITM 1.0005 standard of Airbus [14]. The information on the tests is presented in a recent paper by the authors [9] and is not included in this paper. For the Mode I fatigue tests, all DCB samples were tested under displacement control at a frequency of 5 Hz and a tension-tension displacement ratio R=0.1. The delamination growth rate data was generated by applying the maximum displacement (δ_{Imax}) corresponding to G_{Imax}/G_{IC}=0.5 for all material sets. G_{IC} values for all material sets under static Mode I fracture toughness tests were recently determined [11] and taken into consideration. The tests were conducted for a predetermined number of 50 k cycles. During the tests, a travelling microscope was utilized to measure the crack length at the end of precise loading cycles while loads and delamination lengths were recorded at the same time. From the fitted curves to the propagation data arose from experimental results, the Paris' law coefficients (m and c) were calculated as well as the da/dN equations representing region II delamination growth were determined.

  doi:10.5075/epfl-298799_978-2-9701614-0-0

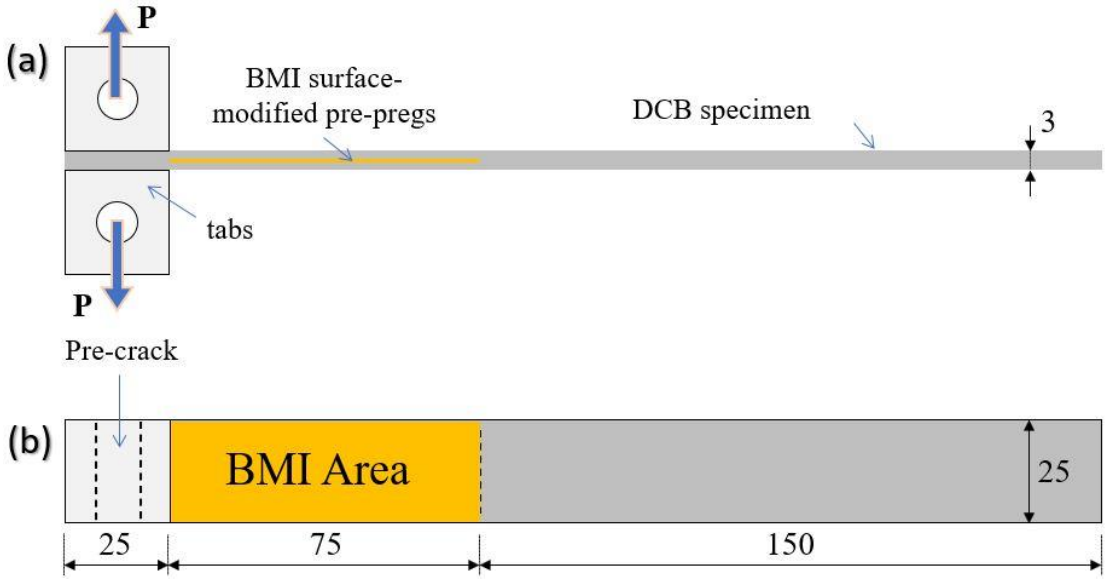

Figure 1. Schematic representation of a modified double cantilever beam (DCB) test configuration; (a) side view, (b) top view. Dimensions in millimeter (mm).

3. Results and discussion

3.1 Mode I threshold toughness determination using onset life tests

The Mode I fatigue tests for all material sets were performed under constant amplitude tension-tension displacement control while the utilized cyclic load frequency was that of 5 Hz. In addition, the minimum to maximum displacement ratio (R) was set to be 0.1. The edges of the specimens were painted in white and scaled to observe the crack growth while the specimens were connected to the test machine by self-aligning tabs as Figure 1 suggests. The corresponding information that is related to the load and displacement values with respect to the number of cycles were automatically stored by the Instron machine by using a software.

For the determination of the Mode I threshold onset life, the ASTM: D6115 [15] standard was taken into consideration. This standard suggests two criteria for the determination of the threshold onset life; the increase of the compliance by 1% and 5% respectively against to the compliance recorded at the first cycle (N=1). Figure 2, provides the compliance with respect to number of cycles for all CFRP types. Based on these, the number of cycles measured at 1% and 5% of the compliance increase has been taken into account to determine the initiation threshold. For all tests, the δ_{max} values was selected to apply a G_{max} of 50% of G_{IC} while the δ_{min} value was determined from R=0.1.

  doi:10.5075/epfl-298799_978-2-9701614-0-0

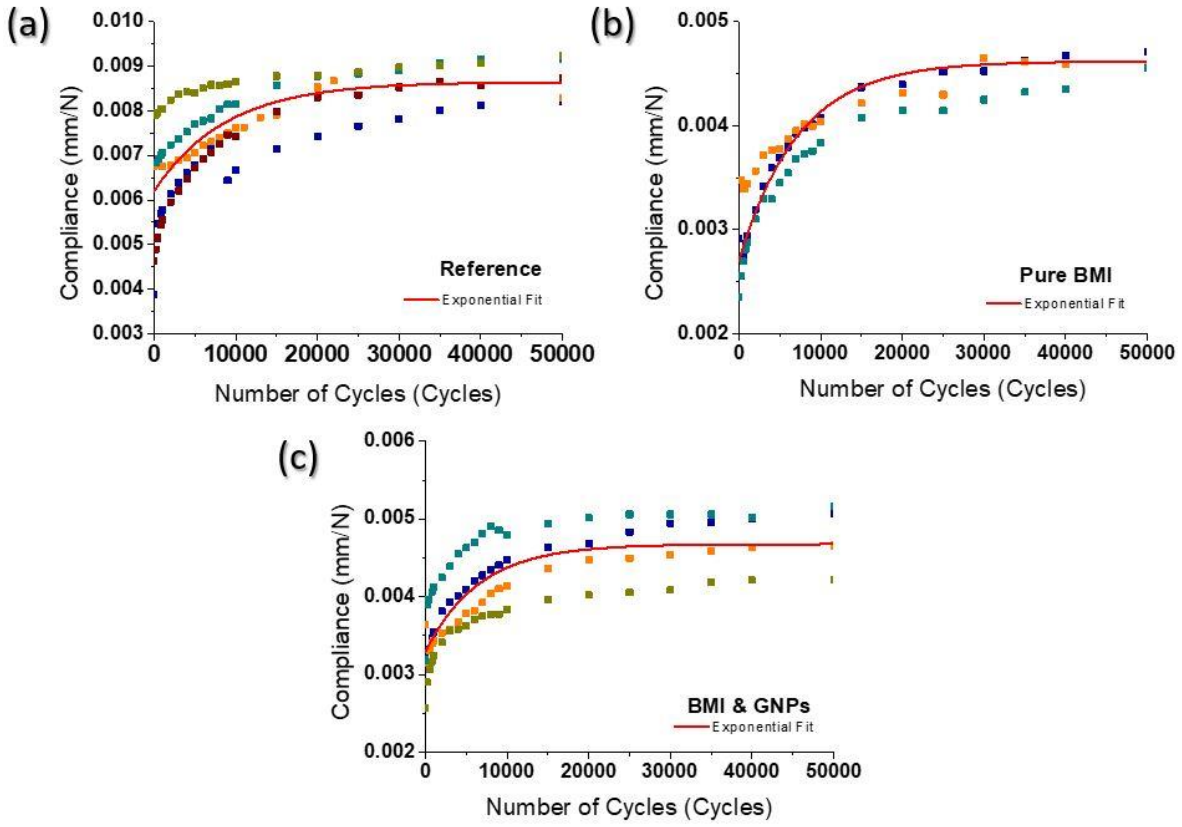

Figure 2. Compliance versus number of cycles for (a) the reference, (b) the BMI modified and (c) the BMI and GNP modified CFRP samples, during initiation tests for loading at G_{max} = 50%G_{IC}.

For the determination of the delamination threshold fracture toughness (G_{th}), the plots of the G_{Imax}/G_{IC} values versus the number of cycles (N) which measured at 1% and 5% increase of the compliance during the onset life fatigue tests were taken into consideration for all CFRPs. Figure 3 provides the plots of G_{Imax}/G_{IC} values with respect to log N for 1% and 5% criteria for the collected data of all the CFRP samples which tested. The first data points for all CFRPs were taken from Mode I quasi-static tests. For the current work, the Shivakumar et al. [16] power law curve was fitted to the data and the fitted equations are provided also in Figure 3 for all CFRP types. The authors also obtained the strain energy release rate (SERR) at N = 10^6 while at the same procedure was followed for the needs of the current investigation. Based on the obtained equations, the calculated threshold strain energy release rate (G_{th}) at N = 10^6 was calculated to be 0.35G_{IC}, 0.23G_{IC} and 0.34G_{IC} for the reference, the BMI modified and the BMI & GNP respectively. Based on these, when the applied SERR is bellow the calculated values the crack speed is very low and the crack will not propagate up to 100 k Cycles.

  doi:10.5075/epfl-298799_978-2-9701614-0-0

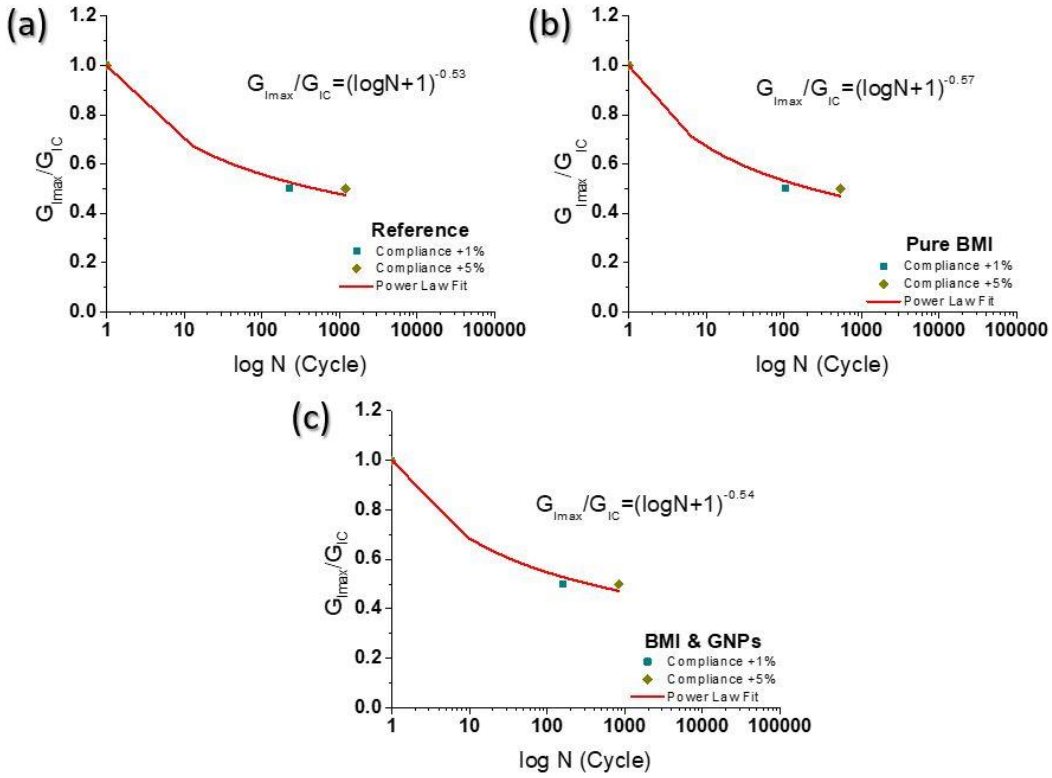

Figure 3. Variation of onset fatigue life with G_{Imax}/G_{IC} for (a) the reference, (b) the BMI modified and (c) the BMI and GNP modified CFRP samples, during initiation tests for loading at G_{max} = 50%G_{IC}.

3.2 Delamination growth of CFRPs under Mode I fatigue loading

For the delamination growth investigation of the three CFRP types the same set-up and the same specifications were utilized as in the case of the onset life tests. Based on these, all CFRP specimens which were pre-cracked during the onset life tests were further utilized for the Mode I fatigue delamination growth tests while the new initial delamination lengths were recorded. The delamination growth data were obtained by applying also δ_{max} value corresponding to G_{Imax}/G_{IC} = 0.5 and the tests were run for a predetermined number of 50 k cycles. During the tests, a travelling microscope was also utilized for the calculation of the crack length versus the number of cycles during the fatigue procedure. At the end of specific sets of ΔN the following values N, ΔN, α, Δα, P_{Imax} and δ_{Imax} were identified. From the recorded results dα/dN, G_{Imax} and G_{IR} values were determined. The G_{Imax} value was determined by using the following Eq.(1):

$$G_{Imax} = \frac{3P_{Imax}\delta_{Imax}}{2b(a+|\Delta|)} \quad (1)$$

where $|\Delta|$ was calculated during the Mode I quasi-static interlaminar fracture toughness tests, α is the crack length and b is the width of the sample. Based on these, Figure 4 provides the delamination crack growth for the three CFRP specimens; (a) the reference, (b) the BMI modified and (c)the BMI & GNP modified one, respectively. The tests data as well as the equation are bounded by the following limits: G_{Imax}/G_{IR}=0.1 and G_{Imax}/G_{IC}=1. From the resulted fitted curves to the propagation data, the coefficients that are related to the Paris' law were determined to be m = 6.38 and C = 12 x 10^{-2} for the reference CFRP, m = 2.37 and C = 0.4 x 10^{-2} for the BMI modified CFRP and m= 7.68 and C= 88.29 for the BMI & GNP modified CFRP. Finally, the dα/dN

equations representing the delamination growth region II are provided also in Figure 4 for all CFRPs.

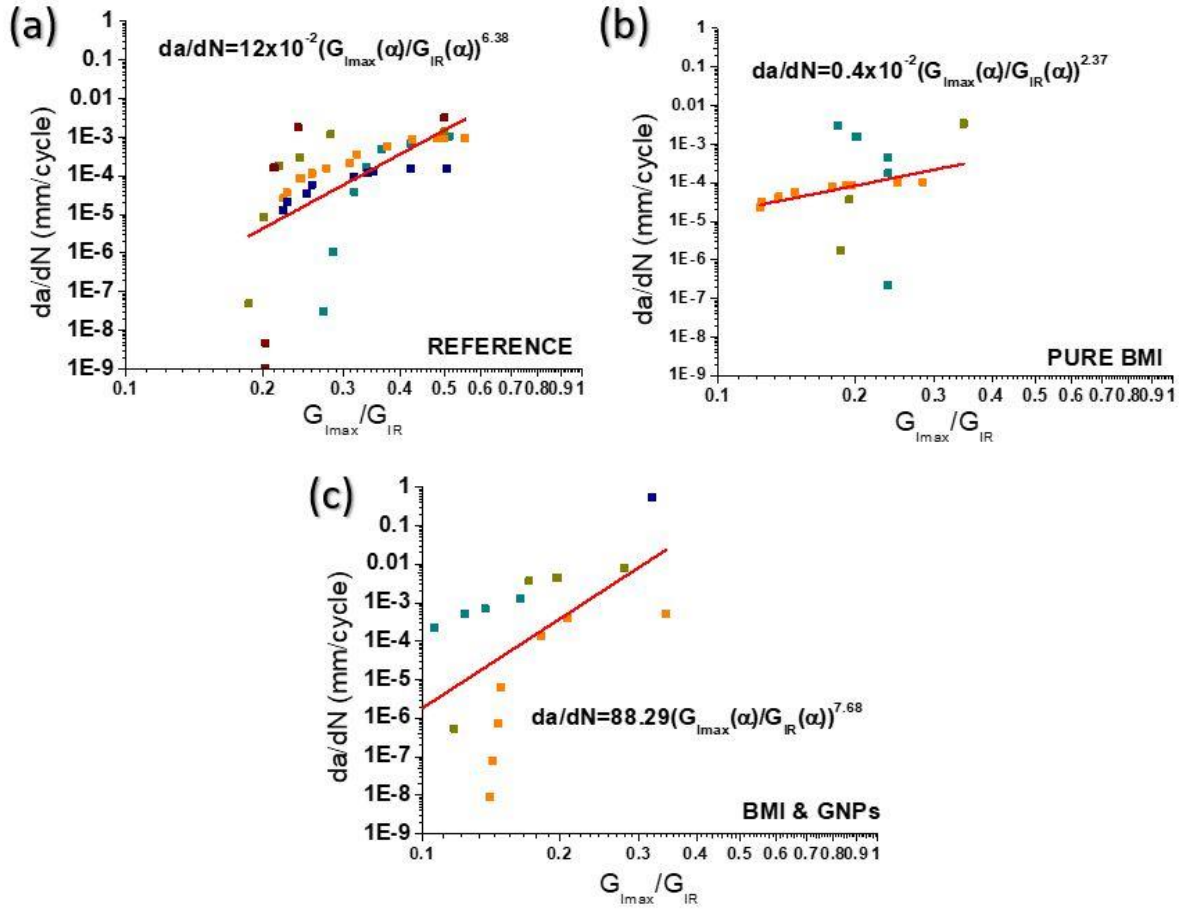

Figure 4. Crack propagation of (a) the reference, (b) the BMI modified and (c) the BMI & GNP modified DCB CFRP specimens, respectively.

4. Conclusions

In the current investigation, fatigue life estimation for delamination growth of modified CFRPs with BMI resin (nanomodified or not) under mode I loading conditions was assessed. The CFRPs' modification was successfully conducted by the incorporation of five surface-modified pre-pregs into the mid-thickness area of the composite. The pre-pregs' modification was performed through SEP technique and three types of CFRPs were manufactured; the reference, the BMI modified and the BMI & GNP modified one. After manufacturing, fatigue onset life tests were conducted for all CFRPs in order the G_{th} values to be determined for the subcritical region. Afterwards, constant amplitude cyclic Mode I fatigue tests with displacement control were conducted for all CFRPs to determine the the delamination crack growth (dα/dN) with respect to the maximum cyclic energy release rate (G_{Imax}). Experimental results revealed that the BMI modified CFRPs exhibited the best resistance to delamination as GNPs seem to negatively affect the composites.

Acknowledgements

This research is co-financed by Greece and the European Union (European Social Fund—ESF) through the Operational Program «Human Resources Development, Education and Lifelong

  doi:10.5075/epfl-298799_978-2-9701614-0-0

Learning» in the context of the project “Reinforcement of Postdoctoral Researchers-2nd Cycle” (MIS-5033021), implemented by the State Scholarships Foundation (IKY).

5. References

1. Al-Khudairi O, Hadavinia H, Waggott A, Lewis E, Little C. Characterizing mode I/mode II fatigue delamination growth in unidirectional fibre reinforced polymer laminates. Materials and Design 2015; 66:93-102.
2. Masters JE. Improved impact and delamination resistance through interleafing Key Engineering Materials 1989; 37:317–48.
3. Stevanovic MM, Stecenko TB. Mechanical behaviour of carbon and glass hybrid fibre reinforced polyester composites Journal of Materials Science 1992; 27:941–946.
4. Dransfield KA, Jain LK, Mai YW. On the effects of stitching in CFRPs–I. mode I delamination toughness Composites Science and Technology 1998; 58:815–27.
5. Gilbert EN, Hayes BS, Seferis JC. Interlayer toughened unidirectional carbon prepreg systems: effect of preformed particle morphology Composites Part A: Applied Science and Manufacturing 2003; 34:245–52.
6. Mouritz AP. Review of z-pinned composite laminates Composites Part A: Applied Science and Manufacturing 2007; 38:2383–97.
7. Aksoy A, Carlsson LA. Interlaminar shear fracture of interleaved graphite/epoxy composites Composites Science and Technology 1992; 43:55-69.
8. Kennedy JP, Castner KF. Thermally reversible polymer systems by cyclopentadienylation. I. A model for termination by cyclopentadienylation of olefin polymerization. Journal of Polymer Science Part A: Polymer Chemistry 1979; 17:2039–2054.
9. Kostopoulos V, Kotrotsos A, Tsantzalis S, Tsokanas P, Christopoulos, AC, Loutas T. Toughening and healing of continuous fibre reinforced composites with bis-maleimide based pre-pregs. Smart Materials and Structures 2016; 25:84011 (12 pp.).
10. Kotrotsos A, Tsokanas P, Tsantzalis S, Kostopoulos V. Healing of carbon fiber reinforced plastics by Diels–Alder based polymers: Effects of healing agent concentration and curing cycle. Applied Polymer Science 2019; 136(19):47478 (p. 12).
11. Kotrotsos A, Rouvalis C, Geitona A, Kostopoulos V. Toughening and Healing of CFRPs by Electrospun Diels–Alder-Based Polymers Modified with Carbon Nano-Fillers. *Journal of Composite Science* 2021; 5:242(1-12).
12. Kotrotsos A, Michailidis G, Geitona A, Tourlomousis F, Kostopoulos V. Toughening and Healing of CFRPs by Diels-alder Based Nano-modified Resin Through Melt Electro-writing Process Technique.
13. Kostopoulos V, Kotrotsos A, Geitona A, Tsantzalis, S. Low velocity impact response and post impact assessment of carbon fibre/epoxy composites modified with Diels-Alder based healing agent. A novel approach. Composites Part A Applied Science and Manufacturing 2021; 140:106151(1-11).
14. AITM 1.0005. Airbus industry test method, Carbon fiber reinforced plastics, Determination of interlaminar fracture toughness energy, Mode I, **1994**, *Issue 2*.
15. D 6115–97. Standard Test Method for Mode I Fatigue Delamination Growth Onset of Unidirectional Fiber-Reinforced Polymer Matrix Composites, 2004.
16. Shivakumar K, Chen H, Abali F, Le D, Davis C. A total fatigue life model for mode I delaminated composite laminates. Int J Fatigue 2006;28:33–42.

  doi:10.5075/epfl-298799_978-2-9701614-0-0

PROGRESSIVE FATIGUE DAMAGE DETECTION AND ASSESSMENT IN COMPOSITE SPECIMENS USING RANDOM VIBRATION RESPONSE SIGNALS

Theodoros Varouxis[1,2], Konstantinos Tserpes[1], Spilios Fassois[2]

[1]Laboratory of Technology & Strength of Materials, Department of Mechanical Engineering & Aeronautics, University of Patras, Patras 26500, Greece
Emails: t.d.varouxis@gmail.com, kitserpes@upatras.gr Web Page: http://ltsm.mead.upatras.gr
[2]Stochastic Mechanical Systems and Automation Laboratory, Department of Mechanical Engineering & Aeronautics, University of Patras, Patras 26500, Greece
Email: fassois@upatras.gr Web Page: http://www.smsa.upatras.gr

Abstract: *The problem of random vibration-based fatigue damage detection and assessment for a population of 8 nominally identical composite specimens under population, test rig, and environmental uncertainty is addressed. Eight damage states created by fatigue tests that are 10 000 cycles apart from each other are specifically considered via a Multiple Model Representation methodology employing a single vibration response signal. The achievable performance is systematically assessed via thousands of Test Cases and is shown to be ideal, reaching 100% correct detection rate for 0% false alarm rate, for the detection problem, and very good, reaching 91.07% to 97.75% correct classification rate, for the damage assessment problem. The results of the study reveal the high potential of automated, on-board, natural vibration-based Structural Health Monitoring for populations of composite structures.*

Keywords: Composite materials; fatigue; vibration testing; Structural Health Monitoring

1. Introduction

Composite materials have found widespread applications in aerospace and other sectors in recent decades [1], and this have stirred high interest in the development of appropriate Structural Health Monitoring (SHM) technology [2]. In this context, the detection and assessment of fatigue damage via random vibration based SHM methods is attractive as it offers potentially high performance, automation, functionality under normal operating conditions, that is without interrupting normal operation, while it also benefits from the availability of natural excitation and inexpensive and reliable measurement equipment.

Yet, the currently available methods are mostly focused on diagnosing specific types of damage, such as delamination or impact damage, mostly under limited uncertainty (for instance for a single structure). The diagnosis of fatigue damage has, thus far, received limited attention, also under limited uncertainty and using natural frequency shifts [3]. Yet, the effects of uncertainty, stemming from experimental, operational, environmental conditions, and also from a population of nominally identical structures, have been shown to be very important and may drastically affect diagnostic performance. These types of uncertainty have been considered in recent studies (such as [4]) by one of the authors and co-workers in the context of impact-induced damage detection.

  doi:10.5075/epfl-298799_978-2-9701614-0-0

The present study aims at tackling the challenging problem of vibration-based progressive fatigue damage detection and assessment in a population of 8 composite structures under population, test rig, and environmental (such ambient temperature) uncertainty and 8 tension-tension, displacement-controlled, damage states that are 10 000 cycles apart from each other. Towards this end a Multiple Model Representation (MMR) type methodology [4] is postulated based on a single random vibration response signal, with the fatigue damage detection and assessment performance evaluated via a systematic and statistically reliable procedure based on thousands of Test Cases. Ultrasonic C-scans are also employed for providing insight into each fatigue damage state.

2. Methodology

The methodology, depicted in the flowchart of Fig. 1, consists of three distinct processes applied to each one of the 8 specimens: (I) Interrupted (every 10 000 cycles) fatigue testing, (II) Ultrasonic C-Scan performed during each interruption, and (III) vibration testing performed at the outset with the Healthy (H) state of each specimen and during each fatigue interruption (along with the C-Scan). The objective of random vibration testing is to provide signals to be used for accumulated fatigue damage detection and assessment.

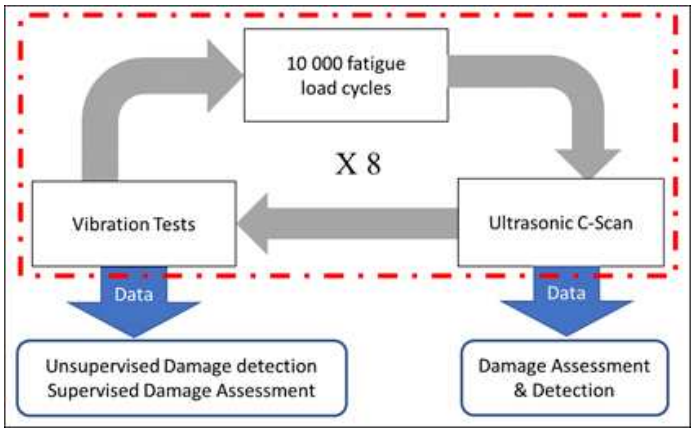

Figure 1. Flowchart of the methodology.

3. The Specimens, the Interrupted Fatigue Testing, and the C-Scans

3.1 The population of composite specimens

The study uses a population of 8 IMA/M21E prepreg composite specimens. The lay-up is (±45/90/0/0/90/±45/0/90)s with the specimen dimensions following the ASTM D3479/D3479M, ASTM D3039/D3039M, and ISO 527-4 standards. A specimen sketch along with its basic nominal dimensions is presented in Fig. 2. It is noted that although the 8 specimens are manufactured as nominally identical, this is not exactly the case due to inevitable material and manufacturing uncertainty.

3.2 The interrupted fatigue tests

A tension test was initially conducted, according to the ASTM D3039/D3039M standard, to measure the Young's modulus and tensile strength of the composite material. The measured values are 49.07 MPa and 950.36 MPa, respectively. Tension-tension displacement-controlled fatigue tests were subsequently conducted for each specimen on an MTS 250 kN universal

  doi:10.5075/epfl-298799_978-2-9701614-0-0

testing machine (Fig. 3a) using a stress ratio R=0.1, a maximum stress equal to the 60% of the tensile strength, and a 5 Hz frequency. Based on the literature [5] these loading characteristics lead to a fatigue life of 100 000 cycles for the specific composite material; yet a fatigue life of 80 000 cycles was observed. Fatigue testing was interrupted every 10 000 cycles, with an ultrasonic C-scan and random vibration testing conducted during each interruption, as well as under the initial (Healthy, H) state. This gave rise to a total of 9 health states, the Healthy H and 8 damage states designated as $FD\_01, FD\_02, \dots, FD\_08$ (also see Table 1).

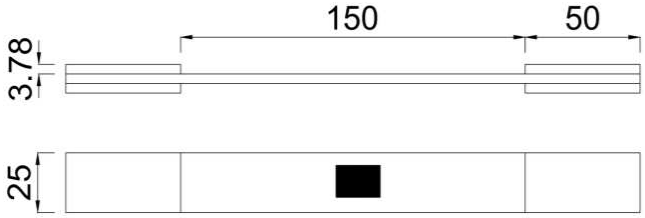

Figure 2. Composite specimen nominal dimensions including the end tabs (dimensions according to the ISO 527-4 standard). The black rectangle indicates the reflective patch used for laser-based vibration measurement.

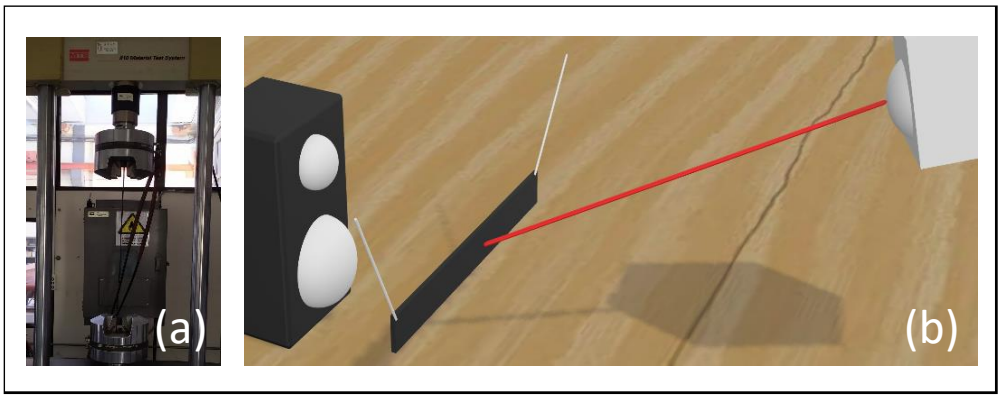

Figure 3. (a) The MTS 250 kN servohydraulic testing machine. (b) Schematic representation of the vibration test rig.

Table 1. The health states, the numbers of random vibration response signals and their characteristics.

Fatigue state	Applied fatigue cycles	No. of signals per specimen	Total no. of signals across all 8 specimens
H	0	70	560
FD_0X	$10\,000 \times X$	30	240

H: Healthy state; FD_0X: Fatigue state X ($X = 1,2, \dots, 8$ progressive fatigue states); 8 specimens
Vibration signal characteristics: Sampling frequency 4 266.67 Hz; Signal length 128 000 samples (30 s)

3.3 Fatigue damage assessment via ultrasonic C-scans

Ultrasonic C-scans were performed for each specimen and under each one of the health states. C-scanning is a form of Non-Destructive Testing capable of determining the presence, position, and shape of damage in CFRP composites [6], although one of its main drawbacks is its inability to detect fiber or matrix cracking in a CFRP with fiber cracking being one the main causes for

  doi:10.5075/epfl-298799_978-2-9701614-0-0

loss of stiffness. In the present context C-scans are run as an off-line assessment method in order to provide useful insight into the extent of corresponding fatigue damage.

Indicative ultrasonic C-scan results are, for specimen 5, indicatively presented in Fig. 4. Based on this, the progressive fatigue damage accumulation is obvious. It is further observed that the transition from FD_02 to FD_03 (from 20 000 to 30 000 fatigue cycles) is characterized by the highest difference between any two consecutive states. This may be attributed to the fact that ultrasonic C-scans are sensitive to detecting delamination, rather than fiber or matrix cracking, with the latter two constituting the predominant failure mechanisms in early stages of fatigue with delamination following [6].

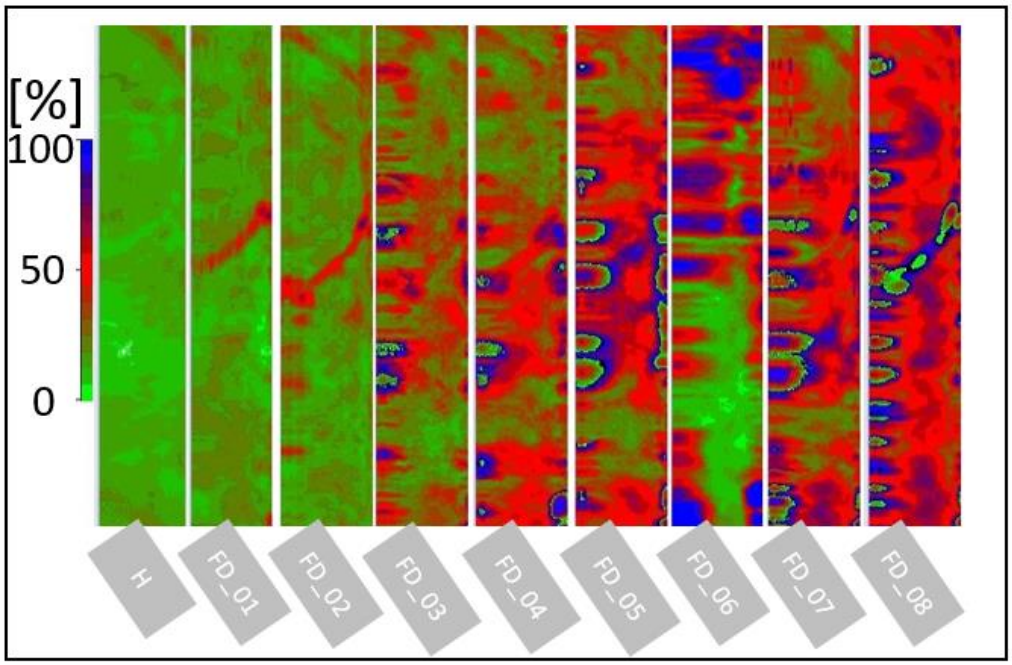

Figure 4. Indicative fatigue damage ultrasonic C-scan based evaluation for specimen 5 (left to right, from Healthy H to FD_08).

4. The Vibration Test Rig and the Measured Signals

The vibration test rig is schematically presented in Fig. 3b. Each specimen is, in each health state ($H, FD\_01, \dots, FD\_08$), suspended via elastic chords simulating free-free boundary conditions. Approximate white noise random excitation is acoustically provided via a set of speakers driven via a MATLAB-running computer. The random velocity vibration response is measured on a single point on each specimen (see Fig. 2) using a Polytec OFV-5000 laser vibrometer equipped with the OFV-505 single point vibration sensor and a National Instruments CompactDAQ Chassis carrying an NI-9234 data acquisition card. Each signal is lowpass filtered within the 0 - 2 133 Hz range, sampled at 4 266.67 Hz, sample mean corrected, and normalized by its own sample standard deviation. The signal length is 128 000 samples, corresponding to 30 s. 70 random vibration response signals per specimen are obtained from the Healthy (H) state of each specimen, and 30 per specimen from each one of the 8 damage states ($FD\_01, \dots, FD\_08$); a summary is presented in Table 1.

  doi:10.5075/epfl-298799_978-2-9701614-0-0

5. The Random Vibration Based Methodology for Fatigue Damage Detection and Assessment

The postulated vibration-based methodology for fatigue damage detection and assessment is to be based on a single random vibration response signal measured on any specimen of the population under any, a-priori unknown, structural state. The objective of the methodology is twofold: (1) Damage detection, that is determining whether a tested specimen is in its Healthy (H) state or is in any of the 8 fatigue damage states ($FD\_01, \dots, FD\_08$), and, in case damage has been detected, (2) damage assessment, that is the determination of the specific (out of the 8) precise damage state. Following training, in an initial Baseline Phase, the methodology is fully automated in its actual operation (Inspection Phase) requiring no human intervention. It is also unsupervised for the 1st (damage detection) problem, implying that training in the Baseline Phase is based on random vibration signals obtained under the Healthy (H) state of each specimen, but supervised for the 2nd (damage assessment) problem, implying that training in the Baseline Phase is based on random vibration signals obtained under each one of the 8 FD states.

The methodology is of the Multiple Model type [4] founded upon the following elements: (i) A data-based, partial, representation of the structural dynamics based on which a proper damage-sensitive feature is obtained; (ii) a corresponding feature space; (iii) a Multiple Model Representation (MMR) of the dynamics for each health state, say $M_H, M_{FD1}, \dots, M_{FD8}$, under population, experimental, and environmental uncertainty, and (iv) a proper `distance metric' $D(\cdot,\cdot)$ between any MMR and any single point in the feature space representing the model, say m_u of the partial dynamics of a specimen under test (the subscript u designating unknown health state).

The particular selections made in this study are: (i) The data-based partial representation of the dynamics is of the AutoRegressive (AR) type of order n [8] and the damage-sensitive feature consists of the AR parameter vector, (ii) the feature space is that spanned by the AR parameters, (iii) each MMR consists of p conventional AR models, that is $M_i := \{AR_1, \dots, AR_p\}$ ($p = p_1$ for the detection problem and $p = p_2$ for the damage assessment problem), and the distance metric $D(M, m_u)$ is defined as the minimum Kullback-Leibler pseudo-distance [4,7] between the elements of M and m_u. In an initial BASELINE (TRAINING) PHASE and for the damage detection problem, the p_1- dimensional MMR, M_H, of the healthy dynamics is constructed, while for the damage characterization problem 8 p_2- dimensional MMRs, $M_{FD1}, \dots, M_{FD8}$, each one for each one of the 8 FD states, are constructed. Then in the INSPECTION (OPERATIONAL) PHASE, given a random vibration response signal from any member of the population under unknown health state and uncertainty, a conventional AR model m_u is constructed, and damage detection and assessment (if required) decisions are made as follows (l designating a user-selected threshold and iff standing for if and only if) – also see Fig. 5:

If $D(M_H, m_u) \leq l$ the specimen is in Healthy state; else in a Damaged state (Damage Detection).
A damaged specimen is in state $i^\star \in [1, \dots, 8]$ iff $i^\star = \min_i D(M_i, m_u)$ (Damage Assessment)

  doi:10.5075/epfl-298799_978-2-9701614-0-0

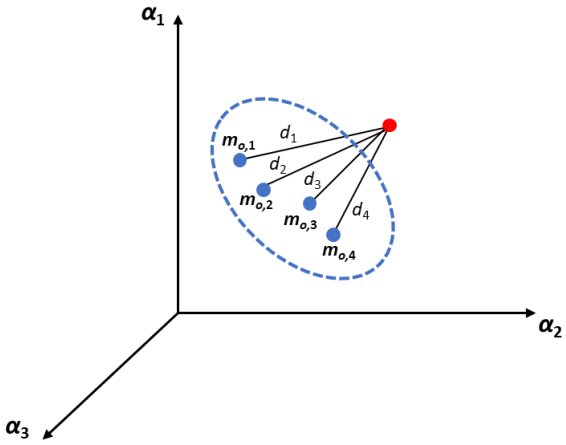

Figure 5. Schematic depiction of the Multiple Model Representation (MMR) methodology for damage detection. The Healthy MMR is surrounded by the blue line and the current specimen in unknown state is designated as m_u [4].

6. Performance Assessment

6.1 The assessment procedure and random vibration signal modeling

Performance assessment is based on a systematic and statistically reliable procedure in which $p_1 = 2$ Healthy vibration signals from each specimen are employed in the Baseline Phase and 68 Healthy and 30 per damage state per specimen signals are employed in the Inspection Phase for the damage detection problem. For fatigue damage assessment $p_2 = 15$ vibration signals from each specimen and damage state are employed in the Baseline Phase, and another 15 from each specimen and damage state are employed in the Inspection Phase. A total of 10 rotations, in which the Baseline Phase signals are interchanged with Inspection Phase signals, are also run in both cases to eliminate effects that could result from any particular selection of the Baseline Phase signals. Performance assessment is thus based on 24 640 and 9 600 Inspection Test Cases for the damage detection and the damage assessment problems, respectively. Complete details are provided in Table 2.

Random vibration response signal modeling [8] leads to an AR(70) representation achieving very good prediction accuracy (0.82% RSS/SSS) in the healthy case.

6.2 Assessment results and discussion

The damage detection results, based on 24 640 Inspection Test Cases (Table 2), indicate excellent ability in correctly determining the presence or not of damage from vibration signals obtained under the Healthy or any FD state. The performance is in fact ideal, leading to a 100% correct detection rate (True Positive Rate, TPR) for 0% false alarm rate (False Positive Rate, FPR).

Damage assessment results, based on 9 600 Inspection Test Cases, are presented in Fig. 6 via correct and incorrect classification rates for each fatigue damage state ($FD\_01, \dots, FD\_08$). Evidently, the results are very good as a correct classification rate ranging from 91.07% to 97.75% (depending on the damage state) is attained, with mean rate of 96.14% over the complete composite specimen population, while the incorrect classification rate is between 2.25% to 8.93%.

  doi:10.5075/epfl-298799_978-2-9701614-0-0

Table 2. Numbers of Baseline and Inspection Signals employed for damage detection and assessment.

	No of Baseline signals (per specimen)	No of Baseline signals (8 specimens)	No of Inspection Signals (per specimen, H and 8 FD states)	No of Inspection signals (8 specimens, H and 8 FD states)	Total no of Inspection signals (8 specimens, H and 8 FD states, 10 rotations)
Damage detection	$p_1 = 2$ H	**16** H	68 H + 240 FD = 308	544 H + 1 920 FD = **2 464**	5 440 H + 19 200 FD = 24 640
	No of Baseline signals (per specimen and FD state)	No of Baseline signals (8 specimens and 8 FD states)	No of Inspection Signals (per specimen and FD state)	No of Inspection signals (8 specimens and 8 FD states)	No of Inspection signals (8 specimens × 8 FD states × 10 rotations)
Damage assessment	$p_2 = 15$	**960**	15	**960**	960 × 10 = 9 600

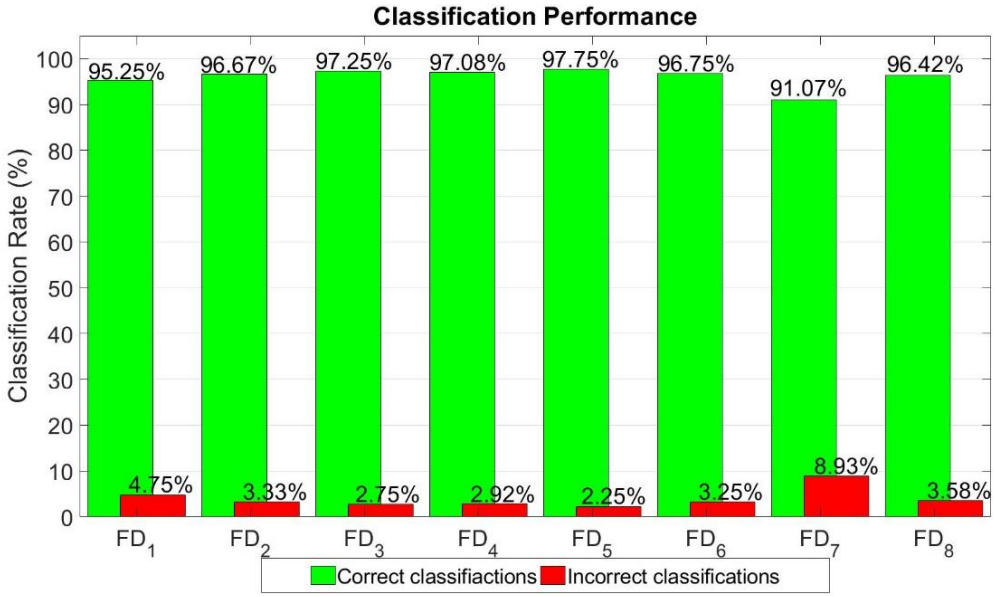

Figure 6. Damage assessment performance evaluation: Correct classification rates (green) incorrect classifications rates (red) for each fatigue damage state ($FD\_01, \ldots, FD\_08$). *[1 200 Test Cases per damage state.]*

7. Concluding Remarks

The problem of random vibration-based fatigue damage detection and assessment for a population of 8 nominally identical composite structures under population, test rig, and environmental uncertainty, and for 8 damage states that are 10 000 cycles apart from each other, has been considered via an MMR type methodology employing a single vibration response signal. The achievable performance has been systematically and reliably assessed via thousands of Test Cases. The main conclusions drawn from the study are: (a) In spite of the population and other uncertainty present, the postulated methodology has been shown to be

  doi:10.5075/epfl-298799_978-2-9701614-0-0 published under CC BY-NC 4.0 license

very effective for both damage detection and assessment using a single, naturally arising, random vibration signal and is also suitable for fully automated on-board operation. (b) Ideal damage detection performance, reaching 100% correct detection rate for 0% false alarm rate, has been achieved under unsupervised operation. (c) Very good damage assessment performance, reaching 91.07% to 97.75% correct classification rate, has been achieved under supervised operation. The results of the study reveal the high potential of automated, on-board, natural vibration based Structural Health Monitoring for fatigue damage in populations of composite structures.

8. References

1. Pantelakis S, Tserpes K (Eds.). Revolutionizing aircraft materials and processes. Springer. 2020.
2. Speckman HR, Roesner H. Structural health monitoring: innovative applications for structural material systems. Sampe Europe Technical Conference 2006; Toulouse, France.
3. Aidi B, Philen MK, Case SW. Progressive damage assessment of centrally notched composite specimens in fatigue. Composites Part A: Applied Science and Manufacturing 2015; 74:47-59.
4. Vamvoudakis-Stefanou KJ, Sakellariou JS, Fassois SD. Vibration-based damage detection for a population of nominally identical structures: Unsupervised Multiple Model (MM) statistical time series type methods. Mechanical Systems and Signal Processing 2018; 111:149-171.
5. Feng Y, Ma B, Zhang T, Zhang T, He Y, Jiao S. Reliability fatigue life and a new S–N curve model of composite laminates under tensile-tensile fatigue load. Applied Composite Materials 2021; 28(1):129-148.
6. Hasiotis T, Badogiannis E, Tsouvalis NG. Application of ultrasonic C-scan techniques for tracing defects in laminated composite materials. Strojniški vestnik-Journal of Mechanical Engineering 2011; 57(3):192-203.
7. Press WH, Teukolsky SA, Vetterling WT, Flannery BP. Numerical recipes: The art of scientific computing, 3rd edition. Cambridge University Press. 2007; pp. 756–758
8. L. Ljung, System identification: Theory for the user. 2nd edition. Prentice Hall PTR. 1999; pp. 498-514.

  doi:10.5075/epfl-298799_978-2-9701614-0-0

HELICOIDAL LAYUPS AND INTERLEAVED HYBRIDS: A NOVEL DESIGN METHODOLOGY FOR IMPACT-RESISTANT COMPOSITES STRUCTURES

Victor Medeau[a], M. Erfan Kazemi[a], Emile Greenhalgh[a], Soraia Pimenta[a], James Finlayson[b] and Silvestre T Pinho[a]

a: Faculty of Engineering, Imperial College London, UK – vmedeau@ic.ac.uk
b: Composites - Structural Systems Design, Rolls-Royce. UK

Abstract: The aim of this study is to propose a design methodology for improved impact resistant composite structures at constant weight. A large range of materials and configurations have been manufactured following the proposed methodology, aiming at a consistent areal weight. The proposed designs were tested under high velocity impact, using a range of velocity between 140 and 300m/s. The results indicate a strong increase in ballistic limit and specific energy absorption when using the proposed hybrid configurations. Helicoidal layups on pure CFRP laminates have been found to improve the absorbed energy by respectively 22 and 55% for thin and thick plies compared to a [60/0/-60] CFRP baseline. Using the methodology presented, further optimized hybrid configurations were designed leading to improvements of up to 134% compared to the pure CFRP baseline. Fractography and C-scan analyses highlight the presence of more diffuse damage, the creation of helicoidal matrix cracks and the delay of the onset of fibre failure.
Keywords: High-Velocity Impact; Hybrid composite; Helicoidal layup; Damage tolerance

1. Introduction

Carbon fibre reinforced polymers (CFRP) have recently become widely used in load-bearing primary structures of aircrafts, due to their high modulus and light weight compared to their traditional metallic counterparts. Further aircraft weight reduction goals are leading to the application of composites in more challenging non-primary structures, such as the Fan Containment casing of turbofan engines. Specifically, in the case of a fan blade-off (FBO) event, the casing must be able to withstand the high energy being transmitted by the portion of the blade ejected into it. During FBO, the casing must preserve its structural integrity and contain any debris to avoid a catastrophic failure of the engine or the aircraft. For such applications, the use of monolithic CFRP solutions is not optimal, due to their inherent brittleness and relatively poor damage tolerance. Material hybridisation [1] and non-conventional layups [2,3] are two of the strategies that can be used to address the relatively poor HVI resistance of CFRPs.

The aim of this study is to propose a design methodology for improved impact resistant composite structures at constant weight. This design methodology will be applied to both thin-ply and thick-ply material and demonstrate significant improvement over a [60/0/-60] layup baseline in both cases.

2. Methodology

A large range of materials and configurations have been manufactured as part of this study, aiming at a consistent areal weight. The manufactured specimens were then compared under High-Velocity Impact (HVI) loading, looking at the energy absorption and the ballistic limit. The tests were carried out using a gas gun with a hardened-steel ball impactor, with a range of impact velocity from 100 to 300 m/s. The target consists of 150 mm × 100 mm panels, with a

  doi:10.5075/epfl-298799_978-2-9701614-0-0

target areal weight of 0.95 g/cm2. Due to the hybrid nature of some configurations and the range of material considered in the study, the resulting thickness of the panels varies from one configuration to another one (see Table 1). The panels were impacted at their centre using a 4 point simply supported test rig. High-speed cameras were used to track the projectile velocity before and after impact and calculate the energy absorption.

The methodology used to design the hybrid configuration focuses on:

1. a "material by design" approach, wherein materials are selected and placed along the thickness of the laminate based on their mechanical performance under the local stress state (see Figure 1 a.);

2. non-conventional helicoidal layups, to diffuse damage and maximise the absorbed energy (see Figure 1 b.);

3. interleaved blocks of the hybrid materials, to control the delamination planes and the compliance of the specimen during the impact event (see Figure 1 c.).

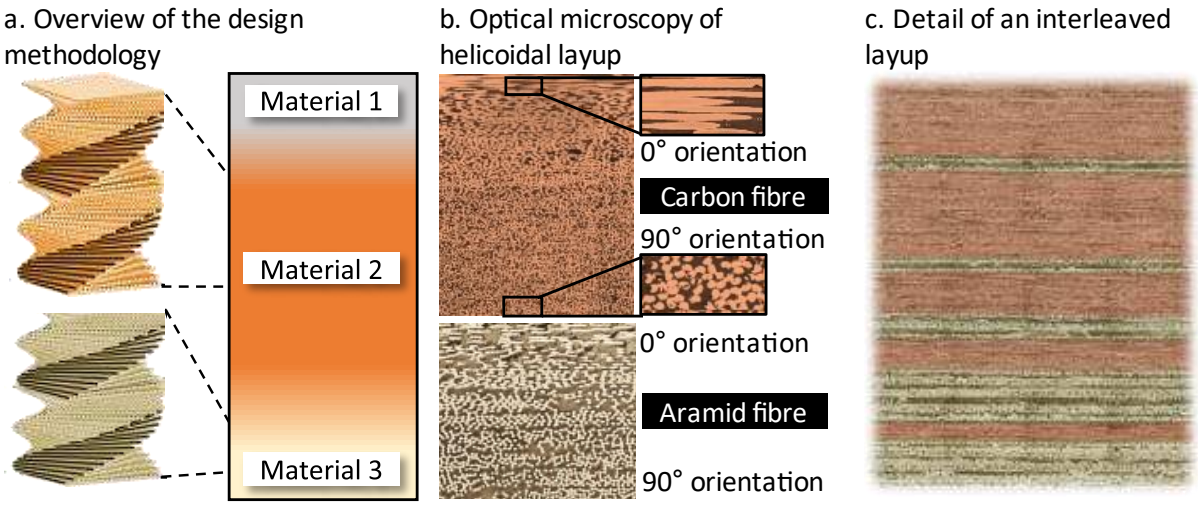

Figure 1. Hybrid design using helicoidal layup and interleaved configuration

The materials selected include CFRP, both using thin and thick ply prepregs, aramid and glass fibre reinforced polymers, titanium foils, and shape memory alloy enhanced CFRP. The ratio of hybrid (non-CFRP) material introduced was kept <50 % by weight. Following a preliminary study, titanium and Zylon aramid fibre were selected amongst the initial list [4,5,6]. Titanium sheets were used on the impact face, to delay the crushing failure caused by the poor through-the-thickness compressive performance of CFRP and redistribute the initial stresses created by the impactor through the whole laminate. Zylon was used towards the distal face to delay the final tensile fibre failure thanks to its higher strain to failure than that of carbon fibres.

Helicoidal layups (see Figure 1 a-b.) were used on both carbon and aramid fibre prepregs, with pitch angles of smaller than 5° for thin-ply materials and smaller than 30° for thick-ply materials. Such stacking sequences have been shown to delay the catastrophic failure of the specimen, redistribute the stresses and promote diffuse matrix cracking and delamination [3].

  doi:10.5075/epfl-298799_978-2-9701614-0-0

Finally, we studied the effect of interleaved alternating blocks of materials (see Figure 1 c.) and the size of those blocks. The details of the configurations manufactured are presented in Table 1.

Table 1: Overview of the configurations manufactured (QI = [60/0/-60], Hel. = helicoidal layup)

	Materials			Hybrid ratio by weight	Thickness (mm)	Areal weight (g/cm2)
	1 (Top)	2 (Center)	3 (Back)			
1.Thin-ply Baseline	-	Skyflex 20 gsm QI	-	0	5.5	0.84
2. Thin-ply Helicoidal	-	Skyflex 20 gsm Hel.	-	0	5.1	0.77
3. Thin-ply Proposed	Titanium	Skyflex 20 gsm Hel.	Zylon 25 gsm Hel.	44%	7.0	1.04
4. Thick-ply Baseline	-	Confidential CFRP QI	-	0	1*	0.94
5. Thick-ply Helicoidal	-	Confidential CFRP Hel.	-	0	1*	0.94
6. Thick-ply Proposed	Titanium	Confidential CFRP Hel.	Zylon 50 gsm Hel.	43%	1.06*	1.12

*Thick-ply thicknesses normalized by to baseline specimen

3. Results

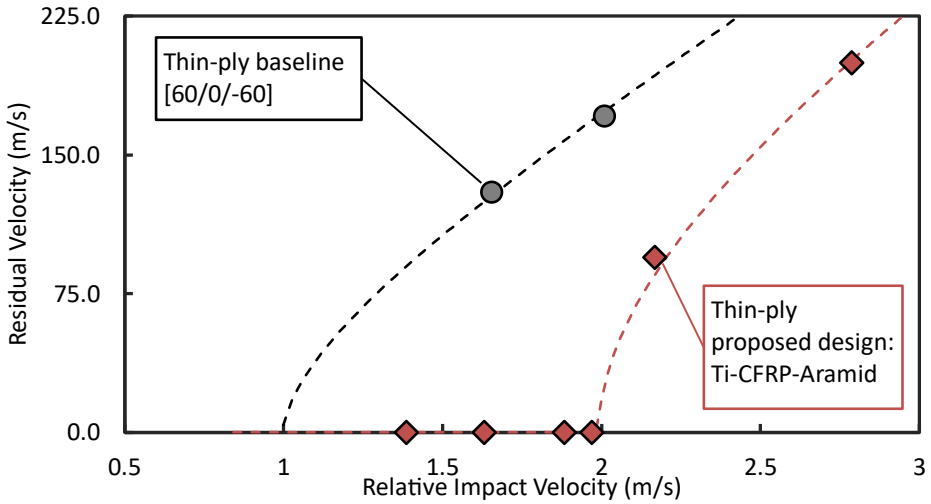

Figure 2: Selected experimental results of impact and residual velocities of the thin-ply baseline and proposed design (normalized by the ballistic limit of the baseline). The dashed lines represent the L-J curve

Figure 2 presents selected experimental results for the [60/0/-60] baseline configuration and the proposed hybrid design using thin-ply prepregs. When penetration is achieved, the residual velocity is plotted against the impact velocity. An analytical curve is fitted to the experimental data using the Lambert-Jonas equation [7]:

$$v_{\mathrm{res}} = A(v_{\mathrm{ini}}^{n} - v_{50}^{n})^{1/n} \quad (1)$$

where v_{ini} is the initial impact velocity, v_{res} the residual velocity and v_{50} the ballistic limit. Figure 2 highlights a strong increase in the ballistic performance of the improved configuration over the pure carbon baseline.

The corresponding specific energy absorption capability for all 6 configurations is presented in Figure 3. By using a helicoidal layup rather than a traditional [60/0/-60] layup, the energy absorption can be improved by 22 % and 55 % relatively for thin and thick plies.

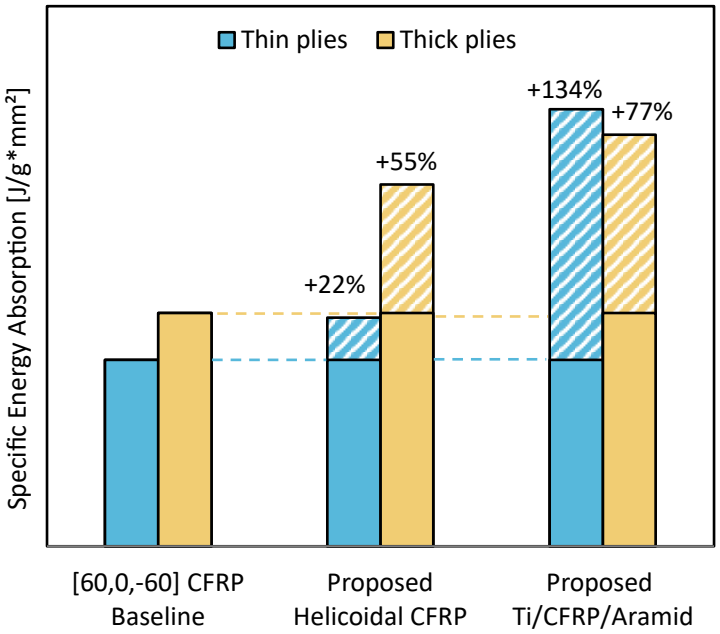

Figure 3: Specific energy dissipation improvement over a pure CFRP [60/0/-60] for thin and thick-ply configurations

Figure 4 highlights the change in damage mechanisms between the two layups on thin-ply specimens. For a conventional [60/0/-60] stacking sequence, it can be determined from a cross-section fractography along the impact plane (Figure 4 a.) that the specimen fails in a brittle manner under shear plugging. Damage stays confined in the region of impact. This correlates with the low energy absorption since shear plugging has been reported to be a low energy dissipating failure mechanism [8]. As seen from the back face damage after impact (Figure 4 c.), a large portion of the specimen was not involved in the failure process. C-scan analysis of the panels after impact (Figure 4 e.) confirms that damage stays confined to the impact region.

By contrast, helicoidal panels exhibit more complex and diffuse failure mechanisms. Figure 4 b. shows significant delamination and matrix cracking away from the impactor path. Plies toward the distal face of the specimen appear to have failed under tensile failure rather than shear plugging. Furthermore, the low pitch angle encouraged crack migration from one ply to the other, resulting in large helicoidal shaped cracks. This results in an increased compliance of the panel during the impact, stress redistribution, widely spread damage at the distal face (Figure 4 d.) and significant delamination and matrix cracking being detected by the C-scan analysis (Figure 4 f.). All those additional failure mechanisms and the shift from shear to tensile failure at the distal face can explain the improved energy absorption capability.

  doi:10.5075/epfl-298799_978-2-9701614-0-0

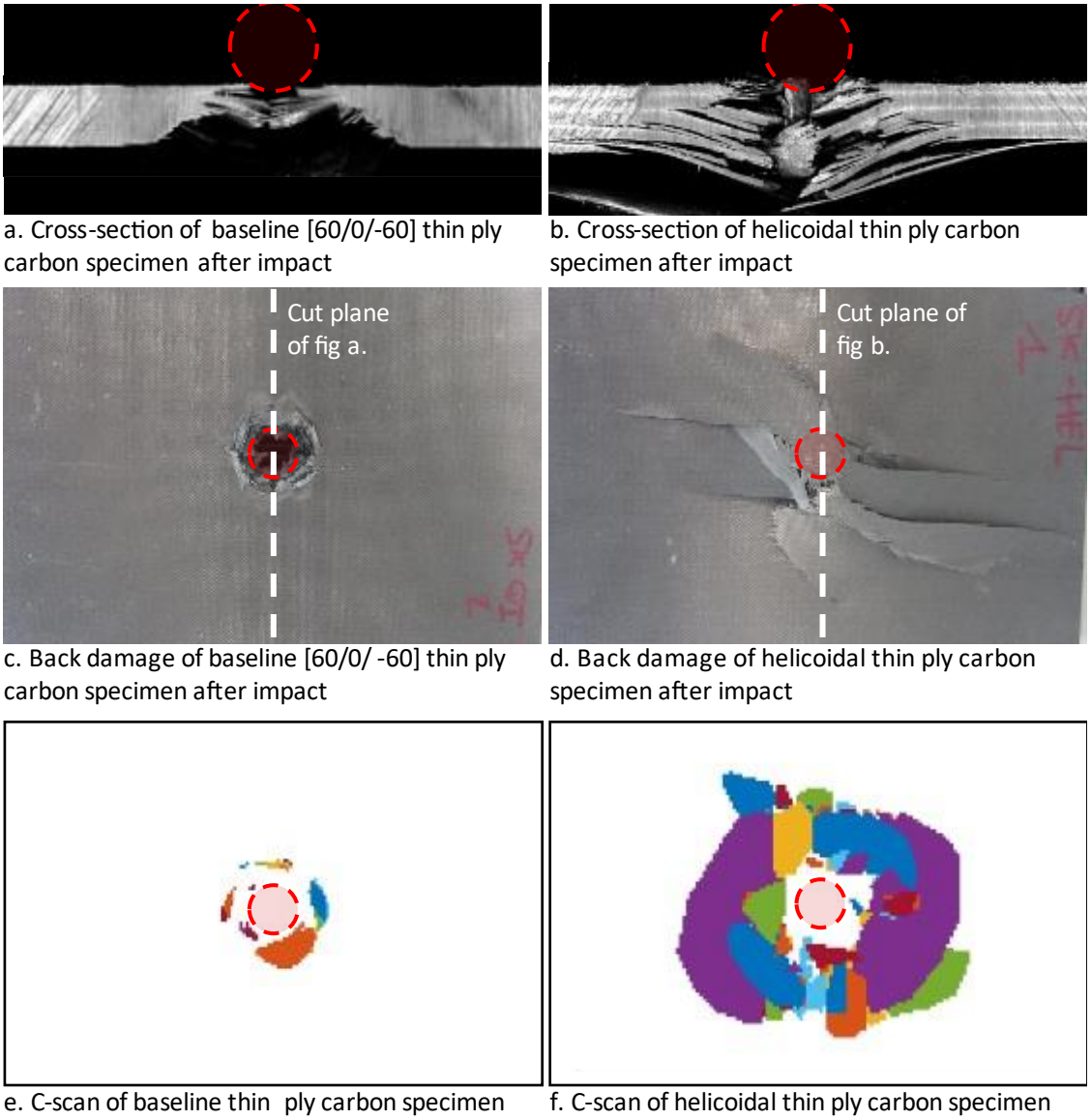

a. Cross-section of baseline [60/0/-60] thin ply carbon specimen after impact

b. Cross-section of helicoidal thin ply carbon specimen after impact

c. Back damage of baseline [60/0/ -60] thin ply carbon specimen after impact

d. Back damage of helicoidal thin ply carbon specimen after impact

e. C-scan of baseline thin ply carbon specimen

f. C-scan of helicoidal thin ply carbon specimen

Figure 4: Comparison of the damage mechanisms using a conventional and helicoidal layup for thin-ply CFRP

Further analysis of the position of the delamination detected by the C-scan analysis reveals the 3D helicoidal nature of the migrating crack created by the low-pitch angle stacking sequence (Figure 5). The delaminated area creates a continuous surface that is growing as it propagates toward the distal face, increasing the energy dissipated through delamination.

When combined with a hybrid design, further improvement in the energy absorption capability can be achieved over the [60/0/-60] baseline. The outer titanium layer creates an initial diffusion of the stresses and delays the apparition of the brittle failure at the top of the CFRP block. The helicoidal layup can subsequently spread the damage and dissipate more energy through delamination and matrix cracking. The increased compliance and stress distribution improve the efficiency of the back layer or aramid prepreg. Finally, interleaved blocks of different materials create interfaces along which more delamination can grow, further increasing the compliance of the panel during the impact event. Evidence of this mechanisms using post impact fractography will be presented at the conference. The design methodology shows good

  doi:10.5075/epfl-298799_978-2-9701614-0-0

improvements in specific energy dissipated when applied to both thin and thick-ply prepregs of respectively 134 % and 77 % (Figure 3).

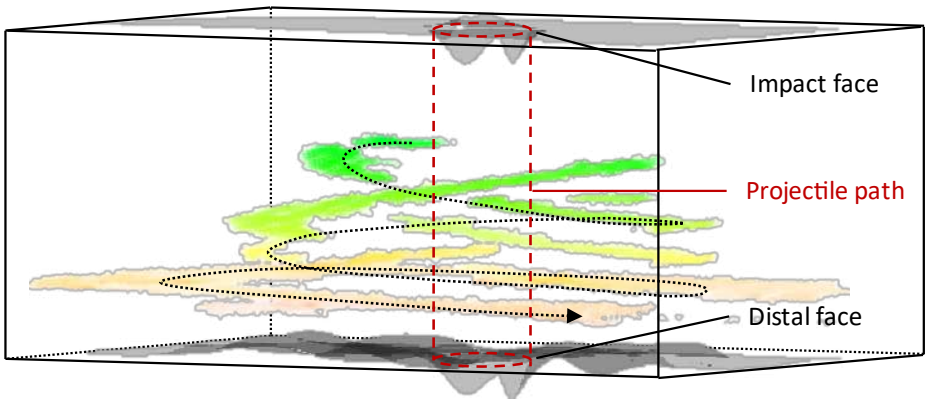

Figure 5: 3D view of the helicoidal nature of the delamination and matrix cracking obtained by ultrasonic C-scan on a thin-ply CFRP laminate

4. Conclusion

In this study, we presented a novel design methodology to improve the impact resistance of hybrid CFRP panels under high-velocity impact. The methodology relies on:

1. a “material by design” approach, wherein materials were selected and placed based on their mechanical performance under the local stress state;
2. non-conventional helicoidal layups; and
3. interleaved blocks of hybrid materials.

Following an initial study, titanium sheets and aramid fibre prepregs were selected to hybridize baseline [60/0/-60] CFRP specimens. Several configurations were manufactured aiming at a constant areal weight and impact at 100-300 m/s using a steel ball impactor.

This study highlights a strong improvement in the damage resistance capability of the proposed design at a constant weight, using both thin and thick-ply prepregs. The final energy absorption capability was increased by 134 % and 77 % respectively for the two material systems due to a change in the failure mechanisms from brittle shear plugging to diffuse damage, matrix crack migration and tensile failure.

Acknowledgements

The funding from Innovate UK under the UKRI FANDANGO project No. 113232 (https://gtr.ukri.org/projects?ref=113232) is gratefully acknowledged. We also thank Prof. Nik Petrinic and Dr. Yanhong Chen at the University of Oxford for their involvement in kindly carrying out the impact tests on the Ti/CFRP/Aramid thin-ply panels presented here.

5. References

1. P.J. Hazell et al., A study on the energy dissipation of several different CFRP-based targets completely penetrated by a high velocity impactor, Composites Structures, 91, p.103-109, 2009.

2. J.L. Liu et al., The response of bio-inspired helicoidal laminates to small projectile impact, International Journal of Impact Engineering, 202, 142:103608.
3. L. Mencatelli et al., Ultra-thin-ply CFRP Bouligand bio-inspired structures with enhanced load-bearing capacity, delayed catastrophic failure and high energy dissipation capability, Composites Part A, 2020, 129:105655.
4. E. Kazemi, V. Medeau et al., Ultra-thin-ply structures with enhanced load-bearing capacity, delayed catastrophic failure and high energy dissipation capability, to be published.
5. H. Nakatani et al., Damage characterization of titanium/GFRP hybrid laminates subjected to low-velocity impact, Composites Part A, 2011, 42:772-781.
6. J.M. Pereira et al., Ballistic Impact Response of Kevlar 49 and Zylon under Conditions Representing Jet Engine Fan Containment, Journal of Aerospace Engineering, 2009, 22:240-248.
7. J.P. Lambert, G.H. Jonas, Ballistic Res. Lab., Rep. BRL-R-1852, Aberdyn, Maryland, USA, 1976
8. L. Alonso et al., A finite element approach to model high-velocity impact on thin woven GFRP plates, International Journal of Impact Engineering, 2020, 142:103593.

  doi:10.5075/epfl-298799_978-2-9701614-0-0

ANALYSES OF TIME-DEPENDENT DAMAGE WITHIN CARBON WOVEN-PLY REINFORCED THERMOPLASTIC COMPOSITES LAMINATES AT HIGH TEMPERATURE

David, Bouscarrat[a], Mathieu, Calvat[a], Benoit, Vieille[a], Martin, Lévesque[b]

a: Normandie Univ, UNIROUEN, INSA Rouen, CNRS, Groupe de Physique des Matériaux, 76800 St Etienne du Rouvray, France – david.bouscarrat@insa-rouen.fr
b: Polytechnique Montreal, Mechanical Engineering Dept., Laboratory for Multiscale Mechanics, C.P. 6079, succ. Centre-ville, Montreal, QC H3C 3A7, Canada

Abstract: *As fiber-reinforced thermoplastic matrix composites (PMCs) are gaining interest in aeronautics, it is a major concern to increase their service life. For these materials, it is essential to study the coupling between their mechanical time-dependent behaviour and damage mechanisms, especially at temperatures above their glass transition. To do so, specific cyclic creep (CC) tests at 120°C were performed to monitor damage development through acoustic emission (AE) and edge replications after each creep cycle. X-ray computed micro-tomography (XµCT) scans were also achieved after mechanical testing to characterize damage and its spatial distribution throughout the laminate. In order to analyze the data from edge replications and XµCT scans, a post-process was developed to highlight damage development.*

Keywords: Thermoplastic; mechanical testing; creep; damage monitoring; clustering.

1. Introduction

Economic and environmental actual challenges require the industry to reduce their costs but also their greenhouse gases. For that, the transportation has been used lighter materials such as fiber-reinforced composite materials and especially thermoplastic (TP) matrix composites (PMCs). Their mechanical properties have been widely studied for the past forty years [1-4]. However, the coupling between their time-dependent mechanical behaviour and damage mechanisms is little studied, especially above their glass transition. This issue is essential from the point of view of the durability of composite structures in an aircraft engine environment.

In this study, angle-ply (AP) 5-harness satin weave carbon/ polyphenylene sulfide (5HS C/PPS) laminates were solicited under several creep cycles with incremental duration at 120°C. Damage occurring within those laminates was monitored through different technics. Acoustic emission (AE) provides an in-situ information about damage development. Edge replication enables to quantify damage development on the edges after each creep cycle. Ex-situ X-ray computed micro-tomography (XµCT) enables to quantify damage throughout the whole laminate.

To differentiate between damage development and/or phases (i.e., bundle and matrix), recent studies have been using neural network [5-6]. But neural network usually requires large data to be trained with, which can be either labelled by hand or by an algorithm. We propose a post-process to handle the problem of image segmentation into different classes. This algorithm relies on a gaussian mixture models (GMM) used in addition with descriptor calculation based on the original image. This aims to highlight damage development as well as their spatial distribution with XµCT scans and with edge replications.

  doi:10.5075/epfl-298799_978-2-9701614-0-0

2. Material and protocol

2.1 Materials and specimen

The material used in this work is a carbon fabric reinforced polyphenylene sulfide. The fabric is a balanced 5-harness satin weave of T300 3K carbon fibres provided by Soficar. The Fortron® 0214 polyphenylene sulfide (PPS) matrix was supplied by Ticona. Its glass transition temperature (T_g) is around 90°C [7]. 7-ply laminates were manufactured by hot press consolidation (Dedienne Multiplasturgy) from 0.317 mm thick prepregs with a 50% volume fraction of carbons fibres. The 600×600 mm² laminates were waterjet-cut to obtain dumbbell specimens with a stacking sequences $[(\pm45)_{3s}(\pm45)]$. Figure 1 illustrates the specimen geometry.

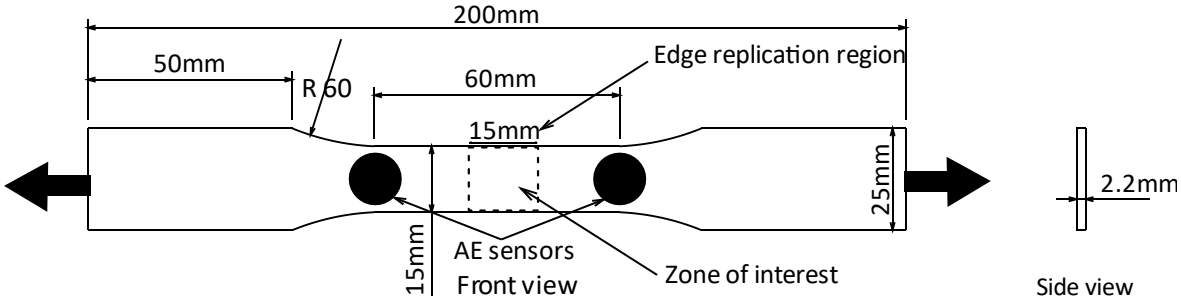

Figure 1: Illustration of dumbbell geometry machined by waterjet.

2.2 Experimental procedure

Specific cyclic creep (CC) tests were performed at three different stress values σ_0: 40, 60 and 100 MPa. Two versions of CC tests were conducted, one without edge replication (Figure 2.a) and another with edge replications (Figure 2.b). The first consists in a conditioning cycle at the chosen stress level σ_0 followed by five creep cycles at σ_0 of respective time: 15, 30, 45, 60 and 480 minutes. Each creep stage is followed by a recovery time at least three times longer than the creep time. Finally, a last cycle is performed up to the same stress value. These tests were performed at a temperature of 120°C similar to the service conditions of an aircraft engine nacelle. The second test is the same except that, after each creep stage, edge replications were performed under a constant loading of 100 N at 50°C for one hour. Edge replications were carried out by applying vinylpolysiloxane to monitor the surface damage development [8]. For both types of tests, damage development was monitored through acoustic emission. AE sensors were 60 mm apart, as illustrated in Figure 1. After the tests with edges replications, XµCT analyses were performed to characterize the damage and its spatial distribution within the whole laminate, which is not possible with the surface information from edge replications.

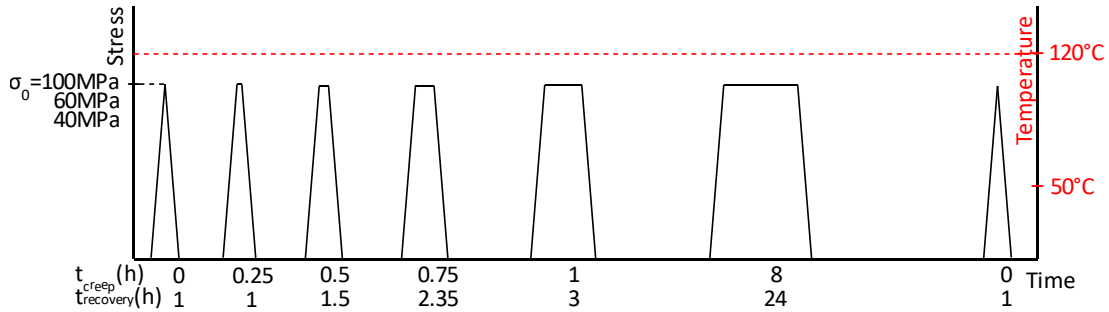

(a)

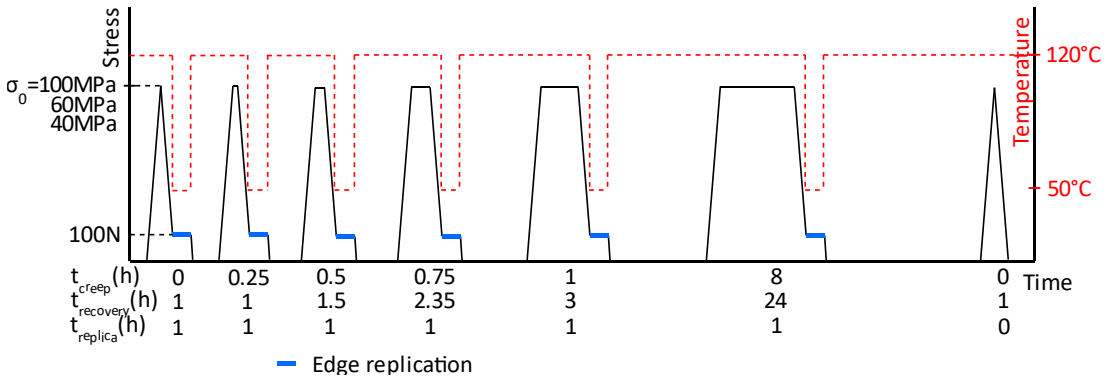

(b)

Figure 2. Specific cyclic creep tests at 120°C and 40, 60 and 100 MPa (a) without edge replications or (b) with edge replications.

2.3 Numerical procedure

Edge replications and XµCT provide grey-level images (2D or 3D). It is generally not sufficient to highlight damage development by considering only the grey level. The combination of different materials (i.e., matrix and carbon bundles) and damage results in overlapping grey-level distributions that are usually too complex to dissociate. In this study, two methods were used to try to detect and quantify damage.

The first one is a simple morphological image approach. The microscopic observation is binarized and subjected to a morphological image process, which consists of an erosion followed by a dilation using the same structuring element (rectangle [4px 2px]).

The second one is based on a clustering approach. The main idea is to calculate new descriptors from the grey-level images: based on classical morphology operations (erosion, dilation, …) or local mathematical operations (entropy, median, standard deviation, skewness, …). As these processes can lead to very different ranges of values, results must be standardized to be handled by cluster analysis. Firstly, a K-means algorithm is used to provide centroids for the following gaussian mixture models (GMM). The number of classes can be either fixed or determined through optimization of a given criterion such as Dunn index [9] or Davies-Bouldin index [10]. As the GMM only gives belonging probabilities to the different gaussian (i.e., the different classes), strict classes are determined from the maximum probability density function (PDF) with respect to the different gaussian distributions. Once strict classes attributed, morphology operations are applied to remove isolated pixels. Finally, the contour (or surface) is reconstructed through the marching squares (or marching cubes [11]) algorithm. Several descriptors can then be calculated either on each contour (classes surface/volume fraction, major/minor axis length/orientations, …) or on the whole set of reconstructed contours (covariogram [12], …).

3. Results

3.1 Mechanical behaviour

Using the assumption of infinitesimal strains, the true axial strain is decomposed using Eq. (1):

$$\varepsilon = \varepsilon_{ve} + \varepsilon_{vp} \quad , \tag{1}$$

with ε being the total true axial strain (i.e., at the end of creep stages), ε_{ve} the viscoelastic true strain, including the instantaneous elastic part, and ε_{vp} the viscoplastic true strain (i.e., at the end of recovery stages). Although high total strain has been measured (e.g., up to 12% for the 100 MPa test), the infinitesimal strains assumption is used here as a first approximation.

Figures 3.a, 3.b and 3.c show the variation of the axial true strain, the viscoelastic true strain and the viscoplastic true strain, respectively, as a function of time. A noticeable time-dependent behaviour is observed from the true total strain. Once decomposed, it seems that the main source of this time-dependent behaviour is the viscoplastic component. The largest part of the viscoelastic strain takes place during the first 15 min of creep, whereas viscoplastic strains continue after 15 min, especially at 100 MPa. For example, at 100 MPa, the viscoplastic strain increases of about 1% at 15 min of creep and another 1% between 15 min and 630 min of cumulative creep time.

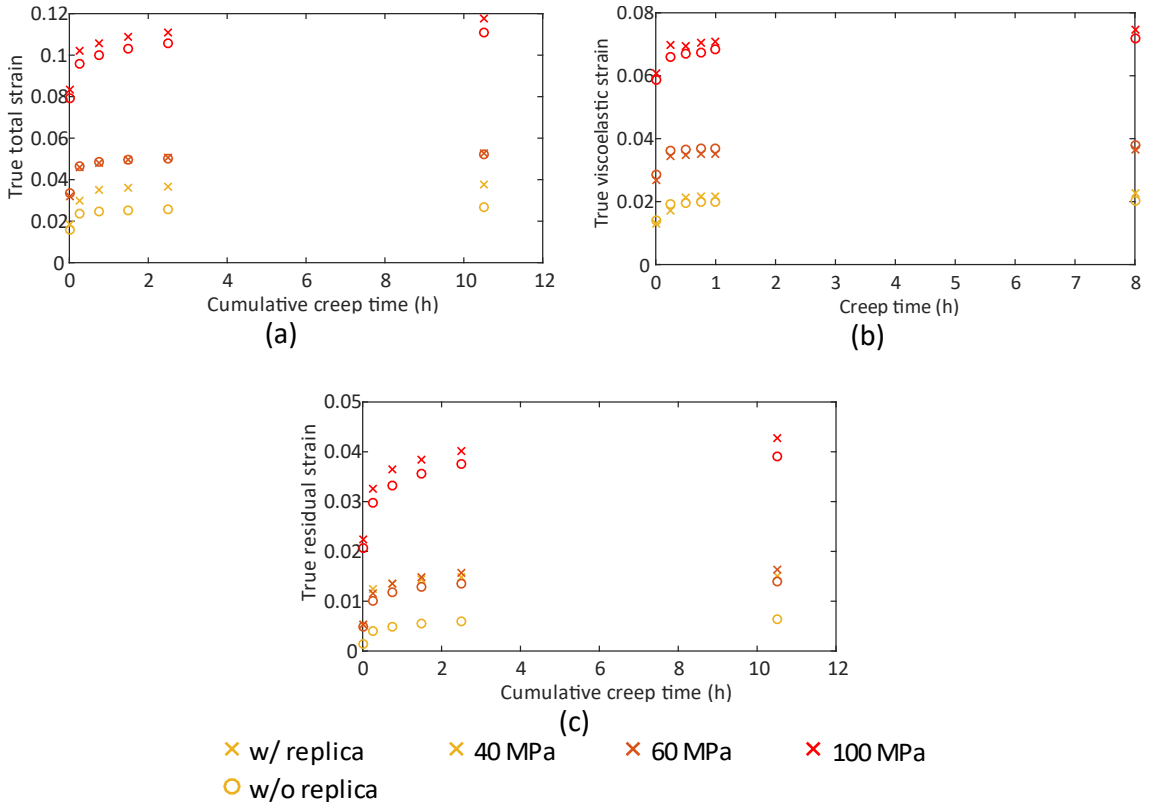

*Figure 3. V*ariation of (a) the total true strain, (b) the viscoelastic true strain, (c) the viscoplastic true strain.

3.2 Tomography

Tomographic observations from different regions (i.e., intra-bundle region, inter-bundle intra-ply region and inter-bundle inter-ply region) for a specimen tested at 100 MPa are presented in Figure 4. Two main damage mechanisms are observed: intra-bundle and inter-bundle cracking. These cracks are more easily detected within outer plies than inner one, because the latter are more constrained by neighboring plies. Interfacial cracks seem to preferentially develop within intra-ply region, and more precisely at the crimp regions, compared to inter-ply ones. These mechanisms are also observable at 40 and 60 MPa.

  doi:10.5075/epfl-298799_978-2-9701614-0-0

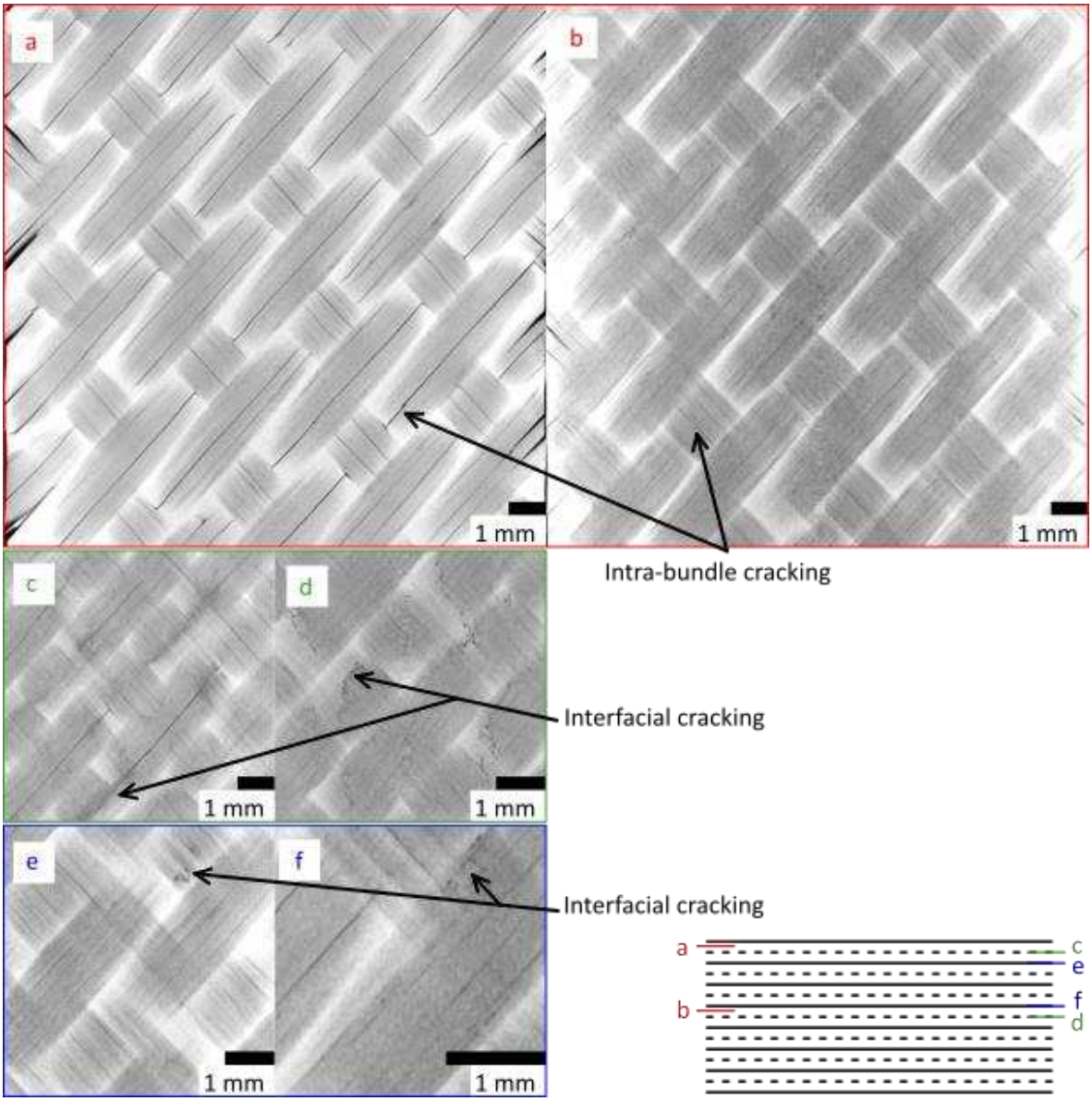

Figure 4. Ex-situ tomographic observations of an AP C/PPS subjected to a CC test at 100 MPa at 120°C: (a) slice within the intra-bundle region of the first ply, (b) slice within the intra-bundle region of the fourth ply, (c) slice within the inter-bundle region of the first ply, (d) slice within the inter-bundle region of the fourth ply, (e) slice within interlaminar region between the first and second plies and (f) slice within interlaminar region between the third and fourth plies.

Figure 5 illustrates four slices of 800 by 800 pixels on which are represented the damage class based on the clustering approach. For this analysis, original grey-level data in conjunction with x, y and z gradient were calculated from nine slices of 800 by 800 pixels from the previous 100 MPa test. Two optimal centroids were then calculated through the K-means algorithm using the Davies-Bouldin index criterion. Then final classes were obtained from the GMM with the damage class standing for intra-bundle cracking. No further morphology operation was applied on identified classes. For the chosen variables and the given volume, the algorithm allows to highlight some of the damage development for the 45° orientation but not the -45° one, unfortunately. This damage class represents 1.3% over the nine slices.

  doi:10.5075/epfl-298799_978-2-9701614-0-0

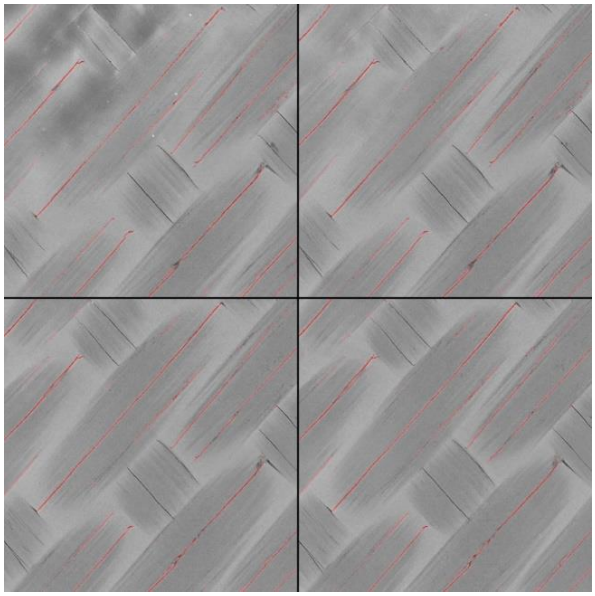

Figure 5: Illustration of the damage class highlighted in red on 4 subsequent slices from the specimen tested at 100 MPa.

3.3 Acoustic emission

Figures 5.a, 5.b and 5.c show the AE activity using the cumulative AE events after each cycle for the 40, 60 and 100 MPa tests, respectively. As expected, the higher the stress the higher of detected AE events (factor 10 between 40 and 60 MPa but also between 60 and 100 MPa).

The AE events are separated into three groups according to the mechanical steps during which they occurred: the loading steps, the creep steps and the other detected AE events (i.e., during an unloading or a recovery step) are in green, orange and red, respectively. The data in blue represents all the detected events. Firstly, AE events detected during unloading and recovery steps are not significant compared to the others, which tends to prove that friction-based/unwanted AE events are negligible during those tests. Secondly, most of the AE events from loading steps occurs during the first two cycles, which results cumulative AE events for this group to reach a plateau. Further loading steps do not result in damage development. Finally, the cumulative AE events from creep steps keep increasing during the entire test, which seems to underline potential time-dependent cracking. The variation of the cumulative AE events during creep is similar to the variation of the true residual strain presented in Figure 3.c.

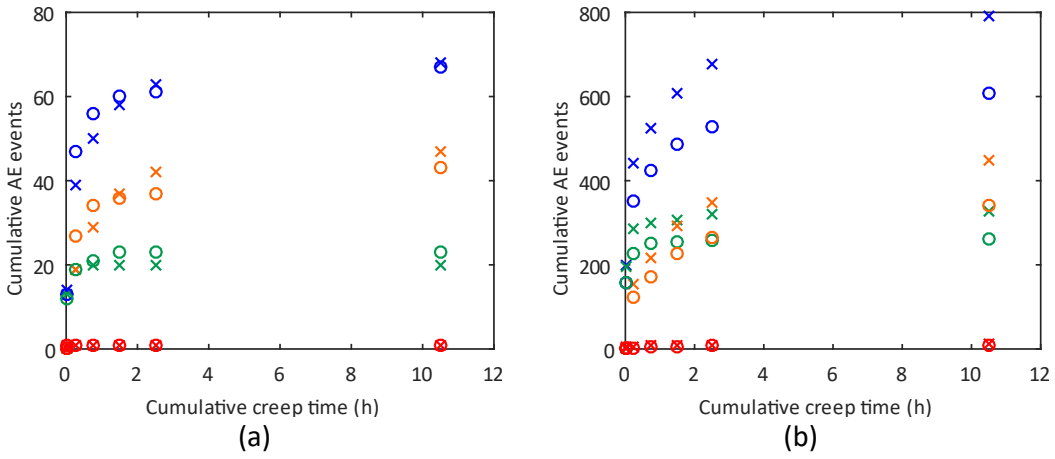

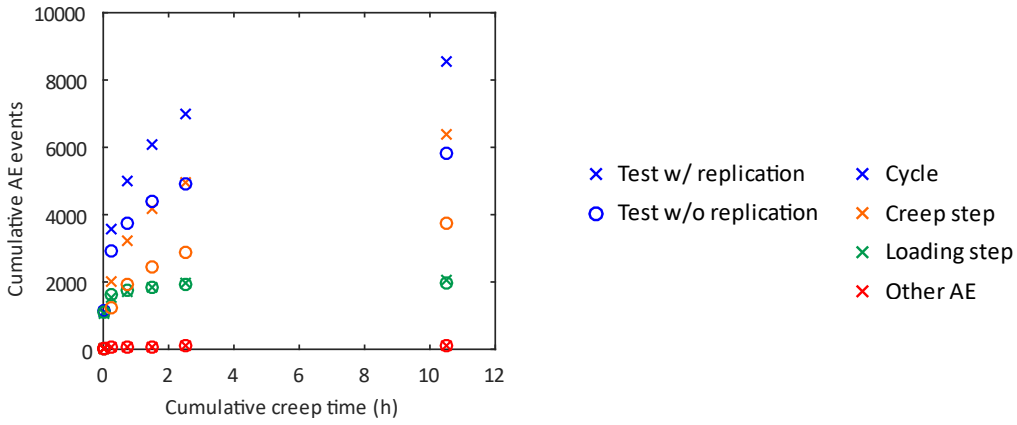

(c)

Figure 5. AE activity (i.e., cumulative AE events) within a 15 mm centered region during (a) 40 MPa, (b) 60 MPa and (c) 100 MPa CC tests on 5HS C/PPS at 120°C.

3.4 Edge crack density

Figure 6 shows the variation of the cracked surface density as a function of creep time for each stress level based on the simple morphological image approach. Due to the method used to estimate edge crack density, tendencies are not well defined for the 40 and 60 MPa tests, but the higher the stress the higher the edge crack density. Furthermore, it seems that the edge cracked surface densities from the 40 and 60 MPa are constant after the conditioning cycle. In contrast, the 100 MPa test show a monotonic increase in the cracked surface on the edge with creep time.

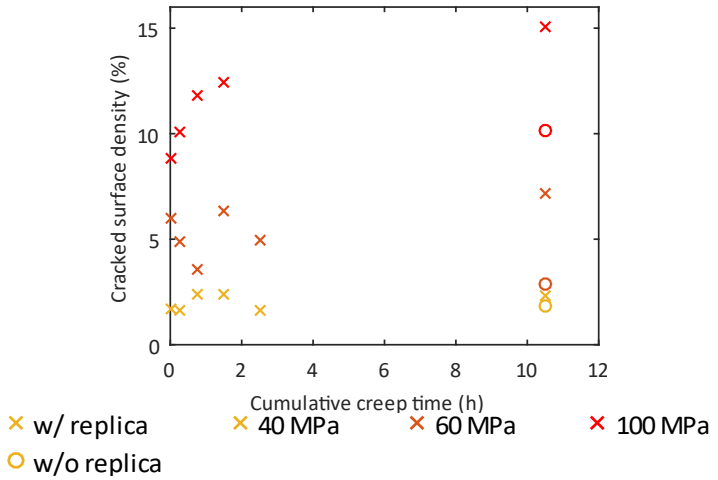

Figure 6. Variation of the cracked surface density as a function of creep time for each stress level based on the simple morphological image approach.

4. Conclusions

The purpose of this study was to investigate possible time-dependent damage in AP 5HS C/PPS laminates at $T>T_g$. During these tests, strain partition was used in conjunction with different techniques to monitor damage development during mechanical tests (acoustic emission and edge replications) or after tests (XµCT scans). The following conclusions can be reached from the previous results:

- The largest part of the viscoelastic strain takes place during the first 15 min of creep, whereas viscoplastic strains continue after 15 min, especially at 100 MPa.

  doi:10.5075/epfl-298799_978-2-9701614-0-0

- Tomographic observations highlighted that the two main damage mechanisms (i.e., intra-bundle and inter-bundle cracking) occurs at the three stress levels throughout the laminates. The clustering approach gives encouraging results for the identification of damage using XµCT scans, however improvements are needed to correctly quantify its distribution.
- AE seems to highlight time-dependent damage at the three stress levels. However, surface crack density at the edges using the simple morphological image approach seems to only confirm this observation at 100 MPa. Further analyses using the clustering approach should confirm or refute the previous observations.

Acknowledgements

The authors would like to express their gratitude to Christophe Bouvet and Pierre Journoud (Institut Clément Ader, Toulouse) for the tomographic observations.

5. References

1. Damore A, Pompo A, Netti P, Masi E, Nicolais L. Non-Linear Viscoelastic Behavior of Poly-Ether-Ether-Ketone (PEEK) and PEEK-Based Composites. Journal of Reinforced Plastics and Composites 1993;12(3):327-40.
2. Ma CCM, Tai NH, Wu SH, Lin SH, Wu JF, Lin JM. Creep behavior of carbon-fiber-reinforced polyetheretherketone (PEEK) [±45]4s laminated composites (I). Composites Part B: Engineering 1997;28(4):407 17.
3. Albouy W, Vieille B, Taleb L. Experimental and numerical investigations on the time-dependent behavior of woven-ply PPS thermoplastic laminates at temperatures higher than glass transition temperature. Composites Part A: Applied Science and Manufacturing 2013;49:165 78.
4. Erartsin O. Time-dependent, matrix-dominated failure of continuous fiber-reinforced thermoplastic composites. Enschede: University of Twente, 2020. 151 p.
5. Rogala T, Przystałka P, Katunin A. Damage classification in composite structures based on X-ray computed tomography scans using features evaluation and deep neural networks. Procedia Structural Integrity. 2022;37:187-94.
6. Xiao C, Buffiere JY. Neural network segmentation methods for fatigue crack images obtained with X-ray tomography. Engineering Fracture Mechanics. 2021;252:107823.
7. Aucher J. Etude comparative du comportement de composites à matrice thermoplastique ou thermodurcissable. INSA de Rouen; 2009.
8. El Mourid A. Mechanical Behavior of a Triaxially Braided Textile Composite at High Temperature. École Polytechnique de Montréal; 2014.
9. Dunn J. A fuzzy relative of the isodata process and its use in detecting compact well-separated clusters. Journal of Cybernetics 1973; 3: 32–57.
10. Davies DL, Bouldin DW. A cluster separation measure. IEEE Transactions on Pattern Analysis and Machine Intelligence 1979; PAMI-1: 224–227.
11. Wu Z, Sullivan Jr JM. Multiple material marching cubes algorithm. International Journal for Numerical Methods in Engineering. 2003;58(2):189-207.
12. Doumalin P, Bornert M, Crépin J. Caractérisation de la répartition de la déformation dans les matériaux hétérogènes. Mechanics & Industry. 2003;4:607-17.

  doi:10.5075/epfl-298799_978-2-9701614-0-0

Composites Meet Sustainability – Proceedings of the 20th European Conference on Composite Materials,
ECCM20. 26-30 June, 2022, Lausanne, Switzerland

MECHANICAL CHARACTERIZATION OF 3D-PRINTED COEXTRUDED CONTINUOUS CARBON-FIBER THERMOPLASTIC

Guilherme Machado, Aurélien Maurel-Pantel, Christian Hochard

Aix Marseille Univ, CNRS, Centrale Marseille, LMA, Marseille, France – machado@lma.cnrs-mrs.fr

Abstract: *This study aims to investigates the in-plane mechanical properties of continuous fiber-reinforced polymer fused filament parts based on a thermoset-thermoplastic bi-matrix material. This relatively new 3D printing concept has the potential to combine the advantages of separate thermoset and thermoplastic-based, fused filament fabrication methods and to advance continuous fiber-reinforced polymer 3D printing toward higher mechanical performances printed parts. The experimental mechanical properties (stiffness and strength) of the flat composite specimens in tensile (longitudinal and transverse), and in-plane shear are studied. In all tests strain fields were obtained by digital image correlation method (DIC).*

Keywords: 3D-Printed composites; mechanical properties; continuous fiber; X-ray.

1. Introduction

Additive manufacturing (AM, commonly referred to as 3D-printing) have a demonstrated capacity for flexible production polymer components, offering exceptional flexibility in achieving complex geometries. While AM itself is a wide field with different materials and methods, the fused filament fabrication method (FFF) can be considered as the most widely used technology because of its cost convenience and simplicity. However, low mechanical performance of unreinforced thermoplastic polymers is the main issue for industrial applications. More recently, research on methods for 3D-printing of continuous fiber-reinforced polymers (CFRP) were developed. It offers significant improvement in mechanical properties compared to discontinuous fibers. There are, up to date, few commercial machines available for 3D-printing with continuous fiber based on FFF method. This evidences the fact that 3D-printing with continuous fibers is still a rising technology with no standard paradigm. Compared to traditional fiber-reinforced composites manufacturing techniques, printed CFRP are also based on stacking a series of discrete layers however no expensive tooling is required. As reinforcements can be accurately placed, the laminated structure of composite parts can be further optimized in each layer, allowing for an increase in design freedom and mechanical performance.

These new advances in the FFF process have been allowed the use of high-performance materials in many industries, and consequently, it is very important to well know their mechanical properties for the proper composite structural design. Although several studies have presented important investigations on the mechanical properties characterization of printed fiber-reinforced thermoplastic, gaps have still remained. For example, most part of works reported the elastic properties for the whole laminate instead of the lamina. Tensile strength is the most studied mechanical property. Transverse elastic properties for fiber-reinforced filaments are rare. In many instances, information about the layup sequence, infill density, fiber volume fraction, number of thermoplastic floor/roof layers were not entirely presented, each of which could result in noticeable difference in the resulted mechanical properties. In view of above, the present work intended to evaluate how close printed CFRP behaves like a traditional

  doi:10.5075/epfl-298799_978-2-9701614-0-0

shear moduli were established by testing CFRP-FFF specimens manufactured using a recent technology proposed by Anisoprint [1].

2. Materials and manufacturing

2.1 Specimen manufacturing

All specimens were printed using an Anisoprint Composer-A3 continuous fiber composite printer (Anisoprint LCC, Russia). It provides a bi-matrix concept, based on preliminary impregnation of fiber in the form of a tow into an epoxy thermoset matrix [2]. The printer head are equipped with two nozzles. A standard nozzle, called *plastic extruder* for conventional thermoplastic filaments and a co-extrusion nozzle called *composite extruder*. This second one has two inputs: one for the reinforcing fiber and the other for thermoplastic filament. Reinforcing fiber and plastic are fed separately. Due to the co-extrusion process, three filaments (two plastic, one continuous fiber) are necessary for the operation of the machine. Specimens are reinforced with a carbon fiber, which has 1.5k filaments per fiber tow. Each carbon fiber tow has an effective diameter of 0.35mm and its linear density is 145tex. The pre-impregnated carbon fiber tow volume fraction is about 60%. It is significantly reduced by the integrated co-extrusion process. During the printing, the composite carbon fiber was embedded into thermoplastic polyamide (PA12) matrix (CFC-PA by Polymaker, China). The PA12 filament has an effective diameter of 1.75mm, and its density is 1.17g/cm^3. Similarly Smooth-PA (also PA12) with 1.06 g/cm^3 (Smooth-PA by Polymaker, China) was used in shell zone.

In 3D-printing of composite laminates, any stacking sequence can be easily achieved. However, there are some distinctions to be considered when reading 3D-printed specimen lay-ups. The printed specimens can be viewed as “sandwich” laminates consisting of a core of continuous carbon fiber reinforced thermoplastic layers (CFTSTP) and a shell of Smooth-PA (TP), in a smaller amount, with two or more layers of floor (bottom layers), roof (top layers) and perimeter layers. Mechanical properties of composite specimens highly depend on the orientation of fibers. Intrinsic anisotropy of composites requires determination of properties at different directions. To determine the Young’s modulus and strength, specimens with fibers oriented at 0° (TS-0), 90° (TS-90), and 45° (TS-45) are manufactured and tested to find longitudinal, transverse and shear properties, respectively. Quasi-isotropic (TS-Qiso), 0°/90° (TS-0/90) and single 0° ply (TS-Sply) specimens were also manufactured. Default process parameters suggested by the manufacturer were used.

Uniaxial tensile tests were performed on hourglass specimens [3] follow the nominal dimensions shown in Fig. 1. Samples had a gage zone defined by the nominal gage length g=15mm, width w=15mm and nominal thickness t=3.6mm. Speed of testing was controlled by the crosshead movement at 1mm/min. Three specimens per sample were tested. Drawings of the different fiber orientations are presented in in Fig. 2. The global directions are represented by the coordinate system XYZ and the local material directions are represented by the coordinate system 123. The global direction X is the load direction. The layup sequence and sample codes of the composite specimens are presented in Table 1. Finally, effective section dimensions are obtained by X-ray tomography as shown in Fig. 3. This allows to calculate the cross-sectional area ratios of thermoplastic (TP) shell layers (V^s) and reinforced carbon fiber thermoset-thermoplastic (CFTSTP) layers (V^c).

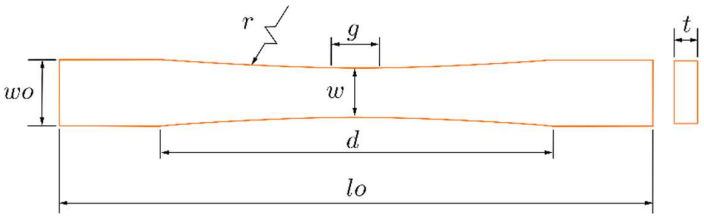

Figure 1. Uniaxial tensile printed specimen, where: Width overall w_o = 20 mm, Width of narrow section w=15 mm, Length overall l_o=200mm, Distance between grips d=120 mm, Radius r=721.25 mm.

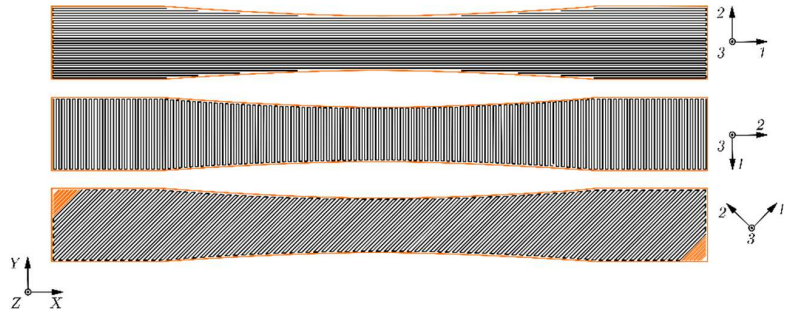

Figure 2. Schematic representation of base "ply" configurations: 0°, 90° and 45°, with respect to the loading direction X (PA shells in orange and internal fiber filling in black).

Table 1: Stacking sequence and deposition pattern for the manufactured specimens. Thickness t in mm measured by X-ray tomography.

Sample name	Floor layers (TP)	Core layers (CFTSTP)	Roof layers (TP)	V^c	Properties
TS-0 t=3.8	$[\pm45°]_2$ t=0.3	$[0°]_8$ t=3.2	$[\pm45°]_2$ t=0.3	0.78	E_1^X, σ_1^X
TS-90 t=3.8	$[\pm45°]_2$ t=0.3	$[90°]_8$ t=3.2	$[\pm45°]_2$ t=0.3	0.78	E_2^X, σ_2^X
TS-45 t=3.8	$[\pm45°]_2$ t=0.3	$[(\pm45°)_4]_S$ t=3.2	$[\pm45°]_2$ t=0.3	0.78	G_{12}^X, σ_{12}^X
TS-0/90 t=3.8	$[\pm45°]_2$ t=0.3	$[(0°/90°)_4]_S$ t=3.2	$[\pm45°]_2$ t=0.3	0.78	-
TS-Qiso t=3.8	$[\pm45°]_2$ t=0.3	$[(0°/90°/+45°/-45°)_4]_S$ t=3.2	$[\pm45°]_2$ t=0.3	0.78	-
TS-Sply t=3.7	$[\pm45°]_{10}$ t=1.65	$[0°]_1$ t=0.4	$[\pm45°]_{10}$ t=1.65	0.10	-

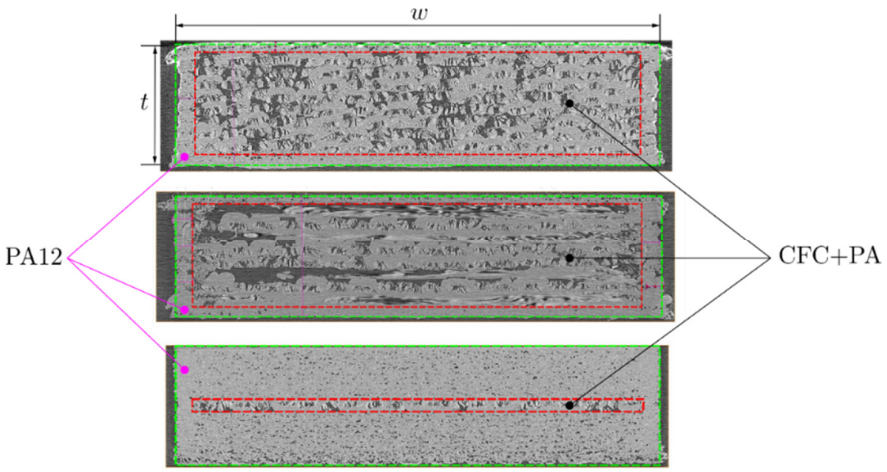

Figure 3. Example of cross section obtention for samples TS-0, TS-0/90 and TS-Sply. TP shell layers (floor,

2.2 Lamina mechanical properties

As previously mentioned, the printer software requires some pure PA layers at the top, bottom and perimeter of all printed composite parts. It implies that is not possible to directly measure the mechanical properties of the carbon fiber composite lamina. In this context, a simple method based on mixture distribution. Thus, substituting, the longitudinal elastic modulus of reinforced layers (CFC-PA) can be written as:

$$E_i^c = E^s + \frac{1}{V^c}\left(E_i^X - E^s\right) \quad (1)$$

where E_i^c, E^s and E_i^X are respectively the elastic moduli of reinforced core layers, shell layers and homogeneous equivalent material. The index i denotes the elastic modulus that is being determined in function of the tested specimen, as shown in Table 1. To compute the in-plane shear elastic properties of reinforced lamina, the stress over reinforced core layers must be written in function of the longitudinal stress over the representative volume, then:

$$\sigma_{12}^c = \frac{\varepsilon^X}{V^c}(E_{12}^X - V^s E^s) \quad (2)$$

where ε^X and E_{12}^X are, respectively, the longitudinal strain and modulus measured specifically over the in-plane shear composite specimens. Therefore, the in-plane shear modulus of reinforced lamina can be determined [3] by:

$$G_{12}^c = \frac{1}{2}\frac{\Delta\sigma_{12}^c}{\Delta\gamma_{12}} \quad (3)$$

3. Experimental testing results

Fig. 4 presents the engineering stress–strain curves recorded throughout the tensile test for composite specimens. For all tested directions, it can be noticed a good consistency between the elastic modulus of the tested specimens. Regarding the tensile strength, no significant variations were observed, with exception of TS-Qiso tests. For TS-90 and TS-45 specimens have not failed within 5% strain. Thus, the data were truncated to the 5% strain mark and ultimate tensile strengths were not computed. The recorded data during the experiments have been processed and the average values for composite specimens are reported in Tables 2.

The tensile (E_1^c and E_2^c) and in-plane shear (G_{12}^c) elastic moduli for the CFTSTP laminae alone were computed according to Eqs. (1) and (3) and are presented in Table 2. It is worth to say that $E^s = 1500\ MPa$ is the measured elastic modulus of 100% PA specimen (curves are not presented). When compared (without any normalization) to typical values for thermoplastic composites elastic moduli, the results illustrated in Table 2 present modest values. However, considering the fiber volume fraction and consequently perform a ratio of elastic moduli (longitudinal and transverse) to the fiber volume fraction, the composite material tested in the present work provide good results. Reference values [4] for CF/PA6 thermoplastic composites are about $E_1 = 98.2\ GPa$, $E_2 = 7.4\ GPa$, $\sigma_1 = 1308.9\ MPa$, for a fiber volume fraction $V^f = 43.1\ \%$. Using standard process parameters, the achieved V^f by CFRTSTP long fiber technology is around 20.5%. It can be inferred from the data in Table 2 that, the stiffness of TS-Qiso is directly proportional to the number of 0° layers, which seem to work independently of other directions. This observation can be explained by the lack of consolidation between layers.

  doi:10.5075/epfl-298799_978-2-9701614-0-0

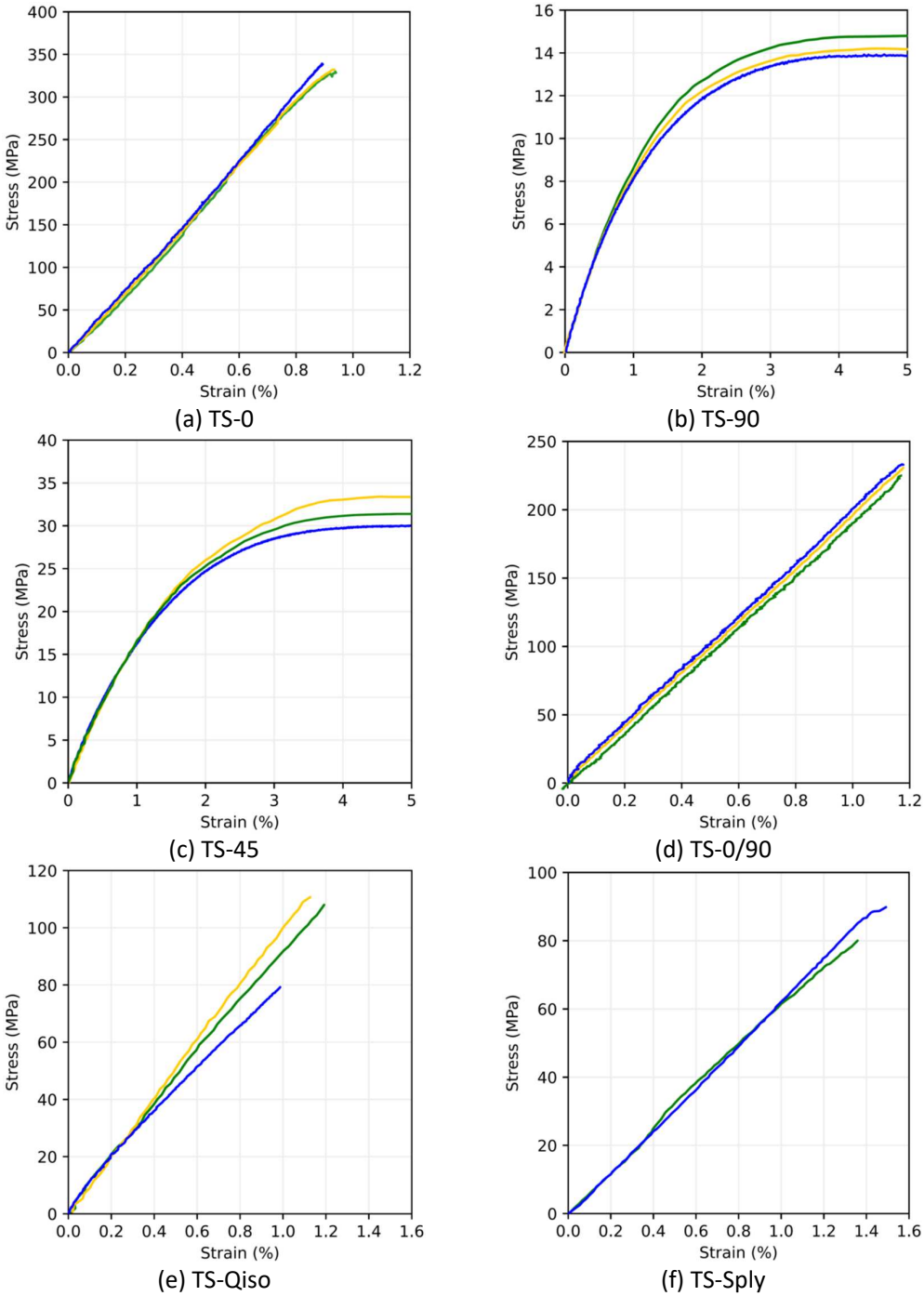

Figure 4. Tensile engineering stress–strain curves for composite specimens.

Table 2: Experimental results elastic moduli and ultimate strengths.

Sample name	Homogeneous equivalent material		CFTSTP core	
	Elastic modulus avg (GPa)	Ultimate strength avg (MPa)	Elastic modulus (GPa)	Ultimate strength (MPa)
TS-0	$E_1^X = 36.5$	$\sigma_1^X = 332$	$E_1^c = 46.3$	$\sigma_1^c = 424$
TS-Sply	$E_1^X = 6.2$	$\sigma_1^X = 84.9$	$E_1^c = 47.9$	$\sigma_1^c = 655.3$
TS-90	$E_2^X = 1.0$	$\sigma_2^X = 14.3$	$E_2^c = 0.85$	-
TS-45	$G_{12}^X = 0.49$	$\sigma_{12}^X = 15.8$	$G_{12}^c = 0.47$	-
TS-0/90	18.7	226	23.5	284
TS-Qiso	9.4	98.6	11.6	121.75

4. Conclusion

The mechanical performance of 3D printed continuous fiber reinforced thermoplastic composites was studied. With the actual state of 3-D printed CFRTSTP long fiber technology, composite parts cannot fully compete in terms of the maximum achievable elastic modulus and ultimate strength, against the high-performance thermoplastic composites manufactured by the classical methods where high fiber volume fraction can be reached (40-65%). Thus, classical laminate design approach seems to be inappropriate. However, 3D-print long fiber technology combines the high specific strength/stiffness of composite materials with unique capabilities of manufacturing complex geometries. As reinforcements can be accurately placed, the laminated structure of composite parts can be further optimized in each layer, allowing for an increase in design freedom and mechanical performance, reducing the effort required to produce light-weight parts manufactured with minimum wastage of materials.

5. References

1. Azarov AV, Antonov FK, Vasil'ev VV, Golubev MV, Krasovskii DS, Razin AF, et al. Development of a two-matrix composite material fabricated by 3D printing. Polym Sci Ser D. 2017 Jan;10(1):87–90.

2. Adumitroaie A, Antonov F, Khaziev A, Azarov A, Golubev M, Vasiliev VV. Novel Continuous Fiber Bi-Matrix Composite 3-D Printing Technology. Materials. 2019 Sep 17;12(18):3011.

3. Cocchi A, Montagnier O, Hochard C. Study of hourglass-shaped specimens for the analysis of compression behaviour in fibre direction of FRP composites using compression and four-point bending tests. Compos Part Appl Sci Manuf. 2021 May;144:106332.

4. Sims DF. In-Plane Shear Stress-Strain Response of Unidirectional Composite Materials. J Compos Mater. 1973 Jan;7(1):124–8.

5. Ma Y, Ueda M, Yokozeki T, Sugahara T, Yang Y, Hamada H. A comparative study of the mechanical properties and failure behavior of carbon fiber/epoxy and carbon fiber/polyamide 6 unidirectional composites. Compos Struct. 2017 Jan;160:89–99.

IN-SITU FULL-FIELD MEASUREMENTS FOR 3D PRINTED COMPOSITES UNDER INTERLAYER DELAMINATION

Alessandra, Lingua[a], Nicola, Picirelli[b], Daniel, Therriault[a], Martin, Lévesque[a]

a: Laboratory for Multiscale Mechanics (LM2), Mechanical engineering department, Polytechnique Montréal, Montréal, Québec H3T 1J4, Canada – alessandra.lingua@polymtl.ca
b: Safran Composites, Safran Group, 33 Avenue de la Gare, Itteville 91760, France

Abstract: *The increasing interest in 3D printed composites for more sustainable, reliable, and lightweight aerospace structural components entails the need to understand and model their mechanical behavior under loading. The meso and microstructure of 3D printed composites, including porosity, defects, and weak interfaces, only detectable with in-situ characterization techniques, drive their failure mechanism. We propose a microstereoscopic digital image correlation based characterization approach to study the interlayer delamination of high-performance carbon fiber reinforced parts manufactured by fused filament fabrication and promote the development of modeling tools. We deliver full-field displacement and strain measurements at the crack tip of miniature compact tension specimens printed using 30 wt% carbon fiber reinforced polyetheretherketone. We tested specimens with 0°- 90° and* ± 45° *layers stacking to investigate the influence of the mesostructure on the local deformations under mode I load. Fractography contributed to a further understanding of the local interface failure mechanism.*

Keywords: Additive Manufacturing; Composites; Characterization; Digital Image Correlation; Fracture mechanics

1. Introduction

The interplay of composite materials and 3D printing enables the manufacturing of lightweight, high-strength components for more sustainable structural aerospace solutions [1]. The reinforcement embedment in a polymer matrix ensures the mechanical properties and functionalities required in operating conditions, reducing the final part weight and thus the CO2 emissions [2]. Moreover, as opposed to injection molding or casting, additive manufacturing delivers the final part design, although complex, without any massive machining or post-processing, cutting off drastically the material waste [3]. Extrusion-based techniques, such as fused filament fabrication (FFF), are currently the most widespread 3D printing approach as they deliver complex parts through a relatively cheap and straightforward process [4]. FFF envisages the layer by layer deposition of the molten thermoplastic filament on a heated platform, following the geometry defined in the computer-aided design file and based on the printing parameters specified during slicing [5]. Short fibers (mainly carbon and glass fibers) can be embedded in the polymer matrix before feeding the heated nozzle for the effective reinforcement's impregnation and dispersion [6],[7]. The semi-crystalline thermoplastic polyetheretherketone (PEEK) is chosen as a matrix when high strength, chemical and thermal resistance, or biocompatibility are primary requirements [8].
The multiscale failure mechanism of FFF composites is complex as it involves both the delamination of weak interfaces due to the incomplete layers' adhesion during deposition, the porosity-driven crack nucleation, and the fiber-matrix debonding [9],[10]. Moreover, the fibers'

  doi:10.5075/epfl-298799_978-2-9701614-0-0

directional deposition and hardly controllable dispersion yield the final part anisotropy [11]. Multiscale characterization is essential to understand the influence of the architecture, layup, and meso and microvoids on the damaging of 3D printed carbon fiber reinforced PEEK, thus guiding the design of reliable aerospace structural components[12]. Moreover, experimental data are required to support the development of constitutive models for FFF composites in operating conditions to support the testing phase. Due to the relatively recent introduction of short fiber composites as a feedstock material for extrusion-based processes, the majority of the works in the literature focuses on the identification of the printing and material parameters maximizing the elastic properties under tensile and flexural load [13–15]. However, local characterization approaches are necessary to investigate the effect of the architecture and the multiscale porosity on the final part failure mechanism under loading [16,17]. Few authors emphasized the suitability of contactless characterization approaches, such as digital image correlation (DIC) and X-ray tomography, to identify the local phenomena causing the FFF composites' failure and investigate the fibers' role in the damage mechanisms [1,9,18]. DIC is an optical characterization technique that exploits the correlation between a reference and a deformed speckle pattern, applied on the specimen surface prior to testing to estimate the displacement distribution based on image matching [19]. The local strains are then derived for each subset, and smoothing techniques deliver a continuous field all over the inspected region of interest.

In this work, we present a contactless in-situ characterization approach to study the interlayer fracture of high-performance composites manufactured by FFF. The primary failure mechanism for such parts is thus the interlayer delamination due to the incomplete molecular diffusion during deposition and thus weak bond between deposited layers [1,20]. We deliver full-field displacement and strain measurements in the vicinity of the delamination front by microstereoscopic digital image correlation for specimens with 0°- 90° and ± 45° stacking. We analyze the specimens' macroscopic response, along with the local strain distribution at the interface, to identify the local phenomena arising during delamination, such as secondary interface failure or fiber breakage. Scanning electron microscopy contributed to validate the observations drawn from the strain contour plots and macroscopic responses.

2. Materials and methods

2.1 Specimens manufacturing

We designed miniature compact tension (CT) specimens, adapting the ASTM E 180-20 standard to meet the constraints in terms of region of interest size for the stereoscopic imaging ($\sim$ 7 x 7 mm^2) and material consumption minimization due to the high materials costs and its complex recycling. Figure 1a shows the specimens' geometry, including a 600 μm thick notch to ensure the crack propagation within the observed region of interest in the proximity of the specimen mid-plane. We selected 30 wt% carbon fiber reinforced (CF) TECAFIL Victrex PEEK, supplied by Ensinger, as a feedstock material, due to the high fibers infill and elastic properties, suitable for high-performance applications. Prior to printing, the filaments were dried under vacuum at 60 °C for at least 6 hours to prevent air moisture absorption. We manufactured the miniature CT specimens in the AON3D M2 printer to attain the bed and chamber temperatures of 180 °C and 120 °C, respectively, required for the CF PEEK extrusion and adhesion during printing.

  doi:10.5075/epfl-298799_978-2-9701614-0-0

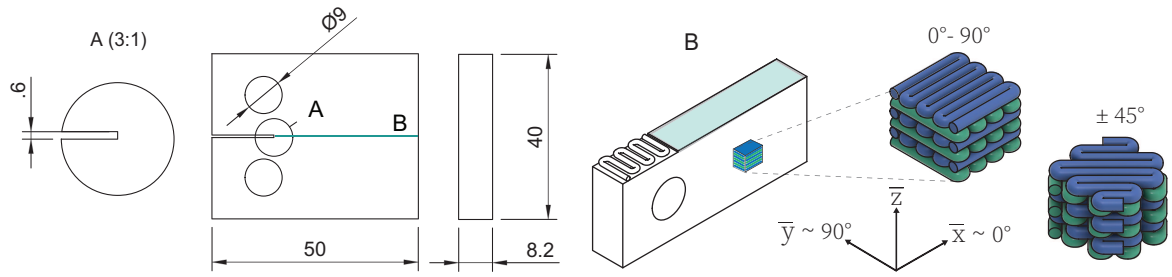

(a) (b)

Figure 1. Miniature CT specimen design (a) and stacking sequences (b). (a) The crack propagation is constrained at the specimen's mid-plane by the presence of a 600 µm thick notch (A), manufactured by removing the support (B) after printing. (b) We characterized specimens with 0°- 90° and ± 45° layers stacking to identify the role of the architecture on the interlayer delamination. The 0°, 90° directions coincide with the $\bar{x}$ and $\bar{y}$ directions, respectively, in the global reference system. All the dimensions are in mm.

The feedstock material supplier suggested a higher chamber temperature (~ 250 °C) to maximize the fracture properties, however unattainable with the AON3D M2 extruder. We installed a 400 µm diameter nozzle on the Dyze design extruder, and we chose a 200 µm layer height to increase the final part dimensional accuracy. We printed the specimens at a nozzle temperature of 440 °C and 35 mm/min speed to hinder the layers' interface cooling after the extrusion. Figure 1b illustrates the two different deposition patterns that we considered, namely ± 45° and 0°- 90°, defined in the slicer Simplify3D for the GCode generation to study the fracture mechanics of specimens with a different mesoscale architecture. The 0° and 90° directions are coincident with the $\bar{x}$ and $\bar{y}$ directions in the global reference system, respectively. Each printing job envisaged the manufacturing of a single specimen to reduce the layers cooling time and thus maximize the adhesion. After manufacturing, we mechanically removed the support at the notch using a metallic razor blade. The support removal introduced a pre-crack at the notch tip, in agreement with the mechanical pre-cracking guidelines of the ASTM E1820-20 standard, due to the interfaces' brittleness. We polished the specimens' surface using the Buehler Metaserv 2000 grinder-polisher and the CarbiMetTM silicon carbide abrasive paper with decreasing grit sizes of 100, 240, and 320. We applied mat white paint on the polished specimen' surface, and once dried, we nebulized carbon black ink using an airbrush to obtain a fine non-periodic speckle pattern over the region of interest for correlation.

2.2 In-situ characterization during mode I delamination

Figure 2a illustrates the imaging setup supplied by Correlated Solutions, including a stereomicroscope with high-resolution cameras installed (1), the microscope head (2) to align the field of view with the region of interest on the specimen surface, and a precision movement platform to control the x, y, z movement and dampen the vibrations (3). We monitored a surface of ~ 8.5 x 7.2 mm^2 around the delamination front and performed DIC measurements over a region of interest of 6.5 x 5 mm^2, meshed according to the step and subset defined for the full-field displacement and strain measurements, as shown in Figure 2b and 2c, where a representative *xy* strain contour plot is shown. The software VicSnap remotely controlled the images acquisition at a frame rate of 4 FPS during the specimen mechanical loading with the Insight Electromechanical testing machine at a speed of 0.5 mm/min.

  doi:10.5075/epfl-298799_978-2-9701614-0-0

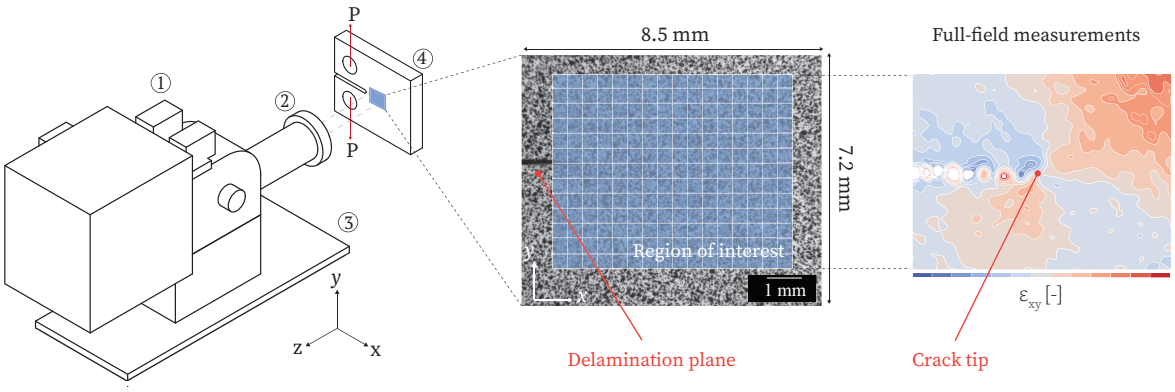

Figure 2. Imaging setup for microstereoscopic digital image correlation and analysis approach. The stereomicroscope module includes two Grasshopper high-resolution cameras (1) and a support platform (3) to dampen the vibrations and control the x, y, and z microscope movement to align the field of view (2) with the region of interest on the specimen surface(4). The software Vic-3D implements a local approach based on the region of interest meshing in subsets over which the correlation problem is solved (c) to deliver full-field displacement measurements through smoothing techniques (d).

We selected the testing speed, the frame rate, and the region of interest size to successfully track the rapid crack advancement over the specimens' surface caused by the brittleness of the interface.

2.3 Images post-processing

We analyzed the images using the software for local correlation Vic3-D V7.2.4 (Correlated Solution) and exported the nodal data for the displacement and strain contours plotting with Python. We focused on the *y* component of the displacement (V) and Lagrangian strain (ε_{yy}), parallel to the opening load direction. The high-speed cameras allowed to capture the crack advancement at different time steps to investigate the strain distribution evolution with time, despite the high crack propagation speed.

2.4 Fractography

We inspected post-mortem the specimens' cross-section and fracture surface by scanning electron microscopy using the Hitachi-TM3030Plus tabletop microscope. The specimens were cut using liquid nitrogen and coated with chromium prior to their inspection for the interaction with the electrons beam.

3. Results and discussion

Figure 3 presents the full-field measurements obtained for specimens with ± 45° stacking undergoing interlayer delamination for three time steps after the peak load. No information is lost over the selected region of interest, thanks to the careful selection of the analysis parameters (subset size, step, thresholds, and filters). The quasi symmetric V contour plot highlighted the effective load transfer from the electromechanical machine pins to the specimen midplane. The crack length was directly measured in the V contour plot, and its variation from 1.1 mm (A) to 2.8 mm (C) was tracked during delamination. The ε_{yy} contour plot shape conformed to the butterfly lobes distribution conventionally observed at the crack tip of compact tension specimens undergoing mode I failure [21].

  doi:10.5075/epfl-298799_978-2-9701614-0-0 published under CC BY-NC 4.0 license

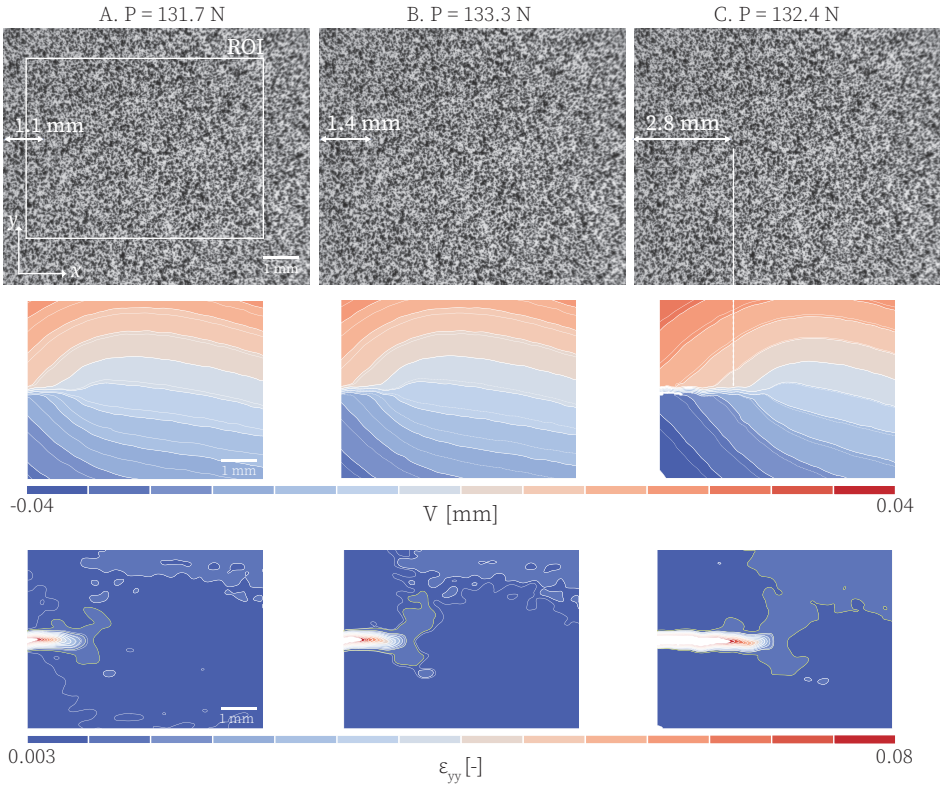

Figure 3. Full-field displacement and strain measurements over a region of interest of 6 x 5 mm² around the propagating crack on the surface of CT specimens with ± 45° stacking. The quasi-symmetric V displacement field revealed the effective load transfer at the specimen midplane during delamination. The ε_{yy} local distribution at the crack tip follows the butterfly lobe shape expected for specimens undergoing mode I failure.

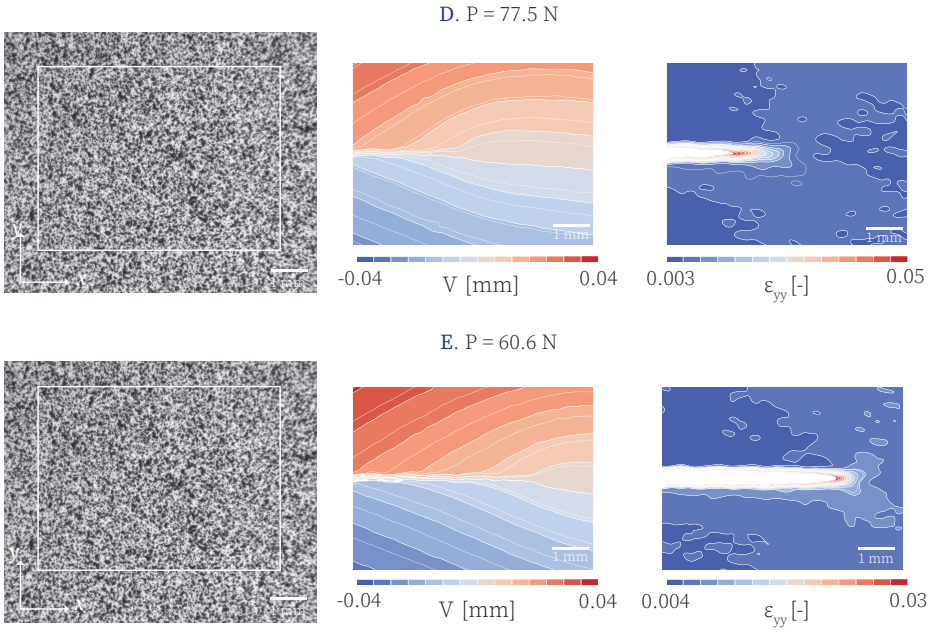

Figure 4. Full-field displacement and strain measurements on the surface of specimens with 0°-90° stacking undergoing interlayer failure. The quasi-symmetric V distribution confirmed the effective load transfer at the specimen's midplane. The ε_{yy} lobes distribution is affected by measurements noise that can be attributed to the rigid body motion caused by the sudden crack propagation or to the simultaneous damage of parallel interfaces.

  doi:10.5075/epfl-298799_978-2-9701614-0-0

The strain concentration area is localized in the near proximity of the rapidly propagating crack and progressively growing until the lobes shape regularity is partially lost, in C, probably due to the simultaneous damage nucleation and propagation on a parallel layers' interface. The displacement and strain spatial resolutions were 673 and 676 µm, respectively. Figure 4 shows the full-field measurements found for 0°- 90° interfaces for two time steps after the peak load and suggests the comparison with the measurements previously described for specimens with ± 45° stacking. The V distribution is quasi symmetric, further validating the mechanical loading setup effectiveness. The contour plots revealed that the crack rapidly propagated from D to E in 0.5 s. The ε_{yy} butterfly lobes distribution described for ± 45° interfaces was observed for 0°- 90° interfaces too (with a spatial strain resolution of 663 µm), despite the measurements noise, probably due to the failure of different weak interfaces or to the vibrations deriving from the sudden delamination. The local ε_{yy} values recorded for specimens with 0°- 90° stacking are lower than those observed for specimens with ± 45° oriented layers, in agreement with the force-displacement response recorded by the Insight loading machine, shown in Figure 5a. The macroscopic specimens' response highlighted the specimens' brittle failure behaviour, independently from the stacking. Moreover, after failure, the force-displacement curve step behavior, highlighted in yellow, revealed the simultaneous delamination of different weak layers interfaces parallel to the specimen mid-plane. The A, B, C, D, and E points highlight the force and displacement values at which the DIC measurements previously described were performed. Figure 5b illustrates the ± 45° stacking specimens' fracture surface ($\bar{x}$ - $\bar{y}$) and cross-section ($\bar{y}$ - $\bar{z}$) inspected by scanning electron microscopy (SEM) after failure.

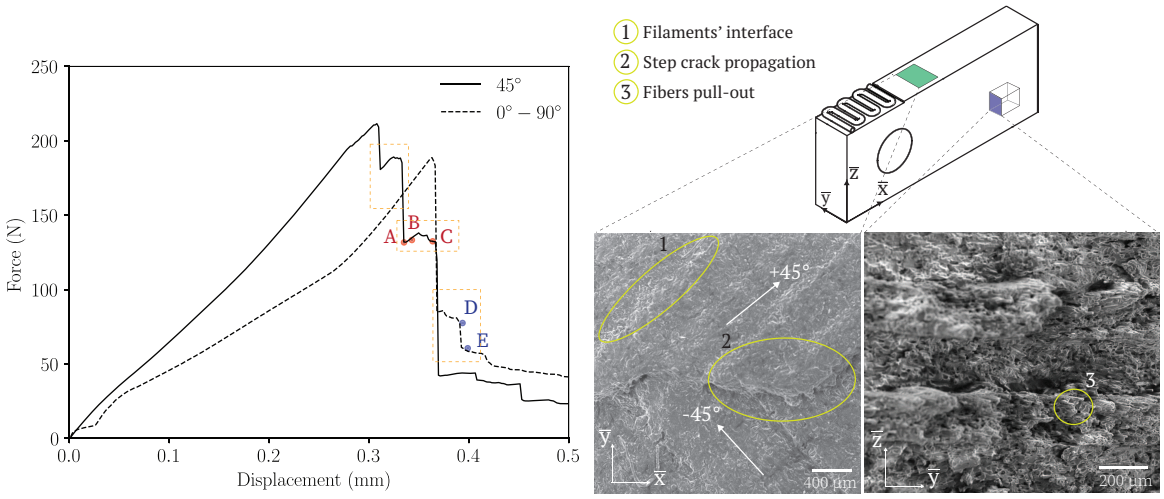

(a) (b)

Figure 5 Representative force-displacement response recorded by the electromechanical testing machine for specimens with ± 45° and 0°- 90° stacking (a) and fractography (b). Higher fracture energy is involved in the brittle delamination of ± 45° interfaces due to the filaments' misalignment with the crack propagation direction. The points A, B, C, D and E correspond to the presented full-field measurements. A step macroscopic response is recorded, revealing the progressive failure of different interfaces in the proximity of the specimen midplane. The hypothesis is confirmed by the ± 45° stacking specimens' fracture surface inspection by SEM, highlighting the crack path deviation on the adjacent interface. The cross-section image reveals the fibers' alignment with the deposition direction and the presence of multiscale porosity.

  doi:10.5075/epfl-298799_978-2-9701614-0-0

The fracture-surface inspection shows that the crack propagated on different planes, highlighting the difficulty of controlling the crack path when under loading due to the weakness of the interlayer molecular bond. There is no evidence of fiber pull-out during interlayer failure, and the interfilament interfaces are recognizable on the smooth fracture surface. The cross-section SEM image highlights the fibers' alignment with the ± 45° deposition directions as well as the presence of multiscale porosity between and within filaments. The step crack propagation on different layers' interfaces and the sudden brittle failure is one of the possible causes of the measurements noise affecting the full-field contour plots.

4. Conclusions

We presented and validated an in-situ approach to locally characterize the failure of FFF composite interfaces, highlighting the weakness of the layers' interfaces under mode I load. We showed that the interlayer fracture mechanics is related to the specimens' mesoscale architecture, characterized by weak interfaces and multiscale porosity.
The brittle delamination of specimens with ± 45° stacking involved higher fracture energy and local deformations at the crack tip, when compared to specimens with 0°- 90° stacking. Microstereoscopic digital image correlation delivered full-field mesoscale measurements on the surface of compact tension specimens to study the local crack propagation mechanism. The crack tracking highlighted the rapid delamination due to the interface brittleness. The availability of full-field high-resolution measurements supports and promotes the development of a constitutive interface model for 3D printed composites. However, further characterization is required to validate the observations drawn from the first tests, with an increased stereomicroscope magnification and various layers stacking. Moreover, the investigation of the intralayer delamination could deliver a thorough understanding of the role of the meso and microstructure in the interface damage under loading.

Acknowledgements

We acknowledge the financial and technical support of the Safran Industrial Research Chair on Additive Manufacturing of Organic Matrix Composites (AMOMC), and the financial support of the Natural Sciences and Engineering Research Council of Canada.

5. References

1. Yavas D, Zhang Z, Liu Q, Wu D. Interlaminar shear behavior of continuous and short carbon fiber reinforced polymer composites fabricated by additive manufacturing. Composites Part B: Engineering. 2021;204:108460.
2. Fidan I, Imeri A, Gupta A, Hasanov S, Nasirov A, Elliott A, et al. The trends and challenges of fiber reinforced additive manufacturing. Int J Adv Manuf Technol. 2019;102(5–8):1801–18.
3. Wang X, Jiang M, Zhou Z, Gou J, Hui D. 3D printing of polymer matrix composites: A review and prospective. Composites Part B: Engineering. 2017;110:442–58.
4. Ngo TD, Kashani A, Imbalzano G, Nguyen KTQ, Hui D. Additive manufacturing (3D printing): A review of materials, methods, applications and challenges. Composites Part B: Engineering. 2018;143:172–96.
5. Gao X, Qi S, Kuang X, Su Y, Li J, Wang D. Fused filament fabrication of polymer materials: A review of interlayer bond. Additive Manufacturing. 2021;37:101658.

  doi:10.5075/epfl-298799_978-2-9701614-0-0

6. Tekinalp HL, Kunc V, Velez-Garcia GM, Duty CE, Love LJ, Naskar AK, et al. Highly oriented carbon fiber–polymer composites via additive manufacturing. Composites Science and Technology. 2014;105:144–50.
7. Goh GD, Yap YL, Agarwala S, Yeong WY. Recent Progress in Additive Manufacturing of Fiber Reinforced Polymer Composite. Adv Mater Technol. 2019;4(1):1800271.
8. Spoerk M, Savandaiah C, Arbeiter F, Traxler G, Cardon L, Holzer C, et al. Anisotropic properties of oriented short carbon fibre filled polypropylene parts fabricated by extrusion-based additive manufacturing. Composites Part A: Applied Science and Manufacturing. 2018;113:95–104.
9. Yu S, Bale H, Park S, Hwang JY, Hong SH. Complex anisotropic fracture behaviors of 3D-printed fiber-reinforced composites based on multi-scale hierarchical microstructure. Composites Science and Technology. 2022;218:109176.
10. Li, Zhao, Li, Yang, Wang. Flexural Properties and Fracture Behavior of CF/PEEK in Orthogonal Building Orientation by FDM: Microstructure and Mechanism. Polymers. 2019;11(4):656.
11. Brenken B, Barocio E, Favaloro A, Kunc V, Pipes RB. Fused filament fabrication of fiber-reinforced polymers: A review. Additive Manufacturing. 2018;21:1–16.
12. Singh S, Ramakrishna S, Berto F. 3D Printing of polymer composites: A short review. Mat Design & Process Comms [Internet]. 2020 [cited 2022];2(2). Available from: https://onlinelibrary.wiley.com/doi/10.1002/mdp2.97
13. Reverte JM, Caminero MÁ, Chacón JM, García-Plaza E, Núñez PJ, Becar JP. Mechanical and Geometric Performance of PLA-Based Polymer Composites Processed by the Fused Filament Fabrication Additive Manufacturing Technique. Materials. 2020;13(8):1924.
14. Ning F, Cong W, Hu Y, Wang H. Additive manufacturing of carbon fiber-reinforced plastic composites using fused deposition modeling: Effects of process parameters on tensile properties. Journal of Composite Materials. 2017;51(4):451–62.
15. Ning F, Cong W, Qiu J, Wei J, Wang S. Additive manufacturing of carbon fiber reinforced thermoplastic composites using fused deposition modeling. Composites Part B: Engineering. 2015;80:369–78.
16. Parandoush P, Lin D. A review on additive manufacturing of polymer-fiber composites. Composite Structures. 2017;182:36–53.
17. Yavas D, Zhang Z, Liu Q, Wu D. Fracture behavior of 3D printed carbon fiber-reinforced polymer composites. Composites Science and Technology. 2021;208:108741.
18. Zhang Z, Yavas D, Liu Q, Wu D. Effect of build orientation and raster pattern on the fracture behavior of carbon fiber reinforced polymer composites fabricated by additive manufacturing. Additive Manufacturing. 2021;47:102204.
19. Schreier H, Orteu JJ, Sutton MA. Image Correlation for Shape, Motion and Deformation Measurements [Internet]. Boston, MA: Springer US; 2009 [cited 2020]. Available from: http://link.springer.com/10.1007/978-0-387-78747-3
20. Bellehumeur C, Li L, Sun Q, Gu P. Modeling of Bond Formation Between Polymer Filaments in the Fused Deposition Modeling Process. Journal of Manufacturing Processes. 2004;6(2):170–8.
21. Anderson TL. Fracture Mechanics: Fundamentals and Applications. 2005;630.

  doi:10.5075/epfl-298799_978-2-9701614-0-0

IMPACT DAMAGE TOLERANCE OF THERMOSET COMPOSITE WITH HYBRID YARNS: ADVANCED MANUFACTURING PROCESS

Jinseong Park[a], Vivek Koncherry[a], David William Lloyd[a], Prasad Potluri[a]*

a: jinseong.park@postgrad.manchester.ac.uk

Abstract: *The aim of this study was to improve the impact damage tolerance of thermoset composites by using thermoplastic dry fibre. Hybrid yarns made of polypropylene fibre and carbon fibre were produced with different yarn structures. A bespoke hybrid yarn manufacturing machine has been developed for commingled and wrapped yarns. The impact behaviour and mechanical properties of the 3D composites were evaluated through a drop-weight impact test and compression after the impact test (CAI). Damage areas in the composites were analysed through the C-scan image analysis. The use of hybrid yarn increased impact damaged area at C-scan analysis and decreased dent depth. Therefore, even though the damaged area of wrapped yarn composite was increased compared to neat carbon fibre composites, the impact damage tolerance of wrapped yarn composites was improved.*

Keywords: impact damage tolerance; hybrid yarn; polypropylene multifilament; thermoset composite; automatic production process

1. Introduction

Carbon fibre thermoset composites have become competitive with steel because of their light weight, ease of fabrication, and corrosion resistance (1). These characteristics of composites are suitable for load-bearing structures and are applied to various industrial applications, such as aircraft and marine vessels. Thermosets form high crosslinked structures during curing time and increase modulus and failure strength. However, this causes brittleness resulting in low impact resistance to crack (2). Hence, barely visible impact damage from low velocity impact can occur during composites manufacturing and in use (3). This significantly diminishes the stiffness and strength of composites (4), and this damage of polymer composites can result in an interlaminar fracture (delamination), intralaminar fracture (transverse matrix cracking and debonding between fibre and fibre fracture (3,5). Hence, it is essential to enhance the impact damage tolerance of thermoset composites.

The damage tolerance of thermoset composites can be improved through the development of fabric architectures, resin modification, and interleaving thermoplastic materials (2,6). Firstly, the 3D structure displays the highest damage resistance and tolerance among unidirectional (UD), 2D plain weave and 3D weave structures (7). The damage of 3D structure composites is remarkably localised in the plane, and it shows the lowest damaged area (8,9). In contrast, damage of UD composites after impact appears along the fibre direction and shows the biggest damaged area compared to 2D and 3D woven composites (8). Secondly, thermoset resins are modified by adding thermoplastic particles (10) or liquid rubber (11) to enhance the mechanical properties of thermoset composites. The fracture toughness and impact strength of composites are improved by blending thermoplastic polysulfone particles and epoxy resin compared to neat epoxy resin (10). Furthermore, the nitrile liquid rubber and epoxy resin mixture also decreased

  doi:10.5075/epfl-298799_978-2-9701614-0-0

the delamination area in the thermoset composites (11). Lastly, interleaving materials such as films (12), particles (13), veils (14), and hybrid yarn (15) have been used with thermoset resin to improve impact damage tolerance. In particular, thermoplastics are mainly used as the third phase because of their high impact damage tolerance and good chemical stability (16). The thermoplastic poly ethylene-co-acrylic acid (PEAA) films or polyester veils are inserted at the centre of plies and included in thermoset composites to increase damage tolerance (12,17).

PP fibres are used in many industries due to their low price and high performance (21); furthermore, because PP fibre helps to improve the impact damage tolerance of composites (15), it is used to produce hybrid yarns with reinforcement fibres. The hybrid yarn combined with reinforcement and matrix fibres is made by different techniques such as commingling, co-spinning, co-wrapping, and co-twisting. They are generally used for thermoplastic composites through the consolidation process. However, recently dry hybrid yarns have been used to increase the impact damage tolerance of thermoset composites. Commingled yarns of glass fibres and polypropylene (or nylon) fibres used to manufacture thermoset composites increased compressive strength (15,18). However, commingled yarn reduces the mechanical properties through the manufacturing process because reinforcement fibres and polymer fibres are mingled by air nozzle, and damage of fibres are caused by air pressure (19,20). Therefore, this study manufactured wrapped yarns as well as commingled yarns to minimise fibre damage and increase impact damage tolerance of thermoset composites. Generally, the impact damage tolerance was evaluated by the compression after impact (CAI) test.

2. Materials and methods

2.1 Hybrid yarn manufacturing

400 tex x 1 carbon fibre and 17 tex x 2 PP multifilament were used to manufacture commingled and wrapped yarns. Continuous 6K carbon fibre (T700SC-6000-60E) and polypropylene multifilament (Duron CF) were supplied by Toray and Drake Extrusion, respectively. This research developed an automatic hybrid yarn manufacturing machine to produce commingled and wrapped yarns based on the traditional manufacturing method (21). The bespoke machine for this research involves let off, de-sizing, wrapping, commingling and winding zones, as shown in Figure 1. a, b.

2.1.1 Commingled yarn

The de-sizing process of PP multifilament was used to enable the PP filaments to be opened more by air pressure and to improve fibre distribution (Figure 1. c). A water bath designed by the University of Manchester was used (22) with tap water (24°C) at 1.5N tension. After passing the de-sizing bath, PP fibres passed through an infrared heater (100°C), a heat gun (120-130°C), and an air cooler to dry fibres. The original (Figure 2. a) or de-sized PP (Figure 2. b) were used to produce commingled yarn with an air nozzle at 2 bar. The let-off and production speeds for commingled yarn were fixed through the preliminary test at 0.22 m/s and 0.18 m/s.

2.1.2 Wrapped yarn

The single wrapped yarn was produced at 50 wraps per metre (w/m) with a hollow spindle.The wrapping density was controlled by the rotation speed of the PP fibre bobbin (360 rpm) and pulling roller speed (28rpm), and winding speed (25 rpm). The double wrapped yarn was also

produced at 50 w/m with two hollow spindles. The single wrapped yarn presents one pattern where PP yarns wrap around the core fibre at one side (Figure 2. c). In contrast, double wrapped yarn shows different patterns because two different PP yarn wraps the carbon fibres in different directions (Figure 2.d).

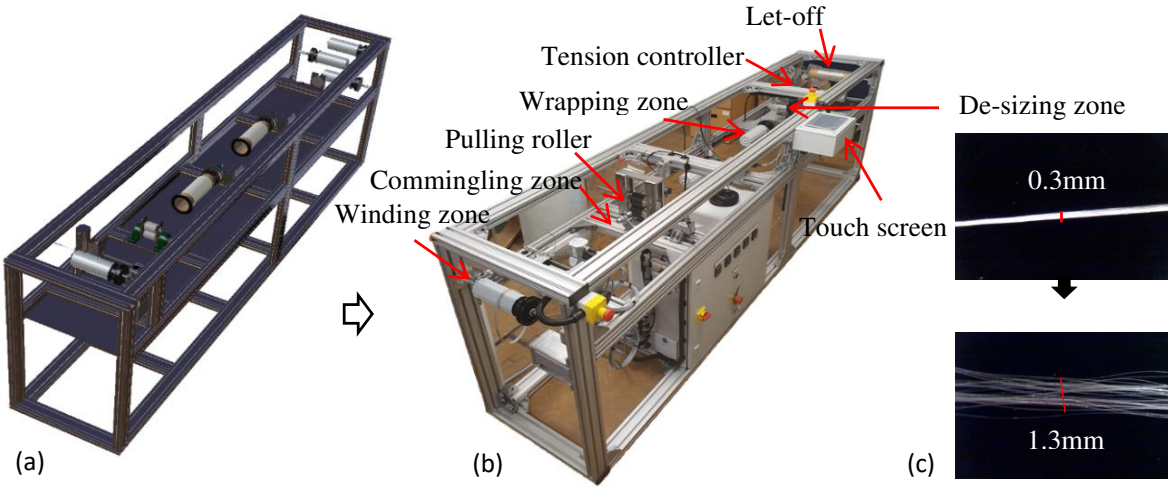

Figure 1 Machine development process to manufacture hybrid yarns: (a) initial CAD drawing, (b) actual machine and (c) PP fibre after and before the de-sizing process

2.2 Composite manufacture

3D structure preforms are manufactured on the robotic tow placement device developed by The University of Manchester (23). The tow density on the pinned flat frame for tow placement was fixed at 8 tows/cm in both warp and weft directions. 3D [90/0/90/0/90/0/90] structure preforms consisted of 7 layers. In particular, the 3D structure consisted of 4 warp and 3 weft layers held by the 6K CF through-thickness binder (Figure 2 e-h). The hybrid yarns were used in warp and weft direction, and neat carbon fibres were used for the binder.

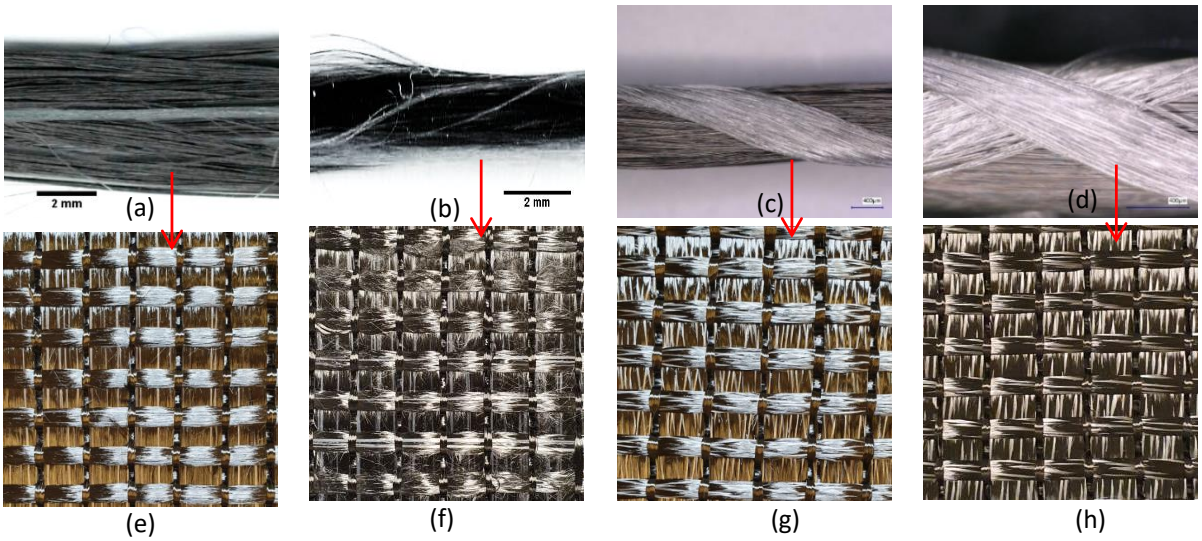

Figure 2 3D composite preforms with hybrid yarns: (a) commingled yarn, (b) de-sized PP commingled yarn, (c) single wrapped yarn, (d) double wrapped yarn, (e) commingled yarn preform, (f) de-sizing PP commingled yarn preform, (g) single wrapped yarn preform, and (h) double wrapped yarn preform

  doi:10.5075/epfl-298799_978-2-9701614-0-0

Preforms were infused by the vacuum bagging method with IN2 epoxy resin (77%wt) and AT30 slow epoxy hardener (23%wt). These components were prepared in a weight ratio of 100:30 in separated cups and degassed under vacuum for 3hr. They were mixed for 2 min and then degassed again under vacuum for 15 min. This vacuum bagging process was carried out at room temperature. The resin mixture was delivered into the preform for 0.5-1hr and left for 24hr after closing the inlet. Once the resin infusion process was finished, samples were heated in an oven at 60°C for 6hr to cure the composites fully. The physical properties of 3D structure composites with commingled (C), de-sized PP commingled (DC), single wrapped (SW), and double wrapped (DW) yarn can be seen in Table 1. The composite density was calculated from the weight of specimens in air and distilled water at room temperature following ASTM D792-20 standard test methods (24). Fibre volume fraction (FVF) was calculated based on the Rule of Mixtures for density which is calculated from the measured and known density of composites (25).

Table 1: Physical properties of 3D structure wrapped yarn composites

Sample name	Wrap density (w/m)	No. of yarns	Thickness (mm)	Density (g/cm^3)	FVF	
					CF	PP
3DCF	-	-	3.1±0.1	1.384 ±0.012	0.60	-
3DCF-2PP-C	-	2	3.4±0.1	1.344 ±0.032	0.60	0.02
3DCF-2PP-DC	-	2	4.0±0.4	1.330 ±0.005	0.52	0.02
3DCF-2PP-SW50	50	2	3.5±0.1	1.382 ±0.034	0.55	0.02
3DCF-2PP-DW50	50	2	3.4±0.1	1.351 ±0.031	0.57	0.02

2.3 Testing

The specimen dimensions for the impact test and CAI tests were 55 x 89mm, which was developed for the specimen scale of the CAI test by Prichard and Hogg [28]. The prepared samples were set on a CEAST 9350 drop-weight impact machine with a hemispherical radius of 20 mm and a total mass of 2kg. 3D structure composites were subjected to 10J nominal impact energy. An INSTRON 5969 machine was used for the CAI test with a constant crosshead displacement of 0.5mm/min and a 50kN load cell. The accumulated damaged area by the impact was assessed through the Ultrasonic C-Scan (Midas NDT Ltd.) with a probe frequency of 1MHz and scanning speed of 150mm/s. The damaged area data and images of samples from C-Scan were obtained by using Zeus v3 software. Dent depth after impact was measured by a digital depth gauge.

3. Results & discussion

3.1 Impact test

The force-displacement impact curves of 3D structure commingled and wrapped yarn composites at 10J are shown in Figure 3, and their impact test results are summarised in Table 2. The hybrid yarn composites almost reach up to 5.5kN, and then the curves reverse after the

impactor rebounded from the composites. The peak force and displacement of the 3D structure CF composite (3DCF) show the highest value among the composite samples. However, 3DCF shows rough curves until it reaches the highest peak force compared to hybrid yarn composites. The absorbed energy of almost all of the samples shows similar values; however, double wrapped yarn composites show significantly decreased recovered energy.

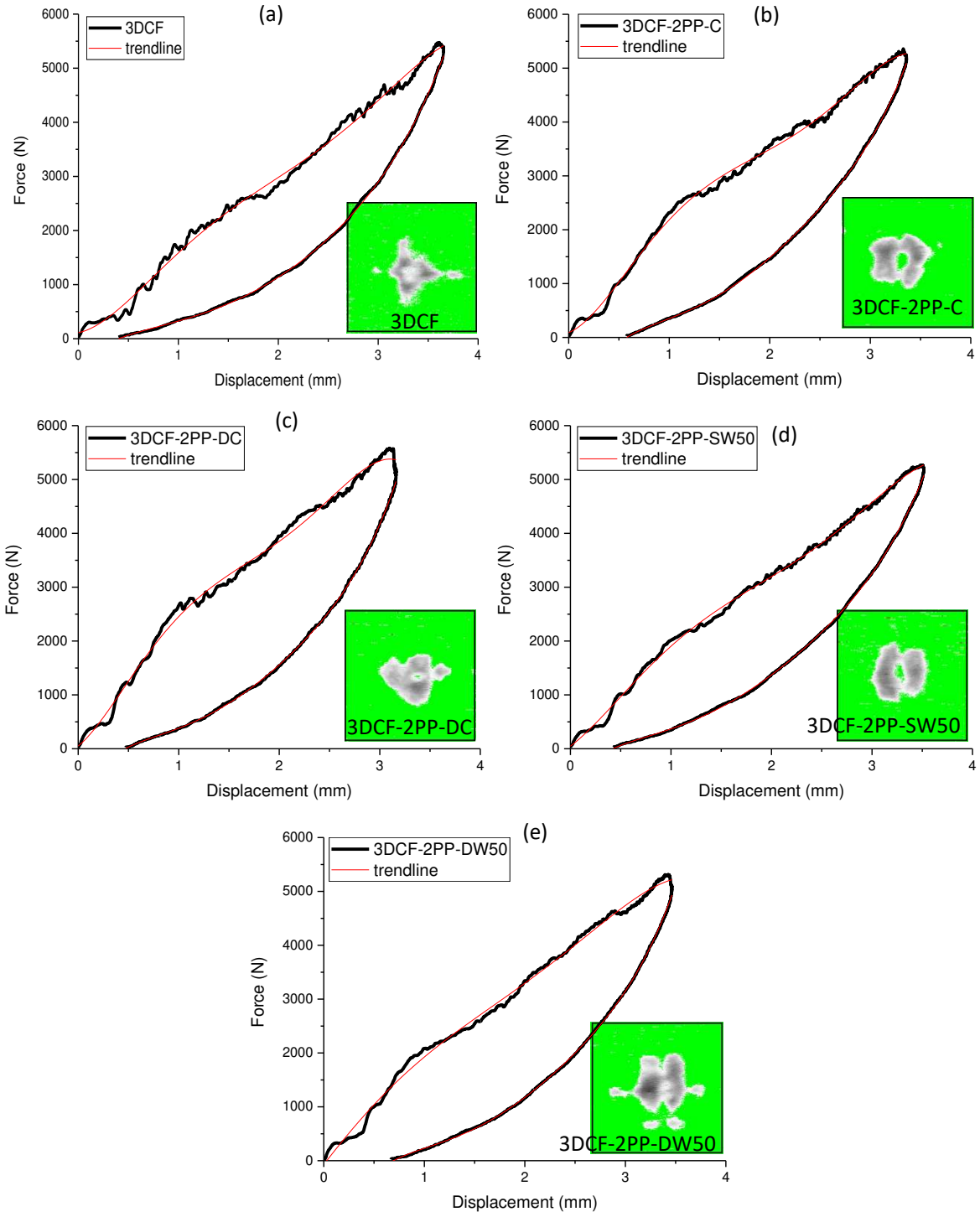

Figure 3 Typical force-displacement curves of (a) neat CF, (b) commingled yarn, (c) de-sized PP commingled yarn, (d) single wrapped yarn, and (e) double wrapped yarn composites at 10J impact energy

  doi:10.5075/epfl-298799_978-2-9701614-0-0

Table 2: Summary of impact test results of 3D structure composites with hybrid yarns at 10J

Sample	Peak force (N)	Peak displacement (mm)	Residual displacement (mm)	Absorbed energy (J)	Recovered energy (J)
3DCF	5524.0±64.8	3.6±0.1	0.5±0.1	4.7±0.1	5.3±0.1
3DCF-2PP-C	5460.8±117.4	3.3±0.1	0.5±0.1	5.0±0.2	5.0±0.2
3DCF-2PP-DC	5477.5±113.6	3.1±0.0	0.5±0.1	5.5±0.2	4.4±0.2
3DCF-2PP-SW50	5498.3±204.4	3.3±0.2	0.4±0.0	4.8±0.1	5.2±0.1
3DCF-2PP-DW50	5231.9±155.3	3.5±0.1	0.7±0.1	5.7±0.2	4.3±0.2

3.2 C-scan

The accumulated damaged area of 3D structure composites shows round shapes, as shown in the insets to Figure 3. The calculated damaged areas from Ultrasonic C-scan images and dent depth are shown in Figure 4. a. The damaged areas are increased, and dent depth is decreased by hybrid yarns in the composites. A possible explanation for this result might be that impact energy is dissipated by the thermoplastic fibres and 3D structure (7,26). The double wrapped yarn composites (3DCF-2PP-DW50) have the highest impact damage area among the hybrid yarn composites.

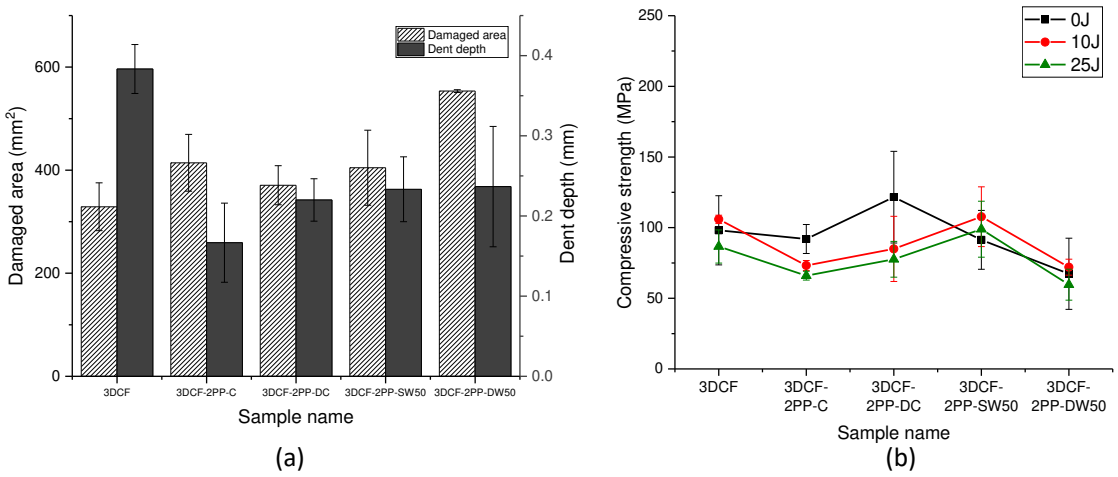

Figure 4 Compressive strength of 3D structure hybrid yarn after 0J, 10J and 25J impact test

3.3 CAI test

The compression test of 3D structure composites was performed after 0J, 10J and 25J impact tests. Figure 4. b illustrates the compressive strength of hybrid yarn composites. The failure of specimens after impact started at the impact area. However, because the failure of unimpacted specimens (0J) is generated near the boundary of the compression tool, undamaged laminates cannot provide a true measure of compression strength. This research performed a compression

test on undamaged specimens at the same test set-up of the CAI test to compare the compressive strength between neat CF composites and hybrid yarn reinforced composites even though it cannot obtain actual values. Single wrapped yarn shows the highest compressive strength after impact among the composites samples. Compressive strength of commingled yarn and developed commingled yarn composites decreased by 25% and 13% compared to neat carbon fibre composites after the 10J impact test. This may be because of CF damage during production. A significant difference was found between commingled and wrapped yarn composites. The compressive strength of single-wrapped yarn composites increased by 10% after the 10J impact test. However, double wrapped yarn composites decreased by 27% against neat carbon fibre composites. Even though double wrapped yarn shows the widest damage area in Figure 4. a, it presents the lowest compressive strength. This confirms the significance of hybrid yarn structure in enhancing damage tolerance.

4. Conclusion

This study investigated the impact damage tolerance and behaviour of thermoset composites by manufacturing hybrid yarns. Impact damage tolerance of single-wrapped yarn composites increased as impact energy was dispersed in the composites. However, commingled and double-wrapped yarn composites decreased damage tolerance because of carbon fibre damage during the yarn manufacturing process and overlapped wrapped yarn structure. The compressive strength of commingled yarn composite was slightly improved after PP fibre de-sizing. However, it is still lower than neat CF composites. Therefore, this result shows that PP multifilament spreads impact energy; however, damage tolerance can be increased when a proper hybrid yarn structure is applied.

5. References

1. Zhou G, Greaves LJ. Damage resistance and tolerance of thick laminated woven roving GFRP plates subjected to low-velocity impact [Internet]. Impact behaviour of fibre-reinforced composite materials and structures. Woodhead Publishing Ltd; 2000. 133–185 p. Available from: http://dx.doi.org/10.1533/9781855738904.133
2. Sonnenfeld C, Mendil-Jakani H, Agogué R, Nunez P, Beauchêne P. Thermoplastic/thermoset multilayer composites: A way to improve the impact damage tolerance of thermosetting resin matrix composites. Compos Struct [Internet]. 2017;171:298–305. Available from: http://dx.doi.org/10.1016/j.compstruct.2017.03.044
3. Sohn MS, Hu XZ, Kim JK, Walker L. Impact damage characterisation of carbon fibre/epoxy composites with multi-layer reinforcement. Compos Part B Eng. 2000;
4. Shyr TW, Pan YH. Impact resistance and damage characteristics of composite laminates. Compos Struct. 2003;
5. Cantwell WJ, Morton J. The impact resistance of composite materials - a review. Composites. 1991;
6. Shah SZH, Karuppanan S, Megat-Yusoff PSM, Sajid Z. Impact resistance and damage tolerance of fiber reinforced composites: A review. Composite Structures. 2019.
7. Potluri P, Hogg P, Arshad M, Jetavat D, Jamshidi P. Influence of fibre architecture on impact damage tolerance in 3D woven composites. Appl Compos Mater. 2012;19(5):799–812.
8. Potluri P, Hogg P, Arshad M, Jetavat D, Jamshidi P. Influence of fibre architecture on impact damage tolerance in 3D woven composites. Appl Compos Mater. 2012;19(5):799–812.

9. Saeedifar M, Saleh MN, El-Dessouky HM, Teixeira De Freitas S, Zarouchas D. Damage assessment of NCF, 2D and 3D woven composites under compression after multiple-impact using acoustic emission. Compos Part A Appl Sci Manuf. 2020;
10. Sun Z, Xu L, Chen Z, Wang Y, Tusiime R, Cheng C, et al. Enhancing the Mechanical and Thermal Properties of Epoxy Resin via Blending with Thermoplastic Polysulfone. 2019; Available from: www.mdpi.com/journal/polymers
11. Ricciardi MR, Papa I, Langella A, Langella T, Lopresto V, Antonucci V. Mechanical properties of glass fibre composites based on nitrile rubber toughened modified epoxy resin. Compos Part B Eng. 2018 Apr 15;139:259–67.
12. Lu WH, Liao FS, Su AC, Kao PW, Hsu TJ. Effect of interleaving on the impact response of a unidirectional carbon/epoxy composite. Composites. 1995 Mar 1;26(3):215–22.
13. Tsai SN, Carolan D, Sprenger S, Taylor AC. Fracture and fatigue behaviour of carbon fibre composites with nanoparticle-sized fibres. Compos Struct. 2019 Jun 1;217:143–9.
14. Gheryani AA, Fleming DC, Reichard RP. Nonwoven polyester interleaving for toughness enhancement in composites. J Compos Mater. 2019;
15. Selver E, Potluri P, Hogg P, Soutis C. Impact damage tolerance of thermoset composites reinforced with hybrid commingled yarns. Compos Part B Eng [Internet]. 2016;91:522–38. Available from: http://dx.doi.org/10.1016/j.compositesb.2015.12.035
16. Sorrentino L, Sarasini F, Tirillò J, Touchard F, Chocinski-Arnault L, Mellier D, et al. Damage tolerance assessment of the interface strength gradation in thermoplastic composites. Compos Part B Eng. 2017;
17. Magniez K, Chaffraix T, Fox B. Toughening of a carbon-fibre composite using electrospun poly(hydroxyether of bisphenol A) nanofibrous membranes through inverse phase separation and inter-domain etherification. Materials (Basel). 2011;
18. Hogg PJ. Toughening of thermosetting composites with thermoplastic fibres. Mater Sci Eng A. 2005;412(1–2):97–103.
19. Choi B-D, Diestel O, Offermann P. Commingled CF/PEEK Hybrid Yarns for Use in Textile Reinforced High Performance Rotors. 12th Int Conf Compos Mater [Internet]. 1999;796–806. Available from: http://www.iccm-central.org/Proceedings/ICCM12proceedings/site/papers/pap528.pdf
20. Alagirusamy R, Ogale V. Commingled and air jet-textured hybrid yarns for thermoplastic composites. J Ind Text. 2004;33(4):223–43.
21. Mankodi HR. Developments in hybrid yarns [Internet]. Specialist Yarn and Fabric Structures: Developments and Applications. Woodhead Publishing Limited; 2011. 21–55 p. Available from: http://dx.doi.org/10.1533/9780857093936.21
22. Koncherry V, Potluri P, Fernando A. Multifunctional Carbon Fibre Tapes for Automotive Composites. Appl Compos Mater. 2017;
23. Koncherry V, Park JS, Sowrov K, Matveev M, Brown LP, Long AC, et al. Novel manufacturing techniques for optimised 3D multiaxial orthogonal preform. In: ICCM International Conferences on Composite Materials. 2019.
24. ASTM D 792-20. Standard Test Methods for Density and Specific Gravity (Relative Density) of Plastics. Annu B ASTM Stand. 2020;
25. Deborah Chung DL. 3 - Polymer-Matrix Composites: Structure and Processing [Internet]. Second Edi. Carbon Composites. Elsevier Inc.; 2017. 161–217 p. Available from: http://dx.doi.org/10.1016/B978-0-12-804459-9/00003-8
26. Safri SNA, Sultan MTH, Jawaid M, Jayakrishna K. Impact behaviour of hybrid composites for structural applications: A review. Composites Part B: Engineering. 2018.

EXPERIMENTAL INVESTIGATION ON BEARING BEHAVIOR AND FAILURE MECHANISM OF HYBRID THIN/THICK-PLY COMPOSITE LAMINATES

Mohamed Sahbi Loukil[a], Mats Bergwall[b], Deepthi Prasad[a], Florence Moreau[c], Mikael Segersäll[a], Zlatan Kapidzic[d]

a: Division of Engineering Materials, Linköping University, 581 83, Linköping, Sweden – email: Mohamed.loukil@liu.se
b: RISE SICOMP, Box 271, SE-94129, Piteå, Sweden
c: Oxeon AB, Företagsgatan 24, SE-504 64, Borås, Sweden
d: Saab AB, SE-581 88, Linköping, Sweden

Abstract: *The effect of using thin plies to increase the bearing strength of composite laminates was investigated. Five different composite laminates were manufactured using a single material system with varying proportions of thin plies (100% thick-ply, 50% thin-ply and 100% thin-ply). Bearing tests were performed and the results from the tests are investigated. The results show that performance in terms of bearing strength at onset of damage, and ultimate bearing stress increase proportionally with the increasing amount of thin plies within the stack. Microscopic examination of the failure modes for all laminates was performed at the center of the hole to determine the dominant failure mode. Transition zone was investigated where both thin and thick plies were designed so that the thin plies are used only when more strength is required.*

Keywords: Thin Ply; Matrix crack; Bearing strength, Hybrid laminate.

1. Introduction

Composite materials have found usage in many industrial applications and more recently they are increasingly used in aerospace panels and airframes. The use of composites in the aerospace industry is justified by their excellent specific modulus and strength. When a composite laminate is loaded in tension with increasing load it will eventually fail (macroscopically). The failure is preceded by initiation and evolution of several microdamage modes and if the amount of damage increases during, for example the service life of the structure, laminate thermo-elastic properties are reduced. Several studies have been published describing the effect of damage development in composite laminates on the thermo-elastic properties [1-5]. Hence, it is desirable to suppress the damage development, especially the initiation of transverse cracks, which is typically the origin for the successive damage modes: delaminations and fiber breaks. One way to realize this effect is by reducing the thickness of the plies in the laminate which will effectively increase the transverse tensile strength of a ply. The general effect of an increased first crack formation strain in thin layers of laminates in tension is described in [6, 7]. Another example of the thin-ply effect was demonstrated by Sihn et al. [8], who performed an experimental campaign comparing the mechanical properties of conventional laminates to thin-ply laminates. In this study it was observed that without special resins, the thin-ply laminate composites suppress microcracking, delamination and splitting damage for static, fatigue and impact loadings. In [9], quasi-isotropic laminates were prepared using both standard prepregs and thin-ply prepregs in order to examine the effect of ply thickness on the damage accumulation processes. Clear difference on the damage accumulation process between

  doi:10.5075/epfl-298799_978-2-9701614-0-0

standard laminates and thin-ply laminates was identified; fiber fractures occurred in thin-ply laminates. The effect of ply thickness on the crack propagation mechanism was discussed by Saito et al. [10] with respect to the energy release rate of the intralaminar transverse crack calculated using finite element analysis. They verified the crack suppression effect using thin ply and they concluded that this effect is apparently caused by a decrease in the energy release rate at the crack tip in the thin layer. Numerical studies presented in [11-13] analyzing the influence of ply thickness on the in-situ strengths showed a significant improvement in transverse cracking and delamination resistance when using thin-ply based laminates.

The use of thin plies is beneficial; however, it is very costly to make a part with 100% thin plies. For that reason, it is desirable to achieve a hybrid solution, where thin plies are used where they can contribute the most performance to the structure and conventional plies are used otherwise The work in [14,15] demonstrated that for laminates with a combination of thin and thick plies, both the amount and the distribution of thin plies influences the failure behavior and failure loads. Several experiments were performed on unnotched as well as notched and bearing loaded specimens and the effect was also found to be depending on loading condition.

One potential application where the crack suppression characteristics of thin-ply laminates may be advantageous, is in bolted joints where composite structures are subjected to bearing loads. The effect of using thin plies to increase the bearing strength of composite laminates has been investigated in [16]. The results show that performance in terms of bearing stiffness, strength at onset of damage, and ultimate bearing stress increase proportionally with the increasing amount of thin plies within the stack. Shifting from a 100% conventional ply laminate to a 100% thin-ply laminate gave an increase of 47% in the strength at onset of damage.

The current study sets out to evaluate the performance of thin-ply material, specifically in bearing strength, in a series of laminates manufactured with a single material system.

2. Layups and testing

2.1. Material selection and layups

This study consists of 3 materials provided by the Swedish SME Oxeon: Textreme 80 (thin-ply), Textreme 160 (thin-ply), and UD (thick-ply). For a volume fraction about 60%, the thickness of one layer of Textreme 80 (T80), Textreme 160 (T160) and UD (thick-ply) is 40 micrometers, 80 micrometers and 128 micrometers respectively.

With a combination of thick and thin plies, the following 5 laminates were manufactured in an autoclave.

Laminate ID 1: This laminate is made of 50% Textreme 80 (T80) and 50% of 100%UD thick-ply.

Laminate ID 2: This laminate is completely made of Textreme 80 (T80) which is 100% T80 thin-ply.

Laminate ID 3: This laminate is made of 100% UD which is 100% thick-ply.

Laminate ID 4: This stack consists of 100% Textreme 160 (T160) which is 100% T160 thin-ply.

Laminate ID 5: This laminate is made of 50% Textreme 160 (T160) and 50% of 100% UD thick-ply.

Table 1 shows the layups used in testing. UD thick-ply is showed in bold text.

1000/1211 ©2022 Loukil et al. doi:10.5075/epfl-298799_978-2-9701614-0-0 published under CC BY-NC 4.0 license

Table 1: Layups description for laminates tested.

Laminate ID	Materials used	Lay-up
1	50% T80	$[((0/90)/\mathbf{45}/(0/90)/\mathbf{-45}/(0/90))_3]s$
2	100% T80	$[((0/90)/(45/-45))_{10}]s$
3	100% UD	$[(\mathbf{0/90/45/-45})_3]s$
4	100% T160	$[((0/90)/(45/-45))_5]s$
5	50% T160	$[((0/90)/\mathbf{45/-45}/(0/90)/\mathbf{45/-45}/(0/90))_{1,5}]s$

2.2. Bearing test and standards

Bearing strength is defined as the maximum stress load that the unit can bear before the structure fails. The bearing stress of the composite laminate at each data point is calculated using the equation 1.

$$\sigma = \frac{P}{k*D*h} \quad (1)$$

Where σ is the bearing stress, P is the bearing force, k is the force per hole factor, D is the hole diameter, h is the thickness of the test specimen.

Ultimate bearing strength F is calculated according to the equation 2.

$$F = \frac{Pmax}{k*D*h} \quad (2)$$

Where *Pmax* is the maximum applied bearing force prior to bearing failure.

All mechanical testing process follows a particular standard. Here, bearing test is performed according to ASTM D5961. This standard consists of 4 different procedures A, B, C, D. And amongst these, procedure A, double-shear tensile loading as in figure 1 is used.

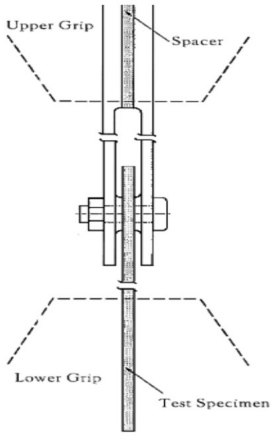

Figure 1: Bearing test assembly.

According to this procedure, a flat, constant rectangular cross-section specimen with the centerline hole is located near the end of the specimen and is loaded at the hole in the bearing. The bearing force is created by loading the assembly in tension in a testing machine.

3. Results

3.1. Bearing tests

The main aim of the work was to investigate the bearing strength of all the five layups mentioned above.

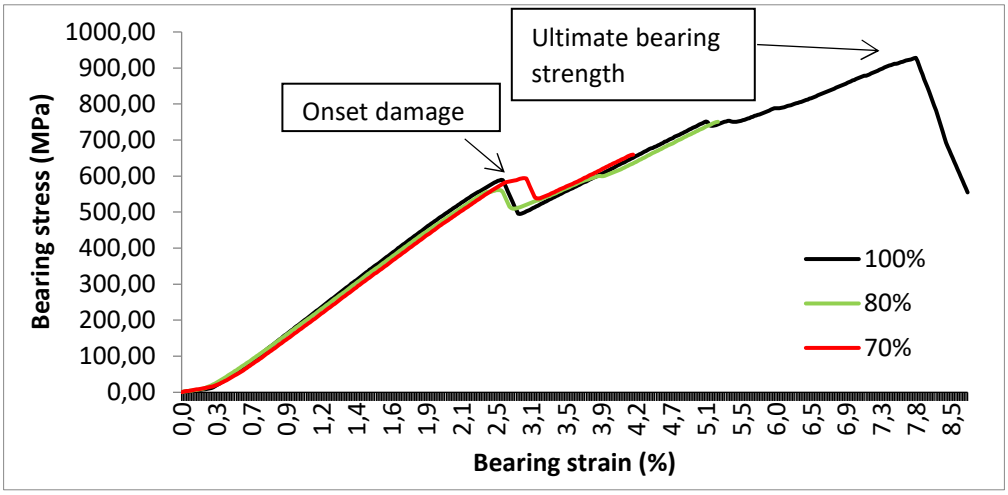

Figure 2: Bearing stress/strain curve of 100% T80 loaded at 70%, 80% and 100% of its ultimate load.

Figure 2 shows the example of the bearing stress/strain curve of materials which were loaded up to 70%, 80% and 100% of each layup's ultimate strength.

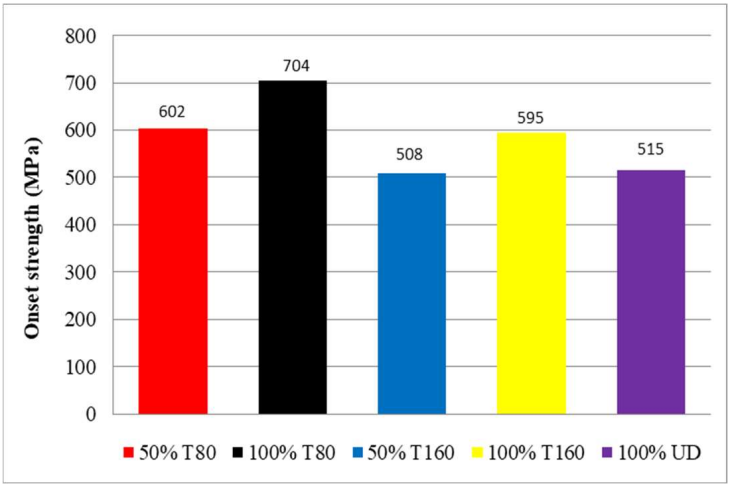

Figure 3: Onset strength of all layups

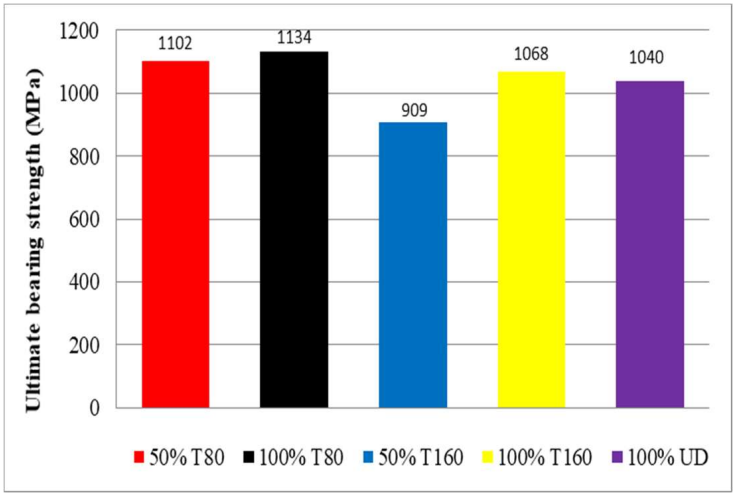

Figure 4: Ultimate bearing strength of all layups.

  doi:10.5075/epfl-298799_978-2-9701614-0-0

The Figure 3 and Figure 4 show the graph of onset strength and ultimate bearing strength (UBS) respectively of all the five layups obtained after the compensation made with respect to fiber volume fraction. It is clearly seen from the compiled data that the values of onset strength and the UBS of 100% T80, with completely thin plies is the highest.

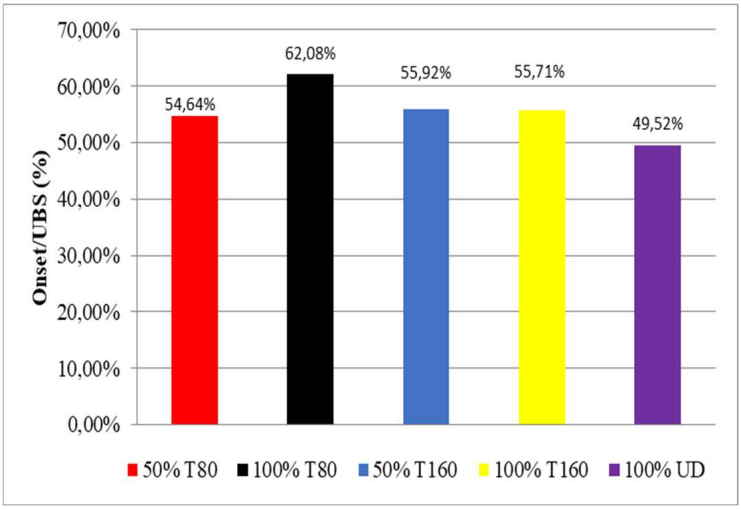

Figure 5: Ratio of onset strength to ultimate bearing strength for all layups.

Figure 5 shows the ratio of the onset strength to ultimate bearing strength. It is seen that 100% T80 has the higher ratio i.e, the onset strength to ultimate bearing strength of the layup is 62% of the ultimate strength which is a very good value as the layup can take more load within the elastic limit when compared to the other layups and this is the biggest advantage of using the thin plies. All Textreme layups used in this work i.e, 50% T80, 50% 160, 100% T160 are under the same group as they have the onset strength 55% of its ultimate strength.

3.2. Microscopic failure analysis

The main objective in this section is to investigate damages at the initial point of failure and to characterize the modes of failure present in the tested specimen.

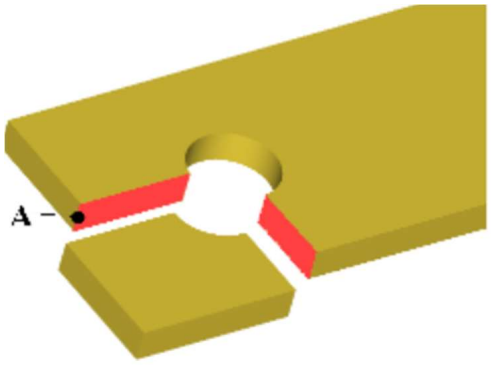

Figure 6: Area investigated with the optical microscope for damage.

Point A in Figure 6 shows the edge where the specimens are investigated for damage under the optical microscope.

  doi:10.5075/epfl-298799_978-2-9701614-0-0

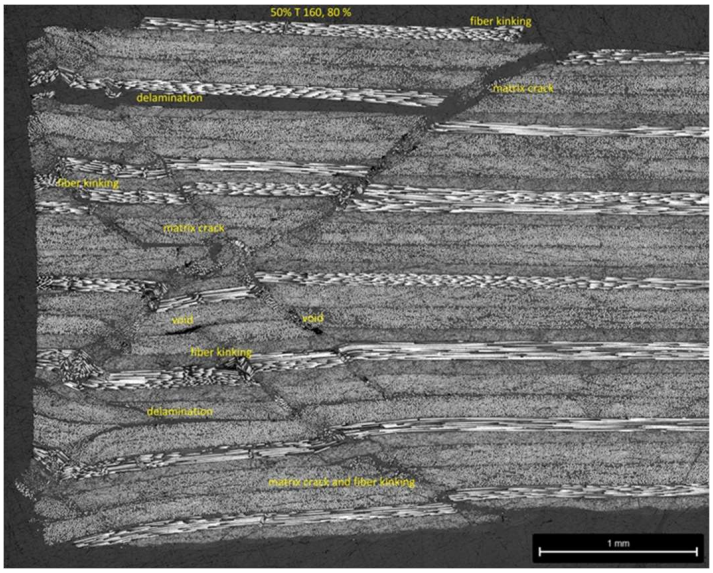

Figure 7: Fractography of 50% T160 and the damages caused at 80% of its ultimate loading.

An example of microscopy image for laminate ID5 is showed in Figure 7. Fiber kinking combined with transverse cracks and delamination were observed as the main failure modes close to the hole for all samples. The interaction between these failure mechanisms forms shear cracks along the whole thickness. Similar failure modes were detected by [16,17] where damage in composite laminates was investigated as a function of applied loads in bolted joint specimens. It was shown that at very high applied bearing stress, both matrix cracking and fiber kinking were observed.

3.3. Transition zone of hybrid laminates

As it is shown above, the use of thin plies is beneficial, the most obvious solution to increase the bearing strength is to use a laminate with 100% thin plies. This strategy has some obvious drawbacks in terms of cost. Thin-ply materials are considered more expensive than conventional standard thickness pre-preg materials. If thin-ply is used for a part, more layers are needed for the same total thickness and thus more time is required in production. For applications where performance is paramount, but costs are still required to be competitive, it would be desirable to achieve a hybrid solution, where thin plies are used where they can contribute the most performance to the structure and conventional plies are used otherwise. In this section, transition zone is introduced where both thin and thick plies are designed so that the thin plies are used only when more strength is required. Laminates with three different types of joints (Overlap joint, Butt joint and Edge joint) were considered as it is showed in Figure 8. In this case, to the left is the thin-ply and to the right is the thick-ply.

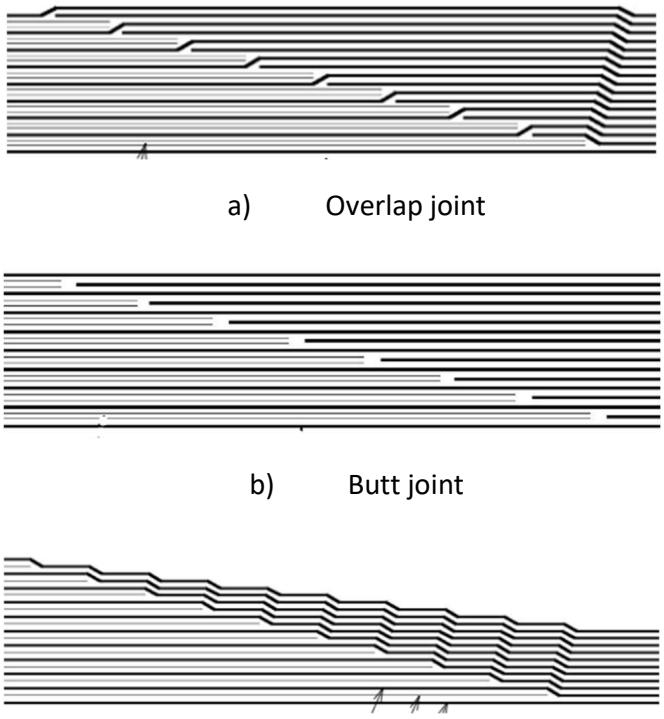

a) Overlap joint

b) Butt joint

c) Edge reinforcement

Figure 8: Types of joints used in the transition zone

Specimens were prepared and tested to determine the tensile strength. Out of seven specimens, five were loaded up to their ultimate strength and the rest is loaded up to 70% of their ultimate load to check for the damages. It was clearly shown that the specimens do not display any onset damage, so it was difficult to see the growth of damage, and there was no apparent damage present in the specimens.
The results are presented in Table 2, where edge reinforcement shows the highest strength.

Table 2: Tensile stress and maximum load values obtained from the tensile test.

Material used and the join method	Maximum load (kN)	Tensile stress at max load (MPa)	Total thickness of layup (mm)
UD thick +T160, lap joint	38.8	502	3.1
UD thick+T160, butt joint	38.19	501	3.04
UD thick +T160, edge reinforcement	32.73	843	1.55

4. Conclusion

Using a double lap shear loading setup, the rectangular test specimens with different lay-up sequences were loaded into the bearing through the fastener. 100% T80 outperformed all layups with highest onset strength of 704.03MPa and highest ultimate bearing strength of 1134.13MPa when compared to all five layups. Fiber kinking combined with transverse cracks

  doi:10.5075/epfl-298799_978-2-9701614-0-0

and delamination were observed as the main failure modes close to the hole for all samples. Transition zone was investigated where both thin and thick plies were designed so that the thin plies are used only when more strength is required, and the highest strength was obtained for edge reinforcement.

5. References

1. Berthelot JM. Transverse cracking and delamination in cross-ply glass-fiber and carbon-fiber reinforced plastic laminates: static and fatigue loading, Applied Mechanics Review 2003; 56(1):111-147.
2. Kashtalyan M, Soutis C. Analysis of composite laminates with intra and intrelaminar damage, Progress in Aerospace Sciences 2005; 41:152-173.
3. Varna J, Berglund LA. Thermo-elastic properties of composite laminates with transverse cracks. Journal of Composites Technology & Research 1994; 16:77-87.
4. Varna J, Berglund LA. Multiple transverse cracking and stiffness reduction in crossply lamintes. Journal of Composites Technology & Research 1991; 13:2 97-106.
5. Loukil MS, Varna J, Ayadi Z. Engineering expressions for thermo-elastic constants of laminates with high density of transverse cracks, Composite Part A: Applied Science and Manufacturing 2013; 48(1):37-46
6. Parvizi A, Garrett KW, Bailey JE. Constrained cracking in glass fibre-reinforced epoxy cross-ply laminates. Journal of Materials Science 1978; 13:195-201
7. Dvorak GJ. Analysis of first ply failure in composite laminates. Engineering Fracture Mechanics 1986; 25:763-770
8. Sihn S, Kim RY, Kawabe K, Tsai SW. Experimental studies of thin-ply laminated composites. Composites science and technology 2007; 67:996-1008
9. Yokozeki T, Kuoda A, Yoshimura A, Ogasawara T, Aoki T. Damage characterization in thin-ply composite laminates under out-of-plane transverse loadings Composite structures 2010; 93:49-57
10. Saito H, Takeuchi H, Kimpara I. Experimental evaluation of the damage growth restraining in 90 layer of thin-ply CFRP cross-ply laminates. Advanced composite Materials 2012; 21:57-66
11. Camanho PP, Davila CG, Pinho ST, Iannucci L, Robinson P. Prediction of in situ strengths and matrix cracking in composites under transverse tension and in-plane shear, Composites Part A: Applied Science and Manufacturing 2006; 37:165-176.
12. Arteiro A, Catalanotti G, Melro A, Linde P, Camanho P. Micro-mechanical analysis of the in situ effect in polymer composite laminates, Composite Structures 2014; 116:827-840.
13. Amacher R, Cugnoni J, Botsis J, Sorensen L, Smith W, Dransfeld C. Thin ply composites: Experimental characterization and modelling of size effects. Composites science and technology 2014; 101:121-132
14. Furtado C, Arteiro A, Catalanotti G, Xavier J, Camanho PP. Selective ply-level hybridisation for improved notched response of composite laminates. Composite Structures 2016; 145:1-14
15. Arteiro A, Catalanotti G, Xavier J, Linde P, Camanho PP. A strategy to improve the structural performance of non-crimp fabric thin-ply laminates, Composite Structures 2018; 188:438-449
16. Cameron CJ, Larsson J, Loukil MS, Murtagh T, Wennhage P. Bearing strength performance of mixed thin/thick-ply quasi-isotropic composite laminates. Composite Structures 2021; 261:113312.
17. Camanho PP, Lambert MA. Design methodology for mechanically fastened joints in laminated composite materials. Compos Sci Technol 2006; 66:3004-20.

  doi:10.5075/epfl-298799_978-2-9701614-0-0

ASSESSMENT OF ALUMINUM FOILS INTERLEAVING ON THE CRYOGENIC IMPACT RESPONSE OF CFRPs: CROSS-PLY, THIN-PLY AND HYBRID CONFIGURATIONS

Claudia, Sergi [a], Nicola, Ierardo [b], Luca, Lampani [c], Andrea, Calzolari [d], Teodoro, Valente [a], Fabrizio, Sarasini [a], Jacopo, Tirillò [a]

a: Department of Chemical Engineering Materials Environment, Sapienza University of Rome & UdR INSTM (Rome, IT), claudia.sergi@uniroma1.it
b: European Space Agency – Space Transportation Systems – VEGA and Space Rider Engineering ESA-ESRIN
c: Department of Mechanical and Aerospace Engineering, Sapienza University of Rome
d: ITW Test and Measurement Italy, Instron CEAST Division

Abstract: *The aerospace field benefited from CFRPs extraordinary mechanical properties to develop lighter components, like cryogenic pressure vessels. The main issue with the production of CFRP cryogenic tanks is the reduction of fuel leakages due to percolation phenomena. This work assessed two strategies in an attempt to decrease walls permeability while preserving CFRPs impact response in cryogenic conditions. The first strategy envisaged the manufacturing of different CFRPs configurations characterized by the same thickness, but a different plies number. It was observed that thin-plies display an impact resistance much lower than traditional CFRPs, but the use of sandwich-like laminates, where thin-plies form the inner core, allows to increase plies number while preserving composite mechanical properties. The second strategy entailed aluminum foil interleaving which does not influence laminates impact response, but slightly reduces their residual flexural properties. This problem can be fixed by increasing aluminum surface roughness and resulting mechanical interlocking with the matrix through oxidation treatments.*

Keywords: CFRP, Aluminum foils interleaving, low-velocity impact, cryogenic conditions, damage tolerance

1. Introduction

Thanks to a successful combination of lightness and high mechanical properties, polymer matrix composites are widespread in most industrial sectors such as automotive, naval, aviation and aerospace. The main goal of all these fields is to decrease structures weight while preserving stiffness and strength. In 1970s, the aerospace industry identified the great potential of polymer composites for the substitution of aluminum in cryogenic pressure vessel production thus funding many research studies on glass fiber reinforced epoxy [1].

Meanwhile, high-strength and high-modulus carbon fibers were progressively developed [2] and, as a result of their unparalleled high specific mechanical properties, they became a cornerstone in high-technology industries such as aerospace for the development of carbon fiber reinforced polymers (CFRPs) [3]. Despite their unique mechanical performance, CFRPs are characterized by a poor interlaminar fracture toughness which makes them dramatically prone to impact damage. This weakness becomes even more critical in severe conditions like the ones

  doi:10.5075/epfl-298799_978-2-9701614-0-0

reached in cryogenic propellant tanks [4,5]. Furthermore, cryogenic pressure vessels must be designed to minimize propellant leakages by reducing their permeability throughout the walls.

To this aim, the present work evaluated different CFRP configurations to minimize propellant leakages while preserving the impact strength of the composites. Bechel and Kim [6] and Sandoval Rosales [7] demonstrated that thin-ply configurations are characterized by a higher resistance to crack initiation under cyclic stress, included thermal cycling, than traditional CFRPs. At the same time, thin ply CFRPs display a completely different impact damage mode, i.e., an early fiber breakage due to delamination delay and matrix cracking, which significantly reduces their impact resistance [8]. In light of this, the hybridization of plies with different thickness might be a suitable way to reduce propellant permeability while preserving structure integrity as a consequence of impact events. In this sense, Sasikumar et al. [9] provided some preliminary results carrying out impact tests at room temperature. In this study plies hybridization feasibility was assessed in cryogenic impact conditions, performing tests at room temperature, -40 °C and -70 °C and considering three different CFRP configurations, i.e., standard plies (RC), thin plies (TP) and sandwich-like configurations.

Another approach to prevent propellant leakages through tank walls entails the introduction of metallic barriers throughout the composite laminates. Wei et al. [10] assessed the feasibility of aluminum foils interleaving on CFRP laminates for cryogenic propellant tanks disclosing an increase of 15 times in CFRP gas barrier properties. In view of this, aluminum foils interleaving was assessed in the present work for all CFRP configurations evaluating its effect on laminates impact response at room temperature and in cryogenic conditions.

Furthermore, Wei et al. proved that aluminum oxidation through NaOH treatment allows to increase foils surface roughness thus improving the interfacial strength with the carbon prepregs through mechanical interlocking. In the present study, aluminum oxidation was optimized, and the treated foils were interleaved in the three CFRP configurations to assess their impact response always at room temperature and in cryogenic conditions.

The impact campaign was supported by a post-impact analysis to evaluate composite damage extent, i.e., permanent indentation and delaminated area, through profilometry and C-scan, and their residual mechanical properties through 4-point bending tests.

2. Materials and methods

2.1 Materials and composites manufacturing

All CFRP laminates were manufactured by vacuum bagging and cured in autoclave using a cross-ply configuration [0/90]. Standard plies laminates used as reference (RC) were manufactured with the unidirectional carbon/epoxy prepreg Arovex®180 (150 g/m^2) provided by Zyvex Technologies, while thin-ply laminates (TP) were manufactured with the unidirectional carbon/epoxy prepreg ThinPregTM 402 (30 g/m^2) provided by North Thin Ply Technology. In particular, RC laminates were produced with 16 plies according to $[0/90]_{4s}$ stacking sequence while TP laminates were produced with 60 plies according to $[0/90]_{15s}$ stacking sequence. Concerning hybrid sandwich-like laminates, the outer layers of the composite were manufactured with 4 plies of RC each, while the core of the laminates was manufactured with 30 plies of TP according to the configuration shown in Figure 1. The average thicknesses of the laminates are 1.85 mm for RC, 1.87 mm for TP and 1.82 mm for sandwich-like.

  doi:10.5075/epfl-298799_978-2-9701614-0-0

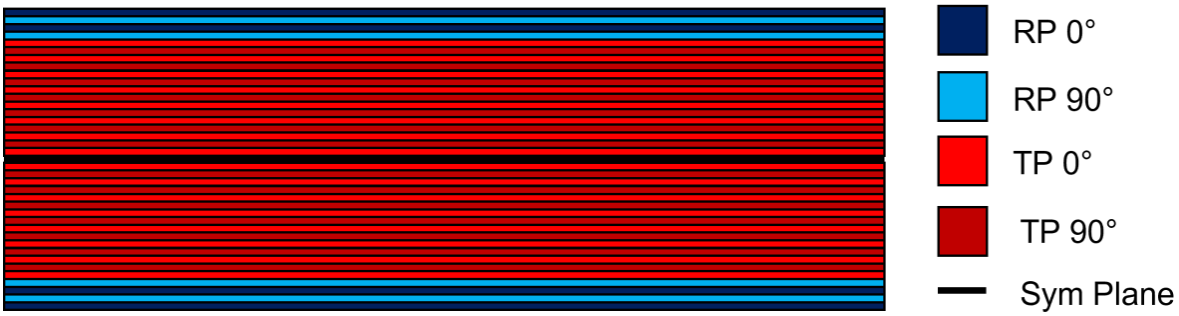

Figure 1: Sketch of the hybrid laminates with the sandwich-like configuration. RP: Regular-Ply, TP: Thin-ply

The aluminum interleaved laminates were produced by inserting four aluminum foils in each composite according to stacking sequence [0/90/0/90/0/90/i/0/i/90]s for RC laminates, stacking sequence $[0/90/i/0/90/0/90/i/0/90/0/90]_S$ for the twenty central plies of TP laminates and stacking sequence $([0/90/0/90]_{RC}/i/[0/90/0/90]_{TP}/i/[0/90/0/90/0/90/0]_{TP})_S$ for hybrid sandwich-like composite. Aluminum foils with a 10 μm thickness were used to keep as constant as possible specimens' thickness. In particular, average variations of 80 μm in the overall thickness were observed for all laminate configurations.

Aluminum foils oxidation was carried out through NaOH water solution at different operating temperatures, times and solution concentrations in order to optimize surface roughness while preserving foil integrity. The three different treating conditions employed are summarized in Table 1.

Table 1: Operating conditions used to carry out aluminum oxidation.

Temperature / **Concentration**	**25 °C**	**65 °C**
0.2 M		X (30 seconds)
1.25 M	X (30 seconds)	X (20 seconds)

The best results were achieved with the 1.25 M concentration and the 25 °C temperature which allow to obtain an increase of 92.5 % in Ra roughness and of 113 % in Rq roughness with respect to the as-received aluminum foils, while preventing the formation of undesired residual oxidative products. These treatment parameters were selected to oxidize the aluminum foils destined for CFRP interleaving.

2.2 Impact and post-impact analysis

Impact tests were performed in a Instron drop weight tower at room temperature, -40 °C and -70 °C. Samples were pre-conditioned for 1 hour at the testing temperature. A hemispherical impactor of 12.7 mm diameter and a circular sample holder with an unsupported area of 40 mm were used. Specimens with a length of 150 mm and a width of 100 mm were used, as per the typical puncture and damage impact tests requirement for automotive testing protocols. The impact energy levels used for each configuration are summarized in Table 2. All configurations available were tested at 5 J to have a direct comparison of laminates impact response, damage extent and residual mechanical properties.

Table 2: Impact energy levels used for each CFRP configuration.

Aluminum Interleaving / Configuration	None	Untreated Aluminum	Oxidized Aluminum
RC	5 J, 7.5 J	5 J	5 J
TP	2.5 J, 5 J	2.5 J, 5 J	2.5 J, 5 J
Sandwich-like	5 J, 7.5 J	5 J	5 J

Laminates damage extent was assessed through profilometry and C-scanning. In particular, permanent indentation depth was evaluated through a laser profilometer by Taylor Hobson while delaminated areas were evaluated through OmniScan MX2 ultrasonic scan. Finally, the residual flexural properties were evaluated according to ASTM D6272 through 4-point bending tests performed in a Zwick/Roell Z010 machine with a support span of 120 mm, a load span of 60 mm and a test speed of 2.5 mm/min.

3. Results and discussion

3.1 CFRP configurations comparison

The first aim of the work was to assess ply thickness hybridization to increase plies number in the laminates to minimize propellant leakages while preserving the impact performance. Figure 2 shows the force-time and energy-time curves of all CFRP configurations impacted at room temperature and -70 °C. TP structures are characterized by an impact response completely different from RC ones as already acknowledged in many research works (8). In particular, they display a much lower peak force and a much higher contact time. This must be ascribed to the intrinsic lower bending stiffness of TP laminates, almost 30 % lower, which entails a lower capacity of the material to store energy elastically due to the lower elastic limit. This strong difference in behavior must be also due to the different damage mechanism of the two types of laminates, as confirmed by the damage mode shown in Figure 3. The first energy dissipation mechanism in standard plies RC is delamination, which does not affect fiber or matrix integrity thus preserving the elastic response of the material. On the contrary, TPs are characterized by an improved interlaminar strength and dissipate energy mainly through fibers breakage thus preventing their elastic response and leading sooner to material penetration.

The penetration of impactor in TP laminates causes a higher permanent indentation which is 7.5 and 14.5 times higher than RC ones at room temperature and -70 °C, respectively. This analysis is further corroborated by energy evolution as a function of time at 5 J. In fact, RC configuration absorbs only a scant amount of the impact energy thus confirming the elastic response of the laminates while TP configuration absorbs almost all the impact energy thus leading to the premature penetration of the laminates.

Observing sandwich-like composites response curves and damage mode, it is possible to acknowledge a behavior closer to RC meaning that this configuration is actually an effective solution to increase the number of plies in the composite without affecting excessively the impact performance of the laminate. Moreover, sandwich-like composites are characterized by superior residual flexural strength with respect to RC ones, thus ensuring improved reliability in case of impact events.

  doi:10.5075/epfl-298799_978-2-9701614-0-0

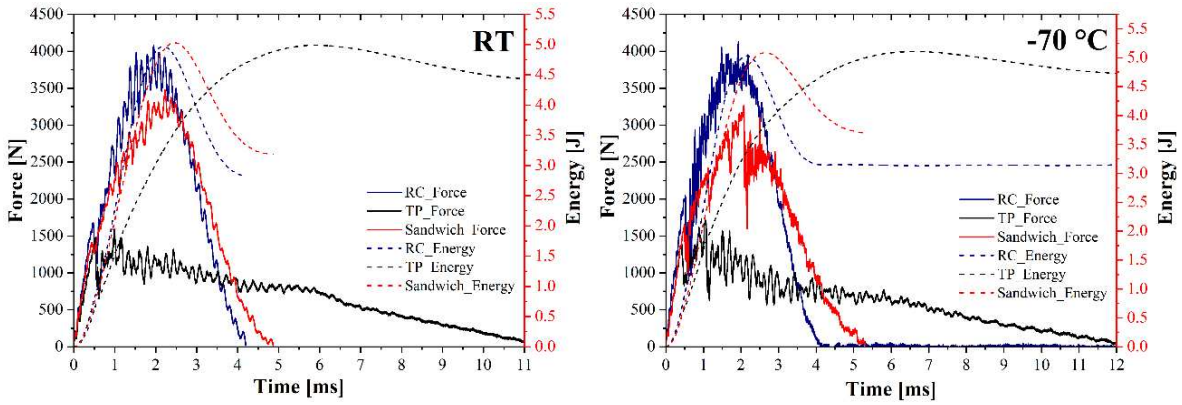

Figure 2: Force-Time and Energy-Time curves of RC, TP and Sandwich configurations impacted at 5 J at room temperature and -70 °C

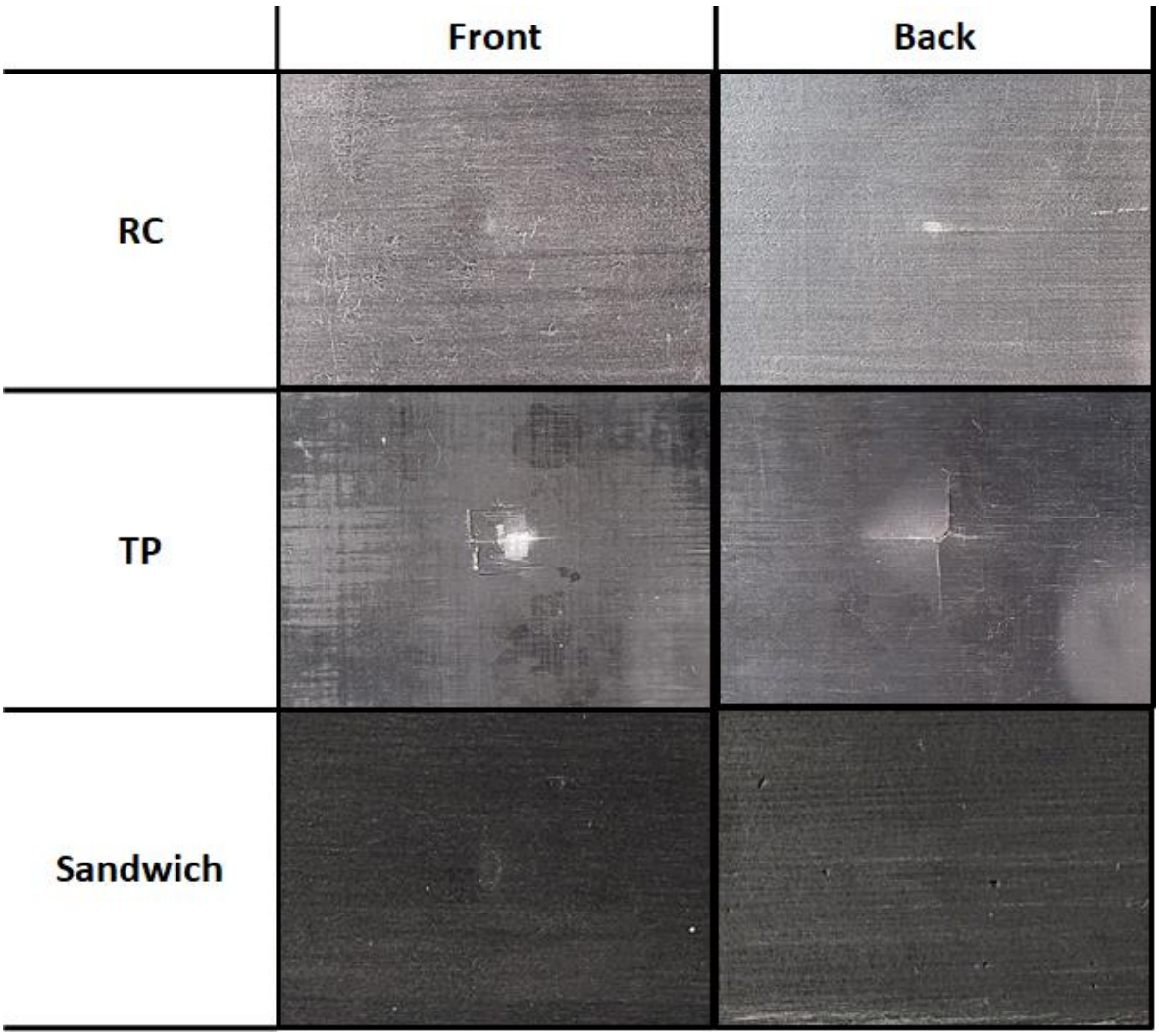

Figure 3: Damage mode of RC, TP and sandwich-like composites after a 5J impact at room temperature

  doi:10.5075/epfl-298799_978-2-9701614-0-0

3.2 Aluminum interleaving effect

As demonstrated by the impact response curves shown in Figure 4, aluminum foils interleaving does not alter laminates impact response, and no significant changes can be detected for neither as-received nor oxidized aluminum foils. Concerning the post-impact response, as-received and NaOH treated foils do not modify substantially the damage mode and the residual flexural properties of TP laminates while some differences can be observed for RC ones. In particular, non-treated aluminum slightly decreases the residual flexural strength of the composites probably due to an easier propagation of impact induced cracks at foil prepreg interface. This phenomenon is reduced with oxidized aluminum which ensures the same residual flexural properties of non-interleaved RCs thanks to the higher surface roughness that promotes the mechanical interlocking with the epoxy matrix. This means that oxidized aluminum is an effective strategy to reduce fuel leakage without jeopardizing the impact and post-impact performance of the composite structure.

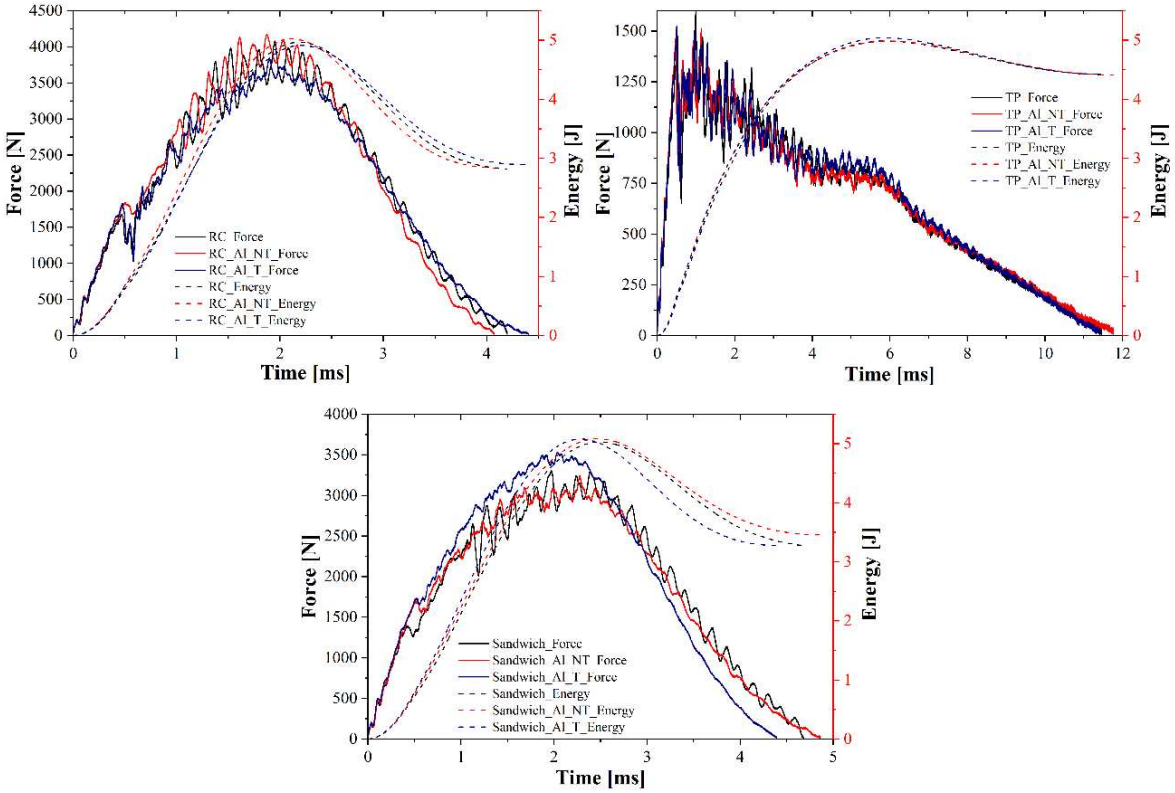

Figure 4: Force-Time and Energy-Time curves of RC, TP and Sandwich configurations without Al foil interleaving, with as received Al interleaving (NT) and oxidized Al (T) interleaving impacted at 5 J at room temperature

4. Conclusions

The present work assessed two different strategies two reduce fuel permeability and leakages in CFRPs composites, meant to cryogenic pressure vessel manufacturing, while preserving their impact and post-impact properties which are the main point of weakness of these materials. In particular, the effect of plies number and thickness was investigated through different CFRPs configurations, i.e., RC, TP and hybrid sandwich-like, together with the effect of aluminum foils interleaving.

  doi:10.5075/epfl-298799_978-2-9701614-0-0

Concerning the effect of plies number and thickness, it was proved that thin plies are characterized by a much lower impact strength than traditional CFRPs with the same thickness both at room temperature and in cryogenic conditions and this must be ascribed to a drastic change in the damage mode. At the same time, sandwich-like hybrid laminates, produced with a thin plies inner core and traditional CFRPs skins, are able to ensure an impact response and residual flexural properties comparable with RC ones thus preserving the overall mechanical performance while increasing plies number to prevent fuel loss.

Considering the effect of aluminum foils interleaving, it is possible to conclude that it does not affect substantially the impact response of CFRPs and it allows to retain the same residual flexural strength as a consequence of NaOH treatment. Oxidation increases aluminum surface roughness thus promoting mechanical interlocking with CFRP prepregs and increasing the energy necessary for crack propagation.

In conclusion, sandwich-like CFRPs interleaved with oxidized aluminum foils are an interesting solution to improve cryo-tanks retaining performance while preserving their mechanical functionality.

Acknowledgements

The activities described in the present paper have been carried out in the frame of the VEGA-Evolution preparatory program under the authority of the European Space Agency. The authors thank and acknowledge the Agency for the given support.

5. References

1. Kasen MB. Mechanical and thermal properties of filamentary-reinforced structural composites at cryogenic temperatures 1: Glass-reinforced composites. Cryogenics (Guildf). 1975;327–49.

2. Park SJ, Lee S-Y. History and structure of carbon fibers. In: Carbon Fibers. Springer, Dordrecht; 2015.

3. Morino Y, Shimoda T, Morimoto T, Ishikawa T, Aoki T. Applicability of CFRP materials to the cryogenic propellant tank for reusable launch vehicle (RLV). Adv Compos Mater. 2001;10(4):339–47.

4. Gomez-del Rıo T, Zaera R, Barbero E, Navarro C. Damage in CFRPs due to low velocity impact at low temperature. Compos Part B. 2005;36:41–50.

5. Aoki T, Ishikawa T, Kumazawa H, Morino Y. Cryogenic mechanical properties of CF/polymer composites for tanks of reusable rockets. Adv Compos Mater. 2001;10(4):349–56.

6. Bechel VT, Kim RY. Damage trends in cryogenically cycled carbon/polymer composites. Compos Sci Technol. 2004;64(12):1773–84.

7. Sandoval Rosales BA. Thin-ply CFRP for cryogenic fuel tank applications. 2019.

8. Arteiro A, Furtado C, Catalanotti G, Linde P, Camanho PP. Thin-ply polymer composite materials: A review. Compos Part A Appl Sci Manuf. 2020;132(105777).

9. Sasikumar A, Trias D, Costa J, Blanco N, Orr J, Linde P. Effect of ply thickness and ply

level hybridization on the compression after impact strength of thin laminates. Compos Part A Appl Sci Manuf [Internet]. 2019;121:232–43. Available from: https://doi.org/10.1016/j.compositesa.2019.03.022

10. Wei R, Wang X, Chen C, Zhang X, Xu X, Du S. Effect of surface treatment on the interfacial adhesion performance of aluminum foil / CFRP laminates for cryogenic propellant tanks. Mater Des [Internet]. 2017;116:188–98. Available from: http://dx.doi.org/10.1016/j.matdes.2016.12.011

  doi:10.5075/epfl-298799_978-2-9701614-0-0

IMPACT PERFORMANCE OF OUT OF DIE UV CURED PULTRUDED PROFILES FOR VESSEL STRUCTURES

Imanol, Ruiz de Eguino[a]; Ivan, Saenz-Dominguez[b]; Iosu, Tena[a]; Ander, Arruti[a]; Mariasun, Sarrionandia[a]; Jon, Aurrekoetxea[a]*

a: Mechanical and Industrial Production Department, Mondragon Unibertsitatea, Loramendi 4, 20500, Mondragón, Spain
b: Irurena Group, Ctra. de Tolosa s/n, 20730, Azpeitia, Spain

* Corresponding author: iruizdeeguino@mondragon.edu

Abstract: *Out of die ultraviolet (UV) cured pultrusion is an automated process for manufacturing bent profiles that can replace the labour-intensive processes currently employed for manufacturing stiffeners for vessels structures. As the applied pulling forces are lower than in conventional pultrusion, profiles with low longitudinal fibre content can be manufactured, improving the transverse mechanical properties of the pultruded composites. Since impact response is significantly relevant for naval applications, in this paper, the low-velocity impact performance of a multiaxially reinforced UV pultruded profile has been compared to that of a typical pultruded composite. The impact resistance achieved for the multiaxial reinforcement configuration showed an 85% higher perforation energy threshold and a 100% higher maximum peak force than in the reference one. The damage tolerance of the multiaxial configuration was also higher, as when suffering a 30 J impact retained 60% of the stiffness, whereas the conventional pultruded composite only did 45%.*

Keywords: Impact behaviour; Pultrusion; Reinforcement configuration; UV curing; Damage tolerance

1. Introduction

The manufacturing processes currently employed in composite vessels are eminently manual, representing a high production cost for the shipyards. Moreover, the applied manufacturing technologies require highly skilled labour, present low production rates, and do not ensure repeatable mechanical properties, negatively affecting the robustness of the process. The consequences of these issues become even more noticeable in the specific case of the vessel hull or superstructure. These structures consist of a stiffened skin where each stiffener must have a different geometry adapted to the required shape. The stiffening profiles are manufactured by manually laminating over expanded polyurethane preforms, which are previously machined to the specified geometry and bonded to the skin [1]. The lack of robustness of this process leads to the oversizing of the vessel structures, not to mention that preforms do not have any function in service. Therefore, introducing automated and flexible technologies for manufacturing composite vessel structures would provide a competitive advantage to the European shipyards.

Pultrusion is one of the most automated and productive processes for manufacturing composite profiled shapes [2]. However, their use is limited because just straight or constant radius

stiffeners can be manufactured by thermally cured pultrusion [3–7]. A feasible option for manufacturing profiles with a variable curvature is curing the pultruded composite out of the die by employing UV radiation. This approach is implemented in the out of die UV cured pultrusion technology [8,9]. Additionally, the pulling forces applied in this process are lower than in conventional pultrusion since the profile is cured out of the die. Thus, the amount of fibre reinforcement that must be oriented towards the longitudinal direction to bear with the applied pulling force can be reduced. Therefore, pultruded profiles manufactured by out of die UV cured pultrusion can offer enhanced transverse mechanical properties as more fibre reinforcement can be placed with that orientation. This feature is especially beneficial for naval applications, where stiffeners have to be able to withstand complex loading conditions, as well as being exposed to unintended impacts.

Hence, the present paper analyses how the impact response of stiffeners could be improved when taking advantage of the greater freedom for defining the profiles reinforcement configuration provided by out of die UV cured pultrusion. For doing so, a multiaxially reinforced pultruded composite made of quadriaxial non-crimp fabrics and unidirectional roving has been subjected to drop weight low-velocity impact tests. The impact behaviour reported for this reinforcement configuration has been compared to that of a typical pultruded composite. The peak load evolution, the damage, penetration and perforation thresholds, and the after impact residual stiffness of both reinforcement configurations have been experimentally determined to perform such a comparative study.

2. Methodology

2.1 Materials

The pultruded composites analysed in the present study were made of a photocurable vinyl ester acrylate resin provided by Irurena Group (IRUCRIL GFR-30 LED) and had a 3 mm thick and 75 mm wide flat plate geometry. The two different reinforcement configurations, illustrated in Figure 1, were tested. A reinforcement configuration consisting of a thick roving (4800 TEX) central layer surrounded by stitched continuous strand mat (CSM) tapes (300 g/m^2) typically employed in conventional pultrusion [10–12] was set as a reference; while the multiaxial reinforcement configuration had a thinner roving (4800 TEX) core with two quadriaxial non-crimp fabric tapes (600 g/m^2) placed on each side. The mat tapes in the reference configuration are 25 % of its reinforcement, while the multiaxial configuration has a 40 % of the fibre reinforcement placed in non-longitudinal orientations.

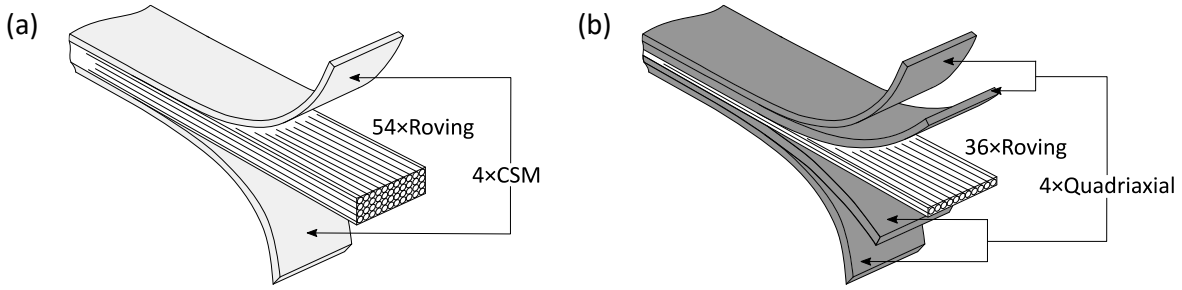

Figure 1. Reinforcement of the studied pultruded laminates: (a) reference and (b) multiaxial configuration.

1016/1211 doi:10.5075/epfl-298799_978-2-9701614-0-0

2.2 Manufacturing process

The out of die UV cured pultrusion (Robtrusion®) line developed by the Polymer and Composites Technology Research Group from Mondragon University and Irurena Group was used for manufacturing the tested composites. This machine uses a resin open bath to impregnate the fibre reinforcement, which is then shaped and compacted in a die with a 100 mm length. Two FireJet FJ240 UV LED sources (Phoseon) placed at the top and bottom of the profile right at the exit of the die are used to cure the composite. A KR 510 R3080 (Kuka) robot arm is employed to pull the profile following a straight path with a velocity of 1.2 m/min.

To ensure that all the tested specimens had the same curing degree, they were subjected to a post-curing of 3 hours at a temperature of 100 ºC. Additionally, the ASTM D3171 standard was followed to experimentally determine the fibre, resin, and void volumetric content in order to assure that the quality of both analysed reinforcement configurations was alike.

2.3 Low-velocity impact tests

A drop weight Fractovis-Plus (CEAST) machine was used to perform the low-velocity impact tests. Initial drop heights ranging from 50 mm to 1000 mm and striker masses from 2 kg to 20 kg were set to define the applied incident impact energies ranging from 1 J to 200 J. A clamping ring with 40 mm inner and 60 mm outer diameters held the square specimens cut from the manufactured profiles during the impact events. These specimens were impacted with a 20 mm diameter hemispherical instrumented striker equipped with a 20 kN load cell, and an anti-rebound system ensured that they were impacted just once. The progress of the contact force generated between the striker and the specimen during the impact event was reported. The absorbed energy was computed by integrating the force versus time curves [13] following the next equations,

$$a(t) = \frac{F(t)}{m} \cdot \mathrm{g} \tag{1}$$

$$v_0 = \sqrt{2\mathrm{g}h} \tag{2}$$

$$v(t) = v_0 + \mathrm{g}t - \int_0^t \frac{F(t)}{m} dt \tag{3}$$

$$\delta(t) = v_0 t + \frac{\mathrm{g}t^2}{2} - \int_0^t \frac{F(t)}{m} d^2 t \tag{4}$$

$$E(t) = \int_0^{\delta(t)} F(\delta) d\delta \tag{5}$$

where $F(t)$ is the contact force curve, $a(t)$ is the acceleration experienced by the impactor, m is the mass of the impactor, g is the gravitational acceleration, t is the time, v_0 is the initial impactor velocity, h is the initial height of the impactor, $v(t)$ is the impactor velocity curve, $\delta(t)$ is the specimen deflection and $E(t)$ is the absorbed energy curve.

A multi-parameter analysis has to be addressed to assess the impact behaviour of composites [14]. Usually, the peak force and dissipated energy as a function of the incident impact energies are reported. But additionally, the three-impact test method proposed by Feraboli *et al.* [14] was applied in this work. This method is based on the fact that the contact time experienced for a subcritical impact is a property of the striker and specimen stiffness and allows to experimentally determine the residual transverse stiffness of the composite specimens in the

1017/1211 doi:10.5075/epfl-298799_978-2-9701614-0-0

same way as the Compression After Impact standard test (ASTM D7136) does. It consists of a first subcritical impact performed to measure the impact contact time when no damage is generated, followed by a second supercritical impact which induces damage in the specimen, and finally, a third subcritical impact equal to the first one. Considering that the impact conditions are the same, the enlargement in the contact time measured for this third subcritical impact with respect to the one experienced in the first impact can only be a consequence of a decrease in the specimen's stiffness. Therefore, the residual stiffness of the composite can be quantified from the ratio between the contact times registered in the subcritical impacts performed when the specimen was undamaged and when it had already been damaged.

As the tested specimens are not opaque, the extent of the generated delamination damage could be analysed with the backlighting technique [15]. Computer vision was applied to avoid any subjectivity when determining the delaminated areas.

3. Results and discussion

3.1 Fibre and void content

The high fibre content and low porosity obtained in the pultruded composites manufactured by out of die UV cured pultrusion evidence the process quality. As collected in Table 1, a similar fibre content was achieved for the reference and the multiaxial configurations, making them suitable to study the effect of the reinforcement configuration on their impact response.

Table 1: Fibre and void volume content for each pultruded composite.

Pultruded composite	Fibre volume content [%]	Void volume content [%]
Reference	62.8 ± 0.3	0.3 ± 0.1
Multiaxial	62.1 ± 0.7	1.3 ± 0.2

3.2 Impact resistance

The trends followed by the impact response of both reinforcement configurations can be studied from the peak force and dissipated energy plots. As usual in thin composite plates [14], the peak force evolution from Figure 2 shows how it increases with the impact energy as long as only delamination damage is experienced and reaches a plateau when fibre breakage starts. A 13400 N maximum peak force is obtained for the multiaxial reinforcement configuration, while the reference configuration gets to a 6800 N maximum.

Three regimes can be differentiated according to the permanent deformations generated in the specimens in the dissipated energy plot from Figure 3. In the first regime, the low incident impact energies are not enough to dent the specimen surface and the striker rebounds. Therefore, the dissipated energy is below the 1:1 dashed line representing the available impact energy. The dissipated energy quadratically increases throughout the first regime until a point where the striker no longer rebounds, beginning with the second regime. From this point on, specimens are penetrated by the striker, and all the incident impact energy is dissipated. Finally, in the third regime, the incident impact energy is enough to perforate the specimens, and the dissipated energy reaches an asymptote.

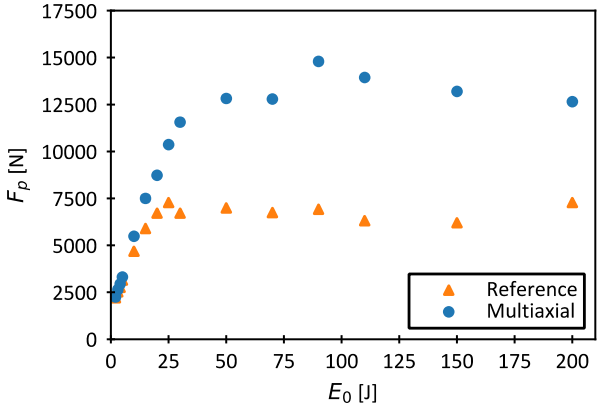

Figure 2. Peak force plot for the reference and multiaxial configurations.

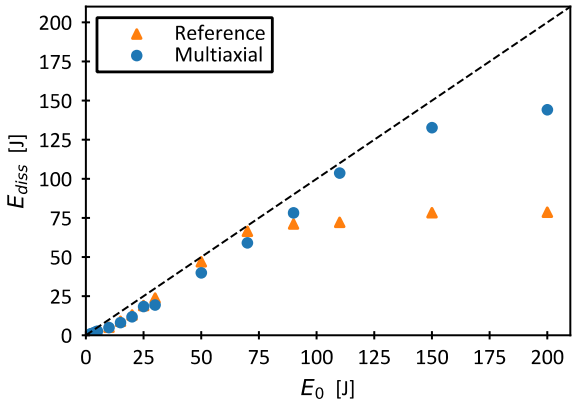

Figure 3. Dissipated energy plot for the reference and multiaxial configurations.

The critical impact energy above which the specimens experience damage is almost the same for both reinforcement configurations, as it is determined mainly by the resin fracture toughness. However, the improvement in the impact resistance provided by the multiaxial reinforcement configuration is evidenced by the considerably higher penetration and perforation impact energy thresholds achieved in comparison to the reference configuration. These characteristic impact energies are collected in Table 2.

Table 2: Delamination, penetration and perforation energy thresholds for the reference and the multiaxial configurations.

Pultruded composite	Critical energy [J]	Penetration threshold [J]	Perforation threshold [J]
Reference	1.2	50	75
Multiaxial	1.3	115	140

As the testing conditions are the same for both reinforcement configurations, the energy dissipated in the rebound region is related to the extent of the delamination generated in the specimens [14]. Hence, the delamination observed in Figure 4 for a 25 J impact are alike for both reinforcement configurations because the energy dissipated is similar in the two cases. A

1019/1211 doi:10.5075/epfl-298799_978-2-9701614-0-0

considerable delamination growth is noticed either in the multiaxial and the reference configurations along the pultrusion direction due to the bending stiffness difference between the tape and roving layers for that direction. However, in the multiaxial configuration, the delamination does not grow as much as in the reference one in the transverse direction.

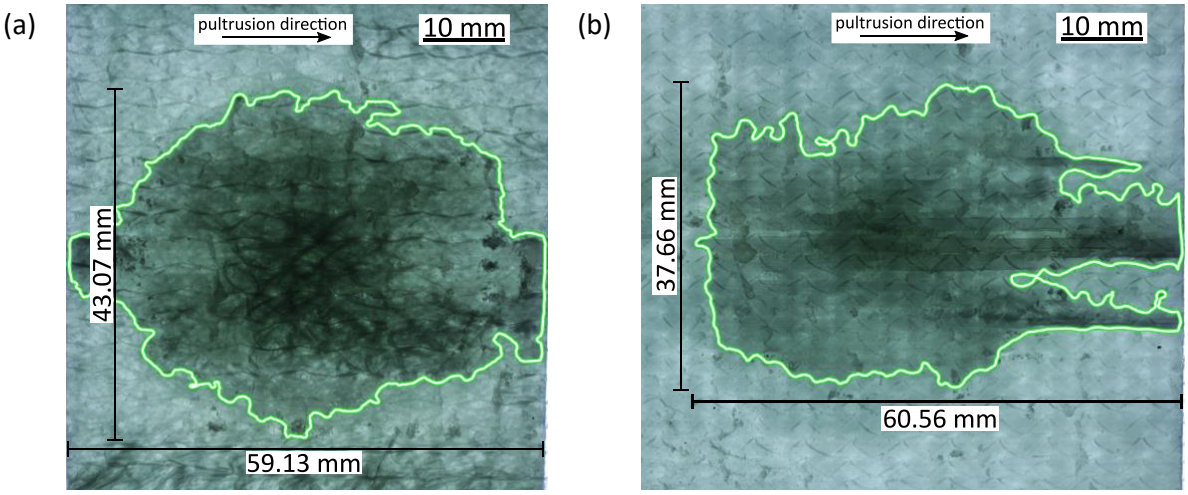

Figure 4. Delamination contours for the 25 J impact energy on the (a) reference and (b) multiaxial reinforcement configurations.

3.3 Damage tolerance

The mechanical performance loss caused by the impact events has to be assessed to completely address the impact response improvement provided by the multiaxial reinforcement configuration. Thus, the damage tolerance of both studied reinforcement configurations has been analysed, experimentally determining their post-impact residual stiffness when just delamination damage is experienced. As plotted in Figure 5, for low energy impacts close to the delamination threshold, that is to say, up to 10 J impacts, a similar decrease is observed in the residual stiffness of both configurations. From that impact energy on, the residual stiffness retained by the multiaxial configuration remains constant with a value of 60 % of the original one, while the reference configuration steadily losses stiffness, up to a point where for a 30 J incident impact energy, just 45 % is left.

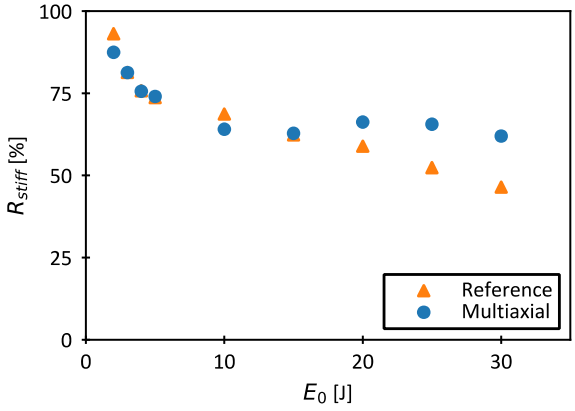

Figure 5. Residual stiffness plot for the reference and multiaxial reinforcement configurations.

1020/1211 doi:10.5075/epfl-298799_978-2-9701614-0-0

4. Conclusions

The high quality of the pultruded composites manufactured by out of die UV cured pultrusion was contrasted. Two high fibre content profile configurations were satisfactorily manufactured, presenting a restrained void content, which gives an example of the reinforcement configurations that can be implemented in the profiles produced with this technology.

The drop weight low-velocity impact tests performed in specimens from both reinforcement configurations showed how, at incident energies close to the delamination threshold, the effect of the reinforcement configuration is not appreciated. However, as higher impact energies are applied, the improvement in the impact resistance and damage tolerance procured by the multiaxial reinforcement configuration arises. A 100 % higher maximum peak force, a 125 % higher penetration threshold, and an 85 % higher perforation threshold were obtained in comparison to the reference configuration. Additionally, the capacity of retaining stiffness after suffering an impact event is better in the multiaxial configuration, which even when presenting delamination of a considerable extent, still maintained 60 % of its original stiffness.

So, the present work evidence that apart from the productive benefits that an automated process like out of die UV cured pultrusion would provide to the manufacturing of stiffeners for vessels structures, other benefits related to the enhancement of their impact response could be attained.

Acknowledgements

The results described in this paper have been generated inside the scope of the FIBRE4YARDS project. This project has received funding from the European Union's Horizon 2020 research and innovation programme under grant agreement No 101006860. The authors also thank the financial support provided by the Basque Government (AVACO ZL-2021/00703; IT883-16; AVANSITE KK-2020/00019).

5. References

1. Davies P, Choqueuse D, Bigourdan B, Gauthier C, Joannic R, Parneix P, et al. Design, manufacture and testing of stiffened panels for marine structures using adhesively bonded pultruded sections. Proceedings of the Institution of Mechanical Engineers Part M: Journal of Engineering for the Maritime Environment. 2004;218(4):227–34.
2. Vedernikov A, Safonov A, Tucci F, Carlone P, Akhatov I. Pultruded materials and structures: A review. Vol. 54, Journal of Composite Materials. SAGE Publications Ltd; 2020. p. 4081–117.
3. Aranberri I, Landa M, Elorza E, Salaberria AM, Rekondo A. Thermoformable and recyclable CFRP pultruded profile manufactured from an epoxy vitrimer. Polymer Testing. 2021 Jan 1;93:106931.
4. Minchenkov K, Vedernikov A, Safonov A, Akhatov I. Thermoplastic pultrusion: A review. Polymers (Basel). 2021 Jan 2;13(2):1–36.
5. Struzziero G, Maistros GM, Hartley J, Skordos AA. Materials modelling and process simulation of the pultrusion of curved parts. Composites Part A: Applied Science and Manufacturing. 2021 May 1;144:106328.
6. Liu TQ, Feng P, Wu Y, Liao S, Meng X. Developing an innovative curved-pultruded large-scale GFRP arch beam. Composite Structures. 2021;256.

7. Malnati P. Curved pultrusions enter production. CompositesWorld 5 [Internet]. 2020;20–3. Available from: https://www.compositesworld.com/articles/curved-profiles-radius-pultrusion
8. Britnell DJ, Tucker N, Smith GF, Wong SSF. Bent pultrusion - A method for the manufacture of pultrudate with controlled variation in curvature. In: Journal of Materials Processing Technology. Elsevier; 2003. p. 311–5.
9. Tena I, Sarrionandia M, Torre J, Aurrekoetxea J. The effect of process parameters on ultraviolet cured out of die bent pultrusion process. Composites Part B: Engineering. 2016;89:9–17.
10. Baran I, Carlone P, Hattel JH, Palazzo GS, Akkerman R. The effect of product size on the pulling force in pultrusion. In: Key Engineering Materials. Trans Tech Publications Ltd; 2014. p. 1763–70.
11. Baran I. Pultrusion processes for composite manufacture. In: Advances in Composites Manufacturing and Process Design. Elsevier Inc.; 2015. p. 379–414.
12. Safonov AA, Carlone P, Akhatov I. Mathematical simulation of pultrusion processes: A review. Vol. 184, Composite Structures. Elsevier Ltd; 2018. p. 153–77.
13. Shah SZH, Karuppanan S, Megat-Yusoff PSM, Sajid Z. Impact resistance and damage tolerance of fiber reinforced composites: A review. Composite Structures. 2019 Jun 1;217:100–21.
14. Feraboli P, Kedward KT. A new composite structure impact performance assessment program. Composites Science and Technology. 2006 Aug;66(10):1336–47.
15. Glossop NDW, Tsaw W, Measures RM, Tennyson RC. Image-enhanced backlighting: A new method of NDE for translucent composites. Journal of Nondestructive Evaluation. 1989 Sep;8(3):181–93.

HYGROTHERMAL INTERFACIAL DEGRADATION OF FLAX FIBRE MICRO-COMPOSITES USING MICRO-DROPLET TEST

Royson Dsouza[a], Alexandros Prapavesis[b], Markus Kakkonen, Essi Sarlin[a], Aart Vuure[b] and Mikko Kanerva[a]

a: Tampere University, Faculty of Engineering and Natural Sciences, PO Box 589, FI-33014 Tampere University, Finland – Royson.dsouza@tuni.fi
b: Departement of Materials Engineering, KU Leuven, Kasteelpark Arenberg 44, bus 2450, B-3001 Leuven, Belgium
c: Fibrobotics Oy, Finland

Abstract: *The key disadvantage that hinders the implementation of natural fibre composites such as flax, is its questionable long-term durability when subjected to different moisture conditions. This study aims to investigate the durability of interfaces at microscale in flax fibre composites using the micro-droplet test method, focusing on the performance after cycling between high and low humidity levels. Elementary flax fibre with epoxy droplets is subjected to hygroscopic cycling between 30% RH and 80% RH for half, one, four, eight and twelve cycles respectively. These samples are further tested using microbond test measuring approximately 30 droplets per hygroscopic cycle, providing huge amount of data to precisely study the interfacial adhesion. Interfacial shear strength is calculated using linear regression fit and numerical stress-based analysis. An increasing trend for first half cycle followed by interfacial degradation of up to 40% is observed until 12 hygroscopic cycles. Interface toughness is studied for every alternate cycling cases.*

Keywords: flax fibre; microbond; adhesion; durability; hygroscopic cycling.

1. Introduction

The current environmental issues have led to the use of natural fibre reinforcements to promote sustainability and circular economy. Natural fibre reinforcements have many advantages over inorganic fibres, having high specific properties with low density coupled with low carbon footprint. Given the availability and excellent mechanical properties, flax fibres (Linum Usitatissimum) are a substitute for synthetic fibres. In terms of stiffness, they are at par with glass fibres, while having ~40% lower density leading to higher specific properties. However, the key disadvantage that hinders their implementation in bio-composites is their sensitivity to moisture absorption [1]. The cell wall of the elementary fibres consists of four different layers of cellulose micro fibrils embedded in a matrix of hemicellulose and lignin. The cell wall also contains a hemicellulose and pectic component, which is predominantly amorphous hydrophilic polysaccharides. These components are highly accessible to water molecules and have a high OH to C ratio [2]. When the fibre is exposed to moisture (humid environment), the cell wall absorbs moisture, and the water molecules accumulate between the micro-fibrils causing the fibre to swell. In contrast, the fibre shrinks when exposed to dry environments. Those hygroscopic instabilities lead to damage developed during the material's lifetime when it is exposed in realistic environments which follow a cycling fluctuation between high and low humidity levels.

  doi:10.5075/epfl-298799_978-2-9701614-0-0

The consecutive wet-dry cycles induce tensile and compressive stresses in reinforced composites. A significant drop in transverse tensile strength is observed when the flax fibre composite (FFC) is subjected to six consecutive wet-dry cycles [3]. The fibre-matrix debonding was quite significant at the laminate level. Similar observations were made by Laetitia et. al wherein a 20% drop in transverse tensile strength was observed within one week of aging [4]. Although, there is a clear indication of the interfacial degradation, the humidity aging mechanisms in FFC's have mostly been studied at the macroscale.

Localized interfacial study can be carried out using micromechanical techniques such as the microbond (MB) test [5]. The MB test can be used to study the local interfacial shear strength (IFSS) as well as interfacial toughness (critical energy release rate) to some extent of precision by using analytical models. MB test has been widely used to study the IFSS of flax fibre with epoxy/PP/PLA droplets [6, 7]. Existing literature on aging test using water immersion technique shows subsequent drop in IFSS as a function of immersion time using microdroplet tests [8]. To the best of our knowledge, the current state of the art does not provide any scientific literature on interfacial degradation of flax fibre at microscale with hygroscopic humidity cycling.

In this work hygroscopic cycling process is carried out for single flax fibre-epoxy samples. A high precision microbond test is carried out to study the local interfacial degradation. To determine the IFSS, the slope of the linear regression fitting using maximum force (F_{max}) and Zhandarov's approach (stress-based analysis) using debond force (F_d) was carried out. Interfacial toughness (G_{ic}) is determined using an energy-based approach. A critical study on frictional sliding force as well as accurate determination of debond force using force-strain derivative is presented in this paper.

2. Materials and methods

2.1 Sample preparation

Elementary flax fibres were carefully extracted from commercially available FLAXTAPE© fabric (provided by Lineo NV, France). Fibres with diameters 15µm to 20 µm are only chosen for the test. No prior treatment is applied to the fibre. The epoxy system Epikote 828 LVEL together with a 1,2-diaminocylcohexane (Dytek DCH-99) hardener from Hexion was used with a 100/15.2 mixing ratio, following the manufacturer's guidelines. The droplets were deposited on the elementary flax fibre using a steel filament of diameter 20 µm. This entire process is carried out in a controlled environment at standard conditions (23º C, 50%RH). After deposition of the

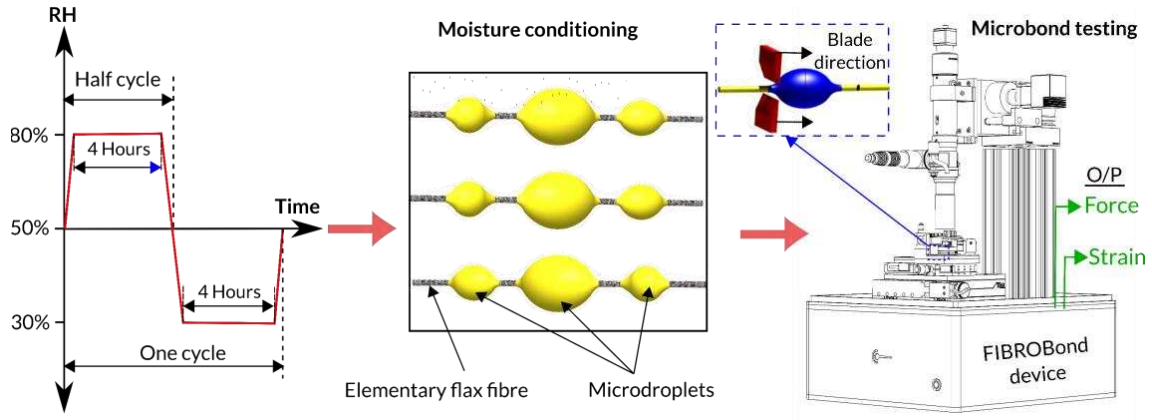

Figure 1. Experimental process of hygroscopic cycling and testing.

droplet on the single flax filament the epoxy left to cure for three hours at 150º C under inert atmosphere (N_2).

2.2 Hygrothermal exposure

The desired humid environment was achieved using desiccators containing saturated salt solutions which were prepared following the ASTM E104 [9]. The high relative humidity (RH) environment achieved using a saturated Potassium Chloride (KCl) solution with a RH point of 80% at 60 ºC, and the low humidity using a saturated Magnesium Chloride (MgCl) solution with a RH point of 30% at 60º C. One hygroscopic cycle is represented by exposure to high RH followed by exposure to low humidity for 4h each (Fig. 1). The exposure time was selected based on the approximate time needed for the salt solution to re-equilibrate back to its conditions after opening the desiccator, plus the time needed for the saturation of a fully exposed single flax fibre.

2.3 Microbond test

MB test was performed using FIBRObond device (manufacturer – Fibrobotics Oy, Finland). The technical details of the device can be found in reference [10]. Load was measured using 1N load cell with frequency of 1kHz and the blade speed is kept constant at a rate of 0.008 mm/s. Approximately 35 to 40 droplets were tested per cycle. It's a well-known fact that the MB test with flax fibres leads to significant scatter of maximum force (F_{max}) due to asymmetric shape of the fibre, variation of fibre diameter and the variation of surface properties along the length of the fibre. To reduce the error source, the diameter of the fibre was measured close to the droplet ends before testing, for every individual droplet. Apart from the measured load, corresponding fibre strain was measured using Fibre Bragg grating sensor using a specialized sample holder [11]. The test was carried out at standard room conditions.

2.4 Interfacial shear strength and interfacial toughness

Two different approaches for the determination of the IFSS from the recorded results of the microbond test are used in this study. In the first approach, F_{max} is plotted as a function of embedded area (A_{emb}) and a linear regression is used to determine the IFSS from the slope [10, 12]. In the second approach stress-based model introduced by Zhandarov et. al is used to estimate the IFSS using debond force (F_d) [13, 14]. The analytical model of stress-based analysis consists of a Nayfeh shear-lag parameter (β) given by,

$$\beta = \left[\frac{2}{r_f^2 E_f E_m} \left(\frac{E_f V_f + E_m V_f}{\frac{V_m}{4G_f} + \frac{1}{2G_m}\left(\frac{1}{V_m} ln \frac{1}{V_f} - 1 - \frac{V_f}{2}\right)} \right) \right]^{\frac{1}{2}} \quad (1)$$

Where E_f, $E_m$are the elastic modulus G_f, G_m are the axial shear modulus V_f, V_m are the volume fractions, of the fibre and droplet respectively and r_f is the radius of the fibre. Eq. (1) results in negative β^2values for very small droplets and cox shear lag parameter was used for such droplets. The cox shear lag parameter is given by, $\beta = \left[2G_m/E_f \ln\left(V_f^{-1}\right)\right]^{1/2}$. Here we follow the traditional approach of this technique, wherein the F_d which is a "kink" in force-displacement curves is selected. Generally, this technique is the easiest and fastest but leads to larger standard deviation (references) of IFSS but could be significantly reduced if the F_d is

determined accurately. The kink in force-displacement curves might not be clearly distinguishable for all the curves but could be determined quite precisely with force-strain plots. From our previous publication, it was clear that this kink generally gives a sharp peak when force-fibre strain derivatives are taken. Finite element simulations have also confirmed the peak being onset of damage at the interface. For the droplets where the kink is clearly not visible, we use this similar analogy by taking the first derivative of force strain curve to precisely estimate the F_d. On this basis, local IFSS (τ_d) can be estimated using Eq. (2) given by,

$$\tau_d = \frac{F_d \beta}{2\pi r_f} \coth(\beta l_e) + \tau_{ther} \tanh\left(\frac{\beta l_e}{2}\right) \quad (2)$$

and τ_{ther} is given by $\tau_{ther} = \left(\beta r_f E_f (\alpha_f - \alpha_m)\Delta T\right)/2$, where α_f and α_m are the co-efficient of thermal expansion of the fibre and the droplet respectively and ΔT is the difference between the test temperature and stress-free temperature (-90° C in our case). Frictional stress (τ_{fric}) is calculated using the equation, $\tau_{fric} = 2\pi r_f A_{emb}/F_{fric}$.

To estimate the critical energy release rate (G_{ic}), we use the analytical model of Scheer and Nairn which is simple in nature with a direct approach [15]. Using this, G_{ic} can be calculated using Eq. (3) given by,

$$G_{ic} = \left(\frac{F_{max}}{\pi r_f^2} + \frac{D_{3s}\Delta T}{C_{33s}}\right)^2 \frac{r_f C_{33s}}{2} \quad (3)$$

Where $D_{3s} = 0.5\left(\alpha_f - \alpha_m\right)$ and $C_{33s} = 0.5\left(E_f^{-1} + V_f V_m^{-1} E_m^{-1}\right)$. Deviation of results using Eq. (3) in comparison to finite element models as previously observed [16], but this initial estimate is good for the comparison with different cycles.

3. Results and discussions

3.1 Estimation of F_d using force-strain derivatives

The first derivative of force strain curve ($\partial F/\partial \varepsilon$) shows significant first peak which indicates the damage initiation F_d (Fig. 2 c-e). Similar peaks were observed in Ref [16] which indicated damage initiation at the interface and it was further confirmed using finite element analysis. The peak

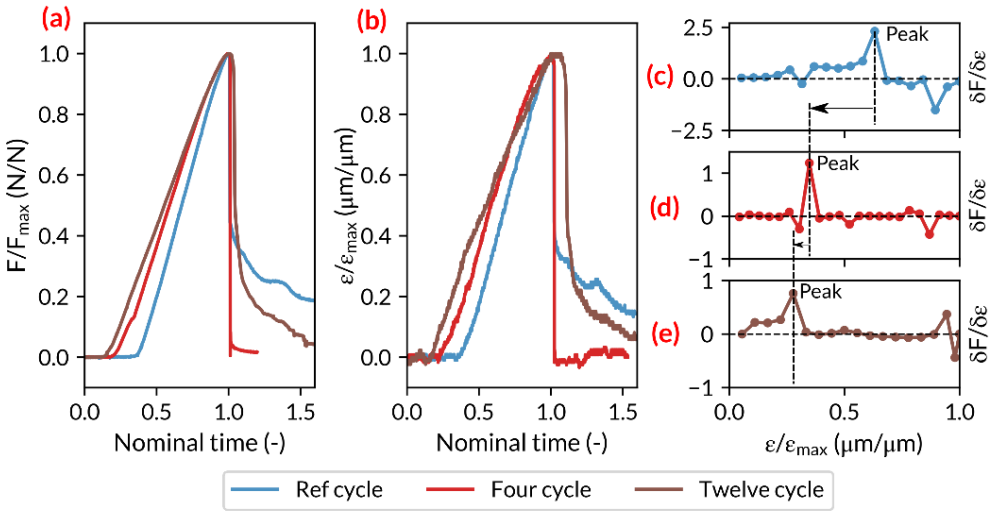

Figure 2. (a) Normalized force-time curves; (b) normalized strain time curves; (c-e) first derivative curves as a function of strain

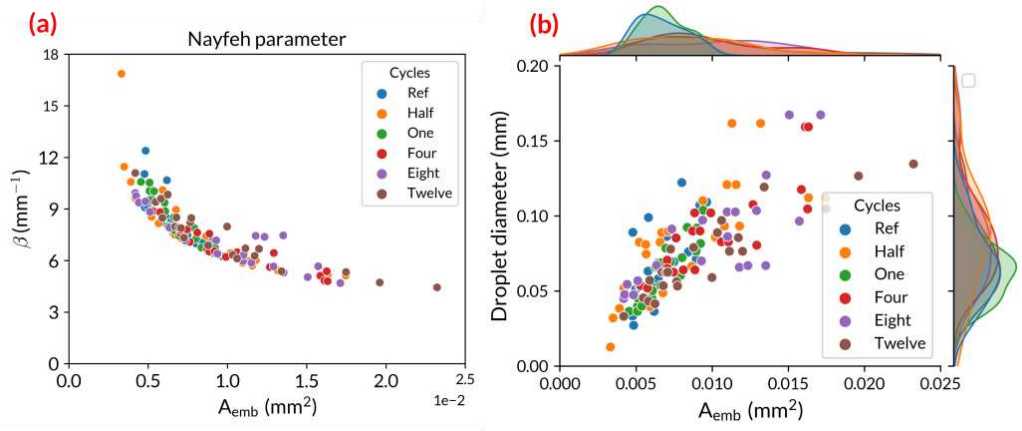

Figure 3. (a) Nayfeh parameter and (b) distribution of droplet diameters- as a function of embedded length

shifts backwards as the hygroscopic cycles increases, giving a clear indication of the decline of F_d. This is critical for the analytical model of stress-based analysis, as local IFSS can be measured with minimal standard deviation using F_d obtained using this process.

3.1 Analytics of stress-based analysis

The Nayfeh parameter β presented in Eq. (1) is plotted as a function of embedded area as shown in Fig. 3. The trend line of β agrees well with the published literature. Very few droplets (~ 6) showed negative β values, for which β parameter of Cox was used. The plot of droplet diameter as a function of embedded area (Fig. 3 (b)) shows that, with the increase in number of moisture cycles increasingly larger droplets can be tested. The probability of the droplet diameters is largely seen between 0.04 to 0.13 mm for all cycles.

3.2 Frictional force

The Weibull probability plot shown in Fig. 4 (a) and (b) indicates that there are two groups of friction forces. In first group, F_{fric} increases as droplet A_{emb} increases whereas in the second group F_{fric} is almost close to zero irrespective of A_{emb}. This is due to the fact that there are several droplets on a single fibre and as the tested droplets are far away from the fixed position

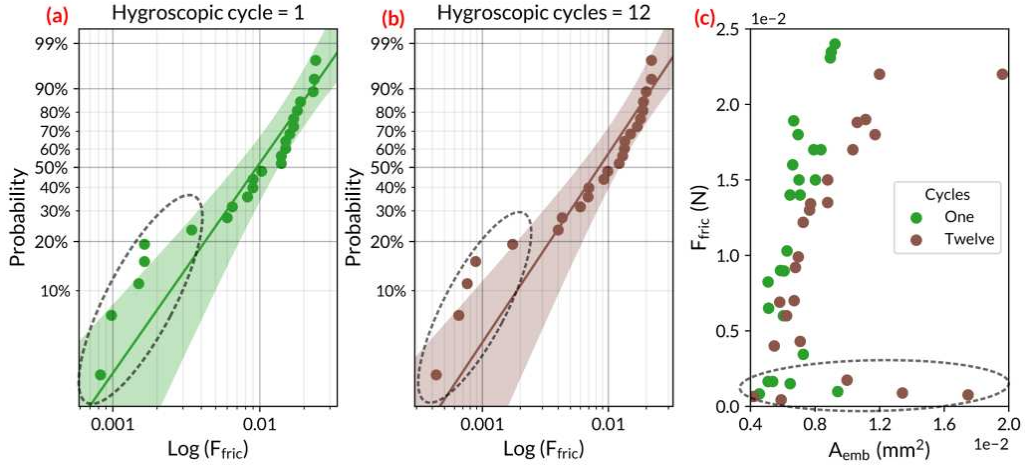

Figure 4. Plots to illustrate the two frictional stress groups during the MB test.

of the fibre, large amount of elastic energy is stored in the fibre. When these droplets debond from the fibre this elastic energy transforms to kinetic energy, detaching the droplet with minimum friction. Around 4 to 6 droplets per cycle are observed with such behavior. For the estimation of τ_{fric} , these droplets are discarded.

3.3 MB test results

The IFSS obtained using linear regression fit and stress-based approach predict similar results (Fig. 5 a, b). The IFSS increases for half cycle by 5% and then gradually decreases up to 55% for

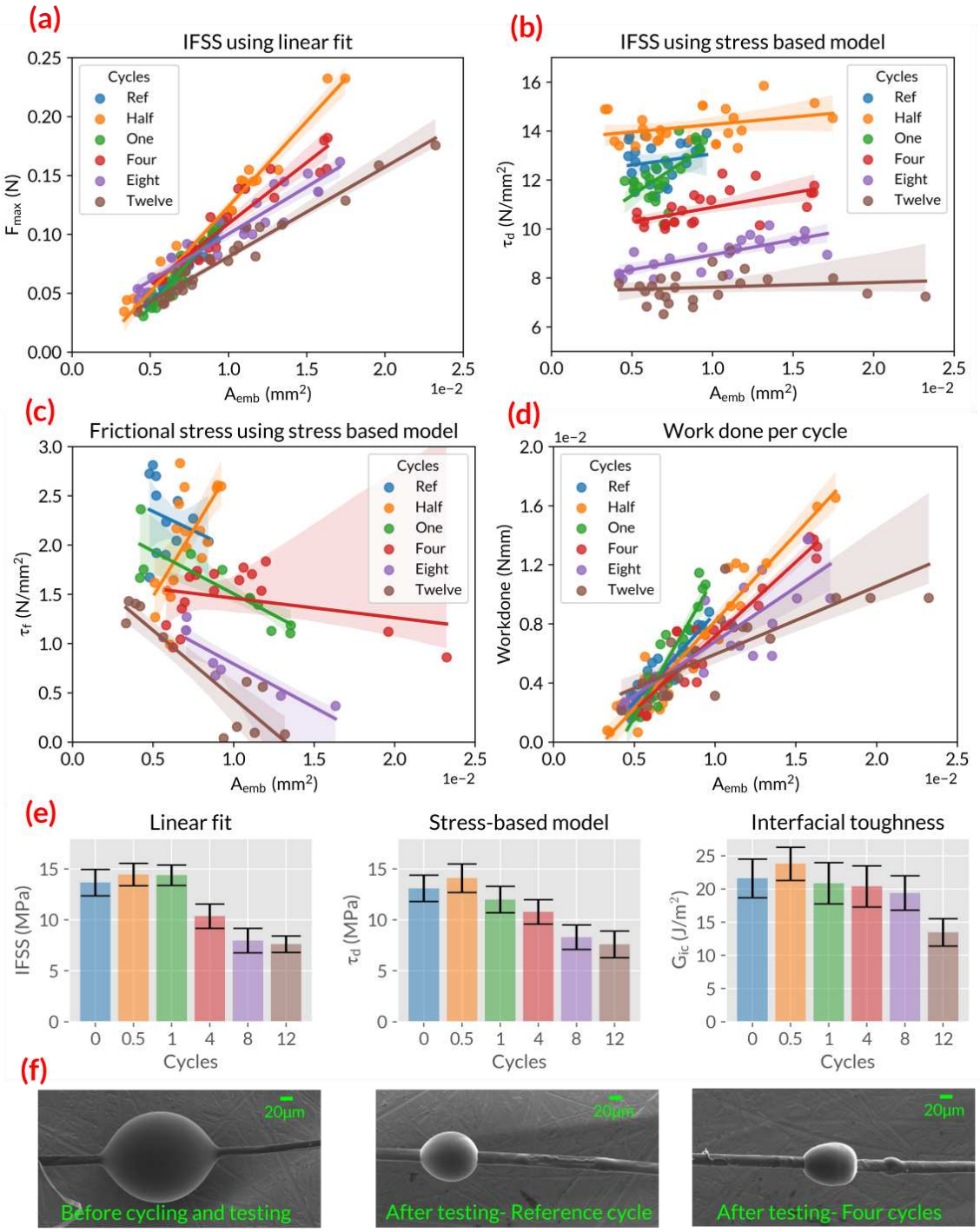

Figure 5. (a)-(d) Measurement results of MB test; (e) variation of IFSS, τ_d and G_{ic} for different cycles; (f) SEM images of the droplets.

twelve cycles. In addition, the work done to debond the droplet decreases with increase in hygroscopic cycles indicating the weak interface. The increase of IFSS for half a cycle by 5% might be due to the post curing effect on the droplet which causes the droplets to shrink, in turn improving the interfacial strength. But the gradual decrease of IFSS and work done is a clear indication of interfacial degradation when subjected to hygroscopic cycles. It is also interesting to see that the frictional stress also decreases when the cycles are increased (Fig 5 (c)). As the free surface of the fibre is exposed directly to the moisture variations, there is a possible removal of pectin from the fibre surface. Longer exposure times would result in removal of pectin in larger concentrations and residual stresses from the sample preparation (e.g. slight shrinkage of matrix) tend to relax in any system and environment with residual stresses. Scanning electron microscopy (SEM) images clearly show the plasticization of the droplet. When the droplet is exposed to moisture for longer period, the moisture diffuses through the epoxy droplet causing it to plasticize. This also explains the reason behind the interfacial toughness which does not change significantly up to eight cycles. With twelve hygroscopic moisture cycles, the load bearing capacity of the interface is so weak, that this also results in significant drop of interfacial toughness.

The degradation of the interface can be explained due to the significantly higher hygroscopic dimensional instability of the fibre compared to the matrix which leads to swelling (80% RH) of the fibre constrained by the matrix leading to stress generated at the interface followed by shrinkage (30% RH) leading to interfacial debonding. Furthermore, the flax surface is covered with highly polar –OH bonds where the moisture may penetrate and degrade the adhesion by forming hydrogen bonds between the –OH groups and the water molecules. Hence, the adhesion between fibre and matrix would weaken.

4. Conclusions

In this research, the interfacial degradation of flax fibre-epoxy, with a systematic procedure of sample preparation as well as high precision testing is presented and supplemented by analytical models. Following important conclusions can be drawn:

- Estimation of $\boldsymbol{F_d}$ using force-strain derivatives serves as an excellent tool to accurately estimate the $\boldsymbol{\tau_d}$ which serves as an important input to the stress-based model.
- A progressive degradation of interfacial shear strength is observed when subjected from one to twelve hygroscopic cycles.
- Analysis of friction reveals a drop in frictional stress with increasing hygroscopic cycles because of moisture exposure for longer duration; it is hypothesized that this could be attributed to, possible removal of pectin from the surface of flax fibres.
- The micro-mechanical behaviour of the epoxy transitions from an initially elastic to a softer plastic deformation of the droplets after hygroscopic exposure, due to the water diffusion into the droplet.

Acknowledgements

This project has received funding from the European Union's Horizon 2020 research and innovation programme under the Marie Skłodowska -Curie grant agreement No 764713. This work made use of Tampere Microscopy Centre facilities at Tampere University.

  doi:10.5075/epfl-298799_978-2-9701614-0-0

5. References

[1] Moudood A, Hall W, Öchsner A, et al. Effect of Moisture in Flax Fibres on the Quality of their Composites. *J Nat Fibers*; 16. Epub ahead of print 2019. DOI: 10.1080/15440478.2017.1414651.

[2] Hill CAS, Norton A, Newman G. The water vapor sorption behavior of natural fibers. *J Appl Polym Sci*; 112. Epub ahead of print 2009. DOI: 10.1002/app.29725.

[3] Koolen G, Soete J, van Vuure AW. Interface modification and the influence on damage development of flax fibre - Epoxy composites when subjected to hygroscopic cycling. In: *Materials Today: Proceedings*. 2019. Epub ahead of print 2019. DOI: 10.1016/j.matpr.2020.01.183.

[4] Van Schoors L, Cadu T, Moscardelli S, et al. Why cyclic hygrothermal ageing modifies the transverse mechanical properties of a unidirectional epoxy-flax fibres composite? *Ind Crops Prod*; 164. Epub ahead of print 2021. DOI: 10.1016/j.indcrop.2021.113341.

[5] Miller B, Muri P, Rebenfeld L. A microbond method for determination of the shear strength of a fiber/resin interface. *Compos Sci Technol*. Epub ahead of print 1987. DOI: 10.1016/0266-3538(87)90059-5.

[6] Raj G, Balnois E, Baley C, et al. Role of polysaccharides on mechanical and adhesion properties of flax fibres in flax/PLA biocomposite. *Int J Polym Sci*; 2011. Epub ahead of print 2011. DOI: 10.1155/2011/503940.

[7] Le Duigou A, Kervoelen A, Le Grand A, et al. Interfacial properties of flax fibre-epoxy resin systems: Existence of a complex interphase. *Compos Sci Technol*; 100. Epub ahead of print 2014. DOI: 10.1016/j.compscitech.2014.06.009.

[8] Le Duigou A, Davies P, Baley C. Exploring durability of interfaces in flax fibre/epoxy micro-composites. *Compos Part A Appl Sci Manuf*; 48. Epub ahead of print 2013. DOI: 10.1016/j.compositesa.2013.01.010.

[9] ASTM E104. Standard Practice for Maintaining Constant Relative Humidity by Means of Aqueous Solutions 1. *ASTM Int*.

[10] Laurikainen P, Kakkonen M, von Essen M, et al. Identification and compensation of error sources in the microbond test utilising a reliable high-throughput device. *Compos Part A Appl Sci Manuf*; 137. Epub ahead of print 2020. DOI: 10.1016/j.compositesa.2020.105988.

[11] Dsouza R, Antunes P, Kakkonen M, et al. Microscale sensor solution for data collection from fibre-matrix interfaces. *Sci Rep* 2021; 11: 1–12.

[12] Liu B, Liu Z, Wang X, et al. Interfacial shear strength of carbon fiber reinforced polyphenylene sulfide measured by the microbond test. *Polym Test*; 32. Epub ahead of print 2013. DOI: 10.1016/j.polymertesting.2013.03.020.

[13] Zhandarov S, Mäder E, Gohs U. Why should the 'alternative' method of estimating local interfacial shear strength in a pull-out test be preferred to other methods? *Materials (Basel)*; 11. Epub ahead of print 2018. DOI: 10.3390/ma11122406.

[14] Zhandarov S, Mäder E. Determining the interfacial toughness from force-displacement curves in the pull-out and microbond tests using the alternative method. *Int J Adhes Adhes*. Epub ahead of print 2016. DOI: 10.1016/j.ijadhadh.2015.10.020.

[15] Scheer RJ, Nairn JA. A Comparison of Several Fracture Mechanics Methods for Measuring Interfacial Toughness with Microbond Tests. *J Adhes*. Epub ahead of print 1995. DOI: 10.1080/00218469508014371.

[16] Dsouza R, Antunes P, Kakkonen M, et al. 3D interfacial debonding during microbond testing: Advantages of local strain recording. *Compos Sci Technol*; 195. Epub ahead of print 2020. DOI: 10.1016/j.compscitech.2020.108163.

NON-DRIED FLAX FIBRE REINFORCED THERMOPLASTIC COMPOSITES IN WET ENVIRONMENTS

Farzin, Javanshour[a], Alexandros, Prapavesis[b], Rama Kanta, Layek[c], Aart Willem, Van Vuure[b], Essi, Sarlin[a]

a: Department of Materials Science and Environmental Engineering, Tampere University, Tampere, Finland – farzin.javanshour@tuni.fi
b: Department of Materials Engineering, KU Leuven, Heverlee, Belgium
c: Department of Separation Science, LUT University, Lahti, Finland

Abstract: *The long-term performance of natural fibre reinforced thermoplastic (NFRP) composites is critical for developing more sustainable structures. The defects developed in NFRP due to fibre swelling and shrinkage in wet service conditions constitute a significant issue. Here, a method for restricting the in-service swelling and shrinkage of NFRP is proposed. The NFRP composites were processed with swollen fibres stored in moist conditions before thermoplastic resin infusion. The swelling of water-saturated NFRP was decreased up to 56% by non-dry fibres. The similar in-plane shear strength and transverse tensile strength of NFRP composites processed with oven-dried and preconditioned fibres (at 50% RH) showed the in-situ polymerisation of poly (methyl methacrylate) (PMMA) to be insensitive to moisture. Processing composites with preconditioned fibres (at 90% RH) decreased the water immersion ageing sensitivity for in-plane shear properties of NFRP from 30% to nearly zero.*

Keywords: Biocomposites; Adhesion; Durability; Mechanical testing; X-CT analysis

1. Introduction

Flax fibre reinforced thermoplastic (NFRP) composites offer low density, good stiffness and damping properties for structural applications [1,2]. The thermoplastic infiltration is often realised at elevated temperatures (above 100 °C). The intrinsic moisture bound to hydrophilic fibres is removed by oven-drying to avoid processing induced porosities due to fibre moisture evaporation. The water absorption of composites processed with oven-dried fibres can create residual stresses (up to 11 MPa, for 50% RH [3]) due to the high radial swelling coefficient of flax fibres ($\beta_{f,r}$: 1.9 [4]). Such residual stresses can create matrix cracking and debonding around fibre and matrix interface [4]. The hydrothermal swelling of NFRP can be restrained by using high stiffness polymer matrix systems [5] and potentially using swollen (namely non-dry) fibres [6]. The advantages of processing NFRP with non-dry fibres are not yet explored.

In this article, the hydrothermal durability of non-dry flax fibre reinforced poly (methyl methacrylate) (PMMA) thermoplastic composites was investigated. It was hypothesised that in-situ polymerisation of PMMA could be insensitive to water molecules as the MMA monomers are emulsion polymerised in an aqueous medium [7]. The microstructure of composites was studied by X-ray computed tomography. The hydrothermal durability of composites was studied by the water immersion method. The effect of ageing on the interfacial adhesion of composites was studied based on quasi-static in-plane shear and transverse tensile testing.

  doi:10.5075/epfl-298799_978-2-9701614-0-0

2. Materials and methods

Non-crimp flax yarn fabrics of unidirectional (UD) types with an areal density of 300 g/m^2 were provided by Bcomp (Fribourg, Switzerland). A liquid thermoplastic resin based on methyl methacrylate (Elium® 188, Arkema, Colombes, France) and an organic dibenzoyl peroxide powder with phthalate (BP-50-FT1, United Initiators GmbH, Pullach, Germany) with 3 wt% initiator to resin ratio were used as the polymer matrix system. The in-situ polymerisation of Elium® 188 was realised at 23 °C to reduce moisture evaporation present in non-dry flax fibres. The resin system in this article (Elium® 188) was named PMMA throughout the text.

Flax fibre reinforced PMMA composite panels with a fibre volume fraction (V_f) of 40% were manufactured based on the vacuum-assisted resin infusion (23 °C, 0.6 bar vacuum pressure) method. After infusion, composites were placed in a hydraulic press with steel-made spacers (2 mm in thickness) to assure consistent thickness values. Composites manufactured with oven-dried fibres (115 °C, 2 h), fibres preconditioned at 50% RH (23 °C, 24 h), and fibres preconditioned at 90% RH (23 °C, 24 h) were respectively labelled as Dry, RT, and RH. The moisture content of fibres was measured by an analytical balance (model GR-202, A&D Ltd, Tokyo, Japan). For these measurements, the average weight for three pieces of fabrics (10 mm × 10 mm; width × length) was measured consecutively after oven-drying and humidity conditioning. The weight gains of RT and RH fabrics after conditioning were respectively 8.1 ± 0.2 wt% and 16.8 ± 0.2 wt% compared to oven-dried (Dry) fabrics. After manufacturing, composite laminates were stored at 50% RH (23 °C) for three months to reach equilibrium before ageing and mechanical testing. Upon reaching equilibrium, the composites' microstructure and fibre volume fraction were characterised by X-ray computed (X-CT) tomography (Phoenix Nanotom, General Electric, Germany). All humidity conditioning protocols were performed in a humidity chamber (model VC 0018, Vötschtechnik, Balingen, Germany).

The hydrothermal ageing of composites was performed by immersing the panels into a sealed container filled with deionised water at 23 °C for 40 days. Prior to the water immersion ageing, the free edges of composites panels were sealed with PMMA resin. The weight gain of the panels was measured in 2 h intervals during the first day and then in 24 h intervals for the remaining period. The surface water of the panels was wiped before weight measurements. The thickness swelling of the panels right after the saturation point was measured with a micrometre. Composite panels were then stored in 50% RH (23 °C) for two months to reach equilibrium.

Quasi-static tensile testing was carried out with a universal tester (model 5967, Instron, MA, USA). The effect of water immersion ageing on the interfacial adhesion in composites was examined based on quasi-static transverse tensile testing (with $[90]_4$ composite lay-up, 500 N load cell, and 1 mm/min crosshead movement rate) and in-plane shear testing of composites (with $[+45/-45]_{SE}$ lay-up, 30 kN load cell, and 5 mm/min crosshead movement rate) according to ASTM D3039 and ASTM D3518 standards, respectively. Full-field deformation was measured with a stereo optical extensometer (StrainMaster Compact, LaVision, Göttingen, Germany).

Rectangular-shaped specimens with dimensions of 150 mm × 25 mm × 2 mm and 200 mm × 25 mm × 2 mm (length × width × thickness) were prepared respectively for transverse tensile and in-plane shear testing. Specimens were cut from the composite panels with a band sawing machine (model RBS904, Ryobi). Tapered glass epoxy tabs were used to reduce the stress concentration at the gripped section of the specimens.

  doi:10.5075/epfl-298799_978-2-9701614-0-0

3. Results and discussions

3.1 X-ray computed (X-CT) tomography of composites

The internal microstructure of flax PMMA composites processed with oven-dried (namely Dry) fibres and precondition fibres (namely RH) after three months of stabilisation at 50% (23 °C) are presented in Figure 1. Both composites are almost free of voids regardless of the initial fibre moisture content during flax PMMA resin infusion. The void-free structure of composites indicates that the in-situ polymerisation of PMMA is not sensitive to the presence of moisture. The moisture insensitivity of the resin can be relevant to the synthesis type of methyl methacrylate, which is emulsion polymerisation in an aqueous medium [7]. Minimal traces of interfacial debonding between fibre and matrix are evident within fibre yarns in Dry composite (Figure 1A). Those limited debonding lines (cracks) in Dry-type composite can be related to the swelling of oven-dried flax fibres during the stabilisation period at 50% RH. On the contrary, highly swollen RH fibres have shrunk during the drying (stabilisation) period at 50% RH (Figure 1B). The extensive interfacial debonding lines (cracks) within fibre yarns are evident for RH-type composite. The average size of crack openings (width) in RH is 9.7 ± 3.1 µm, which is 177% higher than the average crack opening size in Dry-type composite (3.5 ± 0.3 µm). The large debondings can dramatically reduce the interfacial shear strength of RH composites. The results here accentuate the significance of hygroscopic residual stresses in non-dry flax PMMA composites due to flax fibres' high radial swelling coefficient ($\beta_{f,r}$: 1.9 [4]).

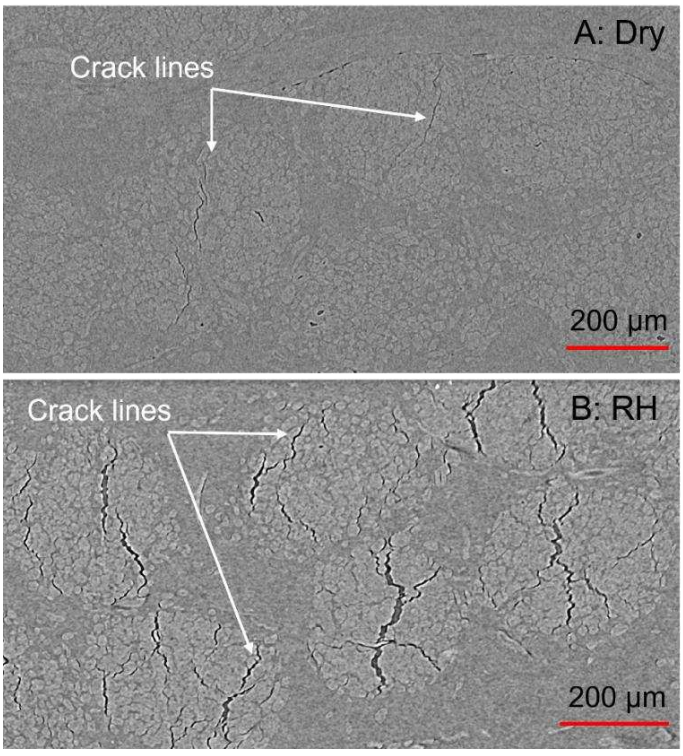

Figure 1. Non-destructively captured microstructure of composites based on X-CT after three months stabilisation period at 50% RH (23 °C).

3.2 Water sorption characteristics of composites

The water sorption-time histories of flax PMMA composites are presented in Figure 2A. After reaching equilibrium (at 50% RH, 23 °C for three months), the composites' moisture content is

  doi:10.5075/epfl-298799_978-2-9701614-0-0

shown as zero water sorption. Composites stabilise after the first 4 days of rapid water sorption and reach the saturation point with weight gain of 9.6% (Dry), 9.1% (RT), and 8.9% (RH) after 28 days. Processing composites with swollen (non-dry) RT and RH fibre reduces the thickness swelling at the saturation point of flax PMMA by 47% and 56%, respectively (Figure 2B). In conclusion, processing composites with swollen (non-dry) fibres limited the hygroscopic swelling and shrinkage of composites which can reduce the hygroscopic residual stress-induced defects.

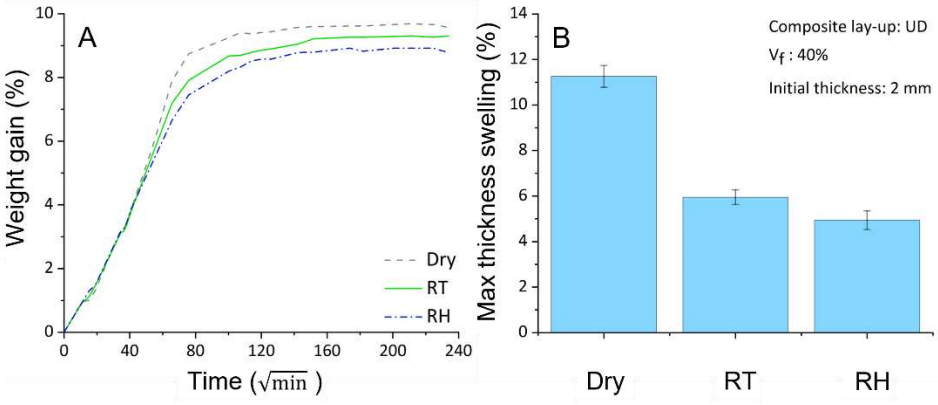

Figure 2. Water sorption-time history (A) and thickness swelling of composites (B)

3.3 Transverse tensile properties of composites

The transverse tensile strength (S_T) and elastic modulus (E_T) values of flax PMMA composites are presented in Figure 3. Before water immersion ageing, composites processed with oven-dried fibres (namely Dry) and conditioned fibres at 50% RH (namely RT) have similar transverse tensile strength (Dry: 14.5 ± 0.3 MPa, and RT: 13.7 ± 0.5 MPa) and elastic modulus (Dry: 3.1 ± 0.3 GPa, and RT: 3.1 ± 2 GPa) values. It is worth noting that the transverse tensile moduli of Dry and RT composites are in the same range as the tensile elastic modulus of the matrix (E_{PMMA}: 3.17 ± 0.2 GPa). Similar S_T and E_T values of RT and Dry composites show that in-situ polymerisation of PMMA is not sensitive to fibre moisture during resin infusion. However, the RH composites processed with non-dry fibres conditioned at 90% RH have 38% and 48% lower S_T and E_T than Dry composites. RH's inferior S_T and E_T values can be ascribed to the debonding cites between fibre and matrix (see Figure 1) due to the shrinkage of highly swollen RH fibres from 90% RH during manufacturing to 50% RH during the stabilisation period.

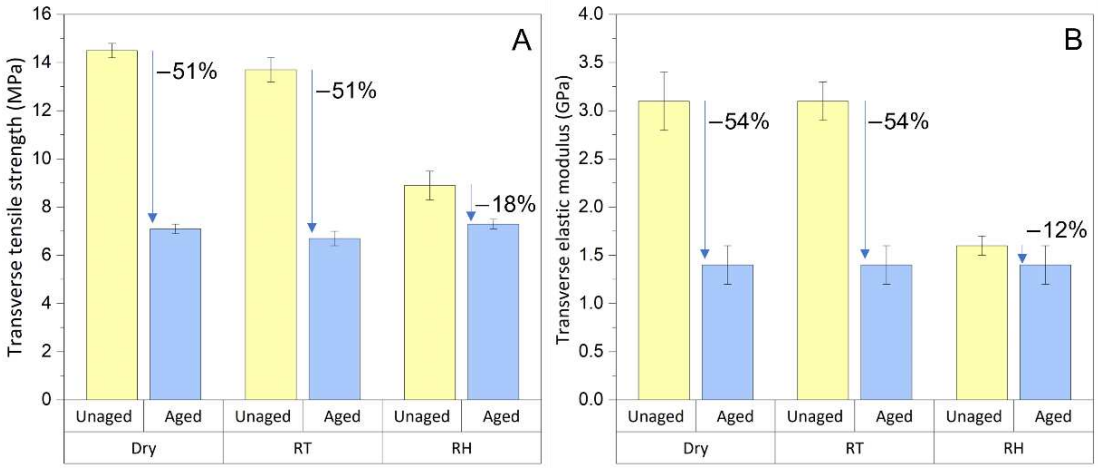

Figure 3. Transverse tensile strength (A) and elastic modulus (B) of flax PMMA composites

In Figure 3, the S_T and E_T properties of Dry and RT composites deteriorate by approximately 50% after one ageing cycle, including 40 days of water immersion, followed by a stabilisation period of 2 months at 50% RH (23 °C). For the similar ageing cycle, the deterioration in S_T (18%) and E_T (12%) properties of RH composites is notably limited compared to Dry and RT. Interestingly, the S_T and E_T properties of Dry, RT, and RH are in the same range after one water immersion ageing cycle.

In summary, the processing of flax PMMA composites with non-dry fibres conditioned at 50% RH did not alter composites' interfacial adhesion (based on S_T values). Especially, similar E_T values of Dry and RT composites indicated that in-situ polymerisation of PMMA is not sensitive to moisture. After one cycle of water immersion ageing, the S_T and E_T values of composites were in the same range regardless of the initial moisture content of fibres during the resin infusion. The mechanical performance of RH composites was relatively stable before and after the water immersion ageing.

3.4 In-plane shear properties of composites

The typical representative in-plane shear stress-strain curves of flax PMMA composites with $[+45/-45]_{SE}$ lay-up are presented in Figure 4. In this section, the offset in-plane shear strength (τ_{12}^{offset}) is defined as the stress value at 0.2% engineering shear strain. The maximum in-plane shear strength (τ_{12}^{max}) is defined as the stress value at 5% engineering shear strain according to the testing standard (ASTM D3518). The shear chord modulus of elasticity (G_{12}^{Chord}) is determined in the engineering shear strain range of 2000 $\mu\varepsilon$ to 6000 $\mu\varepsilon$.

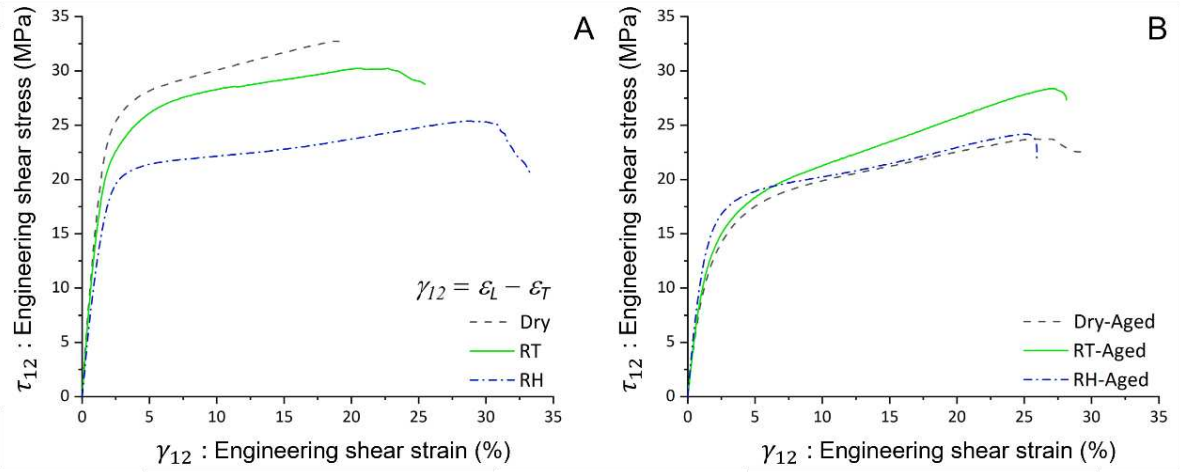

Figure 4. In-plane shear stress-strain plots of flax PMMA composites before water immersion ageing (A) and after ageing (B)

Before water immersion ageing (Figure 5), Dry and RT composites have similar τ_{12}^{max} and G_{12}^{Chord} values. The RH composites manufactured with highly swollen fibres conditioned at 90% RH have respectively 23% and 18% lower τ_{12}^{max} and G_{12}^{Chord} values than the Dry specimens processed with oven-dried fibres.

  doi:10.5075/epfl-298799_978-2-9701614-0-0

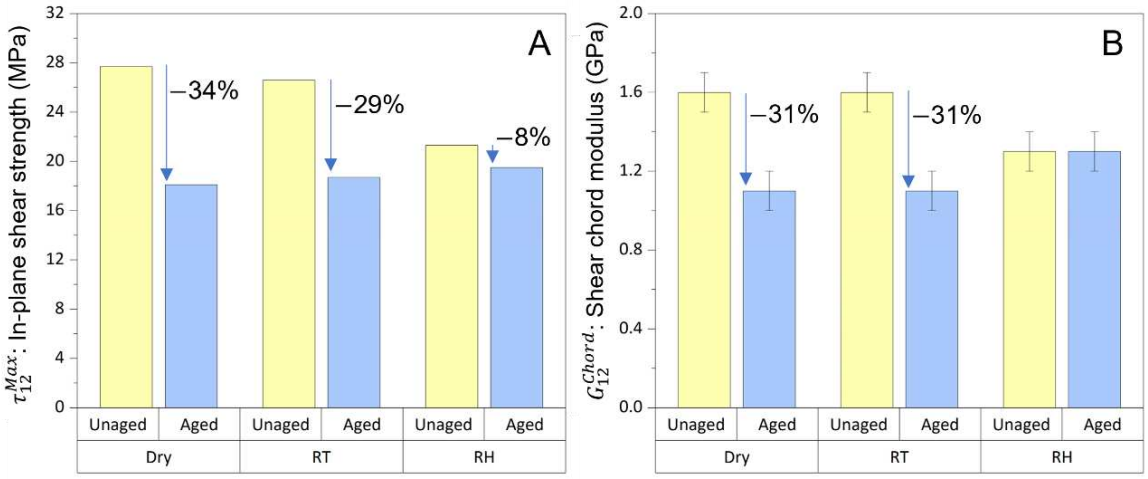

Figure 5. Effect of water immersion ageing on τ_{12}^{Max} (A) and G_{12}^{Chord} (B) values of composites

In Figure 5, one ageing cycle (water immersion and stabilisation) reduces the τ_{12}^{max} and G_{12}^{Chord} of Dry and RT by approximately 30%. Ageing has only a minor effect (8%) on the τ_{12}^{max} of RH composites. Interestingly, the G_{12}^{Chord} of RH is not sensitive to ageing and offers a higher G_{12}^{Chord} value (by 18%) compared to aged Dry and RT. Composites processed with oven-dried and non-dried fibres present similar τ_{12}^{max} values after one ageing cycle. It is worth noting that the in-plane shear strength of composites is less sensitive to the hydrothermal ageing than the transverse tensile strength (see Figures 3 and 5). The overall in-plane shear performance of flax PMMA composites is summarised in Table 1.

Table 1: In-plane shear properties of flax PMMA composites with $[+45/-45]_{SE}$ lay-up

Composite	G_{12}^{Chord} (GPa)	τ_{12}^{Offset} (MPa)	τ_{12}^{Max} (MPa)	$\gamma_{12}^{Failure}$ (%)
Dry	1.6 ± 0.1	17.6 ± 0.7	27.7 ± 0.9	19.4 ± 1.2
Dry-Aged	1.1 ± 0.1	8.6 ± 0.4	18.1 ± 0.7	29.6 ± 1.3
RT	1.6 ± 0.1	16.6 ± 0.4	26.6 ± 0.3	27.6 ± 1.3
RT-Aged	1.1 ± 0.1	13.2 ± 0.6	18.7 ± 0.4	28.6 ± 1.4
RH	1.3 ± 0.1	13.2 ± 0.8	21.3 ± 0.5	34.4 ± 1.9
RH-Aged	1.3 ± 0.1	12.3 ± 0.8	19.5 ± 0.3	26.1 ± 1.5

In summary, the results in this article presented a possibility to tailor the hygroscopic expansion and hydrothermal durability of flax PMMA composites based on the initial fibre moisture content during the in-situ polymerisation. The findings here can be beneficial for manufacturing natural fibre reinforced thermoplastics (NFRP) for various applications such as 3D/4D printing [8] and out of autoclave processing of large NFRP products. The fatigue testing of flax PMMA composites after water immersion ageing will be performed in future work to understand the effect of non-dry fibres on the interfacial adhesion over dynamic loading ranges.

  doi:10.5075/epfl-298799_978-2-9701614-0-0

4. Conclusions

This article showed that flax PMMA thermoplastic composites manufactured with oven-dried and non-dry fibres conditioned at 50% RH offer similar interfacial adhesion properties. Composites processed with preconditioned fibres at 50% RH (namely RT) and 90% RH (namely RH) had respectively 47% and 56% lower thickness swelling due to water sorption compared to NFRP with oven-dried fibres (namely Dry). Lower thickness swelling of non-dry composites can reduce the hygroscopic residual stresses and debond cites between fibre and matrix in wet service conditions. For both Dry and RT composites, the transverse tensile strength (S_T) and in-plane shear strength (τ_{12}^{Max}) respectively reduced by 50% and 30% after a water immersion ageing cycle. The RH composites were least affected by ageing in S_T (by - 18%) and τ_{12}^{Max} (by - 8%). After one ageing cycle, the S_T and τ_{12}^{Max} of all three types of composites were in the same range regardless of the initial fibre moisture content during the manufacturing. Interestingly, the shear chord modulus of elasticity (G_{12}^{Chord}) of RH composites was not affected by the ageing cycle and was 18% higher than aged Dry and RT.

Acknowledgements

This project was funded by the European Union's Horizon 2020 research and innovation programme under the Marie Skłodowska-Curie grant agreement No 764713-FibreNet.

5. References

1. Liu T, Butaud P, Placet V, Ouisse M. Damping behavior of plant fiber composites: A review. Compos Struct. 2021 Nov 1;275:114392. Available from: https://doi.org/10.1016/j.compstruct.2021.114392.

2. Javanshour F, Prapavesis A, Pärnänen T, Orell O, Lessa Belone MC, Layek RK, et al. Modulating impact resistance of flax epoxy composites with thermoplastic interfacial toughening. Compos Part A Appl Sci Manuf. 2021 Nov 1;150:106628. Available from: https://doi.org/10.1016/j.compositesa.2021.106628.

3. le Duigou A, Merotte J, Bourmaud A, Davies P, Belhouli K, Baley C. Hygroscopic expansion: A key point to describe natural fibre/polymer matrix interface bond strength. Compos Sci Technol. 2017 Oct 20;151:228–33. Available from: https://doi.org/10.1016/j.compscitech.2017.08.028.

4. Lu MM, Fuentes CA, Van Vuure AW. Moisture sorption and swelling of flax fibre and flax fibre composites. Compos Part B Eng. 2022 Feb 15;231:109538. Available from: https://doi.org/10.1016/j.compositesb.2021.109538.

5. Fruleux T, Castro M, Sauleau P, Matsuzaki R, Le Duigou A. Matrix stiffness: A key parameter to control hydro-elasticity and morphing of 3D printed biocomposite. Compos Part A Appl Sci Manuf. 2022 May 1;156:106882. Available from: https://doi.org/10.1016/j.compositesa.2022.106882.

6. Lu MM, Van Vuure AW. Effects of water immersion ageing on composites made of non-dry flax fibres. Mater Today Proc. 2020 Jan 1;31:S206–8. Available from: https://doi.org/10.1016/j.matpr.2019.11.061.

  doi:10.5075/epfl-298799_978-2-9701614-0-0

7. Krys P, Matyjaszewski K. Kinetics of Atom Transfer Radical Polymerization. Eur Polym J. 2017 Apr 1;89:482–523. Available from: https://doi.org/10.1016/j.eurpolymj.2017.02.034.

8. Le Duigou A, Correa D, Ueda M, Matsuzaki R, Castro M. A review of 3D and 4D printing of natural fibre biocomposites. *Mater Des*. 2020 Sep 1;194:108911. Available from: https://doi.org/10.1016/j.matdes.2020.108911.

DAMAGE TOLERANT THIN-PLY BOULIGAND CFRP STRUCTURES

*J. Körbelin[a], P.Goralski[a], B. Kötter[a], F. Bittner[b], H.-J. Endres[b], and B. Fiedler[a]**

a: Institute of Polymer and Composites, Hamburg University of Technology, Hamburg, Germany,
b: Institute of Plastics and Circular Economy, Leibniz University Hannover, Hannover, Germany

* Corresponding author (fiedler@tuhh.de)

Keywords: Bouligand structures; Hybrid Composite; Thin-Ply; CFRP

Open access full paper: *Körbelin, Johann and Goralski, Philip and Kötter, Benedikt and Bittner, Florian and Endres, Hans-Josef and Fiedler, Bodo (2021). Damage tolerance and notch sensitivity of bio-inspired thin-ply Bouligand structures. Composites Part C: Open Access. 5. 100146*

Abstract

Different bio-inspired Bouligand thin-ply Carbon-Fibre-Reinforced Polymer (CFRP) laminates with a pitch angle as low as 2:07° are realised, which is the smallest pitch angle realised in literature. The angle is therefore close angles found in biological microstructures. Low-Velocity Impact (LVI) and residual compressive strength tests determined the damage tolerance of the structures. Investigated were interlaminar fracture toughness and two different metal foil-Bouligand-CFRP-hybrids. The low pitch angle results in significantly higher residual strengths than 45° quasi-isotropic (QI) layups, despite the significantly lower proportion of 0° fibres. Higher fracture toughness and hybridisation with steel layers lead to reduced matrix damage without increasing residual compressive strength. In-plane plane tension properties are determined with a pitch angle of 2:59°. The results reveal that the unnotched tensile strength is significantly lower. However, only helicoidal, sub-critical matrix cracking and no delamination occur before final failure. The sub-critical matrix cracking leads to almost no notch sensitivity and a similar open-hole-tensile strength to 45°-QI layups despite the low number of 0°-fibres.

  doi:10.5075/epfl-298799_978-2-9701614-0-0

ACCELERATED AGEING AND MOISTURE ABSORPTION IN POLYMER COMPOSITES

Jasmine Bone[a], Antony Maxwell[b], Graham Sims[b], Charlotte Foreman[a], Robert Dorey[a], Stephen Ogin[a]

a: University of Surrey, Guildford, UK
b: National Physical Laboratory, Teddington, UK

Abstract: *There has been extensive development in the offshore and marine industries of the use of polymer composite materials and understanding the durability of these materials is a significant challenge. Numerous test methods exist for the accelerated ageing of polymeric materials at the laboratory scale, but tests employing a combination of exposure conditions (e.g. at elevated temperature, under pressure, under a mechanical load) are lacking.*

In this work elevated temperatures are used to accelerate the ageing of polymer composite specimens when exposed to different combinations of immersion in water, pressure and mechanical loading. The results show that the behaviour of the material exposed to different combinations of exposure conditions, produces changes in residual properties (i.e. flexural modulus flexural strength and T_g) which are complex. Of immediate significance to understanding the behaviour of composites in a marine environment is the observation of a very significant decrease in the rate of moisture absorption for specimens tested under a pressure of 300 bar.

Keywords: Durability; moisture diffusion; pressure; mechanical properties; degradation

1. Introduction

There is a significant industrial need to develop suitable test methods and models to understand the ageing of polymer composite materials. In subsea environments, materials are subjected to exposure to moisture, pressure, and mechanical loading. Under these conditions, maintenance and repair of structures is challenging and therefore it is essential to ensure the long-term performance, often required up to 25 years, in order to maintain both safety and cost effectiveness. To achieve this, it is necessary to understand the degradation mechanisms occurring in the material and the subsequent deterioration of material properties.

It has been shown that absorption of water into a composite reduces the mechanical properties such as a reduction in tensile strength (1–3), interlaminar shear strength (4), flexural strength and modulus (5,6). The glass transition temperature (T_g) of a polymer is also reduced with moisture ingress due to plasticization (7–10). Therefore, it is essential to understand how water diffuses into a composite material in different environments, and how the exposure conditions affect the relationship between moisture absorption and property degradation. Of interest in this work is the effect of pressure on moisture absorption, and the effect of load.

Accelerated ageing tests can be used to evaluate the likely long-term behaviour of a material/component under service conditions. This is achieved by increasing the severity of test conditions in the laboratory to reduce the test time. However, such an approach is only effective provided the degradation mechanisms do not change under the accelerated conditions. In

  doi:10.5075/epfl-298799_978-2-9701614-0-0

addition, any synergy effects between exposure conditions with respect to the degradation mechanisms must be considered, for example the effect of applied pressure and/or mechanical load on the moisture absorption.

The most widely used method of evaluating the long-term exposure of a material to water is to accelerate uptake using elevated water temperature. Typically, these conditions will range from ambient temperatures to 60°C, dependent on the T_g of the material (11) although it is advisable not to test above T_g-20°C (12,13) so as not to alter any material properties during ageing. This is due to the potential decrease in T_g due to prolonged immersion in water, where an increase in molecular mobility disrupts hydrogen bonding and van der Waals interactions in the polymer chain, plasticising the matrix (14)(9). There are two competing mechanisms by which pressure may affect water uptake, firstly by accelerating the diffusion by forcing more water into the material, but secondly by reducing the amount of water able to enter the composite due to compression of the material (8,12,13,15–18). This compression reduces the free volume available for water to occupy.

A simple approach to explore the effect of load during moisture ageing is to apply a tensile stress to a specimen while immersed in water. A recent study (19), found that the application of a preload to a material before immersion at 60°C had a small effect on water uptake in the composite material; an increase of 6% preloaded compared to 5% uptake in an undamaged material. Applying a tensile load during exposure at 60°C in water had a much greater effect, where water uptake increased up to 9% by weight, and some specimens failed prematurely. Other work has shown that low loads have only a small effect on the diffusion into the material, where deformation is still in the elastic region, but significantly higher loading (which produce damage in the material such as resin cracking) leads to more channels for moisture ingress (16,20,21).

However, exposure of composite specimens both pre-stressed and immersed in water while subjected to a flexural load have shown that application of load can decrease the water uptake (22). Pultruded CFRP specimens were subjected to 30% or 50% bending strain, with increasing strain decreasing the moisture uptake. This was attributed to the bending decreasing the free volume in the material, removing channels for moisture to diffuse. Under a flexural load, one surface is in tension and the other in compression, therefore, to reduce this free volume as in this case, the compressive effects must dominate.

In this paper, various experimental results are presented for the effect on moisture uptake and the reduction in mechanical properties (flexural strength, flexural modulus and T_g) for specimens exposed to 60°C immersion in water, and with the addition of a pressure of 300 bar pressure, and/or a flexural load equivalent to 25% of the flexural strength.

Methodology

1.1 Materials

The carbon fibre epoxy composite material used in this study was obtained from Exel Composites. This material was a unidirectional (UD) pultrusion of dimensions 2 mm thickness, 50 mm width and 1 m in length. All test specimens were cut to size from these strips prior to exposure using a CompCut diamond saw. The material was tested as received, as well as in the conditioned state following various accelerated ageing procedures.

  doi:10.5075/epfl-298799_978-2-9701614-0-0

1.2 Accelerated ageing

Composite specimens were immersed in distilled water in a water bath at 60°C, as outlined in the standard ISO 62 (23), or immersed in pressure vessels at 60°C and 300 bar. Some specimens were also loaded during ageing using a four-point bend flexure jig within the water baths at 60°C, and pressure vessels at 60°C and 300 bar. A load equivalent to 25% of the unaged material failure load in flexure was applied under four-point loading. At least three repeat specimens were subjected to ageing and testing. Specimens were immersed for pre-determined time intervals of between 2 and 112 days, and the moisture content was determined by gravimetric measurements.

$$Moisture\ content(\%) = \frac{m_w - m_d}{m_d} \times 100\% \quad (1)$$

Here, m_w is the mass of the aged specimens and m_d is the mass of the unaged specimens prior to any testing. After immersion, samples were wiped to remove any surface water prior to weighing. All specimens were stored at room temperature in distilled water.

1.3 Characterisation of degradation

The water uptake in the composite materials was modelled using a Langmuir Style Hindered Diffusion model, and diffusion coefficients calculated (24). Four-point bend flexure tests were performed following BS EN ISO 14125 (25). Specimens were cut to dimensions 2 mm x 15 mm x 100 mm. Tests were conducted on an Instron mechanical test machine (4507/5570R) with a 20 kN load cell, and a crosshead speed of 2 mm/min.

Dynamic mechanical analysis (DMA) measurements were performed to determine the glass transition temperature, T_g, of the composite material. Measurements were performed at a heating rate of 3°C/min in flexure on a TA instruments Q800 Dynamic Mechanical Analyser.

2. Results and discussion

3.1 Moisture uptake in the polymer composite

The increases in moisture content (weight %) in the CF epoxy composite over time when exposed in water at 60°C, and in water at 60°C and at a pressure of 300 bar, are shown in Figure 1(a). It can be seen there is overlap in the data points for moisture absorption at very low exposure times (up to 4 days), at which point the curves deviate with significantly less moisture ingress for pressurised specimens. It seems that for this material, pressure slows diffusion of water. This is, of course, reflected in a significant reduction in diffusion coefficient, calculated using Langmuir diffusion modelling (24); Figure 1(b) shows the data fitted to the Langmuir model. Under pressure in water at 60°C, the diffusion coefficient is 27.4 $x10^{-13}$ m^2s^{-1}, whereas in water at 60°C (normal atmospheric pressure), it is 165.5 $x10^{-13}$ m^2s^{-1}. This effect needs to be studied in a wider range of materials.

In the literature, it has been suggested that bending during immersion decreases the free volume in the resin, so there is reduced penetration of water (22), and contrastingly that bending during immersion increases the diffusion coefficient (26). On the other hand, the application of tensile stress during water exposure has been shown to have a large effect on diffusion and lead to premature failure (19), though this is a simpler loading condition.

  doi:10.5075/epfl-298799_978-2-9701614-0-0

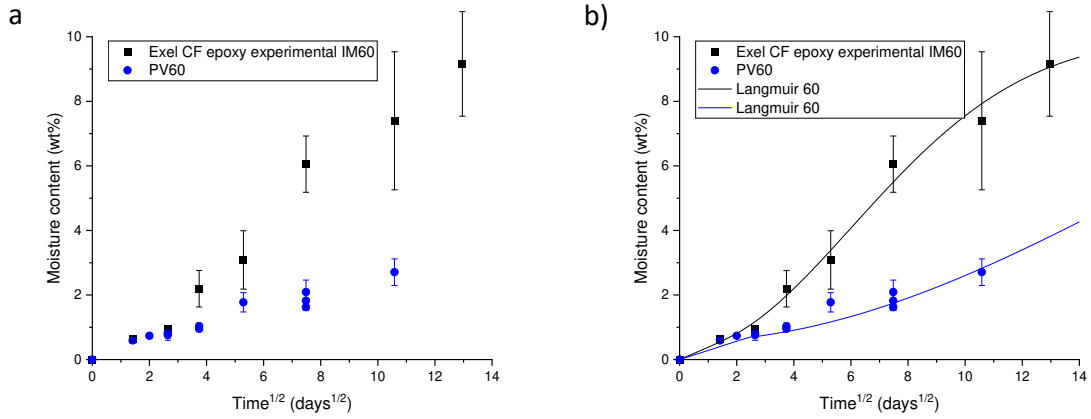

Figure 1 Experimental moisture uptake in the Exel CF epoxy composite when exposed at a) *60°C in water and 60°C and 300 bar in pressure vessels, and* b) *plotted with the best fit Langmuir model curves*

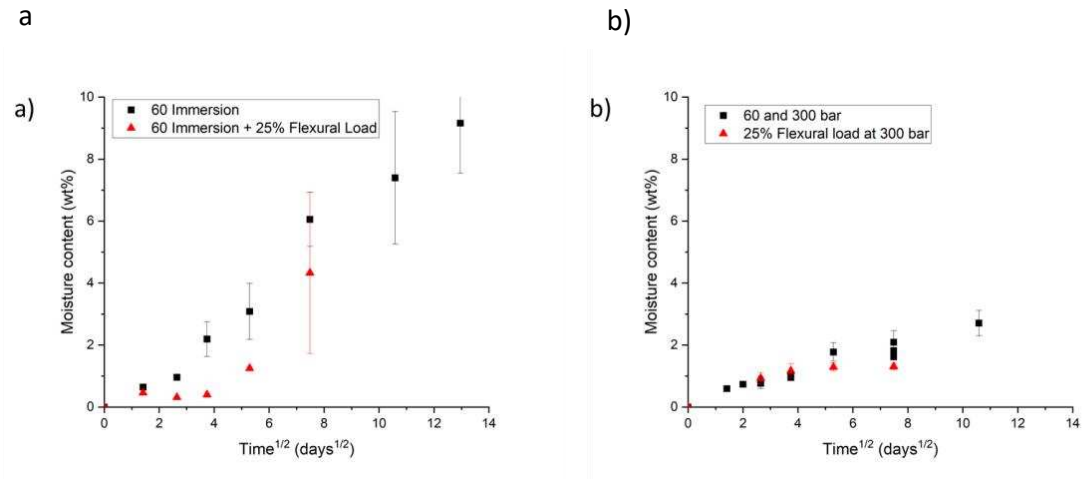

Figure 2 (a) Experimental moisture uptake in Exel CF epoxy composite when exposed in water at 60°C and when exposed to 25% flexural load in water at 60°C; (b) moisture uptake in a pressure vessel at 60°C and 300 bar and when exposed with 25% flexural load at 60°C and 300 bar

Figure 2(a) shows the moisture uptake for the Exel CF epoxy material specimens exposed at 60°C in water (same data as in Figure 1(a) and under the same conditions with an applied flexural load (25% of the flexural load to failure). This data clearly shows a reduced moisture uptake initially for specimens under the flexural load, although after about 56 days the moisture content of specimens under load or without load is similar. For specimens exposed to 300 bar pressure and the flexural load (Figure 2(b)), the additional flexural load again does not appear to reduce reduces the moisture uptake initially, but at longer exposure times (after about 14 days), the additional load reduces the moisture uptake.

3.2 Effect of exposure conditions on property changes

The reduction, as a consequence of accelerated ageing, in the initial values of the flexural strength, flexural modulus and T_g as a result of the various ageing conditions are shown in for the Figures 3, 4 and 5. In all cases, the percentage property retention is shown plotted as a function of exposure time, and a function of moisture content, for the various conditions.

  doi:10.5075/epfl-298799_978-2-9701614-0-0

Figure 3 shows that when simply exposed in water at 60°C, the flexural modulus is not reduced to the same extent as the flexural strength and the T_g. At shorter exposure times, up to about 14-days exposure (2.2% moisture content), there is a larger reduction in T_g and flexural strength, but the flexural modulus is not affected. After 28 days exposure (5.3 days$^{1/2}$) the strength and T_g continue to decrease but at a slower rate, to about 55% and 65% respectively, and the flexural modulus is reduced to about 77% of the unaged value.

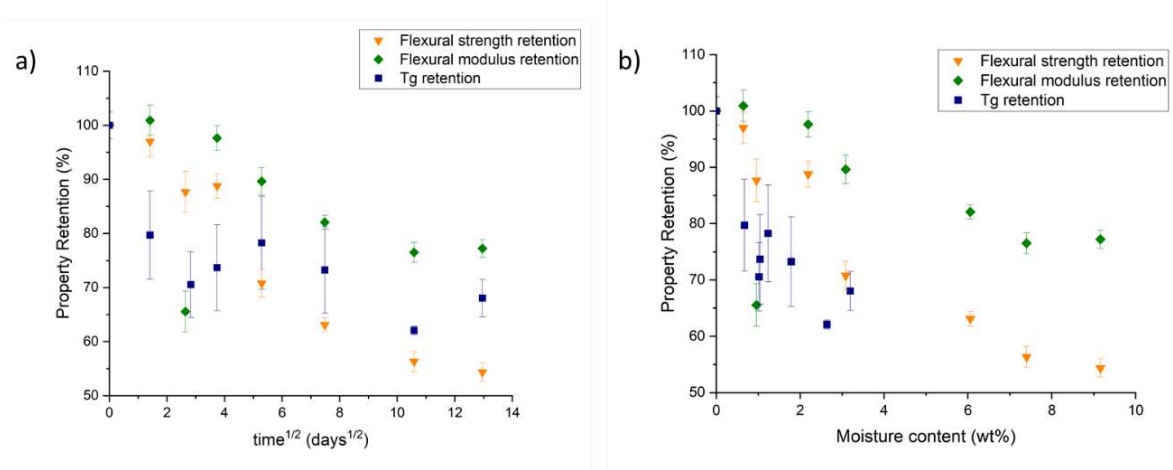

Figure 3 Changes in material properties of the Exel CF/epoxy composite exposed in a water bath at 60°C with (a) increased exposure time and (b) increasing moisture content normalised to pre aged values

The change in properties due to exposure in water at 60°C and 300 bar pressure (Figure 4) shows that the flexural modulus is approximately constant (after an initial reduction to about 92%) up to 14 days exposure and 1% moisture content, and only a further decrease with prolonged ageing to about 86%, even with a moisture content of 3%. The flexural strength, on the other hand, shows a progressive decrease in value with increased moisture content; for up to 1% moisture content, the flexural strength reduced to 80% of the unaged value, and with continued exposure (up to 112 days and about 3% moisture content) the reduction is to about 62% of the unaged strength. The glass transition temperature in these tests is only available up to 28 days exposure, but the T_g reduced significantly in over this exposure period to about 67% of the unaged value. It is not clear why the moisture degraded the strength to such a large extent, but not the stiffness, although the large reduction in T_g is perhaps indicative of significant changes in the matrix.

  doi:10.5075/epfl-298799_978-2-9701614-0-0

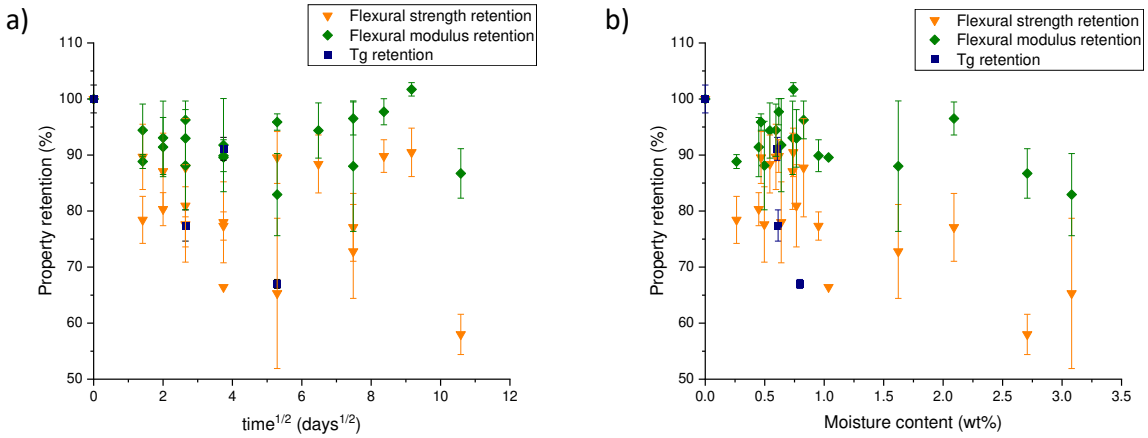

Figure 4 Changes in material properties of the Exel CF/epoxy composite exposed in a pressure vessel at 60°C and 300 bar with (a) increased exposure time and (b) increasing moisture content normalised to pre aged values

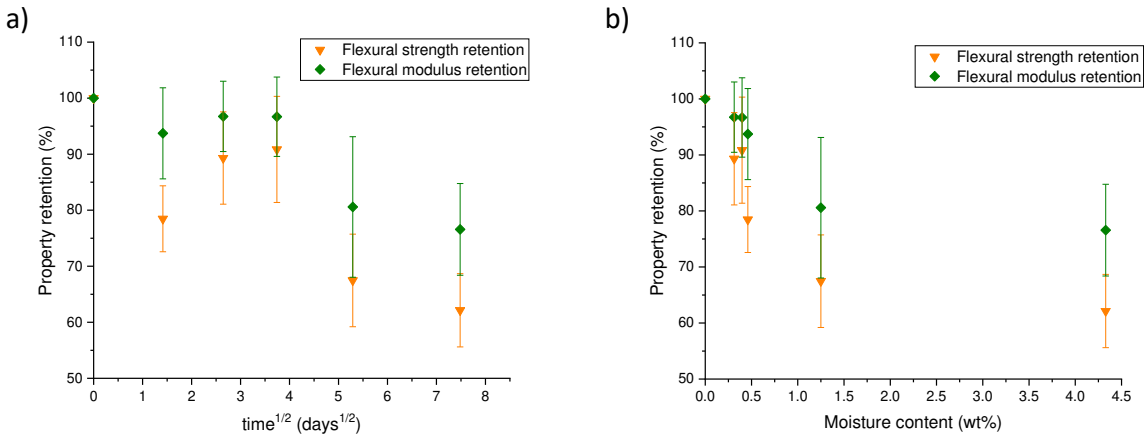

Figure 5 Changes in material properties of the Exel CF/epoxy composite exposed in water baths at 60°C and 25% flexural load with (a) increased exposure time and (b) increasing moisture content normalised to pre aged values.

When exposed at 60°C, 300 bar and 25% flexural load (Figures 5(a) and (b)), the test results again show an interesting equivalence of the trends in the flexural strength and flexural modulus with increasing exposure, although the strength retention is consistently about 15% less than the modulus retention.

Comparing the results for exposure at 60°C, 300 bar, with and without load applied, the interesting result that emerges is that the modulus retention for the exposure with the applied load is significantly worse (by about 10%) than when the load was not applied during the exposure. This may be because the fibre/matrix interface has been additionally degraded when the flexural load is applied in addition to the 300 bar and 60°C.

3. Conclusions

Moisture uptake in the CF epoxy composite was significantly reduced as a function of time when 300 bar pressure was added to the conditioning at 60°C in water. The further addition of an applied load (25% of the flexural load to failure in 4-point bending) showed moisture uptake was unchanged up to about 16 days exposure but was then significantly lower after this point for the specimens with the applied load. Interestingly, for specimens immersed at 60°C with or without

  doi:10.5075/epfl-298799_978-2-9701614-0-0 published under CC BY-NC 4.0 license

the same applied flexural load, the effect of the applied load reduced the moisture uptake from the beginning of the exposure, though by 56 days it was found that the moisture levels were about the same.

The change in material properties after exposure to various conditions showed a complex pattern. For specimens at 60°C with and without an applied pressure of 300 bar, the flexural modulus reduced much less with exposure for specimens at 60°C and 300 bar than the flexural strength and T_g. On the other hand, for specimens exposed at 60°C with a flexural load, the trends in the reduction of flexural modulus and strength were the same, although the reduction in flexural strength was consistently about 15% higher.

Acknowledgements

The authors are grateful to John Hartley from Exel Composites for donating material for testing. This research was was supported by the Engineering and Physical Sciences Research Council UK [EPSRC Centre for Doctoral Training in Micro- and NanoMaterials and Technologies (MiNMaT - EP/L016788/1), University of Surrey, Element Materials Technology and the National Measurement System (NMS) of the UK Department for Business, Energy and Industrial Strategy (BEIS).

4. References

1. Shen CH, Springer GS. Effects of Moisture and Temperature on the Tensile Strength of Composite Materials. *J Compos Mater* 1977;11:2–16.
2. Krauklis AE, Gagani AI, Echtermeyer AT. Hygrothermal aging of amine epoxy: Reversible static and fatigue properties. *Open Eng* 2018;8:447–454.
3. Gu H. Behaviours of glass fibre/unsaturated polyester composites under seawater environment. *Mater Des* 2009;30:1337–1340.
4. Kootsookos A, Mouritz AP. Seawater durability of glass- and carbon-polymer composites. *Compos Sci Technol* 2004;64:1503–1511.
5. Zhang X, Wang Y, Wan B, Cai G, Qu Y. Effect of specimen thicknesses on water absorption and flexural strength of CFRP laminates subjected to water or alkaline solution immersion. *Constr Build Mater* 2019;208:314–325.
6. Afshar A, Alkhader M, Korach CS, Chiang FP. Effect of long-term exposure to marine environments on the flexural properties of carbon fiber vinylester composites. *Compos Struct* 2015;126:72–7.
7. Cavasin M, Sangermano M, Thomson B, Giannis S. Exposure of glass fiber reinforced polymer composites in seawater and the effect on their physical performance. *Materials* 2019;12.
8. Duncan, B.C., and Broughton, W.R., Absorption and Diffusion of Moisture In Polymeric Materials, NPL Measurement Good Practice Guide No 102, 2007
9. Zhou J, Lucas JP. Hygrothermal effects of epoxy resin. Part II: Variations of glass transition temperature. *Polymer*. 1999;40(20):5513–22.
10. Gu H. Dynamic mechanical analysis of the seawater treated glass/polyester composites. *Mater Des*. 2009;30(7):2774–7.
11. Alam P, Robert C, Ó Brádaigh CM. Tidal turbine blade composites - A review on the effects of hygrothermal aging on the properties of CFRP. *Compos Part B Eng*, 2018;149(April):248–59.
12. Broughton WR, Maxwell AS. *Accelerated Environmental Ageing of Polymeric Materials*, NPL Measurement Good Practice Guide No . 103, 2007
13. Davies P. *Towards More Representative Accelerated Aging of Marine Composites*, in Advances

  doi:10.5075/epfl-298799_978-2-9701614-0-0

in Thick Section Composite Sandwich Structures, Springer, 2020, p 507–527
14. Zhou JM, Lucas JP. Hygrothermal effects of epoxy resin. Part I: the nature of water in epoxy. *Polymer*. 1999;40(20):5505–12.
15. Graham-Jones J, Summerscales J. *Marine Applications of Advanced Fibre-Reinforced Composites*, Elsevier, 2016
16. Davies P, Rajapakse YDS. *Durability of Composites in a Marine Environment 2*. Springer International Publishing; 2018.
17. Maxwell AS, Broughton WR. *Survey of Long-Term Durability Testing of Composites, Adhesives and Polymers*, NPL Report MAT 85, 2017
18. Davies P, Rajapakse Y. *Durability of Composites in a Marine Environment*, Springer, 2014
19. Humeau C, Davies P, Jacquemin F. An experimental study of water diffusion in carbon/epoxy composites under static tensile stress. *Compos Part A Appl Sci Manuf*. 2018;107.
20. Weitsman Y. Coupled damage and moisture-transport in fiber-reinforced, polymeric composites. *Int J Solids Struct*, 1987;23(7):1003–25.
21. Perreux D, Suri C. A study of the coupling between the phenomena of water absorption and damage in glass/epoxy composite pipes. *Compos Sci Technol*. 1997;57(9–10):1403–13.
22. Kafodya I, Xian G, Li H. Durability study of pultruded CFRP plates immersed in water and seawater under sustained bending: Water uptake and effects on the mechanical properties. *Compos Part B Eng*. 2015;70:138–48.
23. BS EN ISO 62: 2008, Plastics -- Determination of water absorption
24. Bone JE. *On the effect of accelerated ageing and moisture absorption in polymer composites.* EngD Thesis, University of Surrey, UK, 2021
25. ISO 14125: 1998, Fibre-reinforced plastic composites — Determination of flexural properties.
26. Hong B, Xian G, Li H. Comparative study of the durability behaviors of epoxy- and polyurethane-based CFRP plates subjected to the combined effects of sustained bending and water/seawater immersion. *Polymers*. 2017;9(11).

  doi:10.5075/epfl-298799_978-2-9701614-0-0

MICRO-DAMAGE AND ULTIMATE FAILURE ANALYSIS OF HYBRID THIN-PLY CARBON/GLASS LAMINATES

Alens, Šņepsts[a], Andrejs, Pupurs[a], Mārtiņš, Irbe[a], Viesturs, Lācis[a]

a: Riga Technical university – andrejs.pupurs@rtu.lv

Abstract: *The present study investigates ultimate failure of hybrid thin-ply laminates. Hybrid laminates were manufactured from layers of carbon fiber and glass fiber fabrics using vacuum infusion of epoxy resin. Different lay-up configurations having single, double and quadruple layers of carbon and glass fiber layers were designed to parametrically investigate the ultimate strength and strain to failure under uniaxial tensile loading. In addition laminate specimens were polished to study the micro-damage mechanisms in the laminate layers. Results indicate an increased tensile strength and strain to failure when carbon and glass/epoxy layers are distributed into thinner layers compared to laminates with equal amount of carbon and glass/epoxy layers assembled into thicker layers.*

Keywords: thin-ply laminates; carbon/glass fiber hybrids; experimental testing; micro-damage

1. Introduction

Polymeric composite materials, such as glass and carbon fiber reinforced polymers, over the recent decades, have been increasingly used in modern lightweight high-performance structures such as airplanes, wind turbine blades, cars and sports equipment due to their unique combination of high stiffness and low density. However, despite the increase of use of composites in many high-performance applications, the development of micro-damage such as fiber/matrix interface debonds, matrix cracks, delaminations and fiber breaks in composite layers during the service life is a significant limiting factor. Matrix cracks in transverse layers are typically the first damage mode to occur in the laminate layers due to weak properties in the transverse direction to the fibers and is a main cause for the appearance of subsequent damage modes such as delaminations and fiber breaks. Hence, to delay the final failure, it is highly desirable to suppress the initiation and development of transverse matrix cracks. In this context, laminates with thin plies, developed in the recent decade [1,2], is a promising new development direction for composite materials, which is expected to give superior damage resistance compared to conventional composite laminates due to increased in-situ transverse strength. There have been several studies demonstrating a significant increase of transverse strength and delayed or nearly suppressed micro-cracking in thin-ply carbon/epoxy laminates [3,4]. However, the increased strength and delayed micro-cracking leads to a much more brittle final failure of the laminate which is not desirable in many applications [3]. One typical approach of decreasing the brittleness of the composite laminate failure is fiber or layer hybridization – the use of at least two different types of fibers in the composite. Typical example widely investigated in the literature is carbon/glass hybrid laminates, where the carbon fiber layers provide the stiffness of the laminate, while the glass fibers, which have a much higher failure strain, lead to a significantly more ductile failure behavior of the composite [5,6].

  doi:10.5075/epfl-298799_978-2-9701614-0-0

As mentioned above, the thin-ply laminates and layer hybridization lead to a significant improvement in composite failure properties, however, rather few attempts have been made in the literature to combine both thin-ply architecture and the hybrid glass/carbon lay-up into a single laminate, e.g., [7,8]. According to [7] hybridization of thin carbon and glass fiber layers may lead to an improvement of 20% in the failure strain. Furthermore, the thin plies suppress unstable delamination and it becomes possible to avoid a significant load drop, when the brittle component, such as carbon fiber layer, breaks [8].

2. Materials and lay-ups

Thin-ply laminates were manufactured using Textreme carbon fiber thin-ply plain weave fabrics from Oxeon (Sweden) with areal weight of 100g/m^2 and glass fiber plain weave fabrics from Interglas (Germany) with an areal weight of 80g/m^2. Epoxy resin LY1564 with XB 3404-1 hardener was used as the matrix. Composite plates were hand stacked into desired lay-ups and vacuum infusion technique was used for epoxy infusion into the stacked fabrics (Fig.1).

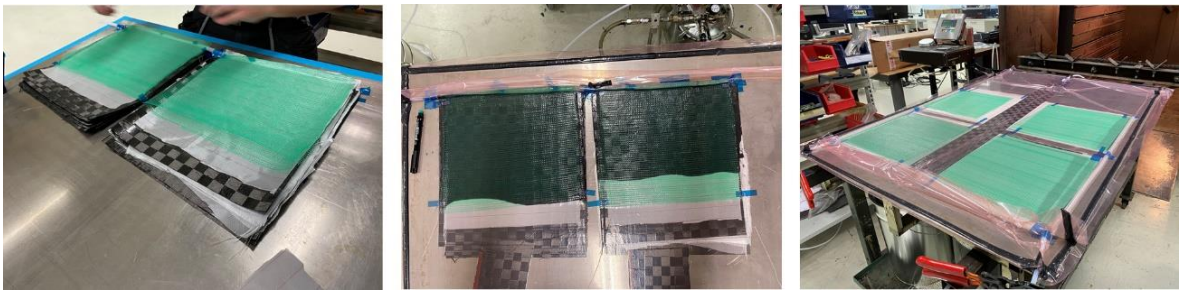

Figure 1. Manufacturing of hybrid thin-ply laminates with vacuum infusion

To enhance the flow of resin through the densely packed fabrics, small size metal pins were used to provide better flow conditions prior to the vacuum infusion process. The hybrid composite plates were cured in an oven at 80°C temperature for 8 hours. Hybrid carbon/glass laminates with various combinations of single, double and quadruple carbon and glass fiber layers were manufactured. All plates consisted of 16 layers. The lay-ups and their notations are schematically shown in Fig.2.

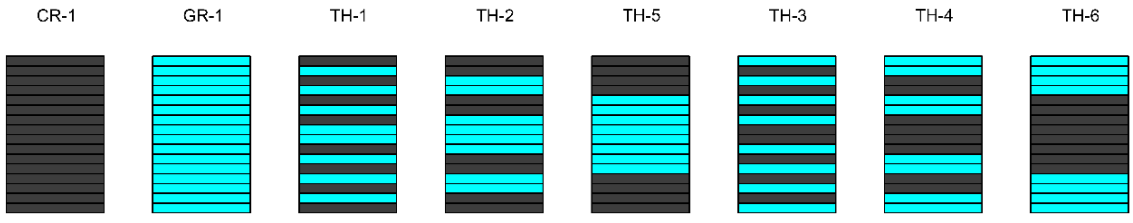

Figure 2. Schematic illustration of hybrid thin-ply laminate lay-ups

In Fig.1. CR-1 and GR-1 denote carbon/epoxy and glass/epoxy reference materials respectively. TH-1 to TH-6 are the used notations for hybrid carbon and glass/epoxy laminate plates with different layer configurations and thickness ratios. Notably the hybrid composite plates TH-1 to TH-6 all consist of 8 layers of carbon/epoxy and 8 layers of glass/epoxy layers.

3. Experimental tests

Standard size tensile test specimens (according to ASTM D3039) were prepared to perform experimental tests for determination of elastic tensile modulus, maximum tensile strength and ultimate strain to failure of reference and hybrid composite laminates. Specimen ends were reinforced with glass fiber composite tabs to prevent failure within grips of the testing machine during loading. Mechanical tests were performed on Zwick/Roell Z150 universal testing machine equipped with 150 kN capacity load cell. Tensile strain was measured using non-contact video-extensometer from Messphysik with gage length of 50 mm. Tests were performed at a rate of tensile strain equal to 1% per minute consisting of initial loading-unloading step up to 0.30% for measurement of elastic tensile modulus followed by loading step until the ultimate failure. 3 test specimens from each laminate lay-up were tested.

4. Results and discussion

4.1 Uniaxial tensile tests

The stress-strain curves from tensile tests are shown in Fig.3-6. Carbon/epoxy reference material and the hybrid thin-ply laminates (TH-1 – TH-6) exhibit distinctively linear behavior up to the point of failure. Glass/epoxy reference material (GR-1 in Fig.3) exhibits non-linear behavior as well as brittle failure. Overall the stress-strain curves demonstrate high repeatability and low scatter in maximum stress and strain values.

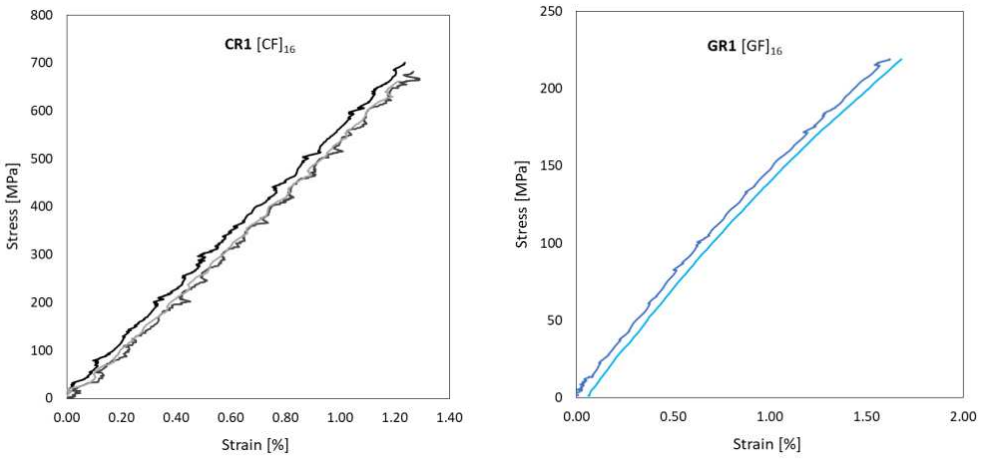

Figure 3. Stress-strain curves for reference materials (CR-1 and GR-1)

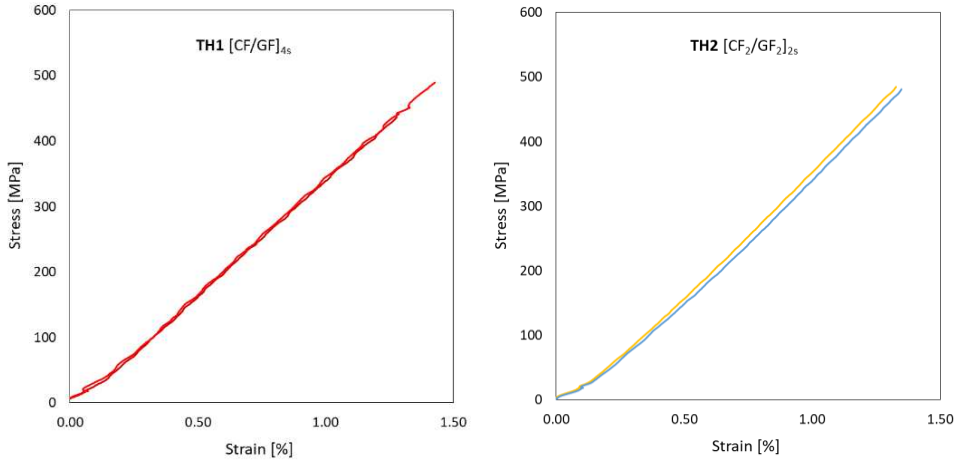

Figure 4. Stress-strain curves for hybrid composite laminates (TH-1 and TH-2)

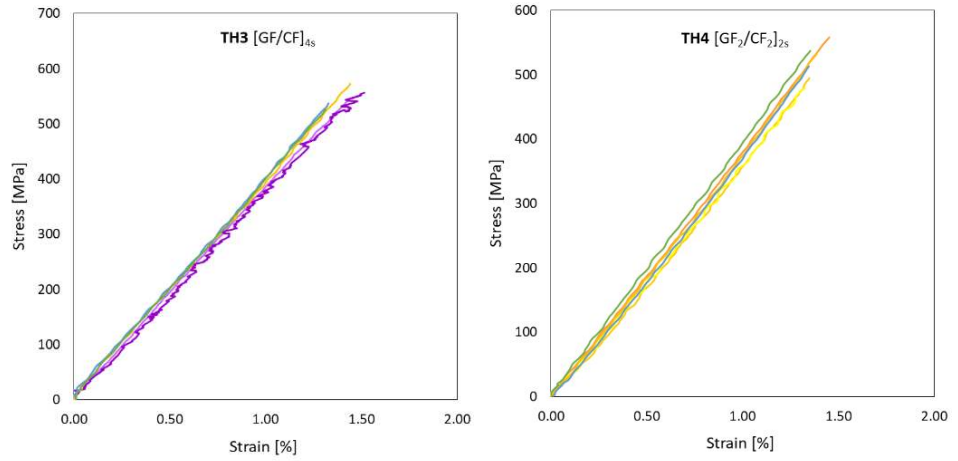

Figure 5. Stress-strain curves for hybrid composite laminates (TH-3 and TH-4)

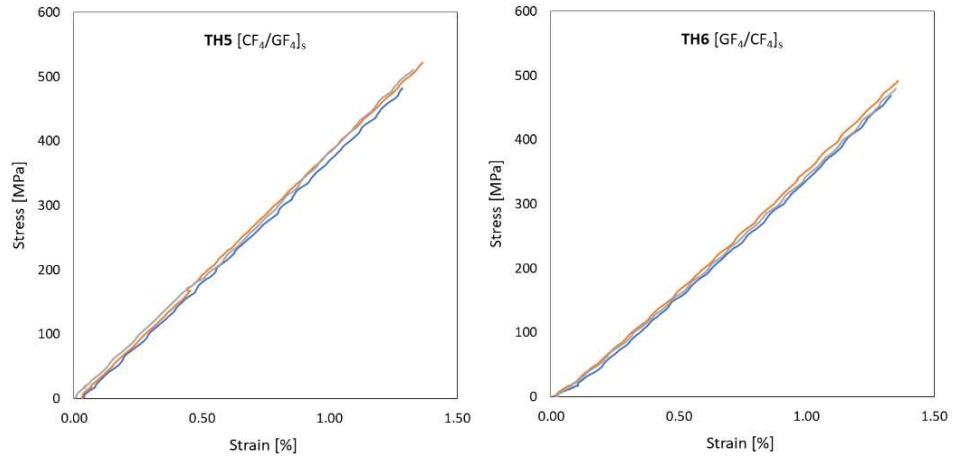

Figure 6. Stress-strain curves for hybrid composite laminates (TH-5 and TH-6)

Fig. 7 summarizes the elastic modulus values for all composite plates, including reference materials. Although hybrid laminates TH-1 to TH-6 have different lay-ups, the amount of carbon/epoxy and glass/epoxy layers in them is equal, hence the elastic modulus for these materials should theoretically be equal. Fig.7 shows a little discrepancy of elastic modulus.

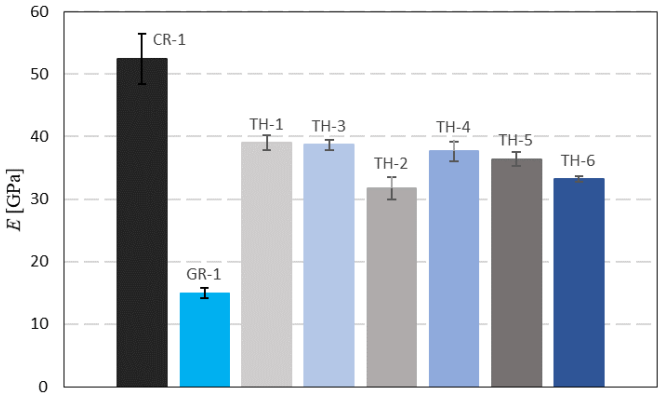

Figure 7. Elastic tensile modulus for reference materials and hybrid composites

Fig.8 summarizes the maximum tensile strength results for different laminate lay-ups, including reference materials. The results in Fig.8 demonstrate a trend that the laminates with carbon and glass/epoxy layers distributed in thinner units (e.g. TH-1 and TH-3) exhibit higher strength compared to laminates with thicker carbon and glass/epoxy layers (e.g., TH-5, TH-6).

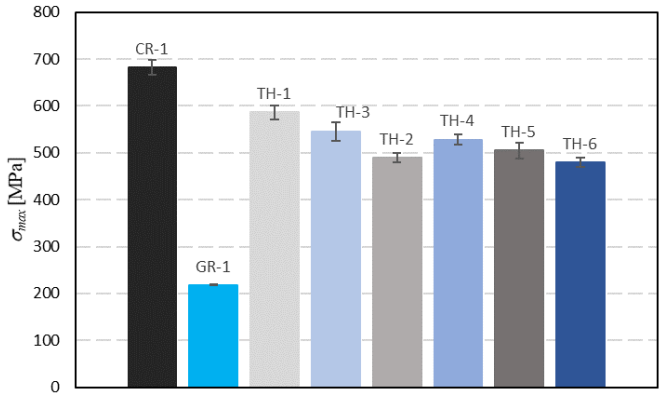

Figure 8. Ultimate tensile strength for reference materials and hybrid composites

A similar trend was observed regarding the maximum strain to failure, summarized in Fig.9. The hybrid laminates with thinner layers (e.g., TH-1, TH-3) exhibited larger strain to failure than the hybrid laminates with thicker layers (e.g., TH-5, TH-6).

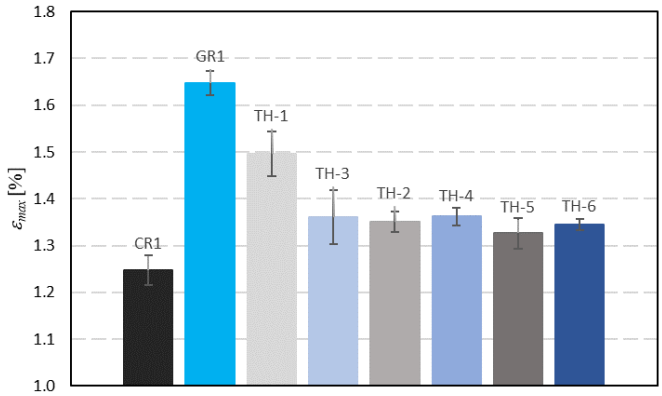

Figure 9. Maximum tensile strain at failure for reference materials and hybrid composites

  doi:10.5075/epfl-298799_978-2-9701614-0-0

Results are also summarized in terms of numerical values in Table 1 where the average values of elastic modulus, tensile strength and maximum strain to failure are shown.

Table 1: Summary of test results.

Lay-up	Notation	E [GPa]	σ^{max} [MPa]	ε^{max} [%]
$[CF]_{16}$	CR-1	52.48	681.48	1.25
$[GF]_{16}$	GR-1	15.04	218.15	1.65
$[CF/GF]_{4s}$	TH-1	39.05	586.27	1.50
$[GF/CF]_{4s}$	TH-3	38.66	545.90	1.36
$[CF_2/GF_2]_{2s}$	TH-2	31.73	490.24	1.35
$[GF_2/CF_2]_{2s}$	TH-4	31.99	510.90	1.37
$[CF_4/GF_4]_s$	TH-5	36.41	505.16	1.33
$[GF_4/CF_4]_s$	TH-6	33.18	479.79	1.34

5. Conclusions

Present study was conducted to investigate the potential enhancement of laminate strength and strain to failure using thin-ply hybrid laminate lay-ups with different layer thicknesses. Hybrid carbon/epoxy and glass/epoxy laminates with different lay-ups were manufactured using vacuum infusion method. Present results show a notable increase of both the tensile strength and strain to failure for laminates with distributed carbon/epoxy and glass/epoxy layers compared to laminates with relatively thicker layers. Tensile test results also exhibited an overall brittle failure of hybrid composite materials, however, very good repeatability of the obtained strength and strain to failure values.

Acknowledgements

This work has been supported by the European Regional Development Fund within the Activity 1.1.1.2 “Post-doctoral Research Aid” of the Specific Aid Objective 1.1.1 “To increase the research and innovative capacity of scientific institutions of Latvia and the ability to attract external financing, investing in human resources and infrastructure” of the Operational Programme “Growth and Employment”, project No.1.1.1.2/VIAA/3/19/408.

6. References

1. Sihn S, Kim RY, Kawabe K, Tsai SW. Experimental studies of thin-ply laminated composites. Composites Science and Technology 2007; 67(6):996-1008.
2. Camanho PP, Arteiro A, Turon A, Costa J, Guillamet G, Gonzalez E. Structural integrity of thin-ply laminates. JEC Composites Magazine 2012; 49(71):91-92.

3. Guillamet G, Turon A, Costa J, Renart J, Linde P, Mayugo JA. Damage occurrence at edges of non-crimp-fabric thin-ply laminates under off-axis uniaxial loading. Composites Science and Technology 2014;98:44-50.
4. Cugnoni J, Amacher R, Kohler S, Brunner J, Kramer E, Dransfeld C, Smith W, Scobbie K, Sorensen L, Botsis J. Towards aerospace grade thin-ply composites: Effect of ply thickness, fibre, matrix and interlayer toughening on strength and damage tolerance. Composites Science and Technology 2018; 168: 467-477.
5. Manders PW, Bader MG. The strength of hybrid glass/carbon fibre composites - Part 1 Failure strain enhancement and failure mode. Journal of Materials Science 1981; 16(8):2233-2245.
6. Swolfs Y, Gorbatikh L, Verpoest I. Fibre hybridisation in polymer composites: A review. Composites Part A: Applied Science and Manufacturing 2014; 67:181-200.
7. Wisnom MR, Czél G, Swolfs Y, Jalalvand M, Gorbatikh L, Verpoest I. Hybrid effects in thin ply carbon/glass unidirectional laminates: Accurate experimental determination and prediction. Composites Part A: Applied Science and Manufacturing 2016; 88:131-139.
8. Swolfs Y, Meerten Y, Hine P, Ward I, Verpoest I, Gorbatikh L. Introducing ductility in hybrid carbon fibre/self-reinforced composites through control of the damage mechanisms. Composite Structures 2015; 131:259-265.

THE EFFECT OF FILAMENT WINDING PARAMETERS ON DAMAGE EVOLUTION IN CARBON FIBER REINFORCED PLASTIC FOR HIGH-PRESSURE HYDROGEN VESSELS

Masahito Ueda[a], Naruki Ichihara[a], Tomohiro Yokozeki[b], Takeshi Watanabe[c], Yusuke Tsuchiyama[c], Yuta Urushiyama [c]

a: Nihon University – ueda.masahito@nihon-u.ac.jp
b: The University of Tokyo
c: Honda Motor Company, Ltd

Abstract: *The effect of the resin content of towpreg and traverse rate in the filament winding process on the damage evolution of carbon fiber reinforced plastic was experimentally studied. Totally five types of coupon specimens were prepared by filament winding process. Plate-type mandrels for filament winding were prepared to make the coupon specimens. The stacking sequences of the coupon specimens were [0/90]2s, [±45]2s, and [±67.5]2s. Then, mechanical testing was performed to obtain damage evolution curves based on continuum damage mechanics. Cross-sectional observation revealed the difference in void amount and the distribution, and a bias of the resin-rich region depended on the manufacturing parameters. Damage evolution was similar for the specimens not dependent on the manufacturing parameters. However, the shear and transverse damage coupling behavior depended on the processing parameters.*

Keywords: Polymer matrix composite; Hydrogen vessel; Filament winding

1. Introduction

A high-pressure hydrogen vessel is one of the key components for fuel cell vehicles. The Type IV vessel is made of a carbon fiber reinforced plastic (CFRP) with polymer liner and metallic boss, which store hydrogen gas at 70 MPa. The high safety factor is generally used in commercially available vessels because of the variation in the strength, which increases the weight and cost. An accurate prediction technique of the product lifetime, as well as the reduction of variation in the strength, is required to realize the lightweight vessels.

The filament winding process is exclusively used to manufacture the vessels to keep fiber continuity throughout a vessel. However, the winding process of towpreg on the rounded surface results in variation in the fiber microstructure and many defects such as voids, uneven resin-rich regions, fiber misalignment, fiber waviness, and residual stress in the CFRP.

Damage initiation and evolution in the CFRP due to loading are predicted based on continuum damage mechanics [1,2]. The phenomenological technique is easy to implement in finite element simulation [3]. The applicability was studied for aerospace-grade CFRPs, and thus the technique is also useful for the lifetime prediction of the CFRP vessel. However, it is known that the mechanical properties of CFRP strongly depend on the manufacturing process. The effect of variation in the microstructure and defects caused during the filament winding process on the damage evolution behavior needs to be studied.

1055/1211 doi:10.5075/epfl-298799_978-2-9701614-0-0

In this study, the effect of the resin content of towpreg and traverse rate in the filament winding process on the damage evolution of CFRP was experimentally studied. The resin content of the towpreg and traverse rate during the winding process was changed. Totally five different manufacturing conditions were adopted. Using the conditions, coupon specimens of [0/90]s, [±45]s, and [±67.5]s lamination were manufactured. Then, mechanical testing was performed to obtain elastic and plastic properties, and damage evolution curves based on continuum damage mechanics. Cross-sectional observation revealed the specific void distribution depended on the manufacturing parameters. The experimental results showed that damage evolution was similar for the specimens not dependent on the manufacturing parameters. However, the shear and transverse damage coupling behavior depended on the processing parameters.

2. Materials and method

2.1 Materials and specimen preparation by filament winding

A towpreg was manufactured using carbon fiber tow and Epoxy resin. The towpreg was supplied to the filament winding machine. In order to model damage evolution, a continuum damage mechanic (CDM) approach was used in this study. Three types of stacking sequence, [0/90]2s, [±45]2s, and [±67.5]2s were selected following the Ladeveze's CDM model [1, 2]. The towpreg was winded on plate mandrels to obtain flat specimens. For [0/90]2s lamination, a square plate mandrel was used (Fig. 1a). The direction was rotated orthogonally at every lamination of a single ply. In the continuous winding of the towpreg, the towpreg needs to traverse from side to side of the plate mandrel. Consequently, the actual angle of [0/90]2s lamination was [0.4/-90.4]2s in this study as a standard condition. The difference in angle between nominal and actual stacking sequence may be small enough that does not affect the experimental results. [0/90]2s coupon specimens were cut out along the fiber direction. [±45]2s flat coupons specimen was also obtained by obliquely cutting out from the [0/90]2s laminate. For [±67.5]2s lamination, a hexagonal plate mandrel was used as shown in Fig. 1(b). The hexagonal plate mandrel was rotated orthogonally at every lamination of a single ply. The actual fiber angle was [67.9/-67.9]2s for the same reason.

Then, the towpreg-winded mandrel was placed between steel plates and lapped by a bagging film. The towpreg was consolidated under vacuumed.

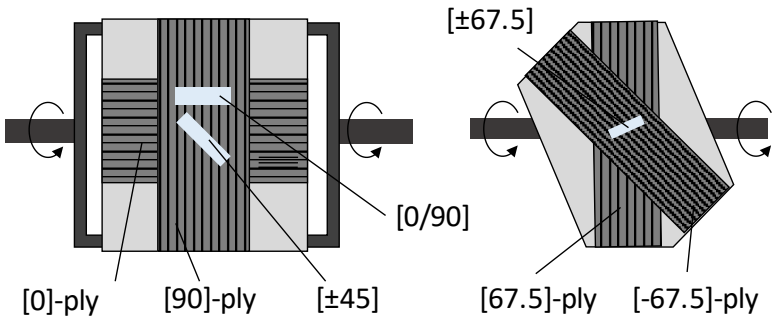

(a) [0/90]2s and [±45]2s specimens (b) [±67.5]2s specimens

Fig. 1 Filament winding process.

The specimens were cut into 250mm x 15mm for [0/90]2s laminates and 250mm x 25mm for [±45]2s and [±67.5]2s laminates after consolidation following the ASTM D3039. The thickness was different depending on the processing parameters. End tabs of glass fiber reinforced epoxy composite were attached to both ends of the specimen. Strain gauges were attached along the loading direction and the transverse direction on both faces of the specimen, and their average value was taken as the applied strain.

2.2 Processing parameters of filament winding

The processing parameters were changed to study the effect on the damage evolution. Three types of towpreg were prepared by changing the resin contest. 26 wt% was set to be a standard and high resin content (30 wt%) and low resin content (22 wt%) towpreg were prepared. Here, the total number of fibers in a single tow is pre-determined, the low and high rein content condition towpreg contain less and more volume of resin as compared to the standard condition towpreg. Three traverse rates in the winding process were studied. The traverse rate of 6 mm/rev was set to be a standard that aligns the towpreg without a gap. A high traverse rate of 8 mm/rev and a low traverse rate of 4 mm/rev was selected, which made gaps and overlaps of towpreg.

Optical micrographs of the [0/90]2s specimens with different processing conditions are shown in Fig. 2. The standard condition showed a relatively uniform fiber distribution without a large void. For the low resin content condition, voids may be included within the towpreg, which remained in each ply. Furthermore, long voids were observed between plies. This may be caused by the thickness variation of towpreg. The void within and between plies increased the thickness as compared to the standard condition specimen.

For the high resin content condition, voids in plies were reduced as compared to that of low resin content. However, resin-rich regions and voids exist between plies. Excessive resin content also degraded the quality of the winded CFRP laminate.

For the low traverse rate condition, the laminate became thicker as compared to the standard condition because of overlapping of towpreg. In contrast, the laminate became thinner for the high traverse rate condition because of a shortage of materials. Large voids were found in a ply which was caused by gaps between towpreg. The total amount of fiber was also smaller than the other conditions because of the gaps.

2.2 Mechanical testing

A universal testing machine (AG-IS 150kN, Shimadzu) was used at a testing speed of 1.25 mm/min. Monotonic tension tests were performed for all the specimens to obtain elastic properties and cyclic tension tests were performed for [±45]s and [±67.5]s specimens to obtain plasticity and damage properties. In the 1st and 2nd cycle in the cyclic test, 30 % and 40 % of the failure load was applied and unloaded. After that, the load was increased by 10 % at every successive loading cycle until the specimen broke.

3. Results and discussion

3.1 Damage evolution of the standard condition specimen

  doi:10.5075/epfl-298799_978-2-9701614-0-0

Figures 3 show the shear damage curve of the [±45]2s specimens of the standard condition, which was derived from the shear stress-shear strain diagram by the repeated tensile test. The shear damage derived from the shear stress-shear strain diagram by the repeated tensile test of [±67.5]2s specimens was also overlaid in Fig. 3 by selecting the appropriate coupling parameter (b2). The plots by [±67.5]2s specimens were only located in the low damage area because the failure strain was small. Shear damage starts at $\sqrt{Y}$ ≈0.1 and increased linearly, and the final fracture occurred when the shear damage was about d_{12} = 0.6. The results indicated that the shear damage evaluation of the CFRP can be arranged by using the continuum damage mechanics.

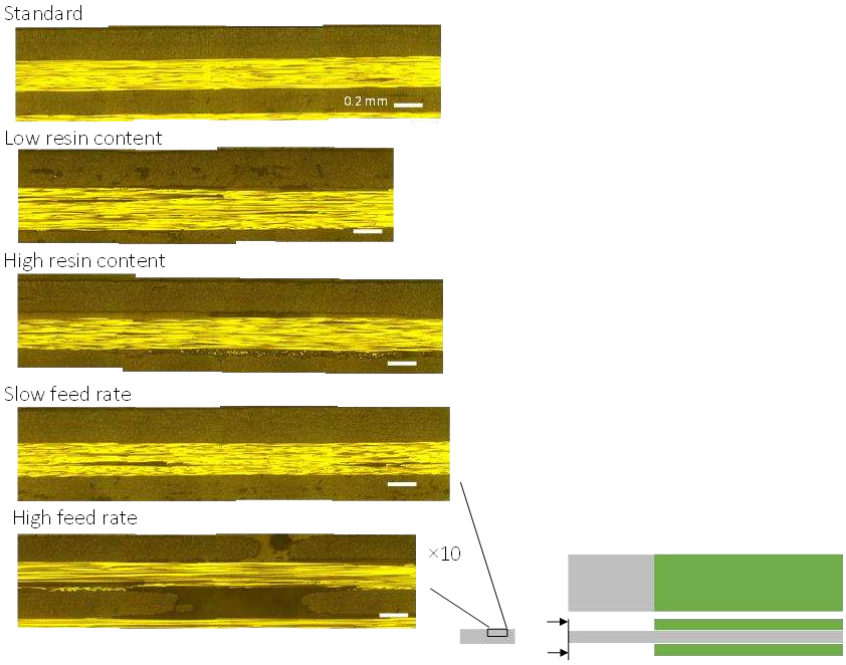

Fig. 2 Cross-sectional observation.

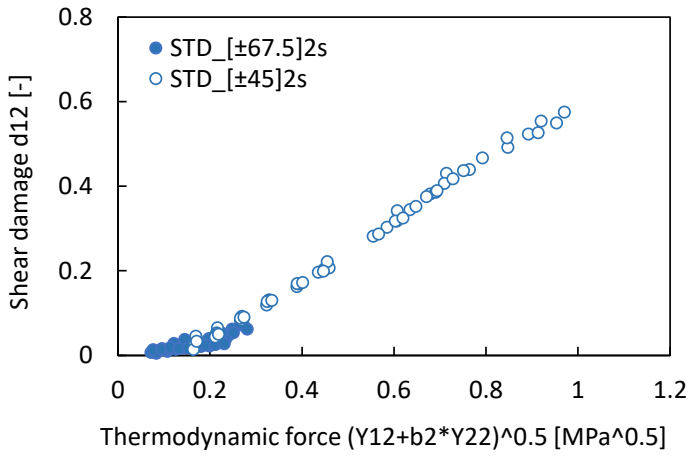

Fig. 3 Shear damage evolution of the standard condition specimens

3.2 The effect of processing parameters on damage evolution

Shear damage curves of the [±45]2s specimens with different processing parameters were also obtained. Figure 4 shows shear damage evolutions of five types of specimens with different processing parameters. Almost the same shear damage evolution was observed regardless of the processing parameters. The difference in voids amount and the distribution, and a bias of the resin-rich region were less likely to affect the shear damage behavior. However, the critical shear damage depended on the processing parameters. Average critical shear damage was d_{12} = 0.3 for the specimen with the low resin content condition, which was the lowest among the five types of specimens. The total amount of resin was small and the shear deformation is less likely to occur even under high stress. Thus, the processing parameter affects the product lifetime.

The shear damage was also derived from the shear stress-shear strain diagram by the repeated tensile test of [±67.5]2s specimens, which was overlaid in Fig. 4 by selecting the appropriate coupling parameter (b2). Here, the different coupling parameter was used dependent on the processing parameters. The shear damage evolution can be expressed by a unified curve when the different coupling parameters were used. However, this means that the coupling behavior of the shear damage and transverse damage was different depending on the processing parameters.

Figure 5 shows the shear damage curves of the [±67.5]2s specimens, in which coupling parameter b2 was not used ignoring the transverse damage development. The coupling parameter b2 was relatively large for the low resin content condition. This indicates that the transverse damage has a large effect on thermodynamic force as compared to the shear damage for the low resin content specimens. The damage coupling between the shear and transverse damage was affected by the processing parameters.

4. Conclusions

The resin content of towpreg and traverse rate in the filament winding process was changed to study the effect on the damage evolution of CFRP. The shear damage behavior of [±45]2s specimens was almost the same not dependent on the processing parameter indicating that the shear dominant damage behavior was insensitive to the processing parameter. However, the critical shear damage depended on the processing parameters, which affects the product lifetime. Shear and transverse damage coupling parameters were also dependent on the processing parameters. The variation in processing parameters changes the damage evolution behavior under simultaneous shear and transverse damage development situation.

5. References

1. Ladevèze P. A damage computational method for composite structures. Computers & Structures 1992; 44(1-2): 79-87.
2. Ladevèze P, LeDantec E. Damage modelling of the elementary ply for laminated composites. Composites Science and Technology 1992; 43(3): 257-267.
3. Ichihara N, Ueda M, Urushiyama Y, Todoroki A, Matsuzaki R, Hirano Y. Progressive damage simulation for a 3D-printed curvilinear continuous carbon fiber-reinforced thermoplastic based on continuum damage mechanics. Advanced Composite Materials 2020; 29(5): 459-474.

  doi:10.5075/epfl-298799_978-2-9701614-0-0

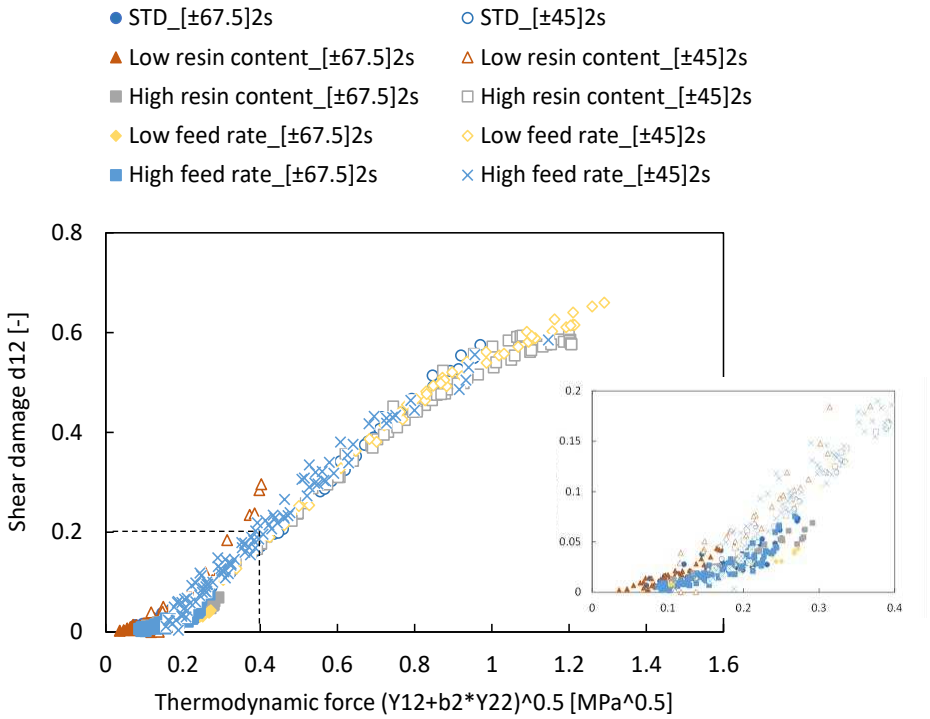

Fig. 4 Shear damage evolutions of different processing parameter specimens

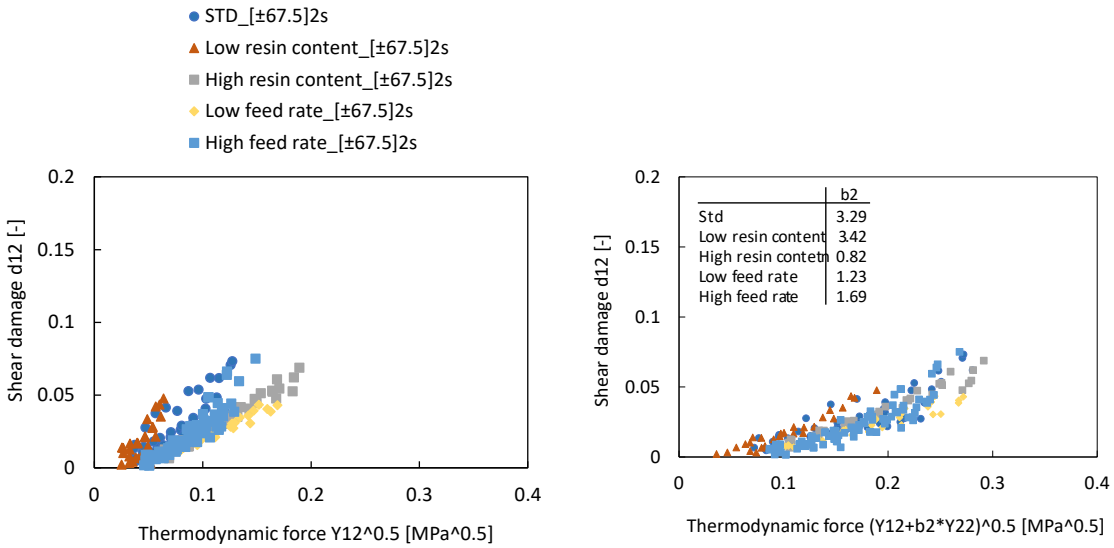

*(a) Arranged by shear thermodynamic force Y12 (b) Arranged by coupled thermodynamic force Y12+b2*Y22*

Fig. 5 Shear damage evolutions of [±67.5]2s *specimens.*

  doi:10.5075/epfl-298799_978-2-9701614-0-0 published under CC BY-NC 4.0 license

INFLUENCE OF KEROSENE FLAME ON IN SITU MECHANICAL PROPERTIES OF HYBRID FIBERS REINFORCED PEEK COMPOSITE LAMINATES

Benoit Vieille[a], Alexis Coppalle[b], Adem Alia[a], Eliot Schuhler[b], Avinash Chaudhary[b], David Bouscarrat[a], Nicolas Delpouve[a]

a: Normandie Univ, UNIROUEN, INSA Rouen, CNRS, Groupe de Physique des Matériaux,

76800 St Etienne du Rouvray, France – benoit.vieille@insa-rouen.fr

b: Normandie Univ, UNIROUEN, INSA Rouen, CNRS, CORIA, 76800 St Etienne du Rouvray, France

Abstract: this work aims at investigating the influence of kerosene flame exposure (1100°C and a heat flux of 116kW/m²) on the in-situ creep mechanical behavior and residual mechanical properties in tension of hybrid carbon/glass fibers reinforced Poly Ether Ether Ketone (PEEK) laminates. A one-of-a-kind experimental bench combining a tensile mechanical loading and a kerosene burner has been designed and instrumented to study the evolution of various physical quantities to be tracked. These include temperature, loss of mass, deformation, stress, which are fundamental for understanding the mechanisms brought into play. By means of an infrared camera, the back-surface temperature of laminates subjected to kerosene flames is mapped during thermal decomposition. Compared to virgin specimens, the residual tensile mechanical properties significantly decrease as a function of the flame exposure time (5-10-15 min): -30% and -50% in axial stiffness and strength, respectively.

Keywords: Thermoplastic; Hybrid fibers; Kerosene flame; Mechanical testing

1. Introduction

In recent years, numerous aircraft accidents have placed the "fire" issue as a primary concern of aeronautical manufacturers [1]. Understanding/predicting the fire response of composite materials and, ultimately, of structures and assemblies, is therefore essential. This raises the need for the development of adapted experimental characterization means. To date, the influence of fire on the structural properties of thermoplastic (TP) matrix composites has been little studied [2-4]. The vast majority of works has focused on thermoset (TS) matrix composites [5]. The flammable nature and rapid thermal decomposition of TD matrices have favored the emergence of TP composites (lower flammability, higher decomposition temperatures, better residual mechanical properties after fire exposure), but the question of multi-physics couplings within Organic Matrix Composites under critical conditions (flame) remains open, as well as for scale change effects (from constituents to elementary ply, structures and assemblies).

The use of thick layups can significantly enhance the fire resistance in several structural applications. In transport or other lightweight applications this approach runs counter to the principal design objectives [6]. According to many references [7-11], there is a significant reduction in mechanical performance of polymer matrix composites during exposure to flame, with a particular interest in creep-induced failure [6]. However, due to the inherent thermal

  doi:10.5075/epfl-298799_978-2-9701614-0-0

decomposition of polymer, polymer composite parts often quickly form a layer of protective char and can then sustain a significant proportion of strength over extended periods of time [6]. This results from the onset of pyrolysis that has an endothermic nature and helps to reduce the temperature. A preliminary study was conducted on hybrid carbon/glass fibers reinforced PEEK thermoplastic matrix laminated composites (CG/PEEK) [12]. The influence of a prior kerosene flame exposure (116 kW/m2 and 1100 ◦C), on the residual mechanical properties (in tension and in compression) was examined as a function of exposure time (5–10-15 min). From this work, it is possible to conclude that the mechanical properties in tension are severely affected (-50% in stiffness and -70% in strength) by prolonged exposures to kerosene flame (15 min) with respect to as-received specimens. Flame exposure time (ranging from 5 to 15 min) seems to have very little influence on tensile properties and the effect is moderate on compressive properties. The barrier formed by an extensive thermally-induced delamination contributes to relatively preserve the structural integrity of the plies near the back-surface. The mechanical loading is taken up by the 0◦ fibers in non-delaminated areas of the specimens, resulting in preserving the residual mechanical properties in tension and in compression.

This context and the analysis of the literature clearly demonstrate the lack of insight, of representative experimental data, of numerical tools but also the absence of a methodology dedicated to the study of the mechanical behavior of composite structures and their assemblies under flame. The main objective of the present work is therefore to dissociate the different phenomena occurring within PEEK-based laminates subjected to combined flame and mechanical loading. It will thus be possible to build a scientifically grounded basis for the design of aeronautical structures combining structural bearing capabilities and improved resistance to fire. For this purpose, this work examines the influence of kerosene flame exposure on the in-situ creep mechanical behavior and residual mechanical properties in tension of hybrid CG/PEEK laminates. The influence of a kerosene flame exposure (116 kW/m^2 and 1100 °C) on the composites structural integrity was examined as a function of exposure time (5-10-15 min).

2. Materials and experimental set-up

2.1 Materials and specimens

The laminates used in this study are obtained by thermo-compression [12]. They consist of a PEEK thermoplastic matrix reinforced with a 5-harness satin weave carbon fiber fabric (Tenax® - E HTA40 3K). They have two outer glass fabric (5-harness satin weave) reinforced PEEK plies denoted $(0/90)_G$. 16 plies laminates with a quasi-isotropic lay-up $[(0/90)_G,(0/90),(\pm45),(0/90),(\pm45),(0/90),(\pm45),(0/90)]_S$ have been tested. The CG/PEEK laminates average thickness is about 4.5 mm. 300mm long tensile specimens with a dog-bone geometry were cut by water jet from 600x600 mm² plates.

2.2 Kerosene flame exposure

The burner shown in Figure 1 is a domestic device (Cuenod manufacturer). The kerosene is injected in a nozzle generating a hollow cone spray with an angle equal to 80° and a maximum flow rate of 0.3 g/s. This flow rate is controlled with a mass flow meter (MINI CORI-FLOW™ - Bronkhorst), and it can be adjusted. Airflow is also controlled with a mass flow meter (EL-FLOW® Prestige - Bronkhorst). The air to fuel ratio has been selected at 0.85 of the stoichiometric value, in order to obtain heat flux and temperatures values close to the standard values (116 kW/m^2 and 1100 °C) at the sample location. The flame at the exit of the turbulator is a wide and turbulent jet. Therefore, a 50 mm diameter steel tube is installed after the turbulator to channel the hot combustion gases on the exposed area of the sample (Figure 1).

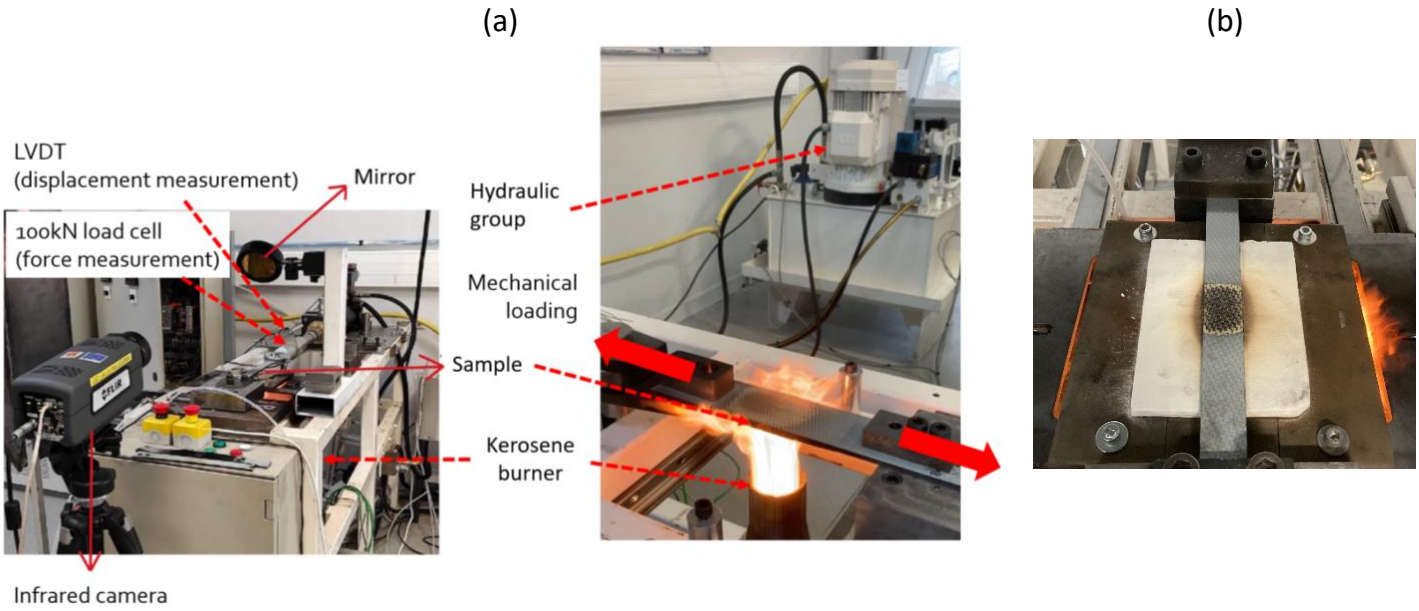

Figure 1. In situ tensile behaviour of CG/PEEK laminates subjected to a kerosene flame during mechanical loading: (a) description of the experimental bench – (b) protective shield limiting the thermal decomposition of the specimen

2.3 Combined mechanical-thermal loadings

Firstly, specimens were subjected to a creep tensile loading during a kerosene flame exposure without any protective shield (Figure 1b). The axial displacement was measured using a Linear Variable Differential Transformer (LVDT) sensor. During the test, the temperature distribution on the back-side of the specimens is monitored by means of an infrared camera and a mirror. Secondly, a protective shield associated with a ceramic thermal insulation layer was designed to limit the thermal decomposition of the specimens with an exposure area of 40*10mm² during kerosene-flame exposure (Figure 1b). Four samples have been tested in the following configurations:

- As received (referred to as virgin state),
- After a 5 min exposure to a kerosene flame while subjected to a 20kN creep loading,
- After a 10 min exposure to a kerosene flame while subjected to a 20kN creep loading,
- After a 15 min exposure to a kerosene flame while subjected to a 20kN creep loading.

2.4 Mechanical characterization of residual tensile properties

The purpose of these mechanical tests is to evaluate the residual tensile properties after flame exposure under tensile loading. Monotonic tensile tests were then performed using a 100kN capacity load cell of a MTS 810 servo-hydraulic testing machine in displacement-controlled mode (1mm/min) at Room Temperature (RT).

3. Results and discussion

In critical service conditions, composites parts may be subjected simultaneously to fire and mechanical loading. Therefore, a particular attention is paid to creep-induced failure. From the thermogravimetric analyses conducted in [12], the onset of thermal decomposition T_{onset} of CG/PEEK laminates increases (from 583 to 627°C) when the heating rate increases (from 10 to

1063/1211 ©2022 Vieille et al. doi:10.5075/epfl-298799_978-2-9701614-0-0 published under CC BY-NC 4.0 license

200 K/min). The knowledge of the pyrolysis temperature is crucial to explain the mechanical contribution of the PEEK matrix in the response of each individual ply of the laminates. According to the classical laminates theory, the tensile load is primarily borne (about 73% of the mechanical load) by the woven (0/90°) plies in CG/PEEK laminates whose stacking sequence is quasi-isotropic.

3.1 Thermo-mechanical response of CG/PEEK laminates without a protective shield

Surprinsingly, the macroscopic response of the specimen is characterized by primary creep, followed by secondary creep locally disrupted by the failure of the plies with (0/90°) fibers (Fig. 2b). Indeed, the mechanical response of QI laminates being fiber-dominated, no time-dependent behavior should be observed. In comparison with virgin specimens (Figure 2a), those exposed (without a protective shield as shown in Fig. 1b) for 17 min to a kerosene flame and a 10kN constant tensile loading (Figure 2c), show a creep response, which is characterized by a gradual failure of the 0/90° fibers that is correlated to the thermal decomposition of the laminates plies (Fig. 2b). The breakage of 0° fibers comes along with a sudden increase in the axial strain until the tensile load is transferred to the undamaged plies.

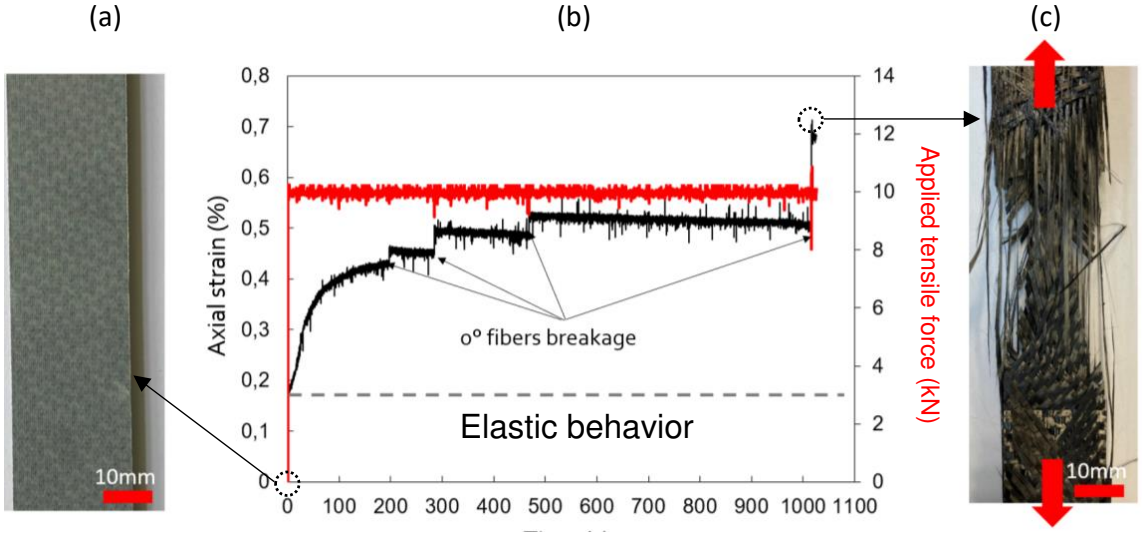

Figure 2. Creep mechanical response of CG/PEEK quasi-isotropic laminates exposed to a kerosene flame for 17 min (without a protective shield): evolution of the axial strain with the thermal decomposition of the laminates' plies (b) and macroscopic observations of the virgin and damaged states (a)-(c)

From the *post-mortem* macroscopic observations of the specimen after a 17 min exposure to kerosene flame (Figure 3), it appears that the role played by the laminates'plies differ from one to another. Flame exposure leads to a significant temperature gradient through-the-thickness of the QI laminates. In the early phase of flame exposure (about 100s), an important softening of the PEEK matrix occurs within the plies. This results in the primary creep stage of the laminates. Once the PEEK matrix has locally deformed, the tensile load is taken up by the plies with (0/90°) fibers. Between the breakage of each (0/90°) plies, the laminates is therefore characterized by a steady creep state whose creep rate is virtually null. In other words, it means that the (±45°) plies whose mechanical behavior is dominated by the PEEK matrix do

not a play a significant role from the macroscopic response standpoint (Figure 2). Then, depending on the thermal decomposition of each ply (function of the exposure time), the bearing capabilities of the plies is gradually degraded. The complete ablation (resulting from the oxydation of the fibers and the pyrolysis of the PEEK matrix) of the outer G/PEEK ply is even observed after a while. The plies exposed to the kerosene flame are the first to fail (Figure 3). The observation of the fractured plies also confirm that the (±45°) plies are not significantly deformed as the (±45°) plies do not rotate when the tensile load is transferred from one ply to another. When all the (0/90°) plies have fail, only the last two (±45°) plies located close to the back surface are characterized by a significant rotation of the fibers along the axial direction. The microscopic observation of the laminates' edge in the thermally-degraded area shows extensive delamination (Figure 3).

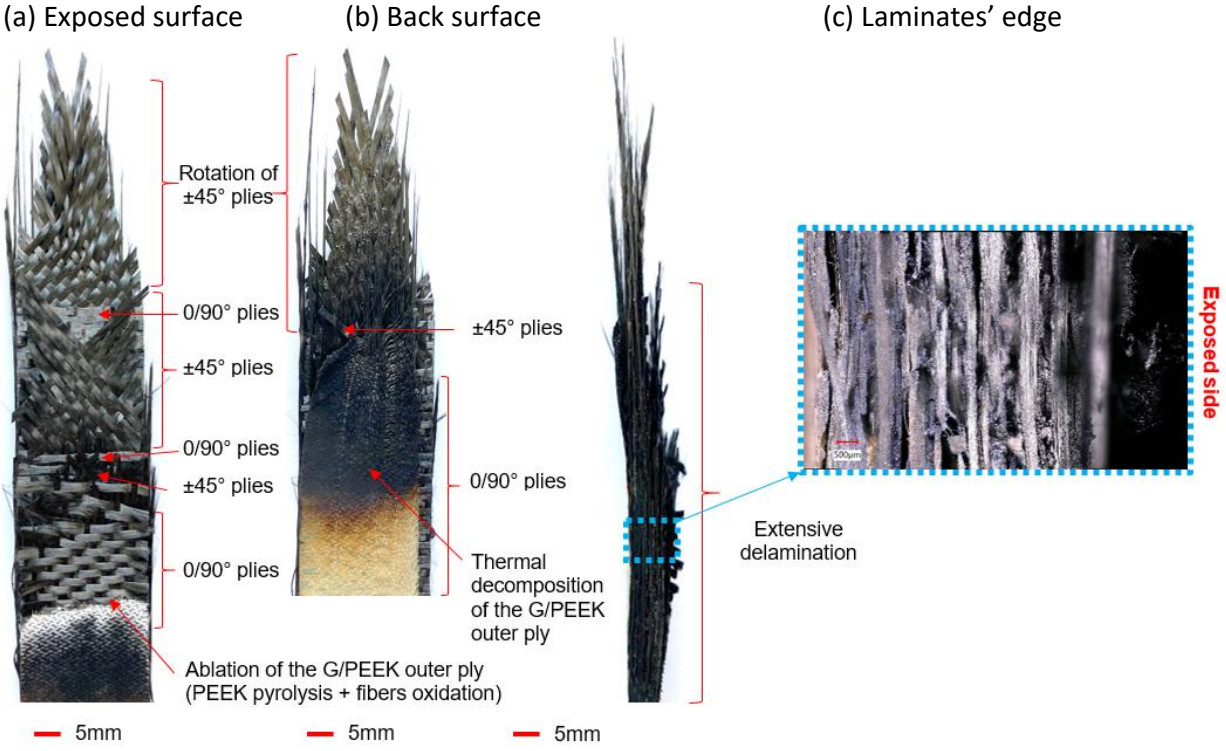

Figure 3. Post-mortem macroscopic observations of a CG/PEEK hybrid specimen subjected simultaneously to a 10kN tensile creep loading and a kerosene flame for 17 minutes (without a protective shield): (a) Exposed surface – (b) Back surface – (c) Laminates' edge

3.2 Thermo-mechanical response of CG/PEEK laminates with a protective shield

When it comes to specimens partly protected by a thermal shield during flame exposure, it appears that the creep response to a 20kN tensile force is virtually characterized by no time-dependent behavior (as pointed out by the blue dotted line). It therefore suggests that an extended time exposure to the kerosene flame results in a temperature gradient within the laminates' plies whose effect is not observable on the macroscopic response of the specimen. In addition, it means that the structural integrity is well preserved during the whole test as the majority of the laminates' plies are undamaged and they are still capable to bear the tensile load. Of course, the 20kN applied tensile force corresponds to a relatively low tensile stress (about 177 MPa) with respect to the residual ultimate strength of CG/PEEK specimens (about

785 MPa) subjected to a prior similar thermal agression without mechanical loading [12]. Finally, the instantaenous strain (about 0.34%) associated with the 20kN creep tensile load applied at the beginning of the test (when the temperature within the specimen is basically at room temperature) allows the estimation of the axial stiffness of the specimen whose value remains virtually a constant (about 52,17 GPa when considering the Hooke's law $E_x = \sigma_x/\varepsilon_x$), confirming that the elastic properties of the material are not signicantly degraded during flame exposure.

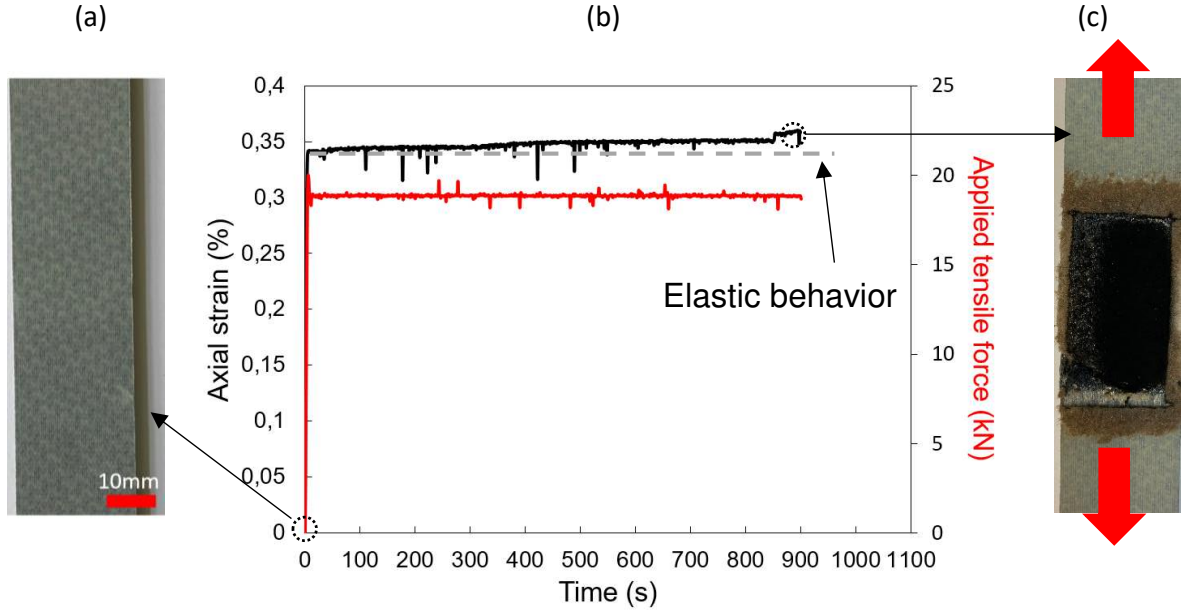

Figure 4. Creep mechanical response of CG/PEEK quasi-isotropic laminates subjected simultaneously to a 20kN tensile creep loading and a kerosene flame for 15 min (with a protective shield): evolution of the axial strain with the thermal decomposition of the laminates' plies (b) and macroscopic observations of the virgin and damaged states (a)-(c)

Compared to the case of a flame exposure without a protective shield, a CG/PEEK specimen subjected to a flame for 15 min is significantly less degraded as the laminates' edges are not directly aggressed by the flame (Figure 5a). A layer of char is observed on the exposed surface and the thermally-degraded area is efficiently limited by the protective shield. It is worth recalling that the layer of char resulting from the local thermal decomposition (pyrolysis of the PEEK matrix and oxidation of the fibers) contributes to the protection of adjacent layers and allows the specimen to sustain a significant proportion of the strength (with respect to the virgin state) over extended periods of time. On the back surface, melted PEEK matrix is observed as well as porosities steming from the exhaust of pyrolisis gases (Figure 5b). Finally, the microscopic observation of the laminates' edge reveals bubles of melted matrix though which came out some pyrolisis gases (Figure 5c). The outer protective layer of char preserves the cohesion of the plies underneath and the delamination is only observed on the outer back surface between the G/PEEK and the C/PEEK ply. It is therfore expected that the structural integrity of the laminates is maintained and it should reflect on the residual tensile properties of the specimens exposed to a kerosene flame for different durations.

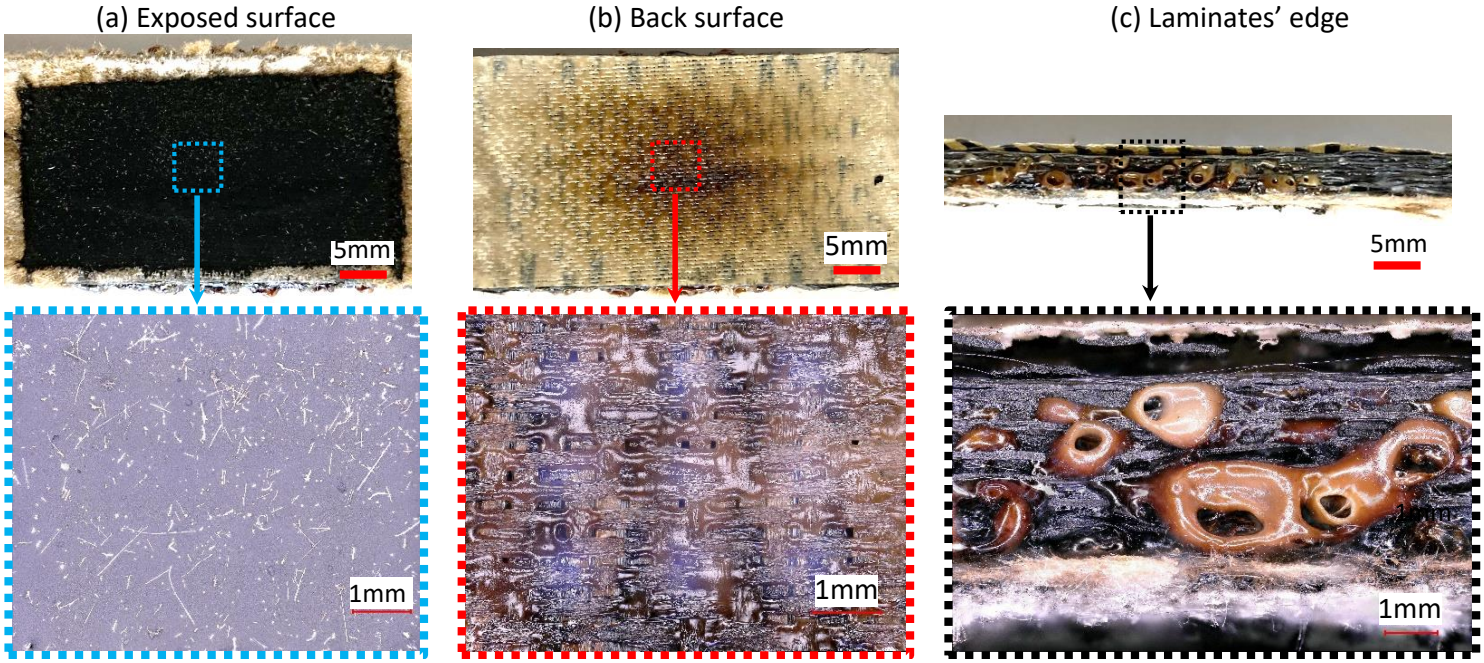

Figure 5. Macro and microscopic observations of a CG/PEEK hybrid specimen subjected simultaneously to a 20kN tensile creep loading and a kerosene flame for 15 minutes (with a protective shield): (a) Exposed surface – (b) Back surface – (c) Laminates' edge

In order to quantify the residual structural capabilities of the CG/PEEK, monotonic tensile tests were conducted on specimens exposed to prior combined loading (flame + tensile creep) with a protective shield. The macroscopic responses show that the tensile behavior is virtually elastic brittle in both virgin and thermally-aggressed specimens (Fig. 6a). Compared to virgin specimens, the tensile properties significantly decrease after a 15 min flame exposure under a 20kN creep loading in tension: - 30% in the axial stiffness and -50% in the axial strength (Fig. 6b).

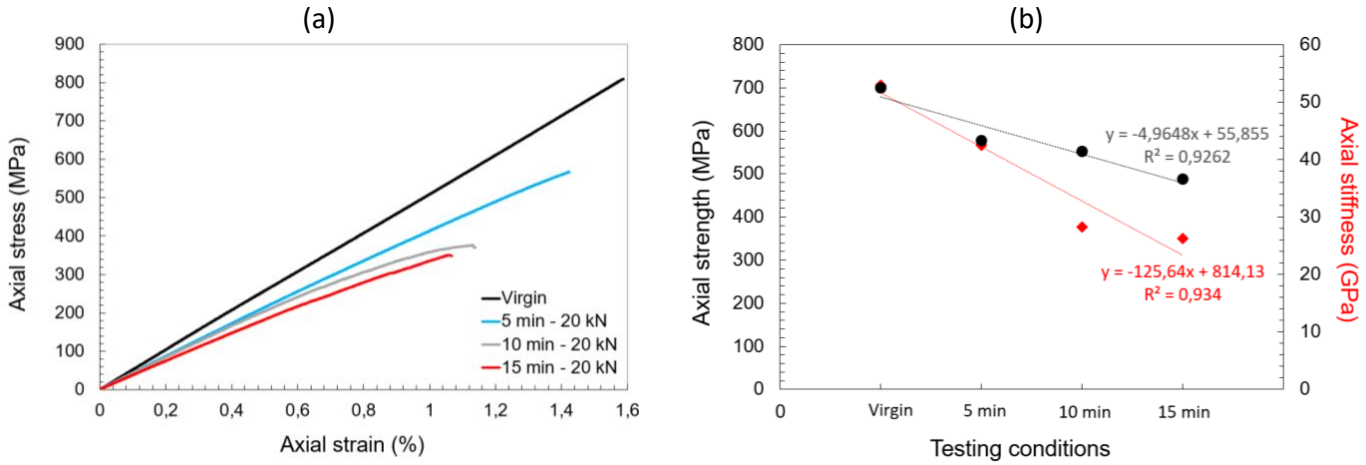

Figure 6. Tensile behaviour of CG/PEEK hybrid laminates: comparison of virgin specimen vs post flame exposure specimen (5-10-15 min exposure under a 20kN tensile force): (a) Macroscopic stress-strain response – (b) Changes in tensile properties

To better understand the contribution of the plies to the mechanical behavior of quasi-isotropic laminates, it is necessary to know the temperature distribution during flame exposure. It is only possible to monitor the temperature changes on the back surface of the specimen by means of thermocouples stuck to the surface or by means of infrared thermography. The emissivity of the specimen changes because of the thermal decomposition of the material, as a result the temperature measurement via IR thermography is not accurate anymore. Figure 7 shows the temperature distribution during flame exposure (Fig. 7a) which has been obtained using a thermocouple stuck to the surface (Fig. 7b) The thermocouple is unstuck from the surface after a 5 min exposure, therefore preventing to further measure the temperature during the entire test. The temperature reached on the back surface is about 400°C (far from T_{onset} =583°C). A thermo-phosphorescence technique is actually developed to measure the surface temperature of pyrolyzed materials. It consists in using a phosphor powder coated on the back surface of the specimens. This surface is then excited by a laser (~4-6ns) during flame exposure. The intensity of the phosphorescence signal decays exponentially with time and the surface temperature can be deduced from the decay time [13].

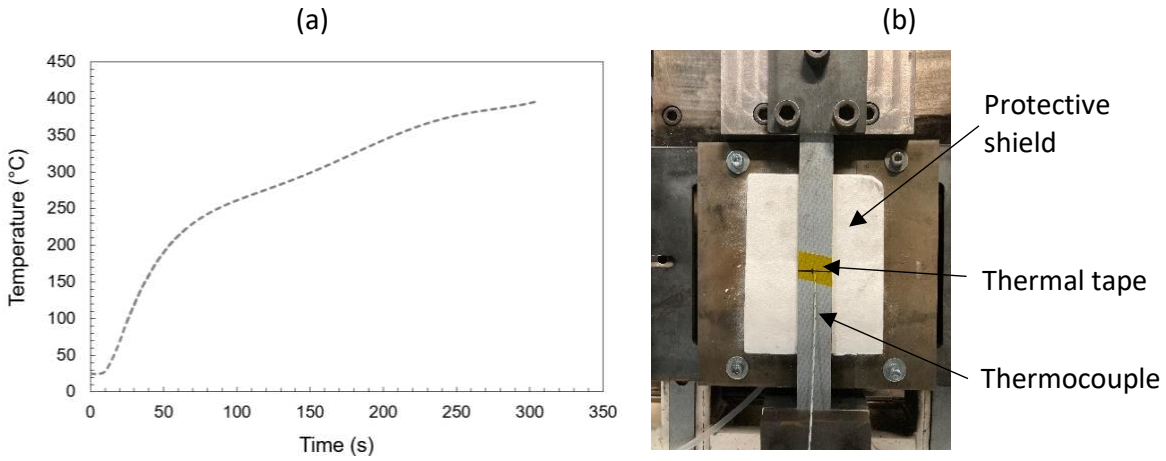

Figure 7. Measurement of the temperature on the back surface of CG/PEEK hybrid laminates subjected simultaneously to a 20kN tensile creep loading and a kerosene flame for 15 minutes: (a) temperature vs time evolution – (b) experimental set-up

4 Conclusions

The main objective of the present study was to separate the influence of different physical phenomena at play within carbon glass reinforced PEEK laminated composites subjected simultaneously to a kerosene flame and a mechanical loading. The underlying idea is to reproduce at the laboratory scale the critical conditions in service (fire scenario in aircrafts' engines). Thus, a specific fire bench was specifically developed to induce a calibrated thermal aggression by a kerosene flame (1150°C and 116kW/m² heat flux – in agreement with the certification requirements) along with a tensile creep loading. Two test configurations were considered to adjust the criticality of the flame exposure: with or without protective thermal shield.

  doi:10.5075/epfl-298799_978-2-9701614-0-0

From the obtained results, the following conclusions can be drawn: (i) the thermo-mechanical response is directly correlated to the flame exposure time – (ii) the thermo-mechanical response significantly differs depending on the boundary conditions – (iii) the contribution of the plies to the structural integrity of the laminates clearly depends on the position of the plies as well as their initial orientation – (iv) the decrease in the residual tensile properties (- 30% in the axial stiffness and -50% in the axial strength) is not catastrophic in the most severe conditions (after a 15min exposure) with respect to the as-received material – (v) The formation of layer of char resulting from the local thermal decomposition (pyrolysis of the PEEK matrix and oxidation of the fibers) contributes to the protection of adjacent layers and allows the specimen to sustain a significant proportion of the strength over extended periods of time.

The influence of the tensile creep force on the deformation mechanisms needs to be further investigated to identify the critical loading conditions from which the structural capabilities of the laminates are reduced. At last, the temperature measurement being a key point to study the thermo-mechanical coupling under severe thermal aggression, it is necessary to implement a phosphor thermometry technique to accurately monitor the back side temperature evolution during the thermal decomposition of the composite material.

Acknowledgements

The work presented in this study is the result of the RIN (R´eseau d'Intérêt Normand) project AEROFLAMME (Behaviour of **AERO**nautical Composites under **FLAM**me and **ME**chanical Loading) financed by the Normandy Region and the FEDER (European Regional Development Fund).

5 References

1. ISO 2685:1998. Environmental test procedure for airborne equipment — Resistance to fire in designated fire zones, 1998.
2. E. Schuhler, A. Coppalle, B. Vieille., J. Yon, Y. Carpier. Behaviour of aeronautical polymer composite to flame: A comparative study of thermoset- and thermoplastic-based laminate. Polymer Deg & Stab 2018, 152 : 105-115.
3. B. Vieille, A. Coppalle, L. Le Pluart, E. Schuhler, A. Chaudhary, B. Rijal, A. Alia, N. Delpouve. Kerosene flame behaviour of C/PEKK composite laminates: influence of exposure time on residual mechanical properties. Comp Part B 2021, 222 : 109046.
4. E. Schuhler, A. Chaudhary, A. Coppalle, B. Vieille. Fire behaviour of composite materials using kerosene burner tests at small-scales. Fire Safety Journal 2021, 121: 103290.
5. A.P. Mouritz, A.G. Gibson. Fire Properties of Polymer Composite Materials. Solid Mechanics and its Applications, Springer, Dordrecht, 2006.
6. A.M. Korsunsky, A.J.G. Lunt, J. Dulieu-Barton. On the reinforced polymer composites with optimised strength and fire resistance - In Memory of Arthur Geoffrey Gibson. Materials & Design, Volume 212, 2021, 110244.

  doi:10.5075/epfl-298799_978-2-9701614-0-0

7. A.P. Mouritz, A.G. Gibson. Fire Properties of Polymer Composite Materials. Solid Mechanics and its Applications. Dordrecht: Springer; 2006.
8. P.T. Summers, B.Y. Lattimer, S.W. Case. Compressive failure of composite plates during one-sided heating. Compos Struct 2011;93(11):2817–25.
9. L.A. Burns, S. Feih, A.P. Mouritz. Compression Failure of Carbon Fiber-Epoxy Laminates in Fire. J Aircr 2010;47(2):528–33.
10. J.V. Bausano, J.J. Lesko, S.W. Case. Composite life under sustained compression and one-sided simulated fire exposure: characterization and prediction. Compos Part Appl Sci Manuf 2006;37(7):1092–100.
11. S. Feih, A.P. Mouritz. Tensile properties of carbon fibres and carbon fibre–polymer composites in fire. Compos Part Appl Sci Manuf 2012;43(5):765–72.
12. B. Vieille, A. Coppalle, E. Schuhler, A. Chaudhary, A. Alia, N. Delpouve, A. Bourdet. Influence of kerosene flame on fire-behaviour and mechanical properties of hybrid Carbon Glass fibers reinforced PEEK composite laminates. Composite Structures, Volume 279, 2022, 114786.
13. A. Omrane, F. Ossler, M. Aldén, U. Gtoransson, G. Holmstedt. Surface temperature measurement of flame spread using thermographic phosphors. Fire Safety Science 2003, 7: 141-152.

  doi:10.5075/epfl-298799_978-2-9701614-0-0

COMPARISON OF INFLUENCE OF HYDROTHERMAL AGING ON THE MECHANICAL PROPERTIES GLASS AND CARBON LONG FIBER-REINFORCED POLYAMIDE 6

Benedikt M. Scheuring[a], Leo,Hoffmann[a], Wilfried V. Liebig[a], John Montesano[b], Kay A. Weidenmann[c]

a: Karlsruhe Institute of Technology, Institute for Applied Materials – Material Science and Engineering, Engelbert-Arnold-Straße 4, 76131, Karlsruhe, German
email: benedikt.scheuring@kit.edu
b: University of Waterloo, Department of Mechanical and Mechatronics Engineering, Composites Research Group,295 Phillip Street, N2L 3W8 Waterloo, Canada
c: University of Augsburg, Institute of Materials Resource Management, Werner-von-Siemens-Straße 6, 86159, Augsburg, Germany

Abstract: *In this study, the effect of absorbed water on the mechanical properties of long fiber reinforced thermoplastics (LFT) is investigated. The matrix system used was polyamide 6 reinforced with glass fibers (GF) and carbon fibers (CF). Two conditioning procedures are investigated, storage at 23°C in distilled water and storage at 70°C and 80%rH. The aim is to determine the influence of the fiber type on the degradation of the mechanical properties by absorbed water. For this purpose, the mechanical properties of uncontaminated specimens are compared with specimens that have been immersed in water or a humid and warm environment for different periods of time. The failure mechanism of selected specimens were investigated by fracture surface analysis in the SEM and differences were determined.*

Keywords: Long fiber-reinforced thermoplastics; Polyamide 6; Environmental degradation; hydrothermal aging; Mechanical properties

1. Introduction

LFT based on polyamide have been widely used in various applications due to their excellent processing ability, their good mechanical properties and their good recyclability. In addition, LFT composites consist of fibers and thermoplastic matrix, which both can be recycled and reused. Due to the lower costs and relatively good mechanical properties, glass fibers are mainly used as reinforcement material in the LFT process for a long time. [1] Through the stricter regulations regarding emissions in the automotive sector, the demands on weight have become even greater and allow greater financial leeway, so the demand for discontinuously reinforced plastics with C-fibers as reinforcement has become higher in the last 10 years [2]. The LFT-D process is particularly suitable in order to obtain a high benefit from the stiffer C-fiber, as long fiber lengths can still be achieved in this process and better properties of the C-fiber can thus be used [2,3]. However, carbon fibers are still much more expensive and significantly more CO_2 is emitted during production. [4]

In the case of polyamide, a hygroscopic thermoplastic, used as a matrix system the absorbed water has a significant influence on the mechanical properties. Thus, the water molecules that accumulate between the chains at the bipolar amide group, cause the material to soften, i.e. the tensile strength and modulus of elasticity decrease. [5] This effect can be reduced by adding

  doi:10.5075/epfl-298799_978-2-9701614-0-0

reinforcing fibers, but is still present. In previous studies, mainly focused on short fiber reinforced polyamide composites, the mechanical properties under the influence of absorbed water have already been investigated in various tests, e.g. tensile tests, creep tests and impact tests [5-8]. The investigations refer to either glass fibers [5, 6] or carbon fibers [7, 8].
With both fiber types, a considerable reduction of tensile strength and modulus of elasticity has been observed after hydrothermal aging [5-8]. However, the influence of the reinforcement fiber type on the water uptake and the degradation by hydrothermal aging has never been investigated under the same process conditions. Also, the influence of long fibers as in the LFT process has not been investigated yet.

The aim of this study is therefore to determine whether a similar reduction in mechanical properties occurs under the influence of absorbed water in LFT materials. In addition, it will be investigated whether the fiber type has an effect on the water absorption and the reduction of mechanical properties and how the absorbed water influences the fracture behavior.

2. Material and Manufacturing

The LFT-D plates were manufactured by the Fraunhofer ICT in Pfinztal, Germany. The glass fibers used in the process were Johns Manville StarRov ® 895 2400 and the carbon fibers used were ZOLTEK PX3505015W-61. Both of the fibers, according to the data sheets, are particularly suitable for the use with polyamides. The fibers were fed directly into the impregnating extruder as roving with the melted polyamide. Both material types were manufactured with the same polymer flow rate of 25 kg/h and a planned fiber volume content of vol. 25%.

The 3mm thick plates were pressed on a press by Diffenbacher (type COMPRESS PLUS DCP-G 3600/3200 AS) in a mold with the dimensions 400mm x 400mm. A side insert was selected so that the finished sheet can be divided into 2 areas, the charge area and the flow area shown in Fig.2-1.

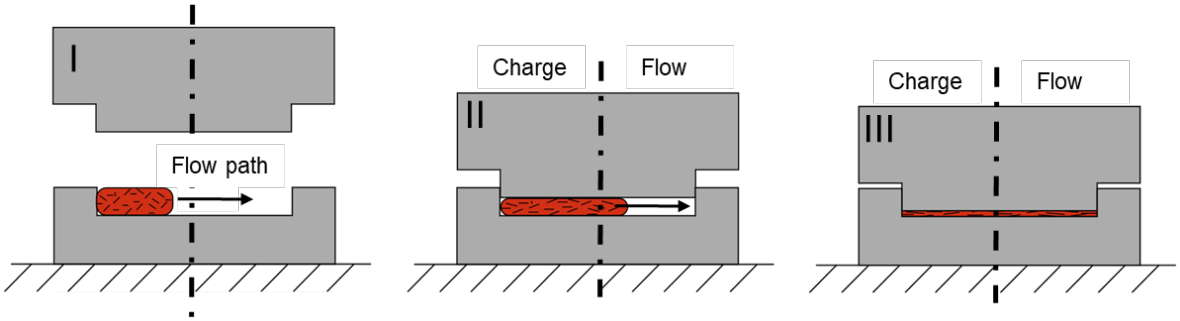

Figure 2-1. Compression molding process with side insert and flow path, which divides the plate into charge and flow area

3. Experimental methods

3.1 Specimen preparation

The samples were cut from the pressed plates in an iCUTwater smart of the company imes-icore with a pressure of 1500bar, a cutting speed of 900mm/min and a flow rate of 250g/min of cutting sand Classic Cut 120 garnet of the company GMA. Since the surface in the charge area of the plates is very rough (due to fibers leading up to the surface), which strongly influences the water absorption, all samples for this work were taken from the flow area. The orientation of all tensile specimens is 0° to the flow path, in which the greatest influence of the fiber reinforcement could be observed due to the flow induced fiber orientation. After cutting, the samples were dried for at least 240 hours in an oven with dryer function at 50°C. For the water absorption according to DIN 62, square specimens with a side length of 61mm were cut. The tensile specimens were rectangular specimens with dimensions of 15x200mm.

3.2 Fiber content measurement

Fiber content measurements were carried out at the Fraunhofer ICT in Pfinztal. The matrix of 16 samples with a diameter of 25 mm were ashed in a TGA701 (LECO Corporation, St. Joseph, Michigan, USA) and measured by weight before and after the ashing process. For the CF-LFT investigations, a very gentle method was used at 430°C under a nitrogen atmosphere.

3.3 Water uptake

The water absorption was investigated on all specimen geometries from 3.1 when immersed in distilled water at 23°C according to DIN EN ISO 62. Since conditioning to the saturation state takes longer than originally assumed, additional tensile samples were stored in a climate chamber at 70°C and 80% relative humidity. The values are based on DIN EN ISO 1110, which describes the accelerated conditioning of polyamides. In order to have a better comparison, the water absorption was related to the weight percentage of the matrix. For this purpose, the results of TGA measurements were used to determine the fiber mass content ($m\%_{fiber}$) of the individual LFT types. The water content was then calculated according to formula 1, where M_0 is the sample mass in dry state at time $t = 0$ and M_t at time t .

$$M_{Matrix}^{Water}\,(\%) = \frac{(M_t - M_0 * m\%_{fiber}) - M_0 * (1 - m\%_{fiber})}{M_0 * (1 - m\%_{fiber})} * 100 \quad (1)$$

3.4 Mechanical test:

The tensile tests were performed according to DIN EN ISO 527-4 2020 on a Zwick Roell Universal testing machine with a 20kN load cell and an external extensometer multi-eXtens for the strain detection.

4. Results and Discussion

In Table 1 the average results with deviation of the TGA data can be seen. The results were used to determine the water absorption on the polymer mass contained in the composite to compare the water absorption of the different materials.

  doi:10.5075/epfl-298799_978-2-9701614-0-0

Table 1: Results of fiber content measurements via TGA.

Material	Ø wt.% total	deviation in %	Ø vol.% Fiber
CF-LFT	29,58	±3,07	21,04
GF-LFT	43,18	±3,29	25,79

It is noticeable that the 25vol% planned value for the glass fiber LFT was hit very accurately, while it was slightly lower for the C-LFT. This may also be due to the analysis method, since the separation between the ashing of fiber and matrix is much more difficult to define for the C-fibers. Therefore, some of the C-fibers may have been ashed before the final measurement, which in result can lead to a too low fiber content.

Figure 4-1 shows the water absorption of the different LFT materials in distilled water at 23°C and in a climatic chamber at 70°C and 80%rh normalized with formula 1 and the data from the TGA to the PA6 content in the compound. In each case, the mean value of 5 samples is given.
It can be seen that the water absorption of the respective material types behaves very similarly in each conditioning method and no major influence of the fibers can be detected. The slightly higher water absorption of the GF-LFT in all tests can be attributed to the results of the TGA, which can easily underestimate the fiber content of C-fibers.

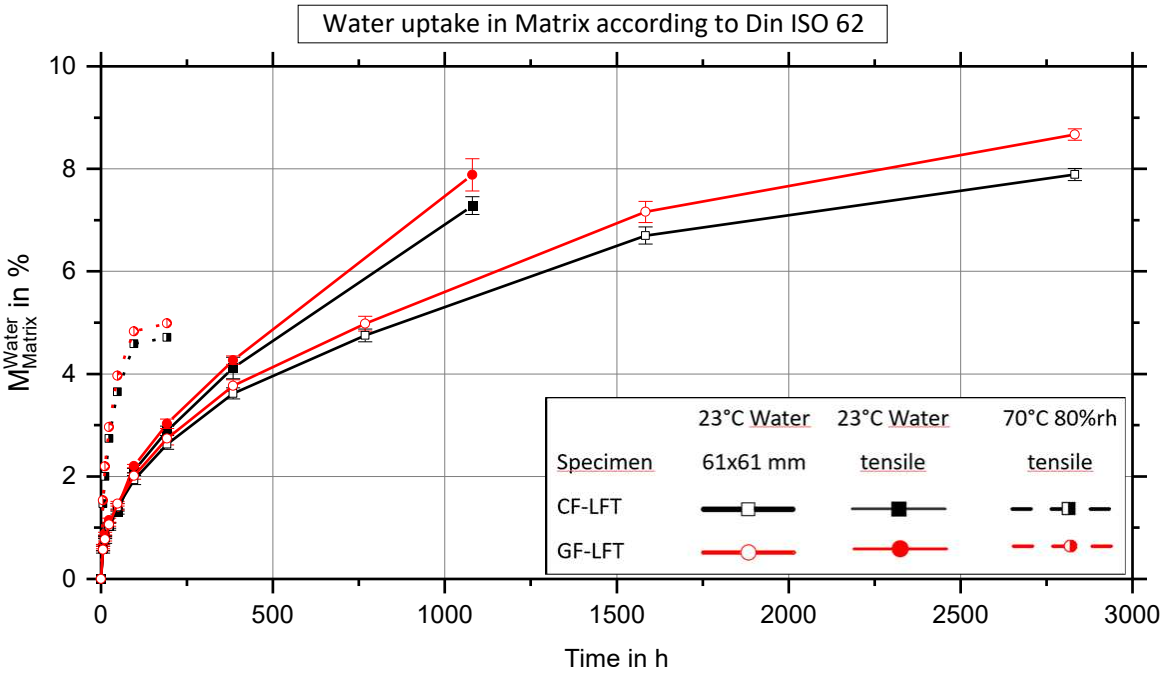

Figure 4-2. Water absorption of the different LFT parts according to DIN EN ISO 62 in distilled water at 23 °C and according to DIN ISO 1110 in a climate chamber at 70°C and 80%rh normalized to matrix content over time in h

It is noticeable that the amount of absorbed water of the tensile specimens in 23°C water increases significantly faster than those of the DIN62 specimens. This can be explained by the fact that the tensile specimens have a relatively higher cutting edge length to volume ratio whereby more rough spots are on the surface. This clearly shows that the diffusion coefficient

is not homogeneous, but that more water diffuses into the samples via the rough cut surfaces. The even faster water absorption of the specimens in the climatic chamber also shows the temperature dependence of diffusion. During conditioning in the climatic chamber, the tensile specimens take on a saturation state at an early stage. This reveals that the absorbed water is uniformly distributed over the entire volume of the specimen. Whereas in the case of specimens placed in water, mainly the peripheral areas are contaminated with water.

The influence of the water on the mechanical properties of the individual materials is shown in figure 4-3. The tensile strength and the modulus of elastisity of the tensile specimens stored in water are shown on the left side and those of the specimens conditioned in the climatic chamber on the right side of the figure.

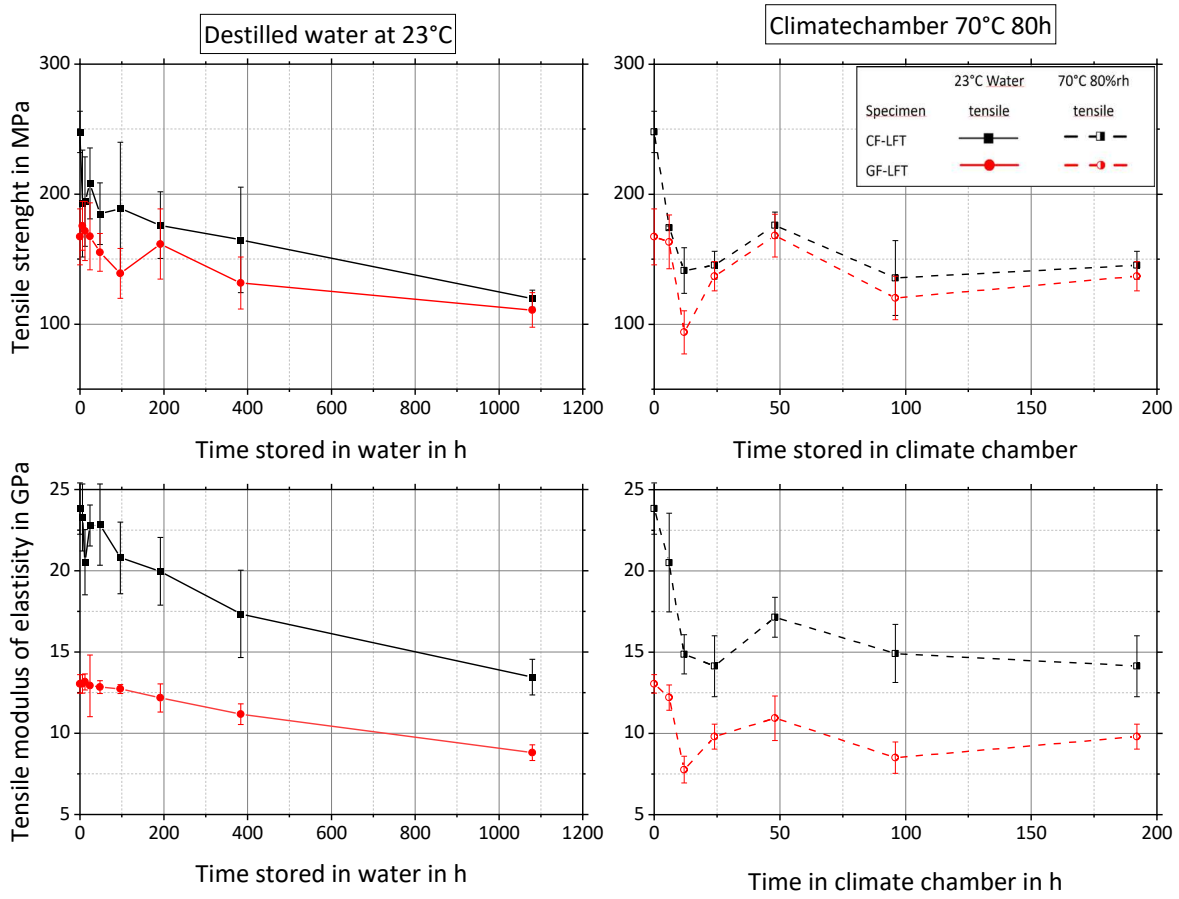

Figure 4-3. Tensile strength and modulus of elasticity of CF-, GF-LFT over time stored in distilled water at 23°C in h

It can be seen that the tensile strength of both materials is significantly reduced under the influence of absorbed water in both conditioning methods. For the samples conditioned in the climatic chamber, as soon as saturation is reached after approx. 96h and even before, the tensile strength of both materials is almost identical at about 140MPa. This clearly shows that the C-fiber reinforced PA6 has a much higher sensitivity to absorbed water as the reduction of the tensile strength in C-LFT is about 41% and in G-LFT about 19%. The same behavior can be observed when stored in water, where after 1080h of exposure to water, the tensile strength of both materials take on a very similar value at about 125MPa. So, the reduction is even more

significant with 52% in the CF-LFT and 34% in the GF-LFT. The even greater reduction can be attributed to the greater amount of absorbed water.

The modulus of elasticity of both materials is also significantly reduced, although the values do not approximate here, but a significantly higher stiffness of the CF-LFT can still be seen after 1080h. The reduction of modulus of elasticity is about 40% for C-LFT and only about 25% for G-LFT for storage in the climatic chamber and about 44% for CF-32% GF-LFT for storage in water. This can be attributed to the fact that the force introduction into the fiber is still sufficient at low strains and the stiffness of the fiber still plays a greater role than is the case with the failure.

In order to better understand the failure of the individual materials, SEM analyses of the fracture surfaces were carried out for selected specimens (in dry codition and after 96h in the climate chamber), which are shown in figure 4-3.

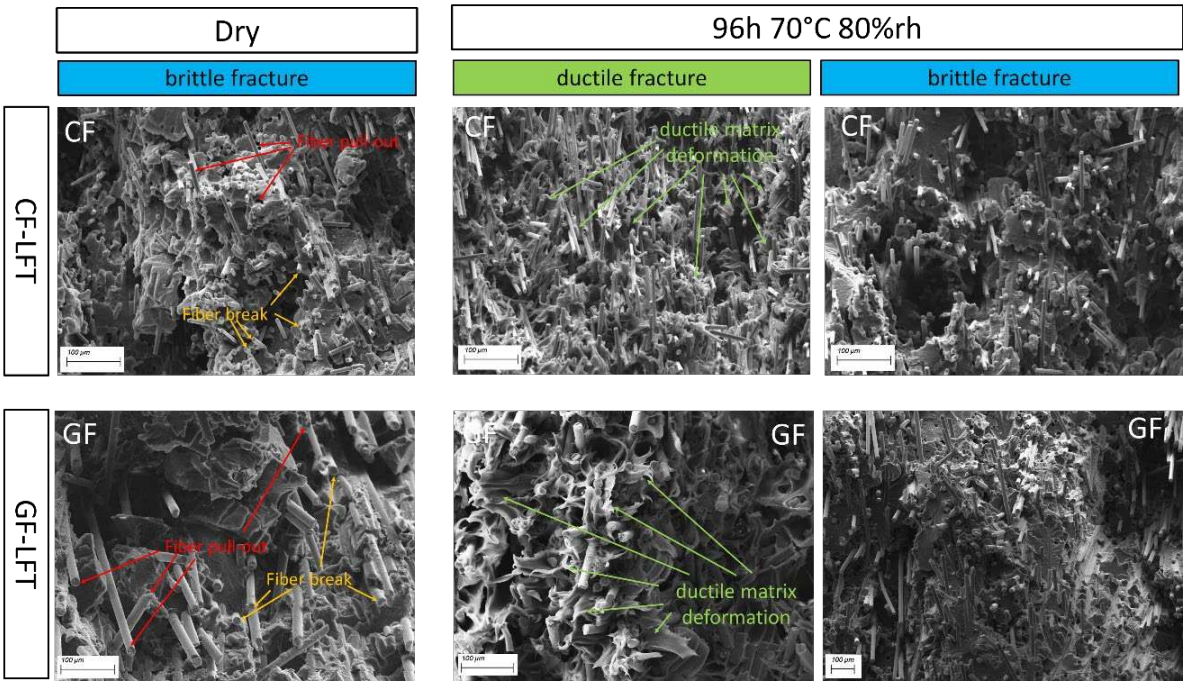

Figure 4-3. SEM images of the fracture surface after the tensile test in dry condition and after 96h in the climatic chamber at 70°C and 80%rh

In the case of the dry samples, for both material systems a brittle fracture behavior with matrix cracks transverse to the loading direction is exclusively observed on the total fracture surface. Both fiber breakage and fiber pull out can be observed, as shown in the fracture surface details of the dry specimens in Figure 4-3. In comparison, on the fracture surfaces of the specimens stored in the climate chamber, a ductile matrix failure can be observed. This can be seen in the highly deformed matrix around the fibers. This can be attributed to the PA6 becoming softer and more ductile due to the absorbed water. It is noticeable that on the same fracture surface at other points, a brittle fracture area can be observed again.

Figure 4-4 shows the fracture surfaces of the same specimens as in Figure 4-3 with low magnification. It can be seen that in both cases a fiber bundle is visible in the middle layer of the

specimen. It is noticeable that the part with ductile failure is always located around the area, where a fiber bundle could be found.

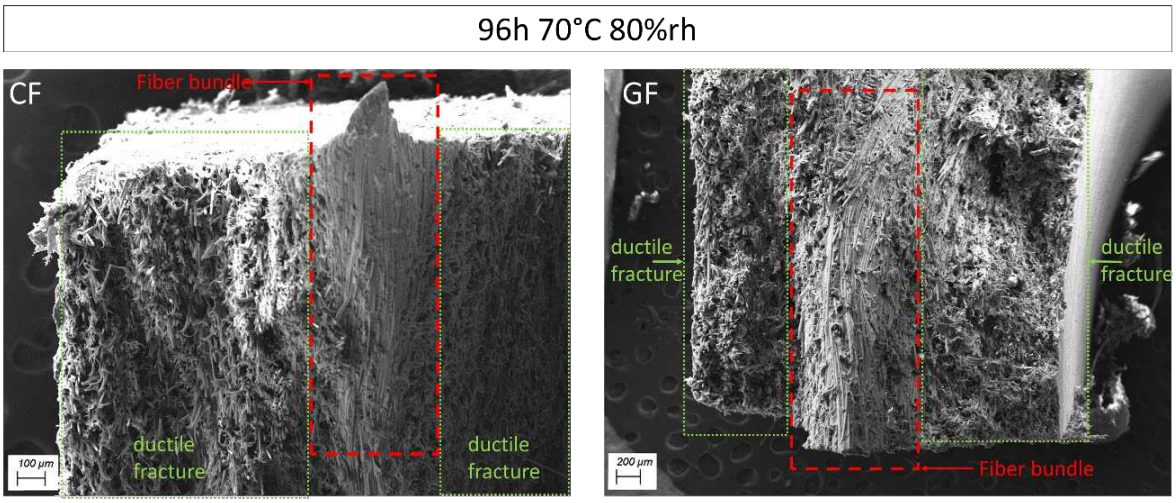

Figure 4-4. SEM images of the fracture surface after the tensile test after 96h in the climatic chamber at 70°C and 80%rh were the damage induction can be localized by the ductile failure modes

Therefore, it can be assumed that there is an increase in stress around the fiber bundle, which leads to a ductile deformation of the matrix. After a crack has developed in the ductile area, however, the remaining fracture surface undergoes brittle fracture, since the crack opening causes the stress in the remaining area to increase very rapidly. The occurrence of ductile failure at the crack initiation coincides with the investigations by Sato et.al. [9] of short glass fiber reinforced PA6 in SEM insitu experiments.

5. Conclusion

It was shown that for both conditioning methods, CF-LFT shows a much higher sensitivity to absorbed water than GF-LFT in terms of reduction of tensile strength and tensile modulus of elasticity. In terms of tensile strength, the behavior of the two materials was even almost identical after extended aging time. With regard to the modulus of elasticity, on the other hand, higher stiffness was still observed with the CF-LFT.
In both materials, a change in the failure behavior could be determined on the basis of fracture surface analyses. Thus, a considerable amount of ductile failure occurred with absorbed water, through which the damage initiation could be localized.

6. Acknowledgements

The work reported in this work has been developed in the framework of the International Research Training Group GRK 2078 "Integrated engineering of continuous-discontinuous long fiber reinforced polymer structures" (CoDiCoFRP) founded by the German Research Foundation (DFG).

7. References

1. Ning H, Lu N, Hassen AA, Chawla K, Selim M, Pillay S. A review of Long fibre thermoplastic (LFT) composites. International Materials Reviews 2019;65(3):164–88. https://doi.org/10.1080/09506608.2019.1585004.
2. Ishikawa T, Amaoka K, Masubuchi Y, Yamamoto T, Yamanaka A, Arai M et al. Overview of automotive structural composites technology developments in Japan. Composites Science and Technology 2018;155:221–46. https://doi.org/10.1016/j.compscitech.2017.09.015.
3. W. Krause, F. Henning, S. Tröster, O. Geiger, and P. Eyerer. LFT-D — A Process Technology for Large Scale Production of Fiber Reinforced Thermoplastic Components.
4. Chawla KK. Composite Materials. Cham: Springer International Publishing; 2019.
5. Pastukhov LV, Kanters MJW, Engels TAP, Govaert LE. Influence of fiber orientation, temperature and relative humidity on the long-term performance of short glass fiber reinforced polyamide 6. J Appl Polym Sci 2021;138(19):50382. https://doi.org/10.1002/app.50382.
6. Chaichanawong J, Thongchuea C, Areerat S. Effect of moisture on the mechanical properties of glass fiber reinforced polyamide composites. Advanced Powder Technology 2016;27(3):898–902. https://doi.org/10.1016/j.apt.2016.02.006.
7. Karsli NG, Aytac A. Tensile and thermomechanical properties of short carbon fiber reinforced polyamide 6 composites. Composites Part B: Engineering 2013;51:270–5. https://doi.org/10.1016/j.compositesb.2013.03.023
8. Sang L, Wang C, Wang Y, Hou W. Effects of hydrothermal aging on moisture absorption and property prediction of short carbon fiber reinforced polyamide 6 composites. Composites Part B: Engineering 2018;153:306–14. https://doi.org/10.1016/j.compositesb.2018.08.138.
9. Sato N, Kurauchi T, Sato S, Kamigaito O. Microfailure behaviour of randomly dispersed short fibre reinforced thermoplastic composites obtained by direct SEM observation. J Mater Sci 1991;26(14):3891–8. https://doi.org/10.1007/BF01184987

STATISTICAL LIFE PREDICTION OF UNIDIRECTIONAL CFRP UNDER CREEP TENSION LOAD BY ACCELERATED TESTING METHODOLOGY

Masayuki Nakada[a], Yasushi Miyano[b], Yoko Morisawa[b], Kazuro Kageyama[b]

a: Materials System Research Laboratory Kanazawa Institute of Technology – nakada@neptune.kanazawa-it.ac.jp
b: Materials System Research Laboratory, Kanazawa Institute of Technology

Abstract: *This study examines the statistical life prediction of unidirectional CFRP under creep tension load by our developed accelerated testing methodology (ATM). Four kinds of resin impregnated carbon fiber strand (CFRP strand) are selected as unidirectional CFRP which consist of two kinds of PAN based carbon fiber, and two kinds of matrix resin, thermoset epoxy and thermoplastic epoxy. Statistical life of these four kinds of CFRP strand under creep tension load are evaluated by ATM and these characteristics are discussed. As results, it can be found that our ATM is applicable to predict the long-term creep strength of these CFRP strands. The creep strengths decrease concomitantly with increasing elapsed time according with the time-dependent relaxation modulus of corresponding matrix resin.*

Keywords: CFRP; durability; tensile creep strength; viscoelasticity; accelerated testing

1. Introduction

Carbon fiber reinforced plastics (CFRP) have been used for primary structural members of airplanes, ships, automobiles, and other vehicles, for which high reliability must be maintained during long-term operation. Therefore, an accelerated testing methodology (ATM) is anticipated strongly for long-term life prediction of CFRP structures exposed to actual environmental temperatures, water, and other influences.

The mechanical behavior of matrix resin of CFRP, so-called viscoelastic behavior, exhibits time and temperature dependence, not only above the glass transition temperature T_g, but also below T_g. Consequently, it can be inferred that the mechanical behavior of CFRP depends strongly on the time and temperature [1-4]. Our earlier reports have proposed formulations of statistical static, creep, and fatigue strengths of CFRP based on matrix resin viscoelasticity [5, 6].

In our earlier work [7], the long-term prediction of statistical creep strength under tension loading along the longitudinal direction of unidirectional CFRP was performed by measuring the statistical static tensile strengths of resin impregnated carbon fiber strand (CFRP strand) and the matrix resin viscoelasticity at various temperatures. Results demonstrated that the experimental creep strength agrees well quantitatively with the predicted values. Therefore, the statistical long-term creep strength of CFRP strands can be predicted using statistically determined static strength of CFRP strands and viscoelastic behavior of matrix resin.

In this paper, four kinds of CFRP strand are selected as unidirectional CFRP which consist of two kinds of PAN based carbon fiber, Torayca T300 and T700, and two kinds of matrix resin, thermoset epoxy (EP) and thermoplastic epoxy (TPEP). Statistical life of these four kinds of CFRP strand named as T300/EP, T300/TPEP, T700/EP and T700/TPEP under creep tension load are

  doi:10.5075/epfl-298799_978-2-9701614-0-0

evaluated by ATM and these characteristics are discussed. First, the static tensile strengths of four CFRP strands are measured statistically at various constant temperatures and the relaxation moduli for two matrix resins are also measured at various constant temperatures. Second, the statistical creep tensile strengths for four CFRP strands are predicted by substituting the measured data into the formulae of these strengths on our developed ATM and the validity of prediction is cleared by compared with the creep tensile strengths measured directly by creep tests. Finally, the characteristics of statistical long-term creep strengths of four CFRP strands are discussed.

2. Formulations

The formulation of statistical static strength σ_s of CFRP based on the matrix resin viscoelasticity, was presented in an equation in our earlier paper [7], as shown below.

$$\log\sigma_s = \log\sigma_0 + \frac{1}{\alpha}\log[-\ln(1-P_f)] + n_R \log\left[\frac{E_s^*(t,T)}{E_r(t_0,T_0)}\right] \quad (1)$$

Therein, P_f signifies the failure probability, t denotes the failure time, t_0 represents the reference time, T stands for the temperature, T_0 stands for the reference temperature, σ_0 and α respectively denote the scale parameter and the shape parameter on the Weibull distribution of static strength. In addition, n_R is the viscoelastic parameter. Therein, E_r and E_s^* respectively represent the relaxation and viscoelastic moduli of matrix resin. The viscoelastic modulus E_s^* for the static load with a constant strain rate is calculated as presented below.

$$E_s^*(t,T) = E_r(t/2\,,T) \quad (2)$$

Statistical creep strength σ_c can be ascertained by shifting the master curve of static strength with log A based on Christensen's theory for viscoelastic crack kinetics [8]. Therefore, the master curve of creep strength can be presented as the following equation [7].

$$\log\sigma_c = \log\sigma_0 + \frac{1}{\alpha}\log[-\ln(1-P_f)] + n_R \log\left[\frac{E_c^*(t,T)}{E_r(t_0,T_0)}\right] \quad (3)$$

In this equation, E_c^* represents the viscoelastic modulus for a constant stress load.

$$E_c^*(t,T) = E_s^*(At,T) = E_r(At/2\,,T) \quad (4)$$

The shifting amount log A, as ascertained from slope k_R of logarithmic static strength against the logarithmic failure time curve, is calculated using the following equation.

$$\log A = \log\left(1+\frac{1}{k_R}\right), \qquad k_R = n_R m_R \quad (5)$$

Therein, m_R represents the slope of logarithmic relaxation modulus of matrix resin against the logarithmic time curve.

3. Molding of CFRP strands and testing methods

Two kinds of CFRP strand, T300/EP and T700/EP using thermoset epoxy resin (EP) were molded by filament winding method [7]. The other two kinds, T300/TPEP and T700/TPEP using thermoplastic epoxy resin (TPEP) were molded using pultrusion method [9]. Table 1 shows the

  doi:10.5075/epfl-298799_978-2-9701614-0-0

carbon fiber and the mechanical properties used for this study [10]. Table 2 shows the matrix epoxy composition and the curing conditions for four kinds of CFRP strand.

The CFRP strand specimen configuration is presented in Fig. 1. The diameter and gage length of CFRP strands are, respectively, approximately 1 mm and 200 mm. The glass transition temperature T_g of the thermoset epoxy resin was 160 °C and of the thermoplastic epoxy resin was 102 °C as ascertained from the peak of loss tangent against temperature at 1 Hz using dynamic mechanical analysis (DMA). Static and creep tension tests for CFRP strands of four kinds were conducted under several levels of constant temperature using our developed testing system [7].

Table 1: Carbon fiber and the mechanical properties.

Carbon fiber	Density [g/cm^3]	Yield [g/1000 m]	Elastic modulus [GPa]	Tensile strength [MPa]
T300-3000	1.76	198	230	3,530
T700-6000	1.80	400	230	4,900

Table 2: Composition and curing schedule of CFRP strand.

CFRP strand	Composition of resin (weight ratio)	Cure schedule
T300/EP and T700/EP	Thermoset epoxy (100) Hardener (104) Cure accelerator (1.0)	70 °C × 12 h +150 °C × 4 h +190 °C × 2 h
T300/TPEP and T700/TPEP	Thermoplastic epoxy (100) Cure accelerator (6.5)	150 °C × 0.5 h

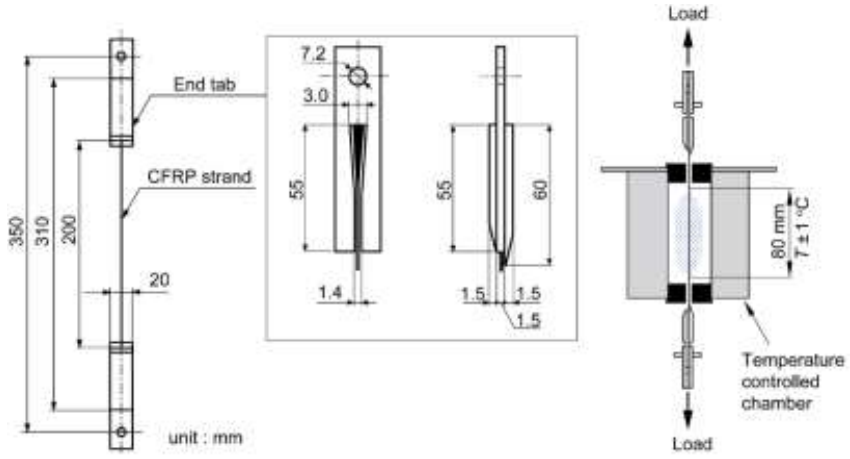

Figure 1. Configuration of tensile tests for CFRP strand specimens

4. Results and discussion

4.1 Relaxation modulus of matrix resin

Relaxation moduli were measured at various temperatures for EP and TPEP resins. Figure 2 shows the relaxation moduli at 1 min for EP and TPEP resins versus temperature. Figure 3 shows the master curve of relaxation moduli at reference temperature T_0= 25 °C which were obtained by shifting relaxation moduli at each temperature horizontally and vertically based on the time-temperature superposition principle.

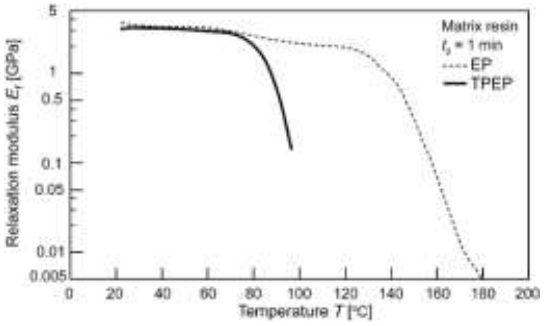

Figure 2. Relaxation moduli of matrix resins EP and TPEP versus temperature

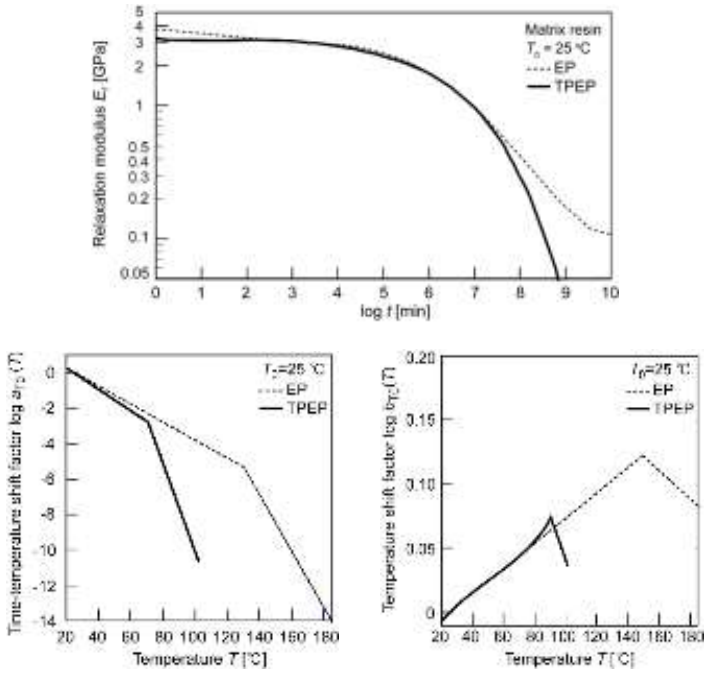

Figure 3. Master curves of relaxation moduli and shift factors for matrix resins EP and TPEP

4.2 Determination of strength parameters of CFRP strands by static tests

Static tension tests for CFRP strands were conducted at various temperatures with cross-head speed of 2 mm/min. The tensile strength σ_s is obtained using the following equation.

$$\sigma_s = \frac{W_{max}}{t_e}\rho \tag{6}$$

In this equation, W_{max} represents the maximum load [N]. In addition, ρ and t_e respectively denote the carbon fiber density [kg/m^3] and the yield of the carbon fiber strand [g/1000 m].

Figure 4 shows the static strength versus temperature for CFRP strands. The static strengths decrease markedly with increasing temperature. The static strengths for T300/TPEP and T700/TPEP are relatively lower than those for T300/EP and T700/EP, respectively, although the same carbon fiber is used. This is caused by the molding method for CFRP strand.

The Weibull distributions for static strength at various temperatures are depicted in Fig. 5 for the CFRP strands. In this figure, α_s is the shape parameter and β_s is the scale parameter of the CFRP strand. Although the scale parameter decreases according to the temperature rise, the shape parameter maintains an almost constant value for the CFRP strand to the temperature rise. Shape parameter α_s and scale parameter β_s at temperature T = 25 °C in this figure can be inferred as shape parameter α, scale parameter σ_0 of static strength at the reference temperature T_0 = 25 °C, and the reference failure time t_0 = 1 min used in Eq. (1).

Figure 6 portrays the dimensionless static strengths of CFRP strands σ_s/σ_0 against the dimensionless viscoelastic modulus of matrix resin E_s^*/E_{r0}. The relation of σ_s/σ_0 against E_s^*/E_{r0} can be represented as a straight line with slope of n_R, which is the viscoelastic parameter in Eqs. (1), (3) and (5). Parameters σ_0, α and n_R for CFRP strand are presented in Table 3. The parameter n_R is controlled by the shape parameter of carbon mono filament based on the Rosen's failure model [11]. It can be seen that the n_R in Table 3 is clearly different with type of carbon fiber.

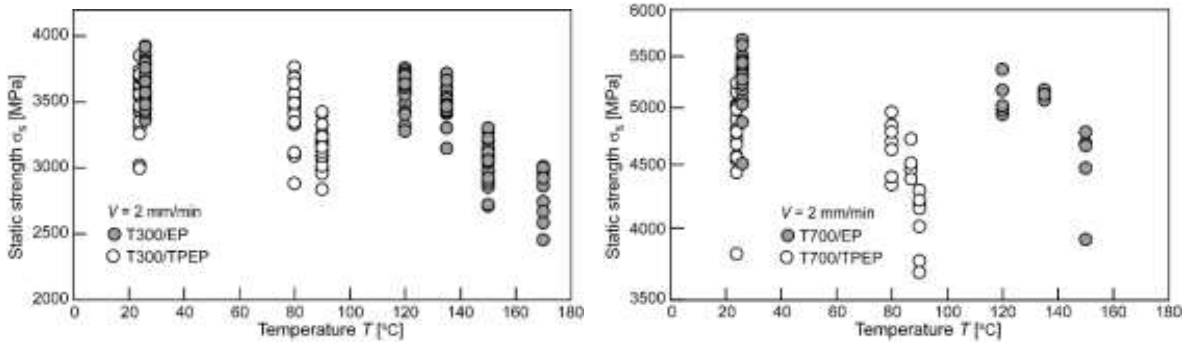

(a) T300/EP & T300/TPEP *(b) T700/EP & T700/TPEP*

Figure 4. Static strengths of CFRP strands versus temperature

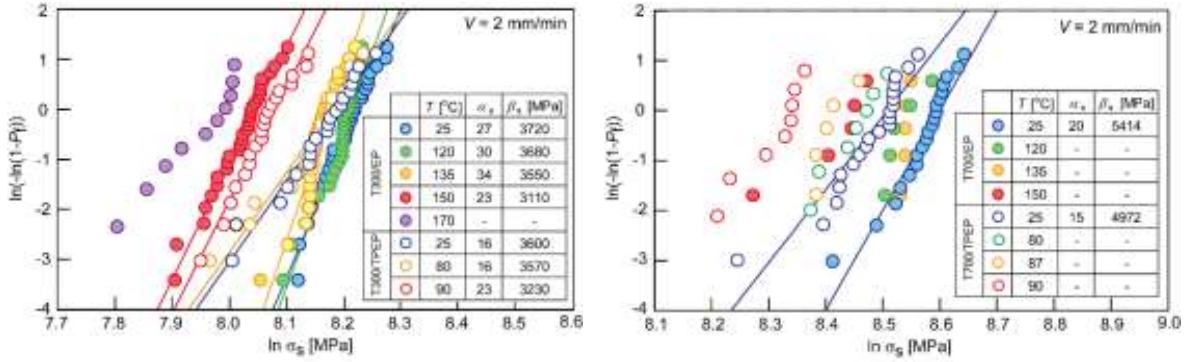

(a) T300/EP & T300/TPEP *(b) T700/EP & T700/TPEP*

Figure 5. Weibull distributions of static strength of CFRP strands

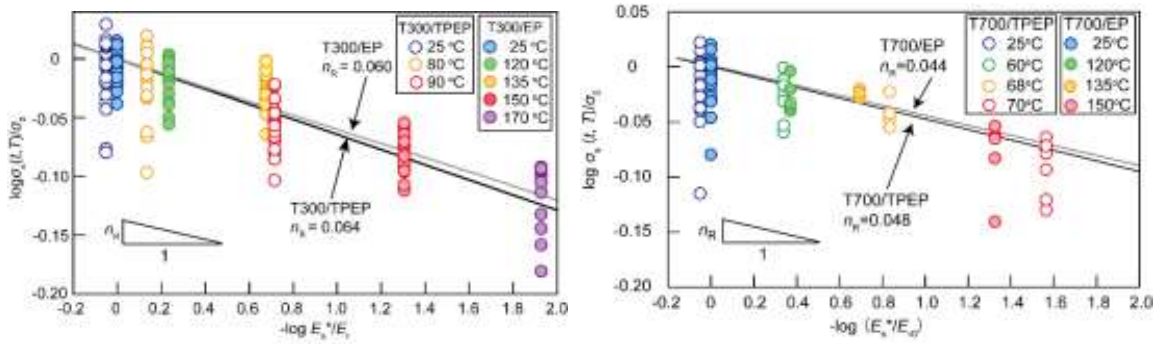

(a) T300/EP & T300/TPEP *(b) T700/EP & T700/TPEP*

Figure 6. Determination of viscoelastic parameter n_R

Table 3: Parameters of statistically determined static and creep strengths for CFRP strands.

	σ_0 [MPa]	α	n_R	m_R
T300/EP	3,720	27	0.060	0.280
T700/EP	5,414	20	0.044	0.222
T300/TPEP	3,600	16	0.064	0.166
T700/TPEP	4,972	15	0.048	0.176

4.3 Statistical creep failure time of CFRP strands

Creep failure tests of CFRP strands were conducted respectively at a constant stress level and at a constant temperature. Results of the creep failure tests are presented in Fig. 7. The predicted tensile creep strength σ_c calculated by substituting the parameters in Table 3 into Eq. (3) are also shown in Fig. 7. The predicted statistical creep failure time agrees well with the experimentally obtained data.

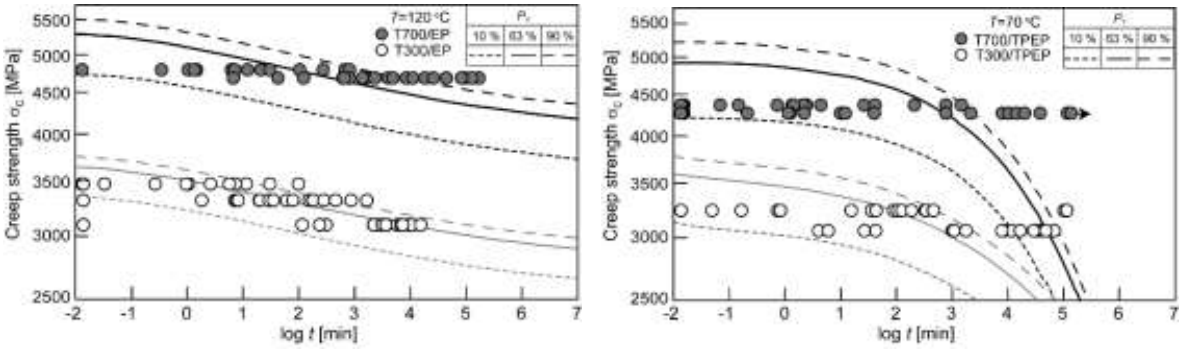

(a) T300/EP & T700/EP *(b) T300/TPEP & T700/TPEP*

Figure 7. Statistical creep failure time for CFRP strands

4.4 Prediction of long-term creep strength

Prediction of long-term statistic tensile creep strengths for CFRP strand used for this study is performed by substituting the viscoelastic properties of matrix resin in Fig. 3 and the material parameters for CFRP strand of Table 3 into Eq. (3). Figure 8 shows the predicted long-term relaxation modulus of matrix resin and the statistic tensile creep strength of CFRP strands at T = 25 °C. These figures clarified that the creep strengths of CFRP strand decrease concomitantly with increasing elapsed time according with the time-dependent relaxation modulus of corresponding matrix resin.

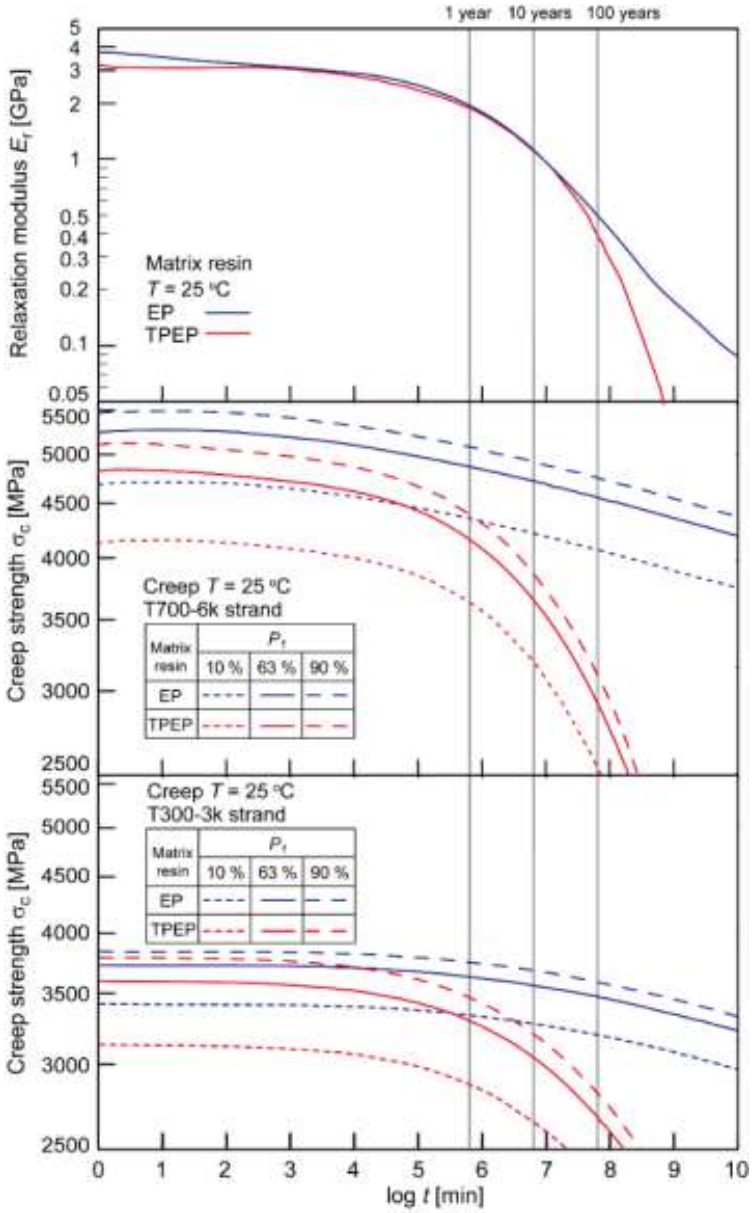

Figure 8. Prediction of long-term relaxation modulus for matrix resin and tensile creep strength for CFRP strands

  doi:10.5075/epfl-298799_978-2-9701614-0-0

5. Conclusion

This study examines the statistical life prediction of unidirectional CFRP under creep tension load by our developed accelerated testing methodology (ATM). Four kinds of resin impregnated carbon fiber strand (CFRP strand) are selected as unidirectional CFRP which consist of two kinds of PAN based carbon fiber, Torayca T300 and T700, and two kinds of matrix resin, thermoset epoxy (EP) and thermoplastic epoxy (TPEP). Statistical life of these four kinds of CFRP strand under creep tension load are evaluated by ATM and these characteristics are discussed. As results, it can be found that our ATM is applicable to predict the long-term creep strength of these CFRP strands. The creep strengths decrease concomitantly with increasing elapsed time according with the time-dependent relaxation modulus of corresponding matrix resin.

Acknowledgements

This paper is based on results obtained from a project, JPNP14004, commissioned by the New Energy and Industrial Technology Development Organization (NEDO).

References

1. Aboudi J and Cederbaum G. Analysis of Viscoelastic Laminated Composite Plates. Composite Structures 1989; 12: 243–256.
2. Sullivan J. Creep and Physical Aging of Composites. Composites Science and Technology 1990; 39: 207–232.
3. Gates T. Experimental Characterization of Nonlinear, Rate Dependent Behavior in Advanced Polymer Matrix Composites. Experimental Mechanics 1992; 32: 68–73.
4. Miyano Y, Nakada M, McMurray MK and Muki R. Prediction of Flexural Fatigue Strength of CFRP Composites under Arbitrary Frequency, Stress Ratio and Temperature. Journal of Composite Materials 1997; 31: 619–638.
5. Miyano Y, Nakada M, and Cai H. Formulation of Long-term Creep and Fatigue Strengths of Polymer Composites Based on Accelerated Testing Methodology. Journal of Composite Materials 2008; 42: 1897–1919.
6. Nakada M and Miyano Y. Advanced Accelerated Testing Methodology for Long-Term Life Prediction of CFRP Laminates. Journal of Composite Materials 2015; 49: 163–175.
7. Miyano Y and Nakada M. Accelerated testing methodology for durability of CFRP, Composites Part B 2020; 191: 107977.
8. Christensen R and Miyano Y. Stress Intensity Controlled Kinetic Crack Growth and Stress History Dependent Life Prediction with Statistical Variability. International Journal of Fracture 2006; 137: 77–87.
9. Nakada M, Miyano Y, Morisawa Y, Nishida H, Hayashi Y and Uzawa K. Prediction of statistical life time for unidirectional CFRTP under creep loading. Journal of Reinforced Plastics and Composites 2019; 38: 938–946.
10. TORAY INDUSTRIES, INC. Web https://www.cf-composites.toray/resources/data_sheets/#anc1 Accessed 25 Feb. 2022.
11. Miyano Y and Nakada M. Accelerated testing methodology for durability of CFRP, Composites Part B 2020; 191: 107977.

  doi:10.5075/epfl-298799_978-2-9701614-0-0

EFFECT OF WATER SORPTION IN NEAT POLY(ETHER KETONE KETONE) AND ITS CARBON FIBER REINFORCED COMPOSITE

Gwladys, Lesimple[a], Bruno, Fayolle[a], Stéphane, Bizet[b],
Thibaut, Benethuiliere[c], Eric, Monteiro[a], Ilias, Iliopoulos[a]

a: Laboratoire PIMM, Arts et Metiers Institute of Technology, CNRS, Cnam, HESAM Universite, 151 boulevard de l'Hopital, 75013 Paris (France) – gwladys.lesimple@ensam.eu
b: Arkema, CERDATO, 27470 Serquigny, France
c: Hexcel Reinforcements, 38630 Les Avenières, France

Abstract: *Poly(ether ketone ketone) (PEKK) is a high performance thermoplastic polymer with excellent mechanical properties, which aims to replace epoxy currently widely used as matrices in aircraft composites. Knowing the aircrafts service life, it is of great importance to evaluate the durability of its constitutive materials. In this paper, water sorption of both PEKK neat resin as well as in its continuous carbon fiber composite (C/PEKK) is fully characterized using both water immersion and dynamic vapor sorption (DVS) methods. Water transport in PEKK follows Henry's law whereas a clear deviation from this behavior is observed in C/PEKK at high relative humidities. Water diffusion in unidirectional consolidated C/PEKK has been modeled using finite element method based on water transport parameters determined in neat PEKK.*

Keywords: Thermoplastic; PEKK; water transport; CFRP; DVS

1. Introduction

Continuous carbon fiber reinforced thermoplastics are gaining in interest in the aeronautic field in the last decades. High performance thermoplastics such as poly(phenylene sulfide) (PPS), poly(ether imide) (PEI) and poly(aryl ether ketone) (PAEK) have the major advantage to be weldable, recyclable and have less constraining storage conditions than thermosets. Poly(ether ether ketone) (PEEK) is the most common polymer from the PAEK family whereas PEKK was developed later. During their use phase, the composite parts of an aircraft can come into contact with different aggressive environments such as temperature, humidity, radiations, aeronautic fluids, etc. Thus, it is necessary to assess the potential effects of these latter on the material.

Thermoplastics exhibit better chemical resistance than epoxy matrices which are currently widely used in aircraft structures. Several studies showed that epoxy resins can absorb up to 10 wt% water (1–4). This is mostly due to the high polarity of chemical groups contained in epoxy resins leading to hydrogen bonding to water molecules. This significant water uptake induces irreversible damage in both epoxy-based composites such as swelling leading to a reduction in delamination fracture (5). Moreover, micro cracks as well as intralaminar cracks are frequently observed (6,7). Water sorption in neat resin is usually described as fickian whereas it deviates from fickian behavior in carbon fiber reinforced epoxy composites due to irreversible damages (8–10).

Water sorption in neat PEEK and its carbon fiber reinforced composite has been studied by several authors since the 1980s. In water immersion, neat PEEK and C/PEEK follow Fick's law and absorb up to 0.55 wt% and 0.4 wt% water respectively (11–14). Very few literature provides data

  doi:10.5075/epfl-298799_978-2-9701614-0-0

on water transport in C/PEKK (15,16) and no paper was found in the case of neat PEKK. The present study aims to investigate water sorption mechanism in neat PEKK matrix as well as in C/PEKK composite using both water immersion and dynamic vapor sorption methods.

2. Experimental

2.1 Materials

Neat PEKK with a T/I ratio of 70/30 was provided by Arkema. Films of 50 µm thickness are used for dynamic vapor sorption (DVS) measurements whereas 2 mm-thick plates are used for gravimetric measurements. Composite tapes (thickness 0.200 mm and controlled porosity) made of unidirectional continuous carbon fibers (AS7) and PEKK 70/30 are provided by Hexcel Reinforcements. The tapes have a porosity level of 3% and 9% and a carbon fiber volume content of 60v%. Tapes consolidated using a press applying 7 bars are considered non porous.

2.2 Gravimetric measurement

For gravimetric measurements, samples of size 50x50 mm² are cut in the PEKK plates and composite tapes using a band saw and a diamond saw respectively. They are dried in an oven at 120°C during 48 hours prior to water immersion. The samples are immersed in distilled water at 30°C, 50°C and 70°C, in sealed glass jars placed in a temperature-controlled water bath, until saturation. The samples are regularly surface-dried with paper towel and weighed using a Mettler Toledo analytical balance. The water uptake is measured using the following equation:

$$w(t) = \frac{m(t) - m_0}{m_0} \quad (1)$$

With *m(t)* the mass of the sample at time *t* and m_0 the initial mass of the dried sample.

2.3 Dynamic Vapor Sorption

For DVS measurements, samples of size 25x15 mm² are cut in the PEKK film and tapes. The samples are placed in the DVS apparatus, hanged by a hook in the chamber which is controlled both in temperature and relative humidity (RH). The sample is weighed *in situ*. A RH cycle of following 0%-10%-0%-30%-0%-50%-0%-70%-0%-90%-0% is applied at constant temperature (70°C). Each RH step is applied until a plateau is observed in the sample mass.

3. Results and discussion

3.1 Water sorption in neat PEKK

Water transport parameters in neat PEKK have been determined through water immersion (*Figure 1*). Water sorption is found to follow Fick's law:

$$\frac{dw}{dt} = D\frac{\partial^2 w}{\partial x^2} \quad (2)$$

With *D* the diffusion coefficient of water in the polymer and *x* the position from the sample surface.

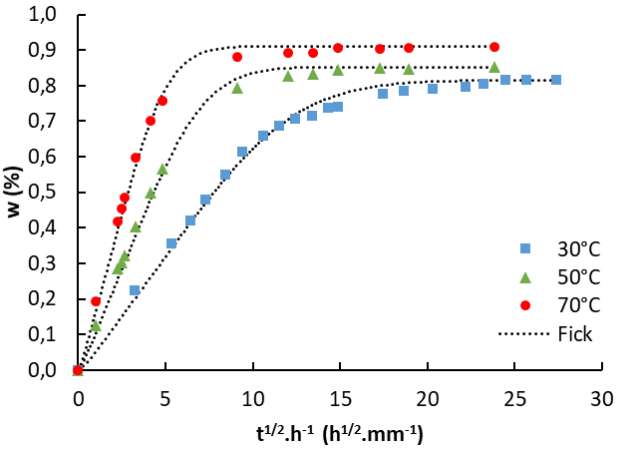

Figure 1. Water uptake in neat PEKK as a function of the square root of time divided by the sample thickness, measured by water immersion at 30°C, 50°C and 70°C.

Moreover, DVS measurement at different relative humidities ranging from 10% to 90% RH shows that water uptake in PEKK follows Henry's law such that (see also *Figure 2*):

$$C_\infty = Sp_{vap} = \frac{w_\infty \rho_p}{M_f} \tag{3}$$

With p_{vap} the water vapor pressure, S solubility of water into the polymer, ρ_p the polymer density and M_f the molar mass of water. This result is consistent with the low amount of water absorbed since PEKK is moderately polar.

3.2 Water sorption in composite

Water immersion as well as DVS were performed on a consolidated tape. The water uptake given is corrected from the mass fraction of PEKK in the composite in order to easily compare w_∞ with neat PEKK.

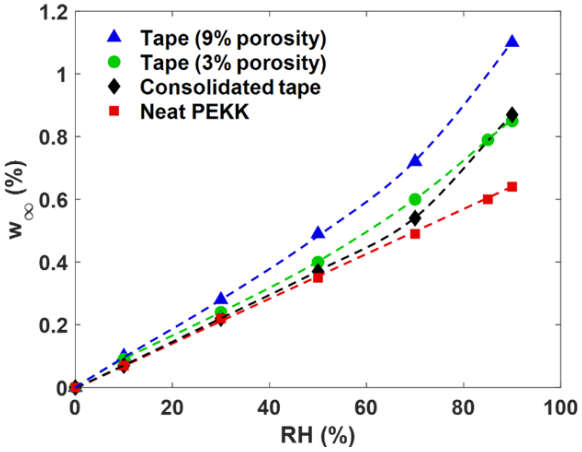

Figure 2. Water uptake at saturation as a function of the relative humidity measured by DVS at 70°C for neat PEKK, consolidated tape and porous tapes. Water uptake measured in composite is corrected with the PEKK matrix content.

The consolidated unidirectional composite does not follow fickian behavior (*Figure 3*). The diffusion mechanism seems to include two steps: first water sorption is driven by diffusion in the PEKK matrix, then the sorption rate decreases corresponding possibly to the filling of residual micro-voids (17).

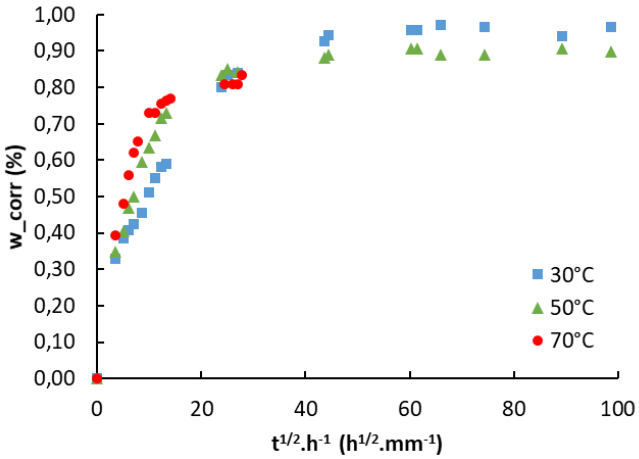

Figure 3. Water uptake in a C/PEKK consolidated tape as a function of the square root of time divided by the thickness, measured by water immersion at 30°C, 50°C and 70°C. Water uptake measured in composite is corrected with the PEKK matrix content.

DVS measurement on the consolidated tape shows a deviation from Henry's law at high relative humidities i.e. from 70% RH (*Figure 2*). This phenomenon which is not observed in neat PEKK, is typical of water clustering in micro-voids and is in accordance with the non fickian diffusion in C/PEKK.

Table 1: Diffusion coefficient and water uptake at saturation in neat PEKK and C/PEKK measured by water immersion.

	PEKK		C/PEKK	
T (°C)	$Dx10^{12}$ ($m^2.s^{-1}$)	w_∞ (%)	'Apparent' $Dx10^{12}$ ($m^2.s^{-1}$)	w_∞ (%)/$w_{\infty,corr}$ (%)
30°C	0.4 ± 0.1	0.82 ± 0.02	0.4 ± 0.1	0.33 ± 0.02/0.97 ± 0.06
50°C	1.1 ± 0.1	0.85 ± 0.01	0.7 ± 0.1	0.31 ± 0.02/0.91 ± 0.06
70°C	2.2 ± 0.2	0.91 ± 0.01	1.0 ± 0.2	0.28 ± 0.01/0.82 ± 0.03

Concerning water uptake, the composite absorbs the same amount of water as neat PEKK up to 70% RH where w_∞ starts greatly increasing due to the filling of cavities.

The same measurements are carried out on unconsolidated tapes with 3% et 9% porosity in order to highlight de effect of porosity on water sorption mechanism. As expected, water uptake as a function of relative humidity in both porous tapes deviate from Henry's law. Moreover, the higher the porosity, the lower the relative humidity at which the deviation starts. Water immersion confirms the void filling in unconsolidated tapes (*Figure 4*).

  doi:10.5075/epfl-298799_978-2-9701614-0-0

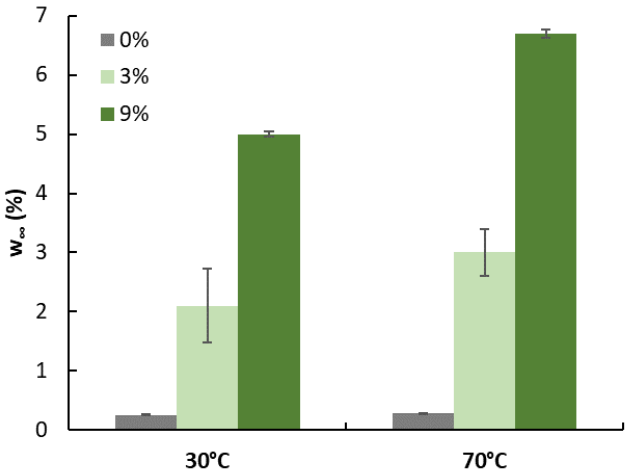

Figure 4. Water uptake in C/PEKK tapes, consolidated (0%) and unconsolidated (3% and 9% porosity) measured by water immersion at 30°C and 70°C.

The total water uptake is in accordance with the void content nevertheless, cavities do not seem to be fully filled with liquid water when saturation plateau is reached.

3.4 Water transport model in unidirectional C/PEKK

Since the tapes do not follow a fickian behavior, we propose to model by finite element method (FEM) water transport in unidirectional consolidated composite. The composite is simulated by incorporating continuous cylinders representing impermeable carbon fibers. Their localization is based on micrographs of the samples used within the framework of this study. The water transport is assumed to be completely driven by water diffusion in the PEKK matrix (with diffusion coefficient D) with neither capillary nor cavity filling mechanisms. As expected, the 2D model shows a slower diffusion of water in the composite compared to the neat PEKK (*Figure 5*).

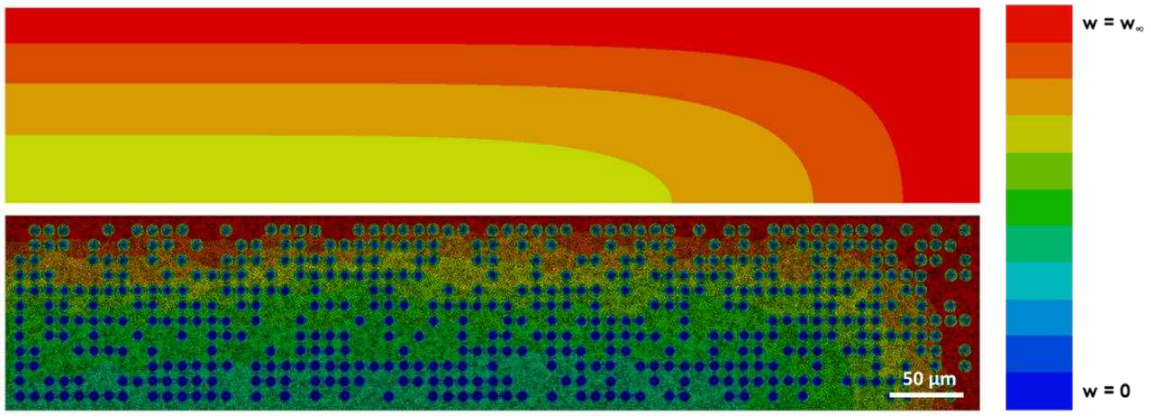

Figure 5. Water diffusion in neat PEKK (top) and C/PEKK (bottom) at the same exposure time. The top right corner of a sample is represented.

Carbon fibers, indeed, slow down the diffusion by extending the diffusion path for water into the composite. The 'apparent' diffusion coefficient, measured on the first linear part of the sorption curve, is lower in the composite than in PEKK (*Table 1*).

1091/1211 ©2022 Lesimple et al. doi:10.5075/epfl-298799_978-2-9701614-0-0 published under CC BY-NC 4.0 license

4. Conclusions

Water sorption mechanism in carbon fiber reinforced PEKK tapes in unconsolidated and consolidated states was investigated. Preliminary study showed that neat PEKK absorbs less than 1 wt% water and that water diffusion follows fickian behavior and Henry's law from 0 to 90% relative humidity. Exposure of C/PEKK consolidated tape to humidity shows a deviation from Henry's law at high relative humidities, typical of the presence of water clustering in micro voids. Increase of the phenomenon using tapes with controlled porosity confirms the filling of cavities at high relative humidities. Water sorption in C/PEKK does not follow classical fickian behavior due to the presence of carbon fibers and voids, leading to more complex sorption mechanisms. We have successfully proposed a FEM modelling to simulate water transport in C/PEKK by taking into account water transport in neat PEKK and fiber geometry.

Acknowledgements

This work was conducted under the framework of HAICoPAS, a PSPC project (projet de recherche et développement structurant pour la compétitivité). BPI France is acknowledged for funding the PhD work of G. Lesimple (project number: PSPC.AAP-7.0_HAICoPAS). The authors thank Arkema, Hexcel for fruitful discussions and the Industrial Chair Arkema (Arkema/CNTS-ENSAM-Cnam) for partial support.

5. References

1. Popineau S, Rondeau-Mouro C, Sulpice-Gaillet C, Shanahan M. Free/bound water absorption in an epoxy adhesive. Polymer. 2005;46:10733–40.
2. Mensitieri G, Apicella A, Kenny JM, Nicolais L. Water sorption kinetics in poly(aryl ether ether ketone). J Appl Polym Sci. 1989;37(2):381–92.
3. Humeau C, Davies P, Jacquemin F. An experimental study of water diffusion in carbon/epoxy composites under static tensile stress. Composites Part A: Applied Science and Manufacturing. 2018;107:94–104.
4. Davies P, Boisseau A, Choqueuse D, Thiebaud F, Perreux D. Durabilité des composites pour énergie marine renouvelable. In: AMAC, editor. 17èmes Journées Nationales sur les Composites (JNC17) [Internet]. Poitiers-Futuroscope, France; 2011 [cited 2022 Jan 17]. p. 34. Available from: https://hal.archives-ouvertes.fr/hal-00597897
5. Lucas JP, Zhou J. The effects of sorbed moisture on resin-matrix composites. JOM. 1993 Dec 1;45(12):37–40.
6. Yekani Fard M, Raji B, Pankretz H. Correlation of nanoscale interface debonding and multimode fracture in polymer carbon composites with long-term hygrothermal effects. Mechanics of Materials. 2020 Nov 1;150:103601.
7. Zhou J, Lucas JP. The effects of a water environment on anomalous absorption behavior in graphite/epoxy composites. Composites Science and Technology. 1995;53(1):57–64.
8. Alessi S, Pitarresi G, Spadaro G. Effect of hydrothermal ageing on the thermal and delamination fracture behaviour of CFRP composites. Composites Part B: Engineering. 2014 Dec 1;67:145–53.

  doi:10.5075/epfl-298799_978-2-9701614-0-0

9. Humeau C, Davies P, Jacquemin F. Moisture diffusion under hydrostatic pressure in composites. Materials & Design. 2016 Apr 15;96:90–8.

10. Todo M, Nakamura T, Takahashi K. Effects of Moisture Absorption on the Dynamic Interlaminar Fracture Toughness of Carbon/Epoxy Composites. Journal of Composite Materials. 2000;34(8):630–48.

11. Boinard E, Pethrick RA, MacFarlane CJ. The influence of thermal history on the dynamic mechanical and dielectric studies of polyetheretherketone exposed to water and brine. Polymer. 2000;41(3):1063–76.

12. Batista NL, Rezende MC, C.Botelho E. The Influence of Crystallinity on the Weather Resistance of CF/PEEK Composites. Appl Compos Mater. 2021 Feb 1;28(1):235–46.

13. Stober EJ, Seferis JC, Keenan JD. Characterization and exposure of polyetheretherketone (PEEK) to fluid environments. Polymer. 1984;25(12):1845–52.

14. Ma C-CM, Lee C-L, Chang M-J, Tai N-H. Hygrothermal behavior of carbon fiber-reinforced poly(ether ether ketone) and poly(phenylene sulfide) composites. I. Polymer Composites. 1992;13(6):448–53.

15. Mazur RL, Cândido GM, Rezende MC, Botelho EC. Accelerated aging effects on carbon fiber PEKK composites manufactured by hot compression molding. J Thermoplast Compos Mater. 2016;29(10):1429–42.

16. Juska T. Effect of Water Immersion on Fiber/Matrix Adhesion in Thermoplastic Composites. J Thermoplast Compos Mater. 1993;6(4):256–74.

17. Alam P, Robert C, Ó Brádaigh CM. Tidal turbine blade composites - A review on the effects of hygrothermal aging on the properties of CFRP. Composites Part B: Engineering. 2018 Sep 15;149:248–59.

  doi:10.5075/epfl-298799_978-2-9701614-0-0

DEVELOPMENT OF A TEST RIG FOR THE TEMPERATURE-DEPENDENT DETERMINATION OF COMPOSITE MATERIAL PROPERTIES AT CRYOGENIC TEMPERATURES

Leonard Gabele[a], Anna Trauth[a], Markus G. R. Sause[a]

a: Augsburg University, Institute of Material Resource Management (MRM),
Am Technologiezentrum 8, 86159 Augsburg, Germany
email: leonard.gabele@mrm.uni-augsburg.de

Abstract: *Fiber reinforced polymers are a common material choice for applications in the cryogenic thermal regime such as vessels to store liquid hydrogen or oxygen for spacecraft or satellite propulsion systems. To ensure safety during usage of these components, a comprehensive material characterization at cryogenic temperatures is essential for design and construction. For that purpose, cryogenic liquids, e. g. liquid nitrogen or helium, and the insertion of the entire test rig (immersion) to cool down the specimen are commonly used. However, this approach limits the test procedure to the respective boiling temperature of the cryogenic liquid and produces substantial costs in the case of helium. Therefore, this work introduces a new concept for the measurement at variable temperatures between 20 K and room temperature by cooling via a closed loop helium Gifford-McMahon cryocooler for the characterization of composite materials.*

Keywords: carbon fiber reinforced polymers; cryogenic; characterization; mechanical properties; cryostat

1. Introduction

For space applications, liquid hydrogen and liquid methane are used as working or propulsion gases in addition to liquid oxygen. Furthermore, both liquid nitrogen and liquid helium are cryogenically stored to be available as working gases. This way, the respective storage systems are thermally and mechanically stressed in the range of cryogenic temperatures. In addition, the temperature exposure of composite structures in space also requires knowledge of the mechanical characteristics in the lowest temperature range to be able to operate them safely. Therefore, comprehensive material characterization at cryogenic temperatures is essential for design and construction of space systems. In the case of composite materials, the measurement of tensile, compression and shear properties are considered as baseline. Moreover, testing of joints and fracture mechanics evaluation, as well as the ability to test cylindrical (e. g. filament wound) samples are seen as a requirement for widespread use of composites in space applications. Hohe et al. have provided a review which highlights the comprehensive research that has been conducted in the last decades. The reports on mechanical experiments to determine stiffness, strength and fracture toughness of fiber reinforced materials with partially contradictory results indicate that multiple and conflicting effects are active on the microscopic level. The most important mechanism is the development of thermally induced residual stresses due to the mismatch in the coefficient of thermal expansion of the fibers and the matrix [1]. In this context, the fibers with their larger stiffness and negative thermal expansion coefficient in axial direction constrain the thermal contraction of the matrix, leading to substantial residual

  doi:10.5075/epfl-298799_978-2-9701614-0-0

stresses in the interface. As a result, micro-crack networks may develop in the matrix of fiber reinforced plastics (FRP) laminates when exposed to a cryogenic environment. Opposing effects are an increase in strength and stiffness of the matrix material if cooled down to the cryogenic regime [1]. Furthermore, some contradictory evidence is found that the strength of the fiber and matrix interface also increases [1].

For the testing of FRP at low temperatures, the use of cryogenic liquids like liquid nitrogen (77 K) or liquid helium (4.2 K) and the insertion of the entire test rig (immersion) in these liquids are widespread [1, 2, 3]. The test rig with a prepared sample is immersed in the bath and cooled down before mechanical characterization is carried out. However, this procedure limits the test to the respective boiling temperature of the cryogenic liquid and produces high costs in the case of helium [1, 2, 3]. Other approaches use a controllable thermal bridge for a variable coupling to a cryogenic liquid bath. This allows to slightly vary the test temperatures; however, the base temperature is fixed by the choice of the cryogenic liquid. More recent approaches use indirect cooling by utilizing the cooling power of the exhaust vapor of a cryogenic liquid to cool the test fixture to defined temperatures between room temperature and the respective boiling temperatures [1, 4]. Due to the excessive use of cryogenic liquids, new approaches aim to use refrigeration machines to achieve cryogenic temperatures in a closed loop cooling circuit. For this purpose, a Gifford-McMahon cryocooler offers a good compromise between cooling capacity and efficiency [5]. Zhang et al. developed such a liquid helium-free cryogenic test stand by integrating two Gifford-McMahon cryocoolers. These are connected to the sample chamber via copper thermal bridges. Cooling of the sample is achieved by convection from the sample to the sample chamber, which is charged by helium gas. The system can provide a continuous, tuneable sample temperature from room temperature down to 16.8 K within 8 hours with a maximum temperature gradient on the sample of 0.3 K [6].

In addition to the reliable and fast generation of a defined temperature down to 20 K, the combination with secondary test methods is also a major challenge for the correct measurement of mechanical properties of FRP. For the correct measurement of displacement, a major drawback of the usual designs is the lack of a device that enables to measure deformation directly on the specimen in cryogenic conditions. Traditionally, strain gauges are used at room temperature, but they are quite difficult to handle at cryogenic temperatures. Special equipment is needed to be able to measure in this temperature range at all and proper coupling to the sample within the bath must be given and suitable temperature compensation is required, which all proves difficult in practice. Furthermore, strain gauges only provide data for its local position on the sample. In recent studies, displacement and strain are more frequently measured by means of digital image correlation (DIC), which provide data for the entire visible surface without requiring contact to the sample. In case of cryogenic measurements, integration of DIC is only possible when no cryogenic liquids are used, as these will obstruct the visibility due to bubble formation and artefacts due to liquid turbulences. Zhang at al. show great success by utilizing optical windows which allow direct sight on the sample within the cryostat [6]. However, DIC only allows the detection of deformations at the surface of the material and does not consider stress accumulations inside. For this reason, an additional measurement system is needed for comprehensive material characterization. For the application of FRP as pressure vessels, the formation of first inter-fiber fractures is a design-relevant damage scenario since the pressure vessel loses its permeation barrier [7]. In this respect, the accompaniment of mechanical test procedures by acoustic emission (AE) analysis for the detection of failure onset

  doi:10.5075/epfl-298799_978-2-9701614-0-0

and damage evolution has become an acceptable standard and is also feasible at cryogenic temperatures [1, 8].

Thus, this study presents a new versatile testing rig that shows some major improvements in comparison to the systems described above and includes both secondary test methods DIC and AE. For easier access and sample handling, cooling is solely provided by heat conduction, reducing test procedure complexity, and allowing precise control of the temperature of the sample. Furthermore, to improve the testing speed, sample exchanges shall be made in the cryogenic state.

2. Development of the testing rig

2.1 Requirement and demand analysis

Our aim is the design of a flexible testing rig to measure material properties in the cryogenic temperature regime. For testing and validation of the system, materials are considered that meet the requirements and needs of the aerospace and space industry. Since there is increasing interest in FRP based pressure vessels for the storage of liquid hydrogen and oxygen and the associated weight reduction of the propulsion system of rockets and future aircraft, the new testing rig is specifically designed to be suitable for the testing of FRP. With respect to the technical requirements for the testing rig, the following basic specifications were set:

- Target temperature range: 20 K to 293 K
- Load capacity: 50 kN
- Closed liquid helium circuit for reduced usage of cryogenic liquids
- Direct optical strain measurement by means of DIC
- Integration of AE measurement
- Sample exchange in cryogenic state allowing for testing of several samples within one cooling cycle
- Modular design: different test setups can be integrated into the available testing space
- Temperature gradient across the sample: < 10 % in the cryogenic temperature regime
- Cooling time: < 10 h

2.2 Concept

As shown in Fig. 1 (left), the force is introduced into the sample via a load deflection within the testing machine. The motion of the moving crosshead is directly transferred to the specimen via a push/pull rod. The moving parts are connected to the cryostat cover via a steel bellow, which ensures the vacuum-tight sealing of the Dewar but also limits the maximum vertical movement to 14 cm. On the opposite side of the specimen, the base plate acts as a fixed end, which is connected to the cryostat cover via a load cage. The cover itself is supported by the load frame of the testing machine. The entire construction is designed to operate at a load of 50 kN with a safety factor of 2, while still maintaining minimal thermal coupling to the outside. This is achieved by minimizing cross-sections and utilizing materials with low thermal conductivity at all possible locations. To allow for a different test setup, the sample holders can be mounted individually. All conventional test methods, which fit into the inner testing space, can thus theoretically be implemented in the cryostat with specifically designed test fixtures.

  doi:10.5075/epfl-298799_978-2-9701614-0-0

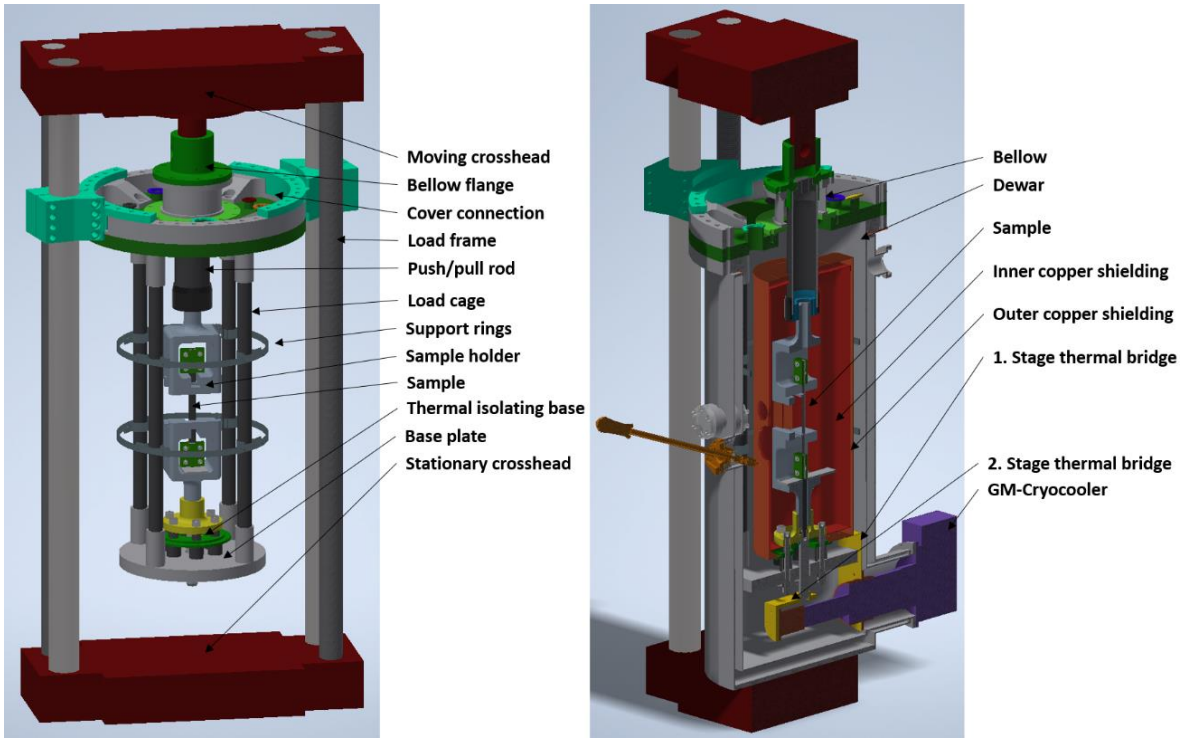

Figure 1. Detailed view of the load transmission path within the cryostat with tensile testing rig (left) and details of the thermal management of the cryostat (right)

For cooling, the Dewar is vacuumized to eliminate heat convection and the temperature of samples, fixtures and shielding is then reduced by the GM-Cryocooler. As shown in Fig. 1 (right), the first stage provides cooling to the outer shielding and operates as a heat shield by absorbing thermal radiation from the Dewar walls. To increase performance, another inner shield is connected to the second stage to further minimize heat radiation effects. Cooling of the sample is achieved by solid-state conduction utilizing a copper rod, which directly connects the second stage of the cryocooler with the sample.

For secondary measurements, which accompany the testing procedure, there are several vacuum feedthroughs for electrical connections of AE sensors and the DIC light source. Furthermore, the Dewar is equipped with two viewing ports to allow direct observation of the sample by DIC. To allow manual access to the inner parts of the cryostat while being assembled, a manipulator is integrated as well. This should enable samples to be changed during operation. The temperature can be further adjusted by a two-point controller using a heating element integrated at the second stage of the cryocooler.

2.3 Mechanical testing setup

The major parts of the mechanical testing setup have been proof-tested and immersed in a pool of liquid nitrogen. In case of the load cage and the push/pull rod, special emphasis is given towards reducing heat conduction into the cryostat chamber. This is achieved by minimizing cross-sections and utilizing GFRP tubing. These are adhered to customized developed thermally shrink-fitted and adhesively bonded metal sleeves at the respective ends for mechanical attachment to the surroundings. Individual testing of the hybrid GFRP tubes in Tab. 1 shows sufficient load capacity for both tensile and compressive force. As the load cage is composed of four tubes, the required safety factor of 2 at a maximum operational load of 50 kN is achieved. Further evaluation by means of FEM shows that with the given load the test rig would suffer

from buckling load, resulting in early deviations from linear behavior and potential damage of the hybrid GFRP structure. To achieve sufficiently high buckling loads under compression, support rings are added as seen in Fig. 2. Inside the base plate, custom-made GFRP spacers are used to provide thermal decoupling between the sample fixture and the load cage to allow for variation of temperature at the sample position. The mechanical load itself is carried by stainless steel screws, which are inserted through the spacers. Therefore, these GFRP spacers solely experience compression loads and have small height, therefore buckling causes no problems. In terms of stiffness, the whole load cage experiences only minimal displacement at the maximum load of 50 kN: Maximum deformation result in 1.2 mm of displacement in the horizontal plane at the base plate (transverse motion), while providing linear displacements in vertical direction proportional to the applied load (axial motion).

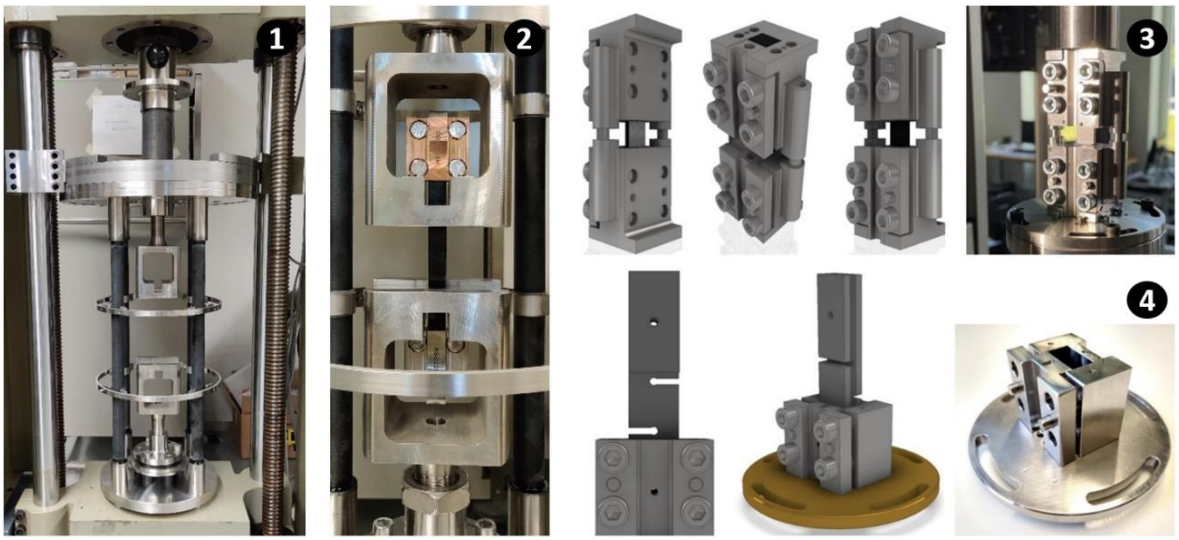

Figure 2. Validated mechanical testing setup: 1) mechanical testing frame; 2) tensile test fixture suitable to mount sample dimensions based on DIN EN ISO 527-5; 3) compression test fixture based on DIN EN ISO 14126; 4) shear test fixture for 12-direction and 23-direction

Table 1: Mechanical test results of the thermal isolating GFRP parts within the mechanical setup

Load	Force [kN]
Load cage (individual tube) - Tensile	25,0
Load cage (individual tube) - Compression	25,8
Thermal isolation base (individual spacer) - Compression	40,0

As described earlier, for FRP testing the measurement of tensile, compression and shear properties are considered as baseline. Moreover, testing of joints and fracture mechanics evaluation, as well as the ability to test cylindrical (e. g. filament wound) samples is seen as a requirement for widespread use of composites in space applications. To accommodate for these requirements, several sample holders have already been designed for the use in the cryostat, as shown in Fig. 2. Tensile test fixtures suitable to mount sample dimensions based on DIN EN ISO 527-5, compression test fixtures inspired from DIN EN ISO 14126 and shear test fixtures for 12-direction and 23-direction have been tested and validated for FRP at room temperature, as well as within liquid nitrogen to show proper sample failure modes. Furthermore, test fixtures for fracture mechanics evaluation of mode 1 and mode 2, as well as tensile adhesion and single-lap

shear of adhesives are currently under development. All these testing procedures are meant to be complemented by AE and DIC measurements. In case of the AE measurements, a suitable VS375-LT sensor has been developed, which can be used at cryogenic temperatures [8]. Results show that the noise of the cryocooler inside the cryostat does not interfere with the AE measurement. As indicated in Fig. 1, 3D-DIC measurements will be possible with a two-camera system. As light source, an LED mounted outside the cryostat is chosen, which provides sufficient illumination to the sample via a fiberglass cable. Thus, the dissipated heat of the LED can be effectively kept out of the cryostat. Furthermore, there is no necessity for an additional viewing port, reducing the introduced heat radiation from outside the cryostat. For that reason, the optical windows are chosen as small as possible, effectively allowing a field of vision from approximately 10 cm in horizontal and vertical orientation. If no visual contact with the sample is necessary, the outer copper shielding can additionally be shut via the manipulator, removing all heat radiation entering the cryostat via the windows.

2.4 Thermal simulation

To design the whole cryostat system, a dedicated thermomechanical model was developed. For the thermal simulation, the geometry of the cryostat is imported into COMSOL Multiphysics. The thermal model includes heat transfer in solids and surface-to-surface radiation with a general surface emissivity value of 0.2. This value is a conservative estimate of clean surfaces for machined steel and copper. Heat convection is assumed to be negligibly small in the vacuum state. As initial condition, temperature of all parts is set to room temperature. The same holds true for the outer surface of the cryostat for the total duration of the simulation. As cooling power, the data of the GM-Cryocooler RDK-415D2 from Shi Cryogenics Group is chosen. The parameters are fully provided by the manufacturer for stage 1 and stage 2, respectively. Important material properties like heat conduction and heat capacity are included in the model considering temperature-dependent values from 4 K to 300 K.

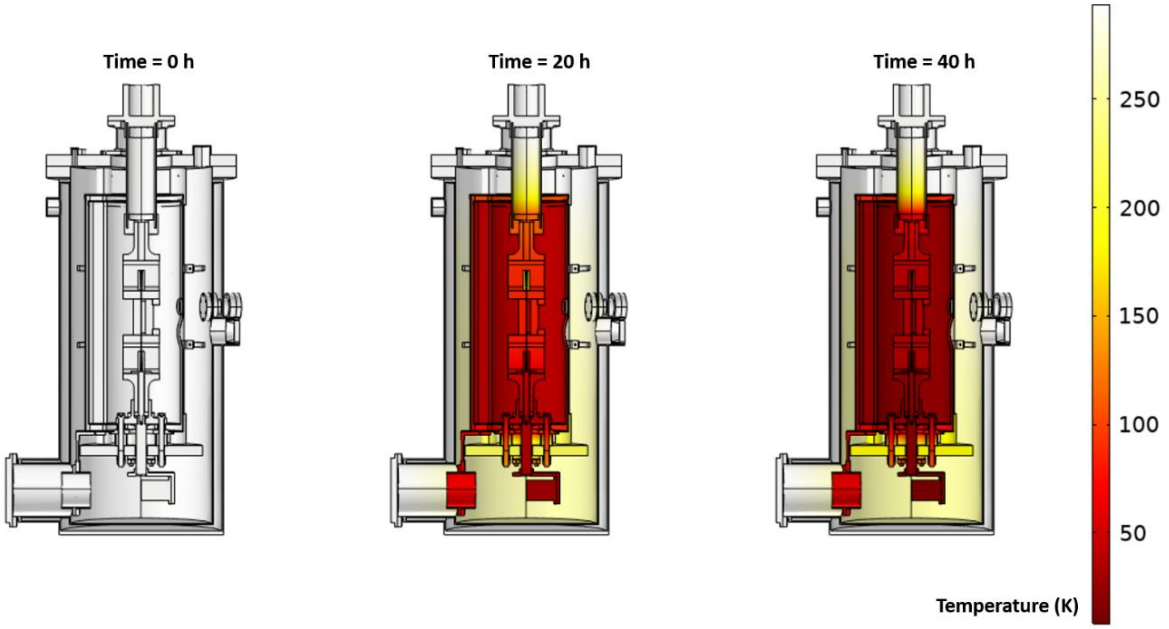

Figure 3. Simulation of the temperature inside the cryostat at the beginning of cooling, after 20 h and 40 h

Fig. 3 shows the temperature distribution of the cryostat at 0 h, after 20 h and after 40 h of cooling. Sufficient thermal isolation via the pulling rod and load cage seems to be provided.

1099/1211 ©2022 Gabele et al. doi:10.5075/epfl-298799_978-2-9701614-0-0 published under CC BY-NC 4.0 license

Thermal radiation shielding of the testing volume is achieved. Fig. 4 shows an evaluation of temperatures at stage 1, stage 2 and the sample position inside the cryostat. This simulation indicates that thermal equilibrium is reached after 48 hours. Stage 2 reaches 20 K within 21.5 h and a minimum temperature of 7.7 K can be achieved. As the sample is connected to stage 2 via a thermal bridge, the temperature slightly lags behind. 20 K is reached after 32 h with a minimum temperature of 16.4 K after 48 h.

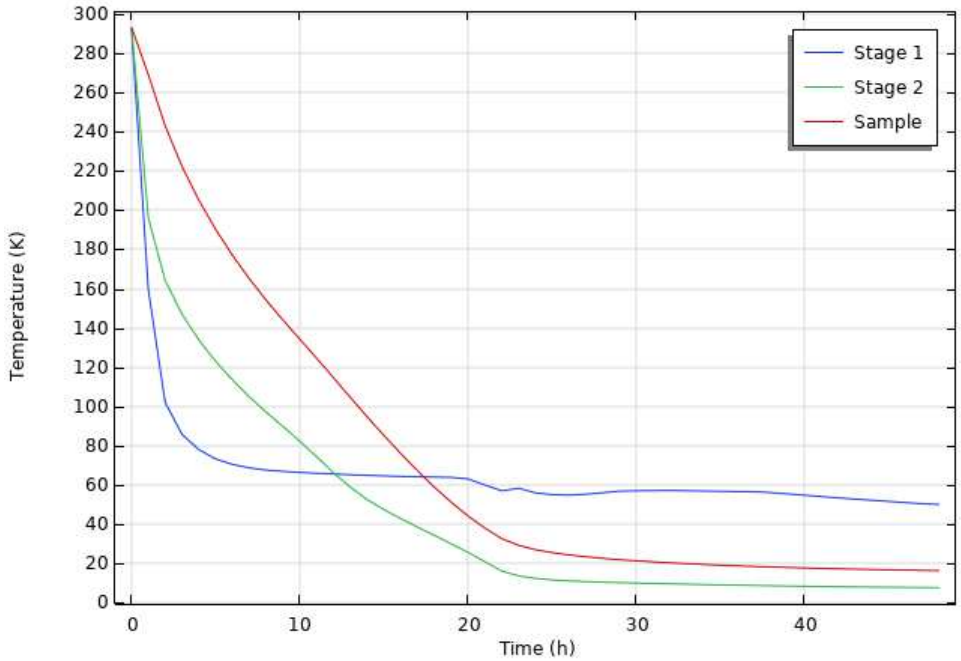

Figure 4. Temperature development of the cryocooler's first stage, second stage and the sample

3. Discussion

As is shown in Fig. 4, sample temperatures around 20 K can be reached. This is comparable to the results achieved by Zhang et al. [6], who also achieve stable 20 K in their experiments. Due to larger cross sections of the load cages and sample holders, to be able to withstand 50 kN of force and only utilizing one cryocooler instead of two, the cooling time increases from 8 h to 32 h in our configuration. To accelerate the cooling time to the desired values, the interior chamber can additionally be flushed with cold gas N_2, preventing the interior walls from quickly heating up to ambient temperature. The necessary cooling time can thus be significantly reduced, since the new initial temperature is at around 77 K. Furthermore, the mass of the material can be reduced by further topology optimization, therefore reducing the stored heat in the beginning. Moreover, the cooling power can be improved by integrating additional cryocoolers into the system, therefore potentially also lowering the sample's temperature of thermal equilibrium.

Otherwise, the following requirements of the testing rig prove to be implementable. DIC and AE measurements have been proven to be viable options and are ready for test runs. The modular design for carrying out different test procedures is integrated. Limiting factors for the test setups are the field of view of the DIC, the available space within the inner copper shielding, as well as the maximum vertical movement limited by the bellow deflection. Nevertheless, tensile, compression and shear test setups have been successfully implemented and tested. The

  doi:10.5075/epfl-298799_978-2-9701614-0-0

mechanical testing frame proves to be ready for use. It shows minimal compliance and satisfying load capacity, while also providing sufficient thermal isolation.

The handling of the samples has not been taken into account so far and needs further investigation. As the primary goal is the testing of FRP, strategies for thermal coupling and uniform cooling of the samples are of great significance. FRP are characterized by low thermal conductivity, which will result in an increasing temperature gradient across the sample. Furthermore, the handling of several samples at once must be further elaborated.

4. Conclusion

The development of a new testing rig for FRP at cryogenic temperatures is based on the requirements specified above. Based on the thermal simulation, the target temperature of 20 K can theoretically be reached by further improving the cooling power, while reducing the mass to cool by optimizing mechanical components within the setup. Special care is required regarding sample coupling, cooling and the resulting temperature gradient. In this field, investigation is still in progress. The mechanical setup is validated and ready for use. Testing of tensile, compression and shear of FRP has been implemented. Furthermore, experimental setups for the fracture mechanics testing of mode 1 and mode 2, as well as tensile adhesion and single-lap shear testing of adhesives are under development.

Acknowledgements

This work has been conducted within the framework of the projects “MakeKryo” and “MakeKryo II”, which is funded by the German Federal Ministry for Economic Affairs and Climate Action in the “National Space Program” of the German Aerospace Center (DLR) collaboration.

5. References

1. Hohe J, Neubrand A, Fliegener S, Beckmann C, Schober M, Weiss K et al. Performance of fiber reinforced materials under cryogenic conditions – A review. Composites Part A, 2020.
2. Geiss G. Einfluss von Tieftemperatur und Wasserstoff auf das Versagensverhalten von Glasfaser-Verbundwerkstoffen unter statischer und zyklischer Belastung. Universität Karlsruhe (TH), 2001.
3. Nicholls-Lee R F, Bostock T D, Watt P. Fully submerged composite cryogenic testing. 18th International Conference on Composite Materials (26/08/11) 2011.
4. Rizov V, Shindo Y, Horiguchi K, Narita F. Mode III interlaminar fracture behavior of glass fiber reinforced polymer woven laminates at 293 to 4 K. Appl Compos Mater 2006; 13:287-304.
5. Radebaugh R. Cryocoolers: the state of the art and recent developments. J. Phys.: Condens. Matter 2009; 21:164-219.
6. Zhang H C, Huang C J, Huang R J, Li L F. Liquid helium free cryogenic mechanical property test system with optical windows. IOP Conf. Series: Materials Science and Engineering 2017; 278.
7. Timmerman J F, Hayes B S, Seferis J C. Cryogenic Microcracking of Carbon Fiber/Epoxy Composites: Influences of Fiber-Matrix Adhesion. J. Compos. Mater. 2003; 37:21:1939-1950.
8. Sause M, Schmitt S, Nagaev I, Tratting H. Schallemissionsprüfung an Faserverbund-werkstoffen bei kryogenen Temperaturen. SCHALL 21 2021.

  doi:10.5075/epfl-298799_978-2-9701614-0-0

INVESTIGATION OF MODE I FRACTURE TOUGHNESS OF CARBON FIBER REINFORCED POLYMERS AT CRYOGENIC TEMPERATURES

Holger Häfele[a,], Anna Trauth[a], Markus G.R. Sause[a]*

a: Augsburg University, Institute of Material Resource Management (MRM), Am Technologiezentrum 8, 86159 Augsburg, Germany
* Corresponding author: holger.haefele@mrm.uni-augsburg.de

Abstract: *The research in this paper presents new possibilities to investigate fracture behavior of unidirectional carbon fiber reinforced polymer (CFRP) laminates exposed to very low temperatures (77 K). Therefore, a modified configuration for the Double Cantilever Beam (DCB) test was used (Mode I). For specimens based on ASTM D 5528, characteristic values for fracture toughness could be determined by using the evaluation-method of the modified compliance calibration (MCC) described in the mentioned standard. The chosen test configuration provides consistent measurements due to linear increasing compliance and it allows the evaluation of fracture toughness values. In this work, unidirectional reinforced laminates were tested without the usage of additional units bonded with the specimen for load introduction.*

Keywords: carbon fiber reinforced polymers; cryogenic; characterization; mechanical properties; fracture toughness

1. Introduction

New applications and possibilities for future energy storage by cooling gases like hydrogen and oxygen to liquids require a comprehensive understanding of temperature dependent material behavior of composite materials at cryogenic temperatures. Liquified gases have a high energy to weight ratio and can be considered in novel concepts for mobility and transportation instead of conventional fossil fuels. For design and construction of vessels, to store liquified gases, it is indispensable to investigate material characteristics at storage or application temperature, respectively. The increase in strength and stiffness of CFRP-materials at low temperatures deserves a special consideration and were reported in past studies [1,2]. Multiscale and micromechanic analyses [3,4] are already used to predict and validate measurements as well as correction models. The underlying effects reported in the mentioned studies are also manifested in fracture toughness by increasing loads for crack growth [5]. Crack growth is based on delamination between different fiber layers. Hence, it is necessary for design and construction of components to refer on reliable predictions of delamination resistance. Studies with various test configurations for delamination fracture in pure and mixed mode are listed in a review done by Tay [6]. Tay describes problems of mode separation in addition to the fairly well-established DCB test methods. According to Tay, the problem is that there is always a fraction of mode I in other established fracture mechanics tests (e.g. the End-Notched Flexure test). A reliable mode I test thus appears indispensable to interpret other tests as well. However, at cryogenic temperatures, the empirical data collected at our group shows general issues with load induction using bonded blocks.

  doi:10.5075/epfl-298799_978-2-9701614-0-0

Thermally induced stresses of the various bonded materials results in low test loads that can be transferred to the specimen before failure of the bonding occurs. Other methods of load introduction, such as bolted laminates, are not specified in the established standard and cause other problems.

Sápi and Butler [7] reviewed results for low and cryogenic temperature fracture toughness properties of laminated composite materials. They clearly identify the matrix as dominating the failure of laminated composites. In most cases of the studies reviewed by Sápi and Butler, the resins stiffness and strength increased with decreasing temperature for static tests. But only half of the resins under investigation showed increased values for fracture toughness of composites. Sápi and Buter show that the distinction is independent of fiber type, ply type and resin generation. They attribute this to possible discrepancies in the experimental approaches used.

The results of improved strength and modulus is partly in contrast to the generally increased values for strength, modulus and fracture toughness of polymers reviewed by Chen et al. [8]. They show results of developments of nanoparticle and modified polymers which aimed to achieve higher cryogenic performance. Values found at room temperature are compared with values at cryogenic temperatures. Chen et al. attribute discrepancies by the utilized methods to improve the cryogenic performance of the polymers to enhance ductility and reduce thermal stresses.

In conclusion, the reviews presented lead to the assumption that variations of the test procedure can be responsible for differing values. These might be variations in preparations, test execution, data reduction methods, thermal stresses, and the chosen test configuration. A.J. Brunner [9] separates those sources of scatter in fracture toughness testing data in an extrinsic and intrinsic class. As a significant extrinsic source, the evaluation method and the test setup are mentioned, respectively. Another focus is given to the load cell and displacement transducer.

In conclusion, further developments of materials require established and reliable test methods to investigate fracture toughness. One of the key motivations is the possibility of materials having new or unpredicted failure mechanisms at low temperatures. This leads to the consideration that general conditions of standard test methods could impede further investigations of materials, especially in cryogenic environments.

The ongoing project “MakeKryo II” focuses on the previously mentioned fracture behavior of CFRPs. For this, specimens were tested in a bath of liquid nitrogen. By using wire bent splints that were passed through a hole in the specimen, adhesively bonded elements for load induction could be avoided. Within this work, a modified setup was developed and implemented. The chosen test configuration provides characteristics to determine fracture toughness in crack opening mode I in accordance with the evaluation equivalent to ASTM D 5528 or DIN EN ISO 15024.

  doi:10.5075/epfl-298799_978-2-9701614-0-0

2. Specimen and preparation

The specimens were 220 mm long and 25 mm wide based on ASTM D 5528, respectively. Laminates were fabricated with a unidirectional layup of an epoxy-based prepreg and a foil at the center plane to introduce an initial crack starter.

The initial crack had a length of 40 mm in center plane of the 4.45 mm thick specimen. A sketched representation of the specimen is shown in Figure 1.

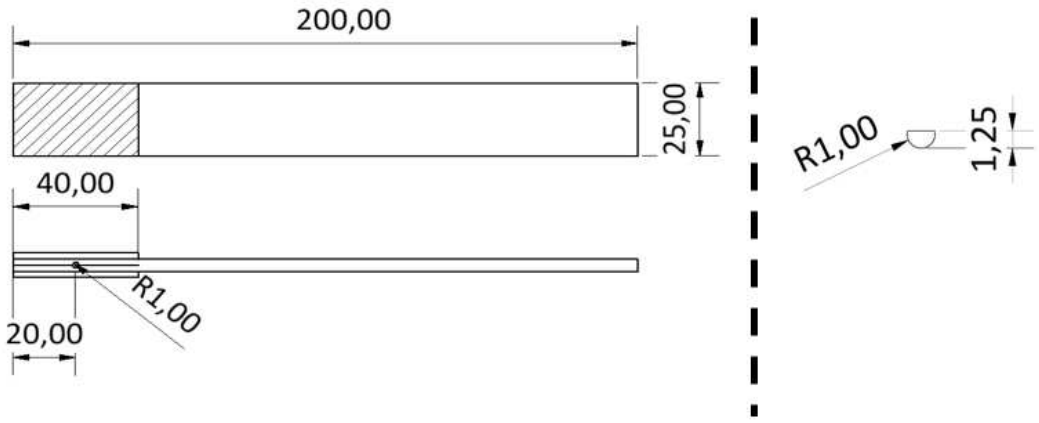

Figure 1: DCB-Specimen with aluminum reinforcement (left) and wire-splint cross-section (right)

Cap reinforcements of aluminum of equal length as the pre-crack were used to avoid premature damage around the load introduction area. 20 mm away from the edge of the sample, a hole with 2 mm diameter was drilled perpendicular through the sample. A measuring scale with markings 5 mm apart was attached to record crack growth by optical means.

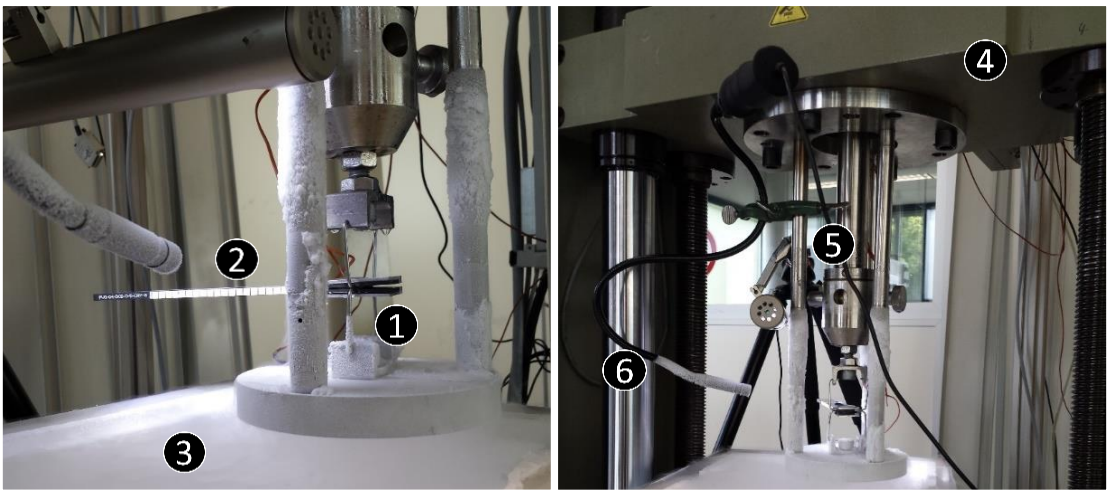

*Figure 2: Test configuration (1-*load fixture with s*plint, 2-Specimen, 3-*Bath of LN2*, 4-Traverse, 5-Rod, 6-Camera)*

3. Testing procedure

DCB tests were performed in accordance with ASTM D 5528. The force was introduced by a wire bent splint with a diameter of 2 mm, one sided grinded to reach a half-circle cross-section as exemplified in Figure 1. The crosshead speed was set to 5 mm/min.

Crack growth was recorded by a digital camera system (Voltcraft BS-10) which was inside the testing chamber. The whole test configuration was immersed into the testing chamber filled with liquid nitrogen. Exemplary images of the digital camera system are shown in Figure 3.

Figure 3: Image recordings with initial crack visible on the left and after crack progression on the right

Specimens were clamped between a fixed rod and a load cage (cf. Figure 2). The rod was connected to a load cell and the load cage was joined with the crosshead of a universal test machine.

4. Results and discussion

Mode I interlaminar fracture toughness G_{Ic} was calculated using the MCC-method (Eq. (1)) as described in ASTM D 5528. This method was chosen based on the recommendation of Kageyama and Hojo [10] for being a method with less dispersions in the results obtained. The following equations were used to determine fracture toughness G_{Ic}:

$$G_{Ic} = \frac{3P^2C^{2/3}}{2Abh} \qquad \text{with} \qquad C = \frac{\delta}{P} \tag{1}$$

Where P is the delamination onset load measured by a load cell and C is the compliance as the ratio of displacement δ to applied load P. The slope of the compensation line, A, is formed by delamination length a divided by the specimen thickness h (a/h) as a function of $C^{1/3}$. In consideration of the large displacement, this correction of the measured apparent fracture toughness values is necessary [11]. The large displacements are due to the low stiffness of the wire-splint and the stiffening of the specimen by aluminum caps.

Figure 4 represent exemplary measured values of applied force and opening displacement of the test series. The load drops are associated with sudden crack growth. Koloor et al. [12] describes that the nonlinear behavior near the first peak results from a pocket filled with epoxy resin in the as-fabricated specimen. The study shows a gradual decrease in load following the peak value that is attributed to the toughness of the resin close to the notch front. The evaluation of the recorded images lead to values for delamination length required as for the stiffness correction value. Using the digital image analysis program ImageJ, the distance between the crack tip and the path marker was evaluated sequentially for each image recorded.

  doi:10.5075/epfl-298799_978-2-9701614-0-0

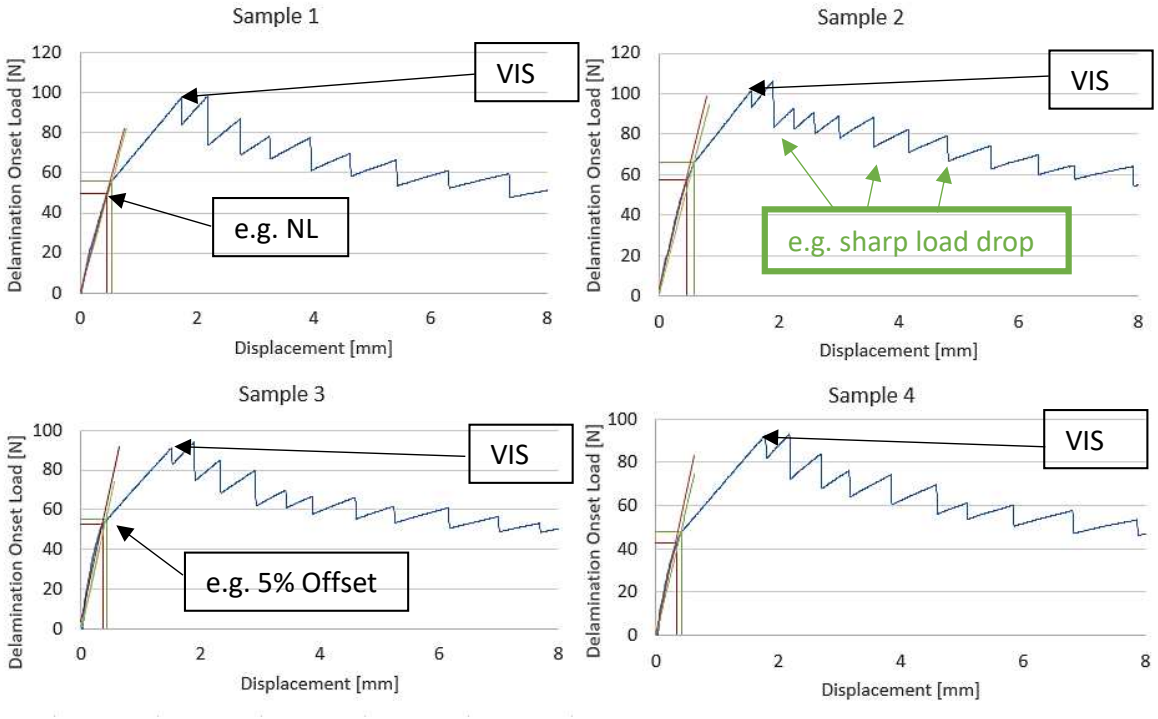

Figure 4 : Load-displacement curves

The results of the measurements are shown in Figure 4, where NL in red indicates the point of initial deviation from linearity. 5 % Offset in green is a line with a 5 % compliance reduction and the intersection with the load-displacement curve. VIS identifies the visual initiation value for the first delamination as visually observed. Due to the brittle matrix, VIS coincides with the first macroscopic load drop. Figure 5 shows the calculated compliance.

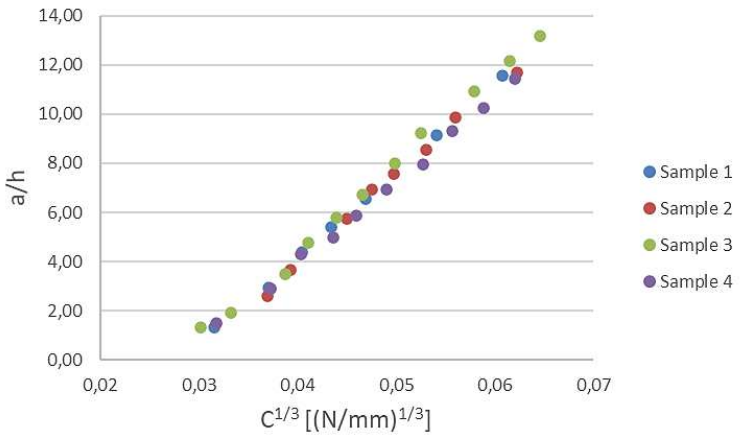

Figure 5: Compliance plot for calibration of fracture toughness evaluation

It is noticeable that the compliance increases relatively linear even at high displacements despite of the effect of severe deflections of the wire-splint. As a result, there is no nonlinear variation of compliance with increasing delamination lengths. The coherence of the slopes indicates a high reproducibility of the setup and thus the reliability of the measured values.

  doi:10.5075/epfl-298799_978-2-9701614-0-0

G_I was evaluated with Eq.(1), the corresponding R-curves are shown in Figure 6 with the corresponding G_I values for NL, 5%/MAX and VIS indicated in the exemplary diagrams as red rectangle (NL), green circle (5%/MAX) and orange circle (VIS).

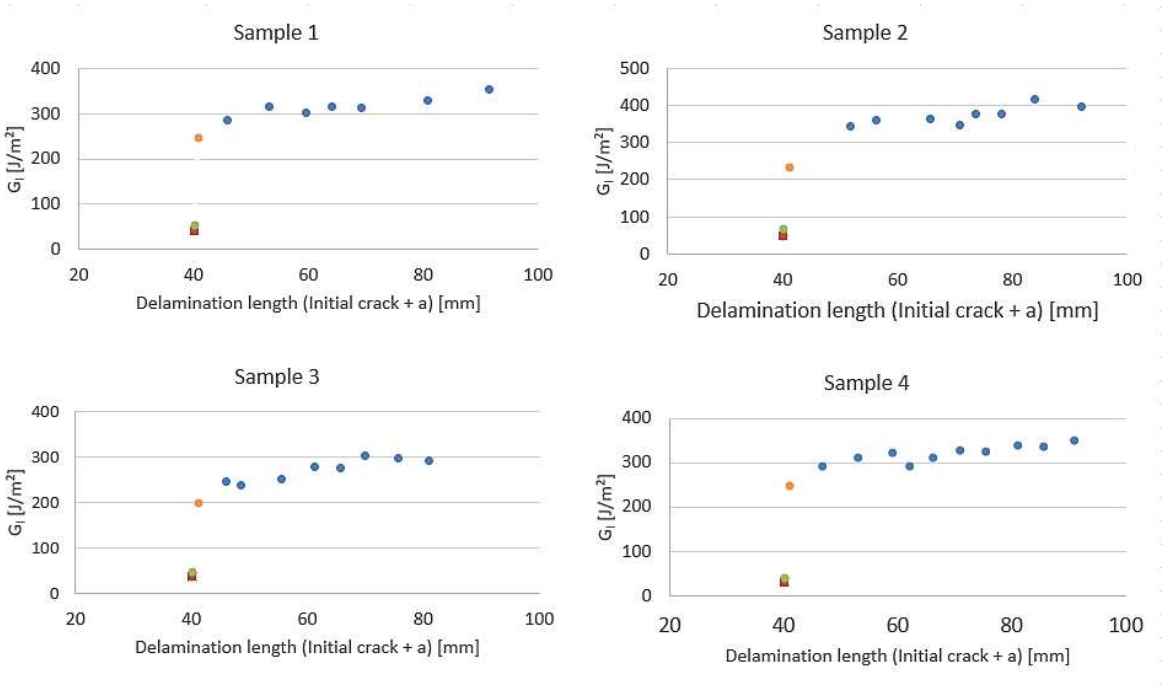

Figure 6: Energy release rate values plotted vs. delamination length. Red-NL value, green-5 % offset value, yellow-VIS value.

The VIS values (rounded) for fracture toughness G_I of the individual samples evaluated with the MCC-method Eq. (1) described in ASTM D 5528 are shown in Table 1.

Table 1: Determined values of VIS fracture toughness

Sample	G_I [J/m²]
1	247
2	235
3	200
4	246
Mean Value	277,6

The results obtained must take into account that high cooling rates due to the immersion of samples in liquid nitrogen from room temperature could lead to thermal degradation and sudden thermal stresses, which have not been considered in the present study.

  doi:10.5075/epfl-298799_978-2-9701614-0-0

Yokozeki et al. [13] found a method that is expected to be useful for evaluation of the interfacial fracture toughness of layered materials subjected to severe thermal loadings at cryogenic temperatures by using Nairn´s formulation [14]. The correction of these thermally induces stresses could be an important step for further studies at cryogenic temperatures.

5. Outlook

The chosen test configuration with a load cage connected to the crosshead of a universal testing machine relies on a liquid nitrogen bath at 77 K for immersing fixture and samples. However, other media with various boiling temperatures like liquid oxygen and helium may also be considered. To bypass limitations of the described test procedure that only allows fixed test temperatures given by the cryogenic medium, an optimized setup in a cryostat with a closed-cycle two staged 4K cryocooler is currently under development. With this cryostat, digital image correlation (DIC) can be used to record delamination onset and crack growth in higher resolutions and accuracy. Moreover, DIC enables to investigate strain distributions around the crack tip and residual thermal stresses while cooling down the sample, so effects of thermally induced stresses may also be considered in the future.

6. Conclusion

A new configuration for determination and investigation of the mode I fracture toughness in liquid nitrogen without the usage of adhesively bonded blocks has been developed. Furthermore, the applicability of the test method with a wire bend splint as load inducing element was shown. The splint was passed perpendicular through the specimen and opened the crack. Results could be evaluated by calculations in accordance to proven standards. The linearity of the compliance as a function of delamination length using the Modified Compliance Calibration Method indicates a high reproducibility of the setup and thus reliability of the obtained values.

7. Acknowledgment

Part of this work was supported by the project “MakeKryo” and “MakeKryo II”, which is funded by the German Federal Ministry for Economic Affairs and Climate Action in the “National Space Program” of the German Aerospace Center (DLR) collaboration.

8. References

1. Okayasu M, Tsuchiya Y. Mechanical and fatique properties of long carbon fiber reinforced plastics at low temperature. Journal of Science: Advanced Materials and Devices. 2019: p. 557-583.

  doi:10.5075/epfl-298799_978-2-9701614-0-0

2. Sánchez-Sáez S, Gómez-del Rio T, Barbero E, Zaera R, Navarro C. Static behavior of CFRPs at low temperature. Composites Part B: Engineering. 2002: p. 383-390.

3. Ren Mf, Zhang Xw, Huang C, Wang B, Li T. An integradet macro/mirco-scale approach for in situ evaluation of matrix cracking in the polymer matrix of cryogenic tanks. Composite Structures. 2019: p. 201-212.

4. Sankar BV. Micromechanical Analysis of Composite Laminates at Cryogenic Temperatures. Journal of Composite Materials. 2005: p. 1077-1091.

5. Kalarikkal SG, Sankar BV, Ifju PG. Effect of Cryogenic Temperature on the Fracture Toughness of Graphite/Epoxy Composites. Journal of Engineering Materials and Technology. 2006: p. 151-157.

6. Tay TE. Characterization and analysis of delamination fracture in composites: An overview of developements from 1990 to 2001. Applied Mechanics Reviews. 2003 Jan 15.

7. Sápi Z, Butler R. Properties of cryogenic and low temperature composite-A review. Bath, United Kingdom:; 2020.

8. Chen D, Li J, Yuan Y, Gao C, Cui Y, Li S, et al. A Review of the Polymer for Cryogenic Application: Methods, Mechanisms and Perspectives. Polymers. 2021.

9. Brunner A. 35 years of standardization and research on fracture of polymers, polymer composites and adhesives in ESIS TC4: Past achievemts and future directions. Procedia Structurals Integrity. 2021: p. 443-455.

10. Kagayema K, Hojo M. Proposed methods for interlaminar fracture toughness tests of composite laminates. 5th US/Japan Conference of Composite Materials. 1990 Jun 24-27: p. 227-234.

11. Monden A, Sause MGR, Horn S. Surface modified steel/epoxy-based cfrp hybrid laminates under mode I, mode II and mixed-load load conditions. 17th European Conference on Composite Materials. 2016.

12. Koloor SSR, Hussin H, Tamin MN. Mode I Interlaminar Fracture Characterization of CFRP Composite Laminates. Advanced Materials Research. 2012 Mar 15: p. 552-556.

13. Yokozeki T, Ogasawara T, Aoki T. Correction method for evaluation of interface fracture toughness of DCB, ENF and MBB specimens with residual thermal stresses. Composite Science and Technology. 2008: p. 760-767.

14. Nairn JA. On the calculation of energy release rates for cracked laminates with residual stresses. International Journal of Fracture. 2016: p. 267-293.

  doi:10.5075/epfl-298799_978-2-9701614-0-0

STRUCTURAL HEALTH MONITORING IN ADDITIVE MANUFACTURED STRUCTURES BY TOTAL ELECTRICAL RESISTANCE MEASUREMENTS

Wilfried Liebig[a], Markus Muth[a], Michael Seitz[a], Florian Wittemann[b], Patrick Weiss[c]

a: Karlsruhe Institute of Technology, Institute for Applied Materials,
Engelbert-Arnold-Strasse 4, D-76131 Karlsruhe, Germany, wilfried.Liebig@kit.edu
b: Karlsruhe Institute of Technology, Institute of Vehicle System Technology,
Rintheimer Querallee 2, D-76131 Karlsruhe, Germany
c: Fraunhofer Institute for Chemical Technology,
Joseph-von-Fraunhofer Strasse 7, D-76327 Pfinztal, Germany

Abstract: *Structural health monitoring is an often-used method for in situ damage detection in systems caused by mechanical loads. State of the art is to implement conductive paths in a structure and to measure respective resistance. By using several paths, it is possible to locate damages, but this procedure accompanied by a great expenditure of time. In this work, the authors present a method to reduce the monitoring effort, by only measuring the total resistance of an electrical parallel connection. Therefore, specimens are manufactured in a two-component additive layer manufacturing (Arburg Plastic Freeforming) process by using an ABS polymer where one of the components is modified with carbon nanotubes to be electrically conductive. By applying electrical paths differing in resistance, conclusions can be made about the damage state of individual paths during the overall resistance measurement under mechanical load.*

Keywords: Structural health monitoring; Additive manufacturing; Nanoparticles

1. Introduction

The usage of composite materials for applications, where single material systems are insufficient, becomes more important. Fibre-reinforced or nanoparticle modified polymers are promising alternatives. One challenge of using such composite materials is the monitoring of their reliability. Therefore, Viets et al. [1] present a monitoring method with electrical conductivity. Within this work, a polymer material is modified with nanoparticles to become electrically conductive. Impact damages have been dedicated and localized by multiple measure points. Nevertheless, the measurements need great effort and a special measure methodology is needed for the conductive parts. Mannov extended this approach by using only a certain number of conductive paths [2]. Through this methodology a damage can be dedicated by measure of only one single path, but still all paths have to be regarded separately.

The here presented work presents a methodology to reduce the effort by measuring only the global system resistance. The realisation is done by an Arburg Freeformer, which is able to perform additive manufacturing with two materials. For structural health monitoring (SHM) with only measuring the global resistance, the individual conductive paths have different electrical resistances and are parallel connected. Therefore, different aspects must be considered in forecast studies. This includes the general feasibility of conductive paths with nanoparticle polymers in an additive manufacturing process, the identifying of manufacturing parameters, which influence the electrical resistance and the electro-mechanical behaviour of the material

  doi:10.5075/epfl-298799_978-2-9701614-0-0

system under mechanical load. Finally, the methodology is realised with specimens in a four-point-bending test.

2. Materials and experimental study

2.1 Materials and sample preparation

All specimens are manufactured with an Arburg Freeformer. The Freeformer is based on the "Arburg Plastic Freeformer" principle (APF), patented by Arburg GmbH and Co. KG, Loßburg, Germany. Parts out of the APF process are built up layer by layer with thermoplastic materials. Unlike conventional fused filament fabrication processes, the placement of the material is not by a continuous strand, but by the semi-continuous placement of polymer drops along the printing path with a frequency of 40 Hz – 200 Hz. Similar to injection moulding processes, the material is plasticised in a screw extruder to buffer a defined mass of melt for printing under pressure (< 80 MPa). The dwell time of the melted material varies from a few minutes up to more than half an hour.

The Freeformer is equipped with two plasticization units, which enables the possibility of two component manufacturing. The bulk material is an ABS Terluran GP 35 by INEOS GmbH, Köln, Germany. The modified, conductive material is based on PC-ABS Bayblend T85 XF by Bayer MaterialScience AG, Leverkusen, Germany. The material is modified by adding 15 wt.-% carbon nanotubes (CNT) NanoCyl NC 7000. The compounding is performed according to manufacturer's guidelines.

The conductive material is completely embedded in the bulk material for two reasons. One is to optimize the adhesion between the two components, the other is to isolate the conductive path from environmental conditions. A symmetrical lay-up is chosen to minimize the specimen's warpage due to deviating material properties. Therefore, the conductive paths are either in midplane or in identical distance to the midplane.

Five identical specimens are produced simultaneously within one printing procedure. The specimens are aligned to the x-axis of the printer and the certain layer of each specimen is printed before starting with a new layer. The printing is divided in two steps. At first, the geometry's contour (perimeter contour) is printed and afterwards, the surface built up this way is filled with polymer drops. The placement done in parallel paths and usually the printing direction within one layer is perpendicular to the surrounding layers. The droplets are placed perpendicular, along and with an offset of 45° towards the longitudinal axis of the conductive path.

A defined length of the conductive path enables the possibility to define the resistance by the cross-section area. The cross-section area can be varied by the width within one layer, or by multiple layers (height). The following variants are compared: 8 mm width and 1 layer; 4 mm width and 2 layers and 2 mm width and 4 layers. One layer is approximately 0.2 mm high. The printing strategy with ±45° produced the most isotropic, homogeneous and reproducible electrical resistances.

  doi:10.5075/epfl-298799_978-2-9701614-0-0

2.2 Characterisation of mechanical and electrical properties

The mechanical characterization is performed on a 200 kN testing machine from Zwick/Roell GmbH and Co. KG, Ulm, Germany equipped with a 20 kN load cell. Quasi-static tensile tests are performed with mechanical clamping jaws. Figure 1 shows the geometry used for testing of the pure single materials (ABS and conductive) and two component specimens. The testing velocity is chosen to be 2 mm/min in all tests, the clamping distance is set to 80 mm.

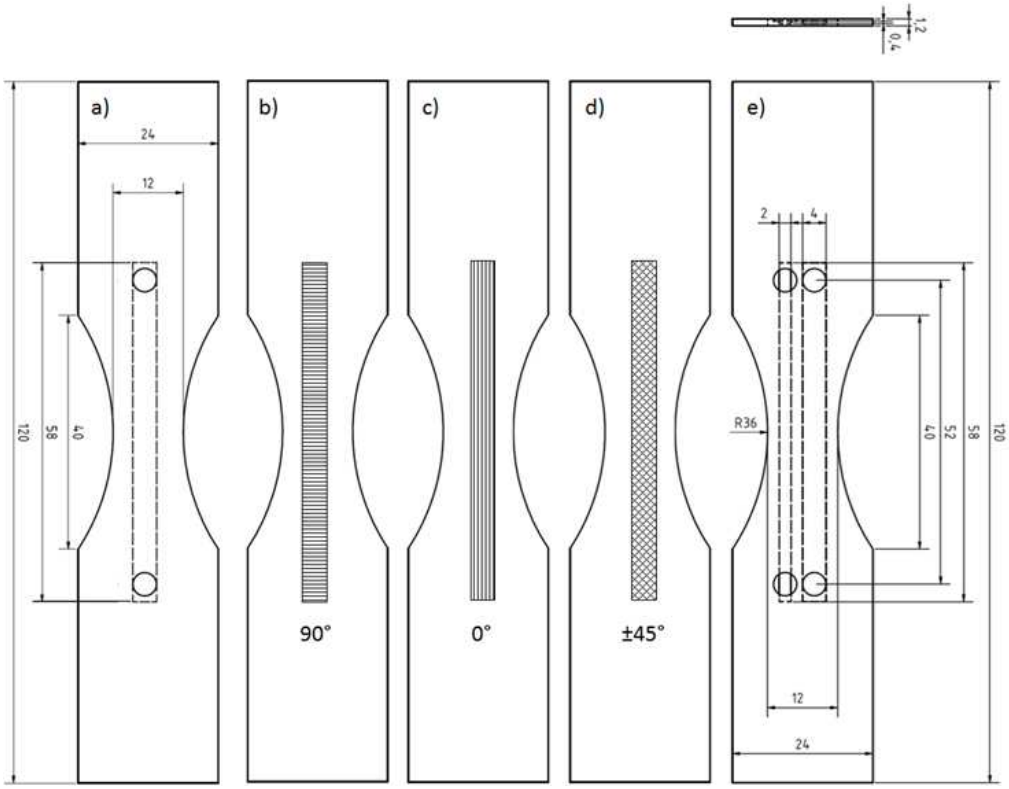

Figure 1. Shape of the dog bone specimens used a) to d) with one conductive path, b) to d) represent different printing directions of the conductive path and e) with two conductive paths.

The bending tests are performed on a four-point in-house developed testing machine, having a maximum testing force of 25 kN. The distance between the inner supports in the four-point-bending test is chosen to be 12 mm, while the distance of the outer supports is 36 mm. The testing built up and the geometry of the specimens is shown in Figure 2. The bending tests are performed with the small conductive path under pressure (as shown in Figure 2) and upside down (small path under tension).

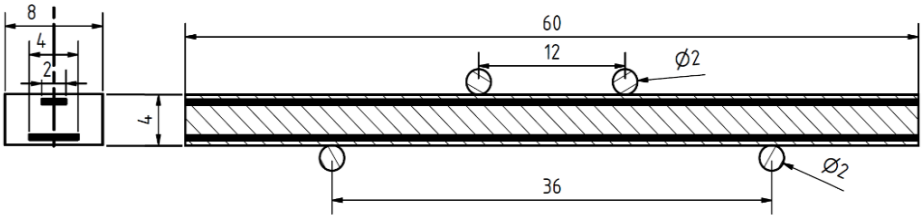

Figure 2: Front view of the specimen geometry for bending tests (left) and clamped specimen for four-point bending test (right). Conductive paths are visualized in solid black.

  doi:10.5075/epfl-298799_978-2-9701614-0-0 published under CC BY-NC 4.0 license

For the electrical resistance Ohm's law is assumed. It is monitored with a Peaktech 4075 true RMS multimeter of PeakTech Prüf- und Messtechnik GmbH, Ahrensburg, Germany during all tests. There is a synchronization at the beginning of electrical and mechanical data. Silver lacquer is applied between the end of the conductive path and the edge of the specimen to connect the path to the measuring equipment. The connection to the multimeter is realized with alligator clips. The resistance of the equipment has been determined in forecast measurements and is subtracted from the final results. Furthermore, it should be mentioned, that only the in-plane properties of the printed parts are investigated in this work.

3. Results

3.1 Electrical resistance as a function of layout of conductive paths

Owing to the anisotropic character of each printed layer, anisotropic mechanical and electrical properties are expected. Therefore, the printing direction (cf. Figure 1) and the number of printed, conductive layers must be considered. The influence of the printing direction on the electrical behaviour is shown in Figure 3a), the scatter beams indicate the distribution of five specimens.

For a printing direction parallel to the longitudinal axis of the conductive path (0°) the electrical resistance shows the smallest value of about 678 Ω ± 254 Ω. With deviation of the printing angle towards the longitudinal axe, the resistance increases to 779 Ω ± 66 Ω at ±45° and 925 Ω ± 118 Ω at 90°. The printing direction of ±45° shows the best reproducibility, therefore, this printing strategy is chosen for ongoing investigations.

Figure 3b) shows the influence of the cross-section's aspect ratio on the electrical behaviour. The highest resistance of 846 Ω is determined for the highest aspect ratio (width 8 mm and one layer). Nevertheless, the great amount of scatter prohibits a definite conclusion. Reducing the aspect ratio by building the cross-section with two printed layers, also reduces the resistance. The resistance built up with a width of 4 mm by two layers is only 396 Ω, for a realization of an even smaller aspect ratio with a width of 2 mm and a height of 4 layers, the resistance offers the smallest value of about 324 Ω.

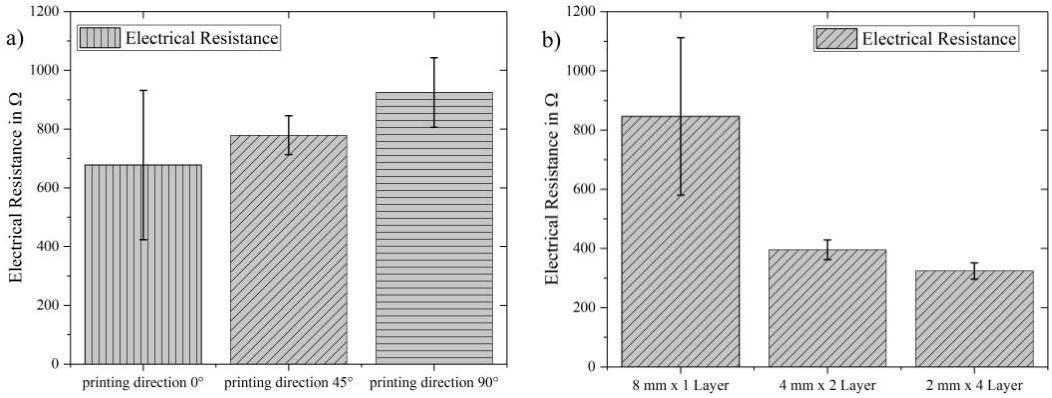

Figure 3: Electrical resistance with scatter beams of the conductive paths, a) as a function of printing direction and b) for identical cross-section area but different layer-built ups. The shading highlights the printing strategy.

The resistance with a width of 8 mm behaves not as expected (≈ 400 Ω), but is in the scale of the 4 mm wide specimen (cf. Figure 3), although this conductive path's cross-section is only half as

  doi:10.5075/epfl-298799_978-2-9701614-0-0

large. The specimen with 4 mm and two layers shows most sensitive result, while the resistance of the 2 mm 4 layers specimen is even lower than expected. Therefore, the minimum height for all ongoing investigations is set to be two layers.

3.2 Tensile test

Tensile tests are performed to quantify changes of the electrical resistance under mechanical load. Figure 4 shows the tensile stress and gauge factor (GF). GF is defined as ratio of relative change in electrical resistance to the mechanical strain. The GF has a sharp increase at about 2.5 % strain of more than one order of magnitude. Above 2.5 % strain the GF increases linear until fracture at about 5.3 % strain. The tensile strength of the two-component specimen is about 33 MPa ± 1 MPa, the fracture elongation is about 5.70 % ± 0.24 %.

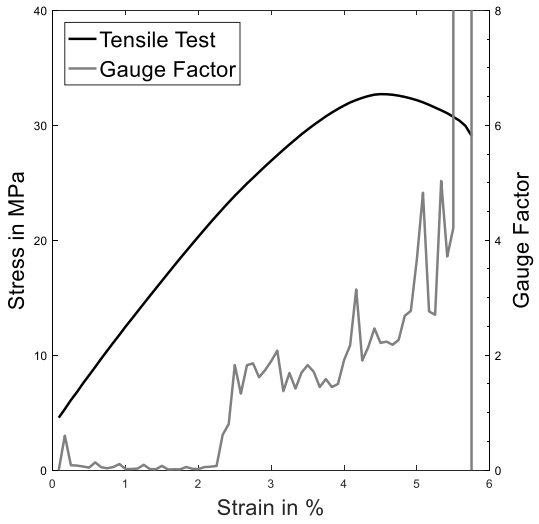

Figure 4: Tensile test of a specimen with in situ measurement of the electrical resistance. Tensile stress (black) and gauge factor (grey) as function of strain.

Table 2 shows the average GFs of the first (strain < 2.45 %) and second area (strain ≥ 2.45 %). At the switchover point of 2.45 % strain the GF increases more than 22 times from 0.095 to 2.106.

Table 2: Evaluated Gauge Factors for a 4 mm width and two layers high conductive path with ±45° printing direction. Determined with five specimens.

Strain at change in %	GF_0	GF_1
2.45 ± 0.04	0.095 ±0.032	2.106 ± 0.547

3.3 Bending tests

For the four-point-bending tests, specimens with two conductive paths of different cross-section areas and therefore different individual electrical resistances are investigated, see Figure 2. The paths are connected in parallel, only the global resistance R_{global} is measured.

Figure 6 shows stress and electrical resistance over strain of two identical specimens. On the left side, the specimen is clamped the way that the path with larger cross-section is under tension

  doi:10.5075/epfl-298799_978-2-9701614-0-0

(cf. Figure 2), on the right side the test setup is upside-down. The positioning of the specimen reveals a significant influence on change of R_{global} during bending. For larger cross-section under tension R_{global} stays nearly constant until 0.6 % edge strain. R_{global} increases from 400 Ω at 0.4 % edge strain to 1500 Ω at 5.8 % edge strain. Above 5.8 % the path with larger cross-section is damaged and hence no more conductive. R_{global} stays constant at 1500 Ω (being the resistance of the path with smaller cross-section) until fracture.

In the upside-down case also a change of R_{global} is detectable. Although R_{global} changes only about 56 Ω between initial value and fracture, being an increase of 15 %. Therefore, R_{global} increases right from the beginning of the test. A maximum is reached for 3.7 % edge strain and R_{global} slightly decreases above.

The mechanical properties are also influenced by the positioning of the conductive paths. The maximum edge stress and fracture elongation for the larger cross-section under tension are slightly above compared to the upside-down case (44 MPa to 41 MPa and 6.9 % to 6.0 %), since the relation of CNT-ABS and pure ABS under tension is different in the two cases.

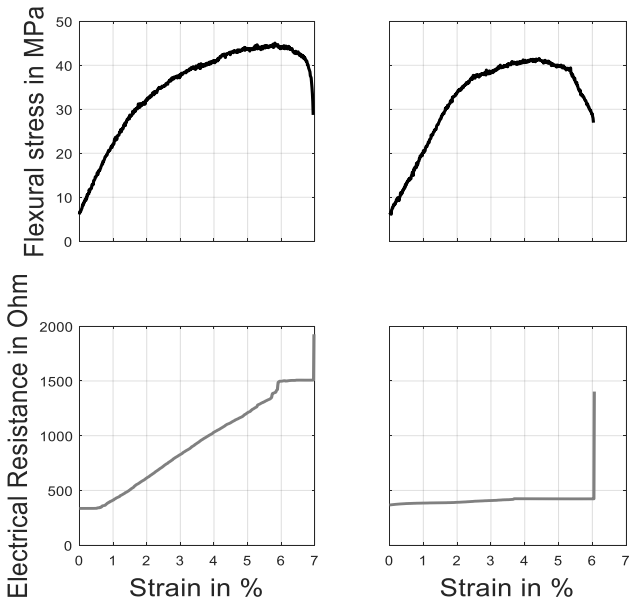

Figure 6: Stress (black) and electrical resistance (grey) of a bending test of a specimen with two conductive paths (with different cross-section areas). Path with larger cross-section under tension on the left and under pressure on the right.

4. Discussion

4.1 Influence of manufacturing aspects on conductive paths and specimens

The reproducible manufacturing of electrically conductive parts in an APF process is validated. Nevertheless, the correlation between resistance and cross-section geometry are not always meaningful. One reason might be the influence of the APF process on material properties. A number of process parameters, which might be a reason for this are identified:

- First of all, the geometry of specimens printed with 0°/45°/90° direction and the specimens' orientation in the Freeformer's coordinate system. Due to the layer setup,

the resistance in z-direction be influenced differently, than the in-plane resistance. This aspect is not investigated within this work.

- Perimeter contours and filling strategy of each component are printed differently in the APF process. The placement of the droplets for the perimeter contour is discrete and with constant frequency. Discrete in this case means every drop has a definite coordinate in the G-code. The filling of the contour is performed with variable velocity, which is varied to be proportional to the length of the (straight) filling path. Thereby, the placement frequency is also dynamic and the distance between two drops is constant. Therefore, it is impossible to define discrete coordinates for a drop in a filling path. The resistance of perimeter contour and filling structure are supposed to be different, due to different printing parameters. The amount of this influence depends on the geometry of the printed part.
- The storage time of polymer melt may vary. In the case of two component printing, both materials are plasticized simultaneously, but printed sequentially within one layer. This leads to longer storage times (agglomeration of nanoparticles) of the less used material.

4.2 Mechanical properties

Tensile tests

The addition of 15 wt.-% CNT influences both, electrical and mechanical properties of the ABS. An increase of tensile strength and Youngs' modulus correlates with a decrease of fracture elongation and ductility. The mechanical characteristics of both monomaterials can be monitored by monitoring the electrical conductivity of the composite. The gauge factor, being the ratio of resistance change and actual absolute resistance, sharply increases above 2.5 % strain about by more than 20 times in the tensile tests. The rapid increase results from cracks, which show a significant influence on the electrical behaviour of the conductive path. Until reaching the tensile strength, no mayor change of the gauge factor is detectable.

The difference of the mechanical properties of monomaterials and compound results from the production. Due to the unsuitability of the CNT-ABS for single component printing, no information about the compounds interface exists and it is neglected within this work, although there is an influence from the interface to the mechanical properties of the compound.

Bending tests

The bending tests show the possibility of locating a load in situ by knowing the global resistance of parallel connected conductive paths with different single resistances. Tension load on the path with smaller single resistance results in a greater change of the global resistance, while the influence of the path with higher resistance is less. Consequently, it is possible to conclude the single path's state, by only measuring the global resistance. This aspect offers the opportunity to reduce the effort for SHM significantly, by lowering the number of required measurements without lowering the amount of information. This reduce of effort is the essential statement of this work.

5. Conclusion

A new approach for structural health monitoring is presented. The conductive paths differ in their electrical resistance, are connected in parallel and only the global resistance is measured

  doi:10.5075/epfl-298799_978-2-9701614-0-0

for monitoring. Even though only one measurement is required, damage and deformation can be detected in place and time by analysing the resistance change in combination with the different individual resistances of the connected paths. Also, the feasibility of structure health monitoring with additive manufactured structures is verified.

Polymer specimens are manufactured in a two-component additive layer manufacturing process and the conductive paths are printed directly into the specimens. Thermoplastic ABS and a PC/ABS blend is used for manufacturing and the conductive parts are realized by mixing in carbon nanotubes in to the ABS. Tensile tests are performed to characterize the electrical and mechanical behaviour of the monomaterials. Tensile tests on the two component specimens characterise the electro-mechanical behaviour. Four-point-bending tests are performed on specimens with two conductive paths and only the total resistance is measured. Due to the base value and change rate of the global resistance, it can be clearly detected, whether the high resistance part is under pressure and the low resistance part is under tension, or vice versa. Therefore, mechanical loads can be located and even quantified, if there is a reference value for the initial global and the individual resistances.

The new approach sets the foundation for reducing the effort of structural health monitoring with consistent quality. Further investigations should be done with more than two paths, more difficult geometries and more complex load cases to validate the method on a higher level. The influence of printing strategies, process parameters and the compounds interface on the electro-mechanical behaviour should be further investigated.

6. References

1. Viets C. 2014 Piezoresistive polymers and fibre-reinforced polymer composites based on carbon nanoparticles. Ph.D. thesis, Technische Universität Hamburg-Harburg, Germany. [In German]
2. Mannov E. 2015 Structural health monitoring of nanoparticle modified glass fibre-reinforced polymers under the influence of temperature and humidity. Ph.D. thesis, Technische Universität Hamburg-Harburg, Germany. [In German]

  doi:10.5075/epfl-298799_978-2-9701614-0-0

CURE MONITORING OF CARBON FIBER REINFORCED POLYMERS USING A SPECIFIC IMPEDANCEMETRY METHOD

Huikangyue BAO [a], Philippe MARGUERÈS and Philippe OLIVIER

a: huikangyue.bao@univ-tlse3.fr

Abstract: *In this work, a cure monitoring method based on electrical impedance (Z) measurements is proposed for the manufacturing of airframe structures made of CFRP. This approach is based on the correlation between rheological and electrical properties of CFRP during curing [1-3]. The method enables us not only to monitor the degree of cure, but also to detect any faults during manufacturing. According to impedance reference signatures, curing processes could be controlled, resulting in cost savings and quality improvements of composites for aeronautics. A home-made low-cost multi-channels bench is developed to measure surface or bulk impedance changes of CFRP in real time. Therefore, the method could be applied in SHM of airframe structures. The proposed approach does not require a dedicated sensor because the composite is used as a sensor of its own state. Combination of embedded instruments and self-sensing materials could be of great interest for smart materials development.*

Keywords: Carbon-fiber reinforced thermosetting composites, cure monitoring, electrical impedancemetry, SHM, self-sensing, functionalization.

1. Introduction

Carbon Fiber Reinforced Polymers (CFRP) have been increasingly successful in the aeronautical industry due to their high performances. The quality of composite structures depends greatly on their manufacturing process. Hence, it is necessary to improve the manufacturing reliability, reproducibility, and implementation of quality assurance by protocols of monitoring. In this context, numerous experimental methods for the purpose of monitoring the changes in a composite material, not only during curing but also under mechanical loading, have been developed since 1970s. Fiber Bragg Grating (FBG), ultrasonic or IR sensors [4-8] can be used to follow the matrix phase changes during curing or detect damages initiation/propagation in real time. Many authors focused on electrical techniques such as Eddy current testing [9-11] during curing or mechanical loading. All these approaches require at least one sensor, attached to the surface, or embedded in the material. In this paper, we are interested in electrical impedance measurements which could be used not only during manufacturing but until the end of the life cycle of composite structures. Here no external sensor is needed while the material itself is used as a sensor of its own physical state. Measurements are performed through a specific instrumentation developed for the purpose.

The first part of this paper presents some experimental results of cure monitoring and fault detection with a preliminary instrumentation exhibiting the feasibility of the proposed approach. In the second part, a new home-made low-cost multi-channels bench is proposed according to measurement quality, portability, and transferability specifications. Several impedance analyzers PmodIA and K-type thermocouples have been selected to ensure cure monitoring by electrical and thermal measurements. First results obtained with this bench are presented before conclusion and perspectives.

  doi:10.5075/epfl-298799_978-2-9701614-0-0

2. Preliminary study: cure monitoring and issue detection

The preliminary study is based on T700/M21 unidirectional prepregs produced by Hexcel Composite France. The thickness of a single ply of prepreg is 256µm and the diameter of the carbon fiber is 7µm. The carbon fibers realize high electrical conductivity, but the matrix is considered a quasi-insulating material. As a result, the carbon fibers exhibit resistive properties while the matrix exhibits capacitive properties in the case of electrical signal excitation. As a thermoset matrix, epoxy resin will undergo several physical chemical transitions during curing. At the beginning of the temperature rise, the resin changes from a viscous to a liquid state exposing the lowest viscosity. The first transition is gelation where resin changed into gel state. The second transition is vitrification where resin changed into glass state near the end of curing. Changes in thermomechanical and rheological parameters of matrix can be measured to highlight those transitions. Figure 1 shows changes in the degree of cure (α), the viscosity (µ), storage (G') and loss (G") shear modulus and their tangent delta (tan (δ)) of the M21 matrix as a function of time and temperature.

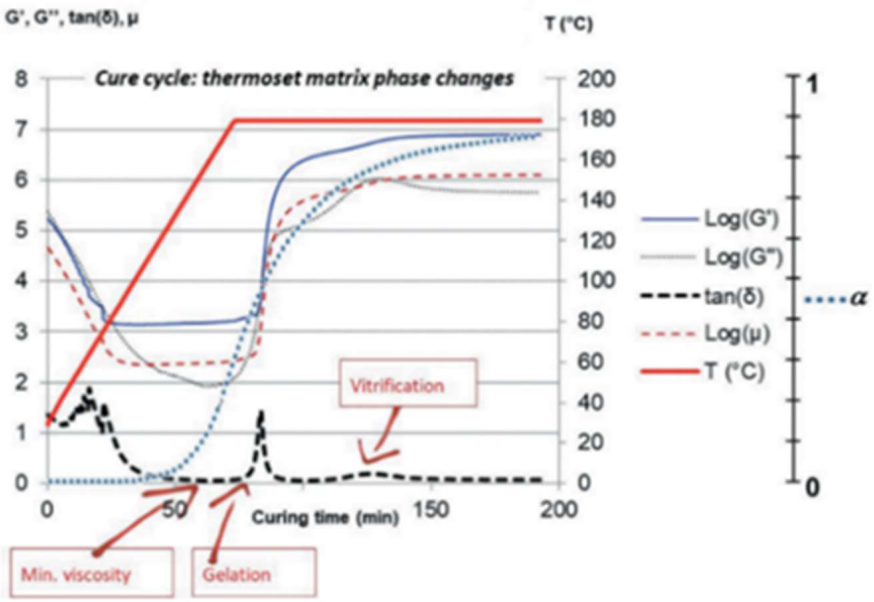

Fig. 1. M21 epoxy matrix phase changes during curing followed by rheology and differential scanning calorimetry. Measured parameters: storage (G') and loss (G") shear modulus, their ratio Tan (δ), viscosity (µ) and degree of cure (α) [12].

For the purpose of ensuring manufacturing reliability and optimizing product quality, these parameters of thermoset matrix must be followed in real time. Moreover, the mechanical behavior of CFRP structure in service should also be followed. In this context, various electrical measurement methods are developed for monitoring CFRP in different stage of its life cycle. Some authors are interested in measuring the capacitance changes (ΔC) of thermoset matrix during curing to detect degree of cure [13-15], some others focus on measuring the resistance changes (ΔR) of carbon fibers for the purpose of damage detection [16-18].

In our research, the electrical impedance measurement (spectral analysis) is preferred because it enables us to obtain information on both the carbon fiber and the matrix simultaneously. Furthermore, this method could be used for monitoring CFRP structure not only during curing but also in service. In other words, it is a SHM method of CFRP throughout its whole life cycle.

  doi:10.5075/epfl-298799_978-2-9701614-0-0

According to our previous works [1-3, 12, 19-23], phase changes of CFRP during curing is correlated to electrical impedance changes (Δ|Z| and Δθ) at the same time (eq.1).

$$Z = |Z|e^{j\theta} \quad (1)$$

where |Z| is the module (Ω), θ the argument (degree) and j the imaginary number.

When the CFRP structure is excited by an alternative electrical signal, |Z| and θ are functions of the signal frequency (f). It exhibits typical resistive behavior (θ tending to 0°) in the low frequencies band but capacitive behavior (θ tending to -90°) in the high frequencies band because a CFRP is a mixture of carbon fiber (electrically conductive) and a polymeric matrix (insulator). A network model made of resistances R (carbon fibers and contacts inter-fibers) and capacitances C (thin zone of insulating matrix) is proposed and shown (Fig. 2). This model enables us to correlate microstructural changes of CFRP structure to its electrical behavior.

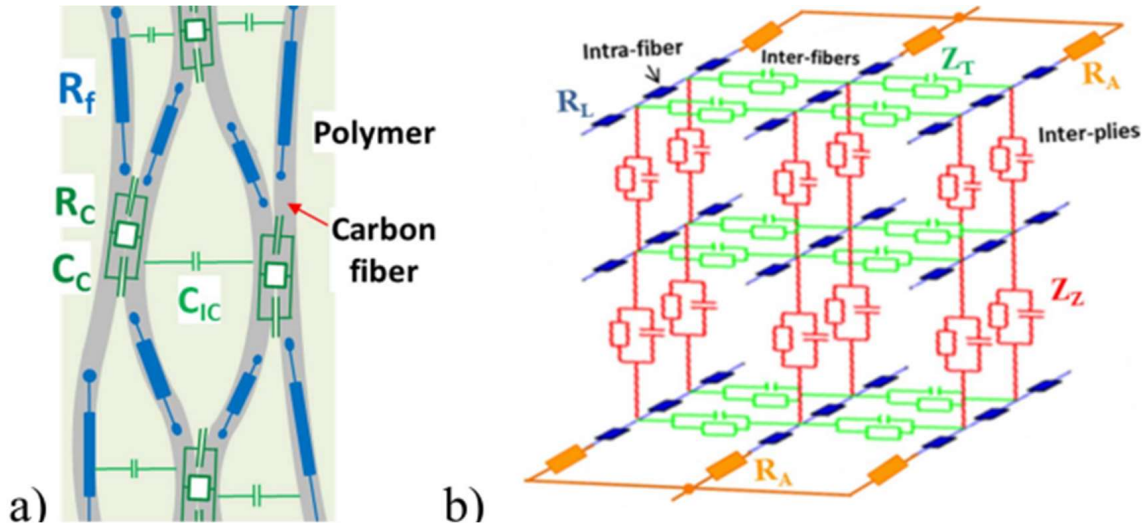

Fig. 2. Physical modelling (a) and 3D network modelling (b) of a unidirectional (all the carbon fibers are aligned in the same direction) CFRP structure [3].

|Z| and θ of parallel RC circuit in the model can be calculated by equations (2) and (3).

$$\theta = \frac{R}{\sqrt{1+\omega^2 R^2 C^2}} \quad (2)$$

$$|Z| = -arctan\,(\omega RC) \quad (3)$$

where ω is the electrical signal pulse (rad/s) with $\omega=2\pi f$ (Hz), R the material resistance (Ω) and C the capacitance (F), and j imaginary number.

In previous works [3, 21, 24], a mono-channel impedance analyzer Hioki IM3570 was used for the purpose of CFRP cure monitoring. The electric conduction between the bench and the CFRP structure is ensured by embedded copper electrodes. The thin and flexible copper tapes (50-µm thick) are embedded between the chosen plies of a laminate (Fig. 3). The surface area of the electrode must be carefully reduced for minimizing its interface resistance. The global access resistance (electrode/fiber interface and feed wire) was less than 1Ω. These copper electrodes will remain thereafter to monitor the CFRP structural health in service. Moreover, the temperature signature of cure cycle in the oven or in the autoclave can be obtained by a temperature measurement module based on K-type thermocouple.

  doi:10.5075/epfl-298799_978-2-9701614-0-0 published under CC BY-NC 4.0 license

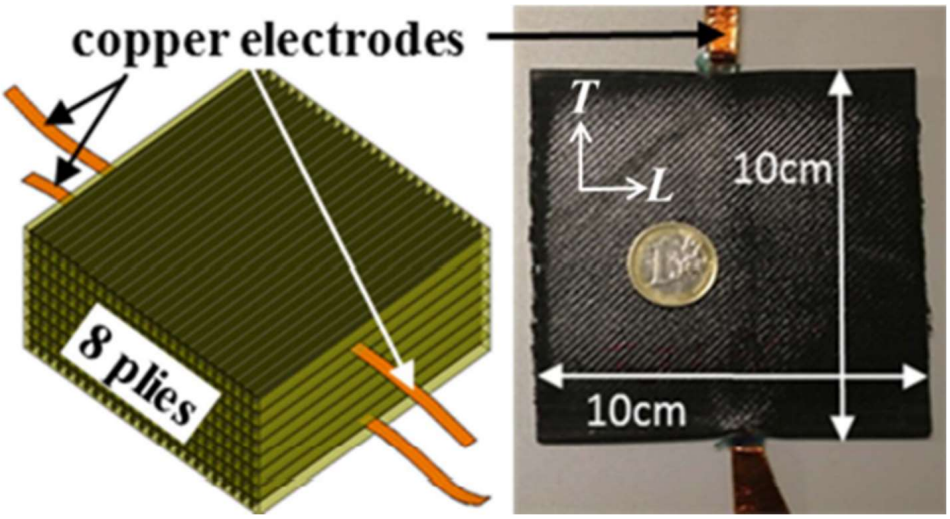

Fig. 3. Through-the-thickness conduction: electrodes placement in 8 UD T700/M21 plies [0°8]. Electrodes located between plies 1–2 and 7–8 perpendicular to the fibers [21].

The measurement results of previous works [1-3, 12, 21, 22] in cure monitoring and manufacturing issue detection are presented. This approach is based on the correlation between changes in through-the-thickness impedance modules during curing (Δ|Zz|) and several points characterizing the thermoset matrix behavior. These 14 rheological characteristic points (point A to point N) were used to follow the epoxy matrix phase changes during a cure cycle. Furthermore, these points can be found during oven and autoclave curing by measuring Δ|Zz| and their first and second derivatives |Zz'| and |Zz"| (Fig. 4.a).

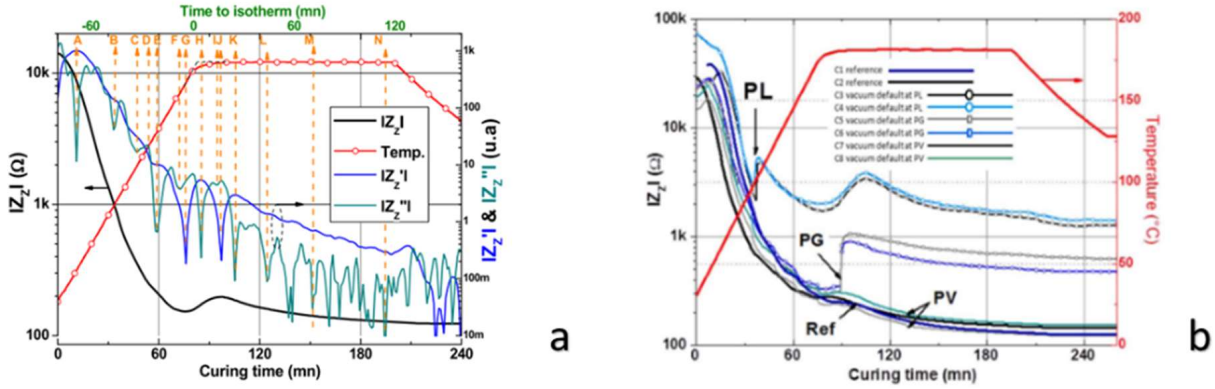

Fig. 4. Changes in |Zz|, |Zz'| and |Zz"| (10 kHz) of UD [0°8] laminate during curing in oven (a); changes in |Zz| (10 kHz) of 8 samples with vacuum fault effect detected (b) [12].

In the CFRP manufacturing processes, the various bagging products like release films, peal plies, bleeding plies and breathing clothes are necessary for the cure cycle in oven or autoclave. An experiment has been implemented to demonstrate that any leak occurring in the vacuum bag during curing could be detected. Six cure cycles were performed with manufacturing issues while two cure cycles were performed without issues. Hence, there are three different times chosen of the leaks: the first near minimum viscosity (PL), the second near gelation (PG) and the last near vitrification (PV). The manufacturing issue can be detected by the curve of Δ|Zz| during curing (Fig. 4.b). The vacuum bag leaks occurring near minimum viscosity or near gelation has caused a change in |Zz|. Furthermore, when a leak occurs in early stages of the cure cycle, |Zz|

  doi:10.5075/epfl-298799_978-2-9701614-0-0 published under CC BY-NC 4.0 license

value of the laminate with issue is higher than the laminates cured without issue. Nevertheless, the leaks can be detected but the |Zz| value remains at the same level with the reference cure cycles. The higher sensibility in |Zz| measured is required.

All these previous works are based on the analyzer Hioki IM3570. It's bulky, expensive, mono-channel, no sensible in time domain (it spent too much time on the data acquisition) and difficult to be transferred. Thus, a new bench which should respect following specifications: portable, low-cost, multi-channel, synchronized or sensible enough in time domain, possible of 4 points configuration and easy to be transferred, is required to the further research.

3. Design and development of new bench

The new bench which has 8 channels for electrical impedancemetry and 2 channels for temperature measurement has been developed for the purpose. The impedancemetry channels can be connected to copper electrodes embedded into CFRP structures via BNC connectors. These channels are built around PmodIA modules which are known as low-cost and miniature spectral analyzers. The CFRP is excited with a known alternative voltage (V-out), and the response (V-in) is analyzed by the signal processor integrated in PmodIA. The results of |Z| and θ are calculated from V-in. Furthermore, V-in is converted to digital signal by a 12-bits analog digital converter (ADC) integrated in PmodIA. A multiplexer (MUX) is used as a switch between 8 channels. The digital signal transmission from PmodIA to PC is implemented by a data acquisition board (DAQ). Finally, the results |Z| and θ are dis-played in the interface LabVIEW. The simplified signal processing chain is shown in figure 5.

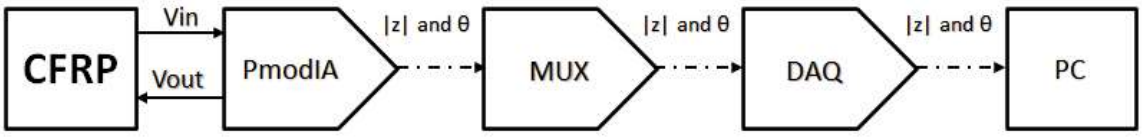

Fig. 5. The signal chain from CFRP under test to PC.

The frequency sweep range of PmodIA is chosen from 5kHz to 50kHz in our approach. The measurement range on |Z| from 5Ω to 1MΩ with an adequate accuracy (relative error<5%) is validated by a set of tests as follows.

- Pure R circuit equivalent to carbon fiber in longitudinal direction.
- Pure C circuit equivalent to pure thermoset matrix.
- RC parallel equivalent to cellule of 3D network model.
- RC cascade equivalent to transverse and through-the-thickness conduction.

In the context of cure monitoring of CFRP, the impedance higher than 1MΩ is not useful, but the impedance lower than 5Ω might be of interest to ensure longitudinal (along fibers) electrical measurements. The |Z| under 5Ω is unmeasurable for the PmodIA in 2 points configuration because of parasite elements that could be eliminated by 4 points configuration.

Hence, an extension circuit identified as Analog-Front-End (AFE) has been designed and connected to PmodIA for the purpose. It consists of two parts: a current source and an instrumentation amplifier (INA). The signal V-out is converted to a current which excites the CFRP. Furthermore, the voltage across CFRP is measured by instrumentation amplifier and sent to PmodIA. The parasite elements are eliminated because of the separation of the excitation source and the measurement device. The range on |Z| is now extended to [0.1Ω;1MΩ].

  doi:10.5075/epfl-298799_978-2-9701614-0-0

4. Preliminary experimental results with new bench

Preliminary experiments have been implemented in order to determine different characteristic times of the bench: the data acquisition time (T_a) of PmodIA and the switching time (T_s) of the multiplexer. *Ta* depends on signal processing speed of the impedance analyzer. Moreover, the switching time (T_s) depends on the I²C communication protocol which spends only a few microseconds in data transmission. The testing material used is a cured laminate made of 8 UD T700/M21 plies [0°$_8$] with two embedded copper electrodes to ensure electrical transverse measurement. A frequency sweep from 5kHz to 50kHz with 10 sweeping steps is implemented to ensure measurement T_a and T_s. Each step is repeated 100 times to ensure measurement accuracy but could increase T_a. The Hioki IM3570 is used for comparison with the same configuration of frequency sweep. Results are given in the table 1.

Table 1: Data acquisition time and switching time of the bench and Hioki

Characteristic Time	The bench	Hioki IM3570
Data acquisition time Ta	1.23s	More than 1 minute
Switching time Ts	< 0.1ms	100ms

Another experiment is implemented on the same laminate to measure the response time (*Tr*) when the CFRP is undergoing a simple mechanical loading: a manual point bending stress in its the central area. The instant deformation of laminate can be converted to a change of module |Z| in transverse (Fig. 6). Here a quasi-continue monitoring mode is applied: the step of frequency sweep is minimized to 0.1 Hz (511 steps of sweep imposed by PmodIA). The response curve exhibits a significant Δ|*Z*| and a *Tr* of 776.16ms highlighting the feasibility to monitor CFRP structure not only during curing but also under mechanical loading. A set of normalized mechanical tests will be performed in the future in order to correlate electrical impedance measurement to mechanical properties.

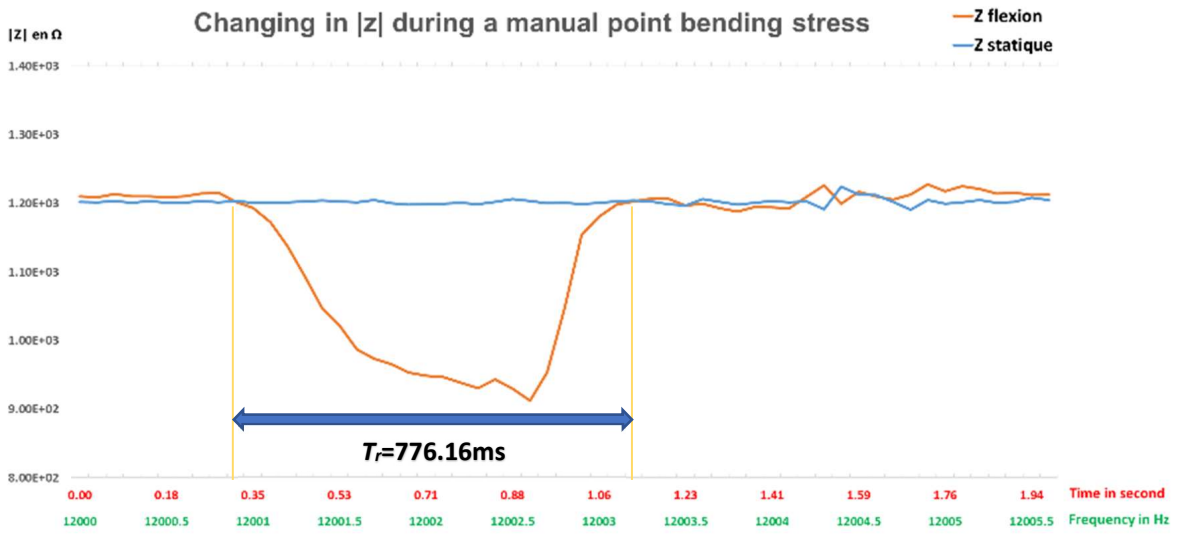

Fig. 6. Changing in |Z| during a manual point bending stress on cured laminate T700/M21 [0°$_8$]

  doi:10.5075/epfl-298799_978-2-9701614-0-0

5. Conclusion et perspectives

In this paper, the feasibility to ensure cure monitoring and SHM of CFRP using electrical impedancemetry has been presented. A new homemade bench has been developed for the purpose taking into account specifications such as portability, low-cost, short sampling time, accuracy and 2 points or 4 points configurations. Obtained measurements cover ranges from 5kHz to 50kHz in frequencies and from 0.1 to 1M in impendences. An Analog-Front-End has been designed and connected to the PmodIA to realize the 4 points configurations. 8 channels based on PmodIA and 2 channels based on K-type thermocouple enable the bench to implement the multi-physic measurement. Obtained measurements on standard samples but also cured laminated exposed good agreement with those obtained using an impedance analyzer and a higher capacity in data acquisition speed than using the Hioki IM3570 (few seconds vs few minutes for 8 channels).

To validate this new bench, a set of cure and mechanical monitoring will be implemented. An electrical-mechanical modelling would be developed in further studies to design a virtual material able to describe changes not only during curing but also during mechanical loading. Experimental and numerical results will be discussed and in a case of good agreement an inverse approach could be proposed.

6. References

1. Sonia Sassi, P.M., Thierry Camps, Mahamadou Mounkaila, Philippe Olivier, Cure Monitoring and SHM of Carbon Fiber Reinforced Polymer Part II : Multi-Physical Correlations. 2014.
2. Marguerès, P., T. Camps, and P. Olivier, Impédancemétrie électrique pour le monitoring de composites carbone/époxy. Revue des composites et des matériaux avancés, 2014. 24(2): p. 207-220.
3. Mounkaila, M., et al., Modelling the electrical behaviour of carbon/epoxy composites and monitoring changes in their microstructure during oven and autoclave curing using electrical impedancemetry. Smart Materials and Structures, 2018. 27(8).
4. Mulle, M., et al., Assessment of cure residual strains through the thickness of carbon–epoxy laminates using FBGs, Part I: Elementary specimen. Composites Part A: Applied Science and Manufacturing, 2009. 40(1): p. 94-104.
5. Mulle, M., et al., Assessment of cure-residual strains through the thickness of carbon–epoxy laminates using FBGs Part II: Technological specimen. Composites Part A: Applied Science and Manufacturing, 2009. 40(10): p. 1534-1544.
6. Takeda, S.-i., Y. Aoki, and Y. Nagao, Damage monitoring of CFRP stiffened panels under compressive load using FBG sensors. Composite Structures, 2012. 94(3): p. 813-819.
7. Garnier, C., et al., The detection of aeronautical defects in situ on composite structures using Non Destructive Testing. Composite Structures, 2011. 93(5): p. 1328-1336.
8. Zhang, Z., et al., Visualized characterization of diversified defects in thick aerospace composites using ultrasonic B-scan. Composites Communications, 2020. 22.
9. Menana, H. and M. Feliachi, 3-D Eddy Current Computation in Carbon-Fiber Reinforced Composites. IEEE Transactions on Magnetics, 2009. 45(3): p. 1008-1011.
10. Mizukami, K., et al., Detection of in-plane and out-of-plane fiber waviness in unidirectional carbon fiber reinforced composites using eddy current testing. Composites Part B: Engineering, 2016. 86: p. 84-94.

  doi:10.5075/epfl-298799_978-2-9701614-0-0

11. Xu, X., et al., Interlaminar contact resistivity and its influence on eddy currents in carbon fiber reinforced polymer laminates. NDT & E International, 2018. 94: p. 79-91.
12. Margueres, P., et al., Carbon fibres reinforced composites. Electrical impedance analysis: a gateway to smartness. International Journal of Smart and Nano Materials, 2020. 11(4): p. 417-430.
13. MATSUO, M., Electric, Dielectric and Magnetic Properties of Polymer and Carbon Fillers. 2008.
14. Takaomi INADA, A.T., Smart Cure Monitoring Method of Carbon/Epoxy Laminates using Electric Capacitance Change with Applied Alternating Current Frequency. Key Engineering Materials, 2005. Vols. 297-300: p. p. p2903 -2908.
15. Hardis, R., et al., Cure kinetics characterization and monitoring of an epoxy resin using DSC, Raman spectroscopy, and DEA. Composites Part A: Applied Science and Manufacturing, 2013. 49: p. 100-108.
16. J.C. Abry, S.B., A. Chateauminois , M. Salvia, G. Giraud, In situ detection of damage in CFRP laminates by electrical resistance measurements. Composites Science and Technology, 1999. 59.
17. Xia, Z., et al., Quantitative damage detection in CFRP composites. Composites Science and Technology, 2003. 63(10): p. 1411-1422.
18. Xia, Z.H. and W.A. Curtin, Damage detection via electrical resistance in CFRP composites under cyclic loading. Composites Science and Technology, 2008. 68(12): p. 2526-2534.
19. Marguerès, P., et al., Preliminary experimental study on the electrical impedance analysis forin-situmonitoring of the curing of carbon/epoxy composite material for aeronautical and aerospace structures. Measurement Science and Technology, 2013. 24(9).
20. Sassi, S., et al. Suivi de cuisson de composites Carbone/Epoxy par impédancemétrie électrique. 2013. Nantes, France.
21. Mahamadou Mounkaila, T.C., Sonia Sassi, Philippe Marguerès, Philippe Olivier, Christophe Escriba, Jean-Yves Fourniols, Cure Monitoring and SHM of Carbon Fiber Reinforced Polymer Part I : Impedance Analysis and Multiphysic Sensitivity. 2014.
22. Sassi, S., et al., Determination of anisotropic geometrical parameters for the electrical characterization of carbon/epoxy composite during oven curing. Composites Part A: Applied Science and Manufacturing, 2016. 80: p. 204-216.
23. Sassi, S., Instrumentation distribuée résidente pour l'optimisation de la fabrication et le suivi de matériaux composites pour pièces structurales pour l'aéronautique et le spatial, in Thèse. 2016, Université Toulouse III Paul Sabatier.
24. Mahamadou, M., Analyse impédancemétrique pour le suivi de cuisson ou de santé des structures composites carbone/époxyde : Vers des matériaux intelligents pour le PHM des structures composites, in Thèse. 2016, Université Toulouse III Paul Sabatier.

  doi:10.5075/epfl-298799_978-2-9701614-0-0

FLEXURAL TOUGHENING OF WAVE SHAPED SHORT PLASTIC FIBERS IN A CEMENTITIOUS MORTAR

Giuseppe Gullì[a], Davide Palamara[b], Francesco Grungo[a], Luigi Calabrese[a]

a: Tradimalt S.p.A., Via Nazionale, 1, 98049 Villafranca Tirrena – Italy
b: Department of Engineering, University of Messina, Contrada di Dio Sant'Agata, 98166 Messina, Italy; lcalabrese@unime.it ,

Abstract: *In this paper, the effect of wave-shaped polymeric fibers at varying aspect ratio and fiber content on the flexural behavior of fiber reinforced mortars (FRM) was studied. Three weight fraction (from 0.5 w.t.%, up to 1.0 w.t.%) and two aspect ratios (L/d 37 and L/d 46) were assessed by performing three-point bending tests. Compared to unfilled M10 mortar, the maximum flexural strengths of the composite samples increases up to 67.8% thanks to the addition of plastic fibers. At low fiber content, the increase of the flexural strength is very limited for I20 fibers with an incidence of 6.9 % for the M10-I20-05 batch. Furthermore, the toughness index (TI) values are in the range of 20-50 for the FRCM. Moreover, despite the unfilled mortar where a brittle failure occurs, FRCMs composites exhibited a ductile-like behavior with large residual strength after fist crack activation also at low plastic fiber content.*

Keywords: wave-shaped fibers; mortar; flexural; toughness; cracking behavior

1. Introduction

Cementitious materials, such as mortars or concretes, due to their price, availability, durability, strong compressive strength and stiffness have long been widely used as building materials. Despite their widespread use, some drawbacks still represent an alarm sign that must be taken into account. Brittleness, poor tensile strength or sensitivity to humidity can represent limiting factors that reduce the durability and functionality of the material at medium and long term. In this context, several efforts have been performed to identify effective solutions in order to improve the performance in terms of toughness and ductility of mortars or concretes.

An approach that has shown great potential is the addition of reinforcing fibers aimed at improving the mechanical stability of the mortar. Fiber-reinforced mortars (FRM) and concretes (FRC) represent a relevant research topic for the engineering construction design and maintenance because the addition of fibers to mortars significantly changes their mechanical properties, such as toughness, compression and tensile strength [1].

Several fibers type, based on metallic, polymeric or ceramic materials are widely applied in the manufacturing of FRM or FRC materials [2] [3] [4]. The choice of adding high modulus and strength fibers (such as metallic, carbon or glass fibers) is effective in order to obtain a significant increase in the concrete strength, however their intrinsic brittle behavior could limit the improvement in toughness and ductility of the material [5]. On the other hand, polymeric fibers, characterized by low strength and high flexibility, are a potentially more effective option to improve ductility preserving the increase of the crack activation resistance for the FRMs [6]

On the mortars, the crack evolution, the choice of a fiber geometry, able to increase the interlocking with the matrix, can further enhance the reinforcing action of the fiber limiting the

  doi:10.5075/epfl-298799_978-2-9701614-0-0

crack formation and propagation. Although the wide potential in the use of corrugated polymeric fibers to increase the toughness and resistance of cementitious materials, few works in the literature have paid attention to this aspect, often correlating its use on hybrid FRC configurations [7] [8]. Consequently, an improvement of knowledge on corrugated polymer FRC or FRM is a benefit able to enhance the scientific soundness of this research topic.

On this concern, the aim of the paper is to assess the effect of corrugated shaped polymeric fibers (with two different aspect ratio) at varying fiber contents on flexural behavior of a fiber reinforced cementitious mortar in order to improve ductility and flexibility of the material. Based on the characteristics of load–deflection curve, the flexural behavior analysis involves first crack load and deflection, maximum peak load and deflection, and toughness indexes. Furthermore, a relationship between FRC microstructure, mechanical behavior and fracture mechanism in order to better identify the best choice in terms of mechanical stability and toughness was carried out.

2. Experimental part

2.1 Materials and sample preparation

Composite mortars constituted by mixing commercial polymeric fibers in a mortar having a compressive strength of 10 MPa (M10) were realized. These mortars are mainly used as a background plaster. As fiber reinforcement, a wave-shaped chopped polypropylene plastic fiber was added.

The mortars were prepared and mixed in the laboratory using selected binders and aggregates and stored under standard conditions (22 ° C -60%). The mortars contain the following raw materials: Portlad II/A-LL 42.5 R cement, natural hydraulic lime NHL 5, silica sand (max grain size 2 mm), cellulose ether and starch ether. The mixing process, between water and mortar (ratio 17:100), took place inside a leaf mixer. The fibers are slowly dispersed into the mixer to ensure, during the mixing phase an excellent fiber dispersion. The amount of mixing water remained the same for all samples. At the end of the mixing phase, the fresh concrete was immediately cast in metal molds (4 cm x 4 cm x 16 cm). After 2 days, the specimens were removed from the molds and left for an additional 26 days in controlled temperature and humidity conditions, according to EN 1015-11 standard. In particular, in order to better assess the effect of the reinforcement in the mechanical behavior of the composite mortar, mixture formulations at varying fiber content (0.5 wt.%, 0.7 wt.% and 1.0 wt.%) and aspect ratio (length 20 mm and 25 mm) were realized. Details of all the produced batches are summarized in Table 1.

Table 1: Codes, fiber content and length for all investigated FRC batches

Code	Fiber Length [mm]	Fiber Content [wt.%]
M10	--	--
M10-I20-05	20	0.5
M10-I20-07	20	0.7
M10-I20-10	20	1.0
M10-I25-05	25	0.5
M10-I25-07	25	0.7
M10-I25-10	25	1.0

  doi:10.5075/epfl-298799_978-2-9701614-0-0

As reference, an unreinforced M10 mortar was prepared. All batches were coded by using a "M10-" acronym prefix followed by an "I" letter and number indicating the length of the chopped fiber (in mm). Finally, a last number is referred to the fiber reinforcement content (in wt. %). E.g., the M10-I20-07 batch indicates composite mortar constituted by 0.7 % of chopped plastic fibers with 20 mm length. The code M10 is referred to the unreinforced cementitious mortar.

2.2 Material Characterization

Three-point load bending (TPB) test has been carried out on prismatic samples (cross section 40 mm x 40 mm and length 160 mm) for each mixture by varying the amount of wave-shaped polymer fibers. The flexural test was performed on a universal electro-hydraulic testing machine (UTM), Uniframe250 (Controls, Milan, Italy), equipped with a 250 kN load cell. The span length for the three-point bending test was set equal to 100 mm. In order to avoid local displacement mismatch among testing fixtures, a pre-loading of 2 N was applied for all tests. A load-controlled set-up was monotonically applied on the prismatic beam at 10 N/s. All tests were per-formed in accordance to EN 1015-11 standard. Three replicas for each batch were per-formed.

3. Results and discussion

In Figure 1 the evolution of the load displacement curve at varying fiber content for 20 mm and 25 mm fiber length are shown (Figure 1a and Figure 1b respectively).

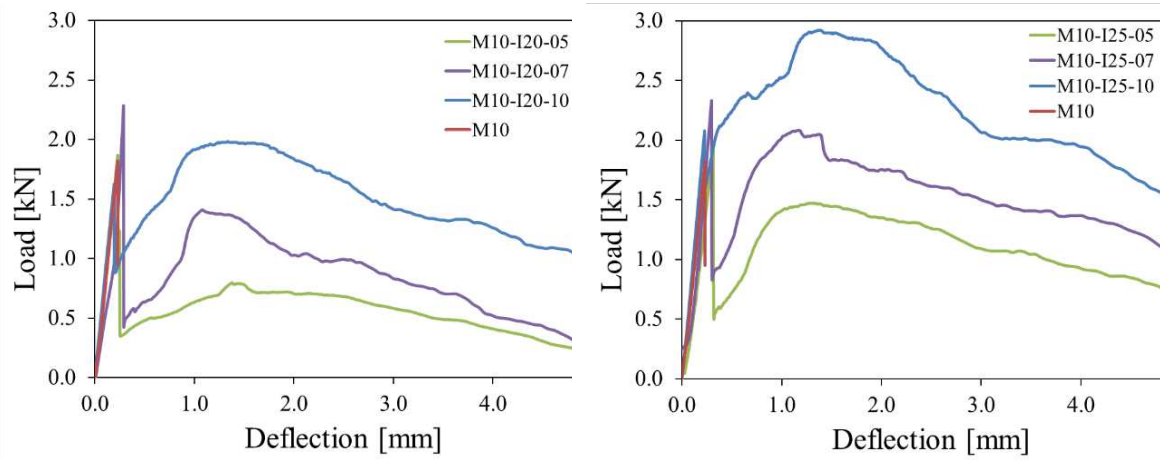

a) b)

Figure 1: Effects of fiber volume fraction and aspect ratio on the flexural stress-strain curves for composite mortars with (a) l=20 short fibers (b) l=25 short fibers as reinforcement.

At low deflection, when the stress state is not suitable to trigger the fracture of the matrix, all the specimens have a very similar linear trend. This states that due to short fibers addition, up to 1 wt.%, no significant effect on the flexural stiffness of the mortar is achieved. Subsequently the onset of the first crack in the matrix, the fiber content plays a significant role in performances increasing the residual strength of the specimen. This effect is all the more relevant the higher the fiber content.

Furthermore, samples with higher aspect ratio fibers (l = 25mm) show better flexural behavior. In fact, the fiber length has a beneficial effect both in the residual loads and mortar ductility. All composite samples with I25 fibers highlighted better strength and ductility than the

  doi:10.5075/epfl-298799_978-2-9701614-0-0

corresponding ones with the same fiber content. The larger fiber surface in I25 fibers improves the interfacial fiber/matrix bond increasing the pull-off strength.

By increasing corrugated fiber volume fraction and length, bridging action improves significantly. The crack opening resistance in the reinforced mortars is favored by a suitable interfacial shear strength that exalt the stress transfer efficiency at the fiber-matrix interface [9]. Consequently, increasing the fiber content both flexural strength and deflection at failure are increased. Evaluating the data reported in Figure 1, the increase in performance due to fiber addition is more relevant in deflection at failure (>5mm for the reinforced composites) than the maximum flexural load (for 1.0% I25 fibers about 68 % higher than unreinforced one).

Table 2 summarized the main flexural performance parameters of the mortars on the three-point flexural test. P_{FP} and δ_{FP} are the first peak load and deflection. Analogously, P_{MP} and δ_{MP} are the load and deflection at the maximum peak of the flexural curve. $P_{L/20}$ indicates the residual load at the net deflection of L/20. Finally, $T_{L/20}$ is the toughness calculated as area under the load vs net deflection curve from 0 to L/20.

Table 2: Flexural loads, deflections and toughness for all composite mortars

	P_{FP} [N]	δ_{FP} [mm	P_{MP} [N]	δ_{MP} [mm]	$P_{L/20}$ [N]	$T_{L/20}$ [J]
M10	1740±108	0.23±0.004	1740±108	0.23±0.004	--	0.19*±0.01
M10-I20-05	1774±84	0.23±0.02	1860±60	0.23±0.02	234±56	2.81±0.6
M10-I20-07	1570±105	0.25±0.03	2012±136	0.25±0.03	388±156	4.12±xx
M10-I20-10	2286±184	0.22±0.02	2286±184	1.31±0.02	838±125	7.02±xx
M10-I25-05	2218±207	0.24±0.05	2218±207	0.33±0.09	758±246	5.51±1.14
M10-I25-07	2304±307	0.23±0.03	2507±166	0.80±0.58	1.515±399	9.50±1.73
M10-I25-10	2080±208	0.22±0.02	2920±165	1.02±0.34	1.703±647	12.37±2.84

* Energy determined at the maximum deflection.

The results highlight that the bending loads (in terms of peak and loads, indicated as P_{FP}, P_{MP}, and $P_{L/20}$ respectively) and deflections (at maximum load deflection and residual deflection, δ_{MP}, $\delta_{L/50}$ and $\delta_{L/20}$, respectively) increase at increasing fiber volume fraction increases due to the increased load capacity of the fiber to suffer applied loads. This phenomenon can be ascribed to the coupled action of crack-bridging effect carried out by the corrugated fibers at the crack and load-carrying capabilities favored by the interlocked bond strength between polymeric fiber and cementitious mortar [10]. This trend is not observed by analyzing the first peak-load related parameters (P_{FP} and δ_{FP}). The deflection at the first-crack formation δ_{FP} does not show a fiber volume dependence. The first-peak load, P_{FP}, on the other hand, shows, although with a non-monotonous trend, a slight increase due to the polyester fibers addition. These two parameters can be correlated to the triggering of cracks on the matrix [11]. Consequently, they are more influenced by the properties of the cementitious binder (which do not change) than the fiber, whose action is mainly carried out during the propagation stage of the cracks.

The typical fracture morphology of M10 and FRM under bending test is shown in Figure 2. As attended, the cracking process of the unfilled M10 mortar is characterized by a singular and narrow fracture line that is triggered in the bottom side of the sample and extended catastrophically toward the topside along the load direction, leading to a catastrophic brittle fracture. No evidence of secondary cracks can be highlighted, confirming the low tensile

  doi:10.5075/epfl-298799_978-2-9701614-0-0

strength stability of the material. Meanwhile, comparing the fracture pattern of M10-I20-10 and M10-I25-10 samples, the I25 FRM exhibited a better fracture morphology than the I120 one. Longer fibers favor larger amount secondary fracture mechanisms than shorter ones. Indeed, in I25 samples, the fracture tends toward a more irregular profile with relevant noticeable synergistic contributes e.g. internal cracks, bridging …. This indicates that different dissipative energy contributes occurred during the bending. Moreover, due to the greater fiber length, higher force is required to pull out the fibers, enhancing the bridging phenomenon even for very large cracks. This has broad benefits not only on the mechanical performances of the mortar but also on its safety features. The fiber-reinforced mortar, even if extensively damaged, preserves a residual structural stability, which limits local detachment from the wall, with clear benefits for the residents of the housing unit in adverse accidents.

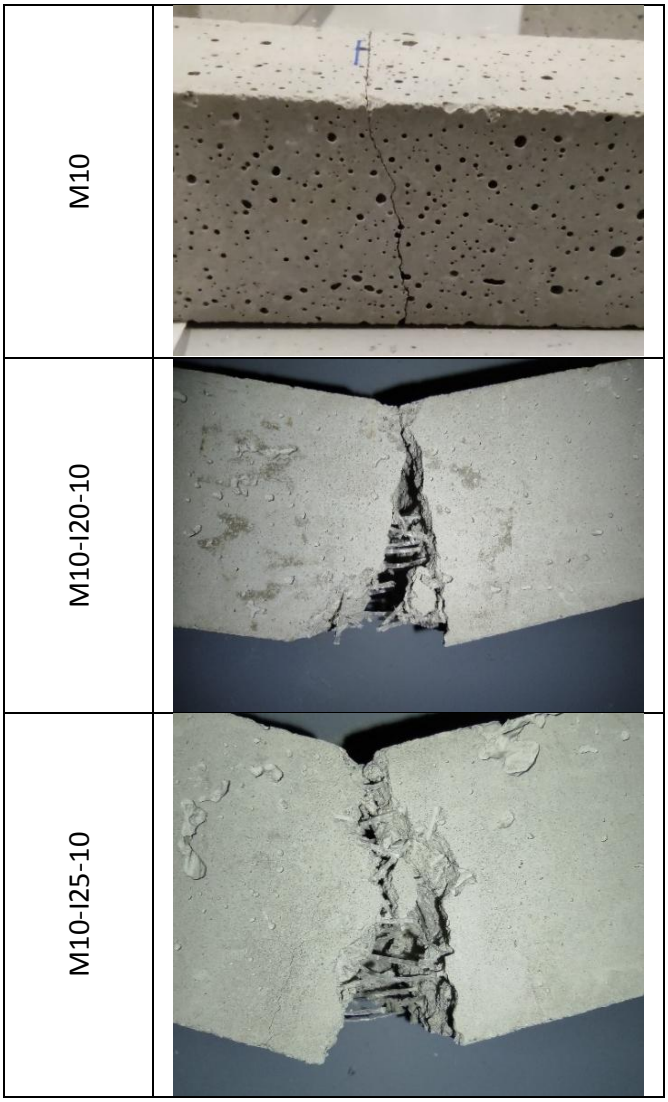

Figure 2: Fracture surfaces of plain mortar and corrugated fiber reinforced mortars.

4. Conclusions

In this paper the effect of corrugated shaped polymeric fibers (with two different aspect ratio) at varying fiber contents (0.5 wt.%, 0.7 wt.%, and 1.0 wt.%) on flexural behavior of a fiber reinforced cementitious mortar was assessed in order to improve the material ductility and flexibility. The flexural performance, in terms of flexural strength, deflection, toughness, of FRM

  doi:10.5075/epfl-298799_978-2-9701614-0-0

increases at increasing fiber content and L/D aspect ratio. Compared to unfilled M10 mortar, the maximum flexural strengths of the composite samples increases up to 31.4% and 67.8% for the I20 and I25 fibers, respectively. At low fiber content, the reinforcing action on the flexural strength is very limited for I20 fibers with an incidence of 6.9 % for the M10-I20-05 batch. Instead M10-I25-05 (characterized by long corrugated polymer fibers) the flexural strength increased of 27.5%. Different considerations can be drawn by analyzing the toughness property. Fiber-reinforced mortars with wave fibers induce a significant increase in toughness even for very low fiber content addition. FRM with 0.5 wt.% fibers reaches $TI_{L/20}$ toughness values in the range of 20-50. The maximum values are reached for M10-I25-10 batch characterized by 1 wt.% of 25 mm long fibers. Furthermore, compared to unfilled M10 mortar, the FRMs exhibited a ductile fracture pattern.

Acknowledgements

This work was supported by the by P.O. FESR Sicilia 2014/2020 (Axis 1, Action 1.l.5 ''Support for the technological advancement of companies through the financing of pilot lines and actions for early validation of products and large-scale demonstrations'') Project 082030000276 SMART-ART “Sviluppo di metodi avanzati di restauro, diagnostica e telecontrollo per la conservazione del patrimonio artistico architettonico”, CUP G79J18000620007.

5. References

1. Ahsan Habib, Razia Begum MMA. Mechanical properties of synthetic fibers Reinforced Mortars. Int J Sci Eng Res 2013; 4:923–27.
2. Brandt AM. Cement based composites : materials, mechanical properties, and performance. Wiltshire (United Kingdom): Taylor & Francis; 2009.
3. Zeng Y, Tang A. Comparison of effects of basalt and polyacrylonitrile fibers on toughness behaviors of lightweight aggregate concrete. Constr Build Mater 2021; 282:122572.
4. Blazy J, Blazy R. Polypropylene fiber reinforced concrete and its application in creating architectural forms of public spaces. Case Stud Constr Mater 2021; 14:e00549.
5. Pakravan HR, Latifi M, Jamshidi M. Hybrid short fiber reinforcement system in concrete: A review. Constr Build Mater 2017; 142:280–294.
6. Halvaei M, Jamshidi M, Latifi M. Investigation on pullout behavior of different polymeric fibers from fine aggregates concrete. J Ind Text 2014; 45:995–1008.
7. Li B, Chi Y, Xu L, Shi Y, Li C. Experimental investigation on the flexural behavior of steel-polypropylene hybrid fiber reinforced concrete. Constr Build Mater 2018; 191:80–94.
8. Corinaldesi V, Nardinocchi A. Mechanical characterization of Engineered Cement-based Composites prepared with hybrid fibres and expansive agent. Compos Part B Eng 2016; 98:389–396.
9. Kheradmand M, Mastali M, Abdollahnejad Z, Pacheco-Torgal F. Experimental and numerical investigations on the flexural performance of geopolymers reinforced with short hybrid polymeric fibres. Compos Part B Eng 2017; 126:108–118.
10. Wu Z, Shi C, He W, Wu L. Effects of steel fiber content and shape on mechanical properties of ultra high performance concrete. Constr Build Mater 2016; 103:8–14.
11. Yazıcı Ş, İnan G, Tabak V. Effect of aspect ratio and volume fraction of steel fiber on the mechanical properties of SFRC. Constr Build Mater 2007; 21:1250–1253.

  doi:10.5075/epfl-298799_978-2-9701614-0-0

INFLUENCE OF MANUFACTURING PROCEDURE ON MECHANICAL PROPERTIES OF CONTINUOUS FIBER REINFORCED THERMOPLASTICS

Florian Mischo[a], Andreas Kenf[b], Markus Kammler[b], Sebastian Schmeer[b]

a: Leibniz-Institut für Verbundwerkstoffe, Kaiserslautern – florian.mischo@ivw.uni-kl.de
b: Leibniz-Institut für Verbundwerkstoffe, Kaiserslautern

Abstract: *Continuous fiber reinforced thermoplastics (cFRTP) increasingly find their way into structural components, for example in the automobile sector, due to both their lightweight and recycling potential. For characterization and application, machining is necessary to get the final shape of the product. In both cases, a negative influence of the machining procedure on the product's properties has to be avoided. Because machining procedures are diverse, the influence of differently generated surface roughness on matrix dominant material properties is analyzed. This research focuses on the transverse tensile strength of unidirectional carbon fiber reinforced polycarbonate as a very sensitive property for edge effects. Its value correlates with the average roughness and standard deviation of manufactured edge surfaces.*

Keywords: continuous fiber reinforced; thermoplastic composites; composite manufacturing; surface roughness; material characterization

1. Introduction

Thermoplastic composites indicate a major lightweight construction potential and are of great interest to key industries. Because of their re-meltability and realization of short production cycle times, they offer the opportunity to make an important contribution to the environmental compatibility and competitiveness of new products. [1] In this material class, continuous fiber-reinforced thermoplastic composites (cFRTP) play a special role. Due to their excellent mechanical properties, they are particularly suitable for use in structural load-bearing components [2], also in large scale automobile applications. [3]

Machining is an important step for the application of these materials. Not only in terms of finishing cFRTP parts but also because of test specimen manufacturing necessary for material characterization generating data for the design process. Nevertheless, especially for composites, machining is a challenging task (anisotropic, non-homogeneous material, abrasive fibers [4]) and risk exists to cause damage to the material. [5] Therefore, optimizing machining processes is state of research and the influence of manufacturing parameters on the material's surface quality as well as service life of the tooling (e.g. for milling/drilling [4,6–9], water jet cutting [10–13], sawing [4,14], laser cutting [10,15]) is extensively investigated. The results leading to guidelines and benchmarks, mainly focusing on thermoset materials. [16–19]

Standardization is necessary for minimizing machining influences and generating comparable material characterization values, which are important for the industrial application of cFRTP. ISO 2818 [20] defines recommended parameters for the machining of plastics regarding different specimen geometries and procedures. In terms of tensile testing cFRTP, ISO 527 [21] refers to this standard and defines to document the chosen specimen manufacturing procedure in the test report to assure comparability or identify deviation in results. Same applies for the appropriate ASTM standard, ASTM D 3039 [22]. Therefore, the question arises which influences

  doi:10.5075/epfl-298799_978-2-9701614-0-0

different surface roughnesses (due to varying manufacturing procedures) have on the mechanical testing results, especially for matrix dominant material values. HADDAD [23] focusses on this topic for compression and inter laminar shear values for thermoset materials. This research examines cFRTP's surface roughness induced by milling, sawing and water jet cutting regarding its influence on transverse tensile properties.

2. Material

The material used is a polycarbonate based continuous carbon fiber reinforced composite tape (CF-PC-UD). The fiber volume content is 44 % and the initial tape thickness 0.17 mm. For specimen manufacturing according to ISO 527-5, plate material (300 x 300 mm²) is manufactured consisting of a stacked tape layup $[0_6]_s$ to reach the targeted plate thickness of 2 mm. The manufacturing process is an industry-oriented thermoforming process in a hot press.

3. Specimen manufacturing procedures

It should be noted that the given and upcoming absolute roughness values do not necessarily represent optimal results of the manufacturing procedures, but of the tools used in this study. With different tools, better results are achievable, as shown in many benchmark tests. The focus of this study is to induce different, characteristic roughness values by procedure, not optimizing the process itself.

Table 1: Manufacturing parameters.

Milling parameter (in co- and counter rotation)		**Water jet cut parameter**		**Circular sawing parameter**	
Tool	Single tooth cutter (Ø 4 mm); polished flute	Abrasive	Quartz sand	Tool	Circular saw blade, synthetic diamond coated (Ø 125 mm)
Feed rate [mm/s]	5	Abrasive flow [g/min]	450	Saw blade speed [rpm]	6 000
Spindle speed [rpm]	30 000	Nozzle diameter [mm]	0.35		Use of cooling lubricant
Axial depth of cut [mm]	1	Focusing nozzle diameter [mm]	1.0		
		Pressure [bar]	3 800		

For transverse tensile testing according to ISO 527-5 (specimen size: 250 x 25 x 2 mm³), three different specimen manufacturing procedures were chosen to induce different edge surface roughness values. Milling with a single tooth cutter and polished flute (to reduce thermal stress on the material without use of cooling lubricant) in co- and counter rotation, abrasive water jet cutting, and circular sawing with a synthetic diamond coated saw blade. Table 1 gives an overview of the used manufacturing parameters.

  doi:10.5075/epfl-298799_978-2-9701614-0-0

For milling, the final manufacturing parameters result from a parameter study to increase tool life and ensure comparability of the manufactured specimen edges while using one single cutter. [24] This study shows, inter alia, the average surface roughness according to the milling/fiber direction (figure 1) with its minimum parallel to the UD fiber direction. In this work, milling direction 2 transverse to fiber direction (see figure 1) is addressed.

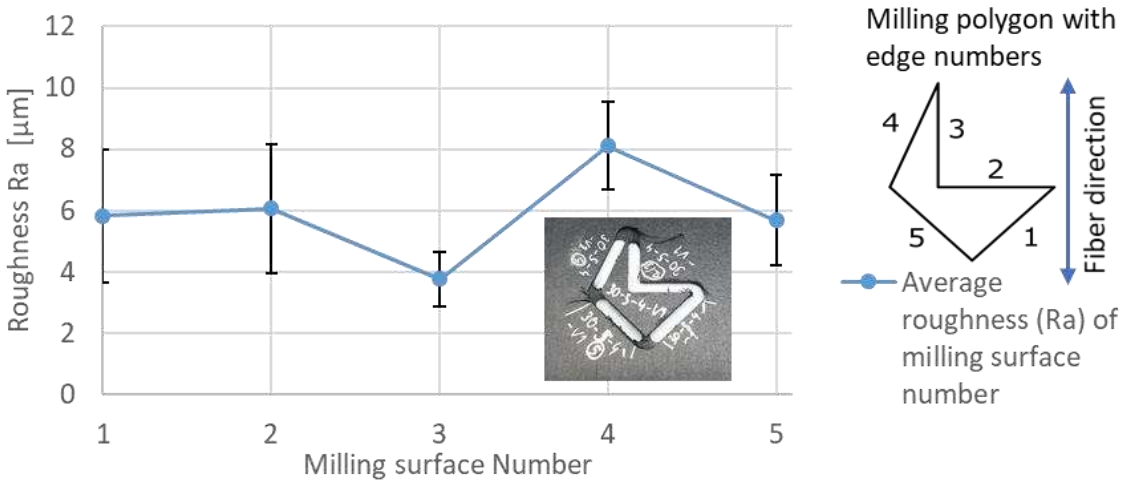

Figure 1: Average surface roughness (Ra) of CF-PC-UD depending on milling direction [24]

A minimum number of six specimens are manufactured for each machining procedure to ensure statistical significance in tensile testing and roughness analysis.

4. Analyzation of surface roughness

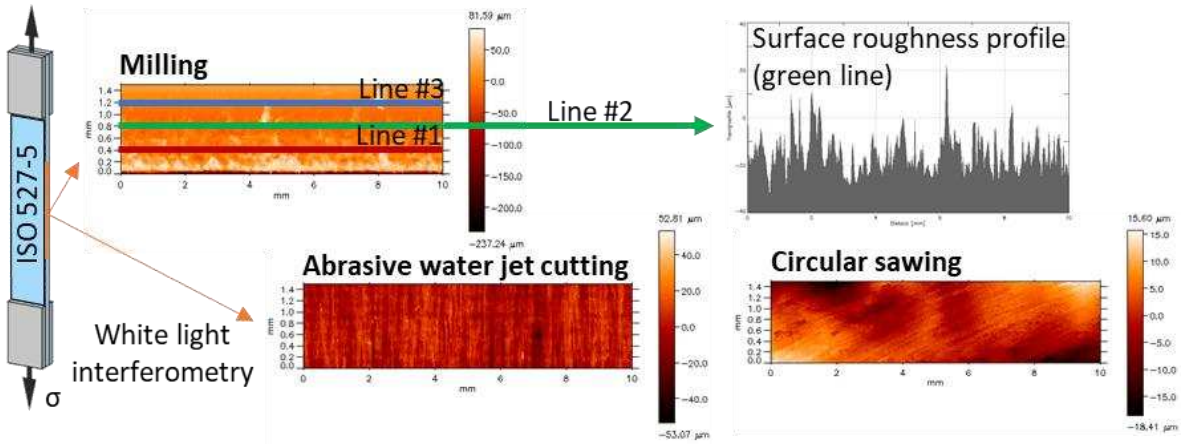

Figure 2. White light interferometry on transverse tensile specimens (ISO 527-5 [21]), 3D roughness analysis and derivation of path profile on section planes

Before testing the rectangular specimens, the roughness on a minimum of four specimens per machining procedure is examined. For roughness analysis, white light interferometry is used due to its fast measurement speed and ease of use being a non-destructive and contactless measurement method. [25,26] For this study, the white light profilometer *FRT MicroProf* by *Fries Research & Technology GmbH* is used with a resolution of 1.0 µm laterally and 0.003 µm vertically.

  doi:10.5075/epfl-298799_978-2-9701614-0-0 published under CC BY-NC 4.0 license

Figure 2 shows the analysis position on a specimen's edge, generating 3D roughness profiles of the surface over an area of 10 x 1.5 mm². 2D roughness profiles on three section planes are derived with coordinates of 0.4 (red line; line no. 1), 0.8 (green line; line no. 2) and 1.2 mm (blue line; line no. 3) in width direction of the 3D-profile (see figure 2). The generated 3D-profiles consist of 300 x 60 pixels, measured at 100 Hz within a vertical sensor measuring range of 300 µm.

To describe the machined surfaces the standardized values of the arithmetical mean deviation of the profile (Ra) and the average surface roughness (Rz) are derived from the generated profiles. [27] In addition, the material ratio curve (according to ISO 4287 [27]) is generated for each profile. The aim of this curve is the visualization of the roughness homogeneity as well as the average notch sharpness of the profiles by analyzing the curve gradient G_{mrc} around the turning point of the material ratio curve (see figure 3). G_{mrc} is calculated according to Eq. 1 using 10 data points around the curve's turning point:

$$G_{mrc} = \frac{\Delta x_i}{\Delta y_i}, with\ i \in [i_{turning\ point-5}, \dots, i_{turning\ point+5}] \quad (1)$$

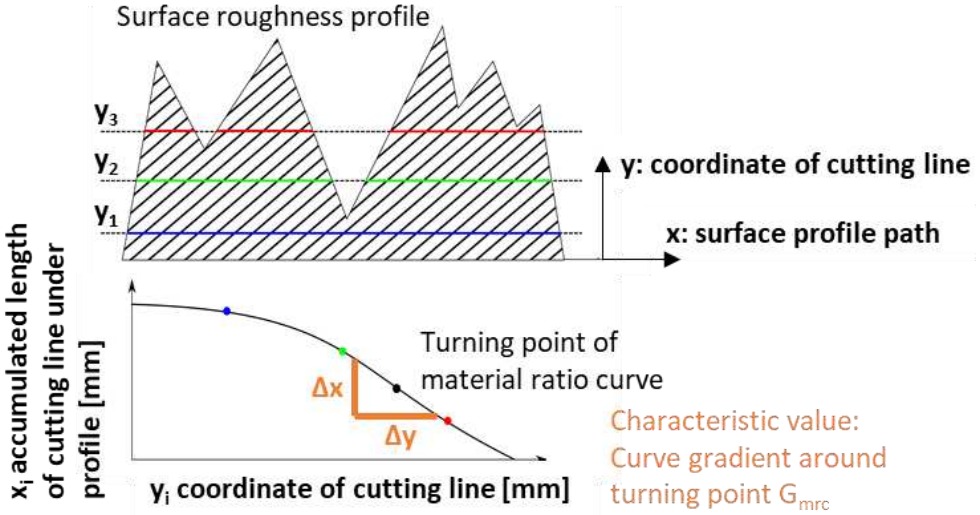

Figure 3. Analyzation of specimens' surface roughness profiles using material ratio curve (according to ISO 4287 [27]) and derivation of characteristic values

The material ration curve is generated by using 100 cutting lines y_i (i = {0, …, 100}), equally distributed over the individual overall height of the surface roughness profile.

5. Results

Figure 4 shows the average relative transverse tensile strength of the specimens in relation to the average edge surface roughness values Ra and Rz. A correlation can be seen. With increasing roughness of Rz by factor 10 and Ra by factor 14 (from Ra = 1.49 ± 0.89 µm [Rz = 11.01 ± 7.92 µm] to Ra = 20.03 ± 16.12 µm [Rz = 112.94 ± 69.28 µm]) the transverse tensile strength of CF-PC-UD decreases by 34.5 %. It is also visible that the average roughness values of milling in co- and counter rotation show a high standard deviation. The inhomogeneity of these surfaces is also visible in the 3D roughness profile in figure 2 as well as in the exemplary 2D profiles in figure 5. The average roughness of milling (e.g., for co-rotation) in the section planes of line no. 3 (Ra = 1.01 ± 0.68 µm [Rz = 9.37 ± 5.64 µm]) and no. 2 (Ra = 0.98 ± 0.32 µm [Rz = 9.04 ± 3.81 µm]) are

  doi:10.5075/epfl-298799_978-2-9701614-0-0

lower than of line no. 1 (Ra = 13.64 ± 1.29 µm [Rz = 91.55 ± 9.95 µm]). Because the material region around line no. 1 is milled in the last cut, the reason for higher roughness is related to more intense vibrations enabled by previous material removal and the resulting loss of stiffness in these areas.

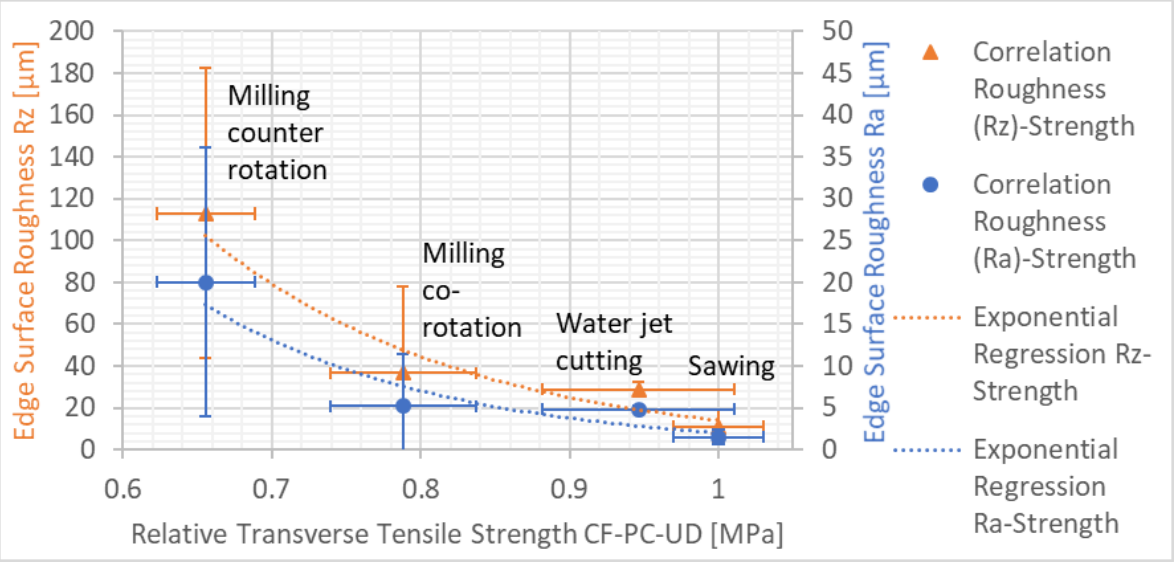

Figure 4. Correlation of specimen's edge surface roughness and transverse tensile strength (relative) of CF-PC-UD

By comparing almost equal average roughness values of milling in co-rotation (Ra = 5.21 ± 6.28 µm [Rz = 36.65 ± 41.03 µm]) and water jet cutting (Ra = 4.83 ± 0.38 µm [Rz = 28.88 ± 3.52 µm]) in figure 4, it becomes clear that the surface homogeneity (standard deviation) plays an important role in terms of tensile strength estimation. The relative strength of the water jet cut specimens (0.95) is higher than the value of the specimens milled in co-rotation (0.79). Therefore, the regions with highest roughness values on a specimen surface act as notches and define the maximum transverse tensile strength.

Figure 5 shows exemplary material ratio curves of each manufacturing procedure in the pictures of the bottom row. The black dot indicates the turning point of each curve and the orange marked region the region of the gradient calculation.

With a higher roughness of the profile the absolute value of the gradient decreases in figure 5. Plotting the average gradients of every manufacturing procedure shows a positive correlation of the gradient with the measured mean value of the transverse tensile strength (see figure 6). In comparison of the gradient in figure 6 and the roughness values in figure 4, an inverse tendency is visible but with the same result. Only the average gradient of milling in co-rotation seems to be an outlier in figure 6. But taking the standard deviation into account, as mentioned before, the result is plausible indicating the high potential of specimen manufacturing by milling in case of a homogenous manufacturing result. Therefore, the gradient of the material ratio curve seems to be a more sensitive value regarding the valuation of the surface roughness and its homogeneity.

  doi:10.5075/epfl-298799_978-2-9701614-0-0 published under CC BY-NC 4.0 license

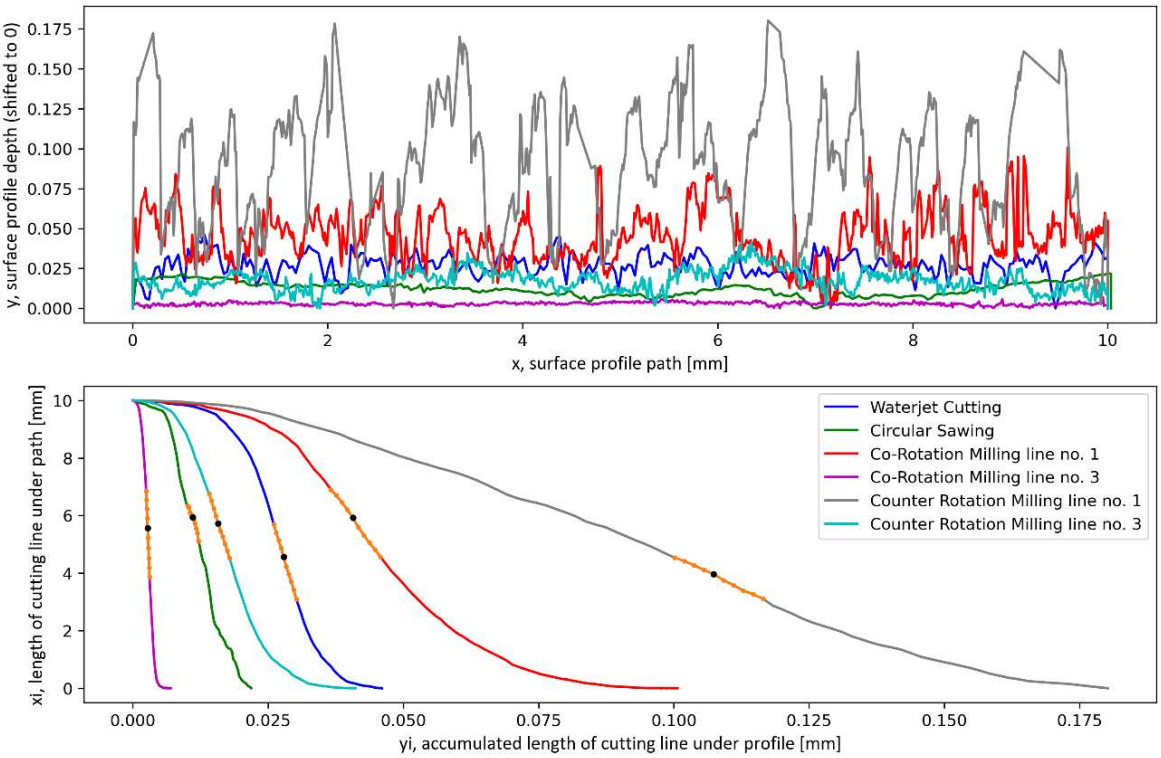

Figure 5. Exemplary surface roughness profiles (top) and associated material ratio curves (bottom) with turning point (black) and gradient derivation region (orange)

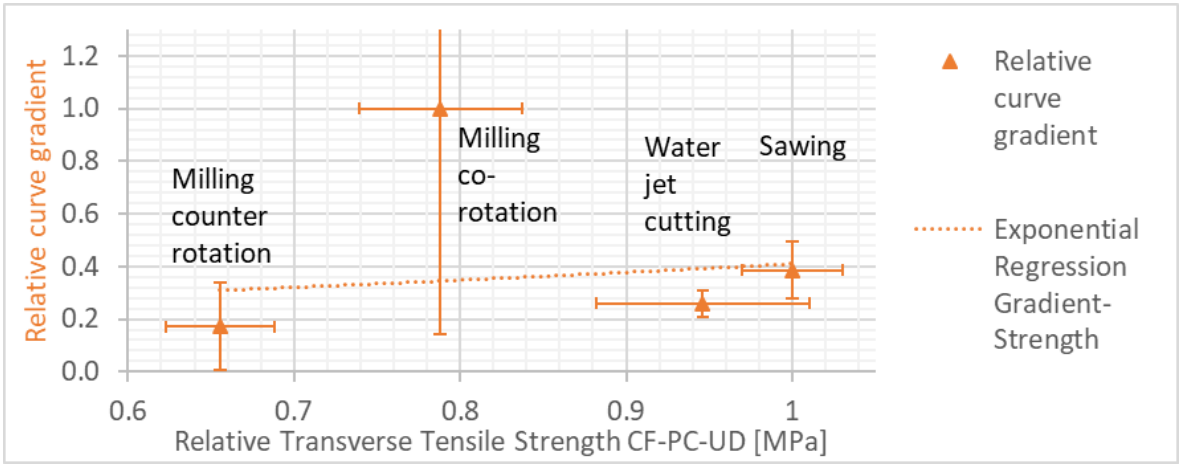

Figure 6. Correlation of curve gradient and transverse tensile strength of CF-PC-UD (relative values)

6. Summary and conclusion

The correlation of the tensile strength and surface roughness shows with increasing roughness values (Rz x 10) a tensile stress decrease of up to 34.5 %. In terms of machining CF-PC-UD perpendicular to fiber direction, a surface roughness of Ra ≤ 5 µm (Rz ≤ 30 µm) is recommended. In addition to the average surface roughness, the standard deviation of all measurements along the specimens' edges is an important indicator of a homogeneous machining result and has to be minimized to reach significant test data. It could be shown that the material curve ratio's

  doi:10.5075/epfl-298799_978-2-9701614-0-0

gradient around the curve's turning point sensitively indicates the surface roughness of a profile in addition to Ra and Rz values.

Acknowledgements

This research is part of the project „Chara-TPC – Establishing a material characterization center for thermoplastic composites (TPC) in Rhineland-Palatinate", funded by the European Regional Development Fund (ERDF) and the Ministry of Economics, Transport, Agriculture, and Viticulture (MWVLW; Funding reference: 84005413).

7. References

[1] Alshammari BA, Alsuhybani MS, Almushaikeh AM, Alotaibi BM, Alenad AM, Alqahtani NB et al. Comprehensive Review of the Properties and Modifications of Carbon Fiber-Reinforced Thermoplastic Composites. Polymers (Basel) 2021;13(15).

[2] Premium AEROTEC. Premium AEROTEC zeigt Zukunftspotenzial von CFK mit thermoplastischer Matrix: Weltweit erster Demonstrator für A320-Druckkalotte steht im Mittelpunkt des ILA-Auftritts.

[3] ElringKlinger AG. ElringKlinger erhält Großserienauftrag für ein globales LeichtbauProjekt; 2016.

[4] Abrate S, Walton DA. Machining of composite materials. Part I: Traditional methods. Composites Manufacturing 1992;3(2):75–83.

[5] Zemann R, Sacherl J, Hake W, Bleicher F. New Measurement Processes to Define the Quality of Machined Fibre Reinforced Polymers. Procedia Engineering 2015;100:636–45.

[6] Erturk AT, Vatansever F, Yarar E, Guven EA, Sinmazcelik T. Effects of cutting temperature and process optimization in drilling of GFRP composites. Journal of Composite Materials 2021;55(2):235–49.

[7] Liu D, Tang Y, Cong WL. A review of mechanical drilling for composite laminates. Composite Structures 2012;94(4):1265–79.

[8] Gordon S, Hillery MT. A review of the cutting of composite materials. Proceedings of the Institution of Mechanical Engineers, Part L: Journal of Materials: Design and Applications 2003;217(1):35–45.

[9] Teti R. Machining of Composite Materials. CIRP Annals 2002;51(2):611–34.

[10] Abrate S, Walton D. Machining of composite materials. Part II: Non-traditional methods. Composites Manufacturing 1992;3(2):85–94.

[11] Alberdi A, Artaza T, Suárez A, Rivero A, Girot F. An experimental study on abrasive waterjet cutting of CFRP/Ti6Al4V stacks for drilling operations. Int J Adv Manuf Technol 2016;86(1-4):691–704.

[12] Alberdi A, Suárez A, Artaza T, Escobar-Palafox GA, Ridgway K. Composite Cutting with Abrasive Water Jet. Procedia Engineering 2013;63:421–9.

[13] Lemma E, Chen L, Siores E, Wang J. Study of cutting fiber-reinforced composites by using abrasive water-jet with cutting head oscillation. Composite Structures 2002;57(1-4):297–303.

[14] Hintze W, Klingelhöller C, Langhof O. Curved sawing of thin lightweight components. Prod. Eng. Res. Devel. 2015;9(1):51–9.

  doi:10.5075/epfl-298799_978-2-9701614-0-0 published under CC BY-NC 4.0 license

[15] Staehr R, Bluemel S, Jaeschke P, Suttmann O, Overmeyer L. Laser cutting of composites—Two approaches toward an industrial establishment. Journal of Laser Applications 2016;28(2):22203.
[16] Davies A, Foreman A, Shaw R, Sims G. Measurement Good Practice Guide No. 38: Fibre Reinforced Plastic Composites – Machining of Composites and Specimen Preparation; 2001.
[17] Bleicher F, Zemann R, Sacherl J, Hake W. Fibrecut Benchmark 2014, Technische Universität Wien; 2015.
[18] Bleicher F, Zemann R, Sacherl J, Hake W. Fibrecut Benchmark 2013, Technische Universität Wien; 2014.
[19] Finkeldei D, Wiesinger G, Bleicher F, Ott F, Hager H, Smuda P et al. Workshop zum 3. Benchmark: Results of the 3rd FiberCut Benchmark; 2018.
[20] DIN Deutsches Institut für Normung e.V. Plastics - Preparation of test specimens by machining(DIN EN ISO 2818: 1996). Berlin: Beuth Verlag GmbH; 1997.
[21] DIN Deutsches Institut für Normung e.V. Part 5: Test conditions for unidirectional fibre-reinforced plastic composites(DIN EN ISO 527-5:2009-10). Berlin: Beuth Verlag GmbH; 2010.
[22] ASTM International. Standard Test Method for Tensile Properties of Polymer Matrix Composite Materials(ASTM D 3039/D 3039M – 00). West Conshohocken: ASTM International; 2002.
[23] Haddad M, Zitoune R, Eyma F, Castanié B. Influence of Machining Process and Machining Induced Surface Roughness on Mechanical Properties of Continuous Fiber Composites. Exp Mech 2015;55(3):519–28.
[24] Kammler M. Untersuchung zu spanenden und abtragenden Bearbeitungsverfahren von Faser-Thermoplast-Verbund Plattenmaterial zur Herstellung von Flachprobekörpern für die Materialcharakterisierung. IVW-Report: Student work, TU Kaiserslautern; 2021.
[25] Roy T. Blunt. White Light Interferometry – a production worthy technique for measuring surface roughness on semiconductor wafers. In: Proceedings of CS MANTECH Conference, Vancouver, Canada; 2006.
[26] DIN Deutsches Institut für Normung e.V. Geometrische Produktspezifikation (GPS) – Oberflächenbeschaffenheit: Flächenhaft – Teil 604: Merkmale von berührungslos messenden Geräten (Weißlicht-Interferometrie)(DIN EN ISO 25178-604:2013). Berlin: Beuth Verlag GmbH; 2013.
[27] DIN Deutsches Institut für Normung e.V. Geometrische Produktspezifikation (GPS) – Oberflächenbeschaffenheit: Tastschnittverfahren – Benennungen, Definitionen und Kenngrößen der Oberflächenbeschaffenheit(DIN EN ISO 4287:2010-07). Berlin: Beuth Verlag GmbH; 2010.

  doi:10.5075/epfl-298799_978-2-9701614-0-0

AUTOMATED MULTI-NDT METHOD

Jules, Recolin[a], Oriane, Fedrigo[b], Romain, Hodé[c], Guillaume, Pors[d]

a: CETIM (Centre Technique des industries mécaniques) – jules.recolin@cetim.fr
b: CETIM (Centre Technique des industries mécaniques)
c: CETIM (Centre Technique des industries mécaniques)
d: CETIM (Centre Technique des industries mécaniques)

Abstract: *This paper deals with the operating principle of a multi-NDT test bench aimed at automatically test wind turbine blade sections. This bench uses two NDT methods, infrared thermography (IRT) which is a global method and phased array ultrasonic (UTPA) which is a volumic method. The interest of using UTPA than conventional ultrasonic testing (UT) is to cover more surface for a single line of scan. This allows shorter scans durations.*

Concerning the test course, the IRT method aims first to detect suspicious areas and UTPA comes next for sanctioning the indications previously detected. This way, the test cycle is shorter than a classic robotized UTPA scan and offers more precision in sizing defects than only an IRT method. This project follows on tests carried out manually in 2019 at CETIM.

Keywords: Non-Destructive Testing; Automation; Infrared thermography; Ultrasonic phased array

1 Introduction

The CETIM developed an innovative solution for testing sections of wind turbine blades. the solution includes automated and robotized methods and is based on the communications between acquisition stations. The goal of this bench is to demonstrate CETIM's know-how, to propose innovative solutions to contributors, but also to increase its competences on the subject. In this sense a multi-NDT test bench designed at automatically check wind turbine blade sections has been developed. The test will be done first by infrared thermography (IRT) and then will be completed by UTPA. the interest of the IRT method is to allow short acquisition time for large tested surfaces. However, it could be difficult to size defects well. In this sense, UT requires longer time of acquisition for large areas but allows a better sizing. By combining these two methods and using their benefits, the test of a part should be less time consuming without sacrificing the quality of the test. This project follows on from tests carried out manually in 2019 at the CETIM.

2 Presentation of the inspection process and of the bench's set-up

2.1 Bench's scenario

To set-up the bench, it is first necessary to define the global inspection process. Thus, the physical set-up of the test bench and the definition of a global scenario of the demonstration have been created. The demonstration is done in two steps. First, an IRT acquisition is

  doi:10.5075/epfl-298799_978-2-9701614-0-0

performed allowing the detection of suspect areas. In a second time, robotized UT scans are performed based on the information of IRT detection. Finally, an automated sanction is done based on alarms generated by the UT acquisition system.

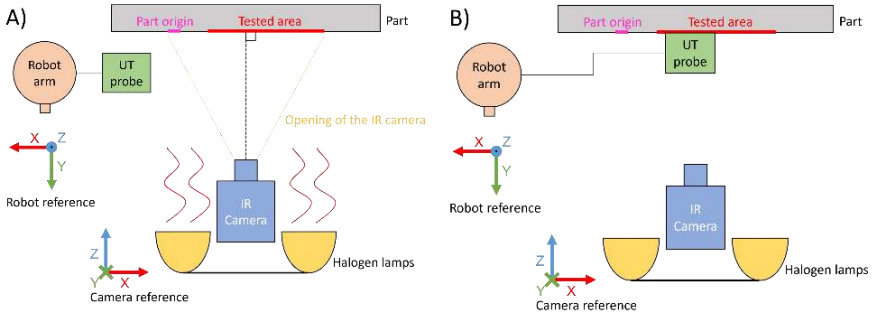

Figure 1. Test bench course, A) Halogens heat the part and an IRT acquisition is performed, B) the UT acquisition system mounted on the robot arm scans the suspicious areas detected previously by IRT allowing the sanction of the part

2.2 Data flows

Until the goals, the global course and the measurement setups defined, flows and types of information transiting through the system has been defined. The informations are communicated by the different inputs and outputs available on the following devices:

- Robot controller
- Control system and software of the IRT acquisition station
- UT acquisition station and its attached software

The bench can be modelled by a set of nodes exchanging data flows. A representation of these flows is shown below.

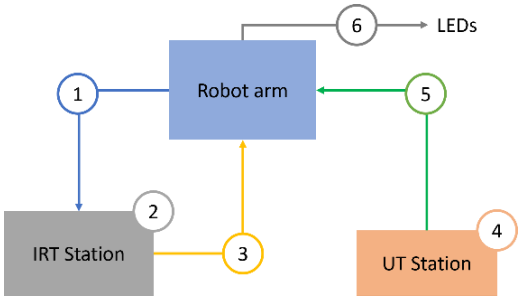

Step	Function	Information
1	Start trigger	Transistor-Transistor Logic (TTL) link used to start a test cycle
2	IRT acquisition	Recording and processing images of the part heat
3	Suspect area information	Ethernet link used to pass position, size, and scale of the detected suspect areas
4	UT acquisition	Scan of the suspicious areas by UTPA

  doi:10.5075/epfl-298799_978-2-9701614-0-0

5	UT alarms	TTL link used to inform the robot if an indication is detected
6	Sanction	TTL links used to inform the operator of the test result

Figure 2. Data flows and course of a testing cycle

One of the interesting developments of the bench concern the detection and transmission of suspect areas. An automatic treatment has been set up in this sense using the available plugin of the IRT acquisition software. This detection is based on the phase values of the fast Fourier transform (FFT) of the IRT acquisition and allows the creation of polygons around each suspicious area.

Then, for each suspect zone which has been detected, extreme coordinates are extracted. these values allow to determine an area to be scanned characterized by an origin, a height, and a length. The resulting of this treatment is a batch of areas parameters ready to be used by the robot (cf step 1 and 2, fig.3).

This batch is then sent to the robot via TCP/IP and a linear scanning path is created. It is characterized by a start scan point relative to a start position of the robot and a length following the X axis (cf step 3, fig.3).

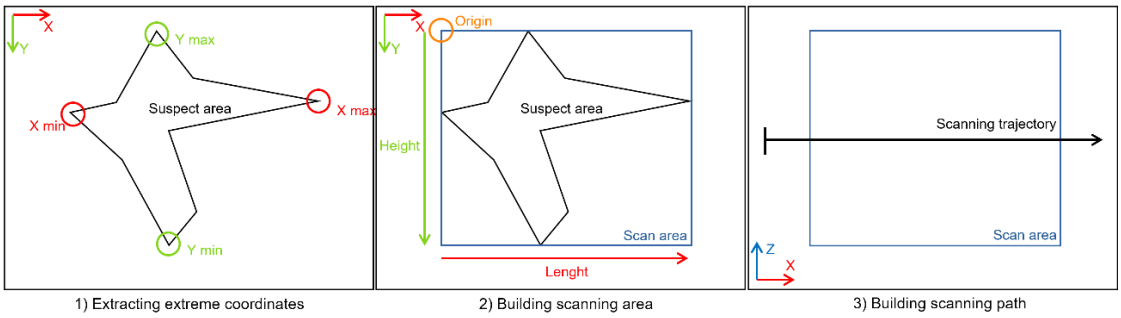

Figure 3. Suspect area treatment

The created path is defined as:

$$RobotStartPosition\begin{pmatrix} X0 \\ Y0 \\ Z0 \end{pmatrix}$$

$$DefectOrigin\begin{pmatrix} OriginX \\ OriginY \end{pmatrix}$$

$$StartScan\begin{pmatrix} X \\ Y \\ Z \end{pmatrix} = \begin{pmatrix} X0 - OriginX * ScaleFactor + WedgeWidth \\ Y0 \\ (\frac{1}{2} HeightScanArea - OriginY) * ScaleFactor \end{pmatrix}$$

$$ScanLength = LenghtScanArea * ScaleFactor + 2\,WedgeWidth$$

A scaling factor is applied to the calculated values to correct the gap between the dimensions of areas on the IRT image and the real ones. This scaling operation is done by measuring a standard distance on the IRT image (pixels) and physically (millimeters).

  doi:10.5075/epfl-298799_978-2-9701614-0-0 published under CC BY-NC 4.0 license

This type of scanning path work on the tested part. Indeed, the indications are about circular and as high as the length of the probe active surface. Hence, the entire indications are scanned. For bigger indications, it could be interesting to set up a slotted scan path.

3 Application case

Following the developments, trial have been carried out on a sample part.

3.1 Tested part

The part is a section of a wind turbine blade canopy on which is bonded a spare box. the bonding zone contains artificial defects detectable by IRT and UT. The test is done on the area of 118x365 mm noted fig 4.

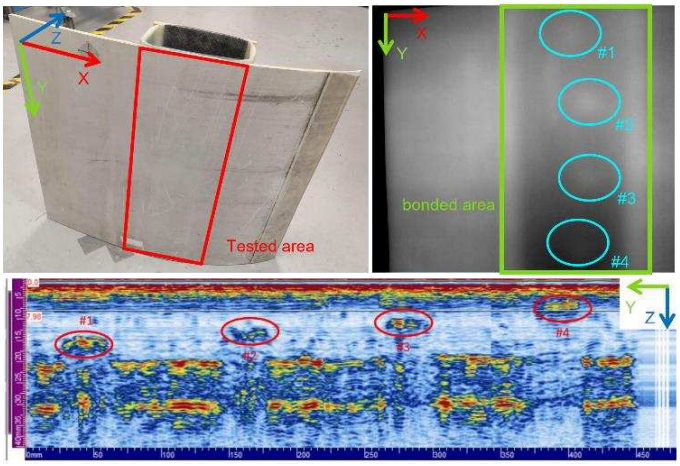

Figure 4. Used part sample

Some interesting information is to be noted before presenting results. This part composed of glass fiber and glue which are low heat conductor, the time of acquisition must be long. To shorten the IRT cycle, only the two defects cooler to the surface are considered (#3 and #4).

3.2 Results

As expected, two suspect areas have been detected by IRT (Fig.5). the scans areas and the resulting scan paths have been realized by the robot. The resulting B-Scans are given in Fig.5.

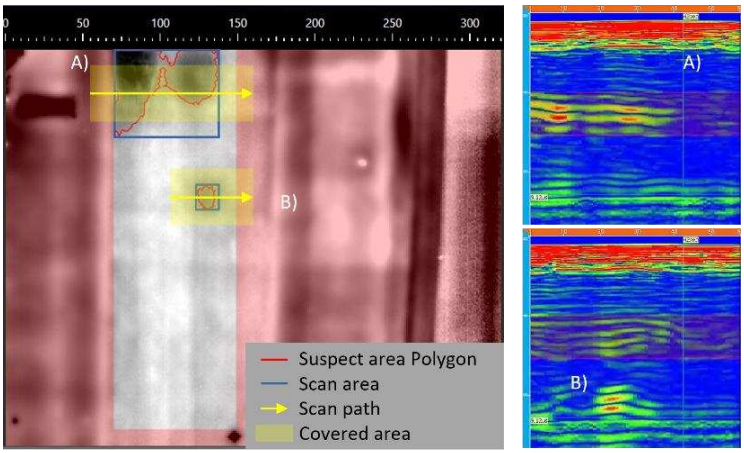

  doi:10.5075/epfl-298799_978-2-9701614-0-0 published under CC BY-NC 4.0 license

Figure 5. IRT (left) and UT (right) acquisitions results

On the automated acquisition (presented in Fig.5), a noisy area which is corresponding to the reflexion of the halogens lamps during the heat is considered. The UTPA scan remove the doubt on this area during the robot scan, but it has for consequence to decentering scan so the A) covered areas is not as extensive as the defect.

3.3 Efficiency of the system

During trials it seems that IRT acquisitions are much longer than UTPA scans. To quantify the performances of the system, it has been compared to theorical estimations of the time of acquisition for a classic slotten robot scan. Following scans parameters have been considered.

Designation	Parameter
Speed	16.7 mm/s
Acceleration	1200 mm/s²
Step	57.5 mm
Scanned area	118x365 mm
Multi-NDT method duration	300 s (defects free)

The results of this comparison are given in Fig.6. The X and Y axes represent dimensions of a given scanned area and the color bar corresponds to the time of acquisition for a classic scan a. Theorical time of scan for the actual scanned area of 118x365 mm is 70.3 s. The time for the multi-NDT method being 300 s, it means that it isn't efficient to apply this method on this area compared to a classic robotized scan. For these parameters of scan, the multi-NDT method could be efficient if a classic scan is longer than 300 s. Graphically it means that the part dimensions must be above the red curve. For this case the balanced dimensions are equivalent to a square with sides of 505 mm length.

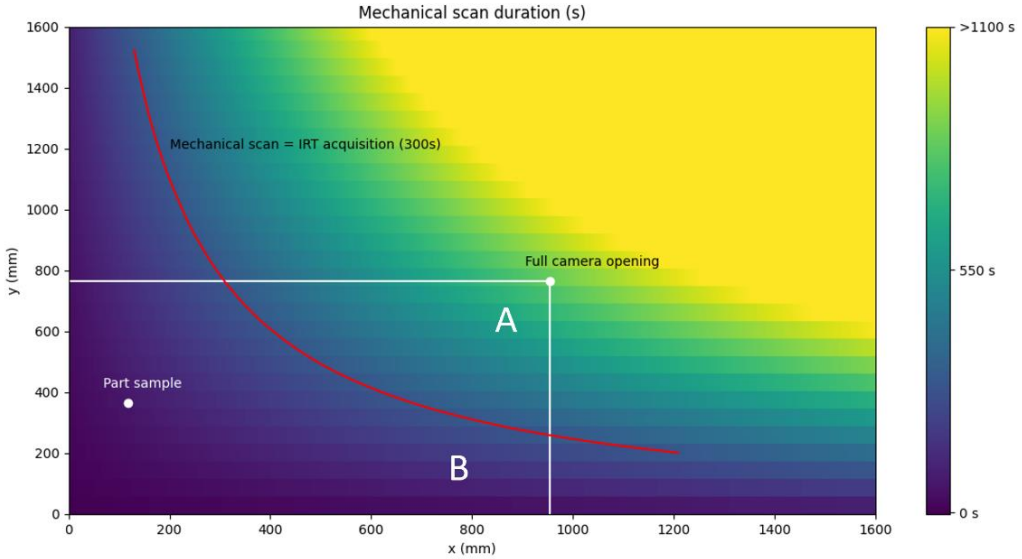

  doi:10.5075/epfl-298799_978-2-9701614-0-0

Figure 6. Efficiency of the system, A) Dimensions of the tested area for which the multi-NDT method being more efficient than a classic UT scan and included in the full camera opening in experimental conditions, B) Dimensions of the tested part for which the multi-NDT method being less efficient than a classic UT scan and included in the full camera opening in experimental conditions

In fig.6, the A) area which is delimited by the balance curve and limits of full IRT camera aperture corresponding to the dimensions of the tested area for which the multi-NDT method in experimental conditions being more efficient than a classic UT scan. Inversely, the B) area is corresponding to dimensions of the tested part for which the multi-NDT method in experimental conditions being less efficient than a classic UT scan. The B) area is 76.2 % of the full camera opening area. This result mean that, in experimental conditions, the tested area must take up to 76.2 % of the full camera covered surface to be efficiently tested by the multi-NDT method.

The efficiency determination doesn't take account the defects present in the part. Testing one suspect area with the multi-NDT method takes about 10 s. For more precision, the defect occurrence frequency and their mean length must be known.

This analysis is exclusively applicable for the tested part in experimental conditions. New estimations must be done if the multi-NDT method is applied to a new type of part.

4 Conclusion

The bench is operational for proof of concept. The communications are efficient, and trial have been carried out. Searched defects are found and UTPA scans are made on suspicious locations allowing sizing and automated sanctions of the indications. However, the method isn't performant for the actual used part. Indeed, the time for the IRT acquisition is too long for show. In addition, the part must cool for few minutes after every cycle before launching a new one. One easy way to overpass this issue is to use a metallic part or a thin one to allow short acquisition and cooling time. The use of parts including larger areas to test could also lead to a better efficiency of the method. However, this way, indications could have a worse resolution and uncertainties on suspicious areas locations and lengths could be higher.

5 References

1. Qualification du contrôle par ultrasons multiéléments et thermographie IR de pâles d'éoliennes ; Oriane FEDRIGO, Guillaume PORS, Nicolas TERRIEN; 2019

  doi:10.5075/epfl-298799_978-2-9701614-0-0

EFFECT OF AERONAUTIC FLUID SKYDROL ON NEAT POLY(ETHER KETONE KETONE) AND ITS CARBON FIBER REINFORCED COMPOSITE

Gwladys, Lesimple[a], Bruno, Fayolle[a], Stéphane, Bizet[b],
Thibaut, Benethuiliere[c], Ilias, Iliopoulos[a]

a: Laboratoire PIMM, Arts et Metiers Institute of Technology, CNRS, Cnam, HESAM Universite,
151 boulevard de l'Hopital, 75013 Paris (France) – gwladys.lesimple@ensam.eu
b: Arkema, CERDATO, 27470 Serquigny, France
c: Hexcel Reinforcements, 38630 Les Avenières, France

Abstract: *High performance thermoplastics such as poly(ether ketone ketone) are currently under development to replace thermoset matrices in composite parts of aircrafts. These composites are likely to be exposed to aggressive environments during their use phase. In this study, the effect of an aeronautical hydraulic fluid (Skydrol) is investigated by immersion of neat PEKK and carbon fiber reinforced PEKK (C/PEKK) in the fluid. Gravimetric measurements show no saturation plateau after 8000h immersion of neat PEKK. The effect of layup sequence of the composite is considered. Anomalous fluid sorption is observed in non-unidirectional composite. Tensile testing performed on neat PEKK shows very low degradation in mechanical properties after exposure to Skydrol.*

Keywords: PEKK; composite; hydraulic fluid; ageing

1. Introduction

High performances thermoplastics arouse interest to replace epoxy matrices in continuous carbon fiber composites for aeronautics. Contrary to thermoset resins, thermoplastic matrices have a long shelf life, allow welding of the composite parts and are recyclable. Poly(aryl ether ketone) (PAEK) is a family of high performance thermoplastics of which poly(ether ether ketone) (PEEK) has been extensively studied in the past 30 years (1–3). Another PAEK polymer, poly(ether ketone ketone) (PEKK) has gained in importance in recent years thanks to the possibility of modifying its melting temperature (T_m) while keeping a high glass transition temperature (T_g) (4,5).

During the use phase of the composite parts, the material can come into contact with different fluids necessary for the operation of the aircrafts such as water, fuel, de-icing, hydraulic fluid, etc. Hydraulic fluid is particularly aggressive for epoxy resins that are currently widely used as matrices in carbon fiber reinforced composites in the aeronautic field. Several studies showed the formation of chemical bonds between the epoxy resin and the hydraulic fluid which is usually composed of phosphate esters (6). Moreover, a study from Sugita et al. (7) on an epoxy adhesive and a C/epoxy composite shows that he adhesive absorbs around 180 wt% Skydrol after 555 days immersed in hydraulic fluid at 85°C. Immersion in hydraulic fluid at room temperature seems far less aggressive. The C/epoxy composite absorbs less than 1 w% and up to 3 wt% Skydrol at room temperature and 70°C respectively.

Stober et al. (8) showed very high resistance of neat PEEK to Skydrol with an uptake of ca. 1 wt% and complete reversibility of sorption. It is essential to understand the behavior of PEKK matrix

  doi:10.5075/epfl-298799_978-2-9701614-0-0

in hydraulic fluids before investigating the C/PEKK composite. The present study focuses on sorption behavior of neat PEKK as well as C/PEKK immersed in hydraulic fluid and the effect on mechanical properties.

2. Experimental

2.1 Materials

Neat PEKK plates were provided by Arkema with a T/I ratio of 70/30. The injected plates are used for gravimetric measurements and have a size of 10x10x2 mm^3. Composite laminates are made of unidirectional continuous carbon fibers (AS7) impregnated with PEKK 70/30, provided by Hexcel Reinforcements. Composite laminates of layup sequences $[0]_8$ and $[0/90]_{2s}$ (both consisted of 8 plies and referred as 'unidirectional' and 'cross-ply') are consolidated out of autoclave (*Figure 1*).

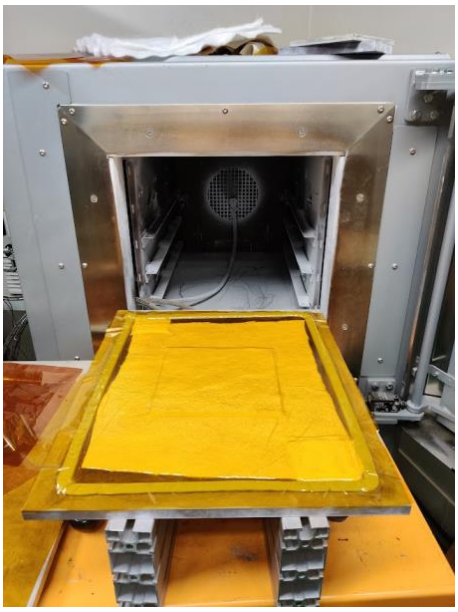

Figure 1. Oven used for out of autoclave consolidation of C/PEKK composite.

Samples of size 50x50 mm^2 are cut in the neat PEKK plates and composite laminates using a band saw and diamond saw respectively. The hydraulic fluid used in this study is Skydrol LD4, composed of different phosphate esters.

2.2 Gravimetric measurement

Neat PEKK and composites samples are dried in an oven at 120°C during 48 hours and crystallized at 200°C during 4 hours prior to Skydrol immersion. The samples are immersed in Skydrol at 70°C, in sealed glass jars placed in a temperature-controlled water bath. The samples are regularly surface-dried with paper towel and weighed using a Mettler Toledo analytical balance. The weight uptake is measured using the following equation:

$$w(t) = \frac{m(t) - m_0}{m_0} \quad (1)$$

  doi:10.5075/epfl-298799_978-2-9701614-0-0

With *m(t)* the mass of the sample at time *t* and m_0 the initial mass of the dried sample. The mean weight uptake is averaged on four samples and two samples for neat PEKK and C/PEKK respectively.

2.3 Tensile testing

Tensile tests are performed on neat PEKK 7002 (ISO 527 1BA 2 mm-thick specimens) before (referred as 'dry') and after ageing in Skydrol. The specimens are immersed in Skydrol at 70°C in sealed glass jars as for gravimetric samples. Poly(tetrafluoroethylene) holders allow maintaining the samples vertically. Tensile tests are carried out using an Intron 5966 machine at 1 mm/min.

2.4 X-ray tomography

X-ray microtomography imaging is carried out on the Anatomix beamline at Synchrotron SOLEIL (9). The samples are cut in the thickness of the C/PEKK composites using a diamond wire saw to a size of 2x2x5 mm^3. Two volumes corresponding to a cylinder of diameter 1.3 mm and height 1.3 mm have been investigated in each sample at different locations.

3. Results and discussion

3.1 Skydrol sorption in neat PEKK

Weight uptake of neat PEKK immersed in Skydrol at 70°C shows a constant increase during the first 300 days of exposure (*Figure 2*). A maximum is observed at this point corresponding to a weight uptake of 0.28 ± 0.01 wt% with no saturation plateau. As the exposure is still in progress, no conclusion will be made at this point on the existence of a plateau.

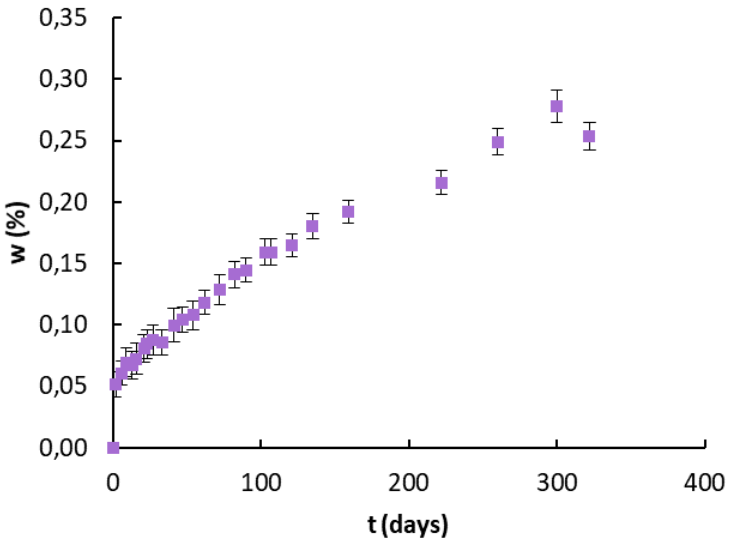

Figure 2. Weight uptake of neat PEKK as a function of immersion time in Skydrol at 70°C.

  doi:10.5075/epfl-298799_978-2-9701614-0-0

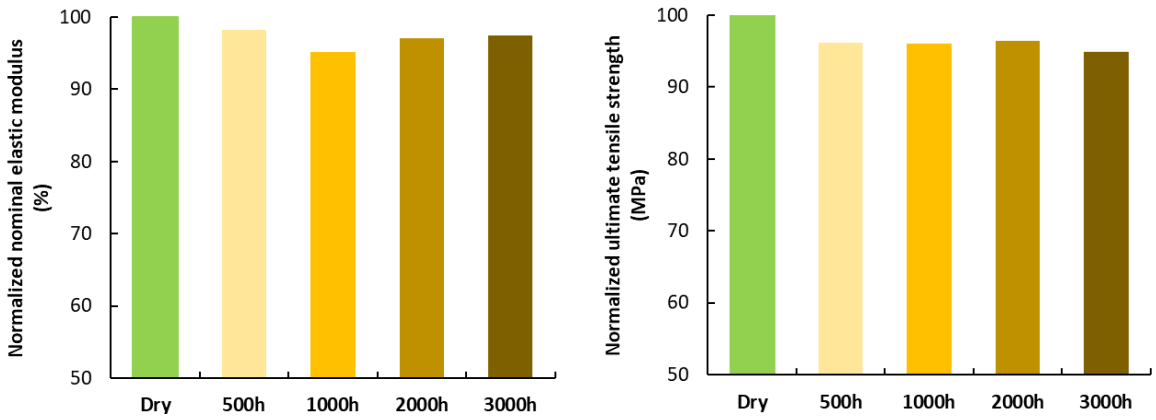

Figure 3. Elastic modulus and ultimate tensile strength of neat PEKK before and after exposure to Skydrol at 70°C.

Tensile tests performed on neat PEKK exposed to Skydrol at 70°C show very low decrease in elastic modulus (-3%) and ultimate tensile strength (-5%) after 3000 hours of exposure (*Figure 3*). These results are consistent with the low absorption of Skydrol (0.17 wt%). Thus, Skydrol do not seem to degrade neat PEKK after 3000 hours of immersion.

3.2 Skydrol sorption in C/PEKK

Exposure of C/PEKK unidirectional and cross-ply ($[0/90]_{2s}$) composite to Skydrol at 70°C show very different behaviors in terms of weight uptake (*Figure 4*). Unidirectional composite absorbs almost no Skydrol, corresponding to the quantity of fluid absorbed by neat PEKK. Nevertheless, cross-ply composite part absorbs around ten times more Skydrol than unidirectional layup.

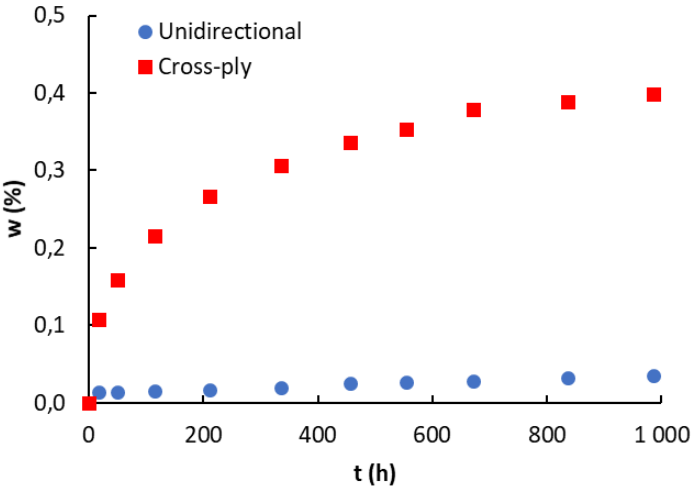

Figure 4. Weight uptake of unidirectional and cross-ply composite *C/PEKK as a function of immersion time in Skydrol at 70°C.*

Fluid sorption in composite is a complex mechanism, taking into account different phases of the material such as the matrix, the fibers, the interface between matrix and fibers, possible voids, etc. Our previous results show low fluid sorption in neat PEKK. We can assume that carbon fibers do not absorb fluid. As the unidirectional C/PEKK absorbs low amounts of Skydrol as observed in neat PEKK, the interface between matrix and fibers does not seem to be a preferential site for

  doi:10.5075/epfl-298799_978-2-9701614-0-0

fluid sorption. Finally, a hypothesis would be that cross-ply C/PEKK has a non-negligible, although low, void content that Skydrol can penetrate and fill in.

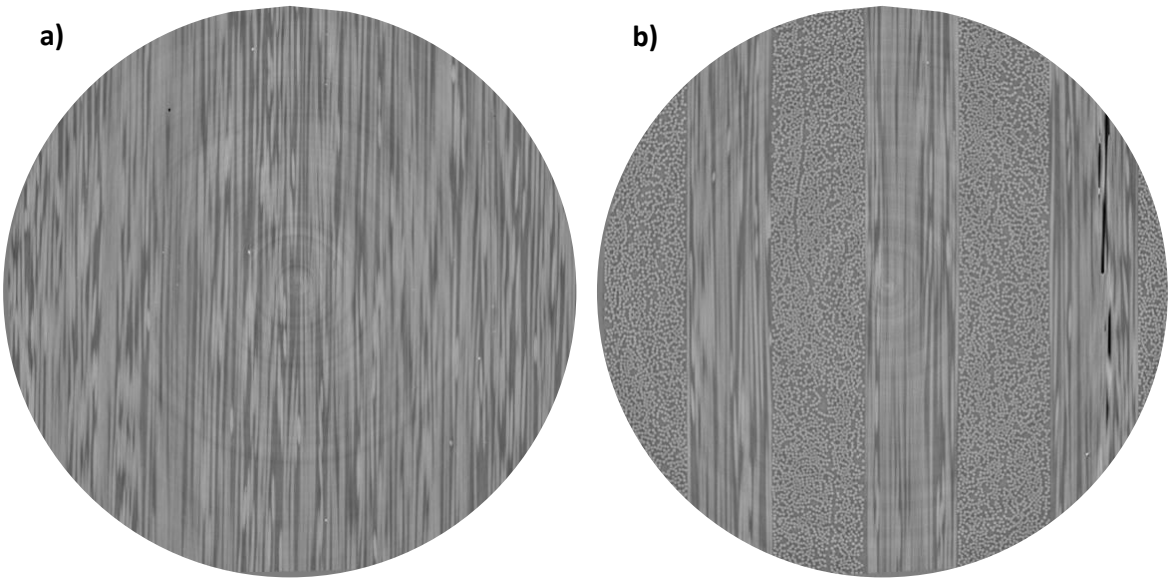

Figure 5. X-ray tomography imaging of C/PEKK (a) unidirectional and (b) cross-ply laminates.

X-ray tomography confirms the negligible porosity content in unidirectional C/PEKK (*Figure 5*a.). Furthermore, cross-ply composite layup seems to hinder the filling of micro cavities with the molten resin during the consolidation process, resulting in some porous areas in the composite. X-ray tomography brings to light the high anisotropy of porosities which are located in the direction of fibers (*Figure 5*b.). Moreover, the distribution of cavities is particularly heterogeneous. As the Skydrol has a low surface tension (28.2 $mN.m^{-1}$ at 25°C), the fluid can easily fill in the micro cavities leading to an increase in weight uptake when the composite is fully immersed.

4. Conclusions

The present study focusses on the sorption of Skydrol by neat PEKK and C/PEKK composite by immersion in the fluid at 70°C. It has been shown that the diffusion of Skydrol in neat PEKK is very slow and that the weight uptake is lower than 0.30 wt% after 300 days. Mechanical properties of PEKK are preserved after 3000 hours. Immersion of unidirectional composite shows Skydrol uptake in the order of magnitude of the matrix capacity of sorption whereas cross-ply composite exhibit abnormally high weight uptake. X-ray tomography showed the presence of relatively porous areas in the cross-ply composite which constitute the main cause for such fluid uptake. Further investigation on C/PEKK mechanical properties are planned.

Acknowledgements

This work was conducted under the framework of HAICoPAS, a PSPC project (projet de recherche et développement structurant pour la compétitivité). BPI France is acknowledged for funding the PhD work of G. Lesimple (project number: PSPC.AAP-7.0_HAICoPAS). The authors thank Arkema, Hexcel for fruitful discussions and Industrial Chair Arkema (Arkema/CNTS-ENSAM-Cnam) for partial support. We acknowledge SOLEIL for provision of synchrotron radiation and we would like to thank Timm Weitkamp and Mario Scheel for assistance in using beamline

Anatomix (proposal no. 20210363). ANATOMIX is an Equipment of Excellence (EQUIPEX) funded by the Investments for the Future program of the French National Research Agency (ANR), project NanoimagesX, grant no. ANR-11-EQPX-0031.

5. References

1. Blundell DJ, Osborn BN. The morphology of poly(aryl-ether-ether-ketone). Polymer. 1983;24(8):953–8.
2. Courvoisier E, Bicaba Y, Colin X. Water absorption in PEEK and PEI matrices. Contribution to the understanding of water-polar group interactions. AIP Conf Proc. 2016;1736(1):020036.
3. Juska T. Effect of Water Immersion on Fiber/Matrix Adhesion in Thermoplastic Composites. J Thermoplast Compos Mater. 1993;6(4):256–74.
4. Gardner KH, Hsiao BS, Matheson RR, Wood BA. Structure, crystallization and morphology of poly (aryl ether ketone ketone). Polymer. 1992;33(12):2483–95.
5. Tencé-Girault S, Quibel J, Cherri A, Roland S, Fayolle B, Bizet S, et al. Quantitative Structural Study of Cold-Crystallized PEKK. ACS Appl Polym Mater. 2021;3(4):1795–808.
6. Buggy M, O'byrne K. The Effects of Skydrol (A Hydraulic Fluid) on the Curing of Tetraglycidyl 4,4'-Diaminodiphenyl Methane Diaminodiphenyl Sulfone-Based Resins. J Appl Polym Sci. 1996;62(11):1869–76.
7. Sugita Y, Winkelmann C, La Saponara V. Environmental and chemical degradation of carbon/epoxy lap joints for aerospace applications, and effects on their mechanical performance. Composites Science and Technology. 2010 May 1;70(5):829–39.
8. Stober EJ, Seferis JC, Keenan JD. Characterization and exposure of polyetheretherketone (PEEK) to fluid environments. Polymer. 1984;25(12):1845–52.
9. Weitkamp T, Scheel M, Giorgetta JL, Joyet V, Roux VL, Cauchon G, et al. The tomography beamline ANATOMIX at Synchrotron SOLEIL. J Phys: Conf Ser. 2017 Jun;849:012037.

  doi:10.5075/epfl-298799_978-2-9701614-0-0

BRAIDING CHARACTERISATION AND OPTIMISATION: COMPLEX GEOMETRIES

B.Grimes[1,2], M.Thompson[2], P.Giddings[1], N.A Warrior[2]

1: National Composites Centre, Bristol, UK – beth.grimes@nccuk.com
2: Composites Research Group, The University of Nottingham, Nottingham,UK

Abstract: *For simple prismatic geometries, such as cylinders, the addition of a twist to fibre tows at the pre-braiding, bobbin winding stage is seen to result in beneficial changes in the fibre architecture of a braided preform. This research considers the effects of braiding on a non-prismatic, frusto-conical cross-section by analysing the key process metrics of tow width, braid angle and braid thickness. The present study demonstrates that whilst some variabilities were observed, adding twist to fibre does not make a significant difference to braid architecture for non-prismatic geometries, but does reduce processing-induced tow damage and is therefore of benefit in improving the final part quality.*

Keywords: Braiding, twist, complex geometry

1. Introduction

Braid architecture simulations are built on generalised assumptions for the tow geometry[1]. This results in discrepancies between key process variables such as cover factor and braid thickness of the designed braid and manufactured preform.

Localised variations in braid architecture and process-induced tow damage are detrimental to the final quality of the manufactured preform. One of the ways tow widths can be influenced is by adding twist to the fibre during the rewinding stage of the process. Torun et al determined that increasing the number of twists reduces the tow diameter producing a more compact structure[2] and that a small number of additional twists offered favorable processability benefits.

It is well accepted that the tow rewinding stage of the braiding process is critical to resultant product quality[3]. State-of-the-art rewinding machines can control multiple parameters including rewinding speed, rewinding tension and tow twist to produce a high-quality bobbin package. Torun et al recommended no more than 10 twists per metre (Tpm) to reach a compromise between tow diameter and friction benefits for a 12K carbon fibre tow.

A geometrical cross-sectional change in the component has been shown to increase the level of variability in braid architecture, for example Du and Popper demonstrated an increase in preform uniformity when section gradient is converging [4]. The authors' previous work has demonstrated that the inclusion of an additional twist during the bobbin rewinding stage reduces braided tow geometry variability [5]. This present research builds on [5] by investigating the effects of fibre tow twist on the braid architecture of a component with changing cross section. The information in this study is aimed at improving the quality and performance of braided composites.

  doi:10.5075/epfl-298799_978-2-9701614-0-0

2. Methodology

2.1 Material Bobbin Rewinding

Standard modulus HST45 12K carbon fibre was wound using the CEZOMA VLS87 winding machine and accompanying Eurocarbon Twist Cabinet at the National Composites Centre (NCC). Three different sets of bobbins were wound with three different levels of twist: 0, 5 twists and 7 twists per metre (Tpm). The rewinding tension was maintained for each set of bobbins and the rewinding speed was constant at 1000 rpm. Anticlockwise bobbins were wound in an anticlockwise direction (or Z-twist) and clockwise bobbins were wound with a clockwise twist (S-twist) to produce a balanced braided preform.

2.2 Preform Manufacture

Two sizes or scales were considered. For the large-scale study, preforms were manufactured using the 192-carrier axial Eurocarbon braider at the NCC. For the small-scale study the preforms were manufactured on the 48-carrier Steeger braider at the UoN.

The fibres were braided onto a continuous axisymmetric mandrel incorporating two stages – a cylindrical section and a frusto-conical section with a transition angle of 10°. For the large-scale study nominal mandrel diameter was 200mm and maximum diameter 350mm, for the small-scale study 50mm and 87.5mm respectively. By switching the located end of the mandrel in the gantry, the transition therefore becomes either a converging (reducing) or diverging (increasing) cross-section. Manufacturing trials were completed with the mandrel in both orientations. The braiding machine was operated in a fully loaded configuration to create a biaxial braid with a regular braid pattern. The process parameters, carrier speed and take-up speed were varied to produce single layer preforms with a constant braid angle of 45°

In the large-scale study braids were single ply and in the small-scale study multi-ply preforms of four layers were manufactured.

2.3 Braid Architecture Measurement

An Apodius RS6 Scanner was used to measure the thickness of layers in the small-scale braided preforms.

Manual images and images taken using the in-process monitoring system at the NCC were used to monitor the characteristics of the braid architecture. Parameters such as braid angle and tow width were measured using image processing software ImageJ.

3. Results

The outputs from the investigation are summarised in the following section. The results highlight the importance of tow material preparation on the resulting fibre architecture of the braided preform.

3.1 Tow Width Variability

Tow widths for the constant, increasing or decreasing cross-sectional change are shown in Figure 1. The twisted fibre tows generally resulted in a smaller tow width than the untwisted tow (roughly 2mm compared to 3.5mm), with a significantly reduced variability (roughly ± 0.3mm

  doi:10.5075/epfl-298799_978-2-9701614-0-0

compared with more than ± 0.6 mm). No clear trends for the effects in cross section change were seen - differences between prismatic, diverging and converging sections were within the range of observed variability. The variability of the tow width leads to localised defects in the braid architecture, this results in irregularity in cover factor which in turn leads to inconsistent mechanical properties.

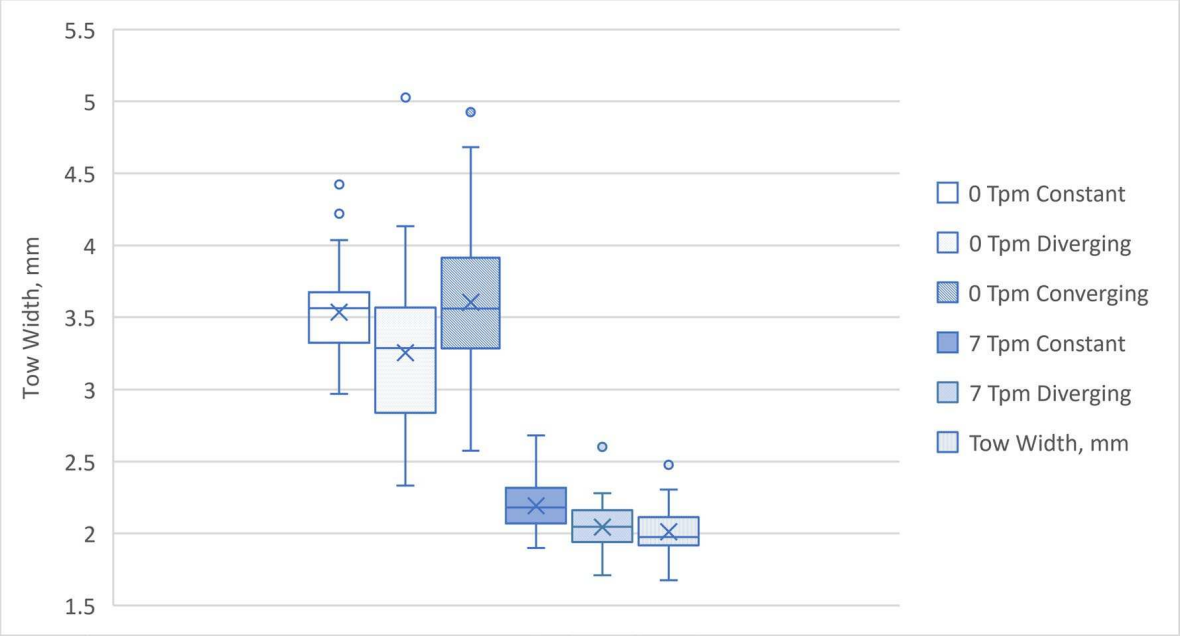

Figure 1 Tow width range for different cross-section changes

3.2 Braid Architecture Variability

Figure 2a and Figure 2b demonstrate the influence of the direction of transition, increasing or decreasing (2b) diameter on the braid angle (for the programmed constant braid angle of 45 degrees), where the yellow orange and red lines represent the converging cross-section and the three blue lines represent the diverging section and where the sloped section of the component is between 200-600mm of the axial length.

Figure 2a shows that for untwisted fibres, braiding on a diameter of decreasing, converging cross-section achieves a more consistent braid angle closer to the programmed braid angle, within ± 2 degree. The braid angle deviation for the diverging cross-sectional diameter was notably higher, reaching 4 degrees at its peak.

Figure 2b shows that for twisted fibres, braiding on a diameter of decreasing, converging cross-section also achieves a more consistent braid angle - within ± 1 degree of the programmed angle. For the diverging cross-section, the braid angle deviation was again higher, reaching 6 degrees.

A braid angle variation of ± 1 degree is generally perceived to be a tolerable range in aerospace manufacture.

  doi:10.5075/epfl-298799_978-2-9701614-0-0

(a)

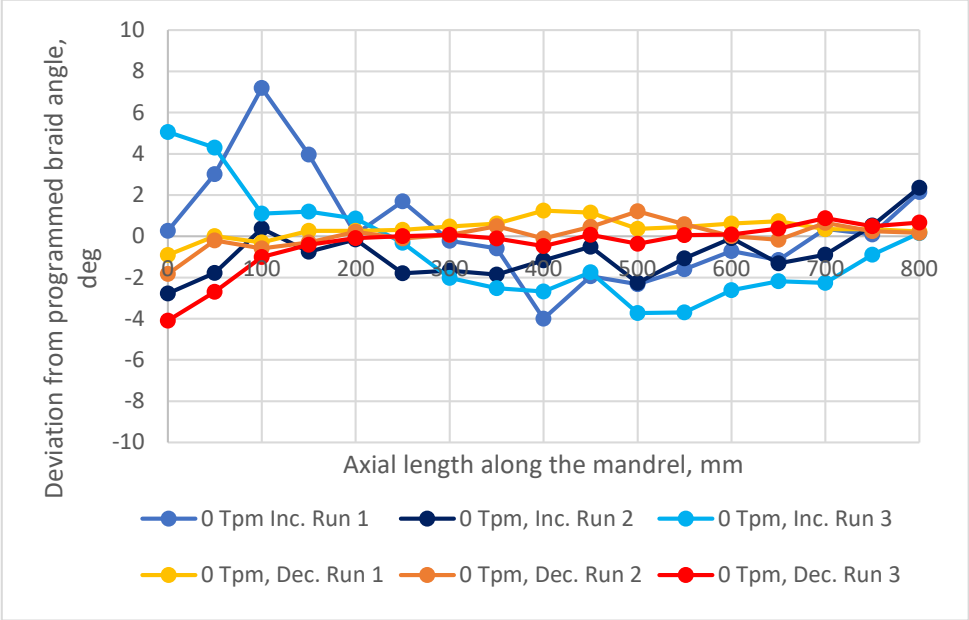

(b)

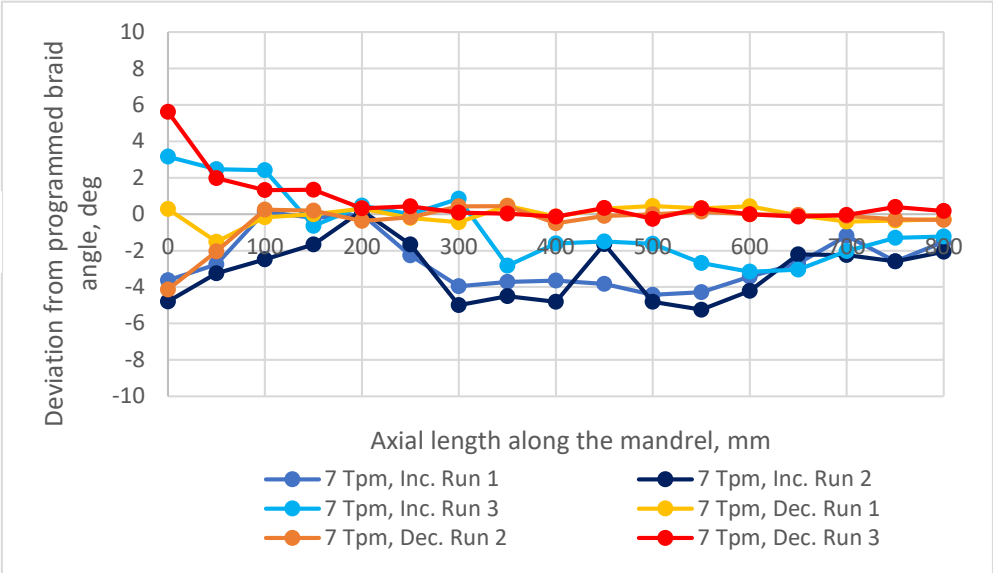

Figure 2 Deviation from programmed braid angle : (a) untwisted fibre tows, (b) twisted fibre tows

3.3 Layer Thickness

In the small-scale study, multi-ply preforms of four layers were manufactured. Table 1 shows the average layer thickness recorded for each layer. An increase in layer thickness was seen in the twisted preforms, 0.668 mm ± 0.067 compared to 0.570 mm ± 0.074 for the diverging transition and 0.689 mm ± 0.076 compared to 0.584 mm ± 0.141 for the converging sections. However, the overlap in standard deviation suggests that these differences were not statistically significant. The variability in layer thickness showed no difference for either the inclusion of a twist or the direction of the transition. The additional twist to fibres did not appear to influence the nesting of the subsequent layers with each additional layer in a 0.2-0.4 mm increase in preform thickness.

Table 1 Average layer thickness of braided preform

Number of Layers	0 Tpm Diverging	0 Tpm Converging	5 Tpm Diverging	5 Tpm Converging
1	0.570 ± 0.074	0.584 ± 0.141	0.668 ± 0.067	0.689 ± 0.076
2	0.813 ± 0.069	0.820 ± 0.087	1.017 ± 0.334	0.959 ± 0.108
3	1.213 ± 0.008	1.058 ± 0.096	1.386 ± 0.104	1.300 ± 0.065
4	1.430 ± 0.006	1.364 ± 0.104	1.700 ± 0.079	1.521 ± 0.035

3.4 Fibre Processability

Figure 3 shows examples of the accumulation of processing defects for the untwisted preform. The images highlight the visible fibre damage shown by the red boxes.

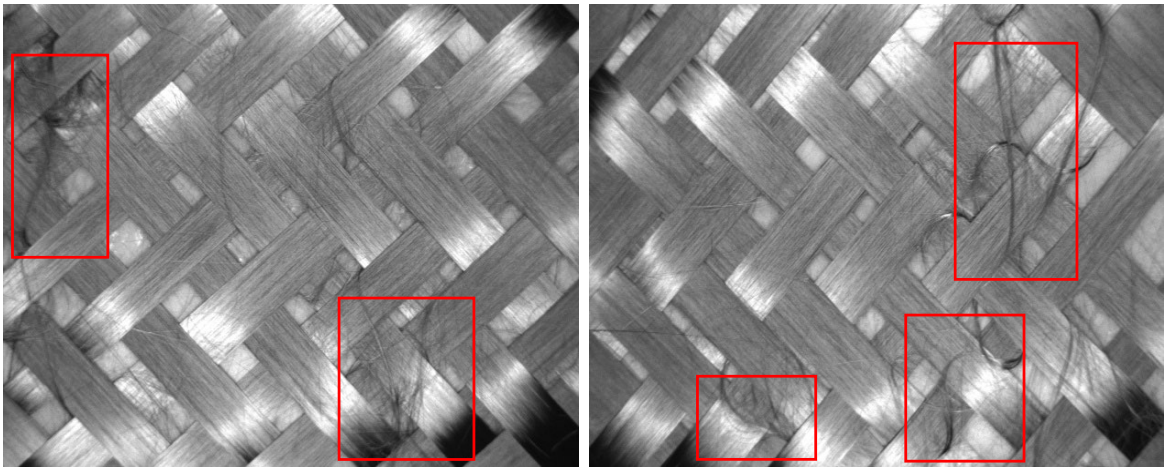

Figure 3 Images from the in-process monitoring system of untwisted preforms

Figure 4a and 4b shows a visual comparison of the impact of adding twist to carbon fibre tows. Figure 4a demonstrates the preform manufactured with 0 Tpm fibres and Figure 4b demonstrates the preform manufactured with twisted fibres. Greater visible damage such as filamentation and fibre breakage (fuzz) is noticeable in Figure 4a.

Figure 4 Images of the braided preforms (a) untwisted, (b) twisted

Figure 5 demonstrates a collection of images taken during the manufacturing process on the 192-carrier braider. Image (a) and (b) show significant levels of filamentation in the braid cone, (c) demonstrates the influence of inconsistent tension levels and (d) shows filamentation causing process interruptions. These filaments catch on the mechanisms of the machine which cause the level of fibre damage to escalate. This results in inconsistent tow tension which leads to tow breakages.

(a) (b) (c) (d)

Figure 5 Images of processability problems

4. Conclusions

This research investigates the influence of the addition of a twist to carbon fibres during the rewinding process and its resultant impact of the manufacture of a frusto-conical preform. Two different manufacturing set-ups were both considered: small scale (48-carrier) and large scale (192-carrier). Two different levels of twist were used in each configuration: 0 and 5 Tpm for the small-scale manufacture and 0 and 7 Tpm for the larger machine. Changes in tow width and braid angle were measured to analyse the variability of the braid architecture. The observations and the key points are outlined below summarised in terms of tow geometry, braid architecture variability and fibre processability.

- Tow Geometry:
  - Direction of the slope influenced the spread of the tow for the untwisted fibre. On a diverging cross-section change the tow width reduced and a converging cross-section changed the tow spread.
  - The tow width of the twisted tow remained constant for both straight and changing geometrical features.
  - Variability of the tow width increased for the untwisted fibres on the geometrical change in cross-section.
- Braid Architecture Variability:
  - Braiding on a converging cross-sectional change produced a more repeatable braid angle, close to the programmed value of 45 degrees.
  - The addition of twist to the fibres had no discernible impact on the braid angle of the preform.
- Layer Thickness:

  doi:10.5075/epfl-298799_978-2-9701614-0-0

  - The initial layer of the braid saw an increase in thickness with twisted fibres.
  - The direction of transition did not influence the magnitude or variability of the thickness of the braided preform.
- Fibre Processability:
  - Surface 'fuzz' caused by fibre filamentation during braiding was seen in the untwisted preforms, resulting in visible processing defects and a greater number of fibre breakages and entanglements.

Acknowledgements

This research work was supported by contributions from the National Composites Centre, the ESPRC Centre for Doctoral Training in Composites Manufacture (Grant EP/L015102/1) and the EPSRC Future Composites Manufacturing Research Hub (Grant EP/P006701/1).

References

1. J. H. Van Ravenhorst, "Design Tools for Circular Overbraiding of Complex Mandrels," Degree of Doctor Dissertation, University of Twente, 2018
2. Torun A, Hoffmann G, Mountasir A, Cherif C. Effect of twisting on mechanical properties of GF/PP commingled hybrid yarns and UD-composites. Journal of Applied Polymer Science. 2011;123(1):246-256
3. C. Ebel, M. Brand and K. Drechsler, "Effects of fiber damage on the efficiency of the braiding process," in *TexComp-11*, Leuven, Belgium, 2013.
4. Du GW, Popper P. Analysis of a Circular Braiding Process for Complex Shapes. J Text Inst [Internet]. 1994 [cited 2019 Jun 18];85(3):316–37. Available from: http://www.tandfonline.com/action/journalInformation?journalCode=tjti20.
5. Grimes B et al, The effect of twist on braid architecture and stability, SAMPE Europe 2021

  doi:10.5075/epfl-298799_978-2-9701614-0-0

EXPLICIT MODELLING OF MATRIX DAMAGE IN A LAMINATED COMPOSITE COMPARISON BETWEEN LINEAR FRACTURE MECHANIC AND COHESIVE ZONE MODEL

Jean, Vereecke[a], Christophe, Bois[a], Jean-Christophe[a], Wahl[a], Erwann, Le Goff[b], Florian, Lavelle[c]

a: Institut de Mécanique et d'Ingénierie (I2M), 15 rue de Naudet, 33175 Gradignan - jean.vereecke@u-bordeaux.fr
b: Structure composite, ArianeGroup, Saint-Médard-en-Jalles, France
c: Direction des Lanceurs, Centre National d'Études Spatiales (CNES) Paris, France

Abstract: *Permeability of carbon fiber reinforced polymer is strongly related to its damage state. In order to identify fracture properties on which cracking kinetics depend, we choose to combine experimental and virtual tests by modelling explicitly all transverse cracks. Two modelling tools are compared, the cohesive zone model (CZM) and finite fracture mechanics (FFM). Both models are based on a double criterion of energy and strength. Each potential crack is assigned a couple of material parameters (critical fracture energy, strength failure limit) derived from a probability distribution. The spatial distribution of parameter pairs follows the evolution of an experimental fiber volume rate to ensure the continuity of the mechanical properties along the sample.*

Keywords: Cohesive Zones; Fracture Mechanics; Cracking; Damage; Variability

1. Introduction

Recently, the use of carbon fiber composites for cryogenic propellant storage has been the subject of numerous studies for the development of reusable lightweight launchers. Without the presence of sealing liner, composite must ensure strength and permeability criteria itself. Feasibility studies have shown that intra-laminar cracking is inevitable and even favored by cryogenic conditions and by the pressurization of the tank. The accumulation of this type of damage is likely to generate leakage points long before the burst failure. The strong relationship between the permeability of a laminate and its transverse cracking rate has been demonstrated in the literature [1, 2]. The analysis and the prediction of transverse cracks network in laminated composite subjected to thermomechanical loadings are therefore of considerable interest for the design of liner-less composite tank.

Experimental approaches based on mechanical tests cannot allow alone to identify the cracking process of a composite laminate since this one come from a combination of many factors inherent to the material (microstructure heterogeneity, local defects), the laminate (ply thicknesses and orientations), stress due internal pressure and thermal residual stress [3]. Virtual tests consist in performing finite element simulations that consider the actual damage morphology within a representative cell of the material. Simulation can be used to evaluate the influence of the increasing damage on the elastic properties at upper scale through a homogenization method and further to build damage propagation laws.

The modeling of matrix damage such as transverse cracking can be done at several scales. At the microscopic scale, virtual test can be used to study the effect of the fiber arrangement, the interface strength or the matrix behaviour on the crack onset and propagation [4]. This approach

  doi:10.5075/epfl-298799_978-2-9701614-0-0

is relevant to study small volume cell with one or few cracks due to computation time. To study transverse cracks distribution in one ply or damage interaction between several plies, mesoscopic scale simulation is required. In such simulations, each ply is represented by homogeneous orthotropic properties. Nevertheless, the intrinsic variabilities of the material can be introduced throughout a large representative volume using graded properties for the material or discrete properties for potential cracks. Meso-scale damage mechanisms (transverse cracking, micro-delamination at crack tips) can be considered [5, 6, 7].

In this paper, we compare the responses of two explicit models of transverse cracking at the meso-scale. One uses the cohesive zone model (CZM), which is due to [8] and [9] and which is widely used in the literature to model the cracking mechanisms of composite materials. The other is based on finite fracture mechanics (FFM) [10, 17]. Both models work on the basis of a double energy-strength criterion [11]. This double criterion is illustrated in Fig. 1 thought the influence of ply thickness on the transverse cracking strain threshold. The cohesive zone method verifies sequentially: initiation and propagation, whereas the FFM verifies both criteria simultaneously.

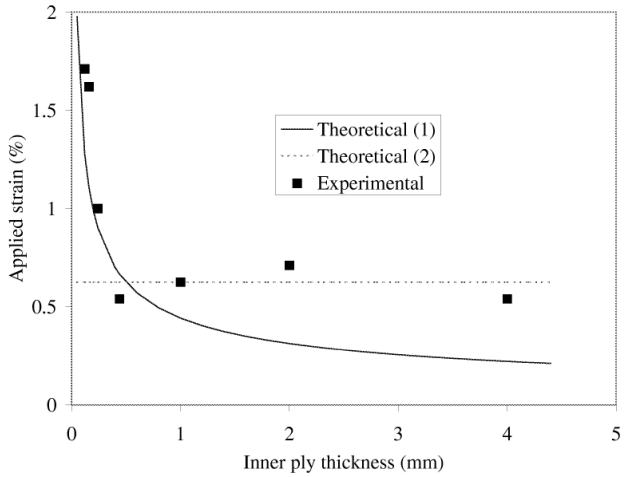

Figure 1. Theoretical (1) denotes the energy criterion, theoretical (2) the stress criterion, they are compared to the [12] results [11].

2. Presentation and implementation of the two models

Both CZM and FFM require to assume the location of cracks which are susceptible to develop within the material contrary to extended finite element method (XFEM) or crack band theory. Presupposed cracks are named potential cracks later. In the literature, two ways are proposed to defined potential transverse cracks. One can either consider a periodic distribution of cracks, or, and this is mostly the case, one considers a random distribution of potential cracks. It is worth noting that by increasing the density of potential cracks, the two methods move towards each other. The way how the number, the location and the mechanical properties of potential cracks are defined is detail in section 2.3. Integrating variability on the critical energy release rate as well as on the tensile strength prevents simultaneous creation of cracks during the computation.

Purely transverse loading (mode I cracking process) is addressed in thus study. A [0/90/0] laminate is therefore loaded in 0-degree direction in order to damage the central ply. The cell

  doi:10.5075/epfl-298799_978-2-9701614-0-0

geometry, length L and width w, is illustrated in Fig. 2. The thickness of the 90-degree ply will take different values in order to activate either one or the other criterion.

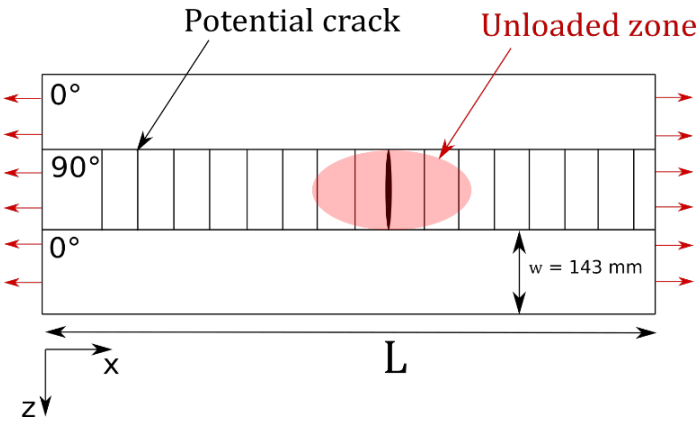

Figure 2. Geometry of the multi-cracked cell associated to a [0/90/0] laminate

2.1 Finite Fracture Mechanics (FFM)

Fracture mechanics is dedicated to the study of the mechanical behavior of cracked materials subjected to loading. Irwin [13] developed the concepts of Griffith [14], Inglis [15] and Westergaard [16]. Griffith noted that when a cracked material is subjected to mechanical loading, its potential energy decreases as the cracked area increases. The propagation of a crack is allowed by releasing the energy necessary to create the fracture surface. Irwin then established a fracture criterion based on surface energy: a crack is created when the energy released by the sample per surface unit exceeds a critical value called the critical energy restitution rate. The calculation of this energy is detailed below. When this criterion is applied for transverse cracking process in composite laminates, it is suitable for thin plies but underestimates the cracking threshold of thick plies, which is why Leguillon [11] proposes to couple the energy criterion with a stress criterion. An extension of this double criterion proposed by [17] will be used as a basis for our modeling.

A cell containing potential cracks is modeled by considering perfect interfaces, infinitely rigid and without thickness. A homogeneous longitudinal deformation is applied to the cell. The calculation aims at determining the appearance sequence of each crack. At a given damage state (*n* cracks created), we determine the level of loading required for each potential crack to validate both criteria. The strength criterion provides a loading level $\varepsilon_{xx}^{\sigma}$ and the energy criterion provides a loading level a loading level ε_{xx}^{W}. The use of discrete fracture mechanics involves validation of both criteria, thus the theoretical crack appearance strain is $\varepsilon_{xx}^{f} = \max(\varepsilon_{xx}^{\sigma}, \varepsilon_{xx}^{W})$.

Calculation of ε_{xx}^{W}

The internal energy stored in the laminate that contains n cracks can be reduced to the elastic energy W_n. Assuming that only the compliance of the damaged ply is influenced by the creation of a new crack, it follows:

$$\delta W = W_n - W_{n+1} \quad (1)$$

  doi:10.5075/epfl-298799_978-2-9701614-0-0

Where W_{n+1} the elastic energy of the laminate including the additional crack and δW is the energy released by the considered crack. Linear fracture mechanics assumes that the dissipated energy is proportional to the area created $\delta a = tw$.

$$\delta W = G_I^c tw \tag{2}$$

where G_I^c is the mode I critical energy restitution rate.

In an elastic calculation, the elastic potential energy is proportional to the square of the strain applied to the cell ε_{xx}. Let:

$$\begin{cases} W_n = \lambda {\varepsilon_{xx}}^2 \\ W_{n+1} = \tilde{\lambda} {\varepsilon_{xx}}^2 \end{cases} \tag{3}$$

where λ and $\tilde{\lambda}$ are proportional coefficients.

The difference in internal energy between the two cracked cells provides the strain ε_{xx}^W at which the crack is created. Combining Eq. (1), (2) and (3) gives:

$$\varepsilon_{xx}^W = \sqrt{\frac{G_I^c tw}{\lambda - \tilde{\lambda}}} \tag{4}$$

Calculation of $\varepsilon_{xx}^{\sigma}$

The normal stress σ_n is integrated over each potential crack following method developed by [17]. These quantities are linear as a function of the strain applied to the laminate:

$$\bar{\sigma}_n = \frac{1}{S}\int_S \sigma_n \, d\sigma = \alpha \varepsilon_{xx} \tag{5}$$

where α is a proportional coefficient.

The strength criterion gives:

$$\bar{\sigma}_n = \sigma_n^f \tag{6}$$

where σ_n^f is the tensile strength in mode I.

Injecting Eq. (5) into Eq. (6) gives:

$$\varepsilon_{xx}^{\sigma} = \frac{\sigma_n^f}{\alpha} \tag{7}$$

At a given damage state, stresses are calculated for all remaining potential cracks to determine the strain at failure $\varepsilon_{xx}^{\sigma}$. Then, the energy potentially released by each crack is calculated in turn to determine ε_{xx}^W and finally ε_{xx}^f. The minimal value of ε_{xx}^f on all the potential cracks gives the crack created at this step and added to build the new initial state required to start the next calculation step.

2.2. Cohesive Zone Model (CZM)

The concept of cohesive zones was first introduced by [8] and [9]. It is commonly used in the modelling of delamination initiation and propagation in composite materials. The behaviour of a cohesive zone is governed by a tensile-separation law illustrated in Fig. 3. The stress and displacement of the interface are related by a linear relationship of slope K, corresponding to

the stiffness of the interface. This stress increases during loading until it reaches a maximum value, called the initiation stress σ_i, which constitutes the crack initiation criterion. As soon as this criterion is activated, the stiffness degrades according to an energy criterion describing the evolution of stiffness loss. The zone in which the initiation criterion is verified but the stiffness is only partially reduced is called the process zone. It constitutes a transient place in which the material passes from a healthy state (without loss of stiffness) to a completely damaged state (of zero stiffness).

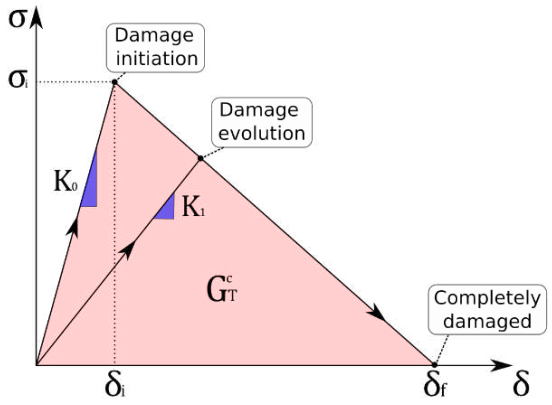

Figure 3. Traction-separation law used in CZM

In the case of mixed loading, the cohesive behaviour depends on the three directions of displacement jump at the interface, so a coupling of the modes is necessary. The initiation criterion form used in this work is quadratic

The evolution of the damage from an energy criterion with linear softening allows a good representation of the intra-laminar crack propagation in laminated composites [18], [19]. When the loading is mixed, [20] have shown the relevance of using the criterion of [21] for carbon-epoxy composites.

Numerical parameters

Stiffnesses define the linear relationships between the out-of-plane stresses and the interface displacement jump. In order not to disturb the overall stiffness of the laminate, they must be sufficiently large without generating numerical difficulties. In our study, the cohesive zones concern intra-laminar cracking and delamination. In his study on delamination, [22] proposes to express the normal stiffness of the cohesive elements as a function of the out-of-plane Young's modulus of the laminate and the thickness of the substrates.

$$K_{33} = \frac{\alpha E_3}{t} \tag{8}$$

Where t is the smallest thickness of the laminate on either side of the delaminating interface, E_3 is the Young's modulus in the out-of-plane direction of the composite material and α is a fitting parameter which must be well above 1. For values of α above 50, the overall stiffness is not influenced by the value of K_{33}. As in the work of [7] and [23], we will take the value $5.10^6 N/mm$ for delamination and transverse cracking.

  doi:10.5075/epfl-298799_978-2-9701614-0-0

Numerical models containing time-dependent degradation of mechanical properties can present convergence difficulties in implicit codes such as ABAQUS/Standard. [24] proposes the use of a viscous regularisation coefficient τ which acts as a delay effect on the damage, it is expressed in seconds and must be small in front of the calculation time increment in order not to influence the simulation results. In the following, we will take $\tau = 10^{-4}s$.

The multi-crack geometry used is the same as the previous one. Cohesive interfaces are positioned at each potential crack and a homogeneous deformation is applied to the cell. [7] estimates with a comparison with fracture mechanics that a transverse crack is created when its central node is completely damaged.

3. Implementation of material variability

The experimentally obtained cracking kinetics shows at its beginning a slow and progressive crack rate evolution. This phase may be due to lower local cracking thresholds that can be represented as defects or local weaker areas in the ply. A probabilistic Weibull-type distribution is chosen following the example of [1, 5, 25, 26, 27]. This distribution allows to apply various fracture properties to each potential crack. A large number of potential cracks is necessary to ensure the representativeness of the chosen distribution.

In the slow evolution and accumulation phases of the cracking process, the creation of a crack is followed by a local unloading around the crack pushing back the cracking thresholds of the neighbourhood. [7] shows that a random distribution of material properties leads to a dependence of the response on the number of potential cracks. Indeed , increasing the number of potential cracks results in a large number of low strength cracks. These cracks are created first at low loading levels and unload others potential cracks making up the rest of the distribution. This bias shifts and distorts the cracking kinetics.

One solution is to implement a continuous spatial distribution of energy and strength criteria. The work of [27, 28, 29, 30] highlights the correlation between fibre volume rate (FVR) and mode I crack propagation. We rely therefore on microscopic images taken on the edge of [0/90] cross-laminates to evaluate the FVR along a composite ply. The images are binarized and then thresholded using the image processing software ImageJ, the white pixels represent the matrix, the black pixels the fibres. The fibre volume ratio corresponds to the proportion of black pixels in the area of interest [31]. The scan is performed with windows of different heights ranging from $71\ \mu m$ to $858\ \mu m$ over 20mm in length. Below $286\ \mu m$ the frequency domain study shows that only noise is added, above $572\ \mu m$ a part of the spectrum is lost. We therefore rely on the volume rate distribution obtained with $286\ \mu m$ windows.

A set of 10^4 values allows a good representativeness of the criterion distribution (strength or energy). It is sorted then projected on the TVF spatial distribution. Since convergence and sensitivity studies show that 250 potential cracks of 20mm length give good results, the spatial distribution is gridded into 250 parts, each value corresponding to a potential crack. Fig. 4 shows an example of the TVF spatial distribution (blue) and criteria extrated with this method (red).

This selection of strength and energy restitution rate and their distribution ensures continuity of properties across the length of the laminate. It also provides sets of properties representative of the initial probability law. The authors will ensure that the modelling results are independent of the ply chosen for the fibre volume rate distribution.

  doi:10.5075/epfl-298799_978-2-9701614-0-0

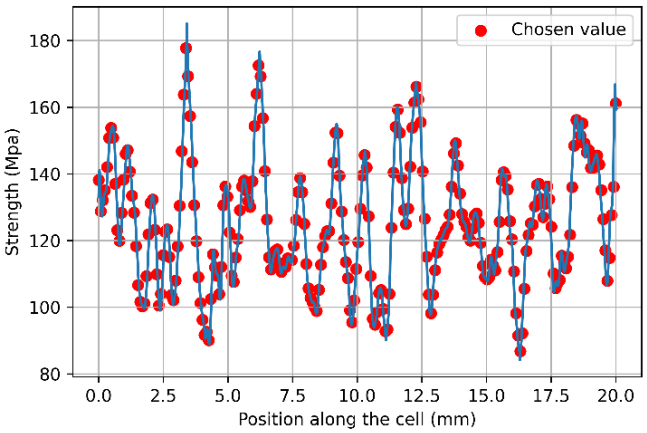

Figure 4. Normal strength criterion according to the position along the ply

4. Results and discussion

The elastic and cracking properties of the material are derived from the experimental characterisation in [7]. The cracking property distributions are identified by calibration to the cracking kinetics. The distribution of strength limits is identified from the cracking kinetics of thick plies, driven by the strength criterion, while those of thin plies allow the identification of the energy criterion.

As shown in Fig. 5, the fracture mechanics correctly reproduces the experimental kinetics. The predominant fracture criterion is dependent on ply thickness and the three phases of kinetics are observed: slow cracking rate, quick cracking rate and cracking saturation. However, the instantaneous creation of cracks through the ply thickness prevents non-realistic competition between two nearby potential cracks.

The cohesive zone model represents a different cracking mechanism depending on the thickness of the ply. For thick plies, the strength criterion drives the cracking process, therefore the among of energy released at crack on-set is large enough to generate a quick propagation of the crack though the thickness. This prevents non-realistic competition between two nearby potential cracks, as for FFM. For thin plies, once the strength criterion is reached for a potential crack, the cohesive zone is progressively damaged since the energy released is quite low. The stiffness loss is thus not sufficient to generate a significant stress unloading around the crack. In this way, when the strain applied to the ply rises, the strength criterion of nearby potential cracks, which are close to each other, is in turn reached. In spite of distributed cracking properties, all the potential cracks have their damage level growing nearly simultaneously. Such a process is clearly unrealistic and prohibits displaying a relevant cracking kinetics. A low potential crack density (lower than $2\ mm^{-1}$ in the present case) is required to create a gap between strength of nearby potential cracks and prevents cracks initiate nearly simultaneously and discharge each other during damage propagation.

  doi:10.5075/epfl-298799_978-2-9701614-0-0

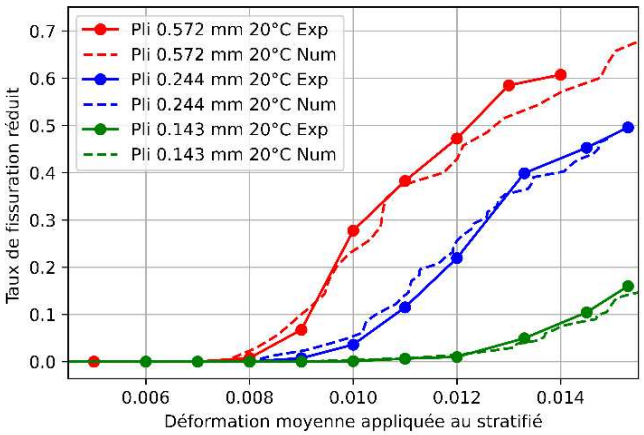

Figure 5. Reduce crack rate according to the laminate strain – Experimental and numerical results

5. Conclusion

This study aims at identifying from virtual tests the fracture properties associated to the transverse cracking process of a unidirectional ply. Two modelling approaches are evaluated: Finite Fracture Mechanics and Cohesive Zone Model. A method to define the spatial distribution of fracture properties required for the discrete modelling of the accumulation of transverse cracks is proposed.

In term of numerical method, fracture mechanics model requires a large number of elastic calculations whereas with cohesive model a single simulation provides the final damaged state. However, elastic calculations are significantly less time expensive compared to simulation including damage model. Moreover, for FFM the number of calculations can be reduced by selecting only relevant cracked states at each calculation step.

The sequential verification of the double criterion and the progressive damage induced by the framework of cohesive zones has shown limitations in the representation of matrix cracking of thin plies. Finite fracture mechanics allows the brittle cracking process to be represented independently of the ply thickness.

In future work, FFM will be used for other cracking phenomena such as interactions between cracked plies. Thus it will be used to better understand the propagation of cracks through the different layers of the laminate. This new model will be a further step in the prediction of damage and leakage rates for cryogenic storage.

Acknowledgements

The authors would like to thank the CNES, the French space agency, and ArianeGroup for their financial support.

References

1. Laeuffer, H., Arbaoui, J., Bois, C., Lavelle, F., Perry, N., & Wahl, J.-C. (2017). A new device to measure permeability evolution under pressure loading: Application to CFRP pipes. Measurement, 98, 68–76.
2. Yokozeki, T., Ogasawara, T., & Ishikawa, T. (2006). Evaluation of gas leakage through composite laminates with multilayer matrix cracks: Cracking angle effects. Composites Science and Technology, 66(15), 2815–2824.
3. C. T. Herakovich, J. G. Davis, Jr., and J. S. Mills, Thermal microcracking in Celion 6000/PMR-15 Graphite/Polyimide. Thermal Stresses in Severe Environments (1980) 649-664.
4. Naya, F., González, C., Lopes, C. S., Van der Veen, S., & Pons, F. (2017). Computational micromechanics of the transverse and shear behavior of unidirectional fiber reinforced polymers including environmental effects. Composites Part A: Applied Science and Manufacturing, 92, 146–157.
5. D.M. Grogan, C.M. O Bradaigh, and S.B. Leen. A combined XFEM and cohesive zone model for composite laminate microcracking and permeability. Composite Structures, 120 :246-261, February 2015. ISSN 02638223.
6. F.P. van der Meer, C.G. Dávila, MODELING TRANSVERSE CRACKING IN LAMINATES WITH A SINGLE LAYER OF ELEMENTS PER PLY, ECCM15, 2012.
7. Tanguy Briand. Caractérisation et modélisation de la relation entre l'endommagement et la perméabilité dans un composite stratifié en condition cryogénique. Thèse de doctorat, Université Bordeaux, 2020.
8. G.I. Barenblatt. The Mathematical Theory of Equilibrium Cracks in Brittle Fracture. In Advances in Applied Mechanics, volume 7, pages 55-129. Elsevier, 1962.
9. D.S. Dugdale. Yielding of steel sheets containing slits. Journal of the Mechanics and Physics of Solids, 8(2) :100-104, May 1960.
10. Weißgraeber, P., Leguillon, D., & Becker, W. (2016). A review of Finite Fracture Mechanics: Crack initiation at singular and non-singular stress raisers. Archive of Applied Mechanics, 86(1 2), 375–401.
11. Dominique Leguillon. Strength or toughness? A criterion for crack onset at a notch. European - Journal of Mechanics - A/Solids, 21(1) :61-72, January 2002.
12. A. Parvizi and J.E. Bailey. On multiple transverse cracking in glass fibre epoxy cross-ply laminates. Journal of materials science(13) :6, 1978.
13. G. R. Irwin. ONSET OF FAST CRACK PROPAGATION IN HIGH STRENGTH STEEL AND ALUMINUM ALLOYS. Technical Report NRL-4763 ; PB-121224, Naval Research Lab., Washington, D.C., May 1956.
14. A. Griffith. VI. The phenomena of rupture and ow in solids. Phil. Trans. R. Soc. Lond. A, 221(582-593) :163-198, January 1921.
15. C. E. Inglis. Stresses in A Plate Due To The Presence of Cracks and Sharp Corners. Scribd, 1913.
16. H. M. Westergaard. Bearing Pressures and Cracks : Bearing Pressures Through a Slightly Waved Surface or Through a Nearly Flat Part of a Cylinder, and Related Problems of Cracks. Journal of Applied Mechanics, 6(2) :A49-A53, June 1939.

  doi:10.5075/epfl-298799_978-2-9701614-0-0

17. Pietro Cornetti, Nicola Pugno, Alberto Carpinteri, David Taylor, Finite fracture mechanics: A coupled stress and energy failure criterion, Engineering Fracture Mechanics, Volume 73, Issue 14, 2006.
18. Erwann Le Goff, Christophe Bois, and Hervé Wargnier. A progressive intra- and inter-laminar damage model to predict the effect of out-of-plane confinement on pin-bearing behaviour of laminated composites. Journal of Composite Materials, 51(4) :433-450, February 2017.
19. Thomas Vandellos, Nicolas Carrere, Cédric Huchette, and Eric Martin. Vers un modèle de zones cohésives adapté à l'étude du délaminage dans les composites stratifiés. 2011
20. P. P. Camanho, C. G. Davila, and M. F. de Moura. Numerical Simulation of Mixed-Mode Progressive Delamination in Composite Materials. Journal of Composite Materials, 37(16) :1415-1438, August 2003.
21. M.L. Benzeggagh and M. Kenane. Measurement of mixed-mode delamination fracture toughness of unidirectional glass/epoxy composites with mixed-mode bending apparatus. Composites Science and Technology, 56(4) :439-449, 1996.
22. A. Turon, C.G. Davila, P.P. Camanho, and J. Costa. An engineering solution for mesh size effects in the simulation of delamination using cohesive zone models. Engineering Fracture Mechanics, 74(10) :1665-1682, July 2007.
23. Paul Van Der Sypt. Analyse et modélisation des chemins d'efforts et de la dégradation des assemblages de type HYPER joints. February 2020.
24. Ireneusz Lapczyk and Juan A. Hurtado. Progressive damage modeling in fiber reinforced materials. Composites Part A: Applied Science and Manufacturing, 38(11) :2333-2341, November 2007.
25. Chunsheng Lu, Robert Danzer, and Franz Dieter Fischer. Fracture statistics of brittle materials: Weibull or normal distribution. Phys. Rev. E, 65(6) :067102, June 2002.
26. Endel V. Iarve, Mark R. Gurvich, David H. Mollenhauer, Cheryl A. Rose, and Carlos G. Davila. Mesh-independent matrix cracking and delamination modeling in laminated composites. Int. J. Numer. Meth. Engng., 88(8) :749-773, November 2011.
27. John A. Nairn. Matrix Microcracking in Composites. In Comprehensive Composite Materials, pages 403-432. Elsevier, 2000.
28. M. Dong and S. Schmauder. Transverse mechanical behaviour of _ber reinforced composites-FE modelling with embedded cell models. Computational Materials Science, 5(1-3) : 53-66, February 1996.
29. Victor Feret, Hossein Ghiasi, and Pascal Hubert. Effect of Fibre Volume Fraction on Mixed-Mode Fracture of a Fabric Carbon/Epoxy Composite. Appl Compos Mater, 20(4) :415-429,August 2013.
30. G. Pappas and J. Botsis. Intralaminar fracture of unidirectional carbon/epoxy composite: experimental results and numerical analysis. International Journal of Solids and Structures, 85-86 :114-124, May 2016.
31. Aurélie Pilato. Caractérisation des structures composites bobinées épaisses, application à l'étude du comportement de réservoirs de stockage d'hydrogène. 2011

BUILDING AND CHARACTERIZATION OF SYMMETRIC STRUCTURAL BATTERY

Shanghong Duan[a], Fredrik Lindelöw[a], Zhaoyang Li[a], Ziyao Ma[a], Yibo Liu[a], Johanna Xu[a], David Carlstedt[a], Marcus Johansen[a], Leif Asp[a]

a: Department of Industrial and material science, Chalmers university of technology, duan.shanghong@chalmers.se

Abstract: *Recently, a structural battery with multifunctional carbon fibre anode has been reported. The energy density of active material is not fully extracted due to the low ionic conductivity inside the battery. To identify the main region that attributes to the low ion transportation, we assemble a symmetric structural battery with one anode layer in the centre sandwiched between two cathode layers. Such a design can also be treated as a combination of two asymmetric batteries with one full thickness cathode layer plus one half thickness anode layer. Thus, the travelled distance of lithium ions is shortened only in the anode part. It is found that the area energy density of the symmetric structural battery is doubled compared to a reference asymmetric battery. Thus, the additional cathode layer activates the double amount of carbon fibres in the anode. A plausible reason is that only the carbon fibres next to the separator is activated in the battery.*

Keywords: Carbon fibre; structural battery;

1. Introduction

Carbon fibre reinforced polymer (CFRP) composites are usually used in lightweight applications due to the high specific modulus of the carbon fibre from a mechanical point of view. The crystalline microstructure of the carbon fibre is very similar to graphite, which is the most frequently used commercial battery anode material. Several research groups have explored the similarity from an electrochemical point of view and proved that the carbon fibre, especially the polyacrylonitrile-(PAN-) based carbon fibre is capable to be an alternative anode [1-3]. A solid-state battery equipped with the carbon fibre anode is expected not only to store electric energy but also to carry mechanical load. An analytic study shows that a structural battery can reach an elastic modulus of 117 GPa in the fibre direction [4]. On a system level, employing such a battery in an electric vehicle would reduce the total weight by 20 to 30% [5].

Recently, Asp et al. built a first structural battery, which possesses Young's modulus of 25 GPa in the fibre direction and an energy density of 24 Wh/kg [6]. The battery employs a commercial cathode foil, carbon fibre anodes, a glass fibre paper separator and a bi-continuous polymer electrolyte system. Even though this recently developed structural battery outperforms other similar products [7-9], there is still a large gap between its real and theoretical properties [6]. Especially, its energy density only reaches 30% of the theoretical value. The cycling curves of the structural battery have indicated a high overpotential caused by poor ion conductivity. Hence, the battery cannot be fully charged/discharged. The poor ion conductivity can relate to the anode part, cathode part, separator part or interfaces between them. The crucial region is still unknown and needs to be identified for future improvement.

  doi:10.5075/epfl-298799_978-2-9701614-0-0

In the present study, a symmetrical stacked structural battery is manufactured and compared with a reference battery [6]. The symmetrical stacked battery has two cathodes on both sides of the carbon fibre anode. Therefore, the stacked battery can be treated as two reference batteries with a half thickness carbon fibre anode. The area energy density of the stacked battery is almost twice as high as that of the reference cell. Furthermore, the overpotential of the stacked battery is much smaller than the reference cell, which indicates that by decreasing the thickness of the carbon fibre anode to 50%, the inner resistance of the structural battery can be decreased.

2. Experiment

2.1 Materials

The structural batteries are made using same materials as Asp et al [6]. T800SC-12k carbon fibre tows from Oxeon AB, Sweden, are used as anode material. Single-side $LiFePO_4$ (LFP) coated aluminum foils with energy capacity of 1 mAh/cm^2 are purchased from Customcells. Whatman GF/A glass microfiber filter paper is selected as separator for its high porosity and stable performance. Bi-continuous polymer structural battery electrolyte (SBE) is made of Bisphenol A ethoxylate dimethacrylate (M_n: 540 g/mol) and a liquid electrolyte mixture. The liquid electrolyte solvent is mixed by 50:50 wt% ratio ethylene carbonate (EC) (Sigma Aldrich) and propylene carbonate (PC) (Sigma Aldrich). 0.4 M lithium trifluoromethanesulfonate (LiTf) (99.99%) (Sigma Aldrich), 0.6 M lithium bis(oxalato) borate (LiBoB) (Sigma Aldrich) are dissolved as lithium salt. In addition, thermal initiator 2,20-azobis (2-methylpropionitrile (AIBN) is pre-dissolved in 1 wt% in the liquid electrolyte.

2.2 Battery manufacturing

Two different types of structural batteries are made: stacked battery and reference battery. The reference cell is made following the procedures described in Asp et al. [6]. The stacked battery contains two cathode foils at each side of the carbon fibre anode. To make a stacked battery, a pouch bag is prepared outside the glovebox as shown in Fig. 1. Electric insulating tapes are taped at the edges of the pouch film to prevent the connections between the current collectors and an aluminium film inside the pouch film. Hot melt tapes are placed to ensure the sealing of the pouch bag. Carbon fibre anode is 2 cm in length (~13 mg) and glued on a copper current collector using silver conductive paint from PELCO®. Separators are placed on both sides of the carbon fibre anode. Then the cathode foils (~25 mg / each) are placed outside of the separators and connected with aluminium current collectors. To fix the positions of cathode foils, their conners are fixed by Teflon tape. The pouch bag is dried at 50 °C under vacuum overnight. The dried pouch bag is transfer to glovebox and SBE mixture is added directly on separators to ensure a proper wetting. After vacuum sealing, the pouch bag is cured at 90 °C for 90 minutes.

  doi:10.5075/epfl-298799_978-2-9701614-0-0

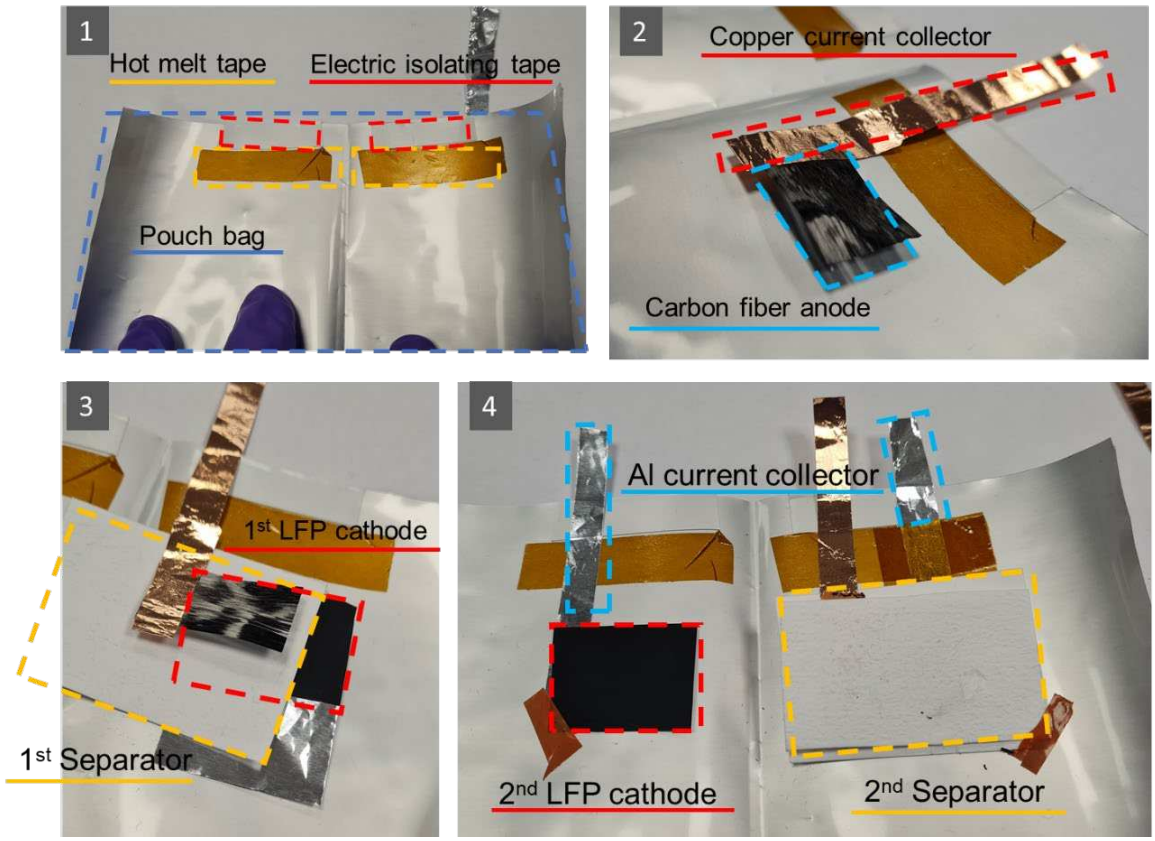

Figure 1. Manufacturing procedures of the pouch bag of the stacked structural battery

2.3 Battery test

The batteries are cycled under C/10 rate using Neware CT-4008-5V10mA-164 battery cycler. The voltage window is set between 2.00 to 3.55 V. The cycling current is calculated based on the theoretical energy capacity of carbon fibre anode (372 mAh/g). 2 hours rest is set between charging/discharging phases.

3. Result and discussion

The stacked battery and the reference battery have the same area and are cycled using the same current. The cycling curves of the two batteries are plotted in Fig. 2. It is obvious that the stacked battery has a larger total energy capacity. Its last cycle discharging capacity is 1.1 mAh, whereas the last cycle discharging capacity of the reference cell is 0.5 mAh. The larger energy capacity of the stacked battery is mainly attributed to the additional cathode material. Moreover, the over potential of the stacked battery is significantly lower than that of for reference cell, which contributes to the larger capacity as well, since the travel distances of the lithium ions in the two batteries only differ in the anode part. The shorter travel distance in the anode of the stacked battery lowers the over potential very efficiently. However, the energy density improvement is limited in the stacked battery (Table. 1). It is because the carbon fibre anode is not the main weight contributor in the structural battery. The area mass of the stacked battery is almost twice as high as the reference battery.

  doi:10.5075/epfl-298799_978-2-9701614-0-0

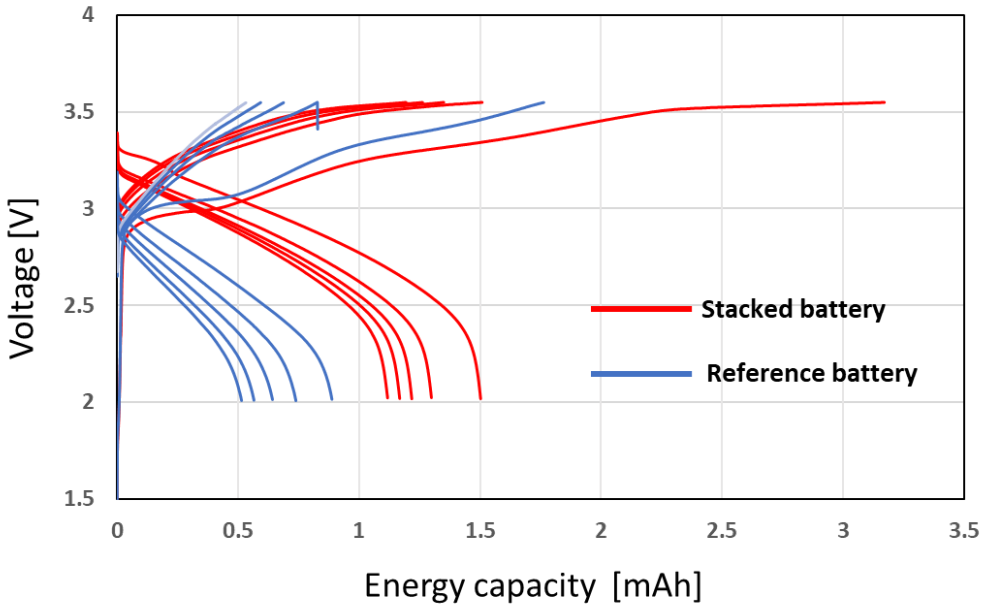

Figure 2. Cycling curves of stacked battery and a reference cell

Table 1: The area energy capacity and energy density of the batteries.

ID number	Area energy capacity [mAh/cm^2]	Energy density [Wh/kg]
Reference battery	0.166	8.7
Stacked battery	0.370	10.4

The doubled area energy capacity means the additional cathode foil in the stacked battery activates the double amount of carbon fibre anode as the reference battery. As shown in Fig. 3, one stacked battery can be considered as a combination of two reference batteries, in which the thickness of the carbon fibre anode is reduced by 50 %. Each thin anode reference battery has approximately the same capacity as the reference battery even though less carbon fibre anode is used. This can be explained by the outer half part of the carbon fibre ply is not activated in in the reference battery. That is, the lithium cannot reach the top part of the carbon fibre ply due to the small volume fraction of SBE in the anode or high interface resistance between the carbon fibre and SBE. When another cathode is added on the top side, the carbon fibres at the outer part can be activated.

  doi:10.5075/epfl-298799_978-2-9701614-0-0

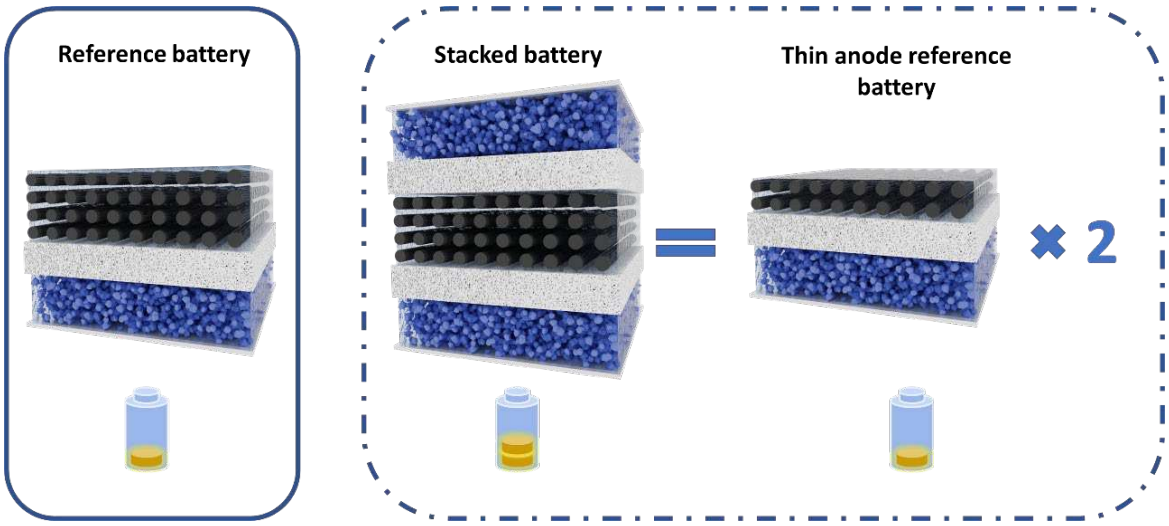

Figure 3. Comparison of the reference battery and the stacked battery.

4. Conclusion

In the present study, a symmetrical stacked structural battery is manufactured, and its electrochemical performance is characterised and compared with a reference cell. The results show that the stacked battery has an energy area capacity that is twice as high as that of the reference cell. The results indicate that less than 50 % of the carbon fibre anode is activated in the reference cell. The low activation level can be due to low/limited ionic conductivity and dense fibre distribution in the carbon fibre anode. As a consequence, the lithium-ions cannot reach the carbon fibres away from the separator. Since a thinner carbon fibre ply is not available as of today, a lose spread carbon fibre ply is suggested as a better choice for the future structural battery.

Acknowledgements

We acknowledge the funding provided by USAF, EOARD Award No. FA8655-21-1-7038 and the Swedish National Space Agency, project no. 2020-00256.

5. References

1. Lee JK et al. Electrochemical properties of PAN-based carbon fibers as anodes for rechargeable lithium-ion batteries. Carbon 2001; 39:1299-1305.
2. Kjell MH et al. PAN-Based Carbon Fiber Negative Electrodes for Structural Lithium-Ion Batteries. J. Electrochem. Soc. 2011; 158:A1455.
3. Fredi G et al. Graphitic microstructure and performance of carbon fibre Li-ion battery electrodes. Multifunct. Mater. 2018; 1:A015003.
4. Carlstedt D, Marklund E, Asp LE, Effects of state of charge on elastic properties of 3D structural battery composites. Compos. Sci. Technol. 2019; 169:26-33.
5. Carlstedt D, Asp LE. Performance analysis framework for structural battery composites in electric vehicles. Composite Part B: Engineering 2020; 186:107822.

  doi:10.5075/epfl-298799_978-2-9701614-0-0 published under CC BY-NC 4.0 license

6. Asp LE et al. A Structural Battery and its Multifunctional Performance. Adv. Energy & Sustaninability Research 2021; 2:2000093.
7. Liu P, Sherman E, Jacobsen A. Design and fabrication of multifunctional structural batteries. J. Power. Soc. 2009; 189:646-650.
8. Men C et al. Multifunctional structural ultrabattery composite. Nano Lett. 2018; 18:7761-7768.
9. Moyer K et al. Carbon fiber reinforced structural lithium-ion battery composite: Multifunctional power integration for CubeSats. Energy Storage Materials 2020; 24: 676-681.

  doi:10.5075/epfl-298799_978-2-9701614-0-0

DEVELOPMENT OF SUSTAINABLE CONTINUOUS CARBON FIBER REINFORCED POLYMERS

Alberto Santiago, Miguel Ángel López-Manchado, Raquel Verdejo

Instituto de Ciencia y Tecnología de Polímeros, ICTP-CSIC, C/ Juan de la Cierva, 3, 28006 Madrid, Spain – santiagobethencourt.alberto@gmail.com

Abstract: *Fiber reinforced polymers (FRP) are steadily gaining more popularity in applications that require high performance materials such as aerospace, automotive, sports or civil engineering. As a consequence of the high-volume demand, it is necessary to propose new alternatives for the FRP waste management. In this study, we present a thermoplastic liquid resin as a solution for this problem, which enables the manufacture of composite materials with commonly used techniques in this sector. Besides, FRP based on this resin can be thermoformed at low temperature while polymer and fiber can also be easily recovered without compromising their properties*

Keywords: Composite materials; sustainability; thermoplastics; recycling; carbon fiber.

1. Introduction

Since the use of fiber reinforced polymer materials began to expand in the 20th century, their use in different sectors has grown exponentially, replacing conventional materials such as wood or metal in countless applications; as an example, in Europe alone, 1141 kt of FRP were produced in 2019 [1]. This effect is mainly due to its excellent strength-to-weight ratio in combination with other characteristics such as high fatigue and corrosion resistance and good dimensional stability [2]. These materials consist of a reinforcing agent, commonly short or continuous fibers (carbon, glass, aramid or natural fibers, among others) embedded in a thermoplastic or thermosetting polymeric matrix. Such wide range of configurations enables the materials on demand for each application, even presenting superior properties to those of steel, as shown in Figure 1 [3]. They are therefore found in aviation, ships, wind generators, sports equipment and even in orthopedics prostheses.

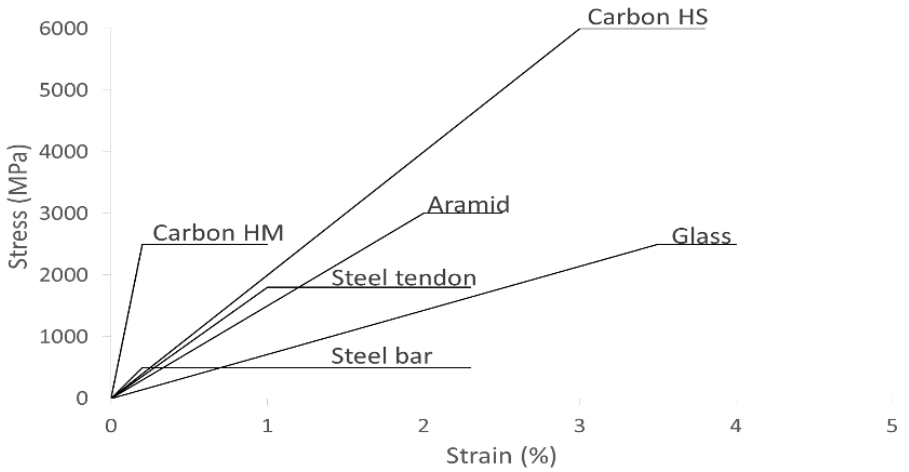

Figure 1. Typical FRP materials VS mild steel [3].

  doi:10.5075/epfl-298799_978-2-9701614-0-0 published under CC BY-NC 4.0 license

This significant raise in FRP consumption has led to an increase in the percentage of composite wastes at the end of its service life, which the European Union has begun to regulate in the last decade to prevent their accumulation in landfills and prioritize their recycling [4]. Normally, high-performance FRPs consist of continuous fibers in combination with a thermosetting matrix. In addition, the liquid nature of these resins facilitates the impregnation on the fiber fabrics at room temperature. However, recycling these materials is a challenge for the industry since the techniques developed so far, remarkably reduce the properties of the recovered fiber, which relegates the use of these fabrics for applications of low structural requirements [5,6] and completely eliminates the polymer.

Consequently, the composite sector is looking for alternatives such as providing self-healing capacity to the material, the use of natural fibers or the substitution of thermosets by thermoplastic matrices or biopolymers [7,8]. The most developed alternative in the industry is the use of thermoplastics owing to their high chemical resistance and shorter processing times compared to thermosetting resins. Still, their main advantage comes from their chemical nature. In contrast to the highly cross-linked network structure of thermosets, thermoplastic structures are composed of linear and branched molecular chains that can move freely. This feature gives them better post-service performance, facilitating their repair [9] and the thermoforming of FRP sheets [10], which facilitates the reuse of the material once its service life is over [11]. In contrast, the processing of FRP based on thermoplastics is more complex, since high temperatures and pressures are required in order to properly impregnate the fiber, which implies investing in expensive techniques and equipment [12] and limits the production of high fiber content composite materials. A promising alternative is the development of thermoplastic reactive resins. Arkema has developed Elium, a liquid thermoplastic (100–500 mPa·s) that can be processed with the same processes as epoxy resins, e.g. vacuum infusion, resin transfer molding (RTM), and wet com- pression molding [13]. Using this resin, they have manufactured a functional boat prototype and a wind generator blade [14]. However, the polymerization of Elium is a highly exothermic redox process with a short pot-life, which hinders the impregnation processes of composite materials. This communication introduces the use of a new thermoplastic liquid resin. We have developed and patented a liquid thermoplastic resin, named Akelite [15], that solves these shortcomings. Therefore, in this study, the processability and mechanical properties of continuous carbon fiber reinforced polymers (CFRP) based on Akelite resin will be compared with two commercial resins; a thermoplastic resin by Arkema and an Epoxy resin by Resoltech. Besides, the recyclability of CFRP based on Akelite resin was studied.

2. Experimental

2.1 Materials

Akelite resin was synthesized in the Institute of Science and Technology of Polymers (Madrid, Spain) by the Polymer Composite Group; the epoxy resin used (Resoltech 1050) and its catalyst (Resoltech 1053s) were purchased from Castro Composites (Pontevedra, Spain); the thermoplastic resin (Elium 180®) and its benzoyl peroxide initiator (Perkadox GB50X) were purchased from Arkema S.A. (Barcelona, Spain). An unidirectional (UD) carbon fiber fabric (12k, 340 g/m^2) was purchased from INP96 (Madrid, Spain).

  doi:10.5075/epfl-298799_978-2-9701614-0-0

2.2 Fabrication of CFRP laminates

Four-layer laminates of UD carbon fiber and the different resins were manufactured by vacuum assisted resin infusion molding (VARIM) at room temperature (see Fig. 2). The cure protocol followed the suppliers' recommendations and were as follows: Elium 180® with 3%wt of Perkadox GB50X was polymerized at 60°C for 2 hours, followed by a post-curing step of 1 hour at 80°C; epoxy and hardener were mixed in a ratio of 100:35 and were then cured at 80°C for 3 hours; Akelite based laminates were manufactured at 60°C for 2 hours in the presence of 3%wt of benzoyl peroxide.

Figure 2. Vacuum assisted resin infusion molding.

2.3 Recovery of carbon fabrics

The carbon fiber composites based on Akelite were immersed in a common solvent for 2 days and the four layers were easily separated and left to dry at room temperature. This process recovered the fibers and the polymer in optimum conditions.

2.4 Mechanical properties of CF laminates

All specimens were machined on a NEURTEK BRILLIANT 220 precision cutting machine and at least ten specimens for each type of material were obtained for each test.

Three-point flexural tests, both in 90° and 0° directions, were performed in accordance to ASTM D 790. The test was carried out in a universal test machine INSTRON 2204 at a constant cross-head speed of 1 mm/min. The Charpy impact tests in 0° direction were performed in a pendulum impact testing machine CEAST in accordance to UNE-EN ISO 179 at a constant hammer speed of 2.9 m/s.

3. Results and discussion

Table 1 shows the flexural and impact response of the composite materials in transversal (90°) and longitudinal (0°) directions. There are no significant differences in the maximum flexural strength and modulus of the three different materials. Meanwhile, both thermoplastic composites performed better in terms of impact, which is ascribed to the better impact behavior of thermoplastics [16]. Thus, these results suggest that it is possible to manufacture structural

  doi:10.5075/epfl-298799_978-2-9701614-0-0

CFRP based on thermoplastic resins with similar or even superior mechanical properties than epoxy resins. It is relevant to note that this is achieved using commercial carbon fabrics without a specific sizing and using the same conventional transformation techniques for the fabrication of CFRP based on thermosetting resins.

Additionally, the main advantages of these composites based on thermoplastics (FRTP) are that they can be thermoformed, they are easy to repair, parts can be joined without the use of adhesives and both components, fiber and polymer, can be easily recovered with good properties and reuse them for the manufacture of new high-performance composite materials. All these characteristics cannot be achieved with conventional FRP and thermosetting matrices. That is what makes this FRTP 100% circular, favoring a closed circle in the circular economy of composite materials and plastics.

Table 1: Mechanical properties of the materials.

Laminate	Flexural Modulus, GPa		Flexural Strength, MPa		Impact Strength, kJ/m²
	0°	90°	0°	90°	0°
Akelite	53±4	5.1±0.5	1045±50	78±4	73±11
Elium	54±4	5.6±0.3	1076±56	77±7	75±9
Epoxy	59±7	6.6±0.8	957±67	90±5	59±6

An already finished piece can be thermoformed at low pressures by heating the material over 100°C. This allows adapting to the desired shape (see Fig. 3) and the process can be repeated indefinitely. Moreover, we can easily join already polymerized parts by applying heat and pressure without the need of any type of adhesive.

Figure 3. Thermoformed piece.

Yet, this material can be easily recycled by a gentle and suitable method for industrial scale. By dissolving the laminate in a common solvent at room temperature, we can recover the fiber fabrics and the polymer in optimal conditions (Fig. 4). The recycled material can be reprocessed to obtain a new FRP that can mechanically perform similar properties to the original one, resulting in a closed cycle process which barely generates any waste.

  doi:10.5075/epfl-298799_978-2-9701614-0-0

Figure 4. CF layers recovery.

4. Conclusions

A thermoplastic liquid resin that combines the advantages of thermosetting and thermoplastic matrices has been developed. It demonstrates that the properties of FRP based on this resin can perform positively as those based in commercial resins. In addition, both the polymer and the fiber can be recycled and recovered without compromising their properties. Still there is a long path to go to achieve the long-awaited goal of no FRP waste. However, the results obtained in this study are very promising and launch a range of possibilities to pursue in order to achieve this goal.

Acknowledgements

The authors acknowledge the grant PDC2021-120853-I00 funded by MCIN/AEI/ 10.13039/501100011033 and by the "European Union NextGenerationEU/PRTR".

5. References

1. Bledzki AK, Seidlitz H, Goracy K, Urbaniak M, Rösch JJ. Recycling of carbon fiber reinforced composite polymers—review—part 1: Volume of production, recycling technologies, legislative aspects. Polymers (Basel). 2021; 13(2):1–13.
2. Rajak DK, Pagar DD, Menezes PL, Linul E. Fiber-reinforced polymer composites: Manufacturing, properties, and applications. Polymers (Basel). 2019; 11(10):1667.
3. Abbood IS, Odaa S aldeen, Hasan KF, Jasim MA. Properties evaluation of fiber reinforced polymers and their constituent materials used in structures - A review. In: Materials Today: Proceedings. Elsevier BV 2021; 1003–8.
4. Parlamento Europeo C de la UE. Directiva (UE) 2018/850 del Parlamento Europeo y el Consejo de 30 de mayo de 2018 por la que se modifica la Directiva 1999/31/CE relativa al vertido de residuos. D Of la Unión Eur Ser L [Internet]. 2018;2018(150, 14 de junio):100–8. Available from: https://eur-lex.europa.eu/legal-content/es/TXT/?uri=CELEX%3A32018L0850
5. Anane-Fenin K, Akinlabi E, Akinlabi ET. Recycling of Fibre Reinforced Composites: A Review of Current Technologies. Proc DII-2017 Conf Infrastruct Dev Invest Strateg Africa. 2017; (October):7.
6. Sukanto H, Raharjo WW, Ariawan D, Triyono J. Carbon fibers recovery from CFRP recycling process and their usage: A review. IOP Conf Ser Mater Sci Eng. 2021; 1034(1):012087.
7. Santiago Bethencourt A, Peñas Caballero M, Hernández Santana M, Verdejo Márquez R, López Manchado MÁ. Materiales compuestos "eco-friendly." Rev. plásticos Mod. Cienc. y Tecnol. polímeros 2021; 121:766.

  doi:10.5075/epfl-298799_978-2-9701614-0-0

8. Peñas-Caballero M, Hernández Santana M, Verdejo R, Lopez-Manchado MA. Measuring self-healing in epoxy matrices: The need for standard conditions. React. Funct. Polym. 2021; 161:104847.
9. Davies P, Cantwell WJ, Jar PY, Bourban PE, Zysman V, Kausch HH. Joining and repair of a carbon fibre-reinforced thermoplastic. Composites 1991; 22(6):425–31.
10. Sachs U, Akkerman R. Viscoelastic bending model for continuous fiber-reinforced thermoplastic composites in melt. Compos Part A Appl Sci Manuf. 2017; 100:333–41.
11. Mamanpush SH, Li H, Englund K, Tavousi Tabatabaei A. Extruded Fiber-Reinforced Composites Manufactured from Recycled Wind Turbine Blade Material. Waste and Biomass Valorization 2019; 11:1–10.
12. Ivanov SG, Beyens D, Gorbatikh L, Lomov S V. Damage development in woven carbon fibre thermoplastic laminates with PPS and PEEK matrices: A comparative study. J Compos Mater. 2017; 51(5):637–47.
13. Obande W, Mamalis D, Ray D, Yang L, Ó Brádaigh CM. Mechanical and thermomechanical characterisation of vacuum-infused thermoplastic- and thermoset-based composites. Mater Des. 2019; 175:107828.
14. Cousins DS, Suzuki Y, Murray RE, Samaniuk JR, Stebner AP. Recycling glass fiber thermoplastic composites from wind turbine blades. J Clean Prod. 2019; 209:1252–63.
15. Verdejo R. Polímeros reforzados con fibras basados en matrices termoplásticas. Spain; PCT1641.1572, 2021.
16. Arikan V, Sayman O. Comparative study on repeated impact response of E-glass fiber reinforced polypropylene & epoxy matrix composites. Compos Part B Eng. 2015; 83:1–6.

  doi:10.5075/epfl-298799_978-2-9701614-0-0

THERMAL STABILITY OF ELIUM® RESIN AND ITS COMPOSITES

Emmanuel Richaud[a], Pierre Gerard[b]

a: Laboratoire PIMM, Arts et Metiers Institute of Technology, CNRS, Cnam, HESAM University, 151 boulevard de l'Hopital, 75013 Paris, France – emmanuel.richaud@ensam.eu
b: Arkema, Laboratoire Composites, Groupement de Recherche de Lacq, 64170 Lacq, France.

Abstract: *This paper deals with the thermal ageing of ELIUM® based composites filled with mineral fillers (aluminium trihydrate in particular) and corresponding matrices. The ageing of thin films and thick blocks was investigated by gravimetry. The comparison of matrices with an incremental complexity highlighted the effect of comonomers and thermal stabilizers. In all cases, unzipping was shown to be the predominant source of mass loss but oxidation seems also to be involved in the case of ageing under air. The existence of this latter was confirmed by the existence of a brown surface layer. This oxidized layer was shown to be deeper for filled composites than unfilled matrices, suggesting that fillers favor the oxygen diffusion into the bulk.*

Keywords: Acrylic resin; Aluminium Trihydrate; Thermal oxidation; Kinetic modeling;

1. Introduction

ELIUM® resin is increasingly used as matrix for composites with the advantage of a low viscosity reactive mixture containing methyl methacrylate [1,2] which can be polymerized at moderate temperature using an organic peroxide [3]. It can thus be easily processed using the common tools used for thermoset matrix based composites (infusion, RTM…). Another of its great advantage is that the monomer can be recovered by the classical depolymerization method allowing to recover feedstock. Its use can for example be envisaged for manufacturing several parts needed for satisfying the societal need of low carbon energy: wind blades [4], or liquid hydrogen tanks [5].

ELIUM® resin suffers, however, from the well-known poor flame resistance common to all the members of the acrylic polymers family, such as PMMA for instance. This deficiency can be solved, for example, using flame retardants, among them aluminum trihydrate. Another issue is the relatively low feedback in terms of long term stability. In particular, the lifetime prediction makes necessary to determine the degradation rate, which can be achieved using a kinetic model based on the degradation mechanism.

Finally, the aim of this paper is to establish a first kinetic model for ELIUM® resin, and check its validity for Flame Retardant additivities resin. Since composites are usually thick parts, we will also address the so called diffusion limited oxidation effect. For that purpose, thin and thick samples of various kinds of ELIUM® resin (differing by the content of comonomers, stabilizers, and Flame retardant fillers) will be isothermally aged at several temperatures under several atmospheres (under nitrogen or in presence of oxygen) so as to derive a first kinetic model.

2. Materials and methods

Three kinds of unfilled acrylic resins were studied here as 4 mm thick plates samples:

  doi:10.5075/epfl-298799_978-2-9701614-0-0

- ELIUM® V1 is an acrylic resin synthesized from a MMA syrup.

- ELIUM® V2 is synthesized from the same reactive mixture than V1 (MMA syrup) to which butanediol dimethacrylate and methacrylic acid were added.

- ELIUM® V3 is made from ELIUM® V2 reactive mixture with an antioxidant package.

Composites (denoted by ELIUM® ATH) were made of ELIUM® V3 loaded with aluminium trihydrate (62% in weight) and Zinc borate (6% in weight). 4 mm thick plates were isothermally aged in ventilated ovens at 180°C.

50 µm thin films of ELIUM® V1 and V2 were obtained by micrototomy. They were in situ aged in TGA cell at temperatures ranging from 230 to 270°C either under pure nitrogen or pure oxygen flow.

4 mm thick ELIUM® V1, V2 V3 and ATH plates were isothermally aged in ventilated ovens at 180 under air. Their ageing was followed by gravimetry and microscopic observations. For ELIUM® ATH samples, 10 mm blocks were used for the microscopic observations.

To better understand the degradation of this composite, the stability of aluminium trihydrate and zinc borate was also investigated under air at those temperatures by gravimetry.

3. Results and discussion

3.1 Stability of thin films of pure ELIUM® resin under nitrogen

The stability of ELIUM® V1, V2 and V3 resin was first investigated by mass loss curves directly recorded in TGA cell. Examples are given in Figure 1 for ELIUM® V2 resin. It can be seen that samples display (i) a first very quick mass loss step expected to correspond to VOC loss in low content, (ii) an auto-decelerated mass loss step (Figure 1). Some T_g measurements were realized by DSC on ELIUM® V1 resin. It was verified that, even after significant level of mass loss (up to 40%). This mechanism was ascribed to an end chain unzipping mechanism [6].

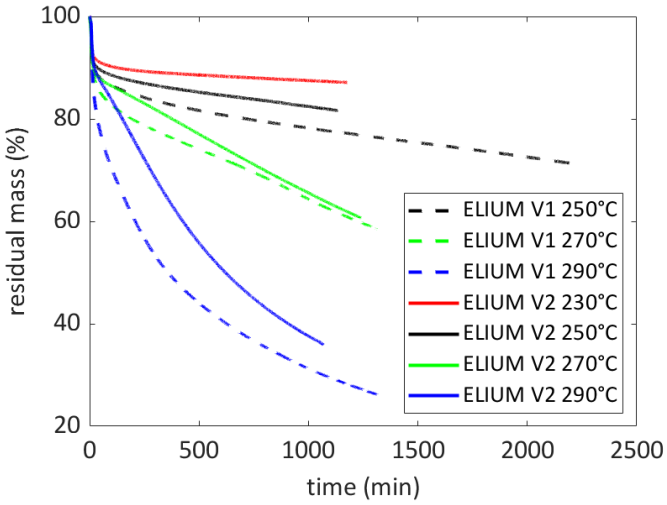

Figure 1. Mass loss curves of thin ELIUM® samples recorded by TGA under inert atmosphere.

In a first approach, its kinetics was depicted by the following equation:

  doi:10.5075/epfl-298799_978-2-9701614-0-0

$$\frac{m}{m_0} = \frac{m_{v_0}.\exp(-k_v.t)+m_{p_0}.\exp(-k_{unzipping}.t)}{m_{v_0}+m_{p_0}} \quad (1)$$

m_{v0} and m_{p0} corresponding respectively to the initial mass of residual VOC's and of polymer, k_v being the rate constant for the volatilization of VOC's and $k_{unzipping}$ corresponding to the apparent rate constant for the overall unzipping process.

This latter was estimated for both ELIUM® V1 and V2 and found higher for ELIUM® V1, in good agreement with the well-known role of acrylic comonomers for slowing down the unzipping rate as illustrated for example in PMMA [7].

3.2 Stability of thin films of pure ELIUM® resin under oxygen

In presence of oxygen, the mass loss curves display the same shape at early stage, but a strong auto-acceleration of mass loss is observed (Figure 2). The depletion of T_g was here clearly higher under air than under inert atmosphere indicating that a random chain scission occurs

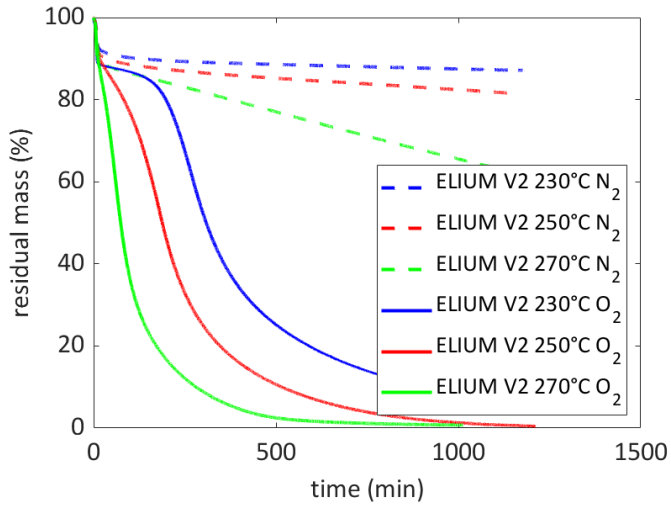

Figure 2. Mass loss curves of thin ELIUM® V2 samples recorded by TGA under N_2 or O_2 atmosphere.

3.3 Stability of thick blocks of ELIUM® resin and its composites under air

Those investigations were used to understand the ageing behavior of thick blocks of ELIUM® and its composites at high temperatures under air, i.e. in conditions closer to the service condition of organic composites. Figure 3 depicts the mass loss of 4 mm blocks.

ELIUM® V1 resin, which has neither comonomers nor antioxidants, is the less stable meanwhile there is a weak difference between ELIUM® V2 and V3 resins. The difference in terms of mass loss between ELIUM® V1, V2 and V3 is very visible on the first stage (before 100 days). After this duration, the apparent mass loss rate seems to reach a value which is almost constant for the 3 systems under investigation at longer times.

There is no evidence of the very strong auto-acceleration associated to oxidation suggesting that the oxidation plays only a negligible role on mass loss.

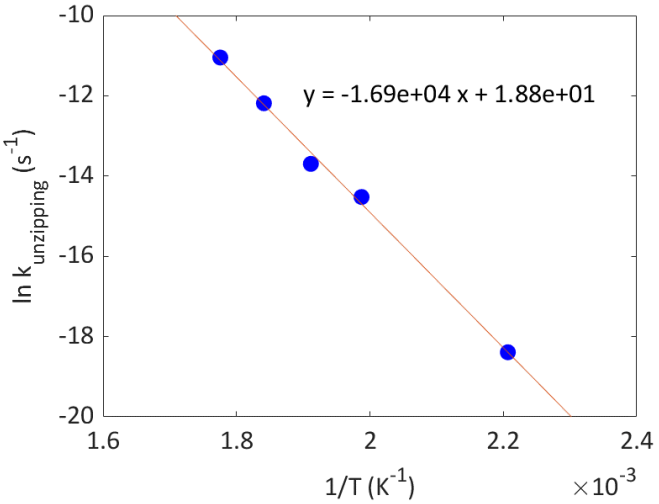

Figure 3. Arrhenius diagram of unzipping rate constant estimated for ELIUM® V2 samples from TGA under N_2 (from Figure 1).

For example, the extrapolation of $k_{unzipping}$ from estimated from Figure 1 allows a very reasonable fitting of ELIUM® V2 and V3 (Figure 4). The slight difference between experimental curves and simulation could be testimony of the existence of a minor oxidation process with a negligible effect on mass loss. Interestingly, the fact that antioxidants present in ELIUM® V3 do not modify the mass loss rate compared to ELIUM® V2 also confirms this hypothesis.

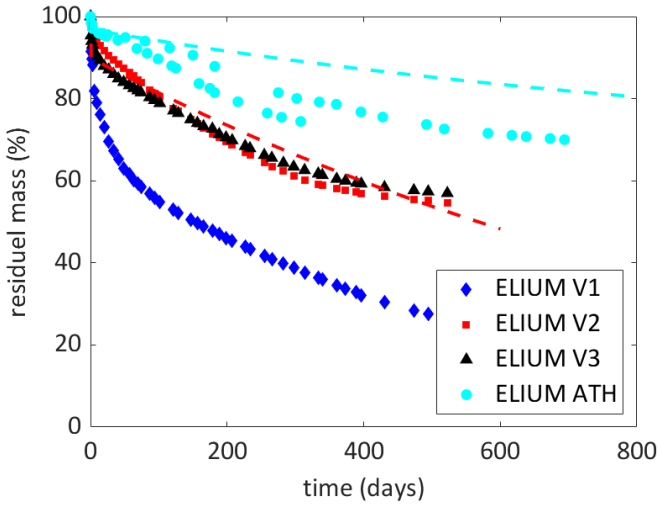

Figure 4. Mass loss curves of 4 mm thick ELIUM® V1, V2, V3 and ELIUM ATH samples at 180°C under air. Dashed lines correspond to simulated mass loss using Eqs. 1 and 2.

ELIUM® ATH composite is the more stable formulation, which can be discussed in the following, having in mind that ELIUM® resin on one side, and fillers on the others, can degrade. To better understand the behavior of this composite, fillers were aged alone (Figure 5). They can be

  doi:10.5075/epfl-298799_978-2-9701614-0-0

observed to be almost stable at the temperature under investigation, keeping in mind that, for example, aluminium trihydrate degraded by dehydration:

$2Al(OH)_3 \rightarrow Al_2O_3 + 3H_2O$ so that the total process induces a mass loss equal to 35%.

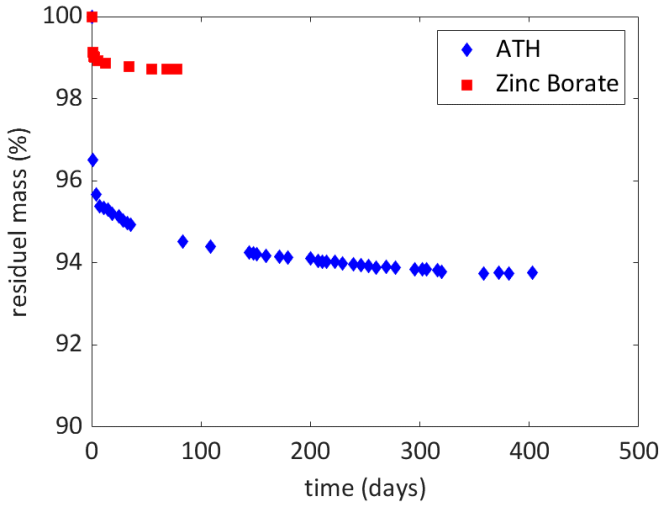

Figure 5. Mass loss curves of zinc borate and aluminium trihydrate at 180°C under air.

The mass loss of A-ATH was thus simulated using:

$$\frac{\Delta m}{m_0} = w_A.\left(\frac{\Delta m}{m_0}\right)_A + w_{ATH}.\left(\frac{\Delta m}{m_0}\right)_{ATH} + w_B.\left(\frac{\Delta m}{m_0}\right)_B \quad (2)$$

where A, ATH and B respectively correspond to ELIUM® resin, aluminium trihydrate, and zinc borate, and w_i are the relative fraction in weight of each component and $(\Delta m/m_0)$ their relative mass loss. The mass loss of ELIUM® composite was thus predicted using Eq 1 for the mass loss of ELIUM part, $k_{unzipping}$ extracted from Figure 3 (as a direct extrapolation of values derived from TGA measurements under inert atmosphere at 230-290°C), $(\Delta m/m_0)_{ATH}$ and $(\Delta m/m_0)_B$ from Figure 4.

The discrepancy between experimental results and this very simple simulation can be interpreted by two ways:

- either the extrapolated $k_{unzipping}$ value is not reliable.

- or there is a “synergy” between degradation of ELIUM® resin and degradation of fillers. One could imagine, for example, that ATH favors the degradation of acrylic group, or that degradation products of ELIUM polymer degrade the ATH filler.

- either oxidation has a more pronounced effect in A-ATH blocks than in ELIUM® samples of comparable thickness, which can be discussed in terms of thickness of degraded layers

This last hypothesis was discussed from the thickness of oxidized layers observed by optical microscopy (Figure 6). The following observations were made:

  doi:10.5075/epfl-298799_978-2-9701614-0-0

- for ELIUM® V2 and ELIUM® V3, the overall thickness decreases in line with unzipping and oxidation induced mass loss.

- the existence of dark edges is characteristic of the oxidation of surface layers, meanwhile the progressive browning observed in the “core” region of the thick blocks is testimony of the existence of chemical modifications in zones where no oxidation occurs.

- the thickness of degraded layer is slightly higher for ELIUM® V3 than for ELIUM® V2. Keeping in mind that the thickness of oxidized layer (TOL) can be approximated from:

$TOL^2 = Pe_{O2}/r_{OX}$, Pe_{O2} being the oxygen permeability and r_{OX} the rate of oxygen consumption in surface, results given in Figure 6 may come from the fact that either stabilizers inhibit the polymerization and induce a lower “crosslinking density in ELIUM® resin, and thus a high value for oxygen permeability or (ii) stabilizer decrease the oxidation rate in surface.

In the case of ELIUM® ATH, a white surface layer is observed. This layer could be constituted of ATH, this latter being almost stable at 180°C (Figure 4) or Al_2O_3. The degraded layer is slightly more degraded (1.5 – 2 mm) than for unfilled resins (about 1-1.2 mm). Since ELIUM® ATH is made from ELIUM® V3, the only possible explanation is that the presence of filler favors the diffusion of oxygen from edge to the bulk.

4. Conclusions

This paper describes the thermal ageing of ELIUM® and its composites. By using an incremental approach, it was observed that this polymer is more stable when comonomers are added, provided those latter slow down the possible thermally induced unzipping. On the contrary, thermal stabilizer hardly slow down the degradation kinetics, which was explained from the fact that thermal unzipping predominates over oxidation effect. In the case of particle filled composites, the oxidation seems increases, in link the possible increase of oxygen diffusivity due to fillers presence.

  doi:10.5075/epfl-298799_978-2-9701614-0-0

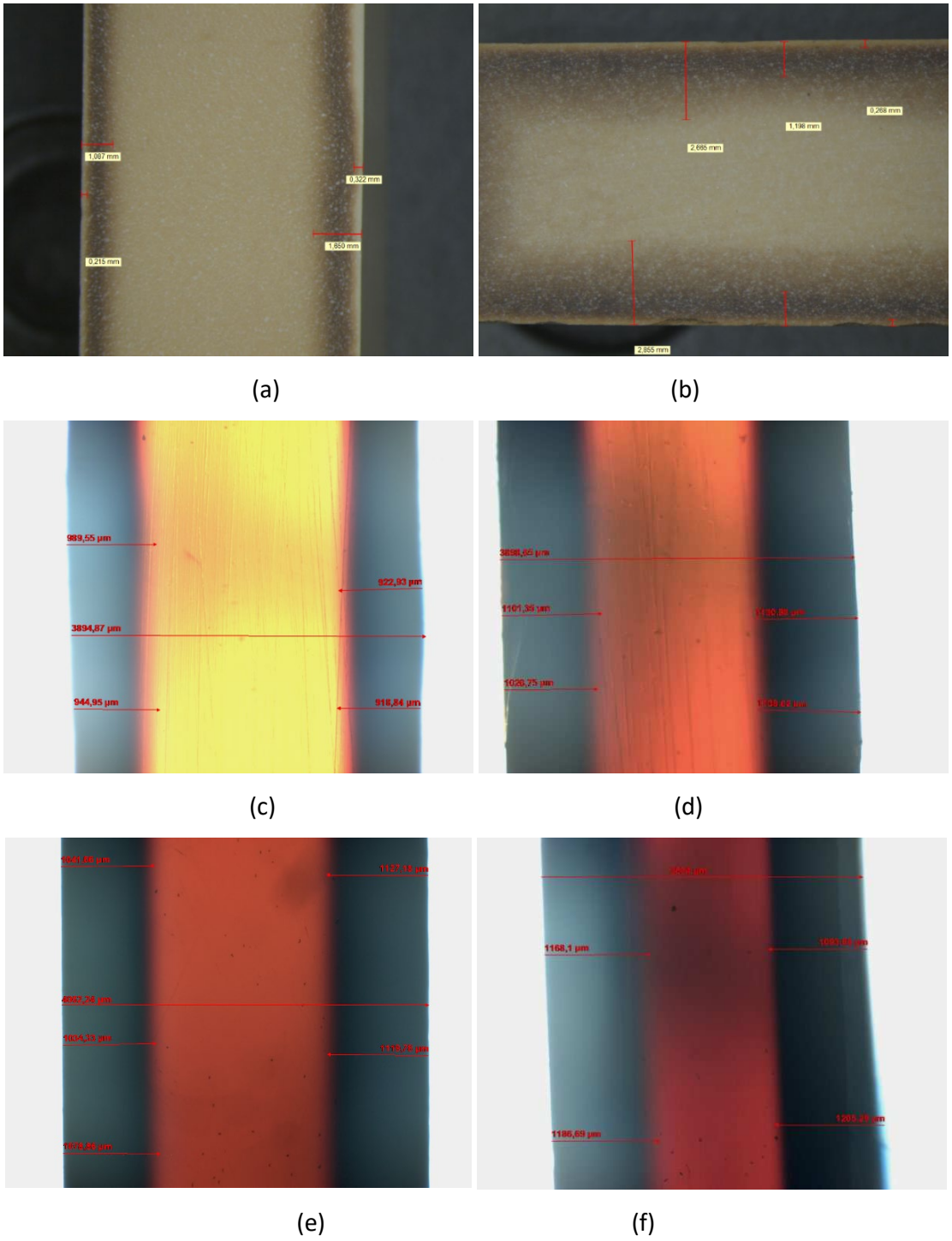

(a) (b)

(c) (d)

(e) (f)

Figure 7. Microscopic observations of ELIUM® ATH aged 1 month (a) and 4 months (b), ELIUM® V2 aged 1 month (c) and 3 months (d), ELIUM® V3 aged 1 month (e) and 11 months (f) at 180°C under air (thickness of samples is close to 4 mm for ELIUM® V2 and ELIUM® V3 and 10 mm for ELIUM® ATH).

5. References

1. Arhant M, Davies P. In « Marine Composites - Design and Performance » Woodhead Publishing Series in Composites Science and Engineering. 2019. Pages 31-53. Chap 2 - Thermoplastic matrix composites for marine applications.
2. Bhudolia SK, Perrotey P, Joshi SC. Optimizing Polymer Infusion Process for Thin Ply Textile Composites with Novel Matrix System. Materials 2017; 10:293.
3. van Rijswijk K, Bersee HEN. Review : Reactive processing of textile fiber-reinforced thermoplastic composites – An overview. Composites: Part A 2007; 38:666-681.
4. Dorigato A. Recycling of thermosetting composites for wind application. Advanced Industrial and Engineering Polymer Research 2021; 4:116-132
5. https://www.arkema.com/japan/en/products/product/incubator/elium/elium-resin-for-composite-hydrogen-tanks/
6. Chebil MS, Bouaoulo G, Gerard P, ElEuch S, Issard H, Richaud E. Oxidation and unzipping in ELIUM resin: Kinetic model for mass loss. Polymer Degradation and Stability 2021; 186:109523
7. Bate DM, Lehrle RS. A new approach for measuring the rate of pyrolysis of cross-linked polymers: evaluation of degradation rate constants for cross-linked PMMA. Polymer Degradation and Stability 1998; 62:67-71.

  doi:10.5075/epfl-298799_978-2-9701614-0-0

STUDIES ON THE SHEAR BEHAVIOR OF TUBULAR BRAIDED FABRICS DURING THE STRETCHING PROCESS

Jinlei, Li[a,b], Gildas , L'Hostis[a,b], Nahiène, Hamila[c], Peng ,Wang[a,b]

a:*University of Haute-Alsace, Ensisa, Lpmt, F-68000 Mulhouse, France* – jinlei.li@uha.fr
b: *University of Strasbourg, France*
c: *Enib, IRDL, F-29000 Brest, France*

Abstract: *Tubular fabrics are increasingly used in composite parts due to their structural integrity. In this study, the Flax/PA12 fibres reinforced fabrics have been performed in the uniaxial tensile test to analyze the deformation and shear behavior. The results show that in the process of fabric stretching, the interwoven yarns approach each other, the included angle is reduced and the shear behavior occurs. The change of the shear angle is closely related to the deformation of the fabrics. At the same time, the length of the yarn remains unchanged with the increase of the shear angle during the stretching process. When the shear angle reaches a certain value, the length of the yarn increases and begins to be stretched. Moreover, during the stretching process, the fabrics undergo a pure shearing stage, stretching and shearing stage, and stretching stage.*

Keywords: tubular braided fabrics; textile composites; shear behavior; stretching process

1. Introduction

Textile composites have been widely used in special-shaped parts due to their excellent properties. Currently, most composite parts are produced by resin transfer molding (RTM) or thermoforming processes [1,2]. During these two manufacturing processes, textile reinforcements forming plays an important role as the first step in the process of manufacturing composite parts. Forming quality of textile reinforcements strongly influences on the mechanical performance of final composite parts [3–8]. Therefore, the mechanical properties of the reinforcements during the preforming process are important. Among textile reinforcements, braided fabrics are gaining increasing attention due to their widespread use in the manufacture of advanced.

A variety of researchers have mainly attached importance to the mechanical properties of braided fabrics. However, most studies focus on flat fabrics. Tubular fabric as a special structure of braided fabric has not been widely carried out yet in the published literature. The tubular braided fabrics obtained by circular braiding provide a high level of both structural integrity and strength to braided composites[9]. And then, it increases the application range of braided fabrics. Not only limited to the aviation and automotive industries, but also have applications in industries such as medicine and sports [10]. The mechanical response of tubular fabrics during the preforming process is critical, which determines the strength of the entire structure. Similar to flat fabrics, tensile behaviour is one of the most important mechanical properties, its characterization was largely analyzed by tensile tests. When the fabric is subjected to tensile load, the interwoven yarns rotate and move closer to each other, a shearing behavior occurs. At the same time, it is accompanied by lateral contraction. And the lateral contraction is symmetrically distributed along the stretching direction.

  doi:10.5075/epfl-298799_978-2-9701614-0-0

The objective of this paper is to study the mechanical properties of tubular braided fabrics under the tensile test. In particular, the shear behaviour of the yarn is characterized. At the same time, the distribution of shear angle along the fabric axial direction is also discussed.

2. Materials and methods

2.1 Materials

The materials used in this study are provided by Schappe Technique. The type of the tubular braided fabrics was Flax/PA12, which were commingled with 64% of flax fibres and 36% of PA12 fibres. The main properties of the Flax/PA12 are noted in Table 1. The length of the specimen is 40 mm (excluding the gripper regions), the diameter of the specimen is 50mm. It is defined that half of the angle of interwoven yarns (β) is the braid angle of the fabrics. During the braiding process, the braid angle can be fixed to 55° (β/2) through the chosen parameters. After the braiding, it can get the tubular braided fabrics (see Fig.1)

Figure 1. Structure of sample

Table 1: The main properties of the tested braided fabrics.

Parameters	
Type of fabric	Biaxial twill 2-2
Area density (g/m2)	376 ± 5
Thickness (mm)	2.06
Braid angle (β/2)	55°

2.2 Stretching process

The tensile tests of tubular braided fabrics were conducted on a INSTRON experimental machine at the LPMT laboratory. The experimental setup is shown in Fig. 2. Both ends of the specimen are fixed on the stretching machine by clamps, and the stretching machine applies force at a uniform speed along the axial direction of the fabrics. The tests are performed at a constant displacement rate of 10 mm/min. The force of deformation and a constant displacement applying on the specimens can be recorded by a force detector, which is linked to the upper jaw.

The force-displacement data are saved on the computer for analysing and post-processing. To accurately analyze the shear deformation characteristics of the tubular fabrics and the change of the shear angle, the three-dimensional scanning software GOM is used to scan the sample (seen in Fi.2). At the same time, it also observes the test process in real-time and records the changing state of the sample with the stretching process.

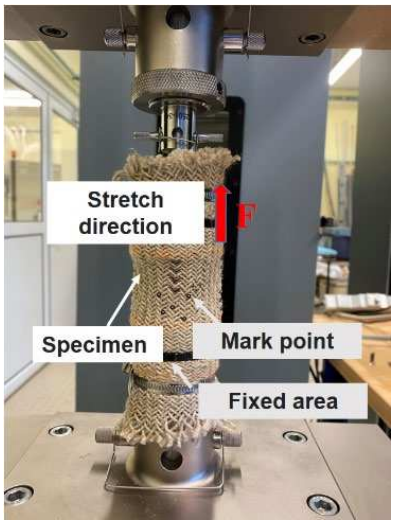

Figure 2. Tensile test on tubular fabrics

3. Results and discussion

In this section, the deformation characteristics of tubular fabrics under tensile load are studied. Four zones of the tubular fabric in the axial direction are selected to analyse, as shown in Fig.3. Due to the symmetry, the shearing characteristics of the whole fabric can be obtained by studying the shear angle distribution of the upper half. The experimental results are shown in Fig.4. The tubular fabric will eventually show a radially contracted shape after the tensile test. It can be noted that the deformability of tubular fabrics depends strongly on the stretching deformation. The radial shrinkage of the fabric is increased along with the fabric extension, resulting in different degrees of shear deformation area.

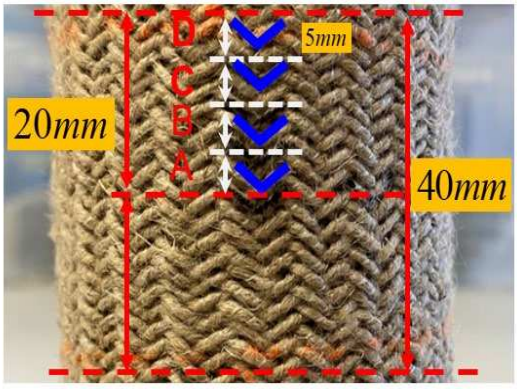

Figure 3. Regional division of tubular fabrics

(a) (b)

Figure 4. Tested tubular braided fabric, (a) before the test and (b) during the test

3.1 Distribution characteristics of the shear zone

Under the tensile load, the shear angle changes in different zones of the tubular fabrics are shown in the Fig.5. It can be seen that when the fabric is stretched, the tensile deformation increases, and shear behavior occurs. The shear angle shows a trend of increasing first and then unchanged. In the early stages of the test, the interwoven yarns are rotated towards each other due to the tensile load. Due to the large shear space between the yarns, the shear angle increases rapidly. When the interwoven yarns contact each other through the shearing process, there is a mutual extrusion effect in the transverse direction of the yarns. This compressive force will reduce the width of the yarns, thereby reducing the increase in the shear angle. Before the fabric failing, the in-plane shear angle hardly changes. At the same time, it can be seen that the shear angles of different zones of the fabric are also different. The shear angle of the middle zone of the fabric is larger than that of the two end zones, and the shearing occurs earlier.

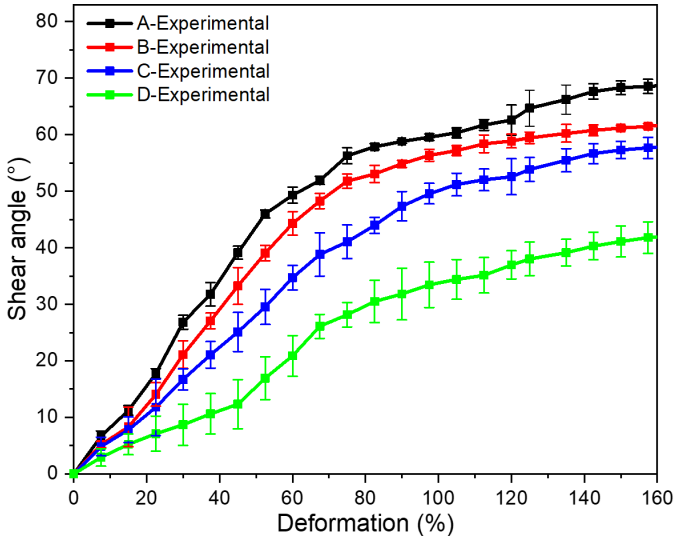

Figure 5. Shear angle distribution in different zones

3.2 The shear mechanical properties of tubular braided fabric

Fig.6 presents load-deformation curves for Flax/PA12 tubular braided samples obtained by extension tests. The curves can be divided into three parties before reaching the maximum shear *load. At first, with the deformation increases, the load increases relatively slowly. This shows* that at the beginning of the experiment, the shear area of the fabric is larger, and a smaller load is needed at this stage to achieve a larger amount of deformation. As the tensile deformation continues to increase, the shear space of the interlaced offset yarns continues to decrease. At this time, the continuous shearing behaviour of the interlaced offset yarns will generate a transverse compressive force along the radial direction of the yarn, and the load will increase rapidly and enter the second stage. When the stretching displacement continues to increase, the shearing space decreases until it no longer exists. The end of the shearing behaviour may be accompanied by the stretching phenomenon, and then the third stage is entered.

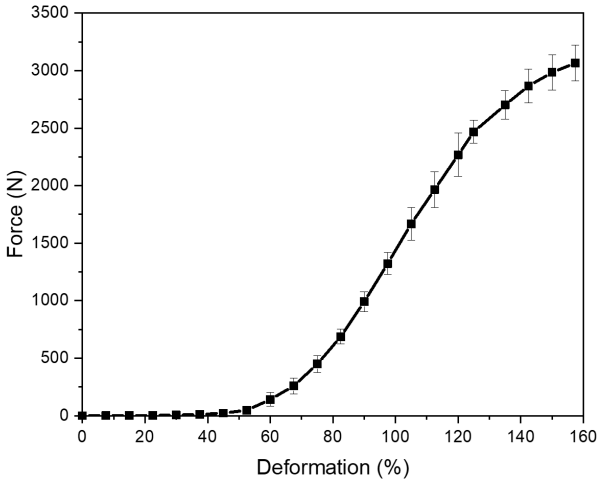

Figure 6. Load vs. displacement of Flax/PA12 specimen during the test

In order to analyse the shear behaviour of tubular braids under tensile load more accurately, the tensile response of a single yarn of the fabric has also been studied. As described in section 2.2, after the tubular fabric is fixed on the stretching machine, mark points are made on a single yarn. Meanwhile, the GOM software can be used to identify the mark point and obtain the length change of a single yarn during the entire stretching process.

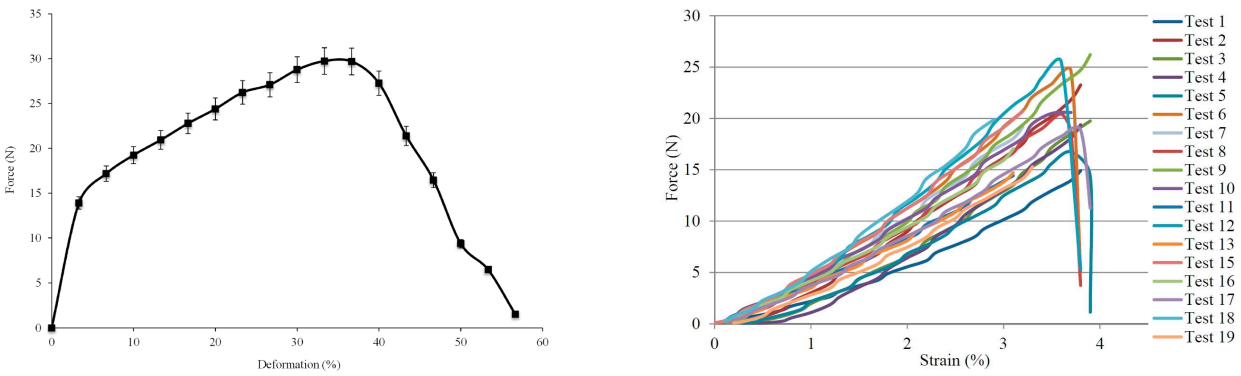

(a) (b)

Figure 7. Tensile results. a) single flax/PA12 yarn and b) pure flax yarns

  doi:10.5075/epfl-298799_978-2-9701614-0-0

Combining with the tensile result of a single flax/PA12 yarn at room temperature (Fig.7a) [11], it can be seen that when a single yarn is deformed at about 3%, there will be a steep increase in force, which is similar to the results of pure flax yarn under tensile force, as shown in Fig. 7b [12]. So, the pure Flax breaks after a shorter deformation with a rapid increase under the tensile force during the test. Therefore, it shows that the third stage in the stretching process of the tubular fabric is caused by the fracture of Flax under the action of the tensile load, and the subsequent tensile load is carried by the PA12. At the same time, it is also the reason for the change in the load slope and causes the third stage of the load-deformation curve (Fig.6). In this stage, the shear angle changes slowly and the shearing action ends. The fabric shearing characteristic in this stage is defined as a pure stretching process.

4. Conclusion

The shear behavior and mechanical properties of the tubular braided fabrics under tensile load is analysed in the present study. The shear angle of the fabric gradually decreases from the center of the fabric to the two ends, which means that the closer the area in the axial direction to the center of the fabric, the larger shear space in this area, and the easier it is to shear under the same load. The shear angle also increases faster. On the other hand, the obtained results reveal that the tubular fabric undergoes three stages of pure shearing, shearing and stretching coexistence, and pure stretching during the tensile process. This is caused by the shear between yarns and the breakage of pure flax.

Acknowledgements

This work was supported by the China Scholarship Council (CSC).

5. References

1. Ruiz E, Trochu F. Flow modeling in composite reinforcements. Compos Reinf Optim Perform. 2011 Jan 1;588–615.

2. Campbell F. Manufacturing Technology for Aerospace Structural Materials. Manuf Technol Aerosp Struct Mater. 2006;

3. Bickerton S, Šimáček P, Guglielmi SE, Advani SG. Investigation of draping and its effects on the mold filling process during manufacturing of a compound curved composite part. Compos Part A Appl Sci Manuf. 1997 Jan 1;28(9–10):801–16.

4. Bel S, Hamila N, Boisse P, Dumont F. Finite element model for NCF composite reinforcement preforming: Importance of inter-ply sliding. Compos Part A Appl Sci Manuf. 2012 Dec 1;43(12):2269–77.

5. Boisse P, Hamila N, Vidal-Sallé E, Dumont F. Simulation of wrinkling during textile composite reinforcement forming. Influence of tensile, in-plane shear and bending stiffnesses. Compos Sci Technol. 2011 Mar 22;71(5):683–92.

6. Liu LS, Zhang T, Wang P, Legrand X, Soulat D. Influence of the tufting yarns on formability of tufted 3-Dimensional composite reinforcement. Compos Part A Appl Sci Manuf. 2015 Nov 1;78:403–11.

7. Wang P, Legrand X, Boisse P, Hamila N, Soulat D. Experimental and numerical analyses of manufacturing process of a composite square box part: Comparison between textile

  doi:10.5075/epfl-298799_978-2-9701614-0-0

reinforcement forming and surface 3D weaving. Compos Part B Eng. 2015 Sep 1;78:26–34.

8. Wang P, Hamila N, Boisse P. Thermoforming simulation of multilayer composites with continuous fibres and thermoplastic matrix. Compos Part B Eng. 2013 Sep 1;52:127–36.

9. Rawal A, Saraswat H, Kumar R. Tensile response of tubular braids with an elastic core. Compos Part A Appl Sci Manuf. 2013;47(1):150–5.

10. Ayranci C, Carey J. 2D braided composites: A review for stiffness critical applications. Compos Struct. 2008;85(1):43–58.

11. Xiao S, Wang P, Soulat D, Gao H. Thermo-Mechanical Characterisations of Flax Fibre and Thermoplastic Resin Composites during Manufacturing. Polym 2018, Vol 10, Page 1139 [Internet]. 2018 Oct 12 [cited 2022 Mar 20];10(10):1139. Available from: https://www.mdpi.com/2073-4360/10/10/1139/htm

12. Omrani F, Wang P, Soulat D, Ferreira M. Mechanical properties of flax-fibre-reinforced preforms and composites: Influence of the type of yarns on multi-scale characterisations. Compos Part A Appl Sci Manuf. 2017 Feb 1;93:72–81.

  doi:10.5075/epfl-298799_978-2-9701614-0-0

MECHANICAL CHARACTERISATION OF SOME POLYMERS USED IN 3D PRINTING

Andrey Aniskevich[a], Edmunds Zīle[a], Olga Bulderberga[a], and Daiva Zeleniakiene[b]

a: Institute for Mechanics of Materials, University of Latvia, Riga, LV-1004, Latvia – Andrey.Aniskevich@pmi.lv
b: Department of Mechanical Engineering, Kaunas University of Technology, Kaunas, Lithuania

Abstract: *With the advancement of fused deposition modelling (FDM), there is a great need for new high-performance materials capable of meeting the requirements of different engineering applications. This study focuses on the comparative evaluation of mechanical characteristics of such thermoplastic polymers processed by FDM as PLA (several variants), PC, PA, ABS, TPU95A, PP, CPE, PET-G, PEI, and PEKK. Tensile properties of "as-produced" filaments, extruded mono-fibres, and unidirectional printed specimens are compared. The compatibility of different polymer types for hybrid structures is evaluated in the adhesion tests.*

Keywords: Fused deposition modelling; Density; Tensile modulus; Strength

1. Introduction

Fused deposition modelling (FDM) is a rapidly growing 3D printing technology utilising a thermoplastic filament that is melted and then extruded through a nozzle. The digitally controlled nozzle deposits the liquefied material on the platform to build the part in a layer-by-layer manner. A wide range of materials is used in FDM 3D printing. Polylactic acid (PLA) is a compostable, biodegradable, high-strength, high-modulus thermoplastic made from renewable sources. Zhao et al. [1] demonstrated that printing parameters significantly influence the tensile strength and Young's modulus of the printed PLA material. Acrylonitrile butadiene styrene (ABS) is a widely used thermoplastic material in FDM due to its good melt fluidity, acceptable stiffness and strength, and resistance to wear and impact. ABS was one of the first materials used for 3D printing. Petruse et al. [2] performed tensile tests of 100 specimens printed from ABS material and determined that fibre orientation has the most significant influence on the physical properties. Polyetherimide (PEI) is becoming a popular material for FDM printing due to its adhesive properties and chemical stability. Gilmer et al. [3] noted that, while PEI is of great interest because of its desirable mechanical properties and high use temperatures, it also creates a more challenging modelling problem with higher thermal gradients and greater potential thermal processing window compared to more traditional FDM materials, such as ABS and PLA. An exceptional chemical and thermal resistance combined with outstanding mechanical properties make polyetherketoneketone (PEKK) an interesting material for high-end applications. Polyethylene terephthalate glycol (PETG) is characterised by notable tensile toughness, transparency, flexibility, high processability and excellent chemical resistance. Guessasma et al. [4] studied the printability of PETG for fused deposition modelling. The study reported that PETG could be printed within a limited range of printing temperatures (240–250 °C). Co-polyester (CPE) is a very strong and versatile material with growing popularity in filament form for FDM printing. Abouzaid et al. [5] investigated the printability conditions of a co-polyester based polymer. A strong relationship was found between thermal cycling, tensile

  doi:10.5075/epfl-298799_978-2-9701614-0-0

properties and printing temperature. Polypropylene (PP) is a semicrystalline polymer extensively used in packaging, furniture production, medical and automotive applications. Carneiro et al. [6] addressed the potential of PP as a candidate for FDM. They found that the thickness of the layers had little influence on the mechanical performance of the samples, but the infill degree had a dramatic and linear effect on the mechanical properties. Thermoplastic elastomers such as thermoplastic polyurethane (TPU) have low modulus, high flexibility and high elongation to breakage. These are commonly used to produce medical parts with good mechanical performance [7], strain sensors etc. TPU has a low glass transition temperature and high crystallisation rate and, thus, are suitable for FDM processing. Polyamide (PA) is commonly referred to as nylon. As indicated by Zhang et al. [8], FDM fabricated products based on pure PA are seriously warped, distorted, and lack of shape stability due to the accumulation of shrinkage stress generated from the crystallisation of polymer, which then severely restricts the application of PA in 3D printing. Polycarbonate (PC) is a transparent material resistant to very high temperatures, slightly flexible and highly resistant to impacts. Similar to other thermoplastics, parts printed from PC are also highly anisotropic in tensile and shear properties. Cantrell et al. [9] found that depending on the raster orientation in the flat build PC samples, the moduli and strengths varied by up to 20%.

Knowledge about the basic mechanical properties of the source filaments and simple specimens is of key importance for further predicting printed structure properties and their reliable design. The aim of this study focuses on the comparative evaluation of mechanical characteristics of such thermoplastic polymers processed by FDM as PLA (several variants), PC, PA, ABS, TPU95A, PP, CPE, PET-G, PEI, and PEKK. Tensile modulus and strength of “as-produced” filaments, extruded mono-fibres, and unidirectional printed specimens are compared. The compatibility of different polymer types for hybrid structures is evaluated in the adhesion tests.

2. Experimental procedure

2.1 Materials and printer settings

Ultimaker 3D printers S5 and 2+Connect (Ultimaker B.V., The Netherlands) with a 0.4 mm diameter nozzle were used to produce the specimens from the filament of 2.85 mm diameter. The nozzle and bed temperatures depend on the material and are given in Table 1. The print head speed was 20 mm/s. The layer thickness was set at 0.1 mm for most specimens, as seen in Table 1. In all cases, the infill pattern was set “Lines”, fibre width (“Line width”) was set to 0.35 mm, and infill density was set to 100%. Shell and Top/Bottom thickness settings were set to zero. These printer settings provided the unidirectional orientation of all filament fibres in all specimens and uniform within any specimen’s cross-section.

Table 1: List of tested materials.

Material, Short name, grade	Supplier	Nozzle temperature, ℃	Bed temperature, ℃	Layer thickness, mm
Polylactic acid, PLA Tough White 20231	Ultimaker	225	70	0.1
PLA Tough Black 202300	Ultimaker	225	70	0.2
PLA Red	Devil Design	200	60	0.1, 0.3
PLA Super Blue	Devil Design	200	60	0.1

  doi:10.5075/epfl-298799_978-2-9701614-0-0

PLA LAVA*, CY190415lyjzys2	Hello3d	200	60	0.1
PLA conductive**, CDP12805 Batch 171201	Proto-pasta	200	60	0.1
Polyethylene terephthalate glycol, PET-G, White	Devil Design	235	85	0.1
Acrylonitrile butadiene styrene, ABS, White 1622	Ultimaker	240	85	0.1
Co-polyester, CPE, White UM-9703-A	Ultimaker	240	70	0.1
Polycarbonate PC, White 1642	Ultimaker	270	110	0.1
Polypropylene, PP, Natural	Ultimaker	225	70	0.1
Thermoplastic polyurethane, TPU95A, White 1755	Ultimaker	223	70	0.1
Polyamide PA, Nylon Transparent 1647	Ultimaker	245	70	0.1, 0.2
Poly(ether ketone ketone) PEKK, Antero 800NA	Stratasys	395	180	0.25
Polyetherimide, PEI, ULTEM 9085 CG	Stratasys	385	180	0.25

* Thermochromic.

**Filled with carbon black.

2.2 Single extruded fibres

A series of samples of a single extruded fibre with an average diameter of 0.42 ± 0.06 mm and length of approx. 140 mm was tested in tension. Tensile tests were performed on the ZWICK 2.5 machine with a 10 mm/min test speed. The tensile strain was calculated by a grip-to-grip separation with a starting value of 100 mm. Elastic modulus was calculated in the strain range of 0.05–0.25%.

2.3 Fabrication of specimens for tensile tests

Standard ISO_527-2_1B dog-bone specimens having a length of 150 mm and cross-section size in the working zone of 3×10 mm were used for tensile testing. Tensile tests were performed on the ZWICK 2.5 machine with a 1 mm/min crosshead displacement rate. The tensile strain was measured using a clip-on extensometer with a base length of 30 mm. Pre-load of 0.5 N was applied to all samples. Elastic modulus was calculated in the strain range of 0.05-0.25%. Strain measurement was switched on grip-to-grip separation above the value of 0.7% and related to the starting value of 110 mm. Three to five specimens were tested for each series, and average data were used. These standard dog-bone specimens had an angle θ between the fibre direction and specimen longitudinal axis equal to 0 and 90°. Specimens with θ = 0° allow the

  doi:10.5075/epfl-298799_978-2-9701614-0-0

determination of the longitudinal elastic modulus and longitudinal strength. Transverse elastic modulus and transverse strength were determined on the specimens with θ = 90°.

The geometry of adhesion/cohesion specimens is shown in Figure 1. “Dog-bone”-like specimens had square cross-sections of 10 × 10 mm from both ends to be fixed in a testing machine. This cross-section was gradually transformed into a circular one of 10 mm diameter in the middle of a specimen. All specimens have a circular groove in the middle to facilitate failure in this location. The groove is also a location where the different printing materials are joined. The adhesion contact area was a circle of 8 mm in diameter.

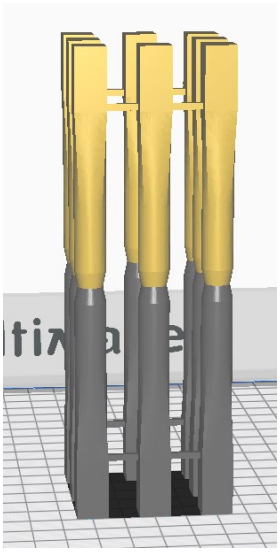

Figure 1. Adhesion/cohesion test hybrid samples

3. Experimental results and discussion

3.1 Density

The FDM process inevitably introduces voids in the produced material. A typical cross-section image of printed material (example of PLA Red) showing the voids is presented in Figure 2. To assess the effect of the printing process on the extruded mono-fibres and printed part, density measurements were performed, and the obtained results are shown in Figure 3. The manufacturer’s data were taken from the Technical Data Sheets (TDS) or the manufacturer’s websites.

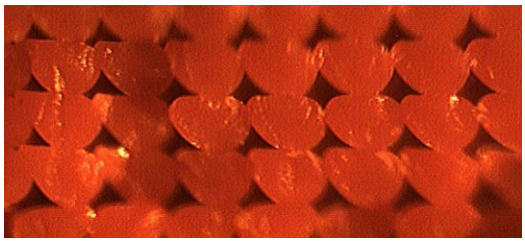

Figure 2. Typical sample cross-section image (example of PLA Red)

The filament density was calculated assuming its cylindrical form using weight (± 0.00001 g), measured diameter ca. 2.85 mm (± 0.001 mm), and length ca. 100 mm (± 0.01 mm). Results for three specimens were averaged. No systematic deviation of TDS and measured data was

  doi:10.5075/epfl-298799_978-2-9701614-0-0

revealed, although disagreement ranged from -2 to +3%. The average difference between the TDS data and the measured density of "as-produced" filaments was 1.7%. The density of extruded fibre was also calculated for a cylinder with the same accuracy of measurements for specimens of ca. 1000 mm length. For all materials, the density of extruded fibre is higher than the filament density. The average difference is 4.4% (TPU95A White was excluded due to the anomaly in results), indicating a polymer's slight compaction during the extrusion.

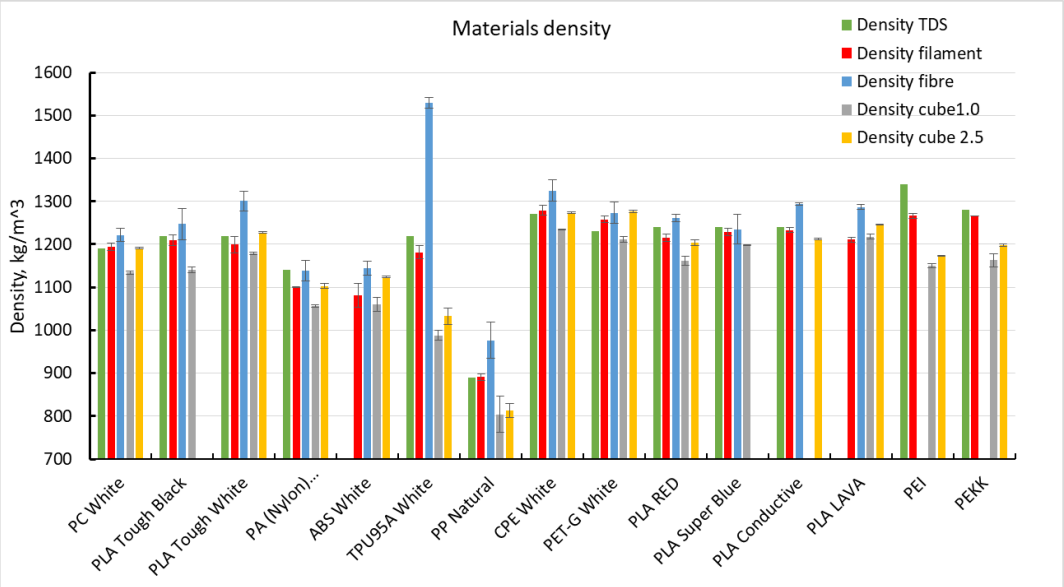

Figure 3. The density of tested materials

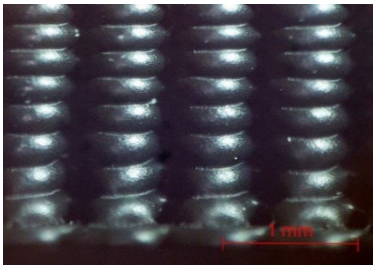

Figure 4. Typical side face of the printed cube with an edge length of 1 cm (example of PLA Tough Black)

Two types of cubes were printed out: one group had an edge length of 1 cm, the other one of 2.5 cm. The cubes with an edge length of 1 cm were used to determine the "production" density of the printed material as the effect of cube side face unevenness due to the printing process (see Figure 4) was taken into account. The faces of the cube with an edge length of 2.5 cm were polished to determine the "true" density of the same structure. Due to the rough side faces, the "production" density was always lower than the "true" density on average by 3.6%.

3.2 Comparative Tensile modulus and strength

Experimental results on the tensile modulus are presented in Figure 5. In most cases, the modulus of "as-produced" filaments was lower than the modulus of the extruded mono-fibres by 12% on average. In the case of PLA materials, this difference was significant up to 20-30%, but for the PC, ABS, PP, CPE, and PET-G materials, the difference between the moduli was small (1–2%) or negligible. For the PEI and PEKK materials, these data were not available. The effect

  doi:10.5075/epfl-298799_978-2-9701614-0-0 published under CC BY-NC 4.0 license

mentioned above can be explained by the polymer molecular orientation, in which the polymer chains change their alignment above the glass transition temperature. As seen from the experiments, this can significantly affect the modulus of the extruded mono-fibre, as orienting polymer chains further improve the strength and modulus in the orientation direction [10]. The FDM printing process is similar to the methods used in conventional manufacturing to produce high modulus, high strength polymers. As seen from the experiments, the molecular orientation effects are dependent on the bulk material type. The PA (Nylon Transparent) material will be retested in future studies as the currently obtained experimental results show anomalous characteristics.

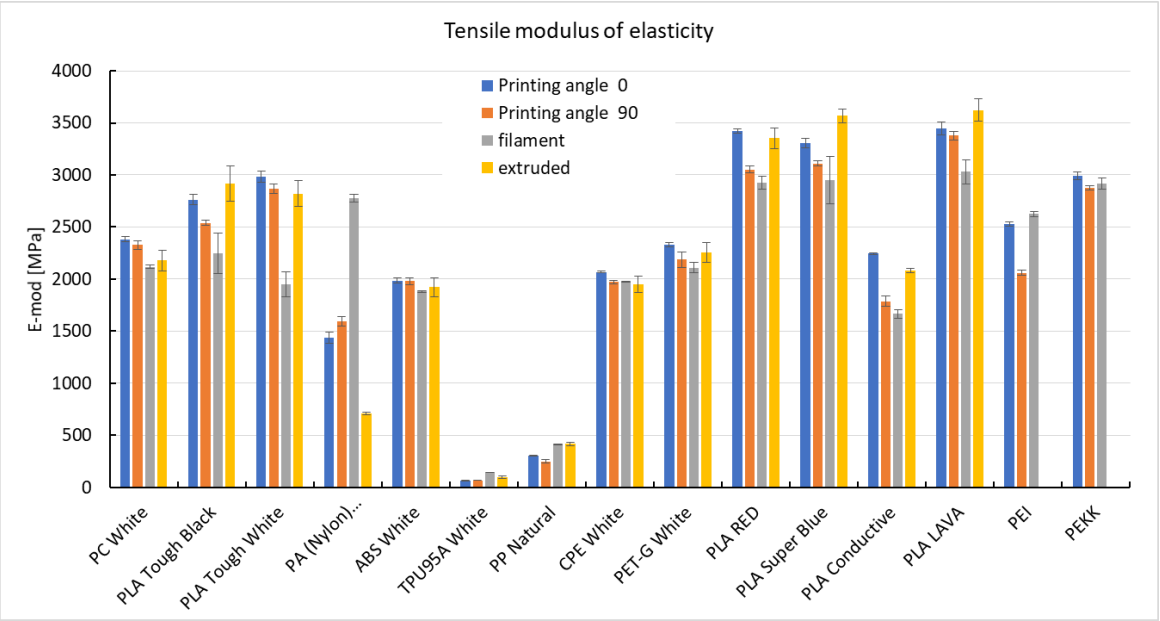

Figure 5. Experimental values of tensile modulus

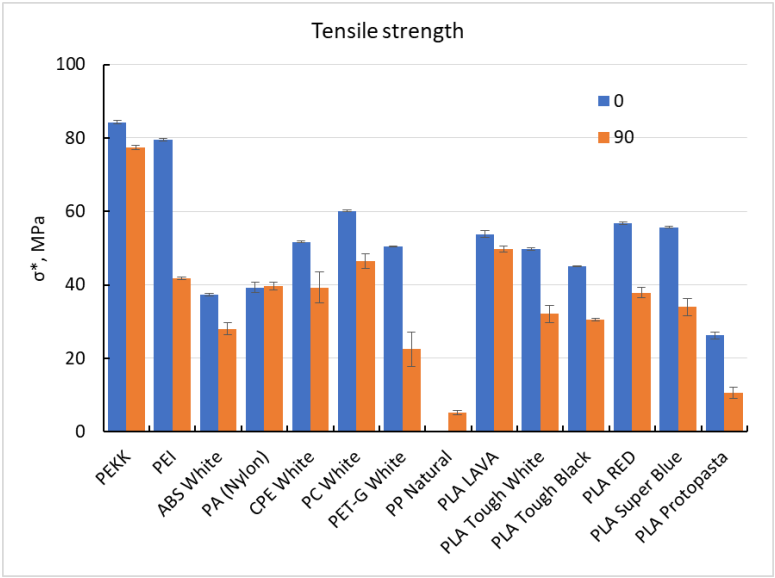

Figure 6. Experimental values of tensile strength

Due to the presence of voids, the transverse elastic modulus (θ = 90°) of the printed structure was always lower than its longitudinal modulus (θ = 0°), except for the anomalous PA (Nylon

Transparent) material. The same behaviour can be observed for the tensile strength (see Figure 6). The transverse modulus and strength were lower than longitudinal ones on average by 7.5 and 30%, respectively.

3.3 Cohesion/Adhesion

Adhesion tests were performed to evaluate the compatibility of different polymer types. Test results are presented in Figure 7. The strength of PLA Tough Black / Tough White pair is lower than the strength of pure Tough Black and Tough White specimens, indicating the possible influence of different colourant additive mix at the interface between extruded fibres. Interestingly, the PLA LAVA / Tough White pair has the same strength as the pure Tough White specimen even though PLA LAVA contains special additives which change their molecular structure with temperature changes, thus changing the colour of the printed object. Further studies will be devoted to determining the effect of chemical additives. The adhesion test of PLA Conductive Protopasta – PLA Tough White showed a very low result.

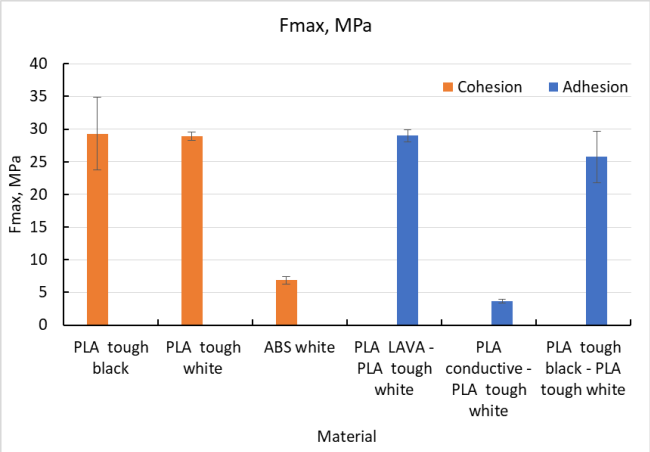

Figure 7. Tension test results of cohesion/adhesion specimens

Analysis of fracture surfaces showed that half of the specimens had clear adhesion fracture with no traces of the second component for hybrid contact of PLA Tough White- PLA Tough black. Another half of the specimens had mainly cohesion fracture character with traces of PLA White on the surface of PLA Black. A similar result was obtained for hybrid contact of PLA Tough White – PLA LAVA. Half of the specimens had adhesion fracture with weak traces of the White component on PLA Lava surface. Another half of the specimens had mainly cohesion fracture character with clear traces of PLA White on the surface of PLA Lava. Finally, all specimens for the hybrid of PLA Tough White – PLA Conductive Protopasta had evident cohesion fracture through PLA Conductive with traces of black-on-white.

4. Conclusions

This paper performed a comparative evaluation of the mechanical characteristics of PLA, PC, PA, ABS, TPU95A, PP, CPE, PET-G, PEI, and PEKK thermoplastic polymers processed by FDM. The following conclusions have been drawn:

- For all materials, the density of extruded fibre is higher than the filament density. The average difference is 4.4%. Additionally, the “production” density is always lower than

  doi:10.5075/epfl-298799_978-2-9701614-0-0

the “true” density on average by 3.6% due to the presence of rough surfaces naturally occurring during printing.

- In most cases, the elastic modulus of “as-produced” filaments is lower than the modulus of the extruded mono-fibres by 12% on average. In the case of PLA materials, this difference is significant (20-30%).
- Due to the presence of voids, the transverse elastic modulus and strength of the printed structure are always lower than its longitudinal modulus and strength.
- Tests showed that adhesion at hybrid PLA contact is only slightly affected by the presence of colourant additives in one of the parts. However, huge adhesion reduction was observed when one of the parts contained conductive particles.

Acknowledgements

This research was supported by ERDF Project No. 1.1.1.1/19/A/031 “OPTITOOL, Decision Tool for Optimal Design of Smart Polymer Nanocomposite Structures Produced by 3D Printing”.

5. References

[1] Zhao Y, Chen Y, Zhou Y. Novel mechanical models of tensile strength and elastic property of FDM AM PLA materials: Experimental and theoretical analyses. Mater Des 2019;181:108089. https://doi.org/10.1016/j.matdes.2019.108089.

[2] Petruse RE, Puşcaşu S, Pascu A, Bondrea I. Key factors towards a high-quality additive manufacturing process with ABS material. Mater Today Proc 2019;12:358–66. https://doi.org/10.1016/j.matpr.2019.03.136.

[3] Gilmer EL, Anderegg D, Gardner JM, Sauti G, Siochi EJ, McKnight SH, et al. Temperature, diffusion, and stress modeling in filament extrusion additive manufacturing of polyetherimide: An examination of the influence of processing parameters and importance of modeling assumptions. Addit Manuf 2021;48:102412. https://doi.org/10.1016/j.addma.2021.102412.

[4] Guessasma S, Belhabib S, Nouri H. Printability and Tensile Performance of 3D Printed Polyethylene Terephthalate Glycol Using Fused Deposition Modelling. Polymers 2019;11:1220. https://doi.org/10.3390/polym11071220.

[5] Abouzaid K, Guessasma S, Belhabib S, Bassir D, Chouaf A. Printability of co-polyester using fused deposition modelling and related mechanical performance. Eur Polym J 2018;108:262–73. https://doi.org/10.1016/j.eurpolymj.2018.08.034.

[6] Carneiro OS, Silva AF, Gomes R. Fused deposition modeling with polypropylene. Mater Des 2015;83:768–76. https://doi.org/10.1016/j.matdes.2015.06.053.

[7] Haryńska A, Gubanska I, Kucinska-Lipka J, Janik H. Fabrication and Characterization of Flexible Medical-Grade TPU Filament for Fused Deposition Modeling 3DP Technology. Polymers 2018;10:1304. https://doi.org/10.3390/polym10121304.

[8] Zhang X, Fan W, Liu T. Fused deposition modeling 3D printing of polyamide-based composites and its applications. Compos Commun 2020;21:100413. https://doi.org/10.1016/j.coco.2020.100413.

[9] Cantrell JT, Rohde S, Damiani D, Gurnani R, DiSandro L, Anton J, et al. Experimental characterization of the mechanical properties of 3D-printed ABS and polycarbonate parts. Rapid Prototyp J 2017;23:811–24. https://doi.org/10.1108/RPJ-03-2016-0042.

[10] Bigg DM. Mechanical property enhancement of semicrystalline polymers?A review. Polym Eng Sci 1988;28:830–41. https://doi.org/10.1002/pen.760281303.

STXM: NANOSCALE 2D/3D CHEMICAL IMAGING

Benjamin Watts[a], Simone Finizio, Jörg Raabe

a: Paul Scherrer Institute, Forschungsstrasse 111, 5232 Villigen-PSI, Switzerland –
benjamin.watts@psi.ch

Abstract: *Scanning transmission X-ray microscopy (STXM) uses a focused X-ray beam to measure spectra and images with a spatial resolution better than 50 nm. The application of various spectroscopic effects allows STXM to achieve strong, natural contrast mechanisms based on materials properties such as elemental composition, molecular structure, molecular orientation, oxidation state, and/or magnetisation. Since X-ray absorption spectra combine linearly, STXM can be used to quantitatively map a variety of chemical and physical properties in composite materials at the nanoscale. Further, a set of projection images can be used to reconstruct the sample volume in 3D.*

Keywords: X-ray; Microscopy; Nanoscale; Imaging; 3D

1. Introduction

Materials characterisation is crucial for materials development and as the materials we create become more complex, further advanced characterisation techniques are needed to assess how well the intended properties and structures have been achieved. X-ray imaging has been an important materials characterisation technique for many years due to its penetrative power and high resolution due to the very short wavelengths. Bright synchrotron radiation sources have allowed X-ray imaging to progress into nanoscale spatial resolution, 3D imaging, and tunable contrast mechanisms [1,2]. In particular, soft X-ray spectroscopy provides many opportunities to interrogate the chemical and physical properties of a material, and its combination with nanoscale spatial resolution in an X-ray microscope produces image contrast that allows unique views into the structures and properties of a material [3]. Here, we present the working principles of scanning transmission X-ray microscopy (STXM) alongside example research from the PolLux STXM [4] (Paul Scherrer Institute, Switzerland) that is relevant to the field of composite materials. Synchrotron-based instruments such as PolLux are readily available to all researchers through a “user facility” access model [5].

2. Experimental Method

2.1 Soft X-ray Spectroscopy

Soft X-ray spectroscopy is a powerful tool for materials characterisation that probes the electronic structure of a specific element to provide chemical and physical information. X-rays interact with matter via the electrons and so any understanding of X-ray spectroscopy must be based on electronic states and transitions [6]. On a wide scale, the X-ray absorption spectrum of a material usually involves a gradual reduction in intensity as the photon energy increases (i.e. increasing penetration power), with discrete step increases at photon energies corresponding to the binding energy of electron shells (i.e. the X-ray has enough energy to eject the electron from the atom) associated with the constituent atoms of the sample. At this level, the X-ray absorption spectroscopy (XAS) only provides information on the samples elemental composition

  doi:10.5075/epfl-298799_978-2-9701614-0-0

and density. However, if we examine the "fine structure" occurring close to the steps (called absorption edges) then we can observe resonance peaks that correspond to specific electronic transitions from the same initial core state, to final states that are empty in the excited atom [6]. The examination of these near-edge resonances is called either near-edge X-ray absorption fine structure spectroscopy (NEXAFS) or X-ray absorption near-edge spectroscopy (XANES) and therefore indirectly indicates the chemical state of the element as the final states of the resonances correspond to types of bonding the atom is participating in [6]. For example, NEXAFS resonances at the Fe L-edge (near 700 eV) allow one to differentiate between Fe^{2+}, Fe^{3+} and metallic states [7]. This is particularly powerful for organic samples as carbon K-edge (near 300 eV) NEXAFS spectra display resonances corresponding to the anti-bonding molecular orbitals of the sample material [1,3,6].

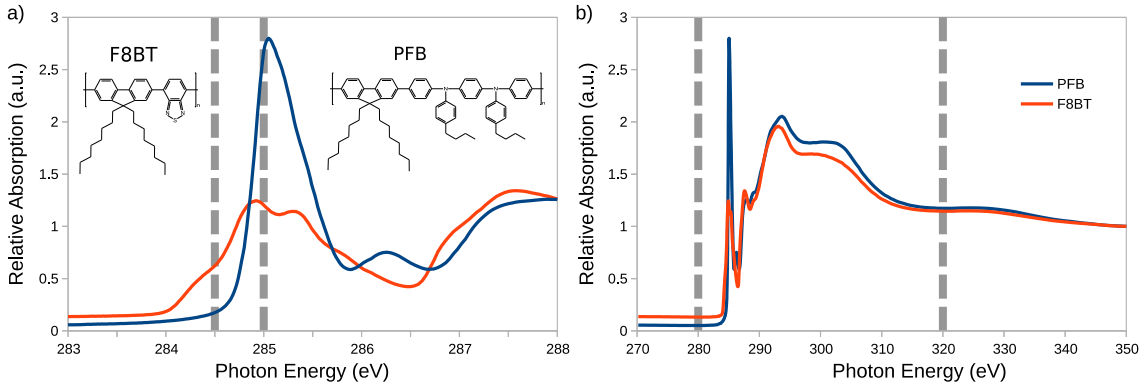

Figure 1. Molecular structures and NEXAFS spectra of PFB and F8BT a) showing detail of the pi resonances and b) a wider view of the C K-edge spectral region. Dashed vertical lines indicate the X-ray photon energies of the images in Figure 2a.*

Figure 1 shows the molecular structures and NEXAFS spectra of two polymers: poly[(9,9-dioctylfluorenyl-2,7-diyl)-co-bis(N,N'-(4,butylphenyl))bis(N,N'-phenyl-1,4-phenylene)diamine] which goes by the acronym PFB, and poly[(9,9-dioctylfluorenyl-2,7-diyl)-co-(1,4-benzo-{2,1',3}-thiadiazole)] which goes by the acronym F8BT. These spectra display a step-increase in X-ray absorption between 280 eV and 320 eV (that can be regarded as photo-excited electronic transitions to the vacuum continuum) and a set of peak resonances that can be attributed to transitions to discrete bound states. The general attributions of the resonance peaks is presented in Table 1.

Table 1: General positions of C K-edge resonances [8].

Photon Energy (eV)	Electronic Transition	Associated Bond
285	$C1s \rightarrow \pi^*_{C=C}$	Double-bonded carbon
286	$C1s \rightarrow \sigma^*_{C-N}$	Carbon – nitrogen single bond
287	$C1s \rightarrow \sigma^*_{C-H}$	Carbon – hydrogen bond
293, 300	$C1s \rightarrow \sigma^*_{C-C}$	Carbon – carbon bond

  doi:10.5075/epfl-298799_978-2-9701614-0-0

In both spectra, the resonances between 284 eV and 286 eV are attributed to C1s→π*$_{C=C}$ transitions, meaning that the final states correspond to the π-type anti-bonding states of the carbon-carbon double bonds. In the case of PFB, these resonances occur at the same energy, resulting in a single sharp peak. In F8BT, however, the π*$_{C=C}$ resonances are split into slightly different energies, resulting in a group of peaks that are overall shorter and wider. The spectral differences between PFB and F8BT means that X-ray measurements conducted at a photon energy of 284.5 eV or 285 eV will show stark differences between these materials.

A further useful property of X-ray spectroscopy is that intermolecular effects are not significant and so the spectrum of a mixed sample is a simple linear combination of the component spectra [6,8]. An exception to this rule is dichroism effects that can be observed in special circumstances. In linear dichroism, the spatial arrangement of the final-state molecular orbital gives a preferred direction for the electronic transition and so the strength of the corresponding resonance depends on the relative orientation of the X-ray polarisation [1,6,9]. X-ray magnetic circular dichroism (XMCD) causes the resonance strength to depend on the local magnetisation since the local field biases the unoccupied final-states towards electrons of a particular spin [3].

2.2 Scanning Transmission X-ray Microscopy

Scanning transmission X-ray microscopy (STXM) uses a very simple optical setup to sequentially measure a set of pixels having particular sample positions (for images) and incident X-ray energy (for spectroscopy) [9]. Focusing is performed with a Fresnel zone plate to produce spot sizes typically of about 30 nm, but can also be as small as 7 nm [10]. Nanoscale positioning precision and repeatability is achieved via laser interferometer metrology and feedback of the signal to the scanning stages [4].

While the lack of parallelism in the STXM hardware slows the measurement process, it also makes it very easy to mix spectroscopy and imaging to produce hyperspectral data (i.e. colour pictures) that provide information beyond the simple shape and density of the sample materials. An illustrative example can be found in the characterisation of a polymer blend film in which the components have similar density and elemental composition. Extending the example of PFB and F8BT discussed in the previous section, Figure 2a displays raw STXM images measured at photon energies, where the 285 eV image shows markedly different contrast due to the strong absorption by the PFB component. These polymers have semiconducting properties and are blended together to form the active layer in a photovoltaic solar cell [11]. Since we know the spectra of each component in the sample, we can use analysis techniques like singular value decomposition to calculate a quantitative composition map (Figure 2b), and with further information of the component materials (e.g. mass density and formula, or the thickness of a reference sample) also calculate the thickness map (Figure 2c) [9]. Such analyses can be applied to sample of any number of components, so long as the number of input images is greater than the number of components. Alternative analytical approaches (e.g. principle component analysis and clustering) can be applied to datasets for which reference component spectra are not available [9].

  doi:10.5075/epfl-298799_978-2-9701614-0-0

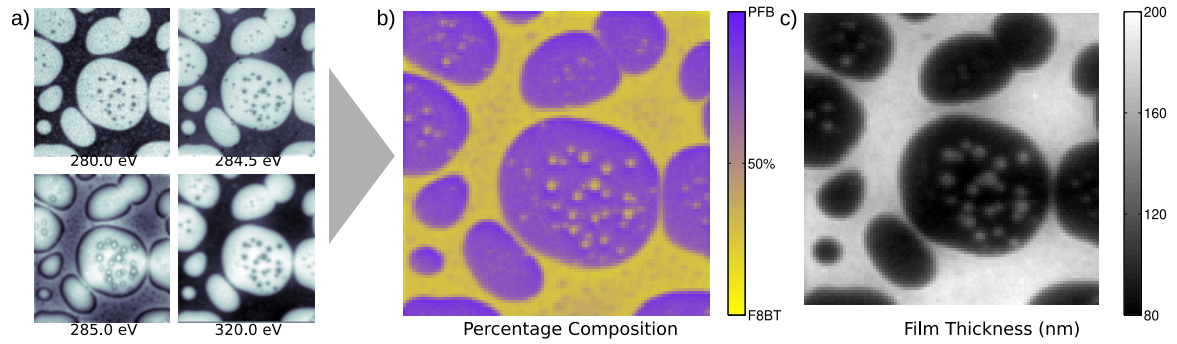

Figure 2. a) Images measured at strategic photon energies show contrast based on the absorption spectra of the component materials (see Figure 1). Combining the set of images with knowledge of the component spectra allow calculation of b) composition and c) thickness maps. Reproduced from [12].

3. Results

3.1 Engineering PLA Toughness

Polylactic acid (PLA) is a major commercial biodegradable plastic, however its brittleness remains a concern in many applications. Melt-blending with a PLA-based thermoplastic elastomer (PLAE) significantly results in a material with significantly better toughness [13]. NEXAFS spectra and STXM images of 20% and 30% PLA/PLAE blends (microtome slices of bulk material) are presented in Figure 3 and reveals a change in structural morphology of the PLAE inclusions. These structures were found responsible for the improved mechanical properties of the blend [13].

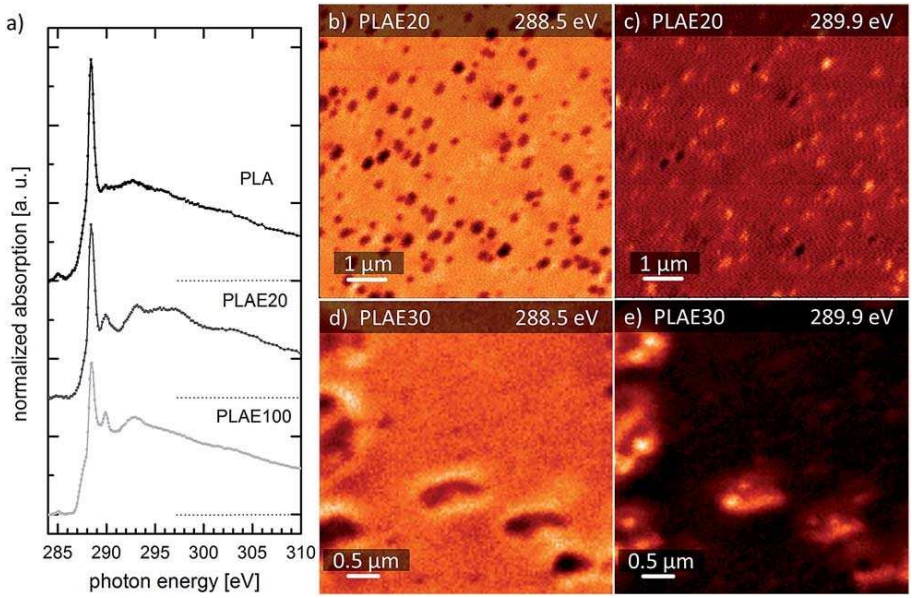

Figure 3. a) NEXAFS spectra of PLA, PLA blended with 20% PLAE, and PLAE. STXM images of 20% (b,c) and 30% (d,e) PLA/PLAE blends measured at 288.5 eV (b,d) to highlight the PLA matrix and 289.9 eV (c,e) to highlight the PLAE inclusions. Reproduced from [13].

3.2 Functional Microspheres

Polymer microspheres find many applications as carriers of material that can be released by some external trigger depending on the functionalisation design. For example,

  doi:10.5075/epfl-298799_978-2-9701614-0-0

superparamagnetic magnetite nanoparticles allow triggering by an external magnetic field [14]. In order to ensure that the functional design is correctly implemented, it is important to confirm distribution of the nanoparticles. This has been performed via 3D imaging in a STXM using the 60° laminography geometry (similar to tomography, but with a tilted rotation axis so as to allow a flat sample support) at 711 eV for optimum absorption contrast of the magnetite (Fe L_3-edge resonance) [14]. Figure 4 presents data from a single magnetite nanoparticle-coated polyvinylacetate microsphere that reveals the shape of the object and the relatively even distribution of magnetite nanoparticle agglomerates.

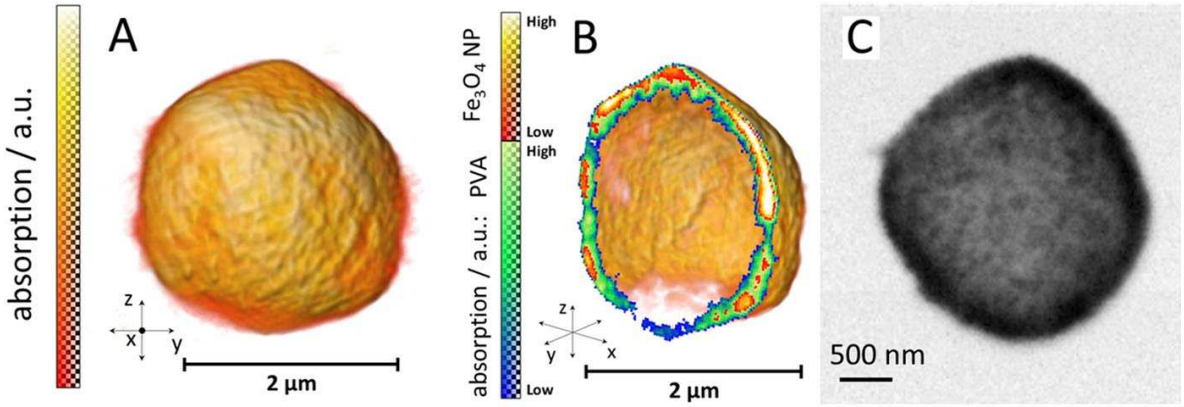

Figure 4. 3D reconstruction of an air-filled PVA microsphere coated with magnetite nanoparticle agglomerates imaged by soft X-ray laminography. a) Volume rendering of the whole sphere and b) the cut sphere with a modified colour scale to distinguish between the polymer shell (blue/green) and the magnetite agglomerates (red/white). c) raw STXM image. Reproduced from [14].

3.3 Porous Electrospun nanofibers

Porous electrospun nanofibers find a number of applications. Coating such fibers with metal oxides provides selective separation membranes [15]. 3D STXM imaging of porous polystyrene (PS) electrospun nanofibers coated with ferric acetylacetonate was performed via focal-stack imaging at 705 eV (weak absorption by Fe) and 712 eV (strong absorption by Fe). Figure 5a shows a 3D model reconstructed from data measured at 712 eV, while figure 5b shows the model reconstructed from the difference between the 712 eV and 705 eV data sets in order to isolate the X-ray absorption by iron.

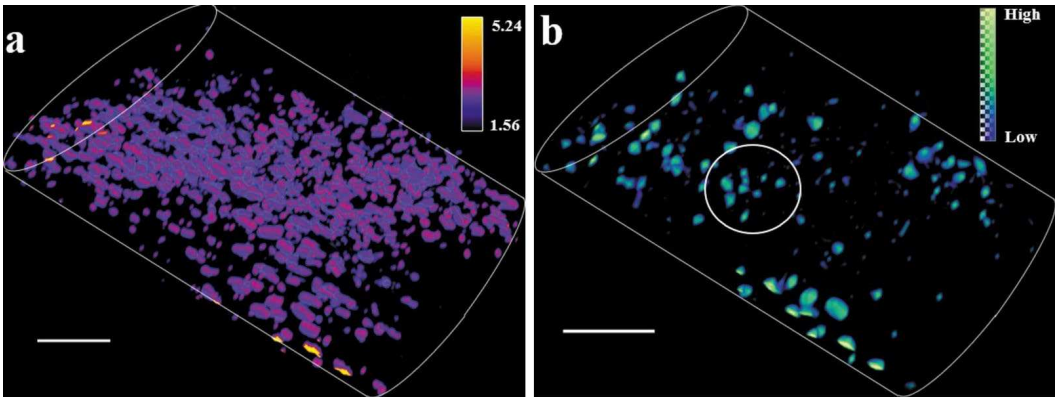

Figure 5. 3D reconstruction of a porous PS nanofiber coated with ferric acetylacetonate presented as a) density, and b) Fe distribution. Scale bars are 1 micron. Reproduced from [15].

  doi:10.5075/epfl-298799_978-2-9701614-0-0

3.4 Carbon Fiber Crystallisation

The physical properties of carbon fibers is strongly affected by the crystalline microstructure, however, most conventional imaging techniques are unable to see such details [16]. By tuning the photon energy to a NEXAFS resonance displaying linear dichroism, STXM images produce contrast based on the crystal orientation [9,12]. In this case, the crystals are essentially graphite, which has a layered structure of hexagonally arranged (i.e. sp^2 hybridised electron orbtials) C atoms. The $\pi^*_{C=C}$ anti-bonding orbital lies in the out-of-plane direction and so the corresponding resonance at 285.4 eV shows high absorption when the electric field vector of the linearly polarised X-ray beam is oriented perpendicular to the graphite layers and low absorption when oriented parallel to the layers. Similarly, the 292 eV C1s→$\sigma^*_{C\text{-}C}$ resonance lies within the plane of the graphite layers and so displays the opposite trend in absorption strength with respect to the electric field orientation of the X-ray beam.

Figure 6 presents TEM and STXM images of carbon fiber cross-sections (measured at BL-13A of the Photon Factory, Japan). The carbon fibers were produced from either polyacrylonitrile (PAN) or pitch-based materials [16]. The pitch-based carbon fibers show strong contrast that inverts when the X-ray polarisation is rotated by 90°, consistent with linear dichroism for graphitic crystals with the sheets oriented along the fiber axis. On the other hand, the PAN-based fiber shows no dichroic contrast and so its graphitic crystals must either be smaller than the STXM resolution, or oriented with the sheets perpendicular to the fiber axis (which is unlikely since the weak interlayer bonds would give the fiber a very low tensile strength).

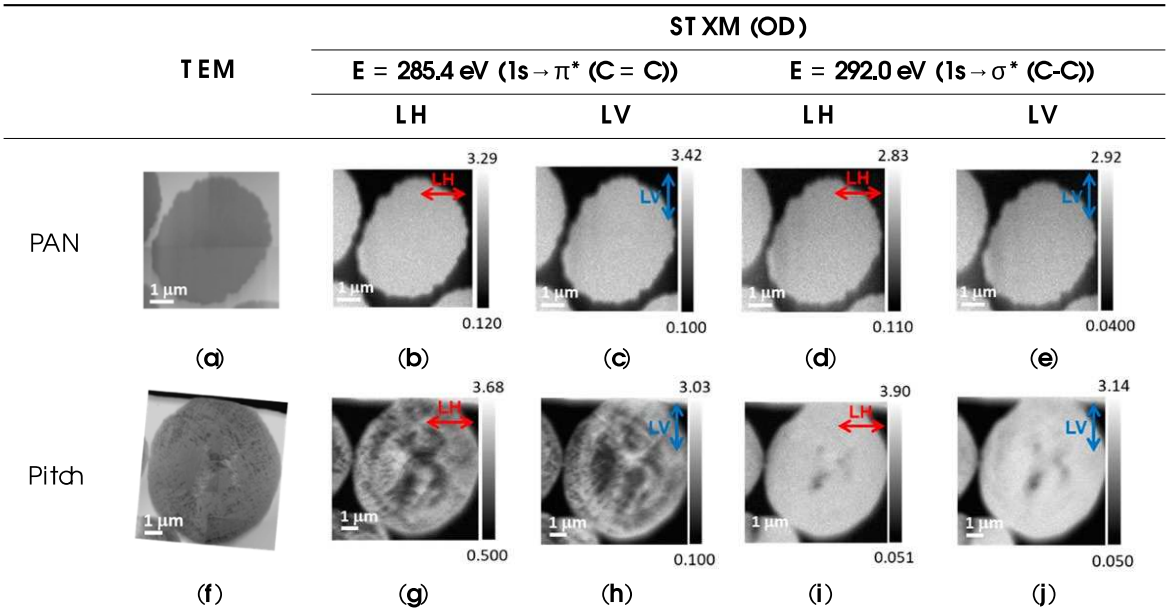

Figure 6. A comparison of images of cross-sections from (a-e) PAN- and (f-j) pitch-based carbon fibers. (a,f) TEM (bright field) images. STXM optical density images measured at photon energies of (b,c,gh) 285.4 eV and (d,e,i,j) 292 eV and with linear horizontal (LH) and linear vertical (LV) polarised X-ray beams. Reproduced from [16]

  doi:10.5075/epfl-298799_978-2-9701614-0-0 published under CC BY-NC 4.0 license

4. Conclusions

Scanning transmission X-ray microscopy (STXM) provides opportunities to to produce nanoscale maps (2D or 3D) with a variety of quantitative contrast mechanisms. The technique allows differentiation of highly similar materials, such as polymers and other organic materials, highlight particular elements or oxidation states, and to observe physical properties like molecular orientation.

STXM instruments require the brightness and tunable photon energy of synchrotron radiation and so are of limited number. However, synchrotron facilities are typically government funded and run as so-called “user facilities” where anyone can apply for access to the instruments free of charge (on condition that the results are published – proprietary access typically requires fees). The “Way For Light” website [17] catalogues all of the synchrotron-based instruments in europe and can be a valuable discovery tool (a search for “STXM” will bring up links for PolLux alongside similar instruments). Further synchrotron facilities around the globe can be found on the “Lightsources” website [18]. Since each instrument will have unique advantages and optimisations, contacting the beamline scientists is highly recommended for ensuring the best suited instrument is selected for your scientific case.

Acknowledgements

The PolLux end station was financed by the German Ministerium für Bildung und Forschung (BMBF) through contracts 05K16WED and 05K19WE2.

5. References

1. Stampanoni M, Menzel A, Watts B, Mader KS, Bunk O. Chimia 2014; 68:66-72. DOI: 10.2533/chimia.2014.66
2. Jacobsen C. X-ray Microscopy (Advances in Microscopy and Microanalysis). Cambridge: Cambridge University Press. 2019. DOI: 10.1017/9781139924542
3. Ade H, Stoll H. Near-edge X-ray absorption fine-structure microscopy of organic and magnetic materials. Nature Materials 2009; 8: 281–290. DOI: 10.1038/nmat2399
4. Raabe J, Tzvetkov G, et al. PolLux: A new facility for soft x-ray spectromicroscopy at the Swiss Light Source. Review of Scientific Instruments 2008; 79:113704. DOI: 10.1063/1.3021472
5. https://www.psi.ch/en/sls/users-proposals
6. Stöhr J. NEXAFS spectroscopy. Springer-Verlag. 1992. DOI: 10.1007/978-3-662-02853-7
7. Miot J, Benzerara K, et al. Iron biomineralization by anaerobic neutrophilic iron-oxidizing bacteria. Geochimica et Cosmochimica Acta 2009; 73(3):696-711. DOI: 10.1016/j.gca.2008.10.033
8. Watts B, Swaraj S, et al. Calibrated NEXAFS spectra of common conjugated polymers. Journal of Chemical Physics 2011; 134:024702. DOI: 10.1063/1.3506636
9. Ade H, Hitchcock AP. NEXAFS microscopy and resonant scattering: Composition and orientation probed in real and reciprocal space. Polymer 2008; 49:643-675. DOI: 10.1016/j.polymer.2007.10.030
10. Rösner B, Koch F, et al. Exploiting atomic layer deposition for fabricating sub-10 nm X-ray lenses. Microelectronic Engineering 2018; 191:91-96. DOI: 10.1016/j.mee.2018.01.033

11. McNeill CR, Watts B, et al. X-ray Microscopy of Photovoltaic Polyfluorene Blends: Relating Nanomorphology to Device Performance. Macromolecules 2007; 40:3263-3270. DOI: 10.1021/ma070132d
12. Watts B, Ade H. NEXAFS imaging of synthetic organic materials. Materials Today 2012; 15(4):148-157. DOI: 10.1016/S1369-7021(12)70068-8
13. Cai S, Zeng C, et al. Enhanced mechanical properties of PLA/PLAE blends via well-dispersed and compatilized nanostructures in the matrix. RSC Advances 2016; 6:25531-25540. DOI: 10.1039/C6RA01367H
14. Witte K, Späth A, et al. From 2D STXM to 3D Imaging: Soft X-ray Laminography of Thin Specimens. Nano Letters 202; 20:1305-1314. DOI: 10.1021/acs.nanolett.9b04782
15. Ma L, Xu Z, Guo Z, Watts B, Lin J, Zhang X, Tai R. Three-dimensional fast elemental mapping by soft X-ray dual-energy focal stacks imaging. J. Synchrotron Rad. 2021; 28:924-929. DOI: 10.1107/S1600577521002903
16. Harano T, Takeichi Y, et al. Observation of Distribution of π-Orbital-Oriented Domains in PAN- and Pitch-Based Carbon Fibers Using Scanning Transmission X-ray Microscopy. Applied Sciences 2020; 10:4836. DOI: 10.3390/app10144836
17. https://www.wayforlight.eu/
18. https://lightsources.org/

ECCM
26-30 JUNE
2022
LAUSANNE
SWITZERLAND

ECCM20 - Proceedings

ISBN: 978-2-9701614-0-0
DOI: 10.5075/epfl-298799_978-2-9701614-0-0